



Issue



First



Prev



Issues



Next



Last



Issue



Send

Encyclopedia of Nanoscience and Nanotechnology

Volume 10 Number 1 2004

- | | | |
|------------------------|--|------------|
| ▶ view | Soft and Hard Magnetic Nanomaterials
<i>Juli"n Gonz"lez; Oksana Chubykalo; Jes"s M. Gonz"lez</i> | <u>1</u> |
| ▶ view | Sol-Gel Derived Nanocrystalline Semiconductor Oxide Gas Sensors
<i>Satyajit Shukla; Sudipta Seal</i> | <u>27</u> |
| ▶ view | Solid Lipid Nanoparticles and Nanostructured Lipid Carriers
<i>R. H. M"ller; M. Radtke; S. A. Wissing</i> | <u>43</u> |
| ▶ view | Solid-State Synthesis of Carbon Nanotubes
<i>Hua Chun Zeng</i> | <u>57</u> |
| ▶ view | Sonochemical Synthesis of Nanomaterials
<i>S. Sundar Manoharan; Manju Lata Rao</i> | <u>67</u> |
| ▶ view | Stealth and Biomimetic Core-Corona Nanoparticles
<i>Ruxandra Gref; Patrick Couvreur</i> | <u>83</u> |
| ▶ view | Stilbenoid Dendrimers
<i>Herbert Meier; Matthias Lehmann</i> | <u>95</u> |
| ▶ view | Strain Effects in Manganite Nanostructured Thin Films
<i>W. Prellier; B. Mercey; A. M. Haghiri Gosnet</i> | <u>107</u> |
| ▶ view | Structural Characterization of Single-Walled Carbon Nanotubes
<i>Daniel E. Resasco; Jose E. Herrera</i> | <u>125</u> |
| ▶ view | Structure of Mesoporous Silica
<i>Wuzong Zhou</i> | <u>149</u> |
| ▶ view | Structure of Nanoclusters by High-Resolution Transmission Electron Microscopy
<i>J. Urban</i> | <u>161</u> |
| ▶ view | Structures of Epitaxial Quantum Dots
<i>X. Z. Liao; J. Zou; D. J. H. Cockayne</i> | <u>175</u> |
| ▶ view | Superhard Nanocomposites
<i>Gregory M. Demyashev; Alexander L. Taube; Elias Siores</i> | <u>191</u> |
| ▶ view | Superplasticity in Nanoceramics | <u>237</u> |

M. Pal; D. Chakravorty

- [▶ view](#) Supramolecular Coordination Polymers **247**
Jing-Cao Dai; Zhi-Yong Fu; Xin-Tao Wu
- [▶ view](#) Surface Functionalization of Semiconducting Nanoparticles **267**
Marie-Isabelle Baraton
- [▶ view](#) Surface Nano-Alloying **283**
Ruxandra Vidu; Nobumitsu Hirai; Shigeta Hara
- [▶ view](#) Synthesis of Covalent Nanoparticles by CO₂ Laser **301**
Nathalie Herlin-Boime; Martine Mayne-L'Hermite; Cécile Reynaud
- [▶ view](#) Synthesis of Inorganic Nanowires and Nanotubes **327**
S. Sharma; H. Li; H. Chandrasekaran; R. C. Mani; M. K. Sunkara
- [▶ view](#) Synthesis of Metal Chalcogenide Nanoparticles **347**
Jun-Jie Zhu; Hui Wang
- [▶ view](#) Synthesis of Nanomaterials Using Microemulsion Process **369**
Suresh C. Kuiry; Sudipta Seal
- [▶ view](#) Synthetic Nanoinorganics by Biomolecular Templating **381**
S. Behrens; E. Dinjus; E. Unger
- [▶ view](#) Techniques in Electrochemical Nanotechnology **393**
P. Schmuki; S. Maupai; T. Djenizian; L. Santinacci; A. Spiegel; U. Schlierf
- [▶ view](#) Theory of Semiconductor Quantum Devices **411**
Rita Claudia Iotti; Remo Proietti Zaccaria; Fausto Rossi
- [▶ view](#) Thermal Conductivity of Semiconductor Nanostructures **425**
Alexander A. Balandin
- [▶ view](#) Transition Metal Acetylide Nanostructures **447**
Thomas M. Cooper
- [▶ view](#) Transition Metal Nanocluster Assemblies **471**
K. Sumiyama; T. Hihara; D. L. Peng; S. Yamamuro
- [▶ view](#) Transition Metal Atoms on Nanocarbon Surfaces **509**
Antonis N. Andriotis; Madhu Menon
- [▶ view](#) Transition Metals-Based Nanomaterials for Signal Transduction **519**
Bamaprasad Bag; Parimal K. Bharadwaj
- [▶ view](#) Transport in Self-Assembled Quantum Dots **537**
S. W. Hwang; Y. J. Park; J. P. Bird; D. Ahn
- [▶ view](#) Transport in Semiconductor Nanostructures **547**
H. Leijn; R. Riera; J. L. Marín; R. Rosas
- [▶ view](#) UHV-SPM Nanofabrication **581**

G. Palasantzas; J. Th. M. De Hosson; L. J. Geerligs

- [▶ view](#) Unconventional Nanolithography **595**
Kahp Y. Suh; Dahl-Young Khang; Y. S. Kim; Hong H. Lee
- [▶ view](#) Vacuum Nanoelectronics **613**
Ning-Sheng Xu
- [▶ view](#) Visible-Light-Sensitive Photocatalysts **639**
Hiromi Yamashita; Masato Takeuchi; Masakazu Anpo
- [▶ view](#) X-Ray Characterization of Nanolayers **655**
Dirk C. Meyer; Peter Paufler
- [▶ view](#) X-Ray Microscopy and Nanodiffraction **681**
S. Lagomarsino; A. Cedola
- [▶ view](#) X-Ray Photoelectron Spectroscopy of Nanostructured Materials **711**
J. Nanda; Sameer Sapra; D. D. Sarma
- [▶ view](#) Yttrium Oxide Nanocrystals: Luminescent Properties and Applications **725**
Fiorenzo Vetrone; John-Christopher Boyer; John A. Capobianco
- [▶ view](#) Zinc Oxide Nanostructures **767**
Chun-Hua Yan; Jun Zhang; Ling-Dong Sun

Copyright © 2004 American Scientific Publishers

Soft and Hard Magnetic Nanomaterials

Julián González

*Facultad de Química, Paseo Manuel de Lardizabal 3,
20018 San Sebastián, Spain*

Oksana Chubykalo, Jesús M. González

*CSIC, Cantoblanco, Madrid, Spain and UCM-RENFE-CSIC,
Las Rozas, Madrid, Spain*

CONTENTS

1. Introduction
 2. Soft Nanocrystalline Materials
 3. Hard Nanocrystalline Materials
 4. Micromagnetic Numerical Simulations
 5. Conclusions
- Glossary
References

1. INTRODUCTION

Magnetic materials today constitute, from the standpoint of the size of their world market and in the narrow concurrence with the semiconducting materials, one of the major groups of functional materials. They are involved in a broad range of technologies, from electromechanics to those related to information recording. Although it is difficult to find a common point underlying this large set of applications and devices, the occurrence of hysteresis in their response to an applied magnetic field could be considered the most representative feature of the magnetic materials phenomenology. Magnetic hysteresis can be described by two quantities, namely, the remanence and the coercive force. For a given set of phases, present in a particular material and characterized by particular values of saturation magnetization, order temperature, and magnetocrystalline anisotropies, the coercivity and remanence depend on many different extrinsic parameters, from the phase morphology (crystallites size and shape) to the distribution of defects present in them and, particularly, the characteristics of the intergranular and interphase couplings. The basic consequences of this are the possibility of optimizing and, in some cases, tailoring the properties of a material for a particular application, during the last century, most of the research efforts in the field

were concentrated on the control of the micro- and nanostructures of a relatively reduced set of relevant phases. It also is important to state that, whereas the coercivity of the technologically used magnetic materials covers six decades (from ca. 5×10^{-6} T up to ca. 5 T), the remanence values are bound by the value of the saturation magnetization, and the whole range of technologically relevant magnetic materials varies from 0.5 T up to ca. 2 T.

The introduction in the technologically relevant magnetic materials of structural correlation lengths of the order of the nm has several important consequences. First, and in the particular case of the nanoparticulate and the nanocrystalline materials, it results in a significant increase of the surface (grain boundary)-to-(particle/grain) volume atomic ratio. Since the moments present at the surfaces and grain boundaries are characterized by a co-ordination different from that corresponding to the bulk materials, the local values at these regions of the magnetization, order temperature, exchange constant, and anisotropy can be significantly different from those corresponding to bulk-like regions and largely influence and even rule the global behavior of the system. Second, the reduction of the crystallite size crucially influences, through the reduction of the absolute number of defects present inside the structurally coherent regions, the global value of defect sensitive properties as, very relevantly, the coercivity. Finally, and most importantly, the nanostructuration brings about the problem of the interphase coupling at length scales comparable with the magnetic correlation lengths, i.e., the exchange and dipolar correlation lengths, given the width of a domain wall in a bulk and planar uniaxial systems, respectively. Since the coupling is largely ruled by the characteristics of the exchange interactions at the grain boundaries, and since, for the time being, the control of those properties could only be achieved heuristically, it is not exaggerated to state that the main goal of the present research on the magnetic properties of nanostructured materials could be the achievement of better control of the magnetic properties of the intergranular regions.

To support this statement, we will focus on the discussion of the implications of the particularities of the intergranular coupling on the hysteretic behavior of nanocrystalline materials. First, we will cover the case of the (mainly single phase) reduced magnetocrystalline anisotropy materials, in which the dipolar correlation length frequently can be much larger than the crystallite size (ca. 15 nm), thus resulting in an extremely soft behavior linked to the occurrence of exchange-induced averages of the local anisotropy. The second section will be dedicated to the demagnetization process of high anisotropy, single- and multiphase nanocrystalline materials characterized by exchange correlation lengths comparable with or smaller than the crystallite size. In this case, the goal is either the reduction of the intergranular coupling (single-phase materials) aiming at the increase of coercivity or the achievement of large remanences linked to the occurrence of strong coupling between hard and soft grains, the latter having dimensions comparable with their exchange correlation length. We will end this chapter by reviewing the state of the art of the micromagnetic modeling, a numerical technique allowing both the analysis of systems for which (as it is the largely majority case today) there are not experimental data on the local magnetic properties and the implementation of elements of device design. This last section also will include a discussion of the influence on the performance of magnetic recording media of the control of the intergranular exchange.

2. SOFT NANOCRYSTALLINE MATERIALS

2.1. Introduction to the Soft Magnetic Materials

Nanocrystalline materials, obtained by devitrification of the precursor amorphous alloy, displaying soft magnetic character (high magnetic permeability and low coercivity), have been the subject of increasing attention from the scientific community, not only because of their potential use in technical applications but also because they provide an excellent setting in which to study basic problems in nanostructures formation and magnetism [1–8]. In fact, these materials provide a crucial point in opening up new fields of research in materials science, magnetism, and technology, such as metastable crystalline phases and structures, extended solid solubilities of solutes with associated improvements of mechanical and physical properties, nanocrystalline, nanocomposite and amorphous materials that, in some cases, have unique combinations of properties (magnetic, mechanical, corrosion, etc.). Technological development of the fabrication technique of the amorphous precursor material and studies of the structure, glass formation ability, and thermodynamics, and magnetism of amorphous alloys were intensively performed in 1960s and 1970s. These aspects have been analyzed extensively in few review papers and books [9–11].

Most commercial and technological interests have been paid to soft amorphous and nanocrystalline magnetic materials. Initially, it was believed that ferromagnetism could not

exist in amorphous solids because of a lack of atomic ordering. The possibility of ferromagnetism in amorphous metallic alloys was theoretically predicted by Gubanov [12] and the experimental confirmation of this improbable prediction was the main cause of the sudden acceleration of research on amorphous alloys from about 1970 onward, this onrush of activity was due both to the intrinsic scientific interest of a novel and unexpected form of ferromagnetism and also to the gradual recognition that this is the key to the industrial exploitation of amorphous ferromagnetic alloys. The amorphous alloy ribbons obtained by the melt-spinning technique have been introduced widely as the soft magnetic materials in the 1970s. Their excellent magnetic softness and high wear and corrosion resistance made them very attractive in the recording head and microtransformer industries. In contrast with the flood of work on magnetic behavior, the study of electrical transport (i.e., magnetoimpedance effect) is very recent and is making significant progress.

Conventional physical metallurgy approaches to improving soft ferromagnetic properties involve tailoring the chemistry and optimizing the microstructure. Significant in the optimizing of the microstructure is recognition that a measure of the magnetic hardness (the coercivity, H_c) is roughly inversely proportional to the grain size (D) for a grain size exceeding ~ 0.1 to $1 \mu\text{m}$ (where the grain size exceeds the domain wall thickness). In such cases, grain boundaries act as impediments to domain wall motion, and, thus, fine-grained materials usually are magnetically harder than large grain materials. Significant developments in the understanding of magnetic coercivity mechanisms have led to the realization that for very small grain size $D < \sim 100 \text{ nm}$ [13–21], H_c decreases rapidly with increasing grain size. This can be understood by the fact that the domain wall, whose thickness exceeds the grain size, now samples several (or many) grains so that fluctuations in magnetic anisotropy on the grain-size length scale are irrelevant to domain wall pinning. This important concept suggests that nanocrystalline and amorphous alloys have significant potential as soft magnetic materials.

In this section, we explore issues that are pertinent to the general understanding of the magnetic properties of amorphous and nanocrystalline materials. As the state of the art for amorphous magnetic materials is well developed and much of which has been thoroughly reviewed [11, 22–24], we will concentrate on highlights and recent developments. The development of nanocrystalline materials for soft magnetic applications is an emerging field for which we will try to offer a current perspective that may well evolve further with time.

The development of soft magnetic materials for applications requires the study of a variety of intrinsic magnetic properties as well as development of extrinsic magnetic properties through an appropriate optimization of the microstructure. As intrinsic properties, we mean microstructure insensitive properties. Among the fundamental intrinsic properties (which depend on alloy composition and crystal structure), the saturation magnetization, Curie temperature, magnetic anisotropy, and magnetostriction coefficient are all important. In a broader sense, magnetic anisotropy and magnetostriction can be considered as extrinsic in that,

for a two-phase material (in aggregate), they depend on the microstructure.

A vast literature exists on the variation of intrinsic magnetic properties with alloy composition. Although new discoveries continue to be made in this area, it can be safely stated that a more wide open area in the development of magnetic materials for applications is the fundamental understanding and exploitation of the influence of the microstructure on the extrinsic magnetic properties. Important microstructural features include grain size, shape, and orientation; defect concentrations; compositional inhomogeneities; magnetic domains; and domain walls. The interaction of magnetic domain walls with microstructural impediments to their motion is of particular importance to the understanding of soft magnetic behavior. Extrinsic magnetic properties important in soft magnetic materials include magnetic permeability and coercivity, which typically have an inverse relationship. Thorough discussions of soft magnetic materials are available [25–28, 29].

2.2. Microstructural Characterization

An important part of the recent developments corresponding to nanostructured materials is related to those obtained by controlled crystallization, either by annealing the amorphous single phase or by decreasing the cooling rate from the liquid of metallic systems. Typically, in these nanostructures, precipitate sizes range between 5 and 50 nm embedded in an amorphous matrix with nanocrystal volume fractions of 10 to 80%, which means particle densities of 10^{22} to 10^{28} m^{-3} .

We present the most relevant aspects of the nanocrystallization process of Fe-based nanocrystalline alloys as a two-phase system, namely α -Fe or α -Fe(Si) grains embedded in a residual amorphous matrix, which, being ferromagnetic, results in a material with extremely good soft magnetic properties. The microstructural analysis of the primary crystallization of Fe-rich amorphous alloys usually has been done by using conventional techniques such as differential scanning calorimetry (DSC), X-ray diffraction (XRD), transmission Mössbauer spectroscopy (TMS), and transmission electron microscopy (TEM). In this way, through the combined structural analysis of these techniques, useful information, such as the dependence of the microstructure upon time and temperature of treatment, can be obtained.

The kinetics of metastability loss of the disordered system above glass transition, i.e., under less than equilibrium conditions, is a key subject, because it provides new opportunities for structure control by innovative alloy design and processing strategies. Several examples include soft and hard magnets and high-strength materials [30–32]. Most studies focus on the crystallization onset as a measure of kinetic stability under heat treatment and recognise the product phase selection involved in nucleation and the role of competitive growth kinetics in the evolution of different microstructural morphologies [33, 34]. Differential scanning calorimetry has become quite effective as a means of studying the nature of nanoscale structures and their stability. It has been established that the initial annealing response allows one distinguish between a sharp onset for a nucleation and growth or a continuous grain growth of pre-existing grains [35]. Kinetic

data on the transformation often are obtained from this technique.

Figure 1 shows the DSC curves of the as-prepared amorphous alloy ($\text{Fe}_{73.5}\text{Cu}_1\text{Nb}_3\text{Si}_{17.5}\text{B}_5$, trademark *Finemet*), as well as of that of alloy previously annealed for 1 hour at 703 K and 763 K, respectively [36]. For the as-prepared alloy, the calorimetric signal shows some relaxation before the exothermic nanocrystallization process, as well as with the Curie temperature of the amorphous phase ($T_C^{\text{qmc}} \approx 595 \text{ K}$). When the sample has been annealed at 703 K, relaxation is no longer apparent in the calorimetric signal, the Curie temperature is shifted about 15 K, to higher values, and the nanocrystallization process is slightly advanced in temperature (2 K). On further increasing the annealing temperature, the calorimetric signal shows no clear changes in the Curie temperature of the annealed sample with respect to annealing at 703 K. However, a clear shift of the nanocrystallization onset toward higher temperatures (40 K) can be observed, as well as a significant decrease of its area [36]. Consequently, DSC measurement permits evaluation of the maximum temperature to prevent partial crystallization during previous heating and the maximum heating rate to control the temperature of the sample by analyzing the transformation peak connected to the primary crystallization.

Calorimetric measurements, however, give information about microstructural development. Microstructure determination by the use of several techniques (XRD, TMS and TEM) allows us to complete the understanding of the mechanisms of the primary crystallization. Transmission Mössbauer spectroscopy has the main advantage of giving local information of an active element (Fe nuclei in these alloys). Because Fe is present both in the nanocrystalline precipitates and in the disordered matrix, TMS provides information on local ordering in both phases, which can be correlated with the changes in the short-range order of the amorphous phase and with the composition of nanocrystalline phase. X-ray diffraction and TEM provide a

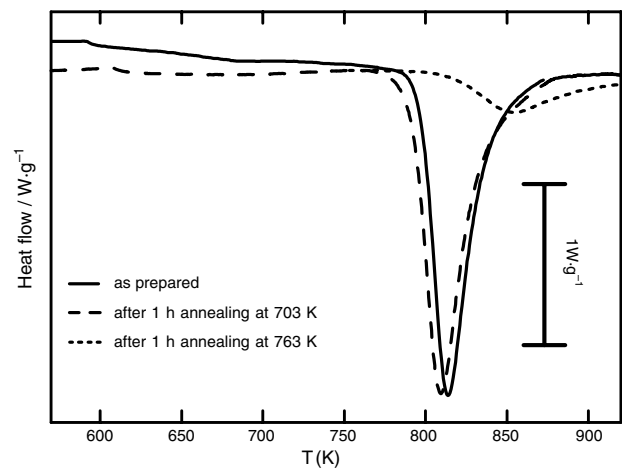


Figure 1. DSC signals of $\text{Fe}_{73.5}\text{Si}_{13.5}\text{B}_5\text{Cu}_1\text{Nb}_3$ alloy obtained after heating at 40 K/min. For the as-quenched amorphous alloy (solid line); after 1 h isothermal annealing at 703 K (dashed line) and at 763 K (dotted line). Reprinted with permission from [37], M. T. Clavaguera-Mora et al., *Progress in Materials Science* 47, 559 (2002). © 2002, Elsevier Science.

close look at the developed microstructure and permit the characterization of the precipitates, showing their morphology and grain-size distribution.

Figure 2(a–c) shows a TEM image of a *Finemet* alloy after heating at 763 K at three annealing times (3, 10, and 30 minutes), while Figure 2(d) corresponds to the case (b) with increasing contrast, which allows the shape and size of the precipitates to be determined [37]. As can be seen, the microstructure is characterized by a homogeneous, ultra-fine grain structure of α -Fe(Si), with grain sizes around 10 nm and a random texture, embedded in a still amorphous matrix. The formation of this particular structure is ascribed to the combined effects of elements as Cu (which promotes the nucleation of grains) and Nb, Ta, Zr, Mo,—(which hinders their growth) and their low solubility in α -Fe(Si) [38–40]. Nevertheless, the size and morphology of the nanocrystals in these alloys, as well as their distribution, could be analyzed by the application of local probe techniques. These techniques, such as scanning tunneling microscopy (STM) and atomic force microscopy (AFM) provide three-dimensional (3D) topographic images at the nanometer level [41, 42] and represent powerful tools to study the surface properties and structures of metals and alloys.

2.3. On the Ferromagnetism in Amorphous and Nanocrystalline Materials

There are, when concerning the magnetic order in materials having structural disorder (such as is the case of amorphous and nanocrystalline alloys), some fundamental questions related to the existence of such a well-defined magnetic order. Ferromagnetic interactions of the magnetic materials can be immediately considered as ferromagnetic structures. In this naive idea, the magnetic anisotropy effects have been neglected. Magnetic moments tend to arrange their orientations parallel to each other via exchange interactions; they

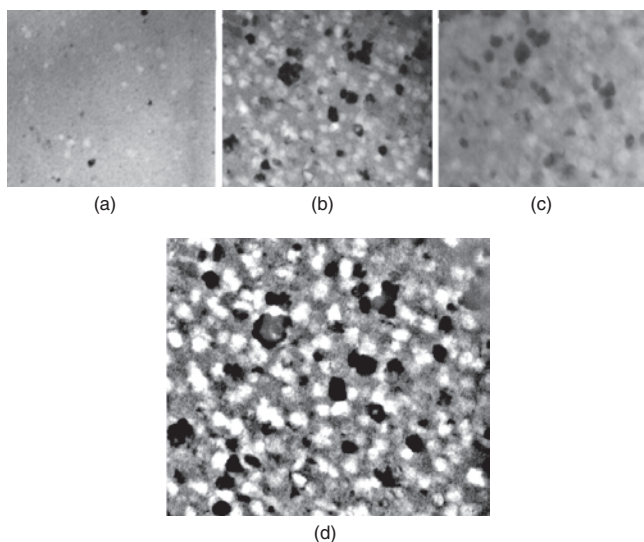


Figure 2. TEM images of *Finemet* samples after (a) 3 min; (b) 10 min; (c) 30 min annealing at 763 K; and (d) is the case (b) after contrast increasing. Reprinted with permission from [37], M. T. Clavaguera-Mora et al., *Progress in Materials Science* 47, 559 (2002). © 2002, Elsevier Science.

do this when lying along a magnetic easy axis that is in the same direction at every point in the material. However, if the easy axis orientation fluctuates from site to site, a conflict between ferromagnetic coupling and anisotropy arises. As long as we imagine lattice periodicity, a ferromagnetic structure is a consequence of ferromagnetic exchange interactions, the strength of the anisotropy being irrelevant. In this situation, we are assuming a major simplification, namely, the direction of the easy axis is uniform throughout the sample. With this simple picture, we present crucial questions related to the influence of an amorphous structure on magnetic order.

Regarding the magnetic order in amorphous and nanocrystalline materials, we know that it stems from two contributions: exchange and local anisotropy. The exchange arises from the electron–electron correlations. The mechanism of the electrostatic interactions between electrons has no relation to structural order and is sensitive only to overlapping of the electron wave functions. With respect to magnetic anisotropy, it also originated by the interaction of the local electrical field with spin orientation, through the spin-orbit coupling. Therefore, magnetic anisotropy also is a local concept. Nevertheless, the structural configuration of magnetic solids exerts an important influence on the macroscopic manifestation of the local anisotropy. As a consequence, when the local axes fluctuate in orientation owing to the structural fluctuation (amorphous and nanocrystalline materials as examples), calculations of the resultant macroscopic anisotropy become quite difficult.

In the case of amorphous ferromagnetic alloys, the usual approach to the atomic structure of a magnetic order connected to a lattice periodicity is not applicable. These materials can be defined as solids in which the orientation of local symmetry axes fluctuate with a typical correlation length $l = 10$ Å. The local structure can be characterized by a few local configurations with icosahedral, octahedral, and trigonal symmetry. These structural units have randomly distributed orientation. The local magnetic anisotropy would be larger in the units with lower symmetry. In general, these units are characterized by fluctuations of the orientation local axis. It is remarkable that with these types of structures, the correlation length, l , of such a fluctuation is typically the correlation length of the structure and ranges from 10 Å (amorphous) to 10 nm (nanocrystals) and 1 mm (polycrystals).

Fluctuations in the interatomic distances associated with the amorphous structure also should contribute to some degree of randomness in the magnetic interactions of the magnetic moments. Nevertheless, such randomness is expected not to affect the magnetic behavior qualitatively [11, 43]. Moreover, random distribution of the orientation of the easy axis drastically affects the magnetic properties. The random anisotropy model developed by Alben et al. [44] provides a successful explanation of how the correlation length, l , exerts a relevant influence on magnetic structure. The important question is What is the range of orientational correlation of the spins? Let L be the correlation length of the magnetic structure. If we assume $L > l$, the number of oriented easy axes in a volume L^3 should be $N = (L/l)^3$.

The effective anisotropy can be written as:

$$K_{eff} = K/N^{1/2} \quad (1)$$

where K is the local anisotropy where strength is assumed to be uniform everywhere. By minimizing the total energy with respect to L , the following expression can be deduced:

$$L = (16A^2)/(9K^2l^3) \quad (2)$$

where A is the exchange stiffness parameter. If we consider $A = 10^{-11}$ J/m and $l = 10^{-9}$ m, which are typical values of ferromagnetic metallic glasses [45], L in equation (2) becomes $10^5/K^2$. For 3D-based alloys, we can take the value of K corresponding to crystalline samples ($\sim 10^4$ J/m³) leading to L around 10^{-9} m, which is equal to the structural correlation length of an amorphous material.

In addition, the random anisotropy model provides the following expression for the average macroscopic anisotropy:

$$\langle K \rangle = K^4 l^6 / A^3 \quad (3)$$

Equation (3) points out that the macroscopic structural anisotropy is negligible in 3D amorphous alloys ($\langle K \rangle \sim 10^{-9}$ K); this is a consequence of the averaging of several local easy axes, which produces the reduction in magnitude.

Special attention has been paid, in the last decade, to the study of nanocrystalline phases obtained by suitable annealing of amorphous metallic ribbons owing to their attractive properties as soft magnetic materials [1, 15, 19–21, 23, 46–48]. Such soft magnetic character is thought to have originated because the magnetocrystalline anisotropy vanishes and there is a very small magnetostriction value when the grain size approaches 10 nm [1, 12, 46]. As was theoretically estimated by Herzer [12, 46], average anisotropy for randomly oriented α -Fe(Si) grains is negligibly small when grain diameter does not exceed about 10 nm. Thus, the resulting magnetic behavior can be well described with the random anisotropy model [12, 19, 23, 46–48]. According to this model, the very low values of coercivity in the nanocrystalline state are ascribed to small effective magnetic anisotropy (K_{eff} around 10 J/m³). However, previous results [19, 21, 49] as well as recently published results by Varga et al. [50] on the reduction of the magnetic anisotropy from the values in the amorphous precursors (~ 1000 J/m³) down to that obtained in the nanocrystalline alloys (around 300–500 J/m³), is not sufficient to account for the reduction of the coercive field accompanying the nanocrystallization. The enhancement of the soft magnetic properties should, therefore, be linked to the decrease of the microstructure–magnetization interactions. These interactions, originating in large units of coupled magnetic moments, suggest a relevant role of the magnetostatic interactions, as well a role in the formation of these coupled units [19, 49]. In addition to the suppressed magnetocrystalline anisotropy, low magnetostriction values provide the basis for the superior soft magnetic properties observed in particular compositions. Low values of the saturation magnetostriction are essential to avoid magnetoelastic anisotropies arising from internal or external mechanical stresses. The increase of initial permeability with the formation of the nanocrystalline state is closely related to a simultaneous decrease of the saturation magnetostriction. Partial crystallization of amorphous alloys leads to an increase of the frequency range, where the permeability presents high values [51]. These high values in the highest

possible frequency range are desirable in many technological applications involving the use of ac fields.

It is remarkable that a number of workers have investigated the effects on the magnetic properties of the substitution of additional alloying elements for Fe in the Fe_{73.5}Cu₁Nb₃Si_{13.5}B₉ alloy composition, *Finemet*, to further improve the properties, e.g., Co [52–56], Al [20, 57, 58], varying the degree of success. Moreover, it was shown in [20] that substitution of Fe by Al in the classical *Finemet* composition led to a significant decrease in the minimum of coercivity, $H_c^{\min} \approx 0.5$ A/m, achieved after partial devitrification, although the effective magnetic anisotropy field was quite large (around 7 Oe) [59]. The coercivity behavior was correlated with the mean grain size, and a theoretical low effective magnetic anisotropy field of the nanocrystalline samples was assumed in contradiction with those experimentally found in [49, 50, 58].

Although amorphous Fe-, Co-, and Ni-based ribbons are slightly more expensive compared with conventional soft magnetic materials, such as sendust, ferrites, and supermalloys (mostly due to the significant content of Co and Ni), they found considerable applications in transformers (400 Hz), ac powder distributors (50 Hz), magnetic recording as a magnetic heads, and magnetic sensors. The main reason for using amorphous alloys such as soft magnetic materials is a saving of the electric energy wasted by magnetic cores. Besides, the combination of high magnetic permeability and good mechanical properties of amorphous alloys may be used successfully in magnetic shielding and in magnetic heads [51]. Production of about 3 millions heads per year in Japan in the mid-1980s has been reported [51].

The internal stresses, as the main source of magnetic anisotropy in amorphous and nanocrystalline materials, are due to the magnetoelastic coupling between magnetization and internal stresses through magnetostriction. Consequently, these materials are interesting for field- and stress-sensing elements because the Fe-rich amorphous alloys exhibit high magnetostriction values ($\lambda_s \approx 10^{-5}$) and, therefore, many of magnetic parameters (i.e., magnetic susceptibility, coercive field, etc.) are extremely sensitive to the applied stresses.

The discovery of Fe-rich nanocrystalline alloys carried out by Yoshizawa et al. [1] was important owing to the outstanding soft magnetic character of such materials. Typical compositions of the precursor amorphous alloys, which, after partial devitrification, reach the nanostructure character with optimal properties, are FeSi and FeZr, with small amounts of B to allow the amorphization process, and smaller amounts of Cu, which act as nucleation centers for crystallites, and Nb, which prevents grain growth. This effect is provided by Zr in FeZr alloys. After the first step of crystallization, FeSi or Fe crystallites are finely dispersed in the residual amorphous matrix. In a wide range of crystallized volume fraction, the exchange correlation length of the matrix is larger than the average intergranular distance, d , and the exchange correlation length of the grains is larger than the grain size, D . Magnetic softness of Fe-rich nanocrystalline alloys is due to a second complementary reason: the opposite sign of the magnetostriction constant of crystallites and residual amorphous matrix,

which allows reduction and compensation of the average magnetostriction.

Figure 3 shows the thermal variation of the coercive field (H_c) in a *Finemet*-type (Ta-containing) amorphous alloy. This behavior is quite similar to that shown in the case of Nb-containing ones and particularly, evidences the occurrence of a maximum in the coercivity linked to the onset of the nanocrystallization process [60, 61].

Considering the grain size, D , to be smaller than the exchange length, L_{ex} , and the nanocrystals are fully coupled between them, the random anisotropy model implies a dependence of the effective magnetic anisotropy $\langle K \rangle$, with the sixth power of average grain size, D . The coercivity is understood as a coherent rotation of the magnetic moments of each grain toward the effective axis leading to the same dependence of the coercivity with the grain size [16]:

$$H_c = p_c \frac{\langle K \rangle}{J_s} = p_c \frac{K_1^4 D^6}{J_s A^3} \left(\langle K \rangle = \frac{K_1^4 D^6}{A^3} \right), \quad (4)$$

where $K_1 = 8 \text{ kJ/m}^3$ is the magnetocrystalline anisotropy of the grains, $A = 10^{-11} \text{ J/m}$ is the exchange ferromagnetic constant, $J_s = 1.2 \text{ T}$, is the saturation magnetic polarization and p_c is a dimensionless prefactor close to unity. The predicted D^6 dependence of the coercive field has been widely accepted to be followed in a D range below L_{ex} (around 30 to 40 nm) for nanocrystalline Fe-Si-B-M-Cu (M = Iva to Via metal) alloys [21, 46, 62–65]. A clear deviation from the predicted D^6 law in the range below $H_c = 1 \text{ A/m}$ was reported by Hernando et al. [19]. Such deviation was ascribed to effects of induced anisotropy (e.g., magnetoelastic and field induced anisotropies) on the coercivity could be significant with respect those of the random magnetocrystalline anisotropy. As a consequence, the data of $H_c(D)$ were fitted by assuming a contribution from (i) the spatial fluctuations of induced anisotropies and (ii) $\langle K_u \rangle$ to H_c (i.e., a dependence $H_c = \sqrt{(a^2 + (bD)^6)}$ was found with

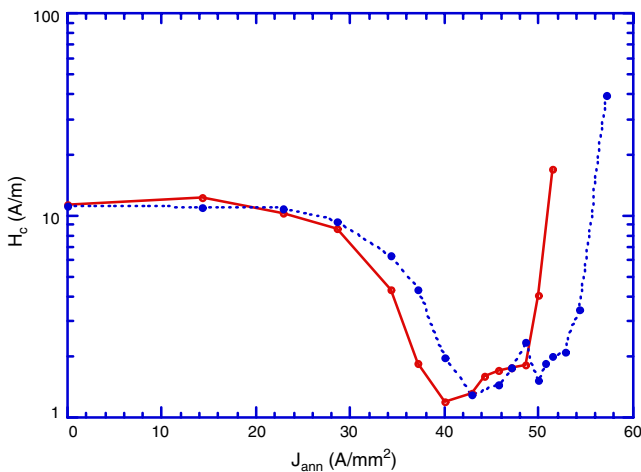


Figure 3. Evolution of the coercive field, measured at room temperature, as a function of the current density after: (o) 1 min and (□) 10 min of annealing time. Reprinted with permission from [21], N. Murillo and J. González, *J. Magn. Magn. Mater.* 218, 53 (2000). © 2000, Elsevier Science.

$a = 1 \text{ A/m}$ representing the contribution originating from the induced anisotropies).

To investigate the effect of the grain size on coercivity, this dependence of $H_c(D)$ in alloys treated by Joule heating was obtained. Experimental results on this dependence are shown in Figure 4 [21]. The fitting of this dependence appears to follow, surprising, a rough dependence of the $H_c \propto D^{3-4}$ type (the best regression was found fitting the D^3 law). It must be noted that our data of $H_c(D)$ correspond to a grain size variation between about 10 to 150 nm. As it is well known, an analysis of this $H_c(D)$ data in terms of the random anisotropy model is only justified if the grain size is smaller than L_{ex} and, hence, could not be applicable (in the framework of the random anisotropy model) to the range grain size above L_{ex} , which results in being only two points of our data in Figure 4 [21]. These points should correspond to a magnetic hardening due to the precipitation of the iron borides. In this case, the random anisotropy model should be applied by taking into account the volume fraction and the different anisotropy of the iron borides. This indicates that $\langle K_1 \rangle$ should vary as D^3 , contrary to the theoretical D^6 law. This indicates that H_c is mainly governed by $\langle K_1 \rangle$, which varies as D^3 , contrary to the theoretical D^6 law. This contradiction of the $H_c(D)$ law between the theory and the experimental has recently been explained by Suzuki et al. [62] considering the presence of long-range uniaxial anisotropy, K_u , which influences the exchange correlation value and length, and yields an anisotropy average given by:

$$\langle K \rangle = K_u + \frac{1}{2} \cdot \frac{\sqrt{K_u} \cdot K_1 \cdot D^3}{A^{3/2}} \quad (5)$$

The second part of (5) corresponds to $\langle K_1 \rangle$ and if K_u is coherent in space or if its spatial fluctuations are negligible to $\langle K_1 \rangle$, this second part ultimately determines the grain size influence on the coercivity. Such influence changes from the D^6 law to a D^{3-4} one when the coherent uniaxial anisotropies dominate over the random magnetocrystalline anisotropy. An additional point in order to justify the Eq. (5)

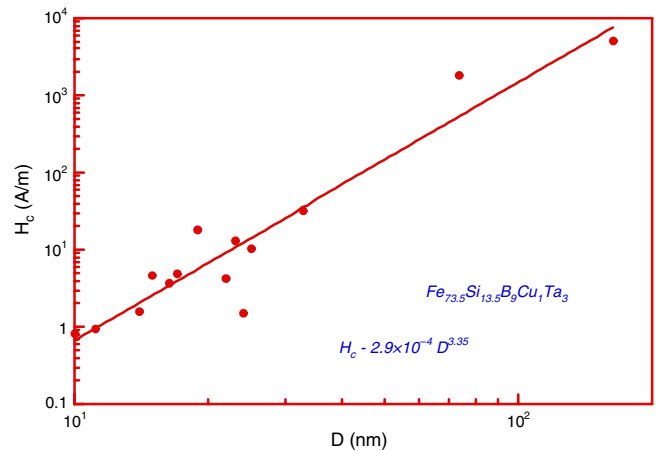


Figure 4. Dependence of the coercive force, H_c , with the average grain diameter, D , for the two studied compositions ($\text{Fe}_{73.5}\text{Si}_{13.5}\text{B}_9\text{Cu}_1\text{Nb}_3$ and $\text{Fe}_{73.5}\text{Si}_{13.5}\text{B}_9\text{Cu}_1\text{Ta}_3$). Reprinted with permission from [21], N. Murillo and J. González, *J. Magn. Magn. Mater.* 218, 53 (2000). © 2000, Elsevier Science.

is connected with the fact that the results of Figure 4 were obtained in samples treated by the Joule heating effect. This kind of annealing could induce some inhomogeneous magnetic anisotropy, which could be responsible for this significant change of the grain size dependence of the coercive field. This argument is supported by the remanence ratio, which is achieved by these samples of values around 0.50. As a consequence, it can be assumed that the presence of more long-range uniaxial anisotropies are larger than the average magnetocrystalline anisotropy (K_1). It should also be noted that Eq. (5) can, interestingly, account for the occurrence of dipolar and deteriorated exchange intergrain interaction and thus can be more realistic than the simple anisotropy averaging, since those features are involved in the accomplishment of a nanocrystallization process.

An interesting study can be one related with the dependencies of the magnetization in partially crystallized samples. Figure 5 displays such dependencies. In Table 1, the evolution with the annealing time of the average grain size, D , the Si atomic percentage diffused in the Fe crystalline lattice, and the crystalline phase percentage are listed. It has been mentioned that in samples annealed with short times (0.5 to 5 minutes), there was no evidence of crystallization. In samples treated for long times, the Si content was of the order of 20% at and slightly larger in the samples having a larger grain size.

On the other hand, the current density dependence of the coercivity for *Finemet-type* alloys results in a very interesting study (illustrated by the Fig. 6). Such dependencies exhibit a peak of coercivity in nanocrystallized samples (treated for 60–720 minutes). This peak of coercivity occurs above the Curie point of the residual amorphous phase. The intensity and the width of the peak strongly depend on the annealing current density. It must be mentioned that the current density above the Curie point of the amorphous matrix being paramagnetic and with its thickness is high enough to avoid exchange interactions between the grains, the nanocrystalline sample can be magnetically considered

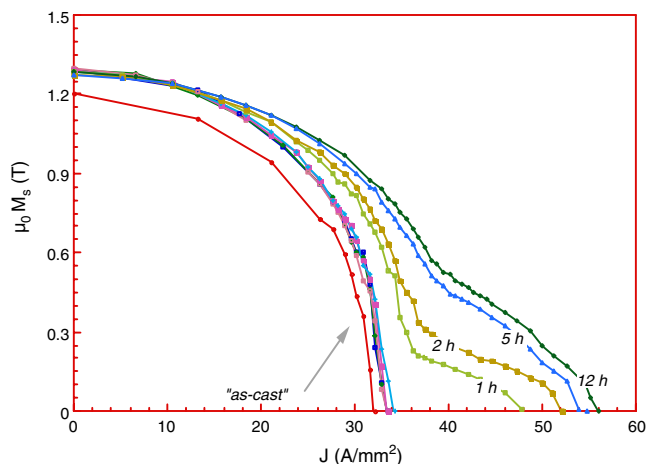


Figure 5. Current density dependence of the saturation magnetisation of samples previously treated at 40 A/mm² with 0, 0.5, 1, 2, 5, 60, 120, 300, and 720 min. Reprinted with permission from [62], J. González, *J. Mater. Res.* 18, 1038 (2003). © 2003, Materials Research Society.

Table 1. Evolution with the annealing time of the percentage of crystalline phase, percentage of Si content inside bcc phase, and average grain size of Fe_{73.5}Cu₁Nb₃Si_{13.5}B₀ amorphous alloy ribbon treated by current annealing at 40 A/mm².

T_{ann} (min)	% crystalline phase	% of Si content inside bcc phase	Average grain size (nm)
60	60	19	12
120	65	21	15
300	70	21	15
720	78	22	17

as an assembly of isolated or weakly magnetostatic interactive single domain particles.

The coercivity behavior can be interpreted in the framework of the two-phase model [47]. At room temperature, the system is soft because the exchange between crystallites is large enough to make the correlation length larger than both the intergranular distance and the grain size. As the current density rises and approaches the Curie point of the residual amorphous matrix, the exchange constant decreases, and some grains start to be weakly coupled. The exchange correlation length decreases and the crystallites progressively start to act as pinning centers.

It is interesting to mention the variations on the Curie point with the annealing time (Fig. 6) [62], corresponding to either the remaining amorphous matrix or the nanocrystalline phase. In the temperature range below the Curie temperature of the residual intergranular amorphous phase (T_C^{am}), the nanocrystallites are coupled magnetically via the exchange interaction acting over the bcc–amorphous–bcc coupling chain. However, this coupling chain is diminished in the temperature range above T_C^{am} , and the nanocrystalline alloys behave as an assembly of isolated magnetic particles in which the magnetically hardest domain configuration is expected. Consequently, we observe a significant increase in H_c in the temperature range above $\sim T_C^{\text{am}}$ [16]. This effect is a possible disadvantage of the nanocrystalline soft

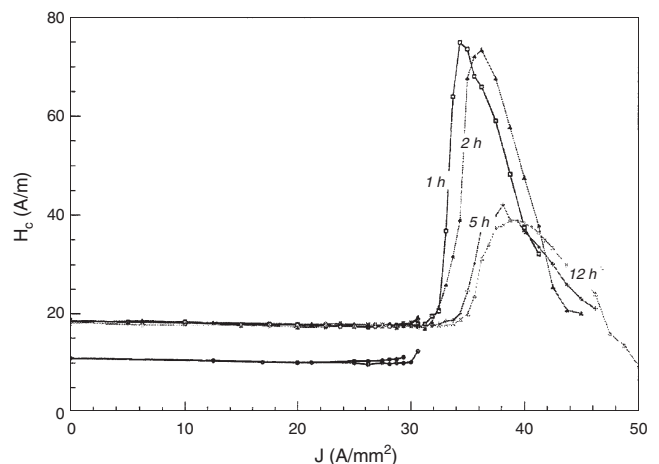


Figure 6. Variations of coercive field with current density of samples previously treated at 40 A/mm² with 0, 0.5, 1, 2, 5, 60, 120, 300, and 720 min. Reprinted with permission from [62], J. González, *J. Mater. Res.* 18, 1035 (2003). © 2003, Materials Research Society.

magnetic alloys from the application viewpoint. On the other hand, the intergranular residual amorphous phase plays an important role. The presence of the residual amorphous phase is essential to maintaining the metastable thermodynamical equilibrium of the nanostructure. This behavior should be understood, taking into account the compositional change of the amorphous matrix (with progressive loss of Si and Fe with the annealing time), which can significantly change the Curie point of this phase. Unavoidable mixing of atoms at the interface nanocrystal–amorphous gives rise to the formation of thin layers of alloys with unknown compositions. It has been proposed that the exchange penetration is likely to be the main cause of the Curie temperature enhancement of the matrix, but with contributions from a magnetostatic interaction as well as compositional sharp gradients of the interface. Unfortunately, the lack of knowledge about the nature of this interface opens an interesting question related to the coupling between two phases with a large interface area as is the case of these soft magnetic nanocrystalline Fe-base alloys.

2.4. Processing of Nanocrystalline Alloys. Induced Magnetic Anisotropy

The magnetization characteristics of *Finemet*-type nanocrystalline magnets (FeCuNbSiB alloy) similar to those of metallic glasses, also can be well controlled by the magnetic anisotropy induced by field annealing, stress annealing, and stress plus field annealing. Magnetic field annealing induces uniaxial anisotropy with the easy axis parallel to the direction of the magnetic field applied during the heat treatment. The magnitude of the field-induced anisotropy in soft nanocrystalline alloys depends upon the annealing conditions (that is, if the magnetic field is applied during the nanocrystallization process or firstly the sample is nanocrystallized and then submitted to field annealing) [63, 66] and on the alloy composition (relative percentage content of Fe and metalloids) [67]. Nevertheless, this field-induced anisotropy is induced at a temperature range of 300 to 600 °C (above the Curie temperature of the residual amorphous matrix and below that of the Curie temperature of the α -Fe(Si) grains. Thus, the anisotropy induced during nanocrystallization should primarily originate from the bcc grains. The amorphous matrix has a rather inactive part, since its Curie temperature is far below the typical field annealing temperature.

The evolutions of the different types of anisotropy induced in a typical alloy susceptible to being nanocrystallized, as a function of current density (thermal treatment carried out by current annealing technique under action of stress and/or field) are shown in Figure 7. As can be seen, stress and stress plus field induced anisotropies increase with the current density (temperature) up to a maximum value at 45 A/mm², which may be related to a maximum of the coercive field. The increase of induced magnetic anisotropy up to 45 A/mm² could be ascribed to an increase in the intensity of the interactions between the metallic atoms, and, consequently, an increase of the induced anisotropy could be expected. This argument is linked to the internal stress relaxation produced by thermal treatment in the metallic glasses. Similarly, field-induced

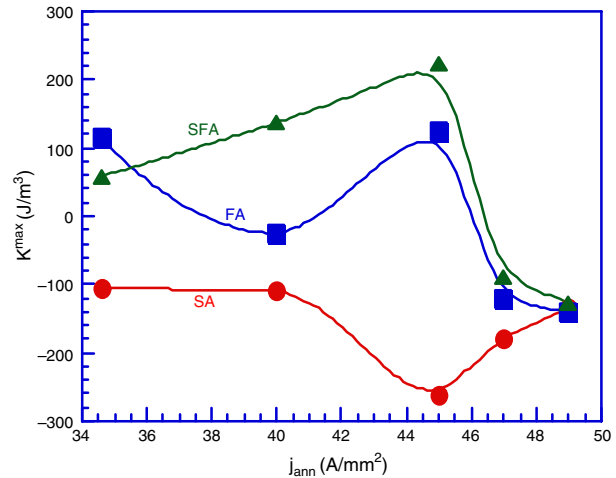


Figure 7. Maximum magnetic anisotropies versus current annealing intensity induced in Fe_{73.5}Cu₁Nb₃Si_{15.5}B₇ samples. Reprinted with permission from [76], C. Miguel et al., *Phys. Status Solidi A* 194, 291 (2002). © 2002, Wiley-VCH.

anisotropy decreases with the current density down to minimum value. Such minimum is observed again at around 45 A/mm². For current densities higher than that of the maximum, induced anisotropy monotonically decreases with current annealing density.

Studies on the stress-induced anisotropy [68–76] indicate that resembling behaviors as those in metallic glasses also can be found in *Finemet* type nanocrystalline magnets. Although the occurrence of this effect has been well confirmed, nevertheless, its origin seems to be not entirely understage at present. Herzer proposed [70] an explanation, claiming that this anisotropy is of a magnetoelastic nature and is created in the nanocrystallites α -Fe(Si) grains due to tensile back stresses exerted by the anelastically deformed residual amorphous matrix. The above conclusion seems to be highly probable because of a strong correlation between the stress-induced anisotropy and the magnetostriction of the nanocrystallites found by Herzer [70]. However, Hofmann and Kronmüller [72] and Lachowicz et al. [73] suggested an alternative explanation of the origin of the considered anisotropy. They adapted the Néel's calculations of atomic pair directional ordering proposed by Néel [77] to the conditions of the investigated material, obtaining a theoretical value of the energy density of the stress-induced anisotropy of the same order of magnitude as that observed experimentally. Consequently, besides the magnetoelastic interactions within the nanocrystallites suggested by Herzer, the directional pair ordering mechanism in α -Fe(Si) grains is also a very probable origin of the stress-induced anisotropy in *Finemet*-type material.

The occurrence of dipolar and deteriorated exchange intergrain interaction also should be considered to explain the origin of the stress-induced anisotropy in the nanocrystalline alloys [19, 49]. This leads to a more realistic situation than the simple anisotropy averaging, since those features are involved in the accomplishment of a nanocrystallization process. In this way, the procedure to obtain the weighted average anisotropy nicely proposed by

Alben et al. [42] strongly depends on the degree of magnetic coupling. This stress anisotropy is induced, as has been noted previously, inside the grains. The maximum value (around 1000 J/m^3) is clearly lower than 8000 J/m^3 , corresponding to the magnetocrystalline anisotropy of the α -Fe(Si) grains; therefore, the origin of the stress anisotropy should be strongly connected to the internal stresses in the FeSi nanocrystals. An interesting question should be one related to the coupling between these two phases with a large interface area such as is the case of Fe-rich nanocrystalline alloys. For this, a deep knowledge about the nature of the interface results are to be determinant. Unavoidable mixing of atoms of the interface gives rise to the formation of thin layers of alloys of unknown composition, which makes this study complicated.

2.5. Saturation Magnetostriction Behavior

The effective magnetostriction, λ_s^{eff} , observed in nanocrystalline alloys at different stages of crystallization, has been interpreted as a volumetrically weighted balance among two contributions with opposite signs originating from the bcc-FeSi grains (λ_s^{cr}) and residual amorphous matrix (λ_s^{am}) according to Herzer [42]:

$$\lambda_s^{eff} = \lambda_s^{cr} + (1 - p)\lambda_s^{am} \quad (6)$$

where p is the volumetric fraction of the crystalline phase. Therefore, assuming negative and positive sign as for the nanocrystalline and amorphous phase, respectively, the variations of λ_s^{eff} (including the change of sign observed in some nanocrystalline composition) can be interpreted as a consequence of the variations of the p parameter. Although this simple approximation gives the qualitative explanation of the effective magnetostriction in Fe-based nanocrystalline alloys [42], it does not consider many effects occurring in the real materials. More exact calculations take into account that the magnetostriction of the residual amorphous phase is not constant but depends on the crystalline fraction due to the enrichment with B and Nb [61, 78]. Consequently, Eq. (6) can be modified in the form [78]:

$$\lambda_s^{eff} = \lambda_s^{cr} + (1 - p)(\lambda_s^{am} + kp) \quad (7)$$

where k is a parameter that expresses changes of the magnetostriction in the residual amorphous phase with evolution of the crystallization. In many cases, even this model does not fit the experimental results, demonstrating that the effective magnetostriction in nanocrystalline material cannot be described by a simple superposition of the crystalline and amorphous components [61]. In the case of the FeZrBCu nanocrystalline system in which the bcc-Fe phase is formed, the model described does not fit the experimental data, even through the $\lambda_s^{am}(p)$ dependence as was shown by Slawska-Waniewska and Zuberek in [79, 80]. They considered this to be an additional contribution to the effective magnetostriction, which arises from the enhanced surface to volume ratio describing interfacial effects [79–83]. Therefore, the Eq. (7) of the effective magnetostriction could be approximated by:

$$\lambda_s^{eff} = p\lambda_s^{cr} + (1 - p)(\lambda_s^{am} + kp) + p\lambda_s^s S/V \quad (8)$$

where the last term describes the effects at the interfaces and depends on the surface-to-volume ratio for the individual grain, as well as on the magnetostriction constant λ_s^s , which characterizes the crystal-amorphous interface.

Equation (8) is the basic dependence, which can be used to interpret the experimental data on the effective magnetostriction in Fe-based nanocrystalline alloys at different stages of crystallization. The composition of the Fe(Si) grains (depending on the annealing temperature) should be considered, giving rise to different values of the magnetostriction constant for the crystalline phase. The appropriate values of λ_s^{cr} can be obtained from the compositional dependence of the saturation magnetostriction in the polycrystalline α -Fe_{100-x}Si_x, shown in Figure 8 [42, 84]. Thus, the first term in the Eq. (8) can be treated as the well-defined one.

Figure 9 presents the crystallization behavior and accompanying changes in the magnetostriction of the classical *Finemet* (Fe_{73.5}Cu₁Nb₃Si_{13.5}B₉) alloy published by Gutierrez et al. [85]. The analysis of these data, according to Eq. (8), allows (i) estimation of the contribution from the crystalline phase (see Fig. 8a, where the values of λ_s^{cr} were found from the combined Figs. 8 and 9a), and then (ii) fitting of the experimental ($\lambda_s^{eff} - p\lambda_s^{cr}$) on p dependence in Eq. (8). The results, both experimental points and the fitted curve (solid line) are shown in Figure 9b.

Assuming spherical α -Fe(Si) grains, with radius R , the last term of Eq. (8) can be expressed as $3\lambda_s^s/R$, and the magnetostriction constant, which describes the interface λ_s^s , can be estimated. For the soft nanocrystalline alloys (*Finemet* and FeZrBCu alloys) [42, 61, 79], $R = 5 \text{ nm}$, and, thus, λ_s^s has been found to vary in the range $4.5\text{--}7.1 \times 10^{-6} \text{ nm}$. These results are one order of magnitude smaller than values of the surface magnetostriction obtained in multilayer systems. However, investigations of Fe/C multilayers have shown that not only the value but also the sign of the surface magnetostriction constant depends on the structure of the iron layer, and it has been found that for crystalline iron, λ_s^s (bcc-Fe) = $45.7 \times 10^{-6} \text{ nm}$, whereas, for the amorphous iron, λ_s^s (am-Fe) = $-31 \times 10^{-6} \text{ nm}$ [86]. Thus, the value of the interface magnetostriction obtained in the nanocrystalline systems is within the range of the surface magnetostriction constant estimated for thin iron layers. It should be noted that, contrary to Fe/c multilayers, in the nanocrystalline materials, both the crystalline and amorphous phases are

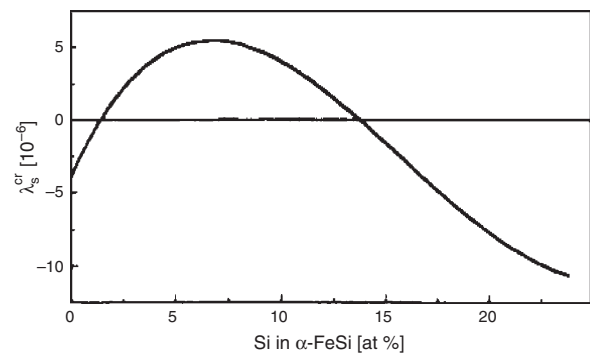


Figure 8. Saturation magnetostriction of the polycrystalline α -Fe_{100-x}Si_x. Reprinted with permission from [80], A. Slawska-Waniewska et al., *Mater. Sci. Eng. A (Supplement)*, 220 (1997). © 1997, Elsevier Science.

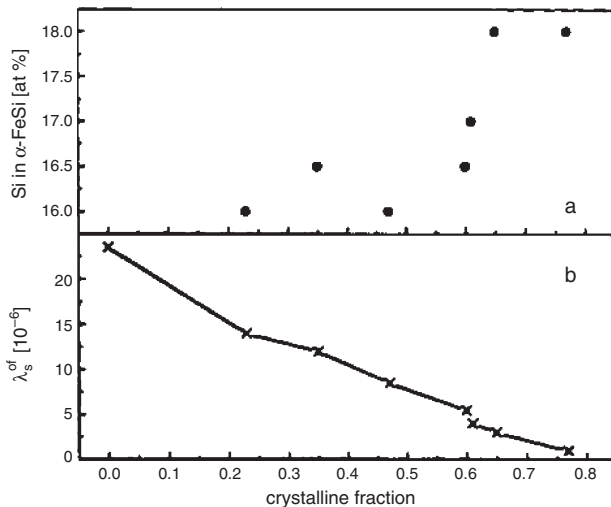


Figure 9. Si content in α -Fe(Si) grains (a) and magnetostriction of the $\text{Fe}_{73.5}\text{Cu}_1\text{Nb}_3\text{Si}_{13.5}\text{B}_9$ alloy (b) versus crystalline fraction. Reprinted with permission from [80], A. Slawska-Waniewska et al., *Mater. Sci. Eng. A (Supplement)*, 220 (1997). © 1997, Elsevier Science.

magnetic, and they are coupled through exchange and dipolar interactions. It must thus be expected that the magnetic interactions in the system can affect the magnetoelastic coupling constant at the grain–matrix interfaces. In addition, the structure and properties of the particular surfaces that are in contact, as well as local strains at the grain boundaries also should be considered.

The problem of the surface/interface magnetostriction, however, requires further studies, which, in particular, should include measurements at temperatures above the Curie point of the amorphous matrix, where only ferromagnetic grains should contribute to the effective magnetostriction, simplifying a separation between bulk and surface contributions.

3. HARD NANOCRYSTALLINE MATERIALS

3.1. An Introduction

Permanent magnets are devices capable of producing, during a time of the order of several years and without any on-service energy input, a magnetic field whose magnitude is at least in the order of the tens of T. The devices, based on fields produced by permanent magnets, are ubiquitous in modern technology; a good example of this point is that in a modern car, it is typically possible to identify up to 30 different magnets [87]. In most of the cases (the exception are those in which the magnets are used to produce a field gradient), the figure of merit characterizing the device is the so-called energy product of the permanent magnet [88]. If the permanent magnet is used as a part of a magnetic circuit in which the magnetization is essentially uniform, the energy product gives the magnetic energy density, stored in a thin air gap introduced in the circuit and limited by surfaces (the poles) perpendicular to the average magnetization (the energy product also is proportional to the square

of the induction created in the gap). In addition to a sufficiently high energy product, a permanent magnet should exhibit (especially those used in the automotive industry) a weak decrease of the coercive force with the increase of the temperature and good corrosion resistance properties.

Modern permanent magnets are based on the so-called hard magnetic phases, that is on phases difficult to demagnetize. A hard phase should present, at the temperatures of interest from the standpoint of the applications [89], (i) a coercive force large enough to preserve the remanence from either on-service or spurious demagnetizing effects (it is possible to show that, in a uniform magnetization circuit, the stability of the remanence is granted by a coercivity larger than half the magnitude of the remanence), (ii) a remanence as large as possible (in a polycrystalline hard material, the remanence value results from the saturation magnetization value and from the degree of macroscopic texture of the grain orientation distribution), and (iii) a magnetic transition temperature high enough so as to be compatible with the temperature increases occurring during the use of the magnet.

The optimization of this set of properties can, first of all, be correlated to an adequate choice of the structure and intrinsic properties of the hard phase. The induction of a large coercivity is linked to the occurrence of a large magnetic anisotropy. For the coercivity values required by modern applications, the anisotropy can only be of a magnetocrystalline origin [90]. The magnetocrystalline anisotropy results from the electrostatic interaction between the charge distribution of the atoms bearing the localized magnetic moments responsible for the macroscopic magnetization and the crystalline electric field created by the ions surrounding those magnetic atoms. Requisite for the observation of large magnetocrystalline anisotropy is the existence of a large spin-orbit coupling in the atoms having magnetic moments [91]. This large spin-orbit coupling has, as a consequence, the fact that any modification of the orientation of the moments is linked to a rotation of the charge linked to the orbital part of the total moment and, consequentially, to a variation of the energy of interaction between that charge and the ions in its neighborhood (the relative orientation(s) resulting in a minimum of this interaction energy are called easy axes and those corresponding to maxima, hard axes). Considering this initial requisite, it is possible to identify the complete Rare-Earth series as a group of elements with a potential to either be used as or to form hard phases [92] (the rare-earth elements have large spin-orbit interactions and the Rare-Earth ions exhibit, with the only exception of Gd, large asphericities which make the crystalline field interactions highly dependent on the charge orientation).¹

The achievement of a large saturation magnetization is linked to the identification of a highly packed atomic structure in an element or compound formed by atoms bearing the larger possible magnetic moments and having the smallest possible atomic volume. Due to their large atomic volumes, which is not compensated by their often large atomic moments, the rare-earths are, in respect to the elevated

¹ The occurrence of uniaxial anisotropies (corresponding to hexagonal, tetragonal, or rhombohedral crystal structures) is an additional requisite for the achievement of elevated coercivities.

magnetization, in a clear disadvantage with respect to the transition metal magnetic elements and, specially, in comparison with Co and Fe (which, in turn, have, due to the very small spin-orbit coupling, a reduced magnetocrystalline anisotropy).

The third requisite, that corresponding to the elevated order temperature, also excludes the rare-earths since the small magnitude of the exchange interactions between the elements of the series results in the fact that the rare-earth with the larger Curie temperature is Gd, the most spherically symmetric rare-earth ion, which goes paramagnetic at ca. 300 K, an order temperature incompatible with any practical application. It is thus possible from this discussion to discard any magnetically pure element as a potential hard magnetic phase.

A hard phase must, consequently, at least be a binary compound joining in a single structure high anisotropy, magnetization, and order temperature [93]. The intermetallic transition metal–rare earth alloys are thus clear candidates for a hard magnetic behavior and, in fact, hexagonal phases of the SmCo system exhibit coercivities in single-phase, polycrystalline samples of up to 4 T at room temperature (these phases can bear remanences of the order of 1 T, have reasonably good corrosion properties, and can be used up to ca. 650 K without a large deterioration of their hysteretic properties). The main problem with the extensive use of SmCo magnets is related to the limited availability of Co and its high (and highly fluctuant) price.

Phases alternative to the SmCo ones and not containing Co are the ordered tetragonal FePt (exhibiting coercivities smaller than those obtained in SmCo) and, more importantly, the ternary tetragonal NdFeB, the phase having the better hard properties achieved up to the moment.

In this section, we will review the basic characteristics and behaviors of these hard phases, the links between the demagnetization properties and the phase distribution and morphology, the influence of the demagnetization mode in the optimization of the preparation methods, and will finish with the analysis of the way of overcoming the limitations of the hysteretic properties related to the values taken by the intrinsic quantities: the induction of different types of nanostructures.

3.2. Magnetization Processes and the Phase Distribution

On the origin of the possibility of controlling the demagnetization behavior are the particularities of the demagnetization process. In the particular case of a polycrystalline material, demagnetization takes place in a complex way (Fig. 10), involving some (or all) of the stages in the sequence nucleation–expansion–propagation–pinning–depinning [94]. We will describe these stages, as well as their dependence on the extrinsic characteristics of the materials.

The nucleation process corresponds to the first (occurring at a smaller demagnetizing field) irreversible departure of the distribution of the magnetic moments present in a certain region (typically a grain) of a material from the configuration associated to the remanent state. That departure, depending on the main phase properties, could involve either the formation of a reversed region limited

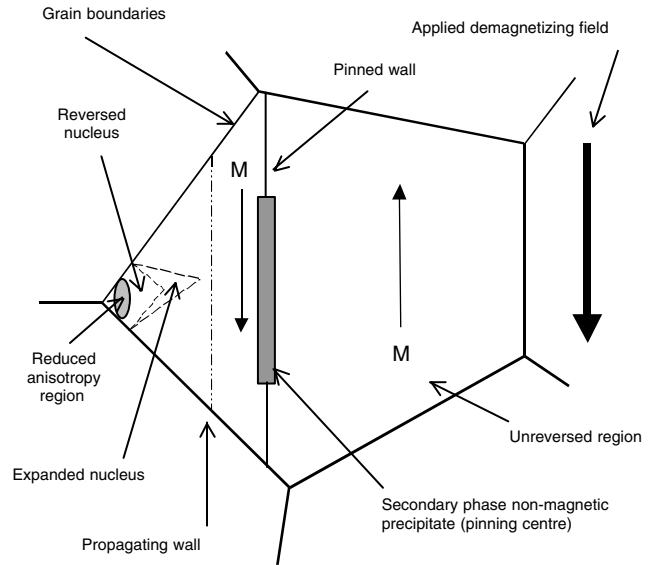


Figure 10. Schematic illustration of the intragrain demagnetization sequence (nucleation–nucleus expansion–propagation–pinning stages).

by a domain wall or that of an extended inhomogeneous local magnetization distribution, which corresponds to the onset of the global reversal process and takes place preferentially at (i) points where local demagnetization fields are more intense (as the edges and corners in well-crystallized, polyhedral grains) and (ii) points where the local anisotropy and/or exchange are significantly reduced with respect to their values in a free-from-defects area of the main phase (to be effective, these sites of preferential nucleation should have transverse dimensions of the order of the magnetic moments structures formed upon nucleation). In the most general case, the occurrence, at a given field value, of nucleation does not have as a consequence the complete reversal of the magnetization of the sample. This is so just because the growth in size of the total or partly reversed regions requires the input of energy in the system due to the fact that, in general, the moments in those regions do not point along easy axes (as required to minimize the anisotropy energy) and/or are not fully parallel (which is the configuration minimizing exchange and dipolar energies). It is thus necessary to increase the magnitude of the demagnetizing field in order to balance the increase of the energy of the distribution of magnetic moments required by the growth in size of the localized reversed region from which the global reversal proceeds. This process is denominated by nucleus expansion and takes place, reversibly, up to an applied field value for which the nucleus can steadily grow in size (that field is called the propagation field). In the particular case of the hard magnetic materials, the nucleation and propagation fields can be significantly different.

Once the condition of steady expansion of the reversed nucleus is achieved, the magnetization reversal can only be stopped if the structures involved in the propagation (e.g., a domain wall limiting the reversed area) get trapped in regions where they have an energy lower than that corresponding to the previously swept areas. Those pinning centers are associated with secondary phases

of deteriorated crystallinity regions where the anisotropy and/or the exchange energies are lower than those of the well-crystallized main phase (planar structures as second phase precipitates are especially effective as pinning centers). If a propagating nucleus gets trapped in one of these pinning points, in order to proceed with the reversal process, it is necessary to increase the applied demagnetizing field in the magnitude required to unpin the propagating structure (the depinning field is related to the characteristics of the difference on the anisotropy, exchange and dipolar energies between the pinning center, and the well-crystallized areas).

From this discussion, it is clear that the field required to fully reverse the magnetization of a grain in a polycrystalline hard material coincides with the maximum of the nucleation, propagation, and depinning fields.

As for the complete reversal of the magnetization of a polycrystalline material, the crucial role corresponds to the intergranular regions (Fig. 11). Those intergranular regions (grain boundaries separating main hard-phase grains) could have a differentiated structure (thus, being a secondary phase) or could just correspond to the main phase structure accumulating defects and additive elements so as to provide the transition between the crystallographic orientations of different main-phase grains. In both cases, the most important points are (i) the occurrence and type of the exchange interactions in the intergranular structure and (ii) the thickness of the grain boundary. These two points will be analyzed in detail in the next section but, for the moment, we can say that:

- (a) If the main phase grains are perfectly exchange coupled through the grain boundaries, the global coercive force will correspond to the coercivity of the grain having the smallest reversal field (the structures propagating in the reversal of that grain will not have any hindrance to propagate across the sample). This is a particularly undesirable case, since the coercivity is linked to the region in the material having the most deteriorated magnetic properties.
- (b) If the main phase grains are partially exchange coupled (either if they are uniformly coupled through an

intergranular exchange constant that is a fraction of that of the main phase, case A, or if they are nonuniformly coupled, case B), the increase in volume of the reversed regions will find either pinning centers (case A, stopping the walls inside the grain boundaries) or propagation barriers (case B, stopping the grains outside the grain boundaries) at the grain boundaries. The global coercivity will be a convolution of the distribution of grain reversal fields and of the depinning fields of the grain boundary regions (this is a particularly complex case since the reduced exchange at the grain boundaries also can influence the distribution of nucleation fields).

- (c) If the main phase grains are fully exchange decoupled, the global coercivity directly results from the distribution of grain reversal fields. This case is, in principle, preferred for the optimization of the hard materials since, as we will see in the next section, it is compatible with the state of the art about the control of the properties of the intergranular regions and ensures the achievement of coercivities directly related to the structure and properties of the main phase.

It is clear that the detailed knowledge of the actual demagnetization mechanism taking place in a concrete material is the key to the achievement of a relevant optimization of its hysteretic properties and that the basic mechanism for that purpose is the control of the phase distribution and morphology. This information is, nevertheless, quite elusive to simple and straightforward analysis and, usually, can only be partially obtained. To that purpose, the most commonly analyzed data are those corresponding to the temperature dependence of the coercive force [95], due to the availability of models correlating in simple terms the magnetic properties and some microstructural features. The conclusions of those models [96, 97], initially proposed by Brown, and basically adequate to describe nucleation-ruled magnetization reversal processes, can be summarized in Eq. (9)

$$H_c(T) = \alpha H_K(T) - N_{eff} M_s(T) \quad (9)$$

where $H_C(T)$ is the temperature dependence of the coercivity, α and N_{eff} are parameters fitting the experimental coercivity data, $H_K(T)$ is the experimental temperature dependence of the anisotropy field, and $M_S(T)$ is the experimental temperature dependence of the magnetization. Equation (9) simply states that at all the temperatures, the coercive force can be obtained from the anisotropy field of the main phase (the maximum observable coercivity in that phase) multiplied by a factor (lower than the unity) that contains all the sources of deterioration of the local coercivity and decreased in the local demagnetizing field at the site of the reversal onset. The fitting parameter α can be factorized on the contributions of the texture of the grains of the main phase, the occurrence of either complete intergranular exchange or perfect grain decoupling, and the local reduction of the anisotropy related to the occurrence of poor crystallinity or soft regions. As for the N_{eff} parameter, the local demagnetizing factor, it can be larger than the unity since it does not necessarily describe fields originated by uniform magnetization distributions [98].

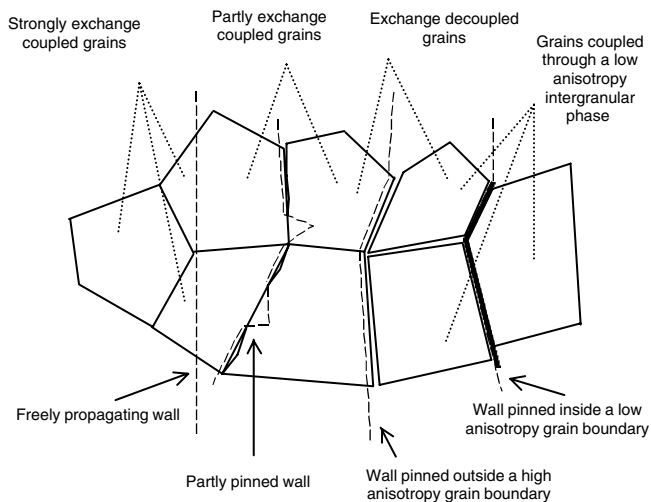


Figure 11. Domain wall propagation across differently exchange coupled grains.

Despite its simplicity (it reduces the complex influence of the phase distribution to only two parameters), Eq. (9) almost universally describes the temperature dependence of the coercivity [99] and is very useful to analyze the behavior of a series of samples prepared under similar conditions. A typical example of this type of study is the analysis of the influence of additive elements on the grain decoupling that (provided other influencing factors are maintained constant) should correspond to an increase of α with the increase of the decoupling. Also, the achievement of better crystallinities, resulting in better defined grain edges and corners can be correlated easily to the increase of N_{eff} .

The occurrence of pinning–depinning processes can be quite unambiguously identified from the measurement (usually carried out in highly textured samples) of the angular dependence of the coercivity [100]. If the main phase grains in these samples are well exchange coupled, the presence of depinning walls can be pinpointed from the observation of a monotonous increase of the coercivity with the increase of the angle ϕ formed by the direction of the saturation remanence and the applied demagnetizing field. That increase is related to the increase of the pressure exerted over the pinned walls by the applied field that is proportional to $1/\cos\phi$. In contrast with the reversal mechanisms linked to pinning, a nucleation-ruled reversal usually exhibits an angular dependence of the coercivity characterized by an initial decrease with the increase of ϕ , a minimum and a further increase, a behavior resembling (but, in general, not mimicking) the angular dependence of the coercivity predicted for systems demagnetizing according to coherent rotation mechanisms.

Finally, in what concerns the analysis of the magnetic properties, the measurement of the relaxational properties (those related to the thermally activated magnetization reversal) can yield and estimate (the so-called activation volume) of the size of the region involved in the onset of the reversal process [101]. That estimate can be useful to try to identify the characteristics of the points at which the nucleation occurs but, generally, the discussions based on the measurement of the magnetic viscosity are not very conclusive.

3.3. Hard Nanocrystalline Materials

The most consolidated reason to reduce the size of the grains of the main phase in a hard magnetic material is related to the previously discussed influence of the defects on the promotion of the magnetization reversal. This point is clear if the occurrence in the material of a uniform density of defects is assumed. In this case, the reduction of the grain size will result in a reduction of the number of defects per grain, and, regarding the nucleation processes, the lower the number of defects, the larger the nucleation field. Typical average grain sizes of materials optimized following this idea are in the range of 10 to 100 nm.

The nanocrystalline structure is induced by means of four main techniques:

- (i) Mechanical alloying and mechanical grinding. These two techniques are characterized by the introduction in the starting materials (either pure elements in the

case of the alloying or a prealloyed material in that of the grinding) of a large amount of mechanical energy that results in a large increase of their free energy (linked both to large deformations and to a high degree of intermixing). From that high-energy state, the material can decay (either spontaneously or after a low temperature treatment) to lower energy configurations, as those corresponding to an extended solid-state solution, metastable phases, and stable phases. Mechanical alloy has been widely used to produce NdFeB and, to a lower extent, SmCo. It is an inexpensive technique, resulting in a powdered material having typical grain sizes of the order of 10 nm that allows to process large amounts of materials and whose only drawback is the impossibility of producing highly textured magnets.

- (ii) Rapid quenching from the melt. This preparation technique usually involves the quenching of a quasi-amorphous material and an ulterior treatment that allows crystallizing the main phase in grains of the order of 50 to 100 nm. The mechanical alloying mainly has been used to prepare NdFeB and does not result in macroscopically anisotropic materials. It is, nevertheless, possible in this case to produce a high-quality textured material by hot mechanic working of the quenched materials (these textured samples are not nanostructured).
- (iii) Physical vapor deposition techniques used to grow thin and thick hard magnetic films. Although, there is a large variety of physical vapor deposition techniques (laser ablation, evaporation, molecular beam epitaxy, etc.), the most promising and widely used is sputtering. Generally speaking, the nanostructure is induced either by room temperature deposition of a quasi-amorphous phase, followed by a high temperature thermal treatment, or by direct deposition at moderately high substrate temperatures. The most relevant hard phase deposited by using sputtering has been NdFeB [102], although, recently there is a lot of activity on SmCo-based phases [103].
- (iv) Electrodeposition. Although limited in the achievable compositions (basically CoNiP, CoP, and FePt), this is by far the technique that allows the higher film deposition rates and also that allows an easier implementation [104]. As in other cases, it is possible to deposit amorphous films that afterward are crystallized or, directly and depending on the composition of the film and deposition bath, nanocrystalline films.

In addition to the increase of coercivity linked to the reduction down to the nm scale of the main hard-phase grains, the induction of nanocrystallinity in permanent magnet materials has, as a consequence, the increased influence on the demagnetization processes of the grain boundary regions. As we will discuss, that influence can bring about the possibility of major optimizations of the properties of these materials.

Let us consider first a single-phase nanocrystalline material: a high anisotropy phase for which the domain wall width, L , is larger than the grain boundary thickness, d , but smaller than the average grain size, D . Typical examples of

that kind of material are the NdFeB-based alloys obtained by controlled crystallization of an amorphous precursor. The crystallization process used to prepare those samples usually is implemented by rapidly heating the precursor material up to the treatment temperature (typical heating rates are in the range of the tens of thousands of degrees per minute), keeping them at that temperature for a few minutes and cooling them down at a rate of variation of the temperature comparable to that used during the heating process. This treatment strategy aims at the enhancement of the crystallite nucleation process and, simultaneously, to the reduction of the grain growth (both basic crystallization mechanisms typically have independent kinetics) and results in a very fine and homogeneous nanostructure, characterized, in the case of the NdFeB-based materials, by average grain sizes of the order of a few tens of nm and, also, by very clean (free from defects) grain boundaries, with a typical thickness of the order of a few interatomic distances. The rapid heating also can avoid a significant precipitation of unwanted secondary phases (as, mainly, α -Fe in the case of the considered system). In fact, the control of the heating rate during the crystallization process seems to be crucial since, for instance, in the case of the $\text{Nd}_x\text{Fe}_y\text{B}_{100-x-y}$ alloys, the coercive force measured in the as-crystallized material varies from a value close to zero, corresponding to heating rates of the order of $10^\circ\text{C}/\text{minute}$ up to a value of 4 T in the optimally treated sample, that crystallized by using a heating rate of $1.5 \times 10^4^\circ\text{C}/\text{minute}$ [105].

The relevant point is that the presence in these materials of very thin grain boundaries, free from defects to a large extent, result in the occurrence of strong intergranular exchange coupling. Thus, in the boundary region limiting two grains having different easy axes orientations, a structure of magnetic moments allowing a gradual transition between those easy axes directions is formed (Fig. 12). Those domain wall-like structures have two relevant effects on the hysteretic parameters. On the one side, and taking into account that the transition structures have a typical transverse dimension of the order of L and are larger than the grain boundary thickness, they result on a remanence, M_r , enhancement (with respect to the value corresponding

to an isotropic uniaxial material). The enhancement is linked to the fact that the moments forming the transition structure point away from their associated easy axis direction and closer to the direction of the previous saturation. On the other side, they produce a significant coercivity decrease, related to the fact that they act as very effective nucleation sites (Fig. 12) for the reversal of the magnetization (the reversal process can, alternatively be seen as corresponding to the depinning from the grain boundary region of the domain wall-like structures). The combination of these two effects is, nevertheless interesting in general because it can result in an increase of the maximum energy product, $(\text{BH})_{\text{max}}$, the parameter giving the figure of merit of a permanent magnet material (for a coercive force value sufficiently high so as to effectively support the remanence, the maximum energy product is proportional to $\mu_0 M_r^2/4$). Let us finally say that the first single-phase materials exhibiting a significant remanence enhancement contained Si and Al additions, and it was believed that the occurrence of small grains strongly exchange coupled was linked to the presence of those additives. Today it is clear that both the nanostructure and the remanence enhancement are a consequence of a nucleation ruled crystallization process originating with narrow grain boundaries.

Going now into the case of the multiphase nanostructured materials and, as has been discussed previously, the basic idea behind the use of rare-earth transition metal intermetallic phases for the preparation of permanent magnet materials was the achievement of a combination of high magnetic anisotropy with high magnetization values at room and higher temperatures (a property linked to the large transition metal exchange and Curie temperature). This combination also can be implemented by adequately coupling a high anisotropy phase (as, mainly, a rare-earth transition metal intermetallic) with a phase exhibiting high magnetization (usually a transition metal, a transition metal intermetallic, or a transition metal-metalloid alloy). The point has been analyzed in detail, and it is well established that the requisites to achieve such a coupling are linked to the nanostructure of the phases. It is necessary to produce an intimate phase mixture, essentially consisting of hard grains embedded into a soft phase and strongly exchange coupled to it. Since the dominating exchange coupling both in the hard phase and in the soft one is the transition metal-transition metal one, the effective magnitude of the intergranular coupling is ruled both by the boundary thickness and by the amount of disorder present at the boundary. In the case of an intense hard-soft coupling, the optimum thickness of the soft phase in between two hard grains corresponds to half the hard-phase domain-wall width.

This optimum value results from a twofold compromise: first, it should correspond to a large polarization of the magnetization of the soft phase along the direction of the magnetization of the neighboring hard grains and, consequently, to a high remanence (this, in principle, could be achieved even with a large soft-phase thickness, provided the interphase coupling could be large enough), and, second, it should preserve, as much as possible, the coercivity of the hard phase (which limits the soft-phase thickness, since it should be kept below the soft-phase exchange correlation length to avoid the easy complete magnetization reversal

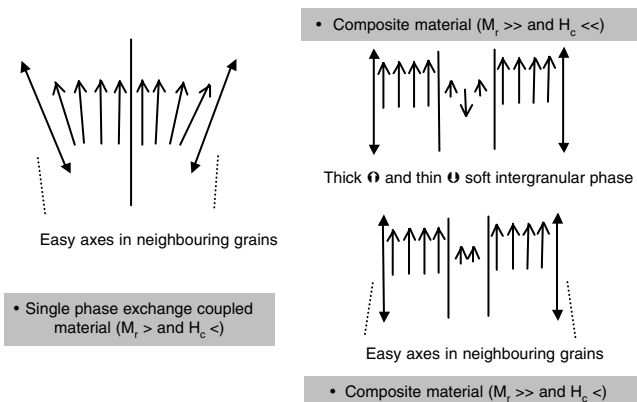


Figure 12. Influence on the remanent magnetization and the coercive force of the occurrence of direct exchange coupling (single phase material) and of coupling through intergranular phases having different thicknesses (composite materials).

inside the soft phase, which could propagate into the hard one due to the large interphase coupling). As for the average hard-phase grain dimensions and, again, in order to achieve high remanences, they should be slightly larger than the hard-phase exchange correlation length. There exist a quite broad group of hard–soft composites meeting (to a different extent) the requirements corresponding to the optimized hysteretic behavior. They are based on the $\text{Nd}_2\text{Fe}_{14}\text{B}$ and SmCo_5 phases and contain as soft phase $\alpha\text{-Fe}$ and Fe_3B .

To end this section, we will discuss the case corresponding to the presence of antiferromagnetic phases at the intergranular region. It recently has been shown [106] that in mechanically ground samples formed by SmCo and NiO (the antiferromagnetic phase), the intimate mixture of both phases results in a remarkable increase of the coercivity with respect to that measured in the NiO -free SmCo samples. The origin of this increase has been associated with the exchange coupling between the hard and the antiferromagnetic phase that transmits the anisotropy of the latter to the easily reversible moments on the edges and corners of the SmCo grains.

4. MICROMAGNETIC NUMERICAL SIMULATIONS

4.1. Introduction

A quantitative treatment of the correlation between the microstructure and magnetic properties in nanostructured materials requires numerical and computational techniques. These techniques, in many senses, are complimentary to the experimental ones, especially in understanding of the magnetization reversal mechanisms, which define the nanostructured material performance. The experimental studies, such as magnetic imaging, have serious difficulties in controlling the magnetic properties down to several nanometers scale in space or down to nanosecond scale in time. At the same time, the modeling of reversal modes propagation both in space and time in this scale is possible. The use of computational techniques such as *micromagnetics* provides a way to obtain a realistic relation between the microstructure and magnetic properties in many cases.

By using this technique, the magnetic properties of a nanostructured material, relevant to its application, such as coercivity and remanence, dynamical switching time, and thermal stability could be predicted qualitatively in relation to nanostructure. The rapid variation of many extrinsic and intrinsic parameters is accessible by using numerical techniques and is useful in understanding the qualitative tendency in the material behavior when one constitutes the design of materials with determined properties. As an example, the micromagnetic simulations have been shown to be extremely useful techniques in the study of the performance of magnetic media used for magnetic recording.

In general, many factors influence the magnetic properties of a nanocrystalline magnetic film, e.g., the grain size and shape, anisotropy distribution, the grain boundary properties, magnetic impurities, etc. The potential of an analytical approach is limited to a small number of very simplified cases. The simulations represent the only alternative to experimental techniques. At the same time, the

micromagnetic simulations require an input of the intrinsic media parameters in the micromagnetic code from measurements. However, in many cases and especially in granular materials, the experimental techniques are unable to provide the knowledge of the microstructure with the desired details. This is especially true for the treatment of the grain boundary in nanostructured materials where normally there is no detailed knowledge of many intrinsic parameters such as exchange or anisotropy. This limits the potential accuracy of micromagnetic predictions. For example, the coercivity value, which is a result of very complicated interplay between intrinsic and extrinsic magnetic medium parameters, calculated numerically, rarely coincides with the experimental value. At the same time, this also constitutes a strong point of the numerical simulations since it allows the flexibility and control in varying the intrinsic parameters (such as different intergrain boundary models), which are not accessible by experimental techniques, with the aim of a final comparison of the results with the experimental measurements.

We will describe the principle utilities and results of the so-called micromagnetic simulations in relation to the magnetization reversal processes in nanostructured magnetic materials. Section 4.2 will describe briefly the classical micromagnetics. In Sections 4.3 to 4.5, we present results on the role of zero-temperature micromagnetic simulations in understanding the magnetization reversal processes in nanostructured magnetic materials. Section 4.6 is devoted to simulations of magnetic recording medium performance. In Section 4.7, we present the results of the micromagnetic simulation guiding the optimization of magnetic behavior of nanocomposite (soft-hard) magnetic materials. Finally, Sections 4.8 and 4.9 are devoted to “nonclassical” micromagnetics, i.e., to the dynamical behavior of the nanostructured media and to the effects of temperature.

4.2. General Principles of Micromagnetics

Classical (zero-temperature) micromagnetics describe magnetic materials in a nanometric lengthscale where each discretization unit is represented by a large magnetic moment that could be described in a semiclassical approximation, i.e., no quantum effects are taken into account. The principle of micromagnetics is due to Brown [107] who derived the micromagnetic equations for the equilibrium properties. The method consists in discretizing the magnetic film in finite differences [108–110] or finite elements [111–114], writing the energy contribution of each magnetic discretization unit, and minimizing the total energy of the system. No temperature effects or dynamics are included at this stage. The total energy normally comprises the contributions of Zeeman energy (external field):

$$E_{ext} = - \int_V \vec{H}_{ext}(\vec{r}) \vec{M}(\vec{r}) dV \quad (10)$$

where $\vec{M}(\vec{r})$ is the magnetization of the specimen and V is its volume; the energy of anisotropy in the uniaxial case has the expression:

$$E_{ani} = - \int_V K(\vec{r}) [\vec{m}(\vec{r}) \vec{e}(\vec{r})]^2 dV, \quad (11)$$

where K is the anisotropy constant, $\vec{e}(\vec{r})$ is a unit vector that defines its direction, and $\vec{m}(\vec{r})$ is the unit magnetization vector; the energy of exchange:

$$E_{ex} = \int_V A(\vec{r})[(\nabla m_x)^2 + (\nabla m_y)^2 + (\nabla m_z)^2] dV \quad (12)$$

where A is the exchange constant, and the magnetostatic energy:

$$E_{\text{magn}} = -\frac{1}{2} \int_V \vec{M}(\vec{r}) \vec{H}_{\text{magn}}(\vec{r}) dV \quad (13)$$

The magnetostatic energy, which has the nature of very long-range decaying interactions, requires the most effort of the computation. It should be found by solving the Poisson equation of motion (SGSM units are used):

$$\vec{H}_{\text{magn}} = -\nabla U_{\text{magn}}, \quad \Delta U_{\text{magn}}^{\text{inside}} = 4\pi \nabla \vec{M}, \quad \Delta U_{\text{magn}}^{\text{outside}} = 0, \quad (14)$$

where U_{magn} is the magnetostatic potential inside and outside the magnetic body, with the boundary conditions:

$$U_{\text{magn}}^{\text{inside}} = U_{\text{magn}}^{\text{outside}}, \quad \frac{\partial U_{\text{magn}}^{\text{inside}}}{\partial \vec{n}} - \frac{\partial U_{\text{magn}}^{\text{outside}}}{\partial \vec{n}} = 4\pi \vec{M} \vec{n} \quad (15)$$

and \vec{n} defines the unit vector, normal to the surface of the magnetic sample. At the present time, two main methods have become widely used for its calculation: the Fast Fourier transform [115, 116] and FEM-BEM (finite element-boundary element method), which directly solves the Poisson equation [111–114]. For the energy minimization, the conjugate gradient method [113, 114] or the relaxation method [108, 109] are very useful. Another way to minimize the energy is the integration of the equation of motion of the magnetization (the Landau–Lifshitz–Gilbert equation) with a large damping constant [117]. The advantage of this method is that it provides the dynamical information for the magnetization motion together with the static information.

For simulation of a nanostructured material, it is important to generate numerically the geometrical microstructure (crystalline grain structure). Although at the beginning, many calculations used regular hexagonal arrays [118, 119], lately, it has been widely accepted that the Voronoi discretization [111, 112, 120, 121] naturally and realistically describes the nanostructure with the desired log-normal distribution. Figure 13 represents an example of such a structure generated for micromagnetic simulations. Another way to introduce the nanostructure into the calculation is the use of closely packed spherical particles [122, 123] with log-normal distribution.

The role of the magnetization-discretization length has been discussed intensively in the literature. Depending on the desired size of calculations, more or less details in the magnetization distribution are required. As a consequence, the micromagnetic calculations have been performed in systems by using different discretization scales, ranging from one discretization element equal to one grain [119, 124], passing through the grains with special discretization at the intergrain boundaries [111], and down to atomistic models [125]. However, it must be noted that there exist two

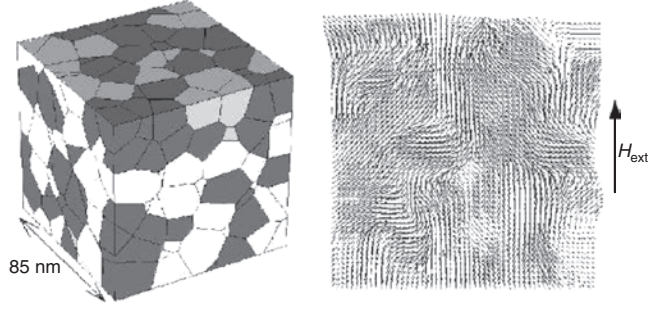


Figure 13. Example of a micromagnetic model with finite element soft-hard grain structure in a two-phase $\text{Nd}_2\text{Fe}_{14}\text{B}/\text{Fe}_3\text{B}$ magnet. Right: Magnetization distribution in a slice plane for zero applied field. The arrows denote the magnetization direction projected on a slice plane. (courtesy of T. Schrefl).

characteristic material length parameters: the width of a domain wall, $\delta_w = \sqrt{A/K}$ (where A is the exchange parameter and K is the uniaxial anisotropy strength) and the exchange correlation length $L_{ex} = \sqrt{A/M_s^2}$, where M_s is the saturation magnetization value. Depending on the value of the anisotropy, these lengths are comparable with or even smaller than the grain sizes of polycrystalline films. If they are smaller, the assumption of a single-domain grain is not always valid. Also and importantly, the thickness of the film could be ignored when the film is thinner than these characteristic lengths. The other problem is that, generally speaking, magnetostatic potential always has a 3D character. The complete 3D calculations are a very time-consuming task and result in a reduced size of a simulated magnetic element. However, in some cases, when the magnetization vector is expected to lay in the plane, the calculations may be restricted to a 2D model [111].

Furthermore, the model could be made much more realistic so as to include explicitly inhomogeneously arranged magnetic moments inside each grain [111, 112], special treatment of boundaries [126], inclusion of magnetically soft phases between hard grains [111, 127], surface roughness [120], etc.

4.3. Hysteresis and Magnetization Reversal

Static and dynamic micromagnetic modeling provided useful information for understanding domain formation and the switching mechanisms in polycrystalline nanostructured materials. The micromagnetic simulations confirm that the polycrystalline microstructure influences these mechanisms, leading to different remanence and coercivity of the hysteresis loop. By controlling the microstructure, different shape hysteresis loops can be obtained, i.e., different magnetic properties can be designed according to the requirement of the application. The texture (distribution of anisotropy directions of individual magnetic grains) also significantly affects the morphology and dynamics of reverse domains. For example, the hysteresis loop normally is round for a textured sample (with unique anisotropy direction) and may have steps (Barkhausen jumps) for an untextured one (with distribution of easy axes directions).

Generally speaking, when the applied field is reduced from the saturation value, the competitive effects of magnetic (exchange and magnetostatic) interactions and the random magnetocrystalline anisotropy lead to magnetization ripple when the magnetization deviates locally from its saturation value [112, 128, 129]. Figure 14 supposes to simulate a hysteresis cycle of a permalloy-based thin film and a standard Kerr-microscopy image. The ripple formation and its changes through the hysteresis cycle are clearly appreciated. The remanence value decreases monotonically with an increase of the ripple angle—the greater the misalignment of grains is due to the anisotropy randomness, the less is the remanence of the corresponding polycrystalline film [130].

In general, two competitive mechanisms influence the development of the coercivity: the nucleation and the pinning. *Nucleation* occurs normally at the places where some local conditions (for example, reduced internal field at the sharp corners of a magnetic element) favors such a process. Modeling of the demagnetization process, for example, in Co bars [112] with the grain structure described by Voronoi polyhedra, shows [128, 129] that as the field increases toward the negative directions, the ripple becomes more pronounced, with the consequent formation of vortices at the ends of the bars. The magnetization vortex, together with a domain wall, is the most elementary structure resulting from nucleation and magnetization reversal. Expansion of reversed regions during hysteresis is achieved through their motion and annihilation in the magnetic element.

Furthermore, in nanostructured samples (for example, simulations of FePt materials [130]), multiple nucleation centers due to “magnetic charges” inside the grains with large deviations of easy axes take place. This drastically reduces the nucleation field in comparison to a textured sample.

Once the magnetization reversal nucleus is formed, it propagates in the form of some collective microstructure (domain wall or a vortex). The *pinning* effects the propagation. The same way as the grains with a large misalignment of easy axes could induce the nucleation, they also can serve as pinning centers [130]. The greater the misalignments between grain easy axes are, the more difficult it is for a domain wall to cross the boundary and thus the greater is

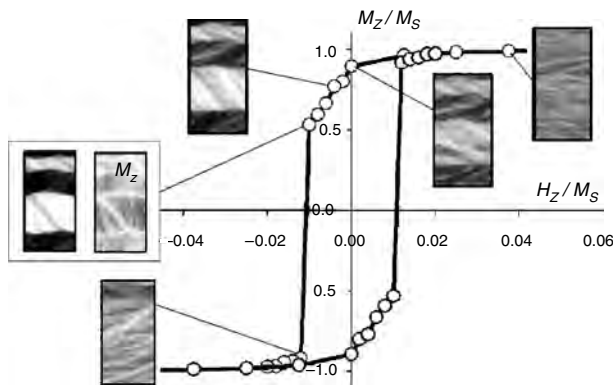


Figure 14. Simulation example of a hysteresis cycle in a Permalloy thin film with $\langle D \rangle = 40$ nm average grain diameter, random anisotropy, and an additional easy-axis anisotropy. The ripple structure is clearly visible and becomes more pronounced with the increase of an external field. (Courtesy of D. Berkov).

the external field that is necessary to push the domain wall through it. If the texture is small, there are fewer nucleation centers. However, once a domain of a reversed direction is nucleated, it sweeps the entire film quickly, producing the complete reversal. Consequently, the squareness of the hysteresis loop is high, and the coercive field is large. Figure 15 illustrates the variation of the coercive field as a function of the system texture in a one-dimensional system of grains. More complete micromagnetic simulations in 3D FePt films with 3D easy axes orientation [130] also have shown that the coercivity decreases for more randomness of the easy axes distribution so that it is maximum for a textured sample. However, intermediate texture and a random easy axes sample have revealed almost the same coercivity. This is explained by the competition between nucleation of domains and their motion.

Depending on the particular microstructure realization [128], different reversal mechanisms could occur. This results in dispersion of coercive fields, which may be especially evidenced in small-size magnetic nanoelements [128].

4.4. The Role of the Magnetic Interactions

The magnetization reversal is a collective process that involves the interaction of magnetization in different grains. The micromagnetic simulations allow one to predict the influence of the interactions by slowly varying their strength, which is not accessible by any experimental technique. They even allow separating the influence of different contributions, such as to take into account separately magnetostatic or exchange ones [111]. The presence of interactions, together with the microstructure, drastically influences the remanence and coercive field. At $T = 0$ K for a system of noninteracting grains with easy axes randomly oriented, the Stoner-Wolfarth theory [131] shows that the hysteresis loop has a reduced remanence $M_r/M_s = 0.5$. In general, the values M_r/M_s less than 0.5 have been reported, which was attributed to interaction effects [132, 133].

It should be noted that the exchange energy contribution evaluation experiences significant arbitrariness for

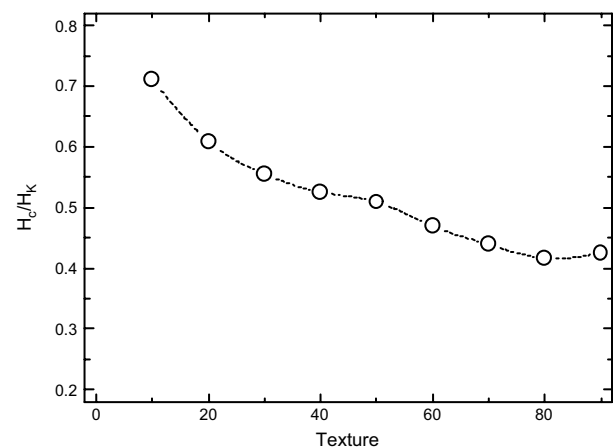


Figure 15. Results of a micromagnetic simulation of the coercive field as a function of the system texture (the apex angle, in degrees, of the cone in which the easy axes are distributed). (Courtesy of R. Smirnov-Rueda).

nanostructured materials. This is due to the lack of precise experimental knowledge of the exact exchange value at the grain boundary. The magnetic grain boundary is influenced by the break of atomic bonds, which leads to different values of exchange integrals at different points of space. The higher the degree of perfection of the grain boundary structure, the higher is the exchange interaction across the boundary and thus the stronger is the coupling between neighboring grains. The exchange energy contribution may be found to be a function of the position inside grain [125, 134], since there may exist migration of nonmagnetic atoms toward the grain boundary (such as Cr in Co grains in typical thin films used for magnetic recording). In these films, there is evidence that the exchange value also depends on the angle between easy axes of two neighboring grains [125]. The atomistic models, in which exchange integrals are evaluated at each point, are necessary to correctly take into account the grain boundary. The latter becomes an extremely technically complicated problem for modern state of the art.

As a consequence, different phenomenological models [113, 114, 119, 124, 135] have been suggested to describe the exchange strength in nanostructured materials. Provided the average strength of their “exchange field” is the same, they should give the same influence of the “exchange” contribution, on average, in granular material. Detailed calculations are still necessarily to reveal the differences between different models. Generally speaking, different values for intergrain and intragrain exchange parameters also should be supposed. For granular materials, the intergrain exchange phenomenological model, which is based on the surfaces exchange [124] (strength of the exchange proportional to the surface of the contact grains), is considered to be a rather realistic description. Some preliminarily atomistic calculations in a model of a chain, which takes into account the difference of the concentration of Cr in CoCr films typically used for magnetic recording, has revealed that for Cr rich grain boundaries (more than 30% of Cr), the intragrain exchange parameter could be taken as almost constant [125].

In general, remanence enhancement is attributed to intergrain exchange interactions. Since exchange coupling of neighboring grains favors the nucleation of reversed domains, remanence enhancement generally is achieved at the expense of coercivity [136, 137]. Figure 16 presents simulations of different hysteresis cycles for various exchange parameters $C^* = H_{ex}/H_K$ (strength of the exchange field versus the anisotropy field) in a Co-based granular media. These effects are confirmed by multiple micromagnetic simulations [111, 138–143], although quantitatively stronger decrease of coercivity or stronger increase of the remanence has been predicted. The latter may be attributed to different evaluations of the magnetostatic energy present in the system or to different exchange models. The consequent decrease of remanence for very large exchange values is attributed to cooperative effects, for example, formation of vortices). Figure 14 supposes to simulate a standard Kerr-microscopy image. As expected, the average scale of the observed ripple structure increases strongly with the exchange coupling at grain boundaries.

Calculations show that the magnetostatic interactions in a granular material also influence the coercivity and remanence due to formation of magnetic charges at the grain

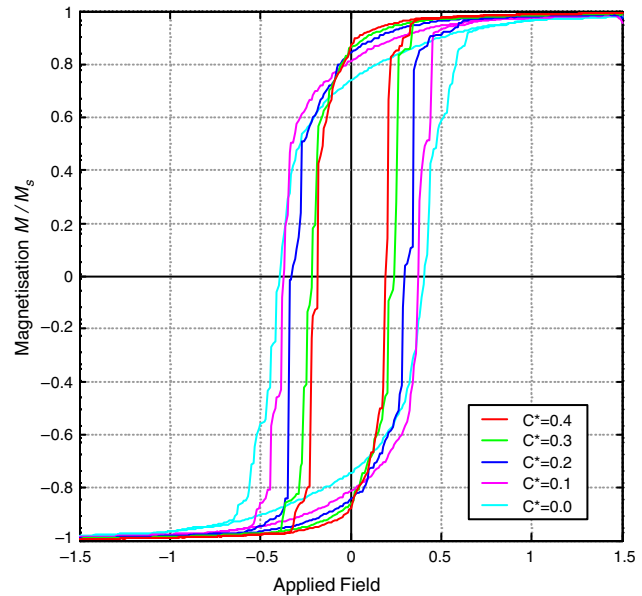


Figure 16. Simulated hysteresis cycles in a Co-based granular material with different strength of the exchange interactions modeled by an effective parameter C^* , introduced by the group of R. Chantrell (see text) (the effective exchange decreases from the top remanence to bottom). The decrease of remanence and coercivity is clearly observed. Reprinted with permission from J. D. Hannay et al., *J. Magn. Magn. Mater.* 193, 245 (1999). © 1999, Elsevier Science.

boundary [111]. More detailed micromagnetic calculations [111, 138, 144, 145] show that the decrease of coercivity occurs with increasing magnetostatic interactions. The effect is smaller for uniform grain structure [111]. However, if there is a distribution of grain sizes, the decrease of the coercivity is more pronounced. It has been demonstrated that the magnetostatic interactions are responsible for a reduction in the low-temperature remanence [111, 138]. However, in a Co-based film used for longitudinal magnetic recording with random anisotropy distribution and uniform grain sizes, it has been found that the dipolar interactions tend to enhance the remanence [144, 145] that was attributed to an extra effective easy axis arising from dipolar interactions and lately was suggested to be the case of systems with regular lattice (no grain size distribution) [146].

4.5. Influence of the Grain-Size Distribution

The grain size influences crucially the remanence and coercivity of nanostructured materials. Indeed, in large grains, internal magnetization distribution with domain walls at the grain boundary may be formed. Calculations of Ref. [111], by using randomly oriented anisotropy distribution, in-plane magnetization, and equal-size grains in $Fe_{14}Nd_2B$ magnets showed that in interacting grains, the remanence enhancement (with respect to that for noninteracting grains) increases with the average grain diameter, and this is more prominent for grains with diameter <20 nm. However, coercivity also is significantly reduced. This is explained by means of competitive effects between magnetocrystalline anisotropy and exchange interaction at the grain boundary. Only the magnetic moments within the boundary region, which is of the order of the domain wall, could enhance

remanence; its volume fraction is more significant for small grains. However, these strongly inhomogeneous microstructures favor the nucleation of reversed domains and, therefore, decrease the coercivity. Figure 17 presents the grain size dependence of the demagnetization curves, the distribution of the magnetization for NdFeB soft-hard magnets, and the magnetization distribution at the remanence. More inhomogeneous magnetization structures at the boundaries of large grains are clearly observed.

Similarly, for Co nanoelements [128], three grain sizes without size dispersion were investigated. The nanoelements, consisted of 8-nm grains, exhibit strongly pinned magnetization until the coercive field is reached and, consequently, is a very squared loop. In larger grains (12-nm Co), the reversible magnetization changes occur inside grains (within the boundary region) in the field prior to the coercive one that resulted in Barkhausen jumps. It was observed, during the simulation, that the magnetization within individual grains was strongly uniform in the case of 8-nm grains and less homogeneous in the case of 12-nm grains.

In reality, the nanostructured materials typically present a log-normal grain-size distribution. It has been showed that a small dispersion of the grain sizes may lead to an enhanced remanence and may preserve a high coercive field [111].

4.6. Micromagnetics of the Magnetic Recording Media

Micromagnetic calculations have been recommended as a useful tool to optimize the nanostructured magnetic media performance. This is especially true for the magnetic recording process, where simulation of the written track could help to understand, qualitatively, the tendency to

improve the media characteristics. The conventional longitudinal recording media (nanostructured granular CoCrPt and CoCrTa thin films) have been intensively modeled in the past [119]. The performance of the new high anisotropy media (such as SmCo, CoPt, FePt), together with the new ways of magnetic recording (such as perpendicular recording), is currently under the intensive investigation, in which the long-scale micromagnetic calculations serve as one of the tools.

Magnetic recording simulations have some peculiarities in comparison to a standard hysteresis modeling. This includes the simulation of the read and write processes, which may be done by using some well-established approximations such as the Karlquist or Lindholm [147, 148] fields for the recording head and the approximation for the magneto-resistive head used for the reading process. At the same time, more realistic modeling includes the head models explicitly, together with the micromagnetic processes, which happen simultaneously in the recording head and in the media [149]. The latter is especially necessarily for the perpendicular recording media, where the soft magnetic underlayer also should be included in the realistic model [141, 150, 151]. The aim of the simulation is normally the calculation of the signal-to-noise (SNR) ratio, which for different models, may be found summarized in Ref. [124]. The results strongly depend on the linear recording density, normally measured in kfc (kilo floppy changes per inch).

One of the major limitations of magnetic recording medium performance is the medium noise. The most important noise source is the bit transition, which is influenced by the finite size of the grains, their anisotropy values and orientations, and their size distribution. The efforts to optimize the longitudinal recording performance, both experimental and theoretical, have showed that the magnetic media suitable for high density recording require reduction of the average grain diameter and a more uniform grain-size distribution. The SNR varies inversely as the square of the transition parameter and the cross-track correlation length [119, 152]. For high-quality recording media, these parameters are approximately proportional to the grain diameter, which is achieved for smaller grains. At the same time, the exchange interactions would broaden the magnetization profile at the boundary transition. In the longitudinal recording media, the intergranular exchange is largely responsible for transition noise because of the cross-track correlations it causes [119, 153, 154]. The isolation of individual grains is achieved experimentally by the segregation of Cr at the grain boundaries. More detailed simulations show that the signal, as a function of an exchange parameter, is increased [119, 124, 153, 154] for small exchange values, the same way the noise coming from the transitions also is increased. The competition between signal and noise is very complicated and depends on the read-write parameters. It is possible that some small amount of exchange may be present in recording media without endangering the SNR [122, 153]. The SNR also is very influenced by the large dispersion of the grain sizes (normally log-normal), which leads to a zigzag character of the transition and to the coupling of the small grains to large ones that deteriorate both the signal and the noise. Simulations show that the absence of the grain-size distribution may lead to the difference in the SNR parameter up to 1 dB

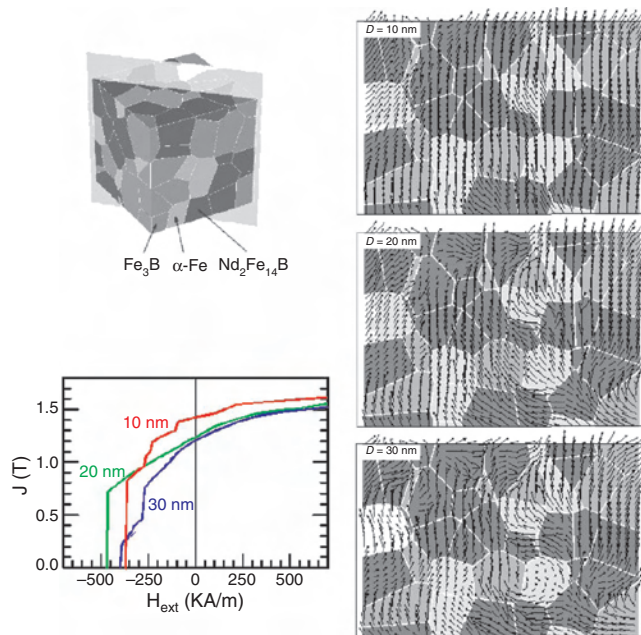


Figure 17. Grain size dependence of the demagnetization curves of 125 polyhedral grains for hard-soft magnets (40% $\text{Nd}_2\text{Fe}_{14}\text{B}$ [dark scale map], 30% Fe_3B , 30% $\alpha\text{-Fe}$ [bright scale map]) and magnetization distribution for zero applied field. (Courtesy of T. Schrefl).

for noninteracting grains and up to 4 dB at the presence of small exchange [155] for intermediate recording densities (~ 100 kfc). Another very important factor is the random character of the anisotropy directions. The presence of some texture may lead to a drastic enhancement of the signal. Indeed, the calculations show that, for a uniform grain size distribution and moderate exchange, the gain of approximately 2 dB could be expected [145] for a textured sample with intermediate recording density (~ 100 kfc). This gain is much larger for larger recording densities. For log-normally distributed grains, the effect may be even more dramatic as to reach 7 dB at 200 kfc.

One of the main limitations to further increase the magnetic recording density is the presence of thermal effects. In the efforts to decrease the transition noise, the grain size has become so small as to make the effective energy barrier (KV in the approximation of noninteracting grains where V is the grain volume), separating the two magnetization states (“up” and “down”) to be comparable to the thermal energy. This is called the *superparamagnetic limit* and is currently the main limitation for conventional longitudinal recording. The intensive search for high-anisotropy media and new ways of magnetic recording (such as the thermally assisted one) is currently under progress.

Nanocrystalline perpendicular films with easy magnetization directions close to the normal of the film and with high magnetocrystalline anisotropy are attracting the increased interest of researchers as possible candidates for perpendicular recording. This is due to the narrow dispersion of the easy axes distribution, typically a Gaussian one with small dispersion (of the order of 5 degrees). The small grain size and perpendicular arrangement of the easy magnetization axes allow one to obtain greater recording densities, whereas the higher magnetocrystalline anisotropy increases the ferromagnetic thermal stability of the small grains.

In perpendicular recording media with a strong orientation of crystalline easy axes, intergranular exchange coupling also increases the squareness of perpendicular loops, which generally results in sharper transitions. As a result [151], media SNR may be enhanced because of the reduction of the transition parameter. With a further increase of the exchange coupling, reduction of the transition parameter becomes less significant, since the transition noise increases. In Ref. [151], the optimal exchange constant was found.

4.7. Composite Materials

Few micromagnetic calculations have been performed in soft nanostructured magnetic materials. One of the possible explanations is that due to the small value of the anisotropy, the discretization length in soft magnetic materials is so small that the possible total size of the calculations is very limited. In Ref. [123], the micromagnetic simulations have been performed for magnetic permeability of composite soft materials (thoroughly mixing iron powder). The initial susceptibility was shown to increase as a function of packing density in a highly nonlinear manner and was shown to decrease as a function of the intrinsic susceptibility. Interestingly, the computational results were significantly different from the mean-field approximation, which indicates an important contribution of the nearest-neighbor interactions.

At the same time, the nanostructured soft-hard magnetic systems such as, for example, exchange-spring permanent magnets, have become a topic of interest since a mixture of hard and soft phases reduces the rare-earth content while preserving good magnetic properties. Reversal mechanisms in these systems can be interpreted schematically as two-step processes: the initial magnetization reversal is dominated by the reversible nucleation in the soft phase, while irreversible processes, which characterize the coercivity mechanisms, occur at larger field values and are determined by the hard phase. The micromagnetic calculations (e.g. Figs. 13, 17, 18) have been performed to predict qualitatively the ratio between soft and hard phases optimal to establishing a high coercivity and remanence. By using a 1D micromagnetic model, Kneller and Hawig [157] found that the optimum microstructure for improved magnetic properties of a hard magnet would be hard grains embedded in a magnetically soft matrix with lateral dimensions of both phases about equal to the domain-wall width of the hard phase.

Later simulations [111] (Fig. 13) in soft-hard composites (grains of α -Fe and $\text{Fe}_{14}\text{Nd}_2\text{B}$) showed that the remanence was increased as a function of the volume fraction of magnetically soft grains, and this enhancement is higher for smaller grains. Remarkably, unlike pure hard nanostructured materials, the coercivity, although reduced, was high (of the order of 1 T; Fig. 18) for microstructures that have magnetically soft phase grain smaller than twice the domain-wall width of the hard grain (10-nm grains in the case described above). For NdFeB magnets, coercivity and remanence [158] also were calculated by using soft magnetic grain of α -Fe surrounded by hard magnetic grains with random easy axes. If the intergrain exchange constant were reduced by $1/10^{\text{th}}$ of its bulk value, irreversible switching of the magnetization was shown to shift by more than 259 kA/m toward higher values of the opposite field, since the grains become more decoupled. Figure 18 presents results of micromagnetic simulations for different soft-hard contents and different grain sizes by using a micromagnetic model similar to that of Figure 17.

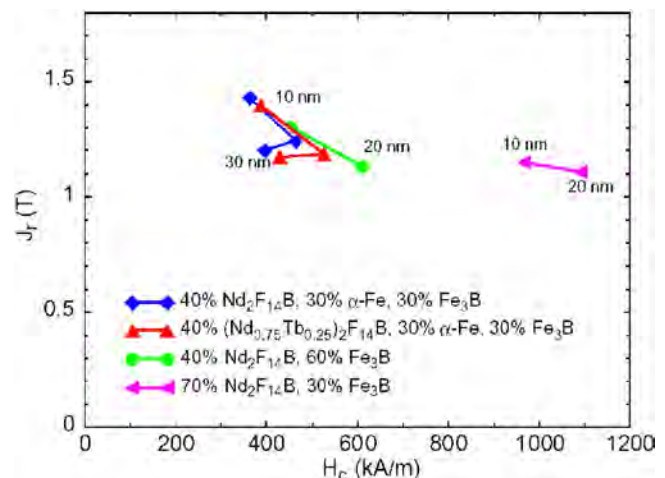


Figure 18. Micromagnetic results for remanence and coercivity for different soft-hard magnets with different grain sizes. (Courtesy of T. Schrefl).

Rave et al. [127], and T. Schrefl and J. Fidler [159] have investigated the effect of different initial states on the initial magnetization curve of nanocrystalline permanent magnets. Namely, calculations for α -Fe/Nd₂Fe₁₄B and Fe₃B/Nd₂Fe₁₄B composites [159] have showed that the thermally demagnetized state that stores a higher amount of exchange energy, leads to an increase of the initial susceptibility as compared to dc initial state. The α -Fe/Nd₂Fe₁₄B composite [159] has shown the improved saturation behavior that is attributed to the exchange field provided by α -Fe grains that already are oriented parallel to the field direction.

4.8. Magnetization Dynamics

The precise understanding of switching processes of nanomagnets is important for magnetic heads, sensors, and spin electronics applications. Since the speed of the data read-write process is increasing, the calculation of the high-speed switching in magnetic recording media is currently becoming a matter of considerable importance, because of the potential limitation on data rates that this phenomena produces.

The theoretical treatment of the magnetization dynamics at zero temperature starts from the integration of the Landau–Lifshitz–Gilbert equation [112, 120]

$$\frac{d\vec{M}}{dt} = -\gamma\vec{M} \times \vec{H}_{eff} - \frac{\alpha\gamma}{M_s}\vec{M} \times (\vec{M} \times \vec{H}_{eff}) \quad (16)$$

where γ is the gyromagnetic factor, α is the damping parameter, M_s is the saturation magnetization value, and $\vec{H}_{eff} = -\delta E/\delta\vec{M}$ is the total effective field, which includes external field, anisotropy, exchange, and magnetostatic contributions. This equation contains a term describing the precession of the magnetic moment around the internal field direction and a phenomenological damping term. Since the period of the precessional motion of a magnetic moment is of the order of 10^{-11} s, the total elapsed time of these calculations is of the order of ns [120]. However, the potential applications related to this rate of the magnetization switching are rapidly approaching this scale. The dynamical calculations, even if used to calculate the magnetization minima do not always lead to the same micromagnetic structure due to the presence of the precession, which takes the system magnetization out of thin film plane and makes other magnetization minima accessible. For example, calculations in soft-hard nanocrystalline NdFeB-based permanent magnets have shown that the gyromagnetic precession of the magnetization reduces the coercive field by about 10% as compared to the coercive field obtained with static micromagnetic calculations [158].

The precessional response and the magnetization damping govern the upper limit of the switching speed. One of the experimental characterizations of high speed switching is related to dynamic coercivity measurements in which the remanent magnetization and coercivity are measured as a function of the duration and intensity of the applied field pulse [160] (Fig. 19). The calculations related to this experimental procedure have shown that in a granular materials with noninteracting grains, the remanent magnetization curves as a function of the reverse peak duration are very sensitive to the value of the damping constant [122]. For

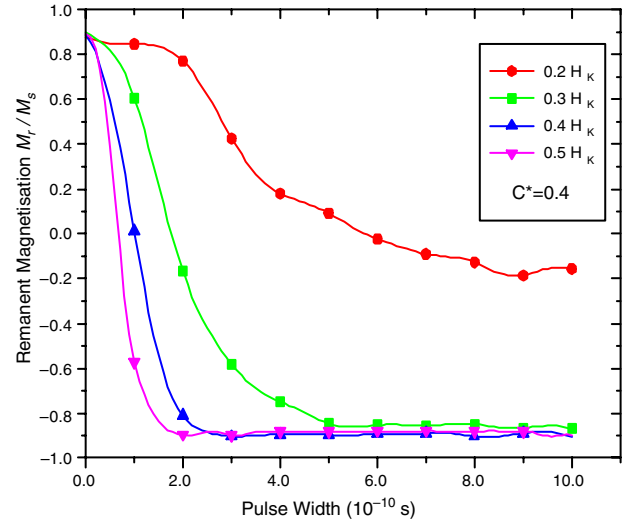


Figure 19. Simulation of the dynamic coercivity experiment in an interacting Co-based granular media using a micromagnetic model of the group of R. W. Chantrell [135]. The remanent magnetization is represented as a function of squared pulse duration for different applied field values. Reprinted with permission from J. D. Hannay et al., *J. Appl. Phys.* 85 5012 (1999), © 1999, American Institute of Physics.

small damping case, $\alpha = 0.05$ (Fig. 20), the peaks in the remanent magnetization as a function of the pulse duration have been observed due to precessional motion [120].

The exchange interactions seem to reduce or remove these peculiarities (Fig. 19), which may be interpreted in terms of the effective increase of the damping. Generally,

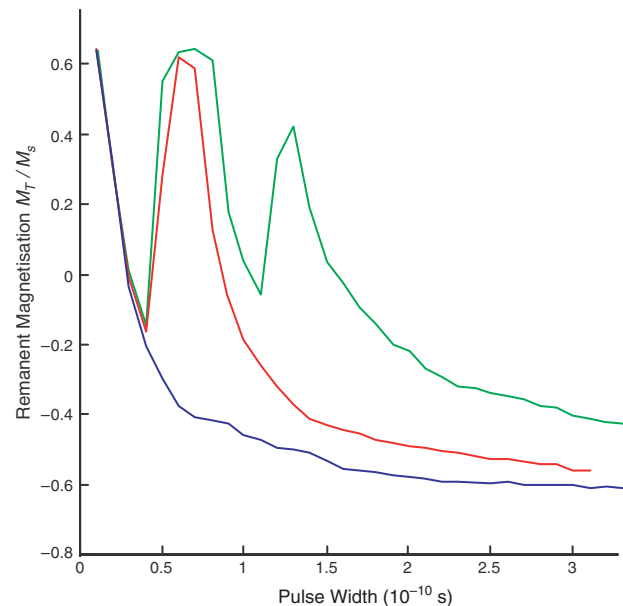


Figure 20. Remanent magnetization for a typical dynamic coercivity experiment in a non-interacting Co-based media for different values of the damping varied from $\alpha = 0.2$ (left curve) to $\alpha = 0.05$ (right curve). For small damping values the magnetization oscillation due to precessional motion are observed. Reprinted with permission from J. D. Hannay et al., *J. Appl. Phys.* 85, 5012 (1999). © 1999, American Institute of Physics.

increasing intergranular exchange coupling will initially slow down the reversal process because of larger correlated magnetization fluctuations. The switching time normally is increased in the presence of exchange and this effect is increased with increasing field rise time [161, 162]. However, similar to static properties, the applied field required to switch the highly exchanged coupled medium is lower than that required to switch the zero exchange coupled system [122].

The dynamic coercivity parameters have been investigated as a function of the characteristics of the applied field. Different types of the field-rise pulse with different durations were supposed. For example, uniform exponential field for switching was investigated in Ref. [161]. Although experimentally, the switching time normally is considered as inversely proportional to the switching field, numerical simulations showed that the field rise time has a major effect on the switching time of the medium and the above relation is true for the head field rise time larger than 0.3 ns or in the range H_{\max}/H_K 0.5–0.6.

For magnetic recording media switching, it has been shown that, in the case of a squared field pulse [162] and for small damping $\alpha < 0.4$, the perpendicular media switches slower than the longitudinal. The fundamental reason why the longitudinal media switches faster than the perpendicular one is the demagnetization field of the media, which produce an additional torque. In longitudinal media, this field is perpendicular to the reversal direction and provides an additional reversal torque. For perpendicular media, the demagnetizing field is parallel to the reversal direction and does not give an additional reversal torque.

Surface irregularities and grain structure drastically change the reversal mechanisms [112]. For perfect magnetic elements, the high stray field at the particle ends causes the nucleation and determines the switching process. For granular structured material, the nucleation inside a particle occurs, which determines a faster switching process [120]. The surface roughness further decreases the switching time [120, 163, 164], since, at rough surfaces, vortices could be nucleated at particle ends.

4.9. Temperature Effects

Temperature fluctuations play an important role in magnetization switching. In the presence of temperature fluctuations, the switching is faster, since a small energy barrier separating different magnetization minima could be overcome by thermal fluctuations. Two regimes should be distinguished here: dynamical and statistical (Fig. 21).

Dynamical regime corresponds to small time scale (less than nanoseconds) and to low-energy barriers. The magnetization dynamics in the presence of thermal fluctuations is modeled by the stochastic Landau–Lifshitz–Gilbert equation of motion, augmented by a thermal random field \vec{H}_{therm} , whose properties are determined by the fluctuation–dissipation theorem [165] (Langevin equation):

$$\begin{aligned} \langle H_{\text{therm}}^i \rangle &= 0, \quad \langle H_{\text{therm}}^i(t) H_{\text{therm}}^j(t + \tau) \rangle \\ &= \frac{2\alpha k_B T}{\gamma V M_s (1 + \alpha^2)} \delta(\tau) \delta_{ij} \end{aligned} \quad (17)$$

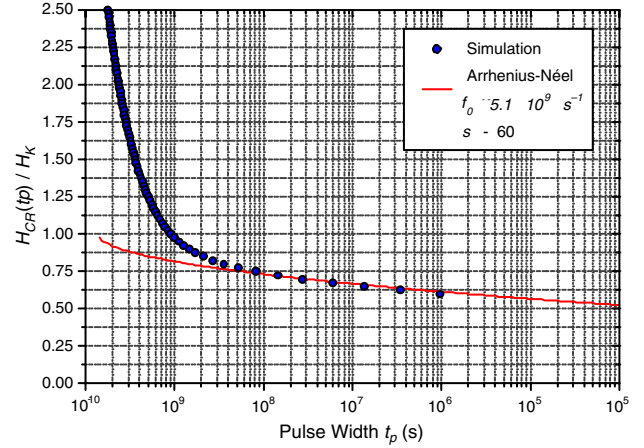


Figure 21. Coercive field as a function of an applied field duration for a Co-based media. Two regimes are observed: dynamical for short pulses duration and statistical (exponential): for large time durations where it coincides with Arrhenius–Néel asymptote [165] (solid line).

where k_B is the Boltzmann constant, T is the temperature, and the indices i, j numerate both field components and different grains.

A nonexponential magnetization decay (Fig. 21) takes place in this regime, even for a system of noninteracting grains. Interactions change the relaxation form significantly and usually lead to the temporal dependence of the magnetization, which is slower at the beginning and then faster than that for noninteracting grains [165].

Large time scales correspond to large energy barriers and to the statistical regime, or magnetic viscosity. In this regime, the thermal behavior of granular materials is described as similar to the theory of small magnetic particles switching [160, 166, 167]. Namely, each grain is described by the two energy levels with the relaxation process between these two states governed by the Arrhenius–Neel law with the switching rates $\tau_{\pm}^{-1} = \tau_0 \exp(-\Delta E_B^{\pm}/k_B T)$, where ΔE_B^{\pm} are the energy barriers separated by the two minima. In the absence of interactions and the external field, the two energy barriers are equal to KV . The master equations for the magnetization change could be solved directly to give the exponential magnetization decay for a system of equal grains and the logarithmic decay for uniform energy barrier distribution.

In the presence of the external field, the energy barriers could be calculated by using the Pfeiffer [168] or Victora [169] approximations. However, in reality, all the grains are interacting, which means that the energy barriers are dependent on the magnetization state at each moment and could be calculated only numerically. Often some approximations are used as, for example, interactions are included in the form of an internal field in the Pfeiffer approximation as an additional external field [138]. Obviously, this is valid only if the strength of interactions is small. Moreover, for large interaction strength, the reversal in forms of clusters of grains should be expected, which makes the one particle approximation invalid.

The influence of the thermal effects in the statistical regime has been mostly investigated in the case of weakly interacting grains, where the energy barriers could be easily evaluated. In this case, the Monte Carlo–based models

[138, 170–172] or the equivalent solution of the Master equation [160, 173] have been developed. It has been shown that in most of cases, the interactions broaden the energy barrier distribution. The remanence is influenced by thermal effects, it is slightly lower than for a nonthermal case [138]. Furthermore, remanence is decreased as a function of temperature [134], and the interactions increase the effect [138]. With magnetostatic interactions present at low temperatures, this decrease is faster and, at a later stage, slower. This is interpreted as arising from an increase in the effective barrier distribution brought about by the effect of interactions [138] and is caused by the different influence of magnetostatic interactions at small and large grains. While, for small grains, they act as demagnetising field, reducing the energy barriers and, consequently, the remanence; for large grains, they lead to more stable magnetization clusters and, consequently, to the remanence enhancement [138]. This is a consequent of the dispersion of energy barrier distribution.

As for exchange interactions, they also differently influence the energy barrier, corresponding to large and small particles, and this influence depends on the angle between the grains easy axes. Generally speaking, the energy barrier is increased for the particles with almost aligned easy axes and is decreased for those with a large angle between them. This also causes the broadness of the energy barrier distribution. There also are evidences that the average blocking temperature is increased as a function of exchange parameter [174].

The influence of interactions on the thermal decay is especially important for the magnetic recording media. Due to the fact that the longitudinal recording media is almost noninteracting, the individual grain energy barriers are practically proportional to their volumes. Since, to achieve the optimal SNR with high recording density, the grain size of the medium should be reduced, the recording density will approach the so-called superparamagnetic limit when the energy barrier separating the two minima is of the order of the thermal energy, and, therefore, the data recording will be unstable. The current longitudinal media is rapidly approaching the time when this effect will be significant. This has led to the necessity of the extensive investigation and search for alternatives in the magnetic recording. The micromagnetic calculations could play an important role in the determination of the factors relevant to recording stability versus temperature. It has been established, for example, that the grains size and easy axes distribution play crucial roles in this process. The textured medium with narrower size distribution would potentially be more stable. A bias-exchange coupled media has demonstrated higher thermal stability. The perpendicular recording media, being almost a textured granular material, and having a larger grain volume due to increased thickness, has been predicted to be much more stable in comparison to the longitudinal media.

5. CONCLUSIONS

To conclude this chapter, and in order to highlight the most relevant point in our exposition, we would like to come back to an idea already mentioned in the introduction: the crucial role on the achievement of controlled (and optimized) hysteretic properties of the grain boundary regions.

As we have discussed, the occurrence of strong exchange intergranular coupling in nanocrystalline systems having large exchange correlation lengths, results in a dramatic softening of the material arising from the effective average of the local anisotropies. Differently from this, in the case of the single phase, high anisotropy materials, used to produce permanent magnets, it is highly desirable to reduce as much as possible the intergranular exchange in order to hinder the propagation of a local reversal induced by a moderate demagnetizing field at an anisotropy defect. In the case of the recording media, the role of the exchange coupling is even more subtle: it should, in principle, be kept as reduced as possible in order to reduce the bit size, but a moderate amount of coupling could also account for an improvement in the signal-to-noise properties of the material. Finally, and now in relation to composite nanocrystalline materials, it again is the interphase exchange magnitude that is the main factor ruling the achievement from the properties of the individual phases, enhanced hysteretic behavior.

Although all these effects (and many other similar) are qualitatively well understood, we are still today quite far from effectively tailoring the grain boundary properties to meet the different requirements involved in an optimization process. Thus, it is a clear priority for the research in the field of the nanocrystalline materials to develop experimental techniques to locally determine the grain boundary structure and properties and, in parallel to this, to implement realistic quantitative simulations of the influence on the global properties of the intergranular regions. If these goals are reasonably achieved, it is possible to foresee the possibility of getting, both from single phase and composite materials, ranges of hysteretic properties much broader than those available today.

GLOSSARY

Exchange correlation length One of the two most relevant magnetic characteristic lengths. It gives the typical distance along which a small local departure from a homogeneous magnetization configuration extends due to exchange interactions. It coincides, in a uniaxial system, with the thickness of a wall separating two domains with antiparallel magnetizations and having the so-called Bloch-type structure (corresponding to the rotation of the moments inside the wall in a plane perpendicular to that containing the moments of the neighboring domains).

Magnetic anisotropy In the most general sense, the dependence of the magnetization process of a given magnetic material on the applied field direction. In the particular case of single crystal, that dependence is linked both to the spin orbit coupling and to the symmetry of the crystal field at the site of the ions bearing magnetic moments (magnetocrystalline anisotropy). In other cases, the occurrence of magnetic anisotropy could be linked to the occurrence of large anisometries (shape anisotropy), either applied or residual stresses (magnetoelastic anisotropy) and/or chemical disorder (“pair ordering” anisotropy).

Magnetic domains Homogeneous magnetization regions formed in a sufficiently large magnetic system in order to minimize the magnetostatic energy. Two neighboring

domains are separated by a transition structure named the domain wall. In a nanostructured system, the role of the domains in the magnetostatic energy minimization often corresponds to extend heterogeneous magnetization structures as those appearing in an isolated nanoparticle at the remanent state (“S” and “C” states, “flower state,” etc.).

Magnetic interactions In a localized moments picture short- (a few interatomic distances) and long-range moment couplings associated with the exchange coupling and with the magnetostatic fields, respectively.

Magnetic viscosity It is commonly observed as a time decay of the magnetization of an ordered magnetic material, measured at constant applied demagnetizing field and temperature. In a nanostructured magnetic material, and due to distribution of magnetic properties, thermally activated decay takes place in a time scale ranging from picoseconds up to several tens of years. The effects of the temperature fluctuations have become important in relation to the high-density magnetic recording, where they could cause thermal instability of the recorded information.

Magnetization dynamics Magnetization processes taking place at short time scale (from pico- to nanoseconds), including the magnetization precession around the local field direction. The precession leads to important effects in fast magnetization dynamics, such as spinwave phenomenology, relevant to magnetic recording applications.

Magnetization reversal process Process corresponding to the applied field induced evolution from the saturation remanence state to the fully reversed one (in which the local magnetization points parallel to the demagnetizing field). It can take place either locally or in a collective way, and, in the most general case, involves a sequence including reversed nucleus formation, nucleus expansion, nucleus steady propagation, and nucleus wall pinning/depinning stages. In a given material, the relationship between the characteristics of the reversal process and the material nanostructure (including here, dimensions, shape, and defect structure) determines the possibilities of tailoring its hysteretic behavior.

Magnetoelasticity Modification of the magnetization process of a magnetically ordered material associated to the presence in it of mechanical stresses.

Magnetostatic correlation length One of the two most relevant magnetic characteristic lengths. It gives the typical distance along which a small local departure from a homogeneous magnetization configuration extends due to the magnetostatic interactions. It coincides, in a uniaxial system, with the thickness of a wall separating two domains with antiparallel magnetizations and having the so-called Néel-type structure (corresponding to the rotation of the moments inside the wall in a plane parallel to that containing the moments of the neighboring domains).

Magnetostriction Variation of the dimensions of a magnetically ordered material submitted to different applied fields.

Micromagnetic modeling Theoretical modeling of magnetic materials at nanoscale based on total magnetic energy minimization considerations. This allows one to predict qualitatively the variation, in a given magnetic material, of the hysteretic properties (mainly those of the coercivity and the remanence) associated to both intrinsic and extrinsic parameters.

Remanence Residual magnetization value measurable at zero applied magnetic field in a magnetically ordered material after submitting it to a saturating field.

Saturation coercive force or saturation coercivity Applied demagnetizing field value required to reduce to zero the magnetization of a magnetically ordered material after saturating it.

Soft and hard magnetic materials Traditional classification of the technologically relevant magnetic materials based on their coercive force values. Soft magnetic materials exhibit reduced coercivities (from 1 A/m up to a few KA/m), whereas, the hard ones are difficult to demagnetize and are characterized by coercive force values in excess of the MA/m.

Spontaneous magnetization In a ferromagnetic material formed by localized moments, the magnetization corresponding to the complete parallelism of all the moments in the system. In the case of a ferromagnetic system exhibiting order linked to itinerant electrons, the magnetization corresponding to the largest unbalance between the populations of the majority (spin up) and the minority (spin down) bands. The spontaneous magnetization at a given temperature coincides fairly well with that measured when the material is submitted to sufficiently large (saturating) fields. In the case of entities having nanometric dimensions, the division into domains is not favorable and, therefore, the local remanent magnetization is approximately equal to the spontaneous one.

REFERENCES

1. Y. Yoshizawa, S. Oguma, and K. Yamauchi, *J. Appl. Phys.* 64, 6044 (1988).
2. K. Suzuki, A. Makino, A. Inoue, and T. Masumoto, *Mater. Trans., JIM* 32, 93 (1991).
3. M. Knobel, D. R. dos Santos, I. L. Torriani, and R. S. Turtelli, *Nanostruct. Mater.* 2, 399 (1993).
4. A. Danzig and N. Mattern, *Phys. Status Solidi A* 147, 335 (1995).
5. B. G. Kim, J. S. Song, H. S. Kim, and Y. W. Oh, *J. Appl. Phys.* 77, 5298 (1995).
6. M. L. Fdez-Gubieda, I. Orue, F. Plazaola, and J. M. Barandiarán, *Phys. Rev. B* 53, 620 (1996).
7. M. Kopcewicz, A. Grabias, and D. L. Williamson, *J. Appl. Phys.* 82, 1747 (1997).
8. M. E. McHenry, M. A. Willard, and D. E. Laughlin, *Progress Materials Science* 44, 291 (1999).
9. P. Duwez, in “Progress in Solid State Chemistry of Alloy Phases” (H. Reiss, Ed.), Vol. 3, p. 377. Pergamon Press, Oxford, 1966.
10. H. Jones, *Rep. Progress Phys.* 36, 1425 (1973).
11. F. E. Luborsky, in “Amorphous Metallic Alloys” (F. Luborsky, Ed.), Butterworth, 1983.
12. A. I. Gubanov, *Fizika* 2, 502 (1960).
13. G. Herzer and H. R. Hilzinger, *J. Magn. Magn. Mater.* 62, 143 (1986).
14. G. Herzer and H. R. Hilzinger, *Phys. Scr.* 39, 639 (1989).
15. G. Herzer, *IEEE Trans. Magn.* 25, 3327 (1989).
16. G. Herzer, *IEEE Trans. Magn.* 26, 1397 (1990).
17. G. Herzer, *J. Magn. Magn. Mater.* 112, 258 (1992).
18. G. Herzer and H. Warlimont, *Nanostruct. Mater.* 1, 263 (1992).
19. A. Hernando, P. Marin, M. Vázquez, J. M. Barandiarán, and G. Herzer, *Phys. Rev. B* 58, 366 (1998).
20. M. Frost, I. Todd, H. A. Davies, M. R. J. Gibbs, and R. V. Major, *J. Magn. Magn. Mater.* 203, 85 (1999).
21. N. Murillo and J. González, *J. Magn. Magn. Mater.* 218, 53 (2000).

22. A. Hernando, V. Madurga, M. C. Sánchez-Trujillo, and M. Vázquez, "Proceedings of the Symposium: Magnetic Properties of Amorphous Metals," North-Holland, Amsterdam, 1987.
23. A. Hernando and M. Vázquez, in "Rapidly Solidified Alloys" (H. H. Liebermann, Ed.), p. 553. Marcel Dekker, New York, 1993.
24. R. C. O'Handley, in "Amorphous Magnetism II" (R. A. Levy and R. Hasegawa, Eds.), p. 379. Plenum Press, New York, 1977.
25. R. M. Bozorth, "Ferromagnetism." Van Nostrand, New York, 1951.
26. C. W. Chen, "Magnetism and Metallurgy of Soft Magnetic Materials." Dover, New York, 1986.
27. S. Chikazumi, "Physics of Magnetism." Kreiger, Malabar FL, 1978.
28. B. D. Cullity, "Introduction to Magnetic Materials." Addison-Wesley, Reading MA, 1972.
29. R. Boll, in "Materials Science and Technology, a Comprehensive Treatment" (K. H. J. Buschow, Ed.), Vol. 3B 399, 1994.
30. A. Inoue, A. Takeuchi, A. Makino, and T. Masumoto, *Sci. Rep. RITU* A42, 143 (1996).
31. X. H. Lin, W. L. Johnson, and W. K. Rhim, *Mater. Trans., JIM* 38, 473 (1997).
32. A. P. Tsai, T. Kamiyama, A. Inoue, and T. Masumoto, *Acta Mater.* 45, 1477 (1997).
33. J. H. Perepezko, B. A. Mueller, and K. O. Ohsaka, in "Undercooled Alloy Phases" (H. H. Liebermann, Ed.), p. 17. Marcel Dekker, New York, 1993.
34. R. Trivedi, *Mater. Sci. Eng., A* 178, 129 (1994).
35. L. C. Chen and F. Spaepen, *Nature* (London) 336, 366 (1988).
36. T. Pradell, J. Zhu, N. Clavaguera, and M. T. Clavaguera-Mora, *J. Appl. Phys.* 83, 5171 (1998).
37. M. T. Clavaguera-Mora, N. Clavaguera, D. Crespo, and T. Pradell, *Progress in Materials Science* 47, 559 (2002).
38. Y. Yoshizawa and K. Yamauchi, *J. Jpn. Inst. Met.* 53, 241 (1989).
39. U. Köster, U. Schünmann, M. Blank-Bewrsdorff, S. Brauer, M. Sutton, and G. B. Stephenson, *Mater. Sci. Eng., A* 133, 611 (1991).
40. G. Herzer, *Phys. Scr.* T49, 307 (1993).
41. N. J. Di Nardo in "Nanoscale Characterization of Surfaces and Interfaces." Wiley-VCH, Weinheim, 1994.
42. D. R. Salinas, S. G. García, J. B. Bessone, and A. R. Pierna, *Surf. Interface Anal.* 30, 305 (2000).
43. K. Handrich, *Phys. Stat. Sol.* 32, K55 (1969).
44. R. Alben, J. J. Becker, and M. C. Chi, *J. Appl. Phys.* 49, 1653 (1978).
45. R. C. O'Handley, *J. Appl. Phys.* 42, R15 (1987).
46. G. Herzer, *Scr. Metall. Mater.* 33, 1713 (1995).
47. A. Hernando, M. Vázquez, T. Kulik, and C. Prados, *Phys. Rev. B* 51, 3581 (1995).
48. J. M. González, C. de Julián, F. Cebollada, A. K. Giri, and J. González, *J. Appl. Phys.* 81, 4658 (1997).
49. J. M. González, N. Murillo, J. González, J. M. Blanco, and J. Echeverría, *J. Mater. Res.* 11, 512 (1996).
50. L. K. Varga, L. Novák, and F. Mazaleyrat, *J. Magn. Magn. Mater.* 210, L25 (2000).
51. K. Mohri, *IEEE Trans. Magn.* 20, 942 (1984).
52. L. Pascual, C. Gómez-Polo, P. Marín, M. Vázquez, and H. A. Davies, *J. Magn. Magn. Mater.* 203, 79 (1999).
53. A. Slawska-Waniewska, L. Malkinski, A. Wisniewski, H. K. Lachowicz, T. Kulik, and J. Latuch, *Mater. Sci. Forum* 269–272, 871 (1998).
54. P. Quintana, E. Amano, R. Valenzuela, and J. T. S. Irvine, *J. Appl. Phys.* 75, 6490 (1994).
55. P. García-Tello, N. Murillo, J. González, E. Amano, R. Valenzuela, and J. M. González, *J. Magn. Magn. Mater.* 203, 211 (1999).
56. M. A. Willard, D. E. Laughlin, M. E. McHenry, D. Thoma, K. Sickafus, J. O. Cross, and V. G. Harris, *J. Appl. Phys.* 84, 6773 (1998).
57. S. H. Lim, W. K. Pi, T. H. Noh, H. J. Kim, and I. K. Kang, *J. Appl. Phys.* 73, 6591 (1993).
58. B. J. Tate, B. S. Parmere, I. Todd, H. A. Davies, M. R. J. Gibbs, and R. V. Mayor, *J. Appl. Phys.* 83, 6335 (1998).
59. G. R. Aranda, C. Miguel, P. García-Tello, and J. González, *J. Appl. Phys.* 89, 6422 (2001).
60. M. Vázquez, P. Marín, H. A. Davies, and A. O. Olofinjana, *Appl. Phys. Lett.* 64, 3184 (1994).
61. N. Müller and N. Mattern, *J. Magn. Magn. Mater.* 136, 79 (1994).
62. J. González, *J. Mater. Res.* 18, 1035 (2003).
63. K. Suzuki, G. Herzer, and M. Cadogan, *J. Magn. Magn. Mater.* 177, 949 (1998).
64. K. Suzuki and J. M. Cadogan, *Phys. Rev. B* 58, 2730 (1998).
65. K. Suzuki and J. M. Cadogan, *J. Magn. Magn. Mater.* 203, 229 (1999).
66. G. Herzer, in "Nanostructured and Non-Crystalline Materials" (A. Hernando and M. Vázquez, Eds.), p. 449. World Scientific, Singapore, 1995.
67. G. Herzer, *J. Magn. Magn. Mater.* 133, 1 (1994).
68. N. Murillo, J. M. Blanco, J. González, and M. Vázquez, *J. Appl. Phys.* 74, 3323 (1993).
69. O. V. Nielsen, J. R. Petersen, and G. Herzer, *IEEE Trans. Magn. Mag-30*, 1042 (1994).
70. D. Herzer, *IEEE Trans. Magn. Mag-30*, 1800 (1994).
71. L. Kraus, V. Haslar, O. Heczko, and K. Zaveta, *J. Magn. Magn. Mater.* 157/158, 151 (1996).
72. H. K. Lachowicz, A. Neuweiler, F. Poplawski, and E. Dynowska, *J. Magn. Magn. Mater.* 173, 287 (1997).
73. B. Hofmann and H. Kronmüller, *J. Magn. Magn. Mater.* 152, 91 (1996).
74. C. Miguel, N. Murillo, and J. González, *J. Appl. Phys.* 88, 6623 (2000).
75. C. Miguel, A. P. Zhukov, and J. González, *J. Non-Cryst. Solids*, 287, 355 (2001).
76. C. Miguel, A. P. Zhukov, and J. González, *Phys. Status Solidi A* 194, 291 (2002).
77. M. L. Néel, *J. Phys. Radium* 15, 225 (1954).
78. K. Twarowski, M. Kurzmanski, A. Slawska-Waniewska, H. Lachowicz, and G. Herzer, *J. Magn. Magn. Mater.* 150, 85 (1995).
79. A. Slawska-Waniewska, R. Zuberek, and P. Nowicki, *J. Magn. Magn. Mater.* 157/158, 147 (1996).
80. A. Slawska-Waniewska, R. Zuberek, J. González, and H. Szymczak, *Mater. Sci. Eng., A (Supplement)*, 220 (1997).
81. H. Szymczak, R. Zuberek, and J. González, *J. Magn. Magn. Mater.* 191, 199 (1999).
82. T. Szumata, R. Zuberek, J. González, A. Slawska-Waniewska, and H. Szymczak, *J. Magn. Magn. Mater.* 203, 262 (1999).
83. C. W. Nan, J. H. Huang, and G. J. Weng, *J. Magn. Magn. Mater.* 233, 219 (2001).
84. T. Yamamoto, "Development of Sendust." Chiba, Komiyama Pr., 1980, p. 27.
85. J. Gutierrez, P. Gorria, J. M. Barandiarán, and A. García-Arribas, in "Nanostructured and Non-Crystalline Materials" (A. Hernando and M. Vázquez, Eds.), p. 500. World Sci. Publ., Singapore, 1995.
86. R. Zuberek, H. Szymczak, R. Krishnan, C. Sela, and M. Kaabouchi, *J. Magn. Magn. Mater.* 121, 510 (1993).
87. "The Concerted European Action on Magnets – Final Report" I. V. Mitchell, J. M. D. Coey, D. Givord, I. R. Harris, and R. Hanitsch, Eds. p. ii. Elsevier, London, 1989.
88. J. M. D. Coey, in "Rare-Earth Iron Permanent Magnets" (J. M. D. Coey, Ed.), p. 8. Clarendon Press, Oxford, 1996.
89. J. M. D. Coey, in "Rare-Earth Iron Permanent Magnets" (J. M. D. Coey, Ed.), p. 47. Clarendon Press, Oxford, 1996.
90. H. Kronmüller in "Supermagnets: Hard Magnetic Materials" (G. J. Long and F. Grandjean, Eds.), p. 461. Kluwer, Dordrecht, 1991.
91. R. J. Radwanski and J. J. M. Franse, *Phys. Rev. B* 36, 8616 (1987).
92. J. M. D. Coey, in "Rare-Earth Iron Permanent Magnets" (J. M. D. Coey, Ed.), p. vii. Clarendon Press, Oxford, 1996.
93. K. H. J. Buschow, *J. Less-Common Met.* 118, 349 (1986).

94. D. Givord, Q. Lu, F. P. Missell, M. F. Rossignol, D. Taylor, and V. Villas-Boas, *J. Magn. Magn. Mater.* 104–107, 1126 (1992).
95. S. Hirosawa, Y. Tsubokawa, and R. Shimizu, “10th Int. Workshop on Rare-Earth Magnets and Their Applications” p. 465. The Society of Non-Traditional Technology, Tokyo, 1989.
96. W. F. Brown Jr., in “Micromagnetics,” p. 68. Interscience Publishers, 1963.
97. H. Kronmüller, *J. Magn. Magn. Mater.* 7, 341 (1978).
98. H. Kronmüller, K. H. Durst, S. Hock, and G. Martinek, *J. Phys. (Paris)* 49, C8–623 (1988).
99. D. W. Taylor, V. Villas-Boas, Q. Lu, M. F. Rossignol, F. P. Missell, D. Givord, and S. Hirosawa, *J. Magn. Magn. Mater.* 130, 225 (1994).
100. D. Givord, Q. Lu, M. F. Rossignol, P. Tenaud, and T. Viadieu, *J. Magn. Magn. Mater.* 83, 183 (1990).
101. J. M. González, A. K. Giri, C. de Julián, M. Vélez, and J. L. Vicent, *J. Mater. Res.* 12, 2643 (1997).
102. F. J. Cadieu, *J. Appl. Phys.* 61, 4105 (1988).
103. F. J. Cadieu, *J. Appl. Phys.* 83, 6247 (1998).
104. F. Cebollada, J. M. González, C. de Julián, and S. Suriñach, *Phys. Rev. B* 56, 6056 (1997).
105. V. E. Martín, J. Bernardi, J. Fidler, F. Cebollada, and J. M. González, *J. Alloys Comp.* 191, 127 (1993).
106. J. Sort, J. Nogués, S. Suriñach et al., *Appl. Phys. Lett.* 79, 1142 (2001).
107. W. F. Brown, “Micromagnetics.” Interscience Publisher, John Wiley, New York, 1963.
108. A. E. LaBonte, *J. Appl. Phys.* 79, 2450 (1990).
109. D. V. Berkov, K. Ramstock, and A. Hubert, *Phys. Stat. Sol.* 137, 207 (1993).
110. M. Gibbons, *J. Magn. Magn. Mater.* 186, 389 (1998).
111. T. Schrefl, J. Fidler, and H. Kronmüller, *Phys. Rev. B* 49, 6100 (1994).
112. T. Schrefl, J. Fidler, K. Kirk, and J. Chapman, *IEEE Trans. Magn. Mag-33*, 4182 (1997).
113. T. R. Koeler and D. R. Fredkin, *IEEE Trans. Magn. Mag-28*, 1239 (1992).
114. T. Koehler, *Physica B* 203, 302 (1997).
115. S. W. Yuan and H. N. Bertram, *IEEE Trans. Magn. Mag-28*, 2031 (1992).
116. K. Ramstock, T. Leibl, and A. Hubert *J. Magn. Magn. Mater.* 135, 97 (1994).
117. T. Schrefl, J. Fidler, C. Kirk, and J. N. Chapman, *J. Appl. Phys.* 85, 6169 (1999).
118. S. W. Yuan and H. Bertram, *Phys. Rev. B* 44, 12395 (1991).
119. H. N. Bertram and J.-G. Zhu, *Solid State Physics Review* 46, 271 (1992).
120. D. Suess, V. Tsiantos, T. Schrefl, W. Scholtz, and J. Fidler, *J. Appl. Phys.* 91, 7977 (2002).
121. A. W. Spargo, P. H. Ridley, G. W. Roberts, and R. W. Chantrell, *J. Appl. Phys.* 91, 6923 (2002).
122. J. D. Hannay, R. W. Chantrell, and H. J. Richter, *J. Appl. Phys.* 85, 5012 (1999).
123. N. S. Walmesley, R. W. Chantrell, J. G. Gore, and M. G. Maylin, *J. Appl. Phys.* 87, 5541 (2002).
124. O. Chubykalo, B. Lengsfeld, J. Kaufman, and B. Jones, *J. Appl. Phys.* 91, 3129 (2002).
125. B. Valcu and H. N. Bertram, *J. Appl. Phys.* 91, 764 (2002).
126. G. J. Parker, C. Cerjan, and D. W. Hewett, *J. Magn. Magn. Mater.* 214, 130 (2000).
127. W. Rave, D. Eckert, B. Gebel, A. Handstein, R. Schafer, and K.-H. Müller “Proceedings of the XIV International Workshop on Rare Earth Magnets and their Applications, Sao Paulo, Brasil, (F. P. Missel et al., Ed.), p. 297. World Cientific, Singapore, 1996.
128. A. W. Spargo, P. H. Ridley, G. W. Roberts, and R. W. Chnatrell, *J. Appl. Phys.* 91, 6923 (2002).
129. T. Schrefl, *J. Magn. Magn. Mater.* 207, 66 (1995).
130. Y. M. Jin, Yu. U. Wang, A. Kazaryan, Y. Wang, D. E. Laughlin, and A. Khachatryan, *J. Appl. Phys.* 9, 6172 (2992).
131. E. P. Wohlfarth, *Proc. R. Soc. London, Ser. A* 232, 208 (1955).
132. F. Soffge and E. Schmidbauer, *J. Magn. Magn. Mater.* 24, 54 (1981).
133. S. Mahmood and I. Abu-Aljarayesh, *J. Magn. Magn. Mater.* 118, 193 (1993).
134. B. Valcu, Y. Takahashi, and H. N. Bertram, *J. Appl. Phys.* 92, 6094 (2002).
135. J. D. Hannay, N. S. Wamsley, and R. W. Chantrell, *J. Magn. Magn. Mater.* 193, 245 (1999).
136. A. Hernando, I. Navarro, and J. M. González, *Europhys. Lett.* 20, 175 (1992).
137. T. Schrefl, H. F. Schmidts, J. Fidler, and H. Kronmüller, *J. Magn. Magn. Mater.* 124, 251 (1993).
138. M. El-Hilo, R. W. Chantrell, and K. O’Grady, *J. Appl. Phys.* 84, 5114 (1998).
139. J. Zhu and H. N. Bertram, *J. Appl. Phys.* 63, 3248 (1988).
140. D. V. Berkov and N. L. Gorn, *J. Appl. Phys.* 83, 6350 (1998).
141. M. Mansuir and R. Giles, *IEEE Trans. Magn. Mag-24*, 2326 (1989).
142. J. G. Zhu and H. N. Bertram, *J. Appl. Phys.* 63, 3248 (1988).
143. J. J. Miles and B. K. Middleton, *IEEE Trans. Magn. Mag-26*, 2137 (1990).
144. C. Dean, A. Hart, D. A. Parker, R. W. Chantrell, and J. J. Miles, *IEEE Trans. Magn. Mag-27*, 4769 (1991).
145. J. G. Zhu and H. N. Bertram, *J. Appl. Phys.* 63, 3248 (1988).
146. N. S. Wamsely, C. Dean, A. Hart, D. A. Parker, and R. W. Chantrell, *J. Magn. Magn. Mater.* 170, 81 (1997).
147. O. Karlquist, *Trans. Roy. Inst. Technol.* 86, 1 (1954).
148. D. A. Lindholm, *IEEE Trans. Magn. Mag-13*, 1460 (1977).
149. K. Senanan, J. Xue, and R. H. Victora, *J. Appl. Phys.* 91, 8013 (2002).
150. T. Schrefl, M. Schabes, and B. Lengsfeld, *J. Appl. Phys.* 91, 8662 (2002).
151. L. Guan and J.-G. Zhu, *J. Appl. Phys.* 91, 8363 (2002).
152. H. N. Bertram, in “Theory of Magnetic Recording.” Cambridge University Press, Cambridge, 1994.
153. H. Azou and H. N. Bertram, *IEEE Trans Magn. Mag-36*, 16 (2000).
154. J.-G. Zhu, *IEEE Trans. Magn. Mag-29*, 195 (1993).
155. O. Chubykalo, B. Lengsfeld, and B. Jones, *IEEE Trans. Magn. Mag-37*, 1363 (2001).
156. H. Zhou and H. N. Bertram, *IEEE Trans. Magn. Mag-35*, 2712 (1999).
157. E. F. Kneller and R. Hawing, *IEEE Trans. Magn. Mag-27*, 3588 (1991).
158. T. Schrefl, H. Roitner, and J. Fidler, *J. Appl. Phys.* 81, 5567 (1997).
159. T. Schrefl and J. Fidler, *J. Appl. Phys.* 83, 6262 (1998).
160. D. Weller and A. Moser, *IEEE Trans. Magn. Mag-35*, 4423 (1999).
161. A. Torabi, H. Zhou, and H. N. Bertram, *J. Appl. Phys.* 87, 5669 (2000).
162. Q. Peng and H. N. Bertram, *J. Appl. Phys.* 81, 4384 (1997).
163. T. Schrefl, J. Fidler, K. J. Kirk, and J. N. Chapman, *J. Appl. Phys.* 85, 6169 (1999).
164. J. Gadbois and J.-G. Zhu, *IEEE Trans. Magn. Mag-31*, 3802 (1995).
165. R. Chantrell and J. Hannay, *J. Magn. Soc. Japan* 21, 283 (1997).
166. R. Street and J. C. Wooley, *Proc. Phys. Soc. London Sec. A* 62, 662.
167. X. Battle and A. Labarta, *J. Phys. D: Appl. Phys.* 35, R15 (2002).
168. H. Pfeiffer, *Phys. Status Solidi A* 122, 377 (1990).
169. R. Victora, *Phys. Rev. Lett.* 63, 457 (1989).
170. Y. Kanai and S. H. Charap, *IEEE Trans. Magn. Mag-27*, 4972 (1991).
171. S. H. Charap, P.-L. Lu, and Y. He, *IEEE Trans. Magn. Mag-33*, 978 (1997).
172. A. D. Liu and H. N. Bertram, *J. Appl. Phys.* 89, 2861 (2001).
173. Y. Zhang and H. N. Bertram, *IEEE Trans. Magn. Mag-34*, 3786 (1998).
174. R. W. Chantrell, M. Wongsam, J. D. Hannay, and O. Chubykalo, *Comp. Mat. Science* 17, 483 (2000).

Sol–Gel Derived Nanocrystalline Semiconductor Oxide Gas Sensors

Satyajit Shukla, Sudipta Seal

University of Central Florida, Orlando, Florida, USA

CONTENTS

1. Introduction
 2. Sol–Gel Process
 3. Synthesis of Nanocrystalline SnO₂ via Sol–Gel
 4. Characterization of Sol–Gel Coated SnO₂ Thin Films
 5. Gas Sensing Characteristics of Sol–Gel Derived Nanocrystalline SnO₂ Thin Films
 6. Other Semiconductor Oxides
 7. Conclusions
- Glossary
References

1. INTRODUCTION

Gas sensors are small devices, which can sense particular gas in a gaseous environment. Gas sensors based on various mechanistic principles, such as Schottky diode, optical, metal nano-wire, solid and polymer electrolyte, thermoelectric, surface acoustic wave, micro-cantilever, diamond-quartz crystal microbalance, thermal conductivity, and resistance-based, have been investigated in the literature. Semiconductor oxide sensors based on resistance-change mechanism are, however, the most popular ones among this group due to their simple operational principle and the simple measurement system associated with them. Hence, one of the primary goals of the present chapter is to review the current understanding of the working principle of the semiconductor oxide sensors based on resistance-change mechanism.

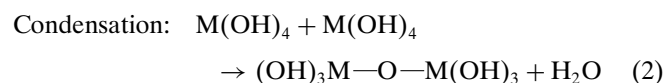
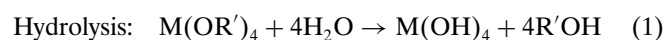
In the previous decade, different semiconductor oxides as gas sensors have been synthesized in different forms (thin and thick films, and pellets) using variety of techniques,

such as spray pyrolysis, chemical vapor deposition, ion-assisted deposition, sputtering, evaporation, arc plasma, metal organic deposition, and sol–gel, to sense different gases for environmental safety and pollution control. This chapter primarily focuses on reviewing the fundamentals of the sol–gel technique for synthesizing semiconductor oxide gas sensors, especially in the nanocrystalline form. The present chapter summarizes the gas sensing properties of different semiconductor oxides synthesized via sol–gel technique as reported in the last decade by different research groups around the world. In the beginning, the reports on the most popular sol–gel derived semiconductor oxide sensor are reviewed, followed by the summary of the gas sensing data reported for the other sol–gel derived nanocrystalline semiconductor oxides.

2. SOL–GEL PROCESS

2.1. Fundamentals of Sol–Gel Processing

The sol–gel synthesis process [1, 2] involves the hydrolysis and the condensation of metal alkoxide (M(OR')_n), where M is the metal, O the oxygen, and R' the organic group. Since the metal alkoxide and water are insoluble in each other, they are dissolved in a common alcoholic solvent in order to carry out the reaction. The alkoxide group (OR'), being highly electronegative, creates a partial positive charge on the central metal atom. On the other hand, in the water molecule, there exists a partial negative charge on the oxygen atom. As a result, metal alkoxides are highly reactive to water. The water molecule attacks the central metal atom, which results in the hydrolysis of the alkoxide. The hydrolysis and the condensation reactions are generally described as:



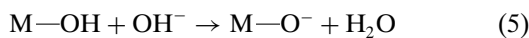
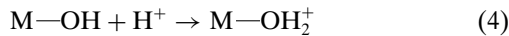
The result is the formation of the M—O—M bond within the solution. The kinetics of the hydrolysis and the condensation reactions are governed mainly by the ratio (R) of molar concentrations water to alkoxide. In general, low R-value (<3) is suitable for thin-film formation while large R-values (>3) generate powder particles.

Once the oxide particles grow in the solution, they are likely to collide with each other due to Brownian motion and this may cause excessive aggregation of the particles. Forming a stable colloidal suspension of oxide nanoparticles (sol) is hence essential. In a colloid, the dispersion forces (van der Waals force of attraction) exist between the particles, which tend to aggregate the particles. For a colloidal particle, the dispersion force is the summation of dispersion forces of all the atoms within the particle. Hence, for colloidal particles of nanometer size, the attractive dispersion force becomes significant and can cause flocculation of colloids. The attractive dispersion force also depends on the shape of the particles. For particles having plate-like shape separated by distance “ h ,” the attractive potential is given by [1]

$$V_A = -A/12\pi h^2 \quad (3)$$

where A is the Hamaker constant and is the material property and h the distance away from the particle surface. It can be noted that for plate-shaped particles, the attractive force decays in proportion to $1/h^2$ while for atoms it decays as $1/h^6$. Hence, the decay of dispersion force with “ h ” is slower for the plate-shaped particles than for atoms. Moreover, for spherical particles, the dependence of the attractive dispersion force on “ h ” is logarithmic; hence, the dispersion force decays more slowly for spherical particles than for plate-shaped particles (at least for small separations comparable to the radius of sphere). The attractive dispersion force between two spherical particles (of size say in the nanometer scale) can extend over the distances of nanometers, and hence, can cause coagulation of particles. Hence, the closest approach of the particles must be avoided to prevent coagulation.

On the other hand, in a colloid, the repulsive electrostatic force is created by the electrical double layer associated with the colloidal particles. The hydrous oxides generally have OH groups on their surface. The protonation and deprotonation of the M—OH bonds result in the creation of a charge on the particle surface:



These H^+ and OH^- ions are thus the charge-determining ions. Whether the particle is positively or negatively charged or is neutral, depends upon the pH of the solution. The pH at which the charge on the particle is zero is called the “point of zero charge (PZC).” At $\text{pH} < \text{PZC}$, the particle is positively charged, while for $\text{pH} > \text{PZC}$, the charge on the particle is negative.

This surface charge of the colloidal particle then attracts ions (known as “counter-ions”) of opposite charge in the

solution. These counter-ions bind to the particles via van der Waals force as well as electrostatic potential of charge-determining ions. The water molecules are also attracted towards the surface charge and are held by van der Waals force as well as by hydrogen bonds. Hence, in a colloid, the particle surface charge is screened by the counter-ions. The charge-determining ions and counter-ions create an electrical double layer. This electrical double layer, associated with every colloidal particle, is responsible for generating a repulsive force between two neighboring particles, thus avoiding flocculation of particles, and thus, produces a stable sol.

This stable sol is then used for producing either nanocrystalline powder by removing the solvent by heating or nanocrystalline thin films. For the latter, spin-coating and dip-coating techniques have been extensively used for producing quality thin films.

2.2. Sol-Gel Spin-Coating Process

Spin-coating is used for many applications where relatively flat substrates or objects are coated with a thin layer of material. In spin-coating, Figure 1, the material, in the form of a stable sol, to be made into coating is deposited onto the substrate surface and spun off to leave a uniform layer. There are four key stages in the sol-gel spin-coating process, Figure 2 [3]:

(1) Stage 1: This step involves the deposition of the sol onto the substrate surface, Figure 2. This can be done using a nozzle that pours the sol out, or the sol could also be sprayed onto the surface. Usually this dispense stage provides a substantial excess of coating solution (sol) compared to the amount that will ultimately be retained in the final coating. For many solutions, it is often beneficial to dispense the sol through a submicron-sized filter to eliminate particles that could lead to flaws.

(2) Stage 2: This step involves aggressive fluid expulsion from the substrate surface by the rotational motion, Figure 2. In this step, the substrate is accelerated up to its final desired rotational speed. Because of the initial depth of the fluid on the wafer surface, spiral vortices may briefly be present during the early stage of substrate rotation, as a result of the twisting motion caused by the inertia exerted by the top of the fluid layer. As the substrate below rotates faster and faster, eventually, the fluid thickness difference

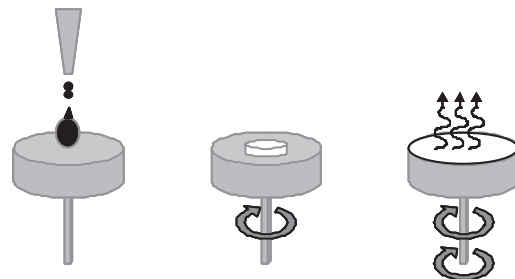


Figure 1. Schematic of the sol-gel spin-coating process.

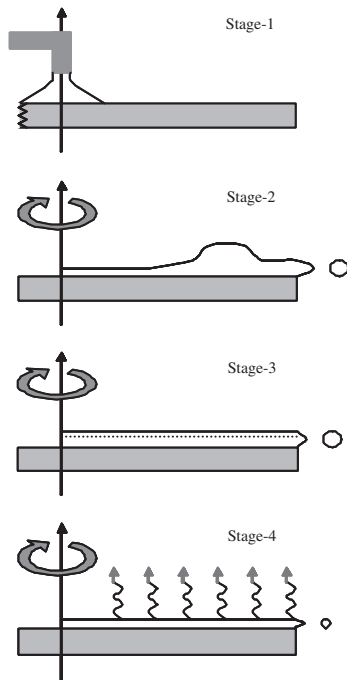


Figure 2. Different stages in the sol-gel spin-coating process.

vanishes. Ultimately, the wafer reaches its desired speed and the fluid is thin enough that the viscosity shear drag exactly balances the rotational accelerations.

(3) Step 3: This step involves gradual fluid thinning, Figure 2, which is generally uniform. The stage begins when the substrate is spinning at a constant rate and fluid viscous force dominates the fluid thinning behavior. With the sol containing volatile solvents, it is often possible to observe interference colors “spinning off,” and doing so, progressively move slowly as the coating thickness is reduced. Edge effects are often seen because the fluid, flowing uniformly outward, must form droplets at the edge to be flung off. Thus, depending on the surface tension, viscosity, and rotation rate, there may be a small bead of coating thickness difference around the rim of the final wafer. If the liquid exhibits Newtonian viscosity and if the fluid thickness is initially uniform across the wafer, then the fluid thickness profile at any following time will also be uniform, leading to a uniform coating under ideal circumstances.

(4) Step 4: This step involves coating-thinning by the solvent evaporation, Figure 2. The coating thickness, at this stage, is inversely proportional to the square root of the rotation speed, that is, thickness $\sim [1/\text{speed}]^{1/2}$. In addition, the sol properties, such as viscosity and concentration, also affect the coating thickness. The fourth stage is when the substrate is spinning at a constant rate and solvent evaporation dominates the coating-thinning behavior. As the prior stage advances, the fluid thickness reaches a point where the viscosity effects yield only a minor net fluid flow. At this point, the evaporation of any volatile solvent species becomes the dominant process occurring in the coating. At this point, the coating effectively “gels” because as

these solvents are removed, the viscosity of the remaining sol rises, effectively freezing the coating in place.

2.3. Sol-Gel Dip-Coating Process

Sol-gel dip-coating is a process where the substrate to be coated is immersed in a liquid and then withdrawn with a well-defined withdrawal speed under controlled temperature and atmospheric conditions, Figure 3 [4]. Vibration-free mountings and very smooth movement of the substrate are essential for the dip-coating process. The coating thickness is mainly defined by the withdrawal speed, the solid content, and the sol viscosity.

The dip-coating route can be divided into three stages: (i) pulling phase, (ii) drying, and (iii) densification.

(i) *Pulling Speed*: The entrainment of the draining fluid (sol) film during the dip-coating process establishes a layer, which increases in thickness with the substrate withdrawal speed. Draining and simultaneous evaporation accompanying pulling, strongly influences the thickness as well as the resulting solid volume fraction of the densified film. The thickness-speed relation is directly linked to the complex time-dependent exchanges near the meniscus. The higher humidity and viscosity of the sol increase the film thickness under given pulling rate.

(ii) *Drying*: Drying is necessary in order to remove the solvent completely before densification of the film to avoid any cracking. Minimum drying temperature of 150 °C is required for complete solvent removal from the thin films. During the drying stage, the structure of the deposited film depends on the competition between two phenomena such as evaporation, which compacts the film, and the condensation reactions (elimination of —OH groups), which strengthen the film, increasing its resistance to compaction.

(iii) *Densification*: Annealing temperature range of 200–600 °C with annealing time of 30–60 min are generally selected for final densification and crystallization of thin films. Increasing annealing temperature reduces the film thickness. The average nanocrystallite size and its distribution increase with increasing annealing temperature. The atomic density of the film and its refractive index also increase with increasing annealing temperature.

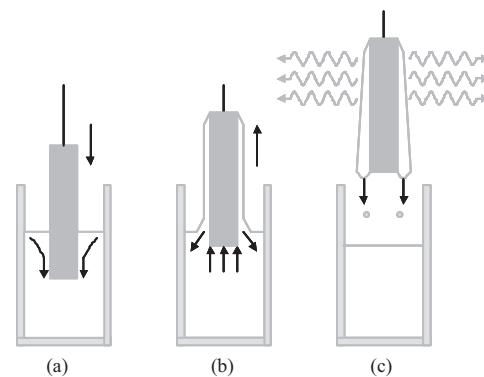


Figure 3. Steps involved in the sol-gel dip-coating: (a) dipping, (b) withdrawal and concurrent deposition, and (c) evaporation.

2.4. Sol-Gel Coating Processes and Gas Sensors

The sol-gel coating processes described above have been investigated to synthesize nanocrystalline semiconductor gas sensors (typically tin oxide (SnO_2)) in the last decade by several groups [5–37]. Other gas sensors, such as thin films of alumina (Al_2O_3) [38], iron oxide (Fe_2O_3) [39, 40], indium oxide (In_2O_3) [41–45], magnesium oxide (MgO) [46], molybdenum oxide (MoO_3) [47–49], niobia (Nb_2O_5) [50], silicates impregnated with ruthium (Ru) complex [51], organically modified silicates [52], titania (TiO_2) [53–58], barium strontium titanate ($(\text{Ba,Sr})\text{TiO}_3$) [59, 60], lead zirconate titanate ($\text{Pb}(\text{Zr,Ti})\text{O}_3$) [60, 61], tungsten oxide (WO_3) [62], zinc oxide (ZnO) [63], zirconia/yttria stabilized zirconia (ZrO_2/YSZ) [64–67] have also been synthesized using the sol-gel technique. The fundamental gas sensing mechanism and the reported results associated with the semiconductor metal oxides are reviewed in detail.

Environmental pollution and security in the work and domestic ambient atmospheres represent acute problems with a high social impact. The need for solid-state chemical sensors, and more specifically gas sensors, in areas such as manufacturing process control, monitoring of toxic and combustible gases in emissions, and domestic and manufacturing safety, has led to extensive research in the area of semiconductor metal oxide gas sensors. SnO_2 is the most widely used commercial gas sensor today as it represents good compromise between price, stability, and reliability of material together with a relatively low sensor operating temperature (230 °C), fast response, and high mechanical strength. SnO_2 has also been utilized in many other applications such as liquid crystal display, solar cells, protective coatings, and catalysts [68–70]. SnO_2 gas sensors in the thin- or thick-film forms are very attractive due to their small size, simple construction, low cost, and low weight. The demand for thin-film type SnO_2 gas sensor devices is also expected to grow because of their lower power consumption and their easy integration into other devices [71, 72]. Applications of SnO_2 sensors have been expanded into the fuel industry, environmental protection, and biotechnology. SnO_2 based semiconductor type devices have been widely used for the prototype gas sensors for detecting inflammable gases. In view of their potential applications to a high-performance micro-sensor integrated in a silicon chip [73], thin-film type SnO_2 gas sensors have drawn much interest.

2.5. Advantages of Sol-Gel Process

Sol-gel technique, as a method for synthesizing thin- or thick-film gas sensor, offers several advantages [1, 2]: (i) The sol-gel technique is simpler and cheaper than others, (ii) it allows an easy coating of large and complex shaped substrates (if the angles are not too sharp), (iii) the process is inexpensive with respect to the initial investment of the production plant and the running cost, (iv) it produces no perturbations of devices in the case of deposition on top, (v) it offers easy control of film thickness and porosity, (vi) it can produce ultrafine films, (vii) it is a low-temperature process, (viii) the large surface area can be obtained on both films and powders that enhance the sensing properties,

(ix) it can easily modify the composition with uniformly dispersed dopants and/or modifier that can enhance the sensitivity and the selectivity towards specific gas species, (x) the process is potentially easy to scale up, (xi) the technology is well suited for the production of thin-film sensors because of its relatively low processing cost and the ability to control the film morphology, (xii) it is well suited for the preparation of thin sensitive layers for MOS-based gas sensors, (xiii) it offers easy deposition of thin films by spin- or dip-coating methods, (xiv) sol-gel produced thin films consist of porous interconnected nanosized particles, while PVD and sputtering produce compact films with reduced gas sensitivity, (xv) sol-gel spin-coated SnO_2 can be patterned onto the silicon-based sensor structure; these spin-coating and patterning steps are compatible with silicon-based micro-fabrication processes, (xvi) particle size can be controlled through careful control of the film calcination temperature; good porosity, and improved surface to volume ratio, due to nanosized particles, result in high sensitivity to various reducing gases, (xvii) highly energetic procedures such as RF sputtering and vacuum evaporation deposit SnO_2 crystallites in high energy state, which take a long time to stabilize; in contrast to this, the sol-gel process deposits more stable SnO_2 thin films on an alumina or silica glass by dip-coating or spin-coating from a SnO_2 sol.

2.6. Disadvantages of Sol-Gel Process

The sol-gel process has a few limitations, too. The real application of this synthesis route for the serial devices needs efforts in R&D. Much work and time are needed in optimizing the stability of the sol, the durability, and the reproducibility of the results for the production of sensor devices. Moreover, the alkoxide precursors are generally costlier. In spite of these disadvantages, the sol-gel process has been proven to be a highly applicable and industrially viable process for synthesizing nanocrystalline SnO_2 gas sensors in the form of thin films.

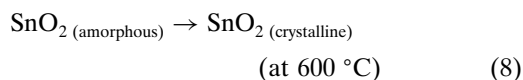
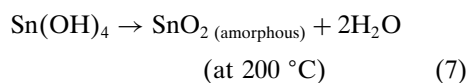
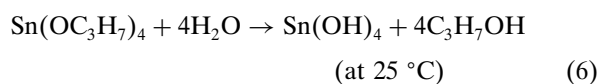
3. SYNTHESIS OF NANOCRYSTALLINE SnO_2 VIA SOL-GEL

Two sol-gel synthesis routes (or precursors) are generally used for producing SnO_2 thin films; first is the hydrolysis of tin alkoxide [8, 34, 74, 75] and the second is the hydrolysis of tin(IV) chloride [5, 6, 9–19, 21–26, 29, 30, 33, 37, 76]. SnO_2 thin films can also be prepared from an aqueous SnO_2 sol, which is synthesized via tin(IV) chloride hydrothermal treatment [16]. Semiconductor SnO_2 gas sensor can be fabricated into three types of devices: (i) sintered block [12, 16, 19], (ii) thick film [27, 28], and (iii) thin film [5–11, 13–18, 20–24, 26, 29–31]. Of these, sintered block and thick-film devices have been commercialized successfully. Thin-film devices, however, have not been brought into practical use, in spite of their advantages claimed over the above devices, that is, (i) fast response, (ii) low fabrication cost, (iii) ease of miniaturization, and (iv) compatibility with microelectronic circuitry. It is suspected that this situation has resulted from

a difference in the preparation technology for the gas sensing material.

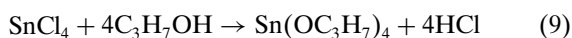
3.1. SnO₂ Thin Films Using Alkoxide Precursor

SnO₂ semiconductor thin film coated on the glass substrate via sol-gel dip-coating technique is described here [77]. The glass substrate is ultrasonically cleaned, first in acetone and then in iso-propanol. The pre-cleaned substrate is then dipped in the solution of tin-isopropoxide (0.23 M) in iso-propanol and toluene, using a dip-coater with a withdrawal speed of 150 cm/min. The gel films are dried at 200 °C for 1 h in air. The substrate is dip-coated again using the same solution under similar conditions and then dried again at 200 °C for 1 h in air. The dried gel film is then fired at 600 °C in air. The film is heated at a rate of 30 °C/min up to the firing temperature, held at that temperature for 1 h, and then cooled to room temperature inside the furnace. The sequence of chemical reactions during gelling, drying, and crystallization, for the film having stoichiometric composition, can be summarized as



3.2. SnO₂ Thin Films Using Non-Alkoxide Precursor

Alkoxides are usually very costly. However, this problem can be overcome by using the cheap, commercially available non-alkoxide precursors, namely SnCl₄, without further purification or modification. Following procedures are generally followed to prepare pure and modified SnO₂ thin films by means of sol-gel technique utilizing non-alkoxide precursors. In the first method [5, 13, 14], tin tetrachloride (SnCl₄) is first dissolved in propanol (or any other alcohol) forming a solution of tin compounds of type SnCl_x(OC₃H₇)_y, (typically stannic trichloride mono propoxide propyl alcoholate and tin dichloride di-propyl alcoholate):



Due to heat evolution, the solution is allowed to cool down to room temperature. Water-propanol mixture is then added to this for hydrolysis reaction. Another dilution with butanol may be followed to obtain desired SnO₂ equivalent wt %.

In another method [76], SnCl₄ is dissolved in deionized water (1 L) and the mixture is stirred for 24 h to obtain Sn(OH)₄ precipitate:



This precipitate is separated using a centrifuge and washed several times using deionized water to remove the H⁺ and

Cl⁻ ions until pH > 5. The precipitate is then peptized in deionized water with high pH (>11), which is obtained by adding appropriate amount of NH₄OH. The resulting sol is suitable for thin-film formation.

3.3. SnO₂ Thick Films via Sol-Gel

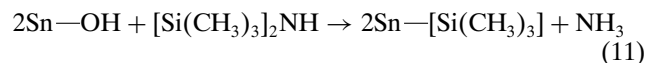
The SnO₂ thick films via sol-gel method begins with the preparation of nanosized SnO₂ powder [27, 28]. The sol prepared via various methods, described above, is suitable for nanosized SnO₂ powder preparation. The sol is converted to nanosized powder by heating it at higher temperature (150–200 °C) to remove the solvent and water completely. Amorphous nanosized SnO₂ powder obtained in this way is then mixed with water and suitable binder such as polyvinyl alcohol (PVA) polymer. The resulting paste is then applied on a suitable substrate (typically Al₂O₃) to form a thick film of nanosized SnO₂ suitable for gas sensing.

3.4. SnO₂ Pellets via Sol-Gel

Pellets of SnO₂ powder are formed by mixing the nanosized SnO₂ powder with PVA polymer and pressing this mixture into a pellet [12, 16, 19]. The pellet is then sintered at higher temperature, at which the polymer is decomposed, producing a porous nanocrystalline SnO₂ pellet suitable for gas sensing.

3.5. Controlling Growth of SnO₂ Nanocrystallites

Two approaches have been reported to control the growth in the size of the nanocrystallites during the high-temperature exposure [16, 78]. The first approach [78] is based on replacing the surface OH group with another functional group that does not condense as OH groups and that could eventually form the “pins” at the grain boundaries during high-temperature exposure. Hexamethyldisilazane (HMDS; [Si(CH₃)₃]₂NH) is a OH scavenging reagent because it replaces the OH groups in the SnO₂ gel to form noncondensing methyl siloxyl group, and when decomposed in air above 300 °C, it transforms to extremely small SiO₂ particles, which could serve as the “pinning” for the SnO₂ particles. When heated at 150 °C for 1 h, HMDS vaporizes and reacts with the surface OH groups by following reaction:



The methyl siloxyl group decomposes after firing at 200–500 °C for 1 h in air, producing Sn—O—Si bond on the surface, which is not condensing as the surface OH groups. Moreover, the process produces extremely tiny SiO₂ particles over SnO₂ nanoparticles, which act as “pinning sites” for the grain boundary movement during densification, thus avoiding excessive growth at higher temperature. In the second method [16], the alkaline Sn(OH)₂ sol is subjected to the hydrothermal treatment in an autoclave at 200 °C for 3 h. Such hydrothermally treated sol particulates are more resistant to grain growth as compared to untreated sol.

4. CHARACTERIZATION OF SOL-GEL COATED SnO_2 THIN FILMS

Typical SEM micrograph of nanocrystalline SnO_2 thin film coated on a Pyrex glass substrate is shown in Figure 4 [77]. The SnO_2 thin film appears to be relatively smooth. At some locations, few cracks are observed on the film surface, which are characteristic features of the sol-gel dip-coated thin films.

Typical broad-scan XPS spectrum, within the B.E. range of 0–1100 eV, obtained for the nanocrystalline SnO_2 thin film dip-coated on the Pyrex glass substrate is shown in Figure 5a [77], which primarily shows the presence of Sn and O on the glass surface after the dip-coating process. Typical narrow-scan analysis of Sn (3d) spectra, within the B.E. range of 480–500 eV, is presented in Figure 5b. Sn $3d_{5/2}$ B.E. level of 485.8 eV is observed in Figure 5b, which is in between the Sn $3d_{5/2}$ B.E. values of 484.9 eV and 486.7 eV reported for pure Sn and SnO_2 , respectively [79]. Hence, the observed Sn $3d_{5/2}$ B.E. value of 485.8 eV is attributed to the presence of Sn-oxidation state less than +4. The O:Sn relative atomic ratio of ~ 1.6 is calculated from the survey spectrum and is in agreement with the Sn $3d_{5/2}$ B.E. value. The nonstoichiometric O:Sn ratio suggests the presence of oxygen vacancies [80], which is responsible for the n-type semiconductor property of the film.

Typical TEM images, obtained from the FIB-milled TEM sample of the nanocrystalline SnO_2 thin film dip-coated on the Pyrex glass substrate, are shown in Figure 6 at different magnifications [77]. The thickness of the nanocrystalline SnO_2 thin film can be directly measured via these micrographs. Various regions corresponding to Pt, Au-Pd (both originating from the FIB-milling procedure), SnO_2 (originating from the sol-gel dip-coating process), and the glass substrate are marked appropriately. The SnO_2 thin film appears to be smooth and highly continuous. No cracks are visible within the film, although slight variation in the film thickness is noted in these images. The average SnO_2 thin-film thickness is observed to be within the range of ~ 100 – 150 nm.

Typical AFM images of the nanocrystalline SnO_2 thin-film sol-gel dip-coated on the Pyrex glass substrate, at low and high magnifications, are presented in Figure 7a and 7b, respectively [77]. The nanocrystalline SnO_2 thin film is observed to be made up of nanoparticles having near-spherical shape and uniform particle size distribution. Very dense packing of nanoparticles is noted in these micrographs. The average nanoparticle size is estimated to be

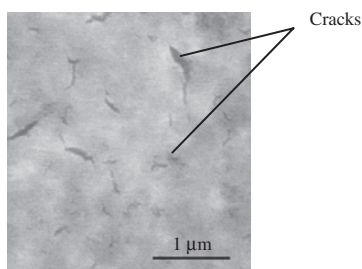


Figure 4. SEM micrograph of SnO_2 thin-film gas sensor [47].

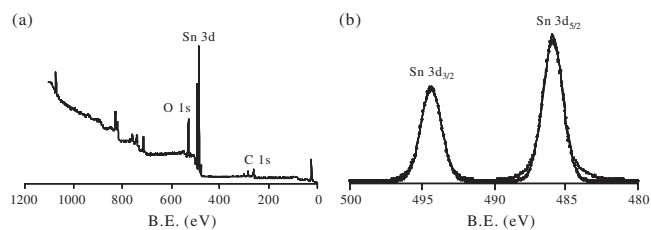


Figure 5. Broad-scan (a) and narrow-scan (b) XPS analysis of SnO_2 thin-film gas sensor [47].

within the range of 15–20 nm and is comparable with the resolution limit of AFM determined by the AFM-tip radius.

Typical HRTEM images obtained from the FIB-milled TEM sample are presented in Figures 8a and b at different magnifications. Selected-area electron diffraction (SAED) pattern obtained from the center of the nanocrystalline SnO_2 thin film is presented in Figure 8c [77]. From these images, it is obvious that the sol-gel dip-coated SnO_2 thin film is highly dense and nanocrystalline in nature. The nanocrystalline SnO_2 thin film–glass substrate interface is visible in Figure 8a. No porosity or cracks are visible at the interface, which suggests very adherent nature of the sol-gel dip-coated nanocrystalline SnO_2 thin film. Porosity and cracks are not observed within the nanocrystalline SnO_2 thin film at nanoscale level, indicating very dense packing of the SnO_2 nanocrystallites within the thin film, which is in agreement with the AFM analysis. The average SnO_2 nanocrystallite size of ~ 6 – 8 nm is measured from these HRTEM images. The nanocrystallite size distribution is observed to be very narrow. SAED pattern, Figure 8c, shows continuous and diffused ring patterns, which suggests the nanocrystalline nature of SnO_2 thin film.

The variation in the average nanocrystallite size as a function of calcination temperature, within the range of 100–1000 °C, reported for the sol-gel derived nanocrystalline SnO_2 thin films or powders is presented in Figure 9 [9, 12–14, 21, 22, 25]. It can be observed that, within the calcination temperature range of 100–700 °C, the grain growth is marginal and lies within the range of 3–20 nm. However, above 700 °C, rapid grain growth is observed. Grain size as high as 300 nm is observed at the calcination temperature of 1000 °C. The activation energy for the grain growth, for high (700–1000 °C) and low temperature ranges (100–700 °C), can be determined from the

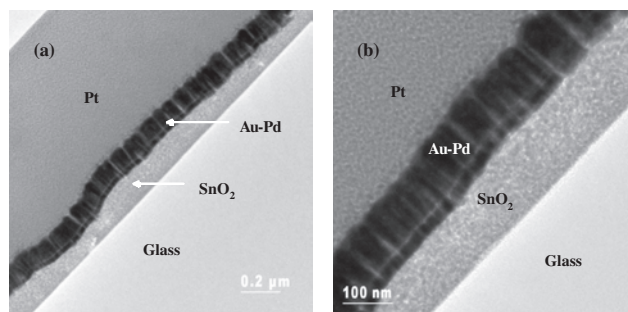


Figure 6. TEM micrographs of SnO_2 thin-film gas sensor at low (a) and high (b) magnifications [47].

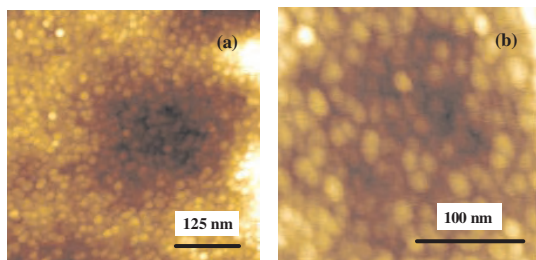


Figure 7. AFM micrographs of SnO₂ thin-film gas sensor at low (a) and high (b) magnifications [47].

activation energy plot, Figure 10. The activation energy values of 91 kJ/mol and 9 kJ/mol are determined for high and low calcination temperature regions, respectively. Very low activation energy value (9 kJ/mol) observed in the lower temperature range (100–700 °C) is attributed to the possible generation of excess oxygen-ion vacancy concentration in the SnO₂ nanoparticles, as reported for other oxide particles [81].

5. GAS SENSING CHARACTERISTICS OF SOL-GEL DERIVED NANOCRYSTALLINE SnO₂ THIN FILMS

5.1. Mechanism of Gas Sensing

When a freshly prepared sol-gel derived nanocrystalline SnO₂ semiconductor thin film is exposed to air, physisorbed oxygen molecules pick up electrons from the conduction band of SnO₂ and change to O_{ads}⁻ or O_{2(ads)}⁻ species. Consequently, a positive space-charge layer forms just below the surface of SnO₂ particles, which creates a potential barrier between the particles increasing the electrical resistance of the nanocrystalline SnO₂ film, Figure 11 [82].

However, when a reducing gas comes in contact with the nanocrystalline SnO₂ film, it gets oxidized via reaction with

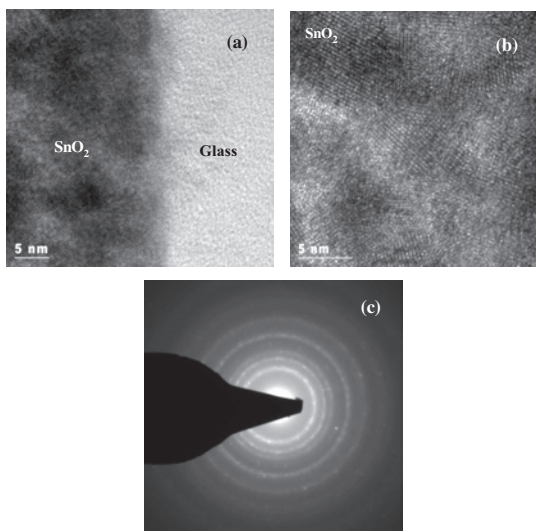


Figure 8. HRTEM images (a, b) and SAED pattern (c) of SnO₂ particles within a gas sensor thin film [47].

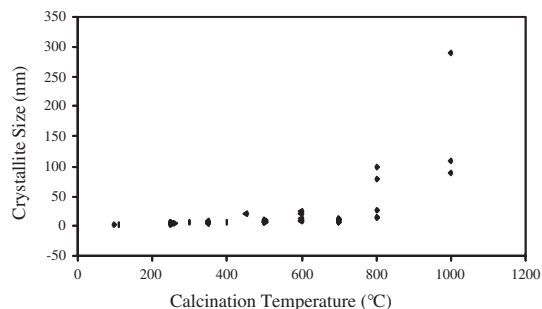


Figure 9. Effect of calcination temperature on the crystallite size for the sol-gel derived nanocrystalline SnO₂ [9, 12–14, 21, 22, 25].

the surface adsorbed O_{ads}⁻ or O_{2(ads)}⁻ species and subsequently electrons are reintroduced into the electron depletion layer, leading to decrease in the potential barrier. The sensitivity of the nanocrystalline SnO₂ thin film is usually determined by the ratio $(R_a - R_g)/R_g$, where R_a and R_g are the resistance of the sensor in air and reducing gas, respectively.

A typical response of the nanocrystalline SnO₂ sensor is schematically shown in Figure 12. The figure shows that the sensor exhibits a resistance “ R_a ” in air. When the reducing gas comes in contact with the sensor, its resistance decreases rapidly initially, then decreases at lower rate with increasing time and attains a steady-state resistance value (R_g). The total time taken by the sensor to attain 90% of the steady-state value is known as the “response time” of the sensor. If the air is flown back over the sensor, it retains its original resistance in air. The time required to reach 90% of the original resistance is known as the “recovery time” of the sensor. The gas sensitivity, response time, and recovery time are the three most important parameters of the nanocrystalline gas sensor. During the preparation of the nanocrystalline SnO₂ thin film, the sol-gel synthesis parameters are optimized to maximize the gas sensitivity and to minimize the response and recovery times.

5.2. Summary of Reported Results

Various parameters such as nanocrystallite size, calcination and operating temperatures, film thickness, and amount of porosity, have been reported to affect the gas sensitivity of the sol-gel derived nanocrystalline SnO₂ thin film. Figure 13 shows the effect of the nanocrystallite size on the

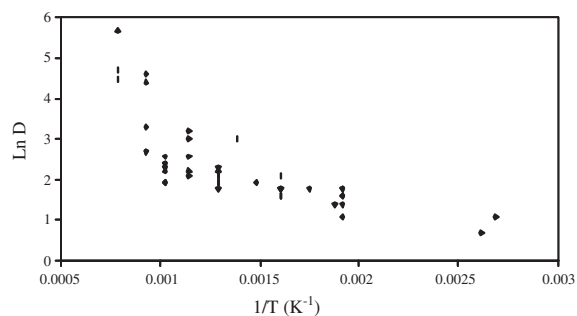


Figure 10. Activation energy determination plot for the sol-gel derived nanocrystalline SnO₂. D-crystallite size (nm).

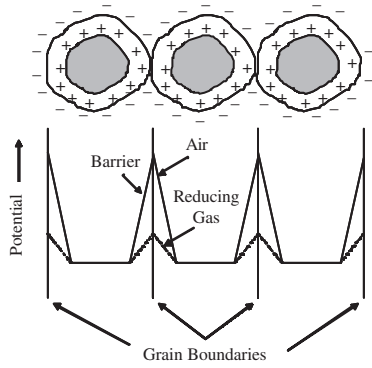


Figure 11. A model showing the variation in the potential barrier of the nanocrystalline SnO₂ gas sensor due to change in the environment [52].

gas sensitivity of the sol-gel derived nanocrystalline SnO₂ thin film [9, 12–14, 21, 22, 25]. The gas sensitivity is observed to be enhanced drastically below a nanocrystallite size of ~10 nm while the gas sensitivity is almost independent of the nanocrystallite size above this size range. The enhancement in the gas sensitivity below ~10 nm crystallite size has been attributed to the “grain-control” resistance mechanism, which enhances the transducer function of the sensor [83, 84].

A semiconductor gas sensor has two functions [84]. First is the receptor function, which recognizes or identifies a chemical gas component. The receptor function in this case is played by the surface oxygen. If a metal or a metal oxide is added onto the surface as a surface modifier, it may also influence the receptor function. The receptor function of a semiconductor is thus determined by the ability of the semiconductor surface to interact with a reducing gas component. The second function of a semiconductor gas sensor is a transducer function, which transforms the chemical signal into an electrical signal. In this case, the electrons generated via chemical reaction are conducted through the gas sensor material. As these conduction electrons have to overcome the potential barrier induced by the space-charge layer, the microstructure of the semiconductor gas sensor plays an important role to control the transducer function. The magnitude of this potential barrier for the electronic conduction strongly depends on the ratio of the nanocrystallite size (D) to the space-charge layer thickness (L).

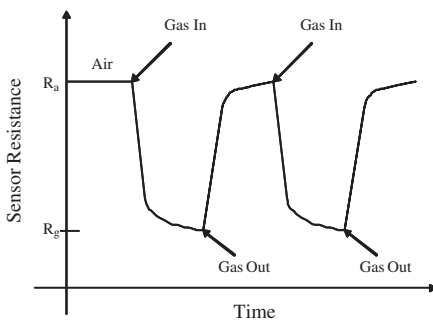


Figure 12. Schematic diagram describing the variation in the sensor resistance with the change in the environment.

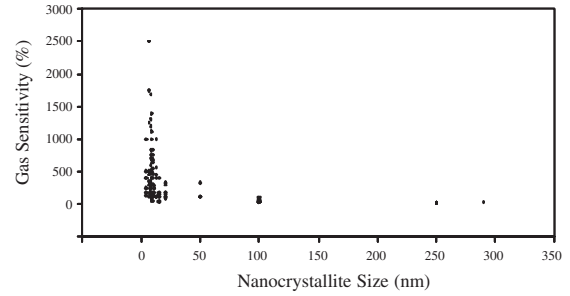


Figure 13. Variation in the gas sensitivity as a function of nanocrystallite size [9, 12–14, 21, 22, 25].

In a semiconductor gas sensor, the nanocrystallites are connected to each other via necks forming aggregates (large-sized particles). The large-sized particles are in turn connected to the neighbors via grain boundary contacts. When the nanocrystallite size is very large ($D \gg 2L$), the conduction electrons have to overcome the potential barrier induced by the space-charge layer at each grain boundary contact, Figure 14a. In this situation, the resistance of the gas sensor is determined by the resistance offered by the grain boundary contacts, which is independent of the grain size. Hence, when the nanocrystallite size is very large compared to the space-charge layer ($D \gg 2L$), the sensitivity of an oxide semiconductor sensor is independent of the nanocrystallite size.

As the nanocrystallite size decreases, the space-charge layer penetrates deeper into each of the nanocrystallites. When the nanocrystallite size approaches the space-charge layer thickness ($D \geq 2L$), the space-charge layer forms channels at each neck within a particle, Figure 14b. As the conduction electrons must move through these channels, they experience additional potential barrier in addition to the potential barrier existing at the grain boundaries. Under these constraints, the resistance of the gas sensor is determined predominantly by the neck resistance. As the neck size is observed to be proportional to the nanocrystallite

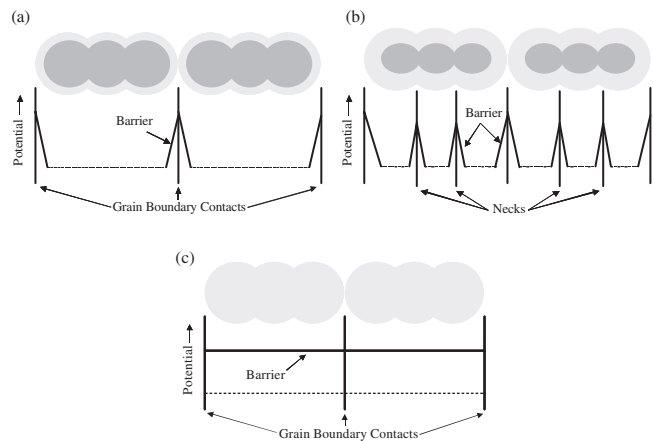


Figure 14. Resistance-control models for the sol-gel derived nanocrystalline SnO₂ thin film under different conditions: (a) $D \gg 2L$, (b) $D > 2L$, and (c) $D < 2L$. D -crystallite size and L -space-charge layer thickness [54].

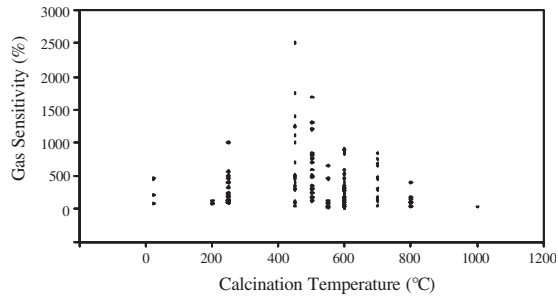


Figure 15. Variation in the gas sensitivity as a function of calcination temperature [5, 8, 9, 12–14, 17, 21, 22, 25].

size, the sensitivity of the gas sensor is dependent on the nanocrystallite size for $D \geq 2L$.

As the nanocrystallite size reduces below twice the space-charge layer thickness ($D < 2L$), the entire nanocrystallite becomes depleted of electrons. The space-charge layer then penetrates into the nanocrystallite completely, Figure 14c. The electrical resistance of the gas sensor increases abruptly and is controlled mainly by the grain resistance under this situation. In this region, the ratio of electron concentration in gas (n_g) to that in air (n_a) within a nanocrystallite decreases as the distance from its surface increases. As a result, when $D < 2L$, the sensitivity of the gas sensor increases with decreasing nanocrystallite size in this range.

Thus, the nanocrystallite size (D) relative to the space-charge depth (L) is one of the most important factors affecting the sensing properties of a semiconductor oxide gas sensor. For a thin sputtered SnO_2 film and sintered powders, the space-charge depth has been calculated to be ~ 3 nm at 250 °C [85, 86]. Hence, for the sol-gel derived nanocrystalline SnO_2 gas sensor, very high sensitivity is theoretically expected just above and below the nanocrystallite size of ~ 6 nm.

Figure 15 shows the effect of the calcination temperature on the gas sensitivity for the sol-gel derived nanocrystalline SnO_2 thin-film sensor [5, 8, 9, 12–14, 17, 21, 22, 25]. The maximum gas sensitivity is observed to be reported at the calcination temperature of 450 °C. Above and below this calcination temperature range, the gas sensitivity decreases. The sol-gel derived nanocrystalline SnO_2 thin film is always amorphous at room temperature. Hence, the calcination treatment at higher temperature is necessary to crystallize

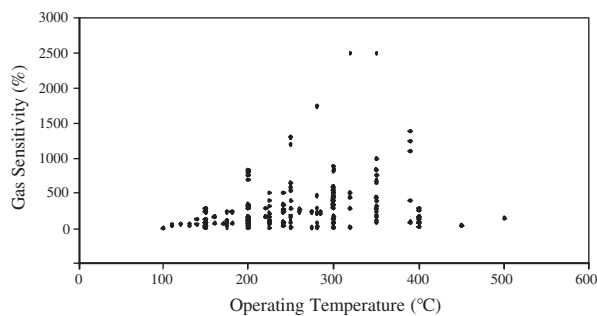


Figure 16. Variation in the gas sensitivity as a function of operating temperature [5, 8, 9, 12–14, 17, 21, 22, 25].

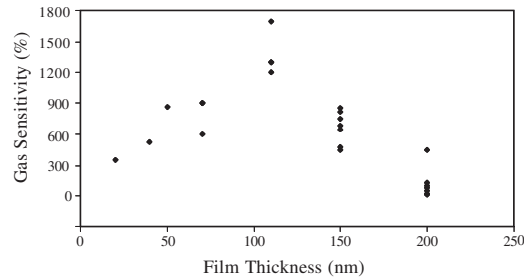


Figure 17. Variation in the gas sensitivity as a function of film thickness for sol-gel derived nanocrystalline SnO_2 film [5, 9, 13, 17, 21].

the film. At the same time, higher calcination temperature results in the grain growth, Figure 9, which may decrease the gas sensitivity. Hence, due to the optimum balance between the amount of crystallization and the degree of grain growth, the maximum sensitivity value is observed at the intermediate calcination temperature of 450 °C. Decrease in the film thickness with increasing calcination temperature would also tend to enhance the gas sensitivity.

The dependence of the gas sensitivity on the operating temperature, within the range of 100 – 500 °C, is shown in Figure 16 [5, 8, 9, 12–14, 17, 21, 22, 25]. The gas sensitivity increases with increasing operating temperature, reaches the maximum value at 320 – 350 °C, and then decreases with further rise in the operating temperature. The electrical resistance of the sensor is also known to follow similar behavior as a function of operating temperature [82]. Within the lower operating temperature range of 100 – 320 °C, the adsorption of the oxygen ions dominates, which decreases the conduction electron density in the film, which favors the high gas sensitivity. On the other hand, in the higher temperature range, 350 – 500 °C, desorption of the oxygen ions dominates, thus reducing the conduction electron density, which reduces the gas sensitivity. The low activation energy for the reaction between the reducing gases and the adsorbed oxygen ions at higher operating temperatures is also a major factor for increased gas sensitivity at higher operating temperatures. On the other hand, instability in the microstructure at high operating temperatures can lead to reduced gas sensitivity at higher operating temperatures.

The variation in the gas sensitivity as a function of the film thickness is shown in Figure 17 [5, 9, 13, 17, 21]. The graph shows that the maximum gas sensitivity appears at the film thickness of ~ 110 nm, while above and below this thickness, the gas sensitivity decreases. To explain the thickness dependence, a single-crystal thin-film model has been suggested [87], which excludes the effects of microstructure.

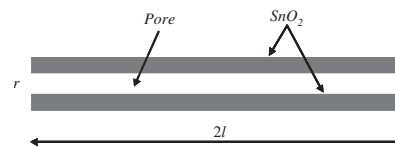


Figure 18. Model of SnO_2 thin film having straight channel structure [55].

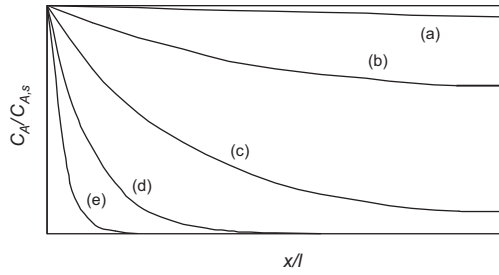


Figure 19. Generalized gas concentration profiles within SnO₂ thin film, film having straight channel structure, with increasing function of $l(k/D_K)^{1/2}$ (from ‘a’ to ‘e’).

The sensitivity (S) defined by this model is given as

$$S = n_s / (n_B t) \quad (12)$$

where n_s is the density of electrons per unit area that are returned to SnO₂ particle surface by the oxidation of gas with the surface-adsorbed oxygen ions (O⁻) and n_B is the electron density per unit volume in the film bulk. The model predicts that the gas sensitivity would increase with decrease of the film thickness. In contrast to this behavior, for the film thickness less than ~110 nm, a markedly lower gas sensitivity, which decreased with decreasing film thickness, exists. The amount of porosity in the sol-gel derived nanocrystalline SnO₂ thin films has also been reported to decrease drastically below the film thickness of 70–200 nm [8, 88]. Very compact films exhibit low surface areas, and as a result, they offer reduced number of the active sites for the oxidation reactions with reducing gases and would decrease the gas sensitivity with decreasing film thickness below the critical thickness range. The decrease in the gas sensitivity with increase in the film thickness can also be explained based on the following model [88].

Consider a porous film having thickness $2l$ and represented by a straight channel structure as depicted in Figure 18. Each channel is assumed to be a round pore of radius r and length $2l$. The gas molecules diffuse into the pores by Knudsen mechanism from both the sides of the film. The Knudsen diffusion coefficient (D_K) under these

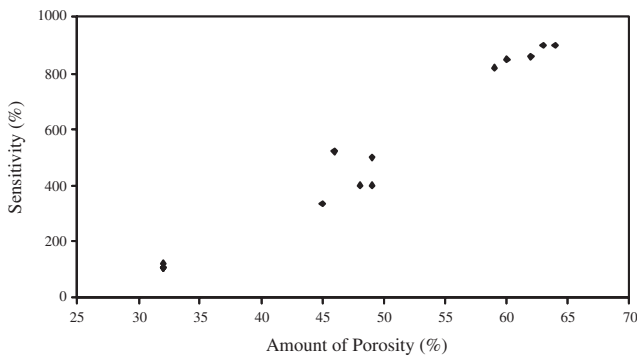


Figure 20. Variation in the gas sensitivity as a function of amount of porosity for the sol-gel derived nanocrystalline SnO₂ film [8, 12].

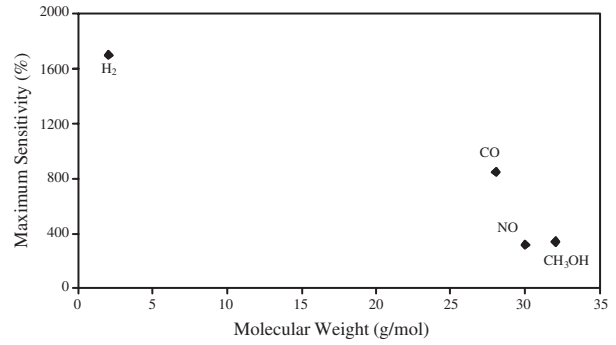


Figure 21. Variation in the maximum gas sensitivity of the sol-gel derived nanocrystalline SnO₂ thin film as a function of molecular weight of various gases [5, 9, 21, 22].

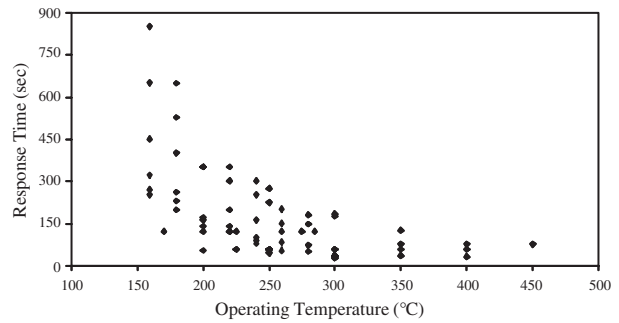


Figure 22. Variation in the response time of the sol-gel derived nanocrystalline SnO₂ thin film as a function of operating temperature [5, 8, 9, 12, 13, 18, 21].

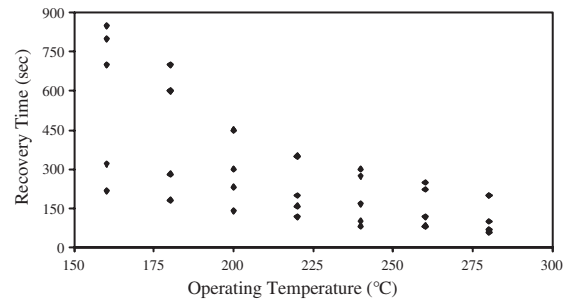


Figure 23. Variation in the recovery time of the sol-gel derived nanocrystalline SnO₂ thin film as a function of operating temperature [5, 9, 12, 18, 21].

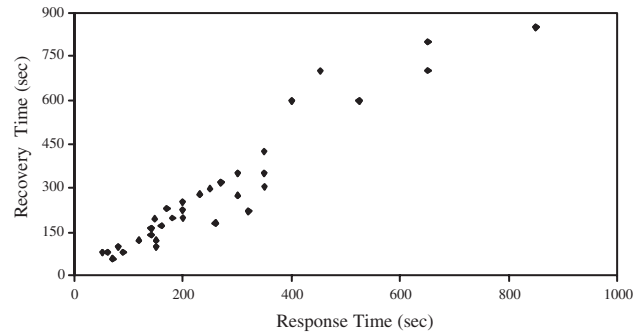


Figure 24. Variation in the recovery time of the sol-gel derived nanocrystalline SnO₂ thin film as a function of response time [5, 9, 12, 18, 21].

Table 1. The gas sensing properties of the sol-gel derived other nanocrystalline semiconductor oxides.

(A)								
Sensor	Precursors	Calcination temp. (°C)	Gas (ppm)	Film thickness (nm)	Crystallite size (nm)	Operating temp. (°C)	Sensitivity (%)	Ref.
Zinc Oxide	Zinc Acetate	300–500	CH ₄	4000	300–600	300	750	[63]
Zinc Oxide-Pd ²⁺ Catalyst							1500	
Barium Strontium Titanate	—	475	H ₂ (5–1000)	125	—	250	18–900	[59, 60]
Lead Zirconate Titanate	Lead Acetate Trihydrate, Zirconium Acetylacetonone, Titanium Isopropoxide	410	H ₂ (1000)	160	—	175	1600	[60, 61]
Titania	Titanium Butanol Alkoxide	—	O ₂ (10 ⁻²⁸ –10 ⁻³ atm)	—	—	600–1000	1,000,000–100,000	[90]
	Titanium Butoxide	800	O ₂ (0.0496–1 atm)	300,000	80	640	143	[91]
Titania-Niobium Oxide	Titanium Butoxide, Niobium Ethoxide	600	O ₂ (10,000)	55	55–60	190	682	[53]
				60			2233	
Titania	Titanium Sulfate, Niobium Chloride	600	H ₂ (500)	Disc 5.0 mm diameter, 0.5 mm thick	12	450	480	[56]
Titania-Niobium Oxide			CO (500)		11	400	225	
			H ₂ (500)				570	
			CO (500)				375	
Titania	Tetraethyl Ortho-Titanate	500	CH ₃ OH (100 ppm)	—	3–30 nm	400	700	[55]
			C ₂ H ₅ OH (100 ppm)			500	1700	
			NO ₂ (4 ppm)			400	2110	
			CO (300 ppm)			500	3666	
						400	50	
						400	50	
	Titanium Isopropyl Alkoxide	500	H ₂ O (80%)	300–400	<100	40	9900	[92]
Indium Oxide	—	800	CH ₄ (40)	Pellister Type	—	—	2	[93]
			CO (40)				2	
			C ₂ H ₅ OH (45)				54	
			NH ₃ (15–1100)				1–19	
Indium Oxide-Pt			CH ₄ (40)				4	
			CO (40)				56	
			C ₂ H ₅ OH (45)				66	
			NH ₃ (15–1100)				7–312	
Indium Oxide-Au			CH ₄ (40)				4	
			CO (40)				16	
			C ₂ H ₅ OH (45)				38	
			NH ₃ (15–1100)				2–125	
Indium Oxide	Indium Nitrate	500	O ₃ (100 ppb)	—	8	300	150,000	[94]

continued

Table 1. Continued

(A)									
Sensor	Precursors	Calcination temp. (°C)	Gas (ppm)	Film thickness (nm)	Crystallite size (nm)	Operating temp. (°C)	Sensitivity (%)	Ref.	
Indium Oxide-Ni ²⁺	—	600	NO ₂ (1)	<100	10–25	150	3000	[95]	
			CO (50)			400	25	[95, 96]	
			NO ₂ (1)			150	4200	[96]	
			CO (50)			400	12		
Indium Oxide	Indium Nitrate	697 400–700	NO ₂ (0.2–4)	100	10	247	300–2500	[97]	
			NO ₂ (1)	100	5	150	2000	[44]	
					6		3000		
					20		6000		
Indium Oxide-Mo ⁶⁺	—	—	O ₃ (0.2)	—	20–25	100	2000	[43]	
					15–20	130	2000		
Indium Oxide	—	800	CH ₄ (20,000)	Pellister Type	—	—	27	[42]	
Indium Oxide-Ni ²⁺			CO (20,000)				14		
Molybdenum Oxide-Titania	Molybdenum Propoxide-Titanium Butoxide	450	O ₂ (120)	100	20–100	330	200	[98]	
			O ₂ (1000)				800		
			O ₂ (10,000)				8000		
Molybdenum Oxide	Molybdenum (V) Isopropoxide, Tungsten (VI) Ethoxide	500	O ₂ (1000)	—	—	370	4040	[62]	
Molybdenum Oxide-Tungsten Oxide (25 at. %)			O ₂ (100)			420	1010		
Molybdenum Oxide-Tungsten Oxide (50 at. %)			O ₂ (10,000)			320	190		
Molybdenum Oxide-Tungsten Oxide (25 at. %)							160		
							2290		
Molybdenum Oxide	Molybdenum (V) Isopropoxide, Titanium Butoxide	500	O ₂ (10,000)	—	—	370	3900	[48]	
Molybdenum Oxide-Titania (5 at. %)							200		
Molybdenum Oxide-Titania (25 at. %)							1600		
Molybdenum Oxide-Titania (50 at. %)						320	300		
Molybdenum Oxide-Titania (25 at. %)			CO (25)			300	200		
							CO (200)	250	
							CO (400)	290	
							NO ₂ (0.5)	130	
							NO ₂ (2)	270	
Tungsten Oxide	Tungsten (VI) Ethoxide	500	O ₂ (1000)	—	—	420	750	[62]	
Tungsten Oxide-Molybdenum Oxide (5 at. %)	Tungsten (VI) Ethoxide-Molybdenum (VI) Isopropoxide	500	O ₂ 100	—	—	320	140	[62]	
							O ₂ 1000	290	
							O ₂ 10,000	680	
			O ₂ 1000			420	440		
			O ₂ 100			320	170		
Tungsten Oxide-Molybdenum Oxide (25 at. %)			O ₂ 1000			420	360		
							O ₂ 10,000	860	
							O ₂ 1000	340	

continued

Table 1. Continued

(B)					
Sensor	Gas (ppm)	Operating temperature (°C)	Response time (sec)	Recovery time (sec)	Ref.
Titania	O ₂ (10,000)	190	90	120	[53]
Titania-Niobium Pentoxide			180	66	
Titania	H ₂ (500)	450	<120	<120	[56]
Titania-Niobium Pentoxide			<120	<120	
Titania	CH ₃ OH (100)	400–500	30	<60	[55]
	C ₃ H ₅ OH (100)		120	60	
Indium Oxide	NH ₃ (30)	—	16	37	[93]
	NH ₃ (1000)		12	30	
Indium Oxide-Pt	NH ₃ (30)		5	37	
	NH ₃ (1000)		5	37	
Indium Oxide	O ₅ (100)	300–350	60	600	[94]
Indium Oxide	NO ₂ (1)	150	30–60	>720	[96]
Indium Oxide-Ni ²⁺		250	30–60	<180	
Indium Oxide	NO ₂ (1)	200	<60	900	[44]
Indium Oxide	O ₅ (0.4)	200	60	90	[43]
	NO ₂ (0.4)		60	240	
Indium Oxide-Molybdenum Oxide	O ₅ (0.4)		90	180	
	NO ₂ (0.4)		60	360	
Indium Oxide-Nickel Oxide	CO (500–20,000)	—	<5	15	[42]
Molybdenum Oxide-Titania	O ₂ (120)	330	180	—	[98]
	O ₂ (1000–10,000)		1200	—	
Molybdenum Oxide	O ₂ (1000)	370	60	300	[48]
Molybdenum Oxide-Titanium Oxide (5 at. %)			210	180	
Molybdenum Oxide-Titanium Oxide (25 at. %)			72	180	
Molybdenum Oxide-Titanium Oxide (50 at. %)		320	114	138	
Molybdenum Oxide	O ₂ (1000)	370	66	210	[62]
Molybdenum Oxide-Tungsten Oxide (5 at. %)		—	—	—	
Molybdenum Oxide-Tungsten Oxide (25 at. %)		420	210	240	
Molybdenum Oxide-Tungsten Oxide (50 at. %)			90	150	
Tungsten Oxide			240	240	
Tungsten Oxide-Molybdenum Oxide (5 at. %)			324	360	
Tungsten Oxide-Molybdenum Oxide (25 at. %)			360	180	

conditions is expressed as follows for a straight round pore [89],

$$D_K = 9700r \times (T/M)^{1/2} \quad (13)$$

where r is the pore radius, T the absolute temperature (K) and M the molecular weight of the gas. As the gas molecules diffuse into the film, they react with the adsorbed oxygen ions (O⁻) on the way. This process is expressed by the following transport equation:

$$\partial C_A / \partial t = D_K (\partial^2 C_A / \partial x^2) - k C_A \quad (14)$$

where x is the distance from the film surface, C_A the concentration of an inflammable gas at x , and k the rate constant

of the surface reaction. When the steady state is reached, C_A no longer changes with time:

$$D_K (\partial^2 C_A / \partial x^2) - k C_A = 0 \quad (15)$$

The concentration profile of the reducing gas molecules (A) can be obtained by solving this equation. Two boundary conditions are required to determine the two integration constants involved. These are $C_A = C_{A,S}$ at $x = 0$ and $x = 2L$. Under these boundary conditions, Eq. (10) can be solved to give

$$C_A = C_{A,S} \left[\frac{\sinh(x(k/D_K)^{1/2}) + \sinh((2L-x)(k/D_K)^{1/2})}{\sinh(2L(k/D_K)^{1/2})} \right] \quad (16)$$

Figure 19 is a generalized profile, which gives the relations between $C_A/C_{A,S}$ and x/l for changing $l(k/D_K)^{1/2}$ as a parameter. It is clearly observed that for fixed k/D_K , the flat profile is exhibited by thin films (low $l(k/D_K)$). On the other hand, for thick films (high $l(k/D_K)$), the concentration of the gas molecules within the film is restricted to the near surface region. As the gas molecules are likely to diffuse throughout the film thickness, thin films exhibit large sensitivity relative to thick films. For a given film thickness, large pore radius would increase the Knudsen diffusion coefficient, and hence, would favor the flat concentration profile, thus enhancing the gas sensitivity. Figure 20 shows the effect of the amount of porosity on the gas sensitivity of the sol-gel derived nanocrystalline SnO₂ thin films [8, 12]. It is observed that the increased amount of porosity within the thin films also increases the gas sensitivity, which is in accordance with the above model.

Further, the molecular weight of the gas molecules also tends to affect the Knudsen diffusion coefficient, Eq. (8). Hence, the gases having lower molecular weight, such as H₂, are likely to exhibit higher sensitivity than those having higher molecular weight (for example, CO, NO, and CH₃OH). In Figure 21 [5, 9, 21, 22], the maximum sensitivity reported for these gases is plotted as a function of their molecular weights. Decrease in the maximum gas sensitivity with increasing molecular weight is evident in Figure 21, which also supports the prediction of the above model.

The effect of operating temperature on the response and recovery time, for the sol-gel derived nanocrystalline SnO₂ thin-film sensor, is shown in Figures 22 [5, 8, 9, 12, 13, 18, 21] and 23 [5, 9, 12, 18, 21], respectively. It is observed that both the response and recovery time decrease with increasing operating temperature and this behavior is primarily attributed to the reduced activation energy for the involved chemical reactions at higher operating temperatures. In agreement with this, the recovery time is observed to increase with increasing response time, Figure 24.

5.3. Other Major Issues

Following are the major issues associated with the sol-gel derived nanocrystalline SnO₂ thin-film sensor, which need to be yet resolved: (i) very low stability of SnO₂ nanocrystals during operation at elevated temperature, (ii) poor selectivity of the sol-gel derived nanocrystalline SnO₂ thin-film sensor towards specific gas, and (iii) lower sensitivity and higher response and recovery time at lower operating temperatures, specifically at room temperature.

6. OTHER SEMICONDUCTOR OXIDES

The results of the other sol-gel derived semiconductor oxide thin films are summarized in Table 1. It is to be noted that much attention has been given towards the sol-gel synthesis of SnO₂ thin films as a gas sensor relative to the other semiconductor oxides listed in Table 1. The limited data currently available in the literature for other oxides, however, do suggest that the gas sensing characteristics of these

oxides are similar to those exhibited by SnO₂ as discussed in detail earlier. Further improvement in the gas sensing properties of these semiconductor oxides, using sol-gel technique, needs extensive research in near future.

7. CONCLUSIONS

Sol-gel is an extremely versatile technique to produce the nanocrystalline semiconductor oxide gas sensors. These characteristics may open many possibilities for wide development of gas sensors that are based on the sol-gel processing and that can be market competitive with the existing technologies and materials. Although the sol-gel technique has been associated with some disadvantages, the large number of advantages associated with it is continuously providing greater impetus for an advanced research to utilize this technique for the development of novel materials for novel applications.

GLOSSARY

Activation energy Describes the amount of energy required for a given thermodynamical process.

Condensation A chemical reaction, which involves elimination of water as a product.

Dip-coating A thin film deposition process using sol-gel precursors, which involves dipping the substrate vertically into the solution (or sol) and then withdrawing it with definite speed under controlled atmosphere.

Hydrolysis A chemical reaction, which involves the reaction between metal alkoxide and water.

Nanocrystalline Tiny crystalline particles of size in the nanometer range. (1 nm = 10⁻⁹ m).

Precursor A starting chemical for a conducting a given chemical reaction.

Receptor function It is related to the ability of the sensor surface to chemically react with the gas to be detected.

Recovery time It is the total time taken by the thin film sensor element to regain its 90% of its original electrical resistance in air, when the surrounding controlled atmosphere containing the reducing gas is replaced by pure air.

Response time It is the total time taken by the thin film sensor element to reduce its electrical resistance, in the presence of a reducing gas, by 90% of its original resistance in air.

Sensitivity It is defined as the ratio of the electrical resistance of the thin film sensor element in the presence of air to that in the presence of the atmosphere containing the reducing gas.

Sol-gel Wet chemical process involving the hydrolysis and the condensation reactions as a result of chemical reaction between water and metal alkoxide in an alcoholic solvent.

Space charge layer Electron depletion region formed on the surface of semiconductor oxide particle as result of chemisorption of the oxygen-ions (O₂⁻ and O⁻ ions).

Spin-coating A thin film deposition process using sol-gel precursors, which involves dropping few drops of the sol on the substrate surface, which is subsequently rotated along

the vertical axis with definite speed for specific amount of time to form a thin film adherent to the substrate surface.

Transducer function It is related to the ability of the sensor element to conduct the electrons generated due to the chemical reaction between the sensor surface and the reducing gas to be detected.

ACKNOWLEDGMENTS

Authors would like to thank Mechanical, Materials and Aerospace Engineering Department and Advanced Materials Analysis and Processing Center (AMPAC) at University of Central Florida, Orlando for continued support. Sudipta Seal is thankful to National Science Foundation, Office of Naval Research through the Young Investigator Award (ONR-YIP 2002), Florida High Tech Corridor, NASA-Glenn, Florida Space Grant Consortium, Siemens Westinghouse, Energy Strategy Associates, USNR Coal Resources, *psiloQuest*, US Filter, Pratt and Whitney, Lucent Technologies, for supporting his research activities in nanomaterials processing.

REFERENCES

1. C. J. Brinker and G. W. Scherrer, "Sol-Gel Science: The Physics and Chemistry of Sol-Gel Processing." Academic Press, San Diego, 1990.
2. L. Klein, "Sol-Gel Technology for Thin Films, Fibers, Preforms, Electronics, and Speciality Shapes, Part II." Park Ridge, New Jersey, 1988.
3. D. E. Bornside, C. W. Macosko, and L. E. Scriven, *J. Imaging Tech.* 13, 122 (1987).
4. C. J. Brinker, A. J. Hurd, P. R. Schunk, G. C. Frye, and C. S. Ashley, *J. Non-Cryst. Solids* 147–148, 424 (1992).
5. R. Rella, A. Serra, P. Siciliano, L. Vasanelli, G. De, A. Licciulli, and A. Quirini, *Sensors and Actuators B* 44, 462 (1997).
6. M. S. Selim, *Sensors and Actuators B* 84, 76 (2000).
7. J. P. Chatelon, C. Terrier, and J. A. Roger, *J. Sol-Gel Sci. Technol.* 10, 55 (1997).
8. S.-S. Park and J. D. Mackenzie, *Thin Solid Films* 274, 154 (1996).
9. Z. Jin, H.-J. Zhou, Z.-L. Jin, R. F. Savinell, and C.-C. Liu, *Sensors and Actuators B* 52, 188 (1998).
10. C. Terrier, J. P. Chatelon, and J. A. Roger, *J. Sol-Gel Sci. Technol.* 10, 75 (1997).
11. J. P. Chatelon, C. Terrier, and J. A. Roger, *J. Sol-Gel Sci. Technol.* 10, 185 (1997).
12. V. Jayaraman, K. I. Gnanasekar, E. Prabhu, T. Gnanasekaran, and G. Periaswami, *Sensors and Actuators B* 55, 147 (1999).
13. G. De, A. Licciulli, C. Massaro, A. Quirini, R. Rells, P. Siciliano, and L. Vasanelli, *Sensors and Actuators B* 55, 134 (1999).
14. A. Licciulli and S. Mazzarelli, *J. Sol-Gel Sci. Technol.* 21, 195 (2001).
15. F. Quaranta, R. Rella, P. Siciliano, S. Capone, C. Distanto, M. Epifani, and A. Taurino, *Sensors and Actuators B* 84, 55 (2002).
16. N. S. Baik, G. Sakai, N. Miura, and N. Yamazoe, *Sensors and Actuators B* 63, 74 (2000).
17. F. Quaranta, R. Rella, P. Siciliano, S. Capone, M. Epifani, L. Vasanelli, A. Licciulli, and A. Zocco, *Sensors and Actuators B* 58, 350 (1999).
18. R. Rella, P. Siciliano, S. Capone, M. Epifani, L. Vasanelli, and A. Licciulli, *Sensors and Actuators B* 58, 283 (1999).
19. A. Dieguez, A. Romano-Rodriguez, J. L. Alay, J. R. Morante, N. Barsan, J. Kappler, U. Weimar, and W. Gopel, *Sensors and Actuators B* 65, 166 (2000).
20. A. Dieguez, A. Vila, A. Cabot, A. R. Rodriguez, J. R. Morante, J. Kappler, N. Barsan, U. Weimar, and W. Gopel, *Sensors and Actuators B* 68, 94 (2000).
21. J. W. Hammond and C.-C. Liu, *Sensors and Actuators B* 81, 25 (2001).
22. G. Zhang and M. Liu, *Sensors and Actuators B* 69, 144 (2000).
23. P. Siciliano, *Sensors and Actuators B* 70, 153 (2000).
24. S. Capone, P. Siciliano, F. Quaranta, R. Rella, M. Epifani, and L. Vasanelli, *Sensors and Actuators B* 69, 230 (2000).
25. A. Cabot, J. Arbiol, J. R. Morante, U. Weimar, N. Barsan, and W. Gopel, *Sensors and Actuators B* 70, 87 (2000).
26. Z. Jin, H.-J. Zhou, Z.-L. Jin, R. F. Savinell, and C.-C. Liu, *Sensors and Actuators B* 52, 188 (1998).
27. A. Chiorino, G. Ghiotti, F. Prinetto, M. C. Carotta, D. Gnani, and G. Martinelli, *Sensors and Actuators B* 58, 338 (1999).
28. A. Chiorino, G. Ghiotti, M. C. Carotta, M. Gallana, and G. Martinelli, *Sensors and Actuators B* 59, 203 (1999).
29. S. Capone, M. Epifani, F. Quaranta, P. Siciliano, and L. Vasanelli, *Thin Solid Films* 391, 314 (2001).
30. S. Capone, P. Siciliano, F. Quaranta, R. Rella, M. Epifani, and L. Vasanelli, *Sensors and Actuators B* 77, 503 (2001).
31. C. Cobianu, C. Savaniu, P. Siciliano, S. Capone, M. Utriainen, and L. Niinisto, *Sensors and Actuators B* 77, 496 (2001).
32. C. Cobianu, C. Savaniu, O. Buiu, D. Dascalu, M. Zaharescu, C. Parlog, A. V. D. Berg, and B. Pecz, *Sensors and Actuators B* 43, 114 (1997).
33. A. Cabot, A. Vila, and J. R. Morante, *Sensors and Actuators B* 84, 12 (2002).
34. A. Wilson, J. Wright, J. Murphy, M. A. M. Stroud, and S. C. Thorpe, *Sensors and Actuators B* 18–19, 506 (1994).
35. J. C. Giuntini, W. Granier, J. V. Zanchetta, and A. Taha, *J. Mater. Sci. Lett.* 9, 1383 (1990).
36. M. Ando, S. Suto, T. Suzuki, T. Tsuchida, C. Nakayama, N. Miura, and N. Yamazoe, *J. Mater. Chem.* 4, 631 (1994).
37. D. J. Yoo, J. Tamaki, S. J. Park, N. Miura, and N. Yamazoe, *J. Electrochem. Soc.* 142, L105 (1995).
38. R. Lalauze, E. Visconte, L. Montanaro, and L. Pijolat, *Sensors and Actuators B* 13, 241 (1993).
39. H.-T. Sun, C. Cantalini, M. Faccio, and M. Pelino, *Thin Solid Films* 269, 97 (1995).
40. S. Tao, F. Gao, X. Liu, and O. T. Sorensen, *Mater. Sci. Eng. B* 77, 172 (2000).
41. B.-F. Quan, F.-M. Liu, A.-W. Li, and L.-H. Chen, *J. Funct. Mater.* 32, 407 (2001).
42. M. Ivanovskaya and P. Bogdanov, *Sensors and Actuators B* 53, 44 (1998).
43. M. Ivanovskaya, A. Gurlo, and P. Bogdanov, *Sensors and Actuators B* 77, 264 (2001).
44. A. Gurlo, M. Ivanovskaya, N. Barsan, M. Schweizer-Berberich, U. Weimar, W. Gopel, and A. Dieguez, *Sensors and Actuators B* 44, 327 (1997).
45. G. Vaivars, J. Kleperis, J. Zubkans, G. Vitins, G. Liberts, and A. Lasis, "International Conference on Solid-State Sensors and Actuators, and Eurosensors IX, Proceedings, IEEE," 1995, Vol. 1, p. 870.
46. P. Mishra, B. L. Yadav, S. K. Shukla, G. K. Parashar, R. K. Shukla, L. M. Bali, and G. C. Dubey, *Proc. SPIE* 4746 II, 1203 (2002).
47. Y. Li, M. K. Ghantasala, K. Galatsis, and W. Wlodarski, *Proc. SPIE* 3892, 364 (1999).
48. K. Galatsis, Y. X. Li, W. Wlodarski, E. Comini, G. Faglia, and G. Sberveglieri, *Sensors and Actuators B* 77, 472 (2001).
49. K. Galatsis, Y. X. Li, W. Wlodarski, E. Comini, G. Faglia, and G. Sberveglieri, "Conference Record—IEEE Instrumentation and Measurement Technology Conference," 2001, Vol. 1, p. 425.
50. R. Ochoa and R. Miranda, in "Better Ceramics Through Chemistry VI, Materials Research Society Symposium Proceedings," 1994, Vol. 346, p. 553.

51. A. K. McEvoy, C. M. McDonagh, and B. D. MacCraith, *Proc. SPIE* 2508, 190 (1995).
52. J. Lin, S. Moeller, and E. Obermier, *Sensors and Actuators B* 5, 219 (1991).
53. M. Z. Atashbar, H. T. Sun, B. Gong, W. Wlodarski, and R. Lamb, *Thin Solid Films* 326, 238 (1998).
54. E. Comini, G. Faglia, G. Sberveglieri, M. Z. Atashbar, and W. Wlodarski, "Conference on Optoelectronic and Microelectronic Materials and Devices, Proceedings, COMMAD" 1999, p. 302.
55. C. Garzella, E. Comini, E. Tempesti, C. Frigeri, and G. Sberveglieri, *Sensors and Actuators B* 68, 189 (2000).
56. G. S. Devi, T. Hyodo, Y. Shimizu, and M. Egashira, *Sensors and Actuators B* 87, 122 (2002).
57. E. Traversa, *J. Intell. Mater. Syst. Struct.* 6, 860 (1995).
58. Y. X. Li, W. Wlodarski, E. Comini, G. Sberveglieri, C. Cantalini, S. Santucci, M. Passacantando, and K. Galatsis, *Sensors and Actuators B* 83, 276 (2002).
59. W. Zhu, O. K. Tan, Q. Yan, and J. T. Oh, *Sensors and Actuators B* 65, 366 (2000).
60. W. Zhu, J. Deng, O. K. Tan, and X. Chen, *Key Eng. Mater.* 214–215, 183 (2002).
61. J. Deng, W. Zhu, O. K. Tan, and X. Yao, *Sensors and Actuators B* 77, 416 (2001).
62. K. Galatsis, Y. X. Li, W. Wlodarski, and K. Kalantar-Zadeh, *Sensors and Actuators B* 77, 478 (2001).
63. G. Tan, J. Wu, and X. Wu, *J. Mater. Sci. Technol.* 13, 302 (1997).
64. Z. Peng, M. Liu, and E. Balko, *Sensors and Actuators B* 72, 35 (2001).
65. M. A. Villegas, *Thin Solid Films* 382, 124 (2001).
66. A. D. Brailsford, M. Yussouff, and E. M. Logothetis, *Sensors and Actuators B* 44, 321 (1997).
67. G.-L. Tan and X.-J. Wu, *Thin Solid Films* 330, 59 (1998).
68. E. Llobet, X. Vilanova, J. Brezmes, R. Alcubilla, J. Calderer, J. Sueiras, and X. Correig, *Meas. Sci. Technol.* 8, 1133 (1997).
69. K. Nomura, H. Shiozawa, T. Takada, H. Reuther, and E. Richter, *J. Mater. Sci. Mater. Electron.* 8, 301 (1997).
70. S. S. Park and J. D. Mackenzie, *Thin Solid Films* 258, 268 (1995).
71. J. R. Brown, M. T. Cheney, P. W. Haycock, D. J. Houlton, A. C. Jones, and E. W. Williams, *J. Electrochem. Soc.* 144, 295 (1997).
72. K. D. Schierbaum, U. Weimar, and W. Gopel, *Sensors and Actuators B* 7, 709 (1992).
73. U. Dibbern, *Sensors and Actuators B* 2, 63 (1990).
74. Y. Takahashi and Y. Wada, *J. Electrochem. Soc.* 137, 267 (1990).
75. K. Takahata, in "Chemical Sensor Technology" (T. Seiyama, Ed.), Vol. 1, p. 39. Kodansha, Tokyo, 1988.
76. P. Mulvaney, F. Grieser, and D. Meisel, *Langmuir* 6, 567 (1990).
77. S. Shukla, S. Patil, S. C. Kuiry, S. Seal, Z. Rahman, L. Ludwig, and C. Parish, *Sensors and Actuators*, to be published.
78. N.-L. Wu, S.-Y. Wang, and I. A. Rusakova, *Science* 285, 1375 (1999).
79. J. F. Moulder, W. F. Stickle, P. E. Sobol, and K. D. Bomben, in "Handbook of Photoelectron Spectroscopy: A Reference Handbook of Standard Spectra Identification and Interpretation of XPS Data" (J. Chastain, Ed.). Perkin-Elmer Corp. Physical Electronics Division, Minnesota, .
80. S. P. Lee, *Sensors and Actuators B* 15–16, 379 (1993).
81. X.-D. Zhou and W. Hueber, *Appl. Phys. Lett.* 79, 3512 (2001).
82. Y. Shimizu and M. Shigara, *MRS Bull.* 18 (1998).
83. C. Xu, J. Tamaki, N. Miura, and N. Yamazoe, *Sensors and Actuators B* 3, 147 (1991).
84. S. Seal and S. Shukla, *JOM* 54, 35 (2002).
85. C. Xu, J. Tamaki, N. Miura, and N. Yamazoe, *J. Electrochem. Soc. Jpn.* 58, 1143 (1990).
86. H. Ogawa, M. Nishikawa, and A. Abe, *J. Appl. Phys.* 53, 4448 (1982).
87. H. Winddishmann and P. Mark, *J. Electrochem. Soc.* 126, 627 (1979).
88. G. Sakai, N. S. Baik, N. Miura, and N. Yamazoe, *Sensors and Actuators B* 77, 116 (2001).
89. C. N. Satterfield, "Mass Transfer in Heterogeneous Catalysts." MIT Press, Cambridge, MA, 1970.
90. M. Li and Y. Chen, *Sensors and Actuators B* 32, 83 (1996).
91. L. Gao, Q. Li, Z. Song, and J. Wang, *Sensors and Actuators B* 71, 179 (2000).
92. G. Gusmano, G. Montesperelli, P. Nunziante, E. Traversa, A. Montenero, M. Braghini, G. Mattogno, and A. Bearzotti, *J. Ceram. Soc. Jpn. Int. Ed.* 101, 1066 (1993).
93. V. Romanovskaya, M. Ivanovskaya, and P. Bogdanov, *Sensors and Actuators B* 56, 31 (1999).
94. M. Epifani, S. Capone, R. Rella, P. Siciliano, and L. Vasanelli, *J. Sol-Gel Sci. Technol.* 26, 741 (2003).
95. M. Ivanovskaya, P. Bogdanov, G. Faglia, and G. Sberveglieri, *Sensors and Actuators B* 68, 344 (2000).
96. P. Bogdanov, M. Ivanovskaya, E. Comini, G. Faglia, and G. Sberveglieri, *Sensors and Actuators B* 57, 153 (1999).
97. A. Gurlo, M. Ivanovskaya, A. Pfau, U. Weimar, and W. Gopel, *Thin Solid Films* 307, 288 (1997).
98. Y. Li, K. Galatsis, W. Wlodarski, M. Ghantasala, S. Santucci, and M. Passacantando, *J. Vac. Sci. Technol. A* 19, 904 (2001).

Solid Lipid Nanoparticles and Nanostructured Lipid Carriers

R. H. Müller, M. Radtke, S. A. Wissing

Free University of Berlin, Berlin, Germany

CONTENTS

1. Introduction
 2. Solid Lipid Nanoparticles
 3. Structural Features of Nanostructured Lipid Carriers (NLCs)
 4. Production Technology
 5. *In Vitro* Tolerability
 6. *In Vivo* Tolerability
 7. Drug Release and *In Vivo* Degradation
 8. Applications and Final Dosage Forms
 9. Cosmetic Applications
 10. Summary
- Glossary
References

1. INTRODUCTION

Nanoparticulate drug carriers in their broadest sense are currently under intensive investigation. Under development are liposomes, oil-in-water (o/w) emulsions, and solid nanoparticles made from polymers or natural or synthetic macromolecules. The use of parenteral o/w emulsions for parenteral nutrition started in the middle of the 1950s; about one decade later, interest started focusing on their use for intravenous drug delivery. Nowadays, drug-loaded intravenous emulsions are established as a carrier system on the market. However, there are only a very limited number of active compounds incorporated in these systems (diazepam, etomidate, and propofol), also resulting in a low number of market products. One of the reasons for this is that the solubility of poorly water-soluble drugs that are of commercial interest is too low in the currently available registered oils (e.g., soya oil, MCT). Potential sales figures do not justify the investment for performing extensive toxicity studies for new oil excipients.

Up to now, a reasonable number of liposomal products have appeared on the market; a decent number is in the

clinical phases. However, the number of products is still far behind the expectations from the 1980s and 1990s of the last century. The reasons for this are manifold; examples are physical stability problems and the high cost of liposomes. Products such as Amphotericin liposomes need to be lyophilized for long-term storage; a tedious reconstitution procedure is necessary (e.g., Ambisome). There are no “cheap” liposomes available; the high costs are a large obstacle for the broad introduction of these carriers to the market. For example, the costs of daily treatment with the product Fungizone are only \$24 a day, and treatment with Amphotericin liposomes as a product is about \$1300 a day [1].

Almost 30 years of intensive research have been invested in nanoparticles since their development by Speiser et al. in the middle of the 1970s. Many review and research articles have reported the benefits of these systems for controlled drug delivery; however, as market products, they are practically nonexistent. Again, the problems are manifold. There is a lack of regulatorily accepted polymers; newly synthesized polymers have many nice features, but require expensive toxicity studies before acceptance by the regulatory authorities. Even polymers regulatorily accepted for use as implants can show cytotoxic effects when delivered as nanoparticles or very small microparticles [2]. Other problems are also the cost of production, especially the lack of large-scale production methods able to be qualified, validated, and leading to a product being acceptable to the regulatory authorities. There are interesting data in academic research; however, there is a lack of concepts to transfer these successes to the industrial scale, and finally to products with benefit for the patient.

To summarize, there is still a definite need for a nanoparticulate carrier system possessing the benefits of the above-mentioned “traditional” carriers, but simultaneously avoiding their major disadvantages. The first concept to realize a really versatile carrier was the development of solid lipid nanoparticles (SLNs) [3, 4]. The SLNs are nanoparticles; the matrix is composed of a lipid that is solid at room temperature, but also at body temperature. One can simply derive the SLNs from o/w emulsions by replacing the

liquid lipid (oil) by a solid lipid. They possess the advantages of the different traditional nanoparticulate carriers. Similar to emulsions and liposomes, they are composed of well-tolerated, accepted excipients, and can be produced on a large industrial scale by a simple high-pressure homogenization process. For topical delivery of SLNs, the full range of excipients in cosmetic and pharmaceutical topical products can be exploited. For oral SLNs, all lipids and surfactants used for tablets, capsules, and other oral products such as microemulsions can be used. For parenteral administration, the lipid matrix can be produced from glycerides that are composed of fatty acids contained in the glycerides of emulsions for parenteral nutrition. Existing production lines for parenteral emulsions can be used to produce SLN dispersions.

A major disadvantage of emulsions and liposomes is the lack of protection for chemically labile drugs; in addition, drug release takes place as a burst (emulsions) or at least relatively fast (from liposomes). In contrast to this, SLNs possess a solid lipid matrix identical to nanoparticles from polymers and macromolecules. The solid matrix slows down drug release; SLNs have many more possibilities of modulating the release [5]. To summarize, SLNs definitely possess major advantages over the existing previous carriers; simultaneously, they also avoid some of their major disadvantages. Another major advantage of SLNs is that they are “low-cost” products. Excipients and production lines are relatively inexpensive, and production costs are not that much higher compared to a parenteral emulsion.

The first patents for SLNs were filed in 1991, one by Müller and Lucks [3] describing the production of SLNs by high-pressure homogenization, and another by Gasco [4] describing the production via microemulsions. Generally, for the high-pressure homogenization technique, the drug is dissolved in the melted lipid, the drug-containing lipid melt is dispersed in a hot surfactant solution by stirring, and the obtained preemulsion is homogenized at a temperature about 5 °C above the melting point of the lipid. The obtained hot o/w nanoemulsion is cooled, the lipid recrystallizes, and forms SLNs. The microemulsion technique involves the formation of a hot microemulsion based on the melted lipid. The drug-containing microemulsion is then poured into cold water, and SLNs are precipitated. The new carrier system attracted much attention, as is clearly indicated by the number of research groups; an overview is given in the first SLN review published in 1995 [6]. The success continued within the first decade of SLN research, clearly evident from the latest two SLN reviews published in 2000 [7] and 2001 [8].

However, the SLNs were the first generation of a solid lipid nanoparticulate carrier. They can be considered as a solid development with interesting applications; however, there was still some room for improvements, which were realized in the next generation, the so-called nanostructured lipid carriers (NLCs) [9]. The basic difference is that, in the NLC concept, controlled nanostructuring of the lipid matrix is performed to increase drug load, physical stability, to give more flexibility in the modulation of drug release, and also to provide an improved, smarter production technology.

This chapter describes the features of the novel NLCs, and highlights the improvements compared to the first-generation SLNs.

2. SOLID LIPID NANOPARTICLES

2.1. Definition

Solid lipid nanoparticles are particles with a mean average size in the nanometer range, which means approximately 50–1000 nm, being composed of a lipid matrix material that is solid at room temperature, but also at body temperature. Originally, the term “solid lipid nanoparticles” and the abbreviation “SLNs” were introduced by Müller and Lucks, the inventors of the patent describing the production of SLNs by high-pressure homogenization [3]. Then this name was also transferred to lipid nanoparticles with a solid matrix, but being produced by using microemulsions, a technique developed by Gasco in Turin [4]. Meanwhile, the term SLNs is used for all lipid nanoparticles with a solid matrix, independent of the method of production. This includes particles being produced by solvent evaporation, precipitation, or phase inversion methods.

Strictly speaking, by definition, nanoparticles are particles with a mean diameter in the nanometer range, that is, below 1000 nm. Microparticles are defined to be in the micrometer range, that is, having a minimum size of 1 μm , and going up to a few hundred micrometers. The upper size limit of microparticles is not unanimously defined. Based on the word “micro”particle, one could define an upper size limit of 1000 μm , that is, 1 mm. However, such large particles might be better described as pellets, and so on. Based on this, larger lipid particles were introduced to the literature as solid lipid microparticles (SLMs) [10]. There is a range of different techniques to produce SLMs, ranging from high-speed stirring techniques to static blenders, and recently, the so-called micromixers [11].

2.2. Production Technologies of SLNs

Looking back at the historic development, the first lipid particles with a solid matrix were produced by the research group of Speiser from Zurich [12], the father of nanoparticles (J. Paris Match). Melted lipid was dispersed in a hot surfactant solution, applying, for example, high-speed stirring. The obtained emulsion was then cooled; the lipid formed solid particles. The disadvantages of stirring techniques in general are the relatively broad size distribution, in addition to the relatively high concentrations of surfactants required to obtain a mean particle diameter in the nanometer range. The product was called “lipid nanopellets,” and intended for oral delivery. A similar process was developed and patented by Domb; particle dispersions were produced, for example, by sonication. He called his system “lipospheres” [13]. The patent by Speiser was not followed up by the owner, Rentschler, in a number of countries where patent protection no longer exists. The lipospheres also found no broad application in pharmaceutical products.

The start of “SLN history” can be seen in 1991, the year in which the patent applications were submitted describing particle production either by high-pressure homogenization or, alternatively, via the microemulsion technique.

High-pressure homogenization is a technique broadly used in different areas; it is also established in pharmaceutical production, for example, for the production of emulsions for parenteral nutrition (Intralipid, Lipofundin). Using this technique overcomes the problem of other nanoparticles, which means the lack of scaling up and large-scale production lines. In addition, the technology leads to a product being relatively homogeneous in size, that is, possessing higher physical stability of the aqueous dispersion (in general, polydisperse dispersions show a greater tendency to aggregate or coalesce). Briefly, the lipid is melted, dispersed by high-speed stirring in a hot surfactant solution of identical temperature, and then the obtained preemulsion is passed through a high-pressure homogenizer (cf. details in Section 4). For the production of SLNs by the microemulsion technique, the matrix lipid is melted, and a surfactant and cosurfactant and water are added in such concentrations that a microemulsion results [14]. The size of the microemulsion region in the phase diagram is a function of temperature, which means that a microemulsion can convert to a different system when, for example, reducing the temperature. Therefore, for particle production, the microemulsion needs to be kept at an elevated temperature during the process. For particle formation, the hot microemulsion is poured into cold water. This leads to a “breaking” of the microemulsion; it converts to an ultrafine nanoemulsion. Reasons for the breaking of the emulsion are the dilution with water and the reduction in temperature, narrowing the microemulsion region. A typical microemulsion composition is 10–15% lipid, 15–25% surfactant, 2–10% cosurfactant, and 73–50% water [15]. A disadvantage of the microemulsion method is the dilution of the particle suspension by water; typically, the concentrations are distinctly below 1% particle content. In the case of processing to a final dosage form, a very large amount of water needs to be removed, which is inconvenient.

Other approaches to produce SLNs should be only briefly mentioned, for example, the solvent evaporation method. This is a method analogous to the production of polymeric nanoparticles and microparticles by solvent evaporation. The lipid is dissolved in an organic solvent which shows little or no miscibility with water (e.g., chloroform or methylene chloride). The organic solution is dispersed in an aqueous surfactant phase, and the solvent is then removed by evaporation [16].

Alternatively, a solvent can be used which is miscible with water. The solvent is saturated with water, and the water phase is saturated with solvent. Then the water-saturated organic phase is used to dissolve the lipid; after this, an o/w emulsion is prepared. Due to the saturation of the water phase with the organic solvent, no solvent diffuses from the droplets into the water phase. Removal of solvent from the droplets and particle formation is obtained by adding additional water to the emulsion, and extracting the solvent by this [17].

A very interesting approach from the physics end is the separation method, developed by the research group of Benoit. This method is a two-step method. First, all components were placed on a magnetic stirrer using a temperature program from room temperature to, for example, 85 °C. This was followed by progressive cooling to 60 °C.

Three temperature cycles (85–60–85–60–85 °C) were applied to reach the inversion process defined by the temperature range. In step 2, an irreversible shock was induced by dilution with cold water. This fast cooling–diluting process leads to the formation of stable nanoparticles [18].

2.3. Structure of the Lipid Matrix

A range of very different lipids has been used to produce SLNs ranging from highly purified lipids, for example, tristearin [19], to mixtures of mono-, di-, and triglycerides, including monoacid glycerides, but also polyacid glycerides. In general, a melting-point depression is observed when transforming the bulk lipid to nanoparticulate form. This melting-point depression is described in the Thomson equation, which itself is derived from the Kelvin equation [20]:

$$\ln \frac{T}{T_0} = \frac{2\gamma V_s}{r\Delta H}$$

T represents the melting point of the nanocrystal, and it is always smaller than T_0 , the melting point of the bulk material. The molar volume of the substance is characterized by V_s , r is the radius, ΔH is the molar melting enthalpy, and γ is the interfacial energy of the crystal.

An additional melting-point depression occurs when a foreign compound is dissolved in the lipid matrix, for example, a surfactant will partition from the water phase to the lipid phase; drug-loaded SLNs show a melting-point depression in case the molecular-dispersed drug is present.

It is well known from lipids that the melting point and recrystallization point can be different, especially in the case of chemically polydisperse lipids. When producing SLNs, the difference can easily be 10–20 K or more. It is known that some lipids such as Dynasan 112 (trilaurin) show a very pronounced supercooling when producing SLNs. Crystallization does not take place anymore at room temperature; it can only be induced when cooling down to a freezing temperature (original melting point of lipid: 43–47 °C) [21].

Lipids show as polymorph forms α -, β' -, and as the most stable modification β . In the case of polylipidglycerides, a transition occurs from β' to β_i , and then to β , which means that another intermediate polymorph form is present. Most bulk lipids are obtained in β modification, or at least predominantly in β modification. In many cases, the production of SLNs leads to a change in the relative fraction of the polymorphic forms. Depending on the chemical nature of the lipid and the production conditions, different fractions of α and β' modification are obtained. On the one hand, this can lead again to a reduction of the melting point, or more precisely, a change in the form and shift of the melting peak. On the other hand, it might be that the created polymorph forms are not long-term stable, which means that there is a gradual transform to more stable modifications, and hence, an increasing content of β'/β_i , and finally β . Of course, this is not desired, because the change in lipid structure can cause:

1. drug expulsion during storage, and
2. a change in the release profile of the incorporated drug.

To avoid such undesired effects, lipid mixtures should be chosen which transform relatively quickly to more stable modifications directly after particle production (i.e., within 1–3 days). It is also perfectly acceptable or can even be exploited to trigger drug release when the generated fractions of the different polymorphic forms remain unchanged during storage, and do not transform back to the β modification of the bulk lipid.

Drug expulsion from lipid matrices is a very well-known phenomenon from suppositories for many years [22]. There are a number of different possibilities as to how drugs can be incorporated in the lipid particle matrix. In general, when a crystal is formed, foreign molecules can be incorporated:

1. by replacing host molecules in the lattice by a guest molecule, or
2. by being incorporated in between host molecules (however, for this, the guest molecule needs to be less than 20% in size of the host molecule) [23].

In addition, drugs can be localized in between the lipid lamellae, which then results in an increase of the lattice spacing d , detectable by WAXS investigations [24]. There is also the possibility that the drug is present in the form of amorphous clusters, mainly localized in the imperfections of the crystal. In general, drug accommodation is improved the more imperfections are present in the lipid crystals. This was very nicely demonstrated by Westesen et al. when producing SLNs from highly purified tripalmitate. Drug expulsion occurred immediately after production [25]. Drug loading can be increased by using rather crude lipid mixtures, for example, as being used in cosmetic preparations. An even further improved drug loading can be achieved by controlled nanostructuring of the lipid matrix, that is, creating as many imperfections as possible (cf. Section 3). Depending on the nature of the lipids used for blending the lipid matrix, different types of nanostructured lipid carriers will be obtained.

To sum up, the crystalline nature of the lipid matrix is the dominant factor determining drug loading, type of release profile, and also long-term stability of the particles regarding drug release, and subsequently, bioavailability. Therefore, the crystalline status needs to be closely monitored when developing drug formulation. Routine methods are differential scanning calorimetry (DSC) and wide-angle X-ray (WAXS) and small-angle X-ray (SAXS). WAXS provides information on the distance between the fatty acid chains of the glycerides, and as a consequence, on the lipid modification. SAXS provides information on the distance between two methyl end groups being in comparable positions in the crystal lattice. From this information, the distance between the lipid layers can be derived.

It was found that the crystalline status is also related to the physical stability of SLN dispersions, which means the absence or induction of particle aggregation, and finally, gel formation. It was observed that particle aggregation was accompanied simultaneously by a transform of high energetic polymorphic forms (i.e., mainly α) to more stable lipid modifications [26]. In general, the next step after particle aggregation is viscosity increase, and the formation of soft, and finally, relatively rigid gels (because the viscosity increase is also a function of the lipid particle concentration). Obviously, the particles form a network; formation of the network is promoted by a transform-induced

change of the particle shape (from more spherical to elongated shapes); prearrangements of the surfactant/surfactant mixtures at the different sides of the elongated particles lead to bridging when the particles get in contact. A very detailed discussion of gel-forming mechanisms can be found in [27–29].

2.4. Drug Incorporation Models and Release

Three different models of how drugs can be incorporated into SLNs have been developed. The first particles produced were characterized by a burst release; a first *in vitro* prolonged release was reported for particles loaded with prednisolone [5]. Basically, three incorporation models are proposed [30]:

1. drug-enriched shell type
2. drug-enriched core type
3. homogeneous matrix of solid solution.

These incorporation models are shown in Figure 1. The type of SLN depends on the chemical nature of the drug and lipid, the solubility of drug in the melted lipid, the nature and concentration of surfactants, the type of production (hot versus cold homogenization), in general from the production temperature.

A drug enrichment in the shell is achieved when SLNs are produced via the hot homogenization technique and the drug concentration in the melted lipid is low. During the cooling process of the hot o/w nanoemulsion, the lipid will precipitate first, leading to a steadily increasing concentration of drug in the remaining lipid melt with an increasing fraction of lipid solidified. A drug-free lipid core is formed when the drug reaches its saturation solubility in the remaining melt; an outer shell will solidify, containing both drug and lipid. The enrichment in the outer area of the particles causes a burst release.

Drug enrichment in the core can take place when the drug concentration in the lipid melt is high and at the (or relatively close to) saturation solubility. Cooling down of the hot oil droplets will, in most cases, reduce the solubility of the drug in the melt; when the saturation solubility is exceeded, the drug precipitates, and leads to the formation of a drug-enriched core.

A solid solution can be obtained when SLNs are produced by the cold homogenization method. A lipid blend can be produced, containing the drug in a molecular disperse form. After solidification of this blend, it is ground in its solid

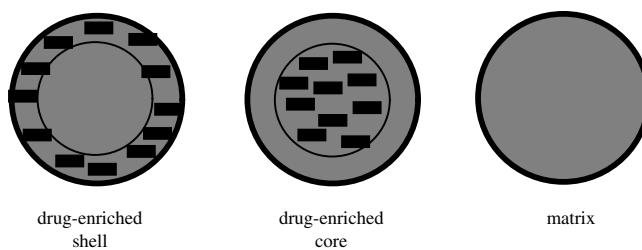


Figure 1. Incorporation models for SLNs. Drug-enriched shell (left), drug-enriched core (middle), and homogeneous matrix (right).

state, thus avoiding or minimizing the enrichment of drugs in different parts of the lipid particle. The percentage of drug localized in the outer shell can be adjusted in a controlled way by altering the production parameters.

Figure 2 shows the redistribution effect occurring during the SLN production by the hot homogenization technique [31]. Dispersing the drug-containing lipid melt in a hot aqueous surfactant solution will lead to a distribution of the drug into the aqueous phase (according to the solubility and partitioning coefficient). If the aqueous phase contains a higher surfactant concentration, in most cases, this leads to a better solubility of the lipophilic drug in the water phase (e.g., by solubilization), and thus, a more pronounced distribution of drug to the water phase. Furthermore, the solubility in the water phase can be further increased by choosing higher production temperatures; thus, even more of the drug will go to the water phase. An opposite effect occurs when the produced hot nanoemulsion is in the cooling process. The solubility in the aqueous phase decreases. Lipids start to precipitate, forming a lipid core with a lower drug concentration than in the original drug-containing lipid melt. Further cooling leads to a further reduction of the drug solubility in the water phase, and redistribution back to the lipid phase; however, due to the formation of the solid lipid core, only the outer shell is accessible for the drug to localize. In general, most of this drug is considered to be released in the form of a burst. This means that the extent of burst can be controlled by controlling the amount of drug in the shell. zur Mühlen and Mehnert [30] could show nicely the dependence of the extent of burst release as a function of production temperature and surfactant concentration. Burst release can be avoided by the cold homogenization technique.

To summarize, the drug-release profile depends on the type/structure of the SLN nanoparticle created. This allows adjustment of the drug-release profile by controlled production of a certain SLN type. Especially for active compounds which should exhibit a prolonged/very little release, the drug-enriched core type is most suitable, for example, molecular sunscreens [32].

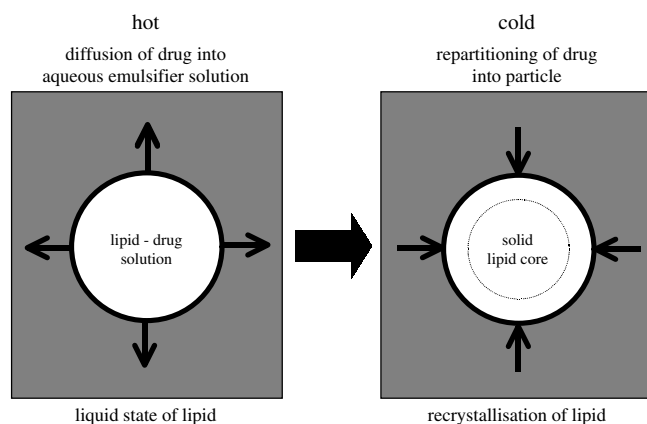


Figure 2. Redistribution effects during the production process of SLNs using the hot homogenization technique. For explanations, see text. Adapted with permission from [31], R. H. Müller et al., *Adv. Drug Del. Rev.* 54, S131 (2002). © 2002, Elsevier.

2.5. Examples of Drugs Incorporated in SLNs

Table 1 gives an overview of the different drugs incorporated in SLNs by different research groups. It is a table taken from [7], which was updated by the latest publications.

To give but a few examples of the effects of the drugs incorporated in SLNs mentioned in Table 1, an increased

Table 1. Drugs incorporated in SLNs by different research groups.

Drug	Corresponding author/research group	Ref.
Oxytetracycline	Domb	[81]
Bupivacaine		[82]
DEET		[83]
Timolol	Gasco	[84, 85]
Deoxycorticosterone		[86]
Idarubicin		[87, 88]
Doxorubicin		[87, 89]
(D-Trp-6)LHRH		[90]
Pilocarpine		[71]
Thymopentin		[91]
Diazepam		[92]
Gadolinium (III) complexes		[93]
Progesterone		[94]
Hydrocortisone		[94]
Tobramycin		[95, 96]
Cyclosporine A		[36]
Paclitaxel		[97]
Retinol	Gohla	[41, 98]
Coenzyme Q10		[38]
Vitamin E palmitate		[99]
DEET	Hekimoglu	[100]
Aciclovir	Lukowski	[101, 102]
Diazepam		[103]
Prednisolone	Mehnert	[5, 30]
Tetracaine		[30, 104]
Etomidate		[30, 104, 105]
Cyclosporine A	Müller	[106]
Sunscreens		[32, 107]
Nimesulide	Patravale	[108]
3'-azido-3'-deoxythymidine palmitate	Phillips	[109, 110]
Azido thymidine palmitate		[111]
Oxazepam	Westesen	[25]
Diazepam		[25]
Cortisone		[25]
Betamethasone valerate		[25]
Prednisolone		[25]
Retinol		[25]
Medadione		[25]
Coenzyme Q10		[25, 112]
Camptothecin	Yang	[34, 35]
Nimodipine		[113]
Piribedil	Yazan	[114]
Cyclosporine A	Zhang	[115]
Paclitaxel		[116]
5-fluorouracil		[117]

uptake in the brain was observed for IV-administered paclitaxel-containing SLNs. Here, the avoidance of capture by liver and spleen macrophages was achieved by the low surface hydrophobicity of the particles. Further, the efficacy of paclitaxel in SLNs was found to be 100-fold greater than free paclitaxel on MCF-7 cells, while on HL60 cells, a lower sensitivity was achieved with paclitaxel in SLNs [33]. It could be shown for camptothecin that an increased uptake was found in the brain [34]. This can be explained by the adsorption of blood proteins such as ApoE which mediates the adherence to the endothelial cells of the blood brain barrier.

Camptothecin is also an example of orally delivered SLN formulations [35]. It was demonstrated that the drug was effectively protected from hydrolysis, and that *in vitro* sustained release was achieved for up to a week. Another example for successful oral drug delivery is cyclosporine A. *In vitro*, a pseudozero order was determined [36]; in an *in vivo* study with pigs, it was found that prolonged release with low variations in the blood levels was possible [37].

For dermal administration, it can be shown that the incorporation of molecular sunscreens leads to improved protection levels due to a decrease in penetration into the skin [32]. This was achieved by producing SLNs with a drug-enriched core. For coenzyme-Q10-containing SLNs, increased skin penetration, and thus increased effects, can be achieved by formulating the drug-enriched shell type. Furthermore, the chemically labile drug can be stabilized by incorporation into the protective solid matrix [38].

3. STRUCTURAL FEATURES OF NANOSTRUCTURED LIPID CARRIERS

SLNs produced by high-pressure homogenization at elevated temperature (hot homogenization technique) are formed during the cooling process of the hot o/w emulsion as mentioned above.

To summarize occurring disadvantages, the immediate formation of a perfect crystal or formation during the long-term storage can cause drug expulsion. To avoid this, a less ordered lipid matrix with many imperfections is desirable for better accommodation of the drug, especially to avoid drug expulsion during storage. This approach was realized in the NLCs.

SLNs are made from solid lipids, in very special cases even highly purified lipids, which means that at least the lipid molecules are relatively similar, allowing the formation of structures with few imperfections. In contrast to this, NLCs are produced from lipid blends made from chemically very different molecules, which means mixing solid lipids with liquid lipids (oils, e.g., MCT). Due to the different chain lengths of the fatty acids and the mixture of mono-, di-, and triglycerides, the matrix is not able to form a highly ordered structure. There are many imperfections which are able to accommodate the drug. NLCs based on this principle are called the “imperfect crystal type” (type I).

The occurrence of crystallization was identified as the basic mechanism leading to drug expulsion. Consequently, one can avoid drug expulsion by avoiding lipid crystallization, which means creating solid particles of an amorphous lipid structure. This can be achieved by mixing special lipids

which no longer recrystallize after homogenization and cooling down, for example, hydroxyoctacosanylhydroxystearate and isopropylmyristate [39]. This is the “amorphous type” of NLCs (type II).

For a number of drugs, the solubility in liquid lipids (oils) is higher than in solid lipids. A typical example is retinol [40]. Conventional SLNs could only be loaded with 1% retinol [41]. Therefore, to improve the loading capacity, the “multiple type” of NLCs (type III) was developed. This type is derived from water-in-oil-in-water emulsions, which means that it is, in fact, an oil-in-fat-in-water dispersion. Tiny oil nanocompartments are created inside the solid lipid matrix of the lipid nanoparticles. Of course, it is not possible to create tiny oily nanocompartments in lipid nanoparticles of, for example, a diameter of 300 or 400 nm by mechanical means. The trick is that these nanocompartments are generated by a phase-separation process. A melted lipid and a hot oil are blended; the prerequisite is that the two lipids show a miscibility gap at the used concentrations approximately at 40 °C. A hot o/w nanoemulsion is produced at higher temperature (80 °C); the lipid droplets are cooled when reaching the miscibility gap, and the oil precipitates, forming tiny oil droplets in the melted solid lipid. Subsequent solidification of the solid lipid as a solid nanoparticle matrix leads to fixation of the oily nanocompartments. The solubility of a number of drugs in the oil is higher, for example, the drug load of retinol could be increased from 1% in SLNs to about 5% in the multiple NLC type [41].

To summarize, there are three different types of NLCs offered:

- I. imperfect crystal type
- II. amorphous type
- III. multiple type.

Comparing SLNs and NLCs, one can summarize that the novel NLCs can be used for any purpose that the SLNs have previously been exploited for. However, using the NLC system can provide additional benefits, such as drug load and avoidance or minimization of drug expulsion during storage because the spatially very different molecules are less capable of forming perfect crystalline structures.

It has been published that aqueous dispersions of SLNs are physically stable for up to three years [42]. However, it is also described that particle aggregation can occur in case a suboptimal surfactant mixture has been employed. Especially for surfactant mixtures having lecithin as one component, particle aggregation or even gel formation can occur [29, 43] (Table 2). However, for certain reasons, it might be desirable to use just a certain surfactant mixture, for example, in case the surfactants are regulatorily accepted. Examples are combinations of lecithin with Tween 80 or Poloxamer 188 for IV administration.

Also, for other administration routes, it is desirable that the lipid particle dispersions maintain their high dispersivity. To fully exploit the benefits of lipid nanoparticle dispersions, they should be finely dispersed in the gastrointestinal tract after administration as a capsule, tablet, or drink suspension. Factors leading to particle aggregation are the free diffusion of the particles, random collision and flocculation, or aggregation when overcoming the electrostatic or steric repulsion. Aqueous SLN dispersions according to the patent

Table 2. Long-term stability data of SLN formulations stabilized with different surfactants. PCS mean diameter and polydispersity index (PI).

Emulsifier Lipid	1% Lipoid S 75 + 0.5% Poloxamer 188				5% Poloxamer 188			
	2.5% Witexsol E85		2.5% Compritol 888 ATO		2.5% Witexsol E85		2.5% Compritol 888 ATO	
	Size (nm)	PI	Size (nm)	PI	Size (nm)	PI	Size (nm)	PI
Day 1	119.9	0.192	208.4	0.212	191.3	0.215	216.1	0.264
Year 1	142.1	0.230	1.0	0.523	201.3	0.217	219.3	0.270
Year 2	165.3	0.266	gel		225.1	0.223	217.5	0.266
Year 3	gel		gel		223.3	0.235	219.5	0.281

by Müller and Lucks possess a particle (solid) content of 0.1 to a maximum of 30%. The lower concentrated dispersions in particular show good diffusibility of the particles and potential random collision. However, SLN and NLC dispersions can be produced with a solid content above 30% up to 95%. The high particle concentration leads to a dense packing of the particles; depending on the concentration, they form a pearl-like network or an even denser hexagonal packing. The pearl-like network can be compared to the structure of gels formed by Aerosil or Bentonit (Montmorillonit). In such a network, particle diffusion is minimized, the particles are fixed in a certain structure, and aggregation does not occur or is less pronounced. Physical stability studies were performed by producing lipid nanoparticle dispersions with increasing lipid content. When diluting the highly concentrated particle dispersion after storage, finely dispersed lower concentrated suspensions were obtained. This means that such highly concentrated lipid particle dispersions can be produced that are optimal for storage. Producing the lipid particle dispersions, for example, in oils or PEG 600 instead of water, such dispersions can be directly filled into soft gelatine capsules. In the stomach, the capsule dissolves, the concentrated lipid particle dispersion is diluted, and releases finely dispersed particles for drug delivery.

Physical stabilization of the dispersivity of particles can also be achieved by spray drying (Fig. 3, upper part) or lyophilization (Fig. 3, lower part). There are no basic differences between SLNs and NLCs in these processes; we refer to the publications regarding spray drying [44, 45] and lyophilization of SLNs [46, 47].

4. PRODUCTION TECHNOLOGY

As mentioned earlier, the production of SLNs is performed by dispersing the drug-containing melted lipid in a hot aqueous surfactant solution by stirring and subsequent high-pressure homogenization. The original teaching of the SLN patent by Müller and Lucks is that only lipid concentrations up to a maximum of 30% can be employed; using a higher lipid concentration leads to the formation of creams with a bicoherent structure. Surprisingly, it was found that when even homogenizing concentrations of 70 or 80% lipid, no bicoherent structures were obtained, but definite nanoparticles. Therefore, the new NLC application contains—apart from a product claim of a nanostructured lipid particle—a production process claim describing the formation of lipid nanoparticles when employing solid concentrations above 30% up to 95%.

Of course, a lipid concentration of 80% cannot be produced in a one-step production process by high-pressure homogenization. For this, a two-step process is employed. In the first step, a stock lipid nanoparticle dispersion of 60% lipid content is produced. In the second step, melted lipid is added stepwise, and dispersed after each addition by high-speed stirring in the nanoparticulate stock dispersion. The principle of this process is shown in Figure 4. A 1000 g stock dispersion is produced by high-pressure homogenization containing 600 g of lipid in the form of nanoparticles and 400 g of water (first step). In the next step, an additional 100 g of lipid are added, which means dispersed in the 400 g water, leading to a total of 1100 g particle dispersion, now containing 700 g of lipid particles and still 400 g of water. In the next step, again, 100 g of melted lipid are dispersed in the 400 g of water, leading to a total of 800 g lipid plus still 400 g water, which means that the lipid content increases continuously. The newly added melted lipid is dispersed each time in 400 g water. Repeating this process can produce an 80% lipid nanoparticle dispersion. Of course, parti-

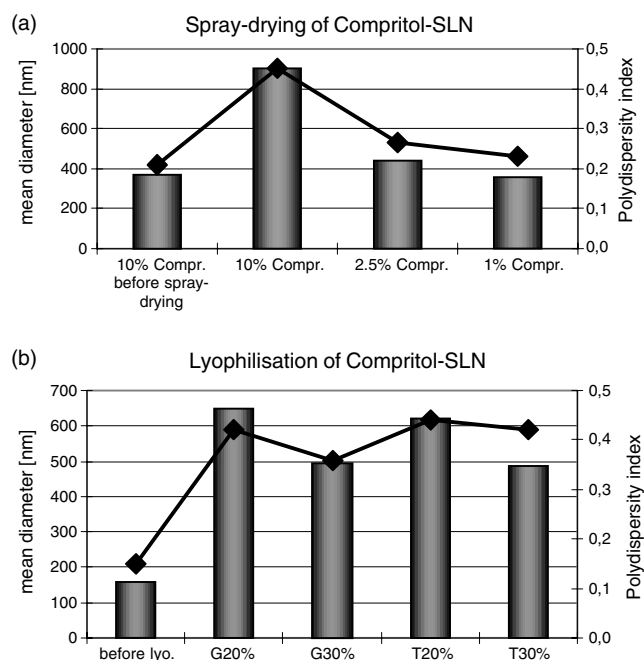


Figure 3. PCS particle size and polydispersity indexes (PIs) of spray-dried (a) and lyophilized (b) SLNs consisting of Compritol. Cryoprotectants: glucose (G) and trehalose (T). Modified with permission from [44], C. Fretas and R. H. Müller, *Biopharm.* 46, 145 C1 Elsevier; and [47], Ph.D. Dissertation, Freie Berlin, 1995.

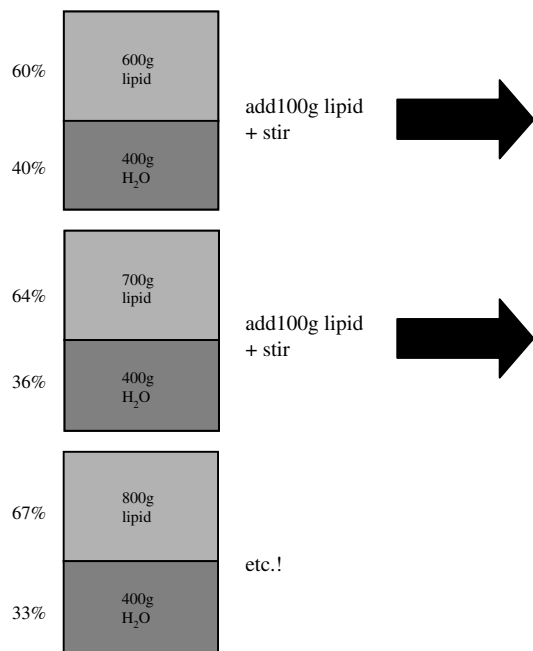


Figure 4. Scheme for the process of highly concentrated nanoparticle dispersions. For explanations, see text.

cle dispersions above 30% are not liquid anymore. They are creamy, gel paste-like with a further increase of lipid concentration, and are more or less solid at approximately 80%.

For the production of NLCs by high-pressure homogenization, any type of high-pressure homogenizer can be used which allows temperature control, which means keeping the preemulsion above the melting point of the lipid. SLNs have been produced by using piston-gap homogenizers of the APV Gaulin type (e.g., Micron LAB 40, LAB 60, and Gaulin 5.5), but also different Avestin homogenizers [48, 49]. The employment of microfluidization is also possible (e.g., Microfluidizer). A comparison of different homogenizers (APV and Avestin) with regard to the production of SLNs by the hot homogenization and cold homogenization techniques was performed [48, 49]. The findings obtained here can be transferred to NLCs. It can be summarized that the hot homogenization technique yields relatively similar results with different homogenizers. Larger differences were found in the cold homogenization technique. However, the reason for this was not insufficient homogenization capacity, but rather the design of the machines. In the case of horizontal tubes for microparticle suspension flow, sedimentation/flotation of lipid particles can occur, blocking the system. Such effects can be avoided by moving such types of homogenizers in a vertical position. Basically, it can be summarized that a good lipid nanoparticulate product is, in principle, achievable with most types of high-pressure homogenizers.

It should be pointed out that all types of machines used for SLN production can also be employed for NLC production. For clinical batch production, a modified Micron LAB 60 system was developed [50]. It makes no difference if a melted solid lipid, a blend of solid lipids (SLNs), or a blend of melted solid lipid and liquid lipid is processed. A 2 kg

batch can be produced within 10 min, and a 10 kg batch within 20 min homogenization time. The unit can be qualified and validated; the material of the unit is pharma grade. The system was developed by dds GmbH (Kronshagen/Kiel, Germany); the first prototype was installed at the company Pharmatec (Milan, Italy), and used to produce the first batch of SLNs for human trials. Figure 5 shows the basic setup of the machine. The central block is the actual homogenizer; in a feeding container, the preemulsion is prepared (arrow), and is passed through the homogenizer block to the product container. After the first cycle, the dispersion is passed back to the first container. A second homogenization cycle follows, leading to the final product within 20 min homogenization time [38, 51].

For some highly potent drugs, even a small batch size such as 10 kg already might be a production batch size. Higher volumes can be produced just by moving to a higher capacity homogenizer, for example, Gaulin 5.5 (150 kg dispersion/h) and a Rannie 118 (up to 2000 kg dispersion/h).

In general, scaling up of a production technique can be difficult in many cases. Results and production conditions from a small lab-scale unit cannot be directly transferred to large-scale units. In contrast to this, scaling up is very simple with piston-gap homogenizers of the APV Gaulin type. The geometry of the homogenization valves is identical or very similar. In addition, the larger machines give even better results with regard to small particle sizes and homogeneity of the particle size distribution. The reasons for this are improved dispersion properties due to the placement of two homogenization valves in series, and improved temperature control compared to the lab machines. For example, to yield an identical PCS diameter, it is required to run three cycles at 500 bar on a Micron LAB 40 (batch size 40 g). It is only necessary to run two cycles at 500/50 bar when employing a LAB 60 (10 kg batch size, pressure of first and second valve, respectively). At identical particle size, the polydispersity index of the larger batch is even lower, indicating a more homogeneous particle population. Against the general experience, scaling up of lipid particle production is relatively easy, and leads to an even better product quality under milder production conditions (less pressure, fewer homogenization cycles).

It is also possible to use the high-pressure homogenization unit under high-security conditions. For this, the production tower can be separated from the master control module,

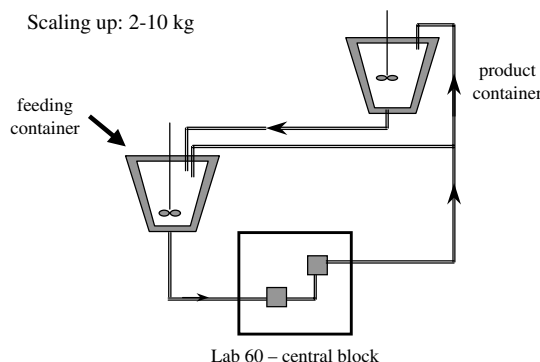


Figure 5. Modified Micron Lab 60 system basic setup.

and placed underneath a laminar air flow. The high-security production unit has been validated for the production of paclitaxel-containing nanosuspensions [52].

To summarize, the same production equipment can be used for the production of SLN and NLC dispersions. The new finding for NLC dispersions is that, despite applying high lipid concentrations, a nanoparticulate product with definite particles is obtained. In a two-step process, highly concentrated dispersions with up to 95% solid content can be produced (solid content defined as solids used for particle production, i.e., solid lipid plus solid surfactant).

5. IN VITRO TOLERABILITY

Cell cultures are increasingly used to assess the potential toxic effects of drugs, excipients, but also delivery systems such as nanoparticles. A rough measure of cytotoxicity is the viability of cells. Of course, cell cultures cannot imitate special elimination mechanisms in the living organism, but at least they provide a general impression of cellular tolerability. *In vitro* determination of cell viability reflected very well the differences between relatively cytotoxic polyalkylcyanoacrylate nanoparticles and much better tolerated polylactic acid (PLA) and PLA/PGA nanoparticles. The EC50 (effective concentration leading to a 50% cell death) was about 20 $\mu\text{g/mL}$ for polymethylalkylcyanoacrylate nanoparticles [53]. Concentrations of about 0.5% were well tolerated in the case of PLA nanoparticles, but the copolymer particles with polyglycolic acid led to 100% cell death [54]. An even better tolerability was found for SLN dispersions; concentrations of 10% in the cell culture led only to a reduction of viability to about 80% [54]. A similar good tolerability can be assumed for NLCs, especially when considering that a part of the solid glycerides of SLNs is replaced by even better tolerated oils, for example, MCT used in parenteral nutrition. Cell culture studies of emulsions for parenteral nutrition showed even less cytotoxicity compared to lipid nanoparticles (viability of peritoneal macrophages after 20 h of *in vitro* culture: emulsion = 97%, SLN = 82–75%) [55].

Of course, cell viability is a very crude measure to assess cytotoxicity. To obtain a deeper insight, it is more appropriate to determine the induction of production of Interleukin 6 and 12, as well as TNF- α . Such cytotoxic effects on the molecular level can lead to a serious disturbance in the living organism. In the last few years, systematic studies were performed to measure these parameters after incubation, with SLNs being composed of different lipids, and also produced from different surfactants [55]. In addition, the size effect on the cytotoxicity was also investigated. These results can be summarized as follows: none of the investigated lipids led to a serious increase in the production of Interleukins or TNF- α when using well-tolerated surfactants (Fig. 6). Again, a similar or even better tolerability can be expected for NLCs.

6. IN VIVO TOLERABILITY

NLCs are a rather young development; the patents were filed in 1999 explaining why limited data are available. However, again one can refer to the results obtained with

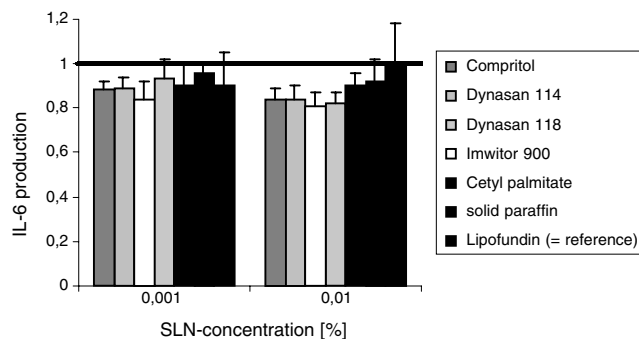


Figure 6. IL-6 production of macrophages treated with different SLN formulations compared to Lipofundin-treated macrophages. Non-treated macrophages are defined as 1. Modified with permission from [80], N. Schöler, Ph.D. Dissertation, Freie Universität Berlin, 2001.

SLNs. The first studies were performed in mice by injecting extremely high doses of SLNs intravenously (1.33 g lipid/kg body weight). In these studies, large volumes of SLNs were injected into mice, which means 0.4 mL [56]. Assuming a blood volume of about 2 mL/mouse, about 20% of the blood volume was injected as highly concentrated SLN dispersion. Calculating the injected amount on the basis of medium human body weight (75 kg) would mean that 100 g of solid lipid were injected as a bolus. Of course, such a calculation cannot be done in a strict sense, but illustrates the heavy lipid load in this tolerability study. Injected particles were made from Compritol, and as a second system made from cetyl palmitate. Only with 10% Compritol dispersions was an increase in the weight of the liver and spleen observed, which was reversible after a few weeks. Cetyl palmitate did not lead to any changes. The difference *in vivo* was explained by the difference in the degradation velocity. Compritol as a lipid with a high fraction of triglycerides is degraded much more slowly; therefore, there is an increase in liver weight. Cetyl palmitate is degraded much faster, thus avoiding a change in the liver weight. This is also a well-known phenomenon when comparing the degradation of LCT and MCT oils. LCT oils are degraded more slowly; during long-term parenteral nutrition, they can increase the liver weight [57]. Transferring these results to NLC means that basically NLCs are even better tolerated than SLNs because they contain fast degrading oils as one component.

Recently, tissue tolerability studies were performed in chickens. SLN particles made from different lipids and stabilized with different surfactants were injected in the pectoral muscle of chickens [58]. The tolerability was compared to injected Freund's incomplete adjuvants. With the SLNs, no or very little tissue alteration was observed, much less than described, for example, for polymeric particles in the literature (of course, distinctly less compared to Freund's incomplete adjuvants). The tolerability was not at all or very little affected by the nature of the lipid; rather, there was a size effect (larger particles disturbed the tissue more Fig. 7, right). From this, it can also be concluded that NLCs will have a similar excellent tolerability.

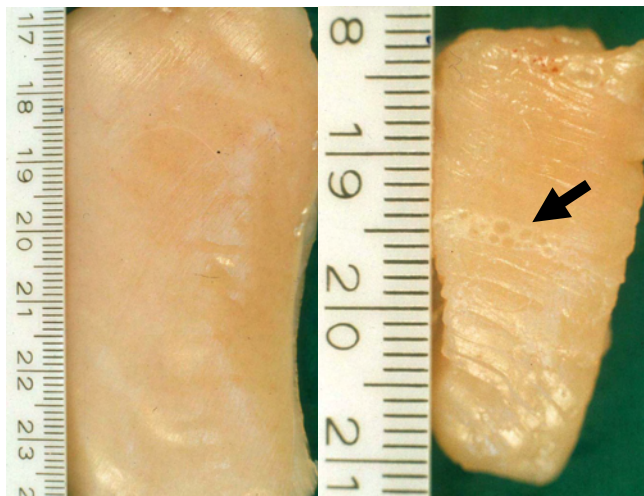


Figure 7. Right: foci of tissue alterations of the pectoral musculature (arrow) after injection of larger Compritol SLN. Left: no tissue alterations are found after injection of control.

7. DRUG RELEASE AND *IN VIVO* DEGRADATION

Drug release from lipid nanoparticles takes place by diffusion; *in vivo*, additionally, degradation of the lipid particle matrix accelerates release. Intensive studies were performed by Mehnert and co-workers, investigating the *in vitro* drug release as a function of the production conditions of SLNs, which means, in fact, localization of the drug inside the SLN matrix [5, 30, 42]. These results can be directly transferred to NLCs, which means whether the drug is localized more in the core, in the shell, or is evenly distributed throughout the matrix.

A full series of studies was performed to investigate the enzymatic degradation of lipid particle matrices as a function of the nature of the lipid, the size of the lipid particles, drug-loaded versus drug-free particles, and the type of surfactant used to stabilize the particles [59–61]. Regarding the dependence of the degradation velocity on the chemical structure of the lipid matrix, it can be summarized that triglycerides are degraded more slowly than diglycerides; the degradation velocity decreases further with increasing length of the fatty acid chain. In addition, it seems to be more difficult for the enzymes to degrade triglycerides because they are composed of very similar fatty acids and similar chain lengths or even identically long fatty acids. It seems to be more suitable to have a fatty acid mixture. In addition, easily accessible molecules such as esters are degraded relatively fast (e.g., the wax cetyl palmitate). Transferring these results to NLCs means that the degradation velocity increases with triglycerides originating from oils because they have shorter fatty acid chains. The higher the percentage of oil in the NLCs, the faster will be the degradation velocity. However, the most important finding was that the degradation velocity is predominantly influenced by the type of surfactant. Lecithin-stabilized particles are degraded relatively fast, especially when they additionally contain sodium cholate in the surfactant mixture. Sodium cholate promotes the anchoring of the lipase–colipase com-

plex, thus promoting degradation. In contrast to this, sterically stabilizing surfactants and polymers slow down the degradation velocity, for example, Tween 80 and cblock polymers such as Poloxamer 188 or Poloxamer 407 [61]. It can also nicely be shown that the degradation time can be adjusted as desired when mixing degradation-enhancing surfactants (fast degradation time) with degradation-delaying stabilizers (e.g., Poloxamer). Depending on the mixture, an intermediate degradation time can be obtained [60].

To summarize, the dominant factors for lipid particle degradation are the surfactants or surfactant mixtures. This means for NLCs that, parallel to SLNs, the degradation can be mainly controlled by the surfactants and the stabilizers used in the production process. After removal of the surfactant mixture, degradation will be enhanced with increasing oil content and vice versa.

8. APPLICATIONS AND FINAL DOSAGE FORMS

Basically, the NLCs can be employed everywhere SLNs were employed previously. Therefore, application routes range from topical to parenteral, including targeting to the brain or the bone marrow. For more detailed general descriptions of the application possibilities of lipid nanoparticles, we refer to some literature reviews [6–8, 30, 45, 62]. In the subsequent paragraphs in particular, some special features of NLCs are addressed.

8.1. Topical Application

SLNs can be admixed to traditional pharmaceutical creams and lotions, which means combining the existing advantages of the traditional dosage form with novel features of SLNs [38]. Of course, the same can be done with NLCs. A previous obstacle was that admixing the SLN dispersions to an existing cream limited the total lipid particle content in the final product because SLN dispersions are only available up to a lipid content of 30%. Replacing 10% of the water phase of a cream by a 30% SLN dispersion led to a final particle concentration of just 3%. The newly developed SLN and NLC dispersions can be produced in much higher concentrations, for example, 50%. In addition, it is possible to produce topical products that are composed solely of NLCs, with no oil droplets present. Concentrations of 40–50% lipid particles led to cream and paste-like products exhibiting similar viscous and elastic properties as traditional systems [63–65]. In addition, it has the advantage that it is a one-step production process; the cream is directly obtained after the homogenization process [66].

NLCs have similar properties as SLNs regarding the occlusion effect [67] and the modulation of drug penetration into the skin [68]. In addition, a triggered drug release is possible. It was found that, when applying NLC to the skin, the loss of water and increase in temperature seem to initiate a crystallization process toward a more ordered structure. This leads to controlled drug expulsion [41]. This could be utilized to generate supersaturated systems, which means loading the particles with a drug, and having the drug additionally dissolved in the dispersion medium at saturation solubility. The formation of the highly ordered structure

leads to drug expulsion; the drug is being expelled into the already saturated outer phase of the cream, which means that a supersaturation occurs with increased penetration into the skin (microemulsion effect without having present the high surfactant concentrations of a microemulsion).

8.2. Oral Administration

SLN dispersions were recommended to be transformed to a dry dosage form, being most convenient for the patient (e.g., tablet, pellets, or gelatine capsules). Despite having SLN particle dispersions up to 30% lipid content, still 70% water remains to be removed, which is a relatively high amount in a drying process. Approaches to obtain dry products are the use of lipid particle dispersions as a granulation fluid in tableting, as a wetting agent in pellet production, or direct filling of nonaqueous SLN dispersions into soft gelatine capsules. These problems have been drastically reduced when producing highly concentrated NLC dispersions, for example, 40 or 50%.

The filling of gelatine capsules with nonaqueous SLN dispersions could generate another problem, which means insufficient loading capacity of the capsule for the drug. The gelatine capsule contains only a certain percentage of lipid particles, and the lipid particles themselves only a certain percentage of the drug. From this, one encountered dosing problems when having single drug doses of about 25 mg and more. This is not at all or is less of a problem when processing highly concentrated NLC dispersions.

8.3. Parenteral Administration

Lipid nanoparticles can be employed for intravenous injection, intraarticular drug delivery (e.g., treatment of arthritis), prolonged drug release after subcutaneous injection, but also for local treatment in body cavities or release from body cavities (e.g., IP). The basic advantages of NLCs for these application purposes are the higher drug load, higher particle concentrations in the dispersions, and thus lower injection volumes and higher flexibility in modulating the drug release profile.

There are also reports in the literature that SLNs can be used for the delivery of drugs to the brain, as mentioned above. Reports describing brain delivery of drugs by SLNs [34, 69] are relatively reluctant to specify the total amount of particles (and drug) delivered. It seems to still be a relatively low percentage; it is more important to have a very high drug loading to use such effects for therapy. NLCs with improved loading compared to SLNs offer the perspective to be successfully exploited for brain delivery.

8.4. Ocular Delivery

The use of polymeric nanoparticles can prolong the retention time of drugs in the eye [70]. Despite these clear reports in the literature, no nanoparticulate products are on the market according to our knowledge. There are two reasons for this from our point of view. First, the profits from ocular products are relatively low; a company is therefore reluctant to replace an existing selling product by a completely new development. In case the product sells well anyway, why

should there be an improved development causing relatively high costs not fully compensated by additional profit? In addition, the use of polymeric nanoparticles would require extensive toxicity studies, too expensive for a small-sale volume product such as eye formulations.

The incorporation of a drug into SLNs and application as SLN dispersion to the eye can clearly enhance the retention time [71]. Recently, the first investigations of SLNs for ocular delivery were published [72]. Due to the excellent tolerability of lipids used for lipid nanoparticle production, for their topical application, only very limited toxicity studies are expected to be required (especially when using excipients accepted for topical use). Drainage to the nasal tract should also be no problem; many surfactants and lipids used in SLNs are also registered for nasal creams. NLCs could also be used for these formulations, again having the advantage of higher drug loads and more flexible modulation in drug release.

9. COSMETIC APPLICATIONS

In the last 3–5 years, increasing attention focused on the use of lipid nanoparticles for cosmetic purposes. Described are the chemical stabilization of chemically labile cosmetic compounds such as retinol [73], and the incorporation of cosmetic compounds such as coenzyme Q10 [74] and vitamin E [75, 76]. In particular, the occlusion effect of lipid nanoparticles improves the penetration of cosmetic compounds in the upper skin layer (of course, it should not penetrate too deeply to prevent any pharmaceutical effects from occurring). The occlusiveness leads to increased skin hydration [77], and the increased skin hydration can reduce the wrinkle depth [7]. Basically, SLNs can be exchanged against NLCs. This is especially desirable when the SLN structure does not allow the envisaged drug loading in the case of admixing the particles to existing creams (e.g., as for retinol).

Applications of lipid nanoparticles are also the controlled release of perfumes (Fig. 8) [78] or the prolonged release of insect repellents [79]. Basically, the lipid nanoparticles can be considered as a novel cosmetic carrier. Considering the

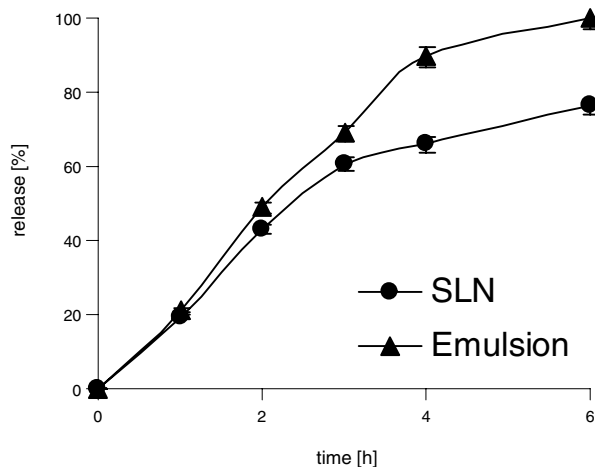


Figure 8. Prolonged release of perfume from SLNs compared to reference emulsion.

cosmetic industry, a real breakthrough with regard to product quality, and especially attention by the customers, was the introduction of liposomes in cosmetic products. A high percentage of the population knows liposomes. Of course, most of them do not know exactly what a liposome is, but there is an association of improved product quality when liposomes are contained. Since that time, no similar cosmetic carrier has been placed on the market. Attempts such as multiple emulsions, thalaspheeres, and microsponge delivery systems (MDS) attracted no similar attention among the public and no similar sale success, and, of course, no similar broad technological application. Therefore, from the marketing and technological points of view, the time might have come for the next broad introduction of a novel cosmetic carrier; the lipid nanoparticles have the potential to be this carrier. However, a prerequisite is that a large cosmetic company with excellent reputation takes up this carrier system.

10. SUMMARY

To summarize, both SLNs and NLCs have a great potential as carrier systems for pharmaceutical applications; as a kind of "spin off" from pharmaceuticals—similar to liposomes—cosmetic exploitation as a new carrier system is possible. A basic advantage of SLNs and NLCs is that these carrier systems were developed having industrial needs and requirements in mind, which means considering the accepted status of excipients, large-scale production facilities, the qualification and validation of production lines, and—very importantly—the costs of goods and the costs of production. The lipid nanoparticles are low-cost systems. A highly attractive feature is the simplicity of the technology; a very simple high-pressure homogenization process has itself been very well established in the pharmaceutical industry for more than half a century. Production equipment is off-the-shelf equipment. Another industrial prerequisite is also fulfilled: exclusivity of the technology, which guarantees a return of investment and protects against generic products.

A very important step for a new technology is that it moves from academic research levels to industry. The SLN[®] technology developed in our labs was acquired by SkyePharma PLC in 1999; it is nowadays one of the nanoparticulate core technologies of SkyePharma (apart from the drug nanocrystals Dissocubes[®]). Industrial developments, and hopefully the products, will now follow. NLCs as the next generation are expected to also find their way to industry. This is highly likely because the first generation has already found acceptance in industry.

The final criterion to judge the success of a technology is the appearance of products on the market, and of course, the number of products that are on the market. Therefore, final judgment of the lipid nanoparticulate carrier systems might be done in 5 or 10 years; at least they seem to be in a pole position in the race for new carrier systems for the market.

GLOSSARY

High pressure homogenization Method for the preparation of SLN and NLC. High shear forces and cavitation in a piston-gap homogenizer lead to particle diminution.

In vitro tolerability Method using cell cultures to assess potential toxic effects. Measures of *in vitro* tolerability include viability of cells, Interleukin 6 and 12 and TNF- α production.

Nanostructured lipid carriers (NLC) Nanoparticles composed of a mixture of lipids solid or liquid at room (body) temperature. The mixture allows higher drug incorporation.

Scaling up Increasing the batch size from lab scale to large scale while ensuring identical batch characteristics.

Solid lipid nanoparticles (SLN) Nanoparticles with a matrix composed of lipids solid at room (body) temperature. Versatile drug carrier system.

Supersaturated systems Used for increased penetration of drugs. By creating a supersaturated system, the thermodynamic activity is increased promoting penetration.

REFERENCES

1. J. M. Hann and H. G. Prentice, *Int. J. Antimicrob. Agents* 17, 161 (2001).
2. A. Smith and J. M. Hunneyball, *Int. J. Pharm.* 30, 215 (1986).
3. R. H. Müller and J. S. Lucks, European Patent EP 0605497, 1996.
4. M. R. Gasco, U.S. Patent 5, 250, 236, 1993.
5. A. zur Mühlen and W. Mehnert, *Pharmazie* 53, 552 (1998).
6. R. H. Müller, W. Mehnert, J. S. Lucks, C. Schwarz, A. zur Mühlen, H. Weyhers, C. Freitas, and D. Rühl, *Eur. J. Pharm. Biopharm.* 41, 62 (1995).
7. R. H. Müller, K. Mäder, and S. Gohla, *Eur. J. Pharm. Biopharm.* 50, 161 (2000).
8. W. Mehnert and K. Mäder, *Adv. Drug Del. Rev.* 47, 165 (2001).
9. M. Radtke and R. H. Müller, *New Drugs* 2, 48 (2001).
10. K. Schalper, S. Harnisch, R. H. Müller, and G. E. Hildebrand, "Proceedings of the International Symposium on Controlled Release of Bioactive Material," 2001, Vol. 28, pp. 1388–1389.
11. G. Hildebrand, J. Tack, and S. Harnisch, WO 2000072955 A1, 2000.
12. P. Speiser, European Patent EP 0167825, 1990.
13. A. J. Domb, U.S. Patent 5, 188, 837, 1993.
14. R. Cavalli, O. Caputo, E. Marengo, F. Pattarino, and M. R. Gasco, *Pharmazie* 53, 392 (1998).
15. R. Cavalli, E. Marengo, L. Rodriguez, and M. R. Gasco, *Eur. J. Pharm. Biopharm.* 43, 110 (1996).
16. B. Siekmann and K. Westesen, *Eur. J. Pharm. Biopharm.* 43, 104 (1996).
17. M. Trotta and F. Debenardi, *Int. J. Pharm.* (in press).
18. B. Heurtault, P. Saulnier, B. Pech, M. Venier-Julienne, J. Proust, R. Phan-Tan-Luu, and J. Benoit, *Eur. J. Pharm. Sci.* (in press).
19. H. Bunjes, K. Westesen, and M. H. J. Koch, *Int. J. Pharm.* 129, 159 (1996).
20. R. J. Hunter, "Foundations of Colloid Science." Oxford University Press, Oxford, 1986.
21. K. Westesen and H. Bunjes, *Int. J. Pharm.* 115, 129 (1995).
22. B. W. Müller, "Suppositorien." Wissenschaftliche Verlagsgesellschaft mbH, Stuttgart, 1986.
23. K. Vadnera, in "Encyclopedia of Pharmaceutical Technology" (J. Swarbrick and J. Boylan, Eds.), pp. 337–352. Marcel Dekker, New York, 1993.
24. K. Larsson, *Fette, Seifen, Anstrichm.* 74, 136 (1972).
25. K. Westesen, H. Bunjes, and M. H. J. Koch, *J. Control. Rel.* 48, 223 (1997).
26. C. Freitas and R. H. Müller, *Eur. J. Pharm. Biopharm.* 47, 125 (1999).
27. K. Westesen and B. Siekmann, *Int. J. Pharm.* 151, 35 (1997).

28. K. Westesen, *Colloid. Polym. Sci.* 278, 608 (2000).
29. C. Freitas and R. H. Müller, *J. Microencapsulation* 16, 59 (1999).
30. W. Mehnert, A. zur Mühlen, A. Dingler, H. Weyhers, and R. H. Müller, *Pharm. Ind.* 59, 511 (1997).
31. R. H. Müller, M. Radtke, and S. Wissing, *Adv. Drug Del. Rev.* 54, S131 (2002).
32. S. Wissing and R. H. Müller, *J. Control. Rel.* 81, 225 (2002).
33. A. Miglietta, R. Cavalli, C. Bocca, L. Gabriel, and M. R. Gasco, *Int. J. Pharm.* 210, 61 (2000).
34. S. C. Yang, L. F. Lu, Y. Cai, J. B. Zhu, B. W. Liang, and C. Z. Yang, *J. Control. Rel.* 59, 299 (1999).
35. S. C. Yang, J. B. Zhu, L. F. Lu, B. W. Liang, and C. Z. Yang, *Pharm. Res.* 16, 751 (1999).
36. E. Ugazio, R. Cavalli, and M. R. Gasco, *Int. J. Pharm.* 241, 341 (2002).
37. S. A. Runge, Ph.D. Dissertation, Freie Universität Berlin, 1998.
38. A. Dingler, Ph.D. Dissertation, Freie Universität Berlin, 1998.
39. R. H. Müller and V. Jenning, *Deutsche Patentanmeldung* 199, 38 (2000).
40. V. Jenning, Ph.D. Dissertation, Freie Universität Berlin, 1999.
41. V. Jenning, M. Schäfer-Korting, and S. Gohla, *J. Control. Rel.* 66, 115 (2000).
42. A. zur Mühlen, Ph.D. Dissertation, Freie Universität Berlin, 1996.
43. C. Freitas, Ph.D. Dissertation, Freie Universität Berlin, 1998.
44. C. Freitas and R. H. Müller, *Eur. J. Pharm. Biopharm.* 46, 145 (1998).
45. R. H. Müller, A. Dingler, H. Weyhers, A. zur Mühlen, and W. Mehnert, *Pharm. Ind.* 59, 614 (1997).
46. E. Zimmermann, R. H. Müller, and K. Mäder, *Int. J. Pharm.* 196, 211 (2000).
47. C. Schwarz, Ph.D. Dissertation, Freie Universität Berlin, 1995.
48. S. A. Wissing, Ph.D. Dissertation, Freie Universität Berlin, 2002.
49. S. Liedtke, S. Wissing, R. H. Müller, and K. Mäder, *Int. J. Pharm.* 196, 183 (2000).
50. T. Schneppe, Ph.D. Dissertation, Freie Universität Berlin, 1998.
51. R. H. Müller, S. A. Wissing, and A. Radoska, *New Drugs* 1, 72 (2001).
52. B. Böhm, Ph.D. Dissertation, Freie Universität Berlin, 1999.
53. C. Lherm, R. H. Müller, F. Puisieux, and P. Couvreur, *Int. J. Pharm.* 84, 13 (1992).
54. S. Maaßen, C. Schwarz, W. Mehnert, J. S. Lucks, F. Yunis-Specht, B. W. Müller, and R. H. Müller, "Proceedings of the International Symposium on Controlled Release of Bioactive Material," 1993, Vol. 20, pp. 490–491.
55. N. Schöler, C. Olbrich, K. Tabatt, R. H. Müller, H. Hahn, and O. Liesenfeld, *Int. J. Pharm.* 221, 57 (2001).
56. H. Weyhers, S. Ehlers, W. Mehnert, H. Hahn, and R. H. Müller, "Proceedings of the 1st World Meeting on Pharmaceuticals, Biopharmaceuticals and Pharmaceutical Technology," Budapest, 1995, pp. 489–490.
57. C. A. Gogos and F. Kalfarentzos, *Nutrition* 11, 339 (1995).
58. C. Olbrich, R. H. Müller, K. Tabatt, O. Kayser, C. Schulze, and R. Schade, *Atla* 30, 1 (2002).
59. C. Olbrich and R. H. Müller, *Int. J. Pharm.* 180, 31 (1999).
60. C. Olbrich, O. Kayser, and R. H. Müller, *Int. J. Pharm.* 237, 119 (2002).
61. C. Olbrich, O. Kayser, and R. H. Müller, *J. Nanopart. Res.* 4, 121 (2002).
62. R. H. Müller, H. Weyhers, A. zur Mühlen, A. Dingler, and W. Mehnert, *Pharm. Ind.* 59, 423 (1997).
63. A. Lippacher, R. H. Müller, and K. Mäder, *Eur. J. Pharm. Biopharm.* 53, 155 (2002).
64. A. Lippacher, R. H. Müller, and K. Mäder, *Int. J. Pharm.* (submitted).
65. A. Lippacher, R. H. Müller, and K. Mäder, *Int. J. Pharm.* 196, 227 (2000).
66. A. Lippacher, R. H. Müller, and K. Mäder, "Proceedings of the 3rd World Meeting on Pharmaceuticals, Biopharmaceuticals and Pharmaceutical Technology," Berlin, 2000, pp. 427–428.
67. S. A. Wissing, A. Lippacher, and R. H. Müller, *Int. J. Cosmetic Sci.* 52, 313 (2001).
68. U. Münster, K. Jores, W. Mehnert, M. Schaller, H. C. Korting, and M. Schäfer-Korting, 6. GD-Jahrestagung, Hamburg, 2002.
69. A. Fundarò, R. Cavalli, A. Bargoni, D. Vighetto, G. P. Zara, and M. R. Gasco, *Pharmacol. Res.* 42, 337 (2000).
70. T. Harmia, P. Speiser, and J. Kreuter, *J. Microencaps.* 3, 3 (1986).
71. R. Cavalli, S. Morel, M. R. Gasco, P. Chetoni, and M. F. Saettone, *Int. J. Pharm.* 117, 243 (1995).
72. M. Fresta, C. Bucolo, A. Maltese, S. Mangiafico, and G. Puglisi, "Proceedings of the 4th World Meeting on Pharmaceuticals, Biopharmaceuticals and Pharmaceutical Technology," Florence, 2002, pp. 939–940.
73. V. Jenning and S. Gohla, *J. Microencaps.* 18, 149 (2001).
74. R. H. Müller and A. Dingler, *Eurocosmetics* 7/8, 19 (1998).
75. A. Dingler, R. P. Blum, H. Niehus, S. Gohla, and R. H. Müller, *J. Microencaps.* 16, 751 (1999).
76. R. H. Müller and A. Dingler, *Pharm. Zeitung* 49, 11 (1998).
77. S. A. Wissing and R. H. Müller, *Eur. J. Pharm. Biopharm.* (submitted).
78. S. A. Wissing, K. Mäder, and R. H. Müller, "Proceedings of the International Symposium on Controlled Release of Bioactive Material," 2000, Vol. 27, pp. 311–312.
79. S. Wissing, K. Mäder, and R. H. Müller, "Proceedings of the 3rd World Meeting on Pharmaceuticals, Biopharmaceuticals and Pharmaceutical Technology," Berlin, 2000, pp. 439–440.
80. N. Schöler, Ph.D. Dissertation, Freie Universität Berlin, 2001.
81. A. J. Domb, *Int. J. Pharm.* 124, 271 (1995).
82. D. B. Masters and A. J. Domb, *Pharm. Res.* 15, 1038 (1998).
83. A. J. Domb, A. Marlinsky, M. Maniar, and L. Teomim, *J. Am. Mosquito Contr. Ass.* 11, 29 (1995).
84. R. Cavalli, R. M. Gasco, and S. Morel, *S.T.P. Pharma Sci.* 2, 514 (1992).
85. M. R. Gasco, R. Cavalli, and M. E. Carlotti, *Pharmazie* 47, 119 (1992).
86. M. R. Gasco, S. Morel, and R. Carpignano, *J. Pharm. Biopharm.* 38, 7 (1992).
87. R. Cavalli, O. Caputo, and M. R. Gasco, *Int. J. Pharm.* 89, R9 (1993).
88. G. P. Zara, A. Bargoni, R. Cavalli, A. Fundarò, D. Vighetto, and M. R. Gasco, *J. Pharm. Sci.* 91, 1324 (2002).
89. G. P. Zara, R. Cavalli, A. Bargoni, A. Fundarò, D. Vighetto, and M. R. Gasco, *J. Drug Target.* 10, 327 (2002).
90. S. Morel, M. R. Gasco, and R. Cavalli, *Int. J. Pharm.* 105, R1 (1994).
91. S. Morel, E. Ugazio, R. Cavalli, and M. R. Gasco, *Int. J. Pharm.* 132, 259 (1996).
92. R. Cavalli, O. Caputo, M. E. Carlotti, M. Trotta, C. Scarnecchia, and M. R. Gasco, *Int. J. Pharm.* 148, 47 (1997).
93. S. Morel, E. Terreno, E. Ugazio, S. Aime, and M. R. Gasco, *Eur. J. Pharm. Biopharm.* 45, 157 (1998).
94. R. Cavalli, E. Peira, O. Caputo, and M. R. Gasco, *Int. J. Pharm.* 182, 59 (1999).
95. R. Cavalli, M. R. Gasco, P. Chetoni, S. Burgalassi, and M. F. Saettone, *Int. J. Pharm.* 238, 241 (2002).
96. A. Bargoni, R. Cavalli, G. P. Zara, A. Fundarò, O. Caputo, and M. R. Gasco, *Pharmacol. Res.* 43, 497 (2001).
97. R. Cavalli, O. Caputo, and M. R. Gasco, *Eur. J. Pharm. Sci.* 10, 305 (2000).
98. V. Jenning, A. Gysler, M. Schäfer-Korting, and S. Gohla, *Eur. J. Pharm. Biopharm.* 49, 211 (2000).

99. A. Dingler, G. Hildebrand, H. Niehus, and R. H. Müller, "Proceedings of the International Symposium on Controlled Release of Bioactive Material," 1998, Vol. 25, pp. 433–434.
100. Y. Yaziksiz-Iskan, S. A. Wissing, R. H. Müller, and S. Hekimoglu, "Proceedings of the 4th World Meeting on Pharmaceuticals, Biopharmaceuticals and Pharmaceutical Technology," Florence, 2002, pp. 789–790.
101. G. Lukowski and P. Pfügel, *Pharmazie* 52, 642 (1997).
102. G. Lukowski and U. Werner, "Proceedings of the International Symposium on Controlled Release of Bioactive Material," 1998, Vol. 25, pp. 425–426.
103. M. Sznitowska, M. Gajewska, S. Janicki, A. Radwanska, and G. Lukowski, *Eur. J. Pharm. Biopharm.* 52, 159 (2001).
104. A. zur Mühlen, C. Schwarz, and W. Mehnert, *Eur. J. Pharm. Biopharm.* 45, 149 (1998).
105. C. Schwarz, C. Freitas, W. Mehnert, and R. H. Müller, "Proceedings of the International Symposium on Controlled Release of Bioactive Material," 1995, Vol. 22, pp. 766–767.
106. L. Penkler, R. H. Müller, S. A. Runge, and V. Ravelli, (1999).
107. S. Wissing and R. H. Müller, *Pharmazie* 56, 783 (2001).
108. A. V. Ambarkhane, H. J. Gala, and V. B. Patravale, "Proceedings of the 4th International Symposium on Innovations in Pharmaceutical Sciences & Technology," Ahmedabad, India, 2000, p. 52.
109. H. Heiati, R. Tawashi, R. R. Shivers, and N. C. Phillips, *Int. J. Pharm.* 146, 123 (1997).
110. H. Heiati, R. Tawashi, and N. C. Phillips, *Int. J. Pharm.* 174, 71 (1998).
111. H. Heiati, R. Tawashi, and N. C. Phillips, *J. Microencaps.* 15, 173 (1998).
112. B. Siekmann and K. Westesen, *Pharm. Res.* 12, 201 (1995).
113. J. Zhu, S. Yang, and K. Cheng, *Zhongguo Yiyao Gongye Zazhi* 30, 441 (1999).
114. M. Demirel, Y. Yazan, R. H. Müller, F. Kilic, and B. Bozan, *J. Microencaps.* 18, 359 (2001).
115. Q. Zhang, G. Yie, Y. Li, Q. Yang, and T. Nagai, *Int. J. Pharm.* 200, 153 (2000).
116. D. B. Chen, T. Z. Yang, W. L. Lu, and Q. Zhang, *Chem. Pharm. Bull.* 49, 1444 (2001).
117. Z. Zhang, B. Yu, and Y. Zeng, *Yaoxue Xuebao* 35, 700 (2000).

Solid-State Synthesis of Carbon Nanotubes

Hua Chun Zeng

National University of Singapore, Singapore

CONTENTS

1. Introduction
 2. Types of Synthetic Methods
 3. Carbon Nanotubes Prepared by Solid-State Reactions
 4. Conclusions
- Glossary
References

1. INTRODUCTION

Over the past decade, carbon nanotubes (CNTs) and related fullerene carbons have gained great attention in materials research due to the novel properties of this class of materials in electrical, magnetic, nonlinear optical, mechanical, and catalytic applications [1–22]. The potential usages of these new forms of carbon have been since proposed for various technological fields spanning from more classical type applications, such as the catalysts in heterogeneous catalysis and carbon adsorbents in separation technology, to display devices, chemical mapping, bio/mechanical sensors/devices, energy storage, and molecular electronic devices/connectors [1–6]. Although tremendous technological progress and research accomplishments have been made since the discoveries of fullerene carbons and CNTs [3, 5, 6], the new developments in nanoscience and nanotechnology research in turn impose us with higher demands and standards for the future nanocarbons preparation. Even today, controlled synthesis of high-quality CNTs is still a problem largely hindering the actual applications of these fascinating materials. In certain application areas such as energy storage and heterogeneous catalysis, furthermore, large quantities of the CNTs are required. Clearly, the further progress of the entire field depends heavily on our ability to develop newer synthetic methodologies for nanocarbon materials with desired quality and quantity.

In this chapter, we will look at a less common aspect of the CNTs fabrication—solid-state synthesis of CNTs. Our attention will be directed to several important case studies, each representing a typical synthetic method. The chapter is thus focused on a comprehensive review on representative synthetic methodologies. It is our aim that the chapter will allow interested readers to have a general picture on various solid-state methods for the CNTs preparation with certain in-depth details.

2. TYPES OF SYNTHETIC METHODS

There have been numerous synthetic methods for nanotubular and other low-dimensional materials [1–6]. For example, the preparation methods of CNTs range from the most common techniques such as high-voltage arc-discharge, double laser vaporization, pyrolysis, and chemical vapor deposition [1–6], to the rare types like synthesis of CNTs under a focused sunlight [5]! Concerning the mass transport during the synthesis, these methods can be broadly divided into two categories—vapor-phase and condensed-phase processes. The vapor-phase methods involve processes in which gaseous reactants are transported through vapor phase and converted into solid/liquid phase in the growing fronts of materials. These methods include arc-discharge [7], thermal decompositions (pyrolysis) [8, 9], chemical vapor deposition [10–12], laser catalytic growth (LCG) [13, 14], and pulsed laser ablation [15, 16], and various physical (possibly also with additional chemical) vapor depositions [17, 18], etc. The technical merits of vapor-phase processes have been laid largely on the production of highly oriented crystalline materials such as thin films with excellent crystal perfection, although their growth rates and thus the product yields are normally not high. Compared to the vapor-phase methods, conventional syntheses with condensed-phase reactions can offer much higher production yields. In this regard, solid-state reactions and electrochemical processes have also been widely used nowadays in nanostructured materials synthesis. In fact, soon after the discovery of the first CNTs [7],

condensed-phase preparation of CNTs had been attempted with an electrolysis method by passing an electric current between carbon electrodes in molten lithium chloride that acted as an electrolyte [19, 20]. Other electrochemical methods, such as anodization processes, have also been utilized in preparations of alumina oxide membranes with controlled 1D channels and individual alumina nanotubes [22]. In recent years, low-energy and environmentally benign processes such as liquid-phase deposition (LPD) analogous to “biomimetic” mineralization, have generated significant interests [23–29] in the nanomaterials research. For instance, TiO₂ crystalline films and nanostructures with desired crystallographic phase(s) have been prepared by hydrolyzing titanium inorganic salts (for example, (NH₄)₂TiF₆, TiF₄, and TiCl₄, etc) in aqueous solution at a low reaction temperature on various substrates including metal oxides and organic polymeric materials [23–29]. It should be mentioned that in the above LPDs, source chemicals exist in the movable forms of molecules (or complexes), ions, or clusters in the liquid phase prior to transport/conversion to solid phases. In this sense, these condensed-phase reactions are analogous to the vapor-phase reactions, except for the solvation effects for the starting chemicals and other known physical processes in the solution phase.

In this chapter, we will limit ourselves only to material syntheses involving conventional solid-state reactions; that is, one or more source chemicals are in the form of solid precursors, and most likely at elevated temperatures or with other external energy inputs (e.g., electrolysis), for the formation of nanotubular materials. Certainly, we realize that a strict classification of the reviewing scope cannot be done so simply, as in many cases multiple reaction steps (and thus possibly multi-techniques) are applied to a particular synthesis. In such cases, the context of “solid-state synthesis” of this chapter is extended to any synthetic processes in which one or more of steps involve solid-state reactions, including dissolutions of solid phases. It should be mentioned that although multiwalled CNTs have been transformed directly from solid carbon precursors without using metal catalysts in high-temperature arc furnaces at 2200–3000 °C [30, 31], the synthesis of this type still belongs to the arc-discharge method in general.

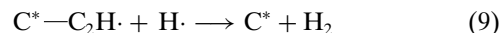
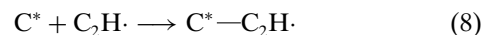
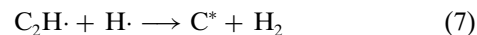
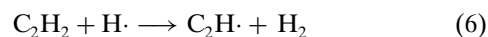
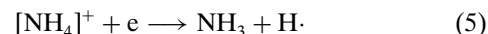
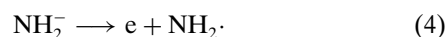
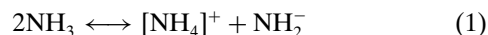
3. CARBON NANOTUBES PREPARED BY SOLID-STATE REACTIONS

3.1. Electrolysis

Although the vapor-phase preparation of CNTs will still remain as a major processing method in the foreseeable future, solid-state synthetic methods become more and more important because of their promise for large-scale production. In 1995, multiwalled CNTs were produced for the first time by the electrolytic conversion of a graphite cathode in molten lithium chloride. By passing an electric current between carbon electrodes, it had been found that formation of CNTs in condensed phase is also possible [19–21]. In these experiments, a high-purity carbon crucible (as the anode, diameter 2.5 cm, depth 3 cm) was filled with around 1 g of LiCl and heated to its melting point at 600 °C in air. A high-purity carbon rod (diameter 3 mm) was immersed in the LiCl melt serving as the cathode for

electrolysis cell. During the reaction, 30 A current was maintained for 1 min. The immersed part of the cathode was eroded (small pits formed on the surface), and particulate materials (10–30 mg) were found dispersed throughout the melt. After the separation and purification, onion-like carbon polyhedral particles and nanotubes (2–10 nm in diameter, and the length longer than 500 nm) were observed with TEM technique. Interestingly, some of the nanotubes are found encapsulated with lithium chloride, oxide, or possibly lithium in their cavities. All nanocarbons prepared in this way are multiwalled, consisting of 5–20 concentric layers. Unlike those prepared with the vapor-phase techniques, the thus-prepared nanotubes are not straight, easily forming loops. Nonetheless, this electrolysis investigation shows important implications for continuous methods of nanotube production, as well as facilitating encapsulation of material within the inner cavities of carbon nanotubes.

The actual mechanism of the formation is not clear at this time. It is noted that the carbon electrode probably dissolves in the molten droplets of alkali metal [19–21]. However, one can also propose that the formation of CNTs may occur not only from pure carbon clusters/aggregates, but also from common hydrocarbon radicals like CH₃· or C₂H· with subsequent dehydrogenation similar to the CVD processes [32]. In addition to the electrolysis methods in fused alkali salts [19–21], a new electrochemical method for multiwalled CNTs from acetylene solution in liquid ammonia has been developed at 233 K (below normal room temperature!) [32]. Single-crystal silicon (*n*-type Si(100) wafers) was used as electrodes and no metal catalysts were further used. It is further proposed that chain radical reactions may be involved in the growth process, and some of these reactions are listed below [32]:



where C* indicates a carbon product from the synthesis (carbon nanotubes, or graphitic and turbostratic carbon, or amorphous carbon). However, unlike the carbon electrode cases [19–21], as the precursor used in this case was a hydrocarbon compound rather than pure carbon element, this electrochemical CNT synthesis does not exactly belong to “solid-state” type, but to a general condensed-phase method.

3.2. Metathesis

Solid-state metathesis reactions have gained considerable attention over the past few years in the synthesis of refractory ceramics and semiconductors [33–36]. Unlike the long-lasting conventional solid-state reactions that encounter

large diffusion barriers, rapid metathesis in solid-state can reach high temperature ($>1000\text{ }^{\circ}\text{C}$) on a very short time scale ($<1\text{ s}$) [37].

Very recently, solid-state synthesis of CNTs via metathesis has also been conducted using carbon halides (e.g., C_2Cl_6), lithium acetylide (Li_2C_2), and catalyst cobalt dichloride (CoCl_2). The chemical reaction can be given as [38]:



The theoretical maximum (exchange) reaction temperature of 2307 K was calculated, based on reaction enthalpy data of Eq. (10). The reactions are self-propagating and can be simply initiated with a heated filament. With 5 mol% (with respect to carbon) of cobalt dichloride added to the precursor compounds, both single- and multiwalled CNTs, along with graphite-encapsulated cobalt nanoparticles, have been synthesized. Some of the multiwalled nanotubes have a length up to 50 nm or more and possess a bamboo-like structure (the morphology similar to that formed from vapor-phase syntheses!). Graphite-encapsulated cobalt nanoparticles, amorphous, and graphitic carbons are also found, noting that the latter two byproducts can easily be removed by washing in concentrated nitric acid. It has been found at lower catalyst concentrations ($<5\text{ mol}\%$) that the yield of single-walled CNTs significantly reduces, while at higher Co concentrations ($>5\text{ mol}\%$), the yield of graphite-encapsulated nanoparticles rises rapidly with no evidence for the formation of single-walled CNTs. Therefore, the 5 mol% CoCl_2 is considered to be an optimal concentration for the formation of CNTs. Among the various catalysts tested (5 mol% FeCl_3 , 5 mol% NiCl_2 , 2–10 mol% CoCl_2) for Eq. (1), it is noted that CoCl_2 is the only case giving single-walled CNTs, although all of them can produce multiwalled CNTs and graphite-encapsulated metal nanoparticles. Without a transition-metal catalyst, on the other hand, only graphitic and amorphous carbons can be formed.

The reaction temperature of these solid-state metathesis reactions can be further regulated. Calculation performed by the same group of researchers indicates that increasing the length of the carbon chain can lower the reaction temperatures. Furthermore, it has been shown that replacing chlorine with fluorine can also reduce the reaction temperature. In principle, hydrogen in substitution of chlorine can further decrease the reaction temperature. This theoretical prediction has been confirmed experimentally using a copolymer of poly(vinyl chloride) and poly(vinylidene chloride) with a 5 mol% of FeCl_3 catalyst to form multiwalled CNTs [38]. It is believed that these reactions, once optimized, will represent an economic synthetic route using cheaper precursors under less-demanding reaction conditions for the CNTs production.

3.3. Thermal Reactions (Pyrolysis)

It has long been known that carbon can retain in carbon-containing ceramic solids after their thermal decompositions owing to insufficient oxidation reactions to CO and CO_2 for the trapped carbon species under atmospheric conditions. For example, significant amounts of carbons were found in organic-compound intercalated hydrotalcites and

sol-gel materials derived via organic routes after heat treatments before the discovery of CNTs [39–43]. As revealed later, these residual carbon phases may also be formed as fullerene-like carbons such as short multiwalled CNTs and polyhedral particles at presence of metal catalysts [44–46].

Carbon materials can be converted from polymeric materials via simple thermal treatments. In particular, these polymeric precursors can be fabricated into various shapes with the assistance of porous solid templates, as illustrated in Figure 1 for a hypothetical array of one-dimensional (1D) channels in synthesis of carbon nanotubes. As early as in 1989, inclusion of polyaniline filaments in zeolite molecular-sieves had been achieved [47]. In 1992, zeolite-Y and mordenite had been utilized as this kind of template materials for radical polymerization of acrylonitrile within their open pores and channels. The thus-prepared polyacrylonitrile (PAN) can be converted into graphite-like conducting carbon filaments via pyrolysis at elevated temperatures [48]. Using the similar solid-state approach, *in-situ* polymerization of acrylonitrile had also been carried out, producing PAN nanotubes within the pores of a nanoporous membrane [49]. In a subsequent heat treatment, the thus-prepared PAN nanotubes underwent graphitization that gave aligned multiwalled CNTs, similar to those depicted in Figure 1.

Very recently, carbon 60 (C_{60}) fullerene nanotubes have also been prepared from the template technique with 1D alumina channels with a density of $10^{11}\text{ channels/cm}^2$ [50]. In this synthetic preparation, the alumina template was repeatedly dipped into a C_{60} containing toluene solution. After several dipping-and-drying cycles, the C_{60} deposited templates were heated at $500\text{ }^{\circ}\text{C}$ for 5 hours in an argon atmosphere and then cooled down to room temperature. The as-grown C_{60} nanotubes after removal of the template (with NaOH solutions) are well aligned (tube diameter 220–310 nm, and tube length $60\text{ }\mu\text{m}$), showing a hexagonal long-range order in accordance with the original 1D channel array (e.g., Fig. 1). The surfaces of these tubes are smooth and clean, and the FTIR investigation shows four typical C_{60} absorption

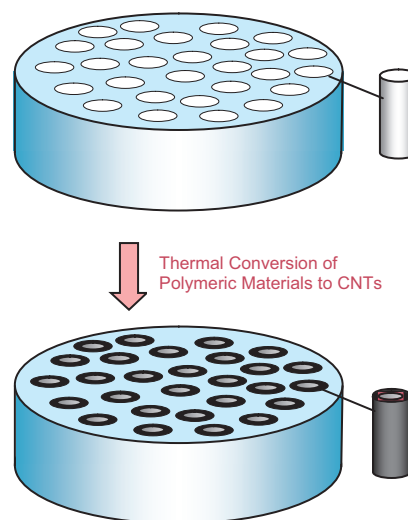


Figure 1. Schematic drawing of porous inorganic template growth of CNTs with prefilled organic materials in the one-dimensional channels and thermal conversion reactions.

bands at 527, 577, 1182, and 1431 cm^{-1} , respectively. The TEM and electron diffraction (ED) observations indicate that the C_{60} nanotubes are polycrystalline, and the structure of nanotubes is a mixed phase of face-centered cubic and hexagonal close-packed arrangements [50]. In view of its versatility, this approach should represent a promising route for formations of other nanotubular structures for various materials including polymer, inorganic, and organic compounds. In particular, this technique could be a general method for thermopolymerization and *in-situ* polymerization under controlled conditions.

Unlike the above cases, in which porous templates were used, nanotubular materials can also be prepared with negatype templates [51, 52]. In particular, micrometer-sized carbon tubes had been prepared by solid-state reactions with polymeric composite fibers that have a novel core-skin structure [53, 54], as described in Figure 2. The composite fibers were fabricated by a typical reaction coating method [55]. Under a nitrogen atmosphere (flow rate at 0.5 L/min), the composite fibers comprising a thermally removable polymer core [e.g., poly(ethylene terephthalate), PET] and a thermally more stable skin (e.g., conducting polymer: polypyrrole, PPy) were heated in a quartz tube oven from room temperature to 1000 °C (at a heating rate of 10 °C/min). Upon this thermal heating, the reactions were carried out at 1000 °C for 0 to 3 hours, respectively, prior to the thermally formed products being cooled down to ambient temperature. This pyrolysis method turned out to be very versatile. It had been used to prepare micrometer- or submicrometer-sized carbon tubes with controllable wall thickness in the range of smaller than 30 nm to a few micrometers and with a few centimeters in length by changing the thickness of the PPy skin coating as well as the diameter of the PET core fibers. More importantly, this method allows us to prepare well-organized two- or three-dimensional structures assembled by carbon tubes several centimeters in length via selecting or preparing appropriate woven polymeric templates [56]. It has been proven that the diameters of the PPy-skinned PET fiber composites are directly proportional to the number of coating treatments. For example, the corresponding weight gain of the composite samples was measured to be 0.66%, 9.3%, 18.7%, and 27.1% (with respect to the original uncoated PET fibers) when 1 to 4 cycles of PPy coating were applied, respectively. As shown in these weight data, the growth of PPy skin on the fresh PET surface (i.e., the first coating cycle) was significantly slower [54]. This weight-variation suggests that different formation mechanisms for different PPy coating layers might be involved.

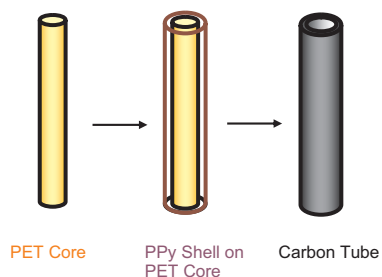


Figure 2. Synthetic process for making micrometer-sized carbon tubes using PET core templates.

By varying the concentrations of PPy and oxidant and reaction time, it is understood that most of PPy particles in the first coating cycle might have initiated and continued their growth in the solution phase, and only those close to the surfaces of PET fiber cores have chance to deposit via chemisorption and/or physisorption. Because of the competition between the solution phase and surface phase, on one hand, the resulting PPy in the first coating layer is thinner. Due to the lower oxidation potential of the first PPy layer, on the other hand, the subsequent coating or polymerization of pyrrole becomes easier. Scanning electron microscopic observations on these thermally treated samples reveal that the cores of composite fiber start to melt at a temperature between 230 and 290 °C and then decompose at 390 °C, leaving behind only carbon microtubes. Both the diameter and thickness of carbon tubes decrease continuously when the heating temperature is increased. Furthermore, since the PPy is thermally more stable than the PET, the resultant carbon tube walls are mainly derived from the PPy skin layers. With a recently developed method for fabrication of crystalline linear polyethylene (PE) nanofibers [57], carbon tubes with diameters in the nanometer regime can be further prepared using these nanometer-core fibers. However, it should be mentioned that the resultant carbon tubes prepared at 1000 °C are largely amorphous. With a further annealing at 1000–2400 °C, the disordered amorphous carbon tube walls can be gradually changed to a highly ordered graphitic phase with preferred orientation. Accordingly, in summary, the temperatures for these thermal reactions can be divided into three different zones: (i) 200–500 °C, formation of precursor tubes, (ii) 500–1700 °C, carbonization of the precursor tubes, and (iii) 1700–2400 °C, graphitization process [58] to increase the crystallinity of the carbon tubes.

Without the solid templates, synthesis of CNTs via direct thermal treatment of polymers (without using catalysts) can also be achieved [59]. The solid precursor used was a transparent brown resin prepared from anhydrous citric acid ($\text{HOOCCH}_2\text{C}(\text{OH})(\text{COOH})\text{CH}_2\text{COOH}$) and ethylene glycol ($\text{HOCH}_2\text{CH}_2\text{OH}$) with a molar ratio of 1:4. The resin was heat-treated at 400 °C for 8 hours in air on an alumina boat followed by natural cooling to room temperature. The CNTs obtained in such a way are multiwalled tubes with diameters ranging from 5 to 20 nm and lengths shorter than 1 μm . In addition to the tubular morphology, small carbon graphitic particles and amorphous sheet-like carbons are also found. Regarding heating condition at 400 °C, several kinetically competing chemical processes are brought to attention: formation reactions of CO, CO_2 , CNTs, graphitic particles, and amorphous sheet-like carbons. It is believed that the decomposition of polymer might generate dangling bonds of carbon for further reconstruction at this temperature. Therefore, the current CNT growth seems to take place as a nonequilibrium solid-state process. The simple synthetic conditions, such as the solid-state reaction, catalyst-free, and mild heat treatment in air atmosphere, are particularly attractive to mass-production of CNTs. It has also been confirmed that the CNTs can also be obtained under vacuum condition or with inert atmospheres for the similar reaction processes.

Solid-state synthesis of CNTs can also be simply conducted with organic compounds such as polymers or large

hydrocarbons and transition metals as catalysts for direct thermal decomposition reactions. In this type of reactions, the CNTs are formed together with the original metal catalysts used in the synthesis. Without a further separation/purification, the resultant mixtures can be viewed naturally as the CNTs/metal nanocomposites. Nonetheless, the product CNTs can be easily separated from product mixtures via acid or thermal treatments after the solid-state catalytic reactions. It had been recently demonstrated that thermal decomposition of polyethylene with nickel catalyst is an efficient method to fabricate large quantities of multiwalled CNTs with fishbone-like morphologies [60]. The content of nickel nanoparticles in the final CNTs/metal nanocomposites is less than 15% by mass, and the mixing of both components is excellent. If desired, the nickel component can be completely removed by thermal processing of the nanocomposites in vacuum at temperatures up to 2800 °C. The CNTs prepared are all multiwalled with lengths of several micrometers, inner channel diameter of 9–12 nm, and outer diameter of 40–50 nm. In particular, these CNTs consist of almost rectilinear sections with lengths of 100–300 nm turned with respect to one another, and their walls are composed in most cases of 40–65 tapered graphene layers with a taper angle along the tubes in the range of 16–35°. Interestingly, the dimensions and shapes of wider sections of the inside channel can be correlated to those of nickel nanoparticles, which are located in most cases at the ends of the nanotubes. In order to have transport measurements, the mixture powders were cold pressed under high pressure of about 25 kBar and shaped into bars with dimensions of $1 \times 2 \times 3 \text{ mm}^3$. It has been found that the electric resistivity (R) of these nanocomposites at room temperature is about $1 \Omega\text{cm}$. The resistance was measured as a function of temperature down to the liquid-helium temperature in magnetic fields of up to 75 kOe. In the low-temperature range of 4.2–100 K, the resistivity of the composite changes according to the law of $\ln R \propto (T_0/T)^{1/3}$ where $T_0 \approx 7 \text{ K}$. The measured magnetoresistance can be interpreted in terms of two-dimensional variable range hopping conductivity. It has been assumed that the space between the inside and outside walls on the nanotubes acts as a two-dimensional medium. These CNTs with nested-cone morphologies are characterized by very high densities of electron states at the Fermi level of about $10^{21} \text{ eV}^{-1}\text{cm}^{-3}$, which is a typical value of metals [60].

Different from the above cases, in which organic solids were used as carbon sources, CNTs can also be synthesized from inorganic carbon-containing solids, such as SiC. For example, an aligned CNT film was formed and investigated from surface decomposition of β -SiC at 1700 °C by *in-situ* transmission electron microscopy [61]. The degree of the orientation in the CNT film depends strongly on the β -SiC crystal planes; CNTs preferentially orient along [111] direction on the $(111)_{\beta\text{-SiC}}$ surface. Later, it was further found that the surface decomposition was progressed by an oxidation reaction with residual oxygen gas, based on the observations of high-resolution electron microscopy and electron energy-loss spectroscopy [62, 63]. Similar syntheses using single-crystal wafers of 6H-SiC with Si(0001) and C(0001) terminations were also carried out, aiming at a mechanistic understanding of the formation of aligned

CNTs [64]. As depicted in Figure 3, the SiC single wafers were heated at a temperature range of 1200–1700 °C for half an hour in a vacuum furnace with an electric resistance heater. On the C-face, vertically aligned CNTs 3–5 nm in diameter and $0.25 \mu\text{m}$ in length were formed after heating. In contrast, on the Si-face, graphite sheets (ca. 5 nm in thickness) parallel to the crystal plane were generated. The CNTs formed on the C-face were about 50 times thicker than the graphitic layers formed on the Si-face under the same decomposition conditions. Based on the experimental results, the difference in carbon products can be further explained. The graphitic sheets formed on the Si(0001) are attributable to an epitaxial growth as graphitic (0001) plane is parallel to the 6H-SiC(0001). On the basis of the two- and three-layer collapse mechanisms [65, 66], the area carbon density of the three condensed layers is around $3.67 \times 10^{15} \text{ atoms cm}^{-2}$, which is close to the carbon density of a graphite layer ($3.80 \times 10^{15} \text{ atoms cm}^{-2}$). For the crystal plane with C-termination, carbon islands could be nucleated at impurity or defect sites, and develop into the larger particles of about 5 nm in size. There are two types of carbon islands, corresponding to spherical and flat caps for the final CNTs. The first one, spherical particles, would be graphitized from the surface. The second one, formed from two to five (flat) graphitic layers, would curve to connect with the carbon atoms on the surface. In particular, the diameter of the nanocaps depends on the SiC decomposition rate, the surface diffusion coefficient of carbon, the cohesive energy of carbon, and the flatness of the SiC surface [64]. As for the decomposing product SiO, the atomic oxidation mechanism of SiC is thought to be plausible. For example, gaseous SiO molecules could be continuously generated at the boundary between SiC and the graphite clusters. Nonetheless, the oxidation or decomposition process of SiC is thought to be rather complicated. The formation of Si—O—C bonding during the SiC oxidation has been investigated theoretically [67]. It has been realized that the atomic difference between the Si- and C-faces of SiC must have played an important role in the SiC decomposition.

In general, controlled synthesis of CNTs in solid state is much more difficult than that in vapor phase, especially

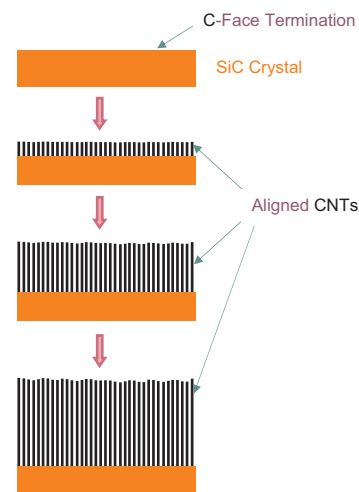


Figure 3. Growth of aligned CNTs using oriented SiC single-crystal wafers as solid precursors.

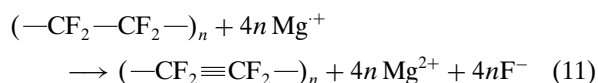
for the preparation of single-walled CNTs. Very recently, this difficulty has been overcome, and aligned single-walled CNTs have been synthesized successfully in solid state. Using the Si-face of hexagonal silicon carbide (6H-SiC) at temperature above 1500 °C [68], two types of CNTs have been grown over the steps or terraces of the SiC. The first type, Y-shaped CNTs, results when the surface morphology is composed of terraces. The CNTs form a web-like network with a predominance of 120° for inter-bundle (or inter-tube) angle. The second type, T-shaped CNTs, is found when the surface is composed of parallel steps. In the latter case, the tubes align either along or perpendicular to the step edges which then give an inter-bundle (or inter-tube) angle of 90°. Most importantly, the CNTs prepared are single-walled with a very narrow distribution of diameters. With AFM manipulation, it is further demonstrated that the CNT bundles can be divided into several smaller tubes. In addition to this, it is also confirmed that the AFM manipulation can bring subsurface segments of tubes to the surface. After reannealing the sample in ultra-high vacuum at 1300 °C, the CNTs can return to a well-ordered configuration. This observation indicates that the ordering of the CNTs is due to a diffusion process occurring after the CNT growth.

Regarding the formation mechanism of these flat-aligned CNTs, it is noted that when the Si termination of 6H-SiC is annealed at very high temperature, silicon will evaporate, leaving behind a carbon-rich surface. With atom-resolved STM technique, it is observed that this C-rich surface possesses the hexagonal C-lattice (i.e., graphite layers), and these initially formed graphite layers are not well-defined graphene sheets but more likely composed of small pieces of graphite layers with a high population of dangling bonds at their edges. Due to the thermodynamic driving force, the dangling carbon bonds can be saturated by folding of the graphene pieces. On the other hand, the thus-formed nanotube segments can act as seeds for the attachment of new carbon atoms, leading to the subsequent nanotube growth [68].

3.4. Electron-Induced Synthesis

Organic compounds containing linear *sp*-bonded carbon chains have been known to be useful reactants for synthesis of carbonaceous materials [69]. It has also long been known that organic compounds and their polymeric materials decompose easily under the irradiation of electron beam during the measurement with electron microscopy. In the nanocarbon investigations, energetic electron beams in TEM have been well known to cause reconstruction (or transformation) of carbon nanoparticles to more compact carbon onions [70]. Very recently, a new process for solid-state synthesis of nanocarbon materials under TEM electron irradiation has been developed, in which polyynes-containing carbons are involved as precursor compound for CNT formation [71, 72].

The polyynes-containing carbon is prepared with an electrochemical reduction between a poly(tetrafluoroethylene) (PTFE) film and a sacrificial magnesium anode [72, 73]:



The above reduction was carried out by a two-electrode method (anode: magnesium; cathode: stainless steel) in tetrahydrofuran, containing lithium chloride and iron (II) chloride as supporting electrolytes [73]. The polyynes-containing carbon was formed on the reduced surfaces (about 1 μm in depth) of PTFE films (10 mm × 10 mm × 60 μm), and the carbonized layer was confirmed to contain the polyynes structure by Raman spectroscopy (e.g., C≡C stretching vibration at 2100 cm⁻¹). The *in-situ* synthesis of CNTs using the carbonized PTFE films can be described in the sequence shown in Figure 4. First, the cross-section specimen was heated towards 800 °C (at the rate of 15 °C/min) without the electron irradiation, during which the remaining PTFE part in the thin film was melted and disappeared at about 350 °C. After an electron irradiation at 800 °C (electron acceleration voltage 100 kV, irradiated charge density about 103 C/cm²), copious amounts of CNTs were formed on the surface of the layer. The length of these CNTs is typically at 1 μm while the outer diameter of these tubules is in the range of 10–50 nm and the inner diameter is of about 8–30 nm. It is noted that graphitization of the shell of the tubules was low although the tubules resembled “CNTs.” Interestingly, the carbon tubules were found only on the substrate side of the polyynes-containing carbon layer, as illustrated in Figure 4. Based on these observations, it is believed that the PTFE layer can protect the polyynes structure in the carbonized layer from the oxidation in moist air. The undamaged polyynes structure and free space are two important factors responsible for the observed CNT growth. When the heating temperature is below ca. 400 °C, the same electron irradiation does not cause any CNT growth. Instead, damages such as bond rupture and loss of mass and crystallinity take place due to the electronic irradiation on the organic materials [71].

Very recently, the same material system has been investigated in a greater depth [72]. The *in-situ* TEM observation indicates that graphene layers are first formed around the magnesium particles (from electrochemical reduction process) with low crystallinity. The metal particles evaporate gradually while a further graphitization takes place upon the heating (600 °C) and irradiation, leading to formations of carbon nanocapsules (CNCs) and nanoparticles (CNPs), as depicted in Figure 5. One important finding in this work is

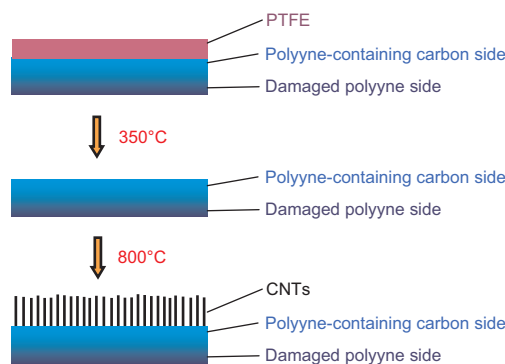


Figure 4. Illustration of process of heating and synthesis of CNTs under an electron radiation: melting of the PTFE film occurs at 350 °C and growth of aligned CNTs starts on the nondamaged polyynes side at 800 °C.

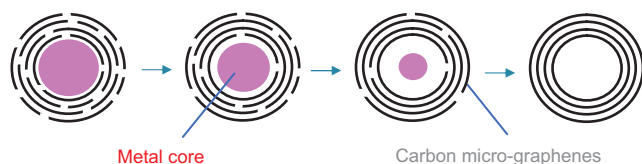


Figure 5. Formation process of carbon nanocapsules and nanoparticles upon the evaporation of magnesium metal core particles under both thermal heating and electron radiation.

differential growth of CNTs from CNCs and CNPs. Under the investigated conditions, CNTs are always grown on the inside of the carbonized layer while CNCs and CNPs are grown on the outside where the magnesium metal particles are supposed to be richer based on the incorporation mechanism during the electrochemical reduction. These metal particles may act as growth cores to form the CNCs and CNPs. Compared to those in the inner layer, polyene-containing carbons in the outside layer are more oxidized (or more damaged), and thus more wettable on the metal particles owing to easy cross-linking. The cross-linking increases the viscosity of the melted carbons, prohibiting the formation of long carbon rods (1D). It has been known that the CNTs are formed from the rod-like carbons after graphitization. Therefore, through this *in-situ* TEM investigation, selective solid-state formations of CNTs and CNCs/CNPs can be explained thoroughly with direct experimental evidences, especially with the degree of graphitization of graphene sheets for all these nanocarbons at various formation stages [72a].

Apart from the selective growth study, the same group of researchers has recently observed the graphitization mechanism during the CNT formation based on the *in-situ* HRTEM investigation [72b]. Their study shows that micrographenes exist from the beginning of the formation process and later change to highly ordered graphene layers through fusion and rearrangement of premature layers. These processes are also accompanied by evaporation of micro-graphenes. In their latest investigation [72c], these researchers found that the CNTs prepared under TEM environment are formed in two steps: rapid formation of rod-like carbons, and slow formation of hollow cavity in parallel with graphitization. In particular, the length and the diameter of the CNTs are defined in the first step, and are not varied any further during the second step, that is, the hollow inner cavity formation.

3.5. Pyrolysis in Mesophase

In contrast to the common gas-phase and solid-phase pyrolytic syntheses for CNTs, fullerene-like carbon nanomaterials can also be prepared with a newly developed pyrolytic method in which well-defined polycyclic aromatic hydrocarbons (PAHs) are used under mild reaction conditions [74]. This approach, to some extent, is similar to the classical liquid-phase carbonization of organic compounds (aromatics, petroleum, and coal-tar pitches) [75, 76]. Very recently, this method has been demonstrated for synthesis of various nano- and microcarbons using the compound hexa-alkyl-substituted hexa-*peri*-hexabenzocoronene (HBC), whose molecular structure is detailed in Figure 6, as a

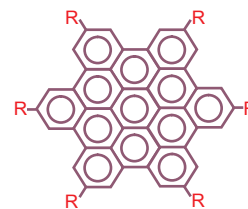


Figure 6. Molecular structures of substituted HBC ($R = \text{CH}_2\text{-CH}_2\text{-C}_{10}\text{H}_{21}$) and unsubstituted HBC ($R = \text{H}$) used as precursor compounds for pyrolysis in the mesophase.

starting precursor. All pyrolysis experiments were carried out in evacuated and sealed quartz ampules by electric heating (rate $2\text{ }^\circ\text{C}/\text{min}$). The starting compound HBC has a large two-dimensional disk-like graphite subunit and exceptional mesomorphic properties. The flexible alkyl chains ($-\text{R}$) around the graphite disks lower the melting points and induce the formation of stable discotic mesophases in a columnar arrangement of the disk-like molecules resulting from a stacking of the π -layers. During the thermolysis at moderate temperatures (e.g., $400\text{ }^\circ\text{C}$, 72 h), even larger structures can be further built up, preserving the liquid crystalline order. In this step, it is believed that the prolonged heat treatment will provide highly oriented structural units, as a consequence of their mobility in the melt. The synthesis also includes thermal oligomerization of the HBC subunits following the cleavage of alkyl side chains with the preservation of the initial mesomorphic order. After these pretreatments, graphitization of the extended PAH structures can occur at a temperature (e.g., $800\text{ }^\circ\text{C}$ or $650\text{ }^\circ\text{C}$, 24 h) much lower than the normally used range of $2000\text{--}3000\text{ }^\circ\text{C}$ [75], which leads to generation of different carbon micro- and nanoparticles in the absence of metal-based catalysts. Different substrates (e.g., quartz and mica) for carbon deposition have been investigated. Many of the carbon objects, such as nanocolumns, nanodonuts, nanosticks, zigzag, and root-like micro-objects, synthesized with this method are new nanocarbon morphologies observed for the first time with this novel method.

One important note in these syntheses that must be mentioned is that the liquid crystalline properties of the precursor organics are required. Without the alkyl side chains (i.e., they are replaced by H, i.e., $R = \text{H}$) in the HBC molecules, an ordered mesophase cannot be formed, which yields black carbon products (disordered and spongy structures) that are completely different from those obtained with the alkyl-substituted HBC after the same pyrolysis treatments. Therefore, a proper control of alkyl chain cleavage and a directional cross-coupling of radical intermediates in an ordered mesophase are key prerequisites for the formation of large mesoscopic structures in the above carbon material preparations [74].

3.6. Hydrothermal Synthesis

Hydrothermal and solvothermal methods have long been used for inorganic materials synthesis. Since the finding of CNTs, these methods have also been utilized widely for separation and purification of as-grown CNTs, including both

single- [77, 78] and multiwalled CNTs [79]. More importantly, hydrothermal processes for the formations of amorphous carbon as well as CNTs had been developed in recent years [80–87].

In these hydrothermal reactions, solid-state carbon-containing materials such as amorphous carbon [84], fullerene carbon (e.g., C_{60} [85]), and polymeric carbon (e.g., polyethylene [86]) have been adopted as starting materials of carbon source. Using amorphous carbon and distilled water, carbon nanocells can be prepared at 600 °C in an autoclave without using metal catalysts [84]. The straight segments of the polygonal cell walls show a well-defined lattice with an interlayer spacing of about 0.33 nm which corresponds to the 002 distance of a graphitic lattice. The graphitic multiwalls grew as a result of the hydrothermal treatment of amorphous carbon. The interpenetrating carbon nanocells form a very porous texture. At 800 °C and 100 MPa, the carbon products showed as aggregates of needle-like or polygonal nanoparticles. The CNTs formed have diameters in the range of tens and lengths in the range of hundreds of nanometers. It is recognized that the mechanism by which amorphous carbon rearranges into curled graphitic onions is more complex than in multisheet graphitic carbon produced in the gas-phase reactions and involves debonding of graphitic clusters from the bulk carbon material due to a catalytic effect of hydrothermal fluids [84].

The behaviors of fullerene C_{60} have also been investigated with the similar hydrothermal treatments in the temperature range of 200 to 800 °C and 100 MPa [85]. It is found that the fullerene molecules can survive in water up to 400 °C for 48 h under the studied hydrothermal conditions. However, they gradually transform to amorphous carbon when the heating temperature or time is increased. Note that C_{60} is thermally stable without water. Molecular dynamic studies have shown that C_{60} is stable up to over 4000 °C in the carbon-only system [88]! At 700 °C, high-quality open-ended multiwalled CNTs are formed in the vicinity of nickel particles (which act as a catalyst). The typical outer diameter of the hydrothermally formed CNTs is about 30–40 nm, and the wall thickness is ca. 5 nm. The observed results clearly indicate that water strongly accelerates the transformation of fullerenes. This hydrothermal process is kinetically controlled, and longer reaction time will shift the stability range to lower reaction temperatures.

Using polyethylene (PE, high density) sheets or ethylene glycol (EG) as a carbon source, the hydrothermal formation of nanocarbons has been investigated in a greater depth with a two-step process [86]. In step one, a post-pyrolysis C—H—O equilibrium is established, and in step two, the growth of graphitic carbon occurs with an increase in reaction pressure. Depending on the size of metal particles (Ni as a catalyst), flake-like graphite or CNTs (70–1300 nm in diameter) were generated. Without using water, the CNTs synthesized had multiple internal caps. On the contrary, very few internal obstructions and a large inner diameter were observed when water was used in the synthesis. The quality of the CNTs is exceptional, while Ni particles in the carbon tube tips can be easily found. The presence of water appears to be responsible for the large internal channels and highly graphitic nature of the carbon deposited. More importantly, high integrity of hydrothermally synthesized

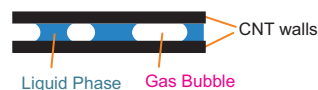


Figure 7. CNTs synthesized with hydrothermal methods. Both gas bubbles and liquid entrappings can be observed in the inner cavity of the as-prepared CNTs.

CNTs is demonstrated by the existence of gas/liquid inclusions trapped inside the tube cavities, as shown in Figure 7.

Regarding the formation mechanism of CNTs under hydrothermal conditions, it has been recognized that the precursor chemistry is not critical in the process, with the most crucial factor being the C—H—O equilibrium established in step one. Because EG/water and PE/water mixtures yield very similar pyrolytic carbon products, it is believed that the C—H—O equilibrium compositions in the two systems are very similar, and the equilibrium species of importance are CO , CO_2 , H_2O , CH_4 , and H_2 in these cases. The injected gaseous species can be converted to desired nanocarbons via catalytic carbon condensation at higher temperatures or pressures. Finally, it should be mentioned that the liquid-encapsulated CNTs synthesized in this type of hydrothermal methods can be used as nanofluidic devices and as lightweight reinforcement for composites [86, 87].

The above hydrothermal synthesis can be further extended to organic solvent conditions (also called solvothermal synthesis). Recently, synthesis of CNTs had been carried out using a so-called “benzene-thermal-reduction-catalysis” route [89]. In this method, a refluxed mixture of $FeCl_3 \cdot 6H_2O$ and $HAuCl_4 \cdot 3H_2O$ (Au:Fe molar ratio = 1:1) in thionyl chloride ($SOCl_2$) and $AgCl$ were used respectively as catalysts. A typical synthesis can be summarized as follows: 8 mL of tetrachloroethylene (C_2Cl_4), 10 mL of benzene, 5 g of potassium, and 100 mg of catalyst precursor were added sequentially into a stainless steel autoclave, which was then heated at 200 °C for 27 h, and cooled down to room temperature naturally. The TEM investigation for the synthesized products indicates that CNTs are produced in a straight form with lengths of 1.8 μm , inner diameters of 60 nm, and outer diameters of 80 nm on average. The walls of CNTs are multiwalled, and the yield is about 15% from the original reagents through electron microscopic observation. In addition to the CNTs, carbon nanorods are also formed with this method, with a yield of about 60%. It is believed that the freshly reduced C_2 (from C_2Cl_4) may also assemble into one-dimension conjugate carbon chain clusters. This could be the reason for the formation of carbon nanorods observed in the presence of Ag catalyst in the synthesis [89].

4. CONCLUSIONS

As summarized above, different solid-state methods for CNT synthesis have been developed over the past decade, offering a wide range of selections for future specific applications. Nonetheless, the current status of solid-state CNT synthesis is just started. Although the solid-state methods promise possibilities for large-scale CNT production, the current research field is still far from its maturity. Many

technical obstacles exist, compared to the existing vapor-phase methods. One of the unsolved difficulties is irregularity and polydispersivity of the CNTs prepared with these solid-state methods. Generally speaking, as exemplified in the previous section, the overall quality of the CNTs is poorer than their vapor-phase synthesized counterparts. The second technical difficulty encountered in the solid-state synthesis is the alignment of the CNTs, because the synthetic processes are normally carried out in a less controllable manner, compared to much more sophisticated vapor-phase CNT fabrications. Furthermore, the solid precursors and starting chemicals used at this time may not be sufficiently economical and environmentally benign, as special design of the precursor molecules and more stringent reaction conditions are usually required.

In order to turn the solid-state syntheses of CNTs into practical approaches, several improvements should be made in the future. First, for example, we may have to search for new solid-precursor materials; perhaps more complex carbon-containing nanocomposites such as organic-inorganic hybrid materials will fulfill the requirements. Second, solid precursors with distinct structural anisotropy or well-defined crystal orientation are ideal candidates for the preparation of aligned CNTs (as demonstrated in Section 3.3). This class of materials may also include layered organic-inorganic self-assemblies in view of their excellent structural anisotropy and richness in carbon content. Third, the mesophase pyrolysis that has shown promising potential for large-scale CNT production is worthy of further investigations. This method may be further improved with introductions of supramolecular templates as CNT cores/micelles or tube-directing reagents in the synthesis to produce CNTs with a better monodispersivity. Perhaps pre-structured inorganic (including metal catalysts) or organic solid templates can also be introduced for carbonization and graphitization in this type of syntheses to achieve oriented growths of CNTs. Fourth, the hydrothermal synthesis of CNTs may further benefit from future investigations on template-directing growths in which organized metal nanoparticles in well-prepared thin films may act as both a catalyst and a nucleation template for aligned CNTs. Furthermore, in addition to the common thermal energy source used, high-energy electrons (as demonstrated in Section 3.4), photons, ions, and other extraordinary energy sources may be introduced to the solid-state synthesis of CNTs in order to generate new types of chemical reactions and thus product organizations.

It is anticipated that the vapor-phase syntheses will continue to take the lead of CNTs preparation in the foreseeable future while the solid-state synthesis merely plays a supplementary role. Nonetheless, it has been well conceived that future commercial applications of CNT materials depend on our development of cost-effective synthetic methods for large-scale CNT production. To this end, the solid-state synthesis of CNTs will gradually gain its strategic importance, and it may eventually take the lead when more sophisticated methods are in place in the future. In a broader sense, some of solid-state methods may be further coupled with gas-phase chemical reactions to devise simultaneous multi-phase processes for CNT synthesis, in taking all the advantages of existing growth techniques, although this newer approach will remain challenging for many years ahead.

GLOSSARY

Carbonaceous mesophase A complex mixture of numerous essentially aromatic hydrocarbons containing anisotropic liquid-crystalline particles.

Carbon nanotubes (CNTs) A new form of graphite-related carbon with “rolling” of graphene sheets into a cylindrical morphology. The materials can be broadly divided into two types: single-walled and multi-walled CNTs.

Electrolysis An electrochemical process involves both reduction (at cathode) and oxidation (at anode) reactions for electrolytes in an electrolytic device.

Electron-induced synthesis Chemical synthesis with assistance of external electrons (e.g., under the radiation of an energetic electron beam).

Hydrothermal synthesis A chemical synthesis carried out under high temperature and pressure conditions. The high pressure is normally self-generated from water vapor (or other chemical solvents, i.e., solvothermal synthesis) at elevated temperatures.

Metathesis The chemical replacement or transposition takes place between two adjacent molecules or two different reactants.

Pyrolysis A chemical process involves thermal decomposition reactions of reactants.

REFERENCES

1. P. M. Ajayan and T. W. Ebbesen, *Rep. Prog. Phys.* 60, 1025 (1997).
2. S. Subramoney, *Adv. Mater.* 10, 1157 (1998).
3. C. N. R. Rao, B. C. Satishkumar, A. Govindaraj, and M. Nath, *Chem. Phys. Chem.* 2, 78 (2001).
4. J. Liu, A. G. Rinzler, H. Dai, J. H. Hafner, R. K. Bradley, P. J. Boul, A. Lu, T. Iverson, K. Shelimov, C. B. Huffman, F. Rodriguez-Macias, Y. Shon, T. R. Lee, D. T. Colbert, and R. E. Smalley, *Science* 101, 1253 (1998).
5. R. Saito, G. Dresselhaus, and M. S. Dresselhaus, “Physical Properties of Carbon Nanotubes.” World Scientific, Singapore, 1998.
6. A. Huczko, *Appl. Phys. A* 74, 617 (2002).
7. S. Iijima, *Nature* 354, 56 (1991).
8. R. Sen, A. Govindaraj, and C. N. R. Rao, *Chem. Phys. Lett.* 267, 276 (1997).
9. R. Sen, A. Govindaraj, and C. N. R. Rao, *Chem. Mater.* 9, 2078 (1997).
10. T. Kyotani, L. F. Tsai, and A. Tomita, *Chem. Mater.* 7, 1427 (1995).
11. T. Kyotani, L. F. Tsai, and A. Tomita, *Chem. Commun.* 701 (1997).
12. T. Kyotani, L. F. Tsai, and A. Tomita, *Chem. Mater.* 8, 2109 (1996).
13. M. S. Gudiksen and C. M. Lieber, *J. Am. Chem. Soc.* 122, 8801 (2000).
14. M. S. Gudiksen, J. Wang, and C. M. Lieber, *J. Phys. Chem.* 105, 4062 (2001).
15. M. H. Huang, Y. Wu, H. Feick, N. Tran, E. Weber, and P. Yang, *Adv. Mater.* 13, 113 (2001).
16. M. H. Huang, S. Mao, H. Feick, H. Yan, Y. Wu, H. Kind, E. Webber, R. Russo, and P. Yang, *Science* 292, 1897 (2001).
17. Z. W. Pan, Z. R. Dai, and Z. L. Wang, *Science* 291, 1947 (2001).
18. Z. R. Dai, Z. W. Pan, and Z. L. Wang, *J. Am. Chem. Soc.* 124, 8673 (2002).
19. W. K. Hsu, J. P. Hare, M. Terrones, H. W. Kroto, D. R. M. Walton, and P. J. F. Harris, *Nature* 377, 687 (1995).
20. W. K. Hsu, M. Terrones, J. P. Hare, H. Terrones, H. W. Kroto, and D. R. M. Walton, *Chem. Phys. Lett.* 262, 161 (1996).

21. G. Z. Chen, X. Fan, A. Luget, M. S. P. Shaffer, D. J. Fray, and A. H. Windle, *J. Electroanal. Chem.* 446, 1 (1998).
22. L. Pu, X. Bao, J. Zou, and D. Feng, *Angew. Chem. Int. Ed.* 40, 1490 (2001).
23. S. Deki, Y. Aoi, O. Hiroi, and A. Kajinami, *Chem. Lett.* 1996, 433.
24. S. Baskaran, L. Song, J. Liu, Y. L. Chen, and G. L. Graff, *J. Am. Ceram. Soc.* 81, 401 (1998).
25. H. Imai, Y. Takei, K. Shimizu, M. Matsuda, and H. Hirashima, *J. Mater. Chem.* 9, 2971 (1999).
26. H. Imai, M. Matsuda, K. Shimizu, H. Hirashima, and N. Negishi, *J. Mater. Chem.* 10, 2005 (2000).
27. K. Shimizu, H. Imai, H. Hirashima, and K. Tsukuma, *Thin Solid Films* 351, 220 (2000).
28. T. P. Niesen, J. Bill, and F. Aldinger, *Chem. Mater.* 13, 1552 (2001).
29. (a) S. Yamabi and H. Imai, *Chem. Mater.* 14, 609 (2002). (b) K. J. Kim, K. D. Benkstein, J. van der Lagemaat, and A. Frank, *J. Chem. Mater.* 14, 1042 (2002). (c) Y. Masuda, Y. Jinbo, T. Yonezawa, and K. Koumoto, *Chem. Mater.* 14, 1236 (2002).
30. A. A. Setlur, S. P. Doherty, J. Y. Dai, and R. P. H. Chang, *Appl. Phys. Lett.* 76, 3008 (2000).
31. S. P. Doherty and R. P. H. Chang, *Appl. Phys. Lett.* 81, 2466 (2002).
32. A. T. Matveev, D. Golberg, V. P. Novikov, L. L. Klimkovich, and Y. Bando, *Carbon* 39, 137 (2001).
33. J. B. Wiley and R. B. Kaner, *Science* 255, 1093 (1992).
34. P. R. Bonneau, R. F. Jarvis, and R. B. Kaner, *Nature* 349, 510 (1991).
35. I. P. Parkin, *Chem. Soc. Rev.* 25, 199 (1996).
36. R. W. Cumberland, R. G. Blair, C. H. Wallace, T. K. Reynolds, and R. B. Kaner, *J. Phys. Chem. B* 105, 11922 (2001).
37. E. G. Gillan and R. B. Kaner, *Chem. Mater.* 8, 333 (1996).
38. J. L. O'Loughlin, C.-H. Kiang, C. H. Wallace, T. K. Reynolds, L. Rao, and R. B. Kaner, *J. Phys. Chem. B* 105, 1921 (2001).
39. A. Oya, Y. Omata, and S. Otani, *J. Mater. Sci.* 20, 255 (1985).
40. A. Oya, Y. Omata, and S. Otani, *Am. Ceram. Soc. Bull.* 65, 776 (1986).
41. A. Oya, K. Matsunaga, and S. Otani, *Appl. Clay Sci.* 3, 145 (1988).
42. A. Oya, H. Mita, and S. Otani, *Appl. Clay Sci.* 5, 13 (1990).
43. T. Hibino, K. Kosuge, and A. Tsunashima, *Clays Clay Miner.* 44, 151 (1996).
44. L. Ji, J. Lin, and H. C. Zeng, *Chem. Mater.* 13, 2403 (2001).
45. Z. P. Xu and H. C. Zeng, *J. Phys. Chem. B* 104, 10206 (2001).
46. Z. P. Xu, R. Xu, and H. C. Zeng, *Nano Lett.* 1, 703 (2001).
47. P. Enzel and T. Bein, *J. Phys. Chem.* 93, 6270 (1989).
48. P. Enzel, J. J. Zoller, and T. Bein, *Chem. Commun.* 633 (1992).
49. R. V. Parthasarathy, K. L. N. Phani, and C. R. Martin, *Adv. Mater.* 7, 896 (1995).
50. H. Liu, Y. Li, L. Jiang, H. Luo, S. Xiao, H. Fang, H. Li, D. Zhu, D. Yu, J. Xu, and B. Xiang, *J. Am. Chem. Soc.* 124, 13370 (2002).
51. P. Hoyer, *Langmuir* 12, 1411 (1996).
52. P. Hoyer, *Adv. Mater.* 8, 857 (1996).
53. C. C. Han, J. T. Lee, R. W. Yang, H. Chang, and C. H. Han, *Chem. Commun.* 2087 (1998).
54. C. C. Han, J. T. Lee, R. W. Yang, and C. H. Han, *Chem. Mater.* 13, 2665 (2001).
55. R. V. Gregory, W. C. Kimbrell, and H. H. Kuhn, *Synth. Met.* 28, C823 (1989).
56. C. C. Han, J. T. Lee, R. W. Yang, H. Chang, and C. H. Han, *Chem. Mater.* 11, 1806 (1999).
57. K. Kageyama, J. I. Tamazawa, and T. Aida, *Science* 285, 2113 (1999).
58. C. C. Han, J. T. Lee, and H. Chang, *Chem. Mater.* 13, 4180 (2001).
59. W.-S. Cho, E. Hamada, Y. Kondo, and K. Takayanagi, *Appl. Phys. Lett.* 69, 278 (1996).
60. V. I. Tsebro, O. E. Omel'yanovskii, E. F. Kukovitskii, N. A. Sainov, N. A. Kiselev, and D. N. Zakharov, *J. Exp. Theoret. Phys.* 86, 1216 (1998).
61. M. Kusunoki, M. Rokkaku, and T. Suzuki, *Appl. Phys. Lett.* 71, 2620 (1997).
62. M. Kusunoki, M. Rokkaku, and T. Hirayama, *Jpn. J. Appl. Phys.* 37, L605 (1998).
63. M. Kusunoki, T. Suzuki, K. Kaneko, and M. Ito, *Philos. Mag. Lett.* 79, 153 (1999).
64. M. Kusunoki, T. Suzuki, T. Hirayama, and N. Shibata, *Appl. Phys. Lett.* 77, 531 (2000).
65. A. J. Van Bommel, J. E. Crombeen, and A. Van Tooren, *Surf. Sci.* 48, 463 (1975).
66. D. V. Badami, *Carbon* 3, 53 (1965).
67. M. D. Ventra and S. T. Pantelides, *Phys. Rev. Lett.* 83, 1624 (1999).
68. V. Derycke, R. Martel, M. Radosavljević, F. M. Ross, and Ph. Avouris, *Nano Lett.* 2, 1043 (2002).
69. J. Hlavatý, L. Kavan, and J. Kubišta, *Carbon* 40, 345 (2002).
70. (a) U. Ugarte, *Chem. Phys. Lett.* 207, 473 (1993). (b) U. Ugarte, *Carbon* 33, 989 (1995).
71. N. Kawase, A. Yasuda, T. Matsui, C. Yamaguchi, and H. Matsui, *Carbon* 37, 522 (1999).
72. (a) A. Yasuda, N. Kawase, F. Banhart, W. Mizutani, T. Shimizu, and H. Tokumoto, *J. Phys. Chem. B* 106, 1247 (2002). (b) A. Yasuda, N. Kawase, F. Banhart, W. Mizutani, T. Shimizu, and H. Tokumoto, *J. Phys. Chem. B* 106, 1849 (2002). (c) A. Yasuda, N. Kawase, and W. Mizutani, *J. Phys. Chem. B* 106, 13294 (2002).
73. N. Kawase, A. Yasuda, T. Matsui, C. Yamaguchi, and H. Matsui, *Carbon* 36, 1234 (1998).
74. L. Gherghel, C. Kübel, G. Lieser, H.-J. Räder, and K. Müllen, *J. Am. Chem. Soc.* 124, 13130 (2002).
75. A. Oberlin, *Carbon* 22, 521 (1984).
76. E. J. Roche, *J. Mater. Sci.* 25, 2149 (1990).
77. K. Tohji, H. Takahashi, Y. Shinoda, N. Shimizu, B. Jeyadevan, I. Matsuoka, Y. Saito, A. Kasuya, S. Ito, and Y. Nishina, *J. Phys. Chem. B* 101, 1974 (1997).
78. Y. Maruyama, T. Takase, M. Yoshida, K. Kogure, K. Suzuki, K. Tohji, H. Takahashi, A. Kasuya, and Y. Nishina, *Fullerene Sci. Technol.* 7, 211 (1999).
79. Y. Sato, T. Ogawa, K. Motomiya, K. Shinoda, B. Jeyadevan, K. Tohji, A. Kasuya, and Y. Nishina, *J. Phys. Chem. B* 105, 3387 (2001).
80. Y. G. Gogotsi and M. Yoshimura, *Nature* 367, 628 (1994).
81. Y. Gogotsi, J. A. Libera, and M. Yoshimura, *J. Mater. Res.* 15, 2591 (2000).
82. J. M. Calderon-Moreno and M. Yoshimura, *Mater. Trans.* 42, 1681 (2001).
83. J. M. Calderon-Moreno and M. Yoshimura, *Key Eng. Mater.* 206, 2159 (2002).
84. J. M. Calderon-Moreno, S. S. Swamy, T. Fujino, and M. Yoshimura, *Chem. Phys. Lett.* 329, 317 (2000).
85. W. L. Suchanek, J. A. Libera, Y. Gogotsi, and M. Yoshimura, *J. Solid State Chem.* 160, 184 (2001).
86. J. Libera and Y. Gogotsi, *Carbon* 39, 1307 (2001).
87. Y. Gogotsi, J. A. Libera, A. Güvenç-Yazicioglu, and C. M. Megaridis, *Appl. Phys. Lett.* 79, 1021 (2001).
88. B. L. Zhang, C. Z. Wang, C. T. Chan, and K. M. Ho, *Phys. Rev. B* 48, 11381 (1993).
89. X. Wang, J. Lu, Y. Xie, G. Du, Q. Guo, and S. Zhang, *J. Phys. Chem. B* 106, 933 (2002).

Sonochemical Synthesis of Nanomaterials

S. Sundar Manoharan, Manju Lata Rao

Indian Institute of Technology, Kanpur, India

CONTENTS

1. Introduction
2. Effects of Ultrasound
3. The Sonochemical Cell
4. Nanomaterials Employing Ultrasound
5. Mesoporous Solids
6. Bionanomaterials
7. Conclusions
- Glossary
- References

1. INTRODUCTION

The use of ultrasound has become an important synthetic tool in 'liquid-solid' reactions, and its ability to enhance chemical reactivity is a widely applicable and emerging laboratory technique. Sonochemistry is the application of ultrasound to chemical reactions and processes. Ultrasound is the part of the sonic spectrum which ranges from about 20 kHz to 10 MHz, and can be roughly subdivided into three main regions: low frequency, high-power ultrasound (20–100 kHz), high frequency, medium-power ultrasound (100 kHz–1 MHz), and high frequency, low-power ultrasound (1–10 MHz). The range from 20 kHz to around 1 MHz is used in sonochemistry, whereas frequencies far above 1 MHz are used as medical and diagnostic ultrasound. Ultrasound offers several potential advances compared to the more traditional synthetic routes. These include:

1. the use of mild ambient temperatures to protect reactants that might be thermally unstable,
2. enhanced mixing and transport properties,
3. the ability to generate unique, high-energy intermediates,
4. the production of materials normally associated with physical extremes, for example, molten metals and plasmas with relatively nominal energy input,
5. decrease of reaction time and/or increase of yield,

6. use of fewer forcing conditions, for example, lower reaction temperature,
7. possible switching of reaction pathway,
8. use of fewer or avoidance of phase transfer catalysts,
9. degassing force reactions with gaseous products,
10. use of crude or technical reagents,
11. activation of metals and solids,
12. reduction of any induction period.

The origin of sonochemical effects in liquids is the phenomenon of acoustic cavitation. Acoustical energy is a mechanical energy, that is, molecules do not absorb it. Ultrasound is transmitted through a medium via pressure waves by inducing vibrational motion of the molecules, which alternately compress and stretch the molecular structure of the medium due to a time-varying pressure. Therefore, the distance among the molecules varies as the molecules oscillate around their mean position. If the intensity of ultrasound in a liquid is increased, a point is reached at which the intramolecular forces are not able to hold the molecular structure intact. Consequently, it breaks down, resulting in the formation of a cavity. This cavity is called the *cavitation bubble*, as this process is called *cavitation* and the point where it starts the *cavitation threshold*. A bubble responds to the sound field in the liquid by expanding and contracting, that is, it is excited by a time-varying pressure. Two forms of cavitation are known: stable and transient. Stable cavitation means that the bubbles oscillate around their equilibrium position over several refraction/compression cycles. In transient cavitation, the bubbles grow over one (sometimes two or three) acoustic cycles to double their initial size, and finally collapse violently.

The size, lifetime, and fate of a cavitation bubble depend on the following parameters: frequency, intensity (acoustic pressure), solvent, bubbled gas, and external parameters (temperature, pressure). However, it should be noted that there is often no simple relationship. Since sonochemistry is the chemistry assisted/enhanced by ultrasound, this means that chemical reactions that take place under more conventional conditions are enhanced or even yield totally different products. The reason for this can be either physical or chemical effects of cavitation.

2. EFFECTS OF ULTRASOUND

2.1. Physical Effects of Ultrasound

Intensive sonication of liquids can generate cavitation bubbles. The bubbles collapse violently, and in doing so, generate high temperatures and pressures within the gaseous contents. There are three different theories about cavitation—the hot spot, the electrical, and the plasma theory. The most popular one is the hot-spot theory. Thus, it has been experimentally shown that the cavitation collapse creates drastic conditions inside the medium for an extremely short time generating temperatures of 2000–5000 K and pressures up to 1800 atm inside the collapsing cavity. This can lead to a reactive chemical environment, as well as the often-observed pulse of light near the end of the collapse phase of the bubble oscillation. As a result, emission of light often accompanies sonochemistry. Such sonoluminescence provides an extremely useful spectroscopic probe of the conditions created during cavitation bubble collapse [1–3] (Fig. 1). As with sonochemistry, sonoluminescence is a consequence of acoustic cavitation. The collapse of bubbles caused by cavitation produces intense local heating and high pressures, with very short lifetimes (Fig. 2). The collapse of bubbles in a multibubble cavitation field produces hot spots with effective temperatures of ca. 1000 atm, and heating and cooling rates above $10 \text{ K} \cdot \text{s}^{-1}$. In a single-bubble cavitation, conditions may be even more extreme [4, 5]. Thus, cavitation can create extraordinary physical and chemical conditions in otherwise cold liquids. Research studies have concentrated on either an isolated single bubble or clouds of many bubbles. The acoustic cavitation bubble is likely to be near spherical in single-bubble sonoluminescence (SBSL), with almost an indefinite number of oscillations being observed, while in multibubble sonoluminescence (MBSL), it will more likely be nonspherical, with only a small number of oscillations before it breaks up. High temperatures of 10^4 – 10^5 K

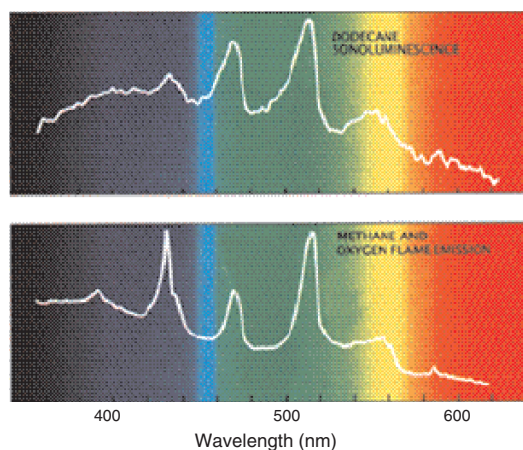


Figure 1. Light resembling that from a gas flame is generated when cold hydrocarbon liquids are exposed to ultrasound; the phenomenon is known as sonoluminescence. The graphs show the spectrum produced by the sonoluminescence of dodecane, $\text{C}_{12}\text{H}_{24}$ (top), and the combustion of methane, CH_4 (bottom). The similarities between the spectra are due to the formation and emissions of diatomic carbon in both cases. Reprinted with permission from [3], K. S. Suslick, *Sci. Am.* 82 (1989). © 1989, Andrew Christic, Slim Films.

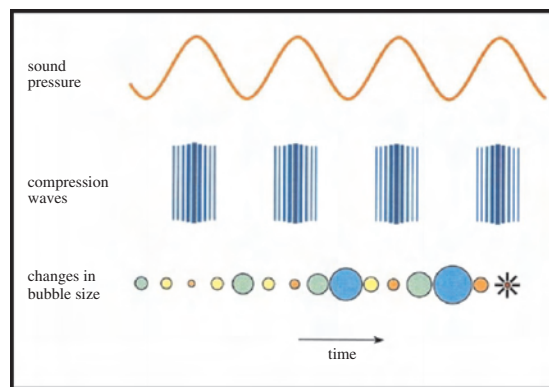


Figure 2. Growth and implosive collapse of the bubble in a sonochemical cell. The initial bubbles absorb dissolved gas from the surrounding liquid, and grow. Once large enough, the bubble resonates and absorbs acoustic energy. It quickly grows over the course of one acoustic cycle until it can no longer sustain itself, and it implodes. Reprinted with permission from [5], S. J. Putterman, *Sci. Am.* 46 (1995). © 1995, American Association for the Advancement of Science.

have been measured in SBSL, while an order of magnitude lower (10^3 – 10^4 K) is more typical of MBSL. The chemical constituents of the bubble interior are also different, typically argon in many of the SBSL experimental studies, while in MBSL, they are related to the vapor of the liquid solution, each of the constituents being identified by the different spectral characteristics. Clearly, such a potentially chemically reactive environment has attracted significant attention from chemists and industrialists, as well as the innate scientific curiosity with such seemingly simple observable phenomena. Nevertheless, the phenomenon is much more complicated than first thought, and the complex nonlinear mathematics, physics, and chemistry make acoustic cavitation and sonoluminescence an exciting area of research.

2.2. Chemical Effects of Ultrasound

The high local temperatures and pressures, combined with extraordinarily rapid cooling, provide a unique means for driving chemical reactions under extreme conditions. A diverse set of applications of ultrasound to enhance chemical reactivity has been explored, with important applications in mixed-phase synthesis, materials chemistry, and biomedical uses. For example, the sonochemical decomposition of volatile organometallic precursors in low-volatility solvents produces nanostructured materials in various forms with high catalytic activities. Nanostructured metals, alloys, carbides and sulfides, nanometer colloids, and nanostructured-supported catalysts can all be prepared by this general route.

The chemical effects of ultrasound [6–8] do not derive from a direct coupling of the acoustic field with chemical species on a molecular level. Instead, sonochemistry and sonoluminescence derive principally from acoustic cavitation: the formation, growth, and implosive collapse of bubbles in liquids irradiated with high-intensity ultrasound [9] (Fig. 3). Bubble collapse during cavitation serves as an effective means of concentrating the diffuse energy of sound: compression of a gas generates heat. When the compression of bubbles occurs during cavitation, heating is more

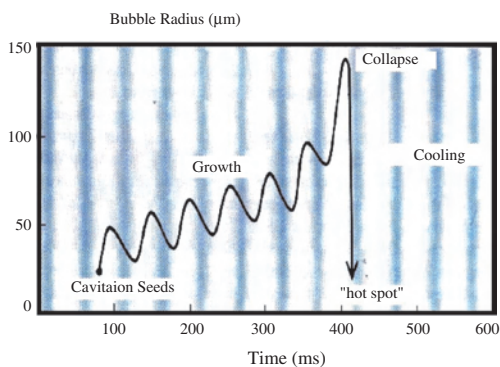


Figure 3. Bubble growth and implosion in a liquid irradiated with ultrasound is the physical phenomenon responsible for most sonochemistry. Intense ultrasound waves generate large alternating stresses within a liquid by creating regions of positive pressure (dark color) and negative pressure (light color). A cavity can form and grow during the episodes of negative pressure. When the cavity attains a critical size, the cavity implodes, generating intense heat and tremendous pressure. Reprinted with permission from [16], K. S. Suslick, *MRS Bull.* 20, 29 (1995). © 1995, Materials Research Society.

rapid than thermal transport, creating a short-lived localized hot spot. There is a nearly universal consensus that this hot spot is the source of homogeneous sonochemistry. Rayleigh's [10] early descriptions of a mathematical model for the collapse of activities in incompressible liquids predicted enormous local temperatures and pressures. Ten years later, Richards and Loomis [11] reported the first chemical effects of ultrasound. Cavitation was heavily studied during the 1950s and 1960s, culminating in a relatively detailed understanding [12–13].

3. THE SONOCHEMICAL CELL

A schematic of the sonochemical apparatus is illustrated in Figure 4. The heart of the sonicator is an element called the transducer. This is a ceramic disk whose crystal structure has a specific direction (in this case, in the vertical direction) in response to an applied ac voltage. In most high-intensity experiments, the transducer is being displaced 20,000 times a second (20 kHz). Since the transducer displacement and the (resulting pressure wave) is relatively small, the signal is amplified by physically coupling the transducer to a stiff, durable mass such as a titanium horn which has the effect of increasing the ultrasonic power by several orders of magnitude, so that over 50 W/cm^2 is typically produced at the sonicator tip. Because the ultrasonic waves are being produced by the metal shaft being vibrated up and down by a small amount 20,000 times a second, frictional heating occurs when the shaft is surrounded by a liquid. In order to keep the temperature inside the cell arrangement close to room temperature, the cell arrangement is thermostated using a cooling bath, resulting in optimum temperature for carrying out most of the sonochemical experiments. Gas and liquid inlets and outlets allow a variety of experiments to be performed under different atmospheres with or without oxygen being present.

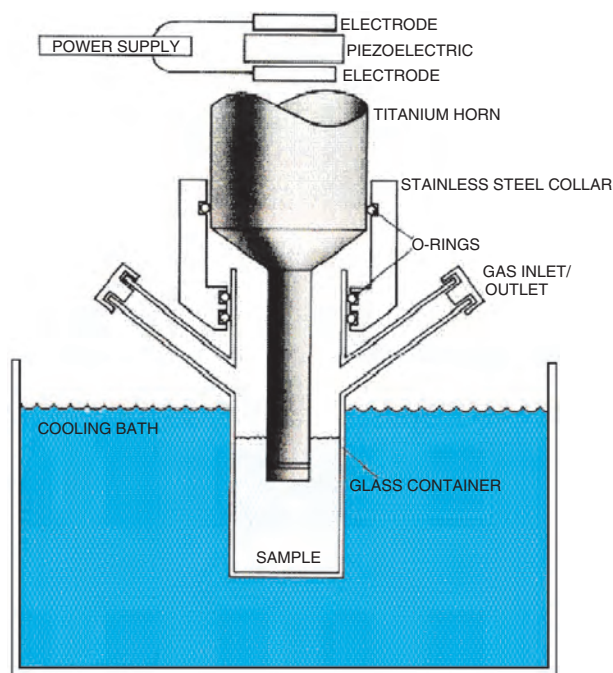


Figure 4. Schematic of the sonochemical apparatus used for carrying out reactions. Ultrasound can easily be introduced into a chemical reaction in which there is good control of temperature and ambient atmosphere. The titanium horn immersed in the reaction liquid is driven by a piezoelectric, which vibrates when subjected to an alternating current electric field. The common piezoelectric ceramic used is PZT, a lead zirconate titanate material. Reprinted with permission from [16], K. S. Suslick, *MRS Bull.* 20, 29 (1995). © 1995, Materials Research Society.

4. NANOMATERIALS EMPLOYING ULTRASOUND

Solids made from nanometer-sized components often exhibit properties distinct from those of the bulk, in part because clusters that small have an electronic structure with a high density of states, but not continuous bands [14, 15]. Such nonstructural materials are of intense current interest, and several preparative methods have been developed for their synthesis. As a general approach to this synthesis of nanophase materials (Fig. 5), extreme conditions of cavitation produce a variety of nanostructured and often-amorphous metals, alloys, and carbides [16–19]. Volatile organometallic compounds decompose inside a collapsing bubble, and the resulting metal atoms agglomerate to form nanostructured materials. The sonochemical synthesis of nanostructured materials is also extremely versatile; simply changing the reaction medium can generate various forms of nanophase materials. When precursors are sonicated in low-volatile alkanes, nanostructured metal powders are formed. If sonication occurs in the presence of a bulky or polymeric surfaced ligand, stable nanophase metal colloids are created. Sonication of the precursor in the presence of an inorganic support (silica or alumina) provides an alternative means of trapping the nanometer clusters. The nanoparticles, once fixed on the surface of these supports, are very active supported heterogeneous catalysts.

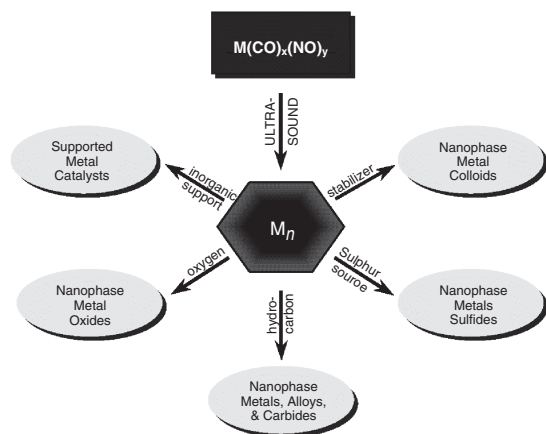


Figure 5. Sonochemical synthesis of nanostructured materials is highlighted. Given the unusual conditions created during cavitation, various potential applications for generating amorphous and nanoscale materials is given, including nanometals, alloys, nanometal colloids and catalysts, and nanometal chalcogenides. Reprinted with permission from [16], K. S. Suslick, *MRS Bull.* 20, 29 (1995). © 1995, Materials Research Society.

4.1. Nanometals

Suslick and Grinstaff were the first to demonstrate the use of ultrasound to prepare amorphous metals. The ultrasonic irradiation of volatile solutions of transition-metal carbonyls (e.g., $\text{Fe}[\text{CO}]_5$, $\text{Co}[\text{CO}]_3\text{NO}$) produces highly porous aggregates of nanometer-sized clusters of amorphous metals [20]. Typically, sonication of 1 μm penta-carbonyl in decane at 0 °C under a flow of argon yielded a dull black powder. Scanning electron micrographs (SEMs) revealed that the powder is an agglomerate of 20 nm particles; transmission electron micrographs (TEMs) further indicated that these 20 nm particles consist of smaller 4–6 nm particles. The amorphous nature of the iron powder was confirmed by several different techniques, including SEM, differential scanning calorimetry (DSC), electron diffraction, X-ray powder diffraction, and neutron diffraction. Initial X-ray powder diffraction showed no diffraction peak; with heat treatment under helium at 350 °C, the diffraction lines characteristic of bcc iron metal are observed. DSC also shows one exothermic irreversible disorder–order transition temperature at 308 °C. The amorphous metal formation appears to result from the extremely high cooling rate during acoustic cavitation.

There had been a long-standing controversy concerning the magnetic properties of amorphous iron, which had not been previously available without a substantial amount of added alloying elements (e.g., boron). Magnetic studies of the sonochemically prepared amorphous iron showed that amorphous iron is a very soft ferromagnet with a saturation magnetization of ca. 173 $\text{emu} \cdot \text{g}^{-1}$ and a Curie temperature in excess of 580 K. The effective magnetic moment is $1.7\mu_B$, with an effective exchange constant of only ca. 30% of crystalline Fe [21–23]. The magnetic properties fall close to those of liquid iron. The neutron-diffraction data confirmed these measurements, and are consistent with a random packing model, as observed for many thin amorphous metal films. The magnetic moment μ of the amorphous iron determined by neutron diffraction data is significantly below

that of crystalline iron, and good agreement with other iron-based alloys on some extrapolation is also observed. Sonochemically synthesized chromium amorphous powders [24] showed interesting particulate characteristics unlike Fe nanopowders. The SEM micrograph (Fig. 6) showed the particles to be monosized and necked to each other in an ordered fashion. Such an arrangement reflects room-temperature sintering effects due to the surface energy of the highly reactive powders. A method from Katabi and co-workers reported the preparation of amorphous Ni powder with a particle size of about 10 nm by sonolysis of neat $\text{Ni}(\text{CO})_4$ with decane as a solvent [25].

Manoharan and Rao [26] reported that nanoscale particles of metallic cobalt clusters are obtained from $\text{Co}_2(\text{CO})_8$ in decalin in a flow of Ar gas. Ultrasonic irradiation of the Co–carbonyl yields a dull black powder, highly pyrophoric when exposed to air. The most striking feature of sonochemically prepared Co is that it exhibits a negative magnetoresistance of the order of $\sim 1.5\%$ at room temperature (Fig. 7). The temperature and magnetic-field dependencies of the conductivity for the nanosized cobalt follow a simple activated behavior. These observations indicate that conduction is by spin-polarized electron hopping between the metallic nanoparticles.

Pol and co-workers [27] reported the synthesis of silver nanoparticles with an average particle size of ~ 5 nm on the surface of preformed silica submicrospheres with the aid of power ultrasound (Fig. 8). Ultrasound irradiation of slurry of silica submicrospheres, silver nitrate, and ammonia in an aqueous medium for 90 min under an atmosphere of argon to hydrogen (95:5) yielded a silver–silica nanocomposite. Control over the size and shape of the silver particles was achieved by a modified pulse sonoelectrochemical method. Such a process yields spherical Ag nanoparticles, Ag nanorods, and elegant, highly ordered dendritic nanostructured silver [28]. It was found that the concentration of both silver nitrate and nitrilotriacetate plays a key role in the formation growth of different shaped nanoparticles. The mechanism of formation of silver nanoparticles from a solution of silver nitrate in an Ar/H_2 (95:5) atmosphere takes into consideration the radical species generated from water molecules by the absorption of

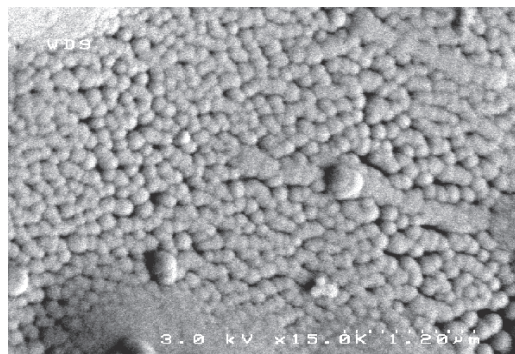


Figure 6. Scanning electron micrograph of sonochemically prepared chromium metal powder shows particles to be monosized and necked to each other in an ordered fashion arising out of high surface energy. Reprinted with permission from [24], M. L. Rao, Ph.D. Dissertation, IIT Kanpur, 2003.

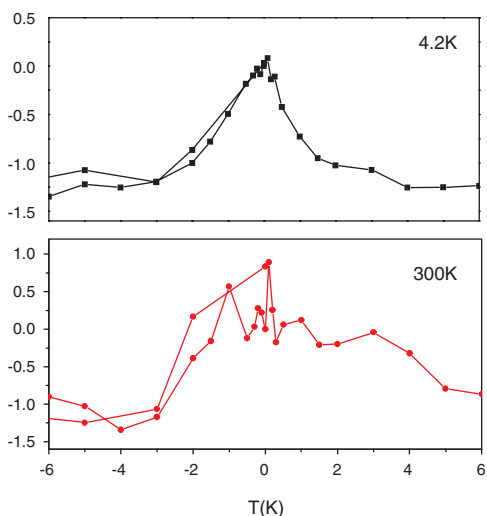


Figure 7. Negative magnetoresistance in sonochemically prepared cobalt metal. Reprinted with permission from [26], S. Sundar Manoharan and M. L. Rao (private communication).

water molecules. An argon–hydrogen atmosphere produces more H radicals than in air, thereby enhancing the reduction of Ag^+ ions under sonochemical conditions [29].

Nanoscale particles of metallic copper clusters have been prepared by the sonochemical reduction of copper (II) hydrazine carboxylate complex (CHC) in an aqueous medium. Ultrasonic irradiation of the CHC under a mixture of argon and hydrogen yielded pure copper metallic nanoclusters, which also explains the scavenging action of hydrogen toward the OH^\cdot radicals, generated from water molecules on the absorption of ultrasound [30].

Arul Dhas and co-workers [31] reported the *in-situ* preparation of amorphous carbon-activated palladium nanoparticles. Such palladium metallic clusters have been prepared (*in-situ*) at room temperature by ultrasound irradiation of an organometallic precursor, tris- μ -[dibenzylideneacetone]-dipalladium [$\text{CH}=\text{CH}-\text{CO}-\text{CH}=\text{CH}_2\text{Pd}_2$] in mesitylene [32]. Mizukoshi and co-workers [33] demonstrated the sonochemical reduction processes of Pt

(IV) ions in water in the presence of various kinds of surfactants, such as sodium dodecylsulfate (SDS) and sodium dodecylbenzenesulfonate (DBS) as anionic surfactants, polyethylene glycol monostearate (PEG-MS) as nonionic, and dodecyltrimethylammonium chloride (DTAC) and bromide (DTAB) as cationic surfactants. An improved colorimetric determination reveals that the Pt (IV) ion is reduced to zero valent metal in two steps: step (1) Pt (IV) ion to Pt (II) ion, and step (2) Pt (II) ion to Pt (0), and after the completion of step (1), step (2) sets in. The average diameter (1.0 nm) of platinum particles prepared from the system of PEG-MS is smaller than those from the aqueous solution of the anionic surfactant SDS (3.0 nm) and DBS (3.0 nm). Diodati and coworkers [34] have reported the non-crystalline phase of palladium by cavitation technique starting from a solution of palladium acetylacetonate and toluene. The microscopic structure of the sample, a very fine powder, was investigated by X-ray diffraction and it showed the characteristic features of a disordered system.

Okitsu and co-workers [35] found that sonochemically prepared metal particles such as Ag, Pd, Au, Pt, and Rh are of nanometer size with a fairly narrow distribution (e.g., about 5 nm for Pd particles obtained from a 1.0 mM Pd (II) in polyethylene glycol monostearate solution). Three different reduction pathways under sonication: (1) reduction by H atoms, (2) reduction by secondary reducing radicals formed by hydrogen abstraction from organic additives with OH radicals and H atoms, and (3) reduction by radicals formed from the pyrolysis of the additives have been identified at the interfacial region between cavitation bubbles and the bulk solution. The reduction of Ag (I) and Pt (II) mainly proceeds through reaction pathway (2). In the cases of Pd (II) and Au (III), the reductions mainly proceed through reaction pathway (3). Similar reports on the synthesis of Ag and Au, and bimetallic particles such as Au/Pd and Pt/Pd were also presented [36–39]. The effect of atmospheric gas on the particle size and size distribution of nanoparticles has been reported [39].

4.2. Nanometal Composites, Ferrofluids, Colloids, and Catalysts

Composite materials containing amorphous iron embedded in poly(methylacrylate), PMA, or poly(methylmethacrylate), PMMA, and amorphous cobalt embedded in PMA were reported by Wizer and co-workers [30, 41], using a sonochemical method. The physical and thermal properties of the composite materials were probed. A significant difference in the solubility of the iron-PMA and cobalt-PMA in various solvents was observed. This difference is accounted for by the stronger interaction existing between the cobalt and the surrounding polymer. For iron-PMA, this interaction is weakened due to the formation of an iron complex. Composites made of PMA and amorphous iron nanoparticles reveal a superparamagnetic behavior.

The existence of aggregates of nanometer clusters in the sonochemically prepared materials suggests the possibility of trapping these particles before they aggregate. The colloids of ferromagnetic materials are of special interest due to their many important technological applications as ferro

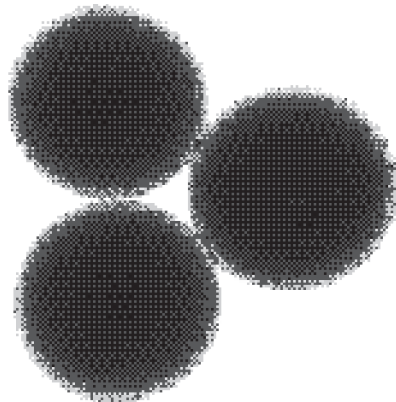


Figure 8. TEM image of silver nanoparticle coated on silica surface. Reprinted with permission from [27], V. G. Pol et al., *Langmuir* 18, 3352 (2002). © 2002, American Chemical Society.

fluid [42]. Such magnetic fluids find uses in information media, magnetic refrigeration, audio reproduction, and magnetic sealing. Exhaustive grinding of magnetite [Fe_3O_4] in ball or vibratory mills for several weeks in the presence of surfactants generally produces commercial magnetic fluids, which produces a very broad particle-size distribution.

Suslick and co-workers [43] developed a new method for the preparation of stable ferromagnetic colloids of iron. High-intensity ultrasound is used to sonochemically decompose volatile organometallic compounds in the presence of colloid-stabilizing ligands such as poly-vinylpyrrolidone (PVP) or oleic acid. A TEM micrograph show that the iron particles have a relatively narrow range in size from 3 to 8 nm for polyvinylpyrrolidone, while oleic acid gives a more uniform distribution at 8 nm. Electron microdiffraction revealed that the particles are amorphous on the nanometer scale as formed, and that, during *in-situ* electron-beam heating, these particles crystallize to bcc iron. Magnetic studies indicate that these colloidal iron particles are superparamagnetic, with a respectable saturation magnetization of $101 \text{ emu} \cdot \text{g}^{-1}$ per iron at 290 K. High saturation magnetization is desirable for magnetic fluid applications, and is highly sensitive to the method of preparation. Bulk amorphous Fe saturates at $156 \text{ emu} \cdot \text{g}^{-1}$ per iron. In comparison, the saturation magnetization of a commercial magnetic fluid is $123 \text{ emu} \cdot \text{g}^{-1}$ [Fe] (Ferrofluids Corp. cat. no. APG-047) [21, 22].

Self-assembled monolayer coatings of amorphous iron nanoparticles binding the thiol chromophore were recently reported by Gedanken and co-workers [44–46]. The coverage of the iron surface by a long alkyl-chain thiol was as good as the coating of the short alkyl-chain thiol. Magnetic proteinaceous microspheres composed of iron oxide filled and coated with globular bovine serum albumin (BSA) were been reported by Levi and co-workers [47]. The magnetic microspheres are prepared from BSA and iron pentacarbonyl, or from BSA and iron acetate.

Suslick et al. [48] probed the catalytic activity of the amorphous iron powder for two commercially important reactions: the Fischer–Tropsch process (hydrogenation of CO), and the hydrogenolysis and dehydrogenation of saturated hydrocarbons. The amorphous iron powder was roughly ten times more reactive than $5 \mu\text{m}$ diameter crystalline powder. Also, the overall activity for cyclohexane dehydrogenation (to benzene) and hydrogenolysis (predominantly to methane) was 30 times greater for the sonochemically produced amorphous iron compared to its crystalline counterpart.

The synthesis and characterization of molybdenum colloidal particles were evaluated using sonochemistry, and starting from different metal precursors, $\text{Mo}(\text{CO})_6$ and $(\text{NH}_4)_2\text{MoS}_4$. Using $\text{Mo}(\text{CO})_6$ as the metal source, particle sizes with an average diameter of 1.5 nm can be obtained using tert-amyl alcohol as a solvent and tetrahydrothiophene as a sulfurating ligand. The characterization of these particles showed that they are composed of molybdenum oxide MoO_3 . Using $(\text{NH}_4)_2\text{MoS}_4$ as a metal precursor, particles with average diameters of 2.5 nm were synthesized using high-intensity ultrasound. The characterization of these particles showed them to be composed of molybdenum sulfide, MoS_2 [49].

4.3. Nanoalloys

Sonochemical techniques can also be used to prepare nanostructured alloys. For example, Fe–Co alloys have been synthesized from the readily available $\text{Fe}(\text{CO})_5$ and $\text{Co}(\text{CO})_5(\text{NO})$ precursors. Simply by altering the ratio of solution concentrations of the precursors, one can control the composition of the Fe–Co alloys. Alloy compositions ranging from pure Fe to pure Co can easily be realized [50]. Shafi and co-workers [51] reported the preparation of nanosized amorphous alloy powders of $\text{Fe}_{20}\text{Ni}_{80}$, $\text{Fe}_{40}\text{Ni}_{60}$, and $\text{Fe}_{60}\text{Ni}_{40}$ sonochemical decomposition of solutions of volatile organic precursors such as $\text{Fe}(\text{CO})_5$ and $\text{Ni}(\text{CO})_4$ in decalin, under an argon pressure of 100–150 kPa at 273 K. The magnetic susceptibility of $\text{Fe}_{40}\text{Ni}_{60}$ and $\text{Fe}_{60}\text{Ni}_{40}$ indicates blocking temperatures of 35 K and a magnetic particle size of about 6 nm. Thermogravimetric measurements of $\text{Fe}_{20}\text{Ni}_{80}$ give Curie temperatures of 322 °C for amorphous and 550 °C for crystallized forms. Differential scanning calorimetry exhibits an endothermic transition at 335 °C from a combination of the magnetic phase transition and alloy crystallization. The Mössbauer spectrum of crystallized $\text{Fe}_{20}\text{Ni}_{80}$ shows a sextet pattern with a hyperfine field of 25.04 T. The same authors have reported the preparation of a Co–In alloy [52].

Nanosized amorphous alloy powders of $\text{Co}_{20}\text{Ni}_{80}$ and $\text{Co}_{50}\text{Ni}_{50}$ have been prepared by the sonochemical decomposition of solutions of volatile organic precursors, $\text{Co}(\text{NO})(\text{CO})_3$ and $\text{Ni}(\text{CO})_4$ in decalin, under an argon pressure of 100–150 kPa, at 273 K. A transmission electron micrograph of the heated $\text{Co}_{20}\text{Ni}_{80}$ sample showed near uniform particles with sizes less than 10 nm. Magnetic measurements indicated that the as-prepared amorphous CoNi alloy particles were superparamagnetic. The observed magnetization, measured up to a field of 15 kG, of the annealed $\text{Co}_{20}\text{Ni}_{80}$ sample ($54 \text{ emu} \cdot \text{g}^{-1}$) was significantly lower than that for the reported multidomain bulk particles ($75 \text{ emu} \cdot \text{g}^{-1}$), reflecting the ultrafine nature of the sample. Thermogravimetric measurements of $\text{Co}_{20}\text{Ni}_{80}$ with a permanent magnet yielded a glass transition temperature of 338 °C for the amorphous form, and a Curie temperature of 565 °C for the crystallized form. The differential scanning calorimetry showed crystallization temperatures of 400 °C for $\text{Co}_{20}\text{Ni}_{80}$ and 365 °C for $\text{Co}_{50}\text{Ni}_{50}$ amorphous samples. The as-prepared amorphous Fe–Ni–Co alloy particles [53] were superparamagnetic, as indicated by the magnetic studies. The observed magnetization measured up to a field of 1.5 kG of the annealed Fe–Ni–Co samples ($75\text{--}87 \text{ emu} \cdot \text{g}^{-1}$) was significantly lower than that for the reported multidomain bulk particles ($175 \text{ emu} \cdot \text{g}^{-1}$), reflecting the ultrafine nature of our sample.

Rao and Manoharan [54] recently reported the effect of short-range order on the magnetic and electronic transport properties of a series of cobalt–platinum alloys. In an amorphous phase, the order parameter differs with different Pt concentrations. The crystallization temperature is accompanied by a structural phase transition (*fcc*–*fcc*) at around 380 °C, as inferred from the DSC studies (Fig. 9). For the Co–Pt binary alloy, transition from the soft magnetic disordered *fcc* phase to an ordered *fcc* structure occurs around 675 °C, as evident from the DSC curve. However,

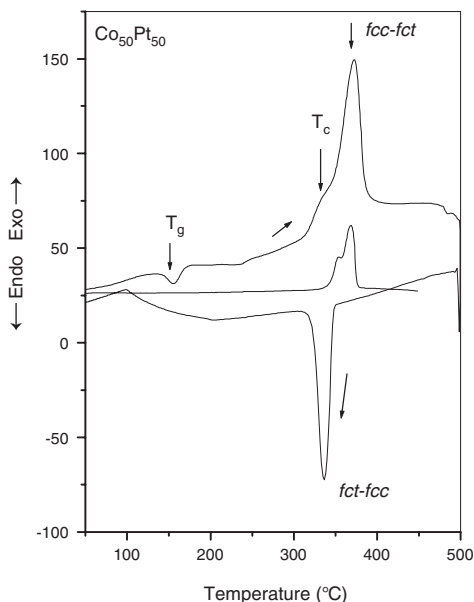


Figure 9. Differential scanning calorimetric curve of amorphous $\text{Co}_{50}\text{Pt}_{50}$ alloy showing glass transition, crystallization, and phase transition. Samples sintered at $900\text{ }^{\circ}\text{C}$ appear to undergo a disorder (α) \leftrightarrow order (ε) \leftrightarrow disorder (α) transformation ($300\text{ }^{\circ}\text{C} \leftrightarrow 650\text{ }^{\circ}\text{C} \leftrightarrow 900\text{ }^{\circ}\text{C}$), resulting in the *fcc* phase *in vivo*. Reprinted with permission from [54], S. S. Manoharan and M. L. Rao (private communication).

samples sintered at $900\text{ }^{\circ}\text{C}$ appear to undergo a disorder (α) \leftrightarrow order (ε) \leftrightarrow disorder (α) transformation ($300\text{ }^{\circ}\text{C} \leftrightarrow 650\text{ }^{\circ}\text{C} \leftrightarrow 900\text{ }^{\circ}\text{C}$), resulting in the *fcc* phase *in vivo*. The cooling curve in the DSC suggests the phase transformation to be reversible. Upon further heating the sample, the endothermic peak due to crystallization is absent, while the *fcc* to *fct* phase transformation does reappear. As a result, heat-treated samples yield only the high-temperature *fcc* phase, which is a disordered alloy; see Figure 10. In a system such as this, the influence of the magnetic field on the electronic transport has shown interesting properties. First, the magnetoresistance ratio (which is defined as $\rho_0 - \rho_H / \rho_0$) of the order of 3% at relatively low fields is observed at 4 K and at 300 K; see Figure 11(a). This is the first observation of negative magnetoresistance in amorphous alloys. Second, with varying compositions of the Pt concentration, the MR ratio oscillates, showing a dependency on the short-range order, Figure 11(b). The same authors also reported the synthesis of Co–Pd alloys using high-frequency ultrasound using organometallic Co–carbonyl and PdCl_2 ; by varying the molar concentrations of the solutions used, a series of alloys, $\text{Co}_{100-x}\text{Pd}_x$ ($0 < x < 100$) have been prepared. Interestingly, all of these nanosized alloys show an interesting conduction mechanism (Fig. 12) [55].

Cobalt-chromium multilayer thin-film systems have been studied in detail due to its potential for application as a read head memory devices. Alloys of amorphous Co–Cr alloys show an interesting phase transition from a pure *hcp* to *fct* to a pure *fct* phase with increasing Cr concentration. Similar magnetoresistive features as the Co–Pt series have been observed in these amorphous alloys [56]. Interesting soft magnetic behavior has been explored in the amorphous form

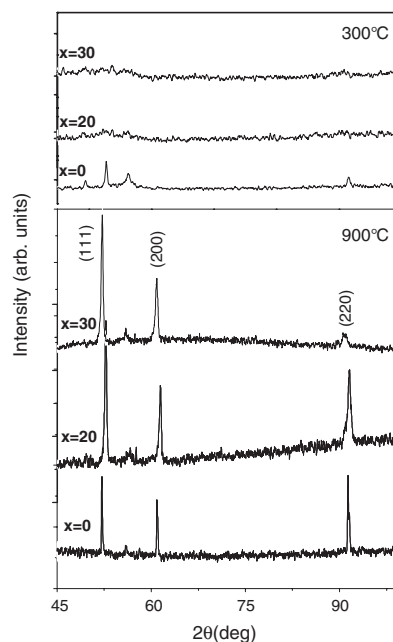


Figure 10. X-ray diffraction patterns of Co–Pt nanoalloys showing a disordered *fcc* phase for the $900\text{ }^{\circ}\text{C}$ heat-treated samples. All the “as-prepared” samples are X-ray amorphous. Reprinted with permission from [54], S. Sundar Manoharan (private communication).

of Fe–Pt alloys, which otherwise is a commercially employed hard bulk magnet [57].

4.4. Nanometal Oxides

A simple and efficient methodology has been established for the selective synthesis of anatase and rutile [58], as well as their mixtures with various precursors using ultrasound irradiation; the products, the particle sizes of which are nanometric ($<9\text{ nm}$), are dependent both upon the reaction temperature and the precursor used; a substantial reduction in reaction time as well as reaction temperature is observed as compared to the corresponding hydrothermal processes. Zhu and co-workers [59] developed a process for the formation of titania whiskers and nanotubes with the assistance of sonication; titanate whiskers are obtained as a slender sheet with a length of about $1\text{ }\mu\text{m}$ and a width of 60 nm ; arrays of titania whiskers with a diameter of 5 nm are prepared from the titanate whiskers; titania nanotubes with a diameter of about 5 nm and a length of $200\text{--}300\text{ nm}$ are also synthesized.

Xu and co-workers [60] reported the magnetic size effects and phase transformation in sonochemically synthesized Fe_2O_3 nanoparticles. Annealing in vacuum at temperatures T_a between 240 and $450\text{ }^{\circ}\text{C}$ produced nanophases of $\gamma\text{-Fe}_2\text{O}_3$ with average particle size ranging from 4 to 14 nm , depending on T_a . Phase transformation into $\alpha\text{-Fe}_2\text{O}_3$ occurred directly by annealing in air, or via an intermediate Fe_3O_4 phase by annealing in vacuum at temperatures higher than $450\text{ }^{\circ}\text{C}$. Mapping the correlation between the magnetic properties and the annealing conditions enables control of the annealing process to obtain nanocrystals of $\gamma\text{-Fe}_2\text{O}_3$, $\alpha\text{-Fe}_2\text{O}_3$, or Fe_3O_4 with different particle sizes and magnetic properties.

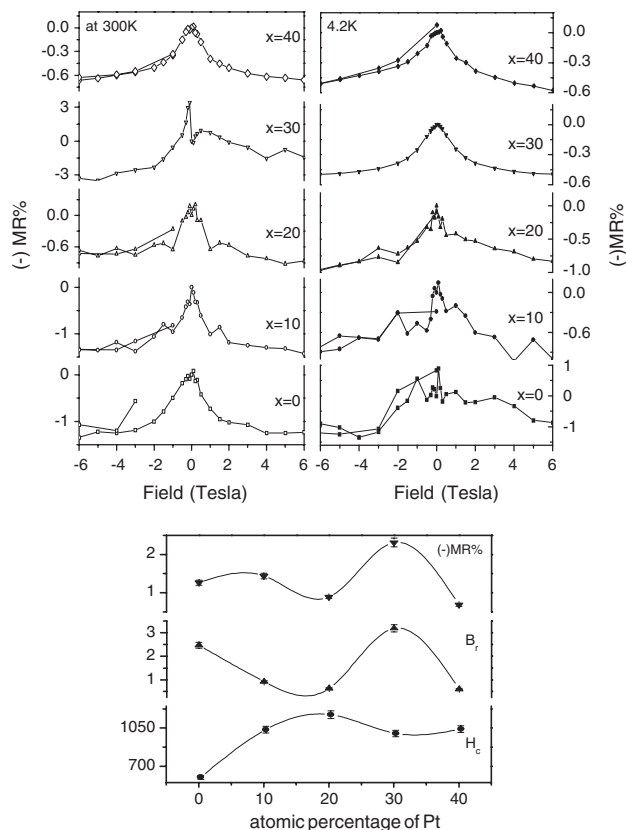


Figure 11. Negative magnetoresistance in Co–Pt alloys prepared using sonochemical decomposition of metal–organic precursors. Magnetoresistance ratio (which is defined as $\rho_0 - \rho_H/\rho_0$) on the order of 3% at relatively low fields is observed at 4.2 K and at 300 K. (b) Variation of magnetoresistance as a function of Pt concentration, with a maximum at 30%. With varying composition of Pt concentration, the MR ratio oscillates showing dependency on the short-range order. Reprinted with permission from [54], S. Sundar Manoharan (private communication).

Sonochemical of aqueous iron(II)acetate in the presence of β -cyclodextrin is reported to yield magnetite nanorods [61]. The as-prepared magnetite nanorods are ferromagnetic, and their magnetization at room temperature is ~ 78 emu/g, as shown in Figure 13. The particle sizes measured from transmission electron micrographs are about 48/14 nm (L/W). A mechanism for the sonochemical formation of magnetite nanorods is discussed. Measurements of the magnetic irreversibility line and time-logarithmic decay of the magnetization are described for sonochemically synthesized three Fe_2O_3 samples composed of regular amorphous, acicular amorphous, and crystalline nanoparticles. The relaxation rate is the largest and the irreversibility temperature is the lowest for the regular amorphous nanoparticles. The crystalline material exhibits the lowest relaxation rate and the largest irreversibility temperature. Prozorov and co-workers [62] developed a phenomenological model to explain the details of the experimental results. The main new aspect of the model is the dependence of the barrier for magnetic relaxation on the instantaneous magnetization, and therefore on time. The time-dependent barrier yields a natural explanation for the time-logarithmic decay of the magnetization. Interactions between particles as well as shape and

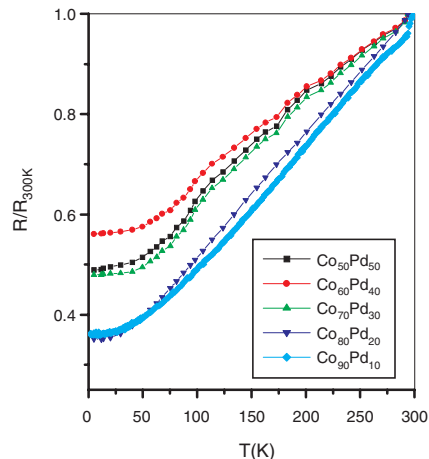


Figure 12. Resistance as a function of temperature for $\text{Co}_{100-x}\text{Pd}_x$ alloys. Reprinted with permission from [55], M. L. Rao and S. Sundar Manoharan (private communication).

crystalline magnetic anisotropies define an energy scale that controls the magnetic irreversibility. Introducing this energy scale yields a self-consistent explanation of the experimental data.

Cao and co-workers [63] showed the method for the preparation of pure amorphous Fe_2O_3 powder with a particle size of 25 nm. Pure amorphous Fe_2O_3 can be simply synthesized by the sonication of neat $\text{Fe}(\text{CO})_5$ or its solution in decalin under an air atmosphere. The Fe_2O_3 nanoparticles are converted to crystalline Fe_3O_4 nanoparticles when heated to 420 °C under vacuum or when heated to the same temperature under a nitrogen atmosphere. The magnetization of pure amorphous Fe_2O_3 at room temperature is very low (<1.5 emu/g), and it crystallizes at 268 °C. Porous nickel and cobalt oxides have been prepared using their alkoxides as an inorganic precursor [64]. The stabilization of the mesostructure is especially critical for divalent elements such

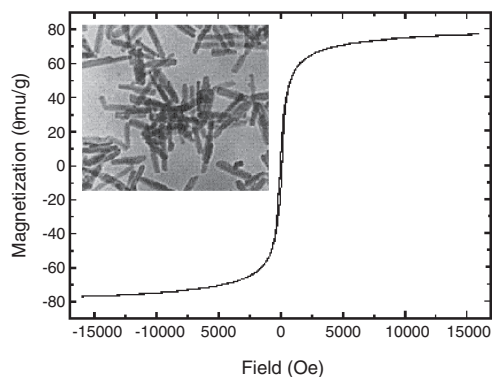


Figure 13. Room-temperature magnetization curve of “as-prepared” magnetite nanorods. Inset to figure shows TEM image of the nanorods with dimension of 40 nm. The particles are rod shaped and well dispersed. The particle size distribution is measured directly from the TEM with dimension 48/14 nm. The extent of agglomeration is minimal. There is no evidence of the formation of amorphous magnetite. Reprinted with permission from [61], R. V. Kumar et al., *J. Appl. Phys.* 89, 6324 (2001). © 2001, American Institute of Physics.

as Ni and Co, which do not form any network structure, like silicates. The lack of a network-forming multivalent bond is the probable reason why no stable mesoporous oxides have been synthesized for divalent elements yet. Octadecylamine has been used as the organic structure-directing agent to prepare Ni and Co oxides. A relatively better surface area has been obtained for the Co oxide, but in Ni, the surface area was less. The porous (solvent-extracted) cobalt oxide has been used as a catalyst in the oxidation reaction of cyclohexane in mild conditions. The catalyst has shown relatively better conversion of cyclohexane into cyclohexanone and cyclohexanol than the nanostructured cobalt oxide catalyst of a regular structure.

Gasgnier and co-workers [65] reported the ultrasound effects on metallic (Fe and Cr), iron sesquioxides (α - γ - Fe_2O_3), calcite, copper, lead, and manganese oxides as powders. Different kinds of materials, such as powders, were submitted to ultrasound after mixing in water, dodecane, or dilute acetic acid (5%). After treatment, first, a decrease of particle sizes, and second, the formation of unexpected and unknown compounds were observed on a mesoscopic scale (CaO from CaCO_3 , for example). For iron and iron oxides, it was found that the magnetic properties (susceptibility and effective magnetic moment) were changed slightly. A shift in the Morin temperature transition for α - Fe_2O_3 was attributed to the formation of impurities. For inorganic oxides (Cu_2O , PbO , Pb_3O_4 , and Mn_3O_4) sonicated in dilute acetic acid, the formation of metallic acetates is easily achieved, and it is rapid (10 s for PbO).

Zhong and co-workers [66, 67] coated molybdenum oxide on submicrospheres of amorphous alumina and crystalline alumina, using a sonochemical method. Blue oxide of molybdenum was found to be formed on the alumina surface, while on amorphous alumina, the presence of an isolated tetrahedrally coordinated Mo oxide species was confirmed. The surface area of the alumina-coated Mo oxide is about 11 times larger than that of the bare alumina. An explanation for this change is offered. Amorphous tungsten oxide was prepared by ultrasound irradiation of a solution of tungsten hexacarbonyl $\text{W}(\text{CO})_6$ in diphenylmethane (DPhM) in the presence of an Ar (80%)- O_2 (20%) gaseous mixture at 90 °C. Heating this amorphous powder at 550 °C under Ar yields snowflake-like dendritic particles consisting of a mixture of monoclinic and orthorhombic WO_2 crystals (Fig. 14). Annealing of the as-prepared product in Ar at 1000 °C causes the formation of a WO_2 - WO_3 mixture containing nanorods (around 50 nm in diameter) and packs of these nanorods. Heating the product in air for 3 h leads to triclinic WO_3 crystal formation, with a basic size of 50–70 nm [68].

$\text{ZrO}_2 \cdot n\text{H}_2\text{O}$ nanopowders were prepared by the ultrasonication approach at room temperature [69]. Photoluminescent properties of the as-prepared ZrO_2 nanoparticles were investigated [Fig. 15(A)]. The use of ultrasound has proven to dramatically reduce the temperature, and makes the reaction conditions very easy to maintain during the preparation. The PL spectra obtained from the as-prepared nano- ZrO_2 samples excited with an excitation wavelength of 254 nm show fluorescence emission. Although the detailed PL mechanism for the nano- ZrO_2 is still under research, the emission appearing at the short-wavelength excitation

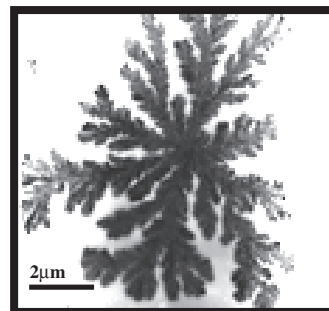


Figure 14. Transmission electron micrograph of WO_2 crystal showing dendrite morphology. Heating the amorphous powder at 550 °C under Ar yields snowflake-like dendritic particles consisting of a mixture of monoclinic and orthorhombic WO_2 crystals. Reprinted with permission from [68], Yu. Koltypin et al., *J. Mater. Chem.* 12, 1107 (2002). © 2002, Royal Society of Chemistry.

has been attributed to the near band-edge transitions. In Figure 15(B), the emissions have been attributed to the involvement of midgap trap states, such as surface defects, and oxygen vacancies arising out of the sonochemical synthesis [70–71]. Cerium oxide (CeO_2) nanoparticles were prepared sonochemically, using cerium nitrate and azodicarbonamide as starting materials, and ethylenediamine or tetraalkylammonium hydroxide as additives. The additives have a strong effect on the particle size and particle size distribution. CeO_2 nanoparticles with a small particle size and a narrow particle size distribution are obtained with the addition of additives, while highly agglomerated CeO_2 nanoparticles are obtained in the absence of additives. Monodispersed CeO_2 nanoparticles with a mean particle size of ca. 3.3 nm are obtained when tetramethylammonium hydroxide (TMAOH) is used as the additive and the molar ratio of cerium nitrate/azodicarbonamide/TMAOH is 1/1/1. Blue shifts of the absorption peak and the absorption edges of the products are observed in the UV-vis absorption spectra as a result of the quantum size effect [72].

4.4.1. Perovskites

Liang and co-workers [73] reported the synthesis of nanostructured LaNiO_3 by coprecipitation under ultrasonic radiation. The effects of ultrasound on the structured properties

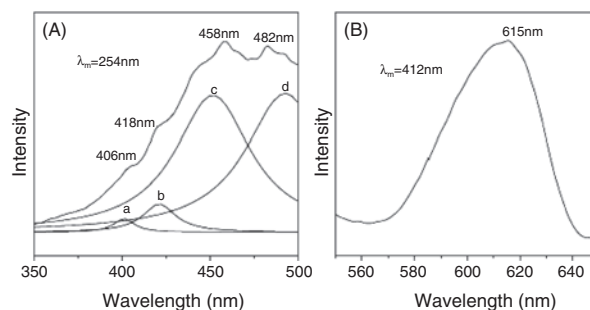


Figure 15. Photoluminescent spectra of t - ZrO_2 nanoparticles (A) excited at 254 nm and (B) excited at 412 nm. Reprinted with permission from [69], J. Liang, et al., *Mater. Res. Bull.* 38, 161 (2003). © 2003, Elsevier Science.

and catalytic activity of LaNiO_3 were reported. The result of TEM showed that the ultrasound could cause a decrease of particle size. The average particle size of LaNiO_3 prepared by sonochemistry is 20 nm. The specific surface area of LaNiO_3 is $11.27 \text{ m}^2 \cdot \text{g}^{-1}$ by BET. The O-ads/O-ads on the surface are 1.25 (ultrasound) and 1.01 (without ultrasound) by XPS. This shows that ultrasound could lead to increased surface content oxide and an increased number of surface crystal oxygen vacancies. The result of TPR showed that LaNiO_3 prepared by sonochemistry has a lower reduction temperature and a larger ratio of surface oxygen to crystal oxygen. The result of the evaluation of catalytic activity showed that ultrasound could increase the catalytic activity of LaNiO_3 for NO decomposition.

An example of a more complicated mixed metal oxide system is the perovskite, $\text{La}_{0.7}\text{Sr}_{0.3}\text{FeO}_3$. This material was synthesized by coprecipitation using both a Five Star Technologies cavitation processor [74] and conventional high-speed mechanical mixing under otherwise similar conditions for comparison purposes. The XRD results for materials obtained from both processes are summarized in Figure 16. The material obtained via the classical precipitation technique is shown at the top of the figure. This pattern shows that large amounts of separate phase compounds are present in addition to the desired perovskite material. The other four XRD patterns were processed for materials obtained by cavitation synthesis under various process conditions. It can be seen that all four of these materials exhibited high phase purity. Another multimetallic perovskite, LaCoO_3 , has also been synthesized using sonochemical processing [75]. XRD analysis confirmed the phase purity of this material with a crystallite grain size of 33 nm. The SEM photograph of this material is shown in Figure 17. The base crystallites that are present in the large agglomerates of this material

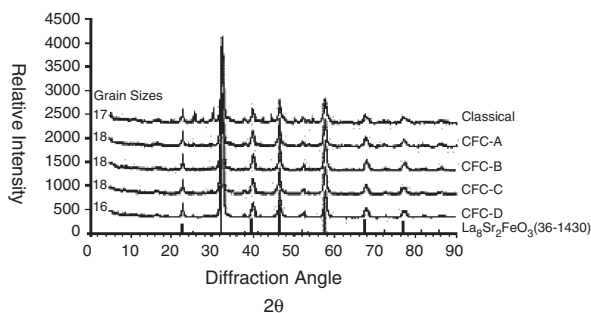


Figure 16. Example of a complicated mixed metal oxide system is the perovskite $\text{La}_{0.7}\text{Sr}_{0.3}\text{FeO}_3$. This material was synthesized by coprecipitation using both a Five Star Technologies cavitation processor and conventional high-speed mechanical mixing under otherwise similar conditions for comparison purposes. The XRD results for materials obtained from both processes are summarized in the following figure. The material obtained via the classical precipitation technique is shown at the top of the figure. This pattern shows that large amounts of separate phase compounds are present in addition to the desired perovskite material. The next four XRD patterns were processed for materials obtained by cavitation synthesis under various process conditions. It can be seen that all four of these materials exhibited high phase purity. Reprinted with permission from [75], W. R. Moser et al., Worcester Polytechnic Institute. © Five Star Technologies.

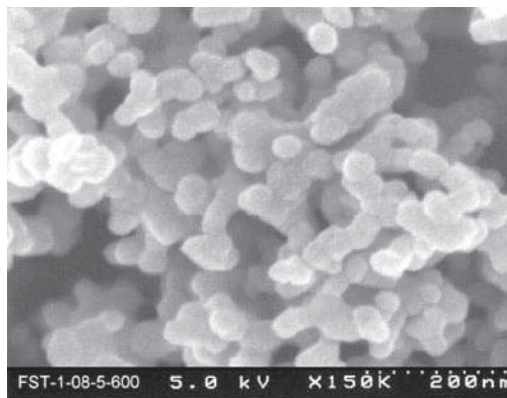


Figure 17. LaCoO_3 , also synthesized using the Five Star processing technologies. XRD analysis confirmed the phase purity of this material with a crystallite grain size of 33 nm. The SEM photograph of this material is shown below. The base crystallites that are present in the large agglomerates of this material are all quite similar in size. The use of such materials with a narrow distribution of primary particles could be quite useful in the development of an effective pore structure for catalytic applications. Reprinted with permission from [75], W. R. Moser, Five Star Technologies. © Five Star Technologies. BHR Group (1999).

are all quite similar in size. The use of such materials with a narrow distribution of primary particles could be quite useful in the development of an effective pore structure for catalytic applications.

4.4.2. Spinel Oxides

Shin and co-workers [76] demonstrated the use of ultrasound in accelerating the crystallization of nanosize ferrite powders. The effects of ultrasonic waves on the crystallization were studied for ferrite powders prepared using the coprecipitation method. The process of crystallization was evaluated employing XRD. The ferrite powder prepared without ultrasonic irradiation by the coprecipitation method was amorphous. However, the ferrite prepared with ultrasonic irradiation for 5 h was observed to crystallize, and the crystallization of the ferrite powder became more enhanced in proportion to the time of ultrasonic irradiation. The ferrite powder prepared with ultrasonic irradiation for 25 h had a higher crystallinity and a larger specific surface area than the ferrite powder calcined at 500°C for 2 h after preparing with coprecipitation. The prepared ferrite powders were a nanosize crystal phase. Jeevanandam and co-workers [77] reported a nanosized nickel aluminate spinel with the aid of ultrasound radiation by a precursor approach. Sonication an aqueous solution of nickel nitrate, aluminum nitrate, and urea yields a precursor which, on heating at 950°C for 14 h, yields nanosized NiAl_2O_4 particles with a size of ca. 13 nm and a surface area of about $108 \text{ m}^2 \cdot \text{g}^{-1}$. Vijayakumar and co-workers [78] reported the synthesis of Fe_3O_4 by sonication of iron (II) acetate in water under an argon atmosphere. The prepared Fe_3O_4 nanoparticles are superparamagnetic, and their magnetization at room temperature is very low ($<1.25 \text{ emu} \cdot \text{g}^{-1}$).

4.4.3. Complex Oxides

Shafi and Gedanken [79] prepared garnet phases by the sonochemical decomposition of the solutions of organic precursors, for the synthesis of nanostructured crystalline single-phase $\text{BaFe}_{12}\text{O}_{19}$ particles. Nanosized amorphous precursor powders for $\text{BaFe}_{12}\text{O}_{19}$, were prepared by the sonochemical decomposition of the solutions of $\text{Fe}(\text{CO})_5$ and $\text{Ba}[\text{OOCCH}(\text{C}_2\text{H}_5)\text{C}_4\text{H}_9]_2$ in decane, under air at 273 K. The amorphous phase, when heated, shows the formation of single-phase $\text{BaFe}_{12}\text{O}_{19}$, and the TEM micrograph revealed near uniform platelets with sizes less than 50 nm. The observed magnetization measured up to a field of 1.5 kG of the nanocrystalline $\text{BaFe}_{12}\text{O}_{19}$ sample ($48 \text{ emu} \cdot \text{g}^{-1}$) was significantly lower than that for the reported multidomain bulk particles ($72 \text{ emu} \cdot \text{g}^{-1}$), reflecting the ultrafine nature of the sample. In a further study, Shafi and co-workers [79] reported the formation of Olympic-ring-like colloidal hexaferrite particles without the use of a surfactant (Fig. 18). The intersection of two rings is amazing, as this is in direct contradiction to the proposed mechanism for the ring formation, based on the dry hole formation on an evaporating thin film completely wetted to the substrate. The creation of this unique feature is attributed to the interplay of magnetic forces with the regular particle-substrate interactions.

4.4.4. Mixed Oxides

The nonhydrolytic reaction of FeCl_3 with $(i\text{-C}_3\text{H}_7\text{O})_4\text{Ti}$ induced by sonication at 353 K forms bimetallic oxides, in which the iron and titanium ions are linked together by oxygen; the product remains amorphous, even when heated at 773 K for 2 h. When heated to 1073 K, the iron ions in

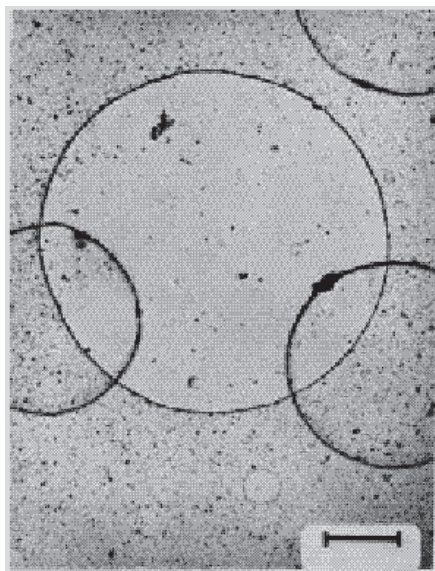


Figure 18. Transmission electron micrographs of amorphous $\text{BaFe}_{12}\text{O}_{19}$ nanoparticles prepared by a sonochemical decomposition technique showing Olympic rings formation. The creation of this unique feature is attributed to the interplay of magnetic forces with the regular particle-substrate interactions. Reprinted with permission from [79], K. V. P. M. Shafi et al., *J. Phys. Chem. B* 103, 3358 (1999). © 1999, Royal Society of Chemistry.

the bimetallic oxide exist in the form of crystalline Fe_2TiO_5 . The Fe_2O_3 in the products obtained by sonicating the mixture of $\text{Fe}(\text{CO})_5$ and $(\text{C}_2\text{H}_5\text{O})_4\text{Ti}$ at 313 K is amorphous; in contrast, when pure $\text{Fe}(\text{CO})_5$ is sonicated under the same conditions, the presence of titanium compounds affects the crystallization of Fe_2O_3 . The amorphous Fe_2O_3 is easily reduced and reacts with TiO_2 , forming FeTiO_3 in the presence of a reducing agent and calcination under vacuum. The particles of the as-prepared products are all of nanometric size, but they aggregate to form $\text{Fe}_x\text{O}_y\text{-TiO}_2$ [80].

4.5. Nanometal Chalcogenides

Xu H. and co-workers [81] reported a novel method for the preparation of copper monosulfide (CuS) and nickel monosulfide (NiS) nanoparticles via a sonochemical route from an aqueous solution containing metal acetate [$\text{Cu}(\text{CH}_3\text{COO})_2$ or $\text{Ni}(\text{CH}_3\text{COO})_2$] and thioacetamide (TAA) in the presence of triethanolamine (TEA) as a complexing agent under ambient air. The as-prepared nanoparticles have a regular shape, a narrow size distribution, and high purity. It is found to be a mild, convenient, and efficient method for the preparation of CuS and NiS nanoparticles. In fact, a sonochemical route has been successfully established to prepare copper selenide nanocrystals with different phases. It is found that the ratio of $[\text{Cu}^{2+}]/[\text{SeSO}_3^{2-}]$ determines the phases of the products. The size of Cu_{2-x}Se nanocrystals can be controlled by using different complexing agents. This route is proved to be a convenient, mild, and energy-efficient route for the preparation of copper selenide nanocrystals with different phases. Mdleleni and co-workers reported the sonochemical synthesis of nanostructured molybdenum sulfide [82]. MoS_2 is best known for its layered structure and as a desulfurization catalyst. MoS_2 was prepared by irradiating solutions of molybdenum hexacarbonyl and sulphur in 1,2,3,5-tetramethylbenzene with high-intensity ultrasound. The MoS_2 was amorphous as initially prepared (see Fig. 19), but subsequently crystallized upon heating at 725 K for 10 h under an atmosphere of flowing He. The sonochemically prepared MoS_2 catalyzes the HDS of thiophene with activities roughly fivefold better than conventional MoS_2 and comparable to those observed with RuS_2 , one of the best

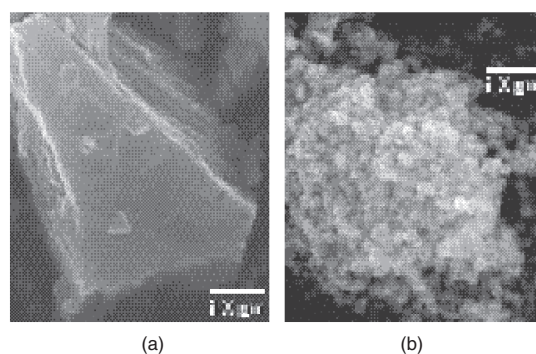


Figure 19. Morphology of MoS_2 prepared by (a) conventional and (b) sonochemical method. Reprinted with permission from [82], M. M. Mdleleni et al., *J. Am. Ceram. Soc.* 120, 6189 (1998). © 1998, American Chemical Society.

prior catalysts. Nikitenko et al. have reported the synthesis of amorphous WS_2 by the ultrasound irradiation of a $W(CO)_6$ solution in diphenylmethane (DPhM) in the presence of a slight excess of sulfur at $90^\circ C$ under argon. Heating the amorphous powder at $800^\circ C$ under argon yields WS_2 nanorods and their packings. The average size of WS_2 nanorods was found to be 3–10 nm and 1–5 μm in thickness and length, respectively [83].

Vijayakumar and co-workers [84] reported the preparation of Ag_2S and CuS -polyvinyl acetate composites. Li et al. developed nanocrystalline silver tellurides in organic solvent systems by high-intensity ultrasonic irradiation at room temperature. Ag_2Te and Ag_7Te_4 are prepared in an ethylenediamine system and an ethanol system, respectively. The ultrasonic irradiation and the solvents are both important in the formation of products [85]. Nanospherical Ag_2S/PVA and nanoneedles of CuS/PVA composite have been prepared by sonochemical irradiation of an ethylenediamine–water solution of elemental sulfur, silver nitrate, or copper acetate in the presence of polyvinyl alcohol. The particles are 25 and 225 nm for Ag_2S/PVA and CuS/PVA nanocomposites, respectively. Both Ag_2S and CuS , being narrow-bandgap nanocrystalline semiconductors, find significant applications in many technological applications, ranging from microelectronics to nonlinear optics, optoelectronics, catalysis, and photoelectrochemistry. Bandgaps of 1.05 and 2.08 eV have been estimated for Ag_2S/PVA and CuS/PVA nanocomposites.

$ZnSe$ nanoparticles about 3 nm in size have been prepared by the sonochemical irradiation of an aqueous solution of seleno urea and zinc acetate under argon [86]. This sonochemical method was found to be a general method for the preparation of other selenides as well. Figure 20 shows the X-ray diffraction pattern of sonochemically processed as-prepared powders after 1, 2, and 3 h of sonication. Zhu and co-workers also reported [87] that $PbSe$ nanoparticles about 12 nm in size were prepared by a pulse sonoelectrochemical technique from an aqueous solution of sodium seleno-sulfate and lead acetate. The effects of changing the various parameters on particle size were discussed, and possible explanations were offered. A bandgap of 1.10 eV was estimated from optical measurement of the nanoparticles.

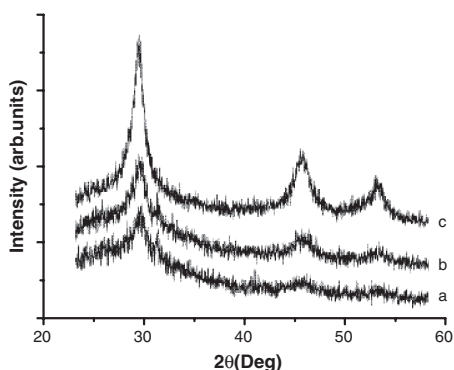


Figure 20. X-ray diffraction patterns of the as-prepared $ZnSe$ after sonication of (a) 1, (b) 2, and (c) 3 h. Reprinted with permission from [86], J. Zhu et al., *Chem. Mater.* 12, 73 (2000). © 2000, American Chemical Society.

Li et al. [88] recently prepared nanophase lead chalcogenides, via the sonochemical route, using $Pb(CH_3COO)_2 \cdot 3H_2O$ and the corresponding elemental chalcogens were used as the reactants, while ethylenediamine (en) was used as the solvent. Ultrasonic irradiation was found to have two main effects: (1) it favored the dissolution of chalcogens (E) and the formation of E^{2-} , and thus accelerated the reaction; (2) it prevented the aggregation of the resulting nanoparticles [89].

The sonochemical preparation of mercury(II) selenide nanoparticles based on the reaction between mercury acetate and sodium selenosulfate in an aqueous system was reported by Wang et al. The products obtained are well dispersed, and the nanoparticles are of small sizes [90].

4.6. Nanometal Carbides and Nitrides and Phosphides

The sonochemical synthesis of nanophase molybdenum carbide from the ultrasonic irradiation of molybdenum hexacarbonyl has been prepared by heating the product at $450^\circ C$ under a helium gas flow. Since the synthesis of Mo_2C is particularly prone to substantial oxygen contamination [91], the sonicated product is subjected to heating in a flow of (1:1) CH_4/H_2 mixture at $300^\circ C$ for 1 h, then at $400^\circ C$ for 1 h, and finally at $500^\circ C$ for 48 h. The flow rate of the CH_4/H_2 mixture was 27.5 cm^3 (STP)/min. After this carburization, excess carbon, hydrogen, and oxygen had been largely removed [92]. Ultrasonic irradiation (22 kHz, Ar atmosphere) of Th(IV) β -diketonates $Th(HFAA)_4$ and $Th(DBM)_4$, where HFAA and DBM are hexafluoroacetylacetone and dibenzoylmethane, respectively, causes them to decompose in hexadecane solutions, forming solid thorium compounds. The rate of the sonochemical reaction increased with the rising β -diketonate volatility, and decreased with the rising hydrocarbon solvent vapor pressure. Solid sonication products consisted of a mixture of thorium carbide ThC_2 and Th(IV) β -diketonate partial degradation products. The average ThC_2 particle size was estimated to be about 2 nm. ThC_2 formation was attributed to the high-temperature reaction occurring within the cavitating bubble. The thorium β -diketonate partial degradation products formed in the liquid reaction zones surrounding the cavitating bubbles [93]. This is the first study of the “direct” effect of power ultrasound on $5f$ -transition elements using volatile Th(IV) β -diketonate precursors.

Li et al. [94] prepared InP nanocrystals with a diameter of ≈ 9 nm under high-intensity ultrasonic irradiation for 4 h from the reaction of $InCl_3 \cdot 4H_2O$, yellow phosphorus, and KBH_4 in the mixed solvents of ethanol and benzene. The sonochemical reaction of $Fe(CO)_5$ and triethylphosphine has been found to produce a solid amorphous iron phosphide of composition FeP . This reaction provides the first use of ultrasound to sonochemically synthesize amorphous phosphide semiconductor materials from organometallic precursors [95]. Unlike the sonication on $W(CO)_6$ and triphenyl phosphine, where the monosubstituted product $W(CO)_5(PPh_3)$ was principally formed [96], sonication of the volatile species $Fe(CO)_5$ and $P(CH_2CH_3)_3$ produced a complete loss of the ligand sets to produce FeP as the principal product. The difference in reactivity is most probably due to the difference

in vapor pressure of the reactant sets, as well as the relative kinetic stability of the carbonyl-substituted species. Both $W(CO)_6$ and triphenylphosphine are solids, and have relatively low vapor pressures, even in solution [97]. $Fe(CO)_5$ and $P(CH_2CH_3)_2$, on the other hand, are both liquids with high vapor pressures, and are expected to be the principal components of the gas-phase composition of the cavities.

Buhro et al. [98] used coreduction of $MoCl_5$ and $SiCl_4$ with an NaK alloy in a hexane dispersion using 600 W, 20 kHz irradiation, followed by annealing at 900 °C to produce nanocrystalline $MoSi_2$ powders with $\approx 90\%$ yield. Consolidation by hot pressing at 1170 °C, 140 MPa for 4 h gives a 78% dense compact with 31 nm average grain sizes and a Vickers microhardness of 1484 (10% kg/mm^2). The microhardness values and compression strengths are 50–70% higher in nanocrystalline $MoSi_2$ than in conventional, coarse-grained $MoSi_2$.

Recently, Suslick et al. [99] developed a new synthetic technique, that is, sonochemical synthesis of nanostructured inorganic materials, to produce Mo_2N with a face-centered cubic structure [hereafter designated as Mo_2N (fcc)]; a stream of NH_3 (Matheson, 99.99%) was passed through the reaction cell at a flow rate of $135\text{ mmol}\cdot\text{s}^{-1}$. Following rapid heating to 500 K, the sample was further heated to 973 K with a linear ramping rate of 30 K, and then maintained at a final temperature for 1 h. Once the reaction was complete, the gas flow was switched to a flow of helium ($25\text{ mmol}\cdot\text{s}^{-1}$) prior to quenching the catalysts.

5. MESOPOROUS SOLIDS

Another closely related field that has been developed by Gedanken and co-workers is the sonochemical coating of submicron ceramic spheres (silica, alumina, and zirconia) by a large variety of nanoparticles. This was done by synthesizing the ceramic spheres by conventional techniques (like the Stobber method for silica particles). The spheres were then introduced in the sonication bath, mixed with the solution of the precursor, and the ultrasonic radiation was passed through the solution for a predetermined time. In this way, nanoparticles of metals (Ni and Co, for example), metal oxides (Fe_2O_3 , Mo_2O_5), rare earth oxides (Eu_2O_3 , Tb_2O_3), semiconductors (CdS, ZnS), and Mo_2C were deposited on a ceramic surface.

Gedanken and co-workers recently developed mesoporous (MSP) materials, and used ultrasound radiation in the deposition of amorphous nanomaterials into the mesopores. They demonstrated that the sonochemical technique can be employed for the synthesis of mesoporous metal oxides. The sonochemical method reduced the time period required for such synthesis by manifold, and also produced more stable structures. Excellent results were obtained with silica, titania, yttria-stabilized zirconia (YSZ), and Fe_2O_3 [100].

Further, a sonochemical method was used to prepare MSP silica [101], MSP YSZ (yttria-stabilized zirconia), and other MSP materials. The sonochemical products were shown to have thicker walls than those synthesized by the conventional methods. MSP titania, prepared under sonochemical conditions, has the highest surface area reported so far. In addition, sonochemistry has been used for the

insertion of amorphous nanoparticles into the mesopores: Mo_2O_5 into the mesopores of MCM-41 (MSP silica) [103], and amorphous Fe_2O_3 [104] in the mesopores of MSP titania. Five physical methods were used to prove that the amorphous nanoparticles are indeed anchored onto the inner walls of the channels. The amount of Mo_2O_5 that was inserted in the mesopores was 45% by weight. An attempt to increase this amount showed that the excess is deposited outside the mesopores.

The sonochemical preparation of air-stable iron nanoparticles having a very high magnetization has been reported. Iron nanoparticles are pyrophoric, and protecting them against oxidation is a challenge. However, the sonication of $Fe(CO)_5$ in diphenylmethane results in iron nanoparticles coated by a polymer. Further annealing of the sample yields the air-stable product [105]. The characterization of the product and the stability studies are based on Mossbauer spectroscopy, XRD, and magnetization measurements. Although some efforts in materials science are still directed toward developing new methods for the fabrication of nanomaterials, more attention is directed these days to the control of the size and shape of the nanoparticles. Various research groups have demonstrated over the years that the control of the particle size is quite easy when using sonochemistry. It is accomplished simply by the variation of the concentration of the precursor in the irradiated solution. The more dilute the solution, the smaller are the particles. The shapes of the products of the sonochemical process are less predictable. A major factor is the presence or absence of a surfactant. We can just mention that shapes such as Olympic nanorings ($BaFe_{12}O_{19}$) [72], nanocylinders ($GaOOH$) [106], nanotubes (TiO_2) [107], nested inorganic fullerenes (Ti_2O) [108], and spheres were among the shapes of the sonochemical products.

Chen et al. developed a simple method for the preparation of Pd particles *in-situ* within the mesoporous silica host by soaking and subsequent irradiation by ultrasound at room temperature. The straightforward process yields composite samples containing Pd nanoparticles, with a mean size of 5–6 nm diameter, located within the pores of the mesoporous silica host [109].

6. BIONANOMATERIALS

Hydroxyapatite ($Ca_{10}(PO_4)_6(OH)_2$, HAp) is one of the most attractive materials for vertebrate and dental implants due to its compositional and biological similarity to native tissues. HAp exists over a compositional range that can be characterized in terms of its Ca/P ratio. Stoichiometric HAp has a Ca/P ratio of 1.67, while calcium-deficient HAp has a Ca/P ratio as low as 1.5. HAp can be prepared in bulk by normal ceramic processing methods using fine powder and a precursor at high temperatures. Such a powder results in easy handling, casting, and sintering, leading to an excellent sintered body. Several investigations on the precipitation of HAp or its precursor phases from Ca^{2+} and PO_4^{3-} bearing solutions and an acid–base reaction at constant composition have been carried out; however, these methods need highly qualified and controlled parameters, such as the nature and composition of the starting materials, and the pH and temperature of the solutions prepared to obtain an

HAp monophase. However, high-intensity ultrasound waves can stimulate the reactivity of chemical species involved, resulting in the acceleration of the heterogeneous reactions between liquid and solid reactants. Ultrasound was irradiated to an aqueous suspension containing phosphoric acid (H_3PO_4) and calcium hydroxide ($\text{Ca}(\text{OH})_2$) to investigate the sonochemical effect on the preparation of hydroxyapatite ($\text{Ca}_{10}(\text{PO}_4)_6(\text{OH})_2$, HAp). The HAp monophase could be synthesized from the suspension sonicated for 60 min [110 and references therein].

1. The HAp monophase can be synthesized from an aqueous suspension containing H_3PO_4 and $\text{Ca}(\text{OH})_2$ with the aid of ultrasonic irradiation under atmospheric pressure, and this synthesis reaction progresses more effectively than that by the heating method.
2. The synthesis reaction for HAp in the ultrasonic field is almost completed by 60 min in the present condition. The completion of the reaction is confirmed by monitoring the equilibrium pH of the suspension to be a neutral value.
3. The ultrasonic irradiation leads to the formation of very fine HAp powder with a relatively narrow size distribution.

7. CONCLUSIONS

Through the process of cavitation, ultrasound performs high-energy chemistry. A variety of applications to the synthesis of nanocrystalline metals, amorphous metals, alloys, nanophasic colloids, and catalysts extend to oxides, nitrides carbides, and chalcogenides. There are other bionanomaterial applications through the synthesis of protein microspheres and HAp. The applications of high-intensity ultrasound to the synthesis of nanomaterial science is not only diverse, but also has been expanding over the past decade. The sonochemical synthesis of amorphous, and more recently nanocrystalline, materials has been investigated for application in magnetic devices requiring magnetically soft materials. Such synthetic conditions result from cavitation collapse, resulting in high local temperatures and pressures with exceptionally high cooling rates. The synthetic conditions and the modified property-related studies have been discussed in this review, with special emphasis on nanometals, alloys, oxides, and chalcogenides.

GLOSSARY

Photoluminescence (PL) Photoluminescence is simply the emission of photons from an excited molecular species, where the excitation of the molecular species is by the absorption of light.

Scanning electron microscopy (SEM) An electron microscopic technique capable of providing structural information over a wide range of magnification. SEM compliments optical microscopy for studying the texture, topography, and surface features over a wide range, from 10^{-2} to $\sim 10^2 \mu\text{m}$.

Single-bubble sonoluminescence and multibubble sonoluminescence (SBSL and MBSL) The acoustic cavitation bubble is nearly spherical in SBSL, with an almost infinite

number of oscillating bubbles being observed, while in MBSL, it is more likely to be nonspherical, with only a small number of oscillations.

Sodium dodecyl sulfate (SDS) Mol formula $\text{CH}_3(\text{CH}_2)_{11}\text{OSO}_3\text{Na}$ is stable, incompatible with strong acids and oxidizing agents, and used as a surfactant to encapsulate nanoparticles.

REFERENCES

1. K. S. Suslick, *Science* 247, 1439 (1990).
2. K. S. Suslick and L. A. Crum, in "Encyclopedia of Acoustics" (M. J. Crocker, Ed.), Vol. 1, Chap. 26, pp. 271–282. Wiley-Interscience, New York, 1997. Also, J. R. Blake, G. S. Keen, R. P. Tong, and M. Wilson, *Phil. Trans. R. Soc. London* 357, 251 (1999).
3. For a brief review, see M. A. Margulis and I. M. Margulis, *Ultrason. Sonochem.* 9, 1 (2002). Also, K. S. Suslick, *Sci. Amer.* 82 (1989).
4. L. A. Crum, *Phys. Today* 47, 22 (1994).
5. S. J. Putterman, *Sci. Am.* 46 (1995).
6. K. S. Suslick (Ed.), "Ultrasound: Its Chemical, Physical and Biological Effects." VCH, New York, 1988. Also, K. S. Suslick, Y. Didenko, M. M. Fang, T. Hyeon, K. J. Kolbeck, W. B. McNamara, M. M. Mdleleni, and M. Wong, *Phil. Trans. R. Soc. London* 357, 335 (1999).
7. K. S. Suslick, in "Encyclopedia of Chemical Technology" (K. Othmer, Ed.), 4th ed., Vol. 26, pp. 517–541. Wiley, New York, 1998.
8. T. J. Mason and J. P. Lorimer, "Sonochemistry: Theory, Applications and Uses of Ultrasound in Chemistry." Ellis Horwood, Chichester, U.K., 1988. Also, T. J. Mason, *Phil. Trans. R. Soc. London* 357, 355 (1999).
9. T. G. Leighton, "The Acoustic Bubble," pp. 531–551. Academic, London, 1994.
10. Lord Rayleigh, *Phil. Mag.* 34, 94 (1917).
11. W. T. Richards and A. L. Loomis, *J. Am. Chem. Soc.* 49, 3086 (1927).
12. E. A. Neppiras, *Phys. Rep.* 61, 159 (1980).
13. H. G. Flynn, in "Physical Acoustics" (W. P. Mason, Ed.), Vol. IB, p. 157. Academic, New York, 1964.
14. D. Weller, *Adv. Mater.* 5, 88 (1993).
15. W. R. Moser (Ed.), "Advanced Catalysts and Nano Structured Materials." Academic, New York, 1996.
16. K. S. Suslick, *MRS Bull.* 20, 29 (1995).
17. K. S. Suslick, in "Handbook of Heterogeneous Catalysis" (G. Ertl, H. Knozinger, and J. Weitkamp, Eds.), Vol. 3, Chap. 8.6, pp. 1350–1357. Wiley-VCH, Weinheim, 1997.
18. K. S. Suslick, in "Encyclopedia of Inorganic Chemistry" (R. B. King, Ed.), Vol. 7. 1994.
19. T. Hyeon, M. Fang, and K. S. Suslick, *J. Am. Chem. Soc.* 118, 5492 (1996).
20. K. S. Suslick and M. W. Grinstaff, *J. Am. Chem. Soc.* 112, 7807 (1990).
21. M. W. Grinstaff, M. B. Salamon, and K. S. Suslick, *Phys. Rev. B* 48, 269 (1993).
22. R. Bellissent, G. Galli, M. W. Grinstaff, P. Migliardo, and K. S. Suslick, *Phys. Rev. B* 48, 15797 (1993).
23. G. J. Long, D. Hautot, Q. A. Pankhurst, D. Van dormael, F. Grandjean, J. P. Gaspard, V. Brios, T. Hyeon, and K. S. Suslick, *Phys. Rev. B* 57, 716 (1998).
24. M. L. Rao, Ph.D. Dissertation, IIT Kanpur, 2003.
25. G. Katabi, X. Cao, A. Gedanken, R. Prozoro, and Yu. Koltypin, *J. Non-Cryst. Solids* 201, 159 (1996).
26. S. Sundar Manoharan and M. L. Rao (private communication).
27. V. G. Pol, D. N. Srivastava, O. Palchik, V. Palchik, M. A. Slifkin, A. M. Weiss, and A. Gedanken, *Langmuir* 18, 3352 (2002).

28. J. Zhu, S. Liu, O. Palchik, Y. Koltypin, and A. Gedanken, *Langmuir* 16, 6396 (2000).
29. R. A. Salkar, P. Jeevanandam, S. T. Aruna, Y. Koltypin, and A. Gedanken, *J. Mater. Chem.* 9, 1333 (1999).
30. N. A. Dhas, C. P. Raj, and A. Gedanken, *Chem. Mater.* 10, 1446 (1998).
31. N. A. Dhas, H. Cohen, and A. Gedanken, *J. Phys. Chem. B* 101, 6834 (1997).
32. N. A. Dhas and A. Gedanken, *J. Mater. Chem.* 8, 445 (1998).
33. Y. Mizukoshi, E. Takagi, H. Okuno, R. Oshima, Y. Maeda, and Y. Nagata, *Ultrason. Sonochem.* 8, 1 (2001).
34. P. Diodatti, G. Giannini, L. Mirri, G. Petrillo, and F. Sachtetti, *Ultrason. Sonochem.* 4, 45 (1997).
35. K. Okitsu, Y. Mizukoshi, H. Bandow, Y. Maeda, T. Yamamoto, and N. Nagata, *Ultrason. Sonochem.* 3, 249 (1996).
36. Y. Nagata, Y. Watanabe, S. Fujita, T. Dohmaru, and S. Taniguchi, *Chem. Commun.* 1620 (1992).
37. S. A. Yeung, R. Hobson, S. Biggs, and F. Grieser, *Chem. Commun.* 378 (1993).
38. Y. Mizukoshi, K. Okitsu, Y. Maeda, T. Yamamoto, R. Oshima, and Y. Nagata, *J. Phys. Chem. B* 101, 7033 (1997).
39. T. Fujimoto, S.-ya. Terauchi, H. Umehara, I. Kojima, and W. Henderson, *Chem. Mater.* 13, 1057 (2001).
40. S. Wize, S. Margel, A. Gedanken, T. C. Rojas, A. Fernández, and R. Prozorov, *J. Mater. Res.* 14, 3913 (1999).
41. S. Wize, P. Prozorov, Y. Cohen, D. Aurbach, S. Margel, and A. Gedanken, *J. Mater. Res.* 13, 211 (1998).
42. B. M. Berovsky, V. F. Medvedev, and M. S. Krakov, "Magnetic Fluids: Engineering Applications." Oxford University Press, 1993.
43. K. S. Suslick, M. Fang, and T. Hyeon, *J. Am. Chem. Soc.* 118, 11960 (1996).
44. A. Gedanken, G. Katabi, Yu. Koltypin, and X. Cao, *J. Cryst. Growth* 166, 1 (1996).
45. G. Katabi, R. Prozorov, and A. Gedanken, *Nanostruct. Mater.* 12, 412 (1999). Also, *Nanostruct. Mater.* 12, 669 (1999).
46. K. V. P. M. Shafi, S. Wize, T. Prozorov, and A. Gedanken, *Thin Solid Films* 318 (1998).
47. S. Avivi (Levi), I. Felner, I. Novik, and A. Gedanken, *Biochim. Biophys. Acta* 1527, 123 (2001).
48. K. S. Suslick, S.-B. Choe, A. A. Cichowlas, and M. W. Grinstaff, *Nature* 353, 414 (1991).
49. B. Moren, O. Vidoni, C. Ovalles, B. Chaudret, C. Urbina, and H. Krentzein, *J. Colloid Interface Sci.* 207, 251 (1998).
50. T. Hyeon, M. Fang, A. A. Cichowlas, and K. S. Suslick, *Mater. Sci. Eng. A* 204, 186 (1995).
51. K. V. P. M. Shafi, A. Gedanken, R. B. Goldfarb, and I. Felner, *J. Appl. Phys.* 81, 6901 (1997).
52. K. V. P. M. Shafi, A. Gedanken, and R. Prozorov, *J. Mater. Chem.* 8, 769 (1998).
53. K. V. P. M. Shafi, A. Gedanken, R. Prozorov, A. Revesz, and J. Lendvai, *J. Mater. Res.* 15, 332 (2000).
54. M. L. Rao and S. Sundar Manoharan (private communication).
55. M. L. Rao and S. Sundar Manoharan (private communication).
56. M. L. Rao and S. Sundar Manoharan, *Solid State Sci.* 5, 821 (2003).
57. M. L. Rao, S. Sundar Manoharan, D. Elefant, and C. M. Schneider, *J. Mater. Res.* (to appear).
58. W. Huang, X. Tang, Y. Wang, Yu. Koltypin, and A. Gedanken, *Chem. Commun.* 15, 1415 (2000).
59. Y. Zhu, H. Li, Yu. Koltypin, Y. Rosenfeld Hacohe, and A. Gedanken, *Chem. Commun.* 24, 2616 (2001).
60. X. N. Xu, Y. Wolfus, A. Shaulov, Y. Yeshurun, I. Felner, I. Nowik, Yu. Koltypin, and A. Gedanken, *J. Appl. Phys.* 91, 4611 (2002).
61. R. V. Kumar, Yu. Koltypin, X. N. Xu, Y. Yeshurun, A. Gedanken, and I. Felner, *J. Appl. Phys.* 89, 6324 (2001).
62. R. Prozorov, Y. Yeshurun, T. Prozorov, and A. Gedanken, *Phys. Rev. B* 59, 6956 (1999).
63. X. Cao, R. Prozorov, Yu. Koltypin, G. Katabi, I. Felner, and A. Gedanken, *J. Mater. Res.* 12, 402 (1997).
64. D. N. Srivastava, N. Perkas, G. A. Seisenbaeva, Y. Koltypin, V. G. Kessler, and A. Gedanken, *Ultrason. Sonochem.* (2002).
65. M. Gasgnier, L. Beaury, and J. Derouet, *Ultrason. Sonochem.* 7, 25 (2000).
66. Z. Y. Zhong, Y. Mastai, R. A. Salkar, Y. Koltypin, and A. Gedanken, *J. Mater. Res.* 15, 393 (2000).
67. P. Jeevanandam, Y. Diamant, M. Motiei, and A. Gedanken, *J. Phys. Chem.* 3, 4107 (2001).
68. Yu. Koltypin, S. I. Nikitenko, and A. Gedanken, *J. Mater. Chem.* 12, 1107 (2002).
69. J. Liang, X. Jiang, G. Liu, Z. Deng, J. Zhuang, F. Li, and Y. Li, *Mater. Res. Bull.* 38, 161 (2003).
70. G. Kortüm, "Reflectance Spectroscopy: Principles, Methods, Applications." Springer, Berlin, 1969.
71. X. C. Wu, R. Y. Wang, B. S. Zou, L. Wang, S. M. Liu, and J. R. Xu, *J. Mater. Res.* 13, 64 (1998).
72. L. Yin, Y. Wang, G. S. Pong, Y. Koltypin, and A. Gedanken, *J. Colloid Interface Sci.* 246, 78 (2002).
73. X. Y. Liang, Z. Ma, Z. C. Bai, and Y. N. Qin, *Acta Phys. Chem. Sinica* 18, 567 (2002).
74. W. R. Moser, J. Find, S. C. Emerson, and I. M. Krausz, "Engineered Synthesis of Nanostructured Materials and Catalysts," Worcester Polytechnic Institute, *Adv. Chem. Eng.* 27 (2001). Also, J. Find, S. C. Emerson, I. M. Krausz, and W. R. Moser, "Hydrodynamic Cavitation as Tool to Control Macro-, Micro, and Nano-Properties of Inorganic Materials," Worcester Polytechnic Institute.
75. W. R. Moser, T. Giang, and S. Nguyen, Worcester Polytechnic Institute; and O. V. Kozyuk, "A New Route to Cavitation Chemistry and Chemical Processing by Controlled Flow Cavitation," Five Star Technologies; BHR Group, 1999 Process Intensification Conference, Oct. 1999. Also, "Synthesis of Supported Silver Nanocrystallites Using Hydrodynamic Cavitation," I. M. Krausz, Worcester Polytechnic Institute; S. C. Emerson, "International Fuel Cells"; J. Find, Fakultät für Chemie; and W. R. Moser, Worcester Polytechnic Institute, Elsevier Science, Nov. 9, 2001.
76. H. C. Shin, J. H. Oh, J. C. Lee, and S. C. Choi, *Phys. Status Solidi A—Appl. Res.* 189, 735 (2002).
77. P. Jeevanandam, Yu. Koltypin, and A. Gedanken, *Mater. Sci. Eng. B* 90, 125 (2000).
78. R. Vijayakumar, Yu. Koltypin, I. Felner, and A. Gedanken, *Mater. Sci. Eng. A* 286, 101 (2000).
79. K. V. P. M. Shafi and A. Gedanken, *Nanostruct. Mater.* 12, 23 (1999). Also, K. V. P. M. Shafi, I. Felner, Y. Mastai, and A. Gedanken, *J. Phys. Chem. B* 103, 3358 (1999).
80. W. Huang, X. Tang, I. Felner, Yu. Koltypin, and A. Gedanken, *Mater. Res. Bull.* 37, 1721 (2002).
81. S. Xu, H. Wang, J. J. Zhu, and H. Y. Chen, *J. Cryst. Growth* 234, 263 (2002).
82. M. M. Mdleleni, T. Hyeon, and K. S. Suslick, *J. Am. Chem. Soc.* 120, 6189 (1998).
83. S. I. Nikitenko, Yu. Koltypin, Y. Mastai, M. Koltypin, and A. Gedanken, *J. Mater. Chem.* 12, 1450 (2002).
84. P. Vijayakumar, O. Palchich, Yu. Koltypin, Y. Diamant, and A. Gedanken, *Ultrason. Sonochem.* 9, 65 (2002).
85. B. Li, Y. Xie, Y. J. Huang, and Y. Qian, *J. Solid State Chem.* 158, 260 (2001).
86. J. Zhu, Y. Koltypin, and A. Gedanken, *Chem. Mater.* 12, 73 (2000).
87. J. Zhu, S. T. Aruna, Yu. Koltypin, and A. Gedanken, *Chem. Mater.* 12, 143 (2000).
88. Q. Li, D. Ming, W. Shao, J. Wu, G. Yu, and Y. Qian, *Mater. Res. Bull.* 2164, 1 (2002). Also, T. Ding, H. Wang, S. Xu, and J.-J. Zhu, *J. Cryst. Growth* 235, 517 (2002).

89. J. H. Zhan, X. G. Yang, D. W. Wang, Y. Xie, and Y. T. Qian, *Inorg. Chem. Commun.* 2, 447 (1999). Also, M. Chen, Y. Xie, J. C. Lu, Y. J. Zhu, and Y. T. Qian, *J. Mater. Chem.* 11, 518 (2001).
90. H. Wang, S. Xu, X.-N. Zhao, J.-J. Zhu, and X.-Q. Xin, *Mater. Sci. Eng. B* 96, 60 (2002).
91. G. S. Ranhotra, G. W. Haddix, A. T. Bell, and J. A. Reimer, *J. Catal.* 108, 24 (1987).
92. K. S. Suslick, T. Hyeon, and M. Fang, *Chem. Mater.* 8, 2172 (1996).
93. S. I. Nikitenko, Ph. Moisy, I. A. Tcharushnikova, P. Blanc, and C. Madic, *Ultrason. Sonochem.* 77, 177 (2000).
94. B. Li, Y. Xie, J. Huang, Y. Lin, and Y. Qain, *Ultrason. Sonochem.* 8, 331 (2001).
95. J. D. Sweet and D. J. Casadonte, Jr., *Ultrason. Chem.* 8, 97 (2001).
96. K. S. Suslick, D. A. Hammerton, and R. E. Cline, *J. Am. Chem. Soc.* 108, 5641 (1986).
97. E. B. Flint and K. S. Suslick, *J. Phys. Chem.* 97, 3098 (1993).
98. W. E. Buhro, T. J. Trentler, R. Suryanarayanan, and S. M. L. Sastry, *Mater. Sci. Eng.* 24, 193 (1995).
99. K. S. Suslick, S. B. Choe, A. A. Cichowlas, and M. W. Grinstaff, *Nature* 353, 414 (1991). Also, K. S. Suslick, T. Hyeon, and M. Fang, *Chem. Mater.* 8, 2172 (1996).
100. D. N. Srivastava, N. Perkas, A. Zaban, and A. Gedanken, *Pure Appl. Chem.* 74, 1509.
101. X. Tang, S. Liu, Y. Wang, W. Huang, Yu. Koltypin, and A. Gedanken, *Chem. Commun.* 2119 (2000).
102. Y. Wang, X. Tang, L. Yin, W. Huang, and A. Gedanken, *Adv. Mater.* 12, 1137 (2000).
103. M. V. Landau, L. Vradman, M. Herskowitz, Y. Koltypin, and A. Gedanken, *J. Catal.* 201, 22 (2001).
104. N. Perkas, Y. Wang, Yu. Koltypin, A. Gedanken, and S. Chandrasekaran, *Chem. Commun.* 988 (2001).
105. S. Nikitenko, Yu. Koltypin, I. Felner, and A. Gedanken, *Angew. Chem. Int. Ed.* (Dec. 2001).
106. S. Avivi, Y. Mastai, G. Hodes, and A. Gedanken, *J. Am. Chem. Soc.* 121, 4196 (1999).
107. Y. Zhu, H. Li, Yu. Koltypin, Y. Rosenfeld Hacoheh, and A. Gedanken, *Chem. Commun.* (in press).
108. S. Avivi, Y. Mastai, and A. Gedanken, *J. Am. Chem. Soc.* 122, 4331 (2000).
109. W. Chen, W. Cai, X. Lei, and L. Zhang, *Mater. Lett.* 50, 53 (2001).
110. W. Kim and F. Saito, *Ultrason. Sonochem.* 8, 85 (2001).

Stealth and Biomimetic Core-Corona Nanoparticles

Ruxandra Gref, Patrick Couvreur

UMR CNRS, Châtenay Malabry, France

CONTENTS

1. Introduction
 2. Biodistribution of Intravenously Administered Particles
 3. Protein-Rejecting Abilities of Poly(ethylene glycol) Coatings
 4. Theoretical Modeling
 5. "Stealth" PEG-Coated Drug Carriers
 6. Detection and Characterization of the PEG Corona
 7. Drug Encapsulation
 8. Biodistribution
 9. Toxicological Considerations
 10. Other Types of Coronas
 11. Active Targeting
 12. Conclusions
- Glossary
References

1. INTRODUCTION

Over the last decades, there has been a growing interest in the development of a drug carrier that is small enough for intravenous administration and that has the ability to bypass the normal physiological defense processes of the organism. This type of "stealth" carrier could, therefore, circulate for prolonged times in blood, opening, in this way, new therapeutic opportunities such as site-specific drug delivery or controlled drug release into the vascular compartment.

For site-specific or targeted drug delivery, the drug carrier should avoid indiscriminate interactions with the mononuclear phagocyte system (MPS), selectively reach the diseased site of action, and release the drug in its active form at a suitable rate and in therapeutic amounts. This concept of "magic bullets" was first imagined by Ehrlich at the beginning of the century. Nowadays, such drug carriers could

be of highest interest in cancer chemotherapy and in many other diseases such as viral infections, which suffer from nonspecific toxicity and poor tissue specificity of drugs.

There are numerous advantages of stealth carriers, for example, the protection of highly sensitive active molecules against *in vivo* degradations, the reduction of their toxic side effects, the increase of patient comfort by avoiding repetitive injections or the use of perfusion pumps, and the achievement of more favorable drug pharmacokinetics. In particular, the successful administration of protein drugs is often problematic, as they are hydrolyzed or denatured in the gastrointestinal tract, and they are quickly metabolized if intravenously injected. Their typical blood half-lives, ranging from 2 to 30 minutes [1], could be improved by encapsulating them into long-circulating drug delivery devices acting as circulating microreservoirs.

Long-circulating particulate carriers loaded with contrast agents could find potential applications in nuclear medicine. Stealth nanoparticles also have been foreseen to be used as "artificial blood" [2].

Many efforts have been devoted to the design of sub-micronic long-circulating drug carriers such as liposomes, nanoparticles, lipid emulsions, micelles, and solid lipid nanoparticles. We focus here on nanoparticles, which are defined as solid colloidal particles ranging in size from 10 to 1000 nm, consisting of macromolecular materials in which the active principle is dissolved, entrapped, or encapsulated, and to which the drug is adsorbed or attached [3]. Nanoparticles are divided in two groups, nanospheres with a polymeric core and nanocapsules with an oily core, containing most of the dissolved drug and surrounded by a polymeric coating.

2. BIODISTRIBUTION OF INTRAVENOUSLY ADMINISTERED PARTICLES

The organ distribution of intravenously administered particles is determined by particle size, shape, and surface properties such as charge and hydrophobicity. Firstly, to

circulate through the smallest capillaries, the particle size should be less than 5 μm , and, to avoid spleen filtering effects, the diameter should be less than 200 nm [4]. However, a small size is not sufficient to confer a long blood half-life. For example, tiny polystyrene nanospheres (60 nm in diameter) disappear from blood within minutes [5]. Similar short blood half-lives have been observed with other types of nanoparticles: albumin [6], poly(lactic acid) (PLA) [7], poly(lactic-co-glycolic acid) (PLGA) [8, 9], and poly(cyanoacrylate) [10], which all were rapidly cleared from blood and accumulated at tissue sites, especially liver and spleen. Indeed, the actively endocytic cells of the MPS play a key role in recognizing as foreign and efficiently clearing injected particles from blood. In particular, given its abundant blood flow, tortuous circulation in the sinusoids and efficacy and abundance of the avidly phagocytic Kupffer's cells, liver is an extremely efficient organ for the removal of injected particles. Under these conditions, it only is possible to deliver drugs to MPS organs and it is not possible to fulfill the aims presented in the introduction.

2.1. Impairing the Phagocytic Capacity of MPS

To avoid the accumulation of the injected particles in the MPS organs, strategies were developed in the early 1980s to impair the phagocytic capacity of macrophages in contact with blood, for example, by injecting large doses of placebo carriers before the administration of the drug loaded carriers [11, 12]. However, these approaches have the inconvenience to impair or to suppress the essential defense system of the body and can have serious consequences, especially in cancer patients. Preferred strategies are particle camouflage from MPS, for example, by modifying their surface to make it "stealth" toward phagocytic cells. For this, surface-engineered nanoparticles have been conceived by taking into account the interactions between the carriers and blood components.

2.2. Opsonins and Dysopsonins

Immediately after intravenous administration, the nanoparticles encounter hundreds of different plasma proteins. A protein layer begins to form within seconds at the nanoparticles' surface after contact with blood. The adsorption of plasma proteins that are capable to interact with receptors on the MPS cells, thus promoting the particle uptake by these cells, is called opsonization.

The complement is considered to be one of the main opsonins involved in the uptake of intravenously administered particles [13, 14]. It comprises about 20 blood proteins that can interact in a complex cascade involving specific binding and proteolytic activation steps [15]. Fibrinogen is also one of the most active plasma proteins involved in phagocytosis [16]. Immunoglobulin IgG and fibronectin also have a strong opsonic activity [17, 18].

Opposite the opsonin family, certain blood components called dysopsonins were shown to inhibit phagocytosis. Such effects mainly were reported in the case of polystyrene particles [19, 20] and liposomes [21]. It was suggested that

the principal factors that result in a dysopsonic action are two serum components, one with a molecular weight below 30 KDa and another one with a molecular weight higher than 100 KDa [22].

It is believed that one key in controlling the particle uptake is the simultaneous reduction of opsonin adsorption and the selective adsorption of dysopsonins [23]. Special attention was given to the mechanism by which particles interact with proteins.

3. PROTEIN-REJECTING ABILITIES OF POLY(ETHYLENE GLYCOL) COATINGS

A great effort has been devoted toward suppressing the adsorption of opsonins at the particles' surface. For this, polymers were covalently bound or adsorbed on surfaces. Among these, poly(ethylene glycol) (PEG) is distinguished as one of the most commonly used polymer for surface modification [2, 24, 25]. This uncharged polyether was reported to have unlimited water solubility at room temperature [24]. In water, the high degree of hydration and large excluded volume induce repulsive forces, advantageous for surface steric stabilization and protein repulsion.

4. THEORETICAL MODELING

Jeon et al. built a mathematical model to explain the protein-rejecting abilities of PEG coatings [26, 27]. The authors considered the case of a hydrophobic surface covered with a brush of terminally attached PEG chains at a distance D from one another [27]. Proteins approaching these surfaces by diffusion were assimilated to homogeneous spherical particles with hydrophobic surfaces. Optimal surface densities to avoid adsorption were calculated as a function of protein radius. For example, in the case of a PEG brush with a molecular weight of 5280 g/mole, the calculated optimal D values were 9–11, 11–15, and 13–17 Å for protein radius, respectively, equal to 20, 40, and 60–80 Å. Furthermore, at optimal surface densities, the longest PEG chain length was best for protein-resistance properties.

More recently, Torchilin et al. [28, 29] built a simple model for understanding the steric repulsion induced by PEG layers. The authors highlighted the importance of polymer flexibility to avoid protein adsorption. Indeed, a polymer chain in solution statistically exists as a distribution or cloud of probable conformations. The higher the polymer flexibility, the higher its ability to occupy, with high frequency, many surrounding locations, which are thus made inaccessible for proteins. By opposition with the very flexible PEG chains, nonflexible polymers terminally attached to a surface form a broad but loose and, thus, protein-permeable cloud.

Szleifer [30] developed a theoretical approach based on the single-chain mean-field theory to study protein adsorption on surfaces grafted with polymers. The polymer-protein-solvent layer at the surface was considered inhomogeneous in the direction perpendicular to the surface. It was found that the main parameter in determining the ability of

a polymeric layer to prevent protein adsorption is the density of the polymer segments close to the surface.

5. “STEALTH” PEG-COATED DRUG CARRIERS

To take advantage of the protein rejecting abilities of PEG, nanoparticles were coated with PEG mainly by polymer adsorption or by covalent grafting. Nondegradable polystyrene (PS) or poly(methyl methacrylate) nanospheres were coated by adsorption of amphiphilic copolymers such as Poloxamer™ and Poloxamine™, composed of hydrophobic poly propylene oxide (PPO) blocks that adsorb on the surface and of hydrophilic PEG blocks, which stick out of the surface [5, 31, 32]. An important reduction of liver accumulation attributed to the PEG coatings was observed [33].

This approach was adapted from model PS nanospheres to degradable PLGA nanospheres coated by adsorption of diblock PEG–PLA copolymers, which advantageously replaced the nonbiodegradable Poloxamer™ and Poloxamine™ surfactants [34].

However, it was emphasized that the adsorbed copolymers might desorb *in vivo*, due to replacement by blood components with a higher affinity for the particle surface, leading eventually to particle recognition by the MPS [35, 36]. Therefore, to obtain stable coatings, polymer grafting is a preferred alternative to polymer adsorption.

Poly(ethylene glycol) grafting on drug carriers was first achieved with liposomes [37, 38], micelles [39], and lately with model polystyrene nanospheres [40, 41] and cross-linked albumin nanospheres [42]. The use of preformed copolymers containing PEG blocks is a very convenient method to directly form PEG-coated nanoparticles. By this way, PEG-coated nanoparticles with biodegradable cores made of polyesters such as PLA [43], PLGA [9], poly(ϵ -caprolactone) (PCL) [44], polyanhydride [44], and poly(alkyl cyanoacrylate) [45] were prepared. Figure 1 shows a nonexhaustive list of the structures of the most employed preformed block copolymers used for the manufacture of stealth nanoparticles. Diblock and triblock copolymers were synthesized since the early 1970s by anionic or ring-opening polymerization of monomers (lactide or ϵ -caprolactone), initiated by the hydroxyl endgroups of PEG [46, 47]. Multi-block copolymers were prepared by coupling one end-group of PEG to polyester chains [48]. The development of surface-modified poly(alkyl cyanoacrylate) (PACA) nanoparticles has been accelerated since the synthesis of a new PEG-containing PACA copolymer (poly(PEGcyanoacrylate-co-hexa decyl cyanoacrylate)), allowing the preparation of nanospheres by methods avoiding *in-situ* polymerization (i.e., nanoprecipitation or emulsification–solvent evaporation) [45]. In these nanospheres, PEG chains are grafted covalently to the surface by the means of PACA anchors forming the core of the particles.

Nanoparticles were formed with the block copolymers listed in Figure 1, mainly by using techniques such as nanoprecipitation, emulsification–solvent evaporation, double emulsion, or salting out.

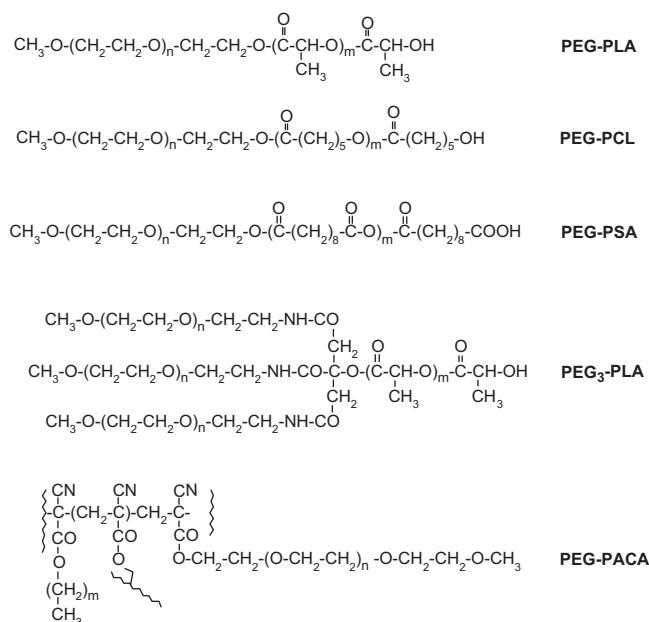


Figure 1. Chemical structures of several PEG-containing block copolymers used to prepare PEG-coated nanoparticles: monomethoxy poly(ethylene glycol)–poly(lactic acid) (PEG–PLA); monomethoxy poly(ethylene glycol)–poly(ϵ caprolactone) (PEG–PCL); monomethoxy poly(ethylene glycol)–poly(sebacic acid) (PEG–PSA); N–PEG₃PLA citric triamide (PEG₃–PLA) and monomethoxy poly(ethylene glycol)–polycyanoacrylate (PEG–PACA).

6. DETECTION AND CHARACTERIZATION OF THE PEG CORONA

All the copolymers listed in Figure 1 are amphiphilic, consisting of hydrophilic PEG blocks and hydrophobic PLA, PLGA, PCL, poly(sebacic acid) (PSA), or PACA blocks. These blocks have different affinities for the organic and aqueous phases that are put in contact in the preparation methods previously described. Therefore, it generally is assumed that these blocks would migrate preferentially toward the aqueous phase (PEG) or the organic phase (hydrophobic block) during the nanoparticle preparation, leading, after solvent evaporation, to the formation of core(hydrophobic polymer)-shell(PEG) nanoparticles [9, 43–45]. Different configurations (Fig. 2) would thus be obtained: (i) “brush” with diblock (PEG–R) or multiblock (PEG–PACA) copolymers, (ii) “loops” using triblock R–PEG–R copolymers, (iii) “bunch” with R–PEG₃ copolymers, and (iv) “star” PEG using the “star” copolymers previously described [48]. In practice, the presence of the PEG coating on the nanoparticles was evidenced by “direct” and “indirect” techniques.

6.1. “Direct” Techniques

Surface analysis techniques, such as time-of-flight secondary ion mass spectrometry and X-ray photoelectron spectrometry, detect the presence of PEG chains at the surface of PLGA [9], PACA [49], and polystyrene [50] nanospheres. In the case of deuterated polystyrene particles coated with Poloxamers™, small-angle neutron scattering is used to determine the thickness of the adsorbed Poloxamer layer and

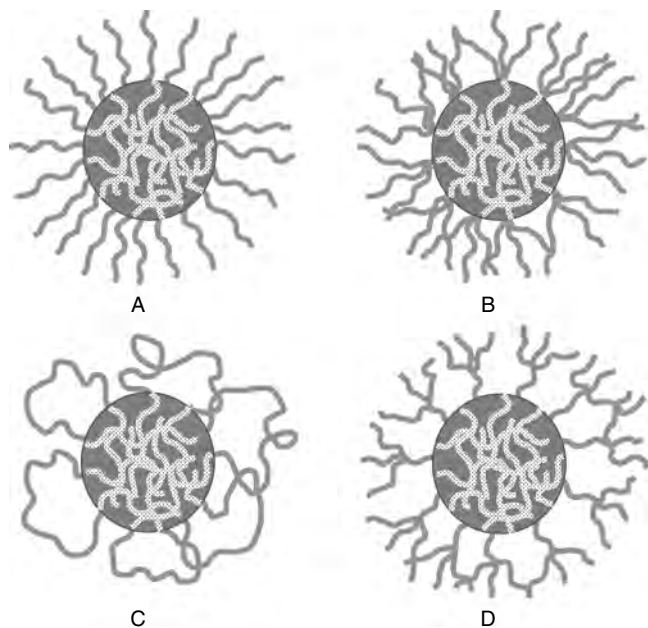


Figure 2. Different configurations of the PEG chains at the surface of the nanoparticles prepared by using block copolymers: “brush” (A), “bunch” (B), “loop” (C), and “star” (D).

to show high surface coverage; the PEG chains were in an extended configuration [51]. ^1H NMR spectroscopy provided a direct evidence of the presence of PEG chains on nanoparticles made of diblock PLGA-PEG or multiblock PLA-(PEG)₃ copolymers [52]. The PEG moieties extended out from the nanoparticles’ cores into the suspending media and exhibited chain mobility similar to that of PEG in solution.

To determine the amount of PEG located at the nanoparticles’ surface, a method was set up to detach, in a controlled manner, the PEG coating. To hydrolyze the ester bridges between PEG and PLA, an alkaline solution was added to a suspension of PEG-PLA nanoparticles. First, the PEG corona was detached, and then the PEG chains embedded in the PLA matrix were revealed. Results led to the conclusion that the PEG chains were practically all located at the nanoparticles’ surface (as in Fig. 2, case “brush”).

6.2. “Indirect” Techniques

Besides these “direct” techniques, a number of “indirect” techniques were used to establish the presence of the PEG coating and to test its efficacy. Indeed, the PEG corona greatly influences the nanoparticles’ properties, such as: (i) surface charge and hydrophobicity, commonly obtained, respectively, by electrophoretic mobility measurements and by hydrophobic interaction chromatography and (ii) interaction with proteins (model proteins, complement, or competitive adsorption of plasma proteins) and cells.

6.2.1. Reduction of Protein Adsorption

Albumin is a model protein commonly used to study the protein-resistance properties of surfaces [53]. A 15-fold reduction of albumin adsorption was found with

PEG-coated PEG-PLA nanospheres compared to PLA ones [54]. Similar albumin-rejecting abilities were observed in the case of PLGA nanospheres surface modified by adsorption of PEG-PLA diblock copolymers [55].

Fibrinogen was used as a model blood protein to test the efficacy of the PEG coating on PEG-PACA nanospheres [49]. After freeze-fracture, the adsorbed fibrinogen layer could only be visualized at the surface of PACA nanospheres but not at the surface of the PEG-coated ones, showing the protein-rejection properties of these last ones.

As it has been previously emphasized, complement is one of the main opsonins responsible for the nanoparticles uptake by MPS. Studies have been devoted to complement consumption by PEG-coated nanospheres [56–59].

In the case of PEG-PLA nanospheres, complement consumption was expressed as a function of the PEG surface density [56]. The nanospheres possessing an estimated average density exceeding 0.2 PEG molecules per square nanometer were found to consume very low amounts of complement, whereas PEG-PLA nanospheres possessing a lower PEG surface density consumed very high amounts. This threshold in complement consumption reduction corresponds to a distance between two terminally attached PEG chains of about 2.2 nm [56]. Moreover, contrary to the PLA nanospheres, due to their PEG coating, the PLA-PEG nanospheres were remarkably inert toward coagulation factors and calcium ions [57]. When prepared by another method (double emulsion), the PEG-PLA nanospheres exhibited the same behavior with regard to complement consumption as the nanospheres previously described [56, 57], prepared by nanoprecipitation. Complement consumption was higher and faster in the case of PLA nanospheres than in the case of PEG-coated ones and decreased with increasing the PEG surface density.

In the case of PEG-coated poly(isobutyl cyanoacrylate) nanoparticles, it was found that complement consumption was affected by the PEG-surface density, as well as by the PEG configuration at the surface (“loop” or “brush,” see Fig. 2) [59].

After intravenous administration, the nanospheres simultaneously interact with a large number of proteins. Two-dimensional gel electrophoresis (2D-PAGE) provides a unique possibility to simultaneously detect hundreds of plasma proteins competitively adsorbing onto the nanoparticles’ surfaces [60, 61]. Pioneer studies showed the interest of this technique in the case of PLA nanospheres and on PLA nanospheres surface modified by PEG [62]. Spots of the apolipoproteins A-IV and E were found on the PLA nanospheres but not on the PEG coated ones. It was, therefore, hypothesized that these specific apolipoproteins might play a role in the recognition process of the nanospheres by the MPS.

Two-dimensional gel electrophoresis was successfully used in the case of nanospheres made of PEG-PLGA diblock copolymers [63]. It was shown that the PEG coating effectively reduced the total amount of protein adsorbed onto the nanoparticles’ surface. Similar findings were reported in the case of PEG-PACA nanospheres [49].

The adsorption of plasma proteins was studied by 2D-PAGE onto nanospheres made by using a series of diblock copolymers: PEG-PLA, PEG-PLGA and PEG-PCL, where

the molecular weight of both hydrophilic and hydrophobic blocks was varied [64]. This allowed varying of both the PEG surface density and the nature of the core. A threshold was found, in terms of PEG molecular weight, between 2000 and 5000 g/mol, resulting in maximum reduction of plasma protein adsorption. This result is in agreement with previous studies in the literature [65] suggesting a PEG molecular weight around 3500 g/mol to minimize albumin and fibrinogen adsorption on poly(ethylene terephthalate). However, even at maximal PEG-surface density, the adsorption of proteins could not be completely prevented. Furthermore, for each protein adsorbed, a threshold for the PEG chain length required for maximum reduction of adsorption was found. Finally, a distance D between two terminally attached PEG chains was determined to minimize protein adsorption. This distance (around 2 nm) was in agreement with the threshold found to avoid complement activation [56] and with theoretical predictions [27, 30]. Finally, it was found that the nature of the core plays a main role by determining the nature and amount of the adsorbed plasma proteins.

6.2.2. Interaction with Phagocytic Cells

The ability of various PEG-coated nanoparticles to avoid the uptake by phagocytic cells extracted from human donor blood (such as monocytes and lymphocytes) or by phagocytic cells in culture (J774 and THP-1) has been extensively studied [43, 62, 64, 66–68].

The uptake of PLA nanospheres both by monocytes and by lymphocytes was reduced when the particles were coated during their preparation process with PEG [62, 66]. After incubation with human monocytes in serum and in plasma, the *in vitro* cellular uptake of PEG-coated PLA nanospheres was found to be related to the PEG chain length and surface density [67]. Both PEG configurations (“loop” and “brush,” see Fig. 2) were found to have equivalent abilities to reduce cellular uptake.

The phagocytosis by human polymorphonuclear cells (PMN) of a series of PEG–PLA nanospheres with various PEG surface densities was studied [64]. Interestingly, the same threshold (distance of about 2 nm between two terminally attached PEG chains) was found to simultaneously minimize plasma protein adsorption, zeta potential, and uptake by PMN cells. The uptake kinetics of PLA and PEG–PLA nanospheres by THP-1 cells was investigated [43]. The PEG–PLA nanospheres were four to eight times less associated to the THP-1 cells than the PLA ones. The necessary distance between two terminally attached PEG 2000 g/mol chains to avoid phagocytosis was found to be in the range of 1.2–1.4 nm.

Similar abilities of the PEG coating to reduce the uptake of phagocytic cells also was found in the case of nanocapsules. The PEG–PLA nanocapsules were about 3- to 13-fold less associated to the macrophage-like cell line J774A1 than the PLA ones [68]. The importance to covalently attach PEG to the surface to obtain stable coatings and, therefore, low uptake was emphasized.

7. DRUG ENCAPSULATION

7.1. Lipophilic Drugs

A variety of model compounds, lipophilic drugs, and macromolecules, such as proteins or DNA, have been encapsulated into PEG-coated nanoparticles by using the polymers listed in Table 1 and by following techniques such as nanoprecipitation, emulsion/solvent evaporation, salting out, or double emulsion.

In the case of lidocaine, the release was governed by the nature of the core (polyester or polyanhydride), by the properties of the coating PEG layer (thickness and density) [44], by the size of the particles, and by the state (crystal and/or molecular dispersion) of the drug inside the matrix [70]. Progesterone release kinetics from nanospheres made of PLA and PLA–PEG–PLA was related to the PEG content in the copolymers and to their polydispersity [71].

The PEG steric barrier at the nanoparticles' surface modified the drug plasmatic half-life and organ distribution [72–75]. A striking example was described in the case of IBP 5823, a drug with a fast hepatic metabolism, which was encapsulated in stealth PEG-PLA and nonstealth PLGA nanospheres [73]. When entrapped in PLGA, the drug had a half-life of only a few minutes and was essentially localized in the liver, intestines, and spleen. The drug plasmatic half-life increased up to 2.5 hours when it was encapsulated in stealth nanospheres. Moreover, in this last case, IBP 5823 was distributed all over the body, and significantly improved pharmacokinetics were found (12-fold increase of the area under the curve of IBP pharmacokinetics, 24 hours after injection).

Hexadecafluoro zinc phthalocyanine, a sensitizer for the photodynamic therapy of cancer, was entrapped in PLA and PEG-coated PLA nanospheres prepared by the salting-out procedure [74]. The biodistribution was assessed in mammary-tumor-bearing mice. After intravenous administration, the PLA nanospheres were rapidly taken up by MPS organs and only small amounts of drug were found in the tumors. On the contrary, the drug-loaded PEG-coated PLA nanospheres stayed in the blood for dramatically increased periods of times (a half-life in the order of 30 h), and the tumor uptake was increased.

Meta-tetra(hydroxyphenyl)chlorin (mTHPC), a photosensitizer with a poor selectivity for tumor tissue, was entrapped in PEG-coated nanocapsules [77]. These carriers were less taken up by the macrophage-like J774 cell line compared to the uncoated PLA ones. Moreover, the drug uptake by mTHPC and HT29 human adenocarcinoma cells was reduced by encapsulation, compared to the drug as a solution.

With the aim to control vascular smooth muscle cell proliferation, paclitaxel was entrapped into PEG–PLGA nanospheres with an average diameter of about 150 nm, prepared by an emulsion–solvent evaporation method [78]. These nanospheres exhibited antiproliferative effects comparable with free paclitaxel. Intravenously administered PEG–PLA micelles loaded with paclitaxel could inhibit more than 98.5% tumor growth [79].

Cyclosporin A (CyA), a highly hydrophobic peptide used in the prevention of xenograft rejection after organ transplantation, was successfully loaded into PLA–PEG and

PLA micro- and nanospheres were prepared following the emulsion-solvent evaporation method [80]. It was shown that *in vitro*, PEG-coated particles displayed a more adequate control of CyA release than PLA particles. This was attributed to their outer hydrophilic PEG layer and to the limited solubility of CyA in aqueous media. It was further hypothesized that the PEG-hydrated coating provided a stationary layer (or reservoir phase) for the diffusion of CyA from the core to the external release medium.

Three tripanocidal drugs (ketoconazole, itraconazole, and D0870) were successfully entrapped in PEG-PLA nanospheres to be used as circulating reservoirs to reach a variety of cells such as muscle and nerve cells of the heart and of the gastrointestinal tract, as well as cells of the MPS, which are invaded by trypanosomes [81]. These nanospheres were administered by the intravenous route for 30 consecutive days in infected mice, leading to a significant cure rate (60–90%).

Procaine hydrochloride was incorporated in nanospheres of 28 to 175 nm made from a series of PLA-PEG copolymers [82].

Recombinant human tumor necrosis factor- α (rHuTNF- α) was loaded into PEG-cyanoacrylate-co-*n*-hexadecyl cyanoacrylate (PHDCA) (PEG-PHDCA) nanospheres following the double emulsion method [83]. Albumin was used to preserve the activity of rHuTNF- α during the preparation process. It was further shown that the half-life of the encapsulated drug could be increased to more than seven hours. [84].

Amoxicillin was entrapped into PEG-coated polyethylcyanoacrylate nanospheres [85]. These PEG-coated nanospheres were less taken up by murine macrophages than the uncoated ones.

Tamoxifen, an antiestrogen used for the treatment of breast cancer, was loaded into PEG-PHDCA nanospheres [86]. The drug essentially was localized at the nanospheres' surface, leading to an unwanted very fast release.

A variety of other applications show the usefulness of PEG-coated micelles as drug carriers of intravenous administration. Indomethacin was loaded up to 42 wt% into PEG-PCL micelles and up to 33 wt% into PEG-PLA micelles prepared by dialysis against water [87, 88]. A sustained *in vitro* release was obtained [88, 89]. Micelles made of PEG-PCL were loaded with the neurotrophic agents [90–92]. Dihydrotestosterone was successfully entrapped by the dialysis method in PEG-PCL micelles of less than 100 nm, showing slow steady release profiles [94]. The released drug maintained its biological activity. Doxorubicin was covalently linked to preformed PLGA-PEG copolymers [79]. Micelles made of these conjugates could better control drug release than micelles with physically entrapped drug.

7.2. Oligonucleotides and DNA

The entrapment of oligonucleotides and DNA in PEG-coated drug carriers is a main challenge. In particular, plasmid DNA has potential as a therapeutic agent, as well as a new vaccination approach. A 13-mer oligonucleotide was entrapped in PEG-PLA nanospheres following the nanoprecipitation method, with encapsulation yields as high as 33%. [76]. To achieve this, an insoluble complex between

the oligonucleotide and an oligopeptide was formed. Plasmid DNA, in the free form or in combination with poly(vinyl alcohol) (PVA) or with poly(vinylpyrrolidone), was entrapped in PEG-PLA nanospheres of less than 300 nm with high efficiencies (60–90%) [96]. However, despite the mild encapsulation conditions, the conversion of the supercoiled form of DNA to the open circular and linear forms was detected.

7.3. Proteins

The attention of many researchers has been devoted to another challenge, the entrapment of macromolecules such as proteins into stealth nanoparticles. It was shown by using a model protein, human serum albumin (HSA), that protein-loaded PEG-coated nanospheres of about 200 nm could be obtained [97, 98] following a preparation method that was an adaptation of the double emulsion water-in-oil-in-water (w/o/w) method for the preparation of microspheres [99]. Microscopic and surface analysis techniques indicated that HSA was well entrapped inside the nanosphere core and that it was not adsorbed on its surface. The HSA loadings of 7–8 wt% was achieved, together with a sustained *in vitro* release, over two weeks [98]. More recently, bovine serum albumin was loaded in 200 nm PEG-PLGA nanospheres, following the double emulsion method, with an entrapment efficiency of about 50% [100]. The albumin half-life in rats was extended from 13.6 min (uncoated nanospheres) up to 4.5 h (PEG-coated nanospheres).

Protein C, a plasma inhibitor that regulates the mechanism of blood coagulation, was successfully entrapped in PEG-PLA nanospheres [101]. Tetanus toxoid (TT), a model antigen known to readily lose its activity during encapsulation and release from microspheres [102], was also efficiently entrapped within PEG-PLA and PLA nanospheres of less than 150 nm [103]. The PEG-coated nanospheres released a greater amount of active antigen than those made of PLA. Moreover, when the TT-loaded nanospheres were administered intranasally in mice, a significant enhancement of the TT concentration in the blood stream was obtained with the PEG-PLA nanospheres [103]. More recently, the potential of TT-loaded PEG-coated nanospheres for oral administration was evaluated [104]. The nanospheres did not degrade in significant amounts in digestive fluids during a 4-hour incubation period, so that the encapsulated TT remained associated to them. After oral administration to rats, the levels of radioactive TT in the blood stream and lymphatics were higher for PEG-coated nanospheres than for PLA nanospheres.

8. BIODISTRIBUTION

The biodistribution of PLA and PEG-PLA nanospheres after intravenous administration was studied in rats [43]. The PLA nanospheres had a circulatory half-life of only 2 minutes, whereas the PEG-coated ones had a dramatically improved half-life (about 6 h). Autoradiography studies confirmed that after 6 hours, a high amount of nanospheres were still in the blood compartment. However, it was observed that the uptake by MPS organs (essentially liver, spleen, and bone marrow) also took place. It was concluded

that the phagocytosis of the PEG-PLA nanospheres was delayed due to their PEG coating, but that the final destination of the particles was always the MPS. More recently, the toxicity of these nanospheres after intravenous administration was investigated in rats [105]. In the case of PLA nanospheres, no toxicity was found at low doses, but at the highest doses investigated (220 and 440 mg/kg), a marked toxicity was observed, together with hematological and biochemical changes. Oppositely, even at these highest doses, no lethality and no clinical changes were observed in the case of PEG-PLA nanospheres.

The blood half-life of PEG-PLGA nanospheres in mice [9] was found to increase with the molecular weight of the coating PEG layer. In parallel, liver uptake was significantly reduced by increasing the PEG molecular weight. Gamma scintigraphy confirmed the dramatic body distribution differences between the long-circulating PEG-PLGA and the PLGA nanospheres, which were sequestered rapidly in liver and spleen. It was shown that both blood clearance and MPS uptake of the PLGA nanospheres were dose-dependent [106]. As this clearance decreased with the increase of the administered dose, it was suggested that MPS saturation occurred. Oppositely, it was shown that blood clearance and MPS uptake of the PEG-PLGA nanospheres were independent of dose.

Cyanoacrylate nanospheres coated with PEG were shown to circulate longer in mice than the uncoated ones [104]. The accumulation of these nanospheres in the liver, bone marrow, and lungs was reduced, whereas 10% of the injected dose reached the spleen 3 hours after injection [107]. Thus, these nanospheres also represent interesting colloidal systems for the targeting of active molecules to the spleen.

All the studies reviewed previously clearly prove the potential of PEG-coated nanoparticles by opposition to the uncoated ones: (i) to increase the blood half-lives, (ii) to reduce MPS accumulation, (iii) to reduce the toxicity, and (iv) to achieve dose-independent pharmacokinetics.

In certain pathological situations, the permeability of the vascular endothelium is dramatically increased because of the inflammatory response resulting from cancers, infections, or autoimmune diseases. This particular histological situation offers interesting perspectives for the targeting of these inflamed tissues with PEG-decorated nanoparticles, since their long circulating properties are believed to increase their chances to extravasate selectively through these leaky vasculatures. Very exciting applications were considered very recently for brain-tissue targeting. Indeed, under healthy conditions, the blood-brain barrier (BBB) limits the passage of solutes and cells from the blood to the central nervous system (CNS). During neurological diseases, BBB permeability, however, increases dramatically, and it has been hypothesized that drug carrier systems such as polymeric nanoparticles could cross the BBB and penetrate into the CNS. In this view, PEGylated polyalkylcyanoacrylate nanoparticles (long-circulating carrier) have been investigated during experimental allergic encephalomyelitis [108]. Brain and spinal cord concentrations of [^{14}C]-radiolabeled PEGylated polyalkylcyanoacrylate nanoparticles were compared with poloxamine 908-coated polyalkylcyanoacrylate nanoparticles, another blood long-circulating carrier and

with conventional non-long-circulating polyalkylcyanoacrylate nanoparticles. The microscopic localization of fluorescent nanoparticles in the CNS also was investigated to further understand the mechanism by which the particles penetrate the BBB. The results demonstrated that the concentration of PEGylated nanoparticles in the CNS, especially in the white matter, was greatly increased in comparison to conventional non-PEGylated nanoparticles [108]. In addition, this increase was significantly higher in pathological situations where BBB permeability was augmented and/or macrophages were infiltrated. Passive diffusion and macrophage uptake in inflammatory lesions seem to be the mechanisms underlying such particle brain penetration. Based on their long-circulating properties in blood and on their surface characteristics that allow cell interactions, PEGylated nanoparticles penetrated into CNS to a larger extent than all the other formulations tested.

By the same way, the vasculature of brain glioma, like that of other solid tumors, may also present some peculiarities that form the basis of increased microvascular permeability. Some of these peculiarities include open endothelial gaps (interendothelial junctions and transendothelial channels; diameter of about 0.3 μm), fenestrations (maximum channel width of 5.5 nm), as well as cytoplasmic vesicles like caveolae (diameter of 50–70 nm) and vesicular vacuolar organelles (diameter of 108 nm \pm 32). An increase in vessel-wall thickness also has been reported, which was attributed to endothelial cell hyperplasia, reflecting an increase in non-selective transendothelial transport. All these characteristics, which may be due in major part to the secretion of the vascular permeability factor VEGF and which can lead to a loss of BBB function in the case of cerebral malignances, would be beneficial for transvascular transport of drugs with the aid of blood long-circulating nanoparticles. This approach has been tested with radiolabeled long-circulating PEG-coated hexadecylcyanoacrylate nanospheres comparatively to non-PEG-coated hexadecylcyanoacrylate nanospheres, after intravenous injection in Fischer rats bearing intracerebrally well-established 9L gliosarcoma [109]. Both types of nanospheres showed an accumulation with a retention effect in the 9L tumor. However, long-circulating nanospheres concentrated 3.1 times higher in the gliosarcoma in comparison with non-PEG-coated nanospheres. The tumor-to-brain ratio of pegylated nanospheres was found to be 11. In addition, a 4- to 8-fold higher accumulation of the PEG-coated carriers was observed in normal brain regions, when compared to control nanospheres. By using a simplified pharmacokinetic model, two different mechanisms were proposed to explain this higher concentration of PEG-coated nanospheres in a tumoral brain: (i) in the 9L tumor, the preferential accumulation of pegylated nanospheres was attributable to their slower plasma clearance, relative to control nanospheres; diffusion or convection was the proposed mechanism for extravasation of the nanospheres in the 9L interstitium, across the altered blood brain barrier: (ii) in addition, PEG-coated nanospheres displayed an affinity with the brain endothelial cells (normal brain region), which may not be considered as the result of a simple diffusion or convection process [109].

In another study [110], PEGylated PHDCA nanoparticles were proposed as a potential efficient drug carrier

for the delivery of active therapeutic molecules to the brain of animals with prion experimental diseases. Again, due to the brain inflammatory process and based on their long-circulating characteristics, these PEGylated particles, indeed, showed comparatively to conventional non-PEGylated nanoparticles, a higher uptake by the brain.

These examples illustrate the potential of core corona PEG-co-hexadecylcyanoacrylate nanoparticles for the targeting of diseased brain tissues.

9. TOXICOLOGICAL CONSIDERATIONS

9.1. Toxicity and Polymer Biodegradation

It is well accepted that polymeric drug carriers for systemic administration to humans need the search for biodegradable polymers. After intravenous administration of nonbiodegradable polymeric particles, the polymer will concentrate in certain intracellular compartments (e.g., lysosomes) or tissues (MPS), inducing severe overloading of nonmetabolized material. Thus, to assess advantages and disadvantages of one polymer in comparison to another, it is essential to identify the way by which the polymeric carrier will be degraded, as well as to approach the release rate and cellular/tissular concentrations of the degradation products. In particular, one has to distinguish between biodegradation and bioerosion. In the biodegradation process (e.g., copolymers of lactic and glycolic acid or some polyaminoacids), the main chain of the polymer will be hydrolyzed either by a chemical or by an enzymatic pathway. In the bioerosion process (e.g., polyalkylcyanoacrylates), the hydrocarbon chain of the polymer remains unchanged, while the enzymatic attack of some lateral functions induces the solubilization of the polymer, leading to a progressive disaggregation of the nanoparticles. These processes are, of course, nonequivalent from the point of view of the toxicity. In the first situation (biodegradation), the metabolization products should be easily filtered through the kidney, whereas in the second (bioerosion), the entire excretion of the polymer material will only occur if nanoparticles have been designed using low molecular weight polymers. But, if the condition of biodegradability/bioerodibility is necessary, it is not sufficient to allow the complete excretion of the polymer. In fact, nanoparticles undergoing cell capture may be hydrolyzed and reduced into small fragments, but, if the degradation products do not cross the lysosomal membrane, they will not be excreted. The above considerations emphasize the molecular weights of the polymer but also the polymer's degradation mechanism, and the diffusibility of its metabolization products have to be identified properly to allow an evaluation of the risk of polymeric overloading *in vivo*. In connection with the molecular weights, one has to bear in mind that the polymeric molecular weight profile may be disrupted when drug molecules are associated with the colloidal system, especially if nanoparticles are prepared by emulsion polymerization of monomers.

9.2. Toxicity and Tissue Distribution

As discussed before, nanoparticles generally are captured by the MPS macrophages after intravenous administration. However, phagocytic stimuli induce macrophages to

secrete a large number of substances, including eicosanoids, active oxygen metabolites from the respiratory burst, and cytokines that may have a strong influence on the inflammatory response. These substances are required for the elimination of pathogenic organisms but are unnecessary and potentially deleterious when the ingested particles are inert and nonpathogenic. The acute phase response may result in impaired defense against infection, hypersensitivity reactions and other unknown undesirable effects. It has been shown that single intravenous injection of PACA or PLA nanoparticles led to an acute inflammatory response, characterized by the increase of serum alpha 1-acid glycoprotein (AGP) levels, an acute phase protein in rats [111]. Now, since the surface coating of the nanoparticles with hydrophilic polymers results in a significant modification of the body distribution profile, it is evident that, as a consequence, it may influence the toxicity of the polymer-drug entity, too. Indeed, altered pharmacokinetic and disposition of the drug should induce novel modalities of cells, tissues, or receptor exposures, as well as novel drug metabolism and drug interactions. For instance, it has been observed that coating PLA nanoparticles with poloxamer 407, poloxamine 908, or poloxamer 338, as well as using PLA-PEG led to minimizing the secretion of inflammatory mediators such as AGP. On the other hand, the evaluation of potential novel toxicities of polymeric site-specific drug delivery systems includes the search for a depression or activation of the MPS when the system is administered intravascularly. For this route of administration, hemocompatibility also needs to be evaluated in terms of embolies due to particle aggregation or of hemolysis due to erythrocyte damages by the nanoparticles or their degradation products.

10. OTHER TYPES OF CORONAS

In the previously reviewed literature dealing with PEG-coated drug carriers, it was emphasized that even at highest surface density and with longest PEG chains (20K), plasma protein adsorption could not be completely avoided [64] and that, even if the blood half-life was dramatically increased, the final destination of the nanoparticles was always MPS [43].

Therefore, a research trend is to develop new types of coatings as alternatives to the PEG ones, to provide the lowest interaction with plasma proteins and MPS. For example, in the case of liposomes, polysaccharides such as dextran and pullulan, and glycolipids (mainly monosialoganglioside GM₁) have been proposed as possible coatings to replace PEG [112, 113]. Other synthetic polymers investigated in the case of liposomes were poly(vinyl pyrrolidone) and poly(acryl amide) (PAA) [114]. Half-clearance times were equivalent for PEG and PAA of equal molecular weight and content in the liposomes. Poly(2-methyl-2-oxazoline) and poly(2-ethyl-oxazoline) were found to be as effective as PEG in prolonging blood circulation time and in minimizing the uptake of liposomes by MPS [115].

In the case of nanoparticles, up-to-date, mainly polysaccharidic coatings were explored as candidates to replace PEG. Pioneering studies dealt with nonbiodegradable nanospheres made of poly(methyl methacrylate) coated with dextran by emulsion polymerization of the acrylic monomer in

the presence of dextran [116]. Stable nanospheres of 220–360 nm were thus obtained. Dextran- and heparin-coated nanospheres were prepared by radical emulsion polymerization of methyl methacrylate, initiated by Cerium ions in the presence of dextran or heparin [117]. These nanospheres had a prolonged blood circulation time compared to the uncoated ones [118]. Furthermore, the presence of the dextran coating reduced the interaction with the complement system [119] and with J774A1 macrophage-like cell lines [120].

In the case of biodegradable polyester nanospheres, an original procedure was proposed to coat their surface with polysaccharides. For this, graft copolymers (dextran with pending PEG chains) were used as surfactants in the nanospheres' preparation by an emulsification and solvent evaporation technique [121]. It was supposed that during particle formation, PEG anchors in the PLGA cores. Nanospheres with a rather large diameter—higher than about 480 nm—were obtained by this method.

Dextran-coated PLA nanospheres of 150–200 nm were prepared by an oil-in-water (o/w) emulsion and evaporation technique, by using dextran grafted with phenoxy groups as emulsion stabilizers [122]. These amphiphilic copolymers are strongly anchored to the nanosphere surface, thus providing protection against interaction with proteins and ensuring particle stability in the presence of salts and during freeze-drying.

More recently, core(polyester)–corona(polysaccharide) nanospheres were directly formed without the need of additional surfactants [123]. These nanospheres, of less than 200 nm, were made by using a new type of comb-like macromolecules, polysaccharides grafted with polyesters. Moreover, because of the presence of many reactive groups, the polysaccharidic coatings should facilitate the coupling of ligands, by comparison with PEG [124].

11. ACTIVE TARGETING

In opposition to the passive accumulation of the nanoparticles at a target site, active targeting aims to direct long-circulating particles to a designated but accessible target. For this, ligands that specifically bind to surface epitopes or receptors located on the target have to be coupled to the surface of the carriers. However, only few examples in the literature deal with this type of targeting.

Functionalized nanospheres were formed by using a novel copolymer, poly(amino poly(ethylene glycol) cyanoacrylate–co–hexadecyl cyanoacrylate) [125]. Folic acid was conjugated to these macromolecules via the PEG terminal amino groups. The specific interaction between the nanospheres and the folate-binding protein was confirmed by surface plasmon resonance.

Recently, a strategy to couple under mild conditions several different ligands at the nanospheres' surface was proposed [126]. This could be useful for complex lock-and-key targeting. For this, biotin was first coupled to the terminus of PEG chains of preformed PEG–PCL copolymers. Biotinylated lectins were coupled to the nanoparticles, after avidin addition. The concept was validated with biotinylated wheat germ agglutinin; its coupling to the nanospheres' surface dramatically enhanced the interaction with Caco2 cells.

12. CONCLUSIONS

Nanoparticle coating with PEG offers therapeutic opportunities that were until recently unrealistic because of the efficient MPS uptake. This type of nanoparticle has significant advantages over uncoated ones, such as decreased MPS uptake, increased blood residence times, and dose-independent pharmacokinetics. A good agreement was found between theoretical thresholds to minimize protein adsorption [27, 30] and experimental thresholds to avoid plasma protein interaction [64], complement consumption [56], and interaction with phagocytic cells [43, 64].

The literature reviewed here showed the possibility of entrapping a variety of compounds in PEG-coated nanoparticles, such as lipophilic drugs, proteins, and oligonucleotides, as well as genetic material. The release was controlled, and it was possible to preserve the biological activity of the entrapped material in PEG-coated nanoparticles to a larger extent than in uncoated nanoparticles.

Given these advantages, The interest of these types of carriers for a variety of therapeutic applications was emphasized. Stealth nanospheres were suggested to be used as circulating depots to continuously deliver drugs to the blood compartment. These carriers could be of interest to deliver drugs to vascular lesions or in pathologies with leaky vasculature such as solid tumors or inflammatory and infectious sites, or to target spleen or lymph nodes. Moreover, it was shown that PEG-coated nanospheres could overcome the nasal [103] and the intestinal [104] barriers, and, therefore, this type of nanoparticles could be administered by noninvasive routes.

It also was demonstrated that PEG-coated nanoparticles could overcome the BBB, which represents an insurmountable obstacle for a large number of drugs [108–110]. Thus, drug-loaded PEG-coated nanoparticles that specifically accumulate in the brain could be especially helpful for the treatment of disseminated and very aggressive brain tumors.

However, it was shown that the PEG-coating only delayed MPS accumulation. Plasma protein adsorption could not be completely prevented, even at the highest PEG-coating layer thickness and density. No surface was yet designed to completely avoid protein adsorption. A challenging research topic is the design of new biomaterials with tailored properties to further reduce the interaction with blood components and MPS. Efforts are directed toward the “biomimetic” approach, which imitates the strategy used by pathogenic agents to escape MPS.

GLOSSARY

Complement System of proteins in the blood, which act in series by the classical or the alternative pathways, to produce a variety of biological effects. The classical pathway consists of nine separate components, of which C1 to C5 are enzymes in an inactive form. The most important products of the enzyme cascade are C3b, C3a, and C5a, which aid engulfment and killing of microbes by phagocytic cells and initiate inflammatory reactions.

Kupffer cell Macrophages which line the blood sinuses of the liver. They are phagocytic and effectively remove foreign particles from the blood.

Macrophage Cell of the mononuclear phagocyte system, derived from blood monocytes which migrate into tissues and differentiate there.

Mononuclear phagocyte system Phagocytic cells derived from bone marrow promonocytes, having the ability to ingest and digest particulate materials, and to express the receptors characteristic of macrophages. Macrophages in the lung, the peritoneal cavity or in the lymph are free to migrate, whereas macrophages such as Kupffer cells or osteoclasts remain *in-situ* for long periods of time.

Nanocapsules Nanoparticles with an oily or aqueous core, containing most of the drug dissolved, and surrounded by a polymeric coating.

Nanoparticle Solid colloidal particle ranging in size from 10 to 1000 nm, consisting of macromolecular materials in which the active principle is dissolved, entrapped, encapsulated, or to which the drug is adsorbed or attached. Nanocapsules are divided in nanospheres and nanocapsules.

Nanospheres Nanoparticles with a polymeric core.

Opsonin Factor present in blood and other body fluids, which bind to particles and increase their susceptibility to phagocytosis.

REFERENCES

- R. Langer, in "Controlled Drug Bioavailability" (V. Smolen, Ed.), Vol 3. Wiley and Sons, New York, 1985.
- S. M. Moghimi, A. C. Hunter, and J. C. Murray, *Pharmacol. Rev.* 53, 283 (2001).
- J. Kreuter, *Pharm. Acta Helv.* 58, 196 (1983).
- S. M. Moghimi, C. Porter, S. S. Davis, and L. Illum, *Biochem. Biophys. Res. Commun.* 177, 861 (1991).
- L. Illum, S. S. Davis, S. Müller, E. Mak, and P. West, *Life Sci.* 40, 367 (1987).
- J. Saphiro, S. Reisner, G. Lichtenberg, and R. Meltzer, *J. Am. Coll. Cardiol.* 16, 1603 (1990).
- D. Bazile, C. Ropert, P. Huve, T. Verrecchia, M. Marlard, A. Frydman, M. Veillard, and G. Spenlehauer, *Biomaterials* 13, 1093 (1992).
- A. Le Ray, M. Vert, J. Gauthier, and J. Benoit, *Int. J. Pharm.* 106, 201 (1994).
- R. Gref, Y. Minamitake, M. T. Peracchia, V. Trubetskoy, V. Torchilin, and R. Langer, *Science* 263, 1600 (1994).
- J. Kreuter, U. Täuber, and V. Illi, *J. Pharm. Sci.* 68, 1443 (1979).
- R. Abra, M. Bosworth, and C. Hunt, *Res. Commun. Chem. Pathol. Pharmacol.* 29, 349 (1980).
- R. Proffitt, L. Williams, C. Presant, G. Tin, J. Uliana, R. Gamble, and J. Baldeschwieler, *Science* 220, 502 (1983).
- J. Scieszka, L. Maggiora, S. Wright, and M. Cho, *Pharm. Res.* 8, 65 (1991).
- G. Borchard and J. Kreuter, *Pharm. Res.* 13, 1055 (1996).
- L. Fries and M. Franck, in "The Molecular Basis of Blood Diseases" (G. Stamatoyannopoulos, A. Nienhuis, P. Leder, and P. Majerus Eds.), p. 450–485. W. Saunders, Philadelphia, 1987.
- K. D. Caldwell, in "Targeting of Drugs 6. Strategies for Stealth Therapeutic Systems" (G. Gregoriadis and B. Mc Cormack, Eds.), p. 1–15. Plenum Press, New York, 1998.
- C. van Oss, M. Woeppel, and S. Marquart, *J. Reticuloendothel. Soc.* 13, 221 (1973).
- K. Yamada, *Annu. Rev. Biochem.* 52, 761 (1983); D. Mosher, *Annu. Rev. Med.* 35, 561 (1984).
- F. Ulrich and D. Zilversmit, *Am. J. Physiol.* 218, 1118 (1970).
- J. Williamson and E. Rowald, *J. Cell Biol.* 47, 228a (1970).
- S. M. Moghimi and H. M. Patel, *Biochim. Biophys. Acta* 984, 384 (1989).
- I. Muir, S. M. Moghimi, L. Illum, S. S. Davis, and M. C. Davies, *Biochem. Soc. Trans.* 19, 329S (1991).
- S. M. Moghimi, I. Muir, L. Illum, S. S. Davis, and V. Kolb-Bachofen, *Biochim. Biophys. Acta* 1179, 157 (1993).
- D. Elbert and J. Hubbel, *Annu. Rev. Mater. Sci.* 26, 365 (1996).
- M. Woodle, in "Poly(ethylene glycol) Chemistry and Biological Applications" (J. Harris and S. Zalipsky, Eds.). ACS Symp. Series, Washington, DC, 1997.
- S. Jeon, J. Lee, J. Andrade, and P. de Gennes, *J. Colloid Interface Sci.* 142, 149 (1991).
- S. Jeon and J. Andrade, *J. Colloid Interface Sci.* 142, 159 (1991).
- V. Torchilin and V. Trubetskoy, *Adv. Drug Delivery Rev.* 16, 141 (1995).
- V. Torchilin, V. Omelyanenko, M. Papisov, A. Bogdanov, V. Trubetskoy, J. Herron, and C. Gentry, *Biochim. Biophys. Acta* 1195, 11 (1994).
- I. Szleifer, *Biophys. J.* 72, 595 (1997).
- S. Tröster and J. Kreuter, *J. Microencapsul.* 9, 19 (1992).
- L. Illum and S. S. Davis, *J. Pharm. Sci.* 72, 1086 (1983).
- L. Araujo, R. Lobenberg, and J. Kreuter, *J. Drug Target.* 6, 373 (1999).
- S. E. Dunn, S. Stolnick, M. C. Garnett, M. C. Davies, A. G. Coombes, D. C. Taylor, M. Irving, S. Purkiss, T. F. Tadros, S. S. Davis, and L. Illum, *Proc. Intern. Symp. Controll. Release Bioact. Mater., Controlled Release Soc.* 21, 210 (1994).
- K. Petrak, in "Pharmaceutical particulate carriers" (A. Roland Ed.). Marcel Dekker, New York, 1993.
- J. C. Neal, S. Stolnik, E. Schacht, E. R. Kenawy, M. C. Garnett, S. S. Davis, and L. Illum, *J. Pharm. Sci.* 87, 1242 (1998).
- A. Klibanov, K. Maruyama, V. Torchilin, and L. Huang, *FEBS Lett.* 268, 235 (1990).
- G. Blume and G. Cevc, *Biochim. Biophys. Acta* 1029, 91 (1990).
- K. Kataoka, G. Kwon, M. Yokoyama, T. Okano, and Y. Sakurai, *J. Controlled Release* 24, 119 (1993).
- S. E. Dunn, A. Brindley, S. S. Davis, M. C. Davies, and L. Illum, *Pharmacol. Res.* 11, 1016 (1994).
- M. Master, A. van Velthoven, W. Norde, and J. Lyklema, *Colloids Surf., A* 83, 255 (1994).
- B. Müller and T. Kissel, *Pharm. Pharmacol. Lett.* 3, 67 (1993).
- D. Bazile, C. Prud'homme, M. Bassoullet, M. Marlard, G. Spenlehauer, and M. Veillard, *J. Pharm. Sci.* 84, 493–498 (1995).
- M. T. Peracchia, R. Gref, Y. Minamitake, A. Domb, N. Lotan, and R. Langer, *J. Controlled Release* 46, 223 (1997).
- M. T. Peracchia, D. Desmaele, P. Couvreur, and J. D'Angelo, *Macromolecules* 30, 846 (1997).
- R. Perret and A. Skoulios, *Makromol. Chem.* 156, 143 (1972).
- K. Zhu, L. Xiangzhou, and Y. Shilin, *J. Appl. Polym. Sci.* 39, 1 (1990).
- A. Domb, R. Gref, Y. Minamitake, M. T. Peracchia, and R. Langer, U.S. Patent 6,007,845, 1999.
- M. T. Peracchia, S. Harnisch, H. Pinto-Alphandary, A. Gulik, J. Dedieu, D. Desmaele, J. d'Angelo, R. H. Muller, and P. Couvreur, *Biomaterials* 20, 1269 (1999).
- G. Harper, S. S. Davis, M. C. Davies, M. Norman, T. F. Tadros, D. C. Taylor, M. P. Irving, J. Waters, and J. Watts, *Biomaterials* 16, 427 (1995).
- T. Cosgrove, P. Griffiths, and P. Lloyd, *Langmuir* 11, 1457 (1995).
- J. Hrkach, M. T. Peracchia, A. Domb, N. Lotan, and R. Langer, *Biomaterials* 18, 27 (1997).
- T. Armstrong, M. Davies, and L. Illum, *J. Drug Target.* 4, 389 (1997).

54. P. Quellec, R. Gref, L. Perrin, E. Dellacherie, F. Sommer, J. M. Verbavatz, and M. Alonso, *J. Biomed. Mater. Res.* 42, 45 (1998).
55. S. Stolnik, S. E. Dunn, M. C. Garnett, M. C. Davies, A. G. A. Coombes, D. C. Taylor, M. P. Irving, S. C. Purkiss, T. F. Tadros, S. S. Davis, and L. Illum, *Pharm. Res.* 11, 1800 (1994).
56. M. Vittaz, D. Bazile, G. Spenlehauer, T. Verrecchia, M. Veillard, F. Puisieux, and D. Labarre, *Biomaterials* 17, 1575 (1996).
57. H. Sahli, J. Tapon-Brethaudiere, A. Fischer, C. Sternberg, G. Spenlehauer, T. Verrecchia, and D. Labarre, *Biomaterials* 18, 281 (1997).
58. M. F. Zambaux, F. Bonneaux, R. Gref, E. Dellacherie, and C. Vigneron, *J. Biomed. Mater. Res.* 44, 109 (1999).
59. M. T. Peracchia, C. Vauthier, C. Passirani, P. Couvreur, and D. Labarre, *Life Sci.* 61, 749 (1997).
60. T. Blunk, D. F. Hochstrasser, J. C. Sanchez, B. W. Müller, and R. H. Müller, *Electrophoresis* 14, 1382 (1993).
61. T. Blunk, M. Lück, A. Calvör, D. F. Hochstrasser, J. C. Sanchez, B. W. Müller, and R. H. Müller, *Eur. J. Pharm. Biopharm.* 42, 262 (1996).
62. J. C. Leroux, P. Gravel, L. Balant, B. Volet, B. M. Anner, E. Allémann, E. Doelker, and R. Gurny, *J. Biomed. Mater. Res.* 28, 471 (1994).
63. R. Gref, A. Domb, P. Quellec, T. Blunk, R. H. Müller, J. M. Verbavatz, and R. Langer, *Adv. Drug Delivery Rev.* 16, 215 (1995).
64. R. Gref, M. Lück, P. Quellec, M. Marchand, E. Dellacherie, S. Harnish, T. Blunk, and R. H. Müller, *Colloids Surf., B* 18, 301 (2000).
65. W. Gombotz, W. Guanghui, T. Horbett, and A. Hoffman, *J. Biomed. Mater. Res.* 25, 1547 (1991).
66. J. C. Leroux, F. De Jaeghere, B. Anner, E. Doelker, and R. Gurny, *Life Sci.* 57, 695 (1995).
67. F. De Jaeghere, E. Allemann, J. Feijen, T. Kissel, E. Doelker, and R. Gurny, *J. Drug Target* 8, 143 (2000).
68. V. Mosqueira, P. Legrand, R. Gref, B. Heurtault, M. Appel, and G. Barratt, *J. Drug Target* 7, 65 (1999).
69. S. Dunn, A. Coombes, M. C. Garnett, S. S. Davis, M. C. Davies, and L. Illum, *J. Controlled Release* 44, 65 (1997).
70. T. Gerner, R. Gref, D. Michenot, F. Sommer, M. Tran, and E. Dellacherie, *J. Controlled Release* 57, 259 (1999).
71. J. Matsumoto, Y. Nakada, K. Sakurai, T. Nakamura, and Y. Takahashi, *Int. J. Pharm.* 185, 93 (1999).
72. H. Redhead, S. S. Davis, and L. Illum, *J. Controlled Release* 70, 353 (2001).
73. T. Verrecchia, G. Spenlehauer, D. Bazile, A. Murry-Brelier, Y. Archimbaud, and M. Veillard, *J. Controlled Release* 36, 49 (1995).
74. E. Allemann, N. Brasseur, O. Benrezzak, J. Rousseau, S. Kudrevich, R. Boyle, J. Leroux, R. Gurny, and J. Van Lier, *J. Pharm. Pharmacol.* 47, 382 (1995).
75. E. Allemann, J. Rousseau, N. Brasseur, S. Kudrevich, K. Lewis, and J. van Lier, *Int. J. Cancer* 66, 821 (1996).
76. C. Emile, D. Bazile, F. Herman, C. Helene, and M. Veillard, *Drug Deliv.* 3, 187 (1996).
77. C. Allen, D. Maysinger, and A. Eisenberg, *Colloids Surf., B* 16, 3 (1999).
78. H. Suh, B. Jeong, R. Rathi, and S. Kim, *J. Biomed. Mater. Res.* 42, 331 (1998).
79. H. S. Yoo and T. G. Park, *J. Controlled Release* 70, 63 (2001).
80. R. Gref, P. Quellec, A. Sanchez, P. Calvo, E. Dellacherie, and M. Alonso, *Eur. J. Pharm. Biopharm.* 51, 111 (2001).
81. J. Molina, J. Urbina, R. Gref, Z. Brenner, and J. Rodrigues Jr., *J. Antimicrob. Chemother.* 47, 101 (2001).
82. T. Govender, T. Riley, T. Ehtezazi, M. C. Garnett, S. Stolnik, L. Illum, and S. S. Davis, *Int. J. Pharm.* 199, 95 (2000).
83. Y. Li, Y. Pei, Z. Zhou, X. Zhang, Z. Gu, J. Ding, J. Zhou, X. Gao, and J. Zhu, *J. Controlled Release* 71, 287 (2001).
84. Y. Li, Y. Pei, Z. Zhou, X. Zhang, Z. Gu, J. Ding, J. Zhou, X. Gao, and J. Zhu, *Biol. Pharm. Bull.* 24, 662 (2001).
85. G. Fontana, M. Licciardi, S. Mansueto, D. Schillaci, and G. Giammona, *Biomaterials*, 22, 2857 (2001).
86. I. Brigger, P. Chaminade, V. Marsaud, M. Appel, M. Besnard, R. Gurny, M. Renoir, and P. Couvreur, *Int. J. Pharm.* 214, 37 (2001).
87. I. G. Shin, S. Y. Kim, Y. M. Lee, C. S. Cho, and Y. K. Sung, *J. Controlled Release* 51, 1 (1998).
88. S. Kim, I. Shin, and Y. Lee, *J. Controlled Release* 56, 197 (1998).
89. S. Y. Kim, I. G. Shin, Y. M. Lee, C. S. Cho, and Y. K. Sung, *J. Controlled Release* 51, 13 (1998).
90. C. Allen, Y. Yu, D. Maysinger, and A. Eisenberg, *Bioconjugate Chem.* 9, 564 (1998).
91. C. Allen, Y. Yu, A. Eisenberg, and D. Maysinger, *Biochim. Biophys. Acta* 1421, 32 (1999).
92. C. Allen, A. Eisenberg, J. Mrcic, and D. Maysinger, *Drug Deliv.* 7, 139 (2000).
93. C. Emile, D. Bazile, F. Herman, C. Helene, and M. Veillard, *Drug Delivery* 3, 187 (1996).
94. C. Allen, J. Han, Y. Yu, D. Maysinger, and A. Eisenberg, *J. Controlled Release* 63, 275 (2000).
95. C. Emile, D. Bazile, F. Herman, C. Helene, and M. Veillard, *Drug Delivery* 3, 187 (1996).
96. M. C. Perez, A. Sanchez, D. Putnam, D. Ting, R. Langer, and M. Alonso, *J. Controlled Release* 75, 211 (2001).
97. P. Quellec, R. Gref, L. Perrin, E. Dellacherie, F. Sommer, J. Verbavatz, and M. Alonso, *J. Biomed. Mater. Res.* 42, 45 (1998).
98. P. Quellec, R. Gref, E. Dellacherie, F. Sommer, M. Tran, and M. Alonso, *J. Biomed. Mater. Res.* 47, 388 (1999).
99. M. Blanco and M. J. Alonso, *Eur. J. Pharm. Biopharm.* 43, 287 (1997).
100. Y. Li, Y. Pei, X. Zhang, Z. Gu, Z. Zhu, W. Yuan, J. Zhou, and X. Gao, *J. Controlled Release* 71, 203 (2001).
101. M. F. Zambaux, F. Bonneaux, R. Gref, E. Dellacherie, and C. Vigneron, *Int. J. Pharm.* 212, 1 (2001).
102. M. J. Alonso, B. Villamayor, M. Tobio, S. Schwendeman, R. K. Gupta, G. Siber, and R. Langer, *Proceed. Intern. Symp. Rel. Bioact. Mater.* 23, pp. 825–826 (1996).
103. M. Tobio, R. Gref, A. Sanchez, R. Langer, and M. J. Alonso, *Pharm. Res.* 15, 274 (1998).
104. M. Tobio, A. Sanchez, A. Vila, I. Soriano, C. Evora, J. Vila-Jato, and M. J. Alonso, *Colloids Surf., B* 18, 315 (2000).
105. J. P. Plard and D. Bazile, *Colloids Surf., B* 16, 173 (1999).
106. Z. Panagi, A. Beletsi, G. Evangelatos, E. Livaniou, D. S. Ithakissios, and K. Avgoustakis, *Int. J. Pharm.* 221, 143 (2001).
107. M. T. Peracchia, E. Fattal, D. Desmaele, M. Besnard, J. Noel, J. Gomis, M. Appel, J. D'Angelo, and P. Couvreur, *J. Controlled Release* 60, 121 (1999).
108. P. Calvo, B. Gouritin, H. Villarroya, F. Eclancher, C. Giannavola, C. Klein, J. P. Andreux, and P. Couvreur, *Eur. J. Neurosci.* 15, 1317 (2002).
109. I. Brigger, J. Morizet, G. Aubert, H. Chacun, M. J. Terrier-Lacombe, and P. Couvreur, *J. Pharmacol. Exp. Ther.* 303, 928 (2002).
110. P. Calvo, B. Gouritin, I. Brigger, C. Lasmezas, J. Deslys, A. Williams, J. P. Andreux, D. Dormont, and P. Couvreur, *J. Neurosci. Meth.* 111, 151 (2001).
111. R. Fernandez-Urussuno, E. Fattal, D. Porquet, J. Feger, and P. Couvreur, *Toxicol. Appl. Pharmacol.* 130, 272 (1995).
112. T. M. Allen, *Adv. Drug Delivery Rev.* 13, 185 (1994).
113. M. Woodle and D. Lassic, *Biochim. Biophys. Acta* 1113, 171 (1992).
114. V. Torchilin and V. Trubetskoy, *Adv. Drug Delivery Rev.* 16, 141 (1995).
115. M. Woodle, C. Engberts, and S. Zalipsky, *Bioconjugate Chem.* 5, 493 (1994).

116. C. Chern, C. Lee, and Y. Tsai, *Colloid Polym. Sci.* 275, 841 (1997).
117. C. Passirani, L. Ferrarini, G. Barratt, J. P. Devissaguet, and D. Labarre, *J. Biomat. Sci.—Polym. E.* 10, 47 (1999).
118. C. Passirani, G. Barratt, J. P. Devissaguet, and D. Labarre, *Pharm. Res.* 15, 1046 (1998).
119. C. Passirani, G. Barratt, J. P. Devissaguet, and D. Labarre, *Life Sci.* 62, 775 (1998).
120. N. Jaulin, M. Appel, C. Passirani, G. Barratt, and D. Labarre, *J. Drug Target.* 8, 165 (2000).
121. A. G. Coombes, S. Tasker, M. Lindblad, J. Holmgren, K. Hoste, V. Toncheva, E. Schacht, M. C. Davies, L. Illum, and S. S. Davis, *Biomaterials* 18, 1153 (1997).
122. C. Rouzes, R. Gref, M. Leonard, A. De Sousa Delgado, and E. Dellacherie, *J. Biomed. Mater. Res.* 50, 557 (2000).
123. R. Gref, J. Rodrigues, and P. Couvreur, *Macromolecules* 35, 9861 (2002).
124. R. Gref, C. Lemarchand, and P. Couvreur, "Proceed. 28th Int. Symp. Controll. Release Bioactive Materials," pp. 23–27. San Diego, 2001.
125. B. Stella, S. Arpicco, M. T. Peracchia, D. Desmaele, J. Hoebeke, M. Renoir, J. D'Angelo, L. Cattel, and P. Couvreur, *J. Pharm. Sci.* 89, 1452 (2000).
126. R. Gref, E. Mysiakine, G. Barratt, and P. Couvreur, *Biomaterials* 24, 4529 (2003).

Stilbenoid Dendrimers

Herbert Meier, Matthias Lehmann

Johannes Gutenberg-University, Mainz, Germany

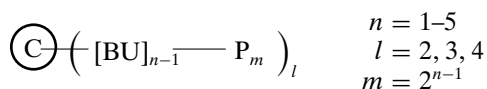
CONTENTS

1. Introduction
 2. Structures of Stilbenoid Dendrimers
 3. Synthesis
 4. Shape and Size
 5. Aggregation and Self-Organization in Mesophases
 6. Electronic Transitions: Absorption and Emission
 7. Energy-Transfer and Charge-Transfer Processes
 8. Photochemistry
 9. Applications in Materials Science
 10. Summary
- Glossary
References

1. INTRODUCTION

Dendrimers represent a class of compounds which is attracting steadily increasing attention. Due to the *uniformity*, *regularity*, and *symmetry*, these compounds are not only aesthetically appealing, but they also possess interesting properties for various applications in materials science [1–18]. This chapter focuses on stilbenoid systems, which means conjugated dendrimers, whose dendrons consist of *trans*-stilbene building blocks. The *branched units* (BU) are either 3,5-divinylphenyl groups or 3,5-bis[2-(4-vinylphenyl)vinyl] groups. The *peripheral benzene rings* (P) are mostly substituted with solubilizing alkoxy or *tert*-butyl groups. The *core* (C) of the dendrimers can consist of a stilbenoid unit, too; but it can also be formed by other (aromatic) chromophores.

The general formula for such dendrimers is



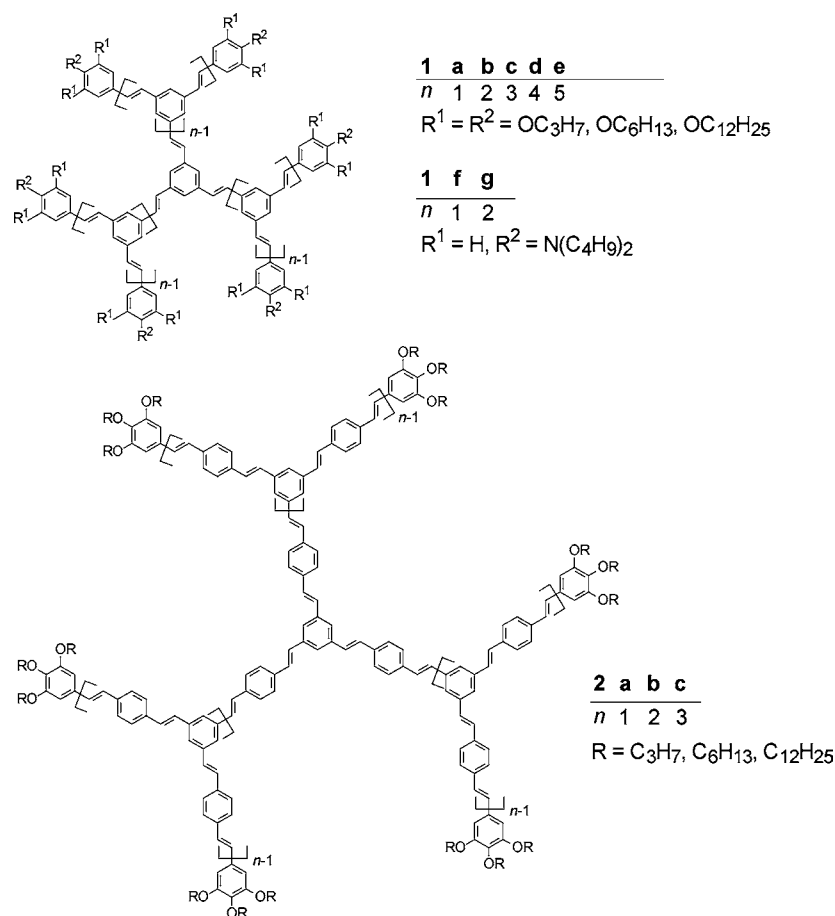
where l is the number of dendrons attached to the core, m is the number of peripheral benzene rings, and $(n - 1)$ is the normal number of the *generation*. The unbranched compound ($n = 1$) therefore has generation 0, but if the stilbenoid core itself has the same branching as the dendrons, the *generation* can be assigned as n ; according to this suggestion, a generation 0 does not exist in the latter case.

The stilbene building blocks permit rotations around the single bonds adjacent to the double bonds, but they do not allow a backfolding of the dendrons. Therefore, the scaffold of the stilbenoid dendrimers is rigid, and the size and shape of a single dendritic particle are persistent within narrow limits. Since a *trans*-stilbene unit is about 0.93 nm long, the stilbenoid dendrimers represent *well-defined nanoparticles* with the diameter of a few nanometers.

The 1,3,5-trisubstitution of the benzene rings in the dendrons implicates a cross conjugation. The electronic interactions among core, branched units, and periphery are small; therefore, these segments can be regarded as individual chromophores. Energy transfers and charge transfers between these regions are possible. Apart from such *intramolecular* processes, *intermolecular energy* and *charge exchanges* should be efficient in stilbenoid dendrimers because there are no large insulating regions as, for example, in benzyl ether or propylene imine-based systems.

2. STRUCTURES OF STILBENOID DENDRIMERS

Until now, the series **1a–e**, shown in Scheme 1, has represented the largest known series of stilbenoid dendrimers with five generations (G-1 to G-5) [19, 20]. Apart from the alkoxy-substituted compounds, the first two generations **1f**, **g** were also prepared with peripheral *p*-dibutylamino groups [21]. Moreover, a variety of compounds exists, which have the 1,3,5-tristyrylbenzene scaffold as **1a** and **1f** and alkyl, acyl, alkoxy, acyloxy, amino, nitro, cyano, and halogeno groups [22–38]. Since they were mostly not prepared in the context of dendrimers, a discussion here is beyond the scope of this chapter.



Scheme 1. Structures of stilbenoid dendrimers.

The compounds **2a–c** resemble in their structure the systems **1**; however, they consist of (*E,E*)-1,4-distyrylbenzene building blocks [23, 39]. Dendrimer **3a** has, like **1** and **2**, a threefold symmetry axis C_3 , and contains (*E,E*)-1,4-distyrylbenzene segments, as well as (*E*)-stilbene building blocks [40]. The same structural concept is realized in the series **4a–d** [41, 42]; however, a nitrogen atom forms the center of the core.

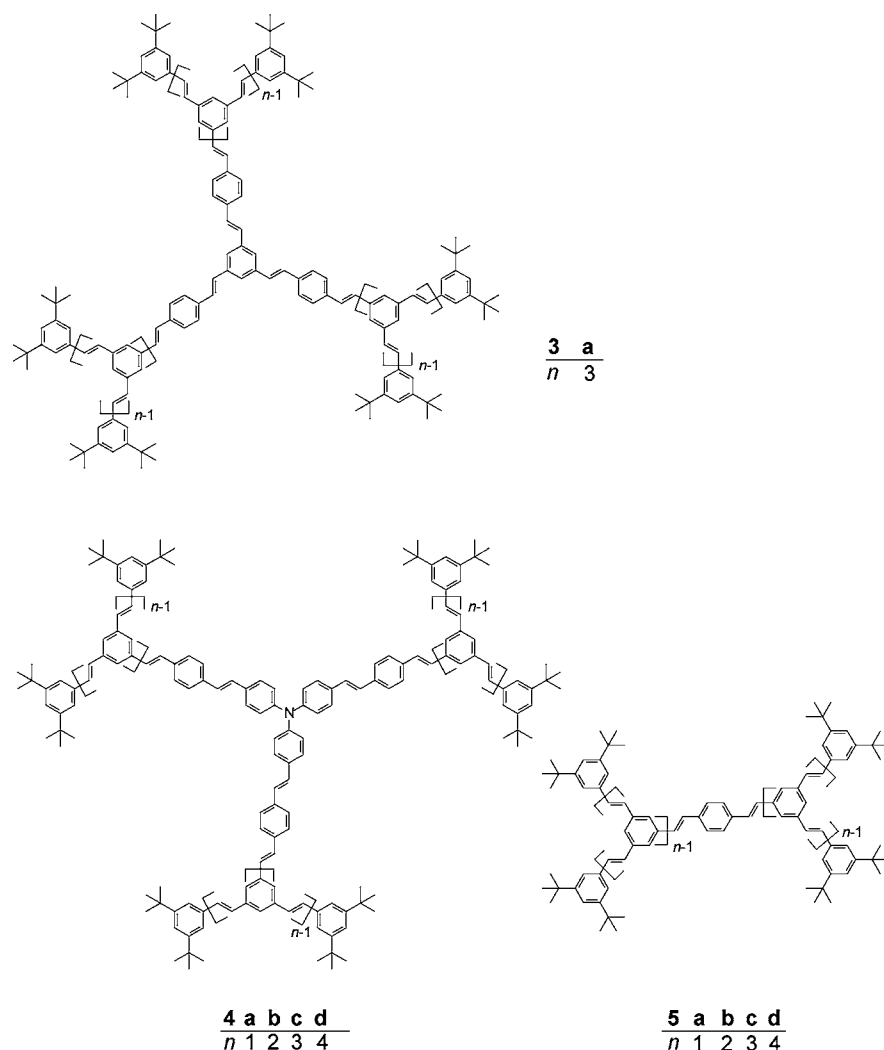
In contrast to the three-arm systems **1–4** ($l = 3$), the dendrimers **5–7** have only two arms ($l = 2$), which are fixed in **5a–d** [43, 44] on a benzene ring, in **6a** [44] and **6b** [44] on an anthracene, and in **7a** [45] and **7b** [45] on a chiral 1,1'-binaphthyl core. The stilbenoid dendrimers **8a** [44] and **8b** [44] are distinguished by four dendrons ($l = 4$) and a porphyrin core.

The dendrimers **1–8** are highly symmetrical, with two-, three-, or fourfold axes C_n . Compounds like **9a–d** [19, 20], **10a, b** [23, 39], and **11a–i** [40, 44] can be regarded as dendrons, that is, as arms of special dendrimers, but they can also be regarded as less symmetrical dendrimers. The focal position in the central benzene rings can be occupied by different chromophores. The fullerodendrimers and their precursors **12a–f** [46] and **12g–k** [47, 48] deserve increasing attention. Finally, the methoxy-substituted compounds **12l** and **12m** belong to this series [24].

3. SYNTHESIS

The synthetic strategies for the preparation of dendrimers comprise *divergent* and *convergent* approaches [1, 2]. The convergent procedures often furnish better results concerning the formation of monodisperse dendrimers because the cumulative effects of failures are excluded. This argument is particularly important for higher dendrimer generations. A unimolecular stilbenoid dendrimer is structurally pure, which means constitutionally and configurationally pure. In this chapter, we would like to discuss the *general features for the preparation of the compounds 1–12* (Scheme 1) without any details.

Wittig–Horner reactions represent the most applied procedures for the generation of stilbenoid dendrimers. Let us consider here the synthesis of the series **1a–e** [19, 20] (see Scheme 2). The diphosphonate **13** with a protected formyl group and the triphosphonate **15** represent the phosphonic ester components and the aldehyde **14** the initial carbonyl component. The Horner reaction **13** + **14** yields the dendron **9a**, whereby the deprotection of the formyl group is a spontaneous part of the work up. The subsequent Horner reaction of **13** and **9a** furnishes the next higher dendron generation **9b**, which is used for **9c**, etc. Thus, the aldehydes **9a–9d** can be prepared in a coupled synthesis with the propagation reagent **13**. The final step for the generation of the



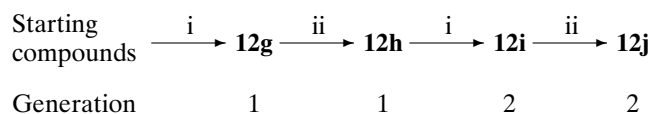
Scheme 1. Continued.

symmetrical dendrimers **1a–e** consists, then, of the Horner reaction of the core component **15** with the corresponding aldehyde.

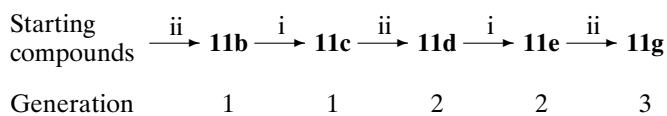
The purification of the dendrons and the control of the final attachment of three dendrons to the core guarantee structural perfection. One- and two-arm systems can be completely excluded by MALDI-TOF mass spectroscopy and *cis* configurations to a detection limit of about 3–5% in ^1H NMR spectroscopy.

The dendrimers **2a–c** and their precursors **10a, b** were prepared in an analogous way [23, 39]. Wittig–Horner reactions were also applied for the preparation of **1f, g** [21], **3a** [40], and in the series **4** [41, 42], **5** [43, 44], **6** [44], **7** [45], **11** [40, 44], and **12** [46–48]. Since the Wittig–Horner reactions are condensation reactions of alkylidenephosphoranes or alkylphosphonates with carbonyl components, it is not possible to keep further present formyl groups intact. Therefore, a *protection–deprotection technique*, as shown above for **13** \rightarrow **9a**, can be applied [19, 20]. Instead of the protected formyl group, one can introduce a cyano group, which is transformed in a subsequent reduction to the formyl group. The alternating sequence of Horner reactions (i) and

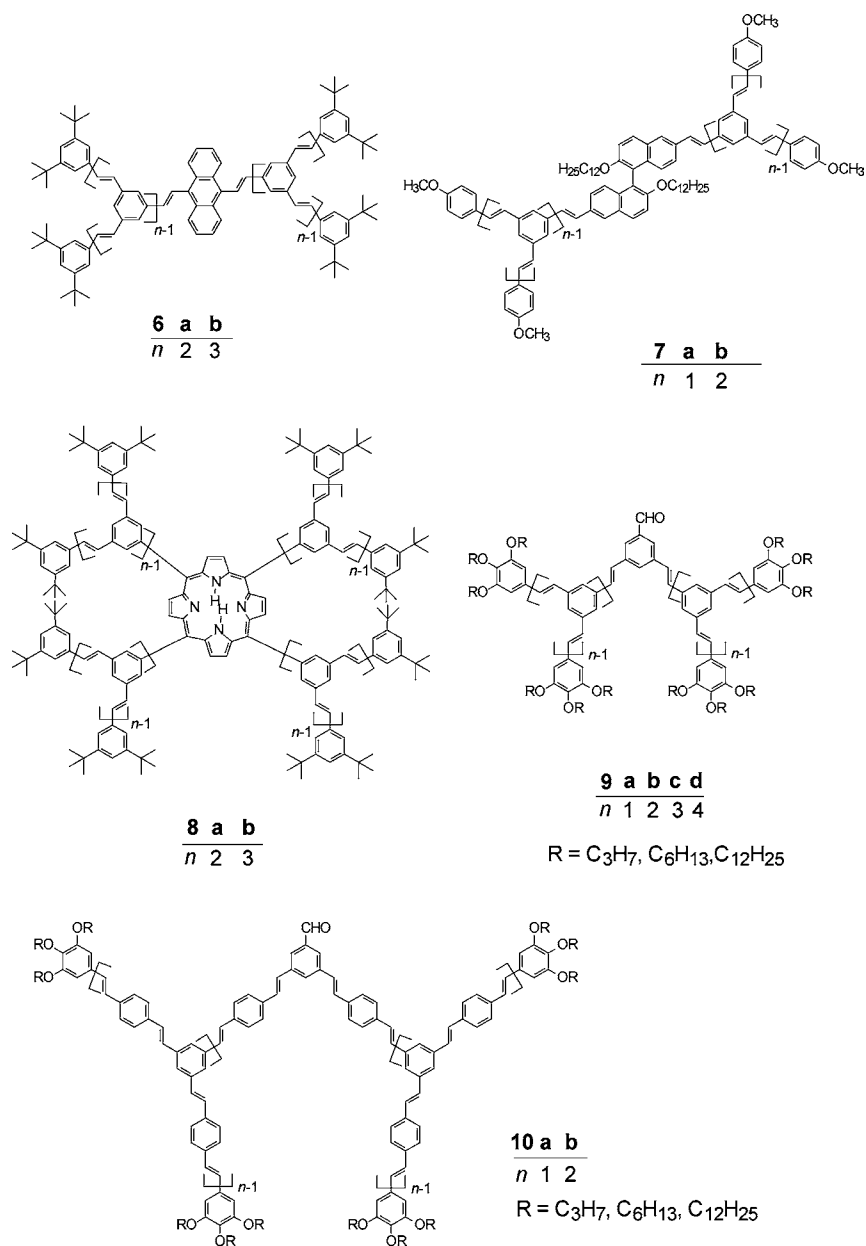
reductions (ii) with diisobutylaluminium hydride was established for the following series [47, 48]:



A combination of Wittig (i) and Heck (ii) reactions was used for the preparation of the following series [44]:

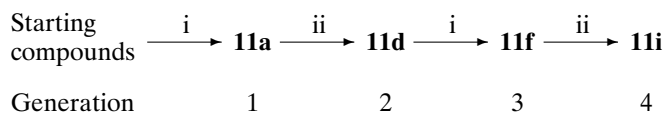


Another strategy makes use of an *orthogonal concept* of alternating reaction steps, which mutually tolerate the involved functionalities and permit the growth of the generation in each step. The first example of such a strategy in



Scheme 1. Continued.

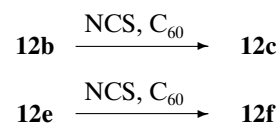
the series of stilbenoid dendrimers consisted of alternating Horner (i) and Heck (ii) reactions [40]:



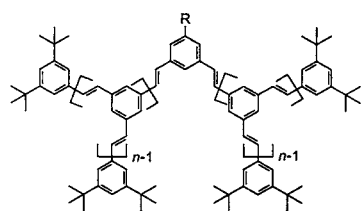
Accordingly, the focal positions in this series are occupied by bromo substituents, which are necessary for the Heck coupling and are tolerated by the Horner condensation, and by formyl groups, which are necessary for the Horner reaction and are tolerated by the Heck process [40].

The attachment of special chromophores in the focal points of dendrimers requires reactions, which keep the molecules

intact. Interesting examples have been found for the attachment of fullerene C_{60} . The aldehydes **12a** and **12d** were first transformed to the *p*-nitrophenylhydrazones **12b** and **12e**, respectively, before the fullerene was fixed in 1,3-dipolar cycloadditions of the *in-situ* generated nitrilimines [46]:

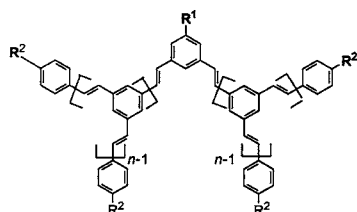


A related, independently developed procedure allows the direct fixation of C_{60} by a 1,3-dipolar cycloaddition with the



11	a	b	c	d	e
<i>n</i>	1	1	1	2	2
R	Br	CHO	CH=CH ₂	CHO	CH=CH ₂

11	f	g	h	i
<i>n</i>	3	3	3	4
R	Br	CHO		CHO

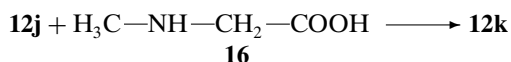


12	a	b	c	d	e	f
<i>n</i>	1	1	1	2	2	2
R ¹	CHO	CH=N-NH-		CHO	CH=N-NH-	
R ²	OC ₁₂ H ₂₅					

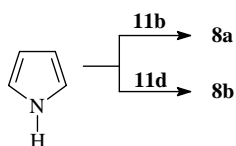
12	g	h	i	j	k	l	m
<i>n</i>	1	1	2	2	2	1	2
R ¹	CN	CHO	CN	CHO		CH ₂ OH	CH ₂ OH
R ²	N(C ₄ H ₉) ₂					OCH ₃	

Scheme 1. Continued.

aldehyde **12j** in the presence of *N*-methyl-glycine (**16**, sarcosine) [47]:



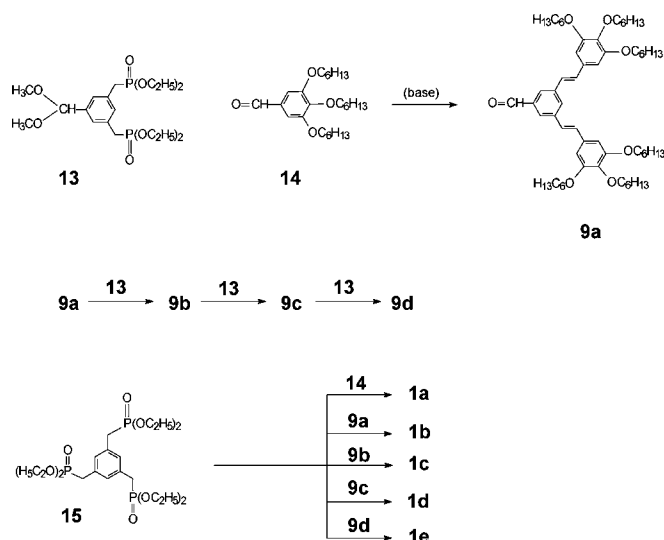
Ultimately, a synthesis will be mentioned here, in which the core is constructed in the final reaction step. The aldehydes **11b** and **11d** were condensed with pyrrole (**17**) in the presence of trifluoroacetic acid. The intermediate chlorins were oxidized with 2,3-dichloro-5,6-dicyano-1,4-benzoquinone [44]. This so-called Lindsey synthesis [49] is an established method for the formation of the porphyrin ring system, which represents the core of the dendrimers **8a**, **b**.



17

4. SHAPE AND SIZE

(*E*)-stilbene and (*E,E*)-1,4-distyrylbenzene, the building blocks of the stilbenoid dendrimers, are *planar molecules*, but their activation barriers for torsions are low because the energy hypersurface is very flat around the planar minima [50, 51]. Thus, one could have the idea that planar cores with stilbenoid dendrons yield altogether planar compounds. However, this is only true for low generations. An X-ray crystal structure analysis of the first generation **1a** (R¹ = R² = OC₃H₇) proved planar molecules, whose torsional angles in the stilbenoid skeleton are, at most, ±6°. The free or dissolved molecule has a *D*_{3h} symmetry [20, 39]. In order to imagine the shape of the higher generations, we developed molecular models of **1a–e** with the CERIOUS 2.0 program [20]. The models revealed that the second generation **1b** is still a flat disk; however, from the third generation onwards, the *steric crowding* becomes so severe that the repulsions force an extension into the third dimension. The



Scheme 2. Coupled and convergent synthesis of the stilbenoid dendrimers **1a–e** ($R^1 = R^2 = \text{OC}_6\text{H}_{13}$).

disk-like shape is transformed to a *cylindrical shape*. Figure 1 illustrates the model of the fifth generation.

The enormous steric interactions are in accord with the fast growing number of atoms and molecular masses with increasing generation n . Table 1 gives a survey over the series **1a–e** with $R^1 = R^2 = \text{OC}_6\text{H}_{13}$.

The dependence of the diameter Θ and the height h of the disks or cylinders on the generation n is shown in Figure 2.

Good indications of the size of the particles can be obtained by gel permeation chromatography (GPC) measurements. The retention time t is an exponential function of the diameter Θ [Eq. (1)]. Figure 3 shows the corresponding curve. The excellent fit parameter ($\chi^2 = 0.012$) reveals the consistency of the Θ values within the series.

$$t = t_0 + t_i e^{-\left(\frac{\Delta G_p}{kT} + \frac{s\Theta}{2}\right)} \quad (1)$$

where $t_0 = (16.63 \pm 0.49)$ min is the retention time corresponding to the total volume of the mobile phase, $t_i = (5.37 \pm 0.47)$ min is the retention time corresponding to the volume of the stationary phase, $e^{(\Delta G_p/kT)} = e^{-0.97 \pm 0.17}$ is the distribution coefficient for the substrate–sorbent interaction, and $s = 0.66 \pm 0.11 \text{ nm}^{-1}$ is the surface area per unit pore volume.

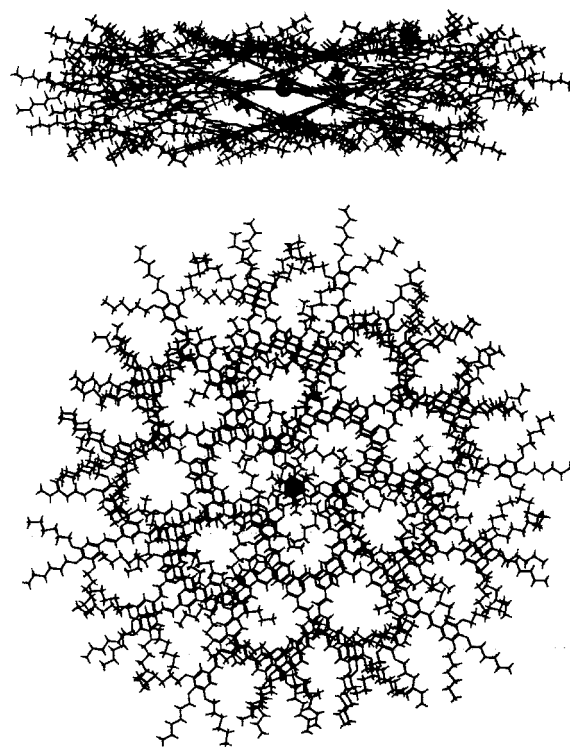


Figure 1. Molecular model of the fifth generation **1e** ($R^1 = R^2 = \text{OC}_6\text{H}_{13}$). View from the side and from above. Reprinted with permission from [20], H. Meier et al., *Chem. Eur. J.* 6, 2462 (2000). © 2000, Wiley-VCH.

5. AGGREGATION AND SELF-ORGANIZATION IN MESOPHASES

The stilbenoid dendrimers exhibit a *high aggregation tendency* in nonpolar solvents. Figure 4 shows the low-field part of the ^1H NMR spectrum of **1b** ($R^1 = R^2 = \text{OC}_{12}\text{H}_{25}$) in CDCl_3 and C_6D_{12} [19, 20]. Chloroform is a good solvent for the compound, and the spectrum in CDCl_3 has a normal resolution. The measurement in C_6D_{12} , however, gives only broad, unresolved signals. The signal broadening is caused by the formation (and dissociation) of aggregates and the restricted mobility of molecules and molecule segments in aggregates. On dilution or warming to 70°C , the spectrum in C_6D_{12} becomes highly resolved.

Other proofs of aggregation make use of fluorescence spectra, fluorescence excitation spectra, or dynamic light scattering measurements. Compound **7a**, for example, in

Table 1. Molecular formula and masses of the stilbenoid dendrimers **1a–e** ($R^1 = R^2 = \text{OC}_6\text{H}_{13}$).

Generation n	Molecular formula $\text{C}_{3(2^{n+3}-6)}\text{H}_{3 \cdot 2^{n+1}-12}(\text{OC}_6\text{H}_{13})_{9 \cdot 2^{n-1}}$	Stilbene units (double bonds) $3(2^n - 1)$	Molecular mass m
1	$\text{C}_{30}\text{H}_{15}(\text{OC}_6\text{H}_{13})_9$	3	1286
2	$\text{C}_{78}\text{H}_{42}(\text{OC}_6\text{H}_{13})_{18}$	9	2800
3	$\text{C}_{174}\text{H}_{96}(\text{OC}_6\text{H}_{13})_{36}$	21	5829
4	$\text{C}_{366}\text{H}_{204}(\text{OC}_6\text{H}_{13})_{72}$	45	11886
5	$\text{C}_{750}\text{H}_{420}(\text{OC}_6\text{H}_{13})_{144}$	93	24000

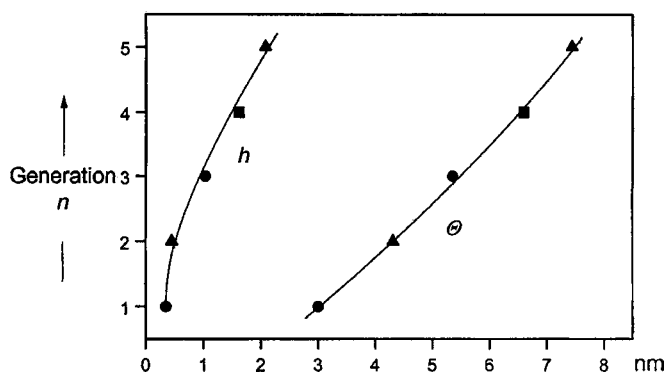


Figure 2. Diameter Θ and height h of the disks or cylinders of **1a–e** ($R = \text{OC}_6\text{H}_{13}$), determined with the CERIU 2.0 software for the molecular models.

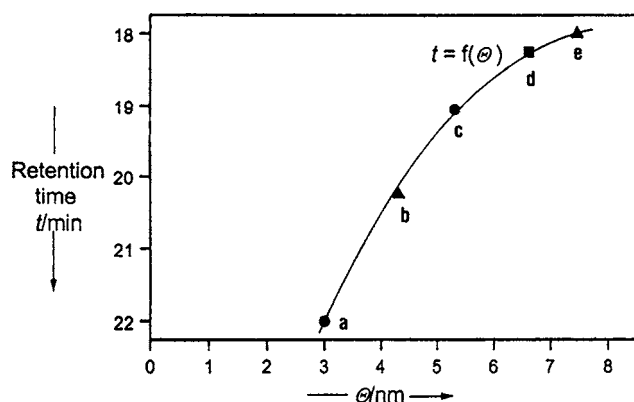


Figure 3. Plot of GPC retention times t versus the molecular diameters Θ of the compounds **1a–e**. Reprinted with permission from [20], H. Meier et al., *Chem. Eur. J.* 6, 2462 (2000). © 2000, Wiley-VCH.

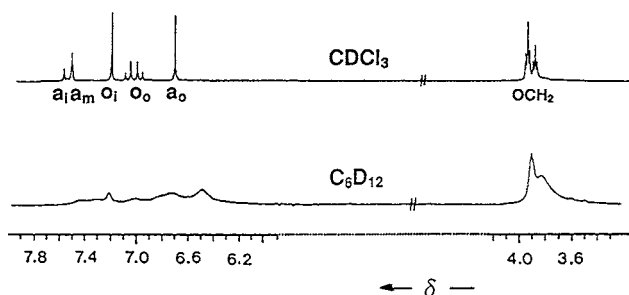


Figure 4. Low-field part of the ^1H NMR spectra of a solution ($4.6 \cdot 10^{-3}$ M) of **1b** ($R^1 = R^2 = \text{OC}_{12}\text{H}_{25}$) in CDCl_3 and C_6D_{12} at room temperature. Signals: a_i : singlet, three inner aromatic protons. a_m : pseudosinglet, nine aromatic protons on the middle rings. a_o : singlet, 12 aromatic protons on the outer rings. o_i : pseudosinglet, six olefinic protons of the inner double bonds. o_o : AB system with $^3J = 16$ Hz, 12 olefinic protons of the outer double bonds. Adapted with permission from [19], H. Meier and M. Lehmann, *Angew. Chem.* 110, 666 (1998); *Angew. Chem. Int. Ed.* 37, 643 (1998). © 1998, Wiley-VCH.

the concentration range between 10^{-5} and 10^{-8} M in dichloromethane, changes the shape, shift, and chromicity of the absorption bands [45].

Thermotropic *liquid crystals* (LC phases) are normally based on calamitic, phasmidic, or discotic mesogens. Spheroidal dendrimers are not capable of generating mesophases unless they are flexible enough to adopt such mesogenic arrangements. An obvious approach to dendritic LC phases consisted, therefore, of the attachment of suitable mesogens on the dendrimer periphery. Poly(propylene imine) dendrimers, for example, functionalized with 3,4-dicycloxybenzoyl groups, exhibit in the first four generations the formation of hexagonal columnar mesophases, whereas the fifth generation fails [52, 53].

In the series of stilbenoid dendrimers, the whole scaffold represents the *mesogen*, provided that a disk-like geometry can be realized. Neat **1a** and **1b** ($R^1 = R^2 = \text{OC}_6\text{H}_{13}$ or $\text{OC}_{12}\text{H}_{25}$) form columnar LC phases [19, 20]. A microphase segregation between the stilbenoid scaffolds and the surrounding region of the alkoxy chains has to be assumed. The π, π stacking of the mesogen as well as the Van der Waals interactions of the sidechains contribute to the *self-organization*. Propoxy chains are obviously not long enough to stabilize such mesophases. According to differential scanning calorimetry (DSC), polarization microscopy, and X-ray scattering, the columnar phases and transitions listed in Table 2 were established [20]. The excellent agreement of calculated and measured Bragg reflections allows a definite characterization of the LC phases.

Figure 5 shows the model of the Col_{hd} phase of **1b** ($R^1 = R^2 = \text{OC}_{12}\text{H}_{25}$). The cell parameter was determined by X-ray measurements.

A variety of further columnar and lamellar mesophases has been found in the series **2**, **9**, and **10** [23, 39].

6. ELECTRONIC TRANSITIONS: ABSORPTION AND EMISSION

The (*E*)-stilbene chromophore shows a strong absorption for the energy-lowest $\pi\pi^*$ transition. Because of the cross conjugation, the influence of the generation of stilbenoid dendrimers on the absorption maxima is very low [20, 23]. The compounds of series **1a–e** ($R^1 = R^2 = \text{OC}_6\text{H}_{13}$), for example, have long-wavelength maxima in dichloromethane at $\lambda = (330 \pm 3)$ nm. The ϵ_{max} values increase linearly with the number of stilbene units; the average value per stilbene unit amounts to $(2.76 \pm 0.30) \times 10^7 \text{ cm}^2 \cdot \text{mol}^{-1}$. The fluorescence maxima in this series were found at $\lambda = (429 \pm 3)$ nm. The (*E,E*)-1,4-distyrylbenzene units in **2a–c** provoke a bathochromic shift in comparison to series **1**. The absorption and emission maxima were observed at $\lambda = (375 \pm 2)$ nm and (445 ± 2) nm, respectively. The average ϵ_{max} value per distyrylbenzene unit amounts to $(4.8 \pm 0.6) \times 10^7 \text{ cm}^2 \cdot \text{mol}^{-1}$. The Stokes shift in series **2** is considerably smaller than in series **1** [23, 39].

The dendrimer series with special cores like **4–8** have typical absorptions of the stilbenoid dendrons (as in **1** and **3**) and bands at larger wavelengths for the excitation of the cores [42, 44, 45]. The same *dual-absorption effect* can be observed for compounds with chromophores (like fullerene)

Table 2. Formation of thermotropic LC phases of stilbenoid dendrimers **1a**, **b**.

Compound	R ¹ , R ²	Phase transitions ^a with $T/\Delta H^b$	
1a	OC ₆ H ₁₃	H	g $\xrightarrow{-15 (T_g)}$ Col _{hd} $\xrightarrow{74/4}$ I
		C	g $\xleftarrow{-18 (T_g)}$ Col _{hd} $\xleftarrow{71/-4}$ I
1a	OC ₁₂ H ₂₃	H	Cr ₁ $\xrightarrow{13/49}$ Cr ₂ -19/-21 $\xrightarrow{38/39}$ Cr ₃ $\xrightarrow{75/10}$ Col _{hd} $\xrightarrow{75/10}$ I
		C	Cr ₁ $\xleftarrow{8/-61}$ Col _{hd} $\xleftarrow{74/-10}$ I
1b	OC ₆ H ₁₃	H	Col _{hd} $\xrightarrow{[c]}$ Col _{ob} $\xrightarrow{144/8}$ I
		C	Col _{hd} $\xleftarrow{[c]}$ Col _{ob} $\xleftarrow{142/-7}$ I
1b	OC ₁₂ H ₂₃	H	Cr $\xrightarrow{11/59}$ Col _{hd} $\xrightarrow{32/4}$ Col _{ob} $\xrightarrow{99/17}$ I
		C	Cr $\xleftarrow{5/-48}$ Col _{ob} $\xleftarrow{91/-17}$ I

^aCr: crystalline state, g: glassy state, Col_{hd}: columnar hexagonal disordered phase, Col_{ob}: columnar oblique phase, I: isotropic phase. Measurement of the second heating process H and the first cooling process C.

^bPhase transition temperatures (onset) T [°C]/transition enthalpies ΔH [kJ · mol⁻¹].

^cDue to very small ΔH values, this transition is only visible in X-ray small-angle scattering.

Source: Reprinted with permission from [20], H. Meier et al., *Chem. Eur. J.* 6, 2462 (2000). © 2000, Wiley-VCH.

attached to the cores in the focal points of the dendrons (series **12**). The influence of functional groups such as CHO, CN, Br, etc., in **9–12** decreases with increasing generation. The fluorescence quantum yield of stilbenoid dendrons is high [21]; nevertheless, their emission can be partly or completely quenched by substituents like Br⁴⁰ or by an efficient energy

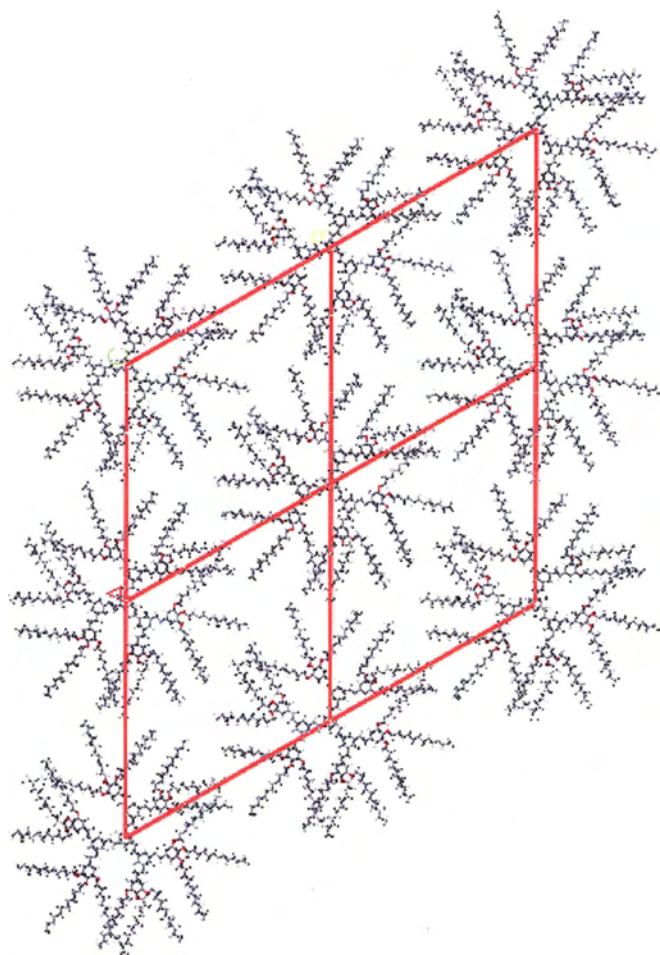


Figure 5. Model of the thermotropic Col_{hd} phase of **1b** (R¹ = R² = OC₁₂H₂₅) with $a = 4.80$ nm.

or charge transfer to the core. The latter effects are discussed in Section 7.

All λ values mentioned above are related to measurements in diluted solutions. The aggregation phenomenon, described in Section 5, can have some impact on the absorption and fluorescence bands—particularly on the long-wavelength tailing of the bands [45]. The comparison of solution measurements and measurements in films, as well as the comparison of photoluminescence (PL) and electroluminescence (EL) led to some elucidation [42, 43]; however, more experiments are necessary for a satisfying understanding of the influence of ground state aggregation and excited state aggregation (excimer formation) on absorption and fluorescence bands.

7. ENERGY-TRANSFER AND CHARGE-TRANSFER PROCESSES

Due to the 1,3,5-trisubstituted benzene rings in the stilbenoid dendrimers, the electronic interactions between the stilbene units are small. Nevertheless, the cross-conjugated dendrons are highly efficient for a singlet energy transfer to a suitable core or to a special chromophore fixed on the focal point of the core.

The compounds **5**, **6**, and **8** are typical examples in which an exothermic energy transfer to the core, which has a red-shifted absorption, is possible. In **5**, **6**, and **8**, an emission of the core can be observed irrespective of the excitation wavelengths [43, 44]. A quantified estimation of the energy-transfer efficiency revealed in these series percentages between 65 and 100% [44].

The compounds **12c** [46] and **12k** [47, 48] permit an energy transfer from the excited stilbene units to the fullerene moiety. Interestingly, compound **12f**, the higher generation of **12c**, does not exhibit a fullerene emission on excitation in the range of the absorption of the stilbene building blocks. Electron transfer was supposed to play a key role in this case [46]. Transient absorption spectroscopy of **12k** revealed that, despite the excitation of the dendrons at $\lambda = 355$ nm, no singlet–singlet absorption of the dendrons could be detected after the 18 ps laser pulse. Instead of that, an absorption at 880 nm was observed, which can

be unequivocally attributed to the fullerene singlet–singlet absorption [47, 48]. On a longer time scale, a triplet–triplet absorption at $\lambda = 700$ nm could be identified. The strong spin-orbit coupling in C_{60} can provoke an *intersystem crossing* $S_1 \rightarrow T_1$.

Moreover, the triplet formation competes with an activated electron transfer, which generates a dipolar radical pair (dendron) $^{+\bullet}$ – $C_{60}^{-\bullet}$. The charge separation of the donor–acceptor system **12k** was established by transient absorption measurements. The radical pair has, in THF and benzonitrile, average lifetimes of 350 and 725 ns, respectively. The fullerene radical anion has a typical NIR absorption at 1000 nm, and the stilbenoid radical cation an absorption at ca. 480 nm in the visible region [47, 48].

Figure 6 summarizes the important photophysical (and photochemical) processes in stilbenoid dendrimers, which have a chromophore (electron acceptor) with a low excitation energy in the core or attached to the focal point. The efficiency of competitive processes, expressed in quantum yields, depends on the special system (core–dendron), but for a consistent rationalization, further experiments are desirable—for example, to the relation of triplet states and charge-transfer states or for irreversible photoreactions of the excited singlet and triplet states.

8. PHOTOCHEMISTRY

Stilbenes belong to the best investigated compounds in photochemistry. Together with the photophysical properties, *E/Z* isomerization reactions, electrocyclic ring closures (with subsequent oxidation to phenanthrenes or higher polycyclic aromatics), cyclodimerizations, and polymerizations/cross-linking processes render the stilbenoid compounds suitable for various applications in materials science and biomedical chemistry [50, 54].

Dendrimers consisting of stilbene building blocks can principally exhibit the above mentioned photoreactions, unless a fast photophysical deactivation (Fig. 6) prevents them. We performed detailed studies in the series **1a–e** and **2a–c**. 1,3,5-tristyrylbenzene has, at room temperature in apolar solvents, a relatively long fluorescence lifetime of 8.3–13.6 ns [55]. Thus, photocyclodimerizations work even in diluted solutions, where (by diffusion) an encounter complex S_0S_1 has to be formed, which reacts regio- and stereoselectively via an excimer to a cyclophane [50, 56, 57]. In more concentrated solutions, aggregation may facilitate the dimerization; however, the photopolymerization by statistical CC bond formations is then favored, too. Scheme 3 shows the

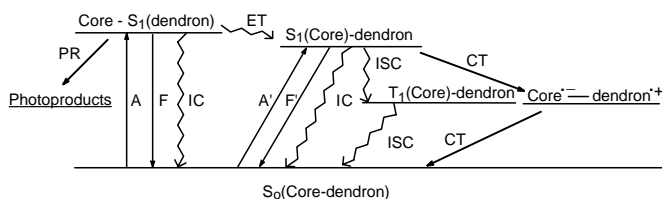
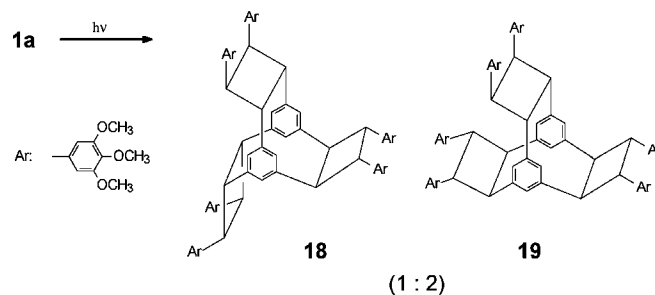


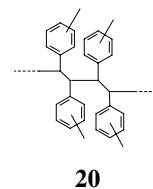
Figure 6. Scheme of the primary and secondary photoprocesses of stilbenoid dendrimers with special core-chromophores. A: absorption, F: fluorescence, IC: internal conversion, ISC: intersystem crossing, CT: charge transfer, PR: photoreaction.

regioselective head-to-head cyclodimerization of **1a** ($R^1 = R^2 = OCH_3$). The process is stereoselective concerning the *trans* configuration, which is preserved in the products; it is not selective concerning the arrangement of the three four-membered rings. The ratio of **18** : **19** depends on the individual system. In the 3,4,5-trimethoxy compound, it is 1 : 2; the statistical distribution of the relevant conformers of the starting compound is 1 : 3.



Scheme 3. Selective photocyclodimerization of **1a** ($R^1 = R^2 = OCH_3$) to the cyclophanes **18** and **19**.

Concerning the selective and statistical CC bond formation, the other systems **1a** with longer alkoxy chains behave in a similar way. Moreover, the UV/Vis spectroscopic investigation of the photochemistry of the higher generations **1b–e** reveals that prolonged irradiation leads to a complete or almost complete disappearance of the typical stilbene absorption, that is, that virtually all olefinic double bonds (Table 1) are finally involved in the process. Figure 7 shows the time-dependent photodegradation of **1b** ($R^1 = R^2 = OC_{12}H_{25}$) in cyclohexane with monochromatic light ($\lambda = 366$ nm). The process is even much faster when UV light with $\lambda \leq 300$ nm is used. On the contrary, the process is slower, as depicted in Figure 7, when a better (and more polar) solvent like THF is used because the aggregation is less efficient. The generation of four-membered rings plays a minor role in the polymerization reactions. The CC bond formation of the olefinic centers occurs in different directions to different neighbor molecules (**20**). The MALDI-TOF mass spectrum, measured after the irradiation, shows the peaks of the oligomer series from the monomer to the pentamer [39].



The UV absorption of the dendrimers **1** in spincoat films is somewhat broader as in solution, and the maximum is shifted by about 10 nm to longer wavelengths. Both effects point to an increased intermolecular interaction. Prolonged irradiation of the films with $\lambda = 350$ nm leads in all cases to a complete or almost complete disappearance of the long-wavelength band. The simultaneous FT-IR measurement reveals the disappearance of the band at 955 cm^{-1} , which corresponds to the typical out-of-plane deformation of *trans*

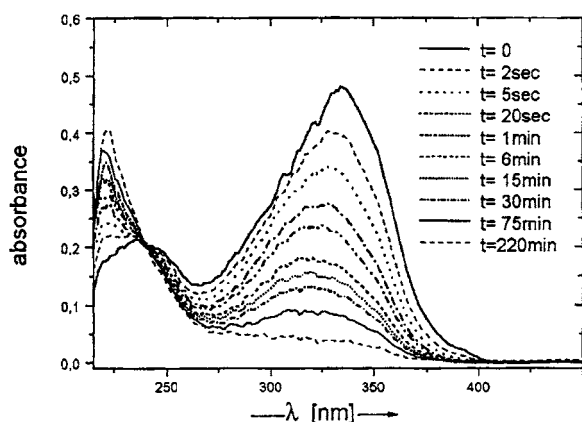


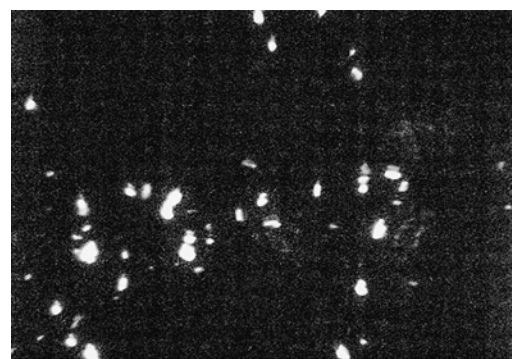
Figure 7. Photodegradation of **1b** ($R^1 = R^2 = \text{OC}_{12}\text{H}_{25}$) in a 4×10^{-6} M solution in cyclohexane with monochromatic light ($\lambda = 366$ nm). Reprinted with permission from [58], R. Petermann et al., *J. Inf. Recording* 25, 259 (2000).

configured stilbene building blocks. On the whole, the reaction is very similar to the solution photolysis [59].

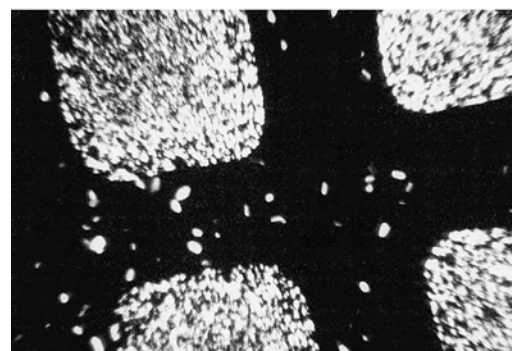
A detailed study was made for the deuterated compounds **1a** ($R^1 = R^2 = \text{OCD}_2\text{-C}_{11}\text{H}_{23}$) and **1b** ($R^1 = R^2 = \text{OCD}_2\text{-C}_{11}\text{H}_{23}$) [60]. The absence of OCH_2 groups allows an integration of the ^1H NMR signals of the CH groups formed in the photolysis. The deuterated system **1a** is photostable ($\lambda = 350$ nm) in the crystalline phases. [Compare Table 2, **1a** ($R^1 = R^2 = \text{OC}_{12}\text{H}_{25}$).] The enhanced mobility in the Col_{hd} phase at 50 °C permits a photooligomerization because it enables an interaction of the olefinic centers within the average singlet lifetime. The generation of the oligomers, proven by MALDI-TOF mass spectroscopy, is accelerated by raising the temperature to 67 °C, and further to 77 °C, where an isotropic phase is present. Figure 8 shows the irradiation through a grating. Small amounts of oligomer formation ($\leq 5\%$) lead to a reversible degradation of the LC phase. Below this limit, the LC phase can be thermally regenerated; the unirradiated zones crystallize at room temperature, whereas the texture of the LC phase is maintained at 23 °C.

According to the ^1H NMR spectrum, the neat compound **1b** ($R^1 = R^2 = \text{OCD}_2\text{-C}_{11}\text{H}_{23}$) already shows a photoreactivity at room temperature because it exists there in a mobile Col_{hd} phase. The reaction rate of the monochromatic irradiation ($\lambda = 350$ nm) is enhanced at 88 °C in the Col_{ob} phase and still higher at 108 °C in the isotropic phase. DSC measurements of the starting compound doped with increasing amounts of (before isolated) photooligomers revealed that, already at 4% oligomer contents, the phase transition temperatures are somewhat lowered; even more pronounced is the effect on the phase transition enthalpies. The ΔH value for the transition $\text{Col}_{hd} \rightarrow \text{Col}_{ob}$ is strongly increased when 4–7% of oligomers are present.

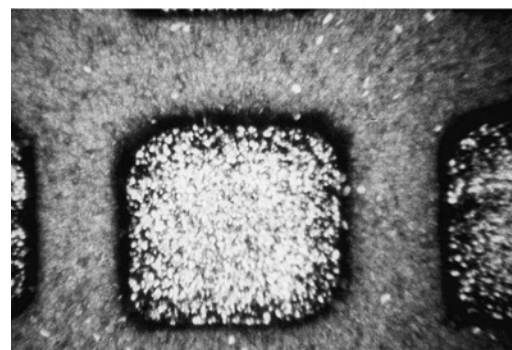
The scaffold of **2** and the other stilbenoid dendrimers exhibit similar photochemical CC bond formations, unless an efficient energy transfer (Section 7) occurs. The main difference in the photochemical behavior between (*E*)-stilbene and (*E,E*)-1,4-distyrylbenzene building blocks consists of high quantum yields for *E/Z* isomerization reactions of the first and very low quantum yields for the latter system. This



(a)



(b)



(c)

Figure 8. Short-term irradiation ($\lambda = 350$ nm) of the Col_{hd} phase of **1a** ($R^1 = R^2 = \text{OC}_{12}\text{H}_{25}$) through a grating. Top: irradiation at 72 °C (homeotropic orientation); middle: regeneration of an LC phase (in a nonhomeotropic orientation) in the irradiated areas on cooling to 50 °C; bottom: starting crystallization of the unirradiated areas at 23 °C.

effect results from the extended conjugation, which influences the π bond orders in the first excited singlet state S_1 [50]. The low intersystem crossing rates $S_1 \rightarrow T_1$ render the *E/Z* isomerization ineffective in the triplet state, too, unless a high triplet population is reached by the energy transfer from a suitable triplet sensitizer. The model of **1e** ($R^1 = R^2 = \text{OC}_6\text{H}_{13}$), shown in Figure 1, demonstrates that there are many *cavities* close to the core in these size- and shape-persistent particles. In dendrimers with less rigid dendrons, the backfolding of the arms prevents the formation of such cavities in the center. The inclusion of guest molecules in the cavities enables a *guest–host chemistry*; particularly guests as

ketones and 1,2-diketones, which can act as *triplet sensitizers*, provoke an efficient *E/Z* isomerization [61]. The incorporation of guest molecules works in the solid state (X-ray crystal structure analysis), in LC phases, and in some cases, even in the vacuum of vapor phases [20].

Finally, it should be mentioned that the stilbenoid compounds are principally sensitive toward oxidation and photooxidation processes [23].

9. APPLICATIONS IN MATERIALS SCIENCE

The formation of liquid crystals and their light-induced phase transitions as *imaging techniques* were already discussed in the Sections 5 and 8. The most important application of stilbenoid dendrimers is in the field of light-emitting diodes (LEDs). A strong photoluminescence together with the high film-forming quality in spin-coating procedures seems to be very promising. The (*E*)-stilbene chromophore has a large HOMO-LUMO gap (bandgap); therefore, (*E,E*)-1,4-distyrylbenzene units, present in **2–5**, are a better choice. We could observe, for example, in a single-layer system (thickness 17.1 nm) of **2b** ($R = C_{12}H_{25}$) a photocurrent on irradiation with a 10 ns laser pulse of $7 \text{ mJ} \cdot \text{cm}^{-1}$. Raising the temperature from 22 to 80 °C led to an increase of the current by a factor of 100 at 200 V. An experiment performed under the same conditions with the related compound **1b** ($R^1 = R^2 = OC_{12}H_{25}$) did not lead to a charge-carrier generation.

More detailed studies have been made for the series **4** [42] and **5** [43]. Poly(3,4-ethylenedioxythiophene) was used as a hole-injecting layer for 100 nm thick dendrimer films of **4a–d** [42]. The ITO–Al device furnished the emission spectra shown in Figure 9. For the lower generations, the *electroluminescence* bands are much broader than the *photoluminescence* band, which was measured in solution. The tailing on the low-energy side is attributed to intermolecular interactions.

At a bias of 4 V, electroluminescence could be observed for all four generations. The external quantum efficiency (EQE) of the device increased exponentially by a factor of 25 on going from **4a** to **4d**. The charge-carrier mobility is reduced with growing generation; consequently, the probability of polaron recombination and electroluminescence

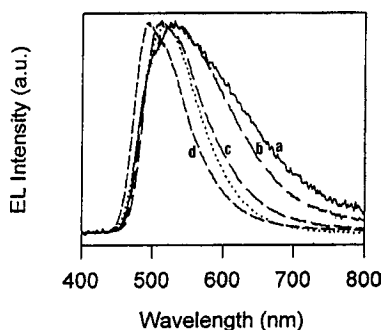


Figure 9. Electroluminescence spectra of **4a–d** (generation 0–3) and solution photoluminescence (dotted line), which does not depend on the generation. Reprinted with permission from [42], J. M. Lupton et al., *Adv. Mater.* 13, 258 (2001). © 2001, Wiley-VCH.

increases. It turned out that the charge transport is essentially determined by the core. The main role of the dendrons in **4a–d** consists of the spacing of the core chromophores, which grows with growing numbers *n* [42].

The ITO–Ca device used for the single-layer dendrimers **5b–d** gave broad electroluminescence emission bands with quantum yields between 20 and 36%. The external quantum efficiencies were measured between 0.01 and 0.09%. A systematic change with the generation could not be found. All three investigated compounds of the series proved to be suitable for an application in LEDs; the best results were obtained for **5c**.

10. SUMMARY

Dendrimers provide a great structural and functional versatility for nanoscale particles. The *stilbenoid dendrimers*, obtained by convergent synthetic strategies, are distinguished by a precise *size* and *shape persistence*. Apart from torsions, their scaffold is rigid, and does not permit a backfolding of the dendrons. The compounds show a high *aggregation* tendency; some of them form *discotic liquid crystalline phases*. The (*E*)-stilbene or (*E,E*)-1,4-distyrylbenzene building blocks give rise to interesting *photophysical* and *photochemical properties*, which favor the compounds for *applications in materials science*. Special attention was directed to stilbenoid dendrimers with low-energy chromophores (and electrophores) in the core or fixed to the core. The opposite strategy, the attachment of different chromophores on the periphery of the stilbenoid dendrons, still has to be studied. Another new and exciting field of research concerns flexible dendrimers with rigid stilbenoid chromophores bound on the periphery [62].

GLOSSARY

Aggregation Accumulation of (equal) molecules to loose complexes.

Discotic mesogens Disk-like molecules as building blocks for liquid crystals.

Electroluminescence Light emission induced by the electric field.

MALDI–TOF Matrix-assisted laser desorption ionization–time of flight measurement (mass spectroscopy).

Mesophase Liquid crystalline phase between the crystalline state (or glassy state) and the liquid phase.

Photoluminescence Light emission after irradiation.

Stilbenoid compounds Compounds which contain stilbene (1,2-diphenylethene) as an essential building block.

ACKNOWLEDGMENTS

We are grateful to the Deutsche Forschungsgemeinschaft, the Fonds der Chemischen Industrie, and the Center of Materials Science of the University of Mainz for financial support.

REFERENCES

1. G. R. Newkome, C. N. Moorefield, and F. Vögtle, "Dendrimers and Dendrons." Wiley-VCH, Weinheim, 2001.
2. J. M. J. Fréchet and D. A. Tomalia, "Dendrimers and Other Dendritic Polymers." Wiley, New York, 2001.
3. S. M. Grayson and J. M. J. Fréchet, *Chem. Rev.* 101, 3819 (2001).
4. S. Hecht and J. M. J. Fréchet, *Angew. Chem.* 113, 76 (2001); *Angew. Chem. Int. Ed.* 40, 74 (2001).
5. F. Vögtle, Vol. Ed., Dendrimers I, II, III and IV, *Top. Curr. Chem.* 197 (1998), 210 (2000), 212 (2001), 217 (2001).
6. F. Vögtle, S. Gestermann, R. Hesse, H. Schwierz, and B. Windisch, *Prog. Polym. Sci.* 25, 987 (2000).
7. K. Inoue, *Polym. Sci.* 25, 453 (2000).
8. A. W. Bosman, H. M. Janssen, and E. W. Meijer, *Chem. Rev.* 99, 1665 (1999).
9. M. Fischer and F. Vögtle, *Angew. Chem.* 111, 934 (1999); *Angew. Chem. Int. Ed. Engl.* 38, 885 (1999).
10. H. F. Chow, T. K. Mong, M. F. Nongrum, and C. W. Wan, *Tetrahedron* 54, 8543 (1998).
11. H. Frey, C. Lach, and K. Lorenz, *Adv. Mater.* 10, 279 (1998).
12. O. A. Matthews, A. N. Shipway, and J. F. Stoddart, *Prog. Polym. Sci.* 23, 1 (1998).
13. D. K. Smith and F. Diederich, *Chem. Eur. J.* 4, 1353 (1998).
14. J. M. J. Fréchet and C. J. Hawker, "Comprehensive Polymer Science, 2nd Supplement," pp. 140–206. Pergamon, Oxford, England, 1996.
15. J. Issberner, R. Moors, and F. Vögtle, *Angew. Chem.* 106, 2507 (1994); *Angew. Chem. Int. Ed. Engl.* 33, 2413 (1994).
16. J. M. J. Fréchet, *Science* 263, 1710 (1994).
17. H. B. Meikelburger, W. Jaworek, and F. Vögtle, *Angew. Chem.* 104, 1609 (1992); *Angew. Chem. Int. Ed. Engl.* 31, 1571 (1992).
18. D. A. Tomalia, A. M. Naylor, and W. A. Goddard, III, *Angew. Chem.* 102, 119 (1990); *Angew. Chem. Int. Ed. Engl.* 29, 113 (1990).
19. H. Meier and M. Lehmann, *Angew. Chem.* 110, 666 (1998); *Angew. Chem. Int. Ed.* 37, 643 (1998).
20. H. Meier, M. Lehmann, and U. Kolb, *Chem. Eur. J.* 6, 2462 (2000).
21. J. L. Segura, R. Gómez, N. Martín, and D. M. Guldi, *Org. Lett.* 3, 2645 (2001).
22. S. J. Rowan and J. F. Stoddart, *J. Am. Chem. Soc.* 122, 164 (2000).
23. M. Lehmann, B. Scharrel, M. Hennecke, and H. Meier, *Tetrahedron* 55, 13377 (1999).
24. E. Díez-Barra, J. C. García-Martínez, and J. Rodríguez-López, *Tetrahedron Lett.* 40, 8181 (1999).
25. R. Benschafut, M. Rabinovitz, Z. Dee-Noor-Barzilay, and A. de Meijere, *J. Phys. Org. Chem.* 12, 333 (1999).
26. G. Mehta, G. Panda, and P. V. V. S. Sarma, *Tetrahedron Lett.* 39, 5835 (1998).
27. J. Groß, G. Harder, F. Vögtle, H. Stephan, and K. Gloe, *Angew. Chem.* 107, 523 (1995); *Angew. Chem. Int. Ed. Engl.* 34, 481 (1995).
28. A. J. Amoroso, J. P. Maher, J. A. McCleverty, and D. M. Ward, *J. Chem. Soc., Chem. Commun.* 10, 1273 (1994).
29. T.-L. Chan, S. Fong, Y. Li, T.-O. Man, and C.-D. Poon, *J. Chem. Soc., Chem. Commun.* 15, 1771 (1994).
30. H.-B. Meikelburger, J. Groß, J. Schmitz, M. Nieger, and F. Vögtle, *Chem. Ber.* 126, 1713 (1993).
31. G. Zerban and H. Meier, *Z. Naturforsch. B* 48, 171 (1993).
32. F. Vögtle, J. Groß, C. Seel, and M. Nieger, *Angew. Chem.* 104, 1112 (1992); *Angew. Chem. Int. Ed. Engl.* 31, 1069 (1992).
33. H. Meier, R. Zertani, K. Noller, D. Oelkrug, and G. Krabichler, *Chem. Ber.* 119, 1716 (1986).
34. W. Winter, U. Langjahr, H. Meier, J. Merkushev, and J. Juriew, *Chem. Ber.* 117, 2452 (1984).
35. J. Juriew, T. Skorochodowa, J. Merkushev, W. Winter, and H. Meier, *Angew. Chem.* 93, 285 (1981); *Angew. Chem. Int. Ed. Engl.* 20, 269 (1981).
36. L. Y. Malkes and N. P. Kovalenko, *J. Org. Chem. USSR (Engl. Transl.)* 6, 1469 (1970).
37. A. E. Siegrist, P. Liechti, H. R. Meyer, and K. Weber, *Helv. Chim. Acta* 52, 2521 (1969).
38. L. Y. Malkes and N. P. Kovalenko, *J. Org. Chem. USSR (Engl. Transl.)* 2, 297 (1966).
39. M. Lehmann, Dissertation, Mainz, Germany, 1999.
40. S. K. Deb, T. M. Maddux, and L. Yu, *J. Am. Chem. Soc.* 119, 9079 (1997).
41. J. M. Lupton, I. D. W. Samuel, R. Beavington, P. L. Burn, and H. Bässler, *Synth. Metals* 116, 357 (2001).
42. J. M. Lupton, I. D. W. Samuel, R. Beavington, P. L. Burn, and H. Bässler, *Adv. Mater.* 13, 258 (2001).
43. M. Halim, J. N. G. Pillow, I. D. W. Samuel, and P. L. Burn, *Adv. Mater.* 11, 371 (1999).
44. J. N. G. Pillow, M. Halim, J. M. Lupton, P. L. Burn, and I. D. W. Samuel, *Macromolecules* 32, 5985 (1999).
45. E. Díez-Barra, J. C. García-Martínez, J. Rodríguez-López, R. Gómez, J. L. Segura, and N. Martín, *Org. Lett.* 2, 3651 (2000).
46. F. Langa, M. J. Gómez-Escalonilla, E. Díez-Barra, J. C. García-Martínez, A. de la Hoz, J. Rodríguez-López, A. González-Cortés, and V. López-Arza, *Tetrahedron Lett.* 42, 3435 (2001).
47. J. L. Segura, R. Gómez, N. Martín, C. Luo, A. Swartz, and D. M. Guldi, *Chem. Commun.* 707 (2001).
48. D. M. Guldi, A. Swartz, C. Luo, R. Gómez, J. L. Segura, and N. Martín, *J. Am. Chem. Soc.* 124, 10875 (2002).
49. J. S. Lindsey, I. C. Schreiman, H. C. Hsu, P. C. Kearney, and A. M. Marguerettaz, *J. Org. Chem.* 52, 827 (1987).
50. H. Meier, *Angew. Chem.* 104, 1425 (1992); *Angew. Chem. Int. Ed. Engl.* 31, 1399 (1992).
51. U. Stalmach, D. Schollmeyer, and H. Meier, *Chem. Mater.* 11, 2103 (1999).
52. J. H. Cameron, A. Facher, G. Lattermann, and S. Diele, *Adv. Mater.* 9, 398 (1997).
53. U. Stebani and G. Lattermann, *Adv. Mater.* 7, 578 (1995).
54. H. Meier, *Angew. Chem.* 113, 1903 (2001); *Angew. Chem. Int. Ed.* 40, 1851 (2001).
55. H. Meier, R. Zertani, K. Noller, D. Oelkrug, and G. Krabichler, *Chem. Ber.* 119, 1716 (1986).
56. J. Juriew, E. Merkushev, T. Skorochodowa, W. Winter, and H. Meier, *Angew. Chem.* 93, 285 (1981); *Angew. Chem. Int. Ed. Engl.* 20, 269 (1981).
57. W. Winter, U. Langjahr, H. Meier, E. Merkushev, and J. Juriew, *Chem. Ber.* 117, 2452 (1984).
58. R. Petermann, C. Schnorpfel, M. Lehmann, M. Fetten, and H. Meier, *J. Inf. Recording* 25, 259 (2000).
59. H. Meier, M. Lehmann, C. Schnorpfel, and M. Fetten, *Mol. Cryst. Liq. Cryst.* 352, 85 (2000).
60. M. Lehmann, H. Meier, I. Fischbach, and H. W. Spiess, publication in preparation.
61. E. Karpouk and H. Meier, publication in preparation.
62. A. P. H. J. Schenning, E. Peeters, and E. W. Meijer, *J. Am. Chem. Soc.* 122, 4489 (2000).

Strain Effects in Manganite Nanostructured Thin Films

W. Prellier, B. Mercey

ISMRA et Université de Caen, Caen Cedex, France

A. M. Haghiri Gosnet

Université d'Orsay, Orsay Cedex, France

CONTENTS

1. Introduction
 2. Growth of Manganite Thin Films
 3. Strain Effects
 4. Applications
 5. Conclusion
- Glossary
References

1. INTRODUCTION

The last decade has seen the emergence of epitaxial metal-oxide films as one of the most attractive subjects for the condensed matter community. The emergence of such interest was primarily stimulated by the discovery of high temperature superconductors (HTSC) and more recently by the discovery of the colossal magnetoresistance (CMR) effect in thin films of manganese oxides $\text{Re}_{1-x}\text{A}_x\text{MnO}_3$ (where Re is a rare earth and A is an alkaline earth) [1–5]. CMR materials exhibit large changes in electrical resistance when an external magnetic field is applied [6, 7].

The doped manganites are mixed-valence with Mn^{3+} ($3d^4$) and Mn^{4+} ($3d^3$). For the octahedral site symmetry of MnO_6 the configurations become $t_{2g}^3 e_g^1$ for Mn^{3+} and t_{2g}^3 for Mn^{4+} . In the double-exchange mechanism, the e_g electrons are considered as mobile charge carriers interactions with localized Mn^{4+} ($S = 3/2$) spins. The carriers hopping avoids the strong on-site Hund rule exchange energy J_{ex} when the spins are aligned ferromagnetically. (Note that if the Mn spins are not parallel or if the Mn–O–Mn bond is bent, the electron transfer becomes more difficult and mobility

decreases.) J_{ex} is much larger than the e_g bandwidth, and thus the conduction electrons are highly spin-polarized in the ground state. With this idea, correlations of the half ferromagnetic character of the CMR materials were found [8]. Theoretical and experimental studies indicate that the small polaron effects including Jahn–Teller distortion also play important roles for the transition and transport measurements as well [9].

These oxide materials are important from a fundamental point of view since they offer a chemical flexibility that enables new structures and new properties to be generated and, consequently, the relations between the structure, electronic, magnetic, and transport properties to be studied.

Since most technological applications require thin films on substrates, the ability to prepare such films and understand their properties is of prime importance. The synthesis of the first HTSC oxide thin films almost 15 years ago generated great interest in the thin films community. This resulted in the development of various techniques, guided by the importance of preparing high quality thin films of superconductor compounds, including sputtering, molecular beam epitaxy (MBE) and metal organic chemical vapor deposition (MOCVD), but the most popular technique is probably pulsed laser deposition (PLD) [10]. This latter method is used extensively to synthesize cuprates and HTSCs, which are now routinely made in laboratories, and it has been easily and rapidly adapted for manganites. Another reason for this quick-transfer technology is that these oxide materials crystallize in a perovskite structure as the HTSCs, and in some sense, they are quite similar [11]. Moreover, the manganite oxides are highly sensitive to any kind of perturbation, and strain effects in particular. This offers the possibility of studying its influence upon various properties such as insulator-to-metal transition temperature (T_{IM}), Curie temperature (T_C), structure, microstructure/morphology, etc.

Thus, the renewed interest in the manganite materials has resulted in a large volume of published research in this field.

In the present chapter, the deposition procedure and its influence (through deposition temperature, oxygen pressure, postannealing, substrate type, ...) upon the magnetotransport properties will be briefly presented. We will particularly discuss the work related to the strain effects such as the substrate-induced strain and thickness dependence of both the structure and their properties.

2. GROWTH OF MANGANITE THIN FILMS

CMR manganite materials are compounds crystallizing in a perovskitelike structure which, apart from manganese and oxygen, contain rare earths and/or lanthanide cations. The prototype compound is $\text{La}_{1-x}\text{Ca}_x\text{MnO}_3$, but there are many other related structures. Numerous studies were performed on the hole doped $\text{La}_{0.7}\text{A}_{0.3}\text{MnO}_3$ manganites (where A = Sr or Ca) since these CMR materials exhibit so far the highest Curie temperatures (often associated with an insulator-to-metal temperature transition). Such high transition, close to room temperature, makes them suitable for applications [12]. As previously said, there are many different compounds due to the fact that the A-site cation can be a lanthanide or a rare earth. Thus, number systems have been studied in the form of thin films (see some examples in Table 1) [13]. To detail the situation in terms of synthesis, this section is divided into three parts. First, in Section 2.1, we will review the parameters that govern the growth of these oxides (temperature, oxygen pressure, etc.), and we will consider the progress made in the synthesis of these materials. We will also focus on the different techniques for the growth of thin films. Then in Section 2.2, we will

discuss the different studies that were carried out to understand the structure and the microstructure of the thin films for the simple perovskite oxides and also for the results of the double ordered perovskites. Finally, some physical measurements will be presented (Section 2.3).

2.1. Simple Perovskite AMnO_3

2.1.1. Pulsed Laser Deposition

The manganite thin films have been mainly prepared using the PLD technique [1, 2, 14, 15]. The principle of this technique is relatively simple. A pulsed laser beam ablates a dense ceramic target of the desired material. In the presence of a background gas (usually oxygen), a plasma is produced and condenses on the heated substrate. Typical lasers used for manganite are excimer Ultra violet (UV) with KrF at $\lambda = 248$ nm [15–17], XeCl at $\lambda = 308$ nm [18], or ArF at $\lambda = 193$ nm [19]. A frequency tripled Nd-YAG at $\lambda = 355$ nm [20] or quadrupled Nd-YAG at $\lambda = 266$ nm [21] may also be used. A cross-beam deposition scheme utilizing two Nd-YAG lasers was also used to grow $\text{Pr}_{0.65}\text{Ca}_{0.35}\text{MnO}_3$ thin films on LaAlO_3 [22]. However, the utilization of high oxygen pressure during PLD growth prevents the use of a reflection high energy electron diffraction (RHEED) system in order to control *in-situ* the different stages of the growth. By a more oxidizing gas (atomic oxygen, ozone, ...) and a differential pumping system, the electron path in the high pressure oxygen atmosphere can be reduced, and thus the specular beam of the RHEED can be monitored in order to observe the oscillations (see Fig. 1 for a typical experimental setup). High quality manganite thin films were fabricated in this way [23, 24]. A persistent intensity of the RHEED is observed and the roughness of the films is low, around one unit cell [23].

Table 1. Examples of various CMR thin films.

Composition	Growth method	Substrates used	Ref.
$\text{La}_{0.7}\text{Ca}_{0.3}\text{MnO}_3$	MBE	SrTiO_3	[43, 178]
$\text{La}_{1-x}\text{Ca}_x\text{MnO}_3$	PLD "on/off-axis"	LaAlO_3 , NdGaO_3 , and SrTiO_3	[1–3, 15, 138, 139, 145]
$\text{La}_{0.7}\text{Ca}_{0.3}\text{MnO}_3$	Sol-gel	MgO	[40]
$\text{La}_{0.7}\text{Sr}_{0.3}\text{MnO}_3$	Sputtering	LaAlO_3	[86]
$\text{La}_{0.7}\text{Sr}_{0.3}\text{MnO}_3$	MOCVD	LaAlO_3	[36]
$\text{La}_{0.8}\text{MnO}_3$	MOCVD	LaAlO_3	[50]
$\text{La}_{0.8}\text{Sr}_{0.2}\text{MnO}_3$	Sputtering	SrTiO_3 bicrystals	[96, 97]
$\text{La}_{0.8}\text{Sr}_{0.2}\text{MnO}_3$	PLD	LaAlO_3 and SrTiO_3	[126]
$\text{Nd}_{0.7}\text{Sr}_{0.3}\text{MnO}_3$	PLD	LaAlO_3	[42, 141]
$\text{Nd}_{0.5}\text{Sr}_{0.5}\text{MnO}_3$	PLD	LaAlO_3	[143]
$\text{Pr}_{0.5}\text{Sr}_{0.5}\text{MnO}_3$	PLD	LaAlO_3	[137]
$\text{Pr}_{0.5}\text{Sr}_{0.5}\text{MnO}_3$	Sputtering	SrTiO_3	[27]
$\text{Pr}_{0.5}\text{Ca}_{0.5}\text{MnO}_3$	PLD	LaAlO_3 and SrTiO_3	[120, 121]
$\text{Sm}_{0.5}\text{Sr}_{0.5}\text{MnO}_3$	PLD	SrTiO_3	[23]
YMnO_3	PLD	NdGaO_3 and SrTiO_3	[119]
$\text{Pr}_{0.7}\text{Ca}_{0.3-x}\text{Sr}_{0.3}\text{MnO}_3$	Sputtering	LaAlO_3	[26]
$\text{Pr}_{0.7}\text{Sr}_{0.3}\text{MnO}_3$	PLD	SrTiO_3 and LaAlO_3	[45, 131]
$\text{Bi}_{1-x}\text{Sr}_x\text{MnO}_3$	PLD	MgO , NdGaO_3 , and SrTiO_3	[120, 121]
$\text{La}_{2-2x}(\text{Ca}, \text{Sr})_{1+2x}\text{Mn}_2\text{O}_7$	Sputtering	MgO	[56, 57, 59]
$\text{La}_{2-2x}\text{Sr}_{1+2x}\text{Mn}_2\text{O}_7$	Laser-MBE	SrTiO_3	[58, 60]
$\text{La}_{3-3x}\text{Ca}_{1+3x}\text{Mn}_3\text{O}_{10}$	Sputtering	MgO	[61]
$\text{Sr}_2\text{FeMoO}_6$	PLD	SrTiO_3	[63–65]

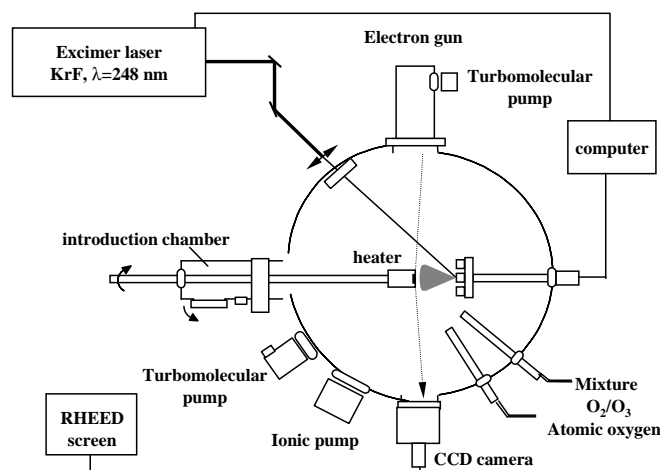


Figure 1. Typical experimental setup of a pulsed laser deposition system used for growing oxides.

2.1.2. Sputtering

A second popular deposition technique is magnetron sputtering, which can be radio frequency [25, 26] or direct current [27, 28]. Reactive sputtering is particularly useful for large-area films, but the deposition of complex oxides, comprising several cations, is difficult because of a possible change in the material composition between the target and the film. Regardless, these two techniques (PLD and sputtering) utilize highly-dense ceramic targets, and the configuration is usually “on-axis.” This means that the plane of the substrate is perpendicular to the particles flux. Samples can also be produced in the “off-axis” configuration by sputtering [29] and PLD [3, 30]. In the case of PLD, this decreases the surface roughness and avoids the formation of droplets associated with laser deposition.

2.1.3. Coevaporation

Ion beam sputtering [31] and electron beam/thermal coevaporation [32] were also utilized. In brief, the films were grown using electron beam sources to evaporate the metals (La, Sr, and Mn usually). By carefully controlling the proper atomic ratio of the metal, one can make films with various compositions. In molecular beam epitaxy, O’Donnell et al. [33] used a block-by-block (BBD) technique, and the films are often oxidized with ozone. This method is remarkably suitable for depositing perovskite oxide films (complex quaternary compounds) of high quality. Briefly, a sequential deposition of separate blocks of the pure elements is used to form each layer of the growing film. In the case of $\text{La}_{0.67}\text{Ca}_{0.33}\text{MnO}_3$, the sequence begins with Ca, followed by La, and lastly Mn this particular sequence has been selected so as to avoid the intermediate formation of others phases (calcium manganese oxides and lanthanum manganese oxides).

2.1.4. Chemical Vapor Deposition

MOCVD [34] was used to prepare high quality thin films of various compositions [35]. Briefly, metal-organic precursors are dissolved in an ether and injected into the

low pressure apparatus. In contrast to the methods previously described, this one does not require a high vacuum but allows deposition at higher oxygen pressure. In the case of CMR films, the 2,2,6,6-tetramethyl-3,5 heptanedionato (TMHD) organometallics used for La, Ca, Sr, and Mn are, for example, respectively tris(TMHD) lanthanum, bis(TMHD) strontium hydrate, bis(TMHD) calcium, and tris(TMHD) manganese [36].

2.1.5. Sol-Gel and Spray Pyrolysis

Chemical deposition has been widely used to prepare oxide films, such as ferroelectrics and semiconductor films [37], since it is a fast and cost-efficient preparation method. In nebulized spray pyrolysis, a solution containing the organic derivatives of the relevant metals in a suitable solvent is nebulized by making use of a CMR transducer. The nebulized spray is slowly deposited on a solid substrate at a relatively low temperature, with sufficient control of the rate deposition to yield the oxide of the desired stoichiometry [38]. This technique is a simple and effective route to prepare oriented, stoichiometric oxide films. To prepare CMR films by sol-gel, a stock solution is prepared from acetates of La, Ca, and Mn in appropriate molar ratio ($\text{La}:\text{Ca}:\text{Mn} = 0.67:0.33:1$ to make a film with a composition $\text{La}_{0.67}\text{Ca}_{0.33}\text{MnO}_3$) which is dissolved into 2-methoxyethanol. With the addition of H_2O , the solution is refluxed at low temperature (80°C) for 24 h and then aged at room temperature for several days. Xerogel is then obtained through further distillation and drying. The thin films are fabricated using a spin coater, from stock solution spun on a substrate. The films are finally pyrolyzed on a hot plate at 400°C after each coating, which is repeated to achieve appropriate thickness. Annealing is sometimes necessary to obtain the optimum properties. One can obtain homogeneous thin films and the processing temperature is considerably lower than conventional methods. Good quality CMR thin films have been prepared by these two methods: nebulized spray pyrolysis [39] and sol-gel [40].

2.1.6. Gases

Various gases, such as O_2 [41], N_2O [42], ozone [43], or a mixture of argon–oxygen atmosphere [26], result in oxygen-stoichiometric films. The background gas pressure is important for the oxidation process. Thus, the emission of the gas-phase oxidation of Mn during pulsed laser deposition of manganites in O_2 and N_2O atmospheres was studied. They show that oxidation both in the gas phase and at the surface is required in order to obtain the optimized properties. It was found that N_2O increases the oxidation of Mn in the plasma plume, leading to an improvement of the magnetic properties of $\text{La}_{0.67}\text{Sr}_{0.33}\text{MnO}_3$ [44].

2.1.7. Deposition Conditions

The deposition conditions (oxygen pressure P_{O_2} , deposition temperature T_S , laser fluence, ...) can drastically influence the properties [45, 46]. For $\text{Nd}_{0.7}\text{Sr}_{0.3}\text{MnO}_3$ grown on (100)- LaAlO_3 [47], the maximum resistivity peak shifts to lower temperatures as the deposition temperature decreases (the optimum T_C of 175 K is obtained for $T_S = 615^\circ\text{C}$). Yamada

et al. [21] have shown that the T_{IM} decreases with either T_S or P_{O_2} in $La_{1-x}Pb_xMnO_3$. The deposition temperature also strongly influences the microstructure of $Pr_{0.7}Sr_{0.3}MnO_3$, since films grown at low temperature exhibit a columnar growth with well-connected grains while those deposited at higher temperature are poorly connected with plateletlike crystals [45].

In addition, it has also been shown that *in-situ* [48] or *ex-situ* [49] oxygen annealing is necessary to obtain the optimized properties. In particular, the postannealing of the films can lead to significant modification of the oxygen content and optimizes the physical properties [50] such as T_{IM} [47], T_C , and the CMR effect [1,3,5]. This annealing effect is necessary to achieve the optimum oxygen concentration of the films. Depending on the nature of the film and on the growth conditions, annealing is used either to fully oxidize the film (oxidative annealing) or to remove extra oxygen (reductive annealing). The effect of annealing was also observed in films annealed in N_2 atmosphere [51]. The T_{IM} transition shifts after the annealing to higher temperature and the MR ratio increases slightly. The magnetic transition also occurs at higher temperature after annealing. For example, the Curie temperature, T_C , is found to increase from 200 K for as-deposited $La_{0.8}MnO_3$ film to 320 K after the fourth thermal treatment (see Fig. 2) [50]. In fact, the changes under annealing can also be seen on the position of the diffraction peak [41]: the out-of-plane parameter decreases, which relates to an increase of the Mn^{3+}/Mn^{4+} ratio [15,50]. This annealing effect can lead to an improvement in physical properties (like in $La_{0.8}Ca_{0.2}MnO_3$ where the T_{IM} value is higher than that of the bulk [52]) but sometimes the resistivity peak is lower by more than 100 K [53]. In fact, Prellier et al. have shown that the entire phase diagram (see Fig. 3) is different in the ferromagnetic region of $La_{1-x}Ca_xMnO_3$ ($0 < x < 0.5$) [15] as compared to the bulk (in terms of transport and magnetic transitions).

Doping is another method used to improve the magnetic properties. For example, enhancement of the properties (T_{IM} and T_C) is observed with silver addition to the $La_{0.7}Ca_{0.3}MnO_3$ target (5 wt%) [54] or with $La_{2/3}Sr_{1/3}MnO_3$ films doped with Ag and grown by dual-beam PLD [55].

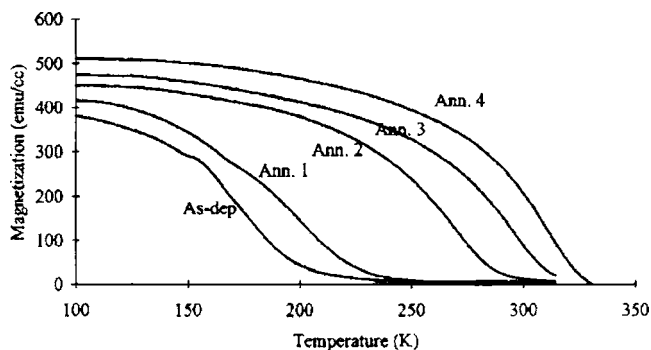


Figure 2. $M(T)$ for as-deposited and postannealed $La_{0.8}MnO_{3-\delta}$ films. Annealing 1—600 °C, 3 h. Annealing 2—600 °C, 24 h. Annealing 3—700 °C, 3 h. Annealing 4—800 °C, 3 h. Reprinted with permission from [50], S. Pignard et al., *J. Appl. Phys.* 82, 4445 (1997). © 1997, American Institute of Physics.

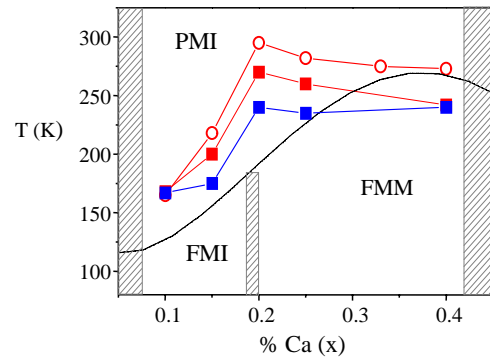


Figure 3. Phase diagram for $La_{1-x}Ca_xMnO_3$. T_C and T_{MI} are taken from the inflection point in $M(T)$ and $\rho(T)$. Dashed line indicates the data from the bulk material. Dashed areas separate the different regions. Solid lines are only guides for the eyes.

2.2. Double and Triple Perovskites: $A_3Mn_2O_7$ and $A_4Mn_3O_{10}$

Although the majority of studies have been done on simple perovskites $AMnO_3$, colossal magnetoresistance also occurs in $(La, A)_3Mn_2O_7$ ($A = Ca, Sr$). These compounds belong to the Ruddlesden–Popper phases whose general formula is $A_{n+1}B_nO_{3n+1}$ (see Fig. 4). Two parents of this family were synthesized in thin film form with $n = 2$ and $n = 3$.

Films of $La_{2-2x}Ca_{1+2x}Mn_2O_7$ ($x = 0.3$) were deposited on (001)-MgO by single-target magnetron sputtering [56,57]. The c -axis oriented films of $La_{2-2x}Sr_{1+2x}Mn_2O_7$ ($x = 0.4$) can be grown on (001)-SrTiO₃ under limited conditions (above 900 °C for the deposition temperature and below 100 mTorr for the oxygen partial pressure) [58] which are different from the typical conditions used for $(La, Sr)MnO_3$ films. On SrTiO₃ substrates, the resistivity curves shows a transition at 100 K which coincides with a magnetic transition for $La_{2-2x}Sr_{1+2x}Mn_2O_7$ films on SrTiO₃ [58]. Films on MgO are a -axis oriented, which means that the long parameter is in the plane of the substrate. These films evidence

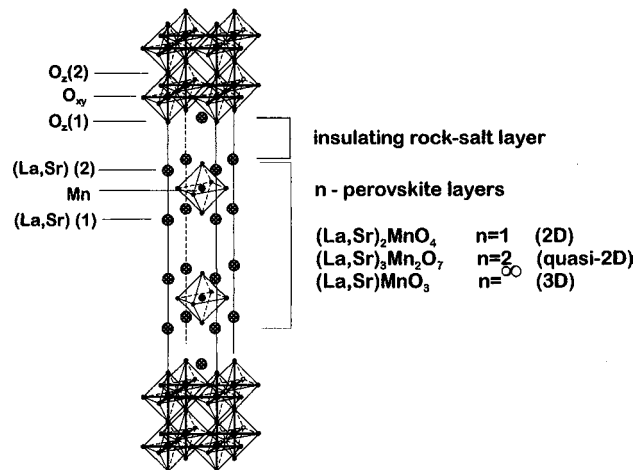


Figure 4. Idealized crystal structure of the layered manganites $La_{n-nx}Sr_{1+nx}Mn_nO_{3n+1}$. Note the intergrowth between insulating rock-salt layers and the perovskite layers. The infinite term ($n = \infty$) corresponds to the $La_{0.7}Sr_{0.3}MnO_3$ perovskite.

two types of ferromagnetic ordering that possibly result from anisotropic exchange interactions for $0.22 < x < 0.55$ [59]. Magnetoresistance is observed in a wide temperature range below the ferromagnetic transitions on MgO and is accompanied by an hysteresis on SrTiO₃ [58]. Epitaxial films of (La,Sr)₃Mn₂O₇ can also be grown artificially by atomic-layer stacking of SrO and (La,Sr)MnO₃ [60].

Contrary to the previous one, the La_{3-3x}Ca_{1+3x}Mn₃O₉ ($x = 0.3$) compound can be stabilized, but only in the form of thin films and not in the form of bulk [61]. Features similar to those reported for the double perovskite ($n = 2$) were also observed for the $n = 3$ compound, indicating a correlation between the dimensionality (or the c -axis bond configuration) and the magnetotransport properties [61].

Thus, it appears that the increase of the c axis reduces the magnitude of the CMR at low temperature and this may be attributed to the increased magnitude of the double-exchange transfer matrix and a better ferromagnetic spin alignment.

2.3. Particular Case of Sr₂FeMoO₆

This chapter focuses on manganite thin films, but it is also interesting to present the results on the ordered double perovskite Sr₂FeMoO₆, even though it does not contain Mn, since it exhibits magnetoresistance [62] with a Curie temperature above 370 K. Films of Sr₂FeMoO_{6-y} were grown using pulsed laser deposition on (001)-SrTiO₃ [63, 64]. They are grown on both (001)- and (111)-SrTiO₃ but in a narrow window near 900 °C and 10⁻⁶ Torr [65]. Asano et al. [63] have shown that by altering the growth conditions they are able to induce either positive (35%) or negative (-3%) magnetoresistance at 5 K under a magnetic field of 8 T. The films show metallic conductivity with a ferromagnetic transition above 400 K [65]. The experimental magnetic moment is calculated to be $4\mu_B$ per formula unit [64], in agreement with the theoretical one [62]. Sr₂FeMoO₆ films also exhibit both an electronlike ordinary Hall effect and a holelike anomalous Hall contribution [66]. More importantly, an intergrain tunneling-type low field magnetoresistance [67], even at room temperature [65, 68], has been reported.

2.4. Structure and Microstructure

It is of prime importance to carry out structural characterization of the films, since it has been shown that in the bulk material, a slight variation of the Mn–O bond length or bond angle drastically modifies the physical properties. Consequently, careful characterization of AMnO₃ films is paramount especially from the crystal structure point of view [69].

One of the best techniques to study the local structure of thin films, as for bulk, is most probably the high resolution transmission electron microscopy (HRTEM). Van Tendeloo et al. [70] have studied the evolution of the microstructure as function of the thickness in La_{0.7}Sr_{0.3}MnO₃ films on LaAlO₃. Close to the interface, both the film and the substrate are elastically strained in opposite directions in such a way that the interface is perfectly coherent. In the thicker films, the stress is partly relieved after annealing by the formation of misfit dislocations. Similar results were found for

La_{1-x}Ca_xMnO₃ [14], where the bottom part of the film, close to the substrate, is perfectly coherent with the substrate, suggesting an important strain, while the upper part shows a domain structure. The perfect epitaxy between the film and the substrate can also be viewed on the cross-section of Pr_{0.5}Ca_{0.5}MnO₃ deposited on SrTiO₃ (Fig. 5). This film is grown in the [010]-direction, that is, $2a_p$, perpendicular to the substrate plane. The cross section along the [110]-direction of the substrate clearly shows the perfect coherence of the interface since the [100]- or [001]-directions of the film match the [110]-direction of the substrate. The lattice parameter length in this direction is $a_p\sqrt{2}$. No dislocation has been detected, whatever the film zone, ruling out definitely such a structural mechanism for explaining the relaxation. A detailed examination allows a mechanism of smooth variation to be proposed. The images indeed show very local variations of the contrast. They appear as point-like defects and waving atomic rows, associated with ion displacements and local distortions of the octahedra. This is exemplified in film areas very close to the interface (circled in Fig. 5); the effect is clearly visible by viewing at grazing incidence. These phenomena are observed in the whole film and generate a tiny mosaicity of the film.

In general, a strain is observed due to the epitaxial growth in very thin films; that is, lattice parameters adopt those of the cubic lattice (see an example of a compressive strain on SrTiO₃ [71]). In ultrathin films (6 nm) of La_{0.73}Ca_{0.27}MnO₃ on SrTiO₃, the crystal structure imposed by the substrate is different than the bulk [71] and leads to disorder effects [72] or the formation of different phases

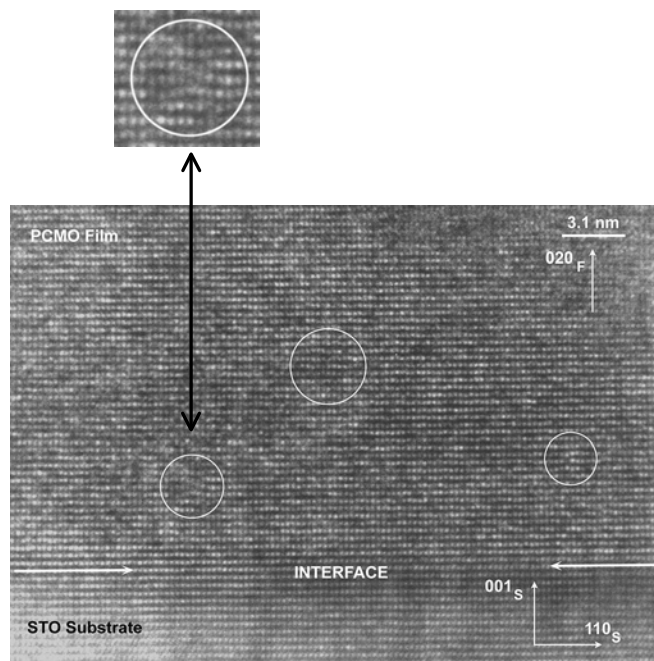


Figure 5. Cross-section (bright field) HRTEM image taken close to the film/substrate interface. No change of the lattice parameters is visible at the interface (marked by white arrows). The white circles (one is exemplified on the top of the image) show a local variation of the contrast. This variations indicate local distortions of the cell and waving atomic rows resulting in the smooth relaxation of the films due to the strains. Subscripts F and S correspond to the substrate and the film respectively.

such as $(\text{La}_{0.7}\text{Sr}_{0.3})_3\text{Mn}_2\text{O}_7$ in $\text{La}_{0.7}\text{Sr}_{0.3}\text{MnO}_3$ films [73]. Microstructural studies also reveal a slight distortion of the $\text{La}_{1-x}\text{Ca}_x\text{MnO}_3$ film, possibly leading to a breakdown of the symmetry from orthorhombic to monoclinic (due to the presence of spots in the electron pattern that are not allowed in the *Pnma* space group) [14]: this suggests that the structural situation might be different in thin film and in bulk material. In contrast, Teodorescu et al. show that the structure and the stoichiometry of the bulk target are perfectly reproduced in $\text{La}_{0.60}\text{Y}_{0.07}\text{Ca}_{0.33}\text{MnO}_{3-\delta}$ thin films [74].

A comparative study between $\text{La}_{2/3}\text{Ba}_{1/3}\text{MnO}_3$ (LBMO) and $\text{La}_{2/3}\text{Sr}_{1/3}\text{MnO}_3$ (LSMO) grown on SrTiO_3 shows that thick LBMO presents a perfect epitaxy and grows coherently strained throughout the film thickness, whereas the LSMO films are composed of two layers separated by an intrinsic interface region containing a high density of defects [75]. Sometimes, secondary phases are observed [18]. In $\text{Pr}_{0.7}\text{Sr}_{0.3}\text{MnO}_3$ [45], the deposition temperature influences the microstructure and is thus directly connected to the T_C , which is depressed maybe due to the role of the grain boundaries.

Returning to the structural characterization of CMR thin films, there are roughly three tendencies that emerge from these studies. The first is that the manganite films are much more sensitive to substrate-induced stress than the analogous cuprate superconductors. The second deals with the presence of two regimes of strain relaxation: one highly strained regime located close to substrate and another above which is more relaxed. It is not clear exactly where the interface is located or even if it exists in every film. The last interesting point that has been shown by several groups is the difference of crystal symmetry (lattice parameters, space group, ...) between the thin film and the corresponding bulk material.

2.5. Nanostructure

The elaboration of submicrometer magnetoresistive (MR) read heads and highly sensitive elements of nonvolatile memories (MRAM) requires patterning processes that are commonly used in the industry of semiconductors. Due to the continued increase in the bit density of magnetic recording, the current challenge consists in the replication of patterns with dimensions lower than 50 nm. The planar processes for thin films patterning are based on two main steps: (i) the pattern definition in a photon or electron sensitive polymer (resist) by lithography and (ii) the transfer of these nanostructures in the manganite film using dry etching (see Fig. 6 which depicts all the steps of the patterning process).

Conventional UV lithography is traditionally used to get patterns higher than 1 μm in size. Patterning at dimensions lower than 50 nm calls for high resolution techniques such as scanning electron beam lithography (SEBL), X-ray lithography (XRL), or nanoimprinting. Today theoretical ultimate resolution limits of SEBL and XRL are well known and replications below 20 nm in the high resolution PMMA (polymethylmethacrylate) resist have been demonstrated experimentally [76, 77]. During SEBL (or XRL), the polymer chains are cut under sufficient electron (or X-rays) doses which reduce locally the molecular weight of the resist and the immersion in a selective solvent dissolves the

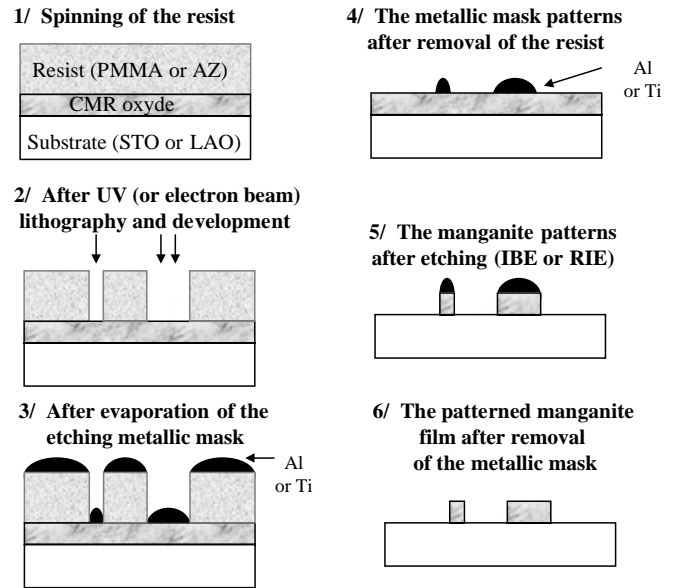


Figure 6. Description of an etching process based on nanolithography (steps 1 and 2) followed by a lift-off process (steps 3 and 4).

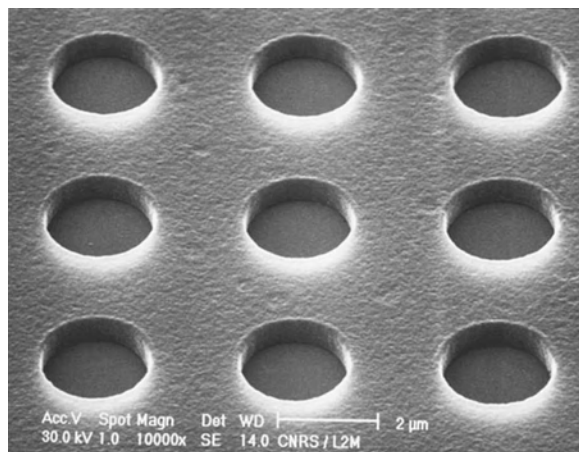
broken chains and reveals the resist patterns (see Fig. 6, step 2). Below 10 nm, the Van der Waals intermolecular forces between the irradiated resist molecules prevent this dissolution and development should be assisted by an ultrasonic (US) agitation. Wide lines of 5 nm can be obtained in 140 nm thick PMMA resist using high resolution SEBL and US development [78]. More recently, nanoimprinting appears as a low cost alternative replication method compared to SEBL and XRL, which need expensive steppers or beam pattern generators. During nanoimprinting, the thin thermoplastic resist film is pressed by a mould which has been previously worked out using SEBL and dry etching. This technique allows elaboration of lines and dots as small as 20 nm in width [79, 80].

After nanolithography, the pattern transfer can be achieved using direct etching, with the resist as mask, or using a metallic lift-off process followed by etching. The lift-off process, which is explained in Figure 6 (steps 3 and 4), is the preferred method for manganite etching since these CMR oxides are very hard materials compared to metals. In contrast to the extensive studies of reactive ion etching (RIE) for the ferromagnetic metallic films, the plasma etching process for manganite materials has not been studied in depth and the literature is very poor. However, these highly spin polarized CMR oxides are very promising materials for realizing spintronics nanodevices.

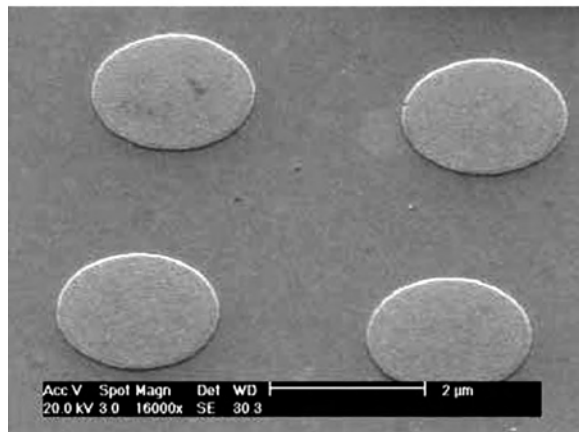
The majority of magnetoresistive nanodevices are thus ordinarily etched using conventional Ar ion beam etching (IBE) after an Al lift-off process. Al is the more frequently used metallic mask since it is easily oxidized and because it appears to be the hardest metal for this application. For IBE of manganites, this bilayer Al/ Al_2O_3 presents the best selectivity (selectivity is the ratio of the manganite etch rate over the Al mask etch rate), which never exceeds the value of 2. To avoid removal of the Al mask in solutions that always attack the manganite film (step 6 in Fig. 6), the etching time is often increased in order to fully etch the Al mask. Typical

micrometer dots etched in a LSMO film using such a lift-off process are shown in Figure 7. Note that both the edge and surface of the LSMO dots are very smooth. This is due to the very smooth morphology of both LSMO and Al films, as well as the high quality of the XRL patterning (see Fig. 7a). With such an optimized IBE process, nanopatterning at a sub-100 nm scale of LSMO films can easily be achieved. The nanodevice presented in Figure 8 exhibits 80-nm-wide contact arms, and 120-nm-wide trenches have been successfully etched on the top of the microbridge [81].

To avoid lateral damages from the high energy Ar bombardment that can modify the magnetoresistive nature of the manganite, RIE is the alternative method. It allows an increase of selectivity for deep etching and also smoother edges. Wang et al. [82] reported fluorine SF₆/Ar and chlorine Cl₂/Ar electron cyclotron resonance etching of Ca-manganites that are very similar to pure Ar IBE with no chemical enhancement. This is attributed to the high melting points beyond several hundreds °C of the reacted products of fluorides and chlorides. Naoe et al. [83] recently proposed a CO/NH₃ gas RIE process with formation of



(a)



(b)

Figure 7. Scanning electron microscope (SEM) pictures of 2- μm -diameter dots patterned in a $\text{La}_{0.7}\text{Sr}_{0.3}\text{MnO}_3$ thin film grown on SrTiO_3 , recorded after (a) the XRL nanolithography replication in the resist (step 2) and (b) the IBE etching (step 6).

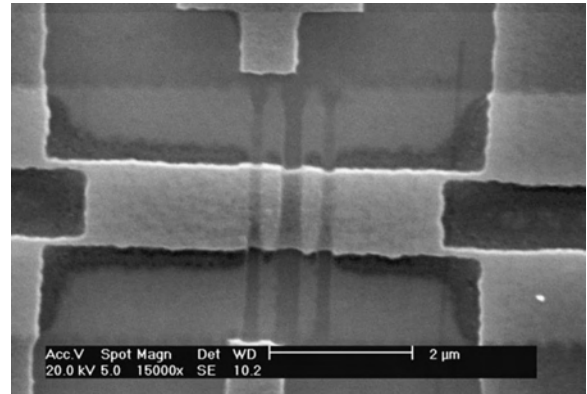


Figure 8. SEM top view of a $\text{La}_{0.7}\text{Sr}_{0.3}\text{MnO}_3$ spin filter patterned using conventional SEBL and high resolution EBL at 200 keV. Reprinted with permission from [81], J. Wolfman et al., *J. Appl. Phys.* 89, 6955 (2001). © 2001, American Institute of Physics.

metal-carbonyls that exhibit low melting points (several tens °C) and a high volatility. These authors demonstrate an enhancement of selectivity up to 4.7 that is comparable to those of ferromagnetic metals, with a significant reduction of the peak-to-peak surface roughness. Such recent RIE processes have not been applied yet to magnetoresistive devices. Thus a comparison of pure Ar and reactive gases etchings in terms of lateral damages in manganite nanodevices cannot be done for the time being.

2.6. Physical Measurements

The standard characterization of CMR thin films consists of resistance measurements versus temperature in zero field and under an applied magnetic field, by using the four probe technique and also in magnetization measurements. Results pertaining to strain effects will be discussed in the next section.

Several groups focused their studies on the surface [84–86]. Extensive thin film surface studies were performed using two complementary techniques: atomic force microscopy and magnetic force microscopy [87]. Work was mostly on $\text{La}_{1-x}\text{Sr}_x\text{MnO}_3$ since this material exhibits the highest Curie temperature. It was also found that the properties of the surface are different from those of the bulk in both the electronic and the composition point of view [86]. For example, the surface termination and the Ca surface concentration depend on the overall Ca concentration in $\text{La}_{1-x}\text{Ca}_x\text{MnO}_3$ films [84] (the La/Ca ratio differs between the surface and in the film). The surfaces of $\text{La}_{0.5}\text{Ca}_{0.5}\text{MnO}_3$ and $\text{La}_{0.66}\text{Ca}_{0.33}\text{MnO}_3$ show a highly ordered grain pattern induced by strains [85], and the $\text{La}_{0.65}\text{Sr}_{0.35}\text{MnO}_3$ surface exhibits a surface phase transition at 240 K (to be compared to 370 K for the bulk) [86].

Grain boundaries (GBS) strongly affect the properties of CMR materials. Low field magnetoresistance (LFMR) has been reported and attributed to the spin-dependent scattering of polarized electrons at the GB [88]. Researchers tried to enhance this property by artificially creating an interface between two elements. We will describe here only the intrinsic effect across natural GB (in polycrystalline thin

films) and across artificial GB (in films deposited on bicrystal substrates). The precise influence of the substrate will be discussed in a separate part. Note that another method has been utilized to create artificial GB by scratching the LaAlO_3 substrate before the deposition of the LCMO film [89]. The MR is subsequent in a field of 2 kOe and varies with the field orientation with respect to the GB.

The simplest way of creating a natural GB is to grow the film on polycrystalline substrates [90]. Most of this work was done by IBM [90, 91] on La–Ca–Mn–O (LCMO) and LSMO films. The $\rho - T$ curve of such films depends on the grain size, as shown on Figure 9: resistivity in zero field decreases when the grain size increases, but the peak temperature of approximately 230 K is almost independent of the grain size [90]. Gu et al. show that the LFMR at low temperature has a dramatic dependence on the nature of the in-plane GB [92]. The reduction of zero-field low-temperature resistivity might be explained by the spin-polarized tunneling across half-metallic grains. Another possibility to obtain polycrystalline samples is to decrease the deposition temperature. The resulting GB results from a lower crystalline quality of the film [93].

Bicrystal substrates having a single GB have also been used to study the transport across a GB. LCMO and LSMO thin films were deposited on bicrystalline SrTiO_3 substrates having a specific misorientation angle [94, 95]. To measure the properties of the GB only, the film was patterned into a Wheatstone bridge. The GB resistance and its magnetic field dependence are strongly dependent on the misorientation angle [95]. The MR increases with an increase of the misorientation angle of the bicrystal [95]. The change of resistance is 3% under 2 mT magnetic field at 300 K for $\text{La}_{0.7}\text{Sr}_{0.3}\text{MnO}_3$. At 77 K, a large bridge resistance (27%) is observed during magnetic field sweeps between ± 200 mT

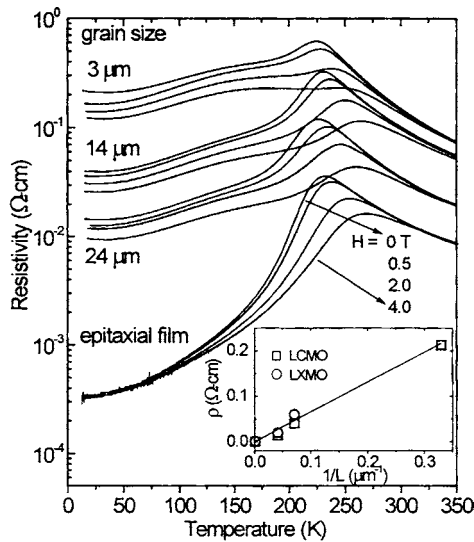


Figure 9. $\rho(T)$ under different magnetic fields for polycrystalline LCMO films with different grain sizes and an epitaxial film. The inset shows the zero-field resistivity at 10 K as a function of the average grain size for $\text{La}_{0.75}\text{MnO}_3$ (LXMO). Reprinted with permission from [88], A. Gupta and J. Z. Sun, *J. Magn. Magn. Mater.* 200, 24 (1999). © 1999, Elsevier Science.

over a temperature range down to 77 K. Steenbeck et al. utilized $\text{La}_{0.8}\text{Sr}_{0.2}\text{MnO}_3$ films grown on SrTiO_3 bicrystals with a misorientation angle of 36.8° [96] or 24° [97]. They found that the GB magnetoresistance occurs at low temperature, separated from the intrinsic MR near T_C , and that the sign of the MR at the GB depends on the domain structure and H [96]. Moreover, current–voltage measurements show that the field dependence might not be related to tunneling [98].

Phase separation was suspected in $\text{La}_{0.4}\text{Ba}_{0.1}\text{Ca}_{0.5}\text{MnO}_3$ films [99] and confirmed by the noise probe method [100] in $\text{La}_{2/3}\text{Ca}_{1/3}\text{MnO}_3$ films; in this work the authors attribute the origin of the random telegraph noise to a dynamic mixed-phase percolative process, where manganese clusters switched back and forth between two phases that differ in their conductivity and magnetization. This spatial inhomogeneity in doped manganite thin films was also investigated in $\text{La}_{1-x}\text{Ca}_x\text{MnO}_3$ [101] using scanning tunneling microscopy. The phase separation is observed below the Curie temperature where different structures of metallic and more insulating areas coexist and are field dependent. This suggests that the insulator to metal transition at T_C should be viewed as a percolation of metallic ferromagnetic domains.

3. STRAIN EFFECTS

The CMR manganites are sensitive to all types of perturbations. In particular, it has been shown in bulk that the internal (through the average size of the A-site cation) or external pressure (via hydrostatic pressure) can strongly influence the magnetotransport properties. Since the beginning of the rediscovery of the CMR effect in Mn-based compounds, many studies have been focussed on the strains in thin films. This is due to the fact that Mn electrons, which determine most of the physical properties, are coupled to the lattice degrees of freedom through the Jahn–Teller trivalent manganese. Thus, strains affect the properties of the manganite thin films, and, in consequence, one needs to correctly understand the effects in order to obtain the desired properties. The following section will discuss the two types of strains: in-the-plane (i.e., substrate-induced strains, Section 3.1) and out-of-plane strain (i.e., thickness dependence, Section 3.2).

3.1. Substrate-Induced Strains

The first important parameter for successful thin film growth is undoubtedly the substrate. For CMR materials, the same substrates as used for the HTSC compounds were utilized. The most commonly used substrates to grow manganite perovskites are MgO (cubic, $a = 0.4205$ nm), SrTiO_3 (STO, cubic, $a = 0.3905$ nm), LaAlO_3 (LAO, pseudocubic, $a = 0.3788$ nm), NdGaO_3 (NGO, orthorhombic with $a = 0.5426$ nm, $b = 0.5502$ nm, and $c = 0.7706$ nm), and Si (cubic, $a = 0.543$ nm). Many authors have investigated the strain effects of the substrate by growing various films on different substrates [102]. They have experimentally [87, 103] or theoretically [104] studied the effect of strains on the magnetoresistive properties of $\text{La}_{0.7}\text{Sr}_{0.3}\text{MnO}_3$ and $\text{La}_{0.7}\text{Ca}_{0.3}\text{MnO}_3$ or on the surface flatness [105] for many substrates. The

physical properties of these materials depend on the overlap between the manganese d orbitals and oxygen p orbitals, which are closely related to the Mn–O–Mn bond angle and the Mn–O distance. As the unit cell of the thin film is modified with respect to the bulk material, the Mn–O distances and Mn–O–Mn angles are altered, inducing variations in the electronic properties. We will review the main characteristics, such as the structure and the physical properties, which are affected by the substrate-induced strains.

3.1.1. Modification of the Structure/Microstructure

The influence of the substrate upon the microstructure/structure, the lattice parameters, the texturation, and also the orientation of the film is discussed in this section.

Using magnetic force microscopy, Kwon et al. [87] showed on $\text{La}_{0.7}\text{Sr}_{0.3}\text{MnO}_3$ a “featherlike” pattern, indicating an in-plane magnetization on (100)- SrTiO_3 , while on (100)- LaAlO_3 , a “mazelike” pattern corresponding to a perpendicular magnetization anisotropy is seen. This kind of study was confirmed and extended recently by Desfeux et al. on other substrates [106].

The influence of the substrate can principally be deduced from the lattice parameters of the film and the effect of strain on lattice parameters has been studied by many groups. These measurements lead to different spin structures. This is evident in $\text{La}_{1-x}\text{Sr}_x\text{MnO}_3$ for which the spin-orbital phase diagram was obtained in the plane of strain-field (c/a ratio) vs doping x using the density-functional electronic calculation [107]. The phase diagram of $\text{La}_{0.67}\text{Sr}_{0.33}\text{MnO}_3$ was also plotted for different substrates [108]. A strong dependence of anisotropy and Curie temperature on lattice strain is observed. The effect of uniaxial strain was studied theoretically by Ahn et al. [109]. Uniaxial strain produces changes in the magnetic ground state, leading to dramatic changes in the band structure and optical spectrum.

Both in-plane and out-of-plane lattice parameters are often modified by strain effects when various substrates are used [110]. In Figure 10, the Θ – 2Θ scan shows that the $\text{Pr}_{0.5}\text{Ca}_{0.5}\text{MnO}_3$ films are single phase and highly crystallized, as seen from the sharp and intense diffraction peaks. It is also found that the films were [010]-oriented (i.e., with the [010] axis perpendicular to the substrate plane) on the STO substrate and [101]-oriented on LAO. Using the X-ray diffraction (XRD) results, the out-of-plane lattice parameter of the substrates was calculated to be 0.3778 nm for STO and 0.3834 nm for LAO. This confirms that the films are under tensile stress on STO (decreasing in the growth direction and expanding in the plane) and under compressive stress on LAO (decreasing in the plane and expanding in the out-of-plane direction) due to the lattice mismatch between the film and the substrate at room temperature (Fig. 11). The strain effects on the out-of-plane lattice parameter of LCMO are enhanced with annealing [111]: the lattice expansion is 2–3 times larger in LCMO/STO than in LCMO/NGO. The stress also influences the bond lengths and bond angles. Miniotas et al. have evaluated the Mn–O and Mn–Mn distances in $\text{La}_{1-x}\text{Ca}_x\text{MnO}_3$ films grown by MBE. The Mn–O bond length was found to be fixed at 0.1975 nm, independent of the substrate types, while the Mn–Mn distance (and

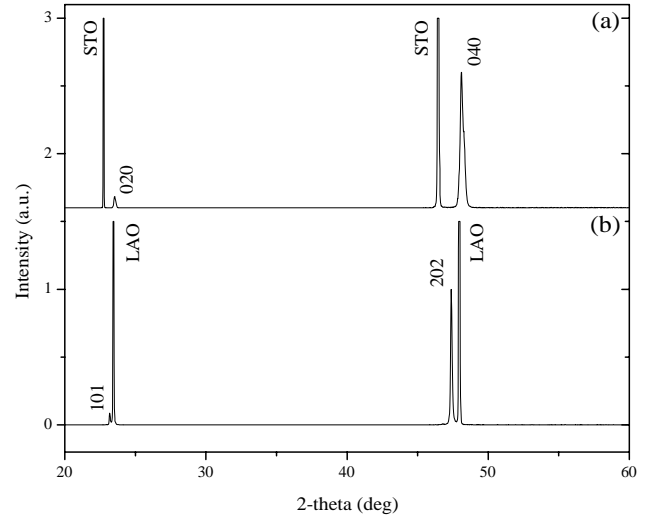


Figure 10. XRD pattern in the range 45–50° of 150-nm-thick $\text{Pr}_{0.5}\text{Ca}_{0.5}\text{MnO}_3$ films on (a) SrTiO_3 and (b) LaAlO_3 . Note the difference in the out-of-plane lattice parameter to the strain effects.

subsequently the Mn–O–Mn bond angle) was calculated to be 0.393 nm for STO and 0.384 nm for LAO [112].

Lattice mismatch (i.e., the difference of parameters between the film and the substrate) influences not only the parameters of the film but also the texturation (or epitaxy), that is, the in-plane alignments. Usually, changes in the in-plane orientation are observed only when the mismatch is small (e.g., LCMO on LAO [113] and is not realized on YSZ [114] or on MgO [115]). Textured $\text{La}_{2/3}\text{Sr}_{1/3}\text{MnO}_3$ films were obtained on Si when buffer layers [17] were used. $\text{La}_{0.7}\text{Ca}_{0.3}\text{MnO}_3$ was grown using a buffer layer of CeO_2 [116] and LSMO with a buffer of YSZ [16] or a double layer $\text{Bi}_4\text{Ti}_3\text{O}_{12}/\text{SiO}_2$ [92]. A highly conducting diffusion barrier layer of TiN has also been utilized recently as a buffer layer [118]. This progress is interesting for technological reasons especially when using Si substrates.

A surprising effect of lattice mismatch is related to the orientation of the films, especially those that crystallize in an orthorhombic perovskite cell. This was first seen on YMnO_3 [119], which is [010]-oriented on SrTiO_3

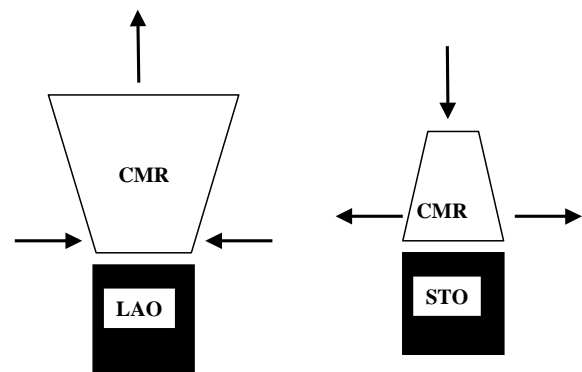


Figure 11. Schematic structure of a film grown under tensile and compressive stress in the plane. Note the compression or the elongation of the out-of-plane parameter depending on the nature of the stress.

but [101]-oriented on NdGaO_3 or LaAlO_3 . Similar results were obtained with $\text{Pr}_{0.5}\text{Ca}_{0.5}\text{MnO}_3$ [41, 120] (see Fig. 12), $\text{Pr}_{0.7}\text{Sr}_{0.3}\text{MnO}_3$ [45], or $\text{Pr}_{0.7}\text{Sr}_{0.3-x}\text{Ca}_x\text{MnO}_3$ [26]. It seems that this orientation can be generalized for every compound that crystallizes in an orthorhombic structure. This dependence on the orientation with the substrate is explained by the lattice mismatch (σ) which should favor one orientation [121]. Indeed, the mismatch between the film and the substrate can be evaluated using the formula $\sigma = 100 * (a_S - a_F)/a_S$ (where a_S and a_F respectively refer to the lattice parameter of the substrate and the film). For $\text{Pr}_{0.5}\text{Ca}_{0.5}\text{MnO}_3$, the smaller mismatch on LaAlO_3 is obtained for the [010]-axis in the plane ($\sigma_{\text{LAO}} = -0.4\%$), that is, the [101]-axis perpendicular to the substrate plane. In contrast, the smaller mismatch on SrTiO_3 ($\sigma_{\text{STO}} = 2.2\%$) found for the [101]-axis is in the plane and thus the [010]-axis normal to the surface of the substrate as found experimentally [121].

3.1.2. Influence on the Physical Properties

Much work has been done on the influence of strain on the transport properties, but we will also describe how the magnetic properties can be changed. Many groups have focused their studies on the modification of the physical properties [122] by the strain effects since the most common properties such as the insulator-to-metal (T_{IM}) transition and the Curie temperatures (T_C) are affected. In Figure 13, Koo et al. show this clear correlation between the substrate

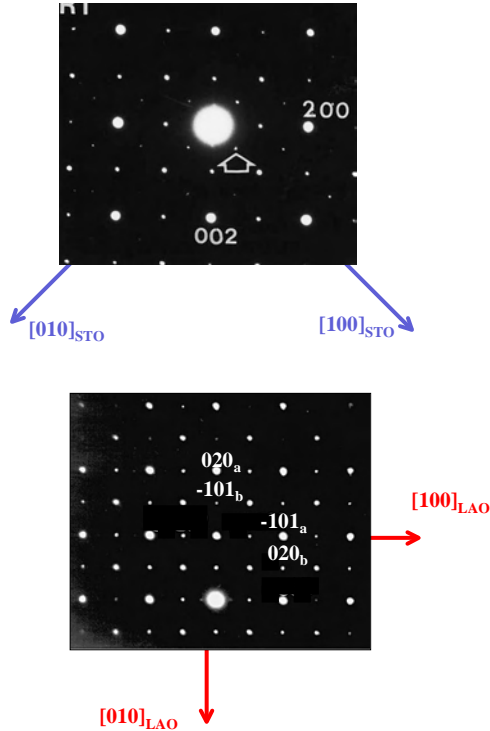


Figure 12. Electron diffraction pattern taken along a direction perpendicular to the substrate plane of a $\text{Pr}_{0.5}\text{Ca}_{0.5}\text{MnO}_3$ films on (a) SrTiO_3 and (b) LaAlO_3 . Note the different orientation between both substrates.

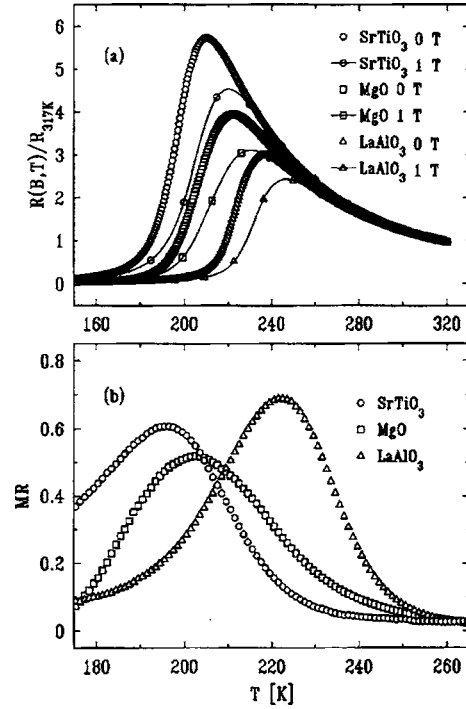


Figure 13. (a) $\rho(T)$ of $\text{La}_{0.7}\text{Ca}_{0.3}\text{MnO}_3$ on various substrates under 0 and 1 T magnetic field. (b) MR defined as $(\rho(0) - \rho(T))/\rho(0)$ normalized to the value at $T = 317$ K. Reprinted with permission from [123], T. Y. Koo et al., *Appl. Phys. Lett.* 71, 977 (1997) © 1997, American Institute of Physics.

and the physical properties for $\text{La}_{0.7}\text{Ca}_{0.3}\text{MnO}_3$ films: the T_{IM} and maximum MR shift to a higher temperature when changing a SrTiO_3 to a LaAlO_3 substrate [123].

Since the crystallinity of these films can be changed, as previously discussed, Gillman et al. [113] have prepared $\text{La}_{1-x}\text{Ca}_x\text{MnO}_3$ ($x = 0.41$) films on substrates with different lattice parameters by liquid delivery metal-organic chemical vapor deposition. Films on LaAlO_3 , closely lattice matched with the substrate, exhibit a high degree of crystallization and a high magnetoresistance ratio as compared to films deposited on Al_2O_3 or Y-ZrO_2 . Similar results were reported for $\text{La}_{0.8}\text{Sr}_{0.2}\text{MnO}_3$, which is epitaxial when grown on (100)- LaAlO_3 and polycrystalline when grown and (100)-Si [122]. Moreover, the T_{IM} increases by 20 K when using (011)- LaAlO_3 rather than (001)- LaAlO_3 . Similar results have been reported for $\text{La}_{2/3}\text{MnO}_{3-\delta}$ films grown on both Al_2O_3 and SrTiO_3 [124] and also for $\text{La}_{0.67}\text{Ca}_{0.33}\text{MnO}_3$ [125]. The T_{IM} is higher and the transition is sharper for material grown on STO (300 K) than on ALO (200 K). Even if the T_{IM} varies a lot, the Curie temperature is found to remain almost constant, independent of the substrate, for many compounds such as $\text{La}_{2/3}\text{MnO}_{3-\delta}$ [124] or $\text{La}_{0.7}\text{Sr}_{0.3}\text{MnO}_3$ [126].

The above evidence implies that T_{IM} is directly connected to the substrate. Often, the transition is at higher temperature and sharper when the mismatch between the film and the substrate is smaller, probably due to a high degree of epitaxy.

Strain not only influences the transport transitions but also the direction of the magnetization (via lattice

deformation): it is found to be in-the-plane for films under tensile stress (for example on SrTiO₃) and out-of-plane for compressive stress (as in the case of LaAlO₃) [87, 126]. Using a wide-field Kerr microscope, magnetic domain orientation and contrast of La_{0.67}Sr_{0.33}MnO₃/SrTiO₃ suggest a magnetic anisotropy with $\langle 110 \rangle$ easy axes [127]. The easy direction is along [110] of the pseudocubic unit cell, that is, diagonal to the O–Mn–O bond direction for La_{0.7}Ca_{0.3}MnO₃ film grown on untwinned paramagnetic NdGaO₃ (001) [128].

The substrate-induced strain can also influence the optical properties, as for La_{0.67}Ca_{0.33}MnO₃ [129]. This can be explained by the fact that the substrate-induced strain results in modification of the Mn–O bonds and Mn–O–Mn bond angles and, thus, in both the corresponding phonon modes and electron–phonon interactions leading to changes in the phonon frequencies and optical conductance. Note that the strains can also induce a surface magnetization as for La_{0.7}Sr_{0.3}MnO₃ [130].

3.1.3. Low Field Magnetoresistance

The strain effect on the LFMR was first studied on polycrystalline La_{0.67}Sr_{0.33}MnO₃ [90, 91]. It was also extensively studied by Wang et al. in Pr_{0.67}Sr_{0.33}MnO₃ [131]. Films with compressive strains (on LaAlO₃) show a large LFMR [132] when the field is applied perpendicularly to the substrate plane (Fig. 12), while they exhibit a positive MR when the film is under tensile stress (on SrTiO₃) [131]. Almost no LFMR is observed when the film is stress-free (on NdGaO₃). O'Donnel et al. confirm that the LFMR depends on the strains and the orientation of the field, by studying highly crystallized La_{0.7}Ca_{0.3}MnO₃ thin films made by molecular beam epitaxy [33]. It was also shown that the LFMR is dominated by the grain boundaries [90, 91] and its sign can be explained by a simple atomic *d*-state model [133]. This idea of anisotropic MR [134] was evidenced by La_{0.7}Sr_{0.3}MnO₃ deposited on (001)-SrTiO₃, (110)-SrTiO₃ [135], and (110)-LaGaO₃. Magnetic anisotropy was also seen recently on La_{0.7}Ca_{0.3}MnO₃ films grown on (001)-NdGaO₃ [128].

3.1.4. Charge-Ordered Manganites

Most of the experimental studies were done on manganites showing an insulator-to-metal transition without field, but it was also shown that substrate-induced strain can affect the properties of charge-ordered (CO) compounds. CO is a phenomenon observed wherein electrons become localized due to the ordering of heterovalent cations in two different sublattices (Mn³⁺ and Mn⁴⁺). The material becomes insulating below the CO transition temperature, but it is possible to destroy this state and render the material metallic by, for example, the application of a magnetic field [136], but an electric field can also induce insulator-metal transitions in thin films of CO manganites [39]. Pr_{0.5}Ca_{0.5}MnO₃ is an example of such a compound. In this case, a tensile stress can decrease the melting magnetic field [41] whereas a compressive strain induces a locking of the structure [120] at low temperature (i.e., under cooling, when the in-plane parameters of the film are equal to the parameters of the substrate, they are kept at this value). This idea of locking was confirmed in Pr_{0.5}Sr_{0.5}MnO₃ where the structural and physical transitions are suppressed under cooling [137],

as compared to the bulk (note that even if the compound Pr_{0.5}Sr_{0.5}MnO₃ is not a typical CO, it has some similarities in the physical properties). In this material, the A-type antiferromagnetic phase with the *Fmmm* structure, which is obtained at low temperature (below 135 K) in the corresponding bulk compound, is not observed in the thin film. The consequence of the absence of structural transitions is that magnetotransport properties are affected. There is no antiferromagnetism (i.e., the A-phase) at low temperature. The material only becomes ferromagnetic insulating. This is one of the very few examples of substrate-induced strain upon the film structure. These results show that the strain effect can destabilized the charge-ordered state for CO materials but, surprisingly, it seems also possible to induce a CO state when the film composition is not a CO type (i.e., if the film has an insulator-to-metal transition without the presence of a magnetic field). This has been shown in a normally metallic La_{0.7}Ca_{0.3}MnO₃ compound where the lattice-mismatch strain effects lead to a strain-induced insulating state [138]. This insulating behavior is related to the coexistence of a metallic state with a possibly charge-ordered insulating state [138, 139].

3.2. Thickness Dependence

3.2.1. Lattice Parameters

The influence of the thickness (*t*) is primary seen upon the lattice parameters of the films (in-plane and out-of-plane parameters). Usually, the volume of the unit cell is conserved in the thin film as compared to the bulk. In order to verify this result, the evolution of the three-dimensional strain states and on crystallographic domain structures was studied on epitaxial La_{0.8}Ca_{0.2}MnO₃ as a function of lattice mismatch with two types of (001)-substrates, SrTiO₃ and LaAlO₃ [140]. Surprisingly, it was shown, using normal and grazing incidence X-ray diffraction techniques, that the unit cell volume is not conserved and varies with the substrate as well as the film thickness (Fig. 14).

But the main result is that for a tensiled film (under expansion in the plane of the substrate), the out-of plane and in-plane parameters gradually increase and decrease,

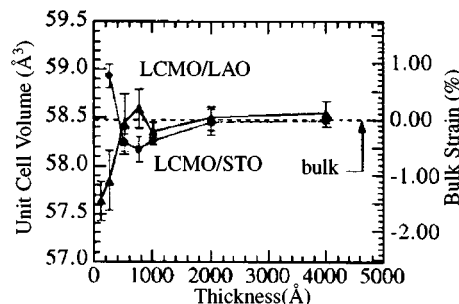


Figure 14. Thickness dependence of the perovskite unit cell volume of epitaxial La_{0.8}Ca_{0.2}MnO₃ films on (001)-LaAlO₃ (triangles) and (001)-SrTiO₃ (circles). Large deviations of the lattice parameters from those of the bulk are observed. As film thickness increases, both in-plane and out-of-plane lattice parameters tend to deviate away from those of the substrates toward the bulk value. Reprinted with permission from [140], R. A. Rao et al., *Appl. Phys. Lett.* 73, 3294 (1998) © 1998, American Institute of Physics.

respectively, as a function of the film thickness [121]. For example, in the case of $\text{Nd}_{2/3}\text{Sr}_{1/3}\text{MnO}_3$ grown on SrTiO_3 , the out-of-plane parameter increases from a value of 0.38 nm for a 20 nm thick film to 0.386 nm for a 100 nm film, which is close to the bulk value [141]. The scenario is the opposite when the film is compressively strained as in $\text{La}_{0.7}\text{Sr}_{0.3}\text{MnO}_3$ on (100)- LaAlO_3 [142]: the out-of-plane parameter decreases from 0.394 nm for a 30 nm thick film to 0.39 nm for a 450 nm thick film, while at the same time the in-plane parameter changes from 0.382 to 0.388 nm. The film is not completely relaxed until it reaches a thickness on the order of 100 nm. In $\text{Nd}_{0.5}\text{Sr}_{0.5}\text{MnO}_3$ deposited on (001)- LaAlO_3 [143], two regimes were observed using XRD: one which was strained (close to the substrate), and a quasi-relaxed component in the upper part of the film, the latter increasing with film thickness.

As previously reported, increasing film thickness leads to a change of the symmetry of the film. This was systematically studied by looking at various film compositions vs thickness by Yu et al. [144]. They found a strong tetragonal lattice strain using HRTEM and XRD characterization. This is more important for a composition in which the bulk structure is orthorhombic, as in $(\text{La}_{1-x}\text{Pr}_x)_{0.7}\text{Ca}_{0.3}\text{MnO}_3$, as compared to $\text{La}_{1-x}\text{Na}_x\text{MnO}_3$ or $\text{La}_{0.7}\text{Sr}_{0.3}\text{MnO}_3$ where the structure is rhombohedral [144].

3.2.2. Physical Properties

The physical properties of manganites [111] such as insulator-to-metal transition [145], magnetoresistance [103], coercive field [146], or microstructure [72, 147] are strongly dependent on the thickness. As an example, the MR value calculated as $\Delta R/R(H)$ for $H = 6$ T exhibits a strong dependence on film thickness as shown in Figure 15 for $\text{La}_{0.7}\text{Ca}_{0.3}\text{MnO}_3$. The curves show a maximum MR for a thickness near 110 nm with a value of $10^6\%$ and, on either side of the peak, the MR ratio is drastically lower. Transport properties are mostly affected and the magnetization is only moderately changed [148] with thickness as seen for $\text{La}_{0.6}\text{Sr}_{0.4}\text{MnO}_3$ deposited on MgO or SrTiO_3 . At an intermediate thickness around 100 nm, the films usually recover the properties of the bulk compounds. Even when the film

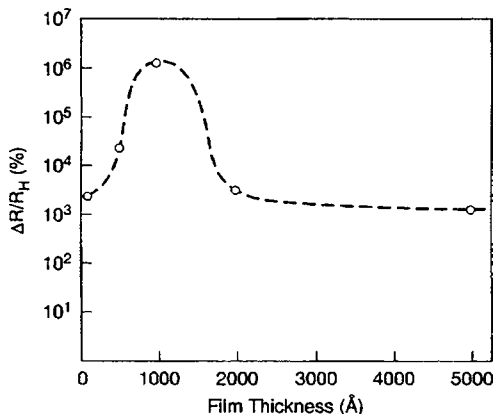


Figure 15. Thickness dependence of the MR for $\text{La}_{0.67}\text{Ca}_{0.33}\text{MnO}_3$ thin films grown on (100)- LaAlO_3 . Reprinted with permission from [103], S. Jin et al., *Appl. Phys. Lett.* 67, 557 (1995) © 1995, American Institute of Physics.

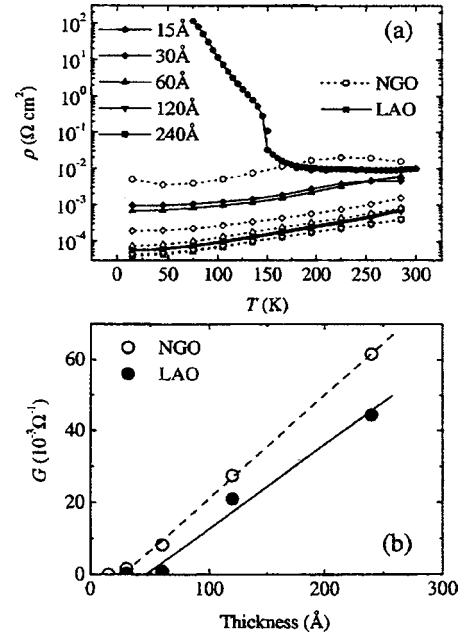


Figure 16. (a) Temperature dependence of the resistivity for $\text{La}_{0.67}\text{Sr}_{0.33}\text{MnO}_3$ films with varying thickness on NdGaO_3 and LaAlO_3 . (b) Thickness dependence of the conductance of films at 14 K. Reprinted with permission from [111], J. Z. Sun et al., *Appl. Phys. Lett.* 74, 3017 (1999) © 1999, American Institute of Physics.

is under low epitaxial stress (case of NGO), T_{IM} varies greatly from 182 (3.5 nm) to 264 K (165 nm), as seen for $\text{La}_{0.7}\text{Ca}_{0.3}\text{MnO}_3$ films [145].

Films thinner than 100 nm have properties different from the bulk and are most of the time unusual. For example thin $\text{La}_{1-x}\text{Ba}_x\text{MnO}_3$ films ($t < 100$ nm) exhibit a T_C higher than in the bulk due to an anomalous tensile strain effect when deposited on SrTiO_3 . Consequently, the resulting film shows room temperature ferromagnetism and an enhancement of the magnetoresistance [19]. In $(\text{La,Ca})\text{MnO}_3$ films, the thinnest films which present full magnetization grow with the b -axis of the structure perpendicular to the substrate, whereas the thicker films grow with the b -axis in the plane of the substrate and do not present full magnetization [72]. Another example of the thickness dependence is seen in $\text{La}_{0.67}\text{Ca}_{0.33}\text{MnO}_3$ on SrTiO_3 , which is ferromagnetic around 150 K but remains insulating [71]. Biswas et al. [139] have explained this behavior by the coexistence of two different phases, a metallic ferromagnet (in the highly strained region) and an insulating antiferromagnet (in the low strain one). This nonuniformity induces, under a magnetic field, an insulator-to-metal transition resulting in a large CMR effect. But the metallic behavior of the bulk $\text{La}_{0.7}\text{Ca}_{0.3}\text{MnO}_3$ can be retained for a thickness down to 6 nm when the SrTiO_3 substrate is treated to obtain an atomically flat TiO_2 terminated surface [149]. For $\text{La}_{0.9}\text{Sr}_{0.1}\text{MnO}_3$ ($t < 50$ nm) on (100)- SrTiO_3 , Razavi et al. [150] reported an unexpected insulator-to-metal transition, most probably due to La deficiency. Nevertheless, Sun et al. [111] have estimated the “dead layer” for $\text{La}_{0.67}\text{Sr}_{0.33}\text{MnO}_3$ to be around 3 nm for NdGaO_3 and 5 nm for LaAlO_3 (Fig. 16). The magnetic, transport, and structural properties of $\text{La}_{0.7}\text{Sr}_{0.3}\text{MnO}_3$ deposited were interpreted recently in terms of a magnetic (1 nm) and an

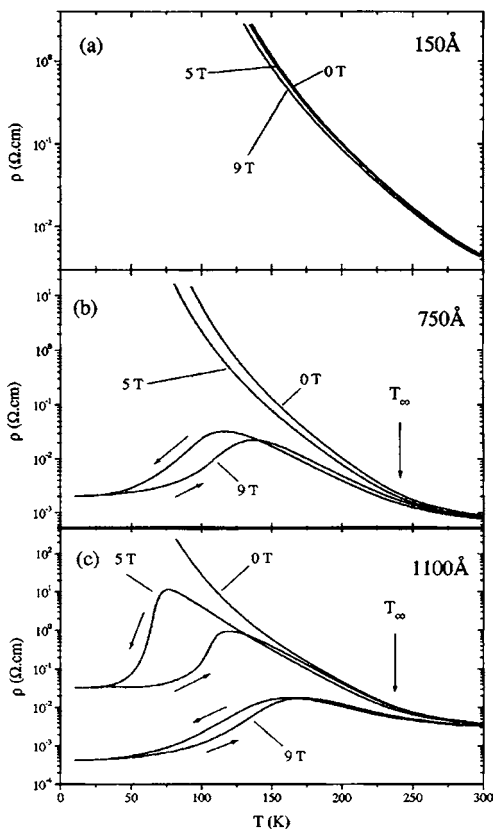


Figure 17. $\rho(T)$ under varying magnetic fields for different thicknesses of $\text{Pr}_{0.5}\text{Ca}_{0.5}\text{MnO}_3$ thin films grown on SrTiO_3 . Arrows indicate the direction of the temperature dependence.

electrical (insulating) dead layer (respectively 1 and 0.4 nm thick) [151].

More recently, the robustness of the CO state was studied by Prellier et al. [121]. In $\text{Pr}_{0.5}\text{Ca}_{0.5}\text{MnO}_3$, the thicker film induced the less stable state; that is, a small magnetic field as compared to the bulk is required to destroy the CO state and induce a metallic behavior (Fig. 17). In $\text{Nd}_{0.5}\text{Sr}_{0.5}\text{MnO}_3$, the (110)-films show a strained and a quasi-relaxed layer. The latter increases with film thickness whereas the strained one has a constant thickness [143]. The coexistence of two strain regimes inside the same film was also seen in $\text{La}_{0.66}\text{Ca}_{0.33}\text{MnO}_3$ films on SrTiO_3 [14] and LaMnO_3 deposited on NdGaO_3 [152]: at the interface a cubiclike dense layer (5 nm thick) is observed while the upper layer shows a columnar growth. These two distinct thickness ranges behave differently with respect to the thickness dependence of the magnetotransport properties [102]; the upper range ($t > 20$ nm) is weakly thickness-dependent whereas the lower one not. These results [102, 107] show the evidence for the effect of Jahn–Teller type distortion and confirm theoretical explanations [104]. In $\text{Nd}_{2/3}\text{Sr}_{1/3}\text{MnO}_3$ films, the release of the strain as the thickness increases [141] results in a first-order phase transition.

Thus, these results show the thickness dependence of the physical properties of the film, but it seems difficult to estimate these changes precisely. For example, considering a $\text{Pr}_{0.7}\text{Sr}_{0.3}\text{MnO}_3$ film deposited on NdGaO_3 , is it possible to

evaluate the T_{TM} and the T_C for 200 nm thick film? There is no report of such calculations, and one of the reasons is that the properties of the film depend not only of the substrate but also on the growth conditions. It will be necessary to answer this question in the future.

The improvement in controlled heterostructures and multilayers is a necessary stage for the realization of many devices and circuits. Structures with new properties such as superlattices were also widely studied.

3.3. Superlattices

Thin film methods offer a powerful and versatile technique for growing new structures, as previously seen for example in cuprates. This is due to strain effects that can stabilize structures which do not exist under classical conditions of pressure and temperature. For example, various metastable perovskites, which cannot be formed in bulk or can only be prepared under high pressure, such as BiMnO_3 [110], YMnO_3 [119], and atomically ordered $\text{LaFe}_{0.5}\text{Mn}_{0.5}\text{O}_3$ [153], are synthesized via a pulsed laser method or by using injection MOCVD-like $\text{NdMn}_7\text{O}_{12}$ [154].

Also interesting is the construction of new compounds, such as artificial superlattices, that show unique physical properties since different types of magnetism can be combined by building the desirable structure at the atomic layer level [155]. Growth conditions such as the oxygen pressure or the deposition temperature are easy to control in the thin film process, allowing the synthesis of metastable phases.

Another approach to obtain exotic properties via new phases is the method of artificial superlattices. Preliminary films were grown by stacking a magnetic layer ($\text{La}_{0.7}\text{A}_{0.3}\text{MnO}_3$ with $\text{A} = \text{Sr}, \text{Ba}, \dots$) and another perovskite, usually an insulator (such as SrTiO_3) [156]. This allows a continuous variation of the in-plane coherency strain in the films [157–159]. High quality films showing a clear chemical modulation by the presence of satellite peaks around the main diffraction peak were obtained [157, 160]. In the case of LCMO, the metallic transition is suppressed and the MR enhanced at low temperature when the thickness of the LCMO layer is decreased to 2.5 nm [158]. The MR ($\text{MR} = 100 * [R(0) - R(H)]/R(0)$) is calculated to be 85% at $H = 5$ T over a wide temperature range (10–150 K). A systematic study of $\text{La}_{0.7}\text{Ba}_{0.3}\text{MnO}_3/\text{SrTiO}_3$ superlattices shows that the decrease of the LBMO layer thickness results in the broadening of the MR peak vs temperature [156]. Such studies also confirm the importance of strains and the relevance of Jahn–Teller electron–phonon coupling in doped manganites, as pointed out by Lu et al. [157]. Following the same idea, $\text{La}_{2/3}\text{Ba}_{1/3}\text{MnO}_3/\text{LaNiO}_3$ multilayers were synthesized. Magnetization measurements show evidence of antiferromagnetic coupling between LBMO layers when the thickness of the LaNiO_3 spacer is 1.5 nm or less [161].

The magnetic exchange interactions have been extensively studied in $\text{La}(\text{Sr})\text{MnO}_3/\text{LaMO}_3$ ($\text{M} = \text{Fe}, \text{Cr}, \text{Co}, \text{Ni}$) [162, 163]. The authors showed that the ferromagnetism is systematically affected by the adjacent magnetic layers via the interface, and they propose an expression of T_C on the basis of the molecular field image. The magnetotransport properties of superlattices such as $\text{La}_{0.6}\text{Pb}_{0.4}\text{MnO}_3/\text{La}_{0.85}\text{MnO}_3$ [164] or $\text{La}_{0.7}\text{MnO}_3/\text{Pb}_{0.65}\text{Ba}_{0.05}\text{Ca}_{0.3}\text{MnO}_3$ [165]

were also investigated. An enhancement of the magnetoresistance is obtained in these materials. Also grown were *c*-axis $\text{YBa}_2\text{Cu}_3\text{O}_7/\text{La}_{0.67}\text{Ba}_{0.33}\text{MnO}_3$ superlattices [166]. Above T_C , the CMR persists up to room temperature, and below T_C the superlattices exhibit a quasi-two-dimensional superconductivity of the $\text{YBa}_2\text{Cu}_3\text{O}_7$ layers coexisting with magnetism in the $\text{La}_{0.67}\text{Ba}_{0.33}\text{MnO}_3$ [166]. An increase in the thickness of the antiferromagnetic $\text{La}_{0.6}\text{Sr}_{0.4}\text{FeO}_3$ layer in between $\text{La}_{0.6}\text{Sr}_{0.4}\text{MnO}_3$ layers induces a strong magnetic frustration around the superlattice interfaces, leading to a reduction of the magnetic temperature transition and of the ferromagnetic volume [159].

Salvador et al. used the PLD technique to create A-site ordering in films of $(\text{LaMnO}_3)/(\text{SrMnO}_3)$ superlattices [167]. An increase of the superlattice period leads to a decrease in the T_C and in T_{IM} or to a low magnetization value.

4. APPLICATIONS

The intense efforts of the condensed matter community in the area of CMR thin films have led to a more precise understanding of the growth of thin film oxides even if the utilization of the materials into devices has not proven to be viable yet. The aim of this chapter is to give an overview of the manganite thin films and, for this reason, we will not go into the details of the realization of devices. A more comprehensive description of the devices made using CMR materials can be found elsewhere [12]. Examples of devices include magnetic field sensors, electric field devices [168], uncooled infrared bolometers [169], or low temperature hybrid HTSC-CMR devices [170]. Some of these are briefly discussed.

A magnetic tunnel junction is a structure composed of two ferromagnetic (FM) layers separated by an insulator barrier (I) and have attracted attention due to their properties of tunneling magnetoresistance (TMR). However, to obtain TMR (FM/I/FM junction) with 100% efficiency, it is necessary to have a perfect half-metal (i.e., a 100% spin polarization). Such a property was confirmed by spin resolved photoemission measurements in the case of the LSMO compound [171]. Junctions with LSMO show a TMR effect [172]. A large MR in 83% at a low field of 10 Oe at 4.2 K in a trilayer film of LSMO/STO/LSMO was observed [173]. Note that the top layer can also be Co [174], half-filled ferrimagnetic Fe_3O_4 [175], or $\text{La}_{0.7}\text{Sr}_{0.3}\text{MnO}_3$ [172]. Using Fe_3O_4 , a positive MR is observed which could be attributed to the inverse correlation between the orientations of the carrier spins in the two FM layers [175].

The electric field effect has been investigated, in which the top layer can be paramagnetic, such as STO [176], or ferroelectric, such as PZT ($\text{PbZr}_{0.2}\text{Ti}_{0.8}\text{O}_3$ [168]), and the bottom layer is a CMR material. But the changes are more profound in the case of PZT where an only 3% change in the channel resistance is measured over a period of 45 min at room temperature which makes this attractive for non-volatile ferroelectric field effect devices [168].

The large temperature coefficient of resistance [TCR, calculated as $(1/R)(dR/dT)$] just below the resistivity peak makes these CMR materials interesting for bolometric detectors [177]. However, for a given material the TCR

decreases as T_C or T_{IM} increases [169]. A TCR of 7%/K is obtained for LCMO at 250 K.

Hybrid structures consisting of HTSC-CMR have also been made for use in spin injection devices [178].

5. CONCLUSION

The structural, magnetic, and transport properties of manganite thin films have been presented in this chapter. As seen, the colossal magnetoresistive oxides display an exciting diversity of behavior in the form of thin films, and an extremely large amount of work has been carried out on thin films showing the great potential of their magnetic and transport properties. It has been shown that the structural and physical properties of these oxides are strongly dependent on the deposition procedure, chemical composition, and applied strain. For this reason, the direct comparison of data between a thin film and a bulk material (ceramic or single crystal) is difficult due to the stress in the thin film.

It has also been shown that devices are interesting and potentially useful for magnetic sensors. Prior to the fabrication of such devices, it will be necessary to characterize the materials more comprehensively, in particular from the view point of the structure and the microstructure. This is clearly evidenced by the fact that intrinsic phenomena such as the substrate-induced strain and the thickness dependence, which are directly related to the thin film process, strongly affect the magnetotransport properties. These results suggest that the local lattice distortions of the Mn–O bonds in the manganite thin films contribute to changes in the physical properties.

There are two main ideas that should be considered in the future based on the recent results. It is now recognized that the strains directly affect the lattice parameters. In addition, researchers have noted that there is a clear relation between the oxygen content (or indirectly the $\text{Mn}^{3+}/\text{Mn}^{4+}$ ratio) and the lattice parameters of the unit cell of the film. Thus, one should ask the following question: what is the relation between the oxygen content and strain? This triangular connection must be investigated precisely and explained in the future. The second main direction is related to the stress, because despite the large amount of work published on manganite thin films, there is still no direct proof of substrate-induced strains: researchers have only found indirect correlations at room temperature. More sophisticated mechanisms going beyond classical concepts (i.e., by looking at the evolution of the structure under cooling) and theoretical work, in particular by quantifying the stress for these oxide films, are required to understand the nature of this class of compounds.

GLOSSARY

Magnetoresistance Change of resistance of a compound when applying a magnetic field. The MR can be positive or negative. The term “colossal” was used for manganite compounds where the effect is several orders of magnitude.

Perovskite Structure of ABO_3 compounds that have been extensively used in the literature. This structure is found in high T_C superconductors, colossal magnetoresistance materials.

Pulsed laser deposition A technique used to grow thin film. Briefly, a laser beam is directed at a solid target. The interaction of the pulsed laser beam with the target produces a plume of material that is transported toward a heated substrate placed directly in the line of the plume.

Strain Results from the difference in lattice parameter between the film and the substrate. This mismatch is responsible for some differences in the properties/structure of a thin film. Films can be under tension (when the lattice parameter of the film is larger than the substrate) or under compression (when the lattice parameter of the film is smaller than the substrate).

ACKNOWLEDGMENTS

We acknowledge Dr. A. Ambrosini, Dr. Ph. Lecoeur, and Professor B. Raveau (Laboratoire CRISMAT, Université de Caen) for fruitful discussions and careful reading of this chapter. We also thank M. Morin for helping with the preparation of the manuscript.

REFERENCES

1. S. Jin, T. H. Tiefel, M. Mc Cormack, R. A. Fastnatch, R. Ramesh, and L. H. Chen, *Science* 264, 413 (1993).
2. S. Jin, M. Mc Cormack, T. H. Tiefel, and R. Ramesh, *J. Appl. Phys.* 76, 6929 (1994).
3. R. von Helmolt, J. Wecker, B. Holzapfel, L. Schultz, and K. Samwer, *Phys. Rev. Lett.* 71, 2331 (1993).
4. R. von Helmolt, J. Wecker, K. Samwer, L. Haupt, and K. Bärner, *J. Appl. Phys.* 76, 6925 (1994).
5. M. McCormack, S. Jin, T. H. Tiefel, R. M. Fleming, Julia M. Phillips, and R. Ramesh, *Appl. Phys. Lett.* 64, 3045 (1994).
6. "Colossal Magnetoresistance Oxides" (Y. Tokura, Ed.). Gordon and Breach, London, 1999.
7. "Colossal Magnetoresistance, Charge Ordering and Related Properties of Manganese Oxides" (C. N. R. Rao and B. Raveau, Eds.). World Scientific, Singapore, 1998.
8. G. M. Zhao, H. Keller, W. Prellier, and D. J. Kang, *Phys. Rev. B* 63, 172411 (2001).
9. A. J. Millis, B. I. Shraiman, and R. Mueller, *Phys. Rev. Lett.* 77, 175 (1996).
10. "Pulsed Laser Deposition of Thin Films" (D. B. Chrisey and G. K. Hubler, Eds.). Wiley Interscience, New York, 1994.
11. T. Venkatesan and R. P. Sharma, *Mater. Sci. Eng. B* 41, 30 (1996).
12. T. Venkatesan, M. Rajeswari, Z. Dong, S. B. Ogalea, and R. Ramesh, *Philos. Trans. A* 356, 1661 (1998).
13. W. Prellier, Ph. Lecoeur, and B. Mercey, *J. Phys.: Condens. Matter* 13, R915 (2001).
14. O. I. Lebedev, G. Van Tendeloo, S. Amelinckx, R. Leibold, and H. U. Habermeyer, *Phys. Rev. B* 58, 8065 (1998).
15. W. Prellier, M. Rajeswari, T. Venkatesan, and R. L. Greene, *Appl. Phys. Lett.* 75, 1446 (1999).
16. Z. Trajanovic, C. Kwon, M. C. Robson, K. C. Kim, M. Rajeswari, R. Ramesh, T. Venkatesan, S. E. Lofland, S. M. Baghat, and D. Fork, *Appl. Phys. Lett.* 69, 1005 (1996).
17. J. Foncuberta, M. Ribes, B. Martinez, V. Trtik, C. Ferrater, F. Sanchez, and M. Varela, *J. Appl. Phys.* 85, 4800 (1999).
18. C. L. Lu, Z. L. Wang, C. Kwon, and Q. X. Jia, *J. Appl. Phys.* 88, 4032 (2000).
19. T. Kanki, H. Tanaka, and T. Kawai, *Solid State Comm.* 114, 267 (2000).
20. A. Gupta, T. R. McGuire, P. R. Duncombe, M. Rupp, J. Z. Sun, W. J. Gallagher, and G. Xia, *Appl. Phys. Lett.* 67, 3494 (1995).
21. Y. Yamada, T. Kusumori, and H. Muto, *J. Appl. Phys.* 88, 6678 (2000).
22. Y. P. Lee, V. G. Prokhorov, J. Y. Rhee, K. W. Kim, G. G. Kaminsky, and V. S. Flis, *J. Phys.: Condens. Matter* 12, L133 (2000).
23. M. Izumi, Y. Konishi, T. Nishihara, S. Hayashi, L. M. Shinohara, M. Kawasaki, and Y. Tokura, *Appl. Phys. Lett.* 73, 2497 (1998).
24. J. Klein, C. Höfener, Y. Lu, J. Klein, M. S. R. Rao, B. H. Freitag, W. Mader, L. Alff, and R. Gross, *J. Magn. Magn. Mater.* 211, 9 (2000).
25. O. J. Gonzalez, G. Bistué, E. Catano, and F. J. Garcia, *J. Magn. Magn. Mater.* 222, 199 (2000).
26. B. Mercey, Ph. Lecoeur, M. Hervieu, J. Wolfman, Ch. Simon, H. Murray, and B. Raveau, *Chem. Mater.* 9, 1177 (1997).
27. P. H. Wagner, V. Metlushko, L. Trappeniens, A. Vantomme, J. Vanacken, G. Kido, V. V. Moshchalkov, and Y. Bruynseraede, *Phys. Rev. B* 55, 3699 (1997).
28. X. T. Zeng and H. K. Wong, *Appl. Phys. Lett.* 66, 3371 (1995).
29. L. M. Wang, H. H. Sung, B. T. Su, H. C. Yang, and H. E. Horng, *J. Appl. Phys.* 88, 4236 (2000).
30. E. Gommert, H. Cerva, A. Rucki, R. von Helmolt, J. Wecker, C. Kuhrt, and K. Samwer, *Appl. Phys. Lett.* 81, 5496 (1997).
31. K. I. Chahara, T. Ohno, M. Kasai, and Y. Kozono, *Appl. Phys. Lett.* 63, 1990 (1993).
32. C. C. Chen and A. de Lozanne, *Appl. Phys. Lett.* 71, 1424 (1997).
33. J. O'Donnel, M. Onellion, M. S. Rzechowski, J. N. Eckstein, and I. Bozovic, *Phys. Rev. B* 54, R6841 (1996).
34. R. Hiskes, S. A. DiCarolis, J. Fouquet, Z. Lu, R. S. Feigelson, R. K. Route, F. Leplingard, and C. M. Foster, *Mater. Res. Soc. Symp. Proc.* 335, 299 (1994).
35. C. Dubourdieu, M. Audier, J. P. Sénateur, and J. Pierre, *J. Appl. Phys.* 86, 6945 (1999).
36. G. F. Snyder, R. Hiskes, S. DiCarolis, M. R. Beasley, and T. H. Geballe, *Phys. Rev. B* 53, 14434 (1996).
37. W. L. Zhong, Y. G. Wang, D. S. Kong, P. L. Zhang, and B. D. Qu, *Thin Solid Films* 237, 160 (1994), R. Rella, A. Serra, P. Siciliano, L. Vasanellie, G. De, and A. Lucciulli, *Thin Solid Films* 304, 339 (1997).
38. A. R. Raju and C. N. R. Rao, *Appl. Phys. Lett.* 66, 896 (1996).
39. V. Ponnambalam, S. Parashar, A. R. Raju, and C. N. R. Rao, *Appl. Phys. Lett.* 74, 206 (1999).
40. S. Y. Bae and S. X. Wang, *Appl. Phys. Lett.* 69, 121 (1996).
41. W. Prellier, A. M. Haghiri-Gosnet, B. Mercey, Ph. Lecoeur, M. Hervieu, Ch. Simon, and B. Raveau, *Appl. Phys. Lett.* 77, 1023 (2000).
42. G. C. Xiong, Q. Li, H. L. Ju, S. N. Mao, L. Senapati, X. X. Xi, R. L. Greene, and T. Venkatesan, *Appl. Phys. Lett.* 66, 1427 (1995).
43. J. O'Donnel, J. N. Eckstein, and M. S. Rzechowski, *Appl. Phys. Lett.* 76, 218 (2000).
44. P. Lecoeur, A. Gupta, P. R. Duncombe, G. Q. Gong, and G. Xiao, *J. Appl. Phys.* 80, 513 (1996).
45. B. Mercey, J. Wolfman, W. Prellier, M. Hervieu, Ch. Simon, M. Hervieu, and B. Raveau, *Chem. Mater.* 12, 2858 (2000).
46. M. Rajeswari, R. Shreekala, A. Goyal, S. E. Lofland, S. M. Baghat, K. Ghosh, R. P. Sharma, R. L. Grenne, R. Ramesh, T. Venkatesan, and T. Boettcher, *Appl. Phys. Lett.* 73, 2672 (1998).
47. G. C. Xiong, Q. Li, H. L. Ju, S. M. Bhagat, S. E. Lofland, R. L. Greene, and T. Venkatesan, *Appl. Phys. Lett.* 67, 3031 (1995).
48. J. Y. Gu, K. H. Kim, T. W. Noh, and K. S. Suh, *J. Appl. Phys.* 78, 6151 (1995).
49. B. C. Nam, W. S. Kim, H. S. Choi, J. C. Kim, N. H. Hur, I. S. Kim, and Y. K. Park, *J. Phys. D.* 34, 1 (2001).
50. S. Pignard, H. Vincent, J. P. Sénateur, J. Pierre, and A. Abrutis, *J. Appl. Phys.* 82, 4445 (1997).
51. H. L. Ju, C. Kwon, Qi Li, R. L. Greene, and T. Venkatesan, *Appl. Phys. Lett.* 65, 2108 (1994).

52. R. Shreekala, M. Rajeswari, R. C. Srivastava, K. Ghosh, A. Goyal, V. V. Srinivasu, S. E. Lofland, S. M. Bhagat, M. Downes, R. P. Sharma, S. B. Ogale, R. L. Greene, R. Ramesh, T. Venkatesan, R. A. Rao, and C. B. Eom, *Appl. Phys. Lett.* 74, 1886 (1999).
53. H. S. Choi, W. S. Kim, B. C. Nam, and N. H. Hur, *Appl. Phys. Lett.* 78, 353 (2001).
54. R. Shreekala, M. Rajeswari, S. P. Pai, S. E. Lofland, V. Smolyaninova, K. Ghosh, S. B. Ogale, S. M. Bhagat, M. J. Downes, R. L. Greene, R. Ramesh, and T. Venkatesan, *Appl. Phys. Lett.* 74, 2857 (1999).
55. J. Li, Q. Huang, Z. W. Li, L. P. You, S. Y. Xu, and C. K. Ong, *J. Phys.: Condens. Matter* 13, 3419 (2001).
56. H. Asano, J. Hayakawa, and M. Matsui, *Appl. Phys. Lett.* 70, 2303 (1997).
57. H. Asano, J. Hayakawa, and M. Matsui, *Jpn. J. Appl. Phys.* 36, L104 (1997).
58. Y. Konishi, T. Kimura, M. Izumi, M. Kawasaki, and Y. Tokura, *Appl. Phys. Lett.* 73, 3004 (1998).
59. H. Asano, J. Hayakawa, and M. Matsui, *Phys. Rev. B* 56, 5395 (1997).
60. H. Tanaka and T. Kawai, *Appl. Phys. Lett.* 76, 3618 (2000).
61. H. Asano, J. Hayakawa, and M. Matsui, *Appl. Phys. Lett.* 71, 844 (1997).
62. K. I. Kobayashi, T. Kimura, H. Sawada, K. Terakura, and Y. Tokura, *Nature* 395, 677 (1998).
63. H. Asano, S. B. Ogale, J. Garison, A. Orozco, Y. H. Li, E. Li, V. Smolyaninova, C. Galley, M. Downes, M. Rajeswari, R. Ramesh, and T. Venkatesan, *Appl. Phys. Lett.* 74, 3696 (1999).
64. W. Westerburg, D. Reisinger, and G. Jakob, *Phys. Rev. B* 62, R767 (2000).
65. T. Manako, M. Izumi, Y. Konishi, K. I. Kobayashi, M. Kawasaki, and Y. Tokura, *Appl. Phys. Lett.* 74, 2215 (1999).
66. W. Westerburg, F. Martin, and G. Jakob, *J. Appl. Phys.* 87, 5040 (2000).
67. H. Q. Yin, J. S. Zhou, J. P. Zhou, R. Dass, J. T. McDevitt, and J. B. Goodenough, *Appl. Phys. Lett.* 75, 2812 (1999).
68. H. Q. Yin, J. S. Zhou, J. P. Zhou, R. Dass, J. T. McDevitt, and J. B. Goodenough, *J. Appl. Phys.* 87, 6761 (2000).
69. W. Prellier and B. Raveau, *J. Phys.: Condens. Matter* 13, 2749 (2001).
70. G. Van Tendeloo, O. I. Lebedev, and S. Amelinckx, *J. Magn. Magn. Mater.* 211, 73 (2000).
71. H. W. Zandbergen, S. Freisem, T. Nojima, and J. Aarts, *Phys. Rev. B* 60, 10259 (1999).
72. J. Aarts, S. Freisem, R. Hendriks, and H. W. Zandbergen, *Appl. Phys. Lett.* 72, 2975 (1998).
73. Y. H. Li, L. Salamanca-Riba, Y. Zhao, S. B. Ogale, R. Ramesh, and T. Venkatesan, *J. Mater. Res.* 15, 1524 (2000).
74. V. S. Teodorescu, L. C. Nistor, M. Valeanu, C. Ghica, C. Sandu, I. N. Mihailescu, C. Ristoscu, J. P. Deville, and J. Werckmann, *J. Magn. Magn. Mater.* 211, 54 (2000).
75. B. Wiedenhorst, C. Höfener, Y. Lu, J. Klein, L. Aff, R. Gross, B. H. Freita, and W. Mader, *Appl. Phys. Lett.* 74, 3636 (1999).
76. C. Vieu, F. Carcenac, A. Pepin, Y. Chen, M. Mejias, A. Lebib, L. Manin-Ferlazzo, L. Couraud, and H. Launois, *Appl. Surf. Sci.* 164, 111 (2000).
77. G. Simon, A. M. Haghiri-Gosnet, J. Bourneix, D. Decanini, Y. Chen, F. Rousseaux, and H. Launois, *J. Vac. Sci. Technol. B* 15, 2489 (1997).
78. W. Chen and H. Ahmed, *Appl. Phys. Lett.* 62, 1499 (1993).
79. S. Y. Chou, P. R. Krauss, and P. J. Renstrom, *Appl. Phys. Lett.* 67, 3114 (1995).
80. A. Lebib, Y. Chen, E. Cambril, P. Youinou, V. Studer, M. Natali, A. Pépin, H. M. Janssen, and R. P. Sijbesma, *Microcircuit Eng.* 61, 371 (2002).
81. J. Wolfman, A. M. Haghiri-Gosnet, B. Raveau, C. Vieu, E. Cambril, A. Cornette, and H. Launois, *J. Appl. Phys.* 89, 6955 (2001).
82. J. J. Wang, J. R. Childress, S. J. Pearton, F. Shari, K. H. Dahmen, E. S. Gillman, F. J. Cadieu, R. Rani, X. R. Qian, and L. Chen, *J. Electrochem. Soc.* 145, 2512 (1998).
83. M. Naoe, K. Hamaya, N. Fujiwara, T. Taniyama, Y. Kitamoto, and Y. Yamazaki, *J. Magn. Magn. Mater.* 235, 223 (2001).
84. J. Choi, J. Zhang, S. H. Liou, P. A. Dowben, and E. W. Plummer, *Phys. Rev. B* 59, 13453 (1999).
85. H. B. Peng, B. R. Zhao, Z. Xie, Y. Lin, B. Y. Zhu, Z. Hao, H. J. Tao, B. Xu, C. Y. Wang, H. Chen, and F. Wu, *Phys. Rev. Lett.* 82, 362 (1999).
86. H. Dulli, E. W. Plummer, P. A. Dowben, J. Choi, and S. H. Liou, *Appl. Phys. Lett.* 77, 570 (2000).
87. C. Kwon, M. C. Robson, K.-C. Kim, J. Y. Gu, S. E. Lofland, S. M. Bhagat, Z. Trajanovic, M. Rajeswari, T. Venkatesan, A. R. Kratz, R. D. Gomez, and R. Ramesh, *J. Magn. Magn. Mater.* 172, 229 (1997).
88. A. Gupta and J. Z. Sun, *J. Magn. Magn. Mater.* 200, 24 (1999).
89. C. Sritiwarawong and M. Ziese, *Appl. Phys. Lett.* 73, 1140 (1998).
90. A. Gupta, G. Q. Gong, G. Xiao, P. R. Duncombe, P. Lecoeur, P. Trouilloud, Y. Y. Wang, V. P. David, and J.-Z. Sun, *Phys. Rev. B* 54, R15629 (1996).
91. X. W. Li, A. Gupta, G. Xiao, and G. Q. Gong, *Appl. Phys. Lett.* 71, 1124 (1997).
92. J. Y. Gu, S. B. Ogale, M. Rajeswari, T. Venkatesan, R. Ramesh, V. Radmilovic, U. Dahmen, G. Thomas, and T. W. Noh, *Appl. Phys. Lett.* 72, 1113 (1998).
93. B. S. Teo, N. D. Mathur, S. P. Isaac, J. E. Evetts, and M. Blamire, *J. Appl. Phys.* 83, 7157 (1998).
94. N. D. Mathur, G. Burnel, S. P. Isaac, T. J. Jackson, B. S. Teo, J. L. McManus-Driscoll, L. F. Cohen, J. E. Evetts, and M. G. Blamire, *Nature* 387, 266 (1999).
95. S. P. Isaac, N. D. Mathur, J. E. Evetts, and M. C. Blamire, *Appl. Phys. Lett.* 72, 2038 (1998).
96. K. Steenbeck, T. Eick, K. Kirsch, K. O'Donnell, and E. Steinbeiss, *Appl. Phys. Lett.* 71, 968 (1997).
97. K. Steenbeck, T. Eick, K. Kirsch, H. G. Schmidt, and E. Steinbeiss, *Appl. Phys. Lett.* 73, 2506 (1998).
98. N. K. Todd, N. D. Mathur, S. P. Isaac, J. E. Evetts, and M. G. Blamire, *J. Appl. Phys.* 85, 7263 (1999).
99. N. H. Hong, J. Sakai, and S. Imai, *J. Appl. Phys.* 87, 5600 (2000).
100. B. Raquet, A. Anane, S. Wirth, P. Xiong, and S. von Molnar, *Phys. Rev. Lett.* 84, 4485 (2000).
101. M. Fäth, S. Freisem, A. A. Menovsky, Y. Tomioka, J. Aarts, and J. A. Mydosh, *Science* 285, 1540 (1999).
102. H. S. Wang, E. Wertz, Y. F. Hu, Q. Li, and D. G. Schlom, *J. Appl. Phys.* 87, 7409 (2000).
103. S. Jin, T. H. Tiefel, M. McCormack, H. M. O'Bryan, L. H. Chen, R. Ramesh, and D. Schuring, *Appl. Phys. Lett.* 67, 557 (1995).
104. A. J. Millis, T. Darling, and A. Migliori, *J. Appl. Phys.* 83, 1588 (1998).
105. N. Okawa, H. Tanaka, R. Akiyama, T. Matsumoto, and T. Kawai, *Solid State Comm.* 114, 601 (2000).
106. R. Desfeux, S. Bailleul, A. Da Costa, W. Prellier, and A. M. Haghiri-Gosnet, *Appl. Phys. Lett.* 78, 3681 (2001).
107. Y. Konishi, Z. Fang, M. Izumi, T. Manako, M. Kasai, H. Kuwahara, M. Kawasaki, K. Terakura, and Y. Tokura, *J. Phys. Soc. Jpn.* 68, 3790 (1999).
108. F. Tsui, M. C. Smoak, T. K. Nath, and C. B. Eom, *Appl. Phys. Lett.* 76, 2421 (2000).
109. K. H. Ahn and A. J. Millis, *Phys. Rev. B* 64, 115103 (2001).
110. E. Ohshima, Y. Saya, M. Nantoh, and M. Kawai, *Solid State Comm.* 116, 73 (2000).
111. J. Z. Sun, D. W. Abraham, R. A. Rao, and C. B. Eom, *Appl. Phys. Lett.* 74, 3017 (1999).
112. A. Miniotos, A. Vailionis, E. B. Svedberg, and U. O. Karlsson, *J. Appl. Phys.* 89, 2134 (2001).

113. E. S. Gillman, M. Li, and K. H. Dahmen, *J. Appl. Phys.* 84, 6217 (1998).
114. R. Shreekala, M. Rajeswari, K. Ghosh, A. Goyal, J. Y. Gu, C. Kwon, Z. Trajanovic, T. Boettcher, R. L. Greene, R. Ramesh, and T. Venkatesan, *Appl. Phys. Lett.* 71, 282 (1997).
115. F. Tsui, M. C. Smoak, T. K. Nath, and C. B. Eom, *Appl. Phys. Lett.* 76, 2421 (2000).
116. W. Zhang, X. Wang, M. Elliott, and I. W. Boyd, *Phys. Rev. B* 58, 14143 (1998).
117. J. Y. Gu, C. Kwon, M. C. Robson, Z. Trajanovic, K. Ghosh, R. P. Sharma, R. Shreekala, M. Rajeswari, T. Venkatesan, R. Ramesh, and T. W. Noh, *Appl. Phys. Lett.* 70, 1763 (1997).
118. D. Kumar, S. Chattopadhyay, Walter M. Gilmore, C. B. Lee, J. Sankar, A. Kvit, A. K. Sharma, J. Narayan, S. V. Pietambaram, and R. K. Singh, *Appl. Phys. Lett.* 78, 1098 (2001).
119. P. A. Salvador, T. D. Doan, B. Mercey, and B. Raveau, *Chem. Mater.* 10, 2592 (1998).
120. A. M. Haghiri-Gosnet, M. Hervieu, Ch. Simon, B. Mercey, and B. Raveau, *J. Appl. Phys.* 88, 3545 (2000).
121. W. Prellier, Ch. Simon, A. M. Haghiri-Gosnet, B. Mercey, and B. Raveau, *Phys. Rev. B* 62, R16337 (2000).
122. K. M. Krishnan, A. R. Modak, C. A. Lucas, R. Michel, and H. B. Cherry, *J. Appl. Phys.* 79, 5169 (1996).
123. T. Y. Koo, S. H. Park, K. B. Lee, and Y. H. Jeong, *Appl. Phys. Lett.* 71, 977 (1997).
124. C. C. Chen and A. de Lozanne, *Appl. Phys. Lett.* 73, 3950 (1998).
125. F. Martin, G. Jakob, W. Westerburg, and H. Adrian, *J. Magn. Magn. Mater.* 196–197, 509 (1999).
126. A. M. Haghiri-Gosnet, J. Wolfman, B. Mercey, Ch. Simon, P. Lecoeur, M. Korzenski, M. Hervieu, R. Desfeux, and G. Baldinozzi, *J. Appl. Phys.* 88, 4257 (2000).
127. P. Lecoeur, P. L. Trouilloud, G. Xiao, A. Gupta, G. Q. Gong, and X. W. Li, *J. Appl. Phys.* 82, 3934 (1997).
128. N. D. Mathur, M. H. Jo, J. E. Evetts, and M. G. Blamire, *J. Appl. Phys.* 89, 3388 (2001).
129. B. Vengalis, A. Maneikis, F. Anisimovas, R. Butkute, L. Dapkus, and A. Kindurys, *J. Magn. Magn. Mater.* 211, 35 (2000).
130. S. E. Lofland, S. M. Baghat, M. Rajeswari, T. Venkatesan, R. Ramesh, R. D. Gomez, C. Kwon, and A. R. Kratz, *IEEE Trans. Magn.* 33, 3964 (1997).
131. H. S. Wang, E. Wertz, Y. F. Hu, and Q. Li, *J. Appl. Phys.* 87, 6749 (2000).
132. H. S. Wang, Q. Li, K. Liu, and C. L. Chien, *Appl. Phys. Lett.* 74, 2212 (1999).
133. M. Ziese and S. P. Sena, *J. Phys.: Condens. Matter* 10, 2727 (1998).
134. Y. Suzuki and H. Y. Hwang, *J. Appl. Phys.* 85, 4797 (1998).
135. L. M. Berndt, V. Balbarin, and Y. Suzuki, *Appl. Phys. Lett.* 77, 2903 (2000).
136. For a review see: C. N. R. Rao, A. Arulraj, A. K. Cheetham, and B. Raveau, *J. Phys.: Condens. Matter* 12, R83 (2000).
137. B. Mercey, M. Hervieu, W. Prellier, J. Wolfman, Ch. Simon, and B. Raveau, *Appl. Phys. Lett.* 78, 3857 (2001).
138. A. Biswas, M. Rajeswari, R. C. Srivastava, T. Venkatesan, R. L. Greene, Q. Lu, A. L. de Lozanne, and A. J. Millis, *Phys. Rev. B* 63, 184424 (2001).
139. A. Biswas, M. Rajeswari, R. C. Srivastava, Y. H. Li, T. Venkatesan, and R. L. Greene, *Phys. Rev. B* 61, 9665 (2000).
140. R. A. Rao, D. Lavric, T. K. Nath, C. B. Eom, L. Wu, and F. Tsui, *Appl. Phys. Lett.* 73, 3294 (1998).
141. A. Barman and G. Koren, *Appl. Phys. Lett.* 77, 1674 (2000).
142. Y. Suzuki, Y. Wu, J. Yu, U. Ruediger, A. D. Kent, T. K. Nath, and C. B. Eom, *J. Appl. Phys.* 87, 6746 (2000).
143. W. Prellier, A. Biswas, M. Rajeswari, T. Venkatesan, and R. L. Greene, *Appl. Phys. Lett.* 75, 397 (1999).
144. O. Yu. Gorbenco, I. E. Graboy, A. R. Kaul, and H. W. Zandbergen, *J. Magn. Magn. Mater.* 211, 97 (2000).
145. T. Walter, K. Dörr, K. H. Müller, D. Eckert, K. Nenkov, M. Hecker, M. Lehmann, and L. Schultz, *J. Magn. Magn. Mater.* 222, 175 (2000).
146. L. B. Steren, M. Sirena, and J. Guimpel, *J. Appl. Phys.* 87, 6755 (2000).
147. G. M. Gross, R. B. Praus, B. Leibold, and H. U. Habermeier, *Appl. Surf. Sci.* 138, 117 (1999).
148. M. Sirena, L. Steren, and J. Guimpel, *Thin Solid Films* 373, 102 (2000).
149. P. Padhan, N. K. Pandey, S. Srivastava, R. K. Rakshit, V. N. Kurkarni, and R. C. Budhani, *Solid State Comm.* 117, 27 (2000).
150. F. S. Razavi, G. Gross, H. U. Habermeier, O. Lebedev, S. Amelinckx, G. Van Tendeloo, and A. Vigliante, *Appl. Phys. Lett.* 76, 155 (2000).
151. R. P. Borges, W. Guichard, J. G. Lunney, J. M. D. Coey, and F. Ott, *J. Appl. Phys.* 89, 3868 (2001).
152. B. Mercey, P. A. Salvador, W. Prellier, T. D. Doan, J. Wolfman, J. F. Hamet, M. Hervieu, and B. Raveau, *J. Mater. Chem.* 9, 233 (1999).
153. K. Ueda, Y. Muraoka, H. Tabata, and T. Kawai, *Appl. Phys. Lett.* 78, 512 (2001).
154. A. A. Bosak, O. Yu Gorbenco, A. R. Kaul, I. E. Graboy, C. Duboudieu, J. P. Senateur, and H. W. Zandbergen, *J. Magn. Magn. Mater.* 211, 61 (2000).
155. H. Tabata and T. Kawai, *IEICE Trans. Electron.* 80, 918 (1997).
156. C. Kwon, K. C. Kim, M. C. Robson, J. Y. Gu, M. Rajeswari, T. Venkatesan, and R. Ramesh, *J. Appl. Phys.* 81, 4950 (1997).
157. Y. Lu, J. Klein, C. Höfener, B. Wiedenhorst, J. B. Philipp, F. Herbstritt, A. Marx, L. Alff, and R. Gross, *Phys. Rev. B* 62, 15806 (2000).
158. M. H. Jo, N. D. Mathur, Jan E. Evetts, Mark G. Blamire, M. Bibes, and J. Fontcuberta, *Appl. Phys. Lett.* 75, 3689 (1999).
159. M. Izumi, T. Manako, Y. Konishi, M. Kawasaki, and Y. Tokura, *Phys. Rev. B* 61, 12187 (2000).
160. Y. Luo, A. Käufler, and K. Samwer, *Appl. Phys. Lett.* 77, 1508 (2000).
161. K. R. Nikolaev, A. Bhattacharya, P. A. Kraus, V. A. Vas'ko, W. K. Cooley, and A. M. Goldman, *Appl. Phys. Lett.* 75, 118 (1999).
162. H. Tanaka, N. Okawa, and T. Kawai, *Solid State Comm.* 110, 191 (1999).
163. H. Tanaka and T. Kawai, *J. Appl. Phys.* 88, 1559 (2000).
164. M. Sahana, M. S. Hedge, V. Prasad, and S. V. Subramanyam, *J. Appl. Phys.* 85, 1058 (1999).
165. S. Pietambaram, D. Kumar, R. K. Singh, and C. B. Lee, *Appl. Phys. Lett.* 78, 243 (2001).
166. G. Jakob, V. V. Moshchalkov, and Y. Bruynseraede, *Appl. Phys. Lett.* 66, 2564 (1995).
167. P. A. Salvador, A. M. Haghiri-Gosnet, B. Mercey, M. Hervieu, and B. Raveau, *Appl. Phys. Lett.* 75, 2638 (1999).
168. S. Mathews, R. Ramesh, T. Venkatesan, and J. Benedetto, *Science* 276, 238 (1997).
169. A. Goyal, M. Rajeswari, S. E. Lofland, S. M. Baghat, R. Shreekala, T. Boettcher, C. Kwon, R. Ramesh, and T. Venkatesan, *Appl. Phys. Lett.* 71, 2535 (1997).
170. A. M. Goldman, V. Vas'ko, P. Krauss, K. Nikolaev, and V. A. Larkin, *J. Magn. Magn. Mater.* 200, 69 (1999).
171. J. H. Park, E. Vesoovo, H. J. Kim, C. Kwon, R. Ramesh, and T. Venkatesan, *Nature* 392, 794 (1998).
172. J. Z. Sun, W. J. Gallagher, P. R. Duncombe, L. Krusin-Elbaum, R. A. Altman, A. Gupta, Yu Lu, G. Q. Gong, and G. Xiao, *Appl. Phys. Lett.* 69, 3266 (1996).
173. X. W. Li, Y. Lu, G. Q. Gong, G. Xiao, A. Gupta, P. Lecoeur, J. Sun, Y. Y. Wang, and V. P. Dravid, *J. Appl. Phys.* 81, 5509 (1997).

174. J. M. De Teresa, A. Barthélémy, A. Fert, J. P. Contour, R. Lyonnet, F. Montaigne, P. Seneor, and A. Vaurès, *Phys. Rev. Lett.* 82, 4288 (1999).
175. K. Ghosh, S. B. Ogale, S. P. Pai, M. Robson, E. Li, I. Jin, Z. Dong, R. L. Greene, R. Ramesh, and T. Venkatesan, *Appl. Phys. Lett.* 73, 689 (1998).
176. S. B. Ogale, V. Talyansky, C. Chen, R. Ramesh, R. L. Greene, and T. Venkatesan, *Phys. Rev. Lett.* 77, 1159 (1996).
177. M. Rajeswari, C. Chen, A. Goyal, C. Kwon, M. C. Robson, R. Ramesh, T. Venkatesan, and S. Lakeou, *Appl. Phys. Lett.* 68, 3555 (1996).
178. V. A. Vas'ko, V. A. Larkin, P. A. Kraus, K. R. Nikolaev, D. E. Grupp, C. A. Nordman, and A. M. Goldman, *Phys. Rev. Lett.* 78, 1134 (1997); V. A. Vas'ko, K. R. Nikolaev, V. A. Larkin, P. A. Kraus, and A. M. Goldman, *Appl. Phys. Lett.* 73, 844 (1998).

Structural Characterization of Single-Walled Carbon Nanotubes

Daniel E. Resasco, Jose E. Herrera

University of Oklahoma, Norman, Oklahoma, USA

CONTENTS

1. Introduction
2. Structural Characterization Techniques
 - Glossary
 - References

1. INTRODUCTION

For centuries, diamond and graphite have been the only known crystalline forms of carbon. However, in recent years, new carbon allotropes have been revealed. Kroto et al. [1] discovered fullerenes in 1985 while Iijima discovered multi-walled carbon nanotubes in 1991 [2] and single-walled carbon nanotubes in 1993 [3]. Single-walled nanotubes were independently and almost simultaneously observed by Bethune et al. [4]. The carbon bonds in fullerenes and nanotubes are more similar to those in graphite than to those in diamond. Diamond has a coordination number of four with sp^3 hybridization while the same as graphite involves three-coordinate carbons, in which three electrons are in sp^2 hybridization and one is delocalized. Fullerenes and nanotubes also have carbon bonds with sp^2 hybridization as graphite, but while the graphite structure is made up of flat planar honeycomb, the structures of fullerenes and nanotubes involve a high degree of curvature. Fullerenes such as C_{60} and C_{70} exhibit a closed-cage carbon structure that is spherical or nearly spherical.

Carbon nanotubes can be formally described as a graphene honeycomb rolled into a single-walled cylinder or into several concentric graphene cylinders. The former are termed single-walled nanotubes (SWNTs) and the latter multiwalled nanotubes (MWNTs). The diameter of a typical SWNT is in the order of a nanometer but its length can be up to several micrometers, or more. Each nanotube can be considered as a single molecule made up of a honeycomb network of covalently bonded carbon atoms. A schematic representation of a SWNT structure is shown in Figure 1. Each SWNT is fully characterized by two integers (n, m).

These integers specify the number of unit vectors \bar{a}_1 and \bar{a}_2 in the graphene structure that constitute the roll-up vector (or chiral vector) $V = n\bar{a}_1 + m\bar{a}_2$. The graphene structure is rolled up such that the chiral vector V forms the nanotube circumference. Therefore, the (n, m) indices determine the nanotube diameter, according to the equation

$$d = (n^2 + m^2 + nm)^{1/2} 0.0783 \text{ nm} \quad (1)$$

At the same time, these indices determine the orientation of the carbon hexagons with respect to the nanotube axis. This orientation is the so-called “chirality” of the nanotube. Nanotubes with indices ($m, 0$) are termed “zigzag” due to the shape of the atomic configuration along the perimeter of such a nanotube. When $m = n$, the resulting nanotubes are called “armchair” because the position of the C atoms arrange in an “armchair” pattern.

Single-walled carbon nanotubes have unique electronic and mechanical properties combined with a very light weight. Depending on their n, m values, which determine their chirality and diameter, nanotubes can be either electrically metallic or semiconductor. At the same time, they have shown evidence for high stiffness (Young modulus), high resilience, and the ability to reversibly buckle and collapse. Therefore, they are promising candidates as components of strong fibers with light weight and high electrical conductivity. At the same time, other characteristics of SWNTs have generated intense attention. For example, due to their high aspect ratio (i.e., high length/diameter ratio and their chemical and mechanical stability they show promise as excellent electron field emitters for commercial applications as flat panel displays and other cold cathode emitters. Nanotubes can be functionalized with a wide variety of chemical groups, which greatly broadens the scope of their applications in diverse fields that range from conductive coatings to fuel cells or from nanosensors to biotechnology.

Carbon nanotubes can be produced by a variety of methods. Iijima first produced nanotubes by arc discharge [2, 3]. The system differed only slightly from that developed earlier by Kratschmer et al. for the production of fullerenes [5].

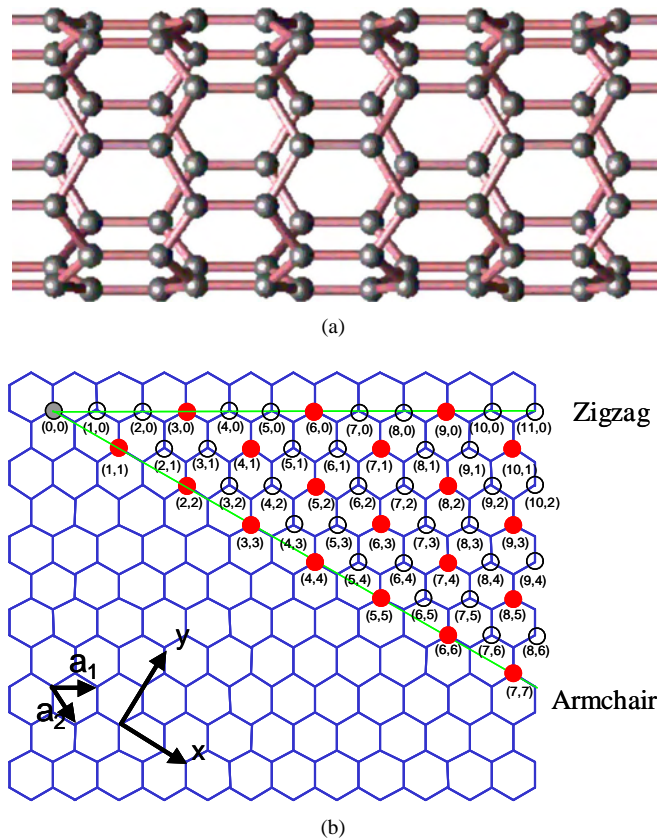


Figure 1. (a) Middle section of a SWNT (<http://www.phys.psu.edu/~crespi/research/carbon.id/public/>). (b) Identification of carbon nanotubes in terms of the indices (n, m) (<http://www.photon.t.uokyo.ac.jp/~maruyana/kataura/chirality.html>). Consider a flat graphene sheet. Vectors n and m placed at the chosen origin $(0, 0)$ determine the specific nanotube. For example, the nanotube $(7, 7)$ can be obtained by drawing a line between the origin $(0, 0)$ and the point indicated as $(7, 7)$ and then cutting the sheet along two lines perpendicular to this line. The cut sheet can then be folded into the $(7, 7)$ nanotube.

A similar system had been employed by Bacon more than 30 years earlier for the production of graphite whiskers [6]. In the system used by Ijima [2], the graphite electrodes were kept separated by a small gap, rather than being in contact as in Kratschmer's method. It was observed that about half of the carbon evaporated from the anode deposited as nanotubes on the negative electrode while the rest condensed in the form of soot. One of the most important observations was that SWNTs were only obtained when metal particles were present in the anode. The metals used in the earlier experiments were cobalt and nickel, packed inside bored graphite rods. Later, other metals and mixtures with lanthanides were found to catalyze the formation of SWNTs as well [7]. In a typical arc discharge apparatus [8], the arc is generated between two graphite rods, which are mounted in a stainless steel vacuum chamber equipped with a vacuum line and a gas inlet. One of the graphite electrodes (cathode) is fixed and it is connected to a negative potential. The other electrode (anode) is moved from outside the chamber through a linear motion feedthrough to adjust the gap between the electrodes. A viewport is mounted on the chamber to allow for a direct observation of the arc discharge.

In a standard operation, a given background pressure is stabilized within the cell by adjusting the incoming flow of an inert gas such as helium and the pumping speed. It has been found that with a continuous flow of He better results are obtained than with a static He pressure. A stabilized voltage of about 20 V is applied while the electrodes are far apart. As the anode is moved in, a gap space is reached (1–3 mm) at which arcing occurs. Depending on the He pressure, the rod diameter, and the gap between the electrodes, the electric current can vary between 40 and 250 A. During the discharge, a plasma is formed generating temperatures of the order of 3700 °C. The temperature is particularly high on the anode surface and this electrode is consumed by vaporization. To keep the proper interelectrode gap constant during operation, the position of the anode must be adjusted manually [9] or by an automated system [10]. The synthesis process lasts only a few minutes [11]. After the synthesis, several types of carbon deposits are obtained: (a) a rubbery soot that condenses on the chamber walls; (b) a weblike structure between the cathode and the chamber walls; (c) a cylindrical deposit on the cathode face; (d) a small collar around the cathode deposits, which contains the highest concentration of SWNTs.

Studies have shown that a number of experimental parameters have important effects on SWNT yield and selectivity. For example, increasing the diameters of both electrodes results in yield and selectivity losses, but decreasing the anode diameter, while keeping the cathode diameter and current density constant, results in an increase in yield [12]. Another critical parameter that greatly affects the SWNT yield is the pressure of the background gas, usually He. While some authors indicate that the yield increases with He pressure [12], other authors have found that beyond a certain pressure, further increase in pressure does not result in an increase in yield [8] and it may even result in yield losses [13]. Not only the yield of SWNTs but also their diameter distribution is affected by the background gas pressure. Saito et al. [14] observed that the distribution of SWNT diameters shifted systematically to small values as the helium pressure decreased. The most frequently occurring diameters were centered at 1.4 nm for the production conducted at 1520 Torr, and it shifted to 0.95 nm for the production at 50 Torr. Among the various experimental parameters, the choice of catalytic additives is of paramount importance. In the first place, the characteristic feature that is common to all SWNT synthesis methods is the participation of a catalyst. So far, no SWNT has been synthesized without the participation of a catalyst.

Smalley et al. showed that single-wall carbon nanotubes SWNTs can also be produced in high yield by laser vaporization of a graphite rod doped with Co and Ni [15]. It was found later [16] that the structure of the carbon species produced in the laser ablation method strongly depends on the background argon pressure that is used. When the pressure is lower than 100 Torr no SWNTs are produced. They are only formed at higher pressures. Apparently, the Ar pressure plays an important role in the heat transfer phenomena and assists in the metal evaporation. Investigation of the carbon/metal target after the ablation showed that at low pressures, the metal evaporation was inhibited. The texture of the target was also found to have an effect on the quantity of

SWNT produced in the laser method. For example, twice as many SWNTs were produced when carbon targets containing Ni and Co nitrates were used as when Ni–Co metals or oxides were employed. This effect was ascribed to the porous structure that results when the Ni or Co nitrates decompose inside the carbon target. At the same time, a better dispersion and smaller particle size of the metals are obtained when using nitrates than when using metals or oxides [17]. Eklund et al. have recently developed a modification of the pulsed laser vaporization technique that, according to the authors, should result in large-scale production of high-quality SWNTs [18]. In this method, ultrafast ablation was achieved by using a high power free-electron laser. The modified setup includes a T-shaped quartz growth chamber placed inside a furnace to keep the chamber at 1000 °C. The laser radiation enters from a sidearm that protrudes out the furnace near the center of the hot zone and strikes the carbon target, which is mounted on a rotating/translating rod. A jet of preheated argon deflects the ablation plume away from the incident laser beam, continuously sweeping the target region. The SWNT soot is then collected from a water-cooled copper coldfinger at the end of the quartz nanotube. A special feature of this method was the use of the free-electron laser operated at a peak laser flux that is about 1000 times greater than the flux used in typical Neodymium(3+)-yttrium-aluminum-garnet laser (Nd:YAG) based systems, but each FEL pulse is only 1/200,000 as long as the typical 10 ns Nd:YAG pulse.

The catalytic decomposition of carbon-containing compounds on appropriate metal catalysts is another method of producing SWNTs. This method, sometimes referred to as CVD (chemical vapor deposition), has a good potential for the production of large quantities of SWNTs at low cost. They also provide the possibility of producing SWNTs on a surface or inside a solid. This method is similar to those used for several decades in the synthesis of carbon filaments. It has been repeatedly demonstrated [19–21] that the diameter of the carbon nanotube is determined by the size of the metal cluster responsible for its growth. It is therefore important to tailor the precursor so that the catalyst particles retain a small size during the SWNT growth. In most studies, even when the metal particles may have had nanometric dimensions before the growth started, they quickly sinter at the high temperatures needed for SWNT synthesis. Laurent et al. [22–27] and Resasco et al. [28–32] have independently designed catalysts which have the common characteristic of being produced only under reaction conditions. Solid oxide solutions such as $Mg_{1-x}Co_xO$ [22] or silica supported Co-molybdates have been found to be effective catalysts when they are reduced *in-situ* by the same carbon-containing reactant that produces the SWNT. Only under specific conditions and using the proper catalyst formulation can SWNTs with high selectivity be produced. Successful examples of SWNT growth by the CVD method are the disproportionation of CO at 850 °C on Co:Mo/SiO₂ (1:2 molar ratio) catalysts [29] and CH₄ decomposition at 1000 °C on a Mg_{0.9}Co_{0.1}O solid solution catalyst [33]. In other cases, the CVD method has resulted in low selective growth of SWNT, with simultaneous formation of other carbon species such as graphite nanofibers and double walled or multiwalled nanotubes [34, 35].

An alternative to the CVD method of catalytic decomposition of carbon-containing molecules has been the so-called “floating catalyst” method. Sen et al. [36] prepared carbon nanotubes by decomposition of ferrocene, cobaltocene, and nickelocene under reductive conditions. In this case, the precursor provides both the carbon and the metal to catalyze the synthesis reaction. Similarly, in other methods benzene or hexane has been added to ferrocene improving the yield [37]. A variation of the floating catalyst method resulted in the commercial process known as HiPCO that produces 10 g/day of high-purity carbon single-walled nanotubes [38]. In this process, SWNTs are grown at high pressure (30–50 atm) and high temperature (900–1100 °C) under flowing CO. The catalyst is iron in the form of small clusters that are generated *in-situ* as continuously added iron pentacarbonyl decomposes in the reactor.

2. STRUCTURAL CHARACTERIZATION TECHNIQUES

A first step in a systematic approach toward improved SWNT production, study, and tailoring of their electronic and mechanical properties is a feedback of information coming from reliable characterization techniques. Several methods have been applied to obtain this information. The techniques comprise local probes such as transmission electronic microscopy (TEM), electron diffraction, scanning electron microscopy (SEM), and scanning tunneling microscopy, combined with tunneling spectroscopy and bulk-sensitive probes such as Raman scattering, optical absorption spectroscopy, and X-ray diffraction. In the subsequent sections some of these methods will be introduced and the kind of information that can be obtained with them will be discussed.

2.1. Electron Microscopy

Observing structures smaller than 1 μm is not possible with light because diffraction effects limit the resolution of optical spectroscopy. So, if information at considerable higher resolution is desired, electromagnetic radiation of shorter wavelengths should be used. Electron beams offer this possibility. Their development over the past 50 years has resulted in electron microscopes that routinely achieve magnification on the order of one million times and can reveal details with a resolution of up to about 0.1 nm.

When an electron beam of energy between 100 and 400 keV hits a sample, many measurable signals are generated. TEM uses the transmitted electrons to form the image while SEM uses the secondary electrons emitted from the sample. Depending on the sample thickness, a fraction of the electrons passes through it without suffering significant energy loss. Since the attenuation of the electrons depends on the density and thickness of the sample the transmitted electrons form a two-dimensional (2D) projection of the sample. This is the basis for TEM imaging. Electrons can also be diffracted by particles if these are favorably oriented toward the electron beam; the crystallographic information that can be obtained from these diffracted electrons is the

basis for electron diffraction. Finally the electrons in the primary beam can collide with atoms in the sample and be scattered back; backscattering is more effective when the mass of the atom increases. If a region of the sample contains heavier atoms (such as metal particles) that the surroundings, it can be distinguished due to higher yield of backscattered electrons. If the electron beam is rastered over the surface and the yield of secondary or backscattered electrons is plotted as function of the position of the primary electron beam it is possible to get three-dimensional images of the samples analyzed. This method is the basis for SEM.

2.1.1. Transmission Electron Microscopy and Electron Diffraction

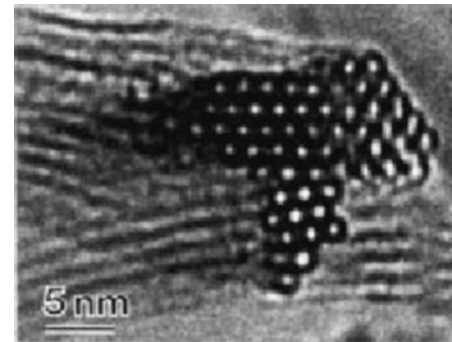
The existence of SWNTs was first confirmed by means of high-resolution electron microscopy and electron diffraction. Due to the small physical size sample and the low atomic number of carbon, classical structural techniques such as X-ray diffraction are difficult to apply to SWNTs. For this reason, TEM has been the most widespread tool for structural characterization of SWNTs.

Figure 2 shows a typical TEM micrograph of a SWNT rope. One of the first observations obtained from TEM was that SWNTs have a tendency to assemble in bundles containing between 10 and 50 aligned nanotubes. It is generally accepted that the SWNTs are held together by van der Waals interactions. Another interesting feature is also observed in Figure 2. A cross-sectional view shows that the individual SWNTs can be clearly distinguished. This is a common observation during TEM analysis and is due to the fact that the SWNT bundles are usually bent and it is possible that a portion of them get oriented parallel to the electron beam, resulting in images of the nanotube ends. TEM images show that the SWNT bundles are typically 5–20 nm in diameter and exhibit a triangular lattice with an inner nanotube distance of around 1.7 nm [15, 39].

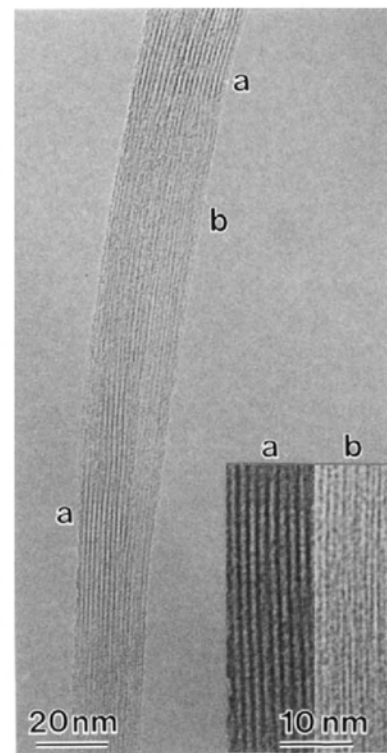
An important precaution to be taken into consideration when performing TEM measurements on SWNT samples is that they are highly susceptible to the 100–200 keV electron beam of the TEM instrument. Beam damage makes it very difficult to carry out electron diffraction studies from isolated SWNTs. Diffractions patterns can be more readily obtained from bundles of SWNTs. By using low electron beam currents it has been possible to obtain good TEM measurements of lattice fringe images and electron diffraction patterns on single-wall nanotubes. These studies have shown that the walls of SWNTs have indeed the local structure of a graphene sheet [3].

The diffraction patterns to be expected from a SWNT sample can be approximated by forming a reciprocal space distribution for a single graphene sheet and rotating it around the nanotube axis to give the scattering power in a set of planes [40]. The interpretation of these electron diffraction patterns becomes easier by the use of computer simulations, which yield the expected diffraction pattern for an individual SWNT with well-defined (n, m) indexes [41–43].

For instance Figure 3a shows the diffraction pattern calculated for a bundle tilted by an angle of 60° with respect to the electron beam [44]. In this simulation, the bundle



(a)



(b)

Figure 2. High resolution TEM images of SWNT bundles produced by arc discharge technique. (a) Cross-section-like view of a polycrystalline bundle. (b) View of a twisted bundle with its axis normal to the electron beam. The inset shows a magnification of fringes related to (11) and (10) lattice planes. Reprinted with permission from [44], L. Henrard et al., *Eur. Phys. J. B* 13, 661 (2000). © 2000, Springer-Verlag.

is assumed to be composed of 55 nanotubes corresponding to eight different helicities: (10, 10), (11, 9), (12, 8), (13, 7), (14, 5), (15, 4), (16, 2), and (17, 0). Two rings of different intensity can be distinguished in the simulated diffraction pattern. Figure 3b shows an electron diffraction pattern experimentally obtained on an isolated straight bundle of SWNTs. The simulation reproduces very nicely the experimental pattern. Since the experimental data could not be simulated with a single chirality, the authors proposed that that SWNT bundles have to be composed of SWNTs with random chirality. The observed patterns need to be compared to the results of the modeling since the computer simulations are not able to carry out the inverse process of

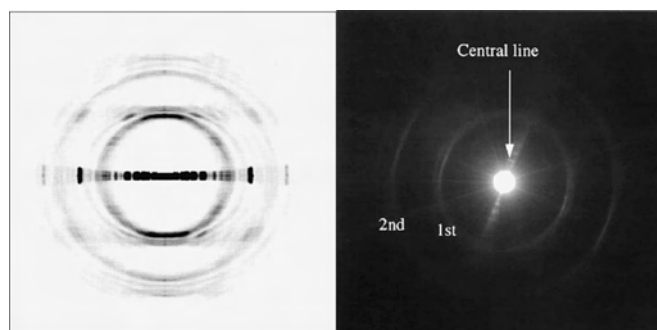


Figure 3. Left: A simulated electron diffraction pattern obtained considering a single bundle composed of 55 nanotubes corresponding to eight different helicities: (10, 10), (11, 9), (12, 8), (13, 7), (14, 5), (15, 4), (16, 2), and (17, 0). Right: Experimental diffraction pattern of an isolated straight SWNT bundle. Reprinted with permission from [44], L. Henrard et al., P. Bernier, *Eur. Phys. J. B* 13, 661 (2000). © 2000, Springer-Verlag.

converting an observed diffraction pattern into a real space structure (n, m) for the atomic sites within the 1D unit cell.

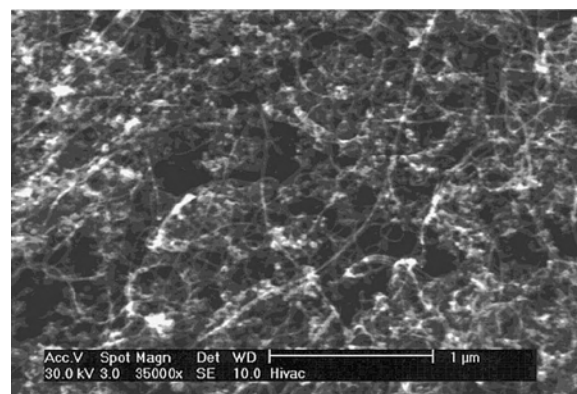
2.1.2. Scanning Electron Microscopy

Scanning electron microscopy is to a certain extent a limited tool to characterize SWNTs, regardless of the high magnifications that can be achieved with SEM instruments. The main problem with the application of SEM to SWNT characterization analysis is that it cannot differentiate between SWNTs and MWNTs. This is mostly due to the tendency of SWNTs to adhere strongly to each other, forming bundles or ropes of 5–20 nm in diameter. In contrast to TEM, SEM cannot resolve the internal structure of these SWNT bundles.

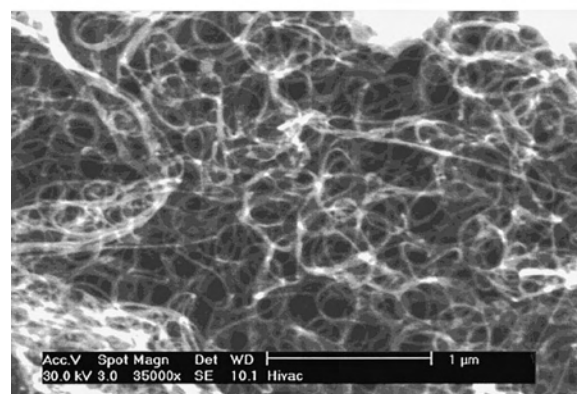
Nevertheless, SEM can yield valuable information regarding the purity of a sample as well as an insight on the degree of aggregation of raw and purified SWNT materials. For instance Figure 4 illustrates how SEM can be used to answer substantive questions about the quality of SWNT samples [45]. Figure 4a shows a SEM micrograph of raw SWNT material produced by laser ablation. The presence of other forms of carbon besides SWNT and the occurrence of a large amount of catalysts particles is apparent. After a gas phase purification step using a gas mixture of H_2 and Cl_2 , Figure 4b shows an improvement in the degree of dispersion as well as in purity since the image predominately shows nanotube ropes. Finally the bright metal particles observed in Figure 4b (cobalt and nickel catalyst), visible after the first gas treatment, can be removed by a subsequent liquid phase treatment in HCl. The final product obtained after this sequential purification process appears to be high-quality single-wall nanotube material.

2.2. Scanning Tunneling Microscopy and Spectroscopy

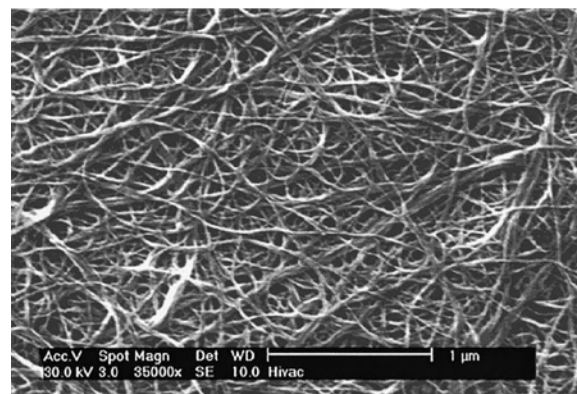
Scanning tunneling microscopy (STM) and spectroscopy (STS) can both be considered as the ultimate technique to assess the electronic properties as well as the structure of individual SWNTs. Although Raman and optical absorption



(a)



(b)



(c)

Figure 4. (a) SEM micrograph of raw SWNT material obtained by laser ablation. (b) The same material in (a) after a gas phase purification treatment and (c) the same material in (b) after a liquid phase purification treatment in HCl. Reprinted with permission from [45], J. L. Zimmerman et al., *Chem. Mater.* 12, 1361 (2000). © 2000, American Chemical Society.

can provide some of the information generated by a STS experiment, the unique advantage of STM and STS is the possibility to probe both the morphology and the electronic structures of SWNT at the atomic level. In this section, some of the most impressive results and applications of this powerful technique are presented. For more details, the reader

is referred to any of the extensive reviews published on this subject [46, 47].

STM and STS are both based on the tunneling effect. In short, a very sharp metal tip is scanned across the surface to be analyzed, which must be conducting, at a distance of the order of typically 1 nm. A bias voltage is applied between the tip and the sample (typically a few millivolts), which leads to a tunneling current of the order of pico- to nanoamperes. This tunneling current is extremely sensitive to the distance between the tip and the sample. Therefore, by measuring the tunneling current while keeping the distance or the bias voltage constant, information on the topography of the surface can be obtained. Moreover, since the tunneling current is also dependent on the electronic structure of the surface (i.e., density of states of the surface being probed) very reliable information about the electronic structure of the sample can be obtained [48].

Figure 5 shows how STM can provide information on a SWNT at the atomic level. In this case, individual SWNTs with different chiral angles were probed [49]. Together with the information on the chiral angle, a direct measurement of the diameter can also be performed. The combination of these two pieces of information provides the (n, m) indexes, which fully characterize the molecular structure of the nanotube. It is necessary to mention that STM images should be carefully analyzed before a direct assignment of the chiral angle and diameter of SWNT can be made. For instance, the geometrical orientation of the STM tip respect to the nanotube greatly influences the image recorded. For a cylindrical structure such as a SWNT, the shortest distance between the tip and the nanotube is perpendicular to the nanotube wall only when the tip is on top of the nanotube. Only in this case the image observed represents the true structure of the probed SWNT. In any other case, the information obtained is that of a stretched lattice [49–51].

While STM can yield insight into the SWNT lattice arrangement, STS provides information on its electronic structure. Tunneling spectroscopy can be performed by recording the current as function of the bias voltage at fixed positions of the STM tip over the sample. That is, in STS the

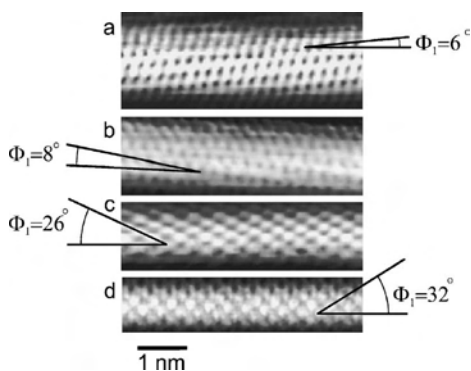


Figure 5. STM images of atomically resolved carbon nanotubes. For each nanotube the apparent angle between hexagon rows and the tube axis is indicated. The 1-nm bar indicates the scale for all four images. (a), (b) Two chiral nanotubes with small chiral angles. (c), (d) Two chiral nanotubes with large chiral angles near 30°. Reprinted with permission from [49], L. C. Venema et al., *Phys. Rev. B* 61, 2991 (2000). © 2000, American Physical Society.

tip is not scanned across the sample. In this way information of the electronic structure of the sample can be obtained with a resolution that is essentially of a single atom. The normalized conductance $(V/I) dI/dV$ is a good measure of the local density of states [48].

These measurements have been used to confirm the predictions made by theory about the diameter and helicity dependence of the electronic properties of SWNTs [52–54]. With the adequate energy range, the experimental density of states (DOS) can be obtained on atomically resolved SWNTs and compared quantitatively with the calculated DOS for specific (n, m) indices. Kim et al. [55] performed the first comparison of this sort, for a nanotube with $(13, 7)$ indices. In Figure 6 the STS data are compared with the theoretical band structure calculations based on a π - π tight binding model [56, 57]. Due to the one-dimensional nature of their band structure, SWNTs exhibit high peaks (or spikes) in the density of states. The experimental data show good agreement between the positions of the spikes and the van Hove singularities determined from these calculations. The agreement between theoretical calculations and STS data was particularly good below the Fermi level, where the first seven singularities corresponded very well. Above the Fermi level some deviations between the experimental data and the calculations were observed. The differences were attributed to band repulsion, which arises from curvature induced hybridization [58, 59].

Figure 6 also shows a similar result obtained by Odom et al. who worked on a small diameter $(10, 0)$ semiconducting nanotube and compared the experimental data with a tight binding theoretical prediction [55–57]. Similar to the results obtained by Kim et al., the normalized conductance

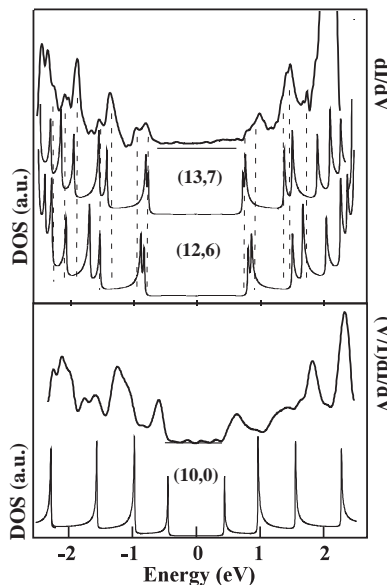


Figure 6. (a) Upper panel: Comparison between the DOS obtained from a STS experiment and a tight binding calculation for a $(13, 7)$ and $(12, 6)$ SWNT. Lower panel: Comparison between the DOS obtained from a STS experiment and a tight binding calculation for a $(10, 0)$ SWNT. Reprinted with permission from [46], T. W. Odom et al., *J. Phys.: Condens. Matter* 14, R145 (2002). © 2002, Institute of Physics Publishing.

exhibited relatively good agreement with the calculated (10, 0) DOS below Fermi level, but a poorer agreement above this level (Fig. 6). The difference was also attributed to curvature-induced hybridization, since the π -only DOS calculation does not include π/σ and π^*/σ^* mixing due to the curvature of the nanotube. This hybridization of π/σ orbitals is believed to produce more pronounced effects on the conduction band than in the valence band and hence this could explain the observed deviations [46, 58].

STS has opened the possibility of performing detailed studies of the electronic structures and perturbation-like quantum effects. For example, the effect of the finite size of the nanotube was studied by experimentally obtaining the DOS of shortened SWNTs [60, 61]. In other studies, the influence of Coulomb charging was also analyzed by STS [62–64]. At the same time more practical issues such as the effect of bending, sidewall functionalization, and how the presence of an intermolecular junction between two SWNT modifies their DOS have been investigated by STM/STS [65, 66]. For instance, studies of atomically resolved STM images have allowed the identification of intermolecular junctions (IMJ) between two different types of SWNTs. Figure 7 shows one of these results. The upper and lower portions of a SWNT with appreciably dissimilar chiral angles are shown. Based on the chiral angle and the SWNT diameter, the (n, m) indices of the upper and lower regions were assigned as (21, -2) (semiconductor) and (22, -5) (metallic), respectively. The STS experiments provided spectroscopic evidence for the overall structure showing that

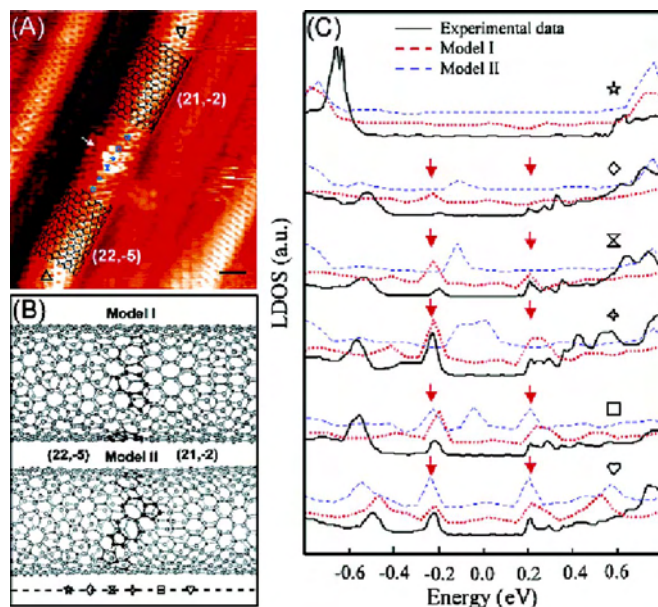


Figure 7. (a) Atomically resolved STM image of a SWNT containing a junction indicated by the white arrow. (b) Models chosen to describe the junction. Model I has three separated 5/7 pairs, and model II has two isolated 5/7 pairs and one 5/7-7/5 pair. The solid black spheres highlight the atoms forming the 5/7 defects. (c) Solid line: spatially resolved dI/dV data acquired at the positions indicated by the six symbols in (a). Thick dashed line: calculated local DOS for model I. Thin dashed line: calculated local DOS for model II. Reprinted with permission from [66], M. Ouyang et al., *Acc. Chem. Res.* 35, 1018 (2002). © 2002, American Chemical Society.

the upper and lower portions corresponded to a semiconductor and metal, respectively. Indeed, as the data presented in Figure 7c show, this junction has a very sharp metal–semiconductor interface where the semiconducting gap between the van Hove singularities decays across the junction into the metallic segment within <1 nm, whereas the distinct spectroscopic features of the metallic nanotube seem to decay more rapidly across the junction interface. The authors modeled the interface in order to compare the calculated and experimentally measured DOS of this junction. Two possible structural models are represented in Figure 7b. The local DOS obtained from a tight binding calculation for model I agreed well with the measured local DOS across the IMJ interface. This result suggests that model I is a reasonable representation of the junction.

Kelly et al. [67] published a report on how STM can provide evidence for sidewall functionalization. The authors showed images of SWNTs whose sidewalls were chemically modified by a two-step synthesis in which they were first fluorinated and then butylated. Noticeable “narrow dark bands” around the walls of the SWNTs that were exposed to aggressive fluorination conditions were observed by STM. Based on these observations and on semiempirical calculations, the authors proposed a sidewall-functionalization mechanism. Unfortunately in this case the results were not supported by tunneling spectroscopy data and seem not to be conclusive. However, this was one of the few reports showing how STM images can provide information on the chemistry of SWNTs.

The big disadvantage of electron microscopy and spectroscopy in this context is that one can never be sure that the observed image is truly representative of the bulk SWNT sample. Consequently a number of bulk sensitive methods that provide information regarding the quality, diameter distribution, and structural properties of a given sample have been employed. These methods comprise Raman spectroscopy, optical absorption, temperature programmed oxidation, and diffraction techniques.

2.3. Raman Spectroscopy

Among the several techniques used to characterize single-walled carbon nanotubes, Raman spectroscopy is perhaps the most powerful tool to get information on their vibrational and electronic structure. Raman spectroscopy is based on the inelastic scattering of visible light by matter. When electromagnetic radiation in the visible range interacts with a substance it may be absorbed by the substance, transmitted, or scattered. Light scattering may be elastic or inelastic. Elastic scattering is the most common phenomenon and occurs without loss of photon energy (i.e., without any change in the frequency of the original wave). In opposition, a very small fraction of the incoming radiation undergoes inelastic scattering, in which the scattered wave results in a different frequency than that of the incoming wave. This frequency difference is called the Raman shift, which can be positive or negative. If, upon collision with a molecule, the photon loses some of its energy, the resulting radiation has a positive Raman shift (Stokes radiation). In contrast, when the incoming photons gain energy the resulting radiation has higher frequencies (anti-Stokes radiation) and a negative Raman shift is observed.

If an adequate instrument is used to measure both the energy of the incoming and outgoing light, it will be observed that both the Stokes and anti-Stokes radiation are composed of discrete bands, which are intimately related to molecular vibrations of the substance under investigation. The information obtained by measuring the Raman shift is therefore most valuable since direct information at the molecular level of the nature of the chemical bonds and symmetry on the substance under investigation can be obtained. In the case of solids, the most elementary processes are associated with degrees of freedom of ions and electrons in crystalline and amorphous solids, with the only exception being long acoustic phonons and acoustic magnons, which are associated with Brillouin scattering [68].

A limitation of Raman spectroscopy is the extremely low quantum efficiency associated with the process (almost 1 photon is inelastically scattered for every 10^6 photons that interact with the sample). Thus, a very intense light source must be used in order to get a signal strong enough to measure satisfactorily the Raman shift. Moreover, since a very precise measure of frequency of the incoming light is needed to calculate the Raman shift, the use of a monochromatic excitation light is preferred. A laser light source satisfies both conditions, monochromaticity and high intensity, and it is then the obvious choice for excitation light source to perform Raman spectroscopy.

The low efficiency of Raman scattering can be counterbalanced by an intensity enhancement due to the so-called resonant Raman effect. This resonant effect occurs when the photon energy of the exciting or scattered light beam matches the energy of an allowed optical electronic transition of a chromophoric group within the sample [69, 70]. Excitation within the absorption band of the sample results then in the selective enhancement of just those vibrational modes on the sample that selectively couple with the oscillating dipole moment induced by the excitation electric field [71]. The intensities of the resonance Raman enhanced bands can increase as much as 10^8 -fold. Thus, it becomes possible to selectively study the vibrational spectra of very dilute samples or chromophores in solids by choosing excitation wavelengths in resonance with a particular analyte chromophore. However, just the intensity of Raman bands associated with this resonant process will be amplified while all other bands will fade away on the spectrum background.

The resonant Raman effect in single-walled nanotubes is very strong due to the sharp spikes present in the one-dimensional electronic density of states. The energy difference between the spikes falls in the visible and near-infrared range [72–77]. Therefore, when the excitation laser energy is close to that of an allowed optical transition between singularities in the one-dimensional density of states of SWNTs the Raman intensity is greatly enhanced [78–80].

The energies of these allowed optical transitions depend on both the diameter and the chirality (and therefore on the metallic or semiconducting character) of the SWNT. Using the tight binding π - π overlap integral as a scaling factor, it has been possible to demonstrate that an inverse proportionality exists between the interband transitions and the nanotube diameter [81–83]. This inverse proportionality has been illustrated in a series of publications, which report the range of the allowed optical transitions for semiconducting

and metallic nanotubes [75, 78, 79]. Of particular interest is the work of Kataura et al. [78] who calculated the one-dimensional energy band structure for SWNTs ranging from 0.6 up to 1.8 nm in diameter. The results of the calculation of the allowed optical transition gap energies between the mirror image spikes of the density of states are reproduced in Figure 8 as function of nanotube diameter.

These theoretical calculations can be used to link nanotube diameters with the energy gaps between singularities in the valence and conduction bands of the electronic density of states of SWNTs. Since the energy gaps are probed through the resonant Raman effect, direct information on the nanotube diameter can be obtained from the Raman spectra. Based on this effect, Raman spectroscopy has provided a particularly valuable tool for examining not just the diameter distribution in a nanotube sample but also the mode frequencies of SWNTs with specific diameters, as well as for evaluating the merits of theoretical modes for the 1D phonon dispersion relation, and for studying the 1D electron DOS through this electron-phonon coupling mechanism [84].

To successfully analyze Raman spectra of SWNT, the vibrational modes of a SWNT need to be evaluated. A first approach considers decomposing these modes into irreducible representations of the point group in which the SWNT belongs [85]. For example, an armchair nanotube belongs to the D_{nh} symmetry group (n being an even integer), and consequently the vibrational modes can be decomposed into the following irreducible representations:

$$\begin{aligned} \Gamma^{\text{vib}} = & 4A_{1g} + 2A_{1g} + 4A_{2g} + 2A_{2u} + 2B_{1g} + 4B_{1u} + 2B_{2g} + 4B_{2u} \\ & + 4E_{1g} + 8E_{1u} + 8E_{2g} + 4E_{2u} + \dots + 8E_{(n/2-1)g} \\ & + 4E_{(n/2-1)u} \end{aligned} \quad (2)$$

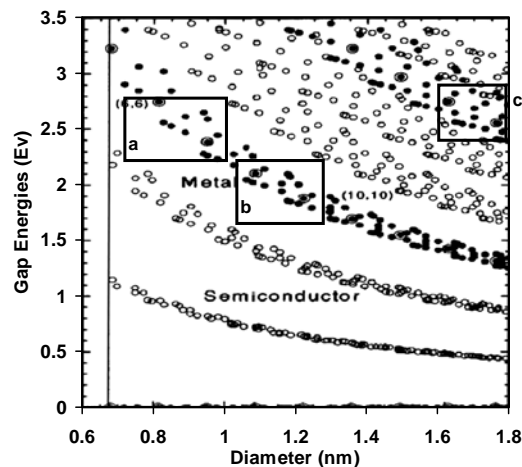


Figure 8. Calculated gap energies as a function of diameter for SWNTs as function of diameter, obtained by Kataura et al. The metallic windows in which metallic tubes are in resonance are presented for (a) SWNTs obtained by arc discharge on a RhPd catalyst, (b) SWNTs synthesized by laser ablation using a Co/Ni catalyst, and (c) SWNTs obtained by CO disproportionation at 950 °C over a CoMo catalyst. Reprinted with permission from [78], H. Kataura et al., *Synth. Met.* 103, 2555 (1999). © 1999, Elsevier Science.

For the case of a (6, 6) armchair nanotube 72 phonon branches are expected and Eq. (2) gives a total of 48 distinct mode frequencies. Appropriate character tables can be used to determine which modes are Raman active. Thus, it can be easily demonstrated that there are 16 Raman active frequencies ($4A_{1g} + 4E_{1g}$ and $8E_{2g}$). Notice that the number of active modes depends just on the SWNT chirality but is independent of nanotube diameter.

Detailed characterization of SWNTs by Raman spectroscopy started with the initial joint efforts of Dresselhaus et al. and Eklund et al. [86], who obtained the Raman spectra of SWNT bundles using several laser excitation energies. They reported a strong enhancement of the Raman intensity due to the diameter-selective resonance Raman effect. This work confirmed the theoretical predictions of the diameter-selective Raman scattering that is a particularly important for the Raman bands associated with the A_{1g} radial breathing mode (RBM) [75, 87–89]. In fact, the presence of the RBM feature in the Raman spectrum is used today as a signature of the presence of SWNTs in the sample. Variations in RBM band shape and position provide information on the nanotube diameters present in a given sample.

Following the seminal work of Dresselhaus et al., the unusual response of this line to changes in excitation energy has been discussed in many articles. *Ab initio* calculations confirmed the inverse proportionality of the A_{1g} mode frequency with the diameter and yielded an appropriate proportionality factor [90, 91]. The RBM band appears in the Raman spectrum below 300 cm^{-1} and has been proposed to be independent of chirality [92]. Bandow et al. calculated the RBM frequencies of all types of SWNTs and found that all frequencies fall on a common line according to the expression [93]

$$\bar{\gamma} = \frac{223.75}{d} \quad (3)$$

where $\bar{\gamma}$ is in units of cm^{-1} and d is the nanotube diameter in nm.

Using this expression one can obtain the diameter of the SWNTs under study just by observing the position of the RBM band. However, a slight correction should be made in this formula since intertube coupling must be considered when the nanotubes are present in a bundle. This correction was achieved by using a Lennard-Jones potential to account for van der Waals interactions among the nanotubes in a bundle [86, 94]. A significant upshift of the RBM was found for nanotubes in bundles with respect to isolated nanotubes. The calculated data were best fitted by the nonlinear phenomenologic relation between the RBM frequency and the nanotube diameter,

$$\bar{\gamma} = \frac{238}{d^{0.93}} \quad (4)$$

where $\bar{\gamma}$ is in units of cm^{-1} and d is the nanotube diameter in nm [95].

This correlation has been widely used to study samples with different diameter distributions [75, 78, 96–98], confirming the diameter dependence of the electronic properties of SWNTs. As a result, the study of the nanotube's diameter by Raman scattering has provided complementary

information to the direct diameter measurements conducted by TEM, STM, and other techniques [99–105].

As mentioned above, the information obtained by Raman spectroscopy is the result of the resonant Raman effect which is particularly strong in SWNTs. Therefore the nanotubes that contribute most strongly to the Raman scattering for a given excitation wavelength are those which are in resonance with the incident or scattered light. Consequently, the spectral shape and position of the Raman RBM do not directly reflect the true diameter distribution in the SWNT sample, but rather the subset of nanotubes that are in resonance with the incident or scattered photon. So the relative intensities of the individual peaks that compose the RBM band are not only associated with the relative concentrations of the different nanotubes in the sample but rather reflect their electronic properties, which in their turn modulate the Raman cross section [106, 107]. This fact has been clearly illustrated by Dresselhaus et al. in a series of publications [73, 75, 108–111]. Figure 9 illustrates the Raman band associated with the radial breathing mode of SWNTs obtained by laser vaporization of a carbon target containing 1 to 2 at% of Ni/Co. In this case, the Raman spectra was obtained with six different laser excitation energies ranging from 1.17 to 2.71 eV [108]. Notice that the band shapes are completely different from one excitation laser to another. This result is consistent with a sample containing

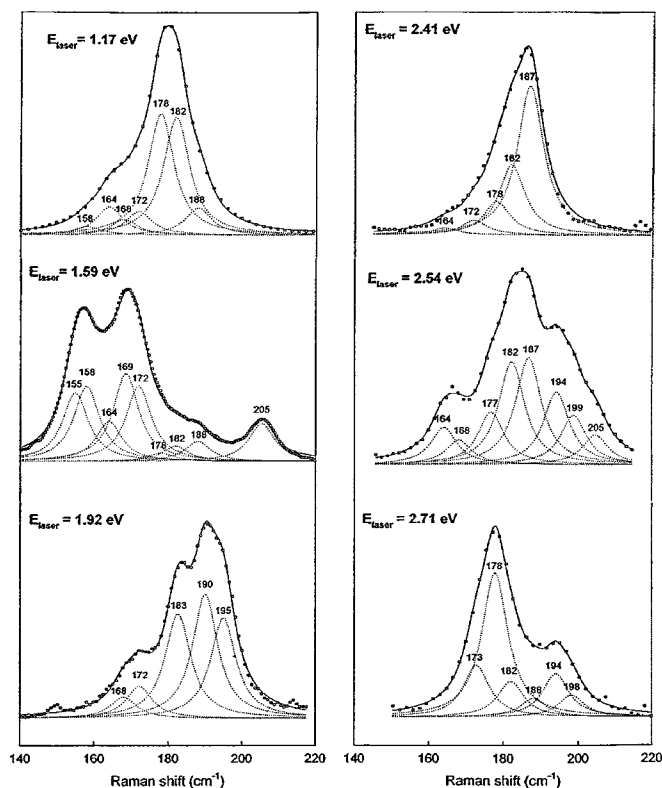


Figure 9. Raman spectra of the radial breathing mode of single-walled carbon nanotubes collected with six different laser lines: 1.17, 1.59, 1.92, 2.41, 2.54, and 2.71 eV. The dotted curves represent individual Lorentzian curves used by the authors to fit the experimental data. Reprinted with permission from [108], M. A. Pimenta et al., *J. Mater. Res.* 13, 2396 (1998). © 1998, Materials Research Society.

carbon nanotubes with different diameters, which resonate at different energies. In this case, the average diameter as determined by TEM of the SWNT was 1.24 nm, but the RBM bands indicate that they range from 1.09 to 1.44 nm.

Figure 10 shows a similar result, on a set of samples produced by catalytic disproportionation of CO over a supported CoMo catalyst at 700 °C [88]. Under these particular conditions the diameter distribution is centered at around 0.9 nm as shown by TEM analysis. Once again the RBM bands show a strong dependence on the laser energy, which confirms the relation among the energy separation on DOS singularities with the nanotube diameter.

The differences in the average peak positions when different lasers are used complicate the analysis. Recently a better understanding of the response of the RBM has been attempted on the basis of an extended experimental and theoretical analysis [82, 112, 113]. The responses of the peak position and of the first and second moments of the spectra were found to oscillate with the energy of the exciting laser. This oscillation was found to be due to the microscopy quantization of the electronic levels as a consequence of the finite size of the nanotubes in the direction perpendicular to the nanotube axis and, as mentioned previously, to the distribution of the states along the nanotube axis into the van Hove singularities. Furthermore, an approximation has been successfully used to evaluate the spectral moments of the RBM Raman response without explicit use of the joined density of states. This simplified model has been used to determine the mean and the width of the diameter distribution of a SWNT sample. A remarkable conclusion is that just a single laser energy could be used to evaluate the first and second moments of the spectra and, therefore, the mean and the width of the diameter distribution of the sample [113].

In principle, the radial breathing mode frequency could provide the identity (n, m) of the individual nanotubes participating in the Raman scattering since the RBM frequency is proportional to the diameter, and the value of the SWNT

diameter depends on the integers (n, m) [39, 114]. However several distinct (n, m) nanotubes can exhibit sufficiently similar diameters so that their RBM frequency differs only by 1–2 cm^{-1} . This prevents one from using the RBM frequencies to determine (n, m) in a sample of SWNTs, since the natural linewidth of the RBM band is 6 cm^{-1} and the individual contributions to the band from nanotubes with similar diameters would be very difficult to resolve [84, 93, 99].

Besides the radial breathing mode band, the Raman spectra of SWNTs also comprise a disorder-induced Raman band (D band), which is a feature common to all sp^2 hybridized disordered carbon materials. This D band appears in the Raman spectra between 1250 and 1450 cm^{-1} and is associated with phonons close to the K point of the graphite Brillouin zone and it becomes Raman active when translational symmetry is lost [110, 111, 115]. The D band also shows a strong dependence on the excitation laser energy, although in this case the dependence is highly linear. Pimenta et al. [116] studied the D band behavior on isolated SWNTs and observed that its intensity appeared to be random from one nanotube to another; although the linear dependence on the excitation laser energy was observed, this was attributed to be more a consequence of the same general trend that is observed for all sp^2 carbon materials. The authors suggested that this phenomenon is linked to phonons that are not at the center of the 1D Brillouin zone of SWNTs and concluded that they become Raman active due to the finite size of the SWNTs or to the presence of defects, which would break the translational symmetry along the nanotube axis [111, 117]. Recently, it has been proposed that the excitation energy dependence of the D band is an intrinsic property of the SWNT, and it has been suggested that the metallic character of an individual nanotube can be inferred from the shape and position of its D band [118].

The D band has been related not just to defects on SWNTs but also to the presence of other forms of disordered carbon such as carbon nanoparticles and amorphous carbon [119]. Its relative intensity has been used as a semi-quantitative indicator of the presence of undesired forms of carbon (i.e., microcrystalline graphite, amorphous carbon, MWNTs, carbon nanofibers). Figure 11 shows an example in which the relative intensity of the D band can be related to the presence of carbon impurities in a SWNT sample. The Raman spectra of SWNTs obtained by a catalytic method over a selective solid catalyst are presented as function of the time on the reaction stream. It is observed that at longer times there is an increase in the intensity of all the Raman bands as a result of the increasing carbon deposition. However, the relative intensity of the D band clearly increases with reaction time, which indicates that undesired forms of carbon start being formed at longer reaction times. The TEM observations on these same samples confirm this conclusion. A higher density of nanofibers and graphite is observed after long reaction times than after short reaction periods [32].

The Raman spectra of SWNTs also contain the typical G band associated with the tangential C–C stretching modes of SWNTs, which consist of two A , two E_1 , and two E_2 phonon modes for chiral nanotubes and one A_{1g} , one E_{1g} , and one E_{2g} mode for armchair or zigzag nanotubes, as predicted by group theory and phonon frequency calculations

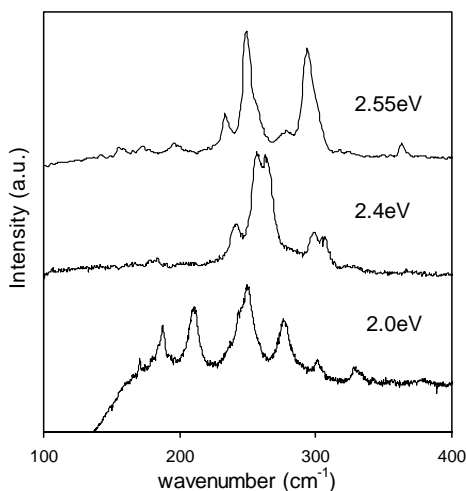


Figure 10. Radial breathing mode resonant Raman spectra of SWNTs grown at 750 °C by CO disproportionation over a Co:Mo catalyst. The laser excitation energies were 2.55 eV, 2.4 eV, and 2.0 eV. Reprinted with permission from [88], J. E. Herrera et al., *J. Nanotech.*, in press. © American Scientific Publishers.

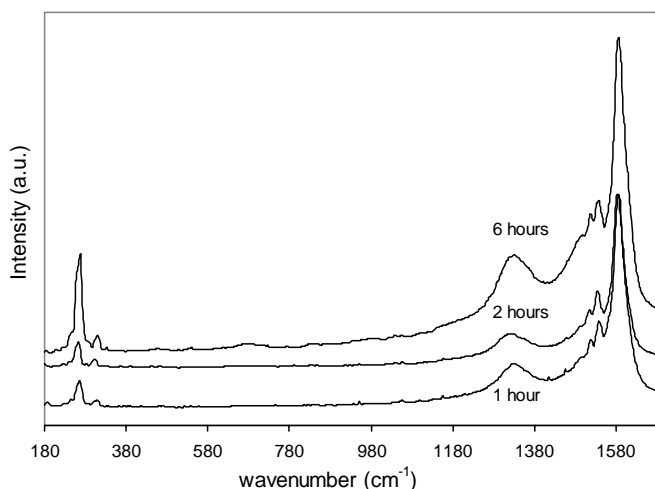


Figure 11. Raman spectra of SWNTs grown at increasing reaction times. The product was obtained at 750 °C over a CoMo catalyst by CO disproportionation. Reprinted with permission from [32], W. E. Alvarez et al., *Chem. Mater.* 14, 1853 (2002). © 2002, American Chemical Society.

[85, 104, 120–123]. This tangential mode *G* band appears in the 1400–1700 cm^{-1} region and involves out-of-phase intralayer displacement in the graphene structure of the nanotubes. In contrast to the *D* band the *G* band is a measure of the presence of ordered carbon and therefore is present on all kind of sp^2 ordered carbonaceous materials (graphite, MWNTs, nanofibers, etc).

In SWNT samples, the most important characteristic of the *G* band is that the analysis of its line shape offers a method for distinguishing between metallic and semiconducting nanotubes [86, 88, 108]. The *G* band of the semiconducting nanotubes has been extensively studied and is well accounted for using Lorentzian oscillators to describe the six Raman active modes that have been spectroscopically identified by polarization studies of the symmetries of the various line-shape components [124, 125]. On the other hand, although Lorentzians can be used to describe the *G* band of metallic carbon nanotubes [75, 126, 127], the lower frequency component of the *G* band spectrum that appears around 1540 cm^{-1} has to be fitted using a Breit–Wigner–Fano (BWF) line shape, due to a downshift and broadening in the tangential *G* band of metallic SWNTs relative to semiconducting SWNTs [78, 128–130].

Brown et al. [131] demonstrated that only these two Raman components were needed to fit the tangential *G* band for metallic SWNTs. Both components were found to exhibit predominant $A(A_{1g})$ symmetry. The differences in their peak frequencies were attributed to a difference in the force constant of vibrations along the nanotube axis (higher force constant) versus circumferential (lower force constant) and to an additional downshifting and broadening of the lower frequency peak due to a coupling of the discrete phonons to an electronic continuum (this continuum is characteristic of any electronic structure that shows metallic-like conduction properties) that resulted in the BWF line shape. However, as in all resonant Raman studies, the presence of this BWF in the Raman spectra will depend on the resonance conditions between the excitation energy and the

DOS of the SWNT present on the sample. Accordingly, in a sample in which SWNTs of different chirality are present it is possible to selectively enhance the Raman efficiency for metallic or semiconducting SWNTs by carefully choosing the laser excitation energy. This method will be illustrated.

Figure 12 shows a wide range resonant Raman spectra of the *G* band for SWNTs obtained by arc discharge using a RhPd catalyst [78]. For laser excitations around 2.4 eV the *G* band takes the shape of a broad and asymmetric peak centered at 1540 cm^{-1} with a BWF line shape. This band shape undoubtedly indicates that metallic nanotubes are in resonance with the laser excitation energy. In this case, the SWNT in the sample had diameters between 0.7 and 1.0 nm, as observed by TEM and inferred from the A_{1g} breathing mode frequencies of the Raman spectra. Consequently, when using laser energies around 1.8 eV, mostly metallic SWNTs are probed and a “metallic window” can be delineated in which the resonance condition for metallic nanotubes with diameter around 0.9 nm takes place. This metallic window is depicted in the Kataura plot of Figure 8.

Pimenta et al. [75] have investigated the line-shape variation of the band attributed to metallic nanotubes as a function of the excitation laser energy. In this study, a large enhancement in the relative intensity of the band centered at 1540 cm^{-1} was observed in the energy range 1.7–2.2 eV. This enhancement is shown in Figure 13, and it was explained in terms of the singularities in the density of states of the metallic nanotubes together with the distribution of

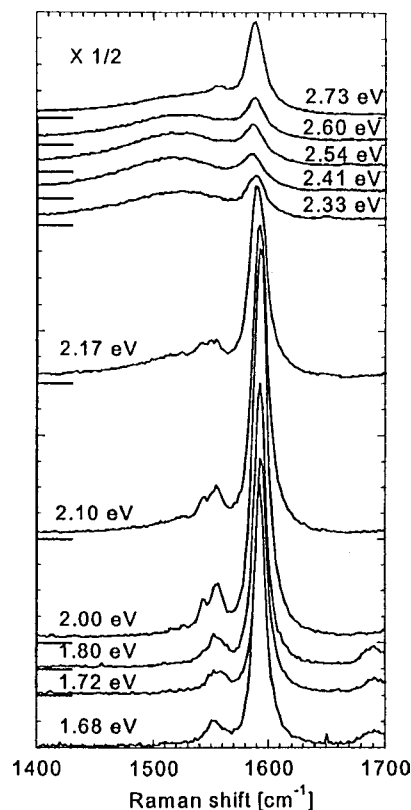


Figure 12. Resonance Raman spectra of SWNTs synthesized using RhPd by arc discharge. The diameter distribution ranges from 0.7 to 1.00 nm. Reprinted with permission from [78], M. Kataura et al., *Synth. Met.* 103, 2555 (1999). © 1999, Elsevier Science.

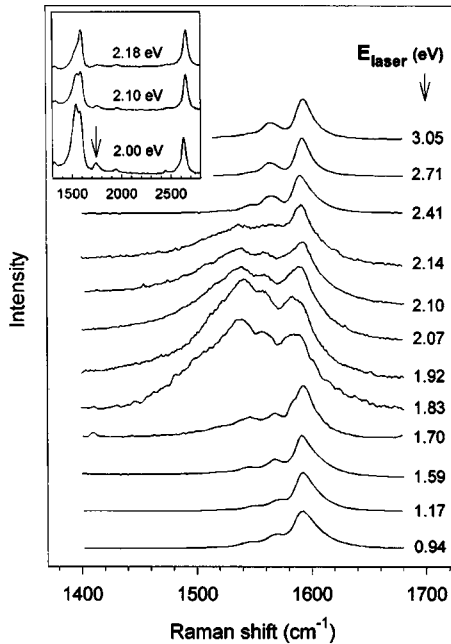


Figure 13. Raman spectra of the tangential modes of SWNTs obtained with several laser energies. The SWNTs were synthesized by laser ablation of a carbon target containing a Ni/Co catalyst. Reprinted with permission from [75], M. A. Pimenta et al., *Phys. Rev. B* 58, R16016 (1998). © 1998, American Physical Society.

diameters of the sample. The nanotubes used in that particular study were obtained by laser vaporization of a carbon target containing 1 to 2% of a Ni/Co catalyst. The diameter distribution obtained from the TEM was in the 1.1–1.3 nm range and, as predicted from the plot in Figure 8, for those diameters the energy region of resonance for metallic nanotubes falls in the range 1.7–2.2 eV. This energy range is in perfect agreement with the range at which the enhancement of the BWF line shape was observed.

As a third example, Figure 14 shows the set of Raman spectra on the *G* band for nanotubes produced by catalytic CO disproportionation at 950 °C on Co–Mo catalysts. Under these conditions, the SWNTs produced have an average diameter of 1.7 nm [32, 88]. Consequently, an enhanced BWF line was observed at higher laser excitation energies (2.4–2.55 eV) than for the previous cases. When a laser with lower excitation energy (e.g., 2 eV) was used, the broad band at 1540 cm^{-1} greatly decreased its relative contribution. This decrease can be explained taking into account that, in this case, one moves out of the metallic window (see Fig. 8).

In spite of all the interesting information that can be obtained from Raman spectroscopy, this technique has an intrinsic limitation related to its resonant character, which permits one to only get information on the nanotubes that are in resonance with the incident or scattered light. Therefore, a full characterization of all the SWNTs in the sample, with different diameters and chiralities, cannot be achieved.

Only on those samples with a narrow diameter distribution or, even better, on isolated SWNTs can Raman spectroscopy provide a full description of the sample. Recently, a series of studies on isolated SWNTs grown over a silicon substrate has been reported. These stud-

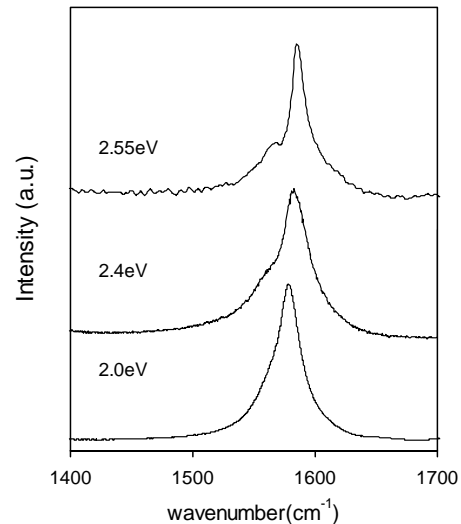


Figure 14. Resonant Raman spectra in the tangential mode (*G* mode) obtained using three different laser excitation energies, for SWNT samples produced by CO disproportionation at 950 °C. Reprinted with permission from [88], J. E. Herrera et al., *J. Nanotech.*, in press. © American Scientific Publishers.

ies have led to the observation of Raman spectra from an isolated nanotube, with intensities under good resonance conditions comparable to those from the silicon substrate, even though the ratio of carbon to silicon atoms in the light beam was approximately only 1 carbon atom to 10^8 silicon atoms [132–137]. All the Raman features observed in previous studies on nanotube bundles were also observed in the spectra of the single nanotubes, including the radial breathing mode, the *G* band, and the *D* band [132, 133]. However, at the single nanotube level, the characteristics of each feature were investigated in greater detail, including its dependence on diameter, chirality, laser excitation energy, and closeness to resonance with electronic transitions [134]. In this case, the uniqueness of the electronic transition energies for each nanotube becomes of particular importance [135]. The high sensitivity of the Raman spectra to diameter and chirality, particularly for the characteristics of the radial breathing mode, which are also uniquely related to the (n, m) indices, provided structural determination of (n, m) at this single nanotube level. The (n, m) assignments made to individual carbon nanotubes have been corroborated by measuring the characteristics of other features in the Raman spectra that are also sensitive to nanotube diameter and chirality. Raman spectroscopy has provided a convenient way to characterize nanotubes for their (n, m) indices, in a manner that is compatible with the measurement of other nanotube properties, such as transport, mechanical, and electronic properties at the single nanotube level, and the dependence of these properties on nanotube diameter and chirality [136, 137].

2.4. Optical Absorption

Another way to probe the electronic properties of SWNTs is through their optical absorption spectra. This technique is based on the well known phenomenon of light absorption

by a chromophore group present in the sample. In the case of SWNTs, when the light sent to the sample matches the energy of an allowed electronic transition between van Hove singularities, light in the visible and near infrared range can be absorbed. The observed absorption peaks are identified with interband transitions $E_{ii}(d_i)$ between the i th van Hove singularity in the valence band (occupied states) to the i th singularity in the conduction band (empty states). Figure 15 shows typical optical absorption spectra of samples synthesized by laser ablation using different catalysts [78, 138]. For the sample obtained by laser ablation using a NiY catalyst (with an average diameter of 1.5 nm) three strong absorption bands at 0.68, 1.2, and 1.7 eV were observed which are related to interband transitions between the first and second van Hove singularities (E_{11}^S and E_{22}^S) for semiconducting nanotubes and E_{22}^M for metallic nanotubes, as can be predicted by observing Figure 8. Notice that the optical absorption spectra for the SWNTs obtained using a RhPd catalyst correspond to SWNTs with much smaller diameters (diameters distributed from 0.68 to 1.00 nm) so the theoretical calculations depicted in Figure 8 predict that the optical absorption peaks should move to higher energies, as is experimentally verified [139].

As mentioned above, the same calculations that relate SWNT diameter with the energy of the optical interband transitions can be used to predict the positions of the absorption bands. The selection rules predict that the optical absorption spectra of SWNT will be dominated by transitions between peaks in the density of states of the valence and conduction bands, with momentum conservation only allowing transitions between pairs of singularities which are symmetrically placed with respect to the Fermi level. Thus, following the van Hove singularities, the energies of the optical transitions in SWNTs are also inversely proportional to

the SWNT diameter. For the first two allowed optical transitions in semiconducting SWNTs, the energy of the optical transitions has been proposed to be proportional to [140]

$$E_{11}^S = 2a_0\gamma/d \quad \text{and} \quad E_{22}^S = 4a_0\gamma/d \quad (5)$$

where γ is the tight binding nearest neighbor π - π overlap integral, which can be calculated from the Raman spectra. For the metallic nanotubes, the energies of the optical transitions have been proposed to be $E_{11}^M = 6a_0\gamma/d$ [81]. However, these calculations were shown to be inaccurate; indeed more recently it has been pointed out that the density of states of the metallic SWNT is also chirality dependent due to a trigonal warp effect [141, 142]. This leads to a splitting of the singularities in metallic nanotubes, which is maximum for the zigzag variety. Therefore, a more careful accounting of the electronic transitions has to be carried out in order to obtain a more accurate model.

One of the great advantages of optical absorption is the possibility of achieving high-energy resolution, which allows the identification of fine structure within the individual absorption features [83]. This fine structure is related to individual SWNTs, or groups of SWNTs with similar diameters. Moreover, it has been proposed that the analysis of such data would offer information as to whether the formation process of SWNT leads to the existence of preferred wrapping angles in the nanotube vector map [56, 81, 83].

In general, the results obtained by optical absorption must be compared with the information obtained by Raman spectroscopy. Since in optical absorption there is no resonance limitation as in Raman spectroscopy, in which a narrow set of SWNTs is probed, the interpretation of the optical absorption information is more straightforward. A true diameter distribution of the sample can be obtained from the absorption spectra. Two different approaches have been proposed to obtain the parameters for the diameter distribution. The first approach is based on the superposition of the full set of DOS functions to represent the quasi-continuous distribution of nanotubes [82]. In this approach, each nanotube is weighted with a Gaussian factor and by using the assumption of constant matrix elements the absorption is obtained from

$$\alpha(E) \propto \sum_{n,m} \exp\left[-\frac{d_{n,m} - d_0}{2\sigma^2}\right] g_{n,m}^2(E) \quad (6)$$

This expression renders characteristic peaks for the optical transitions between the van Hove singularities. Using a fixed value of γ for the π - π tight binding overlap integral and a similar scaling for the first two transitions, d_0 and σ can be fitted to the experimental results. Figure 16 shows how this approach yields information on the diameter distribution for two different SWNT samples. The results obtained using Eq. (6) are shown as dashed lines while the experimental data are superimposed as a continuous line. The two SWNT samples were obtained by laser ablation using a Ni-Co catalyst and by arc discharge using a Ni-Y catalyst. The results of the fitting were $d_0 = 1.38$ nm and $\sigma = 0.11$ nm for the former and $d_0 = 1.47$ nm and $\sigma = 0.12$ nm for the latter. These results are in good agreement with the

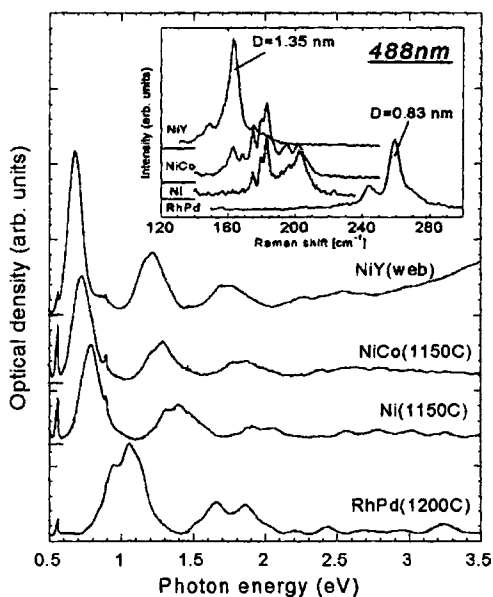


Figure 15. Optical absorption spectra of SWNTs obtained using four different catalysts at different growth temperatures. Inset: Raman spectra obtained on the same set of samples. Reprinted with permission from [78], H. Kataura et al., *Synth. Met.* 103, 2555 (1999). © 1999, Elsevier Science.

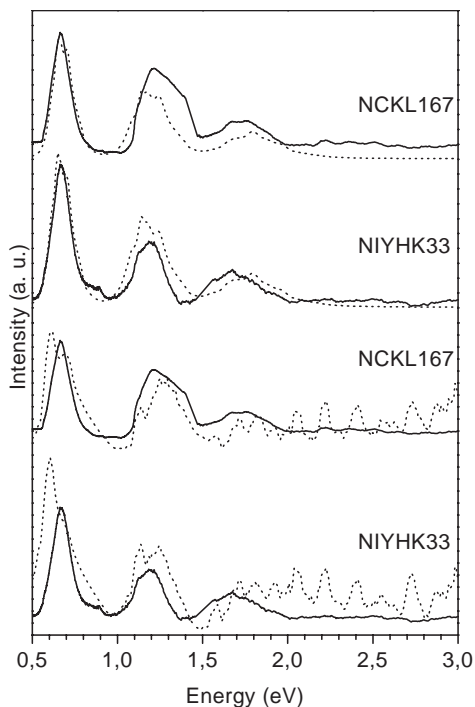


Figure 16. Optical absorption for four different SWNT samples after subtraction of the background (full line). Calculated absorption spectra are shown as dashed lines. The upper two dashed spectra hold for a calculation using the full set of DOS functions. The lower two dashed spectra hold for the approximation according to Eq. (6). Reprinted with permission from [82], H. Kuzmany et al., *Eur. Phys. J. B* 22, 307 (2001). © 2001, Springer-Verlag.

parameters obtained from Raman spectroscopy. The agreement was not only with respect to the RBM band position but also with respect to the line width and intensity.

An alternate analysis of the optical spectra involves an approximation where only the density of states of geometrically allowed nanotubes (chiral angle smaller than 30°) is considered [81]. Again, each nanotube is weighted with a Gaussian probability:

$$\alpha(E) \propto \sum_{n,m,j} \exp\left[-\frac{d_{n,m} - d_0}{2\sigma^2}\right] \times \frac{\delta}{(E - E_{ii}(n,m))^2 + (\delta/2)^2} \quad (7)$$

δ is a small value of the order of 10 meV describing the finite resolution of the spectrometer and the width of the resonant electronic states i due to lifetime effects. $E_{ii}(n,m)$ is a function of the interatomic distance. The π - π overlap integral and the diameters of the SWNTs and their positions ($i = 1, 2, 3$) are taken from the separation between the maxima of the van Hove singularities in the SWNT electronic density of states. The reader is referred to the original work for a full description. The optical absorption data can then be fitted by varying d_0 and σ . It has been said that this is a better approximation than the one described in Eq. 6.

Liu et. al [81] have attempted to draw the vector map of SWNT samples by resolving the fine structure of the optical absorption spectra. Although it is recognized that

an exact assignment of the (n,m) indexes cannot be done solely based on optical absorption data, it was claimed that a reasonable approximation to the chiral angle θ could be obtained. The following equation that describes the absorption profile of a bulk sample of SWNT was proposed:

$$I(E) = f \sum_{n,m} \exp\left[\frac{-(d_{n,m} - d_0)^2}{2(\Delta d)^2}\right] \frac{w}{(E - E_{ii})^2 + (w/2)^2} \quad (8)$$

As in the case of Eq. (7), the energy positions E_{ii} ($i = 1, 2, 3$) are taken from the separation between the maxima of the van Hove singularities in the SWNT electronic density of states [143].

Figure 17 shows the results of one such fitting to the first three absorption peaks of a SWNT sample synthesized by arc discharge using a NiY catalyst. In this case, the authors performed the fitting including all the (n,m) pairs in the SWNT vector map and used a value of 3.0 eV for the tight binding overlap integral. The solid line in the graph represents the experimental data after background subtraction, and the dotted line is the result of the fit. The results of the fit indicated a mean diameter of 1.39 nm and a Δd of 0.09 nm, which was in good agreement with electron diffraction results obtained on the same samples.

For the spectra of the second pair of van Hove singularities, a remarkable improvement was observed in the quality of the fit when only SWNTs with chiral angles between 15° to 30° were used. An example of this improvement is shown in Figure 18. The same improvement was observed on eight different SWNT samples (with different diameter distributions). It was concluded that SWNTs are preferentially formed closer to the armchair rather than zigzag axis during the growth process, a trend previously reported by other authors using electron diffraction and scanning tunneling microscopy [40, 42, 144].

Undoubtedly, since resonance effects do not affect optical absorption, this is a technique more reliable for the quantification of the different kinds of nanotubes present on the sample than Raman spectroscopy. However, it has been

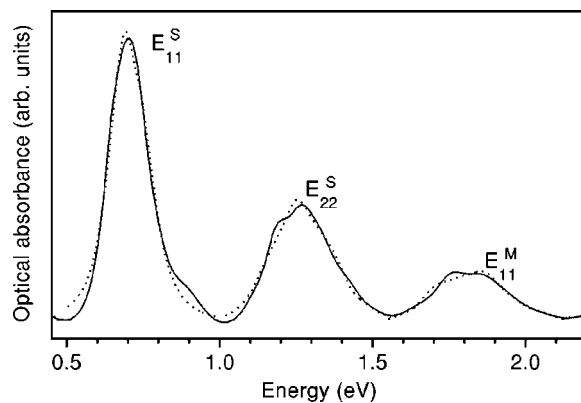


Figure 17. Simulation of the first three optical absorption peaks of sample B with $d = 1.37$ nm using Eq. (8). Nanotubes of all chiralities are included. The solid line is the background subtracted measured spectrum; the dotted line represents the results of the simulation. Reprinted with permission from [81], X. Liu et al., *Phys. Rev. B* 66, 045411 (2002). © 2002, American Physical Society.

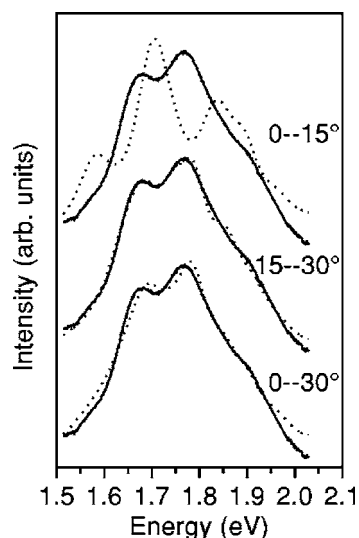


Figure 18. Fitting of the second electronic transition between the second pair of van Hove singularities using Eq. (8); the solid lines are the experimental data (background subtracted) and the dashed lines are the simulation results obtained by using three different SWNT chiral angle distributions (30° stands for the armchair and 0° for the zigzag nanotube). Reprinted with permission from [81], X. Liu et al., *Phys. Rev. B* 66, 045411 (2002). © 2002, American Physical Society.

called to attention by some authors that corrections for the diameter distribution of the SWNTs due to trigonal warping effects need to be considered [142].

Another successful application of optical absorption spectroscopy has been the testing of the electronic structure of SWNTs in the presence of doping agents. For example, it was found that charge transfer induced by either halogen or alkali metal doping causes strong variations in the visible to near infrared range of the absorption spectra [145–147]. An example is presented in Figure 19, in which the absorption spectra of doped SWNTs of *n*-type (Cs) and *p*-type (Br) are reported for different carbon/dopant ratios. It is interesting to notice the disappearance of the absorption bands at 0.7, 1.2 (assigned to semiconducting SWNT), and 1.8 eV (assigned to metallic SWNT). Simultaneous electrochemical measurements showed a concomitant decrease in electrical resistance upon doping. The authors attributed this decrease to electron depletion or filling in specific bands of semiconducting or metallic SWNT. They also proposed an amphoteric doping behavior of SWNTs and claimed that the doping process occurs via charge transfer following a specific sequence. Initially, the transition at 0.7 eV is affected, then that one at 1.2 eV, and finally the feature at 1.8 eV. The extent of the modification depends on the concentration of the dopant [148].

The doping of SWNTs has opened the possibility of tuning the Fermi level of SWNTs by exposing the nanotubes to molecules of different redox potentials. In principle, by choosing an adequate dopant, selective filling or depletion of the density of states can be accomplished. Therefore, the modification of the conducting nature of SWNTs is now a possibility [149]. Optical absorption appears to be the most adequate tool to probe the modifications of the SWNT electronic bands that would occur upon charge transfer.

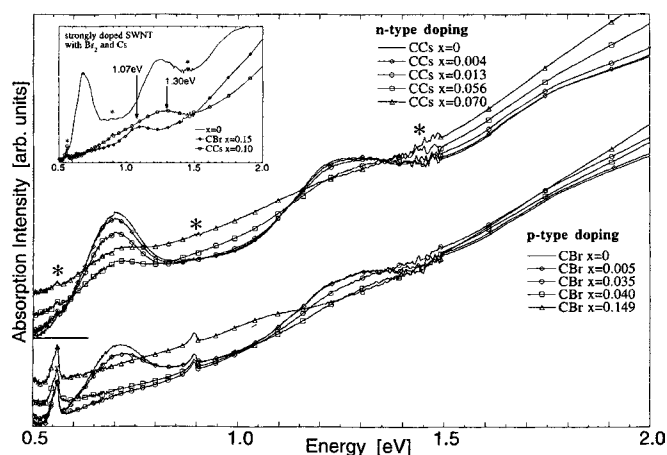


Figure 19. Optical absorption spectra of doped SWNTs for the case of *n*-type (upper set) and *p*-type (lower set). CD, represents the stoichiometry of dopant with respect to carbon (C: carbon, D: dopant, *x*: their ratio). The asterisks indicate absorption due to experimental artifacts. Reprinted with permission from [148], R. Jacquemin et al., *Synth. Met.* 115, 283 (2000). © 2000, Elsevier Science.

2.5. Fluorescence

In direct correspondence to the concepts discussed previously for optical absorption and Raman spectroscopy, the presence of the van Hove singularities in the density of states of SWNTs may result in the emission of radiation at very precise wavelengths if the SWNTs are excited to a higher electronic state through a light induced excitation mechanism. The only condition is the matching between the energy of the excitation light and one of the allowed optical transitions between singularities in the electronic structure of SWNTs. The second condition for emission is that the lifetime of the excited state previous to relaxation is long enough for the process to be measurable. Hence, fluorescence can only be observed on semiconducting SWNTs, in which the absence of a continuum in the density of states at the Fermi level allows a relatively long lifetime of the excited state.

Fluorescence was originally reported on SWNT samples dissolved in organic solvents and integrated in polymer matrices. In those earlier observations, the fluorescence was explained either in terms of electronic structures associated with defects in the nanotubes or in terms of the presence of functional groups that were attached to the SWNT during the functionalization processes [150, 151]. However the absence of fine structure in the emission spectra did not allow linking of the observed emission spectra to the intrinsic electronic structure of SWNTs. A breakthrough in SWNT characterization was recently made by O'Connell et al. [152], who observed fluorescence from SWNT samples consisting of individual nanotubes suspended in aqueous solutions of sodium dodecyl sulfate (SDS). In this suspension, the samples did not undergo any chemical modification. In contrast to the earlier studies, the fluorescence spectra displayed a well-defined fine structure. Figure 20 compares typical emission and absorption spectra for a particular SWNT sample. There is a clear correspondence between each peak in both spectra; that is, each absorption peak in the region of

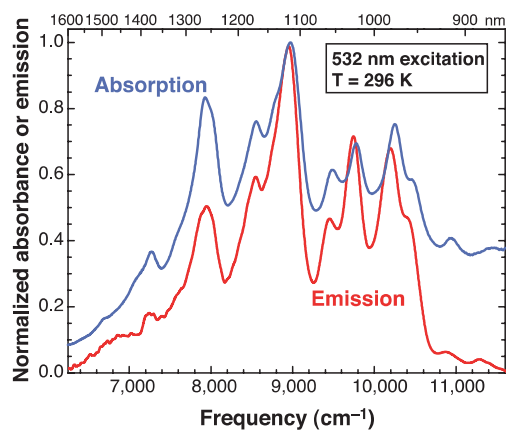


Figure 20. Emission spectrum of individual SWNTs suspended in SDS excited by 8-ns, 532-nm laser pulses, overlaid with the absorption spectrum of the sample in this region of the first van Hove bandgap transitions. Reprinted with permission from [152], M. J. O’Connell et al., *Science* 297, 593 (2002). © 2002, American Association for the Advancement of Science.

the first allowed electronic transition (E_{11}) was also present in the emission spectrum. This correspondence lead the authors to assign the emission spectra to semiconducting SWNTs.

The authors also observed that the photoluminescence intensity was dramatically reduced by aggregation of the SWNT in bundles or by changes on the pH of the SDS solution. This intensity reduction can explain the absence of fine structure on SWNT fluorescence spectra reported in earlier studies.

Another remarkable consequence of this work is that by evaluating the complete excitation–emission matrix in the near infrared to the near ultraviolet range, structural information of individual SWNTs can be obtained. For instance, optical excitation of a SWNT to a second van Hove transition (E_{22}) will be immediately followed by fast relaxation before emission in the first branch transition (E_{11}) is observed. Therefore by monitoring the intensity of the E_{11} transition while varying the excitation energy, the second branch transition E_{22} that gave rise to that particular first branch peak E_{11} can be identified. Figure 21 shows that excitation spectrum for a E_{11} transition of 875 nm. The excitation spectrum showed a distinct second branch (E_{22}) feature centered at 581 nm. The authors were the first to point out that this information could be used to identify the specific indexes (n, m) for every SWNT present in the sample [152]. Soon after, they reported that this goal had indeed been accomplished [153]. They were able to build the entire excitation/emission experimental matrix in the UV-NIR range and each excitation/emission pair was associated with specific E_{11} and E_{22} optical transitions for each individual SWNT. By combining these fluorescence results with the values for SWNT diameter obtained by Raman spectroscopy on the same set of samples and with the results of numerical simulations, a direct assignment of the specific (n, m) nanotube structure for each one of the fluorescence data points peaks was achieved. The measured fluorescence intensity as a function of the nanotube diameter and chiral angle was also obtained. They further assumed that the

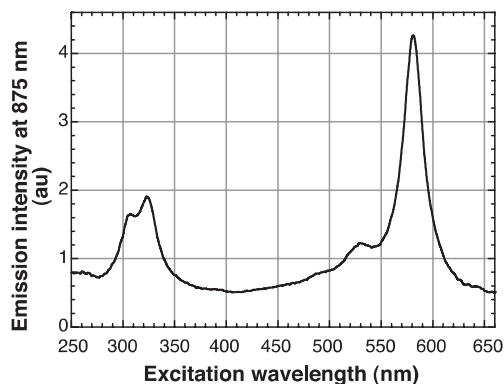


Figure 21. Fluorescence excitation spectrum of the 875-nm bandgap emission feature in a 296 K sample of SWNTs suspended in SDS in H_2O . The strong excitation feature at 581 nm is assigned as the second van Hove absorption of this nanotube species. Reprinted with permission from [152], M. J. O’Connell et al., *Science* 297, 593 (2002). © 2002, American Association for the Advancement of Science.

intensity distribution should closely reflect the distribution of nanotube abundance in the sample. In fact, the variation of quantum yields with diameter or chiral angle has not been clearly established yet, but, as a first approximation, this method provides a direct computation of the distribution of individual SWNT present in a sample. The particular SWNT sample studied by the authors was obtained by CO disproportionation at high pressure, using $Fe(CO)_5$ as a catalyst. The diameter distribution computed for this material was centered at 0.93 nm, while the chiral angle distribution was centered at 30° . The values obtained for the diameter distribution were in good agreement with previous TEM and Raman studies. Of special interest is the result concerning the chiral angle distribution; this outcome is an agreement with previous reports that indicated that SWNT are formed closer to the armchair rather than zigzag structure.

A similar report of photoluminescence in SWNT has been recently reported by another group [154]. In this particular case the SWNT material under study was obtained by pulsed laser vaporization. The authors followed the same methodology described above and obtained a diameter distribution centered at large diameters (around 1.3 nm). Interestingly, the distribution of chiral angles was relatively similar to the one obtained by Bachilo et. al. [153] on SWNT samples produced by the HiPCO process; i.e. a chiral angle distribution with SWNT having a relatively large chiral angles. A new result that again suggests a relative higher stability and abundance of large chiral angle SWNT.

2.6. Temperature Programmed Oxidation

The detailed quantification of the different forms of carbon on a SWNT sample is a difficult task. Electron microscopy can only provide a qualitative description of the type of carbon species produced. Many times, it is hard to determine how representative of the overall production is a given micrograph. At the same time, as mentioned previously, the D/G band ratio in a Raman spectrum can be used as a semiquantitative indication of the presence of undesired (disordered) carbon species. However, Raman spectroscopy does not provide a precise quantification of the

relative amounts of each carbon species present in the sample. In an attempt to make this quantification more precise, Kitiyanan et al. [29] employed temperature programmed oxidation (TPO), a standard technique in catalysis research used to quantify and characterize carbonaceous deposits on heterogeneous catalysts [153, 154]. In a typical TPO experiment, a continuous flow of 5% O₂/He is passed over the catalyst containing the carbon deposits while the temperature is linearly increased (11 °C/min). The evolution of CO₂ produced by the oxidation of the carbon species is monitored by a mass spectrometer. Alternatively, the use of a flame ionization detector (FID) provides a higher carbon sensitivity than the mass spectrometer. In this detection mode, the CO₂ and CO produced during the oxidation can be quantitatively converted to methane in a methanator [155], in which the stream coming from the TPO is mixed with a 50 cm³/min stream of H₂ over a Ni/γ-Al₂O₃ catalyst at 400 °C. The methane produced in the methanator, which exactly corresponds to the CO₂ and CO generated in the TPO, is monitored in a FID. Calibration of the evolved CO and CO₂ with pulses of pure CO₂ or oxidation of known amounts of graphite gives a direct measurement of the amount of carbon that gets oxidized at each temperature. TPO is particularly suitable for the quantitative characterization of SWNTs because SWNTs are oxidized in a relatively narrow temperature range, which lies above the temperature of oxidation of amorphous carbon and below the oxidation of MWNT and graphitic carbon. Thermo-gravimetric analysis (TGA) studies [156] have shown that, in the absence of a catalyst, the ignition temperature of SWNTs is 100 °C higher than that of C₆₀ fullerenes and 100 °C lower than that of MWNTs.

Figure 22 illustrates the TPO profiles of the carbon species produced on a Co:Mo/SiO₂ catalyst, which exhibited high selectivity toward SWNT [29]. This sample presented a small oxidation peak centered at around 330 °C, which can be ascribed to amorphous carbon, and a major peak marked in the figure with an arrow, centered at about 510 °C, which is ascribed to the oxidation of SWNT. Two reference samples

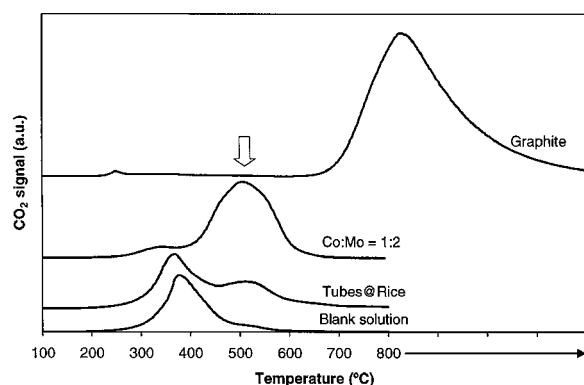


Figure 22. Temperature programmed oxidation of all the carbonaceous species formed over a CoMo/SiO₂ catalyst after disproportionation of CO at 700 °C, compared to similar TPO profiles of a graphite reference and commercial SWNTs obtained from Tubes@Rice. Also included is the TPO of the blank solution, containing a surfactant, in which the commercial SWNTs are dispersed. All the references were physically mixed with bare CoMo/SiO₂ catalyst. Reprinted with permission from [29], B. Kitiyanan et al., *Chem. Phys. Lett.* 317, 497 (2000). © 2000, Elsevier Science.

were compared to this TPO and their profiles are included in the figure. The first reference is a graphite powder physically mixed with the bare Co:Mo catalyst. The oxidation of this form of carbon occurred at very high temperatures, starting at about 700 °C, and completed after holding for 30 minutes at 800 °C. The second reference is a commercial sample of purified SWNTs, obtained from Nanotubes@Rice (Rice University). This sample came in a liquid suspension of 5.9 grams/liter, containing a nonionic surfactant Triton X-100. To conduct the TPO experiment, this suspension was impregnated on the Co:Mo/SiO₂ catalyst to get 0.6 wt% SWNTs on the sample. As shown in Figure 2, the TPO of this impregnated sample exhibited two peaks, a low-temperature one that corresponds to the oxidation of the surfactant and a second one centered at 510 °C, which corresponds exactly to the position ascribed to the oxidation of SWNTs. To corroborate that the first peak was indeed due to the oxidation of Triton, a sample was prepared with a blank solution containing only the surfactant in the same concentration. The TPO shows that indeed that was the case. The quantification of the amount of SWNT in the sample from the CO₂ produced gave a value of 0.64 wt%, in good agreement with the amount of SWNT loaded in the sample (0.6 wt%).

TPO is a quick test for different catalyst formulations. For example, Figure 23 shows the clear synergistic effect exhibited by Co and Mo. In the first place, Mo alone does not produce carbon nanotubes and only exhibits a small low-temperature peak corresponding to amorphous carbon. The term “amorphous carbon” implies carbonaceous deposits, which are not in the form of ordered nanotubes or graphite. The claim that the Mo-alone sample only produced amorphous carbon was substantiated by the absence of graphite or nanotubes in the TEM observations. On the other hand, Co alone is not selective for the production of SWNTs and generates mainly graphitic carbon and MWNTs. Again, these observations were corroborated by TEM. By contrast, the combination of the two metals in appropriate ratio results in high selectivity for SWNTs. TPO has also been used to study the effect of varying the Co:Mo molar

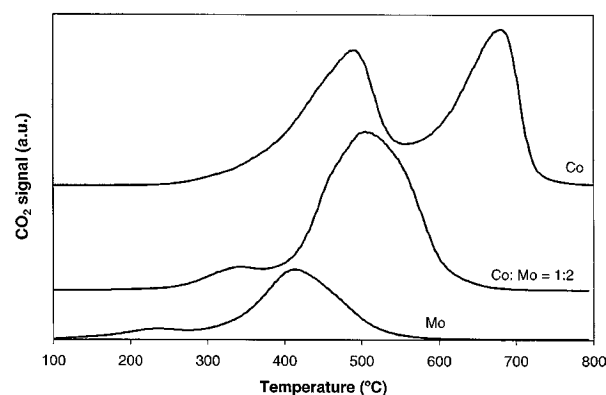


Figure 23. Temperature programmed oxidation of all the carbonaceous species formed over a CoMo/SiO₂ catalyst after disproportionation of CO at 700 °C, compared to monometallic Co/SiO₂ and Mo/SiO₂ catalysts, treated in an identical way. Reprinted with permission from [29], B. Kitiyanan et al., *Chem. Phys. Lett.* 317, 497 (2000). © 2000, Elsevier Science.

ratio in the Co–Mo/SiO₂ catalysts. Figure 24 shows that, in agreement with the TEM characterization, the TPO of the Co:Mo = 1:2 sample indicates that this sample produced mostly SWNTs, with a small amount of amorphous carbon. An increase in the Co:Mo ratio did not enhance the production of SWNTs, but it did accelerate the formation of MWNTs and graphitic carbon, as shown by the increasing size of the peaks in the region 600–700 °C. From the TPO data, selectivity values were estimated by curve fitting. They were 57% SWNT and 31% MWNT for the Co:Mo (2:1), 80% SWNT and 4% MWNT for the Co:Mo (1:1), and 88% SWNT and 4% MWNT for the Co:Mo (1:2). It is important to note that, in all cases, the quantitative data agreed very well with the qualitative observations made by TEM.

2.6.1. In-Situ TPO/Raman

The combination of TPO and Raman provides interesting details about the structure of nanotubes. For example, the application of this combination of techniques to study raw and purified HipCO materials is illustrated in Figures 25 and 26. The TPO analysis of Figure 25 indicates that the amount of carbon present on the samples was 83% and 99%, respectively; the difference represents the amount of Fe removed in the purification process. A comparison between both profiles shows that there are four different carbonaceous species present on the purified material, each one showing a different behavior toward oxidation by O₂. Three of these new carbonaceous species (peak position 600, 700, and 750 °C in the TPO profile) originated during the purification process since the location of the first maximum present on the profile of the purified material (peak at 400 °C) corresponds to the maximum of the TPO of the raw sample. This would indicate that after the purification step a fraction of the material remains in the same state as the raw sample.

The Raman characterization conducted in combination with the TPO is shown in Figure 26. Raman spectra were obtained after *in-situ* partial oxidation steps; that is, the spectra were acquired at room temperature and then after oxidation steps at 400, 500, and 630 °C under the same conditions used to get the TPO profiles. The Raman spectra

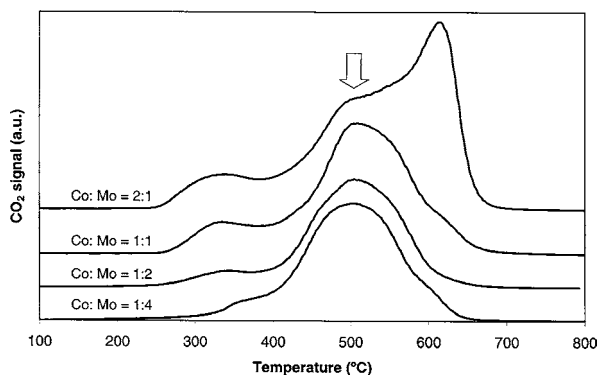


Figure 24. Temperature programmed oxidation of all the carbonaceous species formed over a CoMo/SiO₂ catalyst with four different Co/Mo molar ratios after disproportionation of CO at 700 °C. Reprinted with permission from [29], B. Kitiyanan et al., *Chem. Phys. Lett.* 317, 497 (2000). © 2000, Elsevier Science.

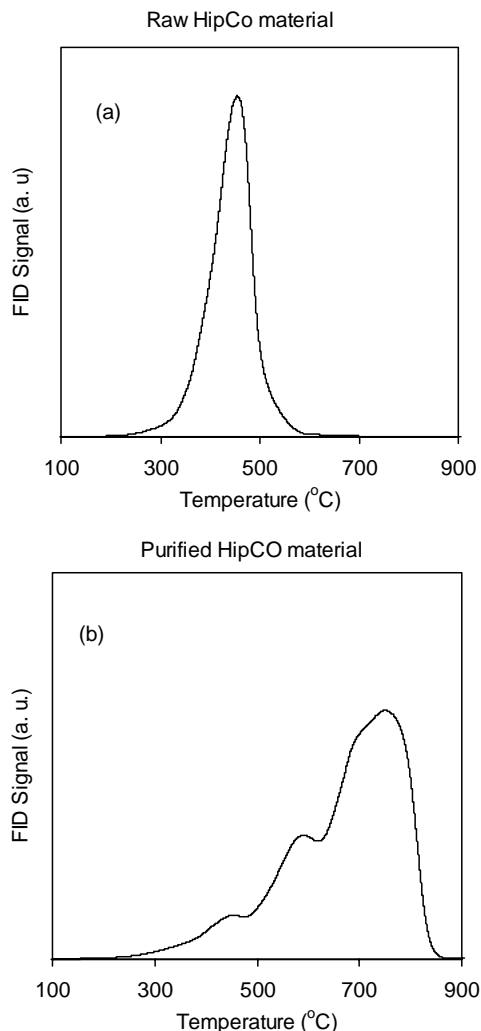


Figure 25. Temperature programmed oxidation profiles of the carbonaceous species present in (a) raw HipCO material and (b) purified HipCO material. The profiles were obtained using a mixture of 5% of O₂ in He at a heating rate of 12 °C/min.

(low *D/G* ratio) indicate that SWNTs are the predominant carbon species present on both purified and raw samples. That is, all of the TPO peaks in the purified material are associated with SWNTs. Consequently, the different TPO peaks in the purified sample are only due to parts of the sample that contain different amounts of residual Fe.

A second example of the combined application of TPO and Raman is a study of two different raw SWNT materials synthesized by CO disproportionation: one obtained over a highly selective Co–Mo metallic catalyst (low Co:Mo ratio) in which SWNTs are the dominant species, and the other obtained over an unselective catalysts (high Co:Mo ratio) in which SWNTs, MWNTs, graphite, and amorphous carbon are present [29]. Figure 27a and b shows the TPO profiles of each material. As expected, the sample obtained over the highly selective catalyst, which contains mostly SWNTs shows a single peak centered at 570 °C. It has been previously shown that under the TPO conditions and while still immersed in this particular catalyst, the SWNTs get oxidized in a relatively narrow temperature range, which lies

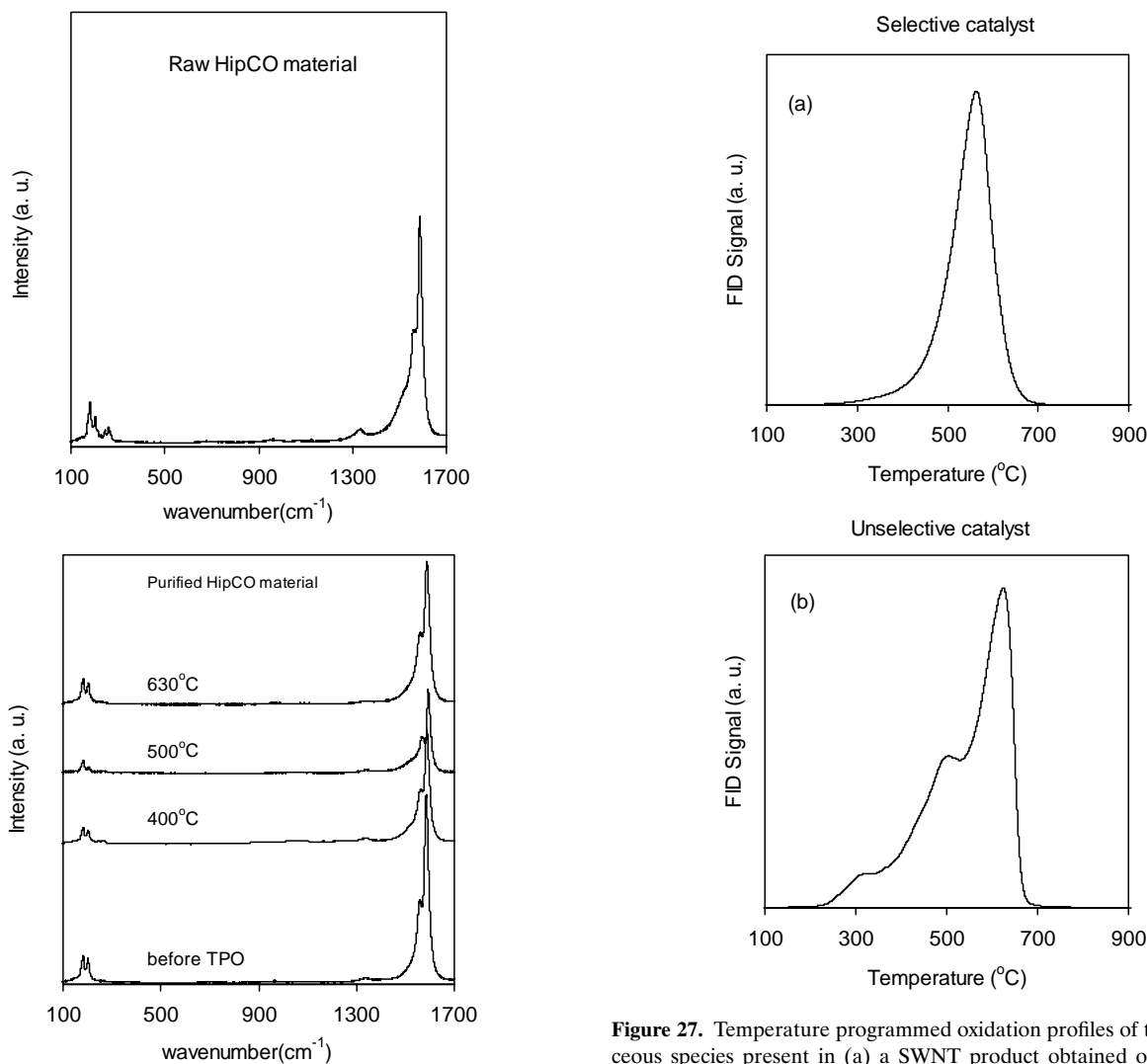


Figure 26. Resonant Raman spectra obtained for (a) raw HiPCO material at room temperature and (b) purified HiPCO material before and after subsequent *in-situ* oxidation steps at 400, 500, and 630 °C. The laser excitation wavelength was 514 nm.

below the temperature in which MWNT, graphite, and carbon fibers are oxidized, but above the temperature at which amorphous and chemically impure carbon species are oxidized [29]. However, an interesting difference is observed in this case on the position of the maximum between the TPO profile obtained for this material and that obtained on the HiPCO raw material (Fig. 25). Even though both profiles exhibit a single peak, the one corresponding to SWNTs obtained on the Co–Mo catalyst appears at more than 100 °C higher temperature than the HiPCO nanotubes. This difference in peak position can only be due to the catalytic effect of the residual metals since the types of carbon species in both samples are similar. The material obtained by the HiPCO process contains an amount of iron catalyst up to 30% in weight [157]. The sample obtained over the Co–Mo catalyst contains less than 5% of Co and Mo metal impurities [28] and, perhaps more importantly, contains a large excess of silica support that may separate the nano-

Figure 27. Temperature programmed oxidation profiles of the carbonaceous species present in (a) a SWNT product obtained over a highly selective Co–Mo catalyst and (b) a low quality product obtained over an unselective Co–W catalyst. The profiles were obtained using a mixture of 5% O₂ in He at a heating rate of 12 °C/min.

tubes from the metal. Consequently, the material obtained by the HiPCO process has a larger amount of metal in close contact with the SWNTs. This metal catalyzes the oxidation of SWNTs during the TPO process and lowers the temperature of the peak.

The corresponding analysis after *in-situ* oxidation steps at 450 and 500 °C under the same conditions used to get the TPO is shown in Figure 28. The spectra show that the sample is indeed composed by high quality SWNTs. There also are some differences after the different TPO stages. A decrease in the contribution of the D band to the whole spectra is observed at higher oxidation temperatures. Before the oxidation at 450 °C some amorphous and chemically impure carbon species may be present. Therefore the first oxidation step eliminates the amorphous carbon material from the samples. This results in the decrease of the relative intensity of the D band in the Raman spectra. However, as shown in Figure 28, a subsequent oxidation step (500 °C) does not change the contribution of the D band to the spec-

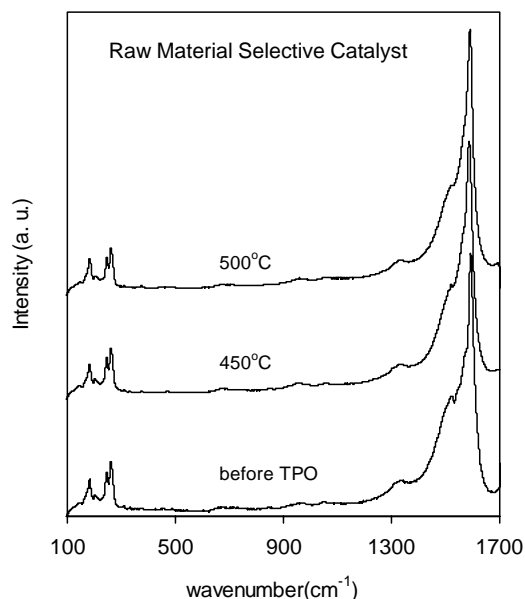


Figure 28. Resonant Raman spectra obtained for the carbon deposits obtained over a highly selective Co–Mo catalyst. The spectra were acquired before and after subsequent *in-situ* oxidation steps at 450 and 550 °C. The laser excitation wavelength was 514 nm.

tra, since at this temperature all amorphous carbon has been removed.

A contrasting behavior is observed for the TPO profile of the material obtained over the unselective catalyst, as shown in Figure 27b. Similar to the TPO of the purified HiPCO material, three peaks are obtained. *In-situ* Raman spectroscopy was used to identify the different kinds of carbonaceous species responsible for each of the TPOs. In this particular case, the spectra were acquired at room temperature and then after subsequent *in-situ* oxidation steps

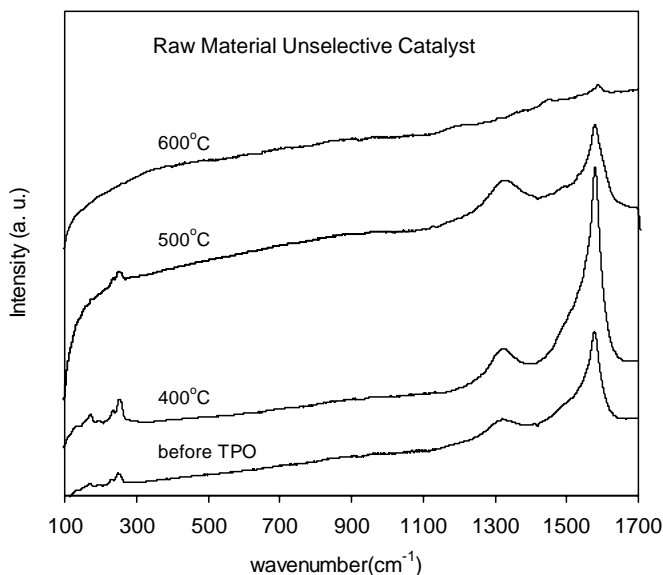


Figure 29. Resonant Raman spectra obtained for the carbon deposits obtained over an unselective Co–W catalyst. The spectra were acquired before and after subsequent *in-situ* oxidation steps. The laser excitation wavelength was 514 nm.

at 400, 500, and 600 °C under the same conditions used in the TPO experiments. Figure 29 shows the corresponding Raman spectra. It can be observed that the relative intensity of the *D* band is much stronger in this case than for any of the other samples. This clearly reveals the low SWNT selectivity this particular catalyst. An interesting variation is observed in the *D/G* ratio as a function of oxidation temperature. After the first oxidation step (400 °C) the *D/G* ratio clearly decreases due to the burning of amorphous carbon, similar to the previous case of the selective sample. However, as the oxidation temperature increases, the *D/G* ratio quickly increases. This increase is to a decrease in the amount of ordered SWNTs compared to the disordered MWNTs and graphite nanofibers that resist oxidation to higher temperatures [158].

GLOSSARY

Density of states (DOS) Solid state physics concept which is defined as the number of allowed energy levels (states) per unit interval of energy.

Electron diffraction Electron microscopic analysis, which can be used to determine the three-dimensional structures of macromolecules at resolutions ranging between 3 and 30 Å. It is based on the diffraction of an electron beam by a specimen.

Multiwalled carbon nanotube (MWNT) Set of graphene honeycombs rolled into several concentric graphene cylinders.

Raman spectroscopy Technique based on the inelastic scattering of electromagnetic radiation (200–1600 nm) by a sample. The wavelength of the scattered light depends on the molecular vibrational modes of the species present of the sample.

Scanning electron microscopy (SEM) Microscopy technique that uses a beam of electrons instead of light. The beam is scanned across the surface of a specimen, while the yield of backscattered and secondary electrons generated in the process are used to form a three-dimensional image. Magnifications can easily exceed 50,000X.

Scanning tunneling microscopy (STM) Microscopy technique that uses a beam of electrons instead of light. A very sharp tip at a small positive potential is scanned across the surface of a specimen, while the tunneling current generated during the process is recoded as a function of the distance between the tip and the sample. Atomic resolution can be achieved when the tunneling current as a function of distance is used to map the specimen.

Single-walled carbon nanotube (SWNT) A graphene honeycomb rolled into a single-walled cylinder.

Temperature programmed oxidation (TPO) A temperature-programmed technique in which the oxidation process is monitored, usually through the measure of the concentration of the oxidation product(s), while the temperature of the process is increased linearly in time.

Transmission electron microscopy (TEM) Microscopy technique that uses a beam of electrons instead of light. The beam of electrons impinge on the sample; the electrons transmitted across the sample are used to form a two-dimensional image.

van Hove singularities Peaks on the density of states of SWNTs that are present on these structures due to their one-dimensional structure.

REFERENCES

1. H. W. Kroto, J. R. Heath, S. C. O'Brien, R. F. Curl, and R. E. Smalley, *Nature* 318, 162 (1985).
2. S. Iijima, *Nature* 354, 56 (1991).
3. S. Iijima and T. Ichihashi, *Nature* 363, 603 (1993).
4. D. S. Bethune, C. H. Kiang, M. S. de Vries, G. Gorman, R. Savoy, J. Vazquez, and R. Beyers, *Nature* 363, 605 (1993).
5. W. Kratschmer, L. D. Lamb, K. Fostiropoulos, and D. R. Huffman, *Nature* 347, 354 (1990).
6. R. Bacon, *J. Appl. Phys.* 31, 284 (1960).
7. Y. Saito, M. Okuda, and T. Koyama, *Surf. Rev. Lett.* 3, 863 (1996).
8. T. W. Ebbesen and P. M. Ajayan, *Nature* 358, 220 (1992).
9. Y. Saito, M. Okuda, and T. Yoshikawa, *Jpn. J. Appl. Phys.* 33, L186 (1994).
10. H. Lange, P. Baranowski, A. Huckzo, and P. Byszewski, *Rev. Sci. Instrum.* 68, 3723 (1997).
11. Y. Ando, X. Zhao, H. Kataura, Y. Achiba, K. Kaneto, M. Tsuruta, S. Uemura, and S. Iijima, *Diamond Relat. Mater.* 9, 847 (2000).
12. X. K. Wang, X. W. Lin, V. P. Dravid, J. B. Ketterson, and R. P. H. Chang, *Appl. Phys. Lett.* 62, 1881 (1993).
13. Y. Ando and S. Iijima, *J. Appl. Phys.* 32, L107 (1993).
14. Y. Saito, Y. Tani, and A. Kasuya, *J. Phys. Chem. B* 104, 2495 (2000).
15. A. Thess, R. Lee, P. Nikolaev, H. Dai, P. Petit, J. Robert, C. Xu, Y. H. Lee, S. G. Kim, A. G. Rinzler, D. T. Colbert, G. E. Scuseria, D. Tomanek, J. E. Fischer, and R. E. Smalley, *Science* 273, 483 (1996).
16. M. Yudasaka, T. Komatsu, T. Ichihashi, Y. Achiba, and S. Iijima, *J. Phys. Chem. B* 102, 4892 (1998).
17. M. Yudasaka, M. Zhang, and S. Iijima, *Chem. Phys. Lett.* 323, 549 (2000).
18. P. C. Eklund, B. K. Pradhan, U. J. Kim, Q. Xiong, J. E. Fischer, A. D. Friedman, B. C. Holloway, K. Jordan, and M. W. Smith, *Nano Lett.* 2, 561 (2002).
19. C. L. Cheung, A. Kurtz, H. Park, and C. M. Lieber, *J. Phys. Chem. B* 106, 2429 (2002).
20. O. Jost, A. A. Gorbunov, J. Moller, W. Pompe, A. Graff, R. Friedlein, X. Liu, M. S. Golden, and J. Fink, *Chem. Phys. Lett.* 339, 297 (2001).
21. Y. Li, W. Kim, Y. Zhang, M. Rolandi, D. Wang, and H. Dai, *J. Phys. Chem. B* 105, 11424 (2001).
22. A. Peigney, Ch. Laurent, F. Dobigeon, and A. Rousset, *J. Mater. Res.* 12, 613 (1997).
23. A. Peigney, Ch. Laurent, O. Dumortier, and A. Rousset, *J. Eur. Ceram. Soc.* 18, 1995 (1998).
24. Ch. Laurent, A. Peigney, and A. Rousset, *J. Mater. Chem.* 8, 1263 (1998).
25. Ch. Laurent, A. Peigney, E. Flahaut, and A. Rousset, *Mater. Res. Bull.* 35, 661 (2000).
26. O. Quenard, E. De Grave, Ch. Laurent, and A. Rousset, *J. Mater. Chem.* 7, 2457 (1997).
27. A. Govindaraj, E. Flahaut, Ch. Laurent, A. Peigney, A. Rousset, and C. N. R. Rao, *J. Mater. Res.* 14, 2567 (1999).
28. D. E. Resasco, W. E. Alvarez, F. Pompeo, L. Balzano, J. E. Herrera, B. Kitiyanan, and A. Borgna, *J. Nanopart. Res.* 4, 131 (2002).
29. B. Kitiyanan, W. E. Alvarez, J. H. Harwell, and D. E. Resasco, *Chem. Phys. Lett.* 317, 497 (2000).
30. J. E. Herrera, L. Balzano, A. Borgna, W. E. Alvarez, and D. E. Resasco, *J. Catal.* 204, 129 (2001).
31. W. E. Alvarez, B. Kitiyanan, A. Borgna, and D. E. Resasco, *Carbon* 39, 547 (2001).
32. W. E. Alvarez, F. Pompeo, J. E. Herrera, L. Balzano, and D. E. Resasco, *Chem. Mater.* 14, 1853 (2002).
33. E. Flahaut, A. Peigney, Ch. Laurent, and A. Rousset, *J. Mater. Chem.* 10, 249 (2000).
34. X. P. Gao, X. Qin, F. Wu, H. Liu, Y. Lan, S. S. Fan, H. T. Yuan, D. Y. Song, and P. W. Shen, *Chem. Phys. Lett.* 327, 271 (2000).
35. P. Coquay, A. Peigney, E. De Grave, R. E. Vandenberghe, and Ch. Laurent, *J. Phys. Chem. B* 106, 13199 (2002).
36. R. Sen, A. Govindaraj, and C. N. R. Rao, *Chem. Phys. Lett.* 267, 276 (1997).
37. R. Sen, A. Govindaraj, and C. N. R. Rao, *Chem. Mater.* 9, 2078 (1997).
38. M. J. Bronikowski, P. A. Willis, D. T. Colbert, K. A. Smith, and R. E. Smalley, *J. Vac. Sci. Technol. A* 19, 1800 (2001).
39. C. Journet, W. K. Maser, P. Bernier, A. Loiseau, M. Lamy de la Chapelle, S. Lefrant, P. Deniard, R. Lee, and J. E. Fischer, *Nature* 388, 756 (1997).
40. J. M. Cowley, P. Nikolaev, A. Thess, and R. E. Smalley, *Chem. Phys. Lett.* 265, 379 (1997).
41. Ph. Lambin and A. Lucas, *Phys. Rev. Lett. B* 56, 3571 (1997).
42. L. Henrard, A. Loiseau, C. Journet, and P. Bernier, *Synth. Met.* 103, 2533 (1999).
43. S. Rols, R. Almairac, L. Henrard, E. Anglaret, and J.-L. Sauvajol, *Eur. Phys. J. B.* 10, 263 (1999).
44. L. Henrard, A. Loiseau, C. Journet, and P. Bernier, *Eur. Phys. J. B* 13, 661 (2000).
45. J. L. Zimmerman, R. K. Bradley, C. B. Huffman, R. H. Hauge, and J. L. Margrave, *Chem. Mater.* 12, 1361 (2000).
46. T. W. Odom, J.-L. Huang, and C. M. Lieber, *J. Phys.: Condens. Matter* 14, R145 (2002).
47. M. Ouyang, J.-L. Huang, and C. M. Lieber, *Annu. Rev. Phys. Chem.* 53, 201 (2002).
48. J. A. Stroschio and W. J. Kaiser, "Scanning Tunneling Microscopy." Academic Press, San Diego, 1993.
49. L. C. Venema, V. Meunier, Ph. Lambin, and C. Dekker, *Phys. Rev. B* 61, 2991 (2000).
50. M. Ge and K. Sattler, *Appl. Phys. Lett.* 65, 2284 (1994).
51. V. Meunier and Ph. Lambin, *Phys. Rev. Lett.* 81, 5888 (1998).
52. J. W. G. Wildöer, L. C. Venema, A. G. Rinzler, R. E. Smalley, and C. Dekker, *Nature* 391, 59 (1998).
53. T. W. Odom, J.-L. Huang, P. Kim, and C. M. Lieber, *Nature* 391, 62 (1998).
54. T. W. Odom, J.-L. Huang, P. Kim, and C. M. Lieber, *J. Phys. Chem. B* 104, 2794 (2000).
55. P. Kim, T. W. Odom, J.-L. Huang, and C. M. Lieber, *Phys. Rev. Lett.* 82, 1225 (1999).
56. N. Hamada, S. Sawada, and A. Oshiyama, *Phys. Rev. Lett.* 68, 1579 (1992).
57. J. Hu, T. W. Odom, and C. M. Lieber, *Acc. Chem. Res.* 32, 435 (1999).
58. X. Blase, L. X. Benedict, E. L. Shirley, and S. G. Louie, *Phys. Rev. Lett.* 72, 1878 (1994).
59. J. C. Charlier and Ph. Lambin, *Phys. Rev. B* 57, R15037 (1998).
60. T. W. Odom, J.-L. Huang, P. Kim, and C. M. Lieber, *J. Phys. Chem. B* 104, 2794 (2000).
61. M. B. Bockrath, D. H. Cobden, P. L. McEuen, N. G. Chopra, A. Zettl, A. Thess, and R. E. Smalley, *Science* 275, 1922 (1997).
62. S. J. Tans, M. H. Devoret, H. Dai, A. Thess, R. E. Smalley, L. J. Geerligs, and C. Dekker, *Nature* 386, 474 (1997).
63. L. C. Venema, J. W. G. Wildoer, H. L. J. T. Tuinstra, C. Dekker, A. G. Rinzler, and R. E. Smalley, *Appl. Phys. Lett.* 71, 2629 (1997).
64. L. C. Venema, J. W. G. Wildoer, J. W. Janssen, S. J. Tans, H. L. J. T. Tuinstra, L. P. Kouwenhoven, and C. Dekker, *Science* 283, 52 (1999).
65. M. Ouyang, J. L. Huang, C. L. Cheung, and C. M. Lieber, *Science* 291, 97, (2001).

66. M. Ouyang, J. L. Huang, C. L. Cheung, and C. M. Lieber, *Acc. Chem. Res.* 35, 1018 (2002).
67. K. F. Kelly, I. W. Chiang, E. T. Mickelson, R. H. Hauge, J. L. Margrave, X. Wang, G. E. Scuseria, C. Radloff, and N. J. Halas, *Chem. Phys. Lett.* 313, 445 (1999).
68. R. Merlin, A. Pinczuk, and W. H. Weber, in "Raman Scattering in Material Science" (W. H. Weber, and R. Merlin, Eds.). Springer Scientific, Berlin, 2000.
69. S. A. Asher, *Anal. Chem.* 65, 59A (1993).
70. S. A. Asher, *Anal. Chem.* 65, 201A (1993).
71. S. A. Asher, *Annu. Rev. Phys. Chem.* 39, 537 (1988).
72. A. Kasuya, M. Sugano, T. Maeda, Y. Saito, K. Tohji, H. Takahashi, Y. Sasaki, M. Fukushima, Y. Nishina, and C. Horie, *Phys. Rev. B* 57, 4999 (1998).
73. M. S. Dresselhaus, G. F. Dresselhaus, and R. Saito, *Solid State Commun.* 84, 201 (1992).
74. E. Richter and K. R. Subbaswamy, *Phys. Rev. Lett.* 79, 2738 (1997).
75. M. A. Pimenta, A. Marucci, S. A. Empedocles, M. G. Bawendi, E. B. Hanlon, A. M. Rao, P. C. Eklund, R. E. Smalley, G. Dresselhaus, and M. S. Dresselhaus, *Phys. Rev. B* 58, R16016 (1998).
76. C. T. White and T. N. Todorov, *Nature* 393, 240 (1998).
77. D. Östling, D. Tománek, and A. Rosén, *Phys. Rev. B* 55, 13980 (1997).
78. H. Kataura, Y. Kumazawa, Y. Maniwa, I. Umez, S. Suzuki, Y. Ohtsuka, and Y. Achiba, *Synth. Met.* 103, 2555 (1999).
79. P. Corio, S. D. M. Brown, A. Marucci, M. A. Pimenta, K. Kneipp, G. Dresselhaus, and M. S. Dresselhaus, *Phys. Rev. B* 61, 13202 (2000).
80. S. Reich and C. Thomsen, *Phys. Rev. B* 62, 4273 (2000).
81. X. Liu, T. Pichler, M. Knupfer, M. S. Golden, J. Fink, H. Kataura, and Y. Achiba, *Phys. Rev. B* 66, 045411 (2002).
82. H. Kuzmany, W. Plank, M. Hulman, Ch. Kramberger, A. Gruneis, Th. Pichler, H. Peterlik, H. Kataura, and Y. Achiba, *Eur. Phys. J. B* 22, 307 (2001).
83. O. Jost, A. A. Gorbunov, W. Pompe, T. Pichler, R. Friedlein, M. Knupfer, M. Reibold, H.-D. Bauer, L. Dunsch, M. S. Golden, and J. Fink, *Appl. Phys. Lett.* 75, 2217 (1999).
84. M. S. Dresselhaus, M. A. Pimenta, P. C. Eklund, and G. Dresselhaus, in "Raman Scattering in Material Science" (W. H. Weber, and R. Merlin, Eds.). Springer Scientific, Berlin, 2000.
85. R. A. Jishi, L. Venkataraman, M. S. Dresselhaus, and G. Dresselhaus, *Chem. Phys. Lett.* 209, 77 (1993).
86. A. M. Rao, E. Richter, S. Bandow, B. Chase, P. C. Eklund, K. A. Williams, S. Fang, K. Subbaswamy, M. Menon, A. Thess, R. E. Smalley, G. Dresselhaus, and M. S. Dresselhaus, *Science* 187, 275 (1997).
87. M. Sugano, A. Kasuya, K. Tohji, Y. Saito, and Y. Nishina, *Chem. Phys. Lett.* 292, 575 (1998).
88. J. E. Herrera, L. Balzano, F. Pompeo, and D. E. Resasco, *J. Nanotech.*, in press.
89. P. M. Rafailov, H. Jantoljak, and C. Thomsen, *Phys. Rev. B* 61, 16179 (2000).
90. D. Sanchez-Portal, E. Artacho, J. M. Soler, A. Rubio, and P. D. Ordejon, *Phys. Rev. B* 59, 12678 (1999).
91. J. Kurti, G. Kresse, and H. Kuzmany, *Phys. Rev. B* 58, R8869 (1998).
92. R. Saito, T. Takeya, T. Kimura, G. Dresselhaus, and M. S. Dresselhaus, *Phys. Rev. B* 57, 4145 (1998).
93. S. Bandow, S. Asaka, Y. Saito, A. M. Rao, L. Grigorian, E. Richter, and P. C. Eklund, *Phys. Rev. Lett.* 80, 3779 (1998).
94. A. M. Rao, J. Chen, E. Richter, U. Schlecht, P. C. Eklund, R. C. Haddon, U. D. Venkateswaran, Y.-K. Kwon, and D. Tomanek, *Phys. Rev. Lett.* 86, 3895 (2001).
95. S. Rols, A. Righi, L. Alvarez, E. Anglaret, R. Almairac, C. Journet, P. Bernier, J. L. Sauvajol, A. M. Benito, W. K. Maser, E. Munoz, M. T. Martinez, G. F. de la Fuente, A. Girard, and J. C. Ameline, *Eur. Phys. J. B* 18, 201 (2000).
96. U. D. Venkateswaran, A. M. Rao, E. Richter, M. Menon, A. Rinzler, R. E. Smalley, and P. C. Eklund, *Phys. Rev. B* 59, 10928 (1999).
97. A. Claye, S. Rahman, J. E. Fischer, G. Sumanasekera, and P. C. Eklund, *Chem. Phys. Lett.* 333 1 (2001).
98. V. G. M. N. I. Hadjiev, S. Arepalli, P. Nikolaev, and B. S. Files, *Appl. Phys. Lett.* 78, 3193 (2001).
99. A. M. Rao, S. Bandow, E. Richter, and P. C. Eklund, *Thin Solid Films* 331, 141 (1998).
100. J. Chen, A. M. Rao, S. Lyuksyutov, M. E. Itkis, M. A. Hamon, H. Hui, R. W. Cohn, P. C. Eklund, D. T. Colbert, R. E. Smalley, and R. C. Haddon, *J. Phys. Chem. B* 105, 2525 (2001).
101. K. A. Williams, B. K. Pradhan, P. C. Eklund, M. K. Kostov, and M. W. Cole, *Phys. Rev. Lett.* 88 165502 (2002).
102. U. D. Venkateswaran, E. A. Brandsen, U. Schlecht, A. M. Rao, E. Richter, I. Loa, K. Syassen, and P. C. Eklund, *Phys. Status Solidi B* 223, 225 (2001).
103. G. S. Duesberg, J. Muster, M. Burghard, H. J. Byrne, and S. Roth, in "Science and Technology of Molecular Nanostructures" (H. Kuzmany, J. Fink, M. Mehring, and S. Roth, Eds.), p. 338. *Am. Inst. of Phys.*, New York, 1999.
104. S. Farhat, M. Lamy de La Chapelle, A. Loiseau, C. D. Scott, S. Lefrant, C. Journet, and P. Bernier, *J. Chem. Phys.* 115, 6277 (2001).
105. E. D. Obraztsova, V. Yu. Yurov, V. M. Shevluga, R. E. Baranovsky, V. A. Nalimova, V. L. Kuznetsov, and V. I. Zaikovskii, *Nanostruct. Mater.* 11, 295 (1999).
106. P. Corio, M. L. A. Temperini, P. S. Santos, J. V. Romero, J. G. Huber, C. A. Luengo, S. D. M. Brown, M. S. Dresselhaus, G. Dresselhaus, M. S. S. Dantas, C. F. Leite, F. Matinaga, J. C. Gonzalez, and M. A. Pimenta, *Chem. Phys. Lett.* 350, 373 (2001).
107. S. Reich, C. Thomsen, G. S. Duesberg, and S. Roth, *Phys. Rev. B* 63, 041401 (2001).
108. M. A. Pimenta, A. Marucci, S. D. M. Brown, M. J. Matthews, A. M. Rao, P. C. Eklund, R. E. Smalley, G. Dresselhaus, and M. S. Dresselhaus, *J. Mater. Res.* 13, 2396 (1998).
109. M. A. Pimenta, A. Jorio, M. Souza, M. S. S. Dantas, A. M. Rao, R. Saito, G. Dresselhaus, and M. S. Dresselhaus, *Bull. Am. Phys. Soc.* 45, March 20–24 (2000).
110. M. A. Pimenta, M. Jorio, S. D. M. Brown, A. G. Souza Filho, G. Dresselhaus, J. H. Hafner, C. M. Lieber, R. Saito, and M. S. Dresselhaus, *Phys. Rev. B* 64, 41401R (2001).
111. R. Saito, M. Fujita, G. Dresselhaus, and M. Dresselhaus, *Appl. Phys. Lett.* 60, 2204 (1992).
112. M. Milnera, J. Kurti, M. Hulman, and H. Kuzmany, *Phys. Rev. Lett.* 84, 1324 (2000).
113. M. Hulman, W. Plank, and H. Kuzmany, *Phys. Rev. B* 63, 81406 (2001).
114. D. Laplaze, P. Bernier, W. K. Maser, G. Flamant, T. Guillard, and A. Loiseau, *Carbon* 36, 685 (1998).
115. F. Tuinstra and J. L. Koenig, *J. Chem. Phys.* 53, 1126 (1970).
116. M. A. Pimenta, A. Jorio, S. D. M. Brown, A. G. Souza Filho, G. Dresselhaus, J. H. Hafner, C. M. Lieber, R. Saito, and M. S. Dresselhaus, *Phys. Rev. B* 64, 41401R (2001).
117. M. S. Dresselhaus, G. Dresselhaus, M. A. Pimenta, and P. C. Eklund, in "Applications of Raman Spectroscopy" (M. J. Pelletier, Eds.), p. 367. Blackwell Science, Oxford, 1999.
118. J. Maultzsch, S. Reich, and C. Thomsen, *Phys. Rev. B* 64, 121407(R) (2001).
119. H. Jantoljak, U. Kuhlmann, C. Thomsen, S. Curran, S. Roth, W. Maser, C. Journet, and P. Bernier, *Mol. Cryst. Liq. Cryst. Sci. Technol. C* 10, 145 (1998).
120. M. S. Dresselhaus, G. Dresselhaus, and R. Saito, *Phys. Rev. B* 45, 6234 (1992).
121. D. Kahn and J. P. Lu, *Phys. Rev. B* 60, 6535 (1999).
122. M. N. Iliev, A. P. Litvinchuk, S. Arepalli, P. Nikolaev, and C. D. Scott, *Chem. Phys. Lett.* 316, 217 (2000).

123. H. Jantoljak, J.-P. Salvetat, L. Forró, and C. Thomsen, *Appl. Phys. A* 67, 113 (1998).
124. A. Jorio, G. Dresselhaus, M. S. Dresselhaus, M. Souza, M. S. S. Dantas, M. A. Pimenta, A. M. Rao, R. Saito, C. Liu, and H. M. Cheng, *Phys. Rev. Lett.* 85, 2617 (2000).
125. G. S. Duesberg, I. Loa, M. Burghard, K. Syassen, and S. Roth, *Phys. Rev. Lett.* 85, 5436 (2000).
126. S. L. Fang, A. M. Rao, P. C. Eklund, P. Nikolaev, A. G. Rinzler, and R. E. Smalley, *J. Mater. Res.* 13, 2405 (1998).
127. A. Kasuya, Y. Sasaki, Y. Saito, K. Tohji, and Y. Nishina, *Phys. Rev. Lett.* 78, 4434 (1997).
128. L. Alvarez, A. Righi, T. Guillard, S. Rols, E. Anglaret, D. Laplaze, and J. L. Sauvajol, *Chem. Phys. Lett.* 316, 186 (2000).
129. T. Hertel and G. Moos, *Phys. Rev. Lett.* 84, 5002 (2000).
130. L. Alvarez, A. Righi, S. Rols, E. Anglaret, J. L. Sauvajol, E. Munoz, W. K. Maser, A. M. Benito, M. T. Martinez, and G. F. de la Fuente, *Phys. Rev. B* 63, 153401 (2001).
131. S. D. M. Brown, A. Jorio, P. Corio, M. S. Dresselhaus, G. Dresselhaus, R. Saito, and K. Kneipp, *Phys. Rev. B* 63, 155414 (2001).
132. M. S. Dresselhaus and P. C. Eklund, *Adv. Phys.* 49, 705 (2000).
133. A. Jorio, A. G. Souza Filho, G. Dresselhaus, M. S. Dresselhaus, R. Saito, J. H. Hafner, C. M. Lieber, F. M. Matinaga, M. S. S. Dantas, and M. A. Pimenta, *Phys. Rev. B* 63, 245416 (2001).
134. G. S. Duesberg, W. J. Blau, H. J. Byrne, J. Muster, M. Burghard, and S. Roth, *Chem. Phys. Lett.* 310, 8 (1999).
135. A. Jorio, R. Saito, J. H. Hafner, C. M. Lieber, M. Hunter, T. McClure, G. Dresselhaus, and M. S. Dresselhaus, *Phys. Rev. Lett.* 86, 1118 (2001).
136. A. G. Souza Filho, A. Jorio, J. H. Hafner, C. M. Lieber, R. Saito, M. A. Pimenta, G. Dresselhaus, and M. S. Dresselhaus, *Phys. Rev. B* 63, 241404R (2001).
137. M. S. Dresselhaus, G. Dresselhaus, A. Jorio, A. G. Souza Filho, and R. Saito, *Carbon* 40, 2043 (2002).
138. H. Kataura, Y. Kumazawa, N. Kojima, Y. Maniwa, I. Umez, S. Masubuchi, S. Kazama, X. Zhao, Y. Ando, Y. Ohtsuka, S. Suzuki, and Y. Achiba, *Am. Inst. Phys. Conf. Proc.* 486, 328 (1999).
139. M. S. Dresselhaus, in "Carbon Filaments and Nanotubes: Common Origins, Differing Applications," Proceedings of the NATO Advanced Study Institute, Budapest, Hungary, 19–30 June 2000 (L. P. Biro, C. A. Bernardo, G. G. Tibbetts, and Ph. Lambin, Eds.), Kluwer, Amsterdam, 2000.
140. H. Kuzmany, B. Burger, M. Hulman, J. Kurti, A. G. Rinzler, and R. E. Smalley, *Europhys. Lett.* 44, 518 (1998).
141. J. W. Mintmire and C. T. White, *Phys. Rev. Lett.* 81, 2506 (1998).
142. R. Saito, G. Dresselhaus, and M. S. Dresselhaus, *Phys. Rev. B* 61, 2981 (2000).
143. T. Pichler, M. Knupfer, M. S. Golden, J. Fink, A. Rinzler, and R. E. Smalley, *Phys. Rev. Lett.* 80, 4729 (1998).
144. T. W. Odom, J.-L. Huang, P. Kim, and C. M. Lieber, *Nature* 391, 62 (1998).
145. S. Kazaoui, N. Minami, R. Jacquemin, H. Kataura, and Y. Achiba, *Phys. Rev. B* 60, 13339 (1999).
146. S. Kazaoui, N. Minami, H. Kataura, and Y. Achiba, *Synth. Met.* 121, 1201 (2001).
147. N. Minami, S. Kazaoui, R. Jacquemin, H. Yamawaki, K. Aoki, H. Kataura, and Y. Achiba, *Synth. Met.* 116, 405 (2001).
148. R. Jacquemin, S. Kazaoui, D. Yu, A. Hassaninen, N. Minami, H. Kataura, and Y. Achiba, *Synth. Met.* 115, 283 (2000).
149. P. Petit, C. Mathis, C. Journet, and P. Bernier, *Chem. Phys. Lett.* 305, 370 (1999).
150. Y.-P. Sun, B. Zhou, K. Henbest, K. Fu, W. Huang, Y. Lin, S. Taylor, and D. L. Carroll, *Chem. Phys. Lett.* 351, 349 (2002).
151. J. E. Riggs, Z. Guo, D. L. Carroll, and Y.-P. Sun, *J. Am. Chem. Soc.* 122, 5879 (2000).
152. M. J. O'Connell, S. M. Bachilo, C. B. Huffman, V. C. Moore, M. S. Strano, E. H. Haroz, K. L. Rialon, P. J. Boul, W. H. Noon, Cr. Kittrell, J. Ma, R. H. Hauge, R. B. Weisman, and R. E. Smalley, *Science* 297, 593 (2002).
153. S. M. Bachilo, M. S. Strano, C. Kittell, R. H. Hauge, R. E. Smalley, and R. B. Weisman, *Science* 298, 2361 (2002).
154. S. Lebedkin, F. Hennrich, T. Skipa, and M. M. Kappes, *J. Phys. Chem. B* 107, 1949 (2003).
155. S. C. Fung and C. A. Querini, *J. Catal.* 138, 240 (1992).
156. Z. Shi, Y. Lian, F. Liao, X. Zhou, Z. Gu, Y. Zhang, and S. Iijima, *Solid State Commun.* 112, 35 (1999).
157. M. Yudasaka, H. Kataura, T. Ichihashi, L. C. Qin, S. Kar, and S. Iijima, *Nano Lett.* 1, 487 (2001).
158. J. Kastner, T. Pichler, H. Kuzmany, S. Curran, W. Blau, D. N. Weldon, M. Delamesiere, S. Draper, and H. Zandbergen, *Chem. Phys. Lett.* 221, 53 (1994).

Structure of Mesoporous Silica

Wuzong Zhou

University of St. Andrews, St. Andrews KY16 9ST, United Kingdom

CONTENTS

1. Introduction
2. Structural Characterization
3. Periodic Phases
4. Nonperiodic Phases
 - Glossary
 - References

1. INTRODUCTION

Porous silicas form a large family of solid state materials. According to the definition accepted by International Union of Pure and Applied Chemistry, they can be grouped into three classes based on their pore diameter (d): microporous ($d < 2$ nm), mesoporous (2 nm $< d < 50$ nm), and macroporous ($d > 50$ nm) silicas.

Microporous zeolites, normally having pore diameters below 1 nm, are widely used as catalysts in industry. They have perfect crystalline framework. For example, zeolite LTA has a cubic unit cell with the cell parameter $a = 1.2$ nm, space group $Pm\bar{3}m$. Twenty-four Si and Al atoms occupy the (24 k) sites (0.370, 0.183, 0) and 48 oxygen atoms occupy the sites of (24 m) (0.110, 0.110, 0.345), (12 h) (0, 0.220, 0.5), and (12 i) (0.289, 0.289, 0) respectively [1]. On the contrary, however, most mesoporous silicas synthesized so far have no ordering at the atomic level (i.e., the frameworks of these materials are amorphous). So-called ordered mesoporous silicas normally refer only the ordering of the mesopores.

Although mesopores can be formed during partial decomposition of zeolites [2] or via other methods, ordered mesoporous silicas did not become an active topic until 1992 when Mobil scientists reported their synthesis of the M41S series materials [3, 4]. Since then tremendous progress has been made in the synthesis of new mesoporous phases and in potential applications of these materials [5].

The most popular formation mechanism of these mesoporous silicas is so called liquid crystal templating (LCT) mechanism [4, 6]. According to this mechanism, the surfactant molecules self-organize into micelles which further

form liquid crystals in the solution. Silicate species then deposit on the surface of the micelles and in the intermicelle space to form a condensed silicate framework. When the surfactant is removed by calcination, an ordered mesoporous silica phase is produced with the same symmetry as the parent liquid crystal. The real mechanism seems to be much more complicated. For instance, during the formation of MCM-41, the most extensively studied mesoporous silica, pure liquid crystals may not exist in the solution. Interaction between individual micellar rods and the silicate species must take place and the presence of silicate layers on the surface of the micellar rods enhances the aggregation of these nanorods as indicated by an *in-situ* ^{14}N nuclear magnetic resonance (NMR) study [7]. Furthermore, Stucky and co-workers believe that the dynamic interplay among ion-pair inorganic and organic species is crucial in the formation of the mesoporous phases [8–12]. Many synthesized mesoporous silicas have indeed structures without known liquid crystal analogs. In transmission electron microscopic (TEM) investigations of series specimens collected after different reaction times, it was proposed that the formation of the micelles and deposition of the silicate species may take place spontaneously [13–15]. Some of the mesoporous phases such as FSM-16 are formed via phase transformation of layered silicates and, therefore, must have a significantly different formation mechanism [16].

In this chapter, we are not going to deal with the arguments on the detailed formation mechanisms of the mesoporous silicas but instead discuss the structures of the final products. In comparison with microporous zeolites, a few important structural features may be expected from the mesoporous silicas. First, the pore structures of most mesoporous silicas retain the symmetries of the liquid crystals, while others do not have liquid crystal analogs but usually simple packed structures with high symmetries. Second, the shape and size of the pores in a mesoporous silica depend on the shape of the micelles and the length of the surfactant molecules. Third, the silica framework is amorphous and its density is variable. Consequently, the structures of the mesoporous silicas become highly tunable with almost an infinite variability.

In the following sections a general review of the structures of most typical mesoporous silicas and their derivatives will be given. Detailed synthetic conditions can be found in the original papers, previous review articles [17, 18], and a chapter by D. Zhao in this encyclopedia. They will not be mentioned in this chapter unless they are necessary in helping us to understand the structures.

2. STRUCTURAL CHARACTERIZATION

The most popular characterization method for the mesoporous silicas is X-ray powder diffraction (XRD). Since the silica frameworks of these materials are amorphous, no reflection peaks with large diffraction angles can be observed. On the other hand, the unit cell dimensions of the mesoporous silicas are very large, normally a few nanometers, and the corresponding XRD patterns contain only one large peak at a low angle together with several extremely weak peaks, as we will see in Figure 3 in the next section. To reveal the unit cell and to determine the space group for a mesoporous silica phase, these weak peaks have to be measured very carefully. In fact, the unit cells and space groups of most mesoporous silicas were determined successfully by using small angle XRD as demonstrated by many examples. However, more detailed structural information of the structures in question cannot be studied by using XRD which is an indirect method and gives insufficient reflection peaks.

Although some disadvantages must be considered, such as strong interaction of electron with the specimen and the two-dimensional nature of the images, TEM is the most powerful technique for investigating the local structures of these materials, benefitting from several advantages [19–24]. First, it offers images of local structures of solids. Therefore, the arrangements of mesopores, defects, surface structures, etc. can be observed directly. Second, TEM examines individual particles, allowing us to identify different phases when the specimen is multiphase. Finally, metal clusters loaded inside the pores can also be imaged directly and their distribution can be investigated by using energy dispersive X-ray spectroscopy (EDX). In most cases of mesoporous silicas, atomic resolution is not required and low magnification in a range from 24,000 \times to 100,000 \times is usually used for recording the images.

Morphology of particles can be studied using scanning electron microscopy (SEM). Because mesoporous silicas are normally insulating materials, the electron beam charging problem should not be ignored if the specimen is in a high vacuum. In order to reduce the beam charging, two methods can be applied. One is surface coating with some conducting materials such as carbon or gold. Another method is to choose a low accelerating voltage (often 1 to 2 kV).

It is obvious that each technique has its own limitations. A complete solution of the structure relies on a combination of various techniques. For example, determination of the pore size in a mesoporous silica by TEM is difficult even for the simplest phase MCM-41. It is because the size of the disks on the image contrast which correspond to the positions of the mesopores if viewing down the [001] zone axis is variable with the lens defocus value, the shape of the pores, etc. In practice, the size of mesopores is determined by

gas adsorption–desorption experiments by using the Barrett–Joyner–Halenda (BJH) method [25]. This method is pretty good for cylindrical pores such as those in two-dimensional hexagonal phases. However, Ravikovitch et al. believe that the conventional BJH method for adsorption–desorption measurement becomes extremely inaccurate for spherical cavities in mesoporous materials. They therefore developed a nonlocal density functional theory (NLDFT) for calculation of the pore sizes of these phases [26].

Elemental mapping of EDX can be used to investigate the distribution of the guest atoms, such as Al, B, and many transition metals, in the framework of doped mesoporous silicas. However, it is difficult to tell whether these atoms are inside the silica framework or deposit on the inner surface of the mesopores. NMR is a better technique to study the local environment of atoms. For example, Al cations are usually tetraordinated inside the silica framework and hexacoordinated when they are not in the framework. ^{27}Al magic-angle-spinning (MAS) NMR can easily differentiate between these two cases [27].

3. PERIODIC PHASES

3.1. MCM-41 ($P6mm$)

MCM-41 is the simplest and most extensively studied mesoporous silica [4]. In a typical example of synthesis, the alkyltrimethylammonium surfactants, $\text{C}_n\text{H}_{2n+1}-\text{N}(\text{CH}_3)_3^+\text{X}^-$ ($\text{X} = \text{Cl}$ or Br , $n = 8–10, 12, 14, 16$), one of so-called anionic surfactants described as S^+I^- , were used. According to the simplest picture of the LCT mechanism, these surfactant molecules form micellar rods (Fig. 1a), which further self-assemble into a hexagonal array (Fig. 1b). Silicate ions deposit on the surface of the micellar rods to form an inorganic framework. When the surfactant molecules are removed, a hexagonal array of unidirectional mesopores appears eventually (Fig. 1c).

Direct structural information can be obtained from the TEM images as shown in Figure 2 [28]. When we view down the pore axis, we can see the hexagonally arranged white disks that correspond to the positions of the pores. If we look along a direction perpendicular to the pore axis, a group of fringes is seen, indicating straight pores. The highest possible space group is $P6mm$. The material has in fact a two-dimensional structure, since its c axis is infinite.

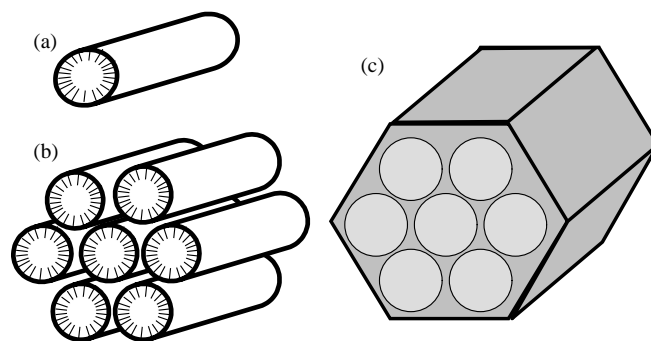


Figure 1. Schematic drawing of (a) a micellar rod, (b) hexagonal array of micellar rods, and (c) MCM-41 mesoporous silica, showing three important steps in the liquid crystal mechanism of the formation of MCM-41.

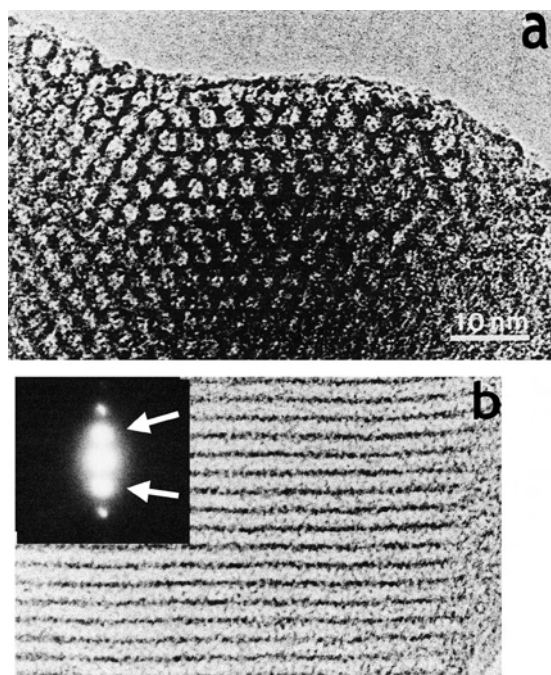


Figure 2. Two principal TEM images of MCM-41, viewing down the (a) channel axis and (b) a direction perpendicular to the channel axis. The arrows in (b) indicate the diffraction spots from the ordering of the mesopores. Reprinted with permission from [28], W. Zhou et al., *Progr. Natural Sci. (Chinese Ed.)* 8, 528 (1998). © 1998, National Natural Science Foundation of China.

Since MCM-41 silica lacks strict crystallographic order at the atomic level and the one-dimensional pore system results in a two-dimensional (2D) hexagonal symmetry, the main structural variations in MCM-41 occur in the pore diameter and the wall thickness. The pore size is affected by several factors. In a highly acidic synthetic system with reactants of tetraethyl orthosilicate (TEOS), HCl, and cetyltrimethylammonium bromide (CTMA^+M^-), the silica-containing liquid crystals have a combination of $\text{CTMA}^+\text{M}^-\text{SiO}^+$. Therefore, the size of M^- , which could be Cl^- or NO_3^- or Br^- , etc., will certainly affect the pore size of the final products. Hydrothermal treatment at different times can also result in different pore sizes [29, 30] (Fig. 3). Obviously, the largest effect on the pore size is from the chain length of the surfactant molecules and addition of auxiliary organics [4, 31]. Although a typical MCM-41 has a pore diameter of about 2 nm and the minimum wall thickness of <1 nm with specific surface area of over $1000 \text{ m}^2/\text{g}$ according to the Brunauer–Emmett–Teller (BET) calculation [4], the range of pore size of MCM-41 can be changed from 1.5 to 10 nm corresponding to the different chain lengths of surfactant molecules.

The shape of the pores in MCM-41 can be either cylindrical or hexagonal. The cylindrical pore structure was proposed based on a classical molecular dynamics simulation approach [32]. The hexagonal pore structure was proposed by Behrens et al. [33]. In the third model, proposed by Garces [34], the pores can be regarded as spherical cages connected by slightly narrower necks. Each model has some experimental evidence to support. However, none of them have been completely proved. On the other hand, due to

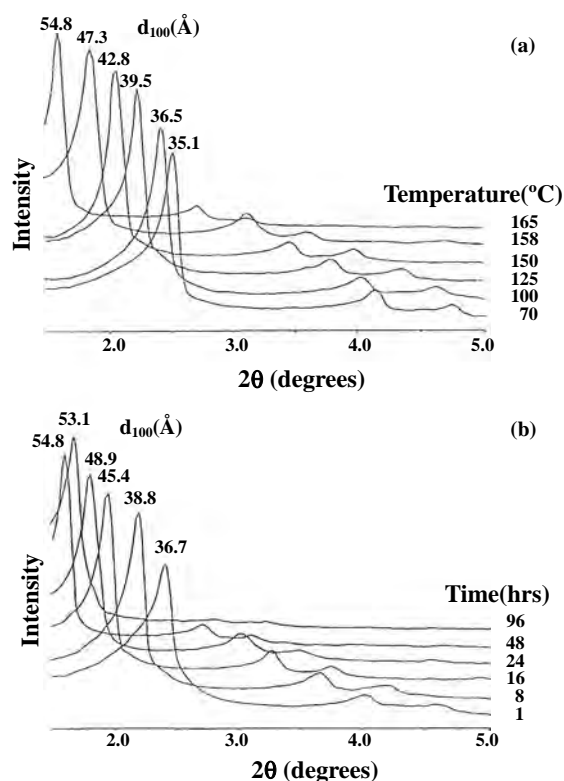


Figure 3. Typical XRD patterns of calcined purely siliceous MCM-41 (a) prepared at different temperatures for 48 h; (b) prepared for different reaction times at 165°C . Reprinted with permission from [29], C. F. Cheng et al., *Chem. Phys. Lett.* 263, 247 (1996). © 1996, Elsevier Science.

the high flexibility of the amorphous wall of MCM-41, the shape of the pores may be variable with different synthetic conditions.

In the last decade, control of particle size and morphology of MCM-41 has been extensively investigated. In addition, derived from the MCM-41 structure, some surface tubular forms with diameters around 30 to 100 nm may appear during a postsynthesis ammonia hydrothermal treatment [35]. Smaller tubular form such as bundle of nanotubes and even single-channel nanotubes with a few nanometer in diameter were also observed on the surface of MCM-41, resulting in a surface *paintbrush* pattern [36].

Similar to zeolites, pure silica materials have no acidic sites and are of limited use for catalysis and metal incorporation. In order to produce acidic mesostructured materials for the application in catalysis, aluminum has been successfully introduced into the framework of MCM-41 [37, 38] and can be detected by EDX commonly equipped in electron microscopes. However, it is very difficult to tell whether Al cations are located inside or outside the wall by using EDX. ^{27}Al MAS NMR confirmed that all Al cations were tetraordinated (i.e., in the framework). XRD and TEM characterizations indicate that the degree of order of the mesopores in MCM-41 is significantly reduced by incorporation of even a few percentage of aluminum into the wall [27].

Incorporation of many other cations into MCM-41 has been investigated in the last decade. Those guest elements

include Ti [39, 40], V [41], Ga [42], B [43], Mn [44, 45], Fe [46, 47], and Sn [48]. The doped materials often have a lower degree of order in comparison with the parent pure MCM-41 silica.

Another method for creating active sites in MCM-41 is introduction of catalytically active metal clusters on the inner surface of the channels. If the metal particles are very small (e.g., in the form of individual atoms) and are evenly distributed in the channels, high resolution TEM (HRTEM) may not give enough image contrast to see them. But the presence of the metal can be confirmed by EDX elemental mapping [49]. When larger clusters (>1 nm) form, they can be detected by HRTEM. It has been shown that direct images can easily differentiate between clusters inside the channels and those on the outer surface of the mesoporous MCM-41 [50]. In the case of $\text{Ag}_3\text{Ru}_{10}$, anchored on the inner surface of the channels, the clusters can be imaged as some dark dots even though they are not ordered [51]. Ordered or partially ordered metal clusters inside the mesopores result in a so-called rosary pattern of image contrast (Fig. 4) [52, 53]. In this case, an average distance of the cluster separation can be calculated. The incorporation of metals inside the MCM-41 channels usually has no significant effect on the original silica framework.

It has been found that MCM-41 templated by the alkyltrimethylammonium surfactants is not the only $P6mm$ phase. For example, using decaoxyethylene cetyl ether [$\text{C}_{16}(\text{EO})_{10}$] with <30 wt% in the reaction system, the product CMI-1 ($P6mm$) has the same structure as MCM-41 with the pore diameter about 4 nm [54]. SBA-3 ($P6mm$) synthesized in an acidic condition using $\text{C}_{16}\text{TMA}^+$ surfactant is also of a MCM-41 type [17]. HMM-1 has a 2D hexagonal structure with a hybrid ethane-silica framework [$(\text{CH}_3\text{O})_3\text{Si}-\text{CH}_2-\text{CH}_2-\text{Si}(\text{OCH}_3)_3$], instead of pure inorganic composition [55, 56]. It is very interesting to find that

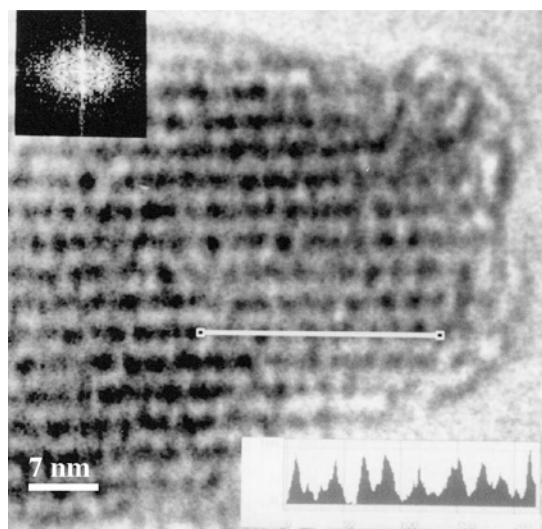


Figure 4. TEM image of MCM-41 loaded with Ru_6 clusters showing a rosary pattern of the image contrast along the pore axis, with its Fourier transform (top inset). The bottom inset shows one-dimensional brightness scanning along the line marked in the image. Reprinted with permission from [28], W. Zhou et al., *Progr. Natural Sci. (Chinese Ed.)* 8, 528 (1998). © 1998, National Natural Science Foundation of China.

these organic/inorganic hybrid mesoporous materials have better ordered mesopore arrangements. The following sections demonstrate more 2D hexagonal phases that are similar to MCM-41.

3.2. SBA-8 (cmm)

Using bolaform surfactant $(\text{CH}_3)_3\text{N}-\text{C}_n\text{H}_{2n}-\text{O}-\text{C}_6\text{H}_4-\text{C}_6\text{H}_4-\text{O}-\text{C}_n\text{H}_{2n}-\text{N}-(\text{CH}_3)_3$ ($n = 4, 6, 8, 10, 12$), the product SBA-8 has a two-dimensional C-centered rectangular structure with typical unit cell parameters $a = 6$ and $b = 3.96$ nm and space group cmm when the surfactant with $n = 12$ was used [57]. A typical SBA-8 structure has pore diameters of 2.65 to 2.91 nm and average wall thickness of about 2 nm with the BET surface area of about $1000 \text{ m}^2/\text{g}$. This structure has a close relation with MCM-41 since the perfect hexagonal cell of MCM-41 is equivalent to a C-centered rectangular cell with $a/b = \sqrt{3}$, while the a/b value in SBA-8 is slightly smaller than $\sqrt{3}$. In other words, SBA-8 consists of arrays of one-dimensional mesopores with a distorted hexagonal symmetry. Although SBA-8 is a thermally stable phase, its uncompleted condensation of the siloxane framework is probably the main reason for the lattice distortion and, indeed, SBA-8 can be transformed into MCM-41 through postsynthesis treatment in water at about 100°C .

It is interesting to see that the bolaform surfactants include two hydrophilic headgroups connected by a hydrophobic chain (i.e., they are amphiphiles), which are different from the alkyltrimethylammonium surfactants normally used for producing MCM-41. They are more similar to gemini surfactants which usually form globular micelles instead of cylindrical rods, resulting in a three-dimensional hexagonal phase SBA-2. It is obvious that such surfactants are not essential to the cmm phase formation. A most recent work by Haskouri et al. reported that SBA-8 could also be synthesized by using cetyltrimethylammonium bromide instead of the rigid bolaform amphiphiles [58].

3.3. FSM-16 ($P6mm$)

Quite different from the formation mechanisms of MCM-41 and SBA-8 mentioned above, FSM-16 is derived from a layered polysilicate without forming any liquid crystals. It was first synthesized by reaction of single layered polysilicate ($\text{NaHSi}_2\text{O}_5 \cdot 3\text{H}_2\text{O}$) with alkyltrimethylammonium chloride [$\text{C}_{16}\text{H}_{33}-(\text{CH}_3)_3\text{N}^+\text{Cl}^-$] [59] and attracted a large attention after the appearance of the M41S series in 1992 [16, 60–62]. A typical FSM-16 has a 2D hexagonal cell with a about 4 nm, pore diameter slightly smaller than 3 nm, and BET surface area over $1000 \text{ m}^2/\text{g}$. These parameters can also be varied by changing the chain length in the surfactants. For example, the use of $\text{C}_{10}\text{H}_{21}-(\text{CH}_3)_3\text{N}^+\text{Br}^-$ leads to the product FSM-10 with smaller pore size and unit cell dimension [62]. Nevertheless, the structure of FSM-16 is almost the same as MCM-41, both having similar pore sizes, surface areas, and hexagonal arrangement of the one-dimensional straight pores.

Although the formation of FSM-16 is due to a structural rearrangement of layered silicates, our knowledge about the detailed procedure of this transformation is still very limited. The originally proposed “folded sheets mechanism”

(FSM) may be an inaccurate description since we do not know whether the sheets of silicates “fold” to form mesopores or some other intermediate phases are involved. According to a HRTEM study, a domain structure was observed during the phase transformation from the layered compound to FSM-16 [63].

On the other hand, if a layered alkyltrimethylammonium–kanemite ($\text{NaHSi}_2\text{O}_5 \cdot 3\text{H}_2\text{O}$) complex was synthesized first followed by a mild acid treatment, novel rectangular arrangements of square or lozenge channels can be formed. The material was denoted as KSW-2 [64], which has flat silicate walls, BET surface area of $1100 \text{ m}^2/\text{g}$, and an average pore diameter of about 2.1 nm. The formation of KSW-2 strongly suggests that the “folded sheets mechanism” is correct at least for this particular case.

3.4. SBA-15 ($P6mm$)

Another important 2D hexagonal mesoporous silica, SBA-15, was synthesized by using triblock copolymers [poly(ethylene oxide)–poly(propylene oxide)–poly(ethylene oxide)], for example, $\text{EO}_{20}\text{PO}_{70}\text{EO}_{20}$, as the structure-directing agents [65, 66]. The structure seems to be similar to that of MCM-41, having a 2D hexagonal unit cell in symmetry of $P6mm$ as detected by XRD and TEM. Its BET surface area can be from 690 to $1040 \text{ m}^2/\text{g}$. One of the significant differences between SBA-15 and MCM-41 is that the pore size (5 to 30 nm) in the former is much larger due to the large surfactant molecules used. The second remarkable feature of SBA-15 is that the wall is much thicker, 3 to 6 nm, which results in a higher hydrothermal stability.

The most extraordinary feature of SBA-15 is that the mesopores are connected by micropores or smaller mesopores through the wall, which has been indirectly proved by TEM observation of metal negative replicas of SBA-15. These replicated structures are consequently three-dimensional. Metal nanorods produced inside the MCM-41 channels, on the other hand, are separated [67]. The micropore volume in SBA-15 can be around $0.1 \text{ cm}^3/\text{g}$ or larger. The formation of these micropores has been proposed. During the aggregation of triblock copolymer surfactant $(\text{PEO})_n-(\text{PPO})_m-(\text{PEO})_n$ and silicate species, the hydrophilic heads (PEO) are deeply occluded within the wall, forming some “corona” regions with relatively low density of silica. These regions become microporous upon calcination [68]. The intrawall micropores can also be detected by the adsorption and desorption method [69]. The existence of nanoscale pores in the wall of SBA-15 is also possible as directly observed by Fan et al. from the TEM images viewed down the directions both along and perpendicular to the principal channel axis [70]. These interchannel micropores and mesopores are randomly located along the [001] direction of SBA-15 and, therefore, could not be detected by XRD. To date, structural control of these pores seems to be much more difficult than controlling the main group of mesopores. Nevertheless, Newalkar and Komarneni reported their experiments of tuning the intrawall micropores by means of salt addition under microwave-hydrothermal conditions [71].

As for MCM-41, investigation of doped SBA-15 has been extensively performed in the last few years, for example, alumina [72, 73], incorporations of Ti [74], V [75], Zr [76],

sulfonic acid groups [77], etc. In comparison with MCM-41, the chemical doping in SBA-15 has less effect on the mesopore structures due to the thicker wall [72, 73].

In addition to loading catalytically active nanoparticles and coating on the inner surface of SBA-15 [78, 79] in order to modify the properties of the material, another important application of the SBA-15 structure due to its relatively large pore size, high stability of the wall, and the existence of microporous connection between mesopores is to use this material as template for fabrication of porous materials of other compositions, such as silica-free Pd [80], Pt [81], carbon [82, 83] frameworks, etc. To achieve 3D porous bulk materials, the microporous bridges in SBA-15 must be filled. Otherwise, separated nanowires would be produced [84]. Most of these 3D porous replicas of SBA-15 mentioned above are either amorphous or polycrystalline. However, 3D porous single crystals (PSCs) of metals and ceramics have been proved to be possible using SBA-15 as template [85, 86]. Figure 5 shows a TEM image of 3D PSCs of Cr_2O_3 prepared in SBA-15. When the silica framework is completely removed by using 10% HF solution, small bridges connecting the Cr_2O_3 nanorods are clearly revealed. The state of the single crystal is confirmed by selected area electron diffraction (SAED) from an area covering many nanorods. Because the structures of these new porous materials are exactly negative replicas of SBA-15, it can be expected that their low-angle XRD patterns should be similar to that of SBA-15 [87].

3.5. SBA-2 ($P6_3/mmc, Fm\bar{3}m$)

SBA-2 was first synthesized by Stucky’s group in 1995 by using Gemini surfactant $\text{C}_n\text{H}_{2n+1}\text{N}^+(\text{CH}_3)_2(\text{CH}_2)_s\text{N}^+(\text{CH}_3)_3(\text{C}_{n-s-1})$ [10]. Based on powder XRD results, the material was believed to consist of discrete supercages in a hexagonal close-packed (hcp) arrangement and the space group was determined to be $P6_3/mmc$. The unit cell dimensions are $a \sim 6 \text{ nm}$ and $c \sim 10 \text{ nm}$ which can be tuned by changing

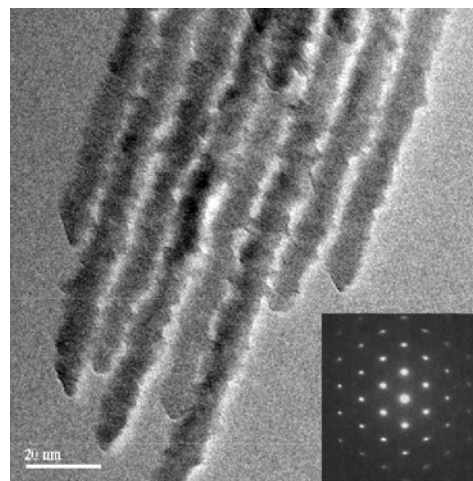


Figure 5. TEM image of 3D porous single crystal of Cr_2O_3 synthesized using SBA-15 as a template which has been completely removed. It is shown that all the nanorods of oxide are linked by smaller bridges. The structure is a negative replication of SBA-15. The inset is the corresponding SAED pattern from the whole particle.

the chain length of the surfactants. It was also mentioned that the shape of the mesopores in SBA-2 is bottle-like. The pore diameter was about 3.5 nm according to the BJH method [25] and no micropore was detectable. Such pore size measurement gave rise to a hypothesis that there must be some mesopores connecting the spherical supercages, which are separated by the silica wall with a minimal thickness of 2.5 nm. Based on TEM observation of some fringes, Zhou et al. proposed a 2D network of mesopores in SBA-2 [88]. This model may not be correct according to the recent adsorption–desorption studies.

Ravikovitch believes that the conventional BJH method for adsorption–desorption measurement becomes extremely inaccurate for spherical cavities in mesoporous materials such as SBA-2. They developed a NLDFT and remeasured the diameter of the cages in SBA-2 with the unit cell dimension of 4.9 nm. The diameter became 4.4 nm, corresponding to a minimal wall thickness of 0.5 nm [26]. In a more recent work, Garcia-Bennett et al. performed adsorption and desorption experiments on several SBA-2 specimens using three different gases, nitrogen, cyclopentane, and mesitylene. It was found that the windows of the supercages in SBA-2 were actually micropores which could be as small as below 0.4 nm so that only small molecules can be adsorbed [89]. The above two experiments indicated that the touch points in between two spherical cages have a very thin wall and some micropores may form without templating during the hydrothermal treatment and/or calcinations. The volume of these micropores is too small to be detected by adsorption–desorption experiments.

The C_{n-s-1} surfactant molecules have a high charge density and large head groups. Globular micelles instead of cylindrical rods form in the solution. Formation of the SBA-2 structure mainly depends on the close packing of the globular surfactant–silicate arrays. Therefore, both hcp (Fig. 6a) and cubic close-packed (ccp) (Fig. 6b) structures are possible and indeed have often been observed in the SBA-2 specimens. Another possible packing structure is body-centered cubic as shown in Figure 6c, which, however, has not been observed in this material.

From analysis of the TEM images of SBA-2, it was found that intergrowth of the hcp and ccp phases is very common. The latter was designated STAC-1 and the highest symmetry would be $Fm\bar{3}m$ [88] (Fig. 7). Such intergrowth can be layered (one-dimensional) along the [001] axis of the hcp phase or the [111] direction of the ccp phase. The intergrowth can also be three-dimensional, forming a domain structure in the particles. Such a domain structure was found in SBA-2 with

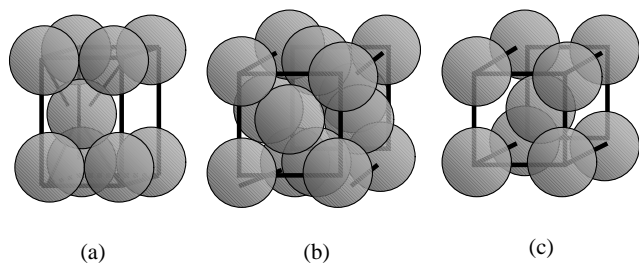


Figure 6. Graphic representations of possible packed structures, (a) hcp, (b) ccp, and (c) body-centered cubic packing.

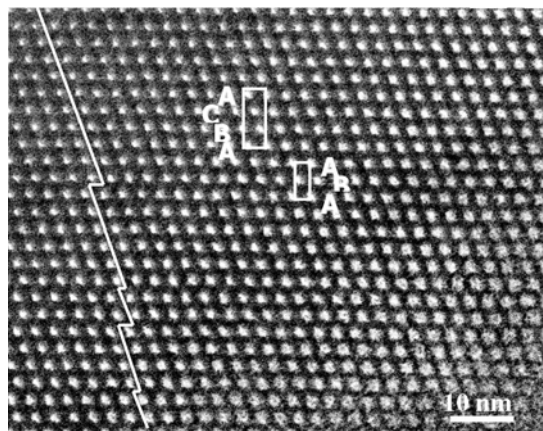


Figure 7. TEM image from SBA-2 showing layered intergrowth of the hexagonal closed packed (ABA) and cubic closed packed (ABCA). The ccp structure dominates the particle.

three different morphologies. One morphology is a large hollow sphere of about 50 to 150 μm in diameter and the thickness of shells is only about 1 to 2 μm . The second is small solid sphere with the diameter in the range of 2 to 3 μm . The third morphology is a sheetlike plate [90, 91].

To date, a pure phase of either hcp or ccp phase SBA-2 has not been synthesized. In the recent report by Garcia-Bennett et al. [89], it was presented that the morphology of the SBA-2 particles could be controlled by changing the acidic/alkali conditions and the concentration of the surfactant. When the surfactant concentration was 40%, large hexagonal prisms were observed. The XRD pattern of this sample can be indexed onto a hexagonal unit cell with $a = 4.3$ and $c = 6.8$ nm. However, the monophasic nature of this so-called hcp SBA-2 has not been confirmed by other techniques.

3.6. SBA-12 ($P6_3/mmc$, $Fm\bar{3}m$)

SBA-12 was synthesized using the oligomeric alkyethylene oxide surfactant Brij 76 ($C_{18}EO_{10}$) [65]. The space group was originally determined to be $P6_3/mmc$, similar to SBA-2. The difference between these two phases is that different surfactants are used, cationic Gemini surfactants for SBA-2 and nonionic oligomeric surfactants for SBA-12. Nevertheless, no significant structural difference was found in between these two phases. For example, a typical calcined SBA-12 has a 3D hexagonal unit cell with $a = 6.34$ and $c = 10.2$ nm. The BET surface area is 1150 m^2/g and the pore volume is 0.83 cm^3/g [66].

It was soon revealed by using TEM that the SBA-12 specimens usually contain mixed hcp and ccp phases, exactly same as we have seen from SBA-2. On the other hand, a functionalized SBA-12, SH-SBA-12, synthesized by Spanish scientists, showed large domains of the ccp phase. Based on good TEM images of single domains, electron crystallographic studies gave a face centered cubic structural model with cell dimension $a = 8.2$ nm [21]. The structure forms with each cavity connected to its 12 nearest-neighbor cavities through openings parallel to the $\langle 110 \rangle$ directions. The ideal

space group is therefore $Fm\bar{3}m$ (Fig. 6b). To date, syntheses of the pure hcp and ccp SBA-12 have not been achieved.

It is noted that the diameter of the pores in SBA-12 was measured to be 6.3 nm when the pore center to pore center distance was about 7.4 nm according to Ravikovitch's nonlocal density functional theory [26]. The corresponding minimum wall thickness is over 1 nm which is larger than that in SBA-2.

Another mesoporous phase with the symmetry of $P6_3/mmc$ is named HMM-2, which consists of an organic/inorganic hybrid framework, the same as the composition of HMM-1 [55, 56].

3.7. MCM-48 ($Ia\bar{3}d$)

MCM-48 was first reported as one of the members in the M41S series using the same surfactant as that for MCM-41 with a different ratio of surfactant to silicate source [3]. Although MCM-48 can be also obtained by phase transformation from MCM-41 [92], the pore system in the former is significantly different from the latter. Its structure can be described using a model of minimal surface of gyroid (Fig. 8), first suggested in 1993 [8] and confirmed a few years later using HRTEM [93, 94] and a newly developed method of electron crystallography [19]. This minimal surface divides space into two identical but separate compartments, forming a so-called bicontinuous cubic with space group $Ia\bar{3}d$. The unit cell parameter is about 8.5 nm. The mean pore size of MCM-48 has been determined according to the nonlocal density functional theory to be 3.1 to 3.3 nm with the wall thickness of 0.8 to 1 nm [95]. The minimal surface can be approximated by the simple analytical function

$$\cos x \sin y + \cos y \sin z + \sin x \cos z = 0$$

MCM-48 is one of few mesoporous silicas which can be produced as relatively large single crystals. For example, MCM-48 particles of a few micrometers in diameter with a unique crystalline morphology of a cube truncated by rhomb dodecahedron was synthesized by Kim et al. [96].

Incorporation of metal cations in MCM-48 can be achieved as successfully as that in MCM-41. The guest cations include Ti, Cr, V [97], Cr [98], Fe [99], Mn, Al [21, 100], Zr [101], B [36], Cu, Zn [102], etc. The degree of

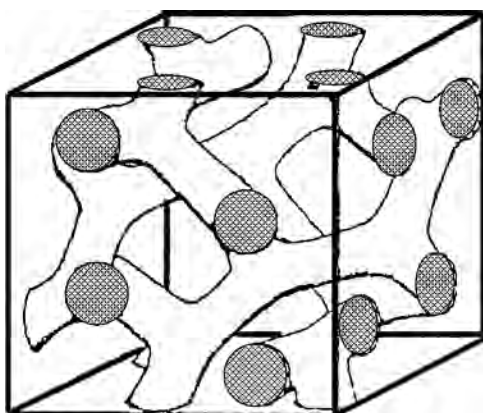


Figure 8. Schematic drawing of the mesopores in MCM-48.

order of the mesopores in MCM-48 usually decreases when the doping level increases.

Encapsulation of metals such as Pd inside the MCM-48 mesoporous system resulted in some nanoball domains [80]. In this case, the metal did not fill completely the pores. Nevertheless, after removing the silicate matrix by a dilute HF solution, pure porous Pd nanoballs were recovered which actually are negative replicas of the MCM-48 structure. If the mesopores of MCM-48 are fully filled by carbon and the silica framework is removed by HF, a 3D carbon negative replica of MCM-48 can be fabricated [103]. The final product is also mesoporous with a quite narrow pore size distribution centered at 2.4 nm and specific surface area of 1200 m²/g. These carbon replicas of MCM-48 can retain the parent symmetry of $Ia\bar{3}d$, designated CMK-1, or changed to $I4_1/a$, designated CMK-4, [24] depending on the silicate source used. The wall structure of the mesoporous carbon can contain graphite domains instead of being completely amorphous. It is interesting to see that micropores of 0.5 to 0.8 nm in diameter exist in the silica wall of MCM-48 so that a 3D framework of carbon becomes possible after removal of the silica framework [104]. This structural feature is similar to that of SBA-15. Three-dimensional porous negative replicas of MCM-48 with other materials, such as crystalline Pt, have also been investigated [105].

3.8. SBA-16 ($Im\bar{3}m$)

SBA-16 is also a cubic phase with a symmetry of $Im\bar{3}m$ and the cell parameter $a = 16.6$ nm when triblock copolymer with large PEO segments, EO₁₀₆PO₇₀EO₁₀₆, was used [66]. The structure of this phase can be regarded as body-centered packing of globular cages (Fig. 6c) as proved by HRTEM [20]. The calcined specimen has a pore size of 5.4 nm, a pore volume of 0.45 cm³/g, and a BET surface area of 740 m²/g. In this case, the corresponding minimal wall thickness is about 9 nm. According to the NLDFT method, on the other hand, the pore size of SBA-16 with the same unit cell dimension is about 8.5 nm and the minimal wall thickness is about 5.9 nm [26]. Both values of the minimal wall thickness are much larger than those in SBA-2 and SBA-12, indicating a weaker interplay between the globular micelles during the assembly of organic and inorganic species. Consequently, the formation of close packed structures does not take place in this synthetic system.

On the other hand, a relatively thicker wall must contain some small channels connecting the spherical cages. Otherwise, gas adsorption on the inner surface would be impossible. As determined by Voort et al., a large amount of micropores exist in SBA-16. The porosity is greatly dependent on the synthetic conditions. When a high ratio of silicate source to surfactant is applied, many microporous nanocapsules will be created [106]. The details of these channel bridges have not been revealed by HRTEM or by other techniques.

In Zhao's first report about SBA-16, they also detected two other cubic phases [66]. One was SBA-11 with symmetry of $Pm\bar{3}m$ and the unit cell dimension of 10.6 nm, prepared using nonionic alkyl PEO oligomeric surfactants, C₁₆H₃₃(OCH₂CH₂)₁₀OH (C₁₆EO₁₀). A typical calcined SBA-11 specimen contains uniform mesopores of 2.5 nm

in diameter and has a BET surface area of 1070 m²/g and a pore volume of 0.68 cm³/g. The second phase, designated SBA-14, was obtained when the surfactants with shorter chains and smaller EO segments were used, such as C₁₂EO₄. The thermally stable SBA-14 contains mesopores with pore diameter of 2.2 nm and a BET surface area of 670 m²/g. However, the space group of this phase was not determined. Both SBA-11 and SBA-14 have not been extensively studied since Zhao's report in 1998.

3.9. SBA-1 ($Pm\bar{3}n$)

SBA-1 has a complicated packing structure of two types of globular cages and was first synthesized by Huo et al. in 1994 [9, 107] using tetraethyl orthosilicate (TEOS) as a silica source and hexadecyltriethylammonium bromide (HTEABr) as the surfactant under strongly acidic conditions. The synthetic conditions were refined by Kim and Ryoo in 1999 to produce an excellent specimen by using a reaction mixture of 1 HTEABr : 5 TEOS : x HCl : 12.5 x H₂O, where x can be varied from 240 to 400 and applied stirring of 4 hours at 273 K [108]. The pore size together with the unit cell dimensions can be varied by choosing different chain lengths in the surfactant. The product using C₁₆H₃₃N(C₂H₅)₃Br as a template has a unit cell parameter $a = 7.6$ nm, pore size of 2.1 nm in diameter by the BJH method, and surface area of 1355 m²/g. However, according to the NLDFT method, the pore size of the similar specimen is about 4.1 nm and the minimal wall thickness is about 0.3 nm [26].

The structure of SBA-1 contains large cages (4 nm in diameter) at positions of (1/2, 0, 1/4), (1/2, 0, 3/4), (0, 1/4, 1/2), (0, 3/4, 1/2), (1/4, 1/2, 0), and (3/4, 1/2, 0), and small cages (3.3 nm in diameter) at the (0, 0, 0) and (1/2, 1/2, 1/2) positions (Fig. 9) [20]. The windows of the cages are also two different sizes. If the synthetic conditions are well controlled, large particles of SBA-1 with decaoctahedral crystal-like shape can be fabricated as demonstrated by Che et al. (Fig. 10) [109].

In the same article, Sakamoto et al. also described for the first time another cubic phase with the same symmetry $Pm\bar{3}n$ but prepared under basic conditions, designated SBA-6 [20]. The unit cell dimension of SBA-6 (14.6 nm) is about double

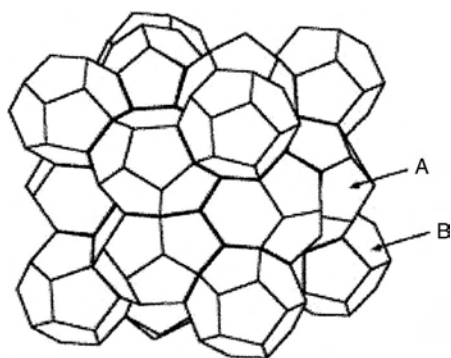


Figure 9. Schematic drawing of the structures of SBA-1 and SBA-6. The large cages and small cages are indicated by A and B respectively. Reprinted with permission from [20], Y. Sakamoto et al., *Nature* 408, 449 (2000). © 2000, Macmillan Magazines Ltd.

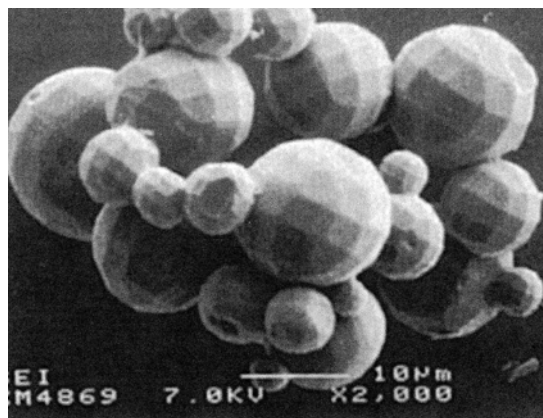


Figure 10. SEM image showing decaoctahedral crystal-like morphology of SBA-1. Reprinted with permission from [109], S. Che et al., *Chem. Mater.* 13, 2237 (2001). © 2001, American Chemical Society.

that of SBA-1, while the wall thickness of the former is much thinner. The diameter of the large cages is 8.5 nm and that of the small cages is 7.3 nm.

Chemical doping in SBA-1 has not been investigated as extensively as in MCM-41. But its 3D porous network is very attractive for potential application in catalysis and it is indeed possible to introduce various metal cations in order to modify the physicochemical properties. Up to date, V, Ti, Mo, and Co have been incorporated into the SBA-1 framework and the original structure with space group of $Pm\bar{3}n$ is maintained very well [110–114]. Among them, the incorporation of vanadium is particularly interesting, not only because the doping level could be quite high (e.g. Si/V < 20) but also because the incorporation of V leads to the formation of secondary mesopores [111].

Synthesis of the $Pm\bar{3}n$ phase with an ethane–silica hybrid framework proved to be successful [115]. The structure is similar to SBA-1 with the unit cell parameter $a = 11.1$ nm, the pore size about 2.9 nm by the BJH calculation, and the BET surface area about 770 m²/g. On the other hand, the pore size was determined to be 5.1 nm by the NLDFT method with a minimum wall thickness of 1.1 nm [26]. The latter method is believed to be more accurate for the packing structures of globular cages.

3.10. FDU-1 ($Im\bar{3}m$) and FDU-2 ($Fd\bar{3}m$)

We discussed the most popular ordered mesoporous silicas in the above sections. There are indeed many other phases which are either difficult to synthesize or have been discovered recently. Two examples are FDU-1 and FDU-2.

FDU-1 has a cubic unit cell with the cell parameter $a = 22$ nm, space group $Im\bar{3}m$, synthesized by Zhao's group [116] using triblock poly(ethylene oxide)–poly(butylene oxide)–poly(ethylene oxide) copolymer, such as EO₃₉BO₄₇–EO₃₉. The pore size is about 12 nm, pore volume about 0.77 cm³/g, and BET surface area about 740 m²/g. The structure is similar to SBA-16 (Fig. 6c) but has a significantly larger pore size and unit cell dimensions, which are the largest among all the known cubic mesoporous silicas.

FDU-2, also reported by Zhao's group recently, has symmetry of $Fd\bar{3}m$. The material was prepared by using tri head group quaternary ammonium surfactants, $[C_mH_{2m+1}N^+(CH_3)_2CH_2CH_2N^+(CH_3)_2CH_2CH_2CH_2N^+(CH_3)_3-3Br]^-$ ($m = 14, 16, 18$), as the structure-directing agents under basic conditions at low temperature [117]. It was assumed that FDU-2, similar to FDU-1, is also a packed structure of globular cages, but the arrangement of the cages is a novel diamond type. Although the proposed structure was supported by XRD and TEM images, the details of the structure have yet to be determined.

4. NONPERIODIC PHASES

In addition to the silicas with ordered mesopores, disordered mesoporous silicas, so-called wormlike phases, form another class of useful materials. These materials have disordered pores (Fig. 11), amorphous silica wall, and, importantly, uniform pore diameters. These materials include MSU [118, 119], TUD-1 [120], HMS [121, 122], KIT [123], Al-MMS [124, 125] series, etc.

MSU mesoporous phases were prepared using a nonionic templating method. For example, they can be synthesized by the hydrolysis of tetraethylorthosilicate in the presence of PEO surfactants, which act as the structure-directing (templating) agents [118]. Hydrogen bonding interactions between the hydrophilic surfaces of wormlike micelles and $Si[(OC_2H_5)_{4-x}][OH]_x$ were assumed to be important. Uniform diameters ranging from 2.0 to 5.8 nm can be tuned by varying the size and structure of the surfactant molecules.

TUD-1 was made by using a small, inexpensive organic template, triethanolamine [120]. The disordering nature of the wormlike material leads to more flexible morphology of the particles. The tunable pore size distribution can be made in the range of 2.5 to 25 nm. Beta-TUD-1 is a new type of material with a corn-shell structure (i.e. a beta-type zeolite with particles size of about 50 to 60 nm is incorporated into TUD-1). The TUD-1 shell is around a few nanometers in thickness, and therefore the material has mesopore-controlled selectivity and zeolite-controlled catalytic activity [126].

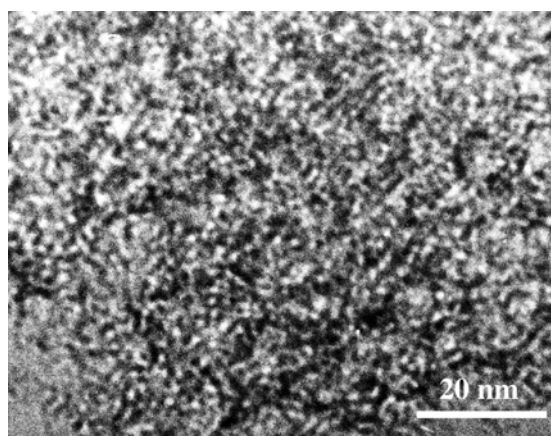


Figure 11. TEM image of wormlike mesoporous TUD-1.

Hexagonal mesoporous silicas were prepared via a non-ionic pathway [121]. Typical XRD patterns of these materials only show one peak at low angle. However, there is a local hexagonal ordering. This is probably why the strange term "hexagonal disordered phases" is used.

KIT-1 was synthesized by an electrostatic templating route using sodium silicate, hexadecyltrimethylammonium chloride, and ethylenediaminetetraacetic acid tetrasodium salt. Its three-dimensional nature was proved by TEM when the pores were partially filled by Pt. Although the mesopores are completely disordered, the pore size of KIT-1 is uniform with the pore diameter of 3.4 nm and peak width smaller than 3 nm at half-height as indicated by N_2 adsorption results. It is noted that the structure of KIT-1 has outstanding hydrothermal and thermal stabilities. For example, it was stable in boiling water for 2 days. Incorporation of Al into the KIT-1 framework has been achieved with the ratio of Si/Al down to 5. The doped materials were also found to have high hydrothermal stability and ion-exchange capacity [123].

Aluminosilicate mesoporous molecular sieves (designated Al-MMS X , where X is the ratio of Si/Al used in the synthesis gel) were prepared at room temperature using the primary amine hexadecylamine as organic templating surfactant. The real ratios of Si/Al in the products are slightly higher than X . The average pore diameters of the materials are in the range from ca. 2 to 2.5 nm determined using the BJH method. The materials should be wormlike indicated by

Table 1. Summary of structures of mesoporous molecular sieves.

Name	Structure type	Space group	Pore diameter (nm)	Ref.
MCM-41	2D-hexagonal	$P6mm$	1.5–10	[4]
CMI-1	2D-hexagonal	$P6mm$	~4	[54]
SBA-3	2D-hexagonal	$P6mm$	~3	[17]
HMM-1	2D-hexagonal	$P6mm$	~3	[55, 56]
SBA-8	2D-orthorhombic	cmn	~3	[57]
FSM-16	2D-hexagonal	$P6mm$	~3	[59]
FSM-10	2D-hexagonal	$P6mm$	~2	[59, 62]
KSW-2	2D-orthorhombic	—	2 to 3	[64]
SBA-15	2D-hexagonal	$P6mm$	5–30	[65, 66]
SBA-2	hexagonal	$P6_3/mmc$,	~4	[10, 26]
	cubic	$Fm\bar{3}m$	~4	[88]
SBA-12	hexagonal	$P6_3/mmc$	~6	[65, 26]
	cubic	$Fm\bar{3}m$	~6	[21]
HMM-2	hexagonal	$P6_3/mmc$	~3	[55, 56]
MCM-48	cubic	$Ia\bar{3}d$	~3	[8, 95]
SBA-16	cubic	$Im\bar{3}m$	~8	[26, 66]
SBA-11	cubic	$Pm\bar{3}m$	~3	[66]
SBA-14	cubic	—	~2	[66]
SBA-1	cubic	$Pm\bar{3}n$	~4 & ~3	[9, 20, 26]
SBA-6	cubic	$Pm\bar{3}n$	~8 & ~7	[20]
FDU-1	cubic	$Im\bar{3}m$	~12	[116]
FDU-2	cubic	$Fd\bar{3}m$	~3	[117]
MSU-X	wormlike	—	2–6	[118, 119]
TUD-1	wormlike	—	2.5–25	[120]
HMS-X	wormlike	—	2–3	[121, 122]
KIT-1	wormlike	—	3.4	[123]
MMS	wormlike	—	2.0 to 2.5	[124]

single-peak XRD patterns. On the other hand, they exhibit higher Brønsted acidity compared to aluminum-containing MCM-41. The Pt-impregnated forms of Al-MMSX become efficient catalysts for the hydroconversion of *n*-heptane. At low Si/Al ratio (e.g., $X = 10$) the materials have total conversions and selectivity comparable to that of USY zeolite (Si/Al = 21) [124]. Further studies of these materials confirmed that these materials with disordered pores can be good candidates for catalysts [125].

The existence of disordered short channels in these worm-like silicas can be detected by TEM observation of samples incorporating with heavy metals such as Pt [123]. The high flexibility of the mesopores in these nonperiodic phases leads to easy control of the morphology [127]. It is also possible to make very small particles [128] for application in the realm of catalysis or homogeneous large area thin films [129] and monoliths [130], which have wide applications in the electrochemical industry.

In summary, during the last 10 years, many ordered mesoporous silicas have been synthesized using several different mechanisms. The structures of most phases have been determined (Table 1). To date, these structures discovered have symmetries of $P6mm$ (two-dimensional), $P6_3/mmc$, $cm\bar{m}$, $Fm\bar{3}m$, $Ia\bar{3}d$, $Im\bar{3}m$, $Pm\bar{3}n$, $Fd\bar{3}m$, etc. Several nonperiodic phases were also fabricated. Variation of the pore sizes in these materials has been extensively investigated. The shapes of pores can be cylindrical, spherical with windows, bottle-like, wormlike, etc. Incorporation of chemically active inorganic or organic groups into the mesoporous particles is an important direction of development in the field of advanced material research.

GLOSSARY

Energy dispersive X-ray spectroscopy (EDX) An analytic method involving exciting atoms using electron beam to emit characteristic X-rays which are sorted out according to their energy to reveal the elemental composition of a specimen.

Mesoporous molecular sieves A class of porous materials with the pore diameter in the range of 2 nm to 50 nm.

Scanning electron microscopy (SEM) A technique for imaging surface morphology of solids using backscattered or secondary electrons.

Selected area electron diffraction (SAED) A technique for observing diffraction patterns from a small specimen area.

Transmission electron microscopy (TEM) A technique for imaging ultramicrostructure of materials by using a transmitted electron beam and diffracted electron beams.

X-ray powder diffraction (XRD) A technique for structure determination based on the scattering of X-rays by matter that is extensively used for the studies of polycrystalline materials and materials possessing long range ordering.

REFERENCES

1. T. B. Reed and D. W. J. Breck, *J. Am. Chem. Soc.* 78, 5972 (1956).
2. S. Carlidge, H. U. Nissen, and R. Wessicken, *Zeolites* 9, 346 (1989).
3. C. T. Kresge, M. E. Leonowicz, W. J. Roth, J. C. Vartulli, and J. S. Beck, *Nature* 359, 710 (1992).
4. J. S. Beck, J. C. Vartulli, W. J. Roth, M. E. Leonowicz, C. T. Kresge, K. D. Schmitt, C. T.-W. Chu, D. H. Olson, E. W. Sheppard, S. B. McCullen, J. B. Higgins, and J. L. Schlenker, *J. Am. Chem. Soc.* 114, 10834 (1992).
5. J. Y. Ying, C. P. Mehnert, and M. S. Wong, *Angew. Chem. Int. Ed. Engl.* 38, 56 (1999).
6. C. F. Cheng, H. He, W. Zhou, and J. Klinowski, *Chem. Phys. Lett.* 244, 117 (1995).
7. C. Y. Chen, S. L. Burkett, H. X. Li, and M. E. Davis, *Microporous Mater.* 2, 27 (1993).
8. A. Monnier, F. Schuth, Q. Huo, D. Margolese, R. S. Maxwell, G. D. Stucky, M. Krishnamurty, P. Petroff, A. Firouzi, M. Janicke, and B. F. Chmelka, *Science* 261, 1299 (1993).
9. Q. Huo, D. I. Margolese, U. Ciesla, P. Y. Feng, T. E. Gier, P. Sieger, R. Leon, P. M. Petroff, F. Schuth, and G. D. Stucky, *Nature* 368, 317 (1994).
10. Q. Huo, R. Leon, P. M. Petroff, and G. D. Stucky, *Science* 268, 1324 (1995).
11. U. Ciesla, D. Demuth, R. Leon, P. Petroff, G. D. Stucky, K. Unger, and F. Schuth, *J. Chem. Soc. Chem. Commun.* 1387 (1994).
12. A. Firouzi, D. Kumar, L. M. Bull, T. Besier, P. Sieger, Q. Huo, S. A. Walker, J. A. Zasadzinski, C. Glinka, J. Nicol, D. Margolese, G. D. Stucky, and B. F. Chmelka, *Science* 267, 1138 (1995).
13. W. Zhou and J. Klinowski, *Chem. Phys. Lett.* 292, 207 (1998).
14. W. Zhou, R. Mokaya, Z. Shan, and T. Maschmeyer, *Progr. Nat. Sci. (Engl. Ed.)* 11, 33 (2001).
15. R. Mokaya, W. Zhou, and W. Jones, *J. Chem. Soc. Chem. Commun.* 51 (1999).
16. S. Inagaki, Y. Fukushima, and K. Kuroda, *Stud. Surf. Sci. Catal.* 84, 125 (1994).
17. Q. Huo, D. I. Margolese, and G. D. Stucky, *Chem. Mater.* 8, 1147 (1996).
18. A. Corma, *Chem. Rev.* 97, 2373 (1997).
19. A. Carlsson, M. Kaneda, Y. Sakamoto, O. Terasaki, R. Ryoo, and S. H. Joo, *J. Electron Microsc.* 48, 795 (1999).
20. Y. Sakamoto, M. Kaneda, O. Terasaki, D. Zhao, J. M. Kim, G. D. Stucky, H. J. Shin, and R. Ryoo, *Nature* 408, 449 (2000).
21. Y. Sakamoto, I. Diaz, O. Terasaki, D. Zhao, J. Perez-Pariente, J. M. Kim, and G. D. Stucky, *J. Phys. Chem. B* 106, 3118 (2002).
22. W. Zhou, *Micron* 31, 605 (2000).
23. J. M. Thomas, O. Terasaki, P. L. Gai, W. Zhou, and J. Gonzalez-Calbet, *Acc. Chem. Res.* 34, 583 (2001).
24. M. Kaneda, T. Tsubakiyama, A. Carlsson, Y. Sakamoto, T. Ohsuna, O. Terasaki, S. H. Joo, and R. Ryoo, *J. Phys. Chem. B* 106, 1256 (2002).
25. E. P. Barrett, L. G. Joyner, and P. P. Halenda, *J. Am. Chem. Soc.* 73, 373 (1951).
26. P. I. Ravikovitch and A. V. Neimark, *Langmuir* 18, 1550 (2002).
27. Z. Luan, C. Cheng, W. Zhou, and J. Klinowski, *J. Phys. Chem.* 99, 1018 (1995).
28. W. Zhou, Z. Dong, and L. Peng, *Progr. Natural Sci. (Chinese Ed.)* 8, 528 (1998).
29. C. F. Cheng, W. Zhou, and J. Klinowski, *Chem. Phys. Lett.* 263, 247 (1996).
30. M. Kruk, M. Jaroniec, and A. Sayari, *J. Phys. Chem. B* 103, 4590 (1999).
31. N. Ulagappan and C. N. R. Rao, *J. Chem. Soc. Chem. Commun.* 2759 (1996).
32. B. P. Feuston and J. B. Higgins, *J. Phys. Chem. B* 98, 4459 (1994).
33. P. Behrens and G. D. Stucky, *Angew. Chem. Int. Ed. Engl.* 32, 696 (1993).
34. J. M. Garces, *Adv. Mater.* 8, 434 (1996).
35. H. P. Lin, C. Y. Mou, and S. B. Liu, *Adv. Mater.* 12, 103 (2000).
36. Z. Y. Yuan and W. Zhou, *Chem. Phys. Lett.* 333, 427 (2001).

37. A. Corma, V. Fornes, M. T. Navarro, and J. Perez-Pariente, *J. Catal.* 148, 569 (1994).
38. R. Schmidt, D. Akporiaye, M. Stocker, and O. H. Ellestad, *J. Chem. Soc. Chem. Commun.* 1493 (1994).
39. A. Corma, M. T. Navarro, and J. Perez-Pariente, *J. Chem. Soc. Chem. Commun.* 147 (1994).
40. P. T. Tanev, M. Chibwe, and T. J. Pinnavaia, *Nature* 368, 321 (1994).
41. K. M. Reddy, I. Mondrakovski, and A. Sayari, *J. Chem. Soc. Chem. Commun.* 1059 (1994).
42. C. F. Cheng, H. He, W. Zhou, J. Klinowski, J. A. Gonclaves, and L. F. Gladden, *J. Phys. Chem.* 100, 390 (1996).
43. A. Sayari, C. Danumah, and I. L. Moudrakovski, *Chem. Mater.* 7, 813 (1995).
44. D. Zhao and D. Goldfarb, *J. Chem. Soc. Chem. Commun.* 875 (1995).
45. Z. Y. Yuan, H. T. Ma, Q. Luo, and W. Zhou, *Mater. Chem. Phys.* 77, 299 (2002).
46. Z. Y. Yuan, S. Q. Liu, T. H. Chen, J. Z. Wang, and H. X. Li, *J. Chem. Soc. Chem. Commun.* 973 (1995).
47. Z. Y. Yuan, W. Zhou, Z. L. Zhang, Q. Chen, B.-L. Su, and L. M. Peng, *Stud. Surf. Sci. Catal.* 141, 403 (2002).
48. A. Corma, M. T. Navarro, L. Nemeth, and M. Renz, *J. Chem. Soc. Chem. Commun.* 2190 (2001).
49. M. J. Danks, H. B. Jervis, M. Nowotny, W. Zhou, T. A. Maschmeyer, and D. W. Bruce, *Catal. Lett.* 82, 95 (2002).
50. D. S. Shephard, W. Zhou, T. Maschmeyer, J. M. Matters, C. L. Roper, S. Parsons, B. F. G. Johnson, and M. Duer, *Angew. Chem. Int. Ed. Engl.* 37, 2719 (1998).
51. D. S. Shephard, T. Maschmeyer, B. F. G. Johnson, J. M. Thomas, G. Sankar, D. Ozkaya, W. Zhou, R. D. Oldroyd, and R. G. Bell, *Angew. Chem. Int. Ed. Engl.* 36, 4 (1997).
52. W. Zhou, J. M. Thomas, D. S. Shephard, B. F. G. Johnson, D. Ozkaya, T. Maschmeyer, R. G. Bell, and Q. Ge, *Science* 280, 705 (1998).
53. D. Ozkaya, W. Zhou, J. M. Thomas, P. Midgley, V. J. Keast, and S. Hermans, *Catal. Lett.* 60, 113 (1999).
54. J. L. Blin, A. Leonard, and B. L. Su, *Chem. Mater.* 12, 3542 (2001).
55. S. Inagaki, S. Guan, Y. Fukushima, T. Ohsuma, and O. Terasaki, *J. Am. Chem. Soc.* 121, 9611 (1999).
56. M. Kruk, M. Jaroniec, S. Guan, and S. Inagaki, *J. Phys. Chem. B* 105, 681 (2001).
57. D. Zhao, Q. Huo, J. Feng, J. Kim, Y. Han, and G. D. Stucky, *Chem. Mater.* 11, 2668 (1999).
58. J. E. Haskouri, S. Cabrera, M. Caldes, C. Guillem, J. Latorre, A. Beltran, D. Beltran, M. D. Marcos, and P. Amoros, *Chem. Mater.* 14, 2637 (2002).
59. T. Yanagisawa, T. Shimizu, K. Kuroda, and C. Kato, *Bull. Chem. Soc. Jpn.* 63, 988 (1990).
60. J. C. Vartuli, C. T. Kresge, M. E. Leonowicz, A. S. Chu, S. B. McCullen, I. D. Johnson, and E. W. Sheppard, *Chem. Mater.* 6, 2070 (1994).
61. S. Inagaki, Y. Fukushima, and K. Kuroda, *J. Chem. Soc. Chem. Commun.* 680 (1993).
62. T. Ishikawa, M. Matasuda, A. Yasukawa, K. Kandori, S. Inagaki, T. Fukushima, and S. Kondo, *J. Chem. Soc. Faraday Trans.* 92, 1985 (1996).
63. Y. Sakamoto, S. Inagaki, T. Ohsuna, N. Ohnishi, Y. Fukushima, Y. Nozue, and O. Terasaki, *Microporous Mesoporous Mater.* 21, 589 (1998).
64. Y. Kimura, T. Kamata, M. Fuziwarra, Y. Takano, M. Kaneda, Y. Sakamoto, O. Terasaki, Y. Sugahara, and K. Kuroda, *Angew. Chem. Int. Ed. Engl.* 39, 3855 (2000).
65. D. Zhao, J. Feng, Q. Huo, N. Melosh, G. H. Fredrickson, B. F. Chmelka, and G. D. Stucky, *Science* 279, 548 (1998).
66. D. Zhao, Q. Huo, J. Feng, B. F. Chmelka, and G. D. Stucky, *J. Am. Chem. Soc.* 120, 6024 (1998).
67. Z. Liu, Y. Sakamoto, T. Ohsuna, K. Hiraga, O. Terasaki, C. H. Ko, H. J. Shin, and R. Ryoo, *Angew. Chem. Int. Ed. Engl.* 39, 3107 (2000).
68. M. Imperor-Clerc, P. Davidson, and A. Davidson, *J. Am. Chem. Soc.* 122, 11925 (2000).
69. P. I. Ravikovitch and A. V. Neimark, *J. Phys. Chem. B* 105, 6817 (2001).
70. J. Fan, C. Yu, L. Wang, B. Tu, D. Zhao, Y. Sakamoto, and O. Terasaki, *J. Am. Chem. Soc.* 123, 12113 (2001).
71. B. L. Newalkar and S. Komarneni, *Chem. Mater.* 13, 4573 (2001).
72. Z. Luan, M. Hartmann, D. Zhao, W. Zhou, and L. Kevan, *Chem. Mater.* 11, 1621 (1999).
73. S. Sumiya, Y. Oumi, T. Uozumi, and T. Sano, *J. Mater. Chem.* 11, 1111 (2001).
74. Z. Luan, E. M. Maes, P. A. W. van der Heide, D. Zhao, R. S. Czernuszewicz, and L. Kevan, *Chem. Mater.* 11, 3680 (1999).
75. Z. Luan, J. Y. Bae, and L. Kevan, *Chem. Mater.* 12, 3202 (2000).
76. B. L. Newalkar, J. Olanrewaju, and S. Komarneni, *J. Phys. Chem. B* 105, 8356 (2001).
77. D. Margolese, J. A. Melero, S. C. Christiansen, B. F. Chmelka, and G. D. Stucky, *Chem. Mater.* 12, 2448 (2000).
78. K. Zhu, Z. Ma, Y. Zou, W. Zhou, T. Chen, and H. He, *J. Chem. Soc. Chem. Commun.* 2552 (2001).
79. J. Sauer, F. Marlow, B. Spliethoff, and F. Schuth, *Chem. Mater.* 14, 217 (2002).
80. H. Kang, Y. Jun, J. Park, K. Lee, and J. Cheon, *Chem. Mater.* 12, 3530 (2000).
81. R. Ryoo, C. H. Ko, M. Kruk, V. Antochshuk, and M. Jaroniec, *J. Phys. Chem. B* 104, 11465 (2000).
82. H. J. Shin, R. Ryoo, M. Kruk, and M. Jaroniec, *J. Chem. Soc. Chem. Commun.* 349 (2001).
83. R. Ryoo, S. H. Joo, M. Kruk, and M. Jaroniec, *Adv. Mater.* 13, 677 (2001).
84. Y. Han, J. M. Kim, and G. D. Stucky, *Chem. Mater.* 12, 2068 (2000).
85. Z. Liu, O. Terasaki, T. Ohsuna, K. Hiraga, H. J. Shin, and R. Ryoo, *Chem. Phys. Chem.* 4, 229 (2001).
86. K. Zhu, B. Yue, W. Zhou, H. He, *J. Chem. Soc. Chem. Commun.* 98, (2003).
87. H. J. Shin, C. H. Ko, and R. Ryoo, *J. Mater. Chem.* 11, 260 (2001).
88. W. Zhou, H. M. A. Hunter, P. A. Wright, Q. Ge, and J. M. Thomas, *J. Phys. Chem.* 102, 6933 (1998).
89. A. E. Garcia-Bennett, S. Williamson, P. A. Wright, and I. J. Shannon, *J. Mater. Chem.* 12, 3533 (2002).
90. H. M. A. Hunter, A. E. Garcia-Bennett, W. Zhou, and P. A. Wright, *J. Mater. Chem.*, 12, 20 (2002).
91. W. Zhou, A. E. Garcia-Bennett, H. M. A. Hunter, and P. A. Wright, *Stud. Surf. Sci. Catal.* 141, 379 (2002).
92. C. C. Landry, S. H. Tolbert, K. W. Gallis, A. Monnier, G. D. Stucky, P. Norby, and J. C. Hanson, *Chem. Mater.* 13, 1600 (2001).
93. V. Alfredsson and M. W. Anderson, *Chem. Mater.* 8, 1141 (1996).
94. V. Alfredsson, M. W. Anderson, T. Ohsuna, O. Terasaki, M. Jacob, and M. Bojrup, *Chem. Mater.* 9, 2066 (1997).
95. K. Schumacher, P. I. Ravikovitch, A. D. Chesne, A. V. Neimark, and K. K. Unger, *Langmuir* 16, 4648 (2000).
96. J. M. Kim, S. K. Kim, and R. Ryoo, *J. Chem. Soc. Chem. Commun.* 259 (1998).
97. W. Zhang and T. J. Pinnavaia, *Catal. Lett.* 38, 261 (1996).
98. C. Pak and G. L. Haller, *Microporous Mesoporous Mater.* 48, 165 (2001).
99. B. Echchahed, A. Moen, D. Nicholson, and L. Bonnevot, *Chem. Mater.* 9, 1716 (1997).
100. J. Xu, Z. Luan, M. Hartmann, and L. Kevan, *Chem. Mater.* 11, 2928 (1999).

101. M. S. Morey, G. D. Stucky, S. Schwarz, and M. Froba, *J. Phys. Chem. B* 103, 2037 (1999).
102. M. Hartmann, S. Racouchot, and C. Bischof, *J. Chem. Soc. Chem. Commun.* 2367 (1997).
103. S. B. Yoon, J. Y. Kim, and J. S. Yu, *J. Chem. Soc. Chem. Commun.* 559 (2001).
104. R. Ryoo, S. H. Joo, and S. Jun, *J. Phys. Chem. B* 103, 7743 (1999).
105. H. J. Shin, R. Ryoo, Z. Liu, and O. Terasaki, *J. Am. Chem. Soc.* 123, 1246 (2001).
106. P. V. D. Voort, M. Benjelloun, and E. F. Vansant, *J. Phys. Chem. B* 106, 9027 (2002).
107. Q. Huo, D. I. Margolese, U. Ciesla, D. G. Demuth, P. Feng, T. E. Gier, P. Sieger, A. Firouzi, B. F. Chmelka, F. Schuth, and G. D. Stucky, *Chem. Mater.* 6, 1176 (1994).
108. M. J. Kim and R. Ryoo, *Chem. Mater.* 11, 487 (1999).
109. S. Che, Y. Sakamoto, O. Terasaki, and T. Tatsumi, *Chem. Mater.* 13, 2237 (2001).
110. L. Dai, Y. Teng, K. Tabata, E. Suzuki, and T. Tatsumi, *Chem. Lett.* 794 (2000).
111. L. Dai, K. Tabata, E. Suzuki, and T. Tatsumi, *Chem. Mater.* 13, 208 (2001).
112. L. Dai, K. Tabata, E. Suzuki, and T. Tatsumi, *Microporous Mesoporous Mater.* 44–45, 573 (2001).
113. S. Che, Y. Sakamoto, H. Yoshitake, O. Terasaki, and T. Tatsumi, *J. Phys. Chem. B* 105, 10565 (2001).
114. A. Vinu, J. Dedeczek, V. Murugesan, and M. Hartmann, *Chem. Mater.* 14, 2433 (2002).
115. S. Guan, S. Inagaki, T. Ohsuna, and O. Terasaki, *J. Am. Chem. Soc.* 122, 5660 (2000).
116. C. Z. Yu, Y. H. Yu, L. Miao, and D. Y. Zhao, *Microporous Mesoporous Mater.* 44, 65 (2001).
117. S. Shen, Y. Li, Z. Zhang, J. Fan, B. Tu, W. Zhou, and D. Zhao, *J. Chem. Soc. Chem. Commun.* 2212 (2002).
118. S. A. Bagshaw, E. Prouzet, and T. J. Pinnavaia, *Science* 269, 1242 (1995).
119. S. A. Bagshaw and T. J. Pinnavaia, *Angew. Chem. Int. Ed. Engl.* 35, 1102 (1996).
120. J. C. Jansen, Z. Shan, L. Marchese, W. Zhou, N. V. D. Puil, and Th. Maschmeyer, *J. Chem. Soc. Chem. Commun.* 713 (2001).
121. P. T. Tanev and T. J. Pinnavaia, *Science* 267, 865 (1995).
122. T. R. Pauly and T. J. Pinnavaia, *Chem. Mater.* 13, 987 (2001).
123. R. Ryoo, J. M. Kim, C. H. Ko, and C. H. Shin, *J. Phys. Chem.* 100, 17718 (1996).
124. R. Mokaya, W. Jones, S. Moreno, and G. Poncelet, *Catal. Lett.* 49, 87 (1997).
125. E. Bastardo-Gonzalez, R. Mokaya, and W. Jones, *J. Chem. Soc. Chem. Commun.* 1016 (2001).
126. Z. Shan, W. Zhou, J. C. Jansen, C. Y. Yeh, J. H. Koegler, and Th. Maschmeyer, *Stud. Surf. Sci. Catal.* 141, 635 (2002).
127. C. Boissiere, A. Larbot, and E. Prouzet, *Stud. Surf. Sci. Catal.* 129, 31 (2000).
128. E. Prouzet, F. Cot, G. Nabias, A. Larbot, P. Kooyman, and T. J. Pinnavaia, *Chem. Mater.* 11, 1498 (1999).
129. Y. Lu, R. Gangli, C. A. Drewien, M. T. Anderson, C. J. Brinker, W. Gong, Y. Guo, H. Soyez, B. Dunn, M. H. Huang, and J. I. Zink, *Nature* 389, 364 (1997).
130. K. M. McGrath, D. M. Dabbs, N. Yao, I. A. Aksay, and S. M. Gruner, *Science* 277, 552 (1997).

Structure of Nanoclusters by High-Resolution Transmission Electron Microscopy

J. Urban

Fritz Haber Institute of the Max Planck Gesellschaft, Berlin, Germany

CONTENTS

1. Introduction
 2. Preparation of Clusters
 3. Computer Simulation of Clusters by the Multislice Technique
 4. Image Processing
 5. Cluster Models and Experimental Results
 6. Oxidation of Cu Clusters
- Glossary
References

1. INTRODUCTION

In recent years, nanoparticles have become the focus of increasing interest. A variety of different techniques are in use to prepare small clusters. The main aim of this chapter is to describe two different techniques for the preparation of clusters in the size range between 1 and 10 nm. However, examples of long needles or rods diameters of a few nanometers and lengths in the micrometer range are presented. The outstanding characteristic behavior in comparison with bulk material depends entirely on the size and geometrical structures of the clusters. These characteristic properties are very important, for instance, in the case of heterogeneous catalysis, to name only one of their important features. High-resolution transmission electron microscopy (HRTEM) is one of the most powerful tools for the structural characterization of particles, even though its interpretation sometimes turns out to be difficult. Computer simulations and the comparison between calculated images and experimental pictures serve as an important technique for overcoming this handicap. Following the description of

some experimental designs for preparing these nanoparticles, techniques for performing these simulations will be discussed in detail. It will also be explained how structural and symmetry information can be obtained with the use of the Fourier transform of the images. From the images in the reciprocal space, much valuable information, such as lattice parameters and lattice angles, can be obtained, which are also described in this chapter. Examples of experimental results will be given. The main focus, however, is on Cu clusters prepared by the inert gas aggregation technique, although materials like Ag and CdS are also discussed. Furthermore, some examples of chemical reaction techniques that result in ligand stabilized clusters are described. The procedure of the chapter is the following: description of the preparation of clusters, computer simulation using the multislice technique, and, finally, comparison between examples of different materials with computer simulations and presentation of the results. Finally, the chemical reactivity of Cu clusters for the oxidation process is discussed.

2. PREPARATION OF CLUSTERS

There are many different techniques (supersonic nozzle beam, seeded beam technique, sputtering, laser evaporation, to mention only a few) for the deposition and preparation of clusters, their nucleation, and growth. A detailed review thereof is given by Gunter et al. [1] and Henry [2]. This chapter, however, is concerned only with two different techniques, which are discussed below.

2.1. Inert Gas Aggregation

One of the most commonly used techniques for the preparation of clusters is inert gas aggregation [3–5]. Most of the particles described in the present review were prepared with this technique. Therefore, it is necessary to deal with specific features in the described experiments. In principle, the experimental setup for the inert gas aggregation technique

is shown in Figure 1. The nucleation cell consists of three main parts: the evaporation area, the nucleation area, and the deposition area with the transfer systems and the preparation chambers. In contrast to systems where helium is used as the nucleation gas [6], the present preparations used argon as the nucleation gas. The material under investigation (generally pure metals but compounds can also be used) is evaporated from an open crucible or a Knudsen cell. The evaporation is performed by direct heating of a tantalum foil wrapped around an Al_2O_3 container. Sometimes, quartz or carbon containers are used. In general, the argon pressure is kept between 10^{-1} and 1 mbar. The condensation of nuclei and further cluster growth take place within an area cooled down by liquid nitrogen, allowing for supersaturation of the metal-argon mixture. The cluster growth is terminated by pumping off the argon gas with a highly efficient helium-cooled cryo-pump. The helium cryo-pump was the reason to use argon as the nucleation gas instead of helium. The clusters are then deposited in the deposition area at 10^{-6} – 10^{-7} mbar pressure on an amorphous carbon film of about 4-nm thickness covering a commercial copper grid as it is used for electron microscopy. The clusters are then transferred under vacuum or under argon gas by means of a transfer system from the reaction chamber to the microscope to protect the clusters against oxidation or further reactions under ambient conditions. The cluster flow is controlled with a microbalance quartzoscillator. Typical deposition rates were 0.1 nm/s. The deposition time was on the order of 1–3 s to avoid coalition either in the cluster beam or on the substrate. Several apertures, one of them variable between 1- and 45-mm diameter, influence the particle size distribution obtained with the nucleation cell. Typical dates for size distributions obtained with the nucleation cell are the following for Ag clusters: mean particle size of 4.5-nm diameter, full width at half-maximum of 1.3-nm diameter. Argon pressure and evaporation temperature also influence the particle growth. The size distribution in the case of the preparation of silver clusters is studied in detail and described elsewhere [7] in a comparison between time-of-flight mass spectroscopy and electron microscopy. With the described

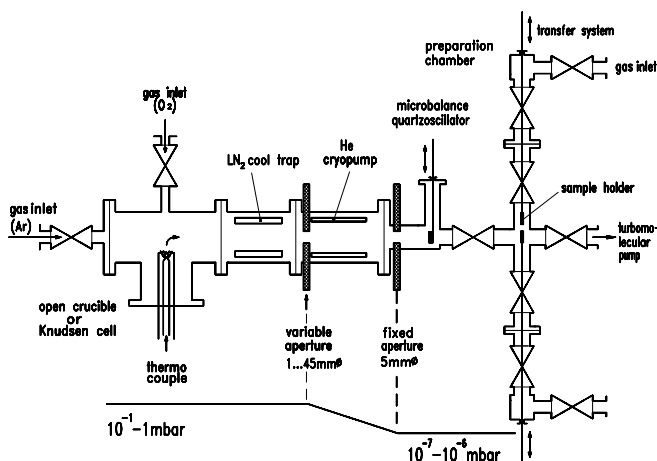


Figure 1. Principle of the nucleation cell for the preparation of clusters by inert gas aggregation. Reprinted with permission from [46], J. Urban et al., *High Temp. Mater. Sci.* 36, 155 (1996). © 1996, Humana Press.

nucleation cell it is possible to prepare clusters consisting of a few atoms up to several thousands of atoms. For the present structural characterization of clusters by HRTEM, a region of 1- to 10-nm diameter could easily be achieved. The number N_0 of atoms in a sphere of diameter D is given by

$$N_0 = \left(\frac{D}{a}\right)^3 \frac{2\pi}{3} \quad (1)$$

a is the lattice parameter for the cubic elementary cell. Therefore, the size region $D = 1, \dots, 10$ nm diameter corresponds for Ag and Au to $N_0 = 31, \dots, 30,800$ and for Cu to $N_0 = 44, \dots, 44,514$.

A typical example of an overview electron microscopic image for Cu clusters is shown in Figure 2. In order also to study reactivity during the evaporation process—prior to the nucleation of clusters—an additional gas inlet into the evaporation region is installed. In the present representation, however, only examples of the inlet of O_2 will be given.

2.2. Colloidal Particles

The preparation of colloidal particles has recently become a focus of great interest, seeing that it seems possible to create particles of narrow size distribution by this technique. A great number of recent publications focus on this subject. Here we refer only to a limited number of papers [8–12]. The examples of colloidal particles given in the present article consist of Cu cylinders and needles (rods) [13–15], triangular CdS particles [16], and spherical CdS particles [17–19]. A detailed description of the different techniques is given in the corresponding references. Here only brief descriptions of the different examples are given:

Cu Particles (Rods and Cylinders)

Copper metal particles are prepared by reduction of $\text{Cu}(\text{AOT})_2$ in $\text{Cu}(\text{AOT})$ -isooctane- NaCl -water colloidal self-assemblies. Hydrazine is used as a reducing agent. The reduction takes place under a N_2 atmosphere.

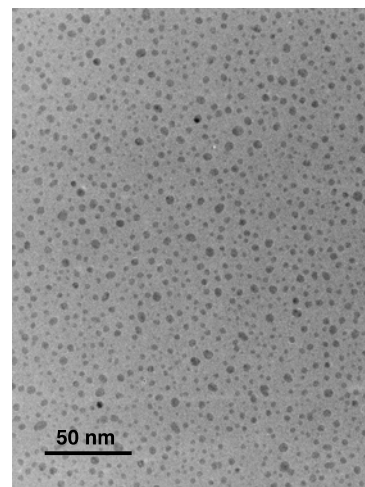


Figure 2. Overview electron micrograph of Cu clusters prepared by the nucleation cell described in Figure 1.

CdS Triangular Particles

Cadmium bis(ethyl-2-hexyl)sulfosuccinate($\text{Cd}(\text{AOT})_2$)/iso-octane/ H_2O is used to prepare CdS nanoparticles. For more details refer to [16].

CdS Spherical Particles

The preparation involves the capping of CdS nanoparticles with the use of mercaptoethanol ($\text{C}_2\text{H}_5\text{OSH}$). The synthesis involves the reduction of CdCl_2 with mercaptoethanol. Na_2S is added to this solution. The reactions are carried out under nitrogen, and the solutions are made in water. After the reaction is completed, the colloid is centrifuged and washed repeatedly in distilled water.

3. COMPUTER SIMULATION OF CLUSTERS BY THE MULTISLICE TECHNIQUE

For calculations of electron microscopic images the multislice technique is the most commonly used approach. The theory was originally developed by Cowley and Moodie [20] and Goodman and Moodie [21]. A more recent approach in a nonrelativistic treatment is given by van Dyk [22], which is briefly reported as follows.

3.1. Thin-Phase Object: The Phase Grating Approximation

This theory goes back to Alpress and Sanders [23], Cowley and Iijima [24], and Hutchison [25].

After the interaction of an electron with wavelength λ with an object with local potential $V(x, y, z)$ the wavelength of the electron varies as λ' :

$$\lambda = \frac{h}{\sqrt{2meE}} \quad \lambda' = \frac{h}{\sqrt{2me(E + V(x, y, z))}} \quad (2)$$

where E is the electrostatic acceleration potential and m and e are the mass and charge of the electron.

Since the electron travels perpendicular to the x, y plane in the z direction, the phase shift change $d\chi(x, y, z)$, traveling through dz , is given as

$$\begin{aligned} d\chi(x, y, z) &= 2\pi dz(1/\lambda' - 1/\lambda) \\ &= \frac{2\pi dz}{\lambda} (\sqrt{(E + V)/E} - 1) \end{aligned} \quad (3)$$

and with $\sigma = \pi/(\lambda E)$ and $V/E \ll 1$ one obtains

$$d(x, y, z) \quad V/(E)dz = V(x, y, z) dz$$

The total phase shift traveling through a thickness q_0 (q_0 is on the order of 0.1 nm) is given by

$$\chi(x, y) = \int_0^{q_0} d\chi(x, y, z) = \sigma \int_0^{q_0} V(x, y, z) dz = \sigma V_p(x, y) \quad (4)$$

where V_p is the projected potential for the whole sample:

$$V_p(x, y) \approx V(x, y)q_0 \quad (5)$$

$V(x, y)$ is an average over the sample in the z direction. The transmission function at the exit of the sample at $z = q_0$ is then

$$\psi(x, y) = \exp(i\sigma V_p(x, y)) \quad (6)$$

Here absorption has been neglected. This can be considered by introducing an imaginary absorption potential, $-i\mu(x, y)$ (cf. Hamid Rahman [26] and Urban et al. [27]). Without absorption and for thin-phase objects the phase grating approximation is given by

$$\psi(x, y) \approx 1 + i\sigma V_p(x, y) \quad (7)$$

3.2. Multislice Approximation

For thick samples the sample can be divided into n slices of thickness q_0 . At the entrance of each slice (x, y) , a spherical wave with amplitude $\psi(x, y)$ and wave vector k is created. The amplitude at the exit of the slice (x', y') is a superposition of all spherical waves:

$$\psi(x', y') = \int \exp(i\sigma V_p(x, y)) \frac{\exp(2\pi ikr(x', x, y', y))}{r} dx dy \quad (8)$$

with

$$r = \sqrt{(x - x')^2 + (y - y')^2 + q_0^2} \quad (9)$$

In the case of $|x - x'|, |y - y'| \ll q_0$ the Fresnel approximation can be used:

$$r \approx q_0 \left(1 + \frac{(x - x')^2}{2q_0^2} + \frac{(y - y')^2}{2q_0^2} \right) \quad (10)$$

Therefore one obtains

$$\begin{aligned} \psi(x', y') &\cong \frac{\exp(2\pi ikq_0)}{q_0} \int \exp(i\sigma V_p(x, y)) \\ &\quad \times \exp\left(\frac{i\pi k}{q_0}((x - x')^2 + (y - y')^2)\right) dx dy \end{aligned} \quad (11)$$

This is a convolution defined as

$$\begin{aligned} f(x) * g(x) &= \int f(x')g(x - x') dx' \\ &= \int f(x - x')g(x') dx' \end{aligned} \quad (12)$$

The electron wave function at the entrance of the first slice is $\psi(x, y, 0)$, and, at the exit, which serves as the

entrance of the second slice, it is $\psi(x, y, q_0)$. Therefore we obtain

$$\begin{aligned} \psi(x, y, q_0) &= \{\psi(x, y, 0) \exp(i\sigma V_p^1(x, y))\} \\ &\quad * \exp\left(\frac{i\pi k}{q_0}(x^2 + y^2)\right) \end{aligned} \quad (13)$$

$$\begin{aligned} \psi(x, y, 2q_0) &= \{\psi(x, y, q_0) \exp(i\sigma V_p^2(x, y))\} \\ &\quad * \exp\left(\frac{i\pi k}{q_0}(x^2 + y^2)\right) \end{aligned} \quad (14)$$

⋮

$$\begin{aligned} \psi(x, y, nq_0) &= \{\psi(x, y, (n-1)q_0) \exp(i\sigma V_p^n(x, y))\} \\ &\quad * \exp\left(\frac{i\pi k}{q_0}(x^2 + y^2)\right) \end{aligned} \quad (15)$$

where $V_p^n(x, y)$ is the projected potential of the n th slice. The propagation of the electron can therefore be calculated successively. With the Fourier theorem of the convolution the convolution product can be replaced by a normal product in the Fourier space. \mathcal{F} is the symbol for the Fourier transform. Therefore one obtains

$$\begin{aligned} \mathcal{F}(x, y, nq_0) &= \mathcal{F}(x, y, (n-1)q_0) \exp(iV_p^n(x, y)) \\ &\quad * \exp\left(\frac{i\pi k}{q_0}(x^2 + y^2)\right) \end{aligned} \quad (16)$$

$$\begin{aligned} &= \mathcal{F}(x, y, (n-1)q_0) \exp(iV_p^n(x, y)) \\ &\quad \times \mathcal{F}\left(\exp\left(\frac{i\pi k}{q_0}(x^2 + y^2)\right)\right) \end{aligned} \quad (17)$$

With fast Fourier transforms the computation time can be remarkably reduced in comparison with the convolution. For the calculation of the images, phase changes due to defocus and spherical or chromatic aberrations must be considered. These effects are not considered here but are discussed in detail by Fejes [28].

For the calculation of the projected potentials, the atomic positions, and hence the structures of the samples, must be known. The calculation is performed by using atomic form factors as published, for instance, by Doyle and Turner [29]:

$$\begin{aligned} V(x, y, z) &= V(\vec{r}) = \mathcal{F}V(\vec{u}), \\ V(\vec{u}) &= \sum_n f_{\text{at}}^n(\vec{u}) \exp(2\pi i \vec{u} \vec{r}_n) \end{aligned} \quad (18)$$

where f_{at}^n are the atomic form factors of atoms at position \vec{r}_n . The whole procedure is described in more detail by Nihoul et al. [30].

4. IMAGE PROCESSING

In addition to real images, the power spectra (PS) are also calculated. The PS is the square of the Fourier transform of the real image. From the PS in the reciprocal space more information on the symmetry of the atomic arrangements can be obtained. Furthermore, in crystalline structures reflections appear in the PS that lie symmetrically distributed on circles around the origin. The reflections always

appear as pairs under an angle of 180° for hkl and $-h-k-l$. From the diameter of the circles the corresponding netplane spacings can be calculated:

$$d_{hkl} = \frac{N_{\text{pix}}(\text{total})\text{pix}}{N_{\text{pix}}(\text{radius})} \quad (19)$$

$N_{\text{pix}}(\text{total})$ is the total number of pixels along the quadratic frame of the PS. This is usually 128, 256, 512, ... $N_{\text{pix}}(\text{radius})$ is the number of pixels between the origin and the reflection in the PS. pix is the pixel size, which depends on the digitizing of the images. The PS also allows the processing of experimentally obtained images for comparison of experimental images with computer simulations. The whole procedure is normally a Fourier filtering of the images [30–32]. Among many other aspects—such as improving the quality of experimental images—image processing by Fourier filtering allows a decrease in the influence of the background, that is, the substrate, in the images and the separation of different structures, which may overlap each other. Examples thereof will be given later.

5. CLUSTER MODELS AND EXPERIMENTAL RESULTS

It has already been pointed out that for the calculation of EM images the projected potentials of the samples must be known. Obviously, to be able to compare experimental images with calculated images the atomic positions in the sample must be known. Generally, certain structures are assumed. We will discuss these structures, which have recently been observed in the case of metals such like Au, Ag, Pd, Cu, etc. Examples are only given for Cu and Ag samples. We will also discuss structures of compounds. For each typical model, examples of EM images as computer simulations and experimental images will be given. The experiments are performed with a Philips CM 200 FEG microscope equipped with a field emission gun (200 kV, $C_s = 1.35$ mm). The calculations are performed with the data of this microscope. In the following, fcc structures in the form of cuboctahedra and hexagonal structures are investigated. Examples of multiply twinned particles with 5-fold symmetry (MTP), that is, icosahedra and decahedra, are also presented. Small clusters consisting of only a few of atoms can be explained by means of the electronic shell model introduced by Knight et al. [33] and Ekardt [34]. However, clusters under the present investigation have the most stable form with closed atomic shells, which are caused entirely by their geometrical arrangement [35]. The stable clusters consist of defined numbers of atoms, that is, magic numbers that depend on the structures.

5.1. Cuboctahedra

Clusters with cuboctahedral structures are particles with fcc symmetry (cf. Wulff [36] and Herring [37]). The magic numbers are the same as those for icosahedra. An N_s -shelled cluster consists of N_0 atoms:

$$N_0 = (10N_s^3 + 15N_s^2 + 11N_s + 3)/3 \quad (20)$$

Therefore, the magic numbers are 13, 55, 147, 309, As mentioned before, there is a relation between the diameter of the cluster and the number N_0 for closed-shell cubic particles assuming a spherical surface:

$$D = a \sqrt[3]{3N_0/2\pi} \quad a \text{ is the cubic lattice parameter} \quad (21)$$

Figure 3 shows a five-shelled cuboctahedron consisting of 561 atoms. Figures 4 and 5 show computer simulations (top) and experimental images (bottom) in the [110] and [001] orientations, respectively. The PS are displayed on the right-hand side. The computer simulation is performed for seven-shelled cuboctahedra (1415 atoms). Calculations and experiments are performed for Cu at room temperature. No image processing is performed in the present case. The particles were prepared with the inert gas aggregation technique. Generally, it was concluded that larger Cu clusters, that is, larger than about 5 nm critical cluster diameter, show the bulk fcc structure, whereas, as shown later, the smaller Cu clusters have icosahedral or decahedral structures. Examples thereof will be given later. This finding is in good agreement with molecular dynamical calculations by Valkealahti and Manninen [38]. A similar behavior but with different critical cluster sizes also exists for Au, Ag, Pd, etc.

5.2. Hexagonal Particles

Examples of two different preparations described above are given for CdS ligand stabilized clusters, that is, one preparation for sphere-like clusters (Figs. 6–9) and the other for flat triangular clusters (Fig. 10). For the spherical particles computer simulations are also performed as shown at the top of the images. For simplicity the calculations are performed for hcp clusters consisting of only one type of atom, whereas the experimental images consist of two types of atoms. Therefore, more reflections appear in the PS of the experimentally obtained CdS images. This is due to the lowering of the symmetry for these samples. The PS in Figures 6–8 are a convincing demonstration thereof. The same applies for the PS of the triangular particle in Figure 10. The calculations are performed for seven-shelled clusters consisting of 2037 atoms. The orientations of the particles are

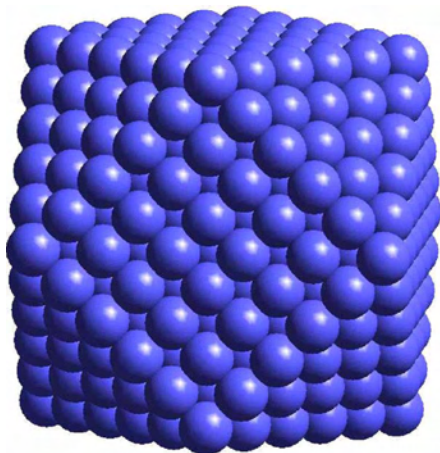


Figure 3. Model of a cuboctahedron consisting of five shells, 561 atoms.

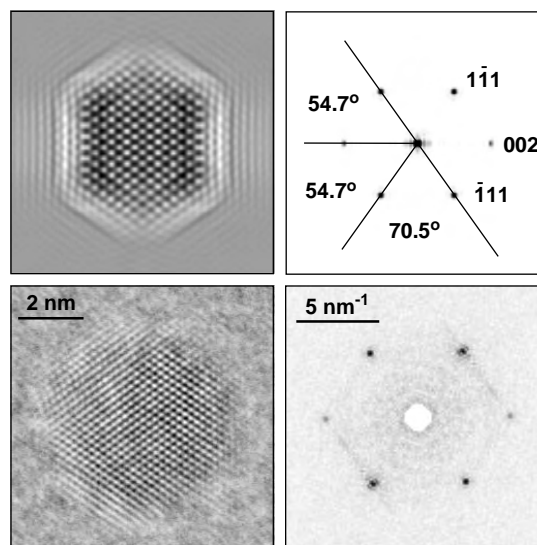


Figure 4. Computer simulation (top) and electron micrograph (bottom), together with the PS on the right-hand side of a Cu cuboctahedron consisting of seven shells, 1415 atoms in the [110] orientation.

[001] (Fig. 6), [011] (Fig. 7), [100] (Fig. 8), [211] (Fig. 9), and [001] (Fig. 10B). It is well known that bulk CdS exists in two structures, sphalerite (cubic) and wurtzite (hexagonal) [17]. In the case of spherical particles both structures were observed. However, only hexagonal examples are shown here. For the triangular particles, however, only hexagonal structures could be observed. To exclude also cubic structures with stacking faults, computer simulations for CdS with different numbers of stacking faults were performed (cf. Fig. 11). The structures, stapling, and orientations for the images in Figure 11a–e (from top to bottom) are as follows:

- a: cubic, abc abc abc, orientation [111]
- b: cubic, abc abc ab, orientation [111]

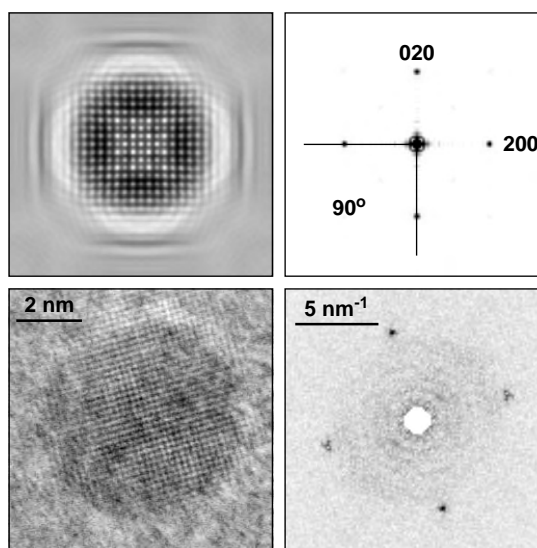


Figure 5. Computer simulation (top) and electron micrograph (bottom) together with the PS on the right hand-side of a Cu cuboctahedron consisting of seven shells, 1415 atoms in the [001] orientation.

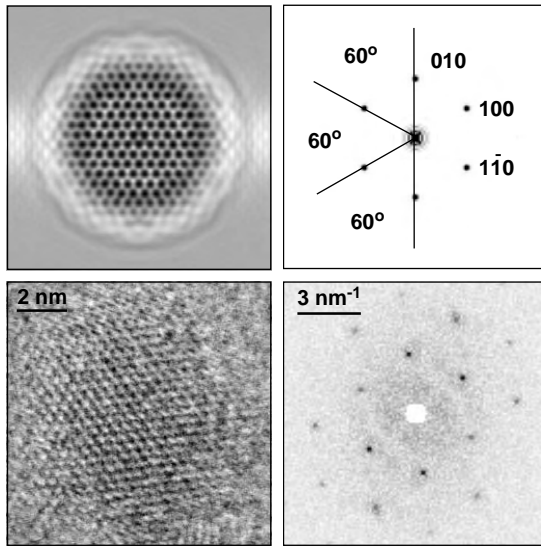


Figure 6. Computer simulation (top) of a hcp structure and electron micrograph (bottom) of CdS and the PS on the right-hand side in the [001] orientation. The simulation consists of seven shells, 2037 atoms.

- c: cubic, abc ab ab, orientation [111]
 d: cubic, ab ab ab, orientation [001]

5.3. Multiply Twinned Particles

Multiply twinned particles are clusters with 5-fold symmetry [39, 40]. Such particles are icosahedra and decahedra. Both types of clusters can be built up from deformed tetrahedral subunits [41, 42]. The subunits have to be deformed to close the necessary gaps that had to be incorporated in the case of ideal tetrahedra (all six edges are equal). These gaps would increase the surface energy. However, it has been reported that such gaps were observed [43]. It is assumed that these clusters are unstable.

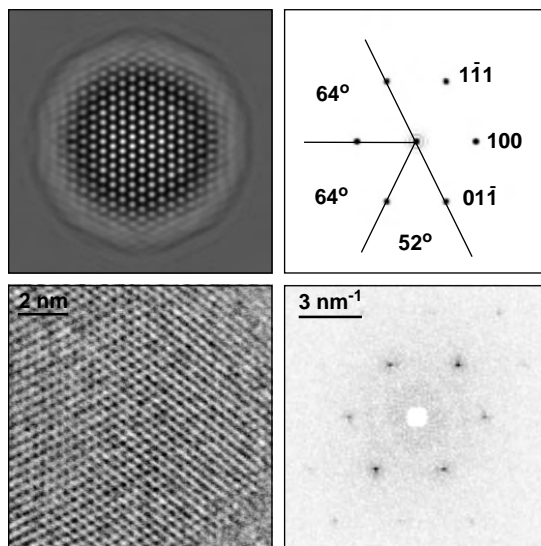


Figure 7. Computer simulation (top) of a hcp structure and electron micrograph (bottom) of CdS and the PS on the right-hand side in the [011] orientation. The simulation consists of seven shells, 2037 atoms.

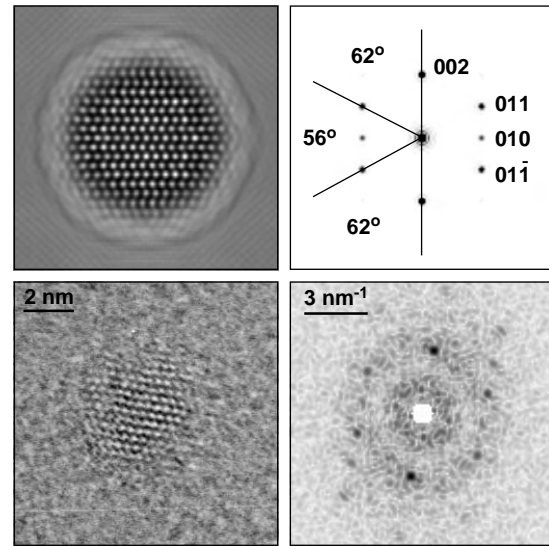


Figure 8. Computer simulation (top) of a hcp structure and electron micrograph (bottom) of CdS and the PS on the right-hand side in the [100] orientation. The simulation consists of seven shells, 2037 atoms.

5.3.1. Decahedra

The decahedron (a model of which is shown in Fig. 12) consists of five subunits. The deformation can be performed in two different ways. Figure 13a shows a deformed tetrahedral subunit consisting of six edges: one x_1 , four x_2 , and one x_3 .

- Case a: $x_2 = x_3$, x_1 is larger by 5% than the other five edges x_2 , x_3 .
 Case b: $x_1 = x_2$, x_3 is larger by 1.8% than the other five edges x_1 , x_2 .

In the latter case (b), five edges for the five subunits have to be deformed, whereas in case a, only one common edge has to be deformed. In both cases the decahedra consist of 10

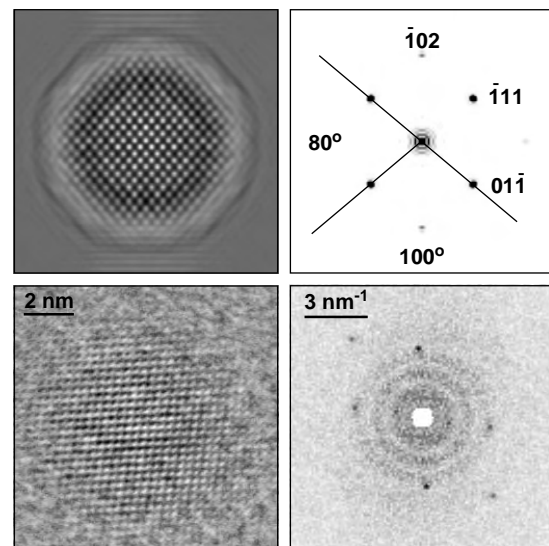


Figure 9. Computer simulation (top) of a hcp structure and electron micrograph (bottom) of CdS and the PS on the right-hand side in the [211] orientation. The simulation consists of seven shells, 2037 atoms.

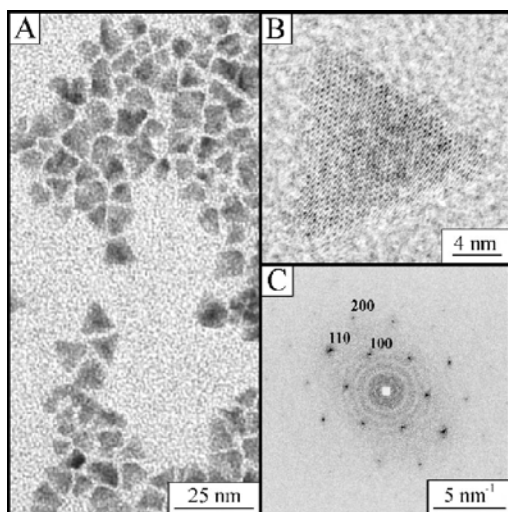


Figure 10. Flat triangular CdS cluster with hexagonal structure in the [001] orientation. (A) Overview image. (B) HRTEM image. (C) PS. Reprinted with permission from [16], N. Pinna et al., *Adv. Mater.* 13, 261 (2001). © 2001, Wiley-VCH.

(111)-planes at the surface. Sometimes (cf. examples below) truncated decahedra (or decahedra with additional intermediate planes) are also discussed. These consist of five additional rectangular (100)-planes. The magic numbers of the nontruncated decahedron are 7, 54, 181, 428, 835... Decahedra do not have a central atom. The tetrahedral angle $2\varphi = 72^\circ$. In terms of the normalized edges $x_1 \dots x_3$ netplane distances can be expressed as follows for the two cases:

$$d_{111} = \alpha x_3 \cos \varphi, \quad d_{200} = \alpha x_3 / (2 \operatorname{tg} \varphi),$$

the normalising factor is $\alpha = a / \sqrt{2}$

Case a: $x_1 = x_2 \sqrt{4 \sin^2 \varphi - 1} / \sin \varphi, \quad x_2 = x_3 = 1$
 Case b: $x_3 = x_1 \sqrt{3} \sin \varphi, \quad x_1 = x_2 = 1$

a is again the lattice parameter of the cubic bulk lattice.

Figure 14 shows a computer simulation and an experimental image together with the PS from top to bottom of a Cu decahedron viewed along the 5-fold axis.

5.3.2. Icosahedra

The icosahedron consists of 20 deformed tetrahedral subunits. Here the deformation is placed such that the three edges x_1 at the surface (cf. Fig. 13b), which terminate one of the 20 triangular (111) surface planes, are larger by 5% than the others. The magic numbers are the same as for the cuboctahedron, that is, 13, 55, 147, 309, ... The tetrahedral angle is again $2\varphi = 72^\circ$.

$$d_{111} = \alpha x_1 \cos \varphi, \quad d_{200} = \alpha x_1 / (2 \operatorname{tg} \varphi), \quad \alpha = a / \sqrt{2}$$

$$x_1 = x_2 \sqrt{4 \sin^2 \varphi - 1} / \sin \varphi, \quad x_2 = 1.$$

A model is shown in Figure 15 that consists of five shells (561 atoms). Computer simulations for seven-shelled Cu icosahedra (1415 atoms) together with experimental images and PS are shown in Figures 16–18 in the 5-fold, 3-fold,

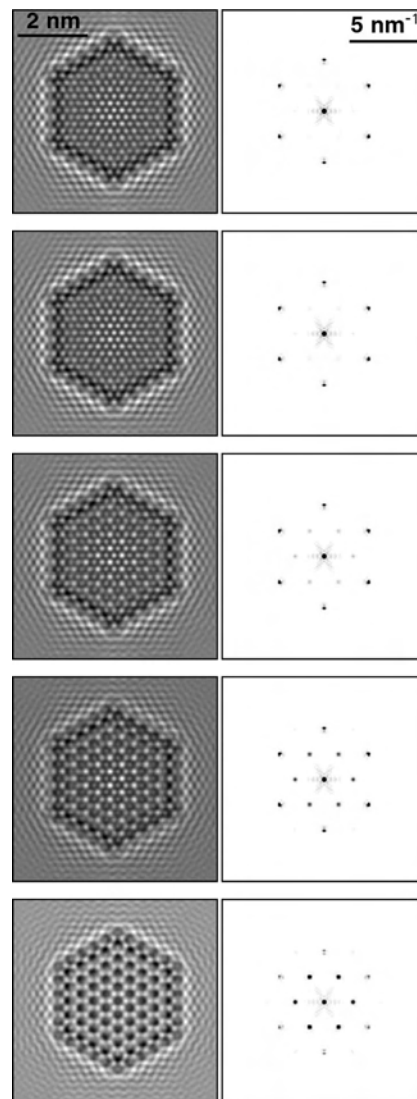


Figure 11. Computer simulation and PS of a CdS cluster in cubic structures with stacking faults in the [111] orientation (a–d) and pure hexagonal structure in the [001] orientation (e). The stapling is: (a) abc abc abc, (b) abc abc ab, (c) abc ab ab, (d) ab ab ab, (e) ab ab ab (from top to bottom).

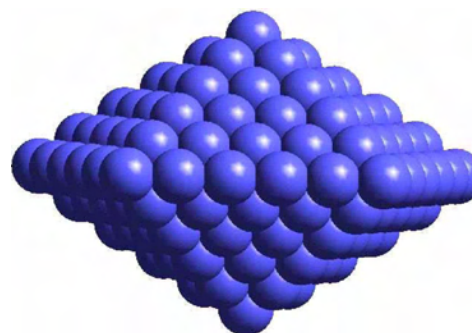


Figure 12. Model of a nontruncated decahedron.

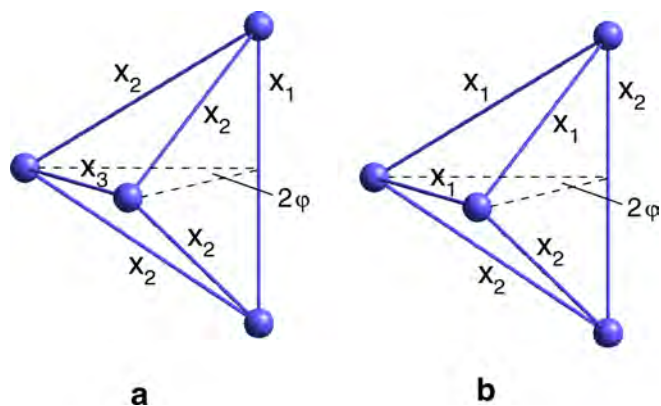


Figure 13. Deformed tetrahedral subunits for the construction of (a) the decahedron and (b) the icosahedron.

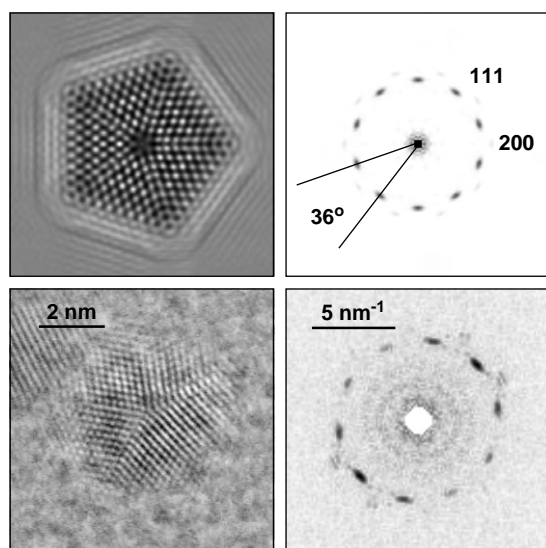


Figure 14. Computer simulation (top) and experimental image (bottom), together with the PS at the right-hand side of a Cu decahedron, viewed along the 5-fold axis.

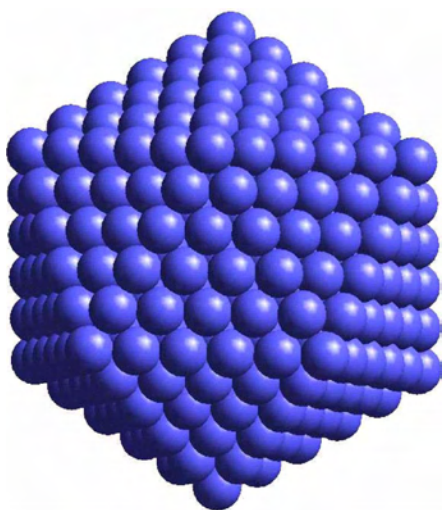


Figure 15. Model of an icosahedron consisting of seven shells, 1515 atoms.

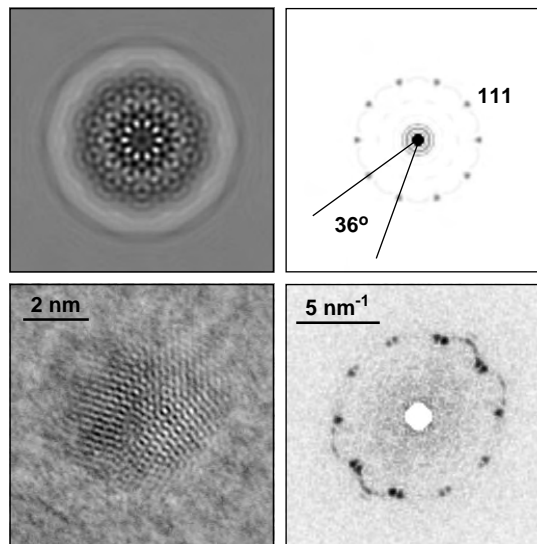


Figure 16. Computer simulation consisting of seven shells, 1415 atoms (top) and electron micrograph (bottom) of a Cu icosahedron viewed nearly along the 5-fold axis.

and 2-fold orientation. The particle in the 5-fold orientation shows a typical ring structure. The orientation of the experimental image is not exactly along the 5-fold axis. The PS for the 3-fold orientation shows a typical 3-fold splitting of the 111 reflections.

5.4. Cu Cylinders and Rods

Colloidal Cu particles are prepared as described above by chemical means. An overview image of such rods is given in Figure 19. Tilt series have been performed around the long axis of the needle. Two typical patterns were observed. Figure 20 shows such a series from top to bottom, $+36^\circ$, 0° ,

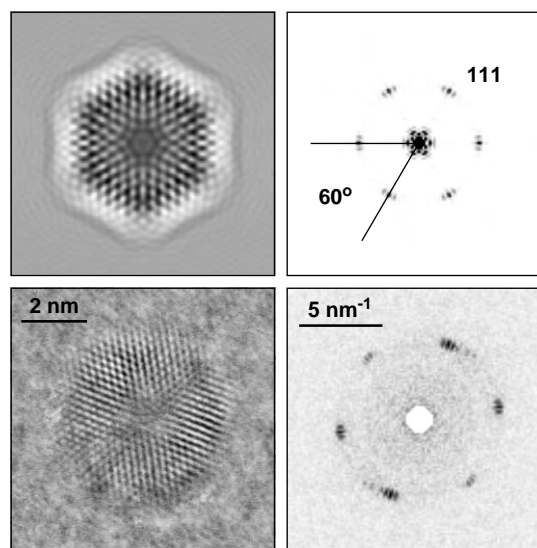


Figure 17. Computer simulation consisting of seven shells, 1415 atoms (top) and electron micrograph (bottom) of a Cu icosahedron viewed along the 3-fold axis.

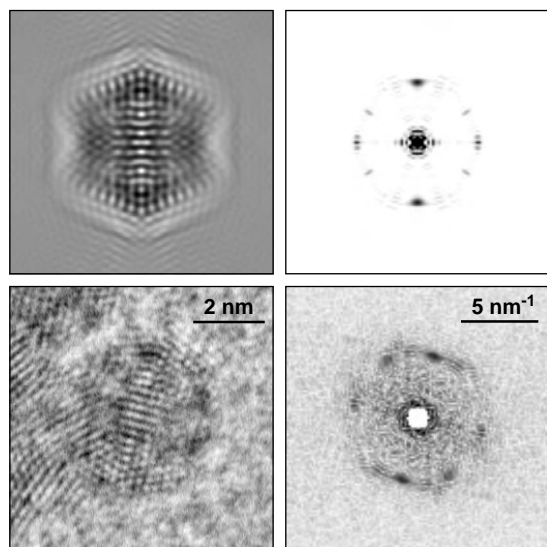


Figure 18. Computer simulation consisting of seven shells, 1415 atoms (top) and electron micrograph (bottom) of a Cu icosahedron viewed along the 2-fold axis.

-36° , together with the PS. As can be seen from the image and from the PS, a repetition of the pattern is performed. Figure 21 shows a tilt series around $+18^\circ$ and -18° from top to bottom. Here lattice lines are shown only on the left-hand side for $+18^\circ$ tilt and on the right-hand side for the -18° tilt. The PS, however, are the same. In Figure 22 a high-resolution image of the zero tilt together with the PS is shown. Three pairs of equatorial reflections are shown, marked 1, 2, 3. In addition, five other reflection pairs outside the equator (marked 4–8) exist. The corresponding lattice parameters are $d_1 = 0.211$ nm, $d_2 = 0.332$ nm, $d_3 = 0.566$ nm, $d_4 = d_7 = 0.184$ nm, $d_5 = d_6 = 0.252$ nm, $d_8 = 0.148$ nm, with an accuracy of $\pm 2\%$. The data of reflec-

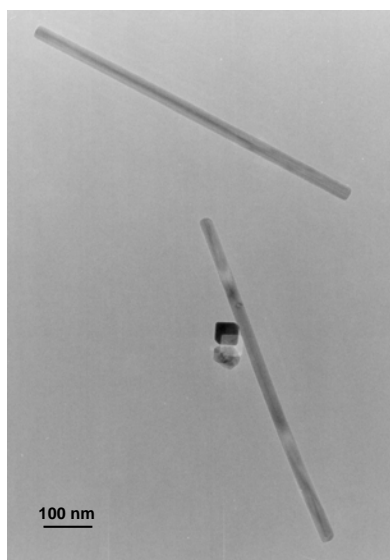


Figure 19. Electron micrograph of long extended rods. Reproduced with permission from [13], A. Lisiecki et al., *Phys. Rev. B* 61, 4968 (2000). © 2000, American Physical Society.

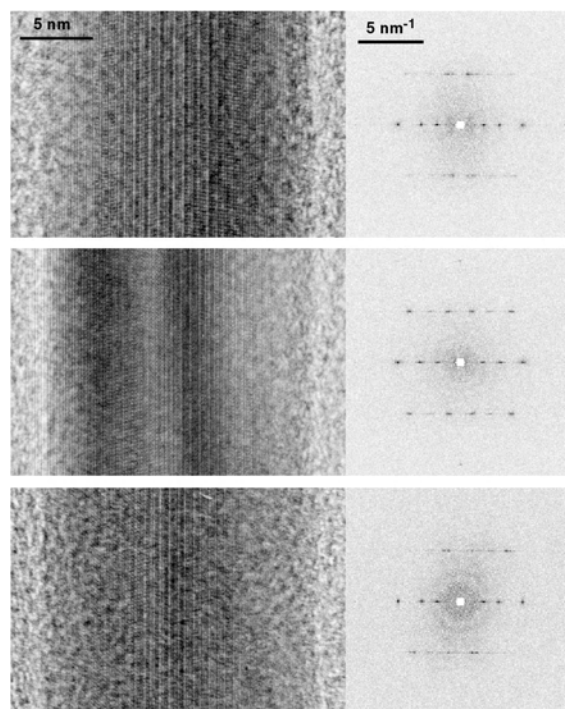


Figure 20. HRTEM images (left) and PS (right) of a Cu rod tilted by, from top to bottom, $+36^\circ$, 0° , -36° . Reprinted with permission from [13], A. Lisiecki et al., *Phys. Rev. B* 61, 4968 (2000). © 2000, American Physical Society.

tions 1, 4, and 7 are very close to the bulk data of Cu of reflections 111, 200, and 020, respectively, that is, 0.2087 nm, 0.1808 nm, and 0.1808 nm. The small deviations can be explained by deformations within the particle, which are also present in the case of MTPs. Furthermore, the existence of the 111 reflection together with the 200 and 020 reflections indicates that the particle must consist of more than one subunit (twinning). In Figure 22 a superstructure

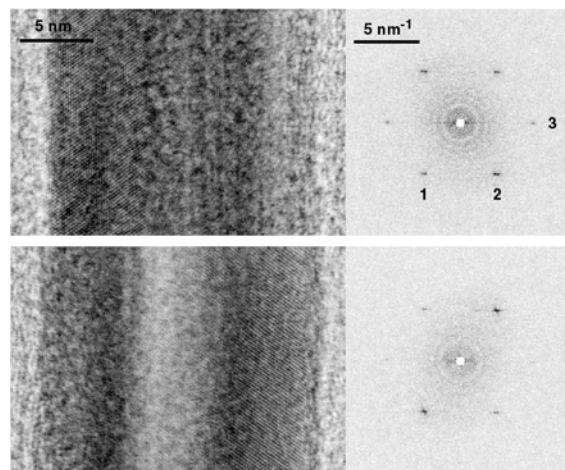


Figure 21. HRTEM images (left) and PS (right) of a Cu rod tilted by, from top to bottom, $+18^\circ$, -18° . Reprinted with permission from [13], A. Lisiecki et al., *Phys. Rev. B* 61, 4968 (2000). © 2000, American Physical Society.

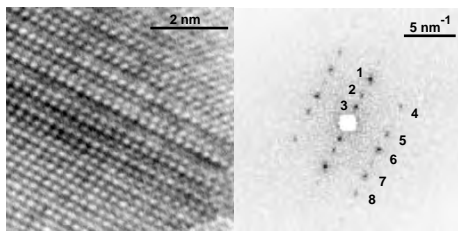


Figure 22. Detail of a Cu rod with the PS to the right. Reflections 1–8 in the PS represent lattice parameters: $d_1 = 0.211$ nm, $d_2 = 0.332$ nm, $d_3 = 0.566$ nm, $d_4 = d_7 = 0.184$ nm, $d_5 = d_6 = 0.252$ nm, $d_8 = 0.148$ nm. The angle between planes representing reflections 5 and 6 is 27° . Reprinted with permission from [13], A. Lisiecki et al., *Phys. Rev. B* 61, 4968 (2000). © 2000, American Physical Society.

can be observed along the long axis. This suggests a fcc structure with stacking faults [44, 45]. Computer simulations, however, showed that reflections 5 and 6 with an angle of 27° could not be explained by such a structure. This is also true for reflections 1, 4, and 7. Furthermore, the repetition of the reflection pattern and in the images at $\pm 36^\circ$ and $\pm 18^\circ$ could also not be explained by an fcc structure with stacking faults. As was demonstrated above, small Cu clusters prepared by inert gas aggregation show the structure of decahedra or icosahedra (cf. also [46]). Therefore, truncated decahedral particles were calculated in different orientations. Figure 23 shows models, computer simulations, and PS for such a structure. From left to right one obtains: viewed along the 5-fold axis, viewed along 0, and $\pm 36^\circ$ and $\pm 18^\circ$. The tilt angles are defined in the model of Figure 24. As can be seen from the images and from the PS, the struc-

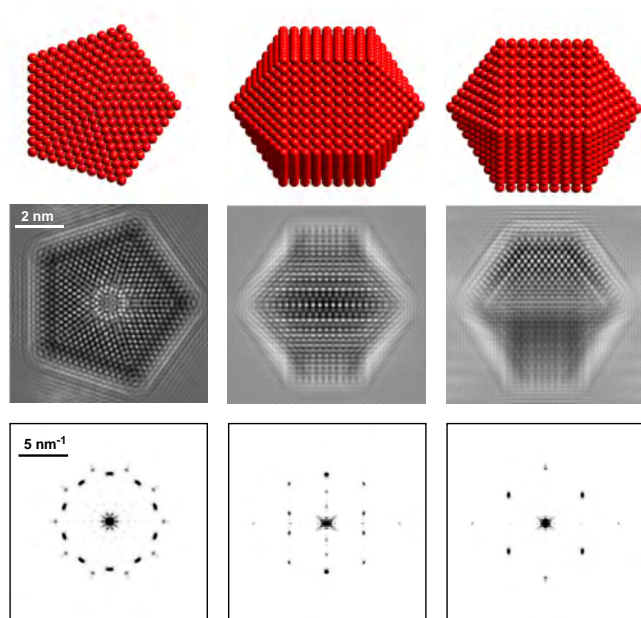


Figure 23. Models, computer simulations, and PS of a truncated decahedron. The orientation is (from left to right) 5-fold axis, [001] direction, and [1-10] direction (parallel to a (001) plane), that is, 0° and 18° , perpendicular to the 5-fold axis for the latter two. Reprinted with permission from [13], A. Lisiecki et al., *Phys. Rev. B* 61, 4968 (2000). Fig. 8. © 2000, American Physical Society.

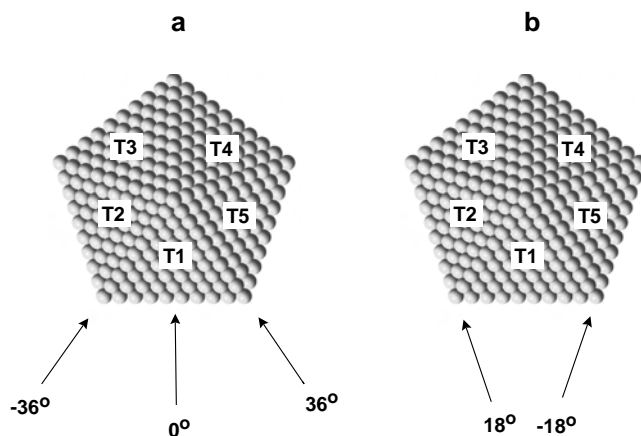


Figure 24. Model of a decahedron viewed along the 5-fold axis with labeled subunits T_1 – T_5 . The arrows indicate the direction of the electron beam. (a) Tilt 0, $\pm 36^\circ$. (b) Tilt $\pm 18^\circ$. Reprinted with permission from [13], A. Lisiecki et al., *Phys. Rev. B* 61, 4968 (2000), Fig. 7. © 2000, American Physical Society.

ture represents exactly the results of the different tilts. This is also demonstrated in the model of Figure 24, where the different subunits are labeled T_1 – T_5 , which are responsible for the different reflections. The different subunits cause single and multiple scattering reflections, all of which can be completely explained. A detailed description is given in [13]. The prepared cylinders show the same structure as the rods. The needles and cylinders show a remarkable behavior under heating. Partial premelting and an extreme lowering of the melting point compared with the bulk are observed. This is discussed in [14, 15].

5.5. Ag Cylinders

Surprisingly, also in the case of Ag clusters prepared by inert gas aggregation but supported by NaCl (100), cylinders were observed [47], whereas the morphology of the clusters in the same beam but deposited on amorphous carbon films was spherulike. The structure of these spherulike clusters resembled cuboctahedra for larger clusters and that of MTPs for smaller clusters. After the deposition of the cluster on the NaCl surface, carbon was evaporated on top of the surface including the cluster. Finally, the carbon film with the clusters was removed by dissolving the NaCl in distilled water. Figure 25 shows an overview image of this preparation with two cylindrical particles. Figure 26 shows an Ag cylinder in high resolution together with the PS. It can be clearly seen that the structure is the same as that for Cu cylinders and rods, that is, truncated decahedral particles. This can be concluded by comparing PS and high-resolution images as shown in Figure 26 with those of Cu rods in Figure 22. It is not clear why cylindrical particles prepared by inert gas aggregation are produced only on NaCl surfaces. Originally, it was concluded that this happens as decoration on terrace steps. However, for such behavior the cylinders should have the same orientation. It is therefore assumed that the interaction of clusters with the chlorine of the substrate causes this effect. Investigation with using other crystalline substrates thereof are in progress.

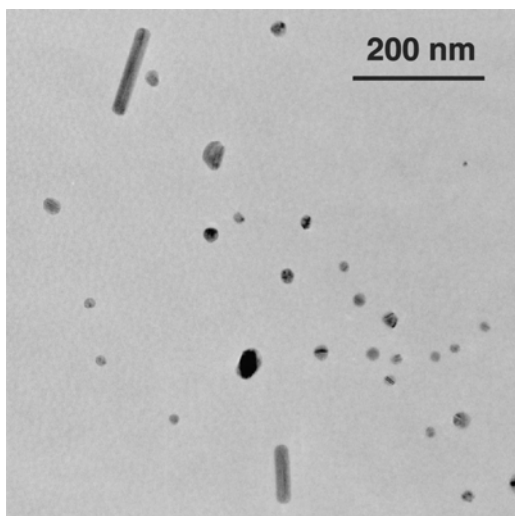


Figure 25. Ag cylinders grown on NaCl (100). Deposition after inert gas aggregation. Reprinted with permission from [47], S. Nepijko et al., *Chem. Phys. Chem.* 3, 140 (2000). © 2000, Wiley-VCH.

6. OXIDATION OF Cu CLUSTERS

The study of chemical reactions in the case of particles prepared by inert gas aggregation is discussed for Cu in the case of oxidation. Two oxides are discussed, cuprite (Cu_2O) and tenorite (CuO), although the latter has not been observed directly. Only one example of a transition between cuprite and tenorite will be shown. Transitional states such as Cu_4O , Cu_8O , Cu_{64}O [48, 49], and paramelaconite (Cu_3O_4) [50] are observed, and complex structures like suboxides are also present. They will not be discussed in the present work. The oxidation can be performed in different ways:

- (a) Additional insertion of O_2 at controlled partial pressure during the evaporation process to argon.

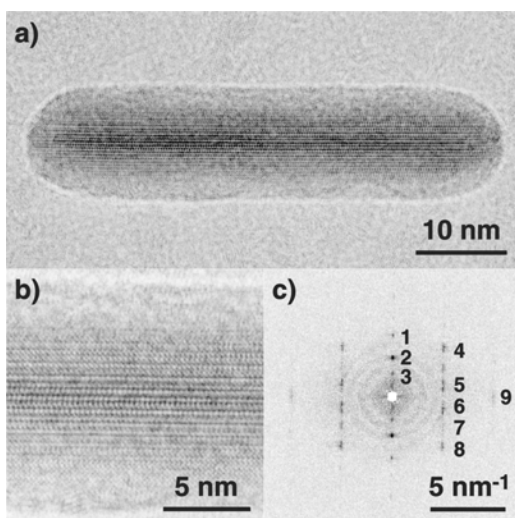


Figure 26. HRTEM image (a) of a Ag cylinder deposited on NaCl (100). (b) Detail. (c) PS. Reprinted with permission from [47], N. Nepijko et al., *Chem. Phys. Chem.* 3, 140 (2000). © 2000, Wiley-VCH.

- (b) Exposure of deposited clusters to oxygen (in the present examples to air at ambient pressure and temperature) for several hours.

In general, it can be concluded that with the addition of very small amounts of oxygen on the order of less than 10^{-3} mbar to the argon at about 1 mbar partial pressure (cf. case (a)), the structure is modified even for smaller particles less than 5 nm in diameter. No icosahedra or decahedra were observed after this treatment. Only cuboctahedral particles with the Cu lattice parameters were detected. The reactivity of these clusters is also decreased. Even after exposure to air at ambient temperature for more than 100 h, splitting the reflections in the PS could very often prove the existence of Cu and oxide. One example is given below. It is assumed that small amounts of oxygen are built into the lattice of Cu, leaving the lattice constants like those of Cu. Therefore, this cannot be deduced by HRTEM. Increasing the amount of oxygen during the evaporation period leads to the creation of both Cu and oxide in the same particle or to the total oxidation of the particle, which can be directly observed from the PS by splitting the reflections or by observing only the cuprite reflections, respectively.

In the other case (i.e., case (b)), preparation without oxygen but exposure to air) this process causes a total oxidation after 100 h at room temperature. Transitional states showing the appearance of Cu and Cu_2O reflections can also be observed after less than 100 h of air exposure. Some examples are given in the following.

Figure 27 shows a transition between Cu and Cu_2O . The preparation was performed without oxygen but after air exposure for 26 h. Two pairs of reflections are observed which represent the 111 reflections of the metal and its oxide. The corresponding planes are slightly misoriented. They form an angle of 2° with respect to each other. The corresponding lattice parameters are 0.218 nm for Cu and 0.253 nm for cuprite (for the bulk materials they are 0.209 and 0.247 nm). Figure 27c and d shows the Fourier filtered image and the PS after filtering. The filtering was performed with both reflections e and f. Images e and f

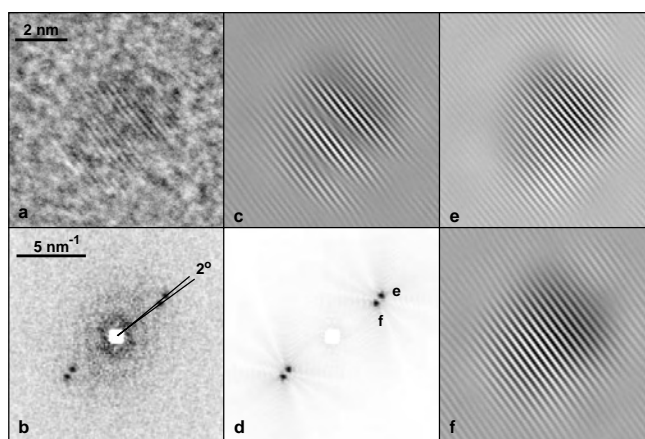


Figure 27. Transition between Cu and Cu_2O . Layered structure tilted by 2° . (a) Unfiltered image. (b) PS of the unfiltered image. (c) Filtered image. (d) PS of c. (e) Filtered image with reflection e only. (f) Filtered image with reflection f only.

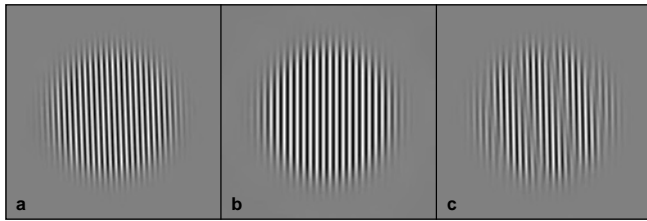


Figure 28. Computer simulation consisting of two layers tilted by 2° with different lattice constants (a, b) to explain Figure 27. (c) Sum of layers a and b.

are Fourier-filtered images with a single pair of reflections e and f, respectively. In Figure 27c moiré fringes are observed, whereas the lattice lines in both images e and f are undisturbed over the total region of the particle. It is concluded that there is a layered structure of the two different lattices causing the moiré fringes. The small deformation of the lattices and their distortion must be introduced to fit the different layers to each other. An optical model is shown in Figure 28.

Figures 29 and 30 show computer simulations of cuprite (top) and experimental images together with PS for preparations without O_2 but after air exposure for 100 h. In Figure 29 cuprite is shown for a cluster in the $[110]$ orientation. The orientation of the cluster in Figure 30 is $[112]$. No splitting of the reflections is observed. This means that the oxidation process for cuprite is terminated.

Figures 31 and 32 also show cuprite clusters in the $[001]$ and $[111]$ orientations. The preparation was performed with 2×10^{-3} mbar O_2 partial pressure and after 100 h of air exposure. There is also no splitting of reflections present, which means that the oxidation process is finished.

Figure 33 shows the image of a cluster prepared with less than 10^{-3} mbar partial pressure of oxygen and after air exposure for 114 h. The splitting of the reflections indicates a transitional state between CuO and Cu_2O . Figure 33c and

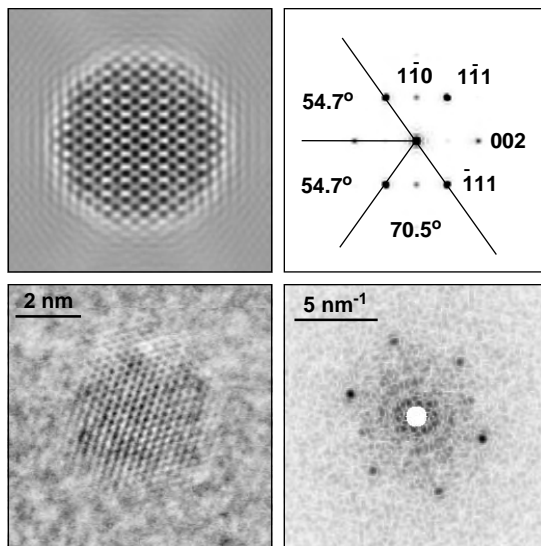


Figure 29. Computer simulation (top) and HRTEM image (bottom) of Cu_2O cuprite with the PS to the left in the $[110]$ orientation.

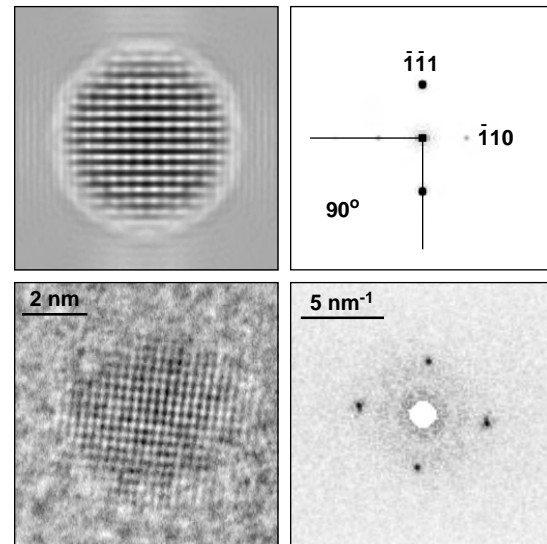


Figure 30. Computer simulation (top) and HRTEM image (bottom) of Cu_2O cuprite with the PS to the right in the $[110]$ orientation.

d again represents the Fourier filtered image and the PS after filtering. Figure 33e and f shows Fourier filtered images of reflection pair e and f, respectively. Reflection pairs e can be identified as tenorite reflections, whereas f represents the cuprite reflections. Both structures are in the $[110]$ orientation. The tenorite reflections are the -111 and 002 reflections. For the cuprite one observes the $-11-1$, -110 , and -111 reflections. The two lattices are turned slightly with respect to each other. There are also small deformations inserted. Since the particle consists of two different oxides, they can only coexist by inserting deformations in comparison with the bulk. This causes a deformation for the cubic cuprite such that the structure becomes orthorhombic. For the tenorite cell a deformation is also observed.

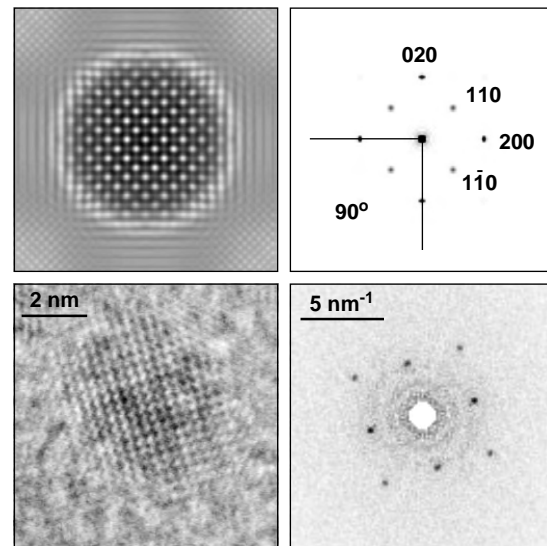


Figure 31. Computer simulation (top) and HRTEM image (bottom) of Cu_2O cuprite with the PS to the right in the $[001]$ orientation.

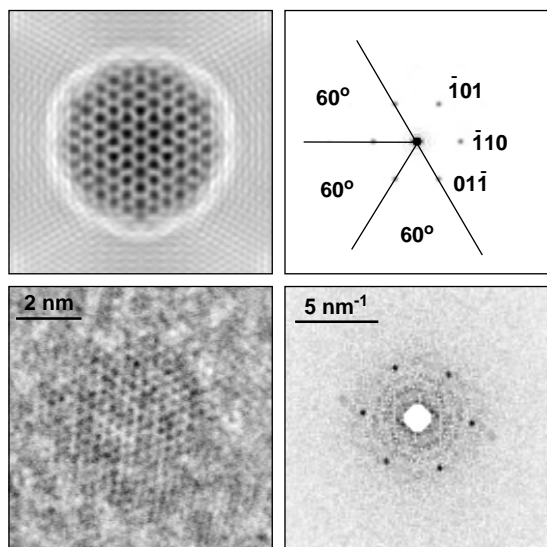


Figure 32. Computer simulation (top) and HRTEM image (bottom) of Cu₂O cuprite with the PS to the right in the [111] orientation.

The following table compares the bulk data with the experimental data obtained from Figure 33.

Tenorite:

Experimental	Bulk
$a = 0.4694 \text{ nm}$	$a = 0.4684 \text{ nm}$
$b = 0.3418 \text{ nm}$	$b = 0.3425 \text{ nm}$
$c = 0.5411 \text{ nm}$	$c = 0.5129 \text{ nm}$
$\beta = 101.2^\circ$	$\beta = 99.47^\circ$

$$\Delta^2 = 7.97 \times 10^{-4} \text{ nm}^2$$

Cuprite:

$a = 0.3930 \text{ nm}$	$a = b = c = 0.4270$
$b = 0.4347 \text{ nm}$	
$c = 0.4076 \text{ nm}$	

$$\Delta^2 = 1.59 \times 10^{-3} \text{ nm}^2$$

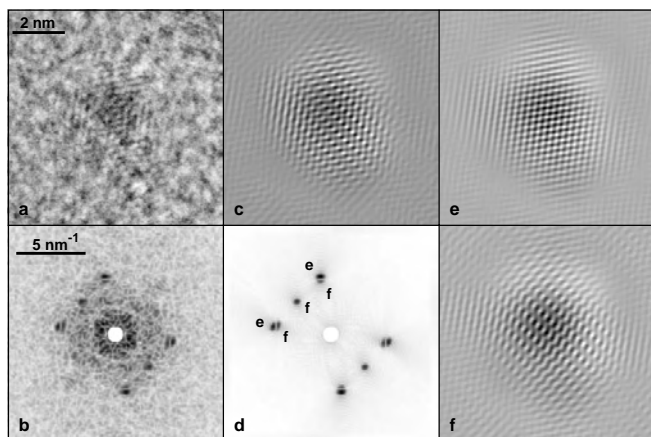


Figure 33. Transitional state in a, b between tenorite, reflections e and cuprite, reflections f in the [110] orientation. (c) Filtered image. (d) Ps of c. (e) Filtered image with reflection e. (f) Filtered image with reflection f.

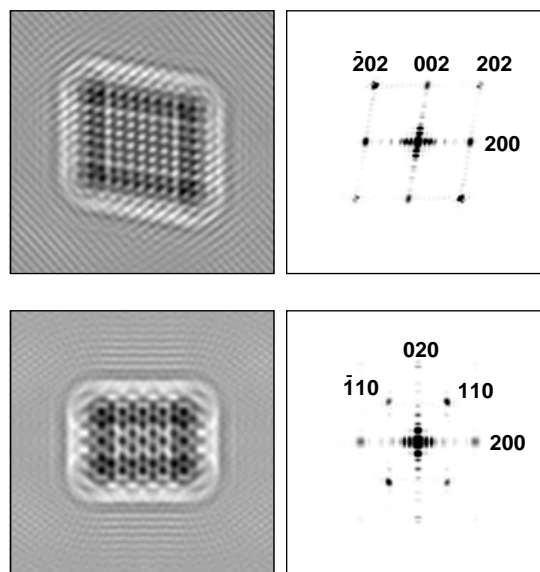


Figure 34. Computer simulation and PS of tenorite. (a) In the [010] orientation. (b) In the [001] orientation.

Δ^2 is the mean square deviation of the cell parameters from the bulk data:

$$\Delta^2 = \Delta a^2 + \Delta b^2 + \Delta c^2$$

Computer simulations together with the PS for tenorite are shown in Fig. 34. The orientations from top to bottom are [010] and [001].

GLOSSARY

Multiply twinned particle (MTP) Particle with 5-fold symmetry

Power spectrum (PS) Square of the Fourier transform of the image

ACKNOWLEDGMENTS

I thank my co-workers Hilde Sack-Kongehl and Klaus Weiss for their continuous cooperation, S. Kulkarni for the preparation of CdS clusters, Isabelle Lisiecki and Marie-Paule Pileni for the preparation of Cu rods and cylinders, Nicola Pinna and Marie-Paule Pileni for the preparation of triangular CdS clusters, and D. N. Jevlev and S. A. Nepijko for the preparation of Ag clusters deposited on NaCl surfaces.

REFERENCES

1. P. L. J. Gunter, J. W. H. Niemantsverdriet, F. H. Ribeira, and G. A. Somorjai, *Catal. Rev. Sci. Eng.* 39, 77 (1997).
2. C. R. Henry *Surf. Sci. Rep.* 31, 231 (1998).
3. H. Abe, W. Schulze, and B. Tesche, *Chem. Phys.* 47, 95 (1980).
4. F. Frank, W. Schulze, B. Tesche, J. Urban, and B. Winter, *Surf. Sci.* 156, 90 (1985).
5. W. Schulze, F. Frank, K.-P. Charlé, and B. Tesche, *Ber. Bunsenges. Phys. Chem.* 88, 263 (1984).
6. J. Mühlbach, E. Recknagel, and K. Sattler, *Surf. Sci.* 106, 188 (1981).

7. J. Urban and B. Tesche, *Thin Solid Films* 137, 325 (1986).
8. I. Lisiecki and M.-P. Pileni, *J. Am. Chem. Soc.* 115, 3887 (1993).
9. J. Tanori and M.-P. Pileni, *Adv. Mater.* 7, 862 (1995).
10. J. Tanori, T. Gulik-Krzywicki, and M.-P. Pileni, *Langmuir* 13, 632 (1997).
11. J. Tanori and M.-P. Pileni, *Langmuir* 13, 639 (1997).
12. M.-P. Pileni, J. Tanori, and A. Filankembo, *Colloids Surf., A* 123–124, 561 (1997).
13. A. Lisiecki, A. Filankembo, H. Sack-Kongehl, K. Weiss, M.-P. Pileni, and J. Urban, *Phys. Rev. B* 61, 4968 (2000).
14. I. Lisiecki, H. Sack-Kongehl, K. Weiss, J. Urban, and M.-P. Pileni, *Langmuir* 16, 8802 (2000).
15. I. Lisiecki, H. Sack-Kongehl, K. Weiss, J. Urban, and M.-P. Pileni, *Langmuir* 16, 8807 (2000).
16. N. Pinna, K. Weiss, J. Urban, and M.-P. Pileni, *Adv. Mater.* 13, 261 (2001).
17. W. Vogel, J. Urban, Nabisha Kundu, and S. K. Kulkarni, *Langmuir* 13, 827 (1997).
18. A. A. Khosravi, M. Kundu, B. A. Kuruvilla, G. S. Shekavat, R. P. Gupta, A. K. Sharma, P. D. Vyas, and S. K. Kulkarni, *Appl. Phys. Lett.* 67, 2506 (1995).
19. Y. Nosaka, Yamagushi, H. Miyama, and H. Hayashi, *Chem. Lett.* 605 (1988).
20. J. M. Cowley and A. F. Moodie, *Acta Crystallogr.* 10, 609 (1957).
21. P. Goodman and A. F. Moodie, *Acta Crystallogr., Sect. A* 30, 280 (1974).
22. D. van Dyk, in “Electron Microscopy” (S. Amelickx, D. van Dyk, J. van Landuyt, and G. van Tandeloo, Eds.), p. 152. VCH, Weinheim, 1997.
23. J. G. Alpress and J. V. Sanders, *J. Appl. Crystallogr.* 6, 165 (1973).
24. J. M. Cowley, S. Iijima, in “The Direct Imaging of Crystal Structures” (H. R. Wenk, Ed.), p. 123. Springer-Verlag, Berlin, Heidelberg, New York, 1976.
25. J. L. Hutchison, in “Lattice Images” (J. A. Venables, Ed.), p. 241. Academic, London, 1976.
26. S. Hamid Rahman, *Z. Kristallogr.* 176, 291 (1986).
27. J. Urban, H. Sack-Kongehl, and K. Weiss, *Z. Phys. D* 28, 247 (1993).
28. P. L. Fejes, Thesis, Arizona State University, 1973; *Acta Crystallogr., Sect. A* 33, 109 (1977).
29. P. A. Doyle and P. S. Turner, *Acta Crystallogr., Sect. A* 24, 390 (1968).
30. G. Nihoul, H. Sack-Kongehl, and J. Urban, *Cryst. Res. Technol.* 33, 1025 (1998).
31. S. Giorgio, G. Nihoul, J. Urban, and H. Sack-Kongehl, *Z. Phys. D* 24, 395 (1992).
32. G. Nihoul, *Microsc. Microanal. Microstruct.* 3, 71 (1992).
33. W. D. Knight, K. Clemenger, W. A. DeHeer, W. A. Saunders, M. Y. Chou, and L. M. Cohen, *Phys. Rev. Lett.* 52, 2141 (1984); 31, 1804 (1985).
34. W. Ekardt, *Phys. Rev. B* 36, 4483 (1987).
35. J. Urban, *Cryst. Res. Technol.* 33, 1009 (1987).
36. G. Wulff, *Z. Kristallogr.* 34, 449 (1901).
37. C. Herring, in “The Use of Classical Microscopic Concepts in Surface Energy Problems: Structure and Properties of Solid Surfaces” (R. Gomer and C. S. S. Smith, Eds.). University of Chicago Press, Chicago, 1952.
38. S. Valkealahti and M. Manninen, *Phys. Rev. B* 54, 9459 (1992).
39. B. G. Bagley, *Nature* 208, 674 (1965).
40. A. L. Mackay, *Acta Crystallogr.* 15, 916 (1962).
41. S. Ino, *J. Phys. Soc. Jpn.* 27, 541 (1969).
42. T. Komoda, *J. Appl. Phys.* 27, 603 (1966).
43. A. E. Romanov, I. A. Polonsky, V. G. Gryanzov, S. A. Nepijko, T. Junghanns, and N. J. Vitrykhovs, *J. Cryst. Growth* 29, 691 (1993).
44. R. Hillebrand, H. Hofmeister, K. Scheerschmidt, and J. Heydenreich, *Ultramicroscopy* 49, 252 (1993).
45. K. Ogawa and S. Kajiwora, *Mater. Trans. JIM* 34, 1169 (1993).
46. J. Urban, H. Sack-Kongehl, and K. Weiss, *Z. Phys. D* 36, 73 (1996); *High Temp. Mater. Sci.* 36, 155 (1996); *Catal. Lett.* 49, 101 (1997).
47. S. A. Nepijko, D. N. Ievlev, W. Schulze, J. Urban, and G. Ertl, *Chem. Phys. Chem.* 3, 140 (2000).
48. R. Guan, H. Hashimoto, K. H. Kuo, *Acta Crystallogr., Sect. B* 40, 560 (1984); *Acta Crystallogr., Sect. B* 41, 219 (1985).
49. R. Guan, H. Hashimoto, and T. Yoshida, *Acta Crystallogr., Sect. B* 40, 108 (1984).
50. M. O’Keefe and J.-O. Bovin, *Am. Mineral.* 63, 180 (1978).

Structures of Epitaxial Quantum Dots

X. Z. Liao

Los Alamos National Laboratory, Los Alamos, New Mexico, USA

J. Zou

The University of Sydney, Sydney, New South Wales 2006, Australia

D. J. H. Cockayne

University of Oxford, Oxford, United Kingdom

CONTENTS

1. Introduction
 2. Shape and Size
 3. Composition
 4. Growth Mechanisms
 5. Summary
- Glossary
References

1. INTRODUCTION

1.1. What are Quantum Dots?

Interest in quantum dots (QDs) stems from the work of Esaki and Tsu [1], who in 1970, reported the direct observation of quantization effects in $\text{Al}_x\text{Ga}_{1-x}\text{As}/\text{GaAs}/\text{Al}_x\text{Ga}_{1-x}\text{As}$ quantum well structures, opening a new chapter of solid-state electronics. A quantum well is a thin layer (film) of one material sandwiched between pieces of another material, where the bandgap of the film is less than the bandgap of the surrounding material (e.g., a thin film of GaAs) (bandgap $E_g = 1.42$ eV) sandwiched between $\text{Al}_x\text{Ga}_{1-x}\text{As}$ (e.g., $\text{Al}_{0.3}\text{Ga}_{0.7}\text{As}$, $E_g = 2.0$ eV). In this heterostructure, any carriers (electrons and holes) that move into the middle (e.g., GaAs) layer are effectively trapped there. In this case, the sandwich structure is analogous to a “well,” where the carriers easily enter but are very difficult to remove. If the thickness of the middle (e.g., GaAs) layer is equal to or smaller than the de Broglie wavelength of the carriers, which is typically about a few tens of nanometers [2] for an electron in a semiconductor, then quantization of the energy levels of the carriers in the well occurs. Only certain

energy levels are allowed (i.e., those for which the well width corresponds to an integral number of half de Broglie wavelengths), so that carriers in the well occupy discrete energy levels.

This quantization of the levels in the well leads to the structure being called a “quantum well.” Obviously, the energy levels in the quantum well can be tuned by changing the dimensions (the width and depth) of the well. For example, by narrowing the well width, the longest allowed wavelength of an electron in the well is shortened and, as a result, the lowest electron energy level becomes higher. The depth of the well is adjustable by changing the composition of the material of the well. It follows that energy levels can be controlled by adjusting the width and composition of the quantum well and the work of engineering the energy levels is called *bandgap engineering*. In this way, devices based on semiconductor quantum well structures, such as lasers, have been successfully manufactured in many key areas of modern technology such as optical communications [3], magneto-optical recording disc drive memory systems [4], and optical printing systems [5].

In the quantum well structure, carriers are confined only in one dimension. By the end of the 1980's, research had been started to further reduce the dimension of semiconductor structures from three (bulk materials) and two (quantum wells) to one (quantum wire) [6] and “zero” (QDs) [7, 8]. So a quantum wire comprises a material of a smaller bandgap geometrically confined in two dimensions within material of a larger bandgap, with the dimensions in two directions being sufficiently small resulting in quantization of the energy levels corresponding to those two directions. Similarly, a QD has the same form but with the dimensions constrained in three dimensions. Carriers in quantum wires and QDs are confined in two and three dimensions,

respectively. The effects of the dimensionality of the confinement on the density of electronic states are illustrated in Figure 1.

The size of semiconductor QDs is usually in the range of a few nanometers to tens of nanometers, containing up to a few hundred thousand atoms. Because carriers in QDs are confined three dimensionally, a QD behaves in many ways like a single giant atom [9–11]. Evidence for the atom-like electronic states of QDs is shown by the narrow photoluminescence linewidth from excitons in a single QD [12–15]. The unusual behavior of optical and transport properties seen in the QDs provides the basis for novel device concepts including large-gain, low-threshold quantum lasers [16, 17], light-emitting diodes [18–20], single-electron logic devices [21], and optical computing quantum units [22, 23].

1.2. Quantum Dot Growth and Important Structural Parameters

Quantum dots have been grown in a wide range of material systems, including elemental [Ge(Si) on Si] [24, 25], III–V (such as InGaAs on GaAs [12], InP on GaAs [26], InAs on InP [27], and nitride [28–31]), and II–VI [9, 32, 33] semiconductors. They can be produced in many ways, including by high-temperature precipitation in molten silicate glass matrices [34–37], by molecular precursor pyrolysis reactions for III–V semiconductor QDs [38, 39], by colloidal chemistry techniques [9, 32, 33, 40–42], from size fluctuations in conventional quantum wells [43–45], by mechanochemical synthesis [46, 47], and by lithographic patterning and etching [48–52]. However, the most important technique for QD growth is coherent island formation through heteroepitaxial growth of lattice mismatched semiconductor materials [24, 25], because this approach combines QD growth with well-established semiconductor integration techniques.

Just as the dimensions of a quantum well and the geometry of the well influence the energy levels of the well, the size and composition profile of a QD and the material of the QD and the matrix can influence the energy levels

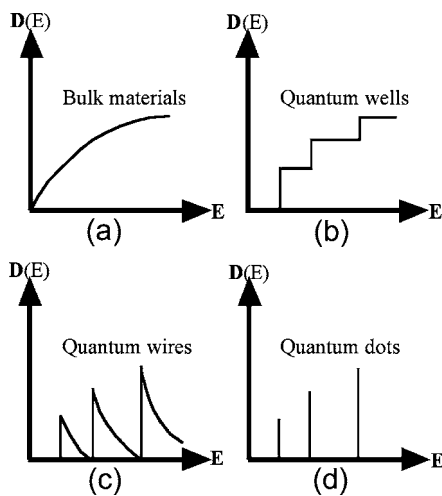


Figure 1. The density of the electronic states $D(E)$ in (a) bulk materials, (b) quantum wells, (c) quantum wires, and (d) QDs. E represents the energy levels.

of the QD. Consequently, the opto-electronic properties of a QD are sensitive not only to all these parameters, but also to the shape of the QD [53–64]. The calculated values for QD ground-state and excited-state emission, and the intersublevel energies, are dependent upon the shape and aspect ratio (i.e., height to base diameter) [65] assumed in the calculation (e.g., conical shaped [66], pyramid-shaped [53, 67–69], and lens-shaped [70] QDs). As a consequence, knowledge of the geometry and chemical composition of QDs is a prerequisite if models are to be used to calculate their electronic and optical properties. It follows from this that understanding the growth mechanisms that control these parameters is crucial for producing device-applicable QDs.

In this review article, the terms “QD” and “island” are used interchangeably, as they often are in the literature, although generally those islands that are of sufficiently small size are properly named QDs.

2. SHAPE AND SIZE

It is not surprising that many different shapes have been reported for different (or even within the same) QD systems because both thermodynamic and kinetic effects play an important role in determining the shape and size of the QDs during the growth of strained heterostructures. The nature (including the material [71], surface anisotropy [72], and orientation [73–75]) and temperature [76–84] of the substrate, the deposition rate [80, 82, 83, 85–87], the chemical form of the epitaxial material, and the ambient conditions all affect the QD growth and lead to dramatically different morphologies even for the same combination of materials [88]. For example, for InAs QDs, increasing the substrate temperature results in larger QDs, a narrower size distribution, a lower QD density, and an increased aspect ratio [76]. This sensitivity to growth conditions explains why, for example, the shapes of the Ge QDs on Si (001), grown by different groups, are often quite different [24, 25].

In this section, we discuss the shapes of QDs in the most important and, therefore, the most widely investigated systems $\text{Ge}_x\text{Si}_{1-x}/\text{Si}(001)$ (Section 2.1) and $\text{In}_x\text{Ga}_{1-x}\text{As}/\text{GaAs}(001)$ (Section 2.2). The shapes of QDs on (001) surfaces in other systems, including the InP and II–VI systems, are discussed together in Subsection 2.3. Because QDs grown on higher index surfaces are quite different from QDs grown on (001) surface, they are also discussed in a separate subsection (2.4).

2.1. Shapes of $\text{Ge}_x\text{Si}_{1-x}/\text{Si}(001)$ QDs

The most frequently reported QD shapes in the $\text{Ge}_x\text{Si}_{1-x}/\text{Si}$ system are pyramid (with square bases) bounded by $\{501\}$ facets, hut (with rectangular bases) bounded also by $\{501\}$ facets [25, 89–92], multifaceted dome (including $\{311\}$, $\{111\}$, and other $\{h11\}$ facets) [88, 93], and dome without facets [24]. Examples of hut, pyramid, and dome QDs are shown in Figure 2.

Pyramids with $\{501\}$ facets are seen at the early stage of $\text{Ge}_x\text{Si}_{1-x}/\text{Si}$ QD growth. As the QD growth continues, pyramids evolve into either huts or domes, depending on the

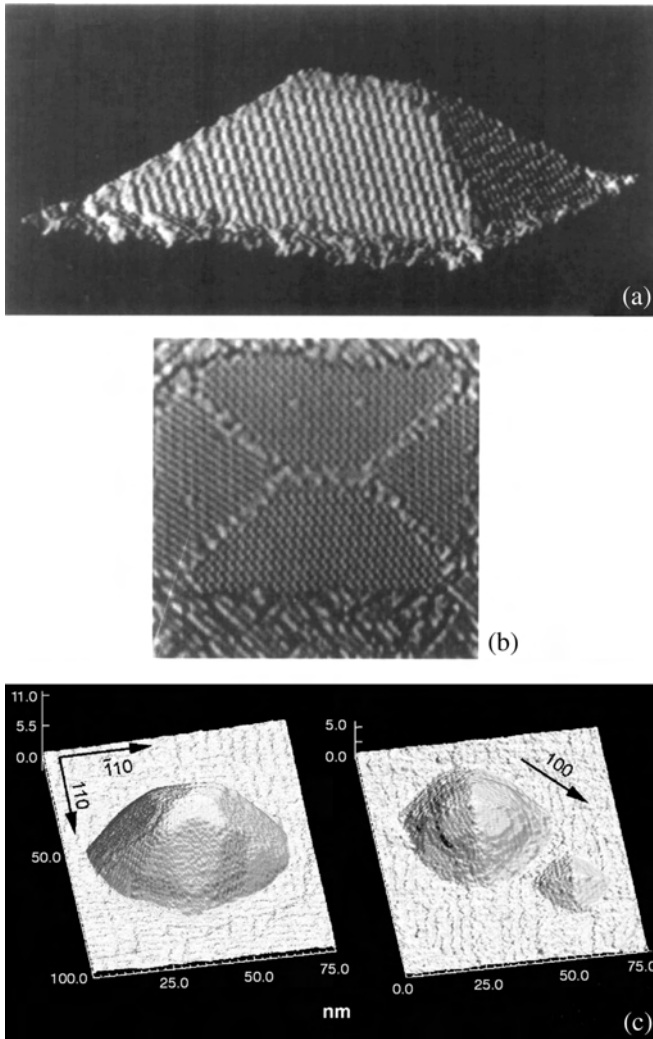


Figure 2. (a) and (b) scanning tunneling microscopy (STM) images of a hut-shaped Ge/Si(001) island. Reprinted with permission from [25], Y.-W. Mo et al., *Phys. Rev. Lett.* 65, 1020 (1990). © 1990, American Physical Society; (c) STM images of Ge/Si(001) islands with (left) a dome-shaped and (right) an island at the transition stage and a small pyramid-shaped. Reprinted with permission from [88], G. Medeiros-Ribeiro et al., *Science* 279, 353 (1998). © 1998, American Association for the Advancement of Science.

growth conditions. At lower growth temperatures, transformation from pyramids into elongated huts with $\{501\}$ facets [25, 94] occurs; at higher temperatures, equiaxial islands (i.e., pyramids and domes) are more stable than huts [95], and the pyramids evolve into domes. The lower-temperature transformation from pyramid into $\{501\}$ -faceted huts has been explained by Tersoff and Tromp [96]. If we consider the case of a high density of adatoms being deposited, diffusion is much more rapid on the substrate than on the QD, so that atoms tend to stick to the QD side-wall and not diffuse to the top facet. As a result, the QD height remains roughly constant. Under these circumstances, for QDs with size smaller than a specific value, the minimum energy, which includes the surface energy and the elastic energy, corresponds to islands of the square shape. Above this value, it is energetically favorable for the QDs to be

elongated in one direction, through a second-order shape transition (the second derivative of the energy, with respect to QD size, is discontinuous), to maintain a smaller lattice strain along the shorter axis of the QDs. Conversely, for high-temperature growth, diffusion is rapid, and so QDs can grow in height. Assuming that the stable configurations are a square-based pyramid (at small QD size) and a dome (at large QD size), as a QD grows, it should adopt increasingly steeper facets (the facets of a dome are steeper than those of a pyramid) [95].

Pyramids and domes can coexist in a system, giving the so-called bimodal size distribution. Many groups have observed the transformation from pyramid to dome. However, interpretation of the experimental evidence, in terms of the nature of the transformation process, remains controversial and, as a result, two different explanations for the transformation have been given.

Medeiros-Ribeiro et al. [88] suggested that pyramid and dome shapes represent two volume-dependant energy minima, separated by a large energy barrier resulting from the interplay between strain relaxation at the facets and stress concentration at the edges. Therefore, the bimodal size distribution reflects two equilibrium states with different energies. From an *in-situ*, scanning tunnelling microscopy (STM) investigation, they observed an abrupt shape change from pyramid to dome, which involves overcoming the energy barrier and a rapid increase in volume. In an annealing experiment involving alloying between a Ge island and the Si substrate, Kamins et al. [97] found that a dome-shaped island can change back to a pyramid, even though the island volume continues to increase substantially. This supports the conclusion that both pyramid and dome are equilibrium shapes.

On the other hand, Ross et al. [98] argued that the pyramid is not a stable shape. In their model, mean field theory is used to give an expression for the island energy E , which depends upon the contact angle and the total volume of the island V . In the case of both pyramids and domes, E decreases monotonically with V , with $E(\text{dome}) > E(\text{pyramid})$ for any $V < V_1$, and $E(\text{dome}) < E(\text{pyramid})$ for any $V > V_1$. Consequently, for a given V , pyramids are predicted to be stable for $V < V_1$ and unstable for $V > V_1$. At the same time, the chemical potential for both pyramids and domes decreases monotonically with V , and for any $V > V_1$ is much lower for domes than for pyramids. Consequently, at $V = V_1$, a pyramid transforms into a dome, and the system chemical potential drops discontinuously causing these islands to grow preferentially, consuming the smaller islands [99]. Using *in-situ* low-energy electron microscopy, they [98] found that the transformation from a pyramid to a dome is a slow process passing through a series of transition shapes. Pyramidal islands have two fates: either transforming to domes or disappearing through a form of Ostwald ripening [100].

Rastelli et al. [101, 102] investigated the evolution process of Ge/Si(001) islands during exposure to a Si flux using STM. They found gradual morphological changes from dome to pyramid, which involve intermediate shapes, caused by the incorporation of Si into the Ge islands—a phenomenon similar to that reported by Kamins et al. [97]. They concluded that the shape of an island is determined by its

volume and average composition and that an island is stable if material exchange with its environment is *kinetically* suppressed. This conclusion is different from that obtained by Williams' group [88, 97] who suggest that pyramids and domes are both *thermodynamically* stable (energy minima).

According to Ross et al. [98, 99], as island growth continues, pyramidal islands will not survive and all islands will end up as domes. Indeed, single-modal, dome-shaped Ge/Si(001) islands with very uniform size distribution have been successfully grown by Wang et al. [103] using molecular beam epitaxy (MBE) at the high growth temperature of 700 °C. The islands are of a square base with edges parallel to $\langle 100 \rangle$ and rounded corners. Extensive investigation showed that most of the islands are uniform in size with a base edge of approximately 95 nm. The reason for the size uniformity in strained island growth has been discussed [99, 104–106] and has been attributed to a self-limiting growth mechanism [107]; the adatom attachment to a large island is slowed down by the build-up of elastic strain around the island perimeter, which allows the size of small islands to catch up with that of the large islands.

Zhang [108] proposed that the above experimental inconsistencies in the stability of GeSi/Si(001) island shapes could be explained in terms of island surface energy anisotropy through its dependence on temperature and material composition [109]. It has been reported that (001), (105), and (103) facets are thermodynamically stable and, therefore, their surface energy densities are local minima [110]. Zhang [108] called these minima the “first, second, and third” minima. Through three-dimensional computer simulations, which took into account the strain energy density, surface energy density, and anisotropy, Zhang concluded that

- (1) in the case where surface energy anisotropy is weak or where there is no anisotropy (which is true for very high temperatures), ripening occurs and islands with different shapes and sizes can coexist. This is consistent with the results of 850 °C controlled annealing experiments of GeSi/Si(001) islands carried out by Ozkan et al. [111];
- (2) when the second minimum is shallow and the energy barrier between the second and the third minima is high, islands are almost uniform in size and self-organize into a regular square array, similar to the experimental results of Floro et al. [112] at 755 °C;
- (3) in the situation where there is a deep second minimum and a high barrier between the second and third minima, islands evolve and coalesce until they reach a state that does not undergo ripening. Large islands are hut-shaped, while small islands are pyramidal-shaped with a square base. This result resembles those observed at temperatures below 330 °C [25, 91, 92];
- (4) if the barrier between the second and third minima is intermediate in height, pyramids or huts appear first, followed by a bimodal size/shape distribution in which both shapes are stable, which is consistent with the results of Ge/Si(001) grown at 550 °C reported by Medeiros-Ribeiro et al. [88];
- (5) with a low barrier between the second and third minima, square base pyramids form first, and then

all islands transform into dome-shaped islands, as observed by Ross et al. at 650 °C [99].

Although many other shapes for $\text{Ge}_x\text{Si}_{1-x}/\text{Si}(001)$ QDs have been reported, including a truncated pyramid with $\{111\}$ facets [113–116], $\{311\}$ faceted [117–119], cone-shaped circular island with $\{711\}$ facets [120], all can be regarded as dome-shaped.

2.2. Shapes of $\text{In}_x\text{Ga}_{1-x}\text{As}/\text{GaAs}(001)$ QDs

Many shapes have been reported for QDs in the $\text{In}_x\text{Ga}_{1-x}\text{As}/\text{GaAs}$ system. One of the most commonly reported is the pyramid with a square base, deduced from plan-view [001] zone-axis transmission electron microscopy (TEM) diffraction contrast images [121, 122]. However, direct interpretation of such images can lead to a wrong conclusion about shape because diffraction contrast in TEM does not directly relate to QD shapes but to the strain field around and within the QDs [123].

Zou et al. [124] presented the first unambiguous shape determination of unburied $\text{In}_x\text{Ga}_{1-x}\text{As}/\text{GaAs}(001)$ QDs using a direct imaging TEM technique. Using a very thick (>300 nm) cross-section TEM sample, images of different side projections (see an example image in Fig. 3) proved that the QDs are lens shaped with a circular base.

Liao et al. [123] studied the shape of buried metalorganic chemical vapor deposition (MOCVD) grown $\text{In}_{0.6}\text{Ga}_{0.4}\text{As}/\text{GaAs}(001)$ QDs using TEM combined with image simulations. As shown in Figure 4, the buried QDs have side projections similar to the unburied QDs reported by Zou et al. [124], suggesting the QDs to be lens shaped. Although plan-view [001] zone-axis images show a square contrast, interpretation of the contrast is not straightforward because image simulations show that lens-shaped QDs can produce a square-shaped image [123] (see Fig. 5).

Other shapes of $\text{In}_x\text{Ga}_{1-x}\text{As}/\text{GaAs}$ QDs have also been reported. For example, using contact mode atomic force microscopy (AFM) with a B-doped Si tip, Yoon et al. [125] reported that MOCVD grown $\text{InAs}/\text{InGaAs}$ QDs are truncated pyramids with four $\{136\}$ facets and with base edges parallel to $\langle 130 \rangle$. Lee et al. [126, 127] reported a similar result using reflection high-energy electron diffraction (RHEED). Combining AFM and RHEED techniques, Kaizu and Yamaguchi [128] also reported $\{136\}$ faceted $\text{InAs}/\text{GaAs}(001)$ QDs grown by solid-source MBE. However, Nabetani et al. [129] interpreted the same RHEED pattern as showing $\{113\}$ facets. An *in-situ* investigation of $\text{InAs}/\text{GaAs}(001)$ QDs by STM [130] revealed a pyramidal QD shape dominated by $\{137\}$ facets. Using a high-resolution grazing incidence small angle X-ray scattering technique, Zhang et al. [131] determined an InAs QD

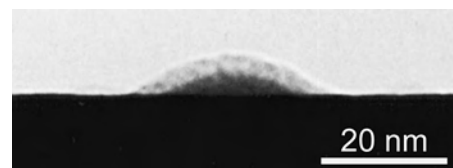


Figure 3. A cross-section TEM image of a side projection of an unburied $\text{In}_{0.6}\text{Ga}_{0.4}\text{As}/\text{GaAs}(001)$ QD.

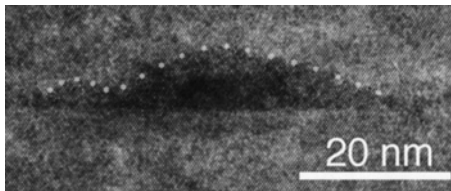


Figure 4. A cross-section high-resolution TEM image of two buried $\text{In}_{0.6}\text{Ga}_{0.4}\text{As}/\text{GaAs}(001)$ QDs observed along $\langle 110 \rangle$. The QD boundaries are marked with white stars.

shape of octagonal-based truncated pyramid with $\{111\}$ and $\{110\}$ sidewalls and a $\{001\}$ top facet. Anders et al. [132] also reported large $\text{In}_x\text{Ga}_{1-x}\text{As}/\text{GaAs}(001)$ QDs bounded by $\{111\}$ sidewalls and a $\{001\}$ top facet.

Moll et al. [133] calculated the equilibrium shapes of $\text{InAs}/\text{GaAs}(001)$ QDs using an approach that includes density functional calculations of microscopic parameters, surface energies, and surface stresses with elasticity theory for the long-range strain fields and strain relaxations. In their calculations, they considered only low-index surface facets $\{001\}$, $\{110\}$ and $\{111\}$. Also, they neglected the island-island interaction and the alloying effect between QDs and the matrix. The equilibrium shapes they presented are islands bounded by an $\{001\}$ top facet and $\{110\}$ and $\{111\}$ side facets. They found that the island shape changes continuously with the island volume. The $\{111\}$ facets are more prominent than $\{110\}$ facets for larger islands. However, most of the experimentally observed shapes in the $\text{InAs}/\text{GaAs}(001)$ system differ from those predicted by Moll et al. They therefore concluded that the growth conditions of these InAs/GaAs QDs do not represent thermodynamic equilibrium but are driven by kinetics, and that it should be possible to achieve thermodynamic equilibrium by choosing appropriate experimental conditions.

2.3. Shapes of QDs in Other Material Systems with $\{001\}$ Surfaces

Using TEM to investigate the shape of MOCVD grown $\text{InP}/\text{GaInP}(001)$ islands, Georgsson et al. [134] found that both buried and unburied islands have truncated pyramidal shapes with a hexagonal base bounded by $\{001\}$, $\{110\}$ and $\{111\}$ facets. Figure 6 shows the cross-section images taken from $[110]$ and $[\bar{1}\bar{1}0]$ of $\text{InP}/\text{GaInP}(001)$ islands together

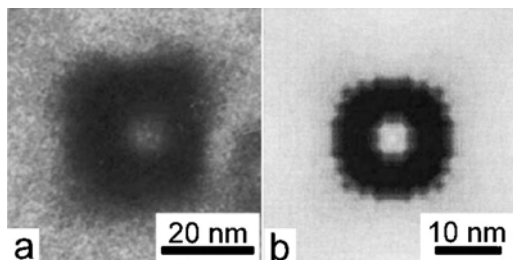


Figure 5. A comparison of an experimental plan-view image of a buried $\text{In}_x\text{Ga}_{1-x}\text{As}/\text{GaAs}$ QD (a) and a simulated image based on a lens-shaped model buried QD (b).

with the schematic shape model deduced from the information provided by plan-view and cross-section TEM images. Theoretical investigations [135] using a hybrid approach that combines density-functional theory calculations of the surface energies and continuum elasticity theory calculations of bulk deformation energies, suggest that the $\text{InP}/\text{GaInP}(001)$ island shape shown in Figure 6 is close to thermodynamic equilibration.

Arlery et al. [136] characterized $\text{GaN}/\text{AlN}(0001)$ QDs in the wurtzite GaN crystal structure using cross-section high-resolution TEM images [136, 137] together with RHEED data [138, 139] and deduced that the QDs are truncated pyramids with a hexagonal base, an aspect ratio of 1/5, and a contact angle between the QD sidewalls and the substrate plane of 30° . Wurtzite GaN QDs with the aspect ratio of 1/5 and zinc-blende GaN QDs with an aspect ratio of 1/10 were also reported by Daudin et al. [140].

Although AFM [141, 142] and optical characterizations [143, 144] have suggested the existence of QD structures in II–VI systems, detailed structural information of II–VI QDs has been rare. The first clear image of II–VI QDs was produced by Arita et al. [145]. They used AFM to investigate CdSe/ZnSe islands grown on $\text{GaAs}(001)$ by MOCVD and showed a structure with $\{311\}A$ facets along the $[0\bar{1}1]$ direction.

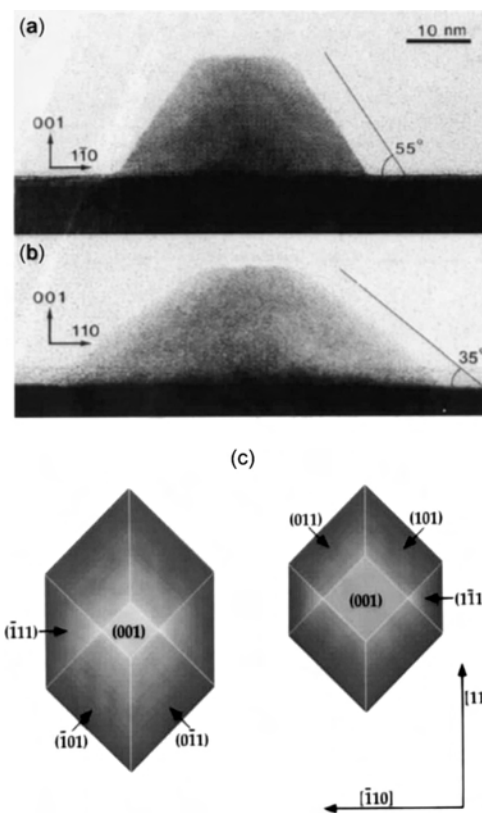


Figure 6. Cross-section TEM images of an unburied $\text{IP}/\text{GaIP}(001)$ island taken from $[110]$ (a) and $[\bar{1}\bar{1}0]$ (b). A schematic model of the island shape deduced from the combination of plan-view and cross-section TEM images is shown in (c). Reprinted with permission from [134], K. Georgsson et al., *Appl. Phys. Lett.* 67 2981 (1995). © 1995, American Institute of Physics and Prof. W. Seifert.

Maehashi et al. [146] fabricated CdSe/ZnSe on GaAs (001) using MBE and characterized the sample using plan-view TEM. They found CdSe QDs with a rhombic base with edges along $\langle 510 \rangle$ and with the long axis of about 20 nm in length along $[1\bar{1}0]$ and the short axis of about 13 nm along $[110]$.

2.4. Shapes of QDs Grown on Surfaces Other Than (001)

The surface structures and surface energies of substrate materials are important parameters in determining the mode of epitaxial growth. Higher index substrates often generate QDs different from those grown on the (001) surface. For example, Lobo and Leon [73] investigated InGaAs QDs on GaAs (11 \bar{n}) ($n = 0, 1,$ and 3) surfaces using AFM. They found trapezoidal islands on $(1\bar{1}0)$ with the parallel edges of each trapezoid lying along $[110]$, equilateral triangular islands on $(111)B$ (they speculated that the island edges might parallel to $\langle 110 \rangle$), lens-shaped islands on $(311)B$, and lens-shaped islands elongated along $[\bar{2}33]$ on $(311)A$. Because of the observation of small lens-shaped islands on (110) and $(111)B$, they argued that large polygonal islands possibly begin as coherent lens-shaped islands and change shape beyond the coherent-incoherent transition (dislocations were seen in these large polygonal islands). Alternatively, the triangular and trapezoidal shapes may be the most energetically favorable for coherent islands and dislocation introduction may occur later.

Among all the investigated substrates with higher index surfaces, substrates with (311) surfaces have produced the highest quality QDs [147], while GaAs substrates with $(111)A$ surface [148, 149] produced no QD. Nötzel et al. [150] grew InGaAs/AlGaAs heterostructure on GaAs(311)B using metalorganic vapor-phase epitaxy. They found that during growth interruption after subsequently growing an AlGaAs buffer layer and an InGaAs layer, the strained InGaAs layer self-organizes into orderly arranged nano disks. The nano disks were found to be covered with AlGaAs, forming clearly faceted islands (see Fig. 7). However, the facet planes were not identified. The fact that no AlGaAs was deposited after the InGaAs was deposited implies lateral mass transport from the AlGaAs buffer layer to the InGaAs QDs. Nötzel et al. later [147] compared the morphologies of InGaAs grown on GaAs($n11$)A/B ($n = 2, 3,$ and 5) with a thick $Al_{0.5}Ga_{0.5}As$ film as the buffer layer. They found that among all of these high-index surfaces (311)B provides the best alignment and uniformity, while (311)A presents wirelike structures with the wire axis approximately along $[233]$.

Lacombe et al. [151] investigated $Ga_{0.2}In_{0.8}As/InP(311)B$ QDs using TEM and AFM and found that the QDs are generally bounded by low-index facets $\{001\}$, $\{111\}B$, and $\{110\}$ which make angles to the substrate surface of 25°, 29°, and 31°, respectively. A very similar shape but with more facets ($\{315\}$ and $(112)B$) on the skirts of QDs has been seen in the MBE grown InAs/GaAs(113)B system by Suzuki et al. [152]. They presented *in-situ* shape determination of the QDs using atomically resolved STM. The shape and facet plane indices determined by Suzuki et al. [152] are shown in Figure 8. The fact that QDs grown on (113)B

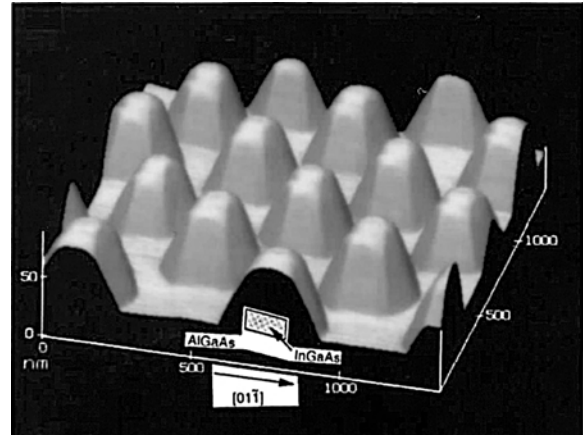


Figure 7. A three-dimensional AFM image of $In_{0.2}Ga_{0.8}As/Al_{0.5}Ga_{0.5}As$ on GaAs(311)B. Reprinted with permission from [147], R. Nötzel et al., *Appl. Phys. Lett.* 65, 2854 (1994). © 1994, American Institute of Physics and Prof. T. Fukui.

have low-index facets is important for QD growth because low-index facets normally have lower surface energies and therefore reduce the barrier for QD formation. This is supported by the observation that $In_{0.8}Ga_{0.2}As$ QDs were easier to form on InP(113)B than on InP(001) [153].

Omi and Ogino [154, 155] grew coherent Ge islands on Si(113) using MBE at 400 °C to 550 °C and found the islands to be wire-shaped, elongated along $[33\bar{2}]$, and bounded by $\{519\}$ facets. The width of the islands is between 16 and 32 nm, while the length is between 10 and 600 nm. They found the wire-shaped islands were transformed from equiaxial islands and they explained the transformation in terms of the theory of Tersoff and Tromp [96]. Zhu et al. [156] also reported Ge/Si(113) islands elongated

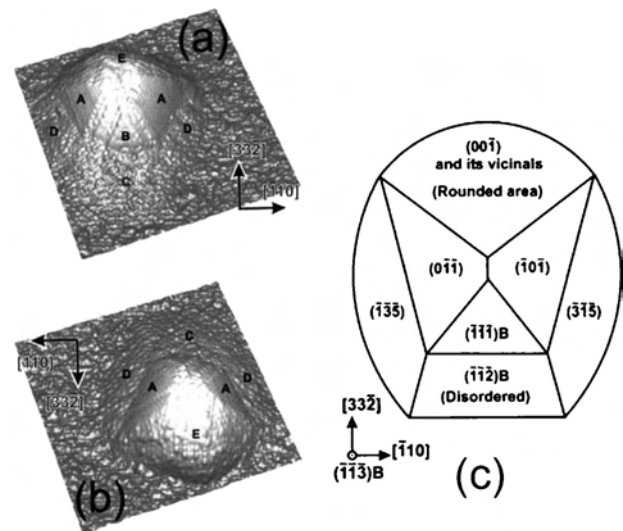


Figure 8. (a) and (b) three-dimensional STM images of an InAs/GaAs(113)B QD with the image size of 42×42 nm² and (c) a schematic model of the QD shape. Reprinted with permission from [152], T. Suzuki et al., *Appl. Phys. Lett.* 80, 4744 (2002). © 2002, American Institute of Physics and Prof. K. Jacobi.

along $[3\bar{3}2]$ but bounded by facets including (111), $\{516\}$, $\{517\}$, and $\{518\}$ with (113) as the top facets.

Atomic force microscopy and TEM investigation [157] revealed that coherent Ge/Si(211) islands grown by MBE are of irregular hexagonal shapes elongated along $\langle 111 \rangle$ and bounded by $\{111\}$ and $\{113\}$ facets, whereas large dislocated Ge/Si(211) islands are mainly bounded by $\{111\}$ and $\{001\}$ facets. Truncated tetrahedral-shaped islands have been observed in Ge/Si(111) [158–160], and they have a triangular base bounded by three $\langle 110 \rangle$ equivalent edges and with (111) as the top facet. The Ge/Si(111) island shape appears to reflect the symmetry of the (111) substrate surface.

2.5. Size

Unfortunately, it is necessary to start this section by pointing out that the word “size,” as used in much of the QD literature, has an imprecise meaning. Sometimes it is used to mean volume (in which case, the better word would be volume), but at other times it is used to mean width. In this latter case, two QDs of equal size (width) can be of different volume as, for example, for a pyramid and a dome. This is an important point where objects of different shape are to be compared (e.g., dome to pyramid). Because of this imprecision in the literature, and because it is not always possible to determine which is meant, we use the word size in the ambiguous sense where ambiguity exists. Of course, where shape remains fixed, volume scales with size; however size is interpreted.

Daruka and Barabási [161] showed that in the S–K mode, when the island growth starts, the equilibrium island size does not increase continuously but jumps discontinuously from zero to a value that depends upon the lattice mismatch and the wetting layer thickness. Spencer and Tersoff [162] also suggested that island formation starts from a fixed width (a minimum island size). Very narrow island size distributions at the early stages of island growth have been observed [103, 163–168] in various material systems and have been attributed to specific models of self-limiting growth [107, 169–171]. When the thickness of deposited materials reaches a certain value, Ostwald ripening occurs [161, 172] and the above narrow size distribution no longer exists. Bimodal size distribution has also been reported [93, 95] and has been discussed in Section 2.1.

In a study of InAs/GaAs QDs grown at different temperatures, Saito et al. [76] showed that QD size depends greatly on growth temperature. They found that with increasing growth temperature, the island density decreases while island size increases and the island size distribution becomes more uniform. The same effect was found in the Ge/Si system [173]. Kinetic Monte Carlo simulations suggest that the QD size distribution immediately after deposition is kinetically controlled, giving smaller islands for lower temperatures and larger islands for higher temperatures [174]. Allowing for variations of the island density, the stability of the combination of larger islands with a lower island density implies the action of Ostwald ripening [175].

Quantum dot size also depends on the orientation of the substrate surface. It has been reported that QDs

grown on some high-index surfaces are smaller, more uniform in size, and of a higher density than QDs grown on (001). For example, under the same deposition conditions, SiGeC QDs grown on Si(311) [75], InP QDs grown on GaInP/GaAs(311)A [74], and InGaAs QDs grown on GaAs(311)B [176] are smaller than their counterparts grown on (001).

2.6. Shape Evolution During Growth

Chen et al. [89] reported that during the two-dimensional (2D) to three-dimensional (3D) transition in a $\text{Ge}_{0.5}\text{Si}_{0.5}/\text{Si}(001)$ QD system, the lateral width and inclination angle of the islands evolve continuously until the island is bounded by stable $\{501\}$ facets. This phenomenon was later confirmed by Vailionis et al. [177] who investigated the 2D to 3D transition during the growth of Ge on Si(001) using STM and found “prepyramids” before the formation of $\{501\}$ -faceted pyramids. The prepyramids have rounded bases and are bounded by steps oriented approximately along $\langle 110 \rangle$. The aspect ratio of the prepyramids varies from 0.03 to 0.05, increasing with increasing island size. When the base width of a prepyramid reaches 16–20 nm, the prepyramid transforms into $\{501\}$ -faceted pyramids. At the point of the transformation from prepyramids to pyramids, the island volume remains approximately constant and Ge atoms in the islands rearrange so that the island width decreases while the island height increases. As the growth continues, pyramids all finally transform into domes.

Both experimental and theoretical investigations have shown that QD shapes change during the growth of the QD [88, 98, 177]. However, different experiments show different evolution processes. For example, by growing Ge QDs on Si (001) in an ultra high vacuum, chemical-vapor deposition system at temperatures of 550 °C and 700 °C, Thanh [178] reported two different evolutions of island shapes:

- (1) from a metastable square-base truncated pyramid formed by $\{501\}$ facets and a $\{100\}$ facet on the top, to a dome with $\{111\}$ facets, and
- (2) from the same metastable shape to a dome with $\{311\}$ facets.

From the study of the growth of $\text{Ge}_{0.8}\text{Si}_{0.2}/\text{Si}$ (001), which proceeds in a similar way to the growth of Ge/Si (001) but with the length scales expanded by the reduced strain, Floro et al. [90, 179] showed that the $\{501\}$ facets are extremely stable over a range of deposition thicknesses. Beyond a certain thickness, the islands with $\{501\}$ facets transform to domes with steep $\{h11\}$ facets. As the film thickens, dome formation continues, and the dome facets approach $\{311\}$. All of the above experimental observations show one point in common: the contact angle between the sidewalls of the islands and the substrate increases with increasing island size. This is consistent with theoretical considerations [162, 175, 180]. For example, Spencer and Tersoff [162] calculated the equilibrium morphology of a coherent epitaxial strained layer grown under the S–K mode, in an isotropic two-dimensional continuum model. Assuming an unafaceted surface and assuming that mass transport caused by surface gradients in the chemical potential occurs only by surface

diffusion, and based on the fact that the equilibrium morphology has a constant chemical potential along the free surface, they concluded that very small islands have a fixed asymptotic width and a vanishingly small aspect ratio. With increasing volume, the island initially grows in the vertical direction which makes the small island have an arbitrarily small aspect ratio. At a larger volume both the island width and aspect ratio continue to increase. The contact angle between the island side-wall and the substrate increases continuously with size and a sufficiently large island approaches a ball shape sitting on top of the wetting layer. On the basis that stable shapes have minimum energy and considering the fully faceted islands, Daruka et al. [180] studied in a two-dimensional model, the equilibrium shape and the shape evolution in the growth of strained islands. They predicted that the first-order shape transition (discontinuous shape change) is a very general phenomenon in island growth. They found that at the smallest volumes there is no island at all; all the material remains in the planar wetting layer. Above a lower transition, the island is stable and consists of shallow side facets. At a critical island volume, the shallow side facets are substituted by steep side facets so that the overall aspect ratio increases discontinuously.

Goldfarb, Briggs et al. [181–183] considered growth in the Ge/Si system at temperatures of 620 °C and 690 °C, using *in-situ* STM observations. At the lower temperature, they reported the formation of huts, while at the higher temperature, strain was initially relieved by hut pits with their apex down. They developed a model of hut growth, with the early stages being limited by surface diffusion. The later stages of growth have the smaller huts dissolving, as in Ostwald ripening, but with the released material reagglomerating rather than contributing to the coarsening of the larger huts. At higher temperatures, the role of true Ostwald ripening increases. This model explained the skewed and bimodal distributions seen in their STM experiments.

2.7. Capping Effect on QD Shape and Size

In many applications, QD islands need to be buried by larger bandgap materials (normally the same material as the substrate). Obviously, strain fields in and around buried QDs are different from those of free-standing QDs. As a result, it is thermodynamically favorable for buried QDs to adopt new shapes to lower the system energy and, if kinetic growth conditions allow, shape change will occur during the QD capping process.

The QD shape change during the capping process has been reported in the Ge/Si [184, 185] and $\text{In}_x\text{Ga}_{1-x}\text{As}/\text{GaAs}$ [186, 187] systems. Sutter and Lagally [188] investigated the morphology evolution process in a GeSi/Si system using low-energy electron microscopy. They found that the GeSi islands expand and undergo a shape change to incorporate a (100)-top facet under a Si flux. They explained that Si deposition results in intermixing between Si and Ge and the intermixing destabilizes {501} facets and a (100)-top facet becomes the thermodynamically stable structure. Atoms from the island top migrate down the sides resulting in the elimination of the {501} facets at the top and outward expansion of the remaining {501} facets in the lower parts

of the islands. They further concluded that while thermodynamic destabilization of the island apex region through intermixing and a reduction in strain drives the island shape change, kinetics limit the actual decay of the island apex. Rapid capping at a low temperature retains the initial island shape, while slow capping at a high temperature results in island height reduction. Figure 9 shows an example of an unburied and two buried Ge/Si(001) islands in an island stack grown by MBE at 575 °C. It is clearly seen that the unburied island has a larger aspect ratio, while the buried islands have larger base diameters, although this interpretation assumes that the sections are taken through the same positions of each QD. For island capping at higher temperatures, island shape changes are expected to be more significant than seen in Figure 9. For example, using an X-ray scattering method, which is capable of resolving buried island shape and strain status, Hesse et al. [189] reported that $\text{Ge}_x\text{Si}_{1-x}/\text{Si}(001)$ islands underwent a significant change in shape and size during a Si capping process at 700 °C. The island base diameter increased from 110 nm to 180 nm, while the island height decreased from 13 nm to 6 nm. The average Ge content in the islands also changed from $x = 0.78$ before the capping process to about $x = 0.37$, implying considerable alloying effect between the islands and the Si capping layer.

Joyce et al. [190] investigated the initial stages of the capping process of InAs/GaAs(001) QDs using RHEED and STM. They found that a significant amount of mass transport and alloying occurred during the GaAs capping process, resulting in a dramatic shape and size change. Quantum dot sidewalls first became shallower and later lost all their crystallographic facets. During the capping process, the QDs increased in volume but reduced in height, elongating significantly along $[\bar{1}10]$.

The capping process has been used to narrow the distribution of QD sizes. For example, Lian et al. [191] deposited a GaAs capping layer on InAs/GaAs(001) QDs first at a low temperature of 530 °C to cover the smaller QDs and then at an elevated temperature of 580 °C. At this higher temperature, the InAs QDs are unstable against evaporation [192]. Because the InAs wetting layer is fully strained and, therefore, is lattice matched with the GaAs substrate, it is energetically favorable for the GaAs capping layer to form initially on the wetting layer. Consequently, in the case

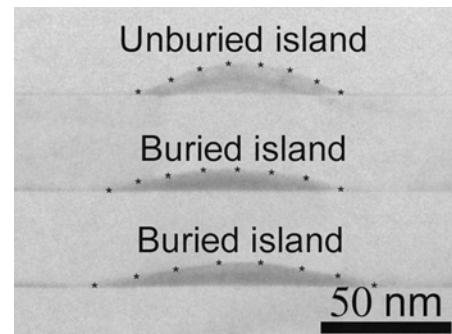


Figure 9. An example of an unburied and two buried Ge/Si(001) islands in a multilayer sample grown by MBE at 575 °C. The QD boundaries are highlighted with black stars.

where adatoms have sufficient surface mobility, a QD will not be covered by the GaAs until the capping layer thickness reaches the QD height. Then, with the high-temperature deposition at 580 °C, the larger QDs will remain uncapped and so will be sublimed, while the smaller QDs will be protected by the capping layer formed at the lower temperature. In this way, a very narrow QD size distribution was obtained and the QD density was decreased.

3. COMPOSITION

Detailed knowledge of composition and its distribution within and around QDs is important for a thorough understanding of the QD growth mechanism and of the structure-property relationship of QDs. However, the determination of quantitative composition profiles of QDs is a very challenging task because of the small size of the QDs. As a result, the composition of QDs has been less investigated compared to their shape and size.

Most investigations of QD composition suggest that the average composition of a QD is not necessarily the composition of the deposited materials, with the evolution of the composition being a complicated process involving alloying with the substrate material, elemental enrichment [193], and segregation.

Tersoff [194] argued that because an enriched larger-misfit component (e.g., In in a InGaAs/GaAs system and Ge in a GeSi/Si system) will significantly reduce the energy barrier of nucleation, and because the subsequent island growth and final growth stage may consume an indium- (or germanium-) depleted film, the resulting island will have a core that is rich in the larger misfit component (In-rich core in InGaAs/GaAs systems, Ge in GeSi/Si (larger atoms at compressive regions)). This results in a so-called “self-capping” process. The predicted self-capping process is illustrated schematically in Figure 10.

Liao et al. [195] presented the first experimental evidence of the elemental enrichment and segregation in QDs. They studied plan-view TEM diffraction contrast images and compared the details of the contrast with that predicted for

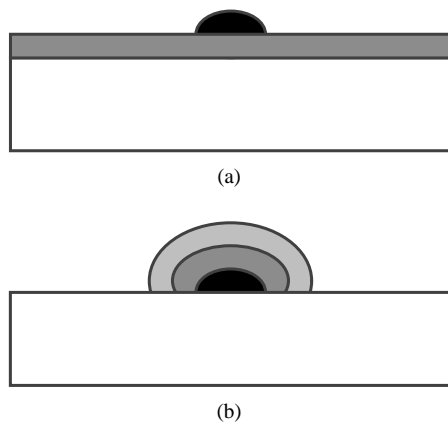


Figure 10. Schematic diagrams showing (a) an indium-enriched island nucleated on the wetting film and (b) the island further growing by consuming progressively In-depleted wetting film. The indium compositions are represented by grey scale with darker areas having higher indium composition. (After Tersoff [194])

QDs modelled using finite element analysis. They found that under the [001] zone-axis imaging condition, the image detail (in the form of Maltese crosses, see Fig. 11) could be used to investigate the elemental distribution with the QD. In this way, they demonstrated In enrichment and segregation in $\text{In}_{0.6}\text{Ga}_{0.4}\text{As}/\text{GaAs}$ QDs.

Walther et al. [196] also reported elemental enrichment and segregation in MBE grown $\text{In}_{0.25}\text{Ga}_{0.75}\text{As}/\text{GaAs}$ (the lowest In concentration at which islanding occurs), using energy-filtering imaging (EFI) in TEM. They observed strong inhomogeneous In enrichment within the islands (up to $x_{(\text{In})} \approx 0.6$ at the apex), resulting in a simultaneous In depletion in the remaining flat layer. Their results also demonstrated strong vertical and lateral In segregation with the highest In content at the island apex.

Krost et al. [197] use high-resolution X-ray diffraction and pole figure analysis to study a 15-fold InAs/InGaAs/GaAs QD stack grown by MOCVD. Through the analysis of the diffuse scattering intensity in the vicinity of the (113) reflection in the symmetric scattering geometry, they found that the In concentration in QDs is more than double the mean In concentration (43%) in the wetting layer, indicating a strong In enrichment during the S–K formation process. Crozier et al. [198] also found strong In enrichment in buried $\text{In}_{0.5}\text{Ga}_{0.5}\text{As}/\text{GaAs}$ QDs grown at 550 °C, with the highest In/As ratio up to 0.8, by measuring quantitatively the composition profiles using electron energy-loss spectroscopy in a scanning transmission electron microscope.

Experimental observation of enrichment and segregation of the larger-misfit component has also been found in the Ge(Si)/Si system by Liao et al. [199]. They deposited pure Ge on Si(001) by gas-source MBE at 575 °C and then investigated cross-section samples using the EFI technique. They found that both the wetting layer and the islands are GeSi alloys, implying that alloying occurred during the deposition process. However, as illustrated in Figure 12, there is a much higher Ge content in the islands than in the wetting layer and the highest Ge content is located at the island center. The observed composition distribution and interfacial morphology (island/substrate interface slightly below wetting layer and the position of the highest Ge content slightly above the wetting layer) in Figure 12 can

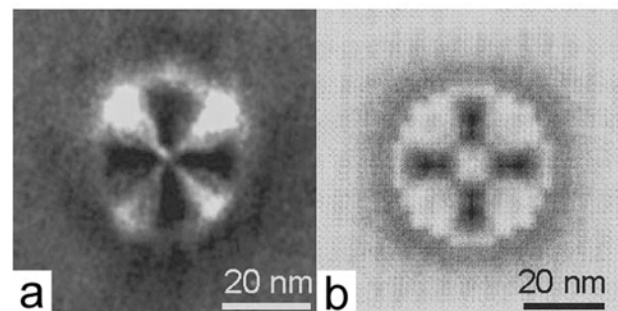


Figure 11. A comparison of an experimental (a) and a simulated (b) image of an $\text{In}_x\text{Ga}_{1-x}\text{As}/\text{GaAs}$ QDs. The simulated image was obtained using a model QD with composition segregation. The conclusion of In enrichment and segregation was reached through the comparison. Reprinted with permission from [124], J. Zou et al., *Phys. Rev. B* 59, 12279 (1999). © 1999, American Physical Society.

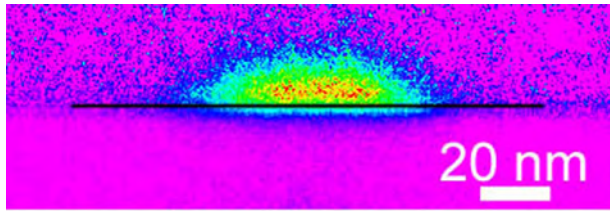


Figure 12. A pseudo-color (spectrum) image showing the Ge/Si distribution within a Ge(Si)/Si(001) island, where the area with the highest Ge content is presented in red color while the lowest is purple. A horizontal black line is drawn along the wetting layer/substrate interface.

be explained by following Tersoff's theoretical analysis [194], while also assuming that alloying occurred during deposition and that interdiffusion between islands and substrate at the island/substrate interface occurred to further release strain energy.

In fact, alloying (a reverse process to elemental enrichment) during the deposition process is a commonly seen phenomenon [200–204]. One of the earliest reports was by Joyce et al. [205] in which they employed STM to study the growth by MBE of InAs QDs on GaAs(001). They measured the volume of the QDs at different temperatures as a function of InAs deposition. They found that a high substrate temperature (>420 °C) resulted in QDs with a much greater volume than the deposited volume, which implies significant mass transport from both the wetting layer and the substrate to the QDs. Furthermore, the wetting layers in the InAs/GaAs system and in the Ge/Si system have been reported to be an (In, Ga)As alloy [149] and a GeSi alloy [206], respectively, with temperature-dependant composition. Chaparro et al. [207] reported that strain-driven alloying in Ge/Si(001) coherent islands results in an increased mean Ge/Si(001) dome size and a delayed onset of island dislocation formation as the growth temperature increases.

Although elemental segregation appears to be common in QD islands, the segregation mode depends on the growth conditions. For example, Liao et al. [208, 209] showed that for Ge(Si)/Si(001) grown by solid-source MBE at 700 °C, the highest Ge content is at the island top, while in another study [199] they showed that Ge(Si)/Si(001) grown by gas-source MBE at 575 °C had the highest Ge content at the island center. The reason for the different segregation modes is discussed later.

There are many other investigations that report elemental segregation with the highest content of a larger-misfit component located either at the island center [210, 211] or at the island top [187, 212–217]. Using high-resolution TEM combined with finite element calculations, Kret et al. [210] investigated $\text{In}_{0.35}\text{Ga}_{0.65}\text{As}/\text{GaAs}(001)$ QDs grown by MBE at 510 °C. They concluded that the In concentration in the island center is significantly high (up to $\sim 50\%$), while the concentration at the island edges is low (down to $\sim 20\%$). Litvinov et al. [211] studied CdSe QDs in a ZnSe matrix grown by MBE on GaAs(001) and used lattice fringe analysis in TEM to evaluate the distribution of Cd (the larger-misfit component in the CdSe/ZnSe system). They showed that the highest Cd content was in the QD center. Rosenauer et al. [215] reported that the lattice mismatch in MBE grown $\text{In}_x\text{Ga}_{1-x}\text{As}/\text{GaAs}(001)$

QDs at 560 °C increases from the bottom towards the top of the QDs. Stangl et al. [216] investigated the composition distribution of GeSi islands grown by MBE on Si(001) at 600 °C using grazing incidence, noncoplanar, scattering X-ray diffraction. They compared the experimental diffraction pattern with patterns calculated, based on the QD strain fields obtained from finite element analysis. Using surface-sensitive X-ray diffraction, Kegel et al. [217] investigated the tomographic nanometer-scale images of 530 °C MBE grown InAs/GaAs(001) QDs. Based on the three-dimensional intensity mapping of selected regions in reciprocal space, they extracted information about the interdiffusion profile along the QD growth direction on a subnanometer scale and found that QD composition varies continuously from GaAs at the island/substrate interface to InAs at the top. From this comparison, they concluded that although pure Ge was deposited, the Ge content varies from 50% at the island base to 100% at the island top. Using electron energy-loss spectroscopy (EELS), Walther et al. [218] showed vertical and lateral Ge segregation in $\text{Si}_{0.8}\text{Ge}_{0.2}/\text{Si}(001)$, where the Ge atoms tend to occupy tensile positions.

Although Tersoff's theoretical investigation [194] predicts islands forming with enriched a larger-misfit component in the center to lower the nucleation barrier, it is energetically favorable to have larger atoms in the regions that are (relatively) more tensile and smaller atoms in more compressive regions [219]. Different atomic mobilities on the surface can also lead to substantial segregation, even when the atomic sizes are identical [219]. Therefore, in the case where kinetic conditions (higher growth temperature, slower deposition speed) allow a system to reach an equilibrium state, QDs will have the segregation mode with the larger-misfit component located at the island top. Otherwise, the enriched larger-misfit component will remain in the center of the QDs. This explains the different observations discussed above.

Because of the dynamic, often nonequilibrium, nature of QD growth, the real situation may be more complicated than is covered by the above discussion. A surprising compositional uniformity in $\text{Si}_{0.8}\text{Ge}_{0.2}/\text{Si}(001)$ islands was reported by Floro et al. [220]. Bimodal composition distribution in InGaAs/GaAs QDs grown using low-pressure MOCVD has been reported by Saint-Girons et al. [221] They demonstrated that the presence of a bimodal inhomogeneous broadening of the photoluminescence was correlated with a bimodal QD contrast distribution in the bright-field [001], plan-view TEM images, which they believe are from In-poor and In-rich QDs.

4. GROWTH MECHANISMS

Most of the QDs produced using strained epitaxial growth adopt the Stranski–Krastanow (S–K) growth mode [222]. There are, however, some including InAs/GaP(001) [223], GaAs/Si(001) [224], ZnTe on ZnSe/GaAs [225], and ZnSe on ZnS/Si(001) and ZnS/GaAs(001) [226], which have been reported to adopt the Volmer–Weber growth mode [227], that is, island growth directly without any prior wetting layer formation. In the classical S–K mode of coherent island formation, one material with a different lattice parameter

and low interfacial energy is initially deposited on a substrate surface, layer by layer, forming a “wetting layer.” When the wetting layer reaches a critical thickness (usually three to five monolayers for pure Ge on Si(001) [25, 228]), island growth starts to partially release the mismatch strain energy between the epitaxial layer and the substrate.

However, the classic S–K mode is too simple to explain fully the complicated experimental observations. Based on a series of TEM studies of high-temperature growth Ge(Si)/Si(001) islands, in which a trench is seen on the substrate surface around a Ge(Si)/Si(001) island and the island/substrate interface is found moving towards the substrate (see Fig. 13), Liao et al. [229] proposed a modified S–K mode for high-temperature growth of Ge islands on Si, as shown diagrammatically in Figure 14. In classical S–K growth, layer-by-layer growth takes place at the initial stage of Ge deposition, as shown in Figure 14(a). However, the layer-by-layer growth at high temperature is accompanied by an alloying process, resulting from Si transport to the wetting layer. Following the layer-by-layer growth, surface migration of both Ge and Si results in island growth (Fig. 14(b)). The formation of the small coherent island only partially releases the misfit strain. With the growth of the island, misfit strain builds up. The strain energy is further reduced by lowering the misfit between the island and the substrate, which could result from the alloying of Si into the Ge island. The transfer of Si into the island can be either through transport from the wetting layer, or directly by bulk diffusion from the bottom of island/substrate interface, or both (as in Fig. 14(c)). The lower mobility of Si than Ge [219] implies that while Ge can be transported from a longer distance, most of the Si consumed comes from areas surrounding the islands. This results in a trench around the island, as illustrated in Figure 14(c). The subsequent island expansion necessarily starts from the bottom of the trenches and the lateral Si migration process continues as the island grows, as shown in Figure 14(d).

The above-mentioned growth mode does not provide a complete picture because the composition profile is not considered. The QD islands investigated above [229] have been found to have highest Ge content at the island top and the lowest Ge content at the island/substrate interface [208, 209, 230]. On the other hand, as discussed earlier, Liao et al. [199] used EFI in the TEM to study “pure” Ge/Si(001) islands grown at a lower temperature of 575 °C.

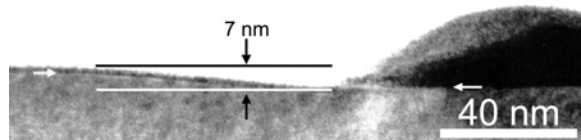


Figure 13. A cross-section bright-field image of a coherent Ge(Si)/Si(001) island grown at 700 °C showing a clear wetting layer. White arrows at the left and right sides of the image mark the wetting layer/substrate interface and the island/substrate interface, respectively. A white line below the wetting layer represents the depth level of the island/substrate interface. A trench with a depth of about 7 nm at the edge of the island is clearly seen. Reprinted with permission from [229], X. Z. Liao et al., *Phys. Rev. B* 60, 15605 (1999). © 1999, American Physical Society.

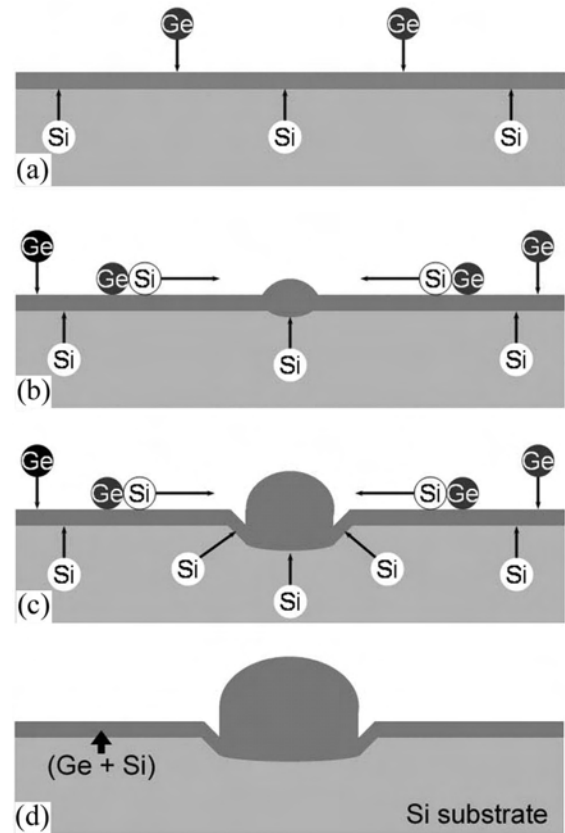


Figure 14. Schematic diagrams of a modified S–K growth mode at different growth stages. Reprinted with permission from [229], X. Z. Liao et al., *Phys. Rev. B* 60, 15605 (1999). © 1999, American Physical Society.

They found that the Ge content in islands is much higher than in the wetting layer and the Ge is nonuniformly distributed within an island with the highest Ge content located at the island center. These results imply alloying, elemental enrichment, interdiffusion, and composition redistribution occurring during the QD island growth process. Higher temperatures and lower growth rate will allow the QD composition to be distributed in such a way that the system can minimize the system energy more efficiently.

Combining all the information on the interfacial structure and composition mentioned above, a more complete image on the S–K island growth mode should be:

- (i) the initial stage of layer-by-layer growth includes an alloying process between the deposited material and substrate material;
- (ii) island nucleation is accompanied by the enrichment of a larger-misfit component of the deposited material and this will result in nonuniform composition distribution with the larger-misfit component concentrating at the center of the island;
- (iii) the alloying process continues during the island growth and this lowers the island/substrate interface; and
- (iv) if growth conditions permit, elements in islands will be redistributed to allow a larger-misfit component

moving up to the top so that minimizing the island strain energy.

Stranski–Krastanow island growth mode normally involves a nucleation process. However, under some temperature and low-lattice, mismatch composition ranges, QDs in the $\text{Ge}_x\text{Si}_{1-x}/\text{Si}(001)$ system can apparently be formed in a so-called “nucleation-free” process involving a gradual evolution of surface roughness driven by misfit strain [231, 232]. Using *in-situ*, low-energy electron microscopy, Sutter and Lagally [231] and Tromp et al. [232] found that faceted $\text{Ge}_x\text{Si}_{1-x}/\text{Si}(001)$ islands can form barrierlessly and continuously from strain-induced surface ripples with bunched steps as sidewalls. The sidewall angle of the ripples increases continuously until it reaches 11° , forming {501} facets. By assuming that the surface-energy anisotropy of strained GeSi allows all surface orientations near (001) with the first facet being {105}, Tersoff et al. [233] explained this phenomenon in terms of the barrierless formation of unfaceted prepyramid islands with low aspect ratio and indistinct edges.

5. SUMMARY

The microstructures of semiconductor QDs, including shape, size, composition, and its distribution, have been widely investigated and the results vary from one system to another. Even within the same system, different authors obtain conflicting results. From this, it is clear that QD growth is highly sensitive to growth conditions; this sensitivity might best be explored by a careful combination of modelling and experiment.

GLOSSARY

Bandgap The energy gap between valence band and conduction band in semiconductor materials.

de Broglie wavelength The wave-like properties of matter can be related to its particle-like properties through $\lambda = h/p$, where h is Planck's constant, λ is called de Broglie wavelength, and p is the momentum.

Dome A solid shape that resembles a hemispherical structure.

Heteroepitaxial growth The growth of near perfect crystal layer/layers on a single crystal substrate in such a way that the crystalline structure of the substrate is preserved in the grown layer/layers. The material/materials grown on top of the substrate and the substrate itself are different materials.

Hut A solid shape with a rectangular base, two similar trapezoidal sides on the long edges of the base, and two similar triangular sides on the short edges of the base. The four sides slope to meet in a line at the top.

Ostwald ripening Large precipitates (islands, in our case) grow larger by consuming small precipitates. As a result of the ripening, the average precipitate size is increased at the expense of precipitate density.

Pyramid A solid shape with a square base and four triangular sides that slope to meet in a point.

Stranski–Krastanow (S–K) growth mode A heteroepitaxial growth mode in which layer-by-layer growth is followed by island growth.

REFERENCES

1. L. Esaki and R. Tsu, *IBM J. Res. & Dev.* 14, 61 (1970).
2. P. M. Petroff and G. Medeiros-Ribeiro, *MRS Bulletin* 21(4), 50 (1996).
3. C. J. Changhasnain, J. P. Harbison, C. E. Zah, M. W. Maeda, L. T. Florez, N. G. Stoffel, and T. P. Lee, *IEEE J. Quantum Electronics* 27, 1368 (1991).
4. A. O. Harm, *Philips J. Res.* 45, 177 (1990).
5. I. Pollentier, L. Buydens, P. Vandaele, and P. Demeester, *IEEE Photonics Technol. Lett.* 3, 115 (1991).
6. E. Kapon, D. M. Hwang, and R. Bhat, *Phys. Rev. Lett.* 63, 430 (1989).
7. R. Dettmer, *IEE Review* 34, 395 (1988).
8. J. N. Randall, M. A. Reed, R. J. Matyi, and T. M. Moore, *J. Vac. Sci. Technol. B* 6, 1861 (1988).
9. A. P. Alivisatos, *Science* 271, 933 (1996).
10. M. A. Kastner, *Phys. Today* 46, 24 (1993).
11. R. C. Ashoori, *Nature* 379, 413 (1996).
12. R. Leon, P. M. Petroff, D. Leonard, and S. Fafard, *Science* 267, 1966 (1995).
13. J.-Y. Marzin, J.-M. Gerard, A. Izraël, D. Barrier, and G. Bastard, *Phys. Rev. Lett.* 73, 716 (1994).
14. P. M. Petroff and S. P. Den Baars, *Superlatt. Microstruct.* 15, 15 (1994).
15. S. Fafard, R. Leon, D. Leonard, J. J. Merz, and P. M. Petroff, *Phys. Rev. B* 50, 8086 (1994).
16. Y. Arakawa and H. Sakaki, *Appl. Phys. Lett.* 40, 939 (1982).
17. N. Kirstaedter, N. N. Ledentsov, M. Grundmann, D. Bimberg, V. M. Ustinov, S. S. Ruvimov, M. V. Maximov, P. S. Kopev, Z. I. Alferov, and U. Richter, *Electron. Lett.* 30, 1416 (1994).
18. M. Grundmann, N. N. Ledentsov, N. Kirstaedter, F. Heinrichsdorff, A. Krost, D. Bimberg, A. O. Kosogov, S. S. Ruvimov, P. Werner, V. M. Ustinov, P. S. Kopev, and Z. I. Alferov, *Thin Solid Films* 318, 83 (1998).
19. Y. S. Tang, C. M. S. Torres, W. X. Ni, and G. V. Hansson, *Superlatt. Microstruct.* 20, 505 (1996).
20. G. S. Solomon, M. C. Larson, and J. S. Harris, *Appl. Phys. Lett.* 69, 1897 (1996).
21. I. Amlani, A. O. Orlov, G. Toth, G. H. Bernstein, C. S. Lent, and G. L. Snider, *Science* 284, 289 (1999).
22. F. H. Julien and A. Alexandrou, *Science* 282, 1429 (1998).
23. C. S. Lent, P. D. Tougaw, W. Porod, and G. H. Bernstein, *Nanotechnology* 4, 49 (1993).
24. D. J. Eaglesham and M. Cerullo, *Phys. Rev. Lett.* 64, 1943 (1990).
25. Y.-W. Mo, D. E. Savage, B. S. Swartzentruber, and M. G. Lagally, *Phys. Rev. Lett.* 65, 1020 (1990).
26. M. Sopanan, H. Lipsanen, and J. Ahopelto, *Appl. Phys. Lett.* 65, 1662 (1995).
27. H. X. Li, T. Daniels-Race, and Z. G. Wang, *Appl. Phys. Lett.* 74, 1388 (1999).
28. T. J. Goodwin, V. J. Leppert, S. H. Risbud, I. M. Kennedy, and H. W. H. Lee, *Appl. Phys. Lett.* 70, 3122 (1997).
29. G. Feuillet, B. Daudin, F. Widmann, J. L. Rouviere, and M. Arlery, *J. Crystal Growth* 190, 142 (1998).
30. M. Arlery, J. L. Rouviere, F. Widmann, B. Daudin, G. Feuillet, and H. Mariette, *Appl. Phys. Lett.* 74, 3287 (1999).
31. A. Petersson, A. Gustafsson, L. Samuelson, S. Tanaka, and Y. Aoyagi, *Appl. Phys. Lett.* 74, 3513 (1999).
32. C. B. Murray, D. J. Norris, and M. G. Bawendi, *J. Am. Chem. Soc.* 115, 8706 (1993).
33. A. A. Guzelian, J. E. B. Katari, A. V. Kadavanich, U. Banin, K. Hamad, E. Juban, A. P. Alivisatos, R. H. Wolters, C. C. Arnold, and J. R. Heath, *J. Phys. Chem.* 100, 7212 (1996).
34. A. I. Ekimov, A. L. Efros, and A. A. Onuschenko, *Solid State Comm.* 56, 921 (1985).
35. L. C. Liu and S. H. Risbud, *J. Appl. Phys.* 68, 28 (1990).

36. N. F. Borelli, D. W. Hall, H. J. Holland, and D. W. Smith, *J. Appl. Phys.* 61, 5399 (1987).
37. U. Woggon, M. Müller, U. Lembke, I. Rückmann, and J. Cesa-nulovicus, *Superlatt. Microstruct.* 9, 245 (1991).
38. M. A. Olshavsky, A. N. Goldstein, and A. P. Alivisatos, *J. Am. Chem. Soc.* 112, 9438 (1990).
39. T. Douglas and K. H. Theopold, *Inorg. Chem.* 30, 594 (1991).
40. O. I. Micic and A. J. Nozik, *J. Lumin.* 70, 95 (1996).
41. U. Banin, G. Cerullo, A. A. Guzelian, C. J. Bardeen, A. P. Alivisatos, and C. V. Shank, *Phys. Rev. B* 55, 7059 (1997).
42. A. A. Guzelian, U. Banin, A. V. Kadavanich, X. Peng, and A. P. Alivisatos, *Appl. Phys. Lett.* 69, 1432 (1996).
43. H. F. Hess, E. Betzig, T. D. Harris, L. N. Pfeiffer, and K. W. West, *Science* 264, 1740 (1994).
44. D. Gammon, E. S. Snow, and D. S. Katzer, *Phys. Rev. Lett.* 67, 2391 (1995).
45. D. Gammon, E. S. Snow, and D. S. Katzer, *Surf. Sci.* 362, 814 (1996).
46. T. Tsuzuki and P. G. McCormick, *Appl. Phys. A* 65, 607 (1997).
47. P. N. H. Nakashima, T. Tsuzuki, and A. W. S. Johnson, *J. Appl. Phys.* 85, 1556 (1999).
48. S. Tarucha, D. G. Austing, T. Honda, R. J. Vanderhage, and L. P. Kouwenhoven, *Phys. Rev. Lett.* 77, 3613 (1996).
49. A. Forchel, H. Leier, B. E. Maile, and R. Germann, *Festkörperprobleme (Advances in Solid State Physics)* 28, 99 (1988).
50. M. A. Reed, J. N. Randall, R. J. Aggarwal, R. J. Matyi, T. M. Moore, and A. E. Wetsel, *Phys. Rev. Lett.* 60, 535 (1988).
51. M. A. Reed, *Scientific American* (January), 118 (1993).
52. M. A. Kastner, *Physics Today* 46 (1), 24 (1993).
53. C. Pryor, *Phys. Rev. B* 60, 2869 (1999).
54. R. Leon, Y. Kim, C. Jagadish, M. Gal, J. Zou, and D. J. H. Cockayne, *Appl. Phys. Lett.* 69, 1888 (1996).
55. H. Jiang and J. Singh, *Phys. Rev. B* 56, 4696 (1997).
56. R. Leon, S. Fafard, D. Leonard, J. L. Merz, and P. M. Petroff, *Appl. Phys. Lett.* 67, 521 (1995).
57. J. L. Zhu, Z. Q. Li, J. Z. Yu, K. Ohno, and Y. Kawazoe, *Phys. Rev. B* 55, 15819 (1997).
58. A. Zunger, *MRS Bull.* 23(2), 35 (1998), and references therein.
59. H. T. Johnson, L. B. Freund, C. D. Akyuz, and A. Zaslavsky, *J. Appl. Phys.* 84, 3714 (1998).
60. R. Heitz, O. Stier, I. Mukhametzhanov, A. Madhukar, and D. Bimberg, *Phys. Rev. B* 62, 11017 (2000).
61. Y. M. Li, O. Voskoboynikov, C. P. Lee, S. M. Sze, and O. Tretyak, *J. Appl. Phys.* 90, 6416 (2001).
62. W. D. Sheng and J. P. Leburton, *Phys. Rev. B* 63, 161301 (2001).
63. V. M. Ustinov, N. A. Maleev, A. E. Zhukov, A. R. Kovsh, A. Yu. Egorov, A. V. Lunev, B. V. Volovik, I. L. Krestnikov, Yu. G. Musikhin, N. A. Bert, P. S. Kop'ev, Zh. I. Alferov, N. N. Ledentsov, and D. Bimberg, *Appl. Phys. Lett.* 74, 2815 (1999).
64. A. E. Zhukov, V. M. Ustinov, A. R. Kovsh, A. Y. Egorov, N. A. Maleev, N. N. Ledentsov, A. F. Tsatsulnikov, M. V. Maximov, Y. G. Musikhin, N. A. Bert, *Semicond. Sci. Technol.* 14, 575 (1999).
65. M. A. Cusack, P. R. Briddon, and M. Jaros, *Phys. Rev. B* 56, 4047 (1997).
66. J. Y. Marzin and G. Bastard, *Solid State Commun.* 92, 437 (1994).
67. C. Pryor, *Phys. Rev. B* 57, 7190 (1998).
68. M. Grundmann, O. Stier, and D. Bimberg, *Phys. Rev. B* 52, 11969 (1995).
69. M. A. Cusack, P. R. Bridden, and M. Jaros, *Phys. Rev. B* 54, R2300 (1996).
70. A. Wojs, P. Hawrylak, S. Fafard, and L. Jacak, *Phys. Rev. B* 54, 5604 (1996).
71. H. X. Li, T. Daniels-Race, and M. A. Hasan, *Appl. Phys. Lett.* 80, 1367 (2002).
72. L. González, J. M. García, R. García, F. Briones, and J. Martínez-Pastor, *Appl. Phys. Lett.* 76, 1104 (2000).
73. C. Lobo and R. Leon, *J. Appl. Phys.* 83, 4168 (1998).
74. C. M. Reaves, R. I. Pelzel, G. C. Hsueh, W. H. Weinberg, and S. P. DenBaars, *Appl. Phys. Lett.* 69, 3878 (1996).
75. R. Jonczyk, D. A. Hits, L. V. Kulik, J. Kolodzey, M. Kaba, and M. A. Barteau, *J. Vac. Sci. Technol. B* 16, 1142 (1998).
76. H. Saito, K. Nishi, and S. Sugou, *Appl. Phys. Lett.* 74, 1224 (1999).
77. A. Stintz, G. T. Liu, A. L. Gray, R. Spillers, S. M. Delgado, and K. J. Malloy, *J. Vac. Sci. Technol. B* 18, 1496 (2000).
78. W. Q. Ma, R. Nötzel, H. P. Schönherr, and K. H. Ploog, *Appl. Phys. Lett.* 79, 4219 (2001).
79. N. N. Ledentsov, V. A. Shchukin, D. Bimberg, V. M. Ustinov, N. A. Cherkashin, Y. G. Musikhin, B. V. Volovik, G. E. Cirlin, and Z. I. Alferov, *Semicond. Sci. Technol.* 16, 502 (2001).
80. A. Raab and G. Springholz, *Appl. Phys. Lett.* 81, 2457 (2002).
81. J. Johansson and W. Seifert, *Appl. Surf. Sci.* 148, 86 (1999).
82. J. Johansson and W. Seifert, *J. Crystal Growth* 234, 132 (2002).
83. J. Johansson and W. Seifert, *J. Crystal Growth* 234, 139 (2002).
84. J. Brault, M. Gendry, G. Grenet, G. Hollinger, J. Olivares, B. Salem, T. Benyattou, and G. Bremond, *J. Appl. Phys.* 92, 506 (2002).
85. J. Johansson and W. Seifert, *Appl. Surf. Sci.* 148, 86 (1999).
86. P. B. Joyce, T. J. Krzyzewski, G. R. Bell, T. S. Jones, S. Malik, D. Childs, and R. Murray, *Phys. Rev. B* 62, 10891 (2000).
87. P. B. Joyce, T. J. Krzyzewski, G. R. Bell, T. S. Jones, S. Malik, D. Childs, and R. Murray, *J. Crystal Growth* 227–228, 1000 (2001).
88. G. Medeiros-Ribeiro, A. M. Bratkovski, T. I. Kamins, D. A. A. Ohlberg, and R. S. Williams, *Science* 279, 353 (1998).
89. K. M. Chen, D. E. Jesson, S. J. Pennycook, T. Thundat, and R. J. Warmack, *Phys. Rev. B* 56, R1700 (1997).
90. J. A. Floro, E. Chason, R. D. Twesten, R. Q. Hwang, and L. B. Freund, *Phys. Rev. Lett.* 79, 3946 (1997).
91. M. Kästner and B. Voigtländer, *Phys. Rev. Lett.* 82, 2745 (1999).
92. A. J. Steinfurt, P. M. L. O. Scholte, A. Ettema, F. Tuinstra, M. Nielsen, E. Landemark, D. M. Smilgies, R. Feidenhansl, and G. Falkenberg, *Phys. Rev. Lett.* 77, 2009 (1996).
93. T. I. Kamins, E. C. Carr, R. S. Williams, and S. J. Rosner, *J. Appl. Phys.* 81, 211 (1997).
94. M. Kästner and B. Voigtländer, *Phys. Rev. Lett.* 82, 2745 (1999).
95. G. Medeiros-Ribeiro, T. I. Kamins, D. A. A. Ohlberg, and R. S. Williams, *Phys. Rev. B* 58, 3533 (1998).
96. J. Tersoff and R. M. Tromp, *Phys. Rev. Lett.* 70, 2782 (1993).
97. T. I. Kamins, G. Medeiros-Ribeiro, D. A. A. Ohlberg, and R. S. Williams, *Appl. Phys. A* 67, 727 (1998).
98. F. M. Ross, R. M. Tromp, and M. C. Reuter, *Science* 286, 1931 (1999).
99. F. M. Ross, J. Tersoff, and R. M. Tromp, *Phys. Rev. Lett.* 80, 984 (1998).
100. W. Ostward, *Z. Phys. Chem.* 34, 495 (1900).
101. A. Rastelli, M. Kummer, and H. van Känel, *Phys. Rev. Lett.* 87, 256101 (2001).
102. A. Rastelli, M. Kummer, and H. van Känel, *Physica E* 13, 1008 (2002).
103. X. Wang, Z. M. Jiang, H. J. Zhu, F. Lu, D. M. Huang, X. H. Liu, C. W. Hu, Y. F. Chen, Z. Q. Zhu, and T. Yao, *Appl. Phys. Lett.* 71, 3543 (1997).
104. J. Drucker, *Phys. Rev. B* 48, 18203 (1993).
105. R. Leon, C. Lobo, J. Zou, T. Romeo, and D. J. H. Cockayne, *Phys. Rev. Lett.* 81, 2486 (1998).
106. K. Yamaguchi, K. Yujobo, and T. Kaizu, *Jpn. J. Appl. Phys.* 39, L1245 (2000).
107. Y. Chen and J. Washburn, *Phys. Rev. Lett.* 77, 4046 (1996).
108. Y. W. Zhang, *Phys. Rev. B* 61, 10388 (2000).
109. C. Rottman and M. Wortis, *Phys. Rev. B* 24, 6274 (1981).
110. Z. Gai, R. G. Zhao, H. Ji, X. Li, and W. S. Yang, *Phys. Rev. B* 56, 12308 (1997).
111. C. S. Ozkan, W. D. Nix, and H. J. Gao, *Appl. Phys. Lett.* 70, 2247 (1997).

112. J. A. Floro, E. Chason, M. B. Sinclair, L. B. Freund, and G. A. Lucadamo, *Appl. Phys. Lett.* 73, 951 (1998).
113. P. O. Hansson, M. Albrecht, H. P. Strunk, E. Bauser, and J. H. Werner, *Thin Solid Films* 216, 199 (1992).
114. M. Albrecht, P. O. Hansson, S. Christiansen, W. Dorsch, H. P. Strunk, and E. Bauser, *Scanning Microscopy* 8, 925 (1994).
115. M. Schmidbauer, Th. Wiebach, H. Raidt, M. Hanke, and R. Köhler, *Phys. Rev. B* 58, 10523 (1998).
116. J. Groenen, R. Carles, S. Christiansen, M. Albrecht, W. Dorsch, H. P. Strunk, H. Wawra, and G. Wagner, *Appl. Phys. Lett.* 71, 3856 (1997).
117. C. Tatsuyama, T. Terasaki, H. Obata, T. Tanbo, and H. Ueba, *J. Crystal Growth* 115, 112 (1991).
118. Y. Koide, S. Zaima, N. Oshima, and Y. Yasuda, *Jpn. J. Appl. Phys.* 28, L690 (1989).
119. M. Tomitori, K. Watanabe, M. Kobayashi, and O. Nishikawa, *Appl. Surf. Sci.* 76/77, 322 (1994).
120. M. Horn-von Hoegen, A. Al-Falou, B. H. Muller, U. Kohler, L. Andersohn, B. Dahlheimer, and M. Henzler, *Phys. Rev. B* 49, 2637 (1994).
121. S. Ruvimov, P. Werner, K. Scheerschmidt, U. Gosele, J. Heydenreich, U. Richter, N. N. Ledentsov, M. Grundmann, D. Bimberg, and V. M. Ustinov, *Phys. Rev. B* 51, 14766 (1995).
122. K. Mukai, N. Ohtsuka, and M. Sugawara, *Jpn. J. Appl. Phys. Part 2-Lett.* 35, L262 (1996).
123. X. Z. Liao, J. Zou, X. F. Duan, D. J. H. Cockayne, R. Leon, and C. Lobo, *Phys. Rev. B* 59, R4235 (1998).
124. J. Zou, X. Z. Liao, D. J. H. Cockayne, and R. Leon, *Phys. Rev. B* 59, 12279 (1999).
125. S. Yoon, Y. Moon, T. W. Lee, H. Hwang, E. Yoon, and Y. D. Kim, *Thin Solid Films* 357, 81 (1999).
126. H. Lee, R. Lowe-Webb, W. Yang, and P. C. Sercel, *Appl. Phys. Lett.* 72, 812 (1998).
127. H. Lee, W. D. Yang, P. C. Sercel, and A. G. Norman, *J. Electron. Mater.* 28, 481 (1999).
128. T. Kaizu and K. Yamaguchi, *Jpn. J. Appl. Phys.* 40, 1885 (2001).
129. Y. Nabetani, T. Ishikawa, S. Noda, and A. Sasaki, *J. Appl. Phys.* 76, 347 (1994).
130. J. Márquez, L. Geelhaar, and K. Jacobi, *Appl. Phys. Lett.* 78, 2309 (2001).
131. K. Zhang, Ch. Heyn, W. Hansen, Th. Schmidt, and J. Falta, *J. Crystal Growth* 227–228, 1020 (2001).
132. S. Anders, C. S. Kim, B. Klein, M. W. Keller, R. P. Mirin, and A. G. Norman, *Phys. Rev. B* 66, 125309 (2002).
133. N. Moll, M. Scheffler, and E. Pehlke, *Phys. Rev. B* 58, 4566 (1998).
134. K. Georgsson, N. Carlsson, L. Samuelson, W. Seifert, and L. R. Wallenberg, *Appl. Phys. Lett.* 67, 2981 (1995).
135. Q. K. K. Liu, N. Moll, M. Scheffler, and E. Pehlke, *Phys. Rev. B* 60, 17008 (1999).
136. M. Arlery, J. L. Rouvière, F. Widmann, B. Daudin, G. Feuillet, and H. Mariette, *Appl. Phys. Lett.* 74, 3287 (1999).
137. F. Widmann, J. Simon, B. Daudin, G. Feuillet, J. L. Rouvière, N. T. Pelekanos, and G. Fishman, *Phys. Rev. B* 58, R15989 (1998).
138. B. Daudin, F. Widmann, G. Feuillet, Y. Samson, M. Arlery, and J. L. Rouvière, *Phys. Rev. B* 56, R7069 (1997).
139. F. Widmann, B. Daudin, G. Feuillet, Y. Samson, J. L. Rouvière, and N. Pelekanos, *J. Appl. Phys.* 83, 7618 (1998).
140. B. Daudin, G. Feuillet, H. Mariette, G. Mula, N. Pelekanos, E. Molva, J. L. Rouvière, C. Adelman, E. Martinez-Guerrero, J. Barjon, F. Chabuel, B. Bataillou, and J. Simon, *Jpn. J. Appl. Phys.* 40, 1892 (2001).
141. S. H. Xin, P. D. Wang, A. Yin, C. Kim, M. Dobrovolska, J. L. Merz, and J. K. Furdyna, *Appl. Phys. Lett.* 69, 3884 (1996).
142. D. Hommel, K. Leonardi, H. Heinke, H. Selke, K. Ohkawa, F. Gindele, and U. Woggon, *Phys. Stat. Solid. B* 202, 835 (1997).
143. F. Flack, N. Samarth, V. Nikitin, P. A. Crowell, J. Shi, J. Levy, and D. D. Awschalom, *Phys. Rev. B* 54, 17312 (1996).
144. Y. Kuroda, I. Suemune, Y. Fujii, and M. Fujimoto, *Appl. Phys. Lett.* 61, 1182 (1992).
145. M. Arita, A. Avramescu, K. Uesugi, I. Suemune, T. Numai, H. Machida, and N. Shimoyama, *Jpn. J. Appl. Phys.* 36, 4097 (1997).
146. K. Maehashi, N. Yasui, T. Ota, T. Noma, Y. Murase, and H. Nakashima, *J. Crystal Growth* 227–228, 1116 (2001).
147. R. Nötzel, T. Fukui, H. Hasegawa, J. Temmyo, and T. Tamamura, *Appl. Phys. Lett.* 65, 2854 (1994).
148. Y. Yamaguchi, M. R. Fahy, and B. A. Joyce, *Appl. Phys. Lett.* 69, 776 (1996).
149. B. A. Joyce, J. L. Sudijono, J. G. Belk, H. Yamaguchi, X. M. Zhang, H. T. Dobbs, A. Zangwill, D. D. Vvedensky, and T. S. Jones, *Jpn. J. Appl. Phys.* 36, 4111 (1997).
150. R. Nötzel, J. Temmyo, and T. Tamamura, *Nature* 369, 131 (1994).
151. D. Lacombe, A. Ponchet, S. Fréchengues, V. Drouot, N. Bertru, B. Lambert, and A. Le Corre, *Appl. Phys. Lett.* 74, 1680 (1999).
152. T. Suzuki, Y. Temko, and K. Jacobi, *Appl. Phys. Lett.* 80, 4744 (2002).
153. D. Lacombe, A. Ponchet, S. Fréchengues, V. Drouot, N. Bertru, B. Lambert, and A. Le Corre, *J. Crystal Growth* 201/202, 252 (1999).
154. H. Omi and T. Ogino, *Appl. Phys. Lett.* 71, 2163 (1997).
155. H. Omi and T. Ogino, *Phys. Rev. B* 59, 7521 (1999).
156. J. H. Zhu, C. Miesner, K. Brunner, and G. Abstreiter, *Appl. Phys. Lett.* 75, 2395 (1999).
157. M. Floyd, Y. T. Zhang, J. Drucker, D. J. Smith, S. Tari, and S. Sivananthan, *Appl. Phys. Lett.* 79, 4518 (2001).
158. N. Motta, *J. Phys.* 14, 8353 (2002).
159. G. Capellini, N. Motta, A. Sgarlata, and R. Calarco, *Solid State Commun.* 112, 145 (1999).
160. F. K. LeGoues, M. Hammar, M. C. Reuter, and R. M. Tromp, *Surf. Sci.* 349, 249 (1996).
161. I. Daruka and A.-L. Barabási, *Phys. Rev. Lett.* 79, 3708 (1997).
162. B. J. Spencer and J. Tersoff, *Phys. Rev. Lett.* 79, 4858 (1997).
163. J. M. Moison, F. Houzay, F. Barthe, L. Leprince, E. Andre, and O. Vatel, *Appl. Phys. Lett.* 64, 196 (1994).
164. D. Leonard, K. Pond, and P. M. Petroff, *Phys. Rev. B* 50, 11687 (1994).
165. D. Leonard, M. Krishnamurthy, C. M. Reaves, S. P. Den Baars, and P. M. Petroff, *Appl. Phys. Lett.* 63, 3203 (1993).
166. N. P. Kobayashi, T. R. Ramachandran, P. Chen, and A. Madhukar, *Appl. Phys. Lett.* 68, 3299 (1996).
167. M. Grundmann, J. Christen, N. N. Ledentsov, J. Böhrer, D. Bimberg, S. S. Ruvimov, P. Werner, U. Richter, U. Gösele, J. Heydenreich, V. M. Ustinov, A. Yu. Egorov, A. E. Zhukov, P. S. Kop'ev, and Zh. I. Alferov, *Phys. Rev. Lett.* 74, 4043 (1995).
168. N. N. Ledentsov, P. D. Wang, C. M. Sotomayor Torres, A. Yu Egorov, M. V. Maximov, V. M. Ustinov, A. E. Zhukov, and P. S. Kop'ev, *Phys. Rev. B* 50, 12171 (1994).
169. A. L. Barabási, *Appl. Phys. Lett.* 70, 2565 (1997).
170. V. A. Shchukin, N. N. Ledentsov, P. S. Kop'ev, and D. Bimberg, *Phys. Rev. Lett.* 75, 2968 (1995).
171. D. E. Jesson, G. Chen, K. M. Chen, and S. J. Pennycook, *Phys. Rev. Lett.* 80, 5156 (1998).
172. I. Daruka and A.-L. Barabási, *Appl. Phys. Lett.* 72, 2102 (1998).
173. J. Drucker and S. Chaparro, *Appl. Phys. Lett.* 71, 614 (1997).
174. M. Meixner, E. Schöll, V. A. Shchukin, and D. Bimberg, *Phys. Rev. Lett.* 87, 236101 (2001).
175. L. G. Wang, P. Kratzer, N. Moll, and M. Scheffler, *Phys. Rev. B* 62, 1897 (2000).
176. K. Nishi, R. Mirin, D. Leonard, G. Medeiros-Ribeiro, P. M. Petroff, and A. C. Gossard, *J. Appl. Phys.* 80, 3466 (1996).
177. A. Vailionis, B. Cho, G. Glass, P. Desjardins, D. G. Cahill, and J. E. Greene, *Phys. Rev. Lett.* 85, 3672 (2000).
178. V. L. Thanh, P. Boucaud, D. Débarre, Y. Zheng, D. Bouchier, and J.-M. Lourtioz, *Phys. Rev. B* 58, 13115 (1998).

179. J. A. Floro, G. A. Lucadamo, E. Chason, L. B. Freund, M. Sinclair, R. D. Twosten, and R. Q. Hwang, *Phys. Rev. Lett.* 80, 4717 (1998).
180. I. Daruka, J. Tersoff, and A.-L. Barabási, *Phys. Rev. Lett.* 82, 2753 (1999).
181. I. Goldfarb, P. T. Hayden, J. H. G. Owen, and G. A. D. Briggs, *Phys. Rev. B* 56, 10459 (1997).
182. I. Goldfarb, P. T. Hayden, J. H. G. Owen, and G. A. D. Briggs, *Phys. Lett.* 20, 3959 (1997).
183. I. Goldfarb and G. A. D. Briggs, *J. Crystal Growth* 198/9, 1932 (1999).
184. E. Mateeva, P. Sutter, J. C. Bean, and M. G. Lagally, *Appl. Phys. Lett.* 71, 3233 (1997).
185. A. Hesse, J. Stangl, V. Holy, T. Roch, G. Bauer, O. G. Schmidt, U. Denker, and B. Struth, *Phys. Rev. B* 66, 085321 (2002).
186. J. M. García, G. Medeiros-Ribeiro, K. Schmidt, T. Ngo, J. L. Feng, A. Lorke, J. Kotthaus, and P. M. Petroff, *Appl. Phys. Lett.* 71, 2041 (1997).
187. A. Rosenauer, W. Oberst, D. Litvinov, and Gerthsen, *Phys. Rev. B* 61, 8276 (2000).
188. P. Sutter and M. G. Lagally, *Phys. Rev. Lett.* 81, 3471 (1998).
189. A. Hesse, J. Stangl, V. Holy, T. Roch, G. Bauer, O. G. Schmidt, U. Denker, and B. Struth, *Phys. Rev. B* 66, 085321 (2002).
190. P. B. Joyce, T. J. Krzyzewski, P. H. Steans, G. R. Bell, J. H. Neave, and T. S. Jones, *Surf. Sci.* 492, 345 (2001).
191. G. D. Lian, J. Yuan, L. M. Brown, G. H. Kim, and D. A. Ritchie, *Appl. Phys. Lett.* 73, 49 (1998).
192. O. Brandt, K. Ploog, L. Tapfer, M. Hohenstein, R. Bierwolf, and F. Phillipp, *Phys. Rev. B* 45, 8443 (1992).
193. T. Yamauchi, Y. Ohyama, Y. Matsuba, M. Tabuchi, and A. Nakamura, *Phys. Rev. Lett.* 79, 2465 (2001).
194. J. Tersoff, *Phys. Rev. Lett.* 81, 3183 (1998).
195. X. Z. Liao, J. Zou, D. J. H. Cockayne, R. Leon, and C. Lobo, *Phys. Rev. Lett.* 82, 5148 (1999).
196. T. Walther, A. G. Cullis, D. J. Norris, and M. Hopkinson, *Phys. Rev. Lett.* 86, 2381 (2001).
197. A. Krost, J. Bläsing, F. Heinrichsdorff, and D. Bimberg, *Appl. Phys. Lett.* 75, 2957 (1999).
198. P. A. Crozier, M. Catalano, R. Cingolani, and A. Passaseo, *Appl. Phys. Lett.* 79, 3170 (2001).
199. X. Z. Liao, J. Zou, D. J. H. Cockayne, J. Wan, Z. M. Jiang, G. Jin, and K. L. Wang, *Phys. Rev. B* 65, 153306 (2002).
200. F. Boscherini, G. Capellini, L. Di Gaspare, F. Rosei, N. Motta, and S. Mobilio, *Appl. Phys. Lett.* 76, 682 (2000).
201. M. O. Lipinski, H. Schuler, O. G. Schmidt, K. Eberl, and N. Y. Jin-Phillipp, *Appl. Phys. Lett.* 77, 1789 (2000).
202. F. Boscherini, G. Capellini, L. Di Gaspare, F. Rosei, N. Motta, and S. Mobilio, *Appl. Phys. Lett.* 76, 682 (2000).
203. G. Capellini, M. De Seta, and F. Evangelisti, *Appl. Phys. Lett.* 78, 303 (2001).
204. M. De Seta, G. Capellini, F. Evangelisti, and C. Spinella, *J. Appl. Phys.* 92, 614 (2002).
205. P. B. Joyce, T. J. Krzyzewski, G. R. Bell, B. A. Joyce, and T. S. Jones, *Phys. Rev. B* 58, R15981 (1998).
206. K. Nakajima, A. Konishi, and K. Kimura, *Phys. Rev. Lett.* 83, 1802 (1999).
207. S. A. Chaparro, J. Drucker, Y. Zhang, D. Chandrasekhar, M. R. McCartney, and D. J. Smith, *Phys. Rev. Lett.* 83, 1199 (1999).
208. X. Z. Liao, J. Zou, D. J. H. Cockayne, Z. M. Jiang, and X. Wang, *J. Appl. Phys.* 90, 2725 (2001).
209. X. Z. Liao, J. Zou, D. J. H. Cockayne, and S. Matsumura, *Ultramicroscopy*, submitted.
210. S. Kret, T. Benabbas, C. Delamarre, Y. Androussi, A. Dubon, J. Y. Laval, and A. Lefebvre, *J. Appl. Phys.* 86, 1988 (1999).
211. D. Litvinov, A. Rosenauer, D. Gerthsen, and N. N. Ledentsov, *Phys. Rev. B* 61, 16819 (2000).
212. A. Rosenauer, D. Gerthsen, D. Van Dyck, M. Arzberger, G. Böhm, and G. Abstreiter, *Phys. Rev. B* 64, 245334 (2001).
213. D. M. Bruls, J. W. A. M. Vugs, P. M. Koenraad, H. W. M. Salemink, J. H. Wolter, M. Hopkinson, M. S. Skolnick, F. Long, and S. P. A. Gill, *Appl. Phys. Lett.* 81, 1708 (2002).
214. K. Tillmann, A. Thust, M. Lentzen, P. Swiatek, A. Forster, K. Urban, W. Laufs, D. Gerthsen, T. Remmele, and A. Rosenauer, *Philos. Mag. Lett.* 74, 309 (1996).
215. A. Rosenauer, U. Fischer, D. Gerthsen, and A. Förster, *Appl. Phys. Lett.* 71, 3868 (1997).
216. J. Stangl, A. Daniel, V. Holy, T. Roch, G. Bauer, I. Kegel, T. H. Metzger, Th. Wiebach, O. G. Schmidt, and K. Eberl, *Appl. Phys. Lett.* 79, 1474 (2001).
217. I. Kegel, T. H. Metzger, A. Lorke, J. Peisl, J. Stangl, G. Bauer, J. M. García, and P. M. Petroff, *Phys. Rev. Lett.* 85, 1694 (2000).
218. T. Walther, C. J. Humphreys, and A. G. Cullis, *Appl. Phys. Lett.* 71, 809 (1997).
219. P. Venezuela and J. Tersoff, *Phys. Rev. B* 58, 10871 (1998).
220. J. A. Floro, E. Chason, L. B. Freund, R. D. Twosten, R. Q. Hwang, and G. A. Lucadamo, *Phys. Rev. B* 59, 1990 (1999).
221. G. Saint-Girons, G. Patriarche, L. Largeau, J. Coelho, A. Mereuta, J. M. Moison, J. M. Gerard, and I. Sagnes, *Appl. Phys. Lett.* 79, 2157 (2001).
222. I. N. Stranski and Von L. Krastanow, *Akad. Wiss. Lit. Mainz Math.-Natur. Kl. Iib* 146, 7979 (1939).
223. R. Leon, C. Lobo, T. P. Chin, J. M. Woodall, S. Fafard, S. Ruvimov, Z. Liliental-Weber, and M. A. Stevens Kalceff, *Appl. Phys. Lett.* 72, 1356 (1998).
224. P. Finnie and Y. Homma, *Phys. Rev. B* 59, 15240 (1999).
225. M. C. Kuo, C. S. Yang, P. Y. Tseng, J. Lee, J. L. Shen, W. C. Chou, Y. T. Shih, C. T. Ku, M. C. Lee, and W. K. Chen, *J. Crystal Growth* 242, 533 (2002).
226. M. C. H. Liao, Y. H. Chang, Y. F. Chen, J. W. Hsu, J. M. Lin, and W. C. Chou, *Appl. Phys. Lett.* 70, 2256 (1997).
227. M. Volmer and A. Weber, *Z. Phys. Chem.* 119, 277 (1926).
228. M. Hammar, F. K. Legoues, J. Tersoff, M. C. Reuter, and R. M. Tromp, *Surf. Sci.* 349, 129 (1996).
229. X. Z. Liao, J. Zou, D. J. H. Cockayne, J. Qin, Z. M. Jiang, X. Wang, and R. Leon, *Phys. Rev. B* 60, 15605 (1999).
230. X. Z. Liao, J. Zou, D. J. H. Cockayne, Z. M. Jiang, X. Wang, and R. Leon, *Appl. Phys. Lett.* 77, 1304 (2000).
231. P. Sutter and M. G. Lagally, *Phys. Rev. Lett.* 84, 4637 (2000).
232. R. M. Tromp, F. M. Ross, and M. C. Reuter, *Phys. Rev. Lett.* 84, 4641 (2000).
233. J. Tersoff, B. J. Spencer, A. Rastelli, and H. von Känel, *Phys. Rev. Lett.* 89, 196104 (2002).

Superhard Nanocomposites

Gregory M. Demyashev, Alexander L. Taube, Elias Siores

Swinburne University of Technology, Hawthorn, Melbourne, Australia

CONTENTS

1. Introduction
2. Strengthening of Nanocomposites
3. State-of-the-Art Superhard Nanocomposites
4. Synthesis of Superhard Nanocomposites
5. Nanostructure Evaluation
6. Superhardness Testing
7. Applications of Superhard Nanocomposites
8. Conclusion
9. Milestones in Superhard Nanocomposites
 - Glossary
 - References

1. INTRODUCTION

Superhard nanocomposites in the form of coatings are a novel class of materials, which have a great potential for a variety of applications. The high hardness of the nanocomposites distinguishes them from microcrystalline and amorphous materials of the same composition. For example, the nanocrystalline coatings of nc-TiN/a-Si₃N₄/nc-TiSi₂/a-TiSi₂ (nc, nanocrystalline state; a, amorphous state) display a very high hardness (up to 105 GPa [1]) although the hardness is only up to 25 GPa [2, 3] if every component is taken separately as a coarse-grained material. Consequently, it is possible to create purposely artificial nanocomposites having a total hardness that significantly exceeds the hardness of the individual components.

Recently, the search for superhard materials has been pointed in a few directions:

- Novel superhard phases, such as predicted superhard carbon nitride (β -C₃N₄) [4–11], hypothetical superhard carbon with a rigid three-dimensional network of sp² hybridization [12–14], hard graphitic-like structures [15, 16], carbon nanotubes [17], super diamond [18, 19], insufficiently explored carbynes [20–23], new possible phases of three-dimensional (3D) C₆₀-based fullerites [24–26], transition-metal dioxides containing

heavy elements [27, 28], superhard boron suboxides [29], superhard cubic BC₂N [30–34], ultrahard MgAlB₁₄ phase based on boron icosahedra [35], nonmolecular polymeric CO₂ solid [36, 37], new spinel-type phase of Ti₃N₄ and SiTi₂N₄ [38], C₆₀ compounds (one- and two-dimensional polymers) [39–44], novel W₃C phase [21, 45], and so on

- Nanocrystallization of hard and superhard materials (e.g., nanodiamond [46–118], diamond-like carbon [119–127], carbon nitride [128–133], c-BN [134–144], B₄C [145–149], silicon nitride [150–155], silicon carbide [156, 157], chromium nitride [158], titanium nitride [159]), trying to obtain their nanostructured state
- Development of artificial superhard nanocomposites, the superhardness of which is solely defined by their optimal nanostructure and composition

In this review, attention is focused on artificial superhard nanocomposites in the form of coatings with hardness higher than 35–40 GPa. The aim of the review is the state of the art in artificial superhard nanocomposites that demonstrate a significant enhancement of their hardness owing to a nanostructured state. A few comprehensive reviews and general papers about the artificial superhard nanocomposites have been published [160–175].

1.1. Nanostructured State

The essential defects of both nanostructured and microcrystalline materials are the intergrain boundaries, which are the junctions between monocrystalline regions in one-phase materials and interphase boundaries in multiphase materials. Side by side with stacking faults and twin boundaries, the intergrain/interphase boundaries are classified as two-dimensional (or planar) defects of the crystal structure. The density of the boundaries in nanocomposites can reach 10¹⁹ cm⁻³ [176]. The high density of the boundaries transforms a microcrystalline structure, which has grain sizes on the micrometer scale, into a new type of structure, the so-called nanostructured materials [177–182], which represent a certain “symbiosis” of the crystal structure and the

planar defects in the form of intergrain/interphase boundaries. Such coexistence of a crystal structure and its planar defects usually results in phenomenal properties, which are radically different from microcrystalline and amorphous materials of the same composition.

The properties of nanocomposites can be changed into either their strengthening such as diffusivity, toughness, and hardness [183] or their slackening such as density and thermoconductivity [183, 184] in comparison with coarse-grained materials of the same composition. Modeling and prediction of the functional properties of nanocomposites is a very important issue as well [185–190]. For example, tantalum carbide and hafnium nitride of NaCl-type structure with stoichiometry of $\text{TaC}_{0.85}$ and $\text{HfN}_{0.75}$ have a hardness of 12 GPa and 16 GPa, respectively. However, close-packed phases of the same stoichiometry, that is, $\xi\text{-Ta}_4\text{C}_3$ and $\xi\text{-Hf}_4\text{N}_3$, have a hardness of approximately 1 GPa and 8 GPa, respectively [191]. The point is that stacking faults are inherent elements of the $\xi\text{-Ta}_4\text{C}_3$ and $\xi\text{-Hf}_4\text{N}_3$ crystal lattices [192–195], that is, three stacking faults per unit cell [192]. The well-ordered stacking faults drastically change the physical properties of such materials [196].

To obtain the nanostructured state, the dimensions of the morphological elements (i.e., the average diameter of grains, thickness of layers, etc.), which form the nanostructured state [176, 179, 180, 197–202], should be within the nanoscale range. The nanoscale sizes of the morphological elements usually cover the range between 2 and 100 nm ($1 \text{ nm} = 10^{-9} \text{ m}$).

As is well known [197, 203–209], when the sizes of the morphological elements become comparable with the characteristic distances related to appropriate physical phenomena (e.g., short-circuit diffusion paths, size of magnetic domains, the effective carrier de Broglie wavelength, Bohr radii of the excitonic states, the electron/photon mean free path, dimensions of defects, a wavelength of light, the superconducting coherence length, etc.), the physical phenomena manifest themselves in nanoscale sizes and the corresponding anomalous features of the nanocomposites may be revealed, for example, diffusion processes [210–216], electrical resistivity [217–219], specific heat [220, 221], thermal expansion [222], optical transparency [197], magnetic properties [177, 223–232], superconductivity [233–235], the group velocities of acoustic phonons [236], laser middle-infrared emission [237, 238], resonant tunneling [239], critical fields/currents in superconductors [240], change in color [241], a solid solubility [242, 243], thermal conductivity [244–246], optical absorption spectra [247, 248], nanosize-dependent luminescence [249, 250], metastable phase formation [251, 252], corrosion resistance [253–255], mechanical properties [256–263] increasing in hardness particularly, and so on. As to coatings with high hardness, when the grain/layer sizes, core of dislocation, sizes of dislocation sources, and boundary thickness become comparable with each other on a nanometer scale, some nanostructured coatings exhibit intriguing high hardness [1]. This brief enumeration demonstrates the variety of properties that depend on morphological elements when they reach nanoscale sizes.

In nature, some living organisms reveal the ability to reproduce hybrid organic–inorganic nanocomposites in the form of shells containing inorganic nanocrystals and

some percentage of organic binders [264–268]. The shells of the living organisms represent nanocomposite materials possessing high toughness. A few examples of such nanocomposites are demonstrated below. *Strombus gigas* shells consist of aragonite (i.e., the metastable orthorhombic polymorph of CaCO_3) in the form of nanolamellae having a length of 1–20 nm and an average width of 5 nm [264]. Red abalone shells consist of a hybrid ceramic–polymer nanocomposite having CaCO_3 crystal sizes in the range of 200–300 nm and a superplastic organic binder 20–30 nm thick [265]. *Cristaria plicata* shells are built from three layers [266]; one of them, the pearl layer, is constructed with many ultrathin hard slices, which have thickness of about 100 nm. The shells of the bivalve mollusk *Cristaria plicata* are ceramic nanocomposite consisting of a polygonal-shaped aragonite (CaCO_3) platelet approximately 500 nm thick. The platelets are connected by a thin ($\sim 30 \text{ nm}$) organic layer of protein–polysaccharide binder [269]. The fine and properly organized nanostructure of the shells has been adapted as an example to develop similar synthetic nanomaterials [270, 271]. For example, the hardness of TiC/Fe nanolayered composite coatings constructed similarly to the shells can reach a hardness of 42 GPa [272].

Here the nanostructured composite (or nanocomposite) coatings in question are generally classified into two groups according to the dimensions of the morphological elements. If the morphological element consists of alternating layers of two different materials within a nanoscale thickness, these coatings are termed nanolayered composite coatings. If the morphological element consists of nanograins, the coatings are termed nanocrystalline composite coatings. In general, the term nanostructured composite coatings includes both types of coatings. Ramified classifications of nanostructured materials can be found elsewhere [273–276].

The first group unites nanolayered composite coatings, or so-called heterostructures or superlattices [277]. Superlattices, which are defined as epitaxial structures inheriting the crystallographic orientation of the prelayer [278], provide a more narrow definition than nanolayered composite coatings. The term nanolayered composite coatings is chosen here because it is the most coincident terminology for nanoscience.

As a rule, nanolayered composite coatings are two-phase nanocomposites consisting of alternating nanolayers of two functionally different materials denoted A and B (Fig. 1). The total thickness ($h_A + h_B$) of the two alternating nanolayers, called the bilayer repeat period (Λ) [277], amounts to a few dozen nanometers (practically up to 40 nm). Important parameters for the description of nanolayered composites include [279]:

- Thickness of bilayer repeat period
- Thickness ratio of nanolayers within the bilayer repeat period
- Degree of interdiffusion and roughness at interfaces

Two other dimensions (length and width) of the nanolayers are unlimited and significantly larger as compared with their thickness. A few hundreds of such alternating nanolayers of different materials create a nanolayered composite coating. The hardness of this nanolayered “sandwich” is considerably enhanced when the bilayer repeat period has

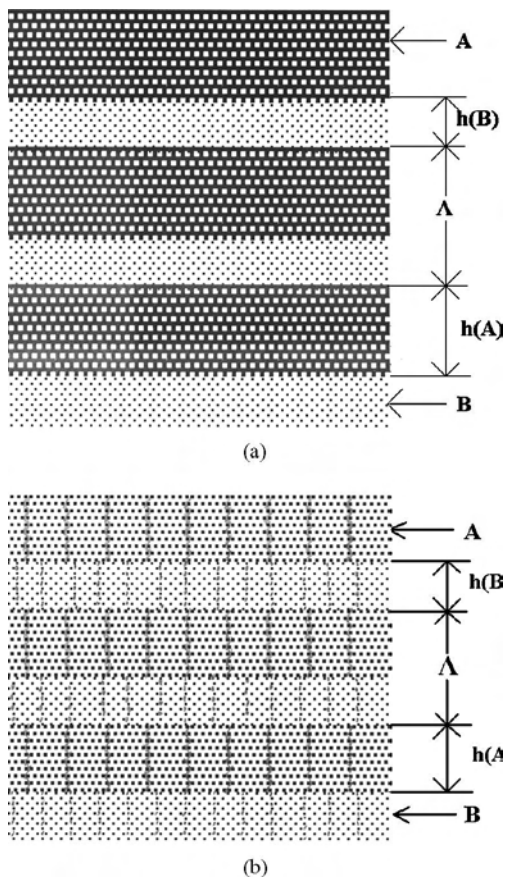


Figure 1. Draft of two-dimensional representation of nanolayered composite coatings: (a) nanolayered composite coatings with monocrystalline structure (monocrystalline type) and (b) nanolayered composite coatings with nanocrystalline structure (nanocrystalline type). Reprinted with permission from [175], G. M. Demyashev et al., in "Handbook of Organic-Inorganic Hybrid Materials and Nanocomposites" (H. S. Nalwa, Ed.), Vol. 2, Chap. 13. American Scientific Publishers, Stevenson Ranch, CA, 2003. © 2003, American Scientific Publishers.

an optimal value for each coupled material forming the nanolayered coating.

It is necessary to distinguish nanolayered composite coatings from both monocrystalline and nanocrystalline types of nanolayered composites (Fig. 1). The discrepancy is similar to the difference between monocrystalline and polycrystalline states. The monocrystalline type (1) has a monocrystalline structure of nanolayers and (2) exhibits an epitaxial crystalline relationship between joined nanolayers [280]. In the case of polycrystalline-type nanocomposites, every nanolayer has, first, a nanocrystalline structure with a number of nanograin boundaries and, second, interfaces between joined nanolayers, which represent an incoherent interphase boundary.

The second group of nanocomposites unites nanocrystalline composite coatings (Fig. 2), which are usually a composition of two or more phases. The term nanocrystalline composite coatings refers to coatings that consist of nanocrystals/nanograins (nc-A) embedded predominantly in an amorphous or low-dimensional matrix (a-B) of another

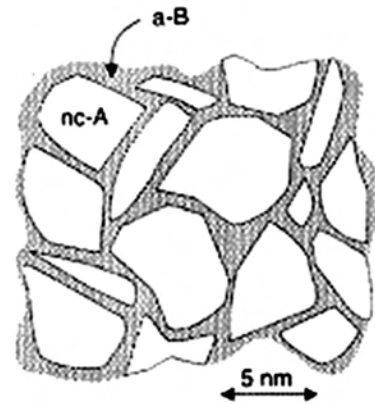


Figure 2. Cross-sectional sketch of as-deposited nanocrystalline composite coatings, where nc-A is nanocrystalline phase A and a-B is amorphous phase B. Reprinted with permission from [281], C. Mitterer et al., *Surf. Coat. Technol.* 120–121, 405 (1999). © 1999, Elsevier Science.

material. Interphase boundaries are inherent elements of nanostructures in multiphase nanocomposites.

On an atomic scale, if atoms are represented by circles (Fig. 3), a two-dimensional representation of nanocrystalline structures can be considered as a mixture of two structural components [176, 283, 284]: nanograins with a crystal lattice of ordered atoms, denoted by black circles, and intercrystallite boundaries, depicted with white circles in Figure 3. The average grain sizes of the nanocrystalline coatings vary from 2 to 100 nm and can contain from 10^2 to 10^8 atoms [285].

Intergrain boundaries are inherent elements of the structure of one-phase coatings. A lot of research has been devoted to intergrain boundaries in nanocomposites [182, 286–297]. The intergrain boundary width of nanocrystalline materials is usually between 0.5 and 1.2 nm [178, 282, 298, 299]. The average atomic density of the boundaries is relatively lower than that in a crystal lattice of nanograins. Atoms in the boundaries, which vary from special close-packed boundaries to widely spaced ones [300, 301], display a wide range of interatomic spacings. The average density of the boundaries can vary from 70% to 85% of the perfect crystal lattice [176], which is from 15% to 30% less than the

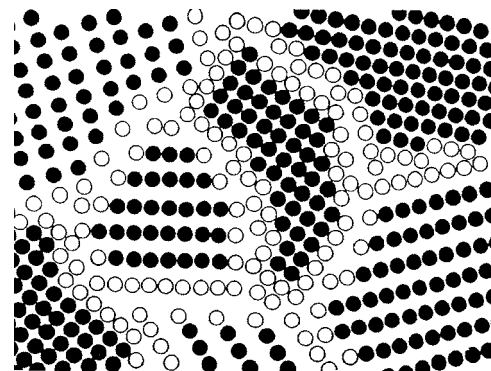


Figure 3. Schematic representation of a nanocrystalline structure on atomic scale: individual nanograins (black circles represent bulk atoms) and nanograin boundaries (white circles represent grain atoms). Reprinted with permission from [282], H. Gleiter, *Prog. Mater. Sci.* 33, 223 (1989). © 1989, Elsevier Science.

atomic density in the perfect crystal structure, depending on the type of bonds encountered in the crystal lattice [197]. The properties of the grains, such as transport, thermodynamic, and mechanical properties, differ from the properties of the boundaries. Therefore, nanocrystalline coatings can be treated as two-component structures, that is, a mixture of nanograins and grain boundaries [284, 302], even in the case of single-phase nanocomposites.

A reduction in grain size leads to an increasing volumetric portion of atoms located in the boundaries. It was found [303] that the volumetric fraction of atoms in the boundaries is 87.5% for 2-nm grain materials, approximately 44% for 3-nm grain materials, about 50% for 5-nm grain materials, approximately 30% for 10-nm grain materials, and only 3% for 100-nm grain materials.

The portion of boundaries (C) in a bulk material can be estimated from [298]:

$$C = 3d/\Delta$$

where Δ is the grain boundary thickness and d is the average grain size. Considering the grains as regular 14-sided tetrakaidecahedrons with the hexagonal faces of the grain boundaries, it was calculated [303] that the intercrystalline (ic) volumetric fraction is

$$V_{ic} = 1 - [(d - \Delta)/d]^3$$

the volumetric portion of the grain boundaries (gb) is

$$V_{gb} = [3\Delta(d - \Delta)2]/d^3$$

and the volumetric part of the triple junctions (tj) is

$$V_{tj} = V_{ic} - V_{gb}$$

where d is the average grain diameter and Δ is the average size of the grain boundaries. Note that $d > \Delta$.

Figure 4 displays the dependence of V_{ic} , V_{gb} , and V_{tj} on the average grain diameter. The volumetric fraction of the triple junctions, which are defined as intersections of three (or more) adjoining grain boundaries [198, 304, 305], becomes an important element of the nanostructure [256, 306]. Triple junctions are considered [307–311] as disclinations depending on the specific crystallographic arrangement of adjoining nanograins. The atomic structure of the boundaries in nanocrystalline materials differs from the atomic structure of the boundaries in coarse-grained microcrystalline materials by rigid-body relaxation [273]. It is clear from Figure 4 why nanostructured materials have been defined as having grain sizes (at least in one dimension) between 2 and 100 nm.

With decreasing grain size, the interatomic distances in the crystal lattice of the nanograins increase, and, as consequence, the density of the nanograins decreases [312, 313]. It was experimentally demonstrated [314, 315] that the crystal lattice expansion mainly exists near the grain boundaries. The crystal lattice expansion of the nanocomposites could be conditional upon nonlinear effects caused by the existence of stress fields [316]. The “ x^{-3} law” for the stress field and a model of the crystal lattice expansion of nanostructured materials caused by vacancies and vacancy clusters

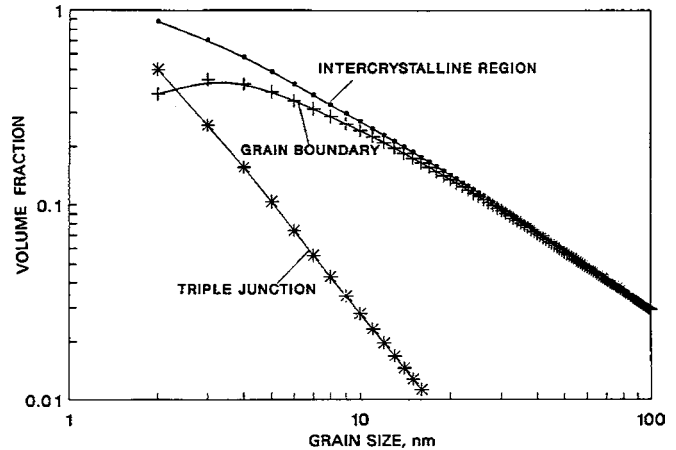


Figure 4. Influence of nanograin size on the calculated volumetric portion of intercrystalline regions, grain boundaries, and triple junctions, assuming an average grain boundary thickness of 1 nm. Reprinted with permission from [198], C. Suryanarayana et al., *J. Mater. Res.* 7, 2114 (1992). © 1992, Materials Research Society.

have been proposed [317]. The calculated deviation of lattice parameters for nanograins [317] in nanocrystalline Ni coatings was found to be in good agreement with the experimental data [312]. The maximum elastic modulus due to lattice distortion was estimated for an optimal nanograin size of 15–20 nm [318].

Nanocomposites belong to nonequilibrium (metastable) structures [211, 319, 320] formed during extreme conditions of synthesis. It was evaluated for Ni–P [321] that the release of heat energy was 339 mJ for 5-nm grain materials, whereas, for 5- μ m grain materials, the heat energy released was only about 0.7 mJ. Similar dependence was obtained for the SiC fiber nanocomposite with an average grain size of approximately 3 nm [322].

Therefore, nanocomposites share the following fundamental features [323]:

- Grains/layers confined to less than 100 nm in at least one dimension.
- Significant atomic fraction associated with interfaces and triple junctions.
- Interaction between the constituent domains.

The nanostructured state was considered [282] a new state of solids equally with

- Amorphous
- Coarse-grained microcrystallines
- Monocrystals

In particular, the important characteristics of nanocomposites that influence hardness include [198]:

- Grains (size, distribution, and morphology)
- Nature and morphology of grain/interphase boundaries
- Structure of intercrystalline regions
- Local composition of nanograins and interfaces
- Porosity of nanostructured composites
- Impurities trapped due to the processing medium

1.2. Superhardness

Hardness, which is a practical parameter for the evaluation of wear resistance of materials, is commonly used for the characterization of the mechanical properties of materials. The hardness of materials depends on both their elastic and their plastic properties.

The hardness of materials, that is, the ability to resist deformation, depends on the type of interatomic bond as well the type of crystal lattice. Superhard nanocomposites demonstrate the kind of results that can be achieved by forming an optimal nanostructure. As will be demonstrated, the hardness of such nanocomposites can be a few times higher as compared with their microcrystalline components or their coarse-grained mixtures.

Conventionally, superhard materials are defined [156, 167] as materials having microhardness between 40 and 80 GPa. In the range of 35–40 GPa, there are a lot of nanostructured coatings that have various functional applications. In this review, the selection of superhard coatings was lowered to 35 GPa in order to consider certain nanostructured coatings that can demonstrate novel developments and potential applications of such superhard nanocomposites. Materials with hardness higher than 80 GPa are classified as ultrahard [168, 324–327].

2. STRENGTHENING OF NANOCOMPOSITES

2.1. Hall–Petch Strengthening Mechanism

The experimental Hall–Petch relationship applied to hardness shows that the hardness of microcrystalline materials increases with a decrease in the average diameter of the grains [328–332]:

$$H = H_0 + k_H/d^{1/2}$$

where d is the average diameter of the grains, H is the hardness, H_0 is the hardness of the monocrystal when $d \rightarrow \infty$, and k_H is the Hall–Petch intensity constant.

Extrapolation of the Hall–Petch relationship to nanostructured materials should show a much higher hardness than that of coarse-grained materials having the same composition. However, limitations should be taken into account [199] since (1) hardness cannot increase indefinitely, (2) relaxation processes in grain boundaries can decrease hardness, and (3) in nanometer-sized grains the Hall–Petch strengthening is not valid for nanograins less than 2 nm [333]. Regarding nanolayered composites, the Hall–Petch strengthening is not as applicable [334] when the bilayer repeat period approaches a few nanometers in size.

Originally, the empirical Hall–Petch relationship [328, 329], which was obtained for coarse-grained microcrystalline mild steel, ingot iron, and spectrographic iron with grain sizes larger than $1 \mu\text{m}$, was based on the conception of dislocation pileup in individual grains. Therefore, the Hall–Petch strengthening for coarse-grained structures is explained in terms of dislocation propagation [335, 336]. For microsized grains, it is easier to activate the dislocation multiplication and propagation at lower stress levels. But dislocation

sources [337–340], for example, the Frank–Read dislocation source, can operate if grains are larger than 15–100 nm [341]. Grains are free of dislocations when grain sizes are smaller than [341, 342]:

$$d_c = (\alpha_1 Gb)/(2\sigma)$$

where α_1 is a geometrical constant with value of about 0.5–1, σ is an appropriate stress, b is the numerical value of Burger's vector, and G is the shear modulus. Similar evaluation of the critical grain size has been given [343]:

$$d_c = Gb/[(1-\nu)H]$$

where H is the hardness and ν is the Poisson ratio. For grains smaller than d_c , material softening should occur because of the introduction of a new deformation mechanism due to refinement of the nanostructure [344].

From the amorphous state through the nanocrystalline state to the microcrystalline state, a schematic diagram of microhardness versus modulation period, which is represented by a bilayer repeat period (Λ) for nanolayered composites and an average nanograin size (d) for nanocrystalline composites, is presented in Figure 5. Interval I of the modulation periods reflects the microhardness anomaly of nanocomposites when the nanostructure and composition of the composites becomes optimal. The critical modulation period corresponds to maximum microhardness. Interval II of the modulation periods corresponds to transformation of the nanostructure into an amorphous state. Interval III corresponds to the classical Hall–Petch relationship.

Various attempts have been made to explain [198, 311, 346–357] the hardness behavior of nanostructured coatings and to modify [333, 341, 343, 358–366] the classical Hall–Petch model, adapting it to nanostructured materials. The critical average nanograin size (d_c), when the hardness reaches a maximum, was calculated [360], and the hardness for grain size $d \geq d_c$ and $d < d_c$ was evaluated. The hardness values are described by the following Hall–Petch equation adapted for nanocrystalline coatings [360, 367, 368]:

$$H_1 = H_0 + k_H d^{-1/2} \quad \text{when } d \geq d_c$$

$$H_2 = k_H (1/2\pi\alpha) [\ln(d/r_{\text{eff}})] d^{-1/2} \quad \text{when } d < d_c$$

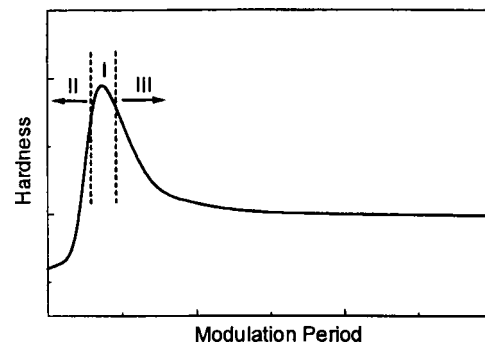


Figure 5. Tendency of the microhardness variation with a bilayer repeat period for nanolayered composite coatings or with a nanograin size for nanocrystalline composite coatings. Reprinted with permission from [345], J. Xu et al., *Thin Solid Films* 370, 45 (2000). © 2000, Elsevier Science.

where $\alpha = \sigma/(Gb^2)$ is a dimensionless constant, σ is the applied shear stress, G is the shear modulus, b is the magnitude of Burger's vector of dislocation, and r_{eff} is the effective cutoff radius.

This model predicts the slope formation and magnitude of the microhardness dependence on grain size. The inverse (or abnormal, or negative) Hall–Petch H_2 gives a good phenomenological agreement with the experimental softening of nanocrystalline materials for $d < d_c$ [333, 369–373]. The inverse Hall–Petch region is sometimes referred to as “Coble creep” [333]. Good agreement with a large set of experimental data has been demonstrated [310, 374]. Thus, the standard Hall–Petch strengthening relationship was adapted to nanostructured coatings. It was proposed [375] that a deformation mechanism such as grain boundary sliding appears at very fine grain sizes approaching the amorphous state ($d < d_c$). The proposed mechanism considers sliding along suitable grain boundaries. The model offers a physical explanation for the softening of nanomaterials at very small grain sizes.

It has been clearly shown for various materials [161, 342, 376–384] that optimization of the nanostructure of the composite coatings, for example, to be free of dislocations, is more important than interatomic bonds in the crystal lattice in order to obtain superhard nanocomposites. The major principles on which the superhardness of the nanostructured coatings is based are as follows:

- Crystal domains of nanoscale size are free of any dislocations or have a small number of dislocations in critical pileup.
- Propagation of dislocations through phase interfaces is strongly hampered.
- Dislocation multiplication sources cannot operate in domains of nanoscale size.

2.2. Other Possible Strengthening Mechanisms

The hardening mechanism of nanocomposites should be more complicated [165, 385, 386] than that in coarse-grained polycrystalline materials. The hardness of nanocomposites is most precisely approximated by the Hall–Petch equation, but currently there is no agreement on the strengthening mechanism of nanocomposites. A few strengthening models of nanostructured materials at nanoscale thicknesses of the bilayer repeat period below the Hall–Petch breakdown were proposed:

- Orowan mechanism [344, 387–393], which shows that dislocation slip can occur by bowing of dislocations within a nanolayer between interfaces [394].
- Koehler mechanism [395], which takes into account a shear modulus mismatch between the nanolayers of nanolayered nanocomposites [396].
- Coherency stress mechanism, which is based on the idea that alternation of in-plane coherency stresses from tensile to compressive between nanolayers resists dislocation movement across nanolayers [397–401].
- Electronic structure model [402–405], which arises from the interaction between the Fermi surface and the Brillouin zones created by the periodicity of nanolayered composites.

It has been estimated [393, 395, 406] that nanolayered composites consisting of two periodically repeated high-strength materials can possess high hardness because the alternating stress fields in the nanolayers prohibit any dislocation movement. The difference in shear moduli means that dislocations have lower energy in the phase with the lower elastic modulus. The role of the second-phase nanolayer, having a higher modulus, is to act as an elastic barrier inhibiting dislocation movement through the nanolayered composite. Therefore, it acts as an elastic barrier to dislocation propagation into the harder layer.

A model of two-component nanolayered coatings has been analyzed for the prediction of the critical shear stress that influences a dislocation slip transmission across the interface [407] as well as crack formation [408]. The investigation was based on a dislocation pileup model in which the Frank–Read dislocation source was considered for dislocation generation. This effect generated by changes in the modulus across the interface in a thin layer indicates strong dislocation interaction with the interface. This analysis is based on [161, 354, 393, 395, 408, 409]:

- Effects of modulus changes through the interfaces
- Coherency stress
- Barriers for dislocation slip across the interfaces

The effect of increasing hardness is controlled by [354]:

- Option of a bilayer repeat period
- Constituent modulus of material nanolayers
- Epitaxy of nanolayers

The movement of dislocations through the interface between two neighboring nanolayers with different shear moduli has also been considered [407], where a dislocation source length was the critical parameter. The mechanism of strengthening, that is, increasing hardness with the bilayer repeat period approaching an optimum value, in nanolayered composite coatings is due to the fact [394–396, 410, 411] that the strain induced prevents a dislocation movement across the interface from a softer material into a harder one and assists the dislocation movement through the interface from the harder material. Therefore, the harder nanolayer is usually free from dislocations or, at least, has a minimum number of them. The critical value (λ_c) of the dislocation spacing in the pileup can be calculated from the equation [341]:

$$\lambda_c = 3Gb/[(1 - \nu)H]$$

where λ_c is the dislocation spacing in the pileup, G is the shear modulus, b is the numerical value of Burger's vector of dislocation, ν is the Poisson ratio, and H is the hardness.

Another suggested explanation of superhardness [277, 412] is that the stress appears because of mismatch in the lattice constants of the two phases which inhibits dislocation movement as well. For example, the residual stresses in the nanolayers of Cu/Cr were found [413] to reach a peak value of approximately 1 GPa for a bilayer repeat period of about 50 nm. The stress level in nanolayered coatings is higher when there is a lattice mismatch. Because the lattice plains fit across the nanolayers of monocrystal type, the mismatch in the spacings should be compensated for by elastic strains

in the nanolayers; that is, one of them must be compressed and the other should be tensed [398]. These strains prevent movement of dislocations across interfaces and, therefore, increase the hardness of the nanolayered coatings. The elastic modulus has been found to be up to 2–3 times greater as compared with homogeneous coatings of the same average composition [404, 405]. When a nanolayered composite coating is on a substrate, the substrate imposes an additional deformation on the nanolayers as well.

A detailed analysis of the strengthening mechanism has been considered elsewhere [414] where a phenomenological model for the one-dimensional elastic reaction of the nanolayered composite coatings was developed. The model demonstrated the capability of reproducing the elastic anomalies, which were then confirmed experimentally. The critical shear stress of two-phase nanolayered coatings for dislocation slip transmission was found [397, 398, 407, 415] to be dependent on layer thickness, shear moduli of the phases, slip conditions of interfaces, properties of dislocation source, and orientation of pileup. An anomalous change of elastic constants of compositionally modulated structures is explained by the different shapes of the Fermi surface [403] and the electronic structure of nanolayered composites [402].

There are a few approaches to explain the superhardness effect in nanolayered composite coatings, namely:

- Strain distribution within individual nanolayers [416, 417]
- Difference in elastic moduli of nanolayers
- Lattice mismatch of nanolayers

The above preconditions help explain aspects of the hardening mechanisms, but a comprehensive explanation of the strengthening phenomenon does not currently exist.

3. STATE-OF-THE-ART SUPERHARD NANOCOMPOSITES

3.1. Superhard Nanolayered Composites

3.1.1. Introduction

This section summarizes the experimental data that reflect the two major distinguishing characteristics of superhard nanolayered composites, namely:

- Superhardness effect
- Stabilization effect

The anomalous increasing hardness of nanolayered composite coatings when the thicknesses of the nanolayers reach optimal values is summarized in Section 3.1.2.

The nanostructured state allows stabilization of some phases in a nanoscale range [418]. The possibility of stabilizing metastable phases by trapping them within nanolayers is considered to be an advantage of nanolayered composite coatings. A few examples of such stabilization are discussed below. It was noticed [419, 420] that zirconium and titanium, having a hexagonal close-packed lattice, can be stabilized with a body-centered cubic (bcc) lattice in the nanolayered composite coating of Nb/Zr and Nb/Ti. The similar phenomenon of pseudomorphic stabilization was observed in

nanolayers of Al/Ti [384, 421, 422] and Ag/Ti [423]. At the smallest bilayer repeat period, both Al and Ti nanolayers were of hexagonal closed-packed structure; for intermediate periods, both Al and Ti nanolayers were of face-centered cubic (fcc) structure. A thermodynamic model was proposed [421] to account for the effect of coherency strains on phase stability. The stabilization of the face-centered cubic Ti phase in a nanolayered composite of Ni/Ti was reported as well [424]. Fe nanolayers in a nanolayered composite of Fe/Ni with equal thickness of Fe and Ni nanolayers are in an fcc and bcc lattice for a bilayer repeat period of 2.76 nm and 12 nm, respectively [425]. A novel epitaxially stabilized CoSi phase with CsCl-type lattice was determined [426]. A crystalline-to-amorphous transition phenomenon is found for a nanolayered composite of Ni/a-Si with a bilayer repeat period below 5 nm [427] and for a Cu/a-Cu₄Zr₃ nanolayered composite [428]. The stabilization phenomenon in nanostructured materials was used to stabilize hexagonal niobium nitride nanolayers, the hypothetical superhard phase β -C₃N₄, the cubic form of aluminum nitride (c-AlN), cubic boron nitride (c-BN), and the metastable cubic form of β -WC_{1-x}. The stabilization phenomenon in superhard nanolayered composites is discussed in Section 3.1.3.

3.1.2. Superhardness Phenomenon in Nanolayered Composites

TiN/MeN (Me = V, Nb, Ta, Ta_xW_{1-x}, V_xNb_{1-x}, Cr, Si)

TiN/VN This type of nanolayered composite coating was one of the first subjects of systematic investigation of the superhardness effect. Monocrystal MgO(100) [377, 397, 429], M2 tool steel [430, 431], high-speed steel [432], cemented carbide (WC, 10wt% Co) inserts [433, 434], and Si wafers [345] served as substrates.

TiN/VN nanolayered coatings with a total thickness of about 2.5 μ m were deposited by reactive magnetron sputtering from two V and Ti targets in nitrogen atmosphere [377]. Deposition of the coatings started with titanium nitride [377, 397] where the TiN nanolayer thickness (h_{TiN}) was varied between 0.75 and 16 nm and the ratio of h_{TiN}/Λ ranged from 0 to 1.

The TiN/VN interfaces were free of misfit dislocations, but dislocation loops with diameter of 8–10 nm extending across a few nanolayers were observed [377]. The TiN/VN nanolayered composite coatings themselves represent a monocrystal-type structure with the alternation of TiN and VN nanolayers [377, 397]. The lattice mismatch of these two nitrides having a NaCl-type crystal structure was estimated to be 2.4% [377]. Equally spaced satellite reflexes located above and below the main Bragg reflection in the [100] direction characterized the bilayer repeat period.

It was found [377] that the microhardness of the TiN/VN nanolayered coating depends on both Λ (Fig. 6) and the ratio of h_{TiN}/Λ (Fig. 7). The highest microhardness of such nanolayered composite coatings was determined to be 55–56 GPa [377, 431, 435] when the bilayer repeat period and thickness of the TiN and VN nanolayers were optimum, that is, $h_{\text{TiN}}/\Lambda = 0.5$ and $\Lambda \sim 5.2$ nm. The microhardness of TiN/VN was found to be significantly higher than the microhardness of each polycrystalline TiN and VN phase as shown on the hardness axis (Fig. 6). It was assumed [377] that the

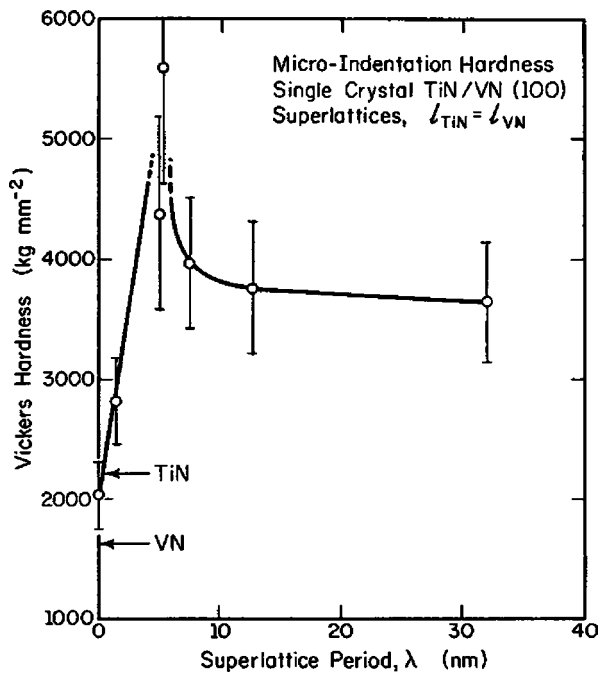


Figure 6. Microhardness of the TiN/VN nanolayered coatings ($h_{\text{TiN}}/h_{\text{VN}} = 1$) with orientation $\langle 100 \rangle$ perpendicular to the substrate versus bilayer repeat period. Reprinted with permission from [377], U. Helmerson et al., *J. Appl. Phys.* 62, 481 (1987). © 1987, American Institute of Physics.

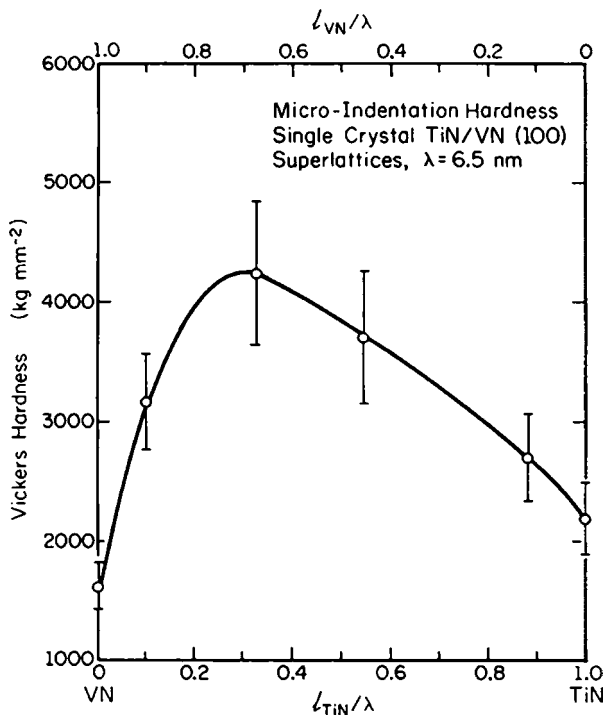


Figure 7. Dependence of the microhardness of the TiN/VN nanolayered composite coatings on the ratio of h_{TiN}/λ when $\lambda = 6.5$ nm and the total coating thickness was $2.5 \mu\text{m}$. Reprinted with permission from [377], U. Helmerson et al., *J. Appl. Phys.* 62, 481 (1987). © 1987, American Institute of Physics.

increase in microhardness is based on a decrease in dislocation mobility.

TiN/NbN A wide range of bilayer repeat period from 1.6 to 450 nm was investigated for TiN/NbN nanolayered composite coatings [397, 436–447], which were grown on different sorts of substrates, for example, monocrystal MgO(100) substrate [397], cemented carbide [434], M2 tool steel [431, 448], and high-speed steel [432], using ultrahigh vacuum reactive magnetron sputtering with a total pressure of about 2 Pa of Ar + N₂ gas mixture [397, 430] and unbalanced magnetron sputtering [432] with the same gas mixture.

The microhardness of the TiN/NbN nanocomposites of nanocrystalline-type structure is a function of the bilayer repeat period (Λ) [430]. The maximum microhardness of 55–57 GPa was achieved when the bilayer repeat period was between 4 and 8 nm [431]. This microhardness exceeds the microhardness of each polycrystalline TiN and VN phase by more than 2.5 times. A compressive residual stress for the TiN/NbN nanolayered composite coatings was evaluated as -1.2 GPa [433, 434]. The interfaces between the nanolayers of the nanocrystalline-type structure [430] were not so perfectly planar and abrupt as they were between nanolayers in the monocrystalline-type nanocomposites [397].

The maximum hardness of 48–49 GPa for the TiN/NbN nanocomposites of monocrystalline type with a thickness of approximately $2 \mu\text{m}$ was achieved when the bilayer repeat period was $\Lambda = 4\text{--}7$ nm and the average layer thickness ratio $h_{\text{TiN}}/\Lambda = 0.3 \pm 0.5$ [397, 432]. The lattice mismatch of TiN and NbN reached 3.6% [397], which is larger than that for TiN/VN. X-ray diffraction indicated [397] that the TiN/NbN interfaces were relatively sharp. No misfit dislocations were observed for the optimal bilayer repeat period.

The electron diffraction pattern consisting of points (Fig. 8a) reaffirmed that the TiN/NbN nanolayered coatings have a monocrystal structure. The satellite reflexes characterized the long-range ordering of the TiN/NbN nanolayered composite coatings. The long-range ordering corresponds to the bilayer repeat period where the dependence is as follows:

- The satellite reflexes are closer to the central peaks if the bilayer repeat period is increased.
- The central peaks have the same intensity if the bilayer repeat period and ratio h_{TiN}/Λ are maintained severely; that is, the nanolayered composite structure is well ordered.

The typical high-resolution transmission electron microscopy image, represented in Figure 8b, verifies that interfacial misfit dislocations were not observed [397]. The NbN nanolayers appear darker than the TiN nanolayers because of the higher atomic number of Nb.

Using a reactive hybrid deposition process consisting of a combination of electron beam evaporation and direct current magnetron sputtering [449], the TiN/NbN coatings with variation of TiN and NbN layers in nanoscale range thickness were obtained. The maximum microhardness was 34 GPa for $h_{\text{TiN}}/h_{\text{NbN}} = 2$ with approximately 33% NbN content. The hardness was found to increase with an increase in the relative thickness of the NbN nanolayer.

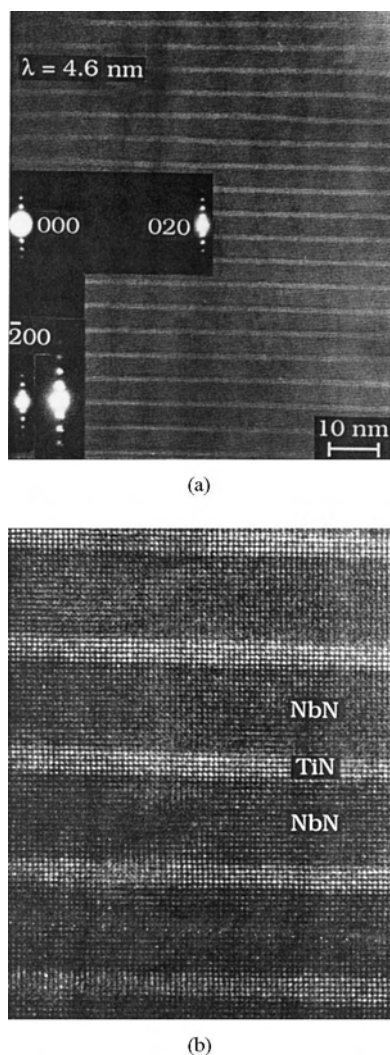


Figure 8. Cross section of the TiN/NbN nanolayered coatings: (a) conventional transmission electron microscopy image and selected-area electron diffraction and (b) high-resolution transmission electron microscopy of the {200} lattice fringe images. Reprinted with permission from [397], M. Shinn et al., *J. Mater. Res.* 7, 901 (1992). © 1992, Materials Research Society.

TiN/TaN The TiN/TaN nanocomposites, having a small lattice mismatch of 2.1%, were grown on cemented carbide inserts [433, 434, 450] and high-speed steel substrate [451, 452]. A microhardness of 39–40 GPa was reported [345, 433, 434] when the bilayer repeat period was 9–12 nm with a ratio of $h_{\text{TiN}}/\Lambda = 0.64$ and the cubic TaN phase was formed. If the tantalum nitride lamella was thicker than 15 nm, hexagonal phases of $\text{TaN}_{0.8}$ and Ta_2N formed [451]. Pseudomorphic stabilization of the cubic TaN phase in nanolayers thinner than 6 nm was reported [451]. The compressive residual stress for the TiN/TaN system was relatively low—3.1 GPa [433, 434].

TiN/Ta_xW_{1-x}N The TiN/Ta_xW_{1-x}N nanocomposites with NaCl structure of Ta_xW_{1-x}N were deposited [345] from Ti and Ta_{0.9}W_{0.1} targets. A maximum microhardness value of 50 GPa for the TiN/Ta_{0.9}W_{0.1}N nanolayered composite coatings was found to conform to $\Lambda = 5.6$ nm and $h_{\text{TiN}}/\Lambda = 0.64$.

TiN/V_xNb_{1-x}N Nanocomposites of TiN/V_{0.6}Nb_{0.4}N composition with monocystal-type structure were deposited on MgO(001) substrates using ultrahigh vacuum reactive sputtering with a computer-controlled shutter for two targets [378]. A maximum microhardness of approximately 41 GPa was achieved when the bilayer repeat period had an optimal value of 10–12 nm [378, 453]. The nanolayers had flat and abrupt interfaces. The composition of the targets was chosen so that the V_{0.6}Nb_{0.4}N and TiN nanolayers did not have a lattice mismatch, which was approximately 0.3%. These results indicate that coherency strains do not play major role in increasing the microhardness of the TiN/V_{0.6}Nb_{0.4}N nanolayered composite coatings.

Later [400], the composition of V_{0.3}Nb_{0.7}N for the TiN/V_{0.3}Nb_{0.7}N nanolayered composite coatings was chosen in order to increase the lattice mismatch, which was 1.7% between TiN and V_{0.3}Nb_{0.7}N. In this case, the hardness increased rapidly and reached a maximum of approximately 51 GPa when the bilayer repeat period was 6 nm. It was concluded [400] that coherency strains, which are larger for TiN and V_{0.3}Nb_{0.7}N, are responsible for the increase in hardness.

Attempts to obtain superhard nanolayered composite coatings of TiN nanolayers in combination with TiAlN and CrN were undertaken [454–459], but the hardness of these coatings was not so impressive. TiN/TiAlN and TiN/CrN nanolayered composite coatings had a microhardness of 23.5 GPa and 29–32 GPa, respectively. It is important to note that coating hardnesses demonstrated strong sensitivity to the nanolayer thickness and to their bilayer repeat period as well.

TiN/CrN Polycrystalline nanolayered composites of TiN/CrN were deposited [460–462], in particular, on M1 tool steel [463]. Nanoindentation of 2- μm -thick TiN/CrN nanolayered composites fixed the maximum hardness of 35 GPa at the bilayer repeat period of 2.3 nm [463].

TiN/a-SiN_x Nanolayered composites of TiN/a-SiN_x were deposited with dual-cathode unbalanced reactive magnetron sputtering [464, 465]. Amorphous nanolayers of SiN_x periodically interrupted the growth of TiN in order to suppress the columnar structure of TiN [465]. A maximum hardness of approximately 45 GPa for the nanolayered composites of TiN/a-SiN_x was achieved [465] for the deposition under optimum conditions, that is, $\Lambda_{\text{TiN}} = 2.0$ nm, $\Lambda_{\text{a-SiN}_x} = 0.5$ nm, and substrate bias ranging from –80 to –90 V.

Nanolayered composite coatings of TiN/FeN [466], TiN/ZrN [467], TiN/CrAlN [468], and TiN/Al₂O₃ [469] composition were synthesized. These nanocomposites did not display a superhardness effect.

VN/MeN (Me = Ti_xAl_{1-x}, Ti_xAl_{0.96-x}Y_{0.04}) A computer-controlled vacuum system combining two physical vapor deposition processes, namely, cathodic arc and unbalanced magnetron with two pairs of TiAl (50:50 at%) and V (99.8%) targets, was used to deposit the VN/Ti_xAl_{1-x}N nanolayered composites [470, 471]. For deposition of the VN/Ti_xAl_{0.96-x}Y_{0.04}N nanolayered composites, the TiAl targets were replaced with the TiAl targets containing 4 at% Y. An Ar + N₂ gas atmosphere was used for sputtering the foregoing targets and the synthesis was carried out under a total pressure of 0.3 Pa.

The VN/Ti_xAl_{1-x}N and VN/Ti_xAl_{0.96-x}Y_{0.04}N nanolayers were deposited on a thin (0.1–0.2 μm) base layer of vanadium nitride for the enhancement of the adhesion of the VN/Ti_xAl_{1-x}N and VN/Ti_xAl_{0.96-x}Y_{0.04}N nanolayered coatings to substrates. Mirror-polished hardened M2 high-speed steel, cemented carbides, and 304L stainless steel served as substrates for measuring the hardness, adhesion, high-temperature tribology, corrosion resistance, and structure of the nanolayered composite coatings [471].

The VN/Ti_xAl_{1-x}N nanolayered composites had a {111} texture at –75 V of bias voltage. The incorporation of small amounts of yttrium into the Ti_xAl_{1-x}N nanolayers transformed the {111} texture of the VN/Ti_xAl_{1-x}N nanolayered coatings into the {110} texture of the VN/Ti_xAl_{0.96-x}Y_{0.04}N nanocomposites [471]. Moreover, increasing the bias voltage higher than –75 V leads to domination of the {111} texture in the VN/Ti_xAl_{0.96-x}Y_{0.04}N nanolayered coatings.

The highest hardness was approximately 39 GPa and 78 GPa for the VN/Ti_xAl_{1-x}N and VN/Ti_xAl_{0.96-x}Y_{0.04}N nanolayered composites having a bilayer repeat period of 3.2 nm and 3.5–4 nm, respectively [170, 471]. The range of the residual compressive stress for both VN/Ti_xAl_{1-x}N and VN/Ti_xAl_{0.96-x}Y_{0.04}N was between –3.3 and –8.5 GPa [471]. Alloying with yttrium increases the compressive residual stress.

CrN/MeN (Me = Nb, Ti_xAl_{1-x})

CrN/NbN Nanolayered coatings of CrN/NbN composition were deposited using combined cathodic-arc and unbalanced magnetron sputtering of Cr and Nb targets on an M2 high-speed steel substrate under a working pressure of 0.3–0.36 Pa [472–478] and on knife blades produced from martensite 420 SS and from 1% carbon steel [479]. The flow rate was selected so that single-phase (NaCl-type) structures of CrN and NbN were co-deposited [472]. The low-angle X-ray diffraction gave evidence [472] that the CrN/NbN nanolayered coatings with a bilayer repeat period in the range of 2.76–7.4 nm were obtained.

The microhardness of the CrN/NbN nanolayered coatings as a function of the nitrogen flow rate was investigated [472]. The CrN/NbN nanolayered coatings had the dominant texture of {200} crystallographic orientation. Both stoichiometric and substoichiometric CrN/NbN nanolayered coatings were formed with the highest microhardness of approximately 56 GPa [170].

The residual compressive stress for the CrN/NbN nanolayered coatings having stoichiometric composition (N/Me~1) was as low as 1 GPa [472], while the compressive stress for the substoichiometric composition (N/Me~0.45) reached 7 GPa.

CrN/Ti_xAl_{1-x}N The CrN/Ti_xAl_{1-x}N nanolayered composite coatings reached the highest microhardness of 60 GPa [170]. The highest value of a compressive residual stress reached –10 GPa for the CrN/Ti_xAl_{1-x}N nanolayered composites [170]. In other cases [480–485], the microhardness of CrN/Ti_xAl_{1-x}N nanolayered composite coatings was only 32–35 GPa. Hardness as a function of the bilayer repeat period demonstrated strong dependence. The optimal bilayer repeat period was found to be 3–4 nm for the highest hardness.

Other nanolayered composite coatings with chromium nitride such as CrN/Cr₂N [486, 487] and CrN/Si₃N₄ were reported [488]. The hardness measured by nanoindentation was approximately 22 GPa for CrN/Cr₂N. The superhardness effect was not observed in CrN/Si₃N₄.

ZrN/Ti_xAl_{1-x}N The ZrN/Ti_xAl_{1-x}N nanolayered composites were deposited using combined unbalanced magnetron sputtering and steered-arc evaporation [170]. The microhardness of the ZrN/Ti_xAl_{1-x}N nanolayered composites was very high and reached a maximum of 55 GPa at a bilayer repeat period of 2.6 nm [170]. In the case of ZrN/Ti_xAl_{1-x}N nanolayered composites, the compressive residual stress was as high as 10 GPa. The ZrN/Ti_xAl_{1-x}N coatings demonstrated a well-defined <100> growth texture.

NbN/TaN Nanocomposite coatings of alternating NbN and TaN nanolayers were prepared, employing the magnetron sputtering technique on stainless-steel wafers [401, 489, 490]. This system of nanolayers was found to be attractive because the NbN (NaCl-type structure) and TaN phases (hexagonal structure) possess different types of crystal lattices and, therefore, different slip systems of dislocation. Transmission electron microscopy of NbN/TaN cross-sections showed that the lattice planes of {111}NbN were coherent with the {11.0}TaN planes.

It has been shown [401] that X-ray diffraction (XRD) of the NbN/TaN nanolayered composites with a small bilayer repeat period is similar to the XRD pattern of single-phase tantalum nitride. The hexagonal niobium nitride structure, as expected [401], was stabilized by the hexagonal TaN nanolayers. Overlapping of the X-ray diffraction lines of niobium nitride and tantalum nitride was also possible [401]. The (200) reflex of cubic NbN on selected-area electron diffraction patterns was present when $\Lambda = 73.2$ nm.

The effect of the thickness of the bilayer repeat period (Λ) on the microhardness of NbN/TaN nanolayered composites has been investigated from $\Lambda = 0$ nm to $\Lambda = 73.2$ nm [401]. The influence of the bilayer repeat period on the microhardness of the coatings exists in a wide range of $\Lambda = 2.3$ –17 nm, and the microhardness reaches a maximum of 51 GPa [401, 490]. This effect differs from the earlier investigated ones where extreme microhardness existed within a narrow band of bilayer repeat period. The coherent stresses and the structural barriers (NbN, NaCl-type structure; TaN, hexagonal structure) for dislocation movement through the NbN–TaN interface are believed [401] to be the main reasons for the extreme microhardness in the broad range of the bilayer repeat period.

Other nanolayered composites of NbN/Si₃N₄ [491] and NbN/Fe₄N [492] have been investigated. Niobium nitride, being a superconducting material, demonstrated superconductivity at a NbN nanolayer thickness of approximately 10 nm. Below this thickness, ferromagnetism of the Fe₄N nanolayers was detected.

Si₃N₄/SiC Nanolayered composites of Si₃N₄/SiC were deposited on Si substrates and cemented carbide inserts by radio frequency (rf) magnetron sputtering [493]. It was determined that the microhardness of Si₃N₄/SiC nanocomposite coatings reaches a maximum of 3700 HV_{0.01} when the bilayer repeat period equals 11.6 nm. The residual stress of the nanocomposite was as low as 2–2.45 GPa.

MeN/Me (Me = Ti, Hf, W, Mo) Nanolayered composites of TiN/Ti [494–506], HfN/Hf [494], (Ti, Al)N/Mo [507, 508], and WN/W [494] were deposited. A radio frequency diode sputtering system [188] was used. The total pressure was about 1.3 Pa for the preparation of TiN/Ti and HfN/Hf and about 2.7 Pa for the WN/W nanolayers. The nitrogen content in the sputtering gas mixture was 20%, 25%, and 50% for the TiN, HfN, and WN nanolayers respectively. The nanocomposite coatings were grown with total thickness varying from 3 to 8 μm .

For TiN/Ti nanolayered composite coatings, a maximum hardness of approximately 37 GPa was reported [494] when the bilayer repeat period was $\Lambda = 16\text{--}18$ nm and the individual nanolayers of TiN and Ti were equivalent to each other, that is, $h_{\text{TiN}} = h_{\text{Ti}} = 8\text{--}9$ nm. The TiN/Ti nanocomposite coatings possess a very narrow range of bilayer repeat period where the hardness has the maximum value. Further reduction of the bilayer repeat period leads to the hardness dropping sharply to approximately 22 GPa when the thickness of each nanolayer is below 7 nm. Later attempts [496, 509] to obtain TiN/Ti nanolayered composite coatings with larger bilayer repeat period [496] and with various ratios of h_{TiN}/Λ [509] gave hardnesses of about 29 GPa and 23 GPa, respectively.

The hardness of HfN/Hf nanolayered composites was also measured [494]. When the bilayer repeat period was equal to 8 nm, the hardness of the HfN/Hf nanocomposite reached a maximum of 50 GPa and remained constant within the range of $\Lambda = 4\text{--}8$ nm. The thickness of the HfN and Hf individual nanolayers remained equal to each other during the experiments ($h_{\text{HfN}} = h_{\text{Hf}}$).

The hardness of the WN/W nanolayered composite coatings reached a value of about 35 GPa [494], which is significantly higher than that of W and WN coarse-grained one-phase coatings. The bilayer repeat period for the maximum hardness varied in the range of $\Lambda = 16\text{--}40$ nm. The individual W and WN nanolayers were equal to each other ($h_{\text{WN}} = h_{\text{W}}$) during the experiments.

Nanolayered composites of (Ti, Al)N/Mo with a bilayer repeat period of approximately 6 nm have a hardness value of 51 GPa [507], which was significantly improved in comparison with the previous attempt [508].

Epitaxial nanolayered composites of NbN/Mo [510, 511] and NbN/W [512, 513] with a bilayer repeat period between 1.3 and 120 nm were deposited on MgO(001) substrate by direct-current (dc) reactive magnetron sputtering. The orientation relationships were (001)Me|| (001)NbN and [110]Me|| [100]NbN. A maximum hardness of approximately 32 GPa was detected at a bilayer repeat period of 2–3 nm. The hardness follows the Hall–Petch relationship: $H = 10.3 + 26.7\Lambda^{-0.38}$ GPa for NbN/Mo and $H = 12.88 + 22.1\Lambda^{-0.3}$ GPa for NbN/W. Other hybrid nanolayered composites of nitrides in combination with metals, namely, AlN/Mo [514], TiN/Pt [515, 516], TiN/Ni [517], TiN/Ag [501], and CrN/Cr [518, 519], were obtained.

TiC/Me (Me = Fe, Mo) Nanolayered coatings of TiC/Me as a composition of TiC with both soft metals (Fe, Al, Cu, Ti) and hard metals (W, Mo) were synthesized using the ion beam sputtering technique [271, 272, 520–525] in order to investigate the mechanical properties of the ceramic–metal

nanolayered composite coatings. The microhardness of the TiC/Me system has been determined [62, 272] and was found to have a great dependence on the bilayer repeat period; in particular, the TiC/Fe nanolayered composite coatings showed the superhardness effect.

Fe/TiC nanolayered composite coatings were deposited on Si wafer using Ar^+ ion beam sputtering of the composite (Ti + C) and Fe targets under a pressure of 7×10^{-3} Pa [62, 272]. The Ti/C ratio of the composite target was selected so that the formation of stoichiometric TiC was realized.

The maximum microhardness of the Fe/TiC nanolayered composite coatings was 42 GPa [272, 522] when the thickness of the Fe nanolayers was about 0.43 of the total thickness of the bilayer repeat period. Simultaneously, the maximum toughness of the Fe/TiC nanolayered composite coatings reached and surpassed TiC over 3 times [62]. In this case, the bilayer repeat period had a value of 14 nm and the components were distributed with $h_{\text{TiC}} = 8$ nm and $h_{\text{Fe}} = 6$ nm. It was found [272, 522] that every particular TiC and Fe nanolayer, in turn, had a nanocrystalline structure. Within the nanograins, the crystallographic coherent arrangement of TiC(200)||Fe(110) was commonly observed [62].

A maximum microhardness of 47.62 GPa for TiC/Mo was reported at $\Lambda = 8$ nm [520]. The bilayer repeat period was investigated in the range of 2–14 nm [520, 521], and the layer thickness was maintained to be equal ($h_{\text{TiC}} = h_{\text{Mo}}$).

Attempts to synthesize nanolayered composite coatings of Mo/TiC were undertaken [526]. Other nanocomposite coatings demonstrated a microhardness dependence on the bilayer repeat period as well. But the microhardness was significantly lower, namely, approximately 21 GPa for Mo/TiC at $\Lambda = 2.5$ nm [526], approximately 24 GPa for W/TiC [272], and approximately 16 GPa for Al/TiC [272].

Nanolayered composites of carbides with other materials, such as TiC/Al₂O₃ [526, 527], TiC/DLC [528], TiC/B₄C [524], W/B₄C [529, 530], TiC/SiC [531], TiC/VC [532, 533], and TiC/Ni₃Al [534], have been obtained. The microhardness of the nanolayered composites demonstrated a strong dependence on the sharpness of the nanolayers and the bilayer repeat period. But their microhardness was moderate and below the conventional superhardness definition or had not been reported.

3.1.3. Stabilization Phenomenon in Superhard Nanolayered Composites

CN_x/MeN (Ti, Zr) The idea of this type of nanolayered composite originated from numerous attempts to synthesize carbon nitride ($\beta\text{-C}_3\text{N}_4$) in the crystalline state, which was predicted to have a hardness higher than that of diamond [4, 5]. Pseudomorphic stabilization between two nanolayers having a similar structure to $\beta\text{-C}_3\text{N}_4$ was proposed [535–537]. The faces of TiN(111) and ZrN(111) were expected to be the best stabilizers because of the good lattice match between TiN(111) or ZrN(111) and $\beta\text{-C}_3\text{N}_4$ (00.1). The mismatch is less than 0.5% between ZrN(111) and $\beta\text{-C}_3\text{N}_4$ (00.1) and approximately 0.7% between TiN(111) and $\beta\text{-C}_3\text{N}_4$ (00.1) [538].

Dual-cathode unbalanced magnetron sputtering with two targets of Zr/Ti and graphite was used for deposition in

an Ar + N₂ gas atmosphere at about 1 Pa [537–539]. The substrates used were Si(100) wafer [536–540], M2 steel [536–539], and high-speed steel [541]. The microhardness of the ZrN/CN_x nanolayered coatings in relation to process parameters such as nitrogen partial pressure, target power, substrate bias, and substrate turntable rotation speed has also been investigated [539]. In particular, the thickness of ZrN and CN_x-nanolayers was controlled by the rotation speed of the holder.

A maximum microhardness of 45–50 GPa for the CN_x/ZrN nanolayered composite coatings, where the bilayer repeat periods were 1.5 nm [539] and 1.39 nm [536], was achieved. The bilayer repeat period corresponding to 20–24 rpm was 1.5 nm [539]. The intermediate nitrogen partial pressure (53–67 Pa) and the high substrate bias (–180 V) were applied to obtain the maximum hardness [539]. The experimental evidence demonstrates the good correlation between nanostructure and microhardness of the ZrN/CN_x nanolayered composites. The ZrN/CN_x nanolayered composite coatings have a polycrystalline-type structure. Both high-resolution transmission electron microscopy of the cross-sectional ZrN/CN_x imaging (Fig. 9a) and selected-area electron diffraction (SAED) (Fig. 9b) confirm the polycrystalline nature of the nanocomposites. Some nanocrystalline regions denoted by an arrow go through the nanolayers (Fig. 9a). The intensive diffuse halo at the middle of the SAED presents clear evidence that the ZrN/CN_x nanolayered composites contain a certain portion of amorphous state, which is common for the carbon nitride phase [542].

TiN/CN_x nanolayered composite coatings have been deposited on high-speed tool steel substrates as well [535, 541, 543–545]. The microhardness of the coatings was found to be in the range of 35–47 GPa [541]. A maximum hardness of approximately 48 GPa for the CN_x/TiN nanocrystalline composites was obtained at a speed of 6 rpm and a substrate bias voltage of –150 V [536]. The TiN/CN_x thickness ratio for maximum hardness should be $h_{\text{TiN}}/h_{\text{CN}_x} = 2.5$ [546].

c-AlN/MeN (Me = Ti, V) Usually, the stable forms of the TiN phase and the AlN phase have a crystal lattice of NaCl type and hexagonal wurtzite type, respectively [547]. The idea of synthesis of these nanolayered composite coatings is to stabilize the cubic form of the aluminum nitride phase. The point is that TiN nanolayers can take part as stabilizers of cubic-type AlN because the AlN phase of NaCl type exists only under high pressure. As expected, the stabilized cubic AlN phase should have a high bulk modulus and high hardness.

Superhard nanolayered composites of AlN/TiN were deposited using reactive magnetron sputtering [548–551], ion-beam-assisted processing [552–555], and pulsed laser deposition [556]. It was established [552] that AlN nanolayers are crystallized in a NaCl-type lattice for a bilayer repeat period of $\Lambda \leq 3$ nm. The AlN/TiN nanolayered composite coatings reach a microhardness of approximately 40 GPa at a repeat period of 2.5 nm [551, 552, 556]. Close to the bilayer repeat period of 2.5 nm, formation of the cubic AlN phase similar to the TiN nanolayers was observed [557]. The cubic AlN phase strongly affects the hardness of the nanolayered composite coating [552]. Selected-area electron diffraction

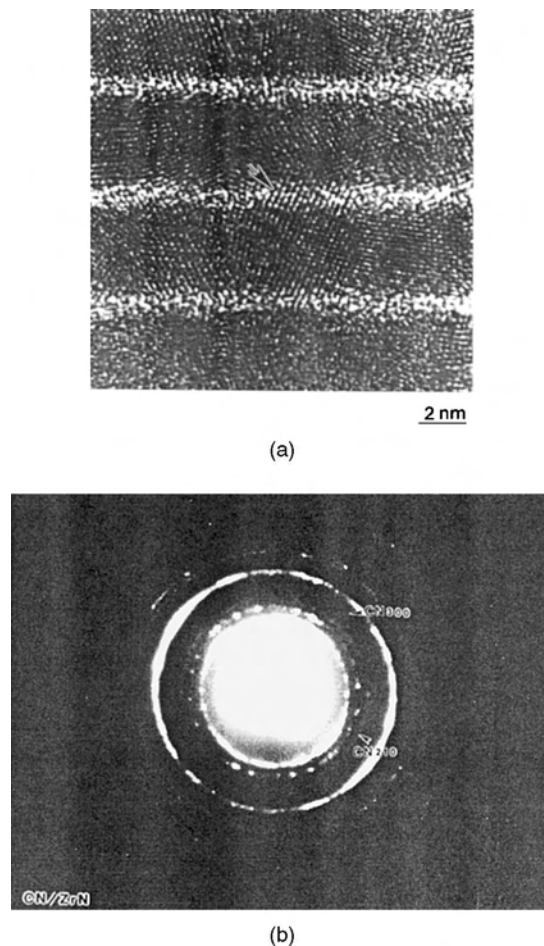


Figure 9. (a) Cross-sectional image of high-resolution transmission electron microscopy of the ZrN/CN_x nanolayered composite coating deposited at a substrate rotation speed of 7 rpm, a nitrogen partial pressure of 0.05 Pa, and a substrate bias of –120 V. (b) Selected-area electron diffraction of the superhard nc-ZrN/nc-CN_x nanolayered coatings. Reprinted with permission from [539], M. L. Wu et al., *Thin Solid Films* 308–309, 113 (1997). © 1997, Elsevier Science.

of the AlN/TiN coatings provided evidence that the coatings are nanocrystalline type with a $\langle 111 \rangle$ growth texture.

The cubic AlN phase was also stabilized in an AlN/TiN(001) nanolayered composite template [558]. Aluminum nitride included in the AlN/TiN(001) nanocomposite of the monocrystal-type structure was stabilized for a c-AlN nanolayer thickness of less than 2 nm as a NaCl-type structure with a lattice parameter of 0.408 ± 0.002 nm. The formation of c-AlN at nanolayer thickness was provided by lower c-AlN/TiN interfacial energy. The lattice mismatch of TiN ($a_{\text{TiN}} = 0.424$ nm) with c-AlN ($a_{\text{c-AlN}} = 0.408$ nm) was 4.8%. The c-AlN/TiN nanolayered composite coatings with $\Lambda = 1.8$ –8 nm were grown on MgO(001) using an ultrahigh vacuum direct-current magnetron sputtering system with Al and Ti targets in a gas mixture of Ar + N₂.

Other attempts to synthesize superhard c-AlN/TiN nanocomposite coatings with high hardness employing magnetron sputtering were not successful [559, 560]. A microhardness of only 23 GPa was obtained at a bilayer repeat period of 1.1 nm.

VN/c-AlN nanolayered composite coatings were developed to improve the wear resistance of cutting tools [561, 562]. The cubic form of aluminum nitride (c-AlN) was stabilized with the help of NaCl-type VN. A maximum hardness of 59–60 GPa was reached when the bilayer repeat period was 3.6 nm with $h_{\text{VN}} = 1.8$ nm and $h_{\text{c-AlN}} = 1.8$ nm. The transformation of the AlN phase from a NaCl structure to a hexagonal wurtzite-type structure for the AlN/VN architecture occurs when the AlN nanolayers are thicker than 4 nm [563].

Nanolayered composite cermet of AlN/W with a bilayer repeat period of 3.5–7 nm were grown by magnetron sputtering on a MgO(001) [564] and Al [565] substrates. The zinc-blended phase (zb-AlN) was formed when $h_{\text{AlN}} \leq 1.5$ nm, and the stabilization was explained as a result of good interfacial matching between W(100) and zb-AlN(011) [564]. Formation of a wurtzite-type structure (w-AlN) was detected when the thickness of the AlN nanolayers was above 1.5 nm [564]. A decrease in the longitudinal elastic response in the direction of the nanocoating growth as a function of bilayer repeat period was observed in AlN/ZrN [565]. The nanocomposite coatings of AlN/NbN did not exhibit any anomalies in dependence on a bilayer repeat period in the range of 3–100 nm [567].

c-BN/TiN Unbalanced magnetron sputtering was used to template cubic boron nitride (c-BN) nanolayers between TiN nanolayers [568] because synthesis of one-phase c-BN coatings is difficult. As in the case of CN_x and c-AlN, the c-BN/TiN nanolayered composite structure was a good template for trapping the metastable c-BN phase between the TiN-nanolayers.

c-BN/TiN nanolayered composites with a hardness of 40–45 GPa were obtained [568]. The bilayer repeat period depended on the substrate bias, sputtering rate of each compound, and nitrogen partial pressure. The nanocomposite coatings remained stable and hard up to 700 °C.

An attempt to stabilize c-BN structures when sandwiched between aluminum nitride nanolayers was undertaken [569]. The nanolayered composite coatings of c-BN/AlN were prepared using reactive direct-current magnetron sputtering of a boron carbide (B_4C) target in argon–nitrogen plasma.

$\beta\text{-WC}_{1-x}/\text{MeN}$ (Me = Ti, $\text{Ti}_{1-y}\text{Al}_y$) WC/TiN nanolayered composites were deposited on Si(100) wafer and cemented carbide (WC–Co 3 at%) using the arc ion-plating system [570]. Although the single-phase WC coatings deposited separately were identified as a mixture of carbon-deficient metastable phases of $\alpha\text{-WC}$ (trigonal) and of $\beta\text{-WC}_{1-x}$ (NaCl type), only $\beta\text{-WC}_{1-x}$ was recognized in the TiN/WC nanolayers; that is, the nanolayered composite coatings can be classified as having $\beta\text{-WC}_{1-x}/\text{TiN}$ composition. In this case, the nanolayers of TiN ($a = 0.4242$ nm, NaCl type) serve as a trap for the stabilization of the metastable phase of $\beta\text{-WC}_{1-x}$ ($a = 0.4235$ nm, NaCl type), that is, stabilization of the metastable structure owing to the templating effect. These phases were matched with a small distortion.

The cross-sectional transmission electron microscopy investigation of $\beta\text{-WC}_{1-x}/\text{TiN}$ nanolayered composites provided evidence that the coatings consist of TiN and $\beta\text{-WC}_{1-x}$ -nanolayers, which are nanocrystalline conglomerates. This was also verified by selected-area electron

diffraction [570]. The residual stress of the as-deposited $\beta\text{-WC}_{1-x}/\text{TiN}$ nanolayered coatings was measured to be up to 7.9 GPa. To decrease this high level of residual stress, three types of intermediate layers, namely WC, Ti, and Ti–WC, were incorporated into the $\beta\text{-WC}_{1-x}/\text{TiN}$ nanolayered coatings. Significant reduction of the residual stress was achieved with the Ti intermediate layer (up to 2.3 GPa) and the Ti–WC intermediate layer (up to 2.2 GPa).

The microhardness of the $\beta\text{-WC}_{1-x}/\text{TiN}$ nanolayered coatings was measured to be in the range of 38–40 GPa. The maximum hardness was achieved when the bilayer repeat period had an optimum value of 7 nm. The Ti–WC interlayer did not have any effect on stress, and the $\beta\text{-WC}_{1-x}/\text{TiN}$ had the same hardness (38–40 GPa) before the interlayer was incorporated.

Nanolayered composite coatings of $\beta\text{-WC}_{1-x}/\text{Ti}_{1-y}\text{Al}_y\text{N}$ were deposited using the multicathode arc ion-plating evaporation of Ti, Al, and WC targets [571]. The approach was similar to the synthesis of $\beta\text{-WC}_{1-x}/\text{TiN}$ nanolayered composite coatings [570]. Silicon wafers of Si(100) and WC–Co(3 at%) served as substrates for the coatings. Steering the arc power density for each target controlled the composition of the coatings. To reduce the residual stress, interlayers of WC, Ti, and Ti–WC were periodically incorporated.

The nanostructure of the coatings is defined by the Al content (y). X-ray diffraction demonstrated that the coatings with $0.35 \leq y \leq 0.57$ Al content and with a bilayer repeat period of 10 nm consisted of $\text{Ti}_{1-y}\text{Al}_y\text{N}$ (NaCl type) and of cubic $\beta\text{-WC}_{1-x}$ (NaCl type). The template effect of the $\text{Ti}_{1-y}\text{Al}_y\text{N}$ nanolayers trapped the metastable phase of $\beta\text{-WC}_{1-x}$. The hardness of the $\beta\text{-WC}_{1-x}/\text{Ti}_{1-y}\text{Al}_y\text{N}$ nanolayered composite coatings reached a maximum of 50 ± 5 GPa when $y = 0.57$. Titanium–aluminum nitride nanolayers had a (111) texture. Increasing the Al content up to $y = 0.57$, the nanolayered composite coatings transformed from a monocrystalline-type structure to a nanocrystalline-type structure with an average grain size of about 10 nm. Increasing the bilayer repeat period up to 20 nm led to the transformation of $\beta\text{-WC}_{1-x}$ nanolayers into $\alpha\text{-W}_2\text{C}$ nanolayers where the $\alpha\text{-W}_2\text{C}$ phase possesses a trigonal lattice.

3.1.4. Summary

Some technological results for the synthesis of superhard nanocomposites are presented in Table 1. First of all, the coatings achieve microhardness greater than or equal to 40 GPa owing to a resultant optimal nanostructure. The bilayer repeat periods vary usually within a narrow range from 0.5 to 17 nm; the ratio of thickness of the first phase (h_1) to the bilayer repeat period (Λ) amounts to 0.3–0.4 predominantly. The exceptions are the nanolayered composites of TiN/Ti, HfN/Hf, WN/W, and TiN/NbN where h_{TiN}/Λ reaches approximately 0.5, TiN/TaN where $h_{\text{TiN}}/\Lambda = 0.34 - 0.64$, and NbN/TaN where the maximum microhardness is achieved when $h_{\text{NbN}} = h_{\text{TaN}}$ and the bilayer repeat period is 0.64. The microhardness data vary approximately as the inverse square root of the bilayer repeat period (Λ) [572]. Their microhardness follows the Hall–Petch strengthening mechanism as applied to nanolayered composites [494].

Some tribological results, which have been achieved, are presented in Table 2. Certain nanolayered composite

Table 1. Summary of the technological characteristics for the synthesis of superhard nanolayered composites.

Composition (type) of nanolayered coating	Maximum microhardness (GPa)	Range of		Coating thickness (μm)	Deposition conditions			
		Λ (nm)	h_1/Λ		Rate ($\mu\text{m/h}$)	Temperature of substrate ($^{\circ}\text{C}$)	Method	Pressure (Pa)
TiN/VN (monocrystalline type)	~56	~5.2	0.3	~2.5	~1	750	MS	0.5
TiN/NbN (monocrystalline type)	48–49	4.6–7	0.3	2.5–3	0.25–0.74	260–700	UMS	1–2
TiN/NbN (nanocrystalline type)	52	5–8	~0.5	3–6	~1	500	MS + IP	0.25–1
TiN/TaN (nanocrystalline type)	39–40	9–12	0.34–0.64	~4	0.5–3.2	70	MS + IP	0.1
TiN/Ta _x W _{1-x} N (nanocrystalline type)	50	5.6	0.34	~2	0.5–3.2	70	MS	0.1
TiN/V _x Nb _{1-x} N (monocrystalline type)	~41	10–12	0.3	~2.5	0.8		MS	~3
VN/Ti _x Al _{1-x} N (nanocrystalline type)	39	3.2		3–5		450	UMS + SAD	
VN/Ti _x Al _{0.96-x} Y _{0.04} N (nanocrystalline type)	78	4		3–5		450	UMS + SAD	
CrN/NbN (nanocrystalline type)	56	2.7–7.4		3–7		250–450	UMS + SAD	4×10^{-3} –0.3
CrN/Ti _x Al _{1-x} N (nanocrystalline type)	60	~3		3–5		450	UMS + SAD	
ZrN/Ti _x Al _{1-x} N (nanocrystalline type)	55	2.6					UMS + SAD	
NbN/TaN (monocrystalline type)	51	2.3–17	1	2	~1	70	MS	0.3–0.4
CN _x /ZrN (nanocrystalline type)	~45	4.5	0.34	4.5	3	200	UMS	1
CN _x /TiN (nanocrystalline type)	~48	0.5–3.1		3–4.5	1.3–2		MS + AD	0.2–1.3
TiN/c-AlN (monocrystalline type)	39	2.5			1.5–3.5	650	AIP MS AIP	1.7–3.9
VN/c-AlN (monocrystalline type)	59–60	3.6	0.5	3–13				
c-BN/TiN	40–45						UMS	
TiN/ β -WC _{1-x} (nanocrystalline type)	38–40	7		~3	4		AIP	
Ti _{1-y} Al _y N/ β -WC _{1-x} (nanocrystalline type)	~50						AIP	
Fe/TiC (nanocrystalline type)	42	14	0.43	0.5–1	0.2–0.7	50–60	IBS	7×10^{-3}
TiN/Ti	~37	16–18	0.5	3–8			RF-MS	
HfN/Hf	~50	8	0.5	3–8			RF-MS	
WN/W	~35	16–40	0.5	3–8			RF-MS	

Note: UMS, unbalanced magnetron sputtering; MS, magnetron sputtering; IP, ion plating; SAD, steered-arc deposition; AD, arc deposition; RF-MS, radio frequency magnetron sputtering.

Source: Reprinted with permission from [175], G. M. Demyashev et al., in "Handbook of Organic-Inorganic Hybrid Materials and Nanocomposites" (H. S. Nalwa, Ed.), Vol. 2, Chap. 13. American Scientific Publishers, Stevenson Ranch, CA, 2003. © 2003, American Scientific Publishers.

coatings possess relatively high compressive intrinsic stress, for example, VN/Ti_xAl_{0.96-x}Y_{0.04}N (-8 GPa), CrN/NbN (-6.5 GPa), CrN/Ti_xAl_{1-x}N (-9.2 GPa), and ZrN/Ti_xAl_{1-x}N (-10 GPa).

In a number of cases [455–457, 559], the nanolayered composites demonstrated comparatively low hardness, contrary to what was expected. For example, the TiN/CrN nanolayered composite coating deposited on the (WC–Co) cemented carbide with a bilayer repeat period of 15–21 nm exhibited a maximum microhardness of only 30 GPa [455–457].

For the deposition of nanolayered composites, very complicated facilities with low efficiency should be used. For example, the coatings of TiN/VN and TiN/NbN were obtained using a computer-controlled shutter [377, 397]. For a typical growth rate of approximately 1 $\mu\text{m/h}$, the required time for Ti/V target exposure for every nanolayer should be less than 1 s, which corresponds to a deposition thickness of less than 0.3 nm [377]. In the case of TiN/NbN nanocomposite coatings [397], the shutter shadowed the Ti/Nb targets for about 0.15 s. This technique should be supplied with a computer-controlled shutter [397] or a rotating substrate

Table 2. Summary of the achievable physicomechanical properties of superhard nanolayered composites.

Composition (type) of nanolayered coating	Maximum microhardness (GPa)	Stress (GPa)	Coefficient of friction	Coefficient of wear ($10^{-15} \text{ m}^{-2} \text{ N}^{-1}$)	Adhesion (N)	Roughness (nm)	Oxidation resistance (up to °C)
TiN/VN (monocrystalline type)	56						
TiN/NbN (monocrystalline type)	~52						
TiN/NbN (nanocrystalline type)	52	-1.1		129 ($\mu\text{m}^3\text{mm N}^{-1}$)	36	15	
TiN/TaN (nanocrystalline type)	40	-3.1		50 ($\mu\text{m}^3\text{mm N}^{-1}$)	38	15	
TiN/Ta _x W _{1-x} N (nanocrystalline type)	50						
TiN/V _x Nb _{1-x} N (monocrystalline type)	~41						
VN/Ti _x Al _{1-x} N (nanocrystalline type)	39	-3.3	0.18-0.4	126	70	66	
VN/Ti _x Al _{0.96-x} Y _{0.04} N (nanocrystalline type)	78	-8.5	0.22-0.65	45	39	53	
CrN/NbN (nanocrystalline type)	56	-6.5	0.23-0.9	5	62	33	850
CrN/Ti _x Al _{1-x} N (nanocrystalline type)	60	-9.2	0.2-0.92	3.1	52	62	900
ZrN/Ti _x Al _{1-x} N (nanocrystalline type)	55	-10	0.6		55	60	
NbN/TaN (monocrystalline type)	51						
CN _x /ZrN (nanocrystalline type)	~45						
CN _x /TiN (nanocrystalline type)	~48		0.05-0.2		10-50		
TiN/c-AlN (monocrystalline type)	39						
VN/c-AlN (monocrystalline type)	59-60						
c-BN/TiN	40-45						
TiN/ β -WC _{1-x} (nanocrystalline type)	40	2.2-2.3			48.5		
Ti _{1-y} Al _y N/ β -WC _{1-x} (nanocrystalline type)	~50						
Fe/TiC (nanocrystalline type)	42						
TiN/Ti	~37						
HfN/Hf	~50						
WN/W	~35						

Source: Reprinted with permission from [175], G. M. Demyashev et al., in "Handbook of Organic-Inorganic Hybrid Materials and Nanocomposites" (H. S. Nalwa, Ed.), Vol. 2, Chap. 13. American Scientific Publishers, Stevenson Ranch, CA, 2003. © 2003, American Scientific Publishers.

holder [430, 432], which helps to regulate the sputtered fluxes for the deposition of nanolayered composites.

In reality, the nanolayered composites are not so perfect [397]. As they need to reach high hardness and have a well-defined bilayer repeat period, sharp interfaces between adjacent nanolayers are often realized [432]. It was demonstrated that interdiffusion between adjacent layers greatly affects the perfection of the nanolayered coatings [436]. High-quality interfaces for dissimilar materials require that deposition rates should be both well controlled ($\pm 1\%$) and well known [573]. An *in-situ* monitoring method based on using a soft X-ray reflectometer has been developed [574],

which allows one control to accurately the thickness of each nanolayer.

Monocrystalline-type TiN/NbN nanolayered coatings have defects such as dislocations, low-angle grain boundaries, and elongated weak-phase defects [397]. These defects can affect the microhardness of the nanolayered composite coatings [436, 575].

Synthesis of nanolayered composites is a long-term process because of the inherent low rate of growth. The deposition of a few micrometers of such coatings takes a few hours, which affects the interdiffusion nanolayers and leads to the intermixing of nanolayers [397]. Extensive X-ray investigation of the interdiffusion in TiN/NbN nanolayered

composites has demonstrated [436] that up to 15% metal substitution occurs within the nanolayers and that the interface width is 0.4–2.0 nm [436, 576].

It is difficult to obtain uniform nanolayered composites of an intricate shape because the technologies are based on the “line-of-sight” phenomenon. Flat samples have been used as substrates [345, 377, 397, 430, 432]. In addition, the nanolayered composites have anisotropic properties [577]. The nanolayered coatings are usually absent in the first 300–400 nm above the substrate [397].

Precise control of the applied sputtering power and the nitrogen partial pressure in front of each target needs to be realized in order to obtain a suitable thickness of nitride nanolayers as well as a stoichiometric composition. For example, NbN deposits require higher nitrogen partial pressure than TiN deposits at the same power level [430, 432].

Modulation of the TiN/NbN composition is not constant. The ratio h_{TiN}/Λ varies with depth in the nanocomposite coatings between 0.1 and 0.3 in different areas [397]. Target poisoning is a very sensitive issue and results in a spontaneous reduction of the bilayer repeat period [578].

Preparation of substrates for deposition of nanolayered composites must be precise [345, 377, 397, 434]. The complicated process of cleaning the workpieces includes a computer-controlled automated cleaning line, several ultrasonic baths, deionized water baths, and vacuum dryers [479].

Summarizing, it is imperative to point out that the superhard nanolayered composites, as well the technologies for their deposition, have a number of weaknesses:

- Difficult to cover complicated-shape substrates
- Sometimes not compatible with polycrystalline substrates
- Difficult to support optimal bilayer period
- Line-of-sight limitations of used methods
- Strong regulation of nitrogen partial pressure for supporting stoichiometry of nanolayers
- Difficult to support the ratio h_{TiN}/Λ
- Complicated preparation of substrates
- Poisoning of the target surface during processing
- Weak adhesion between substrate and nanolayered coatings (special interlayer should be incorporated)
- Highly sensitive total pressure control [472]
- Flatter and better defined interfaces between nanolayers [471]

The above-mentioned current technologies for the deposition of nanolayered composite coatings do not lessen the prospects of the coatings. On the contrary, they stimulate further developments of novel processes for the synthesis of nanolayered composite coatings.

First, synthesis of nanocrystalline composite coatings, which have similar microhardness as nanolayered coatings, should be relatively simpler from the standpoint of deposition processes than synthesis of nanolayered coatings, and, second, nanocrystalline composite coatings are more compatible with polycrystalline substrates. Nanocrystalline composites, which are the subject of the next section, are expected to be more convenient for practical applications.

3.2. Superhard Nanocrystalline Composites

3.2.1. Introduction

Nanocrystalline composites have been classified into groups as follows [168, 175, 324, 382, 579, 580]:

- Nanocrystals of hard materials embedded into an amorphous matrix of originally hard materials such as Si_3N_4 , AlN, and diamond-like carbon
- Nanocrystals of hard materials embedded into an amorphous matrix of relatively soft metals such as Ni, Cu, and Y
- Nanocrystals of hard materials embedded into a matrix of low-dimensional materials such as carbines [21, 175] and carbon nanotubes [581–586].

Nanocrystalline composites (Fig. 2) have a number of advantages over nanolayered composites (Fig. 1). First, nanomodulation of the nanocrystalline composite coatings occurs automatically under optimal conditions [577]. Second, nanocrystalline composites have a much more isotropic structure than nanolayered composite coatings [577]. Third, interdiffusion, which can decrease hardness, can be avoided by employing low-temperature deposition conditions [577]. Fourth, coating intricately shaped substrates by nanocrystalline–amorphous composite coatings should be easier than that by nanolayered composite coatings [325, 579, 587].

3.2.2. Nanocrystalline–Hard–Amorphous–Matrix Nanocomposites

nc-Me_nN/a-Si₃N₄ (Me = Ti, W, V) The synthesis and properties of $\text{Si}_3\text{N}_4/\text{TiN}$ composite coatings have been the subject of scientific and technological interest. The first efforts to co-deposit silicon nitride and titanium nitride were undertaken in the 1980s [588–592]. The TiN/ Si_3N_4 composite coatings were prepared by chemical vapor deposition (CVD) from $\text{SiCl}_4 + \text{TiCl}_4 + \text{NH}_4 + \text{H}_2$ [588–592] and $\text{TiCl}_4/\text{SiH}_2\text{Cl}_2/\text{NH}_3$ [593] at a low pressure of 1.33–10.7 kPa and a relatively high temperature of 1050–1450 °C, which is typical of conventional CVD processes. It has become advantageous to make use of the magnetron sputtering of TiSi targets in order to produce conductive diffusion barriers for copper metallization [594, 595]. The crystal structure of the Si_3N_4 matrix is varied from the amorphous to the α and β type of Si_3N_4 [591, 596]. The average crystallite size of TiN in the amorphous Si_3N_4 matrix from the half-width of X-ray diffraction peaks is estimated to be about 3 nm [588, 591, 592]. It has been reported [588] that the solid solubility of TiN in Si_3N_4 is not significant at such elevated temperatures.

Recently, novel superhard nanocrystalline–amorphous composite coatings of nc-Me_nN/a-Si₃N₄ type with hardness higher than 50 GPa, used as an alternative for diamond-like carbon, were developed by means of plasma-assisted chemical vapor deposition [163, 208, 577, 587, 597–604] and physical vapor deposition (PVD) [605–610]. As is known [277], the diamond-like carbon has:

- High solubility in ferrous materials
- Limits in high-temperature applications, for example, etching by oxygen at high temperatures

- Low threshold of temperature stability, that is, limited by 500 °C
- Low coefficient of thermal expansion, that is, noncompatible with most substrates

As a further extension, the PVD technology was developed to overcome the highly corrosive and flammable precursors (i.e., TiCl_4 , SiCl_4 , SiH_4 , etc.) of CVD processing [605, 606].

The research and development strategy regarding the deposition of nc- $\text{Me}_n\text{N}/\text{a-Si}_3\text{N}_4$ has been extensively described [164, 577, 598, 599] and can be briefly summarized as follows:

- The components of the composite should themselves have high hardness.
- A ternary/quaternary system is used in order to form a nanocrystalline–amorphous composite with very marked interfaces.
- High adhesion of the nanocrystalline–amorphous interface should be realized.
- Relatively low deposition temperatures should lead to nanostructure formation, avoiding interdiffusion during deposition and a structure change in the steel substrates (550 °C).

Small nanocrystals (2–4 nm) of nitrides of refractory transition metals (Ti [605, 606], Zr, Hf, V, Nb, Ta, W [597]) have been embedded in a thin (0.4–0.6 nm) amorphous silicon nitride ($\text{a-Si}_3\text{N}_4$) matrix (Fig. 10).

The approach to deposition of nc-TiN/ $\text{a-Si}_3\text{N}_4$ and nc- $\text{W}_2\text{N}/\text{a-Si}_3\text{N}_4$ provides that these nanocomposites crystallize into two separate phases, which creates an n- $\text{Me}_n\text{N}/\text{a-Si}_3\text{N}_4$ nanocomposite mixture at a relatively low temperature of 500–550 °C from precursors of $\text{TiCl}_4 + \text{SiH}_4 + \text{N}_2 + \text{H}_2$ [1, 577] and $\text{TiCl}_4 + \text{SiCl}_4 + \text{N}_2 + \text{H}_2$ [611] by vacuum plasma-assisted chemical vapor deposition. The deposition temperatures are suitable for using steel substrates without any irreversible changes in their structure during deposition processing. The deposition rate used was 2.5–5 $\mu\text{m}/\text{h}$.

In particular, as the $\text{a-Si}_3\text{N}_4$ content increases up to 16–23 mol%, the hardness reaches a maximum value of approximately 50 GPa, whereas the average size of the nanocrystals becomes minimal at about 4 nm [577]. For this composition, the nanocomposite system reaches a minimum free-energy level when the specific area of the nc-TiN/ $\text{a-Si}_3\text{N}_4$ interface

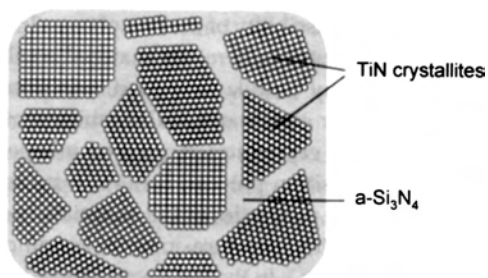


Figure 10. Schematic representation of the nc-TiN/ $\text{a-Si}_3\text{N}_4$ nanocomposite consisting of TiN nanocrystals embedded in an $\text{a-Si}_3\text{N}_4$ amorphous matrix. Reprinted with permission from [166], R. Hauert and J. Patscheider, *Adv. Eng. Mater.* 2, 247 (2000). © 2000, Wiley–VCH.

reaches maximum [208]. Further increasing the $\text{a-Si}_3\text{N}_4$ content leads to an increase in the average nanocrystalline size and a decrease in hardness.

Further vacuum annealing of nanocomposites suggests [612] that the increase in crystallite size during annealing over a temperature of $T/T_{\text{ext}} \geq 0.5$, where T_{ext} is the melting/decomposition temperature, is absent up to 1150 °C during 30 min annealing. For example, the 1150 °C is sufficiently higher than $0.5T_{\text{ext}} \sim 800$ °C for TiN and Si_3N_4 forming the nc-TiN/ $\text{a-Si}_3\text{N}_4$ component. It was concluded [233] that such high temperature stability is due to the absence of solubility of TiN in the interface nc-TiN/ $\text{a-Si}_3\text{N}_4$.

A correlation between the average nanocrystallite size, the content of $\text{a-Si}_3\text{N}_4$, and the hardness of nc-TiN/ $\text{a-Si}_3\text{N}_4$ was experimentally found. The dependence of the average nanocrystallite size on the content of $\text{a-Si}_3\text{N}_4$ reaches the minimum of the nanocrystal size. Therefore, the average nanocrystal size, which is about 9 nm, corresponds to 16–20 mol% of $\text{a-Si}_3\text{N}_4$, and the maximum hardness of the nc-TiN/ $\text{a-Si}_3\text{N}_4$ nanocomposite was found to be about 50 GPa.

Recently, there have been reports on ultrahard nanocrystalline composite coatings of nc-TiN/nc-TiSi₂/ $\text{a-Si}_3\text{N}_4/\text{a-TiSi}_2$ composition [1, 612–614] having a microhardness of 80–105 GPa. The nc-TiN/nc-TiSi₂/ $\text{a-Si}_3\text{N}_4/\text{a-TiSi}_2$ nanocrystalline multiphase composite coatings possess a high elastic recovery up to 90% [1]. Two kinds of ultrahard nanocomposite coatings, namely, nc-TiN/ $\text{a-Si}_3\text{N}_4/\text{a-TiSi}_2$ with about 5 at% Si and nc-TiN/nc-TiSi₂/ a-TiSi_2 with about 17 at% Si, were formed [1]. The nc-TiN/ $\text{a-Si}_3\text{N}_4/\text{a-TiSi}_2$ nanocrystalline composite coatings with a microhardness of 80 GPa consist of TiN nanocrystals with an average grain size of 10–11 nm surrounded by the $\text{a-Si}_3\text{N}_4/\text{a-TiSi}_2$ amorphous matrix. At about 10 at% Si, formation of the TiSi₂ nanocrystalline precipitates commences. The nc-TiN/nc-TiSi₂/ a-TiSi_2 nanocrystalline composite coatings with a microhardness of 90–105 GPa consist of TiN nanocrystals with an average grain size of 4–6 nm and TiSi₂ nanocrystals with an average grain size of 3 nm. This nanocrystalline mixture is surrounded by the TiSi₂ amorphous matrix.

A gas mixture of $\text{WF}_6 + \text{SiH}_4 + \text{N}_2 + \text{H}_2$ has been used as a precursor for high-frequency (13 MHz) plasma chemical vapor deposition of nc- $\text{W}_2\text{N}/\text{a-Si}_3\text{N}_4$ nanocrystalline composite coatings at approximately 100 Pa on Si wafer and stainless-steel substrates [597, 598]. Similar correlations were found for the nc- $\text{W}_2\text{N}/\text{a-Si}_3\text{N}_4$ nanocomposite coatings (Fig. 11). A maximum microhardness of about 50 GPa is achieved when the average nanograin sizes are 3–4 nm and the optimal Si content is approximately 7 at%.

It has been concluded [587, 597] that:

- Nanocrystalline deposits are trying to maximize the specific surface of the interfaces and, therefore, decrease the Gibbs free energy of nanocomposite formation.
- An increase in the $\text{a-Si}_3\text{N}_4$ content above 20–30 mol% leads to a decrease in the hardness of the nanocomposite.
- Deposits gain thermodynamic stability when the total area of the nanocrystalline–amorphous interfaces is maximized and both the average size of the TiN nanocrystals and the average thickness of the $\text{a-Si}_3\text{N}_4$ streaks are minimized.

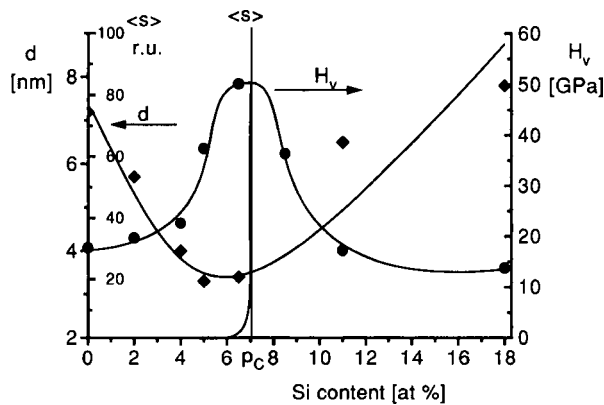


Figure 11. Average nanocrystal size (d) and hardness (H_v) of the nc-W₂N/a-Si₃N₄ nanocomposite versus a-Si₃N₄ content. Reprinted with permission from [615], S. Veprek et al., *Surf. Coat. Technol.* 108–109, 138 (1998). © 1998, Elsevier Science.

The same nc-TiN/a-Si₃N₄ nanocrystalline composite coatings have been deposited using the unbalanced magnetron sputtering technique [166, 605, 606, 616] where two separate Ti and Si targets were utilized. As expected, this physical vapor deposition technique should eliminate any weaknesses associated with plasma-assisted chemical vapor deposition and the use of the gas mixture TiCl₄+SiCl₄/SiH₄, which is hazardous and flammable, as the precursor. The incorporation of chloride into the deposits may induce interface corrosion at elevated temperatures.

As in the case of plasma-assisted chemical vapor deposition, coatings deposited by PVD exhibit a similar structure; namely, the TiN nanocrystallites are surrounded by an amorphous matrix of a-Si₃N₄. The microhardness of the nc-TiN/a-Si₃N₄ coatings, where $0 < x < 1.3$, reaches 38 GPa when the optimal content of silicon is 4–6 at%.

The presence of a-Si₃N₄ has been detected using X-ray photoelectron spectroscopy, whereas selected-area electron diffraction and X-ray diffraction do not provide any evidence of a crystal form of Si₃N₄. However, both X-ray diffraction and the selected-area electron diffraction show the presence of a crystalline form of TiN. The characteristic size of nc-TiN is approximately 20 nm.

The advantages of the nc-Me_nN/a-Si₃N₄ nanocrystalline composite coatings include [208]:

- Thermodynamical stability
- Resistance against oxidation in air at elevated temperatures
- Low-temperature deposition (500–550 °C)
- Compatibility with nonplanar substrates

The weakness of the nc-Me_nN/a-Si₃N₄ superhard nanocrystalline coating is that the solubility of silicon is high in many metal substrates [615]. Thus, the similar disadvantage of diamond-like carbon is not overcome. Replacement of the a-Si₃N₄ phase by boron nitride or aluminum nitride is likely to be one of the possible ways to eliminate the weakness of the nc-Me_nN/a-Si₃N₄ coatings. Such superhard nanostructured coatings, where the amorphous silicon nitride is replaced by BN and AlN, are reviewed in the following sections.

nc-Ti_{1-x}Al_xN/a-AlN As has been noted [615], the disadvantage of nc-MeN/a-Si₃N₄ nanocomposite coatings could be the high solubility of silicon in many metals and alloys. Replacement of the a-Si₃N₄ phase with a-AlN can bring new advantages to the modified coatings.

Superhard nanocrystalline coatings of nc-Ti_{1-x}Al_xN/a-AlN composition have been physically vapor deposited from the alloyed target TiAl (60/40 at%) in an Ar+N₂ gas mixture and at constant total pressure (0.5 Pa) using the unbalanced magnetron technique [617, 618]. It had been found earlier [618] that the Ti_{1-x}Al_xN nanocrystalline composite coatings can be formed in the range of $0.52 \leq x \leq 0.59$. The nc-Ti_{1-x}Al_xN/a-AlN nanocomposite coatings with maximum microhardness up to 47 GPa have been obtained for a stoichiometry of $x = 0.562$ and a substrate temperature of 200 °C. The coatings consist of nanograins (with an average size of ~30 nm) of Ti_{1-x}Al_xN phase bordered by the amorphous AlN phase. This nanocomposite coating exhibits high elastic recovery up to 74%.

The microhardness as a function of the partial pressure of nitrogen is a complicated relationship that is connected with the changes in structure and chemical composition of the Ti_{1-x}Al_xN deposits [617]. A maximum hardness of about 27 GPa and 33 GPa for a 5% and for 37% nitrogen partial pressure, respectively, was obtained when the substrate temperature corresponds to room temperature.

The influence of the substrate temperature was investigated [617]. The highest hardness (~47 GPa) of the nc-Ti_{1-x}Al_xN/a-AlN is achieved around 200 °C. The maximum possible hardness (~47 GPa) of the nc-Ti_{1-x}Al_xN/a-AlN nanocomposite coatings is optimized for an average nanograin size of about 18 nm, although the single-phase coatings of TiN, AlN, and Ti_{1-x}Al_xN have hardness of 21 GPa, approximately 13 GPa, and approximately 30 GPa, respectively, which is significantly lower than the approximate 47 GPa for the nc-Ti_{1-x}Al_xN/a-AlN nanocomposite coatings.

The experiments demonstrated [617] that nanograin size and grain orientation are of fundamental importance for the synthesis of such superhard nanocrystalline coatings. The maximum hardness can be realized if the grains have a suitable average size and the deposits have the appropriate texture. The (111) crystal planes of the nc-Ti_{1-x}Al_xN were parallel to the substrate surface. The structure of the superhard nc-Ti_{1-x}Al_xN/a-AlN nanocomposite coatings characterized by X-ray diffraction can be generalized as nanocomposites, which constitute highly oriented nanograins of TiAlN embedded into an amorphous matrix of AlN.

Nanocomposite coatings of (Ti, Al, Si)N with a Si content of 9.5 at% displayed maximum hardness values of approximately 60 GPa [619].

nc-Mo₂C/(a-C + a-Mo₂N) Superhard nanocomposites of nc-Mo₂C/(a-C+a-Mo₂N) composition have been synthesized during plasma nitriding with a hollow cathode discharge [620]. The conventional direct-current glow discharge [621] was modified with an auxiliary cathode [622] so that the sputtering of molybdenum and graphite into the plasma of a N₂+H₂+Ar gas mixture under 665 Pa pressure was accomplished.

The incorporation of molybdenum and carbon simultaneously into the surface of nitrided steel has enabled the formation of superhard nanocrystalline composite coatings consisting of Mo₂C nanocrystals encircled with an amorphous mixture of Mo₂N and carbon [620]. The structure of such superhard nanocomposite coatings can be expressed as nc-Mo₂C/(a-C+a-Mo₂N).

The highest hardness of 52.5 GPa is achieved when the nanocrystals have (1) predominant orientation of Mo₂C(110) parallel to the substrate surface, that is, a <110> texture, and (2) an average nanocrystal size of 48 nm. It has been explained [620] that such a high microhardness is a result of both the deposition of the nanocrystalline-amorphous composite and the orientation of the hard nc-Mo₂C nanograins only in one direction. For comparison, the hardness of polycrystalline material of Mo₂C is only 16.6 GPa [623].

nc-TiC/DLC It was expected [609, 624–628] that hydrogenated amorphous carbon (a-C:H), having both limited temperature stability up to 400 °C and low hardness of 15–25 GPa, can be improved by adding a nanocrystalline TiC fraction. Generally, amorphous carbon coatings containing transitional metals (Ti, Zr, W) can be obtained with improved tribological properties [629–636]. The combination of a closed-field unbalanced magnetron sputtering of the Ti target in the presence of argon (Ar) and acetylene (C₂H₂) or methane (CH₄) was used for the deposition of various compositions of nc-TiC/a-C:H nanocrystalline composite coatings on single-crystal Si(100) or Si(111) wafers and steel substrates [624–627].

Both the hardness and the toughness [637] of nc-TiC/a-C:H and nc-TiC/a-C [469] nanocomposites are remarkably increased with the incorporation of amorphous non-hydrogenated/hydrogenated carbon into the TiC coatings. The coating hardness in relation to the Ti content is illustrated in Figure 12. The average nanocrystalline size varies from 3–5 nm for Ti content below 43 at% to 20 nm for Ti content higher than 43 at% (Fig. 13). The maximum microhardness of 35 GPa is achieved approximately at a composition of 80% TiC and 20% a-C:H. The average TiC

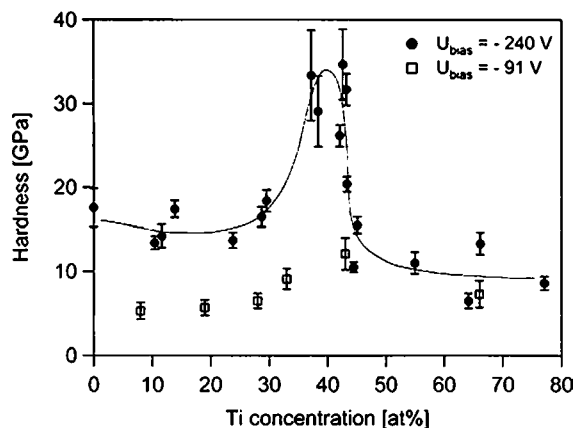


Figure 12. Microhardness of nc-TiC/a-C:H versus Ti content for negative bias of -240 and -91 V. Reprinted with permission from [624], T. Zehnder and J. Patscheider, *Surf. Coat. Technol.* 133–134, 138 (2000). © 2000, Elsevier Science.

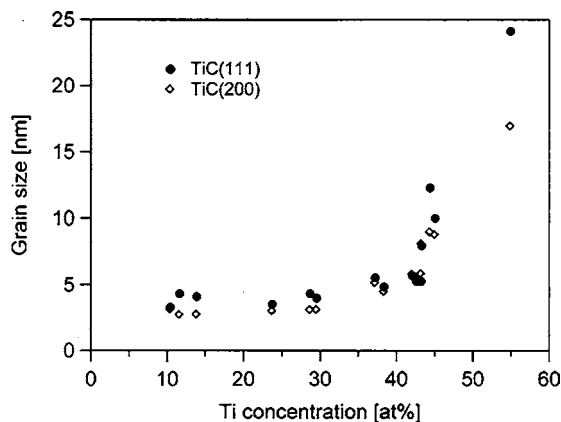


Figure 13. Average nanocrystal size of TiC versus Ti content. Reprinted with permission from [624], T. Zehnder and J. Patscheider, *Surf. Coat. Technol.* 133–134, 138 (2000). © 2000, Elsevier Science.

grain size remains within the limits of 3–5 nm until the maximum microhardness is reached. This maximum of 35–40 GPa corresponds to an average nanograin size of 4–8 nm [469, 624]. The coatings qualified [624] as nanocomposites consisting of nc-TiC embedded in an amorphous matrix of a-C:H, that is, nc-TiC/a-C:H (Fig. 14).

The Ti concentration of approximately 40% is a crucial point for other properties of the nc-TiC/a-C:H nanocrystalline composites. For example, the coefficient of friction is rapidly increased up to 0.6.

Thus, nc-TiC/a-C:H nanocrystalline composite coatings provide high hardness (~35 GPa) and low coefficient of friction (0.25–0.3) at the optimal nanostructure (an average nanograin size of ~5 nm) and composition (80% TiC and 20% a-C:H).

Vacuum-deposited nanocomposite coatings of β-WC nanograins (1–10 nm) embedded in a nonhydrogenated diamond-like carbon matrix were obtained with carbon content between 30 and 90 at% [634]. The nanostructure of β-WC/DLC results in a nanohardness [634] that is twice as hard as that of metal-doped DLC coatings. The distribution

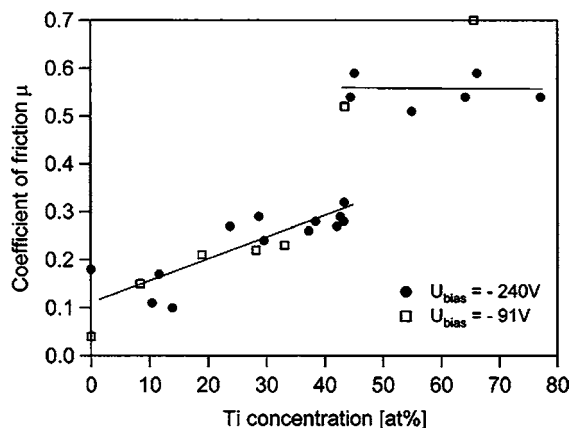


Figure 14. Dependence of coefficient of friction on Ti concentration for U_{bias} = -240 and -90 V. Reprinted with permission from [624], T. Zehnder and J. Patscheider, *Surf. Coat. Technol.* 133–134, 138 (2000). © 2000, Elsevier Science.

and density of nanograins in metal-containing DLC strongly influence the mechanical properties of Me-DLC nanocomposites [638].

Me-B-X (Me = Ti, Hf; X = C, N) This kind of superhard nanocrystalline composite coating was prepared under an optimal ratio and composition from TiB_2+TiC and TiB_2+TiN targets [281, 639–653] as well as from TiB_2 , $\text{Ti}+\text{h-BN}$, and $\text{Hf}+\text{h-BN}$ targets using magnetron sputtering [654–656].

Analysis of the Ti-B-N phase diagram provides evidence [639, 640] that nanocomposite coatings possessing both high hardness and high toughness may be obtained where TiB_2 and TiN coexist and form coherent interfaces [623, 640]. The optimal elemental composition of $\text{Ti}_{0.4}\text{B}_{0.4}\text{N}_{0.2}$ with a concentration ratio of $\text{Ti}:\text{B}:\text{N} = 2:2:1$ can provide a combination of high hardness with high toughness. The phases of TiB_2 and TiN can overcome the superhard mark if the microstructure of the TiB_2/TiN and TiB_2/TiC composites is optimized [639].

A hardness value of up to 40 GPa was obtained for Ti-B-N based coatings containing both TiB_2 and c-BN phases [657]. The highest hardness of approximately 57 GPa for $\text{TiBN}_{0.5}$ has been obtained using magnetron sputtering of the heterogeneous $\text{Ti}/\text{h-BN}$ target for a bias substrate of -150 V and temperature of 400 °C [658]. If the substrate temperature is around 25 °C, the hardness of the as-deposited TiB_2/TiN coatings is about 10 GPa, but the highest hardness is achieved by annealing for 6 h at 800 °C. The highest hardness of the TiB_2/TiN coatings can be realized using the deposition of $\text{TiN}/\text{h-BN}$ nanolayered coatings subject to annealing at 400 °C for 40–200 h [659] depending on the thickness of the $\text{Ti}/\text{h-BN}$ nanolayers. Annealing transforms the soft nanolayers to a superhard (~ 57 GPa) nanocrystalline composite of TiB_2/TiN .

Further investigation of the nanostructure has demonstrated [281, 649] that the nanograin sizes of the TiB_2/TiN and TiB_2/TiC nanocrystalline coatings with compositions of about 35–45 at% Ti, 18–44 at% B, and 20–36 at% N or 22–40 at% C vary between 3 and 5 nm. At low boron content, the coatings represent nanocrystals of TiN or TiC surrounded by a quasi-amorphous TiB_2 phase, that is, nc-TiN/a- TiB_2 or nc-TiC/a- TiB_2 . Increasing the concentration of boron reverses the nanocrystalline composite structure. At higher boron content, the coatings are nanocrystals of TiB_2 embedded by the quasi-amorphous phase of TiN or TiC , that is, nc- $\text{TiB}_2/\text{a-TiN}$ and nc- $\text{TiB}_2/\text{a-TiC}$. A microhardness of approximately 68 GPa was obtained for the TiB_2 nanocrystalline coatings having an average nanograin size of 11 nm. It was expected [281] that such a high hardness results from the high intrinsic stress achieved under intense ion bombardment conditions.

The highest hardness of up to 60 GPa has been obtained for nanocomposite coatings and for the stoichiometry of $\text{TiB}_{1.5}\text{N}_{0.45}$ and $\text{HfB}_{0.85}\text{N}_{0.3}$ [655]. The hardness of the coatings sputtered with bias voltage demonstrates a strong maximum, which corresponds to the lowest deposition rate. Without the bias voltage, a hardness of approximately 30 GPa can only be obtained. The bias voltage (-30 V) causes a decrease in the average nanograin size from 8 to 3.5 nm for $\text{TiB}_x\text{N}_{1-x}$ and from 10.5 to 3 nm for $\text{HfB}_x\text{N}_{1-x}$. The stress of the superhard nanocomposite coatings was negligible.

Nanocomposite coatings of Ti/BN with the presence of a c-BN phase as determined by XRD were deposited by plasma vapor deposition (PVD) and combined PVD/plasma-activated chemical vapor deposition (PACVD) techniques [660].

nc-TiN/a-MeN_x (Me = W, Mo) Nanocomposites of Ti-W-[661, 662] and Ti-Mo-N composition [663] have been deposited using the unbalanced magnetron sputtering technique from W-Ti (30 at%) and Ti-Mo (10 at%) targets in a gas mixture of Ar+N₂ on steel and Si substrates.

The influence of the grain size, chemical composition, and relative content of individual phases on the microhardness of the nanocomposite coatings has been studied. For a nitrogen partial pressure of more than 0.1 Pa, only the single body-centered cubic phase of TiN was identified. The maximum microhardness of approximately 60–66 GPa for the nc-TiN/a-WN_x nanocomposite coatings was achieved for 25 at% nitrogen content and a ratio of $\text{Ti}/\text{W} = 0.32$ [661]. The result was interpreted [661] that when the nitrogen concentration in the coatings reaches approximately 30 at%, tungsten becomes amorphous and nanograins of TiN are formed. The formation of a-WN_x and TiN nanograins of 10–20 nm creates the nc-TiN/a-WN_x nanocomposite with a high hardness [661, 664].

Nanocomposite coatings of the Ti-Mo-N system have a maximum microhardness of approximately 45 GPa, which is achieved when the (111) or (200) texture reveals itself. The presence of the TiN phase only was fixed by X-ray diffraction. As has been stated [663], the coatings of the Ti-Mo-N system behave like nanocomposite coatings of Zr-Cu-N, Ti-Al-N, and Zr-Y-N where the amorphous phase plays the role of a binder. Therefore, the structural composition of the coatings could be classified as nc-TiN/a-MoN_x.

3.2.3. Nanocrystalline-Soft-Amorphous-Matrix Nanocomposites

nc-MeN/a-Ni (Me = Zr, Cr) Coatings of the Zr-Ni-N and Cr-Ni-N ternary systems [663, 665–669], deposited using direct-current magnetron sputtering of Zr-Ni (90/10 at%) and Cr-Ni alloy targets in Ar-N₂ mixture onto steel substrates, correspond to a nanocomposite of nc-MeN/a-Ni type combining a hard nc-ZrN phase (nanograins of 10–50 nm in diameter) embedded in a soft Ni matrix. The nanocomposite coatings displayed the following characteristics [665, 666]:

- Strong influence of the nanostructure and the Ni content in the nanocomposite coatings on their microhardness
- High hardness of up to 57 GPa for Zr-Ni-N and up to 37 GPa for Cr-Ni-N nanocomposite coatings
- The microhardness of the Zr-Ni-N and Cr-Ni-N nanocomposite coatings regulated by variation of partial pressure of nitrogen and negative bias voltage
- The nc-ZrN/a-Ni nanocomposite coating, possessing the highest microhardness, consisted of 4 at% Ni, 50 at% Zr, and 46 at% N.

The investigations demonstrated that the incorporation of nitrogen into the ZrNi deposit transforms the ZrNi alloy into a nc-ZrN/a-Ni nanocomposite. The microhardness of

the nc-ZrN/a-Ni nanocomposite coatings reaches a maximum of about 55 GPa at a nitrogen partial pressure between 0.03 and 0.15 Pa depending on the substrate bias voltage [665].

As stated [665], the influence of the substrate bias on the microhardness is very similar to the influence of the nitrogen partial pressure [665]. The nanocomposite coatings with a microhardness of 51.1 GPa prepared at a substrate bias of -75 V and with a microhardness of 54.6 GPa prepared at a substrate bias of -125 V differ in nanograin size. Therefore, the nanocomposite coatings with 51.1 GPa have an average nanograin size of 23 or 57 nm depending on the method of evaluation. The nanocomposite coatings with 54.6 GPa have an average nanograin size of 14 or 5 nm.

The nc-CrN/a-Ni nanocomposite coating possessing the highest microhardness of up to 37 GPa has been deposited from a Cr target fixed with a Ni ring at a partial nitrogen pressure of 0.08 Pa and a substrate temperature of 300 °C [666]. Later, a microhardness of approximately 45 GPa for the Cr-Ni-N system was achieved [663].

Recently, the origins of the high hardness of ZrN/Ni and CrN/Ni nanocomposites was investigated [669]. It was indicated [669] that the hardness enhancement is due to a high biaxial compressive stress in the ZrN/Ni and CrN/Ni nanocomposites. No hardness enhancement due to the nanostructure formation could be attributed to the ZrN/Ni and CrN/Ni nanocomposites [669].

The attempt to obtain such hard nanocomposite coatings of TiN/Ni has not met with much success [668]. The maximum hardness measured in the TiN/Ni was 10.5 GPa only. It was suggested [668] that the hardness could be increased with decreasing Ni content.

nc-MeN/a-Cu (Me = Zr, Cr, Al, Al-Si) The nc-ZrN/a-Cu nanocomposite coatings were prepared by sputtering the Zr-Cu alloyed target in an Ar+N₂ mixture using an unbalanced direct-current magnetron system under a total pressure of 0.7 Pa [670-673].

The microhardness of the ZrN/a-Cu composite coatings, which contained approximately 1-2 wt% Cu, exceeds 40 GPa [670]. X-ray diffraction displayed a strong reflection from ZrN nanograins and no reflections from copper. The microhardness proved to be very sensitive to the substrate current density and the substrate temperature. The negative substrate bias was found not to have a strong influence on the microhardness, which remains nearly constant for a wide range of negative substrate bias voltages.

A substrate current density (i_s) higher than 0.8 mA/cm² is favorable to obtain nc-ZrN/a-Cu superhard nanocomposite coatings. The range of substrate temperatures (T_s) between 200 and 400 °C provides the deposition of the coatings with microhardness higher than 45 GPa. Among these optimal regimes, the highest microhardness (~54 GPa) of the nc-ZrN/a-Cu containing 1-2 at% Cu corresponds to $T_s = 300$ °C and $i_s = 1$ mA/cm².

These experiments suggest that the incorporation of nitrogen into the deposits leads to the nanocrystalline structure formation of the coatings, where nc-ZrN and a-Cu are components of the nanocomposite. X-ray diffraction indicated only intensive X-ray peaks from ZrN nanograins oriented so that the $\langle 111 \rangle$ texture appears. Copper and its compounds

have no X-ray peaks, which is evidence of the X-ray amorphous state of the Cu matrix. The average nanograin size evaluated from the integral width of the X-ray peaks was 35 nm.

Replacement of Zr on Cr in combination with Cu has provided similar results [672]. The highest microhardness achievable was approximately 35 GPa [672]. The nc-CrN/a-Cu nanocomposite coatings with the highest hardness were sputtered at 300 °C with a substrate bias of -500 V and a substrate ion current density of 1.6 mA/cm². The optimal composition of the superhard nc-CrN/a-Cu nanocomposite coatings was 1 at% Cu, 48 at% Cr, and 51 at% nitrogen. X-ray diffraction did not display the presence of copper and no crystalline Cu phase was observed.

Superhard nanocomposite coatings of the Al-Cu-N [306] and Al-Si-Cu-N [674] systems have been prepared by the unbalanced magnetron sputtering technique from targets composed of Al+(2-12) at% Cu and Al+(5-9) at% Si+(2-12) at% Cu, respectively. A mixture of Ar+N₂ was used under a total pressure of 0.5 Pa. The maximum hardness of approximately 48 GPa is reached at a nitrogen partial pressure of 0.13 Pa and composed of substoichiometric AlN_x (N/Al = 0.77) with an average nanograin size of 9.5 nm [675]. The AlN_x nanograins are surrounded by 8.1 at% Cu, which has an X-ray amorphous state.

nc-ZrN/a-Y Nanocomposite coatings of the Zr-Y-N system can achieve a hardness of up to 47 GPa if they possess both an optimal nanostructure and a composition. An unbalanced magnetron sputtering of the alloyed targets of Zr-Y (80/20 at%) and Zr-Y (93/7 at%) has been utilized for the synthesis of this type of coating [676, 677]. Alloying with yttrium has been found to have a positive influence on reducing the grain size and decreasing the starting temperature of oxidation [678, 679]. Coatings of various compositions of Zr-Y-N were deposited in N₂ and N₂+Ar atmosphere under a total pressure of 0.5 Pa. The typical coating thickness was approximately 3 μm.

The hardness of such coatings suggests dependence on the partial pressure of nitrogen [676]; that is, the partial pressure of nitrogen predominantly influences the nanostructure formation of the coatings. The average nanograin sizes vary between 4 and 20 nm. The superhardness (~41 GPa) is achieved when the average grain size becomes about 20 nm for $P_{N_2} = 0.0025$ Pa. These deposits were characterized by the (200) X-ray texture of the nc-ZrN phase. The embedding phase containing yttrium is X-ray amorphous. The nc-ZrN/a-Y nanocomposites achieve a maximum microhardness when the incorporation of nitrogen becomes higher.

The ratio of N/(Zr+Y) affects the microhardness of the Zr-Y-N coatings [676]. The highest possible microhardness (~45 GPa) is achieved when the ratio of N/(Zr+Y) reaches about 1.

3.2.4. Nanocrystalline-Low-Dimensional-Matrix Nanocomposites

nc-W₃C/nc-Carbynes It was demonstrated [45, 680] that tungsten carbide coatings can be synthesized by low-temperature chemical vapor deposition in a hot-wall reactor

using the precursors of WF_6 , C_3H_8 , H_2 , and Ar as the carrier gas. The process is carried out at atmospheric pressure and within a temperature range of 400–900 °C. The results of such experiments showed [45, 680] that the deposition of tungsten carbide phases depends on the concentration of propane in the gas mixture as well as catalytic pretreatment of the propane.

Equally with the conventional tungsten carbide phases of WC with a simple hexagonal lattice ($a = 0.2907$ nm and $c = 0.2837$ nm) and W_2C with a hexagonal close-packed lattice ($a = 0.30008$ nm and $c = 0.47357$ nm), a novel tungsten carbide phase (~ 0.8 wt% C) was synthesized [45, 680]. On the basis of chemical analysis and X-ray diffraction, the structure of the chemically deposited novel tungsten carbide was identified [680] as a cubic structure of A15 type with a lattice parameter $a_0 = 0.5041$ nm. Later, the novel tungsten carbide phase was classified as the W_3C phase [21, 175]. The A15 lattice has a cubic-type structure with a space group of $Pm\bar{3}n(\#223)$ [681]. Among tungsten compounds, only three phases with the A15 lattice [i.e., $\text{W}_3\text{O}(\beta\text{-W})$, W_3Si , and W_3Re] were known. Because this novel tungsten carbide phase has an unusual lattice of the A15 type, which is typical of superconductors [681], the critical temperature transition to superconductivity was defined experimentally as being equal to 2.55 K [680], which is different from 2.74 K for W_2C and 1.28 K for WC. This novel tungsten carbide phase decomposes to tungsten and W_2C carbide above 1000 °C [680].

This novel W_3C phase differs from the very well established WC and W_2C in terms of properties and is characterized by a very high hardness of approximately 35 GPa [680]. The deposited W_3C coatings have been identified by X-ray diffraction as the single tungsten carbide phase [680].

Selected-area electron diffraction (SAED) indicated the presence of additional diffraction rings [682, 683], which were not fixed by X-ray diffraction. Comparison with the very well known carbon structures [684, 685], and carbides WC and W_2C [299, 686, 687], showed that the extra electron diffraction rings belong to α - and β -carbynes and their mixture—chaoite [22]. Carbynes are little known carbon compounds [22, 23, 685], that is, α - and β -carbynes, chaoite, with sp^1 covalent bonds. The sp^1 hybridized carbon atoms settle down along a straight line, provide symmetry, and form linear chainlike arrangements of carbon atoms.

The lamellar structure of the W_3C deposits was found [21, 175, 682, 683, 688, 689] to be bound up with the co-deposition of carbynes. The coatings represent a composite of the two phases: one being the W_3C phase and the other the α/β -carbynes. This provided a hint on the existence of very fine grain sizes in the deposits. Calculations from extended X-ray peaks using the Scherrer formula [690] showed that the average grain size was 70 nm. Furthermore, direct TEM investigations using the dark and bright fields of the TEM images confirmed (Fig. 15) that (1) the composite deposits have a nanocrystalline structure and (2) they are compounds of nanoscale size of both nc- W_3C phase and nc-carbynes. The W_3C grains measuring in the range of 50–100 nm, in turn, formed microclusters of size 2–5 nm embedded within a very fine (up to 1 nm) carbyne matrix. Carbynes, which were present in the deposits throughout the volume of coatings, usually had size measuring between 2 and 5 nm.

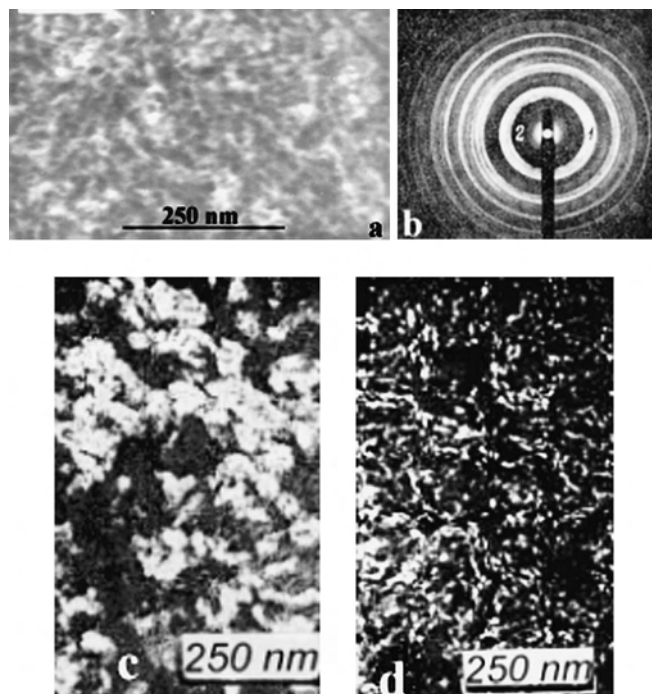


Figure 15. Typical transmission electron microscopy images of the nc- $\text{W}_3\text{C}/\text{nc}$ -carbyne nanocomposite: (a) bright-field imaging, (b) selected-area electron diffraction, (c) dark-field imaging of W_3C nanograins, and (d) dark-field imaging of nc-carbyne nanograins. Reprinted with permission from [21], G. M. Demyashev et al., *Nano Lett.* 1, 183 (2001). © 2001, American Chemical Society.

Two kinds of alternating layers were regularly formed in the composite deposits: on the one hand, layers with higher carbide content, larger sized carbide crystallites (~ 5 nm), and smaller sized W_3C clusters (up to 50 nm); on the other hand, layers with lower carbide content, smaller sized carbide crystallites (~ 2 nm), and larger sized W_3C clusters (up to 100 nm).

Thus, the nanocrystalline structure of the composite coatings in conjunction with the unusual crystal structure of both the W_3C phase (A15-type lattice) and the carbynes (linear chainlike arrangements of carbon with double/triple bonds) was considered to be a major precondition for the high hardness (~ 35 GPa) of the nc- $\text{W}_3\text{C}/\text{nc}$ -carbyne coatings. Repeated hardness measurements of cross sections demonstrated the gradual alternation of the microhardness between 35 and 40 GPa, corresponding to the change of carbynes in the lamellae. These nanocomposite coatings exhibit low internal stress, high temperature stability, low coefficient of friction, good adhesion, and high corrosion protection [21, 175].

Investigation of the temperature stability of these coatings using an *in-situ* heating system of TEM showed [682, 683] that the deposits decompose into tungsten, W_2C carbide, and amorphous carbon at about 1200 °C. This temperature is significantly higher than 1000 °C, as roughly evaluated before [680].

3.2.5. Summary

The main features of nanostructured composite coatings have been summarized as follows [579]:

- Boundaries in the form of an amorphous matrix play a decisive role in the formation and growth of the coatings.
- Superhardness of the nanocomposite coatings strongly depends on the size of the nanograins.
- Nanograins are free of dislocations.

One difference between the superhard nanocrystalline–hard-amorphous-matrix nanocomposite coatings (see Section 3.2.2) and the superhard nanocrystalline–soft-amorphous-matrix nanocomposite coatings (see Section 3.2.3) is that the first ones are brittle and the second ones have a higher toughness [580]. Both types of superhard nanocomposite coatings were represented in the “hardness–toughness” coordinate system [580].

A detailed investigation of the superhard nanocomposite coatings of the nc-MeN/soft-amorphous-phase type demonstrated the dependence of microhardness on [324, 580]:

- Content of the soft amorphous phase
- Kind of element that forms the hard nanocrystalline phase (nc-MeN)

Research demonstrated that the synthesis of ultrahard coatings requires at least three-phase nanocomposites [163, 324, 326]. For example [1], multiphase nanocomposite coatings with microhardness higher than 80 GPa consist of nc-TiN/a-Si₃N₄/a- and nc-TiSi₂. Superhard nanocomposite coatings are characterized by a high elastic recovery (up to 85% for 70 GPa).

The nanocrystalline structure of the superhard coatings gives rise to other tribological properties of the coatings such as coefficient of friction and wear resistance. Incorporation of copper into TiN coatings reduces the coefficient of friction from 0.6–0.7 for TiN to 0.2–0.4 for the nc-TiN/a-Cu nanocomposite coatings [324]. The hardness of the nc-TiN/a-Cu nanocomposite coatings with a frictional coefficient of 0.2–3 ranges between 20 and 30 GPa [168, 324]. One potential disadvantage of the nc-MnN/a-Si₃N₄ nanocrystalline coatings may be the high solubility of silicon in many metals, including ferrous-based metals, aluminum alloys, superalloys, and others [615].

The nc-W₃C/nc-carbyne superhard nanocomposite coatings do not follow a common scheme of formation of superhard nanocomposite coatings such as the nc-MeN/hard phase [615] or nc-MeN/soft phase [580]. First, carbynes are low-dimensional chainlike structures [691]. Second, the nc-W₃C/nc-carbyne nanocomposite coatings achieve the superhardness threshold at a relatively large nanocrystal size (~70 nm). Third, the nc-W₃C/nc-carbyne nanocomposite coatings with large grains (greater than 10 nm) have an unexpectedly low internal stress (0.5–1 GPa), as expected [328].

Currently, it is possible to state that superhard nanocrystalline composite coatings can be synthesized as the following combinations:

- Nanocrystalline–hard-amorphous-matrix composite coatings (see Section 3.2.2.)

- Nanocrystalline–soft-amorphous-matrix composite coatings (see Section 3.2.3)
- Nanocrystalline–low-dimensional-matrix composite coatings (see Section 3.2.4)

The data in Table 3 were compressed as much as possible. Every line of Table 3 represents data from different sources. Table 3 was compiled on the basis of revised publications. The temperature stability is defined as the temperature recrystallization at which the grain growth occurs.

Table 4 presents some performance characteristics of superhard nanocrystalline composite coatings. First of all, attention was paid to their hardness. Data of other important tribomechanical properties are very limited, which means that the application potential of such coatings is still ahead.

4. SYNTHESIS OF SUPERHARD NANOCOMPOSITES

Only technologies that were used for the synthesis of superhard nanocomposites are highlighted here.

The conditions for the deposition of nanolayered composites have been defined as [573]:

$$(R/N_0\nu) \exp(6E_2/kT) > 1$$

where R is the deposition rate, N_0 is the number of sites for absorption having equal absorption energy, ν is the atomic vibration frequency (10^{12} – 10^{13} s⁻¹), E_2 is the adatom–adatom bond energy, k is Boltzmann’s constant, and T is the absolute temperature. Nanolayered composites can be deposited using any method in which the structure is formed by means of atom-by-atom processing [573], and, as consequence, they have a relatively low rate of deposition (Table 1).

Practical rules for the synthesis of nanocrystalline–amorphous composites are as follows [163, 208, 577, 587, 692]:

- A ternary system should be used, which allows for the formation of nanocrystalline–amorphous composites with sharp interfaces.
- The cohesive energy of the interfaces should be high.
- The phases forming the nanograins should be hard.
- Low-temperature deposition should be used in order to avoid interdiffusion.
- The matrix should be amorphous and thin to reduce crack formation/propagation.

Many transitional metal nitrides, borides, and carbides are hard and can serve as nanocrystalline components.

As has been stated [168, 324, 327, 382, 579, 580], there are two basic processes for controlling the grain size in nanocomposite coatings:

- Low-energy ion bombardment
- Mixing by incorporation of additional elements into a base material

Low-energy ion bombardment of growing nanocomposites can effectively change the deposition mechanism. The effect of low-energy ion bombardment, which restricts grain

Table 3. Summary of the technological characteristics for the synthesis of superhard nanocomposites.

Composition of nanocrystalline coating	Maximum microhardness (GPa)	Nanocrystalline		Coating thickness (μm)	Deposition conditions			
		Phase type	Grain size (nm)		Rate ($\mu\text{m/h}$)	Temperature of substrate ($^{\circ}\text{C}$)	Method	Pressure (Pa)
nc-TiN/a-Si ₃ N ₄ (16–20 at% a-Si ₃ N ₄)	~50	nc-TiN	9	~2	2.5–5	500–550	PACVD	100–500
nc-TiN/a-SiN _x (0 < x < 1.3, 4–6 at% Si)	38–47	nc-TiN	~20	1.2–8	0.5	350	UMS	0.5
nc-TiN/a-Si ₃ N ₄ /a-TiSi ₂ (5 at% Si)	80	nc-TiN	10–11	3–11	~1.8	550	PACVD	500
nc-TiN/nc-TiSi ₂ /a-TiSi ₂ (17 at% Si)	90–105	nc-TiSi ₂	~3	3–11	~1.8	550	PACVD	500
		nc-TiN	4–6					
nc-W ₂ N/a-Si ₃ N ₄ (~7 at% Si)	~52	nc-W ₂ N	3–4	2–4	1.4–2.2	500–550	PACVD	100
nc-VN/a-Si ₃ N ₄	~45	nc-VN						
nc-Ti _{1-x} Al _x N/a-AlN (x = 0.562)	~47	nc-TiAlN	18–30	~2.5		25–400	UMS	0.5
nc-Mo ₂ C/(a-C + a-Mo ₂ N)	~53	nc-Mo ₂ C	~48	2		600	GD	665
nc-TiC/a-C : H	~35	nc-TiC	~5	1.5–2		50–150	UMS	2
TiC/TiB ₂	~71	nc-TiC	1–2.5			300–400	UMS	0.8
TiN/TiB ₂	~57	nc-TiN	1–2.5	2–10		300–500	MS	0.8
nc-TiN/a-WN _x	~60	nc-TiN	10–20	3.5	~11	240–430	UMS	0.5
nc-TiN/a-MoN _x	~45						UMS	
nc-ZrN/a-Ni (4 at% Ni)	~57	nc-ZrN	5–14	3–5	3–8	25–300	UMS	0.7
nc-CrN/a-Ni	~37	nc-CrN		~3	3–8	25–300	MS	0.5
nc-ZrN/a-Cu (1–2 wt% Cu)	~54	nc-ZrN	~38	2.5		200–600	UMS	0.7
nc-CrN/a-Cu (~1 at% Cu)	~35	nc-CrN	70–90			25–650	MS	0.5
nc-AlN/a-Cu (~8 at% Cu)	~48	nc-AlN	~9.5	3		25–500	UMS	0.5
nc-ZrN/a-Y	~45	nc-ZrN	~20	3	6–12	200–300	UMS	0.5
nc-W ₃ C/nc-carbynes	~40	nc-W ₃ C	50–100	2–300	10–500	400–900	LTCVD	atm (10 ⁵)
		nc-carbyne	5–50	and more				

Note: PACVD, plasma-assisted chemical vapor deposition; UMS, unbalanced magnetron sputtering; MS, magnetron sputtering; GD, glow discharge; LTCVD, low-temperature chemical vapor deposition.

Source: Reprinted with permission from [175], G. M. Demyashev et al., in “Handbook of Organic–Inorganic Hybrid Materials and Nanocomposites” (H. S. Nalwa, Ed.), Vol. 2, Chap. 13. American Scientific Publishers, Stevenson Ranch, CA, 2003. © 2003, American Scientific Publishers.

Table 4. Summary of some important physical–mechanical properties of superhard nanocomposites.

Composition (type) of nanocrystalline coating	Maximum microhardness (GPa)	Stress (GPa)	Coefficient of friction	Coefficient of wear (m ⁻² N ⁻¹)	Scratch adhesion (N)	Roughness (μm)	Stability/oxidation ($^{\circ}\text{C}$)
nc-TiN/a-Si ₃ N ₄	~50	–0.5					1150/850
nc-TiN/a-Si ₃ N ₄	~38		0.6–1.0	10 ⁻⁵ mm ³ /m			
nc-TiN/a-Si ₃ N ₄ /a-TiSi ₂ (5 at% Si)	80						
nc-TiN/nc-TiSi ₂ /a-TiSi ₂ (17 at% Si)	90–105						
nc-W ₂ N/a-Si ₃ N ₄	~50						
nc-VN/a-Si ₃ N ₄	~45						
nc-Ti _{1-x} Al _x N/a-AlN (0.52 ≤ x ≤ 0.59)	~47		0.25–0.3				
nc-Mo ₂ C/(a-C + a-Mo ₂ N)	~53						
nc-TiC/a-C : H	~35	–1	0.25–0.3	10 ⁻⁷			
TiC/TiB ₂	~71						850–1000/1000/
TiN/TiB ₂	~57						
nc-TiN/a-WN _x	~60						
nc-TiN/a-MoN _x	~45						
nc-ZrN/a-Ni	~55						
nc-CrN/a-Ni	~35						
nc-ZrN/a-Cu (1.2 at% Cu)	~54	–4.0					
nc-CrN/a-Cu	~35						
nc-AlN/a-Cu (8.1 at% Cu)	~47	–1.4					
nc-ZrN/a-Y	~45						
nc-W ₃ C/nc-carbynes	35–40	0.5–1	0.1–0.12			0.5–1	1200/

Source: Reprinted with permission from [175], G. M. Demyashev et al., in “Handbook of Organic–Inorganic Hybrid Materials and Nanocomposites” (H. S. Nalwa, Ed.), Vol. 2, Chap. 13. American Scientific Publishers, Stevenson Ranch, CA, 2003. © 2003, American Scientific Publishers.

growth, has been defined by energy per deposited atom (E_p) [693]:

$$E_p \approx eU_s(i_s/a_D)$$

where U_s is the substrate bias, i_s is the substrate ion current density, a_D is the deposition rate, and e is the elementary charge.

For efficient control of the nanostructure, the value of the substrate ion current density (i_s) should be greater than 1 mA/cm² [382]. Low-energy ion bombardment is a nonequilibrium process, called atomic scale heating, and is accompanied by (1) heating the growing deposit at an atomic scale and (2) applying an extremely fast cooling rate of about 10¹⁴ K/s [327, 382].

For deposition of nanostructured coatings, researchers usually try to increase the rate of nucleation and decrease the growth rate. Low-energy ion bombardment stops grain growth and allows the formation of a nanostructure [382]. Ion bombardment should be used for nanostructure formation cautiously because the residual stress increases with increasing ion bombardment energy [694].

The mixing process is the second method allowing for control of nanostructure deposits [324, 327, 382]. The main parameters that control a nanostructure include the amount and type of additional elements [382]. The following factors play a vital role in the formation of nanocrystalline structures [382]:

- Mutual miscibility/immiscibility of deposit elements
- Ability of the elements to form solid solutions or intermetallics
- Negative/positive enthalpy in alloy formation

The mixing process in comparison with low-energy ion bombardment has no substrate bias, but external heating is necessary [327]. The formation of nanocomposite structures is explained by the co-deposition of two phases. A segregation in binary (or ternary) systems, which is a driving force for the spontaneous self-organization of nanostructure formation [692], is realized by means of narrow boundaries consisting of an amorphous phase.

The revised superhard nanocomposites were prepared by various evaporation/sputtering techniques [161, 168, 169, 170, 272, 281, 324, 345, 353, 377, 378, 397, 401, 430, 432–435, 448, 454, 455–459, 471, 472, 479–483, 496, 509, 526, 535, 539, 541, 543, 557, 559, 568, 573, 579, 580, 605, 606, 609, 615–618, 624, 640–642, 661, 663, 665, 667, 668, 670–672, 675, 677], vacuum arc evaporation [552, 570, 571, 644, 646, 678], ion beam–assisted deposition [555], pulsed laser deposition [625, 637], ion beam implantation [639], plasma-assisted chemical vapor deposition based on different sources of power [1, 469, 577, 597, 598, 600, 643], conventional chemical vapor deposition [21, 45], and so forth. All applicable technologies realize nonequilibrium conditions [579], which can produce the nanostructured state of materials. Comprehensive reviews of vapor processing of nanostructured materials have been published elsewhere [695, 696].

Commonly used methods to produce nanocomposite coatings are plasma-assisted techniques, which provide [45, 577, 697]:

- Low deposition temperatures

- Possibility to control the ion bombardment of the growing coating in order to minimize grain size and compressive stress
- High rate of nucleation and low rate of grain growth simultaneously
- Superfast cooling rates reaching up to 10¹⁴ K/s at an atomic level

Magnetron sputtering technology [698–701] is the most frequently used technique for deposition of nanostructured coatings [702, 703]. The magnetron sputtering systems can have a number of configurations such as direct-current diode electrical circuit, alternating-current sputtering, and radio frequency (13.56 MHz) diode sputtering [696].

The principles of nanocomposite deposition by magnetron sputtering have been considered elsewhere [579, 692]. Magnetron sputtering is a nonequilibrium process with extremely high cooling rates of up to 10¹⁴ K/s that is similar to a quenching process [579]. The direct-current magnetron sputtering process includes [696, 704–706]:

- Sputtering processes
- Direct-current plasma formation
- Transport of species
- Kinetics of coating growth
- Chemical interaction on target and coating surfaces

Direct-current magnetron sputtering (DCMS) systems have been used for growing superhard nanolayered composite coatings such as TiN/VN and TiN/NbN.

If the permanent magnetic fields of magnets located under the target are unbalanced, the magnetic field lines flair toward the substrate, which enhances the ion bombardment of the substrate. This design is referred to as unbalanced magnetron sputtering (UMS).

Unbalanced magnetron sputtering has been used for the deposition of superhard nanolayered composite coatings such as TiN/NbN [432] as well as superhard nanocrystalline composite coatings such as nc-TiN/a-Si₃N₄ [605]. Usually, two pairs of rectangular targets, for example, Nb and Ti targets, are installed in a cylindrical vacuum chamber. A rotation shaft with hanging workpieces [605] has been used as a holder. To obtain nanolayered composite coatings, a bilayer repeat period is controlled by the rotation speed of the workpiece holder.

The UMS has a number of distinctions. The separated targets allow independent regulation of each target in order to adjust the ratio of depositing atoms. The UMS configuration also allows both a high sputtering rate and a high plasma density in the zone of deposition. The planetary rotation of the workpieces provides uniform exposure of the growing coatings [605].

The main advantages of UMS systems are as follows [327]:

- Nonequilibrium process at atomic level
- No problems with sputtering of alloys and their nitrides, carbides, etc.
- Deposited ions with a high energy
- Magnetron systems easily commercialized

The high energy of deposited atoms enables (1) synthesis of high-temperature phases on unheated substrates owing

to high cooling rates ($\sim 10^{14}$ K/s) and (2) formation of nanocomposite coatings of the nc-MeN/soft-amorphous-phase type [327]. Three basic configurations have been used for sputtering of nanocomposite coatings [327]:

- One magnetron with an alloyed target
- Two magnetrons with targets fabricated from different metals, alloys, or compounds
- Pulse-operated dual magnetron

The major advantage of plasma-assisted chemical vapor deposition (PACVD) operating at low pressure is that it allows one to reduce the deposition temperature as compared to a conventional CVD process [707].

Microwave plasma reactors having a specific strength, such as a nonpolluting electrodeless plasma source, are of interest in surface engineering [708, 709]. Microwave plasma systems are devices in which a microwave discharge is employed to yield plasma of desired physical properties. The microwave source design and operation must satisfy three main objectives [710]:

- Filling the discharge tube with the required gas composition, pressure, and flow rate
- Providing distribution and intensity of the required electromagnetic field in order to initiate and sustain the discharge
- Ensuring an efficient power transfer from the microwave source to the plasma

Different designs of low-pressure microwave plasma reactors can be realized, namely [706, 711–714]:

- Jar-type design where the microwave plasma at low pressure in a dielectric jar (quartz or alumina) is sustained
- Tube-type design where a dielectric tube of the same material with low pressure inside is put through a microwave guide

The other microwave plasma-processing configurations have been reviewed elsewhere [715].

The microwave plasma process at atmospheric pressure without any vacuum restrictions is a favorable approach to perform plasma coating deposition and surface modification in run-through processes of large-sized, low-cost products. There are two types of atmospheric pressure microwave plasma discharge setups. One is a waveguide-based design [716, 717]. The other system exploits the microwave resonance phenomenon in which the selected resonance mode fixes the electric field geometry inside the cylindrical resonance cavity [175, 718, 719] to create a region of strong electric field that is Q times greater than that in a waveguide-type setup (Q is the quality factor of the resonance system). The localized electric field, in turn, allows one to control the location of the breakdown and sustains discharge. The microwave resonance plasma torch developed on the basis of a cylindrical resonance cavity surpasses the conventional plasma spray sources in characteristics and is an emerging process for nanotechnology [720–722].

In particular, the microwave resonance plasma torch is based on the cylindrical resonant cavity operating in the TM_{013} mode [175, 718, 719]. This mode in the cylindrical waveguide is of interest to plasma applications because it is

well suited to producing stable axial microwave plasma discharges [723]. The typical unloaded Q factor of TM_{013} mode cylindrical resonators is greater than 50,000 at 2.45 GHz, which makes available a required ionizing electric field density for plasma discharge and uses microwave energy to produce expanding plasma directed through a convergent-divergent nozzle [724]. Different precursors (gases, liquids, powders) and carrier gases (N_2 , Ar, He, etc.) can be utilized for formation of the microwave plasma torch.

The direct-current glow discharge plasma nitriding system allows deposition of superhard nanocomposite coatings [620, 622] and is equipped with both a conventional cathode and an auxiliary cathode. The auxiliary cathode fulfills two functions:

- Intensifying nitriding discharge by additional discharges in the holes of the hollow cathode
- Sputtering auxiliary cathode materials

The sputtered material is integrated onto the surface of nitrided workpieces. The auxiliary cathode is made from materials that should be built in to the nitrided layer in order to form nanocomposite coatings. This technique has been used for the deposition of nc-Mo₂C/(a-C+a-Mo₂C) superhard nanocomposite coatings [620].

Chemical vapor deposition, which is deposition processing of solid coatings on heated surfaces as a result of chemical reactions in a vapor phase, is a commercialized versatile technology [725–727] that has been widely adopted. Hot-wall chemical vapor deposition (HWCVD) is a well-established process [728] that is commonly used for surface engineering. In HWCVD, exterior heating of the reactor walls activates chemical heterogeneous/homogeneous reactions capable of coating deposition on substrates. Therefore, the reaction chamber, substrates, and a reactant gas mixture are under identical thermal conditions. HWCVD is an alternative process to CVD where the reaction chamber remains cold and a substrate is heated [729]. One of the significant strengths of CVD processing is that the technology is not based on the line-of-sight principle, thus, allowing one to coat workpieces of intricate shapes. HWCVD can operate under both atmospheric and low-pressure conditions.

CVD is usually regarded as a high-temperature process, typically taking place above 1000 °C, which is necessary for the activation of chemical reactions. Efforts to eliminate the weaknesses associated with high-temperature CVD have been attempted. A medium temperature CVD, which is carried out at 700–900 °C and use metallo-organic precursors, has been developed. It is possible to carry out low-temperature CVD at 350–700 °C with both inorganic and metallo-organic precursors [730]. Further diminution of the CVD temperature, based on the plasma phenomenon, allows a reduction in temperature of 200–400 °C [731].

The hot-wall reactor can have various designs, depending on the tasks to be performed. In principle, the hot-wall chamber can represent a quartz (or stainless steel) tube located within a resistively heated furnace. For cylindrical reactors, the deposition kinetics has been well developed [732]. The precursors are directed along the axis of the chamber tube and low-temperature CVD processing running at 400–700 °C has been used to obtain nanocomposites of nc-W₃C/nc-carbynes [45, 175].

5. NANOSTRUCTURE EVALUATION

The characterization of nanostructure is an important stage in nanomaterials processing in order to synthesize nanocomposites with the required properties. Owing to the very small sizes of the structural elements (grains, layers), there are peculiarities in the determination of the nanostructure. The commonly used method of light microscopy (LM) does not work in the case of nanostructured materials because the LM resolution is limited to approximately 1 μm . As has been noted [274], direct imaging of a nanostructure with transmission electron microscopy (TEM) and indirect evaluation of nanograin (or nanolayer) size with x-ray diffraction (XRD) are the two basic experimental methods to estimate the nanosizes of grains/layers.

XRD is a standard structural method that has been widely used [690]. There are a number of in-depth publications about X-ray diffraction [733–737]. Here, attention is paid to methods specifically employed for nanostructure characterization of superhard nanocomposites. XRD is utilized for measurement of both the bilayer repeat period in nanolayered composites and the average nanograin size in nanocrystalline composites. The main peculiarity of nanostructure measurement is that nanostructured materials may contain some phases whose crystal structure may be different from that of coarse-grained materials due to the inherent properties of the nanocrystalline state [690, 738]. In the case of nanocomposites, X-ray diffraction allows measurement of the average nanograin size using Scherrer's formula.

TEM [739] is able to image the local nanostructure of thin layers, but the investigated volume of a sample is relatively very small. High-resolution TEM [740] can especially resolve the structure on an atomic level (0.1–0.2 nm), but sample preparation and image analysis are nonroutine tasks.

For the determination of the bilayer repeat period, any method that represents a function of any physical property correlating with the bilayer repeat period, for example, the dependence of the Rayleigh wave velocities on the bilayer repeat period [741], can generally be used for this aim.

Transmission Electron Microscopy Owing to the nanoscale sizes of the grains, investigations of the nanostructure of superhard nanocomposites have some peculiarities. In this case, TEM becomes an irreplaceable tool for nanostructure analysis. TEM is a well-established technique as a direct method for nanostructure studies [742–744]. A recent comprehensive review of the microscopy methods has been published elsewhere [739]. The resolution of modern transmission electron microscopes can reach 0.1–0.2 nm, which allows easy imaging of nanostructures. High-resolution TEM can be realized [740] that resolves separate atoms located in a crystal lattice.

The following features of nanocomposites may be noted from TEM investigations:

- Orientation of nanograins
- Nanograin (or nanolayer) sizes
- Atomic structure of boundaries
- Atomic structure of interphase boundaries

TEM methods were used for the investigation of nanolayered composite coatings such as TiN/VN, TiN/NbN, and TiN/TaN, nanocrystalline composite coatings such as nc-TiN/a-Si₃N₄, nc-TiC/a-C:H, and nc-W₃C/nc-carbynes.

Small-Angle X-Ray Diffraction Small-angle X-ray diffraction is a common method employed for the definition of the bilayer repeat period (Λ) of nanolayered composite coatings [397, 432, 745–747]. Theoretical prediction of the formation of satellite peaks around the Bragg reflection, when the diffracting crystal planes are stacked with nanoscale distance between them, has been presented elsewhere [748, 749]. Measurements rely on the direct scattering with the difference in X-ray refractive index of the two nanolayers. The Bragg reflexes are flanked by superlattice satellites, which are caused by long-range periodicity in the nanolayered composites [279]. The thickness ratio within the bilayer repeat period and the effect of interfacial diffusion as well as roughness at the interfaces can be determined from small-angle X-ray diffraction [279], which agrees to within 5% in the common nanoscale thickness range [750].

The bilayer repeat period could be calculated from the angular position of the positive (θ_+) and of the negative (θ_-) satellite X-ray reflexes relative to the central Bragg reflection θ_B . For these aims, the following equation can be used [218, 235, 751, 752]:

$$\sin \theta_{\pm} = \sin \theta_B \pm (m\lambda/2\Lambda)$$

where λ is the X-ray wavelength, m is the order of the satellite reflections, and Λ is the bilayer repeat period.

A typical low-angle X-ray diffraction that scans around the Bragg reflection from the TiN/NbN nanolayered composite coatings is depicted in Figure 16. The figure displays a low-angle X-ray diffraction for the 90-nm bilayered repeat period of the nanolayered composite coating in which seven diffraction maxima were observed. The weak reflections of the bilayered repeat period are assigned as +1, +2, ..., +7 satellites.

The strength of small-angle X-ray scattering is that the nanolayer thickness can be evaluated even if the nanolayered composite coatings represent amorphous–amorphous or crystalline–amorphous nanolayered structures [218].

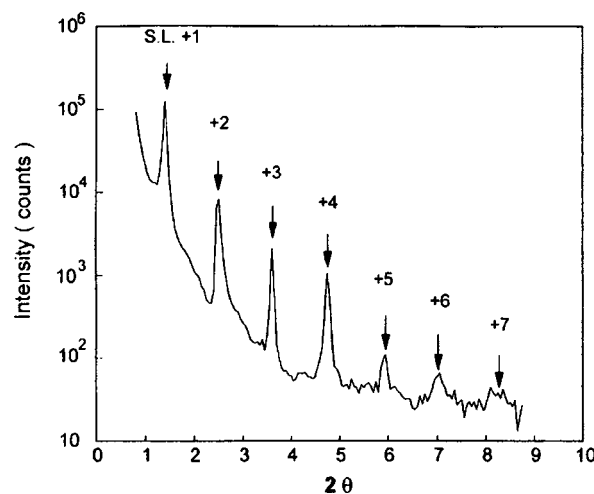


Figure 16. Typical low-angle X-ray diffraction of the TiN/NbN nanolayered composite coating. Reprinted with permission from [432], X. T. Zeng, *Surf. Coat. Technol.* 113, 75 (1999). © 1999, Elsevier Science.

In one report [753] on the estimation of the interface roughness of an island-like structure with a one-monolayer thickness and a lateral size greater than 30 nm, the analysis was performed by broadening the luminescence line widths.

Small-angle X-ray diffraction has been employed for the evaluation of the bilayer repeat period of nanolayered composite coatings such as TiN/NbN [436], ZrN/Ti_xAl_{1-x}N, NbN/TaN, CN_x/TiN, and c-AlN/TiN.

Scherrer's Formula Scherrer's equation is the most frequently used in XRD analysis to determine the average nanocrystalline size and lattice strains in nanocomposites. The nanosizes of the grains result in a broadening of the X-ray peaks in XRD patterns [274, 690, 735, 736, 744]. All three causes, such as nanosize of grains, stress, and distortion, may be simultaneously present, although the broadening of diffraction peaks may cause only one of them. It is possible to separate a nanocrystalline-sized broadening from distortion broadening. The Warren–Averbach method [754, 755], which is based on Fourier analysis and requires accurate approximation of line profiles, allows separating both the particle size and the distortion effects [756].

Scherrer's equation displays the relationship between the average nanocrystalline diameter (D) and the X-ray wavelength (λ), Bragg angle (θ), and peak width at full width at half-maximum after correcting for instrumental broadening (β). It is calculated as follows [690, 735, 736, 744, 757]:

$$D = \lambda(\beta \cos \theta - 4e \sin \theta)^{-1}$$

where e is the lattice strain. The Scherrer's formula allows estimation of the average nanocrystal size if the inhomogeneous strains are absent and the nanograin size distribution is relatively narrow. To separate crystalline-sized broadening from distortion broadening, a simple method which is based on the distinct dependence of the line breadth and expressed as a function of the reciprocal space variable $(2 \sin \theta)/\lambda$, has been described elsewhere [735, 744].

Scherrer's formula was used for measurement of the average sizes of nanocrystals for nanocrystalline composite coatings such as nc-Ti_nN/a-Si₃N₄, nc-Ti_{1-x}Al_xN/a-AlN, and nc-TiN/a-WN_x, nc-ZrN/a-Ni, nc-ZrN/a-Y, and nc-W₃C/nc-carbines.

Scanning Tunneling and Atomic Force Microscopy

Scanning tunneling microscopy (STM) and atomic force microscopy (AFM) are novel methods, which are starting to be used for investigation of nanostructured composites [200, 398, 541, 758–762]. Cross sections of the coatings can be imaged using STM. Fourier analysis of the STM images allows evaluation of the bilayer repeat period [760], which has been found to be in good agreement with X-ray diffraction measurements [278]. As has been noted [278], STM is the most useful tool for measuring a bilayer repeat period that is beyond the resolution of X-ray diffraction, especially when the bilayer repeat period is too large; scanning electron microscopy is appropriate when the bilayer repeat period is too small.

6. SUPERHARDNESS TESTING

Evaluation of hardness of super- and ultrahard coatings presents challenges in nanomaterial characterization. The point is that currently artificial superhard nanocomposite coatings exhibit hardness levels that approach the hardness of diamond. It is known [763] that diamond tips (Vickers, Knoop, Berkovich) are used as indenters in hardness testers. In the case of superhard and ultrahard nanocomposites, the hardness of the material is evaluated by indenters with similar hardness [764, 765].

Currently, two methods have been put forward to solve this problem. The first one is to use in the capacity of nanoindenter a tip possessing hardness significantly higher than that of diamond [766]. The second one is to estimate hardness using methods based on other physical principles [767].

The correct use of microhardness measurements is currently of great concern in materials science for the evaluation of superhard coatings [580]. Finding trustworthy methods to determine the hardness of superhard/ultrahard coatings is a major challenge in the research and development of such coatings [324]. Here, "correctness" implies [580] that the value of microhardness should not depend on the load and not be affected by the substrate.

Hardness is defined as the ability of materials to resist plastic deformation and is measured as a result of plastic deformation [768]. The plastic deformation is created by the diamond indenter, which undergoes a force at any time. It is assumed that the diamond indenter is a *perfectly rigid body*, which has not undergone either plastic or elastic deformation. The diamond indenter satisfies the conditions for the hardness measurement of conventional hard materials that have a moderate hardness.

Usually, the bulk modulus appears in further evaluations of hardness. However, some researchers question the reliability of its usage. It is reckoned [769] that the shear modulus significantly better reflects hardness than the bulk modulus. Indeed, the equation for the calculation of the critical value of dislocation spacing in the pileup includes the shear modulus (not the bulk modulus) and hardness [341]. The relationship between the hardness (H) and the shear modulus (G) is expressed as follows [770]:

$$H = (Gb)/c$$

where b is the numerical value of Burger's vector and c is a constant.

Both a microhardness tester with a diamond indenter of Knoop type [771] and a microhardness tester with a diamond indenter of Vickers type are used to measure plastic microhardness in coatings. A loading force of 50 mN, 100 mN, and 250 mN, which corresponds to a weight of 5 g, 10 g, and 25 g, respectively, is usually chosen to minimize errors due to the influence of a softer substrate than that of the coatings. Scanning electron microscopy (SEM) as well light microscopy (LM) is used to observe and to estimate small indentations at low measuring forces. SEM provides more reliable measurements of the indentation length than LM due to its better resolution over LM. The plastic microhardness of various coatings has been found to be reproducible to within 2 GPa [170].

Hardness is a function of many characteristics [772, 773]. Hardness depends on the test systems (i.e., Vickers, Knoop, etc.) [19], the test regimes (i.e., applied load, duration of the applied load, etc.) [19, 774], and the method of hardness evaluation [19].

As to the microhardness measurement of nanocomposite coatings, there are two issues of major concern. The coatings (see Tables 1 and 3) are, first, very thin and, second, very hard. Their thickness and hardness have a predominant influence on the final result.

The conventional Vickers microhardness tester is not applicable for the hardness estimation of thin coatings because the indenter penetration depth should be approximately 10% of the total coating thickness [775]. A composite hardness model uses an area law-of-mixtures approach, which [776, 777] is applied when the surface displacement is greater than the coating thickness.

Nanoindentation To overcome this challenge, nanoindentation hardness testing (NHT) for thin coatings (10 nm–10 μm) has been developed [778–782], for example, Triboscope Testing System (Hysitron Inc.) [783–785], Nanoindenter[®] (Oak Ridge National Laboratory) [786, 787], Nanoindenter (Nano Systems Inc.) [788], ND-100 [789], CSEM Nano Hardness Tester, and so on. Nanoindentation testing is widely used for hardness measurements [570, 788, 790–798]. Different types of nanoindentation equipment were tested and practically evaluated [799, 800]. Some strengths and weaknesses of the nanohardness measurements have been described elsewhere [789, 801, 802].

Computer-controlled nanoindenters record a load-penetration depth curve automatically in a continuous regime. The normal force (load) varies from 20 μN to 300 mN. A range of penetration from 10 nm to 200 μm was considered in this case.

As reported [803], hardness keeps increasing with decreasing normal force. If hardness measured by nanoindentation is converted into micro-Vickers hardness, the value of the microhardness becomes significantly lower [775]. The nanoindentation requires a correction of Sneddon's solution for indentation [804].

The hardness is usually calculated as the maximum normal force divided by the area of the indentation after subtraction of the elastic deformation [789]. Both a scanning electron microscope [805] and an atomic force microscope [806–808] are used instead of an optical microscope, which is limited by a resolution of about 1 μm , to measure the imprint diagonal.

For correct microhardness measurement, first, the ratio (d/h) of the indenter penetration depth (d) to the total coating thickness (h) should be increased from 10% to 15%, and, second, a correct minimal load (L_{\min}) for a given microhardness should be chosen, that is, $L_{\min} = 50$ mN for about 70 GPa and $L_{\min} = 100$ mN for about 80 GPa [580].

The development of superhard and ultrahard coatings with hardness greater than 70 GPa requires novel methods for hardness evaluation [324]. There are plenty of factors, such as type of indenter [763], substrate effect [809–815], surface adsorption [816], and surface effects [817, 818], that influence microhardness. For example, compressive stress has been found to increase the hardness of the deposited coatings [577].

A new approach to hardness measurements of superhard materials using a scanning force microscope with an ultrahard fullerite C_{60} tip was developed [766]. It has been demonstrated that diamond is plastically deformed under the harder C_{60} fullerite indenter at room temperature. The diamond hardness values were evaluated as 137 ± 6 GPa for (100) diamond face and 167 ± 6 GPa for (111) diamond face. Here, the C_{60} ultrahard fullerite tip can be considered as the *perfectly rigid body*, which is used for hardness testing. A subsequent ultrahard material, which will be harder than the C_{60} ultrahard fullerite, will be utilized for quantitative hardness measurement of the C_{60} fullerite.

Indirect Evaluation of Hardness Because there is currently no other suitable method for hardness testing, comparing the hardness tested by different methods, including indirect methods, can give relatively reliable values of hardness.

The evaluation of hardness from the absorption band tail is a nondestructive technique. The method has been based on the effect of mechanical stress on the optical absorption band tail [767]. The hardness (H) of coatings can be calculated from the following equation [819]:

$$H = 2.9[Y/(1 - \gamma)](100.0/x)^{-n}(\delta a/a)^{1-n}$$

where Y is Young's modulus, γ is the Poisson ratio, $(\delta a/a)$ is the strain, n is the strain-hardening coefficient, and x is the indentational strain.

The absorption coefficient (α) at any frequency (ν) and the absorption coefficient (α_0) at the band edge are used to plot the dependence of α/α_0 on $(E_g - h\nu)$ in order to obtain the strain $(\delta a/a)$ in the coating [820]. The stress (S) in the coating can be also calculated from the equation [819]:

$$S = Y(\delta a/a)(1 - \gamma)$$

This procedure has been used to evaluate the hardness and stress in nanocrystalline diamond coatings [46]. The evaluated hardness of these coatings with Young's modulus $Y = 600$ GPa and Poisson ratio $\nu = 0.11$ has been found to be in good agreement with the hardness estimated by conventional indentation techniques.

Alternatively, Young's modulus for ultrathin coatings can be experimentally measured using the laser-acoustic technique [821, 822]. The laser-acoustic method is a nondestructive method based on measuring the dispersion of surface acoustic waves. In particular, the laser-acoustic technique has been widely adopted in the evaluation of diamond and diamond-like carbon coatings [823–826] as well as multilayered coatings [827].

The brief overview of currently utilized techniques for nanostructure evaluation and for hardness determination has shown that there are distinguishing peculiarities in the application of the different methods in the evaluation of nanostructured coatings. Because of the low thickness and high hardness of nanocomposite coatings, the problem of hardness measurement still persists. The smart principle forming the basis of Mohs' scale, that is, every subsequent hard material surpasses all preceding ones, can be useful for a quantitative hardness evaluation of super- and ultrahard nanocomposite coatings.

7. APPLICATIONS OF SUPERHARD NANOCOMPOSITES

Superhard nanocomposites in the form of coatings have a great potential in applications for the improvement of the performance of working surfaces [828–833]. The current manufacturing industry is in need of cutting tools [834] that can

- Be used without a cutting fluid, that is, green manufacturing
- Resist high tool temperatures ($\sim 1000^\circ\text{C}$)
- Reduce frictional energy, which accounts for some 25%–35% of the total cutting energy

Superhard nanocomposite coatings have been used as thin wear-resistant protection of cutting tools against wear [561, 562, 835–837].

Superhard Nanolayered Composite Coatings The mechanism of wear of superhard nanolayered coatings differs from that of conventional coatings having the same chemical composition [334, 408, 838]. Conventional TiAl–CrN coatings are plastically deformed, resulting in delamination and crack formation beneath the surface at a depth of 50–75 nm [839]. Novel CrN/Ti_xAl_{1-x}N nanolayered composite coatings have been observed to be deformed plastically with the formation of cracks beneath the surface at a depth of 6–8 nm [471, 483, 839]. Figure 17 summarizes the results of wear resistance of such coatings.

Nanolayered composites of TiN/CrN, TiN/NbN, and TiN/TaN composition have been deposited on cemented carbide cutting inserts [433, 434]. They demonstrated 2–5 times higher wear resistance in comparison with TiN coatings and 9–20 times higher wear resistance than cemented carbide (WC + 9 wt% Co). The cutting performance of the cemented carbide cutting inserts, coated with TiN/TaN nanolayered composite coatings, has been estimated for the machining of austenitic stainless steel (AISI/SAE 303/304) [433], which is more difficult to machine than carbon low-alloy steels [840].

TiN/TaN nanolayered composite coatings have demonstrated the best cutting performance [433]. The TiN/TaN nanolayered composite coating was compared with commercially available TiCN and TiAlN as well as with the chemically deposited trilayer coating of TiCN + Al₂O₃ + TiN. The cemented carbide inserts (WC + 11 wt% Co) with TiCN coatings exhibited a high flank wear resistance as well.

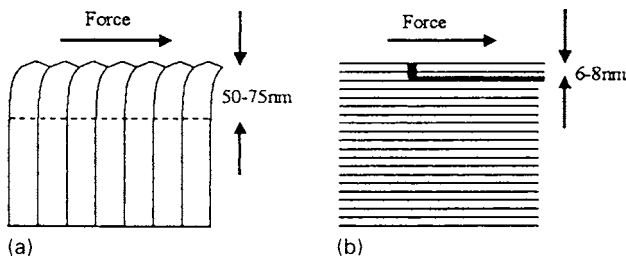


Figure 17. Mechanical failure in conventional (a) and nanolayered composite (b) coatings. Reprinted with permission from [170], W.-D. Munz et al., *Surf. Eng.* 17, 15 (2001). © 2001, Institute of Materials.

VN/Ti_xAl_{0.96-x}Y_{0.04}N nanolayered composite coatings have displayed excellent performance in milling tests [170]. Two fluted ball-nosed cutters were coated by VN/Ti_xAl_{0.96-x}Y_{0.04}N nanolayered composite coatings. Comparisons with conventional TiCN coatings demonstrated that VN/Ti_xAl_{0.96-x}Y_{0.04}N nanolayered composite coatings were responsible for tripling the lifetime of the cutters [170].

The superiority of the novel CrN/NbN nanolayered composite coating is demonstrated in Figure 18 [170]. The nanocomposite coating can provide a good replacement for electroplated hard chromium, which is widely used in industry. The 3- to 5- μm CrN/NbN thin nanolayered composite coating exceeds the 18- μm electroplated hard chromium in wear resistance by a factor of 10 [170]. Currently, CrN/NbN nanolayered composite coatings are successfully applied in forming tools in the manufacturing industry [170], combing roll blades in the textile industry [479], and knife plates in the food industry [170, 479]. Replacing a conventional TiN coating with CrN/NbN increases the lifetime of the forming tools by a factor of 2.5 [170]. The lifetime of combing rolls coated with the 25- μm Ni electroless was 6500 hours, whereas the combing rolls with the 5- μm CrN/NbN nanolayered composite coating had a lifetime of more than 11,000 hours [170]. For polyester fiber cutting, scissors coated with the 5- μm CrN/NbN composite coatings made 3×10^6 cuts in comparison to 1.3×10^6 cuts in the uncoated ones [170]. The CrN/NbN nanocomposite coatings on automotive engine valves increased the lifetime of the valves up to 8000 working hours in comparison with 3000 hours in the uncoated ones [170]. The corrosion behavior of the CrN/NbN nanolayered composite was investigated as well [841].

The CrN/NbN [472] and TiN/AlN [555] nanolayered composites have excellent oxidation resistance at elevated temperatures. The temperature at which the CrN/NbN coatings start to oxidize increases with an increase in the nitrogen flow rate (Fig. 19). The near-stoichiometric composition of the coatings gives rise to temperatures on the order of 820–850 $^\circ\text{C}$.

Drills coated with ZrN/CN_x nanolayered composite coatings have been tested for their cutting life [541]. The ZrN/CN_x nanolayered composite coatings prolong the lifetime of

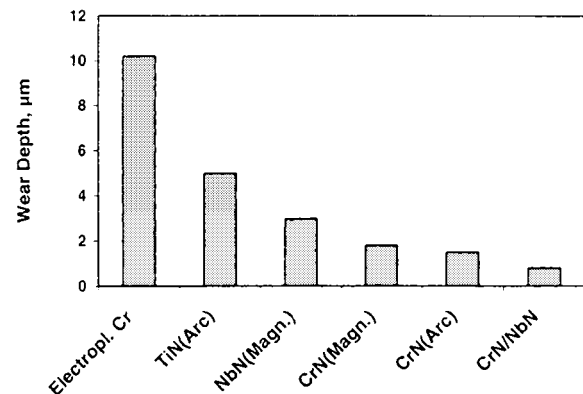


Figure 18. Chart of wear depth for various coatings in pin-on-disk test: load of 5 N; Al₂O₃ ball; 50,000 revolutions. Reprinted with permission from [170], W.-D. Munz et al., *Surf. Eng.* 17, 15 (2001). © 2001, Institute of Materials.

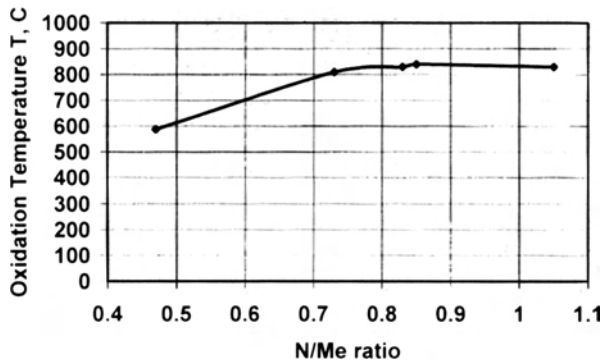


Figure 19. Maximum oxidation temperature of the CrN/NbN nanolayered composite coatings as a function of nitrogen flow rate. Reprinted with permission from [472], P. E. Hovsepian et al., *Surf. Coat. Technol.* 116–119, 727 (1999). © 1999, Elsevier Science.

the drills by more than 50 times [541], which is significantly higher in comparison with conventional TiN coatings which prolong the tool life of coated drills by about 20 times.

Superhard Nanocrystalline Composite Coatings The deformation behavior of nanocrystalline composites is a crucial factor in their applications. A few deformation mechanisms [842, 843] and models [844] for nanocomposites were recently proposed, namely, grain boundary sliding [842, 843], stress-induced mass transfer [333, 368, 845], and rotation of nanograins [846, 847].

The mechanical failure of nanocrystalline–amorphous composites occurs through the formation and propagation of microcracks [328, 848], as illustrated in Figure 20. A critical stress (σ_c) should be applied for the growth of microcracks:

$$\sigma_c = C(2\gamma_s B / \pi a_{\max})^{1/2}$$

where C is a constant depending on the shape of the microcrack, γ_s is the surface energy, B is Young's modulus, and a_{\max} is the maximum size of the microcrack. This results from the fact that smaller cracks require higher critical stress for growing.

The function of an amorphous phase between separated grains in nanocrystalline composite coatings is very important [849]. First, plastic deformation of the nanocrystalline composite coatings is realized in the intergranular amorphous phase, and, second, the existence of the intergranular amorphous phase allows one to maximize the hardness of the nanocrystalline composite coatings.

It has been noted [850] that diffusivity in nanocrystalline copper at room temperature is 14–20 orders of magnitude higher than that of normal microcrystalline copper. The room-temperature diffusivity was measured as being 10^{-20} m²/s, which is higher than the grain boundary diffusivity ($\sim 10^{-24}$ m²/s) and significantly higher than the lattice diffusion ($\sim 10^{-40}$ m²/s). Therefore, high diffusivity in nanocrystalline materials was suggested [365, 851] as an additional mode of plastic deformation leading to softening at very fine grain sizes.

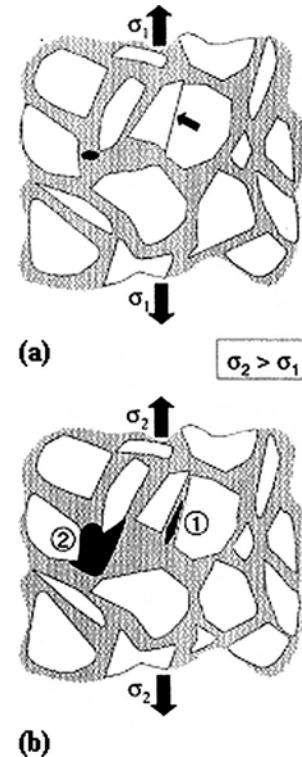


Figure 20. Deformation mechanism of nanocomposite materials: (a) formation of a stacking fault (arrow) and a pore and (b) crack nucleation at stacking fault 1 and crack propagation and debonding of nanocrystals 2. Reprinted with permission from [281], C. Mitterer, et al., *Surf. Coat. Technol.* 120–121, 405 (1999). © 1999, Elsevier Science.

8. CONCLUSION

This review has summarized the experimental results regarding the relationship between superhardness and nanostructure of relevant nanocomposites. These novel superhard nanocomposites have demonstrated the strong dependence of superhardness on optimum nanostructure. This review has confirmed that the hardness of nanocomposite coatings depends on the bilayer repeat period and on the grain size. In fact, the ability to control hardness by changing the nanograin/nanolayer size and composition suggests that nanocomposites can be considered as new types of nanomaterials with tailored high hardness.

It was demonstrated that nanocomposites exhibit a superhardness effect when the sizes of their functional elements (i.e., nanograins, nanolayers) achieve appropriate nanoscale dimensions. The nanostructural architecture of such materials and the fine amorphous or quasicrystalline matrix supplement each other.

There is no sole viewpoint on the extreme increase in hardness of the nanocomposites. Different possible mechanisms have been offered to explain the extreme hardness of optimal sizes of nanolayers and of nanolayered composites, as well as of nanograins for nanocrystalline composites, namely:

- Diffusional creep at room temperature [851]
- Changing grain sizes using thermal treatment [347, 852]

- Crystallographic texture formation with reducing grain size [853]
- Crystalline–amorphous transition [854]
- Domination of triple junctions in nanocrystalline materials [198, 853]
- Consolidation of micropores, roughness, and stringlike surface features in nanocomposite materials [852]
- Dislocation-related explanations [335, 343, 360, 362, 415, 497, 855, 856]
- Coherency and concomitant interfacial misfit dislocations [857]
- Interfacial compositional gradients [161]
- Layer modulus difference [397, 399]
- Effect of the shape of the Fermi surface on the elastic anomaly [402, 403]
- Strain caused by incoherent interfacial stresses [858]
- Possible elastic anomalies of nanolayered composite coatings [453, 566, 567]

Such possible explanations provide enough evidence that this domain of research and development is under progress, and further exciting results are not far off.

9. MILESTONES IN SUPERHARD NANOCOMPOSITES

The following chronological sequence showing the contributions to the research and development of superhard nanocomposites is based on the original published papers.

- 1951** Sylwestrowitz and Hall [859] as well as Hall [328, 860] independently published a set of three papers where the yield stress behavior of mild steel in tensile tests was first presented in the form of a well-known relationship such as $\sigma_0 - \sigma' \sim 1/d^{1/2}$. Explanation of the relationship was given in terms of a grain boundary theory [328].
- 1953** Petch, using polycrystals of mild steel, ingot iron, and spectrographic iron, found [329] that the cleavage strength (σ) depends on the grain size (d) as $\sigma_c = \sigma_0 + k^{-1/2}$. Later, this relationship became known as the Hall–Petch relationship.
- 1970** Koehler showed that it was possible [395] to design superhard composite coatings using thin alternate layers of high and low elastic materials. Such combinations do not allow Frank–Read dislocation sources to operate within the thin-layered composites. Some combinations such as Ni/Cu, MgO/LiF, and W/Ta were considered for the design.
- 1978** Lehoczky, building on Koehler’s proposal [395] and using combinations of Al/Cu [396, 410] and Al/Ag [410], demonstrated that the yield strength of the layered composites, when the thickness of the single layers was within the nanoscale range, is a few times larger than the values given by the rule of mixture for the metal components if the thickness of the layers was reduced from 1000 to 70 nm.
- 1985** Demyashev determined [682] that the novel superhard tungsten carbide (35–40 GPa) previously deposited [45] represents a nanocomposite of nc-W₃C/nc-carbynes where carbynes are chainlike arrangements of carbon atoms.
- 1987** Helmersson et al. were the first to obtain a nanolayered composite of TiN/VN [377], which reached a microhardness of approximately 56 GPa at a bilayer repeat period of 5.2 nm.
- 1988** Birringer and Gleiter summarized the current (at the time) knowledge related to nanocrystalline materials for the first edition of the “Encyclopedia of Materials Science and Engineering” [180].
- 1990** Palumbo et al. showed [303] that the effect of grain size between 2 and 100 nm on the volumetric portion of intercrystalline regions, grain boundaries, and triple junctions is significant.
- 1992** Suryanarayana et al. obtained results [198] similar to [303]. There are critical grain sizes [198] at which nanocrystalline materials reach maximum hardness.
- Scattergood and Koch modernized the Hall–Petch relationship as applied to nanocrystalline materials [360].
- Shinn et al. synthesized a nanolayered composite of TiN/NbN, which had a hardness of 49 GPa at a bilayer repeat period of 4.6 nm [397].
- 1994** Gissler [639] obtained superhard nanocomposite coatings of titanium boron nitride (55 GPa).
- 1996** Setoyama et al. synthesized a superhard nanolayered composite of TiN/AlN (~40 GPa) with NaCl-type AlN for a bilayer repeat period of approximately 3 nm [552].
- Veprek et al. reported nanocrystalline–amorphous composites of nc-TiN/a-Si₃N₄ and nc-W₂N/a-Si₃N₄ [597], which reached a microhardness of approximately 50 GPa when the average nanograin sizes of nc-TiN and nc-W₂N were between 30 and 40 nm.
- 1997** Wu et al. obtained a superhard nanocomposite of CN_x/ZrN with a microhardness exceeding 40 GPa [539].
- 1998** Inspector et al. reported that a superhard nanolayered composite of TiN/BN (~40 GPa) had been obtained [568].
- Selinder et al. obtained a nanolayered composite of TiN/TaN [433], which had a hardness of 39 GPa at $h_{\text{TiN}} = 7$ nm and $h_{\text{TaN}} = 4$ nm.
- He et al. synthesized a hybrid ceramic–metal nanolayered composite of TiC/Fe [272], which reached a microhardness of approximately 42 GPa when $h_{\text{TiC}} \sim 8$ nm and $h_{\text{Fe}} \sim 5$ nm.
- 1999** Diserens et al. reported on a superhard nanocomposite of TiN/SiN_x (38 GPa), which was deposited by reactive unbalanced magnetron sputtering [606].
- Niederhofer et al. reported [612] that a microhardness of 105 ± 20 GPa had been obtained for nanocomposites of nc-TiN/TiSi_x.
- Musil and Hruby reported [618] that a superhard nanocrystalline–amorphous composite of nc-TiAlN/a-AlN with a microhardness of up to 47 GPa had been synthesized.
- Benda and Musil synthesized a superhard nanocrystalline–amorphous composite of nc-Mo₂C/(a-C + a-Mo₂N) with a hardness of about 53 GPa [620].
- 2000** Xu et al. deposited a nanolayered composite of TiN/TaWN having a microhardness of 50 GPa at a bilayer repeat period of 5.6 nm [345].
- Hovsepian et al. synthesized superhard nanolayered composites of TiAlN/CrN (42–78 GPa), TiAl-YN/VN (42–56 GPa), and CrN/NbN (42–56 GPa) [471].

Yoon et al. deposited a superhard nanolayered composite of β -WC_{1-x}/TiN [570], which was as hard as 40 GPa at a bilayer repeat period of 7 nm.

2001 Yoon et al. synthesized a nanolayered composite of β -WC_{1-x}/Ti_{0.43}Al_{0.57}N with a microhardness of approximately 50 GPa [571].

GLOSSARY

Bilayer repeat period (Λ) The total thickness of two different repeating nanolayers, which form a nanolayered composite.

Nanocomposite A composite material having dimensions of morphological elements (i.e., average diameter of grains, thickness of layers, etc.) within the nanoscale range between 2 and 100 nm (1 nm = 10⁻⁹ m).

Nanocrystalline composite A nanocomposite consisting of grains having an average diameter within the nanoscale range.

Nanoindentation Method of hardness evaluation based on a load-penetration depth curve, which is a result of a computer-controlled automatic record where the normal force (load) and the penetration depth vary from 20 μ N to 300 mN and from 10 nm to 200 μ m, respectively.

Nanolayered composite A nanocomposite consisting of layers having a thickness within the nanoscale range. The layers are called nanolayers.

Stabilization phenomenon Stabilization of nonequilibrium crystal phases on the nanoscale range between alternating nanolayers, which are used as a template.

Superhard materials Materials having a microhardness higher than 40 GPa.

Superhardness phenomenon A significant microhardness enhancement higher than 40 GPa in artificial nanocomposites that is solely defined by an optimal nanostructure and composition.

ACKNOWLEDGMENTS

First, we thank Dr. H. S. Nalwa for his kind invitation to contribute to the first edition of the *Encyclopedia of Nanoscience and Nanotechnology*. It has been a great pleasure and honor for us to write this review.

The authors have greatly benefited from many professional scientists who produced the original research and development, which was included in this state-of-the-art review. Hundreds of researchers all over the world have answered our request to send their relevant reprints for this review. The relevant papers are quoted in appropriate sections and the authors gratefully acknowledge all of them for their kind cooperation.

For permission to reproduce the original illustrations from their publications, we thank especially Prof. S. A. Barnett (Northwestern University, Evanston, IL), Prof. Y.-W. Chung (Northwestern University, Evanston, IL), Prof. H. Gleiter (Institute for Nanotechnology, Karlsruhe, Germany), Dr. M. Gu (Shanghai Jiao Tong University, China),

Dr. P. E. Hovsepian (Sheffield Hallam University, UK), Prof. C. Mitterer (Montanuniversitat, Leoben, Austria), Dr. J. Patscheider (Swiss Federal Laboratories for Materials Testing and Research, Duebendorf, Switzerland), Prof. C. Suryanarayana (University of Central Florida, Orlando, FL), Prof. S. Veprék (Technical University Munich, Munich, Germany), Dr. X. T. Zeng (Gintic Institute of Manufacturing Technology, Singapore), as well as the copyright holders: American Chemical Society (C. Arleen Countney), Washington, DC, American Institute of Physics (Mrs. Ann C. Perlman), Melville, NY, Elsevier Science (Mrs. Frances Rothwell), Oxford, UK, Institute of Materials (Mr. Mark Hull), London, UK, Materials Research Society (Mr. Matt Ussia), Warrendale, PA, Wiley-VCH Verlag GmbH (Ms. Claudia Rutz), Weinheim, Germany.

The authors are grateful to Mrs. Mez Wilkinson (Library of Swinburne University of Technology, Melbourne, Australia), Mrs. Fiona O'Donnell (Library of Swinburne University of Technology, Melbourne, Australia), and Miss Stephanie Lavau (Library of Manufacturing Science and Technology Division of CSIRO, Melbourne, Australia) for inestimable information support.

Finally, the authors acknowledge Tina Burke for careful reading and correction of the manuscript.

REFERENCES

1. S. Veprék, A. Niederhofer, K. Moto, P. Nesldek, H. Mannling, and T. Bolom, *Mater. Res. Soc. Symp. Proc.* 581, 321 (2000).
2. B. O. Johansson, J.-E. Sundgren, J. E. Greene, A. Rockett, and S. A. Barnett, *J. Vac. Sci. Technol., A* 3, 303 (1985).
3. B. Aronsson, T. Lundstrom, and S. Rundqvist, "Borides, Silicides and Phosphides." Methuen-Wiley, London, 1965.
4. A. Y. Liu and M. L. Cohen, *Science* 245, 841 (1989).
5. A. Y. Liu and M. L. Cohen, *Phys. Rev. B* 41, 10727 (1990).
6. M. L. Cohen, *Solid State Commun.* 92, 45 (1994).
7. C.-M. Sung and M. Sung, *Mater. Chem. Phys.* 43, 1 (1996).
8. H. Sjöstrom, H. Stafstrom, S. Boman, and J.-E. Sundgren, *Phys. Rev. Lett.* 75, 1336 (1995).
9. A. Badzian and T. Badzian, *Int. J. Refract. Met. Hard Mater.* 15, 3 (1997).
10. K. M. Yu, M. L. Cohen, E. E. Haller, W. L. Hansen, A. Y. Liu, and I. C. Wu, *Phys. Rev. B* 49, 5034 (1994).
11. J. Sung, *Mater. Chem. Phys.* 72, 133 (2001).
12. M. A. Tamor and K. C. Hass, *J. Mater. Res.* 5, 2273 (1990).
13. R. Hoffmann, T. Hughbanks, M. Kertesz, and P. H. Bird, *J. Am. Chem. Soc.* 195, 4831 (1983).
14. A. Y. Liu, M. L. Cohen, K. C. Hass, and M. A. Tamor, *Phys. Rev. B* 43, 6742 (1991).
15. R. G. Lacerda, P. Hammer, C. M. Lepienski, F. Alvarez, and F. C. Marques, *J. Vac. Sci. Technol., A* 19, 971 (2001).
16. S. Hirono, S. Umemura, M. Tomita, and R. Kaneko, *Appl. Phys. Lett.* 80, 425 (2002).
17. M. Popov, M. Kyotani, R. J. Nemanich, and Y. Koga, *Phys. Rev. B* 65, 33408 (2002).
18. R. Riedel, *Adv. Mater.* 6, 549 (1994).
19. A. Zerr and R. Riedel, in "Handbook of Ceramic Hard Materials" (R. Riedel, Ed.), p. xlvi. Wiley-VCH, Weinheim, 2000.
20. A. G. Whittaker, U.S. Patent 4,248,909, 1981.
21. G. M. Demyashev, A. L. Taube, and E. Siores, *Nano Lett.* 1, 183 (2001).
22. R. B. Heimann, in "Carbyne and Carbynoid Structures" (R. B. Heimann, S. E. Evsyukov, and L. Kavan, Eds.), p. 409. Kluwer Academic, Dordrecht, 1999.

23. G. M. Demyashev, A. L. Taube, and E. Siores, *J. Nanosci. Nanotechnol.* 2, 133 (2002).
24. E. Burgos, E. Halac, R. Weht, H. Bonadeo, E. Artacho, and P. Ordejon, *Phys. Rev. Lett.* 85, 2328 (2000).
25. N. Lvova, K. Gogolinsky, V. Reshetov, V. Blank, M. Popov, and G. Pivovarov, *Diamond Relat. Mater.* 7, 427 (1998).
26. N. R. Serebryanaya, L. A. Chernozatonskii, and B. N. Mavrin, *AIP Conf. Proc.* 544, 85 (2000).
27. J. M. Leger, J. Haines, and B. Blanzat, *J. Mater. Sci. Lett.* 13, 1688 (1994).
28. J. S. Tse, D. D. Klug, K. Uehara, Z. Q. Li, J. Haines, and J. M. Leger, *Phys. Rev. B* 61, 10029 (2000).
29. A. R. Badzian, *Appl. Phys. Lett.* 53, 2495 (1988).
30. V. L. Solozhenko, D. Andrault, G. Fiquet, M. Mezouar, and D. C. Rubie, *Appl. Phys. Lett.* 78, 1385 (2001).
31. G. Will and P. G. Perkins, *Diamond Relat. Mater.* 10, 2010 (2001).
32. O. Knotek, E. Lugscheider, and C. W. Siry, *Int. J. Refract. Met. Hard Mater.* 17, 157 (1999).
33. M. Mattesini and S. F. Matar, *Int. J. Inorg. Mater.* 3, 943 (2001).
34. V. L. Solozhenko, S. N. Dub, and N. V. Novikov, *Diamond Relat. Mater.* 10, 2228 (2001).
35. J. E. Lowther, *Phys. Rev. B: Condens. Matter* 322, 173 (2002).
36. C. S. Yoo, H. Cynn, F. Gygi, G. Galli, V. Iota, M. Nicol, S. Carlson, D. Hausermann, and C. Mailhot, *Phys. Rev. Lett.* 83, 5527 (1999).
37. J. Dong, J. K. Tomfohr, O. F. Sankey, K. Leinenweber, M. Somayazulu, and P. F. McMillan, *Phys. Rev. B* 62, 14685 (2000).
38. W. Y. Ching, S.-D. Mo, L. Ouyang, I. Tanaka, and M. Yoshiya, *Phys. Rev. B* 61, 10609 (2000).
39. P. Nagel, V. Pasler, S. Lebedkin, A. Soldatov, C. Meingast, B. Sundqvist, P. A. Persson, T. Tanaka, K. Komatsu, S. Buga, and A. Inaba, *Phys. Rev. B* 60, 16902 (1999).
40. M. E. Kozlov, M. Hirabayashi, K. Nozaki, M. Tolumoto, and H. Ihara, *Appl. Phys. Lett.* 66, 1199 (1995).
41. A. V. Talyzin, L. S. Dubrovinsky, M. Oden, and U. Jansson, *Diamond Relat. Mater.* 10, 2044 (2001).
42. V. D. Blank, S. G. Buga, G. A. Dubitsky, N. R. Serebryanaya, M. Yu. Popov, and B. Sundqvist, *Carbon* 36, 319 (1998).
43. V. D. Blank, A. A. Nuzdin, R. K. Bagramov, and V. M. Prokhorov, *Carbon* 39, 905 (2001).
44. M. E. Kozlov, K. Yase, N. Minami, P. Ons, H.-A. Durand, M. Hirabayashi, K. Nozaki, M. Tokumoto, and H. Ihara, in "Recent Advances in the Chemistry and Physics of Fullerenes and Related Materials" (R. S. Ruoff and K. M. Kadish, Eds.), p. 99. Electrochemical Society, Pennington, NJ, 1995.
45. A. I. Krasowsky, I. L. Sinani, I. V. Kirillov, and Yu. N. Golovanov, USSR Patent 413,753, 1973.
46. K. Chakrabarti, R. Chakrabarti, K. K. Chattopadhyay, S. Chaudhuri, and A. K. Pal, *Diamond Relat. Mater.* 7, 845 (1998).
47. L. Chow, D. Zhou, A. Hussain, S. Kleckley, K. Zollinger, A. Schulte, and H. Wang, *Thin Solid Films* 368, 193 (2000).
48. L. C. Qin, D. Zhou, A. R. Krauss, and D. M. Gruen, *Nanostruct. Mater.* 10, 649 (1998).
49. P. Keblinski, S. R. Phillpot, D. Wolf, and H. Gleiter, *Nanostruct. Mater.* 12, 339 (1999).
50. S. N. Kundu, M. Basu, A. B. Maity, S. Chaudhuri, and A. K. Pal, *Mater. Lett.* 31, 303 (1997).
51. G. Amaratunga, A. Putnis, K. Clay, and W. Milne, *Appl. Phys. Lett.* 55, 634 (1989).
52. G. Amaratunga, S. R. P. Silva, and D. A. McKenzie, *J. Appl. Phys.* 70, 5374 (1991).
53. D. M. Gruen, X. Pan, A. R. Krauss, S. Liu, J. Luo, and C. M. Fosteo, *J. Vac. Sci. Technol., A* 12, 1491 (1994).
54. S. P. McGinnis, M. A. Kelly, S. B. Hagstrom, and R. L. Alvis, *J. Appl. Phys.* 79, 170 (1996).
55. S. A. Catledge, P. Baker, J. T. Tarvin, and Y. K. Vohra, *Diamond Relat. Mater.* 9, 1512 (2000).
56. D. Zhou, F. A. Stevie, L. Chow, J. McKinley, H. Gnaser, and V. H. Desai, *J. Vac. Sci. Technol., A* 17, 1135 (1999).
57. D. Zhou, D. M. Gruen, L. C. Qin, T. G. McCauley, and A. R. Krauss, *J. Appl. Phys.* 84, 1981 (1998).
58. V. I. Konov, A. A. Smiolin, V. G. Ralchenko, S. M. Pimenov, E. D. Obratsova, E. N. Loubnin, S. M. Metev, and G. Sepold, *Diamond Relat. Mater.* 4, 1073 (1995).
59. L. C. Chen, T. Y. Wang, J. R. Yang, K. H. Chen, D. M. Bhusari, Y. K. Chang, H. H. Hsieh, and W. F. Pong, *Diamond Relat. Mater.* 9, 877 (2000).
60. L. C. Nistor, J. Van Landuyt, V. G. Ralchenko, E. D. Obratsova, and A. A. Smolin, *Diamond Relat. Mater.* 6, 159 (1997).
61. K. Chakrabarti, R. Chakrabarti, S. Chaudhari, and A. K. Pal, *Diamond Relat. Mater.* 7, 1227 (1998).
62. D. He, L. Shao, W. Gong, E. Xie, K. Xu, and G. Chen, *Diamond Relat. Mater.* 9, 1600 (2000).
63. T. Sharda, T. Soga, T. Jimbo, and M. Umeno, *Diamond Relat. Mater.* 10, 352 (2001).
64. T. Sharda, M. M. Rahaman, Y. Nukaya, T. Soga, T. Jimbo, and M. Umeno, *Diamond Relat. Mater.* 10, 561 (2001).
65. T. Sharda, T. Soga, T. Jimbo, and M. Umeno, *Diamond Relat. Mater.* 10, 1592 (2001).
66. T. Sharda, T. Soga, T. Jimbo, and M. Umeno, *J. Nanosci. Nanotechnol.* 1, 287 (2001).
67. T. Sharda, T. Soga, T. Jimbo, and M. Umeno, *Diamond Relat. Mater.* 9, 1331 (2000).
68. T. Xu, S. Yang, J. Lu, Q. Xue, J. Li, W. Guo, and Y. Sun, *Diamond Relat. Mater.* 10, 1441 (2001).
69. N. S. Xu, J. Chen, and S. Z. Deng, *Diamond Relat. Mater.* 11, 249 (2002).
70. A. K. Arora, T. R. Ravindran, G. L. N. Reddy, A. K. Sikder, and D. S. Misra, *Diamond Relat. Mater.* 10, 1477 (2001).
71. H. Yoshikawa, C. Morel, and Y. Koga, *Diamond Relat. Mater.* 10, 1569 (2001).
72. A. R. Krauss, O. Auciello, D. M. Gruen, A. Jayatissa, A. Sumant, J. Tucek, D. C. Mancini, N. Moldovan, A. Erdemir, D. Ersoy, M. N. Gardos, H. G. Busmann, E. M. Meyer, and M. Q. Ding, *Diamond Relat. Mater.* 10, 1952 (2001).
73. T.-S. Yang, J.-Y. Lai, C.-L. Cheng, and M.-S. Wong, *Diamond Relat. Mater.* 10, 2161 (2001).
74. T. D. Corrigan, D. M. Gruen, A. R. Krauss, P. Zapol, and R. P. H. Chang, *Diamond Relat. Mater.* 11, 43 (2002).
75. H. Yusa, *Diamond Relat. Mater.* 11, 87 (2002).
76. D. S. Zhao, M. Zhao, and Q. Jiang, *Diamond Relat. Mater.* 11, 234 (2002).
77. A. Heiman, I. Gouzman, S. H. Christiansen, H. P. Strunk, and A. Hoffman, *Diamond Relat. Mater.* 9, 866 (2000).
78. A. Heiman, E. Lakin, E. Zolotoyabko, and A. Hoffman, *Diamond Relat. Mater.* 11, 601 (2002).
79. A. Heiman, I. Gouzman, S. H. Christiansen, H. P. Strunk, G. Comtet, L. Hellner, G. Dujardin, R. Edrei, and A. Hoffman, *J. Appl. Phys.* 89, 2622 (2001).
80. S.-P. Hong, H. Yoshikawa, K. Wazumi, and Y. Koga, *Diamond Relat. Mater.* 11, 877 (2002).
81. R. Haubner and B. Lux, *Int. J. Refract. Met. Hard Mater.* 20, 93 (2002).
82. H.-G. Busmann, A. Pageler, U. Brauneck, and D. M. Gruen, *J. Metastable Nanocryst. Mater.* 8, 255 (2000).
83. K. Teii, H. Ito, M. Hori, T. Takeo, and T. Goto, *J. Appl. Phys.* 87, 4572 (2000).
84. Y. Kurokawa, S. Nomura, T. Takemori, and Y. Aoyagi, *Phys. Rev. B* 61, 12616 (2000).
85. S. Praver, J. L. Peng, J. O. Orwa, J. C. McCallum, D. N. Jamieson, and L. A. Bursill, *Phys. Rev. B* 62, R16360 (2000).
86. A. C. Ferrari and J. Robertson, *Phys. Rev. B* 63, 121405 (2001).

87. H. Ye, C. Q. Sun, H. Huang, and P. Hing, *Appl. Phys. Lett.* 78, 1826 (2001).
88. A. Hoffman, A. Heiman, and S. H. Christiansen, *J. Appl. Phys.* 89, 5769 (2001).
89. S. Jiao, A. Sumant, M. A. Kirk, D. M. Gruen, A. R. Krauss, and O. Auciello, *J. Appl. Phys.* 90, 118 (2001).
90. C. Gu, X. Jiang, Z. Jin, and W. Wang, *J. Vac. Sci. Technol., B* 19, 962 (2001).
91. T. Patrusheva, V. Letunovsky, L. Gorjacheva, A. Gorschkov, V. Sergienko, and E. Jakovleva, *Carbon* 40, 125 (2002).
92. N. Jiang, S. Kujime, I. Ota, T. Inaoka, Y. Shintani, H. Makita, A. Hatta, and A. Hiraki, *J. Cryst. Growth* 218, 265 (2000).
93. N. Jiang, K. Eguchi, S. Noguchi, T. Inaoka, and Y. Shintani, *J. Cryst. Growth* 236, 577 (2002).
94. N. Jiang, K. Sugimoto, K. Nishimura, Y. Shintani, and A. Hiraki, *J. Cryst. Growth* 242, 362 (2002).
95. Z. Y. Chen, J. P. Zhao, T. Yano, T. Ooie, M. Yoneda, and J. Sakakibara, *J. Cryst. Growth* 226, 62 (2001).
96. M. Y. Liao, X. M. Meng, X. T. Zhou, J. Q. Hu, and Z. G. Wang, *J. Cryst. Growth* 236, 85 (2002).
97. S. Chaudhuri, S. N. Kundu, M. Basu, A. B. Maity, and A. K. Pal, *Mater. Lett.* 31, 303 (1997).
98. D. M. Bhusari, J. R. Yang, T. Y. Wang, K. H. Chen, S. T. Lin, and L. C. Chen, *Mater. Lett.* 36, 279 (1998).
99. D. M. Bhusari, J. R. Yang, T. Y. Wang, K. H. Chen, S. T. Lin, and L. C. Chen, *J. Mater. Res.* 13, 1769 (1998).
100. H. Masuda, M. Watanabe, K. Yasui, D. Tryk, T. Rao, and A. Fujishima, *Adv. Mater.* 12, 444 (2000).
101. S. Y. Luo, J.-K. Kuo, B. Yeh, J. C. Sung, C.-W. Dai, and T. J. Tsai, *Mater. Chem. Phys.* 72, 133 (2001).
102. N. Toprani, S. A. Catledge, Y. K. Vohra, and R. Thompson, *J. Mater. Res.* 15, 1052 (2000).
103. S. Kumar, C. M. S. Rauthan, P. N. Dixit, K. M. K. Srivatsa, M. Y. Khan, and R. Bhattacharyya, *Vacuum* 63, 433 (2001).
104. S. Kumar, C. M. S. Rauthan, K. M. K. Srivatsa, P. N. Dixit, and R. Bhattacharyya, *Appl. Surf. Sci.* 182, 326 (2001).
105. J. M. Lopez, F. J. Gordillo-Vazquez, and J. M. Albella, *Appl. Surf. Sci.* 185, 321 (2002).
106. A. Erdemir, G. R. Fenske, A. R. Krauss, D. M. Gruen, T. McCauley, and R. T. Csencsits, *Surf. Coat. Technol.* 120–121, 565 (1999).
107. L. Chow, D. Zhou, A. Hussain, S. Kleckley, K. Zollinger, A. Schulte, and H. Wang, *Thin Solid Films* 368, 193 (2000).
108. M. Hiramatsu, C. H. Lau, A. Bennett, and J. S. Foord, *Thin Solid Films* 407, 18 (2002).
109. Y. Mori, H. Obata, M. Maegawa, G. Katagiri, H. Ishida, and A. Ishitani, *Appl. Phys. Lett.* 67, 694 (1995).
110. E. Mailard-Schaller, O. M. Luettel, L. Diederich, L. Schalpbach, V. V. Zhirnov, and P. I. Belobrov, *Diamond Relat. Mater.* 8, 805 (1999).
111. L. J. Martinez-Miranda, M. P. Siegal, and P. P. Provencio, *Appl. Phys. Lett.* 79, 542 (2001).
112. P. Ascarelli, E. Cappelli, G. Mattei, F. Pinzari, and S. Martelli, *Diamond Relat. Mater.* 4, 464 (1995).
113. K.-I. Kondo, H. Hirai, and M. Yoshida, *Ceram. Eng. Sci. Proc.* 19, 433 (1998).
114. V. I. Konov, A. A. Smolin, V. G. Ralchenko, S. M. Pimenov, E. D. Obraztsova, E. N. Loubnin, G. Sepold, and S. M. Metev, *Diamond Relat. Mater.* 4, 1073 (1995).
115. Y. Fu, B. Yan, N. L. Loh, C. Q. Sun, and P. Hing, *Surf. Eng.* 16, 355 (2000).
116. S. Sattel, H. Ehrhardt, J. Robertson, Z. Tass, D. Wiescher, and M. Scheib, *Diamond Relat. Mater.* 6, 255 (1997).
117. P. Hollman, O. Wanstrand, and S. Hogmark, *Diamond Relat. Mater.* 7, 1471 (1998).
118. L. Vandenbulcke and M. I. De Barros, *Surf. Coat. Technol.* 146–147, 417 (2001).
119. A. A. Voevodin and J. S. Zabinski, *Diamond Relat. Mater.* 7, 463 (1998).
120. A. Goel, D. Kester, D. Bray, P. Persoone, M. Sercu, and D. Neerincx, *Diamond Relat. Mater.* 7, 468 (1998).
121. F. J. Pino, E. Bertran, M. C. Polo, and J. L. Andujar, *Diamond Relat. Mater.* 10, 952 (2001).
122. K.-Y. Lee, K. Fujimoto, S. Ohkura, S. Honda, M. Katayama, T. Hirao, and K. Oura, *Vacuum* 66, 239 (2002).
123. C. Venkatraman, A. Goel, R. Lei, D. Kester, and C. Outtern, *Thin Solid Films* 308–309, 173 (1997).
124. I. A. Faizrahmanov, V. V. Bazarov, V. A. Zhikharev, and I. B. Khaibullin, *Semiconductors* 35, 591 (2001).
125. D. Neerincx, P. Persoone, M. Sercu, A. Goel, C. Venkatraman, D. Kester, C. Hakter, P. Swab, and D. Bray, *Thin Solid Films* 317, 402 (1998).
126. Y. C. Yu, J.-H. Huang, and I.-N. Lin, *J. Vac. Sci. Technol., B* 19, 975 (2001).
127. D. Sheeja, B. K. Tay, S. P. Lau, X. Shi, and X. Ding, *Surf. Coat. Technol.* 132, 228 (2000).
128. H. Sjostrom, L. Hultman, J. E. Sundgren, S. V. Hainsworth, T. F. Page, and G. S. A. M. Theunissen, *J. Vac. Sci. Technol., A* 14, 56 (1996).
129. A. Leonhardt, H. Gruger, D. Selbmann, B. Arnold, and J. Thomas, *Thin Solid Films* 332, 69 (1998).
130. L. C. Chen, K. H. Chen, C. Y. Yang, D. M. Bhusari, J. C. Lin, T. J. Chuang, and M. C. Lin, *Diamond Relat. Mater.* 5, 514 (1996).
131. A. K. M. S. Chowdhury, D. C. Cameron, M. S. J. Hashmi, and J. M. Gregg, *J. Mater. Res.* 14, 2359 (1999).
132. S. Muhl, A. Gaona-Couto, G. Gonzalez, and J. M. Mendez, *Diamond Relat. Mater.* 7, 1605 (1998).
133. J. Konwerska-Hrabowska, S. Mitura, J. Szmids, A. Werbowy, A. Sokowska, and K. Zdunek, *Diamond Relat. Mater.* 5, 564 (1996).
134. J. Loeffler, I. Konyashin, J. Bill, H. Uhlig, and F. Aldinger, *Diamond Relat. Mater.* 6, 609 (1997).
135. A. Chayahara, H. Yokoyama, T. Imura, and Y. Osaka, *Jpn. J. Appl. Phys.* 26, L1435 (1987).
136. S. Komatsu, Y. Moriyoshi, M. Kasamatsu, and K. Yamada, *J. Phys. D: Appl. Phys.* 24, 1687 (1991).
137. S. Ulrich, J. Schwan, W. Donner, and H. Ehrhardt, *Diamond Relat. Mater.* 5, 548 (1996).
138. S. Ulrich, J. Scherer, J. Schwan, I. Barzen, K. Jung, and H. Ehrhardt, *Diamond Relat. Mater.* 4, 288 (1995).
139. M. Mieno and T. Yoshida, *Jpn. J. Appl. Phys.* 29, L1175 (1990).
140. I. Konyashin, J. Loeffler, J. Bill, and F. Aldinger, *Thin Solid Films* 308–309, 101 (1997).
141. I. Konyashin, B. Inkson, J. Bill, F. Aldinger, V. Khvostov, A. Bregadze, M. Guseva, and V. Babaev, *Chem. Vap. Deposition* 4, 125 (1998).
142. D. L. Medlin, T. A. Friedmann, and P. B. Mirkarimi, *J. Appl. Phys.* 76, 295 (1994).
143. K. L. Chopra, V. Agarwal, and D. Vankar, *Thin Solid Films* 126, 307 (1985).
144. P. X. Yan, H. Y. Yu, Z. G. Wu, J. W. Xu, and X. L. Wen, *J. Vac. Sci. Technol., A* 19, 2312 (2001).
145. R. Telle, L. S. Sigle, and K. Takagi, in “Handbook of Ceramic Hard Materials” (R. Riedel, Ed.), Vol. 2, p. 802. Wiley-VCH, Weinheim, 2000.
146. O. Postel and J. Heberlein, *Surf. Coat. Technol.* 108–109, 247 (1998).
147. O. B. Postel and J. V. R. Heberlein, *Diamond Relat. Mater.* 8, 1878 (1999).
148. D. Golberg, Y. Bando, T. Sato, N. Grobert, M. Reyes-Reyes, H. Terrones, and M. Terrones, *J. Chem. Phys.* 116, 8523 (2002).
149. M. U. Guruz, V. P. Dravid, and Y. W. Chung, *Thin Solid Films* 414, 129 (2002).

150. E. Bouyer, M. Müller, R. H. Henne, and G. Schiller, *J. Nanopart. Res.* 3, 371 (2001).
151. X. Junmin and J. Wang, *Mater. Lett.* 49, 318 (2001).
152. W. Z. Zhu, J. H. Gao, and Z. S. Ding, *J. Mater. Sci.* 32, 537 (1997).
153. J. Vlcek, M. Kormunda, J. V. Czek, V. Perina, and J. Zemek, *Surf. Coat. Technol.* 160, 74 (2002).
154. I. Tanaka, F. Oba, T. Sekine, E. Ito, A. Kubo, K. Tatsumi, H. Adachi, and T. Yamamoto, *J. Mater. Res.* 17, 731 (2002).
155. S. Ulrich, T. Theel, J. Schwan, V. Batori, M. Scheib, and H. Erhardt, *Diamond Relat. Mater.* 6, 645 (1997).
156. S. Ulrich, T. Theel, J. Schwan, and H. Erhardt, *Surf. Coat. Technol.* 97, 45 (1997).
157. J. Blum, N. Tymiak, A. Neuman, Z. Wong, N. P. Rao, S. L. Girschick, W. W. Gerberich, P. H. McMurry, and J. V. R. Heberlein, *J. Nanopart. Res.* 1, 31 (1999).
158. P. H. Mayrhofer, G. Tischler, and C. Mitterer, *Surf. Coat. Technol.* 142–144, 78 (2001).
159. I. Konyashin and G. Fox-Rabinovich, *Adv. Mater.* 10, 952 (1998).
160. S. A. Barnett, in “Physics of Thin Films. Advances in Research and Development. Mechanic and Dielectric Properties” (M. H. Francombe and J. L. Vossen, Eds.), Vol. 17, p. 1. Academic Press, Boston, 1993.
161. S. A. Barnett and M. Shinn, *Annu. Rev. Mater. Sci.* 24, 481 (1994).
162. A. Madan and S. A. Barnett, in “Materials Science of Carbides, Nitrides and Borides” (Y. G. Gogotsi and R. A. Andrievski, Eds.), p. 187. Kluwer Academic, Dordrecht, 1999.
163. S. Veprek, *J. Vac. Sci. Technol., A* 17, 2401 (1999).
164. S. Veprek, in “Handbook of Ceramic Hard Materials” (R. Riedel, Ed.), p. 104. Wiley-VCH, Weinheim, 2000.
165. S. Veprek and A. S. Argon, *J. Vac. Sci. Technol., B* 20, 650 (2002).
166. R. Hauert and J. Patscheider, *Adv. Eng. Mater.* 2, 247 (2000).
167. J. Musil, *Surf. Coat. Technol.* 125, 322 (2000).
168. J. Musil and J. Vlcek, *Surf. Coat. Technol.* 142–144, 557 (2001).
169. J. Musil, F. Regent, Z. Soukup, J. Vlcek, and J. G. Han, in “Progress in Plasma Processing of Materials” (P. Fauchais, Ed.), p. 589. Begell House, New York, 2001.
170. W.-D. Munz, D. B. Lewis, P. E. Hovsepian, C. Schonjahn, A. Ehi-asarian, and I. J. Smith, *Surf. Eng.* 17, 15 (2001).
171. A. Badzian, *Mater. Chem. Phys.* 72, 110 (2001).
172. R. A. Andrievski, *Int. J. Refract. Met. Hard Mater.* 19, 447 (2001).
173. R. A. Andrievski and G. V. Kalinnikov, *Surf. Coat. Technol.* 142–144, 573 (2001).
174. L. Hultman and J. E. Sundgren, in “Handbook of Hard Coatings. Deposition Technologies, Properties and Applications” (R. F. Bunshah, Ed.), p. 108., Noyes Park Ridge, NJ, 2001.
175. G. M. Demyashev, A. L. Taube, and E. Siores, in “Handbook of Organic-Inorganic Hybrid Materials and Nanocomposites” (H. S. Nalwa, Ed.), Vol. 2. American Scientific Publishers, Stevenson Ranch, CA, 2003.
176. H. Gleiter, in “Mechanical Properties and Deformation Behavior of Materials Having Ultra-Fine Microstructures” (M. Nastasi, D. M. Parkin, and H. Gleiter, Eds.), p. 3. Kluwer Academic, Dordrecht, 1993.
177. R. Birringer, U. Herr, and H. Gletler, *Trans. Jpn. Inst. Met. Suppl.* 27, 43 (1986).
178. R. Birringer, H. Gleiter, H.-P. Klein, and P. Marquardt, *Phys. Lett. A* 102, 365 (1984).
179. R. Birringer, *Mater. Sci. Eng. A* 117, 33 (1989).
180. R. Birringer and H. Gleiter, in “Encyclopedia of Materials Science and Engineering” (R. W. Cahn and M. B. Bever, Eds.), Vol. 1, p. 339. Pergamon, Oxford, 1998.
181. R. W. Siegel, in “Mechanical Properties and Deformation Behavior of Materials Having Ultra-Fine Microstructures” (M. Nastasi, D. M. Parkin, and H. Gleiter, Eds.), p. 509. Kluwer Academic, Dordrecht, 1993.
182. M. Yu. Gutkin and I. A. Ovid’ko, “Defects and Plasticity Mechanisms in Nanostructured and Non-crystalline Materials.” Yanus, St. Petersburg, 2001.
183. M. Gell, “WTEC Workshop Report on R&D Status and Trends in Nanoparticles, Nanostructured Materials, and Nanodevices in the United States,” 1997, p. 248.
184. H. Chang, H. J. Hofler, C. J. Altstetter, and R. S. Averbach, *Scripta Metall. Mater.* 25, 1161 (1991).
185. J. A. Jaszczak and D. Wolf, *J. Mater. Res.* 6, 1207 (1991).
186. S. Shimogawa and K. Ohtawara, in “Eighth Annual International Conference on Composites Engineering” (D. Hui, Ed.), p. 845. 2001.
187. S. J. Bull, *Thin Solid Films* 398–399, 291 (2001).
188. R. Cremer, K. Reichert, and D. Neuschütz, *Surf. Coat. Technol.* 142–144, 642 (2001).
189. R. Cremer and D. Neuschütz, *Surf. Coat. Technol.* 146–147, 229 (2001).
190. T. Chudoba, N. Schwarzer, and F. Richter, *Surf. Coat. Technol.* 154, 140 (2002).
191. M. A. Khusainov, G. M. Demyashev, and M. M. Myshlyaev, *Izv. Akad. Nauk USSR: Metals* 5, 144 (1990).
192. K. Yvon and E. Parthe, *Acta Cryst. B* 26, 149 (1970).
193. M. A. Khusainov, G. M. Demyashev, and M. M. Myshlyaev, *Izv. Akad. Nauk USSR: Metals* 4, 43 (1991).
194. G. M. Demyashev, M. A. Khusainov, N. N. Repnikov, and R. K. Chuzhko, *Izv. Akad. Nauk USSR: Ser. Fiz.* 9, 1693 (1984).
195. G. M. Demyashev, E. E. Koshchug, N. N. Repnikov, and R. K. Chuzhko, *J. Less-Common Met.* 107, 59 (1983).
196. M. A. Khusainov, G. M. Demyashev, and M. M. Myshlyaev, *Izv. Akad. Nauk USSR: Metals* 6, 160 (1990).
197. C. Suryanarayana, in “High Temperature High Performance Materials for Rocket Engines and Space Applications” (K. Upadhyay, Ed.), p. 61. Minerals, Metals & Materials Society, Warrendale, PA, 1995.
198. C. Suryanarayana, D. Mukhopadhyay, S. N. Patankar, and F. H. Froes, *J. Mater. Res.* 7, 2114 (1992).
199. D. G. Morris, “Mechanical Behaviour of Nanostructured Materials.” Trans Tech, Zurich, 1998.
200. A. S. Edelstein, J. S. Murday, and B. B. Rath, *Prog. Mater. Sci.* 42, 5 (1997).
201. S. Berger, R. Porat, and R. Rosen, *Prog. Mater. Sci.* 42, 311 (1997).
202. C. Koch, in “Nanostructure Science and Technology: Worldwide Status and Trends,” p. 138. Kluwer Academic, Dordrecht, 1999.
203. V. F. Petrunin, *Nanostruct. Mater.* 12, 1153 (1999).
204. A. R. Nozik, in “Semiconductor Nanoclusters—Physical, Chemical, and Catalytic Aspects” (P. V. Kamat and D. Meisel, Eds.), p. 135. Elsevier, Amsterdam, 1997.
205. J. N. Schulman and T. C. McGill, in “Synthetic Modulated Structures” (L. L. Chang and B. C. Giessen, Eds.), p. 77. Academic Press, Orlando, 1985.
206. D. B. McWhan, in “Synthetic Modulated Structures” (L. L. Chang and B. C. Giessen, Eds.), p. 43. Academic Press, Orlando, 1985.
207. H. Dosch, *Appl. Surf. Sci.* 182, 192 (2001).
208. S. Veprek, *Thin Solid Films* 297, 145 (1997).
209. R. A. Andrievski and A. M. Glezer, *Scripta Mater.* 44, 1621 (2001).
210. H. J. Hofler, R. S. Averbach, H. Hahn, and H. Gleiter, *J. Appl. Phys.* 74, 3832 (1993).
211. A. L. Greer and F. Spaepen, in “Synthetic Modulated Structures” (L. L. Chang and B. C. Giessen, Eds.), p. 419. Academic Press, Orlando, 1985.
212. R. A. Masumura and I. A. Ovid’ko, *Mater. Phys. Mech.* 1, 31 (2000).
213. P. P. Chattopadhyay, S. K. Pabi, and I. Manna, *Mater. Chem. Phys.* 68, 80 (2001).
214. X. Y. Zhang, Y. F. Xu, M. L. Yan, L. M. Chao, M. Zhang, J. H. Zhao, W. Y. Wai, and W. K. Wang, *J. Mater. Res.* 14, 984 (1999).

215. M. D. Baro, Yu. R. Kolobov, I. A. Ovid'ko, H.-E. Schaefer, B. B. Straumal, R. Z. Valiev, I. V. Alexandrov, M. Ivanov, K. Reimann, A. B. Reizis, S. Surinach, and A. P. Zhilyaev, *Rev. Adv. Mater. Sci.* 2, 1 (2001).
216. E. J. Gonzalez, J. E. Bonevich, G. R. Stafford, G. White, and D. Josell, *J. Mater. Res.* 15, 764 (2000).
217. Z. D. Liu, J. T. Wang, and J. Zhu, *J. Mater. Sci.* 29, 929 (1994).
218. C. M. Falco and I. K. Schuller, in "Synthetic Modulated Structures" (L. L. Chang and B. C. Giessen, Eds.), p. 339. Academic Press, Orlando, 1985.
219. S. N. Song and J. B. Ketterson, in "Materials Science and Technology: A Comprehensive Treatment" (R. W. Cahn, P. Haasen, and E. J. Kramer, Eds.), Vol. 3A, p. 457. VCH, Weinheim, 1991.
220. E. Helstern, H. Fecht, Z. Fu, and W. L. Johnson, *J. Appl. Phys.* 65, 305 (1989).
221. K. N. Shrivastava, *Nano Lett.* 2, 21 (2002).
222. K. Lu, J. T. Wang, and W. D. Wei, *Scripta Metall. Mater.* 25, 619 (1991).
223. M. C. Cyrille, S. Kim, M. E. Gomez, J. Santamaria, K. M. Krishnan, and I. K. Schuller, *Phys. Rev. B* 62, 3361 (2000).
224. M. Sohma, K. Kawaguchi, and T. Manago, *J. Appl. Phys.* 89, 2843 (2001).
225. J. Tang, K.-Y. Wang, and W. Zhou, *J. Appl. Phys.* 89, 7690 (2001).
226. F. Yang, T. He, J. B. Chen, and F. Pan, *J. Appl. Phys.* 91, 3114 (2002).
227. F. Yang and F. Pan, *Phys. Rev. B: Condens. Matter* 315, 227 (2002).
228. U. Herr, *Adv. Eng. Mater.* 3, 889 (2001).
229. E. Wortham, A. Zorko, D. Arcon, and A. Lappas, *Phys. Rev. B: Condens. Matter* 318, 387 (2002).
230. A. A. R. Fernandes, C. A. Ramos, A. Macedo Teixeira, and E. E. Fullerton, *Phys. Rev. B: Condens. Matter* 320, 175 (2002).
231. A. Butera and J. A. Barnard, *Phys. Rev. B: Condens. Matter* 320, 181 (2002).
232. P. G. Bercoff, M. I. Oliva, E. Borclone, and H. R. Bertorello, *Phys. Rev. B: Condens. Matter* 320, 291 (2002).
233. J. E. Mattson, R. M. Osgood III, C. D. Potter, C. H. Sowers, and S. D. Bader, *J. Vac. Sci. Technol., A* 15, 1774 (1997).
234. N. Canosa and R. Rossignoli, *Phys. Rev. B: Condens. Matter* 320, 319 (2002).
235. I. K. Schuller, *Phys. Rev. Lett.* 44, 1597 (1980).
236. K. Imamura, Y. Tanaka, and S. Tamura, *Phys. Rev. B* 65, 174301 (2002).
237. G. Scamarcio, F. Capasso, C. Sirtori, J. Faist, A. L. Hutchinson, D. L. Sivco, and A. Y. Cho, *Science* 276, 773 (1997).
238. N. Holonyak and K. Hess, in "Synthetic Modulated Structures" (L. L. Chang and B. C. Giessen, Eds.), p. 257. Academic Press, Orlando, 1985.
239. L. Esaki, in "Synthetic Modulated Structures" (L. L. Chang and B. C. Giessen, Eds.), p. 3. Academic Press, Orlando, 1985.
240. S. T. Ruggiero and M. R. Beasley, in "Synthetic Modulated Structures" (L. L. Chang and B. C. Giessen, Eds.), p. 365. Academic Press, Orlando, 1985.
241. A. Hengelein, *Chem. Rev.* 89, 1861 (1998).
242. H. Gleiter and M. Fichtner, *Scripta Mater.* 46, 497 (2002).
243. H. Yasuda and H. Mori, *J. Cryst. Growth* 237–239, 234 (2002).
244. J. A. Eastman, U. S. Choi, S. Li, G. Soyez, L. J. Thompson, and R. J. DiMelfi, *J. Metastable Nanocryst. Mater.* 2–6, 629 (1999).
245. M. V. Simkin and G. D. Mahan, *Phys. Rev. Lett.* 84, 927 (2000).
246. A. A. Kiselev, K. W. Kim, and M. A. Stroschio, *Phys. Rev. B* 62, 6896 (2000).
247. A. F. Khokhlov, I. A. Chuchmai, and A. V. Ershov, *Semiconductors* 34, 344 (2000).
248. D. Chakravorty, S. Banerjee, and T. K. Kundu, *Appl. Surf. Sci.* 182, 251 (2001).
249. A. Konrad, U. Herr, R. Tidecks, F. Kummer, and K. Samwer, *J. Appl. Phys.* 90, 3516 (2001).
250. M. Zacharias, J. Heitmann, R. Scholz, U. Kahler, M. Schmidt, and J. Bläsing, *Appl. Phys. Lett.* 80, 661 (2002).
251. A. A. Levin, D. C. Meyer, A. Tselev, A. Gorbunov, W. Pompe, and P. Paufler, *J. Alloys Compd.* 334, 159 (2002).
252. C. R. Aita, *Surf. Eng.* 15, 195 (1999).
253. D. Szewieczek, J. Tyrlik-Held, and Z. Paszenda, *J. Mater. Process. Technol.* 78, 171 (1998).
254. O. Elkedim, H. S. Cao, and D. Guay, *J. Mater. Process. Technol.* 121, 383 (2002).
255. T. Hakayama, K. Yamamoto, H. Satoh, T. J. Konno, B. M. Clemenc, and R. Sinclair, *Mater. Sci. Eng., A* 198, 19 (1995).
256. A. H. Chokshi, *Scripta Mater.* 34, 1905 (1996).
257. T. Ohji, *Scripta Mater.* 44, 2083 (2001).
258. Y. Gan and B. Zhou, *Scripta Mater.* 45, 625 (2001).
259. T. Sailer, M. Herr, H.-G. Sockel, R. Schulte, H. Feld, and L. J. Prakash, *Int. J. Refract. Met. Hard Mater.* 19, 553 (2001).
260. P. G. Sanders, *Mater. Sci. Eng., A* 234–236, 77 (1997).
261. S. R. Agnew, B. R. Elliott, C. J. Youngdahl, K. J. Hemker, and J. R. Weertman, *Mater. Sci. Eng., A* 285, 391 (2000).
262. K. A. Padmanabhan, *Mater. Sci. Eng., A* 304–306, 200 (2001).
263. F. Ebrahimi, Q. Zhai, and D. Kong, *Mater. Sci. Eng., A* 255, 20 (1998).
264. V. J. Lariaia, M. Aindow, and A. H. Heuer, *Mater. Res. Soc. Symp. Proc.* 174, 117 (1990).
265. M. Sarikaya, K. E. Gunnison, M. Yasrebi, and I. A. Aksay, *Mater. Res. Soc. Symp. Proc.* 174, 109 (1990).
266. L. J. Huang and H. D. Li, *Mater. Res. Soc. Symp. Proc.* 174, 101 (1990).
267. A. H. Heuer, D. J. Fink, V. J. Lariaia, J. L. Arias, P. D. Calvert, K. Kendall, G. L. Messing, J. Blackwell, P. C. Rieke, D. H. Thompson, A. P. Wheeler, A. Vies, and A. I. Caplan, *Science* 255, 1098 (1992).
268. D. L. Kaplan, *Curr. Opin. Solid State Mater. Sci.* 3, 232 (1998).
269. R. Z. Wang, H. B. Wen, F. Z. Cui, H. B. Zhang, and H. D. Li, *J. Mater. Sci.* 30, 2299 (1995).
270. B. J. Tarasevich and P. C. Rieke, *Mater. Res. Soc. Symp. Proc.* 174, 51 (1990).
271. C. H. Liu, W. Z. Li, and H. D. Li, *J. Mater. Res.* 11, 2231 (1996).
272. J. L. He, W. Z. Li, H. D. Li, and C. H. Liu, *Surf. Coat. Technol.* 103–104, 276 (1998).
273. H. Gleiter, *Acta Mater.* 48, 1 (2000).
274. C. E. Krill, R. Haberkorn, and R. Birringer, in "Handbook of Nanostructured Materials and Nanoscience" (H. S. Nalwa, Ed.), Vol. 2, p. 533. Academic Press, San Diego, 2000.
275. H. Gleiter, *Nanostruct. Mater.* 6, 3 (1995).
276. C. Suryanarayana, *Int. Mater. Rev.* 40, 41 (1995).
277. S. Barnett and A. Maden, *Phys. World* 1, 45 (1998).
278. J. A. Switzer, in "Handbook of Nanophase Materials" (A. N. Goldstein, Ed.), p. 63. Dekker, New York, 1997.
279. D.-E. Kim, D.-H. Cha, and S.-W. Lee, *J. Vac. Sci. Technol., A* 15, 2291 (1997).
280. H. Holleck and V. Schier, *Surf. Coat. Technol.* 76–77, 328 (1995).
281. C. Mitterer, P. H. Mayrhofer, M. Beschliesser, P. Losbichler, P. Warbichler, F. Hofer, P. N. Gibson, W. Gissler, H. Hruby, J. Musil, and J. Vlcek, *Surf. Coat. Technol.* 120–121, 405 (1999).
282. H. Gleiter, *Prog. Mater. Sci.* 33, 223 (1989).
283. J. Weissmuller, R. Birringer, and H. Gleiter, in "Microcomposites and Nanophase Materials" (D. C. Van Aken, G. S. Was, and A. K. Ghosh, Eds.), p. 1. Minerals, Metals & Materials Society, New Orleans, 1991.
284. X. Zhu, R. Birringer, U. Herr, and H. Gleiter, *Phys. Rev. B* 35, 9085 (1987).
285. L. Brus, P. Szajowski, W. Wilson, T. Harris, S. Schuppler, and P. Citrin, *J. Am. Chem. Soc.* 117, 2915 (1995).
286. S. R. Phillpot, D. Wolf, and H. Gleiter, *Scripta Mater.* 33, 1245 (1995).

287. S. R. Phillpot, J. Wang, D. Wolf, and H. Gleiter, *Mater. Sci. Eng., A* 204, 76 (1995).
288. S. Ranganathan, R. Divakar, and V. S. Raghunathan, *Scripta Mater.* 44, 1169 (2001).
289. R. A. Andrievski, G. V. Kalinnikov, and D. V. Shtanskii, *Phys. Solid State* 42, 760 (2001).
290. H. Van Swygenhoven, D. Farkas, and A. Caro, *Phys. Rev. B* 62, 831 (2000).
291. C. R. S. da Silva and A. Fazzio, *Phys. Rev. B* 64, 75301 (2001).
292. W. Shulin and Y. Dongsheng, *Ceram. Int.* 21, 109 (1995).
293. L. L. Kazmerski, *Surf. Sci. Rep.* 19, 169 (1993).
294. I. A. Ovid'ko, *Rev. Adv. Mater. Sci.* 1, 61 (2000).
295. K. N. Mikaelyan, I. A. Ovid'ko, and A. E. Romanov, *Mater. Sci. Eng., A* 259, 132 (1999).
296. L. S. Shvindlerman and G. Gottstein, *Mater. Sci. Eng., A* 302, 141 (2001).
297. M. Seefeldt, *Mater. Phys. Mech.* 1, 54 (2000).
298. T. Mutschele and R. Kirchheim, *Scripta Metall. Mater.* 21, 1101 (1987).
299. G. Thomas, R. W. Siegel, and J. A. Eastman, *Scripta Metall. Mater.* 24, 201 (1990).
300. B. Loberg and H. Norden, in "Grain Boundaries Structure and Properties" (G. A. Chadwick and D. A. Smith, Eds.), p. 1. Academic Press, London, 1976.
301. R. W. Siegel, *J. Phys. Chem. Solids* 55, 1097 (1994).
302. C. E. Krill and R. Birringer, in "Metastable, Mechanically Alloyed and Nanocrystalline Materials" (R. Schulz, Ed.), p. 263. Trans Tech, Zurich, 1996.
303. G. Palumbo, S. J. Thorpe, and K. T. Aust, *Scripta Metall. Mater.* 24, 1347 (1990).
304. G. Palumbo, K. T. Aust, and U. Erb, *Mater. Sci. Forum* 225–227, 281 (1996).
305. K. T. Aust, U. Erb, and G. Palumbo, in "Processing and Properties of Nanocrystalline Materials" (C. Suryanarayana, J. Singh, and F. H. Froes, Eds.), p. 11. Minerals, Metals & Materials Society, Cleveland, 1996.
306. V. Y. Gertsman, R. Z. Valiev, N. A. Akhmadeev, and O. V. Mishin, in "Synthetic Modulated Structures" (L. L. Chang and B. C. Giessen, Eds.), p. 739. Academic Press, Orlando, 1985.
307. W. Bollman, *Philos. Mag. A* 49, 73 (1984).
308. W. Bollman, *Philos. Mag. A* 57, 637 (1988).
309. W. Bollman, *Mater. Sci. Eng., A* 113, 129 (1989).
310. D. A. Konstantinidis and E. C. Aifantis, *Nanostruct. Mater.* 10, 1111 (1998).
311. G. Palumbo, U. Erb, and K. T. Aust, *Scripta Metall. Mater.* 24, 2347 (1990).
312. X. D. Liu, H. Y. Zhang, K. Lu, and A. Q. Hu, *J. Phys: Condens. Matter* 6, L497 (1994).
313. R. S. Musalimov and R. Z. Valiev, *Scripta Metall. Mater.* 27, 1685 (1992).
314. D. H. Ping, D. X. Li, and H. Q. Ye, *J. Mater. Sci. Lett.* 14, 1536 (1995).
315. K. Lu, *Nanostruct. Mater.* 12, 559 (1999).
316. A. A. Nazarov, A. E. Romanov, and R. Z. Valiev, *Nanostruct. Mater.* 4, 93 (1994).
317. W. Qin, Z. H. Chen, P. Y. Huang, and Y. H. Zhuang, *J. Alloys Compd.* 292, 230 (1999).
318. K. Lu, H. Y. Zhang, Y. Zhong, and H. J. Fecht, *J. Mater. Res.* 12, 923 (1997).
319. A. L. Greer, in "Mechanical Properties and Deformation Behavior of Materials Having Ultra-Fine Microstructures" (M. Nastasi, D. M. Parkin, and H. Gleiter, Eds.), p. 53. Kluwer Academic, Dordrecht, 1993.
320. D. Turnbull, *Metall. Trans. B* 12, 217 (1981).
321. K. Lu, *Scripta Metall. Mater.* 25, 2047 (1991).
322. Y.-M. Chiang, I. P. Smyth, C. D. Terwilliger, W. T. Petuskey, and J. A. Eastman, *Nanostruct. Mater.* 1, 235 (1992).
323. R. W. Siegel, in "Processing and Properties of Nanocrystalline Materials" (C. Suryanarayana, J. Singh, and F. H. Froes, Eds.), p. 3. Minerals, Metals & Materials Society, Cleveland, 1996.
324. J. Musil and J. Vlcek, in "Proceedings of the First International Congress on Radiation Physics, High Current Electronics, and Modification of Materials" (G. Mesyats, S. Bugaen, and A. Ryabchikov, Eds.), p. 393. Tomsk Polytechnic Univ., Tomsk, Russia, 2000.
325. S. Veprek, *J. Vac. Sci. Technol., A* 17, 2401 (1999).
326. J. Musil, S. Kadlec, J. Vyskocil, and V. Valvoda, *Thin Solid Films* 167, 107 (1988).
327. J. Musil, "Proceedings of the 13th Symposium on Application of Plasma Processes," 2001, p. 31.
328. E. O. Hall, *Proc. Phys. Soc., London, B* 64, 747 (1951).
329. N. J. Petch, *J. Iron Steel Inst.* 174, 25 (1953).
330. E. O. Hall, "Yield Point Phenomenon in Metals and Alloys." Plenum, New York, 1970.
331. R. W. Rice, C. C. Wu, and F. Borchelt, *J. Am. Ceram. Soc.* 77, 2539 (1994).
332. M. A. Meyers and K. K. Chawla, in "Mechanical Metallurgy," p. 494. Prentice Hall, Englewood Cliffs, NJ, 1984.
333. R. A. Masumura, P. M. Hazzledine, and C. S. Pande, *Acta Mater.* 46, 4527 (1988).
334. A. Misra and H. Kung, *Adv. Eng. Mater.* 3, 217 (2001).
335. J. C. M. Li and Y. T. Chou, *Metall. Trans.* 1, 1145 (1970).
336. N. Hansen, *Metall. Trans. A* 16, 2167 (1985).
337. W. T. Read, "Dislocations in Crystals." McGraw-Hill, New York, 1953.
338. S. Amelinckx, "The Direct Observation of Dislocations." Academic Press, New York, 1964.
339. A. H. Cottrell, "Theory of Crystal Dislocations." Gordon & Breach, New York, 1964.
340. J. Friedel, "Dislocations." Pergamon, Oxford, 1964.
341. V. G. Gryaznov, V. A. Solov'ev, and L. I. Trusov, *Scripta Metall. Mater.* 24, 1529 (1990).
342. V. G. Gryaznov, A. M. Kaprelov, and A. E. Romanov, *Scripta Metall. Mater.* 23, 1443 (1989).
343. T. G. Nieh and J. Wadsworth, *Scripta Metall. Mater.* 25, 955 (1991).
344. J. D. Embury and D. J. Lahaie, in "Mechanical Properties and Deformation Behavior of Materials Having Ultra-Fine Microstructures" (N. Nastasi, D. M. Parkin, and H. Gleiter, Eds.), p. 287. Kluwer Academic, Dordrecht, 1993.
345. J. Xu, G. Li, and M. Gu, *Thin Solid Films* 370, 45 (2000).
346. A. M. El-Sherik, U. Erb, G. Palumbo, and K. T. Aust, *Scripta Metall. Mater.* 27, 1185 (1992).
347. G. E. Fougere, J. R. Weertman, R. W. Siegel, and S. Kim, *Scripta Metall. Mater.* 26, 1879 (1992).
348. G. E. Fougere, J. R. Weertman, and R. W. Siegel, *Nanostruct. Mater.* 3, 379 (1993).
349. X. D. Liu, J. T. Wang, and B. Z. Ding, *Scripta Metall. Mater.* 28, 59 (1993).
350. K. Lu and M. L. Sui, *Scripta Metall. Mater.* 28, 1465 (1993).
351. L. Makhele-Lekala, S. Luyckx, and F. R. N. Nabarro, *Int. J. Refract. Met. Hard Mater.* 19, 245 (2001).
352. M. F. Tambwe, D. S. Stone, A. J. Griffin, H. Kung, Y. C. Lu, and M. Nastasi, *J. Mater. Res.* 14, 407 (1999).
353. H. S. Kim, *Scripta Mater.* 39, 1057 (1998).
354. P. Anderson, I.-H. Lin, and R. Thompon, *Scripta Metall. Mater.* 27, 687 (1992).
355. B. P. Kashyap and K. Tangri, *Acta Mater.* 45, 2383 (1997).
356. A. A. Fedorov, M. Yu. Gutkin, and I. A. Ovid'ko, *Scripta Mater.* 47, 51 (2002).
357. M. Verdier, M. Fivel, and B. Gilles, *Adv. Eng. Mater.* 3, 597 (2001).
358. T. Christman, *Scripta Metall. Mater.* 28, 1495 (1993).
359. S. Li, L. Sun, and Z. Wang, *Nanostruct. Mater.* 2, 653 (1993).
360. R. O. Scattergood and C. C. Koch, *Scripta Metall. Mater.* 27, 1195 (1992).

361. V. G. Gryaznov, M. Yu. Gutkin, A. E. Romanov, and L. I. Trusov, *J. Mater. Sci.* 28, 4359 (1993).
362. J. Lian and B. Baudalet, *Nanostruct. Mater.* 2, 415 (1993).
363. I. A. Ovid'ko, *Nanostruct. Mater.* 8, 149 (1997).
364. J. E. Carsley, J. Ning, W. W. Milligan, S. A. Hackney, and E. C. Aifantis, *Nanostruct. Mater.* 5, 441 (1995).
365. N. Wang, Z. Wang, K. T. Aust, and U. Erb, *Acta Metall. Mater.* 43, 519 (1995).
366. T. R. Smith, R. W. Armstrong, P. M. Hazzledine, and R. A. Masumura, *Mater. Res. Soc. Symp. Proc.* 362, 31 (1995).
367. C. C. Koch, *Nanostruct. Mater.* 2, 109 (1993).
368. M. Yu. Gutkin, I. A. Ovid'ko, and C. S. Pande, *Rev. Adv. Mater. Sci.* 2, 80 (2001).
369. J. Schiotz, F. D. Di Tolla, and K. W. Jacobsen, *Nature* 391, 561 (1998).
370. S. Takeuchi, *Scripta Mater.* 44, 1483 (2001).
371. C. A. Schuh, T. G. Nieh, and T. Yamasaki, *Scripta Mater.* 46, 735 (2002).
372. F. Louchet and H. Kung, *J. Metastable Nanocryst. Mater.* 7, 50 (2000).
373. C. Mercer and W. O. Soboyejo, *Scripta Mater.* 35, 17 (1996).
374. J. R. Weertman, M. Niedzielka, and C. Youngdahl, in "Mechanical Properties and Deformation Behavior of Materials Having Ultra-Fine Microstructures" (N. Nastasi, D. M. Parkin, and H. Gleiter, Eds.), p. 241. Kluwer Academic, Dordrecht, 1993.
375. H. Hahn and K. A. Padmanabham, *Philos. Mag. B* 76, 559 (1997).
376. Z. Z. Fang, A. Griffio, B. White, G. Lockwood, D. Belnap, G. Hilmas, and J. Bitler, *Int. J. Refract. Met. Hard Mater.* 19, 453 (2001).
377. U. Helmersson, S. Todorova, S. A. Barnett, J.-E. Sundgren, L. C. Markert, and J. E. Greene, *J. Appl. Phys.* 62, 481 (1987).
378. P. B. Mirkarimi, L. Hultman, and S. A. Barnett, *Appl. Phys. Lett.* 57, 2654 (1990).
379. R. A. Andrievskii, *J. Mater. Sci.* 29, 614 (1994).
380. A. Lasalmonie and J. L. Strudel, *J. Mater. Sci.* 21, 1837 (1986).
381. R. W. Siegel and H. Hahn, in "Current Trends in the Physics of Materials" (M. Yussouff, Ed.), p. 403. World Scientific, Singapore, 1987.
382. J. Musil and J. Vlcek, *Czech. J. Phys.* 48, 1209 (1998).
383. E. Kusano, *Nanostruct. Mater.* 12, 807 (1999).
384. D. Josell, D. van Heerden, D. Shechtman, and D. Read, *Nanostruct. Mater.* 12, 405 (1999).
385. A. Misra, M. Verdier, H. Kung, J. D. Embury, and J. P. Hirth, *Scripta Mater.* 41, 973 (1999).
386. A. S. Argon and S. Veprek, in "Proceedings of the 22nd Riso International Symposium on Materials Science: Science of Metastable and Nanocrystalline Alloys, Structure, Properties, and Modeling" (A. R. Dinesen, M. Eldrup, D. J. Jensen et al., Eds.), p. 183. Riso National Laboratory, Roskilde, 2001.
387. E. Orowan, *Z. Phys.* 82, 235 (1933).
388. E. Orowan, *Z. Phys.* 83, 554 (1933).
389. E. Orowan, *Z. Phys.* 86, 195 (1933).
390. J. D. Embury and J. P. Hirth, *Acta Metall. Mater.* 42, 2051 (1994).
391. J. Hafner, *Acta Mater.* 48, 71 (2000).
392. W. D. Nix, *Mater. Sci. Eng., A* 234-236, 37 (1997).
393. J. W. Cahn, *Acta Metall. Mater.* 11, 1274 (1993).
394. X. Chu and S. A. Barnett, *J. Appl. Phys.* 77, 4403 (1995).
395. S. J. Koehler, *Phys. Rev. B* 2, 547 (1970).
396. S. L. Lehoczky, *J. Appl. Phys.* 49, 5479 (1978).
397. M. Shinn, L. Hultman, and S. A. Barnett, *J. Mater. Res.* 7, 901 (1992).
398. J. Grilhe, in "Mechanical Properties and Deformation Behavior of Materials Having Ultra-Fine Microstructures" (M. Nastasi, D. M. Parkin, and H. Gleiter, Eds.), p. 255. Kluwer Academic, Dordrecht, 1993.
399. M. Shinn and S. A. Barnett, *Appl. Phys. Lett.* 64, 61 (1994).
400. P. B. Mirkarimi, S. A. Barnett, K. M. Hubbard, T. R. Jervis, and L. Hultman, *J. Mater. Res.* 9, 1456 (1994).
401. J. Xu, M. Kamiko, Y. Zhou, R. Yamamoto, G. Li, and M. Gu, *J. Appl. Phys.* 89, 1 (2001).
402. W. E. Pickett, *J. Phys. F: Met. Phys.* 12, 2195 (1982).
403. T. B. Wu, *J. Appl. Phys.* 53, 5265 (1982).
404. G. E. Henein and J. E. Hilliard, *J. Appl. Phys.* 54, 728 (1983).
405. T. Tsakalacos and J. E. Hilliard, *J. Appl. Phys.* 54, 734 (1983).
406. J. E. Krzanowski, *Scripta Metall. Mater.* 25, 1465 (1991).
407. P. M. Anderson and C. Li, *Nanostruct. Mater.* 5, 349 (1995).
408. D. S. Lashmore and R. Thomson, *J. Mater. Res.* 7, 2379 (1992).
409. G. Li, J. Xu, L. Zhang, L. Wu, and M. Gu, *J. Vac. Sci. Technol., B* 19, 94 (2001).
410. S. L. Lehoczky, *Phys. Rev. Lett.* 41, 1814 (1978).
411. J. E. Krzanowski, *Mater. Res. Soc. Symp. Proc.* 239, 509 (1992).
412. C. A. Klein and R. P. Miller, *J. Appl. Phys.* 87, 2265 (2000).
413. A. Misra, H. Kung, T. E. Mitchell, and M. Nastasi, *J. Mater. Res.* 15, 756 (2000).
414. D. R. Gabe and W. A. Green, *Surf. Coat. Technol.* 105, 195 (1998).
415. C. S. Pande, R. A. Masumura, and R. W. Armstrong, *Nanostruct. Mater.* 2, 323 (1993).
416. J. Chaudhuri, V. Gondhalekar, S. Shan, and A. F. Jankowski, *Mater. Res. Soc. Symp. Proc.* 160, 195 (1990).
417. M. Jaouen, J. Pacaud, and C. Jaouen, *Phys. Rev. B* 64, 144106 (2001).
418. A. Chatterjee, S. K. Pradhan, A. Datta, M. De, and D. Chakravorty, *J. Mater. Res.* 9, 263 (1994).
419. W. P. Lowe and T. H. Geballe, *Phys. Rev. B* 29, 4961 (1984).
420. J. Q. Zheng, J. B. Ketterson, C. M. Falco, and I. K. Schuller, *Physica B* 108, 945 (1981).
421. R. Banerjee, X.-D. Zhang, S. A. Gregia, and H. L. Fraser, *Acta Mater.* 47, 1153 (1999).
422. G. Shao and P. Tsakirooulos, "Proceedings of the Eighth International Conference on Composite Engineering," 2001, p. 833.
423. T. Tepper, D. Shechtman, D. Van Heerden, and D. Josell, *Mater. Lett.* 33, 181 (1997).
424. A. F. Jankowski and M. A. Wall, *J. Mater. Res.* 9, 31 (1994).
425. C. Kim, S. B. Qadri, H. Y. Yu, K. H. Kim, B. Maruyama, and A. S. Edelstein, *J. Vac. Sci. Technol., A* 8, 14707 (1990).
426. H. Von Kanel, C. Schwarz, S. Goncalves Conto, E. Muller, L. Miglio, F. Tavazza, and G. Malegozi, *Phys. Rev. Lett.* 74, 1163 (1995).
427. W. H. Wang and W. K. Wang, *J. Mater. Res.* 9, 401 (1994).
428. T. G. Nieh, T. W. Barbee, and J. Wadsworth, *Scripta Mater.* 41, 929 (1999).
429. P. C. Yashar and W. D. Sproul, *Vacuum* 55, 179 (1999).
430. X. Chu, S. A. Barnett, M. S. Wong, and W. D. Sproul, *Surf. Coat. Technol.* 57, 13 (1993).
431. X. Chu, M. S. Wong, W. D. Sproul, and S. A. Barnett, *J. Mater. Res.* 14, 2500 (1999).
432. X. T. Zeng, *Surf. Coat. Technol.* 113, 75 (1999).
433. T. I. Selinder, M. E. Sjostrand, M. Nordin, M. Larsson, A. Ostlung, and S. Hogmark, *Surf. Coat. Technol.* 105, 51 (1998).
434. M. Nordin, M. Larsson, and S. Hogmark, *Surf. Coat. Technol.* 106, 234 (1998).
435. W. D. Sproul, *Surf. Coat. Technol.* 86-87, 170 (1996).
436. A. Madan, P. Yashar, M. Shinn, and S. A. Barnett, *Thin Solid Films* 302, 147 (1997).
437. A. J. Craven, C. P. Scott, M. MacKenzie, P. Hatto, and C. Davies, *Surf. Coat. Technol.* 108-109, 217 (1998).
438. X. T. Zeng, S. Mridha, and U. Chai, *J. Mater. Process. Technol.* 89-90, 528 (1999).
439. J. O. Kim, J. D. Achenbach, M. Shinn, and S. A. Barnett, *J. Mater. Res.* 7, 2248 (1992).
440. L. Hultman, L. R. Wallenberg, M. Shinn, and S. A. Barnett, *J. Vac. Sci. Technol., A* 10, 1618 (1992).
441. W. D. Sproul, *J. Vac. Sci. Technol., A* 12, 1595 (1994).

442. S. Lopez, M.-S. Wong, and W. D. Sproul, *J. Vac. Sci. Technol., A* 13, 1644 (1995).
443. H. Ljungcrantz, C. Engström, L. Hultman, M. Olsson, X. Chu, M. S. Wong, and W. D. Sproul, *J. Vac. Sci. Technol., A* 16, 3104 (1998).
444. C. Engström, J. Birch, L. Hultman, C. Lavoie, C. Cabral, J. L. Jordan-Sweet, and J. R. A. Carlsson, *J. Vac. Sci. Technol., A* 17, 2920 (1999).
445. G. Li, Z. Han, J. Tian, J. Xu, and M. Gu, *J. Vac. Sci. Technol., A* 20, 674 (2002).
446. V. Hainsworth, M. R. McGurk, and T. F. Page, *Surf. Coat. Technol.* 102, 97 (1998).
447. W. D. Sproul, *Vacuum* 51, 641 (1998).
448. X. Chu, M. S. Wong, W. D. Sproul, S. L. Rohde, and S. A. Barnett, *J. Vac. Sci. Technol., A* 10, 1604 (1992).
449. M. Larsson, P. Hollman, P. Hedenqvist, S. Hogmark, U. Wahlstrom, and L. Hultman, *Surf. Coat. Technol.* 86–87, 351 (1996).
450. M. Nordin, M. Larsson, T. Joelsson, J. Birch, and L. Hultman, *J. Vac. Sci. Technol., A* 18, 2884 (2000).
451. M. Nordin and F. Ericson, *Thin Solid Films* 385, 174 (2001).
452. M. Nordin, M. Larsson, and S. Hogmark, *Surf. Coat. Technol.* 120–121, 528 (1999).
453. P. B. Mirkarimi, M. Shinn, S. A. Barnett, S. Kumar, and M. Grimsditch, *J. Appl. Phys.* 71, 4955 (1992).
454. J. H. Hsieh, C. Liang, C. H. Yu, and W. Wu, *Surf. Coat. Technol.* 108–109, 132 (1998).
455. Y. Zhou, R. Asaki, W.-H. Soe, R. Yamamoto, R. Chen, and A. Iwabuchi, *Wear* 236, 159 (1999).
456. Y. Zhou, R. Asaki, W.-H. Soe, R. Yamamoto, R. Chen, and A. Iwabuchi, *Trans. Mater. Res. Soc. Jpn.* 24, 125 (1999).
457. Y. Zhou, R. Asaki, K. Higashi, W.-H. Soe, and R. Yamamoto, *Surf. Coat. Technol.* 130, 9 (2000).
458. M. Nordin, M. Larsson, and S. Hogmark, *Wear* 232, 221 (1999).
459. M. Nordin and M. Larsson, *Surf. Coat. Technol.* 116–119, 108 (1999).
460. Q. Yang, C. He, L. R. Zhao, and J.-P. Immarigeon, *Scripta Mater.* 46, 293 (2002).
461. R. Yamamoto and W.-H. Soe, *Mater. Chem. Phys.* 50, 176 (1997).
462. M. Nordin, M. Herranen, and S. Hogmark, *Thin Solid Films* 348, 202 (1999).
463. P. Yashar, S. A. Barnett, J. Rechner, and W. D. Sproul, *J. Vac. Sci. Technol., A* 16, 2913 (1998).
464. Y.-H. Chen, K. W. Lee, W.-A. Chiou, Y.-W. Chung, and L. M. Keer, *Surf. Coat. Technol.* 146–147, 209 (2001).
465. Y.-H. Chen, M. Guruz, Y.-W. Chung, and L. M. Keer, *Surf. Coat. Technol.* 154, 162 (2002).
466. X.-C. Lu, B. Shi, L. K. Y. Li, J. Luo, X. Chang, Z. Tian, and J.-I. Mou, *Wear* 251, 1144 (2001).
467. C. J. Tavares, L. Rebouta, B. Almeida, J. Bessa e Sousa, M. F. da Silva, and J. C. Soares, *Thin Solid Films* 317, 124 (1998).
468. M. Okumiya and M. Griepentrog, *Surf. Coat. Technol.* 112, 123 (1999).
469. K. Bartsch, H. Liepack, S. Kolozsvari, and A. Leonhardt, "Proceedings of the Eighth International Conference on Composite Engineering," 2001, p. 63.
470. W.-D. Munz, D. Schulze, and F. Hauzer, *Surf. Coat. Technol.* 50, 169 (1992).
471. P. E. Hovsepian, D. B. Lewis, and W.-D. Munz, *Surf. Coat. Technol.* 133–134, 166 (2000).
472. P. E. Hovsepian, D. B. Lewis, W.-D. Munz, A. Rouzaud, and P. Juliet, *Surf. Coat. Technol.* 116–119, 727 (1999).
473. H. W. Wang, M. M. Stack, S. B. Lyon, P. Hovsepian, and W. D. Munz, *J. Mater. Sci. Lett.* 20, 547 (2001).
474. H. W. Wang, M. M. Stack, P. Hovsepian, and W.-D. Munz, *J. Mater. Sci. Lett.* 20, 1995 (2001).
475. H. W. Wang, M. M. Stack, S. B. Lyon, P. Hovsepian, and W.-D. Munz, *Surf. Coat. Technol.* 135, 82 (2000).
476. C. Leyens, M. Peters, P. E. Hovsepian, D. B. Lewis, Q. Luo, and W.-D. Munz, *Surf. Coat. Technol.* 155, 103 (2002).
477. M. Tomlinson, S. B. Lyon, P. Hovsepian, and W.-D. Munz, *Vacuum* 53, 117 (1999).
478. D. C. Cameron, R. Aimo, Z. H. Wang, and K. A. Pischow, *Surf. Coat. Technol.* 142–144, 567 (2001).
479. P. E. Hovsepian, W.-D. Munz, A. Medlock, and G. Gregory, *Surf. Coat. Technol.* 133–134, 508 (2000).
480. I. Wadsworth, I. J. Smith, L. A. Donohue, and W.-D. Munz, *Surf. Coat. Technol.* 94–95, 315 (1997).
481. D. B. Lewis, I. Wadsworth, W.-D. Munz, R. Kuzel, Jr., and V. Valvoda, *Surf. Coat. Technol.* 116–119, 284 (1999).
482. W.-D. Munz, L. A. Donohue, and P. E. Hovsepian, *Surf. Coat. Technol.* 125, 269 (2000).
483. Q. Luo, W. M. Rainforth, and W.-D. Munz, *Scripta Mater.* 45, 399 (2001).
484. M. I. Lembke, D. B. Lewis, and W.-D. Münz, *Surf. Coat. Technol.* 125, 263 (2000).
485. Q. Luo, W. M. Rainforth, L. A. Donohue, I. Wadsworth, and W.-D. Münz, *Vacuum* 53, 123 (1999).
486. S. M. Aouadi, D. M. Schultze, S. L. Rohde, K.-C. Wong, and K. A. R. Mitchell, *Surf. Coat. Technol.* 140, 269 (2001).
487. M. L. Kuruppu, G. Negrea, I. P. Ivanov, and S. L. Rohde, *J. Vac. Sci. Technol., A* 16, 1949 (1998).
488. J. Xu, K. Hattori, Y. Seino, and I. Kojima, *Thin Solid Films* 414, 239 (2002).
489. J. Xu, M. Kamiko, Y. Zhou, R. Yamamoto, G. Li, and M. Gu, *J. Appl. Phys.* 89, 3674 (2001).
490. J. Xu, M. Gu, and G. Li, *J. Mater. Sci.* 35, 3535 (2000).
491. J. J. Jeong, S. K. Hwang, and C. Lee, *Mater. Chem. Phys.* 77, 27 (2003).
492. J. E. Mattson, C. D. Potter, M. J. Conover, C. H. Sowers, and S. D. Bader, *J. Vac. Sci. Technol., A* 15, 2793 (1997).
493. M. Lattemann, S. Ulrich, H. Holleck, M. Stuber, and H. Leiste, *Diamond Relat. Mater.* 11, 1248 (2002).
494. K. K. Shin and D. B. Dove, *Appl. Phys. Lett.* 61, 654 (1992).
495. R. Hubler, A. Schröer, W. Ensinger, G. Wolf, F. C. Stedile, W. H. Schreiner, and I. J. R. Baumvol, *J. Vac. Sci. Technol., A* 11, 451 (1993).
496. E. Kusano, M. Kitagawa, H. Nanto, and A. Kinbara, *J. Vac. Sci. Technol., A* 16, 1272 (1998).
497. J. C. Hu, T. C. Chang, L. J. Chen, Y. L. Yang, S. Y. Chen, and C. Y. Chang, *J. Vac. Sci. Technol., A* 17, 2389 (1999).
498. H. Mu, Y. Yu, E. Z. Luo, B. Sundaravel, S. P. Wong, and I. H. Wilson, *J. Vac. Sci. Technol., A* 18, 2312 (2000).
499. M. Ben-Daia, P. Aubert, S. Labdi, C. Sant, F. A. Sadi, Ph. Houdy, and J. L. Bozet, *J. Appl. Phys.* 87, 7753 (2000).
500. M. Herranen, U. Wiklund, J.-O. Carlsson, and S. Hogmark, *Surf. Coat. Technol.* 99, 190 (1998).
501. X. Ma, X. Li, Y. Sun, L. Xia, M. Sun, and G. Li, *Mater. Lett.* 44, 170 (2000).
502. N. Kikuchi, M. Kitagawa, A. Sato, E. Kusano, H. Nanto, and A. Kinbara, *Surf. Coat. Technol.* 126, 131 (2000).
503. M. Leoni, P. Scardi, S. Rossi, L. Fedrizzi, and Y. Massiani, *Thin Solid Films* 345, 263 (1999).
504. S. Rossi, L. Fedrizzi, M. Leoni, P. Scardi, and Y. Massiani, *Thin Solid Films* 350, 161 (1999).
505. K. Yokota, K. Nakamura, M. Satho, and H. Takano, *Thin Solid Films* 406, 87 (2001).
506. A. Duck, N. Gamer, W. Gesetzke, M. Griepentrog, W. Österle, M. Sahre, and I. Urban, *Surf. Coat. Technol.* 142–144, 579 (2001).
507. C. J. Tavares, L. Rebouta, J. P. Riviere, J. Pacaud, H. Gareme, K. Pishow, and Z. Wang, *Thin Solid Films* 398–399, 397 (2001).
508. C. J. Tavares, L. Rebouta, and E. J. Alves, *Thin Solid Films* 373, 287 (2000).
509. T. S. Li, H. Li, and F. Pan, *Surf. Coat. Technol.* 137, 225 (2001).

510. C. Engstrom, A. Madan, J. Birch, M. Nastasi, and L. Hultman, *J. Mater. Res.* 15, 554 (2000).
511. A. Madan, X. Chu, and S. A. Barnett, *Appl. Phys. Lett.* 68, 2198 (1996).
512. A. Madan, Y. Y. Wang, S. A. Barnett, C. Engstrom, H. Ljungcrantz, L. Hultman, and M. Grimsditch, *J. Appl. Phys.* 84, 776 (1998).
513. A. Madan, S. A. Barnett, A. Misra, H. Kung, and M. Nastasi, *J. Vac. Sci. Technol., A* 19, 952 (2001).
514. V. P. Kobayakov, *J. Mater. Sci.* 32, 4347 (1997).
515. W. Z. Li, H. D. Li, and J. L. He, *Mater. Lett.* 30, 15 (1997).
516. J. L. He, W. Z. Li, H. D. Li, and J. Mater. Res. 12, 3140 (1997).
517. M. Irie, H. Ohara, M. Tsujioka, and T. Nomura, *Mater. Chem. Phys.* 54, 317 (1998).
518. M. Berger, U. Wiklund, M. Eriksson, H. Engqvist, and S. Jacobson, *Surf. Coat. Technol.* 116–119, 1138 (1999).
519. A. Lousa, J. Romero, E. Martínez, J. Esteve, F. Montalà, and L. Carreras, *Surf. Coat. Technol.* 146–147, 268 (2001).
520. J. Wang, W.-Z. Li, and H.-D. Li, *J. Mater. Sci.* 35, 2689 (2000).
521. J. Wang, W.-Z. Li, H.-D. Li, B. Shi, and J.-B. Luo, *Thin Solid Films* 366, 117 (2000).
522. C. H. Liu, W.-Z. Li, and H.-D. Li, *Nucl. Instrum. Methods* 95, 323 (1995).
523. C. H. Liu, W.-Z. Li, H.-D. Li, and Y. H. Li, *J. Vac. Sci. Technol., A* 13, 2210 (1995).
524. A. R. Phani, J. E. Kranowski, and J. J. Nainaparampil, *J. Mater. Res.* 17, 1390 (2002).
525. I. Dahan, U. Admon, N. Frage, J. Sariel, M. P. Dariel, and J. J. Moore, *Surf. Coat. Technol.* 137, 111 (2001).
526. J. Wang, W. Z. Li, H. D. Li, B. Shi, and J. B. Luo, *Surf. Coat. Technol.* 128–129, 161 (2000).
527. H. Memarian, R. C. Budhani, A. A. Karim, H. J. Doerr, C. V. Deshpandey, R. F. Bunshah, and A. Doi, *J. Vac. Sci. Technol., A* 3, 2434 (1985).
528. M. P. Delplancke-Ogletree and O. R. Monteiro, *Surf. Coat. Technol.* 108–109, 484 (1998).
529. A. F. Jankowski, L. R. Schrawyer, M. A. Wall, W. W. Craig, R. I. Morales, and D. M. Makowiecki, *J. Vac. Sci. Technol., A* 7, 2914 (1989).
530. A. F. Jankowski, L. R. Schrawyer, and M. A. Wall, *J. Appl. Phys.* 68, 5162 (1990).
531. S. Qin, D. Jiang, J. Zhang, and J. Qin, *J. Mater. Res.* 17, 1118 (2002).
532. H. Hogberg, J. Birch, M. P. Johansson, L. Hultman, and U. Jansson, *J. Mater. Res.* 16, 633 (2001).
533. H. Hogberg, J. Birch, M. Odén, J.-O. Malm, L. Hultman, and U. Jansson, *J. Mater. Res.* 16, 1301 (2001).
534. W. Hua, X. Wu, D. Shen, H. Lu, and M. Polak, *Appl. Surf. Sci.* 189, 72 (2002).
535. H. Jensen, J. Sobota, and G. Sorensen, *J. Vac. Sci. Technol., A* 16, 1880 (1998).
536. D. Li, X. Chu, S. C. Cheng, X. V. Lin, V. P. Dravid, Y. W. Chung, M. S. Wong, and W. D. Sproul, *Appl. Phys. Lett.* 67, 203 (1995).
537. M. L. Wu, M. U. Guruz, V. P. Dravid, Y. W. Chung, S. Anders, F. L. Freire, and G. Mariotto, *Appl. Phys. Lett.* 76, 2692 (2000).
538. M. L. Wu, X. W. Lin, V. P. Dravid, Y. W. Chung, M. S. Wong, and W. D. Sproul, *J. Vac. Sci. Technol., A* 15, 946 (1997).
539. M. L. Wu, W. D. Qian, Y. W. Chung, Y. Y. Wang, M. S. Wong, and W. D. Sproul, *Thin Solid Films* 308–309, 113 (1997).
540. J. Sobota, G. Sorensen, H. Jensen, Z. Bochnicek, and V. Holy, *Surf. Coat. Technol.* 142–144, 590 (2001).
541. C. S. Liu, D. W. Wu, D. J. Fu, M. S. Ye, P. Gao, Y. G. Peng, and X. J. Fan, *Surf. Coat. Technol.* 128–129, 144 (2000).
542. J. E. Lowther, in “Handbook of Ceramic Hard Materials” (R. Riedel, Ed.), p. 253. Wiley-VCH, Weinheim, 2000.
543. Y. H. Chen, M. M. Lacerda, B. Zhou, and Y. W. Chung, in “Surface Engineering: Science and Technology I” (A. Kumar, Ed.), p. 379. Minerals, Metals & Materials Society, Warrendale, PA, 1999.
544. D. L. Yu, Y. J. Tian, J. L. He, F. R. Xiao, T. S. Wang, D. C. Li, L. Li, G. Zheng, and O. Yanagisawa, *J. Cryst. Growth* 233, 303 (2001).
545. H. Jensen, G. Sorensen, I. Mannike, F. Muktepavela, and J. Sobota, *Surf. Coat. Technol.* 116–119, 1070 (1999).
546. D. Li, X. Chu, S. C. Cheng, X. Lin, V. P. Dravid, and Y. W. Chung, *Appl. Phys. Lett.* 68, 1211 (1996).
547. H. O. Pierson, “Handbook of Refractory Carbides and Nitrides” Noyes Park Ridge, NJ, 1997.
548. H. Jensen, J. Sobota, and G. Sorensen, *J. Vac. Sci. Technol., A* 15, 941 (1997).
549. I. W. Kim, Q. Li, L. D. Marks, and S. A. Barnett, *Appl. Phys. Lett.* 78, 892 (2001).
550. A. Thobor, C. Rousselot, C. Clement, J. Takadoum, N. Martin, R. Sanjines, and F. Levy, *Surf. Coat. Technol.* 124, 210 (2000).
551. Y. Y. Wang, M. S. Wong, W. J. Chia, J. Rechner, and W. D. Sproul, *J. Vac. Sci. Technol., A* 16, 3341 (1998).
552. M. Setoyama, A. Nakayama, M. Tanaka, N. Katagawa, and T. Nomura, *Surf. Coat. Technol.* 86–87, 225 (1996).
553. D.-G. Kim, T.-Y. Seong, and Y.-J. Baik, *Surf. Coat. Technol.* 153, 79 (2002).
554. M. Setoyama, M. Irie, H. Ohara, M. Tsujioka, Y. Takeda, T. Nomura, and N. Kitagawa, *Thin Solid Films* 341, 126 (1999).
555. D.-G. Kim, T.-Y. Seong, and Y.-J. Baik, *Thin Solid Films* 397, 203 (2001).
556. V. Pankov, M. Evstigneev, and R. H. Prince, *J. Vac. Sci. Technol., A* 20, 430 (2002).
557. M. Bernard, A. Deneuve, O. Tomas, P. Gergaud, P. Sandstrom, and J. Birch, *Thin Solid Films* 380, 252 (2000).
558. A. Madan, I. W. Kim, S. C. Cheng, P. Yashar, V. P. Dravid, and S. A. Barnett, *Phys. Rev. Lett.* 78, 1743 (1997).
559. I. Manika, F. Muktepavela, H. Jensen, J. Sobota, and G. Sorensen, *Surf. Coat. Technol.* 100–101, 333 (1998).
560. H. D. Munz, *J. Vac. Sci. Technol., A* 4, 2717 (1986).
561. M. Setoyama, M. Tanaka, A. Nakayama, T. Yoshida, Y. Hashimoto, K. Yamugatu, and M. Kobayashi, U.S. Patent 5478634, 1995.
562. M. Setoyama, M. Tanaka, T. Yoshioka, Y. Hashimoto, K. Yamagata, and M. Kobayashi, U.S. Patent 5503912, 1996.
563. Q. Li, I. W. Kim, S. A. Barnett, and L. D. Marks, *J. Mater. Res.* 17, 1224 (2002).
564. I. W. Kim, A. Madan, M. W. Guruz, V. P. Dravid, and S. A. Barnett, *J. Vac. Sci. Technol., A* 19, 2069 (2001).
565. Q.-C. Zhang, *J. Vac. Sci. Technol., A* 15, 2842 (1997).
566. M. J. Meng, G. L. Eesley, and K. A. Svinarich, *Phys. Rev. B* 42, 4881 (1990).
567. R. Bhadra, M. Garimsditch, and J. Murduck, *Appl. Phys. Lett.* 54, 1409 (1989).
568. A. Inspektor, F. Battaglia, E. Oles, E. Bauer, A. Gates, and U. Schleinkofer, “Proceedings of the Gorham Conference on Wear and Superhard Coatings,” 1998, p. 1.
569. M. S. Wong, C. H. Lee, T. S. Yang, and C. L. Cheng, “12th European Conference on Diamond, Diamond-Like Materials, Carbon Nanotubes, Nitrides and Silicon Carbides,” 2001, Abstract Book, p. 15.8.19.
570. J. S. Yoon, H. S. Myung, J. G. Han, and J. Musil, *Surf. Coat. Technol.* 131, 372 (2000).
571. J. S. Yoon, H. Y. Lee, J. G. Han, S. H. Yang, and J. Musil, *Surf. Coat. Technol.* 142–144, 596 (2001).
572. C. A. Parker, *Metall. Trans. A* 16, 1693 (1985).
573. T. W. Barbee, in “Synthetic Modulated Structures” (L. L. Chang and B. C. Giessen, Eds.), p. 313. Academic Press, Orlando, 1985.
574. E. Spiller, A. Segmuller, J. Rife, and R. P. Haelbich, *Appl. Phys. Lett.* 37, 1048 (1980).
575. M. Shinn, P. B. Mirakarimi, and S. A. Barnett, *Surf. Sci.* 281, 1 (1993).

576. S. M. Durbin, J. E. Cunningham, and C. P. Flynn, *J. Phys. F: Met. Phys.* 12, L75 (1982).
577. S. Veprek and S. Reiprich, *Thin Solid Films* 268, 64 (1995).
578. L. A. Donohue, W.-D. Munz, D. B. Lewis, et al., *Surf. Coat. Technol.* 93, 69 (1997).
579. J. Musil and J. Vlcek, *Mater. Chem. Phys.* 54, 116 (1998).
580. J. Musil, J. Vlcek, F. Regent, F. Kunc, and H. Zeman, *Key Eng. Mater.* 230–232, 613 (2002).
581. K. C. Kwiatkowski, C. M. Lukehart, O. J. Murphy, and S. F. Simpson, *J. Cluster Sci.* 11, 449 (2000).
582. R. Z. Ma, J. Wu, B. Q. Wei, J. Liang, and D. H. Wu, *J. Mater. Sci.* 33, 5243 (1998).
583. W. X. Chen, J. P. Tu, H. Y. Gan, Z. D. Xu, Q. G. Wang, J. Y. Lee, Z. L. Liu, and X. B. Zhang, *Surf. Coat. Technol.* 160, 68 (2002).
584. V. Meunier, C. Roland, J. Bernholc, and M. B. Nardelli, *Appl. Phys. Lett.* 81, 46 (2002).
585. C. L. Xu, B. Q. Wei, R. Z. Ma, J. Liang, X. K. Ma, and D. H. Wu, *Carbon* 37, 855 (1999).
586. H. C. Zeng, in “Handbook of Organic–Inorganic Hybrid Materials and Nanocomposites” (H. S. Nalwa, Ed.), Vol. 2. American Scientific Publishers, Stevenson Ranch, CA, 2001.
587. S. Veprek, P. Nesladek, A. Niederhofer, and F. Glatz, *Nanostruct. Mater.* 10, 679 (1998).
588. T. Hirai and S. Hayashi, in “Proceedings of the Eighth International Conference on Chemical Vapour Deposition” (J. M. Blocher, Jr., G. E. Vullard, and G. Wahl, Eds.), p. 790. Electrochemical Society, Pennington, NJ, 1981.
589. S. Hayashi and T. Hirai, *J. Mater. Sci.* 18, 3259 (1983).
590. K. Hiraga, M. Hirabayashi, S. Hayashi, and T. Hirai, *J. Am. Ceram. Soc.* 66, 539 (1983).
591. T. Hirai and S. Hayashi, *J. Mater. Sci.* 17, 1320 (1981).
592. S. Hayashi, T. Hirai, K. Hiraga, and M. Hirabayashi, *J. Mater. Sci.* 17, 3336 (1982).
593. G. Llauro, R. Hillel, and F. Sibieude, *Chem. Vap. Deposition* 4, 247 (1998).
594. X. Sun, J. S. Reid, E. Kolawa, and M.-A. Nicolet, *J. Appl. Phys.* 81, 656 (1997).
595. Y. Tsuji, S. M. Gasser, E. Kolawa, and M.-A. Nicolet, *Thin Solid Films* 350, 1 (1999).
596. M. Herrmann, H. Klemm, and C. Schubert, in “Handbook of Ceramic Hard Materials” (R. Riedel, Ed.), Vol. 2, p. 749. Wiley-VCH, Weinheim, 2000.
597. S. Veprek, M. Haussmann, and S. Reiprich, *J. Vac. Sci. Technol., A* 14, 46 (1996).
598. S. Veprek, M. Haussmann, S. Reiprich, S. Li, and J. Dian, *Surf. Coat. Technol.* 86–87, 394 (1996).
599. S. Veprek, *Surf. Coat. Technol.* 97, 15 (1997).
600. S. Christiansen, M. Albrecht, H. P. Strunk, and S. Veprek, *J. Vac. Sci. Technol., B* 16, 19 (1998).
601. S. Veprek, S. Reiprich, and L. Shizi, *Appl. Phys. Lett.* 66, 2640 (1995).
602. S. Veprek and A. S. Argon, *Surf. Coat. Technol.* 146–147, 175 (2001).
603. A. Niederhofer, T. Bolom, P. Nesladek, K. Moto, C. Eggs, D. S. Patil, and S. Veprek, *Surf. Coat. Technol.* 146–147, 183 (2001).
604. H.-D. Mannling, D. S. Patil, K. Moto, M. Jilek, and S. Veprek, *Surf. Coat. Technol.* 146–147, 263 (2001).
605. M. Diserens, J. Patscheider, and F. Levy, *Surf. Coat. Technol.* 108–109, 241 (1998).
606. M. Diserens, J. Patscheider, and F. Levy, *Surf. Coat. Technol.* 120–121, 158 (1999).
607. F. Vaz, L. Rebouta, Ph. Goudeau, T. Girardeau, J. Pacaud, J. P. Rivière, and A. Traverse, *Surf. Coat. Technol.* 146–147, 274 (2001).
608. F. Vaz, S. Carvalho, L. Rebouta, M. Z. Silva, A. Paul, and D. Schneider, *Thin Solid Films* 408, 160 (2002).
609. J. Patscheider, T. Zehnder, and M. Diserens, *Surf. Coat. Technol.* 146–147, 201 (2001).
610. R. Hauert, J. Patscheider, L. Knoblauch, and M. Diserens, *Adv. Mater.* 11, 175 (1999).
611. S. Li, Y. Shi, and H. Peng, *Plasma Chem. Plasma Proc.* 12, 526 (1992).
612. A. Niederhofer, P. Nesladek, H.-D. Mannling, K. Moto, S. Veprek, and M. Jiek, *Surf. Coat. Technol.* 120–121, 173 (1999).
613. P. Nesladek and S. Veprek, *Phys. Status Solidi A* 177, 53 (2000).
614. S. Veprek, A. Niederhofer, K. Moto, T. Bolom, H.-D. Mannling, P. Nesladek, G. Dollinger, and A. Bergmaier, *Surf. Coat. Technol.* 133–134, 152 (2000).
615. S. Veprek, P. Nesladek, A. Niederhofer, F. Glatz, M. Jilek, and M. Sima, *Surf. Coat. Technol.* 108–109, 138 (1998).
616. F. Vaz, L. Rebouta, S. Ramos, M. F. da Silva, and J. C. Soares, *Surf. Coat. Technol.* 108–109, 236 (1998).
617. J. Musil and H. Hruby, *Thin Solid Films* 365, 104 (2000).
618. J. Musil and H. Hruby, in “Proceedings of the 14th International Symposium on Plasma Chemistry” (M. Hrabovsky, M. Konrad, and V. Kopecky, Eds.), Vol. 3, p. 1605. International Union of Pure and Applied Chemistry, 1999.
619. S. Carvalho, F. Vaz, L. Rebouta, D. Schneider, A. Cavaleiro, and E. Alves, *Surf. Coat. Technol.* 142–144, 110 (2001).
620. M. Benda and J. Musil, *Vacuum* 55, 171 (1999).
621. B. Edenhofer, *Heat Treatment of Metals* 1, 23 (1974).
622. M. Benda, J. Vlcek, V. Cibulka, and J. Musil, *J. Vac. Sci. Technol., A* 15, 2636 (1997).
623. H. Holleck, *J. Vac. Sci. Technol., A* 4, 2661 (1986).
624. T. Zehnder and J. Patscheider, *Surf. Coat. Technol.* 133–134, 138 (2000).
625. J. S. Zabinski and A. A. Voevodin, *J. Vac. Sci. Technol., A* 16, 1890 (1998).
626. A. A. Voevodin and J. S. Zabinski, *Thin Solid Films* 370, 223 (2000).
627. V. Kulikovskiy, P. Bohac, F. Franc, D. Chvostova, A. Deineka, V. Vorlicek, and L. Jastrabik, *Surf. Coat. Technol.* 142–144, 697 (2001).
628. A. A. Voevodin, S. D. Walck, and J. S. Zabinski, *Wear* 203–204, 517 (1997).
629. U. Wiklund, M. Nordin, O. Wänstrand, and M. Larsson, *Surf. Coat. Technol.* 124, 154 (2000).
630. V. V. Uglov, A. K. Kuleshov, D. P. Rusalsky, J. I. Onate, and S.-Z. Yang, *Surf. Coat. Technol.* 128–129, 150 (2000).
631. B. Feng, D. M. Cao, W. J. Meng, J. Xu, R. C. Tittsworth, L. E. Rehn, P. M. Baldo, and G. L. Doll, *Surf. Coat. Technol.* 148, 153 (2001).
632. B. Feng, D. M. Cao, W. J. Meng, L. E. Rehn, P. M. Baldo, and G. L. Doll, *Thin Solid Films* 398–399, 210 (2001).
633. O. R. Monteiro, M.-P. Delplancke-Ogletree, and I. G. Brown, *Thin Solid Films* 342, 100 (1999).
634. A. A. Voevodin, J. P. O’Neill, and J. S. Zabinski, *Thin Solid Films* 342, 194 (1999).
635. B. Shi, W. J. Meng, L. E. Rehn, and P. M. Baldo, *Appl. Phys. Lett.* 81, 352 (2002).
636. S. J. Park, K.-R. Lee, D.-H. Ko, and K. Y. Eun, *Diamond Relat. Mater.* 11, 1747 (2002).
637. A. A. Voevodin, S. V. Prasad, and J. S. Zbinski, *J. Appl. Phys.* 82, 855 (1997).
638. K. I. Schiffmann, M. Fryda, G. Goerigk, R. Lauer, P. Hinze, and A. Bulack, *Thin Solid Films* 347, 60 (1999).
639. W. Gissler, *Surf. Coat. Technol.* 68–69, 556 (1994).
640. C. Heau, N. Guillon, R. Y. Fillit, and J. Machet, *Surf. Coat. Technol.* 97, 60 (1997).
641. P. H. Mayrhofer and C. Mitterer, *Surf. Coat. Technol.* 133–134, 131 (2000).
642. P. Losbichler, C. Mitterer, P. N. Gibson, W. Gissler, F. Hofer, and P. Warbichler, *Surf. Coat. Technol.* 94–95, 297 (1997).
643. H. Karner, J. Laimer, H. Stori, and P. Rodhammer, *Surf. Coat. Technol.* 39–40, 293 (1989).

644. O. Knotek, F. Löffler, M. Bohmer, R. Breidenbach, and C. Stossel, *Surf. Coat. Technol.* 49, 263 (1991).
645. O. Knotek, R. Breidenbach, F. Jungblut, and F. Löffler, *Surf. Coat. Technol.* 43–44, 107 (1990).
646. M. Tamura and H. Kubo, *Surf. Coat. Technol.* 54–55, 255 (1992).
647. C. Mitterer, M. Rauter, and P. Rodhammer, *Surf. Coat. Technol.* 41, 351 (1990).
648. W. Gissler, T. P. Mollart, and R. Gilmore, in “Protective Coatings and Thin Films: Synthesis, Characterisation and Applications” (Y. Pauleau and P. B. Barna, Eds.), p. 357. Kluwer Academic, Dordrecht, 1997.
649. C. Mitterer, P. Losbicher, F. Hofer, P. Warbichler, P. N. Gibson, and W. Gissler, *Vacuum* 50, 313 (1998).
650. W. Herr, B. Matthes, E. Brozeit, and K. H. Kloss, *Mater. Sci. Eng., A* 140, 616 (1991).
651. H. Holleck and M. Lahren, *Mater. Sci. Eng., A* 140, 609 (1991).
652. H. Ronkainen, I. Nieminen, K. Holmberg, A. Leyland, K. S. Fancey, A. Matthews, B. Matthes, and E. Broszeit, *Mater. Sci. Eng., A* 140, 609 (1991).
653. Y. Quiaoquin, Z. Lihua, W. Lijun, D. Haiqing, and W. Lishi, *J. Mater. Sci. Lett.* 15, 11 (1996).
654. J. F. Pierson, E. Tomasella, and P. Bauer, *Thin Solid Films* 408, 26 (2002).
655. T. Friesen, J. Haupt, P. N. Gibson, and W. Gissler, in “Mechanical Properties and Deformation Behavior of Materials Having Ultra-Fine Microstructures” (M. Nastasi, D. M. Parkin, and H. Gleiter, Eds.), p. 475. Kluwer Academic, Dordrecht, 1993.
656. T. P. Mollart, J. Haupt, R. Gilmore, and W. Gissler, *Surf. Coat. Technol.* 86–87, 231 (1996).
657. C. Rebholz, H. Ziegele, A. Leyland, and A. Matthews, *J. Vac. Sci. Technol., A* 16, 2851 (1998).
658. P. Hammer, A. Steiner, R. Villa, P. N. Gibson, M. Baker, J. Haupt, and W. Gissler, *Surf. Coat. Technol.* 68–69, 194 (1994).
659. T. Friesen, J. Haupt, W. Gissler, A. Barna, and P. B. Barna, *Surf. Coat. Technol.* 48, 169 (1991).
660. P. Holubár, M. Jilek, and M. Síma, *Surf. Coat. Technol.* 120–121, 184 (1999).
661. L. R. Shaginyan, M. Misina, J. Musil, and F. Regent, *Kovine, Zlätine, Tehnologije* 33, 497 (1999).
662. L. R. Shaginyan, M. Misina, J. Zemek, J. Musil, F. Regent, and V. F. Britun, *Thin Solid Films* 408, 136 (2002).
663. F. Regent and J. Musil, *Surf. Coat. Technol.* 142–144, 146 (2001).
664. A. G. Dirks, R. A. M. Wolters, and A. J. M. Nellissen, *Thin Solid Films* 193–194, 201 (1990).
665. J. Musil, P. Karvankova, and J. Kasl, *Surf. Coat. Technol.* 139, 101 (2001).
666. J. Musil and H. Hruby, in “Proceedings of the 14th International Symposium on Plasma Chemistry” (M. Hrabovsky, M. Konrad, and V. Kopecky, Eds.), Vol. 3, p. 1617. International Union of Pure and Applied Chemistry, 1999.
667. J. Musil and F. Regent, *J. Vac. Sci. Technol., A* 16, 3301 (1998).
668. M. Misina, J. Musil, and S. Kadlec, *Surf. Coat. Technol.* 110, 168 (1998).
669. P. Karvankova, H.-D. Männling, C. Eggs, and S. Veprek, *Surf. Coat. Technol.* 146–147, 280 (2001).
670. J. Musil, P. Zeman, H. Hruby, and P. H. Mayrhofer, *Surf. Coat. Technol.* 120–121, 179 (1999).
671. P. Zeman, R. Cerstvy, P. H. Mayrhofer, C. Mitterer, and J. Musil, *Mater. Sci. Eng., A* 289, 189 (2000).
672. J. Musil, I. Leipner, and M. Kolega, *Surf. Coat. Technol.* 115, 32 (1999).
673. P. Zeman, C. Mitterer, P. N. Mayrhofer, and J. Musil, in “Proceedings of the 14th International Symposium on Plasma Chemistry” (M. Hrabovsky, M. Konrad, and V. Kopecky, Eds.), Vol. 3, p. 1647. International Union of Pure and Applied Chemistry, 1999.
674. J. Musil, H. Zeman, and J. Kasl, *Thin Solid Films* 413, 121 (2002).
675. J. Musil, H. Hruby, P. Zeman, H. Zeman, R. Cerstvy, P. N. Mayrhofer, and C. Mitterer, *Surf. Coat. Technol.* 142–144, 603 (2001).
676. J. Musil and H. Polakova, *Surf. Coat. Technol.* 127, 99 (2000).
677. H. Polakova, M. Kubasek, R. Cerstvy, and J. Musil, *Surf. Coat. Technol.* 142–144, 201 (2001).
678. L. A. Donohue, D. B. Lewis, W.-D. Munz, M. M. Stack, S. B. Lyon, H.-W. Wang, and D. Rafaja, *Vacuum* 55, 109 (1999).
679. Z. Yu, A. Jin, C. Liu, L. Yu, and S. Dai, *J. Vac. Sci. Technol., A* 13, 2303 (1995).
680. A. I. Krasovsky, R. K. Chuzhko, V. R. Tregulov, and O. A. Balachovsky, “Fluorine Process of Tungsten Deposition.” Nauka, Moscow, 1981.
681. T. A. Vanderah, Ed., “Chemistry of Superconductor Materials: Preparation, Chemistry, Characterisation, and Theory.” Noyes, Westwood, 1992.
682. G. D. Demyashev, Ph.D. Thesis, Research Institute of Physical Chemistry of the USSR Academy of Sciences, Moscow, 1985.
683. G. M. Demyashev, A. I. Krasovsky, V. P. Kuz'min, M. B. Malandin, and R. K. Chuzhko, *Izv. Akad. Nauk USSR: Non-organ. Mater.* 21, 1155 (1985).
684. H. O. Pierson, “Handbook of Carbon, Graphite, Diamond and Fullerenes.” Noyes, Park Ridge, NJ, 1992.
685. R. B. Heimann, S. E. Evsyukov, and L. Kavan, Eds., “Carbyne and Carbynoid Structures,” p. 215. Kluwer Academic, Dordrecht, 1998.
686. E. K. Storms, “The Refractory Carbides.” Academic Press, New York, 1967.
687. L. E. Toth, “Transition Metal Carbides and Nitrides.” Academic Press, New York, 1971.
688. G. M. Demyashev, E. Siores, and A. L. Taube, “Proceedings of the Eighth International Conference on Composite Engineering,” 2001, p. 183.
689. G. M. Demyshev, A. L. Taube, and E. Siores, “12th European Conference on Diamond, Diamond-Like Materials, Carbon Nanotubes, Nitrides and Silicon Carbides,” 2001, Abstract Book, p. 5.8.24.
690. C. A. Huber, in “Handbook of Nanophase Materials.” Dekker, New York, 1997.
691. M. Springborg, in “Carbyne and Carbynoid Structures” (R. B. Heimann, S. E. Evsyukov, and L. Kavan, Eds.), p. 215. Kluwer Academic, Dordrecht, 1998.
692. S. Veprek and M. Jilek, *Vacuum* 67, 443 (2002).
693. J. Musil, in “Proceedings of the First Meeting of the Ion Engineering Society of Japan (IESJ)” (T. Takagi, Ed.), p. 295. Ionics Publishing, Tokyo, 1992.
694. H. Holleck, M. Lahres, and P. Woll, *Surf. Coat. Technol.* 41, 179 (1990).
695. K. L. Choy, in “Handbook of Nanostructured Materials and Nanoscience” (H. S. Nalwa, Ed.), Vol. 1, p. 533. Academic Press, San Diego, 2000.
696. J. Musil, J. Vyskocil, and S. Kadlec, in “Physics of Thin Films” (M. H. Francombe and J. L. Vossen, Eds.), Vol. 17, p. 79. Academic Press, Boston, 1993.
697. K. D. Leedy and J. M. Rigsbee, *J. Vac. Sci. Technol., A* 14, 2202 (1996).
698. R. F. Bunshah, Ed., “Handbook of Deposition Technologies for Films and Coatings (Coating Processes),” 2nd ed. Noyes, Park Ridge, NJ, 1994.
699. K. K. Schuegraf, Ed., “Handbook of Thin Film Deposition Processes and Techniques (Principles, Methods, Equipments, and Applications).” Noyes, Park Ridge, NJ, 1988.
700. K. Wasa and S. Hayakawa, Eds., “Handbook of Sputter Deposition Technology (Principles, Technology, and Applications).” Noyes, Park Ridge, NJ, 1992.
701. D. L. Smith, “Thin Film Deposition.” McGraw-Hill, New York, 1997.

702. P. B. Mirkarimi, M. Shinn, and S. A. Barnett, *J. Vac. Sci. Technol., A* 10, 75 (1992).
703. J. Musil and J. Vlcek, *Surf. Coat. Technol.* 112, 162 (1999).
704. W. D. Westwood, in "Handbook of Plasma Processing Technology: Fundamentals, Etching, Deposition, and Surface Interactions" (S. M. Rossnagel, J. J. Coumo, and W. D. Westwood, Eds.), p. 233. Noyes, Park Ridge, NJ, 1990.
705. S. M. Rossnagel, in "Handbook of Plasma Processing Technology: Fundamentals, Etching, Deposition, and Surface Interactions" (S. M. Rossnagel, J. J. Coumo, and W. D. Westwood, Eds.), p. 160. Noyes, Park Ridge, NJ, 1990.
706. J. Hopwood, in "Handbook of Nanophase Materials" (A. N. Goldstein, Ed.), p. 141. Dekker, New York, 1997.
707. R. Reif, in "Handbook of Plasma Processing Technology: Fundamentals, Etching, Deposition, and Surface Interactions" (S. M. Rossnagel, J. J. Coumo, and W. D. Westwood, Eds.), p. 260. Noyes, Park Ridge, NJ, 1990.
708. J. Marec and P. Leprince, in "Microwave Discharges: Fundamentals and Applications" (C. M. Ferreira and M. Moisan, Eds.), NATO ASI Series B, Physics, Vol. 302, p. 45. Plenum, New York, 1993.
709. V. M. Batenin, I. I. Klimovskii, G. V. Lysov, and V. N. Troitskii, "Superhigh Frequency Generators of Plasma." CRC Press, Boca Raton, FL, 1994.
710. C. M. Ferreira, M. Moisan, and Z. Zakrzewski, in "Microwave Excited Plasmas" (M. Moisan and J. Pelletier, Eds.), p. 42. Elsevier, Amsterdam, 1992.
711. C.-P. Klages, in "Handbook of Ceramic Hard Materials" (R. Riedel, Ed.), Vol. 1, p. 390. Wiley-VCH, Weinheim, 2000.
712. J. Laimer and S. Matsumoto, *Int. J. Refract. Met. Hard Mater.* 14, 179 (1996).
713. G. Bohm, in "Microwave Discharges: Fundamentals and Applications" (C. M. Ferreira and M. Moisan, Eds.), NATO ASI Series B, Physics, Vol. 302, p. 215. Plenum, New York, 1993.
714. J. Laimer and S. Matsumoto, *Diamond Relat. Mater.* 3, 231 (1994).
715. J. Asmussen, in "Handbook of Plasma Processing Technology: Fundamentals, Etching, Deposition, and Surface Interactions" (S. M. Rossnagel, J. J. Coumo, and W. D. Westwood, Eds.), p. 285. Noyes, Park Ridge, NJ, 1990.
716. A. I. Al-Shamma'a, S. R. Wylie, J. Lucas, and C. F. Pau, *J. Phys. D: Appl. Phys.* 34, 2734 (2001).
717. M. Jasinski, J. Mizeraczyk, Z. Zakrzewski, T. Ohkubo, and J.-S. Chang, *J. Phys. D: Appl. Phys.* 35, 2274 (2002).
718. A. L. Taube and G. M. Demyashev, "Proceedings of the IMPI's 37th Annual International Microwave Symposium," 2002, p. 12.
719. A. L. Taube and G. M. Demyashev, "Proceedings of the 2002 Asia-Pacific Microwave Conference (APMC-2002)," 2002, p. 157.
720. E. Siores, A. L. Taube, and G. M. Demyashev, "Proceedings of the IMPI's 36th Annual International Microwave Symposium," 2001, p. 75.
721. A. L. Taube, G. M. Demyashev, and E. Siores, "Proceedings of the 2001 Asia-Pacific Microwave Conference: Microwaves for New Century," 2001, p. 27.
722. A. L. Taube, G. M. Demyashev, and E. Siores, "Eighth International Conference on Microwave and High Frequency Heating," 2001, Book of Abstracts, p. 49.
723. D. J. Sullivan, J. Kline, C. Phillippe, and M. M. Micci, Current Status of the Microwave Arcjet Thruster, AIAA-95-3065, American Institute of Aeronautics and Astronautics, 1995, pp. 1-15.
724. K. M. McHugh and J. F. Key, *J. Thermal Spray Technol.* 3, 191 (1994).
725. A. Sherman, "Chemical Vapour Deposition for Microelectronics: Principles, Technology, and Applications." Noyes, Park Ridge, NJ, 1987.
726. M. L. Hitchman and K. F. Jensen, in "Chemical Vapour Deposition: Principles and Applications" (M. L. Hitchman and K. F. Jensen, Eds.), p. 1. Academic Press, London, 1993.
727. K. F. Jensen, in "Chemical Vapour Deposition: Principles and Applications" (M. L. Hitchman and K. F. Jensen, Eds.), p. 31. Academic Press, London, 1993.
728. K. J. Huttinger, *Chem. Vap. Deposition* 4, 151 (1998).
729. K. M. Habig, *J. Vac. Sci. Technol., A* 4, 2832 (1986).
730. R. L. Moon and Y.-M. Houng, in "Chemical Vapour Deposition: Principles and Applications" (M. L. Hitchman and K. F. Jensen, Eds.), p. 245. Academic Press, London, 1993.
731. D. W. Hess and D. B. Graves, in "Chemical Vapour Deposition: Principles and Applications" (M. L. Hitchman and K. F. Jensen, Eds.), p. 385. Academic Press, London, 1993.
732. Z. J. Hu and K. J. Huttinger, *Chem. Vap. Deposition* 6, 77 (2000).
733. R. W. James, "The Optical Principles of the Diffraction of X-Rays." Cornell Univ. Press, Ithaca, NY, 1965.
734. H. Lipson and H. Steeple, "Interpretation of X-Ray Powder Diffraction Patterns." St. Martin's Press, New York, 1970.
735. H. P. Klug and L. E. Alexander, "X-Ray Diffraction Procedures for Polycrystalline and Amorphous Materials," 2nd ed. Wiley, New York, 1974.
736. B. D. Cullity, "Elements of X-Ray Diffraction." Wesley, New York, 1978.
737. R. C. Reynolds, Jr., in "Modern Powder Diffraction" (D. L. Bish and J. E. Post, Eds.), Vol. 20, p. 1. Mineralogical Society of America, Washington, DC, 1989.
738. K. Lu and Y. H. Zhao, *Nanostruct. Mater.* 12, 559 (1999).
739. S. Amelinckx, D. Van Dyck, J. Van Landuyt, and G. Van Tendello, "Handbook of Microscopy: Applications in Materials Science, Solid-State Physics, and Chemistry." Wiley-VCH, Weinheim, 1997.
740. D. Shindo and K. Hiraga, "High-Resolution Electron Microscopy for Materials Science." Springer-Verlag, Tokyo, 1998.
741. J. R. Dutcher, S. Lee, J. Kim, G. I. Stegeman, and C. M. Falco, *Mater. Res. Soc. Symp. Proc.* 160, 179 (1990).
742. G. Thomas, "Transmission Electron Microscopy of Metals." Wiley, New York, 1964.
743. L. Reimer, "Transmission Electron Microscopy: Physics of Image Formation and Microanalysis." Springer-Verlag, Berlin, 1993.
744. P. B. Hirsch, "Electron Microscopy of Thin Crystals." Butterworths, Washington, 1965.
745. A. Guinier and G. Fournet, "Small Angle Scattering of X-Rays." Wiley, New York, 1955.
746. G. Gladyszewski, S. Labat, P. Gergaud, and O. Thomas, *Thin Solid Films* 319, 78 (1998).
747. L. M. Goldman, H. A. Atwater, and F. Spaepen, *Mater. Res. Soc. Symp. Proc.* 160, 577 (1990).
748. A. Guinier, in "X-Ray Diffraction in Crystals, Imperfect Crystals and Amorphous Bodies" (P. Lorrian and D. S. M. Lorrian, Eds.), p. 279. Freeman, San Francisco, 1963.
749. D. Fontaine, in "Local Arrangements Studies by X-Ray Diffraction" (J. B. Cohen and J. E. Hilliard, Eds.), Chap. 2. Gordon & Breach, New York, 1967.
750. I. K. Schuller and C. M. Falco, *Surf. Sci.* 113, 443 (1982).
751. A. H. Eltoughy and J. E. Greene, *J. Appl. Phys.* 50, 505 (1979).
752. W. P. Lowe, T. W. Barbee, T. H. Geballe, and D. B. McWhan, *Phys. Rev. B* 24, 6193 (1981).
753. C. Weisbuch, R. Dingle, C. Gossard, and W. Wiegmann, *Solid State Commun.* 38, 709 (1981).
754. B. E. Warren, "X-Ray Diffraction." Addison-Wesley, Reading, MA, 1969.
755. M. Schneider, W. Zeiger, H. Worch, J. Schumann, P. Biscourp, and G. Lange, in "Metastable, Mechanically Alloyed and Nanocrystalline Materials" (R. Schulz, Ed.), Part 1, p. 191. Trans Tech, Zurich, 1996.
756. T. Inami, M. Kobiyama, S. Okuda, H. Maeta, and H. Ohtsuka, *Nanostruct. Mater.* 12, 657 (1999).

757. D. B. Lewis, L. A. Donohue, M. Lembke, W.-D. Munz, R. Kuzel, V. Valvoda, and C. J. Blomfield, *Surf. Coat. Technol.* 114, 187 (1999).
758. N. T. Di Nardo, in "Materials Science and Technology: A Comprehensive Treatment" (R. W. Cahn, P. Haasen, and E. J. Kramer, Eds.), Vol. 2B, Part 2, p. 1. VCH, Weinheim, 1994.
759. J. A. Switzer and T. D. Golden, *Adv. Mater.* 5, 474 (1993).
760. T. D. Golden, R. P. Raffaele, and J. A. Switzer, *Appl. Phys. Lett.* 63, 1501 (1993).
761. R. Garcia and R. Perez, *Surf. Sci. Rep.* 47, 197 (2002).
762. H. C. Barshilia and K. S. Rajan, *Surf. Coat. Technol.* 155, 195 (2002).
763. B. Rother and K. M. Kazmanli, *Surf. Coat. Technol.* 99, 311 (1998).
764. R. Y. Lo and D. B. Bogy, *J. Mater. Res.* 14, 2276 (1999).
765. M. M. Chaudhri, *J. Mater. Res.* 16, 336 (2001).
766. V. Blank, M. Popov, N. Lvova, K. Gogolinsky, and V. Reshetov, *J. Mater. Res.* 12, 3109 (1997).
767. S. N. Kundu, M. Basu, K. K. Chattopadhyay, A. B. Maity, S. Chaudhuri, and A. K. Pal, *Vacuum* 48, 435 (1997).
768. H. Buckle, in "Science of Hardness Testing and Its Research Applications" (J. H. Westbrook and H. Conrad, Eds.), p. 453. ASM International, Metals Park, OH, 1973.
769. D. M. Teter, *MRS Bull.* 23, 22 (1998).
770. S. F. Pugh, *Philos. Mag.* 45, 823 (1954).
771. D. S. Rickerby, A. M. Jones, and B. A. Bellamy, *Surf. Coat. Technol.* 37, 111 (1989).
772. A. Krell, in "Handbook of Ceramic Hard Materials" (R. Riedel, Ed.), Vol. 1, p. 183. Wiley-VCH, Weinheim, 2000.
773. D. Sherman and D. Brandon, in "Handbook of Ceramic Hard Materials" (R. Riedel, Ed.), Vol. 1, p. 66. Wiley-VCH, Weinheim, 2000.
774. R. A. Andrievski, G. V. Kalinnikov, A. F. Potafeev, and V. S. Urbanovich, *Nanostruct. Mater.* 6, 353 (1995).
775. H. Ishikawa, S. Fudetani, and M. Hirohashi, *Appl. Surf. Sci.* 178, 56 (2001).
776. B. Jonsson and S. Hogmark, *Thin Solid Films* 114, 257 (1984).
777. A. M. Korsunsky, M. R. McGurk, S. J. Bull, and T. F. Page, *Surf. Coat. Technol.* 99, 171 (1998).
778. J. B. Pethica, R. Hutchings, and W. C. Oliver, *Philos. Mag. A* 48, 593 (1983).
779. M. F. Doerner and W. D. Nix, *J. Mater. Res.* 1, 601 (1986).
780. N. X. Randall, C. Julia-Schmutz, J. M. Soro, J. von Stebut, and G. Zacharie, *Thin Solid Films* 308–309, 297 (1997).
781. N. X. Randall and A. Harris, *Wear* 245, 196 (2000).
782. T. Sawa, Y. Akiyama, A. Shimamoto, and K. Tanaka, *J. Mater. Res.* 14, 2228 (1999).
783. Y. Yamada, O. Tsuda, and T. Yoshida, *Thin Solid Films* 316, 35 (1998).
784. E. T. Lilleodden, W. Bonin, J. Nelson, J. T. WYROBEK, and W. W. Gerberich, *J. Mater. Res.* 10, 2162 (1995).
785. A. J. Whitehead and T. F. Page, in "Mechanical Properties and Deformation Behavior of Materials Having Ultra-Fine Microstructures" (M. Nastasi, D. M. Parkin, and H. Gleiter, Eds.), p. 481. Kluwer Academic, Dordrecht, 1993.
786. W. C. Oliver, B. N. Lucas, and G. M. Pharr, in "Mechanical Properties and Deformation Behavior of Materials Having Ultra-Fine Microstructures" (M. Nastasi, D. M. Parkin, and H. Gleiter, Eds.), p. 417. Kluwer Academic, Dordrecht, 1993.
787. W. Oliver and G. Pharr, *J. Mater. Res.* 7, 1564 (1992).
788. E. Soderlund and D. J. Rowcliffe, in "Mechanical Properties and Deformation Behavior of Materials Having Ultra-Fine Microstructures" (M. Nastasi, D. M. Parkin, and H. Gleiter, Eds.), p. 463. Kluwer Academic, Dordrecht, 1993.
789. J. Woigard, J.-C. Dargenton, C. Tromas, and V. Audurier, *Surf. Coat. Technol.* 100–101, 103 (1998).
790. J. B. Pethica, in "Ion Implantation into Metals" (V. Ashworth, W. Grant, and R. Procter, Eds.), p. 147. Pergamon, Oxford, 1982.
791. J. L. Loubet, M. Bauer, A. Tonck, S. Bec, and B. Gauthier-Manuel, in "Mechanical Properties and Deformation Behavior of Materials Having Ultra-Fine Microstructures" (M. Nastasi, D. M. Parkin, and H. Gleiter, Eds.), p. 429. Kluwer Academic, Dordrecht, 1993.
792. G. M. Pharr, D. S. Harding, and W. C. Oliver, in "Mechanical Properties and Deformation Behavior of Materials Having Ultra-Fine Microstructures" (M. Nastasi, D. M. Parkin, and H. Gleiter, Eds.), p. 449. Kluwer Academic, Dordrecht, 1993.
793. M. O'Hern, R. H. Parrish, and W. C. Oliver, *Thin Solid Films* 181, 357 (1989).
794. X. Li and B. Bhushan, *Mater. Characterisation* 48, 11 (2002).
795. B. D. Fabes, W. C. Oliver, R. A. McKee, and F. J. Walker, *J. Mater. Res.* 7, 3056 (1992).
796. J. Woigard and J.-C. Dargenton, *J. Mater. Res.* 12, 2455 (1997).
797. J. Mencik, D. Munz, E. Quandt, E. R. Weppelmann, and M. V. Swain, *J. Mater. Res.* 9, 2475 (1997).
798. T. P. Page, W. C. Oliver, and C. J. McHargue, *J. Mater. Res.* 7, 450 (1992).
799. T. Sawa and K. Tanaka, *J. Mater. Res.* 16, 3084 (2001).
800. T. Ohmura, S. Matsuoka, K. Tanaka, and T. Yoshida, *Thin Solid Films* 385, 198 (2001).
801. A. C. Fischer-Cripps, *Vacuum* 58, 569 (2000).
802. J. Musil, F. Kunc, H. Zeman, and H. Polakova, *Surf. Coat. Technol.* 154, 304 (2002).
803. M. R. Sridhar and M. M. Yovanovich, *Wear* 193, 91 (1996).
804. J. C. Hay, A. Bolshakov, and G. M. Pharr, *J. Mater. Res.* 14, 2296 (1999).
805. H. Bangert and A. Wagendristel, *J. Vac. Sci. Technol., A* 4, 2956 (1986).
806. N. X. Randall and J. L. Bozet, *Wear* 212, 18 (1997).
807. M. Goken, M. Kempf, and W. D. Nix, *Acta Mater.* 49, 903 (2001).
808. B. Bhushan and A. V. Kulkarni, *Mater. Lett.* 29, 221 (1996).
809. R. Saha and W. D. Nix, *Acta Mater.* 50, 23 (2002).
810. R. Saha and W. D. Nix, *Mater. Sci. Eng., A* 319–321, 898 (2001).
811. H. L. Wang, M. J. Chiang, and M. H. Hon, *Ceram. Int.* 27, 385 (2001).
812. T. Y. Tsui and G. M. Pharr, *J. Mater. Res.* 14, 292 (1999).
813. T. Y. Tsui, J. Vlassak, and W. D. Nix, *J. Mater. Res.* 14, 2196 (1999).
814. T. Y. Tsui, J. Vlassak, and W. D. Nix, *J. Mater. Res.* 14, 2204 (1999).
815. X. Chen and J. J. Vlassak, *J. Mater. Res.* 16, 2974 (2001).
816. F. Yang, *Appl. Phys. Lett.* 80, 959 (2002).
817. M. S. Bobji and S. K. Biswas, *J. Mater. Res.* 14, 2259 (1999).
818. T.-Y. Zhang and W.-H. Xu, *J. Mater. Res.* 17, 1715 (2002).
819. A. B. Maity, M. Basu, S. Chaudhuri, and A. K. Pal, *J. Phys. D: Appl. Phys.* 28, 2547 (1995).
820. K. K. Chattopadhyay, J. Dutta, S. Chaudhuri, and A. K. Pal, *Diamond Relat. Mater.* 4, 122 (1995).
821. D. Schneider and Th. Schwarz, *Surf. Coat. Technol.* 91, 136 (1997).
822. D. Schneider and B. Schultrich, *Surf. Coat. Technol.* 98, 962 (1998).
823. D. Schneider, Th. Schwarz, H.-J. Scheibe, and M. Panzner, *Thin Solid Films* 295, 107 (1997).
824. D. Schneider, Th. Witke, Th. Schwarz, B. Schoneich, and B. Schultrich, *Surf. Coat. Technol.* 126, 136 (2000).
825. D. Schneider, B. Schultrich, B. Burck, H. J. Scheibe, G. Jorgensen, M. Lahres, and J. Karner, *Diamond Relat. Mater.* 7, 589 (1998).
826. D. Schneider, C. F. Meyer, H. Mai, B. Schoneich, H. Ziegele, H. J. Scheibe, and Y. Lifshitz, *Diamond Relat. Mater.* 7, 973 (1998).
827. D. Schneider, B. Schultrich, H. J. Scheibe, H. Ziegele, and M. Gripenrog, *Thin Solid Films* 332, 157 (1998).
828. S. Veprek and M. Jilek, *Pure Appl. Chem.* 74, 475 (2002).
829. B. Cantor, C. M. Allen, R. Dunin-Burkowski, M. H. Green, J. L. Hutchinsson, K. A. Q. O'Reilly, A. K. Petford-Long, P. Schumacher, J. Sloan, and P. J. Warren, *Scripta Mater.* 44, 2055 (2001).
830. M. Z. Huq and J. P. Celis, *Wear* 225–229, 53 (1999).
831. M. Z. Huq and J. P. Celis, in "Wear of Materials" (D. A. Rigney and R. G. Bayer, Eds.), Part 1, p. 114. Elsevier, Atlanta, 1999.
832. S. Bose, *Mater. Sci. Eng., A* 196, 105 (1995).

833. M. Gell, *Mater. Sci. Eng., A* 204, 246 (1995).
834. F. M. Kustas, L. L. Fehrebnbacher, and R. Komanduri, *Ann. CIRP* 46, 39 (1997).
835. M. Goto, S. Kukino, K. Kikutani, and T. Nakai, U.S. Patent 5712030, 1998.
836. X. T. Zeng, S. Zhang, and L. S. Tan, *J. Vac. Sci. Technol., A* 19, 1919 (2001).
837. U. Wiklund, O. Wanstrand, M. Larsson, and S. Hogmark, *Wear* 236, 88 (1999).
838. D. K. Leung, M. Y. He, and A. G. Evans, *J. Mater. Res.* 10, 1693 (1995).
839. Q. Luo, W. M. Rainforth, and W.-D. Munz, *Wear* 225–229, 74 (1999).
840. M. Nordin, R. Sudstrom, T. I. Selinder, and S. Hogmark, *Surf. Coat. Technol.* 133–134, 240 (2000).
841. H. W. Wang, M. M. Stack, S. B. Lyon, P. Hovsepian, and W.-D. Munz, *Surf. Coat. Technol.* 126, 279 (2000).
842. H. Van Swygenhoven and P. M. Derlet, *Phys. Rev. B* 64, 224105 (2001).
843. V. A. Pozdnyakov and A. M. Glezer, *Phys. Solid State* 44, 732 (2002).
844. R. Chaim, *Scripta Mater.* 44, 1523 (2001).
845. H. S. Kim, Y. Estrin, and M. Bush, *Acta Mater.* 48, 493 (2000).
846. M. Marayama, J. M. Howe, H. Hidaka, and S. Takaki, *Science* 295, 2433 (2002).
847. I. A. Ovid'ko, *Science* 295, 2386 (2002).
848. R. W. Hertzberg, "Deformation and Fracture Mechanics of Engineering Materials," 3rd ed. Wiley, New York, 1989.
849. A. M. Glezer, V. A. Pozdnyakov, V. I. Kirienko, and O. M. Zhigalina, in "Mechanical Properties and Deformation Behavior of Materials Having Ultra-Fine Microstructures" (N. Nastasi, D. M. Parkin, and H. Gleiter, Eds.), p. 781. Kluwer Academic, Dordrecht, 1993.
850. S. Schumacher, R. Birringer, R. Strauss, and H. Gleiter, *Acta Metall. Mater.* 37, 2485 (1989).
851. A. H. Chokshi, A. Rosen, J. Karch, and H. Gleiter, *Scripta Metall.* 23, 1679 (1989).
852. G. W. Nieman, J. R. Weertman, and R. W. Siegel, *Nanostruct. Mater.* 1, 185 (1992).
853. G. McMahon and U. Erb, *Microstruct. Sci.* 17, 447 (1989).
854. J. S. C. Jang and C. C. Koch, *J. Mater. Res.* 5, 498 (1990).
855. S. I. Rao, P. M. Hazzledine, and D. M. Dimiduk, *Mater. Res. Soc. Symp. Proc.* 362 (1994).
856. J. C. M. Li, *Trans. AIME* 227, 239 (1963).
857. D. Baral, J. B. Ketterson, and J. E. Hilliard, in "Modulated Structure Materials" (T. Tsakalakos, Ed.), p. 465. Nijhoff, Dordrecht, 1984.
858. R. C. Cammarata and K. Sieradzki, *Phys. Rev. Lett.* 62, 2005 (1989).
859. W. Sylwestrowicz and E. O. Hall, *Proc. Phys. Soc., London, B* 64, 495 (1951).
860. E. O. Hall, *Proc. Phys. Soc., London, B* 64, 742 (1951).

Superplasticity in Nanoceramics

M. Pal

University of Burdwan, Golapbagh, West Bengal, India

D. Chakravorty

Indian Association for the Cultivation of Science, Jadavpur, Kolkata, India

CONTENTS

1. Introduction
2. Experimental Techniques
3. Systems Investigated
4. Conclusions
- Glossary
- References

1. INTRODUCTION

Superplasticity involving several hundred elongations present in fine-grained polycrystalline metallic systems was first reported by Pearson in 1934 [1]. The systems investigated were eutectic alloys of lead–tin and bismuth–tin, respectively. In the early days of the investigations on the mechanical behavior of polycrystalline metals, expectations were raised for achieving very high strength in materials by reducing the size because of the prediction from the experimental Hall–Petch equation [2, 3]:

$$\sigma_y = \sigma_0 + \frac{K}{d^{1/2}} \quad (1)$$

where σ_y is the yield strength, σ_0 is a friction stress below which no dislocation movement occurs in the material in the absence of grain boundaries, K is a constant, and d is the grain size. However, it was found from experimental results that, in most cases, an opposite effect was present, viz. that the K value showed a decreasing trend as a function of increasing grain refinement, in some cases even showing a negative value [4]. It was shown in the case of ceramic materials that plastic deformation by diffusional creep [5] could be induced in a polycrystalline system by reducing the grain size to a few nanometers. The deformation rate ϵ' of

a polycrystalline material has been shown to be given by [6]

$$\epsilon' = \frac{\sigma\Omega}{d^2kT} \left(B_1 D_v + \frac{B_2 \Delta D_b}{d} \right) \quad (2)$$

where σ is the tensile stress, Ω is the atomic volume, d is the median grain size, B_1 and B_2 are constants, D_v and D_b are the volume and grain boundary diffusivities, respectively, k is Boltzmann's constant, Δ is the grain boundary thickness, and T is the temperature. At low temperatures where $D_b \gg D_v$, the deformation rate is controlled by the second term in Eq. (2), and ϵ' can be increased by reducing the value of d and increasing the value of D_b . Both of these were achieved by preparing a nanocrystalline ceramic, and low-temperature ductility with 100% plastic deformation could be observed in the case of CaF_2 and TiO_2 , respectively [7].

Superplastic structural ceramics have been developed and researched during the last two decades [2–43]. The systems which have been extensively studied are tetragonal zirconia partially stabilized by yttria [8–19], alumina/zirconia [20–27], silicon nitride/silicon carbide [28–35], magnesium oxide [36, 37], uranium dioxide [38], hydroxyapatite [39], and β -spodumene glass–ceramic [40–42]. In this chapter, we give a brief review of the work which has been carried out so far, the theoretical understanding of the properties observed, and some possible future directions of research.

2. EXPERIMENTAL TECHNIQUES

Several methods have been used to prepare nanostructured ceramic materials. Some of these are briefly described in the following paragraphs.

2.1. High-Energy Ball Mill

High-energy ball milling is frequently used for the preparation of nanocrystalline materials. This is sometimes referred to as mechanical alloying or mechanical milling. A nanostructure is obtained by repeated mechanical deformation and alloying as the powder is vigorously shaken in a vial

containing a number of milling balls. The energy transfer to the particles in these mills takes place by a shearing action or impact of the high-velocity balls with the powder. The size of the nanoparticles depends on several factors, namely, milling speed, type, size distribution of balls, ball-to-powder-weight ratio, milling atmosphere, and so on [44]. This process has the advantage of producing large quantities of material, and is already a commercial technology. Contamination from the balls needs to be taken care of.

2.2. Inert Gas Condensation

The most commonly used method for preparing nanosized clusters, especially in the case of metallic systems, is the inert-gas evaporation technique [45]. In this method, the metal whose nanoparticles are to be prepared is kept in a crucible made of very high-purity recrystallized alumina. The crucible is placed inside a glass chamber filled with an inert gas like Ar, N₂, He, and so on, under a pressure of 0.5–4 torr. At first, the metal is heated with the radiation from a graphite heater element to produce a supersaturated vapor. On collision with the gas atoms, the metal atoms rapidly lose energy, and are condensed on a cold surface, forming nanoclusters. For the synthesis of clusters of ceramic compounds, a suitable reactive gas or gas mixture is used in the chamber referred to above.

2.3. Glass–Ceramic

Glass–ceramics are produced by the controlled crystallization of appropriate glasses. The glass specimens are subjected to heat treatment at nucleation and crystallization temperatures, respectively, which lead to the precipitation of the nanocrystalline phases within the glass matrix. The crystallization temperature is determined from differential thermal analysis (DTA). The nucleation temperature is estimated from the glass transition temperature obtained in the DTA curve [46]. Nanoparticles remain protected within the glass matrix from any reaction with the ambient atmosphere.

2.4. Coprecipitation Route

Precipitation within a multicomponent solution system is known as coprecipitation. This process involves the formation of a solid precipitate in a liquid medium, followed by the separation of the solids with a filtration step. This process needs a coprecipitation agent, which can be a solution of inorganic or organic salt. The main condition is that the compound should be insoluble in the mother liquid. Parameters like mixing rate, pH, temperature, concentration, and so on, have to be properly adjusted [47]. Drying and subsequent annealing are required to prepare nanostructured materials by this method.

For the preparation of bulk specimens from the nanocrystalline powder synthesized by any of the previously mentioned techniques, hot pressing has been made use of [48]. In the latter method, both heat and pressure are used to cause densification of porous compacts at a relatively low temperature. The importance of hot pressing is that it ensures limited grain growth. Uniaxial hot pressing and hot isostatic pressing are the most commonly used methods. In

hot pressing, a sintered material is fired for a second time in the presence of a suitable atmosphere. This method suffers from some practical difficulties like die failure, reaction between die and powder, inhomogeneity, and so on.

There are also many other methods for the preparation of structural nanocrystalline ceramics. The properties of these nanoparticles depend on the processing parameters. This should be evident from the subsequent sections.

3. SYSTEMS INVESTIGATED

3.1. Stabilized Zirconia

The creep behavior of a yttria-stabilized tetragonal zirconia polycrystal (Y–TZP) specimen with Y₂O₃ content varying from 2 to 4mol% with grain sizes ranging from 0.36 to 0.85 μm was investigated by Nauer and Carry [49]. The stresses used varied from 2 to 100 MPa. Figure 1 shows the creep strain rate as a function of stress of the Y–TZP specimen with 3mol% Y₂O₃ at 1623 K as measured by the authors. The latter concluded from the analyses of their data that there were two deformation regimes, viz. an interface-reaction-controlled creep at stress lower than 10 MPa, and grain-boundary diffusion-controlled creep at stress greater than 50 MPa. The strain rate $\dot{\epsilon}$ and stress σ are related by the equation

$$\dot{\epsilon} = A\sigma^n \quad (3)$$

where A is a constant and n is referred to as the stress exponent. In the present specimen systems, the stress exponent n was reported to have values around 2.4 in the low-stress region, whereas in the high-stress region, it decreased to 1.4.

Wakai and Nagano [50] studied the deformation in ZrO₂ polycrystals containing 2–8 mol% Y₂O₃ or 12mol% CeO₂ having grain sizes in the range 0.51–14 μm. Tensile creep tests were carried out at temperatures varying from 1370 to 1775 K. The stress exponent n was found to be around 2 for materials having grain sizes less than 1 μm, but the value decreased as the grain size was increased. A model based on grain-boundary sliding was used to explain the behavior. The mechanism envisaged diffusion creep controlled by interface reaction, as well as the diffusion of cations. The

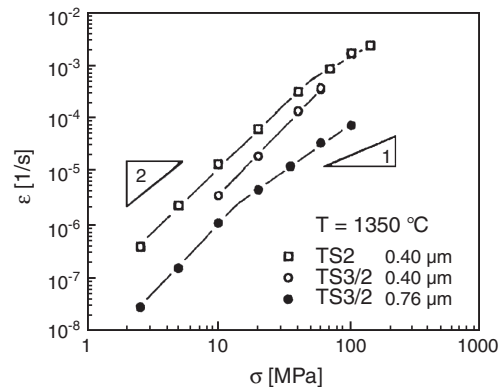


Figure 1. Creep strain rate versus stress curves for 3mol% Y₂O₃ TZP at 1623 K (data for 2mol% Y₂O₃ are shown for comparison). Reprinted with permission from [14], M. Nauer and C. Carry, *Scripta Metall.* 24, 2459 (1990). © 1990, Elsevier Science.

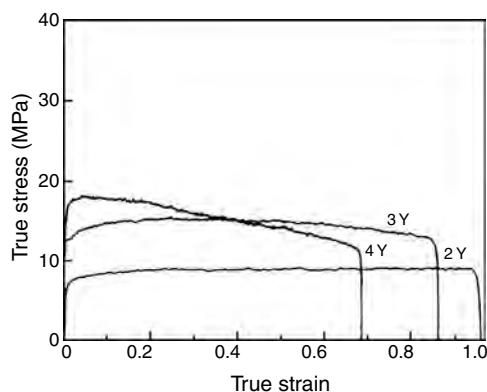


Figure 2. Comparison of true stress–true strain curves for various Y_2O_3 contents at 1723 K and strain rate $2.70 \times 10^{-4} \text{ s}^{-1}$. Reprinted with permission from [50], F. Wakai and T. Nagano, *J. Mater. Sci.* 26, 241 (1991). © 1991, Kluwer Academic.

concentration of the solute ions was shown to have a marked influence on the diffusion of cations. Figure 2 shows the true-stress true-strain curves for different Y_2O_3 -stabilized ZrO_2 polycrystalline specimens as observed at 1723 K and at a strain rate of $2.7 \times 10^{-4} \text{ s}^{-1}$. Superplastic elongations for the specimens are evident. It should be mentioned that ZrO_2 polycrystals with 12 mol% CeO_2 did not exhibit such superplastic elongation.

Bravo-Leon et al. [51] studied the plastic deformation characteristics of Y_2O_3 stabilized- ZrO_2 polycrystals (with the yttria content being 3 and 4mol%, respectively) having grain sizes smaller than $1 \mu\text{m}$ at stresses less than 10 MPa and at temperatures in the range 1573–1723 K. These materials did not show any superplastic behavior, but instead, extensive internal cavitation for a few percent of strain. The data indicated that there was a threshold stress before the grain-boundary sliding mechanism became operative.

Melendo et al. [52] analyzed the published deformation data of yttria-stabilized zirconia polycrystals having grain sizes less than $1 \mu\text{m}$ for temperatures ranging from 1523 to 1723 K. The results have been explained on the basis of a single deformation process characterized by a threshold stress above which grain-boundary sliding takes place. Such stress has been ascribed to the segregation of yttrium atoms at the grain boundaries. For low-purity materials, viz. impurity content greater than 0.1wt%, the stress exponent has been shown to be equal to 2 over the entire range of stress used. The enhancement of the strain rate with an increase in the purity level has been correlated to the existence of an amorphous phase present at the grain boundaries.

Chaim [53] theoretically investigated the plastic deformation characteristics of impure nanocrystalline ceramics using the model of a percolative composite in conjunction with that of grain-boundary sliding. The threshold strain-rate criterion below which plastic deformation would take place in impure nanoceramics was determined utilizing the “glass transition temperature” concept. On the basis of this model, strain rates as high as 10^{-4} s^{-1} were predicted at 873 K for impure yttria-stabilized tetragonal zirconia polycrystals with a grain size of 10 nm.

Bhattacharyya et al. synthesized and characterized nanocrystalline 5mol% yttria-stabilized zirconia for its

compression superplasticity in the temperature range 1363–1523 K [54]. They analyzed the experimental results by the phenomenological as well as the atomistic variants of a model for grain/interphase boundary-controlled superplastic flow [55]. The different deformation parameters arising from the constitutive equations, as well as the activation energies for the rate-controlling process were computed and compared with results of analyses of data obtained from the literature. Both variants of the model were shown to predict the experimental strain rates accurately.

3.2. Zirconia Alumina Composites

Wakai et al. [56] presented compressive deformation data of 80wt% ZrO_2 (3mol% Y_2O_3)/20wt% Al_2O_3 composites in air at temperatures from 1673 to 1823 K. The stress–strain relation at different initial strain rates is depicted in Figure 3. An extraordinarily large deformation (up to -1.8) was observed at strain rates from 10^{-3} to 10^{-4} s^{-1} . The stress exponent was found to vary from 1.2 to 2, and the activation energy was determined to be $620 \pm 40 \text{ kJ/mol}$. During deformation, Al_2O_3 aggregates were found to be generated. This was explained by the model of the grain rearrangement as a result of grain switching during the superplastic flow.

A continuum theory for the non-Newtonian flow of a two-phase composite containing rigid inclusions was developed [57]. It predicted flow suppression by a factor of $(1 - V)^q$, where V is the volume fraction of the rigid inclusion and q is dependent on the stress exponent and the inclusion shape. Stress concentrations in the rigid inclusion were also evaluated. As the stress exponent increased, flow suppression was shown to be more pronounced, even though the stress concentration became less severe. To test this theory, the superplastic flow of zirconia/mullite composites, in which zirconia was the soft, non-Newtonian superplastic matrix and mullite was the rigid phase of various size, shape, and amount, was studied. The continuum theory was found to describe the two-phase superplastic flow reasonably well.

Structural ceramics (Y-TZP, Al_2O_3 , Si_3N_4 , and their composites), which are referred to as superplastic, should be able to withstand biaxial stretching to large strains [58]. It is essential that these ceramics are made of an ultrafine grain size that is stable against coarsening during sintering and deformation. A low sintering temperature is a necessary,

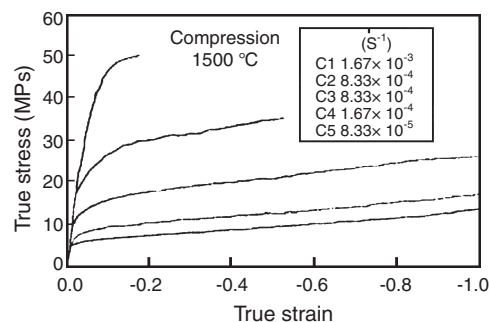


Figure 3. True stress against true strain curves at different initial strain rates (ϵ_0) at 1773 K. Reprinted with permission from [56], F. Wakai et al., *J. Ceram. Soc. Jpn.* 94, 1017 (1986). © 1986, Ceramic Society of Japan.

but not a sufficient, condition for achieving the required microstructure. In many cases, the selection of an appropriate phase, such as a tetragonal phase in zirconia or an α phase in silicon nitride, which is resistant to grain growth, is crucial. Figure 4 shows the forming temperature and time for a few biaxially punch-stretched samples made of various structural ceramics. The quality of as-formed surfaces has been reported to be excellent. These results suggested that the deformation processing of dense ceramics can be carried out at high temperatures using commonly known methods.

The ultrafine grain structure can be preserved during sintering if the grain-boundary mobility can be reduced. This has been shown to occur by introducing suitable dopants into the system. Figure 5 summarizes the grain-boundary mobility values as a function of temperature for different dopings of calcium in zirconia. It is seen that calcium is the most effective dopant for suppressing grain growth in tetragonal zirconia polycrystals (TZPs).

Attempts have also been made to develop superplastic alumina. Grain growth control has been tried by introducing either magnesia, a low melting liquid phase, for example, boron oxide and copper oxide, or charge compensating dopant pairs, for example, Cu^{2+} and Ti^{4+} to alumina so as to reduce the sintering and superplastic-forming temperatures. Typical stress-strain curves for these ceramics are shown in Figure 6. It should be noted, however, that, although the deformation was achieved at temperatures around 1123 K, this was accompanied by abnormal growth of some of the grains. Also, the tensile ductilities were low.

Clarisse et al. [59] reported on the high-temperature creep of three alumina-zirconia composites (alumina volume fraction being 20, 50, and 80%, respectively) and of the end constituents (yttria-partially stabilized zirconia polycrystals and alumina) as a function of stress in the

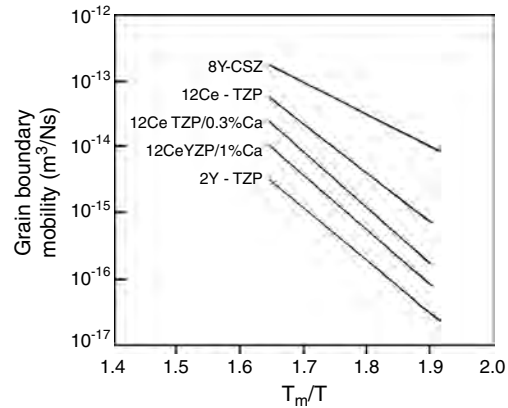


Figure 5. Grain-boundary mobility of TZP and CSZ plotted versus reciprocal homologous temperature (T_m is melting point). Reprinted with permission from [58], I. W. Chen and L. A. Xue, *J. Am. Ceram. Soc.* 73, 2585 (1990). © 1990, American Ceramic Society.

range 4–200 MPa and at temperatures varying from 1548 to 1673 K. The grain sizes in the sample systems were in the range 0.4–2 μm . The deformation of yttria-partially stabilized zirconia polycrystals and alumina were found to arise due to two serial mechanisms, viz. the interface reaction and diffusion at low and high stresses, respectively. The influence of the alumina volume content on the creep rate of the composites has been analyzed by various models. Figure 7 delineates the experimental strain rate fitted with simulated creep rates for different compositions at 1623 K. In this figure, AZ20, AZ50, and AZ80 contain 20, 50, and 80vol% of alumina, respectively, in the composites concerned. Alumina refers to a hot-pressed alumina specimen.

The superplastic behavior of the composite Y-TZP/ Al_2O_3 (20wt%) in uniaxial tension was investigated by Wakai and Kato [60]. The initial strain-rate-dependent stress-strain behavior is shown in Figure 8. The stress exponent and activation energy of the composite were found to be of the same order as those of Y-TZP. The cavitation damage and the creep crack growth could be reduced by keeping the strain rate low enough so that a specimen elongated 100% at an

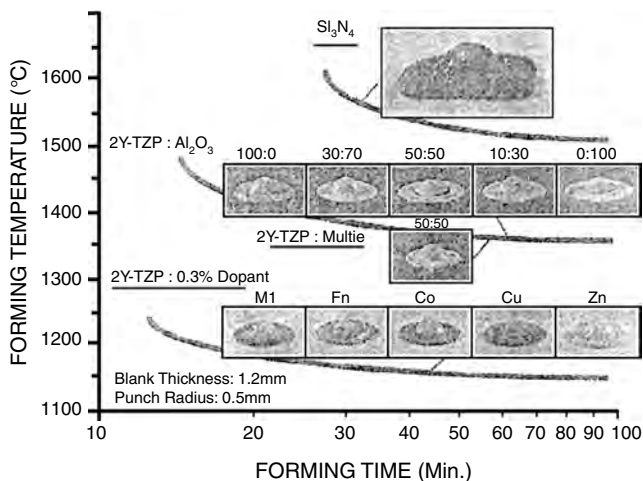


Figure 4. Superplastic-forming temperatures and times of structural ceramics. Hemispherical punch with 6.5 mm radius was used to stretch the initial flat, 1 mm thick disks into the shape shown. Surface finish was excellent and glossy for silicon nitride, zirconia, and zirconia-rich composites. Surface of alumina, although free of visible defects, appeared dull. Under optimal conditions, the forming operation can be completed at even lower temperatures and shorter times. Reprinted with permission from [58], I. W. Chen and L. A. Xue, *J. Am. Ceram. Soc.* 73, 2585 (1990). © 1990, American Ceramic Society.

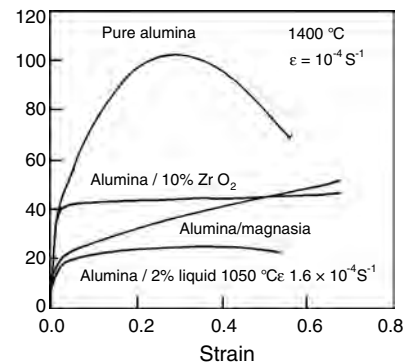


Figure 6. Stress-strain curves for alumina. Strain hardening in pure alumina and magnesia-doped alumina is due to dynamic grain growth. The eventual decrease in stress in pure alumina is a result of cavitation. Note that alumina with 2% liquid was tested at a lower temperature. Reprinted with permission from [58], I. W. Chen and L. A. Xue, *J. Am. Ceram. Soc.* 73, 2585 (1990). © 1990, American Ceramic Society.

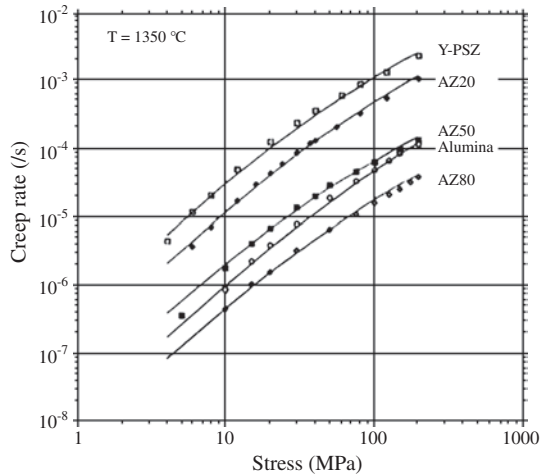


Figure 7. Strain rate versus stress at 1623 K for the five compositions (hot-pressed alumina). Full lines correspond to simulated creep rates. Reprinted with permission from [59], I. Clarisse et al., *Acta Mater.* 45, 3843 (1997). © 1997, Elsevier Science.

elevated temperature maintained a strength of 1800 MPa at room temperature.

Kim et al. [61] demonstrated that a composite ceramic material consisting of tetragonal zirconium oxide, magnesium aluminate spinel, and α -alumina phases exhibited superplasticity at strain rates up to 1 s^{-1} . The composite also exhibited a large tensile elongation, exceeding 1050% for a strain rate of 0.4 s^{-1} . The deformation behavior in the form of a stress-strain curve is presented in Figure 9 at a temperature of 1923 K. The tensile flow behavior and deformed microstructure of the material indicated that the superplasticity was due to a combination of limited grain growth in the constitutive phases and the intervention of dislocation-induced plasticity in the zirconium oxide phase. The starting materials were yttria (3mol%)-stabilized tetragonal zirconia, high-purity α -alumina, and magnesium oxide with particle sizes of 70 nm, 200 nm, and $17 \mu\text{m}$, respectively. Cold-isostatically pressed (at 200 MPa) compacts were sintered at 1673 K for 1 h in air. The microstructure consisted of equiaxed α -alumina, magnesium aluminate spinel, and tetragonal zirconia grains with average sizes of 290, 180, and 180 nm, respectively. Figure 10 gives a typical microstructure of the composite.

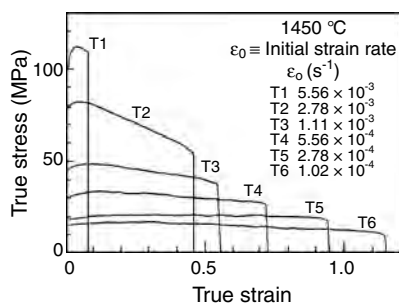


Figure 8. True stress as a function of true strain for a cross-head speed at 1723 K. Reprinted with permission from [60], F. Wakai and H. Kato, *Adv. Ceram. Mater.* 3, 71 (1988). © 1988, American Ceramic Society.

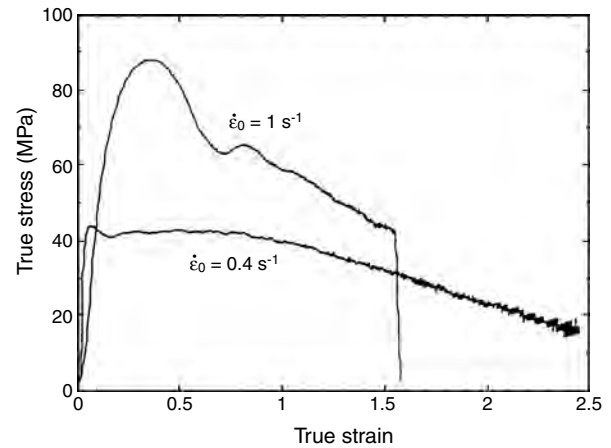


Figure 9. Stress-strain curves at 1923 K. ϵ_0 is the initial strain rate. Reprinted with permission from [61], B. N. Kim et al., *Nature* 413, 288 (2001). © 2001, Macmillan Magazines Ltd.

3.3. Silicon Nitride/Silicon Carbide

Covalent crystal composites made of Si_3N_4 and SiC were prepared by the vapor-phase reaction [33] of suitable precursor compounds. The mixture of the powders obtained was mixed with sintering aids like Y_2O_3 and Al_2O_3 . The resultant powder was hot pressed at 1923 K for 7 h at 34 MPa in a nitrogen atmosphere. The microstructure of the composite consisted of β - Si_3N_4 , α - Si_3N_4 , and β -SiC grains of less than 200 nm diameter. The elongated grains had diameters less than 500 nm. It was suggested that a glassy phase containing Si, O, N, Al, and Y formed during the synthesis of the material. Superplastic elongation by more than 150% was observed at a temperature of 1873 K. At the temperature of stress-strain measurement, the glassy phase referred to above formed a liquid at two and three grain junctions. The superplastic behavior was ascribed to the presence of this liquid phase.

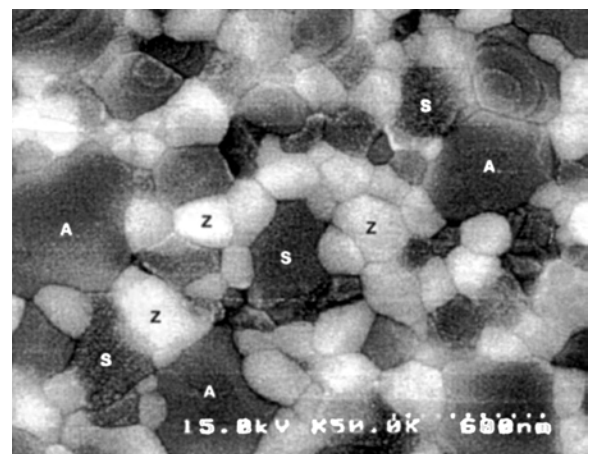


Figure 10. Scanning electron micrograph of the as-sintered microstructure. Grain labels A, S, and Z represent Al_2O_3 , spinel, and ZrO_2 , respectively. Reprinted with permission from [61], B. N. Kim et al., *Nature* 413, 288 (2001). © 2001, Macmillan Magazines Ltd.

Mitomo et al. [34] prepared fine β - Si_3N_4 powder with an average particle size of 280 nm by grinding and centrifugal sedimentation of submicrometer β powder. They obtained finer and uniform grained ceramics from the powder by hot pressing. The average grain size of the ceramic was 210 nm. They showed that this kind of microstructure was desirable for the matrix phases of the *in-situ* composite. A compressive test was performed with an average strain rate of about $1.8 \times 10^{-4}/\text{s}$ at a temperature of 1773 K. They obtained a superplastic deformation at 40 MPa. The conclusion was that mechanical properties of superplastic silicon nitride ceramics could be improved by annealing after deformation.

Silicon carbide powder with an average size of 110 nm has been synthesized by the liquid phase sintering method [35]. These nanoceramic powders have been compacted by hot pressing with the addition of Al_2O_3 , Y_2O_3 , and CaO at 2023 K. The specimens showed superplastic deformation at a strain rate of $5.0 \times 10^{-4}/\text{s}$ at 1973 K. Figure 11 compares the deformation behavior of these nanoceramics with that prepared using submicrometer-sized powder. It is evident that the ceramics with nanosized crystals exhibit a large deformation with a high strain rate, whereas the reference sample (with submicron-sized crystals) shows a much smaller deformation and strain rate.

3.4. β -Spodumene Glass–Ceramic

The glass–ceramic route is an important development in the ceramic field, and has been utilized by many researchers to achieve some useful properties [62].

Two glass–ceramics in the lithium–zinc–silicate system with compositionally similar but morphologically different characteristics containing about 20% residual glass phase were creep tested by Morrell and Ashbee [40]. The testing was carried out both in tension and compression between 873 and 1073 K. High stresses caused low strain failure in both materials, but at low stresses, there was considerable plasticity, with a strain greater than 30% being produced in one material. They applied a model to analyze the behavior, and demonstrated that a stress exponent varying with stress was to be expected, although deformation was still controlled by the glass phase.

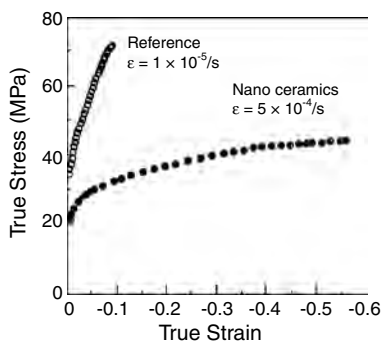


Figure 11. Stress–strain relation of nanoceramic as compared with that of a reference ceramic from submicrometer powder. Reprinted with permission from [35], M. Mitomo et al., *J. Mater. Res.* 11, 1601 (1996). © 1996, Materials Research Society.

Plastic deformation characteristics in two lithium aluminosilicate glass–ceramics were investigated by Wang and Raj [41]. The experiments were carried out under a superimposed hydrostatic pressure and under variable humidity at ambient pressure. The superplastic deformation was shown to be limited either by intergranular cavitation or by the generation and growth of surface cracks. In one of the specimens with a high flow stress, the latter mechanism led to failure. Hydrostatic pressure substantially reduced cavitation in both the specimens, viz. one with a high flow stress and the other with a low flow stress. The tensile ductility, however, increased in the case of the sample with the lower flow stress. The humidity seemed to increase the possibility of a crack propagation mode of failure.

Wang and Raj [42] also reported on large deformations at fast strain rates in fine-grained β -spodumene glass–ceramic materials. It was found that ultrafine-grained ceramics showed high rates of deformation, about 10^{-4} – 10^{-3} s^{-1} at stresses as low as 1–20 MPa. The deformation mechanism was explained as arising due to an increased rate of matter transport through the liquid phase segregated at the grain boundaries. The ceramic was shown to be extremely ductile in compression. In tension, however, elongations as large as 135% in one material and more than 400% in the other were observed. Figure 12 summarizes the data showing the transition from semibrittle to ductile behavior in the case of one of the glass–ceramic compositions. The stress–strain curves are shown as measured under compression. The transition occurs as the temperature is increased.

3.5. Titanium Oxide/Composites

Karch et al. [43] demonstrated that a conventionally brittle ceramic became ductile, permitting large ($\sim 100\%$) plastic deformations at low temperature if a polycrystalline ceramic was generated with a crystal size of a few nanometers. The ductility seemed to originate from the diffusional flow of atoms along the intercrystalline interfaces. The plastic deformation of ceramic materials by diffusional creep is significant only at temperatures close to the melting point, where

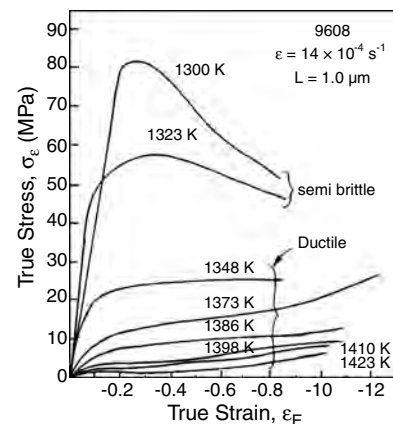


Figure 12. Range of stress–strain curves obtained in compressions; transition from semibrittle to ductile behavior is seen as temperature is increased. Reprinted with permission from [42], J. G. Wang and R. Raj, *J. Am. Ceram. Soc.* 67, 399 (1984). © 1984, American Ceramic Society.

the rate of diffusion is high. The authors in the present work first prepared nanosized titanium particles by an inert-gas condensation technique. The fine titanium particles accumulated on the surface of the cold finger were then oxidized to TiO_2 . The average crystallite size was about 8 nm. The powders were then consolidated by a pressure of 5 GPa at 300 K.

Cui and Hahn [63] showed that nanoceramics could be plastically deformed under tensile stresses at a temperature which was below half of the melting temperature of the material. They prepared TiO_2 nanocrystals of average crystal size around 40 nm by the inert-gas condensation technique. A gas pressure-forming technique was used to vary the stress in the range 2–20 MPa. The deformation was carried out at temperatures varying from 973 to 1073 K. Strain rates as high as $4 \times 10^{-6} \text{ s}^{-1}$ were recorded in their experiments.

Hahn and Padmanabhan [64] also proposed a model based on grain-boundary sliding control of the flow process of nanocrystalline material. This model has been applied both to nanocrystalline metals as well as nanoceramics. A satisfactory agreement between theory and experimental results has been reported.

3.6. Magnesium Oxide/Composites

The mechanical properties of pure magnesia were studied as a function of grain size (1–90 μm) and temperature (303–1773 K) by Vasilos et al. [37]. They showed that the elastic modulus was essentially independent of grain size over the temperature range covered. The transverse bend strength for magnesia revealed a 1/6 power dependence versus grain size at low temperature, that is, $S_{TB} = 50,000 G^{1/6}$. At temperatures above approximately 873 K, the strength of specimens of all grain sizes tested decreased with temperature. Nonlinear load deflection behavior was observed at temperatures above 973 K, and etch pit observations of dislocations produced during deformation and tractate of a large grain magnesia specimen revealed an extensive slip in grain adjacent to the fractured area. The elastic modulus varied from 4.5 to 12.0×10^6 psi in the temperature range 300–1773 K.

Crampon and Escaig [65] investigated the mechanical properties of MgO polycrystal specimens with grain sizes in the range 0.1–1.0 μm at temperatures varying from 1173 to 1423 K. These specimens exhibited a ductility under low compressive stresses which was much larger than that usually observed in these ceramics. Figure 13 shows the stress-strain behavior under compression for a fine-grained MgO specimen at different temperatures. It is seen that, at room temperature, the specimen shows a brittle fracture. Measurable macroplasticity is observed at 1173 K. Extensive plastic strain is shown by the specimens at temperatures 1278–1423 K. The microstructural data indicated a diffusion-accommodated flow.

The mechanical behavior of Mg_2Si particles of dimension 0.7–0.8 μm dispersed in magnesium matrix was investigated by Mabuchi and Higashi [66] through a tensile test. The superplasticity of a high strain rate of $10^{-1}/\text{s}$ was observed in these composites. They noted that a high strain rate was attained in a solid state containing no liquid phase. Their calculation based on the critical strain rate for cavity nucleation indicated that magnesium-based materials have great

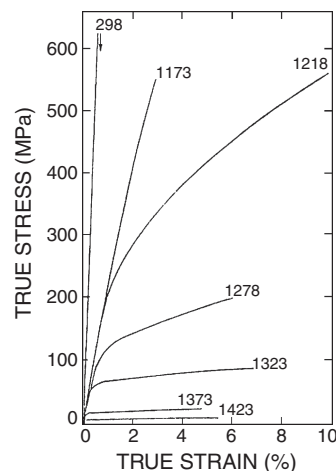


Figure 13. Stress-strain curves in compression at constant strain rate of $\approx 6.7 \times 10^{-6} \text{ s}^{-1}$ as a function of temperature (K). At room temperature, arrow indicates fracture of specimen. Reprinted with permission from [65], J. Crampon and B. Escaig, *J. Am. Ceram. Soc.* 63, 680 (1980). © 1980, American Ceramic Society.

potential for high-strain-rate superplasticity compared with aluminum-based materials.

3.7. Others

Uranium dioxide exhibits two types of creep behavior, depending on the magnitude of applied stress. Chung and Davies [38] reported the low-stress diffusional creep of uranium dioxide of a grain size in the range 2–10 μm over the temperature range 1273–1873 K. The variation of creep rate with grain size is presented in Figure 14. It was found that the creep behavior and creep rates agreed with a deformation model proposed by Ashby and Verrall [67]. This was supported by microscopic observations of grain and pore movements in a superplastically deformed specimen.

Superplasticity in hydroxyapatite for the first time was reported by Wakai et al. [39]. Dense and translucent hydroxyapatite polycrystals ($\text{Ca}_{10}(\text{PO}_4)_6(\text{OH})_2$ with a grain size 0.64 μm) were obtained by hot isostatic pressing at 203 MPa and 1273 K for 2 h in argon. The material exhibited superplastic elongation (>150%) in a tension test at temperatures from 1273 to 1373 K and at strain rates from 7.2×10^{-5} to $3.6 \times 10^{-4} \text{ s}^{-1}$. Extensive strain hardening was observed. True stress versus true strain at 1323 K is presented for hydroxyapatite in Figure 15. The stress exponent of the yield stress was larger than 3.

Interest in the plastic deformation behavior of $\text{YBa}_2\text{Cu}_3\text{O}_{7-x}$ material emanated from their high-temperature superconducting behavior and the need to process them into various shapes by mechanical means. A few studies have been undertaken to delineate the dependence of plastic deformation on temperature and strain rate [68–70].

Extensive investigations were carried out by Yun et al. [70] to understand the superplastic deformation characteristics of $\text{YBa}_2\text{Cu}_3\text{O}_{7-x}$ ceramic specimens with submicrometer grain sizes. The samples were prepared by grinding the commercially obtained powders, and isostatically compacting them into rectangular shapes. The latter were sintered

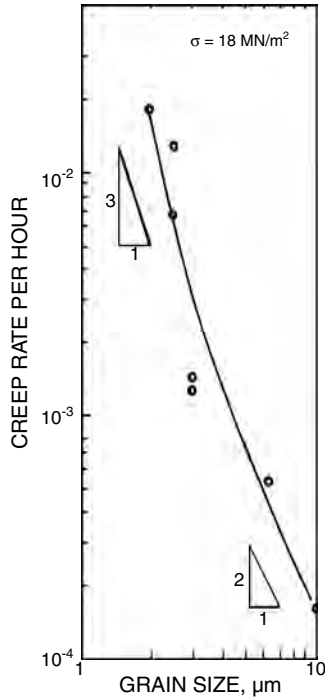


Figure 14. Variation of creep rate with grain size at 1673 K. Reprinted with permission from [38], T. E. Chung and T. J. Davies, *Acta Mater.* 27, 627 (1979). © 1979, Elsevier Science.

finally at around 1173 K. The grain sizes for the specimens had values in the range 0.5–1.4 μm . Deformation studies under compression were carried out at temperatures varying from 1023 to 1148 K. Measurements were done at a constant strain rate ranging from 1.0×10^{-5} to $1.0 \times 10^{-3}/\text{s}$. Figure 16 shows the typical stress–strain curves for the specimens under compression. The extracted values of the stress exponent, the grain size exponent, and the activation energy were found to be 2.0 ± 0.3 , 2.7 ± 0.7 and $Q = 745 \pm 100$ KJ/mol, respectively. From the experimental data, it was

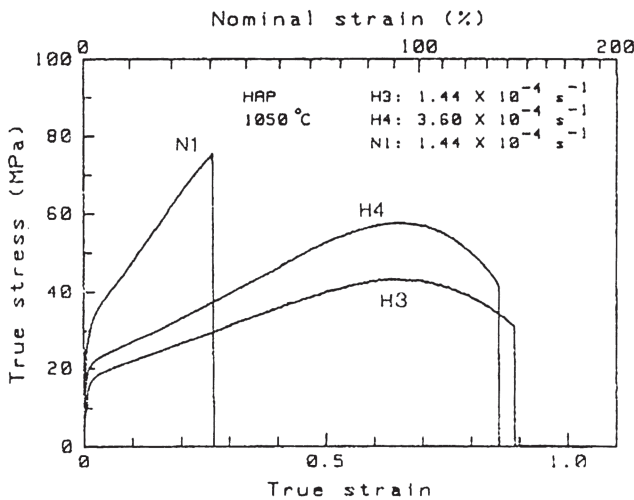


Figure 15. True stress–true strain curves for hydroxyapatite tested at 1323 K. Reprinted with permission from [39], F. Wakai et al., *J. Am. Ceram. Soc.* 73, 457 (1990). © 1990, American Ceramic Society.

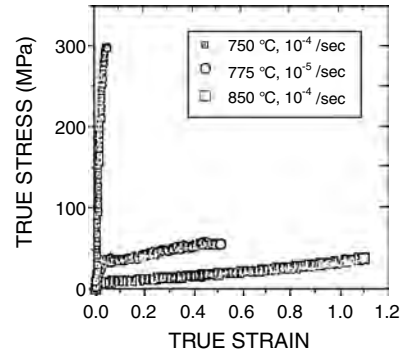


Figure 16. Stress–strain curves of $\text{YBa}_2\text{Cu}_3\text{O}_{7-x}$ samples under compression. Reprinted with permission from [70], J. Yun et al., *J. Am. Ceram. Soc.* 85, 1190 (2002). © 2002, American Ceramic Society.

concluded that the superplastic deformation was controlled by grain-boundary sliding. The latter was accommodated by grain-boundary diffusion.

4. CONCLUSIONS

From the review presented above, it should be evident that the plastic deformation observed in the case of metallic systems is much higher than that found so far in ceramics. Also, the temperature above which superplasticity has been found in ceramic systems is higher than the corresponding temperature in metals. To exploit this property in the forming of different ceramic products, therefore, the greatest challenge will be to either lower the temperature range for the processing steps or develop newer ceramic systems which will provide such possibilities. Also, efforts are likely to be directed toward synthesizing ceramic powders with diameters smaller than what has been achieved so far.

GLOSSARY

Creep rate Creep is defined as the progressive deformation of a material at constant load. The rate at which such deformation occurs is referred to as the creep rate.

Nanoceramics Materials containing oxide and/or nitride phases which have grains of sizes of the order of a few tens to a few hundred nanometers.

Superplasticity Describes the deformation of a solid of a few hundred percent under the influence of a load.

True strain This is given by $\ln(l_i/l_0)$ where l_i is the length at the instant of measurement and l_0 is the original length of the specimen.

True stress The ratio of load applied on a solid and the actual area of cross-section of the same at the instant of measurement.

ACKNOWLEDGMENTS

M. Pal thanks the University Grant Commission of India for extending support for this work. D. Chakravorty thanks C.S.I.R. New Delhi for providing partial financial support.

REFERENCES

1. C. E. Pearson, *J. Inst. Met.* 54, 111 (1934).
2. E. O. Hall, *Proc. R. Soc. London B* 64, 474 (1951).
3. N. J. Petch, *J. Iron Steel Inst.* 174, 25 (1953).
4. S. Takeuchi, *Scripta Mater.* 44, 1483 (2001).
5. C. Herring, *J. Appl. Phys.* 21, 437 (1950).
6. R. L. Coble, *J. Appl. Phys.* 34, 1679 (1963).
7. J. Karch, R. Birringer, and H. Gleiter, *Nature* 330, 556 (1987).
8. F. Wakai, S. Sakaguchi, and Y. Matsuno, *Adv. Ceram. Mater.* 1, 259 (1986).
9. C. M. J. Hwang and I. W. Chen, *J. Am. Ceram. Soc.* 73, 1626 (1990).
10. T. G. Nieh, C. M. McNally, and J. Wadsworth, *Scripta Metall.* 22, 1297 (1988).
11. R. Duclos, J. Crampon, and B. Amana, *Acta Metall.* 37, 877 (1989).
12. T. K. Gupta, J. H. Bechtold, R. C. Kuznicki, L. H. Cadoff, and B. R. Rossing, *J. Mater. Sci.* 12, 2421 (1977).
13. F. Wakai, S. Sakaguchi, and H. Kata, *J. Ceram. Soc. Jpn.* 94, 721 (1986).
14. M. Nauer and C. Carry, *Scripta Metall.* 24, 1459 (1990).
15. A. H. Chokshi, *Mater. Sci. Eng. A* 166, 119 (1993).
16. M. Gust, G. Goo, J. Wolfenstine, and M. L. Mecartney, *J. Am. Ceram. Soc.* 76, 1681 (1993).
17. M. M. R. Boutz, A. J. A. Winnubst, and A. J. Burggraaf, *J. Eur. Ceram. Soc.* 13, 103 (1994).
18. T. Sakuma and Y. Yoshizawa, *Mater. Sci. Forum* 170–172, 369 (1994).
19. F. Wakai, Y. Kodama, and T. Nagano, *Jpn. J. Appl. Phys.* 28, 69 (1989).
20. C. K. Yoon and I.-W. Chen, *J. Am. Ceram. Soc.* 73, 1555 (1990).
21. C. Carry, in “Superplasticity” (B. Baudalet and M. Suery, Eds.), CNRS, Paris, 1985.
22. K. R. Venkatachari and R. Raj, *J. Am. Ceram. Soc.* 69, 135 (1986).
23. P. Gruffel, C. Carry, and A. Mocellin, *Rev. Phys. Appl.* 23, 716 (1988).
24. P. Gruffel, C. Carry, and A. Mocellin, *Sci. Ceram.* 14, 587 (1988).
25. W. R. Cannon, in “Structure and Properties of MgO and Al₂O₃ Ceramics” (W. D. Kinegery, Ed.), American Ceramic Society, Columbus, OH, 1984.
26. T. S. Yeh and M. D. Sacks, *J. Am. Ceram. Soc.* 71, 841 (1988).
27. R. M. Cannon, W. H. Rhodes, and A. H. Heuer, *J. Am. Ceram. Soc.* 63, 46 (1980).
28. F. Wakai, Y. Kodama, S. Sakaguchi, N. Murayama, K. Izaki, and K. Nihara, “MRS Symposium Proceedings on Superplasticity in Metals, Ceramics and Intermetallics” (M. I. Mayo, J. Wadsworth, A. K. Mukherjee, and M. Kobayashi, Eds.), Materials Research Society, Pittsburgh, PA, 1990.
29. L. J. Gauckler, H. L. Lukas, and T. Y. Tien, *Mater. Res. Bull.* 11, 503 (1976).
30. L. J. Gauckler, J. Weiss, T. Y. Tien, and G. Petzow, *J. Am. Ceram. Soc.* 61, 397 (1978).
31. F. F. Lange, E. S. Diaz, and C. A. Andersson, *Ceram. Bull.* 58, 845 (1979).
32. T. G. Nieh, J. Wadsworth, and O. D. Sherby, “Superplasticity in Metals and Ceramics.” Cambridge University Press, Cambridge, 1997.
33. F. Wakai, Y. Kodama, S. Sakaguchi, N. Marayama, K. Izaki, and K. Nihara, *Nature* 334, 421 (1990).
34. M. Mitomo, H. Hirotsuru, H. Suematsu, and T. Nishimura, *J. Am. Ceram. Soc.* 78, 211 (1995).
35. M. Mitomo, Y. W. Kim, and H. Hirotsuru, *J. Mater. Res.* 11, 1601 (1996).
36. S. K. Roy and R. L. Coble, *J. Am. Ceram. Soc.* 51, 1 (1968).
37. T. Vasilos, J. B. Mitchell, and R. M. Spriggs, *J. Am. Ceram. Soc.* 47, 606 (1964).
38. T. E. Chung and T. J. Davies, *Acta Mater.* 27, 627 (1979).
39. F. Wakai, Y. Kodama, and S. Sakaguchi, *J. Am. Ceram. Soc.* 73, 457 (1990).
40. R. Morrell and K. H. G. Ashbee, *J. Mater. Sci.* 8, 1235 (1973).
41. J. G. Wang and R. Raj, *J. Am. Ceram. Soc.* 67, 385 (1984).
42. J.-G. Wang and R. Raj, *J. Am. Ceram. Soc.* 67, 399 (1984).
43. J. Karch, R. Birringer, and H. Gleiter, *Nature* 330, 556 (1987).
44. P. G. McCormick, W. F. Miao, P. A. I. Smith, J. Ding, and R. Street, *J. Appl. Phys.* 83, 6256 (1998).
45. G. Granquist and R. A. Buhrman, *J. Appl. Phys.* 47, 2200 (1976).
46. M. Pal, P. Brahma, D. Chakravorty, D. Bhattacharyya, and H. S. Maiti, *Nanostruct. Mater.* 8, 731 (1997).
47. A. Pathak and P. Paramanik, in “Nanomaterials” (D. Chakravorty, Ed.), pp. 47–70. 2000.
48. H. Lobl, *J. de Phys.* 38, C1-345 (1977).
49. M. Nauer and C. Carry, *Scripta Metall.* 24, 1459 (1990).
50. F. Wakai and T. Nagano, *J. Mater. Sci.* 26, 241 (1991).
51. A. Bravo-Leon, M. J-Melendo, and A. D-Rodriguez, *Scripta Mater.* 35, 551 (1996).
52. M. J-Melendo, A. D-Rodriguez, and A. B-Leon, *J. Am. Ceram. Soc.* 81, 2761 (1998).
53. R. Chaim, *J. Mater. Res.* 14, 2508 (1999).
54. S. S. Bhattacharyya, U. Betz, and H. Hahn, *Scripta Mater.* 44, 1553 (2001).
55. K. A. Padmanabhan and J. Schlipf, *Mater. Sci. Technol.* 12, 391 (1996).
56. F. Wakai, H. Kato, S. Sakaguchi, and N. Murayama, *J. Ceram. Soc. Jpn.* 94, 1017 (1986).
57. C. K. Yoon and I. W. Chen, *J. Am. Ceram. Soc.* 73, 1555 (1990).
58. I. W. Chen and L. A. Xue, *J. Am. Ceram. Soc.* 73, 2585 (1990).
59. I. Clarisse, R. Baddi, A. Bataille, J. Crampon, R. Duclos, and J. Vicens, *Acta Mater.* 45, 3843 (1997).
60. F. Wakai and H. Kato, *Adv. Ceram. Mater.* 3, 71 (1988).
61. B. N. Kim, K. Hiraga, K. Morita, and Y. Sakka, *Nature* 413, 288 (2001).
62. P. W. McMillian, “Glass Ceramics.” Academic, New York, 1964.
63. Z. Cui and H. Hahn, *Nanostruct. Mater.* 1, 419 (1992).
64. H. Hahn and K. A. Padmanabhan, *Phil. Mag. B* 76, 559 (1997).
65. J. Crampon and B. Escaig, *J. Am. Ceram. Soc.* 63, 680 (1980).
66. Mabuchi and K. Higashi, *Phil. Mag. A* 74, 887 (1996).
67. M. F. Ashby and R. A. Verrall, *Acta Metall.* 21, 149 (1973).
68. J. Yun, M. P. Harmer, and Y. T. Chou, *Scripta Metall. Mater.* 29, 267 (1993).
69. G. Bussod, A. Pechenik, C.-T. Chu, and B. Dunn, *J. Am. Ceram. Soc.* 72, 137 (1989).
70. J. Yun, Y. T. Chou, and M. P. Harmer, *J. Am. Ceram. Soc.* 85, 1190 (2002).

Supramolecular Coordination Polymers

Jing-Cao Dai, Zhi-Yong Fu

*Fujian Institute of Research on the Structure of Matter, Fuzhou, Fujian,
People's Republic of China, and Huaqiao University, Quanzhou, Fujian, People's Republic of China*

Xin-Tao Wu

*Fujian Institute of Research on the Structure of Matter,
Chinese Academy of Sciences, Fuzhou, Fujian, People's Republic of China*

CONTENTS

1. Introduction
 2. General Aspects of Design and Construction of Supramolecular Coordination Polymers
 3. Topology and Geometry of Supramolecular Coordination Polymers
 4. Conclusions
- Glossary
References

1. INTRODUCTION

Nanoscale science and technology are a fast-evolving field that has moved to the center of scientific and technological discoveries in recently decades. It is clear in this field that chemistry is a key to its rapid progress [1]. For chemists, and in particular inorganic chemists, widespread attention to the study of compounds in nanoscopic dimensions is being paid to supramolecular architectures, of which coordination polymeric supramolecular architectures are receiving much interest. There have been numerous reports on coordination polymers with novel architectures over the last decade. The interest in the realm of coordination frameworks is due to these compounds possessing fascinating structural diversity and potential applications as function materials [2–4]. The most common strategy for the design and fabrication of this class of framework is based upon the molecular self-assembly from metal ions and bridging ligand molecules containing N donors, such as 4,4'-bipyridine, pyrazine, and related species, and/or O donors, for instance, polycarboxylates, utilizing the spontaneous aggregation of small molecular building

blocks in a solution that recognize each other through multiple molecular recognition sites to generate extended architectures [5]. The challenge in this area is to manipulate building blocks and assemble them into desired architectures—0D, 1D, 2D, or 3D structures—so that the desired properties associated with nanostructural materials can be harvested. Since recent developments in coordination polymeric chemistry have partially alleviated this issue, it seems worthwhile to review the present state of the art. In this chapter, a number of aspects in this area are outlined and discussed in terms of the dimensionality of architectures.

2. GENERAL ASPECTS OF DESIGN AND CONSTRUCTION OF SUPRAMOLECULAR COORDINATION POLYMERS

2.1. From Molecular Building Block to Framework Construction

Like a skyscraper based on the construction of elementary building units, a supramolecular architecture can also be regarded as the aggregation of small molecular building blocks in terms of the local matching rules. A supramolecular architecture is aggregated from discrete small molecular building blocks either by strong coordination bonding or weaker interaction forces, including hydrogen bonding, π - π stacking, and van der Waals interaction. Some polydentate ligands with various geometric fashions are usually chosen as building blocks, including multifunctional organic compounds containing N donors, O donors, S donors, and cyano-donors species among others (Fig. 1), in the rational design and construction of desired supramolecular architectures. Information on the structural and functional features of these building blocks will translate to and store in the resulting supramolecular architectures, thus paving the

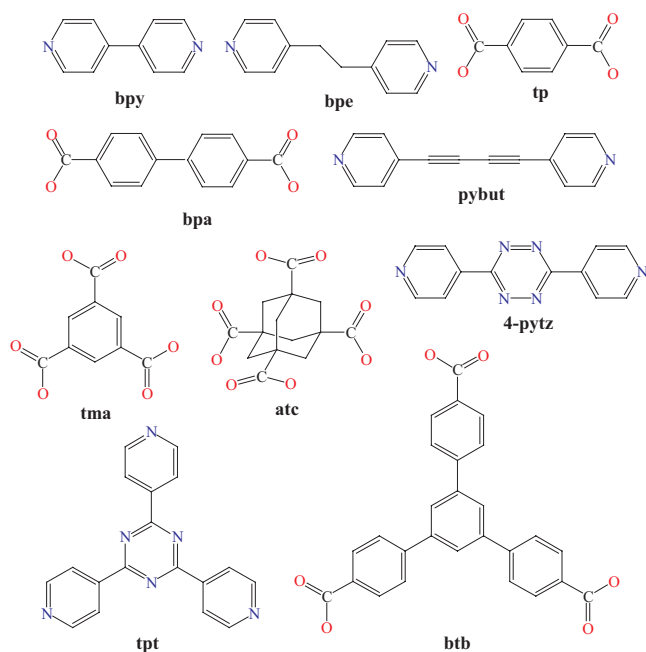


Figure 1. Several organic ligands as building blocks used for supramolecular architectures.

way for establishing connections between molecular building blocks and target structures or/and desired properties of supramolecular species [6]. Despite the final shape of the self-assembled entity being dependent on the metal coordination environment and the coordination orientation of the ligand [7], in fact, the blueprints for target architectures can be predicted in a significant way via the molecular building block approach. For instance, a 1D infinite chain structure in general results from the binding of a two-coordinated metal center and a linear ligand, while a diamondoid framework is commonly built by the tetrahedral coordinated metal center with a spacer ligand. The size and length of the tectonic ligands can also be directly used to offer clues for cavity prediction in some 3D architectures. Therefore, in principle, a limitless number of possibilities exist for the design and construction of supramolecular species with diverse intriguing architectures through exploiting the metal center coordination geometry and the size, shapes, and functionality of the molecular building blocks.

2.2. Structural Topology in Supramolecular Coordination Polymers

The topological conceptual approach offers an advantage for the geometrical exploration of coordination polymers. Structural topology has developed from inorganic network structures into the area of coordination polymeric supramolecular architectures during the past 20 years. From the topological viewpoint, a supramolecular architecture can be reduced to a series of nodes and links; thus, the topological concept used in describing networks is convenient for analyzing and understanding supramolecular architectures. This approach was well established by Wells [8–10] in the early 1990s, and was later developed by Robson and co-workers [11–13]. Complete technical descriptions of the topology of regular and semiregular networks can be found

in Wells's books [8–10] or other literature [14–17]. In this context, some intriguing topologies of supramolecular architectures as well as their novel geometrical structures will be illustrated and discussed in turn.

3. TOPOLOGY AND GEOMETRY OF SUPRAMOLECULAR COORDINATION POLYMERS

3.1. Discrete Coordination Polymers

Discrete coordination compounds are conceptually regarded as zero-dimensional architectures because of their structures showing isolated features. These zero-dimensional architectures have an important structural feature of nanoscopic dimensions in supramolecular chemistry. For example, Hong and co-workers [18] reported a novel metallosupramolecular cube cage coordination compound $[\text{Ni}_6(\text{tpst})_8\text{Cl}_{12}]$ (tpst = 2,4,6-tri[(4-pyridyl)-sulfanylmethyl]-1,3,5-triazine) with O_h symmetry, which possesses a volume of the inner cavity of about 1000 \AA^3 (Fig. 2). This interesting cage compound was synthesized by using the diethyl ether diffusing technique from the reaction of $\text{NiCl}_2 \cdot 6\text{H}_2\text{O}$ and a tpst ligand in a molar ratio of 3:4 in a dmf/MeCN (dmf = *N,N'*-dimethylformamide, MeCN = acetonitrile) medium, while the tpst ligand was designed and prepared from the reaction of 4-picolyl chloride hydrochloride and sodium trithiocyanurate in an MeCN solution [18]. Most structures of these discrete coordination compounds are architectures related to Platonic or Archimedean polyhedra [7, 19–21]. Recently, we demonstrated that the *in-situ* reaction of $\text{Pb}(\text{NO}_3)_2$ with di-2-pyridyl ketone in a molar ratio of 1:1 in water gave a discrete coordination compound, $[\text{Pb}_4(\text{HL})_4] \cdot 8\text{OH} \cdot 5\text{H}_2\text{O}$ ($\text{H}_2\text{L} = (2\text{-C}_5\text{H}_4\text{N})_2\text{C}(\text{OH})_2$), with a disordered Platonic-like structure [22]. In this compound, the bridging ligand H_2L is a hydrolysate of the reactant of di-2-pyridyl ketone, bonding 4-coordinated lead centers by its N donors and O atoms to generate a cubane structure. The IR spectrum of this compound shows that the peaks of the H_2L ligand at $3450, 3020, 1595, 1439, 1383, 1286,$ and 1011 cm^{-1} , and the absence of the expected peak at 1710 cm^{-1} attributed to the carbonyl group are in good agreement with

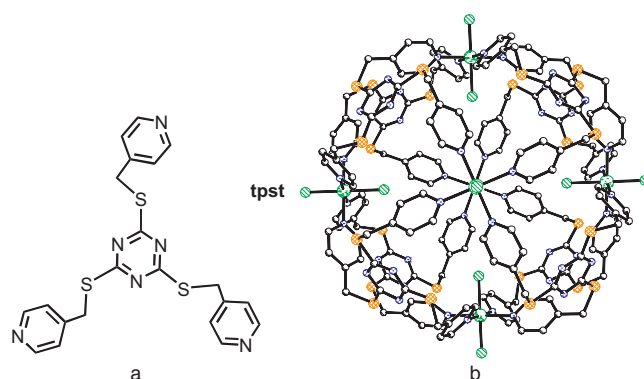


Figure 2. (a) tpst ligand. (b) A nanometer-size metallosupramolecular cube cage— $[\text{Ni}_6(\text{tpst})_8\text{Cl}_{12}]$. Reprinted with permission from [18], M. C. Hong et al., *J. Am. Chem. Soc.* 122, 4819 (2002). © 2000, American Chemical Society.

their crystal structure. Interestingly, some discrete coordination compounds also exhibited infinite architecture via weaker interaction forces. For instance, Chen's group [23] recently described an excellent example of this category of architecture, $[\text{Cu}_2(\text{bpa})_2(\text{phen})_2(\text{H}_2\text{O})_2] \cdot 2\text{H}_2\text{O}$ (bpa = 4,4'-biphenyldicarboxylate, phen = 1,10-phenanthroline), in which each discrete molecular rhombus unit is further interlocked via an aromatic π - π stacking interaction to form a 2D polyrotaxane networks (Fig. 3). This excellent compound came from the product of a simple hydrothermal reaction of $\text{Cu}(\text{NO}_3)_2$, phen, H_2bpa , and Et_3N in a molar ratio of 1:1:1:2 in 10 mL water at 140 °C for 7 days [23].

3.2. One-Dimensional Infinite Chain Coordination Polymers

One-dimensional infinite chains are the most common and simple architectures in coordination polymeric solids. However, even for these commonly one-dimensional infinite

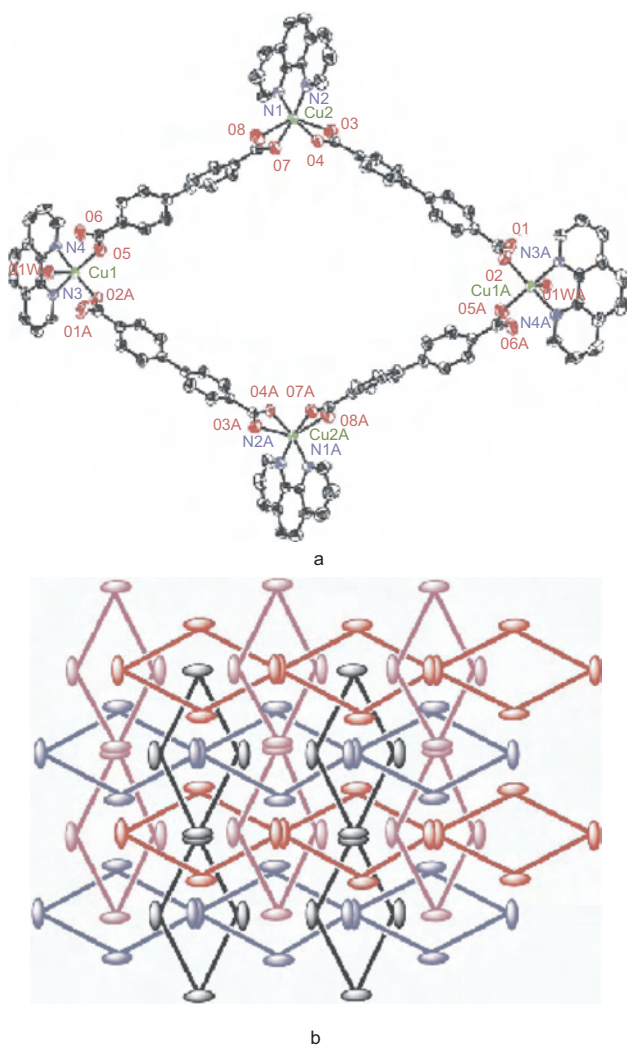


Figure 3. (a) Discrete molecular rhombus of $[\text{Cu}_2(\text{bpa})(\text{phen})]_4$. (b) Schematic presentation of 2D polyrotaxane networks via an aromatic π - π stacking interaction in the compound $[\text{Cu}_2(\text{bpa})_2(\text{phen})_2(\text{H}_2\text{O})_2] \cdot 2\text{H}_2\text{O}$. Reprinted with permission from [23], G.-F. Liu et al., *Chem. Commun.* 1442 (2002). © 2002, Royal Society of Chemistry.

chain polymers, there are still many diversities and intriguing structural features. Generally, there have been five structural types, illustrated schematically in Figure 4, of polymeric solids found in one-dimensional infinite chains: (a) linear chain [24–31], (b) zigzag chain [32–39], (c) helical chain [40–54], (d) molecular ladder [55–66], and (e) molecular railroad [67–69].

3.2.1. Linear Chain Polymers

The linear chain is generally the simplest structural motif for 1D polymers; for example, the hydrothermal reaction of MnCl_2 , 1,3-bis(4-pyridyl)propane (bpp), terephthalate (tp), sodium methoxide, and water in a molar ratio of 1:1:1:2:556 results in a 1D linear chain polymer $\{[\text{Mn}(\text{bpp})_2(\text{tp})] \cdot 2\text{H}_2\text{O}\}_n$ [29]. In this polymer, the Mn centers are bridged to generate a linear infinite chain by tp ligand molecules (Fig. 5). It is rather stable until 200 °C from evidence of the TGA trace [29]. Lu and co-workers [26] prepared another similar 1D linear infinite chain polymer, $[(\text{H}_2\text{O})_2\text{M}(\text{bpy})(\text{bpen})_2] \cdot 1.75(\text{bpen}) \cdot 0.25(\text{bpy}) \cdot 2\text{NO}_3 \cdot 4.45\text{H}_2\text{O}$ (bpy = 4,4'-bipyridine; bpen = *trans*-1,2-bis(4-pyridyl)ethylene; M = Zn, Cd), from the reaction of hydrated $\text{M}(\text{NO}_3)_2$, bpy, and bpen in a molar ratio of 1:1:2 under hydrothermal conditions at 120 °C for 3 days. This polymeric chain possesses unbalanced inclusion guest species (Fig. 6a), and has interestingly been fabricated into nanofibers with the diameter ranging from 60 nm to 4 μm by electrospinning (Fig. 6b).

However, although 1D linear chain polymers are usually the simplest, there are many permutations in the packing feature of these linear chains. Schroder's group [27] described an interesting example of a helical staircase structure formed by a linear chain polymer, $\{[\text{Ag}(4\text{-pytz})\text{NO}_3]\}_n$ (4-pytz = 1,4-bis-(4-pyridyl)-2,3,4,5-tetrazine), obtained from the reaction of AgNO_3 with 4-pytz in a molar ratio of 1:1.07 in a 3 mL MeCN/10 mL CH_2Cl_2 medium. Because of the weak interaction between Ag-pytz chains and NO_3^- anions, adjacent linear Ag-pytz chains are twisted by 60° to stack an excellent helical staircase structure. Suh's group [30] presented another example of a 1D linear chain stacking polymer, $[\text{Ni}(\text{C}_{12}\text{H}_{30}\text{N}_6\text{O}_2)(\text{tp})]_n \cdot 4n\text{H}_2\text{O}$ (Fig. 7). In this polymer, 1D linear chains (Fig. 7b) are formed by a macrocyclic complex $[\text{Ni}(\text{C}_{12}\text{H}_{30}\text{N}_6\text{O}_2)](\text{ClO}_4)_2$ (Fig. 7a) and a tp ligand, and they are packed together to give rise to a 3D plywood-like network by the hydrogen bonding interactions (Fig. 7c). This compound is stable upon

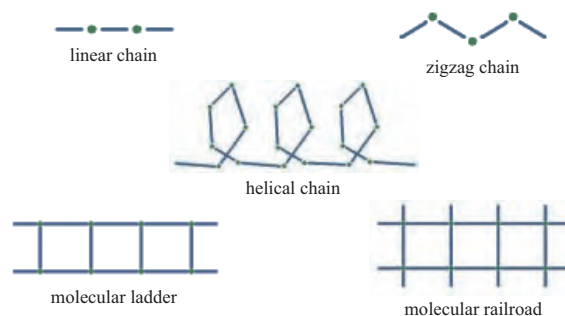


Figure 4. Schematic representation of five 1D infinite chain motifs observed in coordination polymers.

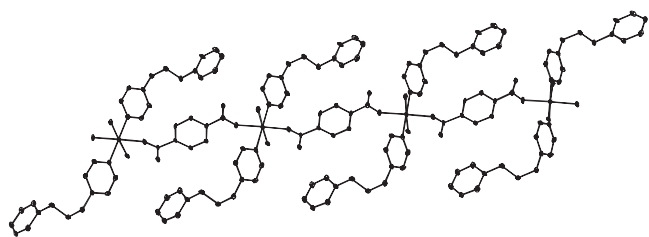
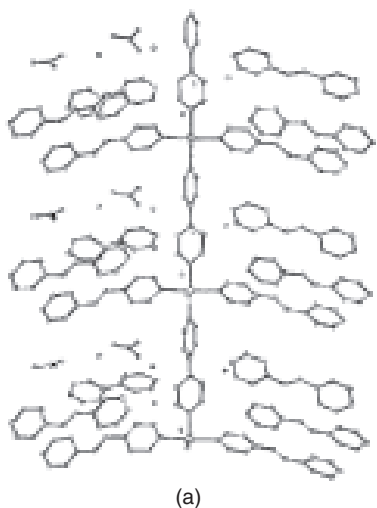
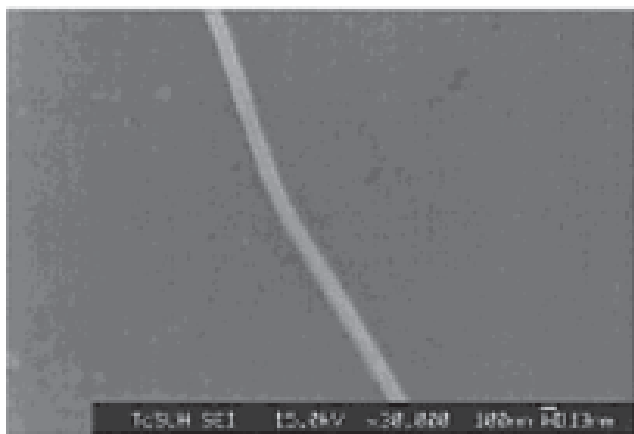


Figure 5. 1D linear chain polymer $\{[\text{Mn}(\text{bpy})_2(\text{tp})] \cdot 2\text{H}_2\text{O}\}_n$.

exposure to the atmosphere, and its IR spectrum shows peaks at 1563 and 1376 cm^{-1} , implying the tp ligand in the unidentate head-to-tail bonding fashion [30]. Hong and co-workers [31] reported an unprecedented linear infinite chain polymer, $[\text{Ag}_7(\text{tpst})_4(\text{ClO}_4)_2(\text{NO}_3)_5]_n$, containing nanosized tubes shown in Figure 8, which were obtained by using the diethyl ether diffusing technique from the reaction of AgNO_3 with tpst in a ratio of 2:1 in dmf/MeOH followed by the addition of AgClO_4 . This novel 1D chain polymer is formed by the basic nanosized tube unit $[\text{Ag}_7(\text{tpst})_4]$ with a

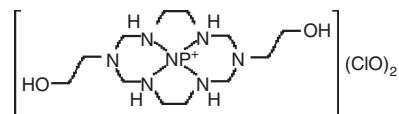


(a)

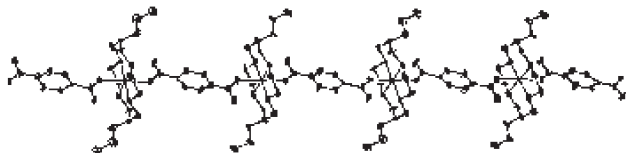


(b)

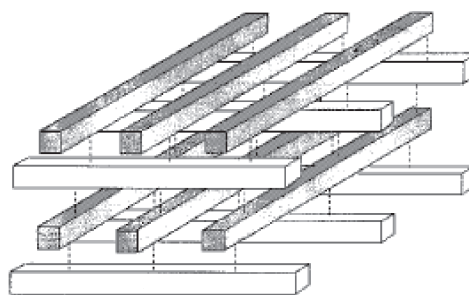
Figure 6. (a) 1D linear chain polymer $[(\text{H}_2\text{O})_2\text{Zn}(\text{bpy})(\text{bpen})_2] \cdot 1.75(\text{bpen}) \cdot 0.25(\text{bpy}) \cdot 2\text{NO}_3 \cdot 4.45\text{H}_2\text{O}$. (b) Its SEM image of electro-spun nanofiber. Reprinted with permission from [26], J. Y. Lu et al., *Inorg. Chem.* 40, 4516 (2001). © 2001, American Chemical Society.



a



b



c

Figure 7. (a) Macrocyclic complex $[\text{Ni}(\text{C}_{12}\text{H}_{30}\text{N}_6\text{O}_2)](\text{ClO}_4)_2$. (b) 1D linear chain polymer $[\text{Ni}(\text{C}_{12}\text{H}_{30}\text{N}_6\text{O}_2)(\text{tp})]_n \cdot 4n\text{H}_2\text{O}$. (c) 3D plywood-like network stacked by 1D linear chain polymer $[\text{Ni}(\text{C}_{12}\text{H}_{30}\text{N}_6\text{O}_2)(\text{tp})]_n \cdot 4n\text{H}_2\text{O}$. Reprinted with permission from [30], H. J. Choi and M. P. Suh, *Inorg. Chem.* 38, 6309 (1999). © 1999, American Chemical Society.

size of $13.4 \times 9.6 \times 8.9 \text{ \AA}$ through sharing silver atoms, in which each basic nanosized tube unit $[\text{Ag}_7(\text{tpst})_4]$ encapsulates two dmf molecules and two perchlorate anions (Fig. 8a).

3.2.2. Zigzag Chain Polymers

The zigzag chain is another simple structural motif found in the 1D infinite polymeric compounds. A primary factor resulting in 1D zigzag chain polymers comes from the coordinated orientation of the metal center. Some representative examples [35] are shown in Figure 9. In these examples, each metal center is coordinated at a certain angle by two μ_2 -bridging ligands to form a zigzag chain. For the first case, 5-coordinated zinc centers are chelated by three nitrogen donors of the terminal ligand 2, 4, 6-tri(2-pyridyl)-s-triazine (tptz), and the remaining two coordination sites are bridged to two linear μ_2 -bpa ligands, resulting in a 1D infinite zigzag polymer $\{[\text{Zn}(\text{tptz})(\text{bpa})] \cdot 4.5\text{H}_2\text{O}\}_n$ (Fig. 9a). Similar to the above case, 2-aminoterephthalate (2-atp) is used as a bridging ligand instead of a bpa molecule to link the 7-coordinated Cd centers to form another zigzag chain example $\{[\text{Cd}(\text{tptz})(2\text{-atp})] \cdot 3\text{H}_2\text{O}\}_n$ (Fig. 9b). The final case of a 1D zigzag chain polymer, $\{[\text{Cd}(\text{tp})] \cdot 7\text{H}_2\text{O}\}_n$, results from a 7-coordinated Cd center chelated by two μ_2 -tp bridging ligands (Fig. 9c). All three polymers were synthesized by hydrothermal reactions

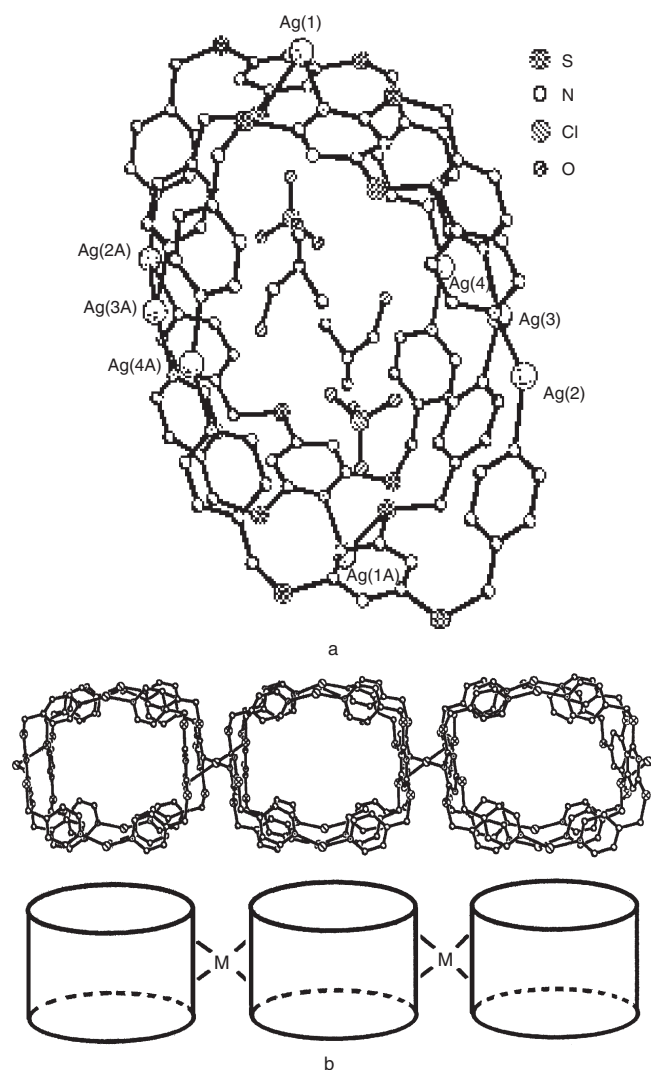


Figure 8. (a) Basic nanosized tube unit $[\text{Ag}_7(\text{tpst})_4]$. (b) 1D linear chain polymer $[\text{Ag}_7(\text{tpst})_4(\text{ClO}_4)_2(\text{NO}_3)_5]_n$. Reprinted with permission from [31], M. C. Hong et al., *Angew Chem., Int. Ed.* 39, 2468 (2000). © 2000, Wiley-VCH Verlag GmbH.

of metal salt with organic ligands at 160 °C [35]. The geometric configuration of a bridging ligand is another important factor for generating 1D zigzag chain polymers. For example, Yaghi's group [37] presented 1D zigzag chain polymers, $\{\text{M}_3(\text{tma})_2 \cdot 12\text{H}_2\text{O}\}$ ($\text{M} = \text{Zn}, \text{Co}, \text{Ni}$; tma = trimesate), fabricated by 6-coordinated metal centers and a tma ligand, a paddle-like molecule. Guilloa's group [39] also documented another similar 1D zigzag chain polymer, $\{[\text{Er}(\text{tma})(\text{H}_2\text{O})_5] \cdot 3.5\text{H}_2\text{O}\}$. These two polymeric crystals were, respectively, obtained by hydrothermal synthesis [37] and by the agar-agar gel crystal growing technique [39].

3.2.3. Helical Chain Polymers

The interest in helical structures of coordination polymers is triggered by examples from nature-like DNA double chains in biology and some helical arrays in pharmacology. The most notable has been the synthesis of chiral helical chain polymers. A representative example is the structure of a 1D chiral helical chain polymer, $\{\text{Ag}[(\text{R,R})\text{-DIOP}(\text{NO}_3)]\}_n$.

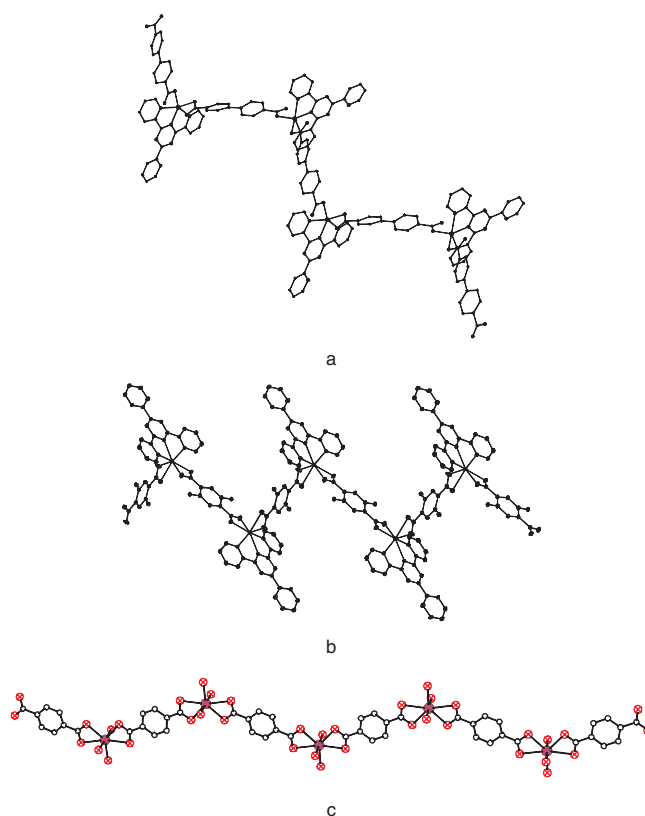


Figure 9. Several examples of 1D zigzag chain polymers. (a) $\{[\text{Zn}(\text{tpzt})(\text{bpa})] \cdot 4.5\text{H}_2\text{O}\}_n$. (b) $\{[\text{Cd}(\text{tpzt})(2\text{-atp})] \cdot 3\text{H}_2\text{O}\}_n$. (c) $\{[\text{Cd}(\text{tp})] \cdot 7\text{H}_2\text{O}\}_n$.

(DIOP=(4R,5R)-*trans*-4,5-bis(diphenylphosphinomethyl)-2,2-dimethyl-1,3-ioxalane) [40]. This polymer was prepared by the reaction of a chiral ligand (R,R)-DIOP and AgNO_3 with an equimolar ratio in methanol media. Its structure consists of an Ag atom coordinated by two P atoms of two adjacent ligands and an O atom of nitrate. The polymer exhibits a chiral right-handed helical array. Another remarkable example of a 1D chiral helical chain polymer, $\{\text{Ni}(\text{bpy})(\text{benzoic})_2(\text{MeOH})_2\} \cdot \text{nitrobenzene}\}_n$, was described by Zaworotko's group [41], as shown in Figure 10. This polymer is grown as a crystal by dissolving nickel acetate and benzoic acid in MeCN and layering with a solution of bpy in MeCN and is surprisingly a chiral double-helical chain generated from simple and achiral building block [41].

Interestingly, a novel helix, $[\text{NC}_5\text{H}_4\text{CN}_4\text{Sn}(\text{C}_2\text{H}_5)_3]_n$, with a very long pitch of screws (40 Å) was described by Bhandari and co-workers [42], as shown in Figure 11. This infinite helical chain was obtained by the cycloaddition reaction of Et_3SnN_3 and 4-cyanopyridine. Even more interesting, the helical structures are still rare in the coordination polymers to date [40–54].

3.2.4. Molecular Ladder, Molecular Railroad Polymers, and Interpenetrating Structures

Molecular ladder [55–66] polymers represent another type of 1D infinite architectures that are different from the above chain motifs in coordination chemistry. Molecular railroads

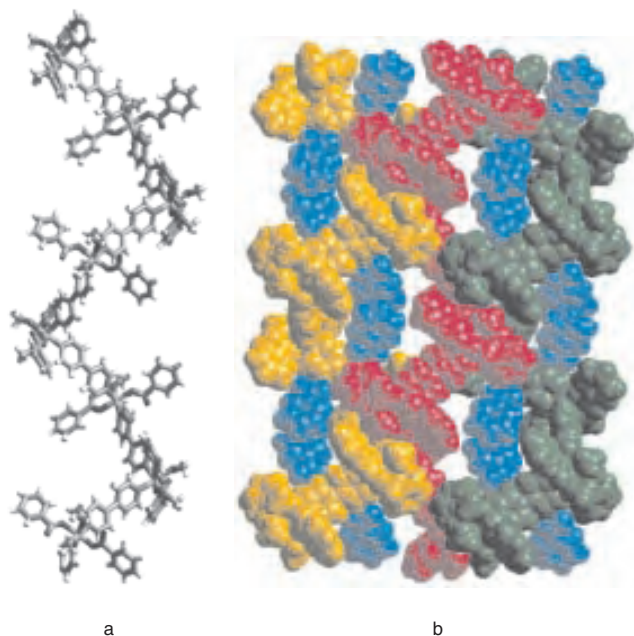


Figure 10. 1D chiral double-helical chain polymer $\{\text{Ni}(\text{bpy})\cdot(\text{benzoic})_2(\text{MeOH})_2\} \cdot \text{nitrobenzene}_n$. (a) Chiral helical structure. (b) Double-helical array. Reprinted with permission from [41], K. Biradha et al., *Angew Chem., Int. Ed. Engl.* 38, 492 (1999). Wiley-VCH Verlag GmbH.

[67–69] are one case of the peculiar molecular ladders, which are ladders bearing additional ligands as sidearms. Generally, most of the molecular ladders [55–65] occur in a T-shaped unit from the quasioctahedral or octahedral geometry of metal centers and rod-like ligands, accompanied by the interpenetrating phenomenon. A remarkable example of the molecular ladder, $\{\text{Cd}(\text{pybz})_{1.5} \cdot (\text{NO}_3)_2\}$ (pybz = 1,4-bis(4-pyridylmethyl)benzene), was reported by Fujita and co-workers [56, 57], as shown in Figure 12, which is a result of allowing an ethanol/water solution of $\text{Cd}(\text{NO}_3)_2$ with pybz in a molar ratio of 2:3 to stand for 10 days at 20 °C [56]. This ladder is generated by a T-shaped unit composed of a 7-coordinated Cd(II) center and three pybz ligands. It is interesting that these ladders are incline interpenetrated to each other to produce a 3D network in the crystal. Figure 13 shows another rare example of a molecular ladder, $\{[\text{Cu}_2(\text{MeCN})_2(\text{pybut})_3](\text{PF}_6)_2\}_n$ (pybut = 1,4-bis(4-pyridyl)butadiyne), based upon tetrahedral coordinated Cu(I) centers and pybut ligands (Fig. 13a), described by Schroder's group [66]. This novel ladder was isolated by layering with diethyl ether diffusing to a deep red solution formed by the reaction of $[\text{Cu}(\text{MeCN})_4]\text{PF}_6$ with pybut in a molar ratio of 1:4 in MeCN/ CH_2Cl_2 media [66]. It displays a 2D network produced by the undulating fivefold interpenetration array (Fig. 13b,c), which was regarded as parallel interpenetration [70–72]. The first molecular railroad polymer, $\{\text{Ni}(\text{bpy})_{2.5}(\text{H}_2\text{O})_2 \cdot (\text{bpy})_{1.5}(\text{ClO}_4)_2(\text{H}_2\text{O})\}$, which was comprised of the same inner rungs and sidearms, was reported by Yaghi and co-workers [68]. A similar molecular railroad polymer was later presented by Ciani's group [67]. It is interesting that molecular railroad polymer were expanded to have different inner rungs and sidearms

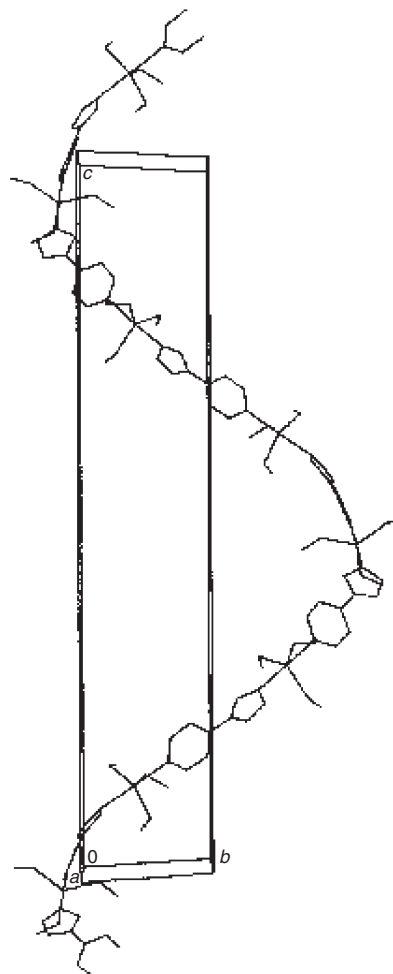


Figure 11. 1D helical chain polymer $[\text{NC}_5\text{H}_4\text{CN}_4\text{Sn}(\text{C}_2\text{H}_5)_3]_n$. Reprinted with permission from [42], S. Bhandari et al., *J. Chem. Soc., Dalton Trans.* 663 (2000). © 2000, Royal Society of Chemistry.

by Chen's group [69]—they prepared two novel railroad polymers, $[\text{M}_2(\text{bpy})_3(\text{H}_2\text{O})_2(\text{phba})_2](\text{NO}_3)_2 \cdot 4\text{H}_2\text{O}$ (M = Cu or Co, phba = 4-hydroxy benzoate), by slowly adding bpy and then phba to a solution of $\text{M}(\text{NO}_3)_2$ in methanol/water media at 60 °C, as shown in Figure 14.

3.3. Two-Dimensional Network Coordination Polymers

In comparison with 1D infinite architectures, 2D network coordination polymers are more complicated supramolecular structures. Some of the 2D architectures, such as the



Figure 12. Molecular ladder $\{\text{Cd}(\text{pybz})_{1.5}(\text{NO}_3)_2\}$. Reprinted with permission from [56], M. Fujita et al., *J. Am. Chem. Soc.* 117, 7287 (1995). © 1995, American Chemical Society.

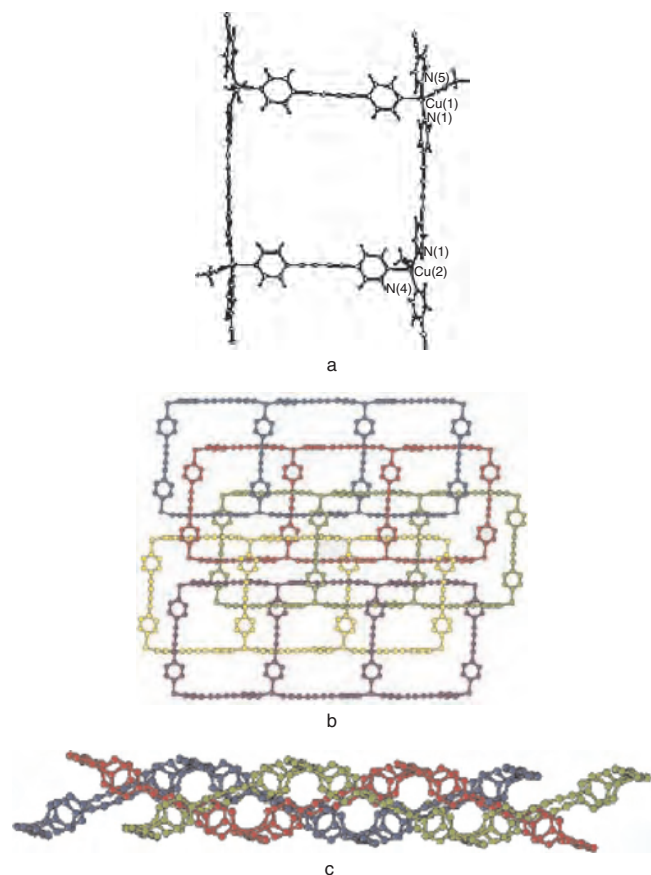


Figure 13. Molecular ladder $\{[\text{Cu}_2(\text{MeCN})_2(\text{pybut})_3](\text{PF}_6)_2\}_n$. (a) Tetrahedral coordinated Cu(I) center. (b) Parallel 2D interpenetration (top view). (c) Undulating nature (side view). Reprinted with permission from [66], A. J. Blake et al., *Chem. commun.* 2027 (1997). © 1997, Royal Society of Chemistry.

square grid [73–85], brick wall [56, 73, 86–92], herringbone [58, 93–95], and bilayer [96–103], have been realized in coordination polymer chemistry.

3.3.1. Square-Grid and 4^4 Networks

Square-grid networks, regarded topologically as a simple 4^4 net, are commonly structural motifs observed in 2D architectures. The first square-grid polymers based on bipyridine ligands were reported by Fujita's group [73]. Many similar square-grid polymers were subsequently prepared by using a bipyridine ligand or related species [74–84]. The polymers $\{[\text{Cd}(\text{bpy})_2(\text{NO}_3)(\text{H}_2\text{O})] \cdot \text{NO}_3 \cdot (4\text{-abp})_2\}_n$ and $\{[\text{Cd}(\text{bpp})_2(\text{H}_2\text{O})_2] \cdot 2\text{H}_2\text{O} \cdot 2\text{NO}_3 \cdot (4\text{-abp})\}_n$ (4-abp = 4-aminobeneophenone) [84], formed by transition metal centers and bipyridine species ligands, are two examples of such grid networks. Both grids were obtained from the reaction of $\text{Cd}(\text{NO}_3)_2$ with bpy or bpp and 4-abp in a molar ratio of 1:1:1 in methanol/water media at room temperature. The IR spectra and ^1H NMR spectra show that the grid compound $\{[\text{Cd}(\text{bpy})_2(\text{NO}_3)(\text{H}_2\text{O})] \cdot \text{NO}_3 \cdot (4\text{-abp})_2\}_n$ comprises bpy and 4-abp in a 1:1 ratio, and the compound $\{[\text{Cd}(\text{bpp})_2(\text{H}_2\text{O})_2] \cdot 2\text{H}_2\text{O} \cdot 2\text{NO}_3 \cdot (4\text{-abp})\}_n$ comprises bpp and 4-abp in a 2:1 ratio, which is in good agreement with their crystal structures [84]. It is notable that these

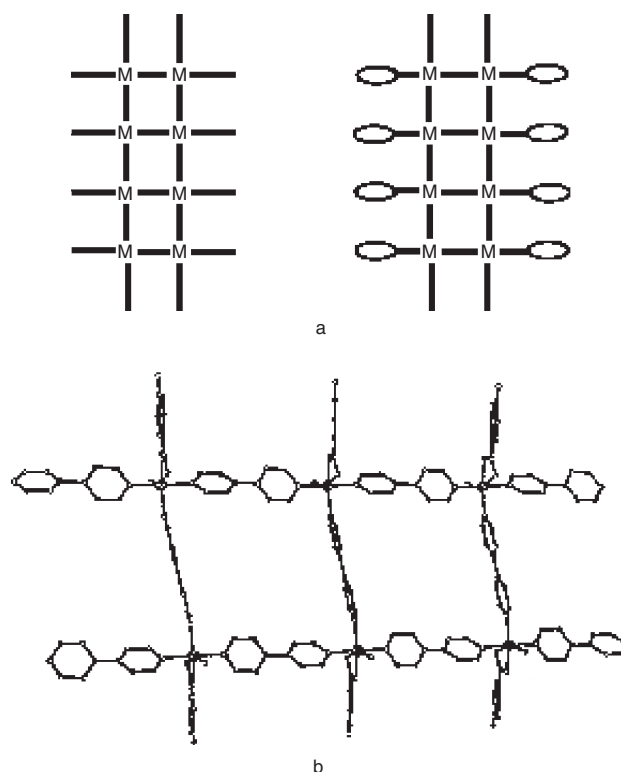


Figure 14. (a) Molecular railroad models with the same inner rungs and sidearms (left), and with different inner rungs and sidearms (right). (b) Molecular railroad polymer $[\text{Cu}_2(\text{bpy})_3(\text{H}_2\text{O})_2(\text{phba})_2](\text{NO}_3)_2 \cdot 4\text{H}_2\text{O}$ having different inner rungs and sidearms. Reprinted with permission from [69], M.-L. Tong et al., *Inorg. Chem.* 39, 2235 (2000). © 2000, American Chemical Society.

two grids possess cavities of about 11.772×11.779 and 10.119×24.233 Å, respectively, and encapsulate an acentric guest molecule—4-abp—and other nitrate and aqua guest molecules. This is significant for providing a robust approach for the design and preparation of nonlinear photoelectronic materials.

Square-grid networks are not just limited to the coordination polymers of bipyridine species ligands. Some linear multifunctional ligands, for example, terephthalate and even trimesate, also can be used to construct grid networks. We have recently demonstrated two examples of grid networks [85] formed by polycarboxylate ligands or hybrid ligands, that is, $\{[\text{Cd}(\text{Htma})(\text{bpy})] \cdot (\text{H}_2\text{tp})_{0.5} \cdot 3\text{H}_2\text{O}\}_n$ and $[\text{Cd}(\text{tp})(\text{bpp})]_n$, as shown in Figure 15. Both polymeric grid networks originate from the products of the hydrothermal reaction of cadmium acetate with polyaromatic acids (H_3tma or H_2tp) and bipyridine species (bpy or bpp) at 200 °C for 4 days. Although these two square-grid networks are topologically isostructures, their structural features are very different because of the difference in the host–guest interaction, interpenetration, stacking fashions, and so on. In the polymer $\{[\text{Cd}(\text{Htma})(\text{bpy})] \cdot (\text{H}_2\text{tp})_{0.5} \cdot 3\text{H}_2\text{O}\}_n$, the interdigitation of the lateral tma ligands from two adjacent 4^4 networks via aromatic π – π interaction and host–guest molecular recognition gives rise to a novel 2D bilayer supramolecular architecture (Fig. 15a), while the polymer $[\text{Cd}(\text{tp})(\text{bpp})]_n$ shows a twofold parallel 2D interpenetration

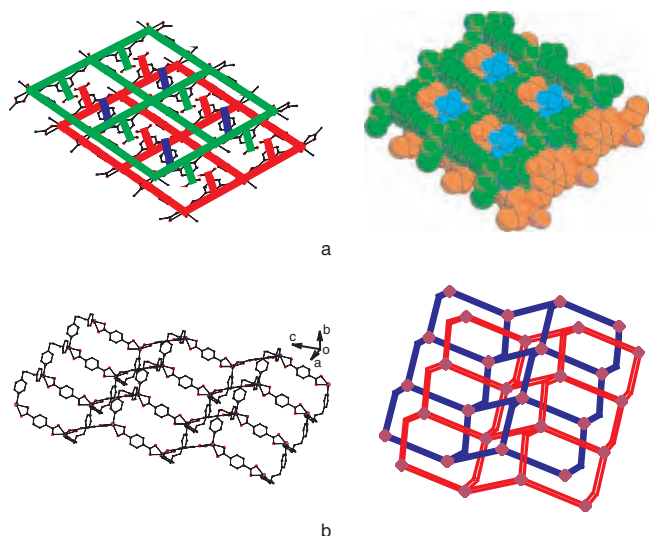


Figure 15. (a) Interdigitation of the lateral tma ligands from two adjacent 4^4 networks via aromatic π - π interaction and host-guest molecular recognition gives rise to a novel 2D bilayer supramolecular architecture fabricated by the polymer $\{[\text{Cd}(\text{Htma})(\text{bpy})] \cdot (\text{H}_2\text{tp})_{0.5} \cdot 3\text{H}_2\text{O}\}_n$. (b) Twofold parallel 2D interpenetration model of 4^4 networks in the polymer $[\text{Cd}(\text{tp})(\text{bpy})]_n$.

model (Fig. 15b) [72]. The elemental analysis data and IR spectra for the two polymers are also consistent with their formulas and their crystal structures, of which the appearance of peaks at 1714 and 1695 cm^{-1} in the polymer $\{[\text{Cd}(\text{Htma})(\text{bpy})] \cdot (\text{H}_2\text{tp})_{0.5} \cdot 3\text{H}_2\text{O}\}_n$ confirms the existence of protonated carboxylate groups in this compound. The TGA traces of the two compounds show that decomposition of the first compound occurs in the 383–538 $^\circ\text{C}$ range and that of the latter in the 297–524 $^\circ\text{C}$ range. Interestingly, the intense fluorescent emission spectra of two polymers at 360, 416, 481, and 513 nm ($\lambda_{\text{ex}} = 311$ nm) for the first compound and at 414 nm ($\lambda_{\text{ex}} = 315$ nm) for the latter compound were observed in the solid state at room temperature, implying that both grid network compounds may be excellent candidates for potential photoactive materials.

3.3.2. Brick-Wall, Herringbone, and 6^3 Networks

From the topological viewpoint, brick-wall and herringbone, as well as honeycomb [92] structural motifs, illustrated schematically in Figure 16, all belong to the 6^3 networks of isostructures, in which the brick-wall and herringbone motifs

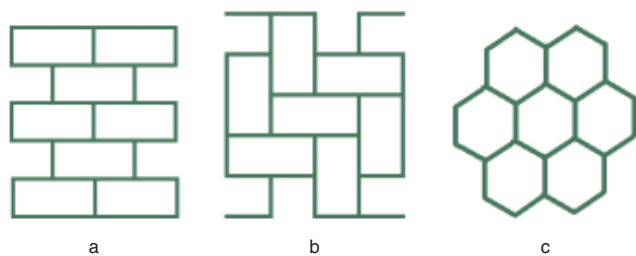


Figure 16. (a) Molecular brick wall. (b) Molecular herringbone. (c) Molecular honeycomb.

are both composed of T-shaped building blocks. The first example of a brick-wall architecture was reported by Fujita et al. [56, 73]. They prepared a molecular brick-wall polymer, $\{[\text{Cd}(\text{pytf})_{1.5}](\text{NO}_3)_2\}_n$ ($\text{pytf} = 1, 4$ -bis[(4-pyridyl)methyl]-2,3,5,6-tetrafluorophenylene), from 7-coordinated Cd(II) cations and pytf molecules in a molar ratio of 2:3 in an ethanol/water solution at 20 $^\circ\text{C}$ for 3 days [56], as shown in Figure 17. This brick-wall displays a triple interpenetration of a 2D sheet architecture. Many examples of analogs of the molecular brick-wall have since been reported by several groups [86–92]. Suh's group [92] demonstrated another example of the brick-wall architecture, $\{[\text{Ni}(\text{C}_{12}\text{H}_{30}\text{N}_6\text{O}_2)]_3(\text{tma})_2 \cdot 18\text{H}_2\text{O}\}_n$ (Fig. 18a), which originate from the reaction product of macrocyclic complex $[\text{Ni}(\text{C}_{12}\text{H}_{30}\text{N}_6\text{O}_2)](\text{ClO}_4)_2$ (also see Fig. 7a) and a tma ligand in dmf/water media by using diffusion techniques. It is notable that the T-shaped unit in this compound is formed by a tma molecule, which differs from that of most brick-wall architectures. Interestingly, adding pyridine in this reaction system will result in a molecular honeycomb 6^3 network, $\{[\text{Ni}(\text{C}_{12}\text{H}_{30}\text{N}_6\text{O}_2)]_3(\text{tma})_2 \cdot 14\text{H}_2\text{O} \cdot 2\text{C}_5\text{H}_5\text{N}\}_n$, which is still rare to date [71] (Fig. 18b). They also demonstrated that the paramagnetic Ni(II) centers of both polymers weakly couple antiferromagnetically through the tma bridges by the investigation of magnetic behaviors (χ_M data) [92].

The herringbone architecture has already been observed in many coordination polymers [58, 89, 93–95]. Figure 19 shows a representative example of a herringbone, polymer $\{\text{Cd}_2(\text{azopy})_3(\text{NO}_3)_4\}_n$ ($\text{azopy} = \text{trans-4,4'}$ -azobis(pyridine)), prepared by Ciani's group [58]. This polymer is obtained from the resulting crystal grown for several days by layering over a solution of cadmium nitrate in acetone with a solution of azpy in dichloromethane in a molar ratio of 3:7, and also displays triply parallel interpenetration of a 2D sheet architecture (Fig. 19b), analogous to Fujita's brick-wall architecture [56].

3.3.3. Bilayer Polymers

The molecular bilayer is a novel structural motif that is still limited [96–103]. Usually, the bilayer architectures are fabricated in the assembly product of a T-shaped building block. The first example of a molecular bilayer in

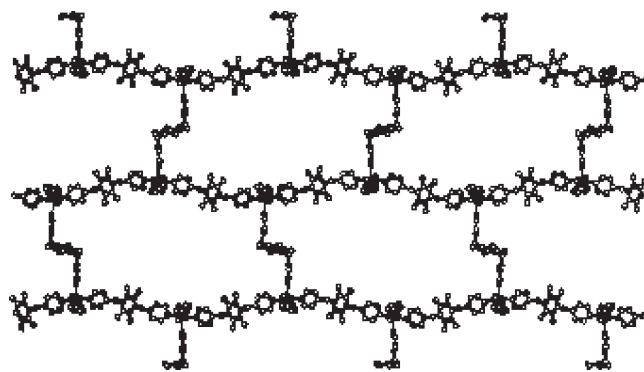


Figure 17. Brick-wall architecture of the polymer $\{[\text{Cd}(\text{pytf})_{1.5}](\text{NO}_3)_2\}_n$. Reprinted with permission from [56], M. Fujita et al., *J. Am. Chem. Soc.* 117, 7287 (1995). © 1995, American Chemical Society.

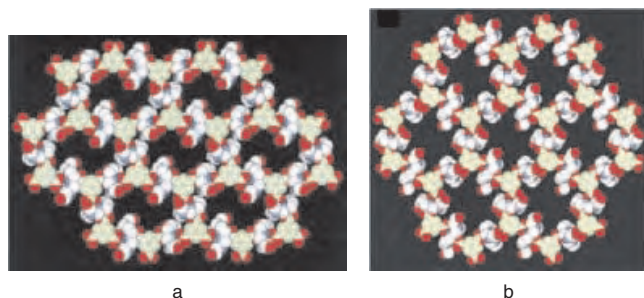


Figure 18. (a) Molecular brick-wall polymer $\{[\text{Ni}(\text{C}_{12}\text{H}_{30}\text{N}_6\text{O}_2)_3 \cdot (\text{tma})_2 \cdot 18\text{H}_2\text{O}]_n\}$. (b) Molecular honeycomb polymer $\{[\text{Ni}(\text{C}_{12}\text{H}_{30}\text{N}_6\text{O}_2)_3(\text{tma})_2 \cdot 14\text{H}_2\text{O} \cdot 2\text{C}_5\text{H}_5\text{N}]_n\}$. Reprinted with permission from [92], H. J. Choi and M. P. Suh, *J. Am. Chem. Soc.* 120, 10622 (1998). © 1998, American Chemical Society.

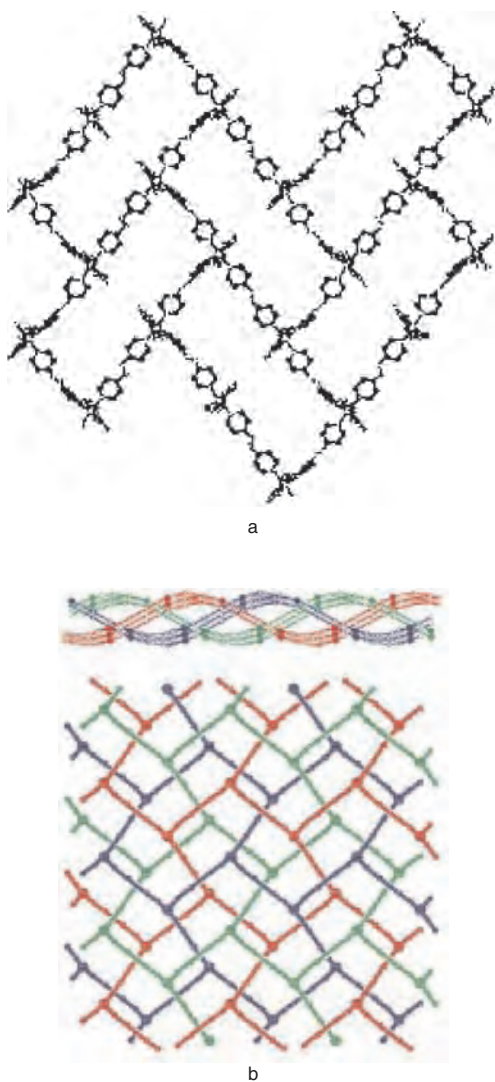


Figure 19. Polymer $\{\text{Cd}_2(\text{azopy})_3(\text{NO}_3)_4\}_n$. (a) Herringbone architecture. (b) Threefold parallel interpenetration. Reprinted with permission from [58], L. Carlucci et al., *Dalton Trans.* 1799 (1999). © 1999, Royal Society of Chemistry.

the polymer $\{[\text{Co}(\text{bpy})_{1.5} \cdot (\text{NO}_3)_2] \cdot \text{CS}\}_n$ was presented by Zaworotko's group [96], prepared through a solution reaction of stoichiometric ratio, in which polymer adjacent bilayers pack in a gear-like fashion. A similar molecular bilayer in the polymer $\{[\text{Cd}_3(\text{tma})_2] \cdot 13\text{H}_2\text{O}\}_n$ (Fig. 20) [97] was obtained from the hydrothermal reaction of cadmium acetate, trimesic acid, and sodium terephthalate in a molar ratio of 3:1:2 at 180 °C for 2 days, in which the polymer exhibits a threefold interdigitation fashion. It is notable that this bilayer consists of two different Cd(II) centers that are linked by tma ligands, in which one Cd(II) center is 5-coordination, and the other Cd(II) belongs to 7-coordination. So the T-shaped unit in this compound is served by a tma molecule rather than the coordinated geometry of metal centers found in other bilayer architectures [96, 98–102]. The TGA trace shows that this bilayer polymer is stable up to 246 °C [97]. Recently, an interesting example of a bilayer architecture, $\{[\text{Ag}(\text{bpe})(\text{bpa})_{0.5}] \cdot \text{H}_2\text{O}\}_n$ (bpe = 1, 2-bis(4-pyridyl)ethane), resulting from the hydrothermal reaction of AgNO_3 , bpe, bpa, and sodium methoxide was formulated [98]. This bilayer architecture displays an unusual fivefold entanglement, and its actual crystal structure belongs to a kind of 2D → 3D parallel interpenetration of “thick” layers, as shown in Figure 21.

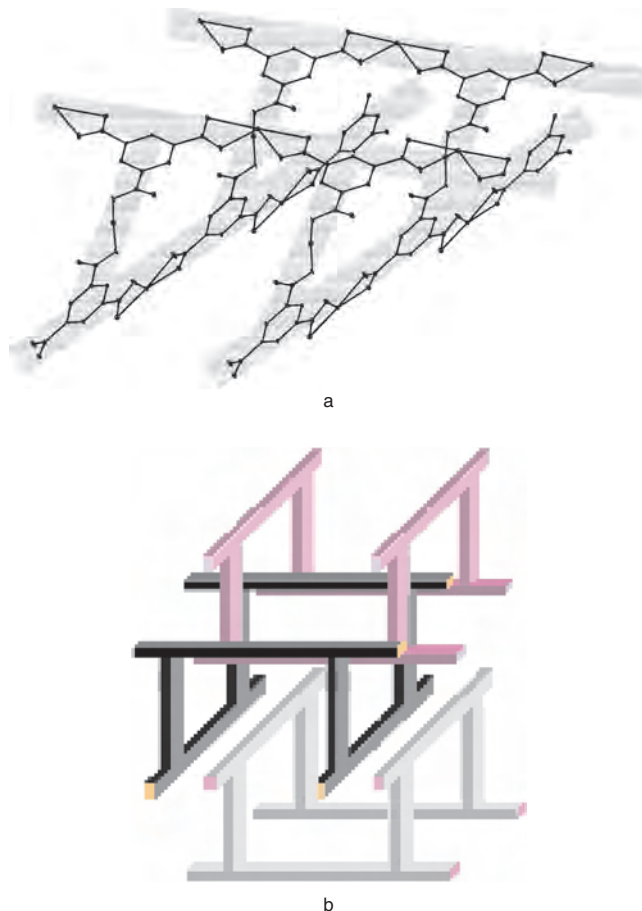


Figure 20. Polymer $\{[\text{Cd}_3(\text{tma})_2] \cdot 13\text{H}_2\text{O}\}_n$. (a) T-shaped molecular bilayer. (b) Threefold interdigitation fashion. Reprinted with permission from [97], J.-C. Dai et al., *Inorg. Chem.* 41, 1391 (2002). © 2002, American Chemical Society.

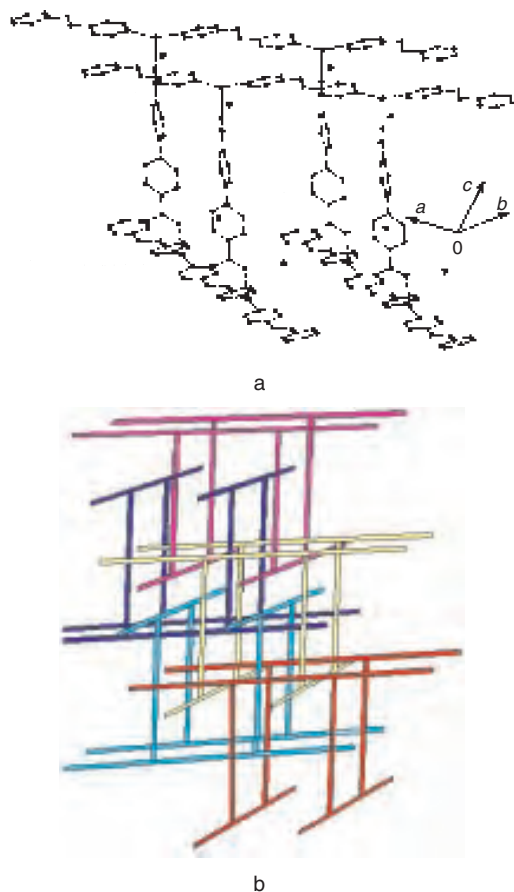


Figure 21. (a) Molecular bilayer architecture of $\{[Ag(bpe)(bpa)_{0.5}] \cdot H_2O\}_n$. (b) 2D \rightarrow 3D parallel interpenetration of fivefold entanglement. Reprinted with permission from [98], Z. Y. Fu et al., *New J. Chem.* 26, 978 (2002). © 2002, Royal Society of Chemistry and the Centre National de la Recherche Scientifique.

The data of TGA and powder XRD reveal the bilayer framework collapse after removal of its crystal aqua molecules [98]. Although most bilayer architectures are fabricated in an assembly product of T-shaped building blocks, there are very few examples of a bilayer architecture constructed by other types of building blocks. One such example of a novel bilayer architecture was first observed in the polymer $\{Cd(isonicotinate)_2(bpe)_{0.5}(H_2O)\}_n$ based on rectangle building blocks [103]. This novel bilayer polymer also originates from a simple hydrothermal approach. In this compound, each Cd(II) center has a slightly distorted $\{CdN_3O_3\}$ octahedral coordinated sphere, completed by three nitrogen donors and three oxygen donors, of which two nitrogen donors and two oxygen donors in the equatorial plane originate from four isonicotinate ligands, and one nitrogen donor and one oxygen donor originate from bpe and water ligands, respectively. Such an octahedral coordinated sphere results in a 2D bilayer architecture with cuboidal box fundamental building units. Interestingly, this structure presents a new remarkable 3D array sustained by the catenation of twofold decked layers. Another interesting example of a bilayer architecture constructed by a non-T-shaped building block was recently demonstrated in the polymer

$\{[Cd(Htma)(bpy)(H_2O)] \cdot (H_2tp)_{0.5} \cdot 2H_2O\}_n$, based on the π - π interactions of two rectangular networks and the host-guest molecular recognition [85] (also see Fig. 15a).

3.3.4. Other 2D Polymers

Besides the 2D architectures mentioned above, there are many other interesting 2D architectures that have been realized. A 2D lamellar structure with an interesting Y-shaped motif, polymer $\{Na_2[Zn(C_2O_4)_{1.5}H_2PO_4] \cdot 2H_2O\}_n$, has been observed in the product from the hydrothermal reaction of $Zn(NO_3)_2 \cdot 6H_2O$, orthophosphoric acid, oxalic acid, and sodium methoxide in a molar ratio of 1:5:5:15 at 115 °C for 1 day [104]. In this polymer, the PO_4 tetrahedra consisting of two terminal hydroxo groups and two μ_2 -O atoms are connected to the ZnO_6 octahedra at two vertices, forming an interesting Y-shaped structural motif. These Y-shaped moieties are further linked to a zigzag layer array and two neighboring layers stack in a tongue-and-groove fashion. This compound exhibits an intense fluorescent emission at 413 nm upon photoexcitation at 310 nm in the solid state, and its complete decomposition occurs in the range of 200–417 °C [104].

Two other 2D lamellar structures occur in the polymers $\{Ag(C_5H_4NS)\}_n$ and $\{[Ag_5(C_5H_4NS)_4(C_5H_5NS)](BF_4)\}_n$ (C_5H_4NS = pyridine-2-thiolate, C_5H_5NS = 1H-pyridine-2-thione) presented by Hong's group [105], which display a graphite-like hexagonal motif (Fig. 22) and an extended 2D layered structure, respectively. Both compounds were prepared by the solution reaction in a stoichiometric ratio. They have also demonstrated that the first polymer is a semiconductor, and the latter an insulator by conductivity determination [105]. In addition, a novel 2D clay-like structure has recently been observed in the polymer $\{Ni_3(tma)_2 \cdot 8H_2O\}_n$ [106], as shown in Figure 23. This structure was obtained by the hydrothermal reaction of nickel acetate tetrahydrate, trimesic acid, and water at 200 °C for 4 days. It has a novel 2D lamellar structure constructed from a tma ligand and a linear trinuclear $\{Ni_3O_{16}\}$ cluster containing three corner-sharing octahedra. The $\{Ni_3O_{16}\}$ cluster consists of three 6-coordinated Ni(II) centers, completed by 16 O donors, of which eight O donors belong to aqua ligands (two μ_2 -O and

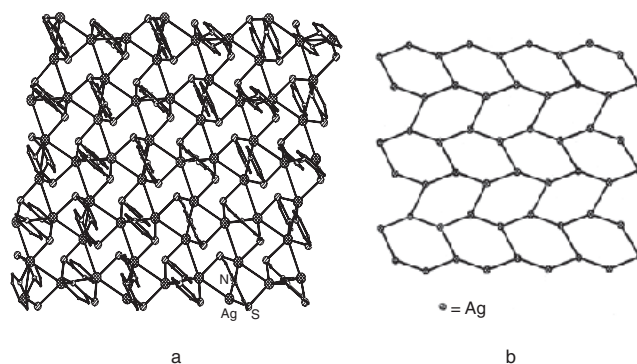


Figure 22. Polymers $\{Ag(C_5H_4NS)\}_n$. (a) View of the lamella structure. (b) Graphite-like motif structure. Reprinted with permission from [105], W.-P. Su et al., *Angew Chem., Int. Ed. Engl.* 39, 2911 (2000). © 2000, Wiley-VCH Verlag GmbH.

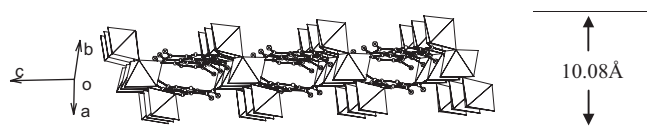


Figure 23. 2D clay-like lamellar structure in polymer $\{\text{Ni}_3(\text{tma})_2 \cdot 8\text{H}_2\text{O}\}_n$.

six μ_t -O), and the other eight O donors are from six different tma ligands. These $\{\text{Ni}_3\text{O}_{16}\}$ clusters and tma ligands are further linked alternatively to generate an interesting 2D clay-like lamellar architecture with 10.08 Å of layered dimension. This clay-like framework is stable up to 428.8 °C [106].

3.4. Three-Dimensional Framework Coordination Polymers

Generally, 3D framework coordination polymers show a more perplexing geometry, structural flexibility, and intriguing topology compared, for instance, to low-dimensional architectures. The design and construction of 3D framework architectures through the copolymerization of metal ions with organic molecules still represents one of the outstanding challenges today. Lately, the designed synthesis of mineralomimetic architectures of coordination polymers analogous to zeolites, clays, quartz, and so on is receiving intensive continuing attention [107–111]. A large number of such supramolecular architectures have been reported. Some good examples are discussed in the next section.

3.4.1. Porous 3D Frameworks

Porous framework materials have found a wide range of technological applications in all aspects of human activity. Many efforts have been devoted to the designed construction of zeolite-like porous polymeric frameworks. Diamondoid frameworks are common and less complex 3D porous structures. Such frameworks result from the assembly of a tetrahedral node with a linear ligand. There have been many examples of diamondoid frameworks reported over the last decades, ranging from single network to 11-fold interpenetration [112–126]. An example of diamondoid frameworks with fivefold interpenetration is the polymer $\{[\text{Co}(\text{bpe})(2\text{-atp})]\}_n$ [126], which comes from the copolymerization of $\text{Co}(\text{NO}_3)_2$, bpe, and 2-atp in the stoichiometric ratio by a hydrothermal approach. In this compound, the tetrahedral geometry is the result of the 5-coordinated Co(II) center by linking to two N donors and three O donors, of which three O donors come from a chelating carboxylate group and a unidentate carboxylate group of two separate 2-atp ligands, while the N donors belong to bpe ligands. Such 4-connected tetrahedral nodes and linear ligands finally give rise to an asymmetrical diamondoid unit. No guest molecules are inserted in this cage of a diamondoid unit, and distortion of the unit results from the employment of different ligands. This diamondoid network presents a novel fivefold interpenetration of hybrid ligands with different tecton lengths, although there have been various interpenetration networks as high as 11-fold. The IR spectrum

of this compound showing characteristic bands at 1618–1549 cm^{-1} and 1421–1396 cm^{-1} are, respectively, attributed to the asymmetric vibration and the symmetric vibration of dicarboxylate groups of a 2-atp ligand, and the splitting of the asymmetric vibration peak confirms that the carboxylate groups have two different coordination fashions, which agree with its crystal structure. In addition, this diamondoid polymer also exhibits high thermal stability (up to 430 °C) and an intense photoluminescence emission at 400 nm upon excitation at 300 nm, suggesting that it might be a good candidate for emitting diode devices [126].

Octahedral frameworks are another common 3D porous structure. An interesting example of an octahedral box occurring in the polymer $\{[\text{Cd}(\text{tp})(\text{bpy})]\}_n$ is shown Figure 24 [127]. This polymer results from the hydrothermal product of $\text{Cd}(\text{CH}_3\text{CO}_2)_2 \cdot 2\text{H}_2\text{O}$, H_2tp , bpy, methenamine, and water in a molar ratio of 3:2:2:2:556 at 200 °C for 4 days. It consists of rectangular sheets of $\{\text{Cd}(\text{tp})\}$ and bpy pillars, in which the $\{\text{Cd}(\text{tp})\}$ sheet is formed by a linear trinuclear $\{\text{Cd}_3\text{O}_{12}\text{N}_6\}$ cluster and a bridging tp ligand (Fig. 24a). The entire octahedral structure possesses three windows of 15.4×10.7 , 11.7×10.7 , and 11.8×11.5 Å, respectively, and exhibits twofold interpenetration (Fig. 24b). The full decomposition of this octahedral compound occurs in the 372–587 °C range [127]. Other examples of twofold interpenetrating octahedral frameworks have been demonstrated by the present authors [126] and others [128]. These structures are very similar to the above octahedral box; the main differences lies in the $\{\text{M}(\text{tp})\}$ ($\text{M} = \text{Co}, \text{Zn}, \text{Cd}$) sheets, as shown Figure 25. An octahedral architecture, $\{\text{Mn}(2\text{-atp})(\text{bpe})_{0.5}\text{H}_2\text{O}\}_n$, with threefold interpenetrating networks, was recently observed in the product of hydrothermal reaction from $\text{MnCl}_2 \cdot 4\text{H}_2\text{O}$, 2-atp, bpe, sodium methoxide, and water at 160 °C for 1 day [129]. This polymer has an interesting paddle-like binuclear $\{\text{Mn}_2\}$ subunit (Fig. 26a), where the distance between two Mn centers is about 3.0 Å, implying a clear metal–metal weak interaction. The largest channel dimensions in a single octahedral framework of this polymer are about 13.6×11.1 Å (Fig. 26b), and the entire architecture displays a threefold interpenetration of octahedral networks (Fig. 26c).

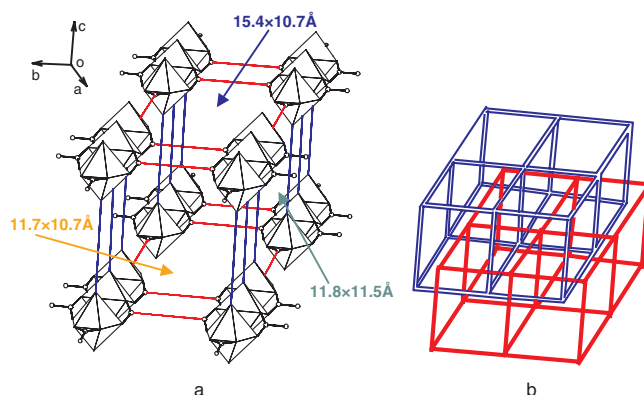


Figure 24. Polymer $\{[\text{Cd}(\text{tp})(\text{bpy})]\}_n$. (a) Cubic framework (red lines indicate the tp struts; blue lines represent bpy struts). (b) Twofold interpenetration.

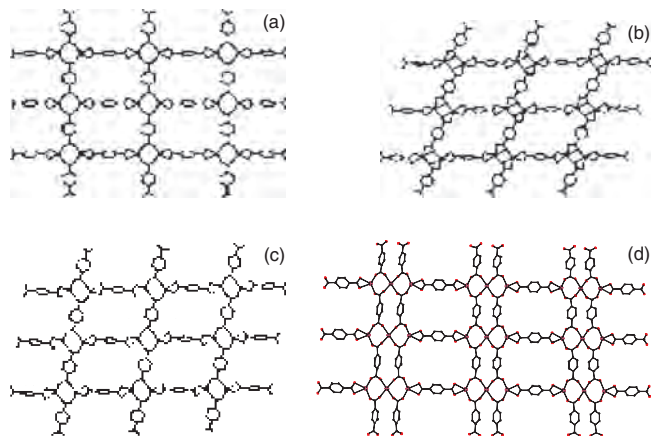


Figure 25. 2D rectangular $\{M(tp)\}$ sheets in some cubic box polymers $\{M(tp)(bpy)\}_n$. (a) $M = Co$. (b) $M = Cd$. (c) $M = Zn$. Reprinted with permission from [128], J. Tao et al., *J. Chem. Soc., Dalton Trans.* 3669 (2000). © 2000, Royal Society of Chemistry. (d) $M = Cd$ (from [127]).

Zaworotko's group presented an example of an octahedral network with noninterpenetration occurring in the polymer $\{[Zn(bpy)_2(SiF_6)]\}_n$ [130]. This rigid cuboidal framework has a channel dimension of $8 \times 8 \text{ \AA}$, while the framework will collapse irreversibly upon an attempt to remove solvent molecules. Recently, Yaghi's group prepared a series of novel primitive cubic frameworks with interpenetration and noninterpenetration based on the polymers $\{Zn_4O(L)_3\}_n$ ($L =$ terephthalate [131] and related species [132]), as shown in Figure 27. It is exciting that these porous compounds possess pores that can be varied from 3.8 to 28.8 \AA , and have an open space ranging from 55.8% up to 91.1% of crystal volume, which far exceeds the most open zeolites; some of these compounds are remarkably stable after removal of the guest.

A number of other 3D porous architectures have also been realized. Figure 28 shows two examples of a 3D porous honeycomb-like architecture observed in the polymers $\{Cd_3(Htma)_3 \cdot 8H_2O\}_n$ [97] and $\{Na[Cd(tma)] \cdot 3H_2O\}_n$ [133]. Both polymers are hydrothermal products under the template effect of methenamine molecules, and they have 1D channel dimensions of about $8 \times 8 \text{ \AA}$ (Fig. 28a) and $7.6 \times 4.2 \text{ \AA}$ (Fig. 28b), respectively. Recently, an interesting 3D porous honeycomb-like architecture topologically related to a borazon 4^66^4 network in the polymer $\{[Cd_4(bpa)_4(bpy)_6] \cdot (bpy)_{0.5} \cdot (H_2O)_7\}_n$ has been demonstrated by our group [134], as shown in Figure 29. This polymer is also synthesized by the hydrothermal approach at $200 \text{ }^\circ\text{C}$ for 4 days, and the network is arranged by a slightly distorted trigonal-bipyramidal subunit, which is seldom observed in the metal-organic polymers [71], and which possesses giant hexagonal channels about $30.5 \times 24.8 \text{ \AA}$ (Fig. 29a). The entire 3D architecture is a fourfold interpenetrating network (Fig. 29b), and the resulting cavities are only about $6 \times 7 \text{ \AA}$, which are filled by encapsulated guests—aqua and bpy molecules.

Williams and co-workers [135] described a highly porous coordination polymer $\{Cu_3(tma)_2(H_2O)_3\}_n$ prepared by the hydrothermal reaction of cupric nitrate trihydrate with trimesic acid in 12 mL 50:50 water/methanol solution at $180 \text{ }^\circ\text{C}$ for half a day. This structure is constructed by

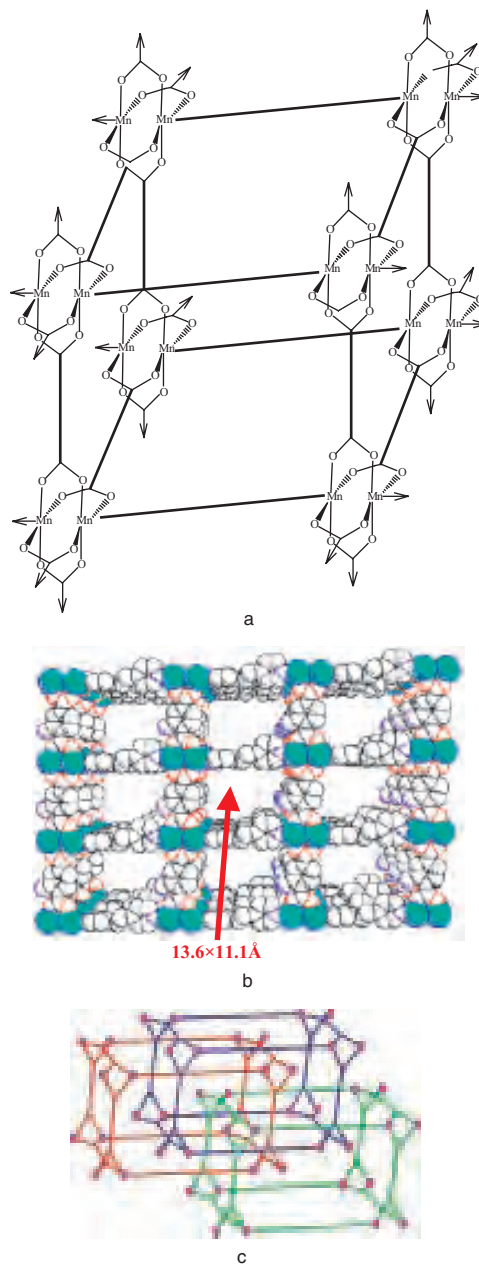


Figure 26. Octahedral architecture in $\{Mn(2-atp)(bpe)_{0.5}H_2O\}_n$. (a) Paddle-like binuclear $\{Mn_2\}$ subunit. (b) Single network. (c) Three-fold interpenetration model.

a common paddle-like binuclear $\{Cu_2\}$ subunit, and has novel nanochannels with fourfold symmetry (Fig. 30). Its open space is up to 40.7% of crystal volume. Yaghi's group also reported a series of 3D porous architectures formed by paddle-like binuclear subunits [136–138], displaying intriguing topologies. They described a chiral Si network topological structure of $SrSi_2$ occurring in the polymer $\{[Zn_2(tma)(NO_3)] \cdot (C_2H_5OH)_5(H_2O)\}_n$, obtained from the reaction of zinc nitrate hexahydrate with trimesic acid in an absolute ethanol media in stoichiometric ratio at room temperature for 6 days [136] (Fig. 31). This structure is a cubic network constructed by a paddle-like binuclear trigonal subunit, and contains 3D channels of 14 \AA diameter, exhibiting

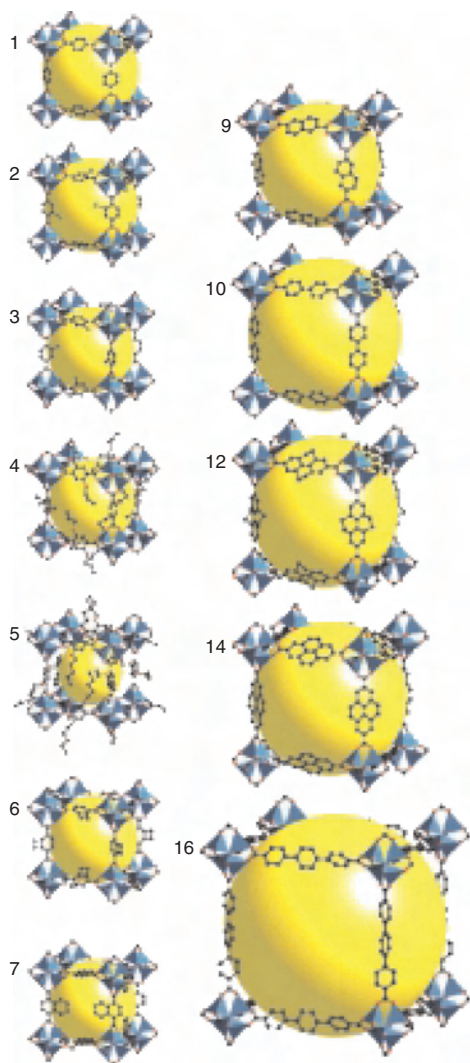


Figure 27. Primitive cubic frameworks in polymers $\{Zn_4O(L)_3\}_n$ ($L =$ terephthalate [131] and related species [132]). Reprinted with permission from [132], M. Eddaoudi et al., *Science* 295, 469 (2002). © 2002, American Association for the Advancement of Science.

a highly selective uptake of alcohol. Another example of a 3D porous architecture based on a paddle-like binuclear subunit reported by them occurs in the polymer $\{[Cu_2(atc)] \cdot 6H_2O\}_n$ ($atc = 1,3,5,7$ -adamantanetetracarboxylate), resulting from the reaction of $Cu(NO_3)_2 \cdot 2.5H_2O$ with H_4atc in a basic aqueous solution at $190^\circ C$ [137]. Its structure is attributed to a 4-connected PtS topological network, and contains 3D channels 6 \AA in diameter. The most interesting 3D porous architecture they recently described is a novel (3,4)-connected Pt_3O_4 topological network observed in the polymer $\{[Cu_3(bt b)_2(H_2O)_3] \cdot (dmf)_9(H_2O)_2\}_n$ ($bt b = 1,3,5$ -benzenetri benzoate), which is prepared from the reaction of $H_3bt b$ with $Cu(NO_3)_2 \cdot 2.5H_2O$ in an ethanol/dmf/water media in the presence of pyridine at $65^\circ C$ for 1 day [138] (Fig. 32). This crystal structure has a surprising extra-large pore of 16.4 \AA diameter resulting from the strong aromatic π - π stacking interactions of two adjacent Pt_3O_4 topological networks, whose cavity size is even larger than that of many

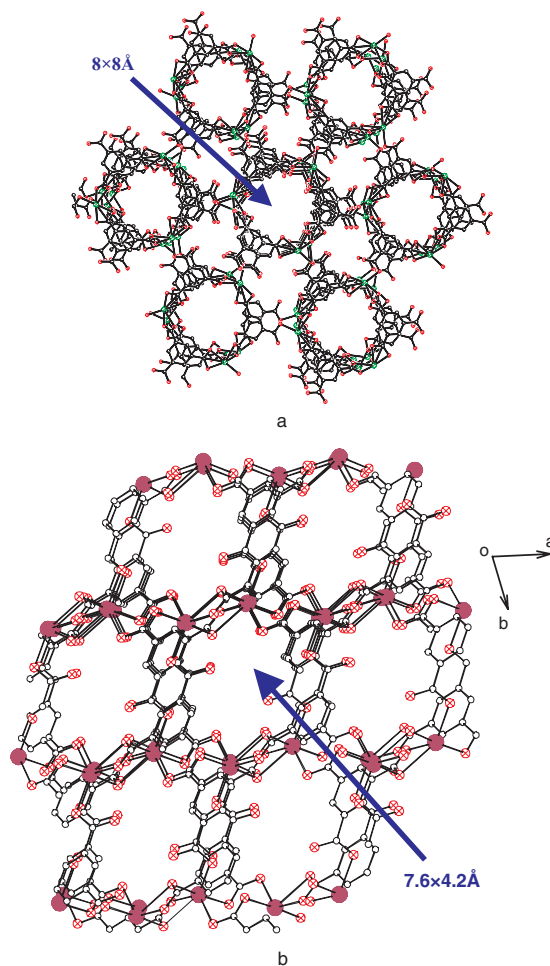


Figure 28. 3D porous honeycomb-like architectures. (a) $\{Cd_3(Htma)_3 \cdot 8H_2O\}_n$. Reprinted with permission from [97], J.-C. Dai et al., *Inorg. Chem.* 41, 1391 (2002). © 2002, American Chemical Society. (b) $\{Na[Cd(tma)] \cdot 3H_2O\}_n$.

other noninterpenetration architectures, although there is a twofold interpenetration network.

Figure 33 presents an interesting example of twofold interpenetration of a novel ribbon-candy-like 3D porous architecture with giant rhombic channels observed in the

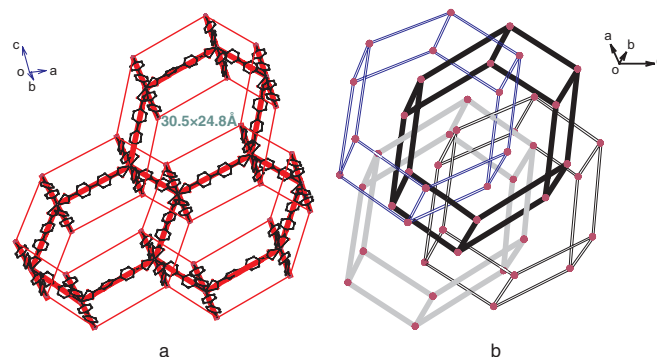


Figure 29. 3D porous honeycomb-like architecture in polymer $\{[Cd_4 \cdot (bpa)_4(bpy)_6] \cdot (bpy)_{0.5} \cdot (H_2O)_7\}_n$. (a) Borazon-like $4^6 4$ topology. (b) Fourfold interpenetrating networks.

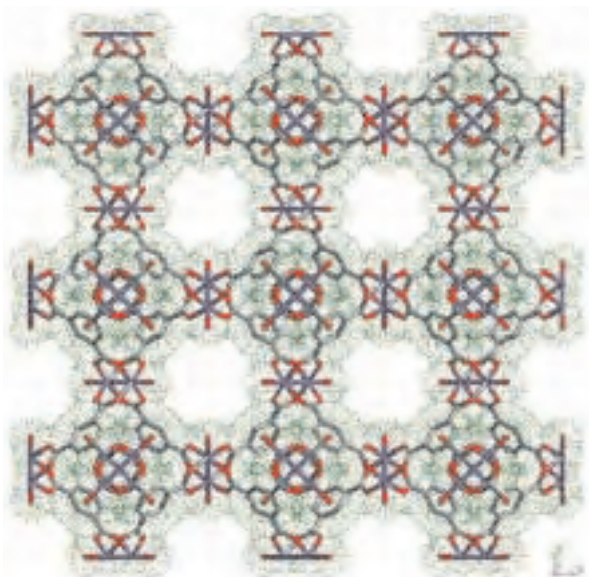


Figure 30. Highly porous coordination polymer $\{\text{Cu}_3(\text{tma})_2(\text{H}_2\text{O})_3\}_n$. Reprinted with permission from [135], S. S.-Y. Chui et al., *Science* 283, 1148 (1999). © 1999, American Association for the Advancement of Science.

polymer $\{[\text{Ph}_3\text{PCH}_2\text{Ph}][\text{Cd}(\text{tp})\text{Cl}] \cdot 2\text{H}_2\text{O}\}_n$ [139]. This polymer is the product of the hydrothermal reaction of cadmium acetate dihydrate with H_2tp , $[\text{Ph}_3\text{PCH}_2\text{Ph}]\text{Cl}$, and water in a molar ratio of 1:1:1:278 at 200 °C for 4 days. In this structure, due to the structure-directing effects of large bulky

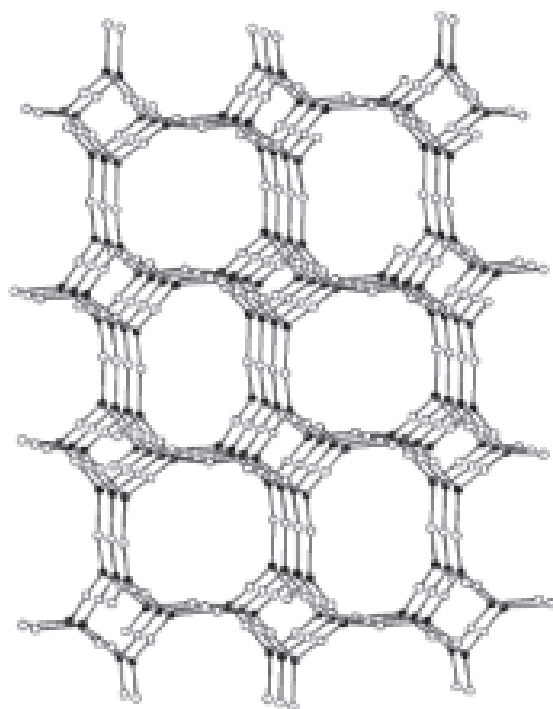


Figure 31. View of a chiral Si network topological structure of SrSi_2 in the polymer $\{[\text{Zn}_2(\text{tma})(\text{NO}_3)] \cdot (\text{C}_2\text{H}_5\text{OH})_5(\text{H}_2\text{O})\}_n$. Reprinted with permission from [136], O. M. Yaghi et al., *J. Am. Chem. Soc.* 119, 2861 (1997). © 1997, American Chemical Society.

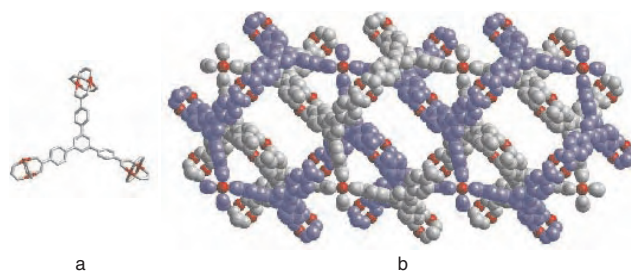


Figure 32. Polymer $\{[\text{Cu}_3(\text{btb})_2(\text{H}_2\text{O})_3] \cdot (\text{dmf})_6(\text{H}_2\text{O})_2\}_n$. (a) Paddle-like binuclear subunit. (b) View of twofold interpenetration Pt_3O_4 topological networks. Reprinted with permission from [138], B. Chen et al., *Science* 291, 1021 (2001). © 2001, American Association for the Advancement of Science.

template cations $[\text{Ph}_3\text{PCH}_2\text{Ph}]^+$, the tp and Cl ligands are coordinated to Cd(II) centers to arrange zigzag rhombic open motifs with a giant cavity of about $33.5 \times 22.7 \text{ \AA}$ (Fig. 33a) rather than a common small square grid, and are further polymerized to yield an interesting ribbon-candy-like 3D porous architecture (Fig. 33b), a topology attributed to the Archimedean $3\text{D } 8^2-10\text{a}$ network (Fig. 33c). The twofold interpenetration result in the final cavities is only about $16 \times 11 \text{ \AA}$ in an actual crystal structure (Fig. 33d). A similar polymer, $\{[\text{Ph}_3\text{PCH}_2\text{Ph}]_2[\text{Cd}_3(\text{tp})_4] \cdot 2\text{H}_2\text{O}\}_n$, exhibiting a 3D porous architecture with 1D rhombic nanochannels, was also recently obtained from the copolymerization of tp ligands and Cd(II) centers based on the template effects of the same cations $[\text{Ph}_3\text{PCH}_2\text{Ph}]^+$ in a stoichiometric ratio under the same hydrothermal condition [140]. Interestingly, in this compound, the Cd(II) centers are aggregated through the

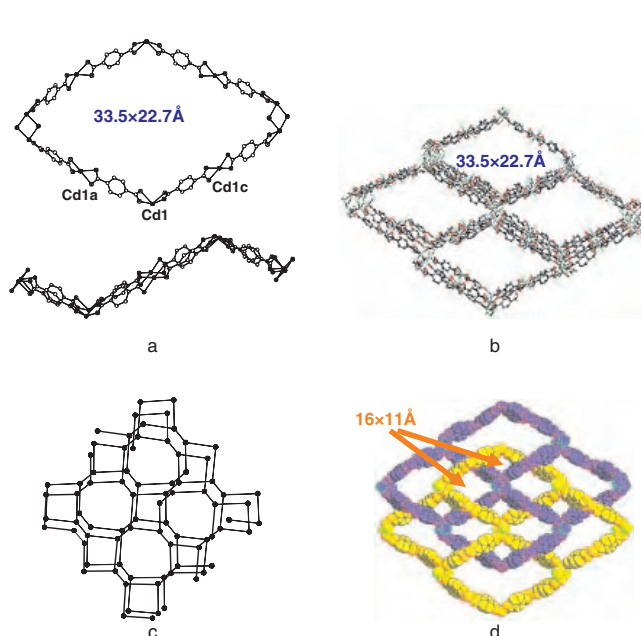


Figure 33. 3D porous architecture of $\{[\text{Ph}_3\text{PCH}_2\text{Ph}][\text{Cd}(\text{tp})\text{Cl}] \cdot 2\text{H}_2\text{O}\}_n$: (a) Top (up) and side (down) view of zigzag rhombic open motifs; (b) An interesting ribbon-candy-like 3D porous architecture; (c) Schematic topology for $3\text{D } 8^2-10\text{-a}$ network; (d) Space-filling view of 2-fold interpenetrating 3D networks showing the rhombic channels of about $16 \times 11 \text{ \AA}$. Reprinted with permission from [139], J.-C. Dai et al., *Chem. Commun.* 12 (2002). © 2002, Royal Society of Chemistry.

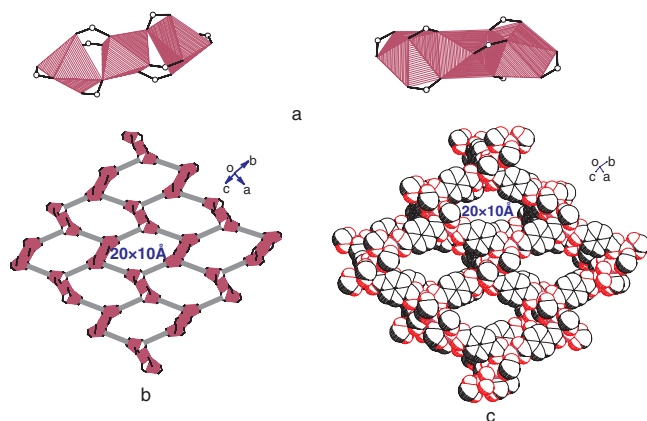


Figure 34. 3D porous architecture of $\{[\text{Ph}_3\text{PCH}_2\text{Ph}]_2[\text{Cd}_3(\text{tp})_4] \cdot 2\text{H}_2\text{O}\}_n$. (a) Two types of trinuclear $\{\text{Cd}_3\}$ clusters—corner sharing of three $\{\text{CdO}_6\}$ octahedra (left) and edge sharing of a $\{\text{CdO}_6\}$ octahedron and two $\{\text{CdO}_7\}$ pentagon pyramids (right) are interlinked through tp tectons to arrange (b), the 2D graphite-like sheet, further pillared by tp ligands to give (c), a 3D porous architecture with a 1D rhombic channel dimension of $20 \times 10 \text{ \AA}$.

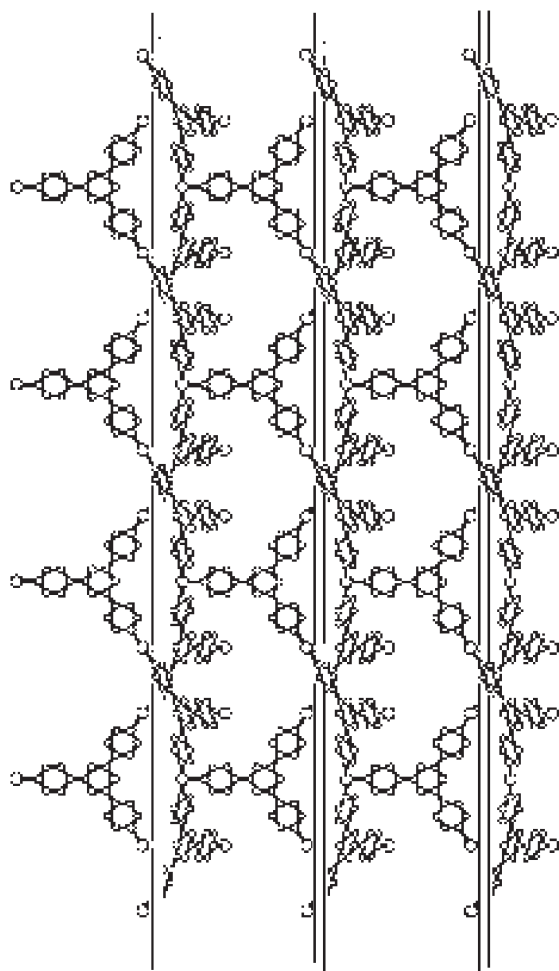


Figure 35. 3D interwoven network with the (12,3) topology of the $\{[\text{Ni}(\text{tpt})(\text{NO}_3)_2] \cdot \text{solvate}\}_n$ polymer. Reprinted with permission from [141], B. F. Abrahams et al., *Angew Chem., Int. Ed.* 38, 1475 (1999). © 1999, Wiley-VCH Verlag GmbH.

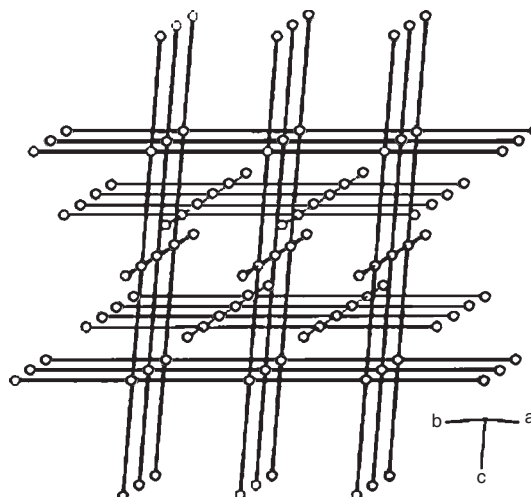


Figure 36. Schematic view of an interesting interpenetration of a 2D square grid into a 3D CdSO_4 -like topological framework observed in $\{[\text{Ni}(\text{bpy})_2(\text{H}_2\text{PO}_4)_2] \cdot \text{C}_4\text{H}_9\text{OH} \cdot \text{H}_2\text{O}\}_n$. Reprinted with permission from [142], Y.-C. Jiang et al., *Inorg. Chem.* 40, 5320 (2001). © 2001, American Chemical Society.

carboxylate groups of coordinated tp ligands into two types of linear trinuclear $\{\text{Cd}_3\}$ clusters (Fig. 34a). Such types of trinuclear $\{\text{Cd}_3\}$ clusters are interlinked through tp tectons to arrange a 2D graphite-like sheet with a rhombic window of dimension of $20 \times 10 \text{ \AA}$ (Fig. 34b). These sheets are further pillared by tp ligands to give a novel 3D porous architecture with a 1D rhombic channel dimension of $20 \times 10 \text{ \AA}$ (Fig. 34c).

3.4.2. Other 3D Frameworks

In addition to the 3D porous architectures, there are a number of other novel 3D frameworks that are worthy of outline. Robson and co-workers reported an excellent 3D interwoven network with the (12,3) topology [141], which shows an interesting self-penetrating phenomenon (Fig. 35). This structure was observed in the polymer $[\text{Ni}(\text{tpt})(\text{NO}_3)_2 \cdot \text{solvate}]_n$ (tpt = tri-4-pyridyl-1,3,5-triazine) obtained from the reaction of $\text{Ni}(\text{NO}_3)_2 \cdot 6\text{H}_2\text{O}$ with a tpt ligand by using

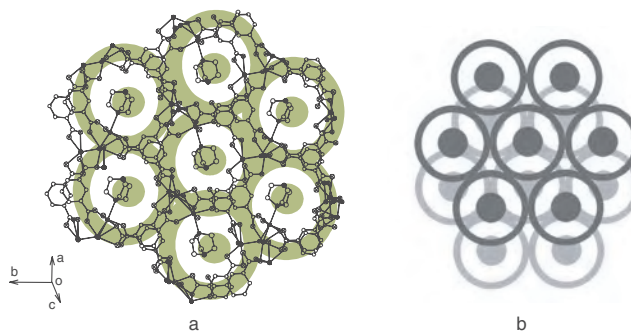


Figure 37. (a) Excellent chicken-wire-like sheet occurring in the polymer $\{\text{Cd}_3(\text{tma})_2(\text{dabco})(\text{H}_2\text{O})_2\}_n$. (b) Stacking of twofold alternate sheets resulting in a novel 3D architecture. Reprinted with permission from [97], J.-C. Dai et al., *Inorg. Chem.* 41, 1391 (2002). © 2002, American Chemical Society.

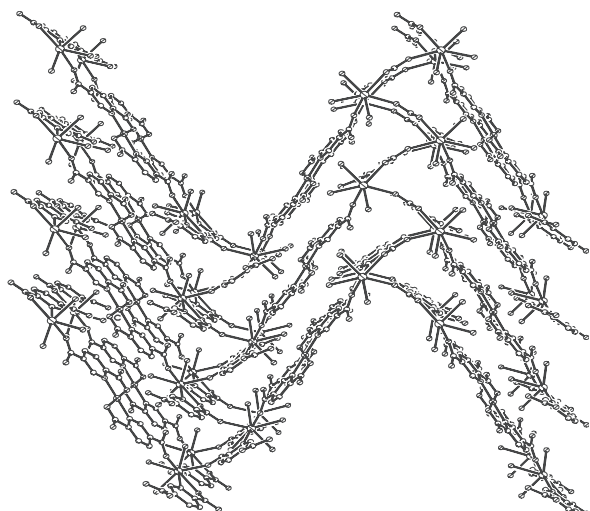


Figure 38. 3D wave-like structure of the heterobimetallic polymer $\{[\text{Gd},\text{Cu}_2(2\text{-pydc})_8(\text{H}_2\text{O})_{12}] \cdot 4\text{H}_2\text{O}\}_n$. Reprinted with permission from [143], Y. C. Liang et al., *Angew Chem., Int. Ed.* 39, 3304 (2000). © 2000, Wiley-VCH Verlag GmbH.

the solution diffused technique [141]. Interpenetration of 3D networks is a common phenomenon in coordination polymers. Usually, interpenetration occurs in the framework of a structure of the same chemical composition and with the same topology. However, Wang's group [142] gave an example of interpenetrating networks of the same chemical composition, but with different topologies. They formulated a crystal structure of the polymer $\{[\text{Ni}(\text{bpy})_2(\text{H}_2\text{PO}_4)_2] \cdot \text{C}_4\text{H}_9\text{OH} \cdot \text{H}_2\text{O}\}_n$, exhibiting an interesting interpenetration of a 2D square grid into a 3D CdSO_4 -like topological framework (Fig. 36). This novel interpenetrating polymer was also a product from the hydrothermal approach at 120 °C for 1 day. An interesting 3D architecture, polymer $\{\text{Cd}_3(\text{tma})_2(\text{dabco})(\text{H}_2\text{O})_2\}_n$ [97], contains an excellent chicken-wire-like motif, as shown in Figure 37. This architecture results from the copolymerization of Cd(II) cations, H_3tma , and dabco molecules in a molar ratio of 3:1:2:278 at 200 °C for 4 days. The formation of such a chicken-wire-like motif in this structure may be due to the template or structure-directing effect of the steric geometry of the dabco molecules. The IR spectrum of this

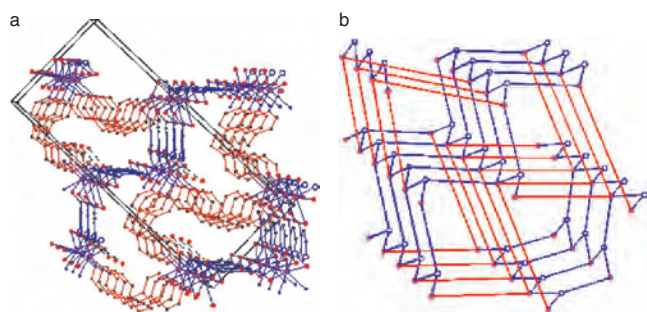


Figure 39. (a) Crystal structure of the polymer $\{[\text{Cd}(3\text{-pydc})(\text{bpp})] \cdot \text{H}_2\text{O}\}_n$. (b) Schematic view of an interesting 3D accordion topology.

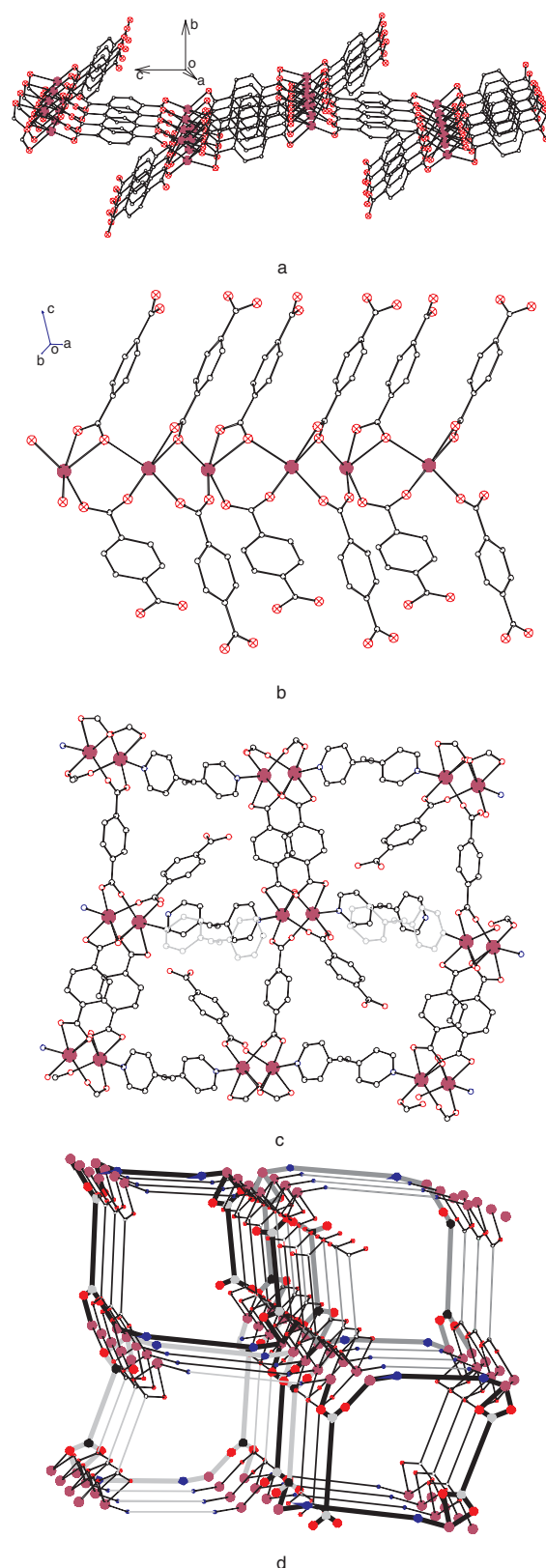


Figure 40. 3D architecture of the polymer $\{\text{Cd}_2[\text{H}(\text{tp})_{2.5}](\text{bpe})\}_n$. (a) Novel 2D abates-like sheets constructed by (b) Cd-tp chains (c), which are further cross linked by bpe bridging ligands to generate (d), an interesting 3D spiral pipe-like structure with a bolt (the bolts are omitted for clarity).

compound shows the expected characteristic bands at 1622–1560 cm^{-1} for asymmetric vibration and at 1439–1371 cm^{-1} for symmetric vibration, in good agreement with its crystal structure. The stability of this architecture is up to 427 °C. In addition, this compound exhibits an intense emission occurring at 437 nm upon excitation of 365 nm in the solid state at room temperature, and a quenching of the fluorescence with $\tau = 3.35$ ns, suggesting it will be an excellent candidate for potential photoactive material [97]. Hong's group described a novel 3D architecture with a wave-like structure occurring in the heterobimetallic polymer $\{[\text{Gd}_4\text{Cu}_2(2\text{-pydc})_8(\text{H}_2\text{O})_{12}] \cdot 4\text{H}_2\text{O}\}_n$ (2-pydc = 2,5-pyridinedicarboxylate) obtained from the reaction of gadolinium oxide, copper oxide, 2,5-pyridinedicarboxylic acid, and water in a molar ratio of 1:2:4:290 at 140 °C for 3 days [143]. This architecture was constructed by interlinking infinite zigzag chains based on the subunit of $[\text{Gd}_4\text{Cu}_2(2\text{-pydc})_8(\text{H}_2\text{O})_{12}]$ (Fig. 38). A novel 3D architecture with interesting accordion cages was demonstrated by our group [144]. This accordion architecture is observed in the polymer $\{[\text{Cd}(3\text{-pydc})(\text{bpp})] \cdot \text{H}_2\text{O}\}_n$ (3-pydc = 3,4-pyridinedicarboxylate) as a hydrothermal product resulting from the copolymerization of Cd(II) cations with the tritopic ligand 3-pydc, as well as ditopic ligand bpp molecules in a molar ratio of 2:2:1 at 150 °C for 7 days. In this 3D architecture, the Cd(II) centers provide the 5-connecting nodes, while the ligands bpp act as 2-connectors and 3-pydc as 3-connectors, respectively. These nodes and connectors are therefore interlinked into a subunit that can also be viewed as a kind of sheet; two edges of the sheet originate from the two rods of bpp 2-connectors, and the other edges come from two rods of 3-pydc 3-connectors. The metal centers, distributed in the sheet, are not all coplanar. Rather, half fall in one plane, and half in an adjacent plane. The cross linking of adjacent layers through the third rod of 3-pydc linkers results in a remarkable 3D framework—accordion cages (Fig. 39). The decomposition of this accordion architecture occurs at about 300 °C. In addition, a similar 3D architecture, $\{\text{Cd}_2[\text{H}(\text{tp})_{2.5}(\text{bpe})]\}_n$, was also recently prepared by heating the cadmium acetate dihydrate with H_2tp , bpe, $[\text{Ph}_3\text{PCH}_2\text{Ph}]\text{Cl}$, and water in a molar ratio of 3:2:2:1:556 at 200 °C for 4 days [145]. Most notable is that this architecture has a novel 2D abates-like sheet (Fig. 40a) constructed by Cd–tp chains (Fig. 40b). These adjacent 2D abates-like sheets are further cross linked by bpe bridging ligands to generate an interesting 3D spiral pipe-like structure with a bolt (Fig. 40c,d). The IR spectrum of this compound shows the expected absorptions for the vibration of a protonated tp ligand at 1705 cm^{-1} , the asymmetric and symmetric vibrations of the carboxylate group of a tp ligand at 1610 and 1394 cm^{-1} , and the vibrations of a bpe ligand at 1504, 1551, and 1574 cm^{-1} . These IR characteristic bands are consistent with their crystal structure. The compound is stable up to 210 °C, and its decomposition is completely finished at about 600 °C.

4. CONCLUSIONS

In conclusion, the rapidly growing chemical and structural diversity of metal–organic coordination polymers is amply illustrated by the many examples cited in the preceding

sections. These polymeric architectures show many of the intriguing structural features and interesting topologies. However, these may only be the tip of the iceberg in the field of supramolecular architectures. Numerous polymers have been prepared, and more and more new architectures are being reported. On the other hand, despite significant progress in the synthesis of numerous coordination polymeric architectures, there are still many “white areas” challenging future research on the designed construction of supramolecules with desired structures and properties, for example, how to control the bridging ligand molecules, adopting a relative orientation suitable for the coordinated sphere of metal centers. There is still a long way to go to fully seek and establish such a successful approach to predict and control the architectures, as well as characteristics and properties of coordination polymers from a combination of metal centers and bridging ligands. The excellent structural features as well as potential useful properties of supramolecular coordination polymers are continuing to fascinate many scientists; therefore, research in this area is still being very actively pursued, and further developments are to be expected. The future expectation in this area is, as Feynman pointed out, “I can hardly doubt that when we have some control of the arrangement of things on a small scale we will get an enormously greater range of possible properties that substances can have” [146].

GLOSSARY

Crystal engineering Design strategy for the construction of predefined crystals with desired structures and properties.

Interpenetrating phenomenon Type of entanglement, which is inextricable and whose disarrangement only can be achieved by breaking the interconnection.

Self-assembly In a reaction system, the spontaneous aggregation of basic molecular fragments that recognize each other through multiple molecular recognition sites to form extended architectures.

Supramolecular architecture Intermolecular structure; a large structure constructed by supramolecular species.

Supramolecular coordination polymers Type of nanostructural materials constructed by metal centers and inorganic/organic ligands based upon a coordinated bond.

Supramolecules Entity beyond the small molecule, which results from the association of two or more chemical species assembled by the intermolecular forces.

ACKNOWLEDGMENTS

The authors thank the State Key Laboratory of Structural Chemistry, Fujian Institute of Research on the Structure of Matter, Chinese Academy of Sciences (CAS), as well as the National Science and Technology of China (001CB1089), the National Science Foundation of China (20273073, 90206040), and the Science Foundation of CAS and Fujian Province (2002F014) for research funding support.

REFERENCES

- E. A. Chandross and R. D. Miller, *Chem. Rev.* 99, 1641 (1999).
- P. J. Hagrman, D. Hagrman, and J. Zubieta, *Angew. Chem., Int. Ed.* 38, 2638 (1999).
- S. R. Batten, *Curr. Opinions Solid State Mater. Sci.* 5, 107 (2001).
- Y.-C. Jiang, Y.-C. Lai, S.-L. Wang, and K.-H. Lii, *Inorg. Chem.* 40, 5320 (2001).
- Z.-Y. Fu, X.-T. Wu, J.-C. Dai, L.-M. Wu, C.-P. Cui, and S.-M. Hu, *Chem. Commun.* 1856 (2001).
- O. M. Yaghi, H. Li, C. Davis, D. Richardson, and T. L. Groy, *Acc. Chem. Res.* 31, 474 (1998).
- S. Leininger, B. Olenyuk, and P. J. Stang, *Chem. Rev.* 100, 853 (2000).
- A. F. Wells, "Three-Dimensional Nets and Polyhedra." Wiley, New York, 1977.
- A. F. Wells, Further Studies of Three-Dimensional Nets, ACA Monograph No. 8, American Crystallographic Association, 1979.
- A. F. Wells, "Structural Inorganic Chemistry." Oxford University Press, Oxford, 1975.
- R. Robson, B. F. Abrahams, S. R. Batten, R. W. Gable, B. F. Hoskins, and J. P. Liu, "ACS Symposium Series 499," 1992, pp. 256-273.
- B. F. Abrahams, B. F. Hoskins, and R. Robson, *J. Am. Chem. Soc.* 113, 3606 (1991).
- S. R. Batten and R. Robson, *Angew. Chem., Int. Ed.* 37, 1460 (1998).
- J. V. Smith, "Structural and Geometrical Crystallography." Wiley, New York, 1982.
- S. Han and J. V. Smith, *Acta Crystallogr. A* 55, 332 (1999).
- M. O'Keeffe and B. G. Hyde, "Crystal Structures I: Patterns and Symmetry." American Mineral Association, Washington, DC, 1996.
- M. O'Keeffe, M. Eddaoudi, H. Li, T. Reineke, and O. M. Yaghi, *J. Solid State Chem.* 152, 3 (2000).
- M. C. Hong, Y. J. Zhao, W. P. Su, R. Cao, M. Fujita, Z. Y. Zhou, and A. S. C. Chan, *J. Am. Chem. Soc.* 122, 4819 (2000).
- B. Olenyuk, J. A. Whiteford, A. Fechtenkotter, and P. J. Stang, *Nature* 398, 796 (1999).
- N. Takeda, K. Umemoto, K. Yamaguchi, and M. Fujita, *Nature* 398, 794 (1999).
- A. Muller, E. Krickemeyer, H. Bogge, M. Schmidtman, and F. Peters, *Angew. Chem., Int. Ed.* 37, 3360 (1998).
- Z.-Y. Fu and X.-T. Wu (to be published).
- G.-F. Liu, B.-H. Ye, Y.-H. Ling, and X.-M. Chen, *Chem. Commun.* 1442 (2002).
- K. B. Yu, S. H. Gou, and X. Z. You, *Acta Crystallogr.* C47, 2653 (1991).
- S. H. Gou, X. Z. You, Z. Xu, Z. Y. Zhou, K. B. Yu, Y. P. Yu, and D. L. Zhu, *Acta Crystallogr.* C47, 1303 (1991).
- J. Y. Lu, K. A. Runnels, and C. Norman, *Inorg. Chem.* 40, 4516 (2001).
- M. A. Withersby, A. J. Blake, N. R. Champness, P. Hubberstey, W.-S. Li, and M. Schroder, *Angew. Chem., Int. Ed. Engl.* 36, 2327 (1997).
- A. J. Blake, N. R. Champness, A. N. Khlobystov, D. A. Lemenovski, W.-S. Li, and M. Schroder, *Chem. Commun.* 1339 (1997).
- Z.-Y. Fu and X.-T. Wu (unpublished result).
- H. J. Choi and M. P. Suh, *Inorg. Chem.* 38, 6309 (1999).
- M. C. Hong, Y. J. Zhao, W. P. Su, R. Cao, M. Fujita, Z. Y. Zhou, and A. S. C. Chan, *Angew. Chem., Int. Ed.* 39, 2468 (2000).
- J. Lu, G. Crisci, T. Niu, and J. Jacobson, *Inorg. Chem.* 36, 5140 (1997).
- C. Chen, D. Xu, and Y. Xu, *Acta Crystallogr.* C48, 1231 (1992).
- A. S. Batsanov, M. J. Begley, P. Hubberstey, and J. Stroud, *J. Chem. Soc., Dalton Trans.* 1947 (1996).
- Z.-Y. Fu, X.-T. Wu, and J.-C. Dai (unpublished result).
- A. J. Blake, N. R. Champness, P. Hubberstey, W.-S. Li, M. A. Withersby, and M. Schroder, *Coord. Chem. Rev.* 183, 117 (1999).
- O. M. Yaghi, H. Li, and T. L. Groy, *J. Am. Chem. Soc.* 118, 9096 (1996).
- R. H. Groeneman, L. R. MacGillivray, and J. L. Atwood, *Inorg. Chem.* 38, 208 (1999).
- C. Daiguebonne, O. Guilloa, Y. Gerault, A. Lecerf, and K. Boubeker, *Inorg. Chim. Acta* 284, 139 (1999).
- B. Wu, W.-J. Zhang, S.-Y. Yu, and X.-T. Wu, *J. Chem. Soc., Dalton Trans.* 1795 (1997).
- K. Biradha, C. Seward, and M. J. Zaworotko, *Angew. Chem., Int. Ed. Engl.* 38, 492 (1999).
- S. Bhandari, C. G. Frost, C. E. Hague, M. F. Mahon, and K. C. Molloy, *J. Chem. Soc., Dalton Trans.* 663 (2000).
- S. R. Batten, B. F. Hoskins, and R. Rocson, *Angew. Chem., Int. Ed. Engl.* 36, 636 (1997).
- W. W. Ellis, M. Schmitz, A. A. Arif, and P. J. Stang, *Inorg. Chem.* 39, 2547 (2000).
- M. C. Hong, W. P. Su, R. Cao, M. Fujita, and J. X. Lu, *Chem. Eur. J.* 6, 427 (2000).
- J. D. Ranford, J. J. Vittal, D. Q. Wu, and X. D. Yang, *Angew. Chem., Int. Ed. Engl.* 38, 3498 (1999).
- W. Jaunky, M. W. Hosseini, J. M. Planeix, A. De Cian, N. Kyritsakas, and J. Fischer, *Chem. Commun.* 2313 (1999).
- R. W. Saalfrank, H. Maid, F. Hampel, and K. Peters, *Eur. J. Inorg. Chem.* 1859 (1999).
- O. Mamula, A. Von Zelewsky, T. Bark, and G. Bernardinelli, *Angew. Chem., Int. Ed. Engl.* 38, 2945 (1999).
- T. Ezuhara, K. Endo, and Y. Aoyama, *J. Am. Chem. Soc.* 121, 1, 3279 (1999).
- C. Kaes, M. W. Hosseini, C. E. F. Rickard, B. W. Skelton, and A. H. White, *Angew. Chem., Int. Ed. Engl.* 37, 920 (1998).
- D. Whang, J. Heo, C. A. Kim, and K. Kim, *Chem. Commun.* 2361 (1997).
- E. Psillakis, J. C. Jeffery, J. A. McCleverty, and M. D. Ward, *Dalton Trans.* 1645 (1997).
- M. A. Withersby, A. J. Blake, N. R. Champness, P. Hubberstey, W. S. Li, and M. Schroder, *Angew. Chem., Int. Ed. Engl.* 36, 2327 (1997).
- M. A. Withersby, A. J. Blake, N. R. Champness, P. A. Cooke, P. Hubberstey, W. S. Li, and M. Schroder, *Inorg. Chem.* 38, 2259 (1999).
- M. Fujita, Y. J. Kwon, O. Sasaki, K. Yamaguchi, and K. Ogura, *J. Am. Chem. Soc.* 117, 7287 (1995).
- M. Fujita, O. Sasaki, K. Y. Watanabe, K. Ogura, and K. Yamaguchi, *New J. Chem.* 22, 189 (1998).
- L. Carlucci, G. Ciani, and D. M. Proserpio, *Dalton Trans.* 1799 (1999).
- C. M. Liu, X. Z. You, and W. Chen, *J. Coord. Chem.* 46, 183 (1998).
- L. Carlucci, G. Ciani, and D. M. Proserpio, *Chem. Commun.* 449 (1999).
- C. B. Aakeroy and A. M. Beatty, *Cryst. Eng.* 1, 39 (1998).
- K. S. Min and M. P. Suh, *J. Solid State Chem.* 152, 183 (2000).
- D. Venkataraman, S. Lee, J. S. Moore, P. Zhang, K. A. Hirsch, G. B. Gardner, A. C. Covey, and C. L. Prentice, *Chem. Mater.* 8, 2030 (1996).
- P. Losier and M. J. Zaworotko, *Angew. Chem., Int. Ed. Engl.* 35, 2779 (1996).
- T. L. Hennigar, D. C. MacQuarrie, P. Losier, R. D. Rogers, and M. J. Zaworotko, *Angew. Chem., Int. Ed. Engl.* 36, 972 (1997).
- A. J. Blake, N. R. Champness, A. N. Khlobystov, D. A. Lemenovskii, W. S. Li, and M. Schroder, *Chem. Commun.* 2027 (1997).
- L. Carlucci, G. Ciani, and D. M. Proserpio, *Chem. Commun.* 449 (1999).
- O. M. Yaghi, H. Li, and T. L. Groy, *Inorg. Chem.* 36, 4292 (1997).

69. M.-L. Tong, H.-J. Chen, and X.-M. Chen, *Inorg. Chem.* 39, 2235 (2000).
70. L. Carlucci, G. Ciani, M. Moret, D. M. Proserpio, and S. Rizzato, *Angew. Chem., Int. Ed. Engl.* 39, 1506 (2000).
71. M. J. Zaworotko, *Chem. Commun.* 1 (2001).
72. S. R. Batten, *Cryst. Eng. Commun.* 18 (2001).
73. M. Fujita, Y. J. Kwon, S. Washizu, and K. Ogura, *J. Am. Chem. Soc.* 116, 1151 (1994).
74. M. Kondo, M. Shimamura, S. Noro, S. Minakoshi, A. Asami, K. Seki, and S. Kitagawa, *Chem. Mater.* 12, 1288 (2000).
75. S. R. Batten, B. F. Hoskins, and R. Robson, *New J. Chem.* 22, 173 (1998).
76. B. F. Abrahams, M. J. Hardie, B. F. Hoskins, R. Robson, and E. E. Sutherland, *Chem. Commun.* 1049 (1994).
77. R. H. Groeneman, L. R. MacGillivray, and J. L. Atwood, *Chem. Commun.* 2735 (1998).
78. M. Aoyagi, K. Biradha, and M. Fujita, *Bull. Chem. Soc. Jpn.* 73, 1369 (2000).
79. S. Subramanian and M. J. Zaworotko, *Angew. Chem., Int. Ed. Engl.* 34, 2127 (1995).
80. D. Hagrman, R. P. Hammond, R. Haushalter, and J. Zubieta, *Chem. Mater.* 10, 2091 (1998).
81. J. Lu, T. Paliwala, S. C. Lim, C. Yu, T. Y. Niu, and A. J. Jacobson, *Inorg. Chem.* 36, 923 (1997).
82. L. R. MacGillivray, R. H. Groeneman, and J. L. Atwood, *J. Am. Chem. Soc.* 120, 2676 (1998).
83. S. H. Park, K. M. Kim, S. Lee, and O. S. Jung, *Bull. Korean Chem. Soc.* 19, 79 (1998).
84. Z.-Y. Fu, P. Lin, W.-X. Du, L. Chen, C.-P. Cui, W.-J. Zhang, and X.-T. Wu, *Polyhedron* 20, 1925 (2001).
85. J.-C. Dai, S.-M. Hu, X.-T. Wu, Z.-Y. Fu, W.-X. Du, H.-H. Zhang, and R.-Q. Sun (unpublished result).
86. L. Carlucci, G. Ciani, and D. M. Proserpio, *New J. Chem.* 22, 1319 (1998).
87. M. Kondo, M. Shimamura, S. Noro, S. Minakoshi, A. Asami, K. Seki, and S. Kitagawa, *Chem. Mater.* 12, 1288 (2000).
88. M. Kondo, A. Asami, K. Fujimoto, S. Noro, S. Kitagawa, T. Ishii, and H. Matsuzaka, *Int. J. Inorg. Mater.* 1, 73 (1999).
89. Y. B. Dong, M. D. Smith, R. C. Layland, and H. C. Zur Loye, *Chem. Mater.* 12, 1156 (2000).
90. Y. B. Dong, M. D. Smith, R. C. Layland, and H. C. Zur Loye, *J. Chem. Soc., Dalton Trans.* 775 (2000).
91. C. V. K. Sharma and R. D. Rogers, *Cryst. Eng.* 1, 19 (1998).
92. H. J. Choi and M. P. Suh, *J. Am. Chem. Soc.* 120, 10622 (1998).
93. R. Masse, J. F. Nicoud, M. Bagieu-Beucher, and C. Bourgeois, *Chem. Phys.* 245, 365 (1999).
94. M. A. Withersby, A. J. Blake, N. R. Champness, P. A. Cooke, P. Hubberstey, and M. Schroder, *New J. Chem.* 23, 573 (1999).
95. Y. B. Dong, R. C. Layland, N. G. Pschirer, M. D. Smith, U. H. F. Bunz, and H. C. Zur Loye, *Chem. Mater.* 11, 1413 (1999).
96. K. N. Power, T. L. Hennigar, and M. J. Zaworotko, *New J. Chem.* 22, 177 (1998).
97. J.-C. Dai, X.-T. Wu, Z.-Y. Fu, C.-P. Cui, S.-M. Hu, W.-X. Du, L.-M. Wu, H.-H. Zhang, and R.-Q. Sun, *Inorg. Chem.* 41, 1391 (2002).
98. Z.-Y. Fu, X.-T. Wu, J.-C. Dai, S.-M. Hu, and W.-X. Du, *New J. Chem.* 26, 978 (2002).
99. A. Rujiwatra, C. J. Kepert, and M. J. Rosseinsky, *Chem. Commun.* 2307 (1999).
100. S. Kitagawa and M. Kondo, *Bull. Chem. Soc. Jpn.* 71, 1739 (1998).
101. C. J. Kepert and M. J. Rosseinsky, *Chem. Commun.* 375 (1999).
102. M. Kondo, T. Yoshitomi, K. Seki, H. Matsuzaka, and S. Kitagawa, *Angew. Chem., Int. Ed. Engl.* 36, 1725 (1997).
103. Z.-Y. Fu, X.-T. Wu, J.-C. Dai, L.-M. Wu, C.-P. Cui, and S.-M. Hu, *Chem. Commun.* 1856 (2001).
104. Z.-Y. Fu and X.-T. Wu (unpublished result).
105. W.-P. Su, M.-C. Hong, J.-B. Weng, R. Cao, and S.-F. Lu, *Angew. Chem., Int. Ed. Engl.* 39, 2911 (2000).
106. J.-C. Dai, S.-M. Hu, X.-T. Wu, Z.-Y. Fu, and W.-X. Du (unpublished result).
107. M. J. Zaworotko, *Chem. Soc. Rev.* 23, 283 (1994).
108. R. Robson and B. F. Hoskins, *J. Am. Chem. Soc.* 112, 1546 (1990).
109. R. Robson, B. F. Abrahams, S. R. Batten, R. W. Gable, B. F. Hoskins, and J. Liu, "Supramolecular Architecture," Chap. 19. American Chemical Society, Washington, DC, 1992.
110. M. J. Plater, A. J. Roberts, J. Marr, E. E. Lachowski, and R. A. Howie, *J. Chem. Soc., Dalton Trans.* 797 (1998).
111. D. Venkataraman, G. B. Gardner, S. Lee, and J. S. Moore, *Nature* 374, 792 (1995).
112. B. F. Abrahams, B. F. Hoskins, J. P. Liu, and R. Robson, *J. Am. Chem. Soc.* 113, 3045 (1991).
113. S. Lopez, M. Kahraman, M. Harmata, and S. W. Keller, *Inorg. Chem.* 36, 6138 (1997).
114. A. J. Blake, N. R. Champness, A. N. Khlobystov, D. A. Lemenovskii, W.-S. Li, and M. Schroder, *Chem. Commun.* 1339 (1997).
115. L. Carlucci, G. Ciani, D. M. Proserpio, and S. Rizzato, *Chem. Eur. J.* 8, 1520 (2002).
116. L. R. MacGillivray, S. Subramanian, and M. J. Zaworotko, *Chem. Commun.* 1325 (1994).
117. T. Otieno, S. J. Rettig, R. C. Thompson, and J. Trotter, *Inorg. Chem.* 32, 1607 (1993).
118. L. Carlucci, G. Ciani, D. M. Proserpio, and A. Sironi, *Chem. Commun.* 2755 (1994).
119. O. R. Evans, R. G. Xiong, Z. Y. Wang, G. K. Wong, and W. B. Lin, *Angew. Chem., Int. Ed. Engl.* 38, 536 (1999).
120. O. R. Evans, Z. Y. Wang, R. G. Xiong, B. M. Foxman, and W. B. Lin, *Inorg. Chem.* 38, 2969 (1999).
121. K. A. Hirsch, D. Venkataraman, S. R. Wilson, J. S. Moore, and S. Lee, *Chem. Commun.* 2199 (1995).
122. Z.-F. Chen, R.-G. Xiong, B. F. Abrahams, X.-Z. You, and C.-M. Che, *J. Chem. Soc., Dalton Trans.* 2453 (2001).
123. O. R. Evans and W. B. Lin, *Chem. Mater.* 13, 2705 (2001).
124. L. Carlucci, G. Ciani, D. M. Proserpio, and S. Rizzato, *Chem. Eur. J.* 8, 1520 (2002).
125. D. S. Reddy, T. Dewa, K. Endo, and Y. Aoyama, *Angew. Chem., Int. Ed.* 39, 4266 (2000).
126. Z.-Y. Fu, X.-T. Wu, J.-C. Dai, S.-M. Hu, and W.-X. Du, *Eur. J. Inorg. Chem.* 2730 (2002).
127. J.-C. Dai, S.-M. Hu, X.-T. Wu, Z.-Y. Fu, and W.-X. Du (unpublished result).
128. J. Tao, M.-L. Tong, and X.-M. Chen, *J. Chem. Soc., Dalton Trans.* 3669 (2000).
129. Z.-Y. Fu and X.-T. Wu (unpublished result).
130. S. Subramanian and M. J. Zaworotko, *Angew. Chem., Int. Ed. Engl.* 34, 2127 (1995).
131. H. Li, M. Eddaoudi, M. O'Keeffe, and O. M. Yaghi, *Nature* 402, 276 (1999).
132. M. Eddaoudi, J. Kim, N. Rosi, D. Vodak, J. Wachter, M. O'Keeffe, and O. M. Yaghi, *Science* 295, 469 (2002).
133. J.-C. Dai, X.-T. Wu, S.-M. Hu, and Z.-Y. Fu (unpublished result).
134. J.-C. Dai, S.-M. Hu, X.-T. Wu, Z.-Y. Fu, and W.-X. Du (to be published).
135. S. S.-Y. Chui, S. M.-F. Lo, J. P. H. Charmant, A. G. Orpen, and I. D. Williams, *Science* 283, 1148 (1999).
136. O. M. Yaghi, C. E. Davis, G. Li, and H. Li, *J. Am. Chem. Soc.* 119, 2861 (1997).
137. B. Chen, M. Eddaoudi, T. M. Reineke, J. W. Kampf, M. O'Keeffe, and O. M. Yaghi, *J. Am. Chem. Soc.* 122, 11559 (2000).
138. B. Chen, M. Eddaoudi, S. T. Hyde, M. O'Keeffe, and O. M. Yaghi, *Science* 291, 1021 (2001).
139. J.-C. Dai, X.-T. Wu, Z.-Y. Fu, S.-M. Hu, W.-X. Du, C.-P. Cui, L.-M. Wu, H.-H. Zhang, and R.-Q. Sun, *Chem. Commun.* 12 (2002).

140. J.-C. Dai, X.-T. Wu, Z.-Y. Fu, S.-M. Hu, and W.-X. Du (unpublished result).
141. B. F. Abrahams, S. R. Batten, M. J. Grannas, H. Hamit, B. F. Hoskins, and R. Robson, *Angew. Chem., Int. Ed.* 38, 475 (1999).
142. Y.-C. Jiang, Y.-C. Lai, S.-L. Wang, and K.-H. Lii, *Inorg. Chem.* 40, 5320 (2001).
143. Y. C. Liang, R. Cao, W. P. Su, M. C. Hong, and W. J. Zhang, *Angew. Chem., Int. Ed.* 39, 3304 (2000).
144. Z.-Y. Fu, X.-T. Wu, J.-C. Dai, W.-X. Du, S.-M. Hu, H.-H. Zhang, and R.-Q. Sun (unpublished result).
145. J.-C. Dai, X.-T. Wu, Z.-Y. Fu, S.-M. Hu, and W.-X. Du (unpublished result).
146. R. P. Feynman, *Eng. Sci.* 22 (1960).

Surface Functionalization of Semiconducting Nanoparticles

Marie-Isabelle Baraton

University of Limoges, Limoges, France

CONTENTS

1. Introduction
 2. Infrared Spectra and Electronic Properties of Semiconducting Nanoparticles
 3. Experimental Procedure
 4. TiO₂ and SnO₂ Nanoparticles as Examples
 5. Conclusions
- Glossary
References

1. INTRODUCTION

Following the successful synthesis of particles with an average size in the nanometer range (nanosized particles, also called nanoparticles), the analyses of their characteristics have led scientists to the conclusion that a decrease of the particle size below 100 nm brings unique properties. Impressive laboratory demonstrations have been widely reported in the scientific and popular press, drawing attention of more scientists, companies, and technology investors.

It is now well recognized that, if the particle size is in the 10-nm range or below, the particle itself can be considered as a surface in three dimensions [1, 2]. For example, in a cube with dimensions less than 3 nm, 50% of all atoms of the particle are surface atoms [3]. As a consequence, the surface properties tend to predominate over those of the bulk. The result can be particularly dramatic when the considered material is a semiconductor because, in this case, the electronic properties are dependent upon surface effects, rather than bulk effects [3]. The electronic properties of a surface are determined mainly by its atomic structure, which in turn depends on the chemical origin of the surface atoms and their mutual arrangement [4]. In addition, the chemical composition of surfaces continuously evolves to balance forces at the interface between the material and its environment. Therefore, at the nanometer size, material properties reflect the nature of unavoidable adsorbates and surface

contaminants and it becomes very difficult to define intrinsic properties that are free and independent of environmental factors [3]. The control of the surface structure and surface chemical composition is therefore a necessary prerequisite for ensuring reliable and reproducible properties of semiconducting nanoparticles and nanostructured devices [5, 6].

Although the surface dominance appears as an important drawback for the electronic properties of nanosized particles, it can be turned into an advantage. Indeed, any process that causes a change in the atomic structure will result in modification of the surface electronic properties [4]. For example, adsorption of foreign atoms or molecules implies rearrangement of surface chemical bonds, and consequently leads to variation of the surface-states density and of the work function. Therefore, it should be possible to tailor the electronic properties of nanosized particles by functionalizing their surface. The possibility of tailoring the surface properties of semiconductors is actually seen as a stimulating challenge [7]. Over the last years, a tremendous research effort has developed, directed at developing procedures suitable to graft organic molecular fragments onto surfaces of nanomaterials (such as Si and SiO_x), leading to stable termination [8 and references within]. The grafting of molecular entities onto whatever surface results in the formation of new bonds and new surface species, thus altering the original atomic arrangement at the surface. But when the surface to be modified is that of a semiconductor material, the grafting may lead to the modification of the surface electronic structure, thus causing charge transfer and electron redistribution between the semiconductor surface atoms, the surface states, and the grafted species [4]. Consequently, the work function will also be modified. Additionally, when the semiconductor sample is a nanosized particle, the surface modification may totally alter the bulk electronic properties. Obviously, control and monitoring of the chemical changes of the surface at the atomic level are strong requirements in order to master the surface functionalization. But in most cases, it should additionally be made sure that the newly introduced surface functionality does not deteriorate the properties of the particle core [9].

This chapter is not intended to review all the studies performed on the chemical functionalization of nanoparticle surfaces or on the passivation of semiconductor surfaces. It is rather devoted to heightening the reader awareness about the difficulties to be faced when functionalizing semiconducting nanoparticles. Indeed, when surface functionalization becomes necessary to (simultaneously or not) optimize the fabrication of a device (e.g., homogeneous dispersion of nanoparticles in an organic matrix), modify the surface chemistry (e.g., control of the surface reactions at the interface), tailor the electrical properties (e.g., enhancement of gas sensor selectivity), the following steps have to be equally and simultaneously mastered:

1. Chemical characterization of the first atomic layer of the nanoparticles surface before and after surface functionalization.
2. Selection of the most appropriate molecules to be used for surface functionalization.
3. Determination of the conditions under which the nanoparticles surface should be pretreated to optimize the functionalization.
4. Monitoring of the surface reactions during the functionalization.
5. Stability of the surface functionalization under the final working conditions of the functionalized semiconductor.
6. Analysis of the consequences on the surface reactivity and on the electrical properties of the semiconducting nanoparticles.

These items will be discussed for titanium oxide and tin oxide nanoparticles selected as examples. Both materials are n-type semiconductors, easily synthesized as nanosized particles by various methods including industrial processes, and widely used in the fabrication of cost-effective chemical gas sensors (see, e.g., [10]). It will be demonstrated that Fourier transform infrared (FTIR) spectroscopy is a powerful tool to fulfill all the six above-listed requirements. Indeed, thanks to their high specific surface area, it is possible to characterize the chemical species at the nanoparticle surface. Additionally, because infrared absorption is affected by the free carrier density of the material, it is possible to simultaneously analyze the surface chemical reactions at the origin of the gas detection mechanism and the resulting variations of the electronic conductivity. This is an important advantage of this characterization technique which allows the rapid screening of the sensing properties of various semiconducting nanoparticles before embarking in the complex fabrication of the device.

The first part of the chapter (Section 2) is devoted to the FTIR technique, its possibilities and performance, including surface chemical analysis and investigation of the electronic properties. Then, in a second part (Section 3), is explained the experimental procedure to control the surface functionalization and to monitor the surface reactions *in-situ*. In Section 4, results on titanium oxide (n-TiO₂) and tin oxide (n-SnO₂) nanoparticles are presented to illustrate the surface functionalization of semiconducting nanoparticles and to discuss its consequences on the gas sensing properties of both materials.

2. INFRARED SPECTRA AND ELECTRONIC PROPERTIES OF SEMICONDUCTING NANOPARTICLES

As a reminder, this section summarizes the fundamentals of infrared spectroscopy and the experimental conditions specific to the surface analysis of nanosized particles. In addition, it is recalled how the modulation of the free carrier density in a semiconductor space-charge region affects the infrared spectrum.

2.1. Fundamentals of Infrared Spectroscopy

It is well known that the infrared spectrum of a molecule originates from the absorption of the infrared energy at discrete wavelengths, thus exciting the interatomic vibrations. A nonlinear molecule consisting of N atoms has $3N$ degrees of freedom, including 3 degrees for translation and 3 degrees for rotation. The remaining $3N - 6$ degrees of freedom correspond to the fundamental vibrations or normal modes and are generally described as bond stretching, bond bending, and torsional modes. These fundamental vibrations lead to absorption bands in the infrared range depending on the symmetry of the vibrations with respect to the symmetry elements of the molecule. In the harmonic oscillator approximation, the frequency of the absorption bands depends on the reduced mass of the vibrating atoms and on the force constant of the bonds (for more details on infrared spectroscopy and spectrometers, see, e.g., [11–14]).

As for mathematical treatment, many of the most important algorithms used in absorption infrared spectroscopy (such as spectral subtraction) rely on the Bouguer–Beer–Lambert law (commonly referred to as Beer's law), according to which the absorbance A of a sample at a given wavenumber λ is linearly proportional to the concentration of the absorber:

$$A(\lambda) = a(\lambda)bc$$

where $a(\lambda)$ is the absorptivity at λ , b is the pathlength, and c is the concentration of the absorber.

When an infrared beam crosses whatever sample, the transmitted beam contains information not only on the interatomic bonds constituting the bulk, but also on the chemical groups at the sample surface. Obviously, the latter are a minority by far. But, when the size of the sample is sufficiently decreased (e.g., nanoparticles), the concentration of the surface groups relative to that of the bulk interatomic bonds significantly increases and the contribution of these surface groups to the overall infrared absorption becomes no longer negligible. This is the reason why transmission infrared spectrometry can be conveniently used for the surface analysis of nanosized particles. However, in most cases, the absorption bands due to the surface groups remain much weaker than those due to the bulk modes. To further increase the absorption of the surface groups, their concentration has to be increased. This is achieved by analyzing the powdered sample without any dilution in an IR transparent material (such as the very popular potassium bromide). Under these conditions, the absorptions due to both bulk and surface groups are simultaneously enhanced,

obviously resulting in a noticeable absorption of the surface groups, whereas the sample becomes opaque in the wavenumber region where the bulk modes absorb.

2.2. Surface Infrared Spectroscopy of Nanoparticles

Because the infrared transmission spectrum contains information on both bulk and surface, it becomes therefore necessary to discriminate the absorption bands due to the bulk modes from those due to the vibrations of the surface groups. From the prior discussion, it is obvious that the most intense absorption bands are due to the bulk modes. But, this does not mean that all the weak bands can be certainly assigned to the vibrations of surface groups. In fact, precise experiments must be performed to discriminate the absorption bands due to surface species from those originating from the bulk (overtones/combinations of bulk modes and eventually impurities trapped in the bulk or closed pores) [15].

The detailed surface characterization procedure of nano-sized particles can be found elsewhere [15–21] but it can be summarized in a brief and simplistic way as follows. The first and obvious step consists in observing the transmission spectrum of the nanoparticles and identifying the absorption bands which cannot be assigned to the bulk modes due to their absorption frequencies. For example, bands in the 1700–1550 cm^{-1} range, which can reasonably be assigned to CO_3^{2-} carbonates groups, should not appear in the transmission spectrum of perfectly pure zirconium oxide. Therefore, the existence of these bands proves that impurities are present either in the bulk or on the surface of zirconia. More generally, the presence of absorption bands at relatively high wavenumbers (above 1000 cm^{-1}) in the transmission spectrum of ceramics can usually be assigned to contaminating organic entities. Indeed, the bulk modes of ceramics generally absorb in the lowest wavenumber range (approximately below 1000 cm^{-1}) due to the high weight of the atoms constituting the bulk. To check whether these foreign chemical species are located on the surface or trapped inside the bulk, the sample is desorbed at increasing temperatures. Usually, surface chemical species are either released (desorbed) or transformed by heating under vacuum. If it is not the case, the foreign species are to be possibly assigned to impurities trapped in the bulk or in closed pores.

The second step of the surface analysis consists in characterizing the surface reactive sites. This is achieved by adsorbing selected molecules (referred to as probe-molecules) onto the surface and by comparing the infrared spectrum of the probe-molecule with that of the gas phase. Depending on the observed spectral modifications, information is obtained on different kinds of sites at the surface, on the acidity or the basicity of these sites, and on their strength. To obtain a complete picture of the surface sites, various complex experiments are necessary with different types of carefully chosen probe-molecules [15, 20, 22, 23]. Additionally, the interaction of probe-molecules with the chemical species identified during the first step constitutes the ultimate proof that these chemical species are located right on the particle surface.

Once the surface is characterized, it is possible to envisage chemical modifications by making appropriate molecules

react with the surface sites or the surface species. It must, however, be kept in mind that the nature, concentration, and reactivity of the surface sites and surface species depend on the temperature and the environmental conditions as well. Therefore, a pretreatment by heating under dynamic vacuum (referred to as *activation*) may be necessary to clear the nanoparticle surface from various impurities and to free surface reactive sites in order to allow the grafting of new molecules or chemical entities on the surface.

2.3. Infrared Absorption by Free Carriers

While surface infrared spectroscopy allows the characterization of the chemical nature of the surface species, the identification of the bonding sites, and the determination of adsorbate geometry through symmetry analysis, absorption due to surface electronic phenomena represents an intrinsic part of the infrared spectrum of semiconductors. Indeed, the semiconducting property originates from the mobility of free carriers which are electrons (n-type semiconductors) or holes (p-type semiconductors) and, according to the Drude–Zener theory [24, 25], these free carriers contribute to the absorption by the material over the whole infrared range. The absorption of the free carriers has been ignored in vibrational studies because it is very broad compared to the sharp vibrational bands [26]. Actually, the obvious application of infrared absorption to vibrational spectroscopy has often masked the useful information that can be derived from absorption due to surface electronic phenomena [27].

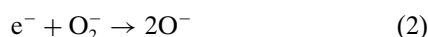
In 1962, Harrick [28] published an article bringing experimental evidence of the contribution of the free carriers to the infrared absorption spectrum of silicon. In that experiment, the absorption of an infrared beam by a silicon wafer is measured while applying an external alternating electric field to the wafer. As a result, the modulating field alters the free carrier density in the semiconductor space-charge region and a broad band (intra-band) appears in the infrared spectrum, characteristics of the free carrier absorption. Most theories predict a λ^n dependence (λ being the infrared wavelength), where n generally equals 2 although variations often occur. The infrared absorption changes due to the free carriers are positive or negative depending on whether carriers are added to or subtracted from the surface. For example, electrons subtracted from the space-charge region of an n-type semiconductor surface will lead to an increase of the infrared transmission (i.e., a decrease of the IR absorption), while electrons subtracted from the space-charge region of a p-type semiconductor surface will lead to a decrease of the IR transmission (i.e., an increase of the IR absorption) [28]. From the above and as stated by Harrick, a measure of the infrared absorption “can be used to monitor the free carrier density in the semiconductor space-charge region and to obtain the spectra of foreign molecules chemisorbed on the surface.”

In Harrick’s experiment, the free carrier density was modulated by an external electric field, but such modulation can also be obtained by varying the gaseous environment of the semiconductor [26]. The variation of the free carrier density, that is, the variation of the electrical conductivity, induced by adsorption of gases is actually the fundamental principle of the gas detection mechanism by chemical

gas sensors based on semiconductors [29]. Therefore, as summarized in Figure 1, it appears that FTIR spectroscopy allows one to follow *in-situ* the reactions taking place at the gas-nanoparticle interface *simultaneously* with the variations of the background infrared absorption which are related to the variations of the electrical conductivity. It then becomes clear that FTIR surface spectroscopy is an excellent method to fundamentally study the gas detection mechanisms taking place in semiconductor-based sensors. It must be stressed that, in this particular case, FTIR spectrometry combines the investigations of two related phenomena (surface reactions and electrical conductivity) involving different thicknesses of the material. Indeed, the surface reactivity concerns only the first atomic layer, whereas the thickness variation of the depletion layer may concern up to several tens of nanometers.

2.4. Application to Gas Sensors

As mentioned earlier, the detection of gases by semiconductor gas sensors is based on the variations of the electrical conductivity induced by adsorption of oxidizing or reducing gases on the semiconductor surface [29]. The adsorption of oxygen on a semiconductor causes a decrease of the electron density in the conduction band due to the formation of negatively charged oxygen species (ionisorbed species), such as O^- or O_2^- [29, 30]:



These oxygen species together with the oxide ions of the lattice play a critical role in all oxidation reactions [31]. It has been demonstrated that O^- is much more active than O_2^- [32, 33]. However, the respective part played by each oxygen species also depends on the reaction temperature as, for example on the SnO_2 surface, the O_2^- species are expected to be the dominant species below 673 K [33]. The oxygen ionosorption, causing an electron transfer from the surface of the particle toward the adsorbed species, leads to

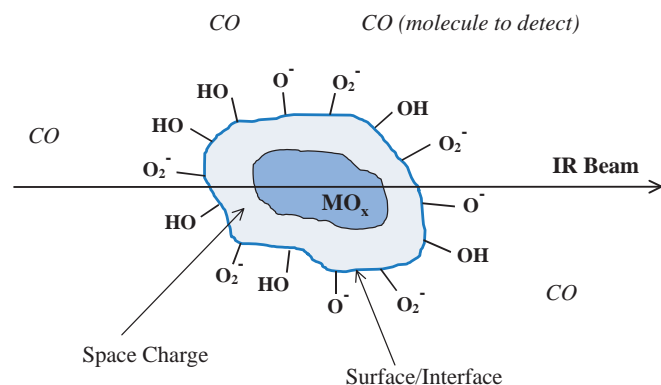
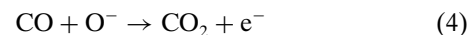
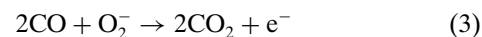


Figure 1. Schematic representation of the analysis of a nanosized semiconducting particle by FTIR transmission spectroscopy. The infrared beam transmitted by the semiconducting nanoparticle contains information on the bulk, the space-charge region, the surface chemical groups, the adsorbed species, and the gaseous environment, *simultaneously*.

the formation of an electron-depleted surface layer (space-charge region).

On the contrary, when a reducing gas, such as CO, adsorbs, electrons are injected into the conduction band. It is generally agreed that CO reacts with ionic oxygen to form CO_2 , releasing electrons in the conduction band [34, 35]. The reactions depend upon the temperature and the ionic state of oxygen:



From these reactions, we note that a competition results between oxygen removing electrons and the reducing gas (CO) restoring electrons [29]. The steady-state value of the conductance is therefore dependent on the concentration of the reducing gas.

The reducing gas can also extract lattice oxygen (O_L^{2-}) from the surface, leaving oxygen vacancies (V_O), which will be further removed by adsorption of gaseous oxygen from the ambient [29]:



The effects of the above-mentioned reactions on the infrared spectrum are twofold:

- The absorption bands corresponding to gaseous CO_2 are observed.
- The background absorption level of the spectrum varies due to the variations of the electron density in the space-charge region, as explained in Section 2.3.

The infrared spectrum of an n-type semiconductor, such as tin oxide or titanium oxide, shows a decrease of the background absorption level under oxidizing gases, whereas an increase of the background absorption level is observed under reducing gases. In terms of infrared energy transmitted by the sample, an increase of the electrical conductivity leads to a decrease of the transmitted infrared energy, whereas a decrease of the electrical conductivity leads to an increase of the transmitted infrared energy.

Therefore, to summarize the above considerations, the study of the evolution of the infrared spectra of semiconducting nanoparticles under various gaseous environments makes it possible to determine the surface reactions at the origin of the electrical conductivity changes.

2.5. Surface Functionalization of Nanoparticles

Even though semiconductor sensors based on metal oxides have been commercialized for many years due to their low cost and their good sensitivity to combustible gases, they suffer from a major drawback, namely a cross-sensitivity to humidity which makes their response unreliable for outdoor operation. Indeed, it has been generally observed that many metal oxide sensors change their response at high humidity level [29, 36]. Water vapor is probably one of the most important factors affecting SnO_2 -based sensor characteristics and may seriously change the baseline value and even produce a false alarm [37]. The influence of water on the gas

sensing mechanism is not totally elucidated, although it is expected that the surface hydroxyl (OH) groups play a major role. Therefore, to reduce the cross-sensitivity to humidity of the final sensor, it has been envisaged to decrease the density of the OH groups at the nanoparticle surface [38]. In addition, surface modifications of semiconducting nanoparticles, such as TiO₂, have been extensively used for improvement of photocatalytic properties, optical properties, dispersibility, among others (see, e.g., [39–41]). On a more general basis, the modification of surface properties by coupling special groups onto the surface is becoming an increasingly popular approach to surface engineering [7, 42, 43].

Because of the presence of broken bonds and atoms in low coordination state, surfaces are highly reactive. Surfaces can be maintained clean only under ultra-high vacuum and become immediately contaminated as soon as the material is in contact with any atmosphere. The most probable contaminant is water which adsorbs to form hydroxyl (OH) groups at the surface. The adsorption of water on an oxide surface is energetically favorable because it terminates the material with the OH single-valent species in agreement with Pauling's valency rule [42, 44]. These OH surface groups play a major role in the chemical and electronic properties of materials and indeed, as mentioned earlier, their involvement in the gas detection mechanism in humid environment has disastrous consequences on the response reliability of metal oxide-based gas sensors.

On the one hand, the surface contamination by humidity cannot be avoided when the material has to be used under regular atmosphere. On the other hand, it is not possible to totally remove the OH groups from the surface without drastic treatments of the material which will inevitably lead to surface reconstruction over several atomic layers and will possibly cause modifications of the bulk structure and properties. As a consequence, the chemical modification/substitution of these OH groups by/for other chemical entities appears as an alternative method to tailor the surface chemistry.

For example, it has been known for several years that the hydrophilic character of a silica surface can be modified by grafting silanes onto the surface ([42, 45–48] among others). The surface OH groups are replaced with methylsilyl groups, thus altering the wetting or adhesion characteristics, the catalytic efficiency, the degree of agglomeration, and additional properties involving surface reactivity. Surface modification by grafting silane agents is also used for passivating slightly oxidized silicon or semiconductor surfaces [42]. In the present chapter, the grafting of silanes onto the tin oxide or titanium oxide surfaces is not intended to totally passivate the surface, but to selectively reduce the attraction for water of oxide surfaces.

However, due to the complexity of the SnO₂ and TiO₂ surfaces, the grafting of silanes onto these semiconductor surfaces is more complicated than in the case of silica. In addition, in the case of semiconductor surfaces, the replacement of OH groups with other chemical entities having different electron affinities and different electron withdrawing powers may substantially affect the surface states and the thickness of the space-charge region [4]. It becomes therefore clear that the modification of a semiconductor surface

by grafting chemical groups requires a chemical investigation of the surface before, during, and after the grafting, and an analysis of the grafting consequences on the electrical properties.

3. EXPERIMENTAL PROCEDURE

This section summarizes the experimental procedure allowing the *in-situ* correlation of the chemical reactions at the surface of semiconductor nanoparticles with the resulting variations of their electrical conductivity. More specific details on the FTIR surface characterization of nanosized ceramic powders and the necessary equipment can be found in [15].

3.1. Surface Analyses

As explained in Section 2.1, the concentration of the surface species has to be increased in order to enhance the intensities of their infrared absorption bands. To this end, the materials are analyzed without any dilution and the pure powders are slightly pressed into thin self-supported or grid-supported pellets. The pressure applied to make such pellets is very dependent on the nature of the material and it should be adjusted at the lowest possible level for each material so that neither the crystalline state nor the stoichiometry is perturbed. The latter is a critical parameter in the case of semiconductors.

The pellets are placed in the small furnace of a vacuum cell. This cell, specially designed to fit in the sample chamber of the spectrometer, allows the IR spectrum to be recorded *in-situ* at any temperature (from room temperature to 773 K) under vacuum or gaseous atmospheres. The cell is connected to vacuum pumps through a nitrogen trap and to gas cylinders and liquid containers. Defined pressures of gases or liquid vapors can be directly introduced inside the cell by using a precision valve system while selected mixtures of gases (or liquid vapors) can be prepared in a separate compartment before introduction.

When the sample is not transparent to the infrared radiation, it is possible to analyze it in diffuse reflectance mode, referred to as diffuse reflectance infrared Fourier transform spectroscopy (DRIFTS) [14, 15]. In this case, loose powders or thick films deposited on opaque substrates can be directly placed in the cup of the specific cell. Like in the transmission mode, an environmental chamber allows the spectra to be recorded *in-situ* at different temperatures under vacuum or different controlled atmospheres. This technique is particularly useful for the study of real sensors in which the sensing layer is deposited on an alumina tile opaque to the infrared radiation [49].

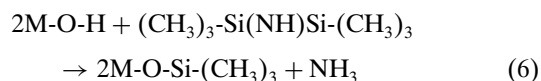
Depending on the targeted experiments, the nanoparticles may undergo a heat treatment under dynamic vacuum (referred to as *activation*) to remove the surface contaminating species that are physisorbed and weakly chemisorbed. These contaminants are mainly water and possibly some synthesis residues such as carbonate or nitrate groups. Surface carbonate groups can also originate from the adsorption of atmospheric carbon dioxide onto basic surface sites. Once these adsorbed species are eliminated, the surface is no longer in equilibrium and becomes *activated*. In other words,

an activated surface, which can only exist under vacuum, presents freed adsorption sites ready to adsorb any new molecules. The nature of the adsorption sites freed on an activated surface depends on the activation conditions (temperature and vacuum). Therefore, the activation conditions must be clearly described and taken into account when comparing the adsorption and reactive sites on the same material characterized by different researchers. In addition, it must be clearly understood that an *activated* surface is different from a *clean* surface. Indeed, a clean surface has never been exposed to environmental contamination (e.g., synthesis or crystal cleavage under ultra-high vacuum conditions) [50], whereas an activated surface is only partly freed from contaminating species. An attempt at complete cleaning by an increase of the activation temperature generally results in surface reconstruction and eventually grain growth.

When semiconducting nanoparticles are to be activated, additional consequences of the heat-treatment process are observed on the IR spectrum. Indeed, a heat treatment under dynamic vacuum usually leads to oxygen desorption from the surface layer of the material. This desorption causes an increase of the free electron density, that is, an increase of the free carrier density in an n-type semiconductor, such as tin and titanium oxides. As a consequence, an n-type semiconductor becomes opaque to the infrared radiation under activation. It is therefore easy to understand that the standard activation process is not always appropriate for surface characterization of n-type semiconducting nanoparticles. To overcome this difficulty, a slightly modified activation procedure has been developed [51], consisting in heating the semiconducting nanoparticles under dynamic vacuum up to 423 K to eliminate physisorbed water and eventually some very weakly bound impurities. Then, the sample is heated up to the chosen activation temperature under a few mbar of oxygen, thus avoiding oxygen desorption. Once the final activation temperature is reached, the cell is evacuated to remove the contaminants which have possibly desorbed from the surface during heating and a new dose of fresh oxygen is introduced to stabilize the stoichiometry. The semiconducting nanoparticles are then cooled under oxygen. This procedure has been applied to tin oxide nanoparticles from which oxygen is relatively easily desorbed. But, in the case of titanium oxide, the increase of the electrical conductivity during activation is not as critical as in the case of tin oxide, and the titanium oxide nanoparticles were activated under the standard conditions, that is, by heating under dynamic vacuum without oxygen addition.

3.2. Surface Functionalization by Grafting

The surface of the nanoparticles has been modified by grafting hexamethyldisilazane (HMDS) to reduce the density of OH groups on the surface. Hexamethyldisilazane is widely used for surface modifications because it exhibits a reasonably high vapor pressure, it is easy to handle, and is environmentally friendly. It usually reacts with hydroxyl groups on metal oxide surfaces by forming ammonia according to the reaction [46, 52–55]:



The OH groups are replaced with O-Si-(CH₃)₃ groups. If the reaction proceeds to completion, no OH group should be left on the surface and the surface is expected to become hydrophobic.

It is obvious that the grafting process is effective only if the OH groups linked to the surface atoms are accessible to HMDS molecules. This means that, as a very minimum condition, water molecules hydrogen-bonded to surface OH groups have to be eliminated. This is the reason why, prior to the HMDS grafting, an activation of the sample is necessary at a temperature sufficiently high to break these hydrogen bonds, that is, 423 K at least.

Thanks to the heatable vacuum cell attached to the FTIR spectrometer, the grafting reactions can be monitored *in-situ*. In order to check the stability of the grafting, it is possible to desorb the grafted sample at various temperatures, adsorb organic compounds, and analyze the behavior of the grafting species under particular environmental conditions. For example, as one of the objectives of the HMDS grafting onto tin and titanium oxides is to decrease the sensor cross-sensitivity to humidity, the stability of the grafted species in presence of water molecules has to be checked at the operating temperature of the real sensors.

In addition to the modification of the surface chemical species, the grafting process itself can eventually be an oxidizing or reducing treatment. In the case of HMDS, ammonia resulting from the grafting reaction may cause a reduction and therefore, an increase of the electrical conductivity of an n-type semiconductor. The consequences will be discussed in Section 4.3 and it must be kept in mind, that an oxidizing/reducing treatment may be necessary after surface functionalization of a semiconductor to restore its original oxidation state. Obviously, the surface grafted species must resist such oxidizing/reducing treatment, or if surface modification occurs in any way, it must benefit the functionalization purpose.

3.3. Evaluation of the Electrical Properties

As explained in Section 2.3, in the case of a semiconductor sample, it is possible to follow the variations of the free carrier density by observing the variations of the background absorption of the infrared spectrum. It must be clear that FTIR spectroscopy does not allow the absolute measurement of the electrical conductivity. However, this technique makes it possible to estimate the amplitude of the variations of the electrical conductivity of semiconductor nanoparticles in presence of oxidizing or reducing gases, that is, to assess the sensing potentiality of a material before embarking in the actual fabrication of the device. In addition, these analyses do not require any metallic electrode whose contact with the semiconductor material is known to perturb the electrical response [56].

While introducing gases into or evacuating the cell, the infrared equipment allows one to measure the infrared energy transmitted by the sample over the total infrared range. Therefore, during any “gas addition-evacuation” sequence, it is possible to quantify and to follow the variations of the transmitted infrared energy corresponding to the variations of the electrical conductivity while studying

the surface reactions and the evolution of the surface chemical groups through the analysis of the infrared spectra. The surface reactions can be directly correlated to the electrical conductivity variations, and this correlation is precisely the fundamentals of the gas detection mechanism by semiconductor-based sensors. As a result, the infrared spectroscopy technique appears as a very valuable tool for the fundamental understanding of resistive gas sensors.

4. TiO₂ AND SnO₂ NANOPARTICLES AS EXAMPLES

As explained in the introduction (cf. Section 1), this section will successively illustrate the following points:

- The characterization of the titanium oxide and tin oxide nanoparticle surfaces, that is, the identification of the surface species.
- The monitoring of the surface functionalization, namely the grafting of HMDS which is expected to reduce the hydrophilic character of the nanoparticle surface.
- The stability of the surface modifications under realistic conditions.
- The consequences of the surface modifications on the electrical properties and the sensing capability.

All these points are necessary steps to control the surface functionalization and master its consequences.

4.1. Surface Characterization of TiO₂ and SnO₂ Nanoparticles

Figure 2a shows the infrared spectrum of a pellet made of slightly pressed titanium oxide nanoparticles (from Degussa, P25). The average primary particle size given by the manufacturer is 21 nm and the material is a mixture of anatase (70%) and rutile (30%) phases. This infrared spectrum has been recorded at room temperature and under dynamic vacuum. The very broad and intense band centered at 3320 cm⁻¹ is assigned to the $\nu(\text{OH})$ stretching vibrations in water molecules and in H-bonded OH groups at the particle surface. The spectrum of the same sample recorded after

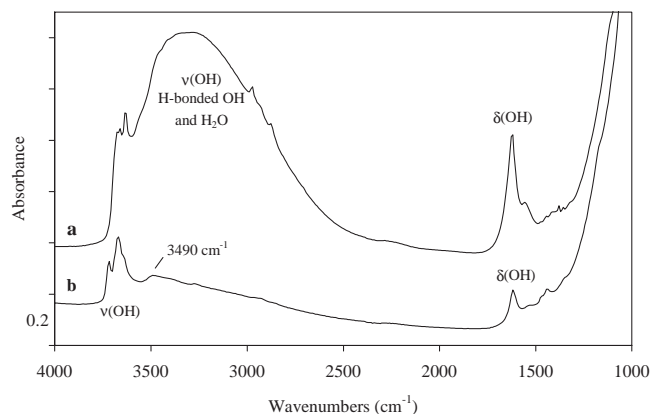


Figure 2. Infrared transmission spectrum of the TiO₂ nanoparticles at room temperature: (a) under dynamic vacuum; (b) after activation at 723 K. (The spectra have been shifted for clarity.)

activation at 723 K is presented in Figure 2b. The disappearance of the very broad band indicates the elimination of water molecules bonded to the surface OH groups [16].

At the end of the activation treatment (Fig. 2b), several bands in the 3780–3600 cm⁻¹ range are observed. All of them are assigned to $\nu(\text{OH})$ stretching vibrations in OH groups attached to titanium atoms at the TiO₂ surface [57, 58]. The multiplicity of these bands indicates that several types of OH groups exist at the surface. According to the literature [58–64], the number and the vibrational frequencies of these OH groups depend on the extent of the dehydroxylation and on the possible presence of impurities, which makes the comparison between different samples and between the results from different works extremely difficult. Moreover, the OH groups on the anatase surface are not exactly the same as those on the rutile surface [63]. It must also be taken into account in the band assignments that a hydroxyl group can be bonded to one titanium atom, or linked to two titanium atoms, or bridged to three titanium atoms. As a consequence, all these OH surface groups have a different reactivity, and it has been proved that most of them are Brønsted acid sites, whereas some other ones are Brønsted base sites [65]. Despite this complexity, the precise assignment of each absorption frequency to a particular type of surface OH groups can be found in several papers (see, e.g., [58–64]). In addition, the broad band at 3490 cm⁻¹ (Fig. 2b) may be assigned to adsorbed undissociated water which is retained on the surface by strong Lewis acid sites, namely coordinatively unsaturated Ti⁴⁺ sites [58, 60]. It must also be noted that the band at 1617 cm⁻¹ is assigned to the associated $\delta(\text{OH})$ bending vibration of undissociated water molecules [60].

The infrared spectrum of tin oxide nanoparticles pressed into a thin pellet is recorded at room temperature and under dynamic vacuum (Fig. 3a). These nanoparticles have been synthesized by laser evaporation of commercial micron-sized SnO₂ powder [66]. The average particle size for this particular powder is 15 nm and the material is crystallized in the rutile form. Due to the high mobility of oxygen, the tin oxide nanoparticles are activated under a low oxygen pressure (50 mbar) in order to avoid oxygen desorption, which would have led to the opacity of the sample to the infrared

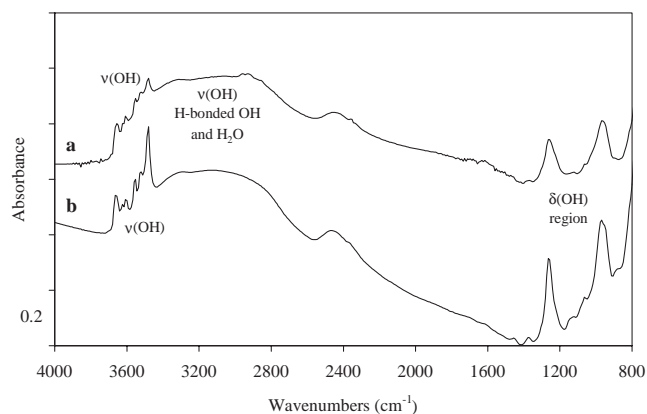


Figure 3. Infrared transmission spectrum of the SnO₂ nanoparticles at room temperature: (a) under dynamic vacuum; (b) after activation at 673 K under 50 mbar O₂. (The spectra have been shifted for clarity.)

radiation (cf. Section 3.1). Figure 3b corresponds to the tin oxide spectrum recorded after activation at 673 K under oxygen. Like in the case of n-TiO₂, a decrease of the broad band centered at 3200 cm⁻¹ is observed, although weaker. It corresponds to the elimination of water molecules adsorbed on the surface. After activation, the multiplicity of $\nu(\text{OH})$ bands, observed in the 3800–3200 cm⁻¹ region, indicates a large number of different types of surface OH groups [67–69]. The different vibrational frequencies of the OH groups originate from the diversity of the coordination types of the surface tin atoms to which the OH groups are bonded. Indeed, it is known that Sn²⁺ and Sn⁴⁺ along with oxygen vacancies can be present on the tin oxide surface [70], thus generating different electronic distributions in the attached OH groups. The bands in the 1500–1000 cm⁻¹ region are assigned to the corresponding $\delta(\text{OH})$ bending vibrations of these OH groups [71].

From the FTIR surface analyses, it not only appears that both TiO₂ and SnO₂ nanoparticles present hydroxyl groups at their surface, but also that several types of OH groups simultaneously exist. They are linked to different surface sites and they have different reactivities. As a consequence, it is necessary to monitor the grafting reactions to know whether all types of OH groups will be involved in the grafting process or whether the HMDS molecules will selectively react, leaving unperturbed OH groups behind.

As previously mentioned, the surface chemical characteristics are very dependent not only on the activation conditions but also on the synthesis parameters and eventually on the storage environment. Therefore, other batches or differently synthesized tin oxide or titanium oxide nanoparticles may present different infrared surface spectra, caused by different surface species or by variations in the relative density of similar surface species (as examples, see discussions in [59] for TiO₂ and [69] for SnO₂). It becomes obvious that a surface analysis of such materials cannot be considered as an absolute reference but should rather be regarded as informative for the investigation of one's own samples.

4.2. HMDS Grafting and Grafting Stability

The surface reaction leading to the modification of the OH groups at the silica surface by grafting hexamethyldisilazane molecules is well known (cf. Section 3.2). This is the reason why HMDS has been used as a test molecule to reduce the hydrophilic character of the titanium oxide and tin oxide surfaces. In the previous section (Section 4.1), it has been shown that both surfaces exhibit the surface OH groups necessary for such grafting reaction to proceed. Obviously, these OH groups have to be made accessible by removing physisorbed water molecules. This is achieved by a thermal pre-treatment (activation), as explained in Section 4.1. As a preliminary approach, the grafting is performed at room temperature by introducing a few mbar of HMDS liquid vapor in the infrared cell containing the activated sample. After a 30-minute contact, the cell is evacuated to remove HMDS in excess. If the functionalized nanoparticles have to be used at a temperature above room temperature, the sample must be thermally desorbed up to this working temperature at least, in order to check the thermal stability of the grafting.

To graft HMDS on titanium oxide, the nanoparticles are first activated at 673 K. Then, after contact between HMDS liquid vapor and the activated surface, the sample is thermally desorbed up to 673 K. All the steps of the grafting process are followed *in-situ* by recording the infrared spectra [54]. Figure 4 shows the evolution of the titanium oxide surface before (Fig. 4a) and after grafting. After HMDS desorption at 673 K (Fig. 4b), most of the $\nu(\text{OH})$ bands disappear, whereas new bands appear, particularly at 2973 and 2914 cm⁻¹, and at 1267 cm⁻¹. They are assigned to the $\nu(\text{CH}_3)$ stretching vibrations and to the $\delta(\text{CH}_3)$ bending vibration of Si-CH₃ groups, respectively [53, 55]. These bands are the proof that HMDS has successfully reacted with the surface OH groups according to reaction (6) (cf. Section 3.2) and that new trimethylsilyl Si(CH₃)₃ groups are linked to the TiO₂ surface. Some surface OH groups are still present but their density is smaller compared to that on the original titanium oxide surface. The difference between these two spectra (Fig. 4c) emphasizes the surface modifications: the negative bands ($\nu(\text{OH})$ and $\delta(\text{OH})$) correspond to the disappearing OH groups, whereas the positive bands ($\nu(\text{CH}_3)$ and $\delta(\text{CH}_3)$) correspond to the new surface species. Note that, due to the very high intensity of the $\delta(\text{CH}_3)$ absorption band compared to the $\nu(\text{CH}_3)$ bands, this $\delta(\text{CH}_3)$ band can be considered as a marker of a successful grafting. Therefore, by grafting HMDS on titanium oxide, the surface species, and consequently the surface reactivity, are modified. These modifications still persist after a desorption at 673 K, thus making it possible to envisage the use of these functionalized nanoparticles at temperatures up to 673 K.

However, because the functionalized TiO₂ nanoparticles are intended to be used in humid atmosphere at relatively high temperature, the stability of the grafted species must be checked under as realistic conditions as possible.

To this end, the HMDS-grafted n-TiO₂ sample has been placed in contact with regular atmosphere at 673 K. Figure 5 compares the infrared spectra of HMDS-grafted n-TiO₂ under vacuum (Fig. 5a) and under air (Fig. 5b) in the

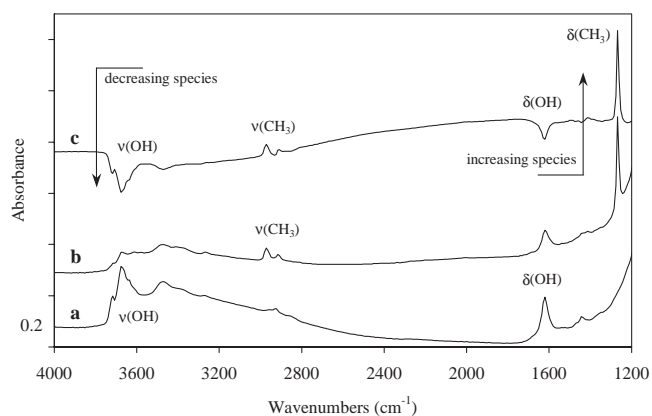


Figure 4. Infrared transmission spectrum of the TiO₂ nanoparticles at room temperature: (a) after activation at 673 K; (b) after HMDS grafting and desorption at 673 K. On spectrum c, corresponding to the difference between spectra a and b, the negative bands indicate the decreasing species, whereas the positive bands indicate increasing and new species. (The spectra have been shifted for clarity.)

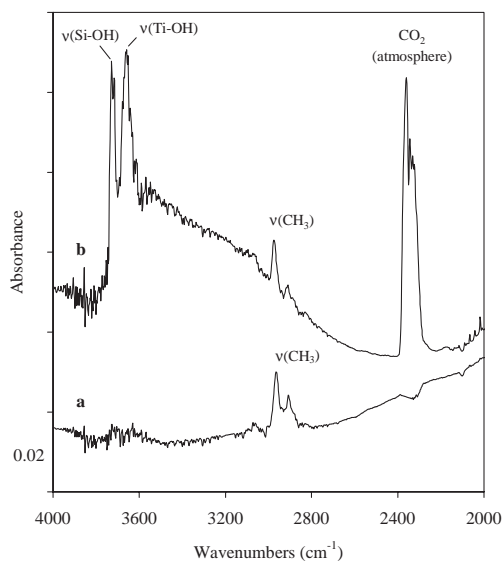


Figure 5. Infrared transmission spectrum of the HMDS-grafted TiO_2 nanoparticles at 673 K: (a) under dynamic vacuum; (b) under air. (The spectra have been shifted for clarity.)

4000–2000 cm^{-1} region at 623 K. The bands of the sample under vacuum are slightly different from those observed on Figure 4b due to the higher temperature. The comparison shows that, under air, two main bands above 3600 cm^{-1} appear to the partial detriment of the $\nu(\text{CH}_3)$ bands. One of these new bands indicates the partial recovery of the original OH groups, whereas the band at 3738 cm^{-1} is assigned the $\nu(\text{OH})$ vibration in silanol (Si-OH) groups at the titanium oxide surface [58, 59]. These silanol groups are formed by reaction of water molecules with the grafted trimethylsilyl groups [38]. It is obvious that the formation of SiOH groups on the n- TiO_2 surface modifies the surface reactivity of the nanoparticles. Indeed, it is known that most of the OH groups linked to titanium atoms at the TiO_2 surface show Brønsted acid characteristics [58, 59], whereas all the OH groups linked to silicon atoms should be similar to the OH groups at the silica surface, which present no or very low Brønsted acidity [58]. It can be concluded that the grafted species are modified by humidity at relatively high temperature, but that the original surface groups and the original surface reactivity of the TiO_2 surface are not restored. It must now be determined whether the changes of the surface due to functionalization are beneficial to the targeted application (cf. Section 4.3).

Identical surface functionalization has been performed on tin oxide nanoparticles and gives similar results (see [55]). But to check whether the grafting procedure can be practically applied to gas sensors in a rapid and cost-effective way, real n- SnO_2 -based sensors have also been functionalized. In such sensors, the sensing layer deposited on an alumina tile is obtained from a paste made of SnO_2 nanoparticles dispersed in α -terpineol. Before operation, the sensor is fired at a maximum temperature of 873 K under a flow of dry air [72]. It is obvious that the real sensors are not transparent to the infrared radiation due to the thickness of both sensing layer and alumina tile. Therefore, these samples are analyzed by diffuse reflectance infrared Fourier transform

spectroscopy (DRIFTS) [14, 49], which allows the surface study of opaque samples (cf. Section 3.1). To graft HMDS on the surface of the sensing layer, the sensor is first placed in an oven at 473 K under flowing air for several hours in order to free the surface OH groups from physisorbed water molecules. Then, liquid HMDS is sprayed on the warm sensor which is then immediately placed in the cell of the DRIFTS environmental chamber. The sensor is then heated at 673 K under oxygen. The diffuse reflectance spectra of the sensing layer at 673 K before HMDS grafting and after the whole grafting process are presented in Figure 6.

Before grafting (Fig. 6a), two particular $\nu(\text{OH})$ stretching absorption bands are clearly visible at 3630 and 3718 cm^{-1} . They correspond to the OH groups linked to the tin oxide surface and to the OH groups of the organic binder, respectively [49]. The band at 3630 cm^{-1} totally disappears under grafting (Fig. 6b), whereas a new band appears at 1270 cm^{-1} assigned to the $\delta(\text{CH}_3)$ bending vibration in Si- CH_3 groups. Like in the case of the titanium oxide nanoparticles, these modifications of the spectrum prove that HMDS has reacted with the surface OH groups and that the grafted species withstand an oxidizing treatment at 673 K. As mentioned earlier, the $\delta(\text{CH}_3)$ band whose intensity is quite high compared to that of the $\nu(\text{CH}_3)$ bands can be clearly seen, whereas the $\nu(\text{CH}_3)$ bands are not observed due to their very low intensity. A closer look at the 3718 cm^{-1} band reveals a shoulder at 3726 cm^{-1} which, like in the case of titanium oxide, is assigned to the $\nu(\text{OH})$ stretching vibration in Si-OH groups. These groups result from the oxidation of part of the trimethylsilyl groups during the heat treatment undergone by the sensor after grafting. Therefore, similarly to the case of the TiO_2 nanoparticles, HMDS can be successfully grafted on n- SnO_2 -based sensors, thus reducing the density of the OH groups at the sensing layer surface, modifying the chemical nature of the surface species and the surface reactivity of the sensor. The HMDS grafting, which withstands temperatures as high as 673 K, is, however, modified by oxidation.

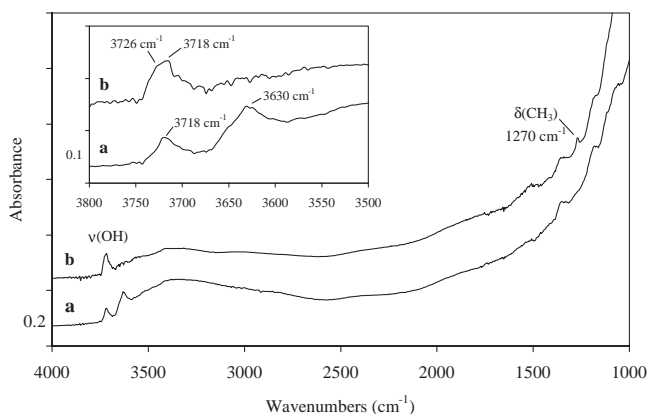


Figure 6. Diffuse reflectance infrared spectrum of a n- SnO_2 -based sensor at room temperature and under vacuum: (a) as received; (b) after HMDS grafting and heating at 673 K under oxygen. (The spectra have been shifted for clarity.)

4.3. Modification of the Sensing Properties

As a final step of our study, the consequences of the surface functionalization on the sensing properties have to be investigated.

Tin oxide is a good example to illustrate the Drude–Zener theory (cf. Section 2.3). In the following, it will be shown how FTIR spectroscopy is a stand-alone technique making it possible to investigate the sensing properties of semiconducting nanoparticles and *simultaneously* analyze the chemical reactions at the origin of the gas detection.

Figure 7 shows the evolution of the infrared spectrum of the tin oxide nanoparticles depending on the gaseous environment at 623 K. The first spectrum (Fig. 7a) has been recorded after an activation under oxygen (cf. Section 3.1) followed by an evacuation. It therefore corresponds to the sample under vacuum. The evacuation at relatively high temperature is a reducing treatment, due to the desorption of oxygen from the surface layer.

On these reduced tin oxide nanoparticles, oxygen is adsorbed at 623 K. The background infrared absorption rapidly and strongly decreases (Fig. 7b). This phenomenon is explained by oxygen adsorption removing oxygen vacancies which had been created by the evacuation (cf. Section 2.4). Simultaneously adsorbed oxygen transforms into ionosorbed species by attracting electrons from the material (cf. Section 2.4). As a result, the density of free electrons decreases as well as the electrical conductivity of the SnO₂ sample. When CO is adsorbed in presence of oxygen (Fig. 7c), the overall infrared absorption increases due to the release of electrons in the conduction band. In addition, the formation of new bands is clearly observed. The complex band centered at 2349 cm⁻¹ corresponds to gaseous CO₂ [73]. The presence of this band is actually the proof that CO has reacted with ionosorbed oxygen species according to the reactions (3) and (4) indicated in Section 2.4:

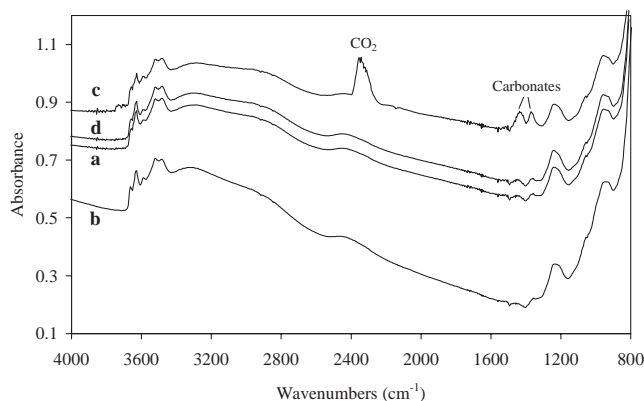
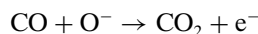
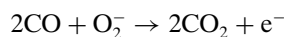
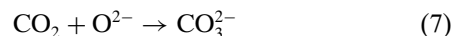


Figure 7. Infrared transmission spectrum of the SnO₂ nanoparticles at 623 K: (a) after activation under oxygen and evacuation; (b) after adsorption of 50 mbar oxygen; (c) followed by addition of 10 mbar CO in presence of oxygen; (d) after evacuation. (The spectra have NOT been shifted.)

However, it should be mentioned that, with the FTIR technique, it is extremely difficult, perhaps even impossible, to determine the type of ionosorbed oxygen species which is involved in the CO₂ formation [31].

Two other bands are noted in the 1500 cm⁻¹ region and are assigned to CO₃²⁻ carbonate groups [74–76]. These carbonate groups are also observed when, under the same conditions, carbon dioxide is adsorbed on the tin oxide surface [77]. It can therefore be concluded that CO oxidation into CO₂ proceeds first and then newly formed CO₂ adsorbs on surface basic sites, leading to surface carbonate groups, according to the following reaction:



It must be noted that, in principle, the formation of carbonate groups does not participate in the variation of the electrical conductivity because the involved electrons remain localized. Only the formation of CO₂ leads to the release of free electrons. Both CO₂ and surface carbonates are eliminated by subsequent evacuation (Fig. 7d).

To better emphasize the modulation of the electron density, the variations of the infrared energy (E_{IR}) transmitted by the tin oxide sample versus gas (O₂ and CO) exposures have been reported in Figure 8. A decrease of the electrical conductivity which corresponds to a decrease of the infrared absorption, that is, to an increase of the transmitted infrared energy, is observed when oxygen is adsorbed. Conversely, an increase of the electrical conductivity, corresponding to a decrease of the transmitted infrared energy, is caused by CO adsorption. A fairly good reproducibility of the E_{IR} variations over the “O₂ addition-CO addition-evacuation” sequences is observed, appearing like a reproducible response. It has indeed been demonstrated that the variations of the infrared background absorption versus gas exposures follow a λ^2 dependence (λ being the infrared wavelength) in agreement with the Drude–Zener theory [78] (cf. Section 2.3). This means that the E_{IR} variations are essentially due to the free carrier absorption and that, as a consequence, they can be directly correlated to the electrical conductivity variations. In addition, it has been proved that this curve (Fig. 8) can be directly compared to the sensor response curve obtained by standard impedance measurements [72]. The lapse of 10 minutes between two

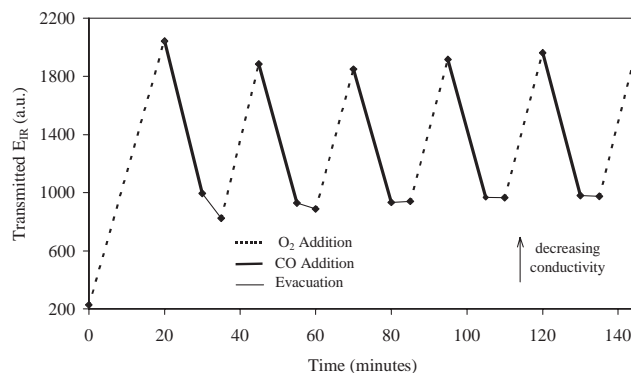


Figure 8. Variations of the infrared energy transmitted by the SnO₂ nanoparticles at 623 K versus gas exposures.

measurements has been chosen to ensure that the system has reached the chemical equilibrium and that the surface reactions are completed. It does not correspond to the response time of the real sensor which actually can be less than 30 seconds [79]. In the following, the E_{IR} variation will be referred to as the “response” of the semiconducting sample by analogy with the sensor response.

From the analysis of this curve, it can be concluded that, with FTIR spectroscopy, one actually measures the integrated contribution to the variation of the free carrier density from each particle independently from the others. To perform such measurement, there is no need for necks between the particles and no need for an electron transfer from a particle to another, contrary to standard electrical measurements. This technique makes it possible to evaluate the amplitude of the electrical conductivity variations that a semiconducting nanopowder can eventually undergo in presence of oxidizing or reducing gases with no need for metallic electrodes that are known to possibly generate perturbations in the gas sensor response [56]. This technique gives precise indications not only on the sensitivity that the final sensor fabricated from these nanoparticles will be able to achieve, but also on the optimized operating conditions, such as working temperature, and on the possible drawbacks, such as drift of the baseline, cross-sensitivity, slow recovery, etc.

As previously demonstrated, the functionalization of the surface causes changes in the surface species, hence in the surface reactivity and possibly in the sensitivity to gases. Because the grafting of HMDS reduces the density of the surface OH groups and the hydrophilic character of the surface as well, it is expected that the surface reactivity in presence of water molecules will be modified. It has therefore been studied whether the response of the semiconducting nanoparticles to CO in absence and in presence of humidity is different for nongrafted and HMDS-grafted nanoparticles.

Series of experiments have been performed on nongrafted and HMDS-grafted n-TiO₂ samples in order to compare their response to the following sequence of gas additions: four pure CO doses (6 mbar), referred to as “dry CO doses,” followed by four doses of CO mixed with a small amount of water vapor (10%), referred to as “wet CO doses,” and then followed by four new “dry CO doses.” The operating temperature is set at 673 K. For sake of simplicity, these preliminary experiments have been performed in an oxygen-free environment. Figure 9 shows the E_{IR} variations versus gas exposures at 673 K for the nongrafted and HMDS-grafted samples.

On the nongrafted n-TiO₂ (Fig. 9, top), the first dose of “dry CO” is added for 10 minutes and causes the expected E_{IR} decrease resulting from the increase of the free carrier density. Simultaneously, the formation of CO₂ is observed on the infrared spectrum [38]. After evacuation of the first CO dose, the transmitted infrared energy does not get back to its original intensity. This is also expected because in absence of an oxidizing atmosphere, the ionized oxygen species used for the CO₂ formation are not regenerated. Then, “dry CO doses” are subsequently added. Each dose causes a decrease of the transmitted infrared energy, whereas each evacuation leads to an increase of the infrared energy. But, the net result is that the sample is steadily

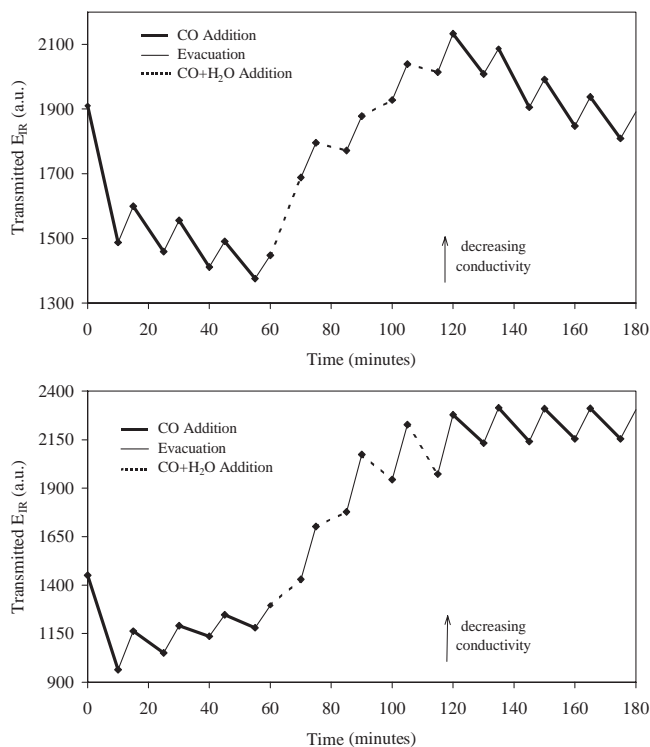


Figure 9. Variations of the infrared energy transmitted by the nongrafted (top) and HMDS-grafted (bottom) TiO₂ nanoparticles at 673 K versus gas exposures.

reduced by the subsequent CO additions. The addition of “wet CO doses” causes a strong decrease of the electrical conductivity although without any reproducibility. In parallel, the infrared spectra show an intensity increase of the $\nu(\text{OH})$ absorption range. The overall effect of the four “wet CO doses” is an oxidation. When “dry CO” is added again, the energy evolution is similar to that observed during the addition of the first “dry CO doses.” Moreover, the baseline drift shows the same downward trend, thus indicating an overall reducing effect.

The second curve (Fig. 9, bottom) corresponds to the same experiment performed on the HMDS-grafted n-TiO₂ sample. As in the previous case, the addition of “dry CO doses” has a reducing effect. Concomitantly, no perturbation can be observed on the IR spectrum and the formation of CO₂ is hardly visible. Like in the case of the nongrafted sample, the oxidation state is not restored by evacuation. But differently, the “addition-evacuation” sequences of “dry CO doses” lead to an overall oxidizing effect. This phenomenon is tentatively explained by an electronic rearrangement at the surface under CO because, in addition to the modification of the surface species, the HMDS grafting by itself has a reducing effect by producing ammonia (cf. Section 3.2). However, further experiments are under way to obtain additional information.

The addition of the first two “wet CO doses” amplifies the oxidizing effect. As explained in Section 4.2, the reaction of water molecules with the Si(CH₃)₃ grafted species leads to the formation of new Si-OH surface groups as proven by the new band appearing at 3738 cm⁻¹ [54, 80]. Then, for the subsequent two “wet CO doses,” the reducing action

becomes preponderant, no further changes are noted in the infrared spectra, and the response to “wet CO” doses seems to stabilize. When “dry CO” is added again, we only note a slight reversible shift of the new Si-OH band. But, surprisingly, the transmitted infrared energy evolution shows a perfectly reproducible response and no drift of the baseline, that is, no change in the oxidation state after the “CO addition- evacuation” sequences. The formation of CO_2 appears slightly more visible.

The mere observation of these curves clearly demonstrates that, by changing the chemical species on the nanoparticle surface, one can affect the response to gases [81]. Even though it seems, from the infrared spectra, that the detection of pure CO somehow involves the surface OH groups [38, 69], their exact role is unclear since their replacement with trimethylsilyl groups does not dramatically change the response to CO. On the contrary, the response to humidity is fundamentally perturbed by the OH groups modification.

In order to check whether the surface functionalization is beneficial to real gas sensors, the sensitivity of the non-grafted and the HMDS-grafted sensors has been investigated at 623 K by DRIFTS. Like in the transmission mode, the diffused infrared radiation contains information on the free carriers and the intensity of the diffused beam decreases when the density of the free carriers increases. It should, however, be noted that DRIFTS is usually less sensitive to electrical conductivity variations than the transmission mode [14]. Due to experimental constraints dictated by the design of the DRIFT accessory, the “gas addition- evacuation” sequence is slightly different from the procedure used to test the TiO_2 nanoparticles in transmission mode. It can be described as follows: oxygen addition, quick evacuation, pure carbon monoxide addition, quick evacuation. This sequence is repeated twice and then pure carbon monoxide is replaced by a mixture of carbon monoxide and water vapor at increasing $\text{H}_2\text{O}/\text{CO}$ ratios (10, 20, 40%). The variations of the diffused infrared energy versus gas exposures are reported in Figure 10 for the non-grafted and HMDS-grafted sensors fabricated from SnO_2 nanoparticles. It can be seen that before grafting (Fig. 10, top), the presence of humidity strongly affects the sensor response toward CO, whereas after grafting (Fig. 10, bottom), the amplitude of the response is fairly stable whatever the humidity content.

The electrical effect of water on semiconductors is rather complex and not clearly understood. The most obvious effect is the direct removal of an electron from adsorbing water molecules, thus causing an increase of the electrical conductivity (reducing effect). However, considering only this effect does not satisfactorily explain the observed electrical consequences [42], as it is the case in the present study. Additional effects should be envisaged to simultaneously occur, such as the dissociation of water molecules into OH^- and H^+ ions which will subsequently react with acidic or basic groups on the surface. Moreover, the presence of the polar water molecules may influence the kinetics of the electron transfer, thus affecting the adsorption of CO and its further oxidation into CO_2 on ionosorbed oxygen [42]. In the particular case of n-TiO_2 and n-SnO_2 , the dissociation of water and the reaction of the resulting OH^- and H^+ ionized species

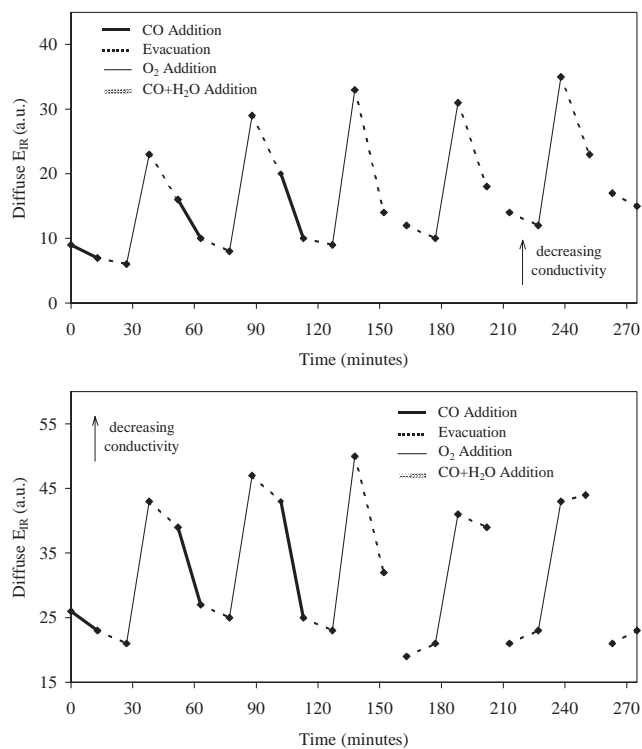


Figure 10. Variations of the infrared energy diffused by the non-grafted (top) and HMDS-grafted (bottom) n-SnO_2 -based sensor at 623 K versus gas exposures.

appears to be one of the preponderant effects responsible for the cross-sensitivity to humidity. Indeed, we have seen that Si-OH surface groups are formed after HMDS grafting and subsequent exposure to either oxygen or water vapor (see Section 4.2 and Fig. 6). These Si-OH groups should have an acido-basicity close to that of the OH groups on a silica surface, that is quite different from that of the Ti-OH or Sn-OH groups originally on the material surface. Consequently, these new Si-OH surface groups dramatically modify the Brønsted acido-basicity of the surface. Whereas the hydroxyl groups on titanium and tin oxides are mostly Brønsted acid [65, 68], all OH groups on the pure silica surface are identical and have an amphoteric character [42]. In other words, when water is adsorbed on a pure silica surface, the tendencies of the surface to give up H^+ protons and to give up OH^- hydroxide ions are similar. We indeed observe that the stabilization of the response of HMDS-grafted n-TiO_2 toward CO in presence of humidity only occurs after the trimethylsilyl groups have transformed into silanol groups. Similarly, the constant amplitude of the response of the HMDS-grafted sensor toward CO whatever the humidity content indicates a stabilizing surface effect by HMDS. Even if the complete mechanism is still unclear, the presence of the new Si-OH groups is believed to play an important part in neutralizing the effect of humidity.

5. CONCLUSIONS

The surface functionalization of semiconducting nanoparticles is a complex task as it requires not only the study of the surface chemistry and the understanding of the surface

reactions which will lead to the appropriate surface modification, but also the investigation of the consequences of the functionalization on the electrical properties. These requirements are not easily met simultaneously because the properties to be analyzed involve the material at very different thicknesses: Surface chemistry and surface reactions concern the very first atomic layers of the nanoparticles, whereas electrical properties usually refer to a surface layer of several nanometers and possibly even several tens of nanometers. Therefore, to establish a direct correlation between surface chemistry and electrical properties, the selected experimental investigation technique must be capable of simultaneously probing two properties at two different thicknesses. This is the major advantage of Fourier transform infrared spectroscopy which, under specific conditions, is particularly relevant for the analysis of the chemical reactions taking place at the very surface of nanosized particles. Simultaneously, in the case of semiconducting nanoparticles, the resulting variations of the electrical conductivity can be probed in real time. This is an important asset for the fundamental understanding of the gas detection mechanism and consequently for the optimization of chemical gas sensors based on semiconductors.

In this chapter, it has been established that specific properties of nanosized particles can be modified on purpose by controlling the surface composition and the surface chemistry. The chemical modification of the surface species on semiconducting nanoparticles generates not only changes in the surface reactivity, but also changes in the work function, that is, changes in the electrical conductivity and in the sensing properties. These changes can be monitored *in-situ* by FTIR spectroscopy and the evolution of the newly formed surface chemical species versus time can give information on the stability and reversibility of the gas sensors, thus allowing the determination of the optimum operating conditions. By tuning the chemical composition of the surface of semiconducting nanoparticles, it can be envisaged to increase the sensor sensitivity and to tailor the sensor selectivity for targeted applications. Fourier transform infrared spectroscopy appears to be one of the ultimate tools to simultaneously control and characterize the performance of the tailored gas sensors.

GLOSSARY

Adsorbate Molecule or chemical entity (purposely or not) adsorbed on a *surface site*.

Cross-sensitivity Linked to insufficient selectivity of a sensing device, it corresponds to the response of sensors to interfering parameters in addition to the targeted parameter to measure. Cross-sensitivity is a usual problem in all kinds of sensors and probably one of the most difficult to minimize.

Drude-Zener theory Theory established by Drude and Zener addressing the interaction of photons with *free carriers* in semiconductors. Induced changes in the density and in the mobility of the carriers either chemically (e.g. by adding impurities) or electrically (e.g. by carrier injection) result in modifications of the material's optical absorption in the infrared and microwave ranges.

Fourier transform infrared (FTIR) spectroscopy Analytical method allowing the identification of a chemical bond by absorption or diffusion of an infrared radiation at precise wavelengths corresponding to the vibrations of this chemical bond.

Free carriers Electrons or holes in metals or semiconductors that are free to move in the solid and are responsible for the electrical conductivity.

Grafting Chemical reaction between a molecule or a chemical entity and a chemical group at the material surface. It leads to a modification of the surface chemical composition and of the surface reactivity. The grafting process is commonly used to eliminate *surface hydroxyl groups* on a material and to tailor the adhesion and wetting properties.

Space-charge region (depleted layer) Surface region depleted of *free carriers* (electrons or holes). The thickness of the depleted layer (related to the Debye length) varies depending upon the nature of the *adsorbates* that can either inject electrons into the conduction band (electropositive adsorbates) or extract electrons (electronegative adsorbates).

Surface acido-basicity Chemical activity of a surface presenting acidic and basic sites. Lewis acid or base sites are able to accept or to donate electron pairs, respectively. Brønsted acid or base sites are able to donate or to capture protons (H^+), respectively.

Surface hydroxyl groups OH groups generated at the surface of all metal oxides by the dissociative adsorption of water. This adsorption is energetically favorable because it terminates the material with OH single-valent species in agreement with Pauling's valency rule. The OH surface groups acting as Brønsted acid or base sites play a major role in the chemical properties of materials.

Surface sites Coordinatively unsaturated surface atoms generated by the termination of a material. These sites are partly responsible for the chemical activity of a surface, such as catalytic properties or adsorption phenomena. In a regular environment, these sites react with surrounding molecules to balance the forces at the interface, thus leading to surface contamination by foreign atoms and chemical species.

ACKNOWLEDGMENTS

The author acknowledges the financial support of the Commission of the European Communities under the BRITE-EURAM III program (SMOGLess Project, Contract BRPR-CT95-0002) and the Information Society Technologies program (INTAIRNET Project, Contract IST-1999-12615). As coordinator of these projects, she is grateful to her partners in the two SMOGLess and INTAIRNET Consortia for exchange of results and samples and for constructive scientific discussions as well.

REFERENCES

1. G. A. Somorjai, "Introduction to Surface Chemistry and Catalysis." Wiley, New York, 1990.
2. G. A. Somorjai, *MRS Bull.* 23, 11 (1998).

3. R. K. Cavin III, D. J. C. Herr, and V. V. Zhirnov, *J. Nanoparticle Res.* 2, 213 (2000).
4. M. Lebedev, *Progr. Surf. Sci.* 70, 153 (2002).
5. K. E. Gonsalves, M.-I. Baraton, R. Singh, H. Hofmann, J. X. Chen, and J. A. Akkara, Eds., "Surface-Controlled Nanoscale Materials for High-Added-Value Applications," MRS Symp. Proc. Series, Vol. 501. Materials Research Society, Warrendale, PA, 1998.
6. B. Panchapakesan, D. L. DeVoe, M. R. Widmaier, R. Cavicchi, and S. Semancik, *Nanotech.* 12, 336 (2001).
7. M.-I. Baraton, Ed., "Synthesis, Functionalization and Surface Treatment of Nanoparticles." American Scientific Publishers, Stevenson Ranch, CA, 2002.
8. M. Bollani, R. Piagge, and D. Narducci, *Mater. Sci. Eng. C* 15, 253 (2001).
9. M. G. Warner and J. E. Hutchison, in "Synthesis, Functionalization and Surface Treatment of Nanoparticles" (M.-I. Baraton, Ed.), p. 67. American Scientific Publishers, Stevenson Ranch, CA, 2002.
10. K. Ihokura and J. Watson, "The Stannic Oxide Gas Sensor—Principles and Applications." CRC Press, Boca Raton, FL, 1994.
11. G. Herzberg, "Molecular Spectra and Molecular Structure." Van Nostrand, Princeton, NJ, 1962.
12. E. B. Wilson Jr, J. C. Decius, and P. L. Cross, "Molecular Vibrations. The Theory of Infrared and Raman Vibrational Spectra." Dover, New York, 1955.
13. B. Schrader, Ed., "Infrared and Raman Spectroscopy. Methods and Applications." VCH, Weinheim, 1995.
14. P. R. Griffiths and J. A. de Haseth, "Fourier Transform Infrared Spectrometry." Wiley, Chichester, 1986.
15. M.-I. Baraton in "Handbook of Nanostructured Materials and Nanotechnology" (H. S. Nalwa, Ed.), p. 89. Academic Press, San Diego, CA, (1999).
16. M.-I. Baraton, in "Nanostructured Materials: Science and Technology" (G. M. Chow and N. I. Noskova, Eds.), p. 303. NATO-ASI Series, Kluwer Academic Publishers, Dordrecht, 1998.
17. M.-I. Baraton, *J. High Temp. Chem. Proc.* 3, 545 (1994).
18. H. P. Boehm and H. Knözinger, in "Catalysis" (J. R. A. Anderson and M. Boudart, Eds.), Vol. 4, p. 39. Springer-Verlag, Berlin, 1983.
19. M. L. Hair, "Infrared Spectroscopy in Surface Chemistry." M. Dekker, New York, 1967.
20. H. Knözinger, *Adv. in Catal.* 25, 184 (1976).
21. A. A. Davydov, "Infrared Spectroscopy of Adsorbed Species on the Surface of Transition Metal Oxides." Wiley, New York, 1984.
22. J. Lercher, C. Gründing, and G. Eder-Mirth, *Catal. Today* 27, 353 (1996).
23. J. C. Lavalley, *Catal. Today* 27, 377 (1996).
24. N. J. Harrick, "Internal Reflection Spectroscopy." Wiley, New York, 1967.
25. A. F. Gibson, *J. Sci. Instrum.* 35, 273 (1958).
26. Y. J. Chabal, *Surf. Sci. Rep.* 8, 211 (1988).
27. J.-N. Chazalviel, B. H. Erné, F. Maroun, and F. Ozanam, *J. Electroanal. Chem.* 509, 108 (2001).
28. N. J. Harrick, *Phys. Rev.* 125, 1165 (1962).
29. R. S. Morrison, in "Semiconductors Sensors" (S. M. Sze, Ed.), p. 383. Wiley, New York, 1994.
30. V. E. Henrich and P. A. Cox, *Appl. Surf. Sci.* 72, 277 (1993).
31. M. Che and A. J. Tench, *Adv. in Catal.* 32, 1 (1983).
32. J. H. Lundsord, *Catal. Rev.* 8, 135 (1973).
33. V. Lantto and P. Romppainen, *Surf. Sci.* 192, 243 (1987).
34. V. E. Henrich and P. A. Cox, "The Surface Science of Metal Oxides." Cambridge Univ. Press, Cambridge, 1994.
35. P. K. Clifford, Mechanisms of Gas Detection by Metal Oxide Surfaces, Ph.D. Thesis, Carnegie Mellon Univ., Pittsburg, 1981.
36. N. Bârsan, M. Schweizer-Berberich, and W. Göpel, *Fresenius J. Anal. Chem.* 365, 287 (1999).
37. K. R. Han, C. S. Kim, K. T. Kang, H. J. Koo, D. I. Kang, and H. Jingwen, *Sensors Actuat. B* 81, 182 (2002).
38. M.-I. Baraton and L. Merhari, *NanoStruct. Mater.* 10, 699 (1998).
39. T. Rajh, O. V. Makarova, M. C. Thurnauer, and D. Crokek, in "Synthesis, Functionalization and Surface Treatment of Nanoparticles" (M.-I. Baraton, Ed.), p. 147. American Scientific Publishers, Stevenson Ranch, CA, 2002.
40. P. Knauth, R. Bouchet, O. Schäf, A. Weibel, and G. Auer in "Synthesis, Functionalization and Surface Treatment of Nanoparticles" (M.-I. Baraton, Ed.), p. 127. American Scientific Publishers, Stevenson Ranch, CA 2002.
41. A. B. Bourlinos, A. Bakandritsos, V. Georgakilas, and D. Petridis, *Chem. Mater.* 14, 3226 (2002).
42. S. R. Morrison, "The Chemical Physics of Surfaces." Plenum Press, New York, 1990.
43. M. Bruening, R. Cohen, J. F. Guillemoles, T. Moav, J. Libman, A. Shanzer, and D. Cahen, *J. Am. Chem. Soc.* 119, 5720 (1997).
44. L. Pauling, "The Nature of the Chemical Bond." Cornell Univ. Press, Ithaca, NY, 1960.
45. F. Garbassi, L. Balducci, P. Chiurlo, and L. Deiana, *Appl. Surf. Sci.* 84, 145 (1995).
46. W. Hertl and M. L. Hair, *J. Phys. Chem.* 75, 2181 (1971).
47. P. Cléchet and N. Jaffrezic-Renault, *Adv. Mater.* 2, 293 (1990).
48. J. M. Chovelon, N. Jaffrezic-Renault, P. Clechet, Y. Cros, J. J. Fombon, M.-I. Baraton, and P. Quintard, *Sensors Actuat. B* 4, 385 (1991).
49. M.-I. Baraton, in "Nanostructured Films and Coatings" (G. M. Chow et al., Eds.), p. 187. NATO-ARW Series, Kluwer Academic Publishers, Dordrecht, 2000.
50. M. Prutton, "Introduction to Surface Physics." Clarendon Press, Oxford, 1994.
51. M.-I. Baraton and L. Merhari, *Mater. Trans.* 42, 1616 (2001).
52. F. O. Stark, O. K. Johannson, G. E. Vogel, R. G. Chaffee, and R. M. Laceyfield, *J. Phys. Chem.* 72, 2750 (1968).
53. F. Chancel, J. Tributou, and M.-I. Baraton, *Key Eng. Mater.* 136, 236 (1997).
54. M.-I. Baraton, F. Chancel, and L. Merhari, *Nanostruct. Mater.* 9, 319 (1997).
55. F. Chancel, J. Tributou, and M.-I. Baraton, in "Surface-Controlled Nanoscale Materials for High-Added-Value Applications," (K. E. Gonsalves, M.-I. Baraton, et al., Eds.), p. 89, MRS Symp. Proc. Series Vol. 501. Materials Research Society, Warrendale, PA, 1998.
56. W. Göpel and K. D. Schierbaum, *Sensors Actuat. B* 26-27, 1 (1995).
57. M. Primet, P. Pichat, and M.-V. Mathieu, *J. Phys. Chem.* 75, 1216 (1971).
58. B. A. Morrow, in "Spectroscopic Characterization of Heterogeneous Catalysis (Part A)" (J. L. G. Fierro, Ed.), p. A161. Elsevier, Amsterdam, 1990.
59. G. Busca, H. Saussey, O. Saur, J.-C. Lavalley, and V. Lorenzelli, *Appl. Catal.* 14, 245 (1985).
60. C. Morterra, *J. Chem. Soc., Faraday Trans. I* 84, 1617 (1988).
61. S.-W. Ho, *J. Chin. Chem. Soc.* 43, 155 (1996).
62. A. A. Tsyganenko and V. N. Filimonov, *Spectrosc. Lett.* 5, 477 (1972).
63. M. Primet, P. Pichat, and M.-V. Mathieu, *C. R. Acad. Sci. Paris* 267B, 799 (1968).
64. D. J. C. Yates, *J. Phys. Chem.* 65, 746 (1961).
65. M. Primet, P. Pichat, and M.-V. Mathieu, *J. Phys. Chem.* 75, 1221 (1971).
66. W. Riehemann, in "Surface-Controlled Nanoscale Materials for High-Added-Value Applications," (K. E. Gonsalves, M.-I. Baraton, et al., Eds.), p. 3, MRS Symp. Proc. Series Vol. 501. Materials Research Society, Warrendale, PA, 1998.

67. E. W. Thornton and P. G. Harrison, *J. Chem. Soc. Faraday Trans. I* 71, 461 (1975).
68. P. G. Harrison and B. M. Maunders, *J. Chem. Soc. Faraday Trans. I* 80, 1341 (1984).
69. S. Emiroglu, N. Bârsan, U. Weimar, and V. Hoffmann, *Thin Solid Films* 391, 176 (2001).
70. D. F. Cox, T. B. Fryberger, and S. Semancik, *Phys. Rev. B* 38, 2072 (1988).
71. J. Tribout, F. Chancel, M.-I. Baraton, H. Ferkel, and W. Riehemann, in "Surface-Controlled Nanoscale Materials for High-Added-Value Applications," (K. E. Gonsalves, M.-I. Baraton et al., Eds.), p. 95, MRS Symp. Proc. Series Vol. 501. Materials Research Society, Warrendale, PA, 1998.
72. G. Williams and G. S. V. Coles, *J. Mater. Chem.* 8, 1657 (1998).
73. G. Herzberg, "Molecular Spectra and Molecular Structure—II. Infrared and Raman Spectra of Polyatomic Molecules," 10th printing. Van Nostrand, Princeton, NJ, 1962.
74. P. G. Harrison and M. J. Willett, *Nature* 332, 337 (1988).
75. M. J. Willett, in "Techniques and Mechanisms in Gas Sensing" (P. T. Mosley, J. W. O. Norris, and D. E. Williams, Eds.), p. 61. Adams Hilger, Bristol, 1991.
76. G. Busca and V. Lorenzelli, *Mater. Chem.* 7, 89 (1982).
77. M.-I. Baraton, in SMOGLESS Final Report, Contract No. BRPR-CT95-0002, unpublished results, 1999.
78. M.-I. Baraton and L. Merhari, *J. Nanosc. Nanotech.*, submitted, 2003.
79. G. Williams and G. S. V. Coles, in SMOGLESS Final Report, Contract No. BRPR-CT95-0002, unpublished results, 1999.
80. M.-I. Baraton, L. Merhari, F. Chancel, and J. Tribout, in "Control of Semiconductor Surfaces and Interfaces," (S. M. Prokes, O. J. Glembochi et al., Eds.), p. 81, MRS Symp. Proc. Series Vol. 448. Materials Research Society, Warrendale, PA, 1997.
81. M.-I. Baraton, in "Nanopatterning—From Ultralarge-Scale Integration to Biotechnology," (L. Merhari, K. E. Gonsalves et al., Eds.), p. 159, MRS Symp. Proc. Series Vol. 705. Materials Research Society, Warrendale, PA, 2002. Å

Surface Nano-Alloying

Ruxandra Vidu

University of California at Davis, Davis, California, USA

Nobumitsu Hirai, Shigeta Hara

Osaka University, Suita, Osaka, Japan

CONTENTS

1. Introduction
 2. Surface Alloying Systems
 3. Applications
 4. Conclusions
- Glossary
References

1. INTRODUCTION

Nowadays, epitaxial growth is one of the most important technologies to obtain uniform and defect-free thin films, which are of utmost importance in the fabrication of nanometer-scale devices with novel properties. Understanding the atomic structures formed at ordered metal surfaces is an important topic in the preparation of epitaxial thin films by electrochemical deposition.

Electrochemical deposition represents an alternate methodology to prepare layered structure compounds at room temperature, which could avoid interdiffusion problems associated with the high temperature required in current deposition techniques. However, the strong adatom-substrate interaction at the metal/ionic solution interface may lead to intermixing at the interface in many underpotential deposition systems. Therefore, many systems cannot be characterized any longer by the conventional growth modes commonly used to describe epitaxial growth, since interdiffusion has been observed to take place at the interface even at room temperature. When favorable conditions are met and surface alloying occurs, it interferes with the underpotential deposition (UPD). However, the two processes can be distinguished one from the other, because the UPD atoms are limited to 1–2 monolayers (ML), while a limit in atom coverage should not theoretically exist for the surface alloy. Moreover, the kinetics of the UPD adsorption

process is much faster than for the alloy formation. Alloy formation is likely to take place under thermodynamically favorable conditions whenever two different metals are in contact with each other. Kolb reviewed state of the art underpotential deposition up to 1978 [1], including the surface alloy formation in the underpotential range. Since then, there are only a few investigations that deal with alloying in the underpotential deposition region compared to the UPD systems.

Different nucleation and growth mechanisms (Stranski–Krastanov [SK] and Frank–van der Merwe) were found to operate in many cases of electrocrystallization and thin film formation of metals (Me) on foreign substrates (S) in systems with underpotential deposition phenomena [2]. Calculations of different thermodynamic contributions to the so-called underpotential shift have been performed by using the embedded atom approach to UPD phenomena [3]. Modern *in-situ* techniques, particularly *in-situ* scanning tunneling microscopy (STM) and atomic force microscopy (AFM) with lateral atomic resolution, have directly shown that two-dimensional (2D) UPD adlayers act as precursors for the subsequent nucleation and growth of a three-dimensional (3D) Me bulk phase. This is reflected in the nucleation kinetics and epitaxial orientation of thin film deposits. The growth mode determines the microstructure and properties of the deposit. Ultrathin Me films and heterostructures (sandwich-structured Me monolayers and surface alloys) can be deposited in the UPD and overpotential deposition (OPD) ranges. The thickness of a thin Me film can be varied between one monolayer and a finite number of monolayers in those systems where the Frank–van der Merwe mechanism operates. The thickness, structure, and composition of heterostructures can be controlled by the substrate, the composition of the electrolyte, and the experimental conditions used. This research field is of great interest for nanotechnology research dealing with structuring and modification of metal surfaces in the nanometer range in vertical and lateral directions.

Electrode processes involving phase formation phenomena usually are studied by using conventional electrochemical methods. These methods provide global information on the electrode behavior but lack information on the local mechanism, kinetics, structure, and morphology of the surface phases formed during electrochemical experiments. Recently, information about the changes in the microstructure and composition of the surface layer became accessible with nanometer scale resolution through the development of *in-situ* techniques such as second harmonic generation, glancing angle X-ray, and electrochemical scanning probe microscopy (SPM). The opportunity to monitor the growth of electrodeposited layers offers answers to some long-standing ambiguities, such as the interaction of the adlayer with the substrate, the mechanism of assembling a monolayer, and the potential dependence of the surface structures. The introduction of SPM techniques to electrochemical systems opened a new research field in surface studies of electrode processes on molecular and atomic levels. Electrochemical methods and/or *in-situ* STM and AFM were used for studying interdiffusion in many systems. These studies suggest that surface alloying formation is a rather common phenomenon of those UPD systems characterized by a strong adatom–substrate interaction. Besides the specific nature of the adatom/substrate atom system, there are several process variables that may promote interdiffusion during electrochemical deposition. Among them, the adsorption of anions such as halides and sulfate/bisulfate on electrode surfaces was found to play an essential role in electrodeposition processes, especially in the underpotential range.

The formation of metal monolayers through underpotential deposition depends on interactions between the electrode surface and the depositing species. Other adsorbable species, if present in solution, will influence the formation of UPD metal films through their adsorption on the electrode surface, taking place simultaneously. For instance, Cu UPD on polycrystalline gold surfaces is significantly influenced by the presence of thiourea in solution [4]. Regarding the UPD and alloy formation of copper on Pd/Pt(111) bimetallic electrodes [5], there are a variety of adsorption behaviors depending on the nature of the anions in solution (HSO_4^- , Cl^- , Br^-). Anions play a decisive role in changing the energetics of some systems [3]. In some particular cases [e.g., copper on Au(111)], the anions may be responsible, to a large extent, for the existence of UPD. Combined electrochemical experiments and SPM observations have demonstrated the effect of adsorbed anions not only on the UPD structures but also on the alloying process occurring in the UPD range. For instance, it was shown that unlike SO_4^{2-} , Cl^- plays an active role in the alloy formation at the Au(110)| Cu^{2+} interface. However, a detailed understanding of the surface alloying process has not yet been reached.

According to the general theory of chemisorption reactions, the kinetics of underpotential deposition of metals includes more than one adsorbed state [6]. An underpotential deposit may consist of partially charged adsorbate [7, 8], as well as completely discharged bulk portions. The change in the double layer charge due to alloy formation

must be introduced into the charge balance. Diffusion-controlled formation of the main part of the partially charged adsorbate points to strong repulsive forces between the adsorbed particles [8]. However, another type of deposit, which consists of completely uncharged metal, also has been detected.

Initial experiments on UPD and surface alloying processes have been performed on polycrystalline metal substrates. The advantage of using polycrystalline electrode surfaces was due, at least in part, to the reduced difficulty of preparing and maintaining a stable surface in comparison with single-crystal electrodes. Although the information gained from these studies was very important for electrochemists, the inherent nature of the polycrystalline surfaces, i.e., the precise identity of the surface under study, raised questions involving surface alloying and weakly adsorbed species. Therefore, numerous studies using well-defined and clean single-crystal electrodes emerged in underpotential deposition studies and improved our understanding of surface alloying.

Although the subject is not covered in this review, it is worth mentioning that the electrodeposition on alloy surfaces offers an exciting possibility of providing information on site-specific chemical interactions between an adsorbate and individual constituents in the alloy. Eventually, this information may be useful in developing a quantitative understanding of how site-specific chemical interactions influence such phenomena as electrocatalysis or dealloying. For instance, copper is known to underpotentially deposit on elemental Au electrodes, but not on Ag electrodes. When Cu is underpotentially deposited on polycrystalline Au–Ag alloys, the charge associated with the adsorption process decreases with increasing Ag atomic fraction in the alloy [9]. Underpotential deposition on an alloy substrate also offers appropriate conditions for studying the structural and energetic aspects of the modified surfaces. Examples include determining the active surface area of an alloy [10], characterization of alloy surface [11], and electrocatalysts [12, 13].

In this review, we examine the alloying process that takes place during the UPD of metal on an electrode surface. The intent is to provide a broad overview of the types of systems that present surface alloying in the underpotential range. The focus will be to systematically evaluate the wealth of data on this subject and to present the most significant findings on surface alloying.

2. SURFACE ALLOYING SYSTEMS

There are several typical metal–substrate (Me–S) systems where alloying in the underpotential region is observed. In order to have a clear picture of these Me–S systems, the identity of the metal substrate was chosen as a scheme for presentation. The list is further broken down by the Me adlayer on a specific substrate. Here we present only typical UPD Me–S systems. Alloy formation has been studied on other substrates as well, such as Fe (e.g., Ni on Fe [14]), Al (e.g., Li on Al [15]), Se (Pb on Se [16]), or Ru (e.g., Cu and Ag on Ru [17]), but these are not typical UPD systems and are not discussed in this review.

2.1. Surface Alloying at Me–Pt Interface

Surface alloying at Me–Pt interface has mainly been studied in connection to the application of Me UPD to electrocatalysis. In particular, heavy metal adatoms increase the catalytic activity of noble and transition metal electrodes for several different types of electrochemical reactions. The enhancement of the electrocatalytic activity of metal electrodes by Me UPD sub- and monolayers permit electron-transfer processes to occur at much lower overpotentials. Additionally, the selectivity of the electrocatalyst surface and the reversibility of redox electrodes are improved.

2.1.1. Ag on Pt Electrode

There is substantial work done with respect to silver UPD onto platinum substrate [18–30]. From early studies of silver deposition on polycrystalline platinum, it was found that 2 MLs of silver were deposited in the UPD region. Potentiostatic and potentiodynamic techniques applied to the electrodeposition of Ag on polycrystalline Pt in 0.1 M HClO₄ at 30 °C have shown that Ag UPD occurs within three well-defined regions: region I (in the 0.9–0.8 V range), associated with the formation of an Ag UPD monolayer; region II, as observed within a small potential window located on the positive potential side of the Ag/Ag⁺ reversible electrode potential; and region III, which corresponds to the bulk deposition of silver [31]. Region II is the most interesting, since it was related to the 2D growth of the Ag UPD layer, but the stripping of bulk silver differs from the stripping of silver electrodeposited in region II. These results have been explained through simultaneous adsorption–desorption, and nucleation and growth processes, the contribution of the growth process increasing as the applied potential approaches the Ag/Ag⁺ reversible potential. Additionally, voltametric results on UPD of silver on polyfaceted and electrochemically faceted Pt (100) electrodes in 0.1 M HClO₄ and 1.0 M H₂SO₄ containing Ag⁺ ions (10^{−5} to 10^{−3} M) have shown different conjugated peaks related to Ag UPD, under practically no interference of O-containing surface species on Pt [32]. Application of the combined adsorption–desorption–nucleation and growth mechanism to this system has led to the conclusion that it is possible that the number of Ag atoms required to attain a complete coverage of the substrate exceeds that of the Ag monolayer.

Later, studies initiated on low-index planes of platinum [e.g., Pt(111), Pt(100), and Pt(110)], confirmed the existence of 2 MLs of silver deposited on the platinum surface prior to bulk deposition. The voltammetric response of a platinum electrode is complicated when the electrode is cycled in the presence of silver cations, because the initial Ag deposition begins in the region where oxygen electroadsorption would occur in the absence of silver cations. Additionally, there was some controversy regarding the observed voltammetric features due to differences in crystal quality and anion interaction [24]. However, there is a general agreement that bulk deposition starts only after two atomic layers of Ag are deposited [1, 20, 31–34]. For both polycrystalline and single-crystal Pt electrodes, two groups of peaks are present in the anodic curves. The first group has been observed within the potential region from 0.6 to 0.8 V/SHE (SHE), which is very

close to the reversible potential for Ag deposition in the same solution (the reversible potential for Ag/Ag⁺ is $E_r = 0.567$ V/SHE), and the second group has been observed within the underpotential region from 0.8 to 1.2 V/VSH (VSH).

Concentration dependence of the underpotential deposition of silver on Pt(111) has been studied by using electrochemical and UHV (UHV) techniques [20]. The voltammetry for deposition of silver on Pt(111) depends on the silver ion concentration but does not follow the Nernstian behavior. Additionally, the adsorption mechanism involved in Ag UPD on Pt depends on Ag concentration, i.e., when silver ion concentration was 10^{−3} M, the electrodeposition took place via adsorption in a well-defined manner, whereas, at a concentration of 5.10^{−6} M, the mechanism involved 3D nucleation and island formation. Two monolayers of silver were deposited at underpotentials. However, the stability of the adsorbed layer and of the second layer during the rinsing procedure was strongly dependent on the silver ion concentration in solution.

The more recent UPD studies of silver on a polycrystalline platinum electrode show that Ag adlayer rearranges and forms a Pt + Ag surface alloy [33, 35]. The potential cycling between the reversible potential of the Ag/Ag⁺ electrode reaction and 1.10 V (SHE) in 10^{−3} M Ag salt in aqueous acid solutions results in the formation of a Ag + Pt surface alloy and the incorporation of Ag into the second layer of Pt atoms. The voltammetric response of the Pt electrode during aging of the UPD layer reflects the formation of the Pt + Ag surface alloy. Deposition/stripping experiments of Ag on the Ag + Pt alloy gives rise to two new pairs of voltammetric peaks in the range 0.93 to 0.75 V, whereas the complete stripping of Ag occurs at 1.15 V. From CV data and *ex-situ* Auger spectra, the proposed atomic model of Pt + Ag surface alloy formation is a surface–atom reordering process, which initiates through a place exchange mechanism involving Ag and Pt surface atoms followed by a slow Ag atom diffusion into bulk Pt [33].

Study of the formation of Ag UPD layers under steady-state conditions shows that the process occurs through several stages [35]. The total amount of Ag deposited in the UPD region is about 2.5 MLs. The two layers differ in their binding energy, as evidenced by the difference in the peak potentials for anodic stripping. A first layer is deposited on top of the Pt atoms in a few minutes. The amount of Ag in this layer slightly exceeds that needed to form a monolayer. The reason for this is thought to be the misfit between the atomic radii of Ag and Pt, which may lead to the formation of a strained UPD layer. The Ag UPD layer is metastable, with Ag adatoms undergoing place exchange to form the Pt + Ag surface alloy. This process reaches the steady state in about an hour, resulting in a modified electrode surface that consists of a mixture of Pt and Ag atoms. The surface alloy is stable, its composition is nearly constant and does not depend on deposition potential. Further deposition of Ag in the underpotential region occurs. The amount of Ag in the second layer is potential dependent and can reach a charge corresponding to 1.5 to 2.0 atomic layers. The two layers formed during Ag deposition on Pt play different roles in the bulk deposition of Ag. While the first layer that forms the surface alloy is totally unaffected by the deposition of

further Ag on top of it, the second, more loosely bound layer is the precursor for bulk deposition. Rearrangements of this second layer, which includes only Ag–Ag bonds, are not involved in the formation of the surface alloy.

The slow surface–atom reordering process plays an important role in the underpotential deposition of Ag on Pt in acid solutions [36]. In the nonequilibrium overlayer, which is formed during the simultaneous reduction of the surface oxide and deposition of a submonolayer of Ag on Pt electrodes, two Ag adatoms block one site available for hydrogen UPD, independent of the surface coverage by silver. During relaxation, the number of hydrogen adsorption sites blocked by Ag decreases. The formation of a surface alloy in the vicinity of imperfections, created by oxide reduction, becomes a primary step in the deposition of Ag.

2.1.2. Pb on Pt Electrode

Numerous bimetallic systems formed by UPD on Pt(hkl) have been investigated, mainly because of their unique structural and chemisorptive properties compared to either of the bulk metal components. The Pb–Pt(111) system in a solution containing Br[−] has been investigated by electrochemical methods in combination with *in-situ* surface X-ray scattering measurements [37]. The results have shown that Pb UPD onto Pt(111) in the presence of bromide is a competitive process with the total amount of Pb deposited at underpotential being less than the amount needed to form a close-packed monolayer of 0.63 ML. Deposition of Pb adatoms was accompanied by desorption of the bromide adsorbed on the Pt surface at higher potentials, leaving coadsorbed bromide both in and on top of the adlayer. An ordered surface alloy was formed in the potential region where the ratio of coadsorbed species was close to one. The formation of this surface alloy was a very slow process of about 2 h and led to an ordered surface structure with a p(2 × 2) unit cell. A physical model for Pb UPD in solution containing Br[−] has been proposed, based on the competitive interaction of metal adatoms and halide anions [21].

2.1.3. Sn on Pt Electrode

Underpotential deposition of tin on Pt(hkl) have been investigated due to its peculiar structural and chemisorptive properties. Adsorption of tin on platinum has been characterized as an uncommon UPD [38]. One of the characteristics of the Sn UPD is that tin induces a strengthening of bonds between platinum and adsorbed hydrogen or oxygen. The electrochemical and catalytic properties of the platinum substrate are irreversibly modified by tin deposition. It is possible to “regenerate” the first monolayers of platinum by voltammetric cycling (0–1.5 V/RHE). However, some of the tin deposit that is found in the oxidized state [Sn(II)], diffuses into the platinum and cannot be desorbed. It is possible that this bulk tin forms a complex compound with platinum and oxygen.

The catalytic properties of the Sn UPD depend on the substrate. For instance, carbon-supported platinum (Pt/C) with an adsorbed layer of underpotential deposited Sn is a much better catalyst for the methanol oxidation reaction than a carbon-supported platinum–tin (PtSn/C) alloy [39]. *In-situ* X-ray absorption (XAS) was used to determine the

differences in the effects that the two methods of Sn addition have on the electronic and structural properties of the catalyst. X-ray diffraction and XAS on Pt indicated that alloying with Sn caused partial filling of the Pt d band vacancies and an increase in the Pt–Pt bond distance. The differences in the activity of the two catalysts for the methanol oxidation reaction are due to the effects of alloying on the Pt electronic structure that inhibit the ability of the Pt to adsorb methanol and dissociate C–H bonds. Another example is offered by the cocatalytic effect of Sn, Mo, and Ru decorating steps of Pt(111) vicinal electrode surfaces on the oxidation of CO. This system has been studied by using a model bimetallic catalyst [40]. Ternary model catalysts also were used to test the synergetic effect of Ru and Sn. The ternary model catalyst behaved like a superposition of the corresponding binary catalysts, probably because separate 2D on Pt(111) or one-dimensional (1D) on Pt(332) islands of Ru or Sn were formed instead of an atomically mixed overlayer [40].

2.1.4. Hg on Pt Electrode

A comparative study of the electrodeposition of Hg on polycrystalline smooth and columnar structured Pt (cs-Pt) substrates was used to identify surface processes on cs-Pt substrates that are not easily detected on conventional smooth Pt [41]. The Hg electrodeposition on cs-Pt results in a nonequilibrium complex deposit consisting of 2D and 3D Hg domains, and Pt–Hg alloy coexisting with bare Pt domains at intercolumnar voids. The mechanism of Hg penetration into bulk Pt consists of two distinguishable steps: the Hg atom shifts to a position underlying the first layer of Pt atoms and then penetrates into bulk Pt. To attain the maximum Hg coordination number in the Pt lattice, the penetration of Hg into bulk Pt should involve an inward shift of Hg atoms underlying the first layer of Pt atoms. The displacement of Hg atoms implies the creation of holes in bulk Pt to allow the Hg atoms' penetration. The driving force for the Hg diffusion into bulk Pt is induced by the chemical potential gradient of Hg built up between the Hg deposit and the bulk Pt. The Hg atom diffusion coefficient into bulk Pt is about $2 \times 10^{-17} \text{ cm}^2 \text{ s}^{-1}$, which is close to those reported for the diffusion of other metal atoms into a solid metal lattice [42].

2.2. Surface Alloying at Me–Au Interface

Au is used extensively as a substrate in UPD studies because of its broad double-layer window, which is free of complications from surface-specific faradaic reactions. Moreover, the gold surface offers relatively easy handling in reactive ambient conditions, such as air or aqueous solutions, and can be easily cleaned. The choice of Au substrate also is based on the fact that gold single crystal surfaces are quickly reconditioned by thermal or electrochemical annealing once their surface experienced from electrochemical exposure. Atomically flat surfaces required for AFM observation with atomic resolution can be obtained by using *in-situ* pretreatment inside the AFM electrochemical cell, just before deposition (Fig. 1). Under potential control, the surface is unreconstructed, providing a known atomic arrangement (Fig. 1b).

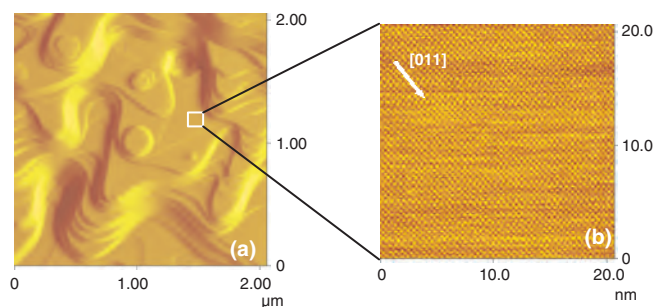


Figure 1. AFM images of Au(100) in 50 mM H₂SO₄ solution (pH = 1) (a) 2 × 2 μm image revealing atomically flat terraces as shown after electrochemical treatment; (b) unfiltered high-resolution image (20 × 20 nm) of Au(100)–(1 × 1) surface. An arrow shows the [011] substrate direction.

This treatment is based on a potential enhanced surface-diffusion process, which quickly changes the Au surface topography, resulting in atomically flat surfaces.

2.2.1. Cu on Au Electrode

The UPD of Cu on Au electrode is one of the most extensively studied systems [43–60]. Experiments on gold electrodes have revealed that the structures of the resulting adlayer, as well as the mechanism of the electrochemical adlayer formation, depend strongly on the anion species in the electrolyte. First-principles energy calculations carried out to study the structure of copper UPD on Au(111) surfaces in sulfuric acid solutions have shown that the proposed honeycomb structure with 2/3 monolayer copper coverage was unstable without the coadsorption of sulfate [58]. In fact, the coadsorbed sulfate binds to copper and much more weakly to clean Au(111) surfaces. Total energy calculations for bisulfate adsorption suggest that even though it is the dominant species in acidic electrolyte, the adsorbed bisulfate may dissociate, leaving sulfate adsorbed on the surface. Simultaneous *in-situ* STM measurements and cyclic voltammetry were used to study, in real time, the initial cycles of potentiostatic copper electrodeposition and subsequent dissolution on a clean gold polycrystalline electrode [61]. The formation of nuclei of an alloy phase was observed after the first cycle. After completion of subsequent cycles, the crystallites changed their size distribution and shape. A shift in peak potential for the anodic current transient has been observed after completion of four subsequent cycles of copper electrodeposition/dissolution. The shift equals the change in potential of the working electrode due to the formation of the alloy phase. The dissolution of the surface alloyed phase can be compared to the selective dissolution of Cu from a copper–gold alloy. The selective dissolution proceeds via Cu transport through an essentially planar Au-rich product layer, which increases over time to hundreds of atom layers in thickness [62]. The TEMs have also shown a few pits, whose diameters are less than 10 nm and whose numbers increase with time, which may account for the higher rate of Cu dissolution.

Metal particles (Cu–Au alloy) with different crystallographic habits, depending on the applied electrode potential, can be formed in the UPD potential region of Cu by electrochemical deposition of Cu and Au [63, 64]. The shape

of the particles is due to a contraction of the Au overlayer, induced by the presence of an incompletely discharged Cu⁺ ion deposited on the Au overlayer of the alloy particles in the UPD region of Cu, comparable to the alkali-metal-induced reconstruction of Au surfaces.

The influence of the Cl[−] addition to the H₂SO₄ solution on Cu UPD on Au(110) has been investigated [47]. In the absence of Cl[−], the general surface topography and the (1 × 1) structure of the nonreconstructed surface was maintained over the entire UPD potential range. This was interpreted as a formation of a (1 × 1) Cu adlayer, with weak and presumably slightly repulsive adsorbate–adsorbate interactions. In Cl[−] containing electrolyte a (2 × 1) structure is reversibly formed and the roughening was interpreted as anion-induced surface alloying.

In order to understand the UPD process and to find applications involving electrodeposition of active metals from nonaqueous solutions, Cu UPD also was studied in solvents other than water. In acetonitrile solutions, the formation of the UPD layer on Au proceeds in two stages [65]. The main differences in the Cd UPD process on textured Au(111) and polycrystalline Au (poly-Au) electrodes in acetonitrile solutions are: (i) the kinetics of formation, i.e., the UPD layer is formed faster, and it is better defined on Au(111) compared to a poly-Au electrode; and (ii) on the well defined surface electrodes, Cd UPD consists of 1 ML, while on poly-Au electrodes, the coverage is about 2 ML. In molten salts, deposition of Cu starts at the steps between the Au terraces in a (8 × 8) [66]. A surface alloy between Cu and Au has been observed, and the defects left on Au after dissolving Cu healed in about 2 h. Oxidation of Cu does not return the surface to its initial appearance, and Cu clusters of 2–3 MLs in height have been observed on the surface.

2.2.2. Ag on Au Electrode

Structural aspects and the mechanism of UPD and OPD of silver on gold single crystal faces have been investigated by different electrochemical techniques and *in-situ* SPM with lateral atomic resolution [67–75]. A fundamental understanding of the factors determining the growth morphologies of the electrodeposited metal films is a key step in elucidating the mechanism of metal epitaxy and alloy formation at the interface in this system.

On Au(100), formation of 2D domains that consist of well-ordered (1 × 1)Ag adlayers and of Au–Ag surface alloy after long-time polarization has been observed [75]. These domains acted as nuclei for the 3D silver phase formation in the OPD range. The growth mechanism depended on deposition potential, i.e., monolayer-by-monolayer growth (i.e., Frank–van der Merwe) at low overpotentials [72, 75] and multilayer growth mode at higher overpotentials [75]. The layers were generated by a spiral growth mode caused by screw dislocations of the real Au(100) substrate. Monte Carlo simulations for the formation and growth of low dimensionality phases during UPD of Ag on Au(100) have been performed [76]. Atomic force microscopy investigations on the atomic structures and growth morphologies of thin Ag films on Au(100) have revealed that in the UPD region, the pseudomorphic (1 × 1)-Ag layer is formed through the c(√2 × 5√2)R45°-Ag structure (coverage, θ = 0.6 ML) in both HClO₄ and H₂SO₄ solutions [72].

It is worth mentioning that UPD of Ag leads to a lifting of the surface reconstruction [75].

Electrochemical STM (EC-STM) has shown that Au(111) surface morphology is substantially altered during repeated cycles in the Ag UPD region [68, 70]. The surface appearance changed after several cycles of Ag deposition and dissolution as monolayer deep pits appeared and grew on the surface. During cycling, the pits expanded rapidly to leave isolated Au islands while the terrace edges retreated. The lateral growth of Au islands was slow, suggesting that the kinetics of the transition process are related to the initial number of surface defects. The surface morphological changes accompanying Ag UPD cycling are clearly reflected in the cyclic voltammograms, which presented dramatic changes in both peak shape and potential. In the presence of a weakly adsorbed anion, i.e., perchlorate anions, repetitive cycling of Ag UPD on the Au(111) electrode resulted in similar alterations in voltammetric peak shape and potential. However, the rate of structural transformation of the Au(111) surface was enhanced in the presence of perchlorate anions. Atomic force microscope images of underpotentially deposited monolayers of Ag on Au(111) have shown that the structure of the monolayer depended on the nature of the electrolyte in which the UPD process occurs, i.e., (3×3) -Ag structure in sulfuric acid and a (4×4) -Ag structure in nitrate- and carbonate-containing electrolytes [70]. Unlike acetate, where a close-packed monolayer was formed, in perchloric acid a more complex structure was observed. Monolayer structures with various packing densities correlate with electrolyte size, except in the case of perchloric acid. However, the packing densities predicted from coulometric measurements did not agree with those actually observed with the AFM. The discrepancy between the two measurements has been ascribed to differing amounts of charge transfer between electrolyte and adatom, which altered the amount of charge needed for UPD lattice formation.

Recent results obtained by using cyclic voltammetry in combination with UHV-based techniques on silver/gold systems have shown that the first stage of Ag UPD strongly depended on the superficial state of the substrate and on the formation of a Ag–Au surface alloy [77]. Potential cycling in the UPD region has introduced surface defects and gradually transformed the surface into a surface alloy phase. Additionally, an unusual temperature dependence of the kinetics of surface alloy formation has been observed. This behavior is due to a self-annealing process of surface defects that takes on the surface and to the rate of surface alloying that strongly depends on the concentration of the surface defects. Regarding Ag dissolution, structure-vacancial disorder of the surface is not easily revealed in the kinetics of decrystallization processes. The stages of the crystal lattice destruction and the surface diffusion of Ag adatoms are replaced, with the time required, by the formation of “cavity nuclei,” which is not typical of copper and its alloys with gold [78]. With an increase in the concentration of a noble metal, decrystallization of silver becomes hampered due to the peculiarities of interatomic interactions typical of binary metallic systems with a negative deviation from Raoult’s law. Atom–atom interactions are masked by the atom–ion inter-

actions manifested in the underpotential adsorption of Ag^+ ions on the alloy surface.

2.2.3. Cd on Gold Electrode

Under potential deposition of Cd mainly has been studied to investigate the initial stages of the electrodeposition of CdTe [79]. In this context, the selection of the substrate on which crystal grows is of major importance. Since fundamental information about Cd electrodeposition on a single crystal is needed to form CdX ($X = \text{S}, \text{Se}, \text{Te}$) compound semiconductor thin films, there are many studies of cadmium electrodeposition on various substrates [42, 80–101], which were performed by using different surface (structure) sensitive methods such as electrochemical techniques, optical second-harmonic generation, low-energy electron diffraction, Auger electron spectroscopy, and SPM.

Cd electrodeposition on gold has been investigated primarily with classical electrochemical methods [102]. From these studies, it was characterized as a system where alloying takes place at a fairly high rate in the underpotential range. However, no structural insight into the origin of the process was available until the *in-situ* EC-AFM study was performed on this system [103]. Generally, at the beginning of the deposition (i.e., 0.65 V/NHE [NHE]), the Au surface is “clean,” meaning, for an electrochemically controlled surface, the Au surface shows the unreconstructed surface of Au (100)– (1×1) structure, the same as the one observed in a Cd^{2+} free electrolyte. The AFM images obtained at 0.05 V/NHE (i.e., approximately 0.1 V more negative than the first UPD peak) revealed a Au(100)– $(0.2 \times 0.2)\text{R}45^\circ$ -Cd structure, with a coverage of 0.5 ML [97]. The Cd surface coverage of 0.5 ML observed by AFM agrees well with the value calculated from coulometric stripping of the adlayer. The first UPD Cd structure is one of the most typical overlayer structures on fcc(100), and similar behavior also has been observed for Cd UPD on Ag single crystals [80], where the formation of an Ag(100)– $c(2 \times 2)$ Cd (equivalent to Ag(100)– $(\sqrt{2} \times \sqrt{2})\text{R}45^\circ$ Cd) structure was proposed for the first Cd adsorption peak on Ag(100). When the potential was scanned back to 0.65 V, the bare Au(100)– (1×1) structure was seen again by AFM, as predicted by the shape of CV. Cd remains adsorbed in a Cd– $(\sqrt{2} \times \sqrt{2})\text{R}45^\circ$ structure on a Au(100) surface up to approximately –0.2 V/NHE. Going to more negative potentials, the adsorption of mobile Cd adatoms increases and, around –0.3 V/NHE, Cd adatom rows rearrange parallel to the [011] direction of the substrate in a structure that is incommensurate relative to the Au(100) substrate. The coverage measured by coulometric stripping of the deposit from –0.3 V/NHE was around 0.7 ML. However, an interpretation of the charge in terms of Cd adsorbate structure seems doubtful, since the formation of a Au–Cd alloy takes place in about the same potential region [102]. Potential and time dependence of the surface structure in this underpotential region is better characterized by polarization experiments and will be discussed later. At –0.45 V, approximately 0.04 V/NHE more positive than the Cd bulk formation potential, the Cd adlayer was completed, showing a (1×1) structure. Again, scanning back the potential to 0.65 V, the Au(100)– (1×1) structure quickly

reappeared. However, after the EC-AFM (EC-AFM) observation was performed for 1–2 min at -0.45 V, the Au(100)– (1×1) structure that appeared was slightly disordered, with nonstraight atom rows, showing that, at this scan size, for these polarization conditions, the surface relaxation is still reversible.

During bulk deposition, small islands nucleate and grow on the terraces, as well as at the step edges (Fig. 2a, b). The growth rate depends on the nucleation site, being higher for the islands that have appeared at step edges. The growth mechanism of the Cd layer follows a SK mode, since it starts as a monolayer and proceeds to grow in an island mode. At atomic-scale observation, on the top of the deposit, the Cd layer shows a hexagonal structure characteristic of Cd(0001) films with an interatomic spacing of 0.3 nm, which is very close to the lattice constant of 0.298 nm along the basal plane (i.e., a axis) for the Cd bulk phase. Stripping the Cd layer by altering the potential back to 0.65 V/NHE leads to

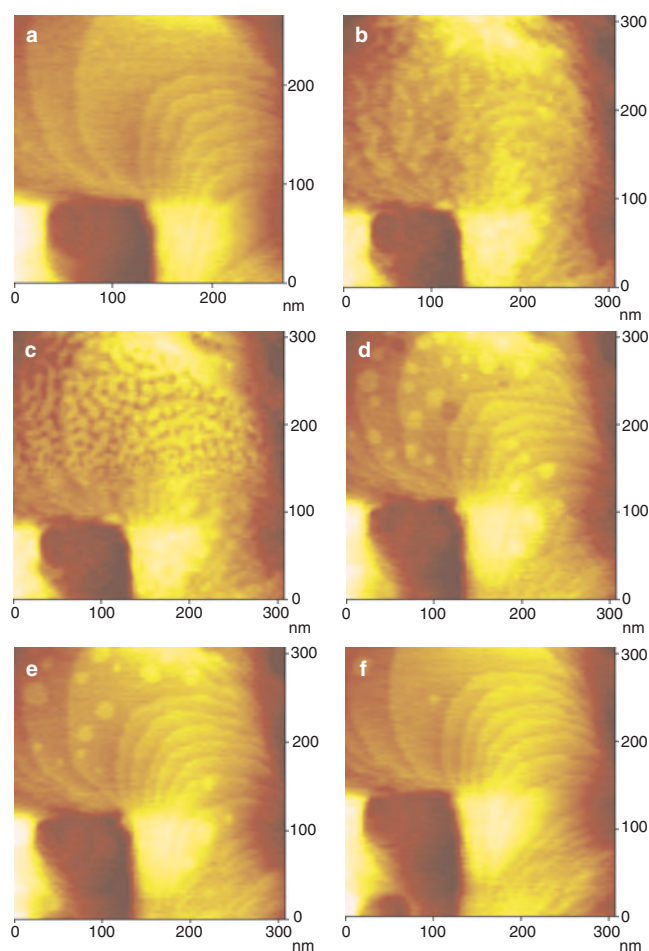


Figure 2. *In-situ* AFM images (310×310 nm) of Cd deposition and stripping. Deposition of Cd ($E = -0.49$ V/NHE) at $t = 0$ s (a) and $t = 120$ s (b), respectively. Stripping of Cd layer ($E = 0.8$ V/NHE) after bulk deposition and stripping of Cd layer (b, c). Note that desorption process of Cd layer leads a rough Au surface of which topography is changing in time: the first image obtained after altering the potential from -0.49 to 0.65 V/NHE (c) and after 300 s at 0.65 V/NHE (d). Changes in topography of the bare Au surface during holding the potential at ca. 0.15 V/NHE at $t = 0$ s (a) and $t = 30$ s (b), respectively.

a rough surface (Fig. 2c). The stripped surface presented many holes and atomic height islands, which have formed together immediately after stripping the Cd layer [103]. This was a direct consequence of alloy dissolution associated with the peak potential that follows after the bulk dissolution peak in a positive scan. Additionally, the evidence of surface mobility of the gold atoms at the observation potential was shown by the continuous topographic change of surface irregularities (i.e., small islands and holes). The disintegration of small gold islands and the growth of larger ones, occurring simultaneously with the enlargement of the diameter of the holes, are mainly due to the 2D Ostwald ripening process, based on statistical fluctuation at the rims (Fig. 2d–f).

The dynamics of the electrode surface topography during alloying also has been investigated by *in-situ* EC-AFM under potential control at -0.4 V and -0.45 V [97]. After 120 s of extended polarization at -0.4 V, no transitional adsorption stages (such as clusters or monoatomically high islands) have been observed. The adsorbed layer shows up as an almost perfect replica of the initial Au(100) surface, with no step edges decoration. Stripping the cadmium adlayer by setting back the potential to 0.65 V leads to a rough surface, similar to that observed after the stripping of the Cd bulk deposit. Stripping induced negligible changes in the step edge line in comparison with the terrace surface on which pits of regular size, randomly distributed around the terrace, have appeared. The area occupied by the holes was estimated as $30 \pm 1\%$ of the terrace area, and the holes have an average depth of 0.5 ± 0.02 nm. By maintaining the potential at 0.65 V for a few minutes only, the surface flatness is quickly restored. Obviously, the step edges do not return to their original lines because the surface diffusion also acts to restore the atomically flat terraces by redistributing the surface atoms. Thus, the surface flatness can be restored more quickly in this case without applying any supplementary surface treatment (e.g., the potential-enhanced surface-diffusion process applied for restoring the surface), since the extent of the surface alloy phase into the gold surface is only about 2 ML. The EC-AFM observation of the alloyed phase formation at -0.45 V/NHE (the potential where high resolution images revealed the Cd– (1×1) structure) for 120 s, followed by stripping, shows both holes and islands, suggesting that the penetration of Cd atoms into the Au(100) surface is a potential-dependent process.

The electrochemical interpretation of a Cd underpotential deposited layer from cyclic voltammetry is complicated by the fact that the competing processes occurring at the interface in the underpotential region give currents that vary with time. Therefore, the nonequilibrium phenomena at the later stage of formation of a monolayer were additionally investigated by long-time polarization experiments within the potential range from -0.35 to -0.45 V/NHE [97]. The shift in peak potential reflects a potential-dependence of Cd concentration in the surface alloyed phase and suggests that an overpotential is required every time for the dissolution of the adlayer(s). The increase in charge associated with the extended polarization at the given underpotential quickly reaches over 1 ML, although the Cd bulk phase deposition has not started yet at this potential.

The surface topography change with time evolves from a smooth to an irregular topography either in the deposition or stripping process, reflecting the kinetics and mechanism of the overall process. However, for the surface alloy formation, the dynamics of the Cd/Au interface topography produced by stripping becomes particularly relevant, as it provides information at the local level, which would otherwise be undistinguishable from deposition morphology and kinetic studies. For example, the EC-AFM images show no changes in surface morphology during the adsorption of more than 1.5 ML of Cd, suggesting that the alloyed phase extends into the surface, i.e., under an adsorbed Cd layer. The surface-roughening pattern seems to be induced by the strong vertical interaction that assists the alloy formation and dissolution at the electrode surface via an exchange process [97]. Unlike other systems, Cd/Au(100) seems to follow an exchange mechanism similar to a turnover process. The rapid increase of the charge at short polarization times demonstrates the existence of a turnover process. The turnover process may be understood as a vertical place exchange process, similar to that involved in the electrochemical oxide formation on a gold single-crystal electrode as the primary step in the oxidation process that causes roughening of the electrode surface. A similar mechanism also was proposed for the formation of Cd UPD layers on Cu(111) in the presence of Cl^- [93], where the underpotential deposited Cd forms a CdCl_2 salt-like bilayer on the surface. The turnover process involved in surface alloy formation is mirrored in the AFM images of stripped surfaces (i.e., the lateral interaction is negligible in comparison with the vertical one, since the holes appear preponderantly on the flat surfaces but not at step edges). These results indicated that an adatom deposited onto a terrace has a higher probability of exchanging places with a substrate atom than an adatom adsorbed near a step edge. Thus, the surface alloyed phase formation involves two processes. One is the turnover process between the Cd adatoms and Au surface atoms, which acts, in fact, as a continuous source for alloy growth, and the other is a substitution process of Au atoms by Cd atoms. During the turnover process, the Au atoms from the topmost surface layer reach the electrode/electrolyte interface awaiting transformation and new adsorbed Cd atoms can find available adsorption sites. Therefore, the amount of underpotential deposited Cd atoms is not limited to 1 ML but increases with polarization time. In this model, for long-time polarization, the extent of the 2D alloyed phase into the surface should be governed by solid state diffusion of either Cd or Au atoms through the vacancy-rich surface alloy (Fig. 3).

From EC-AFM and polarization experiments [98], the formation of surface alloy layers seems to be directly affected by two main factors. One is the interaction energy between Cd and Au atoms on the surface, and the other one is the potential-dependence of Au electrode surface. It is worth mentioning the stability of the first Cd UPD peak on the desorption curves observed during long-time polarization experiments, which shows that the first Cd adlayer is always in contact with the Au substrate. A possible path is the formation of a β -AuCd on Au(100), the geometric misfit between β -AuCd and Au (-18.84%) being less than between Cd and Au (-26.96%). The β -AuCd phase has 11.12%

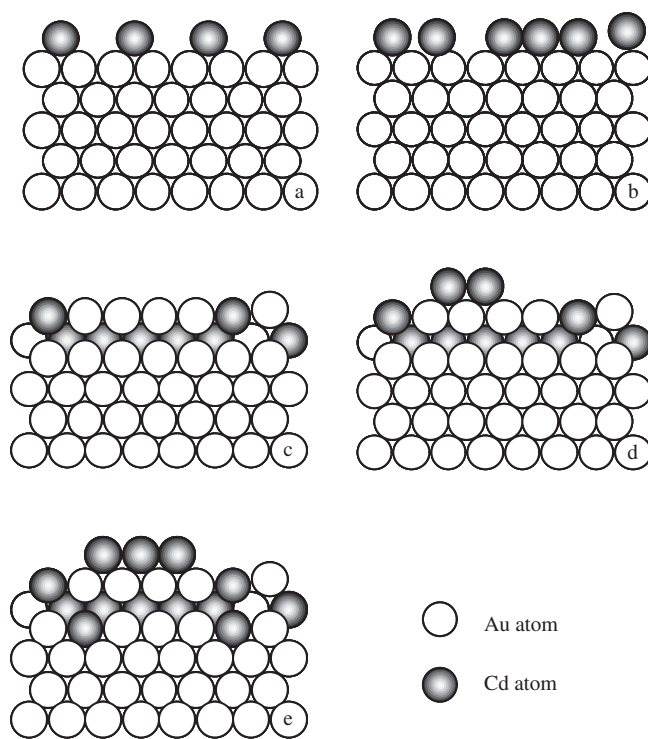


Figure 3. Mechanism of surface alloying process: (a) underpotential deposition; (b) increase of the mobile adsorbed Cd atoms; (c) turnover; (d) turnover and simultaneous slow deposition; (e) diffusion of Cd into the surface, turnover, and simultaneous slow deposition.

expansion relative to the bulk Cd. This expansion favors the structural transformation toward the AuCd surface compound due to the relaxation process at the interface (Fig. 4). Thus, the tendency of surface alloy formation involving the same adsorbed species may be related to adsorbate-induced changes in surface relaxation of fcc (100) surface. The bonding between surface atoms and adsorbed atoms also will affect the bonding to the second layer atoms and, hence, the interlayer separation. The alloy phase releases the strain at the Au/Cd, driving the interface into a nearby low-energy

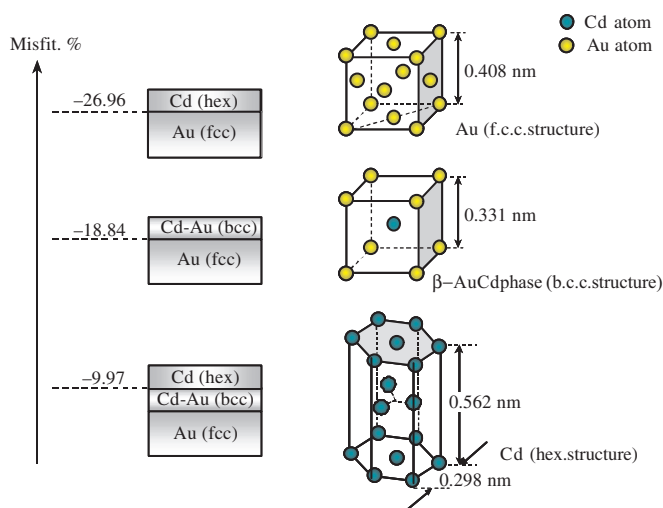


Figure 4. Geometric misfit between Au, Cd, and β -AuCd.

configuration, since the misfit at the AuCd/Au interface is smaller than at the Cd/Au interface. Therefore, the structural transformations associated with the strong interaction between a Cd adatom and an Au atom via a turnover process lead to an adsorbate structure with a potential-dependent kinetic that prevents the establishment of electrochemical equilibrium during the initial monolayer adsorption process.

This behavior is supported by thermodynamic models derived for surfaces [96] that give the surface concentration at a certain deposition time. The fast alloying process that occurs in the surface leads to the formation of an Au–Cd alloy phase of constant composition only within a few monolayers, i.e., the surface layers that sense the presence of the electrolyte side. The same observation applies to the film formed at more positive potentials, where the alloy film shows a constant composition and its thickness is less than that formed at $E = -0.45$ V. However, the film formed at $E = -0.45$ V shows a discontinuity in concentration at $t = 300 \dots 500$ s. The decrease in Cd concentration in the surface phase with deposition time at this potential can be interpreted as a result of an increase in the film thickness. Therefore, the removal of Cd from the alloy phase is affected by kinetic factors, leading to an apparent decrease in Cd concentration in the surface phase. Based on this new kinetic approach, the mechanism proposed for the surface alloying process that occurs in the underpotential region at the metal/electrolyte interface takes into consideration a very thin relaxation layer (“skin”) at the electrode surface. Calculation of the diffusion coefficients of Cd in Au electrode surface has shown that the overall alloying process at Au(100)/Cd²⁺ interface consisted of two processes [42]: one, very fast, which occurred within 2 ML and is characterized by $D \approx 10^{-16}$ cm²s⁻¹; and another one, much slower, which is characterized by $D \approx 10^{-18}$ cm²s⁻¹, suggesting a solid state diffusion process. Additionally, the concentration distribution of Cd into the electrode surface derived from this model has been obtained. The concentration gradient of Cd in the surface alloy demonstrates the existence of a slow relaxation process in the surface.

Alloy formation in the course of UPD of Cd on gold from HClO₄ is well reflected in the results of electrochemical microbalance measurement (EQCM) [90]. The alloy formation and dissolution is a slow process in comparison with the time scale of the usual voltammetric measurements (sweep rates from 5 to 100 mV s⁻¹). The results of the long-time polarization experiments have shown a continuous increase of the amount of underpotentially deposited Cd atoms during reduction and the slow dissolution of the embedded Cd accompanied by surface roughening during oxidation. These observations support the mechanism of surface alloy formation by a turnover process between the adsorbed Cd and the underlying Au atoms, as well as by a solidstate diffusion of these atoms through the alloyed phase.

Specific adsorption of anions in the course of underpotential, bulk depositions and, alloy formation of cadmium on gold has been studied over a wide potential range, corresponding to electrodeposition, alloy formation, underpotential deposition of Cd species [104]. The results have shown that there are distinct sections in the potential dependence of the adsorption of anions that reflect the changes in the state of the electrode surface, the dissolution of the bulk

Cd phase, and the slow elimination of Cd species from the Cd/Au alloy.

2.2.3.1. Inhibition of Hydrogen Evolution Modifications of the upmost layer induced by the adsorbed metal atoms were found to cause extreme changes of the electrode reaction rate by several orders of magnitude. One of the characteristic surface modifications induced by the underpotential deposited atoms deals with the inhibition of hydrogen evolution on the host electrode surface. The UPD of metal atoms on a foreign metal or alloy inhibits the hydrogen evolution reaction [105, 106] and [107] due to the fact that the adlayer shifts the hydrogen evolution reaction to more negative potentials. In the case of Cd–X type semiconductor compounds obtained by electrochemical deposition of atomically controlled thin film on Au, Cd deposition occurs at the most negative potential of any other UPD system studied so far, and the relation with the hydrogen evolution becomes particularly important for this system. This is due because the simultaneous deposition of the two metals UPDs could be assisted by hydrogen codeposition, which affects the quality of the film.

Unlike hydrogen evolution, Cd adsorption is independent of the pH of the solution. The atomic arrangements of Cd adatoms observed during EC-AFM experiments have shown a well-ordered 2D adatom layer in registry with the Au(hkl) substrate structure, as follows: Cd-($\sqrt{2} \times \sqrt{2}$)R45°/Au(100), Cd-(2 × 3)/Au(110) and Cd-c(4 × $\sqrt{3}$)/Au(111). Thus, the symmetry of the substrate predominantly determines the sequence of formation and geometry of the Cd adlayer structure. The surface structure of Cd-c(4 × $\sqrt{3}$)/Au(111) observed by EC-AFM agrees with that reported by Bondos et al. using *in-situ* EC-STM. However, the authors observed an additional Cd overlayer with bands of linear morphology, which is explained by the possibility of coadsorption of electrolyte anions (e.g., SO₄²⁻/HSO₄⁻), along with Cd atoms in the case of strong electrolyte [6].

From the observed UPD structures, the catalytic effect of the substrate structure can be further related with the work function, reticular density, and surface free energy. Independent of whether the reaction path of the hydrogen evolution follows the adsorption and chemical desorption or electrochemical desorption mechanism, specific adsorption of hydrogen atoms is involved. The effect of Cd adatoms on the hydrogen overpotential for the low index faces of an Au electrode can be discussed according to the reaction paths on the two substrates. Cd adatoms raise the hydrogen overpotential at single crystal Au electrode due to the decrease in the amount of adsorbed hydrogen (as a result of the adsorption of Cd adatoms) and the decrease in the heat of adsorption of atomic hydrogen. The displacement of hydrogen evolution to more negative potentials points to a decrease of the adsorption capacity of hydrogen on Au and to the change of energy state of adsorbed hydrogen leading to a change in the ratio of weakly to strongly bonded hydrogen. Regarding the UPD, the retardation mechanism of electrode reaction can be attributed to an interface inhibition caused by specific adsorption of Cd leading to 2D adlayer on the Au electrode surface. Hydrogen adsorption will compete with the strong interaction between Au and Cd, as it is shown by the large underpotential range that usually

is taken as a direct measure for the excess binding energy of Cd adatoms on the Au substrate relative to the binding energy of Cd on Cd.

Unlike Pt, where the hydrogen adsorption is determined by Pt lattice parameter rather than those of isolated Pt atoms (because hydrogen evolution proceeds through a recombination process), in the case of Au covered with Cd UPD, the step determining the hydrogen evolution reaction rate is H_3O^+ ion discharge step and, therefore, can be directly related with the coverage. According to the degree of Cd adatom effect on the hydrogen evolution reaction and, consequently, the decrease in the adsorption activity, the faces of the single crystal can be arranged in the following order: $(110) > (100) > (111)$. It should be noted that this order corresponds to the increase in number density on passing from the (110) to the (111) face ($\rho_{(110)}:\rho_{(100)}:\rho_{(111)} = 1 : 1.41 : 1.63$) in Figure 5. Though the reticular densities of the low index faces of Au single crystal increases in this order, the surface free energy cannot be directly related with this trend, since the surface free energy (γ) of the metallic single crystals faces is given by:

$$\gamma(\text{hkl}) = E_b n \rho(\text{hkl})$$

where E_b is the surface energy per free bond, n is the number of free bonds per surface atoms and $\rho(\text{hkl})$ is the surface atom density. The decrease in the adsorbability of Cd on the faces arranged in the above-mentioned order cannot be associated with the decrease in the free surface energy of these faces but with the number of free bonds in the surface (Fig. 6).

The UPD adlayer formation in relation with an overpotential-deposited H and H_2 evolution reaction is an important process involved in epitaxially electrodeposited metals at potentials negative to the H_2 evolution on the substrate. This gives the possibility of chemical modification of electrode surface in a controlled way with the simultaneous changing of its catalytic properties. In the system Au/Cd^{2+} , $E_{\text{Cd}^{2+}/\text{Cd}}^{2+}$ is more negative than the potential of the hydrogen electrode. However, the hydrogen evolution on $\text{Au}(\text{hkl})$ is strongly inhibited by adsorbed Cd, in a similar way to the bulk Cd phase.

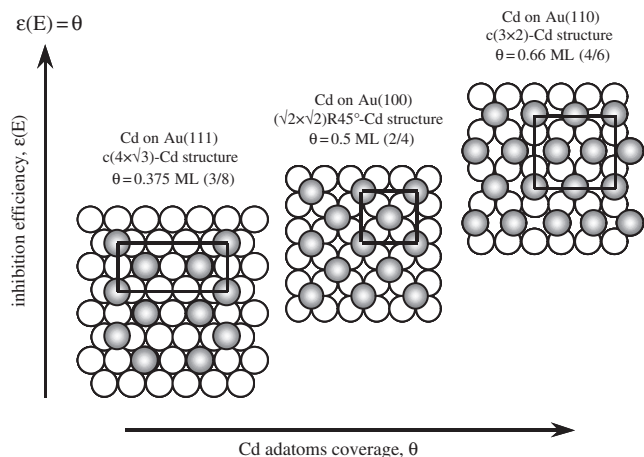


Figure 5. Ball model of the UPD of Cd layer on Au (hkl), illustrating the relationship between UPD Cd coverage and inhibition efficiency.

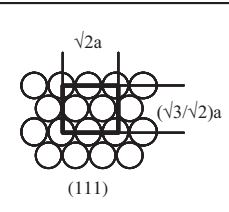
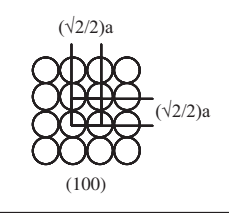
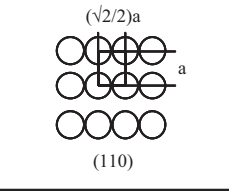
	Atom density	Free bonds in surface	γ/E_B
 (111)	$4/(\sqrt{3}a^2)$	3	6.9
 (100)	$2/(a^2)$	4	8
 (110)	$\sqrt{2}/(2a^2)$	5	7.07

Figure 6. Surface free energy of Au(hkl) surfaces.

2.2.4. Pb on Au Electrode

This system is characterized by a large crystallographic metal/substrate misfit that favors the SK 3D growth mode for the Pb film. Electrochemical studies on the Au surface indicated that the Pb UPD depends strongly on the crystallographic orientation. The UPD of Pb has been found to exhibit a marked influence on the catalytic activity and selectivity of the Au electrode for the electroreduction of nitro groups [108–110]. The UPD process of Pb also has been used to understand the adsorption and reorientation of 2,2'-bipyridine and 4,4'-bipyridine [111] and the factors that influence the atomic structure and compressibility of the Me/S systems [2, 112].

High-intensity synchrotron x-ray radiation has been used for studying the electrochemical solid/liquid interface [113]. Pb deposition results in a roughened surface and alloy formation [113, 114]. The growth of the Pb monolayer begins with diffusion of Pb^{+2} ions to the surface at potentials below the potential of zero charge (PZC) and causes lifting of the $\text{Au}(100)-(5 \times 20)$ reconstruction [113]. Pb atoms are deposited on the (1×1) surface in a $c(2 \times 2)$ structure. Domain sizes are small due to constriction by Au islands formed when the (5×20) is lifted. Irreversible surface defects are observed at -0.32 V/SCE.

In the presence of specifically adsorbed halide ions Cl^- , Br^- , and I^- , the peaks for the initial process of Pb atom deposition are substantially shifted to less positive potentials [115]. Although the effects of the halide ions on the UPD profiles is different, these effects are already significant at high dilution of the UPD added species, and the type of competitive adsorption isotherm depends on the identity of the anion involved.

The importance of local probe techniques for the investigation of the UPD process has repeatedly been emphasized by *in-situ* STM studies that were able to demonstrate that UPD overlayer structures may be different [116]. At low coverage, the electrochemical Pb deposition on Au(100) starts at steps resulting in step decoration. On flat terraces, the formation of overlayer domains with commensurate Au(100)- $c(2 \times 2)$ Pb and Au(100)- $c(3\sqrt{2} \times \sqrt{2})R45^\circ$ Pb structures was observed in the low and medium coverage range. The removal of lead is nearly complete when the total amount in the solution does not exceed the monolayer capacity of the electrode [117]. Simultaneously with the formation of this monolayer, Au-Pb alloys are formed. These alloys (identified by electron diffraction as Au₂Pb, AuPb₂, and AuPb₃) also form when the electrode is held at the UPD potential. The alloy formation can easily be detected from anodic stripping curves, similar to the case of Cd deposition on Au [97]. At higher coverage, these structures with low adatom density transform to a 2D hcp (hcp) Pb overlayer [116]. The strong overlayer-substrate attraction leads to an anisotropic compression of the Pb monolayer reflected in an additional $c(6 \times 2)$ moire superstructure observed at high coverage. In this UPD range first-order phase transitions take place. Unlike Ag substrate, a structural phase transition occurs on Au(100) surfaces. Indications for 2D surface alloy formation were observed after extended polarization starting predominantly at monoatomic steps of the substrate. STM observation [118] has shown that upon Pb stripping, pits form in the Au surface adjacent to Pb deposition sites and the step edges do not return to their original lines. Upon subsequent Pb deposition, the island formation has not been observed on the border in which the pits have formed. Surface roughening mechanism consists of surface alloy formation that results from lateral place exchange between Pb and Au at Au steps, and vertical exchange, Pb and Au switching position within the top two layers, through the flat terraces.

2.2.5. Pd on Au Electrode

The deposition of Pd onto unreconstructed Au(100) was studied by *in-situ* STM and cyclic voltammetry [119]. The electrochemical behavior of the first Pd layer and the growth mechanism for Pd is different on unreconstructed and reconstructed Au (100) surfaces [119]. The presence of small Au islands after dissolution of Pd points toward surface alloy formation in the underpotential region. On unreconstructed Au(110) surface, Pd deposition starts at monoatomic high steps by forming a layer that grows onto the lower terrace [120]. Coulometric data revealed that approximately three monolayer equivalents in the Pd were deposited in the underpotential region. This high coverage and the presence of holes in the Au(110) surface after the complete anodic dissolution of the Pd deposit point to the surface alloy formation. Palladium layers also appear to be rather rough, because there was no strict layer-by-layer growth.

2.2.6. Al on Au Electrode

Underpotential deposition of aluminum and alloy formation on polycrystalline gold electrodes has been studied in molten salts [121]. Cyclic voltammetry and chronopotentiometry suggested that at least two alloys formed. Moreover, there is

a fast phase transformation in the aluminum underpotential region between these intermetallic compounds at room temperature. This transformation with thin gold films was slower than that in bulk gold electrodes. Electrochemical (QCM) studies have stated the correlation between the change in the frequency of the QCM and the amount of electrodeposited Al [122]. The long time required for the mass of the Au electrode to return to its original value after deposition and stripping is consistent with the formation of bulk Al/Au alloys as has been earlier proposed.

2.2.7. Hg on Au Electrode

In-situ surface X-ray diffraction study of the UPD of mercury on Au(111) revealed the existence of three UPD phases at potentials prior to bulk mercury deposition [123]. These phases consist of two well-ordered (hexagonal structure) intermediate states and a fully discharged 2D liquid Hg layer or a monolayer of an amorphous Hg-Au alloy. The first phase appears to be metastable since it changes to a second-ordered phase after a certain time at +0.68 V or after the potential is moved to more negative values (+0.63 V). The second phase has a more compact lattice and appears to be a commensurate (2×2) Hg structure, but it also metastable. Similar to the first one, the second phase can be transformed to a final, fully discharged, state of a 2D liquid Hg layer or an amorphous Hg-Au alloy. The entire Hg UPD process, from Hg²⁺ to the fully discharged metallic Hg layer, agrees with a multistep mechanism based on electrochemical kinetic studies on polycrystalline Au electrodes.

In-situ AFM observation of the Au-Hg alloy formation on gold electrode surface AFM images revealed that small alloy protrusions initially form next to the Au grain boundaries and gradually increase in size as the deposition time increases [124, 125]. These protrusions always are accompanied by the dissolution of gold at the grain boundaries, leaving many apparent pits visible on the amalgamated surface. Based on these AFM observations, a simple model of the Hg/Au amalgam process has been proposed [125].

2.2.8. Sn on Au Electrode

In-situ STM studies on UPD of Sn on Au(100) has revealed that Sn UPD on Au(100) proceeded in three stages [126]: (i) formation of a reversible submonolayer UPD, (ii) surface alloying, and (iii) alloying that extends into the bulk. The formation of the reversible submonolayer UPD proceeds in the form of clusters at potentials close to 0.04 V. The surface alloying takes place at -0.04 V. The process is illustrated by significant changes of steps on the surface. The earlier start of the surface and bulk alloying process is considered to be as a result of enhanced interdiffusion of Sn and Au atoms upon decreasing the potential. In molten salts, the UPD of a Sn monolayer and surface alloy formation also was observed at the Au surface [127].

2.3. Ag Substrate

Surface alloying on Ag has similar features with that on an Au surface. It is interesting to compare metal and alloy growth on these two metal substrates due to their almost

identical lattice constants, which can result in a very similar mismatch with the admetal lattice. However, the electronic differences between Au and Ag surfaces influence the metal growth and alloying process. Additionally, the potential of zero charge differs by several hundred millivolts from Au to Ag, and from one face to another, indicating that the kinetics of various electrochemical reactions also should be strongly affected by the nature and the crystallographic orientation of the electrode surface [128]. Therefore, for developing an atomic and nanoscale understanding of electrochemical processes, only single crystal measurements can furnish meaningful kinetic data. On the other hand, the difference in the surface electronic properties expressed in terms of work function leads to different surface dynamics of an Au and Ag electrode surface in a given electrolyte. It is known that the surface diffusion of Au and Ag atoms in sulfuric acid solution increases as the potential moves away from their PZC [129, 130]. By comparing the process kinetics on Au and Ag electrodes, it can be determined whether excess charge built up on the electrode surface when the potential departs from the value of PZC plays a significant role in the surface alloying process.

2.3.1. Cd on Ag Electrode

Surface alloying during Cd UPD on Ag has similar features with that on Au surface [80, 101, 131, 132]. Cadmium deposition on Ag(100) shows UPD at about -0.25 V/SHE [99]. Cd UPD peak is located at more negative potential than Cd UPD on Au(100) ($E = 0.1$ V [97]), indicating that the interaction at the Ag/Cd interface is smaller than at the Au/Cd interface. The adsorption process during the first UPD is reversible, and its characteristic feature is indicated by a similar peak that appears in the reverse direction during desorption. The structure of Cd UPD is Ag(100)-c(2×2)Cd [equivalent to Ag(100)-($\sqrt{2} \times \sqrt{2}$)R45° Cd] for the first Cd adsorption peak on Ag(100) [80]. Long-time polarization experiments revealed that the peak corresponding to the desorption of the first Cd UPD monolayer does not remain stable over extended polarization conditions, suggesting that the alloying process has affected the first Cd UPD monolayer on Ag(100). This behavior contrasts to the Au(100) surface, where the first Cd UPD adlayer of 0.5 coverage is not affected by the surface alloying process [42]. Additionally, when the polarization potentials are close to the deposition potential, the second desorption peak associated with the alloy removal shifts to more positive potentials with the increase of polarization time, suggesting that the dissolution of the Cd adlayer is affected by kinetic factors. The increase in charge associated with the extended polarization at the given underpotential quickly reaches over 1 to 2 ML and further increases with polarization time. The surface alloying process occurring onto Ag(100) surface during Cd deposition presents a similar time and potential dependence as the Cd/Au(100) system. For a long polarization time, the extent of penetration of the alloyed phase onto the surface is governed by solid-state diffusion of either Cd or Ag atoms through the vacancy-rich surface phase. The real case of surface alloying in the Ag/Ag-Cd/Cd²⁺ system that lead to the formation of a thin surface phase has been characterized by a semi-infinite medium that has a skin

or surface layer having diffusion properties different from those of the rest of the medium. In this model, the surface alloyed layer is viewed as consisting of two regions with different diffusion coefficients. The alloying process at the Cd²⁺/Ag(100) interface consists of two processes: one, very fast, which occurred within 0.4 to 1.4 nm and is characterized by $D \approx 10^{-16}$ cm²s⁻¹, and another one, much slower, which is characterized by $D \approx 10^{-19}$ cm²s⁻¹, suggesting a solid-state diffusion process. At high underpotentials (i.e., $E = -0.35$ and -0.4 V), the surface alloying process is lower and the thickness of the surface "skin" is smaller for Cd/Ag(100) than for Cd/Au(100) but similar at $E = -0.45$ V. These results suggest that there is a potential dependence of the Cd-Au and Cd-Ag atom interaction that is correlated with the stability of the electrode surface. The surface alloy kinetic is enhanced as the potential moves away from the PZC of the electrode surface. Therefore, the instability of Au(100) surface is higher than Ag(100) surface. Therefore, the difference in surface alloying kinetics at Cd/Au(100) and Cd/Ag(100) interfaces streamlines from the known differences in the PZC of the two metals, which is at least 400 mV more negative for Ag(100) than for Au(100) in H₂SO₄ solution [130].

Under potential deposition of Cd on Au(100) and Ag(100) involves two main processes, a relatively fast adsorption/desorption of Cd and a slow deposition of Cd at low underpotentials. The fast adsorption process is accompanied by the formation of a very thin alloy film of which thickness is potential dependent. Additional evidences on the complex mechanism of surface interdiffusion are provided by electrochemical microbalance (EQCM) technique [90]. Unlike Au(100), removing the thinner alloy phase from the Ag surface does not roughen the electrode surface. The kinetic of surface alloy formation is much lower than on Au and the penetration of the alloy phase is smaller. On the other hand, the morphologic changes induced by the removal of the thin surface alloy film formed on Ag(100) might be quickly hidden by a rapid restoration of the surface due to the high surface mobility of Ag atoms or by a simultaneous dissolution of the surface phase. In the case of chloride adatoms, which are adsorbed on the silver substrate when UPD of Cd starts, there is no desorption [133]. They become replaced by Cd adatoms and remain adsorbed and discharged on top of a Cd layer. Alloying of Ag with Cd takes place at potentials close to the reversible potential of Cd.

2.3.2. Pb on Ag Electrode

In-situ STM imaging was used to study the morphologic and structural aspects of 2D UPD Pb layer formation on Ag(100) [116, 134] and Ag(111) [134] surfaces. The UPD process starts at high underpotential by decoration of monoatomic steps with a 1D Pb phase. The decoration extends at the step edges and expands on atomically smooth surface in 2D Pb phase with an incommensurate structure. Formation of overlayer domains with the Ag(100)-c(2×2) Pb structure was observed on flat terraces in the low and medium coverage range. At higher coverage, these structures of low adatom density transform to a 2D hcp Pb layer via a first-order transition. The strong adlayer-substrate attraction and

the high crystallographic Pb–Ag misfit lead to an anisotropic compression of the Pb monolayer reflected in an additional $c(6 \times 2)$ moire superstructure observed at high coverage [116]. In this UPD range, first-order phase transitions take place. On a Ag(111) substrate, the compressed hcp Pb monolayer is incommensurate and isotropically compresses with respect to the substrate, whereas on Ag(100), the hcp Pb layer is anisotropically compressed and is in a higher-order registry with the substrate. The change in surface morphology during UPD and dissolution of Pb is complex. After the initial decoration at high underpotentials, a slow lateral growth of a condensed Pb monolayer starts at monoatomic steps and continues to grow and form 2D islands on atomically flat terraces. The islands are mainly formed on the top of the first condensed Pb monolayer. The dissolution process initiates changes of the shape of the monoatomic step [134], where the alloy phase was formed initially. On Ag(100) surfaces, stable 2D Pb islands on top of the compressed Ag(100)–2D hcp Pb monolayer are observed. Indications for 2D surface alloy formation were observed after extended polarization, starting predominantly at monoatomic steps of the substrate.

2.4. Surface Alloying at Me–Cu Interface

2.4.1. Cd on Cu Substrate

Electrochemical studies of Cd UPD on Cu(111) and Cu(110) from chloride-containing solutions have shown that the process takes place in two steps [135]. On Cu(111), the first step corresponds to the formation of the $(\sqrt{19} \times \sqrt{19})R23.4^\circ$ structure of Cd, and the second one corresponds to the alloying of Cu with Cd. Deposition of the first Cd UPD layer was found to take place by replacing the adsorbed structure of chloride but without chloride desorption, i.e., the chloride remained adsorbed on top of the Cd layer. The alloying process between Cd and Cu was more pronounced on Cu(110) than on Cu(111), although similar electrochemical behavior has been observed.

2.4.2. Pb on Cu Electrode

The deposition of Pb on Cu has been investigated in both sulfuric acid and acid perchlorate solutions. Real-time STM imaging has demonstrated high surface mobility of Cu(100) at 0.05 V in sulfuric acid solutions [136]. That is why *in-situ* STM was unable to reveal the atomic structures of the surface alloys formed by submonolayer Pb atoms, probably because of the lack of a highly ordered arrangement and high surface mobility. The amount of lead deposition influenced the surface morphology, particularly the orientation and unevenness of steps. Deposition of a small amount of Pb vastly decreased kink density and meanwhile caused step realignment. As the coverage of Pb atoms increases, step edges rotate by 45° . As the coverage of lead atoms exceeds 0.5 ML, several structures (including $c(2 \times 2)$, compressed $c(2 \times 2)$, and $(5\sqrt{2} \times \sqrt{2})R45^\circ$) were observed as the coverage of lead is increased from 0.5 to 0.6 ML. The results are similar to those obtained in an ultrahigh vacuum environment.

Formation of an alloy phase during Pb deposition on Cu(100) has been studied in connection to the influence of

chloride adsorption in an acid perchlorate solution [137]. Unlike vacuum deposition, the use of metal UPD and anions as surfactants in the electrochemical deposition of copper provides control over the surfactant coverage and its effect on mesoscopic structure. Upon immersion of a Cu(100) electrode in electrolyte, a $c(2 \times 2)$ Cl adlayer is formed, but, at more negative potentials, an order–disorder transformation occurred. In an electrolyte containing Pb^{2+} , halide adlayer may be completely displaced by lead UPD. Lead adlayer forms either a highly defective $c(2 \times 2)$, $c(5\sqrt{2} \times \sqrt{2})R45^\circ$ or a disordered structure corresponding to a coverage ranging from 0.5 to 0.6. The transformation from the halide to the lead adlayer results in the formation of vacancies and adatoms, which condense to form holes and islands, respectively. These features are consistent with the formation of an alloy phase at low coverage that subsequently dealloys as the coverage approaches 0.5. The extent of the morphologic changes associated with the alloying/dealloying processes is strongly path dependent. Stripping of the lead UPD layer is associated with two oxidation waves. As the potential is increased beyond the peak of the first wave, islands disappear, which may be due to alloy formation occurring coincident with partial desorption of the lead.

Underpotential deposition of Pb or Sn on Cu also has been studied to obtain electroplated Cu–Pb and Cu–Sn alloys, with small amounts of alloyed Pb and Sn from acid solutions that do not contain complexants [138]. Such alloys are of interest as possible on-chip wiring for very-large-scale integration. The UPD process can be used to keep the content of alloying agent small to maintain a low resistivity. The minor component is incorporated in the metallic state, even though the deposition potential is positive to its reversible potential.

2.5. Pd Substrate

2.5.1. Ge on Pd Electrode

Study of the UPD of germanium onto polycrystalline palladium surfaces revealed the Ge + Pd alloy formation [139]. Ge UPD layer on the Pd surface inhibits hydrogen adsorption and hinders hydrogen transport from the bulk of Pd.

2.5.2. Cu on Pd Electrode

Study of the UPD of copper on a palladized Pt electrode has shown that adsorbed Cu atoms form a catalyst on the Pd surface that accelerates Pd corrosion during the desorption of adsorbed Cu [140]. These results suggested alloy formation owing to copper absorption. A mechanism of copper deposition via ionization of presorbed hydrogen has also been proposed.

2.5.3. Bi on Pd Electrode

Study of the interaction between electrodeposited bismuth and polycrystalline palladium surfaces has suggested alloy formation between Bi deposit and Pd substrate [141], and irreversible Bi adsorption on Pd substrate has been demonstrated.

3. APPLICATIONS

Applications of the UPD process, and of the surface alloy formation in particular, include surface modification in nanotechnology. Examples take account of the activity of the bimetallic catalysts [142, 143], the growth of the film (which can be controlled for designing electrocatalysts at an atomic level [144]), interdiffusion in thin films at the alloy surface [145, 146], higher activation of the polycomponent alloy anode [147], etc.

The UPD of appropriate indicator metals Me_1 onto a substrate metal S, which is already covered with a submonolayer or monolayer amount of another metal Me can be used as a microprobe for studying composite metal surfaces [148]. The adsorption energy for an adatom Me_1 on the substrate S is changed in the presence of other adatoms Me on the surface. Metals that show UPD on a foreign metal surface also form monolayers when deposited directly at potentials negative from the Nernst potential, where nucleation and cluster formation would be thermodynamically possible.

Inhibition of hydrogen evolution reaction by an UPD layer finds applications in thin-film deposition and protection against corrosion. The UPD of zinc has been used for mitigation of hydrogen absorption/penetration into steel and alloys (e.g., AISI 4340 steel, Inconel 718 alloys [105], and HY-130 steel [106]). It has been shown that UPDs inhibit the hydrogen evolution reaction and the degree of hydrogen ingress. In the presence of monolayer coverage of zinc on the substrate surfaces, the hydrogen evolution current densities are reduced about 40 to 70 % compared with the values obtained on bare surfaces. The observed effects are due to the kinetic limitations of the hydrogen discharge reaction and the suppression of hydrogen absorption by the deposited monolayers. In the presence of zinc monolayers, the hydrogen entry efficiency in the alloy and the hydrogen entry rate constant also are reduced.

Nanopore preparation in self-assembled monolayers of alkanethiols is another interesting example on how the selective desorption process of an UPD layer can be used to control a nanofeature. The modified electrode possesses characteristics of a nanoelectrode assembly. The method to prepare nanopores in a self-assembled monolayer (SAM) of alkanethiol has been developed on the basis of the observation that UPD of Ag on alkanethiol SAM-coated Au(111) makes numerous islands of Ag atomic monolayers, and UPD of Ag or Cu on SAM-coated Au stabilizes the adsorbed alkanethiol molecules against their reductive desorption in an alkaline solution [149]. The procedure involves several steps: Ag UPD on decanethiol SAM-coated Au(111) to give small islands, selective desorption of decanethiol SAM molecules from the Au surface, Cu UPD on the exposed Au surface, decanethiol SAM formation on the deposited Cu monolayer, and selective desorption of decanethiol SAM molecules from the surface of the Ag islands. Changing the Ag deposition time can control the size and number of the nanopores.

4. CONCLUSIONS

In this review, a number of systems that present alloying at the Me-S interface have been identified and discussed. It is obvious that various surface-sensitive techniques can

provide important insights into the process of surface alloying in the underpotential region. In the past, surface alloying has been observed and studied by standard electrochemical methods in several UPD systems. Recently, many questions on the local surface properties have been answered due to the advent of new *in-situ* techniques with nanoscale and atomic resolution. It is worthwhile comparing the data obtained independently by various research groups on the alloying process from structural, thermodynamic, mechanism, and kinetics point of view. Particularly interesting is the fact that anion adsorption substantiates the hypothesis that the UPDs may largely initiate the surface alloying process at the Me UPD/electrolyte interface. However, a process repeatedly overlooked in the UPD/alloying studies is surface diffusion, which is affected by the accumulation of excess charge on the top atoms or adatoms at the electrode surface during electrodeposition.

It also is worthwhile reflecting on the implications that any change in surface energetics at the atomic level has on a double layer interaction. Current progresses in surface science bring new strategies in designing and “tailoring” advanced materials. Having control over the interface potential becomes a useful tool for synthesizing atomically scaled structures. Nowadays, we have the key technology for building high-quality layered materials “brick-by-brick,” with virtually no surface defect. As an example, a target would be to build up semiconductor superlattices with a periodic structure consisting of alternating ultrathin layers, with a period less than the electron-free path. These kinds of materials are not yet available, but, theoretically, it is shown that such a structure possesses unusual electronic properties. The effort to develop such materials is found in searching for novel phenomena in the quantum regime. The idea is to have control over the surface processes in a way in which we can avoid or promote certain surface reaction in order to create nano-architected 3D interfaces.

GLOSSARY

Activation energy The energy required to initiate a reaction, such as diffusion.

Alloy A metallic substance that is composed of two or more elements.

Amorphous Non-crystalline, without long-range order.

Anisotropy Material characteristic of exhibiting different values of a property in different crystallographic directions.

Annealing A generic term used to denote a heat treatment where the microstructure and properties of a material are altered.

Anodic reaction Electrode reaction equivalent to a transfer of positive charge from the electronic to the ionic conductor; an anodic reaction is an oxidation process.

Atomic packing factor (APF) The fraction of the volume of a unit cell that is occupied by “hard sphere” atoms or ions.

Body-centered cubic (BCC) Within the cubic unit cell atoms are located at corner and center cell positions.

Bonding energy The energy required to separate two atoms that are chemically bonded to each other.

Columnar structure Coarse structure of parallel columns of grains caused by highly directional solidification of molten metal resulting from sharp thermal gradients.

Coordination number The number of atomic or ionic nearest neighbors.

Crystal structure For crystalline materials, the manner in which atoms or ions are arrayed in space; it is defined in terms of the unit cell geometry and the atom positions within the unit cell.

Crystalline The state of a solid material characterized by a periodic and repeating three-dimensional array of atoms, ions, or molecules.

Crystallization Act or process of forming crystals or bodies by elements or compounds solidifying so they are bounded by plane surfaces, symmetrically arranged, and are external expressions of definite internal structure.

Defect structure Relating to the kinds and concentrations of vacancies and interstitials in a ceramic compound.

Diffusion Motion of atoms, ions, or vacancies through a material.

Diffusion coefficient (D) The constant of proportionality between the diffusion flux and the concentration gradient in Fick's first law; its magnitude is indicative of the rate of atomic diffusion.

Diffusion flux (J) The quantity of mass diffusing through and perpendicular to a unit cross-sectional area of material per unit time.

Dislocation A linear crystalline defect around which there is atomic misalignment; plastic deformation corresponds to the motion of dislocations in response to an applied shear stress; edge, screw, and mixed dislocations are possible.

Electrodeposition The deposition of a substance on an electrode by passing electric current through an electrolyte.

Equilibrium (phase) The state of a system where the phase characteristics remain constant over indefinite time periods; at equilibrium the free energy is a minimum.

Face-centered cubic (FCC) A crystal structure found in some of the common elemental metals; within the cubic unit cell atoms are located at all corner and face-centered positions.

Free energy A thermodynamic quantity that is a function of both the internal energy and entropy (or randomness) of a system; at equilibrium the free energy is at a minimum.

Grain An individual crystal in a polycrystalline metal or ceramic.

Hexagonal close-packed (HCP) The unit cell is of hexagonal geometry and is generated by the stacking of close-packed planes of atoms.

Interdiffusion Diffusion of atoms of one metal into another metal.

Isotropic Having identical values of a property in all crystallographic directions.

Metastable Possessing a state of pseudoequilibrium that has a free energy higher than that of the true equilibrium state.

Microstructure The microscopic assemblage of grains, grain boundaries, amorphous phases, pores, and inclusions, that make up a material.

Noble metal A metal with high resistance to chemical reaction, especially oxidation and solution by organic acids.

Nucleation The initial stage in a phase transformation; it is evidenced by the formation of small particles (nuclei) of the new phase which are capable of growing.

Octahedral position The void space among close-packed, hard sphere atoms or ions for which there are six nearest neighbors; an octahedron (double pyramid) is circumscribed by the lines constructed from centers of adjacent spheres.

Ordering Positioning of host and substitution ions in an ordered, repetitious pattern rather than in a random arrangement.

Orientation Arrangements in space of the axes of a crystal lattice with respect to a coordinate system.

Oxidation A reaction in which there is an increase in valence resulting from a loss of electrons; often associated with the corrosion of metals, where the corroded metal forms an oxide; elevated temperatures increase the rate of oxidation.

Phase transformation Changes that can occur within a given material system; how one or more phases in an alloy change into a new phase or mixture of phases; transformation occurs because the initial state of the alloy is unstable relative to the final state.

Polarization Displacement of the centers of positive and negative charge.

Strain The unit of change in the size or shape of a body due to force; a dimensionless number that characterizes the change in dimensions of an object during a deformation or flow process.

Unit cell The smallest repetitive volume that comprises the complete pattern of a crystal.

Vacancy An unfilled lattice site in a crystal structure.

REFERENCES

1. D. M. Kolb, in "Advances in Electrochemistry and Electrochemical Engineering" (T. C. W. Gerischer H. Ed.), p. 125. Wiley, New York, 1978.
2. G. Staikov, K. Juttner, W. J. Lorenz, and E. Budevski, *Electrochim. Acta* 39, 1019 (1994).
3. C. G. Sanchez, M. G. Del Popolo, and E. P. M. Leiva, *Surf. Sci.* 421, 59 (1999).
4. D. N. Upadhyay and V. Yegnaraman, *Mater. Chem. and Phys.* 62, 247 (2000).
5. A. Al-Akl and G. A. Attard, *J. Phys. Chem. B* 101, 4597 (1997).
6. G. Salie, *J. Electroanal. Chem.* 245, 1 (1988).
7. G. Salie and K. Bartels, *J. Electroanal. Chem.* 245, 21 (1988).
8. G. Salie and K. Bartels, *Electrochim. Acta* 39, 1057 (1994).
9. C. McCall, N. Dimitrov, and K. Sieradzki, *J. Electrochem. Soc.* 148, E290 (2001).
10. A. N. Correia, L. H. Mascaro, S. A. S. Machado, and L. A. Avaca, *Electrochim. Acta* 42, 493 (1997).
11. F. Ficiocioglu and F. Kadirgan, *J. Electroanal. Chem.* 346, 187 (1993).
12. C. L. Green and A. Kucernak, *J. Phys. Chem. B* 106, 1036 (2002).
13. B. Beden, F. Kadirgan, A. Kahyaoglu, and C. Lamy, *J. Electroanal. Chem.* 135, 329 (1982).
14. D. B. Lewis, C. E. Lehmborg, and G. W. Marshall, *T. I. Met. Finish.* 79, 60 (2001).

15. L. F. Li, Y. Luo, G. G. Totir, D. A. Totir, G. S. Chottiner, and D. A. Scherson, *J. Phys. Chem. B* 103, 164 (1999).
16. E. A. Streltsov, S. K. Poznyak, and N. P. Osipovich, *J. Electroanal. Chem.* 518, 103 (2002).
17. C. N. Van Huong and M. J. Gonzalez-Tejera, *J. Electroanal. Chem.* 244, 249 (1988).
18. A. Wieckowski, B. C. Schardt, S. D. Rosasco, J. L. Stickney, and A. T. Hubbard, *Surf. Sci.* 146, 115 (1984).
19. J. L. Stickney, S. D. Rosasco, D. Song, M. P. Soriaga, and A. T. Hubbard, *Surf. Sci.* 130, 326 (1983).
20. J. F. Rodriguez, D. L. Taylor, and H. D. Abruna, *Electrochim. Acta* 38, 235 (1993).
21. N. Kimizuka and K. Itaya, *Faraday Discuss.* 94, 117–126 (1992).
22. N. Shinotsuka, K. Sashikata, and K. Itaya, *Surf. Sci.* 335, 75 (1995).
23. N. C. Gibson, P. M. Saville, and D. A. Harrington, *J. Electroanal. Chem.* 318, 271 (1991).
24. P. Zelenay, M. Gamboaaldeco, G. Horanyi, and A. Wieckowski, *J. Electroanal. Chem.* 357, 307 (1993).
25. D. L. Taylor and H. D. Abruna, *J. Electrochem. Soc.* 140, 3402 (1993).
26. J. X. Wang, N. S. Marinkovic, R. R. Adzic, and B. M. Ocko, *Surf. Sci.* 398, L291 (1998).
27. N. S. Marinkovic, J. X. Wang, J. S. Marinkovic, and R. R. Adzic, *J. Phys. Chem. B* 103, 139 (1999).
28. D. Aberdam, C. Salem, R. Durand, and R. Faure, *Surf. Sci.* 239, 71 (1990).
29. D. G. Frank, T. Golden, O. M. R. Chyan, and A. T. Hubbard, *Appl. Surf. Sci.* 48, 166 (1991).
30. D. G. Frank, O. M. R. Chyan, T. Golden, and A. T. Hubbard, *J. Phys. Chem.* 98, 1895 (1994).
31. R. C. Salvarezza, D. V. Vasquez Moll, M. C. Giordano, and A. J. Arvia, *J. Electroanal. Chem.* 213, 301 (1986).
32. B. P. Costa, J. Canullo, D. V. Moll, R. C. Salvarezza, M. C. Giordano, and A. J. Arvia, *J. Electroanal. Chem.* 244, 261 (1988).
33. P. Ocon, P. Herrasti, C. Palacio, M. E. Vela, R. C. Salvarezza, L. Vazquez, and A. J. Arvia, *J. Electroanal. Chem.* 357, 339 (1993).
34. M. E. Martins, R. C. Salvarezza, and A. J. Arvia, *Electrochim. Acta* 36, 1617 (1991).
35. A. Vaskevich, M. Rosenblum, and E. Gileadi, *J. Electroanal. Chem.* 383, 167 (1995).
36. A. Vaskevich and E. Gileadi, *J. Electroanal. Chem.* 442, 147 (1998).
37. N. M. Markovic, B. N. Grgur, C. A. Lucas, and P. N. Ross, *J. Electroanal. Chem.* 448, 183 (1998).
38. E. Lamy-Pitara, L. El Ouazzani-Benhima, J. Barbier, M. Cahoreau, and J. Caisso, *J. Electroanal. Chem.* 372, 233 (1994).
39. S. Mukerjee and J. McBreen, *J. Electrochem. Soc.* 146, 600 (1999).
40. H. Massong, H. S. Wang, G. Samjeske, and H. Baltruschat, *Electrochim. Acta* 46, 701 (2000).
41. M. E. Martins, R. C. Salvarezza, and A. J. Arvia, *Electrochim. Acta* 43, 549 (1998).
42. R. Vidu and S. Hara, *Surf. Sci.* 452, 229 (2000).
43. M. Cappadonia, K. M. Robinson, J. Schmidberger, and U. Stimming, *Surf. Rev. Lett.* 4, 1173 (1997).
44. M. Cappadonia, K. M. Robinson, J. Schmidberger, and U. Stimming, *J. Electroanal. Chem.* 436, 73 (1997).
45. Z. C. Shiand and J. Lipkowski, *J. Phys. Chem.* 99, 4170 (1995).
46. Z. C. Shi, S. J. Wu, and J. Lipkowski, *Electrochim. Acta* 40, 9 (1995).
47. F. Moller, O. M. Magnussen, and R. J. Behm, *Electrochim. Acta* 40, 1259 (1995).
48. T. Hachiya, H. Honbo, and K. Itaya, *J. Electroanal. Chem.* 315, 275 (1991).
49. N. Batina, T. Will, and D. M. Kolb, *Faraday Discuss.* 94, 93–106, (1992).
50. W. Haiss, D. Lackey, J. K. Sass, H. Meyer, and R. J. Nichols, *Chem. Phys. Lett.* 200, 343 (1992).
51. W. Haiss and J. K. Sass, *J. Electroanal. Chem.* 410, 119 (1996).
52. N. Ikemiya, S. Miyaoka, and S. Hara, *Surf. Sci.* 327, 261 (1995).
53. E. Herrero, S. Glazier, and H. D. Abruna, *J. Phys. Chem. B* 102, 9825 (1998).
54. E. Herrero, S. Glazier, L. J. Buller, and H. D. Abruna, *J. Electroanal. Chem.* 461, 121 (1999).
55. A. Tadjeddine and G. Tourillon, *Analisis* 20, 309 (1992).
56. H. Uchida, M. Hiei, and M. Watanabe, *J. Electroanal. Chem.* 452, 97 (1998).
57. M. Legault, L. Blum, and D. A. Huckaby, *J. Electroanal. Chem.* 409, 79 (1996).
58. J. G. Xu and X. W. Wang, *Surf. Sci.* 408, 317 (1998).
59. G. Brown, P. A. Rikvold, and S. J. Mitchell, *Abstr. Pap. Am. Chem. Soc.* 220, 94 (2000).
60. G. Horanyi and M. Wasberg, *J. Electroanal. Chem.* 413, 161 (1996).
61. J. E. T. Andersen and P. Moller, *J. Electrochem. Soc.* 142, 2225 (1995).
62. B. G. Ateya, G. Geh, A. H. Carim, and H. W. Pickering, *J. Electrochem. Soc.* 149, B27 (2002).
63. D. L. Lu and K. Tanaka, *J. Solid State Electrochem.* 1, 187 (1997).
64. D. L. Lu and K. Tanaka, *Phys. Rev. B* 55, 13865 (1997).
65. A. Vaskevich and I. Rubinstein, *J. Electroanal. Chem.* 491, 87 (2000).
66. F. Endres and A. Schweizer, *Phys. Chem. Chem. Phys.* 2, 5455 (2000).
67. S. G. Corcoran, G. S. Chakarova, and K. Sieradzki, *J. Electroanal. Chem.* 377, 85 (1994).
68. C. M. Whelan, M. R. Smyth, C. J. Barnes, G. A. Attard, and X. Yang, *J. Electroanal. Chem.* 474, 138 (1999).
69. C. A. Zell, F. Endres, and W. Freyland, *Phys. Chem. Chem. Phys.* 1, 697 (1999).
70. C. H. Chen, S. M. Vesceky, and A. A. Gewirth, *J. Am. Chem. Soc.* 114, 451 (1992).
71. S. Garcia, D. Salinas, C. Mayer, E. Schmidt, G. Staikov, and W. J. Lorenz, *Electrochim. Acta* 43, 3007 (1998).
72. N. Ikemiya, K. Yamada, and S. Hara, *Surf. Sci.* 348, 253 (1996).
73. S. Takami, G. K. Jennings, and P. E. Laibinis, *Langmuir*, 17, 441 (2001).
74. C. M. Whelan, M. R. Smyth, C. J. Barnes, G. A. Attard, and X. Yang, *J. Electroanal. Chem.* 474, 138 (1999).
75. S. G. Garcia, D. Salinas, C. Mayer, J. R. Vilche, H. J. Pauling, S. Vinzelberg, G. Staikov, and W. J. Lorenz, *Surf. Sci.* 316, 143 (1994).
76. M. C. Gimenez, M. G. Del Popolo, and E. P. M. Leiva, *Electrochim. Acta* 45, 699 (1999).
77. V. Rooryck, F. Reniers, C. Buess-Herman, G. A. Attard, and X. Yang, *J. Electroanal. Chem.* 482, 93 (2000).
78. A. V. Vvedenskii, *Prot. Met.* 32, 539 (1996).
79. B. W. Gregory, M. L. Norton, and J. L. Stickney, *J. Electroanal. Chem.* 293, 85 (1990).
80. H. Bort, K. Juttner, W. J. Lorenz, and G. Staikov, *Electrochimica Acta*, 28, 993 (1983).
81. A. Budniok, *J. Electroanal. Chem.* 123, 365 (1981).
82. L. P. Colletti and J. L. Stickney, *J. Electrochem. Soc.* 145, 3594 (1998).
83. U. Demir and C. Shannon, *Langmuir* 12, 6091 (1996).
84. M. C. dos Santos and S. A. S. Machado, *J. Brazil. Chem. Soc.* 9, 211 (1998).
85. M. L. Foresti, G. Pezzatini, M. Cavallini, G. Aloisi, M. Innocenti, and R. Guidelli, *J. Phys. Chem. B* 102, 7413 (1998).
86. F. Forni, M. Innocenti, G. Pezzatini, and M. L. Foresti, *Electrochim. Acta* 45, 3225 (2000).
87. B. E. Hayden and I. S. Nandhakumar, *J. Phys. Chem. B* 102, 4897 (1998).
88. S. J. Hsieh and A. A. Gewirth, *Langmuir* 16, 9501 (2000).
89. H. Huang, M. Zhao, X. Xing, I. T. Bae, and D. Scherson, *J. Electroanal. Chem.* 293, 279 (1990).
90. G. Inzelt and G. Horanyi, *J. Electroanal. Chem.* 491, 111 (2000).

91. T. E. Lister and J. L. Stickney, *Appl. Surf. Sci.* 107, 153 (1996).
92. T. E. Lister, L. P. Colletti, and J. L. Stickney, *Israel J. Chem.* 37, 287 (1997).
93. C. Stuhlmann, Z. Park, C. Bach, and K. Wandelt, *Electrochim. Acta* 44, 993 (1998).
94. D. W. Suggs and J. L. Stickney, *Surf. Sci.* 290, 362 (1993).
95. D. W. Suggs and J. L. Stickney, *Surf. Sci.* 290, 375 (1993).
96. R. Vidu and S. Hara, *J. Electroanal. Chem.* 475, 171 (1999).
97. R. Vidu and S. Hara, *J. Vac. Sci. Technol. B* 17, 2423 (1999).
98. R. Vidu and S. Hara, *Electrochemistry* 67, 1240 (1999).
99. R. Vidu, N. Hirai, and S. Hara, *Phys. Chem. Chem. Phys.* 3, 3320 (2001).
100. T. Watanabe, O. Kawanami, and K. Honda, *Bull. Chem. Soc. Jpn.* 58, 2088 (1985).
101. X.-K. Xing, P. Abel, R. McIntyre, and D. Scherson, *J. Electroanal. Chem.* 216, 261 (1987).
102. J. W. Schultze, F. D. Koppitz, and M. M. Lohrengel, *Ber. Bunsenges. Phys. Chem.* 78, 693 (1974).
103. R. Vidu and S. Hara, *Scripta Mater.* 41, 617 (1999).
104. G. Horanyi, *J. Solid State Electr.* 4, 177 (2000).
105. G. Zheng, B. N. Popov, and R. E. White, *J. Appl. Electrochem.* 25, 212 (1995).
106. B. N. Popov, G. Zheng, and R. E. White, *Corros. Sci.* 36, 2139 (1994).
107. R. Vidu, Ph.D. thesis Osaka, Japan, 2000.
108. G. Kokkinidis, A. Papoutsis, and G. Papanastasiou, *J. Electroanal. Chem.* 359, 253 (1993).
109. G. Kokkinidis and A. Kelaidopoulou, *J. Electroanal. Chem.* 414, 197 (1996).
110. A. Papoutsis and G. Kokkinidis, *J. Electroanal. Chem.* 371, 231 (1994).
111. X. Q. Zeng and R. Hatton, *Electrochim. Acta* 45, 3629-36 (2000).
112. M. F. Toney, J. G. Gordon, M. G. Samant, G. L. Borges, O. R. Melroy, D. Yee, and L. B. Sorensen, *J. Phys. Chem.* 99, 4733 (1995).
113. K. M. Robinson and W. E. Ogrady, *Faraday Discuss.* 95, 55 (1993).
114. A. Hamelin and J. Lipkowski, *J. Electroanal. Chem.* 171, 317 (1984).
115. J. S. Chacha and B. E. Conway, *B. Chem. Soc. Ethiopia* 11, 31 (1997).
116. U. Schmidt, S. Vinzelberg, and G. Staikov, *Surf. Sci.* 348, 261 (1996).
117. H. J. Schmidt, U. Pittermann, H. Schneider, and K. G. Weil, *Anal. Chim. Acta* 273, 561 (1993).
118. M. P. Green and K. J. Hanson, *Surf. Sci.* 259, L743 (1991).
119. L. A. Kibler, M. Kleinert, and D. M. Kolb, *Surf. Sci.* 461, 155 (2000).
120. L. A. Kibler, M. Kleinert, V. Lazarescu, and D. M. Kolb, *Surf. Sci.* 498, 175 (2002).
121. J. J. Lee, I. T. Bae, D. A. Scherson, B. Miller, and K. A. Wheeler, *J. Electrochem. Soc.* 147, 562 (2000).
122. J. J. Lee, Y. B. Mo, D. A. Scherson, B. Miller, and K. A. Wheeler, *J. Electrochem. Soc.* 148, C799 (2001).
123. J. Li and H. D. Abruna, *J. Phys. Chem. B* 101, 2907 (1997).
124. X. M. Yang, K. Tonami, L. A. Nagahara, K. Hashimoto, Y. Wei, and A. Fujishima, *Surf. Sci.* 319, L17 (1994).
125. X. M. Yang, K. Tonami, L. A. Nagahara, K. Hashimoto, Y. Wei, and A. Fujishima, *Chem. Lett.* 11, 2059 (1994).
126. J. W. Yan, J. Tang, Y. Y. Yang, J. M. Wu, Z. X. Xie, S. G. Sun, and B. W. Mao, *Surf. Interface Anal.* 32, 49 (2001).
127. X. H. Xu and C. L. Hussey, *J. Electrochem. Soc.* 140, 618 (1993).
128. A. Hamelin, T. Vitanov, E. Sevastianov, and A. Popov, *J. Electroanal. Chem.* 145, 225 (1983).
129. N. Ikemiya, M. Nishide, and S. Hara, *Surf. Sci.* 340, L965 (1995).
130. N. Hirai, H. Tanaka, and S. Hara, *Appl. Surf. Sci.* 132, 506 (1998).
131. M. E. Martins, A. Hernandezcreus, R. C. Salvarezza, and A. J. Arvia, *J. Electroanal. Chem.* 375, 141 (1994).
132. Y. Tang and T. E. Furtak, *Electrochim. Acta* 36, 1869 (1991).
133. V. D. Jovic and B. M. Jovic, *Electrochim. Acta* 47, 1777 (2002).
134. J. Sackmann, A. Bunk, R. T. Potzschke, G. Staikov, and W. J. Lorenz, *Electrochim. Acta* 43, 2863 (1998).
135. V. D. Jovic and B. M. Jovic, *J. Serb. Chem. Soc.* 66, 345 (2001).
136. H. C. Wu and S. L. Yau, *J. Phys. Chem. B* 105, 6965 (2001).
137. T. P. Moffat, *J. Phys. Chem. B* 102, 10020 (1998).
138. J. Horkans, I. C. H. Chang, P. C. Andricacos, and H. Deligianni, *J. Electrochem. Soc.* 142, 2244 (1995).
139. I. Bakos, S. Szabo, F. Nagy, T. Mallat, and Z. Bodnar, *J. Electroanal. Chem.* 309, 293 (1991).
140. S. Szabo, I. Bakos, F. Nagy, and T. Mallat, *J. Electroanal. Chem.* 263, 137 (1989).
141. S. Szabo and I. Bakos, *Ach-Models Chem.* 133, 83 (1996).
142. Z. Bodnar, T. Mallat, I. Bakos, S. Szabo, Z. Zsoldos, and Z. Schay, *Appl. Catal. A* 102, 105 (1993).
143. Z. Bodnar, T. Mallat, and A. Baiker, *Catal. Lett.* 26, 61 (1994).
144. S. R. Brankovic, J. X. Wang, and R. R. Adzic, *J. Serb. Chem. Soc.* 66, 887 (2001).
145. F. Lantelme, A. Derja, and N. Kumagai, *J. Electroanal. Chem.* 248, 369 (1988).
146. F. Lantelme and A. Salmi, *J. Phys. Chem. Solids* 57, 1555 (1996).
147. Z. Y. Li, X. Qin, Y. B. Yu, Y. Y. Chen, L. Yi, and L. Yang, *Acta Phys-Chim. Sin.* 15, 381 (1999).
148. S. Stucki, *J. Electroanal. Chem.* 78, 31 (1977).
149. D. Oyamatsu, H. Kanemoto, S. Kuwabata, and H. Yoneyama, *J. Electroanal. Chem.* 497, 97 (2001).

Synthesis of Covalent Nanoparticles by CO₂ Laser

Nathalie Herlin-Boime, Martine Mayne-L'Hermite, Cécile Reynaud

Service des Photons, Atomes, et Molécules, DSM, CEA Saclay, Gif/Yvette France

CONTENTS

1. Introduction
 2. Generalities: Principle and Fundamentals
 3. Experimental
 4. Synthesis of Covalent Nanopowders
 5. Properties and Applications
 6. Summary
- Glossary
References

1. INTRODUCTION

Among the different methods used for the synthesis of nanomaterials, the method based on pyrolysis by CO₂ laser has proved its versatility. Since the first experiments initiated at the Massachusetts Institute of Technology for the synthesis of nonoxide ceramic powders [1–3], it has been applied to the synthesis of a large variety of metals and oxide and nonoxide nanomaterials, such as Si, SiC, Si₃N₄, Si/C/N, Si/C/O, SiO₂, BN, B₄C, TiB₂, ZrB₂, TiO₂, TiC, Al₂O₃, and WC. This technique has also been proved efficient for the deposition of various components but the large majority of the results presented here concern the production of nanopowders. Here, the term “nanopowders” is considered in its widely accepted signification of powders with diameters less than 100 nm, a range in which specific properties generally occur [4].

It is worthwhile to note that laser pyrolysis was specifically developed to synthesize a new class of silicon carbide and nitride powders to obtain ceramic materials with superior properties [1–3]. Indeed, it was demonstrated that the microstructural characteristics of ceramic materials could be drastically improved by using powders with monodispersed particle sizes [5]. Now, in the CO₂ laser pyrolysis process uniform nucleation and growth rates produce uniform powders. Moreover, these new powders were demanded with a small diameter, equiaxed shape, high purity, and controlled stoichiometry. Because laser pyrolysis totally fulfilled this

objective and appears rapidly to be useful for the synthesis of a broad range of materials, this method has met with noticeable interest all over the world.

The CO₂ laser pyrolysis method was developed in different research institutes, mainly in Europe (Italy, France, Germany, Spain, Romania, Switzerland, the Czech Republic, etc.). Some publications concern the development of this technique in Japan, China, and in the United States. Although the efficiency of the process was demonstrated, it has remained until now mainly a laboratory method. To our knowledge, only a few United States companies (Nanogram and Marketech) commercialize products issued from laser pyrolysis. For industrial development, it is necessary to operate in a continuous process. Therefore one main advantage of the technique is the simple design of reactors able to operate under flow conditions and produce homogeneous large numbers of particles [6].

A review of the synthesis devoted to carbide, boride, and nitride materials by this method was published in 1997 [7]. The present paper completes this review by dealing with the synthesis and applications of covalent nanoparticles. It is in four sections: the first one presents the process involved in the laser pyrolysis method, the second section presents the typical experimental setup and the latest technical developments published in the literature, the third section presents some synthesis results, while the last section is more devoted to the evolution of these nanopowders under *ex-situ* treatments and to their applications.

2. GENERALITIES: PRINCIPLE AND FUNDAMENTALS

The laser pyrolysis method is usually classified in the family of gas phase synthesis methods. The principle has been described in several papers [1–3]. Briefly, a stream of reactants is introduced into a reactive chamber, guided by a coaxial inert gas flow. The beam (focused or not) of a CO₂ laser intersects the reactant jet. To induce the reaction, it is required that one of the reactants or a sensitizer (i.e., a

species that absorbs the laser radiation without being dissociated) absorbs the CO₂ laser radiation. The high power of the laser induces large light absorption leading to a rapid increase in the temperature in the gas stream. The resulting effects are dissociation of the reactants and rapid thermalization by collisional transfer; nucleation and growth of nanoparticles can take place in the as-formed supersaturated vapor. Nucleation and growth occur in a very short time (0.1–10 ms). The growth is rapidly stopped as soon as the particles leave the reaction zone. The reaction is materialized by the presence in the interaction zone of a luminescent flame. The nanopowders are carried out of the reaction zone by the gaseous stream and collected onto devices placed in the pumping stream.

Because of the very limited reaction zone and rapid cooling rates, the powders obtained in this wall-less reactor are of high purity and present a low degree of agglomeration. The size is small (usually in the range of 5–50 nm), with a narrow size distribution. Moreover, the average size can be varied by changing the flow rate and therefore the residence time in the reaction zone. Morphologically, the shapes are spherical, with a high specific surface area (>100 m²/g). An example of a powder with a monomodal distribution centered at 22 nm is presented in Figure 1. The stoichiometry, size, and crystallinity can be adapted in a large range and are controlled through the choice of experimental conditions. The products present a good physical and chemical homogeneity.

In the synthesis of nonoxide powders, most of the work deals with the silicon-based materials and the most usual precursor is silane (SiH₄), which strongly absorbs laser radiation. The temperature distribution in the flame is an important parameter of the process. It has been measured with an optical pyrometer [8] or by laser spectroscopy techniques such as CARS (coherent anti-Stokes Raman scattering) [9]. Clearly, this temperature depends on the different

experimental parameters, mainly the chemical system and laser power but also the gas flow rates and pressure.

Even in simple systems dealing with the synthesis of Si or SiC from SiH₄ or SiH₄ + C₂H₂, the detailed mechanisms do not appear to be fully understood. A model proposes decomposition of SiH₄ to elemental Si. After nucleation of Si from the supersaturated vapor, the growth of Si nanoparticles has been explained by collisions [10]. For SiC, a proposed mechanism was also based on the nucleation and growth of Si from supersaturated vapor followed by a carburization step [10, 11]. More recently, a model based on the decomposition of C₂H₂ and SiH₄ followed by growth from collisions and coalescence has been proposed [12]. In the latter model intermediate species, such as Si, C, and SiC₂, are assumed to play a key role in the growth process and direct carburization of silicon is not addressed.

Also, some experimental papers, mainly by the group of ENEA, deal with the dissociation mechanisms involved in the pyrolysis process through detection of intermediate species by various methods. Time-resolved measurement of fragment chemiluminescence and two-photon laser-induced fluorescence (LIF) were used to investigate the role of SiH₂ and Si radicals [13, 14]. Using CARS, the presence of SiC₂ and C₂ radicals as intermediate species in the infrared (IR) synthesis of SiC from a SiH₄/ hydrocarbon mixture was shown [15, 16]. These studies indicate that, depending on the laser fluence, SiH₂ is formed in different electronic states. Only the radicals formed in an excited state appear efficient for the production of Si radicals and therefore the growth of nanopowders [13, 17]. Since the first experiments [2], it has been shown that a minimum power is necessary to induce the production of nanoparticles. This threshold appears to be related to the different dissociation pathways observed for SiH₂. If the power is too low, dissociation occurs via a low energy state of SiH₂, which evolves to Si-based polymers, while for high power, a higher energy state of SiH₂ is attained and evolves toward elemental Si followed by nucleation and growth.

Some authors have presented a possible chemical mechanism involved in the growth of powders from more complex systems, (see, for example [18, 19]). Overall reaction balances, diffusion coefficients, etc., are taken into account, but, from an experimental point of view, these models lack a precise knowledge of intermediate species. In a general manner, it seems that, in the laser pyrolysis process, reaction occurs through collisions between radicals present in the flame.

3. EXPERIMENTAL

In this section, the main experimental characteristics of a typical laser pyrolysis setup are presented together with the different specificities according to the aim either of doing fundamental studies or of achieving high production rates.

3.1. Experimental Setup

A typical laser pyrolysis setup (Fig. 2) is mainly composed of a reaction chamber where the reaction takes place and a collection zone together with a pumping system which ensures permanent gas inlet and product outlet. The pressure is maintained constant and usually near the atmospheric

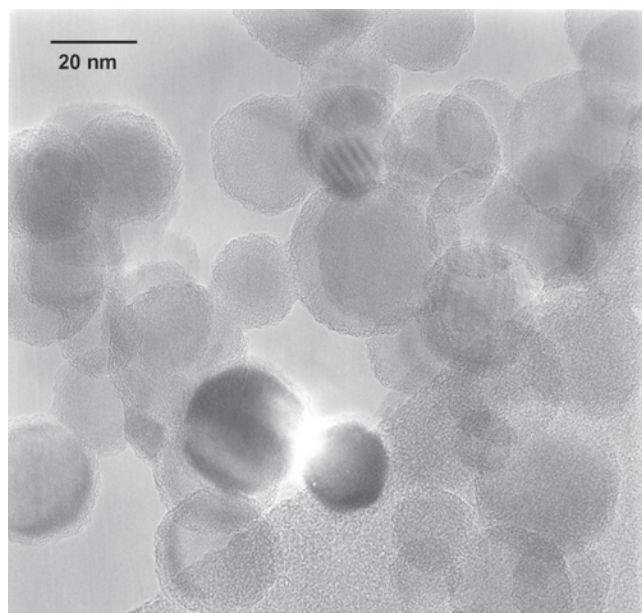


Figure 1. HRTEM image of a typical silicon nanopowder (courtesy of Jean Vicens, LERMAT, Caen).

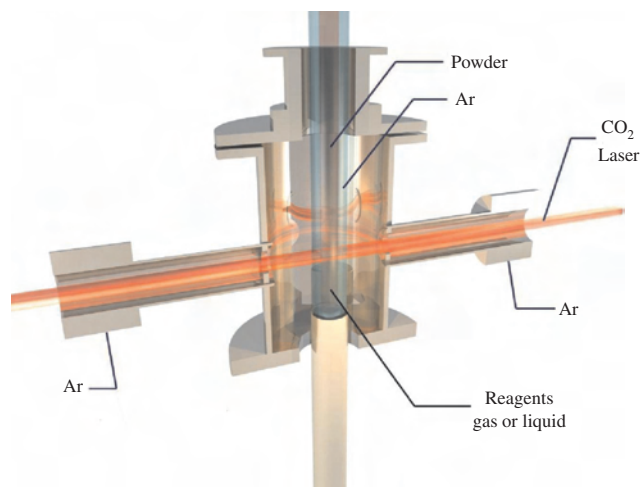


Figure 2. Schematic section of a typical laser pyrolysis reactor.

pressure. The reaction occurs at the intersection of the reactant stream and laser beam delivered by a continuous or a pulsed CO₂ laser, which enters the reactor through KCl or ZnSe windows. A flow of neutral gas protects these windows from dust deposition, which could induce heating and breakdown of the windows.

The stream of reactants usually enters at the bottom of the reactor and is confined in the center of the reactor by a coaxial inert gaseous stream. As there is no interaction between the walls of the reactor and the reaction zone, the choice is very large in building the reactor. Most often, it is a stainless steel chamber which can be evacuated and operated at a fixed pressure through a pumping system. The powders are collected after the reaction zone on several types of filters, including fiber-based and electrostatic precipitation, or on substrates. After a time, these filters are obstructed and in some cases they can be scraped, which allows longer working duration. One paper reports the synthesis of SiC without a pumping system [20] and the powders are collected in a cyclone.

In an original setup, SiCN nanoparticles doped with Al₂O₃ and yttrium were obtained from dual irradiation of a CO₂ and an excimer laser. The produced particles mixed with argon were transferred directly in an aerosol state into a deposition chamber in order to fabricate green compacts in the closed apparatus [21].

The main experimental parameters are briefly presented here and will be illustrated in more detail in the next sections. They are the precursors, which directly influence the chemical composition of the powder, the laser power, which controls the flame temperature and therefore the growing and crystallization of nanopowders, and finally, the flow rates, which control the time of residence in the laser beam and therefore the size of the nanoparticles.

Different characterization methods have been employed in these reactors. *In-situ* characterization of the hot zone or of the reaction products is mainly done by optical methods or time of flight (TOF) mass spectrometry and gives information useful in understanding the chemical processes. For the optical methods, simultaneous HeNe laser light scattering and transmission measurements were used in the

earliest experiments [8], allowing the determination of the local emissivity, number density, and particle diameter in the reaction zone. Optical spectroscopy concerns mainly CARS [9, 16] and laser-induced fluorescence [14] and requires only supplementary windows for excitation and detection of the signal. Some of the results obtained from these studies have been briefly presented in Section 2.

For TOF mass spectrometry, the pyrolysis reactor is coupled through a small conical nozzle to a high vacuum chamber, where a supersonic expansion takes place [22, 23]. An intense He or Ar beam rich in clusters extracted from the reaction flame is formed. These clusters can be obtained in a large range of sizes (from a few tens to several thousand atoms). TOF mass spectrometry allows precise determination of the sizes present in the beam. Therefore, clusters of known size can be easily deposited on different substrates intersecting the beam (low-energy cluster beam deposition (LECBD)). Moreover, since the velocities of the clusters are size-dependent, a size selection system (chopper) can be installed in the way of the supersonic beam, and then deposits of size-selected neutral ultrafine particles can be monitored with very narrow size distribution [24].

These characterization studies have been carried out with pulsed lasers, which offer several advantages when only small quantities of materials are needed. They present a high peak intensity, which is important to induce the reaction. Due to the short reaction time, small particles can be obtained. Finally, synchronization of reaction and detection is more easily achieved. CW lasers appear more adapted to production of large amounts of powders. They are commercially available up to 8000 W. Both continuous (up to 1 kW) and pulsed lasers can be tuned in the range 9.6–11.3 μm.

3.2. Method Development

In the laser pyrolysis method, the reactants are most often used in a gaseous form. In the simplest and most common configuration, commercial gases are directly connected to the reactor and are sent into the reaction zone through mass flow meters. For most process conditions, the reactants are essentially completely consumed. This is particularly important when expansive reactants are used. However, the choice of precursors is influenced by several factors. From an experimental point of view, the energy transfer efficiency from the laser to the precursor is a major parameter. For example, silane, which strongly absorbs the laser radiation, is available in high purity and is extensively used as an Si precursor.

When large quantities of powder are required, the price of the powder is mainly due to the price of the precursor and investigations based on costs of various silicon precursors for the delivery of large quantities have shown that silane remains too expensive for use in ceramic powder synthesis [25, 26]. To decrease the price, other precursors, such as SiH₂Cl₂ [19, 27, 28], have been tested but the absorption of a CO₂ laser by these reactants is very low and they are very corrosive to the experimental setup. Some papers demonstrating the possibility of using silazane or siloxane compounds [29] as silicon precursors were promising for ceramic applications of laser nanopowders, because in these precursors, the price of Si is about 8 times lower than that of silane. In some cases, liquid precursors have been used as vapors.

The precursor is placed in a heated jar and the vapors are carried out to the reaction zone by inert gases such as Ar. For example, with the precursor hexamethyldisilazane ($[(\text{CH}_3)_3\text{Si}]_2\text{NH}$ or HMDS) a conversion efficiency (liquid to powder) of about 60% has been obtained but with low flow rates (7 g/h) and with a low-power laser (135 W) [30]. Higher production rates have been attained (80–120 g/h) when the laser power has been increased to the range of 500–1000 W [31].

The coupling of a laser pyrolysis reactor with an aerosol generator offers an alternative way, which in principle allows the use of liquids with a high vapor pressure which are therefore difficult to use as vapors. A demonstration was published in 1993 [32] using a silazane precursor and an aerosol generator (an ultrasonic atomizer, Sonotek). The delivery rate of the precursor was in the range of 20–30 g/h. In a previous paper, this author claims a production rate of 100 g/h [33]. In 1992, a precursor of the same family (HMDS) was used in a pyrosol apparatus (Pyrosol 7901 type from RBI, Meylan, France). In this case, the liquid precursor is placed in a special glass jar containing a piezoelectric transducer [34, 35]. An intense ultrasonic wave is focused at the surface of the liquid and produces droplets a few micrometer in diameter which are carried out to the reaction zone by inert or reactive gases. The advantage of this pyrosol device is the high amount of reactive gas which can be transferred to the reaction zone (100 g/h) in a laboratory setup. The amount of transfer precursor is dependant on the flow and nature of the carrier gas. The main limitation of this pyrosol apparatus is its restriction to low-viscosity liquids (<5 CP).

Some efforts have been made to demonstrate high production rates. In laboratory installations, a production rate of 100 g/h was demonstrated for SiC in 1988 [36] and production of 500 g/h was obtained at Cise in a plant operating continuously for several hours [37]. More recently the Nanogram Company [38] achieved production rates in the same order of magnitude with the objective of commercializing the products. To achieve high production rates, a major factor is the optimization of the reaction zone. Several experimental solutions have been proposed. Pan et al. [39] proposed a two-reaction zone reactor. The focused laser beam intersects with a stream of reactants on both sides from the focal point. As both interaction zones are identical, this experimental design ensures a homogeneous quality of product. Production rates in the range 90–120 g/h have been achieved for Si/C/N powders from the vapor of a silazane precursor. In the classical design, the nozzle for injection of reactants is a simple cylinder. To increase the production rate, Buerki [40] used a design where the interaction zone is expanded along the laser beam by an elongated design of the introduction nozzle. The Nanogram Company [6] proposes the same design for industrial production.

4. SYNTHESIS OF COVALENT NANOPOWDERS

Table 1 reports results related to the synthesis of covalent or nonoxide powders by CO₂ laser pyrolysis and completes the previous review by Knudsen [7]. The first column

presents the chemical formula of the powder, the second column presents the precursors used in synthesis, and the last column gives some references related to synthesis. As noted before, many studies concern Si-based nanopowders. In addition to classical characterization methods (BET-specific surface area, helium pycnometry, chemical analysis, infrared spectroscopy, transmission electron microscopy, X-ray diffraction, etc.), the nanopowders have been investigated by a large variety of methods sensitive to local organization and bonding [X-ray photoelectron spectroscopy (XPS), NMR, neutron diffraction, extended X-ray absorption fine-structure spectroscopy (EXAFS), XANES, wide-angle X-ray diffraction (WAXS), SAXS, etc.] and the main tendencies are given below. The powders are most often obtained as equiaxed particles and among their common characteristics, the tendency to form weak agglomerates in a chainlike manner must be noted.

4.1. Si-Based Nanoparticles

4.1.1. Si Nanopowders

Silicon powders are obtained mainly from silane, with the exception of the work of Bauer et al. [28], where Si nanopowders were obtained from SiH₂Cl₂. In most cases, a CW CO₂ laser was used to pyrolyse silane, while argon served as a buffer gas and the particles were collected in the gas flow downstream of the reaction zone. Several synthesis results were reported at the beginning of the laser pyrolysis (see Table 1) and then, few new results were published until 1995. In the first publications [1–3, 41–44], it was shown that the particles were pure, spherically shaped, fine (average particle sizes from 20 to 100 nm), and nearly monodispersed. The yield of the synthesis process was >90%. The smallest particles were obtained in the size range of 10–20 nm [44].

The BET equivalent spherical diameter and the diameter measured by transmission electron microscopy (TEM) are found to be nearly equal and the powder densities determined from helium pycnometry are equal to the bulk density. Therefore, silicon nanoparticles exhibit a smooth surface without any closed or opened porosity [3]. Neck formation between particles has been observed by TEM but these necks are exempt of primary bonding because light scattering and photon correlation spectrometer studies of particles dispersed in solutions indicated similar sizes for the dispersed and individual particles [45]. IR spectra of as-produced Si powders show only an Si–H group of bands but as one goes along air exposure, Si–O characteristic bands appear due to oxidation of silicon particle surfaces [46]. Depending upon the reaction temperature, the resulting product can be amorphous, partially crystalline, or fully crystalline [42]. Si powders prepared with an intense unfocused laser beam (600 W/cm²) are pure and well crystallized as deduced from XPS and EXAFS studies [47].

The increasing interest since 1995 in this material, due to the strong photoluminescence (PL) exhibited by silicon nanostructures less than 10 nm in size, has stimulated the synthesis by laser pyrolysis of silicon nanoparticles as small as possible. Using the aerosol growth law [48–50], it was shown that the striking parameters for the scaling of particle dimensions are the initial number of monomers and the residence time of particles in the flame. Therefore, effects of

Table 1. Covalent nanopowders obtained from CO₂ laser pyrolysis.

Powders	Chemical systems	Ref.
Si	SiH ₄	[1, 2, 41–44, 46, 49–51, 121, 187]
Si ₃ N ₄	SiH ₄ + NH ₃	[1, 2, 40, 55, 56, 122, 123, 151]
Si ₃ N ₄	SiH ₂ Cl ₂ + NH ₃	[19, 28]
Si ₃ N ₄	[(CH ₃) ₃ Si] ₂ NH + NH ₃	[58, 59]
Si ₃ N ₄ /Al	SiH ₄ + (CH ₃) ₃ Al + NH ₃	[78]
SiC	SiH ₄ + CH ₄	[2, 11]
	SiH ₄ + C ₃ H ₄ & SiH ₄ + C ₂ H ₆	[56]
	SiH ₄ + C ₂ H ₄	[2, 36, 60]
	SiH ₄ + C ₂ H ₂	[36, 41, 56, 61–63]
	SiH ₂ Cl ₂ + C ₂ H ₄	[27]
	(CH ₃) ₂ Si(C ₂ H ₅ O) ₂ vapor	[124]
	[(CH ₃) ₃ Si] ₂ NH vapor + H ₂	[58, 59]
SiC + Si ₃ N ₄ or Si/C/N	SiH ₄ + CH ₃ NH ₂ + NH ₃	[69]
	SiH ₄ + (CH ₃) ₂ NH + NH ₃	[70, 71]
	SiH ₄ + C ₂ H ₄ + NH ₃	[21, 72–74]
	SiH ₄ + C ₂ H ₂ + NH ₃	[91]
	[(CH ₃) ₃ Si] ₂ NH vapor	[30]
	[(CH ₃) ₃ Si] ₂ NH vapor + NH ₃	[31, 58, 59]
	(CH ₃ SiHNNH) _x with x = 3 or 4 (aerosol) + NH ₃	[29, 33]
	[(CH ₃) ₃ Si] ₂ NH (aerosol) + NH ₃	[26, 84, 85]
	[(CH ₃) ₃ Si] ₂ NH (aerosol) + SiH ₄ + NH ₃	[91]
Si/C/N/Al	SiH ₄ + (CH ₃) ₃ Al + NH ₃	[76, 78]
Si/C/N/Al/Y	[(CH ₃) ₃ Si] ₂ NH (aerosol) + NH ₃ + [OCH(CH ₃) ₂] ₂ Al + [OCH(CH ₃) ₂] ₂ Y	[92, 125]
Si/B	SiH ₄ + B ₂ H ₆	[120, 151]
Si/C/B	SiH ₄ + C ₂ H ₄ + B ₂ H ₆	[9, 60, 126, 144]
SiO ₂ + SiC + C or Si/C/O	(RO) _{4-x} Si(R') _x with x = 0–3, R = C ₂ H ₅ O, R' = CH ₃ , and [(CH ₃) ₃ Si] ₂ O (aerosol)	[35, 68, 127, 128]
Si/C/O/Al	Si(O(C ₂ H ₅) ₄) + [OCH(CH ₃) ₂] ₂ Al	[128]
Si/C/O/Ti	Si(O(C ₂ H ₅) ₄) + [OCH(CH ₃) ₂] ₂ Ti	[128]
C ₃ N ₄ or C/N	C ₂ H ₂ + N ₂ O + NH ₃ + C ₂ H ₄ + SF ₆	[109, 110]
B	B ₂ H ₆	[117]
BN	BCl ₃ + NH ₃	[115, 116]
B ₄ C	BCl ₃ + CH ₄ + H ₂	[114]
	BCl ₃ + C ₂ H ₂ + H ₂	[129]
TiB ₂	TiCl ₄ + B ₂ H ₆	[117]
	TiCl ₄ + BCl ₃ + H ₂	[118]
ZrB ₂	Zr(BH ₄) ₄ (+SF ₆)	[41, 119]
TiC/TiC–SiC	TiCl ₄ + C ₂ H ₄	[109]
WC	WF ₆ + C ₂ H ₂ + H ₂ + SF ₆	[113]
	C ₂ H ₄ + C ₆ H ₆ + Fe(CO) ₅	[99]
Carbon black	SF ₆ + C ₂ H ₂	[98]
	C ₂ H ₄ , C ₃ H ₄ , C ₄ H ₆	[100, 101]
Diamond	C ₂ H ₄	[95–97]
	C ₂ H ₄ + SiH ₄ + H ₂	[95]
Fullerenes	C ₂ H ₂ + SF ₆	[22]
	C ₆ H ₆ + SF ₆	[104]
	C ₆ H ₆ + O ₂ + SF ₆	[104, 105]
	C ₆ H ₆ + N ₂ O + SF ₆	[105]
FeC ₆₀ , FeC ₇₀	Hydrocarbon + Fe(CO) ₅	[108]
	Hydrocarbon + ferrocene	[108]
Fe/C	C ₂ H ₂ + Fe(CO) ₅	[112]
	C ₂ H ₄ + Fe(CO) ₅	[112]

flow rate and silane dilution in inert gas have been studied in detail and reduction in the particle size has been obtained [49, 50].

Using the LECBD technique, ultrafine nonagglomerated neutral Si clusters were deposited on substrates [23, 51] and the diameter could be monitored from 7 down to 2.5 nm with a very sharp size distribution, due to the size selection device. Good agreement was obtained between the size measured *in-situ* by TOF and *ex-situ* by TEM and also *ex-situ* by atomic force microscopy (AFM) image analysis [52]. High-resolution transmission electron microscopy (HRTEM) study [53] showed single crystalline, spherical Si particles almost completely free of planar lattice defects. The particles, covered by thin amorphous oxide shells, are not agglomerated into larger aggregates.

4.1.2. Si₃N₄ Nanopowders

The Si₃N₄ nanopowders can be obtained from gaseous or liquid precursors.

4.1.2.1. Si₃N₄ from Gaseous Reactants The powders are obtained from SiH₄ + NH₃ in a crystallized phase [54, 55] at temperatures above 1300 K or in an amorphous phase at lower temperatures [14, 41]. Buerki et al. [40] investigated the synthesis of Si₃N₄ powders at pressures in the range of 500 to 1500 mbar using different laser lines. With a SiH₄ and NH₃ mixture, irradiated in resonance with SiH₄ or with NH₃, they obtained the same results. The powders are amorphous or partially crystallized and have very high purity. The size measured by TEM is in the range of 18 to 25 nm, with BET surfaces in the range of 55 to 120 m²/g. He achieved a production rate of 18 g/h with a low laser power (50 W). Correlation of the stoichiometry (excess Si) and gas flow rate was studied under different experimental conditions. XPS and EXAFS measurements on powders issued from the same mixture at a laser power of 600 W show a locally and long-range disordered but chemically ordered structure [47]. The presence of hydrogen atoms in nonnegligible proportion in the network is supposed to contribute to the disorder [47]. WAXS and SAXS studies of powders obtained at low pressure (100 Torr) and high laser power density (>200 MW/cm²) indicate a three-phase structure composed of pure crystalline Si, to a lesser extent β-Si₃N₄, and a major phase of amorphous Si₃N₄ [56]. Solid-state ²⁹Si NMR revealed differences between the surface and bulk composition of amorphous Si₃N₄ powders [57]. It was also shown that a hydrated layer rapidly forms at the surface when the powder is exposed to water vapor and the NMR signals were deconvoluted into individual components (Si-OH, Si-OH₂, Si-NH_x, etc.) in order to extract quantitative measurements of the various species present.

Si₃N₄ powders were also obtained from chlorinated species (SiH₂Cl₂ or SiCl₄ + sensitizer) (Table 1). An attempt to produce Si₃N₄ from SiCl₄ and NH₃ was not successful due to an efficient spontaneous reaction forming silicon diimide, Si(NH)₂ [40]. Bauer et al. [19] studied the effect of mixing the reactant gases at different heights before the laser beam. It was found that the flame temperature, morphology, and size of the particles are dependent on this parameter. In the experimental conditions explored here, the flame temperature was measured in the range of 1500–2550 K. The particles often contain Si nuclei and particle size is measured

by TEM in the range of 25–110 nm. Complete nitridation seems difficult to obtain. In order to improve the stoichiometry the amount of NH₃ was greatly increased (multiplied by 2). In this case, a broad distribution of particle sizes was observed and agglomerates were very large. The different effects were interpreted in terms of time of residence and heat transfer.

4.1.2.2. Si₃N₄ from Liquid Reactants Vapors of HMDS mixed with NH₃ were used to produce amorphous Si₃N₄ at a temperature of 1000 °C [58]. In a previous study of the same chemical system, Li et al. [59] measured the reaction temperature with a pyrometer; they found a linear decrease in the reaction temperature when the total gas flow rate increased. Production rates of amorphous Si₃N₄ (96 wt%) up to 120 g/h were obtained at a temperature of 1000 °C. In both studies, it was noted that the surface was highly sensitive to contamination. The main impurities detected at the surface of the powders were CH_x and NH_x, which explains the strong surface absorption of oxygen [58]. Chemical analysis also showed the presence of H₂ (2 wt%) in the powders. When the powders were exposed to air, they contained as much as 15 wt% of oxygen and less than 1% when handled in a glove box.

4.1.3. SiC (B) Nanopowders

4.1.3.1. SiC from Gaseous Reactants The possibility of synthesizing SiC nanoparticles from gaseous precursors was demonstrated in the first publications about laser synthesis [3, 36, 60]. Such nanoparticles have been synthesized by the mixture of SiH₄ with different hydrocarbon gases [36]. Depending on the reactant mixture and laser power, the flame temperature was measured in the range of 1000–1800 °C [36]. Among the different hydrocarbon gases, C₂H₂ does not absorb laser radiation but offers the advantage of a strongly exothermic reaction for SiC formation and gives the highest flame temperature. Conversion efficiency near 100% has been achieved [36, 61]. The amount of powder increases linearly with the gas flow rate and does not change when the pressure is changed in the range of 100–500 Torr [61]. In most cases, the ratio Si/C can be controlled simply by changing the ratio between the reactants. For sintering and material applications, dopants such as B can easily be introduced through the addition of B₂H₆ in the precursor gases [60]. For the same gas flow rates (i.e., the same residence time in the laser beam) an increase in laser power favors an increase in the nanoparticle size [36]. It was shown that increasing the reactor pressure leads to an increased particle diameter [62]. Indeed, the size seems mainly controlled by the time of residence in the laser beam [63] and increases with increasing residence time. Nanopowders with diameters in the range of 10–50 nm were obtained, which is the most common size range obtained by different authors [36, 60, 64].

XRD indicates that the powders are mainly crystallized in the β-SiC phase. The structure has also been studied by XPS and EXAFS [47]. As for the pure Si powders, the results obtained at 600 W of unfocused laser power show that large SiC powders (>25 nm) are pure and well crystallized. With a lower laser power, the SiC sample has a disordered structure and only short-range order exists [47].

NMR gives complementary information on the local structure of the nanopowders. It appears that the smallest particles exhibit an α phase content together with the major β phase, and the amount of α phase decreases when crystallization and size increase [63]. The oxygen content also decreases when crystallization and size increase. The surface chemistry was studied by infrared spectroscopy [65, 66]. The surfaces present silicon and carbon atoms with residual valences, saturated with hydrogen, hydroxyl groups, and doubly bonded oxygen. In air, the reaction with oxygen and water vapor produces a layer of silica on the sample.

SiC nanocrystals were also obtained from a CW chopped laser [20]. The effect of gas flow rates and chop frequency was studied, the latter parameter having the largest influence on the size of the crystallites. In a typical experiment cubic SiC crystallites in the range of 4 nm were obtained inside particles of 10 nm. LECBD [23] was also applied to the synthesis of SiC nanoparticles with different SiH₄/C₂H₂ ratios in the reactant mixture [67]. In this case, the nanoparticles obtained from a stoichiometric mixture contained a substantial portion of free crystalline silicon. In a recent study, different gaseous mixtures were irradiated with a pulsed laser [64]. The effects of the composition of the mixture, laser fluence, pressure, and number of pulses were studied. From SiH₄ + CH₄ or C₂H₆, the main product was amorphous silicon, while it was crystalline SiC from SiH₄ + C₂H₂.

4.1.3.2. SiC from Liquid Precursors Vapors of HMDS mixed with H₂ were used to produce SiC powders, with the aim of removing excess N and C produced during the decomposition of HMDS. The flame temperature was higher than 1200 °C [58, 59]. The powders are partially crystallized in the β phase and contain 0.3 wt% O. SiC was also obtained by IR laser conversion of liquid disiloxane precursors (see for, example [68]).

4.1.4. SiCN and SiCN(AI,Y,O)

SiCN nanopowders have attracted much attention because after sintering they can give a Si₃N₄/SiC composite with enhanced mechanical properties. As in previous cases, powders have been produced from mixture of gaseous reactants or from liquid reactants (Table 1). In all cases, the structure of Si–C–N studied by different local techniques (XPS, EXAFS, XAES, etc.) appears to be more complicated than a binary mixture of SiC and Si₃N₄.

4.1.4.1. SiCN from Gaseous Reactants Different mixtures of gases were used for the synthesis of SiCN nanoparticles (Table 1). The chemical composition of the powder can be controlled by the choice of experimental parameters and in particular the ratio between the different gaseous products used for synthesis [21, 69–73]. Flame temperature was measured in the range of 1450–1900 K for a laser power in the range of 400–600 W [69] and it was in a range as high as 1900–3010 K for a focused laser beam [72, 73]. It is interesting to note that for a given laser power, the flame temperature increases when the NH₃ content increases [72].

A simple way to present the evolution of chemical composition is to use the C/N ratio of the powders compared to the C/N ratio in the reactants. This relationship depends

on the gaseous product used to incorporate N in the powder; in particular, NH₃ does not appear to be a very efficient precursor and imposes the use of a large amount of NH₃ to obtain nitrogen-rich powders. The main effect of NH₃ is to increase the Si₃N₄ content of the powder and this is explained by its decomposition into NH and NH₂ radicals in the laser beam [71]. It is noteworthy that the final products obtained from monomethylamine or dimethylamine have the same composition at the same initial C/N ratio. The C/N ratio in the powder was studied over a large range from 0 < C/N < 2.7 [69, 71, 74], with special interest given to the ratio C/N = 0.2 [69, 74], because superplasticity was observed for nanostructured ceramics with such a composition [75].

It must be noticed that the chemical composition of the bulk and of the surface are rather different [76]. It must also be noticed that in some cases the powders contain free Si and are therefore very sensitive to oxygen contamination [77]. The presence of the amorphous phase also tends to increase the oxidation level [70].

From a structural point of view, IR investigations have shown that interatomic bonds between Si, C, and N are present at the surface [69] and the width of IR bands of the bulk indicates that the sample is not a mixture of SiC and Si₃N₄ [73], as pointed in the Introduction. It was observed that at low laser power (below 50 W), the Si–O bond becomes very important in the IR spectrum of the bulk sample [70].

Depending on the C/N ratio, laser power, and gas mixture, the powders are partially crystallized in the SiC or Si₃N₄ structure and a broad band in the XRD diagram has been attributed to an amorphous phase of silicon carbonitride [72, 76, 78]. The local environment of Si, C, and N atoms has been studied by X-ray-induced photoelectron spectroscopy, from a detailed analysis of the Si 2p, C 1s, and N 1s core levels. Results indicate that Si, C, and N atoms are intimately mixed in these composite particles [47, 72]. Complementary information concerning the structural arrangement around Si atoms has been deduced from extended X-ray absorption fine-structure analysis performed at the Si K edge. The results show that a local C–Si–N₃ structure is formed in SiCN samples [47].

Electronic structure investigated by X-ray photoelectron and soft X-ray emission spectra confirmed previous results [79]. XAES measurements show a nonlinear dependence of the Auger parameter on the carbon fraction, which has also been interpreted in terms of formation of a carbonitride C_x–Si–N_{4–x} phase [76]. Magic angle spinning nuclear magnetic resonance (MAS-NMR) and electron spin resonance (ESR) were also used to clarify the structure of the SiCN composite powders [80]. Particles with low N content are made of very small SiC crystallites with N impurities. When the N content increases, mixed configurations of SiC₃N and SiC₂N₂ appear. In good agreement with previous studies, Dohcevic et al. deduce from a detailed analysis of XRD and IR reflectivity measurements that with N/Si > 1 in the gas phase, C atoms are inserted in substitution in the matrix of amorphous Si₃N₄, giving rise to a ternary compound with an Si local environment of the SiC_xN_{4–x} type [73, 81]. In conclusion, the literature shows that the gaseous mixtures

used to produce SiCN composite powders can be rather different but lead to quite similar results. At low N content, crystalline SiC is the major phase; at high N content, amorphous or crystalline Si₃N₄ is identified. In the amorphous phase obtained at intermediate composition, the local environment around the Si atom contains both C and N.

SiCN nanoparticles were also obtained from dual irradiation of a CO₂ and an excimer laser. It was found that the growth of particles proceeds by CO₂ laser irradiation, and excimer irradiation produces refinement of the nanoparticles initially formed by an ablation mechanism [21].

4.1.4.2. SiCAI, SiCNAl, and SiCNAlYO from Gaseous Reactants

Interest has arisen in the production of Al₂O₃/SiC nanocomposite powders in particular for improved sintering, and several authors have tried to produce such powders by laser pyrolysis. SiCAI powders were synthesized through a reaction between silane, acetylene, and trimethylaluminum. The Al content was studied up to 6 wt% in the powder. XPS and XRD data seem to indicate a nanostructure where Al is involved in bonds with the other constituents [76]. SiCNAl powders were synthesized through a reaction between silane, ammonia, and trimethylaluminum [78]. The Al content was studied up to 2 wt% in the powder. These powders are mainly composed of a matrix of Si₃N₄ with different contents of Al. The identification of chemical bonds involved with the Al element does not appear to be fully understood [78]. SiCN powders doped with Al₂O₃ and yttrium compound were also prepared by Yamada et al. [21] in order to obtain powders with a good aptitude for sintering. An ultrafine Al₂O₃ powder was dispersed in argon gas, and this aerosol was mixed with the aerosol of SiCN nanoparticles between the reaction zone and the collection zone. Y was added in the reaction zone by using a vapor of a yttrium complex (Y(DMP)₃). The sintering aids appear to be uniformly dispersed in the powder.

4.1.4.3. SiCN from Liquid Precursors

Motivation for the use of a liquid precursor was mainly the low price of these precursors compared to silane. The liquid precursors used for the synthesis of Si/C/N powders are mainly silazane precursors and mostly the monomer HMDS. HMDS has been used in the vapor phase after liquid precursor heating or as an aerosol.

Liquid Precursor Used in Vapor Phase Rice [30] demonstrated the possible production of SiCN nanopowders from a vapor of HMDS at different laser powers. The experimental design was very similar to the one used for synthesis from the gas phase, except for modifications concerning the introduction of the liquid reactant which is stored in a special container. Powders obtained by Rice [30] were always of black color and amorphous through XRD. They differed mainly in the H content, which decreases when the laser power increases. With the aim of decreasing the free carbon and increasing the Si₃N₄ content in the powder, Li et al. introduced NH₃ in the reaction zone [31]. The powders were white–gray in color, with a regular shape and an average size of 20 nm. The flame temperature was in the range of 800–1300 °C. Production rates in the range of 40–120 g/h have been achieved in a classical reactor [82]. In a double reactor system, the same order of magnitude (90–120 g/h) was

obtained for the production of powders [39]. The effect of three parameters, NH₃ flow, HMDS flow, and laser power, was studied [31]. The powders were amorphous and sensitive to contamination by air. It was demonstrated that NH₃ flow is the main parameter influencing the N content in the powder and nanopowders were produced with an N/C ratio in the range of 0.36 < N/C < 2.34. This study also showed that high laser power favors SiC formation [31]. The surface properties have been closely studied by IR spectroscopy [82]. The main impurities detected at the surface of the powders were CH_x and NH_x, which explains the strong surface absorption of oxygen. The N/C ratio was extended to the range 0.1 < N/C < 6 [58], with a flame temperature below 1000 °C. It was observed that when the flame temperature was too low, HMDS was not fully decomposed, the rate decreased, and viscous substances mixed with unreacted HMDS were found in the collector.

Liquid Precursor Used as an Aerosol Only a few studies concern the use of an aerosol for powder production. In the design reported by Xiao et al. [29, 33] the powders were produced from an aerosol of a silazane precursor of rather high molecular weight ((CH₃SiHNH)_n, n = 3–4) [29]. The powders were collected on cooled walls. Deposits could also be obtained by this method [33]. The laser power was 700 W, it was focused in the reaction zone, and the reaction temperature was on the order of 2000 K [33]. From a morphological point of view, the powders were round, with a bimodal distribution centered at 44.8 and 119.4 nm. The particles were completely amorphous through XRD and electron diffraction [33]. The IR characterization showed the presence of Si–C–N bonds and evidence for the presence of various hydrogenated bonding (SiH, NH, Si–CH₃). About 70% of the liquid precursor was transformed into powder. A model has been developed for the conversion of the liquid silazane to S–C–N particles [29, 32, 33].

In order to compare laser pyrolysis with other methods used for the synthesis of SiCN preceramic materials, a liquid oligomethylvinylsilazane ([-(CH₃)Si(HC=CH₂)NH-]_n) precursor, which can be used for thermolysis in an oven, was used in a laser pyrolysis setup. The powders are amorphous, and the carbon and hydrogen contents are higher in samples obtained by laser spray pyrolysis. The structure of the powders was studied by NMR and EXAFS. The amorphous network is very comparable for powders obtained by both methods and mainly consists of SiC_xN_{4-x} (x = 0, 1, 2) units and amorphous or sp²-hybridized carbon [83].

The most detailed studies concern the Si/C/N nanopowders obtained from an aerosol of the silazane monomer HMDS and NH₃, with an N/C ratio in the range of 0.7 < N/C < 2.8 [26, 84–86]. The yield of reaction (powder/liquid) is in the range of 40–50%. The powder production rates depend on the gas flow used to carry the aerosol droplets to the reaction zone [26] and on the temperature of the glass jar where the aerosol is produced [86]. Typical values of 30 g/h up to 80 g/h have been achieved [86]. The measured flame temperature was close to 1600 K. The powders are round and monodispersed [26, 85] or with a bimodal distribution [86]. The sizes are in the range of 30–60 nm. The C/N ratio in the powder is closely correlated to the C/N ratio in the reactive phase [85]. The powders always contain free carbon

after decomposition in stoichiometric compounds (SiC and Si₃N₄) [86]. The powders are oxidized by contact with air, as shown by the comparison of bulk and surface analysis [87]. The powders with the highest N content appear to be the most sensitive to pollution by air and O content can reach 10 wt% [88]. As in other studies (see previous section), the IR characterization shows the presence of various hydrogenated bonding (SiH, NH, Si-CH₃) [26]. From a structural point of view, the powders appear to be amorphous through XRD.

The detailed structure and morphology of the powders produced from an aerosol of HMDS have been carefully studied by various techniques (MAS-NMR, XPS, EXAFS, neutron diffraction, etc.) in several papers. Some of the results are summarized in the following. Large peaks observed in the ²⁹Si MAS-NMR spectra show an unstructured massif which can be associated with an amorphous structure. The position of the massif is shifted when the C/N ratio evolves, corresponding to different local environment around the silicon atom [86]. XPS data indicate the existence of local chemical disorder in the as-formed powders [87]. By combining EXAFS and a study of the X-ray absorption near edge structure, it was shown that there is no chemical ordering around Si atoms, and a structural model has been tested to describe the structure of the amorphous as-prepared powders and compared to experimental data [89, 90]. In this model, the powders are composed of SiC_xN_{4-x} tetrahedra and these tetrahedra are bonded through CN bonds [89].

Recently SiCN nanopowders were obtained from a mixture of HMDS, NH₃, and a minor flow of SiH₄. These powders present traces of crystallization, and not surprisingly, the Si content appears higher than that in previous samples, leading to a considerable reduction in the amount of free carbon [91]. It is shown below that these changes in the chemical composition and structure have a drastic effect on the thermal behavior of such powders and give very interesting powders from a sintering point of view.

4.1.4.4. SiCNAIYO from Liquid Precursors With the aim of incorporating sintering aids directly into Si/C/N powders, precursors containing Y and/or Al were dissolved in liquid HMDS. An aerosol was obtained from this solution and carried to the reaction zone. SiCNAIYO powders with (Al + Y)/Si up to 5 at.% were obtained [92]. It must be noted that the introduction of Al and Y does not strongly change the bonding configuration in SiCN powders [92, 93].

4.1.5. SiCBN

Due to the high thermal stability of such materials, some attempts to produce Si/C/N nanopowders including boron atoms in the network were conducted. The powders were obtained from a solution of triethylborate in HMDS carried in the laser beam by an argon/ammonia gas mixture [94]. The powders obtained were amorphous and contained boron but also a very high amount of oxygen.

4.2. C-Based Nanoparticles

4.2.1. Diamonds

The synthesis of nanopowders containing diamonds has been reported by Buerki and Leutwyler [95], by laser decomposition of C₂H₄ or mixtures of C₂H₄ + SiH₄ + H₂. The

flame was yellow to orange and the temperature was in the range of 500–550 °C. A possible reaction pathway for the initial steps of homogeneous nucleation of diamond which is consistent with the experimental results is proposed [96]. The influence of pressure (600–2000 mbar) and reactant gas composition (C₂H₄, C₂H₄-H₂, and C₂H₄-*cis*-decahydronaphthalene) on diamond formation and powder characteristics was studied. The diamonds collected in the powder were characterized by TEM [96, 97]. However, the efficiency of laser pyrolysis in diamond production has not yet been established.

4.2.2. Amorphous Carbon

Few studies deal with the synthesis of hydrogenated carbon-based nanopowders from CO₂ laser synthesis [98–100]. The nanoparticles have been characterized mainly by TEM and IR spectroscopy. In the study of Bi et al. [99] nanoparticles were obtained from an ethylene/benzene mixture with a small percentage of Fe(CO)₅. The particles are agglomerated, nearly amorphous, and spherical, with an average diameter of around 30 nm. HRTEM shows the formation of a small plan of graphene. The H/C ratio is around 0.1 and slightly decreases when the residence time in the flame increases. Nanoparticles have also been produced with CW or pulsed CO₂ lasers from a SF₆/C₂H₂ mixture [98]. With the pulsed laser, particles are amorphous, while some stacks of small graphene layers (basic structural units, BSU) are detected by HRTEM in the particles obtained with the CW laser.

In another study [101], the nanoparticles were obtained from C₂H₄, C₃H₄, or C₄H₆. The nanoparticles are always agglomerated but the agglomeration decreases when the laser power increases. Nanoparticles appear highly aromatic in character whatever the experimental conditions. The H/C ratio was varied in the range of 0.7–0.3. It was demonstrated that whatever the precursor, the particles exhibit the same characteristics and therefore choice of the precursor is not a major parameter. As the flame temperature in the interaction zone increases, the nanoparticles evolve drastically from poorly organized, highly hydrogenated samples toward turbostratic concentric particles of carbon. The multiscale organization of the samples and its evolution with the synthesis parameters are quantitatively determined and correlated to IR properties through an original development of HRTEM image analysis. The multiscale organization does not reduce to the classical view of assemblies of BSU of aromatic bricks. More refined models are proposed where non-stacked aromatic layers play a noticeable role and lead to a better understanding of the sample optical properties. The same conclusions can be drawn when samples are studied as a function of the residence time in the flame [102]. Increasing the residence time favors better organization. Also, the possible contribution to a better understanding of carbon cosmic dust has been discussed from an astrophysical point of view [101, 102].

4.2.3. Fullerenes

Fullerenes were first detected in a laser pyrolysis setup at low pressure from a C₂H₂ flame with SF₆ as a sensitizer [22]. A nozzle was introduced in the reaction zone, which

allowed transfer of carbon clusters and fullerenes to a free molecular beam and analysis of them with a time of flight mass spectrometer. The presence of fullerenes in the soot was also checked by TEM and micro-Raman spectroscopy [22].

Different mixtures of hydrocarbons, such as benzene (+cyclopentadiene), acetylene, or ethylene, have been tested for fullerene synthesis. They were pure or mixed with an oxidizer agent (nitrous oxide or oxygen) and/or a sensitizer (SF₆) [103]. Significant amounts of soot (several grams per hour) containing fullerenes were obtained from a C₆H₆ flame with SF₆ as a sensitizer and with or without an oxidant in the pressure range of 200–760 Torr. The fullerenes were identified by various techniques: infrared and Raman spectroscopy, mass spectrometry, and liquid chromatography [104]. The effect of the SF₆/C₆H₆ mixture and the nature of the oxidant (O₂ or N₂O) were studied. An optimum temperature range was found for the production of fullerenes by the laser synthesis method, in good agreement with measurement in combustion flames and thermodynamical considerations [105]. A strong increase in the fullerene yield (C₆₀ + C₇₀) was observed with decreasing C/O ratio (2.2–1.2) [106]. The lowering of the C/O ratio was also found to dramatically influence the ratio of C₆₀ to C₇₀ through an increase in the C₆₀ yield faster than that in C₇₀. These effects were interpreted by a kinetically based argument. A strong increase in the fullerene content was also observed with decreasing residence time in the reaction flame, and a maximum total yield of 0.23% was reached with high conversion rates (from benzene to soot). Ponderable amounts of C₈₄ were also quantified [106]. In all the previous cases, the powders were polluted by dissociation of the SF₆ sensitizer. A solution was found to obtaining fullerenes without a sensitizer from C₄H₆ + N₂O mixtures [107].

Fullerene/iron complexes were obtained by laser pyrolysis of a gas phase mixture containing hydrocarbon and alternatively iron pentacarbonyl vapors or ferrocene aerosols with N₂O as an oxidant and SF₆ as a sensitizer. The Mossbauer transmission spectrum has evidenced the formation of fullerene phases with iron both inside and outside the cage [108].

4.2.4. C₃N₄

The interest in preparation of carbon nitride materials is generated by ultrahard properties. Some powders were obtained from C₂H₂ + N₂O + NH₃ mixtures with C₂H₄ + SF₆ as the sensitizer. Infrared measurements show the presence of a C–N-bonded phase and the diffraction patterns strongly suggest the presence of crystalline α and β C₃N₄ powders. The powders are always polluted by decomposition of the SF₆ sensitizer [109, 110].

4.2.5. Carbides

Laser pyrolysis has been also used for the synthesis of some metallic carbide nanopowders. The production of titanium-based nanopowders is motivated by advanced ceramic nanocomposites, since mechanical properties of SiC matrices could be significantly improved by the incorporation of

a TiC second phase and vice versa. Nanosized TiC powders were synthesized from a TiCl₄ and hydrocarbons mixture and TiC/SiC composite powders were obtained by the addition of SiH₄. Surface oxidation of both nanopowders is observed under air exposure. Nevertheless, an interesting yield was obtained for nanocomposites with the addition of up to 20% TiC phase [111]. Iron–carbide nanoparticles were formed by sensitized laser pyrolysis of gas mixtures containing iron pentacarbonyl (vapors) and ethylene/acetylene precursors [112]. Iron carbides and iron composites present a particular interest due to their magnetic and catalytic properties, which could be highly enhanced if nanoparticles were used. Nanopowders of WC have been synthesized by laser pyrolysis of a gaseous mixture with WF₆ as a tungsten source, C₂H₂ or C₂H₄ as a carbon source, in the presence of H₂, and with SF₆ as a photosensitizer. In spite of contamination by sulfur and oxygen, WC nanopowders with high specific surface areas (up to 100 m²/g) were obtained after heat treatment in an Ar atmosphere [113]. In the case of the B₄C compound, it has been shown that, by laser-driven synthesis, the stoichiometry of the products is directly related to the stoichiometry of the reactants. Thus, good control of the B₄C hardness can be achieved [114]. Moreover, laser B₄C nanopowders appear significantly more active than commercially available B₄C powders.

4.3. Boron-Based Nanopowders

4.3.1. BN Nanopowders

Boron nitride powders in the nanometric range were obtained from a mixture of BCl₃ and NH₃. The powders present a high specific surface area (up to 230 m²/g). Infrared and Raman spectroscopies were used for characterization regarding bulk structure and the identification of surface species [115]. The morphology was investigated by high-resolution electron microscopy. A variety of roughly spherical particles are revealed, consisting of concentric graphitic shells and ranging in size from 20 to more than 100 nm and in shape from hollow to filled to the center. This onionlike configuration is very similar to that observed in carbon materials. Another morphology made of stacking of a few perfectly flat graphitic sheets (10 to 50 layers, 50 nm in length) is developed after heat treatment [116].

4.3.2. Borides

Some other boron compounds have been obtained from laser pyrolysis. Small-diameter boron and titanium diboride powders were synthesized from vapor phase reactants. Boron powders were synthesized from a BCl₃ + H₂ gas mixtures or from B₂H₆. TiB₂ nanopowders can be formed from TiCl₄ + B₂H₆ gas mixtures [117]. Another process for the preparation of submicrometer-sized titanium diboride has been proposed [7, 118]. Synthesis of fine powders of zirconium boride, ZrB₂, from zirconium borohydride, Zr(BH₄)₄ has been explored as a function of the reaction temperature. ZrB₂ was the only crystalline product identified. Products made at high temperature contained excess boron, while those made at low temperature were boron deficient [119].

Finally, CO₂ laser pyrolysis has been used to prepare ultrafine (<0.1 μm in diameter) boron–silicon powders with different boron concentrations. These powders have been used as a spin-on boron diffusion source for silicon wafers [120].

5. PROPERTIES AND APPLICATIONS

The studies involving Si-based nanoparticles were first motivated by applications in the field of structural ceramics. Therefore, the characterization and evolution of these nanopowders under annealing treatments is of major importance, especially in the SiCN system. In addition, the fabrication of reliable ceramic parts from nanosized powders is strongly dependent on the elaboration step of green bodies. This step involves most often the dispersion of powders in liquid media followed by compaction, filtering, or casting of the suspensions and sometimes the dry compaction of powders. In some cases, materials could be obtained from the nanopowders and the properties of the nanomaterials were evaluated. More recently attention has turned to the optical properties of these powders and from composites issuing from these nanopowders. These different aspects are presented in the next sections.

5.1. Structural Properties of Ceramics

5.1.1. Dispersion of Various Si-Based Nanopowders

The dispersion of different Si-based nanopowders produced by laser pyrolysis has been investigated in various liquid media. Stable powder dispersion is necessary to produce uniform dense ceramic green bodies. Generally two types of dispersion systems are used: pure solvent systems and solvent–dispersant systems. This latter system is known to be more efficient but the dispersing agents are often difficult to eliminate from the green part during binder burnout, particularly with small-diameter powders.

The dispersion of laser-synthesized Si powders has been studied without deflocculants. The aim of this study was to get reaction-bonded silicon nitride (RBSN) parts from a very fine and highly pure silicon powder. In this context, the first interest in silicon dispersion has focused on aqueous slips for casting parts. However, it was demonstrated that aqueous media introduce uncertainties about oxidation which adversely affect the nitrating process to produce RBSN [45 and references therein]. Therefore, the authors chose to study dispersion of silicon in various organic solvents in the absence of surfactants or polymer deflocculants [45]. The liquids involved were aliphatic and aromatic hydrocarbons, alcohol, ketone, ether, carboxylic acid, and aldehyde classes. Dispersion was carried out by subjecting the system (100 mg of Si powder + 15 cm³ of liquid in a glass bottle in an N₂ atmosphere) to an ultrasonic probe for 3 min to mix thoroughly. The control of the dispersion degree was performed through dispersion tests, which consist in evaluating the suspension after standing for 5 days. Good dispersion was observed in liquids having high dielectric constants, such as aliphatic alcohols, ketones, benzyl alcohol, and benzaldehyde. Poor dispersion was observed in liquids having low dielectric constants, such as benzene,

toluene, xylene, isopentyl ether, and propionic and butyric acids. *n*-Propanol was chosen because it can be used for casting silicon powders. Therefore, the state of agglomeration of silicon powders in *n*-propanol subjected to different mechanical dispersing systems was determined through analytical techniques such as TEM, laser–Doppler particle size analysis, and light scattering dissymmetry measurements. The data indicate that the agglomerates are reduced in size when suspensions are subjected to the ultrasonic probe and that the first centrifugal separation leaves a large fraction of the mass suspended as single particles or small agglomerates containing fewer than four or five primary particles. The fracture surface of pellets cast from *n*-propanol suspensions processed as described earlier showed flat surfaces suggesting uniform and defect-free castings.

The dispersibility of both pure SiC powders made by laser pyrolysis and oxidized SiC powders has been examined in pure solvents without dispersants [130]. Powder dispersion was correlated with the following solvent properties: dielectric constant, hydrogen bond index, acid dissociation constant (PK_a), and Lewis acid/base interaction energy. Preparation of suspensions was conducted under a nitrogen atmosphere inside a glove box. A small amount of powder (10 mg) was mixed with the selected solvent (10 cm³) and dispersed by subjecting the suspension to a 40-W ultrasonic probe for 2 min. Sedimentation tests over 5 days were used to determine the stability of the SiC powders dispersed in the various solvents. Coagulation rates were measured by photon correlation spectroscopy (PCS). Packing densities were evaluated from green bodies obtained both by centrifugal casting and by colloidal pressing at 69 MPa. According to this study, the authors demonstrated that oxidized SiC laser powders have acidic surfaces and were dispersed best in basic solvents [130]. Pure laser SiC powders were shown to have basic surfaces and were dispersed best in acidic solvents. Octyl alcohol was established to be the most suitable pure solvent studied for both pure and oxidized SiC powders. Using colloidal pressing with pure SiC powder dispersed in octyl alcohol enables one to get uniform green bodies having around 70% density. The authors concluded that maximum density green bodies can be made with the laser-synthesized powders if they are properly dispersed. Zhou et al. [131] have investigated the dispersion behavior of as-synthesized or oxidized laser nanometric SiC powders in water using ammonium polyacrylate (NH₄PA) as a dispersant. The pH level was adjusted with diluted HCl and NaOH. The solution of NH₄PA was first prepared, and then the powders were added. After a short (1 h)- or long (1 month)-term soaking time, a 10-min ultrasonication (50 W) was used followed by pH readjustment and another 10-min ultrasonication. This procedure was used to obtain a homogeneous suspension with a solid concentration of 1 mg/ml. Sedimentation tests were performed. Zeta potential was measured in diluted suspensions. The authors demonstrated that water alone was insufficient to disperse the as-synthesized powders. The dispersant adsorbed poorly on the powder surface and could offer only a limited contribution to the dispersion. Oxidation of the powders at 500 °C in air eliminated the thin nonwetting carbon layer and improved the adsorption between NH₄PA and the powders, which enhances the suspension stability. A lengthy aging

time in water further increased the dispersion stability with NH₄PA. The optimum conditions for getting well-dispersed and stable suspensions were obtained in using powders oxidized at 500 °C and presoaked in water for 1 month with a concentration of 2.45 wt% of NH₄PA at pH = 9.25.

The dispersion of laser-synthesized Si₃N₄ powder has been investigated in nonaqueous systems. Nilsen et al. [132] selected hexane because it contains no water or oxygen in its structure and it has almost no solubility for water. The aim was to minimize the oxygen and water contents of the powder during consolidation into green bodies. Effectively, the surface of Si₃N₄ in air is one in which an equilibrium of amino and Si–OH groups exists. However, the presence of the Si–O groups is to be avoided in order to keep the inherent properties of Si₃N₄. Steric stabilization is the main mechanism responsible for the stabilization of Si₃N₄ powder in hexane. Steric stabilization is obtained by using long chain polymers that attach to the surface of the particle, with the remaining polymer chain extending into the liquid medium and providing a repulsive barrier to flocculation. The powder surface being basic in chemistry, the polymer dispersant should contain an acidic functional group in order to be attached to the surface of the powder. In this study the authors focused their work on the characterization of the surface of laser-synthesized Si₃N₄ powder and on the selection of a dispersant that would achieve a stable suspension, so as to get a uniformly packed, high-density green compact for densification of “pure” Si₃N₄. Suspensions of 1 vol% of powder in hexane were prepared in a glove box by mechanical agitation for 16 to 18 h followed by ultrasonic agitation for 15 s at 75 W. The dispersing agent called Uniamine T displayed good dispersion characteristics. The main functional group of Uniamine T is an imidazoline which is believed to react with the surface by nucleophilic substitution at the C–N bond in the imidazoline. This dispersing agent exhibits advantageous properties because of its low O content and it does not create Si–O bonds between the powder surface and Uniamine T, as is the case for other dispersants. Zhou et al. [133] reported the dispersion of laser-synthesized Si₃N₄ nanopowders in *N,N*-dimethylformamide (DMF) with triethanolamine (TEA) as a dispersant. The aim was to destroy aggregation and gain stable powder dispersion during the process to guarantee uniform distribution of grains in the matrix. DMF is a high-polarity and strong solvent for many organic polymers and is widely used in industries such as the textile industry. The suspensions were prepared as follows: 0.1 g of Si₃N₄ was added to 10 ml of DMF with different amounts of dispersant from 0 to 10 wt% with reference to the solids, and the suspension was then soaked for from 1 h to 30 days and dispersed in an ultrasonic bath (100 W) for 20 min. The coagulation rates were measured by PCS, and the Z-average sizes of the aggregates were measured at different intervals after ultrasonication with a particle analyzer. The authors demonstrated that Si₃N₄ nanopowders in pure DMF flocculated and settled quickly, but the addition of TEA to DMF led to the stabilization of the suspensions. In addition, it was shown that presoaking the Si₃N₄ powders in media containing dispersant for 1 month is beneficial for dispersion, the optimal concentration of TEA in the suspension being about 1.0 wt%.

SiCN nanopowders obtained by laser pyrolysis have been dispersed in different organic liquids with different dispersants. The aim of this study was to obtain suspensions of Si₃N₄ commercial powders mixed with SiCN nanopowders, in order to elaborate compact green bodies which could be sintered to get Si₃N₄/SiC nanocomposites [134, 77]. Organic liquids have been chosen in order to prevent hydrolysis of silicon nitride-based powders. Suspensions of SiCN nanopowder (50 g/liter) were prepared. Mechanical devices (turbula and ultrasonic probe) and a dispersing agent were chosen in order to, respectively, break down agglomerates and stabilize the suspensions. The evaluation of the most suitable mechanical device and dispersing agent is achieved by sedimentation tests. The optimum concentration of dispersant has been evaluated by viscosity measurements combined with sedimentation tests (Fig. 3a and b). The authors demonstrated that the acetophenone liquid coupled with a PS4 dispersant provided by the ICI Chemical Company was the best medium for dispersing the powder. In addition, the positive effect of the ultrasonic probe on the breakage of agglomerates has been pointed out. Suspensions of commercial Si₃N₄ powder with SiCN nanopowders having a high dry matter content (>50% vol) were prepared. Slip casting in plaster moulds of these suspensions made it possible to prepare green bodies having a compaction rate of 57%. Chen et al. [135] reported the dispersion of laser-synthesized SiCN nanopowders in 15 pure organic liquids. Particle size analysis and sedimentation tests have been carried out. The van der Waals potential energy of interaction between particles and organic molecules was estimated. Poor dispersion was found in nonpolar hydrocarbons, while in polar organic liquids dispersion and stability depend on several parameters (functional groups, dielectric constant, etc.). They also demonstrate that the potential energy of interaction can be used to predicate the stability of the nonpolar hydrocarbon dispersions, while this is not possible in polar organic liquids because of the contribution coming from the electric double layers and solvation layers.

Cerovic et al. [136] reported a study of the dispersion of SiC, SiCN, and Si₃N₄ ultrafine powders in liquids without any dispersant. The stability of suspensions of ceramic nanopowders was investigated in water and organic solvents

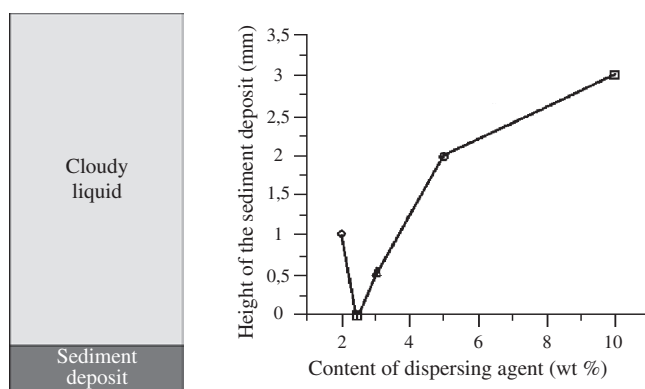


Figure 3. (a) Typical sedimentation test; (b) change in sediment deposit height as a function of dispersing agent content after a 3-day sedimentation test [77].

and suspensions were examined by means of screen sedimentation tests. In addition, experimental results on the settling velocities were related to the calculated values of the total interaction potential energy between the particles interacting over the solvent molecules. The suspensions were obtained by adding 125 mg of powders to 25 ml of selected liquid. The suspensions were then subjected to an ultrasonic bath for 3-min agitation. For aqueous Si₃N₄ suspensions, the suspensions were subjected to an ultrasonic probe with adjustment of the pH at 3 and 10. An order of settling velocity for each powder was determined as a function of the liquid used, and these results were correlated to the interaction potential energy.

5.1.2. SiC-Based Nanomaterials

Some studies concern the effect of annealing treatments on SiC powders but the majority of papers deal with the densification of SiC nanopowders for structural applications. These potential applications have been studied since the first SiC synthesis. Different sintering methods were studied in particular by the German group of Jülich [137] and the main characteristics are given below.

5.1.2.1. Annealing Treatments In the few papers devoted to the characterization of annealed samples, the main interest was to study defects in the structure of SiC samples related to conductivity properties and to vibrational properties of SiC nanopowders in the α or β polytype. Electron paramagnetic resonance (EPR) investigations were performed in SiC nanometric powders annealed between 1200 and 1800 °C [138]. These SiC nanopowders exhibit a substantial electric conductivity [139–141]. The origin of this phenomenon is discussed with respect to structural modifications checked by MAS-NMR, sample composition, and the delocalized paramagnetic centers involved in these materials. Three different paramagnetic defects were deduced from the EPR signal [138]. The g factors were calculated from the spectra, and the defects assignment is discussed with respect to the different SiC forms, namely, α -SiC and β -SiC polytypes as well as amorphous SiC and the carbon present. The coexistence of two paramagnetic centers (DI, DII) localized in the crystalline sites of the SiC polytypes was shown [139]. Delocalized DIII paramagnetic species were partially created by thermal conversion of DII defects with energies not exceeding 13 meV. The spin susceptibility, deduced from EPR measurements, was found to be marked by delocalized paramagnetic species above 150 K and by strongly correlated (DIII) unpaired spins around 30 K. An attempt is made to correlate the delocalized unpaired spins with the electric properties of these materials.

5.1.2.2. Compaction One of the characteristic of the as-formed nanopowders is their very low apparent density (1% of the theoretical density (TD)). The compaction of SiC nanopowders with different amounts of excess Si was studied. Cold uniaxial pressing was used in the range of 10³ to 10⁸ Pa. The densities of the resulting compacts depend on the cube root of the applied pressure for 5 orders of magnitude of pressure. As a result, a mechanism which estimates the number of interparticle bonds and the energy per bond was proposed to explain the compaction process [142].

5.1.2.3. Elaboration Pressureless sintered green bodies without additives having pore sizes of about 20 nm show extreme coarsening without significant densification [143]. Therefore, a large majority of the studies presented here concern powders containing sintering additives. Pressureless sintering of β -SiC powders doped with boron and carbon was shown to lead to dense materials (>97% of theoretical density) very early [61, 144]. At 2050 °C, green compacts with 50% TD made from such powders led to samples with densities as high as 95% of TD. At lower temperature, densification remained important, that is, at 85–90% at 1900 °C and 75–80% at 1800 °C. These densities are higher than the densities obtained from commercial powders [144]. Among the mechanical properties, Vickers microhardness was found to be ≥ 3000 kg/mm² and Young's modulus of 440 GPa was reached. Negligible oxidation in high densified parts occurs up to 1500 °C for a short exposure time [144].

Even with good densification, conventional pressureless sintering led to extreme grain growth and hence the nanophase microstructure was destroyed. Hot isostatic pressing (HIP) was applied to reduce the grain growth and also the sintering temperature by Vassen and Stöver [145, 146]. HIPing of β -SiC with boron and carbon led to a reduction in pore size and to a considerable density increase at temperatures below 1600 °C. The grain size increased with increasing HIP temperature (150 nm at 1500 °C, 350 nm at 1680 °C) [143]. HIPing of the same kind of powders with pressure up to 350 MPa led to samples with more than 95% TD below 1700 °C and grain sizes of 150 nm [146]. The actual oxygen content in the HIPed samples was estimated to be around 2.5 wt%. A white coverage formed on the surfaces after exposure to air. XRD measurements revealed that crystallites of B(OH)₃ formed at the surface. The growth rate is determined by the grain boundary diffusion coefficient of boron to the SiC surface. An estimated grain boundary diffusion coefficient of boron in SiC was many orders of magnitude higher than extrapolated literature values [145]. For SiC, it was shown that the oxide layer on the surface hinders densification. It favors nondensifying sintering mechanisms and hence coarsening of the microstructure. A processing route was developed which removed at least partially the oxygen layer on the surface of the nanophase SiC particles [146]. Reduction in the grain size could finally be obtained by this optimized high temperature heat-treatment of the samples prior to HIP. Samples with densities of more than 97% TD and grain sizes below 80 nm were produced [137, 146]. HIP densification was modeled assuming diffusion to be the dominant mechanism. Vickers hardness and indentation fracture toughness were measured for samples with different densities and grain sizes. The results revealed that, besides grain size, features like density and/or oxygen content can strongly influence hardness and fracture toughness. Similar results have been found for the wear resistance of fine-grained materials. Results of pin-on-disk type experiments showed the importance of a high density of the samples for high wear resistance. Thermal diffusivity measurements were performed for samples with different grain sizes up to 1400 °C. At room temperature, the thermal diffusivity of a 85-nm-grained SiC was smaller by a factor of 4 than the thermal diffusivity of coarse-grained SiC. At higher temperatures,

the difference in the thermal diffusivity of fine- and large-grained materials was reduced [146]. In a recent paper [137], examples of SiC processing, and also TiN, TiC, and Si₃N₄ processing, are given. An overview of the properties (hardness, fracture toughness, thermal diffusivity, and behavior under irradiation) of nanophase nonoxide ceramics is also given and compared with results obtained on samples with slightly larger grain sizes.

Nanoscale SiC powders, produced by laser synthesis from gaseous precursors, have been successfully used to prepare sintered pellets with a β -SiC structure and presenting an enhanced thermal conductivity (>20%) with respect to materials prepared from commercial powders [147]. Sample hardness and toughness, comparable with those of commercial products, confirmed the good sample quality. Such properties make this material promising for thermonuclear application. Thermal shock tests have been performed by irradiating the pellets with a Nd-YAG pulsed laser. The laser power density was increased by reducing the spot size, up to the appearance of a visible surface damage. The measured threshold value is increased by 16% for the newly developed β -SiC compared to the best materials prepared from commercial SiC powders. In another study [148], ceramic composites were developed by hot isostatic pressing of SiC with B₄C, TiC, and C powders. These candidate materials for plasma facing components have been tested at energy densities similar to those expected during disruptions in ITER by using the electron beam facility JUDITH in the KFA. Erosion losses and surface temperature response have been evaluated as a function of energy density and material composition. Correlation of experimental and simulation results for material erosion made it possible to propose a route for material optimization.

In SiC/Al₂O₃ nanocomposites, the amount of SiC dispersed in an alumina matrix is very low (usually in the range of 0.5–5%) and few papers deal with SiC nanopowders issuing from laser pyrolysis. Scitti et al. [149] report elaboration of alumina–SiC nanocomposites starting from ultrafine SiC powders (30/45 nm) and Al₂O₃ powders (60/140 nm). Different amounts of SiC in the range of 0.5–5 vol% were incorporated and the characteristics of the resulting materials compared. The oxygen enrichment in SiC nanopowders was controlled, in order to optimize powder processing. Densification tests of Al₂O₃–SiC powder mixtures were performed by both pressureless sintering and the hot pressing route. The presence of SiC nanoparticles hinders the densification mechanisms. Nearly fully dense materials could be obtained by hot pressing. Improvement in mechanical properties over monolithic alumina was obtained in composites with the 45-nm SiC. The study pointed out the importance of the raw SiC powders in terms of grain size and state of agglomeration. The addition of this ultrafine SiC strongly affected the microstructural evolution, even at low volumetric fractions. The strength of SiC/Al₂O₃ nanocomposites was studied as a function of the volume of SiC nanoparticles with a diameter of 10 nm [150]. Adding 0.7% of nano-SiC leads to a clear enhancement in strength (up to 860 MPa). The coarser SiC particles are located at the grain boundaries, while the smaller ones are within the alumina grains.

5.1.3. Si₃N₄ Nanomaterials: Elaboration

Si₃N₄ ceramics exhibit very attractive intrinsic properties, such as high hardness, high fracture strength and fracture toughness, high thermal shock resistance, and high temperature stability. The first way to get Si₃N₄ sintered materials from laser-synthesized nanopowders was to densify and nitride Si nanopowders under a nitrogen atmosphere in order to produce RBSN.

Danforth and Haggerty [151] reported results of densification and nitriding studies of Si nanopowders and measured the modulus of rupture, fracture toughness, and hardness of reaction-bonded Si₃N₄ samples obtained. First, samples were cold pressed at 6.89 MN·m⁻² and then isostatically pressed at 310 MN·m⁻², producing Si pellets of 40 to 49% of theoretical density. The Si compacts were subsequently densified to more than 70% of theoretical density by heating them at temperatures up to 1350 °C for 10 to 60 min. Nitriding was then performed under a N₂-10% H₂ atmosphere. The addition of boron to the Si powders caused their sintering to be dominated by densification processes. Sintered samples with the lowest density and having fully reacted exhibit microstructures with small pores and grains (~0.1 μm), while samples with the highest density and having incompletely reacted are composed of fine scale features (~0.1 μm) and isolated large scale features (~1 to 5 μm). The hardness values of the materials were increased with nitriding density, and even at lower densities the hardness of samples produced from laser nanopowders was significantly higher than those of commercial materials. For the fully reacted samples having low density, the MOR values are much higher than expected from their relatively low density, thus reflecting their high microstructural quality.

Another work reports the elaboration of Si₃N₄ nanomaterial from Si nanopowder produced by the laser pyrolysis of silane [152]. Powder exhibiting a grain size of 300 nm is stored under an inert atmosphere and then dispersed in methanol using ultrasound. The slurry is subsequently filter pressed in order to remove the liquid and to get a green compact. After drying of the compact, sintering is performed under an N₂ atmosphere. The furnace is heated at 1200 °C and then at 1400 °C. The nitridation reaction is complete for a 6-h duration and makes it possible to produce Si₃N₄ materials which can be posttreated by HIP to get an almost complete densification. The oxidation behavior and microhardness, toughness, and fracture strength were measured on the obtained samples.

Numerous papers report the elaboration of Si₃N₄ materials from Si₃N₄ laser-synthesized nanopowders. For ceramic materials in which the microstructure is composed of very small particle sizes, it has been suggested that the diffusional creep rates (Coble) can be increased by a factor of 10⁹ at low temperatures [153]. Therefore, Pechenik and co-workers [154, 155] developed a densification process of amorphous Si₃N₄ laser-synthesized nanopowders in order to maintain the nanosize morphology until densification is complete. The process is based on the combination of high pressures and low temperatures. The mechanical property measured on the resulting materials was Vickers microhardness. The process was performed on powders both exposed and unexposed to air. First powders were precompact at

0.05–0.07 GPa and then crushed and placed in a molybdenum gasket. The powders obtained were then pressed in a diamond anvil cell (DAC) up to 5 GPa at temperatures varying from –196 (liquid nitrogen) to 500 °C. Some samples were subsequently sintered without pressure at elevated temperatures. Sample hardness is reported as a function of pressing temperature for pressing process of 3 h at 5 GPa. The authors reported an increase in the hardness when the final pressing temperature is increased. In addition, when powders are first pressed at low temperature (ca. liquid nitrogen temperature), a higher hardness (1200 kg/mm²) is observed compared to powders first pressed at room temperature or at 200 °C under outgassing. This behavior is due to high densities (ca. 63% of theoretical density) obtained at low temperature compared to low densities obtained at room or high temperature. The effect of a pressureless sintering treatment applied on the samples pressed in the DAC on the sample hardness is also reported. Hardness increases when sintering temperature increases and reaches a maximum (2000 kg/mm²) in the case of a sample initially pressed at liquid nitrogen temperature and sintered at only 1400 °C for 1 h. This value is higher than the one obtained in the case of the commercial material and may be due to the occurrence of sintering from 1200 °C. It is important to note that these sintering process conditions (relatively low temperatures, without sintering aids) make it possible to produce transparent materials containing 5 to 10 wt% of α -Si₃N₄, the bulk material being amorphous.

Pure Si₃N₄ nanopowders have been used to elaborate dense materials without additives via the HIP process [156–158]. Samples were obtained from powders exposed to the ambient atmosphere and having an oxide layer at the surface or from powders collected, stored, and compacted in a glove box, that is, with minimal oxygen contamination. The native SiO₂ layer acts as a sintering aid during HIPing (1950 °C; 200 MPa) and the exposed Si₃N₄ powder samples HIPed at temperatures in excess of the melting point of SiO₂ lead to dense materials. High-resolution transmission electron microscopy studies indicate that densification occurs via a solution–reprecipitation mechanism. In contrast, samples of unexposed Si₃N₄ powder had to be HIPed to 2050 °C to achieve a density of approximately 70–80%. In this state, the sample consisted of equiaxed β -Si₃N₄ grains, with localized high-density regions. The authors suggest increasing the density of the green compact and understanding the role of minor impurities (Fe, Al, and Ca in quantities less than 0.5%) in order to achieve better final densities for materials without oxygen contamination.

Li et al. [159] studied the densification and sintering of amorphous silicon nitride nanopowders without additives. They used ultrahigh pressures (1 to 5 GPa) and temperatures between room temperature and 1600 °C. The reported results showed effects on the sintering density, the phase structure, the grain size, and the hardness. Prior to the high-pressure experiments, the nanopowders were shaped by uniaxial pressing (400 MPa). The compacts obtained were then densified and sintered using a cubic anvil pressure apparatus generating pressures in the range of 1–10 GPa. The study of compaction behavior (at room temperature for pressure varying between 1 and 5 GPa) demonstrates that green bodies can reach high densities (2.49–2.53 g/cm³) and exhibit

strong bonding characteristics, allowing grinding and polishing. Sintering experiments were performed at temperatures between 500 and 1600 °C. Dense bulk amorphous Si₃N₄ materials (95% relative density) were obtained below the crystallization temperature under sufficiently high pressure. The Vickers hardness of the materials obtained between 800 and 950 °C was in the range of 830–1206 kg/mm². Crystalline Si₃N₄ ceramics which were pure white in color were obtained at sintering temperatures above 1420 °C. For sintering temperatures between 1000 and 1100 °C, the microstructures are mainly composed of α -Si₃N₄, while for temperature between 1100 and 1420 °C, a mixture of α - and β -Si₃N₄ is present, the sintered bodies being almost entirely composed of the β phase for temperatures between 1350 and 1420 °C. Vickers hardness was measured as a function of the sintering temperature. An increase in the hardness was observed for temperatures between 850 and 100 °C, which may be due to the increase in material density. From 1000 °C, the hardness increases slowly and reaches 1648 kg/mm² at 1420 °C. The grain size measured by XRD was 160 nm for a temperature of 1000 °C, which is higher than the starting particle diameter (18 nm). From 1000 to 1350 °C, the grain size increases slowly, and an accelerated growth occurred for temperatures above 1300 °C, which makes it difficult to control grain size below 100 nm. The authors concluded that the densification temperature is 580 °C lower than that previously achieved in HIP sintering, indicating the significant enhancement of densification at relatively low temperature under high pressure.

5.1.4. Si₃N₄/SiC Nanocomposites

According to the attractive properties of Si-based ceramic composites, Si₃N₄/SiC nanocomposites are of great interest for thermomechanical applications. For instance, these nanocomposites were elaborated in order to improve the strength and toughness of the Si₃N₄ matrix or to obtain superplastic ceramics. Different ways have been used to produce Si₃N₄/SiC nanocomposites. Many papers report the mixture of commercial Si₃N₄ powder with either SiC or SiCN nanopowders which, after sintering, often leads to nanocomposites in the micronano system [160]. Other papers are focusing on the preparation of nanocomposites in a nano–nano system by sintering SiCN nanopowders.

5.1.4.1. Annealing Treatments on SiCN Nanopowders

In this latter case, a quite high number of papers report the effect of thermal treatments of SiCN nanopowders on thermal stability, crystallization, phase composition, and grain growth. Although the same elements (Si, C, and N) constitute the powder, changes occurring during thermal treatment can be noticeably different as a function of the laser synthesis parameters.

Nanopowders Produced from Gas Phase Precursors
Lences et al. [161] performed thermal treatments on SiCN nanopowders produced by laser pyrolysis of gaseous mixtures (SiH₄, NH₃, and C₂H₂). The effects of temperature (from 1400 to 1600 °C), time (from 60 to 180 min), and atmosphere (N₂ and/or Ar) were evaluated on phase composition, thermal stability, grain size and crystallite size, and specific surface area. Crystallization tests were performed on

powder compacts. Crystallization starts between 1400 and 1500 °C, and different phases were detected (α and β forms of Si₃N₄, SiC, Si₂N₂O), relative amounts of which depend on temperature, time, and atmosphere. In addition, crystallization involves an increase in the crystallite size and a decrease in the specific surface area. The effects of thermal treatments on both the nature and the amounts of the phases are discussed as a function of the possible reactions occurring. It was shown that preliminary nucleation at 1150 °C has a strong positive influence on the final degree of crystallization.

Heat treatments were investigated for SiC, Si₃N₄, and SiCN nanopowders synthesized by laser pyrolysis of gaseous mixtures (SiH₄ + C₂H₂, SiH₄ + C₂H₂ + NH₃, SiH₄ + DMA + NH₃, respectively) [162]. All heat treatments were performed in two different atmospheres (Ar or N₂) at atmospheric pressure and at 1500 °C for 2 h. The changes in the powder characteristics were followed by chemical analysis, XRD, XPS, and XAES. For SiC powder, heat treatment under an Ar atmosphere does not change any feature, while an N₂ atmosphere induces an insertion of nitrogen atoms replacing carbon atoms. For Si₃N₄ powder, which is amorphous before treatments, annealing under both Ar and N₂ atmospheres involves the crystallization of α - and β -Si₃N₄ phases. Grain growth (from 30 nm to 1 μ m) was noticed after annealing. For SiCN nanopowders, changes occurring during thermal treatments under different atmospheres demonstrate that this mixed phase is unstable and strongly reactive. Under an Ar atmosphere, crystallization of the two main phases, SiC and Si₃N₄, occurs, the relative amount of each phase depending on the C/N ratio of the starting powder. Under an N₂ atmosphere, complete or partial nitriding of the powder occurs and involves the preferential formation of α -Si₃N₄.

The thermal behavior of SiCN nanopowders synthesized by laser pyrolysis of gaseous mixtures (SiH₄ + CH₃NH₂ + NH₃ or SiH₄ + CH₃NH₂) was studied under an Ar or He atmosphere from room temperature to 1500 °C [163]. Two powders exhibiting different C/N atomic ratios (0.22 or 0.87) and different crystallization degrees were used. Thermal behavior is investigated by thermogravimetric analysis/mass spectrometry (TGA/MS) analysis, and crystallization is studied by XRD on annealed powders. Under an He atmosphere, powders are decomposed. The decomposition is emphasized when the powder is partially crystallized, while in the meantime crystallization occurs preferentially into β -Si₃N₄. When the powder is crystallized, the Si phase appears after annealing under He. Under a nitrogen atmosphere, powder which is partially crystalline is significantly nitrated and crystallizes preferentially into α -Si₃N₄. However, nitridation is low for SiCN crystallized powder and exhibits a low C/N ratio. All these results are discussed as a function of the different features of the powders and according to several reactions occurring during thermal treatments [163].

Nanopowders Produced from Liquid Precursors Goncalves et al. [33] reported the synthesis of SiCN nanopowders from a liquid organosilazane monomer. Annealing of the powder was performed in two different gaseous atmospheres (ammonia and nitrogen) at temperatures from 500

to 1100 °C. IR spectroscopy was performed on as-formed and annealed powders, showing that as-formed powders are composed of a lot of different bonds: N–H, Si–H, C–H, Si–CH₃, and Si–N; a broad band between 800 and 1100 cm⁻¹ is also present and could be attributed to a combination of Si–C, Si–N, N–H, and Si–O bonds. Thermal treatment under ammonia involves a decrease in C–H and Si–H peaks, a disappearance of the Si–CH₃ peak (from 800 °C), and the appearance of silicon nitride (from 1000 °C). Under a nitrogen atmosphere, this latter peak is shifted to 1090 cm⁻¹, suggesting a combination of Si₃N₄ and SiC bonds.

Thermal behavior of SiCN nanopowders synthesized by laser pyrolysis of hexamethyldisilazane has been studied by TGA/MS analysis up to 1200 °C [30] under a helium atmosphere. Gas analysis revealed that methane and hydrogen were lost, which is consistent with IR spectra showing both Si–H and Si–CH₃ bonds in the starting powders. In addition, firing tests, performed under an He atmosphere for 3 h up to 2020 °C, show that oxygen and nitrogen were lost. For all firing temperatures, the only crystalline phase formed was SiC.

Annealing of SiCN nanopowders produced from hexamethyldisilazane aerosol was performed for 6 h in a temperature range of 500–1100 °C under an NH₃ atmosphere [29]. IR spectroscopy revealed that, at 500 °C, C–H and Si–H peaks were eliminated and the Si–CH₃ peak decreased in relative height, while at 800 °C, the Si–CH₃ peak completely disappeared and at 1100 °C a pronounced Si₃N₄ peak appeared. The same thermal treatments, carried out under an N₂ atmosphere, showed that the organic groups were eliminated at lower temperature than under an NH₃ atmosphere. At 1100 °C, no evident Si₃N₄ peak was present, but a strong absorption peak appeared at 1090 cm⁻¹, which may be attributed to a combination of Si₃N₄ and SiC bonds.

Crystallization and grain growth were studied after the annealing of SiCN nanopowders synthesized by laser pyrolysis of hexamethyldisilazane with ammonia [164]. Annealing was performed in a graphite resistance furnace with BN crucibles. The powders were compressed up to a density of 30% of the theoretical one and then annealed for 1 h under a nitrogen atmosphere at temperatures between 1473 and 1973 K. The structure was analyzed by XRD and IR spectroscopy. Morphology changes and grain growth were investigated by BET measurements and TEM observations. Crystallization appears at 1773 K, with small amounts of α -Si₃N₄ and β -SiC. Then, at 1873 K, peaks related to these two phases increased and the α -SiC phase with C graphite are formed. When the temperature reached 1973 K, α -Si₃N₄ decreased, while both SiC phases increased. FTIR spectra show that for temperatures up to 1673 K, the broad strong absorption between 800 and 1100 cm⁻¹ decreased in intensity and shifted to lower wave numbers. For higher temperatures, several small absorption bands were distinguished, assigned to Si–N vibrations in crystalline α -Si₃N₄. Regarding particle growth, the decrease in BET-specific surface area with annealing temperature suggests that the particles grow rapidly even before crystallization. Below 1773 K, TEM observations show large clusters, about 100 nm in size, resulting from the shrinkage of particles contacted together. At 1873 K, TEM observations also show that nanocomposite Si₃N₄–SiC particles were formed.

Another study concerning SiCN nanopowders obtained from laser pyrolysis of hexamethyldisilazane reports changes in chemical composition and crystallization of the powders during heat treatment at 1350 and 1550 °C under nitrogen for 1 h [39]. For a 1350 °C annealing temperature, nitrogen content increases, while excess C content decreases compared to the composition of the as-produced powder. When the annealing temperature is raised to 1550 °C, the nitrogen content then decreases even under 105-Pa nitrogen pressure, while excess C content is still decreasing. Concerning the compounds, SiC increases while SiO₂ decreases when the temperature increases, showing that SiO₂ reacts with other phases during annealing. Regarding the structure, XRD shows that heat treatment involves a partial crystallization of the powder. Thus at 1350 °C, β -SiC and α -Si₃N₄ are the major crystalline phases mixed with small amounts of α -SiC and β -Si₃N₄. At 1550 °C, β -SiC becomes the main crystalline phase and the α -SiC peak becomes stronger, while Si₃N₄ phases become weaker. IR spectroscopy confirms these changes in structure. The chemical and structural changes can be explained by reactions occurring in the Si-C-N-O system, involving mainly nitrogen and CO evolution in the presence of excess C under a nitrogen atmosphere.

Cauchetier et al. [26] studied structure, morphology, and size changes occurring during thermal treatments of SiCN nanopowders synthesized by laser pyrolysis of HMDS. Annealing was performed on two different powders (a carbon-rich powder and a nitrogen-rich powder) under argon or nitrogen atmospheres. For the carbon-rich powder, TGA/MS analysis under an argon atmosphere shows a weight loss mainly attributed to the evolution of CH₄, N₂, and CO₂. Changes in chemical composition after annealing under nitrogen indicate that the nitrogen content is increased up to 1400 °C, probably forming Si₃N₄ or Si₂N₂O, while the nitrogen content is decreased and the SiC content is increased from 1400 to 1600 °C. Measurements of specific surface areas on samples annealed under nitrogen reveal a decrease from 133 to 31 m²/g when heating temperatures vary from 25 to 1600 °C, respectively. At 1600 °C, grain growth has occurred, and XRD and IR analysis indicate the presence of both α - and β -SiC phases. For the nitrogen-rich powder, TGA/MS results under an argon atmosphere show a higher weight loss than that obtained for the C-rich powder, which is due to N₂, H₂O, NH₃, and CH₄ evolution. The specific surface area of samples annealed under a nitrogen atmosphere decreases from 125 to 42 m²/g for heating temperatures from 25 to 1500 °C, respectively. From 1500 °C, crystallization occurs and the α -Si₃N₄ phase is formed. The thermal behavior of these two powders is described according to different reactions occurring in the SiCNO system. More detailed results concerning TGA/SM under a nitrogen atmosphere and evolution of the structures of various Si/C/N nanopowders have been presented by Musset [86]. A high weight loss, up to 25%, is observed during heat treatment under N₂ up to 1500 °C. The decomposition of C-rich nanopowders leads to a crystallized SiC major phase at 1500 °C, while the decomposition of N-rich nanopowders leads to a crystallized major Si₃N₄ phase. For intermediate compositions (C/N around 0.75), a SiC/Si₃N₄ composite is obtained. Moreover, a delay in the crystallization is observed

for such intermediate compositions [165]. The local atomic configuration and local order in such SiCN nanopowders annealed at 1500 and 1600 °C under an N₂ atmosphere were studied through XPS analysis [87, 166]. Changes in both chemical composition and local bonding involved in annealing treatments were studied on powders remaining amorphous at temperatures up to 1500 °C. After thermal treatment, a strong evolution in the SiC₄ to SiN₄ ratio was observed, the proportion of SiC₄ groups increasing noticeably with temperature. It could also be noticed that annealing involves a reordering of the network, attested by the sharpening of the Si-2p XPS component. Local evolution was also studied by NMR and X-ray absorption techniques (EXAFS and XANES) [90, 167]. These studies clearly confirm the importance of the local arrangement around Si atoms to describe evolution under thermal treatments. In particular, for intermediate C/N values, the delay in the crystallization temperature corresponds to the formation of very small crystallites distributed into a still amorphous matrix. The observed increase in the crystallization temperature is attributed to a favorable composition corresponding, on average, to a Si-C₂N₂ environment for Si atoms.

As pointed out before, these SiCN nanopowders obtained from liquid HMDS exhibit a high weight loss, which makes them difficult to use for elaboration of materials. In a recent study, the effects of various synthesis parameters (the chemical nature of the precursor and laser power) on the degree of crystallization and on the thermal stability of nanopowders were investigated. Characteristics of powders, such as chemical composition, morphology, structure, and thermal stability, were reported. A correlation between the synthesis conditions and the thermal stability of the powders has been established, and the synthesis parameters enabling good thermal stability up to 1500 °C were determined [91].

5.1.4.2. Elaboration and Properties of Si₃N₄/SiC Nanocomposites

Kaiser et al. [168, 169] elaborated Si₃N₄/SiC nanocomposites from mixture of commercial α -Si₃N₄ powders with up to 20 wt % of β -SiC nanopowders and a sintering additive (Y₂O₃). Powder mixtures were cold isostatically pressed at 400 MPa for 5 min. Subsequent hot isostatic pressing of the green compacts obtained was performed at pressures up to 350 MPa and temperatures above 1700 °C. The resulting materials exhibit densities higher than 98% of theoretical density. Microstructures were observed on fracture surfaces and the hardness and fracture toughness were measured. The formation of equiaxed grains instead of rodlike Si₃N₄ grains occurs for lower HIP temperatures, higher SiC content, and higher dwell time. Nanometer-sized SiC particles are uniformly dispersed in the Si₃N₄ matrix as well as along the grain boundaries. The hardness increases continuously with increasing SiC content. The fracture toughness is not significantly influenced by SiC content.

The same group of researchers [170] reported the elaboration of micro/nano composites and nano/nano composites from mixtures of conventional α -Si₃N₄ powders with β -SiC nanopowders or directly from SiCN nanopowders with or without additives (Y₂O₃, Al₂O₃). Sintering was performed by hot isostatic pressing. The quite complete densification of nanosized powders with additives involves a temperature of 1750 °C and a pressure of 350 MPa for 2 h. Without sintering aids, the temperature and the dwell time are higher

(1900 °C, 2.5 h, respectively). The microstructure of samples was observed, and the mechanical properties evaluated were hardness at room temperature and at temperatures between 800 and 1100 °C, fracture toughness at room temperature, and creep behavior at 1600 °C. For all samples elaborated without additives, hardness decreases continuously with temperature. However, composites containing SiC show better temperature behavior than monolithic Si₃N₄; in particular, the addition of nano-SiC leads to the highest values of hardness. The SiCN nano-nano composite does not show higher creep rates than the micro-nano composite. When powders are sintered with additives, materials exhibit higher creep rates.

Bellosi et al. [171, 172] prepared and characterized Si₃N₄/SiC nanocomposites by adding 30 wt% of SiCN nanopowders to a commercial Si₃N₄ powder or by using only SiCN nanopowders. Sintering aids (Y₂O₃, La₂O₃) were added to the Si-based powders. The powders were mixed in hexane with dispersant and binder either by ultrasonic mixing or by attrition mixing. Densification was carried out by hot pressing under a vacuum at 1850 °C using a pressure of 30 MPa. The density of samples was measured, microstructures were observed, and mechanical properties, such as Young modulus, fracture toughness, and hardness, were evaluated. The relative green density of SiCN nanopowders is lower (35%) than that obtained in the case of Si₃N₄/SiCN mixtures. However, in spite of its poor green density, the SiCN sample achieved complete densification. Regarding the microstructure, the presence of ultrafine powder allowed a substantial refinement of the microstructure at the nanostructural level. For instance, samples obtained with only ultrafine SiCN powder exhibit a final mean grain size of 130 nm. Room temperature flexural strength is higher for samples obtained from attrition mixing (915 MPa) compared to samples issuing from ultrasonic mixing (750 MPa). The low flexural strength (137 MPa) obtained for samples made with SiCN nanopowder to defects related to nonhomogeneous distribution of the additives and to a low dispersion of ultrafine powder. High hardness (17 to 18 GPa) and fracture toughness (3.6 to 4.3 MPa·m^{1/2}) for all materials.

Other studies reported by M. Mayne et al. [173, 174] focused on both the mechanical properties and deformation at high temperature (e.g., superplasticity) of Si₃N₄/SiC nanocomposites. The materials were elaborated from mixtures of commercial Si₃N₄ powder with either SiCN nanopowders (20 wt%) or SiC nanopowders (20 or 40 wt%). Sintering aids (Y₂O₃, Al₂O₃) were added to the mixtures. Densification was carried out by hot pressing in a nitrogen atmosphere, for 2 h, under 35 MPa, for temperatures between 1550 and 1730 °C. Densification was complete from 1550 °C for materials made with SiCN nanopowders, while samples containing 20 wt% of SiC were only densified from 1650 °C. This is due to SiC agglomerates which are not dissolved in the liquid phase during sintering. When SiC or SiCN nanopowders are used, the $\alpha \rightarrow \beta$ Si₃N₄ transformation rate is enhanced compared to that of conventional Si₃N₄ material; SiC nanopowders induce a higher transformation rate than SiCN nanopowders. The microstructures are composed of small and equiaxed grains for Si₃N₄/SiCN samples sintered at 1550 °C, while grain growth occurs at higher temperature and grains become acicular. Si₃N₄/SiC

nanocomposites exhibit different microstructures with small and equiaxed grains which are agglomerated (SiC) and acicular grains (β -Si₃N₄). It is important to note that increasing the amount of SiC involves an inhibition of Si₃N₄ grain growth (Fig. 4a–c) (see, for example [77]). Such microstructures with SiC agglomerates have been analyzed by XPS [175] showing a differential charge effect for the C-1s and Si-2p core levels, while XPS core levels from silicon carbide (Si-C₄ and C-Si₄) are not affected by charge shifts. The authors interpreted these signals as signatures of the structural organization in the compound made of SiC nanoparticles dispersed in a vitreous YSiAlON[C] phase located at the grain boundaries, which made up a conductive cement/skeleton surrounding large silicon nitride grains. Three-point bending strength reaches values from 340 to 850 MPa for Si₃N₄/SiCN materials, while lower values are obtained for Si₃N₄/SiC nanocomposites due to low densification and SiC agglomerates. A bending test at high temperature on the material exhibiting the smallest grain size showed a large deformation without any structural alteration of the surface.

The creep behavior of Si₃N₄/SiC nanocomposites prepared as reported above has been studied by Besson et al. [176]. Compressive creep tests were performed under air at constant temperature ranging from 1250 to 1450 °C under stresses varying from 45 to 180 MPa. The creep behavior of Si₃N₄/SiC nanocomposites was compared to that of Si₃N₄ monoliths elaborated from commercial powders. The results were discussed in terms of creep mechanisms; the stress exponent and the activation energy were evaluated. Therefore, this work revealed mainly that grain boundary sliding accommodated by diffusion through the intergranular glass phase governs creep behavior. The nanocomposite exhibits better creep resistance than the monolith, which can be explained by several phenomena. First, the higher refractivity of the intergranular phase due to the presence of carbon inside can limit creep deformation. Then, the presence of SiC nanoprecipitates inside the grain boundaries obstructs the easy paths of diffusion. Finally

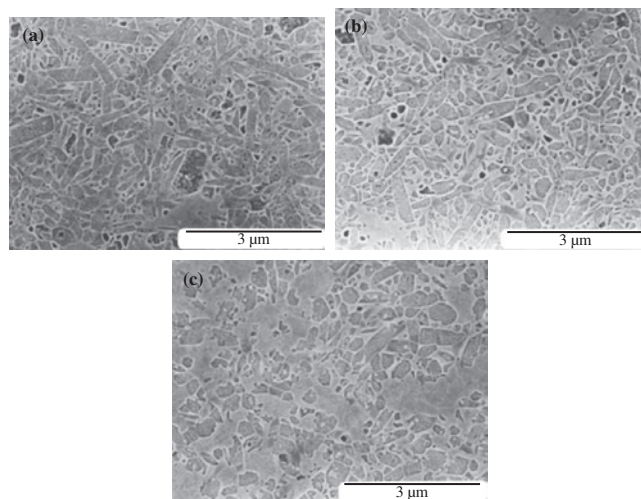


Figure 4. Microstructure of Si₃N₄/SiC nanocomposites elaborated by hot pressing at 1650 °C and exhibiting different SiC contents: (a) 5 wt% of SiC; (b) 10 wt% of SiC; (c) 20 wt% of SiC.

SiC nanoparticles agglomerated and forming pockets do not participate in deformation.

The tensile ductility and rupture behavior of such Si₃N₄/SiC nanocomposites have been studied in the temperature range of 1595–1640 °C under strain rates of $5 \cdot 10^{-5}$ and 10^{-5} s^{-1} [177]. Composites were fabricated in the same way as described above, from a mixture of commercial Si₃N₄ powder and SiCN nanopowders with sintering aids (Y₂O₃, Al₂O₃). The content of SiC in the final composite can be either 10 or 20 wt%. The behavior of composites was compared to that of the Si₃N₄ monolith. The authors demonstrated that the ductility of composites decreased when the SiC content increased in the material and when temperature decreased (Fig. 5). In addition, the ductility of composites was smaller than that of the monolith. However, the ductility of composites is improved when the strain rate is decreased (an elongation of 39% at 1595 °C for 10^{-5} s^{-1} , Fig. 5). This phenomenon is a consequence of the microstructure of composites composed of Si₃N₄ grains embedded in an intergranular phase, the SiC nanoprecipitates being mainly located either along Si₃N₄ grain boundaries or gathered together forming a kind of pocket. At a high strain rate, deformation is controlled by the grain boundary sliding of micro-sized Si₃N₄ grains, and SiC precipitates impede sliding of Si₃N₄ grains, while at lower strain rates the SiC nanoprecipitates contributed to deformation.

Some papers reported the elaboration of Si₃N₄/SiC nanocomposites from SiCN nanopowders mixed with sintering aids. In this context, Lences et al. [161] studied the thermal behavior of powders, the elaboration process, densification, and mechanical properties such as hardness and fracture toughness. Different additive systems and methodologies have been tested for the densification of SiCN nanopowders. SiCN nanopowders are mixed with Y₂O₃ and Al₂O₃ or with AlN and YN. Cylindrical pellets were die pressed. Preliminary tests of pressureless sintering revealed very poor sinterability. Therefore hot pressing was performed at temperatures between 1700 and 1800 °C, under a pressure of 30 MPa for 30 to 60 min. The densification behavior of SiCN nanopowders is different than that of Si₃N₄ commercial powders. The maximum density for SiCN powders is obtained for longer dwell times at 1700 °C than

for Si₃N₄ powders, this being mainly due to the low green density obtained for SiCN and the presence of C in the powder. The microstructure can be composed of α and β phase Si₃N₄, Si₂N₂O, the proportion of each phase depending on the elaboration process involved. In SiCN material which does not contain the Si₂N₂O phase, the microstructure is very fine and composed of equiaxial grains of 50–100 nm. Some crystals up to 0.5 μm can also be observed. High hardness values ($\sim 21 \text{ GPa}$) were measured for samples which do not contain any Si₂N₂O phase. The fracture toughness ($\sim 5 \text{ MPa}\cdot\text{m}^{1/2}$) for nanocomposites is in the same range as that for the Si₃N₄ monolith.

Creep behavior has been studied in Si₃N₄/SiC nanocomposites elaborated by sintering SiCN nanopowders with yttria and alumina [178]. The different powders were mixed in ethanol by sonification and the slurry was homogenized in a polyethylene jar with Si₃N₄ balls. Densification was performed by hot pressing under 35 MPa using different steps, the maximum sintering temperature being 1700 °C. Fully dense (99% of theoretical density) samples were obtained. The microstructure was composed of very fine equiaxed or slightly elongated β -Si₃N₄ grains embedded in an intergranular YSiAlON glassy phase, the mean grain size was around 150 nm, and the maximum size of elongated grains was 450 nm. SiC grains exhibited a spherical shape less than 30 nm and were located either in the Si₃N₄ grains or in the grain boundaries. Compressive creep tests were carried out under an air atmosphere at constant load. Iso-baric tests were conducted at constant temperature between 1150 and 1350 °C under an initial applied stress of 90 MPa, and isothermal tests were achieved at 1350 °C, with stresses ranging from 45 to 180 MPa. For all the creep conditions, the true strain (%) versus time curves showed a short primary stage followed by a pseudo-stationary stage. These nanocomposites exhibited a high ductility compared to Si₃N₄ monoliths or Si₃N₄/SiC micro–nano composites elaborated from a mixture of commercial Si₃N₄ and SiCN nanopowders. The creep deformation of the nanocomposite is three times higher than that of the Si₃N₄ monolith. In addition, its oxidation resistance is better, even better than that of the micro–nano composite. Postsintering heat treatments made possible the development of microstructures with acicular grains and partial crystallization of the amorphous intergranular phase. The creep resistance of such materials obtained is improved, which is promising for future applications.

In a recent study, Si₃N₄/SiC nanocomposites [179] were successfully elaborated from powders synthesized by laser pyrolysis of an aerosol of HMDS. In spite of the high weight loss during heat treatment, dense and homogeneous materials were obtained by hot pressing of the nanopowders with sintering aids. The ductility of the nanocomposites elaborated from these powders is very high due to the small size of the β -Si₃N₄ grains. This study seems promising for the development of materials elaborated from “cheap” powders.

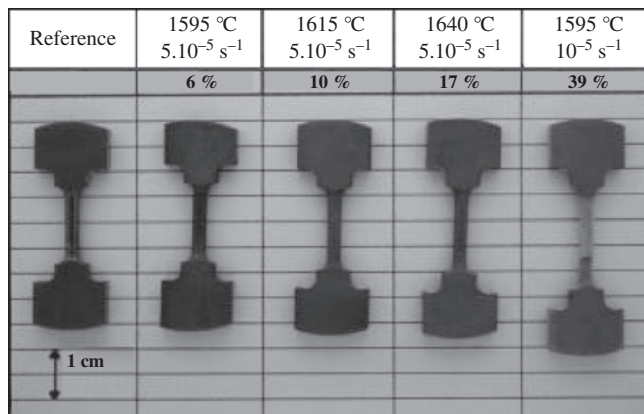


Figure 5. Comparison of elongations obtained for different temperatures and strain rates in the case of a Si₃N₄/SiC nanocomposite exhibiting 10 wt% of SiC [77].

5.2. Optical Properties

There is a great interest in the optical properties of nanoparticles because with size reduction, confinement and surface effects become more and more efficient and considerably affect the electronic and optical characteristics

of nanoparticles. The fundamental understanding of these effects has motivated considerable research activity, including the necessary efforts to synthesize such nanoparticles with very well controlled size and structure. Moreover, applied research with such nanoparticle-based materials or devices is already a very active field. Quantum dots, such as silicon nanocrystals, and nanocomposites issuing from Si or SiC nanopowders are discussed below in relation with their synthesis by laser pyrolysis.

5.2.1. Light-Emitting Silicon Nanocrystals

The discovery of the intense photoluminescence of porous silicon at the beginning of the nineties [180, 181] has triggered great interest in nanostructured silicon. The principal motivation is the possible integration of silicon nanostructures in optoelectronic devices. However, the main challenge is to control the nanoscale size of the structure, because the quantum confinement effect at the origin of the PL is strongly size-dependent. Laser pyrolysis has proved its efficiency for this purpose (see previous section). Since the middle of the nineties, essentially two research groups have specifically used laser pyrolysis to synthesize silicon nanoparticles with controlled size in the range below 10 nm in order to obtain light-emitting silicon nanoparticles. The first group uses a classical experimental setup [182], while the second group uses a pyrolysis source coupled to a molecular beam machine [23]

5.2.1.1. Photoluminescent Si Nanoparticles from a Classical Flow Reactor Attention has been paid to the determination and control of silicon nanoparticle size in a classical laser pyrolysis reactor. WAXS characterization of nanoscale silicon particles has been developed [182]. Light-scattering diagnostics of silicon particle growth has permitted the control of the synthesis in a wide size range [50]. Also, accurate XRD study of spherical silicon nanoparticles has been made, in order to investigate possible structural changes originating from the reduced dimension and the thermal stability of the nanostructured powders [183]. It has been shown that, to reduce the silicon particle size, the residence time has to be reduced drastically. Low pressure, high silane dilution by inert gas, and high flow rate are the different parameters used to reach this objective. However, to control the crystalline structure at the same time is difficult, because flame temperature is very sensitive to the silane flow.

Photoluminescence spectra from Si powders obtained at 200 Torr and different dilutions of silane in argon or helium were reported [50]. However, the size dependence of the PL peak energy is very small compared to the confinement theoretical predictions. In general the PL spectra of these silicon nanoparticles showed two bands, around 1.7 and 1.9 eV. For the smallest nanoparticles (5 and 7 nm in diameter), a supplementary peak is reported at 2.2 eV, and the luminescence can be observed by the naked eye. Particle size analysis by small-angle neutron scattering shows the presence of a second population of very small particles with diameters smaller than 2 nm, to which the high-energy PL peak is attributed. Based on a detailed study using additive characterization methods such as HRTEM and infrared spectroscopy, the origin of the PL has been attributed to a radiative defect, as

a non-bridging oxygen hole center for the high energy peak [184]. In another work [49], Si nanocrystallites were produced that exhibit visible photoluminescence emission after oxidation. The PL intensity and wavelength were sensitive to the temperature of the oxidative heat treatment; the higher the temperature, the higher the energy and intensity of the PL peak.

5.2.1.2. Optical Properties of Size-Selected Silicon Nanocrystals

Instead of collecting the particles on downstream filters in the flow reactor, Ehbrecht et al. [185] introduced a small conical nozzle into the reaction zone, in order to extract orthogonally the growing particles and expand them into the vacuum of a molecular beam machine (see Section 3.1). Particles were deposited on substrates and the presence of silicon particles 3 to 12 nm in diameter was demonstrated. A detailed analysis of the cluster beam by time of flight mass spectrometry has shown that the velocities of the silicon clusters decrease with increasing mass [24, 51]. Thus, it is possible to narrow the size distribution of the deposited particles by using a rotating chopper disk, properly synchronized to the pulsed CO₂ laser and placed in front of the substrate holder. With such a high-performance experimental setup, it was possible to study in great detail the size effects in silicon nanostructures. HRTEM studies [53] showed that silicon nanoparticles exhibit a perfect crystalline core and are surrounded by an amorphous layer of silica. The lattice parameter of the silicon core and the oxide layer thickness are both size-dependent, the latter being around 10% of the particle diameter. These effects have been attributed to a negative interface stress, limiting the curvature of the interface. Thus, at small sizes, Si nanoparticle oxidation must be considered a self-limiting process.

Just after the deposition, nanocrystals do not demonstrate any photoluminescence. However, if the sample is exposed to ambient air, the deposit emits orange-red light when exposed to a laboratory uv lamp at room temperature. The progressive appearance of the PL is due to the passivation action of oxygen at the nanoparticle surface, resulting in the saturation of the dangling bonds which were responsible for nonradiative relaxation. This interpretation is corroborated by the observation of the PL peak blue shift induced by the reduction in the silicon core size [186]. After a few days, bright PL is easily visible to the naked eye. An example is given in Figure 6 in the case of a very thin size-selected deposit. While the measured absorbance of this sample at 266 nm is as low as 7%, it exhibits a red emission clearly visible when illuminated by a uv lamp (Fig. 6).

The size selection capability of the cluster beam apparatus has permitted a detailed analysis of the quantum confinement effects in silicon nanocrystals. The first PL measurements were recorded using sets of deposits with average diameters ranging from 2.8 to 7 nm and a size distribution as narrow as 0.6 nm [52, 187]. In all the cases, the PL spectrum comprises only one peak with a nearly Gaussian shape, and the peak energy is very size-dependent. Comparison with the inverse power law, derived by Delerue and co-workers [188] on the basis of the quantum confinement model, is satisfying. An improved one-phonon confinement model for an accurate size determination of silicon nanocrystals was deduced from such samples [189].

Another sort of sample was prepared by cluster beam deposition employing a clockwise rotating molecular beam chopper that distributed the transmitted nanoparticles on the substrate from left to right according to their size [52, 190]. Within the deposited film, the size of the Si nanoparticles varies from 2.5 to 8 nm, as was determined *in-situ* by time of flight mass spectrometry. The color of the photoluminescence changes with the size of the Si nanocrystals; it varies from yellow–orange to the IR. Full quantitative information on the PL as a function of size was obtained by light emission measurement along a horizontal line with a calibrated PL spectrometer. A plot of the peak positions as a function of the nanocrystal size shows that the data points nicely follow the theoretical prediction made on the basis of the quantum confinement model [188]. Due to the fact that all particle sizes are available in one single sample, the scatter of the data points is noticeably reduced compared to that of earlier studies. The efficiency of the PL process was determined precisely measuring the ratio between emitted and absorbed radiation [190]. A maximum of 0.3 was found for crystallite sizes around 3.5 nm. This very high quantum yield, however, is only a lower limit. Considering that the size selection is not perfect and that the thin films could be contaminated by some larger particles, the true PL yield is estimated to be 90% [191]. This indicates that these Si nanocrystals are very well passivated and that the density of bulk defects is extremely low.

More recently, an ellipsometry study of nc-Si films deposited on suitable substrates has been performed [192]. The refractive index and extinction coefficient were determined in the wavelength range from 240 to 700 nm. It was shown that the optical response of the nc-Si layers can be well described by a Tauc–Lorentz model and that, as for porous silicon, the nc-Si optical indexes significantly deviate from those of bulk silicon. Silicon at the nanometric scale has definitively a specific behavior.

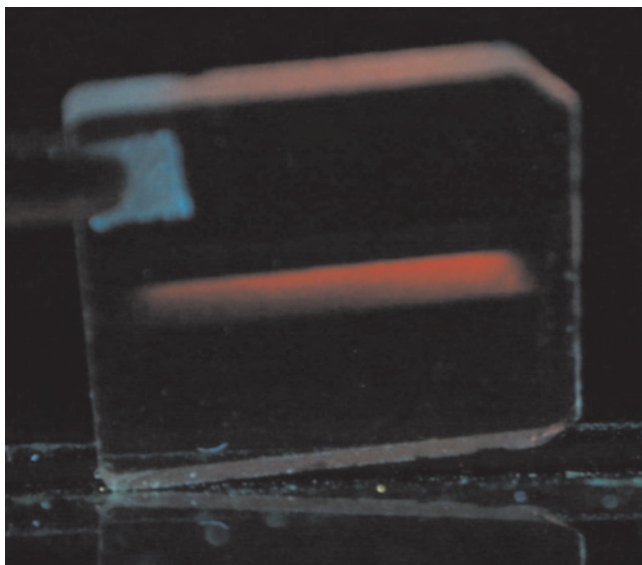


Figure 6. Thin film of silicon nanocrystals deposited on a quartz substrate with size selection in a molecular beam machine [52, 185]. The film is visible through its bright red PL emission under illumination by a uv lamp.

5.2.1.3. Applications of Si Nanoparticles An unexpected application of the photoluminescence properties of nc-Si was found in relation to an astrophysical problem, namely, the identification of a broad emission band observed in the red in many circumstellar and interstellar media, called the extended red emission (ERE). This band was attributed to the PL of an interstellar dust grain component when excited by the uv radiation emitted by a nearby star, but no material in the laboratory was able to fit the ERE properties. Hence, it has been shown that nanometer-size crystals of pure silicon are the best candidate materials [193]. A detailed analysis has shown that indeed, nc-Si allows a complete interpretation of the astronomical data as regards the PL efficiency and the peak wavelength and bandwidth [194]. Thus, taking into account quantum confinement in silicon nanocrystals allows a long-standing astrophysical problem to be solved.

On the technological side, structured films of light-emitting silicon nanoparticles can be produced by cluster beam deposition by shaping the beam with a mask and depositing the nanoclusters at low energy on a sapphire substrate. Upon illumination with ultraviolet radiation, the nanoparticles exhibit strong photoluminescence in the red [195]. To check the resolution that can be obtained by these means, holey carbon films normally used for transmission electron microscopy have been used successfully to create structures with lateral dimensions down to 30 nm. In another experiment, regular patterns of micrometer-sized spots composed of Si nanocrystals have been produced. The PL behavior of these structured films has been studied by laser scanning confocal microscopy [196]. Another interesting application can be found in silicon nanocrystals-based cavities. An active layer of nc-Si is placed in a Fabry–Pérot resonator. It is a plane cavity surrounded by two dielectric mirrors composed of SiO₂ and TiO₂. A noticeable narrowing of the nc-Si PL band is observed as well as a strong light directivity [197].

Finally, there is a great interest in nc-Si containing matrices for optoelectronic applications, such as wave-guide amplifiers. It has been shown that laser-synthesized nc-Si could be integrated into matrices and the resulting material properties have been studied. Composite polycrystalline diamond layers containing light-emitting Si nanoparticles have been prepared by using a chemical-vapor deposition technique coupled with the powder-flowing apparatus. A strong increase in the room temperature PL efficiency in the energy range of 1.6–2.5 eV is observed from Si nanostructures embedded in the diamond matrix. It seems also possible to tune the luminescence wavelength in the yellow–green spectral region by selecting the size of the inserted Si grains [198]. In another study [199], it was shown that incorporation of the Si nanoparticles into a silica matrix by sol–gel technology is not detrimental to the PL (photoluminescence) emission intensity. Micro-Raman mapping and TEM analysis of the nanocomposites have shown the presence of agglomerated nanoparticles (in the sub-micrometer range), as confirmed by dynamic light scattering measurements on colloidal suspensions of as-synthesized powders. Work is in progress in order to improve such promising nanocomposites.

5.2.2. Nanocrystalline SiC

Recent interest has arisen in the possible applications of SiC nanoparticles (np-SiC) in the field of nonlinear optics. As described in previous sections, np-SiC can easily be obtained from laser pyrolysis. With the objective of integrating np-SiC in electro-optical devices, some attempts to decrease the size of the nanoparticles down to the exciton radius have been described [20]. In a first approach, it was shown that the particle diameter can be tuned by the gas flow rate and the chop frequency. Unfortunately, as pointed at in a previous section related to β -SiC nanopowders, the size of the crystallites is decreased up to 4 nm but the size of the particles remains in the range of 10 nm. To further decrease the nanoparticle size, a posttreatment was applied. SiC nanoparticles were oxidized to create a silica layer at the surface, this layer was etched by HF treatment in a further step, and smaller nanocrystals were obtained [20].

Photoinduced optical phenomena in SiC nanocrystallites (with sizes within 10–30 nm) embedded within photopolymer matrices have been studied using experimental nonlinear optics, particularly photoinduced optical second harmonic generation. The SiC hexagonal structural components appear to play a key role in the observed photoinduced nonlinear optical effects. Large values of the nonlinear optical constants open the possibility of enhancing the nonlinear optical susceptibilities [200]. The linear electro-optical effect (LEO) is also experimentally demonstrated in nc-Si incorporated in a polymeric matrix. By using the angle-dependent polarimetric method, in both static and photoinduced regimes, it is observed that embedding nc-SiC within polymer host matrices gives rise to an enhancement in the LEO effective parameters up to 1.325 pm/V. The absence of these phenomena in the separate components suggests that the observed local electro-optical response is intimately driven by the interfacial hyperpolarizabilities appearing between the nc-SiC and the surrounding organic matrix [201]. Stoichiometry and interface effects are shown to play a significant role in the electronic and optical properties of SiC nanoparticles [202]. Finally, Raman and photoluminescence properties of SiC nanoparticles have been studied versus particle size (from 10 to 25 nm), chemical composition, annealing, and oxidation treatments. In the case of quasi-stoichiometric np-SiC, broad red PL emissions seem mainly enhanced by the amorphous fraction of particles and by the surface chemical disorder induced by oxidation. The PL signature could then be used to monitor the physical organization of np-SiC [203].

6. SUMMARY

Laser pyrolysis is a versatile method for the synthesis of various compounds with nanometric size. Important characteristics of the products are their high purity and also their low size dispersion, which make them good candidates for various applications. Moreover, the reactor operates in a continuous flow, which is a key point for industrial development. The resonance condition between the laser emission and the absorption of a precursor appears less and less restrictive with the improvements of laser technology (emission range, power, etc.).

At the laboratory scale, it is clear that the capabilities of the method have not been fully explored. Much development is still possible to increase the quality of the products (control of the surface, synthesis of more and more complex nanocomposite powders by using new precursors or new mixtures of precursors, etc.).

After 20 years of being mainly encountered in research laboratories, laser pyrolysis reactors begin to be developed at the industrial scale. This long delay appears related to the chemical composition of the products (silicon-based powders) easily obtained since the first experiments. In fact, the main application domain for silicon-based nanopowders is structural ceramics. In this field, it is necessary to obtain significant batches of powders for the elaboration of dense pieces made only from nanometric powders. Therefore, very significant improvement in properties must be obtained to overcome economic considerations about the price of precursors. Only recently could good quality powders be obtained from precursors cheaper than silane.

In the very active field of nanomaterials, strong interest has arisen in properties specific to low particle size, such as optical, magnetic, etc., properties. The same tendency can be noted in powders obtained by laser pyrolysis:

- Low particle size (<10 nm) powders have been synthesized. In such particles, quantum confinement effects can appear.
- Composites where metallic nanoparticles are embedded in larger particles have been obtained directly from the decomposition of various precursors.
- Nanocomposites in which nanopowders are incorporated in a matrix have been elaborated after synthesis.

The field of catalysis, more related to oxide materials, has not been presented here but oxide products obtained by laser pyrolysis appear very promising. All these subjects are expanding, as can be seen by the number of publications and by the growing interest in the industrial uses of such composite materials, and this technique will certainly be more developed in the near future.

GLOSSARY

Aerosol Gaseous suspension of very fine particles of a liquid or a solid.

Anneal To treat a material with heat and then cool it. In the present case annealing treatment is used to study structural evolution of nanopowders.

Compaction Increasing the dry density of granular materials by means such as pressure.

Green body Molded shapes of ceramic powders which after sintering will become a solid ceramic material.

Laser pyrolysis Synthesis technique based on the interaction of matter with a narrow beam of coherent powerful and monochromatic radiation emitted by a laser.

Nanoparticles Particles with dimension less than 100 nanometer ($100 \cdot 10^{-9}$ m).

Photoluminescence Luminescence stimulated by visible, infrared or ultraviolet radiation.

Short-range order Regularity in the arrangement of atoms of a disordered material in which the probability of a given type of atom having neighbors of a given type is greater than one would expect on a purely random basis.

Sintering Forming a coherent bonded solid by heating ceramic or metal powders without melting.

ACKNOWLEDGMENTS

We warmly thank all our colleagues in the CEA-Saclay research group, particularly people involved in laser pyrolysis work over the last decade. We are grateful to our colleagues working in other French laboratories, and in different European laboratories, for the fruitful collaborations we have developed.

REFERENCES

- J. S. Haggerty and R. W. Cannon, in "Laser-Induced Chemical Processing", pp. 165–241. Plenum Press, New-York, 1981.
- W. R. Cannon, S. C. Danforth, J. H. Flint, J. S. Haggerty, and R. M. Marra, *J. Am. Ceram. Soc.* 65, 324 (1982).
- W. R. Cannon, S. C. Danforth, J. S. Haggerty, and R. M. Marra, *J. Am. Ceram. Soc.* 65, 330 (1982).
- M. C. Rocco, *J. Nanopart. Res.* 1, 1 (1999).
- E. A. Barringer and H. K. Bowen, *J. Am. Ceram. Soc.* 65, C-199 (1982).
- X. Bi and N. Kambe, Production of particles by chemical reaction, Patent WO9837961, 03 Sept. 1998; see also www.nanogram.com.
- A. K. Knudsen, in "Carbide, Nitride and Boride Materials: Synthesis and Processing" (A. W. Weimer, Ed.), pp. 343–358. Chapman & Hall, London, 1997.
- J. H. Flint, R. A. Marra, and J. S. Haggerty, *Aerosol Sci. Technol.* 5, 249 (1986).
- J. Förster, M. von Hoessling, and J. Uhlenbusch, *Appl. Phys. B* 62, 609 (1996).
- J. H. Flint and J. S. Haggerty, *Ceram. Trans.* 1, 244 (1988).
- K. Sawano, J. S. Haggerty, and H. K. Bowen, *Yogyo-Kyokaiishi* 95, 64 (1987).
- J. M. Lihmann and M. Cauchetier, *J. Eur. Ceram. Soc.* 13, 41 (1994).
- E. Borsella and R. Fantoni, *Chem. Phys. Lett.* 150, 542 (1988).
- E. Borsella, L. Caneve, R. Fantoni, and S. Piccirillo, *Nuovo Cimento* 11D, 487 (1989).
- R. Fantoni, F. Bijnen, S. Piccirillo, and S. Enzo, *Chem. Phys.* 147, 389 (1990).
- R. Fantoni, F. Bijnen, N. Djuric, and S. Piccirillo, *Appl. Phys. B* 52, 176 (1991).
- E. Borsella and L. Caneve, *Appl. Phys. B* 46, 347 (1988).
- G. W. Rice and R. L. Woodin, *J. Mater. Res.* 4, 1538 (1989).
- R. A. Bauer, J. G. M. Becht, F. E. Kruijs, B. Scarlett, and J. Schoonman, *J. Am. Ceram. Soc.* 74, 2759 (1991).
- Y. Kamlag, A. Goossens, I. Colbeck, and J. Schoonman, *Appl. Surf. Sci.* 184, 118 (2001).
- T. Yamada, Y. Tanaka, and T. Suemasu, Y. Kohtoku, *Nucl. Instrum. Methods Phys. Res. B* 121, 378 (1997).
- M. Ehbrecht, M. Faerber, F. Rohmund, V. V. Smirnov, O. Stelmakh, and F. Huisken, *Chem. Phys. Lett.* 214, 34, (1993).
- M. Ehbrecht, H. Ferkel, V. V. Smirnov, O. M. Stelmakh, W. Zhang, and F. Huisken, *Rev. Sci. Instrum.* 66, 3833 (1995).
- M. Ehbrecht and F. Huisken, *Phys. Rev. B* 59, 2975, (1999).
- J. M. Schoenung, *Am. Ceram. Soc. Bull.* 70, 112 (1991).
- M. Cauchetier, O. Croix, N. Herlin, and M. Luce, *J. Am. Ceram. Soc.* 77, 993 (1994).
- M. Suzuki, Y. Nakata, T. Okutani, and A. Kato, *J. Mater. Sci.* 27, 6091 (1992).
- R. A. Bauer, R. Smulders, J. G. M. Becht, P. J. van der Put, and J. Schoonman, *J. Am. Ceram. Soc.* 72, 1301 (1989).
- T. Xiao, P. Strutt, and K. Gonsalves, *Mater. Res. Soc. Symp. Proc.* 206, 557 (1991).
- G. W. Rice, *J. Am. Ceram. Soc.* 69, C183 (1986).
- Y.-L. Li, Y. Liang, F. Zheng, and Z.-Q. Hu, *Mater. Sci. Eng. A* 174, L23 (1994).
- K. E. Gonsalves, T. D. Xiao, and P. R. Strutt, *Indian J. Technol.* 31, 436 (1993).
- K. E. Gonsalves, P. R. Strutt, T. D. Xiao, and P. G. Klemens, *J. Mater. Sci.* 27, 3231 (1992).
- M. Cauchetier and M. Luce, Patent Commissariat à l'Energie Atomique, Process and device for the manufacture of ultrafine inorganic powders by laser aerosol coupling, FR 2677558, 18 Dec. 1992.
- M. Luce, N. Herlin, E. Musset, and M. Cauchetier, *Nanostruct. Mater.* 4, 403 (1994).
- M. Cauchetier, O. Croix, and M. Luce, *Adv. Ceram. Mater.* 3, 548 (1988).
- L. Garifo, *Laser Focus World* 30 (1995).
- X. Bi, S. Kumar, C. Horne, B. Chaloner-Gill, and R. Mosso, Asia-Pacific Optical Conference, Beijing, China, 12–16 November 2001.
- Z. Pan, H. Li, and L. Zhang, *J. Mater. Res.* 13, 1996 (1998).
- P. R. Buerki, T. Troxler, and S. Leutwyler, *High Temp. Sci.* 27, 323 (1990).
- M. Cauchetier, O. Croix, M. Luce, M. Michon, J. Paris, and S. Tistchenko, *Ceram. Int.* 13, 13 (1987).
- R. A. Marra and J. S. Haggerty, *J. Am. Ceram. Soc.* 70, C15 (1987).
- E. Borsella, R. Fantoni, and L. Caneve, in E-MRS Series, vol. 15 (A. Golansky, V. T. Nguyen, and F. Krimmel, Eds.), p. 205. Editions Physique, Les Ulis, France, 1987.
- R. Fantoni, E. Borsella, S. Piccirillo, C. A. Nannetti, R. Ceccato, and S. Enzo, *Appl. Surf. Sci.* 43, 308 (1989).
- S. Mizuta, W. R. Cannon, A. Bleier, and J. S. Haggerty, *Ceram. Bull.* 61, 872 (1982).
- Y.-L. Li, Y. Liang, K.-S. Xiao, F. Zheng, and Z.-Q. Hu, *Nanostruct. Mater.* 5, 1 (1995).
- A. Gheorghiu, C. Senemaud, H. Roulet, G. Dufour, T. Moreno, S. Bodeur, C. Reynaud, M. Cauchetier, and M. Luce, *J. Appl. Phys.* 71, 4118 (1992).
- J. H. Flint and J. S. Haggerty, *Aerosol Sci. Technol.* 13, 72 (1990).
- E. Borsella, S. Botti, M. Cremona, S. Martelli, R. M. Montereali, and A. Nesterenko, *J. Mater. Sci. Lett.* 16, 221 (1997).
- S. Botti, A. Celeste, and R. Coppola, *Appl. Organometal. Chem.* 12, 361 (1998).
- M. Ehbrecht, H. Ferkel, and F. Huisken, *Z. Phys. D* 40, 88 (1997).
- G. Ledoux, O. Guillois, D. Porterat, C. Reynaud, F. Huisken, B. Kohn, and V. Paillard, *Phys. Rev. B* 62, 15942 (2000).
- H. Hofmeister, F. Huisken, and B. Kohn, *Eur. Phys. J. D* 9, 137 (1999).
- M. Aoki, J. H. Flint, and J. S. Haggerty, "Ceramic Transactions, Ceramic Powder Science II," Vol. 1 (G. L. Messing, E. R. Fuller, Jr., and H. Hausner, Eds.), Am. Ceram. Soc., p. 253. Columbus, Ohio, 1988.
- W. Symons and S. C. Danforth, "Advances in Ceramics, Vol. 21, Ceramic Powder Science" (G. L. Messing, K. S. Mazdiyasi, J. W. McCauley, and R. A. Haber, Eds.), p. 249. Am. Ceram. Soc., Westerville, Ohio, 1987.
- E. Borsella, L. Caneve, R. Fantoni, S. Piccirillo, N. Basili, and S. Enzo, *Appl. Surf. Sci.* 36, 213 (1989).
- E. A. Leone, S. Curran, M. E. Kotun, G. Carrasquillo, R. Van-Weeren, and S. C. Danforth, *J. Am. Ceram. Soc.* 79, 513 (1996).
- Y. Liang, Z. Wu, F. Zheng, Q. Xian, and Z. Feng, SPIE, *Int. Soc. Opt. Eng.* 3550, 35 (1998).

59. Y.-L. Li, Y. Liang, K.-S. Xiao, F. Zheng, and Z.-Q. Hu, *Mater. Lett.* 22, 87 (1995).
60. Y. Suyama; R. M. Marra, J. S. Haggerty, and H. K. Bowen, *Am. Ceram. Soc. Bull.* 64, 1356 (1985).
61. F. Curcio, G. Ghiglione, M. Musci, and C. Nanetti, *Appl. Surf. Sci.* 36, 52 (1989).
62. R. Fantoni, E. Borsella, S. Piccirillo, R. Ceccato, and S. Enzo, *J. Mater. Res.* 5, 143 (1990).
63. P. Tougne, H. Hommel, A. P. Legrand, N. Herlin, M. Luce, and M. Cauchetier, *Diamond Relat. Mater.* 2, 486 (1993).
64. J. Najera, J. Vaceres, J. Ferrero, and S. Lane, *J. Eur. Ceram. Soc.* 22, 2371 (2002).
65. P. Quintard, G. Ramis, M. Cauchetier, G. Busca, and V. Lorenzelli, *J. Mol. Struct.* 174, 369 (1988).
66. G. Ramis, P. Quintard, M. Cauchetier, G. Busca, and V. Lorenzelli, *J. Am. Ceram. Soc.* 72, 1692 (1989).
67. F. Huisken, B. Kohn, R. Alexandrescu, S. Cojocaru, G. Ledoux, and C. Reynaud, *J. Nanopart. Res.* 1, 293 (1999).
68. N. Herlin-Boime, F. Ténégal, Z. Bastl, J. Subrt, K. Jursikova, V. Blechta, and J. Pola, *J. Mater. Chem.* 12, 1568 (2002).
69. M. Cauchetier, O. Croix, M. Luce, M. I. Baraton, T. Merle, and P. Quintard, *J. Eur. Ceram. Soc.* 8, 215 (1991).
70. R. Alexandrescu, I. Morjan, E. Borsella, S. Botti, R. Fantoni, T. Dikonimos-Makris, R. Giorgi, and S. Enzo, *J. Mater. Res.* 6, 2442 (1991).
71. E. Borsella, S. Botti, R. Fantoni, R. Alexandrescu, I. Morjan, C. Popescu, T. Dikonimos-Makris, R. Giorgi, and S. Enzo, *J. Mater. Res.* 7, 2257 (1992).
72. M. Suzuki, Y. Maniette, Y. Nakata, and T. Okutani, *J. Am. Ceram. Soc.* 76, 1195 (1993).
73. Z. Dohcevic-Mitrovic and Z. Popovic, *Phys. Stat. Sol. (a)* 181, 347 (2000).
74. E. Borsella, S. Botti, S. Martelli, R. Alexandrescu, M. C. Cesile, A. Nesterenko, R. Giorgi, S. Turtu, and G. Zappa, *Silicates Ind.* 62, 3 (1997).
75. F. Wakai, Y. Kodama, S. Sakaguchi, N. Murayama, K. Isaki, and K. Niihara, *Nature* 344, 421 (1990).
76. R. Giorgi, S. Martelli, S. Turtu, G. Zappa, E. Borsella, and S. Botti, *Surf. Interface Anal.* 22, 248 (1994).
77. M. Mayne, Ph.D. thesis, Limoges University, May 1997, 97LIMO0021; <http://thesenet.abes.fr>.
78. E. Borsella, S. Botti, R. Alexandrescu, I. Morjan, T. Dikonimos-Makris, R. Giorgi, and S. Martelli, *Mater. Sci. Eng. A* 168, 177 (1993).
79. M. Driss-Khodja, A. Gheorghiu, G. Dufour, H. Roulet, C. Senemaud, and M. Cauchetier, *Phys. Rev. B* 53, 4287 (1996).
80. M. Suzuki, Y. Hasegawa, M. Aizawa, Y. Nakata, and T. Okutani, *J. Am. Ceram. Soc.* 78, 83 (1995).
81. Z. Dohcevic, B. Matovic, S. Boskovic, and Z. Popovic, *Philos. Mag. A* 82, 93 (2002).
82. Y.-L. Li, Y. Liang, F. Zheng, K.-S. Xiao, Z.-Q. Hu, and T. Shun, *J. Mater. Sci. Lett.* 14, 713 (1995).
83. A. Müller, N. Herlin-Boime, F. Ténégal, X. Armand, F. Berger, A. M. Flank, R. Dez, K. Müller, J. Bill, and F. Aldinger, *J. Eur. Ceram. Soc.* 23, 37 (2003).
84. N. Herlin, O. Croix, M. Cauchetier, M. Luce, and E. Musset, *J. Phys. IV* 3, 1481 (1993).
85. N. Herlin, M. Luce, E. Musset, and M. Cauchetier, *J. Eur. Ceram. Soc.* 13, 285 (1994).
86. E. Musset, Ph.D. Thesis, Paris-Sud Orsay University, Nov. 1995, 95PA112537, <http://thesenet.abes.fr>.
87. A. Gheorghiu, G. Dufour, C. Senemaud, N. Herlin, E. Musset, M. Cauchetier, and X. Armand, *J. Phys. III* 7, 529 (1997).
88. E. Musset, M. Cauchetier, N. Herlin, M. Luce, A. Gheorghiu, G. Dufour, H. Roulet, and C. Sénémaud, *J. High Temp. Chem. Proc.* 3, 535 (1994).
89. F. Ténégal, A. M. Flank, and N. Herlin, *Phys. Rev. B* 54, 12029 (1996).
90. F. Ténégal, A. M. Flank, M. Cauchetier, and N. Herlin, *Nucl. Instrum. Methods Phys. Res. B* 133, 77 (1997).
91. R. Dez, F. Ténégal, C. Reynaud, M. Mayne, X. Armand, and N. Herlin-Boime, *J. Eur. Ceram. Soc.* 22, 2969 (2002).
92. M. Cauchetier, X. Armand, N. Herlin, M. Mayne, and E. Lefevre, *J. Mater. Sci.* 34, 1 (1999).
93. F. Ténégal, A. Gheorghiu de la Rocque, G. Dufour, C. Sénémaud, M. Mayne, N. Herlin-Boime, X. Armand, and M. Cauchetier, *J. Appl. Phys.* 87, 7864 (2000).
94. X. Armand, N. Herlin-Boime, M. Mayne, and M. Cauchetier, Eds., "European Ceramic Society, Sixth Conference and Exhibition of the European Ceramic Society, Extended Abstracts," Vol. 2. Brighton, 1999, pp. 199–200.
95. P. R. Buerki and S. Leutwyler, *J. Appl. Phys.* 69, 3739 (1991).
96. P. R. Buerki and S. Leutwyler, *Diamond Relat. Mater.* 2, 174 (1993).
97. P. R. Buerki and S. Leutwyler, *Nanostruct. Mater.* 4, 577 (1994).
98. M. Schnaiter, T. Henning, H. Mutschke, B. Kohn, M. Ehbrecht, and F. Huisken, *Astrophys. J.* 519, 687 (1999).
99. X. Bi, M. Jagtoyen, M. Endo, K. Das Chowdury, K. Ochoa, F. Derbyshire, M. Dresselhaus, and P. Eklund, *J. Mater. Res.* 10, 2875 (1995).
100. N. Herlin, I. Bohn, C. Reynaud, M. Cauchetier, A. Galvez, and J. N. Rouzaud, *Astron. Astrophys.* 330, 1127 (1998).
101. A. Galvez, C. Clinard, J. N. Rouzaud, N. Herlin-Boime, and C. Reynaud, *Carbon* 40, 2775 (2002).
102. C. Reynaud, O. Guillois, N. Herlin-Boime, J. N. Rouzaud, A. Galvez, C. Clinard, E. Balanzat, and J. M. Ramillon, *Spectrochim. Acta A* 57, 797 (2001).
103. X. Armand, N. Herlin, I. Voicu, and M. Cauchetier, *J. Phys. Chem. Solids* 58, 1853 (1997).
104. I. Voicu, X. Armand, M. Cauchetier, N. Herlin, and S. Bourcier, *Chem. Phys. Lett.* 256, 261 (1996).
105. R. Alexandrescu, X. Armand, M. Cauchetier, N. Herlin, S. Petcu, and I. Voicu, *Carbon* 36, 1285 (1998).
106. F. Ténégal, S. Petcu, N. Herlin-Boime, X. Armand, M. Mayne, and C. Reynaud, *Chem. Phys. Lett.* 335, 155 (2001).
107. F. Ténégal, I. Voicu, X. Armand, N. Herlin-Boime, and C. Reynaud, submitted for publication.
108. R. Alexandrescu, A. Crunteanu, I. Morjan, S. Petcu, I. Voicu, L. Diamandescu, X. Armand, N. Herlin-Boime, M. Mayne, and C. Reynaud, *Proc. SPIE, Int. Soc. Opt. Eng.* 4430, 196 (2001).
109. R. Alexandrescu, F. Huisken, G. Pugna, A. Crunteanu, S. Petcu, S. Cojocaru, R. Cireasa, and I. Morjan, *Appl. Phys. A* 65, 207 (1997).
110. R. Alexandrescu, S. Cojocaru, A. Crunteanu, S. Petcu, R. Cireasa, I. Voicu, I. Morjan, D. Fatu, and F. Huisken, *Carbon* 36, 795 (1998).
111. R. Alexandrescu; E. Borsella, S. Botti, M. C. Cesile, S. Martelli, R. Giorgi, S. Turtu, and G. Zappa, *J. Mater. Sci.* 32, 5629 (1997).
112. R. Alexandrescu, S. Cojocaru, A. Crunteanu, I. Morjan, I. Voicu, L. Diamandescu, F. Vasiliu, F. Huisken, and B. Kohn, *J. Phys. IV* 9, 537 (1999).
113. L. Bourgeois, G. Barbier, J. C. Vigiú, N. Herlin, and M. Cauchetier, "Fourth Euro-Ceramics," Vol. 1, pp. 225–232. Faenza Editrice, Faenza, 1995.
114. A. K. Knudsen, *Adv. Ceram.*, 21, 237 (1987).
115. M. I. Baraton, L. Boulanger, M. Cauchetier, V. Lorenzelli, M. Luce, T. Merle, P. Quintard, and Y. H. Zhou, *J. Eur. Ceram. Soc.* 13, 371 (1994).
116. L. Boulanger, B. Andriot, M. Cauchetier, and F. Willaime, *Chem. Phys. Lett.* 234, 227 (1995).
117. J. D. Casey and J. S. Haggerty, *J. Mater. Sci.* 22, 737 (1987).
118. A. K. Knudsen, Process for the preparation of submicron-sized titanium diboride, U.S. Patent 4, 689, 129, 1987.
119. G. W. Rice and R. L. Woodin, *J. Am. Ceram. Soc.* 71, C181 (1988).

120. A. Gupta, G. A. West, and J. P. Donlan, *Proc. SPIE, Laser Assisted Deposition, Etching, Doping* 458, 94 (1984).
121. K. M. Khokhlov, D. V. Kolmykov, N. N. Kononov, G. P. Kuz'min, S. N. Polyakov, A. M. Prokhorov, N. A. Sulimov, and O. V. Tikhonovitch, *Laser Phys.* 8, 1070 (1998).
122. Y. Kizaki, T. Kandori, and Y. Fujitani, *Jpn. J. Appl. Phys.* 24, 800 (1985).
123. R. Fantoni, E. Borsella, S. Piccirillo, and S. Enzo, *Proc. SPIE, Int. Soc. Opt. Eng.* 1279, 77 (1990).
124. Y.-L. Li, Y. Liang, F. Zheng, and Z.-Q. Hu, *J. Am. Ceram. Soc.* 77, 1662 (1994).
125. M. Mayne, X. Armand, M. Cauchetier, B. Doucey, D. Bahloul-Hourlier, and P. Goursat, *Advances in Science and Technology (Faenza, Italy), 14(Ceramics: Getting into the 2000s, Pt. B)*, in "Proceedings of the 9th CIMTEC" (P. Vincenzini, Ed.), Techna Srl, p. 211, 1999.
126. J. Förster, M. von Hoesslin, J. H. Schäfer, J. Uhlenbusch, and W. Viöl, "Proceedings of the 10th International Symposium on Plasma Chemistry" (U. Ehlemann, H. G. Lergon, and K. Wiesemann, Eds.), Vol. 1, pp. 1–6. FRG, 1991.
127. H. Martinengo, E. Musset, N. Herlin, X. Armand, M. Luce, and M. Cauchetier, *Silicates Ind.* 61, 9 (1996).
128. N. Herlin, X. Armand, E. Musset, H. Martinengo, M. Luce, and M. Cauchetier, *J. Eur. Ceram. Soc.* 16, 1063 (1996).
129. M. Luce, O. Croix, Y. H. Zhou, M. Cauchetier, M. Sapin, and L. Boulanger, "Euro-Ceramics II," Vol. 1, p. 233. Deutsche Keramische Gesellschaft, Köln, 1993.
130. M. Okuyama, G. Garvey, T. Ring, and J. S. Haggerty, *J. Am. Ceram. Soc.* 72, 1918 (1989).
131. R. Zhou, Y. Jiang, Y. Liang, F. Zheng, and Y. Chen, *Ceram. Int.* 28, 847 (2002).
132. K. Nilsen, S. Danforth, and H. Wautier, "Advances in Ceramics, Vol. 21, Ceramic Powder Science," P. 538. *Am. Ceram. Soc.*, 1987.
133. R. Zhou, Y. Chen, Y. Liang, F. Zheng, and J. Li, *Ceram. Int.* 28, 705 (2002).
134. M. Mayne, D. Bahloul-Hourlier, B. Doucey, and P. Goursat, "Ceramic-Ceramic Composites IV, 4th Int. Conference on Ceramic Composites" (A. Leriche, V. Lardot, D. Libert, and I. Urbain, Eds.), p. 101. *Silicates Industriels*, 1997.
135. Y. Chen, Y. Liang, F. Zheng, R. Zhu, and Z. Feng, *Ceram. Int.* 27, 73 (2001).
136. L. S. Cerovic, S. K. Milonjic, D. Bahloul-Hourlier, and D. M. Kicevic, *Mater. Sci. Forum* 352, 97 (2000).
137. R. Vassen and D. Stöver, *Mater. Sci. Eng. A* 301, 59 (2001).
138. S. Charpentier, A. Kassiba, S. Fusil, X. Armand, M. Cauchetier, J. C. Fayet, and J. Emery, *Appl. Magn. Reson.* 12, 255 (1997).
139. S. Charpentier, A. Kassiba, J. Emery, and M. Cauchetier, *J. Phys. Condensed Matter* 11, 4887 (1999).
140. S. Charpentier, A. Kassiba, A. Bulou, M. Monthieux, and M. Cauchetier, *Eur. Phys. J. Appl. Phys.* 8, 111 (1999).
141. A. Kassiba, M. Tabellout, S. Charpentier, N. Herlin, and J. R. Emery, *Solid State Commun.* 115, 389 (2000).
142. R. Vassen and D. Stöver, *Powder Technol.* 72, 223 (1992).
143. R. Vassen, A. Kaiser, J. Förster, H. P. Buchkremer, and D. Stöver, *J. Mater. Sci.* 31, 3623 (1996).
144. O. Croix, M. Gounot, P. Bergez, M. Luce, and M. Cauchetier, "Mater. Sci. Monogr. 66B(Ceram. Today—Tomorrow's Ceram., Pt. B)," p. 1447. Elsevier Science, Amsterdam, 1991.
145. R. Vassen and D. Stöver, *J. Am. Ceram. Soc.* 79, 1699 (1996).
146. R. Vassen and D. Stöver, *J. Am. Ceram. Soc.* 82, 2585 (1999).
147. A. Donato, E. Borsella, S. Botti, S. Martelli, C. A. Nannetti, M. R. Mancini, and I. Morjan, *J. Nucl. Mater.* 233–237A, 814 (1996).
148. A. Yehia, R. Vassen, R. Duwe, and D. Stöver, *J. Nucl. Mater.* 233–237B, 1266 (1996).
149. D. Scitti, J. Vicens, and A. Bellosi, *J. Mater. Sci.* 37, 3747 (2002).
150. M. Wilhem and W. Wruss, *Ceramic Forum Int.* 75, 40 (1998).
151. S. C. Danforth and J. S. Haggerty, *J. Am. Ceram. Soc.* 66, C58 (1983).
152. J. M. Lihmann, J. S. Haggerty, M. Luce, O. Croix, and M. Cauchetier, *Matér. Mécanique Electricité* 422, 32 (1987).
153. J. Karch, R. Birringer, and H. Gleiter, *Nature* 330, 556 (1987).
154. A. Pechenik, G. Piermarini, and S. Danforth, *J. Am. Ceram. Soc.* 75, 3283 (1992).
155. A. Pechenik, G. Piermarini, and S. Danforth, *Nanostruct. Mater.* 2, 479 (1993).
156. W. Symons, The Effect of Oxygen on the Hot Isostatic Pressing Behavior of Laser Synthesized Silicon Nitride, Ph. D. Thesis, Rutgers University, September 1989.
157. P. Lu, S. C. Danforth and W. T. Symons, *J. Mater. Sci.* 28, 4217 (1993).
158. S. C. Danforth, *Nanostruct. Mater.* 1, 197 (1992).
159. Y.-L. Li, Y. Liang, F. Zheng, X. Ma, and S. Cui, *J. Mater. Res.* 15, 988 (2000).
160. K. Niihara, *J. Ceram. Soc. Jpn.* 99, 974 (1991).
161. Z. Lences, A. Bellosi, and F. Monteverde, *Mater. Chem. Phys.* 41, 46 (1995).
162. R. Giorgi, S. Turtu, G. Zappa, E. Borsella, S. Botti, M. Cesile, and S. Martelli, *Appl. Surf. Sci.* 93, 101 (1996).
163. M. Mayne, D. Bahloul-Hourlier, B. Doucey, P. Goursat, M. Cauchetier, and N. Herlin, *J. Eur. Ceram. Soc.* 18, 1187 (1998).
164. Y.-L. Li, Y. Liang, and Z.-Q. Hu, *Nanostruct. Mater.* 4, 857 (1994).
165. F. Ténégal, B. Bouchet, R. Bellisent, N. Herlin, M. Cauchetier, and J. Dixmier, *Philos. Mag. A* 78, 803 (1998).
166. C. Sénémaud, A. Gheorghiu-de-la-Rocque, G. Dufour, and N. Herlin, *J. Appl. Phys.* 84, 4945 (1998).
167. Y. El Kortobi, H. Sfihi, A. P. Legrand, E. Musset, N. Herlin, and M. Cauchetier, *Colloids Surf. A* 115, 319 (1996).
168. A. Kaiser, R. Vassen, D. Stöver, H. Buchkremer, and J. Förster, *J. Uhlenbusch, Nanostruct. Mater.* 6, 917 (1995).
169. A. Kaiser, R. Vassen, D. Stöver, H. Buchkremer, and W. Kesternich, *Silicates Ind.* 5–6, 111 (1996).
170. A. Kaiser, R. Vassen, D. Stöver, and H. P. Buchkremer, *Nanostruct. Mater.* 8, 489 (1997).
171. A. Bellosi, *Mater. Sci. Forum, Trans. Tech. Publ.* 195, 79 (1995).
172. A. Bellosi, F. Monteverde, S. Botti, and S. Martelli, *Mater. Sci. Forum, Trans. Tech. Publ.* 235–238, 255 (1997).
173. M. Mayne, D. Bahloul-Hourlier, P. Goursat, and J. L. Besson, *C. R. Acad. Sci. Paris* 320, 433 (1995).
174. M. Mayne, D. Bahloul-Hourlier, P. Goursat, and J. L. Besson, Trends in emerging materials and applications, in "4th Euro Ceramics, Basic Science" (A. Bellosi, Ed.), Vol. 4, p. 75, 1995.
175. F. Ténégal, A. Gheorghiu de la Rocque, G. Dufour, C. Sénémaud, B. Doucey, D. Bahloul-Hourlier, P. Goursat, M. Mayne, and M. Cauchetier, *J. Electron Spectrosc. Relat. Phenomena* 109, 241 (2000).
176. J. L. Besson, M. Mayne, D. Bahloul-Hourlier, and P. Goursat, *J. Eur. Ceram. Soc.* 18, 1893 (1998).
177. M. Mayne, T. Rouxel, D. Bahloul-Hourlier, and J. L. Besson, *J. Eur. Ceram. Soc.* 18, 1985 (1998).
178. J. L. Besson, B. Doucey, S. Lucas, D. Bahloul-Hourlier, and P. Goursat, SiCN nanocomposite: creep behaviour, *J. Eur. Ceram. Soc.* 21, 959 (2001).
179. B. Doucey, D. Bahloul-Hourlier, J. L. Besson, P. Goursat, "Key Engineering Materials," 206–213, (Pt. 2, Euro Ceramics VII, 2002), pp. 1081–1084.
180. L. T. Canham, *Appl. Phys. Lett.* 57, 1046 (1990).
181. V. Lehmann and U. Gösele, *Appl. Phys. Lett.* 58, 856 (1991).
182. E. Borsella, S. Botti, M. C. Cesile, P. E. Di-Nunzio, S. Martelli, and A. Nesterenko, *Mater. Sci. Forum* 195, 37 (1995).
183. W. Vogel, S. Botti, and S. Martelli, *J. Mater. Sci. Lett.* 17, 527 (1998).
184. S. Botti, R. Coppola, F. Gourbilleau, and R. Rizk, *J. Appl. Phys.* 88, 3396 (2000).

185. M. Ehbrecht, H. Ferkel, F. Huisken, L. Holz, Y. N. Polivanov, V. V. Smirnov, O. M. Stelmakh, and R. Schmidt, *J. Appl. Phys.* 78, 5302 (1995).
186. G. Ledoux, J. Gong, and F. Huisken, *Appl. Phys. Lett.* 79, 4028 (2001).
187. M. Ehbrecht, B. Kohn, F. Huisken, M. A. Laguna, and V. Paillard, *Phys. Rev. B* 56, 6958 (1997).
188. C. Delerue, G. Allan, and M. Lannoo, *Phys. Rev. B* 48, 11024 (1993).
189. V. Paillard, P. Puech, M. A. Laguna, R. Carles, B. Kohn, and F. Huisken, *J. Appl. Phys.* 86, 1921 (1999).
190. G. Ledoux, J. Gong, F. Huisken, O. Guillois, and C. Reynaud, *Appl. Phys. Lett.* 80, 4834 (2002).
191. F. Huisken, G. Ledoux, O. Guillois, and C. Reynaud, *Adv. Mater.* 14, 1861 (2002).
192. D. Amans, S. Callard, A. Gagnaire, J. Joseph, G. Ledoux, and F. Huisken, *J. Appl. Phys.* 93, 4173 (2003).
193. G. Ledoux, M. Ehbrecht, O. Guillois, F. Huisken, B. Kohn, M. A. Laguna, I. Nenner, V. Paillard, R. Papoular, D. Porterat, and C. Reynaud, *Astron. Astrophys.* 333, L39 (1998).
194. G. Ledoux, O. Guillois, F. Huisken, B. Kohn, D. Porterat, and C. Reynaud, *Astron. Astrophys.* 377, 707 (2001).
195. F. Huisken, B. Kohn, and V. Paillard, *Appl. Phys. Lett.* 74, 3776 (1999).
196. G. Ledoux, D. Amans, J. Gong, F. Huisken, F. Cichos, and J. Martin, *Mater. Sci. Eng. C* 19, 215 (2002).
197. D. Amans, S. Callard, A. Gagnaire, J. Joseph, G. Ledoux, and F. Huisken, *Proc. SPIE*, 4808 (2002).
198. M. L. Terranova, S. Piccirillo, V. Sessa, S. Botti, and M. Rossi, *Appl. Phys. Lett.* 74, 3146 (1999).
199. E. Borsella, M. Falconieri, S. Botti, S. Martelli, F. Bignoli, L. Costa, S. Grandi, L. Sangaletti, B. Allieri, and L. Deper, *Mater. Sci. Eng. B* 79, 55 (2001).
200. I. V. Kityk, J. Boucle, and A. Kassiba, *Nonlinear Opt.* 28, 291 (2001).
201. J. Boucle, A. Kassiba, J. Emery, I. V. Kityk, M. Makowska-Janusik, J. Sanetra, N. Herlin-Boime, and M. Mayne, *Phys. Lett. A* 302, 196 (2002).
202. A. Kassiba, M. Makowska-Janusik, J. Boucle, J. F. Bardeau, N. Herlin, M. Mayne, and X. Armand, *Diamond Relat. Mater.* 11, 1243 (2002).
203. A. Kassiba, M. Makowska-Janusik, J. Boucle, J. F. Bardeau, A. Bulou, and N. Herlin-Boime, *Phys. Rev. B* 66, 155317 (2002).

Synthesis of Inorganic Nanowires and Nanotubes

S. Sharma, H. Li, H. Chandrasekaran, R. C. Mani, M. K. Sunkara

University of Louisville, Louisville, Kentucky, USA

CONTENTS

1. Introduction
 2. Elemental Whisker Synthesis—History
 3. VLS and Related Mechanisms
 4. Nanowire Size Control using Cluster Size
 5. Multiple Nanometer-Scale Nuclei Formation
 6. Synthesis of Whiskers and Nanowires of Inorganic Compounds
 7. Synthesis of Metal Whiskers and Nanowires
 8. Synthesis of Inorganic Nanotubes
 9. Summary
- Glossary
References

1. INTRODUCTION

The relentless pursuit to achieve faster computation speeds has driven the miniaturization of electronic devices to date. Further reduction in the electronic device size requires the creation of nanometer-scale structures [1]. However, the current optical lithography based technology is fast reaching its physical and processing limitations, and will eventually fail to yield nanostructures smaller than 50 nm. This has necessitated the exploration of new routes for creation of bulk amounts of molecular and nanoscale materials, to directly yield individual device components with sizes less than 50 nm. In this regard, two- and three-dimensional rational assemblies of bulk-synthesized nanostructures could present a new route for increasing the packing densities. Similar strategies could be applied to build 3D assemblies for engineering photonic crystals and crystalline and porous matrices for catalysts and sensors.

The nanowires, also known as quasi-1D structures, become interesting in terms of their properties when their

diameter is reduced below a certain length scale characterized by the Bohr exciton size, when the separation distance between electron-hole pair reduces and electronic confinement takes place. This is also referred to as quantum confinement, and is of great interest in studying the excitonic behavior of low-dimensional solids for its effect on electron transport, band structure, and optical properties. In fact, the electronic and optical properties of these low-dimensional solids differ from those at macroscopic scale [2–4]. For example, Si in bulk is an indirect energy bandgap material. When its size is reduced below 5 nm, the non-radiative recombination rate reduces due to quantum confinement, enabling Si to emit visible luminescence at room temperature [2]. Theoretical computations predicted that Si exhibits a direct energy bandgap at nanoscale and the energy bandgap increases with an inverse relationship with the nanocluster size ($\propto d^{1.3}$ for wires) [3]. This quantum confinement effect was predicted to be the strongest for the wire shape compared to films and dots [3].

In addition, the structure of inorganic solids at nanometer scale could be different from its bulk structure. For example, carbon exhibits fullerene, and silicon is predicted to exhibit stable clathrate type structure at nanometer scale. Similar existence of new phases (or structures) for several other inorganic materials cannot be ruled out and is still unknown. Systematic efforts to discover these phases for inorganic solids have led to materials synthesis efforts at nanoscale, followed by thorough structural investigations. In the past, the synthesis efforts for micron-scale whiskers were motivated by superior mechanical properties and applications in composites [5, 6]. However, these techniques were never focused on tight size control. The current motivation in determining the size-constraint effects on both structure and properties for a variety of inorganic materials at nanometer scale has prompted intense research in bulk synthesis methodologies over the last few years. In this chapter, we have tried to provide a comprehensive review on synthesis methods for one-dimensional nanostructures (less than 100 nm in diameter) of various elements and inorganic compounds, along with a historical perspective on synthesis of

the respective micron-scale whiskers. This review intentionally avoids the vast amount of literature that is available on carbon nanotube structures and their synthesis methods, lithography, and template-based techniques for inorganic nanowires. This chapter also discusses the popular mechanisms used to explain the one-dimensional growth of elements that can be extended to compounds in general. Considering the vast, at times redundant, literature on synthesis of various inorganic nanowires and nanotubes, we have summarized and compiled only the notable reports for synthesis of nanowires and nanotubes and the resulting characteristics in Table 1.

2. ELEMENTAL WHISKER SYNTHESIS—HISTORY

The growth of one-dimensional crystals, termed whiskers, was of great interest as early as 1948 [7], due to their better mechanical characteristics compared to the bulk materials [4, 5]. In the 1940s, Frank and his co-workers introduced a spiral growth mechanism to explain enhanced growth rates on certain facets, which were otherwise unexplainable with experimentally attainable vapor-phase solute supersaturation [8]. In this mechanism, the spiral resulting from screw dislocations on certain facets of crystals perpetually generates new layers without the need for new step nucleation events. The enhanced growth in this direction typically leads to the formation of elongated crystals. The basic steps in this vapor-solid (VS) mechanism for one-dimensional growth of crystals, as shown in Figure 1a are (1) adsorption of gas-phase species on the side faces, (2) appearance of screw dislocations at the growing end of the crystal, resulting in perpetual generation of growth steps in the plane perpendicular to the growth direction of the crystal, (3) rapid surface diffusion of the growth species followed by attachment at the whisker tip. Whisker growth of several materials was explained based on this model [8–14]. The growth of mercury whiskers in a field emission tube by an evaporative technique was explained on the basis of this growth model [13]. The spiral growth mechanism is also typically observed in chemical vapor deposition of diamond, and leads to elongated crystals as shown in Figure 1b. This growth mode seems to be active in micron-scale whiskers, and to date no reports exist on clear demonstration of such phenomena in nanowire growth of any material. However, one cannot yet reliably reproduce screw dislocations to yield micron-scale whiskers in bulk quantities.

Throughout the 1950s and early 1960s, experimentally observed growth of whiskers was primarily explained by the above VS mechanism. Carbon filaments were grown using catalytic thermal decomposition of carbonaceous gases such as methane, benzene, cyclohexane, acetylene, and carbon monoxide over Fe, Co, and Ni catalyst particles [15–21]. Iron clusters at tips of the filaments were also observed in one report [15]. Hofer et al. also observed the growth of sub-micron-scale carbon filaments during decomposition of carbon monoxide over Ni catalyst particles [19]. It was contemplated that the one-dimensional growth took place due to preferential deposition of carbon on the $\{111\}$ planes of

the Ni catalyst particles. All of these studies failed to recognize the role of catalyst particle for growth of 1D carbon structure.

The first report on the synthesis of true semiconductor whiskers appeared in 1949. Lyon et al. [22] synthesized 250- μm -thick silicon fibers using reduction of SiCl_4 with Zn vapor at 950 °C. The resulting Si fibers were pure and were 1 cm long and 0.25 mm thick. Using a similar reaction, but with diluted SiCl_4 in Ar or H_2 , Johnson and Amick [23] reported synthesis of thinner (1 μm), single-crystalline silicon whiskers. The reaction was carried out in a tube furnace, and the products were collected at the downstream end. Authors contemplated the reason for 1D growth to be spiral dislocations in the whiskers. In 1961, Greiner et al. [24] reported synthesis of silicon ribbons by a chemical vapor transport technique. Silicon pellets were reacted with iodine and hydrogen at 950 °C, and the resulting vapors were transported to the cooler portion of a sealed quartz tube. The growth direction was observed to be $\langle 111 \rangle$. One-dimensional growth was attributed to the presence of structural defects such as twins along the whisker axis. From the reports of whisker growth using catalytic metals, it became apparent that Frank's dislocation-mediated growth mechanism did not hold in all cases.

Wagner and Ellis [25], in a breakthrough report in 1964, identified the vapor-liquid-solid (VLS) growth mechanism for single-crystal whisker growth (Au particle on $\langle 111 \rangle$ Si, 950 °C, SiCl_4/H_2) and provided clear demonstration of one-dimensional crystal growth due to size confinement of the catalytic cluster solvent medium. In this mechanism, as shown in Figure 2, an impurity forms a molten alloy for selective and preferential deposition from the vapor phase. Silicon and germanium whiskers were grown using this mechanism [26–29]. The VLS type growth was also found to be responsible for whiskers found on the lunar surface [30] and in volcanic eruptions [31].

3. VLS AND RELATED MECHANISMS

The VLS mechanism using transition metal clusters [32–34] consists of four steps: (1) diffusion in vapor phase, (2) chemical reaction at the vapor-liquid interface, (3) diffusion in the liquid phase, and (4) crystallization at the solid-liquid interface. The rate-limiting step could be either chemical reaction at the V-L interface [32] or crystallization [34]. The nature of the limiting step could vary depending upon the temperature and the catalytic nature of the liquid alloy. Wang and Fischman [35] also considered surface diffusion of the adsorbed species on the molten alloy droplet at the whisker tip. They concluded that surface diffusion becomes more important for decreasing whisker diameters, decreasing the solubility of the growth species in the liquid phase, and the increasing ratio of surface diffusion coefficient to bulk diffusion coefficient. The conclusion that can be derived from these empirical studies is that the molten metal cluster at the whisker tip acts in two ways: (1) it reduces the activation energy of the chemical reaction taking place at the vapor-liquid interface, and (2) it enhances the sticking coefficient through dissolution [32].

Table 1. Brief experimental conditions for various nanowires and nanotubes synthesized to date and the resulting nanowire/nanotube characteristics.

Inorganic material	Synthesis method with experimental parameters and Ref.	Resulting wire/tube features
<i>Nanowires</i>		
Si	Thermal chemical vapor deposition (CVD): 320–600 °C, SiH ₄ /He, .01–1 Torr, Au film on {111} Si substrates; [36–38]	10–25 nm diam, 0.5–5 μm long, <111> growth direction, bends and kinks
	Thermal CVD: 640–670 °C, SiH ₄ /SiH ₂ Cl ₂ , Ti islands on (100) and (111) Si substrates; [42]	25 nm mean diam, ~1 μm long
	Laser ablation: Si _{0.9} Fe _{0.1} target, Nd-YAG laser, 1200 °C; [39]	6–20 nm diam, 1–30 μm long, <111> growth direction, 1.5–2.5 nm oxide sheath
	Physical evaporation: Si _{0.95} Fe _{0.05} pellet, 1200 °C, 20 h, 100 Torr, flowing Ar; [40]	12–18 nm diam, 10–100 μm long, crystalline, 2 nm oxide sheath
	Laser ablation and physical evaporation: Si/SiO ₂ mixture: 930–1200 °C, 12 h, 500 Torr, Ar atmosphere; [47–49]	15–20 nm diam, >10 μm long, <112> growth direction, >2 nm oxide sheath, stacking faults and micro-twins
	Supercritical solvent (SCS)-based synthesis: diphenylsilane and alkanethiol stabilized gold catalyst nanoclusters dissolved into the supercritical hexane, 500 °C, 200–270 bar; [45]	4–5 nm diam, >1 μm long, <110> and <100> growth directions, 4 nm thick sheath of carbon and oxygen
	Low-melting metal mediated bulk nucleation: large pools of Ga exposed to a SiH ₄ /H ₂ microwave (MW) plasma, 15 min.–3 h, 10–60 Torr, 400–1100 MW power, 300–600 °C; [73]	10–60 nm diam, 10–100 μm long, <100> growth direction, 0–1.5 nm oxide sheath
Ge	Laser ablation: Ge _{0.9} Fe _{0.1} target, Nd-YAG laser, 820 °C; [39]	3–9 nm diam, twinned nanowires
	Solution-based synthesis: reduction of GeCl ₄ and phenyl-GeCl ₃ by Na in alkane solvent, 275 °C, 2–8 days, 100 atm; [44]	7–30 nm diam, up to 10 μm in length, <110> growth direction, stacking faults
	Laser ablation: Ge/GeO ₂ mixture: 830 °C target temperature, 500 Torr, Ar atmosphere; [48]	16–500 nm diam, >10 μm long, [211] growth direction, >3 nm oxide sheath
	SCS-based synthesis: diphenylgermane and tetraethylgermane, alkanethiol stabilized gold catalyst nanoclusters dissolved into the supercritical cyclohexane, 300–450 °C, 38 MPa; [46]	10–150 nm diam, >1 μm long, <110> and <111> growth directions
Indium tin oxide (ITO)	Electron shower/evaporation: 1 × 10 ⁻⁵ Torr, ITO pellet source; [120, 123]	30 nm diam, 600 nm long
α-Al ₂ O ₃	Evaporation: SiO ₂ /Al source, 1300–1500 °C, 2–4 h, flowing Ar; [122]	100 nm to 10 μm diam, >100 μm long, crystalline
GeO ₂	Physical evaporation: Ge/Fe source, 820 °C, 200 Torr, flowing Ar; [124]	15–80 nm diam, >10 μm long, crystalline
	Carbothermal reduction: GeO ₂ /active carbon mixture, 840 °C, flowing N ₂ , 3.5 h; [126]	50–120 nm diam, >100 μm long, crystalline
TiO ₂	Thermal annealing: Ti(OH) ₄ /NaCl mixture, 730–780 °C, 2 h; [152]	10–50 nm diam, >1 μm long, [001] growth direction
Ga ₂ O ₃	Physical evaporation: Ga source, 300 °C, 100 Torr, flowing H ₂ /Ar, 24 h; [138]	10–150 nm diam, >100 μm long, twinned nanowires
	Carbothermal reduction: Ga ₂ O ₃ /C mixture source, 980 °C, 2 h, flowing N ₂ ; [139]	60 nm mean diam, >100 μm long, crystalline
	Arc-discharge: GaN and Ni/Co or Ni/Co/Y mixture pressed into a hole in a graphite anode, 500 Torr, O ₂ /Ar atmosphere; [142]	33 nm mean diam, >100 μm long, [100] growth direction, rough step edges
	Heating a mixture of Ga, SiO ₂ , and Fe ₂ O ₃ in flowing Ar, 1.2 atm, 1200 °C, 2 h; [140]	20–60 nm diam, >1 μm long, crystalline
	Thermal evaporation: GaN powder, 1100 °C, 2 h, 300 Torr, flowing Ar; [141]	Nanobelts 50–300 nm wide, 20–60 nm thick, >1 μm long, [001] or [010] growth direction
	Direct reaction of oxygen and hydrogen plasma with molten gallium: Microwave power of 600–1200 W, 30–60 Torr, 1–12 h, O ₂ /H ₂ mixtures, 400–600 °C; [65]	10–100 nm diam, >100 μm long, [110] growth direction
Sb ₂ O ₃ and Sb ₂ O ₅	Thermal annealing: Sb ₂ O ₃ powder generated by hydrolysis of SbCl ₃ , 350 °C, 1 h, ambient atmosphere; [153]	Sb ₂ O ₃ nanowires 10–100 nm in diam and 5–15 μm long; Sb ₂ O ₅ nanowires 10–50 nm in diam and 5–25 μm long

continued

Table 1. Continued

Inorganic material	Synthesis method with experimental parameters and Ref.	Resulting wire/tube features
MgO	Heating MgCl ₂ powder at 750 °C for 1.5 h in flowing mixture of H ₂ /Ar; [135]	15–50 nm diam, 1–3 μm long, <111> growth direction
	Heating MgB ₂ powder at 800–900 °C in flowing H ₂ /Ar atmosphere; [137]	15–20 nm diam, ~30 μm long, <001> growth direction
ZnO	Heating a mixture of ZnO and graphite to 900–925 °C under flowing argon atmosphere, with Au-coated silicon substrates in the vicinity; [130]	40–70 nm diam, 10–20 μm long, <001> growth direction
	Heating a mixture of Zn and Se at 1100 °C for 10 h, flowing H ₂ /O ₂ /Ar atmosphere, 100 Torr; [132]	30–100 nm diam, >1 μm long, crystalline
	Thermal evaporation: ZnO powder at 1400 °C for 2 h, 300 Torr, flowing Ar; [133]	Nanobelts 50–300 nm wide, 10–30 nm thick, >100 μm long, [0001] and [01–10] growth directions
SnO ₂	Thermal evaporation: SnO ₂ powder at 1350 °C or SnO powder at 1000 °C, 2 h, 300 Torr, flowing Ar; [133]	Nanobelts 50–200 nm wide, width-thickness ratios of 5–10, >1 mm long, [101] growth direction
In ₂ O ₃	Thermal evaporation: In ₂ O ₃ powder at 1400 °C, 2 h, 300 Torr, flowing Ar; [133]	Nanobelts 50–150 nm wide, >100 μm long, <100> growth direction
	A crystalline InP substrate coated with Au film heated under a flowing O ₂ /Ar atmosphere, 1080 °C, 1.5 h; [143]	15–150 nm diam, >10 μm long, [100] growth direction
CdO	Thermal evaporation: CdO powder at 1000 °C, 2 h, 300 Torr, flowing Ar; [126]	Nanobelts 100–500 nm wide, width-thickness ratios greater than 10, >10 μm long, [100] growth direction
Cu ₂ O	Direct oxidation of Cd/Te film: 450 °C, O ₂ /Ar, 2 h; [149]	40–60 nm diam, >10 μm long, [111] growth direction
	Reduction of copper hydroxide: hydrazine hydrate was used as a reducing agent for Cu(OH) ₂ ; [162]	8 nm mean diam, 10–20 μm long, crystalline
β-PbO ₂	Thermal evaporation: PbO powder at 950 °C, 1 h, 300 Torr, flowing Ar; [144]	Nanobelts 50–300 nm wide, 10–30 nm thick, 10–200 μm long, [010] growth direction
α and β-MnO ₂	Hydrothermal reaction: chemical reaction between MnSO ₄ and (NH ₄) ₂ S ₂ O ₈ at 120 °C, 12 h, adding (NH ₄) ₂ SO ₄ to the systems caused α phase to form; [146]	α phase nanowires 5–20 nm in diam, 5–10 μm long, with growth direction along [110]; β phase nanowires 40–100 nm in diam, 2.5–4 μm long, with growth direction along [110]
Mn ₃ O ₄	Solid-state reaction between MnCO ₃ and NaCl at 850 °C, 2 h; [147]	40–80 nm diam, up to 150 μm long, <211> growth direction
NiO	Solid-state reaction between NiCO ₃ and NaCl at 900 °C, 2 h; [148]	30–80 nm diam, >10 μm long, <110> growth direction
Vanadium oxide	Hydrothermal reaction: reaction of HNO ₃ and NH ₄ VO ₃ aqueous solution followed by heating at 180 °C for 5 h; [150]	Mixture of V ₂ O ₅ · 0.3H ₂ O, V ₂ O ₅ · xH ₂ O (0.3 < x < 1.7) and V ₂ O ₅ phases, 20–85 nm wide, 10–80 μm long, [010] growth direction
Cu(OH) ₂	Chemical reaction between CuSO ₄ and NH ₄ OH followed by reaction with NaOH; [154]	8 nm mean diam, >100 μm long, crystalline
GaN	Laser ablation: GaN/Fe target, 250 Torr, NH ₃ , 900 °C; [82]	~10 nm diam, >1 μm long, [100] growth direction
	HFCVD: Ga ₂ O ₃ /C powder, NH ₃ , 200 Torr, 900 °C, 1 h; [83]	5–12 nm diam, >1 μm long, single crystalline
	Direct reaction of Ga with NH ₃ : 825–925 °C, 15 Torr, 3–4 h; [84]	20–150 nm diam, 500 μm long, [2-1-10] growth direction
AlN	Co-heating Al and AlN: 850–950 °C, 0.1 MPa N ₂ , 1 h; [86]	10–50 nm diam, up to 500 μm long
Si ₃ N ₄	Heating a Si/SiO ₂ powder with/without Fe/Ni, N ₂ /NH ₃ /Ar, 1200 °C, 1 h; [85]	10–70 nm diam, >10 μm long, single crystalline
InN	Ammonothermal reduction of Azido[bis-(3-methylamino)propyl]indium at 400–550 °C, 15 min, 8 mTorr; [68]	10–200 nm diam, 10–100 μm long, crystalline
GaAs	Laser ablation: GaAs power and Ga ₂ O ₃ , Si substrate, 800 °C, 300 Torr; [39]	10–120 nm core diam, 2–10 nm outer sheath, up to 10 μm long, [-11-1] growth direction
	Laser ablation: (GaAs) _{0.95} (Au) _{0.05} target, Si substrate, 800–1000 °C, 100–500 Torr; [93]	19 nm mean diam, up to 10 μm long, <111> growth direction
	Metalorganic chemical vapor deposition (MOCVD): TMG and AsH ₃ in H ₂ , 150 Torr, 500 °C, SiO ₂ patterned, Au-covered GaAs substrate; [91]	10–50 nm diam, <111> growth direction

continued

Table 1. Continued

Inorganic material	Synthesis method with experimental parameters and Ref.	Resulting wire/tube features
	Organometallic reactions: 111 °C, hydrocarbon solvent, (t-Bu) ₃ M (M = In, Ga) and EH ₃ (E = As, P) precursors; MeOH, PhSH, Et ₂ NH, and PhCO ₂ H catalysts; [96]	10–100 nm diam, up to 1 μm long, kinked polycrystalline fibers, [111] growth direction
CdS	Physical evaporation: CdS powder produced from CdSO ₄ and Na ₂ S, Ar atmosphere, 1000 °C; [95]	50 nm diam, several μm long, hexagonal CdS wires grown along [101]; 100 nm diam and tens of μm long, fish-bones shape cubic CdS wires grown along [111]
ZnS	Physical evaporation: ZnS powder, Au-coated Si substrate, Ar atmosphere, 900 °C; [94]	30–60 nm diam, several μm long, <110> growth direction
CdE (E = S, Se, Te)	Solvothermal method: CdCl ₂ or Cd + thiosemicarbazide, mixture was ground and put into autoclave filled with En(Ethylenediamine), 170 °C for 14 h; [97]	20–50 nm diam, 200–1300 nm long
CuFeS ₂	Hydrothermal: CuCl, FeCl ₃ · 6H ₂ O (NH ₄) ₂ S, 200–250 °C for 10 h; [98]	20–40 nm diam, several μm long
ZnTe	Solvothermal method: Zn + Te, Hydrazine hydrate as solvent; [99]	30–100 nm diam, 500–1200 nm long
MIn(S,Se) ₂ (M = Cu, Ag)	Solvothermal method: elements or M(S ₂ CNEt ₂) _x , 195 °C, En(Ethylenediamine) as solvent; [100]	3–50 nm diam, 80–450 nm long
NiE ₂ (E = Se, Te)	Solvothermal method: NiCl ₂ + Se/Te, 160–180 °C, ethylenediamine as solvent; [101]	20–35 nm diam, 90–120 nm long
Sn ₄ P ₃	Solvothermal method: SnCl ₂ + Na ₃ P, 120–140 °C, En(ethylenediamine) as solvent; [102]	~20 nm diam, up to 400 nm long
SbSI	Hydrothermal method: SbCl ₃ + (NH ₂) ₂ CS+I ₂ , 180–190 °C in water for 8–10 h; [103]	20–50 nm diam, up to several microns long
CdWO ₄	Hydrothermal method: CdCl ₂ + NaWO ₄ , 130 °C; [104]	20–40 nm diam, 80–280 nm long
Bi ₂ S ₃	Hydrothermal method: Bi(NO ₃) ₃ · 5H ₂ O + Na ₂ S · 9H ₂ O, 100–170 °C for 2–24 h; [105]	10–50 nm diam, 1–5 μm long, [220] growth direction
β-SiC	Hot filament CVD: powder of Si containing Ni, Cr, Fe impurities and graphite source, filament temperature of 2200 °C, 2 h; [164]	10–30 nm diam, <1 μm in length, <100> growth direction
	Laser ablation: SiC target, KrF excimer laser, 300 Torr, 1100 °C, a graphite substrate dipped in saturated iron nitrate was used at the cooler end of the furnace; [166]	80 nm mean diam, with an amorphous SiO _x shell, >10 μm long, <100> growth direction
	Heating graphite substrate, Si ₂ Cl ₆ -CH ₄ -H ₂ -Ar, 1030 °C, Co impurity; [173]	0.1–1 μm diam, >50 μm long, crystalline
	Reaction using SiCl ₄ , CCl ₄ and Na as a metal co-reductant, 9 MPa, 400 °C; [181]	25 nm mean diam, several μm long, crystalline
	Arc-Discharge: SiC rod containing Fe impurity as anode and graphite plate as cathode; [182]	20–60 nm diam, with 5–20 nm inner core of SiC and SiO ₂ outer core, >1 μm long <111> growth direction
	MWCVD: Fe film on a Si substrate, CH ₄ /H ₂ , 40 Torr, 420–550 W MW power; [183]	15 nm mean diam, 1.5–2.1 μm long, [111] growth direction
	Carbothermal reduction: sol-gel derived silica xerogel containing carbon nanoparticles, 1650 °C, 2.5 h; [187]	20–70 nm diam, a central core of 10–30 nm of SiC and an amorphous SiO ₂ sheath, <111> growth direction
	Heating SiO/graphite mixture, 1500 °C, 12 h; [188]	50–80 nm diam SiC-silica biaxial ([211] and [311] growth directions) and coaxial ([111] growth direction) nanowires
	CVD: Fe-catalyzed decomposition of CH ₄ on Si substrate, 1100 °C; [189]	Helical SiC nanowires with diameter of 10–40 nm and helical periodicity of 40–80 nm covered with a uniform 30–60 nm oxide sheath
TiC	Reaction of CNTs with TiO or I ₂ , 1375 °C, 12 h; [185]	2–30 nm diam, 20 μm long, [111] or [110] growth direction
NbC	Reaction of CNTs with Nb+I ₂ , 730 °C, 12 h; [185]	2–30 nm diam, >1 μm long
Fe ₃ C	Reaction of CNTs with FeCl ₃ , 1350 °C, 12 h; [185]	2–30 nm diam, >1 μm long, amorphous
SiC	Reaction of CNTs with Si and I ₂ , 1200 °C; [185]	2–30 nm diam, >1 μm long, [111] growth direction
BC _x	Reaction of B/B ₂ O ₃ /C at 1650 °C; [185]	2–30 nm diam, >1 μm long, amorphous

continued

Table 1. Continued

Inorganic material	Synthesis method with experimental parameters and Ref.	Resulting wire/tube features
B ₄ C	Heating a mixture of B/B ₂ O ₃ /C, 1650 °C; [214]	50 nm mean diam, 10–100 μm long, [021] and [104] growth directions
	Plasma-enhanced CVD: C ₂ B ₁₀ H ₁₂ /Ar, Fe catalyst, 1100–1200 °C, 50 W; [216]	18–150 nm diam, 13 μm long, crystalline
BC	Same method as above; [217]	Nanosprings with 20–30 nm diam, 31–43 nm pitches, along with nanowires of 20–30 nm diam, amorphous
Al ₄ C ₃	Solid-state reaction of Al/C/Li (Li is the catalyst) at less than 780 °C; [215]	5–70 nm diam nanowires grown in [0001] direction, nanoribbons 5–70 nm thick and 20–500 nm wide grown along the [1–100] direction, 10 μm long
TaC	Carbon nanotubes reacted with Ta and small amounts of I ₂ in Ar atmosphere, 780–1100 °C, 48 h; [219]	14 nm mean diam, up to 1 μm long, crystalline
Ag	Solid-liquid arc-discharge method: an Ag electrode in AgNO ₃ solution, the other Ag electrode momentarily brought into contact with the AgNO ₃ solution while 150 V was applied; [231]	5–15 nm diam, up to 100 nm long, amorphous
<i>Nanotubes</i>		
MoS ₂	Gas-phase reaction between MoO _{3-x} and H ₂ S in flowing H ₂ /N ₂ , 800–950 °C, 1–2 h; [236]	Multiwalled, 2.8–60 nm ID, 10–100 nm OD, up to 5 μm long
	Catalyzed transport: C60 added to MoS ₂ powder and heated for 22 days at 1010 K, 10 ⁻³ Pa, 6 K/cm temperature gradient, iodine as the transport agent; [238]	Single-wall, <1 nm diameter, >100 μm long
WS ₂	Annealing W films on quartz substrates at 1000 °C in H ₂ S in a reducing atmosphere; [233]	Multiwalled, 16 nm OD, ~200 nm long, >four layers
Boron nitride	Arc-melting method: YB ₆ powder source on Cu mold, 200 V acceleration voltage, 125 A, 10 s, 0.025 MPa under flowing N ₂ /Ar; [243]	Multiwalled, 4–10 nm OD, 4–10 layers, 4–6 μm long
	Plasma arc discharge: h-BN and W anode, Cu cathode, 650 Torr, He, 30 V, 50–140 A, >3700 K; [240]	Multiwalled, 1–3 nm ID, 6–8 nm OD, 7–9 walls, >200 nm long
	Plasma arc-discharge: HfB ₂ electrodes, 700 mbar, N ₂ , 60 A DC, 20–40 V, ~3650 K; [241]	Multiwalled, 1.2–4 nm ID, 1–6 layers, >200 nm long
	Plasma arc-discharge: B-Ni-Co electrodes, 380 Torr, N ₂ , 60 A DC, 30–45 V; [245]	Double-walled, 2.7 nm mean OD
NiCl ₂	Dehydrating NiCl ₂ · 6H ₂ O, 400 °C under flowing N ₂ for 30 min, followed by 960 °C under flowing Ar for 30 min; [237]	Multiwalled, 70 nm OD, 6 μm long
TiO ₂	Chemical treatment of sol-gel derived TiO ₂ particles with 5–10 M NaOH: 20–110 °C, 20 h; [257]	~8 nm diam, ~100 nm long
Vanadium oxide	Hydrolysis of a mixture of vanadium triisopropoxide and hexadecylamine, followed by hydrothermal reaction at 180 °C for a week; [256]	Multiwalled, 25–35 nm ID, 50–70 nm OD, up to 2 μm long, nominal composition of VO _{2.40} (C ₁₆ H ₃₃ NH ₂) _{0.34}
	Deposition of V ₂ O ₅ on multiwalled carbon nanotubes (CNT), followed by oxidation of inner carbon layers away at 650–675 °C in air; [252]	Multiwalled, 10–50 nm OD, 1 nm wall thickness, <1 μm long
ZrO ₂	Multiwalled CNTs were coated with ZrO ₂ by reaction with Zr(OPr ⁿ) ₄ in Ar atmosphere, followed by carbon removal by oxidation at 973 K for 2 days; [253]	Multiwalled, 28–38 nm ID, 40–50 nm OD, >10 μm long
Ga ₂ O ₃	Direct reaction of oxygen and hydrogen plasma with molten gallium droplets <100 nm in size: microwave power of 600–1200 W, 30–60 Torr, 1–12 h, O ₂ /H ₂ mixtures, 400–600 °C; [258]	2.5–5 nm ID, 5–15 nm OD, >1 μm long
LaC	DC arc evaporation: lanthanum metal-loaded graphite rod in He atmosphere, 20–30 V, 200 A; [254]	6–8 nm ID, 65–95 nm OD, 0.2–1.5 μm long

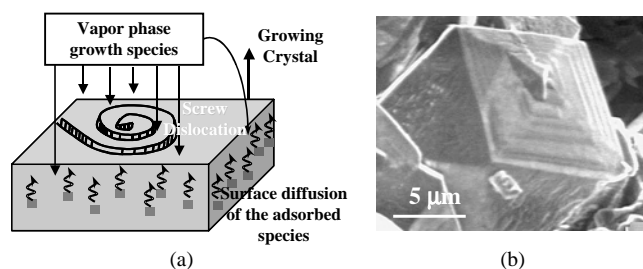


Figure 1. (a) Screw dislocation directed 1D growth of crystals. Vapor-phase species that adsorb on the side faces diffuse rapidly to the growing surface containing the steps resulting due to the screw dislocation. (b) Evidence of a screw dislocation in a vapor-grown columnar diamond crystal. Courtesy: Authors' laboratory.

4. NANOWIRE SIZE CONTROL USING CLUSTER SIZE

The work on whisker growth until the year 1990 focused mainly on micron- to sub-micron-scale diameter whiskers. In the 1990s, the strong interest in nanomaterials, particularly nanowires and nanotubes, intrigued several groups to re-engineer the VLS and VS techniques for synthesizing nanoscale 1D structures of inorganic materials. The first milestone was to generate uniform size distribution of nanometer-scale, transition metal catalyst clusters and to determine ways to disperse them at elevated temperatures. The most popular of these catalysts are gold, iron, and nickel. Westwater and his co-workers [36–38] were the first to report the synthesis of silicon nanowhiskers using a 5-nm-thick gold-film-coated sapphire substrate exposed to silane and Ar mixture at around 335 °C. Upon exposure, the thin gold film converted to nanometer-scale clusters and allowed growth of 15- to 100-nm-thick silicon nanowires. The size of metallic clusters under equilibrium condensation situations is typically on the order of 200 nm. In order to produce uniform size distribution of clusters for sizes less than 200 nm, several nonequilibrium and high energetic condensation processes such as evaporation, laser ablation, and vapor transport were used. Figure 3a and b shows schematics

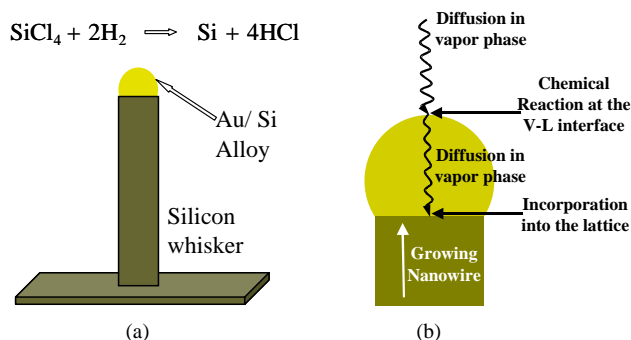


Figure 2. (a) VLS growth mechanism for silicon whiskers using gold as the solvent. Silicon is provided in the gas phase through SiCl_4 over gold cluster supported on a silicon substrate. (b) Schematic depicting various chemical and transport processes taking place in vapor-liquid-solid growth of nanowires: (1) vapor-phase diffusion, (2) chemical reaction at the vapor-liquid interface, (3) liquid-phase diffusion, (4) incorporation into the lattice at the nanowire-liquid interface.

for laser ablation and evaporation laboratory setups, respectively. The physical evaporation system and the vapor transport systems essentially consist of a tube furnace that has a programmed temperature gradient along the length. In most cases, the generated clusters were finally supported on a substrate. In another approach, uniform-sized, molten gold clusters were dispersed in a supercritical fluid medium for increasing the control of size distribution.

Lieber and his co-workers, in a series of papers [39], developed the laser ablation technique with the target composed of a catalyst metal and the material of interest. His group demonstrated the use of catalyst-containing target material for producing nanowires of several inorganic materials including Si, Ge, GaAs, InP, InAs, GaP, and GaN. As shown in Figure 3a (a representation of the typical laser ablation experimental setup), the Si-Fe targets (1) were ablated using a Nd-YAG laser (2) at 1200 °C and the nanowires were deposited downstream on a cold-finger (7). The variables in this method include ablation power, target composition, gas-phase composition, and cold-finger conditions/geometry. The resulting silicon nanowires were found to contain a minimum oxide sheath thickness of 1.5–2.5 nm.

Almost concurrent to the laser ablation method, several groups employed physical evaporation as a way to reduce the catalyst cluster size for synthesizing nanowires. For example, Yu et al. [40] reported silicon nanowire synthesis using physical evaporation of a Si-Fe target (1200 °C, 4 hr, 100 Torr, Ar). The nanowire mass was deposited on the inner walls of the quartz tube. Silicon whiskers were also grown using Au-mediated VLS method vertically on {111} Si substrates for use as atomic force microscopy (AFM) tips [41]. Transition metals other than Fe and Au have also been investigated. Titanium clusters upon reaction with silicon formed titanium silicides that acted as the catalyst for dissolution and subsequent precipitation of silicon in a nanowire form [42]. Ni nanoclusters were used to dissolve Si from underlying silicon substrate to grow amorphous silicon nanowires in a mechanism termed solid-liquid-solid [43].

Both laser ablation and evaporation based techniques typically work under vacuum and primarily utilize gas-phase precursors. Heath and LeGoues demonstrated a liquid solution-based synthesis method [44] for single-crystalline Ge nanowires using sodium in an alkane solvent to reduce GeCl_4 and phenyl- GeCl_3 at elevated temperatures and pressures (275 °C, 2–8 days, 100 atm). The resulting nanowires were 7–30 nm in diameter and up to 10 μm in length. However, a mechanism for one-dimensional crystal growth and the role of sodium were not elaborated. Korgel and his co-workers [45] used supercritical hexane to disperse both the solute material of interest and uniform-sized, alkanethiol stabilized gold catalyst nanoclusters. Figure 3c shows a simplified schematic of the high-pressure reactor used by Korgel's group. For silicon nanowire synthesis, they used silicon precursor, diphenylsilane, dissolved into the supercritical hexane at 500 °C and 200–270 bar pressure. At these temperatures, diphenylsilane decomposes and dissolves into gold clusters to yield silicon nanowires. In another report, Hanrath and Korgel [46] reported synthesis of Ge nanowires using a similar experimental setup at temperatures of 300–500 °C (Fig. 4). Nanowires grown at slightly different temperatures had different growth directions,

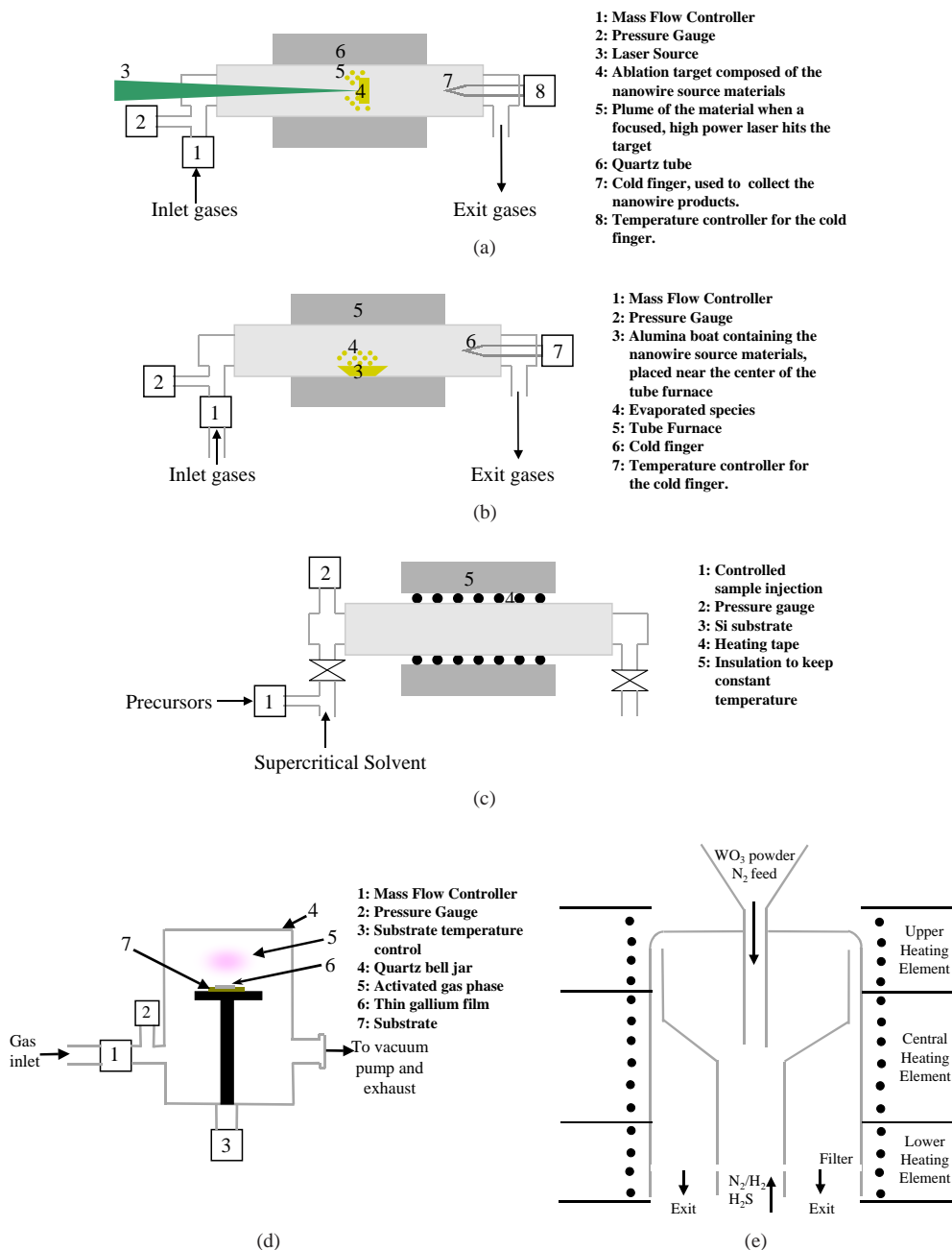


Figure 3. Simplified reactor schematics popularly used for nanowire and nanotubes synthesis using (a) Laser ablation. (b) evaporation: Typically, the nanowire products are collected near the downstream end of the tube furnace, without a specific need for the cold finger. In some cases, nanowires were obtained from the quartz tube inner walls. (c) Supercritical fluids. Courtesy: B. A. Korgel and T. Hanrath, University of Texas, Austin, TX. (d) Activated vapor and low-melting metals: The molten metal film thickness can be arbitrary, ranging from micron to millimeter. (e) Fluidized bed. Courtesy: R. Tenne, Weizmann Institute, Israel.

$\langle 110 \rangle$ or $\langle 111 \rangle$. The growth mechanism is exactly similar to that in the previous VLS techniques except for the fact that the dissolution into molten metal cluster happens from the solution phase rather than the vapor phase, thus giving the name, the solution-liquid-solid (SoLS) method. The supercritical fluid environment offers rapid mass transport of the solute, thus giving much more control on the solution chemistry for the dissolution kinetics and the nanowire growth kinetics. It is not surprising that this method yielded

different growth directions for silicon nanowires by changing the reaction pressure and temperature.

In addition to using catalyst metal particles, micron-scale whiskers were also synthesized using evaporative techniques that used vapor-phase suboxide species as the growth precursors. These reports attributed 1D growth to be according to Frank's screw dislocation based model. Recently, S. T. Lee and his co-workers recognized the oxide cluster-assisted 1D growth. They reported [47] synthesis of silicon

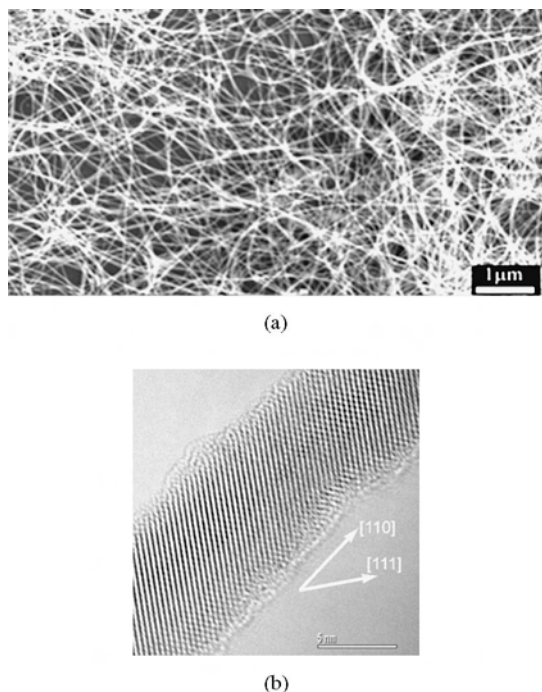


Figure 4. (a) Mass of Ge nanowires synthesized using supercritical fluid-based technique. (b) High-resolution TEM image of a 7-nm-thick Ge nanowire grown along the [110] direction. Micrographs courtesy of B. A. Korgel and T. Hanrath, University of Texas, Austin, TX.

nanowires using a mixture of Si and SiO₂ powder (500 Torr, Ar, 930–1200 °C) and germanium nanowires using a mixture of Ge and GeO₂ [48]. As shown in the schematic in Figure 3b, a quartz chamber with an axial temperature gradient was used to evaporate the source material. The nanowires were deposited either on the inside walls or at the downstream end of the quartz chamber. The generation of gas-phase SiO species and the preferential deposition at the tip due to thick oxide sheath around the growing nanowire were hypothesized to be the main reasons for observed nanowire growth. The resulting nanowires contained substantial oxide sheath and also stacking errors [49, 50]. In addition, in this mechanism, where initial nuclei form upon condensation from the vapor phase, control over the nanowire diameter and diameter distribution is very difficult. Silicon nanoribbons were synthesized using a similar oxide-assisted technique [51], by evaporating SiO powder at 1150 °C, and carrying it to a cooler, downstream end of a tube furnace in 5% H₂/Ar (900 °C) at a total pressure of 0.5 torr. The authors attributed the ribbon growth to lower temperatures and pressures. Pan et al. reported synthesis of semiconducting oxide nanobelts by an evaporation technique [52]. In this technique, evaporation and subsequent chemical vapor transport of metal oxide species from powders resulted in the growth of oxide nanobelts. This technique has been well demonstrated for zinc, tin, indium, cadmium, and gallium oxides. Even though the resulting beltlike morphology is interesting, the growth mechanism is unclear at this time. At the same time, nanobelt morphology is not entirely surprising because similar morphology, that is, micron-scale ribbons, had been reported in whisker literature using a similar technique [24].

The stable configuration of the solid-liquid interface determines the growth direction of the precipitating solid phase [53]. In all the VLS techniques using transition metal clusters, the growth direction for silicon nanowires has been primarily in the $\langle 111 \rangle$ direction. On the other hand, the supercritical SolLS method yielded different growth directions for nanowires such as $\langle 111 \rangle$, $\langle 110 \rangle$, and $\langle 100 \rangle$ directions depending upon the reaction pressure. In the oxide cluster and sheath-assisted techniques, the growth direction was primarily $\langle 211 \rangle$ due to the presence of twins.

A common aspect of all the above techniques is that the nanowire diameter is directly controlled by the cluster size generated either prior to or during the nanowire growth process. This is expected as the transition-metal catalyst clusters or other type of confinement such as suboxide clusters form eutectics with solute material of interest at high concentrations. As an example, Au-Si phase diagram shown in Figure 5a illustrates the eutectic composition of 18.6 at. % Si at 363 °C. The eutectic temperatures limit the minimum temperature for nanowire synthesis using the mentioned processes. In addition, the high eutectic composition expands the molten alloy cluster at higher temperatures, thus making the size of the resulting nanowire larger than the cluster size unevenly depending upon particular conditions. Also, the high eutectic composition of the transition-metal solute alloy limits the maximum solute

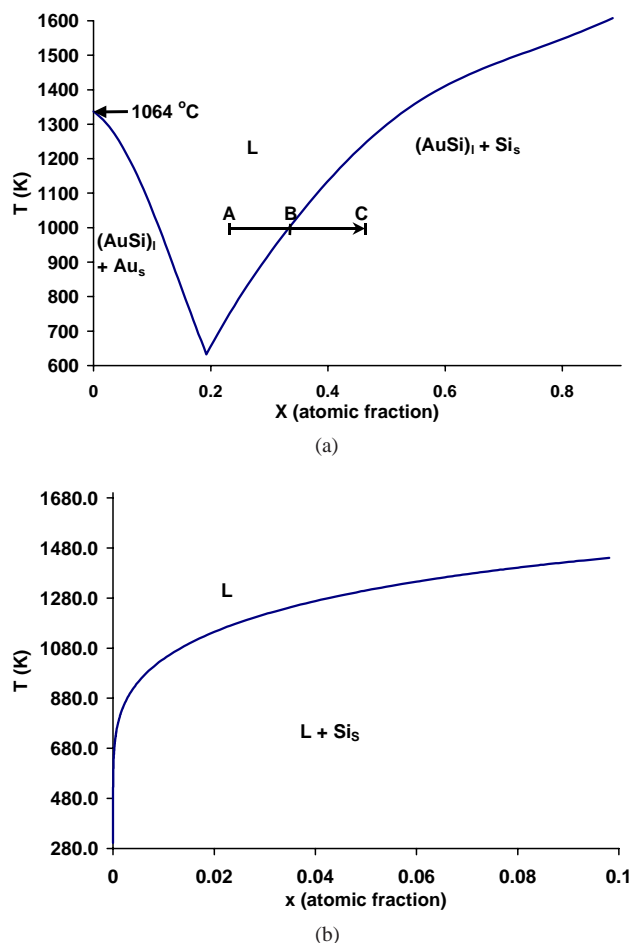


Figure 5. Binary phase diagrams for (a) Au-Si and (b) Ga-Si systems.

supersaturation, necessitating precise control over metal cluster diameter for the uniform diameter distribution of nanowires. There are certain other disadvantages in using high-solubility eutectic systems. For example, nanowires will be extremely useful, if electronic device components can be incorporated directly into individual nanowires. In this regard, attempts have been made to synthesize nanowire superlattices by switching the gas-phase composition during growth using transition metals. These attempts have so far been futile in achieving atomically abrupt junctions along individual nanowires [54–56]. This is expected because of the high retention of solute in the eutectic liquid alloy. In addition, there are no recent attempts or prior reports on metallic nanowire growth using transition-metal catalyst cluster-based VLS synthesis techniques. Recently, core-shell/multishell heterostructures have been generated in nanowires towards building versatile devices [57].

5. MULTIPLE NANOMETER-SCALE NUCLEI FORMATION

The Gibbs' free energy change associated with creation of a spherical nucleus of radius r in a molten metal solvent can be written as

$$\Delta G_T = \Delta G_V \cdot \frac{4}{3} \pi r^3 + \Delta G_S \cdot 4 \pi r^2$$

For the critical nucleus size

$$\frac{\partial}{\partial r} \Delta G_T = 0$$

Therefore

$$r^* = -\frac{2\sigma}{\Delta G_V}$$

where r^* is the critical nucleus radius, σ is the interfacial energy, ΔG_V is the volume free energy driving force (assuming an ideal solution) given by [58]

$$\Delta G_V = -\frac{RT}{\Omega} \ln\left(\frac{C}{C^*}\right)$$

where Ω , C , and C^* represent molar volume, activity coefficients, solute concentration within the liquid alloy and equilibrium concentration, respectively.

Thus, the critical nucleus diameter, d_c , is given by

$$d_c = \frac{4\sigma\Omega}{RT \ln\left(\frac{C}{C^*}\right)}$$

As shown in Figure 5a, in order to isothermally nucleate Si from Au-Si solution, one needs to proceed along the path ABC. Until point B, the dissolved silicon concentration remains less than the equilibrium solubility, making supersaturation, C/C^* , less than unity. A supersaturation of less than 1 will cause the nuclei to dissolve back into the solution. As the Si concentration is further increased along BC, the supersaturation exceeds unity and stable nuclei begin to form. In order to reduce the nuclei size, one needs to achieve increased supersaturation values. In the case of transition-metal-Si systems, such as Au-Si, greater than 40 at. % Si will be needed in an Au pool in order to reduce the nuclei diameters to less than 100 nm (Fig. 6). Multiple

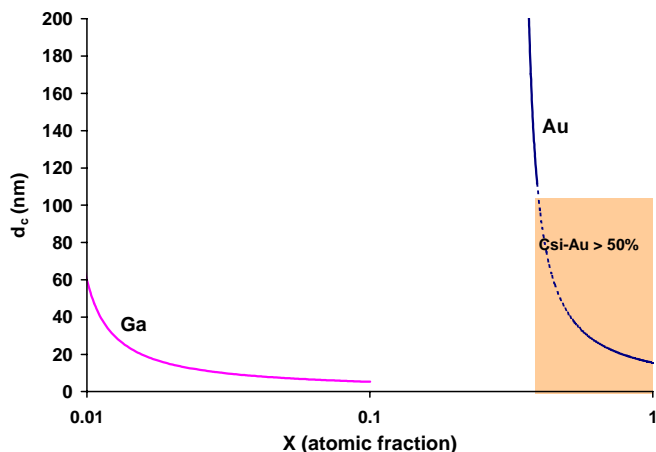


Figure 6. Critical nuclei diameter as a function of the dissolved silicon concentration (at. %) in Ga-Si and Au-Si binary solutions ($T = 1000$ K).

micron-thick silicon whiskers have indeed been grown from a large pool of Au [32]. However, there must be a maximum achievable supersaturation value that could be achieved in the molten metal in order to keep the ideal solution approximation valid. A similar maximum limit has been reported for undercooling in molten melts [59]. In order to satisfy such a requirement of dilute solutions, for modest dissolved Si supersaturations near unity, the nuclei diameter exceeds the molten Au-Si eutectic droplet size at typical conditions [60], causing one nanowire to grow from one Au cluster. The critical nucleus size can be reduced if the solute supersaturation can be increased, which will be possible for metals that form low solubility eutectics with other elements. Gallium, for example [61], forms a eutectic with silicon at about 29 °C with an extremely low silicon fraction of about 10^{-9} (Fig. 5b). At 1000 K, with an arbitrary dissolved silicon concentration of less than 3 at. % in gallium, Eq. (1) yields the critical nucleus diameter to be 10 nm. Figure 6 shows the variation of critical nuclei diameter as a function of dissolved silicon concentration. As can be seen, less than 10 at. % dissolved silicon at 1000 K will result in 5-nm nuclei. These multiple 5-nm nuclei can form in a large pool of gallium, and due to the low solubility and miscibility, can grow out in one dimension. Recently, the authors have demonstrated that the use of low-melting metal melts allows for formation of multiple nanometer-scale nuclei of the solute that gets dissolved from either the vapor phase or from the solid/liquid phases [62–66]. The authors exposed pools of molten metals to activated gas-phase species in a vacuum chamber in order to demonstrate this approach (see Fig. 3d). Since the nanowire diameter is not limited by the metal droplet size, the authors' synthesis technique eliminates the absolute need for creation of nanosized droplets.

In the past, the use of low-melting metals for thermally activated silicon and germanium halides at temperatures below 900 °C was unsuccessful for Si and Ge whiskers [32]. In fact, this study noted that the use of low-melting metals required much higher temperatures than those used for transition-metal catalyst clusters, probably due to the necessary requirement of higher thermal energy for dissociation at V-L interface towards dissolution. These studies pointed out the extreme low solubility as the reason for failure.

In reality, the above results could be explained simply with low or no catalytic activity of the low-melting metals with dehydrogenation or dechlorination reactions at the vapor-liquid interface, but present as the necessary liquid solvent medium. This brings up an interesting question, that is, does one need “true” catalytic action of molten metal alloy for enhancing the dissolution?

The authors’ work on low-melting metals and plasma chemistry at temperatures lower than 500 °C illustrates that the gas-phase chemistry could directly be used for influencing dissolution kinetics at V-L interface selectively. However, due to the low solubility, the nucleation could occur spontaneously forming polycrystalline crusts on top of the metal melt [66, 67]. However, the authors found that if appropriate gas-phase composition is used to disturb the crust formation, then the spontaneity of nucleation could be contained [65]. In this case, the nanometer-scale nuclei surface-out and would grow vertically in one dimension. The surface dynamics of nanometer-scale nuclei could determine the final morphology of one-dimensional structures as illustrated by a schematic in Figure 7. Figure 8a shows a SEM image of the resulting micron-scale gallium oxide tubes. Figure 8b shows a SEM image of the base of a gallium oxide tube. A spiral pattern is clearly seen, indicating unique nuclei agglomeration. Similar results were obtained with addition of hydrogen to nitrogen plasma chemistry for direct synthesis of gallium nitride nanowires and tubes (Fig. 9).

The overall approach in utilizing the noncatalytic, low-solubility eutectics is as follows: (1) vapor-phase decomposition of gas-phase solutes at the vapor-liquid interface using activated gas-phase chemistry, (2) solute dissolution, and (3) phase segregation via nucleation. The authors have demonstrated this approach using gallium-melt with solutes such as nitrogen for the direct synthesis of nitrides, oxygen for the direct synthesis of oxides, and other elements such as silicon and oxygen for the synthesis of silica, crystalline silicon, and amorphous silicon nitride (Fig. 10) [68]. In the case of silicon, the experiments using either solid silicon in contact with a gallium melt or chemical vapor transport of silyl radicals produced nanowires [62]. Silicon nanowires synthesized using molten gallium and silane plasma produced single-crystalline nanowires with no or minimal oxide sheath (Fig. 11). However, the use of silane in hydrogen-rich gas phase with a microwave plasma activation produced a blanket deposition. Another set of experiments using chlorine along with silane in the hydrogen-rich gas

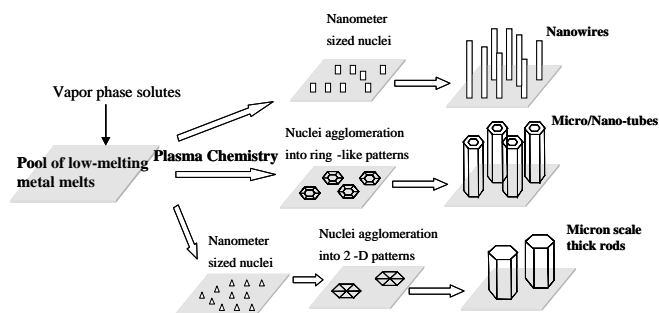
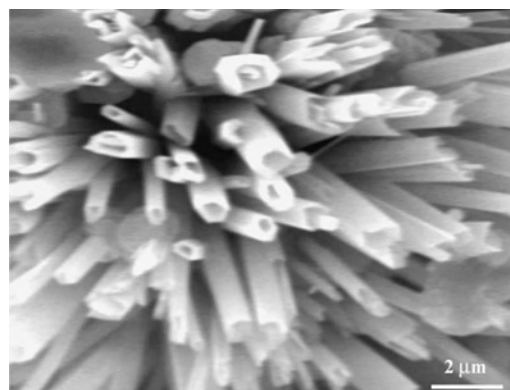
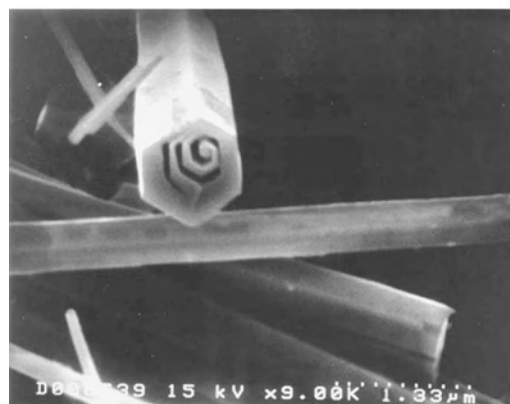


Figure 7. A schematic illustrating the effect of activated gas-phase chemistry over the morphology of one-dimensional metal structures nucleating and growing out of low-melting metal melts.



(a)



(b)

Figure 8. (a) Multiple, micron-scale tubes of beta-gallium oxide synthesized by exposing a molten gallium pool to a gas environment containing oxygen and hydrogen radicals. (b) SEM micrograph of the base of the micron-scale tubes that were unanchored from the molten gallium pool.

phase increased the selective growth of nanowires (Fig. 10e) [68]. The plasma chemistry for radicals seems to mediate the dissolution and re-dissolution kinetics at V-L interface, thus giving a good selectivity. Also, the radical-based gas-phase chemistry seems to reduce the need for catalytic action by the liquid metal alloy cluster. This is essential if one were to take advantage of the class of low-melting metals such as Ga, In, Sn, Bi, and Al and develop a rational foundation for a new class of VLS based techniques, with much more direct control of nanostructure characteristics using gas-phase chemistry. However, this technique is in the beginning stages of development with no or few specific studies either in nanowire or whisker literature. Nevertheless, the whisker literature along with studies on nanowires are discussed in Section 6, which is divided by various groups of inorganic materials.

6. SYNTHESIS OF WHISKERS AND NANOWIRES OF INORGANIC COMPOUNDS

The composition of solid phases that precipitate from molten alloy mixtures could be predicted if pertinent liquidus-solidus phase diagrams are available for the materials of interest. The binary phase diagrams involving metals

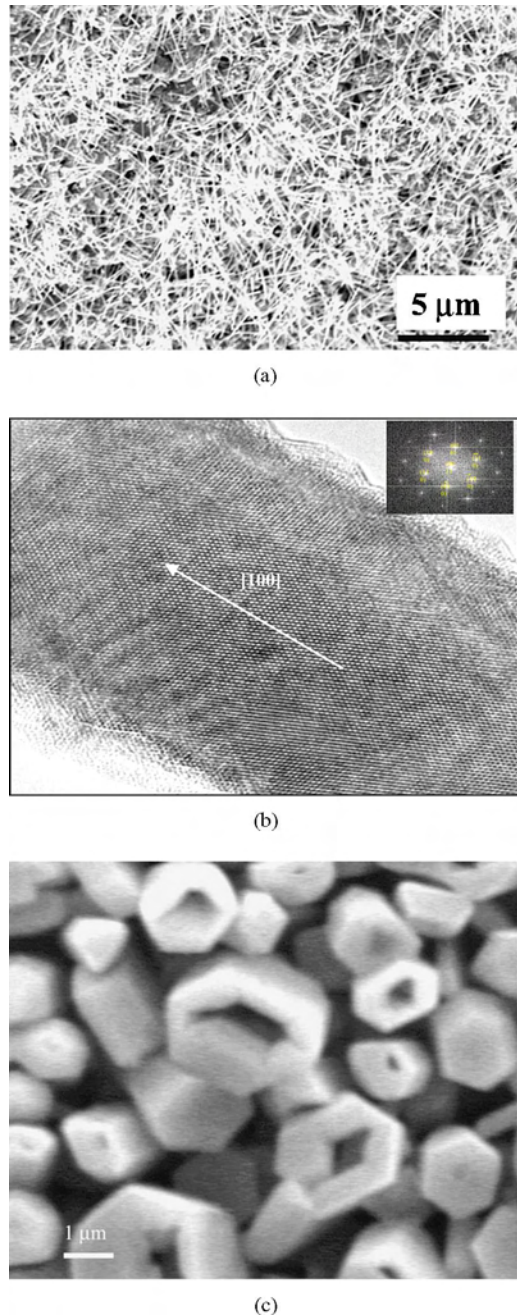


Figure 9. (a) Bulk amounts of GaN nanowires synthesized by exposing a molten gallium pool to a mixture of nitrogen and hydrogen plasma. (b) A high-resolution TEM image of a 60-nm-thick, single-crystalline GaN nanowire grown along the [100] direction. (c) Micron-scale tubes of GaN with hexagonal cross section, synthesized using gallium pool and H_2/N_2 plasma.

and silicon or germanium are readily available, such as those shown in Figure 5. However, the ternary phase diagrams for a variety of inorganic compounds with the metals are not readily available and precipitation of one phase cannot be reliably predicted. In this regard, the experimental evidence for synthesizing several inorganic compounds using either transition-metal catalyst clusters or oxide clusters is necessary and is reviewed in the following sections.

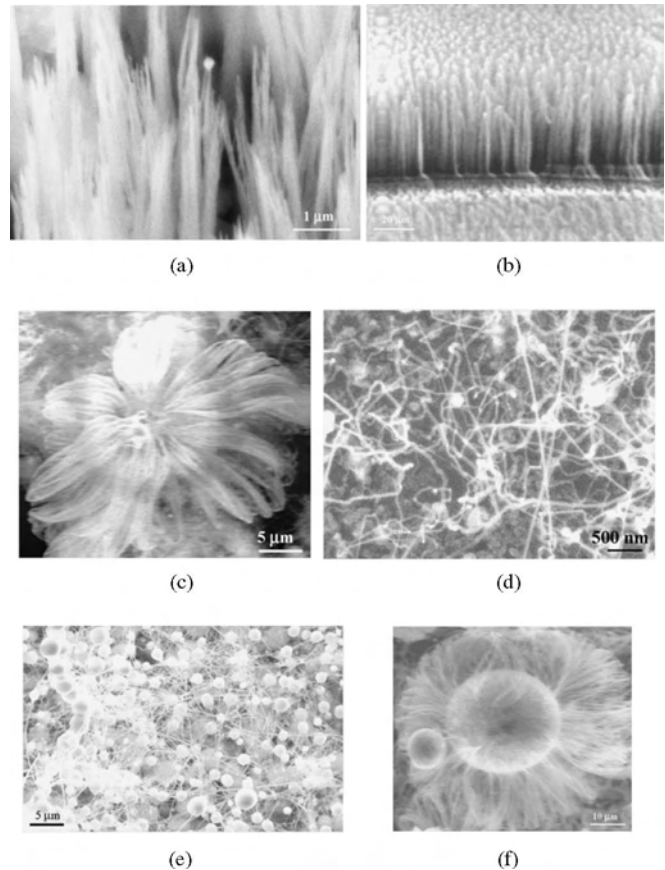


Figure 10. (a) and (b) Crop of Si nanowires synthesized from a pool of molten gallium placed on a silicon substrate and exposed to a diluted hydrogen plasma. (c) Multiple silica nanowires synthesized by providing both silicon and oxygen solutes into molten gallium. (d) Silicon nanowires synthesized using a pool of molten gallium and silane plasma. (e) Silicon nanowires synthesized by modifying the gas-phase chemistry in order to inhibit blanket deposition. Finely ground solid NaCl powder was placed in the vicinity of the gallium pool. (f) Amorphous silicon nitride nanowires grown using molten gallium and a microwave plasma containing silane and nitrogen. Figures (c), (e), and (f) courtesy of the authors' laboratory.

6.1. Nitrides and Other Compound Semiconductors

The synthesis of metal nitride whiskers was reported as early as 1956 [69] and was carried out by either carbothermal reduction or halide reduction followed by reaction with nitrogen. The metal nitrides such as AlN [70], BN [71], HfN [72], InN [73], NbN [74], SiN [75], and TiN [76, 77] were grown using VLS type mechanism. In some of these stated metal nitrides such as InN, the respective molten metal component (In) acted as the molten impurity.

Whiskers of III-V [78–80] and II-VI [81] compound semiconductors had been studied since the first report of the VLS mechanism [25]. Barns and Ellis reported growth of micron-size rectangular blades and ribbons of GaAs and GaP by vapor transport using Au as a catalyst [78]. Curved whiskers [80] had also been observed and the reason for bending was proposed. However, all these studies about

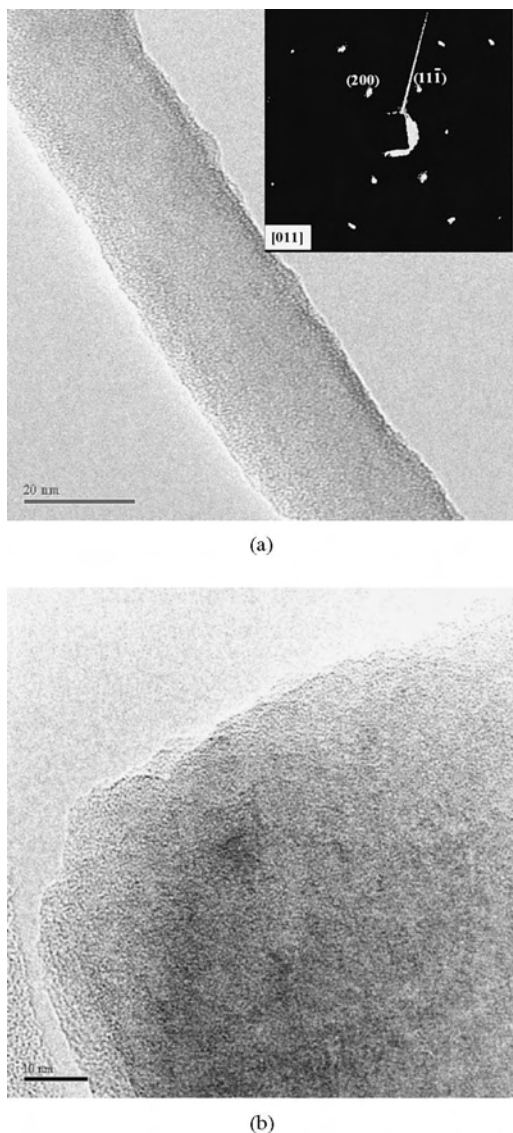


Figure 11. (a) Bright field TEM image of a 25-nm-thick single-crystalline silicon nanowire synthesized using molten gallium and silane plasma. The inset shows a selected area electron diffraction pattern, indicating the nanowire growth direction to be along $\langle 100 \rangle$. (b) High-resolution TEM image of part of a silicon nanowire synthesized using molten gallium and silane plasma. The nanowires had minimal to no oxide sheath.

whiskers had no control over the morphology, width, or length, and no properties were reported.

Nanowires of group-III nitrides were obtained by providing catalyst clusters such as gold and iron using laser ablation [82]. Direct reaction of Ga_2O_3 in NH_3 in a hot filament reactor also resulted in GaN nanowires but with a thick oxide sheath [83]. In this case, the oxide phase assisted in preserving the GaN nuclei by preferentially allowing the reduction of the $\{10\text{-}11\}$ plane of the GaN nuclei. Similarly, the direct reaction of Ga in NH_3 has been demonstrated to result in GaN nanowires [84]. Similar scheme using thermal activation at high temperatures produced Si_3N_4 nanowires using Si or Si/ SiO_2 powder in the ammonia environment [85]. The authors have also reported direct synthesis of

GaN nanowires using molten gallium and nitrogen plasma [66]. Recently, AlN nanowires were synthesized by heating a mixture of Al and AlN under nitrogen atmosphere at 750–850 °C [86].

GaAs quantum wires had been fabricated by ion beam lithography [87], ion etching [88], MBE [89], and MOVPE [90] since the 1980s. But all these structures were anchored on a substrate. Hiruma et al. [91] grew 10- to 50-nm-thick GaAs needle-shaped nanowhiskers on Au-coated SiO_2 patterned GaAs substrate using metalorganic chemical vapor deposition, but the sizes of the nanowhiskers were still not controllable.

GaAs nanowires were synthesized by laser ablating a target composed of gold and gallium arsenide target [39]. Similar results were obtained when oxide-containing GaAs target was ablated using a laser [92, 93]. Nanowires were also synthesized by evaporating the source materials at high temperature in the absence of any transition metals or oxides [94, 95]. The growth method is somewhat similar to the authors' nitride growth technique in which arsenic gets dissolved at high temperatures directly and grows from the basal front. The solution-phase chemistry using either organic [96, 97] or aquatic environments [98–105] has also been used to synthesize III-V and II-VI compound semiconductor nanostructures.

6.2. Oxides

In 1957, Webb and Forgeng reported the synthesis of microns-thick sapphire (alpha-alumina) whiskers by oxidation of molten aluminum at 1300–1450 °C in hydrogen atmosphere [106]. The resulting whiskers were alpha- Al_2O_3 , and had hexagonal cross section. Globules were observed at the growing tips of the whiskers. The authors attributed one-dimensional growth to adsorption and rapid surface diffusion of gas-phase suboxides to the growing tip according to that of the oxide-assisted growth mechanism. BeO whiskers were synthesized [107] by direct reaction of molten Be and water vapor. The authors contemplated that oxygen from the vapor phase diffuses through an oxide-coated Be globule and reacts to form BeO, which eventually diffuses to the whisker-Be interface. Following these early reports, several authors reported synthesis of other metal oxide whiskers, such as ZnO [108, 109], SnO_2 [110], titania [111], and copper oxide [112]. ZnO whisker growth was attributed to screw dislocation-based spiral growth model.

Following discovery of the VLS mechanism by Wagner and Ellis in 1964, there were several reports with VLS-based synthesis of oxide nanowires and nanowhiskers. The increased realization of VLS-type whisker growth can also be attributed to timely improvement in analytical techniques such as electron microscopes, etc. Growth of tungsten oxide [113], NiO [114], cadmium oxide [115, 116], SnO_2 [117], alumina [118], and Cr_2O_3 [119] whiskers was attributed to VLS-type mechanism. The fact that in these reports, the droplet was not always a catalytic impurity, demands detailed investigation of the exact role of a molten droplet at the whiskers tips in enabling 1D growth.

First reports of the synthesis of truly nanoscale oxide whiskers appeared in 1996. Yumoto et al. synthesized ITO whiskers using an e-beam evaporative technique [120].

A predominantly Sn globule at the whisker tips indicated the growth mechanism to be VLS type. Amorphous silica nanowires were synthesized [121] using gas-phase SiO with cobalt as the catalyst in Ar/CO environment at 1500 °C. Since these reports, a variety of oxides have been grown in the nanoscale regime by nonequilibrium processing techniques such as laser ablation and physical evaporation according to either VS or molten impurity-assisted VLS mechanism. These oxides include Al₂O₃ [122], ITO [123], GeO₂ [124–126], tungsten oxide [127, 128], ZnO [129–136], MgO [135–137], gallium oxide [138–142], In₂O₃ [143], β-PbO₂ [144], Cu₂O [145], MnO₂ [146], Mn₃O₄ [147], NiO [148], CdO [149], vanadium oxide [150], and Sb₂O₃ [151]. Additionally, nanowires of TiO₂ [152], Sb₂O₃, and Sb₂O₅ [153] have been synthesized using a microemulsion method. In this method, the structure of the microemulsion defined the growth in one dimension. In a method similar to that reported for synthesis of Cu₂O nanowires [145], Cu(OH)₂ nanowires were synthesized using chemical reaction between CuSO₄ and NH₄OH and NaOH [154]. Recently, the authors have demonstrated bulk synthesis of gallium oxide and silica nanostructures. These studies showed that direct reaction of oxygen and hydrogen plasma with molten gallium enabled multiple nucleation and growth of gallium oxide nanostructures [65]. Similarly, silyl and oxygen plasma over molten gallium pool resulted in multiple nucleation and growth of silica nanowires (Fig. 10c) [68].

6.3. Carbides

Carbides in general are hard, lightweight, high-temperature refractory materials with high thermal conductivity. Whiskers of carbides are interesting due to their use as reinforcing phase in ceramic or metal matrix composites.

6.3.1. Silicon Carbide

Particularly, β-SiC with zinc-blende cubic structure is the most attractive form due to its mechanical and thermal properties. Hexagonal silicon carbide (α-SiC) has also been interesting for applications in high-temperature and high-power electronics. α-SiC whiskers were first synthesized [155, 156] by accident in 1958, using vapor-phase species containing Si and C in the presence of hydrogen onto the walls of a furnace. Similarly, the hydrogen reduction of methyltrichlorosilane [157] and SiO₂-C-H₂ system at high temperatures between 1200 and 1800 °C yielded whiskers containing mixture of α-SiC and β-SiC phases [158].

Following these reports, much of the work has been focused on obtaining control over the growth of SiC whiskers for yield and phase, by using different gas-phase chemistries and different types of transition-metal or other types of catalysts. The popular chemistries for producing α-SiC whiskers included hydrogen reduction of methyltrichlorosilane [159–161]. It was established that the conditions for the formation of α-SiC were very stringent (1400–1450 °C), close to the melting point of silicon; hence molten silicon could have a role in the growth of one-dimensional α-structures. Later studies using carbothermal reduction of silicon dioxide in the presence of transition-metal catalyst clusters illustrated that SiC whisker growth follows that of VLS mechanism. Using the same reactants,

β-SiC was easily synthesized in a broad range of temperature and reactant conditions. β-SiC has been synthesized by carbothermal reduction of silicon dioxide using a range of molten impurities such as Fe [162–166], Ni [167, 168], and Al [169]. In the carbothermal reduction of SiO₂, the partial pressures of SiO_(g) and CO_(g) were found to be important to control the morphology of the SiC whiskers produced. This prompted a number of modifications to the gas-phase composition: usage of SiO_(g)-CO_(g) systems [170], methane [163, 171, 172] and gas-phase sources such as SiCl₄ and Si₂Cl₆ with H₂, CH₄ [173], and economical silica source materials such as agricultural wastes [174–179]. To minimize catalyst contamination in the whiskers, catalyst-free methods such as vapor-solid-assisted growth via molten fluorosilicate [180] and low-temperature self-catalyzed method for using Na as a co-reductant [181] with SiCl₄ and CCl₄ were also proposed.

The progress in SiC nanowire synthesis followed much of the whisker synthesis routes except for reducing the catalyst metal cluster sizes using laser ablation [166], arc-discharge [182], dissolving silicon into iron which remains at the base of the nanowhiskers [183], confined reactions with carbon nanotubes [184–187]. Biaxial SiC-SiO₂ nanowires [188] and co-axial helical SiC-SiO₂ nanowires [189] have also been synthesized. The β-SiC whiskers and nanowires seemed to grow preferentially in ⟨111⟩ direction with either transition-metal catalyst driven or oxide-assisted growth methods [190–194]. Because of this growth direction, as expected, the nanowires and whiskers contain high densities of defects such as twins.

6.3.2. Other Carbides

Other carbides of interest include boron carbide and refractory metal carbides such as ZrC, TiC, GeC, TaC, and NbC. Boron carbide filaments and whiskers were synthesized using boron trichloride, carbon tetrachloride, and metallic impurities at high temperatures (>1400 °C) on graphite substrates [195–199]. A similar gas-phase reaction of YCl₄ (Y = Zr, Ti) with hydrocarbon gas (CH₄ or C₃H₈) and H₂ was used in an argon atmosphere with Ni catalyst to obtain whiskers of ZrC and TiC [200–206] and ZrC fibers [207]. Another common mechanism used in carbides was the carbothermal reduction of oxides at temperatures of about 1500 °C using catalyst and NaCl. This method was used for whiskers of B₄C [208], NbC [209, 210], and TaC [211, 212]. Germanium carbide whiskers were reported to be synthesized from CH₂(GeH₃)₂ by forming Ge-C films on (100) Si [213].

Carbothermal reduction in absence of any catalyst by thermal evaporation of B/B₂O₃/C powder under argon atmosphere was used to grow crystalline nanowires of boron carbide [214]. Lithium-assisted synthesis of Al₄C₃ nanowires using solid-state reaction of Al/C/Li powder at 780 °C was reported [215]. Plasma decomposition of 1,2-dicarbododecaborane (C₂B₁₀H₁₂) at lesser temperatures (<1200 °C) using iron clusters produced nanowires with diameters ranging from 18 to 150 nm. The tip consisted primarily of Fe₂B alloy [216]. The same method also produced amorphous B₄C nanosprings [217]. The growth of this nanospring seemed to follow a similar mechanism as that of helical growth of graphite [218]. Also, unlike nanowires, in which the catalyst diameter is larger than the diameter of

the nanowire, in this case, the catalyst diameter was smaller than the nanospring.

The synthesis of series metallic/nonmetallic carbide nanorods like TiC, NbC, Fe₃C, BC_x apart from SiC was demonstrated using the reaction of carbon nanotubes with gas-phase species (e.g., B₂O₂ for BC_x) [185]. The diameter of the boron carbide nanowire was defined by the diameter of the carbon nanotubes. Other similar work was also reported for NbC, TaC, and TiC [219, 220].

7. SYNTHESIS OF METAL WHISKERS AND NANOWIRES

The vapor-phase schemes primarily involving halide reduction similar to silicon were also applied to metallic whiskers [221] as early as 1956. However, the studies are only a few with no understanding of the growth mechanism, and have primarily been confined to micron-scale whisker growth. Commonly, a metal salt was heated in a tube furnace and transported to colder regions of the furnace in a reducing environment to form whiskers. This technique has been demonstrated for whiskers of Cd [222], Cu [223, 224], Fe [225, 226], Ni [227], Sn [228], In [228], W [229], and Co-Fe [230] alloys systems. In almost all the cases, the whiskers contained a cluster of impurity elements at their tips. However, the detailed information on these clusters at the tips is missing in all the previous reports. The general consensus seems to be that these metallic whiskers grew with the help of another metallic cluster at the tip similar to the traditional VLS mechanism. Only in the case of cadmium, it was conclusively determined that Sn cluster at tip helped the growth. No reports exist on any type of demonstrations or attempts to grow metallic nanowires using the previous reports on whiskers, possibly due to lack of understanding of the growth mechanisms involved. However, Ag nanowires have been synthesized using a solution-based method [231]. A solid-liquid phase arc-discharge was used to generate a colloidal Ag solution that upon aging resulted in short Ag nanowires.

8. SYNTHESIS OF INORGANIC NANOTUBES

The graphitic sheets, when reduced to sizes of a few nanometers, fold to form both cage compounds and tubular structures. This phenomenon does not seem to be limited to carbon. Inorganic materials, both 2D layered and 3D, started to exhibit tubular and closed-shell structures when sizes are restricted to several nanometers or less [232]. However, this is not a universal phenomenon holding true for all 3D inorganic compounds; that is, nanowires of nitrides and oxides have been synthesized to sizes less than 10 nm without forming tubular structures. The nanotubular structures in these materials provide uniform surface throughout and present sites for active functionalization compared to inert surface that carbon nanotubes present in the absence of kinks or defects. In addition, the nanotubular and micro-tubular structures have an increased surface area.

The synthesis procedures for producing nanotubes can be classified into four main groups: (a) reactions with inorganic nanowires such as sulfidization during oxide nanowire growth, (b) coating or doping of carbon nanotubes either after or during growth and then removing of carbon nanotube by oxidation, (c) templating via creation of mesoporous material followed by ionic exchange, and (d) vapor-liquid-solid methods similar to those used in the production of nanowires and carbon nanotubes, that is, metallic or metal-containing compounds aiding the tip growth of nanotubes with vapor-phase precursors.

The tubular and closed-shell structures of 2D layered compounds such as disulfides of tungsten and molybdenum were reported immediately after the discovery of carbon nanotubes. The tungsten disulfide nanotubular structures were obtained by carrying out sulfidization using hydrogen disulfide during the growth of nanoscale tungsten oxide particles. The growth mechanism involves, initially, the formation of tungsten disulfide monolayer on the tungsten dioxide particle, thus forming a shell. The shell formation helps in avoiding the particle coalescence and enables 1D growth through the tip. The competing sulfidization on the shell and the tungsten oxide growth at the tip determine the length of the resulting nanotubes. This technique has been successfully applied to other sulfides [233–236] such as MoS₂. This technique primarily produced multiwalled nanotubes (Fig. 12a) but was extremely amenable for bulk manufacturing (see the reactor schematic in Fig. 3e). Similar studies of layered metal halides (NiCl₂, CdCl₂) such as nickel chloride by dehydration of the respective hydrated compounds in inert gases at different temperatures resulted in particles with fullerene-like structures [237]. Recently, the chemical transport of MoS₂ powder, with iodine as transport agent, and C₆₀ as growth promoter over several days in a closed ampule at 1010 K with 50 K as temperature gradient resulted in single-walled MoS₂ nanotubes, which were stabilized by intercalation of iodine in between the nanotubes [238].

The stability of BN nanotubes was first predicted [239] in 1994 and was first successfully demonstrated [240] in 1995 using an arc-discharge method. Hot pressed BN powder packed into hollow W rod served as the anode and cooled pure Cu rod served as the cathode. The tip of BN nanotube contained tungsten with boron and nitrogen, suggesting traditional VLS mechanism. Following this, several metal boride anode sources, such as HfB₂ [241], LaB₆ [242], YB₆ [243], and ZrB₂ [244] have been demonstrated for the growth of BN nanotubes. Another variation involved packing BN/B₂O₃ powder along with a small amount of transition-metal catalyst, such as Ni, Co [245], V₂O₅, MoO₃ [246], and Fe [247] along with carbon into anode or using B-, O-, N-containing compounds reacting with NiB clusters at high temperature [248]. Boron reacts with nitrogen at the tip of the nanotube to form a sheet of BN around the catalyst. Using this method, both single-walled and multi-walled boron nitride nanotubes were obtained. The synthesis of B_xC_yN_z nanotubes was first achieved by doping carbon nanotubes with boron and nitrogen during arc-discharge synthesis of carbon nanotubes [249]. This method has been extended by directly reacting boron oxide powder and carbon nanotubes at 1523–1623 K under a nitrogen atmosphere

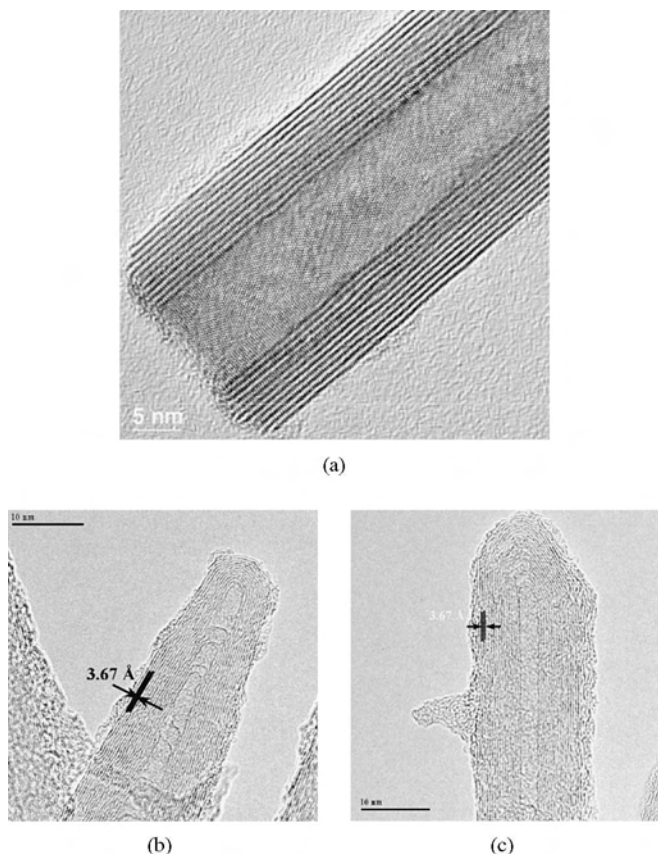


Figure 12. (a) HRTEM image of a WS_2 nanotube synthesized in a fluidized bed reactor. Micrograph courtesy of R. Tenne, Weizmann Institute, Israel. (b) and (c) HRTEM images of Ga_2O_3 nanotubes synthesized using nanometer-scale Ga droplets exposed to a microwave plasma containing hydrogen and oxygen radicals.

to obtain $\text{B}_x\text{C}_y\text{N}_z$ nanotubular structures. In this method, the resulting $\text{B}_x\text{C}_y\text{N}_z$ nanotubes had diameters similar to those of the carbon nanotubes used [250, 251].

The carbon nanotube template technique was first demonstrated for vanadium pentoxide by forming vanadium pentoxide on carbon nanotube and then removing carbon nanotube core by oxidation [252] in air at 650 °C. This technique has been successfully applied to several other metal oxides by forming metal oxide tube around carbon nanotube template using alkoxide precursors in solution and then burning the carbon nanotube [253] core in air at 723 K. Recently, lanthanum carbide nanotubes [254] were synthesized using an arc evaporation setup, in which it was contemplated that La atoms diffuse into the interlayer spaces of multiwalled carbon nanotubes in the early stages and react further to form lanthanum carbide nanotubes.

A similar pretemplating technique (not using carbon nanotubes) has been demonstrated for silica [255], vanadium pentoxide [256], and titania nanotubes [257]. In this method, a metalorganic compound is dissolved together with a template-forming species in alcohol to promote metal oxide nanotube growth within the preformed template. For example, the hydrolysis of vanadium triisopropoxide in hexadecylamine, after aging, resulted in a yellow lamellar structured

composite of surfactant and hydrolyzed vanadium oxide. The treatment of this hydrolysis product under hydrothermal conditions yielded a product of $\text{VO}_{2.4}(\text{C}_{16}\text{H}_{33}\text{NH}_2)_{0.34}$.

Recently, gallium oxide nanotubular structures have been synthesized in the authors' laboratory without the use of catalysts or preformed templates using multiple nucleation out of tiny gallium droplets (less than 100 nm in size) exposed to hydrogen and oxygen plasma system at temperature less than 800 °C (Fig. 12b, c). The tube walls seemed to be composed of $\beta\text{-Ga}_2\text{O}_3$ with layer spacing of 0.367 nm. The tubes were microns in length and the outer diameters ranged from 5 to 15 nm with inner diameters varying from 2.5 to 5 nm. In some cases, the bamboo styled folding of layers was seen. The details of growth mechanism are yet to be understood [258].

Hollow, microtubular crystals of aluminum borate have been synthesized using direct reaction of alumina with boric acid in the presence of nickel chloride [259]. Also, millimeter-long microtubular crystals of $\beta\text{-Ag}_2\text{Se}$ have been synthesized using hydrothermal reaction of silver chloride with selenium in the presence of sodium hydroxide at 155 °C for several hours [260]. However, the formation mechanism for hollow crystals is not entirely clear at this time. Nickel as a catalyst might have played a role in the formation of aluminum borate micron-scale tubular crystals. In the second case, the formation of sodium selenide needles followed by their reaction with silver might have produced the silver selenide hollow crystals.

Direct reaction of nitrogen and hydrogen plasmas with molten gallium produced hollow, tubular crystals of wurtzitic gallium nitride shown in Figure 9, in a similar fashion to gallium oxide tubular structures, shown in Figure 8. Figure 8b shows the base of a gallium oxide tube that was unanchored from the molten gallium pool. A spiral pattern represents unique manipulation of the nuclei agglomeration using activated gas-phase chemistry. Electron cyclotron resonance plasma containing hydrogen and nitrogen [261] was used at 50 mTorr and 900 °C. The external faceting of tubes varied from hexagonal to star-hexagonal (not shown). Though there have been theoretical studies that predict the possibility of GaN nanotubes [262], it has not yet been experimentally demonstrated.

9. SUMMARY

The interest in one-dimensional, nanoscale materials such as nanowires and nanotubes has led in the recent past to intense research towards developing various synthesis methods for producing bulk amounts of these materials. The prior work on whisker technology has provided a rich amount of literature on various inorganic materials synthesis at micron scale. The synthesis methods used for whiskers seemed to be divided into two types of mechanism, that is, transition-metal cluster catalyzed VLS and oxide-assisted growth methods. These two techniques have been primarily used for micron-scale whisker synthesis of several inorganic materials, including elemental semiconductors, metals, and compounds. The whisker size in both these techniques is controlled by the size of the cluster that could be transition-metal cluster or vapor condensed suboxide cluster. The clusters of sizes greater than 0.2 μm are thermodynamically

easier to form and control. In order to produce nanoscale wires, several research groups focused their efforts on how to create nanoscale clusters and disperse them on a support. The most notable techniques have been laser ablation, evaporation, and supercritical fluid processing.

Recently, another technique was demonstrated with nucleation and growth of multiple nanowires from pools and thin films of low-melting metals. In this technique, activated gas-phase chemistry directly controlled the solute dissolution at the V-L interface, and eliminated the need for creation of nanosized clusters. This is a relatively unexplored technique and holds promise towards synthesis of nanostructures with diameters below 5 nm, which is necessary for exploring new phases in several inorganic materials. For example, the synthesis of 1D nanostructures at extremely small scales has allowed discovery of new phases for several inorganic compounds.

At this time, the availability of inorganic nanostructures is limited to only a few laboratories. This has hindered our understanding of the commercial applicability of these nanostructures. Thus, obtaining precise control over the size, size distribution, and morphology of the nanostructures is necessary for scale-up into bulk manufacturing.

GLOSSARY

Catalyst An external impurity confined to nanometer-scale dimensions to selectively enhance the growth of material, thus providing one-dimensionality to the growing structure.

Critical nuclei A nucleus is defined as a thermodynamically stable cluster of molecules. The aggregates smaller than the critical nucleus size will redissolve, and the aggregates larger than the critical nucleus will continue to grow.

Eutectic A eutectic alloy is a mixture of substances having a minimum melting point. For a binary system, the eutectic temperature is lower than the melting points of either of the components.

Nanometer A unit of spatial measurement that is one-billionth of a meter (10^{-9} m).

Nanotube A hollow structure with lengths exceeding the diameter by at least a factor of 100 with the diameters smaller than 100 nm. The walls of the tubular structure may consist of multiple layers of the comprising material.

Nanowire A solid structure with lengths exceeding the diameter by at least a factor of 100 with the diameters smaller than 100 nm.

ACKNOWLEDGMENTS

The authors greatly appreciate financial support from NSF through CAREER Grant CTS 9876251 and US AFOSR through DEPSCoR program (F49620-00-1-0310). One of the authors (RCM) acknowledges Grosscurth Fellowship. The authors thank Prof. B. A. Korgel (University of Texas, Austin, TX) and Prof. R. Tenne (Weizmann Institute, Israel) for providing timely input.

REFERENCES

1. <http://public.itrs.net/Files/2001ITRS/Home.htm>, International Technology Roadmap for Semiconductors, 2001 Edition.
2. A. P. Alivisatos, *Science* 271, 933 (1996).
3. A. Zunger and L. W. Wang, *Appl. Surf. Sci.* 102, 350 (1996).
4. A. M. Saitta, F. Buda, G. Fiumara, and P. V. Giaquinta, *Phys. Rev. B.* 53, 1446 (1996).
5. C. Herring and J. K. Galt, *Phys. Rev.* 85, 1060 (1952).
6. S. S. Brenner, *J. Appl. Phys.* 27, 1484 (1956).
7. R. Iley and H. L. Riley, *J. Chem. Soc.* 1362 (1948).
8. F. C. Frank, *Discussions Faraday Soc.* 5, 48 (1949).
9. G. W. Sears, *Acta Met.* 3, 361 (1955).
10. W. W. Webb and W. D. Forgeng, *J. Appl. Phys.* 28, 1449 (1957).
11. J. M. Blakely and K. A. Jackson, *J. Chem. Phys.* 37, 428 (1962).
12. V. Ruth and J. P. Hirth, *J. Chem. Phys.* 41, 3139 (1964).
13. R. Gomer, *J. Chem. Phys.* 28, 457 (1958).
14. R. L. Schwoebel, *J. Appl. Phys.* 38, 1759 (1967).
15. W. R. Davis, R. J. Slawson, and G. R. Rigby, *Nature* 171, 756 (1953).
16. L. V. Radushkevich and V. M. Luk'yanovich, *Zhur. Fiz. Khim.* 26, 88 (1952).
17. P. A. Tesner and A. I. Echeistova, *Doklady Akad. Nauk. U.S.S.R.* 87, 1029 (1952).
18. W. R. Davis, R. J. Slawson, and G. R. Rigby, *Nature* 171, 756 (1953).
19. L. J. E. Hofer, E. Sterling, and J. T. McCartney, *J. Phys. Chem.* 59, 1153 (1955).
20. R. Bacon, *J. Appl. Phys.* 31, 283 (1960).
21. R. T. K. Baker, M. A. Barber, P. S. Harris, F. S. Feates, and R. J. Waite, *J. Catal.* 26, 51 (1972).
22. D. W. Lyon, C. M. Olson, and E. D. Lewis, *Trans. Electrochem. Soc.* 96, 359 (1949).
23. E. R. Johnson and J. A. Amick, *J. Appl. Phys.* 25, 1204 (1954).
24. E. S. Greiner, J. A. Gutowski, and W. C. Ellis, *J. Appl. Phys.* 32, 2489 (1961).
25. R. S. Wagner and W. C. Ellis, *Appl. Phys. Lett.* 4, 89 (1964).
26. D. W. F. James and C. Lewis, *Brit. J. Appl. Phys.* 16, 1089 (1965).
27. P. R. Thornton, D. W. F. James, C. Lewis, and A. Bradford, *Phil. Mag.* 14, 165 (1966).
28. J. D. Filby and S. Nielson, *J. Electrochem. Soc.* 112, 535 (1965).
29. J. D. Filby, S. Nielson, G. J. Rich, G. R. Booker, and J. M. Larcher, *Phil. Mag.* 16, 565 (1967).
30. J. L. Carter, *Science* 181, 841 (1973).
31. R. B. Finkelman, R. R. Larson, and E. J. Dwornik, *J. Cryst. Growth* 22, 159 (1974).
32. G. A. Bootsma and H. J. Gassen, *J. Cryst. Growth* 10, 223 (1971).
33. E. I. Givargizov, *J. Cryst. Growth* 20, 217 (1973).
34. E. I. Givargizov, *J. Cryst. Growth* 31, 20 (1975).
35. H. Wang and G. S. Fischman, *J. Appl. Phys.* 76, 1557 (1994).
36. J. Westwater, D. P. Gosain, K. Yamauchi, and S. Usui, *Mater. Lett.* 24, 109 (1995).
37. J. Westwater, D. P. Gosain, S. Tomiya, S. Usui, and H. Ruda, *J. Vac. Sci. Tech.* 15, 554 (1997).
38. J. Westwater, D. P. Gosain, and S. Usui, *Phys. Stat. Sol. (a)* 165, 37 (1998).
39. A. M. Morales and C. M. Lieber, *Science* 279, 208 (1998).
40. D. P. Yu, Z. G. Bai, Y. Ding, Q. L. Hang, H. Z. Zhang, J. J. Wang, Y. H. Zou, W. Qian, G. C. Xiong, H. T. Zhou, and S. Q. Feng, *Appl. Phys. Lett.* 72, 3458 (1998).
41. E. I. Givargizov, A. N. Stepanova, L. N. Obolenskaya, E. S. Mashkova, V. A. Molchanov, M. E. Givargizov, and I. W. Rangelow, *Ultramicroscopy* 82, 57 (2000).
42. T. I. Kamins, R. S. Williams, Y. Chen, Y.-L. Chang, and Y. A. Chang, *Appl. Phys. Lett.* 76, 562 (2000).
43. H. F. Yan et al., *Chem. Phys. Lett.* 323, 224 (2000).
44. J. R. Heath and F. K. LeGoues, *Chem. Phys. Lett.* 208, 263 (1993).

45. J. D. Holmes, K. P. Johnston, R. C. Doty, and B. A. Korgel, *Science* 287, 1471 (2000).
46. T. Hanrath and B. A. Korgel, *J. Am. Chem. Soc.* 124, 1424 (2002).
47. N. Wang, Y. H. Tang, Y. F. Zhang, C. S. Lee, and S. T. Lee, *Phys. Rev. B* 58, R16024 (1998).
48. Y. F. Zhang, Y. H. Tang, N. Wang, C. S. Lee, I. Bello, and S. T. Lee, *Phys. Rev. B* 61, 4518 (2000).
49. S. T. Lee, Y. F. Zhang, N. Wang, Y. H. Tang, I. Bello, C. S. Lee, and Y. W. Chung, *J. Mater. Res.* 14, 4503 (1999).
50. S. T. Lee, N. Wang, and C. S. Lee, *Mater. Sci. Eng. A* 286, 16 (2000).
51. W. Shi, H. Peng, N. Wang, C. P. Li, L. Xu, C. S. Lee, R. Kalish, and S. T. Lee, *J. Am. Chem. Soc.* 123, 11095 (2001).
52. Z. W. Pan, Z. R. Dai, and Z. L. Wang, *Science* 291, 1947 (2001).
53. N. Ozaki, Y. Ohno, and S. Takeda, *Appl. Phys. Lett.* 73, 3700 (1998).
54. Y. Wu, R. Fan, and P. Yang, *Nano Lett.* 2, 83 (2002).
55. M. S. Gudikson, L. J. Lauhon, J. Wang, D. C. Smith, and C. M. Lieber, *Nature* 415, 617 (2002).
56. M. T. Björk, B. J. Ohlsson, T. Sass, A. I. Persson, C. Thelander, M. H. Magnusson, K. Deppert, L. R. Wallenberg, and L. Samuelson, *Appl. Phys. Lett.* 80, 1058 (2002).
57. L. J. Lauhon, M. S. Gudikson, D. Wang, and C. M. Lieber, *Nature* 420, 57 (2002).
58. W. A. Tiller, "The Science of Crystallization: Microscopic Interfacial Phenomena." Cambridge University Press, New York, 1991.
59. D. Turnbull, *J. Appl. Phys.* 21, 1022 (1950).
60. J. Hu, T. W. Odom, and C. M. Lieber, *Acc. Chem. Res.* 32, 435 (1999).
61. C. D. Thurmond and M. Kowalchik, *Bell Syst. Tech. J.* 39, 169 (1960).
62. M. K. Sunkara, S. Sharma, R. Miranda, G. Lian, and E. C. Dickey, *Appl. Phys. Lett.* 79, 1546 (2001).
63. S. Sharma, M. K. Sunkara, R. Miranda, G. Lian, and E. C. Dickey, "Proceedings of the MRS Spring 2001 Meeting," 2001, Vol. 676, p. Y.1.6.1.
64. S. Sharma, M. K. Sunkara, G. Lian, and E. C. Dickey, "Proceedings of the MRS Fall 2001 Meeting," 2001, Vol. 703, p. 123.
65. S. Sharma and M. K. Sunkara, *J. Am. Chem. Soc.* 124, 12289 (2002).
66. H. Chandrasekaran and M. K. Sunkara, *MRS Symp. Proc.* 693, 159, 2001.
67. A. Argoitia, C. C. Hayman, J. C. Angus, L. Wang, J. S. Dyck, and K. Kash, *Appl. Phys. Lett.* 70, 179 (1997).
68. S. Sharma and M. K. Sunkara, "Proceedings of the MRS Fall 2002 Meeting," 2002.
69. J. A. Khon et al., *Am. Mineral.* 41, 355 (1956).
70. R. Fu, H. Zhou, L. Chen, and Y. Wu, *Mater. Sci. Eng. A* 266, 44 (1999) and references therein.
71. T. Ishii, T. Sato, Y. Sekikawa, and M. Iwata, *J. Cryst. Growth* 52, 285 (1981).
72. M. Futamoto, I. Yuito, and U. Kawabe, *J. Cryst. Growth* 61, 69 (1983).
73. H. Parala, A. Devi, F. Hipler, E. Maile, A. Birkner, H. W. Becker, and R. A. Fischer, *J. Cryst. Growth* 231, 68 (2001).
74. T. Takahashi, H. Itoh, and T. Yamaguchi, *J. Cryst. Growth* 46, 69 (1979).
75. K. Kijima, N. Setaka, and H. Tanaka, *J. Cryst. Growth* 24/25, 183 (1974).
76. Z. B. Bojarski, K. Wokulska, and Z. Wokulski, *J. Cryst. Growth* 52, 290 (1981).
77. W. Guo, X. G. Ning, J. Zhu, and H. Q. Ye, *J. Cryst. Growth* 106, 400 (1990).
78. R. F. Barns and W. C. Ellis, *J. Appl. Phys.* 36, 2296 (1965).
79. N. Holonyak, Jr., C. M. Wolfe, and J. S. Moore, *Appl. Phys. Lett.* 6, 64 (1965).
80. E. Schonherr and E. Winckler, *J. Cryst. Growth* 32, 117 (1976).
81. S. Simov, V. Gantcheva, P. Kamadjev, and M. Gospodinov, *J. Cryst. Growth* 32, 133 (1976).
82. X. Duan and C. M. Lieber, *J. Am. Chem. Soc.* 122, 188 (2000).
83. H. Y. Peng, X. T. Zhou, N. Wang, Y. F. Zheng, L. S. Liao, W. S. Shi, C. S. Lee, and S. T. Lee, *Chem. Phys. Lett.* 327, 263 (2000).
84. M. He, P. Zhou, S. N. Mohammad, G. L. Harris, J. B. Halpern, R. Jacobs, W. L. Sarney, and L. Salamanca-Riba, *J. Cryst. Growth* 231, 357 (2001).
85. Y. Zhang, N. Wang, R. He, J. Liu, X. Zhang, and J. Zhu, *J. Cryst. Growth* 233, 803 (2001).
86. H. Cong, H. Ma, and X. Sun, *Physica B* 323, 354 (2002).
87. T. Hiramoto, K. Hirakawa, Y. Iye, and T. Ikoma, *Appl. Phys. Lett.* 51, 1620 (1987).
88. A. Scherer, M. L. Roukes, H. G. Craighead, and M. C. Tamargo, *Appl. Phys. Lett.* 51, 2133 (1987).
89. M. Tsuchiya, J. M. Graines, R. H. Ran, R. J. Simes, P. O. Holtz, L. A. Coldren, and P. M. Petroff, *Phys. Rev. Lett.* 62, 466 (1989).
90. H. Asai, S. Yamada, and T. Fukui, *Appl. Phys. Lett.* 51, 1518 (1987).
91. K. Hiruma, T. Katsuyama, K. Ogawa, M. Koguchi, and H. Kakibayashi, *Appl. Phys. Lett.* 59, 431 (1991).
92. X. F. Duan, Y. Huang, Y. Cui, and C. M. Lieber, *Nature* 409, 66 (2001).
93. W. S. Shi, Y. F. Zheng, N. Wang, C. S. Lee, and S. T. Lee, *Adv. Mater.* 13, 591 (2001).
94. Y. Wang, L. Zhang, C. Liang, G. Wang, and X. Peng, *Chem. Phys. Lett.* 357, 314 (2002).
95. X. C. Wu and Y. R. Tao, *J. Cryst. Growth* 242, 309 (2002).
96. T. J. Trentler, K. M. Hickman, S. C. Goel, A. M. Vian, P. C. Gibbons, and W. E. Buhro, *Science* 270, 1791 (1995).
97. S. Yu, Y. Wu, J. Yang, Z. Han, Y. Xie, Y. Qian, and X. Liu, *Chem. Mater.* 10, 2309 (1998).
98. J. Hu, Q. Lu, B. Deng, K. Tang, Y. Qian, Y. Li, G. Zhou, and X. Liu, *Inorg. Chem. Commun.* 2, 569 (1999).
99. Y. D. Li, Y. Ding, and Z. Y. Wang, *Adv. Mater.* 11, 847 (1999).
100. Y. Cui, J. Ren, G. Chen, Y. T. Qian, and Y. Xie, *Chem. Lett.* 3, 236 (2001).
101. B. Li, Y. Xie, J. X. Huang, H. L. Su, and Y. Qian, *Nanostructured Mater.* 11, 1067 (1999).
102. Y. Xie, H. L. Su, B. Li, and Y. T. Qian, *Mater. Res. Bull.* 35, 675 (2000).
103. C. R. Wang, K. B. Tang, Q. Yang, B. Hai, G. Z. Shen, C. H. An, W. C. Yu, and Y. T. Qian, *Inorg. Chem. Commun.* 4, 339 (2001).
104. H. W. Liao, Y. F. Wang, X. M. Liu, Y. D. Li, and Y. T. Qian, *Chem. Mater.* 12, 2819 (2000).
105. W. X. Zhang, Z. H. Yang, X. M. Huang, S. Y. Zhang, W. C. Yu, Y. T. Qian, Y. B. Jia, G. I. Zhou, and L. Chen, *Solid State Commun.* 119, 143 (2001).
106. W. W. Webb and W. D. Forgeng, *J. Appl. Phys.* 28, 1449 (1957).
107. P. L. Edwards and R. J. Happel, Jr., *J. Appl. Phys.* 33, 943 (1962).
108. R. B. Sharma, *J. Appl. Phys.* 41, 1866 (1970).
109. S. D. Sharma and S. C. Kashyap, *J. Appl. Phys.* 42, 5302 (1971).
110. M. Egashira, Y. Yoshida, and S. Kawasumi, *Sensors and Actuators* 9, 147 (1986).
111. T. Oota, I. Yamai, and M. Yokoyama, *J. Cryst. Growth* 66, 262 (1984).
112. C. Kaito, Y. Nakata, Y. Saito, T. Naiki, and K. Fujita, *J. Cryst. Growth* 74, 469 (1986).
113. H. Hashimoto, A. Kumao, T. Eto, and K. Fujiwara, *J. Cryst. Growth* 7, 113 (1970).
114. K. Nakahigashi and Y. Shimomura, *J. Cryst. Growth* 28, 367 (1975).
115. S. Simov, N. Koparanova, G. Metchenov, and D. Genchev, *J. Mater. Sci.* 18, 623 (1983).
116. N. Koparanova, D. Genchev, G. Metchenov, and S. Simov, *J. Mater. Sci. Lett.* 4, 181 (1985).
117. M. Nagano, *J. Cryst. Growth* 66, 377 (1984).
118. M. Schreiner, W. Wruss, and B. Lux, *J. Cryst. Growth* 61, 75 (1983).
119. S. Hashimoto and A. Yamaguchi, *J. Mater. Sci.* 31, 317 (1996).

120. H. Yumoto, S. Onozumi, Y. Kato, M. Ishihara, and K. Kishi, *Cryst. Res. Technol.* 31, 159 (1996).
121. Y. Q. Zhu, W. K. Hsu, M. Terrones, N. Grobert, H. Terrones, J. P. Hare, H. W. Kroto, and D. R. M. Walton, *J. Mater. Chem.* 8, 1859 (1998).
122. V. Valcárcel, A. Souto, and F. Guitián, *Adv. Mater.* 10, 138 (1998).
123. H. Yumoto, T. Sako, Y. Gotoh, K. Nishiyama, and T. Kaneko, *J. Cryst. Growth* 203, 136 (1999).
124. Z. G. Bai, D. P. Yu, H. Z. Zhang, Y. Ding, Y. P. Wang, X. G. Gai, Q. L. Hang, G. C. Xiong, and S. Q. Feng, *Chem. Phys. Lett.* 303, 311 (1999).
125. Y. H. Tang, Y. F. Zhang, N. Wang, I. Bello, C. S. Lee, and S. T. Lee, *Appl. Phys. Lett.* 74, 3824 (1999).
126. X. C. Wu, W. H. Song, B. Zhao, Y. P. Sun, and J. J. Du, *Chem. Phys. Lett.* 349, 210 (2001).
127. Y. Q. Zhu, W. Hu, W. K. Hsu, M. Terrones, N. Grobert, J. P. Hare, H. W. Kroto, D. R. M. Walton, and H. Terrones, *Chem. Phys. Lett.* 309, 327 (1999).
128. W. B. Hu, Y. Q. Zhu, W. K. Hsu, B. H. Chang, M. Terrones, N. Grobert, H. Terrones, J. P. Hare, H. W. Kroto, and D. R. M. Walton, *Appl. Phys. A* 70, 231 (2000).
129. A. Kh. Abduev, A. K. Akhmedov, V. G. Baryshnikov, and Sh. O. Shakhshayev, *Tech. Phys. Lett.* 26, 332 (2000).
130. M. H. Huang, Y. Wu, H. Feick, N. Tran, E. Weber, and P. Yang, *Adv. Mater.* 13, 113 (2001).
131. M. H. Huang, S. Mao, H. Feick, H. Yan, Y. Wu, H. Kind, E. Weber, R. Russo, and P. Yang, *Science* 292, 1897 (2001).
132. Y. C. Kong, D. P. Yu, B. Zhang, W. Wang, and S. Q. Fang, *Appl. Phys. Lett.* 78, 407 (2001).
133. Z. W. Pan, Z. R. Dai, and Z. L. Wang, *Science* 291, 1947 (2001).
134. W. I. Park, D. H. Kim, S.-W. Jung, and G.-C. Yi, *Appl. Phys. Lett.* 80, 4232 (2002).
135. Z. Cui, G. W. Meng, W. D. Huang, G. Z. Wang, and L. D. Zhang, *Mater. Res. Bull.* 35, 1653 (2000).
136. J. Zhang, L. Zhang, X. Peng, and X. Wang, *Appl. Phys. A* 73, 773 (2001).
137. Y. Yin, G. Zhang, and Y. Xia, *Adv. Funct. Mater.* 12, 293 (2002).
138. H. Z. Zhang, Y. C. Kong, Y. Z. Wang, X. Du, Z. G. Bai, J. J. Wang, D. P. Yu, Y. Ding, Q. L. Hang, and S. Q. Feng, *Solid State Commun.* 109, 677 (1999).
139. X. C. Wu, W. H. Song, W. D. Huang, M. H. Pu, B. Zhao, Y. P. Sun, and J. J. Du, *Chem. Phys. Lett.* 328, 5 (2000).
140. C. C. Tang, S. S. Fan, M. L. De La Chapelle, and P. Li, *Chem. Phys. Lett.* 333, 12 (2001).
141. Z. R. Dai, Z. W. Pan, and Z. L. Wang, *J. Phys. Chem. B* 106, 902 (2002).
142. Y. C. Choi et al., *Adv. Mater.* 12, 746 (2000).
143. C. Liang, G. Meng, Y. Lei, F. Phillipp, and L. Zhang, *Adv. Mater.* 13, 1330 (2001).
144. Z. W. Pan, Z. R. Dai, and Z. L. Wang, *Appl. Phys. Lett.* 80, 309 (2002).
145. W. Wang, G. Wang, X. Wang, Y. Zhan, Y. Liu, and C. Zheng, *Adv. Mater.* 14, 67 (2002).
146. X. Wang and Y. Li, *J. Am. Chem. Soc.* 124, 2880 (2002).
147. W. Wang, C. Xu, G. Wang, Y. Liu, and C. Zheng, *Adv. Mater.* 14, 837 (2002).
148. W. Wang, Y. Liu, C. Xu, C. Zheng, and G. Wang, *Chem. Phys. Lett.* 362, 119 (2002).
149. X. S. Peng, X. F. Wang, Y. W. Wang, C. Z. Wang, G. W. Meng, and L. D. Zhang, *J. Phys. D* 35, L101 (2002).
150. D. Pan, Z. Shuyuan, Y. Chen, and J. G. Hou, *J. Mater. Res.* 17, 1981 (2002).
151. C. Ye, G. Meng, L. Zhang, G. Wang, and Y. Wang, *Chem. Phys. Lett.* 363, 34 (2002).
152. G. L. Li, G. H. Wang, and J. M. Hong, *J. Mater. Res.* 14, 3346 (1999).
153. L. Guo, Z. Wu, T. Liu, W. Wang, and H. Zhu, *Chem. Phys. Lett.* 318, 49 (2000).
154. W. Wang, C. Lan, Y. Li, K. Hong, and G. Wang, *Chem. Phys. Lett.* 366, 220 (2002).
155. D. R. Hamilton, *J. Electrochem. Soc.* 105, 735 (1958).
156. W. Brenner, "Silicon Carbide: A High Temperature Semiconductor." Pergamon, Oxford, UK, 1959.
157. R. F. Adamsky and K. M. Merz, *Z. Krist.* 3, 350 (1959).
158. W. F. Knippenberg, *Philips Res. Rep.* 18, 161 (1963).
159. L. Patrick, *Phys. Rev.* 143, 526 (1966).
160. C. E. Ryan, I. Erman, R. C. Marshall, D. P. Considine, and J. J. Hawley, *J. Cryst. Growth* 1, 255 (1967).
161. A. Addamiano, *J. Cryst. Growth* 58, 617 (1982).
162. G. A. Bootsma, W. F. Knippenberg, and G. Verspui, *J. Cryst. Growth* 11, 297 (1971).
163. J. V. Milewski, F. D. Gac, J. J. Petrvic, and S. R. Skaggs, *J. Mater. Sci.* 20, 1160 (1985).
164. X. T. Zhou, N. Wang, H. L. Lai, H. Y. Peng, I. Bello, N. B. Wong, C. S. Lee, and S. T. Lee, *Appl. Phys. Lett.* 74, 3942 (1999).
165. Y. Q. Zhu, W. B. Hu, W. K. Hsu, M. Terrones, N. Grobert, J. P. Hare, H. W. Kroto, D. R. M. Walton, and H. Terrones, *J. Mater. Chem.* 9, 3173 (1999).
166. W. Shi, Y. Zheng, H. Peng, N. Wang, C. S. Lee, and S. T. Lee, *J. Am. Ceram. Soc.* 83, 3228 (2000).
167. I. C. Leu, Y. M. Lu, and M. H. Hon, *Mater. Chem. Phys.* 56, 256 (1998).
168. R. Moene, F. W. Tazelaar, M. Makkee, and J. A. Moulijn, *J. Catal.* 170, 311 (1997).
169. T. Hashishin, Y. Kaneko, H. Iwanaga, and Y. Yamamoto, *J. Mater. Sci.* 34, 2189 (1999).
170. M. Saito, S. Nagashima, and A. Kato, *J. Mater. Sci. Lett.* 11, 373 (1992).
171. H. J. Choi and J. G. Lee, *J. Mater. Sci.* 30, 1982 (1995).
172. T. Belmonte, L. Bonnetain, and J. L. Ginoux, *J. Mater. Sci.* 31, 2367 (1996).
173. S. Motojima, M. Sasegawa, and T. Hattori, *J. Cryst. Growth* 87, 311 (1988).
174. J. G. Lee and I. B. Cutler, *Am. Ceram. Soc. Bull.* 54, 195, (1975).
175. R. V. Krishnarao, M. M. Gpdlljomdo, P. G. I. Mukunda, and M. Chakraborty, *J. Am. Ceram. Soc.* 74, 2869 (1991).
176. R. V. Krishnarao, M. M. Godkhindi, M. Chakraborty, and P. G. Mukundan, *J. Mater. Sci.* 29, 2741 (1994).
177. M. Patel and A. Karera, *J. Mater. Sci. Lett.* 8, 955 (1989).
178. A. Selvam, N. G. Nair, and P. Singh, *J. Mater. Sci. Lett.* 17, 57 (1998).
179. S. Motojima, Y. Owaga, S. Gakei, and H. Iwanaga, *Mat. Sci. Eng. B* 30, 13 (1995).
180. L. Wang, H. Wada, and L. F. Allard, *J. Mater. Res.* 7, 148 (1992).
181. Q. Lu, J. Hu, K. Tang, Y. Qian, G. Zhou, X. Liu, and J. Zhu, *Applied Physics Letters* 75, 507 (1999).
182. Y. B. Li, S. S. Xie, X. P. Zou, D. S. Tang, Z. Q. Liu, and W. Y. Zhou, *J. Cryst. Growth* 223, 125 (2001).
183. Y. Zhang, M. N. Gamo, C. Xiao, and T. Ando, *J. Appl. Phys.* 91, 6066 (1999).
184. D. Zhou and S. Seraphin, *Chem. Phys. Lett.* 222, 233 (1994).
185. H. Dai, E. W. Wong, Y. Z. Lu, S. Fan, and C. M. Lieber, *Nature* 375, 769 (1995).
186. W. Han, S. Fan, Q. Li, W. Liang, B. Gu, and D. Yu, *Chem. Phys. Lett.* 265, 374 (1997).
187. G. W. Meng, L. D. Zhang, C. M. Mo, S. Y. Zhang, Y. Qin, S. P. Feng, and H. J. Li, *J. Mater. Res.* 13, 2533 (1998).
188. Z. L. Wang, Z. R. Dai, R. P. Gao, Z. G. Bai, and J. L. Gole, *Appl. Phys. Lett.* 77, 3349 (2000).
189. H. F. Zhang, C. M. Wang, and L. S. Wang, *Nano Lett.* 2, 941 (2002).

190. R. Stevens, *J. Mater. Sci. Lett.* 7, 723 (1972).
191. H. Iwanaga, T. Yoshie, H. Katuki, M. Egashira, and S. Takeuchi, *J. Mater. Sci. Lett.* 5, 946 (1986).
192. G. McMahon, G. J. C. Carpenter, and T. F. Malis, *J. Mater. Sci.* 26, 5655 (1991).
193. W. S. Seo and K. Koumoto, *J. Am. Ceram. Soc.* 83, 2584 (2000).
194. H. J. Choi and J. G. Lee, *Ceram. Inter.* 26, 7 (2000).
195. S. Mierzejewska and T. Niemyski, *J. Less Common Metals* 8, 368 (1965).
196. C. Jasson and J. O. Carlsson, *Thin Solid Films* 124, 101 (1985).
197. A. W. Mullendore, *AIP Proc.* 140, 41 (1996).
198. M. C. Schouler, M. C. Cheynet, K. Sestier, J. Garden, and P. Gadelee, *Carbon* 35, 993 (1997).
199. K. Kho and T. Nakajima, *Carbon* 36, 913 (1998).
200. K. Kamamura, O. Nittono, and S. Nagakura, *J. Cryst. Growth* 35, 185 (1976).
201. A. Kato, M. Yasunaga, and N. Tamari, *J. Cryst. Growth* 37, 293 (1977).
202. N. Tamari and A. Kato, *J. Cryst. Growth* 46, 221 (1979).
203. A. Kato and N. Timari, *J. Cryst. Growth* 49, 199 (1980).
204. K. Naito, N. Kamegashira, and N. Fujiwara, *J. Cryst. Growth* 45, 506 (1978).
205. R. Mathur and B. M. Gallois, *Mater. Res. Soc. Symp. Proc.* 168, 267 (1990).
206. Z. Wokulski and K. Wokulska, *J. Cryst. Growth* 62, 439 (1983).
207. S. Motojima, H. Asano, and H. Iwanaga, *J. Eur. Ceram. Soc.* 16, 989 (1996).
208. M. Carlsson, F. J. Garcia-Gracia, and M. Johnsson, *J. Cryst. Growth* 236, 446 (2002).
209. J. B. Li, G. Y. Xu, E. Y. Sun, Y. Huang, and P. F. Becher, *J. Am. Ceram. Soc.* 81, 1689 (1998).
210. M. Johnsson, *J. Mater. Sci. Lett.* 19, 1571 (2000).
211. M. Johnsson and M. Nygren, *J. Mater. Res.* 12, 2419 (1997).
212. Y.-J. Chen, J.-B. Li, Q.-M. Wei, and H.-Z. Zhai, *Mater. Lett.* 56, 279 (2002).
213. D. C. Nesting, J. Kouvetakis, and D. J. Smith, *Appl. Phys. Lett.* 74, 958 (1999).
214. R. Ma and Y. Bando, *Chem. Phys. Lett.* 364, 314 (2002).
215. H. F. Zhang, A. C. Dohnalkova, C. M. Wang, J. S. Young, E. C. Buck, and L. S. Wang, *Nano Lett.* 2, 105 (2002).
216. D. Zhang, D. N. McIlroy, Y. Geng, and M. G. Norton, *J. Mater. Sci. Lett.* 18, 349 (1999).
217. D. N. McIlroy, D. Zhang, Y. Kranov, and M. G. Norton, *Appl. Phys. Lett.* 79, 1540 (2001).
218. A. Amerlinckx, X. B. Zhang, D. Bernaerts, X. F. Zhang, V. Ivanov, and J. B. Nagy, *Science* 265, 635 (1994).
219. A. Fukunaga, S. Chu, M. E. McHenry, and M. Nagumo, *J. Mater. Res.* 13, 2465 (1998).
220. Y. Gao, J. Lin, S. H. Elder, and J. W. Virden, *Appl. Phys. Lett.* 74, 3642 (1999).
221. S. S. Brenner, *Acta Met.* 4, 62 (1956) and references therein.
222. A. D. Verma and S. K. Peneva, *J. Cryst. Growth* 3, 700 (1968).
223. M. Yamamoto, Y. Gotoh, and K. Yoshida, *J. Cryst. Growth* 3, 705 (1968).
224. H. J. Latière, H. Caumon, and R. Michaud, *Mem. Sci. Rev. Met.* 64, 169 (1967).
225. S. Kittaka, K. Kishi, and T. Kaneko, *J. Cryst. Growth* 11, 197 (1971).
226. T. Kaneko and S. Kittaka, *J. Cryst. Growth* 42, 171 (1977).
227. T. Kaneko, *J. Cryst. Growth* 44, 14 (1978).
228. D. R. Overcash, C. L. Watlington, M. J. Skove, and E. P. Stillwell, *Physica* 55, 317 (1971).
229. A. G. Starliper and H. Kenworthy, *Electrodep. Sur. Treatment* 2, 249 (1974).
230. Y. Kitano, Y. Komura, T. Iwanari, and R. Kurashige, *J. Cryst. Growth* 24, 354 (1974).
231. Y. Zhou, S. H. Yu, X. P. Cui, C. Y. Wang, and Z. Y. Chen, *Chem. Mater.* 11, 545 (1999).
232. R. Tenne, in "Progress in Inorganic Chemistry" (K. D. Karlin, Ed.), Vol. 50, pp. 269–315. John Wiley & Sons, New York, 2001.
233. R. Tenne, L. Margulis, M. Genut, and G. Hodes, *Nature* 360, 444 (1992).
234. L. Margulis, G. Salitra, R. Tenne, and M. Talianker, *Nature* 365, 113 (1993).
235. M. Hershinkel, L. A. Gheber, V. Volterra, J. L. Hutchison, L. Margulis, and R. Tenne, *J. Am. Chem. Soc.* 116, 1914 (1994).
236. Y. Feldman, E. Wasserman, D. J. Srolovitz, and R. Tenne, *Science* 267, 222 (1995).
237. Y. R. Hachohen, E. Grunbaum, R. Tenne, J. Sloan, and J. L. Hutchison, *Nature* 395, 336 (1998).
238. M. Remskar, A. Mrzel, Z. Skraba, A. Jesih, M. Ceh, J. Demsar, P. Stadelmann, F. Levy, and D. Mihailovic, *Science* 292, 479 (2001).
239. A. Rubio, J. L. Corkill, and M. L. Cohen, *Phys. Rev. B* 49, 5081 (1994).
240. N. G. Chopra, R. J. Luyken, K. Cherrey, V. H. Crespi, M. L. Cohen, S. G. Louie, and A. Zettl, *Science* 269, 966 (1995).
241. A. Loiseau, F. Willaime, N. Demoncey, G. Hug, and H. Pascard, *Phys. Rev. Lett.* 76, 4737 (1996).
242. M. Kuno, T. Oku, and K. Suganuma, *Diamond and Related Materials* 10, 1231 (2001).
243. I. Narita and T. Oku, *Solid State Commun.* 122, 465 (2002).
244. Y. Saito and M. Maida, *Phys. Chem. A.* 10, 1291 (1999).
245. J. Cumings and A. Zettl, *Chem. Phys. Lett.* 316, 211 (2000).
246. D. Golberg, Y. Bando, K. Kurashima, and T. Sato, *Solid State Commun.* 116, 1 (2000).
247. F. L. Deepak, C. P. Vinod, K. Mukhopadhyay, A. Govindraj, and C. N. R. Rao, *Chem. Phys. Lett.* 353, 345 (2002).
248. R. Ma, Y. Bando, T. Sato, and K. Kurashima, *Chem. Mater.* 13, 2965 (2001).
249. O. Stephan, P. M. Ajayan, C. Colliex, Ph. Redlich, J. M. Lambert, P. Bernier, and P. Lefin, *Science* 266, 1684 (1994).
250. D. Goldberg, Y. Bando, W. Han, K. Kurashima, and T. Sato, *Chem. Phys. Lett.* 308, 337 (1999).
251. D. Goldberg, Y. Bando, O. Stephan, and K. Kurashima, *Appl. Phys. Lett.* 73, 2441 (1998).
252. P. M. Ajayan, O. Stephan, P. Redlich, and C. Colliex, *Nature* 375, 564 (1995).
253. C. N. R. Rao, B. C. Satishkumar, and A. Govindaraj, *Chem. Commun.* 16, 1581 (1997).
254. K. Awasthi, A. K. Singh, and O. N. Srivastava, *J. Nanosci. Nanotech.* 2, 67 (2002).
255. H. Nakamura and Y. Matsui, *J. Am. Chem. Soc.* 117, 2651 (1995).
256. M. E. Spahr, P. Bitterli, R. Nesper, M. Muller, F. Krumeich, and H. U. Nissen, *Agnew. Chem. Int. Ed.* 37, 1263 (1998).
257. T. Kasuga, M. Hiramatsu, A. Hoson, T. Sekino, and K. Niihara, *Langmuir* 14, 3160 (1998).
258. U. Graham, S. Sharma, M. K. Sunkara, and B. Davis, *Advanced Materials*, submitted (2002).
259. R. Ma, Y. Bando, T. Sato, C. Tang, and F. Xu, *J. Am. Chem. Soc. Commun.* 124, 10668 (2002).
260. J. Hu, B. Deng, Q. Lu, K. Tang, R. Jiang, Y. Qiang, G. Zhou, and H. Cheng, *Chem. Commun.* 8, 715 (2000).
261. H. Li, H. Chandrasekaran, and M. K. Sunkara, *Journal of Crystal Growth*, submitted (2002).
262. S. M. Lee, Y. H. Lee, Y. G. Hwang, J. Elsner, D. Porezag, and T. Frauenhiem, *MRS Internet J. Nitride Semiconductor Res.* 4S1, G6.3 (1999).

Synthesis of Metal Chalcogenide Nanoparticles

Jun-Jie Zhu, Hui Wang

Nanjing University, Nanjing 210093, People's Republic of China

CONTENTS

1. Introduction
 2. Synthetic Methods
 3. Characterizations
 4. Properties and Applications
 5. Conclusion
- Glossary
References

1. INTRODUCTION

In the past decade, the synthesis, characterizations, and applications of nanodimensional materials have been the focus of interest of many researchers in various fields including chemistry, physics, materials science, biology, and corresponding engineering [1–4]. Nanoparticles usually exhibit unusual electronic, optical, magnetic, and chemical properties significantly different from those of corresponding bulk materials due to their extremely small sizes and large surface-to-volume ratio. They have various potential applications such as catalysis, electronic, optical, and mechanical devices, magnetic recording media, superconductors, high-performance engineering materials, dyes, pigments, adhesives, photographic suspensions, drug delivery, and so on [5]. The rapid development of nanoscience and nanotechnology will bring us a new world [6]. Exploring new methods that involve mild conditions and convenient operations for the preparation of nanosized materials with desirable properties and controllable dimensions and morphologies is currently a great challenge to both synthetic chemists and materials scientists.

Over the past two decades, the synthesis of chalcogenides has attracted significant interest and is still the subject of intense investigations. Conventionally, metal chalcogenides

can be prepared in a variety of ways, the most straightforward of which is the direct combination of the elements at elevated temperatures [7]. This process requires a significant energy input, lasts for a long period of reaction time, and gives little control in material stoichiometry [8]. A low-energy approach is the precipitation of metal chalcogenides from aqueous solutions of metal cations by use of H_2E ($E = S, Se, \text{ or } Te$) [9]. Problems with this method include the use of very toxic reagents and consistently obtaining the product with a high degree of impurity. Molecular precursor methods [10] involve thermal decomposition of a compound containing a $M-S$ or $M-Se$ bond, or involve H_2E as the chalcogenide source [11]. These methods have already been thoroughly investigated and found to be reliable at relatively low temperature (200–350 °C). Bulk materials have also been prepared from the elements by self-propagating high-temperature synthesis [12] and from the reactions of alkali-metal sulfides and metal halides by solid-state metathesis [13]. In recent years, emphasis has been devoted to the synthesis of metal chalcogenides in their nanophased form. This is due to the modern trend of miniaturization, on one hand, and to the unique properties associated with the nanostructures, on the other hand. In the past few years, a number of new methods have been established for the preparation of nanocrystalline metal chalcogenides. Their appearance gives great impetus to the development of nanoscience and nanotechnology. The application of these novel technologies provides convenient and efficient routes to produce nanocrystalline metal chalcogenides with desirable properties and controllable sizes and morphologies. These synthetic methods have already shown their advantages and will play a more and more important role in materials science in the future.

Herein, we present a review about the latest progress in the field of synthesis of metal chalcogenide nanoparticles. This review mainly focuses on some novel synthetic methods for nanocrystalline metal chalcogenides that have been established in the past decade including microwave assisted heating, sonochemical method, sonoelectrochemical method, photochemical synthesis, γ -irradiation method,

microemulsion route, low-temperature solid-state synthesis, solvothermal technique, electrochemical template synthesis, and sol-gel method.

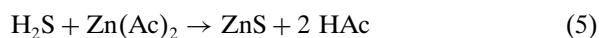
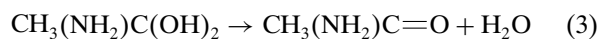
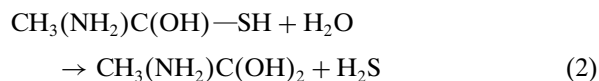
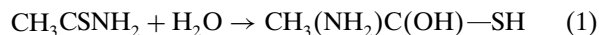
2. SYNTHETIC METHODS

2.1. Microwave Assisted Heating

Microwave heating has been known since the 1940s and widely used in the food industry. Microwaves are electromagnetic waves containing electric and magnetic field components. It is well known that the interaction of dielectric materials, liquids or solids, with microwaves leads to what is generally known as dielectric heating. Electric dipoles present in such materials respond to the applied electric field. In liquids, this constant reorientation leads to the friction between molecules, which subsequently generate heat. Claimed effects of microwave irradiation include thermal effects and nonthermal effects. Microwave irradiation as a heating method has found a number of applications in chemistry. The frequencies allotted for microwave assisted heating are 918 MHz and 2.45 GHz, with the latter frequency being most often used. The latter is also applied in domestic microwave ovens. The microwave ovens used in microwave chemistry range from simple household multimode ovens to large-scale batch as well as continuous multimode ovens. The microwave synthesis, which is generally quite fast, simple, and efficient in energy, has been developed and is widely used in fields such as molecular sieve preparation, radiopharmaceuticals, the preparation of inorganic complexes and oxide, organic reactions, plasma chemistry, analytical chemistry, and catalysis [14]. Though the number of publications related to the application of microwave irradiation in organic chemistry has shown an exponential growth over the past two decades, its extension to inorganic chemistry, on the other hand, has been much slower. It is only quite recently that microwave irradiation has been used in the synthesis of inorganic nanoparticles and keeps showing rapid growth in its application to materials science. Compared with conventional heating methods, microwave assisted heating presents a more rapid and simultaneous environment for the formation of nanoparticles due to the fast and homogeneous heating effects of microwave irradiation. Therefore, microwave assisted heating method has the advantages of short reaction time, high-energy efficiency, and the ability to induce the formation of particles with small size, narrow size distribution, and high purity. In the past few years, microwave assisted heating has been applied in the soft chemical synthesis of various nanocrystalline metal chalcogenides and presents a promising trend in its future development.

Water has a very high dipole moment, which makes it one of the best solvents for microwave assisted reactions. A series of sulfide and selenide nanoparticles have been synthesized by microwave assisted heating method in aqueous solutions. Zhu and co-workers [15] have prepared CdS and ZnS nanoparticles by refluxing aqueous solutions containing CdCl₂ or Zn(Ac)₂ and thioacetamide in the presence of microwave irradiation. The average sizes of the as-prepared CdS and ZnS nanoparticles were ca. 9 nm and ca. 3 nm,

respectively, and both products displayed conspicuous quantum size effects. The reactions occurring during microwave irradiation are believed to be



Equation (1) represents that H₂O reacts with CH₃CSNH₂ to form CH₃(NH₂)C(OH)—SH by microwave heating. Repeating this process would then result in the formation of CH₃(NH₂)C(OH)₂ and H₂S. CH₃(NH₂)C(OH)₂ would immediately lose water to give CH₃CONH₂ (Eq. (3) shows the results). The further H₂S reacts with CdCl₂ or Zn(Ac)₂ to yield CdS or ZnS, respectively. Liao et al. [16] extended this methodology to the microwave assisted preparation of various metal sulfide nanoparticles including CdS, ZnS, CuS, HgS, and Bi₂S₃ by choosing 37.5% formaldehyde aqueous solution as solvent. During the microwave-induced formation of the sulfide nanoparticles, HCHO did not take part in the reactions. However, it acts as the dispersion stabilizer. It was found that the size and morphology of the as-prepared sulfide nanoparticles were different though the same irradiation time and intensity were used. This work showed that microwave irradiation could influence selective nucleation and growth rates of different compounds. Gedanken and co-workers [17] reported the microwave assisted preparation of nanocrystalline selenide semiconductors including CdSe, Cu_{2-x}Se, and PbSe. In this method, CdSO₄, Pb(Ac)₂, or Cu(Ac)₂ reacted with Na₂SeSO₃ in water in the presence of complexing agents with inducement of microwave irradiation to fabricate selenide nanoparticles. In the experiments, several factors were found to have influence on the nature and morphology of the products, such as the pH value, irradiation time, complexing agents, and so on.

Currently, one-dimensional (1D) nanostructured materials have been the focus of scientific research due to their unusual properties and potential uses in both mesoscopic research and the development of nanodevices. Synthesis of metal chalcogenide nanorods (nanowires) or nanoribbons and investigations of their properties arouse considerable interests. Zhu's group has successfully applied microwave irradiation to induce the one-dimensional preferential growth of some II-VI and V-VI group semiconductors and prepared Bi₂S₃ [18] and Sb₂S₃ [19] nanorods and CdS nanoribbons [20] by microwave-induced decomposition of single-source precursors. It was found that microwave-induced decomposition of Bi-thiourea complex in formaldehyde solution and Sb-thiourea complex in N,N-dimethylformamide would lead to the formation of Bi₂S₃ and Sb₂S₃ nanorods, respectively. The observed rod type morphology of the as-prepared Bi₂S₃ and Sb₂S₃ is probably due to the chain type structures of such kind of materials. The formation of uniform nanosized particles demands

a uniform growth environment, and microwave heating afforded this. With microwave irradiation of reactants in polar solvents, temperature and concentration gradients can be avoided, providing a uniform environment for the nucleation. During the process, microwaves not only provided the energy for the decomposition of the complexes, but also greatly accelerated the nucleation. All these were favorable for the formation of uniform and small-sized nanorods. CdCl_2 and 1-pyrrolidine dithio carboxylic acid ammonium salt (APDTC) would react with each other to form an inorganic core cluster complex $[\text{Cd}(\text{APDTC})_2]_2$, which was unstable. Nucleophilic attack by ethylenediamine with the inducement of microwave irradiation would lead to the formation of Cd_2S_2 crystal nuclei. These nuclei were not stable and had the tendency to combine with each other to grow into larger crystals. During the crystal growth process, these Cd_2S_2 nuclei preferentially grew along a unique direction grid, which resulted in the formation of a 1D structure. It was also found that ethylenediamine, which was a strong coordination Lewis base and N-chelation reagent, played an important role in the formation of CdS nanoribbons. When other solvent such as water or ethanol was utilized to replace ethylenediamine, CdS nanoribbons could not be obtained. These results showed that ethylenediamine probably served as a director for the preferential 1D growth of the CdS nanoribbons.

During the formation of the nanoparticles under microwave irradiation, solvents have important influence on the size and morphology of the final products. In different solvents, the collision rate between reactant molecules, the heating rate, and the temperature of the reaction are different. As a result, nanocrystalline particles with different sizes and morphologies could be obtained by using different solvents. Wang et al. [21] established a microwave assisted heating method for the rapid synthesis of spherical β -HgS nanoparticles with different sizes. By using different solvents, the average sizes of the HgS nanoparticles could be controlled in the range of 8 to 23 nm. Murugan and co-workers [22] used a combination of microwave and solvothermal techniques for the synthesis of CdS nanocrystalline powders. The effects of different parameters such as reaction time, temperature, solvent, and molar ratio of Cd^{2+} to thiourea on the formation of CdS powders under microwave-solvothermal conditions were investigated in detail. It was found that solvents had significant effects not only on the different particle sizes, but also on the morphologies and phases of the products.

Metal tellurides are relatively more difficult to prepare than sulfides and selenides due to their much lower reactivity and high toxicity. Palchik et al. [23] used microwave irradiation to activate the reaction between elemental Te and $\text{Cu}(\text{Ac})_2$ or $\text{Hg}(\text{Ac})_2$ in ethylenediamine and synthesized Cu_{2-x}Te and HgTe nanoparticles. The copper telluride prepared by this method was a complex of Cu_{2-x}Te and ethylenediamine, which decomposed into pure Cu_{2-x}Te following annealing at 280 °C. Two probable mechanisms were proposed for the formation of the telluride by microwave irradiation. The first one could be described as a direct interaction between the tellurium and the microwave irradiation. Microwave irradiation could be used to heat metallic powders to very high temperatures, even if they were

dispersed in low-boiling-point solvents. Since Te has some metallic characteristics (resistivity $\rho = 2 \times 10^{-6} \mu \Omega \text{ cm}$), its heating can be a major driving force for the reaction. Te would probably be heated to reach temperatures higher than the boiling point of ethylenediamine (118 °C), leading to the interfacial overheating of the solvent and facilitating the reactions. At an elevated temperature the ethylenediamine could reduce the Te to Te^{2-} , which subsequently reacts with the metallic ions. A second possibility is based on the observation that in microwave boiled solvents, the solvents themselves can undergo profound overheating. This localized overheating effect can reach 13–26 °C in the case of organic solvents. Such an increase in the boiling point has been known to result in an approximately eightfold reaction rate enhancement. Such overheating effects can increase the reduction power of the solvent and reduce the metal ions to the metal in the zero oxidation state. Such metallic powders will strongly interact with microwaves, yielding very high temperatures, which enhance the solid-state reaction of metal with Te. Research is still underway to assess the relative importance of the solvent overheating and microwave-induced “solid-state reactions” in the microwave assisted preparation of metal tellurides.

In the 1980s, Fievet et al. used ethylene glycol as a solvent and reducing agent for the preparation of submicrometer particles of the transition metals. This method is known as the polyol process [24–27]. The mechanism of this reaction, however, is still only poorly understood even though it is known that the reduction is based on the decomposition of the ethylene glycol and its conversion to diacetyl. It has been discovered that the temperature is a dominant factor affecting the reactivity. In these reactions, the temperature influences three factors: (1) reducing potential of polyol compound; (2) rupture and creation of chemical bond; and (3) diffusion. All these factors make the microwave assisted heating method favorable for the fabrication of chalcogenides using ethylene glycol as a solvent. Gedanken's group has already applied microwave irradiation to induce the formation of a series of binary and ternary chalcogenide nanoparticles via the so-called polyol process [28–31]. Polyol solvents like ethylene glycol are very suitable for microwave assisted reactions because of their relatively high dipole moment. Another advantage of using ethylene glycol as a solvent is its reducing power, which can be enhanced with the inducement of microwave irradiation. Palchik et al. [28] prepared CdSe “nanoballs” by a microwave assisted polyol reduction method. The cubic and hexagonal forms of CdSe nanoparticles could be obtained by choosing triethylene glycol and ethylene glycol as the solvent, respectively. The as-prepared “nanoballs” were actually built up of clusters of CdSe with sizes of a few nanometers. Kerner et al. [29] used the microwave assisted polyol reduction method to synthesize agglomerated PbSe and PbTe nanoparticles. It is noteworthy that they also found that such polyol reactions could be induced by ultrasound irradiation and the PbSe and PbTe nanoparticles prepared sonochemically were monodisperse. Grisaru et al. [30, 31] reported the extension of this method to the preparation of ternary selenide nanoparticles, $\text{Cd}_{1-x}\text{Zn}_x\text{Se}$ (Fig. 1). Changing the preparation conditions,

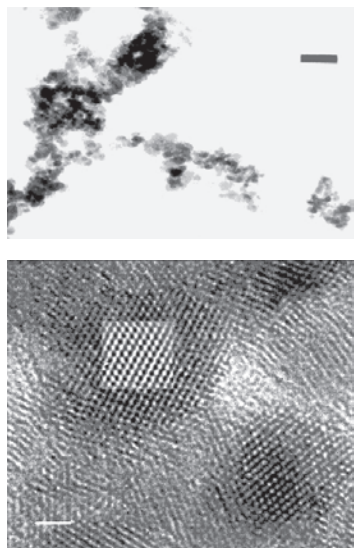


Figure 1. (top) The TEM image of hexagonal $\text{Cd}_{0.8}\text{Zn}_{0.2}\text{Se}$ spheres (bar equals 16 nm). (bottom) The HRTEM image of a hexagonal $\text{Cd}_{0.8}\text{Zn}_{0.2}\text{Se}$ nanoparticle (bar equals 15.7 Å). Inset is an FFT filtered image of the lattice. Reprinted with permission from [30], H. Grisar et al., *Inorg. Chem.* 40, 4814 (2001). © 2001, American Chemical Society.

such as the ratio of Cd and Zn, makes it possible to turn the electronic properties of $\text{Cd}_{1-x}\text{Zn}_x\text{Se}$. Further extension of this method may lead to the fabrication of some other ternary chalcogenide nanoparticles.

2.2. Sonochemical Synthesis

Currently, ultrasound irradiation has become an important tool in chemistry. It provides an unusual mechanism for generating high-energy chemistry with extremely high local temperatures and pressures and an extraordinary heating and cooling rate. Sonochemistry drives principally from acoustic cavitations: the formation, growth, and implosive collapse of bubbles in liquids [32]. When solutions are exposed to strong ultrasound irradiation, bubbles are implosively collapsed by acoustic fields in the solution. High-temperature and high-pressure fields are produced at the centers of the bubbles. The implosive collapse of the bubbles generates a localized hotspot through adiabatic compression or shock wave formation within the gas phase of the collapsing bubbles. The conditions formed in these hotspots have been experimentally determined, with the transient temperature of ~ 5000 K, pressure of >1800 atm, and cooling rates in excess of 10^{10} K/s. These extreme conditions enable many chemical reactions to occur. Ultrasound irradiation differs from traditional energy sources (such as heat, light, or ionizing radiation) in duration, pressure, and energy per molecule. The use of high-intensity ultrasound irradiation to enhance the reactivity of metals as stoichiometric reagent has become a synthetic technique for many heterogeneous organic and organometallic reactions [33], especially those involving reactive metals, such as Mg, Li, or Zn. This development originated from the early work of Renaud and the more recent breakthrough of Luche [34]. The effects

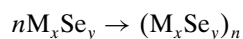
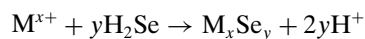
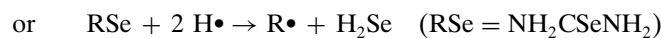
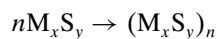
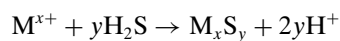
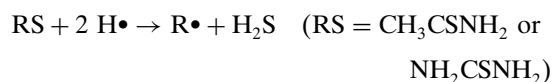
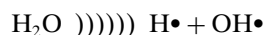
are fairly general and apply to reactive inorganic salts as well. Suslick and co-workers found a variety of sonochemical reactions in liquid-solid mixture synthesis, for example, intercalation into layered inorganic solids [35], synthesis of amorphous metal powders [32], and metal semicarbides [36]. Ultrasound irradiation has also been used to induce hydrolysis to produce various metal oxide nanoparticles [37].

Ultrasound irradiation also offers a very attractive method for the preparation of various nanosized metal chalcogenides. In recent years, it has shown very rapid growth in its application to materials science due to its unique reaction effects. The advantages of this method include a rapid reaction rate, controllable reaction conditions, and the ability to form nanoparticles with uniform shapes, narrow size distributions, and high purities. It has been extensively used to generate novel materials with unusual properties, because in many cases it causes the formation of particles with a much smaller size and higher surface area than those reported by other methods. It has been known that during the sonochemical process, three different regions [38] are formed: (a) the inner environment (gas phase) of the collapsing bubbles, where the elevated temperatures and pressures are produced; (b) the interfacial region between the cavitation bubbles and the bulk solution where the temperature is lower than in the gas-phase region but still high enough to induce a sonochemical reaction; (c) the bulk solution, which is at ambient temperature. Among the three regions mentioned above, it appears that the current sonochemical reaction occurs within the interfacial region, yielding nanoparticles, because of the very high quenching rate experienced by the products. These products present either nanoamorphous or nanocrystalline nature [39, 40], as the results of different conditions formed during ultrasound irradiation.

A wide range of commercial equipment is now readily available for sonochemical research. High-intensity ultrasonic probes (50 to 500 W/cm^2) of the type used for biological cell disruption are the most reliable and effective source for laboratory-scale sonochemistry and permit easy control over ambient temperature and atmosphere. Ultrasonic cleaning baths are less satisfactory, owing to their low intensities (about 1 W/cm^2). For larger-scale irradiations, flow reactors with high ultrasonic intensities are commercially available in 20-kW modular units [32].

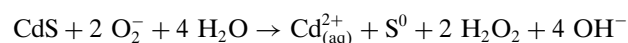
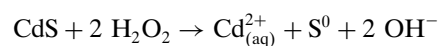
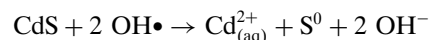
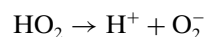
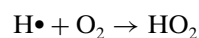
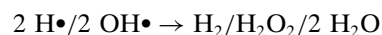
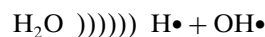
Ultrasound waves that are intense enough to produce cavitations can drive chemical reactions such as oxidation, reduction, dissolution, and decomposition. Other reactions driven by high-intensity ultrasound irradiation, such as promotion of polymerization, have also been reported [32d]. It has been known that during an aqueous sonochemical process, the elevated temperatures and pressures inside the collapsing bubbles cause water to vaporize and further pyrolyze into $\text{H}\cdot$ and $\text{OH}\cdot$ radicals. The sonochemical formation of metal chalcogenide nanoparticles in aqueous solutions is related to the radical species generated from water molecules by the absorption of the ultrasound energy. The *in-situ* generated $\text{H}\cdot$ is highly reducing radicals that can reduce mercaptan or compounds containing $\text{C}=\text{S}$ or $\text{C}=\text{Se}$ bonds, such as thiourea, thioacetamide, and selenourea, to produce H_2S or H_2Se . Then the released H_2S or H_2Se reacts with metal cations to yield metal sulfides

or metal selenides. The sonochemical formation of metal chalcogenide nanoparticles in aqueous solution via such kind of reactions can be summarized as follows:

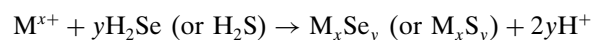
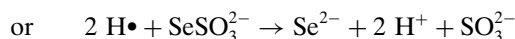
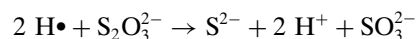
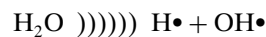


Zhu et al. [41] reported a sonochemical method for the preparation of nanophasic ZnSe. ZnSe nanoparticles of about 3 nm in size have been prepared by the sonochemical irradiation of an aqueous solution of selenourea and zinc acetate under argon. This method is proposed as a general method for the preparation of selenides. It has also been employed for the preparation of CuSe and PbSe nanoparticles. Jeevanandam et al. synthesized nanocrystalline ruthenium sulfide sonochemically by using ruthenium chloride and thiourea as precursors [42]. Sonication of an aqueous solution of ruthenium chloride and thiourea yielded an X-ray amorphous product which yields nanocrystalline ruthenium sulfide of stoichiometry $\text{RuS}_{1.7}$ on heating at 650 °C. The $\text{H}\cdot$ generated from water molecules by absorption of ultrasound not only reduced thiourea, but also triggered the reduction of Ru(III) to Ru(II). The RuS_2 formed an adduct with thiourea and water, $\text{RuS}_2(\text{NH}_2\text{CSNH}_2)_{1.5}(\text{H}_2\text{O})_{1.2}$, which on heating produced nanocrystallites of ruthenium sulfide with nonstoichiometry, $\text{RuS}_{1.7}$. Avivi et al. [43] reported the preparation of nanophased indium sulfide by sonicating an aqueous solution of indium chloride and thioacetamide, the latter serving as the sulfur source. The reaction was carried out at different temperatures. It was found that the sonication of InCl_3 with thioacetamide in an aqueous solution led to different products, depending on the sonication temperature. Sonication at 0 °C yielded In_2O_3 as the major product and In_2S_3 as a minor component. On the other hand, when the reaction is carried out at "room temperature," nanocrystalline In_2S_3 is obtained as the sole product. The products of sonication at 0 °C are obtained in the amorphous form. An explanation for this was offered based on the hot spot mechanism. CuS and NiS nanoparticles have also been synthesized by sonication of aqueous solutions containing metal acetate ($\text{Cu}(\text{CH}_3\text{COO})_2$ or $\text{Ni}(\text{CH}_3\text{COO})_2$) and thioacetamide (TAA) in the presence of triethanolamine (TEA) as a complexing agent under ambient air [44]. Grieser and co-workers [45] described the sonochemical formation of Q-state CdS colloid and the sonochemical dissolution of larger colloid CdS particles. In system containing mercaptopropionic acid, the action of ultrasound produces H_2S and in the presence of Cd^{2+} (aq.) ions, colloidal CdS was formed. The mechanism for the production of H_2S appeared to be predominantly $\text{H}\cdot$ attack on the thio group of the mercaptan, although there

was evidence that the local heating from ultrasound also contributed to H_2S formation. The colloidal particles produced sonochemically clearly showed quantum size effects and were estimated to be less than 3 nm in diameter. The dissolution of colloidal CdS at pH 10.5 appeared to be due to the reaction of H_2O_2 and O_2^- with the colloids. The likely explanation for the dissolution process can be summarized as below:



The $\text{H}\cdot$ generated during an aqueous sonochemical process can also trigger the reduction of $\text{S}_2\text{O}_3^{2-}$ or SeSO_3^{2-} to produce S^{2-} or Se^{2-} ions. The main steps can be described as follows:



Zhu and co-workers [46] have successfully prepared monodisperse lead selenide nanoparticles via a sonochemical route from an aqueous solution of lead acetate and sodium selenosulfate in the presence of complexing agents under ambient air. It was found that when trisodium citrate was used as the complexing agent, the product was spherical nanoparticles with an average size of ca. 8 nm (Fig. 2a).

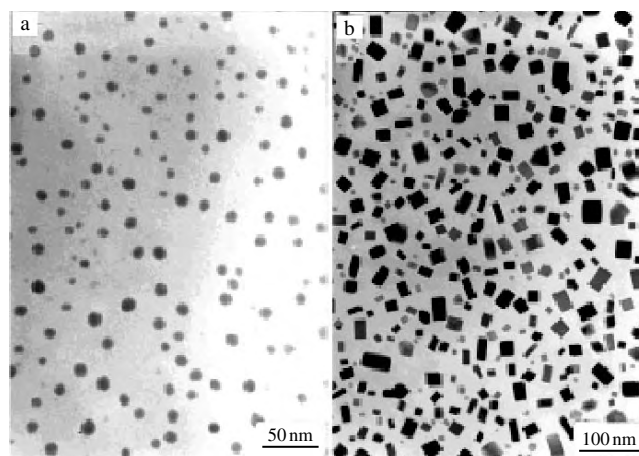
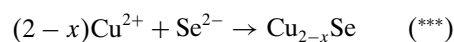
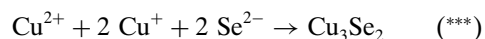
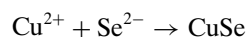
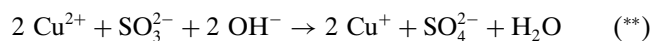
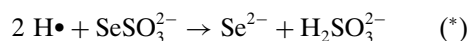


Figure 2. TEM images of (a) monodisperse spherical PbSe nanoparticles prepared sonochemically; (b) monodisperse rectangular PbSe nanoparticles prepared sonochemically. Reprinted with permission from [46], J. J. Zhu et al., *Langmuir* 18, 3306 (2002). © 2002, American Chemical Society.

If potassium nitrilotriacetate was used, the product consisted of rectangles with an average size of ca. 25 nm (Fig. 2b). Several other factors also affected the nature and morphology of the products, such as the pH value, the complexing agents, and the intensity of the ultrasound irradiation. Other selenide nanoparticles including HgSe [47], Cu₃Se₂, Cu_{2-x}Se, and CuSe [48], have also been synthesized sonochemically in aqueous solutions by using sodium selenosulfate as the selenium source. It was interesting that the ratio between Cu²⁺ and SeSO₃²⁻ concentrations played an important role in the phase transformation of copper selenides. In this system, copper selenides with different phases including Cu_{2-x}Se, Cu₃Se₂, and CuSe could be obtained selectively by changing the ratio between Cu²⁺ and SeSO₃²⁻ concentrations. The explanation of this phenomenon was proposed by the authors based on the following reactions:



The *in-situ*-generated H• radicals can react with SeSO₃²⁻ to give Se²⁻. Meanwhile, Cu²⁺ can be reduced by SO₃²⁻ to generate Cu⁺. When the concentration of SeSO₃²⁻ is high enough, the reaction (*) may be the main reaction so that the product is CuSe. The rate of reaction (*) decreased sharply with the decrease of the concentration of SeSO₃²⁻, and when the concentration of SeSO₃²⁻ was decreased, the reaction (**) changed gradually to be the main reaction so that the Cu⁺ generated together with Cu²⁺, leading to the formation of Cu₃Se₂ and Cu_{2-x}Se, as shown in reactions (***). The release of Se²⁻ was a continuous process, which makes the gradual growth of copper selenides nanocrystals. Wang et al. [49] synthesized Bi₂S₃ nanorods (Fig. 3) by a sonochemical method from an aqueous solution of bismuth nitrate and sodium thiosulfate in the presence of complexing agents. Bismuth sulfide nanorods with different

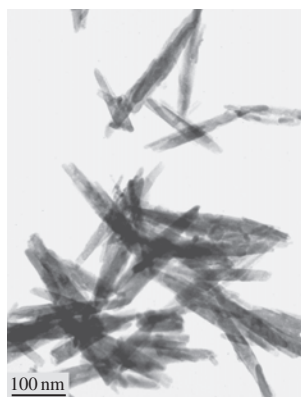
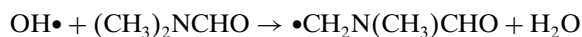
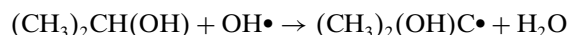


Figure 3. TEM image of Bi₂S₃ nanorods prepared by sonochemical method. Reprinted with permission from [49], H. Wang et al., *J. Phys. Chem. B* 106, 3848 (2002). © 2002, American Chemical Society.

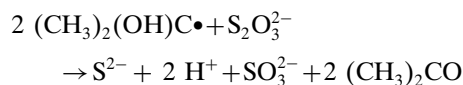
diameters and lengths could be obtained by using different complexing agents including ethylenediaminetetraacetic acid, triethanolamine, and sodium tartrate. When 20% N,N-dimethylformamide (DMF) was used as the solvent, higher yield was observed and smaller sizes of Bi₂S₃ nanorods were obtained. It has been known that in the bulk solution, factors favoring maximum acoustic cavitation and sonochemical yields are low viscosity, high surface tension, low vapor pressure, and high sound speed. DMF is favorable for sonochemical process for it fulfills all of the criteria mentioned. When 20% DMF-water solution was used as the solvent, better yield could be obtained. The DMF accumulated at the interfacial region is likely to outcompete the concurrent process of the removal of OH• radicals:



This is one of the most likely factors responsible for the continuing increase of the sonochemical radical yields. So when 20% DMF-water solution was used as the solvent instead of water alone, the sonochemical process was enhanced, which led to the better yields of the product. Furthermore, the existence of DMF in aqueous solution influences the size and morphology of the product. When 20% DMF-water solution was used as the solvent, the size of the Bi₂S₃ nanorods obtained became much smaller. The decrease in size may be attributed to the faster nucleation rate caused by the enhancement of the sonochemical process. Wang and co-workers [50] employed ultrasound irradiation to fabricate hexagonal and cubic CdS nanocrystallites in aqueous solutions with or without isopropyl alcohol addition at room temperature. If the reactions were carried out in pure aqueous solution, the as-prepared CdS crystallized in hexagonal structure. When the isopropyl alcohol, which was a scavenger of radicals, was added into pure aqueous solution, the final product was cubic phase CdS. In the presence of isopropyl alcohol, a secondary reducing radical (CH₃)₂(OH)C• was formed during sonication via hydrogen abstraction from the (CH₃)₂CH(OH) by OH• radicals through the following reaction:



Being a reducing radical, (CH₃)₂(OH)C• reacts with S₂O₃²⁻ rapidly to form S²⁻ ions:

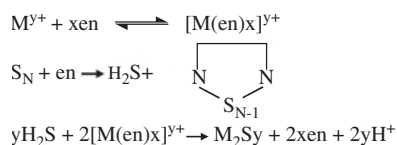


The presence of (CH₃)₂CH(OH) has a great influence on the structure and particle sizes of CdS nanocrystallites. It is known that kinetic factors are important in defining the crystal structure. (CH₃)₂CH(OH) can influence the dissolution and transmission of ions in the solutions, and might lead to the different kinetic factors.

The sonochemical reaction of volatile organometallics in organic solvents was discovered to be a novel approach to nanophasic metal chalcogenides. Mdeleeni et al. [51] reported that nanophasic MoS₂ could be synthesized by irradiating a slurry of molybdenum hexacarbonyl and sulfur in 1,2,3,5-tetramethylbenzene (isodurene) with high-intensity ultrasound (20 kHz) under Ar. The as-prepared

high-surface-area nanostructured MoS₂ was distinct from its conventional counterpart (Fig. 4) and catalyzed thiophene HDS with higher activities than those of the most active materials. Amorphous WS₂ has been prepared by ultrasound irradiation of W(CO)₆ solution in diphenylmethane (DPhM) in the presence of a slight excess of sulfur at 90 °C under Ar [52]. Heating the amorphous powder at 800 °C under argon yields WS₂ nanorods and their packing. The average size of WS₂ nanorods was found to be 3–10 nm in thickness and 1–5 μm in length.

Lelieur and co-workers [53] and Parkin and co-workers [54, 55] have developed a room-temperature liquid-amine route to prepare metal chalcogenides. Reaction of sulfur, selenium, or tellurium with elemental metals in liquid ammonia at room temperature in a pressure vessel produces a series of binary and ternary metal chalcogenides. They pointed out that in sulfur-ammonia solutions, there were various sulfur imido anions (S₂N⁻, S₃N⁻, S₄N⁻) as well as sulfur polyanions (S₆⁻, S₄⁻) and zero oxidation sulfur species (S_xNH₃⁻, x = 1–8). Sulfur could also dissolve in organo-amine to produce colored N,N'-diamine-polysulfide solution and hydrosulfuric acid [56]. Ethylenediamine plays an important role in generating the active sulfur species, such as S²⁻. Meanwhile, ethylenediamine as a strong bidentate ligand can coordinate with metal ions to give stable complexes in the form of chelate compounds [M(en)_x]^{y+}. These chelate compounds would then react with the active sulfur species, leading to the formation of metal sulfides. Metal selenides and metal tellurides would also be produced in a similar way. The whole process can be described as follows:



In most cases, the as-prepared chalcogenides were X-ray amorphous or poorly crystalline, and needed to be annealed to get crystalline products. Ultrasound has the ability to greatly accelerate such reactions, and the products obtained are nanocrystalline. Gedanken and co-workers

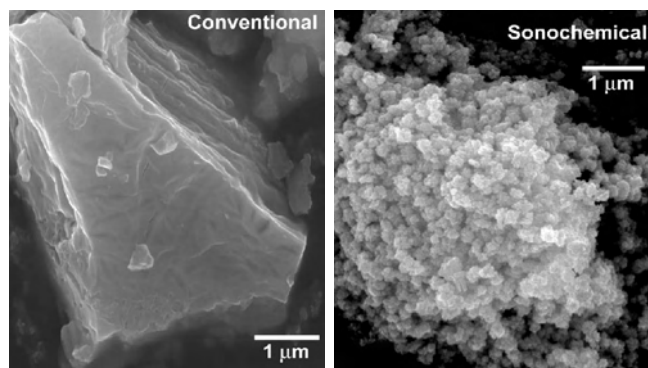


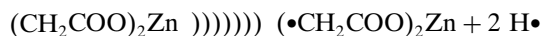
Figure 4. SEM micrographs of (bottom) sonochemical and (top) conventional preparations of MoS₂. Reprinted with permission from [51], M. M. Mdleleni et al., *J. Am. Chem. Soc.* 120, 6189 (1998). © 1998, American Chemical Society.

[57] employed ultrasound irradiation to induce such liquid-ammonia reactions in ethylenediamine and managed to obtain nanocrystalline spherical HgS and rectangular PbS particles. Later, they extended this method [58] and prepared nanospherical Ag₂S/PVA and nanoneedles of CuS/PVA composites by sonication of a 10% ethylenediamine-water solution of elemental sulfur, silver nitrate, or copper acetate in the presence of polyvinyl alcohol (PVA). This method can also be used to prepare other metal sulfides coated with polymers. Qian and Xie's group has synthesized a variety of selenide and telluride nanoparticles sonochemically based on the room-temperature liquid ammonia routes, such as Ag₂Se, CuSe, PbSe [59], Cu₇Te₄, Cu₄Te₃ [60], and Ag₂Te [61]. Ag₂Se, CuSe, PbSe could be prepared by irradiating the mixtures of AgNO₃, CuI, or PbCl₂ with Se in ethylenediamine (en) with ultrasound at 18 kHz, using a commercial ultrasonic cleaner. The products were orthorhombic Ag₂Se, hexagonal CuSe, and cubic PbSe, respectively, and all are well crystallized in nanometers. They have also reported a simple and clean method of producing nanocrystalline silver tellurides in organic solvent systems by high-intensity ultrasonic irradiation at room temperature. Ag₂Te and Ag₇Te₄ were prepared in an ethylenediamine system and an ethanol system, respectively. Sonication of CuCl₂ and Te in ethylenediamine at room temperature for over 3 h leads to the formation of nanocrystalline copper tellurides. Cu₄Te₃ is prepared in a pure ethylenediamine system and Cu₇Te₄ is prepared in ethylenediamine with hydrazine hydrate. Ultrasonic irradiation and the solvents are both important in the formation of products. The use of ultrasound irradiation facilitates the reduction of tellurium to an active form that can react with copper cations at room temperature. In ethylenediamine, which has N-chelating ligands, CuCl₂ can dissolve and form a complex. The system where the reaction is conducted is a heterogeneous system. In liquid-solid solution, the presence of ultrasound can enhance the reactions between metal cations and Te. The effects of interparticle collisions, microjets, and shockwaves can drive high-speed jets of liquid to impinge upon the surface which act to create a localized erosion to produce a newly exposed and highly active surface. Meanwhile, the ultrasound improves mass transport, and causes particle fragmentation that substantially increases the surface activity of the solid products that have a large number of dangling bonds, defects, or traps on their surface. All these factors are favorable to the activation of the reactions and the formation of copper telluride nanoparticles.

Ultrasound irradiation has also been used to induce the polyol process, through which nanocrystalline metal chalcogenides can be produced. Gedanken's group [29] applied high-intensity ultrasound irradiation to induce the reaction between Pb(Ac)₂ and Se or Te in ethylene glycol. The as-prepared PbSe and PbTe were composed of monodisperse rectangular nanoparticles. The conditions resulting from the adiabatic implosion show that the final temperature is inversely proportional to the vapor pressure inside the collapsing bubbles. In the case of nonvolatile solutions the only gas inside the collapsing bubbles will be the solvent vapor. Taking this into consideration will make ethylene glycol an excellent solvent for sonochemistry. On the other hand, the

development of a bubble to its full size is strongly dependent on the viscosity of the solvent. Ethylene glycol in this respect is not a favorable solvent for sonochemistry. Nanocrystalline silver chalcogenides Ag_2E ($\text{E} = \text{Se}, \text{Te}$) can also be synthesized by such a polyol reduction method under sonochemical irradiation [62]. Recently, Zhu and co-workers [63] found that monodisperse PbSe nanocrystals could also be fabricated via ultrasound-induced polyol reduction when polyethylene glycol (PEG)-400 was used as the solvent. The final product was characterized to be PbSe/PEG-400 composite nanocrystals. It was found that PEG played an important role in the formation of PbSe nanocrystals. On the one hand, PEG, like some other polyol solvent, such as ethylene glycol and triethylene glycol, can act as a reducing agent, and on the other hand, it is a dispersion stabilizer which prevents the generated nanocrystals from agglomerating together.

One of the most advanced and intriguing developments in the area of nanoparticles is the coating of semiconductor clusters on a solid support. This can be exploited to synthesize core/shell type materials with unusual optical, electronic, magnetic, and catalytic properties that are more than the sum of their individual components. Although the technology for coating the nanoparticles on rather large substrates is well established, coating on very small substrates, such as submicron-sized particles, still remains a technical challenge. Arul Dhas et al. [64] reported the surface synthesis of ZnS semiconductor nanoparticles coated on submicron-sized SiO_2 by the ultrasound irradiation of a slurry of SiO_2 , zinc acetate, and thioacetamide in water at near room temperature. They paid special attention to the reaction mechanism of the zinc sulfide-silica (ZSS) formation under the given sonochemical conditions. It was noteworthy that in contrast to the use of $\text{Zn}(\text{Ac})_2$, zinc nitrate, zinc chloride, or zinc perchlorate solutions did not show the coating behavior of the resulting ZnS on silica. Therefore, the choice of Zn^{2+} ion source was a particular factor for the sonochemical surface synthesis of ZnS . The formation of $\bullet\text{CH}_2\text{COO}$ radicals ($\bullet\text{Ac}$) in various transition metal acetates, in an appropriate liquid medium, has been known in the literature. Accordingly, the formation of solute radicals under sonochemical conditions can be written as



The solute radicals formed under sonochemical conditions can easily react with the reactive surface silica species (siloxane and silanols), thereby yielding metal implanted silica. The zinc acetate implanted into the silica surface then undergoes ligand exchange, with sulfide ions generated via the sonochemical reduction of thioacetamide, yielding ZnS coated on silica. Once the ZnS is formed, this can act as a nucleating site for the further adhesion of ZnS formed in the bulk solution. Similarly, as described in an earlier publication of Arul Dhas and Gedanken [65], ultrasonic irradiation of a slurry of silica microspheres, cadmium sulfate, and thiourea in an aqueous medium for 3 h under ambient air yielded cadmium sulfide-silica (CSS) composite. Heating the initial amorphous CSS nanocomposite at 150°C for 1 h under a N_2 atmosphere yielded diffraction peaks assignable to the CdS phase. The transmission electron microscopy

image of CSS shows that the CdS nanoparticles homogeneously coated on the silica (SiO_2) carrier. Besides silica microspheres, ultrasound irradiation can also be used to induce the formation of semiconductor nanoparticles coated on the surface of some polymer microspheres. Breen et al. [66] reported that zinc sulfide films could be grown on carboxyl-modified polystyrene microspheres (PS-CO_2) through sonochemical deposition in an aqueous bath containing zinc acetate and sulfide, released through the hydrolysis of thioacetamide. The resulting particles were “optically hollow,” due to a large refractive index contrast between the core and shell materials. Continuous, uniform films were obtained after 3–4 h and reached a maximum thickness of 70–80 nm after 13 h of growth. Aggregation was minimized by subsequent modification of the core-shell particles with mercaptoacetic acid to increase their surface charge and produce good colloidal suspensions. Oscillations in the optical spectra of dilute suspensions of the particles were indicative of interference patterns as expected from Mie light scattering calculations. X-ray diffraction patterns match the zinc blende structure of ZnS and indicate compression in the crystal lattice ($a = 5.305 \pm 0.037 \text{ \AA}$), as compared to the bulk material ($a = 5.406 \text{ \AA}$). Hollow ZnS shells were formed by annealing the core-shell particles in a thermal gravimetric analysis (TGA) oven, at 400°C . A 34% weight loss was observed upon heating, a value approximately equal to that of the polystyrene core. The hollow shells remained intact and readily resuspended in water. Both core-shell and hollow ZnS particles self-assemble to form well-ordered, hexagonal close-packed layers.

In summary, the sonochemical method has been established as a powerful tool to prepare nanosized metal chalcogenides with various morphologies and structures. It shows great prospect in its application in materials science and will play a more and more important role in the preparation of nanostructural materials with desirable properties.

2.3. Sonoelectrochemical Synthesis

The sonochemical method has been widely used in chemistry for some time now. It was discovered as early as 1934 that the application of ultrasound irradiation can increase the rate of electrolytic water cleavage. The effects of ultrasound irradiation on chemical reactions are due to the very high temperatures and pressures developing in and around the collapsing bubbles. Meanwhile, electrodeposition has been proven to be a simple and low-cost method with many advantages to prepare various novel materials with special properties. The electrodeposition process can be controlled more accurately, and the reactions involved are closer to equilibrium than in many gas-phase methods. However, only quite recently have the potential benefits of combining sonochemistry and electrochemistry (sono-electrochemistry) in the preparation of nanosized materials been studied increasingly. The beneficial effects of sono-electrochemical method include acceleration of mass transport, cleaning and degassing of the electrode surface, and increased reaction rate [67, 68]. Generally speaking, sono-electrochemical formation of nanoparticle powders is accomplished by applying an electric current pulse to nucleate the electrodeposition, followed by a burst of ultrasonic vibration that removes

the newly formed particles from the sonic probe cathode. By adjusting the various electrodeposition and ultrasonic parameters, control over the size and morphology of the products can be realized.

Reisse and co-workers [69–73] have described a novel device for the fabrication of metals, alloys, and semiconductors using pulse sonoelectrochemical reduction. This device exposes only the flat circular area at the end of the ultrasonic tip to the electrodeposition solution. The exposed area acts as both the cathode and the ultrasound emitter. A pulse of electric current produces a high density of fine nuclei. This is followed by a burst of ultrasonic energy, which removes the particles from the cathode, cleans the surface, and replenishes the double layer with metal cations by stirring the solution. The metals and metallic alloys were obtained as chemically pure, fine crystalline powders with high surface areas. Reference [73] gives a list of powders prepared by this method, with particle size varying from 10 to 1000 nm depending on the deposition conditions. Reference [73] also reports the first sonoelectrochemical reaction in which a chalcogenide, CdTe, was successfully prepared, by sonoelectrodeposition from an aqueous solution of TeO₂ and CdSO₄.

Gedanken's group has carried out systematic research work on the sonoelectrochemical preparation of metal chalcogenide nanoparticles. They have prepared several nanocrystalline metal chalcogenides including CdSe [74], PbSe [75], and MoS₂ [76] by using a sonoelectrochemical device that is similar to the one described by Reisse and co-workers. The schematics of the experimental setup assembled for the experiments are presented in [74, 75]. A titanium horn acts as both the cathode and the ultrasound emitter. The electroactive part of the sonoelectrode is the planar circular surface at the bottom of the horn. The immersed cylindrical part is covered by an isolating plastic jacket. The sonoelectrode produces a sonic pulse that is triggered immediately following a current pulse. One pulse driver is used to control a potentiostat and a second one controls the ultrasonic processor, which is adapted to work in the pulse mode. The potentiostat is operating in the constant current regime, without using a reference electrode.

By employing such a device, Mastai et al. [74] synthesized CdSe nanoparticles sonoelectrochemically from an aqueous solution containing Na₂SeSO₃ and CdSO₄ in the presence of nitrilotriacetate (NTA) as the complexing agent. The crystal size could be varied from X-ray amorphous up to 9 nm by controlling the various electrodeposition and ultrasonic parameters. The details about the effect of various deposition parameters on CdSe nanoparticles are listed in [74]. PbSe nanoparticles 10–16 nm in size have also been prepared in a similar way by a pulse sonoelectrochemical technique from an aqueous solution containing Pb(Ac)₂ and Na₂SeSO₃ [75]. Several factors that influence the particle size, such as the reaction temperature, ultrasonic intensity, deposition current pulse width, and current density are discussed in detail. It is found that decreasing temperature, shorter pulse duration, higher sonic intensity, and lower current density all lead to a decrease of PbSe particle size.

Since the discovery of the original fullerenes, C₆₀, C₇₀, and multishell closed carbon structures, a wide range of

Table 1. Synthesis of metal chalcogenide nanoparticles.

Synthetic methods	Nanodimensional chalcogenides	Ref.
Microwave assisted heating	CdS	[15, 16, 20, 22]
	ZnS	[16]
	CuS	[16]
	HgS	[16, 21]
	Bi ₂ S ₃	[16, 18]
	Sb ₂ S ₃	[19]
	CdSe	[17, 24]
	Cu _{2-x} Se	[17]
	PbSe	[17, 29]
	Cu _{2-x} Te	[23]
	HgTe	[23]
Sonochemical method	PbTe	[29]
	Cd _{1-x} Zn _x Se	[30, 31]
	ZnSe	[41]
	CuSe	[41, 48, 59]
	PbSe	[29, 41, 46, 59, 63]
	RuS _{1.7}	[42]
	In ₂ S ₃	[43]
	CuS	[44]
	NiS	[44]
	CdS	[45, 50]
	HgSe	[47]
	Cu ₃ Se ₂	[48]
	Cu _{2-x} Se	[48]
	Bi ₂ S ₃	[49]
	MoS ₂	[51]
	WS ₂	[52]
	HgS	[57]
	PbS	[57]
	Ag ² S/PVA	[58]
CuS/PVA	[58]	
Ag ₂ Se	[59, 62]	
Cu ₇ Te ₄	[60]	
Cu ₄ Te ₃	[60]	
Ag ₂ Te	[61, 62]	
PbTe	[29]	
ZnS/SiO ₂	[64]	
CdS/SiO ₂	[65]	
ZnS/polystyrene	[66]	
Sonoelectrochemical method	CdTe	[73]
	CdSe	[74]
	PbSe	[75]
	MoS ₂	[76]
Photochemical synthesis	CdSe	[77]
	PbSe	[78]
	CdS	[79–82]
γ-Irradiation method	CdS	[84, 87, 88, 93, 94]
	Ag ₂ S	[85, 88]
	CdSe	[86]
	Cu ₂ S	[88]
	Cu _{2-x} Se	[89]
	MoS ₂	[90]
	PbSe	[91]
	ZnS	[92, 97]
	NiS	[95]
	PbS	[88, 96]
	CuS	[96]
	PbS/polyacrylonitrile	[98, 103]

continued

Table 1. Continued

Synthetic methods	Nanodimensional chalcogenides	Ref.
	CdS/polyacrylonitrile	[99]
	PbS/(polyvinylacetate)	[100]
	CdS/poly(styrene-alt-maleicanhydride)	[101]
	CdS/polyacrylamide	[102]
Low-temperature solid state synthesis	CdS	[106, 107]
	PbS	[106, 110]
	CuS	[106]
	ZnS	[106, 108, 109]
Solvothermal synthesis	CdS	[111, 119, 121]
	CdSe	[111, 114, 126]
	CdTe	[111]
	ZnSe	[112, 114]
	ZnTe	[113]
	Bi ₂ S ₃	[117, 122]
	Sb ₂ S ₃	[118]
	Ag ₂ S	[120]
	Ag ₂ Se	[120]
	Ag ₂ Te	[120]
	Bi ₂ Se ₃	[122]
	Bi ₂ Te ₃	[122]
	PbS	[122]
	PbSe	[122]
	PbTe	[122]
	NiSe ₂	[123]
	CoSe ₂	[123]
	FeSe ₂	[123]
	CdS/poly(acrylamide-co-styrene)	[124]
	CdSe/poly(acrylamide-co-styrene)	[124]
CdS/polystyrene	[125]	
AgGaS ₂	[127]	
AgInS ₂	[127]	
CuInS ₂	[128, 129]	
CuInSe ₂	[128]	
AgInS ₂	[129]	
Electrochemical template synthesis	CdS, CdSe, CdTe	[131, 134–138]
Microemulsions route	Ag ₂ Se	[140]
	ZnS	[141]
	Cu ₂ S	[142]
	CdSe	[143]
	CdS	[144–147, 151, 154]
	PbS	[153]
	PbS/polymer	[148]
	PbS-coated CdS	[149]
	Ag ₂ S/CdS	[150]
	CdS/CdSe	[143]
Sol-gel synthesis	ZnS	[159, 163, 167]
	GeS ₂	[160]
	WS ₂	[162]
	TiS ₂	[164–166]
	NbS ₂	[164–166]
	CdS	[168]
	CdTe	[169]
Cu ₂ Se	[170]	

related fullerene-like structures, have been identified. Mastai et al. [76] reported the sonoelectrochemical synthesis of MoS₂ fullerene-like nanoparticles (Fig. 5). They have exploited ultrasonic excitation, involving a local burst of very high temperature in and around the collapsing bubbles, to synthesize closed fullerene-like structure of MoS₂ by electrodeposition from thiomolybdate solutions onto an ultrasonic probe at room temperature. Either electrodeposition or ultrasonic irradiation alone results in X-ray amorphous Mo-S products, but the combination of both gives well-crystalline closed structure of MoS₂.

In summary, sonoelectrochemical processes provide a promising method for the preparation of metal chalcogenides and some other nanoparticles with experimental variables which allow control over particle size, morphology, and size distribution. The application of sonoelectrochemical method in nanoscience and nanotechnology has been increasing and will keep increasing in the future due to the advantages of combining electrochemical and sonochemical processes.

2.4. Photochemical Synthesis

It has been known that absorption of photoenergy can change the structure of molecules and induce a variety of photochemical reactions. During recent years, a photochemical technique has emerged as an effective synthetic technique for the preparation of nanosized metal chalcogenides with various morphologies. This method has the advantages of mild reaction conditions and convenient operations, and the equipments involved are simple and cheap. Generally speaking, a low-pressure mercury pillar lamp ($\lambda = 253.7$ nm) and a high-pressure column-like indium lamp ($\lambda = 420$ – 450 nm) are most commonly used as the ultraviolet irradiation and visible photoirradiation source, respectively.

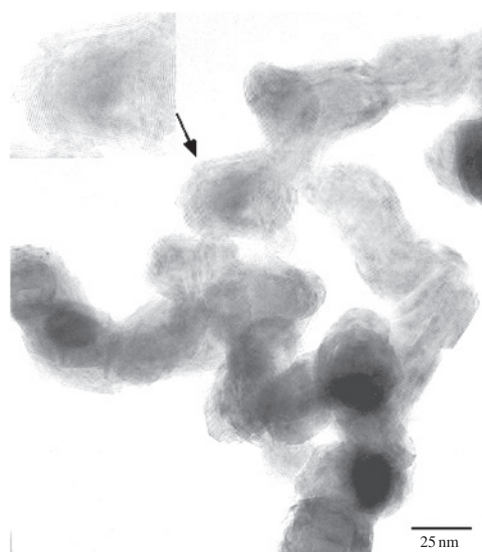
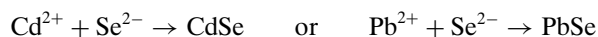
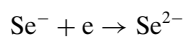
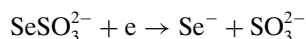


Figure 5. TEM image of the sonoelectrochemically prepared MoS₂ powder. The inset in the top left-hand corner shows part of the image at $\times 2$ magnification. Reprinted with permission from [76], Y. Mastai et al., *Adv. Mater.* 11, 1010 (1999). © 1999, Wiley-VCH.

Zhu's group reported the photochemical synthesis of CdSe [77] and PbSe [78] nanoparticles by employing a high-pressure indium lamp as the visible photoirradiation source. Exposing aqueous solutions containing CdCl₂ (or Pb(Ac)₂) and Na₂SeSO₃ in the presence of complexing agents to photoirradiation for several hours at room temperature would lead to the formation of 7-nm CdSe (or 25-nm PbSe) spherical nanoparticles. The mechanism of the photochemical formation of CdSe and PbSe nanoparticles can be summarized as below:



The formation of CdSe or PbSe nanoparticles may include the above-given three steps through photoirradiation: first, SeSO₃²⁻ is reduced to Se⁻; then Se⁻ is further reduced to Se²⁻; finally, Se²⁻ reacts with metal cations to form metal selenide nanoparticles. The first reaction may be a slow reaction, and the second reaction may be a fast reaction. Both light intensity and irradiation time have influence on the size of the final products. The complexing agents also play an important role: they can retard the rate of the reactions and cause the particle size to be small. The reactions conducted without complexing agents were unsuccessful.

Chen and co-workers [79] established an ultraviolet irradiation method for *in-situ* synthesis of nanocrystalline CdS particles. CdS nanocrystallites with cubic or hexagonal phase structures were prepared at room temperature via precipitation of Cd²⁺ ions with homogeneously released S²⁻ ions, generated from the decomposition of thioacetamide by ultraviolet irradiation reduction. It was found that the solvent has a great influence on the phase structure, the product composition, and the mean size of the CdS nanocrystallites. This technique may be extended to prepare other sulfide semiconductor nanoparticles, including ZnS, Ag₂S, PbS, NiS, and CuS. Based on this approach, Chen's group extended this method to the preparation of nanocrystalline CdS with different morphologies. Mo et al. [80] established a morphology-controlled synthesis of CdS nanocrystallites by introducing poly(vinyl alcohol) (PVA) as the protecting agent, which self-assemble into desirable shapes. CdS spherical nanoparticles, nanodisks, and nanowires were obtained conveniently, and there were some CdS nanotubes that appeared in the CdS nanodisk sample. It is found that the concentrations of Cd²⁺ and thioacetamide have significant effects on the morphologies of products. Hao et al. [81] prepared CdS nanocrystals in selective C₂H₅OH and H₂O solvents using sodium dodecyl sulphate (SDS) as capping material by ultraviolet irradiation technique. The capping material SDS in the solvents with different volume proportions of C₂H₅OH and H₂O has much influence on the morphology of the produced CdS nanocrystals, and the solvent with the volume proportion of C₂H₅OH:H₂O = 9:1 containing 0.2 mol/L SDS was the favorite medium for the formation of CdS nanorods. While the volume proportion of C₂H₅OH:H₂O was changed up to 9.5:1, the dendritic supermolecular CdS nanostructures, known in short as diffusion-limited aggregation (DLA), were obtained. When

the volume proportion of C₂H₅OH:H₂O was down to 6:1, only CdS nanocrystals with irregular morphologies could be formed. It has been demonstrated that surfactant could act as capping material in fabrication of low-dimensional nanocrystals. The physical chemical properties such as polarity (dielectric constants) and softness of different solvents are different according to various volume proportions of C₂H₅OH and H₂O. The difference in properties of the solvents may influence the dissolution and transmission of ions in solution, which may lead to the different cap structures of SDS in the formation of CdS nanocrystals. The SDS in various solvents can produce patterns of the different structures. These different patterns may act as suitable nucleation sites or interact with special crystal planes of the growing CdS nanocrystals, leading to the formation of CdS nanorods and dendritic supermolecular CdS nanostructures. Wu and co-workers [82] synthesized CdS nanowires by a convenient ultraviolet irradiation method using hydroxyethyl cellulose as a soft template at room temperature. In this experiment, the hydroxyethyl cellulose (HEC) is a long-chain macromolecule with many hydroxy groups and the average molecular weight of HEC is approximately 123,000. When HEC is dissolved in water, the HEC is unfolded and the long chain can be easily formed by HEC molecules through hydrogen bonds. The long chains can act as soft templates. When Cd²⁺ ion meets with S²⁻ ions, CdS can grow along these long chains and the CdS nanowire may be formed. S²⁻ ions are from the decomposition of sodium thiosulfate (Na₂S₂O₃) by ultraviolet irradiation. HEC in solution is used as a soft template, which directs the one-dimensional growth of CdS nanowires. This method gives a norm mild chemical route to fabrication of semiconducting nanowires which may be applied in many fields.

2.5. γ -Irradiation Method

γ -irradiation is one of the new and effective methods for synthesis of nanometer materials. It has been extensively used in the preparation of nanocrystalline metals, alloys, oxides, and polymer/metal nanocomposites [83]. Over the past few years, the γ -irradiation method has been extended to the fabrication of chalcogenide nanoparticles.

In γ -irradiation processes, the detailed mechanisms of the formation of nanocrystalline chalcogenides are not very clear up to now. However, some probable reactions may be going under γ -irradiation. It has been known that as a result of γ -irradiation, some reducing radiolytic species, such as solvated electrons or free radicals, are generated. These transient intermediate radiolytic species may react with some chalcogen sources such as S₂O₃²⁻, SeSO₃²⁻, CS₂, thiourea, and thioacetamide, leading to the formation of active S²⁻ or Se²⁻ anions. So far, a variety of metal sulfide and selenide nanoparticles have been successfully synthesized by γ -irradiation method in aqueous or nonaqueous systems [84–97].

Currently, inorganic/organic composites have been playing increasingly important roles in research and in numerous applications. They frequently have special properties, which are combinations of those of their original organic and inorganic components. Among these materials, semiconductive chalcogenide/polymer nanocomposites have aroused more

and more attention. γ -irradiation offers an applicable means by which the polymerization of monomers and formation of inorganic nanoparticles take place simultaneously, leading to the fabrication of inorganic/polymer nanocomposites. However, it is only quite recently that the γ -irradiation has been applied to the synthesis of chalcogenide/polymer nanocomposites. Liu et al. [98] developed a γ -irradiation method to synthesize PbS/polymer nanocomposites by using polymerized bicontinuous microemulsions. The as-prepared nanocomposite has large nonlinear optical response. Besides a polymeric nonionic surfactant, ω -methoxy poly(ethylene oxide)(40) undecyl- α -methacrylate (C-1-PEO-C-11-MA-40), a system consisting of methyl methacrylate (MMA), acrylonitrile (AN), ethylene glycol dimethacrylate (EGDMA), aqueous solutions of $\text{Pb}(\text{NO}_3)_2$ /thioacetamide was selected. High-resolution transmission electron microscopy results indicated PbS nanocrystals with a width of 5 nm and a cubic structure is formed in water domains. A single-beam Z-scan measurement showed that the nanocomposite polymer has a nonresonant and negative nonlinear refractive index (γ) of $6.8 \times 10^{-12} \text{ cm}^2/\text{W}$ at 780 nm. The origin of the large nonlinear optical response is based on the contribution of surface recombination owing to high surface-to-volume ratios of PbS nanoparticles to the optical nonlinearity. In recent years, Qian's group [99–103] has carried out some systematic work in this field and successfully employed γ -irradiation to prepare a series of sulfide/polymer nanocomposites including CdS/polyacrylonitrile composite nanoparticles [99], PbS/(polyvinyl acetate) nanocables [100], CdS/poly(styrene-*alt*-maleic anhydride) nanofibers [101], CdS/polyacrylamide [102], and PbS/polyacrylonitrile [103] composite nanoparticles.

In conclusion, γ -irradiation offers an attractive method for the preparation of nanodimensional chalcogenide particles and chalcogenide/polymer nanocomposites. The ease, reproductivity, and versatility of this synthetic approach will facilitate development of functional nanomaterials and the examination of their structure-property relationships.

2.6. Low-Temperature Solid-State Synthesis

Solid-state chemistry is a fast-developing science, enhanced by its numerous applications in high-technology industries [104]. Though solution-phase synthetic methods are most commonly used in the preparation of nanodimensional materials, solid-state reactions provide an alternative route to prepare nanoparticles. Solid-state reaction methods, especially low-temperature solid reactions, have been developed rapidly in recent years, and have shown their unique advantages in the preparation of nanodimensional chalcogenides, such as the simplicity, low energy cost, and mild conditions. However, up to now, the details about the formation of chalcogenide nanoparticles via low-temperature solid-state reactions are still unclear.

Though low-temperature solid-state synthesis has been long and widely used in a wide variety of fields in chemistry [105], it is only in recent years that considerable progress has been made in its extension to the synthesis of nanodimensional metal chalcogenides. Xin and his research group [106] reported an effective approach based on solid-state metathesis reaction of transition metal hydroxides and

sodium sulfide at room temperature to produce nanocrystals of sulfides. It is known that the structures of the products by solid-state reactions depend on the rate of nucleation and growth of reaction products. The diffusion of solid particles of reactants at ambient temperature is often in short range, and thus helps yield nanosized products. Prompted by this study, Li and co-workers [107] developed a simple solid-state reaction of $\text{Cd}(\text{Ac})_2 \cdot 2.5 \text{ H}_2\text{O}$ and $\text{Na}_2\text{S} \cdot 9 \text{ H}_2\text{O}$ in the presence of polyethylene glycol (PEG) 400 to synthesize CdS nanowires. During this solid-state reaction, the presence of coordinated water in $\text{Cd}(\text{Ac})_2 \cdot 2.5 \text{ H}_2\text{O}$ and $\text{Na}_2\text{S} \cdot 9 \text{ H}_2\text{O}$ helps lower the activation energy and the reaction temperature, since most hydrated metal salts have structures with point defects and relatively lower lattice energies. The NaAc produced in the reactions may form the physical and spacious obstacle around the CdS particles to prevent them from aggregating to larger particles. PEG 400 also plays a critical role in the formation of CdS nanowires. It may interact with $\text{Cd}(\text{Ac})_2 \cdot 2.5 \text{ H}_2\text{O}$ or $\text{Na}_2\text{S} \cdot 9 \text{ H}_2\text{O}$ during the first grinding. After absorbing free water and heat generating by this exothermal reaction, the structure of PEG 400 turns to loose and the PEG 400 molecules extend to form chain structures without any twist. Actually, PEG 400 acts as a soft template in the course of CdS nanowire formation. Similarly, ZnS nanoparticles have also been synthesized by solid-state reaction method at room temperature [108, 109]. It is found that the reaction is affected by the structures of reactants, crystal water, and defects. The as-prepared ZnS nanoparticles show a good sensitivity and selectivity to H_2S gas. Wang et al. [110] reported a novel and simple one-step method for the preparation of ca. 10- to 15-nm PbS nanoparticles by solid-state reaction in the presence of a suitable surfactant $\text{C}_{18}\text{H}_{37}(\text{CH}_2\text{CH}_2\text{O})_{10}$. In the reaction of $\text{Pb}(\text{Ac})_2 \cdot 3 \text{ H}_2\text{O}$ and $\text{Na}_2\text{S} \cdot 9 \text{ H}_2\text{O}$ to produce PbS nanoparticles, free water and NaAc are produced. The surfactant $\text{C}_{18}\text{H}_{37}(\text{CH}_2\text{CH}_2\text{O})_{10}$ dissolves in the free water to form a $\text{C}_{18}\text{H}_{37}(\text{CH}_2\text{CH}_2\text{O})_{10}$ "shell" surrounding PbS particles, preventing them from aggregating to larger particles.

Though the solid-state synthesis of nanoparticles has been developing over the past few years, its application in nanomaterial synthesis still remains quite limited compared with gas-phase or liquid-phase methods. In the field of chalcogenide nanoparticle preparation, it is only restricted to sulfide synthesis at present. A continuous exploration for low-temperature solid-state method for the preparation of selenide and telluride nanoparticles is now under way.

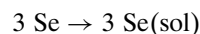
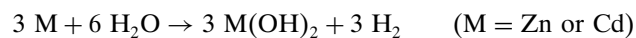
2.7. Solvothermal Synthesis

One of the most promising techniques applicable to the synthesis of the nanocrystalline metal chalcogenides is the solvothermal method. Unlike some other conventional synthetic processes, the solvothermal synthesis involves much milder conditions and softer chemistry conducted at relatively low temperatures. This technique has been widely employed for the crystal growth of many inorganic compounds. An intriguing achievement of this synthetic technique includes the preparation of new phases, inaccessible at high temperatures, because of their thermodynamic metal stability. In recent years, a variety of reports have described the preparation of nanocrystalline metal chalcogenides with

different sizes and morphologies under solvothermal conditions. These reactions are conducted in sealed autoclaves, maintained at a certain range of temperatures (in most cases in the range of 100 °C to 300 °C) for a period of time (from few hours to several days), and requiring relatively high pressures. The solvothermal conditions provide a special environment for various chemical reactions and can induce the formation of nanocrystals with controllable sizes and morphologies.

The most straightforward way to synthesize binary metal chalcogenides is the direct combination of elemental metals and chalcogens (S, Se, or Te) at elevated temperatures, but the products formed via such high-temperature reactions are not nanosized. Li's group has carried out systematic work and found that such elemental-direct reactions can be conducted under solvothermal or hydrothermal conditions at relatively low temperatures, and the products obtained are nanocrystalline. Solvothermal reactions between Cd powders and elemental S, Se, or Te in different organic solvents in the temperature range of 120 to 200 °C have been investigated systematically to prepare a series of cadmium chalcogenide CdE (E = S, Se, Te) nanocrystals [111]. It was found that the characteristics of the products, such as crystal size, shape, and structure, were strongly influenced by the solvent and temperature during the solvothermal processes. In case of CdE, one-dimensional nanorods of CdE with 10- to 40-nm diameters and several micrometers in length were obtained by choosing coordinating solvents such as ethylenediamine and 1,6-diaminohexane as the reaction solvent. When some noncoordinating solvents were used, only spherical nanoparticles could be obtained. The influence of different solvents on the morphologies of the products was systematically investigated, and an outline of the solvent coordination molecular template mechanism for the growth of the nanorods was proposed, though further studies on this mechanism are still in progress. Solvothermal reaction between Zn and Se powders in pyridine at 180 °C would give rise to ZnSe nanoparticles [112]. The formation of nanocrystalline ZnSe results from the combination of Zn and Se by electron transfers. Nanocrystalline ZnS could also be synthesized under similar conditions. Such elemental-direct reactions can also be conducted in aqueous systems under hydrothermal conditions. Li et al. [113] reported the preparation of ZnTe nanorods by a solvothermal process and a subsequent thermal treatment using Zn and Te as the reactants and hydrazine hydrate ($\text{N}_2\text{H}_4 \cdot \text{H}_2\text{O}$) as the solvent. Analysis of the result showed that the produced ZnTe was well crystallized with nanorod morphology, and the yield of this method is up to 80–90%. The hydrazine was found to play a very important role in this reaction process. It acted not only as an electron transfer medium but also as a strong electron provider. Peng et al. [114] reported a hydrothermal elemental-direct-reaction route to nanocrystalline CdSe and ZnSe particles. During the reactions, Zn or Cd powders can first react with water and generate metal oxide (or metal hydroxide) and H_2 . At a temperature of about 180 °C, Se can partially dissolve in water and the dissolved ones may be reduced by the H_2 to produce Se^{2-} . The possible mechanism to produce ZnSe and CdSe under solvothermal conditions

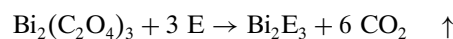
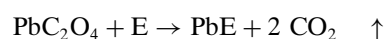
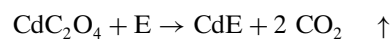
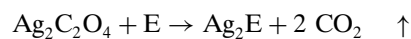
can be presented as follows:



On the basis of the mechanism presented above, this method is predicted to be applicable to other selenide nanoparticles.

Thermal degradation of metal complexes with sulfur-containing ligands seems to be an attractive method for the synthesis of metal sulfides. Several reports refer to thiolato, dithiocarbamate, and thiourea complexes [115]; however, such routes require the use of H_2S or $\text{H}_2\text{S}/\text{H}_2$ at high temperatures. It is well known that thiourea forms metal complex with metal ions in aqueous and alcoholic solutions. Such metal-thiourea complexes can be thermally decomposed to form metal sulfides in forms of thin films and ultrafine particles dispersed in glasses [116]. Yu and co-workers developed a novel one-step solvothermal decomposition process for fabrication of Bi_2S_3 [117] and Sb_2S_3 [118] nanowires. Bi-thiourea and Sb-thiourea complexes have the tendency to decompose under solvothermal conditions to produce Bi_2S_3 and Sb_2S_3 nanowires. The wirelike morphology of the products is possibly due to the inherent chain type structures of Bi_2S_3 and Sb_2S_3 . The *in-situ* generated nuclei could connect with each other and self-assemble into one-dimensional nanostructures. Solvothermal conditions, in which high temperatures are generated, are favorable for the self-assembly of the particles to form connections among them and a great number of such connections provide more opportunities for the formation of nanowires. Similarly, CdS nanowires could be successfully prepared via solvothermal reaction between cadmium salts and thiourea in polyamine solvents, such as ethylenediamine and diethylenetriamine [119]. The polyamines, which contain more than one N-chelating atom in each molecule, play a key role in the formation of the CdS nanowires.

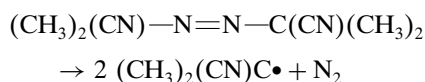
Qian and co-workers [120–122] reported a novel solvothermal approach to prepare a series of metal chalcogenides by reactions between metal oxalates and chalcogens in organic solvents at temperatures ranging from 120 °C to 180 °C. Nanocrystalline Ag_2E [120], CdE [121], and PbE and Bi_2E_3 [122] (E = S, Se, Te) have been synthesized via this route. The reactions can be expressed as the following equations:



Both temperature and solvent have significant effects on the synthesis of the metal chalcogenides. By changing the preparation conditions, control over size and morphology of the products could be realized.

The magnetic and electric properties of many transition metal dichalcogenides have shown large varieties in behavior and have been studied in considerable detail. Typical substances such as ME_2 ($M = Ni, Co, Fe$; $E = S, Se$) are diamagnetic semiconductors, ferromagnetic and anti-ferromagnetic semiconductors. Meanwhile, transition metal dichalcogenides have extensive applications in energy areas such as electrochemistry and catalysis. The large surface areas and high activity of nanomaterials will enhance their applications in these fields. Yang et al. [123] synthesized transition metal diselenides (MSe_2 , $M = Ni, Co, Fe$) through a simple solvothermal-reduction reaction at low temperatures. With increasing temperature, the obtained $NiSe_2$ transformed from initial filament nanocrystallites to final octahedral crystals. The studies on the thermal stability of the as-prepared $NiSe_2$ showed that $NiSe$ acted in an intermediate role in the pyrolysis process. The as-prepared $CoSe_2$ at higher temperature had an orthorhombic structure similar to that of $FeSe_2$. At low temperature, this orthorhombic phase $CoSe_2$, which displayed rodlike shape with the growth direction along (121), coexisted with a trace of the cubic phase $CoSe_2$.

Synthesis and characterizations of inorganic-organic polymer nanocomposites have received much intensive research, owing to their optical, electrical, catalytic, and mechanical properties, and potential applications in microelectronics. The hybridization of organic and inorganic semiconductors is expected not only to permit wide-range selection of emitter and carrier transport materials, but to provide a new approach to construct high-performance electroluminescence devices, taking advantage of organic and inorganic semiconductor characteristics, such as high photoluminescent efficiency of organic materials and high carrier density and low resistivity of inorganic semiconductors. In addition, polymer is also expected to provide good mechanical properties, conferring high kinetic stability on nanometer-sized semiconductor particles. To organize the semiconductor nanoparticles in an orderly fashion in a polymer matrix may afford a potential application of their special properties. Chen and co-workers [124] reported a solvothermal *in-situ* simultaneous copolymerization-decomposition (SCPD) technique for fabrication of poly(acrylamide-co-styrene)-semiconductor CdE ($E = S, Se$) nanorod composite. It is well known that the radical thermal initiator AIBN (2,2'-azobisisobutyronitrile) decomposes at about 45–65 °C, of which the decomposition reaction is described as



In this system, the produced radicals will initiate the copolymerization of the acrylamide and the styrene monomers. The copolymerization process simultaneously accompanies the solvothermal formation of CdE nanorods. Therefore, it was found that the produced CdE nanorods were well dispersed homogeneously in the poly(acrylamide-co-styrene) matrix. Yoshimura and co-workers [125] developed a novel one-step soft solution processing route called the solvothermal-copolymerization technique for *in-situ* fabrication of polystyrene/ CdS nanocomposites embedded with

CdS nanowires in ethylenediamine media at lower temperatures (80–140 °C). In this route, the polymerization of the monomers and the formation of the CdS nanocrystallites occur simultaneously in a certain temperature range. The embedded CdS nanowires, with diameters of 4 to 15 nm and lengths up to several micrometers, have (001) preferential orientation. Both temperature and solvent were found to play a key role in the synthesis of the nanocomposites. The produced novel hybrid nanocomposites display obvious quantum size effects and interesting fluorescence features. The spectroscopic properties of the polystyrene/ CdS nanowire nanocomposites were found to be sensitive to synthetic conditions, including the concentrations of Cd^{2+} or the monomer, temperature, and reaction time.

One of the keys to semiconductor nanoparticle research is the ability to prepare stable (typically through surface passivation—also referred to as capping) monodisperse particles that have very few defects. Gautam et al. [126] presented a convenient and safe one-pot route to capped $CdSe$ nanoparticles making use of common starting materials and inexpensive, low-boiling solvents under solvothermal conditions. The H_2Se required for the reaction was generated *in-situ* through the aromatization of tetralin by Se . The addition of small amounts of dodecanethiol as a capping agent resulted in 3-nm monodisperse nanoparticles with a narrow size distribution. The dark solution obtained from the reaction precipitates solid products when the solvent polarity is increased through the addition of propan-2-ol. The precipitated solid easily redissolves in toluene forming bright orange solutions.

In recent years, the solvothermal technique has been extended to the synthesis of a variety of ternary metal chalcogenide nanoparticles. Among the ternary metal chalcogenides, I-III-VI₂ compounds have been most intensively investigated due to their important technical applications. I-III-VI₂ chalcopyrite semiconducting compounds, such as $AgGaS_2$, $AgInS_2$, $CuInS_2$, and $CuInSe_2$, have been shown to be useful linear and nonlinear optical materials. Nanocrystalline semiconductors $AgGaS_2$ and $AgInS_2$ with particle sizes ranging from 5 to 12 nm have been prepared by a solvothermal reaction of $AgCl$, Ga (or In), and S in the temperature range 180–230 °C [127]. The synthetic reaction can be represented as



Jiang et al. [128] prepared $CuInS_2$ and $CuInSe_2$ nanorods via an elemental solvothermal reaction route. Cui et al. [129] also successfully prepared $CuInS_2$ and $AgInS_2$ nanorods from a stoichiometric mixture of $In(S_2CNEt_2)_3$ and $Cu(S_2CNEt_2)_3$ or $Ag(S_2CNEt_2)_3$, by removal of the thione groups with ethylenediamine at 195 °C in a solvothermal process.

2.8. Electrochemical Template Synthesis

One-dimensional nanostructures, such as nanorods, nanowires, nanowhiskers, and nanotubes, represent the smallest dimensions for efficient transport of electrons and excitons and are ideal building blocks for hierarchical assembly of functional nanoscale electronic and photonic structures.

During the past decade, materials with one-dimensional nanostructures have been the focus of much attention due to their special properties and potential applications. Template synthesis is an elegant chemical approach for the fabrication of nanowires and has attracted more and more attention. Arrays of metal [130], semiconductor [131], conducting polymer nanowires [132], and carbon nanotubes [133] are obtained by electrodeposition or other methods in porous templates such as anodic aluminum oxide (AAO) films and nuclear track membranes. Nanophysics fabrication methods such as molecular beam epitaxy followed by nanolithography of ever-increasing resolution are usually considered to represent the ultimate limit for producing nanoscale materials. However, such nanoscale materials can also be fabricated using a different method, whose key ingredients are templates and electrodeposition. In this method, the desired materials are electrochemically synthesized within the voids of the template materials. The electrochemical synthesis in templates has been taken as one of the most efficient methods in controlling the growth of nanowires because the growth is controllable almost exclusively in the direction normal to the substrate surface. Though there are wide ranges of nanoporous materials, most studies have been performed using AAO membrane as the template.

Routkevitch et al. [131] have fabricated CdS nanowire arrays by a single-step alternating-current electrodeposition in an electrolyte containing Cd^{2+} and S in dimethylsulfoxide (DMSO). They reported that on average the thicker wires (with diameters larger than 12 nm) consisted of a large number of crystallites in the axial direction and rather few in the radial direction, while the thinner wires (with diameters less than 12 nm) were of single crystalline structure. Guo's group [134–138] has prepared cadmium chalcogenide (CdS, CdSe, CdTe) nanowire arrays by direct-current electrochemical deposition in porous AAO templates. The as-prepared nanowires have uniform morphology and present single crystalline nature. TEM and HRTEM images of an individual CdSe nanowire prepared by this method are shown in Figure 6. The diameters of the nanowires can be controlled by the pore diameters of the template. This approach can also be used to fabricate other semiconductor (ZnS, ZnSe, ZnTe, HgS, HgSe, HgTe, GaAs, InP, etc.) nanowires both in aqueous solution and in nonaqueous solution systems.

2.9. Microemulsions Route

Surfactants provide several types of well-organized assemblies that provide specific sizes, geometrical control, and stabilization to particulate assemblies formed within the organized surfactant assemblies. Among the host surfactant assemblies that are available for the formation of nanoparticles are the following: the aqueous micellar solutions, reverse micelles, microemulsion, vesicles, monolayers, Langmuir–Blodgett films, and bilayer liquid membranes. The surfactant host assemblies not only provide favorable sites for the growth of the particular assemblies; they also influence the formation process as well as the chemical properties of the particulate guest, thus unfolding novel chemistries. Fendler [139] has reviewed these aspects in detail and coined a new term “membrane mimetic chemistry.”

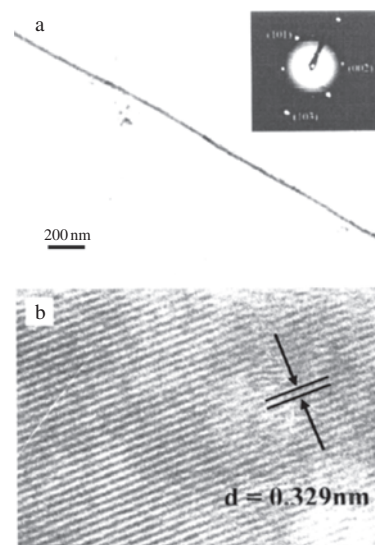


Figure 6. TEM (a) and HRTEM (b) images of an individual CdSe nanowire prepared by direct-current electrochemical deposition in porous AAO templates. Reprinted with permission from [136], D. S. Xu et al., *J. Phys. Chem. B* 104, 5061 (2000). © 2000, American Chemical Society.

Among these surfactant host assemblies, microemulsions are most commonly used in the synthesis of chalcogenide nanoparticles. Microemulsions have been intensively used as spatially constrained microreactors for the controlled growth of inorganic materials. In the case of a microemulsion, the reactions take place in the core of the microemulsions and the hydrophilic head groups of the surfactant molecules. Microemulsions are thermodynamically stable, fluid, optical clear dispersions of immiscible liquids. They provide suitable reaction media for the synthesis of nanoparticles because the droplets of water or oil can be seen as nanoreactors, favoring the formation of small crystallites with a sufficiently narrow size distribution.

In the past few years, a variety of chalcogenide nanoparticles, such as Ag_2Se [140], ZnS [141], Cu_2S [142], CdSe [143], and so on were prepared. Among all chalcogenides, microemulsion synthesis of CdS nanoparticles has been most intensively investigated. Suzuki et al. [144] reported preparation of cadmium sulfide nanoparticles with sharp size-distribution using cadmium diolelyphosphate microemulsion. Cadmium diolelyphosphate (CDOLP) and sodium diolelyphosphate (SDOLP) are expected to form rigid microemulsion droplets; they were used as surfactants in place of sodium bis(2-ethylhexyl) sulfosuccinate (AOT), which has been often used for the preparation of CdS nanoparticles in microemulsion. CdS nanoparticles were prepared by mixing hydrogen sulfide solution with the microemulsion composed of CDOLP and SDOLP. The growth process of the particles through their coagulation is restricted more strongly, and the size distribution of the obtained particles was sharper than those in AOT-microemulsion. Furthermore, in CDOLP/SDOLP microemulsion, the average number of cadmium ions per microemulsion droplet is larger and the number of contaminating “empty” RIE droplets, which contain no particle,

is much smaller than in AOT microemulsion systems. Diolelyphosphates are proper surfactants for the preparation of nanoparticles with sharp size-distribution, because particle coagulation is restricted in the system. The restriction of the coagulation between larger particles is attributed to two mechanisms: (1) It is hard for larger particles to be exchanged between two fusing microemulsion droplets through the "open channel" between them. (2) The microemulsion droplets with the larger particles can hardly coalesce with the other microemulsion droplets. Agostiano and co-workers [145] prepared CdS nanoclusters in a quarternary cetyltrimethylammonium bromide (CTAB)/*n*-pentanol/*n*-hexane/water microemulsion. The presence of cosurfactant (*n*-pentanol), in addition to water, allows the simultaneous modulation of the water droplets dimensions and their exchange dynamics. Moreover, *n*-pentanol has an influence on the stability of CdS clusters, behaving as a capping agent at high concentrations. Recently, CdS nanorods have also been prepared by microemulsion route. Simmons et al. [146] prepared high aspect ratio CdS quantum rods at room temperature in the environment of water-in-oil microemulsions using a combination of two surfactants: the anionic bis(2-ethylhexyl) sulfosuccinate (AOT) and the zwitterionic phospholipid L- α -phosphatidylcholine (lecithin). These highly acicular particles, obtained from a water-in-oil microemulsion containing an equimolar mixture of AOT and lecithin, possess an average width of $4.1 \text{ nm} \pm 0.6 \text{ nm}$, with lengths ranging from 50 to 150 nm. In contrast, conventional spherical CdS quantum dots are obtained from the AOT water-in-oil microemulsion system, with an average particle diameter of $5.0 \text{ nm} \pm 0.6 \text{ nm}$. Mo et al. [147] developed a convenient microemulsion route at room temperature to produce star-shaped CdS patterns, which were composed of rodlike nanoparticles with diameters of 4 to 7 nm and lengths ranging from 150 to 200 nm. It is found that long hydrophobic carbon chain of surfactant molecule is favorable for the formation of fibrillar or dendritic morphology. When surfactant with shorter carbon chain was employed, only spherical CdS nanocrystallites were obtained.

Recent progress shows that the microemulsions can also be employed to prepare chalcogenide nanocomposites. Up to now, a number of chalcogenide nanocomposites have been successfully synthesized in microemulsions, including PbS/polymer [148], PbS-coated CdS [149], Ag₂S/CdS [150] nanocomposites, CdS/CdSe core/shell type nanoparticles [143], and so on.

Over the past few years, the combination of microemulsion with some other synthetic techniques to prepare chalcogenide nanoparticles has been reported. For example, the combination of sonochemistry and microemulsions or micelles provides a promising way to produce different types of nanostructures. The cavitation behavior of ultrasound irradiation can lead to extraction, mixed phase reactions, and emulsification in a liquid-liquid heterogeneous system. Thus, under ultrasound irradiation it is possible that liquid-liquid heterogeneous systems could be emulsified to form microemulsions. Huang et al. [151] described the formation of spherical assemblies of nanocrystalline primary particles of CdS in a CS₂-water-ethylenediamine microemulsion induced by ultrasonic irradiation. CS₂ was employed as the

sulfur source and also as the oil phase in the microemulsion. Under ultrasonic irradiation, the CdS nanoparticles formed *in-situ* at the surface of CS₂ droplets can be dragged inside by the oil surface movement motivated by the surrounding turbulent water flow, which might result in the final spherical nanostructure. Chen and co-workers [152] prepared CdS and CdSe nanorods via the reactions between cadmium chloride and sodium sulfate or sodium selenide in a micellar solution in the presence of sonication. The micellar solution was prepared by introducing appropriate amount of cyclohexane and CTAB into distilled water. The aspect ratios of the nanorods could be changed by changing the amount of cyclohexane. In this case, vigorous sonication could induce the formation of bilayer vesicles, and the formation of CdS or CdSe nanorods in a microemulsion might be attributed to the formation of these rodlike bilayer vesicles. Wang et al. [153] prepared PbS nanoparticles sonochemically in an oil-in-water (o/w) microemulsion system. Sulfur-toluene solution (STS) was chosen as the sulfur source. When STS was mixed with water in the presence of sodium lauryl sulfate (SLS) as the surfactant, a liquid-liquid heterogeneous system was formed. The cavitation behavior of ultrasound irradiation can lead to the formation of an o/w microemulsion of toluene-in-water. This synthetic design was motivated by the known simple interaction between sulfur and ethylenediamine, but it provides special conditions for the formation and growth of the PbS nanocrystals in such a microemulsion system in the presence of high-intensity ultrasound irradiation. Recently, hydrothermal microemulsion synthesis of CdS nanoclusters has also been reported [154]. The reaction of Cd²⁺ ions with S²⁻ ions generated from the decomposition of thioacetamide proceeded in water microdroplets. The mean diameter of the CdS nanoclusters can be varied from 20 to 80 nm by increasing the reaction temperature from 30 to 120 °C. Two intense luminescence bands, that is, green and red, were observed to coexist in the CdS nanoclusters. Their peak positions and relative intensities were found to be sensitive to the size and structure of nanoclusters. These emissions are attributed to surface defects (green emission) and the Cd-Cl composite vacancies (red emission).

2.10. Sol-Gel Synthesis

Sol-gel processing is a promising method for the preparation of nanodimensional materials. The reaction product of the sol-gel synthesis could be either colloidal powders or films. One of the advantages of this method is the ability to control the microstructure of final product by controlling chemical reaction parameters. It was demonstrated that modification of the reaction conditions could significantly affect the structure of the sol-gel product. The connection between the sol-gel process kinetics and the sol-gel product microstructures can be illustrated by the following sequence [155]:

Solvolytic (hydrolysis, thiolysis)

→ condensation → nucleation → growth → aggregation

The prevalent application of sol-gel processing is in the production of metal oxides by one of the two synthetic

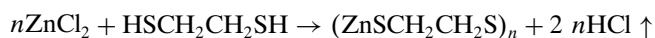
routes. The first route involves the hydrolysis of an alcohol solution of metal alkoxides. This reaction is catalyzed by acid and is very sensitive to the ratio of acid, alcohol, and water in the solution [156]. The second route involves the use of diols and metal salts to form the bridging bonds on the polymer and does not require water or acid [157]. Up to now, most publications related to the sol-gel synthesis have been confined to the preparation of ultrafine oxide powders or thin films. Reports on the sol-gel synthesis of nanosized sulfides, selenides, or tellurides are relatively much scarcer. There are two sol-gel routes that are used most commonly in preparation of metal sulfides. The first one involves a modified sol-gel route in which the conventional alcohol sol is exposed to a stream of H₂S or some other sulfur sources [158]. The other one is the use of thiols in place of alcohol for the formation of sulfides by a modification of the first sol-gel route [159]. In the past few years, by using these two routes, a variety of nanocrystalline sulfides, either in powder form or films, have been successfully prepared by sol-gel method.

Stanic et al. [160] reported a sol-gel method for the preparation of metal sulfides. Synthesis of sulfides was demonstrated by the example of monoclinic germanium disulfide produced by reaction of the sol-gel product with sulfur. The elemental sulfur, in turn, was obtained as the result of oxidation of H₂S in the presence of concentrated sulfuric acid. This sulfur was transported into a toluene solution of germanium ethoxide and found to be homogeneously distributed within the gel. Heat treatment of the sol-gel product yielded single-phase GeS₂. A chemical kinetics study of such a sol-gel processing of GeS₂ from hydrogen sulfide and germanium ethoxide in toluene was also reported [161]. Similarly, tungsten sulfides [162] were synthesized by reaction of different tungsten alkoxides and hydrogen sulfide in toluene. The reaction was performed in toluene solution at room temperature. The sol-gel products were amorphous materials. Stanic et al. [163] also reported a sol-gel process for the chemical synthesis of ZnS at room temperature using zinc tert-butoxide and H₂S as precursors in a toluene solution. The obtained reaction product was a yellow semitransparent gel that dried to a reddish-orange solid. Characterization of the dried gel by XRD, IR, and EDS confirmed that the product is ZnS with a Zn/S atomic ratio approximate to 1:1.

Sriram et al. [164–166] developed a novel thio-sol-gel process for preparing TiS₂ and NbS₂ powders. The mechanism of the reaction of titanium isopropoxide {Ti(OPri)(4)} with H₂S in benzene has been studied using infrared spectroscopy (FTIR), gas chromatography (GC), and chemical analysis. Based on these studies, it has been determined that the precipitate obtained from the reaction forms following a thiolysis-condensation mechanism similar to the hydrolysis-condensation mechanism that operates in the oxide sol-gel process. The precipitate, which is an alkoxy-sulfide, can be converted to TiS₂ by heat treatments in flowing H₂S. The influence of modifying agents, the role of solvents, and the alkoxy group [in Ti(OR)₄] on the formation of the alkoxy-sulfide precipitate have also been presented and discussed. It has been shown that different heat-treatment conditions can be utilized to simultaneously control the morphology of the sulfide powder and its defect

concentration. The performance of these materials as cathodes in secondary lithium batteries has also been evaluated and correlated to the crystallite size distributions and defect concentration. The applicability of this process for the synthesis of NbS₂ has also been demonstrated.

Donahue et al. [167] established a solution-based method for preparing the material through sol-gel processing. Ethanedithiol and zinc chloride were mixed and the resulting sol was heated in a three-step process, producing crystalline wurtzite. Analysis of the sol and its decomposition indicates the following reaction mechanism:



Cao et al. [168] reported sol-gel template synthesis of an array of single-crystal CdS nanowires on a porous alumina template. It shows that sol-gel technique can also be used in template synthesis and the extension of this sol-gel template method to the preparation of some other one-dimensional nanostructural materials is still underway.

Though much progress has been made in the sol-gel synthesis of nanosized sulfides, available reports on the sol-gel synthesis of nanosized selenides and tellurides are still limited. Up to now, only a few selenides and tellurides such as CdTe zirconia films [169] and Cu₂Se in silica glasses [170] have been synthesized via sol-gel process. Exploring new sol-gel routes to produce selenides and tellurides still remains a great challenge.

3. CHARACTERIZATIONS

In the past two decades, a wide variety of techniques have been used in the characterizations of chalcogenide nanoparticles. Herein, we briefly mention some of these techniques that are most commonly used.

- (1) Crystallinity and crystallography analysis:
X-ray powder diffraction (XPRD), selected area electron diffraction (SAED), low energy electron diffraction (LEED), ...
- (2) Observation of dimensions and morphologies:
Transmission electron microscopy (TEM), atomic force microscopy (AFM), scanning electron microscopy (SEM), ...
- (3) Evaluation of composition and purity:
X-ray photoelectron spectroscopy (XPS), ultraviolet photoelectron spectroscopy (UPS), energy-dispersive X-ray analysis (EDAX), inductively coupled plasma (ICP) element analysis, ...
- (4) Methods used in estimation of crystal size [6]:
XPRD (using Debye-Scherrer formula), direct TEM observations, calculation according to the relation between bandgap and particle size, Raman spectroscopy, surface area measurements, ...
- (5) Fine structures:
High-resolution transmission electron microscopy (HRTEM), scanning tunnel microscopy (STM), extended X-ray absorption fine structure (EXAFS), ...
- (6) Spectroscopy characterizations:
Ultraviolet-visible absorbance spectroscopy, ultraviolet-visible reflection spectroscopy, photoluminescence (PL) spectroscopy, ...

4. PROPERTIES AND APPLICATIONS

Metal chalcogenides represent a class of compounds that have a wide range of applications owing to their important nonlinear properties, luminescent properties, quantum size effects, and other important physical and chemical properties [171].

In the past two decades, a growth in publications related to the properties and applications of chalcogenides is accounted. For example, the interest in PbSe, which is a typical narrow-bandgap chalcogenide, can be employed to produce photoresistors, photodetectors, and photoemitters in the IR range, as well as injection lasers [172]. PbSe has also been the object of an inquiry into nanosized effects [173]. The wide-bandgap II-VI chalcogenide semiconductors are of current interest for optoelectronic application light-emitting diodes and optical devices [174]. Among these materials, CdS is the most interesting material because of its high photosensitivity and attractive application in photoconducting cells [175], particularly in the observation of the dependence of these properties on size.

Transition metal dichalcogenides crystallizing in the pyrite structure is another interesting material from both fundamental and technological points of view. For example, ruthenium disulfide has potential applications in energy-related technologies and it is a promising material for thermal catalytic processing as an effective catalyst in petroleum refining and also for photoelectrochemical energy conversion [176]. Ruthenium disulfide is highly stable against photocorrosion and absorbs visible light, and these properties have been exploited in photoelectrochemical energy conversion [177]. It is also used in the photocatalytic decomposition of water [178].

V-VI main-group metal chalcogenides A_2B_3 ($A = Sb, Bi, As$; $B = S, Se, Te$) are a group of important semiconductors, and have applications in television cameras with photoconducting targets, thermoelectric devices, and electronic and optoelectronic devices and in IR spectroscopy [179]. Bismuth sulfide (Bi_2S_3) is a representative V-VI semiconductive material with a lamellar structure whose direct bandgap E_g is 1.3 eV and is useful for photodiode arrays or photovoltaics [180]. It also belongs to a family of solid-state materials with applications in cooling technologies based on the Peltier effect [181]. Antimony sulfide and selenide (Sb_2S_3 and Sb_2Se_3) have also received a great deal of attention due to their good photoconductivity and are regarded as prospective materials for solar energy [182].

Chalcogenide nanoparticles promise to play a major role in a variety of new technologies. The intense interest in this area derives from their unique chemical and physical properties, which give rise to their potential uses in the fields of nonlinear optics, luminescence, electronics, catalysis, solar energy conversion, optoelectronics, and so on. The small dimensions of these chalcogenide nanoparticles result in different physical properties from those observed in the corresponding macrocrystalline bulk materials. As particle sizes become smaller, the ratio of surface atoms to those in the interior increases, leading to the surface properties playing an important role in the properties of the materials [183]. Chalcogenide nanoparticles also exhibit a change in their electronic properties relative to those of the bulk

materials; as the dimensions of the solids get smaller, the bandgap becomes larger. This allows chemists and materials scientists to change the electronic properties of the materials simply by controlling their sizes. Progress in the synthesis of chalcogenide nanoparticles will promote the research on their applications. Meanwhile, advances in the applications will bring new challenges in the synthesis of these materials to both synthetic chemists and materials scientists.

5. CONCLUSION

Metal chalcogenides have attracted considerable interest due to their intriguing properties and structural diversity. In recent years, emphasis has been devoted to their preparation in the nanophased form with two aspects of consideration: one is the modern trend of miniaturization, and the other is the unique property associated with the nanostructures. Herein, several novel synthetic methods for nanocrystalline metal chalcogenides have been reviewed, including microwave assisted heating, sonochemical synthesis, sonoelectrochemical synthesis, photochemical synthesis, γ -irradiation method, low-temperature solid-state synthesis, solvothermal synthesis, electrochemical template synthesis, microemulsion route, and sol-gel synthesis. Though this review cannot cover all the methods for the preparation of metal chalcogenide nanoparticles ever reported in the literature, to some extent, these methods included represent the latest progress in this field. Compared with conventional methods, these novel methods have a variety of advantages and will play an increasingly important role in materials science in the future. However, there is still a long way to go. Exploring new methods that are mild, convenient, efficient, and environmentally friendly to prepare nanosized materials with desirable size, morphology, and properties is still a great challenge to us.

GLOSSARY

Chalcogenide A class of compounds including sulfides, selenides, and tellurides.

Sonochemistry The formation, growth, and implosive collapse of bubbles in liquids.

Sonoelectrochemical synthesis Combination of sonochemistry and electrochemistry in the preparation of nanosized materials.

ACKNOWLEDGMENTS

We thank Prof. A. Gedanken, Department of Chemistry at Bar-Ilan University, Israel, for giving us valuable advice and constructive discussion. We also thank Prof. Hong-Yuan Chen, Ms. Wenbo Zhao, Mr. Jinzhong Xu, Mr. Yu Zhao, Mr. Shu Xu, Mr. Tao Ding, Mr. Xiaofeng Qiu, Ms. Ming Zhang, and Dr. Ming Yang for their kind assistance.

REFERENCES

1. G. A. Ozin, *Adv. Mater.* 4, 612 (1992); G. A. Ozin, *Science* 271, 920 (1996).
2. R. W. Cahn, *Nature* 359, 591 (1992).

3. A. Hagfeldt and M. Gratzel, *Chem. Rev.* 95, 49 (1995); A. Henglein, *Chem. Rev.* 89, 1861 (1989).
4. H. Gleiter, *Prog. Mater. Sci.* 33, 223 (1989); R. Uyeda, *Prog. Mater. Sci.* 35, 1 (1991).
5. D. H. Chen and S. H. Wu, *Chem. Mater.* 12, 1354 (2000), and references cited therein.
6. L. D. Zhang and J. M. Mou, "Science for Nanocrystals." Liaoning Science and Technology Press, Liaoning, 1994.
7. R. Coustal, *J. Chem. Phys.* 38, 277 (1958).
8. Y. M. Gao, P. Wu, J. Baglio, K. M. Dwight, and A. Wold, *Mater. Res. Bull.* 24, 1215 (1989).
9. H. C. Metcalf, J. E. Williams, and J. F. Caskta, "Modern Chemistry." Holt, Reinhart, Winston, New York, 1982.
10. D. M. Wilhelmy and E. Matijevic, *J. Chem. Soc., Faraday Trans.* 563, (1984); C. E. Johnson, D. K. Hickey, and D. C. Harris, *Mater. Res. Soc. Symp. Proc.* 73, 685 (1986); D. M. Frigo, O. F. Z. Khan, and P. O'Brien, *J. Cryst. Growth* 96, 989 (1989); T. Trindade, J. D. De Jesus, and P. O'Brien, *J. Mater. Chem.* 4, 1611 (1994); J. G. Brennan, T. Seigrist, P. J. Carrol, S. M. Stuczynski, P. Reynders, L. E. Brus, and M. L. Steigerwald, *Chem. Mater.* 2, 403 (1990); G. Krauter and W. S. Rees, *J. Mater. Chem.* 5, 1265 (1995).
11. N. L. Pickett, D. F. Foster, and D. J. Cole Hamilton, *J. Mater. Chem.* 6, 507 (1996).
12. H. C. Yi and J. J. Moore, *J. Mater. Sci.* 25, 1159 (1990).
13. I. P. Parkin, *Chem. Soc. Rev.* 25, 199 (1996).
14. A. G. Saskaia, *Chem. Soc. Rev.* 26, 233 (1997), and references cited therein.
15. J. J. Zhu, M. G. Zhou, J. Z. Xu, and X. H. Liao, *Mater. Lett.* 47, 25 (2001).
16. X. H. Liao, J. J. Zhu, and H. Y. Chen, *Mater. Sci. Eng. B* 85, 85 (2001).
17. J. J. Zhu, O. Palchik, S. G. Chen, and A. Gedanken, *J. Phys. Chem. B* 104, 7344 (2000).
18. X. H. Liao, H. Wang, J. J. Zhu, and H. Y. Chen, *Mater. Res. Bull.* 36, 2339 (2001).
19. H. Wang, J. J. Zhu, and X. H. Liao, unpublished data.
20. J. J. Zhu, H. Wang, J. M. Zhu, and J. Wang, *Mater. Sci. Eng. B* 94, 136 (2002).
21. H. Wang, J. R. Zhang, and J. J. Zhu, *J. Cryst. Growth* 233, 829 (2001).
22. A. V. Murugan, R. S. Sonawane, B. B. Kale, S. K. Apte, and A. V. Kulkarni, *Mater. Chem. Phys.* 71, 98 (2001).
23. O. Palchik, R. Kerner, J. J. Zhu, and A. Gedanken, *J. Solid State Chem.* 154, 530 (2000).
24. F. Fievet, J. P. Lagier, and M. Figlarz, *MRS Bull.* Dec, 29 (1989).
25. G. Viau, F. Fievet-Vincent, and F. Fievet, *J. Mater. Chem.* 6, 1047 (1996).
26. G. Viau, F. Fievet-Vincent, and F. Fievet, *Solid State Ionics* 84, 259 (1996).
27. S. Sun, C. B. Murray, D. Weller, L. Folks, and A. Moser, *Science* 287, 1989 (2000).
28. O. Palchik, R. Kerner, A. Gedanken, A. M. Weiss, M. A. Slifkin, and V. Palchik, *J. Mater. Chem.* 11, 874 (2001).
29. R. Kerner, O. Palchik, and A. Gedanken, *Chem. Mater.* 13, 1413 (2001).
30. H. Grisar, O. Palchik, A. Gedanken, V. Palchik, M. A. Slifkin, A. M. Weiss, and Y. R. Hacohen, *Inorg. Chem.* 40, 4814 (2001).
31. H. Grisar, O. Palchik, A. Gedanken, V. Palchik, M. A. Slifkin, A. M. Weiss, and Y. R. Hacohen, *J. Mater. Chem.* 12, 339 (2002).
32. K. S. Suslick, *Science* 247, 1439 (1990); S. J. Doktycz and K. S. Suslick, *Science* 247, 1067 (1990); K. S. Suslick, S. B. Choe, A. A. Cichowlas, and M. W. Grinstaff, *Nature* 353, 414 (1991); K. S. Suslick and G. J. Price, *Annu. Rev. Mater. Sci.* 29, 295 (1999).
33. K. S. Suslick, *Adv. Organomet. Chem.* 25, 73 (1986); J. L. Luche, *Ultrasonics* 25, 40 (1987); T. Kitazume and N. Ishikawa, *J. Am. Chem. Soc.* 107, 5186 (1985).
34. J. L. Luche and C. Damiano, *J. Am. Chem. Soc.* 102, 7926 (1980).
35. K. Chatakoudu, M. L. H. Green, M. Thompdon, and K. S. Suslick, *Chem. Commun.* 900 (1987).
36. K. S. Suslick, T. Hyeon, M. Fang, T. J. Ries, and A. A. Cichowlas, *Mater. Sci. Forum* 225, 903 (1996).
37. N. Arul Dhas and A. Gedanken, *J. Phys. Chem. B* 101, 9495 (1997); R. V. Kumar, Y. Diamant, and A. Gedanken, *Chem. Mater.* 12, 2301 (2000); X. Cao, Y. Koltypin, G. Katabi, I. Felner, and A. Gedanken, *J. Mater. Res.* 12, 405 (1997); J. J. Zhu, Z. H. Lu, S. T. Aruna, D. Aurbach, and A. Gedanken, *Chem. Mater.* 12, 2557 (2000); H. Wang, J. J. Zhu, J. M. Zhu, X. H. Liao, S. Xu, T. Ding, and H. Y. Chen, *Phys. Chem. Chem. Phys.* 4, 3794 (2002).
38. K. S. Suslick, D. A. Hammerton, and R. E. Cline, *J. Am. Chem. Soc.* 108, 5641 (1986).
39. V. Misik, N. Miyoshi, and P. Riesz, *J. Phys. Chem.* 99, 3605 (1995).
40. W. B. McNamara, Y. T. Didenko, and K. S. Suslick, *Nature* 401, 772 (1999).
41. J. J. Zhu, Y. Koltypin, and A. Gedanken, *Chem. Mater.* 12, 73 (2000).
42. P. Jeevanandam, Y. Koltypin, Y. Gofer, Y. Diamant, and A. Gedanken, *J. Mater. Chem.* 10, 2769 (2000).
43. S. Avivi, O. Palchik, V. Palchik, M. A. Slifkin, A. M. Weiss, and A. Gedanken, *Chem. Mater.* 13, 2195 (2001).
44. H. Wang, J. R. Zhang, X. N. Zhao, S. Xu, and J. J. Zhu, *Mater. Lett.* 55, 253 (2002).
45. J. Z. Sostaric, R. A. Caruso-Hobson, P. Mulvaney, and F. Grieser, *J. Chem. Soc. Faraday Trans.* 93, 1791 (1997).
46. J. J. Zhu, H. Wang, S. Xu, and H. Y. Chen, *Langmuir* 18, 3306 (2002).
47. H. Wang, S. Xu, X. N. Zhao, J. J. Zhu, and X. X. Quan, *Mater. Sci. Eng. B* 96, 60 (2002).
48. S. Xu, H. Wang, J. J. Zhu, and H. Y. Chen, *J. Cryst. Growth* 234, 263 (2002).
49. H. Wang, J. J. Zhu, J. M. Zhu, and H. Y. Chen, *J. Phys. Chem. B* 106, 3848 (2002).
50. G. Wang, G. Li, C. Liang, and L. Zhang, *Chem. Lett.* 344 (2001); G. Z. Wang, W. Chen, C. H. Liang, Y. W. Wang, G. W. Meng, and L. D. Zhang, *Inorg. Chem. Commun.* 4, 208 (2001); G. Z. Wang, Y. W. Wang, W. Chen, C. H. Liang, G. H. Li, and L. D. Zhang, *Mater. Lett.* 48, 269 (2001).
51. M. M. Mdleleni, T. Hyeon, and K. S. Suslick, *J. Am. Chem. Soc.* 120, 6189 (1998).
52. S. I. Nikitenko, Y. Koltypin, Y. Mastai, M. Koltypin, and A. Gedanken, *J. Mater. Chem.* 12, 1450 (2002).
53. P. Dubois, J. P. Lelieur, and G. Lepoutre, *Inorg. Chem.* 28, 195 (1989).
54. G. Henshaw, I. P. Parkin, and G. A. Shaw, *Chem. Commun.* 1095 (1996).
55. G. Henshaw, I. P. Parkin, and G. A. Shaw, *J. Chem. Soc. Dalton Trans.* 231 (1997).
56. F. A. Cotton and G. Wilkinson, "Advanced Inorganic Chemistry," 3rd ed. John Wiley & Sons Inc., New York, 1972.
57. J. J. Zhu, S. W. Liu, O. Palchik, Y. Koltypin, and A. Gedanken, *J. Solid State Chem.* 153, 342 (2000).
58. R. V. Kumar, O. Palchik, Y. Koltypin, Y. Diamant, and A. Gedanken, *Ultrasonics Sonochem.* 9, 65 (2002).
59. B. Li, Y. Xie, J. Huang, and Y. Qian, *Ultrasonics Sonochem.* 6, 217 (1999).
60. B. Li, Y. Xie, J. Huang, Y. Liu, and Y. Qian, *Chem. Mater.* 12, 2614 (2000).
61. B. Li, Y. Xie, Y. Liu, J. Huang, and Y. Qian, *J. Solid State Chem.* 158, 260 (2001).
62. R. Harpenness, O. Palchik, A. Gedanken, V. Palchik, S. Amiel, M. A. Slifkin, and A. M. Weiss, *Chem. Mater.* 14, 2094 (2002).
63. T. Ding, H. Wang, S. Xu, and J. J. Zhu, *J. Cryst. Growth* 235, 517 (2002).
64. N. Arul Dhas, A. Zaban, and A. Gedanken, *Chem. Mater.* 11, 806 (1999).

65. N. Arul Dhas and A. Gedanken, *Appl. Phys. Lett.* 72, 2514 (1998).
66. M. L. Breen, A. D. Dinsmore, R. H. Pink, S. B. Qadri, and B. R. Ratna, *Langmuir* 17, 903 (2001).
67. T. J. Mason, J. P. Walton, and D. J. Lorimer, *Ultrasonics* 28, 251 (1990); T. J. Mason, J. P. Walton, and D. J. Lorimer, *Ultrasonics* 28, 333 (1990).
68. T. J. Mason, "Practical Sonochemistry." Ellis Horwood, Chichester, 1991.
69. J. Reisse, H. Francois, J. Vandercammen, O. Fabre, A. K.-D. Messaeker, C. Maerschalk, and J. L. Delplancke, *J. Electrochem. Acta* 39, 37 (1994).
70. A. Durant, J. L. Delplancke, R. Winand, and J. Reisse, *Tetrahedron Lett.* 36, 4257 (1995).
71. C. Dekerckheer, K. Bartik, J. P. Lecomte, and J. Reisse, *J. Phys. Chem. A* 102, 9177 (1998).
72. J. L. Delpancke, V. Dibella, J. Reisse, and R. Winand, *Mater. Res. Soc. Symp. Proc.* 372, 75 (1995).
73. J. Reisse, T. Caulier, C. Dekerckheer, O. Fabre, J. Vandercammen, J. L. Delplancke, and R. Winand, *Ultrason. Sonochem.* 3, S147 (1996).
74. Y. Mastai, R. Polsky, Yu. Koltypin, A. Gedanken, and G. Hodes, *J. Am. Chem. Soc.* 121, 10047 (1999).
75. J. J. Zhu, S. T. Aruna, Yu. Koltypin, and A. Gedanken, *Chem. Mater.* 12, 143 (2000).
76. Y. Mastai, M. Homyonfer, A. Gedanken, and G. Hodes, *Adv. Mater.* 11, 1010 (1999).
77. J. J. Zhu, X. H. Liao, X. N. Zhao, and J. Wang, *Mater. Lett.* 47, 339 (2001).
78. J. J. Zhu, X. H. Liao, J. Wang, and H. Y. Chen, *Mater. Res. Bull.* 36, 1169 (2001).
79. C. Y. Wang, X. Mo, Y. Zhou, Y. R. Zhu, H. T. Liu, and Z. Y. Chen, *J. Mater. Chem.* 10, 607 (2000).
80. X. Mo, C. Y. Wang, M. You, Y. R. Zhu, Z. Y. Chen, and Y. Hu, *Mater. Res. Bull.* 36, 2277 (2001).
81. L. Y. Hao, X. Mo, C. Y. Wang, Y. Wu, D. W. Huang, Y. R. Zhu, Y. Hu, and Z. Y. Chen, *Mater. Res. Bull.* 36, 1005 (2001).
82. S. D. Wu, Z. G. Zhu, J. Y. Tan, and J. C. Gao, *Chem. Lett.* 396 (2001).
83. Y. J. Zhu, Y. T. Qian, X. J. Li, and M. W. Zhang, *Chem. Commun.* 1081 (1997); Y. D. Yin, X. L. Xu, X. W. Ge, C. J. Xia, and Z. C. Zhang, *Chem. Commun.* 1641 (1998); Y. J. Zhu, Y. T. Qian, and W. M. Zhang, *J. Mater. Sci. Lett.* 13, 1243 (1994); Y. J. Zhu, Y. T. Qian, and W. M. Zhang, *Mater. Sci. Eng. B* 23, 116 (1994).
84. X. W. Ge, Y. H. Ni, and Z. C. Zhang, *Radiat. Phys. Chem.* 64, 223 (2002).
85. Y. H. Ni, X. W. Ge, H. R. Liu, Z. C. Zhang, Q. Ye, and F. Wang, *Chem. J. Chinese Univ.-Chinese* 23, 176 (2002).
86. X. W. Ge, Y. H. Ni, H. R. Liu, Q. G. Ye, and Z. C. Zhang, *Mater. Res. Bull.* 36, 1609 (2001).
87. Y. H. Ni, X. W. Ge, H. R. Liu, X. L. Xu, and Z. C. Zhang, *Radiat. Phys. Chem.* 61, 61 (2001).
88. M. Chen, Y. Xie, H. Y. Chen, Z. P. Qiao, and Y. T. Qian, *J. Colloid Interface Sci.* 237, 47 (2001).
89. Z. P. Qiao, Y. Xie, J. G. Xu, X. M. Liu, Y. J. Zhu, and Y. T. Qian, *Can. J. Chem.* 78, 1143 (2000).
90. G. S. Chu, G. Z. Bian, Y. L. Fu, and Z. C. Zhang, *Mater. Lett.* 43, 81 (2000).
91. Y. Xie, Z. P. Qiao, M. Chen, Y. J. Zhu, and Y. T. Qian, *Chem. Lett.* 875 (1999).
92. Y. D. Yin, X. L. Xu, X. W. Ge, Y. Lu, and Z. C. Zhang, *Radiat. Phys. Chem.* 55, 353 (1999).
93. Z. P. Qiao, Y. Xie, X. J. Li, C. Wang, Y. J. Zhu, and Y. T. Qian, *J. Mater. Chem.* 9, 735 (1999).
94. Y. D. Yin, X. L. Xu, X. W. Ge, C. J. Xia, and Z. C. Zhang, *Chem. Commun.* 1641 (1998).
95. G. Z. Bian, Y. D. Yin, Y. L. Fu, Z. H. Wu, T. D. Hu, and T. Liu, *Acta Phys.-Chim. SIN.* 16, 55 (2000).
96. Z. P. Qiao, Y. Xie, J. G. Xu, Y. J. Zhu, and Y. T. Qian, *J. Colloid Interface Sci.* 214, 459 (1999).
97. X. Jiang, Y. Xie, J. Lu, L. Zhu, W. He, and Y. Qian, *Chem. Mater.* 13, 1213 (2001).
98. B. Liu, H. P. Li, C. H. Chew, W. X. Que, Y. L. Lam, C. H. Kam, L. M. Gan, and G. Q. Xu, *Mater. Lett.* 51, 461 (2001).
99. Z. P. Qiao, Y. Xie, J. G. Xu, Y. J. Zhu, and Y. T. Qian, *Mater. Res. Bull.* 35, 1355 (2000).
100. Z. P. Qiao, Y. Xie, M. Chen, J. G. Xu, Y. J. Zhu, and Y. T. Qian, *Chem. Phys. Lett.* 321, 504 (2000).
101. M. Chen, Y. Xie, Z. P. Qiao, Y. J. Zhu, and Y. T. Qian, *J. Mater. Chem.* 10, 329 (2000).
102. Z. P. Qiao, Y. Xie, G. Li, Y. J. Zhu, and Y. T. Qian, *J. Mater. Sci.* 35, 285 (2000).
103. Z. P. Qiao, Y. Xie, Y. J. Zhu, and Y. T. Qian, *J. Mater. Chem.* 9, 1001 (1999).
104. L. Smart and E. Moore, in "Solid State Chemistry," 2nd ed. Chapman and Hall, London, 1996.
105. Y. M. Zhou and X. Q. Xin, *Chin. J. Inorg. Chem.* 15 (1999).
106. X. R. Ye, D. Z. Jia, J. Q. Yu, X. Q. Xin, and Z. Xue, *Adv. Mater.* 11, 941 (1999).
107. Y. T. Chen, Y. Guo, L. L. Kong, and H. L. Li, *Chem. Lett.* 602 (2002).
108. X. S. Niu, Y. L. Liu, and J. Q. Xu, *J. Inorg. Mater.* 17, 817 (2002).
109. X. L. Sun and G. Y. Hong, *Chinese Chem. Lett.* 12, 187 (2001).
110. W. Wang, Y. Liu, Y. Zhan, C. Zheng, and G. Wang, *Mater. Res. Bull.* 36, 1977 (2001).
111. Y. Li, H. Liao, Y. Ding, Y. Fan, Y. Zhang, and Y. Qian, *Inorg. Chem.* 38, 1382 (1999).
112. Y. Li, Y. Ding, Y. Qian, Y. Zhang, and L. Yang, *Inorg. Chem.* 37, 2844 (1998).
113. Y. D. Li, Y. Ding, and Z. Y. Wang, *Adv. Mater.* 11, 847 (1999).
114. Q. Peng, Y. Dong, Z. Deng, X. Sun, and Y. Li, *Inorg. Chem.* 40, 3840 (2001).
115. K. Osakada and T. Yamamoto, *Inorg. Chem.* 30, 2328 (1991); K. Osakada and T. Yamamoto, *J. Chem. Soc., Chem. Commun.* 1117 (1987); R. A. Shaw and W. K. Woods, *J. Chem. Soc. A* 1569 (1971); H. Cui, R. D. Pike, R. Kershaw, K. Dwight, and A. Wold, *J. Solid State Chem.* 101, 115 (1992); R. Nomura, K. Kanaya, and H. Matsuda, *Bull. Chem. Soc. Jpn.* 62, 939 (1989); A. Wold and K. Dwight, *J. Solid State Chem.* 96, 53 (1992); M. Abboudi and A. Mosset, *J. Solid State Chem.* 109, 70 (1994).
116. M. K. Karanjai and D. Dasgupta, *Mater. Lett.* 4, 368 (1986); M. K. Karanjai and D. Dasgupta, *Thin Solid Films* 155, 309 (1987); M. Krunk, E. Y. Mellikov, and E. Sork, *Thin Solid Films* 145, 105 (1986); N. Tohge, M. Asuka, and T. Minami, *J. Non-cryst. Solids* 147-148, 652 (1992).
117. S. H. Yu, L. Shu, J. Yang, Z. H. Han, Y. T. Qian, and Y. H. Zhang, *J. Mater. Res.* 14, 4157 (1999).
118. J. Yang, J. H. Zeng, S. H. Yu, L. Yang, Y. H. Zhang, and Y. T. Qian, *Chem. Mater.* 12, 2924 (2000).
119. S. H. Yu, J. Yang, Z. H. Han, Y. Zhou, R. Y. Yang, Y. T. Qian, and Y. H. Zhang, *J. Mater. Chem.* 9, 1283 (1999).
120. S. H. Yu, Z. H. Han, J. Yang, R. Y. Yang, Y. Xie, and Y. T. Qian, *Chem. Lett.* 1111 (1998).
121. S. H. Yu, Y. S. Wu, J. Yang, Z. H. Han, Y. Xie, Y. T. Qian, and X. M. Liu, *Chem. Mater.* 10, 2309 (1998).
122. S. H. Yu, J. Yang, Y. S. Wu, Z. H. Han, J. Lu, Y. Xie, and Y. T. Qian, *J. Mater. Chem.* 8, 1949 (1998).
123. J. Yang, G. H. Cheng, J. H. Zeng, S. H. Yu, X. M. Liu, and Y. T. Qian, *Chem. Mater.* 13, 848 (2001).
124. Y. Zhou, L. Y. Hao, S. H. Yu, M. You, Y. R. Zhu, and Z. Y. Chen, *Chem. Mater.* 11, 3411 (1999).
125. S. H. Yu, M. Yoshimura, J. M. C. Moreno, T. Fujiwara, T. Fujino, and R. Teranishi, *Langmuir* 17, 1700 (2001).

126. U. K. Gautam, M. Rajamathi, F. Meldrum, P. Morgan, and R. Seshadri, *Chem. Commun.* 629 (2001).
127. J. Hu, Q. Lu, K. Tang, Y. Qain, G. Zhou, and X. M. Liu, *Chem. Commun.* 1093 (1999).
128. Y. Jiang, Y. Wu, X. Mo, W. Yu, Y. Xie, and Y. Qian, *Inorg. Chem.* 39, 2964 (2000).
129. Y. Cui, J. Ren, G. Chen, Y. Qian, and Y. Xie, *Chem. Lett.* 236 (2001).
130. C. R. Martin, *Science* 266, 1961 (1994).
131. D. Routkevitch, T. Bigioni, M. Moskovits, and J. M. Xu, *J. Phys. Chem.* 100, 14037 (1996).
132. L. Piraux, S. Dubois, and S. Demoustier-Champagne, *Nucl. Instrum. Meth. B* 131, 357 (1997).
133. W. Z. Li, S. S. Xie, L. X. Qian, B. H. Chang, B. S. Zhou, W. Y. Zhou, R. A. Zhao, and G. Wang, *Science* 274, 1701 (1996).
134. D. S. Xu, Y. J. Xu, D. P. Chen, G. L. Guo, L. L. Gui, and Y. Q. Tang, *Chem. Phys. Lett.* 325, 340 (2000).
135. D. S. Xu, D. P. Chen, Y. J. Xu, X. S. Shi, G. L. Guo, L. L. Gui, and Y. Q. Tang, *Pure Appl. Chem.* 72, 127 (2000).
136. D. S. Xu, X. S. Shi, G. L. Guo, L. L. Gui, and Y. Q. Tang, *J. Phys. Chem. B* 104, 5061 (2000).
137. D. S. Xu, Y. J. Xu, D. P. Chen, G. L. Guo, L. L. Gui, and Y. Q. Tang, *Adv. Mater.* 12, 520 (2000).
138. Y. Li, D. S. Xu, Q. M. Zhang, D. P. Chen, F. Z. Huang, Y. J. Xu, G. L. Guo, and Z. N. Gu, *Chem. Mater.* 11, 3433 (1999).
139. J. H. Fendler, *Chem. Rev.* 87, 877 (1987).
140. V. Buschmann, G. Van Tendeloo, P. Monnoyer, and J. B. Nagy, *Langmuir* 14, 1528 (1998).
141. T. Hanaoka, T. Tago, M. Kishida, and K. Wakabayashi, *Bull. Chem. Soc. Jpn.* 74, 1349 (2001).
142. S. G. Dixit, A. R. Mahadeshwar, and S. K. Haram, *Colloid Surf. A* 133, 69 (1998).
143. E. C. Hao, H. P. Sun, Z. Zhou, J. Q. Liu, B. Yang, and J. C. Shen, *Chem. Mater.* 11, 3096 (1999).
144. K. Suzuki, N. Mizutani, and M. Harada, *J. Chem. Eng. Jpn.* 32, 588 (1999); K. Suzuki, N. Mizutani, and M. Harada, *J. Chem. Eng. Jpn.* 32, 31 (1999).
145. M. L. Curri, A. Agostiano, L. Manna, M. Della Monica, M. Catalano, L. Chiavarone, V. Spagnolo, and M. Lugara, *J. Phys. Chem. B* 104, 8391 (2000); A. Agostiano, M. Catalano, M. L. Curri, M. Della Monica, L. Manna, and L. Vasaneli, *Micron* 31, 253 (2000).
146. B. A. Simmons, S. C. Li, V. T. John, G. L. McPherson, A. Bose, W. L. Zhou, and J. B. He, *Nano. Lett.* 2, 263 (2002).
147. X. Mo, C. Y. Wang, L. Y. Hao, M. You, Y. R. Zhu, Z. Y. Chen, and Y. Hu, *Mater. Res. Bull.* 36, 1925 (2001).
148. B. Liu, H. P. Li, C. H. Chew, W. X. Que, Y. L. Lam, C. H. Kam, L. M. Gan, and G. Q. Xu, *Mater. Lett.* 51, 461 (2001).
149. B. Liu, C. H. Chew, L. M. Gan, G. Q. Xu, H. P. Li, Y. L. Lam, C. H. Kam, and W. X. Que, *J. Mater. Res.* 16, 1644 (2001).
150. M. Y. Han, W. Huang, C. H. Chew, L. M. Gan, X. J. Zhang, and W. Ji, *J. Phys. Chem. B* 102, 1884 (1998).
151. J. Huang, Y. Xie, B. Li, Y. Liu, J. Lu, and Y. Qian, *J. Colloid Interface Sci.* 236, 382 (2001).
152. C. C. Chen, C. Y. Chao, and Z. H. Lang, *Chem. Mater.* 12, 1516 (2000).
153. H. Wang, J. R. Zhang, and J. J. Zhu, *J. Cryst. Growth* 246, 161 (2002).
154. B. Liu, G. Q. Xu, L. M. Gan, C. H. Chew, W. S. Li, and Z. X. Shen, *J. Appl. Phys.* 89, 1059 (2001).
155. A. C. Pierre, "Introduction to Sol-Gel Processing." Septima, Paris, 1992.
156. C. Brinker and G. Scherer, "Sol-Gel Science." Academic Press, New York, 1990.
157. M. Calzada and S. Milne, *J. Mater. Sci. Lett.* 12, 1221 (1993).
158. N. Tohge, M. Asuka, and T. Minami, *SPIE: Sol-Gel Optics* 1328, 125 (1990).
159. T. Guiton, C. Czekaj, and C. Pantano, *J. Non-Cryst. Solids* 121, 7 (1990).
160. V. Stanic, T. H. Etsell, A. C. Pierre, and R. J. Mikula, *J. Mater. Chem.* 7, 105 (1997).
161. V. Stanic, A. C. Pierre, T. H. Etsell, and R. J. Mikula, *J. Phys. Chem. A* 105, 6136 (2001).
162. V. Stanic, T. H. Etsell, A. C. Pierre, and R. J. Mikula, *Mater. Lett.* 31, 35 (1997).
163. V. Stanic, A. C. Pierre, T. H. Etsell, and R. J. Mikula, *J. Non-Cryst. Solids* 220, 58 (1997).
164. M. A. Sriram, K. S. Weil, and P. N. Kumta, *Appl. Organometallic Chem.* 11, 163 (1997).
165. M. A. Sriram and P. N. Kumta, *J. Mater. Chem.* 8, 2453 (1998).
166. M. A. Sriram and P. N. Kumta, *J. Mater. Chem.* 8, 2441 (1998).
167. E. J. Donahue, A. Roxburgh, and M. Yurchenko, *Mater. Res. Bull.* 33, 323 (1998).
168. H. Q. Cao, Y. Xu, J. M. Hong, H. B. Liu, G. Yin, B. L. Li, C. Y. Tie, and Z. Xu, *Adv. Mater.* 13, 1393 (2001).
169. M. Zelner, H. Minti, R. Reisfeld, H. Cohen, Y. Feldman, S. R. Cohen, and R. Tenne, *J. Sol-Gel Tech.* 20, 153 (2001).
170. V. S. Gurin, V. B. Prokopenko, A. A. Alexeenko, S. Wang, and P. V. Prokoshin, *Mater. Sci. Eng. C* 15, 93 (2001).
171. N. Heron, J. C. Calabrese, W. E. Farneth, and Y. Wang, *Science* 259, 1426 (1993); L. E. Brus, *Appl. Phys. A* 53, 465 (1991); R. Rossetti, R. Hull, J. M. Gibson, and L. E. Brus, *J. Chem. Phys.* 80, 4464 (1984).
172. R. N. Mulik, C. B. Rotti, B. M. More, D. S. Suttrave, G. S. Shahane, K. M. Garadkar, L. P. Deshmukh, and P. P. Hankare, *Indian J. Pure Appl. Phys.* 34, 903 (1996).
173. S. Gorer, A. Albu-Yaron, and G. Hodes, *J. Phys. Chem.* 99, 16442 (1995).
174. M. G. Bawendi, D. J. Carroll, W. L. Wilson, and L. E. Brus, *J. Chem. Phys.* 96, 5649 (1992); R. Rossetti, R. Hull, J. M. Gibson, and L. E. Brus, *J. Chem. Phys.* 82, 552 (1985).
175. A. G. Stanley, "Cadmium Sulfide Solar Cells," Applied Solid State Science 15. Academic Press, New York, 1975.
176. A. M. Redon, *Solar Cells* 15, 27 (1985); T. A. Pecoraro and R. R. Chianelli, *J. Catal.* 67, 430 (1981).
177. R. Heindl, R. Parsons, A. M. Redon, H. Tributsch, and J. Vigneron, *Surf. Sci.* 115, 91 (1982); D. H. M. W. Thewissen, E. A. V. Zouwen-Assik, K. Timmer, A. H. A. Tinnemans, and A. Mackor, *Chem. Commun.* 941 (1984); M. Ashokkumar, A. Kudo, N. Saito, and T. Sakata, *Chem. Phys. Lett.* 229, 383 (1994); M. Ashokkumar, A. Kudo, and T. Sakata, *Bull. Chem. Soc. Jpn.* 68, 2491 (1995).
178. K. Hara, K. Sayama, and H. Arakawa, *Chem. Lett.* 387 (1998).
179. D. Arivuoli, F. D. Gnanam, and P. Ramasamy, *J. Mater. Sci. Lett.* 7, 711 (1988).
180. B. B. Nayak, H. N. Acharya, G. B. Mitra, and B. K. Mathur, *Thin Solid Films* 105, 17 (1983); S. H. Pawar, P. N. Bhosale, M. D. Uplane, and S. Tanhankar, *Thin Solid Films* 110, 165 (1983); L. J. Farrugia, F. J. Lawlot, and N. C. Norman, *Polyhedron* 14, 311 (1995).
181. P. Boudjouk, M. P. Remington, D. G. Grier, B. R. Jarabek, and G. J. McCarthy, *Inorg. Chem.* 37, 3538 (1998).
182. M. T. S. Nair, K. Nair, V. M. Garcia, Y. Pena, O. L. Arenas, J. C. Garcia, and O. Gomez-Daza, *Proc. SPIE—Int. Soc. Opt. Eng.* 3138, 186 (1997); O. Savadogo and K. C. Mondal, *Sol. Energy Mater. Sol. Cells* 26, 117 (1992).
183. T. Trindade, P. O'Brien, and N. L. Pickett, *Chem. Mater.* 13, 3843 (2001).

Synthesis of Nanomaterials Using Microemulsion Process

Suresh C. Kuiry, Sudipta Seal

University of Central Florida, Orlando, Florida, USA

CONTENTS

1. Introduction
 2. Characterization of Physicochemical Properties of Microemulsions
 3. Reaction Kinetics and Mechanisms of Particle Formation in Microemulsions
 4. Nanoparticles Synthesis
 5. Concluding Remarks
- Glossary
References

1. INTRODUCTION

Application of microemulsions has been known for more than a century. Floor cleaning, lubrication for machining and metal working processes, foods, agrochemicals, detergents, paints, cosmetics, pharmaceuticals, and tertiary oil recovery are a few examples of the widespread industrial and domestic applications of microemulsions. Microemulsion was described as special colloidal dispersions by Hoar and Schulman [1]. It is defined as systems of single-phase and thermodynamically stable isotropic solutions composed of water, oil, and one or more amphiphiles. Such definition of microemulsion was put forward by Danielson and Lindman [2], which is widely accepted as reported by Solans and co-workers [3]. The microemulsion can form large numbers of reactors, which can be successfully used to synthesize nanoparticles mainly because these nanoreactors are separated from one another and thereby the growth of the synthesized nanoparticles is restricted. It is a valuable process-tool to synthesize nanoparticles for designing and manufacturing metals, alloys, ceramics, and composite components with improved mechanical, electrical, magnetic, optical, and electronic properties. The use of microemulsions to synthesize monodispersed nanoparticles of platinum group of metals was first reported by Boutonnet et al. [4]. The process of microemulsion to produce nanoparticles is

unique in the sense that it can produce monodispersed particles and it has capability to control not only the size but also the shape of the nanoparticles. Almost all types of nanoparticles can be synthesized with the help of microemulsion method, which has drawn the attention of many researchers for synthesis of nanoparticles in the last decade. Considering the vastness of the available literature on the various aspects of microemulsion, it is almost impossible to accommodate in a single chapter. Therefore, an overview of the microemulsion fundamentals, thermodynamics, kinetics, and physicochemical aspects is presented in this chapter with a view to synthesize nanomaterials. At the end, the available literature on the synthesis of metals, oxides, sulfides, halides, and mixed oxides nanoparticles is also summarized.

1.1. Fundamentals of Microemulsion

The surface tension forces at the boundary between the two immiscible liquids are free to exert their influence equally in all directions [5]; eventually, the dispersed phase assumes the form of spheres in order to have a minimum surface area per unit volume. These spheres may either consist of water or oil. When they are water, the emulsions are called water-in-oil or simply w/o. On the other hand, the emulsions are described as oil-in-water or o/w, when the spheres consist of oil. The formation of emulsion yielded an enormous increase in the surface area of contact between the two immiscible liquids, which in turn requires work to be performed on the system as per the following relation:

$$\text{Work} = -\gamma dA \quad (1)$$

where γ is the interfacial tension between the two liquids when emulsifying agent is present in the system, and dA is the increase in the area of contact between the two liquids. Equation (1) indicates that the emulsification is a strong function of the interfacial energy. The smaller the value of γ is, the smaller is the droplet size. Moreover, a decrease in the value of interfacial energy decreases the amount of

work required for emulsification. When the value of interfacial tension approaches zero, the work term becomes almost zero, which implies that the emulsification process is spontaneous, and such a system of emulsion is termed as microemulsions. However, the work done in emulsion is of mechanical origin, unlike in the case of microemulsions where the work performed for dispersion is mostly chemical in nature. Since changing the chemical composition of the immiscible liquids is neither preferred nor practicable, a chemical substance is introduced into the system that has the ability to reduce the interfacial energy to a great extent at low concentration level. Such material is called the emulsifier or surfactant. Molecules of the surfactant can spontaneously arrange themselves as monomolecular film or monolayer between the two immiscible liquids due to the strong attraction of one portion by the oil and another portion by the water. The hydrophile-lipophile balance (HLB) is the convenient measure of such attractions and counterattractions by the two liquids. Such attraction forces are directly responsible for orienting these molecules perpendicular to the interface and parallel to one another. The surfactant molecule has an aliphatic tail and a polar head, which are normally represented by a zigzag line and a circle, respectively. The polar head is oriented towards the aqueous phase as it is water-soluble. The tail will be dissolved in the oil phase. The circle with a positive sign indicates a cationic surfactant. The polar head and aliphatic tail of the oriented monolayer molecules interact with one another. The forces of attraction and repulsion among the heads are different than among the tails. Among the tails, the London dispersion forces play an important role; they are inversely proportional to the seventh power of the lateral distance between them. On the other hand, the forces operative among the heads mainly depend on the hydrogen bonding with each other and water molecules. As the concentration of the surfactant molecules on the interface increases, the net repulsion forces among the heads and the tails increase, which helps in controlling the curvature of the film and consequently the geometrical shape of the droplets. Co-surfactant, which is either an alcohol or an amine, is used along with the surfactant in order to make the emulsification process more effective. It reduces not only the critical micelle concentration (cmc) but also the interfacial tension above the cmc. Usually cmc is defined as the concentration of micelles at which a sharp change occurs in any of a wide variety of properties of the surfactant solution such as electrical conductance, transference number, surface tension, etc. Co-surfactant helps reduce the rigidity of the film and thereby makes the transition process of film to the microemulsion droplets easy [6]. The surfactant and the co-surfactant interact in such a way as to greatly enhance the interfacial stability by reducing droplet size. A spherical water-in-oil microemulsion droplet is shown schematically in Figure 1. The heads with long and short tails denote the surfactant and co-surfactant, respectively. The water molecules are shown inside the droplet. The diameter of such a spherical droplet in actual practice may vary in the range of 10 to 200 Å. The continuous medium outside the microemulsion droplet is the oil phase.

The surfactants, which are employed for synthesis of materials through microemulsion route, can be classified

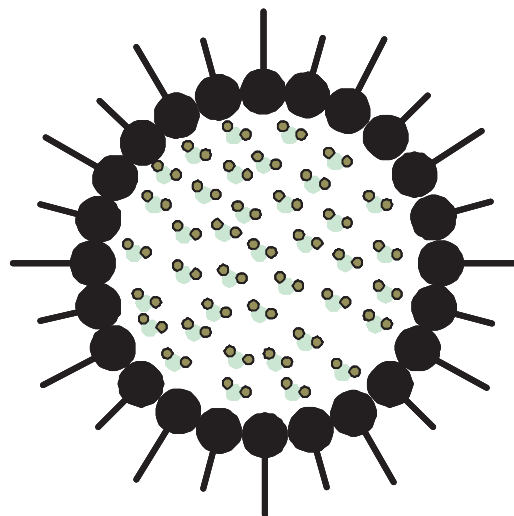


Figure 1. Schematic representation of single water-in-oil microemulsion droplet.

into three groups such as cationic, anionic, and non-ionic [7]. Cetyltrimethylammonium bromide (CTAB), cetyltrimethylammonium bromide (CTAB), and didodecyltrimethylammonium bromide (DDAB) are the examples of cationic surfactant. The anionic surfactants usually used are sodium bis(2-ethylhexyl)sulfosuccinate, which is also known as Aerosol OT or simply AOT, dioleoyl phosphoric acid (DOLPA), sodium dodecyl sulfate (SDS), and potassium oleate. Ionic surfactants with two hydrocarbon chains do not need a cosurfactant to enable them to form microemulsions. AOT and DDAB can form microemulsions without the help of co-surfactant. Polyoxyethylene-(*n*)-dodecyl ether (e.g., tetraoxyethylene dodecyl ether ($C_{12}EO_4$)), polyoxyethylene-(*n*)-nonylphenyl ether (e.g., NP-4, $n = 4$ (Triton N-42); NP-5, $n = 5$ (Triton N-57); NP-6, $n = 6$ (Triton N-60); NP-9, $n = 9-10$ (Triton N-101)), polyoxyethylene-(*n*)-octylphenyl ether (e.g., OP-1, $n = 1$ (Triton X-15); OP-3, $n = 3$ (Triton X-35); OP-5, $n = 5$ (Triton X-45); OP-10, $n = 9-10$ (Triton X-100)), polyoxyethylene-(*n*)-dodecylphenyl ether (e.g., DP-6, $n = 6$), and sorbitan monooleate (SPAN 80) are a few examples of nonionic surfactants used for materials synthesis. Temperature plays an important role in the behavior of the nonionic surfactants because these are water-soluble at low temperatures and oil-soluble at elevated temperatures. The narrow temperature range where the solubility changes is called the phase inversion temperature (PIT) at which the interfacial tension becomes extremely low [8]. The types of microemulsions formed below and above the PIT are oil-in-water and water-in-oil, respectively. A bicontinuous mixture of oil and water, at low surfactant concentrations, may exhibit a three-phase equilibrium with excess water and oil. After the name of P. A. Winsor [9, 10] who investigated the phase equilibria of microemulsions systems extensively, such equilibria of O/W with oil and W/O with water are designated as Winsor I and Winsor II, respectively. A bicontinuous phase of W/O and O/W is known as Winsor III type microemulsion.

1.2. Thermodynamics of Microemulsion

The treatment of the surface chemical behavior of microemulsions system using thermodynamic principles in order to understand the molecular interactions taking place at the interface is quite complex. Hence, it is always subjected to a number of presumptions and simplifications. A few initial studies on the concept of thermodynamical stability and interfacial free energy of microemulsions were initiated by Adamson [11], Ruckenstein and Chi [12], and Wagner [13]. Wagner postulated that a thermodynamically stable emulsion could be obtained only if the concentration of surfactant required for zero interfacial tension is lower than its critical micelle concentration. Microemulsions are thermodynamically stable, unlike emulsions, which are stable due to kinetic restrictions. Ruckenstein [14, 15] and Kegel et al. [16] have attempted to provide the phase behavior of microemulsions with respect to the excess dispersed phases in equilibrium using various thermodynamic variables. Microemulsion is a mixture of oil, water, surfactant, co-surfactant, and electrolyte in which water or oil is dispersed in oil or water as globules of 10 to 100 nm diameter. The surfactant and co-surfactant are mostly located at the interface between oil and water phases. However, these species are also at equilibrium between the two phases. Hence, mixing is not on the molecular level in microemulsion, which restricts the application of principles of solution thermodynamics to a substantial extent. A brief outline of the thermodynamic treatment of the microemulsion will be described mostly from the work of Ruckenstein [15] in this section and readers may refer to the reports [14–16] for details.

Thermodynamics of microemulsions should adequately consider the entropy of the dispersion of the globules in the medium, the free energy of formation of the interface between the two media, the mutual interactions among the globules, and the equilibrium distribution of the surfactant and co-surfactant not only at the interface but also between the two media of the microemulsion. Ruckenstein [15] conveniently decomposed the Helmholtz free energy (f) per unit volume of the entire system into two parts: the free energy (f_0) of dispersion of fixed globules without interactions among them is one, and the free energy (Δf) due to the dispersion of the globules in the continuous phase and to their interactions is the other. Such splitting of the free energy allows one to apply the Gibbs thermodynamics and statistical mechanics for the first and second part, respectively. Now, in order to develop the basic thermodynamic equations for single-phase microemulsion that contains spherical globules of uniform size, Ruckenstein [15] has represented the Helmholtz free energy per unit volume of the microemulsion in the following form:

$$f = f_0 + \Delta f \tag{2}$$

Gibbs thermodynamics provides the following expression for the infinitesimal change of f_0 :

$$df_0 = \gamma dA + C_1 dc_1 + C_2 dc_2 + \sum \mu_i dn_i - p_2 d\phi - p_1 d(1 - \phi) \tag{3}$$

where C_1 and C_2 are the bending stresses associated with the curvatures c_1 and c_2 , respectively; A is the interfacial area per unit volume between the two media of the microemulsion; μ_i and n_i are the chemical potential and the number of molecules of species i per unit volume, respectively; and ϕ is the volume fraction of the surfactant and co-surfactant molecules present at the interface of the globules. The chemical potentials were taken at pressure p_1 for the species present in the continuous phase and at pressure p_2 for those present in the dispersed phase. For spherical shape globules of radius r , $c_1 = c_2 = 1/r$, and $C_1 = C_2 = C/2$. Now using Eqs. (2) and (3), the following relation can be obtained for microemulsions containing spherical globules:

$$df = \gamma dA + C d\left(\frac{1}{r}\right) + \sum \mu_i dn_i - p_2 d\phi - p_1 d(1 - \phi) + d\Delta f \tag{4}$$

The equilibrium state of the microemulsion is completely determined by n_i , the temperature T , pressure p . Therefore, the values of r and ϕ emerge from the condition that f be a minimum with respect to r and ϕ . For the spherical globules,

$$A = \frac{3\phi}{r} \tag{5}$$

Therefore, one obtains

$$\gamma = \frac{r^2}{3\phi} \left(\frac{\partial \Delta f}{\partial r}\right)_\phi - \frac{C}{3\phi} \tag{6}$$

and

$$p_2 - p_1 = \left(\frac{\partial \Delta f}{\partial \phi}\right)_r + \frac{r}{\phi} \left(\frac{\partial \Delta f}{\partial r}\right)_\phi - \frac{C}{r\phi} \tag{7}$$

An additional relationship between p_2 and p_1 is provided by the mechanical equilibrium condition between microemulsion and environment. Considering a variation of dV of the volume V of the microemulsion at constant N_i ($=n_i V$) and T , one can write

$$\gamma d(AV) + VC d\left(\frac{1}{r}\right) - p_2 d(V\phi) - p_1 d[V(1 - \phi)] + d(V\Delta f) - p dV_e = 0 \tag{8}$$

where dV_e is the variation in the volume of the environment which is equal to $-dV$. Combining Eqs. (6)–(8), the following relation can be written:

$$\left(\frac{3\phi}{r}\gamma\right) - (p_2 - p_1)\phi + (p - p_1) + \Delta f = 0 \tag{9}$$

Equations (7) and (9) yield the following relations:

$$p_2 = p + \Delta f + (1 - \phi) \left(\frac{\partial \Delta f}{\partial \phi}\right)_r + \frac{r}{\phi} \left(\frac{\partial \Delta f}{\partial r}\right)_\phi - \frac{C}{r\phi} \tag{10}$$

and

$$p_1 = p + \Delta f - \phi \left(\frac{\partial \Delta f}{\partial \phi}\right)_r \tag{11}$$

Equation (11) demonstrates that the pressure p_1 in the continuous medium of the noninteracting system with free energy f_0 differs from the pressure p , and that the pressure p is equal to the sum between the pressure p_1 and the osmotic contribution due to the free energy Δf . The pressure p acts both in the microemulsion and on the continuous medium of the microemulsion. A globule senses in its immediate vicinity the pressure p_1 of the noninteracting system plus the osmotic pressure due to the free energy Δf . Using Eqs. (6) and (10), the modified Laplace equation, which is valid for the microemulsion, can be written in the following form:

$$p_2 - p = \frac{2\gamma}{r} - \frac{C}{3\phi r} + \Delta f + (1 - \phi) \left(\frac{\partial \Delta f}{\partial \phi} \right)_r + \frac{r}{3\phi} \left(\frac{\partial \Delta f}{\partial r} \right)_\phi \quad (12)$$

In addition to the first two terms on the right-hand side, which are present in the case of a single droplet in a continuum, Eq. (12) contains terms that are due to the entropy of dispersion of the globules in the continuous medium and to the energy of interactions among globules.

In the case of the microemulsion which is in equilibrium with an excess dispersed phase, the composition of the excess dispersed phase is well expected to be the same as that of the dispersed phase. Therefore, the chemical potential of the excess dispersed phase and the dispersed phase is the same. The chemical potential of any species of the microemulsion is equal to its chemical potential in the noninteracting system. The chemical potential in the dispersed phase is expressed in Eq. (4) at pressure p_2 , while the pressure in the excess dispersed phase is equal to the external pressure p to which both the microemulsion and the excess phase are subjected. Therefore, at equilibrium, p_2 should be equal to p . Consequently, Eq. (10) will take the following form:

$$\Delta f + (1 - \phi) \left(\frac{\partial \Delta f}{\partial \phi} \right)_r + \frac{r}{\phi} \left(\frac{\partial \Delta f}{\partial r} \right)_\phi - \frac{C}{r\phi} = 0 \quad (13)$$

The values of r and ϕ for a microemulsion in equilibrium with an excess dispersed phase can be obtained by using Eqs. (6) and (13) with known expressions for γ , C , and Δf . Utilizing the empirical formula of Carnahan and Starling [17] for hard spheres using molecular dynamic simulations as shown in Eq. (14), and combining with Eqs. (6) and (13), the expressions for γ and C may be obtained:

$$\Delta f = -\frac{3\phi kT}{4\pi r^3} \left[1 - \ln \phi - \phi \frac{4 - 3\phi}{(1 - \phi)^2} + \ln \left(\frac{4\pi r^3}{3\nu_c} \right) \right] \quad (14)$$

$$\gamma = \frac{kT}{4\pi r^2} \left[\ln \left(\frac{4\pi r^3}{3\nu_c \phi} \right) - \frac{8\phi - 5\phi^2}{(1 - \phi)^2} + \phi \right] \quad (15)$$

$$C = \frac{3\phi kT}{4\pi r^2} \left[2 \ln \left(\frac{4\pi r^3}{3\nu_c \phi} \right) + \frac{6\phi^2 - 5\phi - \phi^3}{(1 - \phi)^2} \right] \quad (16)$$

where ν_c is the volume of a molecule in the continuous phase. The values of the γ and C were estimated and plotted as functions of r by Ruckenstein [15]. The values of γ and C were found to be very small with increasing value of r . Also for the values of ϕ greater than 0.5, the interfacial

tension exhibited negative values, and hence the interface between the microemulsion and the excess dispersed phase became unstable to thermal perturbations. It can be mentioned here that surfactant, co-surfactant, and hydrophobic phases play an important role in the values of γ and C ; however, Eqs. (15) and (16) do not reflect the effect of these process variables. In reality, development of any mathematical relation that incorporates all these aspects is a remote possibility considering the degree of complexities of the microemulsion system.

2. CHARACTERIZATION OF PHYSICO-CHEMICAL PROPERTIES OF MICROEMULSIONS

In order to obtain a comprehensive view of the physico-chemical properties and structure of the microemulsions, a number of techniques have been utilized so far by various researchers [3, 5]. Phase behavior studies of microemulsions involving at least three components, namely, water, surfactant, and oil [18], can be carried out by measuring various parameters such as solubility, viscosity, and conductivity using simple experimental setup. Study of electrical conductivity has been successfully used to determine the nature of the continuous phase and to pinpoint phase inversion phenomena. Viscosity measurements as a function of the volume fraction have been used to obtain hydrodynamic radius of the droplets, interactions among droplets, and deviations from the spherical shape by fitting the results to appropriate models [19, 20]. Kinugasa et al. [20] have recently derived a simplified expression for the size of the reverse micelle in terms of the water-pool diameter (d_{wp}) as follows:

$$d_{wp} = \left(\frac{6V_W C_W n_{ag}}{\pi C_S} \right)^{1/3} \quad (17)$$

where V_W is the volume of water molecule and n_{ag} is the aggregation number. The terms C_W and C_S are the concentration of water and surfactants, respectively. The aggregation number can be obtained by the following relation of volume fraction of the dispersed spherical reverse micelle (ϕ) which can be obtained by measuring the viscosity of the solution (η), and the viscosity of the solvent (η_0) as reported by Cheng and Schachman [21]:

$$\phi = \frac{\pi N_A C_S}{6n_{ag}} \left[\left(\frac{6V_W C_W n_{ag}}{\pi C_S} \right)^{1/3} + 2L_S \right]^3 \quad (18)$$

$$\frac{\eta}{\eta_0} = 1 + 2.5\phi + 14.1\phi^2 \quad (19)$$

The terms N_A and L_S are Avogadro's number and chain length of a surfactant. The value of L_S for AOT is 1.2×10^{-9} m. Equation (18) suggests that the size of the reverse micelle is a function of the molar ratio of water to surfactant (C_W/C_S). The ratio is denoted by the term W_0 . Kinugasa and co-workers [20] have obtained a correlation between the diameter of the water-pool in nanometers with the W_0 for AOT/water/dodecane system in the domain of $2 < W_0 < 20$ at 25 °C:

$$d_{wp} = 0.29W_0 + 1.1 \quad (20)$$

Usually a microemulsion system under constant pressure is described by a ternary phase diagram in the form of a triangular prism with temperature on the vertical axis, and three components in the three sides of the equilateral triangle. Although most of the phase diagram studies have been limited to the determination of the one-liquid-isotropic phase boundaries, determination of the number and the chemistry of the coexisting phases in equilibrium is equally important in characterizing the microemulsion systems [22, 23].

Numerous scattering techniques have been used in the study of the physicochemical properties of microemulsions [3, 24–28]. Static and dynamic light scattering, small-angle X-ray scattering, and small-angle neutron scattering are popular techniques, to name a few. Generally [3], $I(q)$, the intensity of scattered radiation, is measured as a function of the scattering vector (q) as shown below:

$$I(q) = nP(q)S(q) \quad (21)$$

where n is the number density of the spheres, $P(q)$ is the form factor, and $S(q)$ is the structural factor, which takes into account the particle-particle interaction. The scattering vector is defined as

$$q = \frac{4\pi}{\lambda} \sin \frac{\theta}{2} \quad (22)$$

The independent variables θ and λ in Eq. (22) are the wavelength of the radiation and the scattering angle, respectively. The form factor and the structural factor can be estimated by using appropriate analytical expressions. The lower limit of size that can be measured with these techniques is about 2 nm. The upper limit is about 100 nm for small-angle neutron scattering and small-angle X-ray scattering, and a few micrometers for static and dynamic light scattering techniques. Silas and Kaler [29] have recently investigated the scattering parameters of microemulsions containing water, oil, nonionic surfactant, cationic surfactant using small-angle neutron scattering. Decane and didodecyldimethylammonium bromide were used as the oil and surfactant phase, respectively.

3. REACTION KINETICS AND MECHANISMS OF PARTICLE FORMATION IN MICROEMULSIONS

The nanoparticles can be produced by using microemulsion in various ways such as by mixing of microemulsions containing the reactants necessary for the precipitation or reduction reaction. However, care should be taken to use identical system of microemulsions for each precursor in order to avoid further complexities. The two precursors come in contact with each other upon mixing due to collision and coalescence of the droplets, and thereby the reaction takes place. When the chemical reaction rate is fast, the overall rate of the formation of the particles is expected to be controlled by the rate of coalescence of the microemulsion droplets containing the reactants. In such cases, the interfacial rigidity plays an important role. A relatively rigid interface decreases the rate of coalescence, hence leading to slow reaction rate.

On the other hand, a less rigid interface in the microemulsion enhances the rate of precipitation. It is quite likely that one can control the kinetics of the reaction by controlling the structure of the interface. The structure of the oil, surfactant, and co-surfactant, and ionic strength of the aqueous phase can significantly affect the interfacial rigidity and the reaction kinetics [30, 31]. Figure 2 depicts the formation of particles by using two microemulsion droplets formed from an identical system, one carrying the precursors (R_1) and the other containing the precipitating or reducing agent (R_2). Surfactants play an important role in modifying the interfacial rigidity. Figure 2 indicates that the exchange of the R_1 and R_2 takes place after these two droplets come close together forming the nuclei. Such nuclei are depicted in Figure 2 with the filled circles inside the droplets after their separation at the end of the exchange event. Under certain circumstances, when the size of the nuclei is above the critical size, growth of such nuclei takes place during the next exchange event. The process repeats and the nanoparticles form. However, in reality the situation is more complex because of the influence of various factors such as viscosity, interface rigidity, mobility of the droplets, etc. Several kinetic models have been proposed to explain the particle formation process in microemulsion system [30–40]. Although microemulsion is thermodynamically stable, the droplets are kinetically labile [33]. The droplet size distribution is in a state of dynamic equilibrium. Fletcher et al. [32] proposed that the mechanism of such dynamic equilibrium involves coalescence of the droplets to form short-lived droplet dimers followed by their re-separation. The phenomena of intermicellar exchange and the formation of ultrafine particles have been studied through simulation and stochastic modeling by Natarajan et al. [35]. The study revealed an increase in the particle size with aqueous core size and total aqueous phase volume, and increase in the particle number density with surfactant concentration at fixed aqueous phase to surfactant molar ratio. Bandyopadhyaya et al. [37] put forward a model to calculate the size of fine particles synthesized by the precipitation process in reverse micelles.

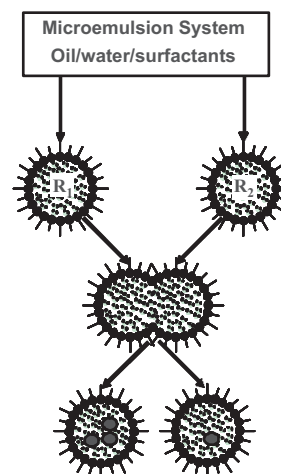


Figure 2. Schematic diagram showing nanoparticle synthesis using water-in-oil microemulsion droplets from the identical system containing the precursor.

Tojo and co-workers [36, 38] studied the formation of particles in microemulsions by Monte Carlo computer simulation. They reported that unimodal and bimodal particle size distributions might be obtained based on the surfactant film flexibility and concentration. The particle size study on the reaction time suggested the occurrence of well-defined nucleation and growth process. Ingelsten et al. [40] investigated the effect of surfactant and temperature on the kinetics of the formation of platinum nanoparticles in water-in-oil microemulsions. The surfactants used were poly(ethylene glycol) monododecyl ethers ($C_{12}E_4$, $C_{12}E_5$, $C_{12}E_6$), and mixtures of the alcohol ethoxylates and AOT. The oil domain was *n*-heptane. The reaction rate for platinum particle formation was approximately the same in microemulsions based on either of the alcohol ethoxylates but considerably lower for microemulsions based on AOT. The average diameter of the platinum particles was found to be about 5 nm, which was consistent with the microemulsion droplet size.

Nanoparticles can also be synthesized by directly adding the reducing or precipitating agent in the form of a liquid solution or a gas to the primary reactant that is present in the microemulsion droplet. In this method, one uses only one type of microemulsion instead of two. The chances of particle growth in this system due to the collision of the microemulsion droplets are minimized in this case because of the increased interface stability. Initially, the precipitating or reducing agent will be accessible to the water core of the microemulsion due to the percolation. Subsequently, nuclei of the precipitate are formed inside the water core, which eventually grow till the precipitation or reduction reaction is almost completed inside the microemulsion droplet. Therefore, the size of the grown particle will be limited by the size of the water droplet that acts as the nanoreactor in such cases. Many times, the diameter of the particle formed inside the water droplet is almost equal to the size of the water droplet. The reaction scheme is shown in Figure 3. Such percolation of the precipitating or reducing agent has been reported for synthesis of various metal-boride and metal-oxide nanoparticles [41, 42]. Recently, Patil et al. [43] synthesized 3- to 5-nm-size ceria nanoparticles using

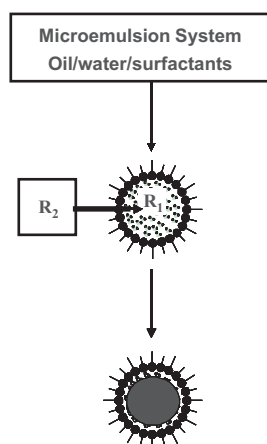


Figure 3. Schematic diagram showing nanoparticle synthesis using single type of water-in-oil microemulsion droplets.

a microemulsion system consisting of AOT, toluene, and water. AOT was dissolved in 50 ml of toluene and 2.5 ml of 0.1 mol/lit aqueous cerium nitrate solution was added. The mixture was stirred for 45 min and 5 ml of 1.5 mol/lit ammonium hydroxide aqueous solution was then added drop by drop. The reaction was carried out for 1 hr and then the reaction mixture was allowed to separate into two layers. The upper layer was toluene containing nonagglomerated ceria nanoparticles and the lower layer was aqueous phase. The particle morphology was studied using HRTEM while the chemical phase analysis was done using EDX system. HRTEM image and the corresponding EDS spectrum taken from the nanoparticles of ceria are shown in Figures 4 and 5, respectively.

4. NANOPARTICLES SYNTHESIS

4.1. Synthesis of Metallic Nanoparticles

López-Quintela and Rivas [44] have reported that ultrafine particles could be obtained with the help of a controlled chemical reaction in microemulsions. Controlling the size of the microemulsion droplet can control the size of such ultrafine particles. By using such procedure, metallic Ni and Ni_3Fe alloy particles were successfully synthesized [44]. Silver nanoparticles were synthesized using microemulsion methodology by Rong et al. [45] with a procedure which involved reduction of aqueous silver salt solution in a water-in-oil microemulsion. The aqueous silver salt micelles in cyclohexane were stabilized by the nonionic surfactant and the same micelles of $NaBH_4$ solution were used for the reduction, keeping identical droplet size and concentration in both sets. The salt concentrations in the aqueous phase were 0.1 M in $AgNO_3$ and 0.05 M in $NaBH_4$, respectively. Porta and co-workers [46] have prepared gold metallic nanoparticles in the micellar core of the clear water-in-oil microemulsions of $NaAuCl_4$ and $NaBH_4$. The microemulsions were produced by using the four components: cetyltrimethylammonium bromide, 1-butanol, *n*-octane, and aqueous solutions of inorganic salts. Arcoleo

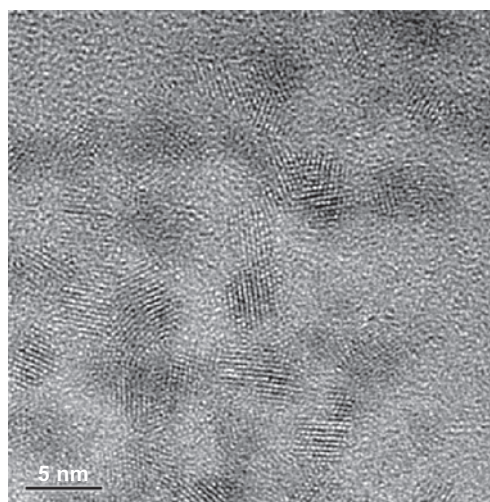


Figure 4. HRTEM image of ceria nanoparticles synthesized using water-in-oil microemulsion.

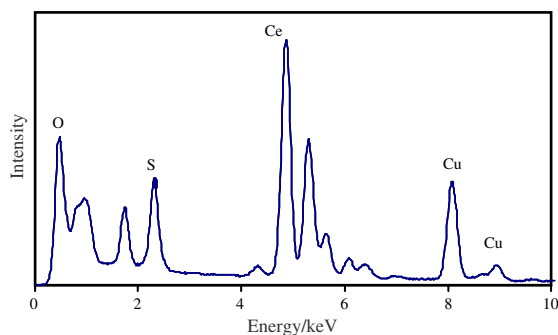


Figure 5. EDS spectrum of ceria nanoparticles synthesized using water-in-oil microemulsion.

and Liveri [47] and Aliotta et al. [48] have successfully synthesized gold nanoparticles aggregates using 0.0103 M tetrachloroauric acid (HAuCl_4), AOT, 0.0624 M hydrazine sulfate (N_2H_4 , H_2SO_4), in an AOT/*n*-heptane solution of 0.295 M. Gold nanoparticles were characterized [47] using atomic force microscopy and it was found that the aggregate size was within the range of 30–100 nm. Calorimetric measurements confirmed [48] the formation of nuclei of gold nanoparticles and their subsequent aggregation in the microemulsions.

In order to probe the phenomenon of size-induced semimetal to semiconductor transition and related quantum confinement effects for optical and electrooptical device applications, crystalline Bi nanoparticles of about 20 nm size were synthesized by Fang et al. [49] using a reverse microemulsion technique. Bismuth (II) nitrate, NaBH_4 , and cyclohexane were used as the precursors. To prevent oxidation of the Bi metallic particles, an *in-situ* polymerization technique used methyl methacrylate as monomer and 2-hydroxyethyl methacrylate as co-monomer with cross-linking by ethylene glycol dimethacrylate. Such polymerization coating protects the bismuth nanoparticles from oxidation during post-synthesis annealing. Figure 6 represents a TEM image of the as-prepared Bi nanoparticles along with an inset-image showing the lattice fringes of a nanoparticle. The size of the nanoparticles was about 20 nm. Figure 7 shows a UV absorption spectrum exhibiting the surface plasmon resonance of nanometer-sized Bi particles in water. After subtracting the contribution of water from the absorption spectrum, an absorption peak was observed [49] at 268 nm, which is similar to the value reported by others [50, 51].

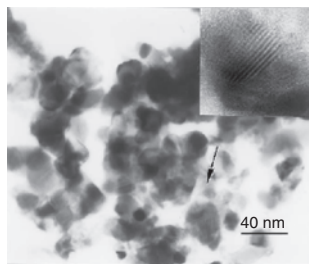


Figure 6. TEM micrograph of bismuth nanoparticles prepared via microemulsion method. Reprinted with permission from [49], J. Fang et al., *Mater. Lett.* 42, 113 (2000). © 2000, Elsevier Science.

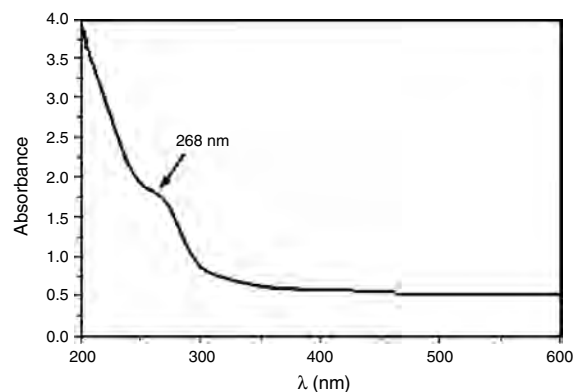


Figure 7. Surface plasmon resonance of nanometer-sized bismuth in aqueous solution. Reprinted with permission from [49], J. Fang et al., *Mater. Lett.* 42, 113 (2000). © 2000, Elsevier Science.

Qiu and co-researchers [52] have synthesized spherical copper nanoparticles in microemulsion system consisting of sodium dodecyl sulfate as a surfactant, isopentanol as a co-surfactant, cyclohexane as the oil phase, aqueous CuSO_4 solution as reactant solution, using NaBH_4 as a reducing agent. Copper particles with size of 3 nm were obtained with a molar ratio of water to surfactant of 2, whereas the size increased to 30 nm at the ratio value of 39. Sodium dodecyl sulfate, isopentanol, and cyclohexane content in the microemulsion were 2 g, 4 g, and 10 ml, respectively. Qi et al. [53] have synthesized well-dispersed copper nanoparticles by reduction of aqueous copper chloride solution using NaBH_4 in the nonionic water-in-oil microemulsion formed by Triton X100, *n*-hexanol, cyclohexane, and water. However, absorption spectra of such synthesized particles revealed the presence of surface monolayer of the copper chloride on copper nanoparticles. Wang et al. [54] have reported a method for preparation of shell-core Cu_2O -Cu nanocomposite particles and pure metallic Cu nanoparticles. The method was based on microemulsion system composed of saturated salt aqueous solution dispersed in iso-propanol and stabilized by polyvinyl alcohol. The synthesis was carried out at various volume ratios of iso-propanol to H_2O ratio. They [54] have concluded that the higher the value of the ratio is, the smaller is the oxide layer in the shell-core [54]. It was also observed that pure Cu metal was obtained at a ratio of iso-propanol to H_2O of 1000 [54].

Iron particles with diameters of less than 100 nm were prepared by Rivas et al. [55] using microemulsions consisting of aqueous solution of FeCl_2 , *n*-heptane, and AOT. The R-values ($R = [\text{H}_2\text{O}]/[\text{AOT}]$) of 5, 10, and 15 along with various concentrations of aqueous phase were used in the study [55] to control the size of the Fe nanoparticles. The reducing agent employed in the synthesis was NaBH_4 . Cain et al. [56] have prepared ferromagnetic α -Fe particles by reducing Fe^{2+} by sodium borohydride in lecithin/cyclohexane/water microemulsion system. Chains of iron spheres, 50–150 nm in diameter, held together by worm-like lecithin assemblies were observed under transmission electron microscope.

Arcoleo et al. [57] characterized the Pd nanoparticles which were synthesized by using microemulsion method in AOT, *n*-heptane along with aqueous solution of $\text{Pd}(\text{NO}_3)_2$ and a hydrazine monohydrate as a reducing agent.

Nanoparticles with a radius of 3–5 nm were obtained from this method with an excellent long-term size stability. They [57] have concluded that formation of such highly stable Pd nanoparticles was possibly attributed to the presence of a novel dimeric surfactant. Berkovich and Garti [58] prepared colloidal Pd particles in the size range of 1–4 nm in a water-organic microemulsion in the presence of the cationic surfactant aliquat 336 (trioctylmethylammonium chloride) in order to study the transfer hydrogenolysis of bromotoluene with sodium formate. Papp and Dékány [59] synthesized nanoparticle of Pd by reduction of palladium acetate with help of ethanol in microemulsion system containing tetrahydrofuran (THF) and tetradodecylammonium bromide (TDAB) surfactant.

Bimetallic particles of Pt and Pd have been prepared [60] by reduction, with hydrazine at ambient temperature, of H_2PtCl_6 and PdCl_2 dissolved in microemulsions consisting of water, hexadecane, and pentachylene glycol dodecyl ether. The diameter of such Pt-Pd alloy particles ranges from 10 to 100 nm. Subsequently, such alloy nanoparticles were used for selective catalyst for isomerization of 2-methylpentane. Wu et al. [61] synthesized various Pt-Pd alloy particles in the size range of 7 to 11 nm. They observed that the nucleation rate of the Pd particles was faster than that of the Pt during reduction of the H_2PtCl_6 and H_2PdCl_4 with hydrazine in the water/AOT/isooctane microemulsions at 25 °C. Synthesis of Pt-Pd alloy nanoparticles in water-in-oil microemulsion was carried out [62] for investigation of the catalytic activity of these particles.

4.2. Synthesis of Nanoparticles of Oxides, Sulfides, and Halides

Synthesis of nanoparticles of oxides, sulfides, halides, and mixed oxides superconductors using microemulsions were reviewed by Pillai et al. [63]. On the other hand, synthesis of nanosized oxide materials has been well covered by Osseo-Asare [7] in a publication on microemulsions.

Song and Kim [64] have synthesized the nanoparticles of tin oxide from water-in-oil microemulsions of water, AOT, and *n*-heptane. The oxide particles thus obtained were calcined at 600 °C for 2 hr. The BET (Brunauer–Emmet–Teller) surface area was found to be 86 m^2g^{-1} . It can be mentioned that BET surface area was found to be 19 m^2g^{-1} for the tin oxide powder, which was prepared by the conventional precipitation process. XRD analysis [65] revealed the size of the tin oxide nanoparticles prepared by the microemulsion method was 40 nm. Singhal et al. [66] have reported a method of producing zinc oxide nanoparticles for varister applications using ethanol-in-oil microemulsions with Zn-AOT as a surfactant which is not only stabilizing the microemulsion but also acting as a source for the metal ions. Coated $\gamma\text{-Fe}_2\text{O}_3$ nanoparticles were prepared by Liu et al. [67] using usual microemulsion method in the system of water in toluene along with surfactants such as sodium dodecyl benzene sulphonate, steric acid, and CTAB. The nanoparticles were characterized using TEM and EXAFS. The size of the nanoparticles was observed to be in the range of 4 to 5 nm. EXAFS study revealed that the Fe-O bond length was extended due to the lattice relaxation. Zirconia nanoparticles were synthesized by

Guo and co-workers [68] to prepare ceramic inks for jet-printing. The synthesis was carried out using the reverse micelle microemulsion system consisting of Triton X-100/*n*-hexanol/cyclohexane/water. Two microemulsions were prepared, one of them with zirconium oxychloride and the other with ammonia solution. Subsequently, ZrO_2 ceramic ink was made by mixing these two microemulsions. The particle size in the reverse microemulsions was in the range of 7–10 nm as studied by TEM. CeO_2 nanoparticles coated by sodium bis(2-ethylhexyl) sulfosuccinate have been prepared by Wu et al. [69] using the microemulsion method. An average particle size of 2–3 nm was revealed by using transmission electron microscopy. Extended X-ray absorption fine structure technique was used to probe the local atomic structures around the absorber Ce. These nanoparticles consist of two parts, that is, the core part and the surface part. The local atomic structures in the surface are quite ordered. The content of the surface part approaches 50% for the 2–3 nm CeO_2 nanoparticles with a surface thickness of about 0.4 nm. The bond length of Ce-O pair of the surface part increases drastically to 2.70 Å, while the bond lengths corresponding to the core part increase by about 0.07 Å, in comparison with the bulk CeO_2 . The bulk CeO_2 has a cubic fluorite structure with eight oxygen atoms located in the neighborhood of Ce with single Ce-O bond length of 2.338 Å. It is postulated that a surface-core model may be used to describe the local atomic structures in the CeO_2 nanoparticles. Ceria nanoparticles in the size range of 3–5 nm were synthesized by Patil et al. [43] for high-temperature oxidation-resistant coating applications. Eu-doped Y_2O_3 nanoparticles, which are known to be one of the most promising red phosphors for field effect diode application, were prepared by Lee et al. [70] in a non-ionic reverse microemulsion. The particles formed by the microemulsion system had a narrow size distribution and round shape with nanosized particles in the size range of 8–16 nm. Dong and Zhu [71] have recently reported the synthesis of stearic acid coated Bi_2O_3 nanoparticles in the size range of 5–13 nm by the microemulsion method for electro-optical applications. They [71] have investigated the optical properties of orange and wine-red colored xylene sol of Bi_2O_3 nanoparticles prepared with 0.005 M and 0.01 M Bi^{3+} solution, respectively. It was found that orange particles had a broader size distribution than that of wine-red bismuth oxide nanoparticles. Figure 8 depicts the bright field HRTEM image of Bi_2O_3 nanoparticles. The circle-mark at the bottom of the image indicates a nanoparticle of about 8 nm size. The presence of edge dislocations is eminent near the interface of the particles, as outlined by a rectangular box. Presence of defects at some other locations is also marked by rectangles in Figure 8. Optical absorption spectra were recorded on an ultraviolet-visible spectrometer between 300–800 nm as shown in Figure 9. After analyzing the spectra, it was found that the absorption edges of orange and wine-red Bi_2O_3 nanoparticles had undergone blue shift of 0.48 and 0.43 eV, respectively. Although exact cause of such blue shift could not be evaluated by Dong and Zhu [71], however, the quantum confinement of the electron and holes usually leads to such shift. The study [71] also revealed that both Bi_2O_3 nanoparticles with orange and wine color show emission peaks at 397 and 420 nm wavelength at room

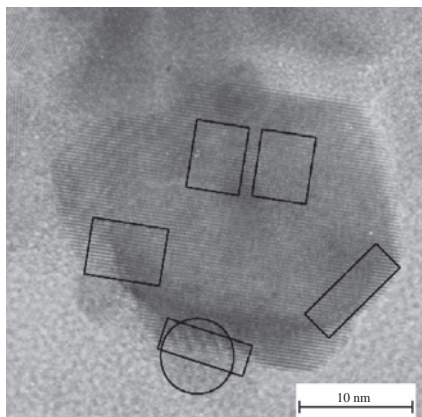


Figure 8. HRTEM image of wine-red Bi_2O_3 nanoparticles. Reprinted with permission from [71], W. Dong and C. Zhu, *J. Phys. Chem. Solids* 64, 265 (2003). © 2003, Elsevier Science.

temperature, which were dependent on the excitation wavelength. Surprisingly such emission behavior was absent in the bulk Bi_2O_3 powder. The quantum size effect and the presence of structural defects are the two possible reasons for such luminescence effect in nanoparticle of bismuth oxide. The photoluminescence spectra of xylene sol of wine-red Bi_2O_3 nanoparticles are reproduced in Figure 10.

Pillai and Shah [72] have synthesized cobalt ferrite (CoFe_2O_4) using water-in-oil microemulsions consisting of water, CTAB as a surfactant, *n*-butanol as co-surfactant, and *n*-octane as the oil phase. Hydroxides were precipitated in the aqueous cores of water-in-oil microemulsions, which were subsequently separated and calcined to give the magnetic oxide. XRD studies confirmed the cobalt ferrite phase with crystallite size less than 50 nm. Magnetic measurements were carried out in vibrating sample magnetometer with a maximum applied field of 5 kOe, and the magnetization curve is shown in Figure 11. The study yielded a saturation magnetization value of $65 \text{ emu}\cdot\text{g}^{-1}$, and a remnant magne-

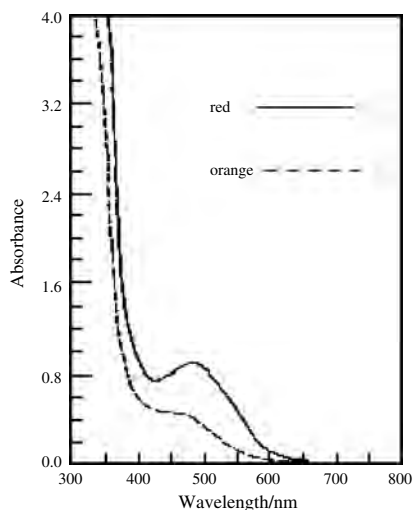


Figure 9. Absorption spectrum of xylene sol of stearic acid coated Bi_2O_3 nanoparticles. Reprinted with permission from [71], W. Dong and C. Zhu, *J. Phys. Chem. Solids* 64, 265 (2003). © 2003, Elsevier Science.

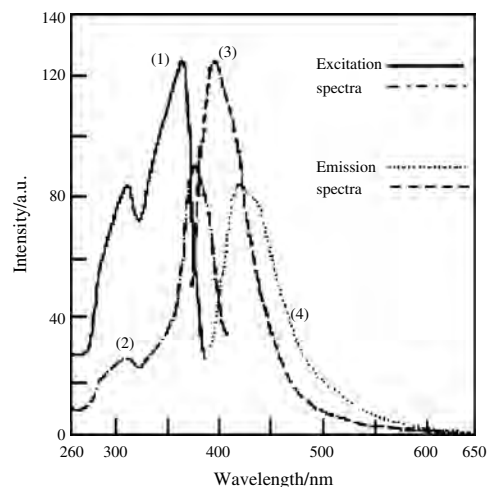


Figure 10. Excitation and emission spectra of xylene sol of wine-red Bi_2O_3 nanoparticles: (1) excitation spectrum detected with emission wavelength of 398 nm; (2) excitation spectrum detected with emission wavelength of 420 nm; (3) emission spectrum excited at 367 nm; (4) emission spectrum excited at 387 nm. Reprinted with permission from [71], W. Dong and C. Zhu, *J. Phys. Chem. Solids* 64, 265 (2003). © 2003, Elsevier Science.

tization of $29 \text{ emu}\cdot\text{g}^{-1}$. Besides, these nanoparticles exhibited a very high coercivity value of the order of 1440 Oe, probably due to enhancement of the magnetocrystalline anisotropy in the presence of cobalt. Pillai and co-workers [73] synthesized barium ferrite ($\text{BaFe}_{12}\text{O}_{19}$) nanoparticles of less than 100 nm size. The process carbonates of Ba and iron were formed in the aqueous cores of the microemulsions consisting of CTAB, *n*-butanol, and octane system, which are separated, dried, and calcined to form nanoparticles of barium ferrite. Nanoparticles of Fe_3O_4 , MnFe_2O_4 , $\gamma\text{-Fe}_2\text{O}_3$, CoFe_2O_4 nanoparticles in the size range of 10–20 nm were also successfully synthesized [74] using microemulsion procedure for magnetic applications.

Jeunieu and Nagy [75] reported syntheses of silver bromide and silver chloride nanoparticles with diameter of 4.6 and 3.2 nm, respectively. The synthesis process was based on a microemulsions system consisting of AOT/*n*-heptane/water and aqueous phase containing the precursors.

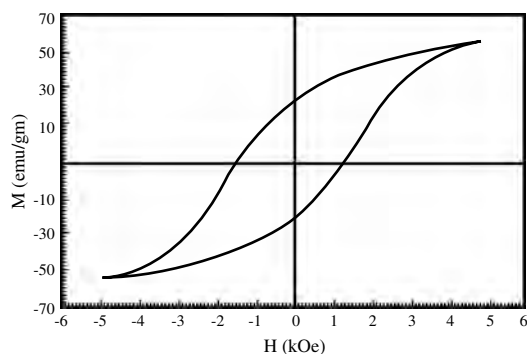


Figure 11. Magnetization curve for cobalt ferrite nanoparticles synthesized using microemulsions. Reprinted with permission from [72], V. Pillai and D. O. Shah, *J. Mag. Mag. Mater.* 163, 243 (1996). © 1996, Elsevier Science.

Sunqing et al. [76] synthesized cerium trifluoride nanoparticles using microemulsions consisting of polybutanedi-imide/cyclohexane/water. The shape of these nanoparticles was found to be spherical and cylindrical with diameter of 25 nm. Cerium trifluoride nanoparticles were reported [76] to have excellent friction-reducing properties.

Cadmium sulfide nanoparticles with uniform size distribution were prepared by Han et al. [77] with the help of an improved inverse microemulsion technique using hexanethiol as co-surfactant, AOT as surfactant, and heptane as the oil phase. CdS nanoparticles exhibited enhanced third-order optical nonlinearities. Agostiano and co-workers [78] reported synthesis of CdS nanoparticles in a quaternary water-in-oil microemulsion formed by a cationic surfactant CTAB, pentanol, *n*-hexane, and water. Two microemulsions containing Cd(NO₃)₂ solution in one and Na₂S in the other were mixed to form the CdS nanoparticles. Sphere-like cadmium sulfide nanoparticles were synthesized by Rong et al. [79] with the reaction of sodium sulfide and cadmium nitrate in a water-in-oil microemulsion system, in which cyclohexane, sodium dodecyl sulfonate (SDS), and pentanol served as oil phase, surfactant, and co-surfactant, respectively. In this work, a water/surfactant molar ratio of 20 was used. The particle size changed as a function of water/surfactant molar ratio. TEM confirmed that the mean diameter of the nanoparticles was 6.25 nm with a standard deviation of 1.4 nm. Boakye et al. [80] reported the synthesis of molybdenum sulfide nanoparticles based on a microemulsion system, which consisted of polyoxyethylene(5)nonylphenyl ether (NP-5), cyclohexane, and aqueous solution of acidified ammonium tetrathiomolybdate. The nanoparticles were found to be in the size range of 10–80 nm.

5. CONCLUDING REMARKS

Microemulsion process is another essential tool for the synthesis of nanoparticles of metals, alloys, and other compounds such as oxides, sulfides, halides, and mixed oxides for various applications, especially nanoparticles in the size range less than 5 nm with a controlled shape and size distribution for a wide range of applications such as catalysis, nanoporous membranes, nanocomposites, and precursor powders for functional ceramics. However, the problem of improving the yield remains to be solved. Moreover, the particles are coated with surfactant, and it is not only difficult to remove the surfactant, but also entails problem of agglomeration and grain growth after the surfactant is removed. Therefore, development of a viable approach for successful removal of the surfactant from the surface of the nanoparticles formed by microemulsion process is needed in order to scale up the process in the industrial scale for production of the nanoparticles.

GLOSSARY

Amphiphiles The substance which has affinity to both water and oil due to its inherent molecular arrangements.

Co-surfactant Either an alcohol or an amine, is used along with the surfactant in order to make the emulsification process more effective.

Critical micelle concentration (CMC) The concentration of micelles at which a sharp change occurs in any of wide varieties of properties of the surfactant solution such as electrical conductance, transference number, surface tension, etc.

Entropy A thermodynamic state or property that measures the degree of disorder or randomness of a system.

Free energy The thermodynamic state function of a system that indicates the amount of energy available for the system to do useful work.

Interfacial tension The surface tension at the interface between two liquids.

Isotropic Exhibiting the same properties in all directions.

ACKNOWLEDGMENTS

Authors would like to thank Mechanical, Materials and Aerospace Engineering Department and Advanced Materials Analysis and Processing Center (AMPAC) at University of Central Florida (UCF), Orlando for continued support. Sudipta Seal is thankful to National Science Foundation, Office of Naval Research through the Young Investigator Award (ONR-YIP 2002), Florida High Tech Corridor, NASA, Florida Space Grant Consortium, Siemens Westinghouse, Energy Strategy Associates, USNR Coal Resources, *psilo*Quest, US Filter, Pratt and Whitney, Lucent Technologies, for supporting his research activities in nanomaterials processing.

REFERENCES

1. T. P. Hoar and J. H. Schulman, *Nature* 152, 102 (1943).
2. I. Danielson and B. Lindman, *Colloids Surfaces* 3, 391 (1981).
3. C. Solans, R. Pons, and H. Kunieda, in "Industrial Applications of Microemulsions" (C. Solans and H. Kunieda, Eds.), p. 1. Marcel Dekker, New York, 1997.
4. M. Boutonnet, J. Kizling, P. Stenius, and G. Maire, *Colloids Surfaces* 5, 209 (1982).
5. L. M. Prince, in "Microemulsions Theory and Practice" (L. M. Prince, Ed.). Academic Press, New York, 1977.
6. J. M. di Meglio, M. Dvolaitzky, and C. Taupin, in "Progress in Microemulsions" (S. Martellucci and A. N. Chester, Eds.), p. 263. Plenum, New York, 1989.
7. K. Osseo-Asare, in "Handbook of Microemulsion Science and Technology" (P. Kumar and K. L. Mittal, Eds.), p. 549. Marcel Dekker, New York, 1999.
8. H. Saito and K. Shinoda, *J. Colloid Interface Sci.* 32, 647 (1970).
9. P. A. Winsor, *Trans. Faraday Soc.* 44, 376 (1948).
10. P. A. Winsor, *Chem. Rev.* 68, 1 (1968).
11. A. W. Adamson, *J. Colloid Interface Sci.* 29, 744 (1969).
12. E. Ruckenstein and J. C. Chi, *J. Chem. Soc. Faraday Trans. II* 71, 1690 (1975).
13. C. Wagner, *Colloid Polym. Sci.* 254, 400 (1976).
14. E. Ruckenstein, in "Progress in Microemulsions" (S. Martellucci and A. N. Chester, Eds.), p. 3. Plenum, New York, 1989.
15. E. Ruckenstein, in "Handbook of Microemulsion Science and Technology" (P. Kumar and K. L. Mittal, Eds.), p. 45. Marcel Dekker, New York, 1999.
16. W. K. Kegel, J. T. G. Overbeek, and H. N. W. Lekkerkerker, in "Handbook of Microemulsion Science and Technology" (P. Kumar and K. L. Mittal, Eds.), p. 13. Marcel Dekker, New York, 1999.
17. N. F. Carnahan and K. E. Starling, *J. Chem. Phys.* 51, 635 (1969).

18. S. Roy and S. P. Moulick, *J. Colloid Interface Sci.* 173, 28 (1995).
19. Th. F. Tadros, in "Surfactants in Solution" (K. L. Mittal and B. Lindman, Eds.), p. 1501. Plenum, New York, 1984.
20. T. Kinugasa, A. Kondo, S. Nishimura, Y. Miyauchi, Y. Nishii, K. Watanabe, and H. Takeuchi, *Colloids Surfaces A: Physicochem. Eng. Aspects* 204, 193 (2002).
21. P. Y. Cheng and H. K. Schachman, *J. Polym. Sci.* 16, 19 (1955).
22. R. G. Laughlin, "The Aqueous Phase Behaviour of the Surfactants," p. 102. Academic Press, New York, 1994.
23. H. Kunieda and K. Shinoda, *J. Dispers. Sci. Technol.* 3, 233 (1982).
24. M. Teubner and R. Strey, *J. Chem. Phys.* 87, 3195 (1987).
25. M. Gradziński, D. Langevin, and B. Farago, *Phys. Rev. E* 53, 3900 (1996).
26. H. Bagger-Jørgensen, U. Olsson, and K. Mortensen, *Langmuir* 13, 1413 (1997).
27. A. Bumajdad, J. Eastoe, P. Griffiths, D. C. Steytler, R. K. Heenan, J. R. Lu, and P. Timmins, *Langmuir* 15, 5271 (1999).
28. O. Glatter, G. Fritz, H. Lindner, J. Brunner-Popela, R. Mittelbach, R. Strey, and S. U. Egelhaaf, *Langmuir* 16, 8692 (2000).
29. J. A. Silas and E. W. Kaler, *J. Colloid Interface Sci.* 257, 291 (2003).
30. M. J. Hou, M. Kim, and D. O. Shah, *J. Colloid Interface Sci.* 123, 398 (1988).
31. C. H. Chew, L. M. Gan, and D. O. Shah, *J. Dispers. Sci. Technol.* 11, 593 (1990).
32. P. D. I. Fletcher, A. M. Howe, and B. H. Robinson, *J. Chem. Soc. Faraday Trans.* 83, 185 (1987).
33. P. D. I. Fletcher and D. I. Horsup, *J. Chem. Soc. Faraday Trans.* 88, 865 (1992).
34. T. Hirai, H. Sato, and I. Komasa, *Ind. Eng. Chem. Res.* 32, 3014 (1993).
35. U. Natarajan, K. Handique, A. Mehra, J. R. Bellare, and K. C. Khilar, *Langmuir* 12, 2670 (1996).
36. C. Tojo, M. C. Blanco, and M. A. López-Quintela, *Langmuir* 13, 4527 (1997).
37. R. Bandyopadhyaya, R. Kumar, K. S. Gandhi, and D. Ramkrishna, *Langmuir* 13, 3610 (1997).
38. C. Tojo, M. C. Blanco, and M. A. López-Quintela, *J. Non-Crystalline Solids* 235–237, 688 (1998).
39. J. Schmidt, C. Guesdon, and R. Schomäcker, *J. Nanoparticle Res.* 1, 267 (1999).
40. H. H. Ingelsten, R. Bagwe, A. Palmqvist, M. Skoglundh, C. Svanberg, K. Holmberg, and D. O. Shah, *J. Colloid Interface Sci.* 241, 104 (2001).
41. J. B. Nagy, in "Handbook of Microemulsion Science and Technology" (P. Kumar and K. L. Mittal, Eds.), p. 499. Marcel Dekker, New York, 1999.
42. Z. Wu, R. E. Benfield, L. Guo, H. Li, Q. Yang, D. Grandjean, Q. Li, and H. Zhu, *J. Phys.: Condens. Matter* 13, 5269 (2001).
43. S. Patil, S. C. Kuiry, S. Seal, and R. Vanfleet, *J. Nanoparticle Res.* 4, 433 (2002).
44. M. A. López-Quintela and J. Rivas, *J. Colloid Interface Sci.* 158, 446 (1993).
45. M. Rong, M. Zhang, H. Liu, and H. Zeng, *Polymer* 40, 6169 (1999).
46. F. Porta, L. Prati, M. Rossi, and G. Scarý, *Colloids Surfaces A: Physicochem. Eng. Aspects* 211, 43 (2002).
47. V. Arcoletto and V. T. Liveri, *Chem. Phys. Lett.* 258, 223 (1996).
48. F. Aliotta, V. Arcoletto, S. Buccoleri, G. La Manna, and V. T. Liveri, *Thermochimi. Acta* 265, 15 (1995).
49. J. Fang, K. L. Stokes, J. A. Wiemann, W. Zhou, J. Dai, F. Chen, and C. J. O'Connor, *Mater. Sci. Eng.* B83, 254 (2001).
50. J. A. Creighton and G. E. Desmond, *J. Chem. Soc. Faraday Trans.* 87, 3881 (1991).
51. M. Gutiérrez and A. Henglein, *J. Phys. Chem.* 100, 7656 (1996).
52. S. Qiu, J. Dong, and G. Chen, *J. Colloid Interface Sci.* 216, 230 (1999).
53. L. Qi, J. Ma, and J. Shen, *J. Colloid Interface Sci.* 186, 498 (1997).
54. C. Y. Wang, Y. Zhou, Z. Y. Chen, B. Cheng, H. J. Liu, and X. Mo, *J. Colloid Interface Sci.* 220, 468 (1999).
55. J. Rivas, M. A. Lopez-Quintela, J. A. Lopez, L. Liz, and R. J. Duro, *IEEE Trans. Magnetics* 29, 2655 (1993).
56. J. L. Cain, S. R. Harrison, J. A. Nikles, and D. E. Nikles, *J. Mag. Mag. Mater.* 155, 67 (1996).
57. V. Arcoletto, M. Goffredi, A. Longo, and V. T. Liveri, *Mater. Sci. Eng.* C6, 7 (1998).
58. Y. Berkovich and N. Garti, *Colloids Surfaces A: Physicochem. Eng. Aspects* 128, 91 (1997).
59. S. Papp and I. Dékány, *Colloid Polymer Sci.* 279, 449 (2001).
60. R. Touroude, P. Girard, G. Maire, J. Kizling, M. Boutonnet-Kizling, and P. Stenius, *Colloids Surfaces* 67, 9 (1992).
61. M.-L. Wu, D.-H. Chen, and T.-C. Huang, *J. Colloid Interface Sci.* 243, 102 (2001).
62. J. Solla-Gullón, V. Montiel, A. Aldaz, and J. Clavilier, *Electrochem. Commun.* 4, 716 (2002).
63. V. Pillai, P. Kumar, M. J. Hou, P. Ayuub, and D. O. Shah, *Adv. Colloid Interface Sci.* 55, 241 (1995).
64. K. C. Song and J. H. Kim, *Powder Technol.* 107, 268 (2000).
65. K. C. Song and J. H. Kim, *J. Colloid Interface Sci.* 212, 193 (1999).
66. M. Singhal, V. Chhabra, P. Kang, and D. O. Shah, *Mater. Res. Bull.* 32, 239 (1997).
67. T. Liu, L. Guo, Y. Tao, T. D. Hu, Y. N. Xie, and J. Zhang, *Nanostruct. Mater.* 11, 1329 (1999).
68. R. Guo, H. Qi, D. Guo, X. Chen, Z. Yang, and Y. Chen, *J. Euro. Ceram. Soc.* 23, 115 (2003).
69. Z. Wu, L. Guo, H. Li, Q. Yang, Q. Li, and H. Zhu, *Mater. Sci. Eng.* A286, 179 (2000).
70. M.-H. Lee, S.-G. Oh, and S.-C. Li, *J. Colloid Interface Sci.* 226, 65 (2000).
71. W. Dong and C. Zhu, *J. Phys. Chem. Solids* 64, 265 (2003).
72. V. Pillai and D. O. Shah, *J. Mag. Mag. Mater.* 163, 243 (1996).
73. V. Pillai, P. Kumar, M. S. Multani, and D. O. Shah, *Colloids Surfaces A: Physicochem. Eng. Aspects* 80, 69 (1993).
74. C. J. O'Connor, C. T. Seip, E. E. Carpenter, S. Li, and V. T. John, *Nanostructured Mater.* 12, 65 (1999).
75. L. Jeunieu and J. B. Nagy, *Colloids Surfaces A: Physicochem. Eng. Aspects* 151, 419 (1999).
76. Q. Sunqing, D. Junxiu, and C. Guoxu, *Wear* 230, 35 (1999).
77. M. Y. Han, L. M. Gan, W. Huang, C. H. Chew, B. S. Zou, C. H. Quek, G. Q. Xu, W. Ji, X. J. Zhang, and S. C. Ng, *Talanta* 45, 735 (1998).
78. A. Agostiano, M. Catalano, M. L. Curri, M. Della Monica, L. Manna, and L. Vasanelli, *Micron* 31, 253 (2000).
79. M. Z. Rong, M. Q. Zhang, H. C. Liang, and H. M. Zeng, *Chem. Phys.* 286, 267 (2003).
80. E. Boakye, L. R. Radovic, and K. Osseo-Asare, *J. Colloid Interface Sci.* 163, 120 (1994).

Synthetic Nanoinorganics by Biomolecular Templating

S. Behrens, E. Dinjus

Forschungszentrum Karlsruhe, Karlsruhe, Germany

E. Unger

Institute of Molecular Biotechnology, Jena, Germany

CONTENTS

1. Introduction
 2. Materials Synthesis with DNA
 3. Materials Synthesis with Protein-Based Biostructures
 4. Conclusions
- Glossary
References

1. INTRODUCTION

It is widely accepted that microelectronics will approach its useful limits due to some fundamental limitations of large-scale photolithography. Commercial requirements to produce increasingly miniaturized microelectronic devices strongly motivates the synthesis of nanoscale systems with alternative techniques. In systems, for example, where metal or semiconductor nanoparticles are regularly arranged in a small spatial distance (approximately 1 nm) in one, two, or three dimensions, tunnel junctions are generated, which allow the handling of single charges by means of single electron tunneling [1]. Manipulations of charges at the single electron level can be utilized to create, for example, switches, transistors, or digital electronic circuits where the absence or presence of single electrons at a certain time and place provides digital information. While conventional approaches (e.g. photolithography) are able to produce miniaturized elements down to about 100 nm, the bottom-up assembly of molecular building blocks enables the construction of much smaller elements, up to about 10 nm. Currently, biological systems and macromolecular components have been explored as building blocks in the bottom-up assembly and generation of micro- and nanometer sized devices and functional elements.

Biomolecular components have been optimized during evolution with respect to their specific molecular recognition capabilities as well as their functionality for distinct biochemical transformations and translocations. Due to these specific recognition capabilities many of these biomolecular subunits are able to self-assemble into complex, well-defined, and extended superstructures. However, most of these biological systems do not possess the required physical properties. Some of these organic-based structures exhibit poor electric conductivities; others are simply insulators.

On the other hand, inorganic materials such as metals or semiconductors display, for example, desired electric properties, but their arrangement into well-defined nanostructures is difficult by conventional techniques. Growth of metals or semiconductors on biomolecular templates, alternatively, is a promising route for producing complex inorganic nanostructures.

Nature designs and manufactures materials with controlled sizes and properties [2]. Living organisms are able to synthesize sophisticated organized inorganic materials by uptake of the necessary precursors from the local environment followed by incorporation into functional structures under strict biological control [3, 4]. Structure and function have been co-optimized phylogenetically.

By biomineralization processes, some organisms provide surprisingly tough and strong building materials; others are able to synthesize chains of magnetic nanoparticles that can act as simple “compass needles” [5]. The synthesis of these biological minerals has been closely related with appropriate templates consisting of complex macromolecular organic frameworks [6, 7]. Specific interactions, selective organic moieties, and biocompatible minerals have evolved. Many *in vitro* studies have demonstrated the importance of, for example, proteins and peptides in controlling the nucleation and growth of inorganic materials in biological systems [8, 9].

In recent years several areas of materials research have been inspired by the study of these biomaterials [10, 11]. Knowledge of biological concepts, functions, and design features has been exploited for the production of new materials and devices with advanced structures and functionalities [12, 13]. At the interface between chemistry, biology, and materials science, the variety of biological molecules, assemblies, and systems offers new synthetic methods for the development of interesting inorganic nanomaterials.

The use of biomolecules for synthesis of nanometer scaled materials focuses on different aspects:

- Biotemplating methods take advantage of the characteristic nanometer dimensions of the biological specimen. Biomolecular components have typical size dimensions from the lower nanometer size range up to several micrometers.
- Biomolecular components represent spatially confined environments with a defined structural topology for the surface-controlled deposition of the inorganic material.
- The surface of biomolecular components consists of specific patterns of functionalities, for example, amino acid residues or the bases of nucleic acids that are able to bind metal ions or nanoparticles by electrostatic interaction or formation of metal–ligand complexes. The adsorbed metals can serve as active sites to build up the solid inorganic nanostructure.
- Another important point is the physical and chemical stability of the biomolecule toward variation of the pH value, high temperatures, or presence of non-native chemicals, because many deposition techniques require “unnatural” reaction conditions.
- The highly specific molecular recognition capabilities of biomolecules conjugated to preformed inorganic building blocks can be exploited for the bottom-up construction of multiplex ordered architectures.
- Up to now, a variety of different biological systems and components have been used to direct the nucleation, deposition, and assembly of inorganic materials into defined micro- and nanostructures.

This chapter is focused on approaches using biomolecular components and assemblies for the synthetic production of nanosized inorganic materials. In the following sections different biological structures and macromolecules will be reviewed that have been used as templates for generating metallic or oxidic nanostructures with, for example, electric properties.

2. MATERIALS SYNTHESIS WITH DNA

DNA molecules, in particular, have been investigated as exciting templates for the bottom-up assembly of periodic arrays from organic and inorganic building blocks [14], for generating nanoelectronic components [15, 16], as well as for nanomechanical devices [17]. The motivation to use DNA derivatives is derived from the unusual combination of the nanosized double-helical structure with appropriate mechanical properties, its molar recognition capabilities, and its polyanionic character. In principle, one can easily synthesize milligram quantities of oligonucleotides

of virtually any sequence in a very straightforward fashion. Preparatory methods for modifying DNA provide many opportunities for the synthesis of molecules with programmed recognition sites and a well-defined surface chemistry to construct organized one-, two-, and three-dimensional arrays of organics or inorganics from 5 nm up to several micrometers. Negatively charged DNA phosphate groups are able to bind metal ions or charged nanoparticles. The hydroxyl groups of the ribose sugar moieties or the nitrogen atoms of the purine and pyrimidine bases can serve as active sites for the formation of organometallic complexes with metal ions. Another interesting property of the DNA double helix is its intrinsic susceptibility to certain external stimuli such as temperature [18] and small ions or molecules [19], which opens the way for future fabrication of nanomechanical devices.

2.1. DNA-Templated Deposition of Metals and Semiconductors

One DNA application being explored is the preparation of nanowires for connecting quantum devices with each other or to electrodes. Charge transport properties of native DNA reported in literature are contradicting [20]; experiments appeared to indicate electronic properties ranging from metallic [21] to insulating behavior [15]. Experiments by Dekker et al. [22] did not show evidence of any electric conductivity for native DNA with various lengths and base pair sequences. It seems unlikely that one can use the intrinsic conductance properties of DNA for single-molecule electronics, so that metallization of DNA will be required to enhance the electric properties of DNA for the production of DNA nanowires for future electronic circuits. Conceptually, the metallization processes of DNA involve two steps: (1) formation of conjugates between DNA template and metal nanoparticles and (2) enlargement of the nanoparticles by electroless plating until they coalesce to form continuous metal wires. The metal particles in (1) can be either nucleated *in-situ* in the presence of the DNA strands or *ex-situ*.

2.1.1. In-Situ Growth of Semiconductors and Metals on DNA Templates

The mechanism of *in-situ* Pt cluster nucleation on DNA templates was studied by first-principles molecular dynamics simulations to understand the role of the DNA molecule in the metallization process and the results have been confirmed by a series of reduction experiments [23]. “Necklaces” of small Pt clusters could be selectively grown on λ -DNA strings using $(\text{CH}_3)_2\text{NH} \cdot \text{BH}_3$ as a reducing agent. These results have suggested that covalently bound Pt(II) ions formed Pt dimers after a single reduction event. Coordination of Pt compounds to DNA has been widely studied due to its relevance to anticancer drugs [24, 25]. These first formed heterogeneous nuclei quickly developed into bigger particles going through an autocatalytic growth process. It was also shown by scanning force microscopy that DNA activation by binding of Pt complexes to the biomolecule prior to reduction is essential for a preferred cluster nucleation at the DNA [26]. In other work, Ford and co-workers

have reported the synthesis of very small Pt nanoparticles on calf thymus DNA using different Pt(II) complexes as precursors followed by ion exchange to remove chemically unbound complexes from solution [27]. The formed Pt²⁺/DNA adducts were reduced with NaBH₄ to generate nanometer-sized Pt⁰ clusters along the DNA backbone. As a result, Pt particles [e.g., derived from dichloro(2,2':6',2''-terpyridine)Pt(II)] were found to be predominantly in the 1 nm size regime. The obtained colloidal Pt/DNA composites showed long-term stability for well over one month when stored at 4 °C. The Pt particles could be enlarged when treating the Pt/DNA composites with an electroless gold plating solution.

A similar two-step procedure has been described for palladium that involved the treatment of λ-DNA with a palladium acetate solution, followed by the addition of (CH₃)₂NH·BH₃ as a reducing agent [28]. Separated Pd clusters with a diameter of 3–5 nm grew on the DNA within a few seconds after the reducing agent was added. After about one minute, a quasi-continuous coverage was achieved with cluster aggregates being around 20 nm in size. By this method, Richter et al. were able to build chains of separated clusters through to wires with a continuous metal coating. Electric properties of continuously coated nanowires measured at room temperature showed metallic transport behavior with a linear dependence of current on voltage [29]. No evidence for a nonconducting region was found at room temperature. Nanowires with a diameter above 50 nm revealed a specific conductivity, which was one order of magnitude below that of bulk palladium, probably due to the granular structure of the wire. At temperatures below 30 K an increase of resistance with decreasing temperature that followed a logarithmic dependence was observed [30]. The behavior was similar to quantum effects observed in a two-dimensional system (such as disordered metallic films) due to weak localization and/or electron–electron interactions. The influence of the organic material of the DNA on the conductance of the nanowires was negligible.

Braun and co-workers have utilized λ-DNA as a template to grow nanometer-scale conducting Ag wires using a three-step deposition process [15]. For investigations of electric properties, the recognition capabilities of DNA were exploited for the targeted attachment of the DNA nanowire to Au electrodes. Hybridization of the DNA molecule with surface-bound oligonucleotides was used to stretch the biopolymer between the two Au electrodes. Through ion exchange, Ag ions were then selectively localized along the DNA skeleton, followed by reducing the ions to form nanometer-sized metallic Ag particles. The DNA-bound Ag aggregates catalyzed further metal deposition using standard hydroquinone reduction procedures. Atomic force microscope (AFM) images revealed a 100 nm wide, 12 μm long wire consisting of 30–50 nm Ag grains deposited contiguously along the DNA backbone. The preparation of thinner Ag wires (<25 nm) only resulted in discontinuous Ag structures. Electrical measurements showed asymmetric current–voltage characteristics of the Ag wire. Approaching zero voltage from large positive or negative bias, a no-current region was observed at near zero bias (0 to ~10 V for positive scan direction, 0 to ~–10 V for negative scan direction). At higher voltages the wire again became conducting.

By depositing more silver and thus increasing the diameter of the Ag wire, the no-current region was reduced from ~10 to ~0.5 V demonstrating that the grain size controls electrical properties in these systems.

Molecular electronics require various geometries at a molecular resolution and accurate device localization. Recently, Keren et al. have demonstrated a sequence-specific molecular lithography on substrate DNA molecules which is shown in Figure 1 [31]. They developed a strategy where the reducing agent was localized along the DNA molecule. Therefore DNA was derivatized with glutaraldehyde. RecA was then used to localize a 2027-base-single-stranded probe molecule on a homologous section in the middle of the aldehyde-derivatized 48,502-base-pair DNA substrate. After incubation with AgNO₃ solution, reduction of the Ag ions occurred by DNA-bound aldehyde groups and yielded tiny Ag aggregates in the unprotected segments of the DNA substrate. The localized RecA proteins prevented Ag deposition and created a gap between the two Ag loaded segments. Further electroless deposition of gold, catalyzed by the Ag nanoparticles, produced two continuous Au nanowires separated by a predefined gap. Electric conductivities were measured for a continuous Au wire, 50 to 100 nm wide and a few micrometers in length, which was prepared by this method. The measurements revealed ohmic characteristics and a wire conductivity that was one-seventh that of bulk gold. This was about four orders of magnitude higher than for the Ag wire in [15].

DNA molecules entrapped in a lipid film were used to grow Ag nanoparticle assemblies in a thin film formed by an ion exchange/reduction process [32]. The Ag ions were entrapped both on the negatively charged DNA backbone and, nonspecifically, in the lipid matrix. During reduction with N₂H₄, Ag ions attached to the DNA backbone formed nanoparticles which were deposited faithfully to the DNA template, whereas the nonspecifically bound ions yielded randomly placed nanoparticles.

Pioneering work on the DNA-templated generation of semiconductor particles was carried out by Coffey and co-workers [33]. Mixing the polynucleotide with Cd ions followed by addition of Na₂S led to the instantaneous formation of CdS nanoparticles in the quantum size regime. The resulting CdS particles were stabilized by the biopolymer

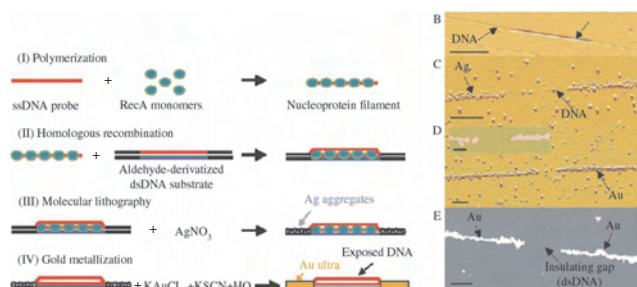


Figure 1. Homologous recombination reaction and sequence-specific molecular lithography on a single DNA molecule. AFM images of (B) RecA bound to aldehyde-derivatized λ-DNA, (C) after Ag deposition, (D) after electroless gold deposition (inset: close-up image of the gap). (E) Scanning electron microscope image after Au deposition. Reprinted with permission from [31], K. Keren et al., *Science* 297, 72 (2002). © 2002, American Association for the Advancement of Science.

allowing storage for more than 17 months. High-resolution transmission electron microscopy (HRTEM) confirmed the formation of polydisperse CdS nanoparticles with an average diameter of 5.6 nm. Optical properties of the particles were characteristic for quantum-confined particles with an absorption edge at 480 nm, which is blueshifted compared to bulk CdS (510 nm). Lattice images and diffraction patterns were consistent with the zinc blende structure of CdS. Interestingly, some unusual structural features were induced by the host nucleotide. Approximately 15% of the particles were found to be hollow-sphere-shaped or hemisphere-shaped CdS structures. However, the role of DNA molecules during nanoparticle formation and their interaction with the formed particles remained ambiguous. Further studies demonstrated that the DNA base sequence, in particular the adenine content, had a significant influence on the size of the formed CdS particles and their resulting optical properties [34]. The adsorptions of different DNA sequences to 40-nm CdS quantum dots were also studied by Mahtab and co-workers [35].

DNA molecules are flexible in solution which results in a lack of control of the mesoscale structure of the material. To overcome this problem, Coffey et al. developed a new strategy where the DNA template was anchored to a solid support [36]. On the substrate a mesoscale ring structure of CdS nanoparticles could be synthesized by using a circular plasmid DNA template, pUCLeu4, which was 3455 base pairs in length with a circumference of 1.17 μm . The developed method consisted of three basic steps: After formation of a Cd^{2+} /DNA complex in solution, the formed complex was bound to a polylysine-coated glass slide and then reacted with a suitable chalcogenide source (e.g., H_2S) to form the desired nanoparticles and array conformation. HRTEM images confirmed the formation of CdS nanoparticles rings. The particles, approximately 5 nm in diameter, were aligned along the DNA backbone but showed neither regular orientations nor regular spacing. The measured circumference of the nanoparticle rings (1.2 μm) closely matched the predicted value for the relaxed conformation of the plasmid DNA molecule.

2.1.2. DNA-Templated Organization of Nanoparticles

Conjugation of Au nanoparticles to biomolecules has widely been used as a standard label to visualize biological structures in electron microscopy and (after enhancement with silver) in light microscopy [37–40]. The combination of the interesting optical and electrical properties of such metal colloids together with the high specificity of biomolecular binding has shown interesting results in nanotechnology.

Several studies have exploited the electrostatic properties of DNA for self-assembly of nanoparticles into linear nanoparticle superstructures. By electrostatic interaction of positively charged, lysine-capped Au nanoparticles (diameter 3.5 nm) and the negatively charged phosphate backbone of DNA, Kumar and co-workers generated two-dimensional arrays consisting of linear, closed-packed nanoparticle assemblies mediated by DNA [41]. The formation of these repetitive lamellar Au/DNA superstructures seemed to be an attempt to maximize the electrostatic interactions in the DNA/particle complex. Using uncapped or

carboxylic acid derived Au particles, which are negatively charged at physiological pH, did not lead to the formation of any superstructure. A method similar to this assembly in solution was based on drop-coated DNA films and lysine-capped Au particles on a solid support, which also led to the formation of quasilinear nanoparticle superstructures [42]. The aggregation of the nanoparticles into quasilinear superstructures was indicated by the appearance of a longitudinal surface plasmon resonance in the ultraviolet-visible (UV-vis) spectrum at 685 nm which was not found for pure nanoparticle films. Torimoto et al. generated one-dimensional chains of positively charged CdS particles by electrostatic binding to a DNA template [43]. The 3 nm CdS nanoparticles were densely packed in a quasi-one-dimensional array, with approximately 1 CdS particle per 10 DNA base pairs. Although both species were negatively charged, Harnack and co-workers could bind $\text{P}(\text{CH}_2\text{OH})_3$ -capped Au nanoparticles (ca. 1–2 nm in diameter) densely to DNA [44]. Hydrogen bonding between the hydroxyl groups of the phosphine ligands and the DNA was expected to be responsible for the binding of the particles. Furthermore, the efficiency of templating could be controlled by the polarity of the solvent used which influenced particle/particle as well as particle/DNA interactions. The bound particles were used as catalysts for further electroless gold plating which provided nanowires with a homogeneous coverage of the DNA by enlarged Au particles, approximately 30–40 nm in diameter, without any obvious gaps between the particles. Electric transport properties were investigated for networks consisting of randomly aligned DNA-templated Au nanowires across 1–4 μm wide electrode gaps. Electric measurements of the networks revealed an overall resistance of 86 Ω and linear ohmic behavior. By cutting selected DNA wires, the resistance of a single wire has been calculated to be 2.4 k Ω . In an alternative approach, Au nanoparticle wires were generated by intercalation of psoralen-functionalized Au nanoparticles into double stranded DNA, followed by the photochemical covalent attachment of the intercalator with the DNA template [45]. Psoralen undergoes a photoinduced $2\pi + 2\pi$ cycloaddition with the thymine residues of DNA, which covalently attaches the psoralen to the DNA.

2.2. DNA-Programmed Assembly of Nanoparticles

The formation of nanostructured materials, both aggregate materials and discrete “nanocrystal molecules,” from oligonucleotide functionalized nanoparticles by sequence-specific hybridization reactions with a DNA template has been extensively studied by several groups. Mirkin and co-workers were able to synthesize three-dimensional DNA/Au colloid hybrid aggregates with unusual optical [46] and electrical [47] properties. Two groups of Au nanoparticles functionalized by different oligonucleotides were exposed to free oligonucleotides with one end complementary to the first group of nanoparticles and the other end to the second one. By DNA hybridization the particles were bound together to form three-dimensional well-ordered aggregates whose optical properties differed significantly from the noninteracting monodispersed particles. The color of the solution mixture ranged from red

in the absence of hybridization through reddish–purple to purple on hybridization, depending on the system. The absorption spectra of the aggregates were characterized by a reduced absorption in the UV, violet, and blue region and by a plasmon peak that was redshifted and broadened relative to that of the monodispersed particles. The optical changes associated with the formation of aggregates could be explained as a collective electromagnetic response involving the electrons of thousands of networked nanoparticles [48]. Thermal melting of the DNA double helix could reverse the assembly process together with the optical properties. The aggregates exhibited characteristic, exceptionally sharp “melting transitions” that could be monitored in the UV-vis spectrum and allowed one to distinguish the fully complementary oligonucleotide from those with mismatches of up to one base pair in the target sequence of the free oligonucleotide [49, 50]. Another technology for the selective detection of DNA was developed by imaging the light scattered by oligonucleotide-functionalized Au nanoparticles, 50 and 100 nm in diameter, on a glass microscope slide [51]. By hybridization with free complementary DNA the functionalized nanoparticles were attached to specific oligonucleotide-treated spots on the slide. Imaging the scattered light of these probes, green light ($\lambda_{\max} = 542$ nm) on a dark background was observed wherever 50 nm Au particles were attached to the slide; orange light ($\lambda_{\max} = 583$ nm) was observed for attached 100 nm Au particles. Amplification of surface bound Au colloids could be obtained by a nanoparticle-promoted reduction of Ag^+ with hydroquinone, which allowed signal read-out using a simple flatbed scanner [52]. In combination with the sharp melting profiles inherent to these oligonucleotide/Au nanoparticle hybrids, these procedures provide highly specific DNA detection technologies with impact on diagnostic applications. Further studies of DNA/Au hybrid materials concerned the influence of the DNA spacer length on the optical properties [53]. Experiments had shown that the DNA linker length kinetically controlled the size of the formed aggregates with slower aggregate growth rates for longer linker molecules, and that the optical properties depended on the size of the formed aggregates. The structures could be transformed into the thermodynamic aggregate products, upon heating just below the aggregate melting temperature for a period of 2 hours. After this annealing process, optical spectra of samples with different linker lengths became nearly identical. Such a DNA-directed assembly strategy was also used to prepare networks of particles comprising oligonucleotide functionalized 8 and 31 nm Au nanoparticles [54]. As a result, extended aggregates of two differently sized particles with a big particle (31 nm) and small particle (8 nm) periodicity were observed. If the ratio of small to big particles was increased to 120:1, “satellite structures” occurred, which consisted of a single 31 nm Au particle surrounded by many 8 nm Au particles (Fig. 2). A method to generate core–shell Au/Ag nanoparticles that could be functionalized with oligonucleotides and aggregated by addition of free oligonucleotide was reported by Cao and co-workers [55]. To create stable oligonucleotide/Ag nanoparticle conjugates, the 11.8 nm Ag particles were covered by a monolayer Au shell to prevent degradation of the Ag particles under conditions used to effect DNA hybridization. These Ag/Au

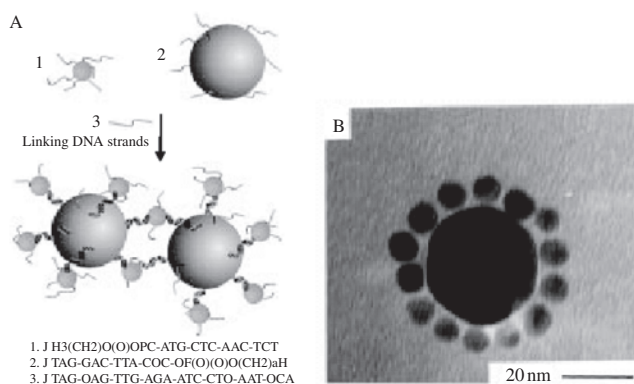


Figure 2. (A) DNA-directed assembly strategy for the production of binary network materials. (B) TEM image of a nanoparticle “satellite structure” obtained by reaction of 8 nm Au particles modified with oligonucleotide 1 (A) and 31 nm Au particles modified with oligonucleotide 2 (ratio 120:1) with free oligonucleotide 3. Reprinted with permission from [54], R. Mucic et al., *J. Am. Chem. Soc.* 120, 12674 (1998). © 1998, American Chemical Society.

core–shell particles provide means to a second colorimetric color change distinct from the previously described Au systems. In a similar approach the aggregate formation of DNA-functionalized CdSe/ZnS quantum dots was observed by addition of the complementary free oligonucleotide [56]. Using mixtures of DNA-modified CdSe/ZnS and DNA-derivatized Au nanoparticles resulted in binary aggregates with “AB” structure. In other work, magnetic nanoparticles consisting of a 3 nm, superparamagnetic $\text{Fe}_2\text{O}_3/\text{Fe}_3\text{O}_4$ core caged by epichlorohydrin cross-linked dextran were conjugated to two different oligonucleotides and assembled by addition of free complementary DNA [57]. After hybridization a decrease of the spin–spin relaxation time (T_2) of adjacent water protons from 63 to 45 ms was observed for these nanoparticle assemblies. Multiple cycles of heating and cooling revealed that the magnetic effects were fully reversible. Such magnetic relaxation nanoswitches consisting of DNA-based magnetic nanoparticle assemblies allowed one to screen DNA-cleaving agents [58]. Treating the magnetic nanoassemblies with DNA-cleaving enzymes lead to redispersed, free nanoparticles and to a concomitant increase in T_2 .

In solution, however, it is difficult to control the size of the formed aggregates. Therefore many attempts have used the recognition properties of DNA for the controlled assembly of oligonucleotide-functionalized nanoparticles on surfaces. Multilayered architectures of double-stranded DNA cross-linked CdS nanoparticles were organized on a Au electrode surface [59]. A set of two populations of DNA-capped CdS nanoparticles was organized layer by layer on the support by adding a soluble free oligonucleotide half-complementary to each population. It was possible to generate a photocurrent by irradiation of the CdS nanoparticles, which was enhanced in the presence of $[\text{Ru}(\text{NH}_3)_6]^{3+}$ electrostatically bound along the DNA backbone. The transition metal complex acted as an electron acceptor for the conduction band electrons and mediated the electron transport from the nanoparticles to the electrode. The generated photocurrent was found to depend on the number

of CdS layers on the electrode which could also be interesting for a future quantitative detection of DNA. In a similar DNA-based strategy, 13 nm Au particles were stepwise grown into layered nanoparticle structures on a glass surface [60]. Zhang and co-workers have used dip pen nanolithography (DPN) combined with wet etching techniques to generate Au nanostructures functionalized with oligonucleotides [61]. By DNA hybridization oligonucleotide modified Au nanoparticles were assembled into defined patterns on the substrate. Even multicomponent nanostructures of 13 and 30 nm Au particles could be obtained by using DPN [62]. Scanning tunneling microscopy and Raman and Fourier-transformation infrared spectroscopy were used to elucidate monolayer morphology, surface coverage, and presence of surface defects such as aggregates or nonselective binding in nanoparticle layers (5 and 10 nm Au particles) assembled through DNA hybridization [63].

For some potential applications (such as nanometer scale electronic devices) stoichiometric organization of metal or semiconductor nanocrystals into defined nanoscale aggregates (e.g., linear chains of nanoparticles) will be required. Well-defined, regularly aligned cluster systems of 1–5 nm dimension for example, would allow investigations on single electron tunneling for potential quantum mechanical devices [64]. To produce nanoparticle oligomers with a well-defined stoichiometry, Alivisatos and co-workers used single-stranded DNA oligonucleotides that were attached to individual Au nanocrystals [65, 66]. Upon addition of a complementary single-stranded DNA template, the nanoparticles assembled into dimers and trimers forming defined “nanocrystal molecules.” However, binding of ssDNA to a particle was a statistical process resulting in inhomogeneous mixtures of free particles, modified particles, and different conjugates. Purification could be achieved using gel electrophoresis [67]. The binding of each strand of ssDNA to a nanoparticle decreased the particle mobility in such a way that highly purified samples of specific conjugates could be isolated from the gel. The conformational modulation of DNA nanomaterial constructs by enzymatic manipulation of such 1.4 nm Au particle dimers was shown by Yun and co-workers [68]. Two 1.4 nm Au particles were conjugated to a thiol-modified, 40-mer duplex DNA strand containing a recognition site for the bacterial DNA methyltransferases *M.EcoRI* and *M.HhaI*. These highly selective bacterial proteins are known to bind to DNA and to induce sequence-specific conformational changes in DNA. In the absence of the proteins the Au–Au separation distance of the Au DNA dimer was found to be 12 nm, corresponding to the calculated length of a native 40-mer duplex DNA strand. The addition of *M.HhaI* did not alter the Au–Au separation distance. However, upon addition of *M.EcoRI* the Au–Au separation distance decreased to 6–8 nm. Each of the measured distances correlated with the expected topological changes of the DNA induced by the binding of the proteins. Evaluating the concentration-dependent histograms of the separation distance for *M.EcoRI* confirmed that the binding affinities were maintained in the Au/DNA hybrids. Treatment of the Au DNA nanoconstruct with the endonuclease *R.EcoRI*, which catalyzes the cleavage of the dsDNA at the same site recognized by *M.EcoRI*, resulted in a random separation distance for the Au nanocrystals. These studies

demonstrated that biofunction and binding affinities were maintained after modification of the DNA with 1.4 nm Au particles.

DNA-programmed assembly methodologies offer the opportunity to tailor the architectural parameters for nanoparticle superstructures, including nanoparticle size and composition, particle periodicity, and interparticle spacing. However, many applications will require precise control of spatial separation of the nanoparticles where flexibility of the DNA strands could be problematic. It is quite likely that more structural rigidity could be achieved using oligonucleotide templates constructed from antiparallel double-crossover components [69].

3. MATERIALS SYNTHESIS WITH PROTEIN-BASED BIOSTRUCTURES

3.1. Bacterial Surface Layers

Bacterial cell surface layers (S-layers) are the outermost component of the cell envelope of many prokaryotic organisms (archaea and bacteria) [70]. They are composed of periodically arranged protein or glycoprotein monomers leading to patterns with precise spatial arrangements of molecules creating regular arrays of physicochemical affinity sites. The highly ordered arrays exhibit oblique, square, or hexagonal lattice symmetries. S-layers are generally 5–15 nm thick and possess pores of identical size and morphology in the range of 2 to 6 nm. S-layer self-assembly processes may lead to the formation of flat sheets, open-ended tubes, or spheres. The possibility to assemble S-layers *in vitro* and the potential for chemical surface modification of S-layers make them an ideal biomolecular template.

Dieluweit et al. have used chemically modified S-layers of *Bacillus sphaericus* to nucleate regularly arranged arrays of Au nanoparticles formed by electron beam irradiation of the corresponding metal salt [71]. In the transmission electron microscope under low electron dose conditions, S-layers incubated with a HAuCl_4 solution revealed a continuous film of grainy Au precipitates. Upon increase of the electron dose, regularly arranged Au clusters were formed in the pore region of the S-layer. Although it is most likely that this observation was a thermal effect, it appeared that a certain density of thiol (introduced by chemical modification) and amino groups on the protein surface was required to initiate Au cluster formation. A square superlattice of uniform 4 to 5 nm sized Au particles could be produced. Electron beam induced growth of nanoparticles was also observed in the case of Pt and Pd on tube-shaped S-layer assemblies after incubation of the template with the corresponding metal salts [72]. The particles exhibited a squarelike shape with a lateral size of 5 to 7 nm.

Crystalline S-layers of *Sporosarcina urea* with square lattice symmetry have been shown to play an active role in the chemical deposition of Pt particles [73]. The template was activated by molecular deposition of Pt from a metal salt solution. NaN_3 from the buffer solution served as a very mild reducing agent. The clusters were heterogeneously nucleated at specific affinity sites on the surface of the S-layer.

The formation of the particles as well as their size was determined by the pores of the template resulting in highly ordered arrays of nanoparticles with particle sizes in the range of 1.9 nm. Using a chemical deposition method two-dimensional arrays of CdS nanocrystals on a S-layer template of *Bacillus stearothermophilus* with domain sizes up to 1 μm could be fabricated [74]. The extent of replication of the underlying protein lattice was found to be significantly less and the particle diameter of the formed particles was found to be smaller if CdS mineralization occurred on an exposed outer face of self-assembled protein subunits instead of an exposed inner face. The inner face has a net negative charge and is less hydrophobic than the charge-neutral outer face suggesting that electrostatic binding of metal ions might be important for the site-directed nucleation. The formed CdS nanoparticles had zinc blende structure with particle diameters in the range of 2 to 8 nm.

Also hexagonally packed intermediate (HPI) S-layers of *Deinococcus radiodurans* have been used for the spontaneous assembly of preformed Au nanoparticles in the range of 10 or 5 nm [75]. This self-assembly process produced μm -sized arrays of regularly spaced nanoparticles that were organized into a hexagonal superlattice. Regular self-assembly of the Au particles was only observed for negatively charged citrate-stabilized Au particles that were smaller than the lattice parameter of the HPI S-layer. Larger or positively charged poly-L-lysine capped particles were randomly distributed across the biomolecular substrate.

The synthesis of planar arrays of quantum dots will represent a crucial aspect in the fabrication of ultrasmall transistors and of materials possessing novel magnetic and optical properties. These results have demonstrated the potential of bacterial S-layers as a specific template to control growth and spatial organization of nanoparticles into two-dimensional arrays.

3.2. Viral and Other Protein Cages

Over evolution, nature has developed a variety of protein compartments that function as transport and storage devices for metal components or materials such as nucleic acids. These protein compartments have been used extensively as spatially confined reaction environments for the synthesis of inorganic materials. The protein coat of viruses, for example, is comprised of hundred to thousands of protein subunits that self-assemble into cage-like or rod-like compartments which enclose the viral nucleic acid. They occur in a wide range of sizes and morphologies and many examples of poly-morphic viruses exist.

The *tobacco mosaic virus* (TMV) is a well-understood system [76]. A TMV particle consists of 2130 identical protein subunits arranged around a single strand of RNA in a helical fashion forming hollow tubes, 300 nm long and 18 nm wide, with a 4 nm wide central channel. The internal and external surface of the protein coat reveals repeated patterns of charged amino acid residues which offer a variety of potential nucleation sites for surface-controlled deposition of inorganic materials. The virus, with its unique geometry and surface functionalities as well as its remarkable thermal and pH stability, has been exploited as a suitable template for several mineralization strategies.

Shenton and co-workers have reported the template-directed synthesis of inorganic-organic nanotubes using the rod-like structure of the TMV [77]. Precipitation of CdCl_2 or $\text{Pb}(\text{NO}_3)_2$ with H_2S in the presence of the TMV led to nanotubes coated by disordered aggregates of CdS (5 nm) or PbS (30 nm) nanocrystals, respectively. Iron oxide mineralization was achieved by addition of NaOH to an acidic $\text{Fe}^{\text{II}}/\text{Fe}^{\text{III}}$ solution in the presence of the TMV which yielded a poorly crystalline Fe^{III} hydrite layer on the external surface of the virus. Thin, 2 nm iron oxide films could be obtained by the slow aerial oxidation of dispersions of the TMV in an anaerobic Fe^{II} solution. Specific metal ion-binding to the numerous glutamate and aspartate surface groups of the virus seemed to direct the preferential deposition of these materials. Sol-gel condensation of $\text{Si}(\text{OCH}_2\text{CH}_3)_4$ led to the formation of a 3 nm SiO_2 shell, uniformly deposited along the outer surface of the viral particle. Arginine and lysine groups on the virion surface (positively charged at pH 2.5) interacted with the formed anionic silica species and led to a preferential deposition of SiO_2 . In other studies, TMV templates have been used to form mesoporous materials. Sol-gel condensation of $\text{Si}(\text{OCH}_2\text{CH}_3)_4$ and $\text{H}_2\text{N}(\text{CH}_2)_3\text{Si}(\text{OCH}_2\text{CH}_3)_3$ within the interstitial spaces of the TMV nematic liquid crystal phase produced highly ordered silica-TMV hybrid mesostructures [78]. The TMV particles were incarcerated within the silica matrix and could be removed by calcinations to produce replicas with hexagonally ordered cylindrical pores, 11 nm in diameter. Lowering the amount of $\text{Si}(\text{OCH}_2\text{CH}_3)_4$ and $\text{H}_2\text{N}(\text{CH}_2)_3\text{Si}(\text{OCH}_2\text{CH}_3)_3$ resulted in a large number of 100 to 150 nm spherical silica particles with unusual mesoporous interiors.

Recently, Lee and co-workers have used a genetically engineered bacteriophage with specific recognition moieties for ZnS crystal surfaces to nucleate and organize ZnS nanocrystals [79]. The virus had a filamentous shape, 880 nm in length and 6.6 nm in diameter, at one end containing a 10 nm peptide insert with ZnS binding affinity. Precipitation of ZnCl_2 with Na_2S in the presence of the long, rod-shaped phage yielded a 2.66 nm ZnS nanocrystal with wurtzite structure at the peptide insert of the phage. Defined by liquid crystal alignment a highly ordered composite material could be prepared.

Spherical viral compartments have also been used as bio-nanoreactors for the growth of inorganic materials. Remarkably monodisperse nanoparticles of polyoxometallate species (paratungstate and decavanadate) with single-crystal nature were obtained by Douglas and Young using the capsid of the *Cowpea chlorotic mottle virus* (CCMV) [80]. The CCMV virion consists of a protein shell of 180 identical coat protein subunits with an outer diameter of 28 nm and an inner cavity of 18 nm containing the viral nucleic acid. Purified viral coat protein subunits can be assembled *in vitro* into empty virion particles. Each of the subunits presents lysine and arginine residues to the inner side of the cavity creating a positively charged interior as an active site for inorganic crystal nucleation and growth. Moreover, the CCMV virus undergoes a reversible pH-dependent swelling which allows a free molecule exchange between the inner viral cavity and the bulk solution (Fig. 3) [81]. This pH-dependent gating mechanism was coupled to the pH-dependent oligomerization

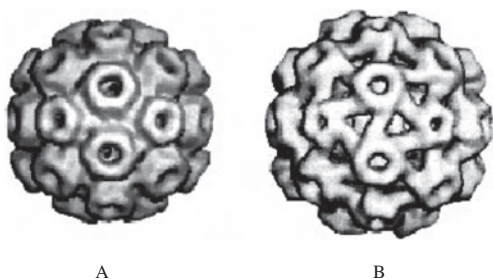


Figure 3. *Cowpea chlorotic mottle virus*. (A) In an unswollen condition induced by low pH. (B) In a swollen condition induced by high pH. Reprinted with permission from [80], T. Douglas and M. Young, *Nature* 393, 152 (1998). © 1998, Macmillan Magazines Limited.

reaction in order to load, crystallize, and entrap polyoxometallate particles of a well-defined size. The empty virions were first loaded with the inorganic precursor ions under conditions ($\text{pH} > 6$) where the virus exists in its open, swollen form. After incubation, the pH was lowered and the pores in the protein shell were closed which induced polyoxometallate oligomerization within the viral cavity. This crystallization process yielded uniform paratungstate or decavanadate nanocrystals 6.7 nm in diameter (Fig. 4). The electrostatic characteristics of the inner viral cavity could be genetically modified from cationic to anionic by replacing, for example, arginine and lysine with glutamic acid [82]. As a consequence the electrostatic characteristics of the interior surface of the cage were changed from cationic to anionic which favored strong interaction with Fe^{II} and Fe^{III} ions. This electrostatically altered viral protein cage promoted the oxidative hydrolysis of Fe^{II} leading to the formation of spatially constrained iron oxide nanoparticles within the cage. Subsequent loading of the viral core with iron atoms resulted in 8.2 or 24 nm iron oxide nanoparticles with the lepidocrocite structure of $\gamma\text{-FeOOH}$.

These results mimic the reactivity of ferritinlike proteins. The iron storage protein ferritin [83] consists of a 6 nm central core of a hydrated iron (III) oxide surrounded by a protein shell. The 24 protein subunits are assembled into a spherical, porous cage of about 8 nm in diameter, termed apoferritin. Iron oxide deposition occurs specifically within this protein cavity which results in spatially confined nanoparticles of a hydrated iron oxide similar to Fe^{III} hydroxide.

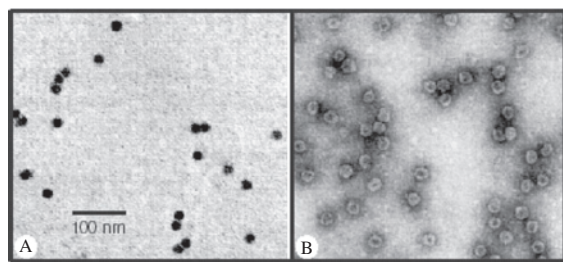


Figure 4. TEM image of paratungstate-mineralized virus particles. (A) Unstained sample showing the paratungstate cores. (B) Negatively stained sample showing the paratungstate core surrounded by the virus protein cage. Reprinted with permission from [80], T. Douglas and M. Young, *Nature* 393, 152 (1998). © 1998, Macmillan Magazines Limited.

It is possible to remove the mineral core by reductive dissolution, so that the empty polypeptide cage can be used as a confined reaction environment for particle synthesis. It has been shown that apoferritin can be reconstituted with a Fe^{III} hydrate core by chemical procedures. Furthermore, successful synthetic reactions have utilized electrostatics to nucleate a range of non-native minerals within the ferritin protein cage [84]. As an example, horse spleen apoferritin could be reconstituted with the ferrimagnetic minerals magnetite (Fe_3O_4) [85] and magnetite/maghemite ($\text{Fe}_3\text{O}_4/\gamma\text{-Fe}_2\text{O}_3$) [86]. Alternatively, Fe^{III} sulfide–ferritin nanocomposites could be synthesized by *in-situ* sulfidation of iron oxide cores reconstituted within the protein [87, 88]. Transmission electron microscopy of the transformed ferritin showed mineralized cores with a diameter of 6.5 nm similar in size to the unreacted ferritin biomaterial. The aerial oxidation of Mn^{II} in the presence of apoferritin lead to the formation of amorphous (MnOOH) cores [89]. X-ray absorption spectroscopy established that the local environment of the Mn closely resembled that in γ - and β - MnOOH [90]. Ferritin-templated hydrolytic polymerization of UO_2^{2+} acetate generated uniform 6 nm UO_2^{2+} hydroxide nanoparticles [89]. Biotinylation of the ferritin surface allowed the formation of supramolecular aggregates of Fe^{III} hydroxide nanoparticles by addition of streptavidin [91]. This aggregation process could be reversed by addition of a 20-fold excess (with respect to streptavidin) of free biotin to the turbid suspension of the aggregates, which resulted in an immediate formation of a clear yellow solution and a dispersion back to the original nonassociated state. Although the obtained systems were highly disordered and did not show any periodic order, ferritin-based arrays could have potential applications in magnetic storage. The focus of these studies on non-iron-containing oxides or non-native iron oxides was directed primarily by similarities between the chemistry of the native biomineral and potential biomimetic counterparts. Wong and Mann have illustrated that ferritin compartments could also be used for a preferential deposition of CdS nanoparticles by a nonhydrolytic chemical reaction [92]. Depending on the Cd^{2+} loading, the resulting polydisperse CdS ferritin nanoparticles had diameters of approximately 2.5 or 4.0 nm with irregular particle morphologies.

Recently, Shenton and co-workers have described another type of bionanoreactor based on the enzyme lumazine synthase, which was used for the biomimetic synthesis of iron oxide nanoparticles analogous to the ferritin system, even though there is no evidence for such a function *in vivo* [93]. Lumazine synthase is a hollow 1MDa bacterial enzyme complex of 60 subunits which is involved in the synthesis of lumazine. The structure of the lumazine synthase from *Bacillus subtilis* has a porous shell with an icosahedral morphology and inner and outer diameters of 7.8 and 14.7 nm, respectively. Aerial oxidation of Fe^{II} loaded capsids yielded $\gamma\text{-FeOOH}$ nanoparticles. Bulk precipitation of iron oxide was strongly inhibited in the presence of the lumazine synthase, because the mineral phase was specifically encapsulated within the internal cavity of the capsid. Interactions between the enzyme and the iron seemed to destabilize the native capsids which then transformed into a broad range of higher order structures in association with discrete nanoparticles of iron oxide. Some of the capsids remained

completely empty while others contained high Fe loadings, suggesting an autocatalytic growth on the surface of developing particles.

3.3. Cytoskeletal Filamentous Assemblies

Microtubules are cytoskeletal protein assemblies ubiquitously present in eukaryotic cells. They are important structures for both cellular architecture and motility. Under appropriate conditions microtubules can be assembled *in vitro* from α β heterodimeric tubulin molecules. They form hollow cylindrical structures consisting of characteristically arranged tubulin molecules with outer diameters of 25 nm and lengths of several micrometers [94]. Depending on the assembly conditions, tubulin can form a variety of other polymorphs (e.g., tubules, sheets, spirals, ribbons, or rings) [95]. Microtubule templates were used to nucleate Pd nanoparticles [96]. The protein assemblies were first incubated with a Pd precursor, followed by reduction of the adsorbed metal ions with a $(\text{CH}_3)_2\text{NH} \cdot \text{BH}_3$ reduction bath which yielded 3.1 nm nanocrystals. The arrangement of nanoparticles reflected the helical structure of the tubulin subunits within the microtubule suggesting a preferential binding of the Pd to histidine residues present in each α and β tubulin subunit at the outer surface of the microtubule (Fig. 5). Increase of the metal concentration leads to a further growth of the particles, so that a quasi-continuous coverage of the tubules was obtained. Nanoparticles of Au, Ru, or Rh could also be heterogeneously nucleated on the surface of microtubules by *in-situ* reduction of the corresponding noble metal salts using reducing agents such as NaBH_4 or NaN_3 . In another approach, preformed Au nanoparticles, which were synthesized by a homogeneous nucleation process in solution, were linked to the surface of the tubular biostructure which yielded microtubules densely covered by nanoparticles. Bimetallic Au/Pd particles in the size range of 3 to 60 nm were obtained by a seed-growth mechanism. Au nanoparticles were first linked to the proteins and covered with Pd by reduction of NaPdCl_4 with Na citrate [97]. In other work, a continuous Ni film could be generated on

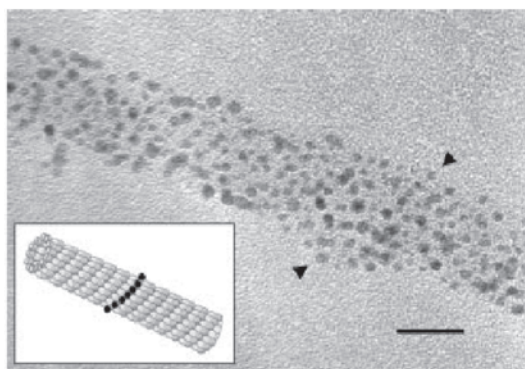


Figure 5. TEM image of 3.1 nm Pd nanoparticles nucleated on the surface of a microtubule. The arrangement of the particles reflects the helical ordering of tubulin subunits in the protein template. Reprinted with permission from [96], S. Behrens et al., *Adv. Mater.* 22, 1621 (2002). © 2002, Wiley-VCH.

microtubules using an electroless deposition technique initiated by a molecular Pd catalyst [98, 99]. The outer diameter of the metallized microtubules was in the range of 50 to 60 nm, corresponding to an average Ni film thickness of 15 nm. Although Ni could diffuse through the activated tubule wall, the tubule lumen was not filled with Ni deposits. The magnetic properties were confirmed by manipulating metallized microtubules in solution or exposed to air with a permanent magnet. A single Ni/microtubule composite could be connected to two Au electrodes for electrical characterization. A metallized microtubule yielded a resistance below 50Ω over the length of $1 \mu\text{m}$ [100].

Motor proteins (e.g., kinesin, dynein, and myosin) “walk” in nm steps along cytoskeletal tracks actively transporting cellular components. These motor proteins provide potential tools to construct shuttles for cargo transport [101]. Especially the kinesin microtubule machinery has been widely explored with its potential application for device transport in defined nanometer steps [102]. Cell-free force-generating linear motors or, more generally, nanoactuatoric units were designed [103] to be able to vectorially transport artificial cargos to predetermined destinations [104].

By binding of nm- or μm -scaled cargos (e.g., gold, silicon, or magnetic particles) [105] and their transfer by optical tweezers from one microtubule system to another, kinesin allows site-directed particle transport.

Besides microtubules, other cytoskeletal fibers such as the 7 nm diameter actin microfilaments or the 12 nm diameter intermediate filaments could be used as a template for the production of metallized nanowires. The narrow diameter and the different protein compositions of these fibers could lead to new nanosized architectures.

3.4. Bacterial Filaments

Using an electroless deposition technique, Pazirandeh et al. produced Ni/rhaphidosome nanotubes [106]. Rhaphidosomes are filamentous structures found in certain bacteria. They are composed of three distinct protein subunits that combine to form tubular structures measuring approximately 25 nm in diameter with a variable length averaging 400 nm. A remarkable stability under extreme conditions, along with their small size and shape, makes them an interesting template for production of nanowires. They could be coated with metal using the electroless deposition technique in which nanosized tin chloride/oxochloride covered Pd catalyst particles were adsorbed onto the rhaphidosome surface, followed by exposure to a commercial nickel-plating bath. The metallized rhaphidosomes were observed as rod-shaped structures that had an average diameter of 35 nm with variable length and appeared to be magnetic.

A bacterial superstructure consisting of coagined multicellular filaments of *Bacillus subtilis* has been used for templating ordered macrostructures in silica and silica-surfactant mesophases [107]. The arrangement of bacterial filaments in the superstructure resembles the hexagonal packing of surfactant cylinders as it occurs during synthesis of the mesoporous silica material MCM-41. Mineralization of the interfilament spaces followed by heating to $600 \text{ }^\circ\text{C}$ produced macroporous fibers of either amorphous silica or ordered mesoporous silica if a silica-surfactant mesophase (MCM-41) was used.

3.5. Protein-Based Assembly of Nanoparticles

Alternatively to DNA, the recognition properties of proteins (e.g., specific antibody–antigen interactions) have been exploited for the assembly of inorganic nanoparticles into metallic or bimetallic nanoparticle aggregates.

Shenton and co-workers used the recognition properties of surface-attached antibodies [108]. Two kinds of antibodies, IgE or IgG, with specificities to dinitrophenol (DNP) or biotin, respectively, were attached to nanoparticles. Addition of bivalent antigens with double-headed functionalities such as homo-(DNP/DNP) or hetero-(DNP/biotin) Janus structures connected by spacers lead to the formation of three-dimensional metallic or bimetallic aggregates. Addition of bivalent DNP/DNP antigen molecules to 12 nm Au particles modified with anti-DNP IgE antibodies led to the formation of large disordered three-dimensional networks of discrete Au nanoparticles. If two groups of Au nanoparticles functionalized by either anti-DNP IgE or anti-biotin IgG were exposed to free DNP/biotin Janus structures, millimeter-long filaments of densely packed, three-dimensional particle networks had been formed. Bimetallic nanoparticle networks were obtained by addition of the hetero-DNP/biotin antigen to a dispersion consisting of Au nanoparticles modified with anti-DNP IgE antibodies and 12 nm Ag nanoparticles functionalized with anti-biotin IgG molecules. TEM images provided evidence for co-assembly into bimetallic networks, but the degree of integration observed was not as high as expected for an assembly directed by molecular recognition.

Other approaches made use of the unique interaction between streptavidin and biotin. Streptavidin has a good chemical and physical stability and biotinylated materials are often commercially available or can be prepared by mild biotinylation procedures. Moreover, a variety of biotin analogs and recombinant streptavidin mutants is available. Connolly and Fitzmaurice used the biotin–streptavidin recognition system to assemble 16 nm Au particles in solution [109]. The Au nanocrystals were assembled using the streptavidin–biotin analog system via two different routes: (1) The Au nanocrystals were modified by chemisorption of a disulfide biotin analog (DSBA), followed by the subsequent addition of streptavidin. (2) The DSBA was bound to streptavidin prior to addition to the Au nanocrystals. Both of these aggregation routes were monitored using dynamic light scattering which yielded a rapid increase in the average hydrodynamic radius and was accompanied by a color change from red to blue upon addition of streptavidin or streptavidin/DSBA. TEM images revealed the presence of aggregates, containing on average 20 nanocrystals. The nanocrystals were separated from other particles by approximately 5 nm, caused by interspersed streptavidin. Small angle X-ray scattering was employed to probe the solution structure of the aggregates, which indicated the presence of trimers of 16 nm diameter hard spheres (Au particles), separated by a minimum distance of 4 nm. A theoretical model has been developed by Connolly and co-workers to explain the effects of ligand–receptor geometry and stoichiometry on the streptavidin-induced aggregation of biotin-modified Au nanoparticles [110]. Niemeyer and co-workers

used covalent conjugates of oligonucleotides and streptavidin for the fabrication of nanostructured supramolecular aggregates [111]. Biotin-derivatized 1.4 nm Au clusters were first coupled to the DNA/streptavidin conjugates, followed by addition of a RNA carrier.

4. CONCLUSIONS

This chapter summarizes a rapidly growing interdisciplinary research field at a crossover of biotechnology and materials science for the production of nanoscale materials. These results illustrate the potential of biological components with their unique chemical and topological properties for the spatial assembly of inorganic materials into well-defined nanostructures. The diversity in size and shape of biomolecular structures offers an exciting alternative to conventional materials synthesis. In the interplay the biological and inorganic components provide charge-compensation, space-filling, and structure-directing roles. Through these studies, new, interesting phenomena, structures, and materials have been identified. These findings support the view that postinformation technologies could emerge at the interface between physical and life sciences.

Although many examples exist where biomolecules have been successfully coupled to a variety of inorganic nanoparticles and materials, there still remains a great demand for new, mild, and selective chemical coupling techniques. A variety of technical obstacles still has to be solved ranging from the currently limited availability of large amounts of, for example, synthetic DNA to the refinement of analytical techniques. Advances in the scale-up of biomolecular precursors such as synthetic oligonucleotides will lead to a reduction in the production costs associated with these methods. Moreover, in many cases the interactions between the biomolecules and the inorganic material (such as the interplay between reactive sites on the surface of the biomolecule and the nucleation and deposition process) are not well understood; future systematic fundamental research will be needed to elucidate the interaction of biomolecules with inorganic materials. Modifying biomolecular structures by genetic engineering will allow one to direct the synthesis of a broad range of new “non-natural” materials. Genetic engineering of biomolecular templates with more suitable shapes and physicochemical properties could yield various advanced materials on the nanometer scale with novel electronic, optical, magnetic, or catalytic properties.

GLOSSARY

Antibody Protein with specific complementary binding sites for an antigen.

Antigen Substance inducing the formation of antibodies in an organism.

Deoxyribonucleic acid (DNA) A macromolecule consisting of one or two strands of linked deoxyribonucleotides.

DNA hybridization Formation of a duplex structure by two complementary single strands of DNA.

Enzyme Protein acting as a catalyst for a specific biochemical reaction.

Nucleotide Monomer of the nucleic acids RNA or DNA. It contains a phosphate group, a sugar group (ribose, deoxyribose), and an organic base (purine or pyrimidine base).

Oligonucleotide Short DNA or RNA strand consisting of a few linked nucleotides.

Protein Natural polymer consisting linked amino acid monomers.

REFERENCES

1. U. Simon, *Adv. Mater.* 10, 1487 (1998).
2. A. Berman, J. Hanson, L. Leiserowitz, T. Koetzle, S. Weiner, and L. Addadi, *Science* 259, 777 (1993).
3. S. Mann, in "Biomaterialization. Principles and Concepts in Bioinorganic Materials Chemistry." Oxford Univ. Press, Oxford, UK, 2001.
4. S. Mann, in "Biomimetic Materials Chemistry." VCH, Weinheim, 1996.
5. I. Šafařík and M. Šafaříková, *Monatsh. Chem.* 133, 737 (2002).
6. S. Mann, D. Archibald, J. Didymus, T. Douglas, B. Heywood, F. Meldrum, and N. Reeves, *Science* 261, 1287 (1993).
7. K. McGrath, *Adv. Mater.* 13, 989 (2001).
8. C. Orme, A. Noy, A. Wierzbicki, M. McBride, M. Grantham, H. Teng, P. Dove, and J. DeYoreo, *Nature* 441, 775 (2001).
9. K. Naka and Y. Chujo, *Chem. Mater.* 13, 3245 (2001).
10. S. Mann, *Nature* 365, 499 (1993).
11. G. Zuccarello, D. Scribner, R. Sands, and L. Buckley, *Adv. Mater.* 14, 1261 (2002).
12. E. Dujardin and S. Mann, *Adv. Mater.* 14, 775 (2002).
13. C. M. Niemeyer, *Angew. Chem. Int. Ed.* 40, 4129 (2001).
14. J. Storhoff and C. Mirkin, *Chem. Rev.* 99, 1849 (1999).
15. E. Braun, Y. Eichen, U. Sivan, and G. Ben-Yoseph, *Nature* 391, 775 (1998).
16. Y. Eichen, E. Braun, U. Sivan, and G. Ben-Yoseph, *Acta Polym.* 49, 663 (1998).
17. C. Niemeyer and M. Adler, *Angew. Chem. Int. Ed.* 40, 3779 (2002).
18. K. Hamad-Schifferli, J. Schwartz, A. Santos, S. Zhang, and J. Jacobson, *Nature* 415, 152 (2002).
19. C. Niemeyer, M. Adler, S. Lehnert, S. Gao, H. Fuchs, and L. Chi, *Chem. Biochem.* 2, 260 (2001).
20. C. Dekker and M. Ratner, *Phys. World* 14, 29 (2001).
21. H. W. Fink and C. Schönenberger, *Nature* 398, 407 (1999).
22. A. J. Storm, J. van Noort, S. de Vries, and C. Dekker, *Appl. Phys. Lett.* 79, 3881 (2001).
23. M. Mertig, L. C. Ciacchi, R. Seidel, W. Pompe, and A. De Vita, *Nano Lett.* 2, 841 (2002).
24. J. Reedijk, *Chem. Rev.* 99, 2499 (1999).
25. E. Jamieson and S. Lippard, *Chem. Rev.* 99, 2467 (1999).
26. R. Seidel, M. Mertig, and W. Pompe, *Surf. Interface Anal.* 33, 151 (2002).
27. W. Ford, O. Harnack, A. Yasuda, and J. Wessels, *Adv. Mater.* 13, 1793 (2001).
28. J. Richter, R. Seidel, R. Kirsch, M. Mertig, W. Pompe, J. Plaschke, and H. Schackert, *Adv. Mater.* 12, 507 (2000).
29. J. Richter, M. Mertig, and W. Pompe, *Appl. Phys. Lett.* 78, 536 (2001).
30. J. Richter, M. Mertig, W. Pompe, and H. Vinzelberg, *Appl. Phys. A* 74, 725 (2002).
31. K. Keren, M. Krueger, R. Gilad, G. Ben-Yoseph, U. Sivan, and E. Braun, *Science* 297, 72 (2002).
32. A. Kumar, V. Ramakrishnan, R. Gonnade, K. Ganesh, and M. Sastry, *Nanotechnology* 13, 597 (2002).
33. J. Coffer, S. Bigham, R. Pinizzotto, and H. Yang, *Nanotechnology* 3, 69 (1992).
34. S. Bigham and J. Coffer, *Colloids Surf. A* 95, 211 (1995).
35. R. Mahtab, J. Rogers, C. Singleton, and C. Murphy, *J. Am. Chem. Soc.* 118, 7028 (1996).
36. J. Coffer, S. Bigham, X. Li, R. Pinizzotto, Y. Gyu Rho, R. Pirtle, and I. Pirtle, *Appl. Phys. Lett.* 69, 3851 (1996).
37. C. Holgate, P. Jackson, P. Cowen, and C. Bird, *J. Histochem. Cytochem.* 31, 938 (1983).
38. G. Danscher, *Histochemistry* 71, 81 (1981).
39. J. Roth, *Histochem. Cell Biol.* 106, 1 (1996).
40. C. Oliver, *Methods Mol. Biol.* 115, 331 (1999).
41. A. Kumar, M. Pattarkine, M. Bhadbhade, A. Mandale, K. Ganesh, S. Datar, C. Dharmadhikari, and M. Sastry, *Adv. Mater.* 13, 341 (2001).
42. M. Sastry, A. Kumar, S. Datar, C. Dharmadhikari, and K. Ganesh, *Appl. Phys. Lett.* 78, 2943 (2001).
43. T. Torimoto, M. Yamashita, S. Kuwabata, T. Sakata, H. Mori, and H. Yoneyama, *J. Phys. Chem. B* 103, 8799 (1999).
44. O. Harnack, W. Ford, A. Yasuda, and J. Wessels, *Nano Lett.* 2, 919 (2002).
45. F. Patolsky, Y. Weizmann, O. Lioubashevski, and I. Willner, *Angew. Chem. Int. Ed.* 41, 2323 (2002).
46. C. Mirkin, R. Letsinger, R. Mucic, and J. Storhoff, *Nature* 382, 607 (1996).
47. S. Park, A. Lazarides, C. Mirkin, P. Brazis, C. Kannewurf, and R. Letsinger, *Angew. Chem. Int. Ed.* 39, 3845 (2000).
48. A. Lazarides and G. Schatz, *J. Phys. Chem. B* 104, 460 (2000).
49. R. Elghanian, J. Storhoff, R. Mucic, R. Letsinger, and C. A. Mirkin, *Science* 277, 1078, (1997).
50. J. Storhoff, R. Elghanian, R. Mucic, C. A. Mirkin, and R. Letsinger, *J. Am. Chem. Soc.* 120, 1959 (1998).
51. T. A. Taton, G. Lu, and C. Mirkin, *J. Am. Chem. Soc.* 123, 5164 (2001).
52. T. A. Taton, C. Mirkin, and R. Letsinger, *Science* 289, 1757 (2000).
53. J. Storhoff, A. Lazarides, R. Mucic, C. A. Mirkin, R. Letsinger, and G. Schatz, *J. Am. Chem. Soc.* 122, 4640 (2000).
54. R. Mucic, J. Storhoff, C. A. Mirkin, and R. Letsinger, *J. Am. Chem. Soc.* 120, 12674 (1998).
55. Y. Cao, R. Jin, and C. Mirkin, *J. Am. Chem. Soc.* 123, 7961 (2001).
56. G. Mitchell, C. A. Mirkin, and R. Letsinger, *J. Am. Chem. Soc.* 121, 8122 (1999).
57. L. Josephson, J. M. Perez, and R. Weissleder, *Angew. Chem. Int. Ed.* 40, 3204 (2001).
58. J. M. Perez, T. O'Loughin, F. J. Simeone, R. Weissleder, and L. Josephson, *J. Am. Chem. Soc.* 124, 2856 (2002).
59. I. Willner, F. Patolsky, and J. Wasserman, *Angew. Chem.* 113, 1913 (2001).
60. T. A. Taton, R. Mucic, C. Mirkin, and R. Letsinger, *J. Am. Chem. Soc.* 122, 6305 (2000).
61. H. Zhang, Z. Li, and C. Mirkin, *Adv. Mater.* 14, 1472 (2002).
62. L. Demers, S. J. Park, A. Taton, Z. Li, and C. Mirkin, *Angew. Chem. Int. Ed.* 40, 3071 (2001).
63. M. Sauthier, L. Carroll, C. Gorman, and S. Franzen, *Langmuir* 18, 1825 (2002).
64. D. Feldheim and C. Keating, *Chem. Soc. Rev.* 27, 1 (1998).
65. C. Loweth, W. Caldwell, X. Peng, A. P. Alivisatos, and P. Schultz, *Angew. Chem. Int. Ed.* 38, 1808 (1999).
66. A. P. Alivisatos, K. Johnsson, X. Peng, T. Wilson, C. Loweth, M. Bruchez, and P. Schultz, *Nature* 382, 609 (1996).
67. D. Zanchet, C. Micheel, W. Parak, D. Gerion, S. Williams, and A. P. Alivisatos, *J. Phys. Chem. B* 106, 11758 (2002).
68. C. Yun, G. Khitrov, D. Vergona, N. Reich, and G. Strouse, *J. Am. Chem. Soc.* 124, 7644 (2002).
69. E. Winfree, F. Liu, L. Wenzler, and N. Seeman, *Nature* 394, 539 (1998).
70. U. Sleytr, P. Messner, D. Pum, and M. Sára, *Angew. Chem. Int. Ed.* 38, 1035 (1999).
71. S. Dieluwweit, D. Pum, and U. Sleytr, *Supramol. Sci.* 5, 15 (1998).

72. M. Mertig, R. Wahl, M. Lehmann, P. Simon, and W. Pompe, *Eur. Phys. J. D* 16, 317 (2001).
73. M. Mertig, R. Kirsch, W. Pompe, and H. Engelhardt, *Eur. Phys. J. D* 9, 45 (1999).
74. W. Shenton, D. Pum, U. Sleytr, and S. Mann, *Nature* 389, 585 (1997).
75. S. Hall, W. Shenton, H. Engelhardt, and S. Mann, *Chem. Phys. Chem.* 3, 184 (2001).
76. G. Stubbs, "The Viruses, Biological Assemblies and Macromolecules" (A. McPherson and F. Journack, Eds.), Vol. 1, p. 149. Wiley, New York, 1984.
77. W. Shenton, T. Douglas, M. Young, G. Stubbs, and S. Mann, *Adv. Mater.* 11, 253 (1999).
78. C. Fowler, W. Shenton, G. Stubbs, and S. Mann, *Adv. Mater.* 13, 1266 (2001).
79. S. Lee, C. Mao, C. Flynn, and A. Belcher, *Science* 296, 892 (2002).
80. T. Douglas and M. Young, *Nature* 393, 152 (1998).
81. J. Speir, S. Munshi, G. Wang, T. Baker, and J. Johnson, *Structure* 3, 63 (1995).
82. T. Douglas, E. Strable, D. Willits, A. Aitouchen, M. Libera, and M. Young, *Adv. Mater.* 14, 415 (2002).
83. P. Harrison and P. Arosio, *Biochim. Biophys. Acta* 1275, 161 (1996).
84. T. Douglas, in "Biomimetic Materials Chemistry" (S. Mann, Ed.), p. 117. VCH, Weinheim, 1996.
85. F. Meldrum, B. Heywood, and S. Mann, *Science* 257, 522 (1992).
86. K. Wong, T. Douglas, S. Gider, D. Awschalom, and S. Mann, *Chem. Mater.* 10, 279 (1998).
87. T. Douglas, D. Dickson, S. Betteridge, J. Charnock, C. D. Garner, and S. Mann, *Science* 269, 54 (1995).
88. F. Meldrum, T. Douglas, S. Levi, P. Arosio, and S. Mann, *J. Inorg. Biochem.* 58, 59 (1995).
89. F. Meldrum, V. Wade, D. Nimmo, B. Heywood, and S. Mann, *Nature* 349, 685 (1991).
90. P. Mackle, J. Charnock, and C. D. Garner, *J. Am. Chem. Soc.* 115, 8471 (1993).
91. M. Li, K. Wong, and S. Mann, *Chem. Mater.* 11, 23 (1999).
92. K. Wong and S. Mann, *Adv. Mater.* 8, 929 (1996).
93. W. Shenton, S. Mann, H. Cölfen, A. Bacher, and M. Fischer, *Angew. Chem. Int. Ed.* 113, 456 (2001).
94. E. Nogales, *Annu. Rev. Biochem.* 69, 277 (2000).
95. E. Unger, W. Vater, and K.-J. Böhm, *Electron Microsc. Rev.* 3, 355 (1990).
96. S. Behrens, K. Rahn, W. Habicht, K. J. Böhm, H. Rösner, E. Dinjus, and E. Unger, *Adv. Mater.* 22, 1621 (2002).
97. S. Behrens, W. Habicht, N. Boukis, E. Dinjus, M. Baum, and E. Unger, *Mater. Res. Soc. Symp. Proc.* 581, 65 (1999).
98. R. Kirsch, M. Mertig, W. Pompe, R. Wahl, G. Sadowski, K. J. Böhm, and E. Unger, *Thin Solid Films* 305, 248 (1997).
99. M. Mertig, R. Kirsch, and W. Pompe, *Appl. Phys. A* 66, 723 (1998).
100. W. Fritzsche, J. M. Köhler, K. J. Böhm, E. Unger, T. Wagner, R. Kirsch, M. Mertig, and W. Pompe, *Nanotechnology* 10, 331 (1999).
101. J. Howard, "Mechanics of Motor Proteins and the Cytoskeleton." Sinauer, Sunderland, MA, 2001.
102. H. Hess, J. Clemmens, D. Qin, J. Howard, and V. Vogel, *Nano Lett.* 1, 235 (2001).
103. R. Stracke, K. J. Böhm, J. Burgold, H. J. Schacht, and E. Unger, *Nanotechnology* 11, 52 (2000).
104. K. J. Böhm, R. Stracke, P. Mühlig, and E. Unger, *Nanotechnology* 12, 238 (2001).
105. E. Unger, R. Stracke, J. Beeg, and K. J. Böhm, "Sensoren im Fokus neuer Anwendungen—Dresdener Beiträge zur Sensorik, Bd. 16" (J. P. Baselt and G. Gerlach, Eds.). Universitätsverlag Dresden, Dresden, 2002.
106. M. Pazirandeh, S. Baral, and J. Campbell, *Biomimetics* 1, 41 (1992).
107. S. Davis, S. Burkett, N. Mendelson, and S. Mann, *Nature* 385, 420 (1997).
108. W. Shenton, S. Davis, and S. Mann, *Adv. Mater.* 11, 449 (1999).
109. S. Connolly and D. Fitzmaurice, *Adv. Mater.* 11, 1202 (1999).
110. S. Connolly, S. Cobbe, and D. Fitzmaurice, *J. Phys. Chem. B* 105, 2222 (2001).
111. C. Niemeyer, W. Bürger, and J. Peplies, *Angew. Chem. Int. Ed.* 37, 2265 (1998).

Techniques in Electrochemical Nanotechnology

P. Schmuki, S. Maupai, T. Djenizian, L. Santinacci, A. Spiegel, U. Schlierf

University of Erlangen-Nuremberg, Erlangen, Germany

CONTENTS

1. Introduction
 2. Resist-Based Approaches
 3. Direct Writing Approaches
 4. Self-Assembly and Templates
 5. Layered Nanostructures
- Glossary
References

1. INTRODUCTION

Electrochemical methods for functionalizing surfaces (mostly metals and semiconductors) have been intensively explored in the last 100 years and have found wide, successful technological application. Electroplating in particular is a long known and well-established technology for the deposit of metals such as Ni, Cu, Au, Zn, Cd, Ag, Fe, etc. on a large scale on conductive substrates [1]. A range of materials can also be deposited in so-called electroless processes [2], where no external voltage source is needed but a reducing agent is in the electrolyte.

In nanotechnology, electrochemical methods are strongly emerging. Some approaches represent simply a “wet” alternative to vacuum deposition techniques such as physical vapor deposition (PVD) or chemical vapor deposition (CVD). In other cases unique features of electrochemical reactions are used for micro- and nanopatterning. A clear advantage of electrochemical reactions is that it is comparably easy and cheap to uniformly cover a nonplanar substrate. In particular, recently discovered special features such as “superfilling” have reached high significance in modern integrated circuit (IC) technologies for via filling [3–5]. In the future, even more important may be the fact that many electrochemical processes are carried out at low temperatures and involve aqueous electrolytes. Both factors are of course extremely important whenever living (bio-organic) matter is involved—thus many view the solid/liquid interface as the interface of the future.

Traditional micropatterning techniques are based on lithography and hence demand a masking process. Apart from the necessity to fabricate masks, these techniques imply that photoresists are provided that are resistant to the deposition or etching environment. Except for masking approaches, direct structuring processes are also being explored, based on either sequential writing processes (comparably slow) or parallel patterning. Such direct parallel patterning is, for example, electrodeposition onto/into templates, and generally a lateral variation of the reactivity (often leading to a variation in the electrical conductivity) of a surface is exploited.

In a narrow sense, true nanostructures may be regarded as lateral surface structures in the submicrometer or even in the maximum 10-nm size range. Therefore, within this chapter, mainly techniques that deal with lateral nanostructuring will be treated. However, layered nanostructures can also be produced electrochemically—this is dealt with briefly at the end of the chapter.

Lateral nanostructuring techniques employing an electrochemical process in conjunction with radiation (either to directly modify a surface or via a resist to transfer a pattern to the surface) must use radiation with a diffraction limit in the nanometer range. Thus, short-wavelength electromagnetic radiation of a sufficiently high energy (e.g., X-rays) or charged particle beams (electron beams (e-beams) or focused ion beams (FIBs)) are the main candidates.

Other writing approaches that can be applied to obtain surface modifications with submicrometer resolution are based on scanning nanoprobes, exploiting mechanical, force, or field-induced interactions of an extremely sharp tip with a surface. Since the 1980s, the invention of the scanning tunneling microscope (STM) [6, 7] and later of the atomic force microscope (AFM) [8] has opened new perspectives for high-resolution visualization of surfaces but also for material structuring at the nanometer scale. The first example of high-resolution surface patterning was the manipulation of individual atoms [9] or molecules [10], giving a significant thrust to nanotechnologies. Also in conjunction with electrochemistry, both STM- as well as AFM-based approaches are widely used.

An often spectacular approach is based on (“natural”) self-organization of nanoscopic features. These features may be holes (pores) or bumps (atoms, molecules, nanospheres), and the reason for self-organization is often the existence of competing reactions or effects. Self-organized structures may be directly created by electrochemistry or serve as templates for electrochemistry.

Finally it should be noted that several recent books are available that treat specific aspects of electrochemical nanotechnology in more detail [11–13].

In the following, this chapter tries mainly to give a broad overview of techniques and approaches used in contemporary electrochemical nanotechnology rather than treating specific approaches in great depth.

2. RESIST-BASED APPROACHES

Optical lithography or photolithography based on a resist exposed to visible or ultraviolet (UV) light is the predominant technique for producing highly accurate and high-volume two-dimensional patterns in the micrometer range. In the IC industry, pattern transfer from masks onto thin films is accomplished almost exclusively with this technique [14].

A lithographic sequence begins with coating substrates with a radiation-sensitive material (often polymer) called a resist. Resists fall into two broad classes: so-called positive and negative. Positive resists such as poly(methylmethacrylate) (PMMA) become more soluble in a developing solvent after exposure because radiation causes local bond breakages and thus chain scission. As a result, the exposed region containing material of a lower mean molecular weight will dissolve during development. Therefore, if a small region of the positive-resist covered film is exposed, a hole will appear in the resist after development. In contrast, negative resists become less soluble in solvent after exposure because cross-linking of polymer chains occurs. In this case, if a region of a negative resist-covered film is exposed, only the exposed region will be covered by resist after development. Subsequently, the resist-free parts of the substrate can be etched, implanted, or covered with another material before the resist is removed. However, the ultimate resolution of photolithography (i.e., the minimum feature size that can be obtained) is around 200 nm because of diffraction, given approximately by the wavelength of the radiation used. Thus, for future resist-based nanotechnology applications, shorter wavelength sources (X-rays or particle beams) have to be used. Of course, this is also true for approaches based on electrochemical material removal (etching) or electrochemical material addition (plating) through a resist-patterned mask.

2.1. X-Ray Lithography and LIGA

Lithography based on X-ray exposure (very short wavelengths) was described in 1972 [15] and has considerably improved the resolution attained so far by photolithography. This technology requires an entirely new combination of source (X-ray radiation typically produced by a synchrotron), mask, resist, and alignment system [16]. X-ray lithography is also capable of producing high-resolution 3D

structures because the resist is highly transparent to X-rays (high-aspect ratio pattern fabrication), and undesired scattering and reflection are negligible. However, its application to large-scale manufacturing is hampered by a variety of technical and economic limitations [17].

A very specific form of X-ray lithography is LIGA, which is an acronym for the German words for lithography, electroplating, and molding developed at the Forschungszentrum Karlsruhe in the mid-1980s [18]. This is a process used to fabricate microstructures with lateral dimensions of the order of several micrometers and high aspect ratio. The schematic sequence of the process is shown in Figure 1. Microelectromechanical systems (MEMS) are made from LIGA-processed metals, ceramics, or plastics. The LIGA process utilizes X-rays from synchrotron radiation as a lithographic light source. Highly collimated, high-energy X-rays from the synchrotron impinge on a patterned mask in proximity to an X-ray-sensitive photoresist, typically PMMA. After development of the resist, the resulting nonconductive mold is filled with metal by electroplating metals such as Cu, Ni, or Au, with use of the metallic substrate as a cathode. The remaining resist is dissolved, leaving the patterned metal structure as the end product. Examples of such

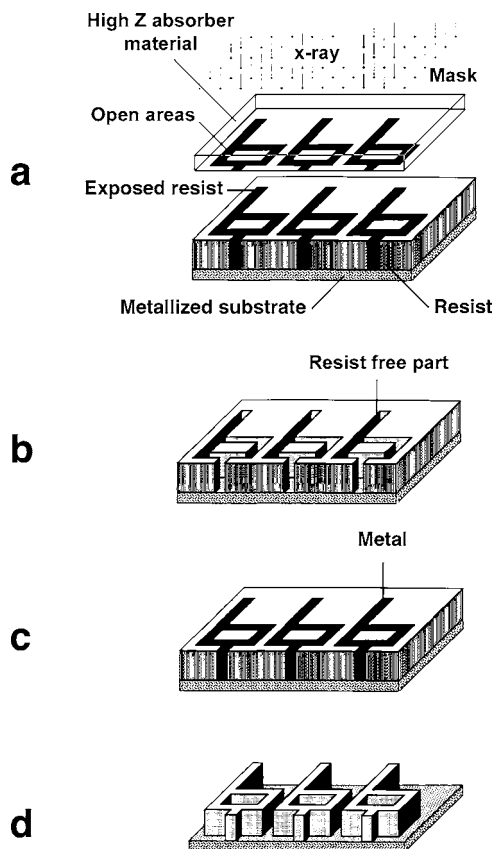


Figure 1. Schematic of the LIGA process. (a) Parallel X-rays from a synchrotron are projected through a mask (patterned with high Z absorber material) onto a resist. (b) The resist is chemically developed at exposed locations. (c) A metal is electroplated in the resist mold to create a metal micropart. (d) The resist is dissolved, leaving a 3D metal micropart. The electroplated part can also be used as a mold for the replication of another material such as plastic or ceramic.

products are shown in Figure 2. The main advantage of the LIGA process lies in the microstructures molded of plastic, metal, and ceramic in nearly any lateral geometry and with a high aspect ratio, with a roughness of the walls of less than 50 nm, and nearly vertical side walls along the entire height of the structures can be produced [19]. LIGA parts typically have 1–10- μm minimum lateral feature sizes, and are from hundreds of micrometers to a few millimeters thick.

2.2. e-Beam Lithography and FIB Lithography

Particle-beam lithography includes techniques that use a focused beam of ions or electrons to write directly into resists or parallel beams combined with stencil masks. FIB lithography and e-beam lithography are resist-based techniques used to generate ultrasmall structures. The process steps are essentially the same as those described for X-ray lithography and photolithography, except that the pattern on the resist can also be obtained by scanning the focused particle beam directly across the surface. This means that the desired structure is written directly into the resist by computer-controlled electromagnetic deflection of the particle beam. Positive or negative resist systems exist [20]; they may be organic or inorganic layers [21]. The dose required to expose resist with ions in terms of $\mu\text{C}/\text{cm}^2$ is usually about two orders of magnitude lower than the dose required for exposure by electrons. This is due to the fact that ions in the 30–200-keV energy range lose most of their energy in the resist, whereas electrons in the 20–100-keV range penetrate deep into the substrate and lose only a small fraction of their energy in the resist. The mechanism of ion exposure of resists is mainly determined by the energy that is transferred from the ions to the electrons in the resist (electronic stopping power) [22]. As mentioned, instead of using a focused beam to expose the resist, it is also possible to use an unfocused beam in conjunction with a stencil mask; in this case, one speaks of electron or ion projection lithography. This

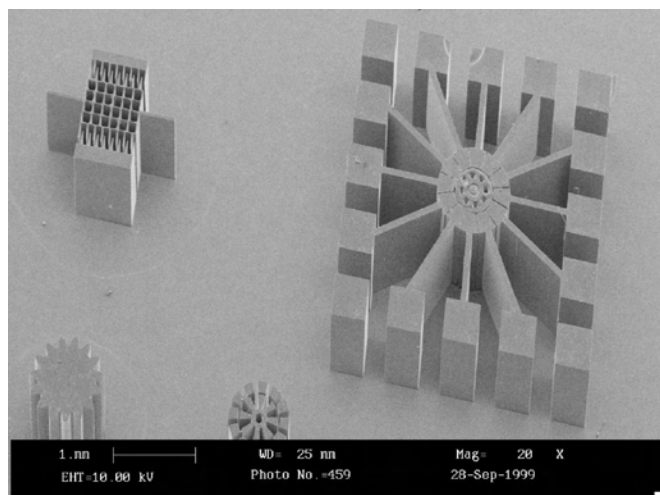


Figure 2. Several microcomponents obtained by LIGA. High-aspect-ratio microstructures in SU-8 resist (height 730 μm) (total scanning/exposure time \approx 2 min; dose \approx 20 J/cm^2). Courtesy of the Synchrotron Radiation Source at Daresbury, UK.

approach can produce features as small as 50 nm [23] and permits a high sample throughput. Because of their excellent resolution, these techniques are possible candidates for sub-100-nm lithography.

E-beam lithography followed soon after the development of the scanning electron microscope (SEM) [24] in 1955 and was one of the earliest processes used for IC fabrication, dating back to 1957 [25]. The key role of e-beam writing in the process is to generate the masks that are used in optical exposure systems (as well as X-ray systems). The actual high-volume device production down to sub-half-micrometer feature size is mainly done with optical systems to expose the whole wafer through masks. However, in specific cases of low-volume manufacture of ultrasmall features for very high-performance devices or prototypes, direct e-beam writing in photoresists is also occasionally used. In addition, there is some activity in so-called mix-and-match lithography, in which the e-beam system is used to expose one or a few levels with especially small features, and optical systems are used for the larger features of the pattern. For all of these reasons, e-beam systems play a significant role in today's advanced manufacturing.

Electron- and ion-based approaches have different advantages over light. In addition to their high resolution, the techniques also do not suffer from optical thin-film interference effects. However, disadvantages of the techniques are that, because of direct writing, they are far too slow for large-throughput production [26]. A weak point of e-beam lithography is electron scattering, which leads to exposure of the photoresist to scattered electrons. A dense array of features may catch enough scattered electrons to seriously overexpose the resist. As a consequence, the resolution of the process is strongly affected by this so-called proximity effect [27–29].

Both approaches (e-beam and FIB lithography) principally can be used in combination with metal electrodeposition to fabricate very small structures (in the sub-100-nm range). Electroplating has been demonstrated to be an alternative to other techniques in the 20-nm scale, including lift-off techniques (see, e.g., [30, 31]). The conventional procedure starts with the deposition of a thin (20 nm) film of chromium or gold (acting as an adhesion and contact layer) on Si or SiO_2 . Then, spin-coated resist is exposed with the use of e-beam or FIB lithography and developed. Subsequently, metal is electrodeposited in the holes formed in the resist. Depending on the electroplating conditions, relatively high-aspect-ratio structures can also be obtained, as shown in Figure 3.

Except for more recent reports of atomic resolution with a proximal probe [32], the resolution of e-beam lithography has been unsurpassed by any other form of lithography.

2.3. STM/AFM Tip-Based Lithography

Patterning of resists can also be carried out with scanning probe techniques (STM/AFM)—in fact, scanning probe lithographies are part of the most promising nanoscale methods [33], as sensitization of a resist layer can be done with a sub-100-nm lateral resolution with the use of various types of scanning probe microscopies.

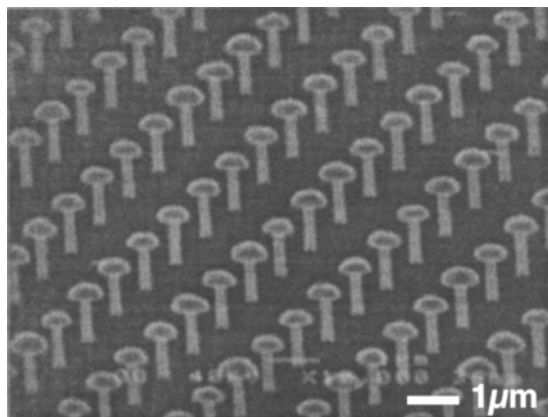


Figure 3. “Mushroom” structures of Au, electrodeposited into e-beam patterned resist. Reprinted with permission from [31], W. Xu et al., *J. Vac. Sci. Technol., B* 13, 2372 (1995). © 1995, American Vacuum Society.

The interactions between the tip of the scanning probe and some sort of resist are typically e-beam based (using the tip as a field emitter) or due to mechanical interaction (scratching).

2.3.1. Electrical Interactions

Scanning probe microscopes can be used for low-voltage e-beam lithography. This was first demonstrated by applying a low voltage between the STM tip and a sample covered with a thin resist layer [34]. With a sharp tip, a highly localized electric field is created at the tip apex and the resist layer. The resist is sensitized, inducing a chemical transformation of the layer. After postexposure bake, the resist layer is developed and chemical or electrochemical reactions can be triggered at the exposed locations with a high lateral resolution. With this technique, it is possible to create 10–20-nm-wide patterns in the resist layer and 20-nm-wide final structures.

This low voltage (5–50 eV) lithography has a better resolution because electrons do not scatter far in the resist layer. The first attempts to use this technique were made in an ultrahigh vacuum (UHV) chamber to avoid dielectric breakdown and hydrocarbon contamination. Noncontact field-emission-mode STM lithography therefore has the drawback of a tedious sample transfer. Moreover, the alignment process is difficult because the imaging process can also lead to resist sensitization. Therefore, contact [35] and noncontact [36] AFM with a conductive tip was explored as an alternative method of exposing a resist layer in air. Usually less than 100 nm thick, resist layers are employed because under these conditions electrons have a low penetration depth. PMMA or other commercial resist films are used in these lithographic processes.

Other sensitive layers can be used, such as self-assembled monolayers (SAMs) (e.g., (aminoethylaminoethyl)-phenylethyl diamine (PEDA); 4-chloromethylphenyl trichlorosilane (CMPTS); trimethylsilyl (TMS)) [37–39] or Langmuir-Blodgett films [40] deposited on semiconductor or metallic surfaces. As already said, the energy of electrons emitted from the tip in STM lithography is low, and there is no

additional focusing device to control the e-beam geometry. Therefore, the smaller the tip-substrate distance, the higher the resolution. In this context, SAMs are very interesting sensitive films, as the distance can be decreased to one molecular monolayer. A two-step process has been proposed [38] in which deposition of a catalyst (Pd) occurs only at the exposed area of the SAM, and selective Ni electroless deposition takes place on the Pd-covered locations, leading to nanometer-scale nickel patterns.

It has also been reported [41] that SAM sensitization can be performed by *in-situ* degradation due to electrochemical reactions induced at the junction between a conductive AFM probe and a monolayer-covered Si sample, leading to nanostructures as shown in Figure 4.

2.3.2. Mechanical Interactions

Sohn and Willet have developed a technique in which a nonconductive tip is used to plough through a layer of a spin-coated resist [42]. After development of the sensitized resist, metallic nanowires (width of 40 nm) can be created. The linewidths can be varied by changing the resist layer thickness, the force, and the development time. With the same approach another group uses an AFM tip to engrave a narrow groove in the top layer of a polyimide film [43] and used this for a mask in an evaporation process. This leads to metallic structures with a 40-nm linewidth. In the same family of patterning procedure, a two-layer resist system consisting of a very thin Ti layer covering a thin PMMA film was used to produce 20-nm-wide structures [44]. The top Ti layer locally scratched by a sharpened AFM tip and the Ti pattern are transferred successively to the PMMA layer and the substrate by reactive ion etching (RIE).

Another technique is based on the creation of nanometer-scale scratches through a thin oxide layer (native or thermal oxide film) covering a silicon surface [45]. The results show clearly that the oxide film acts as a highly efficient mask for the electrochemical deposition, while the scratches are activated locations. Under optimized conditions sub-100-nm metallic structures can be obtained with a very high selectivity on both p- and n-type silicon. Figure 5 shows electrodeposited gold lines on p-Si (the Si is covered by a 10-nm-thick oxide layer that was scratched with an AFM).

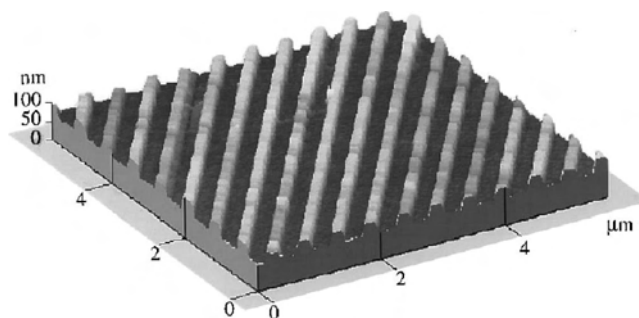


Figure 4. AFM image of etched grooves. This AFM patterning was conducted in 60% relative humidity air at a sample bias of 120 V with a probe scan rate of 500 $\mu\text{m/s}$. The etching was performed for 3 min. Reprinted with permission from [41], H. Sugimura et al., *J. Vac. Sci. Technol., B* 14, 4140 (1996). © 1996, American Vacuum Society.

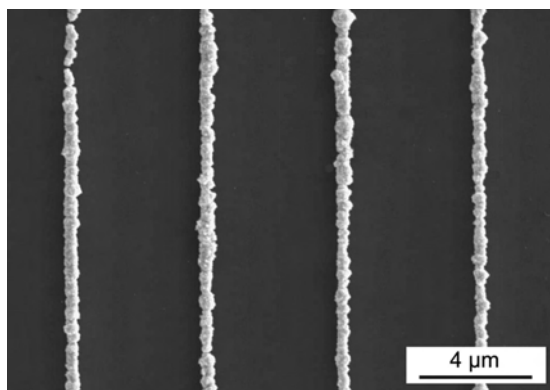


Figure 5. Scanning electron microscope view of Au lines electrochemically deposited on oxide-covered p-Si carrying an array of AFM scratches. Unpublished, from L. Santinacci.

It is noteworthy that AFM scratching and indentation were first used to probe the mechanical properties of the surface and to directly nanomachine surfaces. Hardness, Young's modulus of elasticity, friction coefficient, wear resistance, and adhesion are properties that can now be investigated at the nanometer scale [46].

Even if scanning probe lithography has opened new perspectives through the fabrication of nanosize structures, it suffers the drawbacks of being slow and limited to small areas. Large-scale patterning has recently been proposed [47, 48]. The concept is based on an array of tips mounted on independent piezoresistive cantilevers that are simultaneously used to sensitize the surface. Rapid and centimeter-scale depassivation of a H-terminated silicon surface has been performed (compare Section 3.2), opening perspectives on the use of this multiprobe technique in combination with the SPM-based processes described above. Alternatively, to overcome the writing speed problem of SPM lithographies, it was also proposed that photolithography and AFM lithography be combined [49].

3. DIRECT WRITING APPROACHES

3.1. Nanostructuring with the Electrochemical Scanning Tunneling Microscope

Similar to the UHV-STM, the electrochemical STM (EC-STM) was used in the beginning to map surfaces (topology) directly in the electrolyte (*in-situ*). But already in 1987, the first surface modifications with EC-STM were reported when a substrate surface was patterned in the electrolyte by the application of a voltage pulse and a few nanometer-size holes were achieved in the surface [50]. Lebreton and Wang used a STM in a humid nitrogen atmosphere to create holes in a gold surface [10]. They assumed the presence of water or ethanol and therefore that the reaction was electrochemical. Similar investigations were performed on graphite substrates [51, 52], and holes on Highly Ordered Pyrolytic Graphite (HOPG) surfaces were used as nucleation sites for preferential electrodeposition of metals [53, 54]. Schuster performed "nanoscale electrochemistry" [55] by applying short voltage pulses (100 ns) to a gold substrate in a

copper-containing electrolyte. Depending on the polarity of the pulses, local gold oxidation or copper deposition can be achieved with a lateral dimension of less than 10 nm. Tip-induced deposition of monoatomic high Pd clusters on Pt and Au can be achieved with the application of a tip potential that is slightly negative to the substrate potential [56]. Local dissolution of a copper surface due to electron transfer to the STM tip with the application of a positive potential to the STM tip has been reported [57].

A very reproducible way of producing large numbers and arrays of nanometer-sized clusters was introduced as "tip-induced metal deposition" by Kolb and co-workers in 1993 [58, 59]. They discovered that certain potential steps performed with the EC-STM in the tunneling mode lead to nucleation of small crystallites beneath the STM tip [60]. After optimization, the technique could be used as described in Figure 6 [61]. In a first step, the material to be deposited on the substrate is deposited electrochemically on the apex of the STM tip by the application of a potential slightly negative to the Nernst potential for metal deposition. The tip is then brought close to the surface. At a certain distance, the attractive interaction leads to a jump-to-contact, and a connective neck is formed between the tip atoms and the substrate. When the tip is retracted the connective neck breaks and leaves a small cluster on the surface. The clusters are usually two to four atomic layers in height and are imaged with a lateral width of 6–10 nm. The atomic movement during the jump-to-contact has been simulated for UHV conditions [62, 63] and for the electrochemical Cu/Au(111) system [64]. The simulations confirmed stable metal clusters on the surface when the tip was moved slightly farther than the point of jump-to-contact and assuming underpotential layers to be present on the surface. In the meantime, the generation of large cluster arrays has been shown [65] (see Fig. 7), and the process has been applied to form stable metal clusters made of Pd, Ag, or Pb on various substrates such as Au(111), Au(100), and Ag(111) as well as thiol-covered Au(111) (see, e.g., [66, 67]). In the system Cu/Ag(111), two-dimensional islands were generated by this method [66]. For Ni/Au(111), the production of holes instead of deposition was reported [68]. Up to now, tip-induced metal deposition failed to generate clusters on semiconductor surfaces, as a strong interaction between substrate and tip seems to be a necessary precondition for cluster stability. The stability of these metal nanoclusters has been subject to various studies and has been ascribed to quantum confinement effects [69] or, alternatively, to tip/substrate alloy formation effects [70]. It is noteworthy that under *ex-situ* conditions the decay of such nanoclusters can take place on a time scale of days [71].

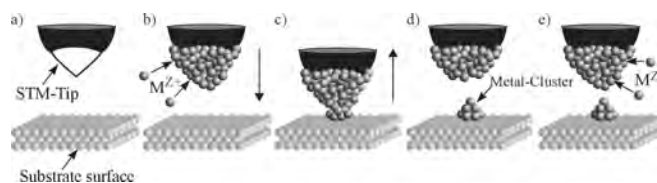


Figure 6. Schematic diagram of the tip-induced metal deposition from a metal-covered STM tip to the substrate, caused by an appropriate tip approach (after [61]).

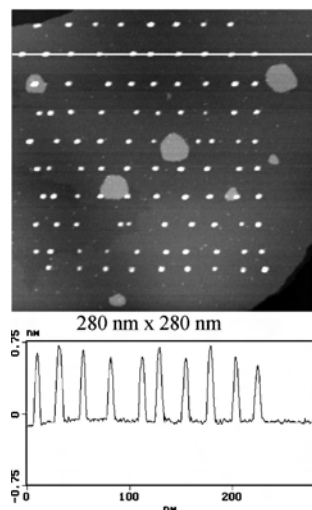


Figure 7. Array of tip-induced Cu clusters on Au(111) and cross sections along marked lines. Taken *in-situ* in 0.05 M $\text{H}_2\text{SO}_4/0.5$ mM CuSO_4 at 10 mV vs. Cu/Cu^{2+} . Reprinted with permission from [71], S. Maupai et al., *Electrochem. Solid State Lett.* 5, C35 (2002). © 2002, Electrochemical Society.

Another method for depositing metallic nanostructures on semiconductor surfaces consists of a two-step process [72]. In a first step, metal, for example, is electrochemically deposited on the STM tip. In a second step, the metal is dissolved by the application of a very positive potential pulse. As the applied substrate potential is held cathodic, a small cluster can be electrochemically deposited on the substrate surface. This method was recently successfully used to generate Pb and Co nanostructures on Si(111) [72, 73]. A variation of the Kolb's tip-induced method was recently used to generate single Pd clusters in Pd-free electrolyte [74] to investigate the properties of single catalytic active clusters by their readiness to reduce hydrogen [75].

3.2. Other Scanning Probe Techniques

Other ways to directly use AFM or STM to create nanoscale patterns on surfaces have been explored. Figure 8 shows nanometer-scale Si structures made by using a conductive AFM tip to write anodic surface oxide on H-passivated Si(100) [76]. The same effect can also be obtained with an STM [77]. Typically, the different chemical reactivity between the substrate and the oxidized locations is utilized for subsequent patterning by wet etching [76, 78] or reactive ion etching (RIE) [79]. The structured surface, however, can also be used as a template for selective deposition [80, 81]. This technique has been successfully employed to pattern semiconductors such as GaAs and GaSb [82, 83]; to selectively oxidize metals such as Ti [84], Cr [85], and Al [86]; and to convert thin dielectric layers such as Si_3N_4 into SiO_2 [87, 88]. Applications such as single-atom point contact devices [89], sub-10-nm scaled field emission transistors [90, 91], single-electron transistors [92], and InAs/AlGaSb heterostructures have been produced. It is noteworthy that using a conducting AFM tip instead of a STM tip offers the advantage that the sensitization process (applied voltage) is decoupled from the feedback control.

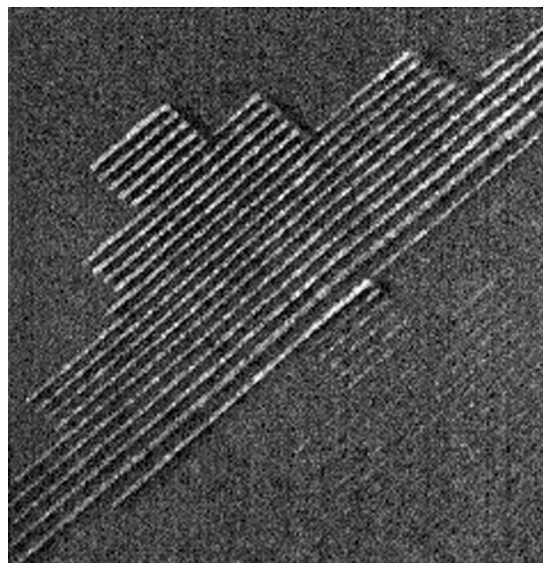


Figure 8. 5×5 μm AFM image of a 120-nm-pitch oxide pattern written by AFM. Local anodic oxidation in air leads to depassivation and oxide formation on H-terminated Si. The top half of the pattern was written at 2.5 V, the bottom position at 1.5 V. The shortest lines were written at $1 \mu\text{m/s}$, and the longest at $10 \mu\text{m/s}$. Reprinted with permission from [76], E. Snow and P. M. Campbell, *Appl. Phys. Lett.* 64, 1932 (1994). © 1994, American Institute of Physics.

Other scanning probes can also be used for patterning. In the scanning electrochemical microscope (SECM), the Faradaic current is used as a local tool [93, 94]. Here the tip is used for localized electrochemistry, as first demonstrated by Bard's group by depositing 200-nm-wide lines of gold or silver on a metallic surface [95]. The amount of Faradaic current depends on the tip-sample distance and on the redox reaction taking place between the tip and the sample. This setup was successfully used to modify electrode surfaces not only by deposition but also by electrochemical etching processes [96–99]. Replacement of the electrolyte with a thin conductive polymer film made it possible to achieve metal structures of copper, silver, or gold with dimensions of about 100 nm [100, 101]. It is possible to increase the resolution of the SECM with a chemical lens, a scavenger that reacts with the tip-generated species, which produces a significant focusing effect on the diffusion field [102].

Recently a new three-dimensional submicrometer machining process based on electrochemical reactions between a scanning tool electrode and the machined surface was also reported [103]. Ultrashort voltage pulses (10 ns) were applied between the tool and the sample. During this short time, double-layer charging occurs only in the region close to the tool electrode, and electrochemical reactions are restricted to areas beneath the tool electrode. With this technique it is possible to perform a local dissolution of metallic and semiconductive surfaces and to selectively deposit metals on silicon.

With the blocking current characteristic of a p-type semiconductor immersed in an electrolyte, it is also possible to obtain light-induced submicrometer electrochemical metal deposition on p-Si with an *in-situ* scanning near-field optical

microscope (SNOM) [104]. The optical tip of the near-field device is used to project light and thereby generate the local photocurrent that triggers the electrochemical reactions.

Local deposition in the submicrometer range with a small capillary tip filled with a metal-containing electrolyte as a probe was also reported [105]. Only the exposed area—limited by the capillary diameter (500 nm)—was in contact with the solution. In this way, copper dots with diameters of 400 nm were electrodeposited on polycrystalline Au surfaces.

3.3. e-Beam or FIB-Induced Deposition

Electron or ion beams can be used to write solid deposit patterns directly on surfaces. Depending on the nature of the particles, electrons, or ions, these techniques are called e-beam-induced deposition (EBID) and focused ion beam-induced deposition (FIBID). The principle is based on the focused particle beam-induced decomposition of adsorbed precursor molecules introduced into the vacuum chamber of the particle-beam instrument. Generally, precursor species that are intentionally injected are CH_4 for diamond-like carbon formation or metallorganic compounds such as $\text{W}(\text{CO})_6$, $\text{Fe}(\text{CO})_5$, AuClPF_3 , and $\text{Rh}_2\text{Cl}_2(\text{PF}_3)_4$ for metal deposition [106, 107]. These techniques are used as a single-step, direct-writing approach.

FIBID can include the deposition of a structure [108, 109] or a local etch [110, 111]. Deposited structures may either be used directly or act as etch resist layers. The second case is called ion-assisted etching: the presence of a reactive gas combined with energetic ions leads to an improved sputter rate.

EBID is more frequently used than FIBID and can be carried out in a conventional or modified SEM or transmission electron microscope (TEM). In general, the materials obtained with EBID show nanocomposite structures with metal nanocrystals of variable size embedded in an amorphous carbon matrix. The metal content of the deposits can be varied depending on the conditions involved during the deposition, such as the type of precursor molecules and the electron current. Consequently, the chemical composition, structure, and physical properties (e.g., electrical conductivity) of such structures can be modified. Since EBID offers the combination of high resolution and 3D structure formation, the technique has found interest particularly in the field of nanodevice development. EBID has recently been used for making special high-aspect-ratio carbon tips for AFM, X-ray mask repair [112], micro-electrical devices [113], micro-field emitters [114, 115], for microswitches [113], conducting lines [116], and defining photonic crystals [117].

A particular use of EBID is its application in combination with electrochemical processes. It has been demonstrated that e-beam deposited carbon contamination patterns only 1 nm in thickness can block electrochemical reactions completely and selectively [118]. The e-beam activates the decomposition of residual hydrocarbon molecules present in the vacuum chamber of the e-beam instrument. The result is a solid, carbon-rich, electrically insulating deposit in the irradiated area. It locally suppresses electrochemical reactions such as the electrodeposition of various materials, including metals and semiconductors [119, 120]. Alternatively, etching

processes such as the formation of porous Si can be masked [121]. Typically, the process can be used to create patterns in the 100-nm range. An example of such nanostructures in the sub-100-nm range is shown in Figure 9.

3.4. FIB Defect or Implant Writing

Because of the direct and highly localized interaction of impinging ions with the substrate, FIBs are frequently used to directly modify material surfaces. Different effects can be achieved by ion bombardment. Depending on the particle energy, ion implantation or surface sputtering can be dominant with the FIB. Ion implantation (typically carried out with energies of several 10 to several 100 keV) is for used, for instance, to locally introduce doping species in a semiconductor. Through self-implantation (e.g., Si^{2+} ions in Si) the main effect is defect creation in the substrate (vacancy-interstitial pairs). At lower energies (typically several 100 to 10 keV), sputtering is dominant.

With the use of a FIB, precise control over all three dimensions is available, and complicated structures can be micromachined by surface sputtering [122–124]. Structures obtained in this way can also be used as micro-imprinting tools [125–127], where either a reactive precursor or the final material is placed on the nano-imprinting tool.

In conjunction with electrochemistry, ion beams can be used to locally change the electrochemical properties of the substrate. It has been observed that ion-beam-induced damage makes semiconductors polarized under blocking conditions more susceptible to electrochemical reactions. This is due to a lowering of the material's Schottky barrier breakdown potential (see Fig. 10). This has been used to locally trigger dissolution reactions on different semiconductors. In Figure 11a an example is shown where selectively within a self-implanted area porous silicon has been formed

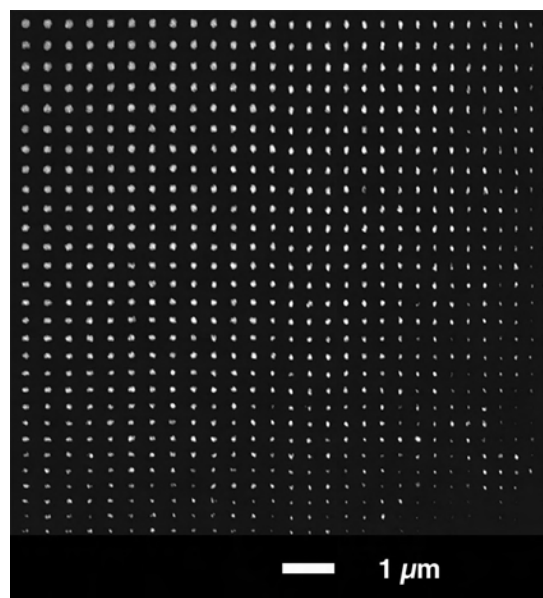


Figure 9. SEM image of gold dots produced by electrodeposition on carbon contamination patterned surface. Contamination patterning was carried out by e-beam writing at 5 keV. Unpublished, from T. Djenizian.

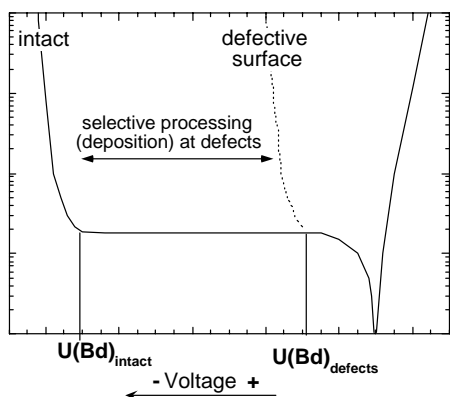


Figure 10. Schematic current density vs. voltage curve for intact and ion-implanted p-Si. Schottky barrier breakdown (and deposition) occurs earlier at defect sites. Reprinted with permission from [130], P. Schmuki and L. E. Erickson, *Phys. Rev. Lett.* 85, 2985 (2000). © 2000, Elsevier Science.

[128, 129]. Later it was also shown that the same FIB sensitization technique can be used to electrodeposit different metals (Cu, Au, Pd, Ni) directly on the damage sites with a resolution of up to 100 nm (see Fig. 11b) [130, 131].

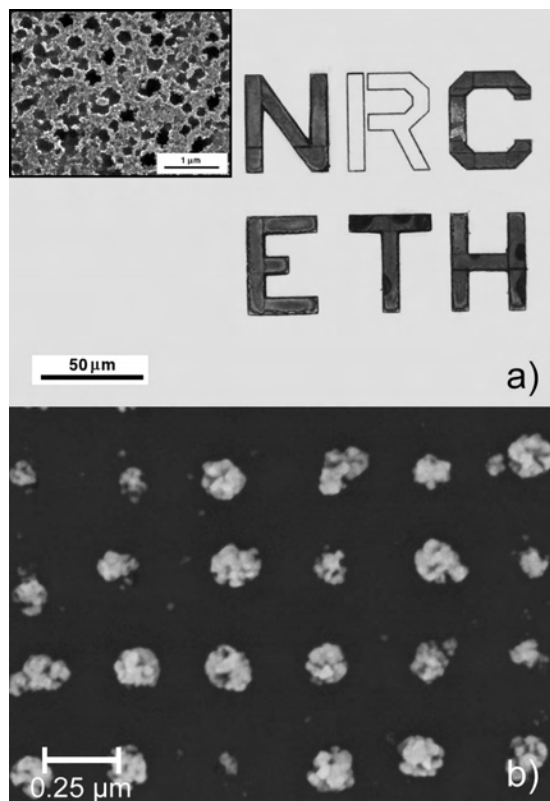


Figure 11. Examples for selective mask and resistless electrochemistry on Si. (a) Porous Si (selective etching) indicating formation of porous, photoluminescent silicon patterns with a resolution in the sub-100-nm region. Reprinted with permission from [128], P. Schmuki et al., *Phys. Rev. Lett.* 80, 4060 (1998). © 1998, American Physical Society. (b) Cu deposits (selective deposition); conditions: $5 \cdot 10^{13}$ Xe⁺/cm²¹ implanted at 75 keV; electrochemistry: 3 s at -2500 mV in 0.05 M H₂SO₄ + 0.01 M CuSO₄ + 0.1 mM BTA. Reprinted with permission from [130], A. Spiegel et al., *Thicroelectron. Eng.*, in press (2003). © 2003, Elsevier Science.

For selective porosification, n-type semiconductors are used (as they show a blocking behavior for anodic polarization). At defect sites, deblocking occurs and charge carriers are available for anodic dissolution of the substrate (e.g., Si in a HF-containing electrolyte). For the selective deposition of metals on semiconductors, p-doped semiconductors have to be used, as they block cathodic polarization.

The opposite approach is used when implanted species are used as etch stoppers. It is well known that dopants such as B and Ga act as effective etch barriers; this effect has been used to obtain Si microstructures delimited by B- or Ga-implanted areas [132–134]. The effect can be enhanced when a photoelectrochemical etch is used; in this case, only very low doses (5×10^9 Ga⁺/cm²) are needed for a selective etch behavior [135]. Interestingly, a similar approach can be used to selectively etch n-GaAs after implantation with Be, Si, or Au ions [136] or to etching p-InP after Ga⁺ implantation [137]; in both cases, the implanted species act as etch barriers.

Electrochemical techniques can also be used to obtain depth profiles of implanted species. This process, called delineation, is quite important for the semiconductor industry, as precise knowledge of the distribution of implanted species is often needed. In this case electrochemistry is used to selectively etch either the substrate or the implanted species. The advantage is that the concentration selectivity can be controlled precisely. Delineation is used for quality control and device characterization [138, 139] as well as to produce working devices [140].

3.5. Micro-Contact Printing

Micro-contact printing belongs to the so-called soft lithography techniques and was developed by Whitesides [141]. An elastomeric stamp or mold, previously shaped on a master, transfers the pattern to the substrate [142]. The master is produced with any serial technique and can contain details in the sub-100-nm range. Micro-contact printing was first demonstrated for SAMs of alkanethiolates on gold and has been extended to other SAM systems [142]. Patterned SAMs can be used as ultrathin resists in selective wet etching or as templates to control wetting, dewetting, nucleation and growth, and deposition of other materials. At present, micro-contact printing is used in different fields, including plastic electronics, integrated optics, microreactors, micromechanics, and MEMS. Sub-micrometer-scale structures have also been fabricated with micromolding in capillaries (MIMIC). Interconnected channels are formed between the stamp and the substrate and filled with a fluid (such as a polymer) via capillary action. After crystallization of the fluid, the stamp is removed, leaving microstructures on the surface [143].

4. SELF-ASSEMBLY AND TEMPLATES

In view of technical applications, nanostructuring techniques that are based on self-organization are very promising, because processes are often of a parallel nature. In combination with electrochemistry, a whole range of approaches have found recent research interest, such as the formation of ordered porous materials or electrodeposition in self-organized templates.

4.1. Porosification of Semiconductors

Large efforts regarding nanostructuring approaches are based on porosification of semiconductors, because of the highly interesting and novel properties of porous semiconductors, such as visible photoluminescence observed for “nanoporous” silicon. Even though porosification can be achieved for many semiconductors (see, e.g., [144, 145]), porous silicon has clearly been a focus of research interest—this of course is due to the dominant role of silicon in IC technology.

Porous silicon is typically produced by electrochemical etching in HF solutions. Generally, electrochemical anodization of semiconductors leads to either an oxidation or a material dissolution process. This dissolution can be homogeneous (electropolishing) or selective (porosification). Selective dissolution typically occurs when, except for the direct anodic dissolution reaction, a current-limiting factor also is present on the semiconductor surface. For n-type semiconductors under anodic bias (in the dark), this current limiting factor is often the blocking space charge layer—the so-called Schottky barrier—formed in the semiconductor in contact with an electrolyte. Dissolution of n-type semiconductors can be carried out under illumination or at sufficiently high potentials (in the dark), leading to breakdown of the Schottky barrier [146].

For p-type semiconductors or n-type semiconductors under illumination and under anodic polarization, the current flow is not limited by the space-charge layer in the semiconductor. In this case, surface reactions such as oxide formation, “hydrogen passivation,” or formation of fluorotransition-state complexes may be rate limiting. In such cases, at sufficiently low anodic potentials, porosification is possible. At higher anodic voltages, such as for Si in HF electrolytes, electropolishing instead of pore formation takes place.

Pore morphology depends on many experimental parameters, such as the dopant type and doping density, the electrolyte, and the electrochemical conditions (e.g., potential and duration of polarization [e.g., 147, 148]).

Basically three different pore morphologies can be distinguished: macroporous systems contain pores with a diameter greater than 100 nm, and micropores have diameters of some nanometers. Between these, one speaks of mesoporous systems. For example, Figure 12 shows a TEM image of microporous p-type Si. The coral-like microstructure of the material is seen to be composed of highly interconnected micropores and a network of the remaining Si structure with typical features in the size range of 2 nm [144]. On the other hand, Figure 13 shows an SEM image of macroporous Si. Highly ordered formation of macropores can be achieved if the surface is first lithographically prepatterned with etch pits (these etch pits serve as highly defined nucleation sites for pore growth) [149, 150]. Subsequent pore formation is then carried out with the use of n-type material and backside illumination. Pore widths are obtained in the range from 0.5 to 10 μm , whereas pore depths up to several 100 μm (through an entire wafer) can be achieved. If the “initiating” etch pits are ordered in arrays, highly ordered arrays of macropores can be produced. The pore growth direction is

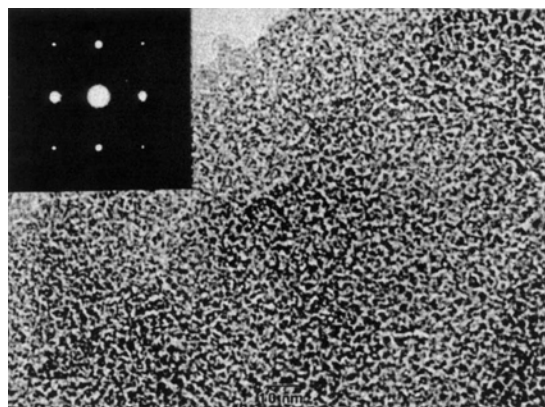


Figure 12. TEM image and diffraction pattern (inset) showing a typical morphology of microporous Si formed by anodizing p-Si in HF. Reprinted with permission from [144], A. G. Cullis et al., *J. Appl. Phys.* 82, 909 (1997). © 1997, American Institute of Physics.

controlled to a large extent by the crystal orientation. Different models have been suggested to explain the initiation and growth of micro- and macropores in silicon (see [151]).

For n-type semiconductors in the dark, selective porosification of the surface can be achieved by presensitization of surface locations with FIB damage writing [129] (see Section 3.4 and Fig. 11a).

As mentioned, nanostructures with a feature size typically smaller than 50 nm can show a whole range of unusual mechanical, electrical, optical, or magnetic properties that are tailored by their own size. For semiconductors quantum confinement effects can lead to a widening of the bandgap. Therefore, microporous semiconductors may show novel optical properties due to this effect (e.g., bulk Si shows no visible photoluminescence (PL), whereas porosified Si can show strong visible PL). Classically, the major interest in porous semiconductors stems from such modified optical properties. Nevertheless, apart from optoelectronic applications, porous semiconductors have also attracted interest for use in many new type of applications, such as lift-off

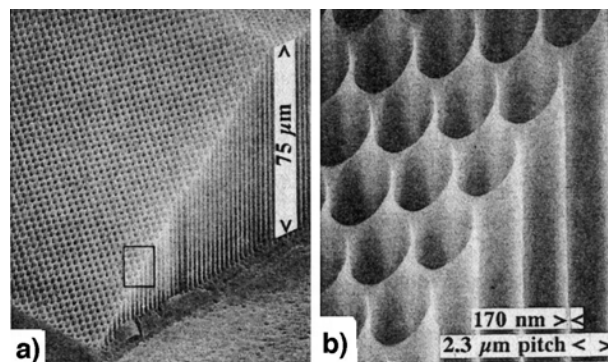


Figure 13. Scanning electron micrographs of a patterned and micro-machined layer of macroporous silicon forming a two-dimensional triangular lattice. A tenfold magnification of the inset in (a) is shown in (b). The edges of the bars were formed by micromechanical etching of the layer. The lattice constant of the macropore array is 2.3 μm , the pore diameter 2.13 μm , and the thinnest parts of the walls are 170 nm. Reprinted with permission from [150], U. Gruning et al., *Appl. Phys. Lett.* 68, 747 (1996). © 1996, American Institute of Physics.

processes for silicon-on-insulator (SOI) technologies [152, 153] and the fabrication of crystalline thin-film Si solar cells [154]. Lately, biology and medicine have become areas of interest in the research on porous semiconductors, in as much as, for example, porous silicon is biocompatible and biodegradable and hence devices based on porous Si could be used for *in vivo* applications [155].

4.2. Porous Alumina as Nanotemplates

Porous alumina layers can be produced by anodization of aluminum in a suitable acidic solution (e.g., sulfuric, phosphoric, or oxalic acid). (An alternative nonelectrochemical method is to press pure alumina powder into disks and sinter it [156]; however, anodization is the more common process.) Typically, anodization of aluminum in the previously-mentioned solutions leads to a formation of disordered porous alumina arrays. Under specific, optimized conditions, however, self-organized structures with an ordered array of uniform-size pores can be achieved [157–159]. Typically, the ordered domains are in the micrometer range. To control pore configuration and periodicity, pre patterning of the Al surface can be used [160], similar to the approach used to produce ordered macroporous silicon. For Al, typically pre patterning is carried out by nanoindentation with the use of a SiC mold with a hexagonally arranged array of pins, formed by e-beam lithography. The shallow indents act as initiation sites for pore formation, and an ordered configuration of channels with a high aspect ratio is produced by subsequent anodization. This process permits a low-cost, high-throughput mass production of ordered nanochannels because the pre patterning process by nanoindentation is simple and fast, and the mold for nanoindentation can be used more than several tens of times. The porous alumina layers produced by anodic oxidation show a packed array of columnar hexagonal cells with central, cylindrical, uniformly sized holes. The Al substrate can be subsequently removed by dissolving it in suitable solutions (e.g., in saturated HgCl_2) to produce porous alumina membranes. An example of such a porous alumina structure is shown in Figure 14.

To use the porous alumina membranes as a template for electrochemical deposition, typically a thin metal layer is evaporated on one side of the porous structure. This metal layer serves either as a catalyst for a subsequent electroless metal deposition step or as a contact for an electrochemical, pore-filling deposition.

Many types of nanocomposites have been fabricated with anodic porous alumina templates. For the preparation of magnetic recording media [161, 162], optical devices [163], functional electrodes [164, 165], and electrochromic [166] or electroluminescence display devices [167], the pores in alumina are filled with a range of metals or semiconductors (for an overview see, e.g., [168, 169]).

On the other hand, the honeycomb structure of anodic porous alumina can also be used as a mold for the fabrication of highly ordered material nanopore arrays by a multiple-step replication [170, 171]. In this approach, a typical sequence consists of first producing a PMMA replica of the porous structure. This can be achieved by injecting the metacrylate monomer into the alumina structure (that is, one side metal covered) followed by UV polymerization [171]. After dissolution of the Al_2O_3 —typically in

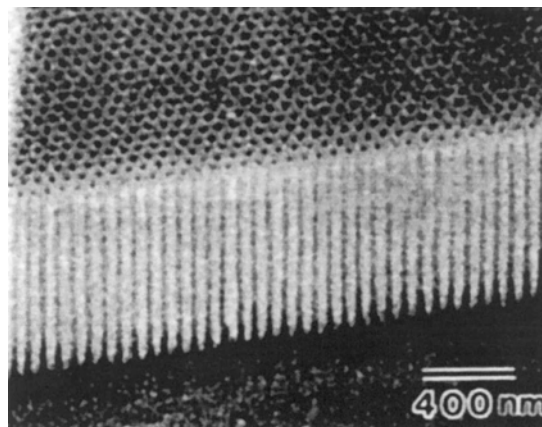


Figure 14. Cross-sectional SEM view of anodic porous alumina. The observation was carried out from the bottom of the porous alumina after removal of the Al and bottom oxide layer. Al was removed by etching in saturated HgCl_2 , and the bottom part of the porous alumina was immersed in 5 wt% phosphoric acid at 30 °C for 25 min. Reprinted with permission from [160], H. Asoh et al., *J. Vac. Sci. Technol., B* 19, 569 (2001). © 2001, American Vacuum Society.

NaOH —metals such as Pt or Au may be deposited around the PMMA template, leading to pore arrays. Fabrication of a Pt pore structure is typically carried out by electroless deposition, with the use of a catalytic metal layer on the PMMA. Then the Pt deposition starts at the bottom part of the PMMA structure and the Pt gradually fills in the cavities. For deposition of Au, typically an electrochemical process is used, with the metal layer on the PMMA as an electrode [171]. An important aspect that distinguishes this two-step method from the conventional one-step pore-filling method is that it permits a full replication of the pore array of anodic porous alumina with desired materials. In this way, it is possible to overcome the disadvantages of using porous alumina, which include insufficient chemical and thermal stability and low mechanical strength [171]. The latter is particularly a problem for very thin (e.g., 10 nm) porous alumina layers.

There has been great interest in the deposition of specific superlattice structures in porous templates. Superlattices are, for example, metal films consisting of alternating layers of ferromagnetic metal and a nonmagnetic metal that exhibit “giant magnetic resistance” (GMR) when the layer thickness is on the order of the appropriate electron mean free path, a few tens of nanometers [172]. An example of electrodeposited nanowires [173, 174] is shown in Figure 15. The nanowires consist of a stack of disks of alternating composition that were deposited in a nanoporous aluminum oxide membrane [175]. Thin permalloy ($\text{Py} = \text{Ni}_{81}\text{Fe}_{19}$) and Fe networks with new magnetic and magneto-transport properties have also been produced in this manner [176].

4.3. Nuclear Track-Etched Membranes as Nanotemplates

One restriction on the use of porous alumina membranes as templates is the limited adjustability of the pore diameter. To overcome this limitation, micro- and nanoporous polymer

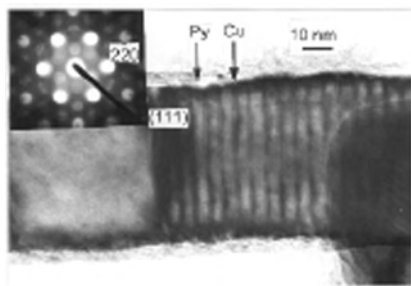


Figure 15. Bright-field TEM images of Permalloy (Py)/Cu multilayer nanowire showing the chemical modulation. The inset shows a diffraction image indicating that single-crystal order across several compositional layers is obtained and thus a “true” superlattice is present. Reprinted with permission from [175], J.-L. Maurice et al., *J. Magn. Magn. Mater.* 184, 1 (1998). © 1998, Elsevier Science.

membranes prepared by nuclear track etching are widely used as templates.

Ion tracks, formed by the interaction of energetic charged particles with matter, have played an important role in the development of modern physics. Tracks of heavy ions in insulators have been investigated for more than three decades. More recently, MeV-GeV ion track production has been used to modify materials in a controlled manner [177–179] and to serve as a tool to engineer material properties at the nanometer to micrometer scale. It has been long known that for polymers a single ion impact can be sufficient to trigger a subsequent chemical (etching) reaction preferentially at the ion track.

Therefore the production of single isolated tracks, but also many overlapping tracks, can be used to modify the physical and chemical properties of polymers. Even more importantly, with the use of an adequate etchant, it is possible to dissolve the chemically modified material in the track at a much higher rate than the undamaged matrix. Hence, chemical etching of defect paths in insulators (e.g., polymers) can be used to produce membrane filters with extremely fine (and straight) pores.

To create nanopores the material is most typically exposed to α -particles emitted from nuclear reactions. The particles initiate damage tracks—with typical energies this leads to damage that is approximately 10 μm deep into the material (e.g., mica, polycarbonate, silica glass, etc.), and after chemical or electrochemical etching of these damage tracks, an array of nanopores will be obtained. These nanopores are randomly distributed, but the morphology and the pore diameter (10 nm to 1 μm) is adjusted by a variation of the chemical and the radiation parameters, and the pore density (1 mm^{-2} to 10^6mm^{-2}) is controlled by the radiation dose (impact density) [182].

The nanotemplates of nuclear track-etched membranes are used, for instance, for the production of nanowires, such as multi- or monolayered Co/Cu, Bi, or Ni nanowires, by electrodeposition from aqueous solutions [183–185]; the nanowires produced in this way have a structure similar to that shown in Figure 15. For Co/Cu nanowires, a thin Cu layer (0.3 μm) is sputter-deposited onto one side of the

membrane and used as the working electrode in a standard three-electrode electrochemical cell (for Bi or Ni nanowires, a thin Au layer is deposited). The production of multilayered nanowires is possible because of the different deposition potentials and the different deposition rates (e.g., in 400-nm pores, the deposition rate of Co is about 60 $\text{\AA}/\text{s}$, ≈ 15 times higher than that of Cu; therefore only a small amount of Cu is codeposited in the Co layer [183]). After the template material (e.g., polycarbonate for Co/Cu and Bi or mica for Ni) is removed in a suitable solution, free-standing nanowires are left. Figure 16 shows SEM and TEM images of a membrane and a single nanowire. As mentioned before, the nanowires show physical properties different from those of corresponding bulk materials. For instance, Bi nanowires show a very large positive magnetoresistance with quasilinear field dependence [184]; for Ni nanowires a reduction of Curie temperature as a function of the nanowire diameter has been observed [185].

Not only porous alumina or track-etched membranes are used as a template or host material; nanochannel glass (NCG) is also used for the fabrication of composites of NCG nanowires and metals [186, 187]. Other materials also have the potential to be used as nanotemplates for electrochemical deposition reactions, such as zeolites [188] or, even more promising, opal with voids in the 50- to 150-nm range that can be filled by various routes (see, e.g., [189]).

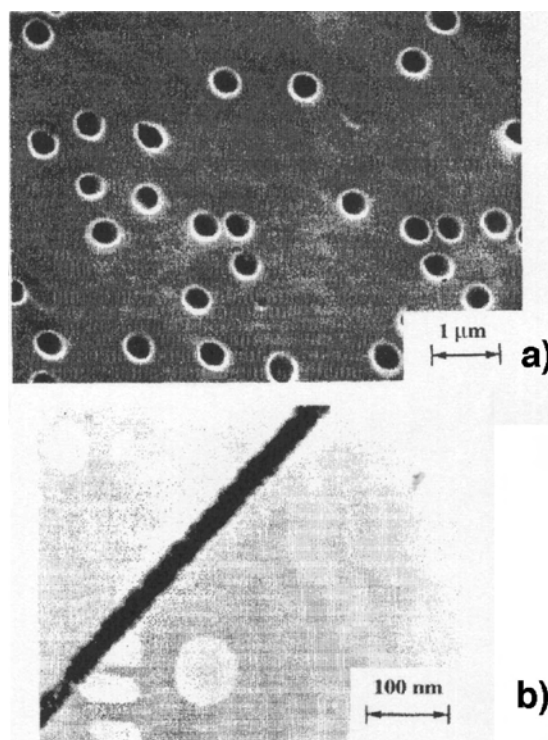


Figure 16. (a) Top-view SEM image of a track-etched polymer membrane with 400-nm-diameter pores. (b) TEM picture of a free-standing 30-nm-diameter nanowire with a layered structure [Co(50 \AA)/Cu(20 \AA)]. Reprinted with permission from [183], K. Liu et al., *Phys. Rev. B* 51, 7381 (1995). © 1995, American Physical Society.

4.4. Nanospheres as Templates

For selective dissolution/porosification or deposition on a nanoscale, it is also possible to build up masks on the surface by other approaches. These masks can be made, for instance, with polymer films (mask aligning) or carbon layers (e-beam lithography). Another possibility for the creation of structurally anisotropic nanoparticles on the surface is nanosphere lithography (NSL). The principle is that the natural self-assembly of a monolayer of nanospheres forms a hexagonally close-packed crystal [190]. Deposition of material (metals) through this colloidal crystal mask, with subsequent removal of the nanospheres, results in an array of evenly spaced, homogeneous nanoparticles known as a periodic particle array (PPA) [191, 192]. The dimensions of these truncated tetrahedral nanoparticles can be tuned by choice of nanosphere diameter and deposition thickness [193]. It is possible to vary the shape of the deposited particle array by forming a double-layer (DL) polymer colloid mask instead of a single-layer mask. The nanosphere lithography mask is created by spin coating of, for example, polystyrene nanospheres onto the substrate of interest. The nanospheres, as a suspension in water, are diluted in a solution before spin coating. The subsequent metal deposition can be carried out by PVD [191] or by electrochemical [194] techniques. Following the metal deposition, the nanospheres can be dissolved in an appropriate solution (e.g., CH_2Cl_2 for polystyrene). The deposited material that penetrates the three-dimensional openings of the single-layer mask remains on the substrate forming the single monolayer PPA pattern. To create a double-layer nanosphere lithography mask, a more highly concentrated suspension of nanospheres is used. Figure 17 shows the schematic procedure of SL and DL nanosphere lithography (images A, B, D, and E) as well as AFM micrographs of the resulting nanoparticle arrays (images C and F). The particle dimensions of the deposited arrays are defined by the mask geometry. Such periodic particle array patterns can be formed on insulator, semiconductor, and metal substrates [191]. For an additional control of the structure size of the deposited particle arrays, the nanosphere arrays can be thinned with RIE [195].

4.5. Atomic-Scale Templates

Atomic-scale inhomogeneities on surfaces can in some cases be exploited to trigger an electrochemical reaction. Typically the reactive sites have either long-range order or statistical distribution. Selective electrodeposition of mesoscale particles was studied in detail by Penner et al. [196, 197]. They managed to deposit metal and nanoparticles that are narrowly dispersed in diameter on graphite basal plane surfaces. In this approach first a voltage pulse with high overpotential is applied for nucleation, and then a second pulse is applied to grow the particles slowly to the desired size. A subsequent chemical conversion led to semiconductor nanocrystals (ZnO [198], CuI [199], and CdS [200]). The chemical transformation involves the oxidation of the metal nanoparticle to the metal oxide and the displacement of the oxide with an anion.

Other attempts to control the crystal size to tailor optoelectronic properties of electrodeposited quantum dots

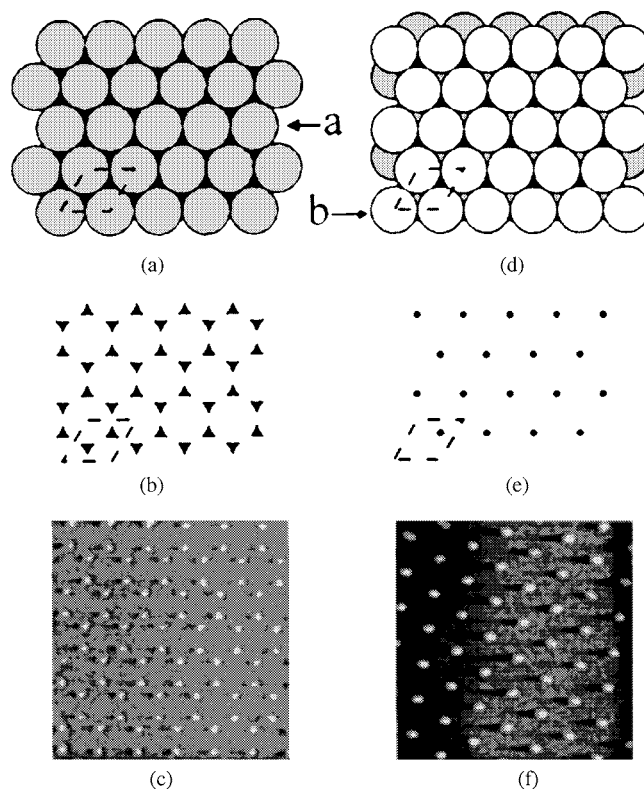


Figure 17. Schematic diagram of single-layer (SL) and double-layer (DL) nanosphere masks and the corresponding periodic particle array (PPA) surfaces. (A) A SL mask. Dotted line = unit cell, a = first layer nanosphere. (B) SL PPA, two particles per unit cell. (C) $1.7 \times 1.7 \mu\text{m}$ constant-height AFM image of a SL PPA with M (deposited metal) = Ag, S (substrate) = mica, D (diameter of nanosphere) = 264 nm, d_m (thickness of deposited metal) = 22 nm, r_d (deposition rate) = 0.2 nm/s. (D) A DL mask. Dotted line = unit cell, b = second layer nanosphere. (E) DL PPA, one particle per unit cell. (F) $2.0 \times 2.0 \mu\text{m}$ constant-height AFM image of a DL PPA with M = Ag, S = mica, D = 264 nm, d_m = 22 nm, r_d = 0.2 nm/s. Reprinted with permission from [191]. J. C. Hulsteeen and R. P. Van Duyne, *J. Vac. Sci. Technol., A* 13, 1553 (1995). © 1995, American Vacuum Society.

were made by Hodes et al. [201–203]. They used chemical and electrochemical deposition techniques to epitaxially deposit CdSe/Au, Cd(Se,Te)/Au, CdSe/Pd, CdS/Au, CdS/Pd, and CdSe/Au-Pd. Nanocrystals with diameters between 2 and 10 nm with controlled spatial distribution and narrow size distribution have been obtained. Effects of semiconductor lattice spacing, substrate lattice spacing, and deposition current on the size distribution and coverage with semiconductor nanocrystals were investigated. The authors also demonstrated size effects on the optical properties of the nanoparticles [201].

A novel type of site-selective nucleation at overpotentials was reported for the systems Ni/Au(111) [204, 205] and Ru/Au(111) [206] demonstrating similarities between electrochemical nucleation and growth and UHV deposition observations [207, 208]. In both cases, the energetically heterogeneous sites of the substrate were used as an atomic-scale template. In the case of Ni deposition regularly spaced monoatomic high islands were achieved by nucleating at “elbow” sites of a reconstructed Au(111) surface. In

the latter case the nucleation of Ru started almost exclusively at the fcc regions rather than at the “elbow” sites of the reconstructed Au(111) surface. Recently site-selective nucleation was also found in the underpotential region for Cd on Au(111) [209]. The first nuclei of Cd can be observed at potentials 300–400 mV positive of the Nernst potential for Cd bulk deposition, decorating exclusively the “elbow” sites and the parallel reconstruction rows (see Fig. 18).

In contrast to those purely electrochemical techniques, structured layers have also been used as atomic-scale templates to obtain periodic arrays *in-situ*. Spatz et al. developed a method to obtain a two-dimensional array of Au clusters on any flat substrate, using Au-containing micelles that are adsorbed regularly on the surface [210, 211]. The diameter of the Au clusters could be adjusted between 1 and 15 nm by using different Au concentrations as electrolytes. The distance between the particles (30–140 nm) could be adjusted by using copolymers of different lengths. Sleytr et al. used proteins, so-called S-layers, as templates for ordered metal deposition [212, 213]. A monolayer of the protein was adsorbed on a surface, and the nanocompartments of the layer were filled with H₂AuCl₄ solution. After reduction of the Au and denaturation of the protein, an array of 4–5-nm Au clusters was obtained.

Several factors act simultaneously to produce a self-assembly made of nanoparticles in 2D and 3D superlattices. A low dispersity in particle size and strong enough interactions between particles are required to induce such organization. Self-organization has been observed, for example, for metallic gold or silver [214, 215], AgS [216], and CdSe [217] nanoparticles with diameters between 2 and 6 nm, that are stabilized and coated with surfactants.

Self-assembly can also be used for a layer-by-layer deposition. This has been reported, for example, for polyelectrolyte-semiconductor nanoparticles in which the surfactant or polyelectrolyte is cationic and the semiconductor particles are negatively charged [218].

5. LAYERED NANOSTRUCTURES

5.1. Monolayers

Almost 20 years ago it was discovered [219] that when gold is immersed in a dilute organosulfur (thiol) solution an organic monolayer is spontaneously chemisorbed on the surface of the gold, producing a SAM. Perhaps the best characterized

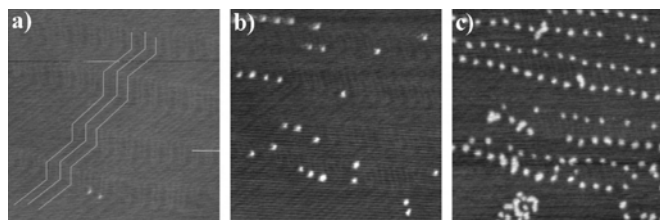


Figure 18. Self-organized underpotential nucleation of Cd on Au(111), starting at elbow sites of herringbone reconstruction (100 nm × 100 nm). Images were taken at (a) 330 mV, (b) 250 mV, (c) 220 mV vs. E⁰(Cd/Cd²⁺). Reprinted with permission from [209], S. Maupai, Y. Zhang and P. Schmaki, *Electrochem. Solid State Lett.* 6, 63 (2003). © 2003, Electrochemical Society.

SAM system is CH₃(CH)_{*n*-1}SH(C_{*n*}) adsorbed on a Au surface. The C_{*n*}/Au system, specifically its surface and chain orientation, has been widely studied [220–223]. These studies clearly show that the S end of the chains is strongly adsorbed to the Au surface and that the chains are highly oriented and densely packed. The number of the *gauche* defects is insignificant. Such homogeneous, well-ordered, and defined electrochemical interfaces find applications in basic and applied research fields ranging from charge transfer studies to coatings potentially useful for reaction inhibition, wear protection, and organic sensors [224].

SAMs, Langmuir-Blodgett multilayers, and Langmuir monolayers have also been used successfully to direct the nucleation and growth of co-aligned crystals. The structure of the organic substrate can be tailored to define the size, shape, and orientation of the growing crystals.

Electrochemical metal deposition on alkanethiol SAMs has been reported in several studies (e.g., [225–227]). Central questions address the interactions between deposit and functional groups of the SAM, the nucleation and growth mode of the metal on the modified surface, and the configuration of the deposit. Short-chain alkanethiol SAMs are much more pervious to ion penetration than long-chain thiol SAMs. *In-situ* STM imaging for copper electrodeposition on such SAMs shows a two-dimensional growth on short alkane thiols and dithiols in the overpotential region, followed by sudden and fast three-dimensional growth [228].

Examples of oriented growth of inorganic crystal films on SAMs can be found for zeolites [229] and oriented ceramic films [230], where the organic multilayers were prepared on gold substrates by adsorption and then chemically modified. The crystal growth was then induced by immersing the sample in a “reaction solution.”

Langmuir monolayers that are formed at the air-liquid interface are another attractive organic matrix for the study of nucleation and growth of a variety of nanocrystalline materials. Langmuir monolayers have been successfully employed to direct the growth of semiconductors as PbS, CdS, or PbSe [231]. The process is to spread the organic surfactant on a metal ion solution in a Langmuir trough. After the surfactant is compressed at a selected surface pressure, the trough is exposed to reactant gas (e.g., H₂S or H₂Se). Diffusion of the gas through the monolayer results in the precipitation of semiconductor particles. A similar process can be used to investigate the biomineralization of different carbonates and sulfates under such a monolayer [232].

Covalently attached organic monolayers on semiconductor surfaces are an emerging area of research in the field of nanoelectronics. Recently, different strategies have been developed to covalently attach organic monolayers to silicon surfaces under various conditions: thermal, electrochemical, photochemical, and catalytic (see, e.g., [233, 234]). These organically modified surfaces are extremely stable in aqueous environments and well passivated and could also be used as resist.

The convergence of surface science and organic chemistry opens new opportunities for the development of new concepts for the design of molecular-scale devices and for the integration of hybrid structures with biologically active

interfaces. Organic monolayers covalently attached to silicon surfaces display various advantages compared with self-assembled monolayers of alkanethiols on gold surfaces and silane monolayers on silicon oxide (SiO_2) that are based on the fact that the Si—C bond is very stable.

5.2. Superlattices

Multiple, alternating thin layers of two different materials are generally called multilayers. Superlattices are a particular type of crystalline multilayer structure in which there is coherent stacking of atomic planes, and periodic modulation of the structure or composition, or both [235]. Electrodeposition became an interesting alternative in the preparation of multilayers and superlattices not only because of the low cost of the equipment required, but also because it may be used in geometries where conventional deposition processes would fail. Whereas dual-bath deposition is the simpler method to design, single-bath deposition is generally used for architectures with a large number of layers or with a very small modulation wavelength. In the single-bath technique the precursor for the layer that is deposited at low overpotentials (layer A) is used in a low concentration compared with that of the precursor for the layer that is deposited at higher overpotentials (layer B). At low overpotentials the deposition is mass-transport-controlled (deposition of layer A), and at higher potentials the mass-transport-limited current is much smaller than the kinetically controlled current, depositing almost pure component B. The superlattice or multilayer can be deposited by pulsing the applied potential or current.

A number of groups have developed methods to electrodeposit metallic superlattices with individual layers as thin as a few Ångströms from a single electrolyte. Examples are Co-Ni-Cu multilayers on Cu [236], Co-Cu on GaAs [237], or other GMR structures discussed in Section 4.2. A review of electrodeposited multilayers for GMR applications is given by Schwarzacher and Lashmore [238].

In addition to metallic multilayers, superlattices of semiconductors and metal oxide ceramics can be deposited by an oscillating electrochemical system. Stickney and co-workers have developed an electrochemical method analogous to molecular beam epitaxy called electrochemical atomic layer epitaxy or ECALE [239, 240]. With automated ECALE, atomic layers of two elements like Cd and Te can be alternately electrodeposited by underpotential deposition to form thin layers of CdTe [241].

Ceramic superlattices based on Tl(III) oxide and a number of other metal oxides were reported recently by Switzer et al. as so-called defect chemistry superlattices [242]. The superlattices are similar in concept to doping on compound semiconductors. It was found that the defect chemistry is a function of applied overpotential: high overpotentials favor oxygen vacancies, whereas low overpotentials favor cation interstitials.

Metal oxide multilayers of cuprous oxide were produced by spontaneous potential oscillations when a fixed current density was applied. Evidence for quantum confinement in the layers was observed by measuring negative differential resistance (NDR) [243].

GLOSSARY

Atomic force microscope A type of microscope in silicon chip which a small probe, consisting of a tiny chip of diamond, is held on a spring-loaded cantilever in contact with the surface of the sample. The probe is moved slowly across the surface and the tracking force between the tip and the surface is monitored. The probe is raised and lowered so as to keep this force constant, and a profile of the surface is produced. Scanning the probe over the sample gives a computer-generated contour map of the surface. The instrument is similar to the scanning tunneling microscope but uses mechanical forces rather than electrical signals. It can resolve individual molecules and, unlike the scanning tunneling microscope, can be used with nonconducting samples, such as biological specimens.

Electrochemistry The study of chemical properties and reactions involving ions in solution, including electrolysis and electric cells. Electrochemistry is concerned with the study of the interface between an electronic and an ionic conductor and, traditionally, has concentrated on (i) the nature of the ionic conductor, which is usually an aqueous or (more rarely) a nonaqueous solution, polymer, or superionic solid containing mobile ions; (ii) the structure of the electrified interface that forms on immersion of an electronic conductor in an ionic conductor; and (iii) the electron transfer processes that can take place at this interface and the limitations on the rates of such processes. Electrochemical processes of high technological significance include dissolution (e.g., corrosion) reactions and deposition (e.g., electrodeposition) reactions.

Ion beam Stream of confined ions accelerated by electromagnetic fields. Typically extracted from a liquid metal tip or from a plasma source. The accelerated ions can be focused by electromagnetic lenses to a focal point in the range of several nanometers. Used for high-resolution cutting, sputtering, or ion implantation.

Scanning tunneling microscope A type of microscope in which a fine conducting probe is held close to the surface of a sample. Electrons tunnel between the sample and the probe, producing an electrical signal. The probe is slowly moved across the surface and raised and lowered so as to keep the signal constant. A profile of the surface is produced, and a computer-generated contour map of the surface is produced. The technique is capable of resolving individual atoms but works better with conducting materials.

Synchrotron A particle accelerator used to impart energy to electrons and protons to carry out experiments in particle physics and in some cases to make use of the synchrotron radiation produced. The particles are accelerated in closed orbits (often circular) by radiofrequency fields. Magnets are spaced around the orbit to bend the trajectory of the particles, and separate focusing magnets are used to keep the particles in a narrow beam. The radiofrequency accelerating cavities are interspersed between the magnets. The motion of the particles is automatically synchronized with the rising magnetic field, as the field strength has to increase as the particle energy increases; the frequency of the accelerating field also has to increase synchronously.

REFERENCES

1. N. V. Parthasaradhy, "Practical Electroplating Handbook." Prentice Hall, Englewood Cliffs, NJ, 1989.
2. G. O. Mallory and J. B. Hadju, Eds., "Electroless Plating, Fundamentals and Applications." American Electroplaters and Surface Finishers Society, Orlando, FL, 1990.
3. D. Edelstein, J. Heidenreich, R. Goldblatt, W. Cote, C. Uzoh, N. Lustig, P. Roper, T. McDevitt, W. Motsiff, A. Simon, J. Dukovic, R. Wachnick, H. Rathore, R. Schulz, L. Su, S. Luce, and J. Slatery, *Tech. Dig. IEEE Int. Electron Devices Meet.* 773 (1997).
4. L. T. Romankiw and E. J. M. O'Sullivan, *SPIE Int. Soc. Opt. Eng.* 197 (1997).
5. P. C. Andricacos, *Electrochem. Soc. Interface* 8, 32 (1999).
6. G. Binnig and H. Rohrer, *Helv. Phys. Acta* 55, 726 (1982).
7. G. Binnig, H. Rohrer, C. Gerber, and E. Weibel, *Phys. Rev. Lett.* 49, 57 (1982).
8. G. Binnig, C. F. Quate, and C. Gerber, *Phys. Rev. Lett.* 56, 930 (1986).
9. D. M. Eigler and L. K. Schweitzer, *Nature* 344, 524 (1990).
10. C. Lebreton and Z. Z. Wang, *Scanning Microsc. J.* 8, 441 (1994).
11. W. J. Lorenz and W. Plieth, Eds., "Electrochemical Nanotechnology." Wiley-VCH, Weinheim, Germany, 1998.
12. J. H. Fendler, "Nanoparticles and Nanostructured Films." Wiley-VCH, Weinheim, Germany, 1998.
13. G. Hodes, Ed., "Electrochemistry of Nanomaterials." Wiley-VCH, Weinheim, Germany, 2001.
14. S. P. Murarka and M. C. Peckerar, "Electronic Materials, Science and Technology." Academic, San Diego, 1998.
15. E. Spears and H. I. Smith, *Electron Lett.* 8, 102 (1972).
16. T. Ueno and J. R. Sheats, in "Microlithography, Science and Technology." Dekker, New York, 1998.
17. R. DellaGuardia, C. Wasik, D. Puisto, R. Fair, L. Liebman, J. Rocque, S. Nash, A. Lamberti, G. Collini, R. French, B. Vampatella, G. Gifford, V. Nastasi, P. Sa, F. Volkringer, T. Zell, D. Seeger, and J. Warlaumont, *Proc. SPIE* 2437, 112 (1995).
18. E. W. Becker, W. Ehrfeld, P. Hagmann, A. Manner, and D. Munchmeyer, *Microelectron. Eng.* 4, 35 (1986).
19. C. R. Friedrich, R. Warrington, W. Bacher, W. Bauer, P. J. Coane, J. Güttert, T. Hanemann, J. Hausselt, M. Hecke, R. Knitter, J. Mohr, V. Pieter, H. J. Ritzhaupt-Kleiss, and R. Ruprecht, *SPIE Int. Soc. Opt. Eng.* 299 (1997).
20. Y. Yamaoka, T. Goto, M. Nakao, S. Kanemaru, and J. Itoh, *Jpn. J. Appl. Phys.* 1 34, 6932 (1995).
21. T. Ohta, T. Kanayama, and M. Komuro, *Microelectron. Eng.* 6, 22 (1987).
22. J. F. Ziegler, J. P. Biersack, and U. Littmark, "The Stopping and Range of Ions in Solids." Pergamon, New York, 1985.
23. J. Melngailis, A. A. Mondelli, I. L. Berry III, and R. Mohondro, *J. Vac. Sci. Technol., B* 16, 927 (1998).
24. K. C. A. Smith and C. W. Oatley, *Br. J. Appl. Phys.* 6, 391 (1955).
25. D. A. Buck and K. Shoulders, "Proceedings of the Eastern Joint Computer Conference," ATEE, 1957.
26. H. C. Pfeiffer and W. Stikel, *Microelectron. Eng.* 27, 143 (1995).
27. L. D. Jackel, R. E. Howard, P. M. Mankiewich, H. G. Craighead, and W. Epworth, *Appl. Phys. Lett.* 45, 698 (1984).
28. H. Schmoranzler, *J. Vac. Sci. Technol., B* 6, 2053 (1988).
29. M. Parikh and D. F. Kyser, *J. Appl. Phys.* 50, 1004 (1979).
30. G. Simon, A. M. Haghiri Gosnet, F. Carcenac, and H. Launois, *Microelectron. Eng.* 35, 51 (1997).
31. W. Xu, J. Wong, C. C. Cheng, R. Johnson, and A. Scherer, *J. Vac. Sci. Technol., B* 13, 2372 (1995).
32. D. M. Eigler and E. I. Schweizer, *Nature* 344, 524 (1991).
33. C. R. K. Marrian, "Technology of Proximal Probe Lithography." SPIE Press, Bellingham, WA, 1993.
34. E. A. Dobsiz and C. R. K. Marrian, *Appl. Phys. Lett.* 58, 2526 (1991).
35. A. Majumdar, P. I. Oden, J. P. Carrejo, L. A. Nagahara, J. J. Graham, and J. Alexander, *Appl. Phys. Lett.* 61, 2293 (1992).
36. K. Wilder, C. F. Quate, D. Adderton, R. Bernstein, and V. B. Elings, *Appl. Phys. Lett.* 73, 2527 (1998).
37. A. Kumar, H. A. Biebuyck, N. L. Abbott, and G. M. Whitesides, *J. Am. Chem. Soc.* 114, 9188 (1992).
38. C. R. K. Marrian, F. K. Perkins, S. L. Brandow, T. S. Koloski, E. A. Dobsiz, and J. M. Calvert, *Appl. Phys. Lett.* 64, 390 (1994).
39. F. K. Perkins, E. A. Dobsiz, S. L. Brandow, T. S. Koloski, J. M. Calvert, K. Rhee, J. Kosakowski, and C. R. K. Marrian, *J. Vac. Sci. Technol., B* 12, 3725 (1994).
40. L. Stockman, G. Neuttiens, C. Van Haesendonck, and Y. Bruynseraede, *Appl. Phys. Lett.* 62, 2935 (1993).
41. H. Sugimura, K. Okiguchi, and N. Nakagiri, *J. Vac. Sci. Technol., B* 14, 4140 (1996).
42. L. L. Sohn and R. L. Willet, *Appl. Phys. Lett.* 67, 1552 (1995).
43. V. Bouchiat and D. Esteve, *Appl. Phys. Lett.* 69, 3098 (1996).
44. S. Hu, S. Altmeyer, A. Hamidi, B. Spangenberg, and H. Kurz, *J. Vac. Sci. Technol., B* 16, 1983 (1998).
45. L. Santinacci, T. Djenizian, and P. Schmuki, *Appl. Phys. Lett.* 79, 1882 (2001).
46. B. Bhushan, "Handbook of Micro/Nanotribology." CRC Press, Boca Raton, FL, 1995.
47. S. C. Minne, S. R. Manalis, A. Atalar, and C. F. Quate, *J. Vac. Sci. Technol., B* 14, 2456 (1996).
48. S. C. Minne, J. D. Adams, G. Yaralioglu, S. R. Manalis, A. Atalar, and C. F. Quate, *Appl. Phys. Lett.* 73, 1742 (1998).
49. H. Sugimura and N. Nakagiri, *Jpn. J. Appl. Phys.* 36, L968 (1997).
50. J. Schneir and P. K. Hansma, *Langmuir* 3, 1025 (1987).
51. T. R. Albrecht, M. M. Dovek, M. D. Kirk, C. A. Lang, C. F. Quate, and D. P. E. Smith, *Appl. Phys. Lett.* 55, 1727 (1989).
52. C. F. Quate, in "Scanning Tunneling Microscopy and Related Methods" (R. J. Behm, N. Garcia, and H. Rohrer, Eds.), NATO ASI Series E: Applied Sciences, Vol. 184, p. 281. Kluwer Academic, Dordrecht, the Netherlands, 1990.
53. W. Li, J. A. Virtanen, and R. M. Penner, *Appl. Phys. Lett.* 60, 1181 (1992).
54. J. V. Zoval, R. M. Stiger, P. R. Biernacki, and R. M. Penner, *J. Phys. Chem.* 100, 837 (1996).
55. R. Schuster, V. Kirchner, X. H. Xia, A. M. Bittner, and G. Ertl, *Phys. Rev. Lett.* 80, 5599 (1998).
56. H. Naohara, S. Ye, and K. Uosaki, *Appl. Phys. A* 66, 457 (1998).
57. Z.-X. Xie and D. M. Kolb, *J. Electroanal. Chem.* 481, 177 (2000).
58. R. Ullmann, T. Will, and D. M. Kolb, *Chem. Phys. Lett.* 209, 238 (1993).
59. D. M. Kolb, R. Ullmann, and T. Will, *Science* 275, 1097 (1997).
60. N. Batina, T. Will, and D. M. Kolb, *Faraday Discuss.* 94, 93 (1992).
61. R. Ullmann, T. Will, and D. M. Kolb, *Ber. Bunsenges. Phys. Chem.* 99, 1414 (1995).
62. U. Landmann, W. Luedtke, N. A. Burnham, and R. J. Colton, *Science* 248, 454 (1990).
63. U. Landmann and W. D. Luedtke, *J. Vac. Sci. Technol., B* 9, 414 (1991).
64. M. G. Del Popolo, E. P. M. Leiva, and W. Schmickler, *Angew. Chem. Int. Ed.* 40, 4674 (2001).
65. G. E. Engelmann, J. C. Ziegler, and D. M. Kolb, *Surf. Sci.* 401, L420 (1998).
66. D. M. Kolb, R. Ullmann, and J. C. Ziegler, *Electrochim. Acta* 43, 2751 (1998).
67. J. C. Ziegler, G. E. Engelmann, and D. M. Kolb, *Z. Phys. Chem.* 208, 151 (1999).
68. D. M. Kolb, G. E. Engelmann, and J. C. Ziegler, *Solid State Ionics* 131, 69 (2000).
69. D. M. Kolb, G. E. Engelmann, and J. C. Ziegler, *Angew. Chem. Int. Ed.* 39, 1123 (2000).
70. S. Maupai, A. S. Dakkouri, M. Stratmann, and P. Schmuki, *J. Electrochem. Soc.* 150, C111 (2003).

71. S. Maupai, M. Stratmann, and A. S. Dakkouri, *Electrochem. Solid State Lett.* 5, C35 (2002).
72. R. T. Pötzschke, G. Staikov, W. J. Lorenz, and W. Wiesbeck, *J. Electrochem. Soc.* 146, 141 (1999).
73. W. Schindler, D. Hoffmann, and J. Kirschner, *J. Electrochem. Soc.* 148, C124 (2001).
74. M. D. Del Popolo, E. Leiva, H. Kleine, J. Meier, U. Stimming, M. Mariscal, and W. Schmickler, *Appl. Phys. Lett.* 81, 2635 (2002).
75. J. Meier, K. A. Friedrich, and U. Stimming, *Faraday Discuss.* 121, 365 (2002).
76. E. Snow and P. M. Campbell, *Appl. Phys. Lett.* 64, 1932 (1994).
77. A. Dagata, J. Schneir, H. Harary, C. J. Evans, M. T. Postek, and J. Bennett, *Appl. Phys. Lett.* 56, 2001 (1990).
78. P. M. Campbell, E. S. Snow, and P. J. McPharr, *Solid State Electron.* 37, 583 (1994).
79. S. C. Minne, P. Flueckiger, H. T. Soh, and C. F. Quate, *J. Vac. Sci. Technol., B* 13, 1380 (1995).
80. H. Sugimura and N. Nakagiri, *Appl. Phys. Lett.* 66, 1430 (1995).
81. E. P. Boonekamp, J. J. Kelly, L. G. J. Fokkink, and D. W. E. Vandenhoudt, *J. Electrochem. Soc.* 142, 519 (1995).
82. M. Ishii and K. Matsumoto, *Jpn. J. Appl. Phys.* 34, 1329 (1995).
83. S. Sasa, T. Ikeda, C. Dohno, and M. Inoue, *Jpn. J. Appl. Phys.* 6B, 4065 (1997).
84. H. Sugimura, T. Uchida, N. Kitamura, and H. Masuhara, *Appl. Phys. Lett.* 63, 1288 (1993).
85. H. J. Song, M. J. Rack, K. Abugharbieh, S. Y. Lee, V. Khan, D. K. Ferry, and D. R. Allee, *J. Vac. Sci. Technol., B* 12, 3720 (1994).
86. K. Matsumoto, M. Ishii, K. Segawa, Y. Oka, B. J. Vartanian, and J. S. Harris, *Appl. Phys. Lett.* 68, 271 (1996).
87. F. S.-S. Chien, J.-W. Chang, S.-W. Lin, Y.-C. Chou, T. T. Chen, and S. Gwo, *Appl. Phys. Lett.* 76, 360 (2000).
88. T. Yasuda, S. Yamasaki, and S. Gwo, *Appl. Phys. Lett.* 77, 3917 (2000).
89. E. S. Snow, D. Park, and P. M. Campbell, *Appl. Phys. Lett.* 69, 269 (1996).
90. P. M. Campbell, E. S. Snow, and P. J. McPharr, *Appl. Phys. Lett.* 66, 1388 (1995).
91. E. S. Snow and P. M. Campbell, *Science* 270, 1639 (1995).
92. K. Matsumoto, M. Ishii, and K. Segawa, *J. Vac. Sci. Technol., B* 14, 1331 (1996).
93. H.-Y. Liu, F. F. Fan, C. W. Lin, and A. J. Bard, *J. Am. Chem. Soc.* 108, 3838 (1986).
94. A. J. Bard, F. F. Fan, J. Kwak, and O. Lev, *Anal. Chem.* 61, 132 (1989).
95. R. F. Fan and A. J. Bard, *J. Electrochem. Soc.* 136, 3216 (1989).
96. C. W. Lin, F. F. Fan, and A. J. Bard, *J. Electrochem. Soc.* 134, 1038 (1987).
97. D. H. Craston, C. W. Lin, and A. J. Bard, *J. Electrochem. Soc.* 135, 785 (1988).
98. D. Mandler and A. J. Bard, *J. Electrochem. Soc.* 136, 3143 (1989).
99. D. Mandler and A. J. Bard, *J. Electrochem. Soc.* 137, 2468 (1990).
100. O. E. Hüßler, D. H. Craston, and A. J. Bard, *J. Vac. Sci. Technol., B* 6, 1873 (1988).
101. O. E. Hüßler, D. H. Craston, and A. J. Bard, *J. Electrochem. Soc.* 136, 3222 (1989).
102. K. Borgwarth and J. Heinze, *J. Electrochem. Soc.* 146, 3285 (1999).
103. R. Schuster, V. Kirchner, P. Allongue, and G. Ertl, *Science* 289, 98 (2000).
104. H. Diesinger, A. Bsiesy, and R. Hérimo, *J. Appl. Phys.* 90, 4862 (2001).
105. L. Staemmler, T. Suter, and H. Böhni, *Electrochem. Solid State Lett.* 5, C61 (2002).
106. F. Cicoira, Electron Beam Induced Deposition of Rhodium Nanostructures, Ph.D. thesis, Swiss Federal Institute of Technology, Lausanne, 2002.
107. P. Hoffmann, I. Utke, and F. Cicoira, 10th International Symposium, "Nanostructures: Physics and Technology," 2002.
108. H. D. Wanzenboeck, A. Lugstein, H. Langfischer, and E. Bertagnolli, *Mater. Res. Soc. Symp. Proc.* PV 624, 163 (2000).
109. H. D. Wanzenboeck, A. Lugstein, H. Langfischer, E. Bertagnolli, M. Gritsch, and H. Hutter, *IEE Conf. Pub.* 473, 485 (2000).
110. C. Flier, I. H. White, M. Kuball, P. J. Heard, G. C. Allen, C. Marinelli, J. M. Rorison, R. V. Penty, Y. Chen, and S. Y. Wang, *Mater. Res. Soc. Symp. Proc.* PV 537, 57 (1999).
111. Y. Lee Hyun, W. Paek Seung, J. Lee Young, and B. Chung Hong, *Proc. Int. Symp. Elec. Insul. Mater.* 151 (1998).
112. K. T. Kohlmann von Platen, M. Thiemann, and W. H. Bränger, *Microelectron. Eng.* 13, 279 (1991).
113. H. W. P. Koops, E. Munro, J. Rouse, J. Kretz, M. Rudolph, M. Weber, and G. Dahm, *Nucl. Instrum. Methods Phys. Res. B* 363, 1 (1995).
114. M. Weber, M. Rudolph, J. Kretz, and H. W. P. Koops, *J. Vac. Sci. Technol., B* 13, 461 (1995).
115. C. Schüssler and H. W. P. Koops, *J. Vac. Sci. Technol., B* 16, 862 (1998).
116. H. W. P. Koops, C. Schüssler, A. Kaya, and M. Weber, *J. Vac. Sci. Technol., B* 14, 4105 (1996).
117. H. W. P. Koops, *Proc. SPIE* 2849, 248 (1996).
118. T. Djenizian, L. Santinacci, and P. Schmuki, *Appl. Phys. Lett.* 78, 2840 (2001).
119. T. Djenizian, L. Santinacci, and P. Schmuki, *J. Electrochem. Soc.* 148, 197 (2001).
120. T. Djenizian, B. Petite, L. Santinacci, and P. Schmuki, *Electrochim. Acta* 47, 891 (2001).
121. T. Djenizian, L. Santinacci, H. Hildebrand, and P. Schmuki, *Surf. Sci.* 524, 40 (2003).
122. K. Gamo and S. Namba, *Microelectron. Eng.* 11, 403 (1990).
123. T. Kaito and T. Adachi, *Jpn. Soc. Prec. Eng.* 53, 857 (1987).
124. A. J. Steckl, S. Balakrishnan, H. S. Jin, and J. C. Corelli, *Microelectron. Eng.* 5, 23 (1986).
125. T. Chraska, M. J. Cabra, S. Mesarovic, D. M. Longo, E. A. Stach, J. C. Bean, and R. Hull, *Mater. Res. Soc. Symp. Proc.* PV 636, 362 (2001).
126. R. Hull and D. Longo, *Proc. SPIE Int. Soc. Opt. Eng.* 3975, 974 (2000).
127. R. Hull, T. Chraska, Y. Liu, and D. Longo, *Mater. Sci. Eng. C* C19, 383 (2002).
128. P. Schmuki, L. E. Erickson, and D. J. Lockwood, *Phys. Rev. Lett.* 80, 4060 (1998).
129. A. Spiegel, L. E. Erickson, and P. Schmuki, *J. Electrochem. Soc.* 147, 2993 (2000).
130. A. Spiegel, W. H. Bzuenger, C. Dzionk and P. Schmuki, *Thiroelectron. Eng.*, in press (2003).
131. A. Spiegel, L. Staemmler, M. Dobeli, and P. Schmuki, *J. Electrochem. Soc.* 149, C432 (2002).
132. B. Schmidt, L. Bischoff, and J. Teichert, *Sens. Actuators, A* 369 (1997).
133. J. Brugger, G. Beljakovic, M. Despont, N. F. de Rooij, and P. Vettiger, *Microelectron. Eng.* 35, 401 (1997).
134. W. Chen, P. Chen, A. Madhukar, R. Viswanathan, and J. So, *Mater. Res. Soc. Proc.* 279, 599 (1993).
135. K. D. Cummings, L. R. Harriott, G. C. Chi, and F. W. Ostermayer, Jr., *Proc. SPIE Int. Soc. Opt. Eng.* 93 (1986).
136. H. Arimoto, M. Kosugi, H. Kitada, and E. Miyauchi, *Microelectron. Eng.* 9, 321 (1989).
137. S. Rennon, L. Bach, H. König, J. P. Reithmaier, A. Forchel, J. L. Gentner, and L. Goldstein, *Microelectron. Eng.* 57 (2001).
138. G. D'Arrigo and C. Spinella, *Mater. Sci. Semicond. Proc.* 4, 93 (2001).
139. C. Spinella, *Mater. Sci. Semicond. Proc.* 1, 55 (1998).
140. G. Garozzo, A. La Magna, S. Coffa, G. D'Arrigo, N. Parasole, M. Renna, and C. Spinella, *Comp. Mater. Sci.* 24, 246 (2002).
141. Y. Xia, J. A. Rogers, K. E. Paul, and G. M. Whitesides, *Chem. Rev.* 99, 1823 (1999).

142. Y. Xia and M. W. Whitesides, *Angew. Chem. Int. Ed.* 37, 550 (1998).
143. E. Chim, Y. Xia, and M. W. Whitesides, *J. Am. Chem. Soc.* 118, 5722 (1996).
144. A. G. Cullis, L. T. Canham, and P. D. J. Calcott, *J. Appl. Phys.* 82, 909 (1997).
145. J. J. Kelly and D. Vanmaekelberg, in "Electrochemistry of Nanomaterials" (G. Hodes, Ed.), p. 103. Wiley-VCH, Weinheim, Germany, 2001.
146. P. Schmuki, L. E. Erickson, D. J. Lockwood, B. F. Mason, J. W. Fraser, G. Champion, and H. J. Labbe, *J. Electrochem. Soc.* 146, 735 (1999).
147. P. Schmuki, J. Fraser, C. M. Vitus, M. J. Graham, and H. S. Isaacs, *J. Electrochem. Soc.* 143, 3316 (1996).
148. P. Schmuki, L. Santinacci, T. Djenizian, and D. J. Lockwood, *Phys. Status Solidi A* 182, 51 (2000).
149. V. Lehmann, *J. Electrochem. Soc.* 140, 2836 (1993).
150. U. Gruning, V. Lehmann, S. Ottow, and K. Bush, *Appl. Phys. Lett.* 68, 747 (1996).
151. S. A. Campbell and H. J. Lewerenz, Eds., "Semiconductor Micro-machining," Vol. 1. Wiley, Chichester, UK, 1998.
152. T. Yonehara, K. Sakaguchi, and N. Sato, *Appl. Phys. Lett.* 64, 2108 (1994).
153. T. Yonehara, K. Sakaguchi, in "Proceedings of Pits and Pores II: Formation, Properties, and Significance for Advanced Materials" (P. Schmuki, D. J. Lockwood, Y. H. Ogata, and H. S. Isaacs), PV 2000-25, p. 313. Electrochemical Society, Pennington, NJ, 2001.
154. R. Brendel and R. Auer, "Porous Semiconductors—Science and Technology 2002 Book of Abstracts," I-5, 90-91, Puerto de La Cruz, 2002.
155. L. Canham and R. Aston, *Phys. World* 14, 27 (2001).
156. S. Chatterjee, S. Basu, D. Chattopadhyay, K. Kr. Mistry, and K. Sengupta, *Rev. Sci. Instrum.* 72, 2792 (2001).
157. A. Despic and V. P. Parkhutik, in "Modern Aspects of Electrochemistry" (J. O. Bockris, R. E. White, and B. E. Conway, Eds.), Vol. 20, Plenum, New York, 1989.
158. D. Al Mawiawi, N. Coombs, and M. Moskovits, *J. Appl. Phys.* 70, 4421 (1991).
159. H. Masuda, M. Yotsuya, M. Asano, K. Nishio, M. Nakao, A. Yokoo, and T. Tamamura, *Appl. Phys. Lett.* 78, 826 (2001).
160. H. Asoh, K. Nishio, M. Nakao, A. Yokoo, T. Tamamura, and H. Masuda, *J. Vac. Sci. Technol., B* 19, 569 (2001).
161. S. Kawai and R. Ueda, *J. Electrochem. Soc.* 122, 32 (1975).
162. M. Shiraki, Y. Wakui, T. Tokushima, and N. Tsuya, *IEEE Trans. Magn.* 21, 1465 (1985).
163. M. Saito, M. Kirihara, T. Taniguchi, and M. Miyagi, *Appl. Phys. Lett.* 55, 607 (1989).
164. C. J. Miller and M. Majda, *J. Am. Chem. Soc.* 112, 1795 (1990).
165. M. J. Tierney and C. R. Martin, *J. Electrochem. Soc.* 137, 3789 (1990).
166. T. Yoshino and N. Baba, *J. Chem. Soc. Jpn.* 1983, 955 (1983).
167. I. Mizuki, Y. Yamamoto, T. Yoshino, and N. Baba, *J. Metal Surf. Finish. Soc. Jpn.* 38, 561 (1987).
168. R. B. Wehrsporn, K. Nielsch, A. Birner, J. Schilling, F. Müller, A.-P. Li, U. Gösele, in "Proceedings of Pits and Pores II: Formation, Properties, and Significance for Advanced Materials" (P. Schmuki, D. J. Lockwood, Y. H. Ogata, H. S. Isaacs, Eds.), PV 2000-25, p. 168. Electrochemical Society, Pennington, NJ, 2001.
169. D. Routkevitch, T. Bigioni, M. Moskovits, and J. M. Xu, *J. Phys. Chem.* 100, 10037 (1996).
170. W. Schwarzacher, *Interface* 20 (1999).
171. H. Masuda, T. Mizuno, N. Baba, and T. Ohmori, *J. Electroanal. Chem.* 368, 333 (1994).
172. H. Masuda and K. Fukuda, *Science* 268, 1466 (1995).
173. L. Piraux, J. M. George, J. F. Despres, C. Leroy, E. Ferain, R. Legras, K. Ounadjela, and A. Fert, *Appl. Phys. Lett.* 65, 2484 (1994).
174. A. Blondel, J. P. Meier, B. Doudin, and J.-Ph. Ansermet, *Appl. Phys. Lett.* 65, 3019 (1994).
175. J.-L. Maurice, D. Imhoff, P. Etienne, O. Durand, S. Dubois, L. Piraux, J.-M. George, P. Galtier, and A. Fert, *J. Magn. Magn. Mater.* 184, 1 (1998).
176. K. Liu and C. L. Chien, *IEEE Trans. Magn.* 34, 1021 (1995).
177. R. Spohr, "Ion Tracks and Microtechnology." Vieweg, Braunschweig, 1990.
178. Proceedings of the First Conference of Ionizing Radiation and Polymers, *Nucl. Instrum. Methods Phys. Res. B* 105 (1995).
179. C. Trautman, *Nucl. Instrum. Methods Phys. Res. B* 105, 81 (1995).
180. C. R. Martin, *Chem. Mater.* 1996, 1739 (1996).
181. R. L. Fleischer, P. B. Price, and R. M. Walker, "Nuclear Tracks in Solids." University of California Press, Berkeley, CA, 1975.
182. P. Wanichapicharl, T. Chitrakarn, W. Sujaritturak, and H. G. Coster, *Sci. Asia* 26, 175 (2000).
183. K. Liu, K. Nagodawithana, P. C. Searson, and C. L. Chien, *Phys. Rev. B* 51, 7381 (1995).
184. K. Liu, C. L. Chien, P. C. Searson, and K. Yu-Zhang, *Appl. Phys. Lett.* 73, 1436 (1998).
185. L. Sun, P. C. Searson, and C. L. Chien, *Phys. Rev. B* 61, R6463 (2000).
186. R. J. Tonucci, B. L. Justus, A. J. Campillo, and C. E. Ford, *Science* 258, 783 (1995).
187. P. P. Nguyen, D. H. Pearson, R. J. Tonucci, and K. Babcock, *J. Electrochem. Soc.* 145, 247 (1998).
188. V. N. Bogomolov, *Sov. Phys. Uspekhi* 21, 77 (1978).
189. S. G. Romanov, D. V. Shamshur, and C. M. Sotomayour Torres, in "Quantum Confinement: Quantum Wires and Dots" (M. Cahay, S. Bandyopadhyay, J. P. Leburton, and M. Razeghi, Eds.), p. 3. Electrochemical Society, Pennington, NJ, 1996.
190. H. W. Deckman and J. H. Dunsmuir, *Appl. Phys. Lett.* 41, 377 (1982).
191. J. C. Hulteen and R. P. Van Duyne, *J. Vac. Sci. Technol., A* 13, 1553 (1995).
192. M. Winzer, M. Kleiber, N. Dix, and R. Wiesendanger, *Appl. Phys. A* 63, 617 (1996).
193. C. L. Haynes, A. J. Haes, and R. P. Van Duyne, *Mater. Res. Soc. Symp. Proc.* 635 (2001).
194. S. Coyle, M. C. Netti, J. J. Baumberg, M. A. Ghanem, P. R. Birkin, P. N. Bartlett, and D. M. Whittaker, *Phys. Res. Lett.* 87, 176801-1 (2001).
195. C. Haginoya, M. Ishibashi, and K. Koike, *Appl. Phys. Lett.* 71, 2934 (1997).
196. H. Liu and R. M. Penner, *J. Phys. Chem. B* 104, 9131 (2000).
197. H. Liu, F. Favier, K. Ng, M. P. Zach, and R. M. Penner, *Electrochim. Acta* 47, 671 (2001).
198. R. M. Nyffenegger, B. Craft, M. Shaaban, S. Gorer, and R. M. Penner, *Chem. Mater.* 10, 1120 (1998).
199. G. S. Hsiao, M. G. Anderson, S. Gorer, D. Harris, and R. M. Penner, *J. Am. Chem. Soc.* 119, 1439 (1997).
200. M. Anderson, S. Gorer, and R. M. Penner, *J. Phys. Chem.* 101, 5895 (1997).
201. G. Hodes, Y. Golan, D. Behar, Y. Zhang, B. Alperson, and I. Rubinstein, in "Nanoparticles and Nanostructured Films" (J. H. Fendler, Ed.), p. 1. Wiley-VCH, Weinheim, Germany, 1998.
202. Y. Golan, E. Ter-Ovanesyan, Y. Manassen, L. Margulis, G. Hodes, I. Rubinstein, E. G. Bithell, and J. L. Hutchison, *Surf. Sci.* 350, 277 (1996).
203. Y. Golan, J. L. Hutchinson, I. Rubinstein, and G. Hodes, *Adv. Mater.* 8, 631 (1996).
204. F. A. Möller, O. M. Magnussen, and R. J. Behm, *Phys. Rev. Lett.* 77, 5249 (1996).
205. F. A. Möller, J. Kintrup, A. Lachenwitzer, O. M. Magnussen, and R. J. Behm, *Phys. Rev. B* 56, 12506 (1997).
206. S. Strbac, O. M. Magnussen, and R. J. Behm, *Phys. Rev. Lett.* 83, 3246 (1999).

207. D. D. Chambliss, R. J. Wilson, and S. Chiang, *Phys. Rev. Lett.* 66, 1721 (1991).
208. S. Helveg, J. V. Lauritsen, E. Lægsgaard, I. Stensgaard, J. K. Nørskov, B. S. Clausen, H. Topsøe, and F. Besenbacher, *Phys. Rev. Lett.* 84, 951 (2000).
209. S. Maupai, Y. Zhang, and P. Schmuki, *Electrochem. Solid State Lett.* 6, 63 (2003).
210. J. P. Spatz, A. Roescher, and M. Moller, *Adv. Mater.* 8, 337 (1996).
211. J. P. Spatz, S. Mossmer, C. Hartmann, M. Moller, T. Herzog, M. Krieger, H. G. Boyen, P. Ziemann, and B. Kabius, *Langmuir* 16, 407 (2000).
212. U. B. Sleytr, M. Sara, D. Pum, and B. Schuster, *Prog. Surf. Sci.* 68, 231 (2001).
213. S. Dieluwweit, D. Pum, and U. B. Sleytr, *Supramol. Sci.* 5, 15 (1998).
214. R. L. Whetten, J. T. Houry, M. M. Alvarez, S. Murthy, I. Vezmar, Z. L. Wang, C. C. Cleveland, W. D. Luedtke, and U. Landmann, *Adv. Mater.* 8, 429 (1996).
215. M. Brust, D. Bethell, D. J. Schiffrin, and C. J. Kiely, *Adv. Mater.* 7, 771 (1995).
216. L. Motte, F. Billoudet, and M. P. Pileni, *J. Phys. Chem.* 99, 16425 (1995).
217. C. B. Murray, C. R. Kagan, and M. G. Bawendi, *Science* 270, 1335 (1995).
218. N. A. Kotov, I. Dekany, and J. H. Fendler, *J. Phys. Chem.* 99, 13065 (1995).
219. R. G. Nuzzo and D. L. Allara, *J. Am. Chem. Soc.* 105, 4481 (1983).
220. R. G. Nuzzo, L. H. Dubois, and D. L. Allara, *J. Am. Chem. Soc.* 112, 558 (1990).
221. M. A. Bryant and J. E. Pemberton, *J. Am. Chem. Soc.* 113, 8284 (1991).
222. M. D. Proter, T. B. Bright, D. L. Allara, and C. E. D. Chidsay, *J. Am. Chem. Soc.* 109, 3559 (1987).
223. A. L. Harris, C. E. D. Chidsey, N. J. Levinos, and D. N. Loiacano, *Chem. Phys. Lett.* 141, 350 (1987).
224. A. Ulman, "Ultrathin Organic Films: From Langmuir-Blodgett to Self-Assembly." Academic, Boston, 1991.
225. J. A. M. Sondag-Huethorst and L. G. Fokkink, *Langmuir* 11, 4823 (1995).
226. O. Cavalleri, S. E. Gilbert, and K. Kern, *Chem. Phys. Lett.* 269, 479 (1997).
227. E. D. Eliadis, R. G. Nuzzo, A. A. Gewirth, and R. C. Alkire, *J. Electrochem. Soc.* 144, 96 (1997).
228. M. A. Schneeweiss, H. Hagenström, M. J. Esplandiu, and D. M. Kolb, *Appl. Phys. A* 5, 537 (1999).
229. S. Feng and T. Bein, *Nature* 368, 834 (1994).
230. B. J. Tarasevich, P. C. Rieke, and J. Liu, *J. Chem. Mater.* 8, 292 (1996).
231. J. H. Fendler and F. C. Meldrum, *Adv. Mater.* 7, 607 (1995).
232. B. R. Heywood and S. Mann, *Adv. Mater.* 6, 9 (1994).
233. R. Boukherroub, F. Bensebaa, S. Morin, and D. D. M. Wayner, *Langmuir* 15, 3831 (1999).
234. J. M. Buriak, *Chem. Rev.* 102, 1272 (2002).
235. J. A. Switzer, R. P. Raffaele, R. J. Phillips, C.-J. Hung, and T. D. Golden, *Science* 258, 1918 (1992).
236. M. Alper, K. Attenborough, V. Baryshev, R. Hart, D. S. Lashmore, and W. Schwarzacher, *J. Appl. Phys.* 75, 6543 (1994).
237. K. Attenborough, H. Boeve, J. de Boeck, G. Borghs, and J.-P. Celis, *Appl. Phys. Lett.* 74, 2206 (1999).
238. W. Schwarzacher and D. S. Lashmore, *IEEE Trans. Magn.* 32, 3133 (1996).
239. B. W. Gregory, D. W. Suggs, and J. L. Stickney, *J. Electrochem. Soc.* 138, 1279 (1991).
240. D. W. Suggs, I. Villegas, B. W. Gregory, and J. L. Stickney, *J. Vac. Sci. Technol., A* 10, 886 (1992).
241. B. H. Flowers, Jr., T. L. Wade, J. W. Garvey, M. Lay, U. Happek, and J. L. Stickney, *Surf. Sci.* 273, 524 (2002).
242. J. A. Switzer, C.-J. Hung, B. E. Breyfogle, M. G. Shumsky, R. Van Leeuwen, and T. D. Golden, *Science* 264, 1573 (1994).
243. J. A. Switzer, C.-J. Hung, L.-Y. Huang, E. R. Switzer, T. D. Golden, and E. W. Bohannon, *J. Am. Chem. Soc.* 120, 3530 (1998).

Theory of Semiconductor Quantum Devices

Rita Claudia Iotti, Remo Proietti Zaccaria, Fausto Rossi

*Istituto Nazionale per la Fisica della Materia
and Politecnico di Torino, Torino, Italy*

CONTENTS

1. Introduction
2. Theoretical Background
3. Application to Quantum
Optoelectronic Devices
4. Conclusions
Glossary
References

1. INTRODUCTION

Continuous progress in microelectronics technology pushes device miniaturization toward limits where the traditional semiclassical transport theory [1] can no longer be applied and more rigorous quantum-transport approaches are required [2]. However, in spite of the quantum-mechanical nature of carrier dynamics in the core region of typical nanostructured devices—like semiconductor superlattices and double-barrier structures—the overall behavior of such quantum systems is often the result of a complex interplay between phase coherence and energy relaxation/dephasing, the latter being primarily due to scattering-induced phase-breaking processes within the device-active region, as well as to the presence of spatial boundaries [3, 4]. It follows that a proper treatment of such novel nanoscale devices requires theoretical modelings able to properly account for both coherent and incoherent, i.e., phase-breaking, processes on the same footing.

The aim of the present paper is to review a general theoretical framework to explain and to predict the performances of different classes of state-of-the-art quantum optoelectronic devices. To this end, we shall present and discuss a fully three-dimensional (3D) microscopic treatment of time-dependent, as well as steady-state quantum-transport phenomena based on the density-matrix formalism. This will allow us to introduce, in a quite natural way, the separation between coherent and incoherent,

i.e., phase-breaking, processes. Moreover, the conventional Boltzmann-transport theory is simply obtained as the semiclassical limit of the proposed density-matrix formalism.

Based on such a general theoretical framework, we shall discuss two different classes of semiconductor-based quantum devices, namely periodically repeated structures (such as quantum-cascade lasers [QCL]) and quantum systems with open boundaries (such as resonant-tunneling diodes).

For the first class of devices, we shall show how a proper use of periodic boundary conditions allows reproduction/prediction of the current-voltage characteristics of state-of-the-art mid- and far-infrared (IR) quantum-cascade lasers, without resorting to any phenomenologic parameter. In particular, such analysis shows that: (i) in steady-state conditions, quantum-transport corrections are negligible, i.e., carrier transport is mainly semiclassical; (ii) carrier-carrier scattering plays an essential role in providing an efficient transport coupling between injection/collection and device active regions, as well as in improving the efficiency of the phonon quantum cascade in far-IR lasing structures.

For the second class of devices, we shall discuss the intrinsic limitations of the conventional Wigner-function formalism used to describe in a microscopic fashion, injection/loss processes in systems with open boundaries, such as double-barrier structures. More specifically, we shall show that the conventional Wigner-function approach leads to the injection of coherent superpositions of scattering states, in clear contrast with the idea of a thermal, i.e., diagonal, injection from the device electrical contacts. To overcome such limitations, we shall present a novel theoretical description of open systems based on a generalized Wigner function. The latter is found to properly reproduce the results of commonly used macroscopic injection/loss models.

The paper is organized as follows. In Section 2, we shall review and discuss the general theoretical framework used for the microscopic modeling of various classes of semiconductor-based quantum devices. In particular, we shall present our fully 3D density-matrix formalism, as well as its semiclassical counterpart, i.e., the conventional

Boltzmann transport scenario. Section 3 will present applications of this density-matrix formalism to two different classes of optoelectronic quantum devices, namely periodically repeated structures (e.g., mid- and far-IR QCL) and quantum systems with open boundaries (e.g., multibarrier structures). In Section 4, we shall finally summarize and draw some conclusions.

2. THEORETICAL BACKGROUND

2.1. Physical System

To properly describe time-dependent as well as steady-state transport phenomena in quantum optoelectronic devices, let us consider a generic electron-phonon system, whose Hamiltonian can be schematically written as:

$$\mathbf{H} = \mathbf{H}_o + \mathbf{H}' = (\mathbf{H}_c + \mathbf{H}_p) + \left(\sum_s \mathbf{H}'_s \right) \quad (1)$$

The single-particle term \mathbf{H}_o is the sum of the noninteracting carrier and phonon Hamiltonians \mathbf{H}_c and \mathbf{H}_p . The many-body contribution \mathbf{H}' may include various interaction mechanisms, e.g., carrier-carrier, carrier-phonon, carrier-light, etc.

More specifically, the single-particle Hamiltonian \mathbf{H}_c describes the noninteracting carrier system within the effective 3D potential profile of our quantum device. By denoting with

$$\phi_\alpha(\mathbf{r}) = \langle \mathbf{r} | \alpha \rangle \quad (2)$$

the wavefunction of the single-particle state α and with ϵ_α the corresponding energy, the noninteracting-carrier Hamiltonian can be written as

$$\mathbf{H}_c = \sum_\alpha \epsilon_\alpha c_\alpha^\dagger c_\alpha \quad (3)$$

Here, the usual second-quantization picture in terms of creation (c_α^\dagger) and destruction (c_α) operators has been used. The generic label α denotes, in general, a suitable set of discrete and/or continuous quantum numbers: for the case of two-dimensional (2D) semiconductor nanostructures considered in this paper (see Section 3), this corresponds to a partially discrete index along the so-called growth direction, where the electron motion is affected by the nanostructure potential profile, plus an in-plane 2D wavevector.

The explicit form of the generic many-body contribution \mathbf{H}'_s in Eq. (1) can be found in Ref. [4]; it depends on the particular interaction mechanism s considered, and typically involves additional degrees of freedom, like phonons, photons, plasmons, etc. From the point of view of the carrier subsystem, such many-body contributions can be divided into two different classes: single-particle terms, including carrier-phonon and carrier-light interactions, and two-body Coulomb interactions.

2.2. Density-Matrix Formalism

To investigate transport as well as energy-relaxation phenomena, our aim is to study the time evolution of single-particle quantities such as total carrier density, mean kinetic energy, charge current, etc. In general, such quantities correspond to a suitable ensemble average of a generic single-particle operator \mathbf{A} , i.e.,

$$\langle \mathbf{A} \rangle = \left\langle \sum_{\alpha_1 \alpha_2} A_{\alpha_1 \alpha_2} c_{\alpha_1}^\dagger c_{\alpha_2} \right\rangle = \sum_{\alpha_1 \alpha_2} A_{\alpha_1 \alpha_2} \langle c_{\alpha_1}^\dagger c_{\alpha_2} \rangle \quad (4)$$

By introducing the single-particle quantity

$$\rho_{\alpha_1 \alpha_2} = \langle c_{\alpha_2}^\dagger c_{\alpha_1} \rangle \quad (5)$$

we get:

$$\langle \mathbf{A} \rangle = \sum_{\alpha_1 \alpha_2} A_{\alpha_1 \alpha_2} \rho_{\alpha_2 \alpha_1} = Tr(\mathbf{A}\rho) \quad (6)$$

The quantity in Eq. (5) is called single-particle density matrix [4]: this is the key ingredient for the study of single-particle properties. Its diagonal elements ($f_\alpha \equiv \rho_{\alpha\alpha} = \langle c_\alpha^\dagger c_\alpha \rangle$) correspond to the usual distribution functions of the semiclassical Boltzmann theory [1] (see below), while the nondiagonal terms ($\alpha_1 \neq \alpha_2$) describe the degree of quantum coherence (or electronic polarization) between states α_1 and α_2 .

In the Heisenberg picture, the time evolution of $\langle \mathbf{A} \rangle$ is fully dictated by the time evolution of the density matrix ρ . Starting from the Heisenberg equations of motion for the destruction operators c_α , i.e.,

$$\begin{aligned} \frac{d}{dt} c_\alpha &= \frac{1}{i\hbar} [c_\alpha, \mathbf{H}] = \frac{1}{i\hbar} [c_\alpha, \mathbf{H}_o] + \frac{1}{i\hbar} [c_\alpha, \mathbf{H}'] \\ &= \frac{d}{dt} c_\alpha \Big|_{\mathbf{H}_o} + \frac{d}{dt} c_\alpha \Big|_{\mathbf{H}'} \end{aligned} \quad (7)$$

it is possible to derive a set of equations of motion for the density-matrix elements $\rho_{\alpha_1 \alpha_2}$ [often called semiconductor Bloch equations (SBE) [4]] whose general structure is given by:

$$\frac{d}{dt} \rho_{\alpha_1 \alpha_2} = \frac{d}{dt} \rho_{\alpha_1 \alpha_2} \Big|_{\mathbf{H}_o} + \frac{d}{dt} \rho_{\alpha_1 \alpha_2} \Big|_{\mathbf{H}'} \quad (8)$$

The time evolution induced by the single-particle Hamiltonian \mathbf{H}_o can be evaluated exactly yielding:

$$\frac{d}{dt} \rho_{\alpha_1 \alpha_2} \Big|_{\mathbf{H}_o} = \frac{1}{i\hbar} (\epsilon_{\alpha_1} - \epsilon_{\alpha_2}) \rho_{\alpha_1 \alpha_2} \quad (9)$$

The resulting dynamics is diagonal within our $\alpha_1 \alpha_2$ representation, i.e., each density-matrix element evolves independently according to:

$$\rho_{\alpha_1 \alpha_2}(t) = \rho_{\alpha_1 \alpha_2}(t_o) e^{\frac{(\epsilon_{\alpha_1} - \epsilon_{\alpha_2})(t - t_o)}{i\hbar}} \quad (10)$$

In particular, the diagonal elements are not affected by the free dynamics, while the nondiagonal density-matrix elements rotate with different frequencies, given by the energy

difference between states α_1 and α_2 . As we shall see, this nondiagonal dynamics, absent in the semiclassical (diagonal) limit, gives rise to a variety of coherent phenomena in quantum optoelectronic devices.

In contrast, the time evolution due to the many-body Hamiltonian $\mathbf{H}' = \sum_s \mathbf{H}'_s$ involves, in general, phonon-assisted as well as higher-order density matrices; Thus, in order to “close” our set of equations of motion [with respect to the single-particle density matrix ρ in Eq. (5)] approximations are needed. A detailed discussion of the various approximation schemes, based on a dynamical expansion in powers of the interaction Hamiltonian \mathbf{H}' , is given in Ref. [4]. In particular, the “mean-field” approximation, together with the Markov limit allows a set of closed equations of motion still local in time to be derived. More specifically, for a number of interaction mechanisms, including carrier–phonon as well as carrier–carrier scattering, their second-order contributions to the time evolution can be cast into the general form:

$$\begin{aligned} \frac{d}{dt} \rho_{\alpha_1 \alpha_2} \Big|_{\mathbf{H}'} = & \sum_{\alpha'} \frac{1}{2} \left[\left(\delta_{\alpha_1 \alpha'} - \rho_{\alpha_1 \alpha'} \right) \gamma_{\alpha' \alpha_2}^{\text{in}} + \left(\delta_{\alpha_2 \alpha'} - \rho_{\alpha_2 \alpha'}^* \right) \gamma_{\alpha' \alpha_1}^{\text{in}*} \right] \\ & - \sum_{\alpha'} \frac{1}{2} \left[\rho_{\alpha_1 \alpha'} \gamma_{\alpha' \alpha_2}^{\text{out}} + \rho_{\alpha_2 \alpha'}^* \gamma_{\alpha' \alpha_1}^{\text{out}*} \right] \end{aligned} \quad (11)$$

Here, the matrices γ can be regarded as generalized in- and out-scattering rates, in analogy to the Boltzmann collision term of the semiclassical theory [1]. They are, in general, complex quantities: their real parts describe incoherent phenomena, like energy-relaxation and dephasing processes, while their imaginary parts lead to modifications of the free coherent evolution in Eq. (10) through nontrivial energy-renormalization effects. Their explicit form for the case of carrier–phonon, as well as carrier–carrier interactions are given in Ref. [5].

The many-body interaction dynamics described by Eq. (11) is intrinsically nonlinear. Indeed, in general, the scattering operators γ are also ρ dependent. In spite of this potential nonlinearity, we can always rewrite Eq. (11) as:

$$\frac{d}{dt} \rho_{\alpha_1 \alpha_2} = \sum_{\alpha'_1 \alpha'_2} \Gamma_{\alpha_1 \alpha_2, \alpha'_1 \alpha'_2} \rho_{\alpha'_1 \alpha'_2} \quad (12)$$

where the scattering tensor Γ is, in general, a ρ -dependent superoperator involving the in- and out-scattering matrices γ in Eq. (11).

By combining Eqs. (9) and (12), the SBE in Eq. (8) can be written as:

$$\frac{d}{dt} \rho_{\alpha_1 \alpha_2} = \sum_{\alpha'_1 \alpha'_2} L_{\alpha_1 \alpha_2, \alpha'_1 \alpha'_2} \rho_{\alpha'_1 \alpha'_2} \quad (13)$$

where the effective Liouville operator

$$L_{\alpha_1 \alpha_2, \alpha'_1 \alpha'_2} = \frac{1}{i\hbar} (\epsilon_{\alpha_1} - \epsilon_{\alpha_2}) \delta_{\alpha_1 \alpha_2, \alpha'_1 \alpha'_2} + \Gamma_{\alpha_1 \alpha_2, \alpha'_1 \alpha'_2} \quad (14)$$

is the sum of two terms: free single-particle evolution plus scattering-induced energy-relaxation/dephasing dynamics.

In the low-carrier-density limit (i.e., $|\rho_{\alpha_1 \alpha_2}| \ll 1$) carrier–carrier scattering, as well as Pauli-blocking phenomena vanish, and the effective Liouville superoperator L becomes

linear, i.e., ρ independent. In this case, the steady-state behavior of the system can be readily obtained by solving the linear homogeneous problem:

$$\sum_{\alpha'_1 \alpha'_2} L_{\alpha_1 \alpha_2, \alpha'_1 \alpha'_2} \rho_{\alpha'_1 \alpha'_2} = 0 \quad (15)$$

2.3. Semiclassical Limit

As anticipated, in the semiclassical limit, the nondiagonal elements of the density matrix ρ are neglected, i.e.,

$$\rho_{\alpha_1 \alpha_2} = f_{\alpha_1} \delta_{\alpha_1 \alpha_2} \quad (16)$$

In this limit, the coherent free evolution described by Eq. (9) reduces to

$$\frac{d}{dt} f_{\alpha} \Big|_{\mathbf{H}_0} = \frac{d}{dt} \rho_{\alpha\alpha} \Big|_{\mathbf{H}_0} = 0 \quad (17)$$

i.e., in the absence of many-body scattering dynamics, the semiclassical distribution function f_{α} is constant in time.

Let us now come to the many-body contribution in Eq. (11); in the semiclassical limit, Eq. (16), it reduces to:

$$\frac{d}{dt} f_{\alpha} \Big|_{\mathbf{H}'} = (1 - f_{\alpha}) \gamma_{\alpha\alpha}^{\text{in}} - f_{\alpha} \gamma_{\alpha\alpha}^{\text{out}} \quad (18)$$

The explicit form of the scattering matrices γ given in Ref. [5] in the semiclassical limit, reduces to

$$\gamma_{\alpha\alpha}^{\text{in}} = \sum_{\alpha'} P_{\alpha\alpha'}^{\circ} f_{\alpha'}, \quad \gamma_{\alpha\alpha}^{\text{out}} = \sum_{\alpha'} P_{\alpha\alpha'}^{\circ} (1 - f_{\alpha'}) \quad (19)$$

where

$$P_{\alpha\alpha'}^{\circ} = \sum_s P_{\alpha\alpha'}^s \quad (20)$$

are total (summed over all scattering mechanisms s) transition probabilities from state α to state α' , as given by Fermi's golden rule:

$$P_{\alpha\alpha'}^s = \left\langle \frac{2\pi}{\hbar} |\langle \alpha', \xi' | \mathbf{H}'_s | \alpha, \xi \rangle|^2 \delta(\epsilon_{\alpha' \xi'} - \epsilon_{\alpha \xi}) \right\rangle_{\xi, \xi'} \quad (21)$$

Here $\langle \dots \rangle_{\xi, \xi'}$ denotes a suitable statistical average over the initial and final set of auxiliary coordinates ξ and ξ' , e.g., phonons, photons, partner carriers, etc.

By combining Eqs. (17), (18), and (19), we then recover the usual Boltzmann transport equation:

$$\frac{d}{dt} f_{\alpha} = \sum_{\alpha'} [P_{\alpha\alpha'} f_{\alpha'} - P_{\alpha'\alpha} f_{\alpha}] \quad (22)$$

where

$$P_{\alpha\alpha'} = (1 - f_{\alpha}) P_{\alpha\alpha'}^{\circ} \quad (23)$$

is the total transition probability P° in Eq. (20), weighted by the Pauli factor of the final state.

The Boltzmann equation in Eq. (22) can then be regarded as the semiclassical limit of the SBE in Eq. (13). This clearly shows that in the semiclassical limit the above quantum scattering model reduces to the conventional Boltzmann theory. As we can see from Eq. (11), also in the quantum case, the

total effect is the result of a balance between in- and out-scattering contributions. In particular, for the case of quasi-elastic processes, it is possible to show [4] that, in analogy to the semiclassical case, the two in and out contributions strongly cancel, thus giving rise to long dephasing times.

As for the quantum case, in the low-density limit ($f_\alpha \ll 1$) the Boltzmann transport equation in Eq. (22) becomes linear; this allows us to obtain the steady-state solution by solving the following homogeneous linear problem:

$$\sum_{\alpha'} \mathcal{P}_{\alpha\alpha'} f_{\alpha'} = 0 \quad (24)$$

with

$$\mathcal{P}_{\alpha\alpha'} = P_{\alpha\alpha'} - \delta_{\alpha\alpha'} \sum_{\alpha''} P_{\alpha\alpha''} \quad (25)$$

The above Boltzmann scattering operator \mathcal{P} can be regarded as the semiclassical counterpart of the effective Liouville superoperator L in Eq. (14).

3. APPLICATION TO QUANTUM OPTOELECTRONIC DEVICES

3.1. Modeling of Periodically Repeated Structures

3.1.1. Fundamentals of Quantum-Cascade Lasers

Since the seminal paper of Esaki and Tsu [6], semiconductor-based nanometric heterostructures have been the subject of impressive theoretical and experimental activity, due to their high potential impact in both fundamental and applied research [2, 7, 8]. One of the main fields of research focuses on exploiting “band-gap engineering,” namely, the splitting of the bulk conduction band into several subbands due to quantum confinement, to generate and detect electromagnetic radiation in the IR spectral region, as already envisioned by Kazarinov and Suris in their early proposal [9].

Quantum-cascade lasers [10–12] are an excellent example of how the principles of quantum engineering can be used to design new materials and related light sources: In these devices, lasing is, in fact, obtained by a suitable design of the structure in which energy levels, optical matrix elements, scattering rates, and relaxation times are properly tailored to maintain a population-inversion condition at the desired emission frequency.

Unipolar coherent-light sources, such as QCLs, are complex devices, whose core is a multiquantum-well (MQW) structure made up of repeated stages of active regions sandwiched between electron-injecting and -collecting regions. When a proper bias is applied, an “electron cascade” along the subsequent quantized-level energy staircase takes place. Several successful designs have been proposed up to now for both the active region and the injector part of the structure. To better present the theoretical approach reviewed in this paper, it can be of some help just to recall the main features of these devices.

As an example, Figure 1 shows the conduction band profile along the growth direction for a QCL emitting in the

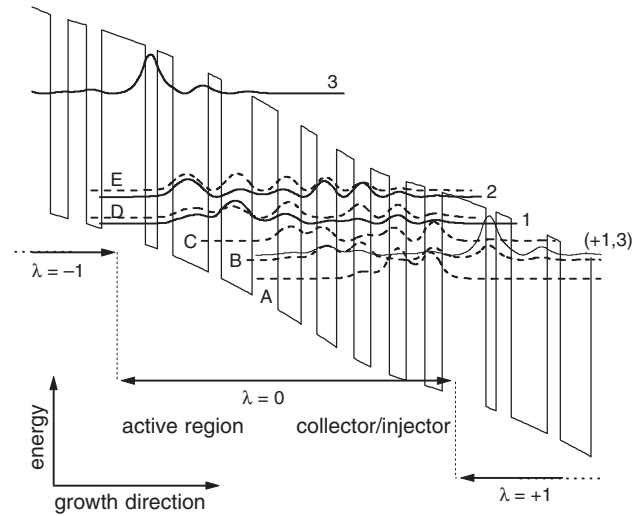


Figure 1. Schematic representation of the conduction-band profile along the growth direction for the diagonal-configuration QCL structure of Ref. [20]. The MQW is biased by an electric field of 48 kV/cm. The levels $\nu = 1, 2, 3$ and $\nu = A, B, C, D, E$ in the active and collector regions (full and dashed lines, respectively) of the simulated stage ($\lambda = 0$) also are plotted together with the corresponding probability densities. The replica of level 3 in the following stage $\lambda = +1$ is shown for clarity. The separation between subbands 1 and 2 matches the optical phonon energy ($\hbar\omega_{LO} \simeq 36$ meV) and the stage length is 453 Å (the figure is in scale). Reprinted with permission from [18], R. C. Iotti and F. Rossi, *Phys. Rev. Lett.* 87, 146603 (2001). © 2001, American Physical Society.

mid-IR portion of the electromagnetic spectrum. The figure presents the generic stage $\lambda = 0$, plus a portion of both the neighboring left and right stages. Also shown are the probability densities of the confined states in the active region ($\nu = 1, 2, 3$) and in the collector/injector ($\nu = A, B, C, D, E$), evaluated within an effective-mass framework. Indeed, taking into account the fully 3D nature of the single-particle Hamiltonian in Eq. (3), as well as of the corresponding eigenfunctions in Eq. (2), the single-particle states $\phi_\alpha(\mathbf{r})$ in this structure are also labeled by the in-plane wavevector \mathbf{k} . This design is based on a three-quantum-well active region: Electrons are injected into subband 3 of the generic stage ($\lambda = 0$) by resonant tunneling and then can relax into lower-energy states in subband 2 and 1. By a proper choice of the geometry, optical matrix elements and scattering rates can be optimized so that a population-inversion condition is established between subbands 3 and 2, corresponding to the lasing transition. Once a photon has been emitted in this stage, the electron is drifted off into the collector, whence it can be recycled into the neighboring stage $\lambda = 1$ to emit a second photon, and so on so forth. It follows that these are intrinsically high-power devices, which can be designed to emit over a wide range of frequencies, just by modifying the geometrical parameters while keeping the same constituent materials.

Since their appearance, QCLs have been the subject of a rapid experimental development in emission wavelength, lasing threshold, output power, and operating temperature [13]. This has stimulated considerable theoretical interest, mainly motivated by the desire to improve the

device performances by optimizing the semiconductor-heterostructure design. Various theoretical models [14] have been proposed to describe gain spectra and characteristics of QCLs. However, these approaches generally resort on macroscopic rate equations to describe the carrier dynamics, whose application does not have a true justification [15]. In contrast, for a detailed understanding of the basic physical processes involved in the operation of these devices, a fully three-dimensional description is needed. Besides, a completely microscopic analysis would really serve as a predictive tool for the evaluation of new designs and strategies.

In the reminder of this section, we shall review and discuss the diverse theoretical approaches commonly used for the description of nonequilibrium carrier dynamics in state-of-the-art QCLs. They range from purely phenomenologic models, to kinetic Boltzmann-like treatments, to fully quantum-mechanical approaches.

3.1.2. Phenomenologic or Macroscopic Modeling

From a theoretical point of view, the intersubband light sources previously described are usually modeled by analogy with n -level atomic systems. Their theoretical description is thus often grounded on purely macroscopic models: the only relevant physical quantities being the various carrier concentrations n_ν , within each subband. Their time evolution can be described by a set of phenomenologic rate equations of the form

$$\frac{dn_\nu}{dt} = \left(g_\nu - \frac{n_\nu}{\tau_\nu} \right)_{i/l} + \sum_{\nu'} (w_{\nu\nu'} n_{\nu'} - w_{\nu'\nu} n_\nu)_s \quad (26)$$

This is the sum of the injection/loss (i/l) contribution in the generic stage, g_ν and τ_ν^{-1} being, respectively, the carrier injection and loss rates for level ν , plus the interlevel-scattering term (s) $w_{\nu\nu'}$ denoting phenomenologic scattering rates connecting levels ν and ν' .

The physical parameters entering Eq. (26) are unavoidably global or macroscopic quantities, i.e., their microscopic evaluation would require the knowledge of the carrier distribution function over the whole three-dimensional \mathbf{k} -space. Indeed, from a microscopic point of view, the carrier concentration/density in a given subband ν is the sum/integral over the in-plane wavevector of the carrier distribution function $f_\alpha = f_{\nu\mathbf{k}}$:

$$n_\nu \propto \sum_{\mathbf{k}} f_{\nu\mathbf{k}} \quad (27)$$

Let us reconsider the Boltzmann equation Eq. (22) written in our specific representation $\alpha = \nu\mathbf{k}$, i.e.,

$$\frac{d}{dt} f_{\nu\mathbf{k}} = \sum_{\nu'\mathbf{k}'} [P_{\nu\mathbf{k}, \nu'\mathbf{k}'} f_{\nu'\mathbf{k}'} - P_{\nu'\mathbf{k}', \nu\mathbf{k}} f_{\nu\mathbf{k}}] \quad (28)$$

By summing the above 3D transport equation over the in-plane wavevector \mathbf{k} , we get:

$$\frac{dn_\nu}{dt} = \sum_{\nu'} (w_{\nu\nu'} n_{\nu'} - w_{\nu'\nu} n_\nu) \quad (29)$$

with

$$dw_{\nu\nu'} = \frac{\sum_{\mathbf{k}, \mathbf{k}'} P_{\nu\mathbf{k}, \nu'\mathbf{k}'} f_{\nu'\mathbf{k}'}}{\sum_{\mathbf{k}'} f_{\nu'\mathbf{k}'}} \quad (30)$$

The effective Boltzmann collision term in Eq. (29) has, indeed, the same form of the one in Eq. (26); however, as clearly shown by Eq. (30), the effective interlevel scattering rates $w_{\nu\nu'}$ are obtained by averaging the microscopic transition probabilities $P_{\nu\mathbf{k}, \nu'\mathbf{k}'}$ over the initial and final in-plane carrier wavevectors \mathbf{k}' and \mathbf{k} . It follows that their values are strongly affected by the actual nature/shape of the unknown in-plane carrier distribution.

For this reason, as pointed out in Ref. [16], this rate-equation scheme can only operate as an *a posteriori* fitting procedure. Indeed, rather than within a multilevel system, the electron dynamics in QCLs occurs within a multisubband structure, and the existence of transverse, i.e., in-plane, degrees of freedom should be properly taken into account.

3.1.3. Three-Dimensional Microscopic Description

As anticipated, to provide a quantitative insight into the details of the carrier dynamics in these unipolar devices—energy-relaxation as well as dephasing processes—a proper treatment of the fully 3D nature of the problem is imperative. As originally proposed in Ref. [16] and generalized in Refs. [17] and [18], this can be done within a kinetic Boltzmann-like approach. In this scheme, the fundamental ingredient is the carrier distribution function f_α . In our MQW structure, α is a global quantum number labeling single-particle states and comprising the stage index λ , the subband index ν within each stage, and the in-plane wavevector \mathbf{k} .

The time evolution of the carrier distribution function f_α is governed by the Boltzmann transport equation Eq. (22), i.e.,

$$\frac{d}{dt} f_\alpha = \sum_{\alpha'} [P_{\alpha\alpha'} f_{\alpha'} - P_{\alpha'\alpha} f_\alpha] \quad (31)$$

Here, $P_{\alpha'\alpha}$ is the scattering probability for a process connecting the state with in-plane wavevector \mathbf{k} in the ν th subband of the λ th stage, to the state $\nu'\mathbf{k}'$ of the λ' th one.

Although Eq. (31) corresponds to the more complete description of the problem and allows one to kinetically study electron dynamics within the full core region of the device, semi-phenomenologic models, in between Eqs. (26) and (31), have been also proposed [16]. They can still provide valuable information on the microscopic carrier dynamics, with the advantage of being much less computer-time consuming. This is valid, in particular, when the region of interest corresponds to a portion of the whole structure, like, e.g., the bare active region of the device. Limiting the kinetic treatment to this subset $\bar{\alpha} = \{\lambda = 0; \nu = 1, 2, 3; \mathbf{k}\}$ of the multisubband structure of Figure 1, the kinetic equation in Eq. (31) can be rewritten as

$$\frac{d}{dt} f_{\bar{\alpha}} = \left[g_{\bar{\alpha}} - \frac{f_{\bar{\alpha}}}{\tau_{\bar{\alpha}}} \right]_{i/l} + \sum_{\bar{\alpha}'} [P_{\bar{\alpha}\bar{\alpha}'} f_{\bar{\alpha}'} - P_{\bar{\alpha}'\bar{\alpha}} f_{\bar{\alpha}}] \quad (32)$$

Here, the first two terms describe injection and loss of carriers with in-plane wavevector \mathbf{k} in miniband ν , while the last one accounts for in- and out-scattering processes between states $\nu\mathbf{k}$ and $\nu'\mathbf{k}'$. Contrary to the macroscopic model in Eq. (26), this formulation provides a description of intra- and interminiband scattering, in the $\bar{\alpha}$ subset, in terms of microscopic ingredients only. However, the injection/loss contributions in Eq. (32), coupling the active region with the injector/collector, are treated on a partially phenomenologic level: The g and Γ functions are defined within the same kinetic picture $\nu\mathbf{k}$ and are adjusted to reproduce the experimentally measured current density across the device.

The kinetic description proposed in Eq. (32) came out to be quite useful to address the microscopic nature of the hot-carrier relaxation within a portion of the structure, e.g., the device active region [16]. However, due to the presence of free-parameters coupling this region of interest to the rest of the device, it does not allow the nature of the physical mechanisms governing charge transport through injector/active-region/collector interfaces to be addressed. To this end, the partially phenomenologic model has to be replaced by the fully microscopic description of the whole MQW core structure in Eq. (31).

The periodicity of the real structure allows one to assume

$$f_{\lambda'\nu\mathbf{k}} = f_{\lambda\nu\mathbf{k}} \quad (33)$$

i.e., the carrier distribution function does not depend on the stage index. Under this assumption, Eq. (31) can then be rewritten as:

$$\begin{aligned} \frac{d}{dt}f_{\lambda\nu\mathbf{k}} &= \sum_{\nu'\mathbf{k}'} [P_{\lambda\nu\mathbf{k}, \lambda'\nu'\mathbf{k}'} f_{\lambda'\nu'\mathbf{k}'} - P_{\lambda'\nu'\mathbf{k}', \lambda\nu\mathbf{k}} f_{\lambda\nu\mathbf{k}}] \\ &+ \sum_{\nu'\mathbf{k}'; \lambda' \neq \lambda} P_{\lambda\nu\mathbf{k}, \lambda'\nu'\mathbf{k}'} f_{\lambda'\nu'\mathbf{k}'} - \sum_{\nu'\mathbf{k}'; \lambda' \neq \lambda} P_{\lambda'\nu'\mathbf{k}', \lambda\nu\mathbf{k}} f_{\lambda\nu\mathbf{k}} \quad (34) \end{aligned}$$

Here, the first term accounts for all intrastage scattering dynamics, while the second and third one correspond, respectively, to injection and loss contributions, coupling this stage with the neighboring ones. They are the microscopic equivalent of the g and Γ functions of the partially phenomenologic model in Eq. (32). To properly “close the circuit” without resorting to phenomenologic parameter, we then impose the periodic boundary conditions previously mentioned, limiting the interstage ($\lambda \neq \lambda'$) scattering to just nearest-neighbor coupling ($\lambda' = \lambda \pm 1$).

3.1.4. Quantum-Transport Approach

So far, no quantum-mechanical effects, such as coherent resonant tunneling between adjacent states, have been considered. In order to see how such coherent phenomena can change the semiclassical scenario presented thus far, we have extended our semiclassical simulation scheme in terms of the density-matrix formalism previously introduced (see Section 2), which allows one to describe, on equal footing, phase coherence as well as energy relaxation and dephasing [4]. In the proposed quantum-transport approach, the basic ingredient is the single-particle density matrix in Eq. (5), written in our $\lambda\nu\mathbf{k}$ representation:

$$\rho_{\lambda_1\nu_1\mathbf{k}_1, \lambda_2\nu_2\mathbf{k}_2} = \langle c_{\lambda_2\nu_2\mathbf{k}_2}^\dagger c_{\lambda_1\nu_1\mathbf{k}_1} \rangle \quad (35)$$

As discussed in Section 2, the time evolution of the single-particle density matrix ρ is governed by the SBE in Eq. (8); the latter can be regarded as the sum of a coherent, i.e., scattering-free, dynamics [Eq. (9)] plus a many-body contribution accounting for energy-relaxation and dephasing phenomena [Eq. (11)].

In view of the in-plane translational symmetry of the carrier system, $\mathbf{k}_1 \neq \mathbf{k}_2$ density-matrix elements are equal to zero; Moreover, we shall neglect interstage ($\lambda_1 \neq \lambda_2$) density-matrix elements. Within such approximation scheme we get:

$$\rho_{\lambda_1\nu_1\mathbf{k}_1, \lambda_2\nu_2\mathbf{k}_2} = \rho_{\lambda_1, \nu_1\nu_2, \mathbf{k}_1} \delta_{\lambda_1\lambda_2} \delta_{\mathbf{k}_1\mathbf{k}_2} \quad (36)$$

Analogous to our semiclassical treatment [Eq. (33)], also for the new quantum-transport formalism, we can adopt the same periodic conditions to “close the circuit”:

$$\rho_{\lambda, \nu_1\nu_2, \mathbf{k}} = \rho_{\lambda', \nu_1\nu_2, \mathbf{k}} = \rho_{\nu_1\nu_2, \mathbf{k}} \quad (37)$$

This allows us to study the time evolution of the density matrix in the $\lambda = 0$ periodicity region only, accounting for both diagonal and nondiagonal scattering processes within region $\lambda = 0$ as well as from and to regions $\lambda = \pm 1$. Similar to the semiclassical scheme, this provides the current-voltage characteristics without resorting to any phenomenologic parameter.

Moreover, since for the considered QCL designs in-plane and along- z carrier dynamics are strongly decoupled, it is possible to adopt a factorization of the density matrix in Eq. (37) according to

$$\rho_{\nu_1\nu_2, \mathbf{k}} = \varrho_{\nu_1\nu_2} f_{\mathbf{k}}^{\parallel} \quad (38)$$

where f^{\parallel} denotes the parallel or in-plane carrier distribution.

Such a factorization scheme allows us to obtain an effective, i.e., one-dimensional (1D) equation of motion for $\varrho_{\nu_1\nu_2}$ of the form:

$$\frac{d}{dt}\varrho_{\nu_1\nu_2} = \sum_{\nu'_1\nu'_2} L_{\nu_1\nu_2, \nu'_1\nu'_2}^{\text{1D}} \varrho_{\nu'_1\nu'_2} \quad (39)$$

the latter, which has again the structure of Eq. (13), involves the 1D effective Liouville superoperator L^{1D} , given by an in-plane average of the Liouville operator L in Eq. (14). Such 1D superoperator, in turn, involves effective 1D scattering matrices, given by an in-plane average of the quantities $\gamma^{\text{in/out}}$ in Eq. (11). As we shall see, such in-plane average can be readily performed within the proposed simulation strategy.

3.1.5. Simulation Strategy

In view of their Boltzmann-like structures, Eq. (31) as well as (32) can be “sampled” by means of a proper Monte Carlo (MC) simulation scheme [1]. Indeed, the latter has proven to be a very powerful technique, allowing the inclusion, at a kinetic level, of a large variety of scattering mechanisms.

More specifically, benefiting from the translational symmetry previously discussed, we can then simulate carrier transport over the central $\lambda = 0$ stage only. Every time a

carrier in state ν undergoes an interstage scattering process (i.e., $0, \nu \rightarrow \pm 1, \nu'$), it is properly reinjected into the central region ($0, \nu \rightarrow 0, \nu'$) and the corresponding electron charge $\pm e$ will contribute to the current through the device. This charge-conserving scheme allows for a purely microscopic evaluation of the device performances such as the gain spectrum or the current-voltage characteristics. The current density j across the whole structure, for example, can be obtained as a pure output of the simulation, just by a proper sampling of the in- and out-stage scattering processes:

$$j \propto \sum_{\nu\nu'\mathbf{k}\mathbf{k}'} \left[\sum_{\lambda' > \lambda} P_{\lambda'\nu'\mathbf{k}', \lambda\nu\mathbf{k}} f_{\lambda\nu\mathbf{k}} - \sum_{\lambda' < \lambda} P_{\lambda'\nu'\mathbf{k}', \lambda\nu\mathbf{k}} f_{\lambda\nu\mathbf{k}} \right] \quad (40)$$

Within such fully 3D MC simulation scheme, it is easy to compute the in-plane average of the generalized in- and out-scattering operators $\gamma^{\text{in/out}}$ in Eq. (11) previously discussed. This is performed by sampling the integral on the in-plane \mathbf{k} coordinate over the usual “free flight + scattering event” sequence of our many-particle simulation by means of a generalized MC sampling strategy [19].

Contrary to Eqs. (31) and (32), the 1D effective quantum transport equation in Eq. (39) is not Boltzmann-like, i.e., the matrix elements of the Liouville superoperator L^{1D} are not positive-definite. Therefore, Eq. (39) cannot be solved by means of a standard particle-like MC simulation, as for the semiclassical case. In contrast, this quantum-transport equation is solved by means of a direct numerical integration based on a time-step discretization strategy.

To properly describe the complex interplay between carrier thermalization and energy relaxation/dephasing in state-of-the-art QCL structures, we have included in our simulation, all relevant interaction mechanisms in a fully 3D fashion: intra- and intersubband carrier–phonon, as well as carrier–carrier scattering processes. In the following, we shall present and discuss simulated experiments based on the semiclassical-transport as well as quantum-transport approaches previously introduced. They are aimed at understanding the nonequilibrium electro-optical response of a variety of QCL designs.

3.1.6. Simulation of Mid-Infrared Quantum-Cascade Lasers

To achieve and maintain a population-inversion regime between the two subbands involved in the optical transition, some clever design of the structure is required. In particular, the intersubband scattering rates have to be properly tailored to efficiently deplete the lower laser states, while preventing electrons from a too fast relaxation out of the upper laser states. This does strongly depend on the frequency ω_{phot} of the emitted light. For QCLs designed to emit in the mid-IR region of the electromagnetic spectrum, such a tailoring of the various relaxation times can be achieved, benefiting from an energy-selective mechanism by which electrons can dissipate their energy: the polar-optical phonon emission. The Fröhlich interaction between electrons and longitudinal optical (LO) phonon modes in polar materials (such as the III–V alloys, which are usually used in state-of-the-art unipolar devices) is characterized by scattering rates that fall as the reciprocal of the squared transferred

momentum, $\Delta\mathbf{k}$. Since LO phonons are characterized by a well-defined energy $\hbar\omega_{LO}$ (their bands can be regarded as dispersionless), an electronic intersubband relaxation process via LO emission is vertical in momentum space and, therefore, highly probable, when the difference in energy between the two subbands matches the phonon energy. On the contrary, when the subbands are more than one phonon far apart, i.e., $\hbar\omega_{\text{phot}} > \hbar\omega_{LO}$, the electronic transition comes out to be diagonal in \mathbf{k} space, and thus less probable than in the previous case.

Let us start our analysis by applying the semiclassical global-simulation scheme in Eq. (31) to state-of-the-art mid-IR QCL structures. In particular, as prototypical device, we have considered the GaAs/(Al,Ga)As-based diagonal-configuration QCL proposed in Ref. [20], schematically depicted in Figure 1. In order to properly model phase-breaking hopping processes, in addition to carrier-optical phonon scattering, all various intra- as well as intersubband carrier–carrier interaction mechanisms have been considered. Other scattering mechanisms, not included in the simulation, are expected to play a minor role [1]. In particular, the interaction with acoustic phonons, in spite of its quasi-elastic nature, does not affect charge transport significantly due to its small coupling constant.

As a starting point, we have investigated the relative weight of the carrier–carrier and carrier–phonon competing energy-relaxation channels. The time evolution of the carrier population in the various subbands, as well as of the total current density in the presence of carrier–phonon scattering are depicted in Figure 2. Parts (a) and (b) refer, respectively, to simulated experiments without and with two-body carrier–carrier scattering. In our “charge conservation” scheme, we start the simulation assuming the total number of carriers to be equally distributed among the different subbands; then the electron distribution functions evolve according to Eq. (31) and a steady-state condition is eventually reached, leading to the desired $3 \rightarrow 2$ population inversion. As we can see, the inclusion of intercarrier scattering has significant effects: It strongly increases intersubband carrier redistribution, thus reducing the electron accumulation in the lowest energy level A and optimizing the coupling between active region and injector/collector (the populations of subbands 3 and B become equal). This effect comes out to be crucial in determining the electron flux through the MQW structure. Figure 2(c) shows the simulated current-voltage characteristics of our QCL device, obtained with (discs) and without (filled squares) carrier–carrier interaction. At the threshold operating parameters estimated in Ref. [20] [marked by an arrow in Fig. 2(c)], the current density in the presence of both electron–phonon and electron–electron scattering mechanisms is about 4 kA/cm². This value is in relatively good agreement with experiments. Indeed, the apparent discrepancy between the theoretical and the experimental ($\simeq 7$ kA/cm²) results is due, we believe, to the different estimate of the potential drop per period required to line up the ground state A of the injector with level 3 of the active region.

The results, plotted in Figure 2, clearly demonstrate that within a purely semiclassical picture, the electron–phonon interaction alone is not able to efficiently couple the injector subbands to the active region ones. While carrier–phonon

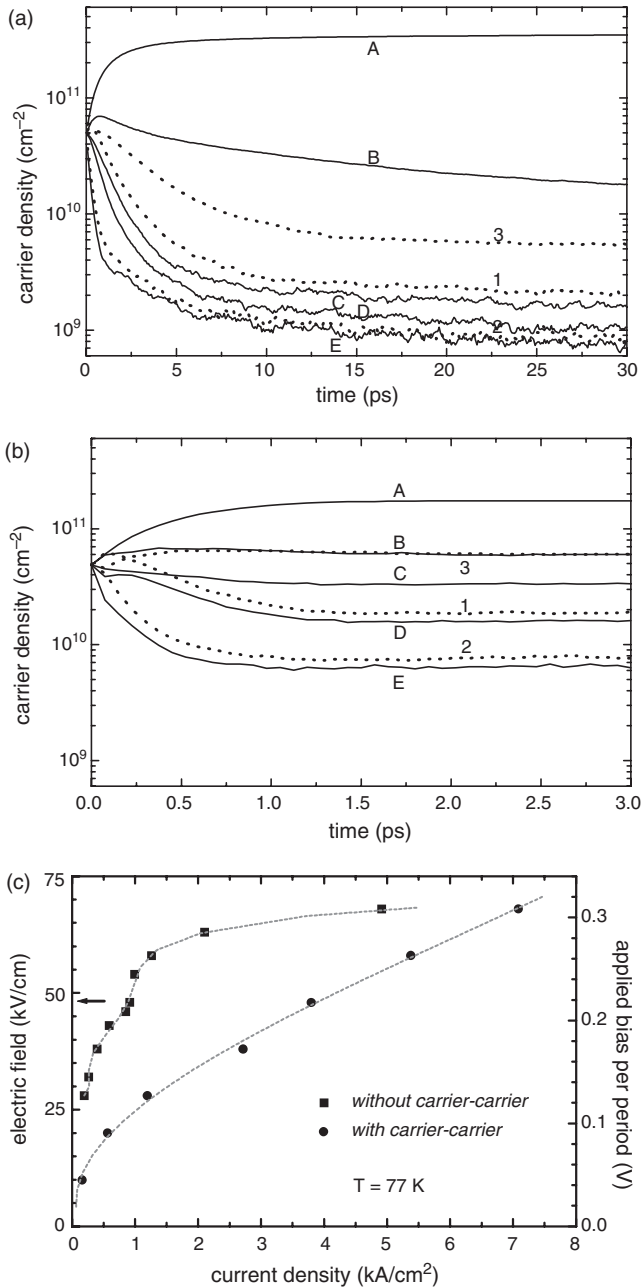


Figure 2. Time evolution of simulated carrier densities in the various subbands of the MQW structure of Figure 1 (full lines: $\nu = A, B, C, D, E$; dotted lines: $\nu = 1, 2, 3$), without (a) and with (b) intercarrier scattering. (c): simulated applied-field vs current-density characteristics of the whole structure at 77 K, in the presence (discs) and absence (filled squares) of carrier–carrier interaction. Threshold applied field (48 kV/cm) is marked by an arrow. Dashed lines are a guide to the eye. Reprinted with permission from [18], R. C. Iotti and F. Rossi, *Phys. Rev. Lett.* 87, 146603 (2001). © 2001, American Physical Society.

relaxation well describes the electronic quantum cascade within the bare active region [16], carrier–carrier scattering plays an essential role in determining charge transport through the full core region. This can be ascribed to two typical features of carrier–carrier interaction, compared to the case of carrier–phonon: (i) this is a long-range two-body interaction mechanism, which also couples nonoverlapping

single-particle states [see Fig. 1]; and (ii) the corresponding scattering process at relatively low carrier density is quasi-elastic, thus coupling nearly resonant energy levels, like states 3 and B.

To focus on the relative weight of the carrier–carrier and carrier–phonon competing energy-relaxation channels, we have investigated the steady-state electron distribution as a function of the in-plane energy, for different carrier densities [17]. Indeed, for low carrier concentrations, intercarrier scattering plays a very minor role and electrons relax their energy via a cascade of successive optical-phonon emissions; for high carrier densities, carrier–carrier scattering is more effective in setting up a heated Maxwellian distribution, with a given temperature T_ν . This is a well-known trend that results from the screened-Coulomb nature of the carrier–carrier interaction potential [1, 4]. The absolute density value corresponding to the transition between these two different regimes, however, depends on the heterostructure details and can be obtained only after performing a direct simulation. Our results clearly show that, for typical operating conditions (sheet density = $3.9 \cdot 10^{11} \text{ cm}^{-2}$), electrons in QCLs thermalize within each subband. Temperatures corresponding to the diverse subbands vary in a quite narrow range ($T_\nu = 600\text{--}750 \text{ K}$), as shown in Figure 3¹. Again, the role of electron–electron interaction is crucial in setting up this behavior: This effect can be mainly ascribed to bi-intrasubband scattering processes, i.e., intercarrier scattering processes coupling electrons in different subbands, without changing their principal quantum number ν . They provide, in fact, a very efficient way of redistributing excess kinetic energy to achieve a common effective temperature. Such temperature results to be about 700 K, to be compared with a lattice temperature of 77 K assumed in the simulation. This heating is a clear fingerprint of a strong hot-carrier regime: the carrier system is not able to dissipate, via optical-phonon emission, the relatively large amount of energy provided by the applied bias.

So far, due to our semiclassical description, no quantum-mechanical effects, such as coherent resonant tunneling between adjacent states, have been considered. To see how such coherent phenomena can change the previously discussed scenario, we have extended our semiclassical simulation scheme in terms of the density-matrix formalism presented in Section 3.1.4, which allows us to describe on the same footing, phase coherence, as well as energy-relaxation and dephasing processes [4].

Comparing the results obtained with the proposed quantum-transport approach to those of the semiclassical global simulation scheme, we find negligible quantum corrections (of a few percentages) to the stationary current density. In the absence of carrier–carrier scattering, we get, e.g., a 2% quantum correction to the result at threshold reported in Figure 2. This is due to the extremely small value of nondiagonal density-matrix elements $\rho_{\nu \neq \nu'}$ (compared to the diagonal ones). The physical interpretation of such a behavior proceeds as follows: Nondiagonal terms of the generalized carrier–phonon scattering operators $\Gamma^{\text{in/out}}$ tend to

¹ It should be noticed that this temperature T_ν has nothing to do with the effective temperature invoked in a macroscopic n -level description, which becomes negative in the case of population inversion.

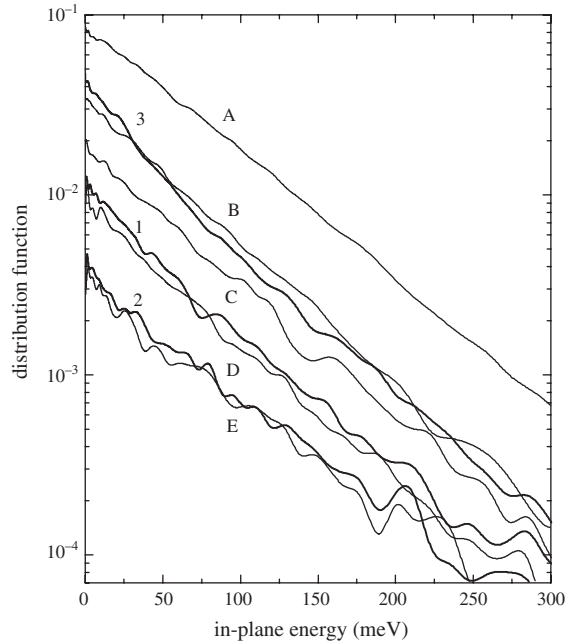


Figure 3. Electron distribution function in-plane energy, for carriers in subbands $\nu = 1, 2, 3$ and $\nu = A, B, C, D, E$ of the MQW structure of Figure 1. Sheet density = $3.9 \cdot 10^{11} \text{ cm}^{-2}$. The slope of each curve provides an estimate of carrier effective temperature in the relative subband, T_ν , which is in the range 600–750 K. Reprinted with permission from [17], R. C. Iotti and F. Rossi, *Appl. Phys. Lett.* 78, 2902 (2001). © 2001, American Institute of Physics.

maintain a nondiagonal density matrix also in stationary conditions. On the other hand, diagonal energy-relaxation and dephasing processes tend to suppress nondiagonal elements on the subpicosecond time scale. Since the average transit time—the time needed by an electron to travel through the device period and thus to be reinjected into the simulation region—is of the order of several picoseconds, the degree of coherence, i.e., the weight of nondiagonal density-matrix elements, in stationary conditions is very small. However, this does not mean that coherent phenomena, such as resonant-tunneling processes, are not present. Figure 4 presents the first simulation of the ultrafast dynamics of a properly tailored electron wavepacket, within the MQW core region of the QCL sketched in Figure 1. Here, the aim is to focus on the injector, active-region tunneling mechanisms. For this reason, the electron system has been prepared at $t = 0$ as a coherent superposition of the two quasi-resonant states (0,B)–(+1,3) shown in Figure 1, to reproduce a charge-density distribution fully localized in the $\lambda = 0$ injector. As clearly shown, the transient dynamics is characterized by a strong interplay between phase-coherence and relaxation (on a picosecond time scale); Only at much longer times, it will eventually reach the stationary transport solution, in which incoherent sequential tunneling is the dominant interwell mechanism. These results suggest that ultrafast optical experiments, like pump-and-probe or four-wave-mixing measurements, should provide a clear fingerprint of such a coherent vs. energy-relaxation carrier dynamics. This is confirmed by recent ultrafast experiments by Eickemeyer et al. [21].

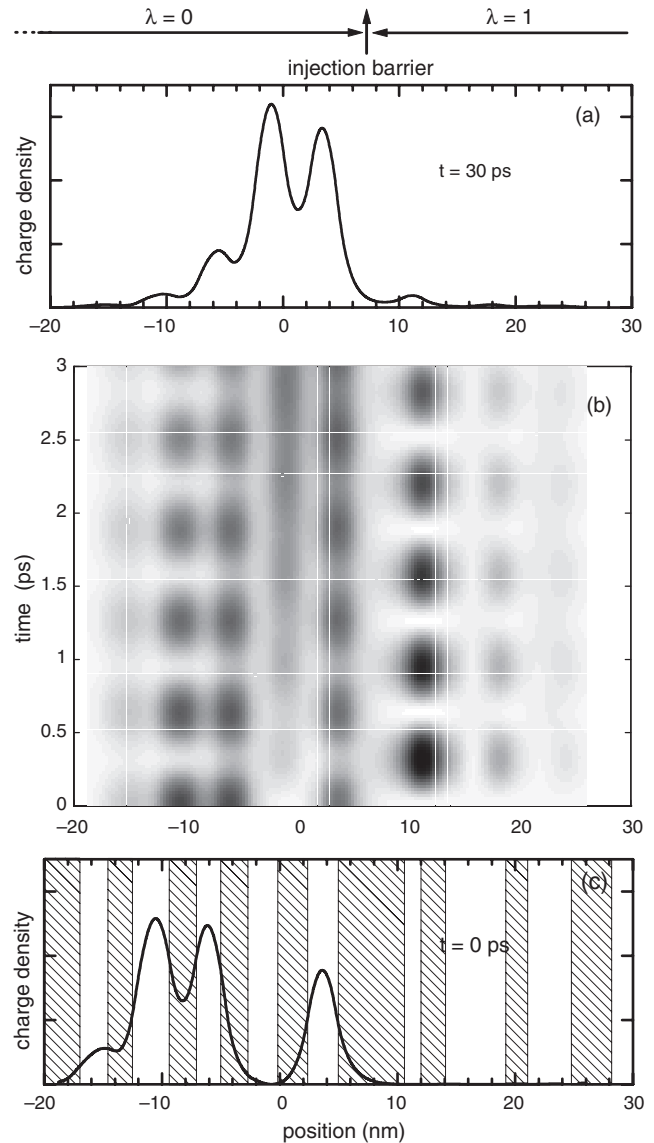


Figure 4. Time evolution of the charge density for an electron wavepacket properly tailored to study the carrier tunneling dynamics across the injection barrier, for the QCL design of Figure 1. At $t = 0$ ps [lower panel (c)], the wavepacket is fully localized in the injector. Shaded regions correspond to (Al,Ga)As barriers in the heterostructure design. The transient dynamics [middle panel (b)] is characterized by a strong interplay between phase-coherence and relaxation processes. At much longer times [upper panel (a)], the system will eventually evolve into the stationary transport solution. Reprinted with permission from [18], R. C. Iotti and F. Rossi, *Phys. Rev. Lett.* 87, 146603 (2001). © 2001, American Physical Society.

On the basis of the previous results, we are able to answer the long-standing controversial question on the nature, coherent versus incoherent, of charge transport in QCLs. For the typical structures considered, energy-relaxation and dephasing processes are so strong to destroy any phase-coherence effect on a subpicosecond time scale; as a result, the usual semiclassical or incoherent description of stationary charge transport is found to be in excellent agreement with experimental results.

3.1.7. Toward THz sources

Since their first demonstration in 1994 [10], the performances of QCLs have experienced tremendous improvements, and the range of emission wavelength has been continuously extended [13]. In principle, QCLs can be designed to emit at any frequency over an extremely wide range, by using the same combination of materials and only varying the heterostructure design. However, the translation of the cascade scheme into devices operating at photon energies below the LO-phonon threshold of the host material ($\hbar\omega_{LO} \simeq 36$ meV in GaAs) is definitely not straightforward. In this configuration, in fact, the main difficulty in achieving a population inversion regime in the active region, is that optical-phonon emission cannot be used to selectively depopulate the MQW excited states, since it acts with equal efficiency on both the upper and the lower laser subbands. On the contrary, the complex and nonintuitive interplay between various competing nonradiative relaxation channels has to be taken into account to properly evaluate the performances of new designs and proposals. In particular, two main targets have to be fulfilled: efficient depletion of the lower laser states and long lifetime in the upper ones.

Although electroluminescence in the THz region of the electromagnetic spectrum has been detected from a variety of quantum-cascade structures in the last years, no evidence of population inversion was achieved, mainly due to slow extraction of electrons from the lower laser states. The parameter-free simulation scheme previously introduced has proved to be an ideal tool to have some insight in the main limitations of these early structures and for the characterization and optimization of novel QCL prototypes [22, 23]. Indeed, our simulated experiments allowed to propose promising designs for which the predicted lasing action was later demonstrated [24].

Our prototypical QCL structure is designed to emit at 4.4 THz ($\lambda \sim 67$ μm) [22]. It is based on a vertical-transition configuration, which is known to lead to larger dipole matrix elements and narrower linewidths, and uses a conventional chirped-superlattice design. Its operating strategy exploits on the same concepts successfully implemented for the shortest-wavelength ($\lambda \sim 17\text{--}24$ μm) mid-IR QCL [25–27]. To minimize the occupation of the lower laser subband, we use a dense miniband with seven subbands, which provides a large phase space where electrons scattered either from the upper laser subband or directly from the injector can spread. The miniband dispersion is chosen as large as possible compatibly with the need of avoiding cross absorption. This suppresses thermal backfilling and provides a large operating range of currents and voltages. Energy relaxation within the first miniband would appear to be hindered by the lack of final states with appropriate energy to allow for LO-phonon emission. Nevertheless, carrier–carrier interaction does beneficially operate as an activation mechanism, since it provides sufficient in-plane momentum for the electrons to open a scattering path via optical phonon to the lower subbands. In the presence of carrier–carrier interaction, electrons efficiently relax into the lower states of the injector, from where they are readily transferred into the upper laser state of the following period. A significant population inversion then results between the subbands of the laser transition [22]. Apart from its strong technologic implications, this

nanostructured device came out to be an ideal context to investigate the complex synergy between carrier thermalization and phonon-assisted energy relaxation. This is indeed the key ingredient for a proper operation of these new light sources.

3.2. Microscopic Modeling of Quantum Systems with Open Boundaries

As anticipated in the introductory part of the paper, in spite of the quantum-mechanical nature of carrier dynamics in the active region of typical nanostructured devices, the overall behavior of such quantum systems is often the result of a complex interplay between phase coherence and energy relaxation/dephasing, the latter being primarily induced by the presence of spatial boundaries [3]. It follows that a proper treatment of open quantum devices requires a theoretical approach able to properly account for both coherent and incoherent, i.e., phase-breaking, processes on the same footing. To this end, a generalization to open systems, i.e., systems with open boundaries, of the SBE in Eq. (8) has been proposed [28]. However, the theoretical analysis in Ref. [28] is primarily related to the interplay between phase coherence and energy relaxation within the device active region. Starting from the analysis presented in Ref. [28], more recently, a detailed investigation of the carrier-injection process (from the electrical contacts into the device active region) has been performed [29].

The aim of this section is to review the microscopic analysis proposed in Ref. [29], which provides a rigorous quantum-mechanical description of the coupling dynamics between the device active region and external charge reservoirs. The latter is able to account for the semiphenomenologic injection models commonly used in state-of-the-art simulations of realistic 1D and 2D open quantum devices [30]. Among such simulation strategies, it is worth mentioning the approach recently proposed by Fischetti and coworkers [31]: By denoting, again, with f_α , the carrier distribution over the electronic states α of the device and with $P_{\alpha\alpha'}$, the microscopic scattering rates (due, e.g., to carrier–carrier and carrier–phonon interaction), the transport equation proposed in Ref. [31] is of the form:

$$\frac{d}{dt}f_\alpha = \sum_{\alpha'}(P_{\alpha\alpha'}f_{\alpha'} - P_{\alpha'\alpha}f_\alpha) + \frac{f_\alpha^b - f_\alpha}{\tau_\alpha} \quad (41)$$

Here, f_α^b denotes the equilibrium carrier distribution in the contacts, while τ_α can be regarded as the device transit time for an electron in state α . As anticipated, in spite of a rigorous treatment of the scattering dynamics (via the standard Boltzmann collision term involving microscopic scattering rates $P_{\alpha\alpha'}$ [1]), the last (relaxation-time-like) term describes carrier injection/loss on a partially phenomenologic level and does not depend on the real position of the device spatial boundaries.

To provide a fully microscopic real-space description of the carrier-injection process, we shall start revisiting the theoretical approach proposed in Ref. [28].

3.2.1. Conventional Wigner-Function Description

The starting point of the microscopic treatment of open quantum systems proposed in Ref. [28] is the SBE for a closed system in Eq. (8):

$$\frac{d}{dt}\rho_{\alpha_1\alpha_2} = \sum_{\alpha'_1\alpha'_2} L_{\alpha_1\alpha_2, \alpha'_1\alpha'_2} \rho_{\alpha'_1\alpha'_2} \quad (42)$$

where the effective Liouville operator given in Eq. (14) is the sum of two terms: coherent (i.e., scattering-free) single-particle evolution plus energy relaxation/dephasing dynamics; The latter is described in terms of the scattering tensor Γ , whose explicit form, given in Ref. [5], involves the microscopic in- and out-scattering rates for the various interaction mechanisms considered. The key idea proposed in Ref. [28] is to apply the usual Weyl-Wigner transform

$$u_{\alpha_1\alpha_2}(\mathbf{r}, \mathbf{k}) = \int d\mathbf{r}' \phi_{\alpha_1}\left(\mathbf{r} + \frac{\mathbf{r}'}{2}\right) \frac{e^{-i\mathbf{k}\cdot\mathbf{r}'}}{(2\pi)^{\frac{3}{2}}} \phi_{\alpha_2}^*\left(\mathbf{r} - \frac{\mathbf{r}'}{2}\right) \quad (43)$$

$[\phi_{\alpha}(\mathbf{r}) \equiv \langle \mathbf{r} | \alpha \rangle]$ denoting the single-particle wavefunction of state α] to the SBE in Eq. (42). In this way, the latter is translated into its phase-space representation \mathbf{r}, \mathbf{k} , which allows the Wigner function [3] to be imposed

$$f(\mathbf{r}, \mathbf{k}) = \sum_{\alpha_1\alpha_2} u_{\alpha_1\alpha_2}(\mathbf{r}, \mathbf{k}) \rho_{\alpha_1\alpha_2} \quad (44)$$

the desired values at the device spatial boundaries according to the well-known ‘‘U scheme’’ depicted in Figure 5. More specifically, to properly impose the desired spatial boundary conditions to the equation of motion for f , we add and subtract a source term

$$S(\mathbf{r}, \mathbf{k}) = v(\mathbf{k}) f^b(\mathbf{k}) \delta(\mathbf{r} - \mathbf{r}_b) \quad (45)$$

where $v(\mathbf{k})$ denotes the negative or incoming part of the carrier group velocity normal to the boundary surface, and $f^b(\mathbf{k})$ is the Wigner function describing the distribution of the injected carriers. By applying the inverse of the Weyl-Wigner transform in Eq. (43) to the new equation of motion for f , we finally get:

$$\frac{d}{dt}\rho_{\alpha_1\alpha_2} = \sum_{\alpha'_1\alpha'_2} \tilde{L}_{\alpha_1\alpha_2, \alpha'_1\alpha'_2} \rho_{\alpha'_1\alpha'_2} + S_{\alpha_1\alpha_2} \quad (46)$$

where the effective Liouville operator \tilde{L} corresponds to the operator L in Eq. (14) renormalized by

$$\Delta L_{\alpha_1\alpha_2, \alpha'_1\alpha'_2} = - \int d\mathbf{r}_b d\mathbf{k} u_{\alpha_1\alpha_2}^*(\mathbf{r}_b, \mathbf{k}) v(\mathbf{k}) u_{\alpha'_1\alpha'_2}(\mathbf{r}_b, \mathbf{k}) \quad (47)$$

and $S_{\alpha_1\alpha_2}$ is the Weyl-Wigner antitransform of the source term in Eq. (45). Equation (46) is the desired generalization to open systems of the SBE in Eq. (42)².

² The open character of the system results in a non-Hermitian correction ΔL to the Liouville operator L , whose effect is equivalent to a purely dissipative process within the simulated region, as originally pointed out in [3].

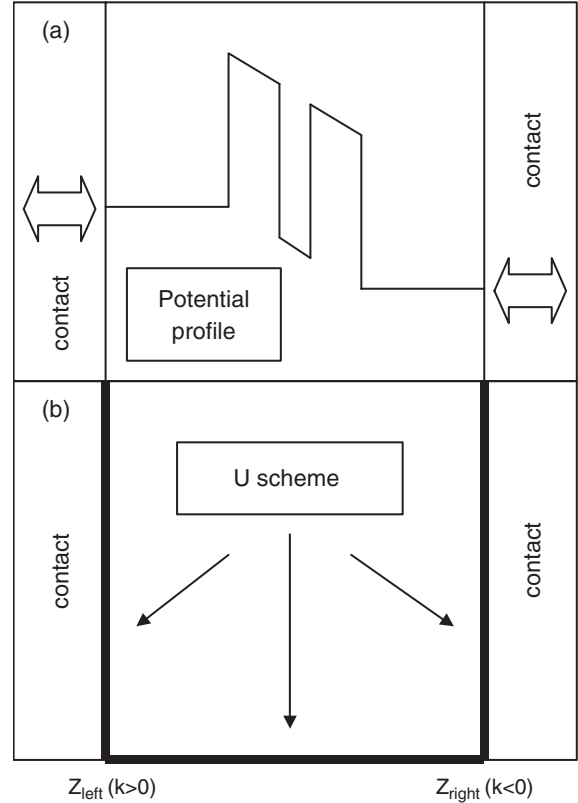


Figure 5. Schematic representation of the device active region sandwiched between its electrical contacts (a) and of the corresponding U boundary-condition scheme for a 1D system. The latter implies, in particular, the knowledge of the incoming Wigner function $f(z_b, k)$, i.e., $f(z_{\text{left}}, k > 0)$ and $f(z_{\text{right}}, k < 0)$.

To validate the theoretical approach presented so far, we shall focus on a very simple semiconductor nanostructure: a single-barrier equidistant from the device contacts (Fig. 6). As basis states α , we adopt the scattering states of the device potential profile; moreover, to better identify the role played by carrier injection, we shall neglect all other sources of energy relaxation/dephasing in the device active region, such as carrier-phonon and carrier-carrier scattering: $\Gamma_{\alpha_1\alpha_2, \alpha'_1\alpha'_2} = 0$ [Eq. (14)]. Under these assumptions, Eq. (46) in steady-state conditions reduces to:

$$\frac{i}{\hbar}(\epsilon_{\alpha_1} - \epsilon_{\alpha_2})\rho_{\alpha_1\alpha_2} - \sum_{\alpha'_1\alpha'_2} \Delta L_{\alpha_1\alpha_2, \alpha'_1\alpha'_2} \rho_{\alpha'_1\alpha'_2} = S_{\alpha_1\alpha_2} \quad (48)$$

Figure 6 shows results for the single-barrier potential profile when carriers are primarily injected from the left. Here, the simulated real-space charge distribution obtained from the phenomenologic injection model in Eq. (41) (dashed curve) is compared to that of the microscopic model in Eq. (48) (solid curves). As we can see, the two models give completely different results. The phenomenologic model gives basically what we expect, since we have significant carrier injection from the left only and since the potential barrier is relatively high, the carrier distribution is mainly located on the left side. In contrast, the microscopic model gives an almost symmetric charge distribution. To understand the

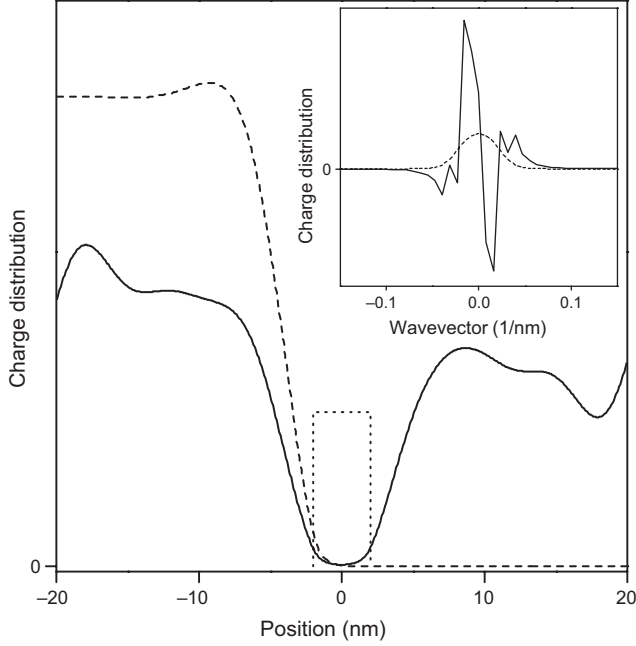


Figure 6. Comparison between the real-space charge distribution obtained from the phenomenologic injection model in Eq. (41) [$n(\mathbf{r}) = \sum_{\alpha} f_{\alpha} |\phi_{\alpha}(\mathbf{r})|^2$ —dashed curve] and the microscopic model in Eq. (48) [$n(\mathbf{r}) = \sum_{\alpha_1 \alpha_2} \rho_{\alpha_1 \alpha_2} \phi_{\alpha_1}(\mathbf{r}) \phi_{\alpha_2}^*(\mathbf{r})$ —solid curve] for a GaAs-based single-barrier structure (height $V_o = 0.5$ eV and width $a = 4$ nm) equidistant from the electrical contacts. In this room-temperature simulation, due to a misalignment $\Delta\mu = 0.2$ eV of the left and right chemical potential, carriers are primarily injected from left. The corresponding charge distribution in momentum space also is reported in the inset (see text).

origin of this unphysical result, let us focus on the nature of the source term in Eq. (46). Contrary to the phenomenologic injection/loss term in Eq. (41), the latter is intrinsically nondiagonal, i.e., the injection of a carrier with well-defined wavevector \mathbf{k} [Eq. (45)] is described by a nondiagonal source contribution $S_{\alpha_1 \alpha_2}$. In other words, we inject into the device active region a coherent superposition of states α_1 and α_2 , in clear contrast with the idea of injection from a thermal, i.e., diagonal, charge reservoir. More specifically, in this case, the generic scattering state α on the left comes out to be an almost equally weighted superposition of $+k$ and $-k$: $\phi_k(z) = a_k e^{ikz} + b_k e^{-ikz}$. This, in turn, tells us that the generic plane-wave state k injected from the left contact also is an almost equally weighted superposition of the left and right scattering states. This is why the charge distribution (solid curve in Fig. 6) is almost symmetric: any electron injected from the left couples to left-scattering, as well as to right-scattering states. The anomaly of the microscopic model is even more pronounced if we look at the carrier distribution in momentum space (see inset in Fig. 6). While, for the phenomenologic model (dashed curve), we get a positive-definite distribution showing, as expected, the two symmetric wavevector components of the scattering state, the microscopic result is not positive definite; this tells us that the boundary-condition scheme considered so far does not provide a “good” Wigner function.

The scenario previously discussed is highly nonphysical; it can be mainly ascribed to the boundary-condition scheme

used so far, which implies injection of plane-wave electrons [see source term in Eq. (45)], regardless of the shape of the device potential profile. This is an intrinsic limitation of the conventional Wigner-function representation \mathbf{r}, \mathbf{k} . It is then clear that, to overcome this limitation, what we need is a boundary-condition scheme realizing diagonal injection over the scattering states α of the device potential profile.

3.2.2. Generalized Wigner-Function Approach

To overcome the intrinsic limitations of the conventional Wigner-function formulation previously discussed, the key idea proposed in Ref. [29] is to extend the Weyl-Wigner transform in Eq. (43) from the \mathbf{k} to a generic basis set $\{|\beta\rangle\}$ according to³:

$$\begin{aligned} \bar{u}_{\beta_1 \beta_2}^{\alpha_1 \alpha_2}(\mathbf{r}) &= \Omega \int d\mathbf{r}' \phi_{\alpha_1}(\mathbf{r} + \frac{\mathbf{r}'}{2}) \chi_{\beta_1}^*(\mathbf{r} + \frac{\mathbf{r}'}{2}) \\ &\times \chi_{\beta_2}(\mathbf{r} - \frac{\mathbf{r}'}{2}) \phi_{\alpha_2}^*(\mathbf{r} - \frac{\mathbf{r}'}{2}) \end{aligned} \quad (49)$$

where Ω denotes the volume of the simulated region. In analogy to Eq. (44), our generalized Wigner function is given by⁴:

$$\bar{f}_{\beta_1 \beta_2}(\mathbf{r}) = \sum_{\alpha_1 \alpha_2} \bar{u}_{\beta_1 \beta_2}^{\alpha_1 \alpha_2}(\mathbf{r}) \rho_{\alpha_1 \alpha_2} \quad (50)$$

By combining Eqs. (44) and (50), the new Wigner function \bar{f} can be easily expressed in terms of the standard one as:

$$\bar{f}_{\beta_1 \beta_2}(\mathbf{r}) = \int d\mathbf{r}' d\mathbf{k}' \mathcal{K}_{\beta_1 \beta_2}(\mathbf{r}; \mathbf{r}', \mathbf{k}') f(\mathbf{r}', \mathbf{k}') \quad (51)$$

with

$$\mathcal{K}_{\beta_1 \beta_2}(\mathbf{r}; \mathbf{r}', \mathbf{k}') = \sum_{\alpha_1 \alpha_2} \bar{u}_{\beta_1 \beta_2}^{\alpha_1 \alpha_2}(\mathbf{r}) u_{\alpha_1 \alpha_2}^*(\mathbf{r}', \mathbf{k}') \quad (52)$$

The new Wigner function then can be regarded as a sort of convolution of the original one with the kernel \mathcal{K} in (52). This may recall a well-established procedure used to obtain positive-definite phase-space quantum distributions, the so-called “smoothing procedure” [32]. However, we stress that this is not the case: (i) here there is no need for a positive-definite function and (ii) contrary to the standard smoothing procedure, the initial and final phase spaces do not coincide ($\mathbf{r}', \mathbf{k}' \rightarrow \mathbf{r}, \beta_1 \beta_2$).

³ Here, the set of basis functions $\chi_{\beta}(\mathbf{r}) \equiv \langle \mathbf{r} | \beta \rangle$ is, in general, different from the basis set ϕ_{α} . It is easy to show that if we consider as basis states $|\beta\rangle$ conventional plane waves, the standard Weyl-Wigner transform in Eq. (43) is recovered. We stress that, contrary to Eq. (43), this new Weyl-Wigner transform is not a unitary transformation corresponding to a simple basis change; it amounts to a nontrivial projection operation involving the real-space Wigner coordinate \mathbf{r} : $\bar{u}_{\beta_1 \beta_2}^{\alpha_1 \alpha_2}(\mathbf{r}) = \langle \beta_1 | \alpha_1 \rangle | \mathbf{r} \rangle \langle \alpha_2 | \beta_2 \rangle$.

⁴ In analogy to the conventional Wigner-function theory [3], the real-space charge distribution (see solid line in Fig. 7) is now given by $n(\mathbf{r}) = \sum_{\beta} \bar{f}_{\beta \beta}(\mathbf{r})$.

By adopting as basis states $|\beta\rangle$ again the scattering states of the device potential profile $|\alpha\rangle$ and assuming a diagonal source term of the form

$$\bar{S}_{\alpha_1\alpha_2}(\mathbf{r}) = v_{\alpha_1} f_{\alpha_1}^b \delta_{\alpha_1\alpha_2} \delta(\mathbf{r} - \mathbf{r}_b) \quad (53)$$

the equation of motion for the new Wigner function \bar{f} in Eq. (50) will be given by

$$\frac{d}{dt} \bar{f}_{\alpha_1\alpha_2}(\mathbf{r}) = \sum_{\alpha'_1\alpha'_2} \int d\mathbf{r}' \tilde{L}_{\alpha_1\alpha_2, \alpha'_1\alpha'_2}(\mathbf{r}, \mathbf{r}') \bar{f}_{\alpha'_1\alpha'_2}(\mathbf{r}') + \bar{S}_{\alpha_1\alpha_2}(\mathbf{r}) \quad (54)$$

with a renormalization $\Delta L_{\alpha_1\alpha_2, \alpha'_1\alpha'_2}(\mathbf{r}, \mathbf{r}')$ given by

$$-v_{\alpha_1} \delta_{\alpha_1, \alpha_2} \delta_{\alpha_1\alpha_2, \alpha'_1\alpha'_2} \delta(\mathbf{r} - \mathbf{r}_b) \delta(\mathbf{r} - \mathbf{r}') \quad (55)$$

We stress that now the source term \bar{S} in Eq. (53) describes diagonal injection over the scattering states (with velocity v_β), as requested. Indeed, if we now integrate Eq. (54) over the real-space coordinate \mathbf{r} , we get again the density-matrix equation in Eq. (46), but now, with a diagonal source term, $S_{\alpha_1\alpha_2} = v_{\alpha_1} f_{\alpha_1}^b \delta_{\alpha_1\alpha_2}$ and a much simpler, i.e., partially diagonal, renormalization term $\Delta L_{\alpha_1\alpha_2, \alpha'_1\alpha'_2} = -v_{\alpha_1} \delta_{\alpha_1\alpha_2} \bar{u}_{\alpha_1\alpha_2}^{\alpha'_1\alpha'_2}(\mathbf{r}_b)$. In the scattering-free case, the stationary solution again is described by Eq. (48). However, due to the diagonal nature of the new source term, as well as of the partially diagonal structure of ΔL , Eq. (48) now has a diagonal solution: $\rho_{\alpha_1\alpha_2} = f_{\alpha_1} \delta_{\alpha_1\alpha_2}$. More specifically, the diagonal density-matrix elements f_α obey the following steady-state equation:

$$\sum_{\alpha'} \mathcal{T}_{\alpha\alpha'} f_{\alpha'} = f_\alpha^b \quad (56)$$

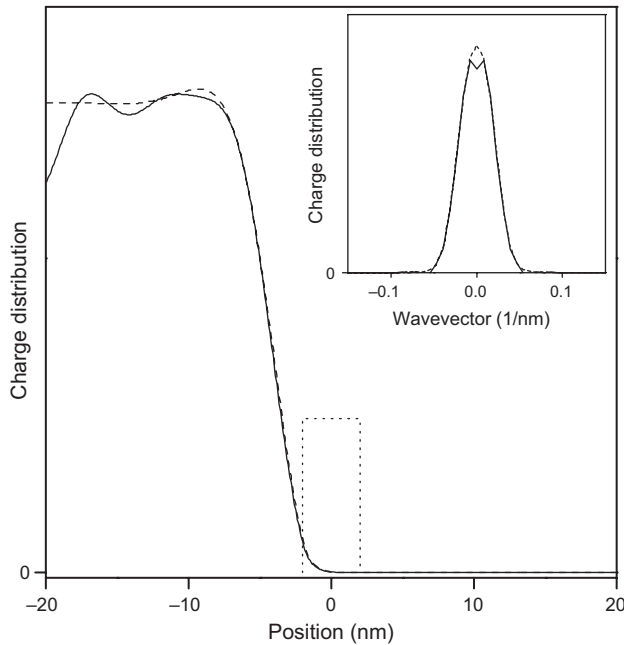


Figure 7. Same as in Figure 6 but for the new microscopic model in Eq. (56) (see text).

with $\mathcal{T}_{\alpha\alpha'} = \bar{u}_{\alpha\alpha'}^{\alpha\alpha'}(\mathbf{r}_b)$. Equation (56) is semiclassical in nature, i.e., it involves diagonal density-matrix terms only. However, contrary to the phenomenologic injection model in Eq. (41), here the distribution function in state α is the result of an “incoherent superposition” from all the injection channels: $f_\alpha = \sum_{\alpha'} \mathcal{T}_{\alpha\alpha'}^{-1} f_{\alpha'}^b$. We finally stress that, by replacing the \mathcal{T} with the identity operator ($\mathcal{T}_{\alpha\alpha'} = \delta_{\alpha\alpha'}$), the phenomenologic injection model in Eq. (41) is recovered. Figure 7 again shows results for the single-barrier potential profile previously considered. Here, the simulation based on the phenomenologic injection model in Eq. (41) (dashed curves) is compared to that of the new microscopic model in Eq. (56) (solid curves). As we can see, the highly nonphysical behaviors of Figure 6 (solid curves) have been completely removed. Indeed, the momentum distribution in the inset is always positive-definite and the two models exhibit a very similar behavior. We find relatively small deviations close to the device spatial boundaries, which can be ascribed to the interlevel injection coupling $\mathcal{T}_{\alpha\alpha'}$ [Eq. (56)], not present in the phenomenologic injection model. This is clearly a fingerprint of our real-space description, where the point-like carrier injection is located at the device spatial boundaries. However, when the device active region is relatively far from the contacts, these deviations can be safely neglected, and the phenomenologic model in Eq. (41) provides reliable results.

At this point, a question needs to be answered: *Would it be possible to describe the diagonal injection over the scattering states in Eq. (53) by means of a “ad hoc” source term $S(\mathbf{r}, \mathbf{k})$ within the standard phase-space?* The answer to this question is yes. However, a closer inspection reveals that such an “ad hoc” function can never be point-like in space, which in turn does not allow to the conventional boundary-condition approach considered so far to be used (Fig. 5), where we impose the value of the Wigner distribution only at the device spatial boundaries by means of an effective point-like source term [Eq. (53)]. Therefore, the generalized Weyl-Wigner representation proposed in Ref. [29] is not only physically sound, but allows all the well-known advantages of the standard boundary condition scheme to be maintained.

4. CONCLUSIONS

In summary, we have discussed state-of-the-art approaches used in the theoretical modeling of optoelectronic quantum devices. The primary goal of the present review article was to provide a cohesive description of basic quantum-transport phenomena, able to explain/predict the performances of new-generation semiconductor quantum devices. To this aim, we have reviewed and discussed a fully 3D microscopic description of time-dependent as well as steady-state quantum-transport phenomena based on the density-matrix formalism. This has allowed us to introduce in a quite natural way, the separation between coherent and incoherent, i.e., phase-breaking, processes. Starting from this general theoretical framework, we have analyzed two different classes of semiconductor-based quantum devices, namely periodically repeated structures (e.g., QCLs) and quantum systems with open boundaries (e.g., multibarrier nanostructures).

For the first class, we have shown how a proper use of periodic boundary conditions allows for reproduction/prediction of the current-voltage characteristics of state-of-the-art mid- and far-IR QCLs, without resorting to any phenomenologic parameters.

For the second class of devices, we have reviewed a rigorous description of quantum-transport phenomena in systems with open boundaries. More specifically, the analysis presented has clearly shown that the conventional Wigner-function formalism leads to unphysical results, such as injection of coherent superpositions of states from the device spatial boundaries. Finally, we have shown how this basic limitation can be removed by introducing a generalization of the standard Wigner-function formulation, able to properly describe the incoherent nature of carrier injection. The latter constitutes a rigorous derivation of the phenomenologic injection models commonly used in the simulation of open quantum devices.

GLOSSARY

Monte Carlo method Stochastic technique based on the generation of random numbers; the method is commonly employed to numerically solve coupled linear and nonlinear rate equations.

Quantum cascade laser Unipolar semiconductor laser based on resonant tunneling as injection mechanism and intersubband transitions as light generation scheme.

Semiconductor Bloch equations Equations of motion describing the time evolution of the single-particle density matrix; generalization to semiconductors of the well-known optical Bloch equations.

Weyl–Wigner transform Unitary transformation connecting the single-particle density matrix with the Wigner function.

Wigner function Quantum mechanical generalization of the classical distribution function in the phase-space.

REFERENCES

1. C. Jacoboni and P. Lugli, “The Monte Carlo Method for Semiconductor Device Simulations.” Springer, Wien, 1989.
2. E. Schöll (Ed.), “Theory of Transport Properties of Semiconductor Nanostructures.” Chapman and Hall, London, 1998.
3. W. Frensley, *Rev. Mod. Phys.* 62, 3 (1990) and references therein.
4. F. Rossi and T. Kuhn, *Rev. Mod. Phys.* 74, 895 (2002) and references therein.
5. T. Kuhn, in “Theory of Transport Properties of Semiconductor Nanostructures” (E. Schöll, Ed.), p. 173. Chapman and Hall, London, 1998.
6. L. Esaki and R. Tsu, *IBM J. Res. Dev.* 14, 61 (1970).
7. J. Shah, “Ultrafast Spectroscopy of Semiconductors and Semiconductor Nanostructures.” Springer, Berlin, 1996.
8. F. Capasso (Ed.), “Physics of Quantum Electron Devices.” Springer, Berlin, 1990.
9. R. F. Kazarinov and R. A. Suris, *Fiz. Tekh. Poluprovodn.* 5, 797 (1971) [*Sov. Phys. Semicond.* 5, 707 (1971)].
10. J. Faist, F. Capasso, D. L. Sivco, C. Sirtori, and A. Y. Cho, *Science* 264, 553 (1994).
11. G. Scamarcio, F. Capasso, C. Sirtori, J. Faist, A. L. Hutchinson, D. L. Sivco, and A. Y. Cho, *Science* 276, 773 (1997).
12. C. Gmachl, A. Tredicucci, D. L. Sivco, A. L. Hutchinson, F. Capasso, and A. Y. Cho, *Science* 286, 749 (1999).
13. F. Capasso, C. Gmachl, R. Paiella, A. Tredicucci, A. L. Hutchinson, D. L. Sivco, J. N. Baillargeon, A. Y. Cho, and H. C. Liu, *IEEE J. Sel. Top. Quantum Electron.* 6, 931 (2000).
14. V. B. Gorfinkel, S. Luryi, and B. Gelmont, *IEEE J. Quantum Electron.* 32, 1995 (1996); L. Friedman and R. A. Soref, *J. Appl. Phys.* 83, 3480 (1998).
15. P. Harrison, *Appl. Phys. Lett.* 75, 2800 (1999).
16. R. C. Iotti and F. Rossi, *Appl. Phys. Lett.* 76, 2265 (2000).
17. R. C. Iotti and F. Rossi, *Appl. Phys. Lett.* 78, 2902 (2001).
18. R. C. Iotti and F. Rossi, *Phys. Rev. Lett.* 87, 146603 (2001).
19. F. Rossi, P. Poli, and C. Jacoboni, *Semicond. Sci. Technol.* 7, 1017 (1992).
20. C. Sirtori, P. Kruck, S. Barbieri, P. Collot, and J. Nagle, *Appl. Phys. Lett.* 73, 3486 (1998).
21. F. Eickemeyer, K. Reinmann, M. Woerner, T. Elsaesser, S. Barbieri, C. Sirtori, G. Strasser, T. Müller, R. Bratschitsch, and K. Unterreiner, *Phys. Rev. Lett.* 89, 047402 (2002).
22. R. Köhler, R. C. Iotti, A. Tredicucci, and F. Rossi, *Appl. Phys. Lett.* 79, 3920 (2001).
23. R. C. Iotti and F. Rossi, *Physica E* 13, 715 (2002).
24. R. Köhler, A. Tredicucci, F. Beltram, H. E. Beere, E. H. Linfield, A. G. Davies, D. A. Ritchie, R. C. Iotti, and F. Rossi, *Nature* 417, 156 (2002).
25. A. Tredicucci, C. Gmachl, F. Capasso, D. L. Sivco, A. L. Hutchinson, and A. Y. Cho, *Appl. Phys. Lett.* 74, 638 (1999).
26. A. Tredicucci, C. Gmachl, M. C. Wanke, F. Capasso, A. L. Hutchinson, D. L. Sivco, S. N. G. Chu, and A. Y. Cho, *Appl. Phys. Lett.* 77, 2286 (2000).
27. R. Colombelli, F. Capasso, C. Gmachl, A. L. Hutchinson, D. L. Sivco, A. Tredicucci, M. C. Wanke, A. M. Sergent, and A. Y. Cho, *Appl. Phys. Lett.* 78, 2620 (2001).
28. F. Rossi, A. Di Carlo, and P. Lugli, *Phys. Rev. Lett.* 80, 3348 (1998).
29. R. Proietti Zaccaria and F. Rossi, *Phys. Rev. B* 67, 113311 (2003).
30. *Special Issue on Computational Electronics, VLSI Design* 13 (2001).
31. M. V. Fischetti, *Phys. Rev. B* 59, 4901 (1999) and references therein.
32. P. Bertrand, J. P. Deremus, B. Izrar, V. T. Nguyen, and M. R. Feix, *Phys. Lett. A* 94, 415 (1983) and references therein.

Thermal Conductivity of Semiconductor Nanostructures

Alexander A. Balandin

University of California-Riverside, Riverside, California, USA

CONTENTS

1. Introduction
 2. Basic Definitions and Concepts
 3. Electronic Thermal Conductivity
 4. Lattice Thermal Conductivity
 5. Size Effects on Thermal Conductivity of Nanostructures
 6. Thermal Conductivity of Specific Types of Nanostructures
 7. Conclusions
- Glossary
References

1. INTRODUCTION

In this section, we outline the factors for the renewed interest to theoretical and experimental investigation of the thermal conductivity of semiconductors and, particularly, to the study of thermal conductivity of nanostructures. The major effects that lead to changes in thermal transport in nanostructures, as compared to thermal transport in bulk semiconductors, are also briefly discussed in this section. Since thermal conductivity is strongly affected even when only one dimension of a semiconductor structure is in the nanoscale range, this article covers results pertinent to quantum wells and superlattices together with such nanostructures as nanowires and quantum dot arrays. The broader coverage is presented also for the reason that most of the experimental data available to date in the field of thermal transport in low-dimensional structures is for superlattices or single-suspended thin films.

1.1. Device Downscaling and the Problem of Thermal Management

In order to achieve increased performance and reduced cost, for the past three decades the semiconductor industry has pursued a strategy of decreasing the characteristic

feature size of devices with each new product generation. Following the projections of the International Technology Roadmap for Semiconductors the gate length of metal-oxide-semiconductor devices should reach the 70-nanometer technology node by the year 2008 [1]. One can conclude that state-of-art Si electronic circuits are already in the nanoscale realm. To support experimental and industrial development and continue the progress associated with the downscaling, novel physical phenomena that emerge at nanoscale have to be thoroughly investigated and incorporated into the nanoscale device simulation tools. The study of novel physics should not be limited to the charge carrier quantum confinement effects only but should also include changes in acoustic phonon transport, due to spatial confinement and their consequences for thermal management at nanoscale. A variety of novel phenomena that emerge at this length scale include, but not limited to, spatial confinement and quantization of phonon modes, decreased phonon group velocity, changed phonon density of states, increased phonon boundary scattering, phonon redistribution due to scattering from rough boundaries, and pronounced thermal boundary resistance due to the increased number of interfaces and the use of dissimilar materials.

The device density multiplied by the energy dissipated and the number of operations per second per device gives the approximate power dissipated per unit chip area. The amount of energy that can be transported away from a given device and a circuit is limited by the thermal conductivity of the circuit material and the environment. The minimum power supply voltage is limited by thermal fluctuations to about $4k_B T/e$ or 0.1 V [2]. Here, k_B is the Boltzmann's constant, T is the temperature, and e is the charge of an electron. When the noise margins are taken into account, it predicts that the supply voltage should be limited to a range from 1.2 V to 2.5 V. Thus, one has to maintain relatively small thermal resistance of the device structure in order to be able to remove generated heat in future ultra-large-scale integrated (ULSI) circuits. An increased number of interconnects and a decreased transistor feature size lead to increased thermal resistance of the integrated circuit and the associated difficulties in heat removal. Following the International Technology Roadmap projections, the total

power consumption in future ULSI circuits will continue to increase despite the planned reduction of the power supply voltage [1]. Higher operating frequency and higher overall capacitance and resistance of larger chips with more on-chip functions mostly drive the predicted increase in power consumption. The expected increase of interconnect density at higher technology nodes may additionally complicate the problem of heat dissipation of a chip. The progress in interconnect technology for the past few years has been associated with the application of multilevel interconnects and growing use of polysilicon. These tendencies make it more difficult to remove heat from a chip and dictate the need for a comprehensive review of nanoscale thermal transport.

The problem of heat dissipation at nanoscale is not only caused by the increased power dissipation density, but also by the various size effects that limit phonon heat conduction as a result of increased phonon boundary scattering [3] and change in the acoustic phonon spectrum [4]. It has been shown that phonon transport in superlattices can be significantly modified due to the formation of mini-bands and emergence of the mini-Umklapp processes associated with transitions between the mini-Brillouin zones [5], as well as modification of phonon dispersion due to phonon spatial confinement induced by the boundaries in nanowires [6] or thin films [4].

1.2. Experimental Evidence of Decreased Thermal Conductivity in Nanostructures

In recent years, many groups reported results of experimental investigation of the lateral thermal conductivity of thin semiconductor films and superlattices [7–14]. A strong decrease of thermal conductivity has been observed in most of cases. Zheng et al. [8] carried out measurements using a suspended microstructure, and found more than an order of magnitude reduction in the lateral thermal conductivity of single thin films in the temperature range from 293 K–413 K. In [10], the authors reported reduction in the in-plane thermal diffusivity of Si/Ge superlattices with period in a wide range from 1–30 nm. Chen et al. [11] reported 2–3 times decrease in the cross-plane lattice thermal conductivity of Si/Si_{0.71}Ge_{0.29} (5 nm/10 nm) superlattices. For the Si/Ge (3.3 nm/3.3 nm) superlattice structures described in [12], the measured value of the thermal conductivity in the in-plane direction was 1.7 W/m-K, while the one in the cross-plane direction was 2.78 W/m-K. The obtained thermal conductivity was considerably lower than those determined using bulk thermal conductivity values for Si, Ge, and Si_xGe_{1-x} alloys. For a comparison, the thermal conductivity of bulk Si is about 149 W/m-K at room temperature.

Beyer et al. [13] reported on experimentally observed strong decrease of the in-plane lattice thermal conductivity in PbTe and Bi₂Te₃-based superlattices compared to bulk materials. The same group has also observed a reduction of the lattice thermal conductivity parallel to the layers of PbTe/PbSe_{0.20}Te_{0.80} superlattice [14]. The choice of material systems for investigation of thermal conductivity in the results cited above is explained by the thermoelectrics context of these works. Lee et al. [15] have demonstrated that in Si/Ge superlattice structure the thermal conductivity is smaller than that in the alloy of the same materials. For the

superlattice periods in the range 3 nm < L < 7 nm, they observed the tendency of the thermal conductivity decrease with decreasing L.

Chattopadhyay et al. [16–17] investigated experimental thickness dependence of thin films made out of amorphous silicon carbon nitride (a-SiC_xN_y) and boron carbon nitride (a-BC_xN_y). These dependencies are shown in Figure 1. For these films, as well as for metallic thin films, they found very strong film thickness dependence of the thermal diffusivity as described by the exponential function $\alpha = \alpha(\infty) - [\alpha(\infty) - \alpha(0)] \exp\{-D/b\}$. Here D is the film thickness, α is the experimentally measured thermal diffusivity at thickness D, b is a constant, $\alpha(0)$ and $\alpha(\infty)$ are the thermal diffusivities for infinitesimally thin film and an infinitely thick layer, respectively. The relation of the thermal diffusivity to thermal conductivity is given later. The values of thermal diffusivities extracted from these measurements reveal very strong thickness dependence. For example, for a-SiC_xN_y on Si substrate the following parameters have been obtained: $\alpha(\infty) = 0.93 \pm 0.04$ cm²/s; $\alpha(0) = 0.36 \pm 0.006$ cm²/s; and $b = 2.7 \pm 0.38$ μ m [17].

1.3. Thermal Conductance at Nanoscale

The increased importance of thermal conductivity research, in view of electronic device downscaling and significant deviation of thermal conductivity values in nanoscale structures from bulk materials, explain the recent attention to this subject and appearance of many topical reviews dedicated to different aspects of the problem. Here, we briefly outline the scope of some of these reviews so that the reader can address those for more in-depth coverage of specific issues in the field, such as instrumentation, thermal boundary resistance, molecular dynamics simulations, etc. Cahill et al. [18] reviewed recent advancements in experimental methods for high spatial-resolution and high time-resolution thermometry, and application of these methods for measurements of thermal transport in low-dimensional structures. The authors of this review focus particular attention on

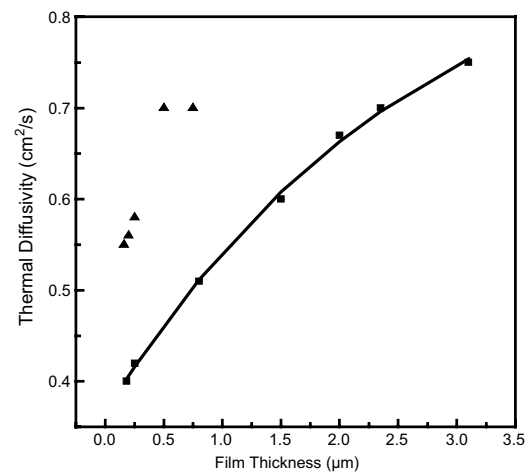


Figure 1. Variation of thermal diffusivity as a function of film thickness for the a-SiC_xN_y (rectangular marks) and a-BC_xN_y (triangular marks) thin films. Reprinted with permission from [17], S. Chattopadhyay et al., *J. Appl. Phys.* 92, 5150 (2002). © 2002, American Institute of Physics.

the scanning thermal microscopy (SThM), which allows one to achieve lateral resolution of 50 nm and a measurement bandwidth of 100 kHz. Chen and Shakouri [19] addressed heat transfer in nanostructures for solid-state energy conversion. In this review, the authors placed emphasis on fundamental issues that distinguish energy transport and conversion between nanoscale and macroscale, as well as heat transfer issues related to device development and property characterization.

Goodson and Ju [20] gave a comprehensive review of heat conduction in single-crystal semiconducting and superconducting thin films and superlattices, polycrystalline diamond films, and highly disordered organic and oxide films. The review of experimental techniques for measurement of thermal conductivity of thin films can be found in [21]. In this review, Mirmira and Fletcher [21] present a summary of different experimental models for thermal conductivity of thin films and comparison of experimental results obtained by different steady state and transient techniques. Balandin and Zou [22] reviewed theoretical approaches to modeling thermal conductivity in semiconductor ultra-thin films (quantum wells) and nanowires. A particular emphasis in their review was on thermal conduction in nanostructures with lateral dimensions much smaller than the phonon mean-free path. In such structures, a strong modification of acoustic phonon spectrum is expected, which affects the lattice thermal conductivity. Quantum effects in ballistic thermal transport through nanowires have been addressed in the review of Ciraci et al. [23]. In this work, the authors addressed quantization effects due to transverse confinement on electronic and phonon thermal conduction. The considered nanostructures included semiconductor nanowires, point contacts, and single-wall carbon nanotubes. In a very comprehensive recent review, Cahill et al. [24] addressed a variety of experimental and theoretical issue pertinent to nanoscale thermal transport.

2. BASIC DEFINITIONS AND CONCEPTS

We start the review of thermal conduction in semiconductor nanostructures with the basic definitions and concepts important for understanding the material of the subsequent sections.

2.1. Thermal Conductivity and Thermal Diffusivity

First, we give a definition of thermal conductivity. In order to induce a heat flow \dot{Q} in a material, one must impose a temperature gradient. The ratio of the heat flow per unit area A to the temperature gradient is defined as the thermal conductivity:

$$K = -\dot{Q}/(A\nabla T) \quad (1)$$

This definition tacitly assumes the validity of Fourier's law of heat conduction, as well as material isotropy, which allows one to avoid tensor notation for thermal conductivity. K , a positively defined quantity and the minus sign that came

from Fourier's law, indicates that the heat flows opposite to the temperature gradient. Strictly speaking, this definition runs into a problem in the ballistic transport regime, for example, at very low temperature or extremely small structures. This problem is related to ambiguities with the concept of temperature in such cases. The temperature, as a measure of the average kinetic energy of a system of particles, is an equilibrium concept. It works in the macroscopic processes of heat flow because one can define a local temperature for large systems. The latter may not be true for the nanometer scale structures. The approach based on Landauer formalism, which allows one to avoid this problem for ballistic flow of heat between two reservoirs [25], may not be very practical for nanodevices at room temperature and above. This is because the phonon mean-free path (MFP) may still be smaller than the distance between reservoirs, and phonon transport is diffusive rather than ballistic. Thus, while the problem of local temperature at nanoscale still needs to be properly addressed, it is customary to extend the definition of eq. (1) to nanostructures.

Thermal diffusivity α , which is a more convenient parameter for experimental measurements, bears a simple direct relationship to the thermal conductivity K through the expression $K = \alpha\rho C$. Here, ρ is the density of the material and C is the specific heat of the material. The units of thermal conductivity are W/cmK, while the units of thermal diffusivity are cm²/s.

2.2. Thermal Boundary Resistance

Another important quantity that needs to be defined is the thermal boundary resistance (TBR), which is also called Kapitza resistance after a scientist who first investigated this effect at low temperature for helium-solid interface [26]. In the remainder of the chapter, we will use both terms interchangeably. The thermal boundary resistance, R_{Bd} , is defined as the ratio of the temperature discontinuity at the interface to the power per unit area flowing across the interface:

$$R_{Bd} = \Delta T/(\dot{Q}/A) \quad (2)$$

The thermal boundary conductivity h_{Bd} is, thus, defined as the ratio of the heat flow per unit area across the interface to the temperature discontinuity at the interface $h_{Bd} = 1/R_{Bd}$. The calculation of the thermal boundary conductivity is analogous to that of the thermal conductivity. The thermal boundary conductivity is determined by the number of phonons (carriers) incident on the interface, the energy carried by each phonon, and the probability that each phonon is transmitted across the interface. While for the calculation of the thermal conductivity, the difficulty is in determining the phonon MFP, that is, the scattering rates, for the calculation of the thermal boundary resistance, the difficulty is in determining the transmission probability. Perhaps the most comprehensive and complete review of the thermal boundary resistance to date was given by Swartz and Pohl [27, 28].

2.3. Lattice Vibrations and Heat Transport

Heat in technologically important semiconductors and nanostructures is mostly carried by the vibrations of crystal lattice, that is, phonons. The heat transport by lattice vibrations is governed by the anharmonicities of the lattice forces, by various imperfections of the crystal lattice and external boundaries. Before going into detail theory, it is beneficial to revisit a very simple concept of the thermal conduction by lattice vibrations given by Debye in order to explain experimental observation that the thermal conductivity in dielectric solids is usually inversely proportional to the absolute temperature. The lattice vibrations can be resolved into traveling waves, which carry heat. The thermal conductivity associate with these waves is $K \sim C_V V_s \Lambda$, where C_V is the specific heat per unit volume, V_s is the sound velocity, and Λ is the attenuation length of the lattice waves. Debye then showed that due to the scattering of the lattice waves, Λ , and correspondingly K , vary as $1/T$, provided that the temperature is not too low so that C_V is constant. This treatment, although far from being rigorous, provides useful physical insight and allows one to explain thermal conductivity values and their variations in many semiconductor materials and experimental situations.

An accurate treatment of the lattice thermal conductivity is based on the concept of a phonon, that is, quantized lattice waves. The theory of phonons can be found in many details in the standard solid-state physics textbooks [29–31]. In simple terms, the usefulness of this concept can be explained in the following way. The atoms in a crystal vibrate around their equilibrium positions, which are arranged in a regular lattice. The atoms are not bound to their equilibrium sites but rather to the neighboring atoms. As a result, the individual atoms do not vibrate independently. The vibrational spectrum of this system of strongly coupled oscillators can be readily found in terms of traveling waves [32]. These traveling waves are normal modes of vibrations of a crystal lattice, provided the lattice is perfect and the interaction forces are harmonic. Each traveling wave is assigned a wave vector \mathbf{q} , frequency ω , and polarization $\boldsymbol{\varepsilon}$. In crystals, to each wave vector \mathbf{q} correspond three waves with mutually perpendicular directions of polarization $\boldsymbol{\varepsilon}$ and three frequencies ω . In general, the direction of $\boldsymbol{\varepsilon}$ bears no simple relation to the direction of \mathbf{q} . In the elastic continuum approximation [31], one polarization direction is parallel to \mathbf{q} (longitudinal wave), while the other two directions are arbitrary but lie in a plane perpendicular to \mathbf{q} (transverse waves). A typical dispersion relation, which is a functional dependence $\omega = \omega(\mathbf{q})$ of the lattice waves (phonons) in bulk semiconductors are shown in Figure 2. For long wavelength vibrations, ω is a linear function of the wave vector \mathbf{q} , and correspondingly, the phase velocity $V_p = \omega/\mathbf{q}$ coincides with the group velocity $V_G = d\omega/d\mathbf{q}$. Three lower modes (see Fig. 2), for which $\omega(\mathbf{q} = 0) = 0$, describe the motion of the crystal unit cell and form the three acoustic branches. The upper modes referred to as optical branches describe the relative motion of atoms in a unit cell. In conventional semiconductors, the contribution of optical branches to thermal transport is negligible because of their low group velocity and high energy of excitation.

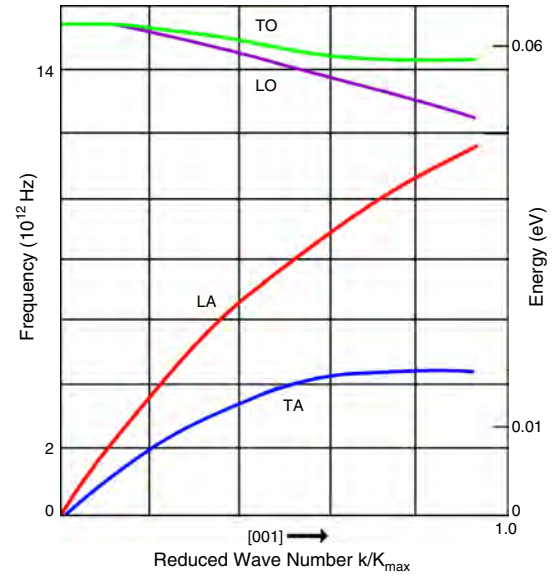


Figure 2. A schematic view of a typical dispersion relation for lattice waves (phonons) in bulk semiconductor.

2.4. Acoustic Phonons in Bulk Semiconductors and Nanostructures

The quanta of lattice vibrations or phonons are introduced more rigorously by applying quantum-mechanical considerations to the normal modes of crystal vibrations [29, 32]. In treating the thermal properties of bulk semiconductors and semiconductor nanostructures, one can speak of a gas of phonons, which are particles of energy $\hbar\omega$ and quasi-momentum $\mathbf{p} = \hbar\mathbf{q}$, obeying Bose–Einstein statistics. In the limit of very small nanostructures (few lattice constants) the concept of phonons encounters a problem related to the definition of the wave packet. Indeed, one can talk of a phonon as a particle as long as he can define a wave packet within the wave vector range Δq , localized within a region $\Delta x \sim 1/\Delta q$. When the feature size of the nanostructure W becomes too small, the ambiguity in $\Delta q \sim 1/W$ may become too large to talk about a “particle-like” phonon. This is similar to some conceptual difficulties with carrier packets in heterostructures and nanostructures discussed in [33]. Yet the approach seems to work even for very small structures and many authors talk about “particle-like” phonons and phonon-boundary scattering in quantum wells with the thickness of a few lattice constants.

A useful concept, which is often used in the context of thermal conductivity, is the so-called dominant phonon approximation [34]. In this approximation, it is assumed that at any temperature the heat is carried predominantly by phonons of a single frequency. One can choose the phonons, which contribute mostly to the specific heat at that temperature, and consider them to be the dominant phonons. Klitsner and Pohl [34] give the following relation to define the dominant phonon frequency f_d :

$$f_d = 4.25(k_B/h)T \approx (90 \text{ GHz} \cdot \text{K}^{-1})T \quad (3)$$

The dominant phonon wavelength, λ_d , is then defined as $\lambda_d = (V_s/f_d)$, where V_s is the sound velocity. The dominant phonon wavelength in Si at 1 K is 65 nm; in Al it is 37 nm.

Acoustic phonon dispersion in semiconductor nanostructures undergoes strong modification and deviates significantly from its bulk form shown in Figure 2. The change in phonon spectrum is particularly strong when the feature size is much smaller than the phonon MFP. Balandin and Wang [4] have shown that the modification of the acoustic phonon dispersion in free-standing quantum wells leads to significant reduction of the in-plane lattice thermal conductivity. The reduction of the lattice thermal conductivity due to acoustic phonon confinement (spectrum modification) has also been predicted for nanowires [6, 35] and other nanostructures. Due to the importance of the issue, a great deal of attention in this review is paid to accurate calculation of the acoustic phonon dispersion in nanostructures.

The two lowest phonon modes (one quasi-acoustic and one quasi-optical) for a free-standing ultra-thin silicon film (quantum well) of different thickness are shown in Figure 3. The mode shown in the upper panel is of the “true” acoustic type ($\omega(\mathbf{q} = 0) = 0$). The mode shown in the lower panel is called quasi-optical, since for this and the higher

modes there exist the cut-off frequencies ($\omega(\mathbf{q} = 0) \neq 0$) for both the thin films and nanowires. The cut-off frequency for the second branch in the nanowire is larger than that in a thin film. This can be explained by the fact that compared to a thin film, a cylindrical nanowire is characterized by the tighter phonon spatial confinement. The quasi-acoustic (upper panel) and the first quasi-optical (lower panel) modes shown in Figure 3 emanate from the longitudinal acoustic phonon bulk branch. It is important to note that the slope of all modes that defines the group velocities are smaller than that of the bulk branch, and as \mathbf{q} increases, it asymptotically approaches values also smaller than the bulk dispersion slope. These facts bear important consequences for the lattice thermal conductivity [4, 36–40]. It is also interesting to note that when the lateral dimension of the thin film decreases, the acoustic phonon dispersion relation approaches the bulk dispersion of the longitudinal modes. However, when the feature size of the well gets larger, the acoustic phonon dispersion approaches that of the transverse modes in the bulk. These phenomena can be explained as the following. The eigenmodes in a thin film are hybrid modes instead of pure longitudinal or transverse modes. When the lateral dimension of thin film approaches zero, the transverse motion is inhibited and only the longitudinal motion remains. On the contrary, when the feature size of the thin film approaches infinity, only the transverse vibrations remain and the longitudinal motion diminishes.

2.5. Phonon Transport Regimes in Semiconductor Nanostructures

There have been several classifications suggested for the phonon transport models in nanostructures. The available models can be roughly divided into particle and wave phonon models. Simkin and Mahan [41] pointed out that when the layer thickness W is much larger than the phonon MFP ($W \gg \Lambda$) the particle model applies, while when it is smaller than the MFP ($W < \Lambda$) the wave theory should apply. Some other researchers assumed that the phonon spectrum modification, which is a “wave affect,” has to be taken into account when the feature size of the nanostructure or the superlattice period is comparable to the dominant phonon wavelength, λ_d , at a given temperature. For example, Chen [42] suggested that for films much thicker than the dominant phonon wavelength ($W \gg \lambda_d$) phonons can still be treated as particles, while the classical size-effect transport regime is reached when the film thickness W is comparable to, or shorter than, the phonon MFP. The term classical size-effect transport regime is understood in a sense that phonon transport is strongly affected by the diffuse phonon-boundary scattering, but the phonon dispersion and MFP still do not deviate from corresponding bulk value.

According to some reported experimental data, the effective MFP of the dominant phonons at room temperature in Si thin films is close to 300 nm [9], which is longer than it was earlier believed. The theoretical values for the effective phonon MFP, in Si calculated from the Debye model, is about 41 nm and about 260 nm from more precise theory which takes into account phonon dispersion [43]. The phonon thermal wavelength, λ_T , estimated from the

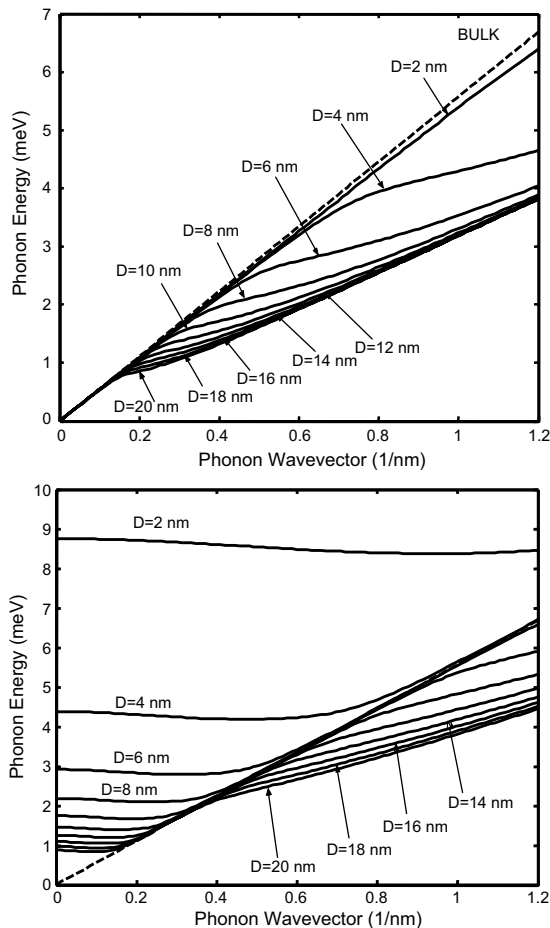


Figure 3. Dispersion of first quasi-acoustic (upper panel) and quasi-optical (lower panel) phonon modes in ultra-thin silicon films (quantum wells) with the film thickness varying from $W = 2$ nm to $W = 20$ nm. Corresponding bulk phonon dispersion is shown with dashed line.

equation $\lambda_T \cong hV_S/(k_B T)$ gives the value of 1.4 nm for silicon at room temperature and reaches 4 μm at $T = 0.1$ K. Some alternative methods to a simple comparison of the feature size with λ_T include an estimation of phonon wavelength, at which phonon group velocity weighted with phonon density of states achieves its maximum or analysis of the spectral dependence of the extinction coefficient [35]. Yet another criterion for the onset of the phonon “wave” or quantum effects is based on the concept of coherence length for phonons defined as $L_{coh} = V\Delta\tau$, where V is the average phonon velocity and $\Delta\tau$ is the phonon coherence time given by [44].

$$\Delta\tau = \int_0^{f_m} |g(f)|^2 df \quad (4)$$

Here, $g(f)$ is the phonon spectrum density and f_m is the phonon frequency at the boundary of the first Brillouin zone. Calculations of the room-temperature coherence length of longitudinal and transverse phonons in bulk GaAs give the values of ~ 1 nm and 2 nm, respectively [3]. These values are close to the thermal phonon wavelength λ_T . The physical meaning of the electron coherence length is rather straightforward and closely related to electron phase-preserving (elastic) and phase-breaking (inelastic) collisions [45]. The latter is not the case for phonons. Due to this reason and because the length scale defined by the coherence length and the thermal phonon wavelength largely coincide, we use λ_T (λ_d) and Λ to define the scale of the problem and phonon transport regimes. Table 1 provides a summary of different acoustic phonon transport regimes. Here, W is the lateral dimension of the structure (bulk sample size, thin film thickness, nanowire lateral size, etc.).

In bulk materials or structures, with W much larger than the phonon MFP, phonon dispersion is unchanged and the dominant phonon-scattering mechanisms that contribute to thermal resistance are the three-phonon Umklapp scattering and the scattering on static imperfection via, for example, mass-difference mechanism. The former is due to the anharmonic nature of the crystal potential and the latter comes from impurities, isotopes, and defects in the material. When the lateral feature size goes down to become comparable to or shorter than the phonon MFP but still much larger than the phonon thermal wavelength, the presence of the

boundaries and interfaces starts to affect phonon thermal transport through diffusive boundary scattering. This is the classical size effect transport regime [3]. A regime, which is more relevant to room temperature nanoscale device operation, is reached when the following inequality holds $\lambda_T \leq W \ll \text{MFP}$. Phonon spatial confinement effect is expected to become dominant when the structure lateral dimension W is much smaller than the acoustic phonon MFP and is approaching the dominant phonon thermal wavelength λ_T . In this regime, phonon dispersion is modified as compared to the bulk, due to the boundary conditions on the equation of motion of the lattice waves. When W is smaller than λ_T , which occurs at very low temperatures, the ballistic transport regime can be achieved, where thermal conductance is quantized with the quantum equal to $\pi^2 k_B^2 T/3h$ [25].

3. ELECTRONIC THERMAL CONDUCTIVITY

In order to present the specifics of thermal conduction in nanostructures, we start with the thermal conductivity results and models for bulk semiconductor crystals followed by the description of its modification in nanostructures such as, for example, quantum wires.

3.1. Electronic Contribution to Thermal Conduction in Semiconductor Crystals

Thermal conductivity of technologically important semiconductors, for example, Si, Ge, GaAs, GaN, etc., is dominated by acoustic phonon (lattice waves) conduction even for highly doped samples. Although in some instances, such as degenerately doped thermoelectrics and very high temperatures, the carrier contribution can become noticeable. In most cases, the charge-carrier contribution to thermal conductivity K_e can be estimated from the Wiedemann-Franz law given by [46]

$$\frac{K_e}{\sigma} = \frac{\pi^2}{3} \left(\frac{k_B}{e} \right)^2 T \quad (5)$$

Here, e is the electron charge, k_B is the Boltzmann constant, T is the temperature, and σ is the electric conductivity. The value of electronic contribution to thermal conductivity of intrinsic or moderately doped Si at room temperature is very small and, thus, it is usually neglected [47]. A similar situation is observed for other technologically important semiconductors. For example, the electronic contribution to thermal conductivity of bulk crystalline GaN is about 1.5×10^{-3} W/cm-K. This is much smaller than the measured values of the total thermal conductivity of GaN, which for the different quality samples is in the range $K = 0.80$ W/cm-K– 1.95 W/cm-K [48]. The electronic contribution to K in semiconductors tends to increase with temperature [47, 49]. In addition to an electron (hole) polar contribution given by eq. (1), at elevated temperatures the electron-hole bipolar contribution starts to play. This contribution can be written as [50]:

$$K_{bp} = \frac{b}{(1+b)^2} \left(\frac{E_G}{k_B T} + 4 \right)^2 \left(\frac{k_B}{e} \right)^2 \sigma T \quad (6)$$

Table 1. Phonon transport regimes.

Scale	Phonon dispersion	Dominant scattering processes
$L \gg \text{MFP}$	bulk dispersion	three-phonon Umklapp point defects
$\lambda_0 \ll L \leq \text{MFP}$	bulk dispersion	three-phonon Umklapp point defects boundary scattering
$\lambda_0 \leq L \ll \text{MFP}$	modified dispersion with many phonon branches populated	three-phonon Umklapp point defects boundary scattering
$L < \lambda_0$	modified dispersion with only lowest phonon branches populated	ballistic transport

where b is the mobility ratio and E_G is the bandgap energy. Glassbrenner and Slack [47] estimated from experimental data that at very high temperatures, which correspond to the respective melting points of Si and Ge, electrons and holes (both polar and bipolar components) are responsible for 40% of the total thermal conductivity, while phonons account for 60%. Similarly, values were obtained in a recent study that used nonstationary thermal conductivity measurement technique [49]. As was mentioned in the beginning, the relative contribution of charge carriers to thermal conductivity is typically somewhat larger for thermoelectric materials. Degenerate doping and correspondingly high-carrier concentrations are used in thermoelectric materials to increase the thermoelectric figure of merit. In optimized bulk thermoelectric materials, the electron contribution to thermal conductivity can reach up to one-third of the total value [51].

3.2. Electronic Thermal Conductance in Quantum Wells and Wires

Electronic thermal conduction undergoes strong modification in nanostructures when the width of the constriction, for example, lateral dimensions of a quantum wire W , is in the range of the Fermi wavelength λ_F . In this case, as is well known, the transverse motion of electrons confined to W becomes quantized [45]. The consequences of electron quantization for electrical and optical properties of nanostructures have been discussed in various textbooks [45, 52] and found many practical applications [52–54]. Investigation of the effects of electron quantization on thermal conductivity is in its infancy, although some important results have already been obtained for the confined ballistic transport regime in quantum wires. Greiner et al. [55] theoretically studied electron thermal conductivity and Lorentz number for one-dimensional ballistic transport. A recent review of the quantum effects in thermal transport through nanowires has been given by Ciraci et al. [23]. It has been shown that one can obtain the approximate expression for a quantum of thermal conduction by simply invoking Heisenberg's uncertainty principle. The precise expression for the quantum of thermal conductance is [23]

$$K_o = \frac{\pi^2 k_B^2}{3 h} T \quad (7)$$

Its approximate value is $10^{-12} T$ [W K⁻¹]. Recalling the value of the electrical conductance in the ballistic quantum limit, that is, the quantum of electrical conductance, $G_o = 2e^2/h$, one can construct the ratio K_o/G_o and obtain an analog of the Wiedemann–Franz law for a quantum transport regime [23]

$$\frac{K_o}{G_o} = \frac{k_B^2}{e^2} T \quad (8)$$

This expression, apart from the numerical factor, coincides with eq. (5) of the “conventional” Wiedemann–Franz law. Thus, one can use eq. (8) to estimate electron contribution to thermal conductivity in very thin semiconductor or metal quantum wires, where electron transport is quantized and ballistic.

If the transport is not entirely ballistic and confined, the electron undergoes scattering events with phonons or imperfections and the problem becomes more complicated. One has to calculate confined electron-confined (or bulk) phonon-scattering rates to obtain a complete picture. Results pertinent to confined electron-confined phonon-scattering rates have been reported [56], although not in the context of thermal transport.

Electronic contribution to thermal conductivity in quantum wells has been examined in detail by Sur et al. [57–58]. It is known that in bulk conductors, the electronic part of the thermal conductivity K_e and electrical conductivity σ are related through the Wiedemann–Franz law (eq. (5)), which can be written as $K_e = LT\sigma$. In the case of degenerate semiconductors the Lorentz number $L = (\pi^2/3)(k_B/e)^2$ does not depend on the material. In the case of nondegenerate semiconductors, the Lorentz number has to be rewritten as $L = g \cdot (k_B/e)^2$, where the parameter g depends on the carrier scattering type. The parameter g is equal to 2 in the case of acoustical phonon scattering; it varies from 2.5 to 3 in the case of LO phonon scattering for the temperatures lower or higher than the Debye temperature [57]. In the 2D systems, the dimensional quantization leads to the formation of the electron energy subbands. Each of these subbands has its own characteristic energy and gives its contribution to the heat transport. Therefore, the relation between K_e and σ may undergo modification. Sur et al. [57] and Casian et al. [58] investigated this problem theoretically taking into account energy band nonparabolicity. They have carried out simulations for PbTe/Pb_{1-x}Eu_xTe quantum wells with effective masses $m_l = 0,620m_0$ and $m_t = 0,053m_0$ for PbTe. The results of numerical calculation of the electronic contribution to thermal conductivity for (100)-oriented quantum well as a function of the well width d are shown in Figure 4. The data is given for different carrier concentrations in the

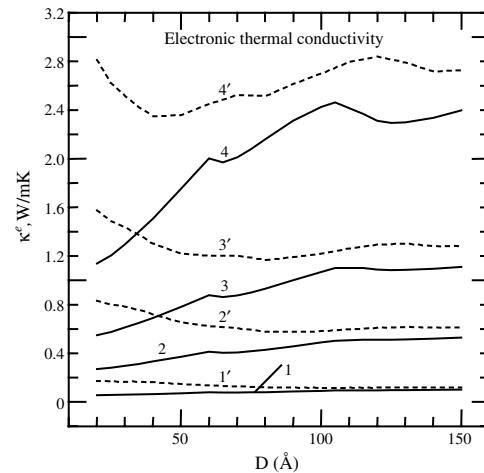


Figure 4. Calculated electronic thermal conductivity of PbTe/Pb_{1-x}Eu_xTe quantum wells as a function of the well width D for the (100) oriented quantum wells (solid curves) and for the (111) oriented wells (dotted curves). Potential barrier height is $U = 171$ meV, Eu content $x = 0.073$, temperature $T = 300$ K. Curves 1 and 1' are for the carrier density $n = 10^{18} \text{ cm}^{-3}$; 2 and 2' for $n = 5 \times 10^{18} \text{ cm}^{-3}$; 3 and 3' for $n = 10^{19} \text{ cm}^{-3}$; 4 and 4' for $n = 2 \times 10^{19} \text{ cm}^{-3}$. Reproduced with permission from Professor A. Casian.

quantum well (curves 1–4). In general, the thermal conductivity curves repeat the shape of the electrical conductivity curves. However, when the concentration increases the shape of K_e , curves becomes nonmonotonous and deviate from that of electrical conductivity.

Figure 5 shows the dependence of the Lorentz number on the quantum well width. One should note that in very thin quantum wells ($d < 50 \text{ \AA}$), there is only one subband occupied and the value of L is close to its bulk value with $g \approx 2.5$. With the increase of d , when the second subband starts to contribute to the transport, a weak peak is observed. Overall, one can conclude that in (100) quantum wells, the multi-subband character of carriers transport has a relatively small effect on the Lorentz number. In (111)-oriented quantum wells, the situation is completely different. In this case, the dimensional quantization leads to a partial lifting of the valley degeneracy. As a consequence, two different sets of subbands appear. One set arises from the longitudinal ellipsoid (longitudinal subbands), while the other set arises from three oblique ellipsoids (oblique subbands). It is seen from Figure 5 that at the small well thickness d , the value of the Lorentz number along (111) direction is considerably larger than that along (100) direction (parameter g is equal or larger than 4). When the carrier concentration is increased, L_{111} decreases due to electron transitions from longitudinal to oblique subbands and the change of their statistics from slightly degenerate to nondegenerate. With the increase of d , the oblique subbands approach the longitudinal ones, which also leads to the decrease in the Lorentz number value. For $d > 140 \text{ \AA}$, the Lorentz number depends very slightly on the QW orientation and tends to its bulk value (in the limit of large d). The nonmonotonous behavior of L_{111} on d is also caused, as in (100) case, by the appearance of new subbands near the top of the potential barrier. But in (111) quantum wells, the number of these subbands is much larger—the population of the states with the high energy is

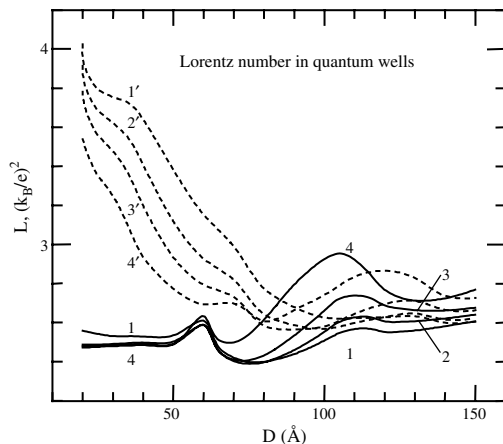


Figure 5. Lorentz number L for $\text{PbTe}/\text{Pb}_{1-x}\text{Eu}_x\text{Te}$ quantum wells as a function of the well thickness D for the (100) oriented quantum wells (solid curves) and for the (111) oriented wells (dotted curves). Potential barrier height is $U = 171 \text{ meV}$, Eu content $x = 0.073$, temperature $T = 300 \text{ K}$. Curves 1 and 1' are for the carrier density $n = 10^{18} \text{ cm}^{-3}$; 2 and 2' for $n = 5 \times 10^{18} \text{ cm}^{-3}$; 3 and 3' for $n = 10^{19} \text{ cm}^{-3}$; 4 and 4' for $n = 2 \times 10^{19} \text{ cm}^{-3}$. Reproduced with permission from Professor A. Casian.

smaller, and as a result, the nonmonotonous behavior is less pronounced than in the (100) case.

4. LATTICE THERMAL CONDUCTIVITY

This section contains a review of the results pertinent to lattice thermal conductivity in bulk crystalline semiconductors and semiconductor nanostructures. Whenever possible, we will provide a brief outline of expected major modifications to the models of thermal conductivity when the size of the structure decreases to nanoscale.

4.1. Theory of the Lattice Thermal Conductivity in Semiconductors

In this section, we describe a standard approach to calculation of the lattice (phonon) thermal conductivity, and give insight into the derivation of these expressions. The details of this derivation can be found in, for example, Klemens [59] and Bhandari and Rowe [30]. Following the standard approach, the thermal conductivity is calculated by an approximate solution of the Boltzmann transport equation for phonons, which uses frequency-dependent relaxation times to represent phonon-scattering processes. This approach has been developed by Callaway [60], Peierls [61], Pomeranchuk [62], and others [30]. The phonon-scattering rates used for bulk crystals were either semi-empirical—obtained from fitting to experimental data some model functions—or calculated from the first principles [59]. It is common to use phonon-scattering rates derived by Klemens from the second-order perturbation theory. Holland [63] modified Callaway's approach by including phonon polarization.

In agreement with eq. (1), the thermal conductivity is related to the phonon heat flux $\mathbf{J} = Q/A$ through the heat conduction equation in the diffusion limit as $\mathbf{J} = -K\nabla T$. From the other side, one can also write down an expression for the heat flux created by a flow of phonons. A phonon of energy $\hbar\omega_i(\mathbf{q})$ and velocity $\mathbf{V}_i(\mathbf{q})$ contributes $\hbar\omega_i(\mathbf{q})\mathbf{V}_i(\mathbf{q})$ to the heat flux. The net phonon heat flux with a small temperature gradient, ∇T , is given by [59]:

$$\mathbf{J} = - \sum_{\mathbf{q}, i} \tilde{N}_{\mathbf{q}, i} \hbar\omega_i(\mathbf{q}) \mathbf{V}_i(\mathbf{q}) \quad (9)$$

where subscript i refers to a particular phonon polarization type, \mathbf{q} is the phonon wave vector, \hbar is the Planck constant, ω is the phonon frequency, $\mathbf{V}_i(\mathbf{q})$ is the phonon group velocity, and $\tilde{N}_{\mathbf{q}, i} \equiv N_{\mathbf{q}, i}^0 - N_{\mathbf{q}, i}$ is the deviation of the phonon distribution, $N_{\mathbf{q}, i}$, from its equilibrium value, $N_{\mathbf{q}, i}^0$. The equilibrium phonon distribution, $N_{\mathbf{q}, i}^0$, is given by the Bose–Einstein distribution

$$N_{\mathbf{q}, i}^0 = \frac{1}{\exp(\hbar\omega_i(\mathbf{q})/k_B T) - 1} \quad (10)$$

Thus, the problem of determining the lattice thermal conductivity is essentially that of obtaining $\tilde{N}_{\mathbf{q}, i}$. Distribution $\tilde{N}_{\mathbf{q}, i}$ can be calculated by solving the phonon Boltzmann

equation. In steady state, the phonon Boltzmann equation can be written as

$$\left(\frac{\partial N_{\mathbf{q},i}}{\partial t}\right)_{\text{drift}} + \left(\frac{\partial N_{\mathbf{q},i}}{\partial t}\right)_{\text{scatt}} = 0 \quad (11)$$

The first term in the above equation represents the change of phonon distribution in the presence of a temperature gradient, and it is given by [30]:

$$\left(\frac{\partial N_{\mathbf{q},i}}{\partial t}\right)_{\text{drift}} = -\mathbf{V}_i(\mathbf{q}) \cdot \nabla N_{\mathbf{q},i} = -(\mathbf{V}_i(\mathbf{q}) \cdot \nabla T) \frac{\partial N_{\mathbf{q},i}}{\partial T} \quad (12)$$

The second term in eq. (12) arises from the change due to scattering by other phonons, impurities, charge carriers, interfaces, boundaries, etc. In the relaxation-time approximation, this term can be written as

$$\left(\frac{\partial N_{\mathbf{q},i}}{\partial t}\right)_{\text{scatt}} = \frac{N_{\mathbf{q},i}^0 - N_{\mathbf{q},i}}{\tau_{C,i}(\mathbf{q})} \quad (13)$$

where $\tau_{C,i}$ is the combined phonon relaxation time. Assuming that the phonon distribution does not deviate strongly from its equilibrium value due to the temperature gradient, one can replace $(\partial N_{\mathbf{q},i}/\partial T)$ by $(\partial N_{\mathbf{q},i}^0/\partial T)$. This is a standard step used for solving such equations. In the bulk, the solution for the linearized phonon Boltzmann equation can be written as

$$\tilde{N} = \frac{\partial N^0}{\partial T} \nabla T \cdot \mathbf{V} \tau_C \quad (14)$$

For convenience, the subscript \mathbf{q} and i are omitted. Substituting eqs. (10) and (14) in eq. (9), and comparing the result with the definition $\mathbf{J} = -\kappa \nabla T$, one can obtain an expression for the regular bulk thermal conductivity. When considering both the resistive and normal processes, the lattice thermal conductivity in the bulk, κ_B , is written as $\kappa_B = \kappa_1 + \kappa_2$, where κ_1 and κ_2 are given by [59, 60, 63]

$$\kappa_1 = \left(\frac{k_B}{\hbar}\right)^3 \frac{k_B}{2\pi^2 V_s} T^3 \int_0^{\theta_D/T} \frac{\tau_{C,B} x^4 e^x}{(e^x - 1)^2} dx, \quad (15)$$

$$\kappa_2 = \left(\frac{k_B}{\hbar}\right)^3 \frac{k_B}{2\pi^2 V_s} T^3 \left\{ \frac{\int_0^{\theta_D/T} (\tau_{C,B}/\tau_N) x^4 e^x (e^x - 1)^{-2} dx \right\}^2 \left\{ \int_0^{\theta_D/T} (\tau_{C,B}/\tau_N \tau_R) x^4 e^x (e^x - 1)^{-2} dx \right\}^{-1} \quad (16)$$

Here, V_s and $\tau_{C,B}$ are the sound velocity and combined relaxation time in the bulk crystal, respectively, and $x = \hbar\omega/k_B T$. In the above equations, one assumes the Debye model for the density of states and the combined relaxation rate is written as $\tau_{C,B}^{-1} = \tau_N^{-1} + \tau_R^{-1}$. In the case of dominant resistive processes, $\kappa_2 \ll \kappa_1$ and $\tau_{C,B} \approx \tau_R$, and κ_B is reduced to the usual Klemens–Callaway formula (given by eq. (15)) for the regular bulk expression for the lattice thermal conductivity. In the bulk, the major important resistive scattering mechanisms are the three-phonon Umklapp scattering and the mass-difference scattering due to impurities and isotopes. The combined relaxation time, $\tau_{C,B}$, is calculated from the bulk dispersion and group velocity.

The approach and formulas outlined here are often referred to as Callaway's model. Its basic assumptions are

summarized as follows: (i) the Debye density of states $g_s(\omega) = \omega^2/(2\pi^2 V^3)$ with no anisotropies or particular structure; (ii) one averaged sound velocity V with no distinction of polarization between longitudinal and transverse phonons; (iii) all phonon scattering processes can be represented by a relaxation time that depends on temperature and frequency; (iv) normal three-phonon processes have a relaxation rate $\tau_n^{-1} = B_2 \omega^2 T^3$ and three-phonon Umklapp processes have the same ansatz for the scattering rate with different material-specific constant; and (v) scattering rates (reciprocal of the relaxation times) are additive for all independent scattering processes. Holland extended the Callaway theory to explicitly include the thermal conductivity by transverse and longitudinal phonons under the assumption that $K_2 = 0$ (see eq. (16)). While applied to the very dispersive semiconductor crystals like Si or Ge, the transverse phonon mode can be further divided into the low-frequency (TO) and high-frequency (TU) ranges to account for the dispersion. The thermal conductivity is then given as [64]

$$\begin{aligned} K &= \frac{1}{3} \sum_{j=L, TO, TU} V_j^2 \int_0^{\theta_j/T} C_{V,j} \tau_{C,j} dx_\omega \\ &= \frac{1}{3} \left(\frac{k_B T}{\hbar}\right)^3 \frac{k_B}{2\pi^2} \sum_{j=L, TO, TU} \frac{1}{V_j} \int_0^{\theta_j/T} \frac{x_\omega^4 \exp\{x_\omega\} \tau_j}{(\exp\{x_\omega\} - 1)^2} dx_\omega \end{aligned} \quad (17)$$

Here $x_\omega = \hbar\omega/(2\pi k_B T)$ is the dimensionless phonon angular frequency—the temperatures θ_j in the integration limit correspond to the cutoff frequencies for the transverse and longitudinal modes. For example, for Si $\theta_{TO} = 180$ K, $\theta_{TU} = 210$ K, and $\theta_L = 570$ K. The combined relaxation times, $\tau_{C,j}$, for three modes consist of various phonon-scattering processes which obey the Matthiessen's rule $\tau_{C,j}^{-1} = \sum_i \tau_{C,j,i}^{-1}$.

From the discussion in this section, it is clear how thermal conductivity can be affected at nanoscale. First, the phonon-boundary scattering rates are expected to increase due to small structure size; second, other scattering rates that depend on phonon group velocity can change due to the change in phonon dispersion; third, the phonon density of states can deviate significantly from its Debye form, again, due to the change in phonon dispersion.

4.2. Phonon Relaxation Due to Crystal Anharmonicity and Defects

As seen from the previous subsection, the important problem in the theory of phonon heat conduction is an accurate estimation of phonon relaxation rates. It is well known that the normal, three-phonon scattering processes, in which the total phonon momentum is conserved, do not contribute to thermal resistance. These processes influence thermal conductivity indirectly by distributing momentum among all phonon modes [59]. Only processes, which do not conserve crystal momentum, directly contribute to the lattice thermal resistance. Such processes, further referred to as resistive, include the three-phonon Umklapp (U) scattering, the impurity (I) scattering, and boundary (B) scattering processes, in which the sum of phonon wave vectors is not conserved but changed by a reciprocal lattice vector. Here, we

outline acoustic phonon relaxation in the above-mentioned resistive processes.

The three-phonon Umklapp scattering is the phonon-phonon interaction due to the anharmonicity of the crystal potential. In a bulk perfect crystal, this is the only resistive process that limits the phonon mean-free path and contributes to the lattice thermal resistance. The scattering rate for Umklapp scattering at high temperature (room and above), which is of interest here, was given by Klemens for bulk samples as [65]

$$\frac{1}{\tau_U} = 2\gamma^2 \frac{k_B T}{\mu V_0} \frac{\omega^2}{\omega_D} \quad (18)$$

where γ is the Gruneisen anharmonicity parameter, k_B is the Boltzmann constant, μ is the shear modulus, V_0 is the volume per atom, and ω_D is the Debye frequency. A more accurate expression for three-phonon Umklapp scattering rates, which takes into account selection rules for phonon transitions between LA and TA branches, can be found in [59]. For confined phonon transport in nanostructures, the above equation has been modified by Balandin and Wang [4] to account for the changed acoustic phonon dispersion and Umklapp scattering selection rules. In high-quality crystalline semiconductors at room temperature and above, three-phonon Umklapp scattering is the dominant resistive process, which results in characteristic $1/T$ dependence of the thermal conductivity.

Phonon scattering rates $1/\tau_p$ on point imperfections such as vacancies, isotopes, and impurity atoms are calculated from the second-order perturbation theory [59]

$$\frac{1}{\tau_p} = \frac{V_0 \omega^4}{4\pi V^3} \Gamma = \frac{V_0 \omega^4}{4\pi V^3} \sum_i f_i \left[\left(1 - \frac{M_i}{\bar{M}}\right)^2 + 8Q_i^2 \gamma_i^2 \left(1 - \frac{R_i}{\bar{R}}\right)^2 \right] \quad (19)$$

where f_i is the relative concentration of the i th atom, M_i and R_i are the mass and radius of the i th impurity atom or defect, respectively, $\bar{M} = \sum_i f_i M_i$ is the average atomic mass, $\bar{R} = \sum_i f_i R_i$ is the average radius, Q_i is the anharmonicity parameter of the linkages in the immediate vicinity of an impurity atom or point defect, γ_i is the Gruneisen parameter of an impurity atom or point defect, and Γ is the measure of the strength of the point-defects scattering. Vacancies are considered to be “atom-like” entities with $M_i = 0$ and $R_i = 0$ [66].

The expressions for scattering on dislocations (extended line defects) derived by Klemens [66]. They are quite complicated and are not reproduced here. The expressions given in [66] include phonon scattering on a dislocation core, as well as scattering on the strain field of dislocation lines. For some material systems, such as GaN and related compounds, the scattering on dislocation is a very important resistive mechanism, which can manifest itself even at room temperature [67–68]. The latter is due to the fact that the dislocation line density is extremely high in GaN films, although the point defect scattering gives the major contribution resulting in significant deviation of the temperature-dependence of the thermal conductivity from $1/T$ law [68–70]. Kotchetkov et al. [67–68, 70] analyzed the relative contribution of each resistive mechanism to the thermal resistivity of

GaN thin films in detail. Figure 6 shows theoretically calculated and experimentally measured dependence of the thermal conductivity of GaN films on Si-doping density. Phonon scattering on semiconductor and nanostructure boundaries, characterized by the scattering rate $1/\tau_B$, is discussed later.

The above equations for phonon-scattering rates were derived for bulk semiconductors. One can extend them to a low-dimensional structure assuming that the lateral dimension of the structure is still larger than the lattice constant. Phonon confinement effects enter these equations through modification of the phonon group velocity, which has to be calculated for each particular geometry and boundary conditions [4, 6, 71]. The phonon selection rules, important for the Umklapp scattering processes, should also be properly modified for a specific nanostructure [4]. In the limiting case of a strictly 1D structure, the phonon frequency dependence in the equation for mass-difference scattering changes to $1/\tau_M \sim \omega^2$ [59]. After the phonon dispersion and group velocity are obtained, one can calculate the scattering rates in different phonon relaxation processes. The combined phonon relaxation rate can be written in a general form as $\tau_C^{-1} = \tau_R^{-1} + \tau_N^{-1}$, where τ_R and τ_N are the relaxation time for the resistive and normal processes, respectively. At a high temperature, one can usually disregard normal processes and assume that all phonon modes are strongly scattered by resistive processes. In this case, $\tau_C^{-1} \approx \tau_R^{-1}$ and the combined relaxation rate can be estimated by the addition of the inverse relaxation times in the following resistive processes:

$$\frac{1}{\tau_C} \approx \frac{1}{\tau_U} + \frac{1}{\tau_P} + \frac{1}{\tau_B} \quad (20)$$

Depending on a particular material system, other resistive processes such as scattering on dislocation can be included in eq. (20). It is interesting to note that the relaxation

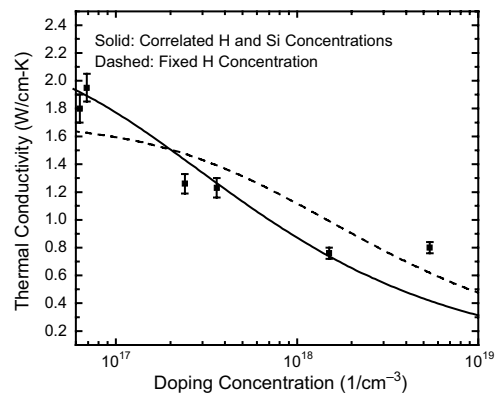


Figure 6. Thermal conductivity of the Si-doped GaN film as a function of doping concentration. The solid curve corresponds to the case when an increase in silicon doping density n_{Si} is accompanied by the increase in the hydrogen n_H impurity concentration. The dashed curve corresponds to the case when the hydrogen impurity concentration is a fixed value $n_H = 2 \times 10^{17} \text{ cm}^{-3}$, and only silicon doping density n_{Si} changes. Note that an order of magnitude increase in the doping density (carrier concentration) leads to about a factor of two decrease in the thermal conductivity. Reprinted with permission from [68], J. Zou et al., *J. Appl. Phys.* 92, 2534 (2002). © 2002, American Institute of Physics.

rate of acoustic phonons on dislocations is also a strong function of the phonon group velocity being inversely proportional to V_G^2 . Thus, phonon spectrum modification in nanostructures strongly affects this scattering mechanism as well.

4.3. Molecular-Dynamics Simulation of Thermal Conductivity

An alternative approach to the calculation of thermal conductivity is an atomistic method that uses molecular dynamics simulation technique. The main limitations of this method are the computational power and sometimes an absence of the knowledge of the interatomic potential. For example, if the simulation domain is of the order of one mean-free path, the computation of the thermal conductivity of bulk crystals would require a calculation of the trajectories of several hundreds of millions of atoms over millions of time steps. The classical molecular dynamics simulation technique adopts Newton's second law to describe the motion of an N -atom system

$$M \frac{d^2 \mathbf{r}_i}{dt^2} = \sum_{j=1, j \neq i}^N \mathbf{F}_{i,j} \quad (21)$$

where M is the mass of an atom, \mathbf{r}_i is the position of the i th atom, and $\mathbf{F}_{i,j}$ is the force exerted from atom j on atom i . The force term is derived from the interatomic potential. One of the commonly used interatomic potentials is the Stillinger–Weber potential [72]. To account for the diamond structure of the crystal lattice in Si, a three-body potential is introduced in addition to the two-body term. The solutions of the equation of motion in eq. (21) with given initial conditions define the trajectory of each particle, that is, the position and velocity as a function of time. This information is then used to calculate the system's temperature, heat flux, and thermal conductivity. The expression for heat flux is derived from the integration of the energy balance equation combined with the definition of the total instantaneous heat flux in the statistical ensemble of constant energy. For two- and three-body potentials, the heat flux is written as [72–73]

$$\mathbf{J}(t) = \frac{1}{V} \left[\sum_{i=1}^N \sum_{j=1, j \neq i}^N \left(\frac{1}{2} \mathbf{r}_{ij} \cdot (\mathbf{F}_{ij} \cdot \mathbf{V}_i) + \frac{1}{6} \sum_{k=1, k \neq i, j}^N (\mathbf{r}_{ij} + \mathbf{r}_{ik}) \cdot (\mathbf{F}_{ijk} \cdot \mathbf{V}_i) \right) \right] \quad (22)$$

where \mathbf{F}_{ij} and \mathbf{F}_{ijk} are the two- and three-body forces, respectively, and V is the system volume. The molecular dynamics simulation technique calculates the lattice thermal conductivity based on the equilibrium fluctuations of the heat flux $\mathbf{J}_0(t)$ [74]. The atomic motion causes both the local and total quantities— $\mathbf{J}_0(\mathbf{r}, t)$, $E_0(\mathbf{r}, t)$, $\mathbf{J}_0(t)$, and $T_0(t)$ —to fluctuate around their equilibrium mean values and follow the local energy balance equation. In the theory of equilibrium fluctuations, a microscopic temperature nonhomogeneity $\delta T(\mathbf{r}, t)$ is created in the system and superimposed on the equilibrium fluctuations of the local temperature

$T_0(\mathbf{r}, t)$. The temperature perturbation leads to a deviation of the average energy of the system, $\delta E(t)$, which causes an instantaneous heat flux, $\mathbf{J}(t)$, in the simulation domain. The resultant heat flux, $\mathbf{J}(t)$, can be expressed in terms of the perturbation of the distribution function. The static thermal conductivity K is given by the Green–Kubo formula according to the fluctuation-dissipation theorem [72–74] as

$$\kappa = \frac{V}{3k_B T_0^2} \int_0^\infty \langle \mathbf{J}_0(0) \cdot \mathbf{J}_0(t) \rangle dt \quad (23)$$

where $\langle \mathbf{J}_0(0) \cdot \mathbf{J}_0(t) \rangle = 1/V \int_V \mathbf{J}_0(0, \mathbf{r}) \cdot \mathbf{J}_0(t, \mathbf{r}) f_0 dV$ is the heat flux auto-correlation function.

The outlined approach can be used for both bulk semiconductors and nanostructures. Volz and Chen [35, 74] have performed molecular dynamic simulation of the lattice thermal conductivity in silicon nanowires based on the Green–Kubo formula. They computed the thermal conductivity of nanowires with a rectangular cross-section area ranging from 2.58 nm²–28.62 nm² for different wire lengths. It was found that the thermal conductivity becomes length independent when the wire is longer than 8.56 nm. These simulation results predicted one to two orders of magnitude reduction in the thermal conductivity of nanowires compared to that in bulk silicon crystals in a wide range of temperatures (200 K–500 K). This predicted reduction is in agreement with the results reported by Zou and Balandin [6] obtained by completely different theoretical approach.

4.4. Thermal Boundary Resistance of Plane Interfaces

Solid-solid thermal boundary resistance plays an important role in determining heat flow in cryogenic and room-temperature applications such as integrated circuits, semiconductor superlattices, and nanostructures. In nanoscale devices, the number of interfaces per unit volume drastically increases, which makes the TBR contribution to the total thermal resistance of the structure even larger. The first approaches to calculate TBR of a single boundary (interface) between two materials have been developed in the 50s and 60s [75–76] and then expanded in the 80s to include interface scattering in the diffuse mismatch model [27–28, 77]. Basically, the same approaches have been applied to semiconductor nanostructures, and more specifically to cross-plane heat flow in superlattices. To date, there have been little theoretical work to augment the formalism for calculating TBR in nanostructures to account for nanoscale effects, such as modification of the phonon velocity, density of states, etc.

The theory of TBR developed for bulk solid-solid interfaces was based on the assumption that the transmission probabilities are independent of temperature on both sides of the interface, which excludes the possibility of anharmonic phonon interactions. Most of the results discussed in literature were obtained for low-temperature using the isotropic Debye solid model. Although the basic formulas are quite general, they can be extended to higher temperatures and nanostructures via proper inclusion of the realistic

phonon dispersion and density of states. The thermal boundary conductance can be written as [27–28]

$$h_{Bd} = (1/2) \sum_j c_{1,j} \Gamma_{1,j} \int_0^{\omega_1} \hbar \omega \frac{dN_{1,j}(\omega, T)}{dT} d\omega \quad (24)$$

where

$$\Gamma_{1,j} = \int_0^{\pi/2} \alpha_{1 \rightarrow 2}(\theta, j) \cos(\theta) \sin(\theta) d\theta$$

Here j is the phonon mode, $c_{1,j}$ is the phonon propagation velocity in medium 1 for phonons in mode j , ω is the phonon frequency, θ is the angle between the incident phonon wave vector and the normal to the interface, $N_{1,j}$ is the product of the phonon density of states and the Bose–Einstein occupation factor, $\alpha_{1 \rightarrow 2}$ is the energy transmission probability from medium 1 to medium 2. There are two main approaches to the calculation of the transmission probability: the acoustic mismatch model [75–76] and the diffuse mismatch model [77]. In the acoustic mismatch model (AMM), one assumes that the phonons are governed by continuum acoustics and that the interface is an ideal plane. In such a case, the transition probability can be expressed through the mismatch between the acoustic impedance $Z_i = \rho_i c_i$ of two media. In the diffuse mismatch model (DMM), the assumption of complete specularity of the AMM is replaced by the opposite requirements that all phonons are diffusively scattered at the interface between medium 1 and 2. In this case, the probability of transmission is determined by the mismatch between the phonon densities of states. The transmission coefficients in such a case and under the assumption of the Debye density of states, can be written as [27–28]

$$\alpha_i(\omega) = \frac{\sum_j c_{3-i,j}^{-2}}{\sum_{i,j} c_{i,j}^{-2}} \quad (25)$$

Here the notation of [27] is preserved, where the subscript $3 - i$ denotes the medium opposite to the medium i .

Recently, a number of models aimed at refinement of AMM and DMM have been reported with the goal of making the calculation procedure more applicable to the low-dimensional structures and high temperatures. Prasher and Phelan [78] proposed a scattering-mediated acoustic mismatch model for the prediction of R_{Bd} at high temperature. This model exploits the analogy between phonon and radiative transport, and it seems to be more accurate in estimating R_{Bd} at high temperatures using one fitting parameter. Chen [79] proposed a model for TBR in the diffuse scattering limit, which can be applied to room temperature and above. Zeng and Chen [80] studied the impact of TBR on phonon heat conduction in thin films. Based on the solution of the Boltzmann transport equation, they found that the total resistance of the thin film depends on both the physical properties of the two adjacent materials and the film thickness.

4.5. Thermal Boundary Resistance of Nanoparticles

The incorporation of the concept of Kapitza resistance, that is, TBR, to the effective medium approximation (EMA) allows one to estimate the lattice thermal

conductivity of polycrystals and nanocomposites without going into details about various scattering processes. In this sense, the Kapitza resistance can be viewed as a connection between the microscopic Klemens–Callaway type and the macroscopic EMA type theories. Table 2 summarizes theoretical and experimental data for TBR of some thermoelectric polycrystals. The data in this table is from Nan and Birringer [81].

The increased importance of the knowledge of boundary resistance at room temperature stimulated recent experimental investigations of TBR in different material systems, including nanoparticle composites. Phase-change material $\text{Ge}_2\text{Sb}_2\text{Te}_3$ (GST) is important for optical data storage media such as rewritable digital versatile disks. The thermal response of the phase-changing, thin GST layer determines the data storage capacity and writing speed. Hence, the accurate values of the TBR of this material with poor thermal conducting layers are required. Kim et al. [82] have measured TBR between sputtered amorphous GST (crystalline GST) and $\text{ZnS}:\text{SiO}_2$ multilayer films in the temperature range from 50 K–300 K using the 3ω method. The boundary resistance in the crystalline GST multilayer was lower than that for the amorphous GST in the whole temperature range. For crystalline GST, they observed a decrease in TBR from about 2×10^{-8} K m²/W at 40 K to 0.6×10^{-8} K m²/W at 300 K. At room temperature, the measured thermal boundary resistance between ZnS nanoparticles (average radius $R = 2$ nm) and SiO_2 matrix is smaller than the typical TBR between metals and dielectrics, that is, $0.5\text{--}3.0 \times 10^{-8}$ K m²/W [83]. Goodson et al. [84] measured TBR of the diamond–Si boundary using Joule-heating and laser-heating methods. The TBR values in the range from $(1.3\text{--}3.5) \times 10^{-8}$ K m²/W have been found. The interest in diamond–Si TBR is due to proposed applications of diamond for passive applications in electronic systems for heat removal. Hu et al. [85] determined TBR for the interface of Si with SiO_2 and with the low k materials. Thermal boundary resistance of SiO_2/Si was about 2.0×10^{-8} K m²/W, while TBR of polystyrene/Si was 10 times larger. Thermal boundary resistance of many low k materials with Si fall between these two values [85].

5. SIZE EFFECTS ON THERMAL CONDUCTIVITY OF NANOSTRUCTURES

The constricted geometry effects on the lattice thermal conductivity in nanostructures can be roughly divided into “classical,” related to increased acoustic phonon-boundary scattering and “quantum,” related to acoustic phonon spectrum modification in nanostructures.

Table 2. Thermal boundary resistance of polycrystals.

Polycrystals	Bulk thermal conductivity (W/mK)	Thermal boundary resistance (m ² K/W)
$p\text{-Si}_{0.8}\text{Ge}_{0.2}$	5.0	4.98×10^{-8}
$\text{Si}_{0.7}\text{Ge}_{0.3}$	6.56	9.5×10^{-8}
$\text{Si}_{0.3}\text{Ge}_{0.7}$	7.84	1.1×10^{-7}
$p\text{-Bi}_2\text{Te}_3/\text{Sb}_2\text{Te}_3$	0.19	1.4×10^{-5}

5.1. Phonon-Boundary Scattering in Thin Films and Nanostructures

In this section, we review the effects of boundary scattering on thermal conductivity of semiconductor nanostructures. The basic assumption here is that the structural lateral dimension W is comparable to or smaller than the phonon mean-free path Λ . At the same time, W is not too small (still well above the thermal phonon wavelength) so that one can disregard the acoustic phonon spectrum modification due to phonon confinement at the nanostructure boundaries.

Theoretical treatment of the phonon-boundary scattering has been initially developed for the low temperature conditions, since in this case the phonon MFP is very large and the effects of boundary scattering are detectable even in large bulk samples. The basics of this formalism were described in detail by Ziman [29] who suggested the following expression for the scattering rate:

$$\frac{1}{\tau_B} = \frac{V_S}{D} \left(\frac{1 - p(\omega)}{1 + p(\omega)} \right) \quad (26)$$

where D is the critical sample dimension, for example, the diameter of a nanowire or the width W of a thin film, V_S is the average phonon sound velocity defined as

$$\frac{1}{V_S} = \frac{1}{3} \left(\frac{2}{V_T} + \frac{1}{V_L} \right) \quad (27)$$

Here V_T and V_L are the sound velocities of the transverse and longitudinal acoustic waves in the sample. When the size of nanostructure is very small and phonon dispersion deviates from its bulk form, instead of bulk sound velocities in the above equations, one has to use phonon group velocities calculated from the phonon dispersion in a given structure [4, 6]. The function $p(\omega)$ represents the probability that the phonon is undergoing a specular scattering event at the interface, and thus quite often p is called the specularity parameter [3, 42]. In the event of a specular scattering, that is, $p = 1$, which corresponds to a perfectly smooth surface, phonons are reflected back from the boundary with the same magnitude but opposite direction in the normal component of the velocity. However, the momentum along the direction of wave propagation is conserved, and thus purely specular boundary scattering does not contribute to the phonon thermal resistance. If the boundary is purely diffusive, that is, $p = 0$, which corresponds to an entirely rough surface, phonons are scattered in all directions, thus reaching a local thermal equilibrium at the boundary. Diffusive scattering contributes to the thermal resistance, in which case eq. (26) reduces to the well-known Casimir limit $1/\tau_B = V_S/D$ [86]. The average value of p is related to the asperity parameter ε , that is, the root mean-square deviation of the height of the surface from the reference surface plane, via the expression [29]

$$p(\omega) = \int P(\varepsilon) \exp \left\{ -\frac{16\pi^3 \varepsilon^2}{\lambda^2} \right\} d\varepsilon \quad (28)$$

where $P(\varepsilon)$ is the probability distribution for ε and λ is the phonon wavelength. Another approximate expression for $p(\omega)$, which is often used is [64]

$$p(\omega) = \exp \left\{ -\pi \left(\frac{2\varepsilon\omega}{V_S} \right)^2 \right\} \quad (29)$$

It is seen from this expression that decreasing the phonon frequency increases the phonon wavelength relative to the surface roughness. As a result, the effective surface roughness appears smaller to the phonons and the probability of specular reflection increases. At molecular beam epitaxy grown GaAs/AlGaAs or Si/SiGe superlattices interface roughness often extends from one to three atomic layers $\delta W \sim 0.3\text{--}0.9$ nm. This roughness is comparable to thermal phonon wavelength and, thus, will cause a mostly diffuse scattering of phonons. Figure 7 shows calculated thermal conductivity in an Si nanowire for different values of the specularity parameter p .

5.2. Phonon Spectrum in Thin Films and Nanowires

In section 2.4, we briefly discussed modification in an acoustic phonon spectrum when one goes from bulk semiconductors to nanostructures. In this section, we address the issue in more detail and focus on the calculation of phonon dispersion and phonon group velocity in several specific cases such as ultra-thin films and nanowires. The calculation of phonon dispersion is one of the key issues in the modeling of thermal transport in semiconductor nanostructures since phonon scattering rates that enter eqs. (14–17) are the functions of the phonon group velocity. Moreover, for very small structures, the Debye density of states has to be substituted with the actual one found from the exact dispersion.

In this and the following section, we review the elastic continuum and atomistic approaches to the calculation of the phonon spectrum in a few specific cases. In the elastic continuum approximation, phonon dispersion close to the

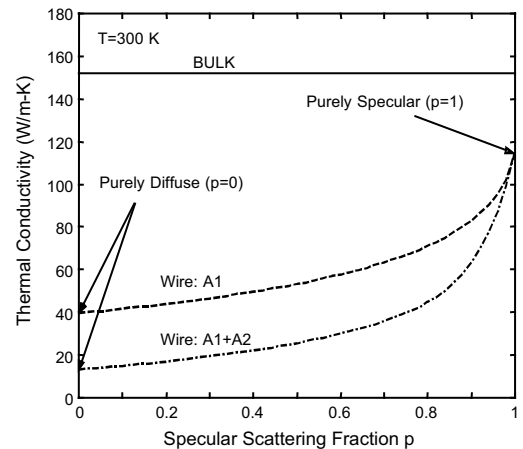


Figure 7. Lattice thermal conductivity at room temperature as a function of specular phonon-boundary scattering fraction p . The results are shown for bulk and the wire of diameter 20 nm. Reprinted with permission from [6], J. Zou and A. Balandin, *J. Appl. Phys.* 89, 2932 (2001). © 2001, American Institute of Physics.

center of the Brillouin zone is calculated by solving the elasticity equation with a given geometry and boundary conditions. The equation of motion of elastic continuum can be written in the vector form as

$$\frac{\partial^2 \mathbf{u}}{\partial t^2} = v_t^2 \nabla^2 \mathbf{u} + (v_d^2 - v_t^2) \nabla(\nabla \cdot \mathbf{u}) \quad (30)$$

where \mathbf{u} is the displacement vector, $v_d = \sqrt{(\lambda + 2\mu)/\rho}$, and $v_t = \sqrt{\mu/\rho}$ are the longitudinal and transverse velocities of acoustic waves in bulk semiconductors, λ and μ are the Lamè constants, and ρ is the density of the material. For nanowires or thin films that are embedded within materials with different elastic properties, the boundary conditions for confined acoustic phonons are such that the displacement and normal components of the stress or the tractional force, are continuous across the surfaces where the elastic properties change discontinuously. The two special cases of the boundary conditions to the surface are the free-standing and the clamped-surface boundary conditions. The former corresponds to a surface between an elastic material and vacuum, but can be used for a “rigid” material embedded within a “softer” material. The latter corresponds to a nanowire or thin film embedded within a rigid material [4]. Quantitatively, the difference in the “rigidity” of materials can be characterized by the acoustic mismatch $\zeta = \rho_2 V_2 / \rho_1 V_1$, between acoustical impedances of the corresponding materials, where ρ_i and V_i are the density and sound velocity of the i th material, respectively. Even similar materials may have rather large acoustic mismatch ζ . For example, mismatch between Si and Ge calculated for longitudinal and transverse sound velocities is 0.75 and 0.71, respectively [87–89]. The mismatch between two very similar materials such as GaAs and $\text{Al}_x\text{Ga}_{1-x}\text{As}$ for a 50% alloy lies in the region of 0.90.

In the case of a free-standing boundary condition, the normal components of the stress tensor vanish and the displacement is unrestricted. On the contrary, for a clamped-surface boundary condition, the displacement is zero while the normal components of the stress tensor are unrestricted. If one considers a generic cylindrical nanowire with a diameter D and an infinite length along the z -axis, the solution of eq. (30) can be written in the following form [90]:

$$\mathbf{u}(r, z, t) = \sum_n \int \mathbf{u}_n(q, r) \exp\{i(qz - \omega_n t)\} \frac{dq}{2\pi} \quad (31)$$

where r and z are the radial and axial coordinates, q is the z -component (along wire axis) of the wave vector, $\mathbf{u}_n(q, r)$ and $\omega_n(q)$ are the eigenmodes and eigenfrequencies, respectively. The longitudinal acoustic waves are coupled modes of the radial and axial modes, which are given by

$$u_r(r, z) = \left[\frac{d}{dr} \{BJ_0(q_d r) + AJ_0(q_t r)\} \right] \times \exp\{i(qz - \omega t)\} \quad (32)$$

$$u_z(r, z) = i \left[qBJ_0(q_d r) + \frac{-q_t^2}{q} AJ_0(q_t r) \right] \times \exp\{i(qz - \omega t)\} \quad (33)$$

where J_0 and J_1 are the ordinary Bessel functions, A and B are two constants that can be determined by the boundary

conditions, and q_d and q_t are two parameters related to ω and q through

$$q_{d,t}^2 = \frac{\omega^2}{v_{d,t}^2} - q^2 \quad (34)$$

The boundary conditions on the normal components of the stress tensor for free-standing nanowires are $\sigma_{r,z} = \sigma_{z,z} = 0$, at $r = D/2$, and those for clamped-surface conditions are $u_z = u_r = 0$, at $r = D/2$. The solutions in eqs. (32–33) have to satisfy these boundary conditions. This results in the following transcendental equations for the confined phonon dispersion of the longitudinal acoustic phonon modes in a nanowire [90–91]

$$(q^2 - q_t^2)^2 \frac{(q_d D/2)J_0(q_d D/2)}{J_1(q_d D/2)} - 2q_d^2(q^2 + q_t^2) + 4q^2 q_d^2 \frac{(q_t D/2)J_0(q_t D/2)}{J_1(q_t D/2)} = 0 \quad (35)$$

for the free-surface boundary conditions and

$$q_d^2 \frac{(q_t D/2)J_0(q_t D/2)}{J_1(q_t D/2)} + q^2 \frac{(q_d D/2)J_0(q_d D/2)}{J_1(q_d D/2)} = 0 \quad (36)$$

for the clamped-surface boundary conditions. Phonon dispersion can be obtained by numerically solving eqs. (35–36) and (34). At each q , there are many solutions for q_d and q_t . Using index n to indicate different branches, we can write the phonon dispersion for each branch as

$$\omega_n = v_{d,t} \sqrt{q^2 + q_{d,t}^2} \quad (37)$$

where ω_n is the phonon frequency for the n th branch. Similarly, one can obtain the dispersion relation of confined acoustic phonons in thin films. Direct comparison of the acoustic phonon dispersion in thin films and nanowires in the context of thermal transport has been given by Zou and Balandin [36–38]. In the ultra-thin film, one can distinguish three different types of confined acoustic waves characterized by their distinctive symmetries: shear waves, dilatational waves, and flexural waves. The shear waves have only one non-zero component of the displacement vector, that is, $\mathbf{u} = (0, u_y, 0)$, which lies in the plane of the thin film and perpendicular to the direction of the wave propagation. Thus, the shear waves can be viewed as the transverse modes in the bulk material. The component of the wave vector that is along the confined direction, that is, the z -axis is quantized and $q_{z,n} = (\pi n/W)$, where W is the width of the thin film or quantum well. The dispersion relation for the shear waves can be written as $\omega_n = v_t(q_x^2 + q_{z,n}^2)^{1/2}$. For simplicity, it is assumed that waves propagate in the x direction. The dilatation waves and the flexural waves have two nonzero components $\mathbf{u} = (u_x, 0, u_z)$. The former are symmetric waves with respect to the midplane, while the latter are antisymmetric waves. Both types of waves have a component in the direction of the wave propagation and hence they can be viewed as a modification of the bulk longitudinal modes.

The dispersion of confined acoustic phonons for the dilational (longitudinal) modes in a freestanding quantum well is given by [92]

$$\frac{\tan(q_d W/2)}{\tan(q_t W/2)} = -\frac{4q_x^2 q_d q_t}{(q_x^2 - q_t^2)^2} \quad (38)$$

where q_d and q_t are defined in eq. (34). Although the confined acoustic phonon spectra in low-dimensional structures are complex, one can always find two distinctive types of confined modes. The first type consists of true acoustic modes for which the relation $\omega(\mathbf{q} = 0) = 0$ holds for any lateral dimension W . The second type consists of quasi-optical modes that have cut-off frequencies (see Fig. 3). The slope of the confined phonon modes that defines the group velocity is smaller than that of the bulk branch for a wide range of the phonon wave vector \mathbf{q} or the phonon energy.

The phonon group velocity can be calculated for each branch by numerical differentiation. In order to calculate the phonon thermal conductivity, we need to find the functional dependence of the phonon group velocity on phonon energy. Also, since different branches have different group velocity-energy dependencies, one has to calculate the phonon group velocity averaged over all contributing branches and different directions. For both the nanowire and thin film, the group velocity almost coincides with the bulk velocity for very small values of the phonon energy. It then drops dramatically with increasing energy and rises up again much more slowly and finally asymptotically reaches a constant value. The asymptotic values for the average phonon group velocity in the silicon nanowire and thin film with the same lateral dimension of 20 nm are 5.39×10^5 cm/s and 5.67×10^5 cm/s, respectively [6, 36–38]. In bulk silicon, the longitudinal sound velocity is 8.47×10^5 cm/s. One should remember that these values are obtained for specific geometry, size, and boundary conditions, and will be different in other structures. It is interesting to note that these asymptotic values of the phonon group velocity calculated for the phonon branches originated from the bulk longitudinal mode are close to the value of the transverse sound velocity in bulk silicon.

5.3. Phonon Spectrum in Quantum Well and Quantum Dot Superlattices

Acoustic phonon dispersion in quantum well superlattices can be found using formalism developed by Rytov for thinly laminated medium [93]. Rytov's model, based on the elastic continuum approximation, is frequently used to identify folded phonon frequencies in the center of the Brillouin zone while interpreting Raman spectra. The phonon dispersion in quantum well superlattices in Rytov's model is given by

$$\begin{aligned} \cos(qD) = & \cos\left(\frac{\omega D_1}{V_1}\right) \cos\left(\frac{\omega D_2}{V_2}\right) \\ & - \frac{1 + \zeta^2}{2\zeta} \sin\left(\frac{\omega D_1}{V_1}\right) \sin\left(\frac{\omega D_2}{V_2}\right) \end{aligned} \quad (39)$$

where $V_i = (C/\rho)^{1/2}$ is the sound velocity in each layer, and $\zeta = \rho_2 V_2 / \rho_1 V_1$ is the acoustic mismatch between the layers, $D = D_1 + D_2$ is the period of the superlattice.

Lazarenkova and Balandin [94–95] have calculated acoustic phonon modes in three-dimensional (3D), ordered quantum dot arrays. They found the phonon dispersion for arbitrary values of the elastic constants of constituent materials solving the general equation of motion

$$\rho \frac{\partial^2 u_i}{\partial t^2} = \sum_j \sum_k \sum_l \frac{\partial}{\partial x_j} c_{ijkl} \frac{\partial u_i}{\partial x_k} \quad (40)$$

where ρ is mass density and T is the stress tensor. The components of the tensor c_{ijkl} are defined by 36 elastic stiffness constants $c_{\alpha\beta}$. The solution of these equations for the 3D-quantum dot superlattice can be expressed in the plane-wave form by the analogy with regular bulk crystals

$$\mathbf{u}(\mathbf{r}, t) = \mathbf{A} \exp[i(\mathbf{q} \cdot \mathbf{r} - \omega t)] \quad (41)$$

where $|\mathbf{q}| = 2\pi/\lambda$ is the phonon wave vector, λ is a phonon wavelength, \mathbf{r} is coordinate vector, t is time, and ω is the phonon frequency. The solution of eq. (40) in bulk material is a linear function as it should be in the continuum approximation. Note that the phonon modes are of a pure compression (longitudinal) type or a pure shear (transverse) type, if and only if the wave propagates along a crystallographic direction of high symmetry; otherwise, it has components of each type. Using the analogy with bulk crystal, one can solve the elasticity eq. (40) for 3D quantum dot arrays with the new quasi-periodic boundary conditions [94]

$$\mathbf{u}(\mathbf{r} + \mathbf{D}) = \exp(i\mathbf{q} \cdot \mathbf{D})\mathbf{u}(\mathbf{r}) \quad (42)$$

Equation (42) constitutes the Bloch–Floquet theorem for the 3D quantum dot superlattice (QDS), where vector $\mathbf{D} = (D_x, D_y, D_z)$ describes the new periodicity of the structure. Figure 8 presents the phonon dispersion in $[[100]]$ quasi-crystallographic direction calculated using finite-difference method (FDM). This quasi-crystallographic direction in QDS is parallel to the $[100]$ crystallographic direction in the host material assuming that the QDS structure is grown on the (001)-oriented substrate. The phonon spectrum in Figure 8 is presented in the extended Brillouin zone scheme to emphasize the existence of two different types of phonon modes in QDS that emanate from bulk acoustic modes. These modes are quasi-acoustic ($\omega(\mathbf{q} = 0) = 0$) and quasi-optical ($\omega(\mathbf{q} = 0) \neq 0$). The quasi-acoustic modes are nothing else but folded acoustic branches of the host material. The multiple reflection of phonons from periodical interfaces leads to a mini-gap formation at the Brillouin zone boundary. The degeneracy due to intersection of different branches is lifted everywhere except for the points of high symmetry. The same figure shows the acoustic phonon dispersion in bulk Si (dashed lines) and bulk Ge (dot-dashed lines) along $[100]$ crystallographic direction. The longitudinal and transverse sound velocities are assumed to be $v_L = 8433.2$ m/s and $v_T = 5844.6$ m/s for Si and $v_L = 4913.8$ m/s and $v_T = 3542.4$ m/s for Ge, respectively. The value of the group velocity for the quasi-acoustic phonons in QDS lies between Si and Ge sound velocities and it is not defined by the volume fractions of two constituent materials (see the dotted lines in Fig. 8). Even in solid alloys, where atoms of two materials are randomly distributed, elastic properties

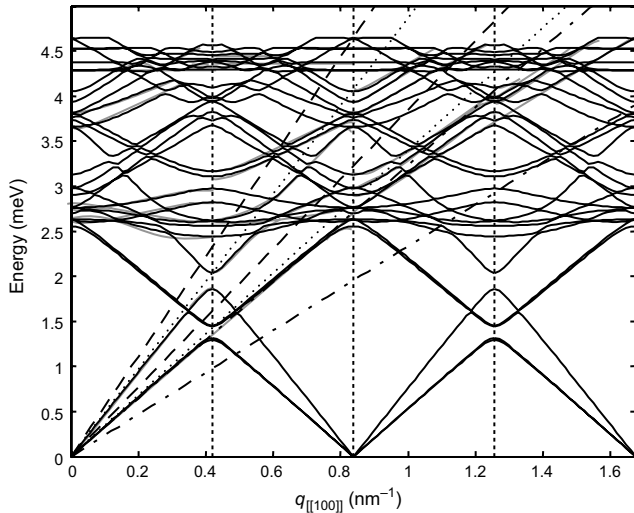


Figure 8. Phonon dispersion in Ge/Si 3D regimented quantum dot superlattice (solid lines) plotted for a structure with the following parameters: $L_x = L_y = 5.0$ nm, $L_z = 2.5$ nm, $H_x = H_y = 2.5$ nm, and $H_z = 1.25$ nm. The dispersion is shown along $[[100]]$ quasi-crystallographic direction. Acoustic phonon dispersion relations in bulk Si and Ge are indicated with dashed and dot-dashed lines, correspondingly. Dotted lines show the acoustic phonon dispersion estimated from the volume fractions of Si and Ge in given QDC. Reprinted with permission from [94], O. L. Lazarenkova and A. A. Blandin, *Phys. Rev. B* 66, 245319 (2002). © 2002, American Institute of Physics.

change almost linearly only in “one-mode behaved” systems such as $\text{Na}_{1-x}\text{K}_x\text{Cl}$, $\text{K}_{1-x}\text{Pb}_x\text{Cl}$, $\text{Ni}_{1-x}\text{CO}_x\text{O}$, etc. The composition dependence of phonon energy in $\text{Si}_x\text{Ge}_{1-x}$ alloy is far from linear. The quasi-acoustic dispersion branches deviate downwards from the linear dependence at higher phonon energy. The transverse mode, which is double degenerate at the zone center, splits at the zone boundary. If the wave propagates along $[[100]]$ quasi-crystallographic direction in QDS with tetragonal symmetry ($d_x = d_y \neq d_z$), two shear modes $[[010]]$ and $[[001]]$ are different. If $d_y > d_z$, the $[[010]]$ mode bends stronger than the $[[001]]$ mode. However, if the phonon wavelength λ is large compared to the QDS period $|d|$ ($\lambda = 2\pi/|q| \gg |d|$) acoustic wave properties are determined by the average medium parameters (effective medium approximation), and the fine structure of the medium does not strongly affect the wave propagation. Indeed, this is clearly in the extended zone presentation when the phonon wave vector approaches the third Brillouin zone, which corresponds to the period of the quantum dot superlattice $d_x = 7.5$ nm along this direction. At this value of the wave vector, the slope of the quasi-acoustic modes that defined the group velocity gets higher.

The quasi-optical modes correspond to “nearly standing” waves. One can view them as created by periodic scatters such as quantum dot interfaces. These modes can be induced inside quantum dots or in the space between them. A “true” standing wave would have a completely flat dispersion relation, which reflects the fact that this wave does not propagate through the crystal. In contrast, the dispersion branches of quasi-optical modes can have a minimum. The latter means that these modes propagate slowly going back and forth. We refer to these modes as quasi-optical since

they have a nonzero energy in the center of the Brillouin zone, that is, a cut-off frequency. At the same time, one should emphasize that these modes are also emanating from acoustic bulk phonon modes. The regular optical phonon modes have much higher energy. In Ge/Si QDS of the considered geometry, the lowest quasi-optical branch has the energy of about 2.6 meV at the zone center. In bulk Si, the longitudinal optical (LO) and transverse optical (TO) phonon energies are $\hbar\omega_{LO}^r = \hbar\omega_{TO}^r = 64.3$ meV. In bulk Ge, they equal to $\hbar\omega_{LO}^r = \hbar\omega_{TO}^r = 37.2$ meV.

The limits of the applicability of the continuum approximation can be estimated from the comparison of the calculated dispersion branches with experimental data and lattice dynamics simulation results. As long as acoustic phonon dispersion remains approximately linear, the phonons can be formally treated in the continuum long-wave approximation. Based on the experimental data provided in [96], we can estimate the lowest limit for Si to be about 10 meV along the $[[111]]$ crystallographic direction and about 5 meV for Ge along the same direction. It corresponds to about one-third (one-fifth) of the Brillouin zone for silicon (germanium). The latter translates to the feature size of 2–3 atomic layers in real space. Thus, our approach is rather accurate for a description of acoustic phonons in QDS of the chosen dimensions. The unit cell of the QDS of ortho-rhombic symmetry is analogous to the unit cell of regular bulk crystal.

Another approach to calculating phonon dispersion in nanostructures is the lattice dynamics approach. The simplest case of lattice dynamics calculation of the phonon dispersion is that of a 1D monatomic linear chain, where one considers a linear chain of identical atoms of mass M positioned at a distance a , the lattice constant connected by some imaginary springs that imitate interaction between atoms. Phonon dispersion can then be obtained from very simple classical treatment. The equation of motion is written in terms of the Hooke’s law for the force between atoms and its solution has to satisfy Bloch’s theorem required by the periodicity condition. The dispersion for the 1D monatomic linear chain takes the following familiar form [29]:

$$\omega = \sqrt{\frac{4C_1}{M}} \left| \sin\left(\frac{qa}{2}\right) \right| \quad (43)$$

The above equation is based on the assumption that the interatomic interaction only exists among nearest-neighbor atoms and C_1 is its force constant. For semiconductor crystals with one atom per unit cell, cell phonon dispersion is represented by the acoustic branches only. If the crystal has more than one atom in the unit cell, the dispersion relation develops additional branches (see Fig. 2). Since in technologically important semiconductors (Si, GaAs, Ge, etc.), optical branches do not contribute significantly to the lattice thermal conductivity, this review included acoustic phonons only.

In semiconductor nanostructures, the equations of motion that describe the system are generally more complicated than in bulk. Hyldgaard and Mahan [97] and Tamura et al. [98] have reported calculations of phonon dispersion in periodic superlattices based on a simple-cubic lattice model and a face-centered cubic (fcc) lattice dynamics model. The lattice dynamics approach allows an accurate calculation of

phonon dispersion in structures with a few atomic layers, but it requires knowledge of interatomic potential and is limited by the computational power.

6. THERMAL CONDUCTIVITY OF SPECIFIC TYPES OF NANOSTRUCTURES

6.1. Lattice Thermal Conductivity of Semiconductor Nanowires

In this section, we describe the change in the in-plane thermal conductivity of semiconductor nanowires due to phonon-boundary scattering and phonon spectrum modification. In addition to a direct contribution to phonon relaxation via the extra resistive scattering mechanism (see eq. (26)), the boundary conditions on the phonon Boltzmann equation in nanowires may lead to a change in the nonequilibrium phonon distribution compared to the bulk. The boundary conditions take the following general form [29]:

$$\tilde{N}(\mathbf{q}, \mathbf{r}_B)_{V_n} = p\tilde{N}(\mathbf{q}', \mathbf{r}_B)_{-V_n} \quad (44)$$

where \mathbf{r}_B is the position at the boundary and V_n is the normal component of the velocity. Equation (44) indicates that of all the phonons arriving at the boundary, only a fraction of p are scattered specularly with reversed normal component of the velocity but the same velocity along the heat conduction direction. The rest are scattered uniformly in all directions and only contribute to the equilibrium distribution. In the two special cases of purely specular and purely diffusive boundary scattering, the boundary conditions are $\tilde{N}(\mathbf{q}, \mathbf{r}_B)_{V_n} = \tilde{N}(\mathbf{q}', \mathbf{r}_B)_{-V_n}$ and $\tilde{N}(\mathbf{q}, \mathbf{r}_B)_{V_n} = 0$, respectively. It has been shown that the above boundary conditions lead to a deviation of the nonequilibrium phonon distribution from its bulk value, and thus a correction to the regular bulk formula for the lattice thermal conductivity. The corrected expression for the lattice thermal conductivity in a nanowire is [99]

$$\begin{aligned} K_{\text{wire}}(T, D, p) &= K_B(T, D, p) - \Delta K_{\text{wire}}(T, D, p) \\ &= \left(\frac{k_B}{\hbar}\right)^3 \frac{k_B}{2\pi^2 V} T^3 \int_0^{\theta_D/T} \frac{\tau_C x^4 e^x}{(e^x - 1)^2} \\ &\quad \times \left[1 - \frac{24}{\pi} G(\eta(x), p)\right] dx \quad (45) \end{aligned}$$

The second term in eq. (45), ΔK_{wire} , is a correction to the regular bulk formula introduced by the scattering from rough boundaries. Function $G(\eta(x), p)$ has been defined in [99] and $\eta(x)$ is the ratio between the lateral dimension D and the mean-free path $\Lambda(x) = V_G(x)\tau_C(x)$. In [99], the thermal conductivity of quantum wires has been calculated using eq. (45) and the bulk value of the phonon velocity. Zou and Balandin [6] modified the calculation by adding the effect of acoustic phonon confinement in nanowires [4, 87–89] by introducing the phonon group velocity determined from the phonon dispersion specific for a given structure geometry and boundary conditions. Figure 9 shows thermal conductivity of a nanowire, including both phonon

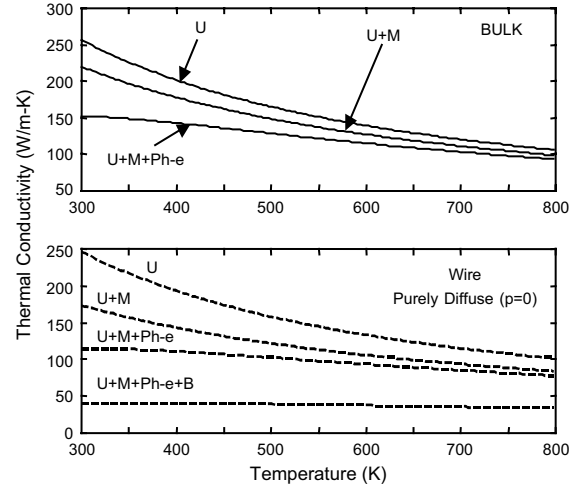


Figure 9. Lattice thermal conductivity in a cylindrical nanowire and bulk silicon. The results for the nanowire are calculated for the case of purely diffuse boundary scattering ($p = 0$). One can see that according to this model the lattice thermal conductivity in the wire is reduced to about 26% of its bulk value at 300 K. The results are obtained for the idealized boundary conditions (free surface) with complete phonon confinement. Reprinted with permission from [6], J. Zou and A. Balandin, *J. Appl. Phys.* 89, 2932 (2001). © 2001, American Institute of Physics.

redistribution and phonon confinement effects for cylindrical nanowire. Since the results were calculated for perfect confinement conditions (free surface boundaries), it gives the lower bound for the actual thermal conductivity. Lu et al. [39, 100], following the approach of [4, 6, 8], obtained the thermal conductivity of rectangular cross-section nanowires taking into account both phonon redistribution and phonon confinement effects. Figure 6 illustrates the relative contribution to thermal resistivity of different scattering process in bulk Si and a nanowire with purely diffuse scattering. Only the phonon confinement effect is taken into account [6].

A similar approach can be used for calculation of the in-plane lattice thermal conductivity of thin films and nanowires of different cross-section. The results have been obtained for the nanowire and thin film with the same lateral dimension of 20 nm, which is above the thermal acoustic phonon wavelength and much less than the acoustic phonon mean-free path reported in [9]. For purely diffuse boundary scattering, the ratio of the lattice thermal conductivity between the wire and the well at room temperature was found to be $\kappa_{\text{wire}}/\kappa_{\text{well}} \approx 0.42$ [38]. Based on their model Zou and Balandin [6] predicted the room temperature thermal conductivity of the cylindrical single crystal Si nanowire of 20 nm diameter to be about 13 W/m-K. This prediction has recently found an excellent experimental confirmation. Li et al. [40] carried out measurements of the single Si nanowires of 22 nm diameter and reported the room temperature thermal conductivity of about 9 W/m-K.

6.2. Thermal Conductivity of Quantum Dot Superlattices and Nanocomposites

In this section, we review thermal conduction in a special type of nanostructure such as QDS, that is, multiple arrays of quantum dots. Conventionally [101–102], the name

“superlattice,” with respect to quantum dot arrays, does not imply strict periodic arrangement of quantum dots. This is unlike quantum well superlattice (QWS), where periodicity along the growth direction is assumed, which distinguishes QWS from multiple quantum well structures [52]. Quantum dots in QDS can be completely random, partially regimented [101–102], or regimented along all three directions [103]. Figure 10 shows an example of partially regimented superlattice with clear vertical correlation of the dot position [104]. Electrical conduction in regimented QDS has been investigated in [105–107]. Thermal conduction in QDS rapidly became an important subfield of research due to theoretically proposed and partially demonstrated experimental applications of these structures in photodetectors, thermoelectric elements, frequency conversion, etc. A review of physical properties of quantum dots and applications of quantum dot superlattices has been given by Wang and Balandin [53].

Experimental data on thermal conductivity in QDS is rather scarce. Since the process of heat conduction in QDS is conceptually similar to that in polycrystalline or composite materials, here we cite some relevant data for different material systems including composite films. Generally, a decrease of thermal conductivity is observed compared to the one in constituent bulk materials. In some cases, the decrease is larger than predicted from the alloy disorder scattering models. Kim et al. [83] measured thermal conductivity of ZnS:SiO₂ composite films, where ZnS nanoparticles of average radius $R = 2$ nm were embedded in an SiO₂ matrix. The volume fraction of the nanoparticles was estimated to be around 64%, which corresponds to the randomly closed-packing density. They found a very small thermal conductivity (order of magnitude) compared to the bulk constituent values. Moreover, the reported thermal conductivity was lower than the conventionally estimated minimum values for disordered ZnS and SiO₂ [83].

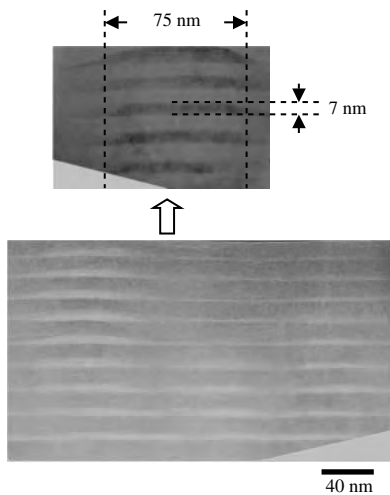


Figure 10. Cross-sectional, high-resolution electron microscope (HREM) image of the 10-period quantum dot superlattice sample. The typical dot base diameter and height were determined to be 75 nm and 7 nm, respectively. Reprinted with permission from [104], J. L. Liu et al., *J. Cryst. Growth* 227–228, 1111 (2001). © 2001, Elsevier Science.

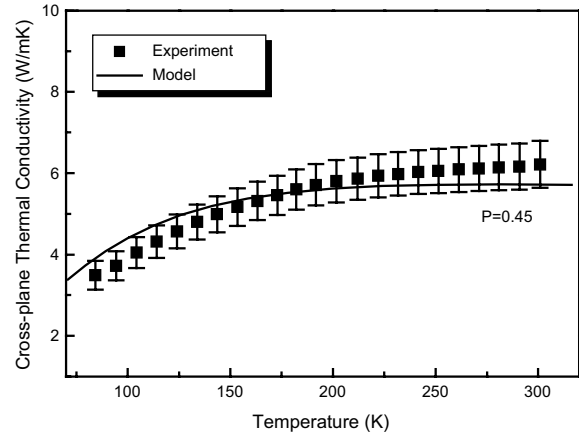


Figure 11. Cross-plane thermal conductivity of the 10-period quantum dot superlattice as a function of temperature. The scattered squares are experiment data, while the solid line is the calculation result using a phonon transport model based on the Boltzmann transport equation that considers partially diffuse and partially specular interfaces. Reprinted with permission from [104], J. L. Liu et al., *J. Cryst. Growth* (2001). © 2001, Elsevier Science.

Lui et al. [104] reported on the measurement of the thermal conductivity of MBE grown Ge/Si quantum dot superlattices (see Fig. 10). The typical dot sizes were determined to be 75 nm in base and 7 nm in height by transmission electron microscopy. A differential 3ω method was employed to measure the thermal conductivity K . At room temperature, K was determined to be 6.2 W/mK and 30.5 W/mK in the cross-plane and in-plane direction, respectively. Temperature-dependent measurements showed that cross-plane thermal conductivity monotonously decreased while in-plane thermal conductivity showed a peak as the temperature decreased from 300 to 80 K. Figure 11 shows the measured cross-plane thermal conductivity of the 10-period quantum dot sample as a function of temperature [104]. The scattered squares are experimental data, while the error bars represent the experiment uncertainty of the thermal conductivity, arising from the data measured with different sizes of metal wires.

Depending on the phonon transport regime, defined by such parameters as the feature size of the structure L , thermal phonon mean-free path Λ and the thermal phonon wavelength λ_T , one can use different models for thermal conductivity in QDS. The choice of the model will also depend on the desired accuracy as well as the availability and accuracy of the initial data such size, shape, interdot distances, interface quality, etc. When the thermal phonon mean-free (MFP) path is smaller than the typical dot size, $\Lambda \ll L$, one can apply a continuum description within the EMA. In this approach, the thermal conductivity of each region of the nanostructured material is represented by its bulk value. Using the simple formula for the phonon thermal conductivity $K_{ph} = (1/3)C_V V_S \Lambda$, where C_V is the heat capacity at constant volume and V_S is the average sound velocity, one can estimate the room-temperature phonon MFP for different materials: $\Lambda(\text{Si}) \approx 52$ nm, $\Lambda(\text{Bi}) \approx 7.5$ nm, $\Lambda(\text{PbTe}) \approx 17.5$ nm, and $\Lambda(\text{SiO}_2) \approx 1$ nm. The actual values of MFP may differ since the above estimate

neglects phonon dispersion (see, for example, [9]). The thermal conductivity of QDS, or other nanocrystalline material in EMA, can be found using Maxwell–Garnett or Clausius–Mossotti approach [108]. For a system of spherical voids ($\xi = 3$) or infinite cylindrical voids ($\xi = 2$) in a material of thermal conductivity K_{bulk} , this approach gives the effective thermal conductivity as

$$K_{\text{eff}} = \frac{(1 - \beta)K_{\text{bulk}}}{1 + \beta/(\xi - 1)} \quad (46)$$

where β is the fractional volume of the voids. This approach represents the geometry of the system very crudely and it is accurate only when the fractional volume of one material is small or the difference in bulk thermal conductivity of the dot-and-barrier materials is small. This approach does not account for regimentation of the dots. Recent examples of the use of this approach include estimates of the phonon thermal conductivity in thermoelectric QDS [109].

An approach for calculating thermal conductivity of crystalline QDS, in the case when the structure feature size W is smaller than the phonon MFP, has been proposed in [110]. It is based on the continuum model and uses a solution of the plane-wave scattering problem on spherical bodies known from acoustics [111]. The approach of [110] explicitly includes all major phonon-scattering process characteristics for a given material system as well as scattering on quantum dots of a semi-spherical shape randomly distributed in-plane. The general expression for an acoustic phonon-scattering rate on quantum dots is written as

$$\frac{1}{\tau_D} = \frac{v_g \sigma_V}{V} \quad (47)$$

where σ_V is the total cross-section of dot ensemble of volume V . The expression for the scattering cross-section σ of a single dot under the assumption that a thermal phonon wave can be represented as a sum of plane waves is given by [111]

$$\sigma = \frac{\pi}{k^2} \sum_{m=0}^{\infty} (2m + 1) |1 + R_m|^2 \quad (48)$$

Here R_m is a reflection coefficient

$$R_m = \frac{h_m^*(ka) + i\beta h_m^*(ka)}{h_m^*(ka) + i\beta h_m(ka)} \quad (49)$$

where $\beta = i \frac{\rho c}{\rho_e c_e} \left[\frac{j_m^*(ka)}{j_m(ka)} \right]$, ρ is density, c is the sound velocity, the subscript e denotes the parameter that corresponds to the dot material, $h_m(ka) = j_m(ka) + iy_m(ka)$, j and y are the spherical Bessel functions of the first and second kind, respectively, and h_m^* is the complex conjugate. In the long-wave and short-wave limits, eq. (48) simplifies to $\sigma \sim 5.6(ka)^4 a^2$ for $ka \ll 1$, and $\sigma \sim 2\pi a^2$ for $ka \gg 1$, respectively. It is seen from these limits that phonon scattering on quantum dots is a process intermediate between the point defect and boundary scattering. It implies that a quantum dot acts like an impurity atom if the dot size is much less than a phonon wavelength in one extreme. In the other limit, when the dot size is much larger than a phonon wavelength, a quantum dot acts like an additional boundary.

Calculations performed using this approach for a Ge/Si quantum dot array predicted a significant decrease of the in-plane lattice thermal conductivity in the wide range of temperatures and dot radii. For example, the room temperature thermal conductivity of Ge/Si QDS with the volume dot fraction of $\delta = 0.05$ and dot radius $R = 4$ nm is about 42 W/m K compared to bulk Si thermal conductivity of 155 W/m K [110]. Thermal conductivity tends to decrease with the decreasing dot size (from $R = 10$ nm to $R = 2$ nm) at a fixed volume dot fraction, and with an increasing dot volume fraction (from $\delta = 0$ to $\delta = 0.14$) at each fixed dot radius. At the same time, its value is always above the alloy scattering limit, which corresponds to the situation when quantum dots degenerate to point impurities and the phonon scattering rate on quantum dots becomes point-defect scattering. This approach has been further extended to include quantum dot regimentation [112]. It has been shown that the long-range ordering of quantum dots enhanced acoustic phonon scattering thus leading to an additional decrease of the lattice thermal conductivity. The additional decrease in the ordered QDS, compared to random QDS, is due to the contribution of the coherent scattering term. For some realistic Ge/Si quantum dot parameters, it was found that regimentation results in about a 30% decrease of the room-temperature lattice thermal conductivity at the volume dot fraction of 0.1. The strength of this coherent acoustic phonon-scattering mechanism depends on the volume dot fraction and acoustic mismatch between the dot and matrix materials.

An accurate approach for calculating the lattice thermal conductivity of QDS with a very small feature size, when $W \ll \Lambda$ and approaches λ_T , should take into account a modification of the acoustic phonon spectra. In such structures, one cannot assume anymore that the phonon dispersion in the matrix and dot material is the same as in constituent bulk. Thus, the crucial part of the calculation of the thermal conductivity in this case will be the modeling of phonon spectra and phonon density of states for QDS [94–95]. For strongly disordered quantum dot superlattices, the assumptions of [110, 112] are not valid anymore. In this case, one can apply “phonon-hopping” models such as described in [113].

7. CONCLUSIONS

We have presented a review of thermal conductivity in semiconductor nanostructures. The review includes general formalism for calculating thermal conductivity in bulk semiconductors and nanostructures, as well as an outline of recent experimental results. It is particularly focused on changes in thermal transport in nanostructures due to increased boundary scattering and a confinement-induced modification of acoustic phonon spectrum. Some specific nanostructures such as nanowires and quantum dot superlattices have been discussed in greater detail.

GLOSSARY

Acoustic impedance A parameter equal to the product of the density of the material and sound velocity in this material.

Acoustic phonon confinement A modification of the acoustic phonon spectrum in semiconductor nanostructures due to acoustic impedance mismatch at the boundaries. Phonon confinement in nanostructures may significantly affect the thermal conductivity.

Acoustic phonon quantization A confinement-induced change in the phonon spectrum manifested via appearance of quasi-optical phonon branches with cut-off frequencies determined by the nanostructure dimensions.

Isotropic continuum approximation Based on the reasoning that at relatively low temperatures most of the phonons, excited in a solid, are confined to the long-wavelength acoustic branches. Within this approximation, details of the crystal structure are ignored and the isotropic linear dispersion relation is used for all the normal modes.

Phonon A quantum of crystal vibrational energy associated with elementary excitations of a lattice. Phonons are quasiparticles that obey Bose-Einstein statistics.

Specular boundary scattering A scattering event when the normal component of the phonon velocity is reversed while the velocity along the heat conduction direction remains the same.

Thermal boundary conductivity Defined as the ratio of the heat flow per unit area across the interface to the temperature discontinuity at the interface between two media.

Thermal boundary resistance (also known as **Kapitza resistance**) Defined as the ratio of the temperature discontinuity at the interface between two media to the power per unit area flowing across the interface.

Thermal conductivity A positively defined quantity, which is the ratio of the heat flow per unit area to the temperature gradient that creates this heat flow.

Thermal diffusivity A parameter equal to the product of the thermal conductivity, density of the material and specific heat of the material.

ACKNOWLEDGMENT

The work on thermal conductivity of nanostructures at the University of California at Riverside has been supported by the National Science Foundation.

REFERENCES

1. The Semiconductor Industry Association: *International Technology Roadmap for Semiconductors*, 1998.
2. P. Hadley and J. E. Mooij, in "Quantum Semiconductor Devices and Technologies" (T. P. Pearsall, Ed.), p. 1. Kluwer Academic Publishers, Boston, 2000.
3. G. Chen, *J. Heat Transfer* 119, 220 (1997).
4. A. Balandin and K. L. Wang, *Phys. Rev. B* 58, 1544 (1998).
5. S. Y. Ren and J. D. Dow, *Phys. Rev. B* 25, 3750 (1982).
6. J. Zou and A. Balandin, *J. Appl. Phys.* 89, 2932 (2001).
7. T. Borca-Tasciuc, W. L. Liu, J. L. Liu, T. Zheng, D. Song, C. Moore, G. Chen, K. L. Wang, M. Goorsky, T. Radetic, R. Gronsky, T. Koga, and M. S. Dresselhaus, *Superlatt. Microstruct.* 28, 199 (2000).
8. X. Y. Zheng, S. Z. Li, M. Chen, and K. L. Wang, in "Micro-Electro-Mechanical Systems (MEMS)," Proceedings of ASME, International Mechanical Engineering Congress and Exposition, pp. 93–98. ASME, New York, 1996.
9. Y. S. Ju and K. E. Goodson, *Appl. Phys. Lett.* 74, 3005 (1999).
10. R. Venkatasubramanian, E. Siivola, and T. S. Colpitts, *Proc. 17th International Conference on Thermoelectrics* 191 (1998).
11. G. Chen, S. Q. Zhou, D.-Y. Yao, C. J. Kim, X. Y. Zheng, Z. L. Liu, and K. L. Wang, *Proc. 17th International Conference on Thermoelectrics* 202 (1998).
12. J. L. Liu, A. Balandin, and K. L. Wang, *Mat. Res. Soc. Symp. Proc.-Thermoelectric Materials* (1998), Vol. 545, p. 111. Materials Research Society, 1999.
13. H. Beyer, J. Nurnus, H. Bottner, A. Lambrecht, T. Roch, and G. Bauer, *Physica E* 13, 965 (2000).
14. H. Beyer, J. Nurnus, H. Bottner, A. Lambrecht, T. Roch, and G. Bauer, *Appl. Phys. Lett.* 80, 1216 (2002).
15. S.-M. Lee, D. G. Cahill, and R. Venkatasubramanian, *Appl. Phys. Lett.* 70, 2957 (1997).
16. S. Chattopadhyay, L. C. Chen, S. C. Chien, S. T. Lin, C. T. Wu, and K. H. Chen, *Thin Solid Films* 420–421, 205 (2002).
17. S. Chattopadhyay, L. C. Chen, S. C. Chien, S. T. Lin, and K. H. Chen, *J. Appl. Phys.* 92, 5150 (2002).
18. D. G. Cahill, K. Goodson, and A. Majumdar, *J. Heat Transfer* 124, 223 (2002).
19. G. Chen and A. Shakouri, *Trans. ASME* 124, 242 (2002).
20. K. E. Goodson and Y. S. Ju, *Ann. Rev. Mater. Sci.* 29, 261 (1999).
21. S. R. Mirmira and L. S. Fletcher, *Trans. AIAA* 12, 121 (1998).
22. A. A. Balandin and J. Zou, in "Quantum Dots and Nanowires" (S. Bandyopadhyay and H. S. Nalwa, Eds.). American Scientific Publishers, Los Angeles, CA, 2002.
23. S. Ciraci, A. Buldum, and I. P. Batra, *J. Phys. Condens. Matt.* 13, R537 (2001).
24. D. G. Cahill, W. K. Ford, K. E. Goodson, G. D. Mahan, A. Majumdar, H. J. Maris, R. Merlin, and S. R. Phillpot, *J. Appl. Phys.* 93, 793 (2003).
25. L. G. C. Rego and G. Kirczenow, *Phys. Rev. Lett.* 81, 232 (1998).
26. P. L. Kapitza, *J. Phys. (USSR)* 4, 181 (1941).
27. E. T. Swartz and R. O. Pohl, *Rev. Mod. Phys.* 61, 605 (1989).
28. E. T. Swartz, Solid-solid thermal boundary resistance, Ph.D. dissertation, Cornell University, Ithaca, NY, 1987 (UMI 8725816).
29. J. M. Ziman, "Electrons and Phonons." University Press, Oxford, 1979.
30. C. M. Bhandari and D. M. Rowe, "Thermal Conduction in Semiconductors." John Wiley & Sons, New York, 1988.
31. J. D. Achenbach, "Wave Propagation in Elastic Solids." North-Holland Series in Applied Mathematics and Mechanics, The Netherlands, 1973.
32. G. P. Srivastava, "The Physics of Phonons." Adam Hilger, New York, 1990.
33. J. Singh, "Physics of Semiconductors and Their Heterostructures." McGraw-Hill, New York, 1993.
34. T. Klitsner and R. O. Pohl, *Phys. Rev. B* 36, 6551 (1987).
35. S. Volz and D. Lemonnier, *Phys. Low-Dim. Struct.* 5/6, 91 (2000).
36. J. Zou and A. A. Balandin, in "Proc. Materials Research Society," April 16–20, San Francisco, CA, 2001. *Mat. Res. Symp. Proc.* Vol. 677, pp. AA6.7.1–6.7.6.
37. J. Zou and A. A. Balandin, Thermal conductivity in semiconductor thin films and nanowires, Device Research Conference, June 25–27, Notre Dame, IN, 2001, pp. 164.
38. J. Zou and A. A. Balandin, Excess heat removal from nanoscale electronic devices, the Sixth International Symposium on Quantum Confinement: Nanostructured Materials and Quantum Devices, September 2–7, San Francisco, CA, 2001. *Electrochemical Society Proceedings Volume* 2001–19 pp. 71–79.
39. X. Lu, J. H. Chu, and W. Z. Shen, *J. Appl. Phys.* 93, 1219 (2003).
40. D. Li, Y. Wu, P. Kim, L. Shi, P. Yang, and A. Majumdar, *Appl. Phys. Lett.* 83, 2934 (2003).
41. M. V. Simkin and G. D. Mahan, *Phys. Rev. Lett.* 84, 927 (2000).
42. G. Chen, *Phys. Rev. B* 57, 14958 (1998).
43. G. Chen, *Internat. J. Therm. Sci.* 39, 471 (2000).

44. C. L. Mehta, *Il Nuovo Cimento* 18, 402 (1963).
45. D. K. Ferry and S. M. Goodnick, "Transport in Nanostructures." Cambridge University Press, Cambridge, 1997.
46. N. W. Ashcroft and N. D. Mermin, "Solid State Physics." Thomson Learning, USA, 1976.
47. C. J. Glassbrenner and G. A. Slack, *Phys. Rev.* 134, A1058 (1964).
48. D. I. Florescu, V. M. Asnin, F. H. Pollak, R. J. Molnar, and C. E. C. Wood, *J. Appl. Phys.* 88, 3295 (2000).
49. E. Yamasue, M. Susa, H. Fukuyama, and K. Nagata, *J. Cryst. Growth* 234, 121 (2002).
50. P. J. Price, *Phil. Mag.* 46, 1252 (1955).
51. C. M. Bhandari, in "Thermoelectrics Reference Book," pp. 55–65. CRC Press, 1995.
52. C. Weisbuch and B. Vinter, "Quantum Semiconductor Structures: Fundamentals and Applications." Academic Press, New York, 1991.
53. K. L. Wang and A. A. Balandin, in "Optics of Nanostructured Materials" (V. Markel and T. F. George, Eds.), pp. 515–550. Wiley & Sons, New York, 2000.
54. A. A. Balandin, F. Madarasz, F. Szmulowicz, and S. Bandyopadhyay, in "Optics of Nanostructured Materials" (V. Markel and T. F. George, Eds.), pp. 467–514. Wiley & Sons, New York, 2000.
55. A. Greiner, L. Reggiani, T. Kuhn, and L. Varani, *Phys. Rev. Lett.* 78, 1114 (1997).
56. A. Svizhenko, A. Balandin, S. Bandyopadhyay, and M. A. Stroschio, *Phys. Rev. B* 57, 4687 (1998).
57. I. Sur, A. Casian, H. Scherrer, and Z. Dashevsky, in "Proc. 19th International Conference on Thermoelectrics," 2000; I. Sur, A. Casian, A. A. Balandin, Z. Dashevsky, V. Kantser, and H. Scherrer, in "Proc. 21th International Conference on Thermoelectrics," 2002.
58. A. Casian, I. Sur, H. Scherrer, and Z. Dashevsky, *Phys. Rev. B* 61, 15965 (2000).
59. P. G. Klemens, in "Solid State Physics" (F. Seitz and D. Turnbull, Eds.), Vol. 7. Academic, New York, 1958.
60. J. Callaway, *Phys. Rev.* 113, 1046 (1959).
61. R. Peierls, *Ann. Physik* 3, 1055 (1929).
62. I. Pomeranchuk, *J. Phys. (USSR)* 4, 259 (1941).
63. M. G. Holland, *Phys. Rev.* 132, 2461 (1963).
64. A. D. McConnell, S. Uma, and K. E. Goodson, *J. Microelectromech. Syst.* 10, 360 (2001).
65. P. G. Klemens, in "Chemistry and Physics of Nanostructures and Related Non-Equilibrium Materials" (E. Ma et al., Eds.), p. 97. Minerals, Metals & Materials Society, Warrendale, PA, 1997.
66. P. G. Klemens, *Proc. Phys. Soc. LXVIII* 12–A, 1113 (1955).
67. D. Kotchetkov, J. Zou, A. A. Balandin, D. I. Florescu, and F. H. Pollak, *Appl. Phys. Lett.* 79, 4316 (2001).
68. J. Zou, D. Kotchetkov, A. A. Balandin, D. I. Florescu, and F. H. Pollak, *J. Appl. Phys.* 92, 2534 (2002).
69. J. Zou, D. Kotchetkov, A. A. Balandin, D. I. Florescu, and F. H. Pollak, "Proc. Materials Research Society, San Francisco, CA, March 2002" (S. Ashok, J. Chevallier et al., Eds.), pp. F8.25–9. MRS Proceedings, Volume 719.
70. D. Kotchetkov, J. Zou, and A. A. Balandin, in "Proc. Materials Research Society," San Francisco, CA, March 2002" (V. Tikare, E. A. Olevsky, and A. Zavaliangos, Eds.), pp. W5.11. MRS Proceedings Volume 731.
71. A. Balandin and K. L. Wang, *J. Appl. Phys.* 84, 6149 (1998).
72. F. H. Stillinger and T. A. Weber, *Phys. Rev. B* 31, 5262 (1985).
73. S. G. Volz and G. Chen, *Phys. Rev. B* 61, 2651 (2000).
74. S. G. Volz and G. Chen, *Appl. Phys. Lett.* 75, 2056 (1999).
75. I. M. Khalatnikov, *Zh. Eksp. Teor. Fiz. (USSR)* 22, 687 (1952).
76. W. A. Little, *Canad. J. Phys.* 37, 334 (1959).
77. E. T. Swartz and R. O. Pohl, *Appl. Phys. Lett.* 51, 200 (1987).
78. R. S. Prasher and P. E. Phelan, *J. Heat Transfer* 123, 105 (2001).
79. G. Chen, *Phys. Rev. B* 57, 14958 (1998).
80. T. Zeng and G. Chen, *Trans. ASME* 123, 340 (2001).
81. C.-W. Nan and R. Birringer, *Phys. Rev. B* 57, 8264 (1998).
82. E.-K. Kim, S.-I. Kwun, S.-M. Lee, H. Seo, and J.-G. Yoon, *Appl. Phys. Lett.* 76, 3864 (2000).
83. E.-K. Kim, S.-I. Kwun, S.-M. Lee, H. Seo, and J.-G. Yoon, *Phys. Rev. B* 61, 6036 (2000).
84. K. E. Goodson, O. W. Kading, M. Rosner, and R. Zachai, *Appl. Phys. Lett.* 66, 3134 (1995).
85. C. Hu, M. Kiene, and P. S. Ho, *Appl. Phys. Lett.* 79, 4121 (2001).
86. H. B. G. Casimir, *Physica* 5, 495 (1938).
87. A. Balandin et al., in "Proc. Internat. Conf. Thermoelectrics," ICT'99, Baltimore, MD, 1999.
88. A. Balandin, *Phys. Low-Dim. Struct.* 1/2, 1 (2000).
89. A. Balandin, *Phys. Low-Dim. Struct.* 5/6, 73 (2000).
90. S. G. Yu, K. W. Kim, M. A. Stroschio, and G. J. Iafrate, *Phys. Rev. B* 51, 4695 (1995).
91. S. G. Yu, K. W. Kim, M. A. Stroschio, G. J. Iafrate, and A. Ballato, *Phys. Rev. B* 50, 1733 (1994).
92. N. Bannov, V. Aristov, V. Mitin, and M. A. Stroschio, *Phys. Rev. B* 51, 9930 (1995).
93. S. M. Rytov, *Soviet Phys.-JETP* 2 (1956), p. 466.
94. O. L. Lazarenkova and A. A. Balandin, *Phys. Rev. B* 66, 245319 (2002).
95. O. L. Lazarenkova and A. A. Balandin, in "Proc. Materials Research Society," San Francisco, CA, March 2002, MRS Proc. Volume 731. (V. Tikare, E. A. Olevsky, and A. Zavaliangos, Eds.), pp. W10.4–7.
96. O. Madelung et al. (Eds.) "Physics of Group IV Elements and II–V Compounds," Landolt-Bornstein, New Series, Group III, Vol. 17, Pt. (a). Springer-Verlag, Berlin, 1982.
97. P. Hylgaard and G. D. Mahan, *Phys. Rev. B* 56, 10754 (1997).
98. S.-I. Tamura, Y. Tanaka, and H. J. Maris, *Phys. Rev. B* 60, 2627 (1999).
99. S. G. Walkauskas, D. A. Broido, K. Kempa, and T. L. Reinecke, *J. Appl. Phys.* 85, 2579 (1999).
100. X. Lu, W. Z. Shen, and J. H. Chu, *J. Appl. Phys.* 91, 1542 (2002).
101. J. L. Liu, W. G. Wu, A. A. Balandin, and K. L. Wang, *Appl. Phys. Lett.* 74, 185 (1999).
102. J. L. Liu, W. G. Wu, A. A. Balandin, and K. L. Wang, *Appl. Phys. Lett.* 75, 1745 (1999).
103. G. Springholz, M. Pinczolis, P. Mayer, V. Holy, G. Bauer, H. H. Kang, and L. Salamanca-Riba, *Phys. Rev. Lett.* 84, 4669 (2000).
104. J. L. Liu, A. Khitun, K. L. Wang, T. Borca-Tasciuc, W. L. Liu, G. Chen, and D. P. Yu, *J. Cryst. Growth* 227–228, 1111 (2001).
105. O. L. Lazarenkova and A. A. Balandin, *J. Appl. Phys.* 89, 5509 (2001).
106. O. L. Lazarenkova and A. A. Balandin, in "Proc. 9th International Symposium on Nanostructures: Physics and Technology," St. Petersburg, Russia, June 18–22, 2001, Ioffe Institute, St Petersburg, 2001 (Zh. Alferov and L. Esaki, Eds.), pp. 294–297.
107. O. L. Lazarenkova and A. A. Balandin, in "Proc. of Symposium on Quantum Confinement VI: Nanostructured Materials and Devices," San Francisco, CA, September 2001, Electrochemical Society Proc., Vol. 2001–19, 2001 (M. Cahay, J. P. Leburton, D. J. Lockwood, S. Bandyopadhyay, and J. S. Harris, Eds.), pp. 238–250.
108. J. C. Maxwell, "A Treatise on Electricity and Magnetism." Dover, NY, 1954.
109. T. C. Harman, P. J. Taylor, D. L. Spears, and M. P. Walsh, *J. Electron. Mater.* 29, L1 (2000).
110. A. Khitun, A. A. Balandin, J. L. Liu, and K. L. Wang, *J. Appl. Phys.* 88, 696 (2000).
111. P. M. Morse and H. Feshbach, "Methods of Theoretical Physics," Part II, pp. 418–430. McGraw-Hill, New York, 1953.
112. A. Khitun, A. A. Balandin, J. L. Liu, and K. L. Wang, *J. Superlatt. Microstruct.* 30, 1 (2001).
113. L. Braginsky, N. Lukzen, V. Shklover, and H. Hofmann, *Phys. Rev. B* 66, 134203 (2002).

Transition Metal Acetylide Nanostructures

Thomas M. Cooper

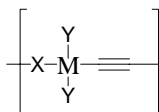
*Materials and Manufacturing Directorate
Air Force Research Laboratory, Wright-Patterson Air Force Base, Ohio, USA*

CONTENTS

1. Transition Metal Acetylides:
An Emerging Nanomaterial
 2. Synthesis of Transition Metal Acetylides
 3. Spectroscopic Characterization
 4. Properties
 5. Applications
- Glossary
References

1. TRANSITION METAL ACETYLIDES: AN EMERGING NANOMATERIAL

In recent years there has been increased activity in the investigation of the synthesis and structure–property relationships of transition metal acetylides, given by the general chemical formula. These compounds contain d^8 transition metals, in most cases platinum, with four ligands bound in a planar structure. The metals bond to at least one acetylenic ligand. The other ligands include phosphines, arsines, cyano groups, acetylenes, and imines.



M = Ni, Pd, Pt; X = C≡C, N; Y = NR₂, PR₃, AsR₃, C≡C

(I)

This chapter will survey the materials science of transition metal acetylides and will show that they are an emerging class of nanomaterials. Several review articles on these compounds have appeared in the literature [1–8]. The reader will see that an amazing number of structures have been synthesized using motif I. These structures include polymers, dendrimers, oligomers, and self-assembled systems. To assist in the understanding of

future, more complex systems, I have emphasized structure–property data for the simpler oligomers and polymers. I will also describe future possibilities for development of the nanotechnology of transition metal acetylides.

2. SYNTHESIS OF TRANSITION METAL ACETYLIDES

2.1. Oligomeric Complexes

2.1.1. PtL₂(PR₃)₂ Bidentate Complexes

Bidentate complexes are synthesized according to the following reaction:

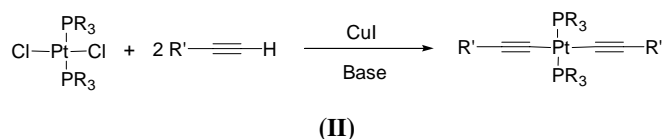
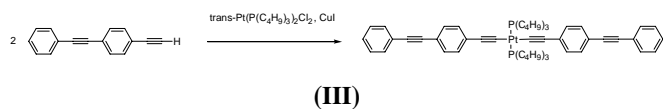


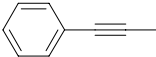

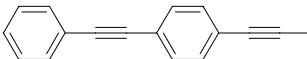
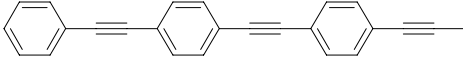
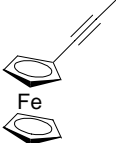
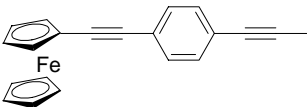
Table 1 lists examples of bidentate complexes. An example of a synthesis of a bidentate complex is given by McKay [9, 10]. The terminal acetylene (2.03 equivalents), Pt complex (1 equivalent), and CuI (0.07 equivalent) is dissolved in a deoxygenated mixture of pyridine and triethylamine with a few drops of tributylphosphine to stabilize the Pt complex. The reaction mixture stirs under nitrogen at room temperature for 18 h. Following purification, the reaction has a 76% yield.

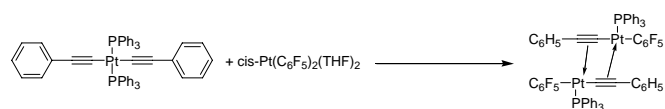


2.1.2. Self-Assembly by π -M Bonding in PtL₂(PR₃)₂ Complexes

Self-assembly by π -M bonding in PtL₂(PR₃)₂ complexes makes possible the formation of nanostructures. A bimetallic double-bridged acetylide complex having η^2 -bonding of two M-C≡CPh units has been prepared [11].

Table 1. Examples of bidentate $\text{PtL}_2(\text{PR}_3)_2$ complexes.

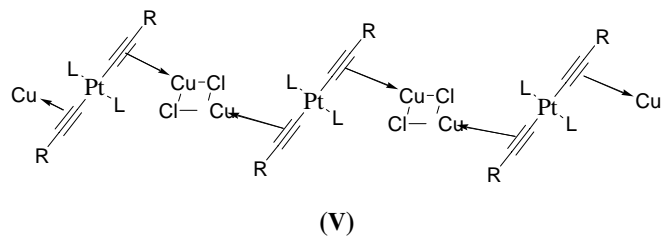
Ligand	Reference
$\text{—}\equiv\text{—H}$	[70]
$\text{—}\equiv\text{—H}$	[67]
$\text{—}\equiv\text{—}\equiv\text{—H}$	[49, 70]
$\text{—}\equiv\text{—Si(CH}_3)_3$	[73]
	[70, 73]
$\text{H}\equiv\text{—}\langle\text{C}_6\text{H}_4\rangle\text{—}\equiv\text{H}$	[49, 70, 108, 117]
$(\text{H}_3\text{C})_3\text{Sn}\equiv\text{—}\langle\text{C}_6\text{H}_4\rangle\text{—}\equiv\text{—}$	[118]
	[73]
$(\text{H}_3\text{C})_3\text{Sn}\equiv\text{—}\langle\text{C}_6\text{H}_4\rangle\text{—}\langle\text{C}_6\text{H}_4\rangle\text{—}\equiv\text{—}$	[118]
	[9, 10, 73, 97–99]
	[73]
	[119]
$\text{H}_2\text{N}\text{—}\langle\text{C}_6\text{H}_4\rangle\text{—}\equiv\text{—}$	[120]
	[121]
$\text{O}_2\text{N}\text{—}\langle\text{C}_6\text{H}_4\rangle\text{—}\equiv\text{—}$	[18]
$\text{H}_3\text{CO}\text{—}\langle\text{C}_6\text{H}_4\rangle\text{—}\equiv\text{—}$	[18]

**(IV)**

The reaction occurs at room temperature for 4 days. The complex forms by rearrangement of phenyl and pentafluorophenyl groups between the two metal centers. The central C_4Pt_2 core atoms are coplanar. Contribution of allenelike resonance forms to the electronic structure causes asymmetric platinum acetylide π -linkages, with the platinum atom being closer (2.261 vs. 2.362 Å) to the acetylinic carbon attached to the phenyl group.

Copper(I) chloride forms a linear co-polymer with platinum acetylide complexes. One equivalent of copper(I) chloride reacts with $\text{cis-}[\text{PtCl}_2(\text{PMe}_2\text{Ph})_2]$ and $\text{Bu}'\text{C}\equiv\text{CH}$ to form a linear

polymeric structure [12]. The structure contains $\text{Pt}(\mu\text{-}\sigma, \eta^2\text{-C}\equiv\text{CBu}')\text{Cu}$ and $\text{Cu}(\mu\text{-Cl})_2\text{Cu}$ linkages. With less CuCl , the complex $\text{cis-}[\text{PtCuCl}(\text{C}\equiv\text{CBu}')_2(\text{PMe}_2\text{Ph})_2]$ forms.

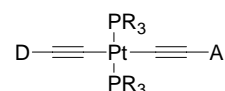
**(V)**

Silver perchlorate complexes of platinum acetylides have also been reported [13]. Treatment of the complex $\text{cis-}[\text{Pt}(\text{C}\equiv\text{C-C}_6\text{H}_5)_2(\text{PPh}_3)_2]$ with 0.5 equivalent of AgClO_4 yields a trinuclear bridged alkynyl derivative (Fig. 1). The vibrational spectra of these complexes show $\text{C}\equiv\text{C}$ frequencies lower than those of the starting platinum acetylide complex, giving evidence for side-on π coordination of the $\text{C}\equiv\text{CR}$ ligands. The crystal structure reveals that each of the $\text{cis-Pt}(\text{C}\equiv\text{CPh})_2(\text{PPh}_3)_2$ units behaves like a bidentate diyne as the Ag atom bonds to the four $\text{C}\equiv\text{C}$ bonds in a tetrahedral arrangement. When $\text{cis-}[\text{Pt}(\text{C}\equiv\text{C-C}_6\text{H}_5)_2(\text{PPh}_3)_2]$ reacts with one equivalent of AgClO_4 , the salt $[\text{Pt}_2\text{Ag}_2\text{-}(\text{C}\equiv\text{CC}_6\text{H}_5)_4(\text{PPh}_3)_4](\text{ClO}_4)_2$ forms. The authors speculate that each silver atom forms a bridge between two $\text{C}\equiv\text{CC}_6\text{H}_5$ units.

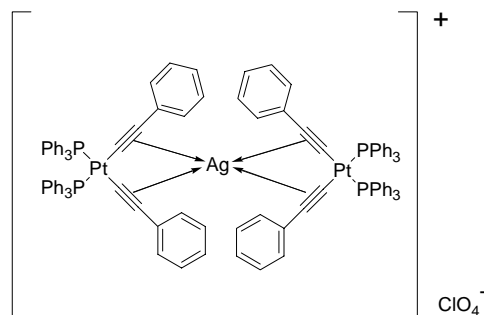
Addition of AgClO_4 to $\text{trans-}[\text{Pt}(\text{C}\equiv\text{CH})_2(\text{PMe}_2\text{Ph})_2]$ results in a 1:1 complex [14]. The crystal structure of the complex reveals a linear polymer with π coordination between the silver atom and two acetylides (Fig. 2). The coordination of the silver ions leads to a zigzag chain with a perchlorate ion in each cavity along the chain.

2.1.3. $\text{PtLL}'(\text{PR}_3)_2$ Asymmetric Complexes

The ability to synthesize asymmetric complexes

**(VI)**

makes possible the development of amphipathic compounds which self-assemble into organized assemblies [15] or placement of the dye in oriented multilayer assemblies [16]. The first

**Figure 1.** Silver perchlorate complex of platinum acetylides [13].

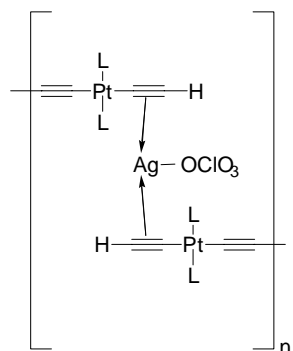
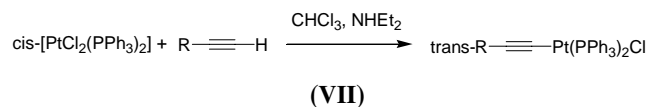


Figure 2. When AgClO_4 is added to $\text{trans-[Pt(C}\equiv\text{CH)}_2(\text{PMe}_2\text{Ph)}_2]$ a linear polymer with π coordination between the silver atom and two acetylides forms [14].

step in the synthesis involves the preparation of the monochloro-acetylide species [17].



Control of the acetylene/base ratio is necessary to prevent formation of the symmetric bis(acetylide) complexes. A 1:1 or slight excess of acetylene will promote formation of the monochloro complex [17]. Because of a charge repulsion effect toward the Cl ligand, successful reaction more likely occurs when the monochloro-acetylide contains electron-donating groups. The unsymmetrical acetylides have been prepared by reacting the monochloro-acetylide with the alkyne in the presence of diethyl amine [18, 19]. Examples of these complexes are listed in Table 2.

Doped PMMA films of these chromophores have been prepared by dissolving 40 mg of PMMA with 2 mg of the acetylide compound in 2 ml chloroform [20]. Spin coating (1200 rpm, 30 s) onto soda lime glass substrates followed by drying at room temperature for 24–48 h results in films having a 1–3 micrometer thickness. Corona poling for 10 min at 80 °C yields oriented films. The order parameters of these films ranges from 0.07 to 0.18 vs. a DR1 standard having an orientation parameter of 0.30.

2.1.4. $[\text{Pt}(\text{PR}_3)_2\text{L}]_n$ Oligomeric Complexes

An early example of an oligomer complex is described by Fujikura and his co-workers [21]. Synthesis is performed by a series of condensations on a growing oligomer in piperidine/toluene 100 °C for 5–10 hr. No CuI catalyst is used in this series. The authors synthesize oligomers up to $n = 4$.

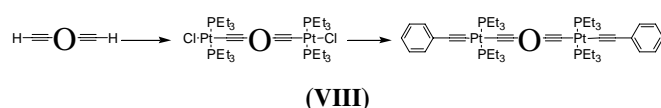
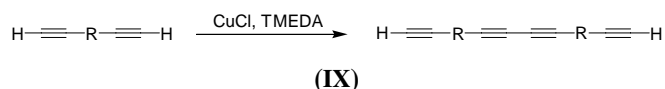


Table 2. Examples of asymmetric $\text{PtLL}'(\text{PR}_3)_2$ complexes.

Complex	Ref.
	[20]
	[20]
	[20]
	[20]
	[20]
	[19]
	[19]
	[18]
	[18]

A series of monodisperse oligomers has been prepared by Glaser–Hay oxidative oligomerization of the terminal acetylene monomer [22] (Fig. 3).



The reaction conditions affect the molecular weight distribution. When the reaction runs at room temperature with two

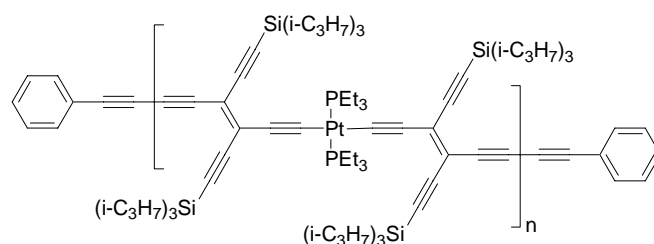
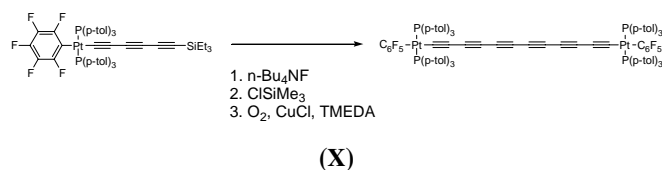


Figure 3. Monodisperse molecular rod [22].

equivalents of the phenylacetylene end-capping reagent immediately added, rods with $n = 1-3$ are prepared. To prepare higher oligomers, the reaction runs at $80\text{ }^\circ\text{C}$ with the addition of the end-capping reagent delayed 10 min. These rods extend in length from 3.3 to 12.1 nm. By delaying addition of the end-capping reagent phenyl acetylene to 20 min, a polymer with 32 repeat units can be prepared. Ultraviolet visible (UV/vis) data and second hyperpolarizability measurements suggest a nearly complete lack of π electron delocalization along the oligomeric backbone. These results suggest the Pt atoms act as true insulating centers and the Pt-C bonds have no π character.

Platinum acetylide chemistry has been used to synthesize compounds with long sp carbon chains with the goal of preparing carbyne, the one-dimensional analog of graphite and diamond. Toward this goal a series of complexes *trans*,*trans*-(C_6F_5)(*p*-tol₃P)₂Pt(C \equiv C)_{*n*}Pt(*p*-tol₃P)₂(C_6F_5), $n = 4, 6, 8$, has been prepared [23]. An earlier analog *trans*,*trans*-(*p*-MeC₆H₅)(*p*-tol₃P)₂Pt(C \equiv C)_{*n*}Pt(*p*-tol₃P)₂(*p*-MeC₆H₅) has been described [24]. The synthesis procedure uses a novel *in-situ* desilylation/coupling protocol, shown for $n = 6$.



The synthesis involves treating the triethylsilyl-protected precursor with $n\text{-Bu}_4\text{N}^+\text{F}^-$ in wet THF, followed by addition of ClSiMe_3 to scavenge F^- ions and running the reaction under Hay coupling conditions. The complex $n = 4$ has a straight rod conformation. Unique features appear in the crystal structures of $n = 6$ and 8 . When $n = 6$, the carbon chain is nearly a semicircle, while $n = 8$ is straighter but has an S-shape. UV/vis spectra of the complexes show vibronic progressions, with the 0-0 band redshifting as n goes from 4 to 8. The extinction coefficient for the $n = 8$ is $600,000\text{ M}^{-1}\text{ cm}^{-1}$.

Very complex structures where sp carbon chains are surrounded by sp^3 carbon double helices have been prepared by a self-assembly technique [25] (Fig. 4). A substitution

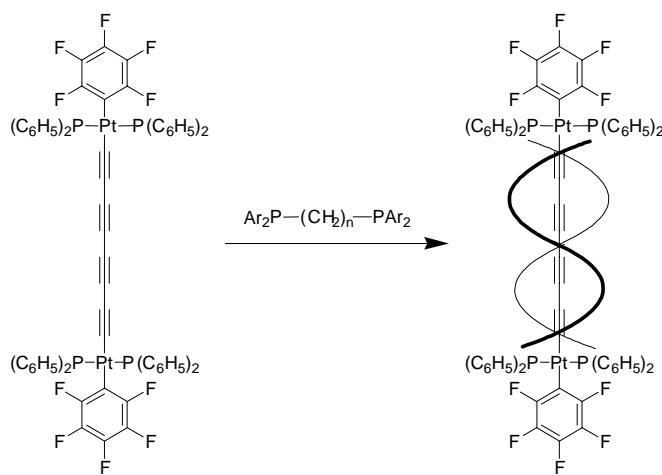


Figure 4. Complex structure having sp alkyne carbon chains surrounded by sp^3 carbon double helices [25].

reaction occurs when the Pt complex is treated with a diphosphane $\text{Ph}_2\text{P}(\text{CH}_2)_n\text{PPh}_2$ under moderately dilute conditions. The authors prepare similar compounds with analogous diphosphanes having *para*-substituted phenyl rings. Variation in the number of methylene groups and triple bonds gives the range of compositions that yields the double helix. The shorter diphosphane ($n = 10, 11$) yields nonhelical structures, while a longer diphosphane ($n = 18$) yields both helical and nonhelical motifs in the unit cell. The ratio of sp^3 carbons to sp carbons is a predictor of structure. The ratio varies from 1.25 for $n = 10$ to 1.75 for $n = 14$. A value of 1.50 is considered the minimum required for helicity.

2.1.5. Cyclic Complexes

Planar platinum metallacyclines with trialkyne pockets have been prepared [26] (Fig. 5). The coupling reaction occurs by reacting a high dilution solution of 2,2',6,6'-tetraethynyltolan with the *cis*-bis(triethylphosphine)platinum dichloride and 5% CuI under nitrogen for two weeks, giving a 66% yield. To inhibit oligomer formation, *cis*-platinum starting materials are used, along with high dilution conditions. This compound of Figure 5 crystallizes in a high symmetry space group. X-ray diffraction measurements show the acetylene C-C-C angles to be nearly linear, while the Pt-C-C angle shows significant deviation from linearity. The reported C-Pt-C angle of 83.1° has significant deviation from 90° . In atoms C_4 and C_{11} , the ^{13}C nuclear magnetic resonance (NMR) splitting pattern indicates coupling to both Pt atoms. The ^{195}Pt - ^{13}C spin coupling extends through four bonds of the enyne framework.

Cyclic Pd-acetylide complexes of *o*-diethynylbenzene have been prepared [27] (Fig. 6) by treating *o*-diethynylbenzene with 2.5 equivalents of $[\text{PdCl}_2(\text{PEt}_3)_2]$ in the presence of CuCl in diethyl amine. In the presence of 1 equivalent of $[\text{PdCl}_2(\text{PEt}_3)_2]$ a cyclic oligomeric complex forms. Because of the greater steric bulk of tributylphosphine, treatment with 1 equivalent of $[\text{PdCl}_2(\text{PBu}_3)_2]$ yields a mixture of oligomeric linear complexes.

Butadiyne heterocyclines containing only platinum and butadiyne fragments have been reported [28]. The complexes may be useful in catenane and rotaxane synthesis, where metal-acetylide polymers and carbon nanotubes thread through the heterocycline. To force a *cis*-geometry at the platinum atom, chelating phosphines are used. The tetraplatinum complex is prepared in high yields following catalytic CuI coupling for five days at room temperature (Fig. 7). The octaplatinum complex contains components which have both *cis*- and *trans*- geometries at platinum. The complex is prepared by reacting the components in the presence of CuI for 36 hr (Fig. 8).

Cyclic platinum acetylide complexes are considered precursors for a transition metal linked carbon network based on

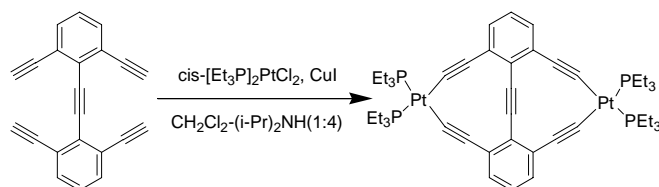


Figure 5. Planar platinum metallacycline with trialkyne pockets [26].

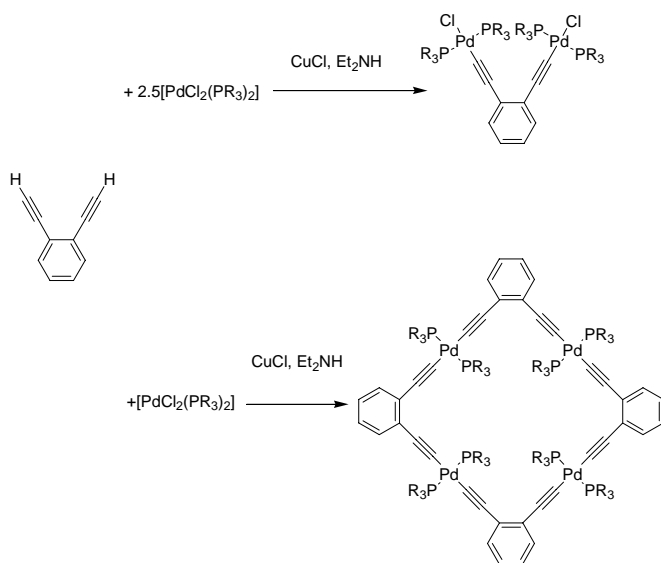


Figure 6. Preparation of cyclic Pd-acetylide complex of *o*-diethynylbenzene [27].

tetraethynylethene [29]. By choice of transition metal and ligands, the reversible formation of σ -bis(acetylide) complexes could lead to a self-assembled metal-acetylide network (Fig. 9). An all-carbon network prepared by reductive elimination at the metal centers and suitable choice of ligands could yield a three-dimensional transition metal acetylide network. A cyclic platinum acetylide complex prepared under Hay coupling conditions yields an orange-red, amorphous solid in 92% yield (Fig. 10). Evidence for this structure is obtained from MALDI-TOF mass spectrometry, where the parent ion has the molecular weight expected for this dimer. ^1H NMR measurements detect no terminal acetylenes and two sets of signals for the di(*t*-butyl)phenyl groups. ^{13}C NMR measurements detect 10 resonances from the tetrakis(tetraethynylethene) substructure. The UV/vis spectrum of this compound shows a broad absorption band extending beyond 500 nm, suggesting significant delocalization of its excited states.

An example of a chiral platinum acetylide shows the wide number of possibilities for synthesis of highly complex structures [30]. These molecular squares contain two types of chiral ligands attached to the transition metal: DIOP [2,3-*O*-isopropylidene-2,3-dihydroxy-1,4-bis(diphenylphosphino)butane] and BINAP [2,2'-bis(diphenylphosphino)-1,1'-bihaphthyl]. Because both DIOP and BINAP are optically active, chiral squares can be prepared. The first square is prepared from the self-assembly of a Pt-acetylide DIOP complex

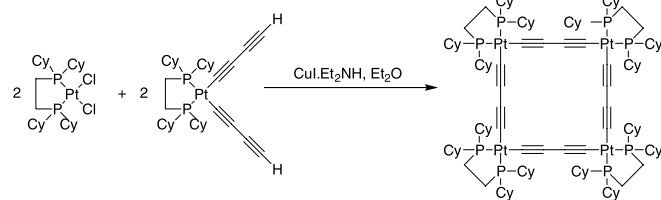


Figure 7. Butadiyne heterocycle containing only platinum and butadiyne fragments [28].

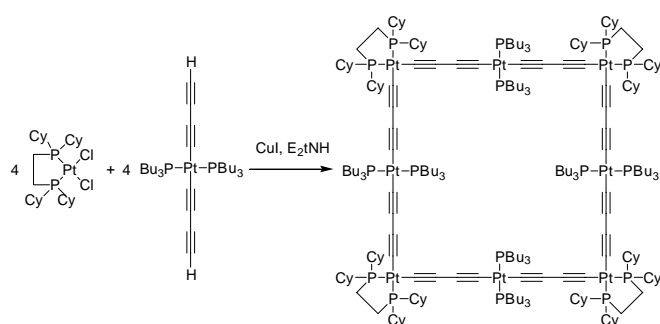
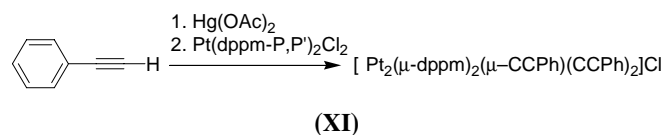


Figure 8. Octaplutonium complex having platinum in both *cis*- and *trans*-geometries [28].

with a Pt-acetylide BIMAP triflate complex. The authors synthesize all combinations of R,S-DIOP and R,S-BINAP complexes, as well as R,S-BINAP Pd(II) complexes. Changes in the structure are monitored by CD spectroscopy. These complexes also exhibit the π -tweezer effect (Fig. 11). Treatment of the square with 2 equivalents of silver triflate results in π -coordinated silver ions. Finally, neutral guests like tetramethyl pyrazine are captured by coordination to the silver ions. These examples show that the structure of platinum-acetylide complexes can be varied through the ligand, the metal, π -coordinated metal ions, and neutral guest.

2.1.6. A-Frame Complexes

A series of A-frame Pt acetylide complexes $[\text{Pt}_2(\mu\text{-dppm})_2(\mu\text{-C}\equiv\text{CR})(\text{C}\equiv\text{CR})_2]^+$ (Fig. 12) have been prepared according to the following reaction scheme [31]:



The chloride salt converts to the perchlorate salt by a metathesis reaction. Face-to-face dinuclear platinum(II) acetylides have the ability to encapsulate metal ions by serving as η^2 -ligands. In particular, the complex $[\text{Pt}_2(\text{dppm})_2(\text{C}\equiv\text{CPh})_4]$ forms a mixed metal tetranuclear complex $[\text{Pt}_2(\text{dppm})_2(\text{C}\equiv\text{CPh})_4]\cdot[\text{Cu}(\text{MeCN})_2] (\text{PF}_6)_2$ [32]. The complex is formed by dissolving $[\text{Pt}_2(\text{dppm})_2(\text{C}\equiv\text{CPh})_4]$ [33] in dichloromethane and gradually

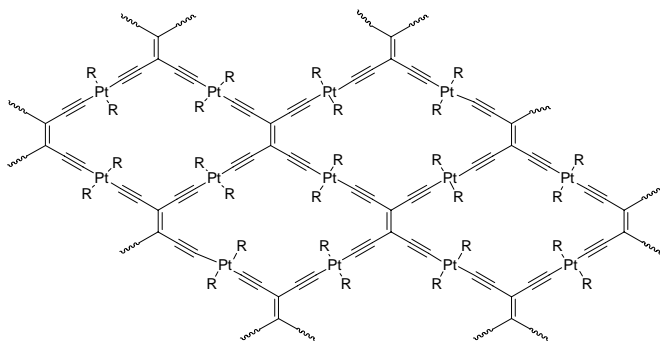


Figure 9. Proposed self-assembled platinum acetylide network [29].

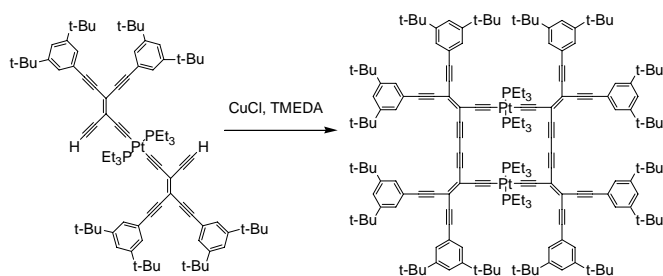


Figure 10. Cyclic platinum acetylide complex prepared under Hay coupling conditions [29].

adding an acetone solution of $[\text{Cu}(\text{MeCN})_4]\text{PF}_6$ to the mixture, with immediate formation of the copper complex (Fig. 13).

Oligomeric A-frame complexes are prepared by reaction of $[\text{Pt}_2\text{Cl}_2(\mu\text{-dppm})_2]$ with 1 equivalent of $\text{HC}\equiv\text{C}\text{Ar}\text{C}\equiv\text{CH}$ in the presence of NaOMe [34]. The reaction yields insoluble, yellow oligomeric complexes. The value of n ranges from 3 for $\text{Ar} = \text{C}_6\text{H}_4\text{-C}_6\text{H}_4$ to 12 for $\text{Ar} = \text{C}_6\text{H}_2\text{Me}_2$. The degree of polymerization is low because the growing oligomer precipitates out of the reaction mixture.

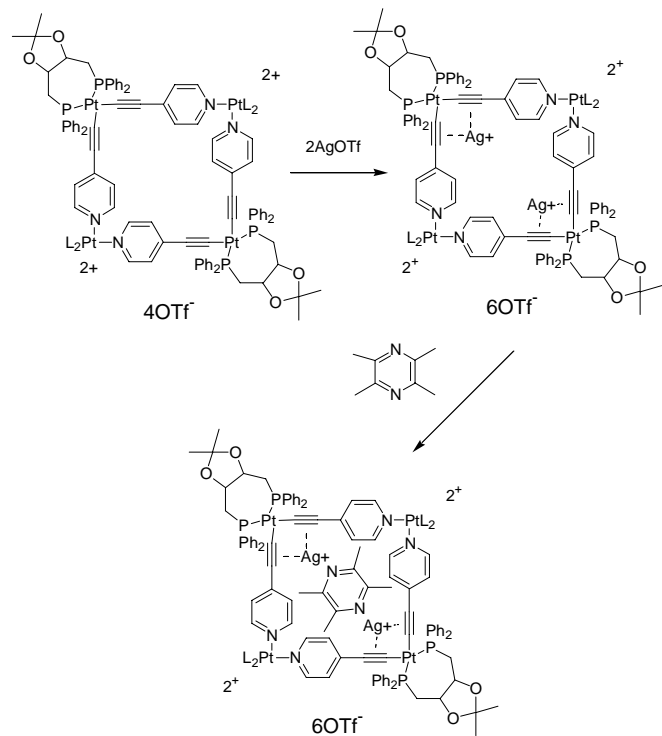
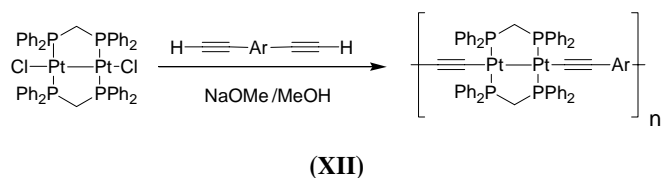


Figure 11. Chiral cyclic platinum acetylide complex exhibiting π -tweezer binding of silver ions and formation of an inclusion complex [30].

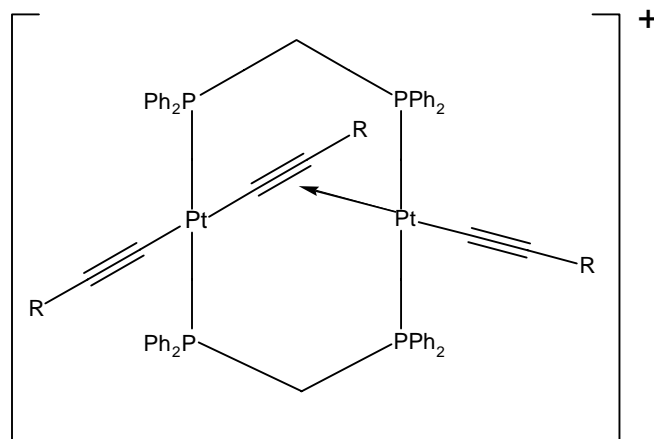


Figure 12. A-frame platinum acetylide complex [33, 75].

2.1.7. Diimine, Terpyridyl, and $[\text{Pt}_2\text{M}_4(\text{C}\equiv\text{CR})_8]$ Complexes

Platinum diimine complexes, having molecular structures as shown in Figure 14, where the compound on the left has the chemical formula $\text{Pt}(\text{dbbpy})(\text{C}\equiv\text{CC}_6\text{H}_4\text{X})_2$ and the compound on the right $\text{Pt}(\text{Rphen})(\text{C}\equiv\text{CC}_6\text{H}_4\text{X})_2$, have been described in a recent review [35]. Synthesis of these compounds is performed in the presence of base and copper iodide catalyst in a procedure similar to complexes with phosphine ligands (Fig. 15).

Platinum(II) terpyridyl acetylide complexes are prepared in a similar manner to diimine complexes [36, 37] (Figs. 16 and 17). In the presence of a terminal acetylene in methanol and base, $[\text{Pt}(\text{trpy})(\text{MeCN})](\text{OTf})_2$ is added and stirred for 12 hours, and then a metathesis reaction occurs through the addition of ammonium hexafluorophosphate, followed by isolation of the salt.

$[\text{Pt}_2\text{M}_4(\text{C}\equiv\text{CR})_8]$ complexes are prepared by treating $[\text{NBu}_4]_2[\text{Pt}(\text{C}\equiv\text{CR})_4]$ with AgClO_4 , CuCl , or $[\text{AuCl}(\text{tht})]$ [38]. The chemistry of these and related complexes has been reviewed [8]. This strategy has also been used to prepare $\text{M} = \text{Ir}$ [39], Tl [40, 41], and Rh [42] complexes.

2.2. Polymeric Complexes

2.2.1. Dendrimers

Dendrimers have been synthesized from a tridentate complex [43] (Fig. 18). The first generation dendrimer is synthesized according to the reaction scheme depicted in Figure 19. The mesitylene is dissolved in piperidine and treated with an excess of the trimer in the presence of CuCl and refluxed, yielding the intermediate. The intermediate is not isolated but treated with an excess of phenyl acetylene and the final complex purified.

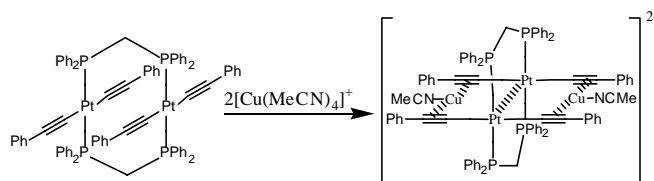


Figure 13. A-frame complex forming π -molecular tweezer with Cu [32].

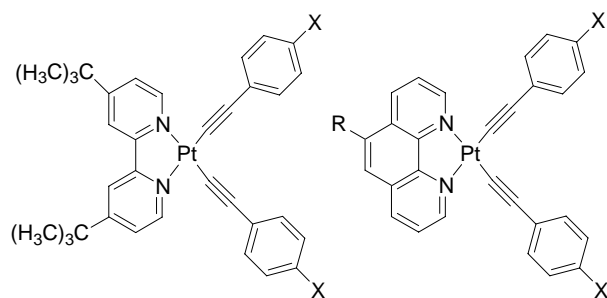


Figure 14. Examples of platinum diimine complexes. The compound on the left has the chemical formula $\text{Pt}(\text{dbbpy})(\text{C}\equiv\text{CC}_6\text{H}_4\text{X})_2$ and the compound on the right $\text{Pt}(\text{Rphen})(\text{C}\equiv\text{CC}_6\text{H}_4\text{X})_2$.

The $^{31}\text{P}\{^1\text{H}\}$ -NMR spectrum of the final complex shows two singlet signals at $\delta = 4.20$ ($J_{\text{Pt-P}} = 2396$ Hz) and 3.80 ($J_{\text{Pt-P}} = 2375$ Hz) at a 1:2 intensity ratio. The former signal is assigned to the inner phosphine ligands and the latter to the outer phosphine ligands.

The second and third generations of this dendrimer have also been prepared. NMR spectroscopy verifies the composition of these dendrimers. For example, the ^1H -NMR spectrum of the second generation dendrimer exhibits two singlets at $\delta = 2.57$ and 3.78 in a 1:2 integral ratio, corresponding to methyl protons of the central mesitylene group and methoxy protons of the end group. The $^{31}\text{P}\{^1\text{H}\}$ -NMR spectrum of the second generation dendrimer exhibits two singlets at $\delta 10.88$ ($J_{\text{Pt,P}} = 2381$ Hz) and 11.10 ($J_{\text{Pt,P}} = 2392$ Hz) in a 2:1 ratio, due to the phosphane groups bound to the six outer and three inner platinum atoms. The third generation dendrimer has a molecular weight of 25,840 and contains 45 platinum atoms. The large size of this molecule places it in nanoscale materials.

A convergent route for a dendrimer composed of platinum acetylide units has been described [44]. The method involves the use of orthogonal trialkylsilyl protective groups to synthesize an acetylene-terminal asymmetric dendron (Figure 20). The increased reactivity of the iodo- vs bromo- substituent allows for selective attachment of the triisopropylsilyl protecting group to the 1-position. Subsequent attachment of trimethylsilyl protective groups and selective deprotection gives two terminal acetylenic groups from which a platinum complex is prepared. Finally, the tri(isopropyl) group is removed by treatment with Bu_4NF at -78 °C.

A pyridine-based dendron has been prepared by similar methods [45] (Fig. 21). A dendrimer prepared by reaction between the core of Figure 18 and the dendron of Figure 21 results in the

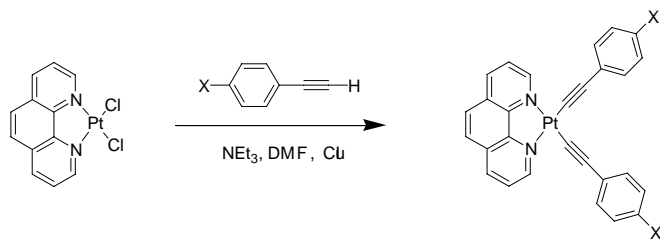


Figure 15. Synthesis of diimine complexes is performed in the presence of base and copper iodide catalyst in a procedure similar to complexes with phosphine ligands [35].

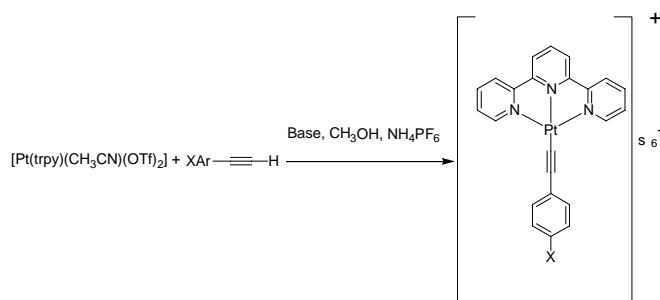
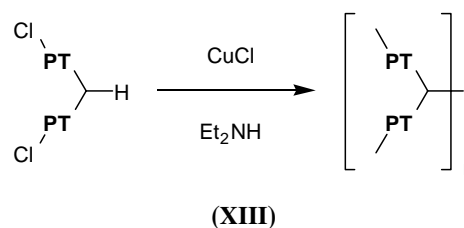


Figure 16. Synthesis of platinum(II) terpyridyl acetylide complexes [36].

displacement of the metal-bound chlorine by the pyridine nitrogen in the presence of $\text{NaB}3,5\text{-(CF}_3)_2\text{C}_6\text{H}_3$. This reaction causes complete ligand exchange (Fig. 22). To increase the lability of the metal-chloride bond in the core, it is necessary to prepare a palladium analog of the core. Treatment of the dendrimer with excess Bu_4NCl in benzene results in quantitative formation of core and dendron. The dendrimer can be regenerated by subsequent addition of $\text{NaB}3,5\text{-(CF}_3)_2\text{C}_6\text{H}_3$. A second generation dendrimer can be prepared by similar methods. This work represents an example of morphology control of dendrimers by chemical stimuli.

In a related study, the dendron described in Figure 20 has been polymerized into a hyperbranched polymer according to the scheme [46].



The polymer has a molecular weight of 32,000, corresponding to 20 monomer units.

2.2.2. Linear Polymers

Linear Pt acetylide polymers are prepared by a dehydrohalogenation reaction developed by Sonogashira [47]. The reaction involves coupling a terminal acetylene to a platinum chloride

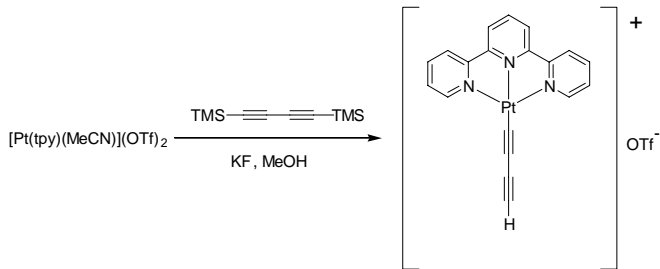


Figure 17. Synthesis of a terpyridyl acetylide complex exhibiting solvent-induced aggregation and solvatochromism [37].

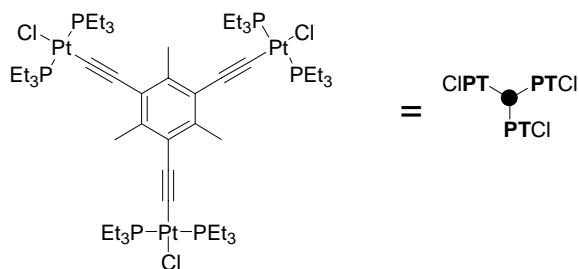
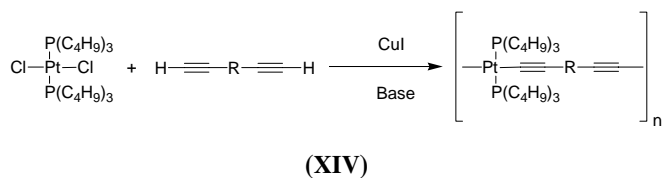


Figure 18. Tridentate platinum acetylide dendrimer core [43].

complex in the presence of a base and a catalytic amount of CuI.



The cuprous iodide serves as a catalyst and the amine base serves as an acid acceptor. There has been an investigation of the effect of reaction conditions on the palladium-containing polymer molecular weight [48]. Condensation in the presence of amines with low $\text{p}K_a$'s like pyridine yields low molecular weight polymers while strongly basic amines like piperidine and diethyl amine yields high molecular polymers. The presence of free tri-*n*-butyl phosphine tends to prevent dissociation of the phosphine ligand from the $\text{Pd}(\text{PBu}_3)_2$ moiety. The type of halogen used in cuprous halides had no effect on the polymer molecular weight. The polymers have a flexible rodlike structure [49, 50] which aggregates into crystallites [51]. Most of the polymers synthesized contain platinum or palladium. A study of nickel-poly-ynes has recently been published [52].

Pyridinium analogs of Pt(II) acetylide polymers [53, 54] show significant changes in their optical properties upon quaternization. Random quaternization occurs when the polymer is stirred with methyl iodide for 48 hours. Triflate analogs can also be prepared by the same method. Upon quaternization, the pyridinium analog's absorption maximum redshifts from 382 to 440 nm. Synthesis of an organometallic polymer with a prequaternized monomer yields a polymer having an absorption maximum at 534 nm.

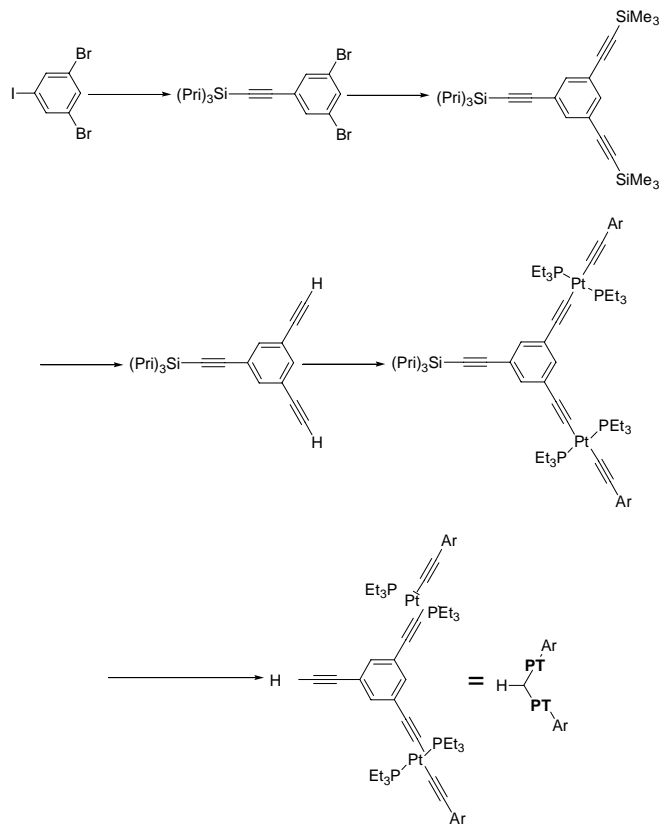
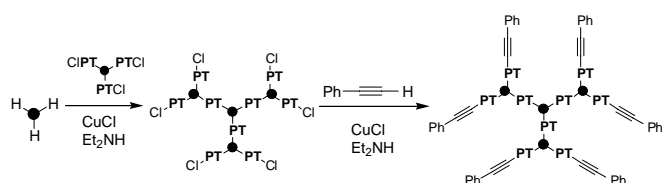
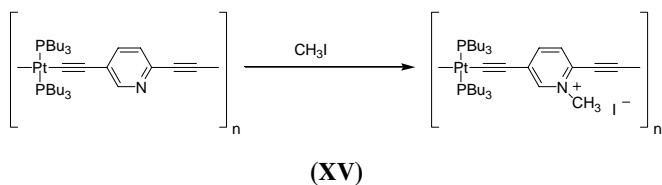


Figure 20. Convergent synthesis of platinum acetylide dendron through the use of orthogonal trialkyl-silyl protecting groups [44]. The symbol "Ar" represents a 4-methoxy-phenyl group.

Introduction of chirality into a polymer gives it potential applications in self-assembly, molecular recognition, ferroelectric liquid crystals, and nonlinear optical materials [55, 56]. Polymers having chiral monomer units have been synthesized from optically active 1,1'-bi-2-naphthol [57] (Fig. 23). The polymer is prepared by refluxing the solution overnight with the condensation reaction being monitored with ^{31}P NMR and GPC. The data show the terminal acetylenes quickly convert to dinuclear organometallic complexes, followed by a slow propagation to the polymer chain. The NMR data show one ^{31}P NMR signal and one set of signals corresponding to the naphthyl group. The platinum polymers have molecular weights ranging from 12,000 to 100,000 daltons, while analogous palladium polymers have molecular weights in the range 5,000–12,000 daltons,

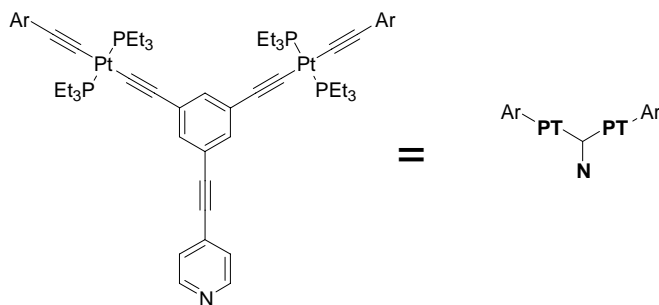


Figure 19. Synthesis of dendrimer from tridentate core [43].

Figure 21. A pyridine-based dendron [45].

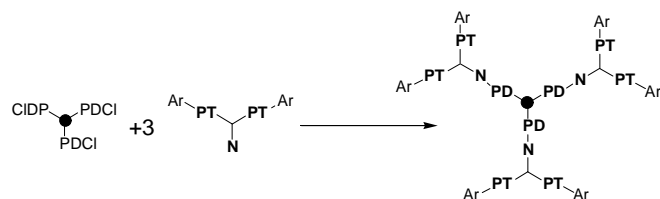


Figure 22. Synthesis of a pyridine-based dendrimer with both platinum- and palladium-containing monomer units [45].

demonstrating the Pt–C≡C bond to be more stable than the Pd–C≡C bond. The optical rotation, $[\alpha]_D$, ranges from -182 to $-364 \text{ 10}^{-1} \text{ deg cm}^2 \text{ g}^{-1}$. It is likely the polymer forms helical structures [58]. Examples of polymers are listed in Table 3.

2.3. Future Directions in Synthesis

Biomimetics ideas can be used to speculate about future directions in acetylide synthesis toward nanomaterials. Tropomyosin provides a well-understood example of a protein that undergoes self-assembly processes [55, 56]. Its primary structure, encoded in the amino acid sequence, promotes self-assembly from an α -helix secondary structure to a coiled-coil dimeric tertiary structure, then to quaternary structures that provide biological function. Similarly, transition metal acetylides have the potential for exhibiting the hierarchical structure seen in proteins. Non-covalent π -M interactions promote formation of novel structures, including polymers, cycles, and octahedral complexes. Platinum acetylide dendrimers are monodisperse nanoparticles having proteinlike dimensions. Nanoscale rod-shaped oligomers and cyclic structures have been synthesized. By incorporating chirality and variable side chain functionality, the wide variety of monomer units described in this chapter are analogous to amino acids. It is possible to synthesize phenyl acetylene ligands having side chain functionality (polar, charged, nonpolar, etc.) that will promote conversion from a primary to secondary structure [59, 60]. Examples of primary-to-secondary structure conversion in the current work include chiral platinum acetylide polymers and oligomers exhibiting secondary structure, including helical conformation [57] and chiral cyclic complex [30].

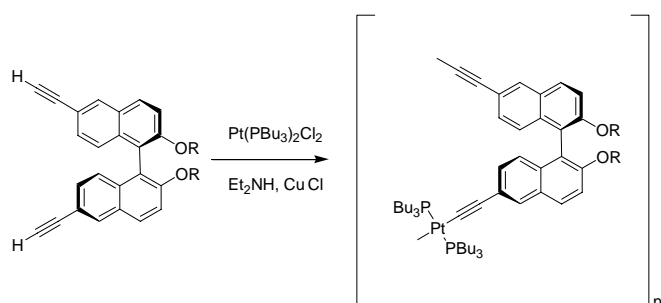
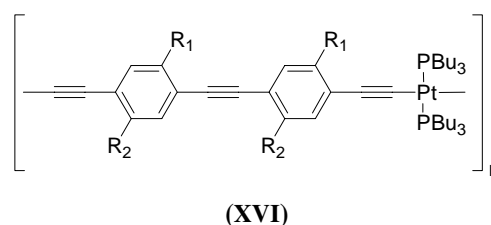


Figure 23. Polymer having chiral monomer prepared from optically active 1,1'-bi-2-naphthol [57].

A hypothetical amphiphathic platinum acetylide polymer,



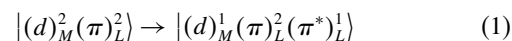
where R_1 is a hydrophobic chain and R_2 is a hydrophilic chain, would very likely form ordered structures that could be processed by the Langmuir–Blodgett and related techniques [61]. Inclusion of a variety of side chains would make possible multifunctional materials having the capacity for supramolecular self-assembly, conversion between chemical, thermal, mechanical, electromagnetic, and electrical energy, and the ability to sense and adapt to the environment [62–64].

3. SPECTROSCOPIC CHARACTERIZATION

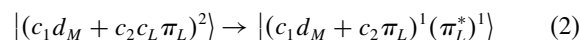
3.1. Introduction to Electronic Structure of Transition Metal Acetylides

Qualitative features of the electronic structure of transition metal acetylides have been determined from extended Hückel calculations [65]. A fragmentation analysis on the complex $M(\text{PH}_3)_2(\text{C}\equiv\text{CC}_6\text{H}_5)_2$, where M is a d^8 transition metal, provides a simple framework to analyze electronic structure and spectroscopy. How does the ML_2^{2+} fragment interact with the yne-fragment $\text{C}_6\text{H}_5\text{C}\equiv\text{C}\cdots\text{C}\equiv\text{CC}_6\text{H}_5$? The $\sigma_{\text{M-C}}$ bond consists of stabilizing interactions between the acetylene lone pair $2p_z$ yne orbitals with the metal d_z^2 and p_z orbitals. The yne-fragment $\text{C}_6\text{H}_5\text{C}\equiv\text{C}\cdots\text{C}\equiv\text{CC}_6\text{H}_5$ also has two π orbitals, π_x and π_y . The filled higher energy π_y orbital interacts with the metal d_{yz} orbital to give a bonding and antibonding $\pi_{\text{M-C}}$ molecular orbital. The highest occupied molecular orbital (HOMO) therefore contains both metal d and ligand π orbitals while the lowest unoccupied molecular orbital (LUMO) contains only ligand π^* orbitals.

In many cases, the HOMO \rightarrow LUMO optical transition of the complex will be a metal-to-ligand charge transfer (MLCT) transition between metal d orbitals and ligand π^* orbitals.



However, in many of the systems described in this review, the HOMO contains ligand π orbitals mixed with metal d orbitals. Optical transitions from the ground to the excited state will then have both MLCT and ligand $\pi\pi^*$ character.



Finally, in compounds where $c_2 \sim 1$, transitions are localized on the ligand.

The theory of MLCT transitions relates the optical transition energy to the redox potential [66] according to the expression

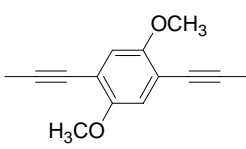
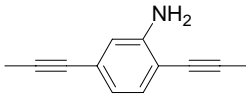
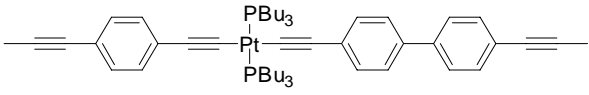
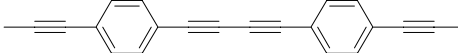
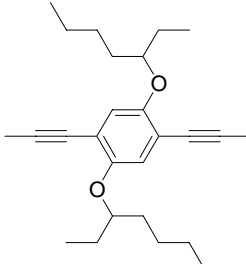
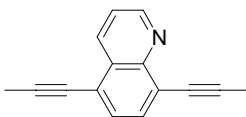
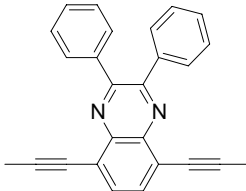
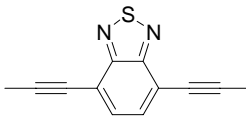
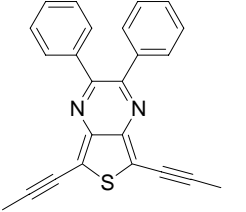

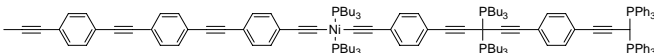
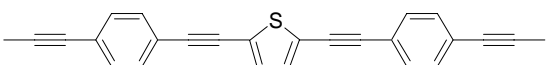
$$h\nu(\text{MLCT}) = \Delta E + C \quad (3)$$

Table 3. Examples of transition metal acetylide polymers $[M(PR_3)_2L]_n$.

Ligand	Ref.
	[48]
	[48]
	[48, 83, 86]
	[49, 82–84, 88, 122]
	[122]
	[51, 91]
	[49, 91, 123]
	[47, 48]
	[48]
	[124]
	[89, 108, 113, 123]
	[108]
	[53, 54, 86, 108]
	[53, 54]
	[53]
	[108]

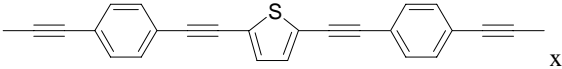
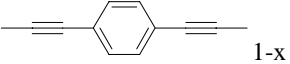
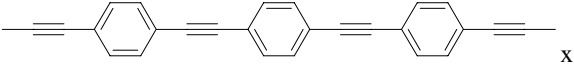
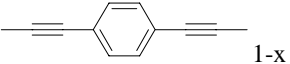
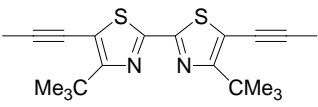
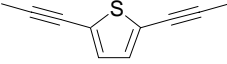
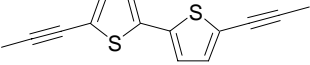
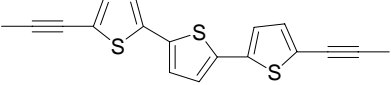
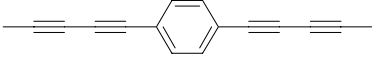
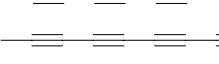
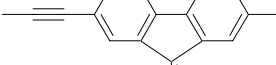
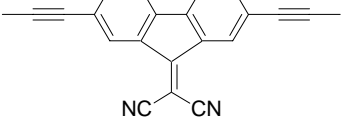
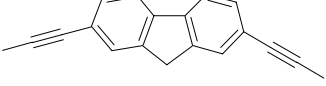
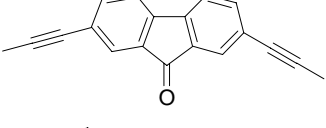
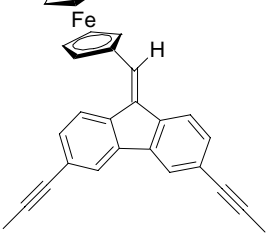
continued

Table 3. Continued

Ligand	Ref.
	[108]
	[108]
	[108]
	[108, 117]
	[88, 89]
	[88, 89]
	[88]
	[88, 89]
	[88, 89]
	[52, 125]
	[52]
	[52, 125]

continued

Table 3. Continued

Ligand	Ref.
	[126]
	
	[126]
	
	[127]
	[86, 87, 89]
	[87, 89]
	[87, 89]
	[91, 123]
	[91, 123]
	[117]
	[94]
	[92]
	[92]
	[93]

continued

Table 3. Continued

Ligand	Ref.
	[125]
	[125]
	[125]
	[128]
	[128]

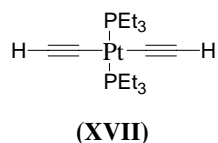
where ΔE is

$$\Delta E = E_{1/2}[M^{III/II}(L)] - E_{1/2}[L^{0/-}(M^{II})] \quad (4)$$

This term describes the oxidation and reduction potentials of the metal and ligand. The constant C has contributions from the solvation energies in the two redox processes, the vibrational excitation energy of the Franck–Condon state, the energy of redox self-quenching of thermally equilibrated excited state singlet $^1[M^{III}L^-]_s^*$ in solution, the solvent reorganization energy, and the difference in solvation energy between the solvent- and vibrationally-equilibrated excited state and the ground state. If $h\nu(\text{MLCT})$ is plotted vs ΔE for a series of ligands, the equation predicts unit slope. If there is configuration interaction between the MLCT state and other states of the same symmetry [Eq. (2)], then this expression breaks down.

3.2. $\text{PtL}_2(\text{PR}_3)_2$ Bidentate Complexes

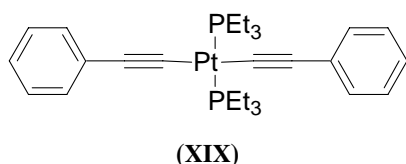
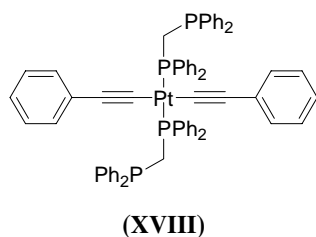
Knowledge of the simplest bidentate Pt-acetylide [67],



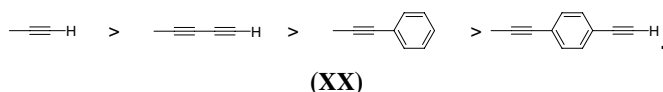
assists in the understanding of more complex systems. The phosphorescence spectrum of **XVII** shows a progression with 2000 cm^{-1} spacing and the relative intensities of the vibronic transitions gives evidence that the triplet state has an increased $\text{C}\equiv\text{C}$ bond length compared to the ground state. From a measurement of the Huang–Rhys factor an acetylinic bond length

change of 0.09 \AA relative to the ground state results in a bond order change from 3 to 2.5 for an MLCT transition from Pt to a π^* orbital. Raman investigation of **XVII** gives information about vibrational reorganizational energies and initial structural changes in the excited state [67]. The most intense Raman band is the $\text{C}\equiv\text{C}$ stretch band (1965 cm^{-1}) and its combination bands with lower frequency Pt–P (409 cm^{-1}) and Pt–C (459 cm^{-1}) stretch modes.

The authors compare the Raman spectra of **XVII** with the compound **XVIII**. The vibrational reorganization energy of **XVII** is considerably smaller than that of **XVIII** and more modes are involved (50% $\text{C}\equiv\text{C}$ stretch contribution vs 70% in **XVIII**). The presence of resonance enhanced Pt–P mode in **XVII** suggests the MLCT transition has Pt–P character. Raman spectra of **XVIII** have less resonance enhancement in the Pt–P stretch frequency, showing the electron-withdrawing nature of the aromatic substituent decreases involvement of the phosphine ligands in the Raman spectrum [68]. The authors speculate the acceptor π^* acetylide orbitals are higher in energy in **XVII** than **XVIII** and nearer in energy to the phosphorus $3d$ orbital, giving the MLCT transition more Pt–P character. An investigation of the 77 K emission spectrum of **XVII** shows strong sensitivity of the emission spectrum with excitation wavelength, pointing toward heterogeneity of the local solvent environment around the chromophore [69]. The small size of **XVII** gives its solvent shell a complex shape, with considerable variation in the microenvironment from individual chromophore to individual chromophore. In contrast, the authors observe less sensitivity in the larger chromophore **XIX**. The larger molecular volume of **XIX** samples a less disordered solvent microenvironment, giving a narrow solvent environment distribution.

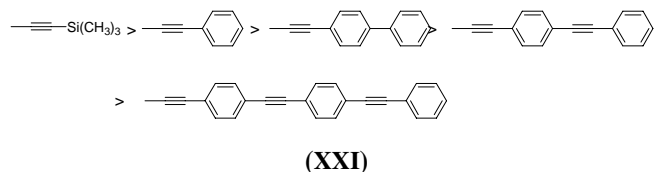


Some structure–property relationships can be determined from literature data [70, 71]. These papers describe a series of bidentate complexes. All these compounds have square planar geometry. The structure variations include *trans*- vs *cis*- orientation of the ligands around the platinum center and variation of the phosphine and acetylene ligands. MLCT transitions have transition energies around 3.7 eV. For both *cis*- and *trans*-conformations, variation in the acetylene gives an MLCT state ordering.



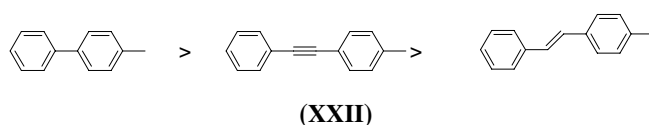
Going from *trans*- to *cis*- conformers, an average 2000 cm^{-1} blueshift occurs in the optical gap. Similarly, conjugation effects on the ligand cause changes in the optical gap. For example, changing the ligand from acetylene to phenylacetylene results in a 2500 cm^{-1} redshift in the optical bandgap. Finally, variation of the phosphine gives the state ordering $\text{PBU}_3 > \text{PEt}_3$. In one example, use of a triphenyl phosphine ligand gives the optical transition energies order $\text{PBU}_3 > \text{PEt}_3 > \text{PPh}_3$. The factors causing the sensitivity of the transition energies to the phosphine ligands have been discussed [72]. Steric and electronic factors originating from the phosphine ligand will influence the transition energies of these compounds.

A systematic study of ground state spectra, fluorescence, phosphorescence, and triplet state absorption on a series of bidentate compounds has been recently published [73]. As the acetylene ligand varies, the MLCT transition energies follow the order.



Similar trends occur in the phosphorescence and the $T_1 \rightarrow T_n$ spectra. The data correlate with a molecular descriptor $N(\text{PE}) = 0.5(N(\text{phenyl units}) + N(\text{triple bonds}))$. The data imply that a triple bond shifts the MLCT energy as much as a phenyl group. The derivative $\Delta E/\Delta N(\text{PE})$ measures the sensitivity of transition energies to changes in molecular structure. A smaller value

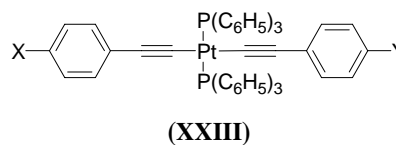
suggests a localized state, while a larger value suggests a delocalized state. From these measurements, S_0 and T_1 states are more localized than the S_1 and T_n states. The results are consistent with the $S_0 \rightarrow S_1$ and $T_1 \rightarrow T_n$ transitions having MLCT character, while the $T_1 \rightarrow S_0$ transition is more localized. A recent publication describing a phenyl ethylene acetylide [74] combines with previous results [73] to show the effect of the linking group on the conjugation of the ligands. The ground state transition energy varies according to



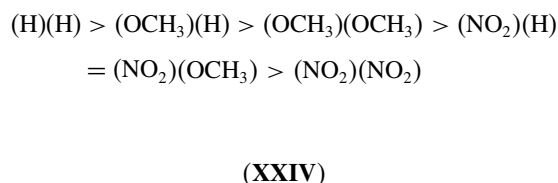
The double bond has higher conjugation across the phenyl groups than the triple bond.

3.3. $\text{PtLL}'(\text{PR}_3)_2$ Asymmetric Complexes

A recent series of symmetrical and unsymmetrical Pt(II) complexes gives substituent effects on the MLCT transition [18] (Table 2).



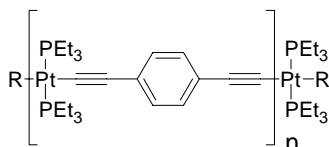
The MLCT transition energy decreases in the order



where the substituents in the parentheses are the 4' substituents on these compounds. Electronic transitions in these compounds appear to be a mixture of MLCT and ligand–ligand charge transfer (LL'CT) states. The HOMO is a combination of metal d orbitals and L ligand π -orbitals. Via back-bonding, electron-donating substituents will tend to add charge to the Pt d orbitals, raising $E(\text{HOMO})$, causing a redshift in the MLCT transition. Electron donation will also raise the $E(\text{HOMO})$ of the L ligand. The LUMO consists of π^* orbitals of the L' ligand. Electron-donating substituents on the acceptor will raise $E(\text{LUMO})$ and electron-withdrawing substituents will lower $E(\text{LUMO})$. The redshifting effect of methoxy groups on the transition energies gives evidence for donation of charge into the electron donor. Nitro groups behave like electron-withdrawing substituents, causing a lowering of $E(\text{LUMO})$. However, the charge transfer effects are not clear, as nitro groups also cause redshifts by increasing electron delocalization.

3.4. [Pt(PR₃)₂L]_n Oligomeric Complexes

Oligomers have three types of end groups, R = Cl-, Ph-C≡C-, and H≡C-Ph-C≡C-.



(XXV)

The $S_0 \rightarrow S_1$ transition energy for the three types of oligomers decreases according to the expression

$$E = E_\infty + \frac{A}{n} \quad (5)$$

where n is the number of monomer units. The value of A has the trend

$$A(\text{Cl}) > A(\text{Ph-C}\equiv\text{C-}) > A(\text{H}\equiv\text{C-Ph-C}\equiv\text{C-})$$

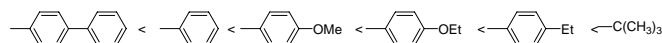
(XXVI)

The value of E is the same for all three end groups and is the same as that of the analogous polymer, 3.2 eV. When $n = 4$, all three types of oligomers have nearly the same transition energy as the polymer.

3.5. A-Frame Complexes

The compounds have an A-frame-like structure with a binuclear d^8-d^8 core analogous to Pt-POP [33, 75]. They also contain a μ -CCR bridgehead (Fig. 12). Raman spectra of the compound R = Ph show three distinct $\nu(\text{C}\equiv\text{C})$ stretches at 2125, 2062, and 2027 cm^{-1} , corresponding to three different acetylide environments [68]. The intensity of the 2027 cm^{-1} band (assigned as the μ -bridging $\text{C}\equiv\text{C}$ stretch vibration) is weakest at the blue edge of the metal-metal bond to ligand charge transfer (MMLCT) band and increases in intensity relative to the other two bands as the excitation line moved toward the red edge of the MMLCT envelope. The results are consistent with the presence of three different, closely lying $\pi^*(\text{C}\equiv\text{CPh})$ orbitals. Vibrational reorganizational energies associated with optical transitions have significant contribution from low frequency vibrations, approximately 60% of the total energy, while the acetylenic $\text{C}\equiv\text{C}$ stretch vibration only contributes 25% of the total energy. This observation suggests considerable conformational flexibility in this compound. Room temperature ^1H NMR spectra of these complexes show nonequivalence of the H_α and H_β methylene protons on the NMR time scale [76]. Similar nonequivalences are observed in the various R groups. The NMR data imply these compounds undergo a σ , π -acetylide exchange “windscreen wiper” process. The nonequivalent protons become equivalent at higher temperatures.

Optical transitions in these A-frame complexes are considered to be MMLCT, a $[(d\sigma^*)^2] \rightarrow [(d\sigma^*)^1(\pi^*)^1]$ transition. Upon excitation, they exhibit intense phosphorescence. Transition energies of the emission spectra give the following trend:



(XXVII)

The sensitivity of the emission energy to ligand conjugation gives evidence for the involvement of the $\pi^*(\text{C}\equiv\text{CR})$ orbital in optical transitions.

Resonance Raman spectra of the related compound **XVIII** exhibits vibrational reorganizational energies distributed very differently from the A-frame compound. In this case, 70% of the total reorganization energy is associated with the acetylenic $\text{C}\equiv\text{C}$ stretch vibration, resulting from higher conformational rigidity [68].

Upon Cu complex formation, (Fig. 13) there changes in bond lengths. The triple bond length increases from 1.19 to 1.21 Å and the Pt...Pt distance decreases from 3.4 to 3.0 Å. These structural changes cause numerous changes in the spectroscopic properties. The acetylene vibrational frequency changes from 2106 to 2024 cm^{-1} , reflecting a decrease in bond order. The absorption spectrum redshifts from 370 to 418 nm. The phosphorescence spectrum also redshifts from 607 to 634 nm. The emission spectrum vibronic spacing decreases from 2220 to 2024 cm^{-1} . The Cu(I) ion behaves as a Lewis acid, increasing the π -accepting ability of the $\text{C}\equiv\text{CPh}$ groups. The HOMO is an antibonding $d\sigma^*$ orbital formed from $\text{Pt}(5dz^2)$ - $\text{Pt}(5dz^2)$ interaction, while the LUMO contains the unoccupied metal p and $\text{C}\cdot\text{CPh}$ π^* orbitals. The major optical transition in these compounds is the $[(d\sigma^*)^2] \rightarrow [(d\sigma^*)^1(\pi^*)^1]$ MMLCT transition. Formation of a Cu complex decreases the Pt-Pt distance and increases the $d\sigma-d\sigma^*$ energy gap, resulting in a smaller HOMO-LUMO gap and the observed redshifts in the optical transitions.

3.6. Diimine Complexes

In order to assign the optical transitions in these compounds, a series of $\text{Pt}(\text{dbbpy})(\text{C}\equiv\text{CC}_6\text{H}_4\text{X})_2$ and $\text{Pt}(\text{Rphen})(\text{C}\equiv\text{CC}_6\text{H}_4\text{X})_2$ complexes have been synthesized and characterized [77]. Absorption spectra of the $\text{Pt}(\text{Rphen})(\text{C}\equiv\text{CC}_6\text{H}_4\text{X})_2$ complexes show a mixture of absorption bands near 400 nm. As the electron-withdrawing ability of the R diimine substituents increases, the low energy tail of the absorption manifold shifts to longer wavelength according to the following order:



(XXVIII)

The redshift associated with increased electron affinity of R is consistent with optical transitions having MLCT character. The absorption spectra of $\text{Pt}(\text{dbbpy})(\text{C}\equiv\text{CC}_6\text{H}_4\text{X})_2$ also shows a mixture of absorption bands near 400 nm. As the electron-donating properties of the X acetylide substituents increases, the low energy tail of the absorption manifold redshifts to longer wavelengths according to the following order:



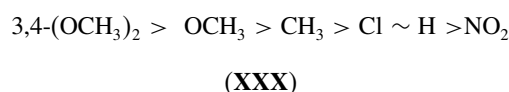
(XXIX)

The redshift associated with decreased ionization potential of X also provides evidence for the MLCT character of optical transitions in these compounds. The emission spectra of these compounds show very similar trends, consistent with a

metal-based HOMO and a π^* diimine LUMO. Another example is a bipyridyl complex of an oligoacetylenic sulfide *cis*-Pt(Me₂bipy){C≡CSC≡C(TIPS)}₂ [78]. The compound has an MLCT transition at 283 nm, originating from the platinum. In contrast, the strongly redshifted fluorescence at 589 nm demonstrates emission from the bipyridyl portion of the complex. A related study of Pt(dbppy)(C≡CC₆H₄X)₂ has been recently published [79]. Transient absorption spectra show a strong absorption in the near UV, bleaching in the 400–450 nm region, and broad, intense absorption through the visible region. The near-UV and visible absorption features are attributed to the bipyridine radical anion present in the MLCT excited state and the 400–450 nm feature resulting from bleaching of the ground state MLCT absorption band. The authors give a detailed analysis of the relation between the nonradiative decay rate constant k_{nr} and spectroscopic parameters including the energy of the zero-zero transition, the average of medium frequency vibrational modes coupled to the MLCT transition, and the Huang–Rhys factor. They found the trends in k_{nr} follow the energy gap law. Through time-resolved infrared spectroscopy, the excited state $\nu(\text{C}\equiv\text{C})$ is probed. The excited state $\nu(\text{C}\equiv\text{C})$ band shifts 24–34 cm⁻¹ relative to the ground state, consistent with decreasing ($d\pi$) Pt → (π^*) – C≡C–Ar back bonding upon excitation from the metal to diimine charge transfer excited state. Another related study [80] investigates Pt(dbppy)(C≡CC₆H₄X)₂ via spectroelectrochemistry and electron paramagnetic resonance (EPR). Absorption spectra of the free radical anion of Pt(^tBu₂dbppy)(C≡CC₆H₅)₂ originates from the bipyridyl anion. EPR experiments also show the unpaired electron on this complex resides on ^tBu₂dbppy.

3.7. Terpyridyl Acetylide Complexes

Structure–property relationships in terpyridyl acetylide compounds have been determined by varying X and measuring spectroscopic properties [36]. The lowest energy ground state transition orders according to



The trend is consistent with the ground state optical transition being a MLCT band where charge transfer to the terpyridyl group occurs. A similar trend is observed in the emission spectra. The authors also synthesize a crown ether derivative, where 4-ethynylbenzo-15-crown-5 is used as the terminal acetylene. Upon addition of alkali metal cations, the MLCT band blueshifts with a well-defined isosbestic point. Binding of Na⁺ gives a 1:1 stoichiometry, while binding of K⁺ has binding of both one and two crown ethers per ion.

3.8. Linear Polymers

The electronic structure of the linear polymers can be qualitatively described by extended Hückel calculations [65]. The authors calculate the band structure for the polymer [(PH₃)₂PtC≡CC₆H₄C≡C]_n. The polymer HOMO contains *d*- π orbitals, while the LUMO is primarily localized on the fragment –C≡CC₆H₄C≡C–. Analysis of the density of states shows considerable metal character in the valence band near the

Fermi level, while there is predominant carbon character in the conduction band. The results are consistent with optical transitions of the polymer having MLCT character.

An *ab initio* calculation on [C≡CPt(PH₃)₂C≡CPt(PH₃)₂C≡C]_x gives similar results [81]. In this study they show the HOMO-1 of this system is a π -like orbital formed both by carbon *p* and platinum *d* atomic orbitals. The HOMO is mainly centered on the Pt atoms and the PH₃ groups. The LUMO has a dominant Pt *d* component with contributions from the nearest C and P neighbors. LUMO + 1 and LUMO + 2 are π orbitals of the carbon chains with some contributions from Pt *d* orbitals. These results support the notion that optical transitions can have both MLCT character and $\pi\pi^*$ transitions delocalized through the Pt atoms.

The spectroscopic properties of Pt–acetylide polymers have been investigated in great detail. A study comparing the properties of platinum and palladium-containing polyynes has been published [82, 83]. The platinum and palladium polymers have qualitatively similar absorption and emission spectra, except all transitions in the palladium polymers are blueshifted from those in the platinum polymers. Singlet absorption, phosphorescence, and photoinduced absorption peaks blueshift 0.22 eV. Photoluminescence from the singlet state blueshifts 0.14 eV, and the weaker triplet absorption peak blueshifts ~0.1 eV. A further detailed study of the Pt-polymer determines the spatial extent of the singlet and triplet excitons [84]. Figure 24 shows optical spectra from XXXI, including transitions from the ground state to the singlet state ($S_0 \rightarrow S_1$) (3 eV), triplet state ($S_0 \rightarrow T_1$) (2.5 eV), from the T_1 state to higher triplet states ($T_1 \rightarrow T_n$) (1.5 eV) and emission from the triplet state ($T_1 \rightarrow S_0$) (2.4 eV). In Figure 24, the transitions labeled with Roman numerals refer to the various types of transitions that occur in conjugated polymers, including charge transfer from a localized molecular orbital to a delocalized molecular orbital, from a delocalized orbital to a localized molecular orbital, between two delocalized orbitals, and a localized transition within a subunit [85]. Molecular modeling of Pt-poly-yne polymers suggests that the metal sites contribute to the delocalization of the π electrons [84]. The authors simulate the optical properties of the Pt-poly-yne by performing calculations on Ni analogs of these polymers. Their INDO calculations show antibonding hybridization between the 3*d* orbitals of nickel and the ligand π -HOMO

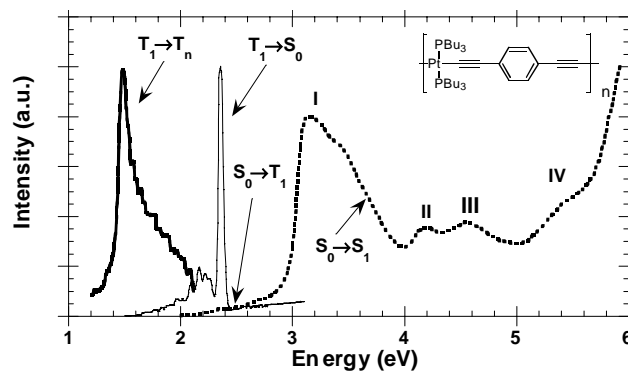
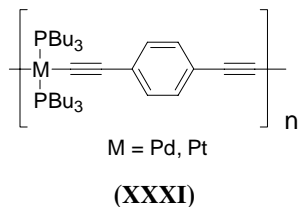


Figure 24. Ground state absorption ($S_0 \rightarrow S_1$), triplet state absorption ($T_1 \rightarrow T_n$), and phosphorescence ($T_1 \rightarrow S_0$) spectra of a platinum acetylide polymer. Adapted with permission from [88], D. Beljonne et al., *J. Chem. Phys.* 105, 3868 (1996) and [84], J. S. Wilson et al., *J. Chem. Phys.* 113, 7627 (2000). © 1996, 2000, American Institute of Physics.

level of the poly-yne derivatives and bonding between the Ni 4*p* orbitals and the ligand π LUMO, suggesting the optical transition is a HOMO \rightarrow LUMO $\pi\pi^*$ transition. They also calculate the dependence of $S_0 \rightarrow S_1$, $S_0 \rightarrow T_1$, and $T_1 \rightarrow T_n$ transition energies on the number of oligomer units. They find the $S_0 \rightarrow S_1$ transition energies to be sensitive to the number of oligomer units and the $S_0 \rightarrow T_1$ transition energy to be independent of the number of oligomer units. They conclude the S_1 exciton to be confined to two repeating units, the T_1 exciton to be confined to a single phenylene ring, and the T_n exciton to be confined to three or more repeating units.



The phosphorescence spectra of these polymers contain a wealth of detail that can be used to gain information about the excited state geometry. Table 4 lists phosphorescence features for XXXI. The vibronic bands were assigned from Raman spectra. The important vibrational modes include C–C stretch (1166 cm^{-1}), C \equiv C stretch (2106 cm^{-1}), aromatic C=C stretch (1596 cm^{-1}), and out-of-plane C–H bend (839 cm^{-1}). The intensity of the vibronic bands can be expressed in terms of the Huang–Rhys parameter S ,

$$I(j \rightarrow i; v = 0 \rightarrow v = n) \propto \frac{e^{-S_v} S_v^n}{n!} \quad (6)$$

where emission occurs from the excited state j , vibrational mode 0 to the ground state i , vibrational mode n . The Huang–Rhys parameter S measures the displacement of the excited-state potential energy surface with respect to the ground state along a normal mode ν and is given as

$$S_v = \frac{E_{\text{rel}}^v}{h\nu_v} \quad (7)$$

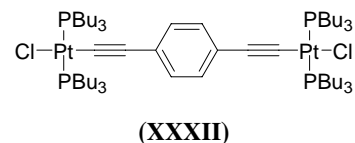
E_{rel}^v is the relaxation energy associated with distortions along v . The total relaxation energy E_{rel} resulting from a vertical transition is a sum over all active modes. From the emission spectra

Table 4. Phosphorescence vibronic bands in the polymer $[-\text{Pt}(\text{PBu}_3)_2\text{C}\equiv\text{CC}_6\text{H}_5\text{C}\equiv\text{C}]_n$.

Phosphorescence feature (eV)	Offset from 0–0 band (cm^{-1})	Assignment
2.273	839	ν_1
2.236	1137	ν_2
2.183	1565	ν_3
2.119	2081	ν_4
2.037	2742	$\nu_2 + \nu_3$
1.987	3146	$2\nu_3$
1.923	3662	$\nu_3 + \nu_4$

Source: Quoted with permission from [84], D. Beljonne et al., *J. Chem. Phys.* **105**, 3868 (1996). ©1996, American Institute of Physics.

for the polymer, the relaxation energy is 0.08 eV associated with distortions from the $T_1 \rightarrow S_0$ transition. For the monomer unit



the relaxation energy is 0.27 eV. The results show less excited state distortion in the polymer than in the monomer unit.

Insight into the extent of delocalization of the various transitions is obtained by comparing polymers and monomer units [86]. In this study, three types of polymers are synthesized, containing pyridine, benzene, and thiophene monomer units. They compare the electron-withdrawing pyridine with the electron-donating thiophene and the “neutral” benzene. Figure 25 shows energy levels determined from the various optical transitions. The energies of the S_1 and T_n states are very sensitive to whether the system is a monomer or polymer. In contrast, the energy of the T_1 state is not sensitive to the degree of polymerization. These show the S_1 and T_n states are delocalized, while the T_1 state is localized. The transition energies are relatively insensitive to the nature of the monomer unit, although the energies are slightly lower in the thiophene-containing polymer.

The optical properties of polymers containing thienyl ring oligomers have been investigated as a function of increasing thiophene content [87]. The energy gap for both the $S_1 \rightarrow S_0$ and $T_1 \rightarrow S_0$ transition energies vary according to the number of thiophene units: $m = 1 > 2 > 3$. The sensitivity of the $T_1 \rightarrow S_0$ transition energies to the number of thiophene units in the monomer units suggests the triplet state is delocalized over several thiophene units rather than being localized on one monomer unit. The phosphorescence intensity relative to fluorescence also decreases dramatically as m increases, due to the decreased influence of the heavy metal center on the larger oligomer units. The results show that as the size of the oligomer

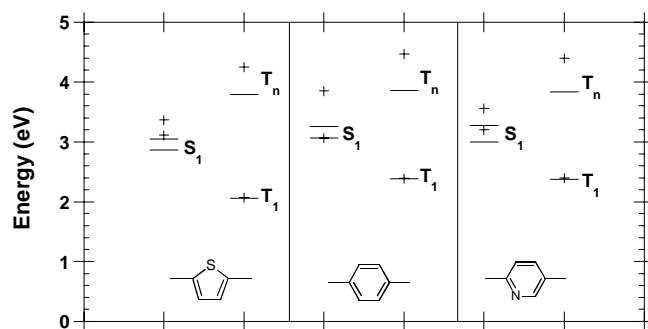
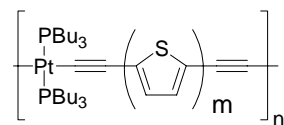


Figure 25. Energy levels for platinum acetylide polymers. Solid lines represent energy levels for the polymers $[\text{Pt}(\text{PBu}_3)_2\text{C}\equiv\text{CRC}\equiv\text{C}]_n$. Crosses represent energy levels for the monomer $\text{Ph}-\text{Pt}(\text{PEt}_3)_2\text{C}\equiv\text{CRC}\equiv\text{C}$ $\text{Pt}(\text{PEt}_3)_2\text{Ph}$. In the S_1 level there are two levels shown. The lower level is determined from photoluminescence, while the upper level is determined from an absorption spectrum. The S_0 level (not shown) is at 0 eV. Adapted with permission from [86], N. Chawdhury et al., *Macromolecules* **31**, 722 (1998). © 1998, American Chemical Society.

increases, the optical transitions of the polymer ligand have more $\pi\pi^*$ character and less metal influence.



(XXXIII)

To further determine the relationship between monomer unit structure and spectroscopic properties, a series of polymers having more conjugation has been synthesized and the energy levels probed by absorption and photoluminescence spectroscopy [88]. These polymers are considered to have more conjugation than the thiophene systems described above. The polymer backbone, including platinum and either 1,4-diethynyl benzene or thiophene units, is kept constant while substituents on the aromatic rings are varied. The monomer units and energy levels determined by the three techniques are shown in Figure 26.

The $S_0 \rightarrow S_1$ transition energies measured from these polymers vary from 1.7 to 3.0 eV. The major low-lying absorption bands are attributed to HOMO \rightarrow LUMO transitions between delocalized polymer orbitals. The 0–0 vibronic band dominates the absorption band throughout the series, indicating a very similar geometry between the singlet ground and excited states. This observation gives evidence for the formation of a well-delocalized exciton in these systems. Photoluminescence includes phosphorescence as well as fluorescence. The energies of both singlet and triplet bands decrease with the polymer optical gap. The S_1-T_1 splitting of 0.7 eV is independent of the spacer. The intensity of triplet emission decreases relative to the singlet intensity as the bandgap decreases.

A related study investigates the relationship between structure and triplet state lifetime [89]. This relationship follows the energy gap law, which gives a relation between the nonradiative decay rate k_{nr} and other variables:

$$k_{nr} \propto \exp(-\gamma\Delta E/\hbar\omega_M) \quad (8)$$

where ΔE is the energy gap between the two states, γ is a function of molecular structure, and ω_M is the maximum vibrational frequency available to the system. A plot of the $\ln(k_{nr})$

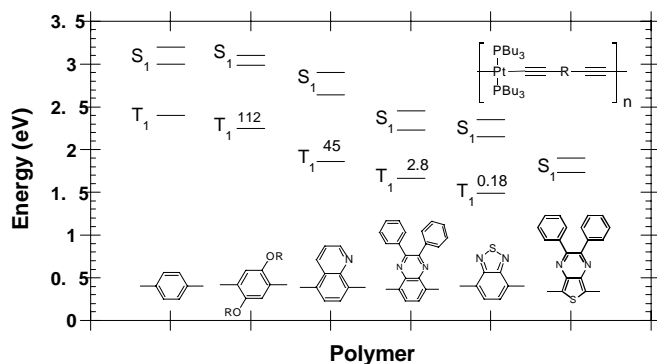


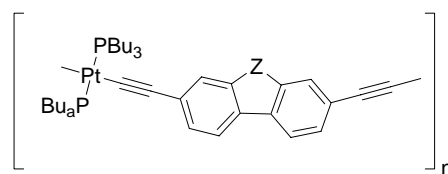
Figure 26. Energy levels for polymers with aromatic monomer units with variable electron-accepting ability. Adapted with permission from [88], J. S. Wilson et al., *J. Chem. Phys.* 113, 7627 (2000). © 2000, American Institute of Physics.

vs the S_0-T_1 gap yields a slope ($=\gamma/\hbar\omega_M$) of -6 eV^{-1} for the polymers and -3.8 eV^{-1} for the monomers. The energy gap law assumes a mechanism of nonradiative decay to be release of energy to the ground state through molecular vibrations. The authors consider benzene and $\text{C}\equiv\text{C}$ stretch modes as efficient in promoting nonradiative decay in these materials. The difference in slopes between the monomers and polymers is attributed to increased distortion of the triplet in the monomer than in the polymer.

A study of the relation between polymer structure and the singlet–triplet energy gap builds on previous work by the same group [90]. Fluorescence and phosphorescence spectra are collected on an extensive series of Pt-containing polymers and the singlet–triplet energy gap is determined. Despite varying the electron density, increasing conjugation length, or the electron affinity on the spacer ring, the singlet–triplet energy gap is always 0.7 eV. A series of model polymers not containing platinum also has a singlet–triplet energy gap of 0.7 eV, although both emission bands redshift 0.55 eV. The exchange energy is proportional to the overlap integral between the π and π^* orbitals involved in the optical transition. The ground and excited states are considered to be delocalized. Electron correlation causes the triplet exciton to be more localized than the singlet exciton. In this series of polymers the delocalization of the states is similar, so the singlet–triplet splitting remains constant. Confinement of the states in the oligomers raises the singlet state energy more than the triplet state, increasing the splitting.

Infrared and Raman spectra have been collected from several rigid rod Pt acetylide polymers, including $[(\text{PBu}_3)_2\text{Pt}-\text{C}\equiv\text{CC}\equiv\text{CC}\equiv\text{C}]_n$, $[(\text{PBu}_3)_2\text{Pt}-\text{C}\equiv\text{CC}_6\text{H}_4\text{C}\equiv\text{C}]_n$, and $[(\text{PBu}_3)_2\text{Pt}-\text{C}\equiv\text{CC}\equiv\text{CC}_6\text{H}_4\text{C}\equiv\text{CC}\equiv\text{C}]_n$ [91]. The spectra can be analyzed by assuming the monomer units have C_{2h} or D_{2h} symmetry. The extent of π conjugation in the backbone is determined from the $\text{C}\equiv\text{C}$ stretch frequency. The measured vibrational frequencies suggest the backbone alternates between $-\text{C}\equiv\text{C}-$ and $-\text{C}-\text{C}-$ bonds with no allenic character. Insertion of a phenyl group tends to further disrupt the conjugation. Near-infrared (IR) FT-Raman spectra show higher frequency vibrations not observed from the IR spectra. In particular $-\text{C}\equiv\text{C}-$ stretch vibrations appear to have resonance enhancement. These vibrations couple with electronic transitions polarized parallel to the polymer chain.

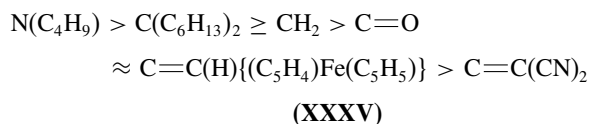
A series of Pt polyynes with 9-dicyanomethylene-substituted fluorene acceptors has been synthesized [92–95]. These polymers have the chemical formula



(XXXIV)

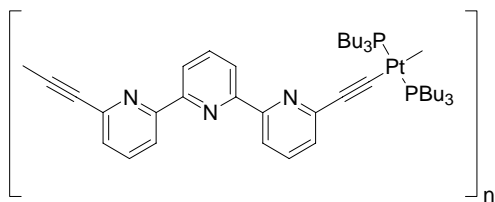
where $Z = \text{C}(\text{C}_6\text{H}_{13})_2$, CH_2 , $\text{C}=\text{O}$, $\text{C}=\text{C}(\text{H})\{(\text{C}_5\text{H}_4)\text{Fe}(\text{C}_5\text{H}_5)\}$, $\text{C}=\text{C}(\text{CN})_2$, and $\text{N}(\text{C}_4\text{H}_9)$. The triple bonds are substituted at the 2,7-positions for all the polymers except $Z = \text{N}(\text{C}_4\text{H}_9)$ where the substitutions are at the 3,6-positions. The

authors measure the HOMO–LUMO gap as the onset wavelength of light absorption in a solid film. The optical gap has the following order:



With reference to $Z = \text{CH}_2$, the 9-dicyanomethylene group enhances conjugation, while $\text{N}(\text{C}_4\text{H}_9)$ and $\text{C}(\text{C}_6\text{H}_{13})_2$ reduce conjugation. All of the polymer films show photoluminescence from 418 to 432 nm with quantum yields ranging from 0.30 to 0.48. Upon cooling to 11 K, $Z = \text{N}(\text{C}_4\text{H}_9)$ and $\text{C}(\text{C}_6\text{H}_{13})_2$ show new lower energy phosphorescence bands at 459 and 554 nm, respectively. None of the other polymers show phosphorescence, even upon cooling. From energy gap law reasoning, this trend can be attributed to increased radiationless decay as the HOMO–LUMO gap decreases [89]. For example, when $Z = [\text{C}=\text{C}(\text{CN})_2]$, the HOMO–LUMO gap is 1.58 eV, a value associated with a rapid radiationless decay rate.

Platinum polyynes with oligopyridines as spacers have been synthesized [96]. An example of this polymer containing a kinked 6,6''-bis(ethynyl)-2,2':6',2'''-terpyridyl spacer shows anomalous spectroscopic properties compared to a rod-shaped 5,5'-bis(ethynyl)-2,2'-bipyridine spacer. The 10 K phosphorescence maximum of the terpyridyl polymer, 2.7 eV, blueshifts 0.5 eV from that of the rigid bipyridine spacer. The room temperature phosphorescence of the terpyridyl polymer redshifts to 2.1 eV, broadens, and loses vibronic structure. A small redshift and minimum loss of vibronic structure occurs in the rod-shaped bipyridyl polymer. Similar but less dramatic effects appear in a kinked 6,6'-bis(ethynyl)-2,2'-bipyridine spacer. The blueshift in the phosphorescence results from twisting of the bipyridyl complex. The redshifted, broadened phosphorescence results from excimer formation.

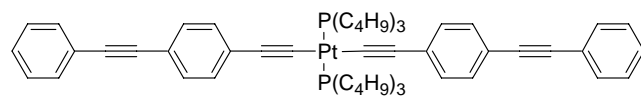


(XXXVI)

4. PROPERTIES

4.1. Oligomers

The physical and optical properties of the oligomer

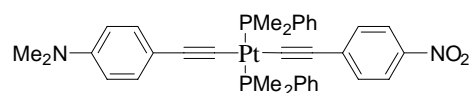


(XXXVII)

have been investigated in detail. The crystal structure of **XXXVII**s [97] gives a dihedral angle of 15.1° between the two phenyl groups resulting in weak conjugation throughout the ligand. Crystals of this compound are biaxially birefringent

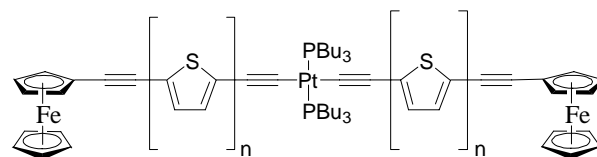
with principal indices of refraction of 1.531, 1.615, and 1.947. Oligomer **XXXVII** exhibits a variety of linear and nonlinear optical properties [9, 98, 99]. The compound has strong singlet absorption at 355 nm and a weak 520 nm absorption feature assigned to be the forbidden $S_0 \rightarrow T_1$ transition. It also exhibits a fluorescence band at 400 nm and phosphorescence at 520 nm. Pump-probe nonlinear absorption experiments confirmed that direct excitation into the triplet state was possible by exciting the 520 nm band.

Second harmonic generation measurements have been made on corona-poled, spin-cast thin films of $\text{PtLL}(\text{PR}_3)_2$ compounds [20]. In particular, compound **XXXVIII** has a significant $\beta = 16 \times 10^{-30}$ esu, a value comparable to disperse red 1 (DR1) ($\beta = 22 \times 10^{-30}$ esu). The result is significant as the β value for compound **XXXVIII** has no resonance enhancement ($\lambda_{\text{max}} = 380$ nm), while that for DR1 results from resonance enhancement ($\lambda_{\text{max}} = 482$ nm). A second study also gives evidence for high nonlinearity of compound **XXXVIII** [19]. EFISH measurements at 1064 nm on compound **XXXVIII** give a $\mu\beta$ value of 670×10^{-48} esu, comparable to DR1 (500×10^{-48} esu). The $\mu\beta$ value is significant, as the EFISH measurements are performed off resonance.



(XXXVIII)

Oligomers containing different types of metals have been studied to determine if a metal bis(acetylide) unit allows for interaction between terminal redox-active groups [100]. Systems that have been investigated include M_1 -spacer- M_1 systems and M_1 -spacer- M_2 -spacer- M_1 . An example of an M_1 -spacer- M_2 -spacer- M_1 system is a platinum (II) complex containing oligothiophene-functionalized ferrocenylacetylene [101]. The number of thiophene units varies from 1 to 3. X-ray crystallography for $n = 2$ shows a rigid-rod structure with coplanar bithienyl rings, a *trans*-arrangement of the two bithiophene groups, and a Fe–Fe distance of 32 nm. Cyclic voltammetry experiments show no metallocene–metallocene interaction. The presence of the platinum center and increased conjugation decrease the oxidation potential of the thiophene units. The optical gap also decreases from 2.90 to 2.44 eV as n increases from 1 to 3. An earlier study of ferrocene-containing complexes $\text{Pt}(\text{FcC}\equiv\text{C})_2(\text{PR}_3)_2$ also shows a moderate interaction between the two ferrocene groups [100].



(XXXIX)

4.2. Terpyridyl and $\text{Pt}_2\text{M}_4(\text{C}\equiv\text{CR})_8$ Complexes

Solvent induced aggregation and solvatochromism have been observed in a Pt(II) terpyridyl complex [37] (Fig. 17). The complex is prepared from the triflate salt, trimethylsilyl-protected

butadiyne, and KF. It crystallizes in two forms: a dark-green form and a red form. The dark-green form is a linear chain with the platinum atoms equally spaced, with short intermolecular Pt–Pt contacts of 3.388 Å. The molecular chain shows a rotation axis from neighbor to neighbor, with a C–Pt–Pt–C torsion angle of 143°. The red form consists of a chain of dimers with alternating Pt–Pt distances of 3.39 and 3.65 Å. The two types of Pt–Pt bonds show a zigzag arrangement with a Pt–Pt–Pt angle of 154° and a rotation of 50° between adjacent molecular planes. Dissolving either form into acetonitrile yields a yellow solution. Addition of increasing amounts of diethyl ether causes the color to change from yellow to green to blue. The MLCT absorption band at 416 nm disappears with a new band appearing at 615 nm with a well-defined isosbestic point. Excitation of the complex results in intense emission at 785 nm that only appears in the presence of ether. The data suggest solvent-induced aggregation of the monomer into an oligomer. The new absorption band is tentatively assigned as an MMLCT band resulting from strong Pt–Pt interactions. The drastic solvent-induced changes in color and emission could have applications in materials science and sensor technology.

A $[\text{Pt}_2\text{M}_4(\text{C}\equiv\text{CR})_8]$ complex whose structure has been solved is the Ag complex, $\text{R} = \text{Bu}'$ [38] (Fig. 27). The six metal atoms have an octahedral arrangement and the Pt atoms have a *trans* orientation to each other. Each platinum atom bonds to four $\text{C}\equiv\text{CBu}'$ groups in a square-planar arrangement. The acetylide $\text{C}\equiv\text{C}$ bonds π -coordinate to the metal atoms. The two $\text{Pt}(\text{C}\equiv\text{CBu}')_4$ groups are labeled “A” and “B.” By looking down the Pt–Pt twofold axis, the two $\text{Pt}(\text{C}\equiv\text{CBu}')_4$ fragments and the four Ag atoms have a staggered conformation with a C(A)–Pt(A)–Pt(B)–C(B) torsion angle of 38°. Continuing to look down the Pt–Pt axis, the Ag atoms are found in the holes between staggered A and B $\text{C}\equiv\text{CBu}'$ fragments.

A detailed investigation of the luminescence and crystal structure has been performed on the $[\text{Pt}_2\text{Cu}_4(\text{C}\equiv\text{CC}_6\text{H}_5)_8]$ complex [102]. The authors show that the color of this complex is a strong function of solvent, concentration, temperature, and precipitation procedure. They find three crystal polymorphs that appear under various conditions: yellow, red, and violet–green. The different colored forms result from the degree of oligomerization, where the yellow form is $[\text{Pt}_2\text{Cu}_4(\text{C}\equiv\text{CC}_6\text{H}_5)_8]$, the red form is $[\text{Pt}_2\text{Cu}_4(\text{C}\equiv\text{CC}_6\text{H}_5)_8]_2$, and the violet–green form is $[\text{Pt}_2\text{Cu}_4(\text{C}\equiv\text{CC}_6\text{H}_5)_8]_3$. The crystal structure of the violet–green polymorph consists of three $[\text{Pt}_2\text{Cu}_4(\text{C}\equiv\text{CC}_6\text{H}_5)_8]$ units linked by two Pt–Pt bonds (Fig. 28). The A and B $\text{Pt}(\text{C}\equiv\text{CC}_6\text{H}_5)_4$ fragments of the two outer cluster units have an eclipsed conformation with a C(A)–Pt(A)–Pt(B)–C(B) torsion angle of 1°. The inner cluster unit is staggered with a torsion angle of 38°. The torsion angle C(outer fragment)–Pt(outer fragment)–Pt(inner fragment)–C(inner fragment) is 44°,

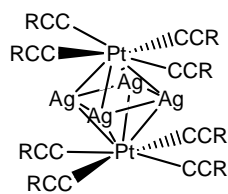


Figure 27. An example of the structure of the $[\text{Pt}_2\text{Cu}_4(\text{C}\equiv\text{CR})_8]$ complex is the Ag complex having $\text{R} = \text{Bu}'$ [38].

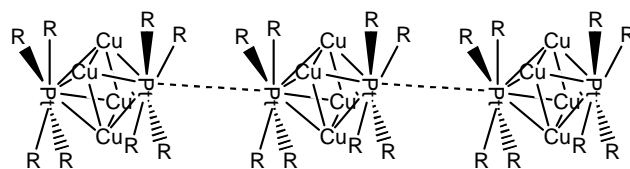


Figure 28. Chemical structure of the violet–green polymorph consisting of three $[\text{Pt}_2\text{Cu}_4(\text{C}\equiv\text{CC}_6\text{H}_5)_8]$ units linked by two Pt–Pt bonds [102].

so that the Pt_2Cu_4 octahedra are successively twisted by 44°. All three polymorphs have intense luminescence, with the wavelength of maximum emission in the solids following the trend $[\text{Pt}_2\text{Cu}_4(\text{C}\equiv\text{CC}_6\text{H}_5)_8]_1$ (550 nm) > $[\text{Pt}_2\text{Cu}_4(\text{C}\equiv\text{CC}_6\text{H}_5)_8]_2$ (715 nm) > $[\text{Pt}_2\text{Cu}_4(\text{C}\equiv\text{CC}_6\text{H}_5)_8]_3$ (806 nm). The intense near-infrared luminescence is attributed to a MMLCT state.

The $[\text{Pt}_2\text{Ag}_4(\text{C}\equiv\text{CBu}')_8]$ complex has been shown to form a linear polymeric aggregate with 2,2'-bipy [103] (Fig. 29). The crystal structure of the aggregate has been determined. The 2,2'-bipy unit is planar, has an *s-trans* conformation, and forms weak contacts with the equatorial Ag centers of adjacent $[\text{Pt}_2\text{Ag}_4(\text{C}\equiv\text{CBu}')_8]$ units. $\text{Pt}(\text{C}\equiv\text{CBu}')_4$ units have an eclipsed conformation, with the C(A)–Pt(A)–Pt(B)–C(B) dihedral angle being 0.5°. The free complex has a staggered conformation. Luminescence occurs in the aggregate and there is a redshift in the emission maximum relative to the free monomer unit. Extended Hückel calculations suggest the HOMO of the monomer unit has contributions from metal *d* orbitals and acetylene π orbitals, while the LUMO has empty metal *d* orbitals, acetylene π^* orbitals, and contributions from Ag *sp* orbitals. The luminescence is considered to be from a MLCT state.

Because platinum is a heavy metal, relativistic effects are significant in platinum acetylides [104]. Relativistic effects include enhancement of spin–orbit coupling leading to rapid conversion from the singlet excited state to the triplet state, shortening of bond lengths, contraction of *s* and *p* orbitals, expansion of *d* and *f* orbitals, and effects on the HOMO–LUMO gap. Through self-assembly processes, Pt···Pt interactions can significantly influence the spectroscopic properties of the platinum acetylide complexes. Examples include A-frame complexes [32], solvatochromism in terpyridyl acetylide complexes [37], and crystal polymorphism in $[\text{Pt}_2\text{Cu}_4(\text{C}\equiv\text{CC}_6\text{H}_5)_8]$ complexes [102]. The optical transitions in these systems include MMLCT transitions, where charge transfers from the Pt–Pt bond to the acceptor. By forming nanomaterials that vary the Pt···Pt distance and the environment around the bond, spectroscopic parameters like quantum yield, transition energies, and excited state lifetimes can be tuned toward an application requirement.

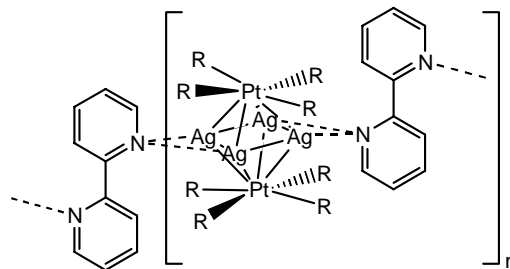
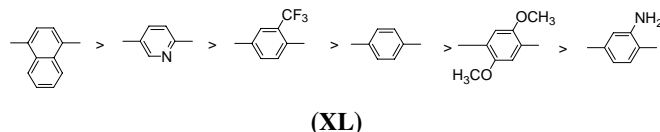


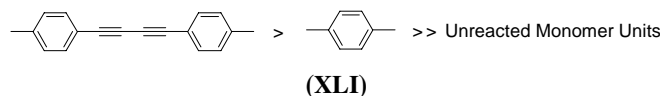
Figure 29. Linear aggregate of the $[\text{Pt}_2\text{Ag}_4(\text{C}\equiv\text{CBu}')_8]$ complex formed in the presence of 2,2'-bipy [103].

4.3. Polymer Nonlinear Optics

Platinum acetylide oligomers and polymers have been investigated for nonlinear optics applications [105–107]. A series of polymers $(\text{Pt}(\text{PBU}_3)_2\text{C}\equiv\text{C}\text{-Ar}\text{-C}\equiv\text{C})_n$ has been synthesized and the real (γ') and imaginary (γ'') components of the third-order hyperpolarizabilities measured by a probe wavelength of 1064 and 532 nm, respectively [108]. The most significant trends are observed in the γ'' values:



Polymers containing electron-withdrawing monomer units have larger γ'' values than those containing electron-donating units. Increasing conjugation will also influence the nonlinearity. The trends indicate the electron-donating or -withdrawing ability as well as increasing conjugation of the monomer units influences γ'' . The trends reflect the interplay between the electron-donating Pt atom and the electron donating/withdrawing ability of the monomer units and its effects on one- and two-photon transition matrix elements.



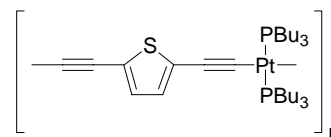
4.4. Polymer Thin Film Properties

Thin film devices can be readily constructed from Pt-acetylide complexes. Films are usually formed by spin casting from a polymer solution. The phase behavior of a Pt polyynone $[\text{Pt}(\text{PBU}_3)_2\text{-C}\equiv\text{C}\text{-C}\equiv\text{C}\text{-Pt}(\text{PBU}_3)_2\text{-C}\equiv\text{C}\text{-C}_6\text{H}_4\text{-C}\equiv\text{C}]_n$ provides an example of solution properties [50]. The authors investigate the orientational characteristics of this polymer in the lyotropic nematic mesophase. The order parameter-polymer volume fraction ($S - v_p$) curve is concave upward, suggesting increasing orientational correlation along the chain with increasing concentration and supporting the idea that the polymer has considerable conformational flexibility. What is the structure of a spin-coated Pt-poly-yne thin film? A near-edge X-ray absorption spectroscopy study has been performed on spin-cast films of the polymer $[\text{M}(\text{PBU}_3)_2\text{-C}\equiv\text{C}\text{-}p\text{-C}_6\text{H}_4\text{-}p\text{-C}_6\text{H}_4\text{-C}\equiv\text{C}]_n$, M = Pt, Pd. X-ray resonances, recorded at grazing (25°) and normal (90°) incidence angles, show a strong polarization dependence. Analysis of the intensity ratios suggests the organic portion of the polymer to be oriented 40° with respect to the surface normal. Electron diffraction measurements on crystallites having 50 nm diameter found in thin films of the polymer $[\text{Pt}(\text{AsBu}_3)_2\text{C}\equiv\text{C}\text{-C}_6\text{H}_4\text{-C}\equiv\text{C}]_n$ have an order parameter of 0.93 and an orthorhombic unit cell with parameters $a = 2.1$ nm, $c = 1.2$ nm, and $90^\circ < \beta < 93^\circ$ [51].

Through the use of X-ray photoelectron spectroscopy, the interface between vapor-deposited Al and a palladium-poly-yne has been investigated [109]. Aluminum is deposited onto a Pt-poly-yne thin film and photoelectron spectra for the Pd $3d$, C $1s$, and Al $2p$ core levels measured as a function of the amount of Al deposited onto the thin film. The Al $2p$ spectra show the presence of positively charged Al atoms near the surface and the formation of Al islands as more metal deposited. When the

Al layer is 30 Å thick, the photoelectron spectrum is that of bulk Al. Broadening and shifts in the Pd $3d$ spectrum also occur during deposition. Finally, the C $1s$ photoelectron spectrum shows no changes during deposition. The data suggest charge transfer from Al atoms to Pd atoms to form Al-Pd. The Al atoms have no effect on the carbon atoms.

Environmental factors like oxygen and water may have effects on the behavior of a photosensitive material. The influence of air exposure on the photocurrent of a Pt-poly-yne cell Al/Pt-poly-yne/ITO has been investigated [110]. They prepare devices containing the polymer

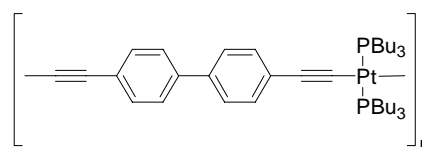


(XLII)

In the presence of ambient air, a new optical absorption feature from 2.5 to 2.8 eV not present under nitrogen appears. Photocurrent measurements in the presence of air show a subgap photocurrent feature below 2.8 eV. Under vacuum there is only a positive dark current in this range. The subgap photocurrent tail is assigned to trap states resulting from the absorption of oxygen or water from air. The authors also observe a moderate reversible photocurrent increase reversible in vacuum, suggesting no chemical change occurs.

5. APPLICATIONS

The properties of platinum acetylide polymers have also been shown to be sensitive to atmospheric moisture [111]. As part of the development of a humidity meter, thin films of the polymer



(XLIII)

are deposited by spin coating onto a surface acoustic wave device. Upon exposure to a humid environment for 15 min, the frequency of the device decreases. Under a dry atmosphere the frequency returns to its original value. The response of the humidity sensor fits a quadratic function in the range of 0–80% relative humidity.

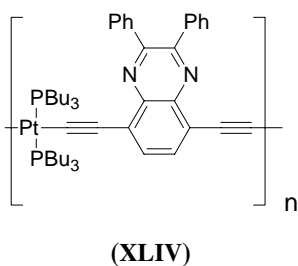
$$\frac{\Delta f}{f} = a(\text{RH}) + b(\text{RH})^2 \quad (9)$$

where f is the frequency of the device and RH is relative humidity. The results show that thin films of platinum acetylides undergo a reversible vapor absorption-desorption process. The effect of water content on the electro-optical properties has not been investigated. A similar device using $[\text{Pt}((\text{PC}_6\text{H}_5)_3)_2\text{C}\equiv\text{C}\text{-C}_6\text{H}_5\text{-C}\equiv\text{C}]_n$ has been recently described [112].

To investigate triplet exciton behavior, a photocell has been fabricated containing a layer structure ITO/Pt-poly-yne ($\pm 7\%$ C_{60})/Al [113]. The photoresponsive device has been described

in a patent [114]. In a cell just containing Pt-poly-yne, photocurrent onset occurs at the threshold of singlet absorption. Upon addition of C_{60} , the quantum yield, measured as the number of charge carriers per incident photons, rises by two orders of magnitude. The position of the photocurrent peak depends upon the applied field. For a forward bias (Al negative), the peak response is 3.25 eV, while for a reverse bias the peak changes sign and shifts to 3.15 eV. This effect also occurs in the presence of C_{60} . The addition of C_{60} results in increased dissociation of the triplet exciton by transfer of the electron to C_{60} . Photoluminescence from the films shows a fluorescence band at 3.2 eV and a phosphorescence band at 2.4 eV. In the presence of 10% C_{60} , the phosphorescence is nearly suppressed, with the phosphorescence lifetime reduced by a factor of 20. These differences reflect the low electron mobility in Pt-poly-yne and domination of the current by hole transport.

A more recent study investigates singlet and triplet exciton generation in an electroluminescent device [115]. A thin film light emitting device (LED) having the layer sequence ITO/PEDOT-PSS/Polymer/Ca/Al has been prepared. The polymer has the following chemical formula.



By measuring electroluminescence and photoluminescence spectra of the LEDs, the authors calculate the fraction of electrically generated singlets, χ_s . Simple spin statistics arguments predict that χ_s would be 25%. The singlet generation fraction for the polymer is 57%, while that for a monomer-containing film is 22%. The measurements suggest that recombination is spin independent for the monomer, but a spin-dependent process favoring singlet formation occurs in the polymer.

A molecular photochemical device based on the platinum diimine chromophore has been proposed [35]. Applications include light-to-energy conversion and sensors. The photochemical device is a three-component donor–chromophore–acceptor (D–C–A) triad depicted in Figure 30. Also shown are additional donors and acceptors that are part of an electrochemical gradient. For electron–hole generation and charge separation, a chromophore absorbs a photon and the electron–hole pair becomes spatially separated. Charge generated by the device could be used to catalyze the oxidation and reduction of other donors and acceptors through dark reactions. A D–C–A (Fig. 31) triad has

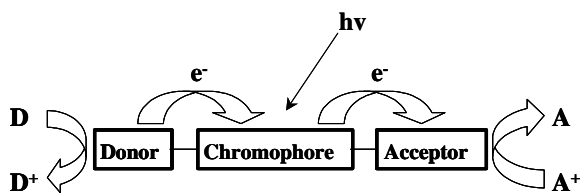


Figure 30. Molecular photochemical device based on the platinum diimine chromophore [35].

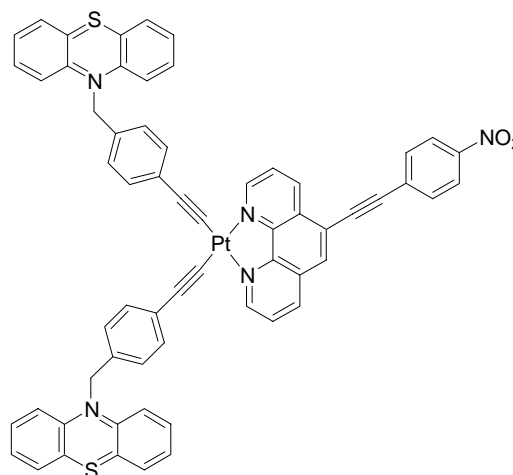


Figure 31. A D–C–A triad showing photoinduced charge transfer behavior [116].

been synthesized and evidence for photoinduced charge transfer has been given [116]. The donor portion of the triad consists of a phenothiazine group and the acceptor is a nitrophenyl chromophore. The authors also synthesize D–C and C–A dyads for comparison experiments. D–C–A, D–C, and C–A exhibit MLCT absorption bands centered around 400 nm, originating from the Pt–diimine complex. Both D–C–A and C–A have an absorption band at 360 nm assigned to the nitrophenyl group, while D–C has no absorption band. Flash photolysis experiments on D–C–A give a strong absorption at 525 nm, weaker absorptions between 390 and 500 nm, and strong bleaching at 360 nm. All bands decay exponentially with a single time constant of 70 ns. The absorption band at 525 nm is assigned to the phenothiazine radical cation. The broad feature from 390 to 500 nm is assigned to the nitrobenzene radical anion and the bleach at 360 nm correlates with the depletion of ground state nitrophenyl. The data are consistent with the formation of a charge separated $D^+–C–A^-$ species. No transients are observed upon irradiation of either D–C or C–A.

GLOSSARY

Acetylide Organometallic complex containing covalent bonds between transition metal and carbon–carbon triple bonds.

Charge transfer transition Optical transition that causes transfer of an electron from a donor to an acceptor.

Phosphorescence Emission of light from a molecule in a triplet excited state to the ground state.

Triplet state Molecular excited state where two electrons have parallel spins.

REFERENCES

1. P. J. Stang and B. Olenyuk, *Acc. Chem. Res.* 30, 502 (1997).
2. R. J. Puddephatt, *Chem. Comm.* 1055 (1998).
3. P. Nguyen, P. Gomez-Elipse, and I. Manners, *Chem. Rev.* 99, 1515 (1999).
4. V. W.-W. Yam, K. K.-W. Lo, and K. M.-C. Wong, *J. Organomet. Chem.* 578, 3 (1999).
5. V. W.-W. Yam, *Acc. Chem. Res.* 35, 555 (2002).

6. R. P. Kingsborough and T. M. Swager, in "Progress in Inorganic Chemistry," Vol. 48 (K. D. Karlin, Ed.), Wiley, New York, 1999.
7. K. D. Ley and K. S. Schanze, *Coord. Chem. Rev.* 171, 287 (1998).
8. J. Fornies and E. Lalinde, *J. Chem. Soc. Dalton Trans.* 2587 (1996).
9. T. J. McKay, J. A. Bolger, J. Staromlynska, and J. R. Davy, *J. Chem. Phys.* 108, 5537 (1998).
10. J. Staromlynska, T. J. McKay, J. A. Bolger, and J. R. Davy, *J. Opt. Soc. Am. B* 15, 1731 (1998).
11. J. R. Berenguer, J. Fornies, F. Martinez, and J. C. Cubero, *Polyhedron* 12, 1797 (1993).
12. S. Yamazaki, A. J. Deeming, M. B. Hursthouse, and K. M. A. Mailk, *Inorg. Chim. Acta* 235, 147 (1995).
13. I. Ara, J. R. Berenguer, J. Fornies, E. Lalinde, and M. T. Moreno, *J. Organomet. Chem.* 510, 63 (1996).
14. S. Yamazaki, A. J. Deeming, D. M. Speel, D. E. Hibbs, M. B. Hursthouse, and K. M. A. Malik, *Chem. Comm.* 177 (1997).
15. E. Nakache, N. Poulain, F. Candau, A. Orecchioni, and J. M. Irache, in "Handbook of Nanostructured Materials and Nanotechnology" (H. S. Nalwa, Ed.), Vol. 5, p. 577. Academic Press, San Diego, 2000.
16. H. E. Katz, G. Scheller, T. M. Putvinski, M. L. Schilling, W. L. Wilson, and C. E. D. Chidsey, *Science* 254, 1485 (1991).
17. A. Furlani, S. Licoccia, M. V. Russo, A. Villa, and C. Guastini, *J. Chem. Soc. Dalton Trans.* 2197 (1984).
18. R. D'Amato, A. Furlani, M. Colapietro, G. Portalone, M. Casalboni, M. Falconieri, and M. V. Russo, *J. Organomet. Chem.* 627, 13 (2001).
19. P. Nguyen, G. Lesley, T. B. Marder, I. Ledoux, and J. Zyss, *Chem. Mater.* 9, 406 (1997).
20. M. Casalboni, F. Sarcinelli, R. Pizzoferrato, R. D'Amato, A. Furlani, and M. V. Russo, *Chem. Phys. Lett.* 319, 107 (2000).
21. Y. Fujikura, K. Sonogashira, and N. Hagihara, *Chem. Lett.* 1067 (1975).
22. P. Siemsen, U. Gubler, C. Bosshard, P. Gunter, and F. Diederich, *Chem. Eur. J.* 7, 1333 (2001).
23. W. Mohr, J. Stahl, F. Hampel, and J. A. Gladysz, *Inorg. Chem.* 40, 3263 (2001).
24. T. B. Peters, J. C. Bohling, A. M. Arif, and J. A. Gladysz, *Organometallics* 18, 3261 (1999).
25. J. Stahl, J. C. Bohling, E. B. Bauer, T. B. Peters, W. Mohr, J. M. Martin-Alvarez, F. Hampel, and J. A. Gladysz, *Angew. Chem.* 41, 1871 (2002).
26. J. D. Bradshaw, L. Guo, C. A. Tessier, and W. J. Youngs, *Organometallics* 15, 2582 (1996).
27. K. Onitsuka, S. Yamamoto, and S. Takahashi, *Angew. Chem.* 38, 174 (1999).
28. S. M. AlQaisi, K. J. Galat, M. Chai, D. G. Ray, P. L. Rinaldi, C. A. Tessier, and W. J. Youngs, *J. Am. Chem. Soc.* 120, 12149 (1998).
29. R. Faust, F. Diederich, V. Gramlich, and P. Seiler, *Chem. Eur. J.* 1, 111 (1995).
30. C. Muller, J. A. Whiteford, and P. J. Stang, *J. Am. Chem. Soc.* 120, 9827 (1998).
31. V. W.-W. Yam, L.-P. Chan, and T.-F. Lai, *Organometallics* 12, 2197 (1993).
32. V. W.-W. Yam, K.-L. Yu, K. M.-C. Wong, and K.-K. Cheung, *Organometallics* 20, 721 (2001).
33. P. G. Pringle and B. L. Shaw, *J. Chem. Soc. Chem. Commun.* 581 (1982).
34. M. J. Irwin, G. Jia, J. J. Vittal, and R. J. Puddephatt, *Organometallics* 15, 5321 (1996).
35. M. Hissler, J. E. McGarrah, W. B. Connick, D. K. Geiger, S. D. Cummings, and R. Eisenberg, *Coord. Chem. Rev.* 208, 115 (2000).
36. V. W.-W. Yam, R. P.-L. Tang, K. M.-C. Wong, and K.-K. Cheung, *Organometallics* 20, 4476 (2001).
37. V. W.-W. Yam, K. M.-C. Wong, and N. Zhu, *J. Am. Chem. Soc.* 124, 6506 (2002).
38. P. Espinet, J. Fornies, F. Martinez, M. Tomas, E. Lalinde, E. Moreno, A. Ruiz, and A. J. Welch, *J. Chem. Soc. Dalton Trans.* 791 (1990).
39. I. Ara, J. R. Berenguer, E. Eguizabal, J. Fornies, and E. Lalinde, *Organometallics* 20, 2686 (2001).
40. J. R. Berenguer, J. Fornies, J. Gomez, E. Lalinde, and M. T. Moreno, *Organometallics* 20, 4847 (2001).
41. I. Ara, J. R. Berenguer, J. Fornies, J. Gomez, E. Lalinde, and R. I. Merino, *Inorg. Chem.* 36, 6461 (1997).
42. I. Ara, J. R. Berenguer, J. Fornies, and E. Lalinde, *Organometallics* 16, 3921 (1997).
43. N. Ohshiro, F. Takei, K. Onitsuka, and S. Takahashi, *J. Organomet. Chem.* 569, 195 (1998).
44. K. Onitsuka, M. Fujimoto, N. Ohshiro, and S. Takahashi, *Angew. Chem.* 38, 689 (1999).
45. K. Onitsuka, A. Iuchi, M. Fujimoto, and S. Takahashi, *Chem. Comm.* 741 (2001).
46. K. Onitsuka, N. Ohshiro, M. Fujimoto, F. Takei, and S. Takahashi, *Mol. Cryst. Liq. Cryst.* 342, 159 (2000).
47. K. Sonogashira, S. Takahashi, and N. Hagihara, *Macromolecules* 10, 879 (1977).
48. S. Takahashi, H. Morimoto, E. Murata, S. Kataoka, K. Sonogashira, and N. Hagihara, *J. Polym. Sci. Polym. Chem. Ed.* 20, 565 (1982).
49. S. Takahashi, M. Kariya, T. Yatake, K. Sonogashira, and N. Hagihara, *Macromolecules* 11, 1063 (1978).
50. A. Abe, N. Kimura, and S. Tabata, *Macromol.* 24, 6238 (1991).
51. A. E. Dray, R. Rachel, W. O. Saxton, J. Lewis, M. S. Khan, A. M. Donald, and R. H. Friend, *Macromolecules* 25, 3473 (1992).
52. M. Yang, Z. Lei, and Z. Cai, *Polymer* 40, 3203 (1999).
53. K. A. Bunten and A. K. Kakkar, *J. Mater. Chem.* 5, 2041 (1995).
54. K. A. Bunten and A. K. Kakkar, *Macromolecules* 29, 2885 (1996).
55. T. M. Cooper, in "Handbook of Nanostructured Materials and Nanotechnology" (H. S. Nalwa, Ed.), vol. 5, p.711. Academic Press, San Diego, 2000.
56. T. M. Cooper and L. V. Natarajan, in "Photonic Polymer Systems: Fundamentals, Methods and Applications" (D. L. Wise, G. E. Wnek, D. J. Trantolo, T. M. Cooper, and J. D. Gresser, Eds.), p. 737. Dekker, New York, 1998.
57. K. Onitsuka, Y. Harada, F. Takei, and S. Tarahashi, *Chem. Comm.* (1998).
58. L. Pu, in "Electrical and Optical Polymer Systems: Fundamentals, Methods and Applications" (D. L. Wise, Ed.), p. 823. Dekker, New York, 1998.
59. J. M. Tour, *Chem. Rev.* 96, 537 (1996).
60. J. S. Moore, D. J. Hill, and M. J. Mio, in "Solid-Phase Organic Synthesis" (K. Burgess, Ed.), p. 119. Wiley, New York, 2000.
61. M. Higuchi, N. Minoura, and T. Kinoshita, *Chem. Lett.* 227 (1994).
62. A. H. Heuer, D. J. Fink, V. J. Lariaia, J. L. Arias, P. D. Calvert, K. Kendall, G. L. Messing, J. Blackwell, P. C. Rieke, D. H. Thompson, A. P. Wheeler, A. Veis, and A. I. Caplan, *Science* 255, 1098 (1992).
63. "Biomolecular Materials by Design" (M. Alper, H. Bayley, D. Kaplan, and M. Navia, Eds.), Vol. 330. Materials Research Society, Pittsburgh, 1994.
64. B. S. Thompson, *SAMPE J.* 32, 38 (1996).
65. G. Frapper and M. Kertesz, *Inorg. Chem.* 32, 732 (1993).
66. A. B. P. Lever and E. S. Dodsworth, in "Inorganic Electronic Structure and Spectroscopy" (A. B. P. Lever and E. I. Solomon, Eds.), Vol. II, p. 227. (1999).
67. L. C. Choi, Y. F. Cheng, C. Yip, D. L. Phillips, and V. W.-W. Yam, *Organometallics* 19, 3192 (2000).
68. W. M. Kwok, D. L. Phillips, P. K.-Y. Yeung, and V. W.-W. Yam, *J. Phys. Chem. A* 101, 9286 (1997).
69. L. Sacksteder, E. Baralt, B. A. DeGraff, C. M. Lukehart, and J. N. Demas, *Inorg. Chem.* 30, 2468 (1991).
70. K. Sonogashira, Y. Fujikura, T. Yatake, N. Toyoshima, S. Takahashi, and N. Higihara, *J. Organomet. Chem.* 145, 101 (1978).
71. I. Collamati and A. Furlani, *J. Organomet. Chem.* 17, 457 (1969).
72. C. A. Tolman, *Chem. Rev.* 77, 313 (1977).

73. T. M. Cooper, D. G. McLean, and J. E. Rogers, *Chem. Phys. Lett.* 349, 31 (2001).
74. K. D. Glusac and K. S. Schanze, *Polymer. Preprints* 43, 87 (2002).
75. D. M. Roundhill, H. B. Gray, and C.-M. Che, *Acc. Chem. Res.* 22, 55 (1989).
76. V. W.-W. Yam, P. K.-Y. Yeung, L.-P. Chan, W. M. Kwok, D. L. Phillips, K.-L. Yu, R. K.-W. Wong, H. Yan, and Q.-J. Meng, *Organometallics* 17, 2590 (1998).
77. M. Hissler, W. B. Connick, D. K. Geiger, J. E. McGarrah, D. Lipa, R. J. Lachicotte, and R. Eisenberg, *Inorg. Chem.* 39, 447 (2000).
78. H. Zhang, A. W. M. Lee, W.-Y. Wong, and M. S. M. Yuen, *J. Chem. Soc. Dalton Trans.* 3675 (2000).
79. C. E. Whittle, J. A. Weinstein, M. W. George, and K. S. Schanze, *Inorg. Chem.* 40, 4053 (2001).
80. C. J. Adams, S. L. James, X. Liu, P. R. Raithby, and L. J. Yellowlees, *J. Chem. Soc. Dalton Trans.* 63 (2000).
81. M. Springborg and R. C. Albers, *Phys. Rev. B* 53, 10626 (1996).
82. H. F. Wittmann, K. Fuhrmann, and R. H. Friend, *Synth. Metals* 55–57, 56 (1993).
83. H. F. Wittman, R. H. Friend, M. S. Khan, and J. Lewis, *J. Chem. Phys.* 101, 2693 (1994).
84. D. Beljonne, H. F. Wittman, A. Kohler, G. S., M. Younus, J. Lewis, P. R. Raithby, M. S. Khan, R. H. Friend, and J. L. Bredas, *J. Chem. Phys.* 105, 3868 (1996).
85. A. Kohler, D. A. dos Santos, D. Beljonne, Z. Shual, J.-L. Bredas, A. B. Holmes, A. Kraus, K. Mullen, and R. H. Friend, *Nature* 392, 903 (1998).
86. N. Chawdhury, A. Kohler, R. H. Friend, M. Younus, N. J. Long, P. R. Raithby, and J. Lewis, *Macromolecules* 31, 722 (1998).
87. N. Chawdhury, A. Kohler, R. H. Friend, W.-Y. Wong, J. Lewis, M. Younus, P. R. Raithby, T. C. Corcoran, A. Al-Mandhary, and M. S. Khan, *J. Chem. Phys.* 110, 4963 (1999).
88. J. S. Wilson, A. Kohler, R. H. Friend, M. K. A.-M. Al-Suti, M. R. A., M. S. Khan, and P. R. Raithby, *J. Chem. Phys.* 113, 7627 (2000).
89. J. S. Wilson, N. Chawdhury, M. R. A. Al-Mandhary, M. Younus, M. S. Khan, P. R. Raithby, A. Kohler, and R. H. Friend, *J. Am. Chem. Soc.* 123, 9412 (2001).
90. A. Kohler, J. S. Wilson, R. H. Friend, M. K. Al-Suti, M. S. Khan, A. Gerhard, and H. Bassler, *J. Chem. Phys.* 116, 9457 (2002).
91. R. D. Markwell, I. S. Butler, A. K. Kakkar, M. S. Khan, A. H. Al-Zakwani, and J. Lewis, *Organometallics* 15, 2331 (1996).
92. J. Lewis, P. R. Raithby, and W.-Y. Wong, *J. Organomet. Chem.* 556, 219 (1998).
93. W.-Y. Wong, W.-K. Wong, and P. R. Raithby, *J. Chem. Soc. Dalton Trans.* 2761 (1998).
94. W.-Y. Wong, K.-H. Choi, G.-L. Lu, and J.-X. Shi, *Macromol. Rapid Commun.* 22, 461 (2001).
95. W.-Y. Wong, G.-L. Lu, K.-H. Choi, and J.-X. Shi, *Macromolecules* 35, 3506 (2002).
96. M. S. Khan, M. R. A. Al-Mandhary, M. K. Al-Suti, A. K. Hisahm, P. R. Raithby, B. Ahrens, M. F. Mahon, L. Male, E. A. Marseglia, E. Tedesco, R. H. Friend, A. Kohler, N. Feeder, and S. J. Teat, *J. Chem. Soc. Dalton Trans.* 1358 (2002).
97. J. Davy, M. E. Gunter, and E. R. T. Tiekink, *Z. Kristallogr.* 213, 483 (1998).
98. T. J. McKay, J. Staromlynska, J. Davy, R., and J. A. Bolger, *J. Opt. Soc. Am. B* 18, 358 (2001).
99. T. J. McKay, J. Staromlynska, P. Wilson, and J. Davy, *J. Appl. Phys.* 85, 1337 (1999).
100. D. Osella, R. Gobetto, C. Nervi, M. Ravera, R. D'Amato, and M. V. Russo, *Inorg. Chem. Commun.* 1, 239 (1998).
101. W.-Y. Wong, G.-L. Lu, K.-F. Ng, K.-H. Choi, and Z. Lin, *J. Chem. Soc. Dalton Trans.* 3250 (2001).
102. J. P. H. Charmant, J. Fornies, J. Gomez, E. Lalinde, R. I. Merino, M. T. Moreno, and A. G. Orpen, *Organometallics* 18, 3353 (1999).
103. I. Ara, J. Fornies, J. Gomez, E. Lalinde, E. Moreno, and M. Moreno, *Organometallics* 19, 3137 (2000).
104. N. Kaltsoyannis, *J. Chem. Soc. Dalton Trans.* 1 (1997).
105. C. C. Frazier, S. Guha, and W. Chen, USA, 1989.
106. S. Guha, K. Kang, and P. L. Porter, *Appl. Phys. B* 53, 308 (1991).
107. S. Guha, K. Kang, P. Porter, J. F. Roach, D. E. Remy, F. J. Aranda, and D. V. G. L. N. Rao, *Opt. Lett.* 17, 264 (1992).
108. P. L. Porter, S. Guha, K. Kang, and C. C. Frazier, *Polymer* 32, 1756 (1991).
109. G. Polzonetti, M. V. Russo, G. Infante, and A. Furlani, *J. Electron Spectrosc. Rel. Phen.* 85, 73 (1997).
110. N. Chawdhury, M. Younus, P. R. Raithby, J. Lewis, and R. H. Friend, *Opt. Mater.* 9, 498 (1998).
111. C. Caliendo, E. Verona, A. D'Amico, A. Furlani, G. Infante, and M. V. Russo, *Sensors and Actuators B* 24–25, 670 (1995).
112. C. Caliendo, I. Fratoddi, and M. V. Russo, *Appl. Phys. Lett.* 80, 4849 (2002).
113. A. Kohler, H. F. Wittmann, R. H. Friend, M. S. Khan, and J. Lewis, *Synth. Metals* 77, 147 (1996).
114. R. Friend and A. Kohler, U.S. Patent 5, 698, 048, 1997.
115. J. S. Wilson, A. S. Dhoot, A. J. A. B. Seeley, M. S. Khan, A. Kohler, and R. H. Friend, *Nature* 413, 828 (2001).
116. J. E. McGarrah, Y.-J. Kim, M. Hissler, and R. Eisenberg, *Inorg. Chem.* 40, 5410 (2001).
117. S. Takahashi, F. Murata, K. Sonogashira, and N. Hagihara, *J. Polymer Sci. Polym. Chem. Ed.* 18, 661 (1980).
118. M. S. Khan, S. J. Davies, A. K. Kakkar, D. Schwartz, B. Lin, B. F. G. Johnson, and J. Lewis, *J. Organomet. Chem.* 424, 87 (1992).
119. K. Onitsuka, X.-Q. Tao, and K. Sonogashira, *Bull. Chem. Soc. Jpn.* 67, 2611 (1994).
120. A. J. Deeming, G. Hogarth, M.-Y. Lee, M. Saha, S. P. Redmond, H. Phetmung, and A. G. Orpen, *Inorg. Chim. Acta* 309, 109 (2000).
121. O. Lavastre, J. Plass, P. Bachmann, S. Guesmi, C. Moinet, and P. H. Dixneuf, *Organometallics* 16, 184 (1997).
122. A. Kohler, M. Younus, M. R. A. Al-Mandhary, P. R. Raithby, M. S. Khan, and R. H. Friend, *Synth. Met.* 101, 246 (1999).
123. J. Lewis, M. S. Khan, A. K. Kakkar, B. F. G. Johnson, T. B. Marder, H. B. Fyfe, F. Wittmann, R. H. Friend, and A. E. Dray, *J. Organomet. Chem.* 425, 165 (1992).
124. M. Younus, A. Kohler, S. Cron, N. Chawdhury, M. R. A. Al-Mandhary, M. S. Khan, J. Lewis, N. J. Long, R. H. Friend, and P. R. Raithby, *Angew. Chem. Int. Ed.* 37, 3036 (1998).
125. M. S. Khan, A. K. Kakkar, N. J. Long, J. Lewis, P. Raithby, P. Nguyen, T. B. Marder, F. Wittmann, and R. H. Friend, *J. Mater. Chem.* 4, 1227 (1994).
126. M. Yang, Z. Lei, M. Wan, Y. Shen, J. Wang, J. Chen, H. Wang, and T. Ye, *J. Appl. Polymer Sci.* 64, 1657 (1997).
127. W.-Y. Wong, S.-M. Chan, K.-H. Choi, K.-W. Cheah, and W.-K. Chan, *Macromol. Rapid Commun.* 21, 453 (2000).
128. O. Lavastre, M. Even, P. H. Dixneuf, A. Pacreau, and J.-P. Vairon, *Organometallics* 15, 1530 (1996).

Transition Metal Nanocluster Assemblies

K. Sumiyama, T. Hihara, D. L. Peng, S. Yamamuro

Nagoya Institute of Technology, Nagoya, Japan

CONTENTS

1. Introduction
 2. Fabrication of Nanoclusters
 3. Cluster Deposition and Assembling
 4. Spectroscopic Characterization
 5. Characteristic Magnetic and Transport Properties of Cluster-Assembled Materials
 6. Concluding Remarks
- Glossary
References

1. INTRODUCTION

Nanoscale-heterogeneous materials have been well known for their excellent functional properties in comparison with uniform (defect-less and/or single crystalline) materials and homogeneous (amorphous or disordered) ones [1]. In basic and applied fields of magnetism, we can find their various examples such as soft magnetic nanocrystalline materials with a high magnetic flux density, magnetic granular materials with giant magnetoresistance, and magnetic recording media. These materials have been mainly produced by quenching and annealing: nanometric scale morphology has been obtained as precipitates from supersaturated solid solution produced initially by vapor, liquid- or solid-quenching. These procedures are versatile and appropriate for mass-production; however, chemical and structural controls are seriously restricted. Precipitated regions leave compositionally depleted regions in their neighborhoods; their size and internal distance cannot be adjusted independently owing to the simple materials balance. In order to overcome this restriction, several fascinating methods are proposed in semiconductor devices and magnetic materials [2]: artificial superlattice films by nanoscale vapor deposition control, nanoscale dots and their one- or two-dimensional arrays by electron beam lithography, focused ion beam techniques and tips of scanning tunneling electron microscope techniques. In this context, nanometer-sized clusters can be used as building blocks to fabricate materials whose microscopic structure is chemically and/or physically tailored on the nanometer scale [3–5].

Small particles have been widely used in history. A typical example is a colorful stained glass, in which optical energy is absorbed by plasmon resonance of conduction electrons in small noble metal particles [6]. A small particle has been first treated as finite size materials in the epoch-making theory by Kubo [7]. In small systems with a 10-nanometer size, the electron energy splitting, which is inversely proportional to the number of containing atoms, cannot be neglected being an order of Kelvin. This leads to anomalous physical properties quite different from the bulk counterparts whose electron energy splitting are roughly assumed to be continuous. For example, Al particles consisting of an odd number of atoms is predicted to be paramagnetic, whereas those consisting of an even number, diamagnetic. This finding encouraged the crystallographic studies, and several systematic physical and chemical experiments conducted by Uyeda [8, 9]. The application-oriented works have been reported on magnetic materials, electronics devices, catalyses, ceramics, etc. [10]. Due to the enormously large surface area, surface lattice softening (surface melting) of small particles [11], and a few 10-micron-size electronic circuit pattern can be directly written by the gas deposition method [12] in which particles are supplied through a small nozzle of a gas evaporation chamber, while small gold particles independently suspended in colloidal liquids are available for very low temperature soldering [13].

The idea of building nanostructured assemblies from nanometer-sized particles was first proposed by Gleiter [14]. A high-pressure mechanical compaction was applied to nanosized particles which were originally synthesized by a gas condensation technique and obtained to be a bulk substance, so-called a noncrystalline material. It is comprised of a number of nanosized crystallites packed together. The materials have a large area of grain boundaries in contrast to the conventional polycrystalline counterparts. Since the grain boundary possesses a different atomic environment, which is characterized by a lack of long-range order, softening of lattice vibration, and low coordination number, it modifies mechanical, electrical, and magnetic properties of the materials [15].

In a field of physical chemistry, there have been increasing studies on nanometer-size, free microclusters showing interesting structures and properties [16]. Specific cluster sizes are very stable and more abundant than their near neighbor sizes in simple metal clusters. This feature is called

a magic number and related to the closed shell structures of the itinerant electrons in the clusters corresponding to the electronic and nuclear closed shell structures of atoms. Such magic number effects have been observed in hierarchic size ranges [17]. In transition metal clusters, in particular, different types of magic numbers based upon an icosahedral and/or closely packed type structures have been observed. The electronic, physical, and chemical properties are also size-dependent at around a nanometer size. The metal-insulator transition in Hg clusters is the famous example: Hg is metallic for larger clusters, while it is insulating for smaller clusters, owing to the change in the bonding mechanism from a metallic-type to a Van der Waals, being ascribed to the obvious quantum-size effect of the discrete electronic levels [18]. By decreasing the cluster size, the magnetic moments are enhanced by localization of electrons and contribution of orbital moments [19]. The domain structure changes from a multiple type to a single one, and very small ferromagnetic clusters become superparamagnetic owing to the thermal fluctuation [20]. When we apply an electric field to a small metal cluster and observe the electric current, we need an additional field corresponding to the charging energy of the cluster in order to break the charge neutrality of the cluster in the transient stage. This Coulomb blockade effect has been extensively studied because it promises the minimum size electronic devices [21]. Since such nanometric clusters and fine particles are located between bulk materials and atoms and molecules, we can expect nonequilibrium structures and anomalous properties related to the instability of their geometrical and electronic structures.

We wish to utilize these extraordinary characteristics of nanometer-size clusters. With the aim of this new paradigm—cluster assembled materials in materials science and engineering—we have to surmount the following steps [5]:

1. development of efficient and versatile cluster source,
2. formation of mono-dispersed size clusters,
3. study of hierarchic magic numbers,
4. simulation and theoretical confirmation of cluster-formation and assembling processes,
5. surface stabilization and/or coating to overcome surface softening and diffusion,
6. concentration and structure control of alloy and compound clusters,
7. development of characterization techniques appropriate for nanometer-size clusters,
8. random and/or periodical assembling,
9. finding of unique structures and properties in cluster assembled materials,
10. application of clusters to other fields.

In this article, we are describing the present status of formation and structures, deposition and assembling, characteristic properties of well-defined size clusters prepared via clean gas phase processes [22].

2. FABRICATION OF NANOCCLUSERS

The nanoclusters can be produced using many experimental techniques. They are not universal, but can be chosen according to the requirements for a specific application.

They are classified into: vacuum syntheses, condensed-phase syntheses, and gas-phase syntheses. Vapor condensation in the ultra-high vacuum system can minimize hydrolysis and oxidation problems that are associated with aqueous methods. The intense flux is enough for film growth to cluster-assembled materials; however, productivity is inferior to the chemical syntheses technique. The condensed-phase technique includes precipitation [23–25], colloidal [26–29], and sol-gel method [30–34]. Such a solution-chemical approach to making nanoclusters offers several attractive features such as homogeneity in size distribution and self-organized assembly, but it has rather low versatility in the choice of the chemical elements, especially if one wants to make alloy clusters. The gas-phase syntheses techniques like inert gas evaporation-condensation [8, 12, 15, 35–41], laser vaporization [42–47], and laser pyrolysis [48–51] are useful for controlling cluster size. In this section, we first mention vacuum syntheses and condensed phase syntheses, and describe gas phase syntheses in details.

2.1. Vacuum Synthesis

In the ion-sputtering source, an ionized cluster beam is produced by bombarding a metal surface with high-energy inert gas ions [52–55]. Kr or Xe gases are used with bombardment energies ranging from about 10 to 20 keV. The temperature of the initially formed cluster in this sputtering source is very high because it does not rely on condensation in an inert gas. Although the cluster-ion intensities are typically exponentially decreasing functions of the cluster size, mass-selected beams with hundreds of atoms per cluster can be produced with sufficient intensities to perform mass spectroscopy analyses. Under optimal conditions for some materials, the intensities are enough to deposit mass-selected clusters.

An ionized cluster beam (ICB) technique has been applied in preparing granular films [56–61]. Figure 1 shows a schematic illustration of this type of source. Metal was evaporated from an inner crucible installed in a molybdenum outer crucible that was heated by electron bombardment. The clusters are thought to be formed by an adiabatic expansion and subsequent cooling when supersaturated atoms are ejected through a crucible nozzle. However, this cooling process is not sufficient to produce large clusters [62] and the

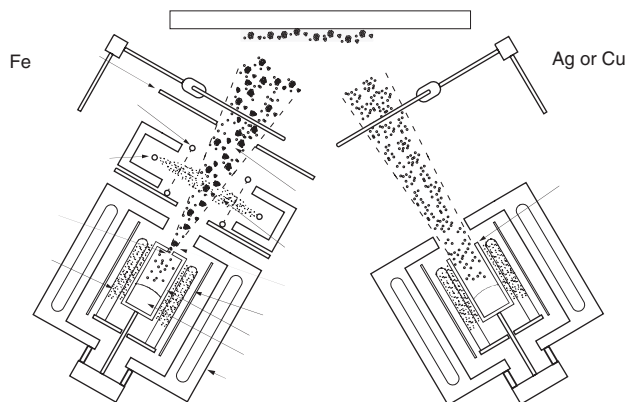


Figure 1. Schematic drawing of ICB deposition apparatus.

initial cluster-ion temperatures are also higher than that synthesized by the gas-phase methods. In previous works, Fe/Ag [58, 59] and Fe/Cu [60, 61] granular films was produced in the ICB technique: Fe clusters were deposited with Ag or Cu vapors simultaneously on a substrate at room temperature. The X-ray absorption fine structure (XAFS) measurements indicated that they vary from fcc γ -Fe to bcc α -Fe in Cu matrix with increasing Fe content x [60]. These experimental results indicate that the Fe clusters formed in this technique should be very small [63]. It seems to be currently accepted that no large clusters (like those consisting of 10^3 atoms) can be generated in the simple supersonic expansion of low pressure metal vapor (~ 1 Torr) in the ICB method [62], though a number of arguments have been done thus far experimentally and theoretically [64–68].

2.2. Condensed-Phase Synthesis

The application to industry in the colloidal clusters has been started in the 19th century. A quantum size effect on the polarized metal cluster by light results in the colored glass. Au and Ag clusters can be dispersed in glass using the Maurer method [45]. $\text{HAuCl}_4 \cdot n\text{H}_2\text{O}$ dissolved soda glass (71.5% SiO_2 , 23% Na_2O , 4% Al_2O_3 , 1% ZnO , 0.13% CeO_2 , and 0.3% Sb_2O_3) is treated in 1400 °C for 8 h. Ultra-violet radiation will be needed in order to nucleate Au clusters, because CeO_2 is activated by this process and can reduce Au ions.

Microemulsion is used as a media for the precipitation of ultra-fine and monodispersed clusters and is based on the nature of the dispersed phase in the microemulsion [69–72]. A microemulsion can be defined as a thermodynamically stable dispersion of two immiscible liquids consisting of microdomains of one or both liquids, stabilized by a monolayer of a surfactant system. The typical immiscible system is water-in-oil microemulsion. The water pools serve as microreactors for the synthesis of the inorganic materials, and restrict the particle growth to a nanoscale. The surfactant system serves to lower the interfacial tension between the dispersed and continuous phases and also the interfacial viscosity of droplets [73, 75–79]. The role of surfactant is very important to generate a self-assembled nanostructure as templating media for the synthesis of novel materials.

The structure of a reverse micelle consists of an aqueous micro-domain facing the polar heads of the surfactant that surrounds this core interacting with the bulk organic solvent (nonpolar) through the hydrophobic chains. The polar cores of the micelles have the ability to solubilize a significant amount of water, which depends on the reversed micellar system properties [80, 81]. Reversed micelles are sometimes referred to as nanoreactors or microreactors due to their structural properties.

2.3. Gas-Phase Synthesis

Several versions of the inert gas aggregation cluster source, in which metal vapor is cooled in inert gas atmosphere, have been developed over the last several decades [8, 12, 15, 35–41]. When the metal vapors are highly supersaturated, they nucleate and grow into large clusters. This source has been used to produce a continuous cluster beam of materials having low melting points, such as alkali and noble

metals. Due to the low temperature of the inert gas, the cluster production proceeds primarily by successive single-atom addition. Since the reevaporation process from the cluster surface is negligible, the cluster abundances are insensitive to the thermodynamic stabilities of the clusters and, consequently, are relatively smooth functions of the cluster size determined mainly by collision statistics.

Laser vaporization sources, illustrated in Figure 2 as an example, produce clusters in the size range from an atom to typically several hundreds of atoms per cluster [42–47, 82, 83]. The second harmonic of a Nd:YAG laser is focused onto a metallic rod which is driven in a slow screw motion. In synchronism with the laser pulse, a short intense helium burst delivered by a fast-pulsed valve cools the laser-produced plasma. The atoms cooled by the helium condense and form small clusters. A further cooling and cluster condensation occurs at the output nozzle of the source because the instantaneous pressure in the source chamber rises high enough to produce an efficient isentropic supersonic expansion at the exit of this chamber. The laser vaporization cluster source successively takes advantage of both cooling mechanisms mentioned above and can work with any solid target even with the most refractory materials.

2.4. Plasma-Gas-Condensation Technique

A plasma-gas-condensation (PGC) cluster source is a combination of sputtering vaporization and gas-condensation techniques [84–97]. It is versatile to vaporize transition metals and refractive elements and enable to control the cluster size by adjusting the sputter yield, the gas pressure and the volume of the cluster growth region.

Figure 3 shows an overview of the present PGC-type cluster deposition apparatus. The metal vapor is generated by a dc magnetron sputtering. A continuous Ar gas stream was injected through the 0.3-mm gap between the shield cover and the target in order to avoid the accumulation of formed particles, which induce the abnormal discharge

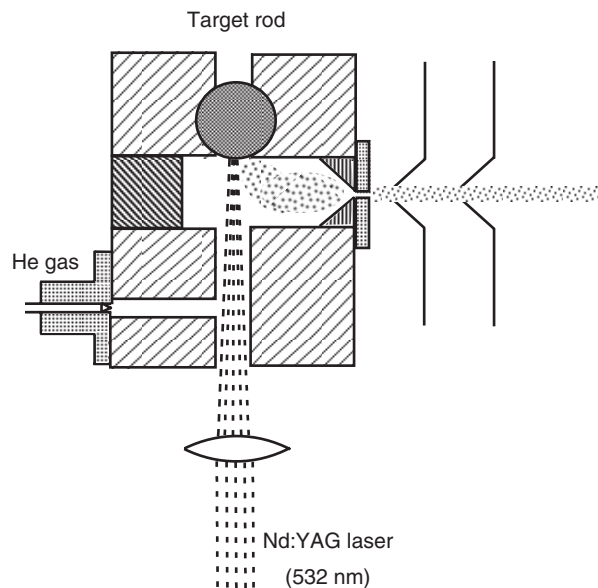


Figure 2. Schematical drawing of laser vaporization source.

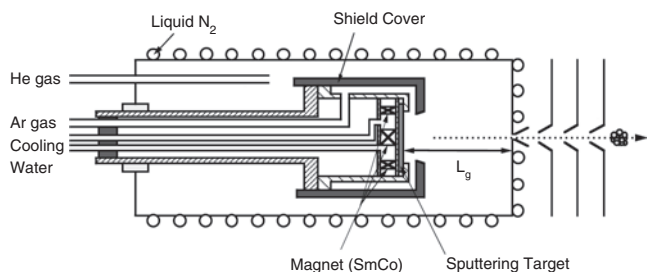


Figure 3. Schematic diagram of PGC type cluster deposition apparatus.

and the short circuit during the glow discharge operation. The metal vapors were generated from a target by dc magnetron sputtering. Clusters nucleate in a high pressure Ar gas atmosphere (0.2–0.7 kPa) and grow in the space between the target and the nozzle (the growth region), whose length, L_g , can be varied by moving the sputtering source back and forth. He gas was also introduced into the sputtering chamber from the backside of the source. The cluster beam was extracted through the nozzle of 5 mm in diameter by differential pumping and further collimated by the three skimmers.

Using the PGC cluster source, monodispersed size transition metal clusters were obtained as shown in Figure 4. The mean cluster size ranges from 5 to 15 nm in diameter with the standard deviation of size distribution less than 10% [84, 85].

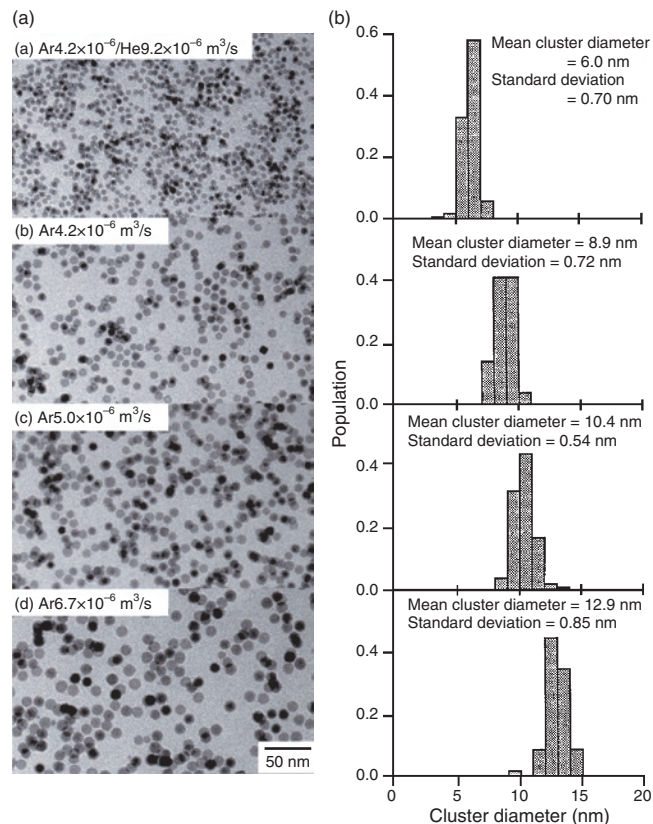


Figure 4. (a) TEM images and (b) size-distribution histograms of Cr clusters produced by plasma-gas-condensation cluster source.

2.5. Cluster Size Control Based on Gas Dynamics

The mass distribution of formed clusters is often measured by means of a time-of-flight mass spectrometer for free clusters and a transmission electron microscope (TEM) for supported clusters on certain substrates. The cluster size estimated from the TEM photograph is usually consistent with the mass distribution measured with a time-of-flight mass spectrometer except for the small clusters ($d < 2$ nm). In the bright-field imaging mode, such small clusters can hardly be distinguished from the background image of the amorphous carbon film. This is particularly true for the clusters whose orientation is not strongly diffracting, with respect to the incident electron beam direction. Another problem is that deposited atoms and smaller clusters can move on the substrate and coalesce to form larger clusters [98–100]. This effect will be observed when a large amount of atoms and smaller clusters ($d < 2$ nm) are produced in the cluster source.

As previously mentioned, the cluster size can be controlled in the PGC cluster source. The important experimental parameters are the sorts of the inert gas, their partial pressure (the mixing ratio) in the cluster source and the sputtering power [94]. According to the inert gas condensation process, the metal vapor is cooled by collisions with the cold inert gas atoms. In an isentropic flow of compressible fluids, a critical pressure p^* can be defined as

$$p^* = p_s \{2/(\gamma + 1)\}^{\gamma/(\gamma-1)} \quad (1)$$

where p_s is the pressure in the cluster source and $\gamma = 5/3$ the ratio of molar heat capacity for the monatomic He and Ar gases [101]. Within our experimental condition, the back pressure after the exit nozzle was much lower than p^* . In this case, the mass flow rate through the nozzle can be formulated by the following equation within the standard gas dynamics [101],

$$\dot{m} = \frac{A_n p_s}{\sqrt{k_B T_s}} \sqrt{\gamma m \left(\frac{2}{\gamma + 1}\right)^{(\gamma+1)/(\gamma-1)}} \quad (2)$$

where k_B is the Boltzmann constant, T_s the gas temperature in the cluster source, A_n the cross-section of the nozzle, and m the atomic mass of the inert gas. The drift velocity of the gaseous species in the cluster source, v_z , can then be estimated by the following equation (the perfect gas equation):

$$v_z = \frac{\dot{m} k_B T_s}{m A_s p_s} \quad (3)$$

where A_n is the cross-section of the cluster source. Combining Eq. (2) with Eq. (3), we can express the residence time of the gaseous species in the cluster source as follows:

$$\begin{aligned} t_s &= L_g v_z^{-1} \\ &= L_g \frac{A_s}{A_n} \sqrt{\frac{m}{\gamma k_B T_s} \left(\frac{\gamma + 1}{2}\right)^{(\gamma+1)/(\gamma-1)}} \end{aligned} \quad (4)$$

When p_s increases, the gases are more compressed at the nozzle and the flow rate of the exit gases increases. Accordingly, t_s becomes independent of p_s for the isentropic flow.

The important parameters to determine the cluster size are the residence time, t_s , and the gas pressure, p_s , in the cluster source. Based upon the cluster growth model by the inert gas condensation, the smaller cluster can be obtained when the residence time becomes shorter, because the total number of cluster-cluster and/or clusters-vapor atom collisions can be proportional to t_s . The t_s value decreases when the He gas is introduced into the cluster source, because the mass and viscosity of the He atom are one order smaller than those of Ar, and He gas is more effectively ejected than Ar gas. The nozzle temperature also influences the cluster size. According to Eq. (4), the residence time increases with decreasing T_s : the gaseous species flow more slowly in the cluster source. Therefore, the peak in the mass spectra shifts toward the lower mass side with increasing He gas flow rate, V_{He} , and T_s .

When the number density of vapor is increased, the clusters become slightly larger. In the first stage of the cluster formation, the atomic vapor condensation is thought to be the dominant process for promoting the cluster growth, where the collision frequency between the vaporized atoms affects the cluster size. With increasing P_w , the density of the vaporized atoms from the sputtering target increases so that the clusters become larger in such a stochastic process. Moreover, when the mixing ratio of the He and Ar gases and t_s are constant, the gas pressure in the cluster source, p_s , can also be an indicative parameter for the cluster size. The mean cluster size increases when increasing Ar gas flow rate, V_{Ar} , (and p_s). This result indicates that the nucleation and growth are promoted by the Ar gas pressure, because the collision frequency among the vaporized atoms and the inert gas increases proportionally to p_s . On the other hand, the sputtering yield is affected not only by the sputtering power P_w but also by p_s . It has been reported that the sputtering yield is suppressed with increasing p_s [102]. This trend can be interpreted as a result of the decrease of the mean-free path of the Ar gas: the incident energy of the Ar ions into the target decreases.

2.6. Cluster Formation and Growth

In the plasma-gas-condensation process, vaporized metal atoms from the target rapidly lose their kinetic energy by collisions with the inert gas atoms. The first step of the cluster growth is embryo formation by thermodynamical fluctuation through three-body collisions. This process is very difficult to analyze through a conventional collision dynamic because there are a lot of unknown factors and a lack of theory. These embryos are so small that they easily evaporate instead of growing to larger clusters [103].

The cluster formation strongly depends on the presence of nucleation centers such as impurity atoms, ions, etc., that is, heterogeneous nucleation. In this process, a large amount of the metal atoms are ionized by penning process [84, 97] and promoting the embryo formation. This dynamic process is predominating the condensation of atoms and clusters [95, 96].

When we consider the cluster growth, there are two major processes: (a) A cluster-cluster collision process: clusters react with each other, and (b) an atomic condensation process: the clusters grow with accepting atoms arrived on their

surface one by one. The model applied for the cluster-cluster collision is simulated by assuming that the clusters grow with conserving the total number of atoms in the system. Here, we need to introduce the supersaturation factor, S , which is related with the cluster radius, r , as follows [104]:

$$\ln S = \ln \frac{P_r}{P_\infty} = \frac{2\Gamma V_a}{k_B T r} \quad (5)$$

where Γ is the surface tension and V_a is the atomic volume. P_r and P_∞ are the equilibrium vapor pressure of the cluster with radius r and that of the plane surface, respectively. In the cluster-cluster collision process, one can neglect the evaporation from the cluster surface, because for large clusters, P_r becomes comparable to P_∞ . The kinetic equation for the collision process is given by the following equation [105]:

$$\frac{dn_k}{d\tau(t)} = \sum_{\substack{i+j=k \\ i \leq j}} C_{i,j} n_i n_j - \sum_i C_{i,j} n_i n_k \quad (6)$$

$$C_{i,j} = \pi(r_i + r_j)^2 \left(\frac{8k_B T}{\pi m_*} \right)^{1/2}$$

Here, n_k is the number of the k -size clusters per unit volume and the coefficient $C_{i,j}$ is a product of the collision cross-section by the mean speed between the i - and the j -size clusters. $r_i = r_1 i^{1/3}$ is the radius of the i -size cluster composed of i atoms, where r_1 is the atomic radius, and $m_* = m_i m_j / (m_i + m_j)$ the reduced mass, where m_i and m_j are the masses of the i - and j -size clusters.

This approach is based on the view that the growth rate for the k -size cluster is the total sum of the increasing number of collisions between i - and j -size clusters ($k = i + j$) and the decreasing number of the k -size cluster to a larger size cluster by collisions. The parameter $\tau(t)$ is the collision frequency [105];

$$\tau(t) = \int_0^t \sqrt{2} \sigma v_{th} \frac{n(\tau)}{V} dt' \quad (7)$$

where σ is the cross-section, v_{th} is the thermal velocity of the clusters, and V is the volume of system. Note that σ becomes larger when a larger cluster meets smaller clusters or vice versa, indicating that the smaller clusters disappear as soon as the larger ones are formed.

The results of this simulation are shown in Figure 5 by the broken lines, which are overlapped well with the size distribution estimated from the TEM results [90]. Here, we obtained $\tau = 120$ for the average cluster size of 2.7 nm. This value corresponds $t = 45$ s in Eq. (7), which is two orders longer than the real traveling time of 0.43 s for $L_g = 170$ mm. The cluster density decreases rapidly as clusters grow up and it takes much longer time for the cluster-cluster collision. Therefore, this collision process is not appropriate to explain the cluster growth in the PGC cluster source.

For the vapor condensation growth, we presume some embryos in the growth region. They can grow into larger clusters by a 2-body collision and the growth rate by adding only atoms that can be expressed as [64]:

$$\frac{di}{dt} = v_z \frac{di}{dz} = \sigma_{a,i} v_{th} n_0 (1 - \eta) \quad (8)$$

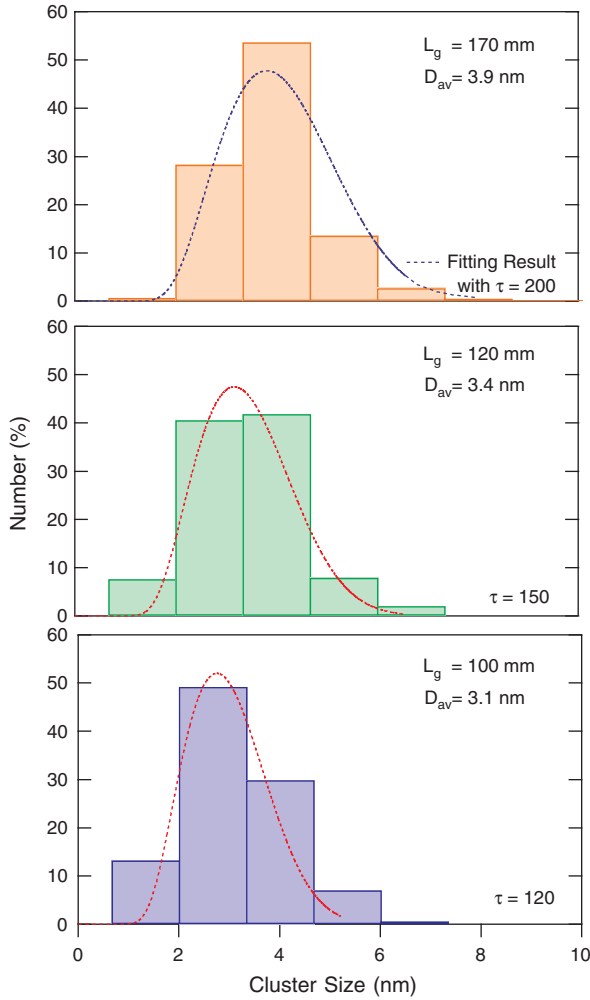


Figure 5. Size distributions of Ni clusters estimated from TEM image. Broken lines are the results of simulation based on cluster-cluster collisions. L_g is the growth length and D_{av} an average cluster size.

where i is the cluster size, v_z is the drift velocity of the materials as we estimated from the flow rate, and n_0 is the vapor density. η is a reevaporation-to-condensation rate factor, which considers the evaporation from the cluster surface. Note that η can be close to 1 if the cluster is small, that is, the reevaporation rate, ϕ_r , is comparable to the condensation rate, ϕ_c , because the latent heat of condensation of metals is large, for example, 4.4 eV for Ni at 0 K and 1 atmosphere. v_{th} is the mean velocity with the reduced mass of the i -size clusters, m_i , and the vapor atom, m_a , $m_* = m_i m_a / (m_i + m_a)$, and $\sigma_{a,i}$ is the collision cross-section between them [104]:

$$v_{th} = \left(\frac{8k_B T}{\pi m_*} \right)^{1/2} \quad \text{and} \quad \sigma_{a,i} = \pi(r_a + r_i)^2 \quad (9)$$

Here, r_a and r_i are the radii of the vapor atom and the i -size cluster.

A practical method of solving the differential equation of Eq. (8) is the estimation of η . A heat flow between the cluster and vapor has been discussed by Knauer [98] for the case of an adiabatic expansion. In his argument, the rate of

heat delivery from vapor to a cluster and that from a cluster to vapor should be equal during the cluster growth. For the PGC process, however, the latent heat can be removed by collisions with high dense inert gas atoms, that is, the clusters are not adiabatically cooled down. A simple explanation for η can be possible because vaporization is generally proportional to the vapor pressure [104]: ϕ_r is proportional to the vapor pressure above a cluster surface with radius r , P_r , (see Eq. (5)) and ϕ_c is commensurate to that of material atoms around the clusters, P_v

$$\eta \propto \frac{\phi_r}{\phi_c} = \frac{P_\infty}{P_v} \exp\left(\frac{2\Gamma V_a}{K_B T r_i}\right) \quad (10)$$

The main assumption here is that the density of vaporized metal atoms does not decrease with the cluster growth, that is, the density of cluster nucleus is low enough, so that they do not markedly consume the vaporized metal atoms during their growth to clusters. Equation (8) can then be solved numerically with setting the initial cluster size, i_0 .

The solutions of Eq. (8) as a function of the traveling length, z , corresponding to L_g , are shown in Figure 6 with different n_0 values with $i_0 = 7$ ($r_a = 1.24 \text{ \AA}$, $M_a = 9.7 \times 10^{-26} \text{ kg}$, $\Gamma = 1.7 \text{ N/m}$, $T = 300 \text{ K}$). The experimental cluster sizes obtained TEM observation are also indicated by the open circles and diamonds in the figure. The experimental cluster size at different L_g overlaps well with the solution lines obtained by assuming the atomic condensation process.

A recent theoretical method based on a combination of direct simulation monte carlo (DSMC) and a cluster collision model has simulated the effects of experimental parameters on size distribution of clusters [106–108]. The cluster

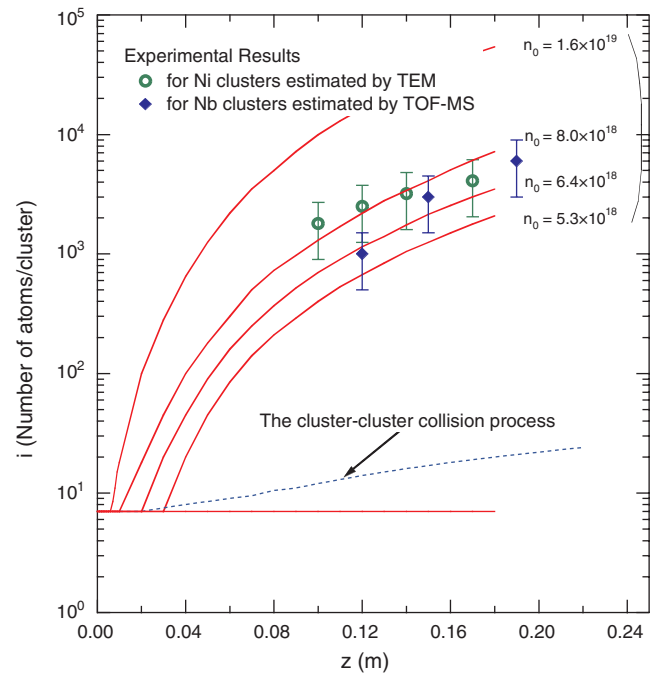


Figure 6. Cluster size-dependence on its traveling length obtained from the numerical solution of differential Eq. (8). n_0 is a vapor density of metal atoms.

size distributions are bimodal and affected by the flight path length, the temperature of the cooling wall, and the ratio of the material vapor to the inert gas. Several types of size distributions under various experimental conditions can be obtained by this model. These results roughly agree with the atomic condensation process [90]. Further work will be done to elucidate the region of magic numbers, by means of a new calculation scheme based on a combination of DSMC and the first-principles method.

2.7. Alloy Cluster Formation

Transition metals and their alloys have attracted much attention in material science. This is because of both the basic interest in research and technological applications as catalysts, optical and electrical devices, and magnetic material. Since the size effects are well understood in pure metal clusters, it becomes interesting to extend these studies to bimetallic clusters.

Depending on the synthesized methods, bimetallic particles form either homogeneous alloy, for example, solid solution and intermetallic compound, or segregated heterogeneous systems, for example, core-shell type. Au-Ag and Pd-Pt clusters have been produced by laser vaporization of alloy targets [109–112]. The optical absorption spectra show presence of the surface plasmon in the Au-Ag clusters, suggesting a heterogeneous structure [109, 110]. For Pd-Pt clusters, ion-scattering spectroscopy and photoevaporation experiments show that the Pd atoms exist mainly on the surface [111, 112]. Such small bimetallic clusters often exhibit the structure and phase stabilities, which are significantly different from those of the corresponding bulk materials. Spontaneous alloying behaviors have been systematically studied [113]. For example, the Zn diffusivity in Au clusters is at least 10 orders of magnitude faster than that in bulk Au. For an Au-Sn bimetallic system, two-phase separation expected from the bulk phase diagram are realized when the cluster size is larger than 10 nm; however, an amorphous-like phase is produced below 6 nm [114]. This result suggests that the cluster size, besides temperature, pressure, and composition, plays an important role in the phase diagram of the nano-bimetallic systems.

The cluster formation processes of the binary alloy systems have been investigated, that is, Ag-Nb, Co-Pd, Co-Al, and Co-Pt, using the PGC-type cluster source [115–117]. Figure 7 shows an experimental setup. Two targets are placed face-to-face, separated by 100 mm. The electric power is supplied independently for controlling the chemical composition of individual elements. The chemical composition and the size of these clusters were very sensitive to the experimental parameters, that is, sputtering power and inert gas pressure. The microscopic alloying in the nanometer-sized clusters is quite an interesting subject, because the chemical bonding in such small clusters is often different from that in bulk solids. For the immiscible Ag-Nb system, we have obtained Ag-Nb alloy clusters with sizes ranging between 5 and 10 nm in diameter [115]. The chemical compositions of clusters are measured by the EDX spectra using nano-electron beams. The estimated compositions are shown as a histogram in Figure 8. Their chemical compositions are broadly dispersed and partitioned into Ag-rich

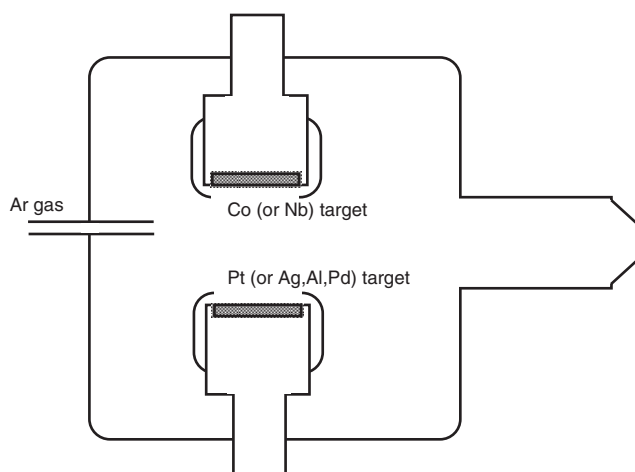


Figure 7. Schematic drawing of a facing-target-type PGC cluster source for preparation of alloy clusters.

and Nb-rich ones, being consistent with the immiscible-type equilibrium phase diagram. The Co-Pd is a homogeneous solid solution in all the compositional ranges of the equilibrium phase diagram. The Co-Pd alloy clusters with the mean cluster size of 6–8 nm show a rather broad distribution (± 10 at.%) around the average composition of 55 at.% Pd. The lattice constants estimated from the electron diffraction are shown in Figure 9(a), which are dependent on the Pd contents and following Vegard's law. The chemical compositions of the isolated cluster are also estimated by EDX spectra and shown in Figure 9(b) as a histogram. In the Co-Al system [116, 117], monodispersed intermetallic alloy clusters of CoAl with the B2 structure were formed for a composition range wider than that predicted by the equilibrium phase diagram, whereas in the Co-Pt system, CoPt alloy clusters formed the disordered fcc phase, which is a

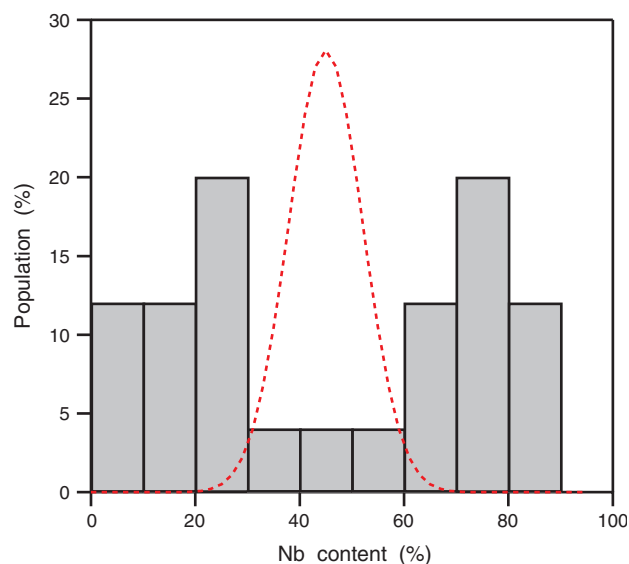


Figure 8. A chemical composition histogram evaluated from the nano-beam EDX spectra for Ag-Nb clusters. The dotted line indicates a binomial distribution for 45 at.% Nb.

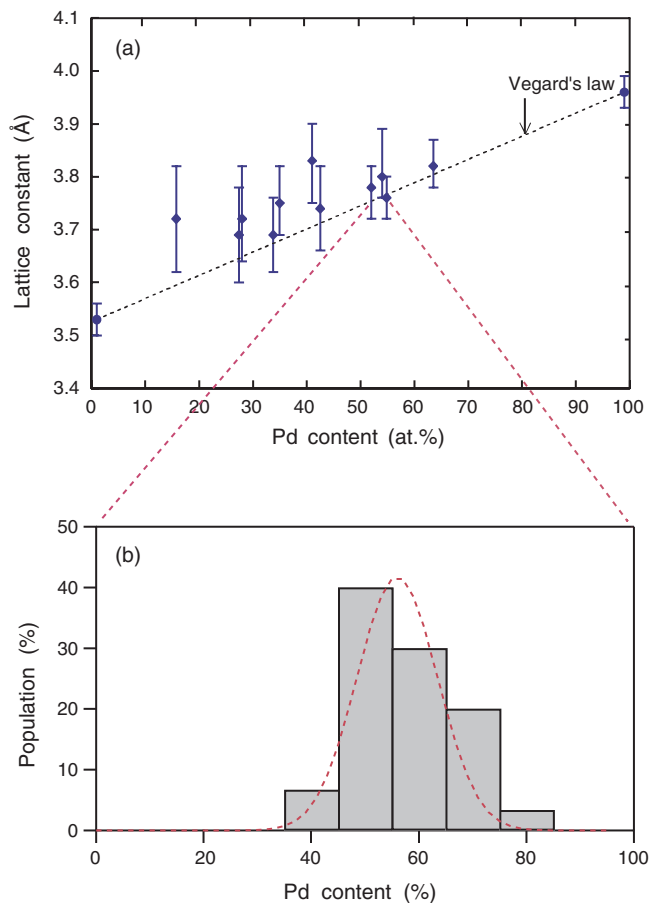
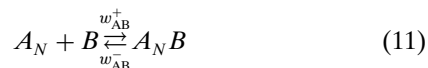


Figure 9. (a) Lattice constants estimated by electron-diffraction patterns as a function of Pd content and (b) a chemical composition histogram evaluated from the nano-beam EDX spectra for Co-Pd alloy clusters. The dotted line indicates a binomial distribution for 55 at.% Pb.

metastable phase at room temperature. The average size of CoAl clusters was about 12 nm, while that of CoPt ones were about 7 nm in diameter.

Considering an atomic condensation process, the cluster formation strongly depends on the presence of nucleation centers such as impurity atoms, ions, etc, that is, heterogeneous nucleation. In this process, a large amount of the metal atoms are ionized [84, 97] and promote the embryo formation [95, 96] as previously mentioned. For simplicity, we neglect this dynamic process and assume that the atoms and growing clusters are in equilibrium with the heat reservoir. The initial A-B alloy cluster formation will have the following reaction:



where w_{AB}^+ and w_{AB}^- are condensation and reevaporation probability, respectively, and we can simply describe as follows:

$$\begin{aligned} w_{AB}^+(i) &\propto z_{AB}(i) \\ w_{AB}^-(i) &\propto N_{\text{sur}} \exp(-E_s/k_B T) \end{aligned} \quad (12)$$

Here, $z_{AB}(i)$ is the collision frequency, N_{sur} is the number of atoms at the cluster surface, and E_s is the binding energy of atoms at the surface. Since E_s is related to the formation enthalpy of the alloy system, the cluster size and the chemical composition distribution are strongly dependent on the alloy formation enthalpy. For this reason, the reevaporation process from the cluster surface cannot be neglected on the cluster formation.

In the plasma-gas-condensation cluster source, the cluster size depends on the length of the growth region. With moving the sputtering target to change the length of the growth region in the cluster source, we measured the mass distribution of the Nb clusters by a time-of-flight high-mass spectrometer. This result indicated that the small clusters containing less than 200 atoms were mainly formed at a 50-mm distance from the target, corresponding to the middle point of the Ag and Nb (Co and Pd) targets in the present apparatus. One can simply take into account the mixing and reaction between two kinds of atoms. Provided that the Nb and Ag clusters, consisting of about 200 atoms, meet at the center position between the sputtering targets, they collide each other and form larger clusters. In the random collision and coalescence processes, the compositional distribution of the Ag-Nb and Co-Pd clusters, $I(m, N)$, as a function of Nb content, m/N ($m = 0, 1, 2, \dots, N$), should be binomial as follows [115]:

$$I(m, N) = \frac{N!}{(N-m)!m!} (1-x)^{N-m} x^m \quad (13)$$

where N is collision times and x the partial molar ratio. Here, we assumed $x = 0.45$ for Ag-Nb and 0.55 for Co-Pd, because the average composition taken by the wide range EDX analyses was almost 45% Nb and 55% Pd, respectively. The binomial distribution obtained for $N = 50$ is shown in Figures 8 and 9(b) by the broken line. The calculated composition distribution is well overlapped on the experimental result for the Co-Pd alloy system; however, it is inconsistent with that obtained for the Ag-Nb system.

Based upon the immiscible-type equilibrium phase diagram of Ag-Nb, the formation of the Ag-rich and Nb-rich clusters suggests that random reaction between Ag and Nb atoms and coalescence of their clusters are markedly suppressed due to their positive formation enthalpy. In the initial growth stage, reevaporation of Ag atoms (Nb atoms) from Nb-rich cluster (Ag-rich cluster) is plausible, because the Ag-Nb chemical bonding is much weaker than the Ag-Ag or Nb-Nb one. Consequently, Ag- and Nb-rich clusters containing their partner elements are formed to be metastable primary solid solutions. This feature is probably attributed to the compositional partition in the nonequilibrium formation process.

2.8. Crystal Structure of Supported Cluster

Besides the cluster size control, the cluster structure control is highly desired. In this context, Cr clusters are interesting because an A15-type metastable phase has been reported in Cr fine particles produced with inert gas condensation [118]. It has been also obtained in films and fine particles

produced by rapid quenching techniques such as sputtering, thermal evaporation, and inert gas-condensation methods [119–122]. It transforms to the equilibrium bcc phase on thermal heating, where the transformation is exothermic [123]. The A15 phase has been also obtained in other VIa group metals, that is, Mo and W, whose equilibrium phases are of a bcc structure [124]. The forming ability of the A-15 phase is very sensitive to the environmental conditions such as the presence of an O₂ and a N₂ impurity and temperature [118–122].

When the cluster size decreases, the contribution of surface energy becomes an important factor in determining the stable crystal structure. An equilibrium shape of a faceted small particle is determined as minimizing the total surface-free energy, G [125–128]:

$$G = \sum \gamma_i A_i \quad (14)$$

where γ_i is a free energy of a particular surface facet of area, A_i . According to the Wulff construction [129], this minimum-energetic shape at constant volume is mathematically equivalent to stating that the normal distance from a common center to any given surface facet is proportional to γ_i . This construction gives the equilibrium shape of a free-floating small particle. The most commonly reported structure of small sizes is a truncated octahedron combining (111) and (100) facets [130–132]. Quite often, single crystals are combined with particles containing simple twins or stacking faults. These are thought to occur either by growth mistakes, by coalescence of multipositioned particles during epitaxial growth or due to internal strain, for instance, by a martensitic transformation [133].

Although small particles ($d < 10$ nm) are often single crystals, a common exception is multiply-twinned particles (MTP) in fcc metals such as Cu, Ag, and Au [125, 134, 135]. The presence of MTP structure depends strongly on how the clusters are prepared. Five tetrahedral packed along (111) faces can be arranged to form a decahedral MTP (pentagonal bipyramid) and 20 units, an icosahedral MTP. The distortion required for a decahedral cluster corresponds to a simple angular gap or wedge of about 7.5°. The distortion for an icosahedral cluster corresponds to six disclinations running along the directions of the center to apexes [127, 128].

The small clusters are fluctuating and do not have a sharp melting temperature. A number of Molecular dynamic calculations have been performed and both structural transformations and coexistence between solid and liquid states (quasi-melting) have been reported [136–139]. There is also some data supporting dynamic structural changes in clusters [140–142]. The phenomenon of the quasi-melting seems to be fairly common in many different materials.

3. CLUSTER DEPOSITION AND ASSEMBLING

3.1. Cluster Deposition

The practical way to build nanostructured assemblies of gas-phase clusters is to deposit free clusters onto a substrate in a controlled manner. This method usually employs a pulsed or

continuous cluster beam source, which is a combination of consecutive carrier gas injections into a cluster source chamber and a subsequent multiple differential pumping process. There are several ways to control the deposition conditions which, hence, affect the structure and properties of resulting assemblies. If clusters are ionized, their kinetic energy is readily controllable by an electric field acceleration [56, 85, 143, 144]. The heat treatment of free clusters prior to the deposition is also effective to tune their atomic structure and external morphology [145, 146]. The deposition of multiple cluster beams (or atomic vapor) of different substances is useful for the fabrication of compositionally tailored nanoscale composites [147–152]. Surface modification of clusters by injecting a small amount of reactive gas gives rise to a core/shell structure, which enhances structural and chemical stabilities and exhibits unique magnetic properties and electron transport phenomena [93, 153–156]. The size selection techniques of incident clusters (*e.g.*, using a quadrupole mass spectrometer) enable one to deposit exactly size-defined clusters on substrates to investigate the size effect on the morphology and other properties [157–162].

3.1.1. Low- and High-Energy Cluster Impact on Surface

The kinetic energy of incident clusters is a primary parameter to control surface mobility of deposited clusters; it induces a lateral migration of the deposits even on a surface of a low-temperature substrate. When the clusters generated in a high-pressure cluster source pass through a small aperture into a higher vacuum chamber by differential pumping, they form a collimated cluster beam. The velocity of the ejected clusters reaches a supersonic regime by the gas expansion. The typical kinetic energy of these clusters is of the order of 10 eV per cluster (*i.e.*, $\sim 10^{-3}$ eV per atom for a cluster consisting of 10^3 atoms) [163], which is sufficiently smaller than its binding energy of the constituting atoms (several eV per atom). Thus, the clusters are softly landed on a substrate surface, preserving their original size and internal atomic structure without fragmentation. The cluster deposition with such low kinetic energy is usually referred to as a low-energy cluster beam deposition (LECBD) [4]. The films made by this method are sooty and porous [156, 164, 165], being analogous to the accumulation of snowflakes, having a low cluster-cluster and cluster-substrate adhesion.

When incident clusters possess a sufficiently high energy, the situation is markedly changed. A simple way to inject such high-speed clusters is achieved by accelerating ionized clusters with an electric field [56, 85, 143, 144]. The accelerating voltage is usually 1–30 kV, which corresponds to the kinetic energy of 1–30 eV for an individual atom of clusters consisting of $\sim 10^3$ atoms. Since this energy is comparable to or larger than the binding energy of the constituting atoms, it results in a deformation of the internal structure and/or partly in a fragmentation into atoms and/or small clusters on impact. These break-up processes effectively fill the micropores in the assemblies, and the released energetic atoms have a high mobility on substrate to effectively find out energetically favorable sites.

As mentioned in the previous section, this idea was first developed by Takagi and Yamada at Kyoto University

[56, 57], using the ionized cluster beam (ICB) deposition technique. They used highly accelerated ionized clusters to fabricate high quality thin films, such as epitaxy [166, 167]. This process is originally designed to deliver highly energetic adatoms onto a substrate surface without any heating process of the substrate, implantation effect of adatoms, and charging problem. However, it recently turns out that only small clusters are generated in the ICB method [62, 64–68].

Based on the same concept, Haberland et al. clearly demonstrated the effect of accelerating energy of incident clusters on its morphology using an alternative sputtering-type cluster source [85]. Molecular dynamic simulations suggested that each impacted cluster makes a local hot spot ($1\sim 2 \times 10^4$ K), which gives rise to a partial melting and mixing of atoms at the cluster/substrate interface [168, 169]. This process does not cause a complete fragmentation of clusters into atoms even at the accelerating energy of 10 keV. They also showed that highly accelerated energetic clusters can fill micron-sized holes on substrates [85]. The films produced are highly dense, smooth, and strongly adhering. A similar energetic cluster deposition via a high-pressure gas expansion also produces a densely packed particle compact (the gas deposition method [170]). The energy threshold dividing the low- and high-energy cluster deposition is approximately 0.1~1 eV per atom [163].

3.1.2. Diffusion and Migration on Surface

Deposited clusters exhibit a surface migration. They resemble adatoms as seen in thin film growth. The temperature dependence of diffusion coefficients indicates that the migration of clusters is a thermally activated process [171]. Atomic diffusion mechanisms are proposed for small 2D clusters that are epitaxially grown on substrates [163, 172–174]. One of them is the periphery diffusion model, where the rearrangement of peripheral atoms diffusing along the cluster edge causes a net displacement of the center of mass [163, 172, 173]. This model was experimentally confirmed by the field ion microscopy studies for small rhodium [172] (or iridium [173]) islands (<20 atoms) epitaxially grown on a rhodium (or iridium) substrate, respectively. However, the periphery diffusion model is not applicable for much larger 2D clusters containing several hundreds of atoms (*e.g.*, Ag clusters on Ag substrate [174]), which exhibit a relatively high mobility. This, in turn, can be accounted for by the evaporation-condensation model that includes the evaporation and subsequent condensation process of peripheral atoms [163, 174].

These two atomic diffusion models, however, cannot explain the very high mobility that was reported for larger 3D clusters of gold and antimony nonepitaxially grown on a graphite surface [175]. Its diffusivity is larger by several orders of magnitude than those observed for small 2D epitaxial islands. A collective atom motion mechanism, where the entire cluster migrates as a rigid object, seems to be more plausible in these systems [163, 175–177]. A weak cluster-substrate bonding is also a key factor for the rapid diffusion [171].

The kind of substrates also affects the surface mobility of clusters. In the case of antimony clusters, the deposits exhibit a high mobility on a highly oriented pyrolytic graphite

(HOPG) substrate, leading to a fractal morphology [4, 175]. In contrast, an amorphous carbon substrate reduces a mobility compared to the HOPG, mainly due to the presence of a higher density of defects on the surface that traps the clusters [4]. No fractal morphology can be seen at all in this case; isolated clusters are instead observed [178]. Such a nearly diffusionless deposition can be regarded as a random pavement process of the substrate.

The morphology of cluster assemblies is accomplished by a specific growth process characterized by their diffusion and coalescence. At the very early stage of deposition, the deposited clusters migrate on the surface and trapped at energetically favorable sites with surface steps or lattice defects. Subsequent deposition gives rise to the growing number of clusters, and the parts of which start to contact each other. The coalescence behavior of the touching clusters is governed by a critical size, above which no merging has occurred [4, 163, 171]. This is arising mainly from the size-dependent melting temperature of clusters. In general, a smaller cluster has a lower melting temperature [179–181], leading to an increased ability to merge. If at least one of the clusters is smaller than the critical size when two clusters meet on the surface, they merge into a single large cluster like Ostwald growth. If both clusters are larger than the critical size, they preserve their original size without merging (memory effect).

3.1.3. Deposition-Diffusion-Aggregation (DDA) Model

A simple model based on the thin-film growth process has been developed by Jensen to simulate the cluster deposition and aggregation phenomena [163]. This model relies on three dynamical processes: deposition, diffusion, and aggregation of clusters on a substrate. In the deposition step, clusters are assumed to be deposited at randomly chosen places with a fixed flux density. All the supported clusters then move on the substrate in random direction at every diffusion time (the diffusion step). If two clusters come to side-by-side positions, they stick to form an immobile aggregate that cannot be reversibly separated (the aggregation step). Detailed computer simulations based on the DDA model suggest that a cluster dimmer becomes immobile on a substrate surface [175]. It is found that the DDA model reasonably reproduces the experimental results for Sb cluster deposition. Comprehensive reviews on the dynamical behavior of deposited clusters on substrates have been presented by Jensen et al. [163, 182].

3.1.4. Matrix Embedment of Clusters

The surface migration of clusters is effectively suppressed by codepositing atomic vapor of different substances. In this method, the deposited clusters are embedded in the vapor-deposited matrix, resulting in physically well isolated clusters [147–152]. Chemically passive isolation was achieved by using inert gas matrices (*e.g.*, Ar gas) on low-temperature substrates [183, 184], on which the thermally activated surface migration is fairly suppressed. In recent years, much attention has been paid to metal cluster assemblies embedded in insulating matrices for the study of electron transport phenomena [151]. The formation of magnetic

granular materials, in which magnetic clusters are embedded in a nonmagnetic matrix, is also an attractive candidate to apply the codeposition technique to study characteristic spin-dependent transport phenomena.

3.1.5. Deposition on Patterned Substrates

An atomic step on a surface acts as a preferential nucleation site against migrating clusters [99, 161]. The diffusion behavior of small silver clusters on the stepped surface of HOPG substrates was extensively studied [143, 144, 158, 161]. These studies showed that the migration of trapped clusters is strongly confined along the edge of the step [99, 161]. Another feature is a reduced mobility of clusters at the step rather than at the flat terrace of the surface, resulting in a reduced ability for clusters to aggregate at the step. All of these features are preferable to form a 1D chain of clusters whose incident size is almost retained [99, 161].

Artificial modification of atomic defect density on surfaces causes the change in morphology of deposits. Ion irradiation on a HOPG substrate creates a number of nanosized hole defects on the surface, which then act as effective traps against migrating clusters. The experiments of gold cluster deposition show an increased nucleation density of small cluster aggregates on an irradiated substrate rather than the characteristic ramified islands (*i.e.*, fractal morphology) seen on a nonirradiated substrate [185]. A focused ion beam nanoengraving technique is applied to create a regular array of nanosized holes, at around which a bunch of clusters are trapped together [185, 186]. This technique has a potential productivity of a 2D array of organized clusters, where clusters are precisely positioned on the surface planed. A lithographically patterned regular structure is also a candidate to control the nucleation sites. Shown are copper clusters that are adsorbed at the sloped edge of a mesa-type resist strip on a silicon substrate [187]. A slanting incidence of clusters against a substrate induces its lateral mobility and lets the deposited clusters fall into lithographically generated gaps [188].

3.2. From Discontinuous to Continuous Networks

3.2.1. Background of Percolation Concept

The self-organizing process of clusters on a substrate can be regarded as a percolation phenomenon, which deals with any kinds of growing connections among constituents. In this theory, the interconstituent connections grow into macroscopic networks over an infinite range as the number of connections is increased. During deposition, the physical properties of cluster assemblies evolve from isolated state to a highly correlated one due to the physical and/or chemical interactions among clusters. Good textbooks and reviews on percolation theory are available in [189–191]. The analytical treatments based on this theory can provide a quantitative understanding of the macroscopically averaged features of complex cluster assemblies during the deposition.

The percolation theory was originally developed by the lattice percolation model, in which each constituent is placed on a regular lattice site and connects adjacent neighbors. In

this model, the networks of site occupation or bond connection are considered. Disorder of constituent sites was then introduced to develop the continuum percolation model, which is suitable to account for the random deposition process of clusters on substrates. In this model, identical circles (or spheres in 3D) are distributed at random with permission of partial overlapping. If two circles (or spheres) are overlapped, they are considered to be connected. Besides these discrete bonding states (connected or disconnected), nonunique bonding strength is also taken into account in the soft-percolation (or fuzzy percolation) model [192, 193], depending on the distance between two sites.

The most distinguishing feature in percolation phenomena is the critical behavior that can be seen near the percolation threshold, at which many physical properties are drastically changed. One of the examples is the geometrical size of networks [189–191]. As the concentration of site occupation or bond connection is increased, the geometrical size of site-occupied or bond-connected networks becomes larger in a nonlinear fashion. At around the percolation threshold, the networks show an extreme exponential growth, spreading out to an infinite range across the system. Another example is a drastic change in electrical conductivity of the percolating systems, which consist of a mixture of conducting and nonconducting constituents [23, 194, 195]. At around the threshold, the conducting paths of electrons steeply grow into a macroscopic scale across the system, giving rise to an insulator-to-metal transition.

This critical behavior can be described by a simple scaling law with a few characteristic parameters such as the critical exponent μ and the percolation density x_c (*i.e.*, the concentration of occupied sites or bonds):

$$P(x) \propto (x - x_c)^\mu \quad (15)$$

where $P(x)$ is the value of a selected physical value and x_c the critical (or threshold) percolation density. The parameters of μ and x_c exhibit an invariant feature [189–191], depending almost only on the spatial dimensionality of the system and being insensitive to other details such as the lattice structure. For instance, theoretical estimations for ordinary lattice percolation systems without overlapping predict that the threshold volume fraction (or surface coverage) is about 0.15 in 3D and 0.45 in 2D [196]. Partial overlapping, seen in the continuum percolation systems, increases these threshold values to 0.29 in 3D and 0.68 in 2D [190]. The attractive interactions among the constituents also modify the threshold values due to the inhomogeneous aggregation of the constituents [197]. The critical exponent μ shows the universal values: $\mu = 1.1\sim 1.3$ in 2D and $1.9\sim 2.1$ in 3D.

3.2.2. Percolation Analysis of Cluster Assemblies

The cluster deposition is considered to be a random site-occupation process of clusters on a substrate, where the isolated clusters are connected to one another to form cluster networks as the deposition is proceeded. This technique provides an ideal percolation system that can never be achieved by the conventional material processes, such as mixing two powders and/or codepositing two vapors; it allows one to

vary the concentration (or coverage) of clusters and the cluster size independently. Here, we will show our results of analyzing the assembling process of Co clusters in terms of the evolution of their morphological, electrical, and magnetic properties [91, 92, 198, 199]. The PGC cluster deposition apparatus [88, 89] described in Section 2 was used to carry out this experiment.

Geometrical Percolation Figure 10 shows typical TEM images of 6.0-nm Co clusters deposited on a carbon-coated TEM grid at the early stage of deposition. The thickness, t , of the deposits is defined by the effective mass that was measured by a crystal quartz thickness monitor. The supported clusters are well separated on the substrate at $t = 1$ nm. As t is increased, they connect each other to form 2D networks. At $t = 4$ nm, the cluster network extends over the observed

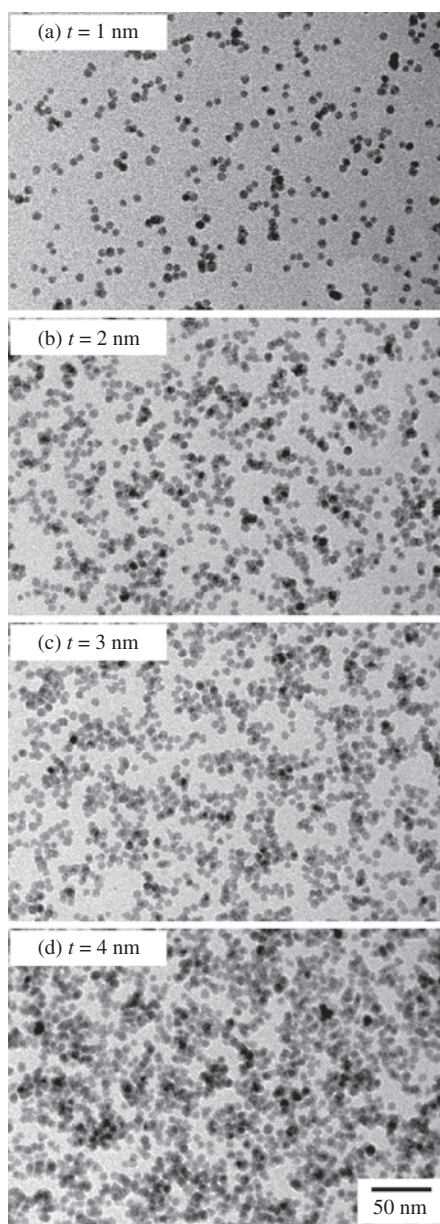


Figure 10. TEM images of 6.0-nm Co clusters deposited on carbon-coated TEM grids as a function of the effective thickness, t .

area of about 1.5×10^5 nm². This indicates that the critical thickness, t_c^{geo} , for geometrical percolation is about 4 nm. The increase in t_c^{geo} is observed with increasing the Co cluster size. This is ascribed to the increased number of atoms in the surface normal direction, which does not contribute to the surface coverage, due to the increased cluster height for larger clusters.

In this Co cluster deposition, the critical coverage, p_c , is found to be independent of the cluster size ($p_c \sim 0.63$) [91, 92], being inconsistent with the theoretical prediction of universality of p_c . However, the value is much larger than the ones theoretically predicted in the ordinary 2D lattice percolation systems ($p_c \sim 0.45$) [196]. This discrepancy is attributed mainly to the partial overlap of the deposited clusters, which results in $p_c \sim 0.68$ in a 2D continuum percolation system of overlapped circles [190]. This value is reasonably close to the present result. Magnetic dipolar interactions could also contribute in part to the increase in p_c [197].

When the cluster size becomes much smaller to become a molecular regime, the percolation characteristics are different from the above results owing to the different mobility and coalescence behavior of the deposits [200]. The Sb_n cluster deposition ($n = 4$ and 1850) on a glass substrate showed that p_c decreases with increasing the cluster size: $p_c = 0.95$ for $n = 4$ and $p_c = 0.48$ for $n = 1850$. For small clusters ($n = 4$), they are easy to migrate on the substrate surface and coalesce into isolated larger clusters by 3D film growth. This increases the percolation threshold. For large clusters ($n = 1850$), they are trapped near their impinging sites, without severe migration, and exhibit pseudo-2D film growth, which effectively paves the substrate surface, leading to a lower percolation threshold.

Electrical Percolation Electrical percolation was studied by the electrical conductivity measurements [91, 92, 199]. Figure 11 shows a typical example of *in-situ* measurement of electrical conductivity, σ , as a function of t during the deposition of 6.0-nm Co clusters. For $t < 4$ nm, σ is negligibly

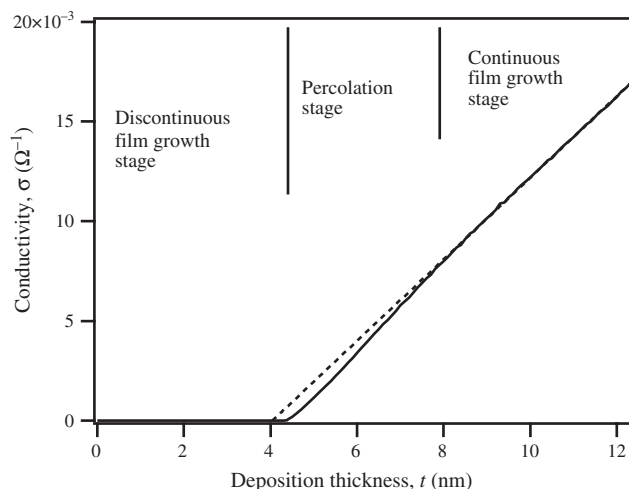


Figure 11. *In-situ* measurement of electrical conductivity, σ , as a function of t during the deposition of 6.0-nm Co clusters on a glass substrate.

small due to the discontinuity of the cluster network (*i.e.*, the discontinuous (2D) film growth regime). At $t \sim 4$ nm, the conductivity σ suddenly starts to increase due to the onset of the formation of macroscopically continuous networks. For $t > 8$ nm, σ increases linearly with increasing t (*i.e.*, the continuous (3D) film growth regime). The percolation stage corresponds to the thickness range of $t = 4\sim 8$ nm, where the measured data deviate from the straight dotted line that is extrapolated from the data for $t > 8$ nm. In this region, the number of conduction paths yields an exponential increase with increasing t . The critical exponent, μ , and the critical thickness, t_c^{elec} , can be evaluated by fitting the data with the scaling law.

The detailed analysis revealed a nonuniversal behavior of the electrical conductivity: the conductivity critical exponent μ increases from 1.1 to 1.8 by increasing the cluster size from 6 to 13 nm [91, 92]. The μ value of 1.8 is almost close to those for 3D percolation [201], although 2D growth of deposits is confirmed by TEM observations. This result can be accounted for by the soft-percolation model, which takes into account the wide distribution of connectivity between clusters [192, 193]. This model suggests that the electrical connectivity between clusters becomes wider for larger cluster size. The origin of such wide connectivity for larger clusters is possibly attributed to the heterogeneous interface structures between clusters (*e.g.*, lattice defects or imperfect contacts), associated with the increase in melting temperature relative to the smaller clusters. Raising the temperature of substrate leads to a delay in the onset of the electrical percolation owing to the mutual coalescence of clusters [199].

Magnetic Percolation Magnetic interactions among clusters also extend to grow into a network during deposition. One of the noticeable features is the enhanced stability of ferromagnetism of the assemblies [198, 202]. For clusters whose size is small enough to exhibit superparamagnetism, the magnetic state of the assembly changes from superparamagnetic for isolated clusters to ferromagnetic for networked clusters as deposition proceeds. Figure 12 shows the evolution of magnetic coercivity, H_c , for Co clusters with

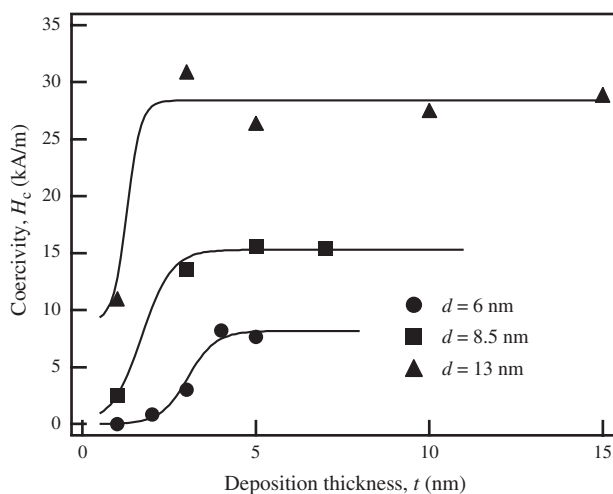


Figure 12. Magnetic coercivity, H_c , for Co clusters with various sizes as a function of t .

various sizes as a function of t . It should be noted that H_c rapidly increases with increasing t at the very early stage of deposition and then saturates. These saturated H_c values do not markedly change for thicker films with a 100-nm thickness [165]. This suggests that the magnetic interactions give the assemblies an additional magnetic anisotropy that effectively suppresses superparamagnetism.

Another feature of the cluster assemblies can be highlighted by comparing the result of Figure 12 with those of magnetic granular films [202], in the latter of which nanometric magnetic granules are precipitated in nonmagnetic matrices via a heat treatment. In the latter films, the H_c markedly enhanced at around the geometrical percolation threshold, and then rapidly decreases with further increasing the content of magnetic materials [202]. This rapid reduction in H_c is attributed to the change of a magnetization mechanism from rotation to wall motion. Based on the fact that H_c is roughly constant for our thicker assemblies of Co clusters, the magnetization mechanism is still in rotation mode as for the isolated clusters. This implies that the original nature of the clusters is well preserved even after they are assembled.

4. SPECTROSCOPIC CHARACTERIZATION

4.1. Transmission Electron Microscopy

Transmission electron microscopy has been widely used to characterize atomic structures and nanoscale morphologies of cluster assemblies. Since electron microscopes operate at high acceleration voltage (usually 100–400 keV), the electron wavelength is much smaller ($\sim 10^{-3}$ nm) than the atomic size and interatomic distance of substances. This gives rise to a good atomic resolution with relatively simple operations, and hence, it becomes almost an indispensable technique for nanoscale structural characterizations in the current cluster research. So far, the application of TEM has been largely limited to noble metal clusters such as gold and silver, mainly because of their chemical stability against oxidation. These clusters are usually well isolated on substrates, resulting in a simple image interpretation. Some review articles on the electron microscopic studies on the cluster structures are available [203, 204]. In this section, we shall give a brief overview on TEM observations of individual transition metal clusters and their assemblies, including some results of noble metals and metalloids. To see general principles on TEM, some good literature is provided [205–207].

4.1.1. Bright- and Dark-Field Imaging

Conventional bright-field imaging is the most common TEM mode to see the shape and size of supported clusters on substrates. Historically, the external shape of gas-evaporated ultrafine particles has been extensively studied by the groups in Japan, largely contributed by researchers at Nagoya University [131, 208–215]. They performed serial structure characterizations for particles of transition metals (V, Cr, Mn, Fe, Co, Ni, Cu, etc.) and alkaline metals (Be, Mg, Ca, etc.), whose typical sizes range from submicron to micrometer order. The particles are usually well faceted

with distinct crystallographic planes. Even a single element particle exhibits multiple particle shapes, depending on their atomic structures and synthetic processes. They reported, for instance, that bcc metal particles (Fe, V, Nb, Ta, Cr, Mo, W) show a single type of crystal habit: the rhombic dodecahedron with (100) planes and its truncated variants [213]. Fcc metal particles (Ag, Au, Co, Ni, Cu, Pd) were found to exhibit the octahedron and its truncated variants when they are a single crystal [131]. Fcc metals also show characteristic twin-related structures when they are not a single crystal. The typical forms are a pentagonal decahedron and an icosahedron, which have been found in vacuum-deposited Au islands on single-crystalline substrates of alkali halides [125, 134, 216]. There, the pentagonal decahedron and icosahedron consist of 5 and 20 tetrahedral crystallites, respectively, which are packed together with their (111) planes bounded [125, 134]. This arrangement generates a twin boundary at each interface and a particle having such twins is called a MTP. Since the tetrahedra cannot fully fill the entire space in the particle, inhomogeneous lattice strains are locally introduced. A similar twin-related form has also been found in needle-shaped Ge precipitates in an Al matrix [217]. There are also other shapes that are related with decahedron: the star decahedron [218], Marks decahedron [203], and the round decahedron [219]. Thermodynamical consideration based on the Wulff construction [220] was provided to account for the appearance of these various external shapes of unsupported particles. The theory requires a minimization of surface-free energy of the particles, resulting in characteristic crystal habits. However, the experimentally observed structures are not necessarily consistent with these Wulff shapes owing to the significant effect of particle growth kinetics [203]. The results are well summarized in [9].

The bright-field imaging is also useful to characterize overall morphology of cluster assemblies, as well as individual particles. When gas-phase clusters are deposited on a substrate, the geometrical connections between the clusters are developed. The connectivity in an early stage of the deposition can be quantitatively evaluated by image analysis of the bright-field micrographs. Using this method, the morphological evolutions during the assembling process of deposited Co clusters were studied in terms of the percolation theory [91, 92]. Assembling processes of other sorts of clusters (e.g., Bi [221, 222] and Sn [178, 200]) have also been observed. The bright-field observations also revealed the characteristic thermal stability and instability of cluster assemblies. The temperature-dependent observations of the morphological change of Co cluster assemblies showed a severe coalescence behavior between contacting clusters at elevated temperatures ($T \geq 250$ K) [199, 223]. Thermally sintered experiments of unsupported FePt clusters in a cluster beam showed that the increased sintering temperature improves the shape and crystallinity of the particles from a poorly crystallized, irregular shape to a regularly faceted, multiply twinned structure [145, 146]. When magnetic clusters having a stable magnetic moment are deposited, they prefer to form chains to reduce the magnetostatic energy [208, 224]. Applying an external magnetic field leads to a strong tendency of forming linear chains along the field

direction. This yields an anisotropic magnetic behavior with respect to the chain direction.

It is a hard task to observe a thick deposit assembly by TEM, largely owing to the difficulty in thinning the fragile specimen through which the electrons are sufficiently transmissible. There is an article in which the cross-sectional view of a softly landed Sb cluster film, showing a granular morphology where the incident cluster size is relatively retained [4]. This morphology is fairly well explained by the ballistic deposition model [225], where incident particles are impinged on the surface and stuck to the supported particles after physical contact.

Dark-field imaging is a complementary technique against the bright-field imaging. It uses only the diffracted beams instead of the nondiffracted (or direct) beam to form the images. The objective lens aperture is necessary to select the diffracted beams. When a specific diffracted beam is chosen, the resulting dark-field image contains bright contrast regions from which the same Bragg diffraction takes place. This technique is powerful in characterizing the atomic structures of polycrystalline particles and in analyzing the structural heterogeneity of multiple-phase clusters. A good example can be seen in the structural determination of MTPs [125, 134, 216].

4.1.2. High-Resolution Electron Microscopy

High-resolution electron microscopy (HREM) is capable of directly imaging local atomic arrangements of clusters. This technique is particularly useful for the structural characterization of nanosized clusters less than 10 nm. Many experiments have reported the frequent appearance of various atomic structures that do not exist in the corresponding bulk substances as equilibrium states. A prominent example is the increased stability of icosahedral and decahedral structures over fcc for smaller clusters. This has been first found in Au clusters [125, 134, 216], followed by other fcc metals such as Ag [226]. High-resolution electron microscopy observation of thermally sintered, unsupported fcc FePt clusters show an increased stability of icosahedral structure as the sintering temperature is increased [145, 146]. Even bcc metals (e.g., Na [227]) has an icosahedral form when the particle size is sufficiently small. Recent computer simulations also support the similar structural transitions from fcc to icosahedral or decahedral structures for various types of potentials as the cluster size is reduced: Lennard-Jones clusters [227–230], Au clusters [231, 232], and Morse potentials [233, 234]. Since the energy difference between the competing forms is very small, slight modifications of surface faceting are sufficient to transform from one structure to another. A recent simulation result pointed out the significance of entropic contribution to the free energy to determine the stable structure of small clusters [235, 236].

Combining the high-resolution imaging and a video recording techniques, *in-situ* observations of dynamic structural change can be carried out. Structural fluctuation of supported Au clusters (~ 2 nm) was first observed by Iijima and Ichihashi [141] and Smith et al. [237] at nearly the same time. They clearly showed the real-time rearrangement of constituting atoms and the transformation between different

forms of the particles. It is interesting to point out that even a 2-nm Au cluster exhibits a distinct crystal habit. The possible reasons for this structural instability have been raised thus far in terms of a Coulomb explosion [238], an Auger cascade [239], a charging effect [141], and an electron beam heating [237, 240]. After these findings, similar experiments have been done using different substances [240, 241].

Another interesting topic of *in-situ* electron microscopy is the *in-situ* experiments in electron microscopes. Mori et al. installed small evaporation sources in a TEM column and observed time-resolved alloying phenomena of small clusters [242–245]. They found that small clusters are spontaneously alloyed in a very rapid fashion that cannot occur in the equilibrium state. These *in-situ* experiments highlighted a marked instability of small clusters even at room temperature.

4.1.3. Electron Diffraction

Transmission electron microscopy also provides reciprocal-space diffraction patterns as well as real-space images. Since electrons have very large scattering cross-sections compared to X-rays and neutrons, a small amount of specimens are sufficient in detecting sizable diffraction intensities. The electron diffraction experiments are performed either in a relatively large region using a selected area aperture (the selected area diffraction) or in a nanometer region using a nanosized probe (the nanodiffraction), the latter of which allows us to examine the atomic structure of a single cluster. The selected area diffraction experiments have been applied to various sorts of clusters, resulting in the findings of a variety of nonequilibrium phases. The high temperature phases in an equilibrium phase diagram occasionally appears in small-sized clusters, such as fcc phase for Co clusters [198, 246] (the hcp phase is stable at room temperature) and chemically disordered fcc phase for stoichiometric FePt clusters [145] (the chemically ordered L1₀ tetragonal phase is stable at room temperature). Entirely different structures from the bulk phases have also been found, like A15 structures for Cr [118], Mo, and W [213] clusters.

4.2. Scanning Probe Microscopy (SPM)

Scanning tunneling electron microscope (STM) and atomic force microscope (AFM) are powerful tools in understanding the surface structure and morphology of all kinds of materials [247, 248]. The nanometer scale surface modification is also possible by controlling the bias voltage, the tunneling current, and the distance between tip and surface in an STM system [249]. The surface atoms and clusters are manipulated by application of high bias voltage which induces the electric field intensity of 10⁸ V/cm and the current density of 10⁶ A/cm². Using the powerful STM technique, we can also study physical properties of material surfaces in nanoscale, such as local density of states (LDOS), friction coefficients, adhesion force, etc. and a magnetic domain structure using a magnetic tip, that is, magnetic force microscope (MFM). An SPM includes all of these sophisticated techniques [250, 251].

One of the central issues of clusters deposited on the substrates is the intercluster interaction—integrity and interaction between cluster and substrate. The lateral dimensions of the transition metal clusters as imaged by the STM depend

on the curvature radius of the tip used. The apparent height of clusters is much closer to the actual cluster diameter or size measured by TEM and mass spectrometry. During the annealing process, surface diffusion of clusters is much enhanced on HOPG substrate, leading to the creation of the fractal-type cluster assemblies [252, 253]. The similar process on the Si(111) surface leads to a surface modification of Si atom sites in close vicinity to clusters up to 850 K. When clusters are deposited on the strongly interacting surface, the cluster shape changes from that of the free cluster in the gas phase. It has been reported that Ag₁₉ clusters are almost spherical in the gas phase probably because the shape is governed by the electronic structure. When Ag₁₉ clusters are soft-landed on a Pt(111) surface, a regular hexagon with a monoatomic height is observed by the STM [254, 255]. The STM measurement of soft-landed Ni₉ clusters on Si(111)-(7 × 7) surface indicates that clusters are fixed to the impinged position, while Ni₃ clusters migrate on the surface and aggregate into characteristic nanometer-sized structure [256]. Mn clusters, whose size is about 2.6 nm, have been deposited on clean Si(111)-(7 × 7) and terminated by a C₆₀ monolayer. They are of irregular shape, but grossly deformed upon adsorption onto the surface. There is no evidence of either cluster coalescence or preferential bonding sites [257].

Electron tunneling between a cluster and a substrate gives rise to an interesting effect, namely, the Coulomb blockade [258, 259]. The energy of the electron-transferred cluster is increased by a charging term, $E_c = e^2/2C$, where C is the capacitance of the cluster, causing a gap for electron tunneling. The steps with voltage widths of e/C (the so-called Coulomb staircase) have been observed in the current-voltage characteristic curve of the nanometer-sized metal clusters such as Au₅₅ and Pt₃₀₉ stabilized by surfactants (organic ligand shells) [260, 261]. The quantum size effect (QSE), which is the discreteness of the energy levels, is also one of the distinctive properties in nanometer-sized clusters. In some ligand-stabilized metal clusters, an additional structure to the regular Coulomb staircase has been observed and ascribed to quantum-sized levels of the cluster [260].

In an STM system, the tunneling electrons that are emitted from the tip and incident on the sample are followed by the inelastic process which induce photoemission at around the tip-sample region [250, 251]. The photoemission spectra represents a particularly versatile channel of information besides the tunneling current. Their intensity, spectral distribution, angular emission pattern, polarization status, and time correlation are accessible by sensitive optical detection methods [262]. For Ag and Cu clusters, the light emission spectra with about 10-nm resolution can be identified when geometric effects are minimized by using a sufficiently small tip [263, 264]. The occurrence of a distinct emission line from alumina-supported Ag clusters can be explained by the decay of a collective electron oscillation (Mie-plasmon resonance) [265]. This emission lines shift to higher energies and their widths increase with decreasing the cluster diameter, because of the reduced screening of the plasmon oscillation due to the Ag 4d electrons and/or an enhanced electron surface scattering rate in small clusters.

The magneto-optical effect, magnetic circular dichroism, has been observed for Co metals with STM-induced luminescence: the degree of polarization to be about 10% [266]. The map of the circular polarization has been directly compared with the STM topography for island-like Ni films, where the highly circular-polarized area is well correlated with Ni particles of 50–70 nm in diameter [267].

4.3. Photoelectron Spectroscopy

A great deal of effort has been devoted to the study of photoelectron spectroscopic studies for the supported metal cluster during the last decades [268–274]. A sufficient sensitivity to detect electrons and an intensive light source from a synchrotron radiation have contributed to investigate the electronic structures of the nanometer-sized clusters [275, 276], although the fraction of emitted electrons from nanometer-sized clusters is expected to be very small. Photoelectron spectroscopy is generally divided into two techniques relating to laboratory photon sources—gas discharge lamps leading to an ultraviolet photoelectron spectroscopy (UPS) and soft X-ray sources that are used for an X-ray photoelectron spectroscopy (XPS). In both cases, photoionization cross-sections are sufficiently small to ensure that the photon penetration depth is large relative to the mean-free path for inelastic scattering of the emitted electrons which therefore ensures the surface sensitivity [277].

The size-dependent electronic structure of metallic clusters is quite interesting because their electronic and chemical properties can vary from those of bulk materials [276, 278, 279]. Au clusters, for example, change from their inert bulk state to a chemically active state when they are in a form of small particles [276, 278, 280]. The synchrotron-based, high-resolution photoelectron spectroscopy (PES) measurement has indicated that Mo nanoclusters are inactive even when exposed to 150 L of oxygen at 300–850 K. However, these Mo nanoclusters are oxidized by reaction with NO₂ at 500 K to form molybdenum oxides, MoO₂ or MoO₃ [281].

Changes in the energy position and width as a function of their size have been observed in the core level spectra and the valence and conduction band spectra of the metal clusters [271–275]. Most experimental studies have been carried out for island-like grown films prepared by thermal evaporation of materials [271–273]. The photoemission spectra from the mass-selected supported clusters have recently obtained [274, 275]. The shifts of core levels and valence bands, as well as a narrowing of the bands, are obtained when the cluster size is decreased [271]. The core-level shifts with the cluster size are interpreted as a size dependence of the initial electronic state, that is, a change in the number of valence *d* electrons. The repulsive Coulomb interaction between core and valence electrons also affects the core-electron binding energies, being sensitive to the valence-electron configuration. Since valence *s* and *p* electrons of transition and noble metals are much more diffused than *d* electrons, the core levels are expected to shift towards lower binding energy with increasing the *d* electron number. The recent study on mass-selected Mn clusters deposited on an HOPG substrate has shown significant changes in the photoemission line shape of the 3s core level relative to bulk Mn [275].

This result can be interpreted as an increase in the Mn magnetic moment in the cluster assemblies, relative to the bulk Mn metal.

It is worthwhile mentioning that the core level shifts observed in supported metallic clusters can stem largely from the charge left on the cluster by electron emission [282]. Ionizing spectroscopy leaves a charge on the clusters, whose contribution to the polarization energy is partially screened by the substrate for the supported clusters. For clusters that weakly interact with conducting substrates [271], the energy shifts in photoemission spectra show that the initial state is much more sensitive to cluster size than the final state. In a Pd_{*n*}/C system [273], the initial-state energy shifts and cluster charging are found to play a minor role because the observed dependence of the spectra is ascribed to mixing of Pd 4*d* and graphite π* electron bands, where the coupling is proportional to the inverse cluster radius. The final one-hole local density of states, however, is modified in a complex way with reducing cluster size because of the increased number of surface and edge atoms. Some experimental results on the same system suggest the cluster charge model. A limited number of photoemission studies have been studied for metallic clusters whose sizes are not well determined. With corroboration of SPM experiment, photoemission spectra have been observed for Pd clusters on carbon substrate where the cluster sizes are less than 1 nm in the mean, indicating a conductance gap in tunneling spectroscopy [283]. Ultraviolet photoemission and bremsstrahlung isochromat (BI) spectroscopic measurements also show the emergence of new states closer to *E_F* with an increase in the cluster size. These results demonstrate the occurrence of a size-dependent, metal-to-nonmetal transition in Pd clusters.

4.4. X-Ray Spectroscopy Based Upon SOR

Using very intense X-ray beams from a synchrotron orbital radiations (SOR) source, oscillations and small humps are well resolved just above and below the X-ray absorption energy edge giving the element-specific geometrical structure (an extended XAFS) and electronic structure (an X-ray absorption near edge structure (XANES)) [284]. In particular, X-ray absorption techniques are so surface-sensitive that they are quite useful in understanding the local structure of dilute samples, such as submonolayer coverages of nanoclusters or nanocluster assemblies deposited onto substrates. Highly polarized, incident X-ray beams also make it possible to understand magnetic states of clusters supported on substrates with detecting helicity changes in the absorption spectra of X-rays passed through magnetic material [285].

4.4.1. XAFS and XANES Spectroscopies

The radial distributions derived for the XAFS signals at the Co and Ni K-edges have been obtained for Co and Ni cluster-assembled films, which were prepared by a laser vaporization cluster source and deposited on polyimide, silicon, and glass substrates [286]. The simple scattering of the photoelectron by the neighbors, and neglecting the multiple scattering, distinguishes atoms in the core of the clusters surrounded by 12 first neighbor shell for the first metallic

neighbors (the first shell) and atoms at the (111) surface surrounded by nine first metallic neighbors on one side (second shell) and by first O neighbors on the other side (third shell). For the second shell, the dilatation of the metal-metal distance is attributed to the interaction of O atoms in the near-surface region of clusters. The simulation of the Ni and Co cluster assemblies indicates that the number of metallic neighbors (the first and second shells), which is related to the surface-volume ratio, is 10.5–11 on average, showing the cluster sizes ranging from 3–5 nm for Ni and Co cluster assemblies with the truncated octahedron (for large clusters) and multiple twinned shapes. In Co cluster assemblies covered with Au films, the decomposition of the XANES spectra reveals coexistence of metallic Co clusters with about 0.6-nm thick CoO layers [287]. Moreover, the detailed peak analyses of assembled Co clusters with 6–14 nm in diameter indicates that the fcc phase is predominant for 6-nm size clusters and the hcp phase is increased for larger sized clusters. These results are consistent with those obtained by the high-resolution TEM observation.

Fe clusters, whose sizes range from 2–20 nm in diameter, have been embedded in noble metal (Ag and Cu) matrices using a ICB cluster source for Fe and a thermal evaporation source for Ag or Cu, and their radial structure function has been estimated from the XAFS spectra measured at the Fe-K edge [59, 60, 288]. In Ag matrices, distorted bcc Fe clusters are formed for an as-prepared state and strain-free bcc Fe clusters after annealing. In Cu matrices, on the other hand, distorted fcc clusters are formed for the dilute Fe concentration region (less than 20 at%) while distorted bcc clusters for the Fe-rich concentration region (more than 60 at%). The decomposition analyses of XANES for Fe clusters embedded in Cu matrices also qualitatively show a continuous reduction in the volume fraction of bcc/fcc between 20 and 60 at% Fe, being in accordance with the spectral analyses of Mössbauer spectra for the same specimens.

X-ray absorption fine structure studies have also done for Co clusters embedded in nonmagnetic Ag, Pt, and Nb matrices using both a laser vaporization, inert-gas condensation cluster source and a thermal evaporation source [289]. They confirm that a pure Co core is conserved to be fcc in all cases. When Co is immiscible with the matrix element (Co/Ag), the cluster/matrix interface is quite abrupt. Even when Co is miscible with the matrix element, an alloying effect is limited to one or two atomic layers of the cluster/matrix interface at an ambient temperature and it is promoted by annealing at higher temperatures.

4.4.2. XMCD Spectroscopy

X-ray magnetic circular dichroism (XMCD) in X-ray absorption spectroscopy (XAS) can determine the atomic spin (m_S) and orbital (m_L) moments by applying magneto-optical sum rules to the data [285, 290–292]. In Fe clusters supported on the substrate, the L edge X-ray absorption spectra were observed using circularly polarized X-rays with their angular momentum parallel or antiparallel to the sample magnetization, where the intensities of the L1 and L2 edge spectra of 3d electrons were measured in the magnetic field applied along parallel or antiparallel to the circularly polarized photon spin. Figure 13 shows size-dependence of

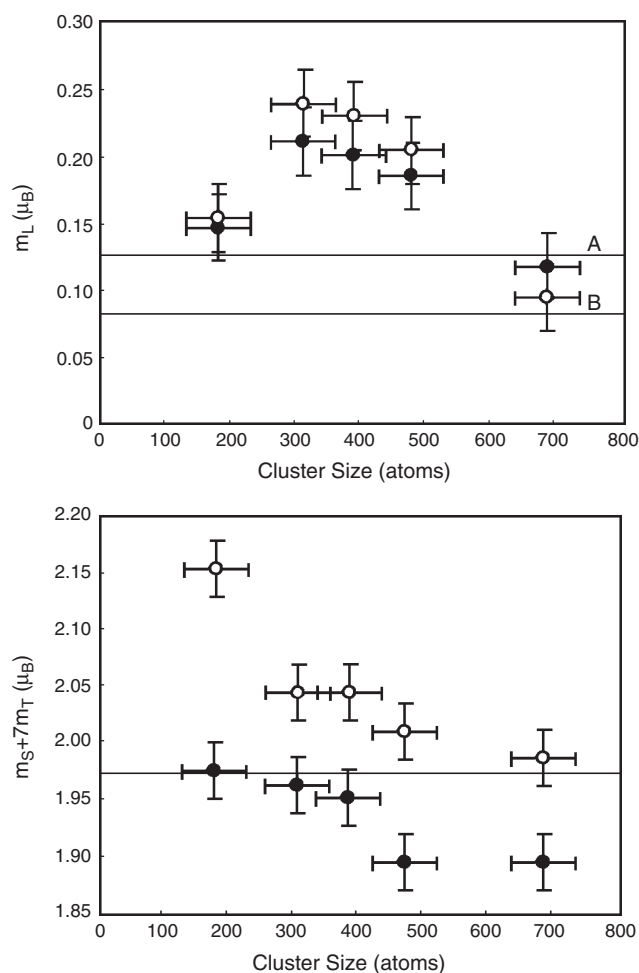


Figure 13. Atomic orbital magnetic moment m_L and spin term $m_S + 7m_T$ as a function of cluster size for Fe clusters on HOPG. The filled square and open circle symbols in both figures represent the measurements taken at $\theta = 0$ and 55° . Lines A and B in the upper figure denote the value measured in the 25-nm MBE film and the typical value of bulk Fe, respectively. Line C in the lower figure indicates the value measured for the MBE film. Reproduced with permission from [296], S. H. Baker et al., *J. Magn. Magn. Mat.* 247, 19 (2002). © 2002, Elsevier Science.

the components, $m_S + 7m_T$ and m_L for Fe clusters, which were prepared by a gas aggregation source (a thermally vaporization source), size-selected by a quadrupole mass filter and deposited on HOPG substrates installed in a UHV chamber [293–296]. m_T is the dipole moment and θ is the angle between the direction of photon beam relative to the sample normal, where $m_T \neq 0$ at $\theta = 0$ and $m_T = 0$ at $\theta = 55$ (the magic angle) for a single crystal or a sample with a rotational symmetry normal to the surface. Comparing two data in Figure 13, the magnetic dipole moment is opposite in sign to the spin moment, contributing about 5% to the sum for measurements normal to the surface. The spin moment of the smaller size Fe clusters is larger than the bulk value. The dipole moment increases with decreasing cluster size, being about two times larger than the bulk value throughout the size range, while it does not show a significant variation with angle. The increase in both m_S and m_L contributions to the magnetic moment can be ascribed to the high

proportion of surface atoms with a low coordination, which produce a narrowing of the d -band responsible for magnetism and an increase in the density of states at the Fermi level, and reduce symmetry and less effective quenching of orbital magnetism by the crystalline field. At low temperatures, the total magnetic moment, $m_S + 7m_L$, in supported Fe clusters is much larger than the bulk value, being ascribed to the enhancement of m_S and m_L and their parallel alignment owing to the positive spin-orbit coupling in the more than half occupation of d -electrons. However, it is not so large as the free cluster values probably due to the cluster-substrate interaction. The XMCD of Fe L edge spectra have been observed for size-selected Fe clusters as a function of the cluster size between two and nine atoms which were deposited in an ultra-high vacuum on perpendicularly magnetized Ni films, where a soft landing was achieved by pre-covering the substrate with argon buffer layers to maintain the selected size [297]. In Fe clusters, whose sizes are less than 10 atoms the enhancement of orbital moments is more significant and the ratio of m_L to m_S reveals an oscillatory size dependence. It has been speculated that the geometrical arrangement and magnetic properties of such small clusters depend on whether they consist of even or odd numbers of atoms.

With increasing coverage of unfiltered Fe clusters with an average size of about 600 atoms deposited on HOPG substrates the value of $m_S + 7m_L$, moreover, increases slightly indicating the dipole moment decreases with an increase in the cluster density, while m_L rapidly decreases due to the increasing proportion of clusters in contact with each other, thus increasing the average atomic coordination [295]. The magnetic remanence estimated by field-dependence of XMCD for the isolated Fe clusters are superparamagnetic even at 40 K, decaying rapidly with increasing temperature, but the magnetic anisotropy is enhanced considerably.

Dichroism is also observed in the $3p$ angle resolved photoemission spectra of the transition metals taken with linearly or circularly polarized photoemission spectra [298]. The former measures the difference in the spectra in response to reversing the alignment between the in-plane sample magnetization and the linear polarization of the XUV light (MLDAD) and the latter between the out-of-plane sample magnetization and angular momentum of circularly polarized light (MCDAD). Since photoemission spectra must be collected in a zero field, the techniques are only applicable to measure the remanence state. At 40 K, the MLDAD signal is zero within experimental error in the isolated Fe cluster. While increasing the coverage, it becomes finite and rapidly increases. This suggests that the interactions between the clusters lead to the coherent shape anisotropy of the films. The remanence becomes larger than the bulk signal, probably due to asperomagnetic configuration in the layered cluster assemblies.

When Fe clusters are coated by Co thin films, Fe spin moments are increased, being about 10% larger than those of the noncoated Fe clusters, but the orbital moment reveals no significant change [294, 298]. Since the XAFS intensity of Co-coated Fe clusters is almost the same as the noncoated one, no significant charge transfers between Fe and Co and an alloy effect is confined to the interface. Therefore, the enhancement of spin moments is attributed to an increase in

the Fe valence band exchange splitting induced by the interaction with the matrix. The m_T contribution is also reduced by Co coating owing to the reduction in the magnetostatic energy.

When Co clusters with 300–9000 atoms are codeposited with Cu atoms on Si (100) substrates, the total magnetic moments are reduced to less than a half value of a deposited Co film, and the orbital moments are enhanced considerably to be comparable to the spin moments [299]. Similar features have been observed for Co clusters formed on Au (111) substrates, under ultrahigh vacuum conditions [300], where the L edge spectra contains no extra peak resulting from chemical core shifts of the p -states and there is little or no contamination of Co atoms. When Co clusters are covered with C films, both the spin and orbital moments are reduced, where the latter reduction is more marked [301]. The Co K-edge spectra also indicate a slight reduction in the orbital moments of $4p$ -electrons being about $1.5 \times 10^{-3} \mu_B$ induced by spin-orbit interactions of $3d$ -electrons on the neighboring sites through the $4p$ - $3d$ hybridization. Several speculations, such as a structural change from fcc to hcp, antiferromagnetic exchange coupling between Co clusters, etc. have been proposed. The careful observation of Cr-L3 edge absorption spectra of Cr clusters (with the sizes less than 10 atoms) whose size are less than 10 atoms indicate that the line broadening and shift are attributable to bimetallic electronic state at the cluster/matrix interface, geometrical structure change, oxidation of surface atoms, etc. [302]. We need more systematic and unique approaches to arrive at a common interpretation of such environment-sensitive aspects of magnetic transition metal cluster assemblies.

4.5. Nuclear Scattering and Resonance Techniques

As discussed in Section 4.1, the thermally activated fluctuation of magnetization in a small particle is described by the an approximate expression for the relaxation time:

$$\tau = \tau_0 \exp(KV/k_B T) \quad (16)$$

where K is a magnetic anisotropy constant, V a volume of a particle, k_B the Boltzmann constant, T the absolute temperature, τ_0 the angular precession frequency in the order of 10^{-9} s [303]. In small cluster assemblies, we observe a ferromagnetic behavior, for a measuring time scale, $\tau_m > \tau$, while a paramagnetic behavior (superparamagnetism) for $\tau_m < \tau$. For $\tau_m \approx \tau$, we can detect a ferromagnetic/superparamagnetic transition at a certain temperature, the blocking temperature T_B . Using conventional magnetic measurement with $\tau_m \approx 1$ – 10^2 s, T_B is of an order of room temperature in small Fe particles whose sizes are 10–20 nm in diameter, depending upon respective anisotropy characteristics. Today, there have been a lot of advanced nuclear scattering and resonance techniques, with which we can choose the observation window, τ_m a very wide range between 10^{-4} and 10^{-12} s to understand the detailed mechanism of magnetic relaxation phenomena, as well as their internal crystalline and magnetic structures.

4.5.1. Neutron Scattering

Neutron scattering is quite an informative method for material characterization because the neutron cross-section is the sum of a nuclear and a magnetic contribution. In a small-angle, neutron scattering experiment of cluster assembled systems, we may obtain the particle sizes, interparticle distance, spin correlations within the particle, and interparticle spin correlations. However, the neutron-matter interaction is so weak and the penetration depth of neutrons in matter is extremely long, so a large amount of specimens is necessary for measurement [304]. This technique has been mainly applied for small particles precipitated in oxide or polymer matrices which are mass productive. With a decreasing temperature of Fe particles with an average diameter of 2 nm embedded in Al_2O_3 matrices, an increase in particle magnetization (an intraparticle term) is dominant down to 100 K, while magnetic correlation between the total spins of neighboring particles (an interparticle term) is dominant below 100 K [305].

Besides the elastic neutron scattering mentioned above, inelastic neutron scattering giving space and time pair correlation of spins is effective in analyzing the spin dynamics, susceptibility, relaxation, etc., where the energy spectra consist in two parts: a central peak (a no-energy-transfer component) and inelastic spectrum (an energy-transfer component) [304]. The energy scale 0.01–100 meV, corresponding to the time scale 10^{-10} – 10^{-12} , is typical of anisotropy energies for the lowest values and of the exchange energies for the highest ones. The energy line width of an inelastic spectrum has been observed as a function of temperature for Fe particles embedded in Al_2O_3 matrices. Above 250 K, the energy line width is temperature-independent, indicating that the magnetic intensity is all contained in the inelastic peak. Below 250 K, it becomes larger and a magnetic intensity occurs in the central peak indicating the slowing down of some magnetic component. There are two characteristic times for the fluctuation of the particle magnetization. A neutron spin-echo-spectroscopy with the time-scale range between 10^{-11} and 10^{-7} s has been further observed at different scattering wave numbers to clarify the slow fluctuation in the Fe particles embedded in Al_2O_3 matrices [306]. The analyses of both the central and satellite components indicate the following relaxation picture: $T \geq K$, there is single-particle fluctuations, while below $T \leq 100$ K, the temperature is less than the magnetic anisotropy energy barrier and the relaxation splits into two components: The slow fluctuation is attributable to the local longitudinal component fluctuating between energy minima and the fast one to the transverse fluctuations around the temporary mean orientation in one of the minima. This correlation leads to a more pronounced freezing of spins in space and time in comparison with the noninteracting particle systems.

4.5.2. Muon Spin Rotation Spectroscopy

Muon spin rotation spectroscopy is another powerful technique in studying spin dynamics of complicated magnetic materials such as spin glass [307, 308]. The spin polarized muons implanted in a sample occupy interstitial sites, precess in the local magnetic field, and decay into positron and two neutrinos. The time-decay spectrum of positrons gives

the muon precession frequencies and the internal magnetic fields of the sample. This technique covers an extremely broad time-scale between 10^{-11} and 10^{-4} s, being comparable to that anticipated for superparamagnetic systems. The kinetic energy of incident muons is so high as an order of MeV that they penetrate thin films and small specimens to be implanted in substrates. So far as concerned with spin dynamics of small particles, this technique has first applied to the specimen, in which a small Co particle precipitated in 0.5-mm thick Cu discs [309].

Recently the low-energy muon beam of orders 0.5–30 keV has been available, where the time-scale set by the muon precession and decay is an order of 10^{-5} s. The low-energy muon rotation has been observed for monodispersed size Fe cluster assemblies prepared in a gas condensation source and embedded in a Ag thin film matrix [310]. Here, the effective Fe concentration was about 0.1% in volume and most of implanted muons stop in the Ag matrix between the clusters. The static distribution of the local fields (dipole fields associated with the magnetic clusters) causes the implanted muons to precess out of step and leads to a decay damping. This experiment indicates that $\tau_0 = 1.2 \times 10^{-8}$ s and $K = 2.3 \times 10^5 \text{ Jm}^{-3}$. The enhancement of K by a factor five is consistent with the enhancement of orbital moments in clusters with the reduced coordination of atoms at the interfaces.

4.5.3. Mössbauer Spectroscopy

The Mössbauer effect is a recoil-free emission and resonant absorption phenomenon of γ -ray between the excited and ground states of a nucleus embedded in a material [311, 312]. This technique is quite powerful in studying specimens containing a reasonable amount of ^{57}Fe atoms, because the half-life of a ^{57}Co radioactive isotope is long (270 days) for conventional laboratory works. Several parameters, such as an isomer shift, a quadrupole splitting, and a magnetic hyperfine field, can be obtained via the data fitting procedure. It is possible to analyze quantitatively the local electronic structure, bonding state, atomic arrangements, magnetic structure, formation phase, phase transition, atomic diffusion, etc. [313].

Relaxation Behaviors Concerned with the magnetic relaxation of Fe nanoparticles, $\tau_m \approx 10^{-8}$ s of ^{57}Fe nuclei, corresponding to the Larmor precession period of the magnetic moment of the nucleus in the excited state (the nuclear moment, $I = 3/2$), which is 14.4 keV higher than the ground state ($I = 1/2$) [312]. A collapse of a hyperfine split spectra can be detected at $T \approx T_B$, being much lower than room temperature in nanosize Fe particles. With a wide temperature range-studies of Mössbauer spectroscopy and AC and DC magnetization measurements of bcc Fe particle assemblies, the average particle size was determined to be about 3 nm, which is consistent with TEM observation and the parameters in Eq. (16) were estimated as follows: $\tau_0 \approx 10^{-10}$ s and $K \approx 1.2 \times 10^5 \text{ Jm}^{-3}$ [313]. Mössbauer spectroscopy has been observed for noninteracting or weakly interacting magnetic particles [315–318, 386]. A maghemite ($\gamma\text{-Fe}_2\text{O}_3$) nanoparticle is superparamagnetic if isolated. However, interparticle magnetic interactions in magnetic particle assemblies lead to spin-glass-like ordering at low

temperatures [316, 386], and the relaxation time decreases with decreasing particle interactions [317–319]. This phenomenon has been often termed superferromagnetism [316].

Spin Canting Characteristics Spin canting of small maghemite particles ($\gamma\text{-Fe}_2\text{O}_3$) [319–328] has been discussed via Mössbauer spectroscopy measurement: nonsaturation behavior of magnetization at 4.2 K even in a magnetic field of 50 kOe is attributable to the existence of random canting of the surface spins caused by competing antiferromagnetic exchange interactions. For small ferrite particles (NiFe_2O_4 [329], CoF_2O_4 [330]), a noncollinear magnetic structure was proposed by Mössbauer spectroscopy experiments: the ferrite particles consist of a core with the usual spin arrangement and a boundary surface layer with atomic moments inclined to the direction of the net magnetization. Similar effects have also been experimentally discussed with corroboration of numerical calculations [331, 403, 404]. The antiferromagnetic superexchange interaction is disrupted at the surface of the ferrimagnetic oxide crystallites because of missing oxygen ions or the presence of other impurity molecules. Such broken exchange bonds between surface spins lead to surface spin disorder, being compatible with a spin-glass-like behavior at the surface. Such spin canting in nanoparticles has long been considered as a surface effect [320–322, 331, 403, 404]; recent Mössbauer spectroscopy experiments of maghemite particles have shown that spin canting is not a surface effect, but rather a finite-size effect that is uniform throughout the whole volume of the particles [326–328] and, consequently, may cause a substantial decrease of the saturation magnetization of small ferrimagnetic particle systems in comparison to that of the bulk material.

Phase Analyses and Surface Oxidations Mössbauer spectroscopy has been extensively studied in the understanding of microscopic precipitation processes and structures of Fe and Co particles in Cu and Au matrices prepared via heat treatments from their supersaturated solutions [60, 332]. The application of this technique to Fe clusters embedded in Ag and Cu matrices (granular alloy films prepared by the combination of ICB and thermal evaporation sources) reveals the following results. At room temperature, broad singlet and doublet lines are observed in the dilute Fe concentration region (in a small Fe cluster size region) and a broad sextet line in the condensed Fe concentration region (in a large Fe cluster size region). At 5 K, a broad ferromagnetic sextet line is observed in the whole concentration for Fe/Ag granular alloy films [332], while very broad singlet, doublet, and sextet lines are detectable in the dilute Fe concentration region, unresolved sextet lines in the intermediate Fe concentration region (at around 20 at% Fe) and broad sextet lines in the Fe rich concentration region for Fe/Cu granular alloy films [60, 333]. These results indicate that Fe clusters are always bcc and ferromagnetic in Fe/Ag granular alloy films, while they are fcc and change from ferromagnetic to antiferromagnetic in the Cu rich concentration region and become bcc and ferromagnetic in the Fe rich concentration region for Fe/Cu granular alloy films.

Presence of oxide surface layers have been discussed using Mössbauer spectroscopy observation for oxidized Fe particles, passivated Fe nanoparticles, and Fe cluster assemblies

[164, 334–346]. Most of the experimental results showed that oxide surface layers are a nonstoichiometric Fe_3O_4 phase and/or a mixture of stoichiometric Fe_3O_4 and $\gamma\text{-Fe}_2\text{O}_3$ phases and they are composed of small crystallites. The spin canting phenomenon mentioned has also been observed in thin oxide layers on metallic Fe cores [334–337].

5. CHARACTERISTIC MAGNETIC AND TRANSPORT PROPERTIES OF CLUSTER-ASSEMBLED MATERIALS

5.1. Magnetic Properties

5.1.1. Theoretical Background

Single Magnetic Domain Particles Review of single domain particles includes those by Bean and Livingston [347], Bean [348], Brown [349], Wohlfarth [350], and Leslie-Pelecky and Rieke [351]. When the size of magnetic particles is reduced to a few tens of nanometers, the formation of domain walls becomes energetically unfavorable and each particle becomes a single magnetic domain. The single domain size (d_{sd}) for spherical particles has been estimated [246]: $d_{\text{sd}} = 24$ (fcc-Co), 40 (hcp-Co), and 24 nm (Fe). Changes in the magnetization can no longer occur through a domain wall motion and instead require the coherent rotation of spins, resulting in larger coercivity (H_c). In this case, H_c is strongly dependent on temperature (T). In order to reverse particle spins, it should have enough thermal energy to surmount the activation energy barrier ($\Delta E = KV$). At high temperatures, where the particles have higher thermal energy, they require a smaller field to reverse the magnetization. This field is equal to H_c for single-domain ferromagnetic particles having no interaction between them and is given by [352]:

$$H_c = \frac{2K}{M_s} \left[1 - \left(\frac{25k_B T}{KV} \right)^{1/2} \right] \quad (17)$$

where V is the volume of the ferromagnetic particle, K the magnetocrystalline anisotropy constant, M_s the saturation magnetization, and k_B the Boltzmann constant. When T approaches zero, H_c approaches $2K/M_s$, that is, $H_{c,0} = 2K/M_s$. Equation (17) predicts that the value of H_c increases as the cluster size becomes larger. For particles with constant size, there is a temperature, called the blocking temperature, T_B , above which the metastable hysteretic response is lost for a particular experimental time, and the particles exhibit a superparamagnetic behavior. For uniaxial particles, T_B can be taken as $KV/25k_B$, and hence, we get

$$H_c = H_{c,0} \left[1 - \left(\frac{T}{T_B} \right)^{1/2} \right] \quad (18)$$

This $T^{1/2}$ dependence has been observed in many nanoparticle systems [156, 353–355].

Packing Fraction In order to form a practical magnet or a specimen for studies, the magnetic nanoparticles must be compacted, with or without a nonmagnetic binder or matrix, into a rigid assembly. Then an important variable is the packing fraction, P_c , defined as the volume fraction of magnetic particles in the assembly. According to the simple theory on a random assembly of single-domain particles with uniaxial anisotropy, the magnetic coercivity is expressed as [356]:

$$H_c(P_c) = H_c(0)(1 - P_c) \quad (19)$$

where $H_c(0)$ is the coercivity of an isolated particle ($P_c = 0$). Some materials obey this simple relation but many do not, because magnetic intercluster interaction generally exists in cluster assemblies [357]. They are more or less strong according to the packing fraction. In any case, long-range magnetic dipolar interaction is always present. If the matrix is metallic, Ruderman-Kittel-Kasuya-Yosida (RKKY) interaction occurs and depends on $1/L^3$, where L is the distance between centers of clusters, as in dipolar interaction. When the matrix is insulating, superexchange interaction could exist at short range according to the structure and nature of the matrix and bonding at the cluster-matrix interface. Those intercluster interactions make the problem complicated. Therefore, a more detailed theoretical analysis on the cluster-assembled system is needed.

Magnetic Relaxation Phenomenon Magnetization reversal may be realized by changing the applied field or by thermal activation. Time-dependence of the magnetization under a constant field is referred to as magnetic viscosity. The magnetic viscosity due to thermal activation is a general property of all ferromagnetic materials. In bulk materials, the time-scale for magnetic viscosity is so large that magnetic viscosity often cannot be significant. However, in fine particle or cluster systems, magnetic viscosity becomes important. Thermally activated magnetic reversal has been investigated intensively, because it might be a limiting factor for the achievable density of conventional magnetic recording media. Especially, in 1988, Chudnovsky and Gunther [358] predicted that at a low temperature, the magnetic moment can quantum mechanically tunnel through the energy barrier U with a probability of $\exp(-B)$, where $B = U/k_B T_{co}$, k_B is Boltzmann's constant and T_{co} is the crossover temperature. Experimentally, the magnetic relaxation phenomena of macroscopic quantum tunneling have been observed in many magnetic systems [359–361]. In a single-domain particle system with a unique value of the anisotropy energy barrier, the magnetization relaxes according to the law $M(t) = M(0) \exp(-\Gamma t)$, where $\Gamma = 1/\tau$ is the transition rate and τ is the relaxation time or decay lifetime. In real systems, there is an energy barrier-height distribution resulting from intrinsic and extrinsic anisotropy, which leads to a logarithmic time relaxation [362]:

$$M(t) = M(t_0)[1 - S(T) \ln(t/t_0)] \quad (20)$$

where $S(T)$ is the magnetic viscosity whose temperature (T) dependence characterizes the relaxation behavior of the system. At a temperature range of $T_{co} < T \ll T_B$, where T_B is

the blocking temperature for the magnetic moment of the particles, $S(T)$ can be written as

$$S(T) = -\left(\frac{1}{M(t_0)}\right) \frac{dM}{d(\ln t)} = n(\langle E \rangle) k_B T \quad (21)$$

where $n(\langle E \rangle)$ is the energy barrier distribution function and $\langle E \rangle$ is the mean-energy barrier within the experimental window. If $n(\langle E \rangle)$ is constant in a certain range of energies, the magnetic viscosity will be linear in T over the corresponding temperature range. The temperature independence of the magnetic viscosity below a critical (crossover) temperature T_B is considered as evidence of macroscopic quantum tunneling in nature. It is predicted theoretically [363] that the crossover temperature from thermal activation regime to quantum tunneling regime scales with the component of magnetic anisotropy normal to the easy axis, so the tunneling effect should be observable at experimentally accessible temperatures only for materials with high anisotropy constants.

Unidirectional Exchange Anisotropy Unidirectional exchange anisotropy (UEA) was first discovered in field-cooled Co/CoO particles more than 40 years ago and shown to be caused by the strong exchange coupling between the ferromagnetic (FM) Co core and the antiferromagnetic (AF) CoO layer [364]. The typical UEA effect is a marked shift of the hysteresis loop against the applied field, commonly referred to as an exchange bias field, H_{cb} , when field-cooling the sample from temperatures above the Néel temperature T_N of the AF to $T < T_N$. This hysteresis loop could be obtained if the energy function was exactly given by

$$E = -K_u \cos \theta \quad (22)$$

where K_u is the UEA constant, and energy minimum occurs at $\theta = 0^\circ$ and energy maximum occurs at $\theta = 180^\circ$. In the hcp cobalt particle, only a direction along c axis ($\theta = 0^\circ$) is stable in an infinite field.

The phenomena related to the UEA effect have also been studied theoretically [365–368] and experimentally [369–375], because they are technologically important to domain stabilizers in magnetoresistive heads [376] and spin-valve-based devices [377]. However, the understanding of the UEA effect has not been well understood because it is very difficult to determine the AF spin structures in interfacial layer contributing to H_{cb} . The first simple model [364] dealt with the unidirectional anisotropy by assumption of a perfect uncompensated plane of the AF at the interface and predicted H_{cb} which was two orders of magnitude larger than the observed ones. Mauri et al. [365] explained the small experimental value of H_{cb} by assuming the formation of a domain wall parallel to the interface which dramatically lowers the energy required to reverse the magnetization. Alternatively, Koon [367] predicted a correct value for H_{cb} as a result of a perpendicular orientation between the FM and AF axes, similar to the classical spin-flop state in bulk AF. The recent polarized neutron diffraction experiment has shown that exchange coupling between the Co and CoO layers is apparently responsible for the increased projection of the AF moments perpendicular to the cooling field direction [373]. Although the theoretical models have

mainly explained the unidirectional anisotropy and obtained the correct order of H_{cb} , they have predicted no effect on the coercivity H_c . Experimentally, the shifted hysteresis loop is always accompanied by an enhancement of the coercivity, which is much larger than the intrinsic value of the FM core [364] and layer [369]. Quite recently, Schulthess and Butler [368] have made a calculation for CoO/FM films using an Heisenberg model and have shown that there are two coupling mechanisms at work, the spin-flop coupling (being responsible for a large coercivity) and FM-AF coupling through uncompensated defects (accounting for exchange bias field).

5.1.2. Co and Fe Cluster Assemblies

For size-monodispersed Co and Fe cluster-assembled films without a nonmagnetic binder or matrix, their magnetic properties have been studied [156, 165, 198, 378]. High-temperature electrical conductivity measurements [379] and TEM observations [156, 165] indicated that in a cluster size range of 6–15 nm, individual Co and Fe clusters are distinguishable at room temperature (RT). This suggests that those clusters in the cluster-assembled films maintain their original size at RT. The actual thickness estimated from a low-magnification cross-sectional SEM image is about $t_a = 800$ nm, while the effective thickness estimated from the thickness monitor was $t_e = 200$ nm, that is, t_a is about four times that of t_e . This implies that the cluster-assembled films are very porous and have a cluster-packing fraction of about 25% ($=t_e/t_a = 200 \text{ nm}/800 \text{ nm}$). On the basis of the aforementioned simple theory (Eq. (19)), such a low-packing fraction leads to a large coercivity. Figure 14 shows the d dependence of H_c at $T = 300$ K for the present Co and Fe cluster assemblies together with that for fcc Co (solid line) and Fe (dash line) nanocrystals estimated from the following equation [380], using the reported values for the bulk Fe and Co [381]:

$$H_c = \frac{P_c K_1^4 d^6}{M_s A^3} \quad (23)$$

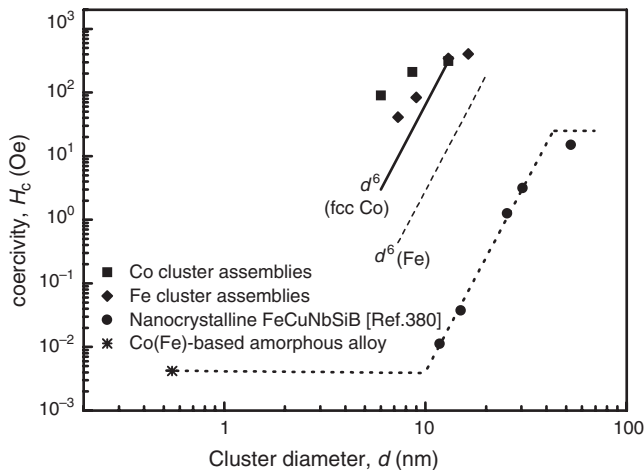


Figure 14. Coercivity, H_c , at $T = 300$ K as a function of the grain diameter d for the Co- and Fe-cluster-assembled films and nanocrystalline materials. The solid and dash lines indicate the results for fcc Co and Fe nanocrystalline materials estimated from Eq. (23), respectively.

where A is the exchange stiffness constant. Clearly, for the Fe cluster assemblies, their H_c values are larger by an order of magnitude than those of the Fe nanocrystals estimated from Eq. (23) for a given d .

On the other hand, in these cluster assemblies, the effect of intercluster interactions strongly affects their magnetic properties. The most striking feature is a superparamagnetic-to-ferromagnetic transition by increasing the film thickness of Co clusters with $d = 6$ nm [198, 378]. Using the K value of bulk materials [381], simple estimation from $T_B = KV/25k_B$ indicates that the superparamagnetic state should appear at RT for Co clusters with $d < 17$ nm (fcc-Co) and $d < 10$ nm (hcp-Co) and for α -Fe clusters with $d < 16$ nm. However, the Co and Fe cluster-assembled films with cluster sizes that are much smaller than these critical sizes show a ferromagnetic behavior [156, 165, 198, 378]. Such ferromagnetic behaviors of the small Co and Fe clusters is ascribed to strong interactions between magnetic nanoparticles that can lead to ordering of the magnetic moments and thus an increase of T_B of the zero-field cooled magnetization [382–386]. This phenomenon has been termed superferromagnetism and the ordering of the magnetic moments of interacting particles may be calculated by use of a mean field model [382–384]. In samples of ferromagnetic or ferrimagnetic ultrafine particles, the magnetic dipole interaction between pairs of particles may be comparable to the thermal energy and can therefore influence the relaxation behavior. The exchange interaction between surface atoms of two magnetically ordered particles in close contact can also result in significant interaction effects. These interacting factors give results not in accordance with the Néel model for superparamagnetic relaxation but can be explained by the formation of an ordered spin-glass-like state [386].

The superparamagnetic-to-ferromagnetic transition with increasing the cluster-assembled film thickness also implies that the effective magnetic anisotropy constant K_{eff} of the clusters is enhanced in thicker cluster-assembled films. Therefore, attempts were made to calculate the value of K_{eff} from the temperature-dependence of the coercivity for Fe cluster-assembled films according to Eqs. (17) and (18) [156]. The results indicated that the Fe cluster-assembled films follow closely H_c versus $T^{1/2}$ law and the fitting is very satisfactory. The value of K_{eff} increases with decreasing the cluster size and is of the order of 10^6 erg/cm³. In the case of $d = 9$ nm, the value of K_{eff} is 3.66×10^6 erg/cm³. Thus, the experimental value (K_{eff}) of the anisotropy constant is larger by an order of magnitude than that (5×10^5 erg/cm³) of the bulk Fe [381].

5.1.3. Core-Shell-Type, Oxide-Coated Co and Fe Cluster Assemblies

Oxide-passivated particles of Co [153, 155, 387–391], CoFe [387, 392, 393], Fe [156, 355, 394–397], and Ni [398, 399] are used to study the UEA effect induced by exchange coupling between the FM metal cores and the AF or ferrimagnetic (FIM) oxide shell layers. For these cluster assemblies, magnetic reversal mechanism and spin structures at a core-shell interface are different from those for simple FM/AF bilayers because of single-domain structure of Co core grains, the

small size of cores and shell crystallites, and real interface roughness, leading to some characteristic properties [153, 155, 156, 389–391, 395, 397]. Their coercivity and hysteresis loop shift induced by field cooling were strongly affected by temperature, cluster size, and oxygen gas flow rate during deposition or volume ratio of the core to shell, as well as the sort of metal core and oxide shell.

Correlation Between H_{eb} and H_c By selecting cluster size and adjusting the thickness of the oxide shells, large H_c and H_{eb} can be obtained. Figure 15 shows the hysteresis loops of the Co/CoO monodispersed cluster assembly with $d = 6$ nm prepared at $R_{O_2} = 1$ sccm after the sample was zero field cooled (ZFC) and field cooled (FC) from 300 to 5 K in a magnetic field, H , of 20 kOe. The direction of H used to measure the loops was parallel to that of the cooling field. For this sample, the thickness of the CoO shell have been estimated to be about 1 nm by direct observation of the high resolution transmission electron microscope, being consistent with the Co core size of about 4 nm estimated from the Langevin fitting to the experimental data above room temperature. The large H_{eb} ($= |H_1^{FC} + H_2^{FC}|/2$) value of 10.2 kOe is detected, which indicates the presence of strong UEA in the present sample. As seen in the inset of Figure 15, H_{eb} increases with increasing the cooling field and almost becomes unchanged when the cooling fields are higher than 10 kOe. On the other hand, the large coercivity H_c ($= |H_1^{ZFC} - H_2^{ZFC}|/2 \approx 5$ kOe) is also obtained for the ZFC case in which the UEA effect is randomized. Clearly, the enhancement of H_c mainly stems from the UEA effect. The correlation between H_{eb} and H_c have been discussed for the Parmalloy/CoO bilayers [374, 375] as a theoretical extension of Malozemoff's model [366]. The UEA effect is interpreted in terms of random exchange fields due to roughness and imperfection at the FM and AF interface, giving the correct order of magnitude for H_{eb} . Recently, the correlation

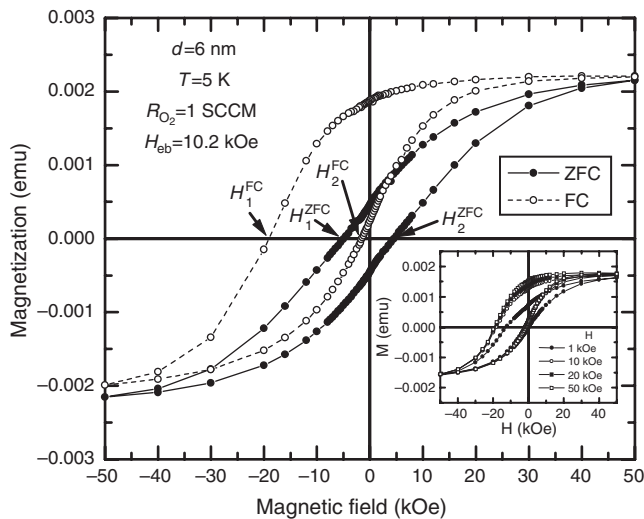


Figure 15. Hysteresis loops of the ZFC and FC Co/CoO monodispersed cluster assembly with mean cluster size of $d = 6$ nm prepared at the O_2 gas flow rate $R_{O_2} = 1$ sccm. The inset shows hysteresis loops after field-cooling the sample in different magnetic fields. Reproduced with permission from [155], D. L. Peng et al., *Phys. Rev. B* 61, 3103 (2000). © 2000, The American Physical Society.

between H_{eb} and H_c for small Co/CoO cluster assemblies have also been discussed experimentally [155]. Figure 16 shows coercivities, H_c and H_c^{FC} ($= |H_1^{FC} - H_2^{FC}|/2$), of the ZFC and FC samples at 5 K as a function of H_{eb} for the monodispersed Co/CoO cluster assemblies with $d = 6$ and 13 nm prepared at different R_{O_2} . Both H_c and H_c^{FC} increase with the increase of H_{eb} , indicating the uniaxial anisotropy is compatible with the UEA. It is noteworthy that the value of H_c^{FC} is about twice as large as that of H_c at a given H_{eb} value. This fact suggests that a magnetization reversal mechanism of rotation exists and an enhanced uniaxial anisotropy parallel to applied field is induced.

Disappearance Temperature of the UEA Effect In the oxide-coated cluster assemblies, a second interesting observation is that the UEA effects often disappear at a temperature (T_d) that are much lower than the Néel temperature ($T_N = 293$ K) of the bulk CoO and the magnetic order-disorder transition temperatures of the bulk Fe oxides (γ - Fe_2O_3 : ~ 1020 K; Fe_3O_4 : ~ 858 K; FeO : ~ 198 K). For the Co/CoO cluster assemblies [153, 155, 390], the UEA effect disappears at $T_d = 150 - 200$ K, while for the Fe/Fe-oxide cluster assemblies [156, 355, 397], it becomes undetectable at about $T_d = 50$ K. For example, Figure 17 shows coercivities, H_c^{ZFC} and H_c^{FC} , of the ZFC and FC sample and exchange bias field H_{eb} as a function of temperature for the oxide-coated Fe cluster assemblies with $d = 9$ nm prepared at $R_{O_2} = 0$ and 3 sccm. For the FC sample, H_c^{FC} is defined as the average of the absolute value of positive and negative fields. The difference in H_c^{ZFC} and H_c^{FC} becomes more significant with decreasing T for both $R_{O_2} = 0$ and 3 sccm. Such a bifurcation effect starts at about $T = 50$ K. H_{eb} also

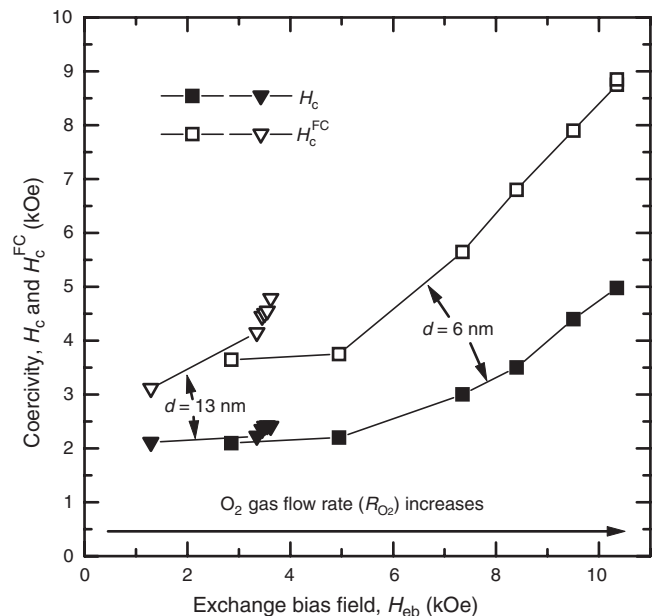


Figure 16. Coercivities, H_c and H_c^{FC} of the ZFC and FC samples at 5 K as a function of the exchange bias field H_{eb} for the Co/CoO monodispersed cluster assemblies with $d = 6$ and 13 nm prepared at different R_{O_2} . Reproduced with permission from [155], D. L. Peng et al., *Phys. Rev. B* 61, 3103 (2000). © 2000, The American Physical Society.

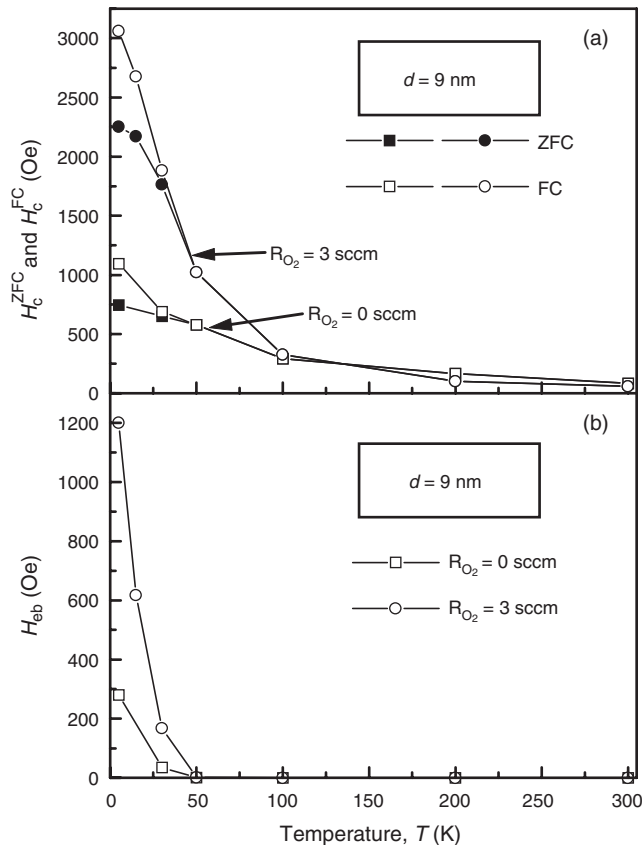


Figure 17. (a) Coercivities, H_c^{ZFC} and H_c^{FC} , of the ZFC and FC samples, and (b) exchange bias field H_{eb} as a function of temperature, T , for the oxide-coated Fe cluster assemblies with $d = 9$ nm prepared at $R_{O_2} = 0$ and 3 sccm. Reproduced with permission from [156], D. L. Peng et al., *J. Appl. Phys.* 92, 3075 (2002). © 2002, American Institute of Physics.

rapidly decreases with increasing T and becomes negligibly small above $T = 50$ K.

Training Effect It is worth mentioning that the dependence of the exchange bias field H_{eb} on repeated magnetization reversals, namely, the so-called training effect, is a diminution of H_{eb} upon the subsequent magnetization reversals [369]. Figure 18(a) shows typical results of the hysteresis loops measured along the field-cooling direction at 5 K for the monodispersed Co/CoO cluster assembly with $d = 6$ nm and $R_{O_2} = 1$ sccm [155]. The successive loops do not coincide with each other and show a decrease in H_{eb} . Figure 18(b) shows the dependence of H_{eb} and the training effect on the training cycle number at 5 K. Here, the training effect was defined as the fraction of the initial value. The decrease of H_{eb} is larger for the second cycle and then become unchanged after further numbers of the training cycles. The training effect is about 89% after the 14th cycle. However, for the monodispersed Fe/Fe-oxide cluster assemblies, the decrease of H_{eb} is very remarkable by increasing the training cycle number, and the training effect is decreased to about 30% after the 13th cycle [156]. This result is clearly different from that of the monodispersed Co/CoO cluster assembly [155]. This suggests that the training effect strongly depends on magnetic properties of the oxide shells, namely, antiferromagnetism or ferrimagnetism.

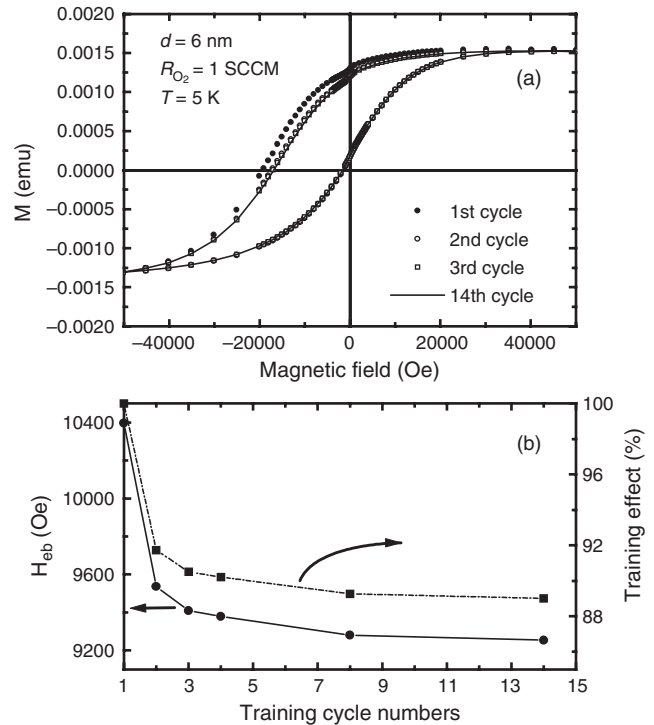


Figure 18. (a) Successive hysteresis loops measured at 5 K along the easy axis after cooling from 300 K in a field of +20000 Oe along the same direction; (b) H_{eb} and training effect as a function of the training cycle number for the monodispersed Co/CoO cluster assembly with $d = 6$ nm. Reproduced with permission from [155], D. L. Peng et al., *Phys. Rev. B* 61, 3103 (2000). © 2000, The American Physical Society.

Spin Disorder at Core-Shell Interface With regard to the origin of the enhanced coercivity or uniaxial anisotropy, disappearance of the UEA effect at lower temperatures, and large training effect, spin disorder states and/or spin glass are highly plausible at around the core-shell interface [153, 155, 156, 355, 369, 391, 397]. At first, Mössbauer spectroscopy studies on surface oxidized Fe nanoparticles revealed that the surface shell consisted of very small crystallites and that a large spin canting characterized the oxide phase [400–402]. Secondly, in ferrite nanoparticles, a surface spin disorder has been experimentally discussed [403, 404], being corroborated by numerical calculations. The antiferromagnetic superexchange interaction is disrupted at the surface of the ferrimagnetic oxide crystallites because of missing oxygen ions or the presence of other impurity molecules. Such broken exchange bonds between surface spins lead to surface spin disorder, being compatible with a spin-glass-like behavior at the surface. In addition, another evidence of the spin-glass-like state has also been given by the alternating-current (ac) magnetic measurement for the Co/CoO cluster assembly with $d = 6$ nm and $R_{O_2} = 1$ sccm [391]. For this sample, the sharp cusps (peaks at freezing temperature T_f) in both ZFC and FC magnetization curves are observed. Since the frequency shift in T_f can offer a good criterion for distinguishing a spin-glass-like material from a superparamagnet, the dependence of the position of the cusp (at freezing T_f) on the frequency of the ac field were measured. The experimental result [391] indicates that T_f depends on the frequency of the ac field and the peak is shifted to the

low-temperature direction with decreasing the frequency of measurement. When the frequency varies between $\omega = 1000$ and 1 Hz, T_f is reduced by about 10%: $\Delta T_f/[T_f \Delta(\log \omega)]$ is about 0.03. These values are the same order as those of the spin glasses and smaller than the values of the superparamagnets [405]. Therefore, the hypothesis of spin disorder at the surface of the oxide crystallites or the interface of the core and oxide shell is applicable for the oxide-coated Fe, Co, and Ni cluster assemblies. According to this hypothesis, the onset of loop shift and bifurcation between H_c^{ZFC} and H_c^{FC} below T_d can be ascribed to a freezing of disorder surface spins of the oxide shell crystallites. The presence of such a disordered spin freezing state leads to not only the loop shift but also the large H_c , which is much larger than the intrinsic value of the FM core, because an ideal interface between the FM core and oxide shell should have no effect on the enhancement of H_c . The training effects also further support such a hypothesis of the spin-glass-like state in the interfacial layers between the FM core and oxide shell. The repeated magnetization reversal at high fields makes the interfacial spins change to a new frozen spin state and decreases the net interfacial uncompensated antiferromagnetic magnetization, causing a decrease of H_{cb} and H_c .

Macroscopic Quantum Tunneling (MQT) Effect Magnetic relaxation measurements were performed for the CoO-coated Co cluster assembly using the following procedure: first, the sample was cooled from 300 K to a lower temperature in low magnetic field, $H_a = 100$ Oe; the field was then reversed to $H_b = -100$ Oe and the variation of the magnetization with time was measured at this temperature. As shown in the inset of Figure 19, the magnetic relaxation follows logarithmic time-dependence (Eq. 20). There is no single exponential time dependence as expected for a collection of identical, noninteracting single-domain clusters aligned in the same direction by a field (*i.e.*, the anisotropy energy barrier is universal throughout the system). This implies a wide distribution of the anisotropy energy, which is ascribed to polycrystalline CoO and a different interfacial state in spite of the narrow cluster size distribution. By least-square fitting of Eq. 20 to the results in the inset of Figure 19, the S value is estimated as a function of temperature and shown in Figure 19. The temperature variation of S at a high temperature range deviates from linearity. However, for $8 < T < 50$ K, S varies linearly with T , extrapolating to zero when $T = 0$, as would be expected for the magnetic relaxation via thermal activation. This indicates that the interaction between the Co cores is smaller than the energy barrier height, probably because the dipole interaction between the Co cores is shielded partially by the AF CoO shell.

The other remarkable feature is that the S values are independent of temperature at $T \leq 8$ K. Such a nonthermal relaxation character below a few Kelvin has been observed in several nanostructured materials with the broad distribution of sizes or anisotropy energy barriers [359–363, 406], being ascribed to the MQT effect of magnetization. The MQT effect is observable at experimentally accessible temperatures only for materials with high uniaxial anisotropy. Indeed, for this CoO-coated Co cluster assembly, $H_c = 5$ kOe (see Fig. 16) and the uniaxial anisotropy constant, $K \approx H_c \times M_s \approx 7.2 \times 10^6$ erg/cm³, which is larger than the

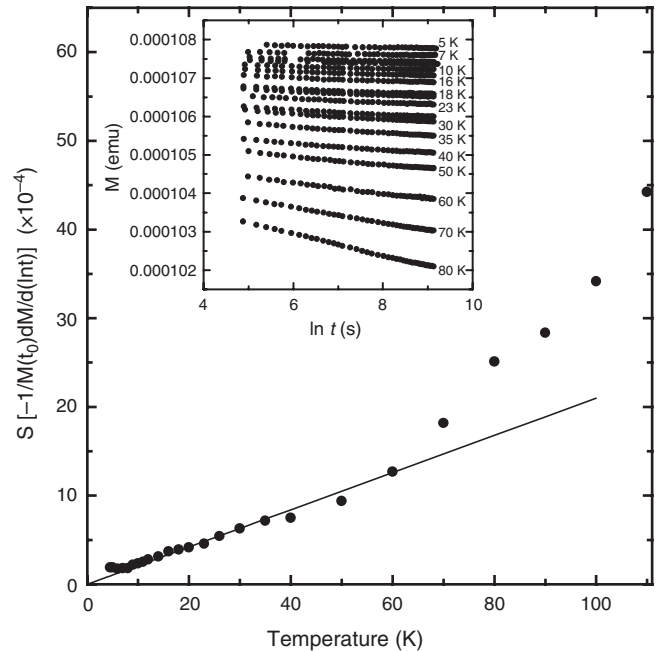


Figure 19. Magnetic viscosity, S , as a function of temperature for the Co/CoO, monodispersed cluster assembly with $d = 6$ nm prepared at $R_{O_2} = 1$ sccm. The inset shows time-dependence of magnetization at different temperatures. Reproduced with permission from [153], D. L. Peng et al., *Appl. Phys. Lett.* 75, 3856 (1999). © 1999, American Institute of Physics.

bulk value ($K = 4.5 \times 10^6$ erg/cm³ and 2.5×10^6 erg/cm³ for bulk hcp and fcc Co, respectively) [407]. Therefore, the high crossover temperature from a thermal activation regime to a quantum tunneling regime, $T_{co} = 8$ K, is ascribed to the enhanced uniaxial anisotropy due to exchange coupling between the FM Co core and AF CoO shell.

5.1.4. MicroSQUID Magnetometry Studies of Individual Magnetic Nanoclusters

As described above, because of the limited sensitivity of conventional magnetic characterization techniques, most of the experimental studies on nanosized particles were carried out on large assemblies of particles, where distributions of particle sizes, shapes, and defects rendered the interpretation quite difficult. From a fundamental point of view, it is very necessary to study the magnetic properties of a single nanocluster. Recently, an ultrahigh sensitivity magnetometry technique based on microSQUID devices has been developed [408] to detect, for the first time, the magnetic signal of one single nanocluster with a size as low as 1000 atoms [409]. Such a challenge is achieved by embedding the Co clusters directly in the metal niobium constituting the superconducting microSQUID loop at low temperature (7 K) to considerably improve the cluster-microSQUID coupling. Thin 20-nm Nb-films with embedded Co-cluster (≈ 3 nm in diameter, fcc-truncated octahedron) were prepared using the low-energy cluster beam codeposition technique and subsequently an electron beam microlithographed to pattern a large number of microSQUID loops. The concentration of Co-clusters is low enough ($< 0.1\%$) to avoid any interaction between them. Magnetic measurement results

showed that a Co-nanocluster embedded in an Nb matrix mainly behaves as a macrospin with a bi-axial anisotropy corresponding to a second-order anisotropy energy [410]. The experimental anisotropy measured for an individual Co-nanocluster is probably related to an interface anisotropy resulting from the symmetry breaking at the cluster surface. The microSQUID magnetic measurements are also complemented with structural studies of the cluster core and surface to understand the origin of magnetic anisotropy in Co-nanoclusters [411]. This clearly emphasizes the dominant role of surface/interface effects in the magnetic properties of nanosize systems.

5.2. Transport Properties and Magnetosistance Effect in Oxide-Coated Metal Cluster Assemblies

5.2.1. Theoretical Background

Weak Localization and Electron-Electron Interactions

The electrical transport behaviors of the metal cluster-assembled films can be changed conspicuously by oxidization of cluster surfaces [93, 154, 412]. That is, the coupling strength between the adjacent clusters can be varied in a wide range by controlling the degree of surface oxidation. This means that the electron transport changes from metallic-like to tunneling-like. For such a disorder system, the low temperature behavior of the resistivity is influenced by weak localization (WL) [413] and/or electron-electron interactions (EEI) [414]. Here, the resistance increases with decreasing temperature owing to the quantum interference of conduction electrons (WL) and/or a disorder-enhanced Coulomb interaction between electrons (EEI). There are different temperature-dependences at low temperatures for two- and three-dimensional systems. At $T = 0$ K, a two-dimensional system cannot be a conductor, being an insulator. The scaling theory [413] predicts that at very low temperatures, the sheet conductance σ of a metallic film deviates from its classic residual value σ_0 as

$$\sigma = \sigma_0 - \left(\frac{Pe^2}{\pi h} \right) \log T \quad (24)$$

where P is a number of the order of unity. The EEI in a disorder potential also results in a similar logarithmic temperature-dependence [414]. Consequently, there is no difference feature between WL and EEI pictures for two-dimensional systems at a very low temperature.

Incipient Anderson Localization In disordered electronic systems, incipient Anderson localization effect is often observed in a transition step from a WL region to an insulating region. Incipient localization was first pointed out by Imry [415]. He extended the scaling theory for a ground state ($T = 0$) [413] to finite temperatures by introducing a temperature-dependent inelastic diffusion length $L_i(T)$ that varies inversely with the temperature. This leads to a crossover of L_i with localization length ξ at a distinct temperature (microscopic conductivity region). A simple

interpolation formula for the conductivity was first given by Girvin and Jonson [416],

$$\sigma = \frac{e^2}{h} \left(\frac{B}{\xi} + \frac{A}{L_i(T)} \right) \quad (25)$$

where A and B are constants of the order of unity. Here, the conductivity scales to its macroscopic value at zero temperature when $L_i \gg \xi$, while it is temperature-dependent with $\sigma \sim (L_i(T))^{-1} \sim T^{p/3}$ for $L_i \ll \xi$. For example, in the region closer to the metal-insulator transition ($0.3 < x < 0.34$), the $\text{Pd}_x\text{C}_{1-x}$ granular films show anomalous resistance behavior with a negative temperature coefficient of resistance (TCR) even at high temperatures [417]. The conductivity behavior changes from $\sigma \sim T^{1/2}$ to $\sigma \sim T^{1/3}$ at low temperatures T_0 , where a crossover of L_i with ξ occurs. This is attributed to incipient Anderson localization due to a diverging ξ which becomes larger than L_i .

Variable Range Hopping Conductivity In disordered electronic systems, another characteristic conductivity behavior is temperature dependence of $\sigma \propto \exp(-b/T^{1/4})$. This relation was first derived by Mott [418] by taking into account the conduction in amorphous semiconductors, in which the electron transport is dominated by the thermal hopping (*i.e.*, phonon-assisted tunneling) between localized states that are randomly distributed with traps-potential fluctuation. The electron can jump from a localized state to a neighboring one, where their wave functions overlap each other. The difference in the eigenstate energies is compensated by the absorption or emission of phonons. This mechanism is valid when the electron coherence length is longer than the localization length, namely, for a strongly localized disorder system.

Tunnel-Type Conductivity For granular materials, when the metal cluster concentration is just below the percolation threshold, the electrical conduction is dominated by the tunneling between metallic clusters. The low-field, tunnel-type electrical conduction in these materials was discussed by Neugebauer and Webb [419]. Most simply, the conductivity is expressed as follows:

$$\sigma \propto \exp\left(-2\kappa s - \frac{E_c}{2k_B T}\right) \quad (26)$$

where s is the tunnel-barrier thickness between the two clusters, κ the tunneling exponent of electron wavefunctions in the insulator, that is, $\kappa = [2m^*(\phi + E_F - E)/\hbar^2]^{1/2}$; m^* the effective electron mass, ϕ the barrier height, E the electron energy, E_F the Fermi level, and \hbar the Plank constant. E_c is the electrostatic energy required to create a positive-negative charged pair in two clusters by tunneling, and gives rise to the Coulomb blockade effect at a low temperature. When the applied voltage and thermal energy are much smaller than E_c , electrons or holes cannot tunnel from one neutral cluster to another without exciting their states from the Fermi level to the levels higher than E_c . When the cluster size is monodispersed and the intercluster distance (namely, the same barrier thickness) uniform, Eq. (26) predicts a simple hopping-type temperature-dependence for the low-field conductivity [419]: $\sigma(T) \propto \exp(-E_c/2k_B T)$.

However, there are also many granular disordered materials [420–422] that exhibit an $\sigma \propto \exp(-b/T^{1/2})$ behavior at a wide temperature range. Such temperature-dependence of the low-field conductivity can be ascribed to a relationship $sE_c = \text{constant}$ between s and E_c [422]. In granular materials produced by codeposition of a metal and an oxide, and subsequent precipitation of magnetic granules on a substrate, there is normally a wide distribution of the cluster size, inter-cluster distance (namely, the tunnel-barrier thickness), and their correlation because precipitated regions leave chemically depleted zones in their neighborhood owing to a simple material balance. Electric current flows in the shortest path depending on temperature.

5.2.2. Conductivity

A typical oxide-coated, Co cluster-assembled system that exhibits the transport behaviors from metallic to tunneling is shown in Figure 20 [154]. The temperature-dependence of resistivity ρ is clearly different for the samples prepared

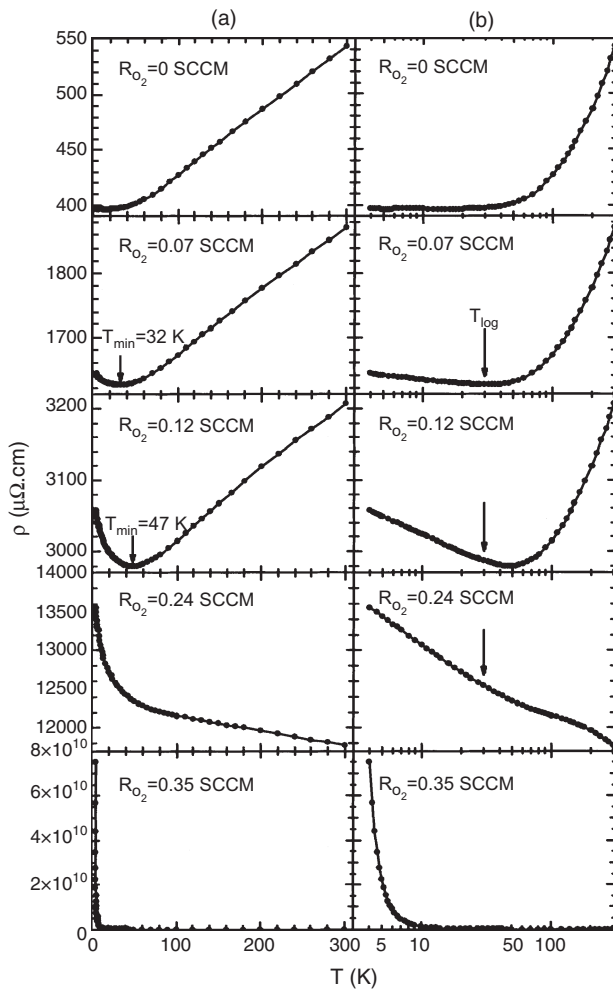


Figure 20. (a) Electrical resistivity, $\rho(T)$, at zero magnetic field as a function of temperature, T . (b) $\rho(T)$ versus logarithmic temperature for the CoO-coated Co-cluster assemblies prepared at $R_{O_2} = 0, 0.07, 0.12, 0.24,$ and 0.35 sccm. Reproduced with permission from [154], D. L. Peng et al., *Phys. Rev. B* 60, 2093 (1999). © 1999, The American Physical Society.

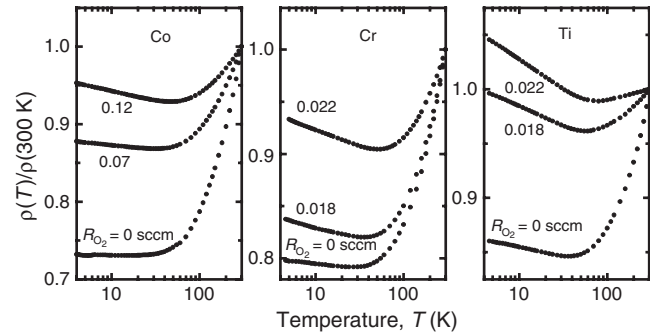


Figure 21. Reduced resistivity, $\rho(T)/\rho(300 \text{ K})$, vs. $\log T$ for Co-, Cr-, and Ti-cluster assemblies prepared at different oxygen gas flow rate R_{O_2} .

at different oxygen gas flow rates R_{O_2} . For $R_{O_2} = 0$ sccm, namely, clean Co cluster assembly, the sample shows ordinary metallic temperature dependence, characterized by the residual resistance at low temperatures and a linear increase with T . The large residual resistance is ascribed to the porous stacking structure of the specimen. For lightly oxidized cluster assemblies ($0 < R_{O_2} < 0.24$ sccm), the resistivity exhibits a minimum at the temperature T_{\min} , which shifts to higher temperatures with increasing R_{O_2} . Above T_{\min} , the samples show the metallic behavior as revealed by the linear temperature-dependence of ρ . Below T_{\log} , the value of ρ logarithmically increases with decreasing T and the increase of $\rho(T)$ becomes more pronounced with increasing R_{O_2} . Such $\log T$ dependence of resistivity in the case of light oxidation of cluster surfaces is similar to $\text{Pd}_x\text{C}_{1-x}$ granular films [423–425]. The same features were also observed in other metal cluster assemblies. For example, Figure 21 shows ρ normalized to the resistivity at $T = 300 \text{ K}$ as a function of the logarithm of T for Co, Cr, and Ti cluster assemblies prepared at low R_{O_2} . Overall, resistivities exhibit $\log T$ dependence below T_{\log} . This characteristic aspect of $\rho(T)$ also becomes more pronounced with increasing R_{O_2} . However, it should be noted that the Cr cluster assemblies show the same temperature-dependence of ρ for much lower R_{O_2} in comparison to the Co cluster assemblies, and Ti cluster assemblies show the same behavior for the lowest R_{O_2} . These differences are attributable to the cohesive energy (ΔH) for Co, Cr, and Ti oxides: $|\Delta H_{\text{CoO}}| < |\Delta H_{\text{Cr}_2\text{O}_3}| < |\Delta H_{\text{TiO}_2}|$ [426].

As seen in Figure 20, when $R_{O_2} \geq 0.24$ sccm, the resistivity minimum disappears and the TCR is negative below room temperature. However, it should be noted that there are obvious differences in the temperature-dependence of ρ between the samples prepared at $R_{O_2} = 0.24$ and 0.35 sccm. For $R_{O_2} = 0.24$ sccm, $\rho(T)$ increases gradually with decreasing T and has the same order of magnitude between $T = 5$ to 300 K , whereas, for $R_{O_2} = 0.35$ sccm, it increases dramatically with decreasing T below $T = 10 \text{ K}$, and the $\rho(T)$ value at 4.2 K is three to four orders of magnitude larger than that at room temperature and about 6–8 orders of magnitude larger than that of the sample prepared at $R_{O_2} = 0.24$ sccm. These results also indicate that the transport mechanism is different between the samples prepared at $R_{O_2} = 0.24$ and 0.35 sccm. For $R_{O_2} = 0.24$ sccm, the conductivity behavior is attributed to incipient Anderson localization or variable range hopping conductivity. Such a transition step in

conduction is also observed in $\text{Pd}_x\text{C}_{1-x}$ granular films [417]. For $R_{\text{O}_2} > 0.3$ sccm, as shown in the next section, the large magneto-resistance effect (spin-dependent, tunnel-type conductivity) was also observed. Further examination on the temperature-dependence of $\rho(T)$ for $R_{\text{O}_2} > 0.3$ sccm shows a $\sigma \propto \exp(-b/T)$ behavior [93], which differs from the well-known temperature dependence of $\sigma \propto \exp(-b/T^{1/2})$ behavior for disordered granular materials [422]. This is ascribed to the uniform cluster size and surface CoO layer (barrier) thickness in the monodispersed Co/CoO cluster assemblies [154]. From the linear part of the plot of $\log \sigma$ versus $1/T$, the E_c values of the Co core clusters are estimated to be $E_c = 5.2, 6,$ and 5.8 meV for $R_{\text{O}_2} = 0.35, 0.4,$ and 1 sccm, respectively, which are in agreement with the calculated value of 5.4 meV using the expression [23]: $E_c = (e^2/2\pi\epsilon_0\epsilon d)[s/(d/2 + s)]$, where ϵ is the dielectric constant (12.9 for CoO), $\epsilon_0 = 8.854 \times 10^{-12}$ F/m, d is the mean diameter of the Co cores (11 nm) and s is the separation between neighboring Co cores (2 nm).

5.2.3. Magneto-Resistance Effect

In oxide-coated magnetic metal cluster assemblies, a giant magneto-resistance (GMR) effect has also been observed [93, 154, 427]. The GMR effect arises from a spin-dependent tunneling effect [428–432]. Electron tunneling between two FM electrodes through an insulating (I) layer depends on the relative orientation of the magnetizations of the electrodes. When the relative orientation of the magnetizations is changed by applying a magnetic field, tunnel-type magneto-resistance (TMR) is expected to occur. In FM-I granular systems, where the magnetic metal granules or clusters are embedded in an insulator matrix, the TMR effect has also been detected [433]. For the oxide-coated magnetic metal cluster assemblies, when the cluster cores are separated completely by the semiconducting oxide shells with a certain thickness, the electrical conduction is dominated by tunneling between metallic cores. This tunnel-type resistance is dependent on the relative orientation of the magnetization in the two cluster cores, thus showing the large magneto-resistance. Therefore, the aforementioned core-shell Co/CoO cluster assemblies exhibit not only a characteristic tunnel-type conductivity but also a typical TMR behavior. The room-temperature resistivities of CoO single crystals are 10^8 – 10^{15} Ω -cm, and the activation energies are 0.73–1.35 eV [434]. Moreover, CoO is an antiferromagnetic semiconductor with the Néel temperature of 293 K. Therefore, the CoO shells play a role in nonmetallic tunneling barrier. Figure 22 summarizes the zero-field resistivity ρ and magneto-resistance (MR) at 30 kOe, measured at 4.2 and 300 K, of the monodispersed Co/CoO cluster assemblies as a function of R_{O_2} , [154]. ρ and MR reveal a rapid increase with increasing R_{O_2} , when R_{O_2} becomes larger than a value (0.24 sccm for the case of the Co/CoO cluster assemblies). Such an abrupt increase in both ρ and MR clearly results from the tunnel-type conduction between metallic Co cores via CoO shell layers. This experimental result also indicates that the MR values at 4.2 K are much larger than those at room temperature. This is ascribed to the Coulomb blockade effect at low temperatures [93, 154].

It is worth further mentioning that the magnetic states (spin order or spin disorder) of the oxide shells results in

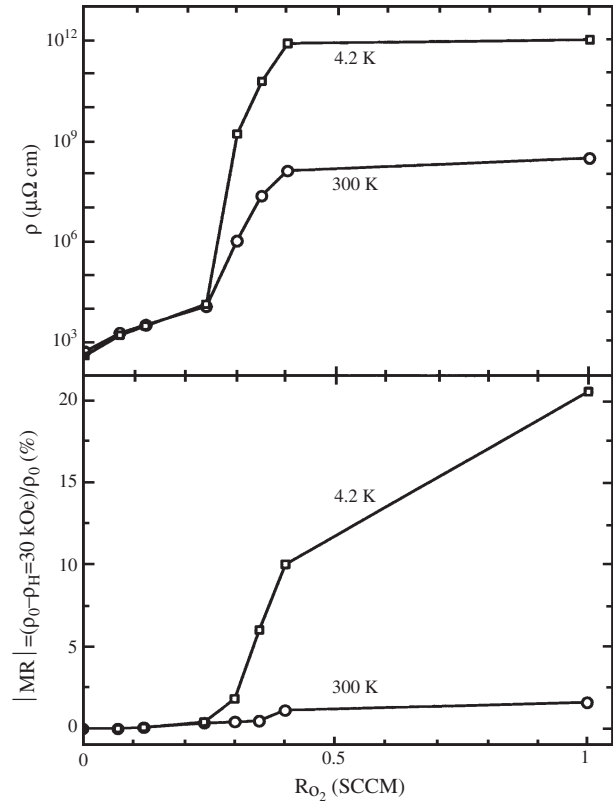


Figure 22. Variation of (a) resistivity, ρ , and (b) the absolute value of the magneto-resistance ratio, $|MR|$, at 300 and 4.2 K for the CoO-coated Co-cluster assemblies as a function of R_{O_2} . Reproduced with permission from [154], D. L. Peng et al., *Phys. Rev. B* 60, 2093 (1999). © 1999, The American Physical Society.

different saturation behaviors in magnetization and MR . For core-shell Fe-Fe oxide systems, for instance, the magnetic field dependence of the MR values exhibits no saturation tendency in field up to $H = 70$ kOe even at low temperatures, disagreeing with the magnetization curves that are of a saturation tendency [427, 435]. This behavior has been interpreted considering spin-disorder surface layers of the oxide grains, interparticle magnetic correlations, and microscopic mechanisms similar to those responsible for the MR in other granular systems.

6. CONCLUDING REMARKS

We have started from the incentive that assembling of monodispersed size transition metal clusters is one of the key technologies in fabricating nanostructure-controlled materials. After mentioning several cluster preparation methods, we have dealt with the plasma gas condensation method in detail: the experimental results and theoretical consideration of formation and growth of size-controlled metal clusters, alloy cluster formation, and nonequilibrium structures in clusters. Then, we have described incidence and deposition of clusters onto the substrate, experimental results and theoretical aspects of cluster-diffusion and -migration on the substrate surface, and codeposition to form cluster-embedded or granular materials. We have discussed how individual clusters first form discontinuous small aggregates and later

continuous networks in terms of the percolation concept, and a possibility of ordered assembly using patterned substrates. Finally, we have displayed the two physical properties of cluster assemblies, magnetic and electrical properties. In small ferromagnetic clusters, a single-domain structure is favorable due to the serious loss of domain wall energy. When the surface of ferromagnetic metal clusters is oxidized, magnetic coupling between the ferromagnetic core and anti-ferromagnetic or ferrimagnetic shell crystallites yields both exchange anisotropy and very large coercivity. The magnetic moment is fluctuated and relaxed thermally at high temperatures and quantum mechanically at low temperature. At low temperatures, moreover, electron localization aspects have been observed in slightly oxidized cluster assemblies, whereas tunneling-type-conductivity and magnetoresistance with Coulomb-Blockade type characters are observed in well-oxidized cluster assemblies. We wish to emphasize that the assembling of monodispersed-size clusters is a prerequisite in highlighting the characteristic properties and their temperature-dependence, that is, the clear crossover of

magnetic relaxation and conductivity between the high and low temperature regimes. All the results that are dealt with in this article are summarized in Table 1.

This chapter demonstrates that we can prepare size-controlled clusters as building blocks and just stand on the entrance to fabricate cluster assembled materials. We are searching new academic and industrial fields to apply small clusters: medical science, drug delivery, catalysis, etc. We should more actively utilize the anomalous properties of much smaller clusters with one or two nanometers in diameter; for instance, atomic moments of Fe, Co, and Ni clusters are 1.5 or 2 times larger than those of their bulk metals [19]. In order to assemble such small clusters without losing their unique characteristics, we have to find stabilization and surface-coating methods other than surface oxidation [436]. Gas-phase syntheses, using vacuum-based systems, are capable in preparing impurity-free and isotropic shape clusters minimizing degradation of unique properties, whereas condensed-phase syntheses will inevitably suffer from inclusion of oxygen and other impurities from surrounding

Table 1. Summary of experimental results for transition metal cluster assemblies.

Elements	Deposition method	Size	Measurement	Ref.
Cr	PGC	6–13 nm	TEM	[88, 89]
Fe	GC	30 nm	Mössbauer spectroscopy	[334, 335]
	GC	9–20 nm	Magnetism	[338]
	GC	5–20 nm	TEM and magnetism	[395]
	SECB	2–5 nm	Magneto-resistance	[58, 59]
	LV	2–6 nm	Magnetism	[164]
	SECB	0.6–1.4 nm	Magnetism and magneto-resistance	[60, 61]
	GC	6–40 nm	Magnetism	[346, 397]
	PGC	7–16 nm	TEM, SEM, magnetism, and magneto-resistance	[156, 431]
Co	GC	180–690 atoms	XMCD	[296]
	GC	5–35 nm	Magnetism	[388–390]
	LV	2–5 nm	Micro-SQUID, magnetism	[408]
	LV	3 nm	Giant magneto-resistance	[151]
	PGC	6–15 nm	TEM, SEM, SAXS, magnetism, and electrical conductivity	[91, 92, 165, 198]
Co-Al	PGC	6–15 nm	Magnetism and magneto-resistance	[153–155]
	PGC	9 nm	TEM and electrical conductivity	[378, 379]
	LV	3 nm	Micro-SQUID, magnetism	[409–411]
	PGC	4.5 nm	TEM and magnetism	[357]
Co-Pt	PGC	13 nm	TEM and EDX	[116]
	PGC	5–8.5 nm	TEM and EDX	[117]
Ni	PGC	2–4 nm	TEM	[90]
Cu	PGC	<3000 atoms	SEM and TOF mass spectroscopy	[85]
Nb	PGC	2–13 nm	TEM and TOF mass spectroscopy	[94]
Nb-Ag	PGC	5–10 nm	TEM and EDX	[115]
Mo	PGC	3 nm	TOF mass spectroscopy	[84]
Ag	PGC	1,7,19 atoms	STM	[254]
	PGC	2,8,19 atoms	STM and fluorescence spectrum	[255]
Ag-Au	LV	1.9–2.8 nm	TEM and optical properties	[109]
	LV	1.5–5 nm	TEM and optical properties	[110]
Pt-Fe	PGC	3–6 nm	TEM and magnetism	[145, 146]
Pt-Pd	LV	1.5–4 nm	TEM and EDX	[111, 112]
Au	LV	2 nm	Optical absorption	[171]

Notes: Notation of deposition methods: PGC: plasma-gas-condensation; GC: gas-condensation; SECB: supersonic expansion cluster beam; LV: Laser vaporation.

environments. However, gas-phase syntheses are unable to prepare ordered lattices and periodical arrangements of clusters and to anisotropically-shape building blocks because of the random formation and deposition procedures, and the simple nucleation and growth processes. Condensed-phase syntheses, such as microemulsion and a colloidal reaction, can give self-organized cluster lattices, and rod and ellipsoidal shape building blocks [5]. Combination of gas-phase and condensed-phase syntheses is appropriate in forming such cluster lattices using their advantages: clusters prepared by gas-phase synthesis can be immersed in a colloidal solution [13, 74]. It is further desired that the crystalline orientation and/or anisotropic shape of size-selected clusters are neatly arranged as were done in liquid crystals and Langmuir–Blodgett films [437]. Therefore, our final goal is to fabricate size-, orientation-, and periodicity-controlled cluster assemblies, because we will obtain extraordinarily unique properties and/or cooperative phenomena originating from the ordered arrangement of the specific nanometer size functional units.

GLOSSARY

Blocking temperature The temperature above which thermal excitation energy becomes so large and overcomes the magnetic anisotropy energy in small magnetic particles. Their magnetization is spontaneously reversed from one easy direction to the other, even in the absence of an applied field.

Coulomb blockade When a condenser size becomes small down to a few ten nanometers, the electric current is induced by a tunneling effect. However, the charging energy, which is necessary in a transient step of the electronic flow, increases with the decrease in the size and blocks the electron tunneling as far as the applied voltage is smaller than the charging energy.

Crystal habit In a small crystal, characteristic crystal shapes are formed via preferential growth of particular crystallographic faces, depending on the atomic structure and the growth condition and surface energy.

Energy dispersive X-ray analysis A chemical analysis method based on the separation of X-ray according to their energies (wave lengths), by use of a lithium-drifted silicon proportional detector.

Exchange coupling Quantum mechanical electrostatic interaction between the electron spins of neighboring atoms in magnetic material. If it is appreciable, the electron spins are aligned either parallelly or antiparallely.

Ferromagnetic/Superparamagnetic transition In a magnetic particle system the magnetic phase changes from superparamagnetism to ferromagnetism with changing the particle size or temperature.

Gas condensation (gas-aggregation) Evaporated vapor atoms, which collide with each other and inert gas atoms, lose their kinetic energies and coalesce each other to form molecules. They further grow up to clusters (small particles) in the inert gas atmosphere.

Isentropic supersonic expansion Supersonic expansion which occurs without any change in entropy, when a gas is expanded through a small hole from a high pressure state

to a vacuum state. Since this adiabatic expansion reduces the relative velocity of gas atoms, clusters are formed.

Macroscopic quantum tunneling The magnetic moment of a small particle behaves as a quantum object rather than a classical vector. Its direction interchanges between the two magnetically easy directions due to quantum tunneling.

Magic number Specific size clusters, which are much more stable than their neighbor size clusters, are called magic numbers, because their electronic structures are analogous to the stable closed shells seen in atoms and in nuclei.

Magnetic viscosity The existence of a time delay between a change in the magnetic field applied to a ferromagnetic material and the resulting change in magnetic induction. The time scale is much longer than explained by the eddy current loss mechanism.

Magneto-optical effect Optical polarization and optical properties of condensed matter are influenced by an applied magnetic field and their magnetic properties because the optical (dipole) transitions between the occupied and unoccupied electronic states are spin-dependent due to the spin-orbit coupling.

Magnetoresistance effect An electrical resistivity change in materials by application of magnetic field. Two groups of conduction carriers are deflected by different amount in the magnetic fields, because they have different masses, different charges or different spins. Since it is impossible to find an electric field that will keep both components of the current going in the same direction, the net current (the resistivity) is changed.

Metal-insulator transition If the average spacing of constituent atoms and/or the electron correlation effect are extremely increased in a metallic system, the metallic state is not sustainable and the system becomes a insulator.

Ostwald growth A particle growth phenomenon in which small particles dissolve and reprecipitate onto large particles to reduce the surface energy of the entire particle system.

Percolation phenomenon A stochastic growing process of random site- or network- systems in which site the occupation numbers or interconnections of constituents extend from a local range to a macroscopic scale when the density of constituents and their interconnections are increased.

Percolation threshold The critical point at which the scale of the local site occupation or network becomes infinite in a percolating system.

Quantum size effect In a condensed matter, whose size is comparable with or smaller than both the mean free path and the effective de Broglie wavelength of electrons, the electron momentum is quantized and the electron states become quasi-discrete, leading to anomalous structural, physical and chemical properties.

Soft-percolation A percolation in a random network system where the strength of the interconnections is not uniform but a function of the distance between the constituents.

Spin glass One of a wide variety of materials that contain interacting magnetic moments and also possess some forms of disorder, in which the temperature variation of the magnetic susceptibility shows a cusp. The temperature corresponding to the abrupt change in slope is generally referred as the freezing temperature.

Superparamagnetism In small (nano-scale) particle magnets, the magnetic spins are exchange-coupled to form a single domain structure, but they are collectively switched or fluctuated by thermal energy.

Supersaturation Thermodynamically unstable condition that is the driving force for both crystal nucleation and growth. Therefore it is the key variable in setting the mechanisms and rates by which these processes occur.

Synchrotron (orbit) radiation Electromagnetic waves are radiated by the centripetal acceleration of relativistically high energy charged particles (electron, positron, proton) along the tangent direction of their orbits. This phenomenon gives rise to a very intensive source of highly polarized waves ranging from ultraviolet to X-ray wave lengths.

Uniaxial anisotropy An energetic preference for the magnetic moment along (parallel or antiparallel to) a specific direction (a crystal axis) in magnetic material.

Universality The critical exponent describing a percolation phenomenon depends only on the dimensionality of the lattice, but not on the system structure.

Vegard's law A linear relation between the lattice parameter and composition of solid solution alloys expressed as the atomic percentage.

Weak localization As a consequence of the interference of electron waves they are scattered weakly by the random potential. Within the classical theory of conductivity which neglects this interference, the residual conductivity at low temperatures is independent of temperature. Once the interference is considered, the perturbation breaks the phase coherence in any manner, showing a temperature-dependent conductivity inherent to the localization.

X-ray absorption fine structure (XAFS) The fine structure in the photon energy spectrum is observed as oscillations just above the X-ray absorption edge of an element. These oscillations contain structural information on the immediate surroundings of the atom undergoing X-ray absorption.

ACKNOWLEDGMENTS

The authors wish to express their sincere thanks to Emeritus Prof. M. Tachiki and Emeritus Professor K. Suzuki of Tohoku University for their valuable guidance and hearty encouragement; Prof. T. J. Konno of Osaka Prefecture University, Mr. K. Wakoh, and Dr. M. Sakurai of Tohoku University for their effective experimental contribution; and Prof. A. Kasuya for his critical discussion. This work has been primarily supported by Core Research for Evolutional Science and Technology (CREST) of the Japan Science and Technology Corporation (JST) and partially supported by the Grant-in-Aid for Scientific Research given by the Ministry of Education, Science, Culture, and Sports of Japan.

REFERENCES

1. A. S. Edelstein and R. C. Cammarata, Eds., "Nanomaterials Synthesis, Properties and Applications," Institute of Physics, 1996.
2. R. P. Andres, R. S. Averback, W. L. Brown, L. E. Brus, W. A. Goddard III, A. Kaldor, S. G. Louie, M. Moscovits, P. S. Peercy, S. J. Riley, R. W. Siegel, F. Spaepen, and Y. Wang, *J. Mater. Res.* 4, 704 (1989).
3. G. Prinz and K. Hathaway, Eds., "Special Issue: Magneto-electronics, Physics Today" April, 24 (1995).
4. P. Mélinon, V. Paillard, V. Dupuis, A. Perez, P. Jensen, A. Hoareau, J. P. Perez, J. Tuauillon, M. Broeyer, J. L. Vialle, M. Pellarin, B. Bauguenard, and J. Lerme, *Int. J. Mod. Phys. B* 9, 339 (1995).
5. K. Sumiyama, Ed., IPAP Conference Series 3, *Proc. Internat. Symp. Cluster Assembled Materials* (2001).
6. O. S. Heavens, "Optical Properties of Thin Solid Films," Dover Publications, New York, 1965.
7. R. Kubo, *J. Phys. Soc. Jpn.* 17, 975 (1962).
8. R. Uyeda, *Proc. Phys. Math. Soc. Jpn.* 24, 809 (1942).
9. R. Uyeda, *Progr. Mat. Sci.* 35, 1 (1991).
10. C. Hayashi, R. Ueda, and A. Tazaki, Eds., "Ultrafine Particles," Mita (in Japanese) 1988.
11. E. Fuchita, M. Oda, and S. Kashu, *Proc. 7th Internat. Conf. Vacuum Metallurgy*, 973 (1982).
12. C. G. Granqvist and R. A. Buhrman, *J. Appl. Phys.* 47, 2200 (1976).
13. H. Murakami, M. Hirakawa, Y. Ohtsuka, H. Yamakawa, N. Imazeki, S. Hayashi, T. Suzuki, M. Oda, and C. Hayashi, *J. Vac. Sci. Tech. B* 17, 2321 (1999).
14. H. Gleiter, *Proc. 2nd Risoe Int. Symp. Metall. Mater. Sci.*, p. 15 (1981).
15. H. Gleiter, *Progr. Mat. Sci.* 33, 223 (1989).
16. S. Sugano, Y. Nishina, and S. Ohnishi, "Microclusters," Springer-Verlag, New York, 1987.
17. H. Haberland, Ed., "Clusters of Atoms and Molecules I & II," Springer-Verlag, New York, 1994.
18. S. Sugano and H. Koizumi, "Microcluster Physics," 2nd ed. Springer-Verlag, New York, 1998.
19. I. M. L. Billas, A. Châtelain, and W. A. de Heer, *J. Magn. Magn. Mat.* 168, 64 (1997).
20. B. D. Curry, "Introduction to Magnetic Materials," Addison-Wesley, London, 1972.
21. B. L. Altshuler, P. A. Lee, and R. A. Webb, Eds., "Mesoscopic Phenomena in Solids," North-Holland, Amsterdam, 1991.
22. P. Milani and S. Iannotta, "Cluster Beam Synthesis of Nano-Structured Materials," Springer-Verlag, Berlin, 1999.
23. B. Abeles, P. Sheng, M. D. Coutts, and Y. Arie, *Adv. Phys.* 24, 407 (1975).
24. A. E. Berkowitz, J. R. Mitchell, M. J. Carey, A. P. Young, S. Zhang, F. E. Spada, F. T. Parker, A. Hutten, and G. Thomas, *Phys. Rev. Lett.* 22, 3745 (1992).
25. J. Q. Xiao, J. S. Jiang, and C. L. Chien, *Phys. Rev. Lett.* 22, 3749 (1992).
26. L. P. Gor'kov and G. M. Eliashberg, *Sov. Phys. JETP* 21, 940 (1965).
27. R. Dupree and M. A. Smithard, *J. Phys. C* 5, 408 (1972).
28. R. D. Maurer, *J. Appl. Phys.* 29, 1 (1958).
29. R. C. McMillan, G. J. King, B. S. Miller, and F. F. Carlson, *J. Phys. Chem. Solids* 23, 1379 (1962).
30. R. Zsigmondy, *Z. Phys. Chem.* 56, 65 (1906).
31. R. H. Doremus, *J. Chem. Phys.* 40, 2389 (1964).
32. S. W. Marshall and R. M. Wilenzick, *Phys. Rev. Lett.* 16, 219 (1966).
33. M. CareyLea, *Am. J. Sci.* 37, 476 (1889).
34. R. M. Wilenzick, D. C. Russell, R. H. Morriss, and S. W. Marshall, *J. Chem. Phys.* 47, 533 (1967).
35. A. H. Pfund, *Phys. Rev.* 35, 1434 (1930).
36. H. C. Burger and P. H. van Cittert, *Z. Phys.* 66, 210 (1930).
37. T. P. Martin and T. Bergmann, *J. Chem. Phys.* 90, 6664 (1989).
38. K. Sattler, J. Mühlbach, and E. Recknagel, *Phys. Rev. Lett.* 45, 821 (1980).
39. D. Rayane, P. Melinon, B. Tribollet, B. Chabud, A. Hoareau, and M. Broeyer, *J. Chem. Phys.* 91, 3100 (1989).
40. W. Schulze, B. Winter, and I. Goldenfeld, *Phys. Rev. B* 38, 2937 (1988).
41. H. G. Limberger and T. P. Martin, *J. Phys. Chem.* 90, 2979 (1988).
42. V. E. Bondybej and J. H. English, *J. Chem. Phys.* 76, 2165 (1982).

43. S. J. Riley, E. K. Parks, C. R. Mao, L. G. Pobo, and S. Wexler, *J. Phys. Chem.* 86, 3911 (1982).
44. R. E. Smalley, *Laser Chem.* 2, 167 (1983).
45. P. Milani and W. A. de Heer, *Rev. Sci. Instrum.* 61, 1835 (1990).
46. S. Maruyama, L. R. Anderson, and R. E. Smalley, *Rev. Sci. Instrum.* 61, 3686 (1990).
47. P. Milani and W. A. de Heer, *Phys. Rev. B* 44, 8346 (1990).
48. P. Ciambelli, G. Bagnasco, L. Lisi, M. Turco, G. Chiarello, M. Musci, M. Notaro, D. Robba, and P. Ghetti, *Appl. Catal. B: Env.* 1, 61 (1992).
49. L. E. Depero, P. Bonzi, M. Musci, and C. Casale, *J. Solid State Chem.* 111, 247 (1994).
50. S. Veintemillas-Verdaguer, O. Bomati-Miguel, and M. P. Morales, *Scripta Mater.* 47, 589 (2002).
51. S. Martelli, O. Bomati-Miguel, L. de Dominicis, R. Giorgi, F. Rinaldi, and S. Veintemillas-Verdaguer, *Appl. Surf. Sci.* 186, 562 (2002).
52. P. Fayet, J. P. Wolf, and L. Wöste, *Phys. Rev. B* 33, 6792 (1986).
53. I. Katakuse, T. Ichihara, Y. Fujita, T. Matsuo, T. Sakurai, and H. Matsuda, *Int. J. Mass Spectrom. Ion Proc.* 67, 229 (1985).
54. W. Begemann, S. Deihöfer, K. H. Meiwes-Broer, and H. O. Lutz, *Z. Phys. D* 3, 183 (1986).
55. W. A. Harbich, S. Fredrigo, and J. Buttet, *Chem. Phys. Lett.* 195, 613 (1992).
56. T. Takagi, I. Yamada, and A. Sasaki, *J. Vac. Sci. Tech.* 12, 1128 (1975).
57. I. Yamada, H. Usui, and T. Takagi, *J. Phys. Chem.* 91, 2463 (1987).
58. S. A. Makhlof, K. Sumiyama, K. Wakoh, and K. Suzuki, *Jpn. J. Appl. Phys.* 33, 1323 (1994).
59. M. Sakurai, S. A. Makhlof, K. Sumiyama, K. Wakoh, and K. Suzuki, *Jpn. J. Appl. Phys.* 33, 4090 (1994).
60. T. Hihara, K. Sumiyama, M. Sakurai, H. Onodera, K. Wakoh, and K. Suzuki, *J. Phys. Soc. Jpn.* 66, 1450 (1997).
61. T. Hihara, K. Sumiyama, H. Onodera, K. Wakoh, and K. Suzuki, *J. Phys. Soc. Jpn.* 66, 1785 (1997).
62. W. L. Brown, M. F. Jarrold, R. L. McEachern, M. Sosnowski, G. Takaoka, H. Usui, and I. Yamada, *Nucl. Instr. Meth. B* 59/60, 182 (1991).
63. T. Hihara, K. Sumiyama, K. Wako, and K. Suzuki, *Jpn. J. Appl. Phys.* 34, 6063 (1995).
64. W. Knauer, *J. Appl. Phys.* 62, 841 (1987).
65. S.-N. Mei, S.-N. Yang, J. Wong, C.-H. Choi, and T.-M. Lu, *J. Cryst. Growth* 87, 357 (1988).
66. J. G. Pruettt, H. Windischmann, M. L. Nicholas, and P. S. Lampard, *J. Appl. Phys.* 64, 2271 (1988).
67. M. Sosnowski, S. Krommenhoek, Jyh Sheen, and R. H. Cornely, *J. Vac. Sci. Technol. A* 8, 1458 (1990).
68. O. F. Hagena, G. Knop, and G. Linker, in "Physics and Chemistry of Fine Systems: From Clusters to Crystals," Vol. II, p. 1233. Kluwer Academic Publishers, Netherlands, 1992.
69. H.-F. Eicke, T. C. W. Shepherd, and A. Steinemann, *J. Coll. Interface Sci.* 56, 168 (1976).
70. P. D. I. Fletcher, A. M. Howe, and B. H. Robinson, *J. Chem. Soc. Faraday Trans. I* 83, 985 (1987).
71. J. P. Chen, C. M. Sorensen, K. J. Klabunde, and G. C. Hadjipanayis, *Phys. Rev. B* 51, 11527 (1995).
72. S. Wu, H. Westfahl Jr., J. Schmalian, and P. G. Wolynes, *Chem. Phys. Lett.* 359, 1 (2002).
73. S. A. Harfenist, Z. L. Wang, M. M. Alvarez, I. Vezmar, and R. L. Whetten, *J. Phys. Chem.* 100, 13904 (1996).
74. R. P. Andres, J. D. Bielefeld, J. I. Henderson, D. B. Janes, V. R. Kolagunta, C. P. Kubiak, W. J. Mahoney, and R. G. Osifchin, *Science* 273, 1960 (1996).
75. S. R. Johnson, S. D. Evans, S. W. Mahon, and A. Ulman, *Supramol. Sci.* 4, 329 (1997).
76. E. E. Carpenter, C. J. O'Connor, and V. G. Harris, *J. Appl. Phys.* 85, 5175 (1999).
77. C. T. Black, C. B. Murray, R. L. Sandstrom, and S. Sun, *Science* 290, 1131 (2000).
78. G. A. Held, G. Grinstein, H. Doyle, S. Sun, and C. B. Murray, *Phys. Rev. B* 64, 012408 (2001).
79. A. Ciach, V. Babin, and M. Tasinkevych, *Coll. Surf. A* 208, 51 (2002).
80. M. Boutonnet, J. Kizling, P. Stenius, and G. Maire, *Coll. Surf.* 5, 209 (1982).
81. C. B. Murray, C. R. Kagan, and M. G. Bawendi, *Science* 270, 1335 (1995).
82. M. Sakurai, K. Watanabe, K. Sumiyama, and K. Suzuki, *J. Phys. Soc. Jpn.* 67, 2571 (1998).
83. M. Sakurai, K. Wakoh, K. Sumiyama, and K. Suzuki, *J. Chem. Phys.* 111, 235 (1999).
84. H. Haberland, M. Karrais, M. Mall, and Y. Thurner, *J. Vac. Sci. Technol. A* 10, 3266 (1992).
85. H. Haberland, M. Mall, M. Moseler, Y. Qiang, T. Reiners, and Y. Thurner, *J. Vac. Sci. Technol. A* 12, 2925 (1994).
86. M. Goto, J. Murakami, Y. Tai, K. Igarashi, and S. Tanemura, *Z. Phys. D* 40, 115 (1997).
87. G. Hohl, T. Hihara, M. Sakurai, T. Oishi, K. Wakoh, K. Sumiyama, and K. Suzuki, *Jpn. J. Appl. Phys.* 33, 1509 (1994).
88. S. Yamamuro, K. Sumiyama, M. Sakurai, and K. Suzuki, *Supramol. Sci.* 5, 239 (1998).
89. S. Yamamuro, K. Sumiyama, and K. Suzuki, *J. Appl. Phys.* 85, 483 (1999).
90. T. Hihara and K. Sumiyama, *J. Appl. Phys.* 84, 5270 (1998).
91. S. Yamamuro, K. Sumiyama, T. Hihara, and K. Suzuki, *J. Phys. Soc. Jpn.* 68, 28 (1999).
92. S. Yamamuro, K. Sumiyama, T. Hihara, and K. Suzuki, *J. Phys. Cond. Mat.* 11, 3247 (1999).
93. D. L. Peng, K. Sumiyama, S. Yamamuro, T. Hihara, and T. J. Konno, *Appl. Phys. Lett.* 74, 76 (1999).
94. T. Hihara and K. Sumiyama, *J. Vac. Sci. Technol. B* 17, 1923 (1999).
95. A. C. Xenoulis, P. Tsouris, G. Doukellis, N. Boukos, E. Valamontes, Y. Chen, and T. Tsakalagos, *Nano Struct. Mater.* 8, 771 (1997).
96. A. C. Xenoulis, G. Doukellis, and T. Tsakalagos, *Nano Struct. Mater.* 10, 1347 (1998).
97. A. C. Xenoulis, G. Doukellis, P. Tsouris, A. Karydas, C. Potiriadis, A. A. Katsanos, and T. Tsakalagos, *Vacuum* 51, 357 (1998).
98. K. Bromann, C. Félix, H. Brune, W. Harbich, R. Monot, J. Buttet, and K. Kern, *Science* 274, 956 (1996).
99. G. M. Francis, L. Kuipers, J. R. A. Cleaver, and R. E. Palmer, *J. Appl. Phys.* 79, 2942 (1996).
100. C. Félix, G. Vandoni, W. Harbich, J. Buttet, and R. Monot, *Surf. Sci.* 331-333, 925 (1995).
101. D. R. Miller, in "Atomic and Molecular Beam Methods" (G. Scoles, Ed.), Vol. 1. Oxford University Press, Oxford, 1988.
102. S. Yatsuya, T. Kamakura, K. Yamauchi, and K. Mihama, *Jpn. J. Appl. Phys.* 25, L42 (1986).
103. A. Milchev and J. Malinowski, *Surf. Sci.* 156, 36 (1985).
104. P. W. Atkins, "Physical Chemistry," Oxford University Press, New York, 1995.
105. J. M. Soler, N. García, O. Echt, K. Sattler, and E. Recknagel, *Phys. Rev. Lett.* 49, 1857 (1982).
106. H. Mizuseki, Y. Jin, Y. Kawazoe, and L. T. Wille, *J. Appl. Phys.* 87, 6561 (2000).
107. H. Mizuseki, Y. Jin, Y. Kawazoe, and L. T. Wille, *Appl. Phys. A* 73, 731 (2001).
108. H. Mizuseki, K. Hongo, Y. Kawazoe, and L. T. Wille, *Scripta Mater.* 44, 1911 (2001).
109. E. Cottancin, J. Lermé, M. Gaudry, M. Pellarin, J. L. Vialle, M. Broyer, B. Prével, M. Treilleux, and P. Mélinon, *Phys. Rev. B* 62, 5179 (2000).

110. M. Gaudry, J. Lermé, E. Cottancin, M. Pellarin, J.-L. Vialle, M. Broyer, B. Prével, M. Treilleux, and P. Mélinon, *Phys. Rev. B* 64, 085407 (2000).
111. J. L. Rousset, A. M. Cadrot, F. J. Cadete Santos Aires, A. Renouprez, P. Mélinon, A. Perez, M. Pellarin, J. L. Vialle, and M. Broyer, *J. Chem. Phys.* 102, 8574 (1995).
112. J. L. Rousset, B. C. Khanra, A. M. Cadrot, F. J. Cadete Santos Aires, A. J. Renouprez, and M. Pellarin, *Surf. Sci.* 352–354, 583 (1996).
113. H. Yasuda and H. Mori, *Phys. Rev. Lett.* 69, 3747 (1992).
114. H. Yasuda, K. Mitsuishi, and H. Mori, *Phys. Rev. B* 64, 094101 (2001).
115. K. Wakoh, T. Hihara, D. L. Peng, and K. Sumiyama, *Nano Struct. Mater.* 11, 1245 (1999).
116. T. J. Konno, S. Yamamuro, and K. Sumiyama, *J. Appl. Phys.* 90, 3079 (2001).
117. T. J. Konno, S. Yamamuro, and K. Sumiyama, *J. Vac. Sci. Technol. B* 20, 834 (2002).
118. K. Kimoto and I. Nishida, *J. Phys. Soc. Jpn.* 22, 744 (1967).
119. C. J. Doherty, J. M. Poate, and R. J. H. Voorhoeve, *J. Appl. Phys.* 48, 2050 (1977).
120. Y. Saito, K. Mihama, and R. Uyeda, *Jpn. J. Appl. Phys.* 19, 1603 (1980).
121. T. Onozawa and K. Takayanagi, *Surf. Sci.* 357–358, 228 (1996).
122. T. Hihara, D. L. Peng, and K. Sumiyama, *Mater. Trans.* 42, 1480 (2001).
123. J. P. Chu, J. W. Chang, P. Y. Lee, J. K. Wu, and J. Y. Wang, *Thin Solid Films* 312, 78 (1998).
124. M. Arita and I. Nishida, *Jpn. J. Appl. Phys.* 32, 1759 (1993).
125. S. Ino, *J. Phys. Soc. Jpn.* 21, 346 (1966).
126. S. Ino, *J. Phys. Soc. Jpn.* 27, 941 (1969).
127. L. D. Marks, *Rep. Prog. Phys.* 57, 603 (1994).
128. H. Fujita and N. Fujita, *Mater. Trans.* 42, 1474 (2001).
129. G. Wulff, *Z. Krist.* 34, 449 (1901).
130. B. E. Sundquist, *Acta Metal.* 12, 67 (1964).
131. T. Hayashi, T. Ohno, S. Yatsuya, and R. Uyeda, *Jpn. J. Appl. Phys.* 16, 705 (1977).
132. J. C. Heyraud and J. J. Metois, *J. Cryst. Growth* 50, 571 (1980).
133. A. R. Tholen, *Surf. Sci.* 106, 70 (1981).
134. S. Ino and D. Ogawa, *J. Phys. Soc. Jpn.* 22, 1365 (1967).
135. J. G. Allpress and J. V. Sanders, *Surf. Sci.* 7, 1 (1967).
136. R. S. Berry, J. Jellinek, and G. Natanson, *Phys. Rev. A* 30, 919 (1984).
137. S. Sawada and S. Sugano, *Z. Phys. D* 20, 259 (1991).
138. H. Matsuoka, T. Hirokawa, M. Matsui, and M. Doyama, *Phys. Rev. Lett.* 69, 297 (1992).
139. C. L. Cleveland, W. D. Luedtke, and U. Landman, *Phys. Rev. B* 60, 5065 (1999).
140. S. Iijima and T. Ichihashi, *Jpn. J. Appl. Phys.* 24, L125 (1985).
141. S. Iijima and T. Ichihashi, *Phys. Rev. Lett.* 56, 616 (1986).
142. D. J. Smith, A. K. Petford-Long, L. R. Wallenberg, and J. O. Bovin, *Science* 233, 872 (1986).
143. S. J. Carroll, S. G. Hall, and R. E. Palmer, *Phys. Rev. Lett.* 81, 3715 (1998).
144. S. G. Hall, M. B. Nielsen, and R. E. Palmer, *J. Appl. Phys.* 83, 733 (1998).
145. S. Stappert, B. Rellinghaus, M. Acet, and E. Wassermann, *Mater. Res. Soc. Symp. Proc.* 704, 73 (2002).
146. B. Rellinghaus, S. Stappert, M. Acet, and E. Wassermann, *Mater. Res. Soc. Symp. Proc.* 705, 315 (2002).
147. J. F. Roux, M. Treilleux, B. Cabaud, G. Fuchs, C. Montandon, and A. Hoareau, *J. Phys. I (France)* 4, 991 (1994).
148. J. F. Roux, B. Cabaud, M. Treilleux, A. Hoareau, and G. Fuchs, *Nanostruct. Mater.* 6, 525 (1995).
149. K. Sumiyama, K. Suzuki, S. A. Makhlof, K. Wakoh, T. Hihara, S. Yamamuro, M. Sakurai, and T. Kamiyama, *Mater. Sci. Eng. B* 31, 133 (1995).
150. K. Ishii, T. Ohba, and T. Hara, *Mater. Sci. Eng. A* 217/218, 232 (1996).
151. F. Parent, J. Tuaille, L. B. Stern, V. Dupuis, B. Prevel, A. Perez, P. Melinon, G. Guiraud, R. Morel, A. Barthélémy, and A. Fert, *Phys. Rev. B* 55, 3683 (1997).
152. Y. Qiang, R. Morel, D. Eastham, J. M. Meldrim, J. Kraft, A. Fert, H. Haberland, and D. J. Sellmyer, in “Cluster and Nanostructure Interfaces” (P. Jena, S. U. Khanna, and B. K. Rao, Eds.), p. 217. World Scientific, Singapore, 2000.
153. D. L. Peng, K. Sumiyama, T. Hihara, and S. Yamamuro, *Appl. Phys. Lett.* 75, 3856 (1999).
154. D. L. Peng, K. Sumiyama, T. J. Konno, T. Hihara, and S. Yamamuro, *Phys. Rev. B* 60, 2093 (1999).
155. D. L. Peng, K. Sumiyama, T. Hihara, S. Yamamuro, and T. J. Konno, *Phys. Rev. B* 61, 3103 (2000).
156. D. L. Peng, T. Hihara, K. Sumiyama, and H. Morikawa, *J. Appl. Phys.* 92, 3075 (2002).
157. H.-V. Roy, P. Fayet, F. Patthey, W.-D. Schneider, B. Delley, and C. Massobrio, *Phys. Rev. B* 49, 5611 (1994).
158. I. M. Goldby, L. Kuipers, B. von Issendorff, and R. E. Palmer, *Appl. Phys. Lett.* 69, 2819 (1996).
159. M. Ehbrecht, B. Kohn, F. Huisken, M. A. Laguna, and V. Paillard, *Phys. Rev. B* 56, 6958 (1997).
160. C. Félix, G. Vandoni, C. Massobrio, R. Monot, J. Buttet, and W. Harbich, *Phys. Rev. B* 57, 4048–4052 (1998).
161. S. J. Carroll, K. Seeger, and R. E. Palmer, *Appl. Phys. Lett.* 72, 305 (1998).
162. S. J. Carroll, S. Pratontep, M. Streun, and R. E. Palmer, *J. Phys. Chem.* 113, 7723 (2000).
163. P. Jensen, *Rev. Mod. Phys.* 71, 1695 (1999).
164. V. Dupuis, J. P. Perez, J. Tuaille, V. Paillard, P. Mélinon, A. Perez, B. Barbara, L. Thomas, S. Fayeulle, and J. M. Gay, *J. Appl. Phys.* 6, 6676 (1994).
165. S. Yamamuro, K. Sumiyama, T. Kamiyama, and K. Suzuki, *J. Appl. Phys.* 86, 5726 (1999).
166. T. Takagi, I. Yamada, K. Matsubara, and H. Takaoka, *J. Cryst. Growth* 45, 318 (1978).
167. T. Takagi, “Ionized-Cluster Beam Deposition and Epitaxy,” Noyes, Park Ridge, NJ, 1988.
168. H. Haberland, Z. Insepov, and M. Moseler, *Z. Phys. D* 26, 229 (1993).
169. H. Haberland, Z. Insepov, M. Karrais, M. Mall, M. Moseler, and Y. Thurner, *Mater. Sci. Eng. B* 19, 31 (1993).
170. Y. Sasaki, K. Shinozawa, H. Tanimoto, Y. Iwamoto, E. Kita, and A. Tasaki, *Mater. Sci. Eng. A* 217/218, 344 (1996).
171. A. Perez, P. Mélinon, V. Dupuis, P. Jensen, B. Prevel, J. Tuaille, L. Bardotti, C. Martet, M. Treilleux, M. Broyer, M. Pellarin, J. L. Vaille, B. Palpant, and J. Lerme, *J. Phys. D: Appl. Phys.* 30, 709 (1997).
172. G. L. Kellogg, *Phys. Phys. Lett.* 73, 1833 (1994).
173. S. C. Wang, U. Kürpock, and G. Ehrlich, *Phys. Phys. Lett.* 81, 4923 (1998).
174. J.-M. Wen, S.-L. Chang, J. W. Burnett, J. W. Evans, and P. A. Thiel, *Phys. Phys. Lett.* 73, 2591 (1994).
175. L. Bardotti, P. Jensen, A. Hoareau, M. Treilleux, and B. Cabaud, *Phys. Phys. Lett.* 74, 4694 (1995).
176. J. C. Hamilton, M. S. Daw, and S. M. Foiles, *Phys. Lett.* 74, 2760 (1995).
177. W. D. Luedtke and Uzi Landman, *Phys. Phys. Lett.* 82, 3835 (1999).
178. G. Fuchs, P. Mélinon, F. Santos Aires, M. Treilleux, B. Cabaud, and A. Hoareau, *Phys. Rev. B* 44, 3926 (1991).
179. M. Takagi, *J. Phys. Soc. Jpn.* 9, 359 (1954).
180. Ph. Buffat and J.-H. Borel, *Phys. Rev. B* 13, 2287 (1976).
181. A. N. Goldstein, C. M. Echer, and A. P. Alivisatos, *Science* 256, 1425 (1992).
182. P. Jensen, A.-L. Barabási, H. Larralde, S. Havlin, and H. E. Stanley, *Phys. Rev. B* 50, 15316 (1994).

183. B. Weitzel and H. Micklitz, *Europhys. Lett.* 12, 123 (1990); *Phys. Rev. Lett.* 66, 385 (1991).
184. S. Fedrigo, W. Harbich, and J. Buttet, *Phys. Rev. B* 58, 7428 (1998).
185. A. Perez, V. Dupuis, J. Tuillon-Combes, L. Bardotti, B. Prével, P. Mélinon, M. Jamet, W. Wernsdorfer, and B. Barbara, in "Nanoscale Materials" (L. M. Liz-Marzán and P. V. Kamat, Eds.), p. 3371. Kluwer Academic Publishers, Boston, 2003.
186. L. Bardotti, B. Prével, P. Jensen, M. Treilleux, P. Mélinon, A. Perez, J. Gierak, G. Faini, and D. Maily, *Appl. Surf. Sci.* (2002) in press.
187. J. Liu, J. C. Barnard, K. Seeger, and E. Palmer, *Appl. Phys. Lett.* 73, 2030 (1998).
188. D. L. Peng, G. Lerondel, T. Hihara, K. Sumiyama, and T. Yao, *Jpn. J. Appl. Phys.* 41, 5726 (2002).
189. D. Stauffer and A. Aharony, "Introduction to Percolation Theory," 2nd ed., Taylor & Francis, London, 1992.
190. V. K. S. Shante and S. Kirkpatrick, *Adv. Phys.* 20, 325 (1971).
191. S. Kirkpatrick, *Rev. Mod. Phys.* 45, 574 (1973).
192. T. Odagaki, *J. Phys.: Condens. Matt.* 1, 1013 (1989).
193. Y. Wachi, T. Odagaki, and A. Puri, *Phys. Rev. B* 50, 13412 (1994).
194. C.-W. Nan, *Prog. Mater. Sci.* 37, 1 (1993).
195. K. Yoshida, *Jpn. J. Appl. Phys.* 30, 3482 (1991).
196. H. Scher and R. Zallen, *J. Chem. Phys.* 53, 3759 (1970).
197. L. J. Duckers and R. G. Ross, *Phys. Lett.* 49A, 361 (1974); L. J. Duckers, *Phys. Lett.* 67A, 93 (1978).
198. S. Yamamuro, K. Sumiyama, T. J. Konno, and K. Suzuki, *Mater. Trans. JIM* 40, 1450 (1999).
199. D. L. Peng, T. J. Konno, K. Wakoh, T. Hihara, and K. Sumiyama, *Eur. Phys. J. D* 16, 329 (2001).
200. P. Mélinon, P. Jensen, J. X. Hu, A. Horeau, B. Cabaud, M. Treilleux, and D. Guillot, *Phys. Rev. B* 44, 12562 (1991).
201. A. B. Harris, *Phys. Rev. B* 28, 2614 (1983).
202. C. L. Chien, *J. Appl. Phys.* 69, 171 (1991).
203. L. D. Marks, *Rep. Prog. Phys.* 57, 603 (1994).
204. M. J. Yacamán, J. A. Accenio, H. B. Liu, and J.-G. Torresdey, *J. Vac. Sci. Technol. B* 19, 1091 (2001).
205. J. C. H. Spence, "Experimental High-Resolution Electron Microscopy," 2nd ed., Oxford University Press, New York, 1988.
206. L. Reimer, "Transmission Electron Microscopy," 4th ed., Springer-Verlag, Berlin, Heidelberg, 1997.
207. D. B. Williams and C. B. Carter, "Transmission Electron Microscopy," Plenum Press, New York, 1996.
208. K. Kimoto, Y. Kamiya, M. Nonomiya, and R. Uyeda, *Jpn. J. Appl. Phys.* 2, 702 (1963).
209. S. Yatsuya, S. Kasukabe, and R. Uyeda, *Jpn. J. Appl. Phys.* 12, 1675 (1973).
210. S. Kasukabe, S. Yatsuya, and R. Uyeda, *Jpn. J. Appl. Phys.* 13, 1714 (1974).
211. R. Uyeda, *J. Cryst. Growth* 24/25, 69 (1974).
212. T. Ohno, S. Yatsuya, and R. Uyeda, *Jpn. J. Appl. Phys.* 15, 1213 (1976).
213. Y. Saito, K. Mihama, and R. Uyeda, *Jpn. J. Appl. Phys.* 19, 1603 (1980).
214. T. Ohno and K. Yamaguchi, *Jpn. J. Appl. Phys.* 20, 1385 (1981).
215. S. Matsumoto and Y. Matsui, *J. Mater. Sci.* 18, 1785 (1983).
216. J. G. Allpress and J. V. Sanders, *Surf. Sci.* 7, 1 (1967).
217. U. Dahmen and K. H. Westmacott, *Science* 233, 875 (1986).
218. J. L. Gardea-Torresday, K. J. Tiemann, G. Gamez, K. Dokken, S. Tehuacanero, and M. José Yacamán, *J. Nanoparticle Res.* 1, 397 (1999).
219. S. Iijima, *Jpn. J. Appl. Phys. Part 1* 26, 357 (1987).
220. G. Wulff, *Z. Kristallog* 34, 449 (1901).
221. F. Santos Aires, M. Treilleux, G. Fuchs, A. Hoareau, P. Melinon, and B. Cabaud, *Z. Phys. D* 12, 149 (1989).
222. C. Montandon, G. Fuchs, M. Treilleux, J. F. Roux, and A. Hoareau, *Nanostruct. Mater.* 4, 353 (1994).
223. D. L. Peng, T. J. Konno, K. Wakoh, T. Hihara, and K. Sumiyama, *Appl. Phys. Lett.* 78, 1535 (2001).
224. A. Tasaki, S. Tomiyama, S. Iida, N. Wada, and R. Uyeda, *Jpn. J. Appl. Phys.* 4, 707 (1965).
225. R. Jullien and P. Meakin, *J. Physique* 39, 873 (1990).
226. B. Pauwels, G. Van Tendelco, W. Bouwen, L. T. Kuhn, P. Lievens, H. Lei, and M. Hou, *Phys. Rev. B* 62, 10383 (2000).
227. T. P. Martin, T. Bergmann, H. Gölich, and T. Lange, *Chem. Phys. Lett.* 172, 209 (1990).
228. D. J. Wales and J. P. K. Doye, *J. Phys. Chem. A* 101, 5111 (1997).
229. R. H. Leary and J. P. K. Doye, *Phys. Rev. E* 60, R6320 (1999).
230. J. P. K. Doye, M. A. Miller, and D. J. Wales, *J. Chem. Phys.* 110, 6896 (1999).
231. C. L. Cleveland, W. D. Leudtke, and U. Landman, *Phys. Rev. Lett.* 81, 2036 (1998).
232. C. L. Cleveland, W. D. Leudtke, and U. Landman, *Phys. Rev. B* 60, 5065 (1999).
233. J. P. K. Doye, D. J. Wales, and R. S. Berry, *J. Chem. Phys.* 103, 4234 (1995).
234. R. S. Berry and B. M. Smirnov, *J. Chem. Phys.* 113, 728 (2000).
235. J. P. K. Doye and F. Calvo, *Phys. Rev. Lett.* 86, 3570 (2001).
236. J. P. K. Doye and F. Calvo, *J. Chem. Phys.* 116, 8307 (2002).
237. D. J. Smith, A. K. Petford-Long, L. R. Wallenberg, and J.-O. Bovin, *Science* 233, 872 (1986).
238. A. Howie, *Nature* 320, 684 (1986).
239. P. Williams, *Appl. Phys. Lett.* 50, 1761 (1987).
240. M. Mitome, Y. Tanishiro, and K. Takayanagi, *Z. Phys. D* 21, 45 (1989).
241. Y. Ooshima and K. Takayanagi, *Prog. Theoret. Phys.* 106, 24 (1991).
242. H. Mori, M. Komatsu, K. Takeda, and H. Fujita, *Phil. Mag. Lett.* 63, 173 (1991).
243. H. Yasuda, H. Mori, M. Komatsu, and K. Takeda, *J. Appl. Phys.* 73, 1100 (1993).
244. H. Yasuda and H. Mori, *Z. Phys. D* 31, 131 (1994).
245. J. G. Lee, H. Mori, and H. Yasuda, *Phys. Rev. B* 65, 132106 (2002).
246. O. Kitakami, T. Sakurai, Y. Miyashita, Y. Takeno, Y. Shimada, H. Takano, H. Awano, and Y. Sugita, *Jpn. J. Appl. Phys.* 35, 1724 (1996).
247. G. Binnig, H. Rohrer, Ch. Gerber, and E. Weibel, *Appl. Phys. Lett.* 40, 178 (1982).
248. G. Binnig, C. F. Quate, and C. Gerber, *Phys. Rev. Lett.* 56, 930 (1986).
249. E. J. van Loenen, D. Dijkkamp, A. J. Hoeven, J. M. Lenssinck, and J. Dieleman, *Appl. Phys. Lett.* 55, 1312 (1989).
250. R. Wiesendanger, "Scanning Probe Microscopy and Spectroscopy; Methods and Applications," Cambridge University Press, Cambridge, 1994.
251. R. Wiesendanger, "Scanning Probe Microscopy; Analytical Methods," Springer-Verlag, Berlin, 1998.
252. R. Czajka, A. Kasuya, T. Hihara, and K. Sumiyama, IPAP Conf. Series 3, *Proc. Internat. Symp. Cluster Assembled Mater.* 137 (2001).
253. R. Czajka, T. Hihara, A. Kasuya, X. Liu, K. Sumiyama, R. Nishitani, and S. Szuba, *Colloids and Surface A202*, 195 (2002).
254. K. Bromann, C. Félix, H. Brune, W. Harbich, R. Monot, J. Buttet, and K. Kern, *Science* 274, 956 (1996).
255. W. Harbich and C. Félix, *C. R. Physique* 3, 289 (2002).
256. W. Yamaguchi, H. Ohashi, and J. Murakami, *Chem. Phys. Lett.* 364, 1 (2002).
257. M. D. Upward, P. Moriarty, P. H. Beton, S. H. Baker, C. Binns, and K. Edmonds, *Appl. Phys. Lett.* 70, 2114 (1997).
258. J. B. Barner and S. T. Ruggiero, *Phys. Rev. Lett.* 59, 807 (1987).
259. M. Dorogi, J. Gomez, R. Osifchin, R. P. Andres, and R. Reifenberger, *Phys. Rev. B* 52, 9071 (1995).
260. J. G. A. Dubois, J. W. Gerritsen, S. E. Shafranuk, E. J. G. Boon, G. Schmid, and H. van Kempen, *Europhys. Lett.* 33, 279 (1996).
261. L. F. Chi, M. Hartig, T. Drechsler, Th. Schwaack, C. Seidel, H. Fuchs, and G. Schmid, *Appl. Phys. A* 66, S187 (1998).

262. N. Nilius, N. Ernst, and H.-J. Freund, *Phys. Rev. B* 65, 115421 (2002).
263. A. Downes and M. E. Welland, *Appl. Phys. Lett.* 72, 2671 (1998).
264. A. Downes, P. Guaino, and P. Dumas, *Appl. Phys. Lett.* 80, 380 (2002).
265. N. Nilius, A. Cörper, G. Bozdech, N. Ernst, and H.-J. Freund, *Prog. Surf. Sci.* 67, 99 (2001).
266. A. L. Vázquez de Parga and S. F. Alvarado, *Phys. Rev. Lett.* 72, 3726 (1994).
267. R. Nishitani, T. Yoshida, H. Arakawa, A. Kasuya, and K. Sumiyama, IPAP Conf. Series 3, *Proc. Internat. Symp. Cluster Assembled Materials* 142 (2001).
268. S.-T. Lee, G. Apai, M. G. Mason, R. Benbow, and Z. Hurych, *Phys. Rev. B* 23, 505 (1981).
269. S.-L. Weng, S. Moehlecke, M. Strongin, and A. Zangwill, *Phys. Rev. Lett.* 50, 1795 (1983).
270. J. Colbert, A. Zangwill, M. Strongin, and S. Krummacher, *Phys. Rev. B* 27, 1378 (1983).
271. M. G. Mason, *Phys. Rev. B* 27, 748 (1983).
272. G. K. Wertheim and S. B. DiCenzo, *Phys. Rev. B* 37, 844 (1988).
273. M. Cini, M. de Crescenzi, F. Patella, N. Motta, M. Sastry, F. Rochet, R. Pasquali, A. Balzarotti, and C. Verdozzi, *Phys. Rev. B* 41, 5685 (1990).
274. H.-V. Roy, P. Fayet, F. Patthey, W.-D. Schneider, B. Delley, and C. Massobrio, *Phys. Rev. B* 49, 5611 (1994).
275. A. M. Keen, C. Binns, S. H. Baker, S. Mozley, C. Norris, and S. C. Thornton, *Surf. Sci.* 352–354, 715 (1996).
276. A. Howard, D. N. S. Clark, C. E. J. Mitchell, R. G. Egdell, and V. R. Dhanak, *Surf. Sci.* 518, 210 (2002).
277. D. P. Woodruff and T. A. Delchar, “Modern Techniques of Surface Science,” Cambridge University Press, Cambridge, 1986.
278. M. Haruta, *Catal. Today* 36, 153 (1997).
279. J. A. Rodriguez, J. Dvorak, T. Jirsak, and J. Hrbek, *Surf. Sci.* 490, 315 (2001).
280. J. A. Rodriguez, G. Liu, T. Jirsak, J. Hrbek, Z. Chang, J. Dvorak, and A. Maiti, *J. Am. Chem. Soc.* 124, 5242 (2002).
281. Z. Chang, Z. Song, G. Liu, J. A. Rodriguez, and J. Hrbek, *Surf. Sci.* 512, L353 (2002).
282. G. K. Wertheim, *Z. Phys. D* 12, 319 (1989).
283. H. N. Aiyer, V. Vijayakrishnan, G. N. Subbanna, and C. N. R. Rao, *Surf. Sci.* 313, 392 (1994).
284. B. K. Teo, “EXAFS: Inorganic Chemistry Concepts 9 Basic Principles and Data Analysis,” Springer-Verlag, Berlin, 1986.
285. J. L. Erskine and E. A. Stern, *Phys. Rev. B* 12, 5016 (1975).
286. J. Tuaille, V. Dupuis, P. Mélinon, B. Prével, M. Treilleux, A. Perez, M. Pellarin, J. L. Vialle, and M. Broyer, *Phil. Mag. A* 76, 493 (1997).
287. H. Sakurai, F. Itoh, H. Oike, T. Tsurui, S. Yamamuro, K. Sumiyama, and T. Hihara, *J. Phys.: Cond. Mat.* 12, 3451 (2000).
288. M. Sakurai, S. A. Makhlof, T. Hihara, K. Sumiyama, K. Wakoh, and K. Suzuki, *Physica B* 208 & 209, 614 (1995).
289. M. Négrier, J. Tuaille-Combes, V. Dupuis, P. Mélinon, A. Perez, and A. Traverse, *Phil. Mag. A* 81, 2855 (2001).
290. C. T. Chen, F. Sette, Y. Ma, and S. Modesti, *Phys. Rev. B* 42, 7262 (1990).
291. B. T. Thole, P. Carra, F. Sette, and G. van der Laan, *Phys. Rev. Lett.* 68, 1943 (1992).
292. P. Carra, B. T. Thole, M. Altarelli, and X. Wang, *Phys. Rev. Lett.* 70, 694 (1993).
293. K. W. Edmonds, C. Binns, S. H. Baker, S. C. Thornton, C. Norris, J. B. Goedkoop, M. Finazzi, and N. B. Brookes, *Phys. Rev. B* 60, 472 (2000).
294. K. W. Edmonds, C. Binns, S. H. Baker, M. J. Maher, S. C. Thornton, O. Tjernberg, and N. B. Brookes, *J. Magn. Magn. Mat.* 220, 25 (2000).
295. K. W. Edmonds, C. Binns, S. H. Baker, M. J. Maher, S. C. Thornton, O. Tjernberg, and N. B. Brookes, *J. Magn. Magn. Mat.* 221, 113 (2001).
296. S. H. Baker, C. Binns, K. W. Edmonds, M. J. Maher, S. C. Thornton, S. Louch, and S. S. Dhési, *J. Magn. Magn. Mater.* 247, 19 (2002).
297. J. T. Lau, A. Föhlich, R. Nietuby, M. Reif, and W. Wurth, *Phys. Rev. Lett.* 89, 057201-1 (2002).
298. C. Binns, S. H. Baker, K. W. Edmonds, P. Finetti, M. J. Maher, S. C. Louch, S. S. Dhési, and N. B. Brookes, *Physica B* 318, 350 (2002).
299. D. A. Eastham, Y. Qiang, T. H. Maddock, J. Kraft, J.-P. Schille, G. S. Thompson, and H. Haberland, *J. Phys.: Cond. Mat.* 9, L497 (1997).
300. H. A. Dürr, S. S. Dhési, E. Dudzik, D. Knabben, G. van der Laan, J. B. Goedkoop, and F. U. Hillebrecht, *Phys. Rev. B* 59, 701 (1999).
301. H. Sakurai, F. Itoh, K. Takano, D. L. Peng, T. Hihara, and K. Sumiyama, IPAP Conference Series 3, *Proc. Internat. Symp. Cluster Assembled Materials* p. 133 (2001).
302. J. T. Lau, A. Achleitner, and W. Wurth, *Surf. Sci.* 467, L834 (2000).
303. L. Néel, *Comput. Rend.* 228, 604 (1949).
304. J. L. Dormann, D. Fiorani, and E. Tronc, “Magnetic Relaxation in Fine-Particle Systems, in Advances in Chemical Physics,” Vol. XCVIII (I. Prigogine and S. A. Rice, Eds.). John Wiley & Sons, Inc., 1997 and references therein.
305. C. Bellouard, I. Mirebeau, and M. Hennion, *Phys. Rev. B* 53, 82, 5570 (1996).
306. H. Casalta, P. Schleger, C. Bellouard, M. Hennion, I. Mirebeau, G. Ehlers, B. Farago, J.-L. Dormann, M. Kelsch, M. Linde, and F. Philipp, *Phys. Rev. Lett.* 1301 (1999).
307. Y. J. Uemura, T. Yamazaki, D. R. Harshman, M. Senba, and E. J. Ansaldo, *Phys. Rev. B* 31, 546 (1985).
308. I. A. Campbell, A. Schenck, D. Herlach, F. N. Gygax, A. Amato, R. Cywinski, and S. H. Kilcoyne, *Phys. Rev. Lett.* 72, 1291 (1994).
309. R. I. Bewley and R. Cywinski, *Phys. Rev. B* 58, 11544 (1998).
310. T. J. Jackson, C. Binns, E. M. Forgan, E. Morenzoni, Ch. Niedermayer, H. Glücker, A. Hofer, H. Luetkens, T. Prokscha, T. M. Riseman, A. Schantz, M. Birke, J. Litterst, G. Schatz, and H. P. Weber, *J. Phys.: Cond. Mat.* 12, 1399 (2000).
311. G. K. Wertheim, “Mössbauer Effect: Principle and Application,” Academic Press, New York, 1964.
312. U. Gonser, “Mössbauer Spectroscopy and Physical Metallurgy in an Introduction to Mössbauer Spectroscopy” (L. May, Ed.) Chapter 8, p. 155 Plenum Press, 1971 and references therein.
313. F. E. Fujita, *Mater. Trans. JIM* 30, 87 (1989).
314. F. Bødker, S. Mørup, M. S. Pedersen, P. Sevdlindeh, G. T. Jonsson, J. L. Garcia-Palacios, and F. J. Lazoro, *J. Magn. & Magn. Mat.* 177–181, 925 (1998).
315. D. P. E. Dickson, N. M. K. Reid, C. Hunt, H. D. Williams, M. El-Hilo, and K. O’Grady, *J. Magn. & Magn. Mat.* 125, 345 (1993).
316. S. Mørup, *Hyperfine Interactions* 90, 171 (1994).
317. S. Mørup and E. Tronc, *Phys. Rev. Lett.* 72, 3278 (1994).
318. P. Prene, E. Tronc, J. P. Jolivet, J. Livage, R. Cherkaoui, M. Nogue, J. L. Dormann, and D. Fiorani, *IEEE Trans. Magn.* MAG-29, 2658 (1993).
319. J. M. D. Coey, *Phys. Rev. Lett.* 27, 1140 (1971).
320. A. H. Morrish, K. Haneda, and P. J. Schurer, *J. Phys. C* 37, 6 (1976).
321. A. Ochi, K. Watanabe, M. Kiyama, T. Shinjo, Y. Bando, and T. Takada, *J. Phys. Soc. Jpn.* 50, 2777 (1981).
322. T. Okada, H. Sekizawa, F. Ambe, and T. Yamada, *J. Magn. & Magn. Mat.* 31–34, 105 (1983).
323. K. Haneda and A. H. Morrish, *IEEE Trans. Mag.* 25, 2597 (1989).
324. Q. A. Pankhurst and R. J. Pollard, *Phys. Rev. Lett.* 67, 248 (1991).
325. F. T. Parker and A. E. Berkowitz, *Phys. Rev. B* 44, 7437 (1991).
326. F. T. Parker, M. W. Foster, D. T. Margulies, and A. E. Berkowitz, *Phys. Rev. B* 47, 7885 (1993).

327. S. Linderoth, P. V. Hendriksen, F. Bødker, S. Wells, K. Davies, S. W. Charles, and S. Mørup, *J. Appl. Phys.* 75, 6583 (1994).
328. B. Martinez, A. Roig, X. Obradors, E. Molins, A. Rouanet, and C. Monty, *J. Appl. Phys.* 79, 2580 (1996).
329. A. H. Morrish and K. Haneda, *J. Appl. Phys.* 52, 2496 (1981).
330. K. Haneda and A. H. Morrish, *J. Appl. Phys.* 63, 4258 (1988).
331. R. H. Kodama, A. E. Berkowitz, E. J. McNiff, and S. Foner, *J. Appl. Phys.* 81, 5552 (1997).
332. S. A. Makhlof, K. Sumiyama, H. Onodera, K. Wakoh, and K. Suzuki, *Nuclear Instr. Methods Phys. Res. B* 76, 197 (1993).
333. T. Hihara, Y. F. Xu, T. J. Konno, K. Sumiyama, H. Onodera, K. Wakoh, and K. Suzuki, *Jpn. J. Appl. Phys.* 36-P1, 3485 (1997).
334. K. Haneda and A. H. Morrish, *Surf. Sci.* 77, 584 (1978).
335. K. Haneda and A. H. Morrish, *Nature* 282, 186 (1979).
336. A. H. Morrish and K. Haneda, *J. Magn. & Magn. Mater.* 35, 105 (1983).
337. I. Tamura and M. Hayashi, *Surf. Sci.* 146, 501 (1984).
338. V. Papaefthymiou, A. Kostikas, A. Simopoulos, D. Niarchos, S. Gangopadhyay, G. C. Hadjipanayis, C. M. Sorensen, and K. J. Klabunde, *J. Appl. Phys.* 67, 4487 (1990).
339. S. Gangopadhyay, G. C. Hadjipanayis, B. Dale, C. M. Sorensen, K. J. Klabunde, V. Papaefthymiou, and A. Kostikas, *Phys. Rev. B* 45, 9778 (1992).
340. S. Gangopadhyay, G. C. Hadjipanayis, C. M. Sorensen, and K. J. Klabunde, *IEEE Trans. Mag.* 29, 2602 (1993).
341. R. Huang, H. Xiong, Q. Lu, Y. Hsia, R. Liu, R. Ji, H. Lu, L. Wang, Y. Xu, and G. Fang, *J. Appl. Phys.* 74, 4102 (1993).
342. A. G. Gavriliuk, V. S. Voitkovsky, O. B. Taiok, V. A. Sidorov, and R. A. Sadykov, *J. Appl. Phys.* 73, (1993).
343. S. Gangopadhyay, Y. Yang, G. C. Hadjipanayis, V. Papaefthymiou, C. M. Sorensen, and K. J. Klabunde, *J. Appl. Phys.* 76, 6319 (1994).
344. Y. V. Baldokhin, P. Y. Kolotyrgan, Y. I. Petrov, and E. A. Shafraunovskiy, *J. Appl. Phys.* 76, 6496 (1994).
345. J. P. Perez, V. Dupuis, J. Tuillon, A. Perez, V. Paillard, P. Mëllinon, M. Treilleux, B. Barbara, L. Thomas, and B. Bouchet-Fabre, *J. Magn. & Magn. Mat.* 145, 74 (1995).
346. L. Del Bianco, D. Fiorani, A. M. Testa, E. Bonetti, L. Savini, and S. Signoretti, *Phys. Rev. B* 66, 174418 (2002).
347. C. P. Bean and J. D. Livingston, *J. Appl. Phys.* 30, 120S (1959).
348. C. P. Bean, in "Structure and Properties of Thin Films" (C. A. Neugebauer, J. B. Newkirk, and D. A. Vermilyea, Eds.), p. 331. Wiley, New York, 1959.
349. W. F. Brown, Jr., "Micromagnetics," Wiley-Interscience, New York 1963.
350. E. P. Wohlfarth, in "Magnetism" (G. T. Rado and H. Suhl, Eds.), Vol. III, p. 351. Academic Press, New York, 1963.
351. D. L. Leslie-Pelecky and R. D. Rieke, *Chem. Mater.* 8, 1770 (1996).
352. B. D. Cullity, "Introduction to Magnetic Materials," p. 415. Addison-Wesley, London, 1972.
353. H. Haberland, M. Moseler, Y. Qiang, O. Rattunde, Y. Thurner, and Th. Reiners, *Mat. Res. Symp. Proc.* 338, 207 (1996).
354. Y. Qiang, Y. Thurner, Th. Reiners, O. Rattunde, and H. Haberland, *Surf. Coat. Technol.* 100–101, 27 (1998).
355. D. Kumar, J. Narayan, A. V. Kvit, A. K. Sharma, and J. Sankar, *J. Magn. Magn. Mater.* 232, 161 (2001).
356. B. D. Cullity, "Introduction to Magnetic Materials," p. 387. Addison-Wesley, London, 1972.
357. D. J. Sellmyer, C. P. Luo, Y. Qiang, and J. P. Liu, in "Handbook of Thin Film Materials" (H. S. Nalwa, Ed.), Vol. 5, p. 337. Academic Press, New York, 2002.
358. E. M. Chudnovsky and L. Gunther, *Phys. Rev. Lett.* 60, 661 (1988); *Phys. Rev. B* 37, 9455 (1988).
359. J. Tejada, X. X. Zhang, and E. M. Chudnovsky, *Phys. Rev. B* 47, 14977 (1993).
360. B. Barbara, L. C. Sampaio, J. E. Wegrowe, B. A. Ratnam, A. Marchand, C. Paulsen, M. A. Novak, J. L. Tholence, M. Uehara, and D. Fruchart, *J. Appl. Phys.* 73, 6703 (1993).
361. J. Tejada, R. F. Ziolo, and X. X. Zhang, *Chem. Mater.* 8, 1784 (1996).
362. B. Barbara, C. Paulsen, L. C. Sampaio, M. Uehara, F. Fruchard, J. L. Tholence, and A. Marchand, "Magnetic Properties of Fine Particles" (J. L. Dormann and D. Fiorani, Eds.), p. 235. Elsevier Science, Amsterdam, 1992.
363. P. C. E. Stamp, E. M. Chudnovsky, and B. Barbara, *Internat. J. Mod. Phys. B* 6, 1355 (1992).
364. W. H. Meiklejohn and C. P. Bean, *Phys. Rev.* 102, 1413 (1956); 105, 904 (1957).
365. D. Mauri, H. C. Siegmann, P. S. Bagus, and E. Kay, *J. Appl. Phys.* 62, 3047 (1987).
366. A. P. Malozemoff, *Phys. Rev. B* 35, 3679 (1987); *J. Appl. Phys.* 63, 3874 (1988).
367. N. C. Koon, *Phys. Rev. Lett.* 78, 4865 (1997).
368. T. C. Schulthess and W. H. Butler, *J. Appl. Phys.* 85, 5510 (1999).
369. C. Schlenker, S. S. P. Parkin, J. C. Scott, and K. Howard, *J. Magn. Magn. Mater.* 54–57, 801 (1986).
370. T. Ambrose and C. L. Chien, *Appl. Phys. Lett.* 65, 1967 (1994).
371. R. Jungblut, R. Coehoorn, M. T. Johnson, J. van de Stegge, and A. A. Reinders, *J. Appl. Phys.* 75, 6659 (1994).
372. J. A. Borchers, Y. Ijiri, S.-H. Lee, C. F. Majkrzak, G. P. Felcher, K. Takano, R. H. Kodama, and A. E. Berkowitz, *J. Appl. Phys.* 83, 7219 (1998).
373. K. Takeno, R. H. Kodama, A. E. Berkowitz, W. Cao, and G. Thomas, *Phys. Rev. Lett.* 79, 1130 (1997).
374. T. Ambrose, R. L. Sommer, and C. L. Chien, *Phys. Rev. B* 56, 83 (1997).
375. D. V. Dimitrov, S. Zhang, J. Q. Xiao, G. C. Hadjipanayis, and C. Prados, *Phys. Rev. B* 58, 12090 (1998).
376. B. Dieny, V. S. Speriosu, S. S. P. Parkin, B. A. Gurney, D. R. Wilhoit, and D. Mauri, *Phys. Rev. B* 43, 1297 (1991).
377. B. Dieny, *J. Magn. Magn. Mater.* 136, 335 (1994).
378. D. L. Peng, T. Hihara, and K. Sumiyama, *Mat. Res. Soc. Symp. Proc.* 676, Y3.16.1 (2001).
379. D. L. Peng, T. J. Konno, K. Wakoh, T. Hihara, and K. Sumiyama, *Appl. Phys. Lett.* 78, 1535 (2001).
380. G. Herzer, *IEEE Trans. Mag.* 26, 1397 (1990).
381. F. Sato, N. Tezuka, T. Sakurai, and T. Miyazaki, *J. Magn. Soc. Jpn.* 17, 886 (1993).
382. S. Mørup, *J. Magn. Magn. Mater.* 37, 39 (1983).
383. S. Mørup, P. H. Christensen, and B. S. Clausen, *J. Magn. Magn. Mater.* 68, 160 (1987).
384. S. Mørup, *Hyp. Int.* 90, 171 (1994).
385. M. Hanson, C. Johansson, M. S. Pedersen, and S. Mørup, *J. Phys.: Condens. Mat.* 7, 9269 (1995).
386. S. Mørup, F. Bødker, P. V. Hendriksen, and S. Linderoth, *Phys. Rev. B* 52, 287 (1995).
387. F. J. Darnell, *J. Appl. Phys.* 32, 186S (1961).
388. S. Gangopadhyay, G. C. Hadjipanayis, C. M. Sorensen, and K. J. Klabunde, *Nanostruct. Mater.* 1, 449 (1992).
389. S. Gangopadhyay, G. C. Hadjipanayis, C. M. Sorensen, and K. J. Klabunde, *IEEE Trans. Magn.* 28, 3174 (1992).
390. S. Gangopadhyay, G. C. Hadjipanayis, C. M. Sorensen, and K. J. Klabunde, *J. Appl. Phys.* 73, 6964 (1993).
391. D. L. Peng, K. Sumiyama, T. Hihara, and T. J. Konno, *Scripta Mater.* 44, 1471 (2001).
392. R. B. Falk and G. D. Hooper, *J. Appl. Phys.* 32, 190S (1961).
393. M. Kishimoto, T. Nakazumi, N. Otani, and T. Sueyoshi, *IEEE Trans. Magn.* 27, 4645 (1991).
394. S. Gangopadhyay, G. C. Hadjipanayis, S. I. Shah, C. M. Sorensen, K. J. Klabunde, V. Papaefthymiou, and A. Kostikas, *J. Appl. Phys.* 70, 5888 (1991).
395. S. Gangopadhyay, G. C. Hadjipanayis, B. Dale, C. M. Sorensen, K. J. Klabunde, V. Papaefthymiou, and A. Kostikas, *Phys. Rev. B* 45, 9778 (1992).

396. S. Gangopadhyay, G. C. Hadjipanayis, C. M. Sorensen, and K. J. Klabunde, *IEEE Trans. Magn.* 29, 2602 (1993).
397. L. Del Bianco, A. Hernando, M. Multigner, C. Prados, J. C. Sanchez-Lopez, A. Fernandez, C. F. Conde, and A. Conde, *J. Appl. Phys.* 84, 2189 (1998).
398. T. Uchikoshi, Y. Sakka, M. Yoshitake, and K. Yoshihara, *Nanostruct. Mater.* 4, 199 (1994).
399. Y. D. Yao, Y. Y. Chen, C. M. Hsu, H. M. Lin, C. Y. Tung, M. F. Tai, D. H. Wang, K. T. Wu, and C. T. Suo, *Nanostruct. Mater.* 6, 933 (1995).
400. K. Haneda and A. H. Morrish, *Surf. Sci.* 77, 584 (1978).
401. S. Linderroth, S. Morup, and M. D. Bentzon, *J. Mater. Sci.* 30, 3142 (1995).
402. L. Bel Bianco, A. Hernando, E. Bonetti, and E. Navarro, *Phys. Rev. B* 56, 8894 (1997).
403. R. H. Kodama, A. E. Berkowitz, E. J. McNiff, and S. Foner, *Phys. Rev. Lett.* 77, 394 (1996).
404. R. H. Kodama and A. S. Edelstein, *J. Appl. Phys.* 85, 4316 (1999).
405. J. A. Mydosh, "Spin Glasses: An Experimental Introduction," p. 66. Taylor & Francis, London 1993.
406. J. Tejada, X. X. Zhang, and Ll. Balcells, *J. Appl. Phys.* 73, 6709 (1993).
407. M. Respaud, J. M. Broto, H. Rakoto, A. R. Fert, L. Thomas, B. Barbara, M. Verelst, E. Snoeck, P. Lecante, A. Mosset, J. Osuna, T. Ould Ely, C. Amiens, and B. Chaudret, *Phys. Rev. B* 57, 2925 (1998).
408. W. Wernsdorfer, K. Hasselbach, A. Benoit, W. Wernsdorfer, B. Barbara, D. Maily, J. Tuillon, J. P. Perez, V. Dupuis, J. P. Dupin, G. Guiraud, and A. Perex, *J. Appl. Phys.* 78, 7192 (1995).
409. M. Jamet, W. Wernsdorfer, C. Thirion, D. Maily, V. Dupuis, P. Mlinon, and A. Perez, *Phys. Rev. Lett.* 86, 4676 (2001).
410. M. Jamet, V. Dupuis, C. Thirion, W. Wernsdorfer, P. Mélinon, and A. Perez, *Scripta Mater.* 44, 1371 (2001).
411. M. Jamet, V. Dupuis, P. Mlinon, G. Guiraud, A. Pérez, W. Wernsdorfer, A. Traverse, and B. Baguenard, *Phys. Rev. B* 62, 493 (2000).
412. S. Kobayashi, *Surf. Sci. Rep.* 16, 1 (1992).
413. E. Abrahams, P. W. Anderson, D. C. Licciardello, and T. V. Ramakrishnan, *Phys. Rev. Lett.* 42, 673 (1979).
414. B. L. Alt'shuler, A. G. Aronov, and P. A. Lee, *Phys. Rev. Lett.* 44, 1288 (1980).
415. Y. Imry, *J. Appl. Phys.* 52, 1817 (1981).
416. S. M. Girvin and M. Jonson, *Phys. Rev. Lett.* 43, 1447 (1979).
417. A. Carl, G. Dumpich, and E. F. Wassermann, *Vacuum* 41, 1183 (1990).
418. N. F. Mott, *J. Non-Cryst. Solids* 1, 1 (1969); "Conduction in "Non-Crystalline Materials," p. 27. Clarendon, Oxford, 1987.
419. C. A. Neugebauer and M. B. Webb, *J. Appl. Phys.* 33, 74 (1962).
420. J. I. Gittleman, Y. Goldstein, and S. Bozowski, *Phys. Rev. B* 5, 3609 (1972).
421. H. R. Zeller, *Phys. Rev. Lett.* 28, 1452 (1972).
422. P. Sheng, B. Abeles, and Y. Arie, *Phys. Rev. Lett.* 31, 44 (1973).
423. A. Carl, G. Dumpich, and D. Hallfarth, *Phys. Rev. B* 39, 915 (1989).
424. A. Carl, G. Dumpich, and D. Hallfarth, *Phys. Rev. B* 39, 3015 (1989).
425. A. Carl, G. Dumpich, and D. Hallfarth, *Thin Solid Films* 193/194, 1065 (1990).
426. L. S. Darken and R. W. Gurry, Eds. "Physical Chemistry of Metals," McGraw Hill, New York, 1953.
427. L. Savini, E. Bonetti, L. Del Bianco, L. Pasquini, S. Signoretto, P. Allia, M. Coisson, J. Moya, V. Selvaggini, P. Tiberto, and F. Vinai, *J. Appl. Phys.* 91, 8593 (2002).
428. M. Julliere, *Phys. Lett.* 54A, 225 (1975).
429. S. Maekawa and U. Gäfvert, *IEEE Trans. Magn.* 18, 707 (1982).
430. J. C. Slonczewski, *Phys. Rev. B* 39, 6995 (1989).
431. J. S. Moodera, L. R. Kinder, T. M. Wong, and R. Meservey, *Phys. Rev. Lett.* 74, 3273 (1995).
432. Jagadeesh S. Moodera and Lisa R. Kinder, *J. Appl. Phys.* 79, 4724 (1996).
433. J. S. Helman and B. Abeles, *Phys. Rev. Lett.* 37, 1429 (1976).
434. M. Roilos and P. Nagels, *Solid State Commun.* 2, 285 (1964).
435. D. L. Peng, T. Asai, N. Nozawa, T. Hihara, and K. Sumiyama, *Appl. Phys. Lett.* 81, 4598 (2002).
436. R. Kato, T. Hihara, D. L. Peng, and K. Sumiyama, *Appl. Phys. Lett.* 82, 2688 (2003).
437. A. W. Adamson and A. P. Gast, "Physical Chemistry of Surfaces," 6th ed. John Wiley & Sons, New York, 1997.

Transition Metal Atoms on Nanocarbon Surfaces

Antonis N. Andriotis

*Institute of Electronic Structure and Laser Foundation for Research and Technology-Hellas,
Heraklio, Crete, Greece*

Madhu Menon

University of Kentucky, Lexington, Kentucky, USA

CONTENTS

1. Introduction
 2. Computational Approach
 3. Catalytic Action of Ni in Growing
Single Wall Carbon Nanotubes (SWCNs)
 4. Organometallic Complexes
- Glossary
References

1. INTRODUCTION

The discovery of the fullerenes and carbon nanotubes brought into consideration the possibility of constructing new materials and devices based on these new forms of carbon. A huge number of investigations has been undertaken in the last 10 to 15 years examining in detail every aspect of the behavior and properties of these materials. The newly discovered magnetic properties of some polymerized forms of C_{60} and the possibility of using single wall carbon nanotubes (SWCNs) as quantum wires or as the basis for building nanoelectronic devices (as, for example, the SWCN-based field effect transistor) have opened wide horizons for research activity in both experiment and theory.

The theoretical challenges are inherently related to two basic properties of these new materials. The first property is that these materials can be produced in a practically defect-free state. The second is that they exist in low-dimension structures, as, for example, two-dimensional (2D) (e.g., graphite), one-dimensional (1D) (e.g., SWCNs), and zero-dimensional (0D) (e.g., C_{60}). The first of these properties allows the researcher to compare experimental results with theory in an unambiguous way. The second allows one to investigate how the properties of carbon materials

depend on the degree of hybridization of the carbon bonding orbitals as this is observed when the dimension and the geometry of the carbon form are changing. However, in some cases, considerable numbers of point defects are present in these new carbon materials, as, for example, in the case of carbon nanotubes in which remnants of catalysts used for their production are present. In addition to that, thermoelectric power measurements have indicated that oxygen adsorption is always present in open air experiments and, as a result, it can significantly modify the transport properties of the nanotubes.

The interaction of transition metal atoms (TMAs) with low-dimension carbon surfaces is of fundamental interest in the search for new materials. In addition to that, the contact resistance between TMAs and SWCNs is of critical importance in nanoelectronics and, more importantly, in spintronics applications. The recent observation [1] of the dynamic behavior of Ni atoms in graphitic carbon onions [2] by *in-situ* atomic resolution electron microscopy revealed the formation of very interesting C–Ni phases. Most important of these findings is that Ni atoms can take substitutional in-plane positions in graphene layers causing only minimal local distortions to the graphene layer. In particular, it was found that a substitutional Ni atom forms Ni–C bonds 0.21 nm long, with a simultaneous displacement of the Ni atom out of the graphene plane by 0.10 nm. The rest of the graphene lattice was found not to suffer any appreciable distortions. These observations, supported by total energy calculations, and the fact that the substitution of a C atom by an Ni atom in a graphene sheet is energetically not favorable (requiring an energy of 9.9 eV) led Banhart et al. [1] to conclude that the Ni atom fills existing vacancies in the graphene sheets when Ni is forced to migrate into carbon onions.

Our recent investigations on the interaction of TMAs with carbon materials of low dimension have revealed many interesting features [3–6]. Of much importance appears to be the contrasting bonding behavior of the 3D TMAs in their interaction with graphite, C_{60} , SWCN, and benzene (Bz) molecules. In addition to that, the TMAs were found to undergo a significant change in their magnetic moment when they interact with graphite, C_{60} , SWCN, and Bz molecules. A striking characteristic feature of this interaction was the quenching of the magnetic moment of Ni on graphite, C_{60} , SWCN, and Bz molecules [3, 4, 7], on the one hand, and the enhancing of the magnetic moment of the early 3D atoms when supported on Bz molecules on the other [7].

2. COMPUTATIONAL APPROACH

In this section we give brief overviews of our theoretical simulation methods.

2.1. Tight-Binding Molecular Dynamics Methodology

The details of our tight-binding molecular dynamics (TBMD) scheme can be found in Andriotis and Menon [8]. Here we give a brief overview.

The total energy U is written in its general form as a sum of several terms [8],

$$U = U_{\text{el}} + U_{\text{rep}} + U_0 \quad (1)$$

where U_{el} is the sum of the one-electron energies E_n for the occupied states:

$$U_{\text{el}} = \sum_n^{\text{occ}} E_n \quad (2)$$

In the tight-binding scheme E_n is obtained by solving the characteristic equation

$$(\mathbf{H} - E_n \mathbf{1})\mathbf{C}^n = 0 \quad (3)$$

where \mathbf{H} is the Hamiltonian of the system.

The Hellmann–Feynman theorem for obtaining the electronic part of the force is given by [8]

$$\frac{\partial E_n}{\partial x} = \mathbf{C}^{n\dagger} \frac{\partial \mathbf{H}}{\partial x} \mathbf{C}^n \quad (4)$$

The total energy expression also derives contributions from ion–ion repulsion interactions. This is approximated by a sum of pairwise repulsive terms and included in U_{rep} . This sum also contains the corrections arising from the double counting of electron–electron interactions in U_{el} [8]. U_0 is a constant that merely shifts the zero of energy. The contribution to the total force from U_{rep} is rather straightforward. One can then easily do molecular dynamics simulations by numerically solving Newton's equation

$$m \frac{d^2 x}{dt^2} = F_x = - \frac{\partial U}{\partial x} \quad (5)$$

to obtain x as a function of time.

Our TBMD scheme for a binary system consisting of elements A and B is based on a minimal set of five adjustable parameters for each pair (A,A), (B,B), and (A,B). These parameters are determined by fitting to experimental data for quantities such as the bond length, the vibrational frequency, and the binding energy of the dimers A_2 , B_2 , AB, the cohesive energy of the corresponding bulk states of the A, B, AB materials, and the energy level spacing of the lowest magnetic states of the dimer and trimer binary clusters consisting of atoms of A and B type. In the absence of experimental data, we fit to data of small clusters obtained using *ab initio* methods. It is apparent that only five parameters are required in the case of a single species system. The generalization to a system containing more than two kind of atoms is also plausible within this approach.

The fixed set of TB parameters [9] is obtained from the universal scheme proposed by Harrison [10] suitably scaled with respect to the interatomic distance [8].

3. CATALYTIC ACTION OF NI IN GROWING SINGLE WALL CARBON NANOTUBES (SWCNs)

Transition metal catalysts such as Ni are known to play a key role in the production of SWCNs. Microscopic details of their interactions with SWCN are, therefore, expected to shed light on the SWCN growth process. While it is tempting to extrapolate known results of interaction of Ni with graphite to the SWCN case by drawing on the similarities between graphite and SWCN, it should be noted that the curvature can be expected to have nontrivial consequences. Indeed, our recent works have shown that such a simple extrapolation can lead to misleading results for bonding geometries, magnetic moments, and other physical properties [3, 4, 11]. An Ni-assisted growth mechanism for SWCN has recently been proposed by Lee et al. [12], who suggested that the mobile Ni catalyst atoms adsorb at the growing edge of the CNT, where they prevent the formation of carbon pentagons and catalyze the continuous formation of carbon hexagons. This was based on their assumption that SWCN samples were devoid of any remaining metal catalysts and, therefore, that the action of Ni is exclusively confined to the tube edge. This is contradicted by recent experiments showing Ni used in the synthesis of SWCN to remain in purified samples even after prolonged treatment in boiling concentrated HNO_3 [13]. Furthermore, chemical analysis, NMR experiments, and HRTEM observations suggest an even distribution of small clusters or isolated atoms of these transition metals within the nanotubes [13]. In an earlier work, we have shown the anomalous behavior of conductivity observed in experiments with SWCN to be due to the effects of residual transition metal catalysts residing in close contact with the nanotube walls [14].

Investigation of the role played by Ni catalyst in the SWCN must, therefore, take full account of all these effects. In order to understand the Ni catalyzed SWCN growth mechanism we study the behavior of substitutional Ni in the presence of external C atoms in graphite and SWCN using TBMD simulations backed by *ab initio* total energy calculations. The graphite is simulated by a portion of a graphene

sheet consisting of 128 carbon atoms. The SWCNs used in our simulations consisted of (5,5) and (10,10) types containing 150 and 320 atoms, respectively. The results obtained were as follows.

(A) **Substitutional Ni in a graphene sheet.** In this simulation we replaced a C atom of a graphene sheet by an Ni atom and allowed the system to relax using the TBMD method [3]. The relaxation resulted in the Ni atom moving slightly outward of the graphene plane with minimal distortions to the rest of the graphene lattice. These results are in very good agreement with the experimental and theoretical results of Banhart et al. [1].

(B) **Substitutional Ni in a graphene sheet in the presence of an additional C atom.** After replacing one C atom in a graphene sheet by an Ni atom (as in (A)) we placed (i) one extra C atom above the Ni atom and (ii) one extra C atom above the center of a hexagon containing one substitutional Ni atom. The TBMD scheme was then used to relax these systems. The relaxation resulted in the extra C atom taking the place of Ni, with the released Ni atom chemisorbing below the plane of graphite. The outcome of these simulations shows that independently of the initial position of the extra C atom, the substitutional Ni atom in the graphene sheet is replaced by a neighboring C atom not belonging to the graphene sheet.

(C) **Substitutional Ni in a SWCN.** We performed TBMD simulations of a substitutional Ni atom in a (5,5) as well as a (10,10) SWCN. In both cases the relaxation resulted in the Ni atom moving into the interior of the nanotube, leaving a C vacancy on the wall, with the distortions of the SWCN confined mainly to the neighbors of the vacancy [6]. In Figure 1 we show a simulation of a substitutional Ni atom in a (5,5) nanotube. It is worth noting that in the relaxed position the Ni atom binds to all the C atoms surrounding the C vacancy created by Ni, with Ni–C bond lengths ranging from 2.03 to 2.08 Å. Thus, the presence of the Ni atom appears to stabilize the C vacancy in the SWCN.

More accurate quantitative results on the stability of the relaxed configuration can be obtained by performing *ab initio* [15] calculations. We calculate total energy of the system using *ab initio* methods starting from the relaxed Ni position shown in Figure 1 and then by moving the Ni atom radially outward to an exterior position in small increments. Figure 2 shows a plot of the total energy obtained at the various Ni positions. From this it is clear that the Ni atom is, in fact, more stable either outside or inside the tube, while its substitutional position is a transition state.

(D) **Substitutional Ni atom in a SWCN in the presence of an additional C atom.** Simulations described in (C) were repeated by including an additional C atom within bonding distance of the substitutional Ni atom. Upon relaxation, the substitutional Ni atom was replaced by the exterior C atom, while the Ni atom broke free and was left encapsulated inside the tube with no bonding to any of the C atoms. The final relaxed geometry shows complete healing of all distortions caused by Ni. A careful observation of the relaxation process suggests that a C vacancy is first created by a substitutional Ni atom; the vacancy then draws into it an external C atom in the atmosphere, annealing the vacancy and freeing the Ni atom. The simulation process is shown in Figure 3.

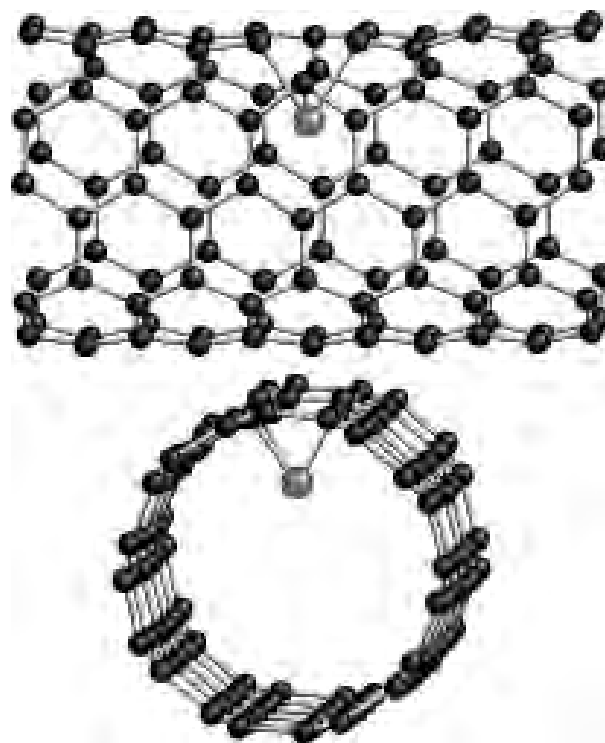


Figure 1. Molecular dynamics simulation of a substitutional Ni atom in a (5,5) nanotube. The relaxation resulted in the Ni atom moving into the interior of the nanotube, leaving a C vacancy on the wall, with the distortions of the SWCN confined mainly to the neighbors of the vacancy. Adapted with permission from [6], A. N. Andriotis et al., *Phys. Rev. Lett.* 85, 3193 (2000). © 2000, American Physical Society.

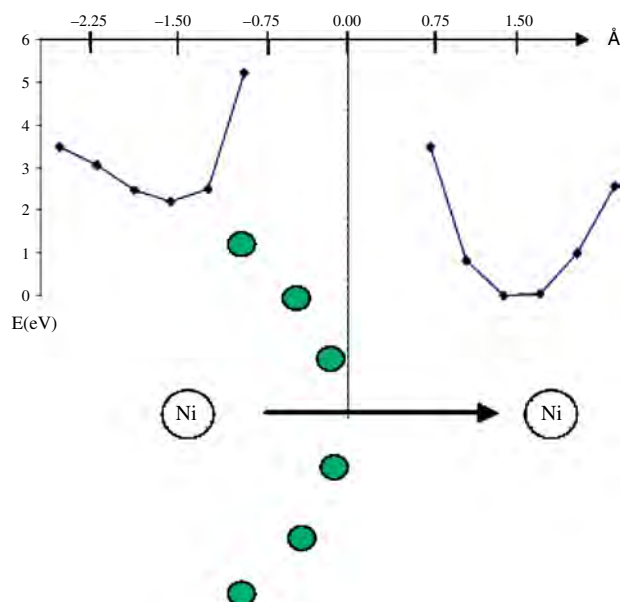


Figure 2. *Ab initio* total energy of the system at various Ni positions starting from the relaxed position shown in Figure 1 and then moving the Ni atom radially outward to an exterior position in small increments. Adapted with permission from [6], A. N. Andriotis et al., *Phys. Rev. Lett.* 85, 3193 (2000). © 2000, American Physical Society.

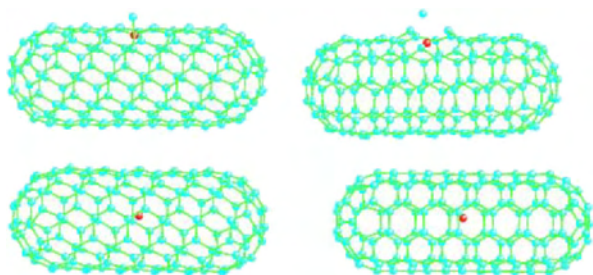


Figure 3. Simulations of the effects of a substitutional Ni atom in a nanotube in the presence of an external C atom. Adapted with permission from [6], A. N. Andriotis et al., *Phys. Rev. Lett.* 85, 3193 (2000). © 2000, American Physical Society.

These results clearly demonstrate the contrasting dynamic behavior of substitutional Ni atoms in graphite and in SWCNs. In particular, they show that, contrary to their behavior in graphite, substitutional Ni atoms are not stable on the SWCNs. Furthermore, our dynamical simulation results allow us to propose a reasonable explanation for the catalytic role of the Ni atoms in the growth process of carbon nanotubes as follows.

- (i) The Ni atoms act as stabilizing agents of the structural defects created in SWCN during the growth process. When other carbon atoms in the atmosphere come within bonding distance of such an Ni-stabilized defect, the defect is annealed, while the freed Ni atom diffuses along the length of the tube either outside or inside.
- (ii) At the end of the tube, the substitutional Ni atom can remain stable, forming part of the hexagonal ring, although with considerable distortions. However, when new hexagons start to form by the incorporation of additional carbon atoms in the atmosphere, the Ni atom exchanges its position with an incoming carbon atom and resets itself by occupying a substitutional position on an exterior ring. The simulation of Ni at the nanotube end is shown in Figure 4. Our *ab initio* total energy calculations support the TBMD results and show that this process is energetically very favorable, with an exothermic release of 7.25 eV.

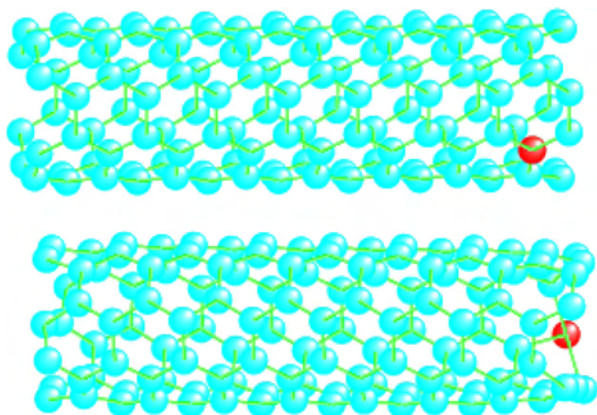


Figure 4. Ni at the nanotube end.

Our mechanism is in striking contrast to that proposed by Lee et al. [12], where the primary role of Ni, acting alone, is to prevent tube closure by inhibiting the formation of pentagons. Furthermore, according to Lee et al. [12], the action of Ni is exclusively confined to the tube edge. In the present work we have shown that an Ni atom cannot act on its own; its action is mediated by existing or created (by the Ni) structural defects. The presence of the Ni atom is necessary either to prevent these defects from spreading across the tube or to anneal them by a swapping process.

Our dynamical simulations also rule out the “scouting” mechanism proposed by Lee et al. [12], in which the Ni atom goes around the tube edge. Our *ab initio* calculations yield an energy barrier of 1.3 eV for Ni hopping from one armchair edge to another. This value for the barrier height is larger by 0.35 eV than the value found by Lee et al. (as deduced from Fig. 1 of Lee et al. [12]). Due to the exponential dependence of the diffusion coefficient on the barrier height, our results correspond (using the assumptions of Lee et al. [12]) to a much smaller (≈ 1 – 2 orders of magnitude) scouting rate of Ni around the tube edge. Our simulations, instead, favor the Ni atom acting initially as a defect stabilizer and subsequently diffusing (by a position-exchange mechanism described earlier) to a substitutional position on an exterior ring. It should be noted that in Lee et al. [12], the growing edge of the carbon nanotube was modeled by a small graphene flake containing only 20–30 atoms. Our TBMD simulations in conjunction with *ab initio* total energy calculations have shown that such a simple interpolation of the results for Ni interaction with graphite to predict similar properties for Ni with nanotubes can lead to qualitatively different results [3, 4, 11].

The encapsulation tendency we find in the case of substitutional Ni in the presence of an incoming C atom is supported by the recent experimental work reported by Dujardin et al. [13], where encapsulation of Ni/Co is suggested as the most probable processes taking place during tube growth. Our simulations, thus, give a detailed description of the possible swapping processes involved in the Ni-assisted catalytic growth of nanotubes.

4. ORGANOMETALLIC COMPLEXES

The interactions of TMAs with various low-dimension forms of carbon has been the subject of recent experimental and theoretical investigations [3–7, 16–27]. All these investigations affirm the contrasting bonding behaviors of the 3D TMAs in their interaction with graphite, C_{60} , SWCN, and benzene molecules beyond any reasonable doubt. In the following sections we review the basic trends found in the interaction of 3D TMAs with low-dimension carbon surfaces.

4.1. Interaction of TMAs with Graphite

Detailed theoretical studies of the interaction of graphite with TMA have shown that the early 3D elements (Sc, Ti, V) are energetically more stable at *hole* sites, while the late 3D elements (Fe, Co, Ni) are found to be energetically more stable on *atop* sites [3, 23].

In our work, graphite is simulated by a portion of a graphene sheet consisting of 128 carbon atoms. This size was

found to be sufficient for ensuring convergence of the results with the cluster size. The relaxation of the transition metal atom on the graphene layer is simulated with the TBMD computational method. Three distinct sites were considered for a single transition metal atom (Ni or V) on graphite. These consist of an Ni atom (i) directly above a C atom (atop site), (ii) above the center of a hexagon (hole site), and (iii) over a C–C bond (bridge site).

At the atop site, the Ni atom induces a significant relaxation in the graphene layer that moves the C atom (lying just beneath the Ni atom) below the graphene plane. The Ni atom bonds to the C atom beneath it and to the three next nearest C atoms (Fig. 5a). At this position, the Ni atom loses $0.98|e|$ of charge to the carbon atoms and also exhibits a magnetic moment of $0.3 \mu_B$.

At the hole site (Fig. 5b), the Ni forms six bonds with the six nearest carbon atoms on relaxation. The strong Ni–C interactions result in considerable distortions in the planar structure beneath the Ni atom. The Ni atom exhibits a magnetic moment of $0.29 \mu_B$ and loses charge to the carbon atoms (approximately $0.44|e|$). The hole site was found to be energetically more stable than the atop site.

Similarly, it was found that the adsorption of V was accompanied by a considerable distortion in the graphene sheet, especially for C atoms in the neighborhood of the V atom. As in the case of the Ni atom, the hole site was the most stable. The total energies for the fully relaxed geometries were obtained using *ab initio* calculations and show the ordering $E_{\text{hole}} < E_{\text{atop}}$. At each adsorption site, the V atom exhibits a magnetic moment and there is appreciable charge transfer to or from the graphite atoms. However, our results do not support the high spin states for V on graphite reported recently [23, 26]. This disagreement may be attributed to surface relaxation effects which have been completely omitted by Duffy and Blackman [23] and Kruger et al. [26].

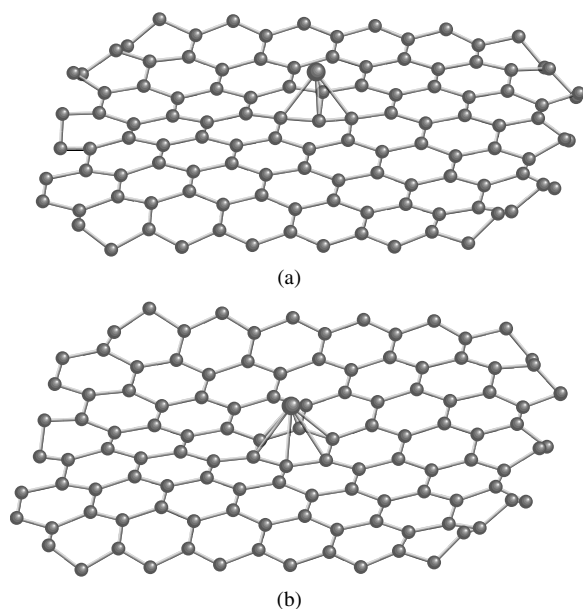


Figure 5. The two stable binding sites for a single Ni on graphite: (a) atop site and (b) hole site.

No bonding was found for either Ni or V on the C–C bridge site of graphite.

4.2. Interaction of TMAs with C_{60} Molecules and SWCNs

The experimental results dealing with the structural properties of small $M_n(C_{60})_m$ clusters, where M denotes a TMA of the 3D series ($m + n < 10$), have revealed that early 3D elements form an $M_1[\eta^6-(C_{60})_2]$ bonding configuration, while the late 3D elements form either an $M_1[\eta^3-(C_{60})_2]$ or an $M_1[\eta^2-(C_{60})_2]$ configuration [16, 18, 19]. Here η^k (k , an integer) denotes that there are k ligand atoms (carbon ring atoms) bonded to the metal (M) atoms. Based on these findings, it was proposed that the early 3D elements form “dumbbell” structures in which the M atom is sandwiched between six-membered rings of C_{60} . It was also proposed that the late 3D elements form bent or ring-type structures in which the M atom forms two or three bonds with each C_{60} molecule. These experimental conclusions were theoretically confirmed by our TBMD simulations of $M_n(C_{60})_m$, $M = \text{Ni}, \text{V}$, ($m + n \leq 5$) clusters [4, 5].

In the case of interaction of Ni with the C_{60} and the SWCN, only the atop and bridge sites were found to be stable on molecular dynamics relaxation. The hole site (i.e., above the center of a hexagonal ring of carbon atoms) is found to be unstable for Ni on the nanotube wall. Instead, an Ni atom, initially placed at a hole site, moves and relaxes on an atop site. This is in striking contrast to the case of the interaction of Ni with graphite, where the hole site was found to be the most stable.

For the $\text{Ni}(C_{60})_2$ cluster we examined the relative stabilities of the linear and bent C_{60} –Ni– C_{60} geometries. A number of distinct stable structures were obtained on relaxation (see Fig. 6). In the first case (Fig. 6a) the Ni atom binds

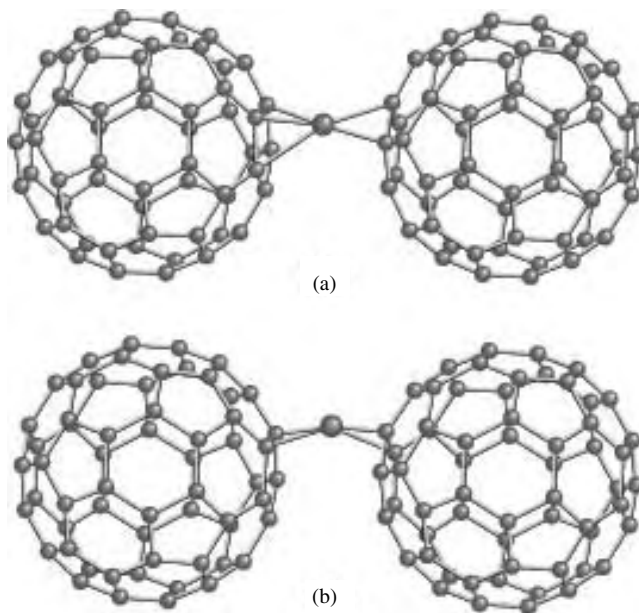


Figure 6. Relaxed geometries for the $\text{Ni}(C_{60})_2$ system. Adapted with permission from [4], A. N. Andriotis and M. Menon, *Phys. Rev. B* 60, 4521 (1999). © 1999, American Physical Society.

at the bridge sites (η^2 ligand) of both C_{60} molecules. The bridge site is over C–C bonds shared by two hexagons. In the second case also the Ni atom binds at the bridge sites on both C_{60} molecules but the bridge sites are now over C–C bonds shared by a pentagon and a hexagon (Fig. 6b). The former geometry is found to be more stable than the latter.

For the $Ni_2(C_{60})_2$ clusters, we studied the following three geometries: the linear geometries $C_{60}-Ni-C_{60}-Ni$ (denoted by D1) and $C_{60}-Ni-Ni-C_{60}$ (denoted by D2) and the geometry $C_{60}-Ni_2-C_{60}$ (denoted by D3, see Fig. 7), in which the Ni_2 dimer binds with its two atoms to both C_{60} molecules. Among these three geometries, D3 was found to be considerably more stable than the other two, followed by D1. In the D3 configuration, the Ni–Ni bond length is 2.47 Å and both Ni atoms exhibit identical behavior described as follows: (i) they gain $0.31|e|$ from the C_{60} molecules, (ii) they exhibit a small magnetic moment of the order of $0.10 \mu_B$, and (iii) they bind at one pentagon bridge site on one C_{60} (η^2 ligand) and at one pentagon atop site on the other C_{60} (η^3 ligand), as shown in Figure 7. The Ni–C bond lengths at the atop site are 2.16, 2.19, and 1.85 Å, while at the bridge site are 1.91 and 1.91 Å. For the sake of comparison it should be noted that in the D2 configuration the Ni atoms loose some charge to the C_{60} 's. Also, the Ni–Ni bond is 2.66 Å and each Ni atom binds to an atop position on one C_{60} molecule.

At the atop site for Ni on nanotube wall (Fig. 8a) the Ni atom forms three Ni–C bonds (1.79, 1.95, and 1.95 Å) and gains electronic charge ($\approx 0.05|e|$) from the carbon atoms, while displaying a magnetic moment of $0.15 \mu_B$.

The Ni atom relaxed at the bridge site (Fig. 8b) forms bonds of 1.76 Å each with the carbon atoms. There is a gain of electronic charge of magnitude $0.179|e|$. The magnetic moment on the Ni atom is $0.10 \mu_B$. The atop site is energetically more favorable by 9.1 eV than the bridge site.

For V on a C_{60} or on a SWCN, we find that V binds at hole, atop, and bridge sites, while the total energies for these sites satisfy the relation $E_{hole} < E_{atop} < E_{bridge}$. Note that for Ni, the hole site was found to be unstable, while the atop site was the most stable on C_{60} [5]. The only similarity here is that the bridge site now becomes stable for both V and Ni as a result of rehybridization due to the substrate curvature. It is also worth noting that our results for V on both graphite and C_{60} indicate the preference for V to act as an η^6 ligand, in contradistinction to Ni, which acts as an η^2 or η^3 ligand [5, 28], in agreement with the experimental findings for both

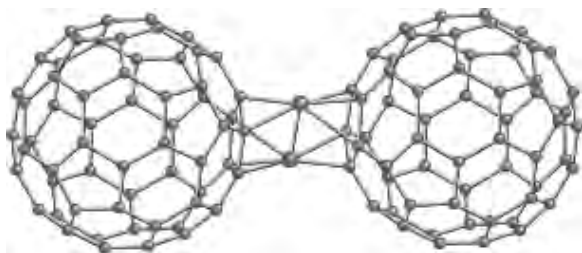


Figure 7. The most stable geometry and the bonding of the $Ni_2(C_{60})_2$ cluster. Adapted with permission from [4], A. N. Andriotis and M. Menon, *Phys. Rev. B* 60, 4521 (1999). © 1999, American Physical Society.

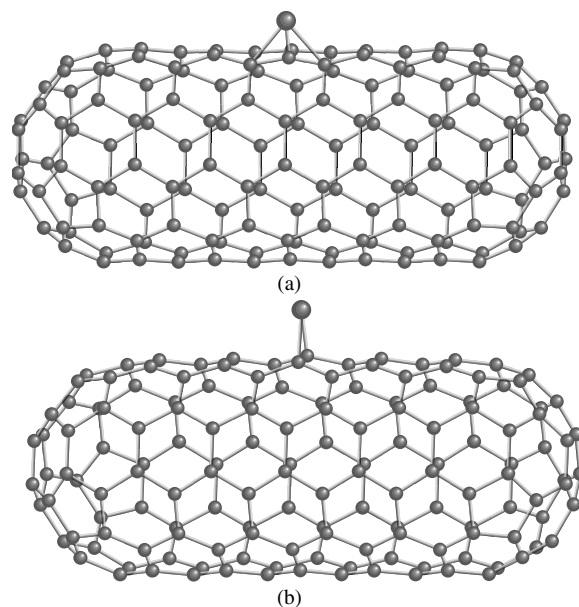


Figure 8. The two stable binding sites for a single Ni on carbon nanotube wall: (a) atop site and (b) bridge site. Adapted with permission from [11], A. N. Andriotis et al., *Chem. Phys. Lett.* 320, 425 (2000). © 2000, Elsevier Science.

Ni and V interacting with C_{60} [16–22]. The V atom on the C_{60} exhibits a net charge and magnetic moment that depend on the adsorption site.

Vanadium is also found to bind two C_{60} molecules. Two of the most stable ground state geometries for the $V(C_{60})_2$ cluster are shown in Figure 9. Among them the most stable exhibits the dumbbell structure, with both C_{60} molecules acting as η^6 ligands (Fig. 9a). It should be recalled that in the case of the $Ni(C_{60})_2$ clusters, the most stable geometry also exhibited the dumbbell structure, but with one C_{60} molecule acting as η^2 ligand and the other as η^3 ligand [4].

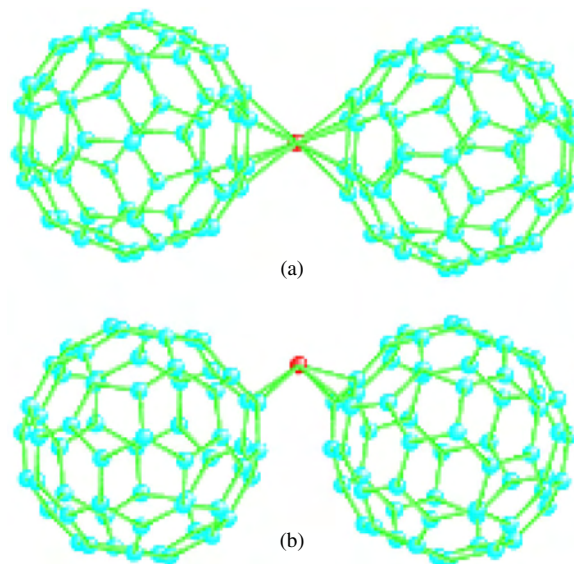


Figure 9. Relaxed geometries for the $V(C_{60})_2$ clusters. Adapted with permission from [4], A. N. Andriotis and M. Menon, *Phys. Rev. B* 60, 9867 (2000). © 2000, American Physical Society.

The qualitatively different behavior found in the case of V and Ni in their interactions with graphite and C_{60} can be attributed mainly to the different occupancies of the adsorbate d orbitals. Another factor contributing to this is the variation in the hybridization strength between the adsorbate d orbitals and the p_z orbitals of graphite (the z axis is perpendicular to the surface). While the occupancy of the d orbitals depends on the adsorbate atom and is affected by interatomic and intra-atomic charge transfer effects, the hybridization strength depends on the point group symmetry of the adsorption site (i.e., C_{6v} for hole; C_{3v} for atop, and C_{2v} for bridge sites), the surface relaxation near the adsorbate, and the adsorbate–substrate distance. The presence of all these factors makes a meaningful quantitative deduction of the contribution of each single factor to the interaction between a 3D element and the graphite (or the C_{60}) seem quite difficult.

4.3. Interaction of TMAs with Benzene Molecules

The experimental results obtained for the interaction of transition metal atoms with Bz molecules further reaffirm the contrasting bonding configuration of the 3D TMA's in their interaction with carbon [20]. Specifically, these results led to the conclusion that the early 3D elements should form structures in which the M atom is sandwiched symmetrically between two Bz molecules in a double η^6 bonding configuration. On the other hand, it was concluded that the late 3D elements should form structures of the “rice ball” type, with η^2 and/or η^3 bonding configurations. In the latter case the TMA is encapsulated in an oysterlike opening or within a small volume surrounded by Bz molecules.

Recently, we reported results of theoretical investigations of TMA–Bz complexes of the form $M_n(\text{Bz})_m$, $M = \text{Ni}, \text{V}$, with $m + n \leq 5$, obtained using *ab initio* computational methods and TBMD [29]. We also used relaxations of the systems to complement our *ab initio* work. Structural optimizations were carried out using both *ab initio* and TBMD methods. While TBMD simulations were used to perform fully symmetry-unconstrained optimizations in all cases, only the smaller clusters were so optimized using *ab initio* methods due to the computational complexity.

For the $\text{Ni}(\text{Bz})_2$ cluster, it was found that Ni prefers the η^2 type bonding with each Bz molecule, following the same general trend found in the bonding configuration of the TMAs with graphite, C_{60} , and SWCN. Our results, however, are at odds with the rice ball structure used to interpret the experimental findings [20]. Instead, we find that the two Bz molecules repel each other and form a Z-like (or steplike) bonding with the Ni atom (Fig. 10) instead of the oysterlike opening of the rice ball structure proposed [20].

Ab initio calculations for the Ni_2Bz_2 cluster are shown in Figure 11a and b for the symmetry-constrained (D_{2h}) and symmetry-unconstrained optimization of this cluster, respectively. The symmetry-unconstrained structure is energetically more stable (by 0.72 eV) than the symmetry-constrained one. In the unconstrained case, each Ni atom exhibits η^2 type bonding to each Bz molecule upon relaxation. The planes of the Bz molecules are not parallel and

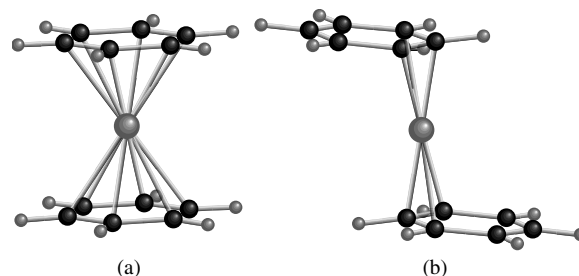


Figure 10. Final structures obtained by performing (a) symmetry-constrained (D_{6h}) and (b) symmetry-unconstrained (C_1) relaxations for the $\text{Ni}(\text{Bz})_2$ complex using *ab initio* methods. Adapted with permission from [29], G. E. Froudakis et al., *Chem. Phys. Lett.* 350, 393 (2001). © 2001, Elsevier Science.

can be thought of as forming an oysterlike opening characteristic of the rice ball structure.

Our *ab initio* studies of $\text{Ni}_3(\text{Bz})_2$ clusters indicated that the segregation of Ni atoms and the formation of an Ni_3 cluster sandwiched between two Bz molecules is energetically more favorable than the steplike structure of Figure 12b.

The relative stability of the Z-like structure is compared with that of the oyster structure in the case of the $\text{Ni}_2(\text{Bz})_3$ complex. From our *ab initio* and the TBMD results (shown in Fig. 13a–c) the oyster structure (Fig. 13a) is found to be isoenergetic with the steplike one (Fig. 13b), the former being more stable by 0.17 eV.

We next study the Ni_4Bz_5 cluster. The resulting relaxed geometry (symmetry unconstrained) for this Ni_4Bz_5 cluster is shown in Figure 14. A striking feature of this relaxed cluster is the helical steplike (“corkscrew”) geometry, indicating that extended $\text{Ni}_m\text{Bz}_{m+1}$ structures may be stable for large m .

Our *ab initio* calculations for the Ni_mBz_n clusters show that each Ni atom gains approximately 0.80 electrons, while the magnetic moment of the Ni atoms is approximately $0.04 \mu_B$ in agreement with Pandey et al. [7].

We repeated the calculations by replacing Ni with V (an early 3D element). In the case of the $\text{V}(\text{Bz})_2$ cluster, our symmetry-unconstrained relaxation resulted in the same

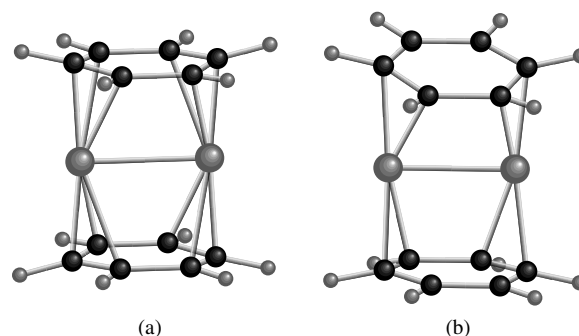


Figure 11. Final structures obtained by performing (a) symmetry-constrained (D_{2h}) and (b) symmetry-unconstrained (C_1) relaxations for the $\text{Ni}_2(\text{Bz})_2$ complex. Note that planes of the Bz molecules are not parallel and can be thought as forming an oysterlike opening characteristic of the rice ball structure. Adapted with permission from [29], G. E. Froudakis et al., *Chem. Phys. Lett.* 350, 393 (2001). © 2001, Elsevier Science.

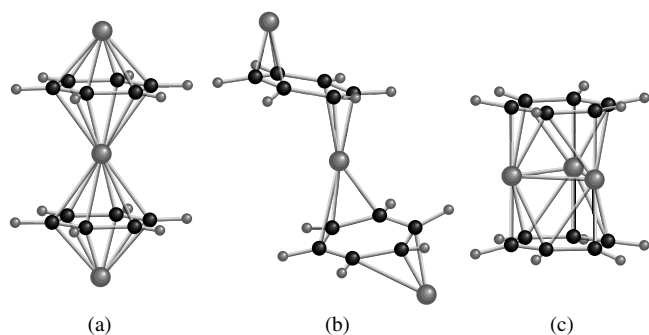


Figure 12. Final structures obtained by performing (a) symmetry-constrained (D_{6h}) and (b), symmetry-unconstrained (C_1) relaxation for the $Ni_3(Bz)_2$ cluster using *ab initio* methods. (c) Symmetry-unconstrained relaxed structure for the $Ni_3(Bz)_2$ cluster obtained by placing three Ni atoms between the planes of the Bz molecules. The relaxed structure has D_{3h} symmetry and is the most stable of the three. Adapted with permission from [29], G. E. Froudakis et al., *Chem. Phys. Lett.* 350, 393 (2001). © 2001, Elsevier Science.

structure as the symmetry-constrained one, that is, similar to that shown in Figure 10a, in which the V atom forms an η^6 type bonding configuration with each Bz molecule. A similar result was obtained in the case of the $V_2(Bz)_2$ complex, that is, symmetry-unconstrained relaxation resulted in a final relaxed structure similar to the symmetry-unconstrained one shown in Figure 11a.

Our results for $Ni_m(Bz)_n$ and $V_m(Bz)_n$ clusters, thus, reaffirm the contrasting bonding behavior between the early and the late 3D elements when they interact with Bz molecules, supporting the conclusion drawn from experiments [20]. Our results, however, do not support the proposed rice ball structure for all the $Ni_m(Bz)_n$ complexes that we studied. Instead, a new structure, namely, the Z- or steplike appears in some complexes to be either more favorable or competing with the oyster structure. We do not claim, however, that this is the most stable one. The purpose of including this result in the present report is to stimulate future investigations about this structure. Our results, thus, make it clear that the structural outcome appears to be dependent on the size of the $Ni_m(Bz)_n$ complex.

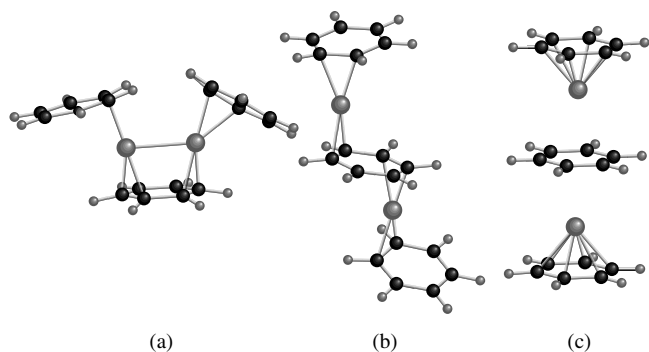


Figure 13. Relaxed $Ni_2(Bz)_3$ structures obtained using our *ab initio* methods. (a) The oysterlike structure and (b) steplike structure, both obtained by symmetry-unconstrained relaxations. (c) The structure obtained using symmetry-constrained relaxation. Adapted with permission from [29], G. E. Froudakis et al., *Chem. Phys. Lett.* 350, 393 (2001). © 2001, Elsevier Science.

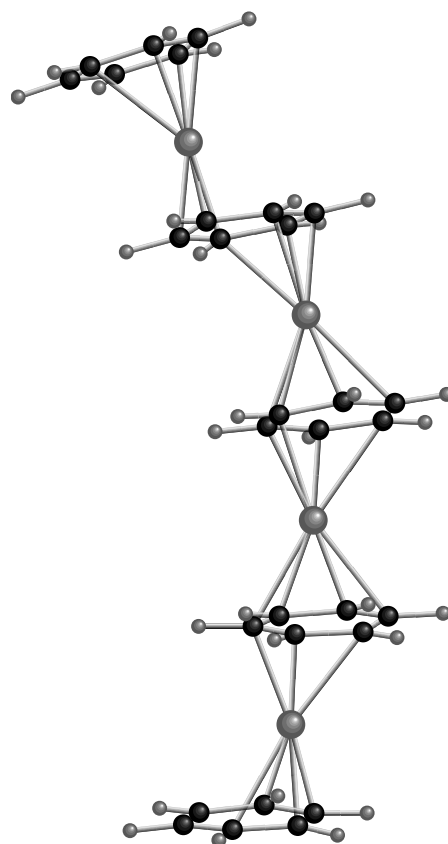


Figure 14. Helical steplike (“corkscrew”) geometry obtained on TBMD relaxation for a Ni_4Bz_5 cluster. The structure gives an indication that extended Ni_mBz_{m+1} structures may be stable for large m . Adapted with permission from [29], G. E. Froudakis et al., *Chem. Phys. Lett.* 350, 393 (2001). © 2001, Elsevier Science.

Additionally, our results also justify the stability of the experimentally traced $M_2(Bz)_2$ and $M_2(Bz)_3$ structures which were found to be very conspicuous in the mass spectra for $M = Ni$ but not for any other 3D elements.

GLOSSARY

Benzene A planar ring consisting of six carbon atoms and six hydrogen atoms.

C_{60} A hollow soccer ball shaped molecule formed by carbon atoms.

Graphene sheet A single layer of planar three-fold coordinated carbon atoms.

Molecular dynamics A structural optimization process using computer algorithm based on electronic structure.

Single wall carbon nanotube (SWCN) Nanotube formed by rolling up a single sheet of graphitic carbon.

ACKNOWLEDGMENTS

The present work is supported through by NSF Grants 98-62485, 99-07463, and ITR-0221916, DOE Grant 00-63857, NASA Grant 00-463937, the EU-GROWTH Research Project AMMARE (G5RD-CT-2001-00478), and the University of Kentucky Center for Computational Sciences.

REFERENCES

1. F. Banhart, J.-C. Chalier, and P. M. Ajayan, *Phys. Rev. Lett.* 84, 686 (2000).
2. D. Ugarte, *Nature* 359, 707 (1992).
3. A. N. Andriotis, M. Menon, G. E. Froudakis, and J. E. Lowther, *Chem. Phys. Lett.* 301, 503 (1999).
4. A. N. Andriotis and M. Menon, *Phys. Rev. B* 60, 4521 (1999).
5. A. N. Andriotis, M. Menon, and G. E. Froudakis, *Phys. Rev. B* 62, 9867 (2000); *Phys. Rev. B* 61, R13393 (2000).
6. A. N. Andriotis, M. Menon, and G. E. Froudakis, *Phys. Rev. Lett.* 85, 3193 (2000).
7. R. Pandey, B. K. Rao, P. Jena, and J. M. Newsam, *Chem. Phys. Lett.* 321, 142 (2000).
8. A. N. Andriotis and M. Menon, *Phys. Rev. B* 57, 10069 (1998).
9. J. C. Slater and G. F. Koster, *Phys. Rev.* 94, 1498 (1954).
10. W. Harrison, in "Electronic Structure and Properties of Solids." Freeman, San Francisco, 1980.
11. A. N. Andriotis, M. Menon, and G. E. Froudakis, *Chem. Phys. Lett.* 320, 425 (2000); *Phys. Rev. B* 62, 9867 (2000).
12. Y. H. Lee, S. G. Kim, and D. Tomanek, *Phys. Rev. Lett.* 78, 2393 (1997).
13. E. Dujardin, C. Meny, P. Panissod, J.-P. Kintzinger, N. Yao, and T. W. Ebbesen, *Solid State Commun.* 114, 543 (2000).
14. A. N. Andriotis, M. Menon, and G. E. Froudakis, *Phys. Rev. B* 61, R13393 (2000).
15. Gaussian 98, Revision A.6, M. J. Frisch, G. W. Trucks, H. B. Schlegel, G. E. Scuseria, M. A. Robb, J. R. Cheeseman, V. G. Zakrzewski, J. A. Montgomery, Jr., R. E. Stratmann, J. C. Burant, S. Dapprich, J. M. Millam, A. D. Daniels, K. N. Kudin, M. C. Strain, O. Farkas, J. Tomasi, V. Barone, M. Cossi, R. Cammi, B. Menucci, C. Pomelli, C. Adamo, S. Clifford, J. Ochterski, G. A. Petersson, P. Y. Ayala, Q. Cui, K. Morokuma, D. K. Malick, A. D. Rabuck, K. Raghavachari, J. B. Foresman, J. Cioslowski, J. V. Ortiz, A. G. Baboul, B. B. Stefanov, G. Liu, A. Liashenko, P. Piskorz, I. Komaromi, R. Gomperts, R. L. Martin, D. J. Fox, T. Keith, M. A. Al-Laham, C. Y. Peng, A. Nanayakkara, C. Gonzalez, M. Challacombe, P. M. W. Gill, B. G. Johnson, W. Chen, M. W. Wong, J. L. Andres, M. Head-Gordon, E. S. Replogle, and J. A. Pople, Gaussian, Inc., Pittsburgh PA, 1998.
16. S. Nagao, T. Kurikawa, K. Miyajima, A. Nakajima, and K. Kaya, *J. Phys. Chem. J. A* 102, 4495 (1998).
17. E. K. Parks, K. P. Kerns, S. J. Riley, and B. J. Winter, *Phys. Rev. B* 59, 13431 (1999).
18. T. Kurikawa, S. Nagao, K. Miyajima, A. Nakajima, and K. Kaya, *J. Phys. Chem. A* 102, 1743 (1998).
19. A. Nakajima, S. Nagao, H. Takeda, T. Kurikawa, and K. Kaya, *J. Chem. Phys.* 107, 6491 (1997).
20. T. Kurikawa, H. Takeda, M. Hirano, K. Judai, T. Arita, S. Nagao, A. Nakajima, and K. Kaya, *Organometallics* 18, 1430 (1999).
21. C. Binns, S. H. Baker, C. Denangeat, and J. C. Parlebas, *Surf. Sci. Rep.* 34, 105 (1999).
22. P. Mathur, I. J. Mavunkal, and S. B. Umbarkar, *J. Clus. Sci.* 9, 393 (1998).
23. D. M. Duffy and J. A. Blackman, *Phys. Rev. B* 58, 7443 (1998).
24. P. Kruger, M. Taguchi, J. C. Parlebas, and A. Kotani, *Phys. Rev. B* 55, 16466 (1997).
25. C. Binns, H. S. Derbyshire, S. C. Bayliss, and C. Norris, *Phys. Rev. B* 45, 460 (1992).
26. P. Kruger, J. C. Parlebas, and A. Kotani, *Phys. Rev. B* 59, 15093 (1999).
27. K. Judai, K. Sera, S. Amatsutsumi, K. Yagi, T. Yasuike, S. Yabushita, A. Nakajima, and K. Kaya, *Chem. Phys. Lett.* 334, 277 (2001).
28. A. N. Andriotis and M. Menon, *Phys. Rev. B* 60, 4521 (1999).
29. G. E. Froudakis, A. N. Andriotis, and M. Menon, *Chem. Phys. Lett.* 350, 393 (2001).
30. A. N. Andriotis and M. Menon, *J. Chem. Phys.* 115, 2737 (2001).

Transition Metals-Based Nanomaterials for Signal Transduction

Bamaprasad Bag, Parimal K. Bharadwaj

Indian Institute of Technology, Kanpur, India

CONTENTS

1. Introduction
 2. Fluorescent Chemosensors
 3. Molecular Information Processing
 4. Photo-Induced Electron Transfer
 5. Transition Metal Ions in Fluorescence Signaling
 6. Nonlinear Optical Effects
 7. Conclusion
- Glossary
References

1. INTRODUCTION

A wide variety of complex biological, as well as artificial structures, can self-assemble [1–4] from a simpler set of molecular subunits in a single step under equilibrium conditions. This has led to the idea that supramolecular interactions such as hydrogen bonding, hydrophobic interactions, aromatic π - π interactions, electrostatic and van der Waals forces can be used for the construction of nanostructures. Conventional synthesis of nano-sized molecules can be achieved by controlled, selective, and sequential formation of covalent bonds. Although this approach continues to generate many large complex structures, synthesis of large nano-sized structures by this approach requires manpower, cost, and investment of time which are really prohibitive [5–7]. Stable and structurally diverse assemblies can be rapidly, accurately, and efficiently synthesized from relatively simple subunits by supramolecular interactions. For the synthesis of nanostructures with metal ions and organic molecules, the metal ions, multidentate organic ligands, and the coordinate bonding are the parameters for directing the self-assembly processes. The metal ions in these structures can play crucial roles. The organic parts alone sometimes may not be able to assemble. Metal ions can attract several units, where these ions can occupy strategic positions made possible through design of the ligand unit(s).

The Gibb's free-energy decrease will be significant upon formation of metal-ligand bonds leading to stable structures. It has been correctly predicted [8] that anything which can be done with a macroscopic thread, such as knitted clothes of various designs, knots, braids, and so on, should be possible in the nanostructures with organic/inorganic ligands and metal ions. Success in producing such structures will depend on understanding and controlling the topological and geometric relationships between molecular modules along with the coordination characteristics of the metal ions, which can all be same or different. When transition metal ions are used, the availability of different oxidation states can be employed to have intelligent systems where signal transduction through processes, such as electron translocation from one part to another, electron delocalization over a large area of the molecule, etc., can be realized. At the present time, metal-driven assembly of organic/inorganic ligands to form giant structures is an area of research that is pursued vigorously in many laboratories in the world, resulting in an explosive growth in the number of published articles. A large number of review articles on this theme are now available [9–25]. When molecules are above a certain size, the intra- and inter-molecular interactions become indistinguishable leading to complex structures such as enzymes in biology [26]. For a biological systems, structures of similar complexity can be realized in metal-ligand ensembles. A direct consequence of increased structural complexity is increased functional complexity, which can be tuned into making intelligent materials [27]. The onus, therefore, rests with chemists to design molecular subunits that can act "smart" to carry out assigned roles, and at the same time, programmable to build the desired nanostructures.

Potentially smart materials can be built [29–31] on the interaction of light (photons) with matter (molecules). Depending on the structural and functional moieties present in the molecule, a wide variety of features can be observed. Overall, it can be made useful in two ways: (i) photons can be stored in a molecule in the form of photo-induced charge-separation, excited states with long half-lives, and so on, or (ii) light energy can be supplied to molecules to

perform light-induced functions such as sensing, molecular-scale signal processing, perturbation of polarizability for nonlinear optics, etc. The light-driven functionalities can be modulated by metal ions. It is this use of light with transition metal complexes that is the subject of this article.

Molecular fluorescence (or luminescence) is a property that can be measured in real-time and in real-space. A photonic molecular device is defined as an assembly of molecular components which, because of the specific arrangement in space and energy, is able to perform light-induced functions. If the fluorescence output of a molecular system can be altered in presence/absence of another molecule or ion acting as an input to the system, it can be used as a sensor or in molecular information processing. In these systems, an intercomponent process, such as electron transfer or energy transfer, must take place upon binding of the input to modify the emission characteristics of the fluorophore.

2. FLUORESCENT CHEMOSENSORS

Chemical sensors [32–37] are miniaturized transducers which are capable of responding to chemical information changes by yielding signals that can be measured. The change in chemical information may originate from a chemical reaction involving an analyte or from a physical property of the system. The chemical information change taking place in the receptor unit is transformed into a form of energy that can be sensed and measured by the transducer unit. These sensors are classified according to the operating principles of the transducer unit as optical, electrochemical, thermal, mass, and so on. For fluorescent chemosensors, the optical transduction of binding analytes with receptors are measured. Chemical sensors have wide-ranging applications in modern life. On-site, real-time monitoring of hazardous chemicals is a longstanding goal [38]. In addition, rapid analysis of metals in large numbers of samples is important for chemical and bioprocess monitoring, as well as for environmental and clinical applications [39–42]. Research has also focused [43–46] on developing sensors for remote monitoring of metal ions that pose serious human and environmental health problems. The nature, as well as the amount of the output signal, can be directly linked to a particular species and its concentration. The design of such systems [47, 48] essentially comprises a signaling (fluorophore) and a guest-binding moiety (receptor). The two components can either be separated by a spacer (Fig. 1a) or can be integrated into one unit (Fig. 1b). The fluorophore, as such, does not show any selectivity. It is the receptor that should show selectivity, and hence is the most difficult component to design. An ideal receptor for a chemical sensor will be one that can recognize a single analyte in the presence of many others. The receptor should be designed with new recognition principles or the existing ones should be fine tuned—both of which are formidable challenges to chemists. For a molecular sensor, the receptor may bind the molecular guest by noncovalent interactions. These interactions are usually weak, and concerted interplay among many sites over a large surface area is the only way to achieve strong and specific binding of the guest molecule [49]. In biological systems, the specificity and precision is derived from the

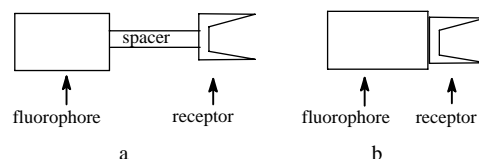


Figure 1. Two different formats for fluorescent signaling.

highly directed mutual recognition displayed by the components of a structure which is possible for large nano-sized biological molecules [50]. To emulate these biological systems, chemists should attempt [51] to make receptors large enough so that the receptor can optimally preorganize itself for the guest binding. It is also expected that interactions of such preorganized molecules are to be highly selective as a guest with a different structure and will require different optimum conformation of the receptor. The same basic idea of preorganization holds when the guest is a metal ion. In this case, the right donor atoms in the receptor should be placed at strategic positions to recognize the coordination properties of the metal ion. A number of approaches [52–55] pertaining to binding a specific metal ion in the presence of several others by a ligand have been reported.

Signal transduction upon analyte binding to the receptor can take place [43] by one or more of the processes:

1. electron transfer
2. charge transfer
3. energy transfer

For the configuration shown in Figure 1a, the spacer plays an important role in the transduction event. Binding of the guest to the receptor is sensed by the fluorophore through bond, space, or both. If the spacer is short and rigid, it keeps the interaction between the fluorophore and the receptor to a minimum. Under such circumstances, the signal transduction mechanism is mostly through bond. With a long spacer, the receptor and fluorophore can come close to each other via folding of the spacer unit making considerable through-space interaction possible. The observed photo-physical changes upon analyte binding can be in terms of

1. appearance of the spectrum
2. emission quantum yield
3. excited-state lifetime

In such systems, signal transduction of a discrete and stoichiometric recognition of the analyte by the receptor is desirable.

3. MOLECULAR INFORMATION PROCESSING

Fluorescence enhancement upon binding of a guest by the receptor can be used [56–58] in molecular-scale arithmetic. The rapid technological advances in electronics and computing that have taken place over the last quarter of a century are based [59–61] on the progressive miniaturization of the components involved. Engineers are able to fabricate progressively smaller structures in order to make complex machines. However, the annual rate of increase in numbers

of transistors on a chip is slowing down as theoretical limits are neared [62], and soon this “top-down” approach will reach its physical limit. Researchers are trying to create “molecular electronics” starting from molecules that can act as wires, transistor-like switches, and logic gates. Chemists can offer this “bottom-up” approach where molecules with fluorescent signaling tags can be used as modules [63–77]. Enhancement of fluorescence upon guest binding by the receptor will give rise to the “1” state, while absence of fluorescence will be the “0” state. Depending upon the input/output functionality, such chemical logics [78] can be divided as *YES*, *NO* logic functions or as *OR*, *AND*, etc. logic gates. A truth-table [79, 80] illustrating some of the logics is shown Figure 2. While several such modules can be covalently linked to make intelligent nanomaterials, the cost of such an endeavor will be prohibitive. By applying the principles of supramolecular chemistry, however, several units can be assembled rapidly in a convergent fashion. The key issue here is to have molecules as large as a nanometer or above. Molecules of this size will exhibit enormous diversity of structures and dynamics which, if modulated by external stimuli, can serve as chemical logics. Besides, with modular chemistry, the fluorophore can be easily varied for higher quantum efficiency, lower energy of excitation, and so on, while the receptor can in principle, be designed to selectively bind a group of ions or molecules. The progress in this area has been slow, although several molecular logic gates [78] and molecular wires [61, 81] have been reported in the last few years. A wide variety of types of molecular wires have been reported [78, 82–96] and several ways [78, 97, 98] to incorporate these wires with molecules have been attempted. However, a discussion of this is beyond the scope of this article.

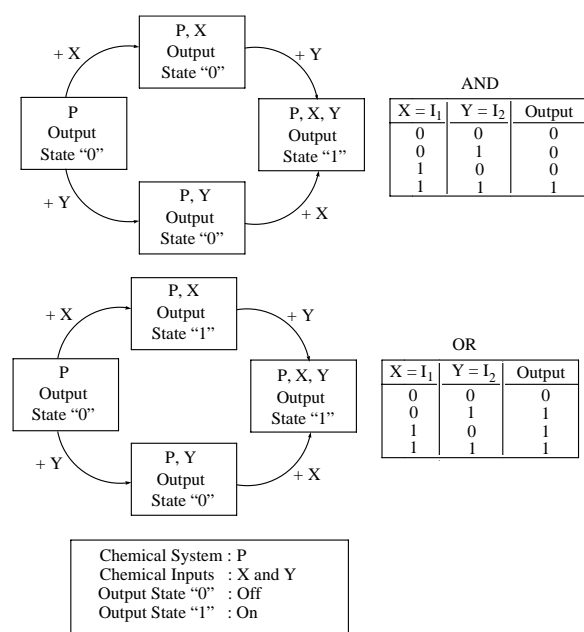


Figure 2. A truth-table illustrating molecular *OR* and *AND* logic gates.

4. PHOTO-INDUCED ELECTRON TRANSFER

Photo-induced intramolecular electron transfer (PET) in fluorescent signaling systems with either format as shown in Figure 1 is the commonly exploited mechanism [99, 100] for fluorescent signaling. The receptor and the fluorophore are chosen, such that the PET between the fluorophore and the receptor (usually a group containing one or more nitrogen atoms) can be modulated. The mechanism can be simply illustrated [101, 102] by a frontier orbital picture as shown in Figure 3. When the lone pair associated with the donor atom is not bonded to a metal ion, proton, or molecular guest, PET from the receptor (i.e., N lone pair) to the excited fluorophore takes place causing a nonradiative decay of the excited state and fluorescence quenching. When a guest engages this lone pair by bonding, the PET process will be blocked causing recovery of the fluorescence. Both fluorescence quenching, as well as enhancement, can be utilized to inform binding of the guest. However, ubiquitous nature of fluorescence quenching reduces their sensitivity as well as their practical utility [103–105]. Therefore, systems with fluorescence enhancement rather than quenching should be the choice in sensor design.

5. TRANSITION METAL IONS IN FLUORESCENCE SIGNALING

Transition metal ions are widespread in nature and their detection in real-time and real-space are of importance [106, 107] from the perspectives of understanding different biological processes and disease control. The use of a transition metal ion in fabricating molecular photonic devices can be an attractive proposition due to availability of various redox states of the metal ion. However, these metal ions effectively quench fluorescence, and a number of mechanisms have been forwarded to rationalize [108, 109] this behavior. These are

1. conversion of electronic energy to kinetic via collisions,
2. heavy atom effects,
3. magnetic perturbations,
4. formation of charge-transfer complexes,
5. electronic energy transfer between the metal ion and the fluorophore etc.

Some of the mechanisms can be discounted by a suitable choice of receptors and metal ions. For the rest to be operative, the fluorophore and the metal ion should have bonding interactions either through the spacer, or the spacers can be

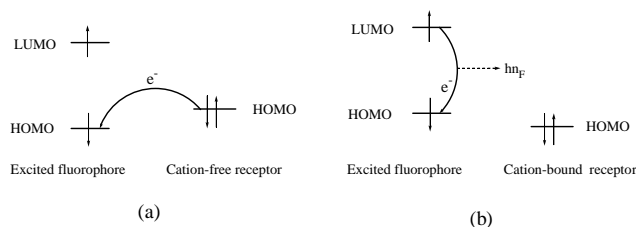
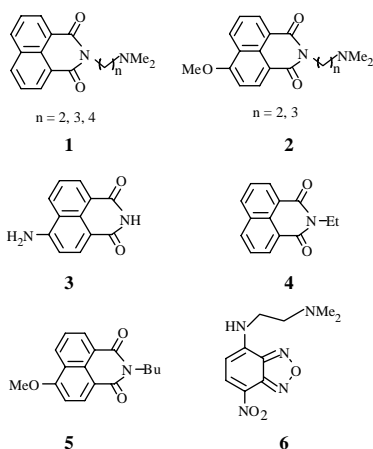


Figure 3. Frontier orbital diagram of the design principle leading to fluorescence ‘off’ and ‘on’ states.

flexible enough for the metal orbitals and the orbitals on the fluorophore of proper symmetry to come closer to make direct overlap. Thus, for transition metal-based fluorescence signaling systems, the receptor should be designed such that the metal ion(s) in the bound state are not accessible to the fluorophore for quenching, that is, making the metal ion-receptor (M-R) interaction significantly greater compared to the metal ion-fluorophore (M-F) communication.

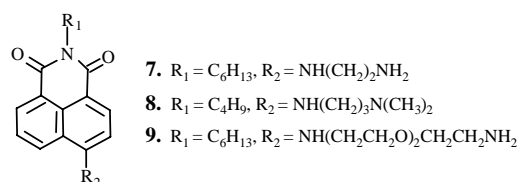
A reduction of M-F communication can be achieved by making the fluorophore electron deficient. Ramachandram et al. [110–112] have reported a number of compounds (**1–6**) based on this design principle. With an electron-deficient fluorophore, the interaction between the fluorophore and the metal ion is not only minimized, but also such fluorophores, being better acceptors for electrons, enhance the PET in the system improving its performance. That the signal transduction in these systems originates from the PET can be proved by the fluorescence decay behavior of these systems. With systems having small spacer units, the PET is through-bond and with systems having long spacers, PET is operational both through-bond and through-space.



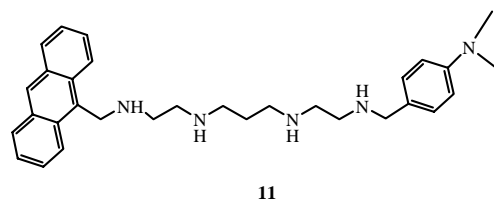
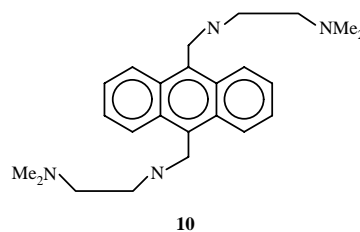
When the receptor is not bonded to a metal ion or proton, a low-fluorescence intensity is observed with each of these compounds. The intensity is, however, found to vary with the nature of the solvent. In the presence of a first-row transition metal ion, the fluorescence intensity is enhanced, which has been attributed to the blockade of the PET process. In some cases, unusually high-fluorescence enhancement (FE) could be observed, which has been accounted for [113] assuming the guest metal ion to be inducing enhancement by more than one means. Preferential solvation of the fluorophore moiety by the water molecules of the hydrated metal salts has been identified as one possible origin of the very high-fluorescence enhancement in these systems. Disadvantages of these systems are unknown complex stoichiometry and low-complex stability. Receptor units (**7–9**) capable of forming chelates with metal ions have been constructed [114] to provide higher stability to the metal binding process.

Compounds (**7–9**) exhibit fluorescence enhancement in presence of Cu(II), Mn(II), and Ni(II). These compounds are suggested to undergo intramolecular quenching via PET

from the distal nitrogen on the 4-substituent. With the addition of the metal ions, blocking of this quenching leads to fluorescence enhancement by a factor of about 50. These systems are quite sensitive to Cu(II) ion; only a sub-ppm level is required to observe enhancement of fluorescence. For other first-row transition metals, higher concentrations are required. Metal salts are known to generate protons when dissolved in an organic solvent. These protons are also capable of blocking the PET process through protonation of the corresponding N atom. It is thus imperative to carry out control experiments to establish that the metal ion and not the proton, blocks the PET showing high fluorescence intensity. The PET in the compound **10** is very effective and in the presence of a Zn(II) ion, it exhibits [115, 116] a 1000-fold enhancement of fluorescence.

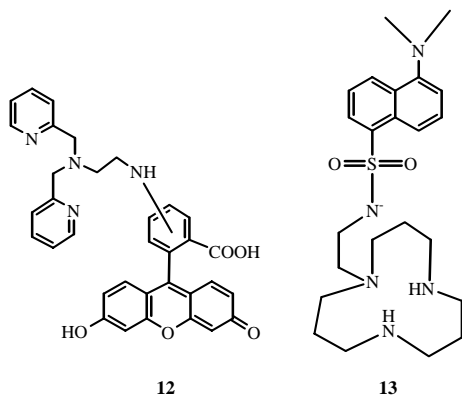


However, a Zn(II) ion has a filled *d* orbital and thus fluorescence quenching mechanism(s) of a typical transition metal ion is nonoperative here. A number of fluorescent probes for the Zn(II) ion have been reported in the literature. The donor (D) and acceptor (A) system connected by a linear tetramine (**11**) exhibits [117] Zn(II)-induced fluorescence enhancement.

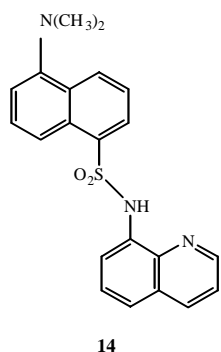


Aminofluoresceins (**12**) have been substituted [118, 119] to have sensors that are highly selective for the Zn(II) ion with 10- to 15-fold enhancement. Dansyl-amidomethyl-[12]aneN₃ (**13**) shows [120] a 5-fold fluorescent enhancement at pH 7.8, which is unaffected in the presence of physiological concentrations of a selective group

of biologically essential metal ions such as Na(I), K(I), Ca(II), and Mg(II).



Compound **14** shows [121] about 20 times enhancement with Zn(II) ion as input.



The first example of the use of fluorescence spectroscopy for probing the environment of the cavity in a coordination polymer was reported recently [122]. Pyrene molecules can enter the cavity and exhibit bipyridine: pyrene exciplex emission (Fig. 4). The presence of Zn(II) ions in the network does not interfere with the exciplex formation. This way, nature of the cavity in a coordination polymer can be probed by emission spectroscopy. Intriguing results are expected when one of the components is fluorophoric in such coordination polymers of transition metal ions, and the positions of the metal ions in the network are such that they do not quench the emission characteristics of the fluorophore.

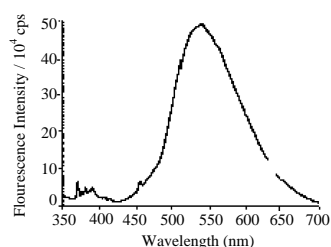
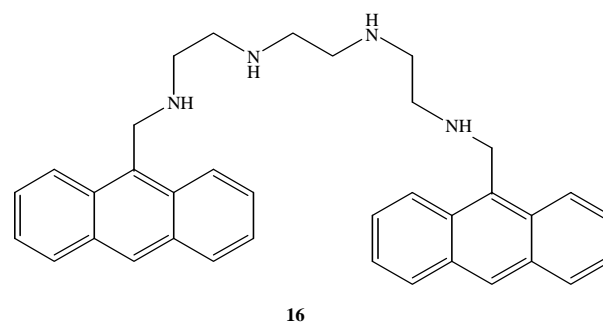
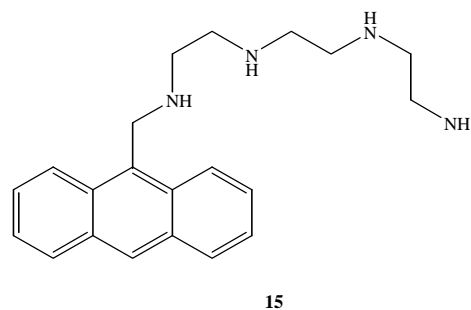


Figure 4. Fluorescence spectrum of pyrene:bipyridine exciplex emission: A spectroscopic probe of the environment of the cavity of an open framework coordination polymer. Reprinted with permission from [122], B. D. Wagner et al., *Chem. Commun.* 2176 (2002). © 2002, Royal Society of Chemistry.

The 9-anthrylpolyamines (**15** and **16**) show 4-6 fold of enhancement [123] in the presence of Zn(II) perchlorate at pH 10.5 in CAPS buffer.



For designing redox switchable fluorescent probe, the redox active thiadiazole/iminothiourea system (**17**) have been used [124, 125]. The 1,2,4-thiadiazole (**A**) can be reduced by Zn in glacial acetic acid to yield the open-chain compound (**B**), which can be oxidized by iodine in chloroform almost quantitatively to the heterocycle (**A**).

The two forms contain distinctly different binding sites. For the form **A**, PET from the methylated N atom to the anthryl group is facile giving a very low quantum yield ($\phi_F \approx 0.0027$) and only Hg(II) shows a significant increase of enhancement (Fig. 5). Cu(II) and Pb(II) show only slight enhancement. Other ions apparently do not bind to the receptor strongly. In case of the open-chain form **B**, a 6-fold enhancement is observed upon addition of Cd(II), and to a minor extent, upon the addition of Zn(II). Following this approach, the same authors reported [126]

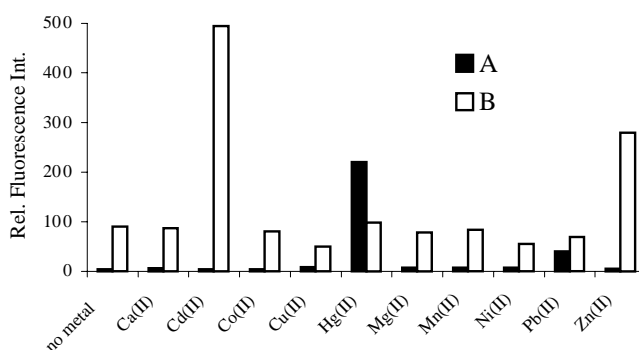
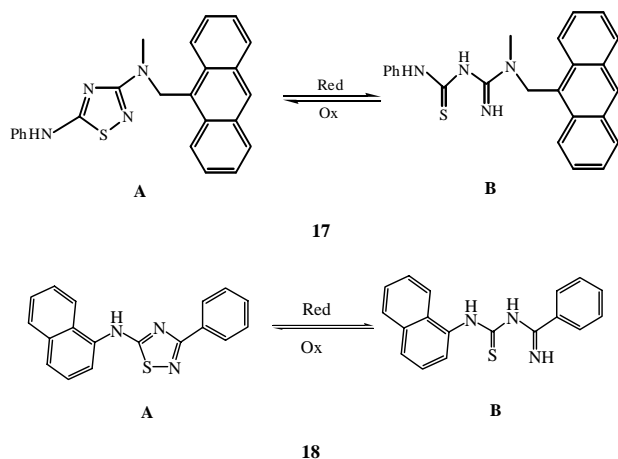


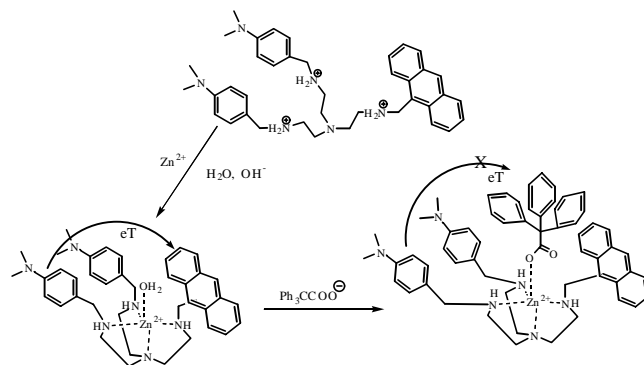
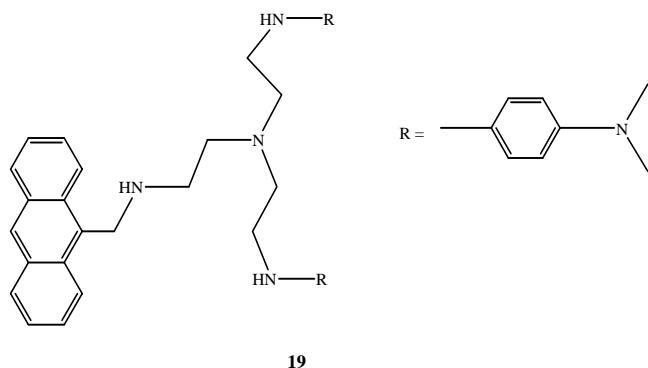
Figure 5. Relative fluorescence intensities of (A) and (B) in the presence of various metal cations. Reprinted with permission from [125], G. Hennrich et al., *J. Am. Chem. Soc.* 121, 5073 (1999). © 1999, American Chemical Society.

a 1,2,4-thiadiazole/iminoyl thiourea redox system, **18**. The heterocyclic oxidized form (**A**) and the open-chain reduced form (**B**) can be converted into each other chemically. While addition of different divalent metal ions such as Ca(II), Hg(II), Mg(II), Ni(II), and Pb(II) to **A** has only minor effects on its fluorescence behavior, the addition of Cu(II) exhibits a high emission intensity enhancement. The highest enhancement (~45 fold with respect to the free ligand) is observed when the metal-to-ligand ratio reaches 1:2. On further addition of Cu(II), an intermolecular excimer is formed. Upon the addition of Hg(II) to the reduced form (**B**), a red shift with a concomitant increase of naphthalene signal is observed immediately. After about 48 h, the initial signal at 334 nm disappear almost completely and a new band appears at 368 nm with a 34-fold enhancement of naphthalene emission. This time-dependent behavior with constant signal intensities reaching in 48 h, is significant with amounts of Hg(II) exceeding a 0.1 equivalent. An excess of Hg(II) (>1 equiv) leads to fluorescence enhancement initially, but undergoes subsequent bimolecular quenching.



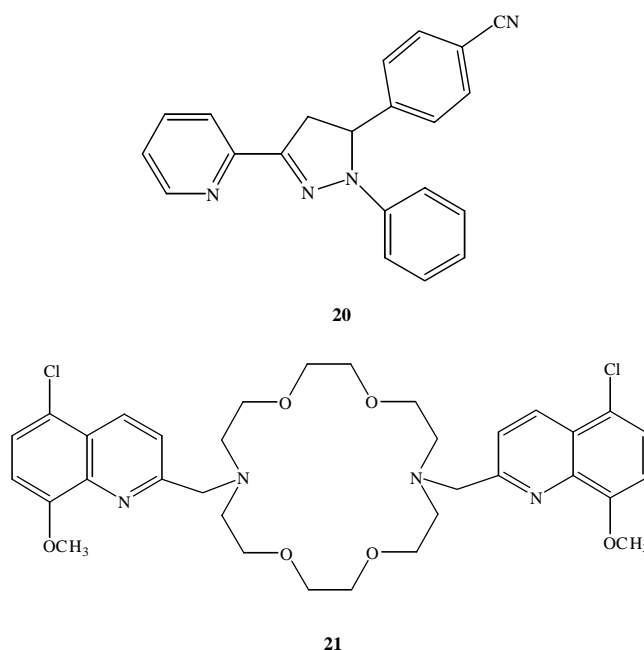
In case of **19**, both Zn(II) and a bulky carboxylate can modulate [127] the PET process. When it is complexed to a Zn(II) ion, the through-bond PET is blocked although the through-space PET is still operational (Scheme 1). As a result, the addition of one equivalent of Zn(II) ion results in a modest enhancement of fluorescence.

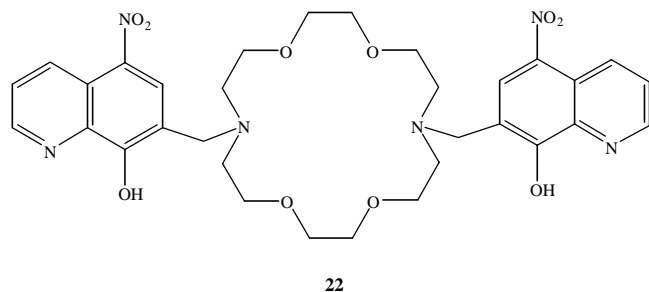
Upon the further addition of an equivalent of triphenylacetate anion, the through-space PET is blocked as the phenyl groups of the acid position themselves in-between the donor and the acceptor (Scheme 1). This results in the further increase in the emission enhancement.



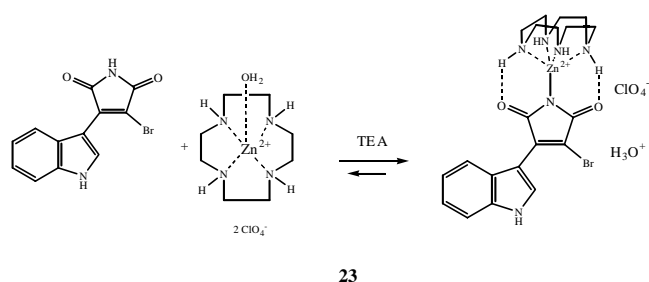
Scheme 1. Pictorial representation of modulation of PET process in the system **19** by both Zn(II) and a bulky carboxylate group. Reprinted with permission from [127], I. Bruseghini et al., *Chem. Commun.* 1348 (2002). © 2002, Royal Society of Chemistry.

The intrinsic fluorescent ligand **20**, exhibits [128, 129] a significant fluorescence enhancement upon the addition of a Zn(II) ion, thus serving as a specific signaling system for this metal ion. Other divalent metal ions quench fluorescence. The fluorophore, 5-chloro-8-methoxyquinoline has been connected to the receptor diaza-18-crown-6 to have the PET system, **21**. As a chemosensor, it selectively binds and responds [130] to Cd(II). Besides, Cu(II), Hg(II), Tl(I), and Pb(II) also form stable complexes with the receptor but do not interfere with the determination of Cd(II), provided that concentrations of these metal ions are not much higher compared to that of Cd(II) in the medium. A large enhancement is also observed with Zn(II), Ca(II) and to a lesser extent with Sr(II) and Ba(II). Interestingly, **22**, where the receptor is the same but the 8-hydroxyquinoline moiety is attached via C-7, is an effective fluorescence sensor [131] for the Hg(II) ion in the presence of other metal ions including Mg(II). However, if the two NO₂ groups are replaced by two Cl groups, the resultant system becomes [132] a chemosensor for Mg(II).

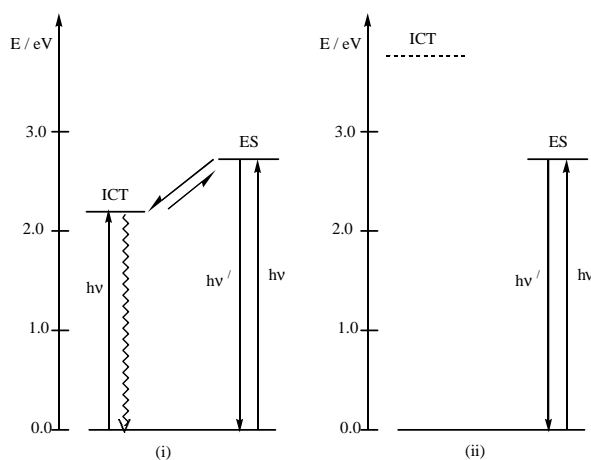




The emission intensity of the indolyl maleimide derivative **23** increases [133] almost 80-fold when it binds (1,4,7,11-tetraazacyclododecane)zinc(II) via supramolecular interactions. The emission enhancement is attributed to significant perturbation of the excited state of **23** upon coordination of the Zn(II) complex. There is a low-lying internal charge transfer (ICT) state with the indole being the donor and the maleimide, the acceptor. This ICT state is in thermal equilibrium with the $\pi-\pi^*$ excited state (Scheme 2). Upon coordination with the macrocycle-bound Zn(II) ion, the maleimide group deprotonates with concomitant weakening of the ICT interaction [134]. This new situation leads to greater quantum yield for the $\pi-\pi^*$ emission. The binding being reversible, it has the potential of acting as a switch.

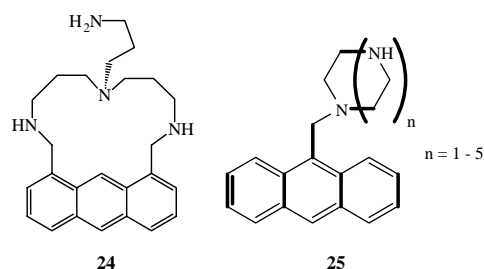


The PET system reported by Yoon et al. with partially immobilized polyamine as the receptor (**24**) act as chemosensors [135] for Hg(II) and Cu(II) ions in aqueous medium.

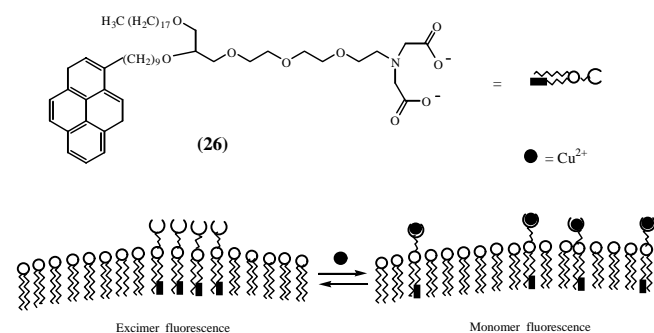


Scheme 2. Schematic energy level diagrams of an indolyl maleimide derivative **23**, (i) in polar solvents and (ii) at low temperature and upon coordination to a Lewis-acidic metal complex. Reprinted with permission from [133], B. K. Kaletas et al., *Chem. Commun.* 776 (2002). © 2002, Royal Society of Chemistry.

Such sensors that can act in aqueous medium are of practical importance. The same group reported [136] few anthrylazamacrocycles (**25**) which show enhancement by factors of 20–190 depending upon the system in an aqueous medium. The lipid **26** with an attached pyrene group [137–138] forms mixed vesicles at pH 7.5 with distearoylphosphatidylcholine. In this mixed vesicle, two or more of **26** can occupy adjacent positions. Upon excitation at 346 nm, the vesicles exhibit two distinct emission bands—one at 377 nm as weak, which is attributable to pyrene monomer emission, and the other at 477 nm due to excimer formation. When a Cu(II) salt is added to the vesicles, the metal is bonded to the iminodiacetate moiety and as a consequence, the excimer emission decrease with concomitant increase of the pyrene monomer emission. Thus, a Cu(II) ion does not quench fluorescence; it just induces a reorganization of the lipid molecules such that most of them are separated. The Cu(II)-induced changes are fast and reversible and can be used for quantitative analysis of the metal ion present.

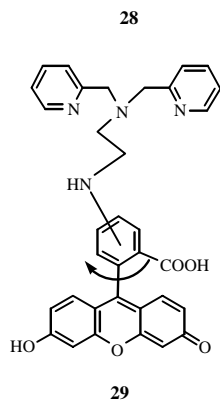
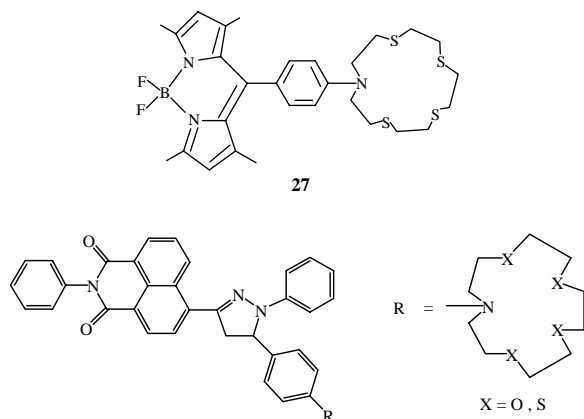


It has been argued [139] that the key factors in the design of fluorescent signaling systems are (1) rigidization of the constituent parts of the system to reduce metal-fluorophore interaction and their preorientation leading to electron decoupling of the fluorophore and the receptor. Based on this design principle, Rurack and Resch-Genger have synthesized a number of fluoroionophores (**27–29**). In **27**, a macrocyclic receptor is virtually electronically decoupled from the fluorophore unit. This compound exhibits [140] a high enhancement of fluorescence in the presence of Cu(II), besides heavy metal ions such as Hg(II) and Ag(I). Other first-row transition metal ions probed did not show any significant enhancement of fluorescence. In **28**, when the macrocycle is azacrown ether, the electron transfer is

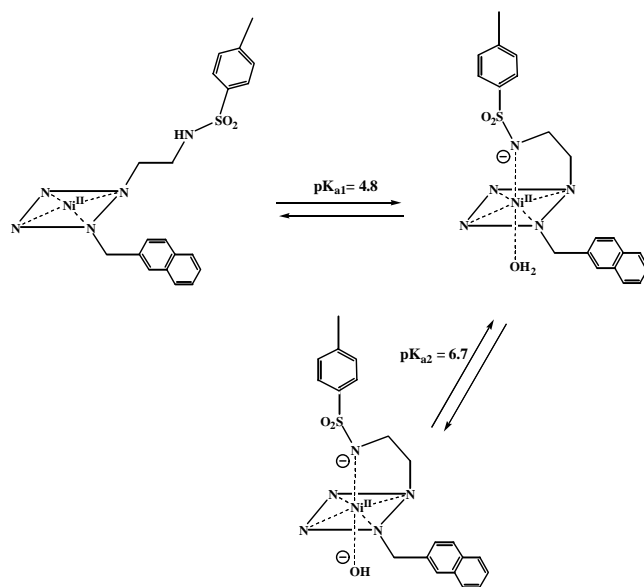


Scheme 3. Change in fluorescence properties of a phospholipid membrane containing **26** upon Cu(II) complexation. Reprinted with permission from [138], R. Kramer, *Angew. Chem. Internat. Ed. Engl.* 37, 772 (1998). © 1998, Wiley-VCH, Weinheim.

suppressed [141, 142] and an increase in the fluorescence quantum yield is observed with known quenchers like Pb(II), as the ionophore does not allow the metal ion and the fluorophore to be in communication. With azathia crown, both Ag(I) and Hg(II) show significant fluorescence enhancement. The fluorophore and the receptor in **29** are not properly oriented and electronically decoupled. The receptor shows [140] selectivity for Zn(II) and exhibits fluorescence enhancement by a factor of ~ 50 .

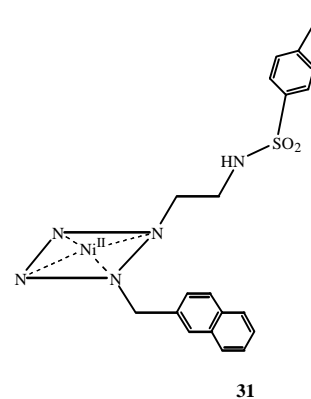
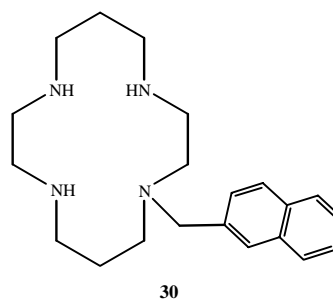


When (cyclam) is attached to a naphthyl group through a methylene spacer (**30**), in the format, “receptor-spacer-fluorophore,” the emission intensity of the fluorophore with Ni(II) ion as input is found [143] to be dependant on the spin-state of metal ion. When the metal ion is high spin with axial ligation, paramagnetic quenching of the fluorescence is observed even though PET from the N atom to the fluorophore is blocked. However, a square-planar diamagnetic Ni(II) ion exhibits a distinctively higher quantum yield as it cannot effectively quench the fluorescence. This signal transduction mechanism of Ni(II) ion has been applied in a system containing a reinforced macrocycle [144] as the receptor (**31**), where a naphthylmethyl group and a sulfonamide group are attached. The reinforced macrocycle does not allow axial coordination to Ni(II) from one side. The sulfonamide moiety itself does not show any coordination behavior; it can, however, deprotonate at a relatively low pH value and can then bind the metal ion anchored in the macrocyclic cavity rendering it in a square-pyramidal, high-spin state (Scheme 4). Of course, there might be a possibility of hexacoordination with a water molecule involved in

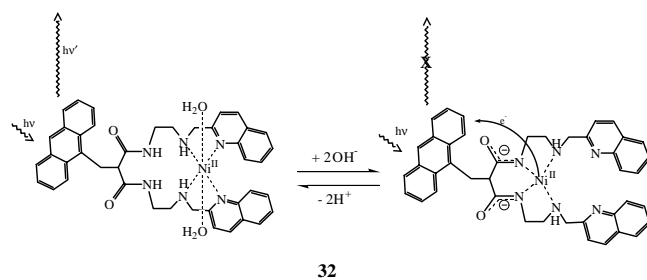


Scheme 4. A schematic representation of detection of geometrical change around Ni(II) in **31** by signal transduction mechanism. Reprinted with permission from [144], L. Fabbrizzi et al., *Inorg. Chem.* 41, 4612 (2002). © 2002, American Chemical Society.

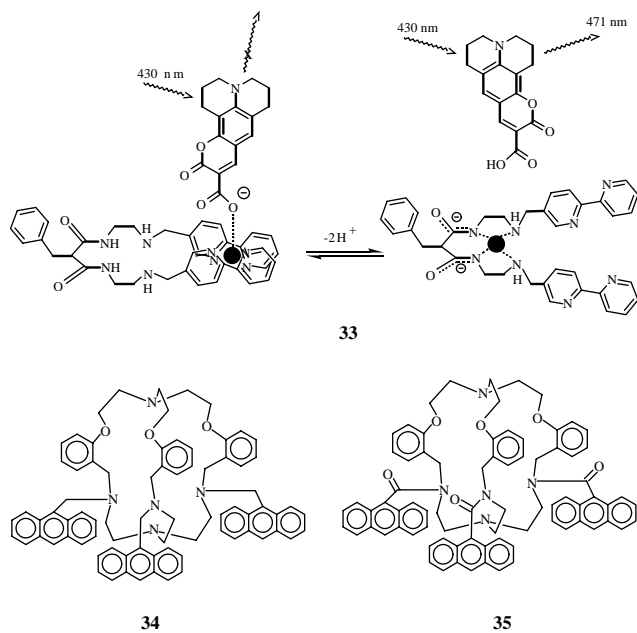
binding. This pH-controlled attachment/detachment of the pendant arm with concomitant change in the spin-state from high-spin to low-spin can be used in the signal transduction mechanism. In the high-spin state, this system exhibits a very low intensity of emission which is measurably increased in the low-spin state. Solid-state X-ray structural data on these and similar systems will be of utmost importance as these systems represent photonic devices whose emission can be mechanically controlled.



Translocation of a metal ion from one compartment to another in a reversible and repetitive manner has been achieved [145, 146] in **32** which contains two distinct binding sites. Amide nitrogens being poor donors, a metal ion such as Ni(II) occupies the site away from the anthracene moiety at pH ~ 7.5 and cannot quench anthracene fluorescence. When the pH is increased to ~ 9.5 , the amide nitrogens are deprotonated and the metal ion moves to the site closer to the fluorophore causing quenching of fluorescence. The translocation of the metal ion can be repeated many times making it a pH-controlled reversible system.



In a related molecule (**33**), the same authors have shown that Cu(II) ion can be translocated intramolecularly [147] by changing the pH of the medium. This translocation can be followed by fluorescence using coumarin-343 as an auxiliary fluorophore as shown in **33**. A metal ion that enters the cavity of a cryptand is isolated from the surroundings. Therefore, fluorescent sensors in the format, “receptor-spacer-fluorophore” built with cryptand as the receptor make the M-F communication negligible, while at the same time M-R interactions become high due to the *cryptate effect* [148]. Two typical cryptand-based molecular fluorescent signaling systems (**34–35**) are shown.



Compound **34** shows [75, 149] a very efficient PET process from the lone pair on the N atom bound to the anthryl moiety. In the presence of a first-row transition metal ion as

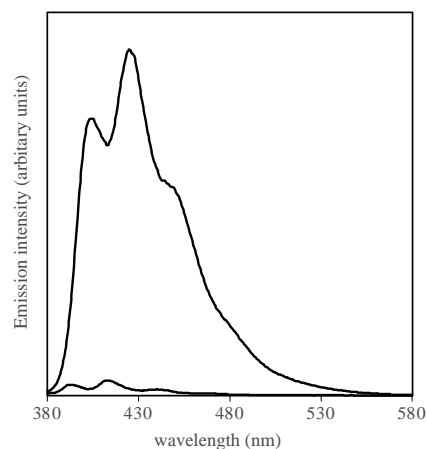
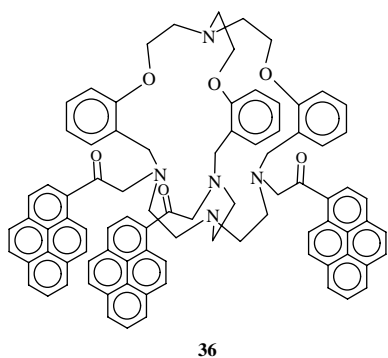


Figure 6. Emission spectra of free **34** and its Zn(II) complex.

input to **34** in dry THF, a strong fluorescence is observed (Fig. 6). The extent of enhancement depends on the nature of the metal ion as well as the receptor cryptand. The enhancement, however, is at least 100 times with respect to the metal free state. The four N donor atoms at the N₄ end of the cavity can bind a metal ion and the strength of this binding is reflected in the emission quantum yield. A metal ion like Co(II), Cu(II), or Zn(II) with tetracoordination, the fluorescence enhancement is maximum due to strong donation of the nitrogen lone pairs. Metal ions like Mn(II), Ni(II), and Fe(III), which prefer higher coordination, also exhibit a high intensity of fluorescence. These metal ions can achieve higher coordination by binding solvent molecules. Zn(II) shows the highest enhancement among the metal ions studied due to its nonquenching nature. The receptor having a poor chemoselectivity, provides an example of an **OR** logic gate [150, 151] with transition metal ions as input. As the anthracene group is not in communication with a metal ion bound inside the cavity, the emission band does not shift by more than 5 nm in the metal complex with respect to the metal free state.

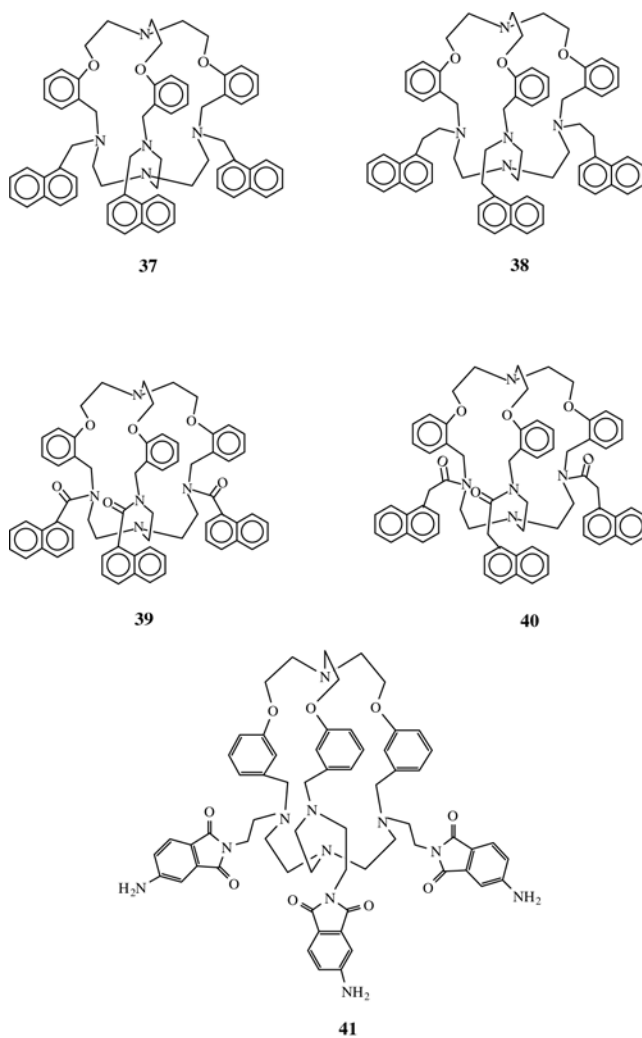
The modular design of fluorescent signaling affords to vary the spacer, receptor, and the fluorophore as well. However, different fluorophores can lead to systems with more complicated emission characteristics. In **35**, a carbonyl group is the spacer in place of methylene [152], which leads to changes in the interaction between the lone pair of nitrogen and the anthracene group. The emission spectra of carbonyl-substituted anthracenes has been found to be greatly influenced by the nature of the carbonyl substituent [153, 154]. Thus, although 9-substituted anthryl ketones are virtually nonfluorescent at room temperature in aprotic solvents, due to a suitably placed (n, π^*) triplet level that enhances intersystem crossing, the anthracene amide carbonyls have the (n, π^*), too high in energy to affect S₁ decay and are fluorescent in nature. Earlier studies revealed [153, 155, 156] that in the ground state (S₀) of 9-substituted carbonyl anthracenes like 9-anthramide and N,N-diethyl-9-anthramide, steric hindrance between the carbonyl group and the ring hydrogens keep the carbonyl group twisted almost 90° out of plane of the anthracene ring, which precludes extensive conjugation between the two. These compounds thus exhibit anthracene-like structured emission. However, the shape as

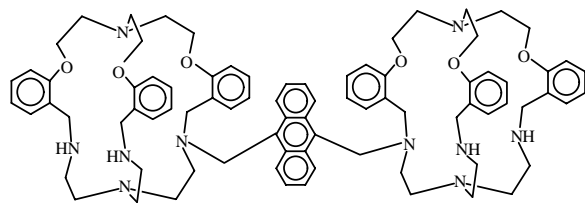
well as position of the emission spectra of 9-anthramide has been found to be quite solvent dependant [153] due to increasing conjugation between the carbonyl group and the anthracene π system. In contrast, the spectra of N,N-diethyl-9-anthramide are solvent independent [157] and show the same structured emission as unsubstituted anthracene due to much higher steric hindrance to rotation of the carbonyl group with respect to the anthracene moiety. The emission spectra of **35** is very similar compared to N,N-diethyl-9-anthramide, indicating restricted rotation of the carbonyl group in the molecule. The restricted rotation has two significant effects: (1) **35** does not show any exciplex like **34**, and (2) the PET process in **34** is less efficient compared to that in **34** due to unfavorable donor-acceptor orientation [158] in the former. Consequently, the quantum yield of emission does not increase more than 20 times upon addition of a metal ion as input. Compound **36** has [159] three pyrene groups attached to the cryptand receptor via $-\text{CH}_2\text{CO}$ -linkages. The metal-free compound exhibits the locally excited (LE) emission of the pyrene moiety. The PET from the N atoms to the pyrene is inefficient due to unfavorable orientation of the spacer and the fluorophore. This molecule also shows a broad structureless band, which begins to build up while the LE emission decreases as the concentration of the compound increases in dry THF. This broad emission is assigned as intramolecular exciplex involving a nitrogen lone pair and the fluorophore, which is another efficient deactivation channel of the donor-acceptor pair. Due to an inefficient PET process in **36**, the recovery of fluorescence (i.e., enhancement observed) seldom rises by a factor of 10.



The efficiency of the PET process in the metal-free **37–40** depends on the nature of the spacer [160]. These systems also provide an excellent opportunity to investigate the possibility of intramolecular exciplex and intramolecular excimer formation as a function of the nature of the spacer unit which allows varying degrees of distance of separation of donor and acceptor, besides flexibility of one with respect to the other. The quantum yield for the exciplex emission is greater for **38** compared to **37** as the nitrogen lone pair, and the naphthalene π orbitals are favorably oriented in **38**. It has been shown that for naphthalene- $(\text{CH}_2)_n$ -amine molecules ($n = 1-4$), the exciplex emission intensity is maximum for $n = 2$ suggesting a most favorable “in-line” approach of the lone-pair electrons of the amine and the π orbitals of naphthalene. The quantum yield of fluorescence monomer emission increases significantly in the case

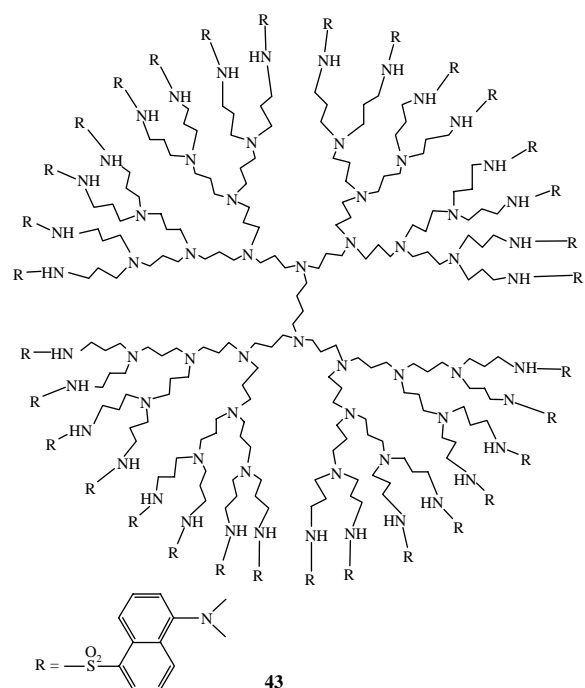
of **37** and **38** upon the addition of a transition metal ion as input. In both cases, the maximum enhancement was found with Zn(II) ion input (~ 9 fold for **37** and ~ 7 fold for **38**) probably due to its nonquenching nature. When an electron withdrawing fluorophore is attached to such a cryptand (**41**), the PET is found [161] not to be very effective in the metal-free state and the fluorescent enhancement does not show more than 20–30 times in the presence of a first-row transition metal ion. This points to the ineffectiveness of an electron withdrawing fluorophore with cryptand receptors where once inside the cavity, the metal ion is isolated from the surroundings and the fluorescence quenching mechanism is not operative. If two receptors [162] are attached to a single fluorophore as in **42**, then both the cavities must be occupied at the same time for fluorescence enhancement leading to an *AND* gate. Such *AND* gates are indeed known in the literature [77, 163–171]. With **42**, an *AND* gate can be realized [172] with transition metal ions as inputs. However, in the concentration range for the fluorescence measurements, it will be almost impossible to establish the situation where only one of the cavities will be occupied. A better design for an *AND* gate will be one where two different types of receptors are connected to a fluorophoric unit.





42

Dendrimers [173–177] with fluorophoric groups at the periphery have been constructed [178–185] for fluorescent signaling by transition metal ions. A fourth generation dendrimer (**43**) with 32 dansyl units at the periphery shows intense fluorescence in the metal-free state [186]. In presence of a transition metal ion such as Co(II), this fluorescence is quenched signaling the presence of the metal ion.



43

6. NONLINEAR OPTICAL EFFECTS

It must be mentioned at the outset that it is not the intention here to discuss molecules with nonlinear optical activity. Rather the discussion is restricted to the modulation of NLO behavior of organic molecules by metal ions. However, it is imperative to present in a rudimentary fashion, the phenomena of nonlinear optical activity for the interested new readers on the subject. A number of excellent books and articles are available on this subject [186–192].

When a molecule is subjected to an oscillating external electric field (light), the induced change in molecular dipole moment (polarization) can be expressed by a power series in the field strength E_j as in Eq. (1) where p_i is the electronic polarization induced along the i th molecular axis, α the linear polarizability, β the quadratic hyperpolarizability, γ the cubic hyperpolarizability, and so on.

$$p_i = \sum_j \alpha_{ij} E_j + \sum_{j \leq k} \beta_{ijk} E_j E_k + \sum_{j \leq k \leq l} \gamma_{ijkl} E_j E_k E_l + \dots \quad (1)$$

For small fields, the quadratic and cubic terms in Eq. (1) can be neglected, so that the induced polarization is proportional to the strength of the applied field, which is the linear optical behavior. However, when a molecule is subjected to an intense electric field such as that of an intense laser light, the second and third terms in Eq. (1) become important and nonlinear optical behavior is observed. Thus, nonlinear optical effects deal with the interaction of applied electromagnetic fields in various materials to generate new electromagnetic fields altered in frequency, phase, or other physical properties. The macroscopic polarization for an array of molecules is given by Eq. (2), where the $\chi^{(n)}$ values are the macroscopic susceptibilities. The macroscopic susceptibilities are related to the corresponding molecular terms α , β , γ by local field factors F , molecular packing density N_s , and appropriate coordinate transformation, $\langle T_{IJK} \rangle$.

$$P_I = \sum_J \chi_{IJ}^{(1)} E_J + \sum_{J \leq K} \chi_{IJK}^{(2)} E_J E_K + \sum_{J \leq K \leq L} \chi_{IJKL}^{(3)} E_J E_K E_L + \dots \quad (2)$$

$$\chi_{IJK}^{(2)} = N_s F \beta_{ijk} \langle T_{IJK} \rangle \dots \quad (3)$$

The discussions are restricted to quadratic NLO effects which lead to frequency doubling (SHG), frequency mixing, and the electrooptic Pockels effects that are of immense technological importance [193, 194].

At the molecular level, compounds likely to exhibit large values of molecular hyperpolarizability β , must have

1. excited states close in energy to the ground state for easy access by visible/infrared light,
2. a large oscillator strength for the transition,
3. a large difference between the ground- and excited-state dipole moments.

Although β in a molecule is closely related to bulk nonlinearity χ^2 in the solid state, large values of β do not mean that the molecule when crystallized, will show a high value of χ^2 . For this, the molecule must crystallize in a noncentrosymmetric space group. It has been a belief for a long time that extended π systems with a considerable molecular dipole character are most promising candidates as second-order NLO materials [192]. Two such dipolar molecules p-NA [196–198] and DANS [199] are illustrated in Figure 7. In the dipolar approach, β is associated with only one HOMO-LUMO electronic transition

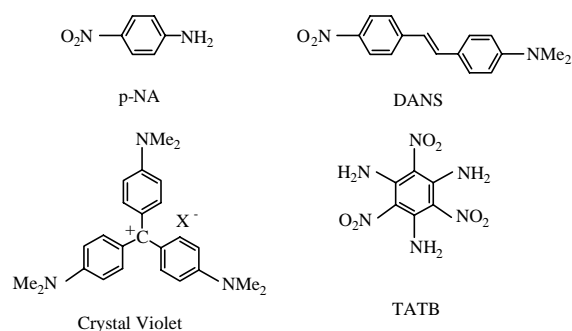


Figure 7. Examples of dipolar and 2D molecules with NLO property.

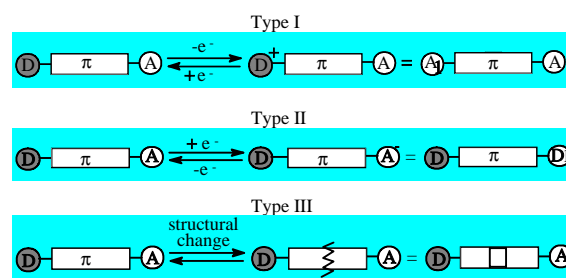
of charge-transfer (CT) character [200]. These molecules lack significant off-diagonal components; hence, β is termed one-dimensional (1D). A major problem [201] of traditional dipolar chromophores is the nonlinearity/transparency trade-off, whereby the desirable increase in second-order polarizability is accompanied by a bathochromic shift [202] of the electronic transition, leading to reabsorption of the second harmonic light, making them ineffective in frequency doubling applications. Moreover, these molecules are difficult to crystallize in noncentrosymmetric space groups. Strategies have been developed during the past decade to circumvent these drawbacks by extending the CT dimension from one to two or even to three [197]. These two- and three-dimensional (2D and 3D) chromophores [203–206] with C_3 , D_3 , or T symmetry, have several advantages:

1. they are more transparent as the lack of a permanent dipole moment results in negligible solvatochromism,
2. enhanced nonlinearity due to coupling of the excited states at no cost of transparency,
3. greater probability of crystallization in a noncentrosymmetric space group due to very low dipole moment.

Based on this principle, several molecules have been designed. Noteworthy among them are 1,3,5-triamino-2,4,6-trinitrobenzene (TATB) [207], crystal violet [208–211], tris(4-methoxyphenyl) cyclopropenyl bromide [208], and triazine derivatives [212, 213], 1,3,5-tricyanobenzene derivatives [214], D- π -A functionalized cryptands [215, 216], etc.

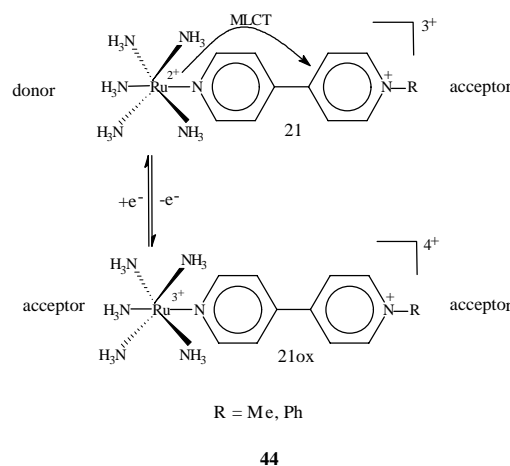
As NLO materials, organic molecules have certain advantages. They are potentially more versatile due to large β values, highly resistant to optical damage, and above all possibilities of designing molecules, highly suitable for SHG applications. In recent years, a number of organic solid-state structures with SHG activity have been synthesized based on crystal engineering principles [217–221]. However, incorporation of metal ions into organic compounds adds a new dimension of study and also introduces many intriguing possibilities [222–229] as NLO chromophores. When an organic molecule showing quadratic nonlinearity can act as a ligand to bind a metal ion, the metal-ligand ensemble can exhibit nonlinear effects quite different from the original molecule. A metal ion plays the role of a transducer by accepting electron density from the ligand moiety, thereby altering polarizability of the latter. The great structural and electronic diversity available in a metal-organic ensemble is likely to introduce into chromophores design strategies, a number of tunable parameters not available with only organic structures. Again, the coordination tendencies of metal ions can be taken advantage of in designing metal-assembled giant structures with NLO activity. With the tremendous advancement in the NLO field, it is anticipated that materials which can modulate or tune the NLO property will find various novel applications. A schematic representation of three different strategies [230] applied for switching of NLO responses in dipolar D- π -A derivatives are given in Scheme 5.

The presence of redox-active metal centers provides extensive opportunities for modulation of NLO responses. Coe et al. have shown [231] that dipolar ruthenium(II) ammine complexes of 4,4'-bipyridinium ligands (**44**) can



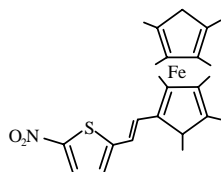
Scheme 5. A schematic representation of different strategies for modulating NLO responses in D- π -A molecules. Reprinted with permission from [230], B. Coe, *Chem. Eur. J.* 5, 2464 (1999). © 1999, Wiley-VCH.

exhibit tunable β values, originating from the intense, low-energy MLCT excitations. The d^6 Ru(II) behaves as a powerful π -donor and can be readily oxidized to the electron-deficient Ru(III) state, electrochemically or chemically. Visible absorption and HRS signals of this complex featuring $[\text{Ru}^{\text{II}}(\text{NH}_3)_5]^{2+}$ as donor is attenuated upon oxidation with a solution of 30% aqueous H_2O_2 and 2 M HCl taken in a 1:1 molar ratio. The complex reverts back to the original Ru(II) state upon reduction with 62% aqueous N_2H_4 solution. The difference in β between **44** and **44ox** is found to be 10–20 fold. Thus, reversible β switching of the molecular NLO responses can be achieved through the redox reaction of a donor (D) group.



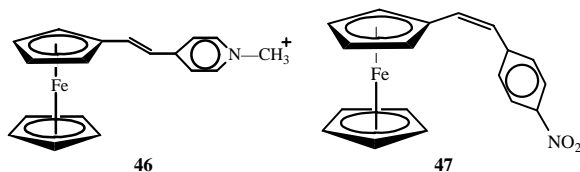
Compounds functionalized with ferrocene units as the electron donor with a conjugated side-arm linked to an acceptor unit have been extensively used for studying SHG in the last decade. Malaun et al. have recently reported [232] an octamethylferrocene donor unit and a nitrothiophene acceptor, linked by an ethylene bridge (**45**). The octamethylferrocene unit reduces at a lower potential compared to ferrocene. One-electron oxidation of **45** upon treatment with 1 equiv. of ferrocenium hexafluorophosphate in MeCN affords $[\mathbf{45}]^+(\text{PF}_6^-)$. The β values of **45** and $[\mathbf{45}]^+$ determined in CH_2Cl_2 at 1064 nm are $316 \pm 32 \times 10^{-30}$ and $25 \pm 5 \times 10^{-30}$ esu, respectively. Thus, compound **45** has SHG efficiency which is about one order of magnitude greater compared to that of $[\mathbf{45}]^+$. The redox interconversion of this

compound thus provides a pathway for modulation of the β value of the complex.



45

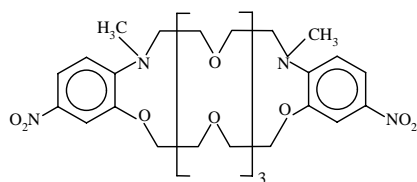
Compound **46** and **47** were found to exhibit [233, 234] very high powder SHG responses: about 220 and 62 times that of area, respectively.



46

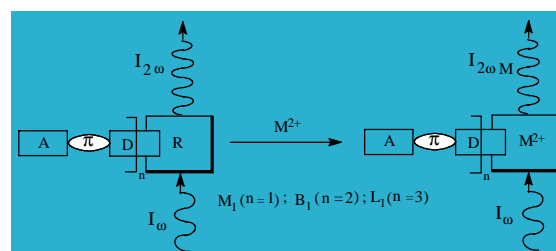
47

Houbrechts et al. have shown [235] that D- π -A functionalized chromophores undergo changes in the intramolecular charge-transfer (ICT) properties upon metal ion binding, which is further responsible for the modulation of its second-order NLO efficiencies. The functionalized crown ether (**48**) show a β value of 38×10^{-30} esu, while its 1:1 metal complexes with Na^+ , K^+ , and Ba^{2+} show β of 32, 27, and 24×10^{-30} esu, respectively. The largest reduction is obtained for Ba^{2+} confirming that the bivalent ion is more efficient in attenuating the electron-donor character of the ring nitrogen atoms. The NLO active 1,3-cone functionalized calixarene, where a significant bathochromic shift of 40 nm is also reported [236]. The cation binding improves the ICT which is reflected in the HRS signal intensity enhancement, although a correct determination of β could not be possible in the absence of a well-defined isobestic point in the absorption spectra.



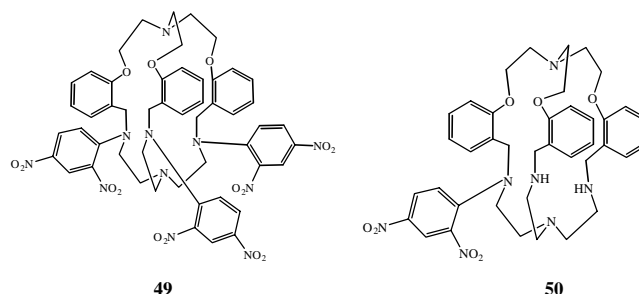
48

Cryptands having a three-fold symmetry axis [237] passing through the two bridgeheads can act as perfect skeletons for designing D- π -A chromophores (**49**). Besides, rigidity of the cryptand cavity can be varied by incorporating different groups in the three bridges. Some of the cryptand molecules can be selectively functionalized with different π -A units (**50**), giving rise to molecules where metal ions can occupy the cavity and bond the N atom attached to the π -A unit, thereby modulating the electrical polarizability of the system (Scheme 6). As the N atom donates its electron density to the metal ion in the cavity, its donating power to the π -A moiety diminishes (Fig. 8). The alkali metal ions such as Li(I), Na(I), and K(I) or the alkaline earth metal ions such



Scheme 6. A sketch for switching of NLO responses in D- π -A functionalized cryptand molecules. R, receptor; D, donor; π , aromatic ring; A, acceptor; n, number of D- π -A units; M^{2+} , metal ions; I_ω , fundamental light; $I_{2\omega}$, second harmonic light; $I_{2\omega M}$, modulated second harmonic light. Reprinted with permission from [237], P. Mukhopadhyay et al., *J. Mater. Chem.* 12, 2786 (2002). © 2002, Royal Society of Chemistry.

as Mg(II) and Ca(II) do not show any change in absorption spectra, since they occupy the upper part of the cryptand core and are thus unable to communicate with the D- π -A chromophore units. Addition of a metal ion such as Ni^{II} , Cu^{II} , Zn^{II} , and Cd^{II} induces an anti-auxochromic shifts in the absorption spectra of the functionalized cryptand molecules, as these metal ions are in direct communication with the D- π -A chromophore units.



49

50

On the gradual addition of metal ion, the absorbance spectra show a well-defined isobestic point, suggesting a 1:1 stoichiometry with the π -A functionalized cryptand. The

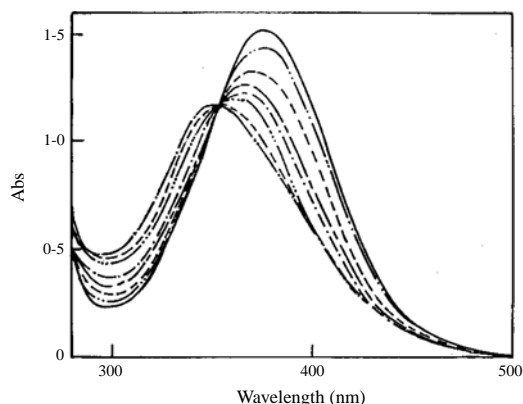


Figure 8. Effect of Cu(II) addition on the UV spectra of B_1 : (-) metal free (5×10^{-5} M); (- · -) Cu(II) (2.5×10^{-5} M); (- -) Cu(II) (5×10^{-5} M); (- · · -) Cu(II) (1.6×10^{-4} M); (- · · ·) Cu(II) (5×10^{-4} M); (- · · · ·) Cu(II) (8×10^{-4} M); (- · · · ·) Cu(II) (1.6×10^{-3} M); (- · · · ·) Cu(II) (5×10^{-3} M). Reprinted with permission from [237], P. Mukhopadhyay et al., *J. Mater. Chem.* 12, 2786 (2002). © 2002, Royal Society of Chemistry.

mono π -A functionalized M_1 exhibits a maximum blue shift in the presence of Cu^{II} ions (21 nm) with respect to the metal ion-free cryptand. Similarly, the bis π -A functionalized B_1 shows a maximum blue shift in the presence of Cu^{II} ions (30 nm). These results indicate that ICT from the amine (donor) to the nitro (acceptor) within the conjugate unit is hindered to the maximum extent as the nitrogen lone pair interacts with the Cu^{II} ion. As expected, the β value decreases with the increase of metal ion concentration, reaches a minimum corresponding to 1:1 stoichiometry, and then remains unaltered (Fig. 9). Maximum modulation of β is achieved with $Cu(II)$ ion. The trisdinitro-substituted cryptand shows no change in the absorption spectra with any of the metal ions as it does not bind a metal ion inside the cavity due to steric as well as electronic reasons. It has been known from our earlier studies [238] on the Ni^{II} complex with the unfunctionalized cryptand L_0 that the metal ion can be removed from the cavity by adding NaCN as the more stable $[Ni(CN)_4]^{2-}$ complex. So the addition of NaCN to either of the Ni^{II} complexed π -A functionalized cryptands results in the restoration of the position and the absorbance of the metal-free cryptands.

Zinc(II) ion has been used [239] as a template to assemble 2,2'-bipyridine based NLO-phores around it for having dipolar and multipolar NLO-active systems (51–53). The free ligands exhibit intense intraligand charge transfer in the visible region which undergoes a bathochromic shift in the complex due to coordination of the N atoms of the bipyridine moiety to $Zn(II)$ ion. The bathochromic shift depends on the number of coordinated ligands and decreases substantially as the ligand:metal ratio increases. This result is significant and shows that a metal ion can substantially modulate the polarizability of NLO chromophores. This strategy of gathering more than one 1-D unit around a metal ion leading to multipolar systems has been used to fabricate a number of NLO chromophores [240–249]. The increase in the quadratic nonlinear optical responses is due to [250–252] the red shift of the intraligand charge transfer transition upon metal coordination. A metal ion, depending on its electronic configuration, can impose a square

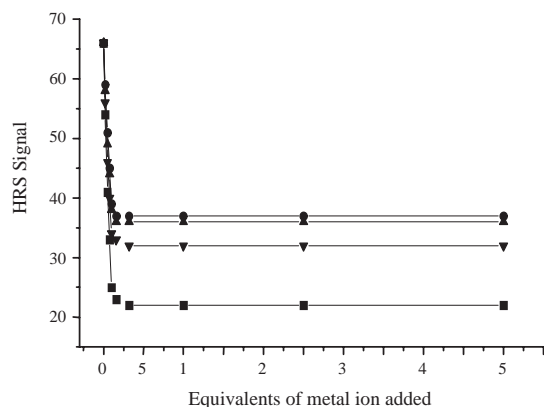
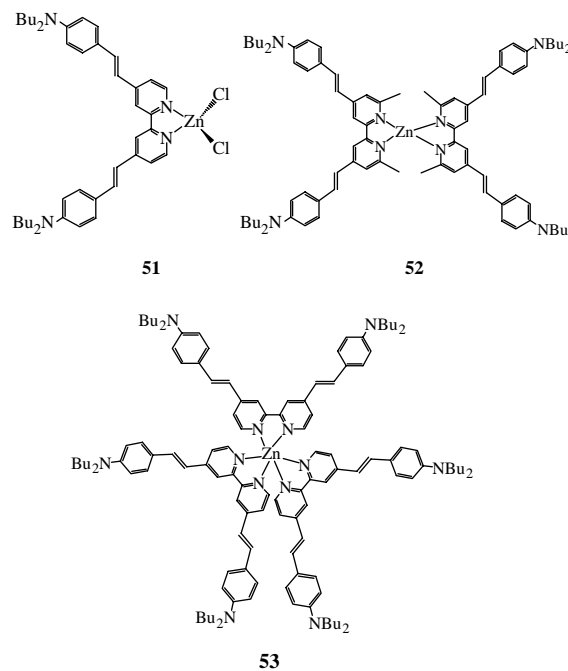


Figure 9. Plot of HRS signal ($I_2\omega/I_2\omega^2$) of M_1 with different metal ion inputs; $M_1 + Ni(II)$ (●); $M_1 + Zn(II)$ (▲); $M_1 + Cd(II)$ (▼); $M_1 + Cu(II)$ (■). Reprinted with permission from [237], P. Mukhopadhyay et al., *J. Mater. Chem.* 12, 2786 (2002). © 2002, Royal Society of Chemistry.

planar geometry and if bound to π -delocalized ligands such as bipyridine or terpyridine, the increase in the nonlinear effects can be substantial [253–255].



7. CONCLUSION

A large volume of work has been done on molecular fluorescent probes especially with alkali and alkaline earth metal ions. It is conceivable that new designer systems can be synthesized for fluorescent signaling with transition metal ions circumventing the quenching nature of these metal ions. Supramolecular chemistry should have a very strong influence in such endeavors. Organometallic systems acting as subunits, by virtue of the large number of available coordination sites about the metal center, can be utilized for directing self-assembly processes to design nanosized structures. In particular, 3D metal ions would appear as versatile candidates because of their capability of imposing many different stereochemical arrangements, depending upon their electronic configuration. Easy change of the redox states of these metal ions will add another dimension in designing. The emission characteristics of a fluorophoric system can be modulated by these metal ions for use in sensing and molecular-scale arithmetic. A combination of optical fiber technology and sensory circuits will make the remote detection of toxic ions possible. There are several problems remaining in this area, waiting to be tackled by the enthusiastic chemists. The foremost being systems that can show reversibility of the emission signal ideally without any fatigue. Besides, the emission signal must be recognized by another system separated in space with the help of a “molecular wire.” A completely organic molecule may not be ideal for this purpose. Introduction of a metal ion is likely to improve its characteristics. For this, either the metal ion should translocate within the molecule, or change in its oxidation state be felt by the fluorophore for the molecular system to act as a switch. While such translocation is

reported to occur chemically, that is, by changing pH or the addition of a complexing anion, completely photochemically reversible systems should be the goal. Such systems will not only be fast in response but the fatigue due to chemical intervention will be absent. Incorporation of transition metal ions into NLO active organic compounds will introduce many new tunable variables as the metal ions can perturb the polarizability characteristics of the organic part. With the advancements made in the technology using nonlinear optical effects, design of NLO chromophores with switchability will enhance their scopes to a great extent.

GLOSSARY

Cryptand A macrobicyclic ligand whose preorganized synthesis through ligand topology, binding ability, and structural rigidity determines the stability, selectivity, and properties of their complexes with metal ions.

Emission quantum yield The ratio of the number of photon emitted to that of the absorbed. It approaches unity if the radiationless rate of deactivation is much less than the rate of radiative decay.

Molecular fluorescence The emission of the excited molecule from a higher excited state to the low-lying ground state after the excitation. The emission occurs at a higher wavelength than that of the absorption.

Nanomaterials The nanosized materials that undergo change in physical, chemical, and mechanical behavior in comparison to bulk materials.

Nonlinear optics (NLO) The phenomenon of optical behavior of materials with the interaction of laser light. When certain molecules are introduced to an applied electromagnetic field, the induced change in the molecular polarizability can be expressed as a nonlinear function of the applied electromagnetic field.

Photoinduced electron transfer (PET) An intercomponent process which is operative between the receptor and the signaling unit. When the signaling unit is a fluorescent fragment, the perturbation of PET modulates the photophysical behavior of the fluorophore and signals the recognition.

ACKNOWLEDGMENT

Partial financial support for this work from the Council of Scientific and Industrial Research, New Delhi, is gratefully acknowledged.

REFERENCES

- G. M. Whitesides, J. P. Mathias, and C. T. Seto, *Science* 254, 1312 (1991).
- D. S. Lawrence, T. Jiang, and M. Levett, *Chem. Rev.* 95, 2229 (1995).
- B. Linton and A. D. Hamilton, *Chem. Rev.* 97, 1669 (1997).
- J. S. Lindsey, *New J. Chem.* 15, 153 (1991).
- K. C. Nicolaou and E. J. Sorensen, "Classics in Total Synthesis." VCH, Weinheim, 1996.
- E. J. Corey and X. M. Cheng, "The Logic of Chemical Synthesis." Wiley, New York, 1989.
- J. H. Fuhrhop, "Membranes and Molecular Assemblies: The Syntactic Approach." Royal Society of Chemistry, Cambridge, 1994.
- D. H. Busch, *J. Inclusion Phenom.* 12, 389 (1992).
- B. J. Holliday and C. A. Mirkin, *Angew. Chem. Internat. Ed. Engl.* 40, 2022 (2001).
- R. W. Saalfrank and B. Demleitner, in "Transition Metals in Supramolecular Chemistry" (J.-P. Sauvage, Ed.). John Wiley & Sons Ltd., New York, 1999.
- G. F. Swiegers and T. J. Malefetse, *Chem. Rev.* 100, 3483 (2000).
- P. J. Stang and B. Olenyuk, *Acc. Chem. Res.* 30, 502 (1997).
- O. M. Yaghi, H. Li, C. Davis, D. Richardson, and T. L. Groy, *Acc. Chem. Res.* 31, 474 (1998).
- M. Fujita, *Coord. Chem. Rev.* 27, 417 (1998).
- J. L. Atwood, J. E. D. Davies, D. D. MacNicol, F. Vögtle, and J.-M. Lehn, Eds., "Comprehensive Supramolecular Chemistry," Vols. 9 & 10. Pergamon, New York, 1996.
- J.-M. Lehn, "Supramolecular Chemistry-Concepts and Perspectives." VCH, Weinheim, Germany, 1995.
- J. S. Lindsey, *New J. Chem.* 117, 8293 (1991).
- P. J. Hagrman, D. Hagrman, and J. Zubieta, *Angew. Chem. Internat. Ed. Engl.* 38, 2638 (1999).
- J. J. Bodwin, A. D. Cutland, R. G. Malkani, and V. L. Pecoraro, *Coord. Chem. Rev.* 216-217, 489 (2001).
- J.-M. Lehn, *Perspect. Coord. Chem.* 447 (1992).
- J. P. Sauvage, *Acc. Chem. Res.* 31, 611 (1998).
- V. Balzani, M. Gomez-Lopez, and J. F. Stoddart, *Acc. Chem. Res.* 31, 405 (1998).
- R. P. Andres, S. Datta, D. B. Janes, C. P. Kubiak, and R. Reifenger, in "Handbook of Nanostructured Materials and Nanotechnology" (H. S. Nalwa, Ed.), Vol. 3, Academic Press, San Diego, 2000.
- F. M. Raymo and J. F. Stoddart, *Chem. Rev.* 99, 1643 (1999).
- E. C. Constable, *Chem. Commun.* 1073 (1997).
- J. M. Berg, J. L. Tymoczko, and L. Stryer, "Biochemistry," 5th Ed. W. H. Freeman & Co., New York, 2002.
- S. I. Stupp and P. V. Braun, *Science* 277, 1242 (1997).
- V. Balzani, in "Modular Chemistry" (J. Michl, Ed.). Kluwer Academic, Dordrecht, 1997.
- V. Balzani and F. Scandola, "Supramolecular Photochemistry." Ellis Horwood, Chichester, 1991.
- J.-M. Lehn, *Angew. Chem. Internat. Ed. Engl.* 27, 89 (1988).
- V. Balzani, Ed., "Electron Transfer in Chemistry," Vol. 5. Wiley-VCH, Weinheim, 2000.
- A. Hulanicki, S. Glab, and F. Ingman, *Pure Appl. Chem.* 63, 1247 (1991).
- A. W. Czarnik, Ed., "Fluorescent Chemosensors of Ion and Molecule Recognition." ACS Symposium Series 538, Washington, DC, 1993.
- B. Valeur, in "Topics in Fluorescence Spectroscopy," Vol. 4, (J. R. Lakowicz, Ed.). Plenum, New York, 1994.
- R. Y. Tsien, *Chem. Eng. News*, July 18, 34 (1994).
- T. D. James, K. R. A. S. Sundanayake, and S. Shinkai, *Angew. Chem. Internat. Ed. Engl.* 35, 1910 (1996).
- F. Szurdoki, D. Ren, and D. R. Walt, *Anal. Chem.* 72, 5250 (2000).
- Z. H. Lin, K. S. Booksh, L. W. Burgess, and B. R. Kowalski, *Anal. Chem.* 66, 2552 (1994).
- M. G. Schweyer, J. C. Andle, D. J. McAllister, and J. F. Vetelino, *Sens Actuators B* 35, 170 (1996).
- I. Oehme and O. S. Wolfbeis, *Mikrochim. Acta* 126, 177 (1997).
- J. Herdan, R. Feeney, S. P. Kounaves, A. F. Flannery, C. W. Stortment, G. T. A. Kovacs, and R. B. Darling, *Environ. Sci. Technol.* 32, 131 (1998).
- O. S. Wolfbeis, "Fibre Optic Chemical Sensors and Biosensors," Vol. I-II. CRC Press, Boca Raton, FL, 1991.
- B. Valeur and I. Leray, *Coord. Chem. Rev.* 205, 3 (2000).
- L. A. Saarl and W. R. Seltz, *Anal. Chem.* 55, 667 (1983).
- Z. Zhujun and W. R. Seltz, *Anal. Chem.* 58, 220 (1986).

46. J. I. Peterson, R. V. Fitzgerald, and D. K. Buckhold, *Anal. Chem.* 56, 62 (1984).
47. R. A. Bissell, A. P. de Silva, H. Q. N. Gunaratne, P. L. M. Lynch, G. E. M. Maguire, C. P. McCoy, and K. R. A. S. Sundanayake, *Top. Curr. Chem.* 168, 223 (1993).
48. J. W. Canary and B. C. Gibb, *Prog. Inorg. Chem.* 45, 1 (1997).
49. D. Philp and J. F. Stoddart, *Angew. Chem. Internat. Ed. Engl.* 35, 1154 (1996).
50. H.-J. Schneider and A. K. Yatsimirsky, "Principles and Methods in Supramolecular Chemistry." John Wiley & Sons, Chichester, 2000.
51. X. X. Zhang, R. M. Izatt, J. S. Bradshaw, and K. E. Krakowiak, *Coord. Chem. Rev.* 174, 179 (1998).
52. R. D. Hancock and A. E. Martell, *Chem. Rev.* 89, 1875 (1989).
53. L. F. Lindoy, "The Chemistry of Macrocyclic Ligands." Cambridge University Press, Cambridge, UK, 1989.
54. P. G. Potvin and J.-M. Lehn, in "Synthesis of Macrocycles: The Design of Selective Complexing Agents" (R. M. Izatt and J. J. Christensen, Eds.), John Wiley & Sons, Inc., New York, 1987.
55. G. J. Brown, A. P. de Silva, and S. Pagliari, *Chem. Commun.* 2461 (2002); A. P. de Silva, H. Q. N. Gunaratne, and C. P. McCoy, *Nature* (London) 42, 364 (1993).
56. D. Steinitz, F. Remacle, and R. D. Levine, *Chem. Phys. Chem.* 3, 43 (2002).
57. F. M. Raymo and S. Giordani, *J. Am. Chem. Soc.* 123, 4651 (2001).
58. J. M. Tour, *Acc. Chem. Res.* 33, 791 (2000).
59. R. M. Metzger, *Acc. Chem. Res.* 32, 950 (1999).
60. M. D. Ward, *J. Chem. Ed.* 78, 321 (2001).
61. D. Haarer, *Adv. Mater.* 28, 1544 (1989).
62. R. R. Birge, Ed., "Advances in Chemistry Series," 240 (1991).
63. F. L. Carter, Ed., "Molecular Electronic Devices II." Dekker, New York, 1987.
64. F. L. Carter, *Physica* 10D, 175 (1984).
65. F. L. Carter, Ed., "Molecular Electronic Devices." Dekker, New York, 1982.
66. C. Joachim, J. K. Gimzewski, and A. Aviram, *Nature* 408, 541 (2000).
67. P. Ball, *Nature* 406, 118 (2000).
68. A. Aviram and M. A. Ratner, *Chem. Phys. Lett.* 29, 277 (1974).
69. T. Gunnlaugsson, D. A. MacDonail, and D. Parker, *Chem. Commun.* 93 (2000).
70. A. P. de Silva and N. D. McClenaghan, *J. Am. Chem. Soc.* 122, 3965 (2000).
71. F. Pina, M. Maestri, and V. Balzani, *Chem. Commun.* 107 (1999).
72. A. Rouque, F. Pina, S. Alves, R. Ballardini, M. Maestri, and V. Balzani, *J. Mater. Chem.* 9, 2265 (1999).
73. A. P. de Silva, I. M. Dixon, H. Q. N. Gunaratne, T. Gunnlaugsson, P. R. S. Maxwell, and T. E. Rice, *J. Am. Chem. Soc.* 121, 1393 (1999).
74. A. Credi, V. Balzani, S. J. Langford, and J. F. Stoddart, *J. Am. Chem. Soc.* 119, 2679 (1997).
75. P. Ghosh, P. K. Bharadwaj, S. Mandal, and S. Ghosh, *J. Am. Chem. Soc.* 118, 1553 (1996).
76. M. Inouye, K. Akamatsu, and H. Nakazumi, *J. Am. Chem. Soc.* 119, 9160 (1997).
77. A. P. de Silva, N. D. McClenaghan, and C. P. McCoy, in "Electron Transfer in Chemistry" (V. Balzani, Ed.). Wiley-VCH, Weinheim, 2000.
78. J. Millman and A. Grabel, "Microelectronics," Chapter 6. McGraw-Hill, New York, 1988.
79. J. Barker, *Chem. Br.* 27, 728 (1991).
80. A. Aviram and M. Ratner, *Chem. Phys. Lett.* 29, 277 (1974).
81. L. M. Tolbert and X. Zhao in "Modular Chemistry" (J. Michl, Ed.). Kluwer Academic Publishers, Dordrecht, 1997.
82. M. D. Ward, *Chem. Ind.* 568 (1996).
83. M. Riordan and L. Hoddeson, "Crystal Fire: The Birth of the Computer Age." W. W. Norton & Co., New York, 1997.
84. H. Taube, *Science* 226, 1028 (1984).
85. W. B. Davis, W. A. Svec, M. A. Ratner, and M. R. Wasielewski, *Nature* 396, 60 (1998).
86. K. Donovan and S. Spagnoli, *Chem. Phys.* 247, 293 (1999).
87. S. Huang and J. M. Tour, *J. Am. Chem. Soc.* 121, 4908 (1999).
88. M. W. Grinstaff, *Angew. Chem. Internat. Ed. Engl.* 38, 3629 (1999).
89. P. Aich, S. L. Lubiuk, L. W. Tari, L. J. T. Delbaere, W. J. Roesler, K. J. Falk, R. P. Steer, and J. S. Lee, *J. Mol. Biol.* 294, 477 (1999).
90. J. Kong, N. R. Franklin, C. W. Zhou, M. G. Chapline, S. Peng, K. J. Cho, and H. J. Dai, *Science* 287, 622 (2000).
91. J. R. Reimers, L. E. Hall, M. J. Crossley, and N. S. Hush, *J. Phys. Chem. A* 103, 4385 (1999).
92. H. L. Anderson, *Chem. Commun.* 2323 (1999).
93. F. Cacialli, J. S. Wilson, J. J. Michels, C. Daniel, C. Silva, R. H. Friend, N. Severin, P. Samori, J. P. Rabe, M. J. O'Connell, P. N. Taylor, and H. L. Anderson, *Nature Materials* 1, 160 (2002).
94. T. Shimomura, T. Akai, T. Abe, and K. Ito, *J. Chem. Phys.* 116, 1753 (2002).
95. P. L. Bum, A. B. Holmes, A. Kraft, D. C. Bradley, A. R. Brown, R. H. Friend, and R. W. Gymer, *Nature* 356, 47 (1992).
96. L. A. Bumm, J. J. Arnold, M. T. Cygan, T. D. Dunbar, T. P. Burgin, L. Jones II, D. L. Allara, J. M. Tour, and P. S. Weiss, *Science* 271, 1705 (1996).
97. G. Leatherman, E. N. Durantini, D. Gust, T. A. Moore, A. L. Moore, S. Stone, Z. Zhou, P. Rez, Y. Z. Liu, and S. M. Lindsey, *J. Phys. Chem. B* 103, 4006 (1999).
98. C. Joachim, J. K. Gimzewski, R. R. Schlittler, and C. Chavy, *Phys. Rev. Lett.* 74, 2102 (1995).
99. A. P. de Silva, H. Q. N. Gunaratne, T. Gunnlaugsson, A. J. M. Huxley, C. P. McCoy, J. T. Rademacher, and T. E. Rice, *Chem. Rev.* 97, 1515 (1997).
100. G. J. Kavarnos, "Fundamentals of Photoinduced Electron Transfer." VCH, Weinheim, 1993.
101. A. Weller, *Pure Appl. Chem.* 16, 115 (1968).
102. R. A. Marcus, *Angew. Chem. Internat. Ed. Engl.* 32, 1111 (1993).
103. K. Cammann, U. Lemke, A. Rohen, J. Sander, H. Wilken, and B. Winter, *Angew. Chem. Internat. Ed. Engl.* 30, 516 (1991).
104. J. Wolfram and M. Sauer, in "Applied Fluorescence in Chemistry, Biology and Medicine" (W. Rettig, B. Strehmel, S. Schrader, and H. Seifert, Eds.). Springer-Verlag, Berlin, 1999.
105. S. Weiss, *Science* 283, 1676 (1999).
106. I. Willner, *Acc. Chem. Res.* 30, 347 (1997).
107. L. Fabbriizzi and A. Poggi, *Chem. Soc. Rev.* 197 (1995).
108. J. A. Kemlo and T. M. Shepard, *Chem. Phys. Lett.* 47, 158 (1977).
109. A. W. Varnes, R. B. Dodson, and E. L. Wehry, *J. Am. Chem. Soc.* 94, 946 (1972).
110. B. Ramachandram and A. Samanta, *Chem. Commun.* 1037 (1997).
111. B. Ramachandram and A. Samanta, *J. Phys. Chem. A* 102, 10579 (1998).
112. B. Ramachandram, G. Saroja, N. B. Sankaran, and A. Samanta, *J. Phys. Chem. B* 104, 11824 (2000).
113. B. M. Aveline, S. Matsugo, and R. W. Redmond, *J. Am. Chem. Soc.* 119, 11785 (1997).
114. K. A. Mitchell, R. G. Brown, D. Yuan, S.-C. Chang, R. E. Utecht, and D. E. Lewis, *J. Photochem. Photobiol. A* 115, 157 (1998).
115. A. W. Czarnik, *Acc. Chem. Res.* 27, 302 (1994).
116. M. E. Huston, K. W. Haider, and A. W. Czarnik, *J. Am. Chem. Soc.* 110, 4460 (1988).
117. L. Fabbriizzi, M. Licchelli, P. Pallavicini, and A. Taglietti, *Inorg. Chem.* 35, 1733 (1996).
118. T. Hirano, K. Kikuchi, Y. Urano, T. Higuchi, and T. Nagano, *J. Am. Chem. Soc.* 122, 12399 (2000).
119. T. Hirano, K. Kikuchi, Y. Urano, T. Higuchi, and T. Nagano, *Angew. Chem. Internat. Ed. Engl.* 39, 1052 (2000).
120. T. Koike, T. Abe, M. Takahashi, K. Ohtani, E. Kimura, and M. Shiro, *Dalton Trans.* 1764 (2002).
121. P. Jiang, L. Chen, J. Lin, Q. Liu, J. Ding, X. Gao, and Z. Guo, *Chem. Commun.* 1424 (2002).

122. B. D. Wagner, G. J. McManus, B. Moulton, and M. J. Zaworotko, *Chem. Commun.* 2176 (2002).
123. J. A. Sclafani, M. T. Maranto, T. M. Sisk, and S. A. V. Arman, *Tetrahedron Lett.* 37, 2193 (1996).
124. G. Hennrich, W. Walther, and U. Resch-Genger, *Eur. J. Org. Chem.* 3, 539 (2000).
125. G. Hennrich, H. Sonnenschein, and U. Resch-Genger, *J. Am. Chem. Soc.* 121, 5073 (1999).
126. G. Hennrich, W. Walther, U. Resch-Genger, and H. Sonnenschein, *Inorg. Chem.* 40, 641 (2001).
127. I. Bruseghini, L. Fabbrizzi, M. Licchelli, and A. Taglietti, *Chem. Commun.* 1348 (2002).
128. P. Wang, N. Onozawa-Komatsuzaki, Y. Himeda, H. Sugihara, H. Arakawa, and K. Kasuga, *Tetrahedron Lett.* 42, 9199 (2001).
129. K. Rurack, W. Retig, and U. Resch-Genger, *Chem. Commun.* 407 (2000).
130. L. Prodi, M. Montalti, N. Zaccheroni, J. S. Bradshaw, R. M. Izatt, and P. B. Savage, *Tetrahedron Lett.* 42, 2941 (2001).
131. L. Prodi, C. Bargossi, M. Montalti, N. Zaccheroni, N. Su, J. S. Bradshaw, R. M. Izatt, and P. B. Savage, *J. Am. Chem. Soc.* 122, 6769 (2000).
132. L. Prodi, F. Bolletta, M. Montalti, N. Zaccheroni, P. B. Sauvage, J. S. Bradshaw, and R. M. Izatt, *Tetrahedron Lett.* 39, 5451 (1998).
133. B. K. Kaletas, R. M. Williams, B. King, and L. de Cola, *Chem. Commun.* 776 (2002).
134. J. Daub, R. Engl, J. Kurzawa, S. E. Miller, S. Schneider, A. Stockmann, and M. R. Wasielewski, *J. Phys. Chem. A* 105, 5655 (2001).
135. J. Yoon, N. E. Ohler, D. H. Vance, W. D. Aumiller, and A. W. Czarnik, *Tetrahedron Lett.* 38, 3845 (1997).
136. E. U. Akkaya, M. E. Huston, and A. W. Czarnik, *J. Am. Chem. Soc.* 112, 3590 (1990).
137. D. Y. Sasaki, D. R. Shnek, D. W. Pack, and F. H. Arnold, *Angew. Chem. Internat. Ed. Engl.* 34, 905 (1995).
138. R. Kramer, *Angew. Chem. Internat. Ed. Engl.* 37, 772 (1998).
139. K. Rurack and U. Resch-Genger, *Chem. Soc. Rev.* 31, 116 (2002).
140. M. Kollmannsberger, K. Rurack, U. Resch-Genger, W. Retig, and J. Daub, *Chem. Phys. Lett.* 329, 363 (2000).
141. K. Rurack, U. Resch-Genger, J. L. Bricks, and M. Spieles, *Chem. Commun.* 2103 (2000).
142. K. Rurack, J. L. Bricks, B. Schulz, M. Maus, G. Reck, and U. Resch-Genger, *J. Phys. Chem. A* 104, 6171 (2000).
143. M. Engesser, L. Fabbrizzi, M. Licchelli, and D. Sacchi, *Chem. Commun.* 1191 (1999).
144. L. Fabbrizzi, F. Foti, M. Licchelli, and A. Poggi, *Inorg. Chem.* 41, 4612 (2002).
145. V. Amendola, L. Fabbrizzi, C. Mangano, and P. Pallavicini, *Acc. Chem. Res.* 34, 488 (2001).
146. V. Amendola, L. Fabbrizzi, C. Mangano, P. Pallavicini, A. Perotti, and A. Taglietti, *J. Chem. Soc. Dalton Trans.* 185 (2000).
147. V. Amendola, L. Fabbrizzi, C. Mangano, H. Miller, P. Pallavicini, A. Perotti, and A. Taglietti, *Angew. Chem. Internat. Ed. Engl.* 41, 2553 (2002).
148. J.-M. Lehn, *Acc. Chem. Res.* 11, 49 (1978).
149. P. Ghosh, P. K. Bharadwaj, J. Roy, and S. Ghosh, *J. Am. Chem. Soc.* 119, 11903 (1997).
150. L. A. Levy, E. Murphy, B. Raju, and R. E. London, *Biochemistry* 27, 4041 (1988).
151. A. P. de Silva, H. Q. N. Gunaratne, and G. E. M. Maguire, *J. Chem. Soc. Chem. Commun.* 1213 (1994).
152. G. Das, P. K. Bharadwaj, M. B. Roy, and S. Ghosh, *J. Photochem. Photobiol. A* 7, 135 (2000).
153. T. C. Werner and J. Rodgers, *J. Photochem.* 32, 59 (1986).
154. R. J. Strugeon and S. G. Schulman, *J. Pharma. Sci.* 65, 1833 (1976).
155. R. S. Shon, D. O. Cowan, and W. W. Schmiegel, *J. Phys. Chem.* 79, 2087 (1975).
156. T. C. Werner, in "Modern Fluorescence Spectroscopy" (E. L. Wehry, Ed.), Vol. 2. Plenum Press, New York, 1976.
157. T. C. Werner and R. M. Hoffman, *J. Phys. Chem.* 77, 1611 (1973).
158. G. J. Kavarnos and N. J. Turro, *Chem. Rev.* 86, 401 (1986).
159. P. Bandyopadhyay, P. K. Bharadwaj, M. B. Roy, R. Dutta, and S. K. Ghosh, *Chem. Phys.* 255, 325 (2000).
160. G. Das, P. K. Bharadwaj, and S. Ghosh, unpublished results.
161. S. Banthia and A. Samanta, *J. Phys. Chem. B* 106, 5572 (2002).
162. B. P. Bag and P. K. Bharadwaj, unpublished results.
163. S. Iwata and K. Tanaka, *Chem. Commun.* 1491 (1995).
164. A. P. de Silva, H. Q. N. Gunaratne, and G. E. M. Maguire, *Chem. Commun.* 1213 (1994).
165. A. P. de Silva, H. Q. N. Gunaratne, and C. P. McCoy, *J. Am. Chem. Soc.* 119, 7891 (1997).
166. H. F. Ji, R. Dabestani, and G. M. Brown, *J. Am. Chem. Soc.* 122, 9306 (2000).
167. A. P. de Silva, H. Q. N. Gunaratne, and C. P. McCoy, *J. Am. Chem. Soc.* 119, 7891 (1997).
168. S. Iwata and K. Tanaka, *J. Chem. Soc. Chem. Commun.* 1491 (1995).
169. M. W. Hosseini, A. J. Blacker, and J.-M. Lehn, *J. Am. Chem. Soc.* 112, 3896 (1990).
170. M. E. Huston, E. U. Akkaya, and A. W. Czarnik, *J. Am. Chem. Soc.* 111, 8735 (1989).
171. F. Pina, M. Maestri, and V. Balzani, *Chem. Commun.* 107 (1999).
172. B. P. Bag and P. K. Bharadwaj, unpublished work.
173. D. A. Tomalia and H. D. Dursi, *Top. Curr. Chem.* 165, 193 (1993).
174. G. R. Newkome, C. Moorfield, and F. Vögtle, "Dendritic Molecules: Concepts, Syntheses, and Perspectives." VCH, Weinheim, 1996.
175. J.-P. Majoral and A.-M. Caminade, *Top. Curr. Chem.* 197, 79 (1998).
176. A. W. Bosman, H. M. Janssen, and E. W. Meijer, *Chem. Rev.* 99, 1665 (1999).
177. F. Zeng and S. C. Zimmerman, *Chem. Rev.* 95, 1681 (1995).
178. V. Balzani, P. Ceroni, S. Gestermann, C. Kauffmann, M. Gorka, and F. Vögtle, *Chem. Comm.* 853 (2000).
179. F. Vögtle, S. Gestermann, C. Kauffmann, P. Ceroni, V. Vicinelli, and V. Balzani, *J. Am. Chem. Soc.* 122, 10398 (2000).
180. V. Balzani, P. Ceroni, S. Gestermann, M. Gorka, C. Kauffmann, and F. Vögtle, *J. Chem. Soc. Dalton Trans.* 3675 (2000).
181. J. Issberner, F. Vögtle, L. de Cola, G. C. Azzellini, and V. Balzani, *Chem. Eur. J.* 3, 706 (1997).
182. T. Aida and D.-L. Jiang, *Nature* 388, 454 (1997); T. Sato, D.-L. Jiang, and T. Aida, *J. Am. Chem. Soc.* 121, 10658 (1999).
183. A. Bar-Haim and J. Klafer, *J. Am. Chem. Soc.* 119, 6197 (1997).
184. K. W. Pollak, J. W. Leon, J. M. J. Fréchet, M. Maskus, and H. D. Abruna, *Chem. Mater.* 10, 30 (1998).
185. T. Gensch, J. Hofkens, A. Herrman, K. Tsuda, W. Verheijen, T. Vosch, T. Christ, T. Basché, K. Mullen, and F. C. de Schryver, *Angew. Chem. Internat. Ed. Engl.* 38, 3752 (1999).
186. S. Houbrechts, E. Hendrickx, T. Verbiest, K. Clays, and A. Persoons, in "Electron Transfer in Chemistry," Vol. 5. Wiley-VCH, Weinheim, 2000.
187. H. S. Nalwa and S. Miyata, Eds., "Nonlinear Optics of Organic Molecules and Polymers." CRC Press, Boca Raton, FL, 1997.
188. P. N. Prasad and D. J. Williams, "Introduction to Nonlinear Optical Effects in Molecules and Polymers." John Wiley & Sons, New York, 1991.
189. S. R. Marder, J. S. Sohn, and G. D. Stucky, "Materials for Nonlinear Optics: Chemical Perspectives." ACS Symposium Series 455, American Chemical Society, 1991.
190. G. H. Wagniere, "Linear and Nonlinear Optical Properties of Molecules." VCH, Weinheim, 1993.
191. D. S. Chemla and J. Zyss, Eds., "Nonlinear Optical Properties of Organic Molecules and Crystals." Academic Press, New York, 1987.
192. P. Günther, Ed., "Nonlinear Optical Effects and Materials." Springer-Verlag, Berlin, 2000.

193. J. Zyss, Ed., "Molecular Nonlinear Optics: Materials, Physics and Devices." Academic Press, Boston, 1994.
194. H. S. Nalwa, Ed., "Handbook of Advanced Electronic and Photonic Materials and Devices," Vol. 9. Academic Press, San Diego, 2001.
195. J.-L. Oudar and D. S. Chemla, *J. Chem. Phys.* 66, 2664 (1977).
196. C. C. Teng and A. F. Garito, *Phys. Rev. B* 28, 6766 (1983).
197. L. T. Cheng, W. Tam, S. H. Stevenson, G. R. Meredith, G. Rikken, and S. R. Marder, *J. Phys. Chem.* 95, 10631 (1991).
198. K. D. Singer, J. E. Sohn, L. A. King, H. M. Gordon, H. E. Katz, and C. W. Dirk, *J. Opt. Soc. Am. B* 6, 1339 (1989).
199. D. Y. Kim, M. Sundheimer, A. Otomo, G. Stegeman, W. H. G. Horsthuys, and G. R. Möhlmann, *Appl. Phys. Lett.* 63, 290 (1993).
200. J.-L. Oudar, *J. Chem. Phys.* 67, 446 (1977).
201. R. Wortmann, P. Kramer, C. Glania, S. Lebus, and N. Detzer, *Chem. Phys.* 173, 99 (1993).
202. J. Zyss and I. Ledoux, *Chem. Rev.* 94, 77 (1994).
203. J. Zyss, *Nonlinear Opt.* 1, 3 (1991).
204. T. Verbiest, K. Clays, C. Samien, J. Wolff, D. N. Reinhoudt, and A. Persoons, *J. Am. Chem. Soc.* 116, 9320 (1994).
205. J. J. Wolff and R. Wortmann, *J. Prakt. Chem.* 340, 99 (1998).
206. M. Joffre, D. Yaron, R. J. Silbey, and J. Zyss, *J. Chem. Phys.* 97, 5607 (1992).
207. I. Ledoux, J. Zyss, J. Siegel, J. Brienne, and J.-M. Lehn, *Chem. Phys. Lett.* 172, 440 (1990).
208. J. L. Bredas, F. Meyers, B. M. Pierce, and J. Zyss, *J. Am. Chem. Soc.* 114, 4928 (1992).
209. Y.-K. Lee, S.-J. Jeon, and M. Cho, *J. Am. Chem. Soc.* 121, 10921 (1998).
210. H. Lee, S.-Y. An, and M. Cho, *J. Phys. Chem. B* 103, 4992 (1999).
211. S. Brasselet, F. Cherioux, P. Audebert, and J. Zyss, *Chem. Mater.* 11, 1915 (1999).
212. P. C. Ray and P. K. Das, *Chem. Phys. Lett.* 244, 153 (1995).
213. R. Wortmann, C. Glania, P. Kramer, R. Matschiner, J. J. Wolff, S. Craft, B. Treptow, E. Barbu, D. Langle, and G. Gorlitz, *Chem. Eur. J.* 3, 1765 (1997).
214. B. R. Cho, S. B. Park, S. J. Lee, K. H. Son, S. H. Lee, J. Yoo, Y. K. Lee, G. J. Lee, T. I. Kang, M. Cho, and S.-J. Jeon, *J. Am. Chem. Soc.* 123, 6421 (2001).
215. P. Mukhopadhyay, P. K. Bharadwaj, G. Savitha, A. Krishnan, and P. K. Das, *Chem. Commun.* 1815 (2000).
216. P. Mukhopadhyay, P. K. Bharadwaj, G. Savitha, A. Krishnan, and P. K. Das, *J. Mater. Chem.* 12, 2237 (2002).
217. V. R. Thalladi, S. Brasselet, H.-C. Weiss, D. Blaser, A. K. Katz, H. L. Carrell, R. Boese, J. Zyss, A. Nangia, and G. R. Desiraju, *J. Am. Chem. Soc.* 120, 2563 (1998).
218. V. R. Thalladi, R. Boese, S. Brasselet, I. Ledoux, J. Zyss, R. K. R. Jetti, and G. R. Desiraju, *Chem. Commun.* 1639 (1999).
219. J. Zyss, S. Brasselet, V. R. Thalladi, and G. R. Desiraju, *J. Chem. Phys.* 109, 658 (1998).
220. P. Gangopadhyay and T. P. Radhakrishnan, *Angew. Chem. Internat. Ed. Engl.* 40, 2451 (2001).
221. K. Huang, D. Britton, M. C. Etter, and S. R. Bryan, *J. Mater. Chem.* 5, 379 (1995).
222. N. J. Long, *Angew. Chem. Internat. Ed. Engl.* 34, 21 (1995).
223. I. R. Whittall, A. M. McDonagh, M. G. Humphrey, and M. Samoc, *Adv. Organomet. Chem.* 42, 291 (1998).
224. D. R. Kanis, M. A. Ratner, and T. J. Marks, *J. Am. Chem. Soc.* 114, 10338 (1992).
225. J. A. McCleverty, in "Transition Metals in Supramolecular Chemistry" (L. Fabbri and A. Poggi, Eds.). Kluwer Academic Publishers, Dordrecht, 1994.
226. W. Lin, Z. Wang, and L. Ma, *J. Am. Chem. Soc.* 121, 11249 (1999).
227. I. G. Voight-Martin, G. Li, A. Yakimanski, G. Schulz, and J. J. Wolff, *J. Am. Chem. Soc.* 118, 12830 (1996).
228. H. S. Nalwa, *Appl. Organomet. Chem.* 5, 349 (1991).
229. S. R. Marder, in "Inorganic Materials" (D. W. Bruce and D. O'Hare, Eds.). Wiley Interscience, Chichester, 1992.
230. B. Coe, *Chem. Eur. J.* 5, 2464 (1999).
231. B. J. Coe, S. Houbrechts, I. Asselberghs, and A. Persoons, *Angew. Chem. Internat. Ed. Engl.* 38, 366 (1999).
232. M. Malaun, Z. R. Reeves, R. L. Paul, J. C. Jeffery, J. A. McCleverty, M. D. Ward, I. Asselberghs, K. Clays, and A. Persoons, *Chem. Commun.* 49 (2001).
233. S. R. Marder, J. W. Perry, W. P. Schaefer, B. G. Tiemann, P. C. Groves, and J. W. Perry, in "Nonlinear Optical Properties of Organic Molecules II" (G. Khanarian, Ed.). *SPIE Proc.* 1147, 1990.
234. M. L. H. Green, S. R. Marder, M. E. Thompson, J. A. Bandy, D. Floor, P. V. Kolinsky, and R. J. Jones, *Nature* 330, 360 (1987).
235. S. Houbrechts, Y. Kubo, T. Tozawa, S. Tokita, T. Wada, and H. Sasabe, *Angew. Chem. Internat. Ed. Engl.* 39, 3859 (2000).
236. E. Kelderman, L. Derhaeg, G. J. T. Heesink, W. Verboom, J. F. J. Engbersen, N. F. van Hulst, A. Persoons, and D. N. Reinhoudt, *Angew. Chem. Internat. Ed. Engl.* 31, 1075 (1992).
237. P. Mukhopadhyay, P. K. Bharadwaj, G. Savitha, A. Krishnan, and P. K. Das, *J. Mater. Chem.* 12, 2786 (2002).
238. P. Ghosh, S. Sengupta, and P. K. Bharadwaj, *J. Chem. Soc. Dalton Trans.* 935 (1997).
239. K. S en echal, O. Maury, H. L. Bozec, I. Ledoux, and J. Zyss, *J. Am. Chem. Soc.* 124, 4560 (2002).
240. C. Fave, M. Hissler, K. S en echal, I. Ledoux, J. Zyss, and R. R eau, *Chem. Commun.* 1674 (2002).
241. E. Kelderman, W. A. J. Starmans, J. P. M. van Duyunhoven, W. Verboom, J. F. J. Emgberson, D. N. Reinhoudt, L. Darhaeg, T. Verbiest, K. Calys, and A. Persoons, *Chem. Mater.* 6, 412 (1994).
242. H. S. Nalwa, T. Watanabe, and S. Miyata, *Adv. Mater.* 7, 754 (1995).
243. E. D. Reka i, J.-B. Baudin, L. Julien, I. Ledoux, J. Zyss, and M. Blanchard-Desce, *Chem. Eur. J.* 7, 4395 (2001).
244. S. Yokoyama, T. Nakahama, A. Otomo, and S. Mashiko, *J. Am. Chem. Soc.* 122, 3174 (2000).
245. T. Thami, P. Bassoul, M. A. Petit, J. Simon, A. Fort, M. Barzoukas, and A. Villaeys, *J. Am. Chem. Soc.* 114, 915 (1992).
246. M. S. Wong, J.-F. Nocoud, C. Runser, A. Fort, M. Barzoukas, and E. Marchal, *Chem. Phys. Lett.* 253, 141 (1996).
247. H. J. Deussen, C. Boutton, N. Thorup, T. Geisler, E. Hendrickx, K. Bechgaard, and A. Persoons, *Chem. Eur. J.* 4, 240 (1998).
248. P. J. A. Kenis, O. F. J. Noordman, H. Sch onherr, E. G. Kerver, B. H. M. Snel uk-Ru el, G. J. van Hummel, S. Karkema, C. P. J. M. van des Vorst, J. Hare, S. J. Picken, J. F. J. Engbersen, N. F. van Hulst, G. J. Vansco, and D. N. Reinhoudt, *Chem. Eur. J.* 4, 1225 (1998).
249. H. J. Deussen, E. Hendrickx, C. Boutton, D. Krog, K. Clays, K. Bechgaard, A. Persoons, and T. Bjornholm, *J. Am. Chem. Soc.* 118, 684 (1996).
250. D. R. Kanis, P. G. Lacroix, M. A. Ratner, and T. J. Marks, *J. Am. Chem. Soc.* 116, 10089 (1994).
251. D. Roberto, R. Ugo, S. Bruni, E. Cariati, F. Cariati, P. C. Fantucci, I. Invernizzi, S. Quici, I. Ledoux, and J. Zyss, *Organometallics* 19, 1775 (2000).
252. S. Bruni, F. Cariati, E. Cariati, F. A. Porta, S. Quici, and D. Roberto, *Spectrochim. Acta, Part A* 57, 1417 (2001).
253. D. Roberto, R. Ugo, F. Tessere, E. Lucenti, S. Quici, S. Vezza, P. C. Fantucci, I. Invernizzi, S. Bruni, I. Ledoux, and J. Zyss, *Organometallics* 21, 161 (2002).
254. D. Roberto, F. Tessere, R. Ugo, S. Bruni, A. Manfredi, and S. Quici, *Chem. Commun.* 846 (2002).
255. M. Bourgoult, K. Baum, H. Le Bozec, G. Pucetti, I. Ledoux, and J. Zyss, *New J. Chem.* 517 (1998).

Transport in Self-Assembled Quantum Dots

S. W. Hwang

Korea University, Seoul, Korea; University of Seoul, Seoul, Korea

Y. J. Park

*Semiconductor Materials Laboratory, Nanodevice Research Center,
KIST, Seoul, Korea*

J. P. Bird

Arizona State University, Tempe, Arizona, USA

D. Ahn

University of Seoul, Seoul, Korea

CONTENTS

1. Introduction
 2. Interaction Between Two-Dimensional Electron Gas and Self-Assembled Quantum Dots (SAQDs)
 3. Tunneling Through SAQDs
 4. Transport Through SAQDs Using STM
 5. Transport Through SAQDs Using Nanofabrication
 6. Selective Growth of SAQDs
 7. *C-V* Measurements
 8. Conclusions
- Glossary
References

1. INTRODUCTION

Transport through low-dimensional semiconductors has been an important and interesting topic since the advent of two-dimensional electron systems (2DES), such as high quality metal-oxide-semiconductor (MOS) [1] and high-electron-mobility-transistor (HEMT) structures [2]. The

density of states (DOS) of low-dimensional semiconductors is drastically different from that of three-dimensional ones and the electron-electron interaction frequently plays a pronounced role in electron transport. There have been important benchmarks in the transport study of such low-dimensional systems, including the observation of the quantum Hall effects [3] in 2DES, conductance quantization [4] in one-dimensional electron systems (1DES), single electron tunneling [5] in closed zero-dimensional electron systems (0DES), and finally, quantum interference effects [6] in open 0DES.

Even though there has been a lot of effort aimed at developing elaborate methods for realizing low-dimensional systems [7], most 1DES and 0DES for *electron transport studies* are still fabricated by lithography of MOS and HEMT structures [8]. Figure 1 shows two examples where low-dimensional systems are realized by lithography and pattern transfer. Figure 1a demonstrates the definition of a quantum dot by the so-called split-gate technique [9]. Here, electron beam (EB) lithography and lift-off of metal gates is performed on a HEMT wafer. Negative biases on the gates can deplete the 2DES underneath and form a small, dot-shaped region connected to the source and the drain reservoir. Figure 1b shows a silicon-on-insulator wire fabricated by etching the top silicon followed by EB lithography. Further definition of two poly-silicon gates that wrap across the wire, and the application of negative biases to them, can

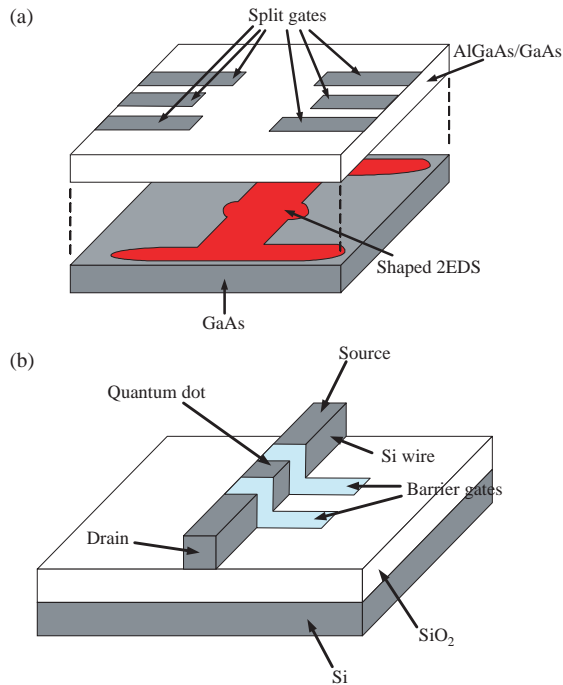


Figure 1. (a) Split-gate-definition of a quantum dot. Negative biases on electron-beam defined metal gates on a HEMT wafer can deplete the 2DES underneath, and form a small dot-shaped region. (b) Poly-silicon wrap gate definition of a quantum dot. Two poly-silicon gates wrapping around the etched silicon can define a quantum dot tunnel-coupled to the source and the drain reservoir.

define a quantum dot connected to the source and the drain reservoir.

Among many interesting approaches to the realization of low-dimensional systems without any *ex-situ* lithography process, self-assembly inside a growth chamber has achieved much success. The self-assembly is different from regrowth techniques in that low-dimensional structures can be grown *in-situ* while the regrowth technique still requires *ex-situ* lithography, except in a few very clever cases [10]. Self-assembled quantum dots (SAQDs) are *in-situ*, automatically grown, quantum dots that are formed on semiconductor substrates and thus represent a self-assembly of 0DES [11]. High-quality, defect-free, 0-D electronic states are expected to exist in SAQDs, since the formation of the dots is achieved in clean growth chambers at high temperatures (T). Furthermore, layers of semiconductors can be grown on top of SAQDs for passivation (these are usually called cap layers). We can expect that the quality of SAQDs are much better than that of regrown systems, or other chemically synthesized 1-D and 0-D semiconductor systems without cap layers [12].

The *in-situ* growth mechanism of SAQDs is strain relaxation of InAs against GaAs surface (the so-called Stranski-Krastanov mode [13]). The basic idea of this approach is that the strain between a thin wetting layer of InAs and the surface of a GaAs substrate can be released by forming small dots of InAs. Figure 2a shows a typical top view of GaAs substrate after the growth of InAs SAQDs. Randomly

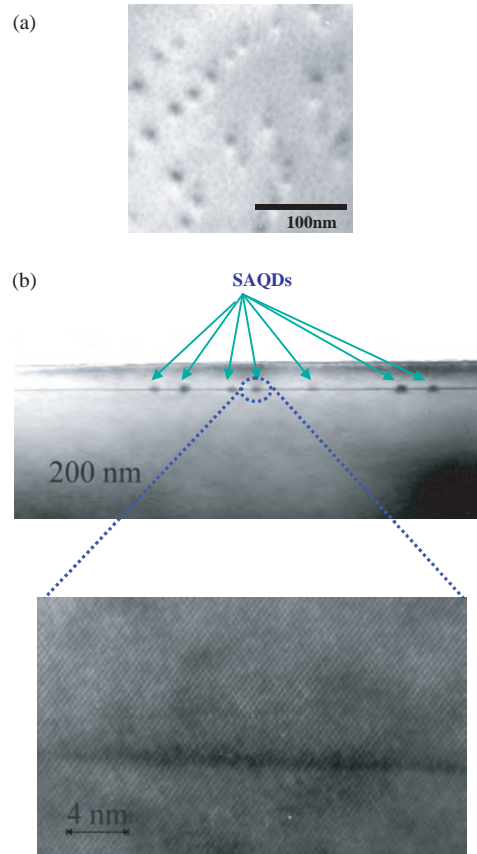


Figure 2. (a) A scanning electron micrograph (SEM) of a GaAs surface after the growth of InAs SAQDs; (b) a cross-sectional TEM of SAQDs. The magnified image clearly shows the formation of a crystalline dot.

distributed SAQDs with an approximate diameter of 20 nm are seen. Figure 2b shows a transmission electron micrograph (TEM) of the SAQDs. The magnified TEM image shows clear crystallization of the dot. The typical size of SAQDs ranges from 5 to 50 nm depending on the growth condition and the condition of the substrate, and the typical height is less than 20 nm. Usually, there is a small distribution in the size and height of the SAQDs, even when they are grown on the same substrate. The size of lithographically fabricated dots is limited by the depletion region, and practically, it is difficult to achieve such a small size. Therefore, the Coulomb charging energy and the quantum energy of SAQDs are expected to be larger than those of lithographically fabricated dots.

To date, much effort has been focused on the optical characterization of SAQDs [14], and there are many possible optical applications [15]. Optical probing is much simpler in terms of device preparation and can be used to study most of the quantized energy states. However, optical probing differs from transport investigations in that it mostly utilizes interband transitions, while the transport through SAQDs involves intraband processes (i.e., states in the conduction band). Furthermore, transport studies are of direct interest for possible electron device applications of SAQDs.

This chapter reviews recent progress in the study of electronic transport in various semiconductor devices incorporating SAQDs. There are many different ways of

incorporating SAQDs into semiconductor devices, and we group them here into several categories. This categorization is mainly for the convenience of discussion. In Section 2, the discussion will focus on transport studies of various 2DES with neighboring SAQDs. Such transport is expected to reveal the interaction between the 2DES and the layer of SAQDs. Tunneling through SAQDs is an important method for studying the electronic states of SAQDs. Several experimental studies, using tunneling structures, will be reviewed in Section 3. Scanning tunneling microscopy (STM) has been mostly used to observe the shapes of SAQDs. On the other hand, it is possible to utilize STM to drive a tunnel current between the tips and SAQDs. There have been a few experimental investigations of the STM current through SAQDs, and in Section 4, these will be introduced. Since SAQDs are automatically formed during epitaxial growth, as shown in Figure 2a, there is no selectivity in their position. For this reason, most of the transport studies that will be discussed in the following sections have been undertaken on devices with a large number of SAQDs. However, present nano-processing technologies have made it possible to fabricate devices with only a few, or single SAQDs. Furthermore, there has been a lot of effort at controlling the position of SAQDs in the growth stage. Transport studies of SAQDs embedded in nano-devices will be discussed in Section 5, and selective growth of SAQDs will be introduced in Section 6. Capacitance-voltage (C - V) measurements are a useful tool for determining energy states in these structures since both charging and discharging of SAQDs affects the capacitance. In Section 7, several C - V measurement studies will be discussed. In Section 8, conclusions will be given as well as a discussion of new issues such as transport through coupled SAQDs and its relation to possible realization of quantum computing.

2. INTERACTION BETWEEN TWO-DIMENSIONAL ELECTRON GAS AND SELF-ASSEMBLED QUANTUM DOTS (SAQDs)

Figure 3 shows a schematic of the device that is used to study the effect of SAQDs on a 2DES. The basic structure is a HEMT device that also features a layer of SAQDs inserted in the middle of the wafer. The growth of the SAQDs can be performed right after the growth of the GaAs buffer, so that the SAQDs reside at the GaAs/AlGaAs hetero-interface, or it can alternatively be inserted in AlGaAs insulator layer. In the first case, the SAQDs will act as direct scattering centers for the 2DES. In the latter case, the SAQDs can act as remote Coulomb scatterers, which smoothly modulate the potential for the electrons. The device for transport measurements can have the form of a transistor as shown in Figure 3, or it may take the form of a Hall bar.

Sakaki et al. studied the effects of InAs SAQDs on the electron transport in a 2DES [16], utilizing a so-called inverted HEMT structure in which the AlGaAs layer was beneath the GaAs layer and the InAs SAQDs were grown in the middle of the upper GaAs layer. They found that the low-temperature electron mobility decreased, while the

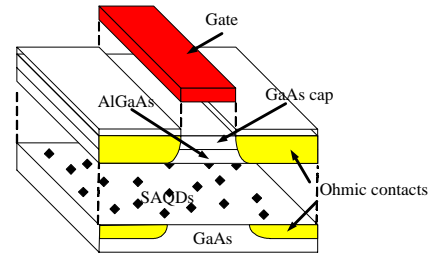


Figure 3. A schematic HEMT FET with a layer of InAs SAQDs at the hetero-interface.

electron concentration increased with a decrease of the distance between the hetero-interface and the layer of InAs SAQDs. This observation was explained by the potential modulation induced by the presence of the SAQDs. Phillips et al. fabricated an FET with InAs SAQDs adjacent to the AlGaAs/InGaAs/GaAs pseudomorphic quantum well channel (the SAQDs were embedded in the AlGaAs layer) [17]. Distinct steps and a negative differential resistance (NDR) were observed in the current-voltage (I - V) characteristics of this structure. Such features could be a manifestation of the resonant transport through quantum energy states, and these authors attributed the existence of these discrete quantum states to the bound states in SAQDs. Kim et al. measured the mobility of several GaAs/AlGaAs quantum wells in which InAs SAQDs were inserted [18], and found that this mobility was a function of the dot density. This observation could be explained using a similar argument as in [16].

A 2DES with an InAs SAQD layer at low T provides us with a good system in which we can study the interplay between disorder and quantum interference. Ribeiro et al. reported a metal-insulator transition at zero magnetic field (B) in such a 2DES [19]. A layer of InAs quantum dots were grown near the 2DES and they studied the T dependence of the diagonal resistance (R_{xx}) at various electron densities. They found a critical density, below which R_{xx} increases with decreasing T (in the insulating regime), while above which R_{xx} decreases with decreasing T (in the metallic regime). Recently, Kim et al. studied high B transport of several HEMT wafers with various different growths of InAs SAQDs at hetero-interfaces [20]. They systematically studied the T dependence of R_{xx} at high B . The transition is again from an insulating behavior to a metallic behavior and they attributed the transition to the short-ranged Coulomb potential originating from the InAs dots.

3. TUNNELING THROUGH SAQDs

Tunneling is the most direct and efficient method to probe quantum energy states in SAQDs. Figure 4 shows a typical tunnel transistor with SAQDs. This particular design has n^+ GaAs contact layers, graded GaAs layers, and AlAs barriers on both sides of the GaAs well with InAs SAQDs. In other types of design, however, the SAQDs can be inserted in the AlAs barriers. The whole structure is then etched into a pillar to form a tunnel diode. When the diameter of this pillar is several hundred μm , the number of SAQDs participating in the vertical transport is large and the measured current will exhibit the averaged properties of the dots. When the

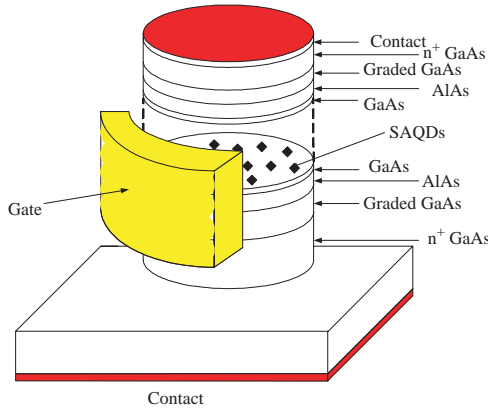


Figure 4. An example of tunnel transistor incorporating InAs SAQDs. This particular example shows a AlAs/GaAs/AlAs double-barrier structure with a SAQD layer grown in the middle of the GaAs quantum well. The metal gate deposited at the sidewall can further deplete the diameter of the active region.

diameter is sub- μm or several hundred nanometers, however, only a few dots participate in the transport and we usually are able to observe the characteristics of individual dots. In this case, a Schottky gate deposited along the periphery of the cylinder can be used to further squeeze the size of the diode. Figure 5 shows a typical differential conductance-voltage (dI/dV - V) characteristic measured from the device with a design similar to Figure 4. The data was taken at $T = 20$ mK and at $B = 18$ T and it shows a clear conductance peak. Such a conductance peak is the result of tunneling through a discrete quantum state in SAQDs. The size of the diode was several hundred μm in this case, and therefore, this characteristic is an averaged behavior of numerous numbers of SAQDs.

Itskevich et al. reported the measurement of the current through a single-barrier GaAs/AlAs/GaAs heterostructure diode at low T [21]. The diode had InAs dots embedded in the AlAs layer. Diodes with various diameters ranging from $30 \mu\text{m}$ to $400 \mu\text{m}$ were fabricated and characterized. They observed current peaks and interpreted them as being due to the resonant tunneling through the quantum states of individual quantum dots. The measured current showed oscillations as functions of B and it originated from the DOS of the 2DES in the emitter accumulation layer. In spite of their interpretation, the sample incorporates a large number

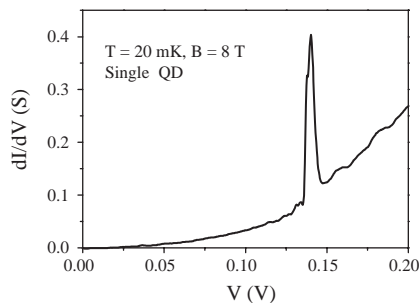


Figure 5. A typical dI/dV - V characteristic measured from the device shown in Figure 4. The data was taken at $T = 20$ mK and $B = 18$ T. The conductance peak is a result of magneto-tunneling through a quantum state of the dot.

of dots (the density of the dots is $2 \times 10^{11} \text{ cm}^{-2}$) and it is rather difficult to think that each current peak originated from an individual SAQD. A similar structure was studied by Narihiro et al. [22] and a resonant peak in the I - V characteristic was observed. The data was interpreted again as being due to resonant tunneling through SAQDs. The magneto-tunneling was also studied and a systematic change of the current shape as a function of B was observed. This magneto-tunneling data was explained by the shift of the Fermi surface of the emitter.

A tunneling structure with SAQDs embedded in the AlAs barrier was used for the careful study of magneto-tunneling through SAQDs. The tunneling current split with the increase of the magnetic field [23]. The splitting with the increase of the magnetic field made it possible to estimate the g -factor of InAs QDs. The observed g -factor ranged from 0.52 to 1.6. This contrasts with the value of bulk InAs (-14.8). The authors suggested that this change might be related to the quantized energy states, which arise due to the small size of the dots. Using a similar sample, the authors of [24] performed tunneling spectroscopy on a 2DES by measuring the tunnel current from the 2DES through the 0-D ground state of a single quantum dot embedded in the barrier of a tunnel diode [24]. The data revealed a structure that resembled the Landau level (LL) fan diagram. The authors also observed a sudden onset of the current as a function of the bias, and interpreted this as arising from a Fermi edge singularity. Thus, it was possible to obtain a quasi-particle lifetime from an LL fan diagram. They also observed the shift of the lowest LL to lower energy and they suggested that it originated from the exchange enhancement of the spin-splitting. The diameter of the mesa in this study was $5 \mu\text{m}$, and it was claimed that most of the dots had ground states above the Fermi energy of the 2DEG at zero bias.

The shape of the electronic wave functions in SAQDs were visualized in a magneto-transport study of SAQDs embedded in a tunneling structure [25]. The magnitudes of the tunneling current peaks were measured as a function of B . Since the increase of B corresponded to the shift of the Fermi surface in the k -space, the dependence of the current on B could be converted to the magnitude of the wavefunction in the k -space.

Under very high B values, the Fermi edge singularity could be observed in the resonant tunneling from highly doped three-dimensional GaAs electrodes through an InAs quantum dot, again embedded in an AlAs barrier [26]. Clear step-like features in the I - V curve with an undershoot were interpreted as the manifestation of the Fermi edge singularity. The observed peak splitting at high B was thought to be from the Zeeman splitting of the dot, and the observed oscillations of the peak position were considered to be from the Landau quantization. From the observed Zeeman splitting, the g factor value of 0.8 was obtained.

4. TRANSPORT THROUGH SAQDs USING STM

Scanning tunneling microscopy is a good tool for studying the transport through SAQDs, since it is possible to achieve access to individual dots on the surface. For the observation

of sample surfaces, a feedback loop has to be switched on to maintain the same current level. However, it is also possible to obtain the I - V characteristics between the sample surface and the STM tip by disconnecting the feedback loop and such a technique is called scanning tunneling spectroscopy (STS).

Rubin et al. performed the first measurement of current through a single SAQD by STM [27]. The technique was specifically called ballistic electron emission microscopy (BEEM). Their measurement showed clear differences between the STM current measured on the wafer with dots and without dots. Recently, more detailed STS measurements were done [28]. While the gap of 1.4 V was observed in the I - V curve on a bare GaAs surface, the gap of 1.25 V was seen in the I - V curve of a SAQD. This value is much larger than that of 0.4 V usually observed in InAs, and this observation was considered as evidence of strong electron confinement. Millo et al. studied the transport through a single InAs nanocrystal quantum dot by using low-temperature STM [29]. They observed a series of staircases in the STM current and the data were consistent with single electron tunneling through quantum states. They were even able to observe two-fold s state and six-fold p state resonances.

5. TRANSPORT THROUGH SAQDs USING NANOFABRICATION

Most of the important transport experiments discussed thus far were undertaken on samples and devices with sizes larger than at least several μm . It is only recently that studies of transport through only a few, or single, SAQDs became possible. Intensive nanometer semiconductor processing is usually needed for the fabrication of such devices.

Using multiple gating, squeezing of a μm -sized tunneling mesa structure has also been demonstrated [30]. This structure utilized four-way gates and local depletion of the dots was achieved by biasing the gates with different voltages (In contrast, Fig. 4 shows an example of one-way gating.). By biasing each gate separately and monitoring the movement of the current peaks, it was possible to relate the current peaks and the particular dot positions.

As shown in the schematic of Figure 6a, Jung et al. fabricated two metal electrodes on a wafer incorporating an InAs SAQD layer [31]. It is clear from the scanning electron micrograph of the actual device of Figure 6b that the size of the gap between the two metal electrodes was comparable to the size of a single SAQD and there was a single dot between the two electrodes. Figure 6c shows the I - V characteristics measured between the two electrodes of this structure at several different temperatures. There is a clear negative differential resistance and they attribute this feature to the resonant tunneling of electrons through the quantum states of the single SAQD.

Figure 7 schematically shows another interesting nano-device for the study of transport through a single SAQD [32]. The dot layer is positioned in the electron channel of an n-doped AlGaAs/GaAs HEMT structure. A point-contact is then fabricated by wet-etching and the size of the channel region was such that it contained at most three dots. While this etched point-contact fabricated from a normal HEMT

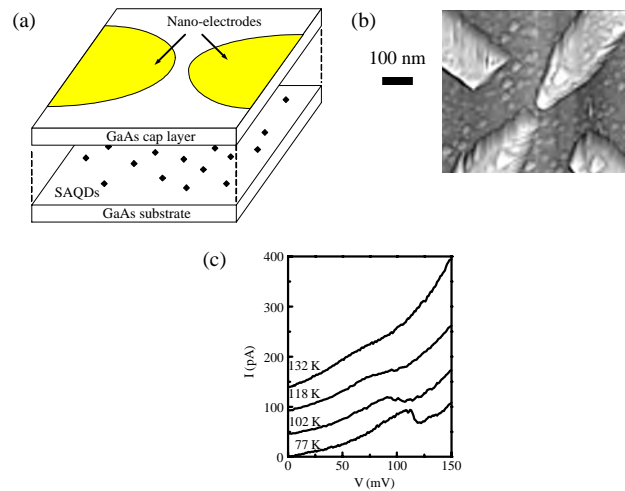


Figure 6. (a) A schematic of the nano-device to study transport through a single SAQD; (b) an SEM of the fabricated device. A single SAQD is located in-between two metal electrodes with the gap of approximately 30 nm [31]; (c) the measured I - V characteristics of the device at various temperatures. Clear NDR can be noticed [31]. Reprinted with permission from [31], S. K. Jung et al., *Appl. Phys. Lett.* 75, 1167 (1999). © 1999, American Institute of Physics.

showed conductance steps, the point-contact fabricated from the HEMT with SAQDs showed resonance peaks. The resonance peaks were interpreted as the conduction through the p-shells in a single SAQD. The authors also studied the effect of B on the transport and found the shift of resonance peak positions. The shift of the peak position with B was consistent with a simple quantum dot model with a harmonic confining potential.

The most standard way of having a small number of dots is fabricating a diode with the smallest possible diameter. Hill et al. fabricated a gated tunnel diode incorporating InAs SAQDs [33]. The diameter of the diode was $0.7 \mu\text{m}$ and the gate bias could further deplete the active area so that they were able to observe current peaks originating from individual dots.

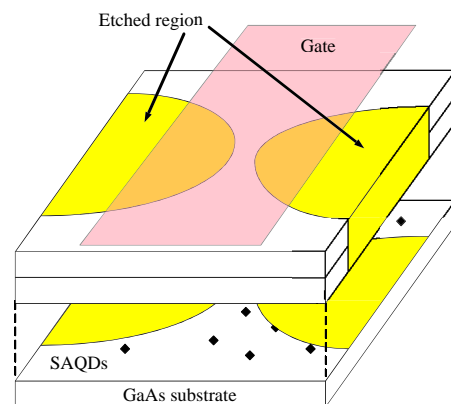


Figure 7. Another type of nano-device which was used to study transport through a single SAQD. A quantum point contact was defined by wet etching from a wafer similar to that in Figure 3.

6. SELECTIVE GROWTH OF SAQDs

The works discussed in the previous section all relied on post-fabrication for the position control of SAQDs. After the growth of InAs SAQDs on the whole wafer, pattern definition was performed to select either a few, or even a single SAQDs for transport study. Since it is considered that the main mechanism for the SAQD formation is strain relaxation, it is possible to selectively position those SAQDs by engineering the surface strain of the substrate.

Such selectivity in the growth of SAQD was first identified by Tsui et al. [34]. They patterned the substrate into a GaAs mesa, and then made facets surrounded by SiO_2 . In this way, they found that SAQDs grew only on the GaAs mesa. In subsequent work [35], the GaAs mesa was reduced to $1\ \mu\text{m}$ wide, but the authors still found a selectivity of InAs dot growth.

Almost perfect site control was achieved by connecting various ultra-high vacuum equipments [36]. These authors used *in-situ* EB patterning and Cl_2 etching to pattern holes on the substrate, and performed subsequent MBE growth without breaking vacuum. In this study, they found that the SAQDs were preferentially self-organized in the patterned holes. Alternatively, Hyon et al. used the oscillating cantilever of an atomic force microscope (AFM) to carve the substrate [37]. They found that the growth position of the SAQDs strongly depended on the slope of the facet of the carved grooves or holes. They could grow SAQDs selectively in the carved grooves or only on top of the hills formed in-between grooves. Figure 8a shows a one-dimensional array of InAs dots grown on top of the carved hill and Figure 8b shows the dots grown only inside the

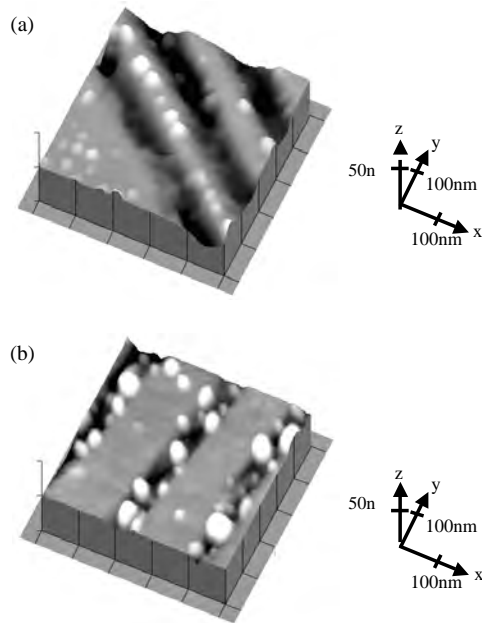


Figure 8. Selectively grown SAQDs after carving a GaAs surface by the AFM cantilever oscillation. Depending on the shape of the carved side-wall, SAQDs can be positioned (a) on top of the hills [37] or (b) inside the grooves [37]. Reprinted with permission from [37], C. K. Hyon et al., *Appl. Phys. Lett.* 77, 2607 (2000). © 2000, American Institute of Physics.

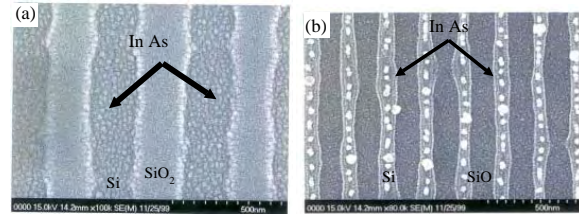


Figure 9. Selectively grown SAQDs utilizing patterned Si/ SiO_2 substrates. (a) The growth of SAQDs occurs only on the Si stripes [39]; (b) when the width of the stripes is narrow enough, 1-D arrays of SAQDs can be achieved [39]. Reprinted with permission from [39], B. H. Choi et al., *Appl. Phys. Lett.* 78, 1403 (2001). © 2001, American Institute of Physics.

grooves. Hahn et al. [38] utilized a SiN_x mask to form a GaAs mesa and grow InAs dots. Depending on the shape and the size of the mesa, they were also able to control the position and even the number of dots on the mesa. Similar selectivity could also be achieved using a layer of SiO_2 covering a Si surface [39]. The nano-patterned SiO_2 was found to successfully block the formation of the InAs SAQDs, and it was therefore possible to grow the dots only on the Si surface. Figure 9a demonstrates that InAs dots are grown only on the region where Si is exposed. As shown in Figure 9b, one-dimensional arrays of the InAs dots can be formed by narrowing the width of the Si stripes.

Recently, it was found that QDs can also be grown on an InGaAs/GaAs superlattice template [40]. The template can provide an appropriate strained layer, since it produces strain fields with high uniformity, enabling the flexible control of alignment of QDs without the need of any complicated pre-processes. The superlattice slightly over the critical thickness affects only the driving of adatoms into local strain relaxed regions. Therefore, a strain relaxation from the misfit dislocations gives rise preferably to the nucleation of QDs. The authors of [40] found that there was a dependence of QD ordering on the number of superlattice periods.

7. C-V MEASUREMENTS

Even though there is no direct electron transfer in C - V measurements, this technique is still an important transport measurement, since the charging and discharging of SAQDs will provide details on the energy level structure of the dots. The first capacitance measurements of InAs dots were done by Medeiros-Ribeiro et al. [41]. They found peaks in the low T C - V measurement which they suggested originate from charging of the s-state. A subsequent experiment by the same group also resolved the p-state in the capacitance measurements [42].

Positively charged defects were shown to be important in C - V measurements. Belyaev et al. measured $C(V)$ and $C(B)$ for many different samples with SAQDs embedded in AlAs [43]. Their data showed a sign of larger positive charges as the thickness of the AlAs layer increases. Recent interesting C - V measurements utilized a pn junction structure [44]. In contrast to previous experiments, these studies revealed a large amount of charges in the pn structure. Therefore, the

Table 1. Detailed information about the InAs SAQDs used in various transport experiments. The growth conditions, size of the dots, average dot density, and the structure of the wafer embedding the SAQDs are shown. The first column displays the category of the device and the reference number.

Type [Ref.]	n ($\times 10^{10}$ cm $^{-2}$)	d (nm)	h (nm)	T ($^{\circ}$ C)	t (ML)	Summary of Layer Structure
2DES [16]	10	10~20	8	450	≥ 1.5	inverted AlGaAs/GaAs, InAs QDs in GaAs layer, δ doping
2DES [17]	5			510	2.5	AlGaAs/InGaAs, InAs QDs in AlGaAs, δ doping
2DES [18]	0.25~0.58	36~28	8~4	530	2.15	GaAs quantum well, InAs QDs in GaAs well, δ doping
2DES [19]	0.3~5					AlGaAs/GaAs, InAs QDs in GaAs layer, δ doping
2DES [20]	0.3	28	4	525	1.61~2.15	similar to [18]
Tunnel [21, 24, 25]	20	10			1.8	InAs QDs embedded in AlAs barrier, GaAs contact layers with graded doping
Tunnel [22]	10			450	1.1~2.2	similar to [21]
Tunnel [23]		10	3			similar to [21]
Tunnel [26]		10~15	3~4			similar to [21]
STM [27]		30	3			InAs QDs embedded in thin GaAs
STM [29]		2~7				solution phase pyrolytic reaction of organometallic precursors
Nano [30]				520~550	0.5 nm	similar to [21], (311)B GaAs substrate
Nano [31]	5	20	5	470	2	InAs QDs in a thin GaAs buffer (MOCVD)
Nano [32]				520	2.1	similar to [19]
Nano [33]	10					similar to [21]
C - V [41]	2			530		InAs QDs with thick layers of GaAs on both sides

electric field was not linear. These authors compared their measurements with the results of self-consistent energy level calculations.

8. CONCLUSIONS

Transport in semiconductor devices incorporating SAQDs is an interesting research topic, since the SAQD is a unique structure obtained automatically during crystal growth. Transport studies of these structures have been undertaken in many different ways such as the study of transport in 2DES with a nearby SAQD layer, tunneling transport through SAQDs, STS on individual SAQDs, transport in various nano-devices incorporating a few or a single SAQD, and C - V measurements. Even though the detailed device structures are different in these experiments, the main outcomes from them are probing the electronic energy states of SAQDs with and without B . In this chapter, we tried to cover all the important experimental progress related to these dots. However, a complete coverage of recent

research would have been impossible since the amount of work is already vast and the field is still actively moving. Finally, Table 1 summarizes all the details related with the SAQDs used in various transport experiments discussed in this chapter.

Recently, transport through coupled quantum-dot systems is of interest, since we can study coherent coupling between two 0DES (such a coupled quantum-dot system is called quantum-dot molecule) and such coherence is recognized as an important ingredient in the development of solid-state quantum computing [45]. Recent progress has made it possible to grow vertically aligned stacked SAQDs [46] and to study the transport through such stacked SAQDs. Figure 10 shows an example of stacked SAQDs. It demonstrates six SAQD layers stacked in the (001) direction. The uniformity and alignment of the dots are quite acceptable. Since the dots can be closely stacked, a much larger interaction is expected in this vertically coupled SAQDs than the case of the lithographically defined coupled quantum dots, where

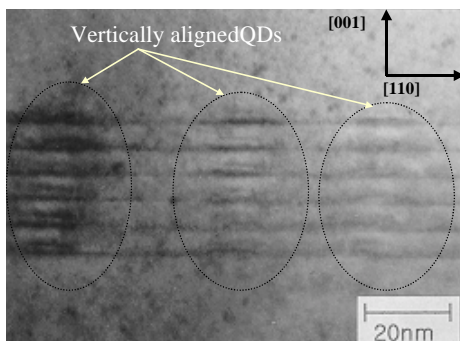


Figure 10. A TEM showing six stacked layers of InAs SAQDs.

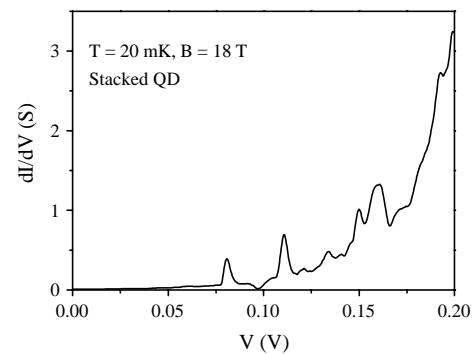


Figure 11. A dI/dV - V characteristic taken from a diode with two stacked layers of SAQDs. The data were taken at $T = 20$ mK and $B = 18$ T.

the finite depletion layer again becomes a limiting factor. There have been some optical experiments demonstrating an entanglement/controlled coupling [47] and a measurement of the relaxation time [48] utilizing self-aligned stacked SAQD systems. However, electronic transport studies through coupled SAQDs have been rarely reported. Figure 11 shows an example of the dI/dV taken from a diode with stacked layers of SAQDs at low T and high B . It shows abundant peaks and rich features which might be expected to originate from quantum coupling between the dots. Future transport studies of such stacked-dot systems will be very interesting.

GLOSSARY

Capacitance-voltage (C - V) measurement A slowly varying ramp voltage and an AC signal are applied to the electrode deposited on the sample to be investigated. Then the AC current is measured to obtain the capacitance as a function of the applied DC bias.

Nano-fabrication Processes for making nano-devices and nano-structures.

Quantum dot A tiny piece of semiconductor whose electrons are isolated from nearby reservoirs. Their sizes range from 1000 nm to several nm.

Scanning tunneling microscope (STM) By monitoring the tunneling current between the scanning probe with a small radius of curvature and the sample surface, we can obtain the topology of the surface in atomic resolution.

Self-assembled quantum dot A quantum dot formed automatically during the crystal growth.

Transport Electronic conduction in semiconductors, devices, or quantum dots. Transport measurement can usually reveal the energy spectrum of the system under investigation.

Two-dimensional electron gas A sheet of electrons confined at the interface between semiconductor and insulator.

ACKNOWLEDGMENTS

This work was supported by the Korean Ministry of Science and Technology through the Creative Research Initiatives Program under Contract No. M10116000008-02F0000-00610, while the work at Arizona State University (ASU) was supported by the Office of Naval Research (N00014-99-1-0326) and the Department of Energy (DE-FG03-01ER45920). The authors thank L. W. Engel in NHMFL, M. H. Son and D. Y. Jeong at *i*QUIPS for providing us unpublished data. S. W. Hwang thanks Prof. D. K. Ferry and Prof. S. M. Goodnick for supporting the preparation of this chapter during his stay in ASU. He also thanks B. Naser and M. Elhassan for careful reading of the manuscript.

REFERENCES

1. T. Ando, A. B. Fowler, and F. Stern, *Rev. Mod. Phys.* 54, 437 (1982).
2. H. L. Stormer, A. Pinczuk, A. C. Gossard, and W. Wiegmann, *Appl. Phys. Lett.* 38, 691 (1981).

3. K. von Klitzing, G. Dorda, and M. Pepper, *Phys. Rev. Lett.* 45, 494 (1980); D. C. Tsui, H. L. Stormer, and A. C. Gossard, *Phys. Rev. Lett.* 48, 1559 (1982); R. E. Prange and S. M. Girvin (Eds.), "The Quantum Hall Effect." Springer-Verlag, New York, 1987.
4. B. J. van Wees, H. van Houten, C. W. J. Beebakker, J. G. Williamson, L. P. Kouwenhoven, D. van der Marel, and C. T. Foxon, *Phys. Rev. Lett.* 60, 848 (1988); D. A. Wharam, T. J. Thornton, R. Newbury, M. Pepper, H. Ahmed, J. E. F. Frost, D. G. Hasko, and D. C. Peakock, *J. Phys.* C21, L209 (1988).
5. J. Scott-Thomas, S. Field, M. Kastner, H. Smith, and D. Antoniadis, *Phys. Rev. Lett.* 62, 583 (1989); A. M. M. Staring, H. van Houten, C. Beenakker, and C. Foxon, *Phys. Rev. B* 45, 9222 (1992).
6. J. P. Bird, R. Akis, D. K. Ferry, and M. Stopa, Magneto-transport as a probe of electron dynamics in open quantum dots, in "Advances in Imaging and Electron Physics" (P. W. Hawkes, Ed.), Vol. 107, p. 1. Academic Press, San Diego, CA, 1999.
7. G. L. Timp, "Nanotechnology." Springer-Verlag, New York, 1998.
8. K. A. Valiev, "The Physics of Submicron Lithography (Microdevices)." Plenum, New York, 1992.
9. H. Z. Zheng, H. P. Wei, D. C. Tsui, and G. Weimann, *Phys. Rev. B* 34, 5635 (1986); T. J. Thornton, M. Pepper, H. Ahmed, D. Andrews, and G. J. Davies, *Phys. Rev. Lett.* 56, 1198 (1986).
10. M. Yoshita, H. Akiyama, L. N. Pfeiffer, and K. W. West, *Appl. Phys. Lett.* 81, 49 (2002).
11. D. Leonard, M. Krishnamurthy, C. M. Reaves, S. P. Denbaars, and P. M. Petroff, *Appl. Phys. Lett.* 63, 3203 (1993).
12. J.-R. Kim, H. M. So, J. W. Park, J.-J. Kim, J. Kim, C. J. Lee, and S. C. Lyu, *Appl. Phys. Lett.* 80, 3548 (2002).
13. A. Ohtake and M. Ozeki, *Appl. Phys. Lett.* 78, 431 (2001).
14. R. Leon, S. Fafard, D. Leonard, J. L. Merz, and P. M. Petroff, *Appl. Phys. Lett.* 67, 521 (1995); Yu. I. Mazur, X. Wang, Z. M. Wang, G. J. Salamo, M. Xiao, and H. Kissel, *Appl. Phys. Lett.* 81, 2469 (2002); S. Kiravittaya, Y. Nakamura, and O. G. Schmidt, *Physica E* 13, 224 (2002).
15. M. C. Bödefeld, R. J. Warburton, K. Karrai, J. P. Kotthaus, G. Medeiros-Ribeiro, and P. M. Petroff, *Appl. Phys. Lett.* 74, 1839 (1999).
16. H. Sakaki, G. Yusa, T. Someya, Y. Ohno, T. Noda, H. Akiyama, Y. Kadoya, and H. Noge, *Appl. Phys. Lett.* 67, 3444 (1995).
17. J. Phillips, K. Kamath, T. Brock, and P. Bhattacharya, *Appl. Phys. Lett.* 72, 3509 (1998).
18. G. H. Kim, D. A. Ritchie, M. Pepper, G. D. Lian, J. Yuan, and L. M. Brown, *Appl. Phys. Lett.* 73, 2468 (1998).
19. E. Ribeiro, R. D. Jaggi, T. Heinzel, K. Ensslin, G. Medeiros-Ribeiro, and P. M. Petroff, *Phys. Rev. Lett.* 82, 996 (1999).
20. G. H. Kim, J. T. Nicholls, S. L. Khondaker, I. Farrer, and D. A. Ritchie, *Phys. Rev. B* 61, 10910 (2000).
21. I. E. Itskevich, T. Ihn, A. Thornton, M. Henini, T. J. Foster, P. Moriarty, A. Nogaret, P. H. Beton, L. Eaves, and P. C. Main, *Phys. Rev. B* 54, 16401 (1996).
22. M. Narihiro, G. Yusa, Y. Nakamura, T. Noda, and H. Sakaki, *Appl. Phys. Lett.* 70, 105 (1997).
23. A. S. G. Thornton, T. Ihn, P. C. Main, L. Eaves, and M. Henini, *Appl. Phys. Lett.* 73, 354 (1998).
24. P. C. Main, A. S. G. Thornton, R. J. H. Hill, S. T. Stoddart, T. Ihn, L. Eaves, K. A. Benedict, and M. Henini, *Phys. Rev. Lett.* 84, 729 (2000).
25. E. E. Vdovin, A. Levin, A. Patanè, L. Eaves, P. C. Main, Yu. N. Khanin, Yu. V. Dubrovskii, M. Henini, and G. Hill, *Science* 290, 122 (2000).
26. I. Hapke-Wurst, U. Zeitler, H. Frahm, A. G. M. Jansen, R. J. Haug, and K. Pierz, *Phys. Rev. B* 62, 12621 (2000).
27. M. E. Rubin, G. Medeiros-Ribeiro, J. J. O'Shea, M. A. Chin, E. Y. Lee, P. M. Petroff, and V. Narayanamurti, *Phys. Rev. Lett.* 77, 5268 (1996).
28. B. Legrand, B. Grandidier, J. P. Nys, D. Stiévenard, J. M. Gérard, and V. Thierry-Mieg, *Appl. Phys. Lett.* 73, 96 (1998).

29. O. Millo, D. Katz, Y. W. Cao, and U. Banin, *Phys. Rev. B* 61, 16773 (2000).
30. D. G. Austing, S. Tarucha, P. C. Main, M. Henini, S. T. Stoddart, and L. Eaves, *Appl. Phys. Lett.* 75, 671 (1999).
31. S. K. Jung, C. K. Hyon, J. H. Park, S. W. Hwang, D. Ahn, M. H. Son, B. D. Min, Y. Kim, and E. K. Kim, *Appl. Phys. Lett.* 75, 1167 (1999).
32. K. H. Schmidt, M. Versen, U. Kunze, D. Reuter, and A. D. Wieck, *Phys. Rev. B* 62, 15879 (2000).
33. R. J. A. Hill, A. Patanè, P. C. Main, L. Eaves, B. Gustafson, M. Henini, S. Tarucha, and D. G. Austing, *Appl. Phys. Lett.* 79, 3275 (2001).
34. R. Tsui, R. Zhang, K. Shiralagi, and H. Goronkin, *Appl. Phys. Lett.* 71, 3254 (1997).
35. R. Zhang, R. Tsui, K. Shiralagi, D. Convey, and H. Goronkin, *Appl. Phys. Lett.* 73, 505 (1998).
36. T. Ishikawa, S. Kohmoto, and K. Asakawa, *Appl. Phys. Lett.* 73, 1712 (1998).
37. C. K. Hyon, S. C. Choi, S.-H. Song, S. W. Hwang, M. H. Son, D. Ahn, Y. J. Park, and E. K. Kim, *Appl. Phys. Lett.* 77, 2607 (2000).
38. C.-K. Hahn, J. Motohisa, and T. Fukui, *Appl. Phys. Lett.* 76, 3947 (2000).
39. B. H. Choi, C. M. Park, S.-H. Song, M. H. Son, S. W. Hwang, D. Ahn, and E. K. Kim, *Appl. Phys. Lett.* 78, 1403 (2001).
40. T. Mano, R. Nötzel, G. J. Hamhuis, T. J. Eijkemans, and J. H. Wolter, *Appl. Phys. Lett.* 81, 1705 (2002).
41. G. Medeiros-Ribeiro, F. G. Pikus, P. M. Petroff, and A. L. Efros, *Phys. Rev. B* 55, 1568 (1997); G. Medeiros-Ribeiro, J. M. Garcia, and P. M. Petroff, *Phys. Rev. B* 56, No. 7 (1997).
42. B. T. Miller, W. Hansen, S. Manus, R. J. Luyken, A. Lorke, J. P. Kotthaus, S. Huant, G. Medeiros-Ribeiro, and P. M. Petroff, *Phys. Rev. B* 56, 6764 (1997).
43. A. E. Belyaev, S. T. Stoddart, P. M. Martin, P. C. Main, L. Eaves, and M. Henini, *Appl. Phys. Lett.* 76, 3570 (2000).
44. R. Wetzler, A. Wacker, E. Schöll, C. M. A. Kapteyn, R. Heitz, and D. Bimberg, *Appl. Phys. Lett.* 77, 1671 (2000).
45. C. H. Bennet and D. P. DiVincenzo, *Nature* 404, 247 (2000).
46. G. S. Solomon, J. A. Trezza, A. F. Marshall, and J. S. Harris, Jr., *Phys. Rev. Lett.* 76, 952 (1996).
47. M. Bayer, P. Hawrylak, K. Hinzer, S. Fafard, M. Korkusinski, Z. R. Wasilewski, O. Stern, and A. Forchel, *Science* 291, 451 (2001).
48. P. Boucaud, K. S. Gill, J. B. Williams, M. S. Sherwin, W. V. Schoenfeld, and P. M. Petroff, *Appl. Phys. Lett.* 77, 510 (2000).

Transport in Semiconductor Nanostructures

H. León, R. Riera, J. L. Marín, R. Rosas

Universidad de Sonora, Sonora, México

CONTENTS

1. Introduction
 2. Carrier Description
 3. Nonequilibrium Carriers
 4. Scattering Mechanisms: Transition Rates
 5. Low-Field Transport
 6. High-Field Transport
 7. Screening of the Scattering Mechanisms
 8. Summary
- Glossary
References

1. INTRODUCTION

Among the nanostructured materials, semiconductor nanostructures may play a crucial role in the fabrication of very small devices, which in turn may allow a very large integration scale already known as nanoelectronics. Such kind of semiconductor structures can be constructed since high quality performance of modern equipment gives the possibility of controlling the crystal growth process up to a few atomic layers (i.e., with a nanometric precision) as well as the chemical composition, according to the required stoichiometric rules. Several techniques have been developed for this purpose, such as metal-organic chemical vapor deposition (MOCVD) and molecular beam epitaxy (MBE), about which a brief explanation can be found in [1]. MBE and MOCVD allow the implantation of donor or acceptor impurities in the desired region of the semiconductor and are known as modulation-doping techniques.

The main feature of these structures is that electrons and holes participating in optical and transport phenomena are basically confined to a certain region, whose dimensions

in one, two, or three directions are of the order of several up to a few tens nanometers. They are called quasi-two-dimensional (Q2D), quasi-one-dimensional (Q1D), or quasi-zero-dimensional (Q0D) systems, respectively, and all of them are also named low-dimensional semiconductor structures or semiconductor nanostructures. Two kinds of such structures can be distinguished: the semiconductor heterostructures and the delta-doped semiconductors, where the electron or the hole confinement can be achieved in different ways, as described in the following examples.

Semiconductor heterostructures are grown with well matching materials from the crystallographic point of view, as the ones formed with III-V binary compounds and ternary alloys (e.g., GaAs/Al_xGa_{1-x}As, where x is the fractional concentration of Al atoms per each Ga atom in the aluminum-gallium arsenide matched on gallium arsenide, whose use is widely extended in actual samples). One of the most studied structures is a modulation-doped double heterostructure B/A/B, where donors are placed in material B (e.g., Al_xGa_{1-x}As) whose conduction-band bottom lies higher than the one of material A (e.g., GaAs). The electrons supplied in the former one are captured in the layer formed by the latter one because of the conduction band offset at the interfaces; therefore, this structure is called a quantum well (QW). The electrons remain trapped in the QW as long as the Fermi level lies below the band offset and scattering processes do not throw them to states with energies above the band offset. In a single heterostructure (SH) of the same materials B/A, n -doped in the same way, the electrostatic interaction between electrons and their partner donors causes a band bending forming a sort of triangular well in the material-A side; thus, electrons are attracted to a very thin layer by the interface. Since the depth of this triangular well is considerably lesser than the one of the rectangular well formed in the double-heterostructure case, electron concentration cannot be too high.

There are also other Q2D systems: the inversion layers in metal-oxide semiconductor (MOS) silicon based structures, where the confinement is similar to the one in SHs; the multiple quantum wells (MQWs) B/A/B/A/B, where one can identify a few noncoupled QWs; and the superlattices (SLs)

B/A/B/A/B... , where one can identify a very large (modeled as infinite) number of coupled QWs. The periodicity of a SL in the direction perpendicular to the interfaces gives rise to a set of minibands instead of single bands, which makes it an especially interesting research object whose properties are widely studied but are beyond the scope of this chapter.

Modulation-doping techniques allow one to construct delta-doped semiconductors, where donors are placed in a very thin layer inside the bulk material (e.g., GaAs). The intentionally attained high donor concentration makes the impurity levels split into an impurity band, and so electrons of this band can move along the layer, but they cannot escape from its approximate limits because of the ion-impurity attraction. This structure is very similar to a QW and, as in that case, electrons remains trapped in the delta-doped layer as long as the Fermi level, which is higher as the electron concentration is larger, lies below a certain effective energy threshold and scattering processes do not throw them to states with energies above this threshold. This way one has another Q2D electron system.

Semiconductor heterostructures B/A are classified according to the relative positions of the valence-band tops. In type I heterostructures the top of the valence band in the material B lies lower than the one in the material A. Then acceptors can be placed in the former to have holes accumulated in the latter one, as in $\text{Al}_x\text{Ga}_{1-x}\text{As}/\text{GaAs}$ heterostructures, where usually phosphorus atoms supply the holes that are mainly confined to the GaAs layer. In type II heterostructures the top of the valence band in the material B lies higher than the one in the material A. Then acceptors can be placed in the latter one to collect the holes in the former one, as in $\text{Si}/\text{Si}_{1-x}\text{Ge}_x$ heterostructures, where frequently boron atoms supply the holes that are mainly confined to the $\text{Si}_{1-x}\text{Ge}_x$ layers. In type III heterostructures the tops of the valence bands in both materials are approximately at the same level and holes cannot be confined, as in the GaSb/InSb heterostructures [2].

Several techniques are used to get a second confinement direction in the so-called quantum wires (QWIs) or quantum well wires (QWWs). Thus, for instance, once a GaAs based QW is grown, by means of electron beam lithography and dry etching, one conforms barriers in the direction perpendicular to the original layer for obtaining etched rectangular QWIs [3]. Similarly, QWIs are also fabricated on $\text{Al}_x\text{Ga}_{1-x}\text{As}/\text{GaAs}$ single heterostructure using laser lithography [4]. Another way is to build a series of $\text{Al}_x\text{Ga}_{1-x}\text{As}/\text{GaAs}$ double heterostructures on nonplanar surfaces by means of a MOCVD or MBE technique to form a V-groove array of QWs [5, 6]. This way at the bottom of each V one has two confinement directions because of the barrier material. These structures are examples of Q1D systems, where freestanding wires are also included.

Electrons and holes in semiconductor nanostructures have de Broglie wavelengths greater than or approximately equal to the lengths in confinement directions of the region they are concentrated. Therefore, their motion in any of these directions bears an essentially quantum character, with discrete values of momentum and energy, while in nonconfined directions it is usually treated as a quasiclassical motion, with continuous values of momentum and energy, which means that instead of conduction and valence bands there are two

respective sets of subbands. This essential feature makes necessary a reformulation of a vast part of the physics in such structures concerning electrons, holes, phonons, and, in general, the whole list of quasiparticles or collective excitations, as well as their interactions and responses to external perturbations. Theoretical and experimental studies show that the carrier confinement leads to the quantum size effects (QSEs), that is, to peculiar characteristics of these systems, ranging from the density of states through the optical and transport properties, due to the size reduction of the transversal dimensions of the region where electrons and holes are concentrated, which is called the conduction channel, since it plays such a role in quasiclassical transport. It must be pointed out that the carrier confinement is not complete, for always there exists a nonzero probability of finding the carriers out of, although very near, the conduction channel.

Transport perpendicular to the interfaces is frequently called vertical transport, because actual heterostructures are grown with interfaces in horizontal planes. This is strictly connected with quantum phenomena, as the resonant tunnel effect, and will not be discussed here. This chapter is concerned with horizontal or parallel transport exclusively, a field of great experimental and theoretical activities. Electrical conductivity, quantum Hall effect, thermoelectric power, Coulomb drag, and many other phenomena attract the attention of thousands of scientists all over the world whose articles are published in dozens of scientific journals. This field could be hardly reviewed in 100 pages, so a specific topic must be selected to introduce the fundamental theory, as well as to give a substantial account of the work concerning this topic basically in the last 20 years.

The construction of two-dimensional electron-gas field-effect transistors, including the MOS field-effect transistor (MOSFET) and the modulation-doped field-effect transistor (MODFET), opened the door for high-speed semiconductor devices [7]. Really, to obtain high-frequency performance in a transistor, one has to limit the transit time through the device. This can be achieved by either decreasing the gate length or increasing the drift velocity of the carriers. Once the gate lengths have been reduced up to micrometer or submicrometer range, the efforts are devoted to the enhancement of the carrier drift velocity. In these semiconductor nanostructures there are two ways of enhancing the carrier drift velocity: by increasing the carrier mobility at relatively low electric fields or by increasing the applied electric field. The latter exhibits a saturation effect and, furthermore, the drift velocity starts to decrease when the electric field increases beyond sufficiently high values, in a region with negative differential conductivity. Therefore, great interest has been put on enhancing the carrier mobility along the conduction channel by reducing, as far as possible, different carrier scattering mechanisms and, consequently, to make possible the fabrication of high-electron-mobility transistors (HEMT's). Nevertheless, the problems related to relatively high electric field, such as energy dissipation, are also important because, despite the fact that the applied voltages can be very low, the micrometric or submicrometric gate lengths make the electric field very high [8]. The MOSFETs are already widely exploited in logical and

memory circuits, but this is not the case with MODFETs for technological reasons [9].

This chapter is mainly concerned with steady-state charge transport along the conduction channel in semiconductor nanostructures, because it is not only of practical interest for nanoscale transistor design but also represents a means for investigating how electrons and holes are scattered by different mechanisms, particularly by phonons, which are important in optical properties to be considered in nanoscale optoelectronic devices.

2. CARRIER DESCRIPTION

2.1. Charge Carriers

For electronic purposes in semiconductor technology charge carriers can be electrons or holes, which are as a rule supplied by donor or acceptor impurities respectively. The creation and annihilation of electron–hole pairs is mainly involved in optoelectronic devices. Modulation-doped techniques allow one to place the impurities conveniently to obtain the required characteristics of the device design. In delta-doped semiconductors impurities are in a very thin layer inside the bulk material, which is itself the conduction channel; and in semiconductor heterostructures impurities are in the barrier material, out of the conduction channel. The latter idea is the milestone for the HEMT fabrication.

The cleanliness of the growth processes together with the inclusion of an undoped region, called the spacer layer, between the doped region and the conduction channel in semiconductor heterostructures aims to reduce substantially the carrier–ion-impurity scattering, apart of other defects, in order to attain high mobilities. Record mobility values have been attained in $\text{Al}_x\text{Ga}_{1-x}\text{As}/\text{GaAs}$ SHs, both for electron mobility $\mu = 14.7 \times 10^6 \text{ cm}^2 \text{ V}^{-1} \text{ s}^{-1}$ reported in [10], at very low temperature ($T = 0.1 \text{ K}$) and ordinary areal concentration ($n_s = 2.4 \times 10^{11} \text{ cm}^{-2}$), as well as for hole mobility $\mu_h = 1.2 \times 10^6 \text{ cm}^2 \text{ V}^{-1} \text{ s}^{-1}$ reported in [11], also at very low temperature ($T = 1 \text{ K}$) and low areal concentration ($n_s = 0.8 \times 10^{11} \text{ cm}^{-2}$).

The study of transport phenomena is carried out, as a rule, in the envelope function approximation of the solid state band theory, namely the effective mass approximation (EMA) for the electrons in the conduction subbands or holes in the valence subbands. The electron and hole effective masses are usually determined experimentally (e.g., from cyclotron resonance experiments) and are considered isotropic, as in direct gap semiconductors with the bottom of the conduction band at the Γ point of the Brillouin zone (e.g., GaAs). Nevertheless, the theory can be applied to indirect gap semiconductors with anisotropic electron effective masses at Δ or L points of the Brillouin zone, as in the case of Si and Ge respectively, by taking an averaged isotropic value, a usual procedure in many calculations. Electrons attract attention in most of the works, certainly because for a given material they are lighter than holes and, consequently, higher mobilities can be expected, which is, as already remarked, a desirable characteristic for high-speed devices. Electron effective mass is denoted as m^* , while the electron charge is $e < 0$. All the derivations for holes in the valence subbands could be accomplished in principle by

the substitution of electron values by the pertinent heavy or light hole effective masses m_{hh}^* or m_{lh}^* and bearing in mind that the hole charge is $e > 0$; besides, one must also take care of the degeneracy at the top of the valence subbands, although it can be suppressed by the strain at the interface due the difference in lattice constants, which is remarkable in Si/Si_{1-x}Ge heterostructures [12]. One deals with acceptor instead of donor impurities in hole transport.

Parabolic subbands are considered, despite the fact that nonparabolicity may be important for very narrow QWs [13]. The introduction of distinct subband effective masses for electrons [14, 15] would complicate a little the derivation of the fundamental equations and would lead to nonremarkable different results of measurable quantities. Similarly, the distinction between the effective masses inside and outside the conduction channel would mean a refinement of calculations, which can be left out of consideration in a first approach to the transport phenomena, although it can be easily introduced in the equation for the envelope wavefunction in the confinement direction or plane [16].

2.2. Carrier Confinement

For the sake of briefness and compact presentation of theory, the 3D vectors are denoted with capital letters, while 2D or 1D vectors will be denoted with small letters. Thus the position is

$$\mathbf{R} = \mathbf{R}_{\parallel} + \mathbf{R}_{\perp} = \mathbf{r} + \boldsymbol{\rho} \quad (1)$$

where the component along the conduction channel, parallel to the interfaces in heterostructures, will be simply $\mathbf{r} = \mathbf{R}_{\parallel}$, while the component perpendicular to the conduction channel, perpendicular to the interfaces in square QWs or cylindrical QWIs, will be simply $\boldsymbol{\rho} = \mathbf{R}_{\perp}$. This way one has

$$\mathbf{r} = x\mathbf{e}_x + y\mathbf{e}_y \quad \boldsymbol{\rho} = z\mathbf{e}_z \quad (2)$$

$$\mathbf{r} = x\mathbf{e}_x \quad \boldsymbol{\rho} = y\mathbf{e}_y + z\mathbf{e}_z \quad (3)$$

in Q2D and Q1D systems respectively. The choice of Cartesian coordinates, with unitary vectors \mathbf{e}_x , \mathbf{e}_y , and \mathbf{e}_z , allows the desired compact presentation of theory, although cylindrical coordinates are to be chosen in order to take advantage of the symmetry in cylindrical QWIs.

The carrier confinement suggests a clear separation in the Hamiltonian of the term related to the motion along the conduction channel and the term related to the confinement direction or plane. Thus the unperturbed one-particle Hamiltonian for electrons is written in the EMA as

$$\hat{H}_0 = -\frac{\hbar^2}{2m^*}(\nabla_{\mathbf{r}}^2 + \nabla_{\boldsymbol{\rho}}^2) + U(\boldsymbol{\rho}) \quad (4)$$

where

$$\nabla_{\mathbf{r}}^2 = \frac{\partial}{\partial x^2} + \frac{\partial}{\partial y^2} \quad \nabla_{\boldsymbol{\rho}}^2 = \frac{\partial}{\partial z^2} \quad (5)$$

$$\nabla_{\mathbf{r}}^2 = \frac{\partial}{\partial x^2} \quad \nabla_{\boldsymbol{\rho}}^2 = \frac{\partial}{\partial y^2} + \frac{\partial}{\partial z^2} \quad (6)$$

in Q2D and Q1D systems respectively. The confining potential $U(\boldsymbol{\rho})$ is frequently modeled in different ways or calculated self-consistently.

The corresponding eigenfunctions (i.e., the electron envelope functions) are

$$\psi_{\alpha\mathbf{k}}(\mathbf{r}, \boldsymbol{\rho}) = A^{-1/2} \varphi_{\alpha}(\boldsymbol{\rho}) \exp(i\mathbf{k} \cdot \mathbf{r}) \quad (7)$$

where α is the subband label and \mathbf{k} is the wavevector for the quasiclassical motion of electrons, which must be understood as

$$\alpha = l = 1, 2, 3, \dots \quad \mathbf{k} = k_x \mathbf{e}_x + k_y \mathbf{e}_y \quad (8)$$

$$\alpha = (n, l) = (1, 1); (1, 2); (2, 1); \dots \quad \mathbf{k} = k_x \mathbf{e}_x \quad (9)$$

with $A = S$, the normalization area, in Q2D systems and $A = L$, the normalization length, in Q1D systems respectively. This way, during the motion between two consecutive scatterings, one has a plane wave for electron free motion along the conduction channel, while another wave describes the electron motion perpendicular to the conduction channel in dependence of the confinement model. Consequently, the electron energy is the sum of two terms,

$$E_{\alpha}(\mathbf{k}) = E + E_{\alpha} = \frac{\hbar^2 k^2}{2m^*} + E_{\alpha} \quad (10)$$

where $E = E(\mathbf{k})$ is the kinetic energy, associated with quasiclassical motion along the conduction channel, and E_{α} is the subband energy, that is, the electron energy at the bottom of the given subband (note the wavevector is measured from the bottom value too).

Such an important characteristic as the density of states (DOS), including a factor 2 because of the spin, is given by

$$\nu[E_l(\mathbf{k})] = \sum_l \nu_l(E) = \sum_l \frac{m^* S}{\pi \hbar^2} \Theta[E_l(\mathbf{k}) - E_l] \quad (11)$$

$$\begin{aligned} \nu[E_{nl}(\mathbf{k})] &= \sum_{n,l} \nu_{nl}(E) \\ &= \sum_{n,l} \frac{L}{\pi \hbar} \left(\frac{2m^*}{E} \right)^{1/2} \Theta[E_{nl}(\mathbf{k}) - E_{nl}] \end{aligned} \quad (12)$$

in Q2D and Q1D systems respectively, where the Heaviside unit step function is

$$\Theta(E) = \begin{cases} 1, & E > 0 \\ 0, & E < 0 \end{cases} \quad (13)$$

and explicitly reflects discontinuities when the total energy crosses subband bottoms. The DOS is not a continuous function of the increasing total energy. It has a staircase form in Q2D systems, with a constant value for each subband, while it diverges as $E^{-1/2}$ when the total energy leaves the bottom of a given subband α and tends to a value proportional to $E_{\alpha}^{-1/2}$ when it approaches the bottom of the following subband in Q1D systems. These behaviors of the DOS in low-dimensional systems can be understood as the first remarkable QSEs. Furthermore, they clearly indicate that transformation of summations in momentum into integrations in energy can be accomplished only for a fixed subband, namely,

$$\sum_{\alpha, \mathbf{k}} F_{\alpha}(\mathbf{k}) = \sum_{\alpha} \int_0^{\infty} \nu_{\alpha}(E) F_{\alpha}(E) dE \quad (14)$$

where $F_{\alpha}(\mathbf{k})$ is any function depending on subband index and wavevector. This transformation leads to all subsequent QSEs, which can be observed in the behavior of many transport and optical properties of low-dimensional systems.

The carrier confinement to the conduction channel has been modeled in different ways, mostly assuming a certain coordinate dependence of the confining potential or calculating it self-consistently. The infinite barrier model (IBM) assumes $U(\boldsymbol{\rho}) = 0$ inside and $U(\boldsymbol{\rho}) = \infty$ outside the conduction channel and leads to analytical expressions for the envelope functions $\varphi_{\alpha}(\boldsymbol{\rho})$, which are strictly confined with no penetration into the barriers, as well as for subband energies E_{α} . This way some progress in calculations can be made before computational methods are necessary. Therefore the IBM has been widely employed for rectangular QWs and QWIs or cylindrical QWIs, although in the latter case the zeros of the Bessel functions have to be found numerically, in order to calculate scattering rates, mobilities, and so on when the attention is mainly paid to QSEs due to electron confinement.

The finite barrier model (FBM) assumes $U(\boldsymbol{\rho}) = 0$ inside and $U(\boldsymbol{\rho}) = U_0 = \text{const}$ outside the conduction channel and leads to analytical expressions for the envelope functions $\varphi_{\alpha}(\boldsymbol{\rho})$, which are partially confined with some penetration into the barriers, and also for subband energies E_{α} , but they include numerically obtained quantized quantities that appear instead of the wavevectors after the solution of transcendental equations. This way little progress in calculations can be made before computational methods are necessary. Nevertheless, the FBM has been also employed for rectangular QWs or QWIs and cylindrical QWIs in order to calculate scattering rates, mobilities, and so on when more realistic results are desired. The barrier height is frequently taken from empirical formulae, for examples, in $\text{Al}_x\text{Ga}_{1-x}\text{As}/\text{GaAs}$ heterostructures $U_0 = 0.693 x + 0.222 x^2$ (eV) [17] and for $x = 0.3$ one has $U_0 = 228$ meV. The FBM has been employed for rectangular QWs and cylindrical QWIs. But it is not suitable for rectangular QWIs because the variables y and z cannot be separated in this case.

Self-consistent (SEL) calculations are often carried out by solving coupled Schrödinger and Poisson equations,

$$\left[-\frac{\hbar^2}{2m^*} \nabla_{\boldsymbol{\rho}}^2 + U(\boldsymbol{\rho}) \right] \varphi_{\alpha}(\boldsymbol{\rho}) = E_{\alpha} \varphi_{\alpha}(\boldsymbol{\rho}) \quad (15)$$

$$U(\boldsymbol{\rho}) = U_e(\boldsymbol{\rho}) + U_f(\boldsymbol{\rho}) + U_{xc}(\boldsymbol{\rho}) \quad (16)$$

$$\nabla_{\boldsymbol{\rho}}^2 U_c(\boldsymbol{\rho}) = \frac{4\pi e^2}{\kappa_0} [n(\boldsymbol{\rho}) - n_D(\boldsymbol{\rho})] \quad (17)$$

where $U_f(\boldsymbol{\rho})$ is a certain model potential, usually the FBM when appropriate, and $U_{xc}(\boldsymbol{\rho})$ is the exchange and correlation potential, which in turn is taken in different ways (e.g., as in [18]). Frequently calculations are carried out in Hartree approximation [i.e., one sets $U_{xc}(\boldsymbol{\rho}) = 0$]. The donor concentration $n_D(\boldsymbol{\rho})$ must somehow be modeled inside and outside the conduction channel. Notice that in modulation-doped heterostructures it is very low inside and quite high outside the conduction channel, while in delta-doped semiconductors it is very high inside and very low outside the

conduction channel. The electron concentration is

$$n(\boldsymbol{\rho}) = \sum_{\alpha=1}^N |\varphi_{\alpha}(\boldsymbol{\rho})|^2 \int_0^{\infty} \nu_{\alpha}(E) dE \quad (18)$$

where N is the number of occupied subband and $\nu_{\alpha}(E)$ is the DOS given in (11) or (12). This way computational methods for numerical calculations are required from the very beginning to find both the envelope function $\varphi_{\alpha}(\boldsymbol{\rho})$, which is partially confined with some penetration into the barriers, and subband energies E_{α} . All of this is supposed to give the more realistic results to interpreted experiments. A detailed comparison of mobility calculations with IBM, FBM, and SEL wavefunctions and energies can be found in [19], where the SEL results of [20], obtained with the Hedin–Lundqvist density functional for exchange and correlation, were employed.

A triangular potential model (TPM) has been also utilized for electron confinement in one direction. It assumes $U(z) = eF_z z$, when an electric field F_z is applied to confine the electrons in this direction. This leads to analytical expressions for the envelope functions and subband energies,

$$\varphi_l(z) = Ai \left[\left(\frac{2m^*}{\hbar^2 e^2 F_z^2} \right)^{1/3} (eF_z z - E_l) \right] \quad (19)$$

$$E_l = \left(\frac{\hbar^2 e^2 F_z^2}{2m^*} \right)^{1/3} \left[\frac{3\pi}{2} \left(l + \frac{3}{4} \right) \right]^{2/3} \quad (20)$$

where $Ai(z)$ are the Airy functions. They have been employed for calculations in SHs or triangular QWs and could be also employed for one of the confinement directions in rectangular QWIs, when in the other direction an IBM is assumed.

Different envelope functions in one confinement direction can be constructed to find the minimum subband electron energy following a variational method. The Fang–Howard variational (FHV) envelope functions for the two lowest subbands are [21]

$$\varphi_1(z) = z \left(\frac{b^3}{2} \right)^{1/2} \exp\left(-\frac{bz}{2}\right) \quad (21)$$

$$\varphi_2(z) = z \left(\frac{3b^3}{2} \right)^{1/2} \left(1 - \frac{bz}{3} \right) \exp\left(-\frac{bz}{2}\right) \quad (22)$$

where the parameter b is chosen by minimizing the subband energy E_1 . It results in $b \propto (m^* e^2 n_s)^{1/3}$. They have been frequently employed for calculations in SHs and inversion layers as well as in one of the confinement directions in rectangular QWIs, when in the other direction an IBM is assumed. A better fit to the TPM wavefunctions, at least to the ground state, is obtained with new variational wavefunctions [22],

$$\varphi_1(z) = z^2 \left(\frac{b^5}{24} \right)^{1/2} \exp\left(-\frac{bz}{2}\right) \quad (23)$$

$$\varphi_2(z) = z^2 \left(\frac{b^5}{24} \right)^{1/2} \left(1 - \frac{bz}{5} \right) \exp\left(-\frac{bz}{2}\right) \quad (24)$$

where the parameter b is also chosen to give the correct ground subband energy.

A parabolic potential model has been also used for confinement in one direction. It assumes $U(z) = \frac{1}{2} D z^2$, where D is an appropriate constant. This leads to analytical expressions for the envelope functions $\varphi_l(z)$, which are the ones of harmonic oscillators (i.e., related to Hermite polynomials), and for subband energies E_l . They have been frequently employed for calculations in the so-called parabolic QWs and it could also be taken in one of the confinement directions in a QWIs, if in the IBM is assumed in the other direction.

2.3. Carrier Statistics

Different scattering mechanisms, such as electron–phonon or electron–ion-impurity interactions, together with electron–electron interaction are responsible for the randomization of momentum and energy values of the electrons in the conduction channel, in such a way that one can think of a gas of noninteracting electrons, in correspondence with the electron gas model of many-body theory (MBT), whose total charge is neutralized by a uniform background of positive charges associated with the ion cores of the crystal. In order to describe the density of the electron gas a generally used parameter r_s must be defined as

$$\pi r_s^2 = \frac{1}{n_s a_B^2} \quad (25)$$

$$2r_s = \frac{1}{n_L a_B} \quad (26)$$

where a_B is the Bohr radius, n_s is the areal electron concentration in Q2D systems, and n_L is the linear electron concentration in Q1D systems. Thus r_s is small for a high-density electron gas and large for a low-density one. In the former case average kinetic energy is much larger than the potential energy due to electron–electron interaction, including exchange and correlation energies, and the electron gas model is expected to be valid [23]. Interacting electrons are considered to be an electron liquid, particularly as in the Fermi liquid theory.

Electron gas is ruled by Fermi–Dirac statistics, which means that the equilibrium distribution function is

$$f^{(0)} [E_{\alpha}(\mathbf{k})] = \left[\exp \frac{E_{\alpha}(\mathbf{k}) - E_F}{k_B T} + 1 \right]^{-1} \quad (27)$$

with k_B the Boltzmann constant, T the temperature, and E_F the Fermi level. The distribution function for the degenerate electron gas can be easily transformed to be written as

$$f_{\alpha}^{(0)}(E) = \frac{1}{\exp[\beta(E - E_{F\alpha})] + 1} \quad (28)$$

in order to have a clear reference to the considered subband and the kinetic energy. Here

$$\beta = \frac{1}{k_B T} \quad \text{and} \quad E_{F\alpha} = E_F - E_{\alpha} \quad (29)$$

Note that $E_{F\alpha}$ is nothing else but the Fermi level measured from the bottom of the subband α . The normalization condition in a low-dimensional system reads

$$N = \sum_{\alpha=1}^N N_{\alpha} = \sum_{\alpha=1}^N \int_0^{\infty} \nu_{\alpha}(E) f_{\alpha}^{(0)}(E) dE \quad (30)$$

where N is the total number of electrons in the conduction channel, N_{α} is the number of electrons belonging to subband α , and N is the number of occupied subbands. From (28) and (30) one obtains the relations between areal n_S or linear n_L concentrations and Fermi level E_F for a degenerate electron gas,

$$\frac{\beta\pi\hbar^2}{m^*} n_S = \sum_{l=1}^N \ln \{1 + \exp[-\beta(E_F - E_l)]\} \quad (31)$$

$$\left(\frac{\pi^2\hbar^2}{2m^*}\right)^{1/2} n_L = \sum_{\alpha=1}^N \Phi_{-1/2}(E_F - E_{\alpha}) \quad (32)$$

in Q2D and Q1D systems respectively. Here the so-called Fermi integral was introduced,

$$\Phi_m(E_{F\alpha}) = \int_0^{\infty} E^m f_{\alpha}^{(0)}(E) dE \quad (33)$$

which leads to analytical results only in the cases of completely degenerate electron gas, when one has the Heaviside unit step function

$$f_{\alpha}^{(0)}(E) = \Theta(E_{F\alpha} - E) \quad (34)$$

or nondegenerate electron gas, when one has the Maxwell-Boltzmann distribution function

$$f_{\alpha}^{(0)}(E) = \exp[-\beta(E - E_{F\alpha})] = \exp(\beta E_{F\alpha}) \exp(-\beta E) \quad (35)$$

This way for completely degenerate electron gas one obtains

$$\frac{\pi\hbar^2}{m^*} n_S = \sum_{l=1}^N (E_F - E_l) \quad (36)$$

$$\left(\frac{\pi^2\hbar^2}{8m^*}\right)^{1/2} n_L = \sum_{\alpha=1}^N (E_F - E_{\alpha})^{1/2} \quad (37)$$

while for nondegenerate electron gas one obtains

$$\frac{\beta\pi\hbar^2}{m^*} n_S = \sum_{l=1}^N \exp[\beta(\xi - E_l)] \quad (38)$$

$$\left(\frac{\beta\pi\hbar^2}{2m^*}\right)^{1/2} n_L = \sum_{\alpha=1}^N \exp[\beta(\xi - E_{\alpha})] \quad (39)$$

in Q2D and Q1D systems respectively. Generally the electron concentration is determined experimentally (e.g., n_S from Shubnikov-De Haas oscillations), and it is frequently a controlled parameter in actual experiments. Thus it is the Fermi level that must be calculated. Notice that in all the cases, except for a completely degenerate electron gas in a Q2D system, these are transcendental equations that must be solved numerically when two or more subbands are occupied. On the contrary, when only the lowest subband is occupied one obtains algebraic equations in all the cases, except for a degenerate electron gas in Q1D systems.

3. NONEQUILIBRIUM CARRIERS

The electron gas can be carried out of equilibrium by the application of an external electric field or by any external action leading to concentration or temperature gradients, as in the case of pulsed lasers. The treatment of nonequilibrium carriers for concrete calculations of transport coefficients, such as mobility, energy-loss rate, or differential thermopower, has mostly been developed in the frame of a quasiclassical theory. This way the quantum problem of finding the transition rates between electron states is as a rule solved by the standard Rayleigh-Schrödinger perturbation theory, mostly limited to the first-order Born approximation. Correspondingly, the statistical problem of finding the nonequilibrium distribution functions is widely treated in the Boltzmann transport equation (BTE) formalism. The many-body effects are then taken into account by the inclusion of the exchange-correlation potential in self-consistent calculations of $\varphi_{\alpha}(\boldsymbol{\rho})$ according to (16), and by means of the screening of the interactions, which scatter electrons from a state into another. The BTE formalism gives not only a clear understanding of transport phenomena, but also a very adequate fitting of experimental data in semiconductor nanostructures, as can be seen in quite a number of works cited.

Many works have been devoted to calculations in the frame of a completely quantum approach of MBT, as in [24–26]. Following the Kadanoff and Baym (KBA) formalism, the equation of motion for the nonequilibrium Green functions and the introduction of the Wigner distribution functions lead to the corresponding system of quantum transport equations, known as quantum Boltzmann equations because they are analogous to the BTEs. Thus, the KBA formalism applied to low-dimensional systems takes into account the finite lifetimes of electron states and the local character of the Wigner distribution functions with respect to the transverse coordinate $\boldsymbol{\rho}$ [27–31], but the obtained results are not very different from the ones obtained following the quasiclassical theory [32]. The so-called memory function approach has also been employed [18, 33]. Finally, a certain dielectric formalism has been developed [34].

3.1. Boltzmann Transport Equations

The multisubband transport theory was originally developed in [35], although not in connection with semiconductor nanostructures, but with multivalley transport. It is reviewed in [21]. In a frame of a MBT approach, it is clear that in general when intersubband scatterings take place, the density matrix has off-diagonal elements between different subbands. When the level broadening due to intersubband scattering is sufficiently small in comparison with subband energy separations, one can neglect such off-diagonal parts and use a diagonal approximation, as in [32], or simply the BTE formalism.

Bearing in mind that the quasiclassical formalism holds exclusively for transport along the conduction channel, it clearly results that in nonequilibrium state the unknown distribution functions $f_{\alpha}(\mathbf{k}, \mathbf{r}, t)$ related to different subbands do not depend on the transverse coordinate $\boldsymbol{\rho}$. Each of

these functions is determined by one kinetic equation, which means they must satisfy a system of BTEs,

$$\left[\frac{\partial}{\partial t} + \frac{1}{\hbar} \nabla_{\mathbf{k}} E \cdot \nabla_{\mathbf{r}} + \frac{e}{\hbar} \mathbf{F} \cdot \nabla_{\mathbf{k}} \right] f_{\alpha}(\mathbf{k}, \mathbf{r}, t) = \widehat{I} f_{\alpha}(\mathbf{k}, \mathbf{r}, t) \quad (40)$$

where \mathbf{F} is the applied electric field (assuming no applied magnetic field) and

$$\nabla_{\mathbf{r}} = \frac{\partial}{\partial x} \mathbf{e}_x + \frac{\partial}{\partial y} \mathbf{e}_y \quad \nabla_{\mathbf{k}} = \frac{\partial}{\partial k_x} \mathbf{e}_x + \frac{\partial}{\partial k_y} \mathbf{e}_y \quad (41)$$

$$\nabla_{\mathbf{r}} = \frac{\partial}{\partial x} \mathbf{e}_x \quad \nabla_{\mathbf{k}} = \frac{\partial}{\partial k_x} \mathbf{e}_x \quad (42)$$

in Q2D and Q1D systems respectively. The right hand side of each equation is the so-called collision integral operator given by

$$\widehat{I} f_{\alpha}(\mathbf{k}, \mathbf{r}, t) = I_{\alpha}^{\text{in}}(\mathbf{k}, \mathbf{r}, t) - I_{\alpha}^{\text{out}}(\mathbf{k}, \mathbf{r}, t) \quad (43)$$

where the incoming to and outgoing from state $|\alpha, \mathbf{k}\rangle$ particle fluxes are

$$I_{\alpha}^{\text{in}}(\mathbf{k}, \mathbf{r}, t) = \sum_{\alpha', \mathbf{k}'} f_{\alpha'}(\mathbf{k}', \mathbf{r}, t) [1 - f_{\alpha}(\mathbf{k}, \mathbf{r}, t)] W_{\alpha'\alpha}(\mathbf{k}', \mathbf{k}) \quad (44)$$

$$I_{\alpha}^{\text{out}}(\mathbf{k}, \mathbf{r}, t) = \sum_{\alpha', \mathbf{k}'} f_{\alpha}(\mathbf{k}, \mathbf{r}, t) [1 - f_{\alpha'}(\mathbf{k}', \mathbf{r}, t)] W_{\alpha\alpha'}(\mathbf{k}, \mathbf{k}') \quad (45)$$

with $W_{\alpha\alpha'}(\mathbf{k}, \mathbf{k}')$ the transition rate between electron states $|\alpha, \mathbf{k}\rangle$ and $|\alpha', \mathbf{k}'\rangle$, which includes all scattering mechanisms considered in the studied problem. Bearing in mind the transformation (14) one realize that BTEs are integrodifferential equations. Note the collision integral operator couples equations to each other. Furthermore, the number of equations is taken equal to the number of occupied subbands.

3.2. Steady-State Transport

The steady-state transport occurs when the applied electric field is $\mathbf{F} = \text{const}$ and, consequently, the current density \mathbf{j} remains constant (the stability can be broken in some circumstances, as will be quoted). One assumes there exist no concentration or temperature gradients in any direction of quasiclassical motion. Thus the nonequilibrium subband distribution functions $f_{\alpha}(\mathbf{k})$ are both \mathbf{r} and t independent and must satisfy the system of BTEs

$$\frac{e}{\hbar} \mathbf{F} \cdot \nabla_{\mathbf{k}} f_{\alpha}(\mathbf{k}) = \widehat{I} f_{\alpha}(\mathbf{k}) \quad (46)$$

coupled each other by the collision integral operators \widehat{I} given by

$$\widehat{I} f_{\alpha}(\mathbf{k}) = I_{\alpha}^{\text{in}}(\mathbf{k}) - I_{\alpha}^{\text{out}}(\mathbf{k}) \quad (47)$$

where the incoming to and outgoing from state $|\alpha, \mathbf{k}\rangle$ particle fluxes in this case are

$$I_{\alpha}^{\text{in}}(\mathbf{k}) = \sum_{\alpha', \mathbf{k}'} f_{\alpha'}(\mathbf{k}') [1 - f_{\alpha}(\mathbf{k})] W_{\alpha'\alpha}(\mathbf{k}', \mathbf{k}) \quad (48)$$

$$I_{\alpha}^{\text{out}}(\mathbf{k}) = \sum_{\alpha', \mathbf{k}'} f_{\alpha}(\mathbf{k}) [1 - f_{\alpha'}(\mathbf{k}')] W_{\alpha\alpha'}(\mathbf{k}, \mathbf{k}') \quad (49)$$

The constant electric field drives the electron gas with a certain drift velocity, which must be redefined for low-dimensional systems because of the subband character inherent to the energy spectrum of involved carriers. Now the determination of $f_{\alpha}(\mathbf{k})$ is required for calculating the drift velocity of the carriers in the α subband,

$$\mathbf{v}_{\alpha}^d = \langle \mathbf{v}_{\alpha}(\mathbf{k}) \rangle = \frac{\sum_{\mathbf{k}} \mathbf{v}_{\alpha}(\mathbf{k}) f_{\alpha}(\mathbf{k})}{\sum_{\mathbf{k}} f_{\alpha}(\mathbf{k})} \quad (50)$$

and the average energy of these carriers in the α subband,

$$\langle E_{\alpha}(\mathbf{k}) \rangle = \frac{\sum_{\mathbf{k}} E_{\alpha}(\mathbf{k}) f_{\alpha}(\mathbf{k})}{\sum_{\mathbf{k}} f_{\alpha}(\mathbf{k})} \quad (51)$$

The current density \mathbf{j} and the electron concentration $n = n_S$, the areal concentration in Q2D systems, or $n = n_L$, the linear concentration in Q1D systems, are quantities that can be measured in experiments and include the contribution of all occupied subbands. The well known expression $\mathbf{j} = env^d$ is still valid in semiconductor nanostructures if a mean drift velocity is defined as

$$\mathbf{v}^d = \frac{\sum_{\alpha} \mathbf{v}_{\alpha}^d n_{\alpha}}{\sum_{\alpha} n_{\alpha}} \quad (52)$$

with n_{α} the areal ($n_{\alpha}^S = n_i$) or linear ($n_{\alpha}^L = n_{ni}$) concentration of electrons belonging to subband α . Similarly, the average energy of the low-dimensional electron gas is defined as

$$\bar{E} = \frac{\sum_{\alpha} \langle E_{\alpha}(\mathbf{k}) \rangle n_{\alpha}}{\sum_{\alpha} n_{\alpha}} \quad (53)$$

It must be clear that the total electron concentration is

$$n = \sum_{\alpha} n_{\alpha} \quad (54)$$

Once the steady-state transport regime is established and maintained, the momentum and the energy continuously supplied by the field to the carriers are transferred to the surrounding scattering centers with the same average rate. The momentum relaxation time τ_{α}^M is defined from the momentum balance as

$$e\mathbf{F} = \frac{m^* \langle \mathbf{v}_{\alpha}(\mathbf{k}) \rangle}{\tau_{\alpha}^M} \quad (55)$$

while the energy relaxation time τ_{α}^E is defined from the energy balance as

$$e\mathbf{F} \cdot \mathbf{v}_{\alpha}^d = \frac{\langle E_{\alpha}(\mathbf{k}) \rangle}{\tau_{\alpha}^E} \quad (56)$$

Both of them are usually evaluated for physical considerations in different transport phenomena.

3.3. Solution of the System of BTEs

The solution of the system of BTEs in semiconductor nanostructures is very complicated, except for relatively low electric fields. Therefore, many calculations related to transport phenomena have been carried out by means of Monte Carlo techniques [36–40], which are very powerful procedures for concrete situations. Nevertheless, most of the calculations are based upon approximate analytical solutions, which allow an essentially physical insight in transport properties of these structures and give sufficiently accurate results to fit experiments in a large number of situations. The analytical solutions are quite general in the low-field regime, but this is not the case in the high-field regime, as will be discussed. The theoretical calculations of the works cited in this chapter are always carried out following analytical solutions of the BTEs. Monte Carlo calculations are explicitly indicated.

One must recall that in thermodynamical equilibrium momenta and energy are randomly distributed among the electrons due to the different scattering mechanisms present in the semiconductor nanostructures. It must be pointed out that the principle of detailed balance (PDB), which holds exclusively in this equilibrium state, reads

$$\begin{aligned} f_{\alpha}^{(0)}(E) [1 - f_{\alpha'}^{(0)}(E')] W_{\alpha\alpha'}(\mathbf{k}, \mathbf{k}') \\ = f_{\alpha'}^{(0)}(E') [1 - f_{\alpha}^{(0)}(E)] W_{\alpha'\alpha}(\mathbf{k}', \mathbf{k}) \end{aligned} \quad (57)$$

which effectively leads to $\widehat{I}f_{\alpha}^{(0)}(\mathbf{k}) = 0$ when there is no applied electric field nor concentration or temperature gradients. For elastic (EL) scatterings, when electron energy does not change, the PDB reduces to

$$W_{\alpha'\alpha}^{\text{EL}}(\mathbf{k}', \mathbf{k}) = W_{\alpha\alpha'}^{\text{EL}}(\mathbf{k}, \mathbf{k}') \quad (58)$$

while for inelastic (NE) scatterings, when electron energy is increased (+) or reduced (−) in a certain amount $\hbar\omega$, the PDB reduces to

$$W_{\alpha'\alpha}^{\text{NE}}(\mathbf{k}', \mathbf{k}) = W_{\alpha\alpha'}^{\text{NE}}(\mathbf{k}, \mathbf{k}') \exp(\pm\beta\hbar\omega) \quad (59)$$

This principle is useful for many derivations, such as the linear approximation to solve the system of BTEs explained in the section devoted to low-field transport.

4. SCATTERING MECHANISMS: TRANSITION RATES

The transition rates appearing in the collision integral operators of the BTEs include all the scattering mechanisms relevant for the considered transport phenomena. Electrons in semiconductor nanostructures can be scattered mainly by phonons (PH) of the acoustic and optical branches, ion impurities (IM) inside and outside the conduction channel, interface roughness (IR) in the boundary between materials forming the heterostructures, and alloy disorder (AL) because of the alien atoms in the host material, for instance, aluminum in $\text{Al}_x\text{Ga}_{1-x}\text{As}$ instead of arsenic in GaAs. Thus one must understand that

$$W_{\alpha\alpha'}(\mathbf{k}, \mathbf{k}') = \sum_{\text{CP}} W_{\alpha\alpha'}^{\text{CP}}(\mathbf{k}, \mathbf{k}') \quad (60)$$

where formally CP = PH, IM, IR, AL. For a given scattering mechanism the transition rates are calculated in first-order Born approximation and, consequently, the Fermi golden rule (FGR) applies to calculate the corresponding transition rates,

$$\begin{aligned} W_{\alpha\alpha'}^{\text{CP}}(\mathbf{k}, \mathbf{k}') = \frac{2\pi}{\hbar} \sum_{j, \mathbf{Q}} |V_{j\alpha\alpha'}^{\text{CP}}(\mathbf{k}, \mathbf{k}'; \mathbf{Q})|_{\text{av}}^2 \\ \times \delta(E + E_{\alpha} - E' - E_{\alpha'} \pm \hbar\omega_{j\mathbf{Q}}) \end{aligned} \quad (61)$$

where the subscript j has different meanings according to the considered interaction. It labels the polarization modes in the case of phonon scattering (CP = PH), the individual ionized impurities in the case of impurity scattering (CP = IM), or the individual alien atoms in the case of alloy disorder scattering (CP = AL). It does not appear in the case of interface roughness scattering (CP = IR), for the statistical correlation between the individual scattering centers taken into account, as will be seen. The Dirac delta function indicates energy conservation. Thus, in an elastic scattering, where the total electron energy is conserved, one simply has $\hbar\omega_{j\mathbf{Q}} = 0$, while in an inelastic scattering the energy gained (+) or lost (−) by the electron is $\hbar\omega_{j\mathbf{Q}}$. Here the subscript “av” means statistical averaging of the scattering centers. In correspondence with (1) now a 3D wavevector is $\mathbf{Q} = \mathbf{q} + \mathbf{q}_{\perp}$, with

$$\mathbf{q} = q_x \mathbf{e}_x + q_y \mathbf{e}_y \quad \mathbf{q}_{\perp} = q_z \mathbf{e}_z \quad (62)$$

$$\mathbf{q} = q_x \mathbf{e}_x \quad \mathbf{q}_{\perp} = q_y \mathbf{e}_y + q_z \mathbf{e}_z \quad (63)$$

in Q2D and Q1D systems respectively.

Screening of the interactions due to the fluctuations of the carrier concentration around the scattering centers must be taken into account. A linear response theory is generally applied to find this effect, whose result is incorporated by means of a screening factor or a matrix dielectric function when transition rates are calculated. Amount the earlier works on this subject one can find a modified Debye model derivation of a screening factor in [41]. The Thomas-Fermi approximation (TFA) and the random phase approximation (RPA) for the matrix dielectric function are widely employed [21]. Thus, the matrix elements for the screened interaction are given by

$$V_{j\alpha\alpha'}^{\text{CP}}(\mathbf{k}, \mathbf{k}'; \mathbf{Q}) = \sum_{\gamma, \gamma'} \varepsilon_{\alpha\alpha'\gamma\gamma'}^{-1}(\mathbf{q}, \omega_{j\mathbf{Q}}) V_{0j\gamma\gamma'}^{\text{CP}}(\mathbf{k}, \mathbf{k}'; \mathbf{Q}) \quad (64)$$

where $V_{0j\gamma\gamma'}^{\text{CP}}(\mathbf{k}, \mathbf{k}'; \mathbf{Q})$ are the corresponding matrix elements for the bare interaction; and $\varepsilon_{\alpha\alpha'\gamma\gamma'}^{-1}(\mathbf{q}, \omega_{j\mathbf{Q}})$ are the elements of the inverted matrix dielectric function. The inversion of a matrix dielectric function is not so simple as it seems at first sight and it is a matter of controversy. Many works avoid this question by making different approximations, particularly the so-called size-quantum limit (SQL) approximation, when only the lower subband is occupied and the intersubband transitions are ignored. The screening of the interactions deserves a special discussion, which can be found in the corresponding section (“Screening of the Scattering Mechanisms”).

4.1. Electron–Phonon Interaction

Electron–phonon interaction plays a very important role not only in transport phenomena but also in a variety of optical phenomena and, consequently, is the subject of a lot of works concerning semiconductor nanostructures. It is generally accepted that acoustic (AC) phonons keep their three-dimensional character, because the elastic constants of materials forming the heterostructures have quite close values. Furthermore, calculations with bulk AC phonons fit very well experimental data of optical and transport coefficients, so one can find very few articles where the problem of AC phonon confinement is considered [43]. On the other hand, optical (OP) phonons bear an essentially confined character, as shown by Raman scattering experiments in layered structures [44]. First explanations to these results were based upon very simple linear chain models [45–48]. Microscopic models have been proposed to find the dispersion relations both in layered and wire structures [49]. However, most of the works have been devoted to continuum models, maybe due to the fact that long wavelength phonons are the ones mainly involved in electron–phonon interaction. Two kind of approaches could be found: dielectric continuum models (e.g., in [50–55]), which consider the matching of electrostatic potential at the interfaces and do not take account of phonon dispersion, and hydrodynamic models (e.g., in [56–60]), which consider the matching of displacements at the interfaces and take account of the phonon dispersion. These models keep the distinction between transverse and longitudinal polarizations and give rise to interface, shear, and confined modes, the latter with different quantized frequencies, which allow quite good interpretation of optical experiments. The main feature of interface modes is the exponential decay of their amplitudes with increasing distance from the interface on both sides. The continuum models have been considered in many calculations of transport properties with satisfactory results, although the consideration of the phonon confinement does not affect the order of magnitude or the different functional dependence of calculated quantities, such as momentum relaxation rates [58], mobility [32], or power loss [61]. But an essential contradiction arises between these two models, because the imposition of matching conditions of one kind leads to the breakdown of matching conditions of the other kind [62]. Therefore, new models have been developed to overcome this contradiction. That is the case of different dispersive continuum theories developed in [63, 64]. For instance, in the latter there are neither purely transverse nor longitudinal polarizations, except at the center of the Brillouin zone, and very complicated dispersion relations, expressed by means of transcendental equations, are obtained. This model, generally with the restriction that the perpendicular to the interface displacement is zero and after some approximations, has been successfully employed in calculations of various optical properties, with acceptable agreement with experiment. However, very few calculations of transport coefficients have made use of this model, mainly because of the analytically unmanageable expressions appearing in derivations, which entails numerical methods from the very beginning [26]. Phonon confinement has been taken into account in several transport properties calculations, but in contrast with optical properties calculations,

it seems that no substantial differences emerge with respect to the consideration of bulk optical phonons.

For the sake of a comprehensive and compact presentation of theory, nonconfined AC and OP phonons are considered in this section. Phonon scattering is essentially inelastic, although for low-field regime acoustic-phonon scattering is considered elastic, which will be discussed later. Electrons are scattered by phonon absorption (+) or phonon emission (–); then it is clear that

$$W_{\alpha\alpha'}^{\text{PH}}(\mathbf{k}, \mathbf{k}') = W_{\alpha\alpha'}^{\text{PH}+}(\mathbf{k}, \mathbf{k}') + W_{\alpha\alpha'}^{\text{PH}-}(\mathbf{k}, \mathbf{k}') \quad (65)$$

according to the FGR (61), where the screened matrix elements are given by (64). The deduction of the interaction Hamiltonian can be found in many textbooks on semiconductor or solid state theory (e.g., in [65, 66]) for bulk phonons. In low-dimensional systems one must take care of separation of the envelope function in the plane-wave part and the confinement part according to (7). The matrix elements for the bare interaction result,

$$V_{0j\alpha\alpha'}^{\text{PH}\pm}(\mathbf{k}, \mathbf{k}'; \mathbf{Q}) = \left[N_{j\mathbf{Q}} + \frac{1}{2} - \left(\pm \frac{1}{2} \right) \right]^{1/2} \times C_{\text{PH}}(\mathbf{Q}) G_{\alpha\alpha'}(\mathbf{q}_{\perp}) \Delta(\mathbf{k} - \mathbf{k}' \pm \mathbf{q}) \quad (66)$$

where $C_{\text{PH}}(\mathbf{Q})$ is the corresponding coupling constant. Here the phonon occupation number $N_{j\mathbf{Q}}$ leads to the Bose–Einstein distribution function $n_B(\hbar\omega_{j\mathbf{Q}})$ after statistical averaging:

$$n_B(\hbar\omega_{j\mathbf{Q}}) = \frac{1}{\exp(\beta\hbar\omega_{j\mathbf{Q}}) + 1} \quad (67)$$

Because of the broken translational symmetry in confinement directions there appears a form factor for the electron–phonon interaction defined as

$$G_{\alpha\alpha'}(\mathbf{q}_{\perp}) = \int \psi_{\alpha'}^*(\boldsymbol{\rho}) \psi_{\alpha}(\boldsymbol{\rho}) \exp(i\mathbf{q}_{\perp} \cdot \boldsymbol{\rho}) d\boldsymbol{\rho} \quad (68)$$

When phonon confinement is considered, instead of $\exp(i\mathbf{q}_{\perp} \cdot \boldsymbol{\rho})$ quite complicated functions can appear even for simple models, as in [67]. Only a very simple confinement model leads to a simple function [58]. The Kronecker delta

$$\Delta(\mathbf{k} - \mathbf{k}' \pm \mathbf{q}) = \begin{cases} 1 & \text{if } \mathbf{k} - \mathbf{k}' \pm \mathbf{q} = 0 \\ 0 & \text{if } \mathbf{k} - \mathbf{k}' \pm \mathbf{q} \neq 0 \end{cases} \quad (69)$$

indicates momentum conservation in the plane or in the axis of translational symmetry for Q2D or Q1D systems respectively.

4.1.1. Acoustic–Phonon Scattering

We are thoroughly considering electrons close to the bottom of the conduction subbands, so electron–phonon interaction involves long wavelength phonons as the main contributors for the scattering processes. For AC phonons the long-wavelength approximation amounts to

$$\hbar\omega_{j\mathbf{Q}} = \hbar u_j Q \quad \text{as } Q \rightarrow 0 \quad (70)$$

where u_j is the sound velocity for the j polarization mode.

For very low temperatures, $T \rightarrow 0$, the Bose–Einstein distribution function is approximated simply by zero, which means there are no AC phonons to be observed. For low temperatures this factor is given by the complete (67) and this is known as the Bloch–Gruneisen regime. For not so low temperatures this factor is

$$n_B(\hbar\omega_{jQ}) \simeq \frac{k_B T}{\hbar u_j Q} \quad \text{when } \hbar u_j Q \ll k_B T \quad (71)$$

and this is known as the equipartition approximation. The latter is the most employed in calculations, which allows advancement in obtaining some analytical expressions. For instance, in GaAs based heterostructures the equipartition approximation works well for $T \geq 4$ K [68].

For mobility calculations the electron–AC-phonon interaction is considered an elastic scattering, which means one must set $\hbar\omega_{jQ} = 0$ in the argument of the Dirac delta function of the FGR. But in the equipartition approximation the small phonon energy is retained to give

$$n_B(\hbar\omega_{jQ}) + 1 \simeq n_B(\hbar\omega_{jQ}) \simeq \frac{k_B T}{\hbar u_j Q} \gg 1 \quad (72)$$

Thus, in the latter approximation, the phonon absorption and phonon emission transition rates equal each other and, consequently, one has

$$W_{\alpha\alpha'}^{AC}(\mathbf{k}, \mathbf{k}') = 2W_{\alpha\alpha'}^{AC+}(\mathbf{k}, \mathbf{k}') = 2W_{\alpha\alpha'}^{AC-}(\mathbf{k}, \mathbf{k}') \quad (73)$$

Furthermore, in the matrix dielectric function one also sets $\omega_{jQ} = 0$ and one talks about static screening according to (64).

For energy loss calculations, the electron–AC-phonon interaction must be considered just a little inelastic or quasielastic scattering, which means that the Dirac delta function in the FGR can be expanded as

$$\delta(E_{\alpha\alpha'} - E' \pm \hbar u_j Q) = \delta(E_{\alpha\alpha'} - E') \pm \hbar u_j Q \delta'(E_{\alpha\alpha'} - E') \quad (74)$$

$$+ \frac{1}{2} (\hbar u_j Q)^2 \delta''(E_{\alpha\alpha'} - E') \quad (75)$$

where $E_{\alpha\alpha'} = E + E_\alpha - E_{\alpha'}$ and [69]

$$\int_{-\infty}^{\infty} g(E') \delta'(E_{\alpha\alpha'} - E') dE' = -g'(E_{\alpha\alpha'}) \quad (76)$$

$$\int_{-\infty}^{\infty} g(E') \delta''(E_{\alpha\alpha'} - E') dE' = g''(E_{\alpha\alpha'}) \quad (77)$$

The elastic approximation, limited only to the first term in the expansion, would prevent AC phonons from participating in electron energy loss, which is important at low temperatures when electrons cannot emit optical phonons.

In both polar and nonpolar semiconductors the local elastic deformations of the media, along which lattice waves of the acoustic branch propagate, give rise to small perturbations of the electron energies. This is the electron–AC-phonon interaction via the so-called deformation potential (DP) coupling, also named nonpolar acoustic interaction.

For cubic crystals this is an isotropic interaction given by the coupling constant

$$C_{DP}(\mathbf{Q}) = \left(\frac{\hbar D_{ac}^2}{2\rho_d u_L V} Q \right)^{1/2} \quad (78)$$

where D_{ac} is the acoustic deformation potential, ρ_d is the material density, u_L is the sound velocity for the longitudinal polarization mode, the only one contributing to acoustic phonon scattering by means of this coupling, and V is the normalization volume. The D_{ac} value must be fixed from experiment (e.g., for GaAs based heterostructures it has been the subject of a quite great controversy [70–72], ranging from 7 to 16 eV depending upon whether the screening of this interaction is taken into account). This question will be reconsidered in sections devoted to mobility and power loss calculations.

In polar semiconductors, when the crystals do not have points of inversion symmetry, local elastic deformations are accompanied by local changes in the electrical polarization of the media, which also give rise to small perturbations of the electron energies. This is the electron–AC-phonon interaction via the so-called piezoelectric (PE) coupling, also named polar acoustic interaction. This is essentially an isotropic interaction even in cubic crystals. Nevertheless, for zinc blende crystals an isotropic approximation is given by

$$C_{jPE}(\mathbf{Q}) = \left(\frac{e^2 h_{14}^2 \hbar}{2\rho u_j \kappa_0 V} \frac{A_j(\mathbf{Q})}{Q} \right)^{1/2} \quad (79)$$

where h_{14} is the only element of the piezoelectric tensor different from zero, κ_0 is the static lattice dielectric constant, and u_j is the sound velocity for the longitudinal (L), $j = 1$, or transverse (T), $j = 2, 3$, polarization modes. The h_{14} value has been also controversial, (e.g., for GaAs based heterostructures [68, 73], ranging from 1.2 to 1.44×10^7 V cm⁻¹). Dealing with bulk phonons a solid angle average of this interaction can be made to obtain $A_j(\mathbf{Q}) = \frac{64}{15} \pi^2$ [74], but one can also find $A_j(\mathbf{Q}) = 1$. Particularly, in a Q2D system formed with heterostructures grown in (0, 0, 1) orientation in crystals with zinc blende symmetry, anisotropy is considered by the factors [75]

$$A_L(\mathbf{Q}) = \frac{9q_z^2 q^4}{2(q_z^2 + q^2)^3} \quad \text{and} \quad A_T(\mathbf{Q}) = \frac{8q_z^4 q^2 + q^6}{4(q_z^2 + q^2)^3} \quad (80)$$

which obviously introduces additional complications in calculations, which do not reveal substantial differences with fully isotropic approximations. For wurzite crystals, as one of the crystal phases of the GaN, there are five components of the piezoelectric tensor different from zero, $h_{15} = h_{24}$, $h_{31} = h_{32}$, and h_{33} , and the isotropic approximation can be found in [42].

4.1.2. Optical Phonon Scattering

Dealing with long wavelength OP phonons, the dispersionless Einstein model is frequently assumed. This amounts to

$$\hbar\omega_{jQ} = \hbar\omega_{j0} \quad \text{as } Q \rightarrow 0 \quad (81)$$

where ω_{j0} is the optical phonon frequency at the center of the Brillouin zone for the L-polarization mode ($j = 1$) and the T-polarization modes ($j = 2, 3$).

For sufficiently low temperatures, $k_B T \ll \hbar\omega_{j0}$, the Bose–Einstein distribution function is approximated simply by zero, which means there are no optical phonons to be absorbed. For other temperatures this factor is given by the complete $n_B(\hbar\omega_{j0})$ after (67). The electron–OP-phonon interaction is essentially an inelastic scattering, so in the argument of the Dirac delta function one must set $\omega_{jQ} = \omega_{j0}$. Furthermore, in the matrix dielectric function one also must set $\omega_{jQ} = \omega_{j0}$ and then talk about dynamic screening according to (64). The screening of this interaction has been frequently ignored (e.g., in mobility calculations for SHs [68] and QWs [32]) or considered as static screening (e.g., in polaron calculations for SHs [76] and QWs [57]), but also the pertinent temperature-dependent dynamical screening has been included in mobility calculations for SHs [77] and QWs [78].

In polar semiconductors the local elastic deformations of the media, along which lattice waves of the optical branch propagate, are accompanied by local changes of the polarization field, which give rise to small perturbations of the electron energies. This is the electron–OP-phonon interaction via the so-called Fröhlich interaction coupling, also named the optical polar interaction. For cubic crystals this is an isotropic interaction, where only the L-polarization mode participates, given by the coupling constant

$$C_{LO}(\mathbf{Q}) = -i \left(\frac{2\pi e^2 \hbar \omega_{LO}}{\kappa^* V} \frac{1}{Q^2} \right)^{1/2} \quad (82)$$

where ω_{LO} is the longitudinal optical (LO) phonon frequency (e.g., for GaAs the most extended value is $\hbar\omega_{LO} = 365$ meV [78], while for GaN $\hbar\omega_{LO} = 928$ meV [79]). Here an effective lattice dielectric constant is introduced as

$$\frac{1}{\kappa^*} = \frac{1}{\kappa_\infty} - \frac{1}{\kappa_0} \quad (83)$$

with κ_∞ the high-frequency and κ_0 the static lattice dielectric constants of the material. The commonly found values for GaAs are $\kappa_\infty = 12.53$ and $\kappa_0 = 10.82$ [78], and for GaN are $\kappa_\infty = 9.5$ and $\kappa_0 = 5.37$ [79].

In both nonpolar and polar semiconductors the local elastic deformations of the media, along which lattice waves of the optical branch propagate, give rise to other small perturbations of the electron energies. This is the electron–OP-phonon interaction via the so-called optical deformation-potential coupling, also named then nonpolar optical (NO) interaction. For cubic crystals this is an isotropic interaction given by the coupling constant

$$C_{NO}(\mathbf{Q}) = \left(\frac{\hbar D_{op}^2}{2\rho_d \omega_0 V} \right)^{1/2} \quad (84)$$

where ω_0 is the optical phonon frequency and D_{op} is the optical deformation potential. This interaction is important for intervalley scattering between Γ and L or X points in the Brillouin zone for III–V compounds and related ternary compounds, where the edge zone LO phonons participate,

and a dispersionless model $\omega_0 = \omega_{LO}$. In GaAs the energy difference between Γ and L valleys is 0.3 eV, while it is 0.47 eV between Γ and X valleys, with the D_{op} values ranging from 4 to 10×10^8 eV cm⁻¹ [80].

4.2. Electron–Ion–Impurity Interaction

The electron–ion–impurity interaction is by far the most important interaction in delta-doped semiconductors and plays the main role in limiting the mobility at low temperatures in semiconductor heterostructures, as will be shown. Impurity scattering arises from the donors (acceptors), which supply electrons (holes) to the conduction channel in the semiconductor nanostructures. This is an essentially elastic scattering, since ions are very much heavier than electrons or holes. The Coulomb interaction between the carriers and the ion impurities, located at $\mathbf{R}_i = \mathbf{r}_i + \boldsymbol{\rho}_i$, is well known in space representation and must be Fourier transformed to obtain the nonscreened Hamiltonian in a form suitable for calculation of matrix elements.

The matrix elements for the bare interaction in a Q2D system are given by

$$V_{0il'}^{IM}(\mathbf{k}, \mathbf{k}'; \mathbf{q}) = C_i^{2D}(\mathbf{q}) G_{il'}^{2D}(\mathbf{q}) \Delta(\mathbf{k} - \mathbf{k}' + \mathbf{q}) \quad (85)$$

where the coupling constant is

$$C_i^{2D}(\mathbf{q}) = \frac{2\pi e^2}{\kappa_0 q S} e^{-i\mathbf{q} \cdot \mathbf{r}_i} \quad (86)$$

with $\mathbf{r}_i = x_i \mathbf{e}_x + y_i \mathbf{e}_y$ and S the normalization area. Because of the broken translational symmetry in the confinement direction there appears the form factor for the electron–impurity interaction as

$$G_{il'}^{2D}(\mathbf{q}) = \int \varphi_l^*(z) e^{-q|z-z_i|} \varphi_l(z) dz \quad (87)$$

The matrix elements for the bare interaction in a Q1D system are given by

$$V_{0i\alpha\alpha'}^{IM}(\mathbf{k}, \mathbf{k}'; \mathbf{q}) = C_i^{1D}(\mathbf{q}) G_{i\alpha\alpha'}^{1D}(\mathbf{q}) \Delta(\mathbf{k} - \mathbf{k}' + \mathbf{q}) \quad (88)$$

where the coupling constant is

$$C_i^{1D}(\mathbf{q}) = \frac{2\pi e^2}{\kappa_0 L} e^{iq_s x_i} \quad (89)$$

with L the normalization length. Because of the broken translational symmetry in the confinement plane there appears the form factor for the electron–impurity interaction as

$$G_{i\alpha\alpha'}^{1D}(\mathbf{q}) = \int \varphi_{\alpha'}^*(\boldsymbol{\rho}) K_0(q|\boldsymbol{\rho} - \boldsymbol{\rho}_i|) \varphi_\alpha(\boldsymbol{\rho}) d\boldsymbol{\rho} \quad (90)$$

where K_0 is the modified Bessel function of the second kind and

$$|\boldsymbol{\rho} - \boldsymbol{\rho}_i| = \sqrt{(y - y_i)^2 + (z - z_i)^2} \quad (91)$$

4.2.1. Background Impurity Scattering

The cleanness of the growth processes reduces the concentration of undesired impurities inside the conduction channels to low enough values, which prevents this mechanism from being relevant in transport phenomena in modulation-doped heterostructures, which has been experimentally verified. However, in delta-doped semiconductors the required impurities are in the conduction channels and are the most important scattering centers. In recent years the intentionally delta-doped QWs, inside the conduction channel, have also been investigated [81–84]. In these cases this mechanism is known as the background impurity (BI) scattering.

Since impurities are somehow distributed inside the conduction channel, the summation on i to find the transition rate is replaced by an integration. In Q2D systems this is done as

$$\sum_i |V_{inn'}^{\text{BI}}(\mathbf{k}, \mathbf{k}'; \mathbf{q})|^2 = \int_{-a}^a n_D(z_i) |V_{inn'}^{\text{BI}}(\mathbf{k}, \mathbf{k}'; \mathbf{q})|^2 dz_i \quad (92)$$

where $n_D(z_i)$ is the profile of volume concentration of donor impurities and $2a$ is the QW width (for a SH, the lower limit must be zero and a must be understood as a certain effective layer width of the formed conduction channel). If necessary, a similar procedure can be done in Q1D systems,

$$\sum_i |V_{iaa'}^{\text{BI}}(\mathbf{k}, \mathbf{k}'; \mathbf{q})|^2 = \int_B n_D(\rho_i) |V_{iaa'}^{\text{BI}}(\mathbf{k}, \mathbf{k}'; \mathbf{q})|^2 d\rho_i \quad (93)$$

where $n_D(\rho_i)$ is the local volume concentration of donor impurities and B is the quantum wire cross section.

4.2.2. Remote Impurity Scattering

Different doping profiles can be achieved by means of modulation-doped techniques in semiconductor nanostructures. The uniformly doped barrier is mostly found, although delta-doped semiconductor heterostructures, with impurities in the barriers, are also investigated [85]. The remote impurity (RI) scattering of electrons comes from the ionized donors placed out of the conduction channel in modulation-doped heterostructures. The inclusion of a spacer layer aims to reduce this mechanism, but this cannot suppress it completely, because the donors must be sufficiently close to the conduction channel to supply the required electrons efficiently. A SH is doped from one side exclusively. For simplicity symmetrically doped QWs and QWIs are considered to present quite general and compact expressions in this section.

Since impurities are somehow distributed outside the conduction channel, the summation on i to find the transition rate is replaced by an integration. In Q2D systems this is done as

$$\sum_i |V_{inn'}^{\text{RI}}(\mathbf{k}, \mathbf{k}'; \mathbf{q})|^2 = 2 \int_{a+s}^{a+s+b} n_D(z_i) |V_{inn'}^{\text{RI}}(\mathbf{k}, \mathbf{k}'; \mathbf{q})|^2 dz_i \quad (94)$$

where $n_D(z_i)$ is the profile of volume concentration of donor impurities, s is the spacer layer width, and b is the depletion

layer width (for a SH the factor 2 must be omitted). In Q1D systems this is done as

$$\sum_i |V_{iaa'}^{\text{BI}}(\mathbf{k}, \mathbf{k}'; \mathbf{q})|^2 = \int_{B^*} n_D(\rho_i) |V_{iaa'}^{\text{BI}}(\mathbf{k}, \mathbf{k}'; \mathbf{q})|^2 d\rho_i \quad (95)$$

where $n_D(\rho_i)$ is the 2D profile volume concentration of donor impurities and B^* is depletion region cross section, whose concrete form depends on the symmetry of the QWI cross section and the desired profile for the modulation-doped region.

4.3. Alloy Disorder Scattering

Ternary compounds are usually fabricated by the substitution of one of the components atoms of a binary compound by atoms of the same group in the periodic table. The alloy disorder is due to the alien atoms in the host material, for instance, aluminum in $\text{Al}_x\text{Ga}_{1-x}\text{As}$ instead of arsenic in GaAs. The alien atoms represent almost point defects in the crystal lattice of the host material, so that a certain short-range scattering potential is modeled as the interaction Hamiltonian. The matrix elements for the bare interaction result [86],

$$V_{0iaa'}^{\text{AL}}(\mathbf{k}, \mathbf{k}'; \mathbf{q}) = C^{\text{AL}}(\mathbf{q}) G_{iaa'}^{\text{AL}}(\mathbf{q}) \Delta(\mathbf{k} - \mathbf{k}' + \mathbf{q}) \quad (96)$$

where the coupling constant is given by the interaction potential D_{AL} with the alien atoms of radius R_0 as follows:

$$C_i^{\text{AL}}(\mathbf{q}) = \frac{4\pi}{3} D_{\text{AL}} R_0^3 \quad (97)$$

According to [86] the alloy potential values are the following: for $x = 0.3$ in $\text{Al}_x\text{Ga}_{1-x}\text{As}$, one has $D_{\text{AL}} = 1.56$ eV; for $y = 0.53$ in $\text{In}_y\text{Ga}_{1-y}\text{As}$, one has $D_{\text{AL}} = 0.55$ eV; and for $z = 0.53$ in $\text{In}_z\text{Al}_{1-z}\text{As}$, one has $D_{\text{AL}} = 0.4$ or 1.3 eV. Here the form factor is

$$G_{iaa'}^{\text{AL}}(\mathbf{q}) = \varphi_{a'}(z_i) \varphi_a(z_i) G_{aa'}(\mathbf{q}) \quad (98)$$

where $G_{aa'}(\mathbf{q})$ is given by (68).

Since alien atoms are somehow distributed inside or outside the conduction channel (e.g., as in $\text{In}_y\text{Al}_{1-y}\text{As}$ / $\text{In}_x\text{Ga}_{1-x}\text{As}$ and $\text{Al}_x\text{Ga}_{1-x}\text{As}$ /GaAs respectively), the summation on index i , which labels the alien atoms, to find the transition rate according to the FGR is replaced by an integration as

$$\sum_i |V_{iaa'}^{\text{AL}}(\mathbf{k}, \mathbf{k}'; \mathbf{q})|^2 = \int_B \frac{1}{2} N_0 x(1-x) |V_{iaa'}^{\text{AL}}(\mathbf{k}, \mathbf{k}'; \mathbf{q})|^2 d\rho_i \quad (99)$$

where $\frac{1}{2} N_0 x(1-x)$ is the concentration of scattering centers, which is taken to be constant, N_0 is the number of atoms per unit volume of the crystal, and B is the region where alien atoms are located.

4.4. Interface Roughness Scattering

Interface roughness arises from the transition region of one or two monolayer between the materials forming the heterostructure because of the effectively random distribution of alien atoms or, as also happens, it is due to inappropriate selection of growth temperatures and deposition rates leading to growth by islanding in 3D rather than advancing terrace edges in 2D. This way, instead of perfect planar interfaces one has irregular ones. Fluctuations along the interface are random and correlated in a Gaussian manner, with root mean square height Δ_0 and correlation length Λ_0 . This is taken into account in the confining potential to derive the corresponding matrix elements [87], which in the case of hard wall potentials leads to [88]

$$V_{\alpha\alpha'}^{\text{IR}}(\mathbf{k}, \mathbf{k}'; \mathbf{Q}) = C_{\text{IR}}(q) G_{\alpha\alpha'}^{\text{IR}}(z_0) \Delta(\mathbf{k} - \mathbf{k}' + \mathbf{q}) \quad (100)$$

where to keep the compact form of presentation the coupling constant is understood as

$$C_{\text{IR}}(q) = \frac{\hbar^2}{2m^*} \left[\pi \Delta_0^2 \Lambda_0^2 \exp\left(-\frac{1}{4} q^2 \Lambda_0^2\right) \right]^{1/2} \quad (101)$$

and the remaining factor as

$$G_{\alpha\alpha'}^{\text{IR}}(z_0) = \left. \frac{d\varphi_\alpha}{dz} \frac{d\varphi_{\alpha'}}{dz} \right|_{z=z_0} \quad (102)$$

with z_0 the corresponding interface coordinate. The parameter values depend on the concrete grown interface (e.g., for a given $\text{In}_y\text{Ga}_{1-y}\text{As}/\text{In}_z\text{Al}_{1-z}\text{As}$ heterostructure they have been estimated as $\Delta_0 = 0.283$ nm and $\Lambda_0 = 10$ nm [88], while for a given $\text{Si}/\text{Si}_{1-x}\text{Ge}_x$ heterostructure they have been chosen as $\Delta_0 = 0.5$ nm and $\Lambda_0 = 10$ nm) [12].

Another approach to the interface roughness scattering has been recently developed in [89], where an effective Hamiltonian is derived taken into account the fluctuations $\Delta_0(\mathbf{r})$ at the interfaces and certain modulated envelope functions in the confinement direction are proposed.

5. LOW-FIELD TRANSPORT

Studying the steady-state transport in semiconductor nanostructures it has been experimentally established that in the graphics of the drift velocity as a function of the applied electric field (v_d vs F) three regions can be clearly distinguished: the one of linear dependence, the one of nonlinear dependence and saturation, as well as the region when drift velocity decreases with increasing field [90, 91]. The latter is the region of negative differential resistance (NDR).

As in the case of bulk semiconductors, there is a linear response of the system to the applied electric field in a range of strength values very attractive for device design, particularly related to the HEMT performance, as was highlighted in the Introduction. Furthermore, the investigation of different scattering mechanisms can be carried out without a series of disturbing phenomena arising in the nonlinear response regime.

One can talk about a low field when experimentally there is a linear dependence between the current density and the applied electric field,

$$\mathbf{j} = \sigma \mathbf{F} \quad (103)$$

where the conductivity $\sigma = \text{const}$. This is the well-known Ohm law. In this case the average energy of the electrons is slightly different from the one of the phonons, which are in thermal equilibrium at the temperature T of the thermal bath. In this regime the energy transfer from the electron system to the phonon system can be disregarded, because this is not so important as the momentum transfer to the different scattering centers, which leads to the resistance of the concrete device.

5.1. Distribution Function in Linear Approximation

Dealing with a low electric field a linear approximation in its strength is enough for the nonequilibrium distribution functions related to the different subbands. Thus for solving the system of BTEs one starts from the assumption that

$$f_\alpha(\mathbf{k}) = f_\alpha^{(0)}(\mathbf{k}) + f_\alpha^{(1)}(\mathbf{k}) \quad \text{and} \quad f_\alpha^{(1)}(\mathbf{k}) \ll f_\alpha^{(0)}(\mathbf{k}) \quad (104)$$

where $f_\alpha^{(0)}(\mathbf{k})$ is the equilibrium distribution function and $f_\alpha^{(1)}(\mathbf{k})$ is a linear term in $F = |\mathbf{F}|$. Particularly in Q2D systems, this can be also understood as the development of $f_\alpha(\mathbf{k})$ in Legendre polynomials, whereas the variable angle ϑ is taken to be the one between \mathbf{k} and \mathbf{F} , up to the second term [92].

The most employed method to solve the BTEs is to set the perturbation to the distribution function in the form

$$\begin{aligned} f_\alpha^{(1)}(\mathbf{k}) &= \frac{e}{\hbar} \mathbf{F} \cdot \nabla_{\mathbf{k}} f_\alpha^{(0)}(\mathbf{k}) \tau_\alpha(\mathbf{k}) \\ &= \frac{e\hbar}{m^*} \mathbf{F} \cdot \mathbf{k} \frac{d}{dE} f_\alpha^{(0)}(E) \tau_\alpha(E) \end{aligned} \quad (105)$$

where $\tau_\alpha(\mathbf{k})$ or $\tau_\alpha(E)$ is just a certain quantity with time dimensions, but without any physical meaning at this stage, depending on energy and not on wavevector direction since all the scattering mechanisms are assumed or approximated by isotropic interactions. In the case of elastic scatterings this assumption corresponds to the so-called relaxation time approximation and a closed form is obtained to calculate $\tau_\alpha(E)$. But when any inelastic scattering is considered, an iterative procedure is commonly followed [92, 93], on the line originally developed in [94, 95], to find $\tau_\alpha(E)$ [also denoted as $\phi_\alpha(E)$ in many works]. Both cases are discussed.

This way, for the steady state transport, taking account of the PDB, straightforward manipulations transform the system of BTEs into a system of integral equations,

$$1 = \sum_{\alpha', \mathbf{k}'} S_{\alpha\alpha'}(\mathbf{k}, \mathbf{k}') \left\{ \tau_\alpha(E) - \eta \frac{k'}{k} \tau_{\alpha'}(E') \right\} \quad (106)$$

where $\eta = \cos \theta$ with θ the scattering angle between \mathbf{k} and \mathbf{k}' for Q2D systems, while $\eta = \pm 1$ for Q1D systems, as well as

$$S_{\alpha\alpha'}(\mathbf{k}, \mathbf{k}') = W_{\alpha\alpha'}(\mathbf{k}, \mathbf{k}') \frac{1 - f_{\alpha'}^{(0)}(E')}{1 - f_\alpha^{(0)}(E)} \quad (107)$$

5.1.1. Elastic Scattering

For any elastic scattering the electron keeps its total energy and $f_{\alpha'}^{(0)}(E') = f_{\alpha}^{(0)}(E)$ as well as $\tau_{\alpha'}(E') = \tau_{\alpha}(E)$, since both quantities depend on the total energy $E_{\alpha}(\mathbf{k})$. Because of the delta Dirac function in the FGR, after going from summation in \mathbf{k}' to integration in E' one obtains the actual relaxation time corresponding to subband α for the considered interaction,

$$\frac{1}{\tau_{\alpha}^{\text{EL}}(E)} = \sum_{\alpha', \eta} S^{\text{EL}}(E, E_{\alpha\alpha'}, \eta) \left\{ 1 - \eta \left(\frac{E_{\alpha\alpha'}}{E} \right)^{1/2} \right\} \quad (108)$$

where $E_{\alpha\alpha'} = E + E_{\alpha} - E_{\alpha'}$ is the kinetic energy in the subband, into which the electron is scattered, and formally EL = DP, PE, AL, IR, according to elastic scatterings introduced. Note here that

$$\sum_{\eta} S^{\text{EL}}(E, E_{\alpha\alpha'}, \eta) \dots = \int_0^{2\pi} S^{\text{EL}}(E, E_{\alpha\alpha'}, \cos \theta) \dots d\theta \quad (109)$$

$$\begin{aligned} \sum_{\eta} S^{\text{EL}}(E, E_{\alpha\alpha'}, \eta) \dots &= S^{\text{EL}}(E, E_{\alpha\alpha'}, 1) \dots \\ &+ S^{\text{EL}}(E, E_{\alpha\alpha'}, -1) \dots \end{aligned} \quad (110)$$

in Q2D and Q1D respectively. When several elastic scatterings are present, the relaxation time, also called transport lifetime or classical relaxation time, is given by

$$\frac{1}{\tau_{\alpha}^{\text{ES}}(E)} = \sum_{\text{EL}} \frac{1}{\tau_{\alpha}^{\text{EL}}(E)} \quad (111)$$

5.1.2. Inelastic Scattering

For any inelastic scattering the electron does not keep its total energy and $f_{\alpha'}^{(0)}(E') \neq f_{\alpha}^{(0)}(E)$ as well as $\tau_{\alpha'}(E') \neq \tau_{\alpha}(E)$, since $E_{\alpha}(\mathbf{k}) \neq E_{\alpha'}(\mathbf{k}')$. Because of the delta Dirac function in the FGR, after going from summation in \mathbf{k}' to integration in E' for the LO-phonon scattering one obtains

$$\begin{aligned} 1 &= \sum_{\alpha', \eta} S^{\text{LO}}(E, E_{\alpha\alpha'}^+, \eta) \left\{ \tau_{\alpha}^{\text{LO}}(E) - \eta \left(\frac{E_{\alpha\alpha'}^+}{E} \right)^{1/2} \tau_{\alpha'}^{\text{LO}}(E_{\alpha\alpha'}^+) \right\} \\ &+ \sum_{\alpha', \eta} S^{\text{LO}}(E, E_{\alpha\alpha'}^-, \eta) \left\{ \tau_{\alpha}^{\text{LO}}(E) - \eta \left(\frac{E_{\alpha\alpha'}^-}{E} \right)^{1/2} \tau_{\alpha'}^{\text{LO}}(E_{\alpha\alpha'}^-) \right\} \end{aligned} \quad (112)$$

where formally $E_{\alpha\alpha'}^{\pm} = E_{\alpha\alpha'} \pm \hbar\omega_{\text{LO}}$ is the kinetic energy in the subband, into which the electron is scattered after absorption (+) or emission (-) of energy $\hbar\omega_{\text{LO}}$. Note that according to (109) or (110) once the summation over η is accomplished, one has a system of algebraic equations. Therefore, this operation must be carried out before any further calculation.

The already mentioned iterative procedure is frequently followed to find the quantities $\tau_{\alpha}^{\text{LO}}(E)$ [96, 97], which in this case cannot be interpreted as relaxation times, since randomization of energy cannot be reached by the exclusive actions of inelastic scattering mechanisms. The following

iterative formula is employed:

$$\begin{aligned} 1 &= \sum_{\alpha', \eta} S^{\text{LO}}(E, E_{\alpha\alpha'}^+, \eta) \left\{ \tau_{\alpha, m}^{\text{LO}}(E) - \eta \left(\frac{E_{\alpha\alpha'}^+}{E} \right)^{1/2} \tau_{\alpha', m-1}^{\text{LO}}(E_{\alpha\alpha'}^+) \right\} \\ &+ \sum_{\alpha', \eta} S^{\text{LO}}(E, E_{\alpha\alpha'}^-, \eta) \left\{ \tau_{\alpha, m}^{\text{LO}}(E) - \eta \left(\frac{E_{\alpha\alpha'}^-}{E} \right)^{1/2} \tau_{\alpha', m-1}^{\text{LO}}(E_{\alpha\alpha'}^-) \right\} \end{aligned} \quad (113)$$

Iterations start from the zero-order iteration $\tau_{\alpha, 0}^{\text{LO}}(E) = 0$, which would correspond to equilibrium, and follow until the step M , when the values converge within the pertinent error. The first-order iteration takes into account scattering out processes exclusively,

$$\frac{1}{\tau_{\alpha, 1}^{\text{LO}}(E)} = \sum_{\alpha', \eta} \{ S^{\text{LO}}(E, E_{\alpha\alpha'}^+, \eta) + S^{\text{LO}}(E, E_{\alpha\alpha'}^-, \eta) \} \quad (114)$$

and it works well at low temperatures, $k_B T \ll \hbar\omega_{\text{LO}}$, when the scattering-in processes due to phonon absorption can be neglected due to the scarcity of LO phonons according to (67), and those due to phonon emission can also be neglected since only a few electrons have energy $\hbar\omega_{\text{LO}}$ or greater. This is known as the low-temperature relaxation-time approximation.

If one considers that most of the electrons have energies very much greater than the phonon energy, the latter is neglected with respect to the former and one simply sets $\tau_{\alpha}^{\text{LO}}(E) = \tau_{\alpha}^{\text{LO}}(E_{\alpha\alpha}^{\pm})$ to obtain the high-energy relaxation-time approximation:

$$\begin{aligned} \frac{1}{\tau_{\alpha}^{\text{HE}}(E)} &= \sum_{\alpha', \eta} S^{\text{LO}}(E, E_{\alpha\alpha'}^+, \eta) \left\{ 1 - \eta \left(\frac{E_{\alpha\alpha'}^+}{E} \right)^{1/2} \right\} \\ &+ \sum_{\alpha', \eta} S^{\text{LO}}(E, E_{\alpha\alpha'}^-, \eta) \left\{ 1 - \eta \left(\frac{E_{\alpha\alpha'}^-}{E} \right)^{1/2} \right\} \end{aligned} \quad (115)$$

It works well at high temperatures, $k_B T \gg \hbar\omega_{\text{LO}}$, when according to the PDB in the form (59), this can be considered an elastic mechanism. This is also known as the high-temperature relaxation-time approximation.

5.1.3. Elastic and Inelastic Scatterings Altogether

When both elastic and inelastic scattering must be considered altogether, the same iterative procedure is followed according to the formula

$$\begin{aligned} 1 &= \frac{\tau_{\alpha, m}(E)}{\tau_{\alpha}^{\text{ES}}(E)} \\ &+ \sum_{\alpha', \eta} S^{\text{LO}}(E, E_{\alpha\alpha'}^+, \eta) \left\{ \tau_{\alpha, m}^{\text{LO}}(E) - \eta \left(\frac{E_{\alpha\alpha'}^+}{E} \right)^{1/2} \tau_{\alpha', m-1}^{\text{LO}}(E_{\alpha\alpha'}^+) \right\} \\ &+ \sum_{\alpha', \eta} S^{\text{LO}}(E, E_{\alpha\alpha'}^-, \eta) \left\{ \tau_{\alpha, m}^{\text{LO}}(E) - \eta \left(\frac{E_{\alpha\alpha'}^-}{E} \right)^{1/2} \tau_{\alpha', m-1}^{\text{LO}}(E_{\alpha\alpha'}^-) \right\} \end{aligned} \quad (116)$$

This situation deserves a brief comment. It is generally argued that owing to inelastic LO-phonon scattering, which cannot randomize energy and so prevent the electron gas from returning to equilibrium, the idea of a relaxation time

is not valid. That is correct when only this kind of scattering mechanism is present, which is an ideal situation. But when there are also present elastic scatterings, as in real systems, randomization of energy is reached and electron gas returns to the equilibrium state once the external agents are switched off. This is a fact; otherwise one could never reobtain the equilibrium state in samples employed in experimental measurements of transport properties, where optical phonons coexist together with acoustic phonons and other scattering centers. Therefore the quantity $\tau_{\alpha, M}(E)$ obtained after the required convergence of the iterative procedure actually is the relaxation time, in spite of the fact that no closed form could be derived to find it and only an approximate value can be calculated.

The low-temperature relaxation time approximation, taking account of (114), results in

$$\frac{1}{\tau_{\alpha}^{\text{LT}}(E)} = \frac{1}{\tau_{\alpha}^{\text{ES}}(E)} + \sum_{\alpha', \eta} \{S^{\text{LO}}(E, E_{\alpha\alpha'}^+, \eta) + S^{\text{LO}}(E, E_{\alpha\alpha'}^-, \eta)\} \quad (117)$$

while the high-temperature approximation, taking account of (115), results in

$$\frac{1}{\tau_{\alpha}^{\text{HT}}(E)} = \frac{1}{\tau_{\alpha}^{\text{ES}}(E)} + \frac{1}{\tau_{\alpha}^{\text{HE}}(E)} \quad (118)$$

5.2. Scattering Rate and Relaxation Rate

Two different quantities are important in the study of transport phenomena: the scattering rate and the relaxation rate, also called the momentum relaxation rate. The former is related to the lifetime of a given electron state, bearing an essential quantum character, while the latter is connected to the mean free pass of an electron in the given state, bearing a quasiclassical character.

The scattering rate of the electron state $|\alpha, \mathbf{k}\rangle$ takes account of the scattering out processes exclusively and is defined as

$$S_{\alpha}(\mathbf{k}) = \frac{1}{\tau_{\alpha}^s(\mathbf{k})} = \sum_{\alpha', \mathbf{k}'} W_{\alpha\alpha'}(\mathbf{k}, \mathbf{k}') \quad (119)$$

where $W_{\alpha\alpha'}(\mathbf{k}, \mathbf{k}')$ includes one or more interaction couplings, according to (60). This is the equivalent of the imaginary part of self-energy in MBT, which gives the level broadening of the energy corresponding to this quantum state. This way the scattering time $\tau_{\alpha}^s(\mathbf{k})$, also known as quantum scattering time or quantum relaxation time, is nothing else but the quasiparticle lifetime of MBT.

On the other hand, the relaxation rate is defined for elastic scattering mechanisms as

$$M_{\alpha}(E) = \frac{1}{\tau_{\alpha}(E)} = \sum_{\alpha', k'} W_{\alpha\alpha'}^{\text{ES}}(E, E_{\alpha\alpha'}) \left\{ 1 - \eta \sqrt{\frac{E_{\alpha\alpha'}}{E}} \right\} \quad (120)$$

where $\tau_{\alpha}(E)$ is the relaxation time, also known as classical scattering time or transport relaxation time, and $W_{\alpha\alpha'}^{\text{ES}}(E, E_{\alpha\alpha'})$ includes one or more of the elastic scatterings, depending on the desired result. According to the comment in previous section, when inelastic scatterings act together with elastic scatterings one can also understand the

relaxation rate as

$$M_{\alpha}(E) = \frac{1}{\tau_{\alpha}(E)} = \frac{1}{\tau_{\alpha, M}(E)} \quad (121)$$

where $\tau_{\alpha}(E) = \tau_{\alpha, M}(E)$ is the convergent value found after M iterations of the formula (116).

Many works have been devoted to finding the scattering rates or the relaxation rates due to the different scattering mechanisms. Most of the works aim to compare different interaction couplings or to establish the role of screening in these interactions. Bulk phonons as well as GaAs based delta-doped semiconductors and $\text{Al}_x\text{Ga}_{1-x}\text{As}/\text{GaAs}$ based semiconductor heterostructures are always considered in the works cited; otherwise it is specially remarked.

Studying the electron–phonon interaction early works on this subject made use of the so-called momentum conservation approximation (MCA) in QWs, considering that the momentum is conserved in confinement directions in spite of the broken translational symmetry [98, 99]. It is argued that the MCA gives the main contribution to the scattering or relaxation rates and, furthermore, analytical expressions for the transition rates are easily obtained. But computational facilities made it unnecessary and more accurate calculations are usually carried out and reveal that this approximation is not so good [67]. In the low-field regime the low-temperature region, where electrons do not reach the LO-phonon emission threshold, is clearly distinguished from the intermediate- and high-temperature regions. A similar situation is found in the high-field regime, bearing in mind the electron temperature. The approximate limits of these regions can be established only after concrete calculations of experimentally measurable quantities and vary from one material to another.

The electron–phonon interaction is investigated in [68]. The FSH variational wavefunction of the lowest subband for a SH is taken to calculate scattering and relaxation rates. The anisotropic factors (80) for PE coupling are used and static screening is taken into account by means of the RPA dielectric function, when only the lowest subband is populated and neglecting intersubband scatterings. An interesting comparison between DP and PE couplings is presented, as illustrated in Figure 1. Notice that the role of the PE scattering is more important as the electron energies are smaller as well as the temperature and areal concentration are lower. The LO coupling is also included, ignoring the screening effect. The numerical results for the inverse of the perturbation function $\tau_{1, M}^{-1}(E)$ [there denoted as $\phi^{-1}(E)$] are compared with the relaxation time obtained in the low-temperature and high-energy approximations, as illustrated in Figure 2. The contribution of acoustic phonons is also displayed. Note that the first approximation works at low temperatures well when the electron energies do not reach the LO-phonon threshold, while the second approximation works well at high temperatures when electron energies are larger than twice the LO-phonon energy.

The IBM wavefunctions for rectangular QWs are employed in [74] to calculate relaxation rates, where also these couplings are compared (there the isotropic version for PE coupling is assumed); furthermore, it can be noticed that the DP relaxation rate coincides with the DP scattering rate, which as a function of the total energy has the same staircase form of the DOS for a Q2D system and presents the same

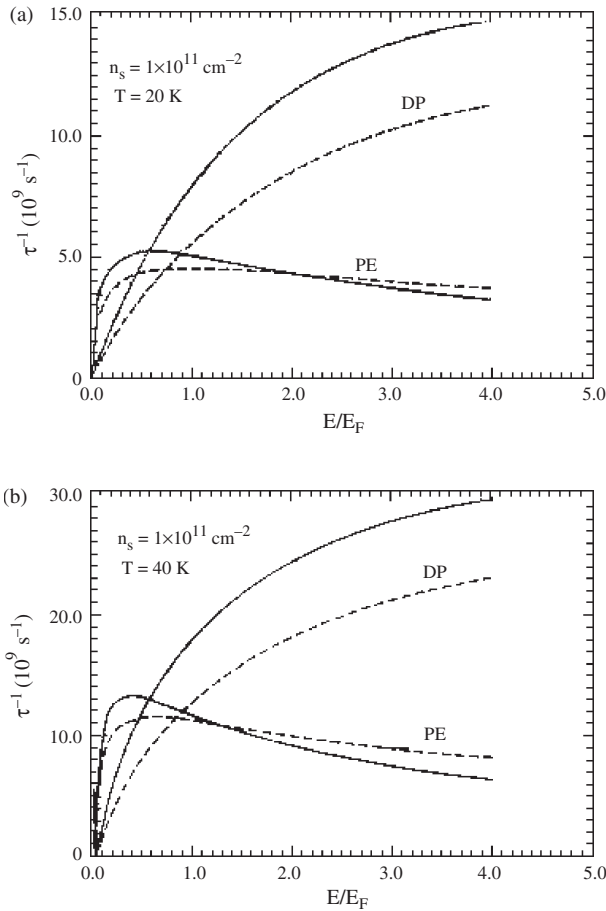


Figure 1. Comparison between DP and PE couplings for two values of temperature. Reprinted with permission from [68], T. Kawamura and S. Das Sarma, *Phys. Rev. B* 45, 3612 (1992). © 1992, American Physical Society.

discontinuities of the DOS for a Q1D system. The screening effect is ignored, since relatively low electron concentrations are considered. Similar calculations are carried out in the KBA formalism with a constant energy level broadening in [97], where one can appreciate that the discontinuities in the DP scattering rate, in both Q2D and Q1D systems, are smeared out because of the finite lifetime of electron states. For a weak piezoelectric material such as GaAs in the conduction channel of a semiconductor heterostructure, both the scattering and the relaxation rates due to the DP coupling are always larger than the ones due to PE coupling, except for very low electron energies, as can be appreciated in Figure 1 taken from [68].

Polar optical phonons always deserve special interest, since they play the main role in transport phenomena at high temperatures and the electron amount. Earlier works on this subject are [100, 101]. For a SH in the just cited [68] the quantity $\tau_{1,M}^{-1}(E)$ [there denoted as $\phi^{-1}(E)$] is calculated and compared with high-temperature and low-temperature approximations $\tau_1^{-1}(E)$ [there denoted as $\tau_{HE}^{-1}(E)$] and $\tau_{1,1}^{-1}(E)$ [there denoted as $\tau_{LT}^{-1}(E)$] respectively. In this work screening was ignored. For a QW the IBM electron confinement is assumed in [67] to calculate the scattering rate and compare with the high-temperature approximation result of

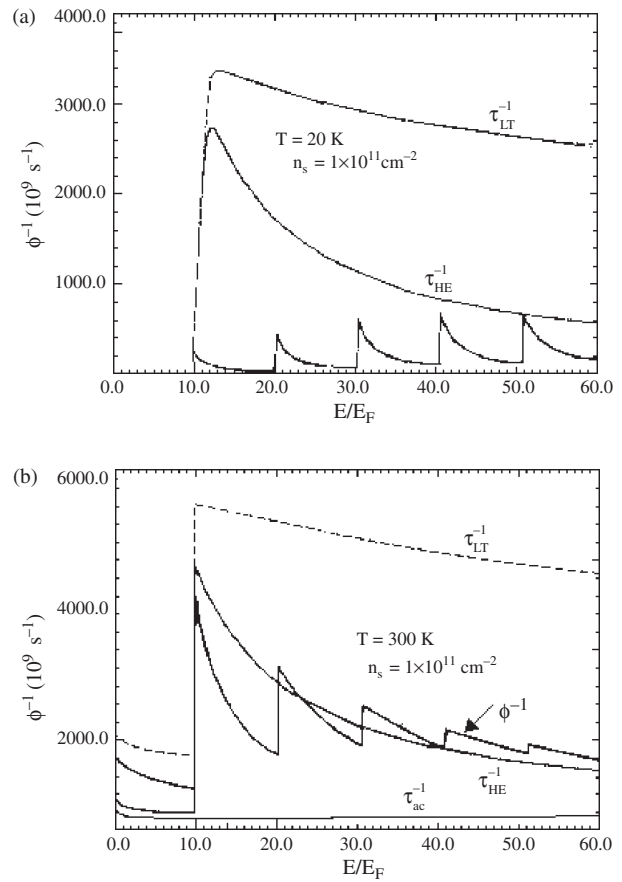


Figure 2. Numerical results for the inverse of the perturbation function $\phi^{-1}(E)$ are compared with the relaxation time obtained in the low-temperature and high-energy approximations. Reprinted with permission from [68], T. Kawamura and S. Das Sarma, *Phys. Rev. B* 45, 3612 (1992). © 1992, American Physical Society.

the momentum relaxation rate; furthermore, the effect of phonon confinement is also investigated according to a simple model which considers LO phonons completely confined to the conduction channel [57]. Similar calculations, with the same electron confinement model, but a different simple phonon confinement model, are carried out in [58]. Comparison of scattering rates and relaxation rates can be found also for QWs [98, 99]. Screening of this interaction is assumed to be small and ignored in these works, because relatively low electron concentrations are assumed. Phonon confinement is also considered in scattering rate calculations of [102], where importance of electron–interface–phonon interaction is highlighted for narrow QWs. For the widely employed material GaAs in the conduction channel of a semiconductor heterostructure, both the scattering and the momentum relaxation rates $\tau_{LT}^{-1}(E)$ and $\tau_{HE}^{-1}(E)$ due to the LO coupling are always larger than the ones due to electron–AC–phonon interaction, via DP and PE couplings together, except for energies below the LO-phonon emission threshold, as can be appreciated in Figure 2 taken from [68].

The electron–ion–impurity interaction is investigated in many works. The difference between the scattering time and the relaxation time is pointed out in [76] for a SH at zero temperature. Important results are presented in [103] for a

QW, where IBM wavefunctions and energies are employed. Analytical expressions of the momentum relaxation rate are obtained for BI and RI scatterings. Screening is ignored in this work. A detailed investigation is presented in [104] for a delta-doped semiconductor, where SEL wavefunctions and energies are employed. Scattering rates due to electron–ion-impurity interaction are calculated for two occupied subbands. Comparison of screened form factors is done when the RPA, diagonal RPA, and TFA matrix dielectric functions are used.

The IBM wavefunctions and energies for a rectangular QWI are used in [105], where also the MCA was applied to obtain analytical expressions for scattering and relaxation rates due to electron–phonon interaction via DP and LO couplings. A similar investigation with the same model is carried out in [106]. In these papers screening is disregarded. The IBM electron confinement for a cylindrical QWI is used in [107, 108] to calculate scattering rates due to acoustic phonons via DP, PE, and LO couplings. In the latter paper the static screening is taken into account by means of the RPA result for the 3D case, when only the lowest subband is occupied and intersubband transitions are ignored. According to these calculations the screening effect for optical phonons is larger than for acoustic phonons, but this may be a misleading conclusion, since a true Q1D dielectric function as well as distinction between static and dynamical screening is required for a more precise evaluation. On the other hand, LO scattering rates are larger than the AC scattering rates, as in the Q2D case in a similar temperature range.

The electron–ion-impurity interaction is investigated in many works. Analytical expressions of the relaxation rate are obtained for BI and RI scatterings in [106] for a QWI, where IBM wavefunctions and energies are employed. Screening is ignored in this work.

5.3. Low-Field Mobility

Theoretical and experimental works have been widely addressed low-field, linear, and dissipationless transport along the conduction channel. As in the case of bulk semiconductors, the usual transport coefficient to characterize the low-field regime in semiconductor nanostructures is the Ohmic or conductivity mobility μ , referred to simply as the mobility and given by

$$\sigma = en\mu \quad (122)$$

where $n = n_S$ is the areal or $n = n_L$ is the linear electron concentration in Q2D or Q1D systems respectively. Notice that the mobility is negative for electrons ($e < 0$) and positive for holes ($e > 0$); this way the conductivity is always positive. For a given subband it must be calculated as

$$\mu_\alpha = \frac{e}{m^*} \langle \tau_\alpha(E) \rangle \quad (123)$$

where

$$\langle \tau_\alpha(E) \rangle = \frac{\sum_{\mathbf{k}} E \left[-\frac{d}{dE} f_\alpha^{(0)}(E) \right] \tau_\alpha(E)}{\sum_{\mathbf{k}} f_\alpha^{(0)}(E)} \quad (124)$$

is the statistically averaged value of the quantity $\tau_\alpha(E)$, which has the meaning of relaxation time when elastic scatterings are involved but is just a time-dimension quantity when calculations involve LO-phonon scattering exclusively, in accordance with the discussion of (116). Note that for a highly degenerate electron gas, when the equilibrium distribution can be approximated by the Heaviside function, one obtains

$$\mu_\alpha \simeq \frac{e}{m^*} \tau_\alpha(E_{F\alpha}) \quad (125)$$

which means that only electrons in a very narrow neighborhood of the Fermi line, in Q2D systems, or the Fermi points, in Q1D systems, participate in charge transport.

Frequently mobility calculations are carried out in the SQL, considering that only the lowest subband is occupied and neglecting intersubband scattering, which means that everywhere one sets $\alpha = \alpha' = 1$, which works quite well for many SHs and narrow QWs or QWIs [109]. The electron concentration cannot be very high in order to ensure the Fermi level lies quite below the bottom of the first excited subband; furthermore, the thermal energy must be low enough to avoid intersubband transitions even after LO-phonon absorption processes.

For multisubband transport, according to (52), the average mobility results [21, 35]:

$$\mu = \frac{\sum_\alpha \mu_\alpha n_\alpha}{\sum_\alpha n_\alpha} \quad (126)$$

It must be pointed out that experimental determinations are carried out through Hall effect measurements, when samples are placed in a constant and uniform low magnetic field B_z perpendicular to the conduction channel. The usual quantity measured is the Hall mobility [110],

$$\mu_H = \sigma R_H = \frac{\sigma F_y}{j_x B_z} \quad (127)$$

where σ is the conductivity when no magnetic field is applied and R_H is the Hall coefficient, which in turn is determined by B_z , the Hall electric field F_y , and the current density j_x along the applied electric field. The Hall mobility is calculated according to an expression similar to (126), but where

$$\mu_\alpha^H = \frac{e}{m^*} \frac{\langle \tau_\alpha^2(E) \rangle}{\langle \tau_\alpha(E) \rangle} \quad (128)$$

The Hall ratio is defined as μ_H/μ . It varies between 1.1 and 1.4 according to several calculations for $\text{Al}_x\text{Ga}_{1-x}\text{As}/\text{GaAs}$ based heterostructures [74, 111] in the commonly found ranges of temperatures, electron concentrations, and QW widths. This ratio is expected to be in similar ranges for other materials. Therefore in the usual log–log graphics quite often-calculated mobilities are compared with measured Hall mobilities.

Mobility calculations or measurements in the low-field regime can be found in a very large number of articles, where a quite enormous amount of results are reported. An important part of these works is devoted to establishing the role of different interaction couplings in limiting the

mobility and the relevance of the screening effect. The temperature and concentration dependence, as well as the QW width, the QWI radius, or the spacer-layer thickness dependence, has been widely investigated both in theoretical and experimental works. Electron transport is investigated and bulk phonons are assumed, and the SQL approximation for calculations is justified, in the works cited; otherwise it is specially mentioned.

The most studied heterostructures are AlAs/GaAs and $\text{Al}_x\text{Ga}_{1-x}\text{As}/\text{GaAs}$, where the supplied electrons or holes are mainly confined to the gallium arsenide. These heterostructures are remarkable by their excellent matching of lattice constants at the interfaces. Pseudomorphic heterostructures, such as $\text{In}_y\text{Al}_{1-y}\text{As}/\text{In}_x\text{Ga}_{1-x}\text{As}$, where the supplied electrons or holes are mostly accumulated in the gallium indium arsenide, are often investigated. In recent years the $\text{Al}_x\text{Ga}_{1-x}\text{N}/\text{GaN}$ heterostructures, where electrons and holes are basically concentrated in the gallium nitride, have also attracted the attention of research work. A vast review of the band parameters for III–V compounds and their ternary alloys, as well as the characteristics of frequently fabricated heterostructures, can be found in a recent review [2].

Mobility has been mostly measured in $\text{Al}_x\text{Ga}_{1-x}\text{As}/\text{GaAs}$ SHs [112–118], including the highest values ever reported [10, 119], which were quoted previously. However, many mobility measurements have been carried out for lateral transport in $\text{Al}_x\text{Ga}_{1-x}\text{As}/\text{GaAs}$ based QWs and SLs [120–132] because these types of semiconductor nanostructures have at least two advantages over the SH type: they can have larger electron concentrations and the conduction channel thickness can be well defined, thus allowing the manipulation of these parameters to find the optimal values of mobility and conductivity. The $\text{Al}_x\text{Ga}_{1-x}\text{As}/\text{GaAs}$ based heterostructures are always considered in the works cited; otherwise it is explicitly indicated.

Electron–phonon interaction has attracted the attention of a lot of works. An interesting investigation is presented in [68] for a SH, with the model and approximations already mentioned in the preceding section. The relative role of acoustic phonons, via DP and PE couplings, and LO phonons can be appreciated and the main conclusion concerns the acoustic deformation potential energy, which is taken as $D_{\text{ac}} = 12$ eV after comparison of the calculated with the experimentally determined parameter α_{ac} in the well known temperature dependence,

$$\frac{1}{\mu_{\text{AC}}} = \frac{1}{\mu_0} + \alpha_{\text{ac}}T \quad (129)$$

in the range 4–40 K when the electron–LO-phonon interaction can be neglected. The piezoelectric constant is taken $h_{14} = 1.2 \times 10^7$ V/cm. A similar temperature dependence of the DP-scattering limited mobility had been obtained before for a QW with simple IBM electron confinement and equipartition approximation for phonons in some works, as in [133], where also expressions for PE-scattering limited and LO-scattering limited mobilities can be found, as well as the one when the optical deformation-potential coupling must be considered. The latter coupling was previously investigated in silicon inversion layers, as in [134]. Although the DP coupling dominates in such a weakly piezoelectric

material as GaAs, the PE coupling cannot be disregarded for accurate calculations.

A detailed study of the phonon-limited mobility is also presented in [78] for a QW, with the IBM wavefunctions and energies and the LO confinement model already employed to calculate scattering rates [67] and mobilities [32] in order to compare with results when bulk LO phonons are considered. The effect of this phonon confinement reveals as an improvement of mobility values in less than 25% for a QW width about 10 nm, but it can be considerably larger in narrow QWs. The full temperature-dependent static and dynamical screening of electron–AC-phonon and electron–LO-phonon interactions is considered by means of the RPA matrix dielectric function. The relative role of DP, PE, and LO couplings can be appreciated; mobility is mainly limited by AC phonons up to 50 K. The screening effect is important not only for electron–AC-phonon interaction, but also for electron–LO-phonon interaction, where this means an increasing of mobility values larger than 30%. The acoustic deformation potential energy is taken as $D_{\text{ac}} = 13.5$ eV and the piezoelectric constant is taken as $h_{14} = 1.44 \times 10^7$ V cm^{−1}. It must be noted that the D_{ac} exact value is quite controversial, as was indicated, but since it must be fixed from experiments it will depend on the models and approximations employed in calculations as well as on h_{14} , which in turn gives rise to further controversy, as can be seen in [68, 135]. Special attention has been paid to the PE-scattering limited mobility in [75, 136] as well as in [137], where the conclusion is drawn that this mechanism dominates over the DP scattering in CdS or ZnO, but not in GaAs, InSb, or InAs based surface layers.

Electron–ion-impurity interaction has been widely investigated. Important efforts in semiconductor heterostructures have been put in the cleanliness of the growth process for avoiding BI scattering, considered in [128, 138] for QWs to estimate its relative role in limiting the mobility. The inclusion of a spacer layer aims to reduce the RI scattering; it has been considered in many works, such as [103] and some others cited.

Mobility calculations and comparisons with their own experiments can be found in [139], where the role of the spacer layer is carefully investigated. The RI scattering is considered together with electron–phonon interaction via DP, PE, and LO couplings. FHV wavefunctions are employed and for elastic scatterings static screening is taken into account by the screening factor of [41]. The screening of the electron–LO-phonon interaction is ignored. The electron–ion-impurity interaction dominates in the low-temperature range up to 40 K, where the mobility is increased by more than an order of magnitude when the spacer-layer thickness varies from 0 through 18 nm. There is reported a maximum value $\mu = 1.5 \times 10^6$ cm² V^{−1} s^{−1} at $T = 1$ K when the spacer thickness is 30 nm. The concentration dependence of the mobility and the contribution of the different scattering mechanisms are also shown. Similar works, where theory and experiments are presented, can be found in [140] for SHs, as well as in [141–143] for QWs.

Multisubband transport in semiconductor heterostructures has been investigated in several works (e.g., in [144–146]). The IBM and the FBM electron confinement are used in [147, 148] for a MQW to calculate the RI-scattering limited

zero-temperature Hall mobility, investigate its dependence on the spacer-layer thickness, and compare with experiments of [120]. The screening effect is considered by a simple TFA dielectric function. The FHV wavefunctions are employed in [149, 150] for a SH to calculate the low-temperature mobility limited by DP, PE, BI, RI, and AL scatterings.

Two-subband calculations and comparison with their own experiments are in [88]. In this work SEL wavefunctions and energies are employed to calculate the two-subband Hall mobility limited by DP, PE, LO, BI, RI, IR, and AL scatterings. Static screening for elastic scatterings is considered in RPA approximation with the finite temperature polarizability according to the Madaugue expression, as reviewed in the section devoted to the screening of the scattering mechanisms. Calculated and measured mobilities as functions of the QW width are presented for an $\text{Al}_x\text{Ga}_{1-x}\text{As}/\text{GaAs}$ based QW and for a pseudomorphic $\text{Al}_x\text{Ga}_{1-x}\text{As}/\text{In}_y\text{Ga}_{1-y}\text{As}$ based QW. The role of the different scattering mechanisms is investigated. The IR and AL scatterings give more contributions for narrow QWs. The latter scattering is by far more important for the $\text{Al}_x\text{Ga}_{1-x}\text{As}/\text{In}_y\text{Ga}_{1-y}\text{As}$ based QW. There is a region where the mobility decreases as the QW width increases, due to the connection of intersubband scattering. This fall is more abrupt at $T = 77$ K than at $T = 300$ K due to the thermal broadening around the Fermi level, which crosses the second subband bottom for a given QW width. After this fall, the mobility increases again with the increasing QW width. In a multisubband model this feature will be repeated as many times as the number of considered subbands, but with a reduction of the fall, as the subband is higher. Such an oscillatory dependence of the measured mobility on the QW width has been reported for a $\text{Al}_x\text{Ga}_{1-x}\text{As}/\text{GaAs}$ based QW in [151].

The role of the alloy-disorder scattering depends on the extension of the envelope functions in the region where alien atoms are distributed. For instance, in a $\text{GaAs}/\text{Al}_x\text{Ga}_{1-x}\text{As}$ based heterostructure electrons are mainly confined to the GaAs material; even SEL envelope functions slightly penetrate into the barrier material and, consequently, the AL scattering play a minor role in the electron-state lifetime or in limiting the mobility. Nevertheless, it has been included in calculations of [133, 141, 142], as well as in [152], where the effects of exchange and correlations are incorporated through local field corrections of many-body effects. This estimation is also supported by mobility calculations carried out in [88, 149, 150] cited previously. However, in $\text{In}_y\text{Ga}_{1-y}\text{As}/\text{In}_z\text{Al}_{1-z}\text{As}$ or $\text{In}_y\text{Ga}_{1-y}\text{As}/\text{Al}_x\text{Ga}_{1-x}\text{As}$ based heterostructures electrons are mainly confined to the $\text{In}_y\text{Ga}_{1-y}\text{As}$ material and, regardless the chosen model for envelope functions and their penetration into the barrier material, the AL scattering plays an important role in electron-state lifetime and in limiting the mobility. This can be appreciated in [150, 153], for SHs and in [88] for QWs. Mobility calculations for $\text{In}_z\text{Al}_{1-z}\text{As}/\text{GaIn}$, $\text{Al}_x\text{Ga}_{1-x}\text{As}/\text{GaAs}$, and $\text{In}_y\text{Ga}_{1-y}\text{As}/\text{InP}$ based QWs are presented in [86], where the importance of this mechanism for narrow QWs is stressed. Similar calculations are carried out for bulk Si and for $\text{Si}/\text{Ge}_x\text{Si}_{1-x}$ in [154], where it is shown that the AL scattering reduces the mobility in an order of magnitude.

The interface-roughness scattering depends on the overlapping of the envelope function with the height of interface fluctuations (Δ_0), so it becomes quite important for narrow conduction channels. This can be clearly appreciated in mobility calculations for QWs [88] and conductivity calculations for QWIs [87]. This mechanism has been included in calculations of [155, 156]. This mechanism is also studied in $\text{In}_y\text{Ga}_{1-y}\text{As}/\text{Al}_x\text{Ga}_{1-x}\text{As}$ based QWs [157] and SHs [158], where experimental measurements are also reported. Thus, the IR scattering presents a clear dependence upon the transverse dimensions of the conduction channels.

The IBM wavefunctions and energies have been widely employed for mobility calculations in rectangular QWIs in [103, 106, 159–161] to investigate the role of BI, RI, DP, and LO scatterings. The latter mechanism is specially considered in [162]. Similar calculations can be found in [74, 137, 163] to investigate the PE scattering in an isotropic approximation. Screening is ignored in all these works. Another sort of IBM electron confinement is used for mobility calculations in cylindrical QWIs in [164, 165] to investigate the role of BI, RI, DP, PE, and LO scatterings. Static screening for a finite temperature is considered for elastic scatterings. The IR scattering is investigated in [166]. Two-subband transport is studied in [167] to investigate RI and IR scatterings. Screening is taken into account in this work by means of the diagonal approximation of the RPA matrix dielectric function; this way the inversion of an eight-index matrix is avoided. The conclusions about the relative roles of the different scattering mechanisms are similar to the ones in Q2D heterostructures. Higher mobility values could be expected if one realizes that, with respect to the Q2D systems, the new direction of quantization imposes an additional restriction to available states for electron scattering. However, comparison depends on the temperature range as well as the selected concentrations and transverse dimensions of the conduction channel.

The characteristics of different types of AlN/GaN and $\text{GaN}/\text{Al}_x\text{Ga}_{1-x}\text{N}$ based heterostructures attract the attention of research work. A special feature on this heterostructures is the possible sheet polarization at the interface depending on the crystal phase of matched materials [168]. The piezoelectric interaction plays an important role in these structures. Hall mobility measurements are presented in [169] for the usual 4–200 K temperature range and considerably high electron concentrations. The experimental values are about $\mu = 2.8 \times 10^3 \text{ cm}^2 \text{ V}^{-1} \text{ s}^{-1}$ up to $T = 80$ K for $n_s = 1.5 \times 10^{13} \text{ cm}^{-2}$, and it falls to $\mu = 0.74 \times 10^3 \text{ cm}^2 \text{ V}^{-1} \text{ s}^{-1}$ at $T = 300$ K for $n_s = 2.1 \times 10^{13} \text{ cm}^{-2}$. One of the highest values reported is $\mu = 6 \times 10^4 \text{ cm}^2 \text{ V}^{-1} \text{ s}^{-1}$ at $T = 0.05$ K for $n_s = 2.4 \times 10^{12} \text{ cm}^{-2}$ [170]. The highest Hall mobility at room temperature is reported in [171], $\mu = 2.019 \times 10^3 \text{ cm}^2 \text{ V}^{-1} \text{ s}^{-1}$ for $n_s \simeq 10^{13} \text{ cm}^{-2}$. Similar measurements are also reported for low temperatures in [172, 173], where the role of the AL scattering is investigated, and in [174], where the maximum intrinsic mobility $\mu \simeq 10^5 \text{ cm}^2 \text{ V}^{-1} \text{ s}^{-1}$ is attained. For very high temperatures, between 300 and 500 K, measured mobilities are reported in [175]. Temperature dependence is experimentally investigated in [176]. Acoustic-phonon limited mobility is calculated in the Bloch–Grüneisen regime, when the phonon population is given by (67), for a GaN based QW in [177], where the results for

the zinc blende and wurzite crystal phases are compared. Self-consistent calculations are carried out in [178] for GaN/ $\text{Al}_x\text{Ga}_{1-x}\text{N}$ and GaN/ $\text{In}_x\text{Ga}_{1-x}\text{N}$ heterostructures, where the increased IR scattering is explained by the enhanced concentration of electrons near the interfaces due to their spontaneous sheet polarization, present in different types of nitride interfaces [168].

The Si/ $\text{Si}_{1-x}\text{Ge}_x$ heterostructures are frequently investigated. The supplied electrons or holes are mainly confined to the Si or to the $\text{Si}_{1-x}\text{Ge}_x$ layers respectively. The mismatch of lattice constants is not negligible and they are known as strained layers. Transport in a silicon QW is investigated in [179], where BI, RI, and IR scatterings are considered. Mobility measurements are reported in [180–182], where high values are attained: $\mu = 1.8 \times 10^4 \text{ cm}^2 \text{ V}^{-1} \text{ s}^{-1}$ at $T = 77 \text{ K}$ and $\mu = 2.83 \times 10^3 \text{ cm}^2 \text{ V}^{-1} \text{ s}^{-1}$ at $T = 300 \text{ K}$.

Mobility calculations and comparison with their own experiment can be found in [183]. The role of the different scattering mechanisms (RI, DP, and IR) can be clearly appreciated by comparison of the calculated and measured values. For electron transport with a concentration around $n_S = 2 \times 10^{12} \text{ cm}^{-2}$ in a silicon channel of a $\text{Si}_{1-x}\text{Ge}_x/\text{Si}/\text{Si}_{1-x}\text{Ge}_x$ QW ($x = 0.38$), when the QW width is $d = 7.5 \text{ nm}$, the results are presented in Figure 3. Three regions can be observed. At very low temperatures, the RI scattering dominates, between 20 and 80 K, both RI and DP scatterings are important, and for higher temperatures, the DP scattering is the main interaction. The contribution of the interface roughness is certainly negligible. For hole transport with a concentration around $n_S = 1 \times 10^{12} \text{ cm}^{-2}$ in

the germanium channel of a $\text{Si}_{1-y}\text{Ge}_y/\text{Ge}/\text{Si}_{1-y}\text{Ge}_y$ QW ($y = 0.4$), when the QW width is $d = 7 \text{ nm}$, the results are presented in Figure 4. Note that in this case the IR scattering is dominant up to 100 K; for higher temperatures the contribution of the DP scattering is also important. Hole mobilities are also calculated in [184] and experimental results are reported in [185, 186]

Heterostructures based on II–VI binary compounds and their alloys are also investigated. In a CdS/ZnSe based QW, where electrons are in the cadmium sulfide, for a QW width of about 4 nm and a concentration $n_S = 1.5 \times 10^{13} \text{ cm}^{-2}$, the mobility does not exceed $380 \text{ cm}^2 \text{ V}^{-1} \text{ s}^{-1}$ at room temperature [187]. An experimental value of $\mu = 6 \times 10^4 \text{ cm}^2 \text{ V}^{-1} \text{ s}^{-1}$ at $T = 2 \text{ K}$ for $n_S = 3 \times 10^{11} \text{ cm}^{-2}$ is reported for a CdTe/ $\text{Cd}_{1-y}\text{Mg}_y\text{Te}$ based QW in [188].

Electron–ion impurity interaction plays the crucial role in limiting the mobility in delta-doped semiconductors, because the delta-doped layer is itself the conduction channel. This means that in these structures the BI scattering is dominant in limiting the mobility and one must expect mobilities lower than in semiconductor heterostructures. But, on the other hand, all the undesirable effects of the interfaces are suppressed, which may be an advantage for certain devices where also considerable high carrier concentrations are required.

Among the highest mobilities in a single delta-doped layer are the ones reported in [189], namely $\mu = 1.26 \times 10^4 \text{ cm}^2 \text{ V}^{-1} \text{ s}^{-1}$ at $T = 77 \text{ K}$ for $n_S = 3 \times 10^{12} \text{ cm}^{-2}$ and $\mu = 1.18 \times 10^4 \text{ cm}^2 \text{ V}^{-1} \text{ s}^{-1}$ at $T = 77 \text{ K}$ for $n_S = 6 \times 10^{12} \text{ cm}^{-2}$.

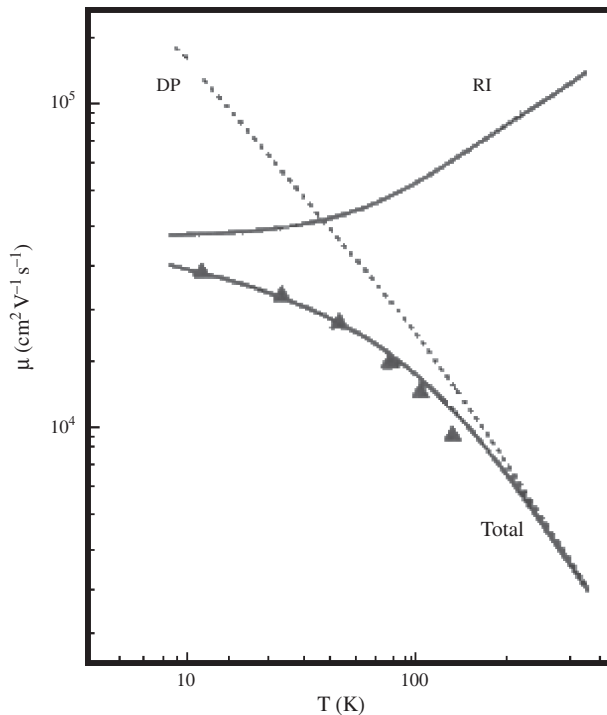


Figure 3. Comparison of mobility calculations and measured values, for electron transport with a concentration around $n_S = 2 \times 10^{12} \text{ cm}^{-2}$ in a silicon channel of a $\text{Si}_{1-x}\text{Ge}_x/\text{Si}/\text{Si}_{1-x}\text{Ge}_x$ QW ($x = 0.38$), when the QW width is $d = 7.5 \text{ nm}$. Reprinted with permission from [183], S. Madhavi et al., *Phys. Rev. B* 61, 16807 (2000). © 2000, American Physical Society.

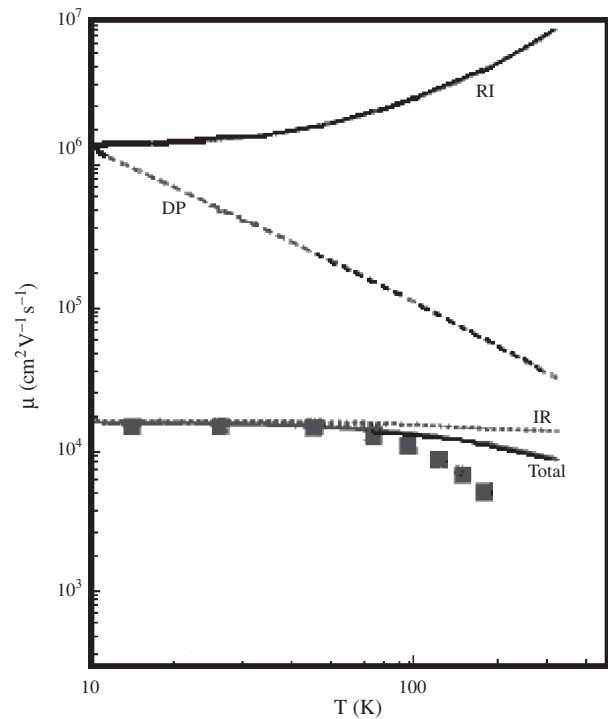


Figure 4. Comparison of mobility calculations and measured values, for hole transport with a concentration around $n_S = 1 \times 10^{12} \text{ cm}^{-2}$ in the germanium channel of a $\text{Si}_{1-y}\text{Ge}_y/\text{Ge}/\text{Si}_{1-y}\text{Ge}_y$ QW ($y = 0.4$), when the QW width is $d = 7 \text{ nm}$. Reprinted with permission from [183], S. Madhavi et al., *Phys. Rev. B* 61, 16807 (2000). © 2000, American Physical Society.

In this work the mobility in a double delta-doped layer is also investigated as a function of the interlayer distance d . For $d = 14.4$ nm a peak mobility $\mu \simeq 1.00 \times 10^4$ cm² V⁻¹ s⁻¹ at $T = 77$ K is observed, but it is lower than the corresponding value in the single delta-doped sample for the similar concentration $n_s = 6 \times 10^{12}$ cm⁻². Experimental results in single, double, and triple delta-doped semiconductors are also reported in [190–192].

A detailed investigation is presented in [193] for this type of Q2D system, where SEL wavefunctions and energies are employed. The BI-scattering limited mobility at zero temperature is calculated for two occupied subbands and the influence of the static screening through the RPA matrix dielectric function is investigated when up to three empty subbands are taken into account. Comparison between the so-called quantum [$\tau_\alpha^s(\mathbf{k})$ is placed in (123) instead of the relaxation time] and transport mobilities is done. Results are in good agreement with experimental data of [194]. Similar calculations, with the same model and approximations, are carried out in [104], where they compare the calculated mobilities when the Thomas–Fermi approximation, the diagonal RPA, or properly RPA matrix dielectric functions are employed. Other mobility calculations in delta-doped semiconductors can be found in [170, 195, 196]. Multisubband calculations, with up to three coupled BTEs, are carried out in [83], where the effect of nonparabolicity is investigated.

The intentionally delta-doped QWs, inside and outside the conduction channel, have also been investigated, since due to the band offsets at the interfaces the extra confinement makes a wider conduction channel or parallel channels, which in principle allows one to have higher concentrations. For instance, a delta-doped channel is fabricated in the barrier of a GaAs/In_yGa_{1-y}As/GaAs QW [85], where mobilities are reported, namely $\mu = 3.3 \times 10^4$ cm² V⁻¹ s⁻¹ at $T = 77$ K and $\mu = 0.55 \times 10^4$ cm² V⁻¹ s⁻¹ at $T = 77$ K for $y = 0.37$. The inclusion of the delta-doped channel inside a QW is most expanded. A GaAs based QW is fabricated with an additional delta-doped channel in the center [81]. Quantum and transport mobilities in such a structure are calculated in [82] including several subbands. Mobility measurements and the concentration dependence are reported at liquid helium temperature in [84], where a GaAs/In_yGa_{1-y}As/Al_xGa_{1-x}As QW is delta doped in the center.

6. HIGH-FIELD TRANSPORT

A nonlinear response of the system to the applied electric field is difficult to investigate bulk materials but has attracted attention in semiconductor nanostructures. Particularly, the size reduction in MOSFETs and MODFETs has to do with the conduction channel or gate length too, varying from a fraction up to several micrometers [7]. This does not lead to QSEs but makes possible the realization of very high electric fields. For instance, applying a gate voltage of 1 V along a conduction channel of length 0.25 μm gives a field strength of 40 kV cm⁻¹, which is a factor of 100 greater than the typical fields to produce hot electrons in bulk materials at room temperature, as stated in an important review on hot electrons presented in [80].

One can talk about high-field transport when a nonlinear dependence between the current density and the applied electric field is found experimentally, that is,

$$\mathbf{j} = \sigma(F)\mathbf{F} \quad \text{with } F = |\mathbf{F}| \quad (130)$$

where the conductivity $\sigma(F) \neq \text{const}$ depends on the module of applied electric field, its strength, for the properties of semiconductor nanostructures are assumed isotropic, except of course when the sample is placed in an external magnetic field. In this case the average electron energy is quite larger than the average energies of phonons, which are considered in thermal equilibrium at temperature T ; therefore they are known as hot electrons. In this regime the energy transfer from the electron system to the phonon system has to be carefully considered.

Hot electrons are involved not only in the nonlinear dependence between the current density and the applied electric field (130), but also in the saturation of the current values and in the NDR. The latter is connected to the negative differential conductivity,

$$\frac{dj}{dF} = \sigma(F) + F \frac{d\sigma}{dF} < 0 \quad (131)$$

and it can also be understood in terms of the negative differential mobility,

$$\frac{dv_d}{dF} = \mu(F) + F \frac{d\mu}{dF} < 0 \quad (132)$$

because this is the form usually established in experiments [90, 91]. Several mechanisms, such as intervalley transitions, real space electron transfer from the well to the barrier, randomization of energy distribution below the LO phonon threshold, electron capture, presumably by the so-called DX centers, and others are invoked to explain this characteristic of hot-electron transport. It must be noted that in some situations the stability of the regime is broken and oscillations of the current density appear for a fixed field, even when strength values are not so high [197]. The NDR and the regime instabilities are reviewed in [80].

6.1. Hot-Electron Distribution Functions

Studying the steady-state transport one could add a quadratic in F term $f_\alpha^{(2)}(\mathbf{k})$ to the expression for the low-field transport (104) to find the perturbation to the equilibrium distribution function. Particularly in Q2D systems, this could be also understood as the development of $f_\alpha(\mathbf{k})$ in Legendre polynomials up to the third term [198]. But this would lead to a rather complicated system of BTEs, and no effort has been made in this line. Approximate analytical solutions have been found in several works. A zero-lattice-temperature approximation for a 2D system can be found in [199]. Two coupled BTEs for a Q2D system have been solved in [200]. Analytical solutions are also given for Q1D systems in [201, 202]. All these solutions depend on the different approximations to solve the system of BTEs, in contrast with the low-field case, when the linear in F form (105) is a general approximation.

Based on physical grounds, the so-called thermal model is usually employed to avoid the problem of solving a system of integral–differential equations. One assumes that the randomization of momenta and energies due to electron–electron (e – e) interaction occurs very much faster than the energy transfer due to electron–phonon (e – p) interaction, a subject that even recently attracted the attention of some investigations [203, 204]. This amounts to considering that the carrier system is internally in equilibrium at an electron temperature T_e larger than the phonon temperature T . Two different situations are distinguished. First, when momenta are randomized faster than energies ($\tau_\alpha^{M(e-e)} < \tau_\alpha^{E(e-e)} \ll \tau_\alpha^{E(e-p)}$), one has an equilibrium distribution function with the electron temperature

$$f_\alpha(\mathbf{k}) = f_\alpha^{(e)}(E) = \frac{1}{\exp[\beta_e(E - E_{F\alpha})] + 1} \quad (133)$$

and, second, when energies are randomized faster than momenta ($\tau_\alpha^{E(e-e)} < \tau_\alpha^{M(e-e)} \ll \tau_\alpha^{E(e-p)}$), one has a shifted equilibrium distribution function with the electron temperature

$$f_\alpha(\mathbf{k}) = f_\alpha^{(e)}(E_d) = \frac{1}{\exp[\beta_e(E_d - E_{F\alpha})] + 1} \quad (134)$$

where

$$\beta_e = \frac{1}{k_B T_e} \quad \text{and} \quad E_d = \frac{1}{2} m^* (\mathbf{v} - \mathbf{v}_d)^2 \quad (135)$$

The electron temperature can be determined experimentally by different procedures, such as the Shubnikov–de Haas method employed in [15, 205] or the mobility comparison method described in [169].

The thermal model has been widely employed both for Q2D and Q1D carrier systems, but in the latter case there is a conflict when calculations are carried out in the SQL approximation. Really, when only the lowest subband is populated and intersubband transitions are disregarded, electron–electron scattering only leads to exchange of momentum and energy between carriers, which are identical particles; this way no randomization can be achieved and the use of the thermal model is inadequate. Therefore, in this particular case it is strictly necessary to solve the remaining BTE [201]. A series of articles has been devoted to this subject [206–208] and the resulting theory can be found in [202].

6.2. Hot-Electron Mobility

Many works have been devoted to high-field, nonlinear, and dissipative transport along the conduction channel. The usual transport coefficients to characterize the high-field regime in semiconductor nanostructures, as in the case of bulk semiconductors, are the field-dependent mobility $\mu(F)$ and the energy loss rate or power loss $P(F)$. It is to the point to remark that the interest in hot-electron transport is motivated for investigating not only the QSEs in the high-field regime, but also the device performance when its gate

voltages and sizes inevitably involve hot electrons. The hot-electron mobility is given by

$$\sigma(F) = en\mu(F) \quad (136)$$

where $n = n_s$ is the areal or $n = n_L$ is the linear electron concentration in Q2D or Q1D systems respectively. For a given subband it must be calculated as

$$\mu_\alpha(F) = \frac{1}{F} \left(\frac{2}{m^*} \right)^{1/2} \frac{\sum_{\mathbf{k}} E^{1/2} \cos \vartheta f_\alpha(\mathbf{k})}{\sum_{\mathbf{k}} f_\alpha(\mathbf{k})} \quad (137)$$

where ϑ is the angle between \mathbf{k} and \mathbf{F} . In the frame of the thermal model $f_\alpha(\mathbf{k})$ is given by (133) or (134), but it has been also found by solving the BTEs in different approximations, than the ones cited.

Note that the drift velocity is $v_d(F) = \mu(F)F$, where according to (52) the field-dependent hot-electron mobility results:

$$\mu(F) = \frac{\sum_\alpha \mu_\alpha(F) n_\alpha}{\sum_\alpha n_\alpha} \quad (138)$$

One can find an enormous amount of articles concerning the high-field transport regime. An important part of these works is devoted to establishing the role of different interaction couplings in limiting the mobility, including the relevance of the screening effect. The electric field and concentration dependence, as well as the QW-width dependence, have been widely investigated both in theoretical and experimental works. Bulk phonons are always considered in the works cited; otherwise it is specially remarked.

Very often theoretical calculations and experimental measurements give the drift velocity instead the hot-electron mobility, since the former is closer to the final interesting result: the response speed of the transistor device. The drift velocity is calculated and measured for an $\text{Al}_x\text{Ga}_{1-x}\text{As}/\text{GaAs}$ based semiconductor heterostructure in [209]. Balance equations in a two-subband model are solved to calculate the drift velocity limited by background impurities (BI), acoustic phonons, via DP and PE couplings, as well as confined LO phonons, and comparison with their own experiment is presented in [210]. Experimental drift velocity values are given in [91], where uniformly doped and delta-doped QWs are investigated, for a typical QW width $a = 10$ nm and a lattice temperature $T = 77$ K, and it is stressed that the electron–impurity interaction becomes significantly smaller for hot electrons than for electrons in thermal equilibrium with the lattice. Saturation of the drift velocity with the increasing electric field is due to the LO-phonon scattering, because the population of hot electrons with energies larger than the LO-phonon threshold is considerably enhanced. A further increase of the electric-field strength even leads to a decrease of the drift velocity, in a region with negative differential mobility (i.e., a region with NDR).

Hall hot-electron mobility and Hall ratio are calculated for $\text{In}_x\text{Ga}_{1-x}\text{As}$ based QWs in [211], where the idea of the iterative procedure to calculate the perturbation to the distribution function is applied, but starting with the zero-iteration value as the equilibrium distribution function with an electron temperature T_e . The IBM wavefunctions are assumed. Screened electron interaction with acoustic

phonons, via DP coupling, ion impurities, namely BI scattering, and alloy disorder scattering are taken into account. For typical QW width $a = 10$ nm, electron concentration $n_s = 6 \times 10^{11} \text{ cm}^{-2}$, and electric field $F = 500 \text{ V cm}^{-1}$, the Hall mobility decreases from 3.8 to $2.2 \times 10^4 \text{ cm}^2 \text{ V}^{-1} \text{ s}^{-1}$ with the increasing lattice temperature from 4 to 15 K, when the external magnetic field is kept between $B = 0.001$ T and $B = 0.01$ T. The Hall ratio does not exceed 1.02 when the former magnetic field is applied.

Multisubband calculations for GaN based QWs are reported in [212] considering electron scattering by acoustic phonons, via DP and PE couplings, as well as by LO phonons. Some approximations lead to an analytical solution of the system of BTEs and hot-electron mobility and mean energy are numerically calculated for several QW widths and plotted as functions of the applied electric field. These quantities are always smaller than the bulk values and in the limit of a very large number of occupied subbands they approach the 3D values.

Drift velocity measurements in GaN/Al_xGa_{1-x}N based heterostructures are presented in [169] for electric fields ranging from several through 10 kV cm^{-1} at $T = 77$ K, as illustrated in Figure 5. The linear dependence is observed up to $F = 1.2 \text{ kV cm}^{-1}$. The saturation value $v_d = 1 \times 10^7 \text{ cm s}^{-1}$ is reached around $F = 7.5 \text{ kV cm}^{-1}$. The NDR is not observed. Hall mobilities are measured as function of the gate voltage (proportional to the electric field) in [213], where the linear, saturation, and NDR regions are clearly observed.

Experiments are carried out for Si_{1-x}Ge_x/Si and Si_{1-y}Ge_y/Ge based QWs in [183]. Measured hot-electron mobility as

a function of the applied electric field of the same silicon channel in the QW of Figure 3, where low-field mobility is displayed, is presented for different lattice temperatures in Figure 6, as reported in [183]. Note that the mobility remains constant, at its low-field value, until the electric field reaches a critical value, beyond which it decreases with increasing electric field. This critical value depends on the lattice temperature. It is around 3 V/cm at $T = 13$ K and around 30 V/cm at $T = 100$ K. Measured high-field hole mobility as a function of the applied electric field of the same germanium channel in the QW of Figure 4, where low-field mobility is displayed, is presented for different lattice temperatures in Figure 7, as reported in [183]. Similar comments as in the case of hot electrons can be understood. The critical values are between 80 and 100 V/cm for temperatures between 13 and 75 K. Notice that the hole mobility decreases faster than the electron mobility.

Several subbands are included in Monte Carlo calculations of hot electron mobility carried out in [214] for rectangular QWs and cylindrical QWIs, where IBM wavefunctions and energies are employed to investigate the role of dimensionality in the results by comparison with the 3D case. The thermal model is assumed for the electron gas. The electron-phonon interaction is considered through the DP, PE, and LO couplings as well as through the nonpolar optical coupling. Screening is also included. The bulk, areal, and linear electron concentrations are related as $n_B = n_s d = n_L \pi \frac{1}{4} d^2$, where d is the confinement length, in order to establish the adequate comparison. Thus, for instance, at a lattice temperature $T = 10$ K the low-field Q2D and Q1D mobilities oscillate around the 3D in a wide range of d , while the high-field Q2D and Q1D mobilities present few

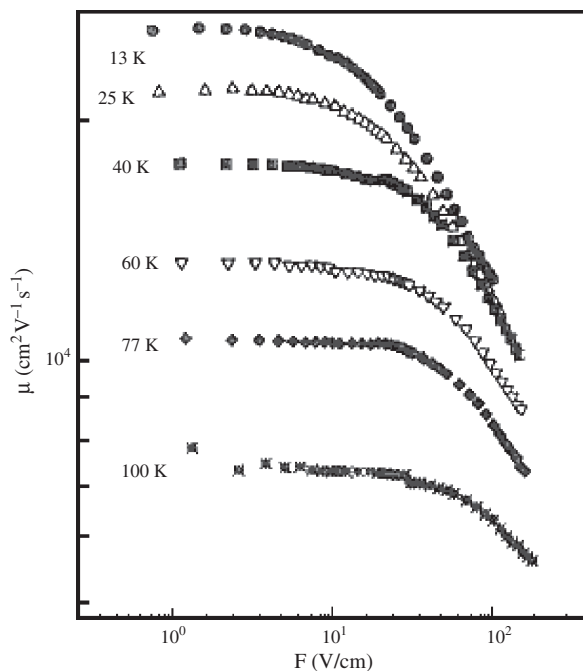


Figure 5. Drift velocity measurements in GaN/Al_xGa_{1-x}N based heterostructures for electric fields ranging from several through 10 kV cm^{-1} at $T = 77$ K. Reprinted with permission from [169], N. Balkan et al., *J. Phys. Condens. Matter* 14, 3457 (2002). © 2002, IOP Publishing.

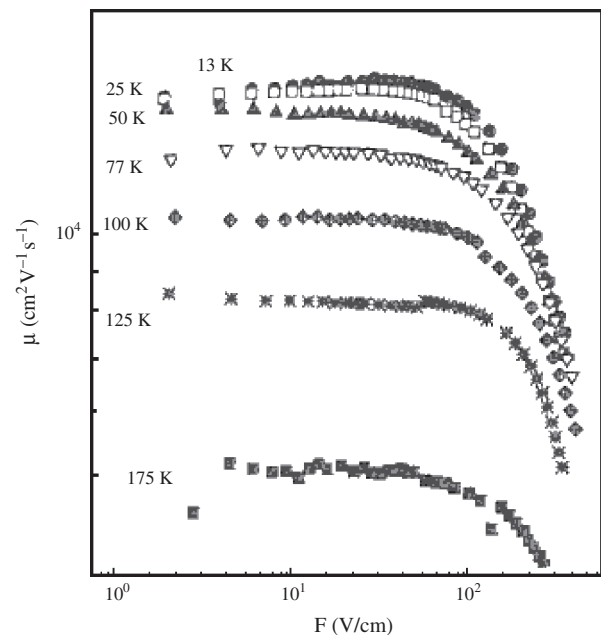


Figure 6. Measured hot-electron mobility as a function of the applied electric field of the same silicon channel in the QW of Figure 3, where low-field mobility is displayed, for different lattice temperatures. Reprinted with permission from [183], S. Madhavi et al., *Phys. Rev. B* 61, 16807 (2000). © 2000, IOP Publishing.

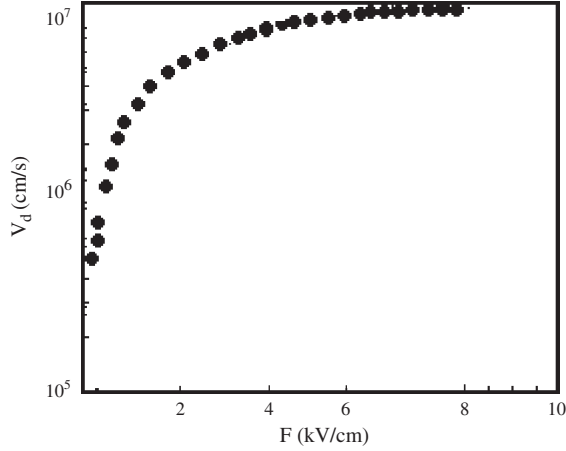


Figure 7. Measured high-field hole mobility as a function of the applied electric field of the same germanium channel in the QW of Figure 4, where low-field mobility is displayed, for different lattice temperatures. Reprinted with permission from [183], S. Madhavi et al., *Phys. Rev. B* 61, 16807 (2000). © 2000, IOP Publishing.

oscillations but are lower than the 3D values, in the same range of d , except around 220 nm, where the Q1D values exceed the 3D ones.

Hot-electron mobility and average electron energy are calculated in [201] for a cylindrical QWI, where IBM wavefunctions and energies are employed. The electron–phonon interaction is considered through the LO couplings. Screening is ignored. The most interesting feature of this work is the discussion of the nonergodicity of the electron system when the SQL approximation is justified. Therefore, the BTE is solved with some approximations. Similar calculations are also carried out in [202] for cylindrical QWIs, basically with the same model, but including the electron–phonon interaction through the DP and LO couplings and the IR scattering. Screening is also ignored. The most interesting feature of this work is the detailed discussion of the solution of the BTE to find the distribution function, since the thermal model is inadequate in this case, and the inclusion of the acoustic phonons, which plays an important role when electron energies do not reach the LO phonon emission threshold.

Drift velocity is experimentally investigated in QWIs fabricated on SHs using laser or electron beam lithography [4]. Saturation of the measured values with the increasing electric field is observed as in the Q2D cases. The second confinement direction in such systems is small enough to have electrons only in the corresponding lowest subband, which cannot reach the first excited subband. Monte Carlo calculations in such kinds of systems are presented in [215], where DP and PE scatterings are included, as well as interface and confined LO-phonon scattering and the role of an applied magnetic field is studied.

The ion-impurity scattering plays a minor role in high-field transport, since as hot-electron energy increases this interaction is weakened and has no effect in limiting the mobility. Hot-electron mobility is basically limited by phonon, alloy-disorder, and interface-roughness scatterings. The contribution of each mechanism depends on the

material, conduction channel dimensions, and experimental conditions. The critical field beyond which the low-field transport regime is broken also depends on the material and experimental conditions.

6.3. Power Loss

In semiconductor nanostructures the dissipation of energy is easier than in bulk materials, because this energy transfer takes place in a small fraction of the total volume of the sample or device. It can be understood that hot-electron experiments in semiconductor nanostructures would have been impossible in bulk materials because of the Joule heating. The hot electrons confined to the conduction channel lose their energies by the interaction with phonons, since the other scattering mechanism bears an elastic character.

The energy-loss rate or power loss is also calculated for a given subband α as

$$P_\alpha(F) = \left\langle -\frac{d}{dt} E_\alpha(\mathbf{k}) \right\rangle = \frac{\sum_{\mathbf{k}} \left[-\frac{d}{dt} E_\alpha(\mathbf{k}) \right] f_\alpha(\mathbf{k})}{\sum_{\mathbf{k}} f_\alpha(\mathbf{k})} \quad (139)$$

and according to (53) one can define the mean power loss as

$$P(F) = \frac{\sum_\alpha P_\alpha(F) n_\alpha}{\sum_\alpha n_\alpha} \quad (140)$$

Power loss is due to both electron–AC-phonon and electron–LO-phonon interactions exclusively. Therefore the energy loss rate per electron can be calculated as

$$-\frac{d}{dt} E_\alpha(\mathbf{k}) = \sum_{\text{PH}} \left\{ \left[-\frac{d}{dt} E_\alpha(\mathbf{k}) \right]_{\text{PH}-} - \left[-\frac{d}{dt} E_\alpha(\mathbf{k}) \right]_{\text{PH}+} \right\} \quad (141)$$

where formally PH = DP, PE, LO. For each scattering mechanism the absorbed (+) and emitted (–) energy rates are

$$\begin{aligned} \left[-\frac{d}{dt} E_\alpha(\mathbf{k}) \right]_{\text{PH}\pm} &= \frac{2\pi}{\hbar} \sum_{\alpha', j, \mathbf{Q}} |V_{j\alpha\alpha'}^{\text{PH}\pm}(\mathbf{k}, \mathbf{k}'; \mathbf{Q})|_{\text{av}}^2 \\ &\quad \times \hbar\omega_{j\mathbf{Q}} [1 - f_{\alpha'}(\mathbf{k}')] \delta[E_\alpha(\mathbf{k}) \\ &\quad - E_{\alpha'}(\mathbf{k}') \pm \hbar\omega_{j\mathbf{Q}}] \end{aligned} \quad (142)$$

When the strength of the applied electric field is not so large, most of the electrons are heated up to energies lower than the LO-phonon energy threshold and they are unable to emit this kind of phonon. This case is often referred to as the warm-electron transport regime and AC phonons are responsible for energy loss.

Theoretical calculations and experimental measurements of power loss can be found in a large number of articles concerning the high-field transport regime. An important part of these works is devoted to establishing the role of different kinds of phonons in the energy loss of the hot-electron system, including the relevance of the screening effect. The electric field and concentration dependence, as well as the QW-width dependence, have been widely investigated both in theoretical and experimental works. Bulk phonons and $\text{Al}_x\text{Ga}_{1-x}\text{As}/\text{GaAs}$ based semiconductor

heterostructures are always considered in the works cited; otherwise it is specially remarked.

Power loss calculations are as a rule carried out with the thermal model for the hot-electron distribution function. Assuming the IBM wavefunctions for electrons, the relative role of DP and LO couplings is investigated in [26, 61], where the phonon confinement is taken into account according to [57, 64]; their results are in good agreement with the experiment of [216].

Power loss has been experimentally determined in $\text{Al}_x\text{Ga}_{1-x}\text{As}/\text{GaAs}$ based semiconductor heterostructures both in SHs [205, 217] and QWs [140, 169, 209, 216, 218] in general by a combination of photoluminescence and Shubnikov–de Haas measurements.

When the plot of $\log P$ vs T_e^{-1} reveals a linear dependence for high electron temperatures, it is explained by nondegeneration of the hot electron gas and the main contribution of the LO-phonon scattering to the energy transfer, which must lead to [80]

$$P = \frac{\hbar\omega_{\text{LO}}}{\tau^E} \left[\exp\left(-\frac{\hbar\omega_{\text{LO}}}{k_B T_e}\right) - \exp\left(-\frac{\hbar\omega_{\text{LO}}}{k_B T}\right) \right] \quad (143)$$

where τ^E is the energy relaxation time and T is the lattice temperature. This electron-temperature dependence is found experimentally in [209, 216], although in their explanations they do not include the lattice-temperature dependence.

In connection with the energy relaxation some comments are to the point. When the electron gas is heated by laser pulses in QWs the energy relaxation can be reached as fast as in 60–200 fs [219–221]. But anomalously slow energy relaxation, after 2 ps for an areal concentration of $5 \times 10^{11} \text{ cm}^{-2}$, can be found when electron gas is heated by an electric field [218]. This is attributed to hot phonons (i.e., to an enhanced population of phonons with respect to the one corresponding to the equilibrium distribution at the lattice temperature). In this case an effective energy relaxation time, which takes into account the finite lifetime of phonons (they can decay into two acoustic phonons via the anharmonic interaction), must be set in (143), as indicated in [80]. However, for lower electron concentrations the energy relaxation time is about 100 fs [80]. This suggests that the hot-phonon effects are connected not only with the high-applied fields, but also with high electron concentrations, which are attained in low-dimensional systems in quite a number of experimental situations.

On the other hand, for low temperatures and degenerate or nondegenerate hot electron gas, electron–AC-phonon interaction dominates and the dependence is given by [80]

$$P \propto (T_e^n - T^n) \quad (144)$$

with $n = 5$ for DP coupling, while $n = 3$ for PE coupling. Thus, for instance, $n = 3$ to fit the measurements reported in [205, 217] for a $\text{Al}_x\text{Ga}_{1-x}\text{As}/\text{GaAs}$ SH and in [15] for a $\text{In}_y\text{Al}_{1-y}\text{As}/\text{In}_x\text{Ga}_{1-x}\text{As}$ based QW, which indicates that the PE scattering dominates the energy loss. Nevertheless, to fit measurements at $T = 0.28 \text{ K}$ reported in [140] for a $\text{Al}_x\text{Ga}_{1-x}\text{As}/\text{GaAs}$ based QW, $n = 3$ or $n = 4$ depending on the electron concentration and the electron temperature region. In this work the role of the PE scattering is stressed.

Power-loss measurements and comparison with a two-subband theory are presented in [15] for a $\text{In}_x\text{Ga}_{1-x}\text{As}/\text{In}_y\text{Al}_{1-y}\text{As}$ SH, as illustrated in Figure 8. They agree that $n = 5$ for DP coupling and $n = 3$ for PE coupling when screening can be ignored. But they found that $n = 7$ for heavily screened DP coupling. They also compare with the 3D power loss calculated according to another expression taken from [80], the dashed line in the figure, and it can be noticed that the first-subband results are very similar, but the second-subband results are quite different.

Recently power-loss measurements in $\text{GaN}/\text{Al}_x\text{Ga}_{1-x}\text{N}$ based heterostructures are presented in [222] for low electron temperatures, when the PE scattering is considered to be the mechanism that dominates the electron–AC-phonon interaction. It is also reported in [169] for electron temperatures ranging from several through a few hundreds degrees at lattice temperature $T = 77 \text{ K}$, as illustrated in Figure 9. The exponential dependence (143) is maintained when $160 < T < 190 \text{ K}$, indicating the prevalence of the LO-phonon scattering. At lower electron temperatures acoustic phonons are to be taken into account, and at higher temperatures the hot-phonon effect becomes important.

Hole power loss is investigated in a $\text{Si}/\text{Si}_x\text{Ge}_{1-x}$ based SH in [223] for very low temperatures. It is argued that the unscreening DP scattering dominates with a deformation potential value $D_{\text{ac}} = 3.0 \pm 0.4 \text{ eV}$.

For Q1D semiconductor nanostructures the power loss depends upon the electron temperature as in (143), when LO phonons give the main contribution, as in (144), when acoustic phonons give the main contribution. The difference with respect to the Q2D case is in the constant coefficients, which includes the confinement length or section areas.

Several subbands are included in calculations of power loss carried out in [214, 224] for rectangular QWs and cylindrical QWIs, with the same approach employed in hot-electron mobility calculations quoted in the preceding subsection. At $T = 4 \text{ K}$ the Q2D and Q1D power loss values oscillate around the 3D values in a range from 0.2 to

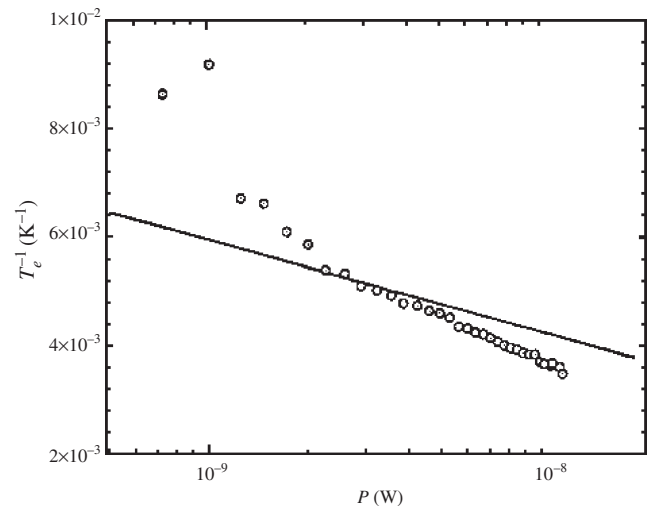


Figure 8. Power-loss measurements and comparison with a two-subband theory are presented for an $\text{In}_x\text{Ga}_{1-x}\text{As}/\text{In}_y\text{Al}_{1-y}\text{As}$ SH. Reprinted with permission from [15], E. Tiras et al., *Phys. Rev. B* 64, 085301 (2001). © 2001, American Physical Society.

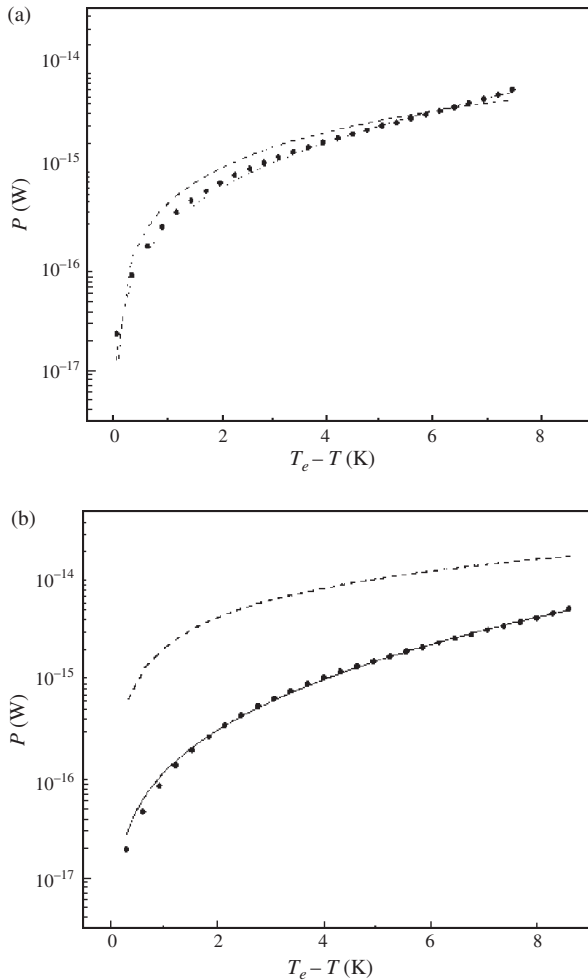


Figure 9. Power-loss measurements in GaN/Al_xGa_{1-x}N based heterostructures for (a) low electron temperatures, (b) electron temperatures ranging from several through a few hundreds degrees at lattice temperature $T = 77$ K. (a) Reprinted with permission from [222], K. J. Lee et al., *Appl. Phys. Lett.* 78, 2893 (2001). © 2001, American Physical Society. (b) Reprinted with permission from [169], N. Balkan et al., *J. Phys. Condens. Matter* 14, 3457 (2002). © 2002, IOP Publishing.

$2 \times 10^{17} \text{ cm}^{-3}$. The electron temperature dependence of the power loss is quite similar in the three cases; nevertheless, the Q1D values are much higher specially when the optical phonons begin to contribute, since the threshold for optical phonon emission is reached first in Q1D case than in the Q2D or 3D cases.

Following the idea of [202] power loss is calculated for a rectangular QWI in [225], where IBM electron confinement is assumed. Nonscreened electron–phonon interaction through the DP and LO couplings are considered for relatively low electron concentrations. Comparison between thermal and nonthermal model calculations (i.e., those accomplished after solving the BTE) makes apparent that the use of the former results in an overestimation of power loss in such Q1D systems. Furthermore, with smaller cross-section area the power loss is lower, in contrast with the results obtained with the thermal model. The latter has been also assumed in several power loss calculations, in the frame of a MBT formalism, as in [226], where bulk LO phonons

were considered, as well as in [227, 228], where the confinement LO-phonon effect was investigated.

7. SCREENING OF THE SCATTERING MECHANISMS

Studying the transport phenomena in semiconductor nanostructures one deals with a Q2D or Q1D electron gas, which is put out of equilibrium by an external agent in the presence of various scattering mechanisms, which in turn are responsible for the randomization of momenta and energy once that external agent is switched off. These very scattering mechanisms are also responsible for local fluctuations of the values associated with the equilibrium state (e.g., the uniform electron concentration), which makes necessary a reconsideration of the scattering mechanisms themselves. Local fluctuations of electron concentration give rise to the screening of the interaction, which causes the scattering from an electron state into another. In a frame of a linear response theory the screening effect is usually taken into account by means of a screening factor or a matrix dielectric function, which can be derived in different approximations. Among the earlier works on this subject one can find a certain screening factor derived following a modified Debye model [41], which has been widely employed in calculations, such as in [88]. The TFA and the RPA are widely treated [21, 35, 144, 198]. Nevertheless, the RPA result has proven to be very adequate to fit experiments, as in [68, 142, 229].

7.1. RPA Matrix Dielectric Function: Self-consistent Field Approach

The self-consistent field approach to derivative the matrix dielectric function for a semiconductor nanostructure follows the method employed in [230] for a QW and in [231] for a QWI, which is essentially the one for 3D systems and seems quite easy to be understood. The starting point to derive the influence of the electron concentration fluctuations, around its uniform value, on the given scattering mechanism is that each interaction coupling must be considered as a local perturbation to the unperturbed electron Hamiltonian. Thus, when only one scattering mechanism is considered the perturbed electron Hamiltonian reads

$$\widehat{H}(\mathbf{r}, \boldsymbol{\rho}; t) = \widehat{H}_0 + \widehat{V}(\mathbf{r}, \boldsymbol{\rho}; t) \quad (145)$$

with \widehat{H}_0 the unperturbed electron Hamiltonian (4) and $\widehat{V}(\mathbf{r}, \boldsymbol{\rho}; t)$ the local perturbation, with the subscript CP indicating a given interaction coupling (formally CP = DP, PE, BI, RI, IR, AL) omitted for brevity. The latter must be understood as

$$\widehat{V}(\mathbf{r}, \boldsymbol{\rho}; t) = \widehat{V}(\mathbf{r}, \boldsymbol{\rho}) \exp[-i(\omega + i\delta)t] \quad (146)$$

with $\delta \rightarrow +0$ (after making $t \rightarrow -\infty$) for adiabatic connection (i.e., the perturbation is switched on quite slowly to keep the thermodynamical equilibrium in the system, although it will give rise to local fluctuations of physical quantities). Here ω is the scattering field frequency.

The fundamental assumption for the self-consistent field derivation of the matrix dielectric function consists in taking the perturbation as the screened scattering potential, that is,

$$\widehat{V}(\mathbf{r}, \boldsymbol{\rho}; t) = \widehat{V}_0(\mathbf{r}, \boldsymbol{\rho}; t) + \widehat{V}_1(\mathbf{r}, \boldsymbol{\rho}; t) \quad (147)$$

where $\widehat{V}_0(\mathbf{r}, \boldsymbol{\rho}; t)$ is the bare scattering potential (bare perturbation), corresponding to the considered interaction coupling, and $\widehat{V}_1(\mathbf{r}, \boldsymbol{\rho}; t)$ is the screening potential (induced perturbation). This induced perturbation as a rule reduces the effect of the external perturbation; although in some cases “antiscreening” effects are reported, as in [232]. For elastic scatterings, such as electron–acoustic-phonon interaction (CP = DP, PE), electron–ion impurity interaction (CP = BI, RI), alloy, and interface roughness scatterings (CP = AL, IR) one must set $\omega = 0$, while for an inelastic scattering, such as electron–optical-phonon interaction (CP = LO), one must keep $\omega \neq 0$.

Some basic definitions must now be noted. The density matrix operator for a mixed state of a quantum system is defined as

$$\hat{\rho}(\mathbf{r}, \boldsymbol{\rho}; t) = \sum_{\alpha, \mathbf{k}} |\alpha, \mathbf{k}\rangle f_{\alpha}(\mathbf{k}, \mathbf{r}, \boldsymbol{\rho}; t) \langle \mathbf{k}, \alpha| \quad (148)$$

where $f_{\alpha}(\mathbf{k}, \mathbf{r}, \boldsymbol{\rho}; t)$ is the probability of occupation of state $|\alpha, \mathbf{k}\rangle$. On the other hand, for a thermodynamical system, when the number of particles does not change, in the canonical ensemble the statistical operator is given by

$$\hat{\rho}(\mathbf{r}, \boldsymbol{\rho}; t) = \exp\{\beta[\Omega - \widehat{H}(\mathbf{r}, \boldsymbol{\rho}; t)]\} \quad (149)$$

where Ω is the thermodynamical potential. According to the ergodic principle the statistical average value of any operator \widehat{A} is calculated as

$$\begin{aligned} \langle \widehat{A} \rangle &= \text{Tr}\{\hat{\rho}(\mathbf{r}, \boldsymbol{\rho}; t)\widehat{A}\} \\ &= \sum_{\alpha, \mathbf{k}} \langle \mathbf{k}, \alpha | \hat{\rho}(\mathbf{r}, \boldsymbol{\rho}; t) \widehat{A} | \alpha, \mathbf{k} \rangle \end{aligned} \quad (150)$$

where $\hat{\rho}$ is given indistinctly by (148) or (149).

For the low-dimensional system under consideration, the unperturbed statistical operator is given by

$$\hat{\rho}_0 = \exp\{\beta[\Omega - \widehat{H}_0]\} \quad (151)$$

and, as can be easily understood, for equilibrium nonperturbed electron gas one has

$$\hat{\rho}_0 |\alpha, \mathbf{k}\rangle = f_{\alpha}^{(0)}(\mathbf{k}) |\alpha, \mathbf{k}\rangle \quad (152)$$

where $f_{\alpha}^{(0)}(\mathbf{k})$ is the Fermi–Dirac distribution function. Similarly, the perturbed statistical operator is given by

$$\hat{\rho}(\mathbf{r}, \boldsymbol{\rho}; t) = \exp\{\beta[\Omega - \widehat{H}_0 - \widehat{V}(\mathbf{r}, \boldsymbol{\rho}; t)]\} \quad (153)$$

and for perturbed electron gas

$$\hat{\rho}(\mathbf{r}, \boldsymbol{\rho}; t) |\alpha, \mathbf{k}\rangle = f_{\alpha}(\mathbf{k}, \mathbf{r}, \boldsymbol{\rho}; t) |\alpha, \mathbf{k}\rangle \quad (154)$$

where $f_{\alpha}(\mathbf{k}, \mathbf{r}, \boldsymbol{\rho}; t)$ is a local nonequilibrium distribution function including some fluctuation around the equilibrium

value. Note that the perturbed statistical operator can be written as

$$\hat{\rho}(\mathbf{r}, \boldsymbol{\rho}; t) = \hat{\rho}_0 \exp[-\beta \widehat{V}(\mathbf{r}, \boldsymbol{\rho}; t)] \quad (155)$$

If the perturbation energy is sufficiently small compared with the thermal energy [i.e., $\langle \widehat{V}(\mathbf{r}, \boldsymbol{\rho}; t) \rangle \ll \frac{i}{2} k_B T$, with $i = 2$ for Q2D and $i = 1$ for Q1D systems] then

$$\hat{\rho}(\mathbf{r}, \boldsymbol{\rho}; t) = \hat{\rho}_0 + \hat{\rho}_1(\mathbf{r}, \boldsymbol{\rho}; t) \quad (156)$$

where it is clear that the perturbation statistical operator $\hat{\rho}_1(\mathbf{r}, \boldsymbol{\rho}; t)$ is linear in $\widehat{V}(t)$, that is,

$$\hat{\rho}_1(\mathbf{r}, \boldsymbol{\rho}; t) = -\beta \hat{\rho}_0 \widehat{V}(\mathbf{r}, \boldsymbol{\rho}; t) \quad (157)$$

Looking for the linear response of the electron gas to the external perturbation, one must start from the single-particle Liouville equation of motion for the statistical operator, which states

$$i\hbar \frac{\partial}{\partial t} \hat{\rho}(\mathbf{r}, \boldsymbol{\rho}; t) = [\widehat{H}(\mathbf{r}, \boldsymbol{\rho}; t), \hat{\rho}(\mathbf{r}, \boldsymbol{\rho}; t)] \quad (158)$$

where as usually $[\widehat{H}(\mathbf{r}, \boldsymbol{\rho}; t), \hat{\rho}(\mathbf{r}, \boldsymbol{\rho}; t)]$ represents the commutator of the operators. By keeping only first-order terms in the perturbation, one obtains

$$i\hbar \frac{\partial}{\partial t} \hat{\rho}_1(\mathbf{r}, \boldsymbol{\rho}; t) = [\widehat{H}_0, \hat{\rho}_1(\mathbf{r}, \boldsymbol{\rho}; t)] + [\widehat{V}(\mathbf{r}, \boldsymbol{\rho}; t), \hat{\rho}_0] \quad (159)$$

that is, the linearized equation of motion for the perturbation statistical operator. Notice that according to (146) and (157) the perturbation statistical operator is

$$\hat{\rho}_1(\mathbf{r}, \boldsymbol{\rho}; t) = \hat{\rho}_1(\mathbf{r}, \boldsymbol{\rho}) \exp[-i(\omega + i\delta)t] \quad (160)$$

with

$$\hat{\rho}_1(\mathbf{r}, \boldsymbol{\rho}) = -\beta \hat{\rho}_0 \widehat{V}(\mathbf{r}, \boldsymbol{\rho}) \quad (161)$$

Then one obtains a time independent linearized equation of motion:

$$\begin{aligned} (\hbar\omega - i\hbar\delta) \hat{\rho}_1(\mathbf{r}, \boldsymbol{\rho}) &= \hat{\rho}_1(\mathbf{r}, \boldsymbol{\rho}) \widehat{H}_0 - \widehat{H}_0 \hat{\rho}_1(\mathbf{r}, \boldsymbol{\rho}) \\ &\quad + \hat{\rho}_0 \widehat{V}(\mathbf{r}, \boldsymbol{\rho}) - \widehat{V}(\mathbf{r}, \boldsymbol{\rho}) \hat{\rho}_0 \end{aligned} \quad (162)$$

Taking matrix elements between electron states $|\alpha, \mathbf{k}\rangle$ and $|\alpha', \mathbf{k}'\rangle$ straightforward calculations yield

$$\langle \mathbf{k}', \alpha' | \hat{\rho}_1(\mathbf{r}, \boldsymbol{\rho}) | \alpha, \mathbf{k} \rangle = R_{\alpha\alpha'}(\mathbf{k} \cdot \mathbf{k}'; \omega) \langle \mathbf{k}', \alpha' | \widehat{V}(\mathbf{r}, \boldsymbol{\rho}) | \alpha, \mathbf{k} \rangle \quad (163)$$

where

$$R_{\alpha\alpha'}(\mathbf{k} \cdot \mathbf{k}'; \omega) = \frac{f_{\alpha'}^{(0)}(\mathbf{k}') - f_{\alpha}^{(0)}(\mathbf{k})}{E_{\alpha'}(\mathbf{k}') - E_{\alpha}(\mathbf{k}) - \hbar\omega - i\hbar\delta} \quad (164)$$

This is a basic relation between the matrix elements of the perturbation part of the statistical operator and the perturbation-potential operator. Note this relation is obtained on the assumption that perturbation energy is

very much smaller than the thermal energy in equilibrium. One also considers that the perturbation is very much smaller than the unperturbed Hamiltonian and, consequently, the Born approximation leads to the FGR (61) to calculate the matrix elements of the scattering potential.

Any of the considered scattering mechanisms is essentially an electromagnetic interaction. Although this is implicit in the derivation of some interactions (CP = DP, IR, AL), it is explicit in the derivation of other interactions (CP = PE, LO, BI, RI). Therefore the associated perturbation produces local changes in the uniform density of electrons associated with the equilibrium state, which are not compensated by the uniform positive background formed by the lattice ion cores. Thus one must pay some attention to the density of particle operator, which can be defined as

$$\hat{n}(\mathbf{r}, \boldsymbol{\rho}) = \delta(\mathbf{r} - \mathbf{r}')\delta(\boldsymbol{\rho} - \boldsymbol{\rho}') \quad (165)$$

whose average value is the perturbed density of electrons

$$n(\mathbf{r}, \boldsymbol{\rho}, t) = \langle \hat{n}(\mathbf{r}, \boldsymbol{\rho}, t) \rangle = \text{Tr}\{\hat{\rho}(\mathbf{r}, \boldsymbol{\rho}, t)\hat{n}(\mathbf{r}, \boldsymbol{\rho})\} \quad (166)$$

which can be easily transformed, taking account of (156) and (157), into

$$n(\mathbf{r}, \boldsymbol{\rho}, t) = n_0 + n_1(\mathbf{r}, \boldsymbol{\rho}, t) \quad (167)$$

where n_0 is the uniform electron density in absence of perturbation [note this is the electron areal concentration n_S or the linear concentration n_L introduced in (25) and (26), which were employed in all the proceeding sections], while $n_1(\mathbf{r}, \boldsymbol{\rho}, t)$ is the induced change of electron density due to the perturbation (the local fluctuations of those quantities). This way the induced charges act upon electrons via the corresponding electrostatic potential, which is nothing else but the screening potential (induced perturbation) \hat{V}_1 in (147).

The average value $V_1 = \langle \hat{V}_1 \rangle$ must satisfy the Poisson equation

$$[\nabla_{\mathbf{r}}^2 + \nabla_{\boldsymbol{\rho}}^2]V_1(\mathbf{r}, \boldsymbol{\rho}, t) = \frac{4\pi e^2}{\kappa} n_1(\mathbf{r}, \boldsymbol{\rho}, t) \quad (168)$$

where κ is the dielectric constant of the material, not including the electron contribution. It must be taken as the static one κ_0 for elastic scatterings by acoustic phonons or ion impurities, as well as for alloy and interface roughness scatterings, and as the high frequency one κ_∞ for inelastic scattering by optical phonons. The Laplace operators are defined in (5) and (6) for Q2D and Q1D respectively. One can easily obtain

$$[-q^2 + \nabla_{\boldsymbol{\rho}}^2]\tilde{V}_1(\mathbf{q}, \boldsymbol{\rho}, \omega) = \frac{4\pi e^2}{\kappa} \tilde{n}_1(\mathbf{q}, \boldsymbol{\rho}, \omega) \quad (169)$$

for the corresponding Fourier components,

$$\tilde{V}_1(\mathbf{q}, \boldsymbol{\rho}, \omega) = \iint V_1(\mathbf{r}, \boldsymbol{\rho}) \exp[-i(\mathbf{q} \cdot \mathbf{r} - \omega t)] d\mathbf{r} dt \quad (170)$$

$$\tilde{n}_1(\mathbf{q}, \boldsymbol{\rho}, \omega) = \iint n_1(\mathbf{r}, \boldsymbol{\rho}) \exp[-i(\mathbf{q} \cdot \mathbf{r} - \omega t)] d\mathbf{r} dt \quad (171)$$

where $d\mathbf{r} = dx dy$, the wavevector is given by (62), the coordinates are given by (2) in Q2D systems. Also $d\mathbf{r} = dx$,

the wavevector is given by (63), and the coordinates are given by (3) in Q1D systems.

Straightforward calculations lead to

$$n_1(\mathbf{r}, \boldsymbol{\rho}, t) = \sum_{\alpha, \mathbf{k}} \sum_{\alpha', \mathbf{k}'} \langle \mathbf{k}', \alpha' | \hat{\rho}_1 | \alpha, \mathbf{k} \rangle \psi_{\alpha' \mathbf{k}'}^*(\mathbf{r}, \boldsymbol{\rho}) \psi_{\alpha \mathbf{k}}(\mathbf{r}, \boldsymbol{\rho}) \quad (172)$$

and the corresponding Fourier transform,

$$n_1(\mathbf{q}, \boldsymbol{\rho}, \omega) = \frac{1}{A} \sum_{\alpha, \mathbf{k}} \sum_{\alpha', \mathbf{k}'} \langle \mathbf{k}', \alpha' | \hat{\rho}_1 | \alpha, \mathbf{k} \rangle \times \varphi_{\alpha'}^*(\boldsymbol{\rho}) \varphi_{\alpha}(\boldsymbol{\rho}) \Delta(\mathbf{k} - \mathbf{k}' + \mathbf{q}) \quad (173)$$

In order to solve Eq. (169) with the induced electron density given by (173), one must take account of the boundary conditions at infinity,

$$V_1(\mathbf{q}, \boldsymbol{\rho} = \pm\infty, \omega) = 0 \quad (174)$$

$$\nabla_{\boldsymbol{\rho}} V_1(\mathbf{q}, \boldsymbol{\rho} = \pm\infty, \omega) = 0 \quad (175)$$

where in Q2D and Q1D systems

$$\nabla_{\boldsymbol{\rho}} = \frac{\partial}{\partial z} \mathbf{e}_z \quad (176)$$

$$\nabla_{\boldsymbol{\rho}} = \frac{\partial}{\partial y} \mathbf{e}_y + \frac{\partial}{\partial z} \mathbf{e}_z \quad (177)$$

respectively. The matching conditions at interfaces in semiconductor heterostructures, when the materials forming the interfaces have different dielectric constants, must also be taken into account, as in [21, 233] for SHs as well as in [230, 233–235] for QWs. In delta-doped semiconductors matching conditions are not required, since the impurities in the very thin layer of the material certainly do not affect considerably the lattice dielectric constant. Nevertheless, in many cases the difference between the dielectric constants is neglected and the solution has the form

$$V_1(\mathbf{q}, \boldsymbol{\rho}, \omega) = \frac{1}{A} \sum_{\alpha, \mathbf{k}} \sum_{\alpha', \mathbf{k}'} \langle \mathbf{k}', \alpha' | \hat{\rho}_1 | \alpha, \mathbf{k} \rangle \times \mathcal{H}_{\alpha\alpha'}(\mathbf{q}, \boldsymbol{\rho}) \Delta(\mathbf{k} - \mathbf{k}' + \mathbf{q}) \quad (178)$$

where, according to [21, 236],

$$\mathcal{H}_{\alpha\alpha'}(\mathbf{q}, \boldsymbol{\rho}) = \frac{2\pi e^2}{\kappa q} \int e^{-q|z-z'|} \varphi_{\alpha'}^*(z') \varphi_{\alpha}(z') dz' \quad (179)$$

$$\mathcal{H}_{\alpha\alpha'}(\mathbf{q}, \boldsymbol{\rho}) = \frac{2e^2}{\kappa} \int K_0(q|\boldsymbol{\rho} - \boldsymbol{\rho}'|) \varphi_{\alpha'}^*(\boldsymbol{\rho}') \varphi_{\alpha}(\boldsymbol{\rho}') d\boldsymbol{\rho}' \quad (180)$$

in Q2D and Q1D systems respectively. In the latter case $K_0(q|\boldsymbol{\rho} - \boldsymbol{\rho}'|)$ is the modified Bessel function of the second kind and

$$|\boldsymbol{\rho} - \boldsymbol{\rho}'| = \sqrt{(y - y')^2 + (z - z')^2} \quad (181)$$

Taking account of the basic relation (164) one gets

$$V_1(\mathbf{q}, \boldsymbol{\rho}, \omega) = \frac{1}{A} \sum_{\alpha} \sum_{\alpha'} \mathcal{P}_{\alpha\alpha'}(\mathbf{q}, \omega) \mathcal{H}_{\alpha\alpha'}(\mathbf{q}, \boldsymbol{\rho}) \langle \alpha' | \hat{V}(\mathbf{q}, \boldsymbol{\rho}, \omega) | \alpha \rangle \quad (182)$$

where

$$\mathcal{P}_{\alpha\alpha'}(\mathbf{q}, \omega) = \sum_{\mathbf{k}} \frac{f_{\alpha'}^{(0)}(\mathbf{k} + \mathbf{q}) - f_{\alpha}^{(0)}(\mathbf{k})}{E_{\alpha'}(\mathbf{k} + \mathbf{q}) - E_{\alpha}(\mathbf{k}) - \hbar\omega - i\hbar\delta} \quad (183)$$

is known as the free electron gas polarizability.

Following the idea of Maldague [237], one can write the Fermi–Dirac distribution function as

$$f_{\alpha}^{(0)}(\mathbf{k}) = \frac{1}{4}\beta \int_0^{\infty} \frac{\Theta(\xi' - E)}{\cosh^2[\frac{1}{2}\beta(E_{F\alpha} - \xi')]} d\xi' \quad (184)$$

where $\Theta(\xi' - E)$ is the zero-temperature Fermi–Dirac distribution function with the Fermi level ξ' . Replacing in (183) and performing the integral over ξ' first, one finds

$$\mathcal{P}_{\alpha\alpha'}(\mathbf{q}, \omega) = \frac{1}{4}\beta \int_0^{\infty} \{ \mathcal{B}_{\alpha}(\mathcal{E}_q, -\hbar\omega_{\alpha\alpha'}; \xi') + \mathcal{B}_{\alpha'}(\mathcal{E}_q, \hbar\omega_{\alpha\alpha'}; \xi') \} d\xi' \quad (185)$$

where the energy-dimension variables are

$$\mathcal{E}_q = \frac{\hbar^2 q^2}{2m^*} \quad \text{and} \quad \hbar\omega_{\alpha\alpha'} = \hbar\omega + E_{\alpha} - E_{\alpha'} \quad (186)$$

The introduced functions are

$$\mathcal{B}_{\alpha'}(\mathcal{E}_q, \hbar\omega_{\alpha\alpha'}; \xi') = \frac{\mathcal{P}^{(0)}(\mathcal{E}_q, \hbar\omega_{\alpha\alpha'}; \xi')}{\cosh^2[\frac{1}{2}\beta(E_{F\alpha'} - \xi')]} \quad (187)$$

and if $\mathcal{E}_q > 2\xi' + \hbar\omega_{\alpha\alpha'} + [(2\xi' + \hbar\omega_{\alpha\alpha'})^2 - (\hbar\omega'_{\alpha\alpha'})^2]^{1/2}$ (this condition leads to $q > 2k'_F$ when $\alpha = \alpha'$ and $\omega = 0$), one has

$$\mathcal{P}^{(0)}(\mathcal{E}_q, \hbar\omega_{nn'}; \xi') = -\frac{m^*S}{2\pi\hbar^2} \left\{ 1 - \left[\left(1 + \frac{\hbar\omega_{nn'}}{\mathcal{E}_q} \right)^2 - \frac{4\xi'}{\mathcal{E}_q} \right]^{1/2} \right\} \quad (188)$$

$$\mathcal{P}^{(0)}(\mathcal{E}_q, \hbar\omega_{\alpha\alpha'}; \xi') = -\left(\frac{2m^*L^2}{\pi^2\hbar^2} \right)^{1/2} \frac{1}{\mathcal{E}_q + \hbar\omega_{\alpha\alpha'}} \quad (189)$$

$$\times \ln \left[1 - \frac{4\xi'\mathcal{E}_q}{(\mathcal{E}_q + \hbar\omega_{\alpha\alpha'})^2} \right] \quad (190)$$

while if $\mathcal{E}_q < 2\xi' + \hbar\omega_{\alpha\alpha'} + [(2\xi' + \hbar\omega_{\alpha\alpha'})^2 - (\hbar\omega_{\alpha\alpha'})^2]^{1/2}$ (this condition leads to $q < 2k'_F$ when $\alpha = \alpha'$ and $\omega = 0$), one has

$$\mathcal{P}_{n'}^{(0)}(\mathcal{E}_q, \hbar\omega_{nn'}) = -\frac{m^*S}{2\pi\hbar^2} \quad (191)$$

$$\mathcal{P}_{\alpha'}^{(0)}(\mathcal{E}_q, \hbar\omega_{\alpha\alpha'}) = 0 \quad (192)$$

for Q2D and Q1D systems respectively.

The zero-temperature polarizability is given by

$$\mathcal{P}_{\alpha\alpha'}^{(0)}(\mathbf{q}, \omega) = \mathcal{P}^{(0)}(\mathcal{E}_q, -\hbar\omega_{\alpha\alpha'}; E_{F\alpha}) + \mathcal{P}^{(0)}(\mathcal{E}_q, \hbar\omega_{\alpha\alpha'}; E_{F\alpha'}) \quad (193)$$

which if $\alpha = \alpha'$ and $\omega = 0$ presents discontinuities at $q = 2k_{F\alpha}$, the Kohn effect reported for Q2D systems [230] and Q1D systems [231]. These discontinuities are smeared out if one takes into account the energy level broadening due to

finite lifetime of quasiparticle states because of the scattering mechanisms, as can be found in [238] for a Q2D system.

The matrix element between subbands γ and γ' results in

$$\langle \gamma' | \widehat{V}_1(\mathbf{q}, \boldsymbol{\rho}, \omega) | \gamma \rangle = \frac{1}{A} \sum_{\alpha} \sum_{\alpha'} \mathcal{P}_{\alpha\alpha'}(\mathbf{q}, \omega) \mathcal{F}_{\gamma\gamma'} \alpha \alpha'(\mathbf{q}) \times \langle \alpha' | \widehat{V}(\mathbf{q}, \boldsymbol{\rho}, \omega) | \alpha \rangle \quad (194)$$

where

$$\mathcal{F}_{\gamma\gamma'} \alpha \alpha'(\mathbf{q}) = \int \mathcal{H}_{\alpha\alpha'}(\mathbf{q}, \boldsymbol{\rho}) \varphi_{\gamma'}^*(\boldsymbol{\rho}) \varphi_{\gamma}(\boldsymbol{\rho}) d\boldsymbol{\rho} \quad (195)$$

Notice the action of the screening potential operator \widehat{V}_1 is just multiplied by a number V_1 .

The basic assumption (147) can be written as

$$\langle \gamma' | \widehat{V}(\mathbf{q}, \omega) | \gamma \rangle = \langle \gamma' | \widehat{V}_0(\mathbf{q}, \omega) | \gamma \rangle + \langle \gamma' | \widehat{V}_1(\mathbf{q}, \omega) | \gamma \rangle \quad (196)$$

Making use of (194), after some manipulation one obtains for the full Fourier transforms in space and time

$$\langle \gamma' | \widehat{V}_0(\mathbf{q}, \omega) | \gamma \rangle = \sum_{\alpha\alpha'} \varepsilon_{\gamma\gamma'\alpha\alpha'}(\mathbf{q}, \omega) \langle \alpha' | \widehat{V}(\mathbf{q}, \omega) | \alpha \rangle \quad (197)$$

Here the matrix dielectric function was introduced as

$$\varepsilon_{\gamma\gamma'\alpha\alpha'}(\mathbf{q}, \omega) = \Delta(\alpha - \gamma)\Delta(\alpha' - \gamma') - \chi_{\gamma\gamma'\alpha\alpha'}(\mathbf{q}, \omega) \quad (198)$$

where the susceptibility was defined as

$$\chi_{\gamma\gamma'\alpha\alpha'}(\mathbf{q}, \omega) = \frac{1}{A} v(q) \mathcal{P}_{\alpha\alpha'}(\mathbf{q}, \omega) \mathcal{F}_{\gamma\gamma'} \alpha \alpha'(\mathbf{q}) \quad (199)$$

with the polarizability given by (183). Notice the normalization area $A = S$ or the normalization length $A = L$ will disappear from the susceptibility when going from summation into integration in (183) according to (11) or (12) respectively. The form factor for the electron–electron interaction given by

$$\mathcal{F}_{ll'nn'}(\mathbf{q}) = \iint e^{-q|z-z'|} \varphi_l^*(z) \varphi_{l'}(z) \varphi_{n'}^*(z') \times \varphi_n(z') dz dz' \quad (200)$$

$$\mathcal{F}_{ll'nn'}(\mathbf{q}) = \iint K_0(q|\boldsymbol{\rho} - \boldsymbol{\rho}'|) \varphi_{\gamma'}^*(\boldsymbol{\rho}) \varphi_{\gamma}(\boldsymbol{\rho}) \times \varphi_{\alpha'}^*(\boldsymbol{\rho}') \varphi_{\alpha}(\boldsymbol{\rho}') d\boldsymbol{\rho} d\boldsymbol{\rho}' \quad (201)$$

for Q2D and Q1D systems, where

$$v(q) = \frac{2\pi e^2}{\kappa q} \quad (202)$$

$$v(q) = \frac{2e^2}{\kappa} \quad (203)$$

respectively. The obtained result for the matrix dielectric function is known as the random phase approximation in MBT, where it can also be derived in a different way. The major defect of the RPA matrix dielectric function is that all exchanges and correlation effects have been disregarded. However, it gives sufficiently good results for the screening of scattering mechanisms in transport theory both in

semiconductor heterostructures [68, 78] and delta-doped semiconductors [104, 170, 193]. Some works are devoted to the enhancement of this result in the line of Singwi–Tasi–Land–Sjolander theory, but they are mainly concerned with elementary excitation spectrum of the electron liquid (interacting electron gas).

7.2. Screened Matrix Elements for a Given Scattering Potential

The just derived equation (197) can be written in an obvious notation as

$$V_{\gamma\gamma'}^0(\mathbf{q}, \omega) = \sum_{\alpha\alpha'} \varepsilon_{\gamma\gamma'\alpha\alpha'}(\mathbf{q}, \omega) V_{\alpha\alpha'}(\mathbf{q}, \omega) \quad (204)$$

which gives each matrix element of the bare scattering potential through the matrix elements of the screened scattering potential. However, what is required is the inverse relation,

$$V_{\alpha\alpha'}(\mathbf{q}, \omega) = \sum_{\gamma\gamma'} \varepsilon_{\alpha\alpha'\gamma\gamma'}^{-1}(\mathbf{q}, \omega) V_{\gamma\gamma'}^0(\mathbf{q}, \omega) \quad (205)$$

where $\varepsilon_{\alpha\alpha'\gamma\gamma'}^{-1}(\mathbf{q}, \omega)$ are the elements of the inverted matrix dielectric function.

The problem of inverting the RPA matrix dielectric function is not so trivial as it seems at first sight. Notice that one deals with a four-index matrix or an eight-index matrix,

$$\varepsilon_{nn'l'l'}(\mathbf{q}, \omega) \quad n, n', l, l' = 1, 2, 3, \dots \quad (206)$$

$$\varepsilon_{nn'li'ij'}(\mathbf{q}, \omega) \quad i, i', j, j' = 1, 2, 3, \dots \quad (207)$$

in Q2D or Q1D systems respectively. This suggests the use of tensor algebra, but it reduces to relabel the matrix indices once, in the first case, or twice, in the second case, to obtain a manageable two-index matrix. But this must be done in the adequate order to obtain the proper mathematical object ruled by the well-known matrix algebra theory. A detailed discussion of how to invert the matrix dielectric function for a Q2D electron gas was presented in [233], where it is shown how the relabeling of a four-index matrix must be carried out in order to be congruent with two-index diagonal unit matrix. A similar procedure may be repeated for a Q1D electron gas.

Many works avoid this question by making different approximations. Concrete calculations are mostly carried out in SQL approximation, when only the lowest subband is considered and the dielectric function is just a number, both in Q2D [149, 150] and Q1D [107, 108, 236] cases. Sometimes strictly 2D or 1D dielectric functions, where no indices appear, have been employed, even for intersubband scattering in Q2D [68, 148] and Q1D systems. Another approximation takes account only of the diagonal terms [167], so that

$$V_{\alpha\alpha'}(\mathbf{q}, \omega) = \varepsilon_{\alpha\alpha'\alpha\alpha'}^{-1}(\mathbf{q}, \omega) V_{\alpha\alpha'}^0(\mathbf{q}, \omega) \quad (208)$$

Finally, in several calculations the matrix dielectric function is actually inverted, of course after limiting the number of considered subbands, which can include some empty ones.

One must be aware that in Q2D systems if the subband index $n = 1, 2, 3, \dots, N$, then the dielectric function matrix has $N^2 \times N^2$ elements, while in Q1D systems if subband indices $n, l = 1, 2, 3, \dots, N$, then the dielectric function matrix has $N^4 \times N^4$ elements. That is the case of multisubband transport calculations in delta-doped semiconductors [104] and semiconductor heterostructures.

However, the just explained method is objected to by some authors [232], who mainly stress that no formal justification is given to cut off the number of considered subbands, even when some empty subbands are included in the dielectric function matrix. They propose a method for a Q2D system, which allows one to obtain the inverted dielectric function $\varepsilon^{-1}(q, \omega; z, z')$. Although they also limit the number of considered subbands, they provide a formal demonstration of the convergence of this method when the number of considered subbands increases to infinity [232, 240]. This result has not been employed in transport calculations. A completely different approach is followed in [34, 241] to directly obtain $\varepsilon_{\alpha\alpha'\gamma\gamma'}^{-1}(\mathbf{q}, \omega)$ for a Q1D system, but concrete calculations are not presented.

8. SUMMARY

Transport in semiconductor nanostructures has been briefly reviewed. Fundamental topics have been selected aiming to give a comprehensive theoretical basis as well as a substantial account of the research work in this area over the last 20 years. The quasiclassical BTE formalism still is widely employed, because it allows a clear understanding and explanation for most of the experimentally determined characteristics of transport properties in these low-dimensional systems. This chapter is focused on steady-state transport because it is particularly important for the investigation of the different scattering mechanisms able to limit the mobility and, consequently, the drift velocity. The latter is directly related to the field-effect transistor design for high-speed devices.

The construction of semiconductor nanostructures has stimulated the search for novel materials as well. The SiGe/Si or SiGe/Ge based heterostructures, as expected, have been widely investigated. But the narrow-gap III–V binary compounds and their ternary alloys, such as the AlGaAs/GaAs based heterostructures, where the record electron and hole mobilities have been reached, have been the most studied low-dimensional systems. Particularly in recent years the wide-gap III nitride binary compounds and their ternary alloys, such as the AlGaN/GaN based heterostructures, have attracted the attention of the researchers. The II–VI binary compounds and their ternary alloys, as the CdMgTe/CdTe based heterostructures, have also been investigated, but not so intensively as the other mentioned materials.

The distinction between low-field and high-field transport regimes, as well as the role of the different scattering mechanisms in limiting the carrier mobility, depends on the materials forming the semiconductor nanostructures, their parameters, and the experimental conditions. Many questions remain open in this research field, which is tightly connected to the size reduction and high quality performance of electronic devices.

GLOSSARY

Acoustic phonon Phonons produced in materials with one atom in each elemental cell.

Charged carrier An electron or a hole.

Conduction band Energy band in a crystalline solid partially filled by electrons.

Effective mass The mass of a particle in a crystalline solid.

Elastic scattering A process in which the scattered particle has the same energy before and after event.

Electron–phonon interaction The coupling between electrons and the oscillations of ions.

Gap Forbidden region for the electrons, which it is determined by the difference of energies between conduction and valence bands.

Hall effect Deviation of the movement of charge carriers due to transverse magnetic field.

Hole The absence of an electron in the valence band.

Inelastic scattering A process in which the scattered particle has different energy before and after event.

Mobility Parameter that characterizes the movement of the carriers in conductors.

Optical phonon Phonons produced in materials with two (or more) different atoms in each elemental cell.

Phonon Collective elemental excitation which describes the oscillations of ions in solids.

Quasi-dimensional system A three-dimensional quantum system in which the movement of carriers is restricted in one, two, or three directions of a few nanometers.

Scattering rate Sum of transition probability per unit time.

Self-consistent field approach A many body theory that considers that particles are moving independently in a mean field due to other particles.

Transition rate Transition probability per unit time.

Valence band Energy band in a crystalline solid completely filled by electrons.

REFERENCES

- J. L. Marín, R. Riera, and R. A. Rosas, in “Handbook of Advanced Electronic and Photonic Materials and Devices” (H. S. Nalwa, Ed.), p. 292. Academic Press, San Diego, 2001.
- I. Vurgaftman, J. R. Mayer, and L. R. Ram-Mohan, *J. Appl. Phys.* 89, 5815 (2001).
- G. Mayer, B. E. Maile, R. Germann, A. Forchel, P. Grambow, and H. P. Meiner, *Appl. Phys. Lett.* 56, 2016 (1990).
- M. Hauser, E. Gornik, C. Wirner, M. Baur, G. Bohm, and G. Weimann, *Semicond. Sci. Tech.* 9, 951 (1994).
- E. Kapon, J. Chisten, E. Colas, R. Bhat, D. M. Hwang, and L. M. Schiavone, in “Nanostructures and Mesoscopic Systems” (W. P. Kirk and M. A. Reed, Eds.), p. 63. Academic Press, San Diego, 1991.
- A. C. Maciel, C. Keiner, L. Rota, J. F. Ryan, U. Marti, D. Martin, F. Morier-Gemout, and F. K. Reinhart, *Appl. Phys. Lett.* 66, 3039 (1995).
- H. Smith and H. Craighead, *Phys. Today* 43, 24 (1990).
- K. Hess, *Phys. Today* 43, 34 (1990).
- A. Fowler, *Phys. Today* 50, 50 (1997).
- V. Umansky, R. de Picciotto, and M. Heiblum, *Appl. Phys. Lett.* 71, 683 (1997).
- M. Henini, P. J. Rogers, P. A. Crump, B. L. Gallagher, and G. Hill, *Appl. Phys. Lett.* 65, 2054 (1994).
- C. J. Emeleus, T. E. Whall, D. W. Smith, R. A. Kubiak, E. H. C. Parker, and M. J. Kearney, *J. Phys. Condens. Matter* 73, 3852 (1993).
- B. R. Nag and S. Mukhopadhyay, *J. Phys. Condens. Matter* 3, 3557 (1991).
- I. Lo, W. C. Mitchel, R. E. Perrin, R. L. Meshan, and M. Y. Yen, *Phys. Rev. B* 43, 11787 (1991).
- E. Tiras, M. Cankurtaran, H. Celik, and N. Balkan, *Phys. Rev. B* 64, 085301 (2001).
- G. Bastard, “Wave Mechanics applied to Semiconductor Heterostructures,” Monographs of Physics Series. Wiley, New York, 1991.
- F. M. Peeters and P. Vasilopolous, *Appl. Phys. Lett.* 55, 1106 (1989).
- N. M. Cho, S. B. Ogabe, and A. Madhukar, *Phys. Rev. B* 36, 6472 (1987).
- H. Leon, F. Garcia-Moliner, and V. R. Velasco, *Thin Solid Films* 266, 38 (1995).
- L. Chico, W. Jaskolki, and F. García-Moliner, *Physica Scripta* 47, 284 (1993).
- T. Ando, A. Fowler, and F. Stern, *Rev. Mod. Phys.* 54, 437 (1982).
- B. K. Ridley, *J. Phys. Conds. Matter* 14, 3469 (2002).
- G. D. Mahan, “Many Particle Physics,” 2nd ed. Plenum Press, New York, 1990.
- S. Das Sarma, J. K. Jain, and R. Jalabert, *Phys. Rev. B* 37, 1228 (1988).
- S. Das Sarma, J. K. Jain, and R. Jalabert, *Phys. Rev. B* 37, 4560 (1988).
- F. Leon-Avila, H. Rodríguez-Coppola, and F. Comas, *Phys. Status Solidi B* 208, 31 (1998).
- O. Ziep and R. Keiper, *Phys. Status Solidi B* 128, 779 (1985).
- O. Ziep, M. Suhrke, and R. Keiper, *Phys. Status Solidi B* 134, 789 (1986).
- R. Keiper and O. Ziep, *Phys. Status Solidi B* 131, K91 (1985).
- C. Prascht and M. Suhrke, *Phys. Status Solidi B* 149, 547 (1988).
- C. Prascht and M. Suhrke, *Phys. Status Solidi B* 154, 315 (1989).
- H. Leon and F. Comas, *Phys. Status Solidi B* 160, 105 (1990).
- W. Y. Lai and C. S. Ting, *Phys. Rev. B* 24, 7206 (1981).
- I. I. Boiko, Yu. M. Sirenko, and P. Vasilopoulos, *Phys. Rev. B* 43, 7216 (1991).
- E. D. Siggia and P. C. Kwok, *Phys. Rev. B* 2, 1024 (1970).
- C. Jacobini and L. Reggiani, *Rev. Mod. Phys.* 54, 645 (1983).
- W. T. Masselnik, *Thin Solids Films* 231, 86 (1993).
- R. P. Joshi, *Appl. Phys. Lett.* 64, 223 (1994).
- J. R. Watting, A. B. Walker, J. J. Harris, and J. M. Roberts, *Semicond. Sci. Tech.* 14, 12 (1999).
- T. Li, R. P. Joshi, and C. Fazi, *J. Appl. Phys.* 88, 829 (2000).
- P. J. Price, *J. Vac. Sci. Technol.* 19, 599 (1981).
- B. K. Ridley, B. E. Foutz, and L. F. Eastman, *Phys. Rev. B* 61, 16862 (2000).
- N. Nishiguchi, *Phys. Rev. B* 50, 10970 (1994).
- M. Cardona, in “Lectures in Surface Science” (M. Cardona and G. Castro, Eds.), Vol. 86, p. 143. Springer-Verlag, Berlin, 1986.
- B. Jusserand, P. Paquet, and R. Regreny, *Superlattice Microst.* 1, 61 (1985).
- C. Colvard, R. Fischer, T. Gant, M. V. Klein, H. Morkoc, and A. Gossard, *Superlattice Microst.* 1, 81 (1985).
- N. Sawaki and I. Akasaki, *Physica B* 134, 494 (1985).
- M. V. Klein, *IEEE J. Quantum Electron.* 22, 1760 (1986).
- S. F. Ren and C. Y. Chang, *Phys. Rev. B* 43, 11857 (1991).
- V. M. Fomin and E. P. Pokatnikov, *Phys. Status Solidi B* 132, 69 (1985).
- F. Bechstedt and R. Enderlein, *Phys. Status Solidi B* 131, 53 (1985).
- L. Wendler and R. Pechstedt, *Phys. Status Solidi B* 138, 197 (1986).
- K. Huang and B. Zhu, *Phys. Rev. B* 38, 13377 (1988).
- N. Mori and T. Ando, *Phys. Rev. B* 40, 6175 (1989).

55. F. Bechstedt and H. Gerecke, *J. Phys. Condens. Matter* 2, 4363 (1990).
56. M. Babiker, *J. Phys. C* 19, 683 (1986).
57. C. Trallero and F. Comas, *Phys. Rev. B* 37, 4583 (1988).
58. B. K. Ridley, *Phys. Rev. B* 39, 5282 (1989).
59. R. Chen, D. L. Lin, and T. F. George, *Phys. Rev. B* 41, 1435 (1990).
60. D. L. Lin, R. Chen, and T. F. George, *Solid State Commun.* 73, 799 (1990).
61. F. Leon-Avila, H. Rodriguez-Coppola, and F. Comas, *Phys. Status Solidi B* 189, 107 (1995).
62. C. Trallero-Giner, F. García-Moliner, V. R. Velasco, and M. Cardona, *Phys. Rev. B* 45, 11944 (1992).
63. K. J. Nash, *Phys. Rev. B* 46, 7723 (1992).
64. R. Perez-Alvarez, F. García-Moliner, V. R. Velasco, and C. Trallero-Giner, *J. Phys. Condens. Matter* 5, 5389 (1993).
65. A. I. Anselm, "Introduction to Semiconductor Theory." Mir, Moscow, 1981.
66. C. Kittel, "Quantum Theory of Solids." Wiley, New York, 1987.
67. H. Leon and F. Comas, *Phys. Status Solidi B* 149, 533 (1988).
68. T. Kawamura and S. Das Sarma, *Phys. Rev. B* 45, 3612 (1992).
69. A. S. Davydov, "Quantum Mechanics," 2nd ed. Pergamon Press, New York, 1976.
70. P. J. Price, *Phys. Rev. B* 32, 2643 (1985).
71. W. Walukiewicz, H. E. Ruda, J. Lagowski, and H. C. Gatos, *Phys. Rev. B* 32, 2645 (1985).
72. B. Vinter, *Phys. Rev. B* 33, 5904 (1986).
73. J. J. Harris, C. T. Foxon, D. Hilton, J. Hewett, C. Roberts, and S. Auzoux, *Surf. Sci.* 229, 113 (1990).
74. F. Comas, C. Trallero, H. Leon, and J. Tutor, *Physica B* 152, 352 (1988).
75. P. J. Price, *Ann. Phys. (N.Y.)* 133, 217 (1981).
76. S. Das Sarma and F. Stern, *Phys. Rev. B* 32, 8442 (1985).
77. X. L. Lei, *J. Phys. C* 18, L593 (1985).
78. H. Leon, F. Leon, and F. Comas, *Phys. Status Solidi B* 170, 449 (1992).
79. D. R. Anderson, N. A. Zakhleniuk, M. Babiker, B. K. Ridley, and C. R. Bennett, *Phys. Rev. B* 63, 245313 (2001).
80. B. K. Ridley, *Rep. Progr. Phys.* 54, 169 (1991).
81. R. A. Mena, S. E. Schacham, E. J. Hanglang, S. A. Alterovitz, and P. G. Young, *J. Appl. Phys.* 78, 6626 (1995).
82. G. Q. Hai and N. Stuard, *Phys. Rev. B* 55, 6708 (1997).
83. L. R. Gonzalez, J. Krupski, M. Pietka, and T. Szwacka, *Phys. Rev. B* 60, 7768 (1999).
84. A. Babinski, J. Siwiec-Matuszyk, J. M. Baranowski, G. Li, and C. Jagadish, *Appl. Phys. Lett.* 77, 999 (2000).
85. W. C. Hsu, C. M. Chen, and W. Lin, *J. Appl. Phys.* 70, 4332 (1991).
86. S. Mukhopadhyay and B. R. Nag, *Appl. Phys. Lett.* 60, 2897 (1992).
87. H. Akarera and T. Ando, *Phys. Rev. B* 43, 11676 (1991).
88. K. Inoue and T. Matsuno, *Phys. Rev. B* 47, 3771 (1993).
89. C. Y. Man and T. M. Huang, *Phys. Rev. B* 61, 12612 (2000).
90. K. Inoue, H. Sakaki, and J. Yoshino, *Appl. Phys. Lett.* 47, 614 (1985).
91. W. T. Masselnik, *Appl. Phys. Lett.* 59, 694 (1991).
92. P. K. Basu and B. R. Nag, *Phys. Rev. B* 22, 4849 (1980).
93. J. B. Roy, P. K. Basu, and B. R. Nag, *Solid State Commun.* 40, 491 (1981).
94. D. L. Rode, *Phys. Rev. B* 2, 1012 (1970).
95. D. L. Rode, *Phys. Rev. B* 3, 3287 (1971).
96. D. Chattopadhyay, *Phys. Rev. B* 33, 7288 (1986).
97. H. Leon, F. Comas, and M. Suhrke, *Phys. Status Solidi B* 159, 731 (1990).
98. B. K. Ridley, *J. Phys. C* 15, 5889 (1982).
99. F. A. Riddoch and B. K. Ridley, *J. Phys. C* 16, 6971 (1983).
100. D. K. Ferry, *Surf. Sci.* 75, 86 (1978).
101. K. Hess, *Appl. Phys. Lett.* 35, 484 (1979).
102. L. Wendler, R. Haupt, F. Bechstedt, H. Rucker, and R. Enderlein, *Superlattice Microst.* 4, 577 (1988).
103. J. Lee and H. N. Spector, *J. Appl. Phys.* 54, 3921 (1983).
104. G. Q. Hai, N. Stuart, F. M. Peeters, P. M. Koenraad, and H. Walter, *J. Appl. Phys.* 80, 5809 (1996).
105. F. A. Riddoch and B. K. Ridley, *Surf. Sci.* 142, 260 (1982).
106. J. Lee and M. O. Vassell, *J. Phys. C* 17, 2525 (1984).
107. B. Tanatar, *J. Phys. Condens. Matter* 5, 2203 (1993).
108. B. Tanatar, *Phys. Rev. B* 48, 12001 (1993).
109. K. B. Wong, M. Jaros, and J. P. Hagon, *Phys. Rev. B* 35, 2463 (1987).
110. R. H. Bube, "Electrons in Solids," 3rd ed. Academic Press, San Diego, 1992.
111. P. K. Ghosh, D. Chattopadhyay, A. Ghosal, and B. G. Mulimani, *Phys. Status Solidi B* 176, 451 (1993).
112. J. C. M. Hwang, A. Katalisky, H. L. Stormer, and V. G. Keramides, *Appl. Phys. Lett.* 44, 864 (1984).
113. E. E. Mendez, P. J. Price, and M. Heiblum, *Appl. Phys. Lett.* 45, 294 (1984).
114. M. A. Paalanen, D. C. Tsui, A. C. Gossard, and J. C. M. Hwang, *Phys. Rev. B* 29, 6003 (1984).
115. J. J. Harris, C. T. Foxon, K. J. Barnham, D. E. Lacklison, J. Hewett, and C. White, *J. Appl. Phys.* 61, 1219 (1987).
116. J. H. English, A. C. Gossard, H. L. Stormer, and K. W. Baldwin, *Appl. Phys. Lett.* 50, 1826 (1987).
117. M. Shayegan, V. J. Goldman, C. Jiang, T. Sajoto, and M. Santos, *Phys. Lett.* 52, 1086 (1987).
118. R. Basco, F. Agahi, and M. L. Kei, *Appl. Phys. Lett.* 63, 1960 (1993).
119. L. Pfeiffer, K. W. West, H. L. Stormer, and K. W. Baldwin, *Appl. Phys. Lett.* 55, 1888 (1989).
120. H. L. Stormer, A. Pinczuk, A. C. Gossard, and W. Weigmann, *Appl. Phys. Lett.* 38, 691 (1981).
121. H. L. Stormer, A. C. Gossard, W. Weigmann, and K. Baldwin, *Appl. Phys. Lett.* 39, 912 (1981).
122. H. L. Stormer, A. C. Gossard, W. Weigmann, and K. Baldwin, *Solid State Commun.* 41, 707 (1982).
123. J. Shah, A. Pinczuk, H. L. Stormer, A. C. Gossard, and W. Weigmann, *Appl. Phys. Lett.* 42, 55 (1983).
124. K. Inoue and H. Sakaki, *Jpn. J. Appl. Phys.* 23, L61 (1984).
125. K. Inoue, H. Sakaki, and J. Yoshino, *Jpn. J. Appl. Phys.* 23, L767 (1984).
126. S. Sasa, J. Saito, K. Naribu, T. Ishikawa, S. Hiyamizu, and M. Inoue, *Jpn. J. Appl. Phys.* 24, L281 (1985).
127. G. Weimann and W. Schlapp, *Appl. Phys. A* 37, 139 (1985).
128. C. T. Foxon and J. J. Harris, *Phillips J. Res.* 41, 313 (1986).
129. H. Burkhard, W. Schlapp, and G. Weigmann, *Surf. Sci.* 174, 387 (1986).
130. Y. Horikoshi, A. Fischer, E. F. Schubert, and K. Ploog, *Jpn. J. Appl. Phys.* 26, 263 (1987).
131. C. Nguyen, K. Enslinn, and H. Kroemer, *Surf. Sci.* 267, 549 (1992).
132. Y. S. Gui, S. L. Guo, G. Z. Zheng, J. A. Zhu, X. H. Fung, K. Qiu, and X. W. Wang, *Appl. Phys. Lett.* 76, 1309 (2000).
133. V. K. Arora and A. Naeem, *Phys. Rev. B* 31, 3887 (1985).
134. D. Roychoud and P. K. Basu, *Phys. Rev. B* 22, 6325 (1980).
135. T. Kawamura and S. Das Sarma, *Phys. Rev. B* 42, 3725 (1990).
136. D. Chattopadhyay, *Phys. Status Solidi B* 135, 409 (1986).
137. P. K. Basu and B. R. Nag, *J. Phys. C* 14, 1519 (1981).
138. J. Lee, H. N. Spector, and V. K. Arora, *J. Appl. Phys.* 54, 6995 (1983).
139. K. Hirakawa and H. Sakaki, *Phys. Rev. B* 23, 8291 (1986).
140. R. Fletcher, E. Zaremba, M. D'Iorio, C. T. Foxon, and J. J. Harris, *Phys. Rev. B* 41, 10649 (1990).
141. C. Guillemot, M. Baudet, M. Gauneau, A. Regreny, and J. C. Portal, *Superlattice Microst.* 2, 445 (1986).
142. C. Guillemot, M. Baudet, M. Gauneau, A. Regreny, and J. C. Portal, *Phys. Rev. B* 35, 2799 (1987).

143. V. Piazza, P. Casarini, S. E. Franceschi, M. Lazzarino, F. Beltran, C. Jacobini, A. Bosacchi, and S. Franchi, *Phys. Rev. B* 57, 10017 (1998).
144. S. Mori and T. Ando, *Phys. Rev. B* 19, 6433 (1979).
145. S. Mori and T. Ando, *J. Phys. Soc. Jpn.* 48, 865 (1980).
146. R. B. Darling, *IEEE J. Quantum Electron.* 24, 1628 (1988).
147. G. Fishman and D. Calecki, *Physica B* 117/118, 744 (1983).
148. G. Fishman and D. Calecki, *Phys. Rev. B* 29, 5778 (1984).
149. W. Walukiewicz, H. E. Ruda, J. Lagowski, and H. C. Gatos, *Phys. Rev. B* 29, 4818 (1984).
150. W. Walukiewicz, H. E. Ruda, J. Lagowski, and H. C. Gatos, *Phys. Rev. B* 30, 4571 (1984).
151. V. G. Mokerov, G. B. Galiev, J. Pozela, K. Pozela, and V. Juciene, *Semiconductors* 36, 674 (2002).
152. A. Gold, *J. Phys. Condens. Matter* 13, 11641 (2001).
153. S. K. Lyo and I. J. Fritz, *Phys. Rev. B* 46, 7931 (1992).
154. V. Venkataraman, C. W. Liu, and J. C. Sturm, *Appl. Phys. Lett.* 63, 2795 (1993).
155. K. Hirakawa, T. Noda, and H. Sakaki, *Surf. Sci.* 193, 365 (1988).
156. M. Wataya, N. Sawaki, H. Goto, I. Akasaki, H. Kano, and M. Hashimoto, *Jpn. J. Appl. Phys.* 28, 1934 (1989).
157. K. Battacharyya, J. O. Orwa, and S. M. Goodnick, *J. Appl. Phys.* 73, 4396 (1993).
158. M. G. Greally, M. Hayne, A. Usher, G. Hill, and M. Hopkinson, *J. Appl. Phys.* 79, 8465 (1996).
159. V. K. Arora, *Phys. Status Solidi B* 105, 707 (1981).
160. V. K. Arora, *Phys. Rev. B* 23, 5611 (1981).
161. V. K. Arora, *Phys. Status Solidi B* 117, 127 (1983).
162. J. P. Leburton, *J. Appl. Phys.* 56, 2850 (1984).
163. F. Comas, C. Trallero, and J. Tutor, *Phys. Status Solidi B* 139, 433 (1987).
164. G. Fishman, *Phys. Rev. B* 34, 2394 (1986).
165. G. Fishman, *Phys. Rev. B* 36, 7448 (1987).
166. J. Motohisa and H. Sakaki, *Phys. Rev. B* 46, 7931 (1992).
167. A. Gold and A. Ghazali, *Phys. Rev. B* 41, 7626 (1990).
168. J. A. Majewski, G. Zandler, and P. Vogl, *J. Phys. Condens. Matter* 14, 3511 (2002).
169. N. Balkan, M. C. Arikian, S. Gokden, V. Tilak, B. Schaff, and R. J. Shealy, *J. Phys. Condens. Matter* 14, 3457 (2002).
170. X. Hu, M. A. Khan, M. S. Shur, R. Gaska, and D. Mande, *Appl. Phys. Lett.* 77, 2551 (2000).
171. R. Gasca, J. W. Yong, A. Osinsky, Q. Chen, M. A. Khan, A. O. Orlov, G. L. Snider, and M. S. Shur, *Appl. Phys. Lett.* 72, 707 (1998).
172. T. Wang, Y. Ohno, M. Lachab, D. Nakagawa, D. Shirihama, S. Sakai, and H. Ohno, *Phys. Status Solidi B* 216, 743 (1999).
173. T. Wang, Y. Ohno, M. Lachab, D. Nakagawa, D. Shirihama, S. Sakai, and H. Ohno, *Appl. Phys. Lett.* 74, 3531 (1999).
174. L. Hsu and W. Walukiewicz, *J. Appl. Phys.* 89, 1783 (2001).
175. J. R. Shealy, V. Kaper, V. Tilak, T. Prunty, J. A. Smart, B. Green, and L. F. Eastman, *J. Phys. Condens. Matter* 14, 3499 (2002).
176. C. R. Elsass, I. P. Schmarkova, B. Heying, E. Haus, P. Fini, K. Maranowski, J. P. Ibbetson, S. Keller, P. M. Petroff, S. P. Den Baars, U. K. Mishra, and J. S. Speck, *Appl. Phys. Lett.* 74, 3528 (1999).
177. N. K. Zakhleniuk, C. R. Bennett, M. Babiker, and B. K. Ridley, *Appl. Phys. Lett.* 75, 1565 (1999).
178. T. H. Yu and K. F. Brennan, *J. Appl. Phys.* 89, 3827 (2001).
179. A. Gold, *Phys. Rev. B* 35, 723 (1987).
180. S. F. Nelson, K. Ismail, J. O. Chu, and B. S. Meyerson, *Appl. Phys. Lett.* 63, 367 (1993).
181. S. F. Nelson, K. Ismail, T. N. Jackson, J. J. Nocera, J. O. Chu, and B. S. Meyerson, *Appl. Phys. Lett.* 63, 794 (1993).
182. K. Ismail, S. F. Nelson, J. O. Chu, and B. S. Meyerson, *Appl. Phys. Lett.* 63, 660 (1993).
183. S. Madhavi, V. Vankataraman, J. C. Sturm, and Y. H. Xie, *Phys. Rev. B* 61, 16807 (2000).
184. B. Laikhtman and R. A. Kiehl, *Phys. Rev. B* 47, 10515 (1993).
185. K. Ismail, J. O. Chu, and B. S. Meyerson, *Appl. Phys. Lett.* 64, 3124 (1994).
186. A. Myronov, *Appl. Phys. Lett.* 80, 3117 (2002).
187. V. Kazukauskas, M. Grun, S. Petillon, A. Storzum, and C. Klingshirn, *Appl. Phys. Lett.* 74, 395 (1999).
188. F. Takano, S. Kuroda, K. Takita, T. Takamasu, Y. Imanaka, and G. Kido, *Physica B* 298, 407 (2001).
189. V. L. Gurtovoi, V. V. Valyaev, S. Y. Shapoval, and A. N. Pustovit, *Appl. Phys. Lett.* 72, 1202 (1998).
190. N. Pan, J. Carter, G. S. Jackson, H. Hendricks, X. L. Zheng, and H. M. Kim, *Appl. Phys. Lett.* 59, 458 (1991).
191. X. Zheng, T. K. Corns, K. L. Wong, and B. Wu, *Appl. Phys. Lett.* 62, 2505 (1995).
192. M. J. Kao, W. C. Hsu, R. T. Hsu, Y. H. Wu, T. Y. Lin, and C. Y. Yang, *Appl. Phys. Lett.* 66, 2505 (1995).
193. G. Q. Hai, N. Stuart, and F. M. Peeters, *Phys. Rev. B* 52, 8363 (1995).
194. P. M. Koenraad, A. C. L. Heessels, F. A. P. Blom, J. A. J. Perenboom, and J. H. Walter, *Physica B* 184, 221 (1993).
195. L. R. Gonzalez, J. Krupsi, and J. Szwacka, *Phys. Rev. B* 49, 11111 (1994).
196. A. B. Henriques, *Phys. Rev. B* 53, 16365 (1996).
197. N. Balkan, R. Gupta, B. K. Ridley, M. Emeny, J. Roberts, and I. Goodridge, *Solid State Electron.* 32, 1641 (1989).
198. B. R. Nag, in "Electron Transport in Compound Semiconductors" (M. Cardona, P. Fulde, and H. J. Queissier, Eds.), Springer Series in Solid State Sciences Vol. 11, Springer-Verlag, New York, 1980.
199. W. Xu, F. M. Peeters, and J. T. Devreese, *J. Phys. Condens. Matter* 3, 1783 (1991).
200. S. Khan-ngern and I. A. Larkin, *Phys. Rev. B* 64, 115313 (2001).
201. J. P. Leburton, *Phys. Rev. B* 45, 11022 (1992).
202. N. A. Zakhleniuk, C. R. Bennet, N. C. Constantinou, B. K. Ridley, and M. Babiker, *Phys. Rev. B* 54, 17838 (1996).
203. S. C. Lee and I. Galbraith, *Physica B* 272, 237 (1999).
204. B. K. Ridley, *J. Phys. Condens. Matter* 13, 2799 (2001).
205. Y. Ma, R. Fletcher, E. Zaremba, M. D'Iorio, C. T. Foxon, and J. J. Harris, *Phys. Rev. B* 43, 9033 (1991).
206. B. K. Ridley and N. A. Zakhleniuk, *J. Phys. Condens. Matter* 8, 8525 (1996).
207. B. K. Ridley and N. A. Zakhleniuk, *J. Phys. Condens. Matter* 8, 8539 (1996).
208. B. K. Ridley and N. A. Zakhleniuk, *J. Phys. Condens. Matter* 8, 8553 (1996).
209. R. Gupta, N. Balkan, and B. K. Ridley, *Phys. Rev. B* 46, 7745 (1992).
210. C. Guillemot, F. Clerot, and A. Regreny, *Phys. Rev. B* 46, 10152 (1992).
211. S. K. Sarkar and D. Chattopadhyay, *Phys. Rev. B* 62, 15331 (2000).
212. N. A. Zakhleniuk, C. R. Bennet, and B. K. Ridley, *Appl. Phys. Lett.* 73, 2485 (1998).
213. X. Z. Dang, P. M. Asbeck, E. T. Yu, G. S. Sullivan, M. Y. Chen, B. T. Dermot, K. S. Boutros, and J. M. Redwing, *Appl. Phys. Lett.* 74, 3890 (1999).
214. X. F. Wang and X. L. Lei, *Phys. Rev. B* 47, 16612 (1993).
215. N. Telang and S. Bandyopadhyay, *Phys. Rev. B* 51, 9728 (1995).
216. C. H. Yang, J. M. Carlson-Swindle, S. A. Lyon, and J. M. Worlock, *Phys. Rev. Lett.* 55, 2359 (1985).
217. A. A. Verevkin, N. G. Pititsina, G. M. Chulkova, G. N. Gol'tsman, E. M. Gershenzen, and K. S. Yngvesson, *Phys. Rev. B* 53, R7592 (1996).
218. J. Shah, A. Pinczuk, A. C. Gossard, and W. Weigmann, *Phys. Rev. Lett.* 54, 2045 (1985).
219. W. H. Knox, C. Hirlimann, D. A. B. Miller, J. Shah, D. S. Chemla, and V. Shank, *Phys. Rev. Lett.* 56, 1191.

220. W. H. Knox, D. S. Chemla, G. Livescu, J. E. Cunningham, and J. E. Hemry, *Phys. Rev. Lett.* 61, 1290 (1988).
221. W. H. Knox, *Solid State Electron.* 32, 1057 (1989).
222. K. J. Lee, J. J. Harris, A. J. Kent, T. Wang, S. Sakaki, D. K. Mande, and J. C. Portal, *Appl. Phys. Lett.* 78, 2893 (2001).
223. G. Ansaripour, G. Braithwaite, M. Myronov, O. A. Mironov, E. H. C. Parker, and T. E. Whall, *Appl. Phys. Lett.* 76, 1140 (2000).
224. X. F. Wang and X. L. Lei, *J. Phys. Condens. Matter* 6, 5667 (1994).
225. F. Leon-Avila, F. Comas, and H. Leon, *Physica B* 304, 276 (2001).
226. V. B. Campos and S. Das Sarma, *Phys. Rev. B* 45, 3898 (1992).
227. V. B. Campos, S. Das Sarma, and M. A. Stroschio, *Phys. Rev. B* 46, 3849 (1992).
228. C. R. Bennet and B. Tanatar, *Phys. Rev. B* 55, 7165 (1997).
229. I. Gorczyca and J. Krupski, *Phys. Rev. B* 52, 11248 (1995).
230. J. Lee and H. N. Spector, *J. Appl. Phys.* 54, 6889 (1983).
231. J. Lee and H. N. Spector, *J. Appl. Phys.* 57, 366 (1985).
232. F. J. Fernández-Velicia, F. García-Moliner, and V. R. Velasco, *Phys. Rev. B* 53, 2034 (1996).
233. H. Leon, R. Riera, J. L. Marín, and E. Roca, *Phys. Low-dimens. Struct.* 7/8, 59 (1996).
234. N. Q. Khanh, *Phys. Status Solidi B* 197, 73 (1996).
235. N. Q. Khanh, *Phys. Status Solidi B* 225, 89 (2001).
236. S. Das Sarma and B. A. Mason, *Phys. Rev. B* 31, 5536 (1985).
237. P. F. Maldague, *Surf. Sci.* 73, 296 (1978).
238. S. Das Sarma, *Phys. Rev. B* 33, 5401 (1986).
239. S. Das Sarma and W. Lai, *Phys. Rev. B* 32, 1401 (1985).
240. F. J. Fernández-Velicia, F. García-Moliner, and V. R. Velasco, *J. Phys. A* 28, 391 (1995).
241. I. I. Boiko, Yu. M. Sirenko, and P. Vasilopoulos, *Phys. Rev. B* 43, 7224 (1991).
242. T. Kawamura, S. Das Sarma, R. Jalabert, and J. K. Jain, *Phys. Rev. B* 42, 5407 (1990).

UHV-SPM Nanofabrication

G. Palasantzas, J. Th. M. De Hosson

University of Groningen, Groningen, The Netherlands

L. J. Geerligs

Delft University of Technology, Delft, The Netherlands

CONTENTS

1. Introduction
 2. Lithography on Atomic Resist
 3. Vapor–Deposition Nanofabrication
 4. Oxide-Based Lithography
 5. Current Technology Applications
 6. Conclusions
- Glossary
References

1. INTRODUCTION

An eminent physicist, Hendrik Casimir, who headed Philips Research (1957–1972) believed that scientific and technological advancement can be described in terms of a *science-technology spiral*. Although science and technology follow separate streams of development, they interact continuously leading to scientific and technological progress. Clearly, research in the field of microelectronics and materials science provide a good example of such interaction. Indeed, results of scientific research are crucial for new technologies, and technological advances stimulate further scientific progress. In the 1980's, the development of pattern generation and the fabrication of advanced semiconductor structures made feasible the study of microscale circuits for the first time. Researchers discovered methods to manipulate single electrons in micron-scale circuits and to observe quantum effects when electrons are confined in small spaces. The advancement of scanning probe microscopy (SPM) techniques allowed the miniaturization down to nanoscale of electronic devices thus opening the possibility for further exploitation of quantum mechanical phenomena at room temperature.

Indeed, in recent years there has been an outstanding development of new methods for micro- and nanofabrication

techniques using SPM [1–15], which will be essential to scientific progress in many areas in physics, materials science, chemistry, and biology. They will form enabling technologies for applications such as nanoelectronics, molecular electronics, micro-optical components, nanoelectro-mechanical systems, catalysis, etc. Advances are strongly aided by the highly engineered and successful lithography techniques that are used in microelectronics. One of the fundamental limits in lithography is imposed by the properties of the resist layer, since for the smallest feature, size one would like the thinnest resist and/or the highest possible contrast. Although today, conventional electron beam lithography is widely used to pattern features with dimensions larger than 10 nm [8], direct writing schemes based on SPM lithography in combination with chemical vapor deposition (CVD) and physical vapor deposition (PVD) schemes of various metals and semiconductors (i.e., for Fe, Pd, Ni, Cd, Si, Al) [1–6, 9–15] have led to feature sizes less than 10 nm.

It is hoped that nanoscale-size metal patterns can be used as model systems to study aspects of nanoscale electronics such as single-electron tunneling [2]. An example design of a nanoscale device is shown in Figure 1 which was made by H desorption by the scanning tunneling microscopy (STM) tip on a hydrogen (H)-passivated Si(100)2 × 1 surface. In such a device, in order to observe charging effects in electronic transport measurements (where the object has to by definition be coupled to the environment), the thermal energy has to be lower than the change in charging energy by single electron transfer. Since, at room temperature, the thermal energy is of the order of $k_B T \approx 0.025$ eV (k_B the Boltzmann constant and T system temperature in Kelvin), the island size has to be below 10 nm in order that the change in charging energy $E_c = q^2/2C$ (with C the island capacitance and q its charge) satisfies the requirement $E_c > k_B T$ [2]. Under this condition, electrons tunnel between the electrodes and the island one-by-one leading to a well-defined charge state. The discrete flow of charged particles gives rise to the so-called Coulomb blockade.

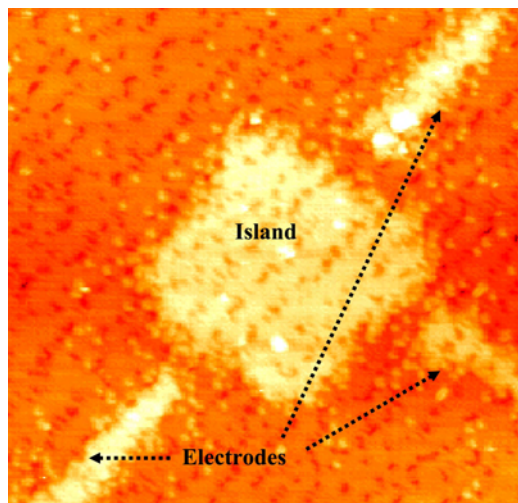


Figure 1. Design of a single electron-tunneling transistor with island size 30×30 nm.

Quantum mechanical effects start playing a dominant role in nanometer-size structures, since the number of energy levels is discrete and rather limited [2, 16]. Consider as a simple example the case of a thin metal film of thickness d (<30 nm) with volume electron density n , and the electron motion quantized along the direction perpendicular to film surface and free along the film plane; then the number N of available electron minibands E_v is given by $nd = (m/\pi\hbar^2)(NE_F - \sum_{v=1,N} E_v)$ with E_F the Fermi level such that $E_N < E_F$. N and E_F can be easily calculated assuming that the electrons are localized in the film by an infinite confining potential well (well-box model), since in this case $E_v = (\hbar^2/2m)(v\pi/d)^2$ with m the effective electron mass [16].

At any rate, an outstanding breakthrough in nanoelectronics would be the connection of SPM-created nanostructures to the macroscopic world through, for example, metallized contacts to allow characterization of their electrical properties. Figure 2 shows a contact pattern written by electron beam lithography on a Si(100) sample and finally metallized by W deposition at a rate 0.2 nm/sec. The next preparation steps involved cleaning and annealing under ultra-high vacuum (UHV) conditions to achieve atomically clean Si(100) 2×1 surface in-between the contact electrodes. Scanning Auger Map (SAM) chemical analysis for Si and W shows also that the surface is clean and suitable for direct lithography (Figure 3).

Finally, besides lithography on Si-supported systems, an electron (e-) beam can also be used as a tool for local oxidation of metal surfaces. Indeed, fundamental and technological interests in the fields of corrosion and catalysis have given an impetus to numerous investigations on the growth of oxide layers on Ni, Ni/Al, and Al/Mg alloy surfaces (i.e., Figure 4 bright spots) [17–23]. These studies can contribute to lithography techniques in microelectronics [24], exchange-bias junctions (ferromagnetic/antiferromagnetic) [25], aerospace technology [26, 27], model systems in catalysis phenomena [17–21], etc.

The previous examples show some possible routes to nanoscale SPM-based lithography, which will be illustrated in more detail in the upcoming sections.

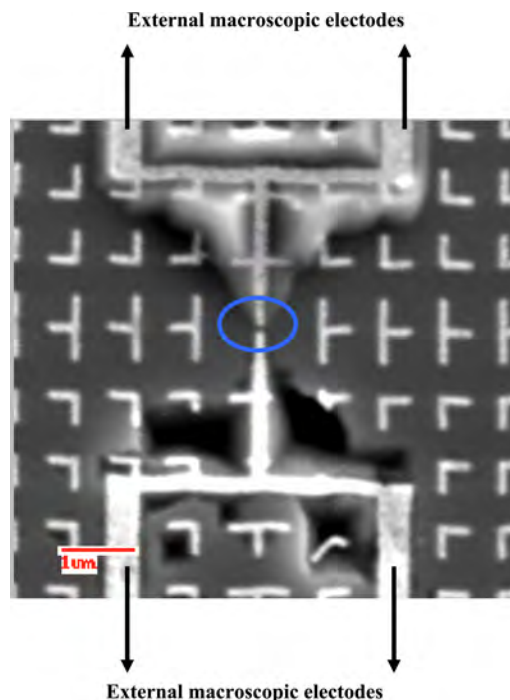


Figure 2. Scanning electron microscopy (SEM) image of a W-silicide electrical contact pattern. The circle shows the area of 100 nm opening where SPM nanostructure design (Fig. 1) and metallization is desirable.

2. LITHOGRAPHY ON ATOMIC RESIST

2.1. Lithography Onto Hydrogen Passivated Si Surfaces

Surfaces formed by a simple truncation of the bulk structure are often energetically unstable, where the high density of unsaturated bonds often leads to local rearrangement and rebonding of surface atoms in order to reduce the density of such dangling bonds. The surface reconstruction reflects a compromise between energy reduction by dangling bond saturation and a cost of increased energy by introduction of surface strain. H-passivation of remaining dangling bonds is commonly applied to Si(001) 2×1 reconstructed surfaces, since an atomically flat surface is preserved (Figure 5a) [1, 2]. In contrast, UHV H-passivation of Si(111) 7×7 reconstructed surfaces leads to rough surfaces [28].

The H-passivated samples were fabricated in UHV, where atomically clean Si(001) 2×1 surfaces were formed by resistive heating to remove the Si-oxide [6]. For example, for the Cobalt experiments that will be described later, the reconstructed Si(100) 2×1 samples were dosed with atomic H from high purity molecular H₂, which was dissociated by a hot (~ 1500 °C) W-filament at a distance ~ 8 cm from the Si substrate. The latter was kept at a temperature ~ 400 °C to ensure monohydride coverage. The passivations lasted 6 min at a chamber pressure $P_{H_2} \sim 3 \times 10^{-6}$ mbar, resulting in a dose ~ 1080 L (1 L = 10^{-6} Torr sec), which suffices to passivate fully the Si(100) 2×1 surface.

For positive sample bias voltage (voltage between surface and STM tip) larger than 6 V, the removal of H atoms (Figure 5b) is related to direct excitation of a bonding/anti-bonding transition of the Si—H bond, while for bias voltages

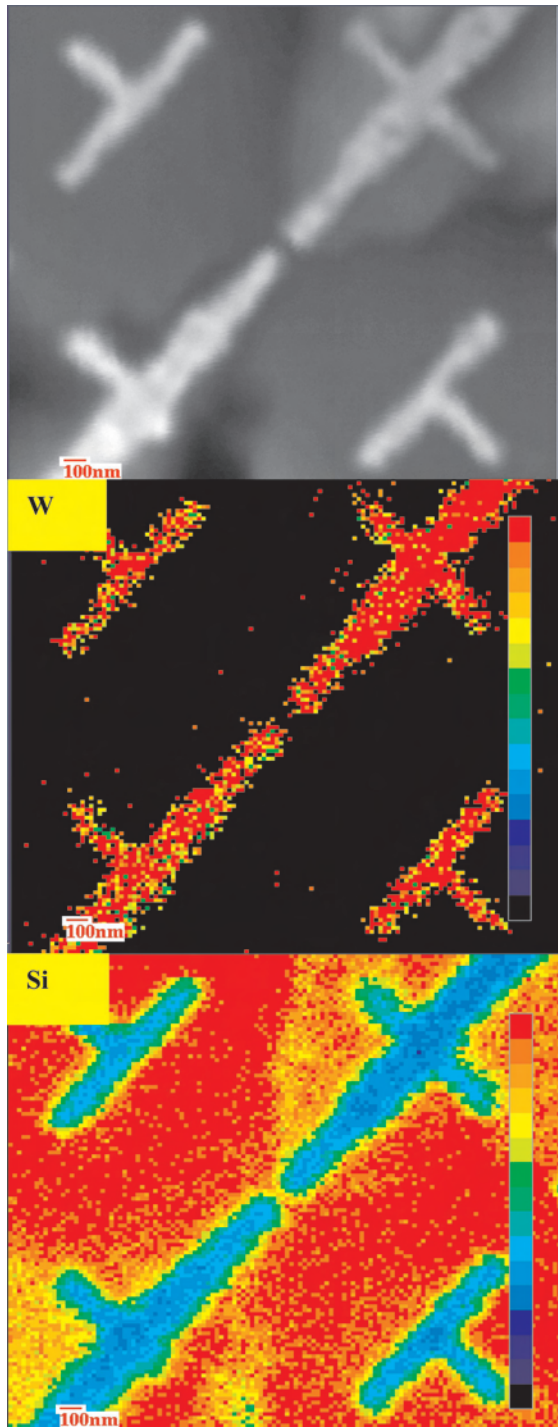


Figure 3. High-resolution SEM image of the central contact electrodes of Figure The sample was annealed for 30 sec at 750 °C and further at 1000 °C for 15 sec to achieve atomically clean Si(001)2 × 1 surface. SAM images of Si (89 eV) and W (163 eV) Auger peaks.

lower than 5 V, the H desorption is related to vibrational heating induced by the inelastic scattering of tunneling electrons with the Si—H 6σ* resonance [1, 2]. At any rate, the shape of the H-depassivated lines depends strongly on the applied sample bias voltage, the electron dose per H-site, and the tunneling geometry (tip shape, tip-sample distance, etc. (Figure 6)). Also note that local desorption of H is also

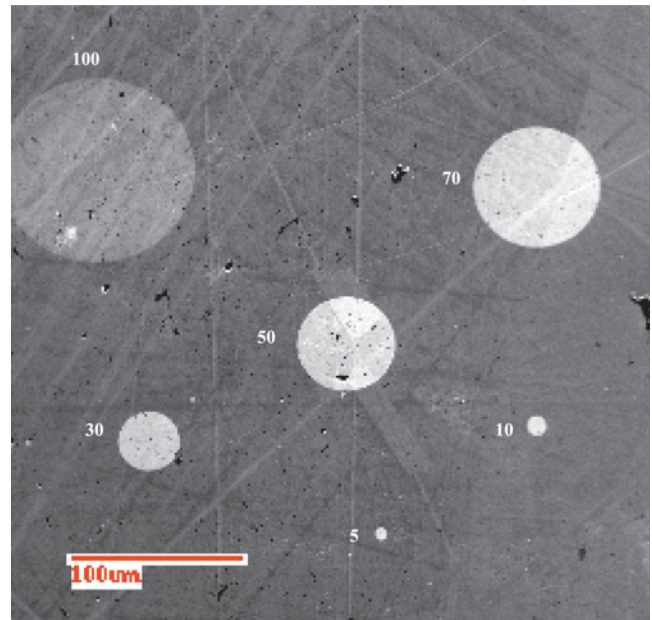
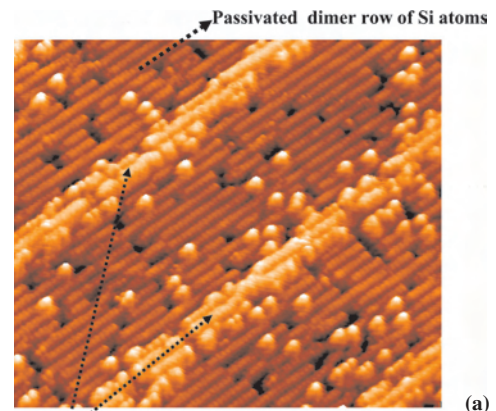


Figure 4. Electron beam-induced oxidation of Ni₃Al with electron beam current of 2.4 nA, accelerating electron voltage 10 keV, and variable electron beam sizes from 5–100 µm. Reprinted with permission from [6], G. Palasantzas et al., *J. Vac. Sci. Technol. A* 19, 2581 (2001). © 2001, American Institute of Physics.



Depassivated dimer rows by the STM tip

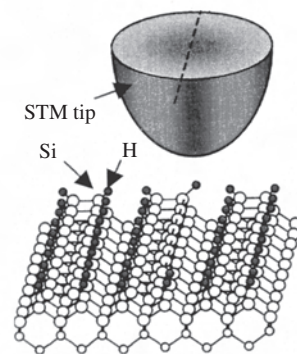


Figure 5. (a) STM tip H-depassivation with current 3 nA, voltage 5.5 V, writing speed 100 nm/sec. Filled state image (bias voltage 1.67 V, tunneling current 0.48 nA). (b) Schematic of the STM tip over the H-passivated Si(001)2 × 1 surface.

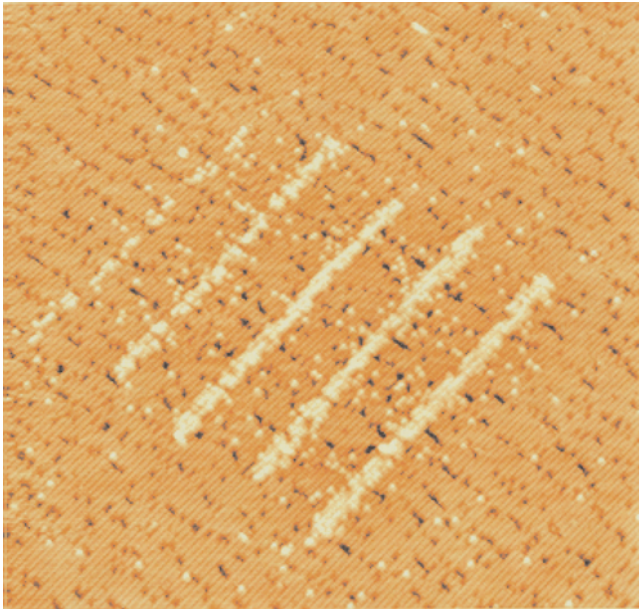


Figure 6. H-depassivated lines with bias voltage 5.5 V, line writing speed 200 nm/sec, and tunneling currents (a) 1 nA, (b) 2 nA, (c) 3 nA, and (d) 4 nA (scan size 85×90 nm).

possible for negative sample bias voltage (filled state). This is believed to be associated with inelastic scattering of tunneling holes with the Si—H 5σ hole resonance. The latter is characterized by a strongly reduced desorption rate [6].

At any rate, an inherent limitation to the resolution of scanning probe lithography on H passivated Si(001) 2×1 surfaces is the area occupied by a single H atom (0.4×0.8 nm on the reconstructed Si(001) 2×1 surface). Finally, another major limitation of scanning probe lithography is the slow writing speed, which, however, can be improved by building arrays of faster STM's [2]. We should also note that electron beam lithography by the STM is similar to classical electron beam where 10–100 keV are used (i.e., within an electron microscope). However, because the effect of the backscattering of electrons by the substrate, the result is a smaller exposed area and lower line width. On the other hand, the electron-sensitive layer has to be very thin (~ 1 –10 nm), depending also on bias voltage, in order to overcome the small penetration depth of the low-energy STM electrons (~ 1 –10 eV) into the resist layer, as well as to overcome the limited tip-sample distance that is imposed by the tunneling process.

2.2. Isotope Effect: The Case of Deuterium

The STM tip-induced desorption process also displays a large isotope effect. Substitution of H by deuterium (D) leads to a D desorption yield (at 300 K), which is about a factor of 50 lower than that of H [2]. The magnitude of the isotope effect is unusually high, while kinetic isotope effects are usually lower by a factor smaller than 10. A number of different mechanisms can give rise to an isotope effect [2]. The higher thermal activation barrier for deuterium, due to its lower zero-point energy, can be ruled out as a reason for the isotope effect since the desorption yield depends on

temperature. Similarly, the lack of temperature dependence of both the yield and the isotope effect exclude also H (D) tunneling through a barrier for a possible a mechanism.

A different mechanism that involves the quenching of an excited state, which leads to large isotope effects, is the related physical mechanism [2]. In this mechanism, the isotope effect is due to the larger mass of deuterium and its influence on the extent of quenching. Both H and D feel the same repulsion moving on the excited-state potential energy curve. However, D moves more slowly and, therefore, it stays in the vicinity of the surface longer, so that the corresponding excited state is more heavily quenched [2]. Therefore, if the isotope effect is the result of an allowed electronic transition and no thermal activation is necessary, no dependence on temperature should be expected, which was in agreement with findings by Foley et al. [2].

3. VAPOR-DEPOSITION NANOFABRICATION

3.1. Aluminum (Al)-PVD Nanofabrication

In this section, we report a basic study of Al PVD nanofabrication by Shen et al. [3]. After verifying by STM a uniform monohydride 2×1 reconstructed surface, Al was evaporated from a coated W filament. Figure 7 shows the pattern on the H-passivated Si(001) 2×1 surface before and after Al deposition, with Figure 8 showing close-up images

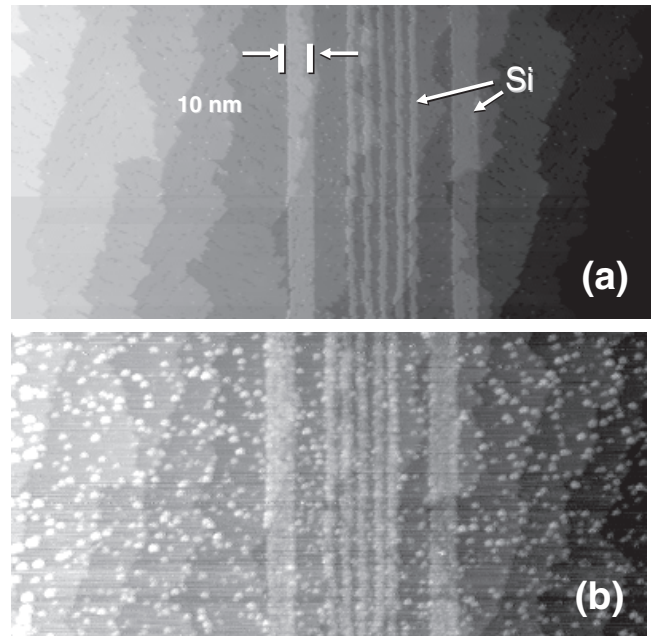


Figure 7. (a) 240×120 nm STM image of a pattern created by STM tip with sample bias 4 V, tunneling current 4 nA, and line dose 2×10^{-3} C/cm. The 10-nm wide lines were made by writing 9 passes with 1 nm pitch, while the thin lines were made by writing a single pass each with 6 nm pitch. The STM image was taken at sample bias 2.2 V, and tunneling current 0.1 nA. (b) Same pattern after deposit of 0.1 ML Al (courtesy J. R. Tucker and T.-C. Shen). Reprinted with permission from [3], T.-C. Shen et al., *Phys. Rev. Lett.* 78, 1271 (1997). © 1997, American Physical Society.

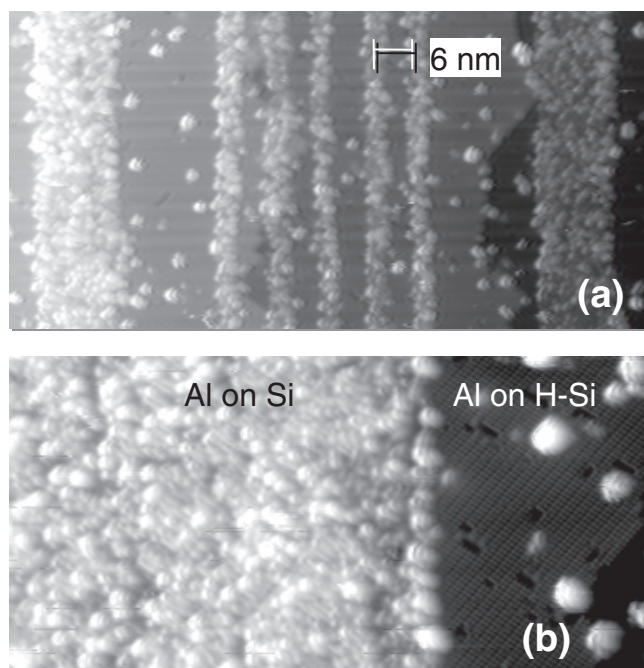


Figure 8. (a) 80×40 nm close-up STM image of Figure 7(b). (b) 40×20 nm STM image of a metallized pattern boundary (courtesy J. R. Tucker and T.-C. Shen). Reprinted with permission from [3], T.-C. Shen et al., *Phys. Rev. Lett.* 78, 1271 (1997). © 1997, American Physical Society.

of the Al metallized areas. Al islands nucleate much more on the bare Si patterns (H-depassivated areas) than on the surrounding monohydride side. The monohydride regions “confined” between bare Si lines were observed to contain fewer and smaller Al clusters than monohydride areas far from the patterns. By varying the width of the confined region, Shen et al. [3] found that the Al cluster density is constant from open regions down to a width of 7 nm. In the pattern of Figure 8a, the smallest confined monohydride areas are ~ 3.5 nm wide and the density of Al clusters is only half that in open regions. The latter implied that the diffusion length of an Al atom on the monohydride surface was between 3.5–7 nm [3].

Figure 8 also shows that the density of Al clusters at the boundary between bare and monohydride Si regions is much higher than in the interior of either. This indicates that Al–Si binding on bare Si(001) is much easier than Al–H–Si binding on the mono-hydride surface, due to the exposed dangling bonds of the Si dimers [3]. Since clusters on the boundary have the same general appearance as those on the monohydride surface, most of the growth of these clusters comes from diffusion of Al adatoms from the monohydride side. Thus, the diffusion length of an Al adatom is much greater on the monohydride side than on the bare Si side [3]. The difference in binding probability between the two surfaces leads to a significantly lower final density of the Al adatoms in the confined monohydride regions and also to smaller cluster sizes.

By greatly reducing the deposition rate and adjusting sample temperature and/or metal species to maximize surface adatom diffusion over the hydrogen termination, it may be possible to approach total selectivity in patterns, 5 nm or

less in feature size. Single-dimer resolution has previously been demonstrated in STM-induced desorption of hydrogen from the monohydride surface [3], so that quasi-atomic patterning of metal lines might be achieved. This method offers a practical means for the linking of metal nanostructures to external contact electrodes (Figure 2), which is more convenient than single-atom manipulation by STM.

3.2. Cobalt (Co)-PVD Nanofabrication

Cobalt merits special attention since it forms a silicide with widespread applications in microelectronic devices (e.g., transistor gates, contacts, interconnects, etc.) due to its low electrical resistivity and small lattice mismatch with Si. Co also has the advantage that all its silicide phases are metallic [29]. In a room temperature (RT) nucleation study of Co on H-(wet)-passivated Si(111) surfaces [30], the growth mode was shown to be dominated by the formation of sparse nonepitaxial islands that grow laterally to merge. In that case, the H-passivated surface did not contain Si adatoms, which constitute the nucleation sites for Co-silicide even at RT [31]. Similar behavior was also observed for Co on H-passivated Si(001), prepared in UHV and studied *in-situ* by STM [32]. This is different from submonolayer growth of Co on bare Si(001), where interstitial Co diffusion and reaction with the Si substrate occurs [33]. Therefore, elimination of nucleation sites yields three-dimensional clusters in the early stages of deposition, indicating that nucleation of highly reactive thin metal films can be strongly altered by the presence of adsorbates (i.e., H) at the metal/Si interface. Nucleation sites on the H-passivated surface are surface defects (e.g., steps, impurities, or some other flaw) [30], or just statistics: if two or more adatoms meet, they form clusters (see Figure 9a and 9c) [3, 32].

Upon submonolayer deposition of Co on a H-passivated Si(100) 2×1 surface at RT, the H-passivation layer stays

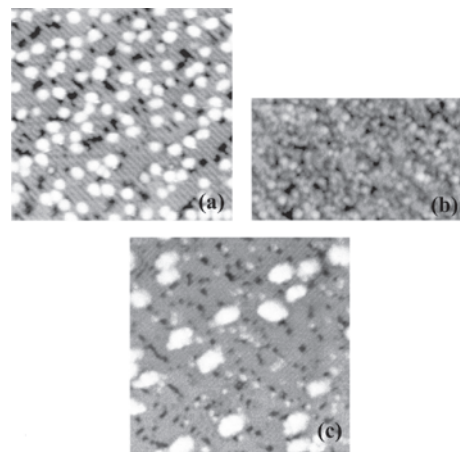


Figure 9. (a) Co clusters on a H-passivated Si(001) 2×1 surface formed after 0.2 ML of Co deposition at RT (scan size 40×40 nm). (b) The same case but on bare Si(001), where Co-Si reaction occurs leading to a disordered surface (scan size 40×22 nm). (c) Deposition of 0.2 ML of Co on H-Si(001) 2×1 surface held at 405°C (scan size 40×40 nm). In all cases for STM imaging the tunneling current was 0.1 nA and sample bias -2 V. Reprinted with permission from [6], G. Palasantzas et al., *Surf. Sci.* 412–413, 509 (1998). © 1998, Elsevier Science.

intact and blocks the reaction of Co with the Si substrate. Figure 9a shows the formation of Co clusters on such a surface. For deposition on the bare Si(100) 2×1 surface, the absence of H allows the interstitial diffusion of Co atoms into Si [33], accompanied by the first silicidation reaction (Figure 9b). In comparison, Al forms a well-ordered dimer-row structure on bare Si(100) for coverage below 0.5 monolayers [3]. Furthermore, a dense concentration of Co in the depassivated lines occurs with respect to the monohydride areas. Co atoms nucleate randomly even rather close to the wire at distances $3 \sim 5$ nm (Figure 10a), which are comparable with the island spacing on the monohydride side. A significant depletion zone around the wire boundary was not observed, which may be different for the case of PVD of Al [3] shown previously.

Device fabrication processing at an elevated temperature is often unavoidable, and its effect on nanostructures can be deleterious. Some metals suffer under high-temperature treatments from the dissolution in Si (e.g., Al/Si structures degrade upon annealing >400 °C [33]), while other metals form upon annealing stable silicides. Co has the advantage that all its silicide phases are metallic [29] while, for example, FeSi₂ is usually semiconducting (depending on the corresponding phase) [34].

Figures 10b and 10c shows a sample where 0.13 ML of Co was deposited at RT on a H-passivated Si(001) surface with depassivated lines of about $\sim 4\text{--}5$ nm wide after which the surface was annealed at 410 °C for 20 sec. The silicidation reaction in the wire area leads to an increase in silicide volume, which leads to a more distinct and compact structure than that formed at RT. The monohydride side remains intact even closely to the wire boundary despite the annealing processes, since H starts to desorb for $T \geq 470$ °C [10].

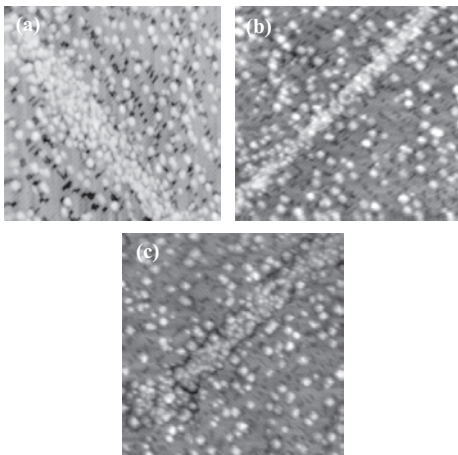


Figure 10. (a) 0.13 ML of Co deposited at RT resulting in wire (patterning parameters as in Fig. 2a) width approximately 8–9 nm. Filled state image acquired with bias -2 V and current 0.12 nA. (b) Co/Si wire deposited at RT and annealed at 410 °C for 20 sec with a wire along the dimer rows (filled state image acquired with bias voltage -1.89 V, current 0.28 nA). (c) Wire perpendicular to dimer rows (filled state image acquired with bias voltage -1.69 V, current 0.34 nA). For (b) and (c) the patterning was performed with current 2 nA, sample bias 7 V, and writing speed 300 nm/sec. Scan size for all STM images is 50×50 nm. Reprinted with permission from [6], G. Palasantzas et al., *J. Appl. Phys.* 85, 1907 (1999). © 1999, American Institute of Physics.

Notably, differences appear when the wire is formed perpendicular (Figure 10b) and along the dimer rows (Figure 10c). In the second case, a more compact structure with more regular boundaries is found. This finding is in good agreement with the shape and appearance of CoSi₂ islands on Si(100) formed at elevated temperature [32], which show edges that are straight on the atomic scale parallel to the dimer rows while they can be rather rough in the perpendicular direction. This is possibly due to different directional surface strain and adatom mobility parallel and perpendicular to the Si dimer rows.

3.3. Palladium (Pd)-PVD Nanofabrication

Since the maximum thickness of well-defined silicide features is limited by the selectivity of the deposition process, Mitsui et al. [35] have investigated the dependence of selectivity on deposition temperature. Upon Pd-PVD on an STM-patterned monohydride terminated Si(001)-(2×1) surface, it was found that Pd growth selectivity is due to the different diffusion lengths on bare and H-terminated surfaces, and that the selectivity increases with increasing temperature from 500 K to 600 K [35]. This is shown in Figure 11, where palladium selectively deposited on a 6 nm wide strip of bare Si(001) on an H-terminated surface. The nanostructure consists of uniform clusters on the bare strip. The selectivity results from the difference in Pd diffusion lengths on bare versus H-terminated silicon. A crystal structure was observed after a 1000 K anneal [35].

3.4. Aluminum (Al) and Iron (Fe)-CVD Nanofabrication

Chemical vapor deposition (CVD) is an alternative to evaporation for material delivery (Figure 12) [35]. In CVD, the growth element arrives at the surface incorporated in a molecular precursor. On appropriately reactive surfaces, the molecule dissociates and deposits the growth element (Figure 12b). Chemical vapor deposition is a popular

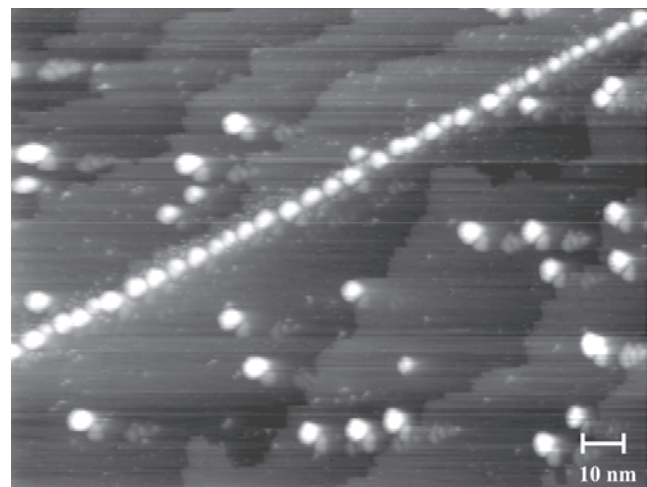


Figure 11. Palladium deposition and fabrication of nanoscale wires with width less than 10 nm on H-Si(001) 2×1 reconstructed surfaces (courtesy E. Ganz).

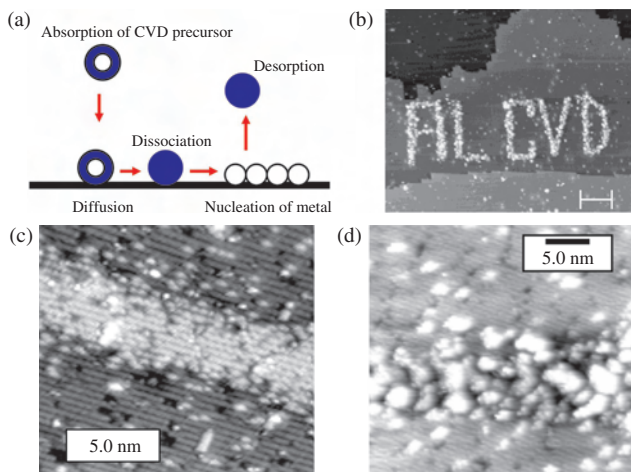


Figure 12. (a) Schematic explanation of the CVD process. (b) STM image of an Al nanostructure CVD fabricated on H resist. The line width is less than 3 nm and the height 0.3–0.5 nm (courtesy E. Ganz). Reprinted with permission from [35], T. Mitsui et al., *J. Appl. Phys.* 85, 522 (1999). © 1999, American Institute of Physics. (c) H-depassivated area prior to Fe CVD by electron beam stimulated desorption with a sample bias of 1.8 V and a line dose of 100 mC/cm. The STM image was taken with sample bias of -2.3 V and tunneling current 0.15 nA (courtesy T. M. Mayer). Reprinted with permission from [5], D. P. Adams et al., *Appl. Phys. Lett.* 68, 2210 (1996). © 1996, American Institute of Physics. (d) STM image after Fe CVD growth taken with a sample bias of -2.3 V and a tip-sample current of 0.15 nA (courtesy T. M. Mayer). Reprinted with permission from [5], D. P. Adams et al., *Appl. Phys. Lett.* 68, 2210 (1996). © 1996, American Institute of Physics.

method for microelectronics device fabrication because of its low cost, high deposition rate, high purity, good conformal coverage, and potential for strong growth selectivity.

3.5. Al-CVD

Mitsui et al. [35] used an Al precursor, dimethylaluminum hydride [DMAH, $\text{Al}(\text{CH}_3)_2$]. This is a promising, new chemical precursor because of its stability, low carbon contamination, and ease of introduction. Al CVD, using DMAH, has been extensively studied over the last few years [4]. Tsubouchi et al. have used DMAH to selectively deliver Al to a silicon surface patterned by electron beam lithography and selective oxidation [5]. The surface was patterned into dihydride terminated and oxidized regions. Under the conditions of their experiment, the DMAH preferentially deposited Al on the hydrogen-terminated surface. However, this is an undesirable negative patterning process, with the Al deposited outside the patterned areas. A variation of this method, which provides a positive patterning process, is rather difficult [36].

An example of Al CVD on H-passivated Si(001) surfaces is shown in Figure 12b. At RT, DMAH is adsorbed intact on the bare Si surface obtained by H desorption. At temperatures above 120 °C, Al deposition began. Indeed, clean Al growth was observed for substrate temperatures between 150 and 300 °C [35]. By contrast with the earlier work on bare Si, it was found that DMAH does not stick on RT monohydride-terminated Si surface. Furthermore, Al deposition was not observed on monohydride

surfaces up to 300 °C. This indicates that DMAH can provide high Al selectivity between bare and monohydride-terminated Si(001) surface at temperatures between 150 and 300 °C [35]. It is important to note that there is no Al growth enhancement along the border between the silicon and hydrogen-terminated regions in Figure 12b. Such an enhancement was observed by Shen et al. [3]. It was attributed to free Al atoms on the H-terminated surface diffusing to and sticking on the bare region. For Al CVD, the DMAH deposits Al only on bare Si regions.

The work by Mitsui et al. [35] demonstrated that this lithography method combines the high selectivity of the CVD precursor DMAH with the precision of an STM-patterned hydrogen resist, where sizes as small as 2 nm can be achieved. Employing computer control in the patterning phase, this process can be used to fabricate complex structures as shown in Figure 12b. The origin of the strong Al selectivity [35] stems from the fact that the $\text{Si}(001)2 \times 1$ reconstructed surface is composed of pairs of Si atoms, each of which are joined by a strong σ -bond and a weak π -bond. The π -bond is only 0.9 eV below the Fermi level, which makes $\text{Si}(001)2 \times 1$ a highly reactive surface [37] on which the DMAH molecules are able to dissociate and deposit Al. In the case of the hydrogen-terminated surface, the π -bond is replaced by two strong Si—H bonds and the surface is passivated. Thus, the DMAH is *unable* to chemically bond or dissociate on such a surface.

3.6. Fe-CVD

Finally, we shall describe the work of Adams et al. on selective CVD growth of Fe nanostructures using a CVD precursor, $\text{Fe}(\text{CO})_5$ [5] on a patterned hydrogen-terminated surface (Figure 12c). Fe is *selectively* deposited onto the patterned areas by pyrolysis of $\text{Fe}(\text{CO})_5$, as is shown in Figure 12d. The Fe lines formed on the clean Si have a rough surface morphology and are most likely polycrystalline. Scanning tunneling microscopy and heavy ion backscattering spectrometry confirmed that that 2 ML monolayers of Fe are locally deposited during a 60 L dose [5]. Separate experiments, by x-ray photoelectron spectroscopy, indicated very small C and O impurity levels, characteristic of pyrolysis onto Si substrates at elevated temperatures [5].

Fe nucleation during CVD growth is dominated by site-specific chemical reactivity of the precursor $\text{Fe}(\text{CO})_5$ with the Si substrate. Former work has shown that decomposition of the $\text{Fe}(\text{CO})_5$ molecule occurs predominantly at Si dangling bond sites [5]. Passivation of the dangling bond sites with hydrogen removes the active site for pyrolysis and effectively raises the activation barrier for nucleation. Notably, the Fe CVD is autocatalytic on Si. For example, the barrier to dissociation of the precursor on an existing Fe cluster is smaller than on the clean Si surface by approximately 0.14 eV on Fe and 0.40 eV on Si [5]. Therefore, once a nucleus is created, it grows rapidly compared to the formation of additional clusters. This highly nonlinear growth rate is advantageous in maintaining the area selectivity of metal deposition on clean Si surfaces [5]. These results for Fe show clearly that nanostructures can be grown by CVD on patterned H-terminated Si surfaces and also for metals

other than Al. Scanning tunneling microscopy confirms that the adsorbed H is still intact as monohydride in unexposed surface areas and is not disrupted by the $\text{Fe}(\text{CO})_5$.

4. OXIDE-BASED LITHOGRAPHY

4.1. Ni-Oxidation

Besides patterning on H-passivated Si surfaces, an electron beam allows direct pattern formation on metal surfaces. This is initially shown in Figure 4 for the case of Ni_3Al surfaces. The apparatus that was used for these studies [7] consists of a UHV (Figure 13b) (base pressure $\sim 4 \times 10^{-8}$ Pa) scanning Auger/electron microscope (field emission JEOL JAMP7800F). Under typical imaging conditions (accelerating voltage 10 keV and electron beam current

$I = 2.4$ nA, which will be used for the e-beam induced oxidation, if not otherwise stated) the attained beam spot size is ~ 15 nm. The AES measurements were performed on polished sample cross-sections, which were cleaned by Ar-sputtering prior to e-beam exposure. Auger depth profile analysis was performed by low-rate Ar^+ sputtering. Oxygen was provided by the UHV atmosphere to initiate chemisorption and direct oxidation under the influence of the e-beam. For Auger maps, it was recorded the ratio (Peak-Background)/Background from the direct spectrum (Figure 13a).

The oxidation of Ni_3Al was described [7] with the model of Li et al. [20], which is based on the premise that the incident electrons create additional nucleation sites around which oxide islands grow. In terms of Auger intensities, this model reads of the form [20] $I_{\text{O}}(t) = A - (A - B)\exp[-kt - (k/\varphi_e\sigma)\{\exp(-\varphi_e\sigma t) - 1\}]$ with φ_e the electron beam density flux ($\text{cm}^{-2} \text{sec}^{-1}$), σ the electron cross-section for the creation of oxide nucleation sites, t the oxidation time, and k an oxidation rate constant. This model describes the oxidation data for e-beam spot sizes $d < 30 \mu\text{m}$ (see Figure 14 for $d = 5, 10 \mu\text{m}$). A is the saturated Auger intensity and B the intensity at chemisorption. For e-beam sizes of $d \geq 30 \mu\text{m}$, the oxidation curve changes its shape and reveals a much slower oxidation process. The latter is also confirmed by the Auger map of O (Figure 13) where the spot intensity decays drastically with increasing e-beam size for $d > 30 \mu\text{m}$. The flux φ_e is estimated by the relation $\varphi_e = I/(\pi d^2/4)$, assuming circular beam spot size of area $\approx \pi d^2/4$ (with d the beam diameter) and I the beam current.

Depth profile analysis (Figure 15) showed that the corresponding Ni-oxide depth decreases with increasing e-beam size. This also offers an alternative way to monitor Ni-oxide thickness in a nanometer range. Such a process can be strongly relevant for the fabrication of anti-ferromagnetic/ferromagnetic junctions [25], and lithography techniques on Ni-based surfaces [2, 7], as well as Ni-oxide formation for catalysis studies [17–21].

The oxidation curves for beam sizes of $d \geq 50 \mu\text{m}$ (Figure 14a) indicate an oxidation process which is characterized by a tilted constant slope area, followed by a saturation (see Figure 14a for $d = 50 \mu\text{m}$). The formation of oxide nuclei by the beam is no longer sufficient to dominate the O chemisorption, and therefore its contribution to the Auger intensity. Thus, we obtain [7]:

$$I_{\text{O}}(t) = A - (A - B)\exp[-kt - (k/\varphi_e\sigma) \times \{\exp(-\varphi_e\sigma t) - 1\}] - C \exp(-k_{\text{ch}}t) \quad (1)$$

by inclusion of chemisorption characterized by a reaction constant k_{ch} . The corresponding fits are shown in Figure 14a for the $d = 30, 50 \mu\text{m}$ oxidation curves. Saturation is necessary for the fit because it yields the parameter A . The fit for the $d = 50 \mu\text{m}$ oxide spot indicates that O chemisorption occurs rather fast with a reaction constant larger than that of the e-beam-induced oxidation. Similar oxidation scenarios have also been observed for other systems with significant affinity to O such as Ni [7, 17–21], Al(111) [38], and Mg (0001) [39], where oxide nucleation occurs long before the saturation of a chemisorbed coverage is reached.

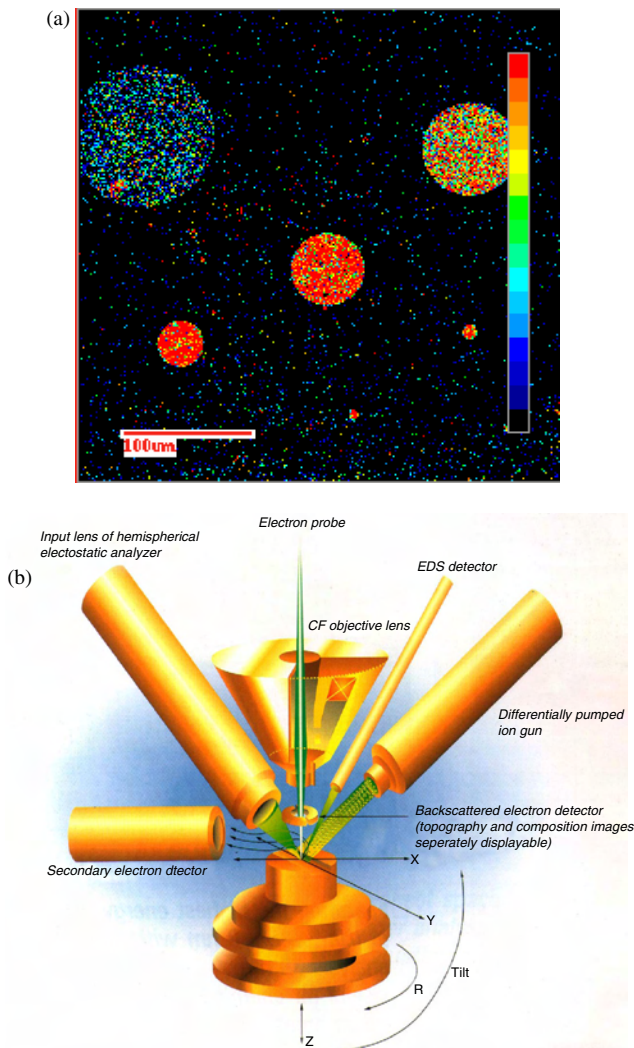


Figure 13. (a) SAM image of O. Data acquired with 100 ms/eV at 40° tilted samples. The typical 15 nm beam spot size was used for SAM imaging. (b) Diagram of the SEM/SAM imaging and data acquisition geometry. Basic components: Secondary electron detector for SEM topography imaging, hemispherical mirror analyzer for Auger imaging-analysis, EDS detector for x-ray bulk microanalysis, ion gun etching for depth profiling, sample stage with its possible motion mechanisms.

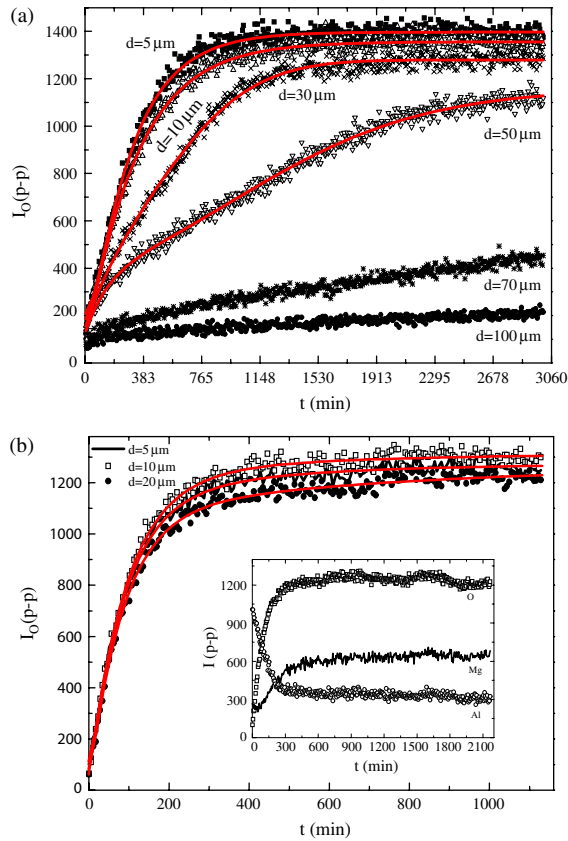


Figure 14. (a) Oxygen peak-to-peak intensity (p-p) vs. oxidation time. Data acquired with 400 ms dwell time (time/eV), 40° tilted samples, and $I = 2.4$ nA beam current. The solid lines are fits by the oxidation model. Reprinted with permission from G. Palasantzas et al., *J. Vac. Sci. Technol. A* 19, 2581 (2001). © 2001, American Institute of Physics. (b) Oxidation curves for oxygen of Al-Mg alloy surface for various e-beam spot sizes d as indicated. The solid lines are the best fits in terms of Eq. (2), and the inset shows an example of the oxidation behavior of all elements (Al, Mg, and O). Reprinted with permission from G. Palasantzas et al., *Appl. Surf. Sci.* 191, 266 (2002). © 2002, Elsevier Science.

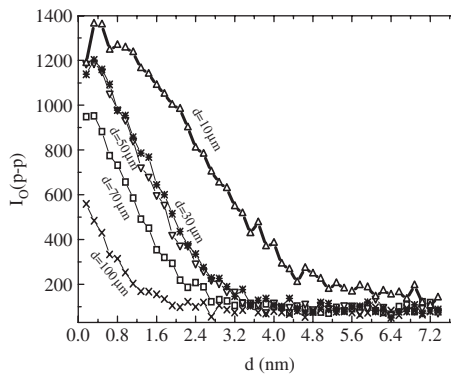


Figure 15. Depth profile analysis with an e-beam spot size of $5 \mu\text{m}$ and 400 ms dwell time. Reprinted with permission from G. Palasantzas et al., *J. Vac. Sci. Technol. A* 19, 2581 (2001). © 2001, American Institute of Physics.

4.2. Al-Mg-Oxidation

Finally, we will examine the case where two (or more) oxidizing elements are present as, for example, in Al-Mg alloy surfaces, where both Al and Mg contribute to the e-beam oxidation process. The present sample surface consisted of a rather random distribution of islands with a bulk composition of (15 ± 1) at % Mg (Mg in solid solution in Al: Al/Mg), where in-between these islands, the corresponding areas have more than double Mg content of (38 ± 1) at % Mg (Al_3Mg_2 , or β -phase). The oxidation took place on the Al_3Mg_2 phase (Figure 14b) and the oxygen curves are shown in Figure 14b and the fits correspond to the more general equation:

$$I_{\text{O}}(t) = A - \sum_{j=1}^N A_j \exp[-(t/\tau_j) - (1/\tau_j)\varphi_c\sigma] \times \{\exp(-\varphi_c\sigma_j t) - 1\} \quad (2)$$

with $N \geq 1$. After saturation, we have $I_{\text{O}}(\infty) = A$, and at $t = 0$, we have $I_{\text{O}}(t=0) = A - \sum_{j=1, N} A_j$, which corresponds to the chemisorption saturation. For the present experiment (Figure 2), there are two elements participating in the oxidation process, namely, Al and Mg, which means that $N = 2$ with indices $1 \equiv \text{Al}$ and $2 \equiv \text{Mg}$. As Figure 14b indicates, the oxidation kinetics surpasses the O chemisorption regime and fast oxide growth dominates the oxidation process. Such an oxidation scenario has also been observed in other systems with significant affinity to O such as Ni [7, 17–21], Al(111) [38], and Mg (0001) [39], where oxide nucleation occurs long before the saturation of a chemisorbed coverage is reached.

At any rate, the Al-Mg alloy oxidation is consistent with the idea that Mg diffusion occurs during the e-beam-induced oxidation of the Al_3Mg_2 surface, which is enhanced by the formation of Al-oxide and Mg-oxide upon e-beam exposure and the high affinity of Mg to O. The activation energy of Mg diffusion in Al_2O_3 -MgO is $Q_{\text{Mg}} \sim 369.9$ kJ/mol, which is smaller than that of O diffusion $Q_{\text{O}} \sim 438.9$ kJ/mol in the same oxide [40, 41], as well as the diffusion prefactor for Mg is much larger than that of O ($D_{\text{O}}^{\text{Mg}} \approx 4.710^2 \text{ cm}^2/\text{sec} \gg D_{\text{O}}^{\text{O}} \approx 8.910^{-1} \text{ cm}^2/\text{sec}$ [40, 41]). These values indicate Mg diffusion and thus segregation through the e-beam-induced oxide layer towards the surface with further MgO formation. Notably, on the areas where Mg is in solid solution, only the oxidation of Al occurs almost without any Mg participating in the oxidation process and/or segregating towards the surface region.

Besides the intense electron beams (keV range) described previously, atomic force microscopy (AFM) also allows selective oxidation of thin metal films to define narrow metal wires by oxidizing unwanted regions of wide metal wires [42]. This process allowed the fabrication of lateral metal-oxide-metal tunnel junctions by introducing thin regions of oxide in an otherwise continuous metal film. By making these junctions very small, the junction capacitance also decreases [2]. These narrow wires can constitute the building blocks from which more complex devices can be built. Recent examples of such devices include a SET transistor by Matsumoto et al. [43], and a metallic point contact by Snow et al. [44].

In the pioneering work by Snow et al. [2, 42, 44], point contacts and tunnel junctions were formed using the AFM

tip to anodise through the cross-section of Al (or Ti) nanometer-scale wires (formed by optical lithography and metal lift-off to pattern 1000-nm-wide \times 5–8-nm-thick metal wires connected to contact pads) while *in-situ* electrical measurements were used as a feedback to guide the anodization. It should be noted that the writing speed and resolution for the AFM-based local oxidation technique is comparable to the results, which have been obtained for the local exposure of a resist layer. However, the local oxidation technique has the important advantage that it works reliably and gives reproducible results (provided that the degree of humidity can be kept constant). Indeed, local oxidation of materials in combination with subsequent pattern transfer has been one of the most successful device fabrication techniques.

5. CURRENT TECHNOLOGY APPLICATIONS

5.1. Effects of Deuterium Desorption on MOS Technology

The studies by Shen and Lyding et al. [1, 2, 45], on H desorption by the STM tip on Si(001) surfaces led to the realization that deuterium was about two orders of magnitude more difficult to desorb than H [2, 46]. An indirect application of these results concern metal-oxide-semiconductor (MOS) transistors with regard to hot carrier degradation effects [2, 47]. In MOS transistors, due to molar volume mismatch at the SiO₂/Si interface, not all of the Si ends up bonded to the oxide resulting in dangling bonds that are becoming charged during transistor operation, thus scattering conduction electrons and shifting voltages used in transistor operation. The dangling bonds are passivated by H after annealing the Si-wafers at \sim 400 °C in H-atmosphere [2]. During transistor operation, however, hot electrons that flow close to the SiO₂/Si interface stimulate H desorption, which leads to reappearance of dangling bonds and transistor degradation. Tests performed by Lucent [47], using deuterium to passivate dangling bonds, indicated increment of the transistor lifetime by an order of magnitude or more [2, 47].

5.2. Silicon-Based Quantum Computer

The challenge to build a quantum computer has been motivated from the formidable computational power such a device could offer. In fact, Si-based proposals, using the nuclear or electron spin of dopants as qubits, are attractive due to the long spin relaxation times involved, their scalability, and the ease of integration with existing silicon technology. Fabrication of such devices, however, requires atomic scale manipulation, which represents an immense technological challenge. It has been demonstrated by O'Brien et al. [48] that it is possible to fabricate an atomically precise linear array of single phosphorus (P)-bearing molecules, as qubits, on a silicon surface with the required dimensions for the fabrication of a silicon-based quantum computer. A quantum bit or qubit is a two-level quantum system which is the building block of a quantum computer.

To date, the most advanced realizations of a quantum computer are qubit ion trap [49] and nuclear magnetic resonance [50] systems. However, scaling these systems to large

numbers of qubits will be difficult [51]. Therefore, making solid-state architectures [52] with their promise of scalability is very important. In 1998, Kane [53] proposed a solid-state quantum computer design using P nuclei (nuclear spin $I = 1/2$) as the qubits in isotopically pure Si ($I = 0$) (Figure 16). One of the major challenges of this design is to reliably fabricate an atomically precise array of P nuclei in Si. Figure 16a shows the process to implement the Kane architecture [48]. This schematic is showing two P qubits in a linear array, incorporated into isotopically pure Si and isolated from surface metal *A* and *J* gates by an insulating barrier. Figure 16b shows a possible process to fabricate an array of P qubits in Si. A low defect density Si(001) 2×1 surface is H-passivated (Figure 17), where after an STM tip is used to selectively desorb H, exposing Si on an atomic scale permitting only one phosphine (PH₃) molecule to adsorb at each of the required sites (Figures 18–20). Finally, low-temperature silicon overgrowth can be used to encapsulate the P array [48]. Although an STM tip has been used for atomic-scale arrangement of metal atoms on metal surfaces [54], rearrangement of individual atoms in a semiconductor system is not straightforward due to the strong covalent bonds involved. Therefore, O'Brien et al. [48] employed the H resist strategy on Si(001) 2×1 .

The requirements for this quantum computer design are very strict. For high-resolution lithography, the Si surface must be atomically flat with a low defect density to allow the formation of a near-perfect resist layer, where one H atom bonds to each surface Si atom (Figure 17). The ability to desorb individual H atoms requires a sharp, large cone angle tungsten tip in order to form desorption sites \sim 1 nm in

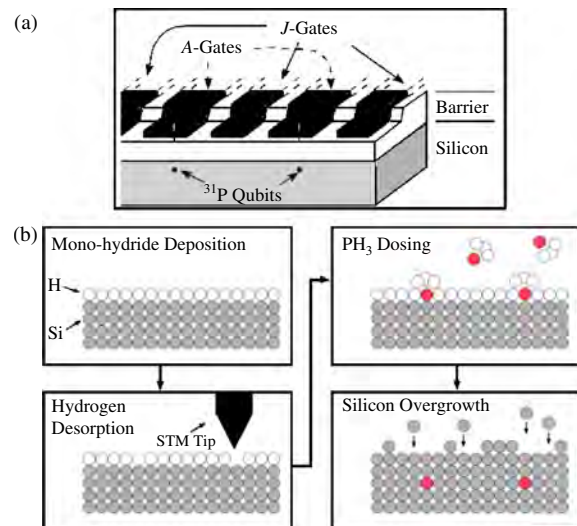


Figure 16. (a) A schematic of the process to fabricate the Kane architecture. Detail of the Kane quantum computer architecture [47] are showing two P-qubits in a linear array, incorporated into isotopically pure Si and isolated from surface metal *A* and *J* gates by an insulating barrier. (b) Process to fabricate an array of P-qubits in Si. A low-defect density Si(001) 2×1 surface is H-passivated. An STM tip is used to desorb H atoms, exposing Si on an atomic scale permitting only one PH₃-molecule to adsorb at each required site (courtesy J. O'Brien). Reprinted with permission from [48], J. L. O'Brien, et al., *Phys. Rev. B* 64, 161401 (2001). © 2001, American Physical Society.

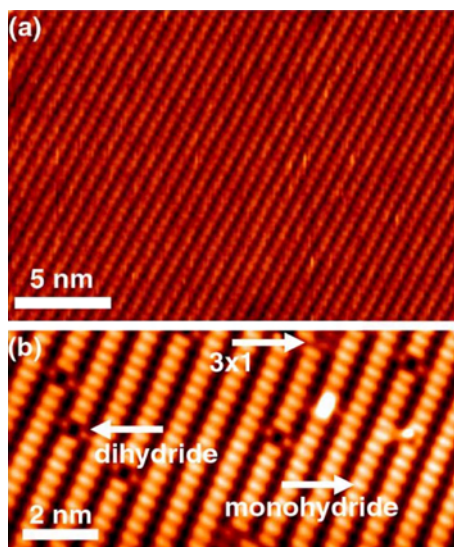


Figure 17. (a) Filled-state STM image of a clean, very low defect density Si(001) 2×1 surface. This image was acquired at a sample bias of 2.1 V and a tunneling current of 0.4 nA. (b) Fully H-terminated Si(001) 2×1 surface. Image acquired at bias 2.5 V and 0.4 nA. The surface is almost entirely 2×1 monohydride, with few sites of 1×1 dihydride and 3×1 trihydride (courtesy J. O'Brien). Reprinted with permission from [48], J. L. O'Brien, et al., *Phys. Rev. B* 64, 161401 (2001). © 2001, American Physical Society.

size. These sites will be subsequently exposed to high-purity PH_3 gas for the required P atom placement (Figure 16b), avoiding the introduction of any spin or charge impurities that would be fatal to quantum computer operation [53]. In order to allow the adsorption of one PH_3 molecule, and therefore only one P atom, it is necessary to desorb an area that exposes *less than or equal to two* Si dimers as is shown in Figure 18a. This is because PH_3 bonds to the Si(001) 2×1 surface with a $c(4 \times 2)$ surface periodicity (Figure 18b). The sticking coefficient of PH_3 molecules on the clean Si surface

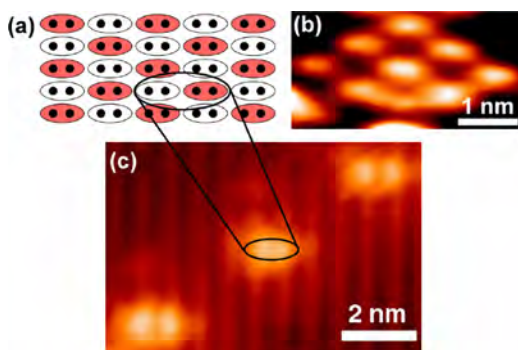


Figure 18. Bonding structure of PH_3 on Si(001) 2×1 . (a) Schematic of the $c(4 \times 2)$ structure of PH_3 bonded to the Si(001) 2×1 surface, where red dimers indicate PH_3 bonding sites. (b) STM image of this structure acquired at a sample bias of 2.3 V and tunneling current 0.2 nA. (c) STM image of three hydrogen desorption sites of H-Si(001) 2×1 -H surface. The highlighted regions in (a) and (c) indicate that only one PH_3 molecule can adsorb at each desorption site (courtesy J. O'Brien). Reprinted with permission from [48], J. L. O'Brien, et al., *Phys. Rev. B* 64, 161401 (2001). © 2001, American Physical Society.

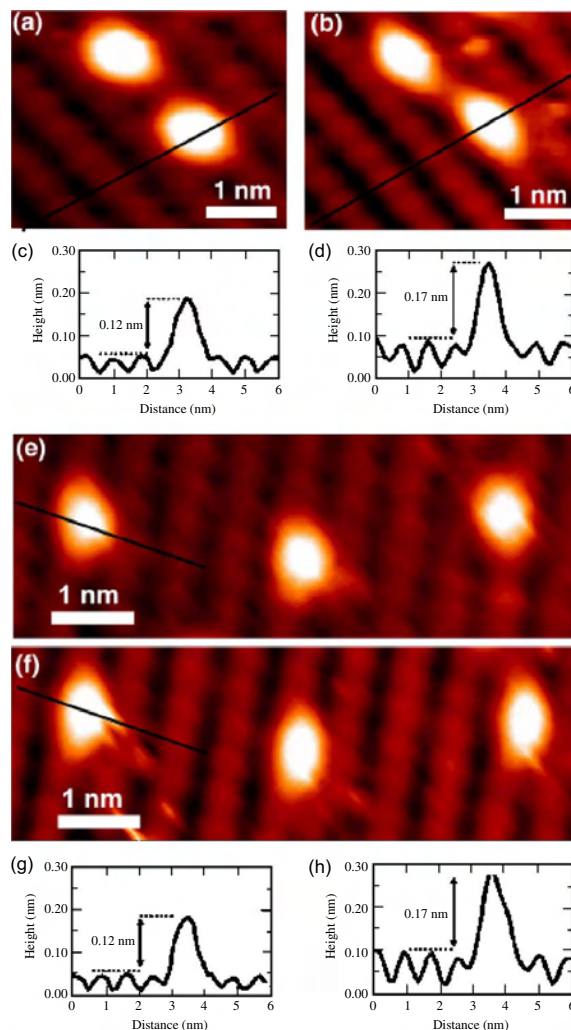


Figure 19. Demonstration of single adsorption through an STM-patterned H resist. STM images of two desorption sites before (a) and after (b) PH_3 dosing. The corresponding line profiles (c) and (d) show a characteristic height increase of 0.05 nm. Three desorption sites before (e) and after (f) PH_3 dosing and corresponding line profiles (g) and (h). STM images were acquired at a sample bias of -1.8 V and tunneling current of 0.4 nA (courtesy J. O'Brien). Reprinted with permission from [48], J. L. O'Brien, et al., *Phys. Rev. B* 64, 161401 (2001). © 2001, American Physical Society.

is 1. Figure 18c shows three smaller than 1 nm in diameter H desorption sites in a row with a pitch of ~ 4 nm on a H-passivated surface.

The ability of the H-passivation layer as a barrier to PH_3 adsorption is demonstrated by the uniform H coverage after PH_3 dosing. As Figure 19a indicates, the bright protrusion at each of the H desorption sites is the signature of the single Si dangling bond, after desorption of just one H atom (in this case from the left side of the dimer: the remaining H on the Si dimer is known to be transient [48] and has been observed to diffuse from one side of the dimer to the other). Figure 19b shows the same area as Figure 19a after exposure to PH_3 gas. Analysis of the line profiles in Figures 19c and 19d shows a characteristic increase of ~ 0.05 nm in the protrusion height after PH_3 dosing [48]. Figures 19d and

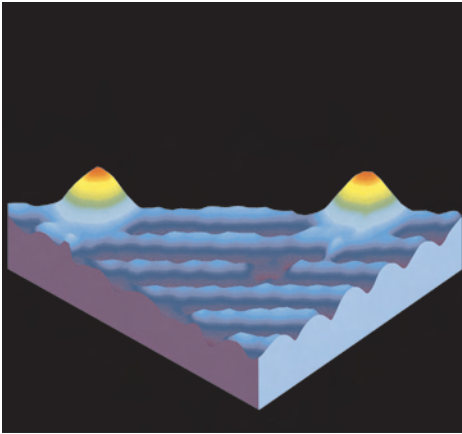


Figure 20. Three-dimensional view of the PH_3 molecule on the $\text{Si}(001)2 \times 1$ surface (courtesy J. O'Brien).

19e show three desorption sites (in a line perpendicular to the Si dimer rows), before and after PH_3 dosing. The height increase confirms the adsorption of a PH_3 molecule and corresponds to the difference between the exposed Si dangling bond and the adsorbed PH_3 molecule. At any rate, O'Brien et al. [48] has answered the critical questions of whether H resist is effective during exposure to PH_3 and whether or not PH_3 will adsorb to an STM-exposed site sufficiently small to achieve one and only one PH_3 molecule at that site. This is an important advance in qubit fabrication for the realization of a scalable Si-based quantum computer.

5.3. SPM Manipulation of Individual Atoms and Molecules

Individual atoms on a surface can be manipulated with an STM microscope due to the strong interaction between the tip and surface at a small working distance [56]. By sliding atoms to exactly controlled positions, a structure can be built atom-by-atom as it was demonstrated in the past by Eigler et al. [56] (see also Figure 21). More examples can be found on the IBM website [57]. Figure 21 shows the direct observation of standing-wave patterns in the local density of states of the $\text{Cu}(111)$ surface. These spatial oscillations are quantum-mechanical interference patterns caused by scattering of the two-dimensional electron gas of the Fe adatoms and point defects. Surface state electrons on $\text{Cu}(111)$ were confined to closed structures (corrals) defined by barriers built from Fe adatoms. The barriers were assembled by individually positioning Fe adatoms, using the tip of a low-temperature STM. A circular corral of radius 71.3 Angstrom was constructed in this way out of 48 Fe adatoms [56, 57].

Such a technique has been the most spectacular demonstration of scanning probe lithography, which allows the possibility of constructing artificial molecules out of their constituent atoms. Apart from individual atoms, molecules can also be manipulated [58]. The manipulation of atoms and molecules is related to a nanofabrication technique that is often called mechanosynthesis, opening the road towards molecular nanotechnology [59, 60].

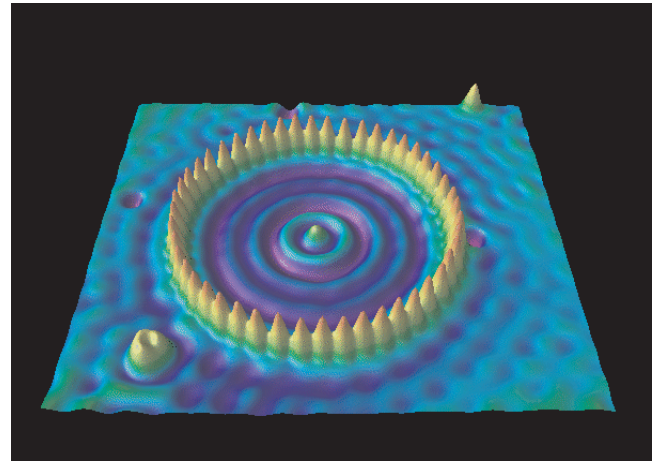


Figure 21. This schematic shows the direct observation of standing-wave patterns in the local density of states of the $\text{Cu}(111)$ surface (courtesy D. Eigler). Reprinted with permission from [57], <http://www.almaden.ibm.com/vis/stm/>. © IBM.

5.4. Local Charge Deposition by Proximal Probe Microscopy

Proximal probe microscopy can be used to perform local charge deposition in Co nanoclusters embedded within insulating matrices such as SiO_2 , and subsequently, to image-injected charge and charge transport [61]. Charge is injected from the probe tip into the sample by application of a

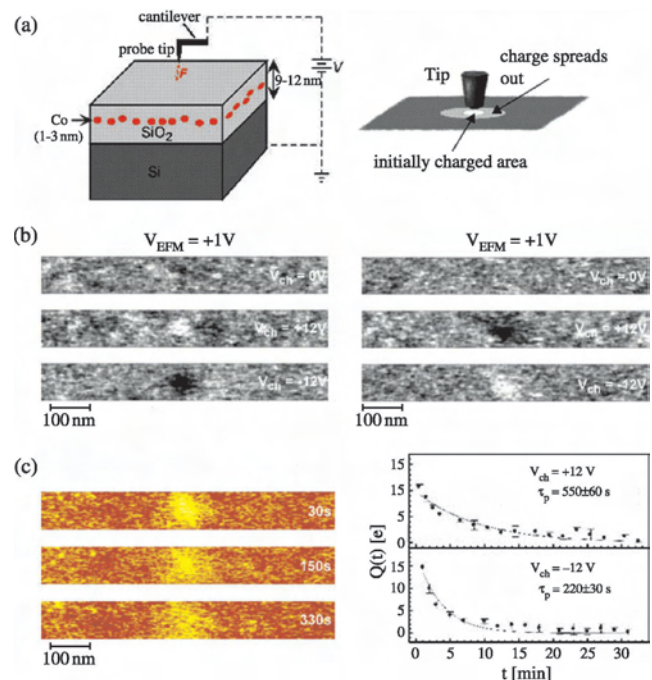


Figure 22. (a) Sample and probe tip geometry for proximal probe charging of Co nanoclusters embedded in SiO_2 , (b) Electrostatic force microscope images of a Co/SiO_2 discontinuous multilayer sample before and after charging at $+12\text{ V}$ and -12 V , (c) Sample charge as a function of time, showing the dependence of discharging time on the sign of the injected charge (figures were obtained from <http://keseey.ucsd.edu/group/PROJECTS/>, and courtesy E. T. Yu).

voltage pulse (Figure 22). Electrostatic force microscopy is then used to image the charged region of the sample. Charge can be injected in a controlled way into areas of radius ~ 20 – 50 nm. It has been observed that in structures with a thin (~ 3 – 5 nm) sputtered SiO_2 layer between the Co clusters and the Si substrate, the discharge time is of several minutes (increasing with increasing SiO_2 layer), and are substantially longer for positively charged clusters than for negatively charged clusters. This observation can be explained semi-quantitatively as a consequence of the single-electron charging energy of a small cluster (cluster radius ~ 1.5 nm) [61] (Figure 22).

The thin film metal/insulator systems, which consist of alternating metallic and insulating layers with the metal layer consisting of a discontinuous assembly of nanoscale clusters, as opposed to a continuous film, can be potentially important in magnetic recording industry because it can display a substantial room-temperature negative magneto-resistance which saturates at low magnetic fields. The observed magneto-resistance arises from spin-polarized tunneling between metallic nanoclusters embedded in the insulating matrix. Such tunneling processes can be highly sensitive to local variations in the structure of both the conducting clusters and the insulating matrix, and it is of considerable interest to probe electrical, magnetic, and transport properties in these structures at the nanometer scale [61].

6. CONCLUSIONS

The transition from microelectronics to nanoelectronics demands the introduction of new fabrication techniques. Indeed, besides self-organization of molecule structures, nanoscale-patterning techniques can play an important role for achieving the micro \rightarrow nano transition. Future electronic devices and circuits will strongly depend on the technological ability to fabricate nanoscale insulating and metallic structures. From the examples mentioned previously, it is clear that SPM is emerging as an important new route for nanofabrication with potential technological relevance for modifying surfaces under UHV conditions. Control at nanometer length scales has already opened the exploration of a new class of device physics. Experiments are also in progress at various nanotechnology research groups to connect nanostructures to macroscopic contacts (i.e., Figure 2) to electrically characterize these nanodevices.

Moreover, electrical studies of nanometer-scale devices will also open the possibility of studying atomistic process of electromigration phenomena, which constitutes an important issue in today's integrated circuit technology. Finally, in terms of proximal probes, these studies have provided the possibility of extending applications in information technology, that is, through quantum computer architectures. We should note, however, that besides the SPM nanofabrication techniques described in this article, other techniques also exist as described in [59].

GLOSSARY

Lithography Writing of device design onto resist layers.

Nanodevices Devices with nanometer scale dimensions (<100 nm).

Quantum computers Computer very fast where the basic operation unit is due to quantum phenomena.

Single electron tunneling transistor (SET transistor) Electrons tunnel "one by one" showing a discrete flow of charge.

SPM nanofabrication Fabrication of nanometer size structures by use of scanning probe microscopes.

ACKNOWLEDGMENTS

We would like to thank Prof. J. R. Tucker and Prof. T.-C. Shen for supplying and giving permission to use the STM images in Figures 7 and 8, useful communication with J. R. Tucker on quantum computing, Prof. E. Ganz for supplying and giving permission to use the STM images in Figures 11 and 12b, Dr. T. M. Mayer for supplying and giving permission to use Figures 12c–12d, Dr. J. O'Brien for supplying and giving permission to use Figures 16–20, Dr. D. Don Eigler for permission to use the web-file image for Figure 21, and Prof. Dr. E. Yu for permission to use his web files for Figure 22. We would also like to thank J. Lyding for useful correspondence, as well as our former collaborators S. Rogge, B. Ilge, and L. Boellaard for their contribution on SPM nanofabrication studies.

REFERENCES

1. T.-C. Shen, C. Wang, G. C. Abeln, J. R. Tucker, J. W. Lyding, Ph. Avouris, and R. E. Walkup, *Science* 268, 1590 (1995).
2. J. W. Lyding, T.-C. Shen, J. S. Hubacek, J. R. Tucker, and G. C. Abeln, *Appl. Phys. Lett.* 64, 2010 (1994); E. S. Snow, P. M. Campbell, and F. K. Perkins, *Naval Research Reviews* Vol. XLIX, 15 (1997); J. W. Lyding, *Naval Research Reviews* Vol. XLIX, 25 (1997); E. T. Foley, A. F. Kam, J. W. Lyding, and Ph. Avouris, *Phys. Rev. Lett.* 80, 1336 (1998).
3. T.-C. Shen, C. Wang, and J. R. Tucker, *Phys. Rev. Lett.* 78, 1271 (1997).
4. K. Tsubouchi and K. Masu, *Thin Solid Films* 228, 312 (1993); K. Tsubouchi, K. Masu, and K. Sasaki, *Jpn. J. Appl. Phys., Part 1* 32, 278 (1993).
5. D. P. Adams, T. M. Mayer, and B. Swartzentruber, *Appl. Phys. Lett.* 68, 2210 (1996); *J. Vac. Sci. Technol. B* 14, 1642 (1996). See also D. P. Adams, L. L. Tedder, T. M. Mayer, B. S. Swartzentruber, and E. Chason, *Phys. Rev. Lett.* 74, 5088 (1995); R. R. Kunz and T. M. Mayer, *J. Vac. Sci. Technol. B* 6, 1557 (1988).
6. G. Palasantzas, B. Ilge, L. J. Geerligs, and J. den Nijs, *J. Appl. Phys.* 85, 1907 (1999); *Micro. Engg.* 46, 133 (1999); B. Ilge, G. Palasantzas, and L. J. Geerligs, *Appl. Surf. Sci.* 144–145, 543 (1999); L. J. Geerligs, S. Rogge, G. Palasantzas, B. Ilge, P. Scholte, and J. de Nijs, *J. Surf. Anal.* 4, 204 (1998); G. Palasantzas, B. Ilge, L. J. Geerligs, and J. M. M. de Nijs, *Surf. Sci.* 412–413, 509 (1998); M. R. Zuiddam, S. Rogge, L. J. Geerligs, E. van der Drift, B. Ilge, and G. Palasantzas, *Micro. Engg.* 41–42, 567 (1998); B. Ilge, Scanning Tunneling Microscopy of Co on Si Surfaces, Ph.D. Thesis, Delft University of Technology, 2000. See also A. W. Dunn et al., *Appl. Phys. Lett.* 71, 2937 (1997).
7. S. A. Koch, D. T. L. van Agterveld, G. Palasantzas, and J. Th. M. De Hosson, *Surf. Sci. Lett.* L67, 476 (2001); G. Palasantzas, D. T. L. van Agterveld, S. A. Koch, and J. Th. M. De Hosson, *J. Vac. Sci. Technol. B* 19, 2581 (2001).
8. M. A. McCord and M. J. Rooks, in "Handbook of Microlithography, Micromachining, and Microfabrication. Volume 1: Microlithography" (P. Rai-Choudhury, Ed.), Chapter 2. SPIE, Washington, D.C., 1997.

9. W. W. Pai, J. Zhang, J. F. Wendelken, and R. J. Warmack, *J. Vac. Sci. Technol. B* 15, 785 (1997); A. D. Kent, T. M. Shaw, S. V. Molnar, and D. D. Awschalom, *Science* 262, 1249 (1993).
10. D. S. Saulys, A. Ermakov, E. L. Garfunkel, and P. A. Dowben, *J. Appl. Phys.* 76, 7639 (1994).
11. S. Rubel, X. D. Wang, and A. L. de Lozanne, *J. Vac. Sci. Technol. B* 13, 1332 (1995).
12. R. M. Silver, E. E. Ehrichs, and A. L. de Lozanne, *Appl. Phys. Lett.* 51, 247 (1987).
13. T. M. H. Wong, S. J. O'Shea, A. W. McKinnon, and M. E. Welland, *Appl. Phys. Lett.* 67, 786 (1995).
14. S. T. Yau, D. Saltz, A. Wriekat, and M. H. Nayfeh, *J. Appl. Phys.* 69, 2970 (1991); A. Laracuenta, M. J. Bronikowski, and A. Gallagher, *Appl. Surf. Sci.* 107, 11 (1996).
15. C. R. K. Marrian, Ed., "Technology of Proximal Probe Lithography," SPIE, Washington, D.C., 1994; C. F. Quate, *Surf. Sci.* 386, 259 (1997).
16. G. Palasantzas and J. Barnas, *Phys. Rev. B* 56, 7726 (1997).
17. J. A. Slezak, B. D. Zion, and S. J. Sibener, *Surf. Sci.* 442, L983 (1999).
18. B. D. Zion, A. T. Hanbicki, and S. J. Sibener, *Surf. Sci.* 417, L1154 (1998).
19. M. J. Stirniman, W. Li, and S. J. Sibener, *J. Chem. Phys.* 103, 451 (1995).
20. W. Li, M. J. Stirniman, and S. J. Sibener, *J. Vac. Sci. Technol. A* 13, 1574 (1995).
21. W. Li, M. J. Stirniman, and S. J. Sibener, *Surf. Sci.* 329, L593 (1995).
22. P. H. Holloway and J. B. Hudson, *Surf. Sci.* 43, 141 (1974).
23. P. H. Holloway and J. B. Hudson, *Surf. Sci.* 43, 123 (1974).
24. E. S. Snow, P. M. Campbell, and F. K. Perkins, *Naval Research Reviews* Vol. XLIX, 15 (1997).
25. J. Nogués and I. K. Shuller, *J. Mag. Mag. Mat.* 192, 203 (1998).
26. S. J. Sibener, R. J. Buss, C. Y. Ng, and Y. T. Lee, *Rev. Sci. Instrum.* 51, 167 (1980).
27. P. N. Peters, H. C. Grogory, and J. T. Swann, *Appl. Opt.* 25, 1290 (1986).
28. J. J. Boland, *Phys. Rev. Lett.* 65, 3325 (1990); *Surf. Sci.* 261, 17 (1992).
29. L. F. Matheiss and D. R. Hamann, *Phys. Rev. B* 37, 10623 (1988); H. von Känel, C. Schwarz, S. Gncalves-Conto, and E. Müller, *Phys. Rev. Lett.* 74, 1163 (1994).
30. M. Copel and R. M. Tromp, *Appl. Phys. Lett.* 65, 312 (1994).
31. P. A. Benett et al., *Phys. Rev. Lett.* 73, 452 (1994); R. T. Tung et al., *Appl. Phys. Lett.* 42, 888 (1983).
32. G. Palasantzas, B. Ilge, L. J. Geelings, and J. M. M. de Nijs, *Surf. Sci.* 412–413, 509 (1998).
33. V. Scheuch, B. Voigtlander, and H. P. Bonzel, *Surf. Sci.* 372, 71 (1996); R. E. Weber, *Appl. Phys. A* 30,1 (1988); H. Meyerheim, U. Dobler, and A. Puschmann, *Phys. Rev. B* 44, 2211 (1991).
34. J. Derrien, J. Chevrier, L. Thanh, I. Berbezier, C. Giannini, S. Lagomarsino, and M. G. Grimaldi, *Appl. Surf. Sci.* 73, 90 (1993).
35. T. Mitsui, E. Hill, and E. Ganz, *J. Appl. Phys.* 85, 522 (1999); Private communication for the Pd PVD nanofabrication structures with E. Ganz.
36. T. Ono, H. Hamanaka, T. Kurabayashi, K. Minami, and M. Esashi, *Thin Solid Films* 281–282, 640 (1996).
37. J. A. Appelbaum, G. A. Baraff, and D. R. Harmann, *Phys. Rev. B* 14, 588 (1976); R. J. Hamers, Ph. Avouris, and F. Bozso, *Phys. Rev. Lett.* 59, 2071 (1987).
38. H. Brune, J. Wintterlin, J. Frost, G. Ertl, J. Wiechers, and R. J. Behm, *J. Chem. Phys.* 99, 2128 (1993).
39. P. A. Thiry, J. Ghijsen, R. Sporken, J. J. Pireaux, R. L. Johnson, and R. Caudano, *Phys. Rev. B* 39, 3620 (1989).
40. K. J. D. MacKenzie and M. J. Ryan, *J. Mater. Sci.* 16, 579 (1981).
41. K. Ando and Y. Oishi, *J. Chem. Phys.* 6, 625 (1974).
42. E. S. Snow and P. M. Campbell, *Science* 270, 1639 (1995).
43. K. Matsumoto, M. Ishii, K. Segawa, Y. Oka, B. J. Vartanian, and J. S. Harris, *Appl. Phys. Lett.* 68, 34 (1996).
44. E. S. Snow, D. Park, and P. M. Campbell, *Appl. Phys. Lett.* 56, 2001 (1990).
45. J. W. Lyding, T.-C. Shen, J. S. Hubacek, J. R. Tucker, and G. C. Abeln, *Appl. Phys. Lett.* 64, 1917 (1990); R. S. Becker, G. S. Higashi, Y. J. Chabal, and A. J. Becker, *Phys. Rev. Lett.* 65, 1917 (1990).
46. J. W. Lyding, T.-C. Shen, G. C. Abeln, C. Wang, E. T. Foley, and J. R. Tucker, *Mat. Res. Soc. Proc.* 380, 187 (1995).
47. J. W. Lyding, K. Hess, and I. C. Kizilyali, *Appl. Phys. Lett.* 68, 2526 (1996); I. C. Kizilyali, J. W. Lyding, and K. Hess, *Elec. Dev. Lett.* 18, 81 (1997).
48. J. L. O'Brien, S. R. Schofield, M. Y. Simmons, R. G. Clark, A. S. Dzurak, N. J. Curson, B. E. Kane, N. S. McAlpine, M. E. Hawley, and G. W. Brown, *Phys. Rev. B* 64, 161401 (2001).
49. C. A. Sackett et al., *Nature* 404, 256 (2000).
50. I. L. Chuang et al., *Nature* 393, 143 (1998); I. L. Chuang et al., *Phys. Rev. Lett.* 80, 3408 (1998); J. A. Jones and M. Mosca, *Phys. Rev. Lett.* 83, 1050 (1999).
51. W. S. Warren, *Science* 277, 1688 (1997).
52. D. Loss and D. P. DiVincenzo, *Phys. Rev. A* 57, 120 (1998).
53. B. E. Kane, *Nature* 393, 133 (1998).
54. M. F. Crommie, C. P. Lutz, and D. M. Eigler, *Science* 262, 218 (1993).
55. R. Vrijen et al., *Phys. Rev. A* 62, 012 306 (2000).
56. D. M. Eigler and E. K. Schweizer, *Nature* 344, 524 (1990).
57. <http://www.almaden.ibm.com/vis/stm/>
58. J. K. Gimzewski et al., *Phys. Rev. Lett.* 72, 1036 (1994).
59. K. E. Drexler, "Nanosystems. Molecular Machinery, Manufacturing, and Computation." John Wiley & Sons, New York, 1992.
60. Ch. Van Haesendonck and L. J. Geerligs, in "Nanotechnology. Towards a Molecular Construction Kit" (A. ten Wolde, Ed.), pp. 84–96. Netherlands Study Centre for Technology Trends (STT), 1998.
61. D. M. Schaadt, E. T. Yu, S. Sankar, and A. E. Berkowitz, *Appl. Phys. Lett.* 74, 472 (1999). See also <http://kesey.ucsd.edu/group/PROJECTS/coclusters.html> The images were taken from the site <http://kesey.ucsd.edu/group/PROJECTS/>

Unconventional Nanolithography

Kahp Y. Suh, Dahl-Young Khang, Y. S. Kim, Hong H. Lee

Seoul National University, Seoul, Korea

CONTENTS

1. Introduction
 2. Basic Concepts of Conventional Lithographies
 3. Unconventional Nanolithographies
 4. Conclusions
- Glossary
References

1. INTRODUCTION

Nanolithography generally refers to a set of lithographic techniques used to fabricate very small features (at scales ranging from 1 to 100 nm) that can be integrated into complex systems. Fascinating and useful phenomena occur in this nanosized regime because the size approaches a fundamental length scale of physical and chemical processes. Examples are quantized excitation [1, 2], Coulomb blockade [3], single-electron tunneling [4], and metal-insulator transition [5]. These interesting phenomena can only be observed in nanostructures where quantum mechanical effects dominate. Actually, the study of phenomena in nanostructures has already evolved into a new field of research that can be termed “nanoscience” [6–9].

In addition to applications in nanoscience, nanostructures are essential to the development of a number of existing and emerging technologies. The ability to fabricate on the nanometer length scale guarantees a continual development in the miniaturization of functional devices. For example, future integrated circuits will require reliable techniques for fabricating nanometer-scale devices. Optical lithography or photolithography, which has been and will be the mainstay of lithography for the near future, is currently used for manufacturing microelectronic structures and typically involves a projection-printing system (usually called a stepper). In the process, the image of a reticle is reduced and projected through a high numerical aperture lens system onto a thin film of photoresist that is spin-coated onto a wafer. The resolution of the stepper (R) is subject to the limitations set by optical diffraction according to the Rayleigh equation [10] that is given by

$$R = k_1 \lambda / NA \quad (1)$$

where λ is the wavelength of the illuminating light, NA is the numerical aperture of the lens, and k_1 is a constant that is determined by the photoresist. The theoretical minimum feature size that is imposed by the relationship is usually the wavelength of the light used. Therefore, extensive efforts have been made to introduce illuminating sources with shorter wavelengths to generate structures with smaller feature sizes [11]. As the structures become increasingly smaller, it also becomes increasingly difficult and expensive to fabricate devices, such that photolithography is expected to be limited to ~ 100 -nm resolution. Because of the limitations the photolithography has for sub-100-nm features, there have been extensive efforts made since the mid-1990s for a technique that can replace photolithography.

If economics is not a major concern, there are technologies already available for sub-100-nm features, such as electron-beam lithography [12, 13], X-ray lithography [14, 15], and scanning probe lithography [16–18], etc. These methods all share the same basic operational principle [19, 20] and only have different exposing skills. The principle is that exposure of an appropriate material to electromagnetic radiation (ultraviolet, deep ultraviolet, extreme ultraviolet, or X-ray) introduces a latent modification (usually a difference in solubility) into the material as a result of a set of chemical changes in its molecular structure. Then this latent modification is subsequently developed into relief structures through etching. When probe tips do the writing, the lithography can be called scanning probe lithography (SPL). SPL uses small (< 50 nm) tips scanned near the surface of a sample in the configuration of scanning tunneling microscopes (STMs) [21], atomic force microscopes (AFMs) [22], scanning electrochemical microscopes (SECMs) [23], or near-field scanning optical microscopes (NSOMs) [24]. Since the first demonstration that STM can be used as a lithographic tool, STMs, AFMs, SECMs, and NSOMs have been used in a variety of ways to perform sophisticated lithography. These tip-based lithographies have advantages of resolving atomic level, realizing features with nearly arbitrary geometries, and patterning over surface topography that deviates significantly from planarity [25]. However, these methods are serial techniques, and they have writing speeds that are typically limited by the mechanical resonance of the tips and the piezoelectric elements that maintain constant separation between the tips and the sample.

To overcome the cost and speed problems, a number of unconventional nanolithographies have emerged, such as nanoimprint lithography (NIL) [26, 27], soft lithography [28–30], capillary force lithography (CFL) [31], and soft molding [32]. Unlike the optical and tip-based lithographies, these methods are economically viable processes and are usually applicable to large-area patterning. The methods are also carried out under physical contact, which basically removes the diffraction problem inherent in optical lithography. As we are interested in unconventional lithographies, these techniques will be reviewed in more detail.

2. BASIC CONCEPTS OF CONVENTIONAL LITHOGRAPHIES

A typical lithographic process consists of three successive steps: (i) coating a substrate with radiation-sensitive polymer layer (resist); (ii) exposing the resist to light, electron, or ion beams; (iii) developing the resist image with a suitable chemical. Exposure can be accomplished by either scanning a focused beam pixel by pixel from a designed pattern or exposing through a mask for parallel replication. Serial beam scanning is used for mask fabrication and single-component fabrication, but it does not meet the throughput required of manufacturing. Industrial techniques must be fast, reliable, and cost-effective. Optical projection lithography with deep UV light is now used for large-scale fabrication. Several techniques have been developed as next-generation lithographies, including extreme UV lithography, X-ray lithography, and projection lithography with either electrons or ions [33, 34]. These methods, generally referred to as top-down methods, are very expensive but sufficiently flexible for new development for the traditional microelectronics industry.

Conventional lithographic exposure involves interactions of an incident beam with a solid material. Absorption of light or inelastic scattering of particles can affect the chemical structure of the resist, which in turn changes its solubility. The response of the resist to the exposure can be either positive or negative, depending on whether the exposed or unexposed portions will be removed from the substrate after development. The next step after lithography is the pattern transfer from the resist to the substrate. There are a number of pattern transfer techniques: selective growth of materials in the trenches of the resist, etching of the unprotected areas, and doping through the open areas of the resist by diffusion or implantation [12]. Both wet chemical etching and dry plasma etching can be used. For a high-resolution pattern transfer, dry etching is more suitable and often requires a metallic layer as a mask. This metal mask is obtained by lift-off, that is, by first depositing a thin metallic layer over the developed resist pattern and then dissolving the resist to leave only the metal portions that are directly in contact with the substrate [35].

Lithography and pattern transfer are used for each level in multilevel fabrication. To increase productivity, optical projection lithography is performed on a large wafer in a step-and-repeat fashion by accurately controlling the sample stage with laser interferometry. The selection of a lithography for production purposes thus hinges on a number

of factors: resolution, throughput, pattern placement, overlay alignment accuracy, etc. However, the control of critical dimensions and the microscopic properties of individual nanostructures are the most important issues. Fabrication of semiconductor integrated circuits is a well-established technology. More information on optical or tip-based nanolithographies can be found elsewhere [36–38].

3. UNCONVENTIONAL NANOLITHOGRAPHIES

In contrast to conventional optical lithography, a contact-based unconventional lithographic process generally consists of three consecutive steps: (i) coating a substrate with a mobile polymer layer (resist); (ii) treating the resist surface chemically or applying a physical force such as pressure, capillary force, solvation force, or electric force; (iii) transferring the pattern on the resist to the underlying substrate. These methods are very cheap and compatible with the optical lithography in that they preserve the lithographic printing strategy. Here we overview several notable unconventional nonphotolithographic methods that can be applied to patterning sub-100-nm features on a large area in a simple and efficient way.

3.1. Imprint Lithography

Embossing a material with a rigid master is an unconventional, low-cost technique for high-resolution pattern replication and has been the standard technique for manufacturing replicas of holograms, diffraction gratings, and compact disks (CDs) [39, 40]. Recently this technique has been reexamined as a method for producing nanometer-sized structures of semiconductors, metals, and other materials commonly used in microelectronic circuitry or information storage, which is called imprint lithography [26, 27].

Imprint lithography generates resist relief patterns in a thermoplastic layer such as polystyrene by physically compressing the resist that has been thermally softened, rather than by modifying the resist's chemical structure by irradiation. A rigid mold is used to physically deform the polymer layer on a substrate. The mold can be made of metal or thermal silicon dioxide produced on a silicon substrate. An anisotropic etching process, such as reactive ion etching (RIE), is used to remove the residual resist in the compressed region for the subsequent hard material pattern transfer. The mold can be reused many times without damage. In typical NIL, the temperature is raised above the glass transition temperature of the polymer (typically 170 °C for polymethylmethacrylate). The resist thickness can vary in the range of 50–200 nm. Structures as small as 6 nm could be produced [41]. Using this technique, Chou et al. have fabricated prototype functional devices such as silicon field-effect transistors (FETs) [42]. More recently, they and other groups have explored this technique as a potential method for producing binary structures for high-density information storage, including arrays of nanometer-sized bars of cobalt or nickel for quantized magnetic disks and nanometer-sized pits in polymer films for optical disks [43]. The initial success

of this technique indicates that it may be worthwhile to reexamine other existing microlithographic techniques for their potential in nanofabrication. More information on nanoimprint lithography can be found elsewhere [44].

However, there are a few problems in the high-temperature process: clean release of the resist from the mold is one of the critical requirements. Usually anti-adhesion agents have been used to achieve clean mold release [26]. Distortion of the imprinted structures or mold features due to the thermal cycle of heating followed by cooling is another problem to contend with. To overcome these shortcomings, room-temperature (RT) imprint methods were proposed, which have given birth to a series of successful low-temperature processes. The easiest method is to use a low-molecular-weight polymer for its low viscosity or high mobility even at low temperature. Examples are standard optical resist S1805 [45], and newly developed hybrane, and hydrogen-bonded polymers. For (RT) processing, there are two useful techniques; one is room-temperature (RT) NIL, by solvent treatment [46], and the other by plastic deformation along with free-volume contraction [47].

3.1.1. Room-Temperature Imprint Lithography by Solvent Treatment

In this method, a film treated with a solvent vapor is pressed with a mold at RT, requiring no heating [46]. It has been shown that the mold or mask patterns down to 60 nm can be transferred well onto polymer film without the polymer adhering to the mold. The vapor treatment of the dried polymer film results in a lowering of both the viscosity and the glass transition temperature, thereby allowing RT lithography.

In RT-NIL by solvent treatment, viscosity plays a crucial role. As is well known, viscosity is a measure of fluidity of any material. The higher the value of the viscosity is, the harder it is for the material to flow. The viscosity of any polymer, especially a thermoplastic polymer, is dependent on many parameters such as temperature, molecular weight and its distribution, concentration, shear rate, and others. The most common way of lowering the viscosity is to heat the material above its glass transition temperature (T_g), at which the solid polymer starts flowing viscously (typically at $T > 1.2T_g$). Because of this fluidity of melt-like polymer above its glass transition temperature, heating the sample has so far been the natural choice for imprinting.

There is, however, another simple way of lowering the viscosity, which involves adding solvent to the polymer to reduce its concentration (thereby reducing the viscosity). Dilute polymeric thin films on substrates by spin coating. In this case, the solution is usually 90–99 wt% solvent. On the other extreme of the concentration scale is the annealed film of polymer that has been spin coated onto the substrate, which does not contain any solvent. Between these two extreme concentrations lies the range within which one can vary the viscosity or the fluidity of the polymer material by adding the solvent to and removing it from the polymer film.

In typical experiments, a solvent is added in a controlled amount to a fully dried polymer film through control of

the time of exposure at a given temperature. The amount of absorbed solvent can also be controlled by changing the temperature. Figure 1 is a schematic for RT-NIL with solvent treatment. First, the annealed substrate is placed in a constant-temperature oven, in which trichloroethylene (TCE) solvent is also placed. Other solvents can also be used, but TCE is chosen because of its relatively high vapor pressure. In this way, the polymer film is allowed to absorb the vapor that is evaporated from the beaker. After this treatment, the substrate is loaded and then pressed at room temperature with a conventional hydraulic press. Applied pressure varies between 30 and 150 MPa, depending on the pressing time of 5–40 min. When the pressure is released, the silicon mold detaches freely without being forced, and no adhered polymer is found on the mold surface. This mold can be reused many times, only needing nitrogen blowing each time it is reused to remove particles from the laboratory environment. Partial drying of the polymeric layer or baking at a low temperature causes difficulties in processing. When partially dried, the adhesion between polymer and substrate becomes poor and the polymer film is lifted off.

The solvent vapor treatment of the polymer film has the following two effects [48, 49]: (1) a plasticization effect, which leads to a decrease in the glass transition temperature [49], thereby lowering the viscosity of the polymer; (2) a dilution effect, which also leads to further lowering of the viscosity. The plasticization effect can be inferred from the following approximate relationship for the glass

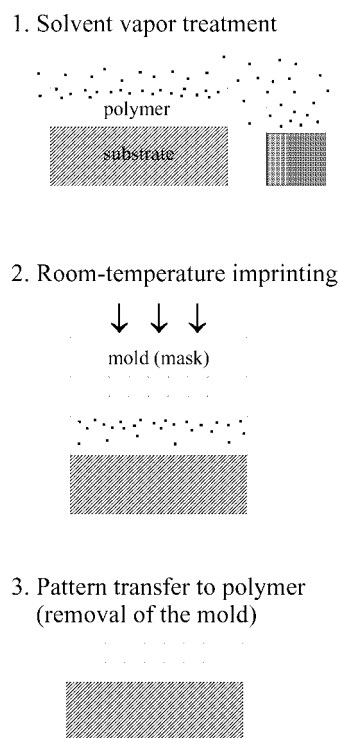


Figure 1. Schematic procedure of RT imprint lithography. Reprinted with permission from [46], D. Y. Khang and H. H. Lee. *Appl. Phys. Lett.* 76, 870 (2000). © 2000, American Institute of Physics.

transition temperature:

$$T_g \approx \frac{T_{gp}}{1 + (X - 1)(1 - \Phi_p)} \quad (2)$$

where X and T_{gs} are given by

$$X \approx \frac{T_{gp}}{T_{gs}} \quad (3)$$

$$T_{gs} \approx \frac{2}{3}T_{ms} \quad (4)$$

Here T_{gp} and T_{gs} are the glass transition temperatures of the pure polymer and the solvent, respectively, T_{ms} denotes the melting temperature of the solvent, and Φ_p is the volume fraction of the polymer. The value of T_{gs} is 378 K for polystyrene, and T_{ms} is 200 K for TCE. Figure 2a shows the plot of the calculated results based on the above three equations. A significant reduction in T_g is seen to result from the presence of the solvent. This decrease makes the polymer more fluid.

The dilution effect can be described in terms of viscosity. When the polymer volume fraction Φ_p is decreased by dilution, there is a corresponding increase in the critical molecular weight M_{cr} , which is the molecular weight at which

entanglements become important in hindering viscous flow. These relationships are

$$\eta \propto M_{cr}'^{-3.4} \quad (5)$$

$$M_{cr}' \propto \frac{M_{cr}}{\Phi_p^{1.5}} \quad (6)$$

Therefore, from Eqs. (5) and (6), one has

$$\frac{\eta(\Phi_p = a)}{\eta(\Phi_p = b)} \propto \left(\frac{a}{b}\right)^{5.1} \quad (7)$$

where $\eta(\Phi_{p1})$ is the viscosity at the volume fraction Φ_{p1} and $\eta(\Phi_{p2})$ is the same at Φ_{p2} . The lowering of viscosity due to the solvent addition is shown in Figure 2b. It can readily be seen from this figure that the viscosity is greatly affected by the volume fraction or the dilution.

The plasticization and dilution effects considered so far show that a small amount of solvent absorbed to a dry, solid polymer can significantly lower the glass transition temperature and the viscosity, thus allowing the compression molding of the solid polymer. The solvent vapor treatment, however, does not always have advantageous effects. In fact, an excess amount of solvent can make the polymer very sticky, which should be avoided.

Figure 3 shows scanning electron micrographs (SEMs) of mold features and the corresponding substrate patterns that were transferred to the polymer film [47]. It is seen that the line-and-space pattern of the nominal 250-nm period does not show straight lines but rather wavy lines. Although the mold pattern is not good because of the limited electron-beam (e-beam) capability, the mold patterns are exactly

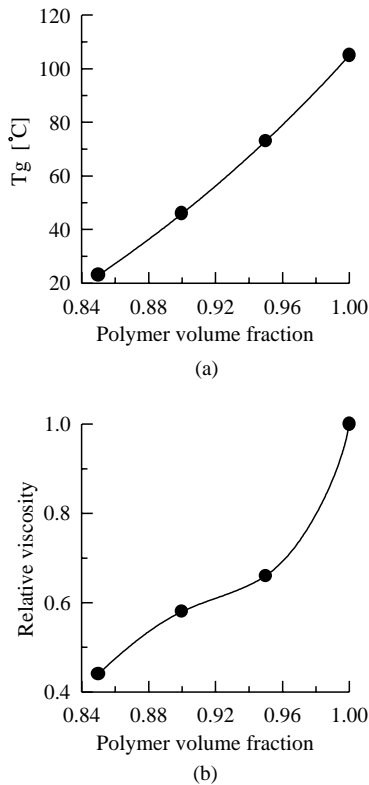


Figure 2. Effects of solvent addition on (a) the glass transition temperature, T_g , and on (b) the viscosity of polymer. In (b) the viscosity was normalized to that of pure solid polymer. Reprinted with permission from [46], D. Y. Khang and H. H. Lee, *Appl. Phys. Lett.* 76, 870 (2000). © 2000, American Institute of Physics.

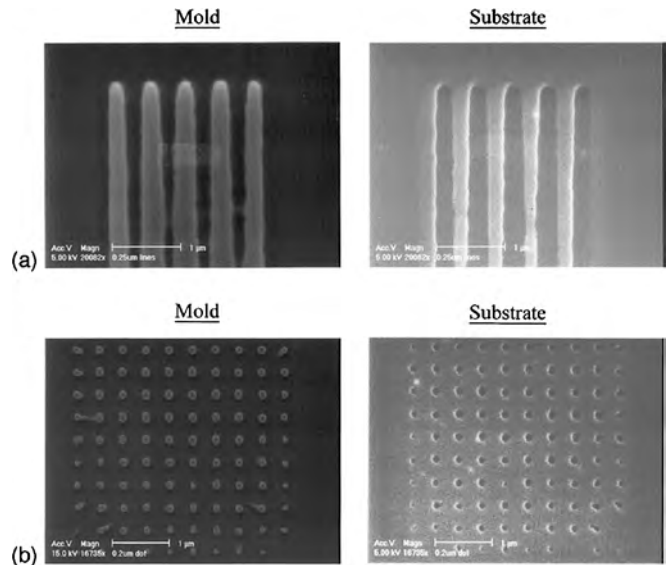


Figure 3. Plane-view SEM images of patterns imprinted in a PS film at room temperature with TCE vapor treatment. (a) 250-nm lines and spaces. (b) 200-nm dots. In each figure the imprinted patterns (right) are exactly the mirror image of the patterns on the mold (left). Thus the two micrographs coincide when folded along the centerline shown in each figure. Reprinted with permission from [46], D. Y. Khang and H. H. Lee, *Appl. Phys. Lett.* 76, 870 (2000). © 2000, American Institute of Physics.

imprinted into the polymer layer, irrespective of their size and shape.

3.1.2. Room-Temperature Imprint Lithography by Simple Compression

Imprint lithography based on plastic flow along with free-volume contraction and plastic deformation of polymer resist is another possible candidate for a RT process [47]. This RT process has the unique feature of enabling step-and-repeat and multiple imprinting, which is impossible in the conventional high-temperature imprint processes.

The RT imprint process presented here involves plastic flow of polymer under compressive stress. According to the cross-sectional AFM results, the void space generated in the polymer by the imprinting is in excess of the overflow of polymer by 10 to 50% by volume, which indicates that not only free-volume contraction and but also plastic deformation plays a major role. In amorphous polymeric materials, a certain number of vacancies, called free volume, must always be present because of the absence of long-range order and chain-like character with finite thickness and persistence. The vacant site fraction, f_v , is given by [50]

$$f_v = (v_s - v_{vs})/v_s \quad (8)$$

where v_s is the specific volume of the amorphous polymer and v_{vs} is the specific volume calculated from van der Waals radii. The value of f_v is in the range of 0.32–0.375 for typical amorphous polymer. The vacant volume, however, is not completely available for thermal motion since not all of the vacant sites are accessible to monomeric units on conformational grounds. The volume available for motion, f_m , is given by [50]

$$f_m = (v_{so} - v_{cso})/v_{so} \quad (9)$$

where v_{so} and v_{cso} are the specific volumes of the amorphous and crystalline polymer, respectively, at 0 K. The value of f_m is in the range of 0.125–0.14 for most polymers. The pattern depth that can be obtained by free volume compaction, therefore, would be given by

$$f_v^{1/3} h \sim f_m^{1/3} h \quad (10)$$

where h is the original thickness of the polymer layer. For example, a polymeric film 100 nm thick can be compressed to a depth of 10–30 nm by the free volume compaction only. If the free volume compaction is completed and the applied stress exceeds the yield stress of the polymer, the pattern depth increases further because of plastic deformation of the polymer.

Typical yield stress of inorganics such as Si or SiO₂ is on the order of 1 GPa, while that of organics (polymers) is 0.05 GPa, which is almost 2 orders of magnitude smaller than the yield stress of inorganics. Young's modulus of inorganics is about 150 GPa, while that of polymer is about 1 GPa, which is also 2 orders of magnitude smaller than that of inorganics [51, 52]. If the applied stress is in the range between the yield stress of polymer and that of the inorganic mold material, further imprinting of the mold features into the underlying polymer layer can be realized through the

plastic deformation of polymer. Therefore a more deeply imprinted pattern is left in the polymer when the plastic deformation is involved.

In typical experiments, the substrate is Si wafer ($\sim 2 \times 2$ cm² in size) and has a top layer of oxide 1 μ m thick. The mold is prepared by e-beam lithography or photolithography. Polystyrene (PS) is used as the thermoplastic resist, which has a very good etch resistance [53]. Etch resistance is essential for the pattern transfer process such as reactive ion etching. The experimentally measured etch rate of SiO₂ is 6 to 10 times greater than that of PS under typical etching conditions.

Prior to spin coating onto a SiO₂/Si substrate with a PS/toluene polymer solution, the substrate is cleaned by nitrogen-blowing, ultrasonification for 5 min in TCE and acetone, and then in isopropylalcohol (IPA), rinsing with deionized water, and blow-drying with nitrogen. The concentrations of polymer solutions in toluene are typically in the range between 0.5% and 10% polymer by weight. After spin coating, the substrate with the polymer film is baked in a vacuum oven at 150 to 200 °C. The thickness of the dried resist layer thus formed on the substrate, as determined by ellipsometry, ranges from 50 nm to 550 nm, depending on the coating conditions.

The PS/SiO₂/Si substrate is loaded and pressed at room temperature for a period of 5 to 20 s with a conventional hydraulic press, at a pressure between 30 and 150 MPa. When the pressure is released, the mold detaches freely without being forced, and no polymer is found adhering to the mold surface when examined by SEM. This mold can be reused directly tens of times for multiple or step-and-repeat imprinting with manual alignments.

One of the unique features of RT imprinting is the large area patterning capability of the step-and-repeat scheme, which is the major reason why photolithography has been the major lithographic tool. In conventional high-temperature (above T_g of polymer) imprinting, the imprinting cannot be repeated sequentially on the same substrate, because the previously patterned features would be destroyed by the heating that follows for the next imprinting. In contrast, a desired pattern can be imprinted many times on the same substrate surface in RT imprinting without causing any distortion of the patterns that were formed previously. Therefore, there is essentially no area limitation in RT imprinting.

Shown in Figure 4 are the large area patterning results that have been obtained over the full area of a $\sim 2 \times 2$ cm² substrate with a 0.5×0.5 cm² mold by imprinting eight times with the step-and-repeat scheme [47]. In these figures, only the two neighboring patterns are shown. Figure 4a shows the large area (at the expense of resolution) view for the two neighboring patterns imprinted by the step-and-repeat scheme for 80-nm lines with 300-nm spacing. The dark central region does not have an imprinted pattern. The bright regions on the left and right sides of the micrograph (Fig. 4a) by SEM are the imprinted patterns. Upon magnification, the patterned left side in Figure 4a reveals the line patterns clearly (Fig. 4b and d), and so does the right side (Fig. 4c and e).

The RT imprinting method can also be used to generate more complex patterns from simpler ones by multiply

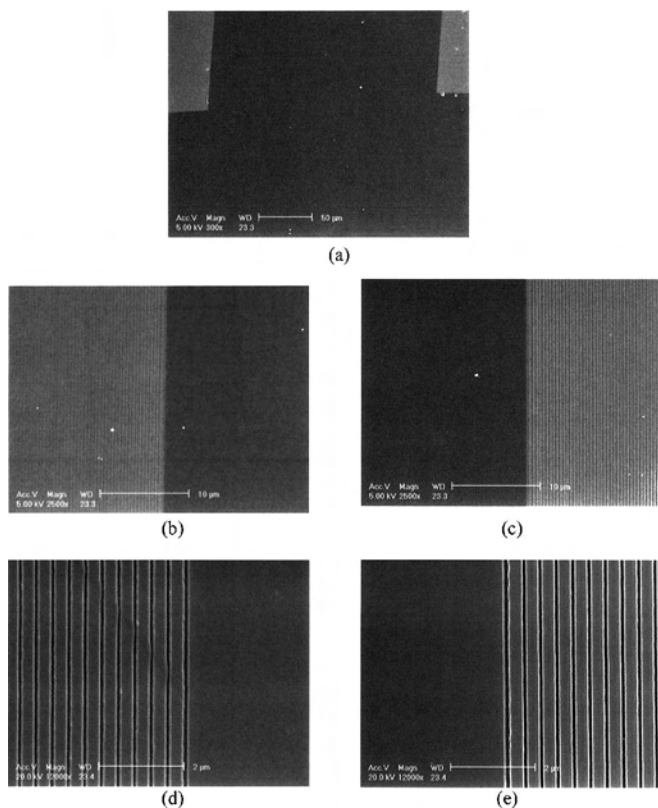


Figure 4. SEM micrographs of a substrate with patterns formed by the step-and-repeat scheme. (a) Two neighboring line (80 nm) and space (300 nm) patterns imprinted with the same mold (brighter regions on the top left/right sides). (b and c) The patterned left and right sides, respectively, of (a) magnified 10 times. (d and e) The images of (b) and (c), respectively, magnified again by 5 times. Reprinted with permission from [47], D. Y. Khang et al., *Adv. Mater.* 13, 749 (2001). © 2001, Wiley-VCH.

imprinting the same region of substrate with the same mold. Such an image is shown in Figure 5 [47]. In this figure, the substrate was first imprinted by a mold with a simple line-and-space pattern (80-nm linewidth and 300-nm spacing). The same region was imprinted again with the same mold, but this time with the mold rotated $\sim 90^\circ$ with respect to the pattern that had been imprinted. The wavy feature of the lines in the figure is not due to the imprinting but rather to the wavy nature of the mold pattern that is caused by the limited capability of the e-beam machine used. In this multiple imprinting scheme, the plastic deformation of polymer in one step may have some effects on the following imprinting step, or vice versa. However, manipulation of the processing conditions such as pressing pressure or polymer film thickness can be used to finely control the surface profile of the multiply imprinted patterns.

The transfer of the pattern imprinted into polymer to the underlying substrate requires a two-step RIE. The first step involves etching of the polymer to create the window for the etching of the underlying substrate. The second step involves etching of the substrate with the polymer remaining on the substrate as the etch mask. An example of pattern transfer by two-step etching is shown in Figure 6 [48]. For comparison purposes, SEM micrographs are shown of the

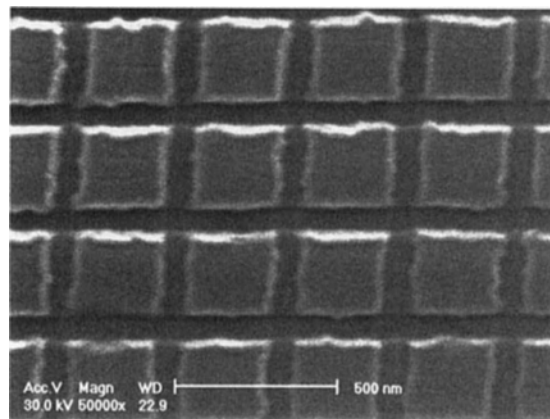


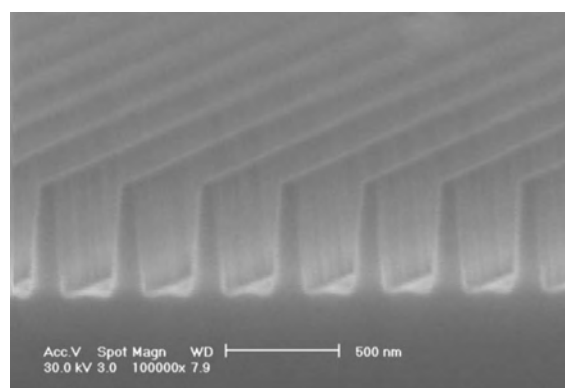
Figure 5. SEM image for the crossing patterns generated by multiple imprinting: 300 nm \times 300 nm square islands generated from crossing line-and-space patterns of 80-nm linewidth and 300-nm spacing between lines. The wavy feature of the imprinted lines differentiates from the mold. Reprinted with permission from [47], D. Y. Khang et al., *Adv. Mater.* 13, 749 (2001). © 2001, Wiley-VCH.

master (Fig. 6a) with which the pattern is imprinted, the pattern imprinted into polymer (Fig. 6b), and the pattern transferred into the underlying SiO₂ substrate (Fig. 6c). The indentation depth resulting from the imprinting ranges from 50 nm to 150 nm, depending on the pressure applied. Since the height of the protruding lines (Fig. 6a) is in excess of 500 nm, only a fraction of the height penetrates into the polymer upon pressing, which in this case is about 100 nm. The first step of etching PS, which was used as the polymer layer, was carried out with CF₄ plasma. After the underlying SiO₂/Si layer had been exposed, the underlying SiO₂ was etched with CHF₃/CF₄ plasma to transfer the pattern to SiO₂. The cross-sectional SEM micrographs in Figure 6 show that a line-and-space pattern is well transferred to a SiO₂ substrate by the two-step RIE process.

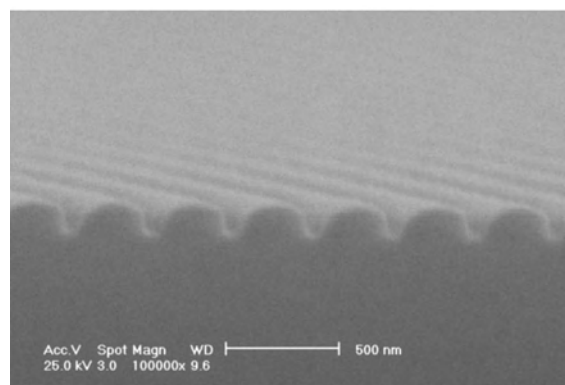
3.2. Soft Lithography

Soft lithography (Fig. 7) is the collective name for a set of lithographic techniques: replica molding (REM), microcontact printing (μ CP), micromolding in capillaries (MIMIC), microtransfer molding (μ TM), solvent-assisted micromolding (SAMIM), and near-field conformal photolithography with an elastomeric phase-shifting mask that has been developed as an alternative to photolithography [28–30].

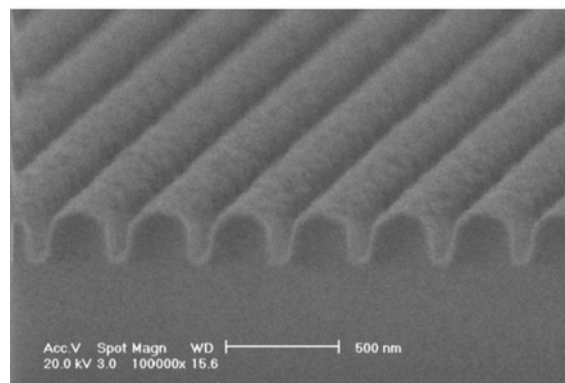
These techniques use a patterned elastomer, usually polydimethylsiloxane (PDMS), as the mold, stamp, or mask to generate or transfer a pattern. Soft lithography offers immediate advantages over photolithography and other conventional microfabrication techniques for applications in which patterning on nonplanar substrates, unusual materials, or large-area patterning are the major concerns. It is especially promising for microfabrication of relatively simple, single-layer structures for uses in cell culture, as sensors, as microanalytical systems, in microelectromechanical system (MEMS), and in applied optics. The initial success of soft lithography indicates that it has the potential to become an important addition to the field of micro- and nanofabrication. Since recent review articles are available that provide detailed information on soft lithography [28–30], we briefly



(a)



(b)



(c)

Figure 6. Cross-sectional SEM images for a line-and-space pattern (80-nm linewidth and 300-nm spacing). (a) Master with which the pattern is transferred. (b) The pattern imprinted into polymer by the imprinting. (c) The pattern transferred to the underlying SiO₂/Si substrate by two-step reactive-ion etching. Reprinted with permission from [47], D. Y. Khang et al., *Adv. Mater.* 13, 749 (2001). © 2001, Wiley-VCH.

outline some of the soft lithographic techniques that can be applied to nanofabrication.

3.2.1. Replica Molding

The capability of REM is greatly enhanced by introducing elastomeric materials as a mold, albeit at some cost in reproducibility (Fig. 7a) [54, 55]. In REM, an elastomer (for

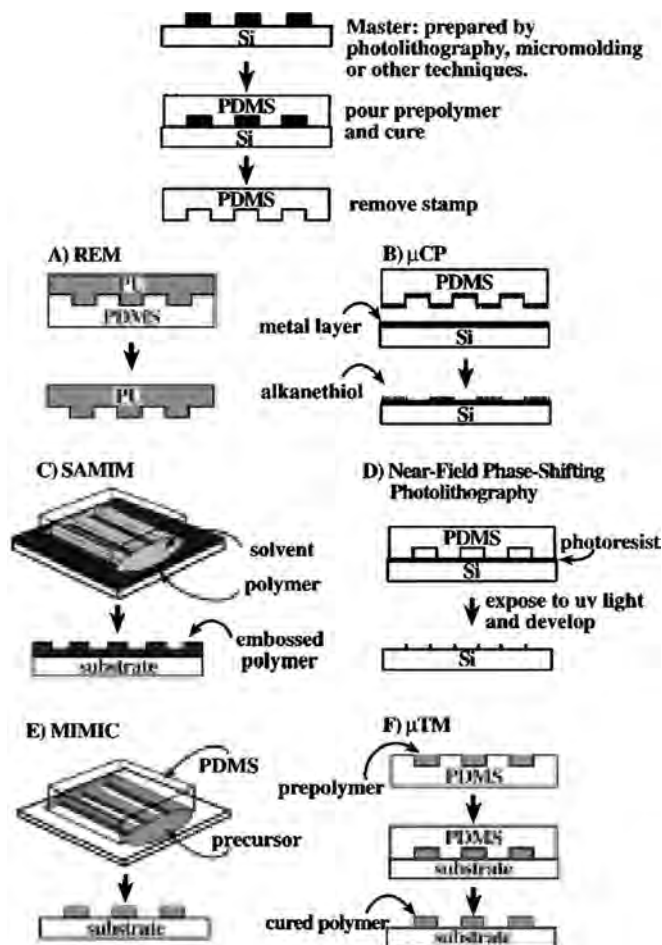


Figure 7. Schematic procedures describing soft lithographic methods and near-field phase-shifting photolithography. Reprinted with permission from [29], Y. Xia et al., *Chem. Rev.* 99, 1823 (1999). © 1999, American Chemical Society.

example, PDMS) is cast against a rigid master, and the elastomeric replica is subsequently used as a mold against which new replicas are produced in organic polymers. The introduction of elastomers into REM makes it easier to preserve small, fragile structures on the original master; the low surface energy (~ 21.6 dyn/cm) of PDMS, in particular, also allows the replica to be separated from the mold easily [56]. An elastomeric mold also offers the opportunity to manipulate the size and shape of structures on the mold by mechanical and thermal deformation. For example, it was reported that the lateral dimension of nanostructures is reduced from ~ 50 to ~ 30 nm by REM when a PDMS mold is compressed mechanically [57].

Figure 8 illustrates the use of REM to generate patterned nanostructures. Figure 8a shows an AFM image of chromium nanostructures on a master that was fabricated with the use of light guiding to pattern the deposition of chromium atoms [58]. Figure 8b shows an AFM image of a polyurethane (PU) replica that was prepared from a PDMS mold cast from this chromium master [57]. Although this process used REM twice, the vertical dimension of the chromium nanostructures was reproduced with an accuracy of better than 5 nm over a substantial area (~ 1 mm²).

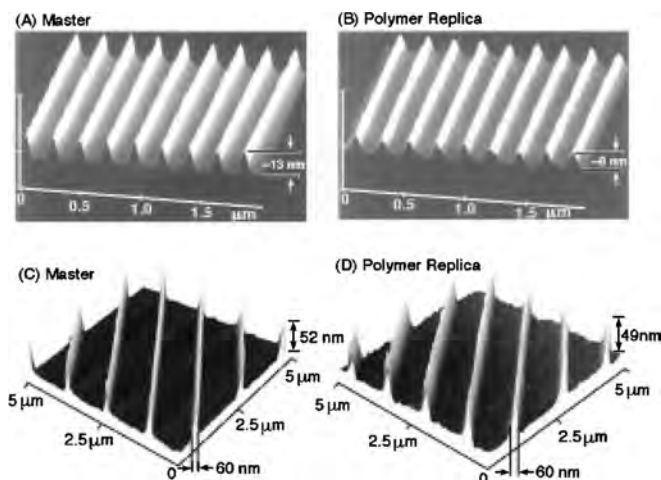


Figure 8. (A, B) AFM images of chromium nanostructures on a master and polyurethane prepared from a PDMS mold cast from this master. (C, D) AFM images of gold nanostructures on another master and a polyurethane replica produced from a different PDMS mold cast from this master. Reprinted with permission from [29], Y. Xia et al., *Chem. Rev.* 99, 1823 (1999). © 1999, American Chemical Society.

Figure 8c shows an AFM image of gold nanostructures on another master. Figure 8d shows an AFM image of nanostructures in PU generated by REM against a PDMS mold cast from this second master. With this procedure, more than 20 copies of PU nanostructures can successfully be produced from a single master: these polymer nanostructures are indistinguishable from each other.

REM against an elastomeric mold has proved to be a practical protocol for producing copies of a master mold: that is, production of multiple copies of indistinguishable nanostructures from a single master, rapidly and economically [57]. The challenge for the future in considering this technique for use in microelectronics or optics is to transfer the structural information present in the polymer into electrical or optical materials, to control distortions in the dimensions of the master and the replicas upon casting and curing of the polymers and during use, and to develop schemes that allow the registration required for multilevel fabrication.

3.2.2. Microcontact Printing

Microcontact printing (μ CP) was mainly developed with self-assembled monolayers (SAMs) of alkanethiols on gold and silver [59, 60]. The procedure for carrying out μ CP in these systems is remarkably simple (Fig. 7b): an elastomeric PDMS stamp, inked with an appropriate solution of alkanethiol, is brought into contact with the surface of a substrate to transfer the ink molecules to those regions of the substrate that contact the stamp. The success of μ CP relies on the conformal contact between the stamp and the surface of the substrate, on the rapid (less than 1 s) formation of highly ordered monolayers as a result of self-assembly [61], and on the autophobicity of the SAM, which effectively blocks the reactive spread of the ink across the surface [62]. Microcontact printing is an additive process that minimizes waste of starting materials. It is intrinsically parallel: patterned SAMs can be formed over relatively large area

($\sim 50 \text{ cm}^2$) in a single impression [63]. It is also applicable to curved substrates and hence is useful for some particular three-dimensional (3-D) fabrication [64–66], although the formation of patterned SAMs is intrinsically a 2-D process. It can also be used on inner surfaces that are not accessible to any plausible projection lithographic scheme [63].

μ CP has been used with a number of systems, including SAMs of alkanethiols on gold [67], silver [60], and copper [68, 69] SAMs of alkylsiloxanes on HO-terminated surfaces [70, 71] and SAMs of RPO_3H_2 on aluminum. Of these, alkanethiols on gold and silver currently give the highest resolution; most other systems have been demonstrated only at scales greater than $1 \mu\text{m}$. μ CP can routinely give patterns of alkanethiolate SAMs on gold and silver with in-plane dimensions on the scale of $\sim 500 \text{ nm}$ and with some difficulty with dimensions $< 100 \text{ nm}$ [72].

The patterned SAMs can be used either as resists in selective wet etching [73] or as templates in selective deposition [71]. Patterned structures can be formed on a variety of materials: metals, silicon, liquids (by dipping or condensation from the vapor), organic polymers (by dipping or polymerization of monomer), and even biological species [74]. Figure 9 shows SEM images of nanostructures of gold and silver that were fabricated by μ CP, followed by selective wet etching. Lateral force microscopy (LFM) shows that the patterned SAMs of hexadecanethiolate on gold have an edge roughness that is less than $\sim 50 \text{ nm}$ [75]. These results indicate that μ CP has the potential for producing structures with lateral dimension less than 100 nm . It is expected that the edge resolution of nanostructures in coinage metals fabricated by a combination of μ CP and wet etching is largely determined by the grain size of the metal films, the etching process, or a combination of these factors. The smallest features fabricated with a combination of μ CP or SAMs

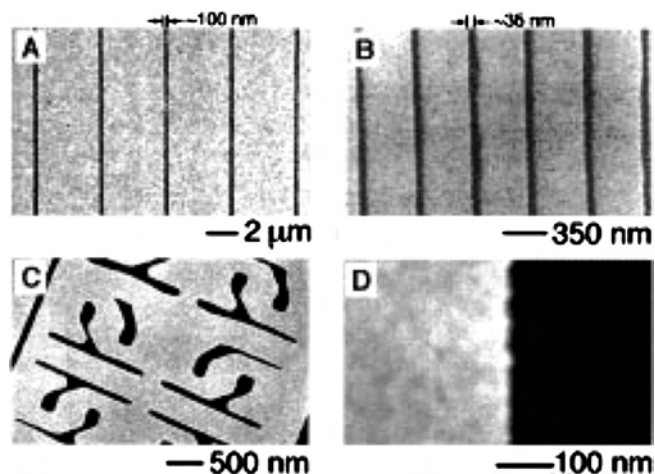


Figure 9. SEM images of nanostructures of gold (A, B) and silver (C, D) fabricated by μ CP with hexadecanethiol, followed by selective wet etching. (A) An array of $\sim 100\text{-nm}$ trenches fabricated in gold by μ CP with controlled reactive spreading of hexadecanethiol under water. (B) Array of $\sim 35\text{-nm}$ trenches fabricated in gold by μ CP with hexadecanethiol. (C, D) Patterned structures in silver with feature sizes of $\sim 200 \text{ nm}$ fabricated by μ CP with hexadecanethiol. Reprinted with permission from [29], Y. Xia et al., *Chem. Rev.* 99, 1823 (1999). © 1999, American Chemical Society.

and wet etching are trenches in gold that are ~ 35 nm wide and separated by ~ 350 nm (Fig. 9b) [72]. The minimum feature size that can be achieved by μ CP has still not been completely defined, and continuing systematic study on the mechanical properties of the stamp and of interactions between the stamp, the ink, and the substrate will be useful for the optimization of μ CP for use in the <100 -nm regime [76].

3.2.3. Solvent-Assisted Micromolding

SAMIM shares operational principles with embossing, except that SAMIM uses a solvent instead of temperature to “soften” the polymeric material and an elastomeric PDMS mold rather than a rigid one to emboss relief structures in the surface of a substrate [77]. In SAMIM (Fig. 7c), a PDMS mold is wetted with a good solvent for the polymer to be embossed and brought into contact with the surface of that polymer. The solvent is selected to dissolve (or “soften”) the substrate without affecting the PDMS mold. After the solvent dissipates and/or evaporates, the mold is removed and a patterned relief structure complementary to that on the surface of the mold remains.

SAMIM has been used with a wide variety of organic polymers: PS, PMMA, Novolac photoresists, poly(vinyl chloride), cellulose acetate, and precursors to conjugated organic polymer [77, 78]. Its only requirement is for a relatively volatile solvent that dissolves the substrate and wets (but does not significantly swell) the surface of the PDMS mold. Other materials can also be added to the solvent; these materials are then incorporated into the resulting relief structures. SAMIM is capable of replicating complex quasi-3-D relief structures over relatively large areas in a single step. Figure 10 shows AFM images of nanostructures that have been generated by SAMIM: parallel lines ~ 60 nm wide and ~ 50 nm high formed in a thin film of photoresist. These features rest on top of a thin underlying polymer film; similar underlying films are also often formed in REM and in embossing. If necessary, this thin film can be removed by RIE in an O_2 plasma without excessive damage to the surface topography that represents the pattern.

An important characteristic of SAMIM is that it is “self-cleaning.” Dust particles on the surface of the stamp tend to remain in the molded polymer. Each cycle of use therefore cleans the mold and limits the influence of adventitious particulates to one cycle of replication. The extent to which the surface of the mold is eventually wetted by and damaged by the polymer being molded remains to be established.

3.3. Capillary Force Lithography

As described earlier, the imprinting method requires a very high pressure, typically on the order of 10^9 Pascals (N/m^2). In addition, a recent study reported [79] that material transport limits the performance of NIL in general, especially when the mold is negative or has recessed features within a large elevated surface level. In this case, the pattern transfer turned out to be unsatisfactory and bubble-like defects were observed, possibly because of a lack of conformal contact.

To solve these problems, Lee and co-workers introduced a new lithographic technique called capillary force lithography

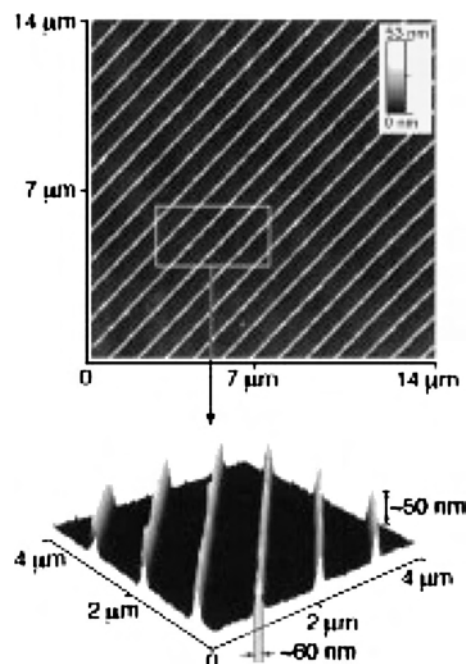


Figure 10. AFM images of polymeric nanostructures fabricated by SAMIM in a thin (~ 0.4 -mm-thick) film of Microposit 1805 spin coated on Si/SiO_2 . Reprinted with permission from [29], Y. Xia et al., *Chem. Rev.* 99, 1823 (1999). © 1999, American Chemical Society.

(CFL) by simply combining some of the features of nanoimprint and soft lithographies [31, 80]. When a patterned (positive or negative) PDMS mold is placed on a polymer surface and heated above the polymer’s glass transition temperature (T_g), capillarity forces the polymer melt into the void space of the channels formed between the mold and the polymer, thereby generating a negative replica of the mold as shown in Figure 11. When the polymer film is thick enough to completely fill the cavity of the mold, a residual polymer layer remains on the substrate as shown in Figure 11a. However, if the polymer film is thin and the interaction between the polymer and the substrate is sufficiently weak, the substrate surface can be exposed as depicted in Figure 11b. In the latter case, a meniscus is observed at the protruding end of the polymer, which is the signature mark of the capillary rise. This experimental procedure is similar to NIL, except that a hard mold is replaced by a soft mold and no pressure is applied.

In CFL, the essential feature of NIL—molding a polymer melt—is combined with the prime element of soft lithography—the use of a PDMS mold. As a result, the advantage of imprint lithography over soft lithography is retained in meeting stringent pattern fidelity requirements, as in the fabrication of integrated circuits, while eliminating the need for extremely high pressure that is needed in imprint lithography.

As is well known, the difference in the thermal expansion coefficient between the PDMS mold and the substrate is very large ($\alpha_{PDMS} \gg \alpha_{sub}$). As a result, the mold tends to separate itself from the polymer surface when the annealing temperature is high. To prevent the separation, the mold can be made soft (curing agent $\sim 6\%$), and the annealing

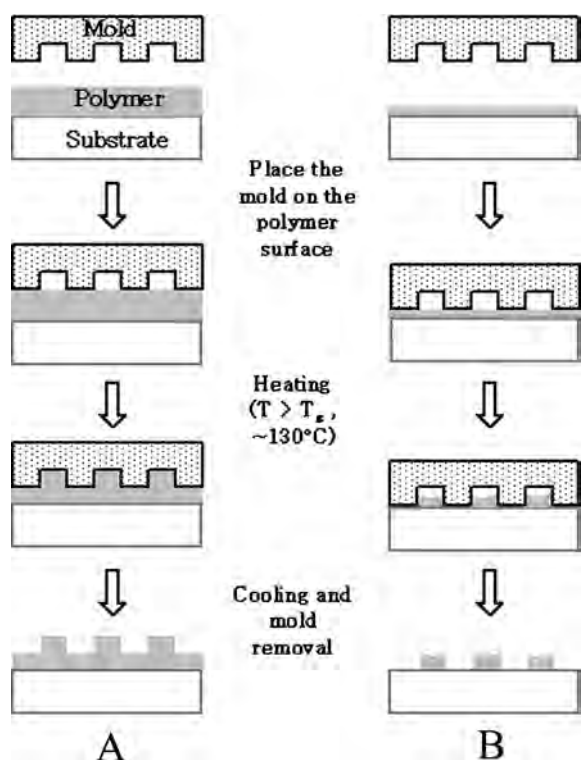


Figure 11. Schematic diagram of capillary force lithography when the film is relatively thick with respect to the mold's step height (A) and when it is thin (B). Reprinted with permission from [80], K. Y. Suh and H. H. Lee, *Adv. Funct. Mater.* 12, 405 (2002). © 2002, Wiley-VCH.

can be carried out gradually from RT to the setting temperature. In this case, no weight or pressure is needed to keep the mold in contact with the surface. However, repeated annealing causes cross-linking of PDMS, thereby leading to poorer wetting properties. It was reported [31] that the same mold can be used about 15 times, but a weak pressure ($\sim 100 \text{ g/cm}^2$) is needed for further use of the mold.

Typically, polymer films of PS ($T_g = 101 \text{ }^\circ\text{C}$) were annealed at $130 \text{ }^\circ\text{C}$, and those of styrene-*b*-butadiene-*b*-styrene (SBS) ($T_g = -36 \text{ }^\circ\text{C}$) at $120 \text{ }^\circ\text{C}$ to make the polymer chain sufficiently mobile. PDMS has a very low reactivity toward polymers, and its elasticity is sufficient to allow its separation from polymeric structures. After annealing for 30 min to 24 h and cooling to ambient temperature, the mold is removed from the surface.

Figure 12 shows SEM images of typical polymer patterns realized by CFL. When the polymer film is thick enough to completely fill the cavity of the mold, a residual polymer layer remains on the substrate as shown in Figure 12a (also refer to Fig. 11a). However, if the polymer film is thin and the interaction between the polymer and the substrate is sufficiently weak, the substrate surface can be exposed as depicted in Figure 12b.

Initial wetting conditions are very crucial when the polymer does not completely fill the cavity of the mold. If the mold leans a little toward one side, an asymmetric structure results such that the meniscus is highly uneven. In this case, the polymer pattern along the channels is not uniform. Moreover, the annealing time should be chosen in such a

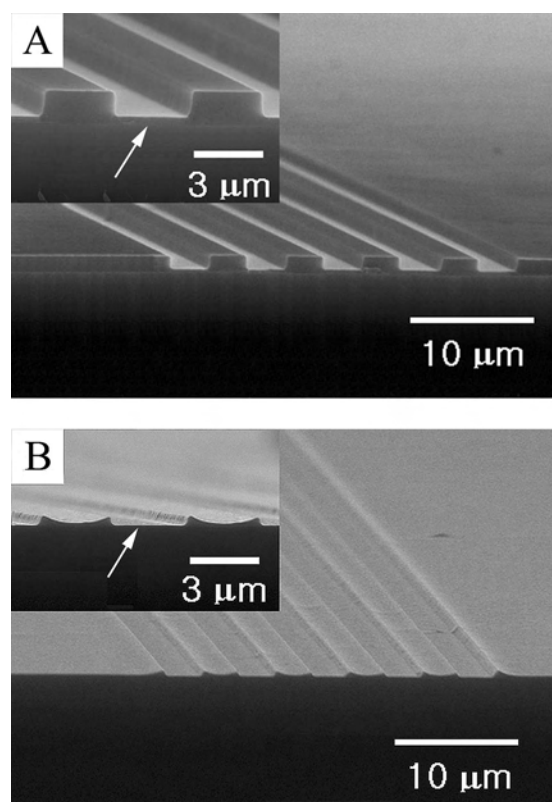


Figure 12. Examples of polymer patterns when the initial film is relatively thick ($1.5 \mu\text{m}$) (A) or thin (180 nm) (B). The arrows in the inset indicate the interface between the polymer and the substrate. Note that the substrate surface can be exposed when the film is relatively thin with respect to the mold's step height. Reprinted with permission from [80], K. Y. Suh and H. H. Lee, *Adv. Funct. Mater.* 12, 405 (2002). © 2002, Wiley-VCH.

way that instability does not set in [81]. For example, polymer films should be annealed for less than about 15 h at $120 \text{ }^\circ\text{C}$ for SBS. A longer annealing time leads to broken or isolated polymer structures.

A simple geometric calculation gives that if the maximum step height (h) of the mold is larger than the polymer thickness (t), that is, $h \geq t$, and only nearby polymeric material participates in the CFL process, the substrate surface can be exposed. However, it has been observed that the whole mass of polymer in contact with the mold spontaneously migrates to planarize the film thickness such that a significantly large mass transport occurs during the CFL. As a result, one may need a mold with a step height much higher than the polymer thickness to safely expose the substrate surface. To verify the exposure of the substrate, a 300-nm Cu line pattern by the Shipley electroless Cu deposition process was fabricated as shown in Figure 13 [31]. For the deposition, a palladium layer was first formed on a silicon substrate. A thin film ($\sim 50 \text{ nm}$) of SBS was then spin coated onto the palladium layer. The CFL process was carried out, and then the substrate was placed in a solution for the deposition. Copper deposits only on the exposed surface where the palladium is exposed and not on the polymer-covered surface. After the growth, the remaining SBS was removed by dissolving in toluene. As-grown Cu lines in Figure 13 verify that

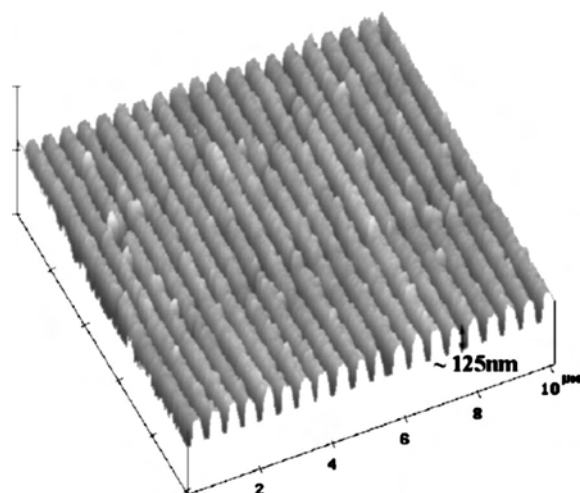


Figure 13. Fabrication of 250-nm Cu lines by a Shipley electroless Cu deposition process. In the process, copper grows only on the exposed surface, thus leading to alternating Cu lines. Reprinted with permission from [80], K. Y. Suh and H. H. Lee, *Adv. Funct. Mater.* 12, 405 (2002). © 2002, Wiley-VCH.

the surface can be exposed by CFL. Considering the poor growth characteristics inherent in the electroless deposition, remarkably good Cu lines are seen to have formed.

Figure 14 shows the cross-sectional SEM images of various three-dimensional and complex polymer structures formed by CFL in one step. As shown in the figure, CFL can preserve the fidelity of the original structure without causing distortions or defects. Furthermore, the edge resolution, which is an important characteristic for the subsequent etching step, is also satisfactory. On the other hand, distorted or textured structures are frequently observed in NIL [26, 27] and SAMIM [77]. If conventional photolithography is used, several mask steps are needed to fabricate the multilevel structures in Figure 14b and d. These results clearly

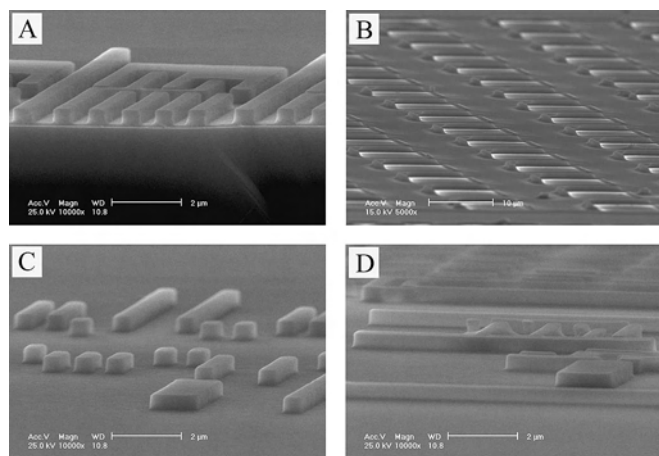


Figure 14. Several examples of three-dimensional and complex structures formed by CFL. Note that the pattern fidelity and edge definition are quite good for all of the structures fabricated. Reprinted with permission from [80], K. Y. Suh and H. H. Lee, *Adv. Funct. Mater.* 12, 405 (2002). © 2002, Wiley-VCH.

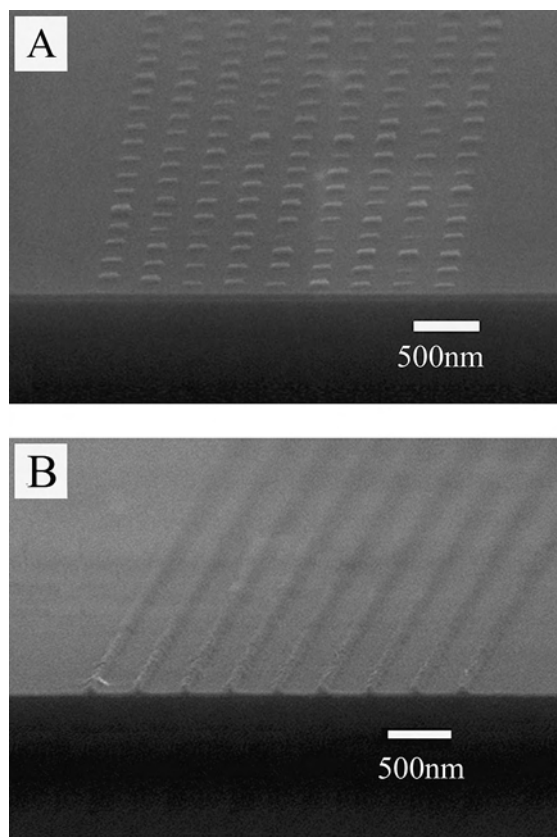


Figure 15. Two structures are shown: (A) 150-nm dots, (B) 100-nm lines. Reprinted with permission from [80], K. Y. Suh and H. H. Lee, *Adv. Funct. Mater.* 12, 405 (2002). © 2002, Wiley-VCH.

demonstrate the effectiveness of CFL in fabricating 3-D and complex structures.

Two examples of nanostructures are shown in Figure 15: one is 150-nm dots (Fig. 15a), and the other is 100-nm lines (Fig. 15b). The dot and line features on the original mold were poor because of limited e-beam capability, which is replicated in the structures formed. In general, however, it becomes very difficult to prepare good molds as the pattern size gets smaller. As PDMS is a very viscous melt (~ 3900 cP), it cannot completely fill up the cavity of the original hard mold when the cavity is deep, which often leads to a rearranged shape of the PDMS mold. In addition, the weak mechanical properties of the PDMS mold lead to broken or isolated structures for smaller features when detached from the original hard mold. For example, an aspect ratio only up to 1.4 and 1.0 could be realized for 800-nm and 400-nm line-and-space patterns, respectively. When the pattern size is smaller than 100 nm, however, the maximum aspect ratio attainable would become less than 0.25, as revealed in some experiments.

However, a recent study has shown that the PDMS mold prepared from mixtures of vinyl and hydrosilane compounds can provide sufficiently good mechanical properties to allow replication of high-density patterns at the 100-nm scale [82]. With further improvement in the mold preparation, CFL may also be effective in patterning high-density sub-100-nm features.

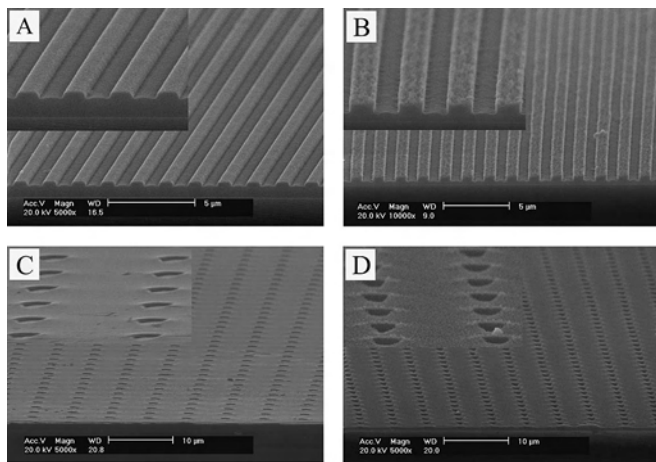


Figure 16. Examples of the pattern transfer to SiO₂ substrate by RIE in one step for an 800-nm line-and-space pattern (5-min etching (A) and 15-min etching (B)) and a 1- μ m dot pattern (before etching (C) and after etching (D)). For the line-and-space pattern, a relatively thin film (60 nm) was used, while a relatively thick film (170 nm) was used for the dot pattern. Reprinted with permission from [80], K. Y. Suh and H. H. Lee, *Adv. Funct. Mater.* 12, 405 (2002). © 2002, Wiley-VCH.

The transfer of a polymer pattern to an underlying SiO₂ substrate by reactive ion etching can be completed in one step as shown in Figure 16 for 800-nm line-and-space and 1- μ m dot patterns. A relatively thin film (60 nm) was used for the line-and-space pattern with a negative PDMS mold; a relatively thick film (170 nm) was used for the dot pattern with a positive PDMS mold. To examine the etching characteristics of the polymer resist, the etching time was varied from 5 min (Fig. 16a) to 15 min (Fig. 16b) for the line-and-space pattern. One notable finding is that the shape of the etched structure is dependent on the etching time due to the meniscus in the original polymer structure. Because of the presence of a meniscus, the minimum point of the meniscus is vulnerable to RIE in that the underlying substrate can be exposed first at that point as the etching time increases. Once the substrate is exposed, polymer and SiO₂ are etched simultaneously, thus leading to a rough surface structure as shown in Figure 16b. Therefore, a thicker film is needed to etch more deeply into the underlying substrate.

The transfer of the dot pattern is shown in Figures 16c (before etching) and 16d (after etching). In this case, there is an ample space between the dots such that the residual film thickness is not negligible. Therefore, the residual polymer is also involved in the etching process, which makes the surface of the etched SiO₂ surface a little rough. However, the pattern is successfully transferred to the underlying SiO₂ without any observable change, as there is little residual polymer present in the patterned, depressed region. The roughness can be eliminated if conventional two-step etching is used.

An important concept of CFL is that wetting of the wall of a PDMS mold by polymer melt lowers the total free energy. If the interaction at the polymer/substrate interface is negligible and the polymer melt is liquid-like, the maximum height the polymer melt can rise to through a narrow channel of width L by capillary action can be obtained by

equating the capillary force with the resistant gravitational force, which gives [83]

$$h_{\max} = \frac{2\gamma_{\text{polymer/air}} \cos \theta}{\rho GL} \quad (11)$$

where h_{\max} is the maximum height, $\gamma_{\text{polymer/air}}$ is the surface tension at the polymer/air interface, θ is the contact angle at the polymer/mold interface, ρ is the density of the polymer, and G is the gravitational constant. From the meniscus of the cross-sectional SEM image, the contact angle is estimated to be about 85°. When we insert into Eq. (11) the surface tension (~ 30 dyne/cm) and density (0.95 g/cm³) of SBS and L of 300 nm, a maximum height of 1.87 m is obtained, which indicates that the height of the patterned polymer can be made quite large. If we take into account the interaction at the polymer/substrate interface and the solid-like properties of the polymer melt, the theoretical maximum height would be reduced. For a more accurate model, further study would be required.

The time it takes for the polymer melt to fill up the void space between the mold and the polymer film can be estimated. If we neglect the effect of gravity, then the surface tension and viscosity of the polymer melt and the size of the capillary determine the rate of flow such that the time is given by [84]

$$t = \frac{2\eta z^2}{R\gamma_{\text{polymer/air}} \cos \theta} \quad (12)$$

where z is the length of capillary to be filled, t is the time, η is the viscosity of the polymer melt, and R is the hydraulic radius (the ratio of the volume of the liquid in the capillary section to the area of the solid and liquid interface), which is approximately one-half the width L . It takes about 30 min for the SBS polymer to completely fill the void in a mold with a step height of 600 nm and a width of 400 nm at 100 °C. The viscosity of the SBS is about 10^6 (Pa · s) from the rheometrics spectroscopy (RMS) measurement at zero shear stress. When we use these values in Eq. (12), the time needed to fill the void in the mold is calculated to be 1377 s (~ 23 min), which is somewhat shorter than the observed value.

3.4. Soft Molding

Soft molding [32] involves placing an PDMS mold on the surface of a spin-coated polymer film with a slight pressure (< 1 N/cm²), allowing the mold to absorb solvent, releasing the pressure, and then letting the mold and the substrate remain undisturbed for a period of time, after which the mold is removed.

Soft molding is a method for forming 3-D micro- and nanostructures that overcomes the difficulties and shortcomings of SAMIM [77] and micromolding [85]. In SAMIM, a polymer film is coated onto a substrate and baked. A patterned PDMS mold is wetted with a good solvent of the polymer, which is then brought into contact with the polymer surface. The solvent on the mold dissolves the polymer, and this dissolved polymer is molded into the channels or cavities formed between the mold and the substrate. There

are two problems with SAMIM when it is applied to form 3-D structures. The first is that the surface of the patterned polymer is highly textured, which may be useful in processes where a high surface/volume ratio is important, as in adhesion and catalysis, but is not desirable at all for forming 3-D structures. The other is that the pattern formed by SAMIM becomes distorted. In particular, the base of a rectangular stripe becomes wider than the top. Furthermore, the structure formed contracts as the solvent evaporates from the molded polymer.

The same problem arises in the method of micromolding [85], which was used to fabricate glass microstructures from sol-gel precursors. The shrinkage problem is further amplified by isotropic shrinkage caused by the annealing step required for the fabrication. For the method to work, there have to be regions where the material to be molded is not present so that the elastomeric mold and the bare substrate are allowed to make contact. Generation of defects is another problem to contend with.

The problems associated with SAMIM and micromolding in forming 3-D structures are essentially solvent-related. If a polymer film spincoated onto a substrate is directly molded by an elastomeric mold without baking, the solvent concentration in the film is initially uniform, relieving any problem associated with the initial nonuniform distribution of solvent. If a solvent is appropriately chosen such that the solvent is readily absorbed into the elastomeric mold and evaporates into air by diffusion through the mold, the fidelity of the structure being molded can be assured. Use of a solvent with efficient absorption and dissipation characteristics and that of a spin-coated polymer film without baking are the two essential features of the method.

Figure 17 illustrates the soft molding process. An elastomeric mold with the desired pattern on its surface is placed on a polymer film, without baking, immediately after the film is spin coated onto a substrate and then pressed slightly at a pressure less than 1 N/cm^2 . After the pressure is released, the mold and the substrate are allowed to remain undisturbed for a period of time, which is on the order of 10 min. During the soft molding, the solvent contained in the polymer film diffuses toward the interface because of the concentration gradient and is absorbed into the mold. The solvent then permeates through the mold and finally evaporates into the air. After the evaporation is completed, the mold is removed, thus finishing the soft molding.

The polymer used is a commercial novolac resin dissolved in propylene glycol methyl ether acetate (PGMEA), which is a typical solvent for photoresists. The polymer was spin coated onto the wafer to a 1.5- to $2.5\text{-}\mu\text{m}$ thickness with 20–30 wt% polymer solution at 3000 rpm for 15 s. In the soft molding of the wet film, the molded 3-D structures are hardened by the time the mold is removed.

Figure 18 shows SEM images of a 3-D structure that was formed by soft molding. Comparison of the master (Fig. 18a) from which the mold was prepared with the polymer replica (Fig. 18b) obtained by soft molding reveals that the original 3-D structure is well transferred to the polymer film without any distortion or defects in a single step. In the soft molding, the solvent in the molded polymer is continuously removed by absorption into a PDMS mold at the interface between the mold and the molded polymer and

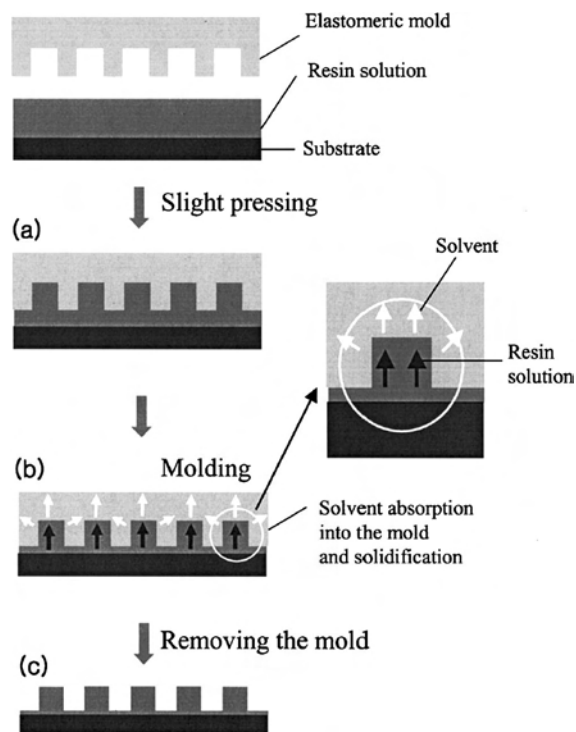


Figure 17. Illustration of the soft molding method. In soft molding (a) an elastomeric mold is placed on a polymer film that is spin coated onto a substrate, which is then pressed down slightly to ensure conformal contact. (b) After the pressure is released, the whole structure is left undisturbed for a period of time for solidification, during which the solvent in the molded structure is absorbed into the mold. (c) The mold is then removed. Reprinted with permission from [32], Y. S. Kim et al., *Appl. Phys. Lett.* 79, 2285 (2001). © 2001, American Institute of Physics.

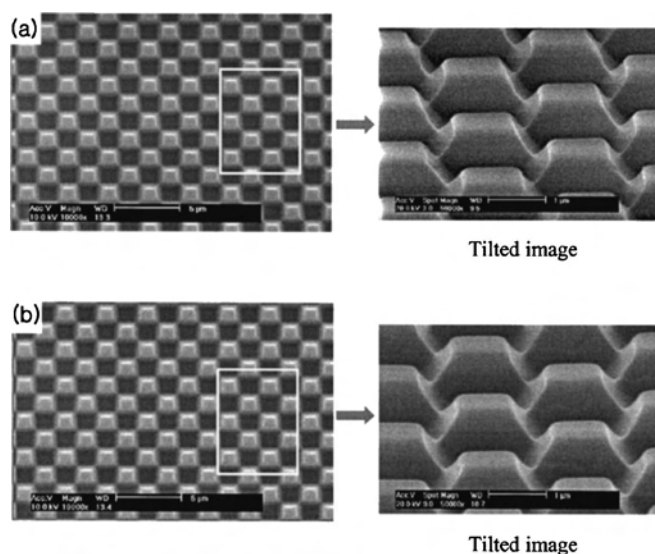


Figure 18. SEM images of (a) the master used for soft molding and (b) the replica fabricated. Reprinted with permission from [32], Y. S. Kim et al., *Appl. Phys. Lett.* 79, 2285 (2001). © 2001, American Institute of Physics.

replenished by solvent diffusion to the interface. The gradual and continuous replenishment of solvent and accompanying polymer to the interface ensures the fidelity of the molded polymer structure. Experimental results show that PDMS can absorb PGMEA up to 27 wt% of its weight. About 30 wt% of the absorbed solvent diffuses out into the air in 1 hour. Although the dissipation rate is not high, the thickness of the polymer layer is negligible compared with that of a PDMS mold such that the mold can more than accommodate all of the solvent in the polymer film. For example, the solvent absorbed into the mold would amount to less than 0.1 wt% of the mold weight even if all of the solvent in the wet polymer film were to be absorbed into the mold without any dissipation. The mold was used more than 20 times without any treatment. PGMEA, which is a widely used solvent for photoresists, is an ideal solvent for soft molding in that it is efficiently absorbed into PDMS, and yet the amount absorbed is not sufficient to cause distortion of the mold. No further processing such as baking is required for the formation of a 3-D structure after the mold is removed.

The 3-D structure thus molded can be used as such since the molded polymer is hardened by the time the mold is removed. If baking is desired, it is carried out at the end of the molding with the mold still in place. It has been found that the original molded structure remains unaltered even with baking.

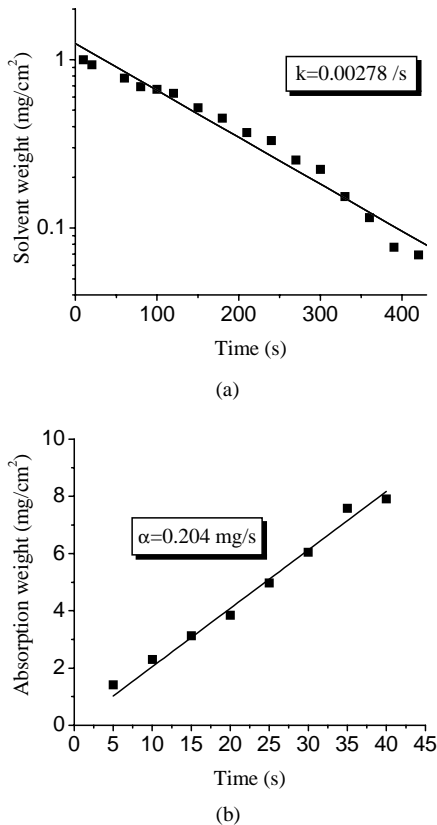


Figure 19. Experimental determination of (a) evaporation parameter k and (b) absorption parameter α . Reprinted with permission from [32], Y. S. Kim et al., *Appl. Phys. Lett.* 79, 2285 (2001). © 2001, American Institute of Physics.

To arrive at a condition under which soft molding can be effective, solvent absorption into the mold and evaporation from the polymer surface are modeled for their rates. Since the film of interest is quite thin, diffusion can be neglected. If it is assumed that the rate of solvent evaporation is proportional to the solvent concentration, then we have

$$\frac{\partial M}{\partial t} = -kM \quad (13)$$

where k is the proportionality constant and M is the solvent concentration in terms of weight per unit area. Equation (13) gives

$$M = M_0 e^{-kt} \quad (14)$$

The experimental data given in Figure 19a show that the first-order kinetics describes the evaporation process well. The solvent weight in Figure 19a was determined experimentally by dividing the weight of the solvent evaporated by the exposed surface area. In the experiment for the rate of absorption by the mold, the mold was floated in a bath filled with the solvent. Since the solvent concentration is constant, the rate of absorption per exposed surface area is independent of the concentration such that

$$\frac{\partial M_a}{\partial t} = -\alpha \quad (15)$$

where α is a constant and M_a is the concentration of the solvent per unit area in the mold. The data plotted in

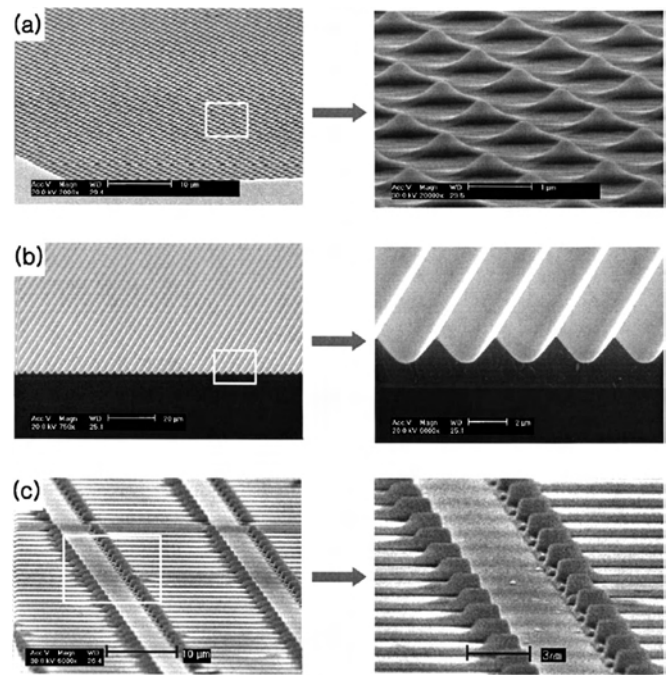


Figure 20. Tilted SEM images of several three-dimensional structures fabricated by soft molding. (a) Circular cones; the enlarged part shows that the base diameter of the cone is approximately 1 µm. (b) Rounded triangular channels with a period of approximately 3 µm. (c) A three-level structure. Reprinted with permission from [32], Y. S. Kim et al., *Appl. Phys. Lett.* 79, 2285 (2001). © 2001, American Institute of Physics.

Figure 19b show that the concentration M_a increases linearly with time. For the soft molding to be successful, the rate of absorption should be larger than the rate of evaporation. Since the evaporation rate is exponential whereas the absorption rate is linear, the initial rates should be used for the condition that the absorption rate be greater than the evaporation rate. It then follows from Eqs. (13) and (15) that

$$\alpha > kM_0 \tag{16}$$

In soft molding, the solvent is absorbed into the mold at the interface between the polymer film and the mold. Therefore, the value of α in the soft molding would be smaller than that of α determined in a bath of solvent. Therefore, the condition should be modified to

$$\frac{\alpha}{kM_0} \gg 1 \tag{17}$$

For the experimental result in Figure 19, novolac in PGMEA was used with PDMS as the mold, for which α is 0.204 mg/s, k is 0.00278/s, and $M_0 = 1.25$ mg/cm². It is seen that $\alpha/(kM_0)$ (= 58.7) is much larger than unity. The same rate laws have been found to apply to other polymer systems such as PS in toluene and PMMA in toluene. For

instance, the values of α and k for the system of PS in toluene are 0.640 mg/s and 0.0312/s, respectively, such that $\alpha/(kM_0)$ (~ 15) $\gg 1$.

Figure 20 shows SEM images of several 3-D structures formed by soft molding. Fabricated circular cones are shown in Figure 20a; the enlarged part reveals that the base diameter of the cone is approximately 1 μ m. Rounded triangular channels with a period of approximately 3 μ m are given in Figure 20b. A fabricated three-level structure is shown in Figure 20c. These results demonstrate the effectiveness of soft molding in the fabrication of 3-D structures.

Soft molding can be made to allow for one-step pattern transfer to the underlying substrate [86]. Shown in Figure 21 are the AFM images of 60-nm-wide lines patterned by soft molding and then transferred to the underlying SiO₂ layer by one-step RIE. Comparison of the transferred SiO₂ pattern (Fig. 21b) with the polymer pattern (Fig. 21a) obtained by soft molding reveals that the polymer pattern is well transferred to the underlying SiO₂ layer without distortion by one-step RIE.

4. CONCLUSIONS

In this chapter we have described a number of unconventional nanolithographic methods. With ever increasing interest in and demand for the fabrication of structures with dimensions less than 100 nm, it is expected that suitable fabricating tools will emerge in the near future. In addition, research in these nanostructures will advance the fundamental understanding of systems with dimensions less than 100 nm for material science, chemistry, and biology.

Historically, photolithography has been the dominant technique for replication. Photolithography will probably continue to provide an attractive solution for replication at scales down to, perhaps, 70 nm with 193-nm (or 157-nm) light and/or performance-enhancing techniques such as phase-shifting masks, off-axis illumination, optical proximity correction, or photoresists based on top surface imaging with silylation and dry development. Projection photolithography with transmission optics seems, however, to be reaching a limit set by the physics of diffraction and the properties of materials.

We have reviewed largely four unconventional nanolithographies: NIL, soft lithography, CFL, and soft molding. These approaches are very promising for future applications in that they are based on physical contact, thus eradicating the diffraction problem. In addition to this inherent advantage, the techniques allow patterning on curved surfaces, patterning a wide range of materials and materials precursors. Demonstrating direct compatibility with materials commonly used in microelectronics, controlling registration and distortion, and reducing the density of defects are areas in which all of these methods require further development before they can be competitive with the much more highly developed photolithographic processes.

NIL is perhaps the most promising method that can allow the fabrication of nanostructures in that it does not have any size limitation (down to several nanometers) and exhibits stringent pattern fidelity. Moreover, the introduction of RT processing makes possible the step-and-repeat process and multiple imprinting, which makes NIL as a strong candidate

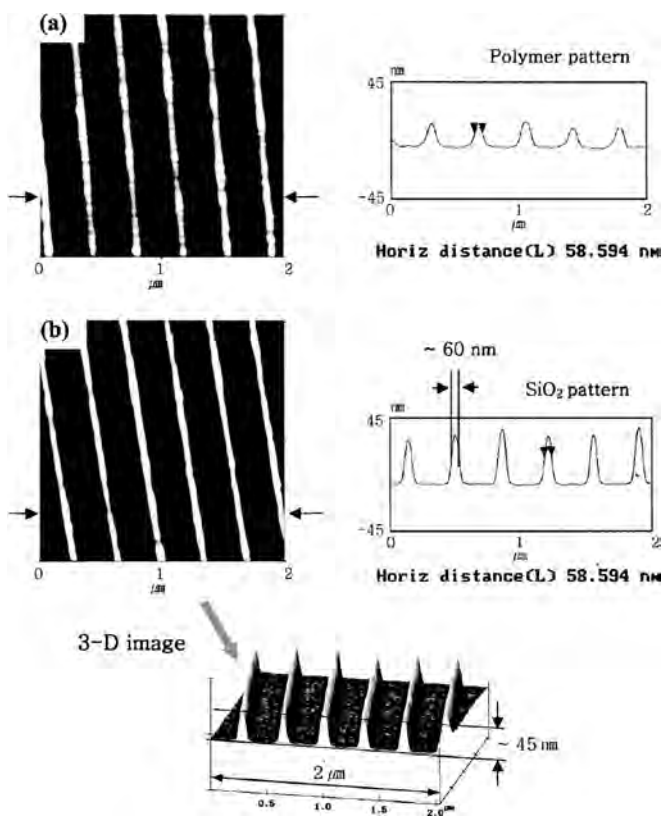


Figure 21. Sixty-nanometer lines transferred into a SiO₂ layer by modified soft molding and one-step RIE. (a and b) AFM images of (a) polymer pattern formed by modified soft molding and (b) the pattern in (a) transferred into an underlying SiO₂ layer by one-step RIE. Reprinted with permission from [86], Y. S. Kim et al., *Appl. Phys. Lett.* 81, 1001 (2002). © 2002, American Institute of Physics.

for nanofabrication. However, several intrinsic problems arising from the use of high pressure are yet to be solved.

Soft lithography has grown extensively since the mid-1990s and has possibly become the most versatile method among the unconventional methods known. Thanks to beneficial material properties of PDMS, soft lithography has already established itself in niche applications in the fabrication of microfluid analytical systems [87] in addition to nanofabrication. As with NIL, a number of issues remain to be solved before soft lithography invades the core applications of photolithography. First, high-resolution (<20 nm) registration with elastomeric materials must be demonstrated. The distortion and deformation associated with elastomeric materials must also be managed, and the pattern transfer must be made exactly reproducible. Second, the quality of the patterns and structures produced must be improved. These patterns, especially for narrow lines, are not yet compatible with the levels of quality required for nanofabrication of complex electronic devices.

CFL is a simple and yet effective tool for patterning. It does away with the high-pressure requirement of imprint lithography while maintaining the excellent pattern fidelity offered by the method. A feature unique to CFL is that photographic lithography involving exposing, developing, and baking can be accomplished in a simple step without involving the RIE that other nonphotographic techniques require. The ease with which 3-D and complex structures can be fabricated is another advantage. For the method to be applicable to high-density patterns with a feature size less than 100 nm and a high aspect ratio, however, better mold preparation techniques should be developed.

Soft molding is a very versatile technique for fabricating 3-D structures. This simple method would be useful for low-cost fabrication of 3-D structures for microoptics, microelectromechanical systems, and microfluidic systems.

Unconventional lithography is in its infancy, and yet the findings have far exceeded expectations. With further development, it would open the door to new discoveries and useful applications in the areas of nanoscience and nanofabrication.

GLOSSARY

Capillarity The interaction between contacting surfaces of a liquid and a solid that distorts the liquid surface from a planar shape.

Elastomer Any of various polymeric materials having the elastic properties of natural rubber.

Imprinting A mark or pattern produced by pressing.

Lithography A printing process in which the image to be patterned is rendered on a surface.

Molding To make a mold of or from molten metal or polymer, for example, before casting.

REFERENCES

1. M. A. Kastner, *Phys. Today* 24 (1993).
2. M. A. Reed, *Sci. Am.* 118 (1993).
3. K. K. Likharev and T. Claeson, *Sci. Am.* 80 (1992).
4. K. K. Likharev, *IBM J. Res. Dev.* 32, 144 (1988).
5. V. Vijayakrishnan, A. Chainani, D. D. Sarma, and C. N. R. Rao, *J. Phys. Chem.* 96, 8679 (1992).
6. H. Rohrer, *Microelectron. Eng.* 32, 5 (1996).
7. W. M. Tolles, *Nanotechnology* 7, 59 (1996).
8. F. A. Buot, *Phys. Rep.* 243, 73 (1993).
9. G. M. Whitesides, J. P. Mathias, and C. T. Seto, *Science* 254, 1312 (1991).
10. S. Okazaki, *J. Vac. Sci. Technol., B* 9, 2829 (1991).
11. M. D. Levenson, *Solid State Technol.* 38, 57 (1995).
12. H. I. Smith and H. G. Craighead, *Phys. Today* 24 (1990).
13. J. M. Gibson, *Phys. Today* 56 (1997).
14. Y. Chen, R. Kupka, F. Rousseaux, F. Carcenac, D. Decanini, M. Ravet, and H. Launois, *J. Vac. Sci. Technol., B* 15, 2489 (1994).
15. J. P. Silverman, *J. Vac. Sci. Technol., B* 16, 3137 (1998).
16. R. Piner, J. Zhu, F. Xu, S. Hong, and C. A. Mirkin, *Science* 283, 661 (1999).
17. S. Hong and C. A. Mirkin, *Science* 288, 1808 (2000).
18. S. C. Minne, G. Yaralioglu, S. R. Manalis, J. D. Adams, J. Zesch, A. Atalar, and C. F. Quate, *Appl. Phys. Lett.* 71, 2324 (1998).
19. W. M. Moreau, "Semiconductor Lithography: Principles and Materials." Plenum, New York, 1988.
20. D. Brambley, B. Martin, and P. D. Prewett, *Adv. Mater. Opt. Electron.* 4, 55 (1994).
21. N. Kramer, H. Birk, J. Jorritsma, and C. Schonberger, *Appl. Phys. Lett.* 66, 1325 (1995).
22. J. A. Dagata, *Science* 270, 1625 (1995).
23. A. J. Bard, G. Denault, C. Lee, D. Mandler, and D. O. Wipf, *Acc. Chem. Res.* 23, 357 (1990).
24. E. Betzig and K. Trautman, *Science* 257, 189 (1992).
25. S. C. Minne, S. R. Manalis, A. Atalar, and C. F. Quate, *Appl. Phys. Lett.* 68, 1427 (1996).
26. S. Y. Chou, P. R. Krauss, and P. J. Renstrom, *Appl. Phys. Lett.* 67, 3114 (1995).
27. S. Y. Chou, P. R. Krauss, and P. J. Renstrom, *Science* 272, 85 (1996).
28. Y. Xia and G. M. Whitesides, *Annu. Rev. Mater. Sci.* 28, 153 (1998).
29. Y. Xia, J. A. Rogers, K. E. Paul, and G. M. Whitesides, *Chem. Rev.* 99, 1823 (1999).
30. Y. Xia and G. M. Whitesides, *Angew. Chem. Int. Ed.* 37, 550 (1998).
31. K. Y. Suh, Y. S. Kim, and H. H. Lee, *Adv. Mater.* 13, 1386 (2001).
32. Y. S. Kim, K. Y. Suh, and H. H. Lee, *Appl. Phys. Lett.* 79, 2285 (2001).
33. J. Canning, *J. Vac. Sci. Technol., B* 15, 2109 (1997).
34. The National Technology Roadmap for Semiconductor Industry Association, 1999.
35. S. M. Sze, "Semiconductor Devices: Physics and Technology." Wiley, New York, 1985.
36. G. Timp, "Nanotechnology." Springer-Verlag, New York, 1998.
37. P. Ball, "Designing the Molecular World." Princeton University Press, Princeton, NJ, 1994.
38. E. D. Regis, "Nano." Bantam Press, London, 1995.
39. M. C. Hutley, "Diffraction Gratings." Academic Press, New York, 1982.
40. M. Emmelius, G. Pawlowski, and H. W. Vollmann, *Angew. Chem. Int. Ed.* 28, 1445 (1989).
41. S. Y. Chou, P. R. Krauss, W. Zhang, L. Guo, and L. Zhang, *J. Vac. Sci. Technol., B* 15, 2897 (1997).
42. L. Guo, P. R. Krauss, and S. Y. Chou, *Appl. Phys. Lett.* 71, 1881 (1997).
43. S. Y. Chou, *Proc. SPIE* 85, 652 (1997).
44. H.-C. Scheer, H. Schultz, T. Hoffmann, and C. M. Sotomayor Torres, "Handbook of Thin Film Materials" (H. S. Nalwa, Ed.), Vol. 5, pp. 1–60. Academic Press, San Diego, 2001.
45. A. Lebib, Y. Chen, F. Carcenac, E. Cambril, L. Manin, L. Couraud, and H. Launois, *Microelectron. Eng.* 53, 175 (2000).
46. D. Y. Khang and H. H. Lee, *Appl. Phys. Lett.* 76, 870 (2000).

47. D. Y. Khang, H. Yoon, and H. H. Lee, *Adv. Mater.* 13, 749 (2001).
48. J. Bicerano, "Prediction of Polymer Properties," 2nd ed. Dekker, New York, 1996.
49. D. W. van Krevelen, "Properties of Polymers," 3rd ed. Elsevier, Amsterdam, 1990.
50. H.-G. Elias, "Macromolecules," Vol. 1. Plenum, New York, 1984.
51. M. Ohring, "The Materials Science of Thin Films." Academic Press, New York, 1991.
52. B. Crist, "Structure and Properties of Polymers" (R. W. Cahn, P. Haasen, and E. J. Kramer, Eds.). VCH, New York, 1993.
53. J. R. Sheats and B. W. Smith, "Microlithography: Science and Technology." Dekker, New York, 1998.
54. Y. Xia and G. M. Whitesides, *Langmuir* 13, 2059 (1997).
55. G. D. Aumiller, E. A. Chandross, W. J. Thomlinson, and H. P. Weber, *J. Appl. Phys.* 45, 4557 (1974).
56. S. J. Clarson and J. A. Semlyen, Eds., "Siloxane Polymers." Prentice Hall, Englewood Cliffs, NJ, 1993.
57. Y. Xia, J. J. McClelland, R. Gupta, D. Qin, X.-M. Zhao, L. L. Sohn, R. J. Celotta, and G. M. Whitesides, *Adv. Mater.* 9, 147 (1997).
58. J. J. McClelland, R. E. Sscholten, E. C. Palm, and R. J. Celotta, *Science* 262, 877 (1993).
59. Y. Xia, X.-M. Zhao, and G. M. Whitesides, *Microelectron. Eng.* 32, 255 (1996).
60. Y. Xia, E. Kim, and G. M. Whitesides, *J. Electrochem. Soc.* 143, 1070 (1996).
61. N. B. Larsen, H. Biebuyck, E. Delamarche, and B. Michel, *J. Am. Chem. Soc.* 119, 3017 (1997).
62. H. A. Biebuyck and G. M. Whitesides, *Langmuir* 10, 4581 (1994).
63. Y. Xia, N. Venkateswaran, D. Qin, J. Tien, and G. M. Whitesides, *Langmuir* 14, 363 (1998).
64. J. A. Rogers, R. J. Jackman, and G. M. Whitesides, *Adv. Mater.* 9, 475 (1997).
65. J. A. Rogers, R. J. Jackman, and G. M. Whitesides, *J. MEMS* 6, 184 (1997).
66. R. J. Jackman, J. L. Wilbur, and G. M. Whitesides, *Science* 269, 664 (1994).
67. A. Kumar, H. Biebuyck, and G. M. Whitesides, *Langmuir* 10, 1498 (1994).
68. T. P. Moffat and H. J. Yang, *J. Electrochem. Soc.* 142, L220 (1995).
69. Y. Xia, E. Kim, M. Mrksich, and G. M. Whitesides, *Chem. Mater.* 8, 601 (1996).
70. Y. Xia, M. Mrksich, E. Kim, and G. M. Whitesides, *J. Am. Chem. Soc.* 117, 9576 (1995).
71. N. L. Jeon, P. G. Clem, A. A. Payne, and R. G. Nuzzo, *Langmuir* 12, 5350 (1996).
72. H. A. Biebuyck, N. B. Larsen, E. Delamarche, and B. Michel, *IBM J. Res. Dev.* 41, 159 (1997).
73. Y. Xia, X.-M. Zhao, E. Kim, and G. M. Whitesides, *Chem. Mater.* 7, 2332 (1995).
74. M. Mrksich and G. M. Whitesides, *Annu. Rev. Biophys. Biomol. Struct.* 25, 55 (1996).
75. J. L. Wilbur, H. Biebuyck, J. C. MacDonald, and G. M. Whitesides, *Langmuir* 11, 825 (1995).
76. E. Delamarche, H. Schmid, A. Bietsch, N. B. Larsen, H. Rothuizen, B. Michel, and H. Biebuyck, *J. Phys. Chem. B* 102, 3324 (1998).
77. E. Kim, Y. Xia, X.-M. Zhao, and G. M. Whitesides, *Adv. Mater.* 9, 651 (1997).
78. J. A. Rogers, Z. Bao, and L. Dhar, *Appl. Phys. Lett.* 73, 294 (1998).
79. H.-C. Scheer, H. Schulz, T. Hoffmann, and C. M. Sotomayor Torres, *J. Vac. Sci. Technol., B* 16, 3917 (1998).
80. K. Y. Suh and H. H. Lee, *Adv. Funct. Mater.* 12, 405 (2002).
81. K. Y. Suh and H. H. Lee, *J. Chem. Phys.* 115, 8204 (2001).
82. H. Schmid and B. Michel, *Macromolecules* 33, 3042 (2000).
83. A. W. Adamson and A. P. Gast, "Physical Chemistry of Surfaces," Chap. 1. Wiley, New York, 1997.
84. D. Myers, "Surfaces, Interfaces, and Colloids." pp. 87-109. VCH, New York, 1991.
85. C. Marzolin, S. P. Smith, M. Prentiss, and G. M. Whitesides, *Adv. Mater.* 10, 571 (1998).
86. Y. S. Kim, J. Park, and H. H. Lee, *Appl. Phys. Lett.* 81, 1011 (2002).
87. D. C. Duffy, J. C. McDonald, O. J. A. Schueller, and G. M. Whitesides, *Anal. Chem.* 70, 4974 (1998).

Vacuum Nanoelectronics

Ning-Sheng Xu

Sun Yat-Sen University, Guangzhou, People's Republic of China

CONTENTS

1. Introduction
2. Vacuum Microelectronics:
Achievements and Trends of Development
3. Novel Nano-Dimensional
Cold-Cathode Materials
4. Vacuum Nanoelectronic Devices
5. Potential Applications
6. Summary
Glossary
References

1. INTRODUCTION

Vacuum nanoelectronics is a frontier subject and a development of vacuum microelectronics. Both vacuum microelectronics and vacuum nanoelectronics are based on operation with electrons in vacuum, but the former deals with devices in microscale while the latter studies the techniques for preparing nano electron-emitters (or nanoemitters) and devices, and the scientific topics about their novel effects and characteristics. The fast growth of recent research activity in vacuum nanoelectronics reflects the rapid development in nanoscience and nanotechnology. In order to prepare a base for presenting the subject of vacuum nanoelectronics and to show the strong relation between vacuum microelectronics and vacuum nanoelectronics, in Section 2 we review the most recent developments in vacuum microelectronics.

The real opportunity to move from vacuum microelectronics to vacuum nanoelectronics came after the discovery of carbon nanotubes [1], which is a novel one-dimensional material formed by sheets of graphite, called graphene, in a tubular form. The carbon nanotubes were later found to possess field emission properties superior to other cold cathode materials studied before [2, 3, 4]; for example, they have extremely low turn-on field and high current density. However, the significance of these findings is far beyond that. It shows to us that we can prepare vacuum electron emitters

in a self-assembly process, or a so-called bottom-up process, rather than only relying on the microfabrication technology, or a so-called top-down technology. Thus, now we often say “synthesis” rather than “fabrication” of cold cathode emitters. This conceptual revolution will have a farther reaching impact than that of the discovery of carbon nanotubes as excellent field emitters. Thus, now one can make one-dimensional nanoemitters of different electronic properties, such as metallic molybdenum [5] and tungsten and their oxide nanowires [6, 7], semiconducting SiC [8], CuS₂ [9], CuO [10], and CuOH [10] nanowires, etc. They have also been shown to have very good field emission performance. Section 3 will describe the recent development in the synthesis and characterization of one-dimensional nanoemitters.

Will the nanoemitters bring to us new physical properties in field emission? This is an important question. From the findings just emerging, one may say “yes.” This largely comes from quantum-size and nano-dimension effects, which will not occur with microscale emitters and devices. Section 3 will also give an account of these new findings. However, the collection of such discoveries is still limited. Thus, more effort is needed. Furthermore, it is also extremely important to explore the application of these effects, because this will lead to widening of the area of application of vacuum electrons. The future of vacuum nanoelectronics will be very dependent on how far it can go in finding novel applications in the coming new era of nanoscience and nanotechnology.

To date, there are only a limited number of successful cases in making vacuum nanoelectronic devices that ideally would use a single nanoemitter and have the dimension of a device structure in nanoscale. Nevertheless, the techniques have been progressing well toward this aim. This often involves exploring a capability enhanced by using a combination of both top-down and bottom-up techniques or completely relies on self-assembly processes. Section 4 will review the recent achievements in this direction.

Section 5 will give several examples of application of using nanoemitters and of the novel potential applications of vacuum nanoelectronics under exploration. More attention will be paid to those applications where vacuum nanoelectronics, if it is used, has apparent advantages over vacuum microelectronics. We intend to use these to show the importance of developing vacuum nanoelectronics.

2. VACUUM MICROELECTRONICS: ACHIEVEMENTS AND TRENDS OF DEVELOPMENT

Microelectronics is a subject that is more familiar to general public, and it is about the science and technology of microscale devices, such as Si-based integrated circuits (chips) or GaAs-based optoelectronic devices. In these devices, the charge carriers are electrons and holes and they move in solid-state materials. Their interaction with solids determines their performance. In vacuum microelectronics, the charge carriers in a device are either electrons (in most cases) or both ions and electrons (in rare cases), and they move in vacuum when the devices operate. The factors limiting their performance are largely related to the field electron emission process, which was formulated in 1928 by two scientists named Fowler and Nordheim [11]. They attributed this phenomenon to a quantum tunneling process, in which free electrons in an atomic clean metal surface are emitted into vacuum.

Before vacuum microelectronic devices became available, the devices that produced vacuum electrons were large in scale, or even bulky. The basic conceptual vacuum microelectronic device was proposed in 1961, when Shoulders [12] published an article entitled "Microelectronics using electron-beam-activated machining techniques." At that time, the success in fabricating four-transistor monolithic chips was just announced. Shoulders, with tremendous vision, proposed to devise vacuum tunneling effect devices. One can see that his proposal was revolutionary.

However, the task to fabricate a working vacuum microelectronic device based on this concept was an extremely difficult one. The reasons include poor microfabrication facility and nonexistence of the relevant technique at that time. Further pressures came from researchers in the field, since they would really believe the future of the direction pointed by Shoulders only after such a device could be made. In this context, the report of successful fabrication of a Spindt cathode had a very significant, extensive, and global impact. The first report on such a success came in 1968, seven years after the concept was published [13]. In Figure 1 we use micrographs from a scanning electron microscope (SEM) of a silicon field emitter array (FEA) to explain the concept of Spindt cathodes. A Spindt cathode is similar to the silicon FEA, but it consists of an array of gated molybdenum tips rather than silicon ones. The apex of a tip is put in the center of a cylindrical open gate aperture in microscale. This

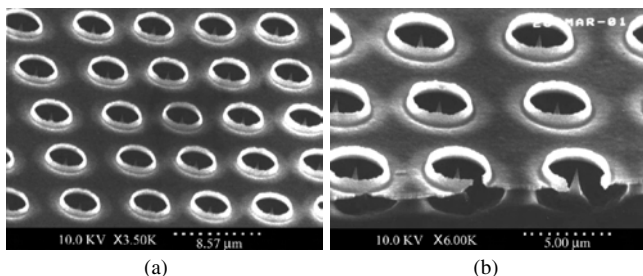


Figure 1. Scanning electron micrographs of a silicon field emitter array using Spindt-cathode structure (a) and its cross-section (b). Courtesy of Dr. Ejaz Huq, Rutherford-Appleton Lab, UK.

device structure was adapted by Spindt for vacuum microelectronic devices from a common electron optic system; therefore we shall call this type of device structure a Spindt-cathode structure.

This success stimulated global enthusiasm in studying this new type of device. Such a move needed to be coordinated, so that a collective effort could be formed to effectively solve both key scientific and technological issues. Henry Gray and Capp Spindt, both from the United States, led a team to establish an international body in the field of vacuum microelectronics. The first International Vacuum Microelectronics Conference (IVMC) was held in Williamsburg, VA, in 1988, and subsequently became an annual meeting of the researchers in the field. In the first IVMC, the term vacuum microelectronics was really established. The subject was then given comprehensive coverage in 1992 in an article entitled "Vacuum microelectronics" by Brodie and Spindt [14], and recently in 2001 in a book with the same title by Zhu [15]. In the following, we shall give only a review on the major achievements that are relevant to our current subject on vacuum nanoelectronics.

Since the invention of the Spindt cathode, the field emitter array has developed as follows.

2.1. Use of Different Emitter Materials

In the original Spindt cathode, molybdenum tips were employed as emitters. But they could not be deposited as crystalline material and were easily contaminated and oxidized. Also, additional facility and steps are required in the microfabrication process. Thus, Gray et al. pursued the silicon field emitter arrays, and they succeeded in 1986 [16]. Since then, one has been able to fabricate field emitter arrays in a monolithic process using the most common microelectronic material (i.e., silicon). As a consequence, the preparation technique of field emitter arrays is closely tied to with the microfabrication process and benefits from its rapid development in the second half of the last century. Since the 1990s, the feasibility of replacing the single crystalline Si wafers with polycrystalline Si films has also been studied. If it is successful, the area of field emitter arrays will not be limited by the size of wafer. In addition, the field emitter arrays may then be prepared with polysilicon deposited on metal films on glass substrates. These could be very useful for field emission displays.

2.2. Development of High Current-Density Field-Emitter Arrays

In the early stages, the areas of application of vacuum microelectronics were similar to those of vacuum electronics (i.e., mainly in vacuum electron sources such as that used in microwave power devices). In these, a high current density is essential. In order to meet this requirement, a lot of effort was spent on how to fabricate high-density tip arrays. In 1983, Spindt reported a 6 mA electron current from 12 Mo tips ($500 \mu\text{A}/\text{tip}$) [17]. Further, if one designs a FEA based on an encouraging result of Van Veen, who obtained $850 \mu\text{A}$ from a single Mo tip at an applied voltage of 205 V [18], a higher density of tip arrays should lead to higher current density. Later, in 1994, Bozler et al. [19] made an array of

tips of $10^9/\text{cm}^2$ density and reported a total current density of $1600 \text{ A}/\text{cm}^2$ obtained after the FEA was cesiated. This FEA was fabricated to have the smallest dimensions (i.e., it had a gate-to-tip distance of 80 nm and tip spacing of 320 nm). To have even higher emitter density, one-dimensional nanowires and nanotubes may be required, and nanotechnology may be needed to produce a finer gate-to-tip distance.

2.3. Development of Surface Cleaning Technique

The high current density electron sources or field emitter arrays often need a surface cleaning process before stable and long-life emission can be sustained. The widely accepted technique was developed by Schowebel et al. [20] based on H_2 plasma etching. The hydrogen ions take away the oxygen from silicon surface and also terminate the dangling bond of the silicon surface. This etching process can be effective only if the etched FEAs will not be exposed to air again since the silicon tip arrays may be oxidized again in air. She et al. [21] recently have developed a procedure to coat the cleaned silicon tip with amorphous diamond nanothin film, the surface of which is chemically inert.

2.4. Invention of Novel Device Structures

In vacuum microelectronics, development of novel device structures is a paramount issue. Several new achievements have been made since the invention of the Spindt-cathode structure [13]. First, Oh invented a method for creating submicrometer gate apertures with microscale lithography [22]. The combination of a submicrometer aperture hole with in the shape of “bird’s beak” (Fig. 2a) is effective in lowering the operation voltage. So this device structure may be adapted for vacuum nanoelectronic devices that employ a nanoemitter.

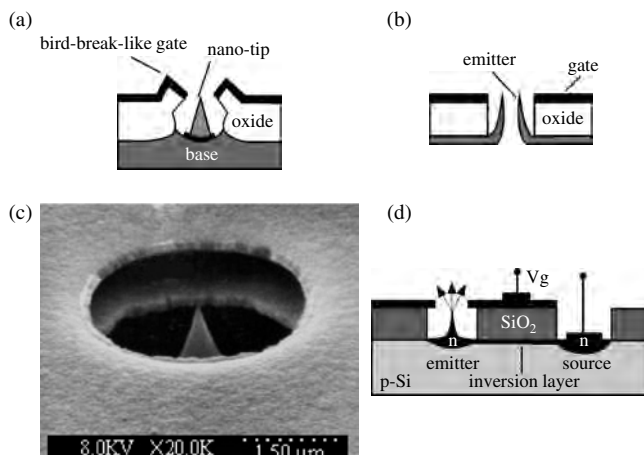


Figure 2. Novel vacuum microelectronic device structures. (a) Illustration of the cross-section of a microtriode having a bird-beak-like gate with a submicrometer aperture hole. (b) Illustration of the cross-section of a microvolcano field ionizer. (c) SEM image of a double-gate microtriode using a silicon field emitter. Courtesy of Dr. Ejaz Huq, Rutherford-Appleton Lab, UK. (d) Illustration of the cross-section (top) of a microtriode with MOSFET structure and its equivalent circuit (bottom).

Second, Spindt developed a microvolcano structure for the field-ionization source of a mass spectrometer [23] (Fig. 2b). Third, silicon field emitter arrays with integrated focus electrodes (Fig. 2c) were also developed [24–26]. If this idea is developed to focus electrons from a single nanoemitter, a bright electron beam with well-defined nano-sized spot may be obtained. Finally, a relatively large number of reports [27, 28] were on MOSFET-structured FEAs (Fig. 2d). The metal oxide semiconductor field-effect transistors (MOSFETs) may be fabricated underneath Si emitters.

Although the development of field emitter arrays and their application was encouraging, two major disadvantages gradually became apparent by the end of 1980s. These include the use of expensive microfabrication facilities and the very limited number of emitter materials (i.e., basically only silicon and molybdenum). Thus, in the 1990s the major focus of the research in vacuum microelectronics was shifted to search for new cold cathode materials that are more robust, easier to prepare, and more friendly when integrated into device structures. There are three noticeable directions: printable composite materials, diamond and related films, and quasi one-dimensional nanomaterials. Since the nanomaterials are one of the major topics of this chapter, for the present section we shall concentrate on the former two kinds of material.

The idea of development of printable composite cathode materials may be traced back to the early 1980s, when two new field emission models [29] were put forward to describe prebreakdown electron emission from naturally occurring microscale emission sites found on the surface of a broad-area vacuum insulated high-voltage electrode. The first is called the MIV model, that is, the metal–insulator–vacuum model [30]. It describes field emission from some forms of insulating microparticles and thin films. This was later verified in the study using Langmuir–Blodgett films. The second is called the MIM model, that is, the metal–insulator–metal model. It describes field emission from some kinds of microsize metallic particles sitting on a metal oxide surface. This was verified in a study of field electron emission from artificially deposited graphite particles on Cu oxide surfaces [31]. These two “simulation” studies had led to the idea of the development of some kinds of ink. The first of such kinds was the resin–graphite composite and was proposed by Xu and Latham [32]. The first set of results was reported in 1989 [33]. This idea was taken up by the Printable Emitter Ltd. to develop a novel type of printable cathode composite, which uses glassy (SiO_2) material as matrix instead of resin [34]. This change in matrix material overcomes the difficulty in maintaining vacuum and stability of emission due to the low vapor pressure of cured resin. In recent years, Samsung has developed several new kinds of printable cathode composites using metallic matrix [35] and photoresist matrix [36], but all kinds use carbon nanotubes (CNTs) as emitters. We shall return to these developments later in Section 5.

Intensive investigation has been also carried out to study field emission from diamond and related films. Hydrogen terminated diamond has a surface negative-electron affinity (NEA) [37], and this is stable even in dry air. The diamond surfaces are chemically stable and mechanically strong [38]. Also, diamond has very high thermal conductivity [38]. The combination of these three advantages has led one to

believe that a low field, robust, highly durable, and long-life field emission electron emitter should possibly be made using diamond.

Vacuum electron emission was first observed from the diamond film sandwiched in a metal–insulator–metal structure [39]. Such a structure was not further developed, since it is not a field emitter structure useful for vacuum microelectronics. Wang et al. [40] carried out a microscopic study of ultraviolet (UV) photo and field electron emission from a small area chemical vapor deposition (CVD) diamond films. At that stage, it was highly suspected that electron emission might come from conductive carbon inclusions embedded in the film. Later, Xu et al. [41–43] first reported on large-area, low-field electron emission from CVD diamond films (Fig. 3a), and also confirmed, using field emission electron energy spectroscopy, that the emission came from diamond rather than metallic carbon inclusions (Fig. 3b). The field emission microscopic images observed from the hot filament CVD film indicated possible emission from the facet of a diamond crystallite in the film (Fig. 3c). Based on these new findings, the first model describing field electron emission from diamond film was proposed [41]. From these early works, the researchers in the field were encouraged, and by 1997, nearly more than 30% of papers presented at the 10th IVMC were about field emission from diamond and related films [44].

To fully benefit from the NEA of the diamond surface, it is necessary to prepare an *n*-type diamond film. Okano et al. obtained strong emission at lowest fields ($0.5 \text{ V}/\mu\text{m}$)

reported so far from N-doped CVD diamond films [45]. However, a reliable technique to prepare *n*-type diamond films with reproducible results seems not yet to be available.

The CVD diamond films often are in polycrystalline form, so that a film of thickness of more than $1 \mu\text{m}$ will consist of diamond crystallites of size in the range of near $1 \mu\text{m}$. As a result, the surface of such a film is rough. Therefore it is difficult to use in a vacuum microelectronic device structure. On the other hand, there are two other types of diamond related film that may be used in a vacuum microelectronic structure. The first is the diamond-like-carbon (DLC) films. The physical property of the film is similar to diamond film and is described by Robertson et al. [46]. The field emission characteristics of the film have been studied by a number of groups [47–51]. In particular, it was found that it is a very good coating for Si tip arrays [51, 52]. Besides enhancing emission, the uniformity, stability, and maximum emission current of the coated Si tip arrays may be much improved. Furthermore, a triode-type emitter array using such a film may be fabricated [53] (Fig. 3d). The second is the nanostructured diamond films [54]. These may be made by a number of methods [54–57]. We shall give a detailed discussion of this type of film, since it may be useful in vacuum nanoelectronics.

From our review, one of the key requirements of vacuum microelectronic devices is to produce emitters using uniform tips with a diameter of less than 100 nm. The one-dimensional nanomaterials such as carbon nanotubes have very high aspect ratio and may be an alternative with great potential. Since the preparation technique relies on self-assembly (i.e., the bottom-up process) rather than microfabrication (i.e., the top-down process), it offers the possibility of synthesis of atomically identical nanosized tips. This possibility may even be extended to building structures with atomic precision. In addition, using one-dimensional nanoemitters, it is possible for one to build up high-density field emitter arrays. Such arrays can be used in electron-beam activated memory, very high-resolution displays, parallel electron-beam writing machines, and vacuum-tube imaging devices. The synthesis, characterization, and use of these nanoemitters will greatly depend on the use of nanotechnology and is beyond the scope of vacuum microelectronics.

By using one-dimensional nanomaterials as nanoemitters, another advantage may be taken: some physical properties that are only related to quantum-sized structures or materials may manifest themselves in field emission. The quantum effect and nanosize effect in field emission may find important applications. The related scientific issues and mesoscopic theory are major interests of nanoscience and cannot be addressed based on the current theory developed for vacuum microelectronics.

Therefore we believe that the development from vacuum microelectronics to vacuum nanoelectronics is logical.

3. NOVEL NANO-DIMENSIONAL COLD-CATHODE MATERIALS

In a vacuum nanoelectronic device, the first basic component is the nanoemitter. Its size should be in nanoscale, so that it is easily built into a vacuum nanoelectronic device

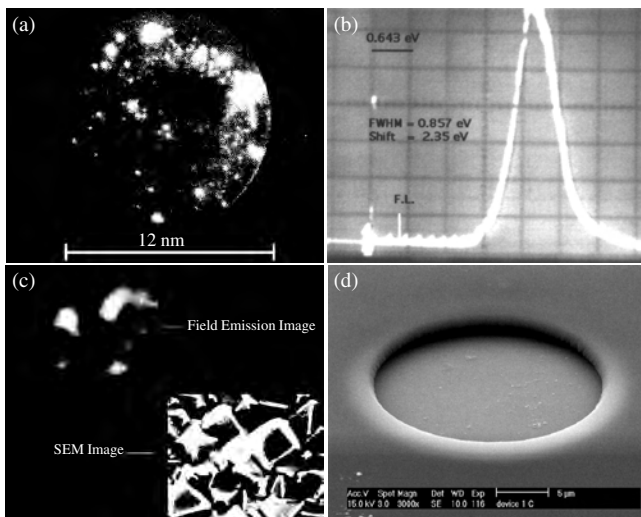


Figure 3. (a) A transparent anode image showing the large-area (12 nm) field electron emission from a hot-filament CVD diamond film. (b) An energy spectrum of field-emitted electrons of the hot-filament CVD diamond film having a large spectral shift from the Fermi level, indicating that the electron was emitted from the insulating diamond film. (c) A field emission microscopic image of the hot-filament CVD diamond film consisting of a square-shape image, indicating that emission might come from a facet of a diamond crystallite of the film, as may be found in the SEM image in the inset. (d) SEM image of a microtriode using DLC film as emitter. Reprinted with permission from [41–43], N. S. Xu et al., *J. Phys. D* 26, 1776 (1993), © 1993, IOP Publishing; *Electron. Lett.* 29, 1596 (1993), © 1993, IEEE; *J. Phys. D* 27, 1988 (1994), © 1994, IOP Publishing.

with size also in nano- or submicrometer scale. In the future, one should be able to fabricate nanoscale triodes in array with separation also in nanoscale; one of the triode structures may just be a nanosized Spindt-cathode structure. The type of nanoemitter may be a one-dimensional nanomaterial including nanotubes, nanowires or nanorods, and nanotips. Others such as quantum dots, nanowedges, thin films in nanothickness (nanothin film), and their combination with one-dimensional nanomaterials may also be considered. Currently, some of the most active research is on quasi one-dimensional nanomaterials such as nanotubes and nanowires, in particular on CNTs. We shall start with carbon nanotubes and then move to nanowires. We also cover nanothin films, since they can be an important coating of nanoemitters.

3.1. Quasi One-Dimensional Nanomaterials

The one-dimensional nanomaterials to be discussed are in reality not ideal one-dimensional materials; for example, the diameter of a carbon nanotube may be more than a few tens of nanometers. Thus, we call them quasi one-dimensional nanomaterials. As mentioned, carbon nanotubes are most attractive, since their new structure may result in some new properties. Further, field emission from semiconductor nanowires has just attracted more and more attention due to possible new effects such as the photofield effect and their novel applications in optoelectronic devices. Finally, the nanowires of traditional cold cathode materials such as molybdenum and tungsten now can also be prepared. Their high melting point is important to high-current emitters. In addition, these may be used to generate spin-polarized vacuum electrons.

3.1.1. Carbon Nanotubes

There already exist a number of books [58, 59] on carbon nanotubes. Also, readers are referred to a sequence of articles published in *Physics World*, on single-wall carbon nanotubes by McEuen [60], on multiwall carbon nanotubes by Schonenberger and Forro [61], on the control growth of carbon nanotubes by Dai [62], and on the application of carbon nanotubes by De Heer and Martel [63], respectively. The fundamental properties and features of carbon nanotubes given in these works are useful for one to fully understand their field emission properties. We shall not give the details here due to space limitations. Instead, we shall mention them in the following when they are relevant.

For reviews on field emission from carbon nanotubes, readers can find relatively wide coverage on the topic in the papers by Xu et al. [64], Bonard et al. [65], and Zhu [66]. In particular, the Bonard et al. article reviews comprehensively the recent five-year developments. Very recently, Baughman et al. [67] have published a comprehensive evaluation on the different applications of carbon nanotubes and their perspectives, including a section on their field emission application. This gives invaluable information and opinions to readers who carry out the related work.

Growth Carbon nanotubes may be in the form of powder or thin film. The powder can be used to make printable inks and the ink may be deposited on a substrate to form

composite emitters [35, 36, 68–70], and the application of these will be described in more detailed in Section 5. Some authors also make a single carbon nanotube emitter from the powder for experimental studies of an individual carbon nanotube [71]. The carbon nanotube film can be used directly as field emitters in cold cathode electron sources, and it may grow in some pattern to become an emitter array.

The CNTs may be prepared in an arc discharge [72–74], by laser ablation [75], and by the catalytic pyrolysis of hydrocarbons [62, 76, 77]. The CNTs prepared using these techniques may be single walled. Figure 4a presents a SEM image of the CNTs of the as-prepared powder, showing that they are randomly distributed.

CVD is the most important technique used for preparation of carbon nanotube films. This process is based on the decomposition of a hydrocarbon gas over a transition metal (as a catalyst). Available techniques include microwave plasma CVD [78], plasma assisted hot-filament CVD [79–81], and thermal CVD [82, 83]. Figure 4 shows SEM images of an aligned CNT film (b) and a nonaligned CNT film (c). Plasma CVD often grows aligned CNTs and thermal CVD can grow both types depending on conditions.

The advantages of using the CVD method over the other techniques include control in direction and location of growth and control in the film structural parameters such as the separation between aligned carbon nanotubes, the length, and the ratio of length over diameter of carbon nanotubes. Growth of CNTs aligned vertically on the substrate surface is very important to vacuum nanoelectronics. Li et al. [82] first grew aligned CNTs up to a few millimeters in length using nanoparticles of catalyst embedded in silica, and later Rinzler et al. [3] prepared similar aligned CNTs on glass substrates, which is suitable for large-area vacuum microelectronics and might be in future vacuum nanoelectronics. Fan et al. [83] further grew vertically oriented tower-like

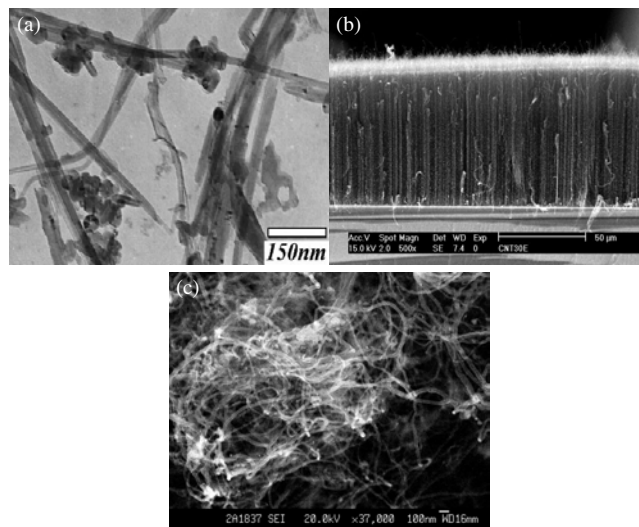


Figure 4. Images of three typical types of carbon nanotube: (a) a TEM image of the carbon nanotube powder as prepared in an arc-discharge process; (b) SEM image of well vertically aligned carbon nanotubes; (c) SEM image of randomly distributed carbon nanotubes. The carbon nanotubes shown in both (b) and (c) were prepared in a thermal CVD process.

bundles of CNTs in array on a Si substrate; these bundles are in fact field emitters. Very recent developments include uniform pattern growth of individual single CNTs on Si substrate by Teo et al. [84] and on the Si tip by She and Xu [85]. Leqagneux et al. [86] have demonstrated the capability of preparing gated single CNT triodes. This is a very important step toward the fabrication of a vacuum nanoelectronic device. Other works [87] on the growth of well-aligned CNT arrays on Si substrates using nanotemplates are also noted.

Field Emission Property In comparison with vacuum microelectronics, one of the major objectives of vacuum nanoelectronics is to develop low-field emitters using nano-dimension materials or structures. When a nanoemitter is used in a device structure of nanoscale, then one may be able to make a low-voltage emitting device. The first targeted objective may be to operate such a device with voltages below 15 V. A main reason that CNT films are considered as a favorite cold-cathode materials is the high aspect ratio, which can result in high field enhancement at the emitting surface of a carbon nanotube of a film. There are many reports on the measurements of field emission from CNTs films, and a comprehensive review on this is given in [65]. Here, we shall only concentrate on the issue of how to optimize the film property for low-field electron emission efficiency.

First, one should minimize the screen effect due to the closed spacing between carbon nanotubes. When the spacing is more than twice the average height of the CNTs of a film, the screen effect may be neglected [88, 89]. On the other hand, if the spacing is too large, the current density may become low. In a classical calculation, to obtain a field enhancement factor in the order of 1000, the height and diameter of a CNT may be 10 μm and 20 nm, respectively, according to the simple relation of height/radius of a CNT. In this case, the spacing should be more than 20 μm , which might be too large. Recently, Deng and Xu investigated a possible solution both experimentally and theoretically [90]. See Figure 5: spaced bundles in pyramid shape of vertically aligned CNTs are prepared in a self-assembly manner using microwave plasma CVD. Their spacing may be controlled by using a different thickness of catalyst and reduction procedure [64]. A theoretical analysis predicts this type of CNT film can balance the screen effect and the low current-density problem [90].

The higher the work function, the higher the threshold field for emission. Multiwall CNTs (MWNTs) have a work function value in the range of 4.89 to 5.6 eV according to Gao et al. [91], which is higher than that of tungsten (i.e., ~ 4.5 eV). Thus, an approach was taken to minimize this effect of high work function of MWNTs. Ma et al. [92] prepared a type of MWNT with nitrogen doping (Fig. 6), and it was found to have good low-field emission property. However, the value of the work function of this type of MWNT will need to be found in a future experiment.

Conditioning by Self-Heating Now, we turn to some typical features that are associated with the nanosize effects (i.e., they may not be possible with microsize emitters).

As-prepared emitters often need conditioning and cleaning. This mainly involves removing the absorbates on surface and even reconstructing the surface. Conventional ways

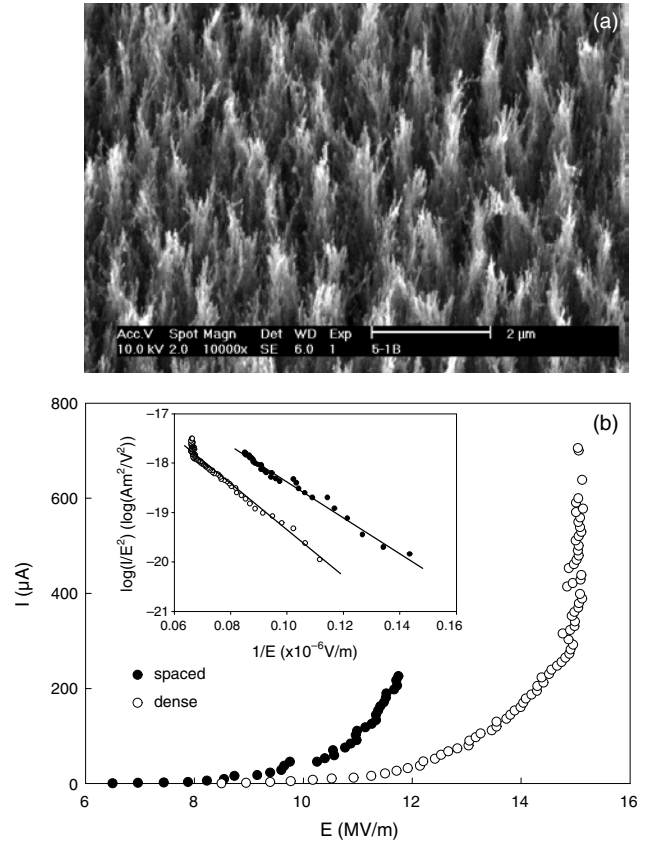


Figure 5. SEM images of pyramid-shape carbon nanotube bundles (a) and their corresponding I - V characteristics (b), showing that the density can be optimized to give a better emission performance.

include field desorption, external heating to high temperature, and their combination. Binh et al. [93, 94] recently discovered that with carbon nanotubes, self-heating is good enough to reach the effect of cleaning. This self-heating is resultant from resistive heating of a carbon nanotube when electron current flows through the nanotube to the emitting surface [95]. Candescent light emission was observed to come from an emitting nanotube, and the energy spectra of the field-emitted electrons were used to measure the temperature of the emitting surface [94]. Findings from an independent theoretical analysis give support to these experimental conclusions [95]. It shows that the temperature of the emitting surface of a carbon nanotube may be high because of its shape and nano-dimension. A temperature of 2000 K may be reached when a current of ~ 2 μA flows through a 40 μm long nanotube of a diameter of 10 nm [94, 95]. To reach such a high temperature in such a small emission current is only possible with a nanotube. Further experimental findings show that conditioning with a temperature of above 2000 K can finally clean the nanotube, judging by the fact that a linear Fowler-Nordheim plot is obtained [93]. Finally, it should be pointed out that their calculation [95] is also suitable to other types of nanotubes and nanowires. Therefore, this finding is very important since self-heating may be adapted as a standard conditioning procedure for vacuum nanoelectronic devices using nanotubes or nanowires.

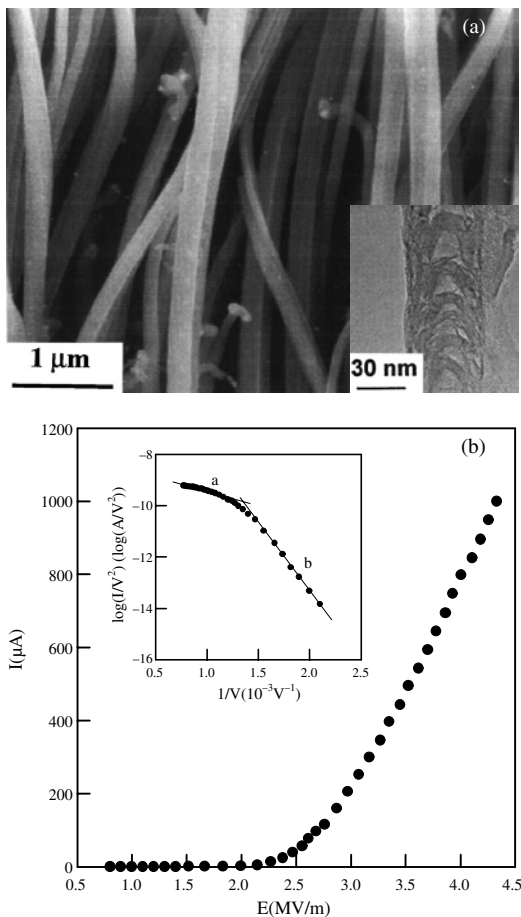


Figure 6. (a) SEM image of the N-doped carbon nanotube film. Inset is a TEM image of a N-doped carbon nanotube showing the polymerized bell structure. (b) The I - V characteristic and its corresponding FN plot. Reprinted with permission from [92], X. Ma et al., *Appl. Phys. Lett.* 75, 3105 (1999). © 1999, American Institute of Physics.

Coherent Emission Processes Another important CNT field emission phenomenon associated with the nanosize effect is observed in their field emission microscopic images. Simply putting a CNT (as cathode) behind a phosphor screen (as anode), the electrons emitted from the CNT may be projected to the screen [92, 96, 97]. Figure 7a is an image from a single CNT and Figure 7b is from a N-doped CNT film [92]. Typical features are the arclike images; some appear with random orientation (Fig. 7b) and some with preferential orientation (Fig. 7a). In fact, this type of field emission image was first reported in 1986 [31, 98]. It was observed from graphite microparticles in a MIM emission regime [29, 31, 98] and carbon fibers [99]. Xu and Latham [31] first attributed the arclike images to coherent scattering of electrons just before they are emitted into vacuum; the process is similar to low-energy electron diffraction in a crystalline matter. We do not know even now if the graphite microparticles and the carbon fibers contain carbon nanotubes or similar structures. So we cannot judge at this point if the emission from the three types of regime may come from the same physical origin.

The arclike field electron emission pattern of a CNT is attributed to the Young's interference of emitted electrons

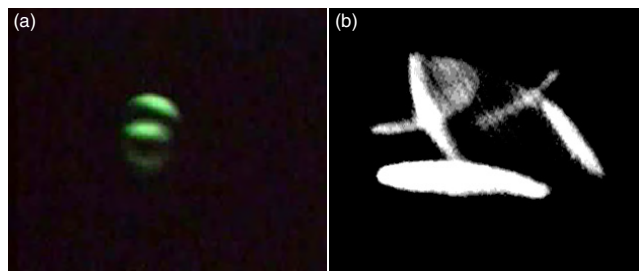


Figure 7. Field emission microscopic images consisting of well-oriented (a) and randomly oriented (b) arclike segments observed from carbon nanotubes. Reprinted with permission from [92], X. Ma et al., *Appl. Phys. Lett.* 75, 3105 (1999). © 1999, American Institute of Physics.

by Oshima et al. [97]. Similar to that proposed by Xu and Latham [31], Oshima et al. [97] also assumed that the electrons are coherent before emission. In simple words, the electrons coming toward the apex of the CNT are in a way like a light beam from a single source with a specific wavelength. When this electron wave passes through the graphite layer of the apex of the CNT, it may be scattered and Young's interference may occur. For some unclear reasons, electrons are emitted only from some points (emission sites) on the surface. Since an electron beam has a finite wavelength, the interference occurs only when emission sites are closed enough. Oshima et al. [97] have shown that the interference happens only when the spacing between emission sites is within a nanoscale region. The strong evidence is shown from an emission image (illustrated in Fig. 8), in which only two closed emission sites of a total four emission sites have interference. This finding is of technical significance because it indicates that it is really possible to develop

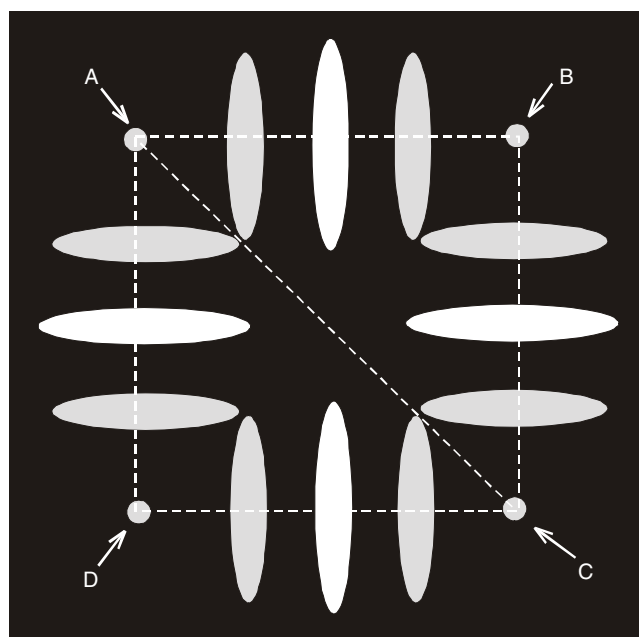


Figure 8. Illustrating how electron beams from two closed emitting sites (e.g., "A" and "B") will undergo Young's interference process, while the far apart emitting sites (e.g., "A" and "C") will not do so.

novel nanobeam electron sources based on the interference of coherent electrons.

Intrinsic Field Emission Property of Single-Wall Carbon Nanotubes Many research activities have been inspired by the study of field electron emission from CNTs, but the experimental data of some key parameters are rather scattered. Typically, both linear and nonlinear Fowler–Nordheim (FN) plots are often observed [100–103]. The reported value of work function is within the range of 5.3–7.3 eV for one arc-discharge MWNT and for a catalytic MWNT film [91, 104, 105]. The field emitted electron energy distribution may be in the form of single or multiple peaks [101, 104]. Thus theoretical studies are required to provide a scientific basis for clarifying these differences. On the other hand, it is also important to understand the intrinsic field emission property of carbon nanotubes of ideal structures, since this is one of the important physical properties of such a new ideal one-dimensional nanomaterial.

In order to achieve this, it is necessary to start theoretical analysis from the very fundamental unit of the CNTs (i.e., a single-wall carbon nanotube). Although there are only a few, previous theoretical studies [106, 107] have set a very good base. Earlier, Filip et al. [106] obtained expressions for the emission current as function of anode voltage and of the energy spectrum of electrons emitted from carbon nanotubes using a parabolic dispersion, limiting themselves to CNTs of diameters of less than 15 nm. All energy spectra appear to be single peaked, but the I – V characteristic is in the form of $\ln I \sim 1/V$ rather than the FN law (i.e., $\ln I/V^2 \sim 1/V$). This latter feature implies that the I – V characteristic is quite different from the usual metals. Their numerical simulation demonstrated that the field enhancement is proportional to the diameter of a CNT, independent of the length of the nanotube.

Recently, Liang and Xu [108] carried out a study of the field emission from a single-wall carbon nanotube (SWNT) in the tight-binding approximation taking into account of the effect of the structure of SWNTs (i.e., the effect of chirality). From this, the energy band structures of different SWNTs are obtained, and the density of states and the distribution of occupied electron states are derived. In the conventional Fowler–Nordheim formulation the I – V characteristic is obtained, energy spectra of emitted electrons are calculated, and their variation with temperature is examined.

Specifically, the calculations show that the I – V characteristics for different chiral nanotubes essentially follow the Fowler–Nordheim law, but the currents depend on the chirality of nanotubes. At the same applied field for the same diameter of tubes, the field-emission line current density j , defined as the total emission current divided by the circumference of the open-end of a SWNT obtained at a specific applied field satisfy two inequalities:

- (1) $j(\text{metallic}) > j(\text{semicond})$ for the open-end SWNTs of the same diameter and chirality;
- (2) $j(d_L) > j(d_S)$ where $d_{L,S}$ represents the diameter of the nanotubes and $d_L > d_S$, for open-end semiconducting SWNTs.

More important, the findings demonstrate that the SWNT possesses unique features in the field emission property,

resulting from its intrinsic physical property. First, the nonlinear behavior in Fowler–Nordheim plots may be attributed to emission of non-Fermi-sea electrons. Second, the variation of emission current with temperature does not follow the relation with a function of T^2 predicted by the conventional field emission theory based on free-electron assumption [109] and exhibits some threshold temperature that sets the starting point of the rapid change of the emission current with temperature. Third, the multipeak energy distributions of electrons emitted from all types of SWNTs are observed. Figure 9 shows the energy spectra of emitted electrons of the three types of SWNTs for both 300 and 2000 K and at different fields. They all have a strong dependence on applied fields, temperature, and chirality. The multipeak spectra of metallic SWNTs (Fig. 9) are another unique feature of nanotubes (i.e., unexpected for common metals). With an increase of applied field, more spectral peaks in the low energy range appear and the peaks become wide (Fig. 9a), while with an increase of temperature, more spectral peaks appear in the high energy side (Fig. 9b). At $T = 2000$ K, the spectra of semiconducting nanotubes (20, 0) reveal a gap between two groups of major peaks (Fig. 9f); this corresponds to the energy bandgap. This is not difficult to measure since a temperature of 2000 K at the tip of an emitting CNT was experimentally found to be easily attended due to self-heating as described previously [95]. This finding is revealed for first time and may be very useful for experimental study of the energy band structure of semiconducting SWNTs.

From the findings summarized previously, we may note that the field emission from SWNTs cannot be treated as that of conventional classes of metals and semiconductors. At the same time, we should point out that these theoretical findings will need experimental evidence for support.

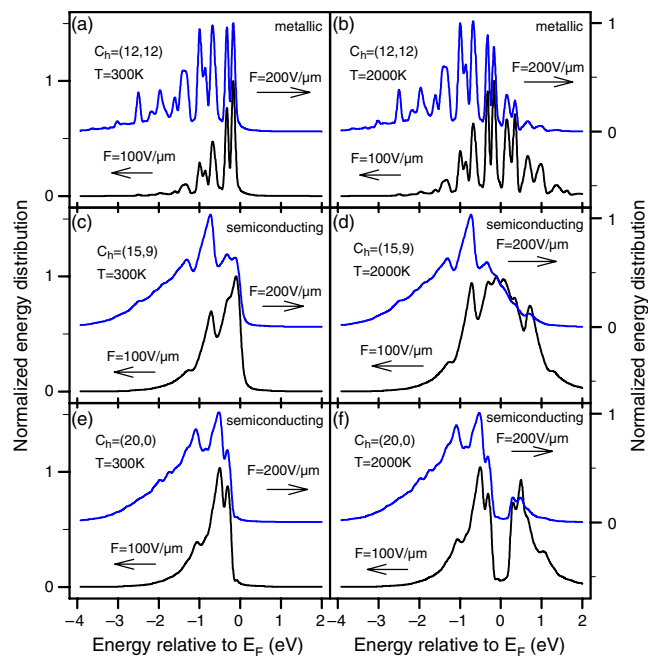


Figure 9. Calculated field emission electron spectra of single-wall CNTs of different chirality.

To succeed in these experiments, SWNTs with well-defined chirality are essential.

3.1.2. Semiconductor Nanowires

The findings on the intrinsic field emission property of single-wall CNTs have strongly demonstrated that the field emission depends on the electronic property of CNTs. We also know that the CNTs may have either metallic or semiconducting properties, depending on their structure. However, one is not yet able to control these properties. On the other hand, field emission from semiconductor nanowires is itself an important subject. As a semiconductor, it will generally have the advantage of a lower surface potential barrier than that of metals due to lower electron affinity. Furthermore, this type of emitter may respond to the external fields such as photons, heat, and magnetic fields more sensitively.

It is only in very recent years that interest has arisen in field emission from semiconductor quasi one-dimensional nanomaterials. Chen et al. [110, 111] was the first to report field emission measurement from semiconductor nanowires, although Pan et al. [112] reported very low field electron emission from SiC nanowires, but the electronic property of the SiC nanowires was not clarified.

Copper-Based Semiconductor Nanowires Cu_2S is a small bandgap semiconductor whose conductivity may be sensitive to visible light band. Recently, it has been found to have good field emission property [110]. The Cu_2S nanowire arrays can be prepared under ambient conditions and room temperature and thus can easily be scaled up [113]. Cleaned Cu foils may be used as substrates. The growth process is based on a gas–solid reaction. The reactor can be simply a glass cylinder with two inlets on one end and one outlet on the other end of the cylinder. One of the inlets is for the flow of an $\text{O}_2/\text{H}_2\text{S}$ gas mixture, and the other is for flow of inert gases such as Ar or N_2 as carrying gases. The outlet may be used to control reactor pressure. A gas mixture of oxygen and hydrogen sulfide may be let into the reactor at a given molar ratio. The total pressure in the reactor may be kept at $\sim 1.05\text{--}1.08$ atm, and at room temperature and under dark conditions. The reaction time often is 10 hours. Figure 10a shows the SEM image of the Cu_2S nanowire array. It consists of straight nanowires with typical diameter of 50–70 nm. These nanowires have a bandgap of ~ 1.26 eV [114], and their conductivity increases significantly with temperature [9]. The uniformity of field emission was shown to be good and the emission was stable. Other small bandgap semiconductor (CuO and CuOH) nanowire arrays have also been synthesized with a similar technique [10] and have been shown to have good emission property [115]. In addition, one emission property in particular that is interesting is shown in Figure 10b, in which a waveform shows how the field emission current may respond to exposure of a visible light. As one may see, the field emission current increases immediately the moment the emitter was exposed to the light, but the decay process was slow. In particular, the decay process carried on until the current level was lower than that before the light was on. This characteristic may be explained like so. The increase in emission

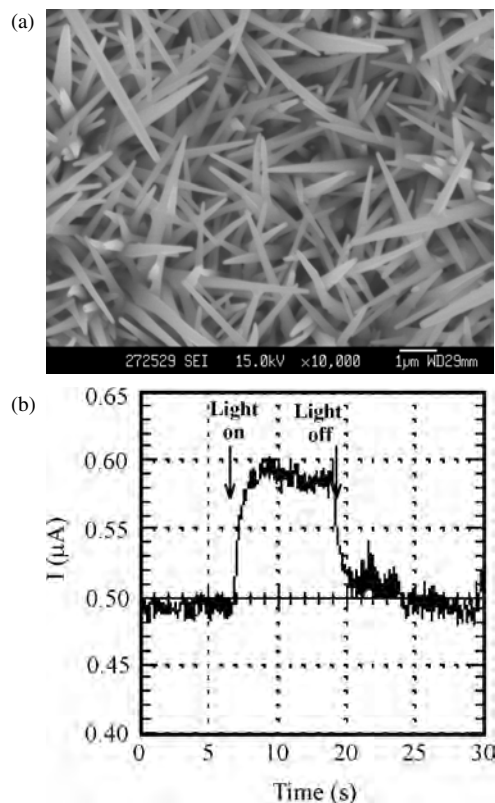


Figure 10. (a) SEM image of a Cu_2S nanowire film. (b) A waveform showing how emission current increases when the visible light is on and decays when the light is off.

current indicates that there is an increase in Fermi-sea electron current density. There are two possibilities. One is due to increase of electrons excited by photons from the valence band to conduction band, and another is due to electrons excited from defects and impurity states in the bandgap. The slow decay indicates that there are deep-level defect and impurity centers. There might be a time interval between the moment when these centers are filled and the moment when the excited electrons are completely emitted. After the excited electrons are emitted but before the centers are filled, the electrons that may possibly be emitted will be in the states of low energies. This is equivalent to saying that the surface potential barrier may be higher. As a result, the emission current is lower. There are still many problems remaining. For example, we do not know the exact nature of the defect and impurity centers. We also do not know if the electrons in valence band can really be excited into the Fermi sea.

SiC Nanowires Several techniques have been developed for synthesizing silicon carbide nanowires [112, 116–121]. Earlier, silicon carbide nanowires were synthesized by filling carbon nanotubes during a reaction between carbon nanotubes and SiO or SiI_2 [116], or by a two-step process involving first generating SiO vapor and then its reaction with carbon nanotubes [117]. Later, Meng et al. prepared SiC nanowires by carbothermal reduction of sol–gel-derived silica xerogel having carbon nanoparticles [118]. Zhou et al. grew SiC nanowires on silicon substrate by hot-filament

chemical vapor deposition [119]. The aligned carbon nanotubes may be used as templates for synthesis of aligned SiC nanowires [112]. This is realized by reaction of carbon nanotubes with Si vapor at elevated temperature under flowing Ar gas. Recently, silicon carbide–silica biaxial nanowires were produced by elevated-temperature synthesis [120]. Deng et al. [8, 121] have developed an alternative approach, in which needle-shape and treelike SiC nanowires may be grown from SiC particles using iron as catalyst in a thermal process. Very recently, aligned SiC nanowires have also been synthesized on large SiC substrates in a catalyst-assisted process.

In the catalyst-assisted process, samples of SiC nanowires may be prepared in a vacuum chamber. Commercially available SiC powder or bulk substrates are placed on a tungsten (W) boat. Iron or aluminum as catalyst is deposited on the surface of the SiC particles or the surface of the substrates. Then, the boat is placed at the center of the vacuum bell jar. The vacuum system is evacuated down to about 5.0×10^{-2} Torr. The boat is gradually heated up by passing current through it and kept at ~ 1700 °C under flowing argon (200 sccm). Typical growth time is less than 30 minutes. The treated SiC samples contained in the W boat are taken out of the chamber when it is cooled down to room temperature.

Depending on the type of catalysts and the conditions of growth, different forms of SiC nanowires may be prepared. Figure 11a (left) is a scanning electron micrograph of the needle-shape SiC nanowires grown on the surface of SiC particles using iron as catalyst. When the Al is used as catalyst, SiC nanotrees (Fig. 11a, middle) may be grown on the surface of particles and aligned SiC nanotrees (Fig. 11a, right) on the surface of bulk SiC substrates. These nanowires can be removed from the surface and placed on the copper or carbon mesh for transmission electron microscopy study. The detailed shape, size, morphology, and internal structures of the nanowires may be analyzed using a transmission electron microscope (TEM). Typical TEM images

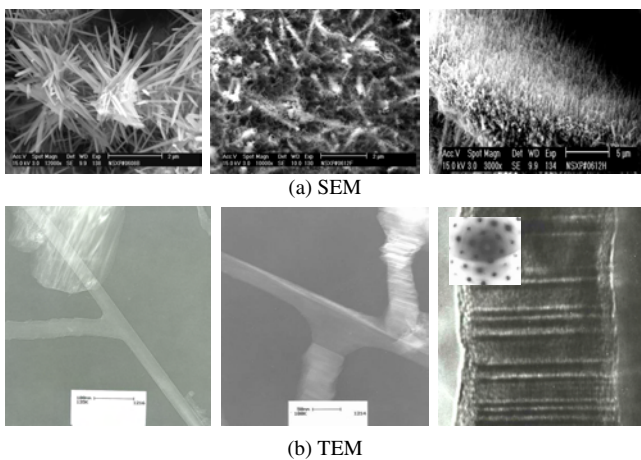


Figure 11. (a) SEM images of needle-shape SiC nanorods (left), SiC nanotrees (middle), and aligned SiC nanotrees (right). (b) TEM images of a Y-shape SiC nanojunction (left), a staggered SiC nanojunction (middle), and the lattice of a SiC nanorod. Reprinted with permission from [121b], S. Z. Deng et al., *Appl. Phys. Lett.* 80, 3829 (2002). © 2002, American Institute of Physics.

(Fig. 11b) show the nanojunctions that are formed by SiC nanowires. Typically, they have two forms in shape, as shown in Figure 11b, where on the left is the TEM micrograph of a SiC nano-Y junction, and the middle is of a nano-staggered junction. The diameter of the branches of these nanojunctions can be either similar or different, typically ranging from 10 to 50 nm, and the length is from 1 to 2 μm (Fig. 11b).

Furthermore, a high-resolution transmission electron microscope may be used to analyze the details of lattice structures of the nanowires that form the nanojunctions (Fig. 11b, right) and the selected area electron diffraction pattern may also be recorded (inset of Fig. 11b, right). From Figure 11b (right), it is determined that these nanorods are β -SiC and that the growth direction is $\langle 111 \rangle$. The nanorods contain stacking faults and twining (Fig. 11b, right). Selected area energy-dispersive analysis of X-ray emission (EDX) shows that the nanorods are pure, containing only Si and C. In addition, it is also found that typically, the free end of nanorods may have a cluster in sphere shape. EDX shows that this cluster contains elements of Si, C, and Al, indicating that it is an alloy of these three compositions. This finding gives rise to strong evidence that supports the vapor–liquid–solid model proposed to explain the mechanism of our growth process [121]. It has some degree of similarity to that proposed by Morales and Lieber [122]. However, this mechanism cannot explain how the SiC nanojunctions are formed, and further investigation is currently undergoing.

Field emission was measured from bunches of needle-shape SiC nanowires. The powder of these nanowires may be easily dispersed and was used to form samples of field electron emitters. Its needle shape of individual nanowires is in favor of field electron emission. Stable emission with current density of 30.8 mA/cm² was observed at fields as low as 9.6 V/ μm , and current density of up to 83 mA/cm² was recorded.

3.1.3. Refractory Metals and Their Oxide Nanowires

Refractory metals have been studied as cold cathode emitter materials for a long time. As a single emitter, now etched tungsten tips have been commercial products for high-resolution transmission and scanning electron microscopes. In the Spindt cathode [13], a cone-shape molybdenum tip was used. Advantages of using the refractory metals include the following. (i) Their many properties such as chemical, physical, electronic, and mechanical properties are already well known. (ii) Their melting points are high, so that their emitters may operate in high current density. (iii) Polarized electron beams may be produced using these emitters [123].

The synthesis of tungsten nanowire powder was first reported by Li et al. [124] and molybdenum nanowires grown on the side of steps and parallel on the surface of substrates were first reported by Zach et al. [125, 126]. These two forms of nanowire are difficult to use as field emitters. The preparation of films of aligned nanowire arrays of both W and Mo was reported by Zhou et al. [5, 6, 127, 128] in a joint meeting of the IVMC and the IFES in 2002. The

field emission properties of these two types of film were also presented. In parallel, Lee et al. [7] carried out a study on the W nanowire film deposition and its field emission characterization.

The process developed by Zhou et al. [127, 128] has not yet been fully disclosed and was detailed in a patent pending and protected under a PCT agreement. But briefly, substrates including Si wafers and stainless steel plates may be used. Pure Mo or W is used as a source of evaporation. In a vacuum chamber and under conditions of flow of inert gases such as Ar, the W and Mo evaporating toward the substrate will grow into film of W and Mo nanowires aligned vertically on the surface of the substrate. They may be treated in a reduction process to remove the oxygen and to turn the refractory metal oxide nanowires into refractory metal nanowires [5]. The technique developed by Lee et al. [7] is based on the self-catalytic process. The W layer may first be deposited on the Si substrate and then the W nanowires may be prepared in a rapid thermal chemical vapor deposition system and under a mixture of Ar and H₂. The mechanism has not yet been clarified.

Figure 12a shows SEM micrographs of the Mo (left) and W (right) aligned nanowire arrays, and the corresponding X-ray diffraction (XRD) spectra in Figure 12b. The latter indicates that the nanowires are crystalline, which cannot be obtained in Spindt cathodes and is difficult to achieve in conventional single W emitters. Figure 13a is a transparent anode image of field emission from the disc sample of MoO₂ nanowire film shown in the inset, which demonstrates the excellent uniformity in emission (i.e., far better than that of CNT films). The field emission microscopic image observed from the film is shown in Figure 13b, which is stable with time. From the I - V characteristic and the corresponding FN plot shown in Figure 13c, one can see that the turn-on field and threshold field are compatible with the best values

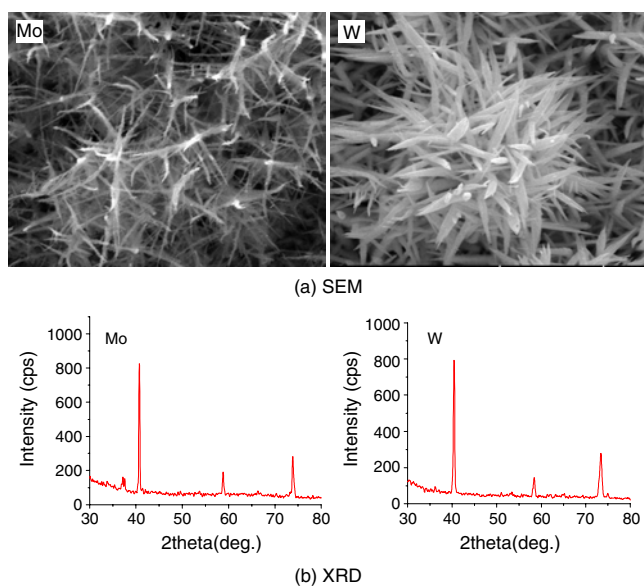


Figure 12. (a) SEM images of Mo nanowires (left) and W nanowires (right). (b) Their corresponding XRD spectra.

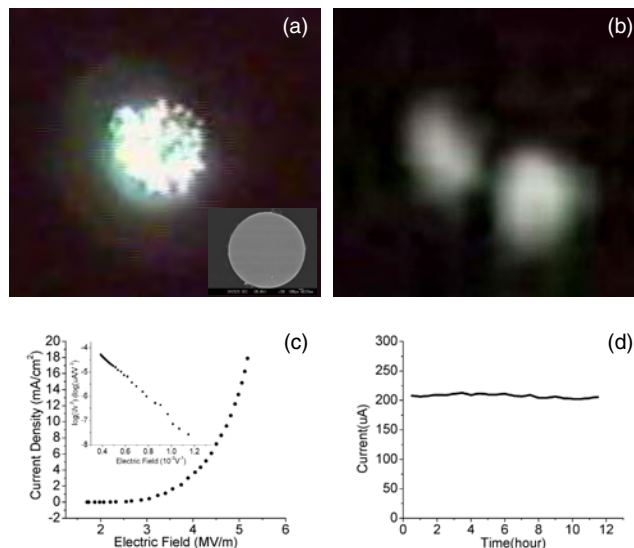


Figure 13. (a) A transparent anode image showing the very uniform electron emission from a MoO₂ nanowire film on a disc sample (inset). (b) The field emission microscopic image of MoO₂ nanowires. (c) The I - V characteristic and FN plot. (d) A I - t plot showing the current stability over time.

in the low range of those measured with CNT films [65]. Also, the current density is high and stable over a long time (Fig. 13d).

3.2. Nanothin Films and Coatings

The nanothin films and coatings that we are interested in often have thickness of less than 100 nm, but if less than 10 nm, they may have important applications in vacuum nanoelectronics, as one may see from the following. As a coating, it may improve the emission stability and enhance the emission if it is applied to nanoemitters such as nanotubes and nanowires. One of the possible applications may be to lower the fields for field emission from CNTs. In this case, the film should be as thin as a few nanometers. Otherwise, it will increase the diameter of the nanoemitters. On the other hand, the nanothin film itself may be used as emitting material in a vacuum nanoelectronic device. In the following, two types of nanothin film are presented.

3.2.1. Amorphous Diamond-Like-Carbon Film

As we have already described in Section 2, since the early 1990s, diamond and related thin films have attracted considerable interest because of their unique physical properties such as low or negative electron affinity, high thermal conductivity, and good mechanical and chemical stabilities. Recent studies [46–52] have indicated that amorphous DLC film may be a promising material for efficient field emission. Compared with other types of diamond, this type of thin film can be deposited at low temperature, the film surface is generally smooth, and it can be deposited on several types of substrate in large area. These superior properties make them potentially attractive for microelectronic and nanoelectronic applications.

The DLC film often is prepared using the filtered vacuum arc plasma deposition technique. Thin films with different thickness may be prepared under similar deposition conditions by varying deposition duration [52]. The working principle of the system and the details of the deposition condition have been described elsewhere [49].

The DLC film often has good contact with a substrate (Fig. 14a) and is uniform within the film (Fig. 14b). It also has a high percentage of sp^3 bonds (Fig. 14c). It is found that thin DLC films (<a few tens of nm) can enhance electron emission, but not the thick film [129, 130]. Figure 15a shows that the DLC film can be deposited on the surface of individual CNTs, while Figures 15b and 15c show the I - V characteristics of the DLC coated CNTs and those without coating. It can be seen that a DLC film of <10 nm can enhance emission but that a thicker film will have negative effect [130].

3.2.2. Nanostructured Diamond Film

Another type of nanothin film is the nanostructured diamond thin film we have already mentioned in Section 2. They are formed by nanosized diamond crystallites. There are a number of techniques for preparing this type of thin film [54–57]. Zhu et al. [54] sprayed repeatedly a liquid that contains diamond nanocrystallites as dispersed aqueous suspension onto a Si surface to deposit a layer of thin film built up by the diamond nanocrystallites. Krauss et al. [55] adapted a microwave plasma chemical vapor deposition technique for preparing this type of thin film and was able to grow them uniformly on Si tips with control thickness, as shown in Figure 16. Xu et al. [56, 57] recently developed a procedure based on electrophoresis method. In this case, it is necessary to first prepare a Si surface with a special technique [131] to generate a high density of nanoprotusions. In

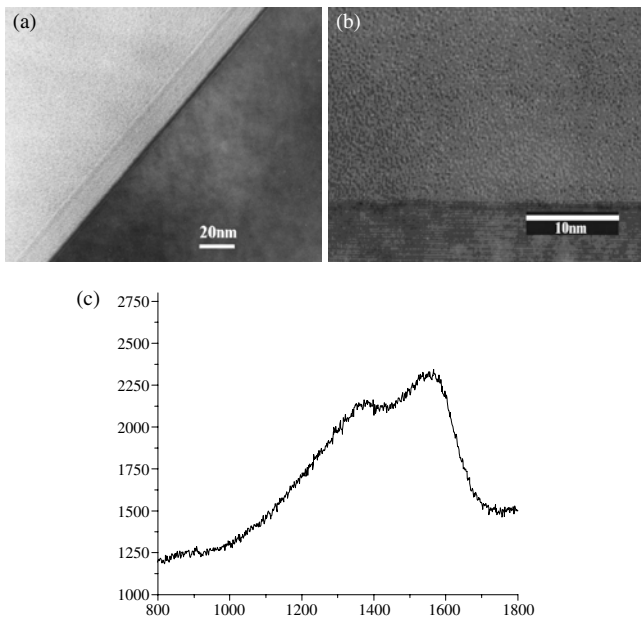


Figure 14. (a) A TEM image showing very good contact between a DLC film and a silicon substrate. (b) A high resolution TEM showing the uniformity inside the DLC film. (c) A Raman spectrum showing a high percentage of sp^3 bonds in the DLC film.

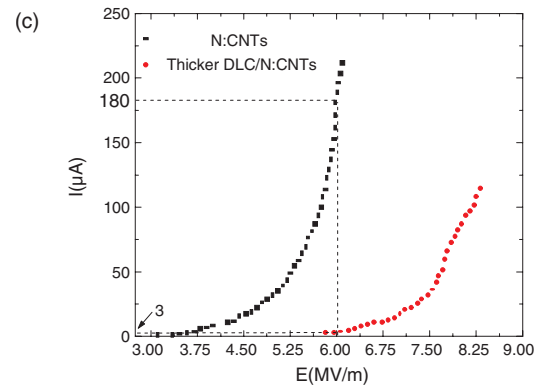
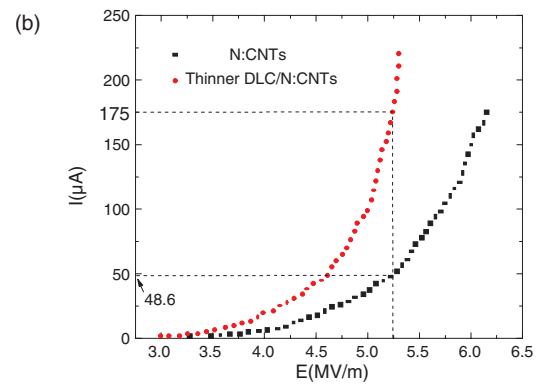
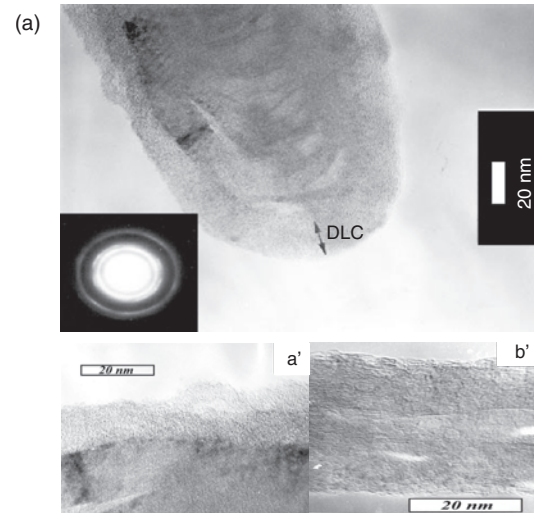


Figure 15. (a) High resolution TEM images showing a DLC coated carbon nanotube; the detailed interface between the DLC film and the nanotube walls is shown in the bottom left image, and this may be compared to that of the walls of an uncoated carbon nanotube shown in the bottom right image. (b) Comparison of I - V characteristics of uncoated carbon nanotubes and those coated with thin DLC film. (c) Comparison of I - V characteristics of uncoated carbon nanotubes and those coated with thick DLC film.

addition, nanodiamond powder is preheated to oxidize the surface of the nanodiamond crystallites [132], so that they may be separated in the solution in the deposition process [56]. These three types of nanostructured film all have good and stable emission. Zhu et al. even went on to develop triodes based on this type of film [54], which will be described

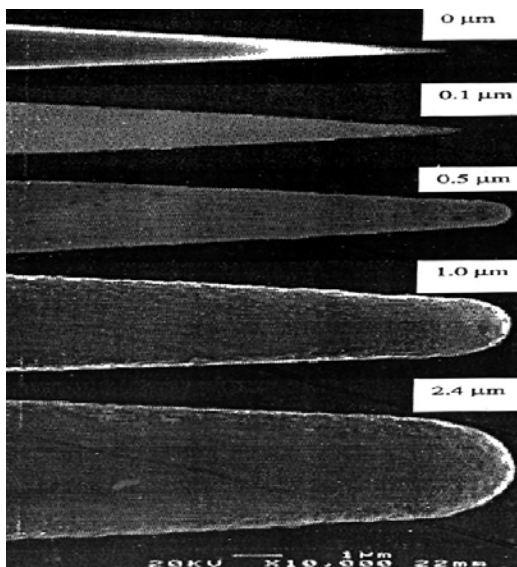


Figure 16. Silicon tips coated with nanostructured diamond film of various thickness. Courtesy of O. Auciello and M. Ding, Argonne National Lab, USA.

in Section 4. From the next section, one can see that, in the nanostructured film and the DLC film, there might be important quantum effects that might have potential application in vacuum nanoelectronics.

3.2.3. Resonance Emission from Nanothin Films

Recently, a theoretical study has been carried out to investigate the effect of DLC film of thickness less than 10 nm [133]. As shown in Figure 17a, the emission regime may be modeled as a MIV microstructure. There are two barriers to this. One is related to the metal–insulator interface and the other is formed by the insulator–vacuum interface. We will name them barrier A and barrier B, respectively. Since an applied field can penetrate into the insulator film, electrons can be injected into the insulator film by the quantum tunneling through barrier A. Then electrons in the insulator are accelerated by the field and finally get enough kinetic energy to go through (or tunnel through) barrier B.

Obviously, the insulator film will stop the emission if the film is too thick. The reason is that the electrons lost their kinetic energy in the scattering with the atoms. However, the film should not be too thin. Otherwise, not enough voltage drop for the acceleration of electrons can be attained. The scale of the thin film considered is 5–10 nm. Assuming that the mean free path (MFP) of electrons in the insulator is more than 10 nm, one can ignore the inelastic scattering. On the other hand, as the nanoscale is one or two orders larger than the atomic scale, the single electron model and the concept of energy band are still applicable.

As the thickness of the insulator film is comparable to or smaller than the MFP of electrons that are transporting in the film, quantum effects become important and need to be considered carefully. Three quantum effects may be found: (1) discretization of the normal energy, (2) resonant

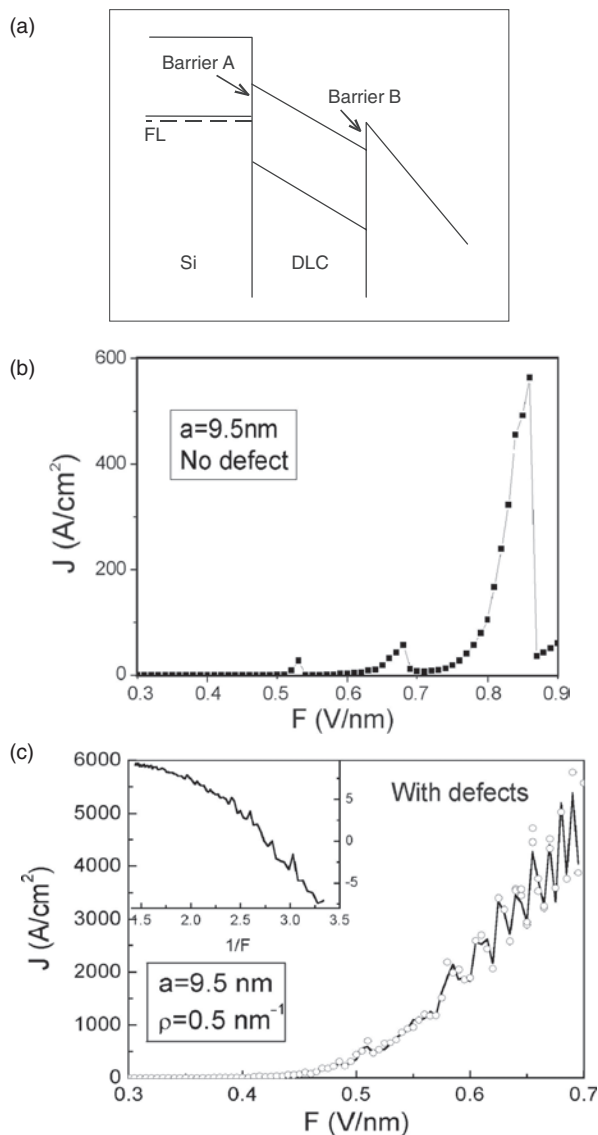


Figure 17. (a) Illustration of a quantum well associated with nano-DLC film on silicon. (b) The resonance peaks that appear at different fields, when the film is assumed to have no defects. (c) The resonance peaks that appear at different fields when the film has defects.

electron emission, and (3) band bending due to the space charges.

A typical band structure is given in Figure 17a. In the quantum well between barrier A and B, the normal energy (the energy of motion in the normal direction of the film) is discretized. For a given band structure, both the normal energy levels and the corresponding wavefunctions can be obtained by solving the one-dimensional Schrodinger equation. When the incident normal energy is equal to the one of the level of the quantum well, resonant emission happens, as shown in Figure 17b and c. Theoretically the transmission coefficient can reach one (i.e., the maximum value) for specific values of thickness and applied field.

This theoretical finding is interesting since these effects are found in both a film with defects and a single crystalline one. But this needs verifying in experiments. Furthermore, a number of coatings such as boron nitride thin film [134] may

also be applied to MWNTs, so the theoretical analysis may also be useful to the emission regime using boron nitride thin film.

4. VACUUM NANO-ELECTRONIC DEVICES

We have presented nanomaterials that may be used as nanoemitters. These nanoemitters can be used in both vacuum microelectronic and vacuum nanoelectronic devices. Currently, there is a technological gap between the synthesis of nanoemitters and the fabrication of vacuum nanoelectronic devices (i.e., there remain many problems in how vacuum nanoelectronic devices may be made). There are not widely accepted device structures and definitions, and we would like to see various novel designs to come in the future. In the following, we present a few considerations for discussion. (i) An ideal single vacuum nanoelectronic device may have structural dimension in nanoscale. (ii) Such a unit may be a basic building block for a vacuum nanoelectronic chip, and it may be in triode form using the Spindt-cathode structure. But it can also be different. (iii) The electron emitter in these devices may be an individual single nanoemitter such as a single carbon nanotube and a single nanowire (i.e., those we have already presented). (iv) The spacing between the gate and the nanoemitter in a triode may be in nanoscale, and the spacing between each triode in the array may be in nanoscale as well. (v) In the design of vacuum nanoelectronic devices, one may pay full attention to the possible quantum effect and nanosize effect and should develop a corresponding nanotechnology to use these effects. (vi) One may pay more attention to applications where high-density electron beams or high-density of emitters and/or nanoemitters are needed. (vii) One should explore applications where light, heat, magnetic fields, and other external fields involved. The current trend is to produce a triode of Spindt-cathode structure but using a single nanoemitter and with nanoscale dimension. However, the number of such studies is still limited.

4.1. Single Nanowire or Nanotube Electron Emitters

Before a vacuum nanoelectronic device may be fabricated, it is essential to develop techniques to locally grow an individual single nanoemitter in an array. For carbon nanotubes, this has been realized by controlling the deposition location of catalyst.

In order to grow CNT emitters at designed positions, thin film deposition and photolithography techniques need to be adapted. So far, several attempts have been made [84, 85]. We may start with how a group of CNTs may be grown locally. Chen developed a procedure for growing CNT emitters in a pattern [135] on the electrodes on Si or quartz substrates. As illustrated in Figure 18, first, a thin layer of metal film such as Ti may be deposited. It is necessary to choose types of thin film that are difficult to become oxidized when the growth of CNTs is performed. Second, this thin film is etched into a form of line electrode using a photolithography technique. Third, the catalyst such as Fe may

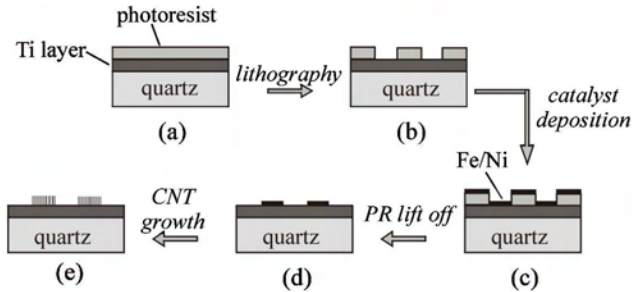


Figure 18. Illustrating a process developed for deposition of an array of carbon nanotube emitters on a large-area quartz substrate.

be deposited in a designed pattern. Finally, CNTs may be grown by thermal CVD. Figure 19a shows the abbreviation of the Chinese characters of the name of Zhongshan University formed by arrays of CNT emitters (Fig. 19b), while Figure 19c is the SEM image of the CNTs in an emitter.

This technique may be refined so that an array of individual single carbon nanotubes may be grown. This involves using a nanolithography technique and plasma-enhanced chemical vapor deposition of carbon nanotubes. Teo et al. [84] have successfully done this. Nickel was used as catalyst. A diffusion barrier layer was first deposited onto the Si substrate, and then the catalyst thin film was deposited onto the barrier layer. The diffusion layer prevents the formation of the NiSi_x so that the Ni nanoparticles were active in the CNT growth process. This treatment was found to ensure 100% yield of CNTs. Both UV lithography and electron-beam lithography were used to define the area of Ni. E-beam lithography is essential for preparing the area of the catalyst in nanoscale. Since the CNTs were required to stand vertically on the surface of the substrate, plasma enhanced CVD (PECVD) was used. As can be seen from Figure 20a, freestanding individual single CNTs were grown in array. Each of the CNTs has diameter in the range of 100–200 nm [84]. From Figure 20b, it is obvious that the

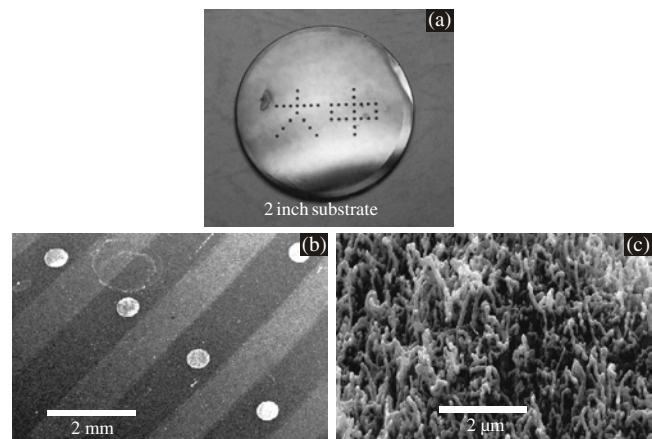


Figure 19. (a) A photo of the abbreviation of the Chinese characters of Zhongshan University formed by the carbon nanotube pixels. (b) SEM image of four carbon nanotube pixels on electrodes. (c) SEM image of the carbon nanotubes of a pixel. Reprinted with permission from [64], N. S. Xu et al., *Ultramicroscopy* 95, 19 (2003). © 2003, Elsevier Science.

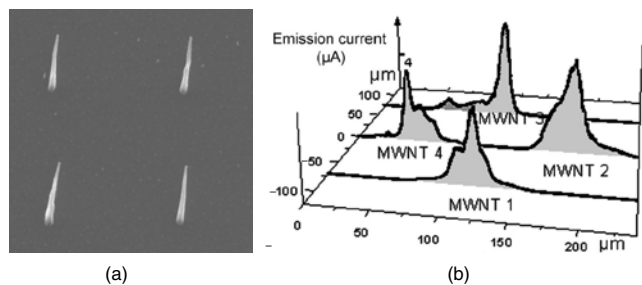


Figure 20. (a) SEM image of an array of four freestanding single carbon nanotubes. (b) The field emission current distribution over the four carbon nanotubes. Reprinted with permission from [93], V. Semet et al., *Appl. Phys. Lett.* 81, 343 (2002). © 2002, American Institute of Physics.

emission from the individual CNTs is quite uniform, and the variation in current is within 30% [93].

She and Xu recently have been investigating ways of growing individual single carbon nanotubes on the apex of a Si tip and have had some successes [85]. The procedure involves several steps using microfabrication rather than a nanolithography technique. Having fabricated a Si tip array, it may then be spin-coated with a photoresist layer. This layer may be removed gradually by exposing it to UV light and with subsequent etching to allow the apexes of the Si tips to come out of the photoresist layer. These apexes are then deposited with catalyst. Having done that, the photoresist may be completely removed. Finally, this treated tip array may be used as a substrate to grow CNTs using a PECVD technique. Figure 21a shows the individual single CNTs on the Si tips. The CNTs have different shapes, lengths, and diameters, so there are still a number of steps needed to be taken to refine this technique. Figure 21b shows a few W nanowires grown on a Si tip, prepared following a similar procedure. This indicates that this technique has wide, potential application. Compared to the technique of Teo et al. [84], its major advantage is that it does not need to use e-beam lithography, which is expensive.

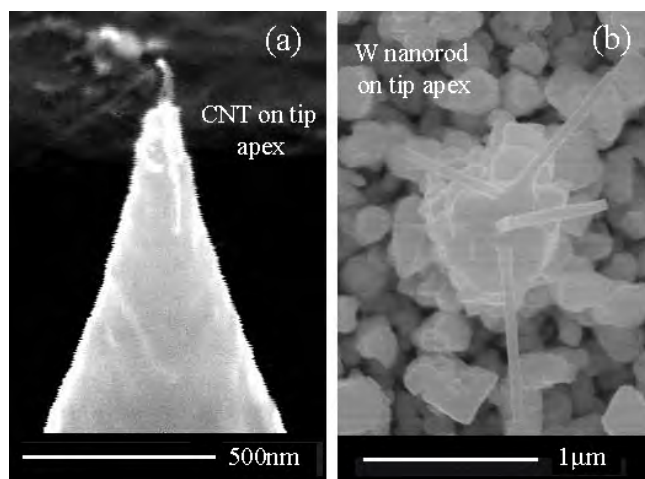


Figure 21. SEM images of a single carbon nanotube (a) and a few W nanowires (b) on the apex of a silicon tip.

4.2. Gated Nanoemitter Electron Sources and Arrays

4.2.1. Single-CNT Triodes and Arrays

There are technological challenges in how to transfer the procedures described previously to the gated device structures, such as the Spindt-cathode structure. In this context, Pirio et al. [136] have made progress in using the technique developed by Teo et al. [84]. The basic process will be described. Referring to Figure 22, the single CNT triode may be fabricated in a self-aligned process [136]. This procedure can ensure that the CNT grows in the center of the extraction gate. It starts with producing a sandwich structure on a doped Si substrate. It has a base metal electrode just on top of the Si substrate, on which a 500 nm silicon dioxide layer may be deposited. The gate electrode may use doped polysilicon and is on top of the SiO₂ layer. A layer of photoresist is coated on the sandwich structure (Fig. 22a). An array of holes may be patterned. The diameter of the hole must be less than 300 nm according to the earlier finding [84]. If this is larger than 300 nm, multiple CNTs will grow in a device [137]. Thus, this pattern needs to be prepared using an electron-beam lithography technique. Furthermore, the pitch of the holes may be determined according to the desired spacing between the holes. A reactive ion etching step using SF₆ gas may be used to isotropically etch the polysilicon gate (Fig. 22b) and wet chemical etching in buffered hydrofluoric acid may be used to isotropically etch the silicon dioxide layer. The latter method can produce microcavities due to undercutting (Fig. 22c). The following procedure is similar to that of Teo et al. [84]. A TiN barrier layer may first be deposited and then the catalyst, that is, Ni (Fig. 22d). The TiN and nickel on top of the gate electrode may be removed in a lift-off process by dissolving the photoresist in acetone (Fig. 22e), and finally the individual single CNT may be grown using PECVD with acetylene and ammonia gases at 700 °C (Fig. 22f). As mentioned, the number of CNTs in the gated hole is dependent on the diameter of the hole initially prepared in the photoresist. If this is less than 300 nm, only one CNT will be grown in the gated hole, as shown in Figure 23a. If it is

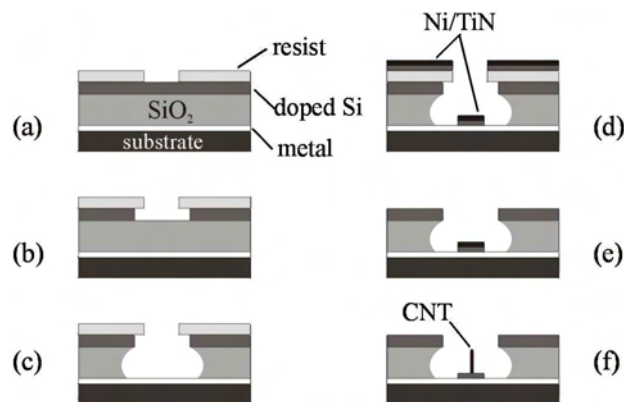


Figure 22. Illustration of the fabrication process of an array of microtriodes using a single carbon nanotube as a nanoemitter. Reprinted with permission from [86], P. Leqagneux et al., *Phantoms Newslett.* 5, 8 (2002). © 2002, CMP Cientifica.

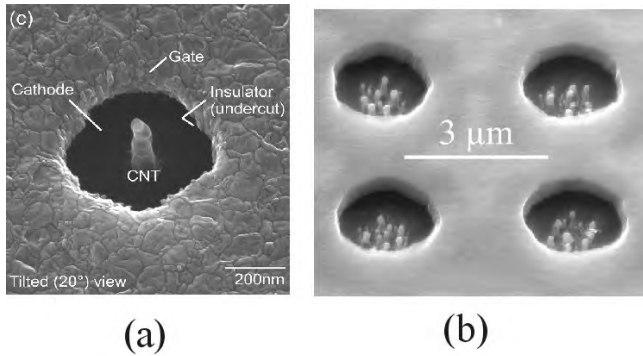


Figure 23. SEM images of a microtriode with a single carbon nanotube nanoemitter (a) and with multicarbon nanotubes (b). Reprinted with permission from [86], P. Leqagneux et al., *Phantoms Newslett.* 5, 8 (2002). © 2002, CMP Cientifica.

larger than that, a number of the CNTs will be grown in the gated hole (Fig. 23b). This latter device will not be an ideal vacuum nanoelectronic device, and its application will be limited to vacuum microelectronics.

Recently, another potentially useful technique was developed by Guilorn et al. [138], who have fabricated a gated device using an individual single carbon nanofiber as nanoemitter. The fabrication sequence is very similar to that followed to make silicon field emitter arrays [139]. As illustrated in Figure 24, electron-beam lithography may be used to define the catalyst site location and size (Fig. 24a) and also the mask for subsequent processing steps. Individual single carbon nanofibers standing vertically on the surface of substrate may be grown using plasma enhanced chemical vapor deposition (Fig. 24b). The carbon nanofibers may

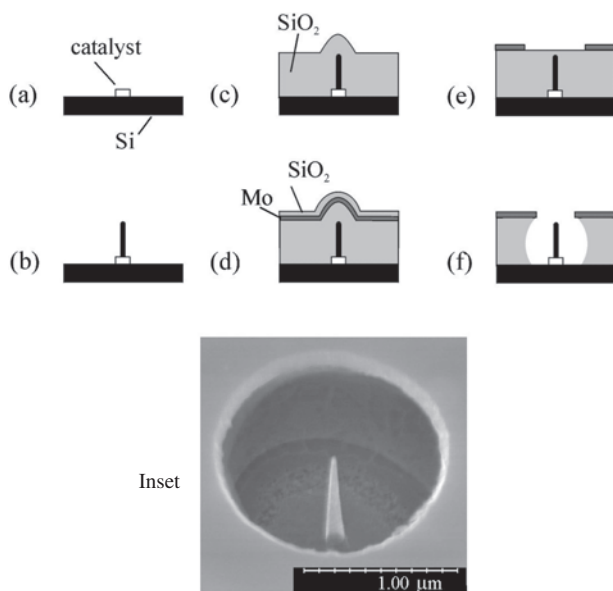


Figure 24. Illustrating how an array of microtriodes using a single carbon nanotube as nanoemitter may be fabricated in a process similar to that employed for making a silicon FEA. Reprinted with permission from [138], M. A. Guilorn et al., *Appl. Phys. Lett.* 81, 3660 (2002); 79, 2503 (2001). © 2001/2002, American Institute of Physics. Inset: the SEM image of a typical single-CNT triode prepared with this process.

have diameters around 30 nm with height of around 1 μm . A layer of SiO_2 with thickness of 1.2 μm may then be deposited onto the whole substrate using a silane-based radio-frequency plasma enhanced CVD process (Fig. 24c). A Mo thin film may be deposited on top of it as a gate electrode (Fig. 24d), and then an additional layer of SiO_2 may be deposited before mechanical polishing may be employed to smooth the top surface of the SiO_2 layer (Fig. 24e). The final step may be to use wet etching with a HF solution to form a microcavity (Fig. 24f). The device made using this procedure was tested to operate at a voltage around 100 V with a stable emission of 1 μA .

Finally, a triode with a Si nano tip can also be fabricated [140]. This was reported before [141], but the concept has been revisited. The process has been developed for fabricating Si field emission arrays [139]. A silicon (100) substrate is needed. The process begins with depositing a set of dot masks, which define where the silicon tips will be prepared (Fig. 25a). The diameter of the dots is around 1 μm . Wet etching may then be carried out using a solvent such as KOH (Fig. 25b). Since the (100) crystal face is etched more quickly than the (111) face, a tip with pyramid shape may gradually form (Fig. 25c). The subsequent sequence is as follows. The masks may be removed by lift-off. Then a silicon dioxide layer may be grown by thermal oxidation. On top of this SiO_2 layer, a metal thin film may be deposited, which is used as a gate electrode. Finally, microholes are etched through to form the triode with Spindt-cathode structure. Alternatively, the orientation-dependent growth process [139] has also been developed to create silicon pyramids. This involves using molecular beam epitaxy. To make Si nanotips, oxidation sharpening is required. This may be done before the mask layer is removed by thermal oxidation. This technique is developed based on the oxidation properties of silicon [142]. When oxidation at around 950 $^\circ\text{C}$, the speed of

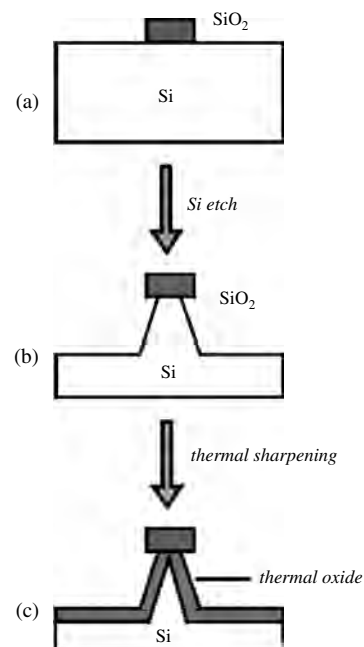


Figure 25. Illustration of the silicon nanotip fabrication process.

oxidation of Si is dependent on the surface conditions. For example, the silicon tip or edge oxidizes slower than the silicon flat surface (Fig. 25c). Figure 26 is an SEM image of a silicon tip, showing the detailed shape of the tip apex. In comparison with triode using a single carbon nanotube, the carbon nanotube emitter may have advantages over a silicon nanotip in material properties and in the intrinsic field emission characteristics outlined in Section 3. Due to these, new applications might be found with the triode using a CNT nanoemitter, such as in coherent electron sources. Nevertheless, the triode with a silicon nanotip may be fabricated using the well-developed microfabrication process, so it may be easy to make. Therefore, one should make a decision on the choice of nanoemitters according to the purpose of application. Meanwhile, it is necessary to develop both techniques further in order to meet future demands of the application.

4.2.2. Gated Diamond Nanotip Arrays and Nanodiamond-Based Triodes

Triodes with modified Spindt-cathode structure using diamond nanotips are a kind of important and potentially useful vacuum nanoelectronic devices. As shown in Figure 27a, a nanotip consisting of polycrystalline diamond is fabricated on the pyramid base of diamond, and it may be gated in the way shown in Figure 27b. Since it has a nanoapex, the field enhancement is high. Due to the low electron affinity of diamond, the low-field emission can be obtained. One more important feature is that it should be able to operate in very high current-density mode due to the high thermal conductivity available in the whole emitter.

An illustration shown in Figure 28 may be used to explain the fabrication process [143]. A *p*-type (100) silicon wafer may be used as a substrate. A SiO₂ layer with a thickness of 1–1.5 μm may first be grown by thermal oxidation. UV photolithography may be used to define the mask for the emitter array, which consists of square holes in the SiO₂ layer (Fig. 28a). The wafer may then be anisotropically etched with an etch-stopped process by wet etching using a potassium hydroxide:normal propanol:deionized water solution (Fig. 28a). This forms inverted pyramid molds in the wafer. It is important then to grow a layer of SiO₂ of thickness

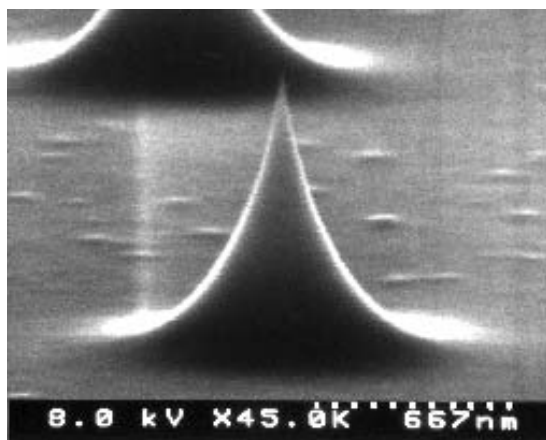


Figure 26. SEM image of a silicon nanotip.

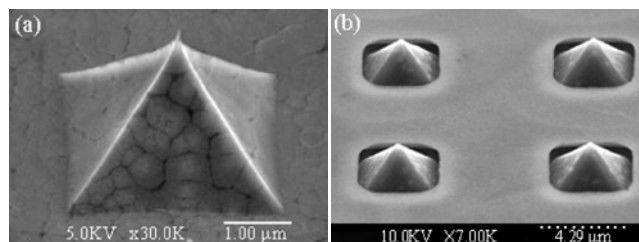


Figure 27. SEM images of a diamond nanotip (a) and a gated diamond nanotip array (b). Courtesy of Professor W. P. Kang, Vanderbilt University, USA.

of 0.7 μm on the mold surface by dry thermal oxidation (Fig. 28b). This process produces a well-sharpened apex on the inverted pyramids. A thick (5–10 μm) polycrystalline diamond film may then be deposited on the substrate by plasma enhanced chemical vapor deposition and they will fill in the inverted pyramid molds (Fig. 28c). Selective etching of the backside of silicon substrate may be performed until the apexes of SiO₂ covering diamond pyramids are exposed (Fig. 28d). Finally, the SiO₂ near the apex region may be etched away to expose the naturally sharpened diamond tips (Fig. 28c). The remaining SiO₂ and silicon form the dielectric spacer and the gate, respectively. The diamond nanotip array on a freestanding diamond diaphragm is finally formed.

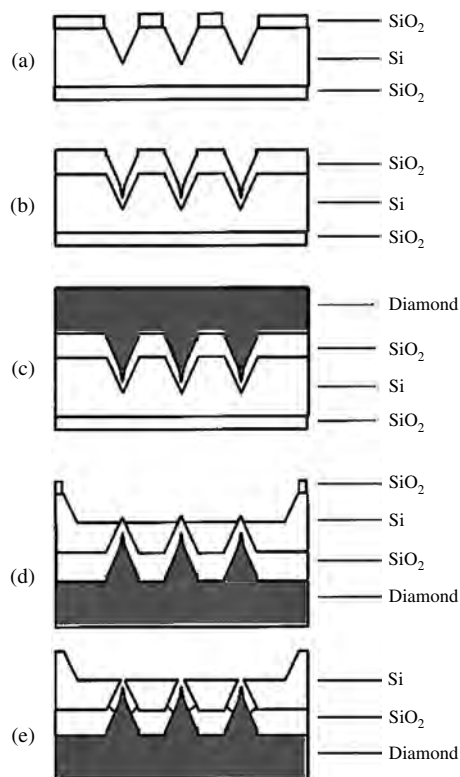


Figure 28. Illustration of the fabrication process of a gated diamond nanotip array. Reprinted with permission from [143], W. P. Kang et al., *J. Vac. Sci. Technol. B* 17, 740 (1999). © 1999, American Institute of Physics.

The triodes described all use nanoemitters standing out of the surface of a substrate. It is worth presenting another type of vacuum nanoelectronic device structure that is very different. This was invented by Zhu et al. [54] and is suitable for vacuum nanoelectronic devices using field emission flat films. Zhu et al. used the nanostructured diamond film as a cold cathode emitter, which has been described in Section 3. The fabrication process may be described using the illustration shown in Figure 29. Having deposited the nanostructured diamond film, spherical nanoballs may be sprayed on top of the film. The silicon dioxide layer and then metal thin film may be respectively sputtered onto the diamond film and the nanoballs. The nanoballs will still stand out of the surface of the SiO₂ film and may be brushed away. Nanoholes are then produced. At the top of the hole, the metal thin film acts as a gate, and the SiO₂ underneath insulates between the structured diamond film and the gate. Only very low fields (less than 5 V/μm) were needed to extract electrons from such devices. Unfortunately, this technique has not been further developed. It is believed that with the new nanotechnology now available, one should be able to make such a technique mature.

4.2.3. AAO Nanotemplate-Based Nanowire- and Nanotube-Emitter Arrays

The techniques described previously are mainly based on a top-down process (i.e., using a microfabrication technique) or a top-down plus bottom-up process, in which nanotubes and nanowires are synthesized. Here, we introduce a method that is mainly based on a self-assembly process (i.e., a bottom-up process). The idea is based on the use of nanotemplates, such as an anodized aluminum oxide (AAO) nanotemplate (Fig. 30a), to create vacuum nanoelectronic devices. As shown in Figure 30c, nanoemitters such as nanotubes or nanowires may be grown inside the nanoholes (Fig. 30b) of the AAO nanotemplate. The walls of the nanoholes may act as an insulating layer between the bottom electrodes and the gate electrodes.

This concept was first pursued by Holland et al. [144–146]. They used glass as a substrate, on which three layers were deposited. The first was the metal film, which might be patterned to be addressable electrodes. The second was a buffer layer, which might be amorphous silicon film. Finally, a layer of aluminum was deposited. To obtain the required nanotemplate, the anodization process must be carried out in a controlled and established manner [144, 145], but essentially following the method described by Furneaux et al. [147, 148]. In their earlier work, Mo nanoemitters with desired

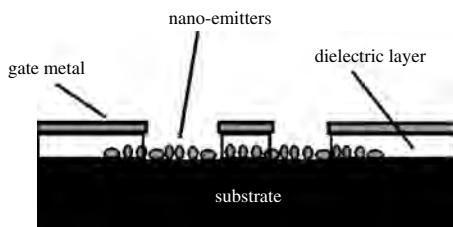


Figure 29. Illustration of a nanotriode using nanostructured diamond film.

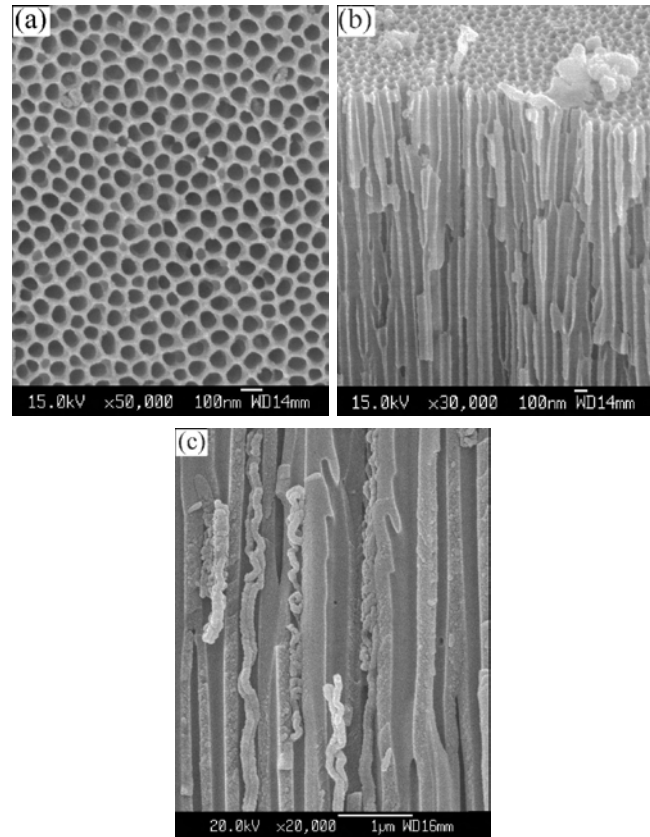


Figure 30. SEM images of an AAO nanotemplate (a), of the cross-section of nanoholes (b), and of the carbon nanofibers in nanoholes.

shape were deposited. However, an important attempt to fabricate a gate electrode has not yet been attempted.

Recently, several studies [149–151] were carried out to develop this but using carbon nanotubes in the nanoholes as emitters. The first study into the field emission from such carbon nanotubes was carried out by Gunther et al. [149]. It was revealed that high-density carbon nanotubes in high-density nanoholes are not good for emission and that low-density carbon nanotubes perform better. This was attributed to the screen effect between the nanotubes [149]. However, if a gate electrode is placed near each nanoemitter, this effect should not be a problem. Nevertheless, this finding indicates that to further develop a technique to create a nanotemplate having nanoholes with predefined pores, cell size and spacing are essential.

5. POTENTIAL APPLICATIONS

5.1. Parallel Electron-Beam Nanolithography

Lithography is a processing technique daily used in the semiconductor industry, in which patterns of integrated circuits are generated. Ultraviolet light lithography is commonly employed in current production lines, but extreme UV or X-ray lithography is under development to meet future needs. These techniques are based on masks. Electron-beam lithography has also been investigated and is a maskless technique; an electron beam directly writes on the resist

coated on a wafer on which integrated circuits are fabricated. There are two advantages of using e-beam lithography. One is low cost due to masklessness and another is that high resolution such as 10 nm could be relatively easily obtained. The drawback has been that it is based on a serial writing process, so that the throughput is low. To meet the production requirement of 25 wafers per hour, the single e-beam technique is 1000 times lower. In order to solve this, a concept based on a parallel e-beam was put forward and demonstrated by Chang et al. [152] and Muray et al. [153] using a vacuum microelectronic technique. Later Binh et al. [154] developed a microgun using a nanotip in tandem with electrostatic lenses integrated in a single silicon chip. Nanometric spot-size and millimeter-size microgun columns were realized in their approach. The problems that need to be addressed immediately include the uniformity of e-beam current and beam diameter in such a multiple-beam system.

In the European Nanolith Project, researchers from France, the UK, and Germany have revisited the parallel e-beam lithography concept and aimed at developing a demonstrator unit based on the vacuum nanoelectronic technique [86]. So far, they have investigated the feasibility of using carbon nanotubes as electron sources and using a localized carbon nanotube growth technique with nanoscale precision as we described in Section 4.

The design concept they have proposed is based on a fixed-focus and fixed-beam position approach, while the parallel e-beam writing head will be moved by a piezo-driven stage to scan over the wafer. As shown in Figure 31, each e-beam gun exposes the desired pixels as an area of 100×100 mm under the gun is scanned by piezo movement. An additional feature in this design is the use of a CMOS circuit connected to control individual e-beam current and diameter. In future, the present hybrid assembly method may be replaced by the monolith integration, in which the CMOS circuit may be built under each gun. The simulation study carried out based on the design shown in Figure 31 reveals that nanometric alignment of CNT in the extraction electrode is very critical if the resolution is to be maintained.

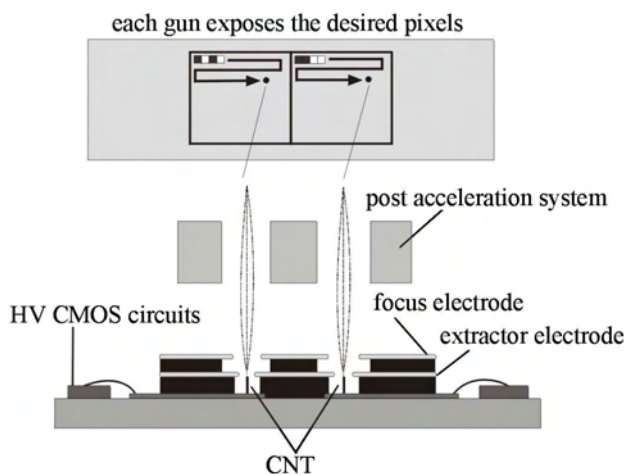


Figure 31. Illustration of an e-beam writing head and how each e-gun exposes the desired pixel. Reprinted with permission from [86], P. Leqagneux et al., *Phantoms Newslett.* 5, 8 (2002). © 2002, CMP Cientifica.

The recent findings of the investigation are encouraging. Regarding the uniformity of emission current from individual CNTs, Semet et al. [93] have found that they can meet the design criteria, as shown in Figure 20b. It has also been shown that a self-heating conditioning process is enough to obtain good Fowler–Nordheim behavior and stable emission [94]. Findings such as shown in Figure 20b demonstrate that a variation of $\Delta I/I$ of only 30% in the FE currents between the different CNTs of a 40×40 array after conditioning can be easily handled by the CMOS circuit. Of course, this, together with the beam spot feature, will need further verifying in the gated CNTs in triode structures such as shown in Figure 23a.

The 30% variation in the emission currents between CNTs in a 40×40 array needs to be taken into account in the system design. In the e-beam writing system, the final uniformity is determined by the total dose of charge received by a unit area of resist. The overall system specifications of CNT emission currents are in the range of 1–10 nA within the exposure time intervals of up to 10 μ s. A CMOS circuit is designed for microgun control. The purpose of the microgun electronics is to ensure a constant current–time product, which is equivalent to a specific value of dose of charge required for resist exposure. This is done by selecting a CNT pixel and controlling the CNT emission current flow within the fixed time interval by switching a high-voltage transistor. If the current of a specific pixel is lower, the time interval needs to be longer. However, if the current is higher, the time interval will be shorter. This design was tested and verified to work in principle [86].

Figure 32a shows a schematic illustration of the first demonstrator by the European group. The e-beam writing head consists of three key elements that is, a microgun array, the CMOS electronics, and a postaccelerating system. The microgun array will have two lines of 16 microguns, and each of them will be an improved version of the gated single CNT triode shown in Figure 32b.

5.2. Field Emission Information Storage

The world generates approximately 10^{18} bytes of unique information per year. This amount increases annually. Currently, information is stored in paper, film, compact disks, and magnetic media in form of tapes or hard disks. Among

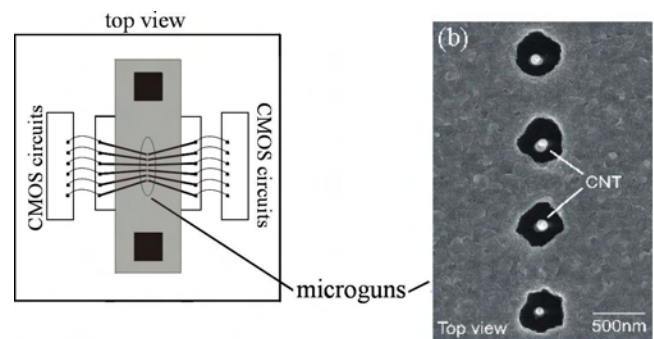


Figure 32. Illustration of the first nanolith demonstrator. Reprinted with permission from [86], P. Leqagneux et al., *Phantoms Newslett.* 5, 8 (2002). © 2002, CMP Cientifica.

these the magnetic storage technique is considered to be the one having the highest limited storage capacity (i.e., 100 Gb/in²). With the present speed of development, this limit may be reached in the near future. Thus, it is desirable to investigate alternative approaches that may be low cost, high capacity, and high efficiency. Thus, an electron-beam based recording approach was proposed [155]. Ultra-high storage density of greater than one terabit per square inch (Tb/in²) may be realized using a field emission information storage device (FEISD) [156]. The success of development of such an ultra-high-density storage device is very much dependent on vacuum nanoelectronics.

Figure 33 illustrates an FEISD, and it consists of three essential components: a field emission tip array, a storage medium, and a micromover. The electron emitters of the tip array should be addressed individually, and each of them is employed to write and read information to and from the storage medium placed under the tips in a microscale proximity. The micromover is capable of positioning the emitters over designed locations of pixels of the storage medium. In a writing process, the storage medium will undergo a phase transition (e.g., from crystalline to amorphous phase). The pixel that has amorphous film will have different electrical resistance. Thus, in a reading process, by recording the currents passing through each pixel and distinguishing their differences, one may retrieve the information stored.

There are a number of technical difficulties in this research. Reported progress has been made by the HP group led by Lam [156]. These studies so far are based on vacuum microelectronics. Two types of device structures, 2-metal and 3-metal devices, were studied and are illustrated in Figure 34. Now, a good emitter material (i.e., Nb-based alloys) has been found, and routinely emission current density of greater than 100 nA per tip and operating voltages of less than 80 V can be obtained and these have met the requirements for FEISDs. However, there are not yet reports on how a FEISD performs when this tip array is used. Also, it is apparent that a vacuum nanoelectronic device will be needed to replace the vacuum microelectronic one if the predicted capacity of ultra-high-density storage of a FEISD will be fully explored. Finally, due to extreme similarity in the technical requirements between the field emission information storage device and the e-beam writing head

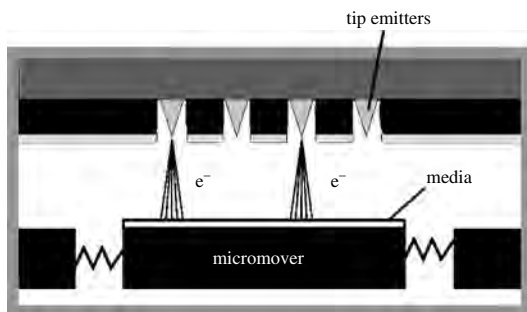


Figure 33. Illustrating the principle of a field emission information storage device. Reprinted with permission from [156], S. T. Lam, in "Technical Digest of the 14th IVMC," Davis, CA, 2001, p. 135. © 2001, AVS-The Science & Technology Society.

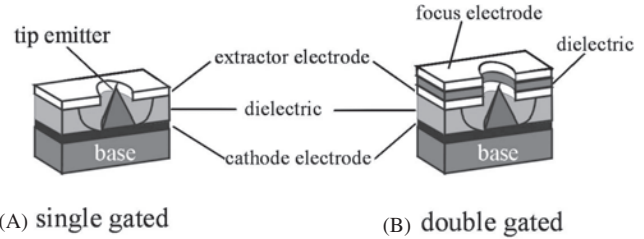


Figure 34. Illustration of the 2-metal (a) and 3-metal (b) devices developed for the FEISD.

of the nanolithography system described, a breakthrough in any of the above two directions will benefit both.

5.3. High Resolution Imaging Devices

Imaging devices have a wide range of applications including digital cameras. Among these, recently there have been a number of reports on the study of vacuum tube imaging devices using cold cathodes as an electron source [157–159]. In such devices, it is possible to reduce size and to obtain high sensitivity. When vacuum nanoelectronic field emitter arrays are used, a high resolution device may be made. An example of such devices uses a selenium photodetector, since this material shows ultrahigh photosensitivity by using avalanche multiplication inside the solid. One way to generate this effect is to use vacuum electrons impinging on the Se film. Figure 35 illustrates a basic device structure. The amorphous Se film is deposited on a transparent conductive film, for example, indium tin oxide, on a glass faceplate. This is used as an anode. Just below the Se film, a cold cathode is placed within a vacuum gap of not more than 100 μm away from and in parallel to the anode. The device is required to work under vacuum conditions. When light illuminates the device, electron-hole pairs are generated in the Se film, and a layer of positive charge will be produced on the surface facing the cathode. This leads to an enhanced field in the vacuum gap and thus on the surface of the cathode. As a result, field emission current from the cathode will increase. These field-emitted electrons bombard the Se film and thus increase the current inside the Se film through avalanche multiplication.

The disadvantages of using cold cathodes include the requirement of ultrahigh vacuum. Recent findings indicate

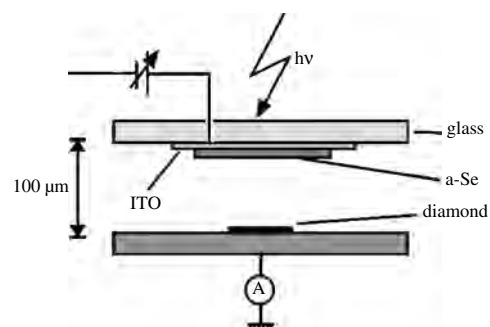


Figure 35. Illustration of a vacuum tube imaging device using field emitters.

that using diamond film as cold cathodes can overcome this and a device with such a cathode was found to show promising performance when it was filled with N_2 gas up to a pressure in the range of 10^{-5} Torr. In the independent study, carbon nanotubes were found to have good emission stability and lifetime in high vacuum conditions, but its application in the vacuum tube imaging devices has not yet been investigated.

A suggestion may be put forward here. In order to increase the sensitivity of the device, the cold cathode materials having good photofield emission properties may be used. One of these has been described in Section 3 (i.e., the CuO nanowire arrays).

5.4. Displays

These potential applications involve not only nanoemitters but also nanoscale device structures. In the displays we are going to describe, nanoemitters are the major concern, and some of them are likely to be commercialized in near future. These mainly include ultra-large-screen displays assembled by using cold cathode lighting elements and field emission display (FED).

Companies such as ISE Electronic Ltd. made lighting elements using hot cathodes. Due to its high brightness, they are used to assemble digital displays for open door sport halls. But their power consumption is high, so ultra-large-screen displays cannot be made of hot cathode lighting elements. Cold cathode lighting elements using silicon tip arrays were made by Chen et al. [160], but the cost and the lifetime of the cold cathodes limit their large volume production. Lighting elements using carbon nanotubes as electron emitters (Fig. 36) have been investigated by both industrial and academic researchers [161–163]. Ynmura and Ohshima at Mie University demonstrated a prototype lighting element using carbon nanotubes and were awarded a silver medal at the 2000 SID conference [161]. In parallel, the study carried out at Zhongshan University with cold cathode lighting elements dated back to 1997. Initially, composite cold cathodes were investigated and the results were first reported in 2000

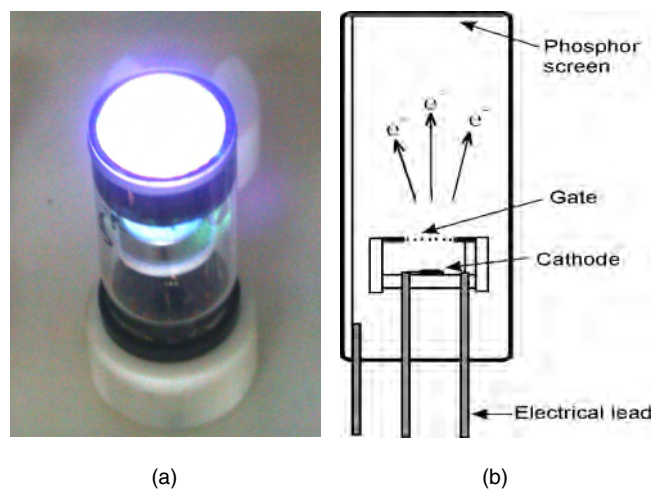


Figure 36. (a) A photo of a lighting element. (b) The illustration of the structure of the lighting element.

[162]. Now, lighting elements of three basic colors (i.e., red, blue, and green) all can be made, and their brightness of greater than $10,000 \text{ cd/m}^2$ can be routinely produced [163]. A full investigation into the frequency characteristics of a cold cathode element was carried out [164]. It is found that the cutoff frequency is mainly limited by the capacitance due to the vacuum gap formed by the cathode and gate electrode, but a cutoff frequency of more than 50 kHz can be obtained without difficulty [164]. Therefore, it is possible to use cold cathode lighting elements to assemble a full-color large-screen display with video frame speed.

It is predicted that flat panel displays are going to replace the current dominating products, that is, cathode-ray tubes and cathode-ray picture tubes; both are hot-filament-based color tubes. Strong emerging flat panel display (FPD) products include plasma discharge panels and liquid crystal displays (LCDs). Organic light-emitting displays (OLEDs) and field emission displays are under intensive investigation as future FPDs.

Figure 37 illustrates a diode-type FED. A faceplate is deposited with many stripes, each of them consists of three-color phosphors. The baseplate is deposited with metal film electrodes. The baseplate and the faceplate form a vacuum gap of less than $100 \mu\text{m}$. The stripes and the electrodes form many cross-points. Cold cathode emitters are grown at the locations of these cross-points. When a potential is applied to one of the cross-points through the stripe and the electrode, the emitters will be excited to emit electrons and when these electrons are accelerated to bombard the phosphors above, light with different color may be generated. In a real display, the emitter array should be gated, and each pixel contains many gated emitters (Fig. 38). The overall emission characteristics of these emitters and the uniformity of the characteristics of all pixels in the display are very important.

Samsung has produced several generations of prototype CNT FEDs [35, 36, 68, 165, 166], including a 9-inch red–blue–green color FED that can operate with video frame speed. The challenging technical issues overcome by Samsung mainly include: (i) development of CNT-based cold cathode electron-emission materials and their application processing techniques and (ii) the development of device fabrication techniques for making gated emitter arrays. The CNT-based cathode materials are printable inks, similar to the idea put forward by Xu and Latham, as already described in Section 3. The early version used an organic-based paste mixed with CNTs [35]. The ink may be printed

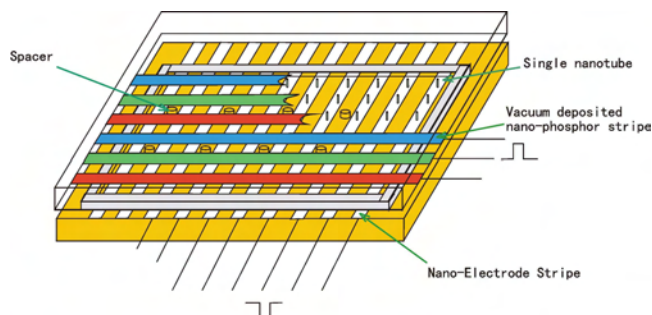


Figure 37. Illustrating the working principle of a FED.

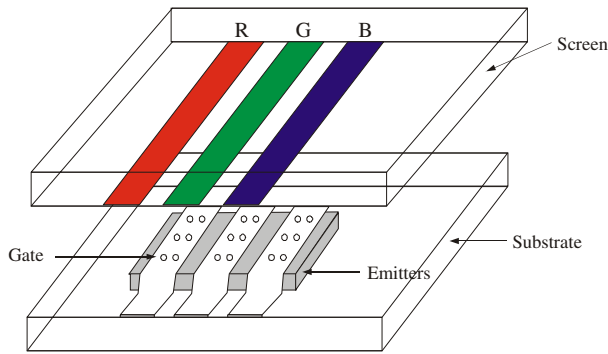


Figure 38. Illustration of a pixel in a real FED.

on a substrate like common screen-printing of thick film. After the heating process, the organic binder was removed, and the CNTs were embedded in the metal electrodes below. A mechanical rubbing process is developed to expose the CNTs embedded in the metal layer. Recently, a new version of inks was developed using a photosensitive material as a base material [166]. After printing, UV light is used to illuminate the printed ink layer through a mask (i.e., in a way similar to UV photolithography in an integrated circuit fabrication process) [166]. For device structures, an earlier version used a modified shadow mask commercially available for CRTs as a control gate electrode [35], but this could not be used to address individual pixels. Later, an under-gate structure was developed, in which the gate electrode of a pixel is placed under an insulating layer below the cathode electrode [165]. A recent structure is similar to common vacuum microelectronic triode structure [68]; each pixel has cylindrical symmetry and the gate electrode is placed above the emitters.

The color CNT-FED produced by Samsung further demonstrates the following advantages of a FED over a LCD display: low power consumption, high brightness, a wide viewing angle, a fast response rate, and a wide operating temperature range. However, it is not possible to know if any company would like to take up these impressive achievements further to make commercially available FED products. The situation is extremely challenging to FED development, since it also faces strong competition from the emerging OLEDs besides the LCDs already on the market.

6. SUMMARY

We have reviewed the available information about a new subject, vacuum nanoelectronics. It is a logical and natural development from vacuum microelectronics. At present, this subject is really in its very early stage of development, and there are strong overlaps with vacuum microelectronics. For example, nanotubes and nanowires as vacuum electron emitters may be employed in both vacuum microelectronic and vacuum nanoelectronic devices. Thus, we do not intend here to define a clear line between vacuum microelectronics and vacuum nanoelectronics. Our real intention is to bring to readers what might be happening in our field in the coming era of nanoscience and nanotechnology and how we may be able to benefit from the rapid development in nanoscience and nanotechnology.

Other authors may cover some of the areas we have discussed in this chapter, such as field emission from carbon nanotubes. However, our major interest focuses on the special aspects, for example, the coherent emission process and the chirality effect. We believe that these properties are the main concern of nanoscience and nanotechnology. So we have paid full attention to them in our chapter.

Finally, the development of vacuum nanoelectronics is so rapid that new findings emerge every day. The information used in our chapter is limited to that available from published results and our own data. We anticipate that many advances in the synthesis of nanoemitters, the design and fabrication of vacuum nanoelectronic devices, and their application will come. Thus, our chapter should be considered as a snapshot of the early phase of the development.

GLOSSARY

Metal-insulator-metal model (MIM model) A theoretical model proposed to explain field-induced electron emission from a metal-insulator-metal microstructure.

Metal-insulator-vacuum model (MIV model) A theoretical model proposed to explain field-induced electron emission from a metal-insulator-vacuum microstructure.

ACKNOWLEDGMENTS

The author first expresses his gratitude to his colleagues, Professor Vu Thien Binh, Dr. D. Pribat, Dr. P. Legagneux, Professor W. P. Kang, Dr. S. T. Lam, Dr. E. Huq, Professor S. Z. Deng, Professor Jun Chen, and Dr. J. C. She, for their valuable information and help the author received in the preparation of this chapter. He also thanks Miss B. Y. Chen for her help in preparation of the manuscript. Finally, he thanks, for the financial support for the research carried out to obtain the findings presented in this chapter, the NSF of China, the Chinese Ministry of Science and Technology and Ministry of Education, and the Department of Science and Technology and the Department of Education of Guangdong Provincial Government.

REFERENCES

1. S. Iijima, *Nature* 354, 56 (1991).
2. L. A. Chernozatonskii, Y. V. Gulyaev, Z. Y. Kosakovskaya, N. I. Sinitsyn, G. V. Torgashov, Y. F. Zakharchenko, E. A. Fedorov, and V. P. Val'chuk, *Chem. Phys. Lett.* 233, 63 (1995).
3. A. G. Rinzier, J. H. Hafner, P. Nikolaev, L. Lou, S. G. Kim, D. Tomanek, P. Nordlander, D. T. Colbert, and R. E. Smalley, *Science* 269, 1550 (1995).
4. W. A. De Heer, A. Châtelain, and D. Ugarte, *Science* 270, 1179 (1995).
5. (a) J. Zhou, N. S. Xu, S. Z. Deng, J. Chen, and J. C. She, in "Technical Digest of the 15th IVMC and 48th IFES," Lyon, France, 2002, p. PM15. (b) J. Zhou, N. S. Xu, S. Z. Deng, J. Chen, J. C. She, and Z. L. Wang, *Adv. Mater.* 15, 1835 (2003).
6. J. Zhou, N. S. Xu, S. Z. Deng, J. Chen, and J. C. She, in "Technical Digest of the 15th IVMC and 48th IFES," Lyon, France, 2002, p. PM16.
7. Y.-H. Lee, C.-H. Choi, Y.-T. Jang, E.-K. Kim, B.-K. Ju, N.-K. Min, and J.-H. Ahn, *Appl. Phys. Lett.* 81, 745 (2002).

8. S. Z. Deng, Z. S. Wu, J. Zhou, N. S. Xu, J. Chen, and J. Chen, *Chem. Phys. Lett.* 356, 511 (2002).
9. S. H. Wang and S. H. Yang, *Adv. Mater. Opt. Electron.* 10, 39 (2000).
10. S. H. Yang, unpublished work.
11. R. H. Fowler and L. Nordheim, *Proc. Roy. Soc. London Ser. A* 119, 173 (1928).
12. K. R. Shoulders, *Adv. Comp.* 2, 135 (1961).
13. C. A. Spindt, *J. Appl. Phys.* 39, 3504 (1968).
14. I. Brodie and C. A. Spindt, Vacuum microelectronics, in "Advances in Electronics and Electron Physics" (P. W. Hawkes, Ed.), Vol. 83, p. 1. Academic Press, New York, 1992.
15. W. Zhu, "Vacuum Microelectronics." Wiley, New York, 2001.
16. H. F. Gray, G. J. Campisi, and R. F. Greene, in "Technical Digest of IEDM," Washington, DC, 1986, p. 776.
17. C. A. Spindt, C. E. Holland, and R. D. Stowell, *Appl. Surf. Sci.* 16, 268 (1983).
18. G. N. A. Van Veen, *J. Vac. Sci. Technol. B* 12, 655 (1994).
19. C. O. Bozler, C. T. Harris, S. Rabe, D. D. Rathman, M. A. Hollis, and H. I. Smith, *J. Vac. Sci. Technol. B* 12, 629 (1994).
20. P. R. Schowebel, C. A. Spindt, I. Bradie, and C. E. Holland, in "Technical Digest of the 7th IVMC," Grenoble, France, 1994, p. 378.
21. J. C. She, N. S. Xu, S. Z. Deng, and J. Chen, *Appl. Phys. Lett.* 83, 746 (2003).
22. C. H. Oh, *J. Vac. Sci. Technol. B* 16, 807 (1998).
23. C. A. Spindt, *Surf. Sci.* 266, 145 (1992).
24. C. A. Spindt, C. E. Holland, A. Rosengreen, and I. Brodie, *IEEE Trans. Electron Devices* 38, 2355 (1991).
25. J. Itoh, Y. Tohma, K. Morikawa, S. Kanemaru, and K. Shimizu, *J. Vac. Sci. Technol. B* 13, 1968 (1995).
26. C. M. Tang, T. A. Swyden, K. A. Thomason, L. N. Yadon, D. Temple, C. A. Ball, W. D. Palmer, J. Marcusie, D. Vellenga, and G. E. McGuire, *J. Vac. Sci. Technol. B* 14, 3455 (1996).
27. T. Hirano, S. Kanemaru, H. Tanoue, and J. Itoh, *Jpn. J. Appl. Phys.* 35, 6637 (1996).
28. A. I. Akinwande, in "Technical Digest of the 15th IVMC and the 48th IFES," Lyon, France, 2002, p. PK01.
29. N. S. Xu, in "High Voltage Vacuum Insulation: Basic Concepts and Technological Practice," Ch. 4. Academic Press, London, 1995.
30. K. H. Bayliss and R. V. Latham, *Proc. Roy. Soc. London Ser. A* 403, 285 (1986).
31. N. S. Xu, Ph.D. Thesis, Aston University, UK, 1986.
32. N. S. Xu and R. V. Latham, private communication.
33. S. Bajic, Ph.D. Thesis, Aston University, UK, 1989.
34. W. Taylor, S. M. Baigrie, H. E. Bishop, M. Brierley, M. K. Bull, A. P. Burden, J. M. Friday, J. J. Gray, C. Hood, C. Howard, P. G. A. Jones, A. Y. Khazov, W. Lee, R. J. Riggs, G. G. Sheehy, R. A. Tuck, and M. S. Waite, in "Technical Digest of the 14th IVMC," Davis, CA, 2001, p. 177.
35. W. B. Choi, D. S. Chung, J. H. Kang, H. Y. Kim, Y. W. Jin, I. T. Han, Y. H. Lee, J. E. Jung, N. S. Lee, G. S. Park, and J. M. Kim, *Appl. Phys. Lett.* 75, 3129 (1999).
36. D. S. Chung, S. H. Park, Y. W. Jin, J. E. Jung, Y. J. Park, H. W. Lee, T. Y. Ko, S. Y. Hwang, J. W. Kim, N. H. Kwon, M. H. Yoon, C. G. Lee, J. H. You, N. S. Lee, and J. M. Kim, in "Technical Digest of the 14th IVMC," Davis, CA, 2001, p. 179.
37. F. J. Himpsel, J. A. Knapp, J. A. Van. Vechten, and D. E. Eastman, *Phys. Rev. B* 20, 624 (1979).
38. J. E. Field, "Properties of Diamond." Academic Press, London, 1979.
39. M. W. Geis, N. Efremow, J. Woodhouse, M. Mcalese, M. Marchy-wka, D. Socker, and J. Hochedez, *IEEE. Electron Device Lett.* 12, 456 (1991).
40. C. Wang, A. Garcia, D. C. Ingram, M. Lake, and M. E. Kordesch, *Electron Lett.* 27, 1459 (1991).
41. N. S. Xu, R. V. Latham, and Y. Tzeng, *J. Phys. D* 26, 1776 (1993).
42. N. S. Xu, R. V. Latham, and Y. Tzeng, *Electron. Lett.* 29, 1596 (1993).
43. N. S. Xu, Y. Tzeng, and R. V. Latham, *J. Phys. D* 27, 1988 (1994).
44. J. D. Lee, in "Technical Digest of the 10th IVMC," Kyongju, Korea, 1997.
45. K. Okano, S. Koizumi, S. Ravi, P. Silva, and G. A. J. Amaratunga, *Nature* 381, 140 (1996).
46. J. Robertson, in "Thin Film Diamond," Ch. 9. Chapman & Hall for the Royal Society, London, 1994.
47. B. S. Satyanarayana, A. Hart, W. I. Milne, and J. Robertson, *J. Appl. Phys.* 71, 1430 (1997).
48. G. A. J. Amaratunga and S. R. P. Silva, *Appl. Phys. Lett.* 68, 2529 (1996).
49. N. S. Xu, J. Chen, and S. Z. Deng, *Appl. Phys. Lett.* 76, 2463 (2000).
50. N. S. Xu, J. Chen, J. C. She, S. Z. Deng, and J. Chen, *J. Phys. D* 33, 2568 (2000).
51. N. S. Xu, J. C. She, S. E. Huq, J. Chen, and S. Z. Deng, *Appl. Phys. Lett.* 73, 3668 (1999).
52. J. C. She, S. E. Huq, N. S. Xu, S. Z. Deng, and J. Chen, in "Technical Digest of the 15th IVMC and the 48th IFES," Lyon, France, 2002, p. OB1.09.
53. N. S. Xu, J. C. She, J. Chen, S. Z. Deng, and J. Chen, *Appl. Phys. Lett.* 77, 2921 (2000).
54. W. Zhu, G. P. Kochanski, and S. Jin, *Science* 282, 1473 (1998).
55. A. R. Krauss, O. Auciello, M. Q. Ding, V. V. Zhirnov, E. I. Givargizov, A. Breskin, R. Chechen, E. Shefer, V. Konov, S. Pimenov, A. Karabutor, A. Rakimov, and N. Suetin, in "Technical Digest of the 13th IVMC," Guangzhou, China, 2000, p. 96.
56. N. S. Xu, J. Chen, Y. T. Feng, and S. Z. Deng, *J. Vac. Sci. Technol. B* 18, 1048 (2000).
57. N. S. Xu, J. C. She, S. E. Huq, J. Chen, S. Z. Deng, and J. Chen, *Ultramicroscopy* 89, 111 (2001).
58. R. Saito, G. Dresselhaus, and M. S. Dresselhaus, "Physical Properties of Carbon Nanotubes." Imperial College Press, London, 1999.
59. M. S. Dresselhaus, G. Dresselhaus, and P. C. Eklund, "Science of Fullerenes and Carbon Nanotubes." Academic Press, San Diego, 1996.
60. P. L. McEuen, *Physics World*, June, 31 (2000).
61. C. Schonenberger and L. Forro, *Physics World*, June, 37 (2000).
62. H. J. Dai, *Physics World*, June, 43 (2000).
63. W. A. De Heer and R. Martel, *Physics World*, June, 49 (2000).
64. N. S. Xu, S. Z. Deng, and J. Chen, *Ultramicroscopy* 95, 19 (2003).
65. J. M. Bonard, H. Kind, T. Stockli, and L.-O. Nilsson, *Solid-State Electron.* 45, 893 (2001).
66. W. Zhu, in "Vacuum Microelectronics," Ch. 6. Wiley, New York, 2001.
67. R. H. Baughman, A. A. Zakhidov, and W. A. de Heer, *Science* 297, 787 (2002).
68. Y. J. Park, D. S. Chung, Y. W. Jin, J. E. Jung, H. S. Kang, J. W. Kim, J. E. Jang, S. N. Cha, S. H. Cho, K. H. Noh, H. R. Seon, C. H. Lee, C. Y. Park, and J. M. Kim, in "Technical Digest of the 15th IVMC and the 48th IFES," Lyon, France, 2002, p. OB4.03.
69. Q. H. Wang, *Appl. Phys. Lett.* 72, 2912 (1998).
70. N. S. Xu, Z. S. Wu, S. Z. Deng, and J. Chen, *J. Vac. Sci. Technol. B* 19, 1370 (2001).
71. M. J. Fransen, T. L. van Rooy, and P. Kruit, *Appl. Surf. Sci.* 146, 312 (1999).
72. T. W. Ebbesen and P. M. Ajayan, *Nature* 358, 220 (1992).
73. S. Iijima and T. Ichihashi, *Nature* 363, 603 (1993).
74. D. S. Bethune, C. H. Kiang, M. S. de Vries, G. Gorman, R. Savoy, J. Vazquez, and R. Beyers, *Nature* 363, 605 (1993).
75. A. Thess, R. Lee, P. Nikolaev, H. Dai, P. Petit, J. Robert, X. Chuhui, L. Y. Hee, K. S. Gon, A. G. Rinzler, D. T. Colbert, G. E. Scuseria, D. Tomanek, J. E. Fischer, and R. E. Smalley, *Science* 273, 483 (1996).

76. M. José-Yacamán, M. Miki-Yoshida, L. Rendó, and J. G. Santie-Steban, *Appl. Phys. Lett.* 62, 657 (1993).
77. A. Cassel et al., *J. Phys. Chem.* 103, 6484 (1999).
78. O. M. Kuttel, O. Groening, and C. Emmenegger, *Appl. Phys. Lett.* 73, 2113 (1998).
79. Z. F. Ren, Z. P. Huang, J. W. Xu, J. H. Wang, P. Bush, M. P. Siegal, and P. N. Provencio, *Science* 282, 1105 (1988).
80. S. K. Chung, S. H. Lim, C. H. Lee, and J. Jang, *Diamond Relat. Mater.* 10, 248 (2001).
81. S. J. Chung, S. H. Lim, and J. Jang, *Thin Solid Film* 383, 73 (2001).
82. W. Z. Li, S. S. Xie, L. X. Qian, B. H. Chang, B. S. Zou, W. Y. Zhou, R. A. Zhao, and G. Wang, *Science* 274, 1701 (1996).
83. S. Fan, M. G. Chapline, N. R. Franklin, T. W. Tomblor, A. M. Cassell, and H. Dai, *Science* 283, 512 (1999).
84. K. B. K. Teo, M. Chhowalla, G. A. J. Amaratunga, and W. I. Milne, *Appl. Phys. Lett.* 79, 1534 (2001).
85. J. C. She and N. S. Xu, unpublished.
86. P. Leqagneux, G. Pirio, E. Balossier, J. P. Schnell, D. Pribat, K. B. K. Teo, M. Chhowalla, D. G. Hasko, G. A. J. Amaratunga, W. I. Milne, V. Semet, V. T. Binh, W. H. Bruenger, H. Hanssen, and D. Friedrich, *Phantoms Newslett.* 5, 8 (2002).
87. W. Hu, D. Gong, Z. Chen, L. Yuan, K. Saito, C. A. Grimes, and P. Kichambare, *Appl. Phys. Lett.* 79, 3083 (2001).
88. J. M. Bornard, N. Weiss, H. Kind, T. Stockli, L. Forro, K. Kern, and A. Chatelain, *Adv. Mater.* 13, 184 (2001).
89. L. Nilsson, O. Groning, C. Emmenegger, O. Kuttel, E. Schaller, L. Schlapbach, H. Kind, J. M. Bonard, and K. Kern, *Appl. Phys. Lett.* 76, 2071 (2000).
90. S. Z. Deng and N. S. Xu, unpublished.
91. R. P. Gao, Z. W. Pan, and Z. L. Wang, *Appl. Phys. Lett.* 78, 1757 (2001).
92. X. Ma, E. Wang, W. Zhou, D. A. Jefferson, J. Chen, S. Deng, N. Xu, and Jun Yuan, *Appl. Phys. Lett.* 75, 3105 (1999).
93. V. Semet, V. T. Binh, P. Vincent, D. Guillot, K. B. K. Teo, M. Chhowalla, G. A. J. Amaratunga, W. I. Milne, P. Legagneux, and D. Pribat, *Appl. Phys. Lett.* 81, 343 (2002).
94. S. T. Purcell, P. Vincent, C. Journet, and V. T. Binh, *Phys. Rev. Lett.* 88, 105502 (2002).
95. P. Vincent, S. T. Purcell, C. Journet, and V. T. Binh, *Phys. Rev. B* 66, 075434 (2002).
96. T. Yamashita, K. Mastuda, T. Kona, Y. Mogami, M. Komaki, Y. Murata, C. Oshima, T. Kuzumaki, and Y. Horiike, *Surf. Sci.* 514, 283 (2002).
97. C. Oshima, K. Mastuda, T. Kona, Y. Mogami, M. Komaki, Y. Murata, and T. Yamashita, *Phys. Rev. Lett.* 88, 38301 (2002).
98. N. S. Xu and R. V. Latham, *J. Phys. D* 19, 477 (1986).
99. D. A. Vilson, Ph.D. Thesis, Aston University, UK, 1981.
100. M. Hirakawa, S. Sonoda, C. Tanaka, H. Murakami, and H. Yamakawa, *Appl. Surf. Sci.* 169–170, 662 (2001).
101. M. J. Fransen, Th. L. van Rooy, and P. Kruit, *Appl. Surf. Sci.* 146, 312 (1999); K. A. Dean, P. von Allmen, and B. R. Chalamala, *J. Vac. Sci. Technol. B* 17, 1959 (1999).
102. N. S. Xu, Y. Chen, S. Z. Deng, Jun Chen, J. C. Ma, and N. G. Wang, *Chin. Phys. Lett.* 18, 1278 (2001); N. S. Xu, Y. Chen, S. Z. Deng, J. Chen, J. C. Ma, and N. G. Wang, *J. Phys. D* 34, 1579 (2001).
103. R. Schlessler, R. Collazo, C. Bower, O. Zhou, and Z. Sitar, *Diamond Relat. Mater.* 9, 1201 (2000); Y. Saito, K. Hamaguchi, K. Hata, K. Tohji, A. Kasuya, Y. Nishina, K. Uchida, Y. Tasaka, and F. Ikazaki, *Ultramicroscopy* 73, 1 (1998); A. N. Obratsov, A. P. Volkov, and I. Pavlovsky, *Diamond Relat. Mater.* 9, 1190 (2000).
104. J. M. Bonard, J. P. Salvetat, T. Stockli, F. Forro, and A. Chatelain, *Appl. Phys. A* 69, 245 (1999).
105. O. M. Kuttel, O. Groening, C. Emmenegger, and L. Schlapbach, *Appl. Phys. Lett.* 73, 2113 (1999); M. Fransen, Ph.D. Thesis, Technical University Delft, 1999.
106. V. Filip, D. Nicolaescu, and O. Okuyama, *J. Vac. Sci. Technol. B* 19, 1016 (2001); V. Filip, D. Nicolaescu, and O. Okuyama, *Ultramicroscopy* 89, 39 (2001).
107. Ch. Adessi and M. Devel, *Phys. Rev. B* 62, R13314 (2000); Ch. Adessi and M. Devel, *Phys. Rev. B* 62, 7483 (2000); Ch. Adessi and M. Devel, *Ultramicroscopy* 85, 215 (2000).
108. S. D. Liang and N. S. Xu, *Appl. Phys. Lett.* 83, 1213 (2003).
109. L. W. Swanson and A. E. Bell, *Adv. Electron Electron Phys.* 32, 193 (1973).
110. J. Chen, S. Z. Deng, and N. S. Xu, *Appl. Phys. Lett.* 80, 3620 (2002).
111. J. Chen, S. Z. Deng, and N. S. Xu, *J. Appl. Phys.* 93, 1774 (2003).
112. Z. W. Pan, H. L. Lai, Frederick C. K. Au, X. F. Duan, W. Y. Zhou, W. S. Shi, N. Wang, C. S. Lee, N. B. Wong, S. T. Lee, and S. S. Xie, *Adv. Mater.* 16, 1186 (2000).
113. S. H. Wang and S. H. Yang, *Chem. Phys. Lett.* 332, 567 (2000).
114. S. H. Yang, unpublished.
115. N. Y. Hang, J. Chen, and N. S. Xu, unpublished.
116. H. J. Dai, E. W. Wong, Y. Z. Lu, S. S. Fan, and C. M. Lieber, *Nature* 375, 796 (1995).
117. W. Q. Han, S. S. Fan, Q. Q. Li, W. J. Liang, B. L. Gu, and D. P. Yu, *Chem. Phys. Lett.* 265, 374 (1997).
118. G. W. Meng, L. D. Zhang, C. M. Mo, S. Y. Zhang, Y. Qin, S. P. Feng, and H. J. Li, *J. Mater. Res.* 13, 2533 (1998).
119. X. T. Zhou, N. Wang, H. L. Lai, H. Y. Peng, I. Bello, and S. T. Lee, *Appl. Phys. Lett.* 77, 1287 (1999).
120. Z. L. Wang, Z. R. Dai, R. P. Gao, and Z. G. Bai, *Appl. Phys. Lett.* 77, 3349 (2000).
121. (a) S. Z. Deng, Z. S. Wu, Jun Zhou, N. S. Xu, J. Chen, and J. Chen, *Chem. Phys. Lett.* 364, 608 (2002). (b) Z. S. Wu, S. Z. Deng, J. Zhou, N. S. Xu, J. Chen, and J. Chen, *Appl. Phys. Lett.* 80, 3829 (2002).
122. A. M. Morales and C. M. Lieber, *Science* 279, 208 (1998).
123. R. Bryl and M. Altman, in “Technical Digest of the 15th IVMC and the 48th IFES,” Lyon, France, 2002, p. PM55.
124. Y. Li, X. Li, Z.-X. Deng, B. Zhou, S. Fan, J. Wang, and X. Sun, *Angew. Chem. Int. Ed.* 41, 333 (2002).
125. M. P. Zach, K. H. Ng, and R. M. Penner, *Science* 290, 2120 (2000).
126. M. P. Zach, K. Inazu, K. H. Ng, J. C. Hemminger, and R. M. Penner, *Chem. Mater.* 14, 3206 (2002).
127. N. S. Xu, J. Zhou, S. Z. Deng, and J. Chen, Chinese patent pending.
128. N. S. Xu, J. Zhou, S. Z. Deng, and J. Chen, Chinese patent pending.
129. J. C. She, S. E. Huq, S. Z. Deng, J. Chen, and N. S. Xu, *J. Vac. Sci. Technol. B* 19, 1059 (2001).
130. Y. Chen, S. Z. Deng, X. G. Zheng, and N. S. Xu, in “Technical Digest of the 12th IVMC,” Germany, 1999, p. 320.
131. N. S. Xu, Jian Chen, and S. Z. Deng, Chinese patent pending.
132. J. Chen, S. Z. Deng, J. Chen, Z. X. Yu, and N. S. Xu, *Appl. Phys. Lett.* 74, 3651 (1999).
133. Z. B. Li and N. S. Xu, *Ultramicroscopy* 95, 75 (2003).
134. C. Kimura, T. Yamamoto, S. Funakawa, M. Hirakawa, H. Murakami, and T. Sugino, in “Technical Digest of the 15th IVMC and the 48th IFES,” Lyon, France, 2002, p. OB3.03.
135. Y. Chen, Ph.D. Thesis, Zhongshan University, Guangzhou, China, 2002.
136. G. Pirio, P. Legagneux, D. Pribat, K. B. K. Teo, M. Chhowalla, G. A. J. Amaratunga, and W. I. Milne, *Nanotechnology* 13, 1 (2002).
137. V. I. Merkulov, M. A. Guillorn, D. H. Lowndes, M. L. Simpson, and E. Voekl, *Appl. Phys. Lett.* 79, 1178 (2001).
138. M. A. Guillorn, A. V. Melechko, V. I. Mevkulov, D. K. Hensley, M. L. Simpson, and D. H. Lowndes, *Appl. Phys. Lett.* 81, 3660 (2002); M. A. Guillorn, A. V. Melechko, V. I. Mevkulov, E. O. Ellis, C. L. Britton, M. L. Simpson, and D. H. Lowndes, *Appl. Phys. Lett.* 79, 2506 (2001).

139. J. Shaw and J. Itoh, in "Vacuum Microelectronics," Ch. 5. Wiley, New York, 2001.
140. M. Ding, H. Kim, and A. I. Akinwande, *IEEE Electron Device Lett.* 21, 741 (2000).
141. D. Temple, H. F. Gray, C. A. Ball, J. E. Mancusi, W. D. Dalmer, G. E. McGuire, and J. L. Shaw, in "Technical Digest of the 8th IVMC," Portland, OR, 1995, p. 113.
142. R. B. Marcus and T. T. Sheng, *J. Electrochem. Soc.* 129, 1278 (1982).
143. W. P. Kang, A. Wisitorsa-at, J. L. Davidson, M. Howell, D. V. Kevus, Q. Li, and F. Xu, *J. Vac. Sci. Technol. B* 17, 740 (1999).
144. E. R. Holland, M. T. Harrison, M. Hung, and P. R. Wilshaw, *J. Vac. Sci. Technol. B* 17, 580 (1999).
145. Y. Li, E. R. Holland, and P. R. Wilshaw, in "Technical Digest of the 12th IVMC," Darmstadt, Germany, 1999, p. 125.
146. Y. Li, E. R. Holland, and P. R. Wilshaw, in "Technical Digest of the 13th IVMC," Guangzhou, China, 1999, p. 86.
147. R. C. Furneaux, W. R. Rigby, and A. P. Davidson, *Nature* 337, 147 (1989).
148. W. R. Ridby, D. R. Cowieson, N. C. Davies, and R. C. Fuineaux, *Trans. Inst. Metal. Finish* 68, 95 (1990).
149. B. Gunther, A. Gohl, and G. Muller, in "Technical Digest of the 13th IVMC," Guangzhou, China, 2000, p. 207.
150. F. Kaldasch, B. Gunther, G. Muller, J. Engstler, and J. J. Schneider, in "Technical Digest of the 14th IVMC," Davis, CA, 2001, p. 25.
151. Q. B. Wu, S. Z. Deng, Jun Chen, J. C. She, and N. S. Xu, in "Technical Digest of the 15th IVMC and the 48th IFES," Lyon, France, 2002, p. PT47.
152. T. H. P. Chang, D. P. Kern, and L. P. Muiay, *J. Vac. Sci. Technol. B* 10, 2743 (1992).
153. L. P. Muray, J. P. Spallas, C. Steller, K. Lee, M. Mankos, Y. Hsn, M. Gmur, and T. H. P. Chang, *J. Vac. Sci. Technol. B* 18, 3099 (2000).
154. Vu. Thein Binh, V. Semet, D. Guillot, P. Legagueus, and D. Pribat, *Appl. Phys. Lett.* 73, 2048 (1998).
155. D. Gibson, Ultra-high density storage device, U.S. Patent 5, 557, 596.
156. S. T. Lam, in "Technical Digest of the 14th IVMC," Davis, CA, 2001, p. 135.
157. M. Nanba, T. Yamagishi, S. Okazaki, K. Tanioka, N. Egami, and F. Sato, *Tech. Rep. IEICE* 96, 13 (1996).
158. M. Nanba, T. Yamagishi, S. Okazaki, K. Tanioka, K. Takayama, M. Tanaka, and S. Itoh, *Tech. Rep. IEICE* 97, 19 (1997).
159. N. Egami, K. Goto, M. Nanba, and S. Okazaki, *Tech. Rep. IEICE* 94, 1 (1994).
160. H. Chen, M. Nakanishi, T. Shimojo, and M. Migitaka, in "Technical Digest of the 10th IVMC," Kyongju, Korea, 1997.
161. M. Ynmura and S. Ohshima, *Diamond Relat. Mater.* 8, 785 (1999).
162. S. Z. Deng, F. Qian, J. Chen, and N. S. Xu, in "Proc. of the 46th IFES," Pittsburgh, 2001.
163. J. Chen, S. Z. Deng, and N. S. Xu, *Ultramicroscopy* 95, 81 (2003).
164. S. Z. Deng, F. Qian, N. S. Xu, and J. Chen, *Ultramicroscopy* 89, 123 (2001).
165. N. S. Lee, J. H. Kang, W. B. Choi, Y. S. Choi, Y. J. Park, H. Y. Kim, Y. J. Lee, D. S. Chung, J. E. Jung, C. J. Lee, J. H. Kim, J. H. You, S. H. Jo, C. G. Lee, and J. M. Kim, in "Technical Digest of the 13th IVMC," Guangzhou, China, 2000, p. 193.
166. C. G. Lee, S. J. Lee, S. H. Jo, J. S. Lee, T. H. Yun, B. G. Lee, J. C. Cha, H. S. Han, S. H. Ahn, K. W. Jung, H. Y. Kim, B. C. Yun, S. M. Park, J. S. Choi, T. S. Oh, S. K. Kang, J. M. Kim.

Visible-Light-Sensitive Photocatalysts

Hiroshi Yamashita, Masato Takeuchi, Masakazu Anpo

*Osaka Prefecture University, Gakuen-cho, Sakai,
Osaka, 599-8531, Japan*

CONTENTS

1. Introduction
 2. Modification of Titanium Oxide (TiO₂)
 3. Mixed Oxides
 4. Zeolite Photocatalysts
 5. Conclusions
- Glossary
References

1. INTRODUCTION

The design of highly efficient and selective photocatalytic systems that can work in the reduction of global air and water pollution is of vital interest [1–25]. Figure 1 shows the solar beam spectrum observed on the earth and Table 1 shows the bandgap energy of several semiconductor photocatalysts. Although several photocatalysts have a bandgap energy small enough to absorb visible light, most of these photocatalysts are not stable or show very small reactivity. Especially, the modified WO₃ and CdS semiconductors are well known as photocatalysts that can operate under visible light, even though they are not stable and have small reactivity [26–41]. On the other hand, sensitization using dye molecules loaded on semiconductor photocatalysts has been successfully and widely applied to utilize solar energy. Although this dye-sensitized system has been developed to be utilized as a Graetzel cell, which can convert solar energy to electronic energy efficiently and directly, the dye molecules are not stable when this system is applied as a photocatalyst under environmental conditions [42–69]. Instead of photocatalysis using semiconductors, it has been reported that some organic compounds and polymers can exhibit photocatalytic reactivity under visible-light irradiation [70–73].

Among semiconductor photocatalysts, the TiO₂ semiconductor is very reactive and stable [1–25, 74–89]. Although utilization of the TiO₂ semiconductor as a photocatalyst has recently attracted a great deal of attention, it can only absorb and utilize ultraviolet (UV) light shorter than 400 nm. The design and development of photocatalysts that

can absorb and utilize visible light are urgent demands and have been hot topics in the research field on photocatalysis for many years.

To design photocatalysts that can operate under visible-light irradiation, modification of the electronic structure of the photocatalysts is indispensable. The following three approaches should be considered to control the electronic structure of semiconducting photocatalysts: (1) modification of the electronic structure by a metal ion implantation [90–99] or metal doping [100–115]; (2) formation of a new valence band instead of O(2p) by the addition of proper atoms [116–132]; and (3) design and modification of the band structure by the formation of solid solutions [133–135]. To design a visible-light-sensitive photocatalyst, metal ion implantation [90–99], plasma irradiation [136–138], metal ion doping [110–115], anion doping [125–132], and the formation of new binary oxides [116–124] and solid solutions [133–135] have been applied. In this review we summarize, these recent applications for the design of visible-light-sensitive photocatalysts.

2. MODIFICATION OF TITANIUM OXIDE (TiO₂)

The utilization of the TiO₂ semiconductor as a photocatalyst has recently attracted a great deal of attention, especially for various environmental applications [1–25, 74–89]. Although TiO₂ is known as one of the most stable and highly reactive photocatalysts, a new concept for the design of a unique photocatalytic system that can operate efficiently not only under UV-light irradiation but also under visible-light irradiation should be developed.

2.1. Physical Process (Dry Process)

2.1.1. Metal Ion Implantation

Ion beam technology using accelerated metal ions has recently been used to design a unique TiO₂ photocatalyst, realizing a breakthrough in the development of an efficient photocatalytic system and the utilization of solar-light energy [90–99, 139–143]. Metal ions are electronic charged atoms

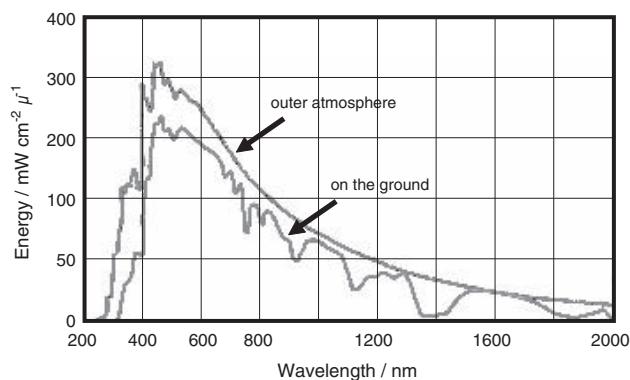


Figure 1. Spectrum of the solar energy observed on earth.

whose kinetic energies can be controlled by the acceleration of metal ions under a controlled electronic field. The ion beam techniques, such as the ion implantation method and the ionized cluster beam (ICB) method, use the accelerated metal ion beam generated by applying the unique properties of metal ions [90–99, 139–143]. By these methods, the metal ions are accelerated in the electronic field and injected into the sample target as an ion beam (Fig. 2). These metal ions can interact in a different manner with the sample target depending on their kinetic energy. In the case of the ion implantation method, metal ions are accelerated enough to have a high kinetic energy (50–200 keV) and can be implanted into the bulk of samples [90–99]. On the other hand, the metal ions (ionized clusters) are accelerated to have a low kinetic energy (0.2–2 keV) in the ICB method and these ions are deposited to form a thin film on the top surface of the sample [139–143]. With these unique properties of the ion beam techniques, well-defined semiconductor materials and thin films have been developed [90–99, 139–143]. Recently, the ion implantation method and the ICB method have been used to prepare an efficient TiO₂ photocatalyst and realize the utilization of visible light. The photocatalytic properties of these unique TiO₂ photocatalysts for the purification of water and air have been investigated.

Metal-Ion-Implanted TiO₂ Semiconductor Powder

TiO₂ photocatalysts cannot absorb visible light and only make use of 3–5% of the solar beams that reach the earth, necessitating the utilization of an ultraviolet-light source.

Table 1. Bandgap energy of semiconductor photocatalysts.

Semiconductor	Bandgap (eV)	Wavelength (nm)	Energy (kcal/mol)
SnO ₂	3.8	326	87.7
ZnS	3.6	344	83.1
ZnO	3.2	388	73.8
WO ₃	3.2	388	73.8
TiO ₂	3.2	388	73.8
SrTiO ₃	3.2	388	73.8
SiC	3.0	413	69.2
CdS	2.5	496	57.7
Fe ₂ O ₃	2.3	539	53.1
GaP	2.25	551	51.9
CdSe	1.7	730	39.2

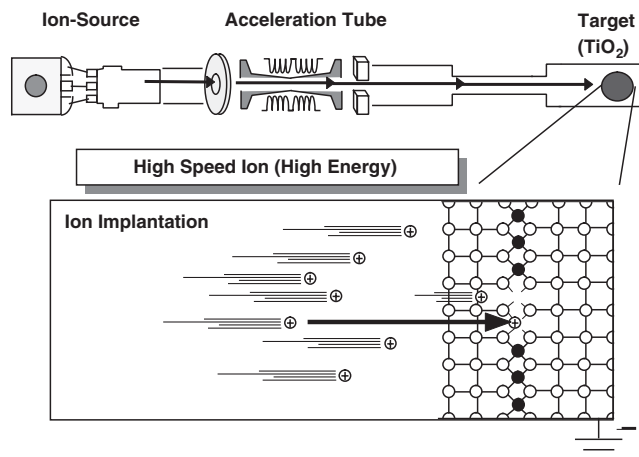


Figure 2. Schematic diagram of the ion beam techniques; metal ion implantation (high-speed ion).

It is, therefore, necessary to develop a modified TiO₂ photocatalytic system that can be applied under visible-and/or solar-light irradiation. Recently, using the advanced metal ion implantation technique, a visible-light-sensitive metal-ion-implanted TiO₂ was developed [90–99]. As shown in Figure 3, the absorption band of the TiO₂ (anatase) implanted with V ions by the ion implantation method with high acceleration energy (150 keV) and calcined in O₂ at 725 K after ion implantation has been found to shift to the visible-light region, the extent depending on the amount of V ions implanted. The V ions implanted within the bulk of TiO₂ can modify the electronic properties of the TiO₂ surface layer. Ion implantation with the other transition metal ions such as Cr, Mn, Fe, and Co is also effective for modifying the properties of TiO₂ to make a large shift in the absorption band to the visible-light region. It can be expected that photocatalytic reactions could be observed under visible-light irradiation on these metal-ion-implanted TiO₂ catalysts. On the other hand, metal-ion (Cr, V)-doped TiO₂ prepared chemically by the impregnation and the sol-gel method could make no shift in the adsorption band of TiO₂. These modifications of the electronic properties of TiO₂ have been made in different ways, depending on the methods of metal ion doping, and metal ion implantation

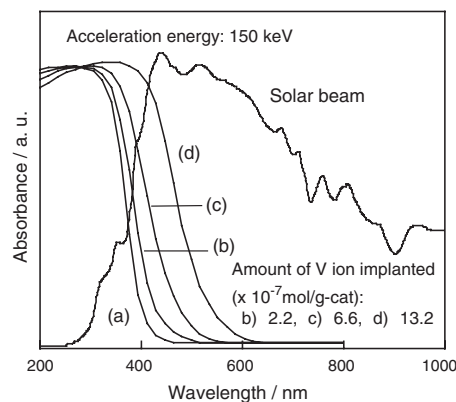


Figure 3. UV-vis spectra of the TiO₂ (a) and the V-ion-implanted TiO₂ (b–d) and the solar spectrum reaching the earth.

is the only smart technique to realize the redshift of the adsorption band of TiO_2 to the visible-light region.

The secondary-ion mass spectrometry (SIMS) analysis of the depth concentration profile of the Cr ions in the Cr-ion-implanted TiO_2 photocatalyst where ion implantation was performed at 150 keV indicated that most Cr ions were implanted within the bulk of the TiO_2 photocatalyst. The deeper the ions were implanted in the bulk of the TiO_2 , the larger the increase in the acceleration energy. Furthermore, X-ray photoelectron spectroscopy (XPS) measurements of the catalysts did not show any evidence of the presence of Cr ions on the TiO_2 surface, indicating that Cr ions are highly dispersed within the bulk of TiO_2 but not on the surface. The use of the metal ion implantation method to modify the bulk electronic properties of TiO_2 photocatalysts without any change in the structure and properties of the top surface of the TiO_2 can be considered as one of the most significant advantages. Usually, the chemical-doped metal ions often work as electron-hole recombination centers to decrease the photocatalytic reactivity. Under UV-light irradiation ($\lambda < 380$ nm), the photocatalytic reactivity for the NO decomposition and the degradation of organic compounds on the metal-ion-implanted TiO_2 is similar to the un-implanted original TiO_2 photocatalyst, indicating that the implanted metal ions do not work as the electron-hole recombination center in the metal-ion-implanted photocatalysts.

Figure 4 shows the time profiles of the photocatalytic decomposition of NO into N_2 , O_2 , and N_2O on the Cr-ion-implanted TiO_2 catalysts under UV-light irradiation ($\lambda > 450$ nm). Visible-light irradiation of the Cr-ion-implanted TiO_2 in the presence of NO at 275 K leads to the direct decomposition of NO into N_2 , O_2 , and N_2O with a good linearity to the irradiation time. The liquid-phase photocatalytic degradation of 2-propanol diluted in water into acetone, CO_2 , and H_2O also proceeded on the V-ion-implanted TiO_2 catalysts under visible-light irradiation ($\lambda > 450$ nm). Under the same conditions of visible-light irradiation, these photocatalytic reactions do not proceed on the un-implanted

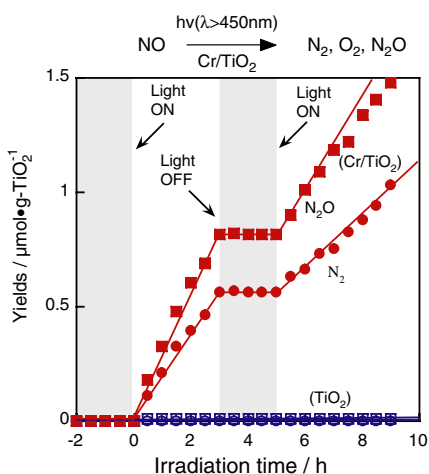


Figure 4. Reaction time profiles of the photocatalytic decomposition of NO into N_2 and N_2O on the Cr-ion-implanted TiO_2 photocatalyst prepared by metal ion implantation under visible-light ($\lambda > 450$ nm) irradiation.

original TiO_2 photocatalyst. Thus, it can be seen that the implantation of metal ions is the determining factor in the use of visible light.

Figure 5 shows the effect of the acceleration energy applied in the ion implantation process and the amount of implanted metal ions on the photocatalytic reactivity for the NO decomposition on the V-ion-implanted TiO_2 photocatalyst under visible-light irradiation. As shown in Figure 5A, with the same amounts of V ion implanted, more efficient photocatalytic reactivity can be observed on the photocatalyst with V ions implanted with a higher acceleration energy within the range investigated. Metal ion implantation within the deeper bulk of the TiO_2 photocatalyst by the higher accelerated energy seems to be suitable for realizing more efficient photocatalytic reactivity under visible-light irradiation. The results in Figure 5B indicate that increasing the amounts of V ions implanted into the deep bulk of the TiO_2 causes an increase in the photocatalytic reactivity under visible-light irradiation, having a maximum at around $0.66 \mu\text{mol} \cdot \text{TiO}_2^{-1}$, and then a decrease with an excess amount of V ions implanted. These results indicate that there is an optimal condition in the depth and amount of implanted metal ions to achieve efficient photocatalytic reactivity under visible-light irradiation.

The field work experiments have been carried out to investigate the photocatalytic reactivity of the metal-ion-implanted TiO_2 photocatalyst under outdoor solar beam irradiation, and the results for the photocatalytic decomposition of NO diluted in air atmosphere are shown in Figure 6. Under outdoor solar beam irradiation, the Cr- and V-ion-implanted TiO_2 photocatalysts show about three times higher photocatalytic reactivity than the un-implanted original TiO_2 photocatalyst. These results clearly show that the application of the metal ion implantation method can realize a photocatalytic system that can utilize visible- and solar-light energy efficiently.

Metal-Ion-Implanted TiO_2 Thin Film TiO_2 thin films prepared mainly by the sol-gel method have been utilized in many fields applying not only their photocatalytic properties but also antibacterial and superhydrophilic properties [2, 21]. It has been desired to develop TiO_2 thin films having efficient photocatalytic reactivity and high mechanical stability in being supported on various substrates in any desired form. Using an ionized cluster beam (ICB) method

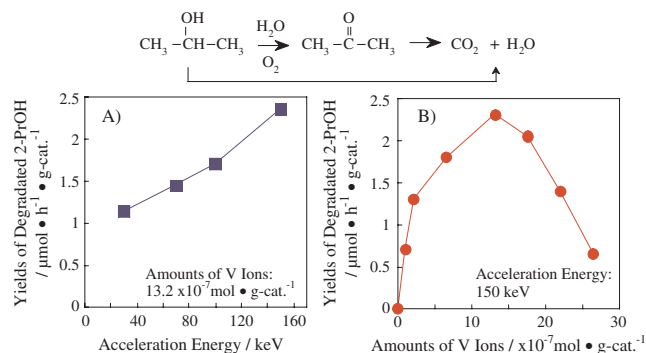


Figure 5. Effects of the acceleration energy (A) and the amount of implanted ions (B) on the reactivity of V-ion-implanted TiO_2 for the photocatalytic degradation of 2-propanol diluted in water.

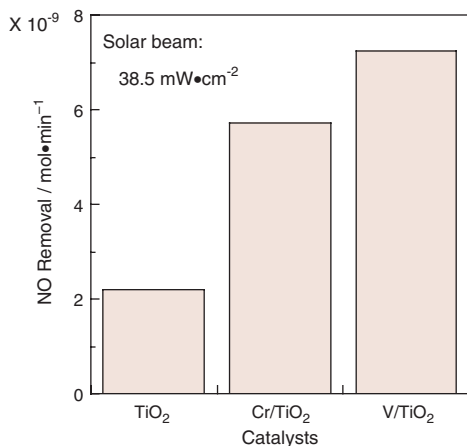


Figure 6. Photocatalytic decomposition of NO on the un-implanted original TiO₂ and the V- and Cr-ion-implanted TiO₂ photocatalysts under outdoor solar beam irradiation.

with low acceleration energy (0.2–2 keV), efficient TiO₂ thin-film photocatalysts can be prepared on various types of substrates such as porous glass plate and activated carbon fiber under mild and dry conditions [139–143]. In the ICB method, the Ti cluster beam is produced by ejecting the Ti vapor ionized by the electrons emitted from the ionization filament and accelerating the produced ionized clusters by an accelerating electrode. Active TiO₂ thin films were produced by impingement of the ionized clusters and oxygen gas onto the support substrate. The advantages of using the ICB method are (1) no contamination because of the dry process in high vacuum, (2) production of highly crystalline films on various substrates without calcination, and (3) well-controlled thickness.

Characterization of these films by means of ultraviolet-visible (UV-vis), X-ray absorption fine structure (XAFS) spectroscopy, scanning electron microscopy (SEM), X-ray diffraction (XRD), and XPS techniques showed that the TiO₂ in transparent thin films having a well-crystallized structure mainly in the anatase phase could be formed on a silica glass plate (PVG) by the ICB method. This TiO₂ thin film also exhibited efficient reactivity for the photocatalytic decomposition of NO into N₂ and O₂ under UV irradiation. The photocatalytic properties and physical properties of the TiO₂ thin films are dependent on the film thickness, and higher reactivity can be observed on the thinner TiO₂ films. TiO₂ thin films prepared on the silica glass plate exhibit higher photocatalytic reactivities than TiO₂ powder and catalysts prepared by the conventional impregnation method. Furthermore, UV irradiation of the TiO₂ thin films in a diluted aqueous solution of propanol, dichloroethane, or phenol led to the efficient decomposition of these organic pollutants finally into CO₂, H₂O, and HCl. These results have clearly shown that the ICB method is useful in the preparation of transparent TiO₂ thin films having efficient photocatalytic reactivity.

To improve the electronic properties of the TiO₂ thin films to absorb visible light, metal ions (V or Cr ions) were implanted into the TiO₂ thin films at high energy acceleration (150 keV) using metal ion implantation. As shown in Figure 7, the UV-vis absorption spectra of these

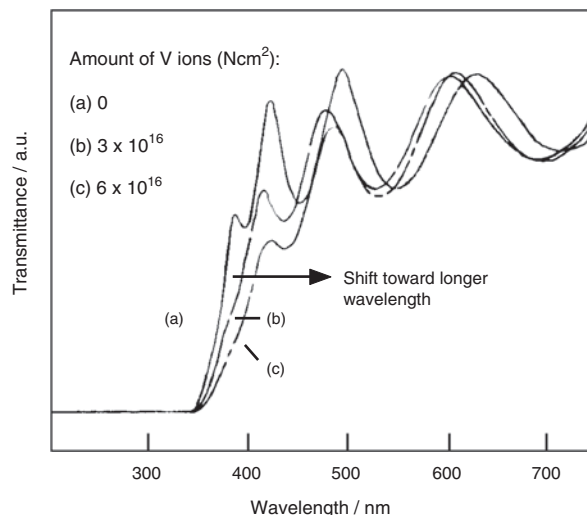


Figure 7. UV-vis spectra (transmittance) of the V-ion-implanted TiO₂ thin-film photocatalysts.

metal-ion-implanted TiO₂ thin films were found to shift toward the visible-light region, depending on the amount of metal ions implanted. They were found to exhibit an effective photocatalytic reactivity for the liquid-phase degradation of propanol diluted in water (Fig. 8) and the decomposition of NO into N₂ and O₂ at 295 K under visible-light ($\lambda > 450$ nm) irradiation, while the un-implanted original TiO₂ thin film does not exhibit reactivity. It was clearly demonstrated that the application of such ion beam techniques as the ICB method and metal ion implantation can allow us to prepare TiO₂ thin films that can work effectively under visible-light irradiation.

Using the transparent TiO₂ thin film, which can operate under visible-light and solar beam irradiation, many innovative solutions can be applied to environmental problems (Fig. 9).

Mechanism in the Metal-Ion-Implanted TiO₂ Metal ion implantation is very effective in modifying TiO₂ semiconductor powder and thin film to absorb and utilize visible light. The local structure of implanted metal ions and their role in the modification of the electronic state of TiO₂ have been investigated using various spectroscopic techniques.

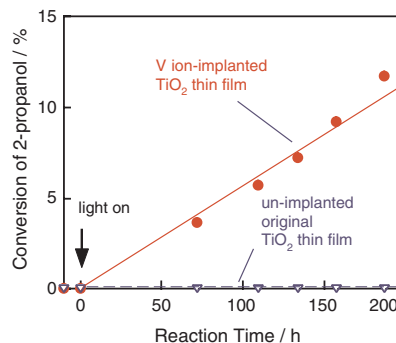


Figure 8. Reaction time profiles of photocatalytic degradation of 2-propanol on the V-ion-implanted TiO₂ thin-film photocatalysts under visible-light irradiation ($\lambda > 450$ nm).

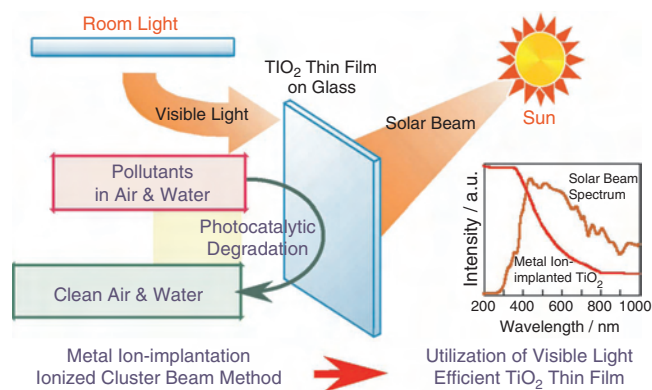


Figure 9. The visible-light-sensitive transparent TiO₂ thin film can provide many innovative solutions to environmental problems.

Figure 10 shows the depth concentration profile of the V ions in the V-ion-implanted TiO₂ thin film deposited on glass plate where ion implantation was performed at 150 keV. Most V ions were implanted within the bulk of the TiO₂ thin films, and the deeper the ions were implanted in the bulk of the TiO₂, the larger the increase in the acceleration energy. XPS measurements of the catalysts did not show any evidence of the presence of implanted metal ions on the TiO₂ surface, indicating that implanted metal ions are highly dispersed within the bulk of TiO₂ but not on the top surface. The use of metal ion implantation to modify the bulk electronic properties of TiO₂ without any change in the structure and properties of the top surface of the TiO₂ can be considered as one of the most significant advantages. On the other hand, metal-ion (Cr, V)-doped TiO₂ prepared chemically by the impregnation and the sol-gel method could make no shift in the adsorption band of TiO₂. These modifications of electronic properties of TiO₂ have been made in different ways, depending on the methods of metal ion doping, and metal ion implantation is the smartest technique to modify TiO₂ to absorb visible light.

Figure 11 shows the XAFS [X-ray absorption near-edge spectroscopy (XANES) and Fourier transform extended X-ray absorption fine structure (FT-EXAFS)] spectra of the Cr-ion-implanted TiO₂ thin film. The analysis of these spectra indicates that in the Cr-ion-implanted TiO₂ the Cr ions

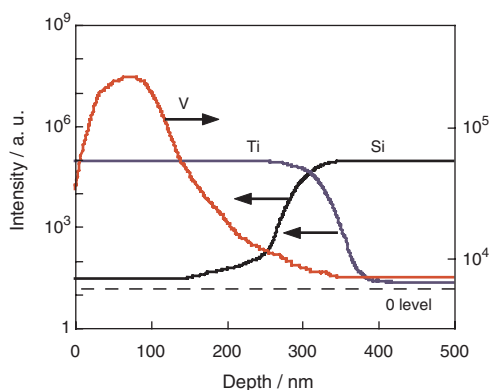


Figure 10. Depth concentration profile of V ions obtained from SIMS measurements with the V-ion-implanted TiO₂ thin film.

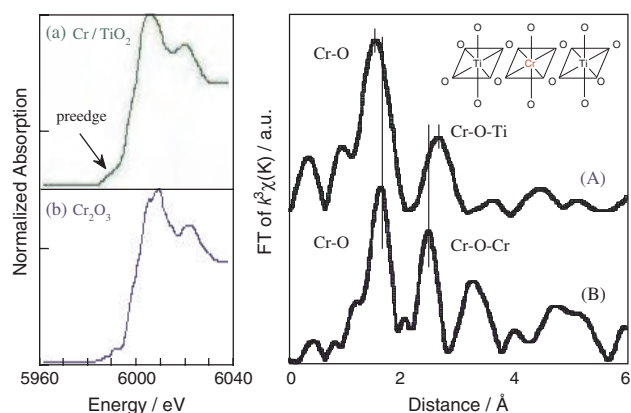


Figure 11. XANES (a, b) and Fourier transforms of EXAFS (A, B) of the Cr-ion-implanted TiO₂ thin film after calcination at 723 K (a, A) and Cr₂O₃ (b, B) as a reference.

are highly dispersed in the lattice of TiO₂ having octahedral coordination. These Cr ions are isolated and substituted with Ti⁴⁺ ions in the lattice positions of the TiO₂. On the other hand, the Cr-doped TiO₂ catalysts chemically prepared by impregnation as well as by the sol-gel method were found to have a mixture of the aggregated Cr oxides having tetrahedral coordination similar to CrO₃ and octahedral coordination similar to Cr₂O₃ [144–147]. Figure 12 shows the electron spin resonance (ESR) spectra of the V-ion-implanted TiO₂ powder catalysts measured before and after calcination in O₂. Distinct signals, which can be assigned to the reticular V⁴⁺ ions, were detected only after calcination at around 723–823 K. These signals due to the reticular V⁴⁺ ions have been observed only with the metal-ion-implanted TiO₂ catalyst after calcination and can exhibit an efficient redshift in their absorption band. On the other hand, the ESR signals assignable to the reticular V ion have never been observed with V-ion-doped TiO₂ prepared chemically by impregnation as well as by the sol-gel method.

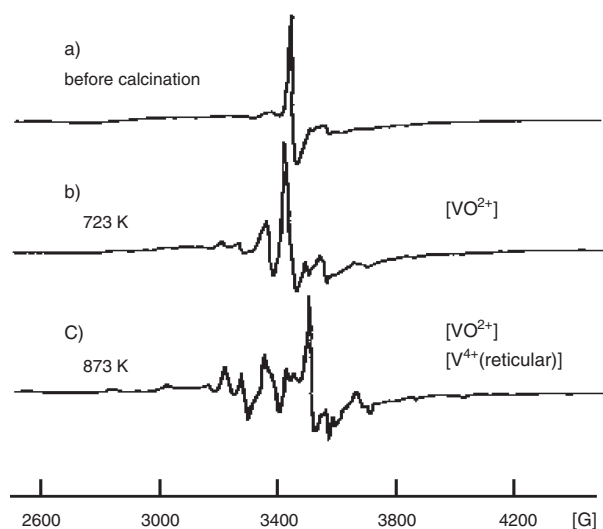


Figure 12. ESR spectra of the V-ion-implanted TiO₂ photocatalysts before calcination (a) and after calcination in O₂ at 723 K (b) and 873 K (c).

These spectroscopic investigations suggest that the substitution of octahedrally coordinated Ti ions in the bulk TiO₂ lattice with implanted metal ions is important for modifying TiO₂ to be able to adsorb visible light and operate as an efficient photocatalyst under visible- and/or solar-light irradiation. To prove this mechanism is induced by metal ion implantation, a theoretical approach using the *ab initio* molecular orbital calculation on the basis of the density functional theory method has been carried out. Because of the capacity of the calculation, the binuclear cluster models having an octahedral coordination similar to the coordination of TiO₂ have been applied. In these cluster models, the metal ions having various electric charges (V⁵⁺, V⁴⁺, V³⁺) are substituted for the Ti⁴⁺ ion octahedrally coordinated in the lattice position of TiO₂ [94]. As shown in Figure 13, the models having V⁴⁺ ions <Ti⁴⁺-V⁴⁺> and V³⁺ ions <Ti⁴⁺-V³⁺> can have an energy gap of Ti(d)-O(d), smaller than that of un-implanted pure Ti oxide <Ti⁴⁺-Ti⁴⁺>. The overlap of Ti(d) and V(d) orbitals is observed with these models. These results indicate that the mixing of the Ti(d) orbital of the Ti oxide and the metal(d) orbital of the implanted metal ions in the low electric charge is essential to decrease the energy gap between the Ti(d) and O(p) orbitals of the Ti oxide. Considering this mechanism, it can be proposed that in the metal-ion-implanted TiO₂ the overlap of the conduction band due to the Ti(d) of TiO₂ and the metal(d) orbital of the implanted metal ions can decrease the bandgap of TiO₂, enabling it to absorb visible light (Fig. 14). The present results indicate that the substitution of Ti ions with the isolated metal ions implanted into the lattice position of the bulk of TiO₂ (Fig. 15) is the determining factor for the utilization of visible light and solar beam.

2.1.2. Magnetron Sputtering

Although the combination of the ICB method and the metal ion implantation method can be applied to prepare TiO₂ thin films that can operate under visible light, it requires

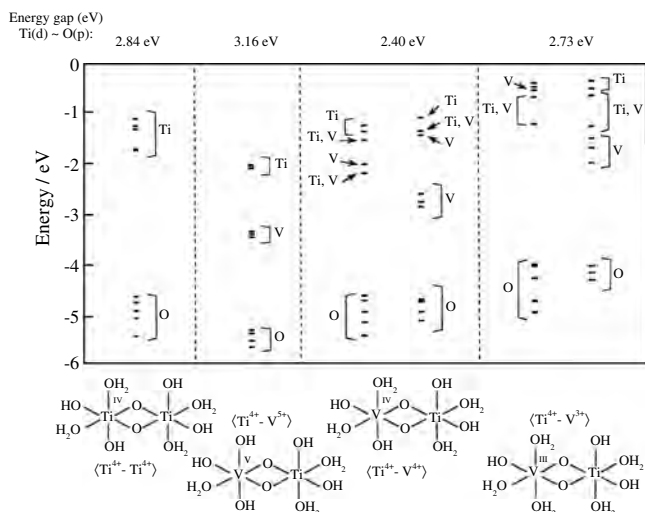


Figure 13. Energy level of higher lying molecular orbital obtained by the *ab initio* molecular orbital calculations with the cluster models of the V-ion-implanted TiO₂ photocatalyst.

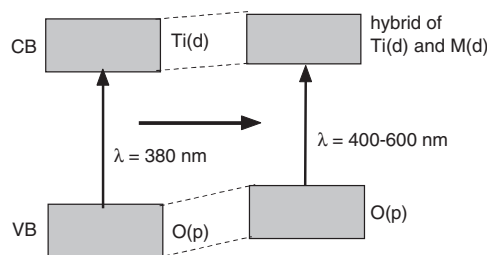


Figure 14. Energy diagram of TiO₂ and metal-ion-implanted TiO₂.

two processes. Recently, it has been found that visible-light-sensitive TiO₂ thin-film photocatalysts can be prepared using a conventional RF magnetron sputtering (RF-MS) deposition method [148]. This is an alternative and more practical preparation method that has been successfully applied to create TiO₂ thin-film photocatalysts that can initiate various significant reactions effectively under visible-light irradiation. In the preparation of TiO₂ thin films using a conventional RF-MS deposition apparatus (Fig. 16), a TiO₂ plate with a rutile structure was used as the source material (sputtering target). Moreover, only Ar was used as the sputtering gas without the coexisting O₂ as the reactive gas in the process chamber. The sputtered particles, such as Ti⁴⁺ and O²⁻, were accumulated on the substrate surface to form the TiO₂ thin films.

Figure 17 shows the UV-vis absorption spectra of the TiO₂ thin films prepared by the RF-MS deposition method with different substrate temperatures. The thin film deposited at 373 K shows high transparency and interference fringes, indicating that stoichiometric and uniform TiO₂ thin films can be prepared. As the substrate temperature is increased, the thin films become more efficient in absorbing visible light. These results clearly indicate that only TiO₂ thin-film photocatalysts that have undergone a modification of their electronic properties are actually able to utilize visible light for some photocatalytic reactions.

UV-light ($\lambda > 270$ nm) irradiation of the TiO₂ thin films in the presence of NO was found to initiate the photocatalytic decomposition of NO into N₂, O₂, and N₂O. The higher the preparation temperatures, the lower the photocatalytic reactivity observed under UV-light irradiation. This is due to the fact that the thin films prepared at relatively lower temperatures are highly transparent and are able to utilize the incident light more efficiently. On the other hand, TiO₂ thin films prepared at relatively higher temperatures (~873 K) exhibited a slightly yellow coloring. This is clear evidence of the efficient absorption of visible light. Visible-light

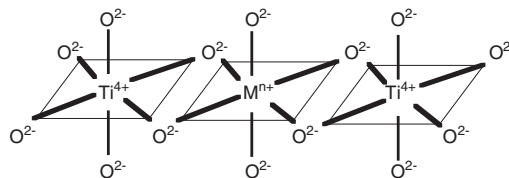


Figure 15. Local structure of metal-ion-implanted TiO₂. Implanted metal ions Mⁿ⁺ (Cr³⁺-Cr⁴⁺, V³⁺-V⁴⁺) are highly dispersed and isolated in the TiO₂ matrix and substituted with octahedrally coordinated lattice Ti⁴⁺ with a low oxidized state.

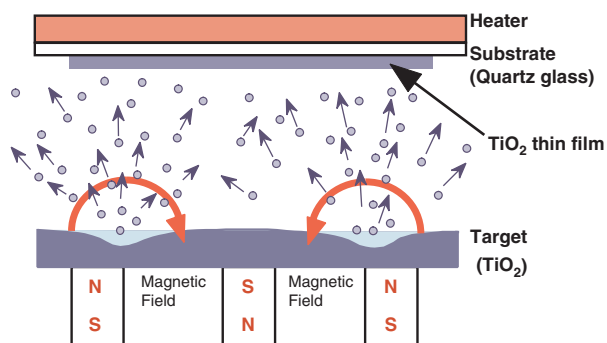


Figure 16. Schematic diagram of an RF magnetron sputtering deposition method.

($\lambda > 450$ nm) irradiation of these TiO_2 thin films in the presence of NO was found to initiate the decomposition of NO into N_2 , O_2 , and N_2O . As the deposition temperature increases, the photocatalytic reactivity under visible-light irradiation became higher, reaching a maximum at 873 K. Moreover, the order of the photocatalytic reactivity under visible-light irradiation corresponds to that of the relative intensity at 450 nm in the UV-vis absorption spectra of these catalysts (Fig. 18). These results clearly show that TiO_2 thin films prepared at relatively higher temperatures (~ 873 K) can work as effective photocatalysts that can absorb and operate efficiently under visible-light irradiation. With this RF-MS technique, TiO_2 with a shortage of lattice oxygen was produced in the bulk of the thin film, which can induce the absorption of visible light.

2.1.3. Plasma Irradiation

It has been reported that the reduction of TiO_2 by hydrogen plasma treatment creates a new absorption band in the visible-light region and is expected to create photocatalytic activity under visible-light irradiation. The TiO_2 semiconductor powder, which has photocatalytic activity in the UV-light region, was treated using microwave and radiofrequency (RF) plasmas [136–138]. The TiO_2 was reduced, thus having an oxygen deficiency. The RF-plasma-treated TiO_2 absorbed visible light between 400 and 600 nm and showed a photocatalytic reactivity in this region, as measured by the

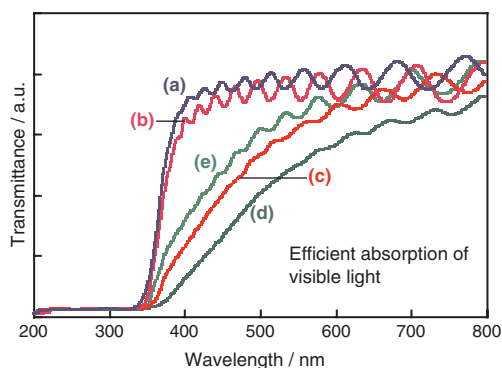


Figure 17. UV-vis absorption (transmittance) spectra of TiO_2 thin films prepared by an RF-MS deposition method. Preparation temperatures (K): (a) 373, (b) 473, (c) 673, (d) 873, (e) 973.

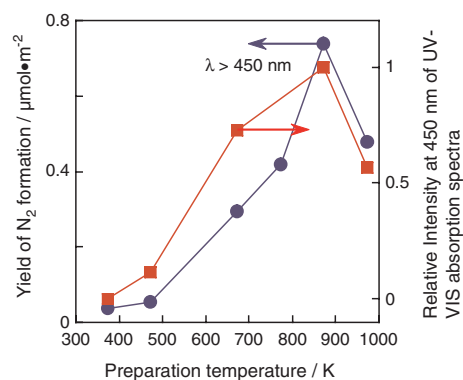


Figure 18. Effects of preparation temperatures on the photocatalytic reactivities for the decomposition of NO under visible-light irradiation and the relative intensity at 450 nm in the UV-vis absorption spectra.

oxidative removal of NO_x from the gas phase. The plasma-treated TiO_2 , which can be easily produced on a large scale, is expected to have a higher efficiency in utilizing solar energy than the raw TiO_2 material.

On the other hand, several researchers have reported that Pt-loaded TiO_2 photocatalysts prepared by a chemical loading method such as conventional impregnation exhibited photocatalytic reactivity for the degradation of organic compounds under visible-light irradiation [154–160]. In these catalysts, the loaded Pt can partially reduce the TiO_2 to generate the lattice oxygen defects, which are similar to those generated by plasma irradiation. Although the detailed mechanism on the absorption of visible light has not been clarified yet, the oxygen defects are probably responsible for the absorption and utilization of visible light.

2.2. Chemical Process

2.2.1. Metal-Doped TiO_2 and ZnS

Photocatalytic water splitting is regarded as artificial photosynthesis. Since the Honda–Fujishima effect using a TiO_2 electrode was discovered, numerous researchers have extensively studied water splitting using semiconductor photocatalysts. Several photocatalysts with wide bandgaps, such as $\text{NiO}_x\text{-Ta}_2\text{O}_5$, $\text{NiO}_x\text{-K}_4\text{Nb}_6\text{O}_{17}$, $\text{NiO-K}_2\text{La}_2\text{Ti}_3\text{O}_{10}$, and NaTaO_3 , have been reported to be highly active for splitting water into H_2 and O_2 under UV irradiation [149–153]. Even in the presence of sacrificial reagents, the well-known photocatalysts that are active under visible-light irradiation are only Pt/CdS for H_2 evolution and WO_3 for O_2 evolution [26–41]. Some modified layered compounds, such as Pt-RbPb₂Nb₃O₁₀ and CdS-K₄Nb₆O₁₇, have also been reported to show photocatalytic reactivity to some extent even under visible-light irradiation [150, 151].

Transition metal ion doping has been applied by many researchers to modify the electronic structure of photocatalysts to utilize visible light. The doping of a foreign element into an active photocatalyst with a wide bandgap to make a donor or an acceptor level in the forbidden band is one of the ways to develop a new visible-light-sensitive photocatalyst (Fig. 19). There are many reports that metal-ion-doped photocatalysts, such as TiO_2 , SrTiO_3 , and ZnS, can absorb and utilize visible light. In particular, the effects of doping of Cr ions into TiO_2 and SrTiO_3 on the photocatalytic

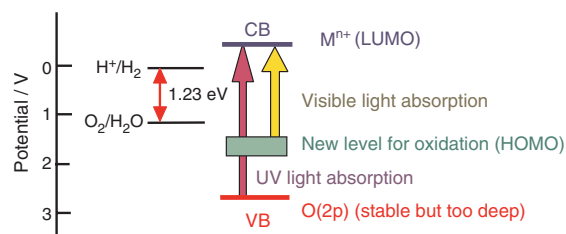


Figure 19. Modified band structure of visible-light-sensitive photocatalysts.

reaction have been widely studied. Although it is easy to put the color to the semiconducting photocatalyst by metal ion doping, in most cases the doped metal ions operate as charge recombination centers, which leads to a decrease in the photocatalytic reactivity.

It has recently been found that TiO₂ and SrTiO₃ co-doped with Sb⁵⁺ and Cr³⁺ ions showed intense absorption bands in the visible-light region and possessed energy gaps 2.2 and 2.4 eV, respectively [101]. TiO₂ co-doped with Sb⁵⁺ and Cr³⁺ ions evolved O₂ from an aqueous silver nitrate solution under visible-light irradiation, while SrTiO₃ co-doped with Sb⁵⁺ and Cr³⁺ ions evolved H₂ from an aqueous methanol solution (Table 2). The activity of TiO₂ photocatalysts co-doped with Sb⁵⁺ and Cr³⁺ ions was remarkably higher than that of TiO₂ doped with only Cr³⁺ ions. This was due to the fact that the charge balance was kept by co-doping of Sb⁵⁺ and Cr³⁺ ions, resulting in the suppression of the formation of Cr⁶⁺ ions and oxygen defects in the lattice, which should work as effective nonradiative recombination centers between photogenerated electrons and holes (Fig. 20).

Table 2. Visible-light-sensitive photocatalysts and their photocatalytic reactivity for water splitting to evolve H₂ and O₂ from aqueous solution.

Photocatalyst	Bandgap (eV)	Sacrificial reagent	Activity (mmol/h)		Ref.
			H ₂	O ₂	
Conventional type					
Pt/CdS	2.4	K ₂ SO ₃	850	—	[100]
WO ₃	2.8	AgNO ₃	—	65	[100]
Doping type					
NiO _x /In _{0.9} Ni _{0.1} TaO ₄		None	17	8	[119]
Pt/SrTiO ₃ :Cr,Sb	2.4	CH ₃ OH	78	—	[101]
Pt/SrTiO ₃ :Cr,Ta	2.3	CH ₃ OH	70	—	[101]
TiO ₂ :Cr,Sb	2.5	AgNO ₃	—	42	[101]
Cu-ZnS	2.5	K ₂ SO ₃	450	—	[100]
Ni-ZnS	2.3	K ₂ SO ₃	280	—	[100]
Cu-TiO ₂	2.0	CH ₃ OH	1.3	—	[114]
New VB formation type					
BiVO ₄	2.4	AgNO ₃	—	37	[100]
AgNbO ₃	2.86	AgNO ₃	—	37	[100]
TaON	2.4	AgNO ₃	—	158	[128]
TaON	2.4	AgNO ₃	—	158	[128]
RbPb ₂ Nb ₃ O ₁₀	2.6	AgNO ₃	—	1.1	[151]
Pt/HPb ₂ Nb ₃ O ₁₀	2.6	CH ₃ OH	3.2	—	[151]
Solid-solution type					
Pt/AgInZn ₇ S ₉	2.4	Na ₂ S + K ₂ SO ₃	940	—	[133]
Pt/In ₂ O ₃ (ZnO) ₃	2.6	CH ₃ OH	1.3	—	[135]

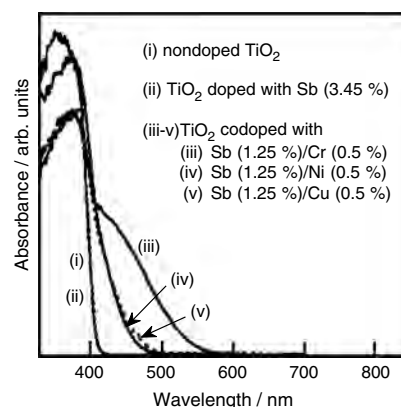


Figure 20. Diffuse reflection spectra of (i) nondoped TiO₂, (ii) TiO₂ doped with Sb (3.45%), (iii)–(v) TiO₂ codoped with (iii) Sb (1.25%)/Cr (0.5%), (iv) Sb (1.25%)/Ni (0.5%), and (v) Sb (1.25%)/Cu (0.5%). Reprinted with permission from [101], W. Kato and A. Kudo, *J. Phys. Chem. B* 106, 5029 (2002). © 2002, American Chemical Society.

ZnS is one of the active photocatalysts for hydrogen evolution from aqueous solutions in the presence of sacrificial reagents even without co-catalysts such as platinum. Although the conduction band level is high enough to reduce H₂O into H₂, ZnS with a bandgap of 3.7 eV can operate as a photocatalyst only under UV irradiation. Cu²⁺- and Ni²⁺-doped ZnS photocatalysts, Zn_{0.9957}Cu_{0.043}S and Zn_{0.999}Ni_{0.001}S, have a pale yellow color and have energy gaps of 2.5 and 2.3 eV, respectively. The absorption bands of these metal-ion-doped ZnS photocatalysts consist of two types of bands. One is a visible-light absorption band due to the transition from doped Cu²⁺ and Ni²⁺ to the conduction band of ZnS and the other is a UV absorption band similar in origin to that of ZnS. Under visible-light irradiation, the H₂ evolution from aqueous potassium sulfite and sodium sulfide solutions can be observed on these doped Zn_{0.9957}Cu_{0.043}S and Zn_{0.999}Ni_{0.001}S photocatalysts (Table 2) [102, 103].

2.2.2. TiON and TaON

By metal ion implantation, Ti⁴⁺ ions in TiO₂ can be substituted with implanted metal ions to modify the electronic state of TiO₂ to absorb visible light. On the other hand, the substitution of O²⁻ ions in TiO₂ with other anions such as N³⁻ and S²⁻ has been applied to modify the electronic state of TiO₂ [125, 126]. The doping of N³⁻ ions into TiO₂ was carried out by heating a TiO₂ sample in the presence of NH₃. Also during the formation of the TiO₂ thin film using the sputtering technique in the presence of N₂, N³⁻-ion-doped TiO₂ thin film was produced directly. It has been found recently that this N³⁻-ion-doped TiO₂ (films and powders of TiO_{2-x}N_x) has revealed an improvement over TiO₂ under visible light ($\lambda < 500$ nm) in terms of the optical absorption properties and photocatalytic reactivity such as photodegradation of methylene blue and gaseous acetaldehyde and hydrophilicity of the film surface (Fig. 21). Nitrogen doped into substitutional sites of TiO₂ has proven to be indispensable for bandgap narrowing and photocatalytic reactivity, as assessed by first-principles calculations and X-ray photoemission spectroscopy. Instead of nitrogen

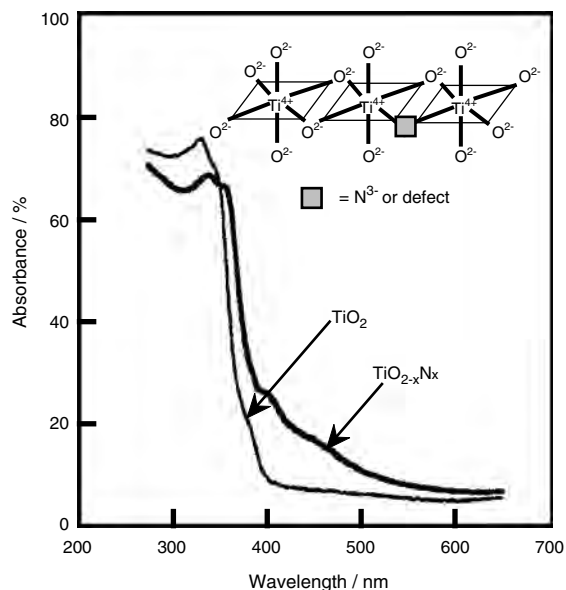


Figure 21. Experimental optical absorption spectra of $\text{TiO}_{2-x}\text{N}_x$ and TiO_2 films. Reprinted with permission from [125], R. Asahi et al., *Science* 293, 269 (2001). © 2001, American Association for the Advancement of Science.

ions, the substitution of the oxygen ions of TiO_2 with carbon and sulfur ions has also been found to be effective in modifying the electronic state of TiO_2 to absorb visible light [126, 132].

A transition metal oxynitride, TaON , and a transition metal nitride, Ta_3N_5 , are also novel photocatalysts responding to visible light [128–130]. Ta_3N_5 and TaON evolve H_2 and O_2 by visible-light ($\lambda < 600$ nm) irradiation in the presence of a sacrificial electron donor and acceptor, respectively, without any noticeable photoanodic or cathodic corrosion, representing candidates for overall water splitting by visible light (Table 2).

3. MIXED OXIDES

3.1. ABO_4 -type Binary Oxide

The valence band of most oxide semiconductors consists of $\text{O}(2p)$ orbitals. The valence band level is about 3 V, which is deep enough to oxidize H_2O into O_2 . Because it causes oxide semiconductor photocatalysts to have wide bandgaps, it is necessary to make a valence band consisting of an orbital other than $\text{O}(2p)$ to develop a visible-light-sensitive photocatalyst. Recently, a binary oxide having an ABO_4 composition, such as BiVO_4 and InTaO_4 , was found to exhibit photocatalytic reactivity even under visible-light irradiation [116–124]. Bi^{3+} with a $6s_2$ configuration is a good candidate for forming such a valence band. The highly crystalline BiVO_4 powders with scheelite (monoclinic) and zircon-type (tetragonal) structures were synthesized selectively by an aqueous process. The BiVO_4 powder with the scheelite structure showed a high photocatalytic activity for O_2 evolution in the presence of a sacrificial reagent (Ag^+) under visible-light irradiation ($\lambda > 420$ nm). The zircon-type BiVO_4 with a bandgap of 2.9 eV mainly showed a UV

absorption band, while the scheelite BiVO_4 with a bandgap of 2.4 eV had a characteristic visible-light absorption band in addition to the UV absorption band (Fig. 22). The UV absorption bands observed in the zircon-type and scheelite BiVO_4 were assigned to the band transition from $\text{O}(2p)$ to $\text{V}(3d)$, whereas the visible-light absorption was due to the transition from the valence band formed by a hybrid orbital of $\text{Bi}(6s)$ and $\text{O}(2p)$ to the conduction band consisting of $\text{V}(3d)$. The photocatalytic activity of the BiVO_4 powder prepared by the aqueous process was much higher than that of BiVO_4 prepared by a conventional solid-state reaction. The highly crystalline powder without significant formation of defects and the decrease in the surface area can be obtained by the aqueous process at room temperature, which led to efficient photoreactivity under visible-light irradiation (Table 2).

Furthermore, it has been found that the Ni doping into InTaO_4 can form $\text{In}_{1-x}\text{Ni}_x\text{TaO}_4$ ($x = 0\text{--}0.2$), which can first induce the direct splitting of water into H_2 and O_2 under visible-light irradiation ($\lambda > 420$ nm) with a quantum yield of about 0.66% at 402 nm even without the sacrificial reagents (Table 2). The bandgap energy is narrowed with Ni doping from 2.6 (nondoped) to 2.3 eV (0.1 Ni doping). This bandgap change in Ni-doped compounds can be attributed to internal transitions in a partly filled Ni d shell.

3.2. Z-Scheme Reaction

This has been studied on water splitting into H_2 and O_2 using two different semiconductor photocatalysts and a redox mediator, mimicking the Z-scheme mechanism of photosynthesis [161, 162]. It was found that the H_2 evolution took place on a Pt-SrTiO_3 (Cr-Ta-doped) photocatalyst using an I-electron donor under visible-light irradiation. The Pt-WO_3 photocatalyst showed an excellent activity of the O_2 evolution using an IO_3^- electron acceptor under visible light (Fig. 23). Both H_2 and O_2 gases evolved in the stoichiometric ratio ($\text{H}_2/\text{O}_2 = 2$) for more than 250 h under visible light using a mixture of the Pt-WO_3 and the Pt-SrTiO_3 (Cr-Ta-doped) powders suspended in NaI aqueous solution. This is the first time that stoichiometric water splitting occurred over oxide semiconductor photocatalysts under visible-light irradiation. A two-step photoexcitation

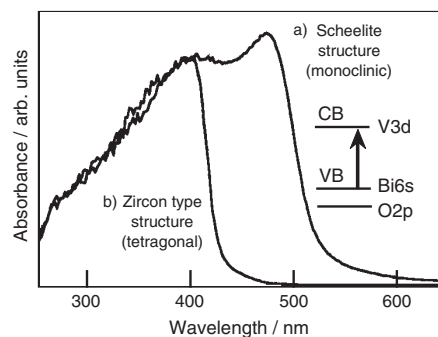


Figure 22. Diffuse reflectance spectra of BiVO_4 prepared by an aqueous process at room temperature (a) Scheelite structure (monoclinic), (b) zircon-type structure (tetragonal). Reprinted with permission from [100], A. Kudo, *J. Ceram. Soc. Jpn.* 109, S81 (2001). © 2001, The Ceramic Society of Japan.

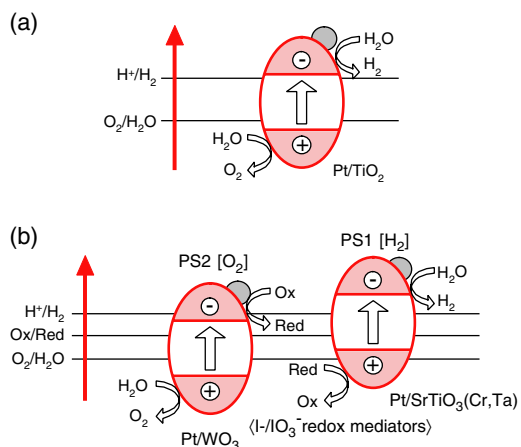
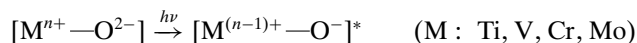


Figure 23. (a) Conventional photocatalytic reaction mechanism (one-step system) and (b) reaction mechanism mimicking Z scheme (two-step system). Reprinted with permission from [162], K. Sayama et al., *J. Photochem. Photobiol., A* 148, 71 (2002).

mechanism using a pair of I⁻/IO₃⁻ redox mediators has been proposed. The quantum efficiency of the stoichiometric water splitting was approximately 0.1% at 427 nm.

4. ZEOLITE PHOTOCATALYSTS

The unique and fascinating properties of zeolites involving transition metals within the zeolite framework or cavity have opened new possibilities for many application areas not only in catalysis but also for various photochemical processes [144–147, 163–230]. The transition metal ions in metallosilicate catalysts are considered to be highly dispersed at the atomic level and also to be well-defined catalysts that exist in the specific structure of the zeolite framework. The well-prepared zeolite sample should contain only the isolated metal ions in the framework. This is of great significance in the design of highly dispersed transition metal oxide catalysts such as Ti [163–190], V [191–200], Cr [144–147], and Mo [201–205], which can be excited under UV irradiation by the following charge transfer process:



These charge transfer excited states, that is, the electron-hole pair states that localize quite near to each other as compared to the electron and hole produced in semiconducting materials, play a significant role in various photocatalytic reactions such as the decomposition of NO into N₂ and O₂ or the degradation of organic impurities in water, the photooxidation reaction of hydrocarbons, and the photoinduced metathesis reaction of alkanes [144–147, 163–229]. These photocatalytic reactions were found to proceed with high efficiency and selectivity, displaying quite different reaction mechanisms from those observed on semiconducting TiO₂ photocatalysts in which the photoelectrochemical reaction mechanism plays an important role. However, the metal oxide moieties included within the framework of zeolite can be activated only under UV irradiation. It is attractive

to develop photocatalyst-included zeolites that can demonstrate their unique photocatalytic properties even under visible-light irradiation.

4.1. Metal-Ion-implanted Ti Zeolite

Although TiO₂ has an octahedral coordination, titanium oxide having a tetrahedral coordination (tetra Ti oxide) can be prepared in a silica matrix such as zeolite and mesoporous silica. Ti zeolites with the tetrahedrally coordinated Ti-oxide species showing unique reactivities for various photocatalytic reactions under UV irradiation (220–260 nm) [163–190, 230] are good candidates for efficient and selective photocatalysts. Although these tetrahedrally coordinated Ti-oxide species can exhibit unique photocatalytic reactivity, they can only adsorb and utilize UV light at around 220–250 nm to form the charge transfer excited state as active species. It is also vital to develop Ti zeolites that can operate efficiently under visible-light irradiation. The application of metal ion implantation [3] to modify the Ti zeolites is very interesting. Recently, it has been found that metal ion implantation with V ions has been applied on Ti zeolites and Ti-containing mesoporous silica to design photocatalysts that can operate under visible-light irradiation.

The metal ion implantation with V ions on Ti zeolites and Ti-containing mesoporous silica was carried out at 150 eV. Figure 24 shows the effect of metal ion implantation on the diffuse reflectance UV–vis absorption spectra of Ti-HMS mesoporous silica having a tetrahedrally coordinated Ti oxide in the framework. As shown in Figure 24, the V-ion-implanted Ti-HMS can absorb light at longer wavelengths (~450 nm), while the original un-implanted Ti-HMS absorbs UV light at a wavelength shorter than 300 nm. These results indicate that metal ion implantation is effective for modifying the Ti-HMS to absorb visible light and exhibit the photocatalytic reaction under visible-light irradiation (Fig. 25).

These metal-ion-implanted Ti zeolites (V/Ti zeolites) and Ti-containing mesoporous silica (V/Ti mesoporous silica) exhibit efficient photocatalytic reactivity for various reactions such as NO decomposition and partial oxidation of hydrocarbons even under visible-light irradiation in keeping the unique photocatalytic properties of the tetrahedrally coordinated Ti-oxide species. The investigations using XAFS analysis on the local structure of active sites and the molecular orbital calculations on the electronic structure of active

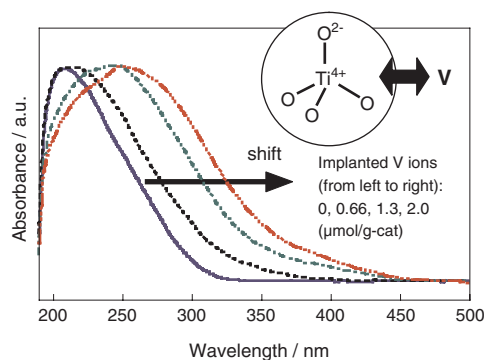


Figure 24. Diffuse reflectance UV–vis absorption spectra of the V-ion-implanted Ti-HMS.

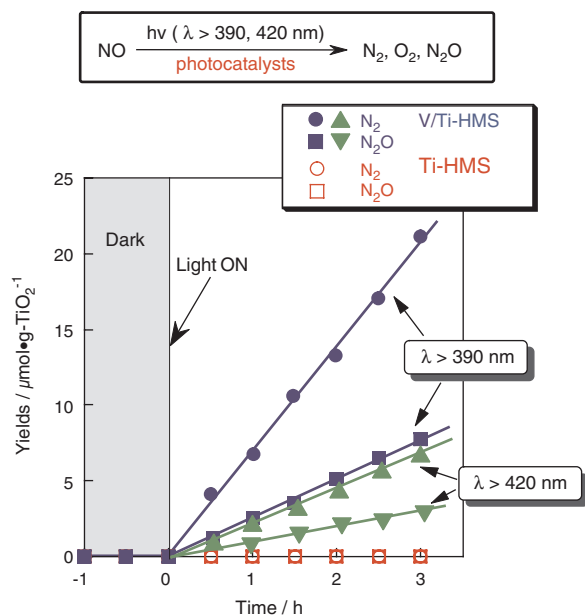


Figure 25. Reaction time profiles of the photocatalytic decomposition of NO on Ti-HMS and V-ion-implanted Ti-HMS under visible-light irradiation ($\lambda > 390$ nm, 420 nm). The amount of implanted V ion: 2.0 $\mu\text{mol/g-cat}$. The yield of N_2 (●, ▲) and N_2O (■, ▼) formation on V/Ti-HMS; the yield of N_2 (○) and N_2O (□) formation on Ti-HMS.

sites have revealed that the direct coordination and interaction between the implanted metal ions and the tetrahedrally coordinated Ti-oxide species can modify the electronic state of the Ti-oxide species to absorb and utilize visible light.

4.2. Cr Zeolite

Highly dispersed Mo- or Cr-oxide catalysts have been shown to exhibit high activities for various photocatalytic reactions such as the photooxidation reaction of hydrocarbons or the photoinduced metathesis reaction of alkanes [144–147, 201–203]. Recently, it has been found that the chemically prepared Cr-containing mesoporous silica molecular sieves (Cr-HMS) having tetrahedrally coordinated isolated Cr-oxide (chromate) moieties can operate as efficient photocatalysts for the decomposition of NO and the partial oxidation of propane with molecular oxygen under visible-light irradiation.

Cr-HMS mesoporous molecular sieves (0.02, 0.2, 1.0, 2.0 wt% as Cr) were synthesized using tetraethylorthosilicate and $\text{Cr}(\text{NO}_3)_3 \cdot 9\text{H}_2\text{O}$ as the starting materials and dodecylamine as a template and calcined in a flow of dry air at 773 K. The results of the XRD analysis indicated that the Cr-HMS has a mesopore structure and the Cr-oxide moieties are highly dispersed in the framework of HMS, while no other phases are formed. Cr-HMS exhibited a sharp and intense pre-edge peak in the XANES region, which is characteristic of Cr-oxide moieties in tetrahedral coordination [144–147]. In the Fourier transforms of the EXAFS spectra, only a single peak due to the neighboring oxygen atoms (Cr–O) can be observed, showing that Cr ions are highly dispersed in Cr-HMS. The analysis of the EXAFS spectrum of Cr-HMS indicated that tetrahedrally

coordinated Cr-oxide (chromate) moieties having two terminal C=O bonds existed as in an isolated state [two oxygen atoms (Cr=O) at 1.57 Å and two oxygen atoms (Cr–O) at 1.82 Å]. The ESR technique was also applied to investigate the coordination state of the Cr-oxide species by monitoring the Cr^{5+} ions formed under UV irradiation of the catalyst in the presence of H_2 at 77 K. After photoreduction with H_2 at 77 K, the Cr-HMS exhibited a sharp axially symmetric signal at around $g = 1.9$ ($g_{\parallel} = 1.880$, $g_{\perp} = 1.945$), attributed to the isolated mononuclear Cr^{5+} ions in tetrahedral coordination. As shown in Figure 26, the UV-vis spectra of the Cr-HMS exhibit three distinct absorption bands at around 250, 360, and 480 nm, which can be assigned to the charge transfer from O^{2-} to Cr^{6+} of the tetrahedrally coordinated Cr-oxide moieties. Without a Cr ion, the HMS exhibited no absorption band above 220 nm. The absorption bands assigned to the absorption of the dichromate or Cr_2O_3 cluster cannot be observed above 550 nm, indicating that tetrahedrally coordinated Cr-oxide species exists in an isolated state. Cr-HMS exhibited photoluminescence spectra at around 550–750 nm upon excitation of the absorption (excitation) bands at around 250, 360, and 480 nm, respectively. These absorption and photoluminescence spectra are similar to those obtained with well-defined highly dispersed Cr oxides anchored onto Vycor glass or silica [144–147] and can be attributed to the charge transfer processes on the tetrahedrally coordinated Cr-oxide moieties involving an electron transfer from O^{2-} to Cr^{6+} and a reverse radiative decay, respectively.

UV-light irradiation ($\lambda > 270$ nm) of the Cr-HMS in the presence of NO led to the photocatalytic decomposition of NO and the evolution of N_2 , N_2O , and O_2 in the gas phase at 275 K. The Cr-HMS also shows photocatalytic reactivity even under visible-light irradiation ($\lambda > 450$ nm). As shown in Figure 27, the N_2 yields increase linearly with the irradiation time. The presence of both Cr-oxide species included within the HMS as well as light irradiation are indispensable for the photocatalytic reaction to take place, and the direct decomposition of NO to produce N_2 , O_2 , and N_2O occurs photocatalytically on the Cr-HMS. Although the reaction rate under visible-light irradiation is smaller than that under

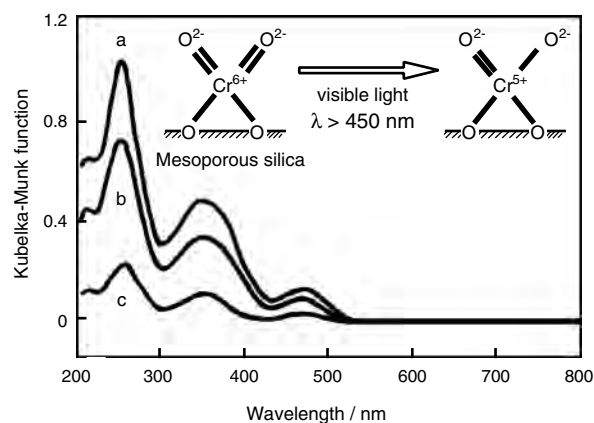


Figure 26. UV-vis spectra of Cr-HMS catalysts: (a) 2.0 wt%, (b) 1.0 wt%, (c) 0.2 wt% as Cr.

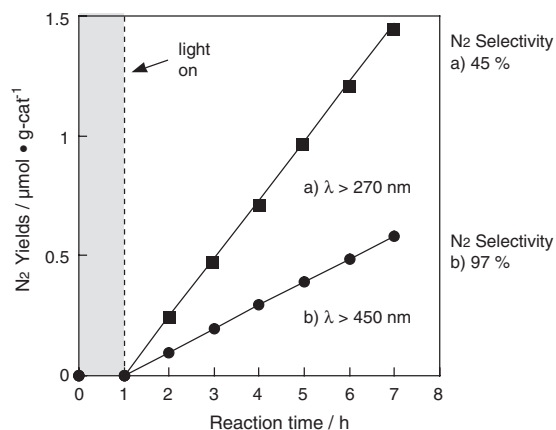


Figure 27. Reaction time profile of N₂ formation in the photocatalytic decomposition of NO on the Cr-HMS catalyst at 273 K (2.0 wt% as Cr) under UV-light irradiation (a, λ > 270 nm) and visible-light irradiation (b, λ > 450 nm).

UV-light irradiation, the selectivity for N₂ formation (97%) under visible-light irradiation is higher than that of UV-light irradiation (45%). These results indicate that Cr-HMS can absorb visible light and act as an efficient photocatalyst under not only UV light but also visible light and especially Cr-HMS can be useful to form N₂ under visible-light irradiation.

The addition of NO into the Cr-HMS led to an efficient quenching of the photoluminescence spectrum of the catalyst, its extent depending on the amount of NO added. These results indicate that the charge transfer excited state of the tetrahedrally coordinated isolated Cr-oxide moieties, (Cr⁵⁺—O⁻)^{*}, easily interact with NO and this photoexcited species plays an important role in the photocatalytic reaction under UV and visible-light irradiation.

On the other hand, light irradiation of the Cr-HMS in the presence of propane and O₂ led to the photocatalytic oxidation of propane. The partial oxidation of propane with a high selectivity for the production of oxygen-containing hydrocarbons such as acetone and acrolein proceeds under visible-light irradiation, while further oxidation proceeds mainly under UV-light irradiation to produce CO₂ and CO. The selectivity of partial oxidation production under visible-light irradiation observed at 12% propane conversion is higher than those observed under UV-light irradiation at 26% conversion and even under UV-light irradiation for the shorter reaction time with 11% conversion. These results indicate that the tetrahedrally coordinated isolated Cr-oxide moieties in HMS can exhibit efficient photocatalytic reactivity for the oxidation of propane under visible-light irradiation with a high selectivity for the partial oxidation of propane.

These results have clearly demonstrated that the Cr-HMS can absorb visible light and act as an efficient and selective photocatalyst under visible-light irradiation. This photocatalytic system with tetrahedrally coordinated Cr-oxide moieties dispersed on mesoporous silica seems to be a good candidate for converting abundant visible- or solar-light energy into useful chemical energy, as well as the metal-ion-implanted tetrahedrally coordinated Ti-oxide moieties dispersed on zeolite and mesoporous silica (Fig. 28).

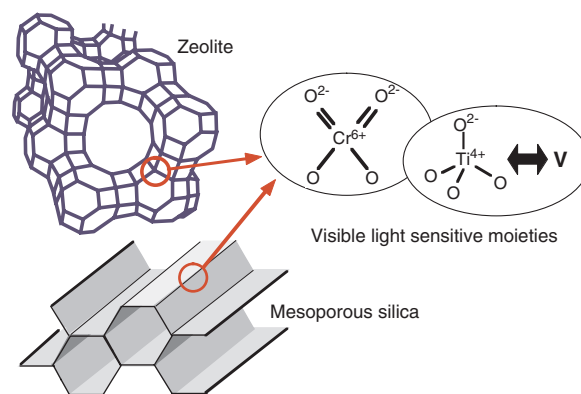


Figure 28. Visible-light-sensitive photocatalysts included within the frameworks of zeolite and mesoporous silica.

5. CONCLUSIONS

In this review, recent applications to the design of visible-light-sensitive photocatalysts are summarized. Large progress has been made in the design of visible-light-sensitive photocatalysts. Especially, the modification of TiO₂ photocatalysts to utilize visible light and the design and development of visible-light-sensitive photocatalysts, which can induce photocatalytic water splitting to produce H₂ and O₂ efficiently, are the most fascinating research topics. Among the various unique attempts to control the electronic structure of semiconducting photocatalysts, the substitution of metal ions (Ti ions in the case of TiO₂) with transition metal ions by metal ion implantation or metal doping and/or the substitution of anions (O ions in the case of TiO₂) with N, S, and C ions (or defects) by chemical methods have been found to be significantly effective (Fig. 29). At the present, many researchers are engaged in applying these techniques to the design of efficient visible-light-sensitive photocatalysts with the assistance of the theoretical molecular orbital calculation and spectroscopic analyses such as XAFS using synchrotron radiation. Furthermore, the application of an advanced dry process such as ion engineering techniques (metal ion implantation, ICB method, magnetron sputtering, etc.) is the new method for the design of unique photocatalysts even in the form of transparent thin films that can operate efficiently not only under UV-light irradiation but

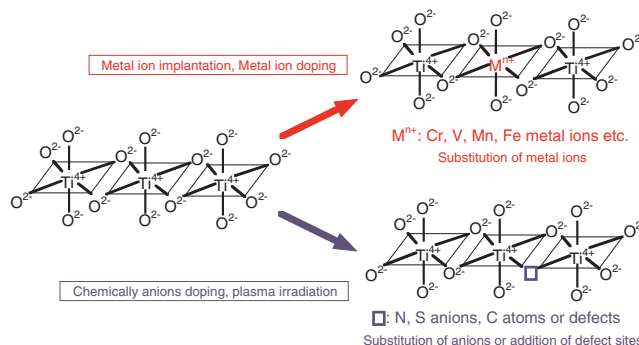


Figure 29. Attempts to control the electronic structure of semiconducting photocatalysts (TiO₂) by the substitution of metal ions or anions to design visible-light-sensitive photocatalysts.

also under visible-light irradiation. The present research has opened the way to many innovative possibilities, significantly addressing urgent environmental concerns, and can also be considered an important breakthrough in the utilization of solar energy.

GLOSSARY

Artificial photosynthesis The set of reactions in which light is harvested as the plants use light to synthesize high-energy molecules. Reactions such as the reduction of CO₂ with H₂O and water splitting to produce H₂ and O₂ can be carried out under visible-light irradiation without plants but using artificial compounds such as semiconductor photocatalysts.

Metal ion implantation A variant of the ion beam techniques in which an accelerated metal ion beam has been used to modify the electronic structure of semiconductors. In this method, metal ions are accelerated in the electronic field and injected into the sample target as the ion beam. These metal ions can interact in a different manner with the sample surface, depending on their kinetic energy. In ion implantation, metal ions are accelerated enough to have a high kinetic energy (50–200 keV) and can be implanted into the bulk of samples. On the other hand, metal ions accelerated to have a low kinetic energy (0.2–2 keV) are deposited to form a thin film on the top surface of the sample. With these unique properties of the ion beam techniques, well-defined semiconductor materials and thin films have been developed.

Photocatalyst The photocatalyst can exhibit the photocatalytic reaction (photocatalysis), which is a catalytic reaction involving light absorption by a catalyst or by a substrate under light irradiation. Photocatalysis on semiconductors such as TiO₂ can be regarded as a light-induced redox process. Under light irradiation with an energy larger than the bandgap energy of the semiconductors, an electron is excited from the valence band to the conduction band, leaving a hole. The electrons formed in the conduction band and the holes formed in the valence band recombine or become trapped in the surface defect sites. These surface trapped holes are powerful oxidants and the trapped electrons can act as good reductants.

X-ray absorption fine structure (XAFS) spectroscopy A technique using X-rays with variable wavelengths as probes to investigate the local atomic coordination structure. The non-destructive *ex-situ* and *in-situ* measurements can be applied to both amorphous and crystalline samples. Extended X-ray absorption fine structure (EXAFS) spectroscopy and X-ray absorption near-edge spectroscopy (XANES) are variants of the X-ray absorption technique.

Zeolite A microporous solid with pore size ranging from approximately 3 to 14 Å. They are composed of aluminosilicates, aluminophosphates, and metal silicates. They have a framework with corner-linked (TO₄) tetrahedra and a void space that forms the channel, cages, and supercages. The term zeolite is now applied to different materials, such as mesoporous silica (pore size, ca. 20–30 Å), that express zeolitic behaviors such as the selective adsorption of small molecules (molecular sieves), ion exchange ability, large surface areas, and perfectly defined pore sizes.

REFERENCES

1. M. Anpo, "Photofunctional Zeolites: Synthesis." Nova, New York, 2000.
2. A. Fujishima, K. Hashimoto, and T. Watanabe, "TiO₂ Photocatalysis." BKC, Tokyo, 1998.
3. M. Schiavello, "Heterogeneous Photocatalysis." Wiley, Chichester, 1997.
4. M. Anpo, "Surface Photochemistry." Wiley, Chichester, 1996.
5. G. Calzaferrri, "Solar Energy Materials and Solar Cells." Elsevier, Amsterdam, 1995.
6. D. F. Ollis and H. Al-Ekabi, "Photocatalytic Purification and Treatment of Water and Air." Elsevier, Amsterdam, 1993.
7. E. Pelizzetti and M. Schiavello, "Photochemical Conversion and Storage of Solar Energy." Kluwer Academic, Dordrecht, 1991.
8. N. Serpone and E. Pelizzetti, "Photocatalysis." Wiley, New York, 1989.
9. Y. Kubokawa, K. Honda, and Y. Saito, "Hikari-Shokubai (Photocatalysis)." Asakura-shoten, Tokyo, 1988.
10. E. Pelizzetti and N. Serpone, "Homogeneous and Heterogeneous Photocatalysis." Reidel, New York, 1986.
11. M. Graetzel, "Energy Resources through Photochemistry and Catalysis." Academic Press, New York, 1983.
12. M. Anpo and M. Che, *Adv. Catal.* 44, 169 (1999).
13. A. J. Bard and M. A. Fox, *Acc. Chem. Res.* 28, 141 (1995).
14. A. Heller, *Acc. Chem. Res.* 28, 503 (1995).
15. A. Hagfeldt and M. Graetzel, *Chem. Rev.* 95, 48 (1995).
16. M. R. Hoffmann, S. T. Martin, W. Y. Choi, and D. W. Bahnemann, *Chem. Rev.* 95, 69 (1995).
17. A. L. Linsebigler, G. Q. Lu, and J. T. Yates, *Chem. Rev.* 95, 735 (1995).
18. K. I. Zamaraev, M. I. Kharamov, and V. N. Parmon, *Catal. Rev.—Sci. Eng.* 36, 617 (1994).
19. P. V. Kamat, *Chem. Rev.* 93, 267 (1993).
20. M. A. Fox and M. T. Dulay, *Chem. Rev.* 93, 341 (1993).
21. A. Heller, *Science* 233, 1141 (1984).
22. A. J. Bard, *J. Phys. Chem.* 86, 172 (1982).
23. T. Inoue, A. Fujishima, S. Konishi, and K. Honda, *Nature* 277, 637 (1979).
24. J. C. Hemminger, R. Carr, and G. A. Somorjai, *Chem. Phys. Lett.* 57, 100 (1978).
25. K. Honda and A. Fujishima, *Nature* 238, 37 (1972).
26. H. B. Yin, Y. Wada, T. Kitamura, T. Sakata, H. Mori, and S. Yanagida, *Chem. Lett.* 334 (2001).
27. H. Fujiwara, M. Kanemoto, H. Ankyu, K. Murakoshi, Y. Wada, and S. Yanagida, *J. Chem. Soc., Perkin Trans. 2*, 317 (1997).
28. J. K. Lee, W. Lee, T. J. Yoon, G. S. Park, and J. H. Choy, *J. Mater. Chem.* 12, 614 (2002).
29. T. Hirai, K. Suzuki, and I. Komasa, *J. Colloid. Interface Sci.* 244, 262 (2001).
30. M. K. Arora, A. S. K. Sinha, and S. N. Upadhyay, *Ind. Eng. Chem. Res.* 37, 1310 (1998).
31. T. Sato, K. Masaki, K. I. Sato, Y. Fujishiro, and A. Okuwaki, *J. Chem. Technol. Biotechnol.* 67, 339 (1996).
32. G. C. De, A. M. Roy, and S. S. Bhattacharya, *Int. J. Hydrogen Energy* 21, 19 (1996).
33. K. Hara, K. Sayama, and H. Arakawa, *Appl. Catal., A* 189, 127 (1999).
34. D. W. Hwang, J. Kim, T. J. Park, and J. S. Lee, *Catal. Lett.* 80, 53 (2002).
35. X. Z. Li, F. B. Li, Yang, and W. K. Ge, *J. Photochem. Photobiol., A* 141, 209 (2001).
36. G. R. Bamwenda and H. Arakawa, *Appl. Catal., A* 210, 181 (2001).
37. T. Ohno, F. Tanigawa, K. Fujihara, S. Izumi, and M. Matsumura, *J. Photochem. Photobiol., A* 118, 41 (1998).
38. K. Sayama, R. Yoshida, H. Kusama, K. Okabe, Y. Abe, and H. Arakawa, *Chem. Phys. Lett.* 277, 387 (1997).

39. C. E. Taylor, R. P. Noceti, J. R. Este, and D. V. Martello, *Stud. Surf. Sci. Catal.* 101, 407 (1996).
40. C. E. Taylor and R. P. Noceti, *Catal. Today* 55, 259 (2000).
41. M. Ashokkumar, *Int. J. Hydrogen Energy* 23, 427 (1998).
42. B. O'Regan and M. Graetzel, *Nature* 353, 737 (1991).
43. A. Kay and M. Graetzel, *J. Phys. Chem.* 97, 96272 (1993).
44. A. K. Ghosh and H. P. Maruska, *J. Electrochem. Soc.* 124, 1516 (1977).
45. A. Kay and M. Graetzel, *Chem. Mater.* 14, 2930 (2002).
46. R. Abe, K. Sayama, and H. Arakawa, *Chem. Phys. Lett.* 362, 441 (2002).
47. T. Sauer, G. C. Neto, H. J. Jose, and R. F. P. M. Moreira, *J. Photochem. Photobiol., A* 149, 147 (2002).
48. M. Saquib and M. Muneer, *Dye Pigments* 53, 237 (2002).
49. A. Furube, T. Shiozawa, A. Ishikawa, A. Wada, K. Domen, and C. Hirose, *J. Phys. Chem. B* 106, 3065 (2002).
50. M. Hara, J. T. Lean, and T. E. Mallouk, *Chem. Mater.* 13, 4668 (2001).
51. J. Bandara, J. A. Mielczarski, A. Lopez, and J. Kiwi, *Appl. Catal., B* 34, 321 (2001).
52. M. Kojima, K. Takahashi, and K. Nakamura, *Photochem. Photobiol.* 74, 369 (2001).
53. K. Szacilowski, J. Oszajca, A. Barbieri, A. Karocki, Z. Sojka, S. Sostero, R. Boaretto, and Z. Stasicka, *J. Photochem. Photobiol., A* 143, 99 (2001).
54. D. Chatterjee and A. Mahata, *Appl. Catal., B* 33, 119 (2001).
55. F. Chen, Y. D. Xie, J. C. Zhao, and G. X. Lu, *Chemosphere* 44, 1159 (2001).
56. Y. M. Cho, W. Y. Choi, C. H. Lee, T. Hyeon, and H. I. Lee, *Environ. Sci. Technol.* 35, 966 (2001).
57. R. Abe, K. Hara, K. Sayama, K. Domen, and H. Arakawa, *J. Photochem. Photobiol., A* 137, 63 (2002).
58. K. Hirano, E. Suzuki, A. Ishikawa, T. Moroi, H. Shiroishi, and M. Kaneko, *J. Photochem. Photobiol., A* 136, 157 (2000).
59. M. Hara, C. C. Waraksa, J. T. Lean, B. A. Lewis, and T. E. Mallouk, *J. Phys. Chem. A* 104, 5275 (2000).
60. K. Gurunathan, *J. Mol. Catal., A* 156, 59 (2000).
61. A. Serban and A. Nissenbaum, *Int. J. Hydrogen Energy* 25, 733 (2000).
62. D. Chatterjee, *J. Mol. Catal., A* 154, 1 (2000).
63. A. Sanjuan, M. Alvaro, A. Corma, and H. Garcia, *Chem. Commun.* 1641 (1999).
64. M. Kimura, A. Takahashi, T. Sakata, and K. Tsukahara, *Bull. Chem. Soc. Jpn.* 71, 1839 (1998).
65. R. Humphry-Baker, C. A. Mitsopoulou, D. Katakis, and E. Vrachnou, *J. Photochem. Photobiol., A* 114, 137 (1998).
66. A. Sanjuan, G. Aguirre, M. Alvaro, and H. Garcia, *Appl. Catal., B* 15, 247 (1998).
67. V. V. Nikandrov, C. K. Gratzel, J. E. Moser, and M. Gratzel, *J. Photochem. Photobiol., B* 41, 83 (1997).
68. F. Franceschi, M. Guardigli, E. Solari, C. Floriani, A. ChiesiVilla, and C. Rizzoli, *Inorg. Chem.* 36, 4099 (1997).
69. E. Bellmann, J. Lobedank, H. Ross, and J. Bendig, *J. Inform. Res.* 23, 43 (1996).
70. Y. Wada, T. Kitamura, and S. Yanagida, *Res. Chem. Intermed.* 26, 153 (2000).
71. Y. Wada, T. Ogata, K. Hiranaga, H. Yasuda, T. Kitamura, K. Murakoshi, and S. Yanagida, *J. Chem. Soc., Perkin Trans. 2*, 1999 (1998).
72. M. Fujita, A. Ishida, S. Takamuku, and S. Fukuzumi, *J. Am. Chem. Soc.* 118, 8566 (1996).
73. D. C. Schmelling, K. A. Gray, and P. V. Kamat, *Environ. Sci. Technol.* 30, 2547 (1996).
74. H. Yamashita, Y. Ichihashi, M. Harada, G. Stewart, M. A. Fox, and M. Anpo, *J. Catal.* 158, 97 (1996).
75. M. Harada, M. Honda, H. Yamashita, and M. Anpo, *Res. Chem. Intermed.* 25, 757 (1999).
76. H. Yamashita, N. Kamada, L. Palmisano, M. A. Fox, and M. Anpo, *Res. Chem. Intermed.* 20, 815 (1994).
77. H. Yamashita, N. Kamada, H. He, K. Tanaka, S. Ehara, and M. Anpo, *Chem. Lett.* 855 (1994).
78. H. Yamashita, A. Shiga, S. Kawasaki, Y. Ichihashi, S. Ehara, and M. Anpo, *Energy Conversion Manage.* 36, 617 (1995).
79. D.-R. Park, B.-J. Ahn, H.-S. Park, H. Yamashita, and M. Anpo, *Korean J. Chem. Eng.* 18, 930 (2001).
80. D. R. Park, J. Zhang, K. Ikeue, H. Yamashita, and M. Anpo, *J. Catal.* 185, 114 (1999).
81. J. L. Zhang, T. Ayusawa, K. Kinugawa, H. Yamashita, M. Matsuoka, and M. Anpo, *J. Catal.* 198, 1 (2001).
82. A. Furube, T. Asahi, H. Masuhara, H. Yamashita, and M. Anpo, *Res. Chem. Intermed.* 27, 177 (2001).
83. A. Furube, T. Asahi, H. Masuhara, H. Yamashita, and M. Anpo, *Chem. Phys. Lett.* 336, 424 (2001).
84. A. Furube, T. Asahi, H. Masuhara, H. Yamashita, and M. Anpo, *J. Phys. Chem. B* 103, 3120 (1999).
85. A. Furube, T. Asahi, H. Masuhara, H. Yamashita, and M. Anpo, *Chem. Lett.* 735 (1997).
86. H. Yamashita, S. Kawasaki, Y. Ichihashi, M. Harada, M. Anpo, G. Stewart, M. A. Fox, C. Louis, and M. Che, *J. Phys. Chem. B* 102, 5870 (1998).
87. H. Yamashita, S. Kawasaki, Y. Fujii, Y. Ichihashi, S. Ehara, S. E. Park, J. S. Chang, J. W. Yoo, and M. Anpo, *Stud. Surf. Sci. Catal.* 114, 561 (1998).
88. H. Yamashita, S. Kawasaki, Y. Ichihashi, M. Takeuchi, M. Harada, M. Anpo, C. Louis, and M. Che, *Korean J. Chem. Eng.* 15, 491 (1998).
89. M. Anpo and K. Chiba, *J. Mol. Catal.* 74, 207 (1992).
90. M. Anpo, *Catal. Surv. Jpn.* 1, 169 (1997).
91. M. Anpo, *Pure Appl. Chem.* 72, 1787 (2000).
92. H. Yamashita, M. Harada, J. Misaka, M. Takeuchi, K. Ikeue, and M. Anpo, *J. Photochem. Photobiol., A* 148, 257 (2002).
93. M. Anpo, S. Kishiguchi, Y. Ichihashi, M. Takeuchi, H. Yamashita, K. Ikeue, B. Morin, A. Davidson, and M. Che, *Res. Chem. Intermed.* 27, 459 (2001).
94. H. Yamashita, M. Harada, J. Misaka, M. Takeuchi, Y. Ichihashi, F. Goto, M. Ishida, T. Sasaki, and M. Anpo, *J. Synchrotron Rad.* 8, 569 (2001).
95. M. Takeuchi, H. Yamashita, M. Matsuoka, M. Anpo, T. Hirao, N. Itoh, and N. Iwamoto, *Catal. Lett.* 67, 135 (2000).
96. H. Yamashita, Y. Ichihashi, M. Takeuchi, S. Kishiguchi, and M. Anpo, *J. Synchrotron Rad.* 6, 451 (1999).
97. M. Anpo, Y. Ichihashi, M. Takeuchi, and H. Yamashita, *Stud. Surf. Sci. Catal.* 121, 104 (1999).
98. H. Yamashita, M. Honda, M. Harada, Y. Ichihashi, M. Anpo, and Y. Hatano, *J. Phys. Chem. B* 102, 10707 (1998).
99. M. Anpo, Y. Ichihashi, M. Takeuchi, and H. Yamashita, *Res. Chem. Intermed.* 24, 143 (1998).
100. A. Kudo, *J. Ceram. Soc. Jpn.* 109, S81 (2001).
101. H. Kato and A. Kudo, *J. Phys. Chem. B* 106, 5029 (2002).
102. O. Hamanoi and A. Kudo, *Chem. Lett.* 838 (2002).
103. A. Kudo and M. Sekizawa, *Chem. Commun.* 1371 (2000).
104. A. Kudo and M. Sekizawa, *Catal. Lett.* 58, 241 (1999).
105. T. Umabayashi, T. Yamaki, H. Itoh, and K. Asai, *J. Phys. Chem. Solids* 63, 1909 (2002).
106. A. Nakayama, E. Suzuki, and T. Ohmori, *Appl. Surf. Sci.* 189, 260 (2002).
107. S. Klosek and D. Raftery, *J. Phys. Chem. B* 105, 2815 (2001).
108. D. Raftery and S. Klosek, *Abstr. Pap. Am. Chem. S219, 35-CATL* (2000).
109. K. Rajeshwar, C. R. Chenthamarakshan, S. Goeringer, and M. Djukic, *Pure Appl. Chem.* 73, 1849 (2001).
110. M. Iwasaki, M. Hara, H. Kawada, H. Tada, and S. Ito, *J. Colloid. Interface Sci.* 224, 202 (2000).

111. N. I. I-Salim, S. A. Bagshaw, A. Bittar, T. Kemmitt, A. J. McQuillan, A. M. Mills, and M. J. Ryan, *J. Mater. Chem.* 10, 2358 (2000).
112. C. A. K. Gouvea, F. Wypych, S. G. Moraes, N. Duran, and P. Peralta-Zamora, *Chemosphere* 40, 427 (2000).
113. T. Ohno, F. Tanigawa, K. Fujihara, S. Izumi, and M. Matsumura, *J. Photochem. Photobiol., A* 127, 107 (1999).
114. Y. Sakata, T. Yamamoto, T. Okazaki, H. Imamura, and S. Tsuchiya, *Chem. Lett.* 1253 (1998).
115. F. Franceschi, M. Guardigli, E. Solari, C. Floriani, A. ChiesiVilla, and C. Rizzoli, *Catal. Lett.* 44, 67 (1997).
116. A. Kudo, K. Omori, and H. Kato, *J. Am. Chem. Soc.* 121, 11459 (1999).
117. A. Kudo, K. Ueda, H. Kato, and I. Mikami, *Catal. Lett.* 53, 229 (1998).
118. S. Kohtani, S. Makino, A. Kudo, K. Tokumura, Y. Ishigaki, T. Matsunaga, O. Nikaido, K. Hayakawa, and R. Nakagaki, *Chem. Lett.* 660 (2002).
119. Z. G. Zou, J. H. Ye, K. Sayama, and H. Arakawa, *Nature* 414, 625 (2001).
120. Z. G. Zou, J. H. Ye, and H. Arakawa, *Catal. Lett.* 75, 209 (2001).
121. Z. Zou, J. Ye, and H. Arakawa, *J. Mater. Res.* 17, 1419 (2002).
122. H. Arakawa and K. Sayama, *Res. Chem. Intermed.* 26, 145 (2000).
123. J. H. Ye, Z. G. Zou, M. Oshikiri, A. Matsushita, M. Shimoda, M. Imai, and T. Shihido, *Chem. Phys. Lett.* 356, 221 (2002).
124. F. Chen and J. C. Zhao, *Catal. Lett.* 58, 245 (1999).
125. R. Asahi, T. Morikawa, T. Ohwaki, K. Aoki, and Y. Taga, *Science* 293, 269 (2001).
126. U. M. K. Shahed, A. S. Mofareh, and B. I. J. William, *Science* 297, 2243 (2002).
127. C. Lettmann, K. Hildenbrand, H. Kisch, W. Macyk, and W. F. Maier, *Appl. Catal., B* 32, 215 (2001).
128. G. Hitoki, T. Takata, J. N. Kondo, M. Hara, H. Kobayashi, and K. Domen, *Chem. Commun.* 1698 (2002).
129. G. Hitoki, A. Ishikawa, T. Takata, J. N. Kondo, M. Hara, and K. Domen, *Chem. Lett.* 736 (2002).
130. G. Hitoki, T. Takata, J. N. Kondo, M. Hara, H. Kobayashi, and K. Domen, *Electrochemistry* 70, 463 (2002).
131. A. Kasahara, K. Nukumizu, G. Hitoki, T. Takata, J. N. Kondo, M. Hara, H. Kobayashi, K. Domen, and A. Tanaka, *J. Phys. Chem. A* 106, 6750 (2002).
132. T. Umebayashi, T. Yamaki, H. Itoh, and K. Asai, *Appl. Phys. Lett.* 81, 454 (2002).
133. A. Kudo, I. Tsuji, and H. Kato, *Chem. Commun.* 1958 (2002).
134. A. Kudo, A. Nagane, I. Tsuji, and H. Kato, *Chem. Lett.* 882 (2002).
135. A. Kudo and I. Mikami, *Chem. Lett.* 1027 (1998).
136. T. Ihara, M. Miyoshi, M. Ando, S. Sugihara, and Y. Iriyama, *J. Mater. Sci.* 36, 4201 (2001).
137. I. Nakamura, N. Negishi, S. Kutsuna, T. Ihara, S. Sugihara, and E. Takeuchi, *J. Mol. Catal., A* 161, 205 (2000).
138. S. Iimura, H. Teduka, A. Nakagawa, S. Yoshihara, and T. Shirakashi, *Electrochemistry* 69, 324 (2001).
139. H. Yamashita, M. Harada, A. Tani, M. Honda, M. Takeuchi, Y. Ichihashi, M. Anpo, N. Iwamoto, N. Itoh, and T. Hirao, *Catal. Today* 63, 63 (2000).
140. H. Yamashita, M. Harada, A. Tani, M. Honda, M. Takeuchi, Y. Ichihashi, and M. Anpo, *Stud. Surf. Sci. Catal.* 130, 1931 (2000).
141. M. Takeuchi, M. Matsuoka, H. Yamashita, and M. Anpo, *J. Synchrotron Rad.* 8, 643 (2001).
142. M. Takeuchi, H. Yamashita, M. Matsuoka, and M. Anpo, *Catal. Lett.* 66, 185 (2000).
143. M. Harada, A. Tani, H. Yamashita, and M. Anpo, *Z. Phys. Chem.* 213, 59 (1999).
144. H. Yamashita, K. Yoshizawa, M. Ariyuki, S. Higashimoto, and M. Anpo, *Stud. Surf. Sci. Catal.* 141, 495 (2002).
145. H. Yamashita, K. Yoshizawa, M. Ariyuki, S. Higashimoto, and M. Anpo, *Stud. Surf. Sci. Catal.* 135, 28P07 (2001).
146. H. Yamashita, K. Yoshizawa, M. Ariyuki, S. Higashimoto, M. Che, and M. Anpo, *Chem. Commun.* 435 (2001).
147. H. Yamashita, M. Ariyuki, S. Higashimoto, S. G. Zhang, J. S. Chang, and S. E. Park, *J. Synchrotron Rad.* 6, 453 (1999).
148. M. Anpo and M. Takeuchi, *Int. J. Photoenergy* 3, 1 (2001).
149. T. Takata, A. Tanaka, M. Hara, J. N. Kondo, and K. Domen, *Catal. Today* 44, 17 (1998).
150. J. Yoshimura, J. Tanaka, J. N. Kondo, and K. Domen, *Bull. Chem. Soc. Jpn.* 68, 2439 (1995).
151. J. Yoshimura, Y. Ebina, J. N. Kondo, K. Domen, and A. Tanaka, *J. Phys. Chem.* 97, 1970 (1993).
152. G. B. Saupe, C. C. Waraksa, H. N. Kim, Y. J. Han, D. M. Kaschak, D. M. Skinner, and T. E. Mallouk, *Chem. Mater.* 12, 1556 (2000).
153. J. H. Wu, S. Uchida, Y. Fujishiro, S. Yin, and T. Sato, *J. Photochem. Photobiol., A* 128, 129 (1999).
154. G. Burgeth and H. Kisch, *Coord. Chem. Rev.* 230, 41 (2002).
155. H. Kisch and W. Macyk, *Chem. Phys. Chem.* 3, 399 (2002).
156. W. Zhao, C. C. Chen, X. Z. Li, J. C. Zhao, H. Hidaka, and N. Serpone, *J. Phys. Chem. B* 106, 5022 (2002).
157. X. Z. Li and F. B. Li, *Environ. Sci. Technol.* 35, 2381 (2001).
158. D. Chatterjee and C. Bhattacharya, *Indian J. Chem., Sect. A* 38, 1256 (1999).
159. T. Abe, E. Suzuki, K. Nagoshi, K. Miyashita, and M. Kaneko, *J. Phys. Chem. B* 103, 1119 (1999).
160. L. Zang, C. Lange, I. Abraham, S. Storck, W. F. Maier, and H. Kisch, *J. Phys. Chem. B* 102, 10765 (1998).
161. K. Sayama, K. Mukasa, R. Abe, Y. Abe, and H. Arakawa, *Chem. Commun.* 2416 (2001).
162. K. Sayama, K. Mukasa, R. Abe, Y. Abe, and H. Arakawa, *J. Photochem. Photobiol., A* 148, 71 (2002).
163. H. Yamashita, K. Ikeue, and M. Anpo, in "ACS Symposium Series 809, Book on CO₂ Conversion and Utilization" (K. Fujimoto and C. Song, Eds.), pp. 330-343. Am. Chem. Soc., Washington, DC, 2002.
164. H. Yamashita, K. Ikeue, T. Takewaki, and M. Anpo, *Top. Catal.* 18, 95 (2002).
165. K. Ikeue, H. Yamashita, and M. Anpo, *Electrochemistry* 70, 402 (2002).
166. K. Ikeue, H. Yamashita, T. Takewaki, and M. Anpo, *J. Phys. Chem. B* 105, 8350 (2001).
167. K. Ikeue, H. Yamashita, T. Takewaki, M. E. Davis, and M. Anpo, *J. Synchrotron Rad.* 8, 602 (2001).
168. K. Ikeue, H. Mukai, H. Yamashita, S. Inagaki, M. Matsuoka, and M. Anpo, *J. Synchrotron Rad.* 8, 640 (2001).
169. K. Ikeue, H. Yamashita, and M. Anpo, *Chem. Lett.* 1135 (1999).
170. H. Yamashita, Y. Fuji, Y. Ichihashi, S. G. Zhang, K. Ikeue, D. R. Park, K. Koyano, T. Tatsumi, and M. Anpo, *Catal. Today* 45, 221 (1998).
171. M. Anpo, S. G. Zhang, Y. Fujii, Y. Ichihashi, H. Yamashita, K. Koyano, and T. Tatsumi, *Catal. Today* 44, 327 (1998).
172. M. Anpo, H. Yamashita, Y. Fujii, Y. Ichihashi, S. G. Zhang, D. R. Park, S. Ehara, S. E. Park, J. S. Chang, and J. W. Yoo, *Stud. Surf. Sci. Catal.* 114, 177 (1998).
173. S. G. Zhang, Y. Fujii, H. Yamashita, K. Koyano, T. Tatsumi, and M. Anpo, *Chem. Lett.* 659 (1997).
174. M. Anpo, H. Yamashita, Y. Ichihashi, Y. Fujii, and M. Honda, *J. Phys. Chem. B* 101, 2632 (1997).
175. M. Anpo, H. Yamashita, Y. Ichihashi, and S. Ehara, *J. Electroanal. Chem.* 396, 21 (1995).
176. J. Zhang, Y. Hu, M. Matsuoka, H. Yamashita, M. Minagawa, H. Hidaka, and M. Anpo, *J. Phys. Chem. B* 105, 8395 (2001).
177. J. Zhang, B. He, M. Matsuoka, H. Yamashita, and M. Anpo, *Stud. Surf. Sci. Catal.* 135, 30P24 (2001).
178. J. Zhang, M. Matsuoka, H. Yamashita, and M. Anpo, *J. Synchrotron Rad.* 8, 637 (2001).
179. J. Zhang, M. Minagawa, T. Ayusawa, S. Natarajan, H. Yamashita, M. Matsuoka, and M. Anpo, *J. Phys. Chem.* 104, 11501 (2000).

180. J. L. Zhang, M. Minagawa, M. Matsuoka, H. Yamashita, and M. Anpo, *Catal. Lett.* 66, 241 (2000).
181. M. Anpo, H. Yamashita, M. Matsuoka, D. R. Park, T. G. Shul, and S. E. Park, *J. Ind. Eng. Chem.* 6, 59 (2000).
182. Y. Ichihashi, H. Yamashita, M. Anpo, Y. Souma, and Y. Matsumura, *Catal. Lett.* 53, 107 (1998).
183. N. U. Zhanpeisov, M. Matsuoka, H. Mishima, H. Yamashita, and M. Anpo, *J. Phys. Chem. B* 102, 6915 (1998).
184. H. Yamashita, S. G. Zhang, Y. Ichihashi, Y. Matsumura, Y. Souma, T. Tatsumi, and M. Anpo, *Appl. Surf. Sci.* 121, 305 (1997).
185. K. T. Jung, Y. G. Shul, M. Anpo, and H. Yamashita, *Korean J. Chem. Eng.* 14, 213 (1997).
186. Y. Ichihashi, H. Yamashita, and M. Anpo, *J. Phys. IV* 7, 883 (1997).
187. M. Anpo, H. Yamashita, and S. Zhang, *Curr. Opin. Solid State Mater. Sci.* 1, 219 (1996).
188. H. Yamashita, Y. Ichihashi, M. Anpo, M. Hashimoto, C. Louis, and M. Che, *J. Phys. Chem.* 100, 16041 (1996).
189. S. G. Zhang, Y. Ichihashi, H. Yamashita, T. Tatsumi, and M. Anpo, *Chem. Lett.* 895 (1996).
190. Y. Ichihashi, H. Yamashita, and M. Anpo, *Stud. Surf. Sci. Catal.* 105, 1609 (1996).
191. S. Higashimoto, M. Matsuoka, H. Yamashita, M. Anpo, and O. Kitao, *Microporous Mesoporous Mater.* 48, 329 (2001).
192. S. Higashimoto, M. Matsuoka, H. Yamashita, M. Anpo, O. Kitao, H. Hidaka, M. Che, and E. Giamello, *J. Phys. Chem. B* 104, 10288 (2000).
193. M. Matsuoka, S. Higashimoto, H. Yamashita, and M. Anpo, *Res. Chem. Intermed.* 26, 85 (2000).
194. M. Anpo, S. G. Zhang, S. Higashimoto, M. Matsuoka, H. Yamashita, Y. Ichihashi, Y. Matsumura, and Y. Souma, *J. Phys. Chem. B* 103, 9295 (1999).
195. S. Higashimoto, M. Matsuoka, H. Yamashita, and M. Anpo, *Jpn. J. Appl. Phys.* 38, 47 (1999).
196. S. G. Zhang, S. Higashimoto, H. Yamashita, and M. Anpo, *J. Phys. Chem. B* 102, 5590 (1998).
197. S. G. Zhang, M. Ariyuki, S. Higashimoto, H. Yamashita, and M. Anpo, *Microporous Mesoporous Mater.* 21, 621 (1998).
198. M. Anpo, S. G. Zhang, H. Mishima, M. Matsuoka, and H. Yamashita, *Catal. Today* 39, 159 (1997).
199. S. Higashimoto, S. G. Zhang, H. Yamashita, and M. Anpo, *Chem. Lett.* 1127 (1997).
200. M. Anpo, S. Zhang, and H. Yamashita, *Stud. Surf. Sci. Catal.* 101, 941 (1996).
201. S. Higashimoto, R. Tsumura, M. Matsuoka, H. Yamashita, M. Che, and M. Anpo, *Stud. Surf. Sci. Catal.* 140, 315 (2001).
202. R. Tsumura, S. Higashimoto, M. Matsuoka, H. Yamashita, M. Che, and M. Anpo, *Catal. Lett.* 68, 101 (2000).
203. S. Higashimoto, R. Tsumura, S. G. Zhang, M. Matsuoka, H. Yamashita, C. Louis, M. Che, and M. Anpo, *Chem. Lett.* 408 (2000).
204. M. Matsuoka, W. S. Ju, K. Takahashi, H. Yamashita, and M. Anpo, *J. Phys. Chem. B* 104, 4911 (2000).
205. M. Anpo, M. Matsuoka, H. Yamashita, W. S. Ju, S. E. Park, and Y. G. Shul, *J. Ind. Eng. Chem.* 6, 133 (2000).
206. N. U. Zhanpeisov, M. Matsuoka, H. Mishima, H. Yamashita, and M. Anpo, *J. Mol. Struct.* 454, 201 (1998).
207. M. Anpo, M. Matsuoka, K. Hanou, H. Mishima, T. Ono, and H. Yamashita, *Korean J. Chem. Eng.* 14, 498 (1997).
208. M. Anpo, M. Matsuoka, K. Hanaou, H. Mishima, H. Yamashita, and H. Patterson, *Coord. Chem. Rev.* 171, 175 (1998).
209. M. Anpo, M. Matsuoka, H. Mishima, and H. Yamashita, *Res. Chem. Intermed.* 23, 197 (1997).
210. H. Yamashita, M. Matsuoka, and M. Anpo, *J. Phys. IV* 7, 941 (1997).
211. M. Matsuoka, K. Takahashi, H. Yamashita, and M. Anpo, *J. Phys. IV* 7, 943 (1997).
212. H. Yamashita, M. Matsuoka, K. Tsuji, Y. Shioya, and M. Anpo, *J. Phys. Chem.* 100, 397 (1996).
213. N. Negishi, M. Matsuoka, H. Yamashita, and M. Anpo, *J. Phys. Chem.* 97, 5211 (1993).
214. M. Anpo, M. Matsuoka, Y. Shioya, H. Yamashita, E. Giamello, C. Morterra, M. Che, H. H. Patterson, S. Webber, S. Quелlette, and M. A. Fox, *J. Phys. Chem.* 98, 5744 (1994).
215. H. Yamashita, M. Matsuoka, Y. Shioya, M. Anpo, E. Giamello, and M. Che, *Stud. Surf. Sci. Catal.* 92, 227 (1995).
216. M. Matsuoka, E. Matsuda, K. Tsuji, H. Yamashita, and M. Anpo, *Chem. Lett.* 375 (1995).
217. M. Matsuoka, W. S. Ju, H. Yamashita, and M. Anpo, *J. Synchrotron Rad.* 8, 613 (2001).
218. M. Anpo, M. Matsuoka, and H. Yamashita, *Catal. Today* 35, 177 (1997).
219. M. Matsuoka, E. Matsuda, K. Tsuji, H. Yamashita, and M. Anpo, *J. Mol. Catal., A* 107, 399 (1996).
220. W. S. Ju, M. Matsuoka, H. Yamashita, and M. Anpo, *J. Synchrotron Rad.* 8, 608 (2001).
221. H. Yamashita, S. Takada, M. Nishimura, H. Bessho, and M. Anpo, *Stud. Surf. Sci. Catal.* 135, 15P07 (2001).
222. H. Yamashita, M. Nishimura, T. Nakajima, M. Hada, H. Nakatsuji, and M. Anpo, *Res. Chem. Intermed.* 27, 89 (2001).
223. H. Yamashita, A. Tanaka, M. Nishimura, and M. Anpo, *Stud. Surf. Sci. Catal.* 117, 651 (1998).
224. H. Nishiguchi, S. Okamoto, M. Nishimura, H. Yamashita, and M. Anpo, *Res. Chem. Intermed.* 24, 849 (1998).
225. H. Yamashita, N. Sato, M. Anpo, T. Nakajima, M. Hada, and H. Nakatsuji, *Stud. Surf. Sci. Catal.* 105, 1141 (1996).
226. T. Fujii, A. Ishii, N. Takusagawa, H. Yamashita, and M. Anpo, *J. Photochem. Photobiol., A* 86, 219 (1995).
227. H. Nishiguchi, K. Yukawa, H. Yamashita, and M. Anpo, *Res. Chem. Intermed.* 21, 885 (1995).
228. M. Anpo, S. Zhang, S. Okamoto, and H. Yamashita, *Res. Chem. Intermed.* 21, 631 (1995).
229. H. Nishiguchi, K. Yukawa, H. Yamashita, and M. Anpo, *J. Photochem. Photobiol., A* 92, 85 (1995).
230. H. Yamashita, K. Kida, K. Ikeue, Y. Kanazawa, K. Yoshizawa, and M. Anpo, *Stud. Surf. Sci. Catal.* 135, 8765 (2002).

X-Ray Characterization of Nanolayers

Dirk C. Meyer, Peter Paufler

Technische Universität Dresden, Dresden, Germany

CONTENTS

1. Introduction
 2. Structural Parameters of Nanolayers
 3. Basic Phenomena Due to Interaction of X-Rays with Flat Surfaces and Nanolayers
 4. Characterization Methods
 5. Nanolayer Materials
- References

1. INTRODUCTION

Thin films behave significantly different from bulk material if the layer thickness is, for example, of the order of several to a hundred nanometers. The influence of surface-near atoms cannot then be neglected depending on the property under investigation. The first few atomic layers are known to deviate notably in atomic, electronic, and magnetic structure from those more distant from the surface. This often includes surface segregation of impurities or surface enrichment of solute species. Moreover, the total number of atoms per unit area is of the order of $4 \times 10^{13} (t/a) \text{ mm}^{-2}$ for a layer of thickness t and lattice parameter a , (i.e., measuring signals proportional to this figure may become too small to be detected). For the preparation of nanolayers a number of methods are available. However, both synthesis and handling of these layers remain challenging tasks because of the need for high-purity materials and for monolayer precision with layer growth.

In addition to that, the great success of nanolayers in the field of microelectronic and optoelectronic devices, for storage of information, as protecting layers, as customized (multilayer) structures, or as coupled systems (e.g., polyelectrolytes/surfactants or protein/lipids) has increased the demand for novel structural analytical tools.

For the characterization of thin films established X-ray analysis methods have been modified and dedicated new techniques were developed which predominantly make use

of the typical characteristics and quality of these samples. Since 1912 [1] it has been well known that X-ray diffraction methods can provide structural information of solids when wavelengths of the order of interatomic distances are employed. Since the scattering cross section of atoms for X-rays is rather weak, the small number of atoms contained within thin layers may prevent diffraction maxima from being detected. A way around insufficient scattering intensity has been found by using longer paths of X-rays within the specimen (i.e., grazing incidence of X-rays) and higher X-ray photon fluxes (e.g., synchrotron radiation sources). Below a critical angle of incidence α_c , with respect to the surface, total external reflection occurs (e.g., $\alpha_c = 0.223^\circ$ for Si wavelength $\lambda = 1.54 \text{ \AA}$ [2]) whereby the totally reflected intensities are significantly larger than in the case of specular reflection above α_c . Exploiting multiple refraction and reflection of X-rays at the surface and the nanolayer/substrate interface in a range of angles of incidence directly above α_c (typically up to 10°), sharp interference patterns may be obtained. The refractive index for X-rays can be written as $n = 1 - \delta - i\beta$ with the dispersion term $\delta \geq 0$ ($\approx 7.6 \times 10^{-6}$ for Si; wavelength $\lambda = 1.54 \text{ \AA}$) and the absorption term β ($\approx 0.17 \times 10^{-6}$ for Si). Thus it is obvious that the values of refractive indexes of solids for X-rays differ in a characteristic manner from those of other photon energies. They are always slightly less than 1. This causes high demands concerning the measuring accuracy to proof and use the associated phenomena.

The availability of intense, highly polarized and energy-tunable X-ray photons from synchrotron sources has enabled significant enhancement of experimental possibilities. As an example, in the case of resonant scattering δ may change by more than a factor 2 [3]. One can cause this situation by the purposeful choice of the energy of X-rays according to element-specific binding energies of the electrons.

For angles of incidence $\alpha_i > \alpha_c$ the penetration depth increases and reaches a maximum value at $\alpha_i = 90^\circ$ of $\lambda/4\beta \approx 10^3\text{--}10^4 \text{ nm}$ for most materials. Thus, by tuning the angle of incidence the analysis can be accomplished depth-resolvedly.

Owing to these properties, analytical methods using X-rays can be applied across the whole variety of materials

irrespective of the chemical composition, microstructure, dimension, and even degree of crystallinity. Depending on the area of application (for an overview we refer to [4]), distinct structural parameters, determinable by means of X-ray analysis methods, are used for the characterization of nanolayers.

In Section 2 we intend to briefly categorize these parameters and provide the reader in Section 4 with details of the appropriate method for obtaining them. Examples of current work on X-ray characterization of different types of nanolayer materials are given in Section 5. Section 3 has been included to introduce X-ray methods to those readers who are not familiar with them. Recognizing the vast variety of analytical methods where X-rays are involved (electromagnetic waves with wavelength range $\approx 1 \times 10^{-2}$ –30 nm), we restricted ourselves to methods exploiting X-rays as both incident and emitted probes. Excitation by/or emission of electrons, for example, will therefore not be dealt with here.

2. STRUCTURAL PARAMETERS OF NANOLAYERS

The structure of nanolayers may be described at different levels of scaling. Here the parameters determinable by means of X-ray analysis methods will be summarized. Scattering of X-rays by atoms is mainly due to the core and the outer electrons (i.e., the electron density distribution in physical space is the structural parameter obtainable at the smallest scale). Also, spin density waves in thin films and multilayers accompanied by strain waves can effectively be studied. It is a very recent development that magnetic moments may also be determined directly by means of X-ray scattering and absorption spectroscopy. By measuring the specular reflectivity with X-rays of energies tuned close to binding energies of electrons, the usually weak magnetic scattering signal may become as large as several percent of the scattering caused by electric interaction. Moreover, it then becomes element specific.

Because of the large amount of data involved, simplifications are often used when exploiting experimentally obtained intensities. Thus, disregarding the electron distribution, in the case of crystalline layers the coordinates of atomic nuclei with respect to a unit cell are taken as characteristics of a certain structure. Noncrystalline layers are structurally characterized by pair-correlation functions indicating the radial distribution of atoms.

If the nanolayer proves multiphase, then both the structures and the quantities of all crystalline phases (including nanovoids) have to be determined in order to characterize the material properly. Characterization thereby, besides the structural identification of crystalline phases, aims also to obtain size, shape, and distribution of the appropriate particles. Supplementary information about the orientation distribution of the crystallites and their texture is needed, when the layer is polycrystalline. Moreover, strains due to internal incompatibilities or external stress can reduce the symmetry of the distorted material as compared with the equilibrium bulk state, so that the strain tensor serves as another set of parameters. It proved useful to distinguish long-range and short-range distortions, where long range means large compared to the unit cell or crystallite diameter.

The understanding of properties at a structural level is essentially facilitated when the roughness of surface and layer/substrate interface is given quantitatively. Finally, the thickness of a nanolayer is the simplest geometric parameter on the nanoscale. Macroscopic material properties, such as the mass density, can be derived partially likewise on the basis of a number of nanoscale parameters.

3. BASIC PHENOMENA DUE TO INTERACTION OF X-RAYS WITH FLAT SURFACES AND NANOLAYERS

3.1. X-Rays and Waves

When X-rays interact with atoms or molecules, energy from the electromagnetic wave is absorbed as well as emitted by them. These processes require extensive mathematical and quantum mechanical treatment. Fortunately, the fundamental ideas are comprehensible using the concept of photons approximated by wave packets. A wave packet is localized in space by superposing several wavelengths λ .

Incident waves coming from an external source may in most cases be well approximated by plane waves, whereas waves emitted by atoms within the solid have to be rather dealt with as spherical waves. In a crystalline solid they may interfere forming an outgoing plane wave. When the amplitude of the single scattered wave is small compared with the incident wave amplitude, then the amplitude of the doubly scattered wave is negligible compared with the singly scattered wave. This simplifies the superposition of scattered X-ray photons in a solid considerably.

Reflection and refraction of X-rays at discontinuities of the refractive index can be analyzed geometrically using the ray concept, which is applicable so long as the discontinuities encountered by the wave packet during its propagation are large compared with its average wavelength. In this respect X-rays behave like visible light as long as absorption of energy can be neglected.

3.2. Interaction of X-rays with Atoms of Matter

The interaction of X-rays with photon energies on the order of 10 keV ("hard X-rays," usually used for X-ray structure analysis) with atoms of matter is limited almost exclusively to their electrons. For quantitative description the attenuation of photons due to the photoelectric effect and scattering processes are to be differentiated as substantial processes. In the case of photoelectric absorption the irradiating photon of energy E extracts a bound electron. A following interatomic electron transition leads to the emission of a fluorescence photon of a characteristic energy. For quantitative description the linear photoelectric absorption coefficient $\tau(E)$ is assigned to this process. Coherent and incoherent scattering of photons is described by the total linear scattering coefficient $\sigma(E)$. The coherent scattering process, with which the energy of the photons and their phase characteristics remain unchanged, is the basis of X-ray interference methods (see Fig. 1).

The interaction effects can be determined quantitatively by measuring the attenuation of a parallel beam of X-ray

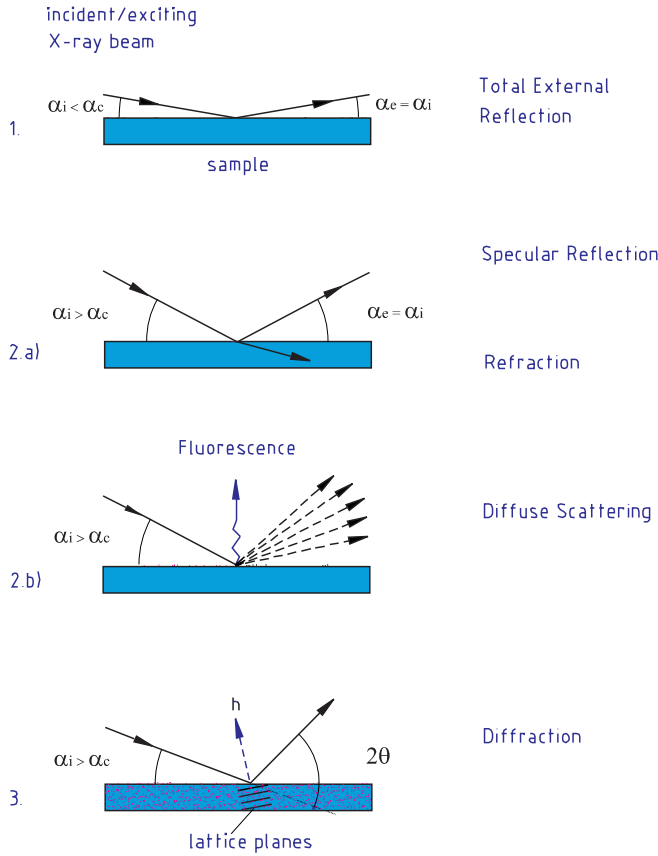


Figure 1. Basic phenomena due to interaction of X-rays (energies in the order of 10 keV) with flat surfaces and nanolayers. X-ray beams directed toward a smooth vacuum/matter interface at angles of incidence α_i below a critical angle α_c will undergo total external reflection (1). For angles of incidence above α_c at ideally smooth interfaces two secondary beams, specular reflected (reflection angle $\alpha_e = \alpha_i$) and refracted ones, arise (2a). The refracted beam is attenuated in the matter, whereby photoelectric absorption is followed by the emission of characteristic fluorescence photons. Deviations from an ideally smooth curvature cause nonspecular diffuse scattering (2b). If matter exhibits long-range order elastic scattering can cause diffraction phenomena (diffraction angle 2θ) (3).

photons with incident intensity $I_0(E)$ in a medium. If these photons penetrate a flat parallel plate of homogeneous isotropic material and thickness t (surface normal of the plate is parallel to the beam direction) the intensity $I(E)$ behind the plate is given by the exponential attenuation law

$$I(E) = I_0(E)e^{-\mu(E)t} \quad (1)$$

with the total attenuation coefficient

$$\mu(E) = \tau(E) + \sigma(E) \quad (2)$$

whereby $\tau(E)$ stands for the contributions of photoelectric absorption and $\sigma(E)$ stands for elastic and inelastic scattering, respectively. The amplitude of the electromagnetic field of X-ray photons, coherently scattered by an atom of atomic number Z , normalized with respect to a free electron, can be described by means of the atomic scattering amplitude f_0 .

The atomic scattering amplitude is a function of the scattering vector Q attributed to a scattered photon. Its modulus Q is usually expressed in dependence on the scattering angle θ and the photon wavelength λ by

$$Q = \frac{4\pi \sin(\theta)}{\lambda}. \quad (3)$$

For the case of forward scattering ($\theta = 0^\circ$) the atomic scattering amplitude corresponds to the number of electrons per neutral atom ($f_0 = Z$). From the viewpoint of classical mechanics the scattering process can be described by a forced oscillation with damping. In extension to the classical model it has to take into consideration that the relativistic mass of the bound electrons increases due to the excitation, whereby the scattering power decreases. This influence can be considered by adding a relativistic correction. The differential equation for the description of a forced oscillation with damping in the model of the harmonic oscillator yields mathematically complex-valued solutions. Thus the atomic scattering has also to be taken as a mathematically complex-valued function. In addition corrections have to be considered, which become substantial for the case of resonance. Energies of resonant interactions correspond to ionization energies of the atoms. The photon gives rise to real and virtual transitions, where it is absorbed and re-emitted. These processes cause the corrections $f'(Q, E)$ and $f''(Q, E)$ to the atomic scattering amplitude. It was shown by experiment that their dependencies on Q are mostly small [5]. Thus the atomic scattering amplitude is usually expressed by

$$f(Q, E) = f_0(Q, E) + f'(E) + if''(E). \quad (4)$$

The values for the individual terms are available in tabulated form. Usually, numerical values are based on the theoretical computations of atomic scattering amplitudes of Cromer and Liberman [6]. The real part $f'(E)$ of the correction to the atomic scattering amplitude and the imaginary part $f''(E)$ are interconnected (self-consistent Kramers–Kronig transform pairs). The physical origin of the causal relationship between both parts was described in detail by Toll [7].

Using the example of nickel ($Z = 28$) typical values and the influence of the distance of photon energy to the absorption edge (ionization energy of a bound state) can be illustrated. The energy of the K -absorption edge of nickel is 8.333 keV. For photons with an energy of 7.500 keV the corrections amount to $f' = -2.076$ and $f'' = 0.579$, respectively. At an energy of 8.340 keV, just below the absorption edge, the appropriate values are $f' = -6.886$ and $f'' = 3.914$, while at an energy of 9.000 keV values of $f' = -6.886$ and $f'' = 3.914$ are to be considered. It can be assumed that for photon energies with significant distance to the absorption edges the amount of corrections die down, whereby $f''(E)$ exhibits a jumplike behavior when exciting ionization energies.

3.3. Interaction of X-Rays with Interfaces

When directing an X-ray beam toward a smooth vacuum/matter interface, like in the case of visible light, specular reflection and refraction (transmission) can be observed as basic phenomena. A deeper understanding and a linkage

to electrodynamics and wave optics is given by the Huygens–Fresnel principle. In the case of X-rays it is characteristic that a refracted beam can only exist in the medium above a critical angle included by beam and surface plane. For angles of incidence below this critical angle total external reflection occurs. The angle characteristic of the reflected beam has to be described by the reflection law. The intensities of the transmitted radiation are attenuated in the medium according to an exponential law, whereby the attenuation coefficient, besides the path length of the beam, covers contributions of all interactions of X-rays with matter as mentioned. The angle of refraction, characteristic of the material as in the case of visible light, observes Snell's law.

For the intensities of the three partial beams (incident, reflected, and transmitted) found at the interface, conservation of energy is required. Considering the continuity conditions of the components of the field vectors at an interface, as demanded by electrodynamics, the amplitudes of the waves are described numerically by reflection factor r and transmission coefficient t (Fresnel equations). The squares of these amplitudes are normally called “reflectivity” and “transmission,” respectively.

3.4. Quantitative Description of Reflection, Refraction, and External Total Reflection

The reflection and refraction of X-rays can be described quantitatively using refractive indices of the media, which form the interface. The refractive index of a medium is a function of the frequency and thus the energy of the photons and is defined through

$$n = \frac{c}{v} \quad (5)$$

whereby c stands for the speed of light in vacuum and v for the phase velocity of the wave in the medium.

For a medium, which contains the chemical elements j with the atomic number Z_j , the atomic weight A_j , and the densities ρ_j , on the basis of the model of the harmonic oscillator with damping, the refractive index n for X-ray photons of the wavelength λ is given by

$$n = 1 - \frac{N_a}{2\pi} r_0 \lambda^2 \sum_j \frac{\rho_j}{A_j} f_j \quad (6)$$

whereby N_a is Avogadro's constant, $r_0 = e^2/mc^2 = 2.818 \times 10^{-13}$ cm is the classical electron radius, and f_j is the element specific atomic scattering amplitude.

In the case of forward scattering of X-ray photons with energies sufficiently different from the ionization energies of the atoms, the approximation $f_j \sim Z_j$ can be used (i.e., in general the atomic scattering amplitude can be estimated by the number of electrons per atom). If the energy of the incident X-ray photons lies in the vicinity of the ionization energy of a species of scattering atoms, contributions of resonant dispersion f_j' and absorption if_j'' must be considered, as already mentioned. Accordingly, the refraction indexes

have to also be described as mathematically complex variables and can be expressed as

$$n = 1 - \delta - i\beta \quad (7)$$

with the parameters of dispersion

$$\delta = \frac{N_a}{2\pi} r_0 \lambda^2 \sum_j \frac{\rho_j}{A_j} (Z_j + f_j') \quad (8)$$

and absorption

$$\beta = \frac{N_a}{2\pi} r_0 \lambda^2 \sum_j \frac{\rho_j}{A_j} f_j'' \quad (9)$$

As already mentioned in Section 1, the values of refractive indexes of solids for X-rays differ in a characteristic manner from those of other photon energies: They are always slightly less than 1 [e.g., for copper ($Z = 29$) and a photon energy of 8.600 keV we have $\delta = 23.0 \times 10^{-6}$ and $\beta = 0.4 \times 10^{-6}$]. Hence for transition of X-rays from vacuum to matter total external reflection occurs below a critical angle of incidence α_c , which is typically smaller than 1° (e.g., for copper $\alpha_c = 0.39^\circ$ at a photon energy of 8.600 keV or $\lambda \approx 1.44$ Å). If the angle of incidence α_i falls short with respect to α_c instead of a refracted beam an exponentially decaying X-ray wave field (“evanescent wave”) develops, the penetration depth of which is typically 5 nm. For the reflected beam the well known law of reflection applies (i.e., the angle of reflection is equal to that of incidence).

3.5. Deviations from an Ideal Interface

Any chemical and structural deviations from an ideal interface lead to deviations from the ideal beam propagation regarded so far. One consequence is loss of intensities of reflected beams accompanied by a redistribution in diffuse scattered contributions. In the case of transition from vacuum into a medium it is directly observable on the vacuum side, thereby allowing for determination of the real structure of the interface as described in Section 4.3.

3.6. Energy Dependent Fine Structure of Absorption and Scattering

Since 1920 it has been well known that X-ray absorption spectra of atoms in solids exhibit energy-dependent oscillating fine structures for energies of about 1 eV above the absorption edges [8, 9]. Similar fine structures in scattered intensities were described for the first time in 1956 [10]. The mentioned fine structures are caused by the interaction of photoelectrons, excited in the case of resonant scattering by the interaction with X-ray photons, with the potentials of neighboring atoms. Thus from a measurement of the fine structures as a function of the energy of exciting X-rays, conclusions on the structural short-range order of the resonant scattering atoms can be drawn. The methods of X-ray absorption fine structure (XAFS) and diffraction anomalous fine structure (DAFS) based on these peculiarities have been developed as routine tools for the determination of structural short-range order. The fine structures

one can imagine to be caused in a simplifying model by the interference of the photoelectron waves emitted by the resonantly scattering atom and backscattered by the neighboring ones. In the case of scattering a virtual photoelectron has to be regarded accordingly. In the quantum-mechanical description one speaks of a structure-dependent change of the transition matrix, which is used for the calculation of the probability of the transition of a bound electron to the state of a free photoelectron.

For the quantitative description of oscillating fine structure all possible scattering paths of photoelectrons must be summed up. The sum over all paths without reflections at the neighbors yields smooth portions $f'_s(E) + if''_s(E)$ which correspond to corrections of the atomic scattering amplitudes mentioned. If the summation runs over all paths with reflections at the neighbors, oscillating contributions $f'_{os}(E) + if''_{os}(E)$ have to be added. The atomic scattering amplitude for atoms with structural ordered environment can therefore be expressed by

$$f(Q, E) = f_0(Q, E) + (f'_s(E) + if''_s(E)) + (f'_{os}(E) + if''_{os}(E)) \quad (10)$$

Following [11] the oscillating portions can be approximated by

$$(f'_{os}(E) + if''_{os}(E)) = f''_s(E)\tilde{\chi}(E) \quad (11)$$

with the complex-valued fine structure function

$$\tilde{\chi}(E) = \chi'(E) + i\chi''(E). \quad (12)$$

In the XAFS and DAFS theory physical quantities are usually expressed in dependence on the wave number of the excited photoelectron waves. The wave number K as a function of the energy of the exciting X-ray photons E and the electron binding energy E_0 (ionization energy of the regarded bound state) is given by

$$K = \sqrt{\frac{2m(E - E_0)}{\hbar^2}}. \quad (13)$$

The complex-valued fine structure function can be calculated by summing all possible scattering paths of photoelectrons to

$$\tilde{\chi}(K) = \sum_{m=1}^N \frac{S_0^2}{KR_m^2} |b_m(K)| \exp[i(2KR_m + \phi_m(K) + 2\delta_c(K))] e^{-2\sigma_m^2 K^2} e^{-2R_m/\Lambda(K)} \quad (14)$$

Here m is the index of a particular scattering path, N is the total number of possible paths, S_0^2 is an amplitude reduction factor due to inelastic losses, R_m is the effective path length of path m (half of the total path length), $b_m(K)$ is the effective curved wave backscattering amplitude for path m with phase shift contribution $\phi_m(K)$, $\delta_c(K)$ is the phase shift of photoelectron waves at the emitting atoms, σ_m^2 is the effective Debye–Waller factor for path m (thermal and structural disorder), and $\Lambda(K)$ is a combined damping factor (mean free path of photoelectron, lifetime of excited state). The imaginary part of the complex-valued fine structure function

corresponds to the XAFS function. Simplifying the approximations of the XAFS function is possible for different cases. The frequency analysis of a measured fine structure, or the numeric fit of a model function to it, allows for the determination of parameters of the structural short-range order of absorbing/resonantly scattering atoms. The backscattering amplitudes and phase shifts are theoretically computed.

Further peculiarities of the interaction of X-rays with long-range ordered media can be observed if the exciting radiation is polarized. These effects arise due to transitions of excited electrons into free energy levels which can be strongly directed in a solid. In the case of resonant scattering the atomic scattering amplitude consequently has to be described as a tensor (“anisotropic anomalous scattering”; see pioneering work by Templeton and Templeton in [12]).

The availability of synchrotron radiation, in particular the high intensity of radiation emitted by these sources, which is available with circular polarization, made possible the observation of weak effects, to be understood as a subset of resonant scattering phenomena. These effects concern magnetic properties; the assigned interaction process is called “magnetic scattering.” The comparatively strongest effects occur in rare-earth elements and in actinides for M-shells. Magnetic scattering and absorption experiments thus enable experiments yielding singular information about magnetic and electronic structures. For a review of pioneering work in the field of X-ray magnetic circular dichroism, the absorptive counterpart of magnetic resonant scattering, and its basics we refer to [13].

4. CHARACTERIZATION METHODS

4.1. X-Ray Diffraction

4.1.1. Introduction

The X-ray diffraction (XRD) method involving powder samples was developed only a short time after the fundamental X-ray interference experiments of single crystals by Laue and co-workers in 1912 [1]. After the descriptive explanation of the diffraction of X-rays by crystals as reflections from lattice planes by Bragg in 1913 [15] further pioneering work was done by Debye and Scherrer in 1916 [16]. For an overview concerning the historical development and fundamentals of XRD we refer to [17, 18]. While the main field of application of this method, besides objectives of single crystal structure analysis, is still on the determination of the Bravais lattice type and lattice parameters of unknown materials as well as the phase composition of materials, the interest in determining parameters of the real structure by XRD has continuously increased.

A substantial milestone in the second half of the 20th century was the introduction of the Rietveld method [19, 20] combined with dedicated indexing procedures. This was due to a renaissance of XRD by opening the field of *ab initio* structure determination for powders and polycrystalline samples. In particular the extraction of information from XRD experiments has extraordinarily profited from the rapid development of computers in the past decades. Apart from the possibilities, which resulted from the availability of synchrotron radiation since the 1980s, also XRD with

conventional X-ray sources could benefit from the development of new instruments. Important innovations were the introduction of parallel beam optics from graded multilayer reflective mirrors (“Göbel mirrors”) [21] and the availability of capillary optics. Additional highlights include the development of position sensitive area and energy resolving detectors and their implementation in XRD setups. Recently particular experiments under nonambient conditions attained much attention.

As in the case of other characterization methods for the investigation of thin layers XRD techniques have been modified and dedicated strategies have been developed. If nanolayers are polycrystalline, they are characterized by grain size and shape, phase composition, texture, and residual stress of the constituent crystallites. For single crystalline layers, their orientation relation with respect to the substrate is in the focus of interest. Concerning XRD investigation of the latter group of samples we refer to Section 4.2.

4.1.2. Conventional XRD

XRD is undisputed as the standard method for the investigation of crystallographic characteristics of materials. An important advantage is low requirements for sample preparation, whereby in most cases the investigation can be performed nondestructively. However, that would not be sufficient to justify the special importance of the method. Rather the high intrinsic precision is the most outstanding benefit, due to the possible precise knowledge of wavelength as the initial parameter. Since the precision is connected to the diffraction angles of reflection used for the calculation of lattice parameters, the possibility to realize large diffraction angles by choosing the appropriate wavelength is important in comparison to other techniques.

X-ray diffraction data restricted to small diffraction angles can provide information on the structure of the scattering objects at lower resolution (i.e., it is sensitive to the cross shapes of molecules, inclusions, or voids). This method has proved to be a powerful probe because of its independence on the structure at atomic scale. So it can be applied to amorphous as well as to crystalline samples. Crucial structural information is derived from anomalous small angle X-ray scattering (ASAXS), because of its ability to provide data related to a certain species separately. As an example, an ASAXS investigation of hydrogenated amorphous Si–Ge alloys deposited by plasma enhanced chemical vapor deposition showed an inhomogeneous distribution of Ge with correlation lengths of about 1 nm [22].

For angle-dispersive XRD experiments (for typical setup see Fig. 2), which are the most common techniques, both radiation from conventional X-ray tubes and radiation emitted by synchrotrons have to be monochromized. While it is possible to employ energy-resolving detectors, which is meaningful particularly when using X-ray tubes, the general way is the monochromization by Bragg reflection of a properly oriented single crystal. For this many techniques using flat or bent crystals or graded multilayer reflective mirrors have been developed. The most common monochromators for use with X-ray tubes are Johannson type collimators with bent curved crystals. They are particularly suitable for established focusing Bragg–Brentano and Seemann–Bohlin

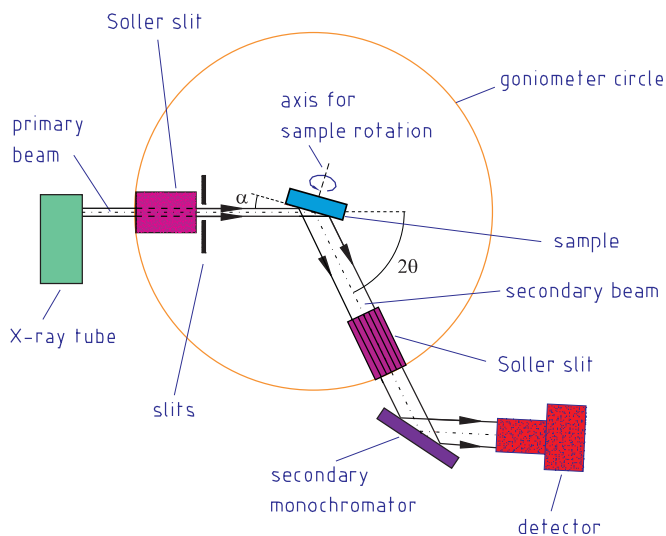


Figure 2. Schematic setup of angle-dispersive X-ray diffraction.

diffractometer geometries. For an overview of the variety of XRD geometries and their individual advantages we refer to [23].

A large spectrum of new XRD applications was opened by the pioneering work of Coster et al. in 1930 [24] which showed that X-ray resonance (“dispersion”) could be useful for studying crystal structures. In the meantime it became obvious that experiments under resonance conditions of interaction of X-rays with atoms of crystals (“resonant anomalous X-ray scattering”) can yield a lot of additional information. Today, resonant X-ray scattering is a routine tool mainly used for overcoming the phase problem in X-ray structure analysis, as well as to achieve a scattering contrast for structures containing chemical elements with similar atomic numbers. Since for these experiments X-rays with defined photon energies according to the ionization energies of the scattering atoms must be available, synchrotrons are the sources of choice for these experiments. Nowadays, resonant scattering is also employed to enhance magnetic scattering. For an exhaustive overview on theory and applications of resonant X-ray scattering we refer to [3].

The experimental setups dedicated to powder samples can be only partly used for the investigation of nanolayers. That is why dedicated strategies were developed, mostly inspired by the low interaction volumes and geometric constraints in the case of nanolayer samples.

4.1.3. XRD of Nanolayers

For the investigation of nanolayers grazing incidence diffraction rather than a conventional focusing Bragg–Brentano setup is appropriate (see an example in Fig. 3). The main goal of grazing incidence setups is to increase the fraction of radiation diffracted from the nanolayer which at the same time causes a reduction of fractions scattered by the substrate. The crystalline structure of the layer can be probed in depth by varying the angle of incidence, what is outlined in more detail in Sections 4.2 and 4.3. The volume contributing to the interference phenomena is limited by the coherence length of radiation, which typically is of the order of 1 μm .

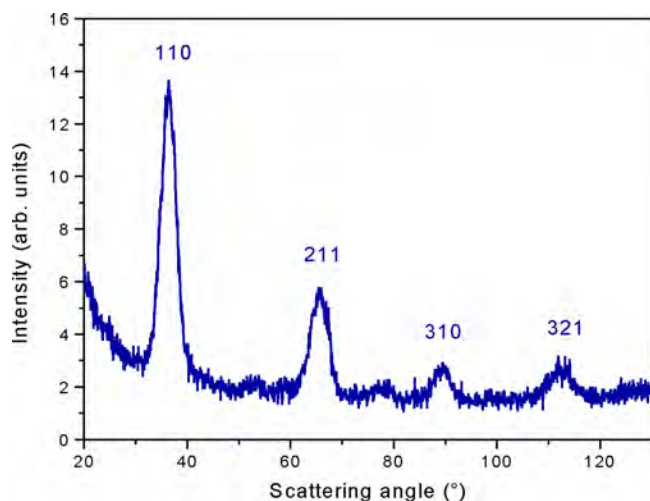


Figure 3. Measured diffracted intensities of a Mo/Si multilayer (40 periods, 2.7 nm Mo + 4.1 nm Si deposited on Si substrate) versus scattering angle. Photon energy was 8905 eV; a fixed angle of incidence of 1.5° was used. Reflection indices of polycrystalline Mo (W-type of structure, space group $Im\bar{3}m$) are indicated, while Si layers appeared to be amorphous.

Generally, stationary nanolayer specimens have to be irradiated with a beam of small divergence in the diffraction plane (horizontal divergence) at angles of incidence typically below 5° . Although this geometry means a loss of advantages of the focusing setups, the detector can be moved, searching for secondary diffracted intensities in the whole range accessible due to the geometrical constraints. To limit the horizontal divergence of the detector, aperture Soller collimators are usually used, often accompanied by secondary crystal monochromators.

For nanolayers the same kind of information as in the case of polycrystals can be obtained. Stronger restrictions exist for textured or single crystal layers due to geometric constraints. This is because only those crystallites which fulfill the Bragg condition at the angle settings predicted by the angle of incidence and the detectable range of scattering angles will contribute to the measured signal. Thus the structure parameters can only be determined for a selection of layer volume, which may be due to a fraction on the order of 1% or less, thereby not being necessarily representative of the layer as a whole. The relative uncertainty of the determination of lattice parameters of nanolayers in conventional setups is in the order of 10^{-3} , whereas changes of parameters can be obtained with a precision of 10^{-4} .

4.1.4. Texture and Stress Measurements

Due to the peculiarities of the deposition methods and the special energetic situation of a large free surface, nanolayers often exhibit fiber textures, whereby the fiber axis is spatially close to the surface normal. In this case XRD measurements in symmetrical geometry will show only one significant kind of reflection, if the fiber axis lies in the scattering plane. In all other cases a complete texture analysis has to be done. Conventionally, this is identical to a pole figure measurement. For this purpose dedicated texture goniometers with Eulerian cradles have been developed (see schematic drawing in

Fig. 4). Thereby the Bragg angle setting is realized by the implemented goniometer. By means of the Eulerian cradle the sample can be rotated independently about two additional axes which are always perpendicular to each other. The definition of the angles ϕ and χ , commonly used, can be seen from Figure 4. Typically, the axis of sample rotation about ϕ is chosen to be in parallel with the surface normal of flat nanolayers. Measurement of a pole figure is then performed by the detection of peak intensities of Bragg reflection by rotating the sample through a wide range of ϕ and χ . Due to the wide range of tilts the spatial resolution is limited to about 1 mm^2 . An improvement can be achieved by appropriate reducing the primary beam cross section by means of capillary optics.

For the spatially resolved analysis of nanolayers by means of XRD a motorized x - y - z specimen stage is used in conjunction with the Eulerian cradle. This stage enables a precise specimen translation in three directions for the mapping investigation of parameters.

Lattice stress can be analyzed with the same experimental setup as for texture measurements. It is determined by evaluating the shift of Bragg angles of selected reflections in dependence on the Eulerian angles ϕ and χ and the changes of widths (more generally the shape) of the diffraction peaks.

The influence of residual stress (internal stress with vanishing external forces) on diffraction behavior depends on the specific group to which it belongs. Shifts of the Bragg reflection maxima, caused by changes of lattice spacings in certain directions, are attributed to “macro residual stresses” ranging far beyond the unit cell. Broadening of the Bragg peaks, on the other hand, is attributed to short-range strain fields, which at a given size of the crystallite may be caused by localized lattice imperfections.

For an overview of stress analysis and the relationship between X-ray methods and other dedicated techniques we refer to [25–27].

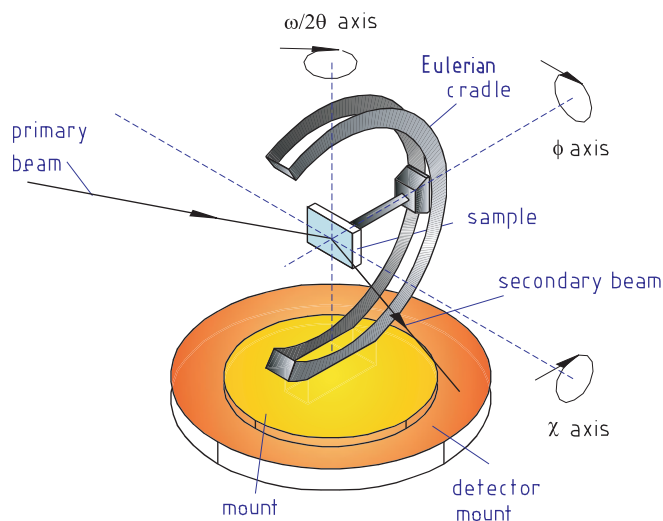


Figure 4. Eulerian cradle for X-ray texture and stress analysis, useful also for single crystal structure analysis. The specimen is rotated through three axes (angles ω , χ , and ϕ with respect to the coordinate system of the goniometer). The detector can be turned around the ω -axis independently (angle 2θ).

4.2. Grazing Incidence Diffraction Analysis

4.2.1. Introduction

For the investigation of nanolayers, X-ray diffraction schemes with grazing incidence and/or exit angles have attracted particular interest. They also allow for the characterization of very thin surface layers of crystals [28–30] (see Figure 5 for basic setup). In the case of plane and smooth surfaces using the “total external reflection” (TER) effect for grazing X-rays, the penetration of radiation inside nanolayers and crystals covers a range from the order of one nanometer to less than a few micrometers. Thus, generally speaking, grazing incidence of X-rays allows for the study of surface structures with atomic depth resolution.

In literature [31] grazing incidence setups are classified into three major types: coplanar “extremely asymmetric diffraction” (EAD), “grazing-incidence diffraction” (GID), and “grazing Bragg–Laue diffraction” (GBL) geometries (see Fig. 6). The first case of coplanar EAD is due to diffraction of lattice planes constituting the Bragg angle with the crystal/nanolayer surface, whereby either the incident or exit beam is grazing [32–35]. For GID the diffraction lattice planes are perpendicular to the surface of the crystal/nanolayer and both the beams are grazing [36–39]. In the third case of GBL a combination of the EAD and GID is realized, involving the diffraction from lattice planes inclined at small angles to the crystal/nanolayer surface normal, so that the corresponding reciprocal lattice vectors (normal of diffraction lattice planes) exhibit small angles to the surface. Under this condition a combination of asymmetric diffraction with either grazing incidence or grazing exit can be realized by a small variation of the angle of incidence or by switching between these two cases in one diffraction experiment [40].

Grazing geometries are widely used in studies of semiconductor crystal surface structures, including epitaxial nanolayers and multilayers. Thereby parameters of real structure, for instance caused by oxidation, ion-implantation, or etching techniques, are the subject of studies for EAD [41–43], GID [44–46], and GBL [47], respectively. For a more exhaustive collection see [31]. Also, charge and spin density waves (e.g. in Cr layers) have been observed making use of strain waves [48].

Recently intensive efforts were made to formulate a general diffraction model covering all grazing geometries. Like in the case of X-ray reflectometry (Section 4.3), quantitative description of X-ray diffraction at grazing incidence

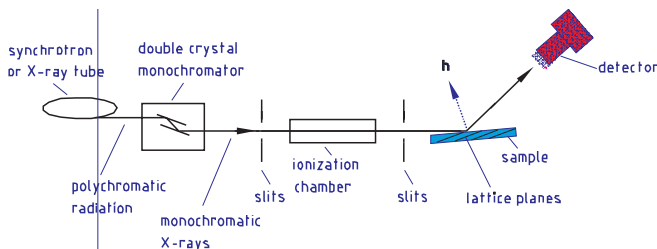


Figure 5. Schematic setup of grazing incidence diffraction at single crystalline samples. Vector h indicates the normal of reflecting lattice planes.

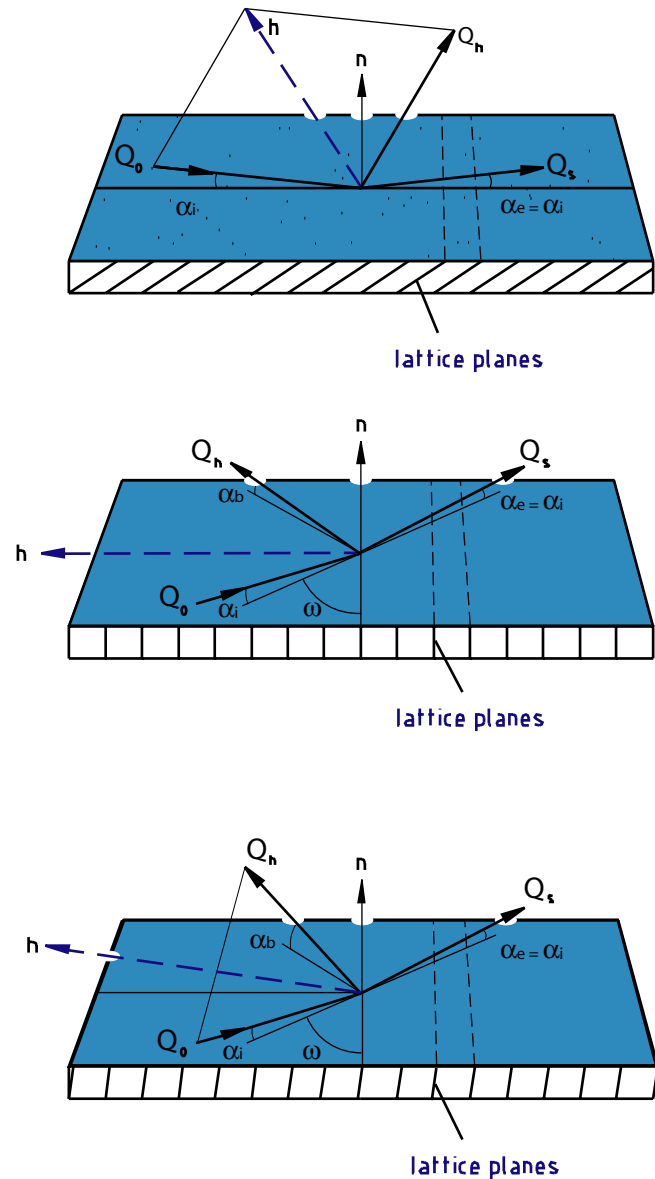


Figure 6. Three major types of grazing incidence setups (after [31]). (a) Coplanar extremely asymmetric diffraction, (b) grazing-incidence diffraction and grazing Bragg–Laue diffraction. Wave vectors Q : Q_0 incident waves, Q_s specularly reflected waves and Q_h diffracted waves. Vector h represents the reciprocal lattice vector according to momentum transfer $Q_0 \rightarrow Q_h$ in reciprocal space, being in the surface normal direction of diffraction lattice planes in real space. The angles α_i and α_e are defined with respect to sample surface (α_i and α_e for specular reflection according to Fig. 1 and α_b inclination in the case of Bragg reflection). ω is the angle of incidence for excitation of Bragg reflection of the crystal/nanolayer.

and/or exit is treated by two models, which differ in principle. The first is based on an extended kinematical approach, frequently called the “distorted wave Born approximation” (DWBA) [38, 44]. The second model uses an extended dynamical theory of X-ray diffraction [32, 39, 46, 49]. Both approaches describe the effects of refraction and specular reflection at crystal surfaces and interfaces of nanolayers in

the case of grazing X-rays. The kinematical theory of X-ray diffraction is applicable to mosaic crystals and thereby, with respect to characterization of nanolayers, to layers thinner than the X-ray extinction depth. Thus the kinematical theory is limited to cases of weak interaction of incident and diffracted X-rays. Strong interaction, due to high intensity of diffracted peaks, is to be described by dynamical theory of X-ray diffraction.

By previous studies a general theory applicable to X-ray diffraction with grazing incidence and/or exit has been accomplished in a matrix form [46, 49–51]. In [31] the matrix dynamical theory was reformulated in a recursion matrix to overcome serious numerical problems with transfer matrices. In addition, [31] presented experimental checks by double-crystal EAD for the case of strained multilayers. Moreover, a linkage to the established scalar models by Parratt [52] and Bartels et al. [53] by reduction of the matrix recursion formulas for cases of X-ray grazing incidence far from the Bragg diffraction condition and for those of Bragg diffraction with no grazing beams was accomplished. The reader can also profit from the discussion on X-ray standing waves in multilayers by Stepanov et al. [31].

4.2.2. Applications

Structural information of nanolayers by means of GID can be obtained by searching for deviations from the ideal bulk scattering of extended crystals and attributing these deviations to the layers. This requires in most cases that the bulk is a good single crystal, so that scattering from it is dominated by Bragg peaks (see an example in Figure 7). Additional scattering can then be attributed to the influence of surface or involved nanolayers. This idea is the basis of the so-called “truncation rod analysis.” The designation is based on the concept of rodlike reciprocal lattice points. Since the

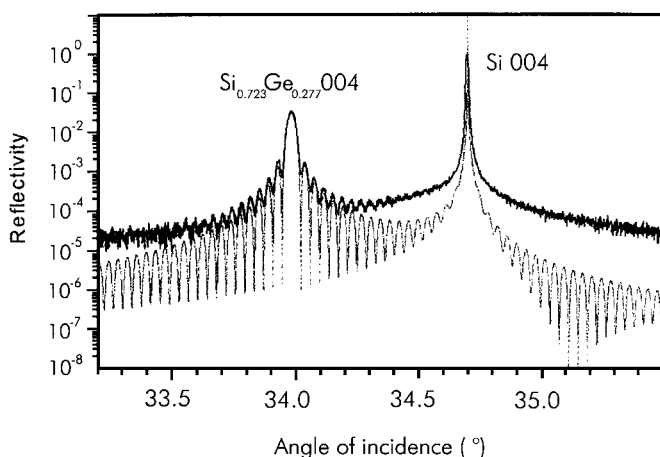


Figure 7. Measured diffracted intensities (black line) and simulation (gray line) of a pseudomorphic SiGe layer (100 nm, epitaxially grown on Si substrate, composition of mixed crystal layer is indicated) versus angle of incidence ω . Because of the relatively large distance between 004 Bragg angles of layer and substrate the detector angle 2θ was moved, too. Photon energy was 8048 eV; the experiment was done using highly parallel radiation. The oscillations in the reflectivity are caused by the interaction of wave fields of single crystalline substrate and layer existing in the vicinity of the Bragg reflection.

method has been extensively used to study surfaces of single crystals and adsorbed monolayers, it was also extended to nanolayers deposited on crystalline substrates (for reviews see [54]).

To obtain quantitative information, the truncation rod profiles have to be fitted to theoretical models. Recently GID has been used to study surface freezing in monolayers [55], self-assembled (chemisorbed) films, and different substrates [56–58]. The method has also proved its efficiency in solving the structure of proteins adsorbed to a phospholipid monolayer [59] or in investigating the structural change of lipids due to adsorption of enzymes [60]. A review of GID studies of thin inorganic films can be found in [61].

4.3. X-Ray Reflectometry

4.3.1. Introduction

The TER of X-rays from solids with smooth surfaces was first reported 10 years after the discovery of X-ray diffraction in crystals [62]. Since that time on the basis of this phenomenon a very efficient analytical method has been developed.

Due to the typically small angles enclosed by X-rays with sample surfaces as a prerequisite for total external reflection of hard X-rays (cf. Section 3.4), there exists an overlap with other methods using the geometries of grazing incidence (see also Section 4.2). This partly leads to ambiguities in the designation of certain experimental techniques. We want to summarize here, under the term “X-ray reflectometry” (XRR), experiments based on the phenomenon of “specular X-ray reflection” (SXR), including the TER and diffuse scattering of X-rays at smooth surfaces/interfaces of samples. When looking at the two phenomena mentioned first, the term “X-ray specular reflection” is frequently used. Diffuse scattering occurs if interfaces are not ideally smooth with respect to the wavelength of X-rays. Experiments using this phenomenon are mostly marked by the synonymous terms “X-ray diffuse scattering” or “X-ray nonspecular reflection.” Fundamental work in this field was carried out in the 1960s. A basis for this is the report by Yoneda [63] on the angle dependent intensity modulation in X-ray diffuse scattering, today usually designated as “Yoneda wings.”

In addition, yet another method should be considered here which aims, frequently in the same experiment, at the excitation of fluorescence radiation in the sample. Accordingly, the method is called “total reflection X-ray fluorescence spectrometry” (TRXF). At present a combined use of XRR and X-ray spectrometry in one and the same experiment is in progress, where mostly for multilayer systems new attractive information is to be expected (see Fig. 8 for basic setup).

A lot of progress was possible in the few last decades due to the availability of synchrotron radiation, as well as the improved quality of the samples produced by modern preparation methods. Simultaneously the theoretical analysis of that experimental data has been developed. For extended reviews we refer here to [64–67] as examples.

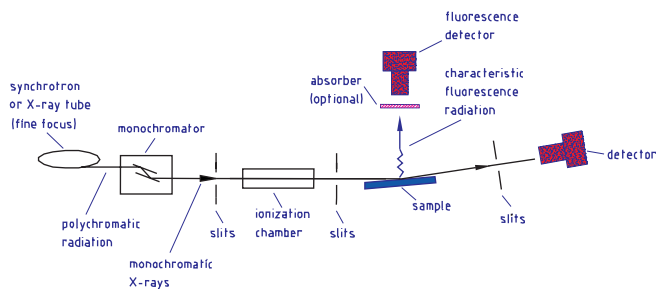


Figure 8. Schematic setup of angle-dispersive reflectometry and total reflection X-ray fluorescence analysis.

4.3.2. Specular Reflectivity

The basic concepts for the theoretical description of external reflection of X-rays at smooth surfaces and interfaces of multilayers were reviewed in [66, 67] (see Fig. 9 for schematic drawing of the origin of interference phenomena in specular reflectivity of nanolayers). Quite substantial pioneering work was done in the 1950s by Parratt [52]. Parratt's formalism requires a recursive calculation of the intensities of the reflected beam. In addition several approximate formulas have been proposed. An analytical formula for calculating X-ray and neutron reflection from thin surface films has been presented by [68]. Another analytical expression

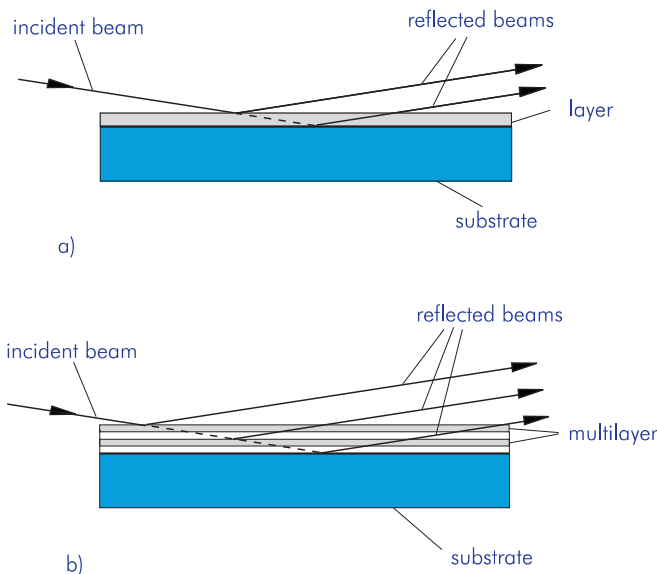


Figure 9. Origin of interference phenomena in specular reflection of nanolayers. (a) A nanolayer with homogeneous optical thickness deposited on a thick substrate with smooth surface can cause two sets of reflected beams with definite phase difference (influence of refraction not indicated in the drawings) giving rise to angle/energy dependent interference phenomena for angles of incidence in the vicinity of the critical angle of total external reflection. Analysis of interference characteristics can yield information on layer thickness, density, and interface roughness. (b) In extension to (a) a number of different nanolayers (multilayer) can cause a corresponding set of reflected beams of an appropriate number. In the case of periodic layer stacking in addition to (a) from the positions of reflection maxima in space of wave vectors the period and from the number of secondary maxima the number of periodic layers can be determined.

is based on a one-dimensional scattering-length-density profile, using a weighted superposition approximation [69]. As outlined in [64], from comparisons of this formula with Parratt's recursion formula, the "Born approximation" (BA), and the DWBA, it was concluded that it is the most accurate one. It is valid in the entire range of wave vector transfer, except for the narrow region around the critical angle of total reflection. Another analytical approximation for the calculation of X-ray reflectivities in the case of multilayers is given in [70], yielding quantitative results which agree well with that of the recursive algorithm according to Parratt (deviations of less than 1% in the vicinity of the critical angle of total external reflection).

The determination of roughness from SXR, like for the nonspecular case, is based on modelling the roughness profiles. In the case of specular reflectivities this can be done with the introduction of a roughness parameter in the Fresnel reflection coefficient. One parameter is sufficient for the description of the influence of roughness on specular scattering. On the other hand this means a rather coarse modelling of the surface. This is due to the fact that for specular reflectivity the scattering vector is always perpendicular to the interface, thereby testing the almost vertical interface roughness. If the model of the vertical roughness profile of the interface is based on the assumption of a Gaussian-like distribution of ideally smooth interfaces the information obtainable is rather limited to the root mean square of this parameter.

A model of Sinha et al. [71] is based on the use of a damping factor for the BA model. An additional linkage to the total reflection X-ray fluorescence analysis is given in [72]. In extension, the modelling of an interface by a series of smooth transition layers has been put forward in [73, 74]. This model is in many cases the comparatively most accurate one and is also useful for the modelling of interdiffusion at interfaces and widely used for the simulation of X-ray specular reflectivities of multilayers. The applicability of different models for the simulation of the roughness can be estimated by the presentation in [64].

Parameters determined from XRR measurements are not affected by an atomic long-range order (i.e., amorphous samples can also be examined). It was Compton who proposed measuring the refractive index by specular reflection in 1922 [75]. Then Kiessig provided pioneering values of the dispersion parameter δ [76] and of the thickness [77] of Ni layers 22 nm thick. The thickness was derived from interference between surface-reflected and layer/substrate interface-reflected beams ("Kiessig fringes"). Since thickness of nanolayers (including layers in multilayer stacks and their number), average electron density, or refractive index can be determined directly from the reflection curves, quantitative analysis including determination of roughness parameters is mostly based on constrained least-squares fitting of model curves to the measured ones (see an example in Fig. 10).

For an accurate analysis the diffuse scattering has to be taken into account, which also contributes to intensities detected at specular angles. The best solution is to measure these contributions under near-specular conditions and to subtract them from the experimentally determined specular reflectivities. The same applies to possible contributions of

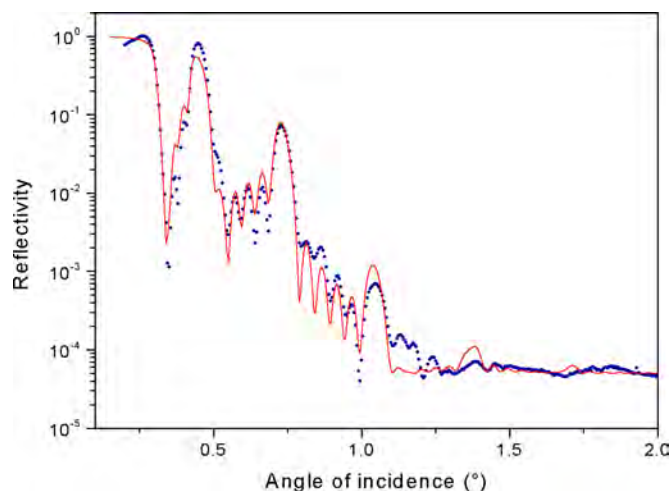


Figure 10. Measured (dotted) and calculated (full line) X-ray specular reflectivities of an Fe/Al multilayer (six periods, 4.3 nm Fe + 10.4 nm Al deposited on Si substrate) versus angle of incidence. Photon energy was 7280 eV above the Fe *K* absorption edge at 7112 eV.

fluorescence radiation excited in the sample. In addition, in each case the systematic influence of sample size must be considered. In particular at the smallest angles only part of the incident beam will hit the sample in the direction of propagation, thus not being available in full for interaction with the sample (also valid for large samples due to the limited detection windows).

The thickness of several layers can be determined with an absolute accuracy of about 0.2 nm. An accurate determination of the distribution of mass densities thereby requires additional information. These may be obtained by taking advantage of experiments under anomalous scattering conditions (scattering contrast) or of additional use of neutron scattering. The accuracy of determination of the interface roughness is strongly influenced by the sample quality on the one hand and the availability of a realistic model of the surface on the other. In the case of magnetic films when using resonant interaction polarization effects can be studied or have to be considered [78, 79].

4.3.3. X-Ray Diffuse Scattering

Diffuse scattering, or nonspecular scattering, can yield the shape function of the interfaces of nanolayers (“in-plane structure”). For the basics of quantitative modelling of X-ray diffuse scattering we refer to overviews in [64–67]. In contrast to the case of X-ray specular reflectivity the interfaces and the roughness parameters are usually described by means of surface shape functions $z(x, y)$ (x, y -plane parallel to the interface). Important parameters, which can be obtained by modelling of experimental intensities, are on the one hand the correlation length, which is due to the distance in the x, y -plane, at which the correlation of structures has decayed with $1/e$ and on the other hand a parameter due to the texture of the interface (known as the Hurst parameter related to the surface fractal dimension). Thereby this texture can be modelled between extreme situations of jagged to slowly oscillating interfaces. In addition, the separation

of compositional and density fluctuations from interfacial roughness can be achieved.

For the determination of interface parameters from diffuse scattering different types of angle scans are possible. Usually longitudinal (near-specular), transverse (rocking curve), radial (detector), and full (source and detector moved) scan geometries are differentiated exhibiting individual sensitivities to certain characteristics. As in the case of X-ray scattering from crystals, X-ray diffuse scattering from interfaces at grazing incidence can be modelled, to a certain extent, by a kinematical approach (BA), where comparable restrictions are valid (phenomena like extinction, refraction, and multiple scattering of X-rays are neglected). Thus the range of validity of this approximation is restricted to the angles of incidence and reflection above the critical angle of total external reflection. For the case of multilayers the BA was extended introducing interface roughness by noncorrelated contributions and correlated ones propagating from layer to layer [80]. Further developments and extensions of the BA for the case of multilayers were presented in [81, 82]. The dynamic approach (DWBA) which overcomes the limitations of the BA by considering refraction and multiple scattering of X-rays was also applied for X-ray diffuse scattering [71]. For the simulation of intensities of diffuse scattering from multilayers, for example DWBA approaches as developed by Sinha [83] are used. For an overview of developments in this field we also refer here to [64].

4.3.4. Total Reflection X-Ray Fluorescence Analysis

From the measurement of X-ray fluorescence excited in nanolayers in the case of total external reflection information can be obtained which is partially comparable to that from specular reflection. Though this offers the possibility of oversampling, it is more interesting for the experimentalist that from fluorescence unique additional information, in particular the spatial distribution of the individual atomic species, can be obtained. An overview of TRXF experiments can be found in [84].

Like in the case of X-ray specular reflectivity common models for quantitative analysis of TRXF in the case of multilayers are based on the matrix approach. They allow for simulation of X-ray fluorescence intensities from structures with concentration modulation.

An important feature of TRXF represents the formation of an “X-ray standing wave field” (XSW) in nanolayers during total external reflection. This standing wave field is formed due to the layered structure and extends also outside the layer. Thereby the X-ray fluorescence excitation is locally connected to the position of the standing wave field which is due to a periodic modulation of the exciting energy. The possibilities which are offered when XSW are combined with other established spectroscopic methods are dealt with in Section 4.7.

To sum up a great potential exists in the combination of features of X-ray reflection, diffuse scattering, and X-ray spectroscopy in one and the same experiment.

4.4. X-Ray Topography

4.4.1. Introduction

Methods which aim at producing images of lattice planes of a crystalline sample by means of Bragg reflected X-rays are summarized under the term “X-ray diffraction topography”. The lattice planes thus assessed may be either bounding planes of the specimen or others inclined to the surface. For pioneering work in this field we refer to [85–90].

In general, X-ray topography gives valuable information on the distribution of strains arising from extended crystal defects or from point defect clusters. When combining topographs of different reflections of the same volume, a spatially resolved picture of the strain distribution may be obtained. Characterization of crystal perfection becomes particularly important if related to the growth history of the sample. For nanolayers note that this information can be obtained depth sensitively, revealing the state of the substrate/layer interface and discovering inhomogeneities within the layers.

In the beginning, only individual Laue reflections, i.e. without specification, of wavelength were employed for X-ray topography. Their nonuniformity gives a direct picture of either local variations of the lattice orientation or of the extinction of X-rays. They are still exploited where the Laue method is applied anyway for structure analysis. Later monochromatic X-ray techniques became pre-dominant because of their higher angular resolution and their applicability to polycrystalline samples. For a detailed description of the development of the method cf. [91–93].

Since topographic contrast can be affected by various factors, a number of different geometries and strategies of X-ray topography have been developed. A substantial classification can be made regarding the use of monochromatic or polychromatic radiation, whereby in the latter case much progress was due to the availability of synchrotron radiation.

For a quantitative understanding the effect of extinction of radiation has to be considered. If the sample can be classified as an “ideally perfect crystal” there is, in addition to the absorption, attenuation of the X-ray beam in the sample exactly for the situation of Bragg reflection. For a sample to be classified as an “ideally imperfect crystal” the influence of extinction can be neglected. Thus an intensity contrast in a Bragg reflected X-ray beam, which is due to a variation in perfection of the crystal lattice, can occur. It is usually called “extinction contrast” or “diffraction contrast.”

As mentioned, image contrast can be due to the misorientation of parts of the sample with respect to the satisfaction of the Bragg condition. This contribution is called “orientation contrast.” The strength of the effect is affected by the range of wavelengths of radiation used and its divergence. A comprehensive treatment of geometry and theoretical foundations of XDT are given in [94, 95]. For an overview of dynamical theory of X-ray diffraction we refer to [96, 97].

The dynamical theory of diffraction is compulsory for perfect crystals. Contrary to the kinematical theory, which deals with the global intensity diffracted by the specimen, the dynamical theory deals with the propagation of the X-rays inside the specimen and investigates the properties of a wave field formed by superposition of all incoming and scattered partial waves. Mathematically, the dynamical theory

is entirely based on Maxwell’s equations of electrodynamics. Generally, the integrated intensities of reflections are smaller for perfect crystals than those for imperfect ones where the kinematical theory applies.

4.4.2. Experimental Setup

For the classification of experimental setups the terms “extended” and “limited beam methods” are normally used. In “extended beam setups” wide areas of a sample are illuminated, whereby the intensities diffracted by a perfect crystal plate would show a homogeneous intensity distribution. In the most common “integrated wave topography” the incident beam is divergent and/or polychromatic. For the subgroup of “white beam topography” a polychromatic beam of low divergence is required. The set up is then a conventional Laue experiment. Mostly with laboratory sources the “Lang topography” technique [98] is used yielding images which are produced by integration over a spatial distribution of divergent waves on the entrance surface of the crystal.

In modern experiments for the enhancement of sensitivity and discrimination of the contributions of background radiation more than one crystal is used in the topographic setup, whereby one crystal can be represented by the sample. If samples are slightly curved due to strain, like wafers with superposed layers or to other effects, a compensation of sample bending can be achieved by slight bending of the first crystal (monochromator). The method is called “curved collimator topography.”

In “limited beam setups” the width of irradiating beams is restricted to about $10\ \mu\text{m}$ in the direction perpendicular to the scattering plane. After diffraction from an ideally perfect crystal an inhomogeneous intensity distribution is detected, which changes sensitively due to the influence of strain fields.

4.4.3. X-Ray Topography of Nanolayers

In conventional X-ray topography an orientation contrast from nanolayers can be detected when using a sufficiently large distance between the sample and image detector (see Fig. 11 for basic setup and Fig. 12 for schematic drawing of origin of image contrast in X-ray topography of nanolayers). For the observation of misorientations usually a minimum layer thickness exists. This is due to the fact that a minimum size of crystal is required to make distorted and perfect parts of a crystal distinguishable by means

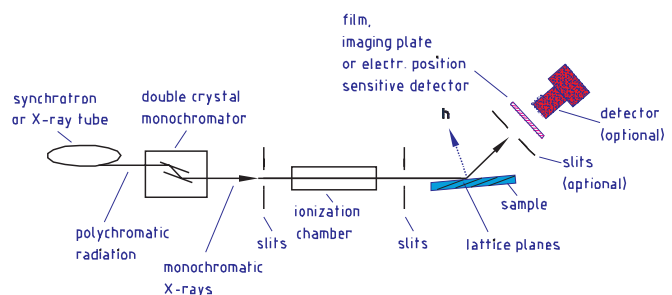


Figure 11. Schematic setup of grating incidence topography of crystalline nanolayers. Vector h indicates the normal of reflecting lattice planes.

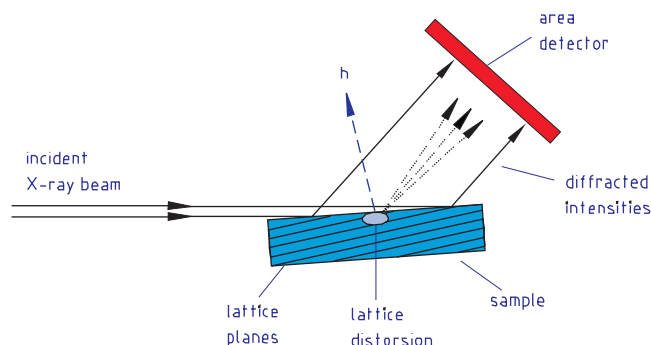


Figure 12. Illustration of the origin of image contrast in X-ray topography of nanolayers. Vector h indicates the normal of reflecting lattice planes.

of the detected integrated reflection intensities. To overcome this limitation dedicated experimental techniques have been developed. When using double crystal setups, which allow for well defined narrow wavelength and angular band-passes, the detectable contrast is determined directly by the misorientation.

Another strategy is to use the interaction of waves scattered by crystalline nanolayers on thick crystalline substrates (see an example in Fig. 13). If the layer is epitaxially linked to the substrate and the difference of lattice parameters is small, they can contribute to the diffracted intensities simultaneously due to the interference of the wave fields of both crystals. The accomplished interference phenomenon (“Moiré effect”) allows for an extremely sensitive detection of weak strains and the possibility to visualize localized defects. In this connection the investigation of epitaxial nanolayers on thick substrates, to be classified as perfect crystals, in transmission geometries using sufficiently hard X-rays, is possible (“Moiré topography”).

As with other X-ray techniques originally developed for investigation of extended crystals also for characterization of nanolayers by means of XDT grazing incident geometries play a key role. Progress in the use of “grazing incidence X-ray diffraction topography” (GIXDT) techniques for the analysis of thin crystalline surface layers has been reported

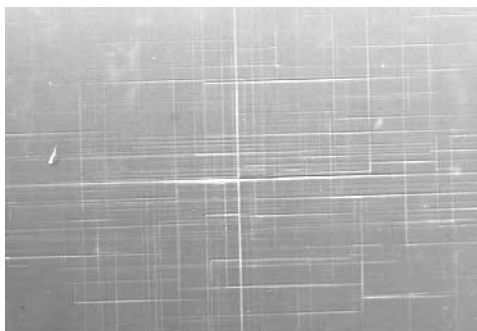


Figure 13. Topographic image (reflected sample area: $\sim 12 \times 8 \text{ mm}^2$) of a pseudomorphic SiGe layer (100 nm, epitaxially grown on Si substrate). Photon energy was 8048 eV; the experiment was done using highly parallel radiation. For exposure the Si 224 reflection, tuned to 60% of maximum intensity, was used. Perpendicular lines are caused by misfit dislocations at the SiGe/Si interface.

by [42, 99–102]. Typically grazing incidence angles are in the order of 0.1° – 1° , mostly larger than the critical angles of total external reflection. From GIXDT experiments information about strain and lattice defects, like dislocations, can be obtained. Thereby typical signal depths extend to the order of micrometers and can be tuned to a certain extent by choosing appropriate angles of incidence. However, in very thin layers, like in epitaxial systems with a layer thickness of some monolayers, the smallest tuneable penetration depth can exceed the overall layer thickness. Normally in such cases grazing incident angles below the appropriate critical angles, for which the penetration depth of radiation lies in the order of 1 nm, are used to image near surface structures [103–105].

Since in common geometries polychromatic radiation is used as standard, in [99] the use of polychromatic radiation for the investigation of very thin layers at angles below the critical angle of total reflection was described (“white beam synchrotron radiation total reflection X-ray topography”). From Laue patterns of topographs features of surface layers up to thickness of 1 nm can be derived.

4.5. X-Ray Absorption Fine Structure Analysis

4.5.1. Introduction

XAFS spectroscopy has developed to be one of the basic tools for the X-ray analysis of nanolayers. By means of X-ray fluorescence analysis the chemical composition can be determined for atomic numbers ≥ 5 . Small concentrations of elements of $\sim 10^{-4}$ can be detected; typical relative accuracy of the content is in the order of 0.1%. As outlined in Section 3 from oscillating fine structure of linear photoelectric absorption coefficient $\mu(E)$ element specific information on parameters characterizing the structural short-range order can be obtained (see illustration of origin of XAFS in Figs. 14 and 15). For exhaustive overviews we refer to [106–108]. The XAFS oscillations can usually be observed at energies up to 1000 eV above an absorption edge. The determination of quantitative structural information from XAFS experiments requires a high resolution measurement of the total attenuation coefficient $\mu(E)$. Since the XAFS is a weak contribution to the total attenuation of X-rays in matter, $\mu(E)$ has to be determined with an accuracy of more than 10^{-3} .

XAFS experiments require X-rays tuneable in energy with a relative energy resolution of typically $\sim 10^{-4}$, detectors with noise smaller than 10^{-3} , and a wide range of linear characteristics of operation. Because of the suitable wide range of X-ray energies/wavelengths synchrotron sources are typically used. Quasi-monochromatic radiation is selected by double crystal monochromators. For experiments with energies in the order of 10 keV for this purpose silicon or germanium single crystals are commonly used.

4.5.2. Transmission and Fluorescence XAFS Experiments

For the monitoring of primary X-ray intensities and transmission XAFS experiments ion chambers are commonly used. For fluorescence XAFS measurements, several kinds

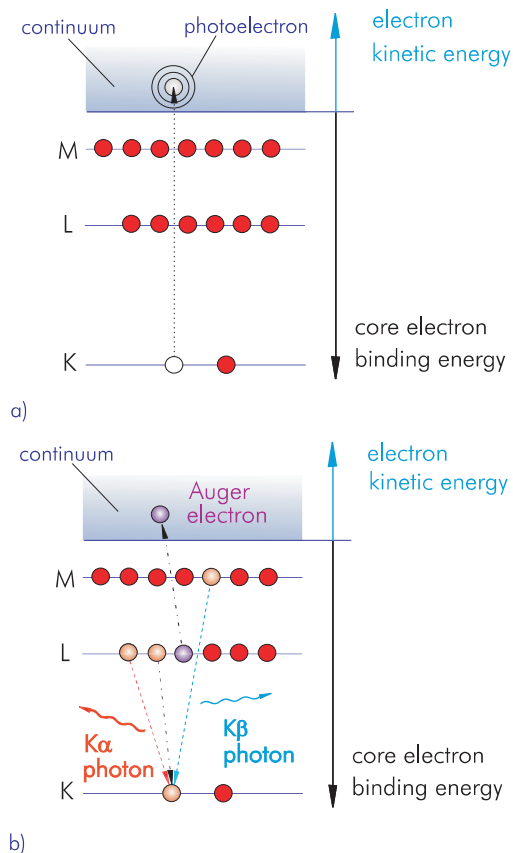


Figure 14. Basic processes behind XAFS experiments. (a) Promotion of a core electron to the energetic continuum by photoelectric absorption of X-rays. From the viewpoint of quantum mechanics the arising photoelectron can be described as a wave propagating out of the excited atom. (b) Decay processes of the excited states: emission of photons of element-specific characteristic energies (fluorescence) and free Auger electrons (kinetic energy element-specific at a given energy of excitation). For indirect measurement of absorption coefficients it is essential that the probability of production of both fluorescence photons and Auger electrons is directly proportional to the absorption probability of X-rays by the atoms.

of detectors are applicable. Mainly in the case of transmission XAFS experiments samples with homogeneous thickness and density (free from pinholes) are required. An optimum sample thickness t for samples with a sufficient concentration of the resonantly absorbing element can be estimated from the condition $\mu(E) t \sim 2.5$ at energies E just above the absorption edge (ionization energy). Typical optimum thickness of concentrated samples is in the order of $10 \mu\text{m}$; for diluted samples (relative concentrations of not less than 10%) it is around a few millimeters.

For XAFS investigations of nanolayers, thick samples, or lower concentrations of resonantly absorbing elements the monitoring of characteristic X-ray fluorescence intensities is the preferred technique (see Fig. 16 for basic setup of fluorescence XAFS and an example of measured fluorescence XAFS in Fig. 17). The resolution limit for diluted samples is approximately 1 ppm. Since in fluorescence XAFS measurements elastically and inelastically scattered components of exciting X-rays and characteristic fluorescence intensities

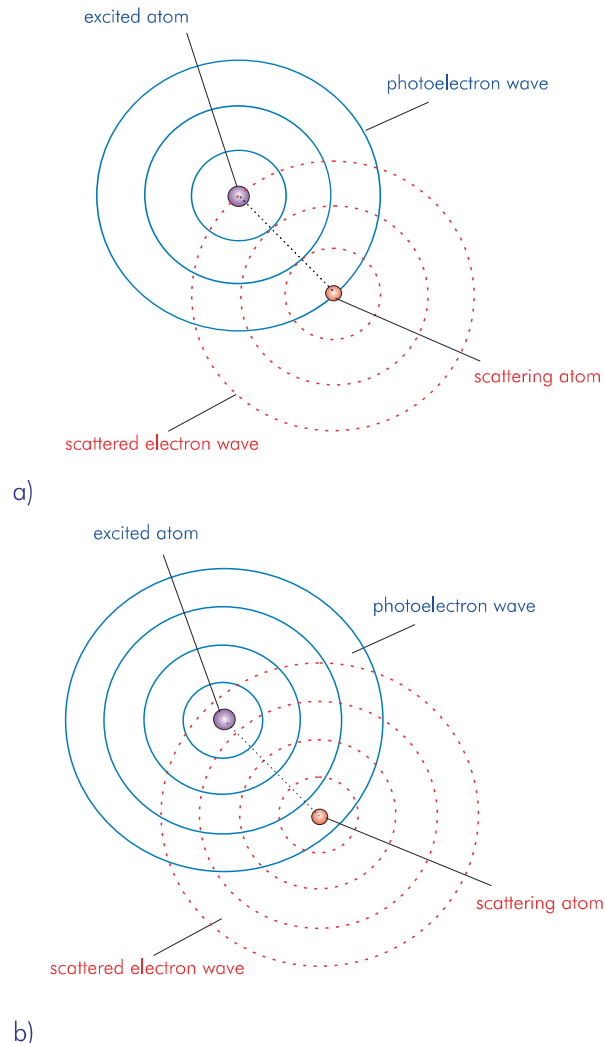


Figure 15. Illustration of the origin of XAFS: outgoing and (back)scattered portions (excited atom is placed into condensed matter) of final state wave functions. The outgoing and (back)scattered contributions interfere depending on the electron wavelength and the interatomic distance. If the energy of incident (exciting) X-rays is scanned across the ionization energy the kinetic energy of the excited photoelectrons is varied. (a) Case of constructive interference. (b) Destructive interference for the same spatial distribution of the atoms as in (a) but at higher kinetic energy of excited photoelectron waves (lower wavelength). The interference modulates the absorption probability, giving rise to oscillations of the coefficient of photoelectric absorption. Since the oscillation characteristics are determined by the interatomic constellation, structural information can be obtained from its quantitative analysis.

of other lines can also give rise to the radiation of interest, a suitable energy resolution of the detection system is required.

In general, two parameters are important for high quality fluorescence XAFS measurements: the solid detection angle and the energy resolution. Only in the case of diluted samples it is suitable to collect as much fluorescence as possible. In all other respects a well defined takeoff angle is demanded in order to allow for correct application of self-absorption corrections. In addition it has to be

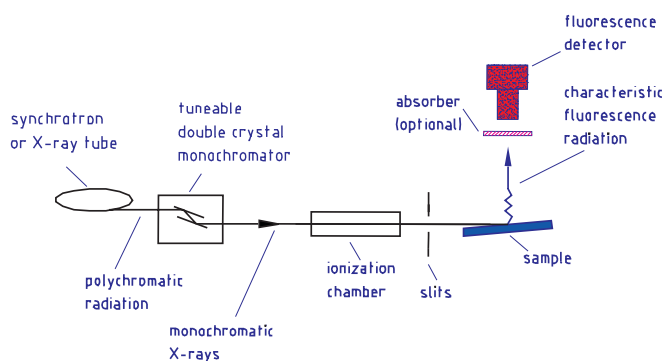


Figure 16. Schematic setup of fluorescence XAFS.

considered that the sometimes dominating radiation contributions, which are elastically scattered by the sample, are not emitted isotropically since the radiation is mostly linearly polarized. Optimal suppression can be achieved by placing the detectors perpendicular to the plane defined by the incident beam and surface normal of the sample. In particular for concentrated samples this also limits the influences of self-absorption expressed by an amplitude damping of the measured fluorescence XAFS.

To reduce contributions of other spectral components physical filters can be placed between sample and fluorescence detector. The material of filters is commonly chosen to profit from the well known selective absorption of chemical elements due to their atomic number. With Z being the atomic number of the resonantly absorbing element of the sample, in most cases of characteristic K -radiation a filter of chemical element with $Z-1$ is useful (commonly called “ $Z-1$ filters”). Due to selective absorption it preferentially absorbs the elastically scattered and $K\beta$ -fluorescence radiation and lets through the $K\alpha$ -fluorescence intensities. To avoid contributions of fluorescence radiation from the filter itself, usually a collimating Soller slit is additionally used.

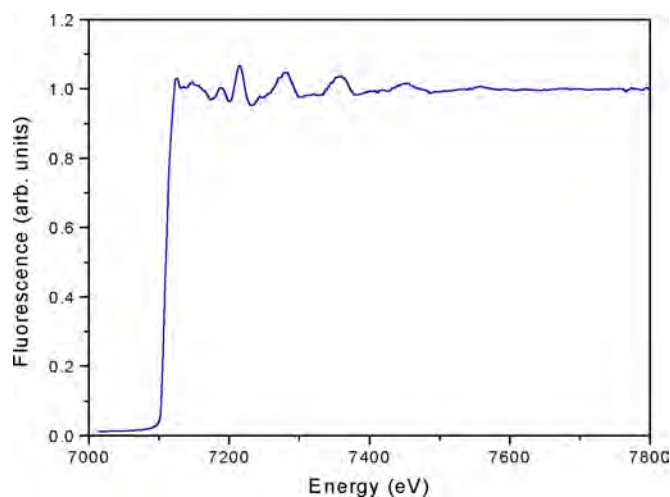


Figure 17. Measured Fe K fluorescence XAFS intensities of an Fe/Al multilayer (30 nm Al + 30 nm Fe + 5 nm Al_2O_3 cover layer, deposited on Si substrate) versus photon energies in the vicinity of the Fe K absorption edge at 7112 eV.

Commonly used energy resolving detectors for absorbed X-ray photons with energy in the order of ~ 10 keV allow for energy resolutions of 200 eV and better. Certain electronic energy resolution requires a finite amount of time, limiting the throughput that can be processed. State-of-the-art detectors at the mentioned energies exhibit typical saturation rates of less than 10^5 absorbed photons per second. In reality at synchrotron sources this upper limit of total intensity, which can be processed by these detectors, often limits the effectiveness of fluorescence XAFS measurements.

4.5.3. Experiment

The determination of the absorption coefficient N can be done in the simplest case by a transmission arrangement, as described at the beginning of Section 3. When a sample with homogeneous thickness ($t \sim 10 \mu\text{m}$) and density is arranged between two ionization chambers and the intensity ratio is monitored, the total attenuation coefficient $\mu(E)$ can be calculated directly. The steps for the separation of contributions of the linear scattering coefficient are represented in detail, for example, in [106, 107]. In most cases the simple transmission arrangement is not applicable for the investigation of nanolayers. Above all, this is due to the fact that an investigation of the layers in most cases is meaningful only if adhering to the substrate. Otherwise a relaxation of strain would occur thus changing the properties of the layer.

The photoelectric absorption coefficient N may alternatively be determined by taking advantage of other transition processes involved such as Auger electrons, secondary electrons (from several internal electron transitions), and fluorescence photons. Even the photo current can be exploited in certain material systems (e.g., semiconductors) [109]. Notably the interlink between photoelectric absorption and coherent scattering of photons can be used in the case of sample systems with translation symmetry to select spatially a certain part of the atoms for fluorescence (cf. Section 4.6).

Due to their small free path length (approx. 2 nm) photoelectrons emitted from surfaces are suitable for investigation of the upper atomic layers of these surfaces (SXAFS surface X-ray absorption fine structure). A clear representation of the characteristics of this method, which requires working under vacuum conditions, is given in [110]. In the case of fluorescence XAFS experiments, the signal depth is given by the penetration depth of the exciting radiation at a given angle of incidence and the absorption of the fluorescence photons on the path to the detector which can be influenced by the detection angle. Using arrangements with small angles in the vicinity of the critical angle of total external reflection, the method can become sensitive to a view monolayers at the surface. The maximum signal depth is limited by the absorption of the radiation and is typically in the order of $10 \mu\text{m}$. If the samples bear surface qualities making them useful for X-ray reflectometry experiments, there is an additional way to detect the energy dependent fine structure of the absorption coefficient N . It is the energy dependent fine structure of specular reflected intensities which are recorded at angles in the vicinity of the critical angle of total external reflection.

The evaluation of fluorescence XAFS measurements, which are commonly used for nanolayers, is described in

somewhat more detail in [111]. Apart from the fundamentals of quantitative analysis aspects of the planning of experiments can be accomplished on this basis.

4.5.4. Analysis

The general approach to an analysis of XAFS spectra implies the intensive use of computers for fast calculations, mostly in an interactive regime. On the basis of the fundamentals described, for instance, in [106, 107] extensive software packages have been developed. One of a widely used code is FEFF [112], enabling *ab initio* simulation of the XAFS signal to be done. The analysis of the absorption coefficient N in the vicinity of the absorption edge [“near edge structure” (XANES), ~ 200 eV above the edge; sometimes the term is also used for resonant characteristics in the direct pre-edge range] is a field in itself aimed at primarily determining the local electronic structure [107]. The energetic position of the absorption edge, mostly attributed to the vanishing second derivative of the curve, is usually used as the origin of the photoelectron kinetic energy.

XAFS data have to be subjected to Fourier transformation to obtain the atomic distribution in physical space. This procedure needs rather sophisticated modelling. Modern approaches take multiple scattering effects of photoelectron waves into account. The photoelectron emitted is not only backscattered directly by the nearest neighboring atoms (scattering angle 180°) but also via multiple scattering by more distant neighbors.

The theoretical backscattering amplitudes and phase shifts can be taken from tables [113], or calculated, for instance by means of the FEFF code [112]. Amplitudes and phase shifts which are calculated on the basis of complex exchange-correlation potentials [114] already involve the contribution from inelastic photoelectron scattering. Additionally they may be extracted from the XAFS spectrum of a standard sample.

The accuracy of the radial distribution depends not only on the model used but also on the distance in physical space taken into account for fitting. For the nearest neighbors typically the interatomic distances can be determined with a precision of 0.01 \AA . The relative uncertainty of the number of backscatterers (coordination numbers) and Debye–Waller factors is in the order of 10%. For the next-nearest neighbors and still longer distance correlations the accuracy deteriorates. Thus the correlation within distances around the absorbing atoms up to $\sim 5 \text{ \AA}$ can be determined by XAFS to an acceptable precision. The limit of spatial sensitivity lies at distances of $10\text{--}15 \text{ \AA}$.

4.6. Diffraction Anomalous Fine Structure

4.6.1. Introduction

The diffraction anomalous fine structure technique represents a combined spectroscopic, structural, and crystallographic method which has developed to become a routine analysis technique since the 1980s. For a description of surveys of DAFS history, theory, experimental methods, data analysis techniques, and some applications we

refer to [11, 115–117]. As outlined in Section 3, energy dependent diffraction and absorption fine structures are closely related by unitarity and causality, with which the DAFS experimental setups and analysis could profit from the established XAFS tools. For a discussion of certain experimental demands we refer to Section 4.5. Due to its special features DAFS spectroscopy has been applied to nanolayers, too. Because DAFS combines absorption spectrometry with diffraction, it offers distinct advantages compared with conventional XAFS (for illustration see Fig. 18).

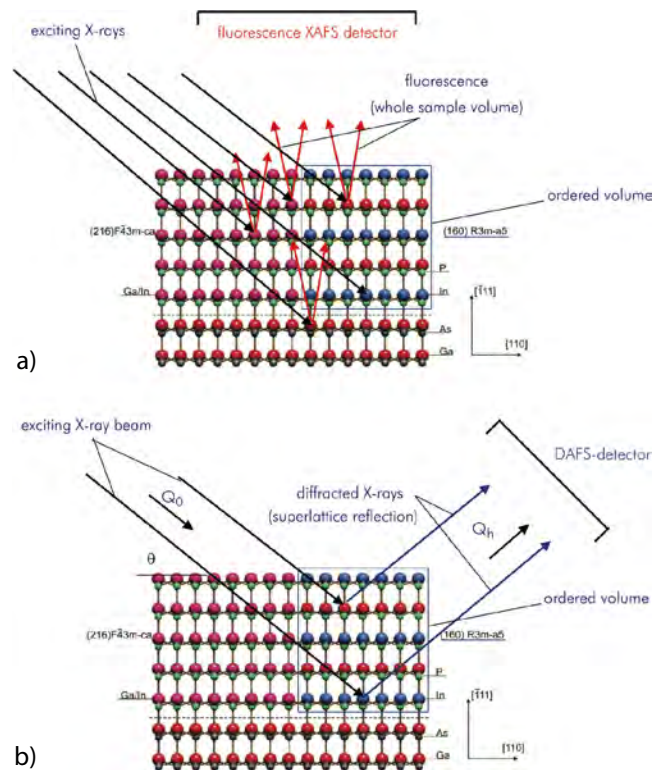


Figure 18. XAFS and DAFS of a partially ordered layer [(Ga,In)P] epitaxially grown on GaAs substrate]. In the case of Ga and In atoms separate shades stand for definite occupation of sites by either Ga or In atoms, whereas mixed ones indicate an occupation at random. (a) Excitation of Ga K fluorescence in the general case involves Ga atoms of both layer and substrate. Especially, volume fractions of the layer, to be distinguished from the rest by another type of crystallographic structure, contribute to the integral fluorescence yield of all atoms of the layer accordingly. Scanning of the energy of incident (exciting) X-rays above the ionization energies (absorption edges) and monitoring of integral fluorescence intensities (fluorescence XAFS) can yield average information of at least all atoms in the layer. (b) Structural short-range order of ordered volume fractions can be determined exclusively by using appropriate Bragg diffraction peaks (superlattice reflections) for DAFS measurements. In the case shown this is possible although the different regions contain the same kind of atoms. Scanning of the energy of incident (exciting) X-rays above the ionization energies (absorption edges) like in (a) and monitoring of Bragg reflection intensities can yield structural information of atoms selective with respect to their assignment to a certain crystallographic structure.

4.6.2. Features of DAFS

One important enhanced feature of DAFS is its diffraction wave vector selectivity. This means that different spatial regions or components of the sample can be selected for analysis when causing Bragg diffraction peaks at separable locations in reciprocal space. In other words, the structural short-range order of each region can be determined exclusively, by using an appropriate Bragg diffraction peak (see Fig. 18 and example of measured DAFS in Fig. 19). This is also possible if these different regions contain the same atomic species. Wave vector selectivity is also important for the analysis of nanolayers. Individual layers of epitaxially grown strained or compositionally modulated layer systems can be selected, but also even buried monolayers [118] have been subject of exclusive investigation of parameters characterizing structural short-range order. Another example is the quantitative characterization of ordered domains in epitaxially grown (Ga,In)P layers [119]. These ordered regions, representing merely a small fraction (a few percent) with identical chemical compositions as their environment, were selected with the use of superlattice reflections caused by ordering. Experiments for the study of strained epitaxial semiconductors by means of DAFS have been reported in [120].

Another important feature of DAFS spectroscopy is its crystallographic site selectivity. This means that short-range order information for inequivalent sites within the unit cell can be obtained selectively. This is possible even when these sites are occupied by the same atomic species. The specific site information can be obtained by the deconvolution of differently weighted contributions of inequivalent sites to the reflections selected. Thus crystallographic knowledge is necessary for the evaluation. In [11] the site selective DAFS investigation of short-range order of Cu atoms occupying two inequivalent sites in an epitaxially grown YBaCuO (001) layer on a MgO (001) substrate was described. In agreement with the orientation of the layer in symmetrical geometry different orders of 001 Bragg reflection were obtained. Site

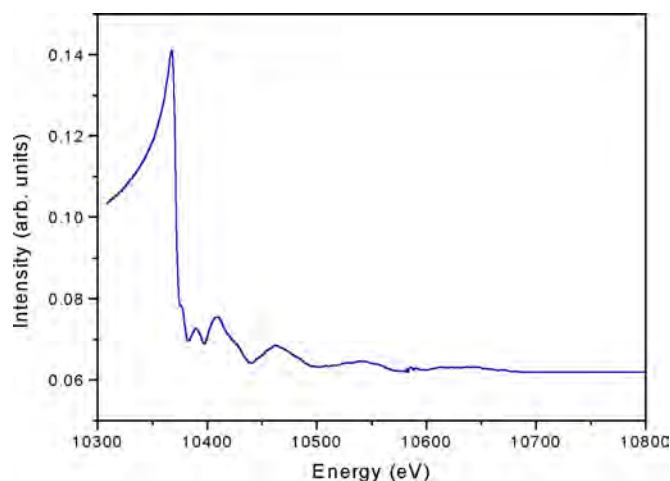


Figure 19. Measured DAFS reflection intensities of superlattice reflection (003 reflection, space group $R3m$; see Fig. 18) caused by partial ordering in a (Ga,In)P layer ($1.69 \mu\text{m}$, epitaxially grown on GaAs substrate) versus photon energies in the vicinity of the Ga K absorption edge at 10,369 eV.

selective information could be obtained by the variability of contributions of Cu atoms at inequivalent sites to the different orders of Bragg reflection.

In the example of DAFS experiments with epitaxially grown (Ga,In)P layers it was shown that the lack of inversion symmetry, typically for the zinc-blende-type structure, has a significant impact on the DAFS signal [121]. This sensitivity of DAFS on the structure polarity, thus on the directions in the crystal at the same magnitudes of the wave vectors, allows for further contributions of the method to structure analysis.

In recent years the enhancement of the relatively weak magnetic dichroism near the absorption edge has been used to provide site-specific local information about the magnetic environment of the resonantly absorbing atom. In the case of multilayers with different magnetic ordering magnetic DAFS makes it possible to distinguish the same atomic species in different layers by means of its magnetic neighborhood. An adequate extension of the information results from the tensor characteristics of the atomic scattering amplitude (see Section 3) which can be tested by means of polarization dependent experiments.

4.6.3. Experimental Setup

DAFS experiments commonly require polychromatic radiation, a tuneable monochromator with energy resolution appropriate for XAFS experiments. In addition an automatic goniometer allowing for alignment of the sample and a DAFS detector to record selected reflections at any photon energy of the DAFS scan are required (constant wave vector scans). For DAFS experiments using sharp Bragg reflections as in the case of single crystals an additional dynamic positioning system (e.g., a piezoelectric tilt table) can be used [121].

Special setups do not require monochromators. The possibility of DAFS experiments using polychromatic synchrotron radiation and a single crystal acting as the sample as well as the monochromator was outlined in [122]. Additionally, polychromatic synchrotron radiation in connection with a suitably curved crystal monochromator allows for an energy dispersive setup [123].

In most cases the parallel detection of fluorescence XAFS intensities is necessary, to be used for the extremely sensitive absorption correction of the DAFS signals. The importance of the absorption correction is due to the fact that the DAFS intensities undergo attenuation causing absorption fine structure comparable with a transmission XAFS experiment. Since this fine structure contains averaged short-range order information of all resonantly absorbing atoms of the sample, without correction of these contributions the selectivity of the DAFS analysis discussed previously would be lost. Energy-dependent background contributions (fluorescence of the sample, radiation scattered at slits or diffusely scattered by the sample) can be measured at angle positions near the Bragg angle.

For practical use the predetermination of Bragg peak positions (angle of incidence and detection angle) at a couple of relevant energies is useful. During the DAFS measurement the peak positions can be adjusted according to a polynomial function determined on the basis of the grid points.

4.6.4. Quantitative DAFS Analysis

The first step of a quantitative DAFS analysis is the background subtraction. Then an absorption correction of the measured reflection intensities must be made. Since the DAFS analysis is usually based on the kinematic theory of X-ray diffraction in the case of single crystals and strong textures extinction corrections have to be applied. An algorithm for extinction correction, which can be applied to the investigation of nanolayers, is described in [124]. The next steps of a complete analysis are the calculation of the smoothed curve (without the fine structure) of the reflected intensities and the adaptation of the medium energy dependent course of the corrected measured intensities to gain the oscillating part, from which the complex-valued fine structure function can be obtained by applying an iterative Kramers–Kronig algorithm (see [11]). Finally the short-range order parameters have to be calculated by modelling the theoretical fine structure function and then comparing it with the experimental one as extracted from DAFS signals. Alternative means for the DAFS evaluation as well as the procedure to obtain site selective information can be seen in [11]. After computation of the complex-valued fine structure function the DAFS analysis can be done by means of the developed procedures of the XAFS analysis, described to a somewhat larger extent in Section 4.5.

For the accuracy of the determinable parameters of short-range order the same statements as in the case of the XAFS apply. Regarding the scattering volumes a lower limit can only be seen regarding the formation of significant Bragg maxima which are interlinked with the number of coherent scatters. The increasing radiation quality of new generation X-ray sources will also lead to further developments in this regard.

4.7. X-Ray Standing Wave Analysis

4.7.1. Introduction

X-ray standing wave fields can be generated when plane wave X-rays undergo reflection or diffraction phenomena. The standard application of XSW experiments is the solution of the phase problem in X-ray single crystal structure analysis and the investigation of lattice position of a certain kind of atom, which can be present in extremely small concentrations (see Fig. 20 for illustration of generation of XSW in the case of Bragg reflection and the origin of depth sensitivity by position dependent excitation of fluorescence intensities). A descriptive representation of appropriate applications can be found in [125]. Since analysis under XSW conditions can allow for extraordinarily sensitive surface analysis and additionally for unique information from thin films and multilayer systems it has been developed to be a powerful tool for the X-ray investigation of nanolayers. A substantial advantage of XSW based analysis is that it does not require vacuum conditions. Due to the nature of X-rays the XSW represent a spatially fixed periodical distribution of electromagnetic field energy. It is remarkable that the spatial period in the case of diffraction at crystals is directly interlinked with the distance of lattice planes. When exciting XSW by using total external reflection at surfaces, the spatial period can be tuned in an extended range. Since

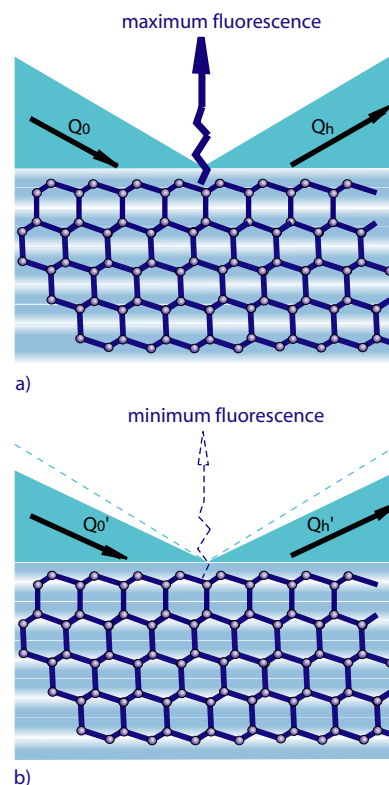


Figure 20. Illustration of the generation of XSW in the case of Bragg reflection and the origin of depth sensitivity by position dependent excitation of fluorescence intensities. If the condition of excitation of a Bragg reflection is fulfilled in addition to the vector of incident waves Q_0 the vector of diffracted waves Q_h can be defined. The XSW represent a spatially fixed periodical distribution of electromagnetic field energy with spatial period directly interlinked with the distance of lattice planes. Simplifying, the creation of the XSW can be imagined by interaction of incident and reflected X-rays, whereby the intensities of the XSW at a particular (equivalent) spatial position can be changed by slightly altering the angle of incidence or the energy of exciting X-rays, respectively. (a) Maxima of XSW (deep colored horizontal regions) according to atomic positions. The correlation between local field strength and absorption/fluorescence excitation causes maximum fluorescence yields from atoms involved. (b) Maxima of XSW in between atomic positions yields lower fluorescence intensities from the atoms considered in (a).

in the case of single crystals the amplitude and the phase of the XSW are derived from the dynamical theory of X-ray diffraction (for an overview see [97]) in complete form, frequently a simple model for a descriptive discussion is used: “the incident and reflected X-rays create the XSW by their interaction.” For a number of applications it is important that the XSW can extend outside of the surface of crystals or nanolayers, where the position sensitive analysis of adsorbates or monolayers becomes possible. The intensities of the XSW at a particular spatial position can be changed by slightly altering the reflection angle, or the energy of exciting X-rays. The position of the XSW can be determined experimentally, whereby the phase is determined relatively. XSW analysis is justified on the possible locally weighted excitation of atoms.

4.7.2. X-Ray Standing Waves in the Case of Multilayers

A complex description is required if both the substrate and layers are to be characterized as single crystallites and the XSW are generated by the excitation of Bragg reflections. An example of this is the epitaxially grown strained layer system. If the lattice parameters of the substrate and layers deviate from each other, the wave field within a given layer cannot be assumed to exhibit the periodicity of its lattice planes correctly. Above all this is the case when the XSW arises primarily from substrate diffraction. For an exhaustive description of the theoretical basis for this situation, which directly presupposes the application of approaches of dynamical theory of X-ray diffraction, we refer to [31].

An interesting field of application for the analysis of nanometer multilayers was opened by coupling the possibilities of the XSW with the method of the fluorescence XAFS. Therefore not the Bragg diffraction of crystalline substrates and layers but instead the total external diffraction and refraction phenomena are used for the generation of the XSW (see Figs. 21 and 22). The advantage of this coupling is that the structural information from fluorescence XAFS can be obtained depth-resolved with respect to the interfaces by tuning the XSW to a certain position during the measurement. Summarizing, the method aims at a locally weighted excitation of the atoms to fluorescence, whose energy-dependent XAFS yields information on their structural short-range order. As a prerequisite plane samples and interfaces of good quality are required. All in all the samples have to be suited for characterization by means of X-ray reflectometry; Regarding the demanded accuracies of beam divergence and sample positioning the experimental setup has to fulfill the same requirements as that in the case of X-ray reflectometry, however, for the spectroscopic part a polychromatic X-ray source with a tuneable monochromator is required. With respect to this device the specifications for XAFS experiments (see Section 4.5) have to be considered. The fundamentals of depth-resolved analysis of structural short-range order by combining Fe-K XAFS and XSW, described using the example of the investigation of the neighborhood of Fe atoms in a sixfold Fe/Al nanomultilayer, can be found in [126]. In addition we refer to earlier publications in this field [127, 128]. For these experiments the shift of the position of the electromagnetic field of XSW perpendicular to the interfaces was used. Therefore the angle of incidence was varied in the vicinity of the first order Bragg reflection of the multilayer stack which occurs slightly above the critical angle of total external reflection.

For quantitative analysis geometrical and physical parameters of the sample, such as single layer thickness, number of periodic repeated layers, roughness parameters of interfaces, and single layer densities, have to be known. They can be determined by fitting a modelled reflection curve to an experimental one (see Section 4.3). Since XAFS experiments are accomplished in the vicinity of the absorption edges (ionization energies of atoms), the strong influence of the resonant scattering has to be taken into account. The next step is to evaluate the XSW distributions within the multilayer stack for different angles of incidence. By varying the angle of incidence in the vicinity of the first order Bragg reflection

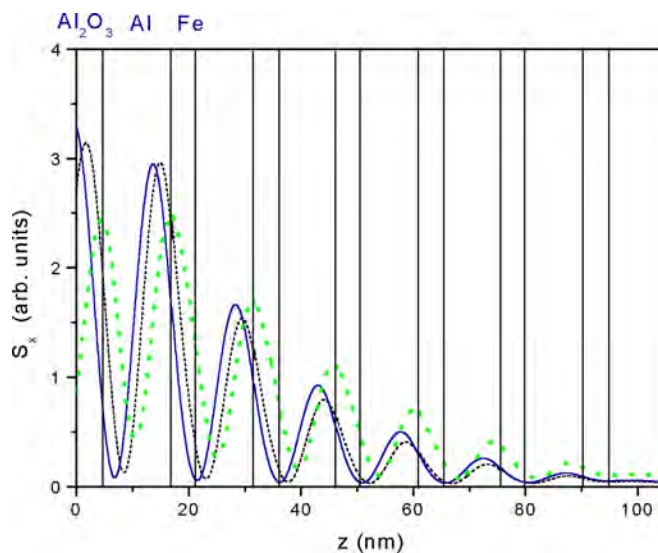


Figure 21. Measured X-ray specular reflectivities (dotted) and Fe *K* fluorescence intensities (full line) of the Fe/Al multilayer specified in the caption of Figure 10 versus angles of incidence. Photon energy was 7580 eV above the Fe *K* absorption edge at 7112 eV. The modulation in fluorescence intensities at angles of incidence in the vicinity of the first order Bragg reflection of the multilayer stack at approx. 0.42° indicates the existence and shift of standing wave fields within the multilayer in this case. Marked positions: (1) maximum of the first order Bragg reflection, (2) inflection point of the course of Fe *K* fluorescence intensities in the vicinity of (1), and (3) maximum of Fe *K* fluorescence.

and thus shifting the position (phase) of the standing wave field within the multilayer stack, the contribution of different regions within certain layers to the excited fluorescence intensities can be distinguished. For depth-sensitive analysis a certain number of XSW positions have to be selected whose adjustment can be done in a reproducible manner. Therefore the first order Bragg reflection of the multilayer, the fluorescence maximum and minimum, and the inflection

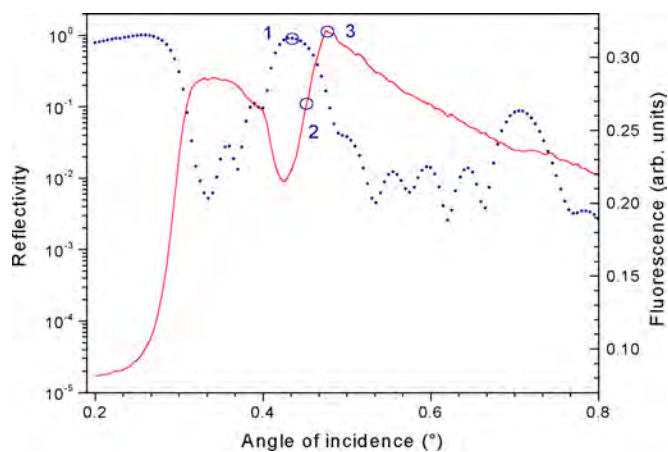


Figure 22. Calculated components S_x of the Poynting vector S (x direction parallel to interfaces) of the Fe/Al multilayer specified in the caption of Figure 10 versus penetration depth z perpendicular to the interfaces (surface: $z = 0$ nm) for different standing wave field positions in the vicinity of the first order Bragg reflection of the multilayer stack as defined by Figure 21 [1 (full line), 2 (dashes), and 3 (dots)].

point of the maximum course in the vicinity of the Bragg reflection are special positions for this procedure. To hold a selected XSW position fixed during the XAFS measurement, with which the energy of the exciting photons is changed, the angle of incidence has to be adjusted accordingly while varying the energy. The energy of incident X-rays and the reflection angle are related by known equations. Due to the influence of refraction the experimental determination of these angle positions at a limited number of energies is preferred. Then a polynomial function can be determined to adjust the scattering angle while tuning the energy step by step during the XAFS measurement.

In general, the energy-dependent fine structure of the photoelectric absorption coefficient N can be extracted from both the fluorescence intensities and from the reflected ones. When the XSW is shifted the contribution of resonantly absorbing atoms and the other (nonedge) atoms to the total attenuation coefficient will change. Therefore the integral field intensities in the individual layers had to be calculated to determine the effective attenuation and photoelectric absorption coefficient N_s for the evaluation of XAFS to be discussed. In [126] this was accomplished by using a recursive matrix approach. The attenuation in the Poynting vector component of the electromagnetic field of the XSW in the stack direction can be used to determine the contribution of different layers to the fluorescence and therefore to the structural information determined from XAFS. Its depth distribution can yield the weights for the local contribution to absorption and thus to fluorescence intensities. To characterize the average neighborhood of resonantly absorbing atoms an XAFS measurement with fixed angle of incidence can be performed. In this case the angle of incidence should be chosen due to small reflectivities; thus only weak interactions between incident and reflected waves cause XSWs with negligibly small spatial intensity modulations.

The accuracy of quantitative parameters characterizing structural short-range order in the neighborhood of resonantly absorbing atoms achieved by the combination of XSW and XAFS is comparable with that of conventional XAFS measurements (see Section 4.5). Regarding the depth resolution it is difficult to state a general limit, since the sample characteristics are important. Generally a high reflectivity of the multilayer Bragg reflection is desirable, because it is equated to the formation of a significant XSW. Additionally, in the case of multilayers a high homogeneity of characteristic parameters of several layers repeated within the stack is a condition for good results. In case of multilayers dedicated for use as mirrors for soft X-ray applications, exhibiting reflectivities of typically 70% in the energy range of 10 keV, approximate monolayer resolution could be achieved for the average parameters [129].

5. NANOLAYER MATERIALS

5.1. Introduction

As already outlined in previous chapters the small number of atoms contained within nanolayers is the main challenge for X-ray characterization. Additionally, the cross section of atoms for X-rays is rather small. In the theoretical

description of the interaction of X-rays with matter in Section 3 it was discussed that the total attenuation of hard X-rays with photon energies in the order of 10 keV is mainly caused by elastic/inelastic scattering and photoelectric absorption. Diffraction and reflection/refraction phenomena are in direct connection to scattering while occurrence of characteristic fluorescence radiation is directly caused by photoelectric absorption. In Section 3 it was shown that, in addition, both scattering and absorption are interconnected by causality.

Regarding X-ray characterization of nanolayers by means of diffraction phenomena in particular the continuous direct dependence of the atomic scattering amplitude on the number of electrons per atom has to be considered. This causes on the one hand challenges for the characterization of nanolayers of elements with low atomic numbers, thereby including the wide range of organic nanolayers in the growing field of biological applications. On the other hand it is difficult to distinguish scattering contributions of atoms with neighboring atomic numbers. A way out is the use of resonant interactions for X-rays with photon energies in the vicinity of ionization energies of the atoms (cf. Section 3.2). If resonant scattering of photons with energies corresponding to K -absorption edges should be applied, for elements with atomic numbers less than ~ 20 the experiments have to be performed under vacuum/inert gas conditions because of significant attenuation of X-rays with these energies in air. This applies to spectroscopic methods, which are based on the detection of fluorescence photons of adequate energies, as well.

Also the absorption cross section for atoms with X-rays, beside edgewise jumps at photon energies due to ionization energies of the atoms, depends directly on the atomic number. Thus, also in this case, the largest challenges exist for the investigations of nanolayers of atoms with low atomic numbers. In particular if the interesting atomic species exhibits a small fraction (lower than ~ 1 at%), simultaneous excitation of fluorescence radiation of the other components can cause low effect/background ratios, which prevent a characterization in justifiable times. In addition, mostly in the case of nanolayers, the contribution of scattered exciting radiation to the background signal can impose further limitation.

Summarizing, limits of X-ray characterization of nanolayers are to be seen in cases of light elements and diluted concentration. To be complete we should mention here the demands for the interface quality and layer homogeneity for X-ray reflection experiments specified already (Section 4). The use of diffraction phenomena requires accordingly ordered volumina. High fluxes and spatial/time coherence of X-rays supplied by synchrotron radiation sources allow for a progressive shift of these limits. In particular with the help of free electron X-ray lasers under construction, in coming decades structural analysis of individual molecules should become possible. In this case it is assumed that, due to the high energy densities, the object of investigation is destroyed after characterization. Also for investigations using conventional synchrotron radiation, in particular in the case of organic specimens, an influence on the structure by the interaction with X-ray photons has to be considered. Apart from a mostly unwanted change of substance nature,

radiation damage can limit the structural information to be extracted from the samples. Contributions on this topic can be found in [130].

In the following we will specify some current work on X-ray characterization of nanolayers which, beyond the examples in the preceding sections, is exemplary for the applicability and resolution of the methods for different classes of specimen and focus of investigation. For an overview the cited papers are arranged according to these aspects in Table 1.

5.2. Examples

Temperature- and time-resolved investigations of thin organic multilayer films [Fe(II)-polyelectrolyte-amphiphile complex, deposited on silicon by means of the Langmuir-Blodgett technique, single layer thickness ~ 5 nm] by means of X-ray scattering were reported in [131]. By using an energy-dispersive setup (geometrical fixed) at a synchrotron radiation source, X-ray reflectivity and in-plane diffraction were recorded simultaneously. After increasing the temperature (273–348 K), transformations of the Langmuir-Blodgett phase could be observed from X-ray reflectivity measurements. Simultaneously detected in-plane diffraction signals indicated changes of the hexagonal arrangement of amphiphilic chains (lattice spacing ~ 0.42 nm).

The structure of hexadecylamine-urease monolayers at the air-water interface has been investigated by X-ray reflectometry and GID studies [132]. The thickness of the two-dimensional crystalline films was determined to be in the order of 0.1 nm (accuracy $\sim \pm 0.01$ nm). From the experimental results, among other facts it was concluded that hexadecylamine, when spread on top of an urease film at the air-water interface, forms a stable, well-organized structure.

The growth of self-assembled monolayers of octadecyltrichlorosilane on oxidized Si(111) substrates from the liquid has been studied *in-situ* by means of X-ray reflectometry [133]. It was found that the film grows through the formation of islands of vertical molecules. Typical layer thickness were in the order of 1 nm.

The generation of large-area X-ray topographs (whole surface of 200-mm-diameter silicon wafers) is described in [134]. By using a horizontally wide monochromatic beam available from a synchrotron radiation source, topographs of the whole surface of the wafers could be obtained with one-shot exposure. From the topographs differences in surface-strain distributions, caused by various steps of silicon wafer manufacturing processes, could be detected. To achieve sufficient sensitivity asymmetric reflections with a glancing angle of 0.26° (above the critical angle of external total reflection of 0.08° at the photon energy of 21.45 keV) were used.

In [135] an anomalous behavior of the specular reflection of X-rays under the condition of noncoplanar grazing incidence diffraction was studied and used for characterization of a native oxide amorphous film on the surface of a Si single crystal. In general, because of the similarity of the electron densities of layer and “substrate,” the determination of parameters of oxide layers by means of specular reflection in symmetric geometry is very difficult. Under conditions of strongly asymmetric diffraction the authors determined the

thickness of the oxide layer with high accuracy (2.8 ± 0.1 nm) and stated the sensitivity of the method to be in the order of one monolayer.

Reactively sputtered Ta₂O₅ nanolayers (thickness ~ 22.4 nm) were investigated by means of reflection mode Ta-L₃ XAFS investigation at several different glancing angles in the vicinity of the critical angle of external total reflection [136]. Also, here the Ta-O bond lengths of the layers were given with an accuracy of ± 0.002 nm, while the appropriate coordination numbers were estimated with an absolute accuracy of ± 0.09 . In comparison to a polycrystalline β -Ta₂O₅ sample the Ta-O distances for the amorphous layers were found to be smaller.

X-ray topography was used to determine the critical thickness of InGaAs epitaxial layers on GaAs [137]. For this purpose the topographs were taken *in-situ* in dependence on the temperature applied.

An indirect determination of the polarity of ferroelectric nanolayers [PbTiO₃ grown on SrTiO₃ (001) substrates, layer thickness 10–40 nm] was accomplished by means of XSWs [138]. The XSWs were generated inside the thin epitaxial layer by excitation of Bragg diffraction and were used for determination of the polarity. This succeeds by the polarization-dependent relative sublattice positions of the Ti and Pb ions. The method allows for detection of relative displacements of sublattice layers within the unit cells in the order of 0.01 nm.

As outlined in Section 4.2 the GID is established for the investigation of epitaxial layers on single-crystalline substrates. In the past few years related objects, self-assembled quantum dots, have been studied extensively. They can be formed if the amount of deposited material is in the order of one monolayer, typically. At an appropriate coverage dislocation-free coherently strained dots are formed. At higher coverage dislocations start to appear, generating relaxed islands on the surface. By X-ray scattering experiments [139] it was shown that for coherently strained islands (InAs on GaAs) the lattice parameter misfit induces a relaxation gradient inside the dots.

Beyond that, an X-ray study of structural changes of self-assembled PbSe quantum dots in PbSe/PbEuTe superlattices [140] should be specified here as an example. From surface-sensitive grazing incidence small angle X-ray scattering (GISAXS) the shape of the freestanding dots could be determined exclusively. Information on shape and chemical composition of the buried dots has been obtained from GID experiments. Another interesting subject accompanying with the growth of strained semiconductor layers is nanowires. When using vicinal substrates, the regularly terraced surfaces can act as templates for subsequent growth of laterally ordered islands; at appropriate conditions wires instead of islands can be formed.

In [141] wide-angle coplanar X-ray diffraction studies on appropriate Si/SiGe wire superlattices are reported. To obtain information on the shape and the lateral correlation, also of buried wires, GISAXS for different information depths was used.

The elastic stress relaxation in Ga_{0.22}In_{0.78}As_{0.80}P_{0.20} quantum wire structures (1% compressively strained) with a wire width of 35 nm and a thickness of 8 nm was investigated by X-ray scattering using asymmetric reflections of the InP

Table 1. Examples for X-ray characterization of nanolayer materials.

Nanolayer class	Material (thickness t)	Characterization method	Focus of investigation	Ref.
Organic multilayers	Fe(II)–polyelectrolyte–amphiphile complex on silicon substrate, $t \sim 5$ nm (single layer)	X-ray reflectometry, X-ray diffraction	transitions of the Langmuir–Blodgett phase in dependence on temperature	[131]
Monolayers at air–water interface	hexadecylamine–urease monolayers at the air–water interface, $t \sim 0.1$ nm	X-ray reflectometry, GID	layer thickness and structure formation	[132]
Self-assembled monolayers	octadecyltrichlorosilane on silicon substrate, $t \sim 1$ nm	X-ray reflectometry	layer growth mode (<i>in-situ</i>)	[133]
Surface layers	silicon wafers, diameter ~ 200 mm	X-ray topography	surface-strain distributions	[134]
Surface layers	native oxide amorphous layers on surface of Si single crystals, $t \sim 2.8$ nm	X-ray reflectometry GID	morphological parameters of the oxide layer	[135]
Sputtered amorphous layers	Ta ₂ O ₅ layers on float glass plates, $t \sim 22.4$ nm	XAFS (reflection mode)	structural short-range order parameters	[136]
Epitaxial layers	(In,Ga)As on GaAs substrate, $t \sim 200$ nm	X-ray topography	critical thickness (<i>in-situ</i>)	[137]
Ferroelectric layers	PbTiO ₃ on SrTiO ₃ substrate, $t \sim 10$ – 40 nm	XSW	polarity	[138]
Quantum dots	InAs on GaAs substrate	GID	strain relaxation gradient inside the dots	[139]
Quantum dots	PbSe dots in PbSe/PbEuTe superlattices (5 periods, $t_{\text{period}} \sim 35$ – 65 nm)	GISAXS	shape and chemical composition of freestanding dots	[140]
Quantum wires	wires in/on Si/SiGe superlattices on Si substrate, 20 periods, $t_{\text{Si}} \sim 10$ nm, $t_{\text{SiGe}} \sim 2.5$ nm	GISAXS	shape and lateral correlation of wires (incl. buried ones)	[141]
Quantum wires	(Ga,In)(As,P) wires on InP substrate, wire width ~ 35 nm, $t_{\text{wire}} \sim 8$ nm	XRD (grazing exit)	elastic stress relaxation in wire structures	[142]
Quantum wires	InAs wires on InP substrates, precursor layer thickness ~ 2.5 monolayers	DAFS (grazing beam geometry)	strain and chemical composition inside the wires and close to the interface	[143]
Epitaxial multilayers	Co/Pt on Pt/Mo buffer layers on Al ₂ O ₃ substrates, $t \sim 0.16$ – 1.07 nm (single layers)	XANES/ XAFS (polarization dep.)	local structure in dependence on thickness	[144]
Quantum wells (strained layer superlattices)	Ge/Si (5 periods) on Si substrate, $t \sim 4$ monolayers (single layers)	XAFS (grazing incidence fluorescence)	influence of mismatch strain on local structure, interface mixing	[146]
Multilayer gratings (lateral patterned multilayers)	(Ga,In)As/InP on InP substrate, grating periodicity ~ 1380 nm, grating depth ~ 432 nm, $t \sim 47$ nm (single layers)	GID XRD	grating parameters, vertical composition profile, strain tensor	[147]

substrate (grazing exit) [142]. The long-range periodicity of the wire positions causes narrow periodic peaks in the direction perpendicular to the wire direction. With an analytical calculation presented in [142] the X-ray diffraction

intensities were described quantitatively and are found to show a good agreement with the experimental data.

InAs/InP (001) self-assembled quantum wires achieved by deposition of 2.5 monolayers of InAs have been investigated

by means of grazing incidence diffraction anomalous fine structure (GIDAFS) [143]. For that reason As *K* GIDAFS spectra were measured at incidence and detection angles close to the critical angle of total reflection of the substrate. Thus information about composition and strain inside the quantum wires and close to the interface could be obtained. The accuracy of bond length obtained from experimental data was in the order of 0.001 nm.

Five epitaxial $[\text{Co}(t \text{ nm})/\text{Pt}(1 \text{ nm})]_{30}$ ($t = 0.16\text{--}1.07 \text{ nm}$) multilayers [prepared on Pt/Mo buffer layers on Al_2O_3 (11–20) substrates] were subjected to polarization dependent Co *K* fluorescence XANES and XAFS investigations to investigate the local structure in the neighborhood of the Co atoms [144]. The results have shown that at the given growth temperature (470 K) no significant interdiffusion can be observed at the Co/Pd interfaces. The structure of the Co layer changes depending on its thickness, whereby a thickness of 0.3 nm can be taken as a threshold. The accuracy of experimentally determined bond length (between ~ 0.250 and $\sim 0.265 \text{ nm}$) was in the order of 0.005 nm.

As outlined in Section 4.5 in fluorescence XAFS experiments the surface sensitivity can be improved significantly by grazing incidence excitation. In principle submonolayer sensitivity can be achieved this way [145]. By means of grazing incidence fluorescence XAFS the local structure around Ge atoms in Ge/Si monolayer strained-layer superlattices (quantum wells) grown on Si(100) substrate have been studied by [146]. The Ge–Ge and Ge–Si bond lengths have been obtained with an accuracy of $\pm 0.001 \text{ nm}$, from which it could be concluded that mismatch strain is accommodated by both bond compression and bond bending in the Ge_4 layer. From coordination numbers, determined with an absolute accuracy of ± 0.2 , conclusions on a substantial interface mixing could be drawn.

Lateral patterned (Ga,In)As/InP multilayers (multilayer gratings) were subjected to analysis of surface shape and the spatial distribution of strain by combined high-resolution X-ray diffraction and GID (coplanar and noncoplanar triple-crystal diffractometry) [146]. Characteristic grating parameters and accuracy determined by GID were grating periodicity (1380 ± 5) nm, grating depth (432 ± 10) nm, thickness of (Ga,In)As layers (47 ± 2) nm, and thickness of InP layers (47 ± 2) nm. These results were compatible with the vertical composition profile obtained by coplanar X-ray diffraction. It was found that elastic strain relaxation causes dramatic deformations of the X-ray diffraction patterns in the measured reciprocal space maps. Different components of the strain tensor could be determined by recording diffraction patterns around different reciprocal lattice points. In [147] a detailed description of the influences of the grating shape, the morphological setup, and the related lattice distortions fields on the X-ray diffraction patterns/maps is given.

5.3. Summary

The examples illustrate that by means of X-ray characterization methods structural parameters of nanolayers (see Section 2) can be obtained nondestructively with an accuracy on the picometer scale. As outlined, characterization of

nanolayers of elements with lower atomic numbers requires a relatively higher experimental effort.

If there is no limitation to the extent of the nanostructures in certain directions, in case of interference methods these parameters are determined by averaging over areas/volumes which are at least limited by the coherence length of the radiation. In reverse this gives a limit for the investigation of correlation length of structures obtainable by means of X-ray methods. As an upper limit the size of $1 \mu\text{m}$ can be considered at usual X-ray sources. This corresponds also to the spot size of X-rays to be achieved with modern optics for a reduction of excitation of samples in two dimensions (local analysis). The morphology of interfaces of nanolayers can be characterized on a scale of 0.1 nm.

As illustrated by the given examples, at suitable sample characteristics a reduction of the investigated volume in one direction down to one monolayer can be achieved. Within these volumes element-specific bond lengths can be determined with an accuracy in the order of one picometer and average coordination numbers with an accuracy of ± 0.01 atoms in the most favorable case.

ABBREVIATIONS

- AAS** Anisotropic anomalous scattering.
- ADX** Angle dispersive X-ray diffraction.
- ASAXS** Anomalous small angle X-ray scattering.
- BA** Born approximation.
- BREFS** Bragg reflectivity extended fine structure (=DAFS).
- CCT** Curved collimator topography.
- CDW** Charge density wave.
- DAD** Dispersive anomalous diffraction.
- DAFS** Diffraction anomalous fine structure.
- DANES** Diffraction anomalous near-edge structure.
- DDAFS** Dispersive diffraction anomalous fine structure.
- DIFFRAXAF** Diffraction X-ray absorption fine structure.
- DWBA** Distorted-wave Born approximation.
- EAD** Extremely asymmetric diffraction.
- EDAFS** Extended diffraction anomalous fine structure.
- EDXD** Energy dispersive X-ray diffraction.
- EXAFS** Extended X-ray absorption fine structure.
- GBL** Grazing Bragg Laue diffraction.
- GID** Grazing incidence diffraction; see also GIXD.
- GIDAFS** Grazing incidence dispersive diffraction anomalous fine structure.
- GISAXS** Grazing incidence small angle X-ray scattering.
- GIXD** Grazing incidence X-ray diffraction.
- GIXDT** Grazing Incidence X-ray diffraction topography.
- MAD** Multiple-wavelength anomalous dispersion.
- NEDAFS** Near-edge diffraction anomalous fine structure (=DANES).
- NEXAFS** Near edge X-ray absorption fine structure (=XANES).
- NSXR** nonspecular X-ray reflectivity.
- NXES** Normal X-ray emission spectroscopy.

REFLEXAFS Reflectivity extended absorption fine structure (=DAFS).

RXES Resonant X-ray emission spectrum.

RXMS Resonant X-ray magnetic scattering.

SANS Small angle neutron scattering.

SAXS Small angle X-ray scattering.

SDW Spin density wave.

SMAD Simultaneous multiple-wavelength anomalous dispersion.

SXAFS Surface X-ray absorption fine structure.

SXR Specular X-ray reflectivity.

TER Total external reflection.

TRXF Total reflection X-ray fluorescence.

USAXS Ultrasmall angle X-ray scattering.

XAFS X-ray absorption fine structure.

XANES X-ray absorption near edge structure.

XAS X-ray absorption spectroscopy.

XDS X-ray diffuse scattering.

XES X-ray emission spectroscopy.

XMCD X-ray magnetic circular dichroism.

XRR X-ray reflectometry.

XSW X-ray standing wave field.

REFERENCES

- M. V. Laue, *Sitzungsber. Bay. Akad. Wiss., Math.-phys. Klasse* 363 (1912).
- M. Tolan, "X-ray Scattering from Soft-Matter Thin Films," p. 7. Springer, Berlin, 1999.
- "Resonant Anomalous X-ray Scattering" (G. Materlik, C. J. Sparks, and K. Fischer, Eds.). Elsevier, Amsterdam, 1994.
- P. F. Fewster, *Rep. Progr. Phys.* 59, 1339 (1996).
- D. H. Templeton, in "Handbook of Synchrotron Radiation" (G. Brown and D. E. Moncton, Eds.), Vol. 3. Elsevier, Amsterdam, 1991.
- D. T. Cromer and D. Liberman, *J. Chem. Phys.* 53, 1891 (1970).
- J. S. Töll, *Phys. Rev.* 104, 1760 (1956).
- H. Fricke, *Phys. Rev.* 16, 202 (1920).
- G. Hertz, *Z. Phys.* 3, 19 (1920).
- Y. Cauchois and C. Bonnelle, *C. R. Acad. Sci. Paris* 242, 100, 1596 (1956).
- L. B. Sorensen, J. O. Cross, M. Newville, B. Ravel, J. J. Rehr, H. Stragier, C. E. Bouldin, and J. C. Woicik, in "Resonant Anomalous X-Ray Scattering" (G. Materlik, C. J. Sparks, and K. Fischer, Eds.), p. 389. Elsevier, Amsterdam, 1994.
- D. H. Templeton and L. K. Templeton, *Acta Crystallogr. A* 38, 62 (1982).
- G. Schütz, M. Knülle, and H. Ebert in "Resonant Anomalous X-Ray Scattering" (G. Materlik, C. J. Sparks, and K. Fischer, Eds.), p. 535. Elsevier, Amsterdam, 1994.
- N. Ishimatsu, H. Hashizume, S. Hamada, N. Hosoizo, C. S. Nelson, C. T. Venkataraman, G. Srajer, and J. C. Lang, *Phys. Rev. B* 60, 9596 (1999).
- W. L. Bragg, *Proc. Cambridge Philos. Soc.* 17, 43 (1913).
- P. Debye and P. Scherrer, *Phys. Z.* 17, 277 (1916).
- "Fifty Years of X-ray Diffraction" (P. P. Ewald, Ed.). Oosthoek, Utrecht, 1962.
- A. Guinier, "X-ray Diffraction in Crystals, Imperfect Crystals and Amorphous Bodies." Dover, New York, 1994.
- H. M. Rietveld, *Acta Crystallogr.* 22, 151 (1967).
- R. A. Young, "The Rietveld Method." Oxford Univ. Press, Oxford, 1993.
- M. Schuster and H. Göbel, *J. Phys. D* 28, A270 (1995).
- G. Goerigk and D. L. Williamson, *J. Appl. Phys.* 90, 5808 (2001).
- J. R. Helliwell, W. Parrish, and J. I. Langford, *Int. Tables Crystallogr. C* 23, 42 (1999).
- D. Coster, K. S. Knol, and J. A. Prins, *Z. Phys.* 63, 345 (1930).
- V. Hauk, *Adv. X-ray Anal.* 39 (1996).
- V. Hauk, "Structural and Residual Stress Analysis by Nondestructive Methods." Elsevier, Amsterdam, 1997.
- "Defect and Microstructure Analysis by Diffraction" (R. L. Snyder, J. Fiala, and H. J. Bunge, Eds.). Oxford Science, Oxford, 1999.
- R. Feidenhans'l, *Surf. Sci. Rep.* 10, 105 (1989).
- H. Dosch, in "Critical Phenomena at Surfaces and Interfaces (Evanescent X-Ray and Neutron Scattering)" (G. Höhler, Ed.), Springer Tracts in Modern Physics, Vol. 126. Springer, Berlin, 1992.
- S. Dietrich and A. Haase, *Phys. Rep.* 260, 1 (1995).
- S. A. Stepanov, E. A. Kondrashkina, R. Köhler, D. V. Novikov, G. Materlik, and S. M. Durbin, *Phys. Rev. B* 57, 4829 (1998).
- S. Kishino and K. Kohra, *J. Appl. Phys.* 10, 551 (1971).
- H. R. Höche, J. Nieber, and O. Brümmer, *Acta Crystallogr. A* 42, 585 (1986).
- A. M. Afanas'ev and O. G. Melikyan, *Phys. Status Solidi A* 122, 459 (1990).
- S. Kimura, J. Harada, and T. Ishikawa, *Acta Crystallogr. A* 50, 337 (1994).
- W. C. Marra, P. Eisenberger, and A. Y. Cho, *J. Appl. Phys.* 50, 6927 (1979).
- A. L. Golovin, R. M. Imamov, and S. A. Stepanov, *Acta Crystallogr. A* 40, 225 (1984).
- H. Dosch, B. W. Batterman, and D. C. Wack, *Phys. Rev. Lett.* 56, 1144 (1986).
- T. Jach, P. L. Cowan, Q. Shen, and M. J. Bedzyk, *Phys. Rev. B* 39, 5739 (1989).
- P. A. Aleksandrov, A. M. Afanas'ev, and S. A. Stepanov, *Phys. Status Solidi A* 86, 143 (1984).
- D. Gao, S. W. Wilkins, A. W. Stevenson, and G. N. Pain, *J. Appl. Phys.* 74, 3126 (1993).
- D. V. Novikov, M. Ohler, R. Köhler, and G. Materlik, *J. Phys. D* 28, A84 (1995).
- V. S. Wang, R. J. Matyi, and K. J. Nordheden, *J. Appl. Phys.* 75, 3835 (1995).
- G. T. Baumbach, S. Tixier, U. Pietsch, and V. Holý, *Phys. Rev. B* 51, 16848 (1995).
- D. Bahr, W. Press, R. Jebasinski, and S. Mantl, *Phys. Rev. B* 51, 12223 (1995).
- S. A. Stepanov, E. A. Kondrashkina, M. Schmidbauer, R. Köhler, J.-U. Pfeiffer, T. Jach, and A. Yu. Souvorov, *Phys. Rev. B* 54, 8150 (1996).
- G. D. Yao, J. Wu, T. Fanning, and M. Dudley, *Adv. X-Ray Anal.* 35, 247 (1992).
- P. Sonntag, P. Bödeker, T. Thurston, and H. Zabel, *Phys. Rev. B* 52, 7363 (1995).
- S. Rugel, G. Wallner, H. Metzger, and J. Peisl, *J. Appl. Crystallogr.* 26, 34 (1993).
- D. W. Berreman and A. T. Macrander, *Phys. Rev. B* 37, 6030 (1988).
- S. A. Stepanov and R. Köhler, *J. Phys. D* 27, 1923 (1994).
- L. G. Parratt, *Phys. Rev.* 95, 359 (1954).
- W. J. Bartels, J. Hornstra, and D. J. W. Lobeek, *Acta Crystallogr. A* 42, 539 (1986).
- I. K. Robinson, *Acta Crystallogr.* 54, 772 (1998).
- B. M. Ocko, X. Z. Wu, E. B. Sirota, S. K. Sinha, O. Gang, and M. Deutsch, *Phys. Rev. E* 55, 3164 (1997).
- I. M. Tidswell, T. A. Rabedeau, P. S. Pershan, S. D. Kosowsky, J. P. Folkers, and G. M. Whitesides, *J. Chem. Phys.* 95, 2854 (1991).

57. P. Fenter, A. Eberhardt, K. S. Liang, and P. Eisenberger, *J. Chem. Phys.* 106, 1600 (1997).
58. P. Fenter, F. Schreiber, L. Zhou, P. Eisenberger, and S. R. Forrest, *Phys. Rev. B* 56, 3046 (1997).
59. S. A. W. Verclas, P. B. Howes, K. Kjaer, A. Wurlitzer, M. J. Weygand, G. Büldt, N. A. Denscher, and M. Lösche, *J. Mol. Biol.* 287, 837 (1999).
60. K. Y. C. Lee, J. Majewski, T. L. Kuhl, P. B. Howes, K. Kjaer, M. M. Lipp, A. L. Waring, J. A. Zadadzinski, and G. S. Smith, *Biophys. J.* 81, 572 (2001).
61. A. Barbier, D. Renaud, O. Robach, and P. J. Guenard, *J. Phys. IV* 8, 203 (1998).
62. A. H. Compton, *Philos. Mag.* 45, 1121 (1923).
63. Y. Yoneda, *Phys. Rev.* 113, 2010 (1963).
64. K. Stoev and K. Sakurai, *Rigaku J.* 14, 22 (1997).
65. D. K. Bowen and M. Wormington, *Adv. X-Ray Anal.* 36, 171 (1993).
66. B. Lengeler and M. Hüppauff, *Fresenius J. Anal. Chem.* 346, 155–161 (1993).
67. V. Holý, U. Pietsch, and T. Baumbach, “High-Resolution X-Ray Scattering from Thin Films and Multilayers.” Springer, Berlin, 1999.
68. X. L. Zhou, S. H. Chen, and G. P. Felcher, *Phys. Rev. A* 46, 1839 (1992).
69. X. L. Zhou and L. He, *Phys. Rev. E* 49, 5345 (1994).
70. M. Manciu, L. Dudas, C. Suergers, and R. Manaila, *J. Appl. Cryst.* 28, 160 (1995).
71. S. K. Sinha, E. B. Sirota, S. Garoff, and H. B. Stanley, *Phys. Rev. B* 38, 2297 (1988).
72. D. K. G. de Boer, *Phys. Rev. B* 53, 6048 (1996).
73. P. Croce and L. Nevot, *Rev. Phys. Appl.* 11, 113 (1976).
74. I. A. Artioukov, V. E. Asadchikov, and I. K. Kozhevnikov, *J. X-ray Sci. Tech.* 6, 223 (1996).
75. A. H. Compton, *Phys. Rev.* 20, 60 (1922).
76. H. Kiessig, *Ann. Phys. (5)* 10, 715 (1931).
77. H. Kiessig, *Ann. Phys. (5)* 10, 769 (1931).
78. V. M. Matveev and V. V. Matveev, *Physica B* 208, 768 (1995).
79. V. M. Matveev and V. V. Matveev, *Physica B* 221, 408 (1996).
80. D. E. Savage, J. Kleiner, N. Schimke, Y. H. Phang, T. Jankowski, J. Jacobs, R. Kariotis, and M. G. Lagally, *J. Appl. Phys.* 69, 1411 (1991).
81. D. G. Stearns, *J. Appl. Phys.* 71, 4286 (1992).
82. G. Gladyszewski and Y. Bruynseraede, *Thin Solid Film* 275, 184 (1996).
83. S. K. Sinha, *Physica B* 173, 25 (1991).
84. R. Klockenkämper, “Total-reflection X-ray Fluorescence Analysis.” Wiley, New York, 1997.
85. W. L. Berg, *Naturwissenschaften* 19, 391 (1931).
86. C. S. Barrett, *Phys. Rev.* 38, 832 (1931).
87. C. S. Barrett, *Trans. Am. Inst. Min. Eng.* 161, 15 (1945).
88. A. Guinier and J. Tennevin, *Acta Crystallogr.* 2, 133 (1949).
89. G. N. Ramachandran, *Proc. Indian Acad. Sci.* 19, 280 (1944).
90. N. Wooster and W. A. Wooster, *Nature* 155, 786 (1945).
91. B. K. Tanner, “X-ray Diffraction Topography.” Pergamon Press, Oxford, 1976.
92. D. K. Bowen and B. K. Tanner, “High Resolution X-ray Diffractometry and Topography.” Taylor and Francis, London, 1998.
93. A. R. Lang, *Techniques and interpretation in X-ray topography*, in “Diffraction and Imaging Techniques in Materials Science” (S. Amelinckx, R. Gevers, and J. van Landuyt, Eds.), 2nd ed. rev., p. 623. North-Holland, Amsterdam, 1978.
94. A. Authier, *Techniques and interpretation in X-ray topography*, in “Diffraction and Imaging Techniques in Materials Science” (S. Amelinckx, R. Gevers, and J. van Landuyt, Eds.), 2nd ed. rev., p. 715. North-Holland, Amsterdam, 1978.
95. A. R. Lang, *Int. Tables Crystallogr. C* 113, 142 (1999).
96. B. W. Batterman and H. Cole, *Rev. Mod. Phys.* 36, 681 (1964).
97. A. Authier, “Dynamical Theory of X-ray Diffraction.” Oxford Univ. Press, Oxford, 2001.
98. A. R. Lang, *Acta Crystallogr.* 12, 249 (1959).
99. P. J. Mc Nally, G. Dilliwai, J. M. Bonar, A. Willoughby, T. Tuomi, R. Rantamäki, A. N. Danilewsky, and D. Lowney, *Appl. Phys. Lett.* 77, 1644 (2000).
100. C. L. Kuo and J. C. Bilello, *J. Appl. Phys.* 62, 137 (1987).
101. G. D. Gao, M. Dudley, and J. Wu, *J. X-Ray Sci. Technol.* 2, 195 (1990).
102. G. D. Gao, S. W. Wilkins, A. W. Stephenson, and G. W. Pain, *J. Appl. Phys.* 60, 2604 (1992).
101. R. Rantamäki, T. Tuomi, P. J. McNally, J. Curley, and A. Danilewsky, *J. X-Ray Sci. Technol.* 8, 159 (1998).
102. M. Dudley, J. Wu, and G. D. Yao, *Nucl. Instrum. Methods B* 40/41, 388 (1989).
103. A. M. Afansae, P. A. Aleksandrov, R. M. Imamov, E. M. Pashaev, and V. Polovinkina, *Phys. Status Solidi A* 90, 419 (1985).
104. T. Kitano, T. Ishikawa, J. Matsui, K. Akimoto, J. Mizuki, and Y. Kawase, *Jpn. J. Appl. Phys.* 2 26, L108 (1987).
105. R. M. Imavov, A. A. Lomov, and D. V. Novikov, *Phys. Status Solidi A* 116, K133 (1989).
106. B. K. Teo, “EXAFS: Basic Principles and Data Analysis.” Springer, Berlin/Heidelberg/New York/Tokyo, 1986.
107. D. C. Koningsberger and R. Prins, “X-Ray Absorption: Principles, Applications, Techniques of EXAFS, SEXAFS and XANES.” Wiley, New York 1988.
108. V. L. Aksenov, A. Yu. Kuzmin, J. Purans, and S. I. Tyutyunnikov, *Phys. Particles Nuclei* 32, 1 (2001).
109. R. F. Boehme, G. S. Cargill III, W. Weber, and T. Jackson, *J. Appl. Phys.* 58, 811 (1985).
110. J. Stöhr, in “X-Ray Absorption: Principles, Techniques and Applications of XAFS, SXAFS, and XANES” (R. L. Prins and D. C. Koningsberger, Eds.). Wiley, New York, 1985.
111. D. C. Meyer, P. Gawlitza, K. Richter, and P. Paufler, *J. Phys. D* 32, 3135 (1999).
112. A. L. Ankudinov, B. Ravel, J. J. Rehr, and S. D. Conradson, *Phys. Rev. B* 58, 7565 (1998).
113. B. K. Teo and P. A. Lee, *J. Am. Chem. Soc.* 101, 2815 (1979).
114. M. F. Ruiz-López, M. Loos, J. Goulon, M. Benfatto, and C. R. Natoli, *Chem. Phys.* 121, 419 (1988).
115. I. Arcon, A. Kodre, D. Glavic, and M. Hribar, *J. Phys. Paris. Colloq.* 48, C9-1105 (1987).
116. H. Stragier, J. O. Cross, J. J. Rehr, L. B. Sorensen, C. E. Bouldin, and J. C. Woicik, *Phys. Rev. Lett.* 69, 3064 (1992).
117. J. Mizuki, “X-ray Absorption Fine Structure for Catalysts and Surfaces” (Y. Iwasaka, Ed.), p. 372. World Scientific, Singapore, 1996.
118. D. J. Tweet, K. Akimoto, I. Horisawa, T. Tatsumi, H. Kimura, J. Mizuki, L. B. Sorensen, C. E. Bouldin, and T. Matsushita, *Jpn. J. Appl. Phys.* 32, Suppl. 32-2, 203 (1993).
119. D. C. Meyer, K. Richter, P. Paufler, and G. Wagner, *Phys. Rev. B* 59, 15253 (1999).
120. M. G. Proietti, H. Renevier, J. F. Berar, V. Dalakas, J. L. Hodeau, G. Armelles, and J. Garcia, *J. Phys. France* 7, C2-749 (1997).
121. D. C. Meyer, K. Richter, A. Seidel, J. Weigelt, R. Frahm, and P. Paufler, *J. Synchrotron Rad.* 5, 1275 (1998).
122. D. C. Meyer, K. Richter, P. Paufler, and H.-G. Krane, *Cryst. Res. Technol.* 29, K66 (1994).
123. U. W. Arndt, T. J. Greenhough, J. R. Helliwell, J. A. K. Howard, S. A. Rule, and A. W. Thompson, *Nature (London)* 298, 835 (1982).
124. D. C. Meyer, A. Kupsch, D. C. Meyer, and P. Paufler, *J. Synchrotron Rad.* 10, 144 (2003).
125. B. N. Dev and G. Materlik, in “Resonant Anomalous X-Ray Scattering” (G. Materlik, C. J. Sparks, and K. Fischer, Eds.), p. 119. Elsevier, Amsterdam, 1994.
126. D. C. Meyer, K. Richter, P. Paufler, P. Gawlitza, and T. Holz, *J. Appl. Phys.* 87, 7218 (2000).

127. S. M. Heald, H. Chen, and G. M. Lamble, *Physica B* 158, 309 (1989).
128. D. C. Meyer, T. Holz, R. Krawietz, K. Richter, B. Wehner, and P. Paufler, *Phys. Status Solidi A* 150, 603 (1995).
129. T. Böttger, D. C. Meyer, P. Paufler, S. Braun, M. Moss, H. Mai, and E. Beyer, *Thin Solid Films* 44/1-2, 165 (2003).
130. Altogether nine papers on radiation damage in *J. Synchrotron Rad.* 9, 327–382 (2002).
131. Y. Bodenthin, J. Grenzer, R. Lauter, U. Pietsch, P. Lehmann, D. G. Kurth, and H. Möhwald, *J. Synchrotron Rad.* 9, 206 (2002).
132. D. Gidalevitz, Z. Huang, and S. A. Rice, *Biophys. J.* 76, 2797 (1999).
133. A. G. Richter, C.-J. Yu, A. Datta, J. Kmetko, and P. Dutta, *Colloids Surfaces A* 198–200, 3 (2002).
134. S. Kawado, S. Iida, S. Yamaguchi, S. Kimura, Y. Hirose, K. Kajiwara, Y. Chikaura, and M. Umeno, *J. Synchrotron Rad.* 9, 166 (2002).
135. V. A. Bushuev, R. M. Imamov, E. Kh. Mukhamedzhanov, and A. P. Oreshko, *J. Phys. D* 35, 1422 (2002).
136. D. Lützenkirchen-Hecht and R. Frahm, *J. Synchrotron Rad.* 8, 478 (2001).
137. B. K. Tanner, P. J. Parbrook, C. R. Whitehouse, A. M. Keir, A. D. Johnson, J. Jones, D. Wallis, L. M. Smith, B. Lunn, and J. H. C. Hogg, *J. Phys. D* 34, A109 (2001).
138. M. J. Bedzyk, A. Kazimirov, D. L. Marasco, T.-L. Lee, C. M. Foster, G.-R. Bai, P. F. Lyman, and D. T. Keane, *Phys. Rev. B* 61, R7873 (2000).
139. I. Kegel, T. H. Metzger, A. Lorke, J. Peisl, J. Stangl, G. Bauer, K. Nordlund, W. V. Schoenfeld, and P. M. Petroff, *Phys. Rev. B* 63, 35318 (2001).
140. V. Holý, J. Stangl, G. Springholz, M. Pinczolits, and G. Bauer, *J. Phys. D* 34, A1 (2001).
141. T. Roch, V. Holý, A. Daniel, E. Höflinger, M. Meduna, T. H. Metzger, G. Bauer, J. Zhu, K. Brunner, and G. Abstreiter, *J. Phys. D* 34, A6 (2001).
142. V. M. Kaganer, B. Jenichen, G. Paris, K. H. Ploog, O. Konovalov, P. Mikulik, and S. Arai, *Phys. Rev. B* 66, 35310 (2002).
143. S. Grenier, M. G. Proietti, H. Renevier, L. Gonzalez, J. M. Garcia, and J. Garcia, *Europhys. Lett.* 57, 499 (2002).
144. C.-H. Lee, K.-L. Yu, P. Y. Cheng, J. C. A. Huang, and W. F. Pong, *J. Synchrotron Rad.* 8, 496 (2001).
145. L. M. Murphy, B. R. Dobson, M. Neu, C. A. Ramsdale, R. W. Strange, and S. S. Hasnain, *J. Synchrotron Rad.* 2, 64 (1995).
146. S. Wie, H. Oyanagi, K. Sakamoto, Y. Takeda, and T. P. Pearsall, *Phys. Rev. B* 62, 1883 (2000).
147. T. Baumbach, D. Lübbert, and M. Gailhanou, *J. Appl. Phys.* 87, 3744 (2000).

X-Ray Microscopy and Nanodiffraction

S. Lagomarsino, A. Cedola

Istituto di Fotonica e Nanotecnologie—CNR, Roma, Italy

CONTENTS

1. Introduction
 2. Production of X-Rays
 3. Optics for X-Rays
 4. X-Ray Microscopy Techniques and Applications
 5. X-Ray Nanodiffraction
 6. Conclusions
- Glossary
References

1. INTRODUCTION

The purpose of this chapter is to give some insight into the field of X-ray microscopy and microdiffraction, which, though initiated decades ago, only in recent years had a strong, and quite explosive, development. The reason is twofold: on one side, the availability of very brilliant X-ray sources, based on synchrotron radiation, fostered practical application of X-ray optics, which were studied theoretically but had a too low efficiency with standard X-ray tubes to attract research beyond the speculative one. On the other side, the “nanoworld” is developing so fast and with so interesting perspectives that many researchers were encouraged to find new and more powerful methods to characterize nanostructures. The large potentialities of X-rays are, therefore, also exploited in this direction. We have to point out that the field of X-ray microscopy and microdiffraction is now so large that it is impossible to give an exhaustive account of all the methods and applications. We will, therefore, try, in the following, to concentrate on works that reached, or are soon likely to reach, submicrometer or nanometer (i.e., below 100 nm) spatial resolution. In this respect, we can speak of nanodiffraction. Good reviews on this subject can be found in the literature [1–3]. A comprehensive state of the art can be found in the proceedings of the Sixth International Conference on X-Ray Microscopy [4].

Strictly speaking, X-rays are already the most powerful microscopy method because, since the twenties, it has been realized that X-rays are diffracted by periodic (crystalline)

arrangement of matter and are, therefore, able to give structural information with an accuracy of the order of fractions of a nanometer (1 nanometer = 10^{-9} m). This is the basis of all the crystallography, including the biomolecular crystallography, which brought in the fifties to reveal the DNA intimate structure. However, in crystallography, the sample is homogeneous and of macroscopic dimensions, therefore, the information is averaged on large volumes. With microscopy or nanodiffraction, we mean the ability to distinguish between microscopic portions of the sample that differ for their structural, compositional, or morphological properties from the rest of the sample. We distinguish the terms microscopy and nanodiffraction in the sense that nanodiffraction (based on Bragg diffraction, see Section 1.1.3) probes the structural properties of matter, i.e., those related to its crystalline, periodic atomic arrangement. With microscopy, instead, we probe the compositional or topographical properties, through a map of electron density obtained by means of absorption or phase variation contrast or through a map of element-specific radiation (fluorescence) or photoelectrons emission. It is interesting that the most advanced microscopy technique, which we will mention at the end of this chapter, is based on diffraction phenomena from nonperiodic structures and, thus, represent the ideal link between Bragg nanodiffraction and standard microscopy.

For pedagogic purposes, the most important properties of X-rays and their interaction modes with matter will be briefly reviewed in the next paragraph. In Section 2, the main characteristics of the X-ray sources will be mentioned, mainly with the purpose to give an idea about the difference between laboratory and synchrotron radiation sources. In Section 3, the X-ray optics able to produce submicrometer beams will be described, while Section 4 will report some of the principle and more promising microscopy technique based on X-rays, together with some example of applications. Finally, Section 5 will describe nanodiffraction techniques, and Section 6 will lead us to the conclusion of the entry.

1.1. Properties of X-Rays

X-rays are part of the electromagnetic (e.m.) wave spectrum, extending in energy from about 250 eV to 50 keV. Due to the simple relation $E = h\nu = hc/\lambda$, where E is the energy; ν , the

wave frequency; λ , the wavelength; c , the light speed, and h , the Planck constant; the same range can be expressed in wavelengths between 50 nm and 0.025 nm. The part at lower energy (up to about 2 keV) is called “soft,” the more energetic, “hard.” Some relevant difference between soft and hard X-rays will be put in evidence. X-rays interact with matter essentially via electrons. An isolated electron subjected to interaction with an X-ray plane wave is instantly accelerated and then radiates as a dipole antenna. The strength of the interaction has been established by Thomson and the ratio between the incident amplitude and the scattered one is proportional to the Thomson scattering length (also called classical electron radius) $r_0 = e^2/mc^2 = 2.82 \times 10^{-13}$ cm. If the electron is bound to an atom, a form factor (atomic scattering factor) must be considered that takes into account the distribution of electrons in the atom. It can be useful to describe, from a phenomenological point of view, three phenomena that take place when X-rays interact with matter and that are at the basis of the microscopy and nanodiffraction techniques: absorption, refraction, and diffraction [5].

1.1.1. Absorption

When an X-ray photon beam having an intensity I_0 impinges on a target of thickness t , the intensity I after the target is simply given by: $I = I_0 e^{-\mu t}$, where μ is called the linear absorption coefficient. The physical phenomenon at the basis of absorption is the photoelectric effect. When an X-ray photon has an energy larger than the binding energy of a given electron shell, the photon is absorbed, and the electrons are ejected with a kinetic energy given in first approximation by the difference between the photon energy and the binding energy. This implies that the absorption coefficient as a function of photon energy is not continuous but has sudden jumps in correspondence of the electron-binding energies of the target elements. The jumps are called absorption edges, and the absorption coefficient before and after the absorption edge can differ from a factor of about 6 to 8 [6]. The absorption edge of the first shell of electrons is called K, the second is L, the third is M, etc. It is important to note that the binding energy and, therefore, the absorption edges, also can have a slight dependence on the valence state of the element (chemical shift). When an electron is ejected, a hole in the corresponding shell is created, which is immediately filled by electrons of the next shell. This gives rise, in turn, to emission of a photon (fluorescence) or to other electrons (Auger electron). In the energy region intermediate between two absorption edges, the absorption coefficient μ is approximately proportional to λ^3 . This implies that μ is very different in the soft and hard regions. To give an example, photons of 25 keV can pass 1 mm of Al with low losses but are completely absorbed by an Al layer 1 micron thick if their energy is 410 eV.

1.1.2. Refraction and Total Reflection

The refraction index r of a material can be expressed by $r = n - i\beta = 1 - \delta - i\beta$. We recall here that $n = (\epsilon_r \mu_r)^{1/2}$, where ϵ_r and μ_r are, respectively, the relative (to the vacuum) dielectric constant and the relative magnetic permeability of the material under consideration. Imagine two mediums, 1 and 2, separated by a plane, smooth interface. An e.m.

wave traveling in medium 1 impinges on the interface at an angle α_1 (Fig. 1a). The beam traveling in medium 2 will make an angle α_2 related to α_1 through the simple formula: $\cos \alpha_1 / \cos \alpha_2 = n_2 / n_1$ where n_1 and n_2 are the real parts of the refraction indexes of mediums 1 and 2.

By using quantum mechanical theory, δ and β for a monatomic material in the X-ray region can be expressed, respectively, as [7]

$$\delta = \lambda^2 (N_0/A) \rho_m r_0 (Z + f') \quad \text{and} \quad \beta = (\lambda/4\pi) \mu \quad (1.1)$$

where N_0 is the Avogadro's number, A is the atomic mass, ρ_m is the density, r_0 is the classical electron radius, Z is the atomic number of the element, and f' is a correction factor related to the rapid variation of the atomic scattering factor for X-rays in proximity of the absorption edges, μ is the linear absorption coefficient; δ is always positive, and this implies that for X-rays, all the materials have a refraction coefficient less than 1. Therefore, if medium 1 is a vacuum (or air) $n_2 < n_1$ and the radiation will travel in the material with an angle $\alpha_2 < \alpha_1$, then, as a consequence, there will be an incident angle $\alpha_1 = \alpha_c$ for which $\alpha_2 = 0$. In this case, the incident beam is totally reflected, and only an evanescent wave can enter into the material, α_c is called the critical angle for total reflection, and it is not difficult to see that $\alpha_c \approx (2\delta)^{1/2}$. Therefore, α_c is proportional to λ and to the square root of Z and ρ_m .

1.1.3. Diffraction

In refraction and reflection, the atoms do not absorb the X-ray photons, but, once excited by them, they reirradiate a X-ray beam of the same energy (in the elastic approximation). The same happens in diffraction. Diffraction is a common phenomenon of an interaction between a wave and an object having dimensions of the same order of magnitude as the wavelength in consideration. Every point of the object, following the principle of Huygens, becomes a source of spherical waves of the same wavelength as the incoming radiation. We can distinguish between Fresnel and Fraunhofer diffraction [8, 9]. If we take a scale factor defined as $d^2/2\lambda$, where d is the object dimension and λ is the wavelength, we can roughly speak of Fresnel diffraction when at least one of the relevant distances source–object (D_1) or object–detector (D_2)—is smaller or of the same order as $d^2/2\lambda$. Fraunhofer diffraction will take place when both the relevant distances are $D \gg d^2/2\lambda$, and, therefore, plane wave approximation is valid. Bragg diffraction is a special case of Fraunhofer diffraction, if many objects interact

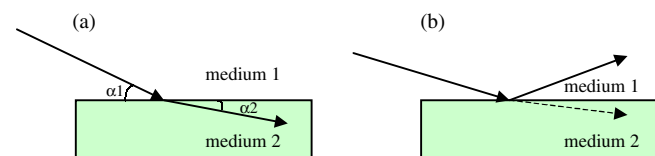


Figure 1. Refraction for X-rays: (a) since the refraction index is <1 , the refracted beam makes an angle α_2 with surface smaller than the incident angle α_1 . (b) Total external reflection: below a given critical angle α_c the beam is totally reflected at the surface and only an evanescent wave penetrates into the material.

with the incoming wave front (that we suppose is a plane wave), the resulting field is the superposition of the spherical wavelets emitted by all the objects. If they are disposed in an ordered array, as in a crystal, the superposition will give rise to constructive interference only for given directions where the wavelets are in phase, otherwise destructive interference will take place. This is the basis of Bragg diffraction. The simple formula that represents the condition for constructive interference was expressed by Bragg in 1913 [10], who considered the crystal as composed of sets of parallel planes of ions. The Bragg law is then

$$\lambda = 2d \sin \vartheta$$

where λ is the wavelength, d is the interplanar distance, and ϑ is the angle of incidence of the incoming (monochromatic) radiation onto the lattice plane.

The diffracted beam is specularly reflected, i.e., it makes the same angle ϑ of the incoming radiation with the planes. Without entering in experimental details, it is, however, important for the comprehension of what follows to consider the difference between a single crystal and a polycrystalline substance. For a single crystal illuminated by a monochromatic plane wave, the Bragg condition for a given set of planes must be accurately determined and adjusted, and the diffracted beam will have a well-defined direction and will give rise to a point in a screen or in a two-dimensional detector that intercepts the diffracted beam. Instead, a polycrystalline substance will always have some grains oriented in the right way to satisfy the Bragg condition (if $2d > \lambda$), and the diffracted beams will lie on a conical surface of aperture ϑ around the axis, which coincides with the incoming radiation. The projection on a screen perpendicular to the incoming beam will then give rise to a circle.

1.1.4. Coherence

An important property of an electromagnetic field, and, therefore, of X-rays, is the coherence. There are two kind of coherence: spatial coherence and time coherence. To define spatial coherence, let us consider two points P_1 and P_2 that lie on the same wave front of an e.m. wave at time $t = 0$. Let $E_1(t)$ and $E_2(t)$ be the corresponding electric fields at these points. By definition, the difference between the phases of the two fields at $t = 0$ is zero. If this difference remains zero at any time $t > 0$, there is a perfect coherence between the two points. If this occurs for any two points of the e.m. wave front, the wave is perfectly coherent (the degree of spatial coherence is 1). Usually, for any point P_1 , the point P_2 must lie within some finite area (coherence area or length) around P_1 to maintain the phase correlation.

From the Van Cittert-Zernike theorem [8] it comes out that the radiation field from a primary incoherent source gains coherence during the propagation. Furthermore, the larger the distance is from the source and the smaller the source size is, the larger is the coherence length. The coherence length l can, therefore, be approximately defined as

$l = \lambda L/s$, where λ is the wavelength; L , the distance source-sample; and s , the transversal source size.

To define temporal coherence, consider the electric fields of the e.m. wave at a given point P , at times t and $t + \tau$. If, for a given time delay τ , the phase difference between

the two field values remains the same for any time t , there is a temporal coherence over a time τ . If this occurs for any delay τ , the wave is perfectly time coherent (the degree of time coherence is 1). If this occurs for a time delay τ $0 < \tau < \tau_0$, there is a partial time coherence, with a coherence time equal to τ_0 .

2. PRODUCTION OF X-RAYS

It is beyond our scope to give a comprehensive account of the available X-ray sources, but we consider it useful to give some basic ideas, to understand the main differences between laboratory sources and synchrotron radiation sources.

2.1. Production of X-Rays Through Interaction of Electrons with Matter

The standard laboratory X-ray tubes are based on the interaction of electrons with matter: an electron beam accelerated to several keV hits a target of a given material and in this way produces strong ionization, with ejection of electrons of the inner shells and production of intense fluorescence whose energy is characteristic of the target element. Moreover, the electrons are decelerated by the bound electrons of the target and, as a consequence, emit a continuous spectrum of radiation (Bremsstrahlung). Therefore, the total spectrum of an X-ray tube is composed of quite narrow peaks of characteristic radiation superimposed on a “white” component. The radiation is emitted in all the directions, but, in general, the target is viewed at a small angle to lower, at least in one direction, the projected dimensions. Typical projected target dimensions are $0.4 \times 0.4 \text{ mm}^2$ for a “point” focus and $0.04 \times 1 \text{ mm}^2$ for a “line” focus. Recently, micro-focus X-ray generators were produced with a source dimension of a few microns in diameter. The drawback is a low value of current necessary to not damage the target. To have an even smaller X-ray source, electrons can be focused by means of electromagnetic lenses. This is what happens, for example, in electron microscopes. Scanning electron microscopes (SEM) have been suitably modified to hit a thin target at the focus position and to generate an X-ray beam with linear dimensions of the order of 0.2μ [11].

2.2. Production of X-Rays Through Interaction of Light with Matter (Plasma Sources)

X-rays also can be generated when an intense laser beam interacts with liquid or solid matter, giving rise to a plasma. The plasma then re-emits a spectrum made of several lines, which depend on the target. A high-power laser such as Nd-YAG is generally used. Thin solid foils can be used as targets, but, in this case, debris, i.e., small solid fragments ejected by the target, can damage sensitive components (such as optical elements) positioned close to the plasma. Moreover, the position of the beam on a solid target must be continuously changed, and the target itself must be removed and changed very often. Recently, microscopic liquid-jet or liquid-droplet targets are used, which eliminate the problem of debris and of regeneration. The target is generated

by forcing a liquid in a capillary nozzle [12, 13]. Typically, sources use ethanol at room temperature or liquid nitrogen at cryogenic temperatures. In the first case, a C line at 3.37 nm is used, while N lines at 2.88 and 2.48 nm are generated in case of liquid nitrogen sources. Typical source dimensions are of the order of 10–20 μ .

2.3. Synchrotron Radiation

Here we want to give just some basic ideas about the mechanism of production of X-rays with synchrotron radiation (S.R.) and S.R.'s main properties. A much more complete presentation, but still clear and concise, is given by D. Raoux in the proceedings of the school "Hercules" [5]. Synchrotron radiation is the e.m. field radiated by accelerated relativistic charged particles. Electrons or positrons are used. Any accelerated charge radiates an e.m. field that, if the particle has a speed $v \ll c$ (c light speed), is isotropic around the acceleration. However, if $v \approx c$, then the relativistic effects dominate and the radiated e.m. field is sharply peaked in the direction of motion of the particles. The cone aperture is $1/\gamma$, where γ is the ratio between the particle energy and its rest mass. For electrons or positrons of energy E expressed in GeV, then $\gamma = 1957 \cdot E$. Thus, for 6 GeV electrons, the aperture is about 80 μ rad. To get a radial acceleration, the easiest way is to hold the particles in a circular orbit of a radius of curvature ρ by means of magnets, which exert the Lorentz force on the charged particles. The synchrotron radiation sources are, therefore, basically storage rings where electrons or positrons have circular orbits, and the radiation is that which originates from bending magnets. The emission spectrum is continuous from infrared radiation up to a critical wavelength λ_c , which depends on ρ and γ . The critical wavelength is defined as the value for which half of the total power is emitted at wavelengths shorter than the critical one; λ_c is given by $\lambda_c = (4\pi/3)\rho/\gamma^3$. To improve the intensity of emission, insertion devices (I.D.) have been conceived, where the charged particles pass through alternating magnetic poles and are, therefore, compelled to have a zig-zag trajectory. At each wiggle, they emit radiation that is, therefore, enhanced in a $2N$ factor, where N is the number of poles. These devices are called wigglers or undulators, and the distinction essentially is due to the relation between the angular deviation α at each wiggle and the aperture $1/\gamma$. Values of $\alpha \gg 1/\gamma$ identify wigglers, while values of $\alpha \approx 1/\gamma$ identify undulators. The radiation emitted by a wiggler is the incoherent sum of the radiation fields emitted by each individual magnet. The spectrum is continuous but shifted at higher energies with respect to that of a bending magnet. Instead, in the undulator regime, the amplitudes of the field radiated at each period of the particle trajectory may interfere, resulting in a periodic radiation field. The spectrum is thus not continuous, but resonances occur at given frequencies (the fundamental and the harmonics). Both in wigglers and undulators, the spectral characteristics depend on the angle with respect to the I.D. axis. In general, a narrow cone around the axis is selected.

What is important in S.R. is not only flux, which is defined as the number of photons per unit time in a given band-pass energy, $F = ph/s/(\Delta\lambda/\lambda)$; $\Delta\lambda/\lambda$, is conventionally taken as

the value of 10^{-3} . Also taking into account the angular aperture (i.e., the collimation), we can speak of brightness that is the flux per solid angle, $\text{Brightness} = ph/s/mrad^2/(\Delta\lambda/\lambda)$. In fact, the size source is of importance, and, therefore, the brilliance becomes the parameter of interest, $\text{Brilliance} = \text{Brightness}/\sigma_x\sigma_y = ph/s/mrad^2/\sigma_x\sigma_y/(\Delta\lambda/\lambda)$, where σ_x and σ_y are the transverse source sizes (horizontal and vertical). The emittance of the source ε is defined as $\varepsilon = \varepsilon_h * \varepsilon_v$, where the horizontal and vertical emittances ε_h and ε_v are defined as $\varepsilon_h = \sigma_x\sigma'_x$, and $\varepsilon_v = \sigma_y\sigma'_y$, where σ'_x and σ'_y are the divergence of the beam in the horizontal and vertical directions, respectively. The figure of merit of a synchrotron is brilliance and emittance. The first should be as high as possible, and the last should be as low as possible. Just to give an idea about numbers, if an X-ray tube has a brilliance of the order of 10^7 , brilliance at an undulator beamline of third generation S.R. can be as high as 10^{20} – 10^{21} . Horizontal and vertical emittances at the European Synchrotron Radiation Facility (ESRF) reached values as low as 4 and 0.025 nm, respectively.

Time structure also is important, at least for time-resolved experiments. Synchrotron radiation is not continuous but is emitted in bunches corresponding to the electron bunches in the storage ring. Duration of a single bunch is, for example, at ESRF in Grenoble, of 20 picosec. Time between bunches depend on the filling mode of the storage ring. For the single-bunch mode (the one generally used for time-resolved experiments), it is about 3 μ s at ESRF. Scientists are now planning S.R. sources of the fourth generation, with impressive performance. They are based on the concept of free electron lasers composed of a linear accelerator of electrons operating at several GeV and long undulators (several tens of meters). Radiation produced by such sources should have brilliance 10 orders of magnitude higher than the present most powerful sources and a time structure with pulses of few tens of femtoseconds (i.e., 10^{-14} s). This should open a new world in many fields, including the one described in this discussion.

3. OPTICS FOR X-RAYS

To perform X-ray microscopy or microdiffraction experiments, the X-ray beam must, in general, be conditioned to have the necessary spatial resolution. In principle, a simple pinhole could do this task, but photon flux would be lost. Therefore, focusing X-ray optics must be used to concentrate photon flux in small dimensions, as lenses do in visible spectrum. This paragraph will describe at a basic level some optical elements for X-rays that are used in microscopy and microdiffraction.

The focusing problem well known in light optics becomes difficult as soon as X-rays are considered because, at short wavelengths, the radiation is very weakly refracted by materials ($1 - n \sim 10^{-5}$ – 10^{-6}), as C. W. Röntgen himself concluded just after having discovered X-rays. The impossibility of using X-ray lenses delayed the beginning of X-ray optics until the development of the dynamical diffraction theory by perfect crystals. Indeed, the use of Bragg diffraction has allowed developing optics based on geometrical focusing by bent or curved elements: crystals, mirrors, or multilayers. These approaches are widely used but, due to the source

size and divergence of laboratory sources, they are capable of reaching a resolution of several microns only.

The advent of S.R. sources and, in particular, the high brilliance of modern high-energy synchrotron storage ring facilities (ESRF, Grenoble France; Advanced photon source (APS), Chicago, IL; Spring 8, Harima, Japan; Elettra, Trieste, Italy; Advanced light source (ALS), Berkeley, CA), gave new impulse to research for innovative X-ray optics. Thus, other focusing optics have been thought as striving for submicrometer beam generation. Presently, there are only five types of X-ray optics producing a submicrometer beam: Fresnel zone plates [14] and Bragg-Fresnel optics [15] based on diffraction, refractive lenses [16] based on refraction, Kirkpatrick-Baez mirrors [17] based on total reflection, and waveguides based on standing waves [18]. Capillaries, which are widely used to shrink the X-ray beam to micrometer dimensions, will not be treated here because their efficiency as a submicrometer beam is very low. The Fresnel zone plates are mostly used in the soft X-ray region, while the other optical elements mentioned before are mostly used in the hard part of the X-ray spectrum. This is due to the fact that in the hard region, fabrication of Fresnel zone plates is more difficult than in the soft region, as will be better illustrated in the following discussion.

The figures of merit useful to compare the performance of the different optics are: (i) the beam size produced, (ii) the coherence of the beam, (iii) the fabrication complexity, and (iv) the gain. This latter is defined as the ratio between the output flux density over the input flux density:

$$G = \frac{I_{\text{exit}}}{I_{\text{inc}}} = \frac{F_{\text{exit}} s_{\text{inc}}}{s_{\text{exit}} F_{\text{inc}}}$$

where F is the flux and s represents the size of the beam; G , that is a dimensional, refers to the performances of a theoretical slit, which reduces the beam from-to the same sizes than the optical element does or, which is the same, it represents the flux density gain and, therefore, an intrinsic property of the optical element. In fact, if the incident beam size s_{inc} increases over the spatial acceptance of the optical element and, therefore, the input flux increases, the gain G remains the same, even if the efficiency decreases.

3.1. Fresnel Zone Plates

Although the first zone plate was constructed by Lord Rayleigh in 1871, the first published work was written by Soret in 1875. However, only Wood, in 1898 [19], carried out the first experiments on zone plates by using visible light, starting the development of this new optics. Baez [20] first suggested the focusing applications of the zone plates in the wavelength region between extreme ultraviolet and soft X-rays in 1961.

3.1.1. Theoretical Principles

The zone plate is so called because it is constructed following the Fresnel-zone law: a plane opaque screen with a circular aperture of radius d illuminated by coherent radiation (i.e., a plane wave) produces, at a generic distance z from it (Fig. 2), the usual diffraction pattern of lighter and darker rings on a screen normal to the z axis.

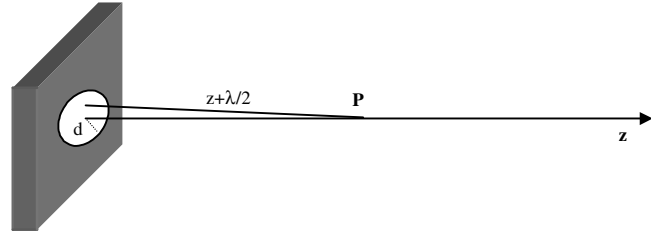


Figure 2. Opaque screen with a circular aperture of radius d . The points on the aperture distant $z + \lambda/2$ from P define the radius of the first Fresnel zone for the point P.

This diffraction pattern is not of interest here, and the analysis will be focused on the diffraction along the z axis alone. The field amplitude $W(z)$ along the z axis oscillates depending on the $d^2/\lambda z$ ratio according to the following relation [8]:

$$W(z) = Ae^{-ikz}(1 - e^{-i\pi N_F}) = -2iAe^{-i(kz + \frac{\pi}{2}N_F)} \sin\left(\frac{\pi N_F}{2}\right) \quad (3.1a)$$

where:

$$N_F = \frac{d^2}{\lambda z} \quad (3.1b)$$

is the Fresnel number. Different regions of the aperture emit radiation, which interferes constructively or destructively depending on the distance z . For any given point P on the $z = 0$ plane (where the aperture is located) depending on the constructive or destructive interference produced in P. These regions are named Fresnel zones.

The first Fresnel zone for the point P distant z from the screen is the circle of radius r_1 :

$$r_1^2 = \left(z + \frac{\lambda}{2}\right)^2 - z^2 \approx \lambda z$$

It identifies the points on the $z = 0$ plane at a distance smaller than $z + \lambda/2$ from P. The radiation emitted from these points interferes constructively in P since the optical path lengths differ by less than $\lambda/2$. The field generated by this circle in P is easily obtained from (3.1a) by taking $d = r_1$ and therefore $N_F = 1$:

$$W_1 = Ae^{-ikz}(1 - e^{-i\pi}) = 2Ae^{-ikz} \quad (3.2)$$

so that its amplitude is two times larger than the field amplitude in the absence of the screen. In other words, if the aperture had a radius $d = r_1$, then the whole radiation passing through it would interfere constructively in P, thus explaining the increased intensity.

The second Fresnel zone is a ring of internal radius r_1 and external radius given by

$$r_2^2 = (z + \lambda)^2 - z^2 \approx 2\lambda z$$

The field produced at P by the points in this second Fresnel zone is obtained by setting $d = r_2$ in (3.1b) and subtracting the field produced by the points in the first zone:

$$W_2 = Ae^{-ikz}[(1 - e^{-2i\pi}) - (1 - e^{-i\pi})] = -2Ae^{-ikz} \quad (3.3)$$

As it is apparent from the negative sign, if the aperture had a radius $d = r_2$, the radiation from the first Fresnel zone would interfere destructively with the radiation coming from the second one and the intensity in P would vanish.

The radius of the generic n th zone is

$$r_n = \sqrt{n\lambda z} \quad n = 1, 2 \dots n_{\max} \quad (3.4)$$

where n_{\max} is the total number of zones.

It is important to notice that the Fresnel zones are independent on the size of the aperture and they only depend on the position of P and on the wavelength.

For a point at distance z , the number N_F in Eq. (3.1b) is the number of Fresnel zones contained in the aperture. In particular, if this number is an even integer, then the interference of the radiation from the various zones is destructive and the intensity in P is zero. If N_F is an odd integer, then the radiation from one whole zone is unbalanced and the intensity is maximal.

The Fresnel zone plate (FZP) (Fig. 3) is a screen of alternately transparent and opaque zones equal in size to the

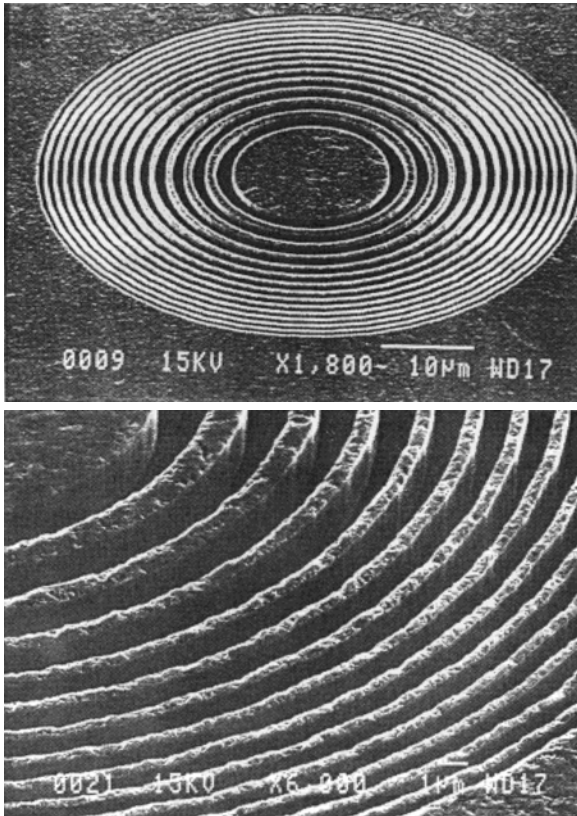


Figure 3. Scanning electron microscopy picture of a zone plate composed of alternately transparent and opaque zones equal in size to the Fresnel zones.

Fresnel zones. In this way, only the radiation from odd or even Fresnel zones is transmitted through the screen.

At the point of observation, the exposed zones produce optical disturbances of the same phase and, therefore, the resultant optical intensity is much greater than that observed in the absence of the screen [see Eq. (3.2) or Eq. (3.3) for the field amplitude coming from the first and second Fresnel zones, respectively]. As a result, the zone plate concentrates the incident intensity in a small region like a lens does.

3.1.2. Focal Distance

Illuminating the screen with a plane wave, for $m \neq 0$, the zone plate produces spherical waves. If r_1 is the radius of the innermost zone, and m is the number of diffracted order, the focal length f_m of a zone plate is given approximately [1] by:

$$\frac{k}{2f_m} = \frac{\pi m}{r_1^2} \Rightarrow f_m = \frac{r_1^2}{m\lambda} \quad (3.5)$$

It is important to notice that the position of the focal point depends on the wavelength. This chromatic aberration is more important than the chromatic aberration in optical lenses, and it is caused by diffraction instead of dispersion as in the case of glass lenses. As a consequence of this aberration phenomenon, a zone plate has to be used with radiation having a $\Delta\lambda$ given by $\frac{\Delta\lambda}{\lambda} = cmn_{\max}$ [1], where c is a constant. Theoretical studies have shown that with $c = 0.5-1$, practically no contrast in the image is lost compared to imaging with quasi-monochromatic radiation [21].

3.1.3. Resolution

The width of the outermost zone of a zone plate can approximately be written as

$$dr_n = \frac{r_n}{2n_{\max}} \quad (3.6)$$

The most important characteristic of the zone plate is the resolution Δ , which can be expressed, according to the Rayleigh criterion [1, 22], as

$$\Delta = 1.22 \frac{dr_n}{m} \quad (3.7)$$

where dr_n is the width of the outermost zone of the FZP. The smaller the dr_n , the better the resolution. Therefore, from Eq. (3.6), to obtain a high resolution FZP, a large number n of zones has to be made. It should also be noted that the spatial resolution depends on the wavelength λ and that the resolution is inversely proportional to the order.

3.1.4. Focal Spot Size

It must be pointed out that the focal spot size Δ_m of the m th order focus is not exactly equal to Δ , because there are other factors contributing to the broadening of the beam. Indeed, for an incident source size Δ_s distant L from the FZP, the focal spot size at a distance f_m from the FZP can be expressed as

$$\Delta_m = [\Delta^2 + \Delta_{i,m}^2 + \Delta_c^2]^{1/2}$$

where $\Delta_{i,m}$ is the magnified source size:

$$\Delta_{i,m} = \Delta_s \frac{f_m}{L}$$

and Δ_c is the chromatic aberration:

$$\Delta_c = D \frac{\Delta E}{E}$$

with D being the diameter of the FZP and $\Delta E/E$, the resolving power of the monochromator.

3.1.5. Efficiency

Another important parameter characterizing a zone plate is the efficiency with which it collects incident photons into its m th order focus. For a FZP of thickness t and laminar zone profiles, the groove efficiency is given by [1]

$$E_{\text{eff}} = \frac{1}{\pi^2 m^2} (1 + e^{-2\eta\phi} - 2e^{-\eta\phi} \cos \phi) \quad (3.8)$$

with:

$$n = 1 - \delta - i\beta \quad \phi = \frac{2\pi\delta t}{\lambda} \quad \eta = \frac{\beta}{\delta} \quad (3.9)$$

where n is the complex refraction index and β is related to the absorption coefficient.

The simplest type of FZP is an amplitude plate composed of zones alternately transparent and opaque to X-rays. In this case, the focusing originates mainly from the relatively different absorption of two neighboring zones. If one only considers the absorption in the material of the absorbing zones ($\delta = 0$), then the two exponential terms of Eq. (3.8) vanish for sufficiently large βt , and one gets theoretical efficiency of an amplitude zone plate, which is $E_{\text{eff}} = 10.1\%$ for the first diffractive order. The efficiency can be considerably improved by using Fresnel phase zone plate (FPZP), which focus X-rays through the relative phase change between two neighboring zones. The FPZP can be realized by choosing an appropriate material with a thickness t such that the retardation ϕ of the incident wave is π in those zones that are opaque in the amplitude FZP. From Eq. (3.9):

$$\delta t = \frac{1}{2}\lambda \quad (3.10)$$

If absorption is ignored, i.e., $\beta = 0$, the groove efficiency, Eq. (3.8) becomes

$$E_{\text{eff}} = 4m^{-2}\pi^{-2}$$

resulting for the first order $E_{\text{eff}} = 40.4\%$.

It should be noted, however, that perfectly transparent phase-shift materials do not exist for X-rays, so that a FPZP is always an amplitude-phase element, and this fact causes a decrease in the focusing efficiency and an increase in the background.

Taking into account the transmittance T of the supporting membrane of the zone plate, one can define the absolute efficiency E_a as

$$E_a = E_{\text{eff}} T$$

3.1.6. Blazed Profile

Another factor reducing the efficiency of a zone plate comes from the very nature of diffractive optics, which leads to the formation of many diffraction orders. Indeed, a significant fraction of incident photons are delivered to the undiffracted zero order and diffraction orders other than the primary first order. A lower contrast and a reduced usable flux are the consequences.

By introducing asymmetries in the grooves [23, 24], it is possible to control the position of the maximum intensity in the order sequence and, therefore, to blaze the optical element. Theoretical research by Tatchyn [25] studied the improvement in focusing efficiency of a zone plate by optimizing the zone profiles. The basic principle of a zone plate with a blazed profile (ZBPB) is that in propagating through a period consisting of two regular Fresnel zones, the rays experience phase delays such that their effective optical path length from the incident surface to the focus is identical. As a consequence, all the rays will constructively interfere at the focus. It may be shown by using Huygens principle or numerical calculation [25–27] that 100% focusing efficiency may be obtained with a parabolic zone profile when the absorption of X-rays is negligible.

Since it is difficult to produce zone plates with an optimal blazed profile, a multisteps profile approximating the ideal one has been used to produce ZBPBs.

In Figure 4 is represented the SEM of a circular gold ZBPB, produced at IFN–CNR (IFN–CNR) of Rome [24], made of four levels.

The calculated focusing efficiency of a 4-step ZBPB can reach 81% by using Be, 73% with Ni, and 50% with Au. The ZBPB in Figure 3 has been tested at APS, and a focusing efficiency of 45% for the linear and 39% for the circular one has been measured and a spot size with full width at half-maximum (FWHM) of $2.2\mu \times 5\mu$ has been found. The relatively large spot size produced by a ZBPB is compensated by the high efficiency.

3.1.7. State of the Art and Fabrication Process

The construction of the first self-supported gold Fresnel zone plate was performed in 1961 by etching followed by gold microelectrodeposition [14]. This zone plate was about 10- μ m thick and had 19 open zones, with an outermost zone width of about 17 μ m.

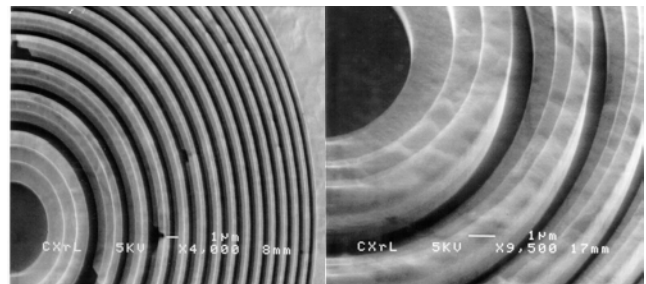


Figure 4. Scanning electron microscopy picture of a circular gold ZBPB.

Development of advanced lithographic techniques has allowed remarkable progress in zone plate fabrication. Holographic [28] and interferometric [29] lithography produced zone plate patterns with hundreds of zones with an outermost zone width as small as 60 nm.

Excellent zone plates have been fabricated by electroplating of nickel into polymer molds [30, 31]. Microzone plates with a minimum outermost zone width of 20, 25, and 30 nm were fabricated [32] with an efficiency of 60%, 71%, and 83% of the maximum theoretical achievable efficiency (9.2%, 16.2%, and 18.0%, respectively). Semiconductors also are commonly used, as they can be structured with high aspect ratios by plasma etching. Germanium lenses optimized for operating at 2.4 keV have been constructed [33] with an efficiency of 60% of the theoretical value (18.3%) and a resolution better than 100 nm.

Figure 5 shows the processing sequence of an electron-beam lithography technique for fabricating zone plate with the central stop.

The pattern generator is programmed to produce the desired patterns. After development, the zone plate is formed by electroplating gold, nickel, or another suitable metal. Advanced reactive ion etching (RIE) processes can be used to transfer the zone plate patterns with an outermost zone width as small as 19 to 55 nm in Ge and Ta.

3.1.8. Hard X-Rays

If high spatial resolution is desirable, some technical considerations have to be taken into account. In the soft X-rays spectral region, zone plates with a focal spot approaching 20 nm and a high efficiency have been developed [31–37]. Nearly all of them in use today are fabricated by using various forms of an electron-beam lithographic technique. These techniques, however, cannot be directly used for producing zone plates for hard X-rays at very high resolution because the thickness required is beyond the fabrication capabilities. Indeed, since the absorption coefficient is inversely proportional to E , thicker opaque zones are required for an amplitude zone plate working at high photon energies. On the other hand, the thickness [Eq. (3.10)] required to obtain a π phase shift in a phase zone plate increases as E increases because δ generally is proportional to $1/E^2$. These facts imply technical problems when hard X-rays are concerned. For a phase zone plate working at 8 keV, the required thickness, when using Au for the opaque regions, is $1.5 \mu\text{m}$. If a resolution of $0.1 \mu\text{m}$ is desirable, an outermost zone width equal to $0.08 \mu\text{m}$ [Eq. (3.7)] for

the first order has to be fabricated. An important technical parameter is the aspect ratio defined as

$$K = \frac{t}{dr_n}$$

representing the ratio between the thickness and the width of the zones.

The K value for the previous requirements is 18.3, which is beyond the capabilities of even state-of-the-art microfabrication facilities with a single step. Several approaches have been developed to effectively obtain the required aspect ratio [38]. One approach used at IFN-CNR consists in growing the FPZP in two steps, duplicating the pattern on another side of a thin membrane on which the first FPZP pattern was made, or on top of it [23, 24]. It is clear that in both cases, it is, in principle, possible to reduce the required aspect ratio for each FPZP pattern by a factor of two. By using this technique, a FPZP working at 8 keV, producing a spot size of 150 nm (FWHM) for the first order and 90 nm (FWHM) for the third one, with a focusing efficiency of 13%, has been constructed and tested [24].

Two other approaches to fabricate FZP for hard X-rays could be mentioned: the sputtered sliced technology and the fabrication of high-aspect linear zone plate by selective etching of Si. In the first approach, layers of different materials (e.g., NiCr and SiO_2) are deposited by sputtering onto a microwire of borosilicate glass. The wire, reinforced by nickel electroplating, is then sliced perpendicular to its axis and then carefully polished to the desired thickness (a few microns). Measured efficiency is of the order of a few percentages, significantly lower than the theoretical value, but this kind of zone plate fabrication preparation is still promising [39]. In the second approach, a linear zone plate, with a staircase profile to increase efficiency, is fabricated in Si. To obtain the required phase difference, the linear zone plate is tilted to increase the light path length ([40], and page 48 in [4]).

3.2. Bragg–Fresnel Lenses

In the previous section, it was remarked that a FPZP allows an efficiency higher with respect to the efficiency obtained with an amplitude FZP. The focusing effect of the FPZP is achieved through the phase retardation of the incident wave by π in those zones that are opaque in the amplitude FZP. Unfortunately, as mentioned earlier, perfectly transparent phase-shift materials do not exist for X-rays, so that such a FZP is always an amplitude-phase element and the focusing efficiency is not as good as theoretically expected.

A solution to this problem consists in working in reflection instead of transmission. This situation can be obtained by using the Bragg diffraction of a perfect crystal, where a FZP is grown. This is what a Bragg–Fresnel lens (BFL) does [41–44]: the wave reflected at a Bragg angle by the lower surface of the BFL zone structure gains an additional phase shift as compared to that reflected by the upper surface. The height of the relief has to be adjusted to have a π phase shift. Notice that the intensity of the beams reflected from the lower or the upper surface is determined by the Bragg

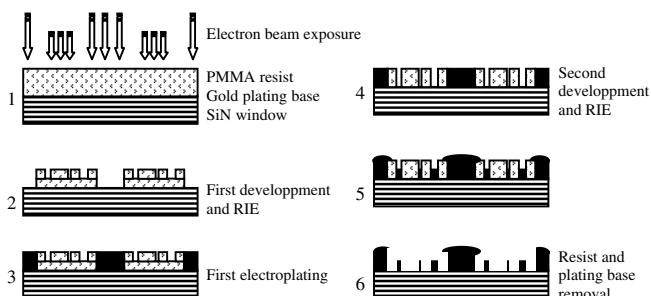


Figure 5. Steps of the fabrication process of a Fresnel zone plate.

condition only, and it is almost unaffected by absorption. Thus, BFL is purely a phase element, and, upon diffraction of the X-ray wave on the BFL zone structure, no amplitude modulation of the reflected wave is observed. Moreover, the BFL phase shift for a certain reflection is independent of the energy, and it is determined by the structure height of the relief only. Diffraction efficiency of the BFL is very close to the theoretical performance and is about 40%. The limiting spatial resolution that can be obtained in BFL is given by the width of the outermost zone of the zone structure, and a fraction of a micron is achievable.

A linear BFL on a flat substrate is analogous to a cylindrical lens in visible light optics and produces one-dimensional focusing of X-rays. Since the phase properties do not depend on energy, the same lens can be applied for a wide range of energy determined only by Bragg's law. A focus spot size of 0.8 μm has been observed by Snigirev [44], and a focus efficiency about 35% was measured.

The curved crystal BFL proposed by Hartman et al. [45], provides a two-dimensional X-ray focusing and both energy tuning and high flux. In this case, sagittal focusing is achieved by the linear BFL, while meridional focusing is produced by the bent BFL crystal substrate, as illustrated in Figure 6. The corresponding flux enhancement is determined both by the increase of the acceptance of the focusing element and by the increase of the crystal bandwidth due to the deformations introduced by the bending.

The minimum focus size in the sagittal direction is determined by the resolution of the BFL (≈0.3 μm). The latter can be decreased significantly for high energies, where the depth-related aberration becomes important, by using Laue geometry. The focal length in the meridional plane of the bent crystal in the symmetric case is

$$F_M = \frac{R \sin \theta_B}{2} = \frac{R\lambda}{4d}$$

where R is the radius of curvature, θ_B is the Bragg angle, and d is the d spacing of the reflection used.

For out-of-plane (sagittal) focusing, the focal length of the BFL is given by

$$F_S = \frac{r_1^2}{\lambda}$$

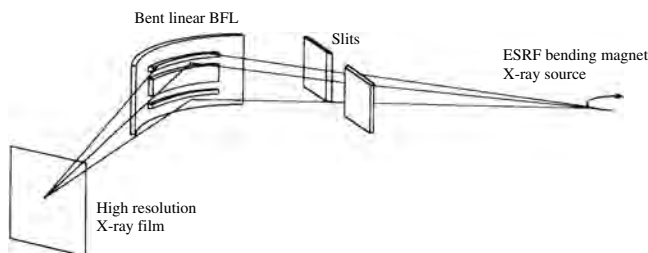


Figure 6. Schematic display of the setup used to obtain a two-dimensional X-ray focusing with a curved crystal BFL. Reprinted with permission from [45], Y. Hartman et al. *Nucl. Instrum. Methods Phys. Res., Sect. A* 385, 371 (1997). © 1997, Blackwell Publishing.

where r_1 is the innermost zone radius. Then the wavelength λ_0 for which the focal lengths are the same is obtained as

$$\lambda_0 = 2r_1 \sqrt{\frac{d}{R}}$$

and, therefore, the focal length is

$$F_M = \frac{R\lambda_0}{4d}$$

Because the parameters of BFL structure are fixed, when tuning the energy, the crystal curvature must be changed, and the sample has to be moved to a different focal length F_M .

A curved crystal BFL has been tested at the optics beamline at ESRF [45] and a two-dimensional focusing of 17.2 keV X-rays was obtained with a focal spot size of 4.5 × 9.1 μm² in vertical and horizontal directions, respectively. The large beam size was compensated by a gain of 300 times in flux density with respect to a flat BFL.

3.3. Compound Refractive Lenses

The X-ray refractive lenses are the focusing elements that more directly adapt the methods developed in visible light optics to X-rays. As discussed in the introduction, this attempt was unsuccessful due to the low refraction index and the strong absorption of the X-rays. In 1948, Kirkpatrick and Baez [17] considered the possibility of a refractive lens for focusing X-rays, and they concluded that it was unfeasible. Suehiro, in 1991 [46], discussed how to realize X-ray refractive lenses, and he proposed the development of spherical refractive lenses with high-Z material. However Michette [47] soon objected that high-Z material, necessary for refracting the X-rays to focalize, would have an absorption that would reduce transmission to an unacceptably low value. In 1993, Yang [48] showed that a single refractive lens made of low-Z material would be characterized by a relatively small radius of curvature and a large aspect ratio of the concave surface. These conditions render fabrication of a single refractive lens very difficult or even impossible.

Finally, in 1996 Snigirev et al. [16] found a simple and effective procedure to build an X-ray refractive lens with low absorption and reasonable focusing distance.

The first principle is that since the X-rays have the refraction index $n < 1$, a hole (that is, the air contained in the hole) drilled in a low-absorbing material can play the role of a lens in visible light. A simple concave lens fabricated as a cylindrical hole drilled in a low-Z material would focalize an X-ray beam. The low-Z material assures a low absorption, while the concave shape will focalize the refracted beams at a distance:

$$F = R/2\delta \tag{3.11}$$

From Eq. (3.11), it is clear that for a feasible radius $R = 300 \mu\text{m}$, the low-Z material, for example, Al ($\delta = 2.8 \times 10^{-6}$ at 14 keV), will produce a focus at 54 m, which is unacceptable for almost all microfocus experiments.

Snigirev et al. [16] built up a compound refractive lens (CRL) consisting of a linear array of many individual lenses

manufactured in a low-Z material (Fig. 7). The lenses, stacked in a row, increase the refractive power; in this case, the focal distance of the array is

$$F = R/2N\delta$$

For the conditions above, a compound lens with $N = 30$ single lenses brings the focus to $F = 1.8$ m, which is widely acceptable.

The diffraction limited resolution of the lens σ_f is defined by an effective lens aperture A :

$$\sigma_f = \lambda r_f / A$$

where r_f is the image distance.

The real gain of the compound refractive lens, taking into account the source size σ_0 and the X-ray absorption in the material, is

$$g = a \frac{A}{\sigma_0} \left(\frac{r_0}{r_f} + 1 \right)$$

where $a = \exp(-\mu N d)$, r_0 is the source distance, and $\sigma_1 = (\sigma_0 r_f / r_0)$ is the real focus size, defined as the demagnified source size.

3.3.1. Parabolic Refractive Lenses

Although these results are very interesting, nevertheless, the focused beam produced by the array of drilled holes did not achieve a submicron dimension.

A substantial improvement in the performance of refractive lenses has been obtained by using as a shape, a double paraboloid of rotation [49]. With modern numerically controlled machines, it is possible to generate a rotational parabolic shape within $1 \mu\text{m}$ and a surface roughness below $0.1 \mu\text{m}$. The main advantages of this new solution are the suppression of the spherical aberrations and the focusing in both directions. By using this new solution, a focal spot size in the submicrometer range can be achieved. Moreover, parabolic profiles can be generated with higher accuracy. Indeed, a parabolic tool always generates a force component normal to the surface, reducing the tendency for micro-cracks and, hence, for profile errors and surface roughness. In contrast, a sphere generates, at the equator line, only shear forces, without compression. It is also clear that the radius of curvature R and the geometrical aperture $2R_0$ are decoupled from one another for a parabola, whereas, they are not for a sphere. Therefore, for a parabolic lenses, it is possible to combine a geometrical aperture of 1 mm with a radius of curvature R of $200 \mu\text{m}$ and below. The smaller the value of R , the lower is the focal length F , and the smaller is the number of lenses needed in a stack.

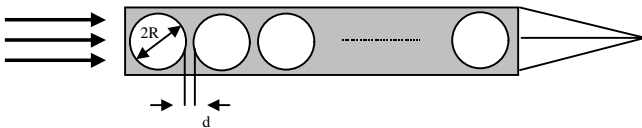


Figure 7. A Compound refractive lens consisting of a number N of cylindrical holes placed close together in a row along the optical axis.

By using a stack of 220 Al lenses with a radius of curvature $R = 209 \mu\text{m}$, a focal distance of 328 mm is obtained. By using an incident radiation of 9.71 keV, a spot of $0.480 \times 5.17 \mu\text{m}$ has been detected at the focus, with a measured gain of 367 [49].

3.3.2. Silicon Planar Refractive Lenses with Minimized Absorption

A recent development of refractive lens fabrication comes from the application of microelectronics technology [50]. Although, in the actual state of the art, a submicrometer beam has not yet been produced by using this technology, nevertheless, the results are promising.

The transmission and, therefore, the gain of the CRL, discussed earlier, is limited by: (i) attenuation in the bridges between adjacent individual lenses, (ii) significant attenuation in the outer parts of the CRL, and (iii) roughness of hole surfaces.

These limitations can be overcome by using a dedicated refractive profile obtained with modern advanced technologies. The silicon microfabrication technique allows the preparation of a dedicated refractive profile by removing passive parts of material, where phase variation is a multiple of 2π within the lens thickness, the so-called kinoform lenses. A planar parabolic lens with minimized absorption is composed of N pairs of segments cut from a parabolic cylinder.

Planar microelectronics technology allows a number of individual lenses to be fabricated onto a single wafer, as with a normal CRL, to shorten the focal distance. The lens with the aperture $A = 150 \mu\text{m}$ consists of $N = 5$ individual lenses, each comprising $p = 10$ pairs of segments. It has been tested at the undulator (ID22) beamline at ESRF by using beam energy of 18 keV [51]. The focal distance is 80 cm, and the focal spot (FWHM) is $1.8 \mu\text{m}$ with a gain of 19. Taking into account the detector point spread function of 1.2 mm, a deconvoluted submicrometric spot size is obtained.

3.4. Total Reflection Optics: Kirkpatrick–Baez Mirrors

An interesting optics to focus hard X-rays is given by grazing incidence total-reflection mirrors. A pair of elliptical mirrors arranged in a crossed mirror geometry (Kirkpatrick–Baez configuration) is able to focus X-rays to submicron size. In Figure 8, a schematic diagram of the system installed at beamline 8C of the storage ring in the Photon Factory (Japan) is shown.

The X-ray beam passing through a Si(111) symmetric double crystal monochromator (CM) is focused by the elliptical mirrors. The radiation incident on the first mirror (M_1) is vertically focused. The reflected beam from M_1 is incident on the second mirror (M_2), which horizontally focuses the beam.

To achieve a focused image, it is necessary to satisfy the focus equations at the center of the first and second mirrors:

$$\frac{1}{p_1} + \frac{1}{q_1} = \frac{2}{R_1 \sin \theta_1}; \quad \frac{1}{p_2} + \frac{1}{q_2} = \frac{2}{R_2 \sin \theta_2}$$

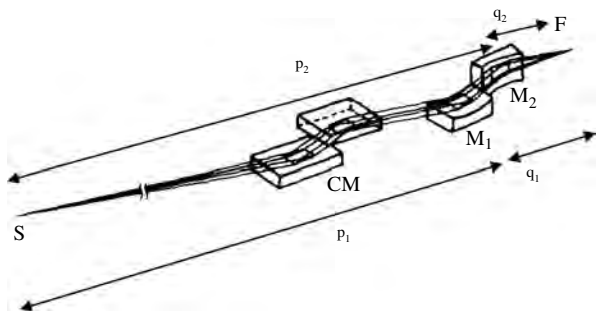


Figure 8. Schematic diagram of the optical system of two crossed Kirkpatrick-Baez curved mirrors to form a demagnified image of a X-ray source.

where p_1, q_1, p_2, q_2 are clear, from Figure 8, R_1 and R_2 are the mirror radii of curvature, and θ_1 and θ_2 are the angles of glancing incidence for the first and second mirror, respectively. For the simple case of cylindrical mirrors, the following conditions are fulfilled:

$$p_2 = p_1 + s \quad q_2 = q_1 - s$$

where s is the distance between mirror centers.

When multilayer mirrors are used, it is additionally necessary to satisfy the Bragg equation for each mirror:

$$2d_1 \sin \theta_1 = 2d_2 \sin \theta_2 = m\lambda$$

where d_1 and d_2 are the periods of the multilayers, and m is the reflection order.

Combining the equations given above, one arrives at the following expression:

$$\frac{d_1 R_2}{d_2 R_1} = \left(1 + \frac{s}{p_1}\right) \frac{\left(K_1 - \frac{s}{p_1}\right)}{K_1}$$

where K_1 is the magnification of the first mirror ($K_1 = q_1/p_1$). In general, the magnification of the second mirror $K_2 = q_2/p_2$ is different from that of the first one, and, for the special case of identical radii and periods, one can find [51]

$$K_1 = \frac{1}{K_2}$$

Kirkpatrick and Baez developed this crossed mirror geometry to eliminate astigmatism of a single spherical (or cylindrical) mirror used at the glancing incidence. The spatial resolution of the Kirkpatrick and Baez system was limited mainly by spherical aberration. Therefore, the mirrors with elliptical cylinder shapes instead of spherical or cylindrical ones are used to remove spherical aberration.

The beam size at the focusing point obtained by Iida and Irano [52] is $0.7 \times 0.9 \mu\text{m}^2$, with a flux of 7×10^5 ph/s/mA.

The advantages, with respect to other focusing optics, are that small aberration optics can be designed, the focusing properties do not depend on the incident X-ray energy, some types of mirror figures can be manufactured with high accuracy, and the working distance from the focusing element to the sample can be relatively long.

Recently, a crossed mirror system has been developed at the ESRF [53]. In this case, two orthogonal Pt-coated silicon substrates are bent into an elliptical shape to fit the experimental condition, such as focal distance and focusing. At about 140 m from the source, the dimensions of the monochromatic beam of 19 keV energy were defined by precise slits $0.2 \text{ mm} \times 0.25 \text{ mm}$ wide. This beam was first reflected by a 170-mm long vertically focusing platinum-coated mirror set at 3 mrad grazing incidence. Then it was focused horizontally onto the sample by the 96-mm-long second mirror.

The measured FWHM were $0.2 \mu\text{m}$ horizontal and $0.6 \mu\text{m}$ vertical. These values were bigger than both the ideal source image and the diffraction-limited spot sizes. Vibrations were clearly identified as a major contribution to blurring. The gain was estimated to 3.5×10^5 .

At Spring-8, (Harima, Japan) a similar system has been installed, and it provides a spot size comparable with that produced in Grenoble. However, the bent system is quite different, since the parabolic shape of the mirrors is obtained during the fabrication process, as schematically illustrated in Figure 9. As can be seen, in this case, a parabolic-shaped mold is prepared and a plane SiO_2 plate is pressed and bent against the surface of the mold. Afterward, the bent SiO_2 plate is plane polished. When the plate is removed from the mold, it returns elastically to its original shape, and a parabolic surface is finished on the upper (polished) plane.

The advantages of this fabrication process are: (i) a compact system due to the absence of the bender system, and a small focal length as a consequence; (ii) small roughness due to the plane polishing instead of a spherical polishing; (iii) smaller slope error than a spherical polishing.

3.5. X-Ray Waveguide

In 1974, Spiller and Segmuller [54] demonstrated, for the first time, the propagation of the X-rays in a waveguide composed of a BN film sandwiched between two layers of Al_2O_3 , but no flux enhancement was demonstrated.

Exploiting previous studies made by Bedzyk et al. [55] on the X-ray standing waves created above a reflecting mirror surface, in 1992, Wang et al. [56] studied the resonance-enhanced effect that takes place inside a two layer system.

In 1993, Feng et al. [57] repropoed the three layer structure of Spiller, with different materials (Si-polymide- SiO_2), and they showed the higher enhancement effect created inside with respect to the two layers structure of Wang. Only in 1995, Feng et al. [58] and Lagomarsino et al. [18] independently proposed the use of this waveguide configuration

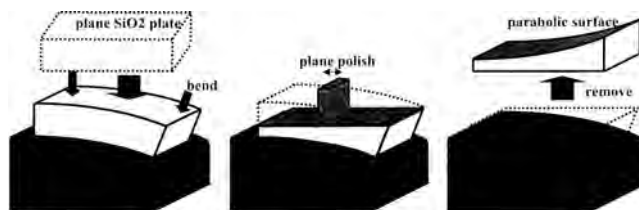


Figure 9. Sketch of the fabrication process steps to realize a parabolic mirror from a mold.

for X-ray microbeam production. Since then, different configurations and different layer materials were used to obtain higher and higher efficiency in the submicrometer beam production. Up to now, the most efficient waveguide [59] is composed of Mo–Be–Mo, and it is able to produce an X-ray beam with one dimension of 37 nm, with a gain of 100.

Very recently a first attempt of a two-dimensional waveguide able to compress the X-ray beam in two dimensions, has been proposed by Pfeiffer et al. [60]. Even if the actual efficiency is still not competitive with others X-ray optics, significant improvements are expected in the near future. Furthermore, the unique characteristics of the beam produced by the waveguides, which will be illustrated in the following sections, allow experiments that were otherwise unfeasible.

3.5.1. Resonance Effect in a Two-Layer Waveguide

An X-ray beam impinging on a surface at an angle smaller than a certain critical angle is totally reflected. The interference between the incident and reflected beams creates a standing wave above the surface with a period D , depending on the incident angle and on the wavelength. In the case of a thin film on a substrate, the interference between the reflected beam from the surface and the reflected beam from the substrate gives rise to new effects, e.g., the Kiessig oscillations. Quite relevant in this regard is the occurrence of a resonance effect inside the deposited film if this has an electronic density smaller than that of the substrate. To better analyze this effect, one should consider the structure in Figure 10.

The incident, reflected, and transmitted amplitudes of the “elementary” electric field are indicated as A_{ij} , R_{ij} , and T_{ij} , respectively, where “ ij ” refers to the interface where the radiation impinges. (e.g., R_{ij} represents the amplitude of the field that impinges from medium i on the interface ij , and it is reflected back in medium i).

Given a thin layer of a light material (e.g., C) deposited on a layer of a heavier material (e.g., Cr), then the following situation occurs [56]: since the critical angle of the lighter material is less than the critical angle for the heavier material, for any wavelength λ , there is an interval where the incident angles θ are larger than the critical angle for medium 2 and smaller than the critical angle for medium 3. This interval also is extended by the fact that the field refracted inside medium 2 reaches the interface with medium 3 at an angle $\alpha_1 < \theta$ (Fig. 10).

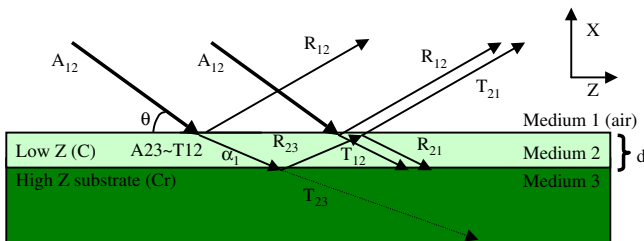


Figure 10. Schematic picture of the incident (A) reflected (R) and transmitted (T) beams at the interfaces of a structure composed of thin film of a light material deposited on a layer of a heavier material.

For any of such angles θ , the X-ray beam can penetrate in the lighter material but is totally reflected from the heavier one. Therefore, the radiation is trapped inside medium 2. The interference of the incident (A_{23}) and reflected (R_{23}) beams creates a standing wave inside medium 2. The period D is given by

$$D = \frac{\lambda}{2 \sin \alpha_1} \quad (3.12)$$

where α_1 is the incident angle at the interface between medium 2 and medium 3, and it differs from the incident angle θ (Fig. 10) because of the refraction in medium 2. It should be remarked that the internal 2–1 interface does not provide total reflection of the incident beam on it. As a consequence, T_{12} and R_{21} beams have different amplitudes. Moreover, the phase shift between them is

$$\begin{aligned} \Delta &= \left(\frac{2\pi}{\lambda} \right) 2d \sin \alpha_1 \approx \left(\frac{2\pi}{\lambda} \right) 2d(\alpha_1) \\ &= \left(\frac{2\pi}{\lambda} \right) 2d(\theta^2 - \alpha_c^2)^{1/2} \end{aligned}$$

where d is the thickness of medium 2, and $\alpha_1 = \sqrt{\theta^2 - \alpha_c^2}$ has been used.

When the incident angle θ is such that the phase shift Δ is a multiple of 2π , the constructive interference between T_{12} and R_{21} creates an enhancement of the field inside medium 2; a resonance effect takes place. This occurs when

$$\Delta = m2\pi \Rightarrow \frac{d}{m} = \frac{\lambda}{2 \sin \alpha_1} \approx \frac{\lambda}{2(\theta^2 - \alpha_c^2)^{1/2}} \quad (3.13)$$

where m is a positive integer.

When a beam traveling in a medium is reflected at an interface with another medium with a higher refraction index, it acquires a phase shift of π [8]. Therefore, when T_{12} and R_{21} interfere constructively, then the R_{12} and T_{21} beams interfere destructively. As a consequence, there is a minimum in the reflectivity curve for each θ fulfilling Eq. (3.13), as it is shown in Figure 11.

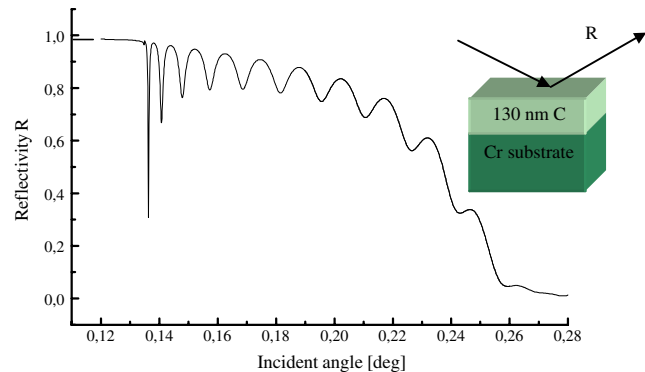


Figure 11. Numerical simulation of the reflectivity curve from the structure represented in the inset. Deep minima occur each time a resonance effect takes place. Calculations are made for an incident energy of 13 keV.

It is interesting to consider the periodicity D of the standing waves created in the film due to total reflection at the 2–3 interface. Since

$$D = \frac{\lambda}{2 \sin \alpha_1} \approx \frac{\lambda}{2 \alpha_1}; \quad \alpha_1 = \sqrt{\theta^2 - \alpha_c^2} \quad (3.14a)$$

$$D \approx \frac{\lambda}{2(\theta^2 - \alpha_c^2)^{1/2}} \quad (3.14b)$$

From Eq. (3.13), it comes out that in resonance conditions:

$$D = \frac{d}{m} \quad (3.14c)$$

and the standing waves have nodes at the interfaces air–medium 2 and medium 2–medium 3. For each θ fulfilling Eq. (3.13) or D fulfilling Eq. (3.14c), a resonant mode is created inside medium 2.

3.5.2. Three-Layer Waveguide: Production of Submicrometer X-Ray Beam

Figure 12 shows a schematic representation of an X-ray waveguide able to produce at the exit, a submicrometer vertical beam with a horizontally unchanged input condition (planar waveguide). A very thin cap layer has been added on top of the two-layer structure described before. In this example the bottom and top layers are made of Mo, and the intermediate layer is made of Be.

At angles more grazing than the critical angle for the air–Mo interface, the incident radiation is totally reflected and only an evanescent wave can travel inside the cap–Mo layer, and it is transmitted in the Be layer (guiding layer). To have maximum efficiency, the cover Mo layer must be very thin (few nanometers) to allow a substantial part of the incoming beam to penetrate. It is important to note that the incident angle α_1 at the Be–Mo interface is smaller than the external incident angle θ because of the refraction inside the Be layer. As in the two-layer system described in the preceding discussion, a resonance occurs for the incident angles that satisfy Eq. (3.13). In correspondence of the resonant modes, minima take place in the reflectivity curve, due to the destructive interference out of the guiding layer, as will be discussed.

Figure 13 represents the calculated intensities for the first three resonant modes excited in the structure of Figure 12.

An important consequence of the guiding process described is that the incident beam impinging on the waveguide is squeezed in one dimension (the vertical dimension in this case) to the thickness of the Be layer, i.e., to fractions

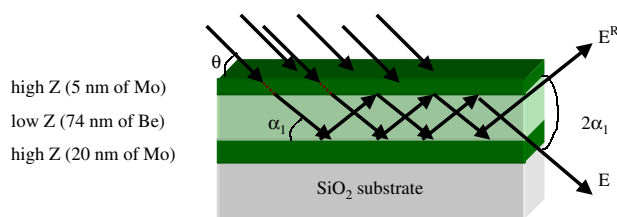


Figure 12. Schematic representation of the X-ray waveguide, which produces a beam with the vertical dimension equal to 37 nm.

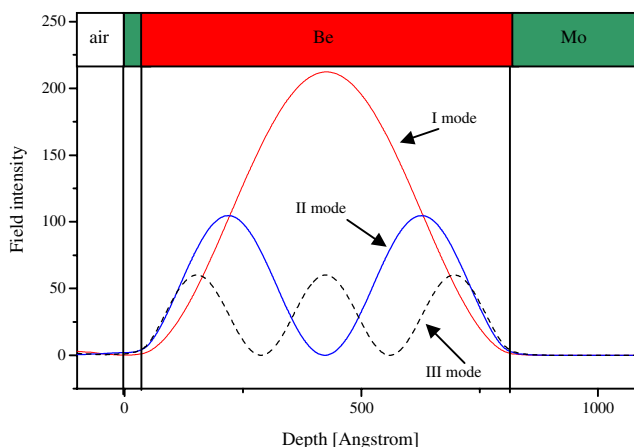


Figure 13. Numerical simulation of the field inside the waveguide represented in Figure 10, for the first three resonances.

of a micron. Thus, the X-ray beam is compressed and the flux density is increased by orders of magnitude [18, 58], as in an optical waveguide. As pictorially represented in Figure 12, two beams exit from the waveguide simply considering reflection at the top and bottom interfaces of the guiding layer. The splitting angle between the two beams is $2\alpha_1$ and, therefore, the splitting angle increases as the incident angle increases.

A waveguide similar to the one represented in Figure 12 has been tested [61] on the microfocus beamline “ID13” at ESRF by using a monochromatic beam at 13 keV.

As is clear from Figure 14, the waveguide beam travels parallel to the surface, while the reflected beam travels at an angle θ with respect to it. Figure 15a and b show both the reflectivity and the waveguided intensity propagated through the Be layer of the waveguide as a function of the external incident angle.

The dots in the curve represent the points measured when using a pin diode at a fixed position (close to the waveguide exit) vs the incident angle. In Figure 15a, the ordinate represents the reflectivity R of the waveguide normalized to the incident signal. In Figure 15b, the ordinate represents the flux exiting from the waveguide (also normalized to the incident flux).

Since the waveguide beam and the reflected beam travel in different directions, separated by θ , a slit in front of the pin diode (Fig. 14), allows to distinguish, at a certain distance from the waveguide, the two beams by simply translating up and down the detector-slit system.

The perfect correlation between the angular position of the maxima of intensity at the exit that corresponds to the excited modes (transverse electric [TE] modes*) and the reflectivity minima confirms that only the efficient coupling gives rise to an exiting beam.

To analyze, in detail, the structure of the different modes exiting from the waveguide, a charged-coupled device (CCD) camera was positioned at 840 mm from the waveguide, and the images for the different resonant angles were

* Due to the linear horizontal polarization of S.R., the electric field of the incoming beam and of the multiply reflected beams in the waveguide stays normal to the incidence plane. Therefore, only the TE modes propagate [8].

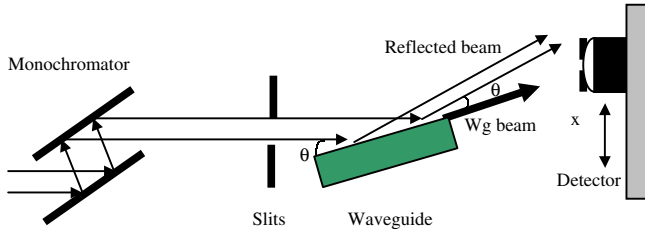


Figure 14. Schematic representation of the set-up used on ID13 at ESRF to test the waveguide.

recorded. The experiment was carried out on the optics beamline BM5 at ESRF with a 17 keV monochromatic incident beam. The results are reported in Figure 16. The five pictures in this figure represent the first five modes exiting from the waveguide for the resonant angles defined by Eq. (3.13). At the same time, in each picture are recorded the direct, the reflected, and the guided beam.

The intensity in the direction of the incident beam must be attributed to the presence of higher harmonics, which are reflected by the channel-cut monochromator and which pass through the substrate.

By rotating the waveguide, the direction of the incident beam always remains the same, while the reflected beam goes up as the incident angle increases. The guided beam always appears midway between the incident and the reflected beams since its direction is parallel to the

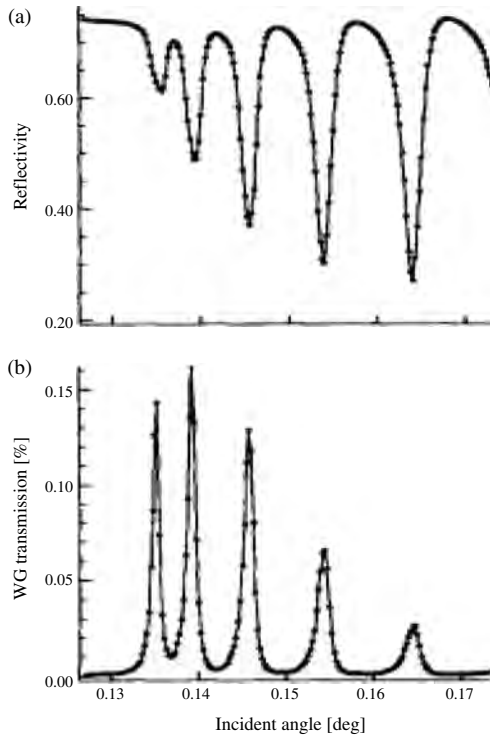


Figure 15. (a) Measured reflectivity R of the waveguide structure as a function of the incident angle and (b) measured intensity I exiting from the waveguide terminal in the direction tangential to the guide surface. Both spectra are normalized to the incident signal and are taken at 13 keV photon energy. The line connects the measured points as a guide for the eye.

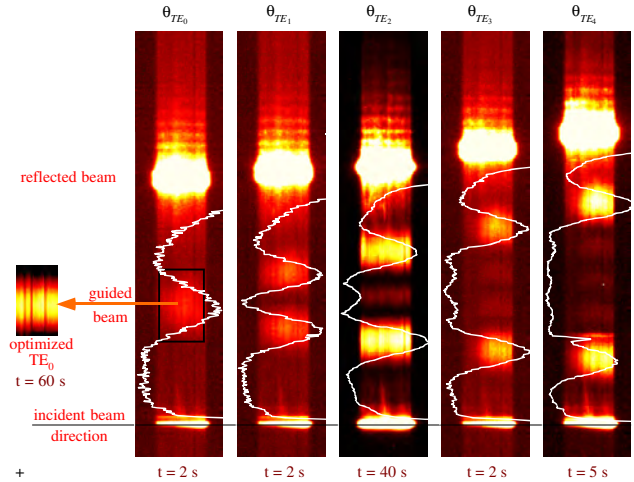


Figure 16. Images of the first five resonant orders exiting from the waveguide recorded with a Frelon CCD camera with $10 \mu\text{m}$ pixel size at a distance of 840 mm from the waveguide end. On the bottom of each picture, the acquisition time is reported. The inset on the left represents the TE_0 mode optimized by using a higher acquisition time.

waveguide surface. This is exactly true for the TE_0 , while, for the higher resonances, two beams exit from the waveguide whose median direction is tangential to the waveguide. This is consistent with the pictorial view in Figure 12 of two beams propagating in the waveguide. Except for the first resonance, it is clear from Figure 16 that the angle between the two beams exiting from the waveguide increases as the mode number increases. In the first picture, representing the TE_0 mode, instead, only one beam is resolved, because, in this case, the splitting angle is comparable to the divergence of each beam.

A detailed study of the guided beam images shows (see the inset of the TE_0 mode in Fig. 16) a nonhomogeneous horizontal profile. This speckle structure is due to the presence of unpolished beryllium windows on the beamline, which deteriorate the quality of the incident beam. The same inhomogeneity cannot be appreciated on the incident and reflected images in Figure 16 because of saturation.

The interference fringes above the reflected beam are a typical phenomenon in total reflection from rough mirror surfaces [62] and are of no concern in the specific physics of interest here.

3.5.3. Mathematical Representation of the Field Inside the X-Ray Waveguide

The field amplitude $E^{(n)}$ [63] at a certain distance x from the middle of the n th layer of a multilayer structure, can be calculated by means of the following expression:

$$E^{(n)}(x) = E_n e^{-ik_z z} e^{ik_x x} + E_n^R e^{-ik_z z} e^{-ik_x x} \quad (3.15)$$

where E_n and E_n^R are respectively the incident and reflected field amplitudes in the middle of n th layer.

In the particular case of a perfectly symmetric waveguide with symmetrically injected radiation (i.e., in the direction parallel to the waveguide) as occurs for an optical waveguide, the modes inside the guiding layer (e.g., Be) must

be odd or even functions. Indeed, in this particular case, $|E_2^R| = |E_2^I|e^{i\varphi}$, in Eq. (3.15) and the field inside the Be can be written:

$$\begin{aligned} E^{(2)}(x) &= E_2 e^{i\frac{\varphi}{2}} (e^{-ik_z z} e^{ik_x x} e^{-i\frac{\varphi}{2}} + e^{ik_z z} e^{ik_x x} e^{i\frac{\varphi}{2}}) \\ &= 2E_2 e^{-ik_z z} e^{i\frac{\varphi}{2}} \left(\cos\left(k_x x - \frac{\varphi}{2}\right) \right) \\ &= 2E_2 e^{-ik_z z} e^{i\frac{\varphi}{2}} \left(\cos\left(\frac{2\pi}{\lambda} \sin \alpha_1 x - \frac{\varphi}{2}\right) \right) \end{aligned} \quad (3.16)$$

where α_1 is the incident angle at the Be–Mo interfaces and

$$|x| < \frac{d}{2}$$

with d equal to the Be thickness and the origin of x taken midway in the Be layer. Since the resonance modes must be of given parity (due to the symmetry of the system) with respect to the center ($x = 0$) of the guiding layer, the relative phase φ between E_2^R and E_2 can only be 0 or π . Therefore, in resonance condition, when the angle α_1 satisfies Eq. (3.13), one has

$$E^{(2)}(x) = 2E_2 e^{-ik_z z} \left(\cos\left(m\pi \frac{x}{d}\right) \right) \quad \text{for } \varphi = 0 \quad \text{and } m \text{ odd} \quad (3.17a)$$

and

$$E^{(2)}(x) = 2E_2 e^{-ik_z z} \left(\sin\left(n\pi \frac{x}{d}\right) \right) \quad \text{for } \varphi = \pi \quad \text{and } n \text{ even} \quad (3.17b)$$

where m and n are positive integers describing the odd and even waveguide modes, respectively.

The case of a real waveguide cannot be considered exactly symmetric because (i) the thickness of the two Mo layers is different and (ii) the radiation is injected in the waveguide from above, so that the upward-moving component of the standing wave has undergone one more reflection. Nevertheless, the Eq. (3.17) satisfactorily describes the field inside the guiding layer.

3.5.4. Propagation Properties of the Guided Beam

In Section 3.5.3., the mode structure inside the waveguide has been studied. In particular, the profiles of the resonances inside the guiding (e.g., Be) layer has been calculated exactly (Fig. 13) and a good approximation of the field has been given in Eq. (3.17).

Therefore, the field intensity of the standing waves created inside the guiding layer in resonance conditions can be approximated by the functions

$$\begin{aligned} I(x) &\propto \left| \cos\left(m\pi \frac{x}{d}\right) \right|^2 \quad m \text{ odd} \\ I(x) &\propto \left| \sin\left(n\pi \frac{x}{d}\right) \right|^2 \quad n \text{ even} \end{aligned} \quad |x| < \frac{d}{2}$$

with m and n being positive odd and even integers, respectively, and d is the Be layer thickness. Clearly, the FWHM is

smaller than d , and, for the first order of resonance ($m = 1$), it can be expressed as

$$\Delta_{\text{theo}} = 2 \frac{d}{\pi} \arccos\left(\frac{1}{\sqrt{2}}\right) = \frac{d}{2} \quad (3.18)$$

The Eq. (3.18) can be considered as the theoretical beam size of the guided beam just at the exit ($z = 0$).

To study the guided beam propagating in free space after exiting the waveguide, one first has to note that, as repeatedly mentioned in the previous sections, two beams exit from the waveguide. In fact, from Figure 12, it is evident that there are two waves inside the Be layer, one progressing in transmission direction (or downward) and the other in reflection direction (upward). At the waveguide exit, these two fields create two different beams separated by an angle:

$$2\alpha_1 = \sqrt{\theta^2 - 2\delta}$$

Therefore, for each resonant mode, two beams exit from the waveguide and their splitting angle increases as the resonance order increases. For a photon energy of 13 keV corresponding to a wavelength of $\lambda = 0.095$ nm and a guiding layer thickness $d = 130$ nm, $2\alpha_1 = 0.037^\circ = 0.64$ mrad for the first order of resonance. Then the angles between the two fields for the higher orders will be multiples of this value.

3.5.4.1. Fresnel Region At the waveguide exit, the two wave vectors are almost normal to the exit surface and thus the fields go out almost unaffected by Be–air refraction. However, due to the limited vertical extent of the wave field at the exit, the beam will undergo a diffraction process (slit diffraction), further enlarging its size [8].

For distances z from the waveguide exit smaller than a critical value

$$z_c = \frac{\pi}{\lambda} d^2$$

where d is the Be layer thickness, the field propagates according to the standard Fresnel diffraction theory. For the wavelength $\lambda = 0.095$ nm and $d = 130$ nm, $z_c \approx 1$ mm. In this regime, the field intensity after a slit of aperture d is given by the expression [8]:

$$|V(x, z)| = \frac{A^2}{2} \left[F\left(\frac{d}{2} + x\sqrt{\frac{2}{\lambda z}}\right) + F\left(\frac{d}{2} - x\sqrt{\frac{2}{\lambda z}}\right) \right]^2 \quad (3.19)$$

where z is the distance from the waveguide and x is the vertical distance from the middle plane of the Be layer with the origin midway in the Be layer, and

$$F(\nu) = \int_0^\nu d\tau e^{i\frac{\pi}{2}\tau^2}$$

is the so-called Fresnel integral.

Despite the complicated analytic structure, from Eq. (3.19), it is possible to retain that as long as $z < z_c$, the F functions are substantially different from zero only for $|x| \leq \frac{d}{2}$, which is inside the geometrical projection of the Be layer section. This is what was expected since close to the waveguide, the deviation from the geometric optics is small.

Furthermore, a detailed study of Eq. (3.19) [8] shows an edge effect that leads to a distribution intensity appearing as tails exceeding the geometrical projection of the Be-layer thickness by an amount

$$\Delta \approx \sqrt{\lambda z}$$

This edge effect depends on the wavelength but is the same for the different orders, and, for photon energy of 13 keV, it is of the order of $\Delta = 0.1 \mu\text{m}$, at a distance of 0.1 mm.

3.5.4.2. Fraunhofer Region Far away from the waveguide, i.e., at a distance $z > z_c$, the intensity distribution is well described by Fraunhofer diffraction or far field approximation. In this regime, for a coherent source, the intensity distribution becomes the square modulus of the Fourier transform of the field distribution of the source

$$I_z(x) = \left| \int_{-\infty}^{\infty} E^{(2)}(x) e^{ik_x x} dx \right|^2$$

where $E^{(2)}$ is the electric field inside the guiding layer and exiting from the waveguide. In the particular case of a symmetric (and symmetrically illuminated) waveguide, the source field distribution $E^{(2)}$ at $z = 0$ is given by the sin-like and cos-like functions of Eq. (3.17a and b) for x inside the Be layer ($-d/2 \leq x \leq d/2$) and zero otherwise. In this simple case, the Fourier transform, giving the field distribution in the Fraunhofer region, is feasible analytically. For the first ($m = 1$) TE_0 mode, e.g., one obtains

$$\begin{aligned} E_z(x) &= E_2 \int_{-\frac{d}{2}}^{\frac{d}{2}} \cos\left(\frac{\pi x}{d}\right) e^{-ik_x x} dx \\ &= E_2 \int_{-\frac{d}{2}}^{\frac{d}{2}} \cos\left(\frac{\pi x}{d}\right) e^{-ik \sin \alpha_1 x} dx \\ &= -\frac{iE_2}{2} \left[\frac{e^{iA^+ \frac{d}{2}} - e^{-iA^+ \frac{d}{2}}}{A^+} + \frac{e^{iA^- \frac{d}{2}} - e^{-iA^- \frac{d}{2}}}{A^-} \right] \end{aligned} \quad (3.20)$$

where the notation $A^\pm = (\pm \pi/d - k \sin \alpha_1)$ has been introduced and where the second equality arises because $k_x = k \sin \alpha_1$, with α_1 being the angle between the wavevector k and the $x = 0$ plane. The resulting intensity distribution is

$$\begin{aligned} I_z(x) = |E_z(x)|^2 &= E_2^2 \left[\frac{\sin^2(A^+ \frac{d}{2})}{A^{+2}} + \frac{\sin^2(A^- \frac{d}{2})}{A^{-2}} \right. \\ &\quad \left. + \frac{2 \sin(A^+ \frac{d}{2}) \sin(A^- \frac{d}{2})}{A^+ A^-} \right] \end{aligned} \quad (3.21)$$

Various observations are now in order. The first two terms in the square brackets are sinc functions, giving rise to two main peaks, while the third term is an interference contribution. The main peaks are located at an angle α_1^{\max} determined by the condition $A^\pm = 0$, and, therefore,

$$\sin \alpha_1^{\max} = \pm \frac{\pi}{kd} = \pm \frac{\lambda}{2d}$$

One can notice that this relation coincides with the resonance condition Eq. (3.13). This observation formally substantiates the pictorial view of Figure 12 according to which two beams (related to the E and E^R components of the field inside the Be layer) exit each one forming an angle α_1 with the $x = 0$ plane.

The FWHM of each main peak can be simply calculated from Eq. (3.21), and, for a given distance z from the end of the waveguide, it is given by

$$\Delta_{\text{theo}}(z) = \frac{\lambda}{2d} z \quad (3.22)$$

Performing the same treatment leading to Eq. (3.20) for a generic mode in Eq. (3.17), it can easily be demonstrated that Eq. (3.22) stays valid at any resonance order. On the other hand, one finds that the two main peaks are separated by a distance

$$\Delta x_m(z) = m \frac{\lambda z}{d}$$

which increases with the order m of resonance.

For the first order TE_0 , the interference term in Eq. (3.21) is positive for $x = 0$ and, therefore, it represents a constructive interference in this position. This positive contribution around $x = 0$ has a width of the order of $\Delta x_{\text{int}}(z) = \lambda z/d$. As a consequence for this TE_0 mode, the two main peaks cannot be resolved, since they are “joined” by this additional peaky structure in the middle.

3.5.5. Coherence

The waveguide is an optical device capable of producing a microbeam with a high degree of coherence. Indeed, the constructive interference that occurs inside the guiding layer in resonance condition necessarily involves only the coherent part of the incident beam. This is clear from the mode structure of the field inside the C layer, which implies strong interference phenomena. However, several effects can degrade this coherence, like roughness and scattering from impurities inside the carbon. An experiment performed at beamline BM5 at ESRF has shown that these effects do not deteriorate the coherence of the guided beam. The experiment consisted in the analysis of the intensity distribution of the waveguided beam in the far field. To this purpose, a CCD camera was used at 840 mm distance from the waveguide end, as it is schematized in Figure 14.

Spectra were taken for the waveguide adjusted to the angles at which the resonant modes give rise to an exiting beam. Experimental profiles of the images recorded for the first five modes (TE_0 – TE_4) are presented in Figure 17, together with the theoretical calculations. These latter are based on Eq. (3.21) and are similar for the higher order modes describing the intensity distribution far away from the waveguide. In particular, at a distance $z \gg z_c$ ($z_c = \pi d^2/\lambda$ is the distance of transition between the Fresnel and Fraunhofer diffraction region), the field is the Fourier transform of the field at $z = 0$ and, therefore, supposing a perfect coherence of the beam at the waveguide exit, the intensity can be written as

$$I^{\text{coh}}(x) = \left| \int_{-\infty}^{\infty} E(\bar{x}) e^{ik_x \bar{x}} d\bar{x} \right|^2 = |\tilde{E}|^2$$

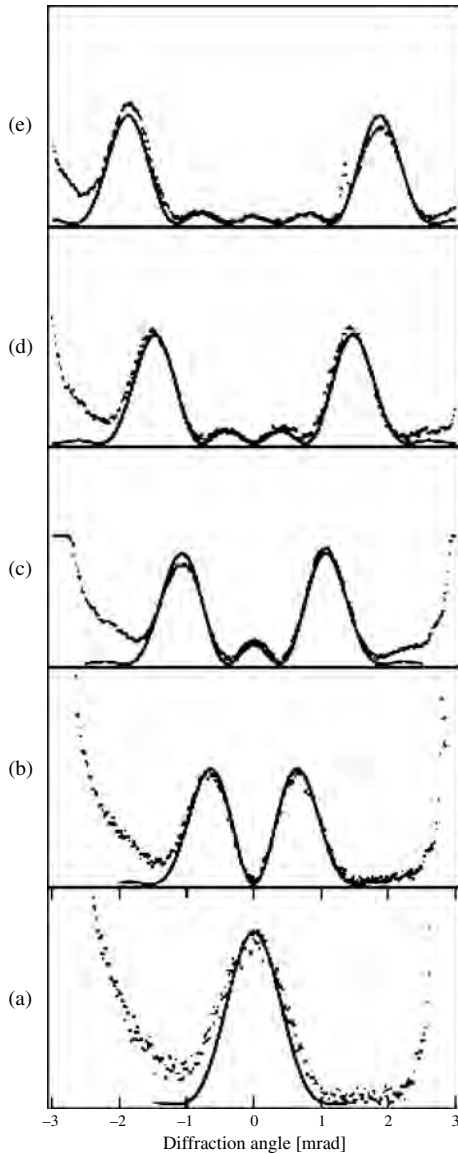


Figure 17. Comparison of the angularly dependent intensity distribution at 840 nm from the waveguide terminal (dots) with the calculated diffraction pattern (solid line) at 13 keV photon energy for the different modes a) TE_0 , b) TE_1 , c) TE_2 , d) TE_3 , and e) TE_4 .

where the electric field E , just at the exit, has the sin-like and cos-like form, as in Eq (3.17).

A high degree of coherence between the two beams is proved by the good agreement between the experimental result and the calculation for the TE modes and, in particular, for the TE_0 one.

3.5.6. Gain

Experimentally, we can measure the transmission T of the object as the ratio between the photon flux F' at the exit of the waveguide and the incident photon flux F . With the known values S and H for the vertical and horizontal dimensions of the incident beam and with the known FWHM size $S' = d/2$ of the exiting beam, the experimental gain is

derived as

$$G = \frac{I_{\text{out}}}{I_{\text{in}}} = \frac{\frac{TF}{Hd/2}}{\frac{F}{SH}} = 2T \frac{S}{d}$$

The highest measured gain ($G = 100$) has been obtained for a waveguide composed of a 74 nm Be layer on a 20 nm Mo and covered with 5.5 nm Mo on silicon substrate, working at 13 keV.

4. X-RAY MICROSCOPY TECHNIQUES AND APPLICATIONS

In the previous section, we have analyzed, in some detail, the main X-ray optics that can provide submicrometer beams. In the following, an overview of applications is given. In Section 4, microscopy (i.e., imaging) techniques are reviewed. In Section 5, nanodiffraction is taken into consideration.

4.1. Experimental Considerations and Instruments

Here we want to describe the basis of the most relevant techniques and instrumentation used in microscopy and nanodiffraction.

4.1.1. Contact Microscopy

The simplest, and more ancient, X-ray microscopy technique is the contact one. The sample is put in tight contact with a sensitive material and is illuminated by an X-ray beam as much collimated as possible. In the first studies, which date back to the beginning of past century [64, 65], the sensitive material was a photographic plate, substituted later by a photoresist layer that allowed for improved resolution [66]. The image is formed through photoabsorption process: the pattern recorded on the photoresist is a map of the variation of a photoabsorption coefficient in the sample. After development, the photoresist, if positive as the poly-methyl-methacrylate (PMMA), the most commonly used, is thinner, if the received dose is higher, i.e., in the more transparent regions of the sample. The recorded pattern can then be viewed by optical or electron microscopy and, more recently, by atomic force microscopy. The resolution r that can be reached with contact X-ray microscopy is mainly limited by diffraction effects, if h is thickness of the specimen $r \approx (h\lambda)^{1/2}$, where λ is the wavelength. Resolutions of the order of 0.1μ are typically reached with this method. Another effect that deteriorates resolution is the penumbra effect due to the angular divergence of the incoming beam.

4.1.2. Projection Microscopy

The working principle of the projection microscopy is quite simple: a point source of X-rays, most often generated by a focused electron beam, project the shadow of the sample put at a distance D_1 from the source onto a screen at a distance D_2 . The magnification M is then simply given by $M = (D_1 + D_2)/D_1 \approx D_2/D_1$, if, as usual, $D_2 \gg D_1$. The resolution limit generally is dominated by the source size s . Substantial improvements have been obtained by using a high brightness field gun scanning electron microscope

(FEG-SEM), which allowed a spot as small as 0.2μ [11]. As the source becomes smaller and smaller, approaching the ideal limit of a point source, the coherence increases, and Fresnel diffraction must be taken into account. This makes the image more complicated than considering photoelectric absorption as only responsible for the contrast. In fact, the phase of the e.m. wave and its modifications must be considered, but the more complex treatment results, in fact, in most of the cases, in an enhanced contrast, as will be discussed later.

The same principle of projection microscopy has recently been applied to the X-ray waveguide, illustrated in Section 3. In this case, the X-ray beam from a S.R. source is compressed in a plane or in a wire through an interferometer effect and comes out from the waveguide with dimensions of the order of few tens of nanometers and a high degree of coherence. Because the high coherence of the beam generated by the waveguide implies necessarily phase contrast effects, an illustration of the potentialities of this method will be given after a discussion on the phase contrast principles.

4.1.3. Full Field and Scanning Microscopy

With the advent of S.R. sources, the projection microscopy that uses point source X-rays generated in modified SEM lost much of its importance. In fact, the high brilliance of S.R. allowed more sophisticated and more performant instrumentation. This is the case of full field X-ray microscope, or simply X-ray microscope (XM), and scanning X-ray microscope (SXM). The modern instruments are in great majority based on FZPs, even if the first instrument of this kind was developed by Kirkpatrick and Baez with mirrors [17]. An instrument that served as a model for many others is the Gottingen XM, installed in the Bessy S.R. source in Berlin [67].

In brief, a condenser FZP receives the radiation and focuses it at the object plane (Fig. 18). The radiation can be, in principle, both monochromatic or polychromatic. Since the FZP focalizes different energies at different distances, a pinhole in the object chamber can act as an energy pass-band filter. The degree of monochromatization is given, in this case, by $\lambda/\Delta\lambda \approx D/2d$, where D is the diameter of the condenser FZP and d , the pinhole diameter. In Figure 18, the instrument at the beamline ID21 of the ESRF

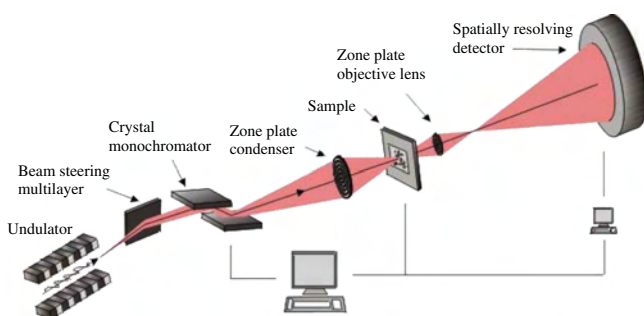


Figure 18. Schematic view of a full field X-ray microscope (from the Web site of Beamline ID21 at ESRF: www.esrf.fr, with permission from J. Susini).

is depicted, which receives radiation already monochromatized. The central stop of the condenser blocks the direct S.R. A micro FZP, with much finer structures and reduced numerical aperture than the condenser FZP, generates a magnified image of the object in the image plane. When working in the soft X-ray region, the spatial resolution can be as good as few tens of nanometers. In the hard X-ray region, however, the limit is for the moment around 150 nm, mainly due to difficulties in fabricating high resolution FZP for high energies (see Section 3.1).

Scanning X-ray microscopes use the high-resolution micro FZP to focalize a monochromatic beam on a submicrometer spot at the sample (Fig. 19). The sample is then mechanically scanned in front of the beam with high accuracy, and the transmitted beam is measured by a high sensitivity detector. The two instruments are complementary and each have their advantages and disadvantages. The micro FZP, which in the XM is behind the sample, has a quite limited efficiency, therefore, only a small percentage of the photons arriving on the sample contributes to the image formation. Moreover, a low efficiency two-dimensional detector such as a photographic plate or a CCD camera must be used. This increases the dose delivered to the sample, which in case of sensitive materials like the biological ones, is quite deleterious. In SXM, instead, no optical elements are behind the sample, and a high efficiency detector can be used. Moreover, secondary effects such as fluorescence radiation can be measured, increasing the quantity of available information. As a counterpart, SXM requires much higher brilliant and coherent sources than the XM to keep the acquisition time reasonable, and, also, the spatial resolution is, in general, worse than that obtainable with XM.

Fresnel zone plates are very efficient in the soft X-ray region, but, at higher energies, their fabrication at high resolution becomes more difficult, and S.R. beamlines working in the hard X-ray region equipped with other optical elements such as refractive lenses [16], waveguides [18] or Kirkpatrick-Baez mirrors [17] are in operation.

4.1.4. Bragg Magnifier

An alternative way to improve spatial resolution is to use, after absorption from the sample, diffraction from an analyzing crystal set in a strong asymmetric reflection [68, 69]. A sketch is shown in Figure 20. The image magnification M is given by the ratio $M = \sin \alpha / \sin \beta$ where α and β are,

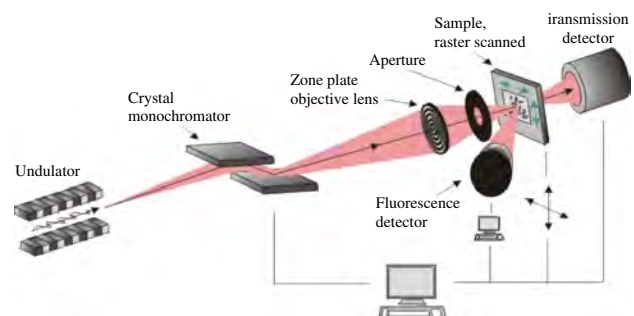


Figure 19. Schematic view of a scanning X-ray microscope (from the Web site of Beamline ID21 at ESRF: www.esrf.fr, with permission from J. Susini).

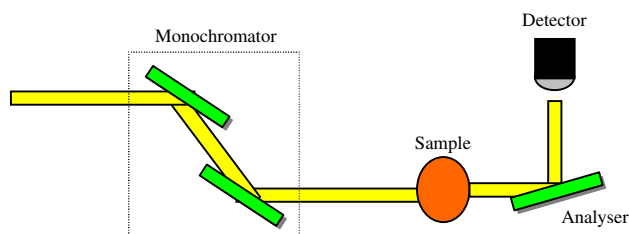


Figure 20. Schematic view of the Bragg magnifier: the beam from the sample impinges on the analyzer crystal at a glancing angle α_1 and the diffracted beam leaves the sample at an angle α_2 with respect to the surface. The magnification M is given by the ratio: $\sin \alpha_2 / \sin \alpha_1$.

respectively, the angles that the diffracted and the incident beams form with the analyzing crystal surface. To predict the exact behavior of the analyzing crystal, the dynamical theory of diffraction in asymmetric conditions should be used [70]. If magnification and high resolution is desired in both directions, as is usually the case, two crossed crystals with surfaces in the horizontal and vertical planes must be used. The resolution that can be reached with this system depends not only on the magnification M , but also on the X-ray source geometrical characteristics, and values of the order of 0.2μ have been claimed [68, 69]. It is worth noting that this method can work easily for hard X-rays, as in [69], where an energy of about 23 keV has been reached, with magnification up to 100 in both directions. Since the detector, as in projection microscopy, is at a certain distance from the sample and analyser, phase contrast effects due to propagation are visible. This will be discussed later in more detail.

4.2. Modes of Operation and Some Examples of Applications

In this section, we will give an overview of the principle methods in use in microscopy, together with some examples of applications. These are not intended to be exhaustive, but just to give an idea about the potentialities of the different methods.

4.2.1. Absorption Contrast

Photoelectron absorption contrast is the usual way matter is imaged in X-ray radiography. The contrast comes from a nonhomogeneous distribution of matter with a different linear absorption coefficient μ and/or with different thickness. As discussed in Section 1, the absorption coefficient is not a continuous function of energy (or λ) but has discontinuities in correspondence with absorption edges. This is usefully exploited to enhance contrast. The most relevant example is in biological matter where the major components are water and organic C compounds. In the wavelength range (the so-called “water window”) between the absorption edges of oxygen ($\lambda = 2.34 \text{ nm} \Rightarrow E \approx 530 \text{ eV}$) and C edge ($\lambda = 4.38 \text{ nm} \Rightarrow E \approx 283 \text{ eV}$), the radiation is weakly absorbed by water but strongly absorbed by organic matter, resulting in good contrast. Most important, this allows hydrated and even (initially) living cells to be studied. The problem of radiation damage will be discussed later. The presence of the water window is the main reason why many microscopes work in the soft X-ray region where most of the activity

deals with biological studies. However, increasing attention and more instruments are now dedicated to the hard region of the spectrum, where thicker samples can be examined and tomographic studies (see below) can be carried out. An example is given in Figure 21, which shows a part of a giant chromosome in a wet state, where the contrast and the spatial resolution are really remarkable [71]. It is worth stressing the importance of the fact that with X-ray microscopy, it is possible to view whole cells in their wet state. However, care must be given to the problem of radiation damage. The important parameter in this respect is dose. Dose is defined as the ratio of energy absorbed in the volume illuminated and the mass pertaining to that volume. It is important to keep the dose as low as possible because, after a certain threshold value, sensitive material is damaged. This also is a serious limitation regarding spatial resolution. Calculations show [2, 11] that, independent on the microscopy method in use, the dose D is proportional to d^{-4} , where d is the minimum feature size detectable (in other words, the spatial resolution). This implies that for biological studies, the ultimate limit in resolution is not given by available flux or optics perfection but by radiation damage. A method that can reduce the threshold dose for radiation damage is to freeze the samples in a state that closely resembles their natural environment (cryomicroscopy). Other methods instead reduce the dose necessary to detect a feature with a given signal–noise ratio. If the radiation damage represents the limit in resolution, enhancing the contrast will also result in improving achievable spatial resolution. One method relies in tagging a probe with nanoparticles of some heavy elements (generally gold) that enhance both absorption and phase contrast [1]. This technique, for example, has been used to immunolocalize proteins or nucleic acids in mammalian cells [72]. This is

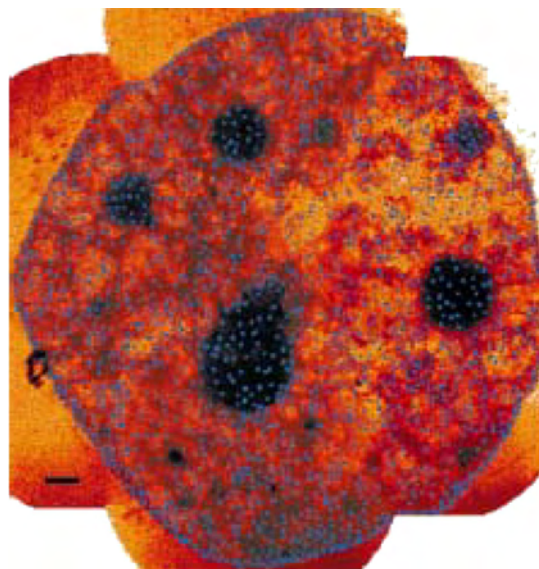


Figure 21. X-ray image illustrating the distribution of pores on the surface of the nucleus of a human mammary epithelial tumour cell (T4). The nuclear pores were labeled by using primary antibodies to a protein from the nuclear pore complex. The contrast has been enhanced by silver. Magnification: 2400x with 20 nm pixel size. Wavelength: 2.4 nm. (Reprinted with permission from [72], W. Meyer-Ilse et al., *J. Microscopy* 201, 395 (2000). © 2000, Blackwell Publishing.

a very important problem in a post-genomic era, where the main task is to determine function of genes. The same labeling with gold also has been used to study tumoral cell [71]. In [71], the investigators show images of the distribution of nuclear pores on the surface of the nucleus of a human mammary epithelial tumor cell at a pixel resolution of 20 nm (Fig. 21). Even if, at the moment, we are not aware of direct applications in the field of nanobiotechnologies, we are confident that these microscopy techniques will give, in the near future, significant contributions as characterization tools in this important emerging field.

Beyond biological studies, X-ray microscopy in absorption mode also has been applied in other fields, for example, characterization of micro- and nanoelectronic materials. The advantages with respect to optical microscopy are not only better spatial resolution but also the possibility to visualize buried layers invisible, both to photons in optical microscopy and to electrons in SEM microscopy, which can only probe surface topography. The open environment accessible to hard X-rays also allows probing devices while active. This is the case, for example, of electromigration (EM) in passivated Cu interconnect structures, where the high values of current density can induce voids in the conducting microstructures or stress [73]. High spatial-resolution (100 nm) studies of EM in passivated Cu interconnections have been carried out in real time [74] with a full field XM. With this technique, it has been possible to record, in real time, an image sequence that allows the study of the time evolution of mass transport that led to formation of voids and interruption of line. Not only was the spatial resolution significantly higher than what could be obtained with optical microscopy, but the X-ray measurements were conducted on passivated layers not accessible to other types of microscopy, therefore, on conditions corresponding to those of the real devices.

In environmental science, X-ray microscopy has been used to study intimate structures of colloidal systems in soil. As an example, the comparison between untreated and thermal-treated soil has shown a drastic change in the soil structure with a buildup of larger particles resulting from the collapse of finer particles due to dehydration, which followed the thermal treatment [75].

4.2.2. Magnetic Circular Dichroism

Atoms with a net magnetic moment show, in the vicinity of absorption edges, a strong circular dichroism, i.e., a relevant difference in absorption coefficient between the left and the right circularly polarized radiation. This difference also appears if the sample is illuminated with circularly polarized photons and the magnetic moment of the sample is directed parallel or antiparallel to the beam direction. This happens, for example, for the L edges of Fe, Co, Ni, etc. Thus, magnetic domains with up and down magnetization can be visualized by X-ray absorption microscopy with a circularly polarized beam at high spatial resolution (≈ 30 nm). This is of high value in studying magnetic nanostructures. A distinct advantage of X-ray microscopy is that the images can be recorded at varying external magnetic fields, allowing a detailed study of the switching of magnetic domains. In this study, a matrix of $1 \mu \times 1 \mu$ dots was prepared in a 0.4 nm

Fe/0.4 nm Gd $\times 75$ multilayer. Images at different external magnetic fields were taken, showing both the domain structure at nanometer scale and the collective switching behavior [76]. Another advantage of X-ray microscopy with respect to other techniques is the element specificity that can give information about magnetic coupling mechanism. Due to the temporal structure of S.R., time-dependent effects, such as spin dynamics, also can be studied [77].

4.2.3. Phase Contrast

Phase contrast arises when the coherence of the beam allows visualization of spatial variations of the real part of the refraction index, which induces changes in the phase of the incident radiation. (Photoelectron absorption is related to its imaginary part, see Section 1.) To understand how phase variations can be imaged, start with a plane wave e^{ikz} traveling along the z direction, impinging on an inhomogeneous sample with refraction index $r(x, y) = 1 - \delta(x, y) - i\beta(x, y)$ and thickness t . If we define $\phi(x, y) = 2\pi\delta t/\lambda$ and $\mu(x, y) = 2\pi\beta t/\lambda$, the sample transmission function $q(x, y)$ is defined as $q(x, y) = e^{i\phi(x, y) - \mu(x, y)}$, and just after transmission from the sample at z_0 , the wavefunction can be expressed as: $f(x, y) = e^{ikz_0} q(x, y)$. The intensity I_1 at z_0 is

$$I_1 = |f(x, y)|^2 = e^{-2\mu}$$

Therefore, any information about the phase is lost. To have detectable contrast due to phase variations, it is necessary either that the beam, which has interacted with the sample, be superposed to a reference beam or the small angular deviation due to the change of phase be detected. In the first case, the interference between the two beams carrying a definite phase difference gives rise to the contrast. The superposition can be obtained in different ways. Here we will mention three methods: Zernike phase contrast [78], Gabor in-line holography [79], and differential interference [80]. Diffraction from an analyzer crystal can be used in the case where the small angular deviation has to be detected.

4.2.3.1. Zernike Phase Contrast Schmahl [1, 81, 82] described in detail the way the Zernike phase contrast method can be applied in the soft X-ray regime. The basic point is the presence of a phase plate put in the back focal plane of the micro FZP, which modifies the phase of the zero order incoming radiation. This causes interference with the first order diffracted radiation from the FZP in the image plane. Careful calculations have been carried out to evaluate the contrast and the dose delivered to the sample [83]. It turns out that the contrast is higher (and in some cases much higher) than the absorption contrast for nearly all wavelengths [1]. More important, especially for sensitive materials like the biological ones and the macromolecules, there is, in general, a strong reduction in the dose required to detect a feature with a given signal-noise ratio, up to three orders of magnitude at shorter wavelengths.

4.2.3.2. In-Line Holography With the term in-line holography, we mean all the techniques based on the interference buildup due to simple propagation in free space. If we start from the transmission function, which gives the field amplitude just after the object, the field f_z at the image plane

after a distance z from the object is given by the Fresnel integral:

$$f_z(x, y) = \frac{i \cdot e^{ikz}}{\lambda z} \int q(X, Y) e^{i\pi\{(x-X)^2+(y-Y)^2\}/\lambda z} dX dY$$

where coordinates X, Y refer to the object plane and x, y to the image plane.

Everything can then be developed in Fourier space, but we do not want to go further in mathematical description. The physical meaning is that, because of Fresnel diffraction, an interference field builds up, caused by the superposition of diffracted waves and a reference wave constituted by the direct field not affected by the object to visualize. This type of holography can be implemented both in the soft [84] and in the hard [85–87] X-ray regions and also with laboratory sources [82, 84]. Both a plane wave [84–86] and a spherical wave [11, 87, 88] can be used, the key point being their degree of coherence. In the first case, there is no magnification, therefore, often, the detector limits the spatial resolution, which, at best, is of the order of 1 micron; in the second case (projection mode), a magnified image of the sample is produced, and better resolution can be obtained.

In holography, three regions can be distinguished: the near field, the Fresnel (or intermediate) field regime, and the far field [11, 89]. To be in one or another region (whose borderlines are only qualitatively defined) depends on the relative magnitude of the defocus distance D and a length scale defined as $D_F = d^2/\lambda$, where λ is the wavelength and d is the linear size of the object under illumination. The defocus distance, however, has a different definition for holography with plane waves or with spherical waves. In illumination with plane waves, the defocus distance $D_{p.w.}$ is just the sample–detector distance D_2 (Fig. 22). Only for $D_2 = D_{p.w.} = 0$, the image is completely free from phase contrast effects. With spherical waves, the defocus distance $D_{s.w.} = D_1 * D_2 / (D_1 + D_2)$. Note that $D_{s.w.}$ approaches $D_{p.w.}$ for $D_1 \gg D_2$. With this in mind, we can describe the effects that arise in the different regions with an unified treatment where the only variable is the defocus distance. In the near-field regime $D \ll D_F$, and the contrast is proportional to

the second derivative of the phase. The contrast is, therefore, particularly enhanced at the edges, while slowly varying phases do not produce practically detectable contrast. A sharp edge is imaged in the near-field with a characteristic black–white fringe. The contrast also is proportional to D , but quite soon, the image becomes more complex entering in the intermediate regime. It also is worth to point out that λ in this regime acts only as a multiplicative factor in the intensity but not in the structure of the fringes [11, 88]. Therefore, polychromatic sources also can be used, and the image contrast will result, in this case, from a weighted sum of the incident spectrum. The image in the near-field regime closely resembles the object, but, to quantitatively determine a projected density, a phase reconstruction process must be carried out. In the approximation of a thin, homogeneous sample, the phase reconstruction can be carried out by using a single defocused image [90]. Figure 23 shows a phase contrast image of latex spheres (a) and the phase retrieved projected density (b) [11]. In the Fresnel region ($D \approx D_F$), a more complex system of fringes set up. In [84], is shown an example of a hologram taken in the soft X-ray region ($\lambda = 2.4$ nm) of zymogen granules, together with its reconstructed image obtained through a computer simulation of the illumination of the hologram with the original reference wave. By using spherical waves and the projection mode, spatial resolution able to visualize nanostructures can be attained. As an example, Figure 24 shows a phase contrast of a gold test pattern on a Si nitride mask 0.3μ wide taken with the X-ray waveguide [87], which provides a highly coherent beam, very well approximated, in the vertical plane, by a spherical wave. Three images are shown for different values of D_1 and different defocus distances and magnifications. Note how the fringes change from one image to the other, and note also how the defect in alignment, barely visible in the SEM image taken at low resolution, is very clearly seen in the X-ray images. The spatial resolution was determined in this case by simulation and resulted to be in the order of 100 nm, mainly due to a nonideal experimental apparatus. This experiment made use of a planar waveguide (see Section 3.5), which has a strong drawback to allow magnification only in one direction (in the cited example, the vertical one). It has been demonstrated that resonance conditions also can be reached in a two-dimensional waveguide [60], providing a coherent point source in the nanometer range. Its implementation as a very powerful projection microscope is in progress. In the Fresnel region, the phase retrieval procedure is much more complex than in the near field. Several algorithms have been proposed to achieve quantitative information. The one developed by Coene et al. [91] needs at least two images of the same object taken at different defocus distances (however, in general, more than two images are taken at different distances to improve the reliability of the phase retrieval). This phase retrieval procedure also can be used in tomography to get a three-dimensional (3-D) image of the sample. An example of such reconstruction in three dimensions will be presented later, when discussing tomography.

The last regime of phase contrast, the far-field or Fraunhofer regime, is that commonly accessed in Bragg diffraction, where constructive interference of atoms give rise to strong peaks. The far-field regime is now of great interest

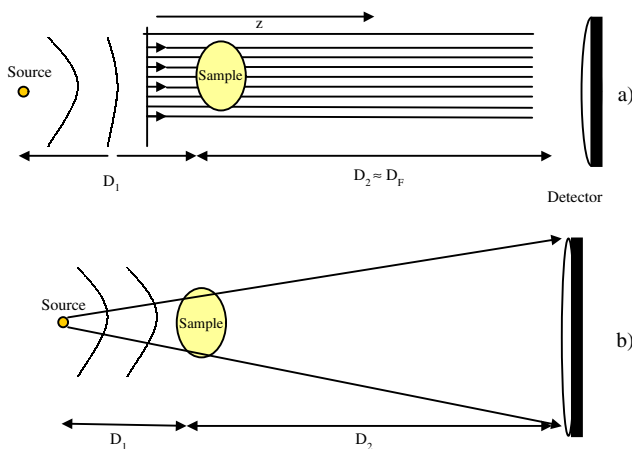


Figure 22. Schematic view of the in-line holography with (a) a plane wave and with (b) spherical wave illumination. The defocus distance in the first case is $D \approx D_F$, in the second case, is $D_{s.w.} = D_1 * D_2 / (D_1 + D_2)$.

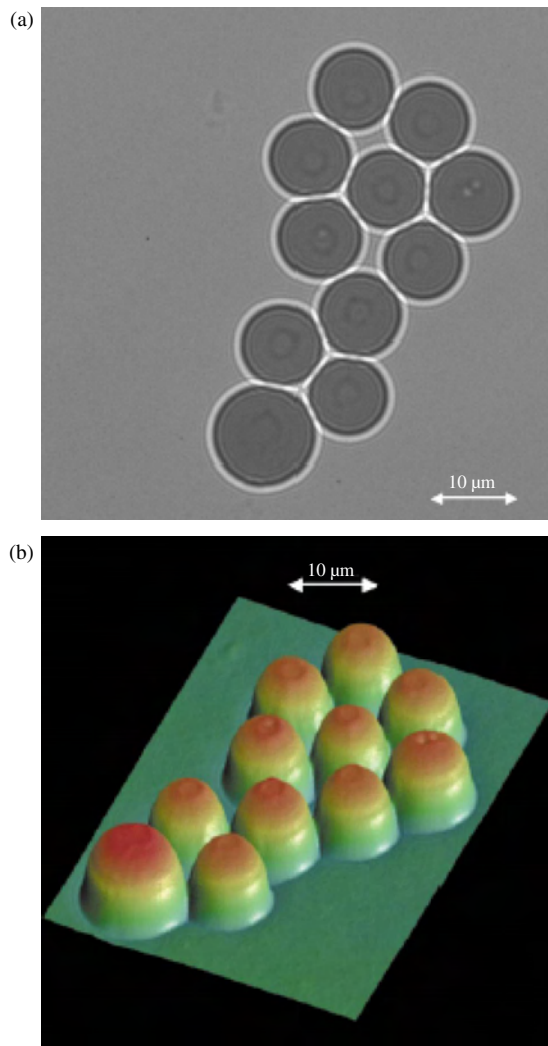


Figure 23. a) Images of a cluster of $\approx 9 \mu$ latex spheres taken with a projection microscope obtained by a modified SEM. Ta target with 15 keV excitation voltage so that the main X-ray energy corresponds to the $\text{TaM}\alpha$ lines at 1.7 keV. Distance electron beam focus sample = 933μ . Both phase and absorption contrast effects are visible. b) projected density of a) obtained by phase-retrieval method. Reprinted with permission from [11], S. C. Mayo et al., *J. Microscopy* 207, 79 (2002). © 2002, Elsevier.

because analysis of Fraunhofer diffraction from single, non-periodic objects could lead to significant improvements in spatial resolution. We will discuss more deeply this subject in the section dedicated to nanodiffraction. It is interesting to note how the borders between microscopy and diffraction lose their rigid character, and the two apparently different methods approach each other to become the expression of the same physical effect.

4.2.3.3. Differential Interference Contrast In this recently developed method [80], interference is created by superposition of two images of the same object created by a zone plate doublet composed by two zone plates very slightly displaced, one with respect to the other. The displacement along the optical axis must be much smaller than the image distance. The lateral displacement must be smaller or of the

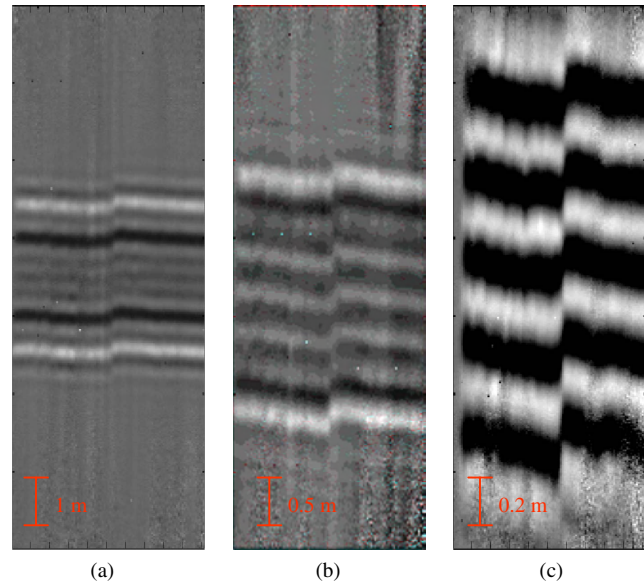


Figure 24. Phase contrast images of a gold test pattern taken with the X-ray waveguide at three different magnifications. Energy ≈ 13 keV. Note the different fringe patterns for the three magnifications and the jump due to a fabrication defect.

same order of the outermost zone width. The superposition of the two images gives rise to a pattern consisting of linear fringes with spacing $s = \lambda A/a$, where A is the distance of their back focal planes to the detector, and a is the lateral displacement of the two zone plates. [80]. Images of low-absorbing nanostructures show impressive improvement of contrast with respect to standard zone plates.

4.2.3.4. Analyzer Crystal Analyzer crystals in Bragg diffraction after transmission of the beam through the specimen can be used for two purposes: magnification of the image or detection of small angular deviations. The first case has been mentioned in a previous paragraph with the term Bragg magnifier. As sketched in Figure 20, the incoming beam impinges on the analyzer crystal at a very grazing incident, while the diffracted beam leaves the crystal at a much larger angle. From dynamical diffraction theory [70], the angular acceptance in the grazing angle incidence is quite large, therefore, small deviations of the incoming beam are accepted. This means that the phase contrast present in the magnified images is due essentially to the same mechanism of the in-line holography discussed earlier [92].

If small deviations of the incoming X-ray beam due to sharp variations of phase have to be detected, a geometry with a less grazing incident beam, or even an asymmetry geometry with the incoming beam at a larger angle with the crystal surface than the diffracted beam must be adopted. As a consequence, the acceptance is much narrower, and, at a certain Bragg angle, the deviated beams are not at all diffracted, while, for a slightly different angular position, only the deviated beams are visible. This is the basis of diffraction enhanced imaging [93, 94]. However this technique, because of the lack of large magnification factors, has the spatial resolution limited by the detector resolution (about 1μ).

4.2.4. Fluorescence Microscopy

One of the most useful and exploited properties of X-rays is its ability to excite fluorescence radiation characteristic of the element probed and, therefore, carry out a nondestructive chemical characterization of materials. The basic mechanism has been illustrated in Section 1. A chemical mapping of the sample, therefore, can be obtained by simply focusing the X-ray beam with some optics (zone plates, refractive lenses, Kirkpatrick and Baez mirrors, waveguides, etc.) and then measuring an X-ray fluorescence spectrum (or a portion of it), while scanning the sample in front of the beam. An interesting example [95] has been obtained at ESRF (ID22) on single human ovarian adenocarcinoma (IGROV1) cell treated with $5 \mu\text{M}$ of iododoxorubicin. The contour map of the treated freeze-dried cancer cell was mapped with a 14 keV polychromatic “pink” excitation. The spatial resolution is essentially that of the optical element used, while the spectral resolution is dictated by the fluorescence detector. The natural evolution of X-ray fluorescence analysis is on one side spectromicroscopy, on the other side, fluorescence tomography. Examples in both fields are given in the following Sections.

4.2.5. Spectromicroscopy

In spectromicroscopy, the chemical mapping is not obtained by measuring fluorescence radiation but rather using the large absorption coefficient changes that occur at the absorption edges of elements. Chemical sensitivity is then obtained, recording images with a scanning or a full-field microscope at a number of different energies appropriately selected to differentiate the chemical components of the system. Each image pixel provides a certain absorption spectrum, which is the weighted sum of the absorption spectra of the different components. The entire image sequence can then provide, after careful analysis, the chemical composition at each sample location, or, conversely, the spatial distribution of each element, with the accuracy of the optical system in use [96], which can be as good as a few tens of nanometers. If a single element has to be put in evidence, subsequent acquisition of two images, one just before and one just after the absorption edge of the element, followed by digital subtraction of the two images, can strongly enhance the contrast and give a clear picture of the spatial distribution of that particular element. Applications of spectromicroscopy span in many fields, e.g., bioscience, material science, environmental science, cultural heritage, etc. Many examples can be found in [4]. Here, we just mention studies of protein adsorption sites on polymers [96] and studies on variations of cross-linking of gels [97]. A very interesting feature of X-ray spectromicroscopy is that it is not only sensitive to chemical composition but also to the chemical environment (valence state) [98]. This comes from the fact that different chemical states can change the energy position of the absorption edge. If images are recorded through an absorption edge with sufficient energy resolution, fine changes in the spectrum can give precise information about the speciation of the chemical components and their spatial distribution in a nondestructive way and under different environmental conditions. This is perhaps one of the most

powerful and unique features of X-ray microscopy. Again, interested readers can find many examples in [4].

4.2.6. Tomography

Up to now, we have considered the sample as a thin slab, and the density information was limited to an x, y plane. However, samples of interest are often three dimensional, and the full object reconstruction is, in many cases, the final goal. Soft X-rays are limited in this respect because their penetration in most materials is very shallow. Hard X-rays are, therefore, needed, and it is not by chance that X-ray microtomography has been developed mainly in these last years, where third generation hard X-ray S.R. sources like ESRF in Europe, APS in the United States, and Spring8 in Japan became operative.

In X-ray microtomography, absorption images are taken for many different angular positions of the samples around an axis perpendicular to the X-ray beam propagation direction, and the images are then computer processed to reconstruct the 3-D object density distribution. To have reliable results, a complete rotation of 360° should be accomplished in steps as small as fractions of a degree. The simplest way is to use a collimated beam and plane waves, but the resolution, is in this case, limited by the detector to $\approx 1 \mu$. To have better spatial resolution, either focusing optics or a projection geometry can be used. With focusing optics, care must be taken that the sample thickness be smaller than the depth of focus. Another critical aspect for resolution is the mechanical perfection of the rotation axis: wobbles during rotation can introduce severe artifacts and difficulties with proper reconstruction. Tomography can be done with high resolution even with table-top laboratory sources now commercially available. In some cases, even tomography at 80-nm resolution on microelectronics integrated circuits (IC) is claimed. Very recent extensions of tomography rely on the possibility to reconstruct the object following its chemical composition (fluotomography) or recording phase contrast images (holotomography). In fluotomography, sections of the samples are taken, measuring the fluorescence spectrum for each section and for each beam position. Difficulties in subsequent analysis are related to the fact that absorption coefficient of both the primary radiation and of fluorescence radiation depends strongly on density distribution, which is the unknown to be found. Special algorithms must, therefore, be developed in order to reliably reconstruct the 3-D composition [99, 100].

A similar problem is encountered in holotomography, where the spatial distribution of the phase and of the absorption coefficient must be reconstructed in 3-D, and, therefore, reconstruction procedures must be followed [101–103]. The phase reconstruction algorithm proposed by Cloetens et al. [103] uses three different distances for each phase-contrast image to reconstruct the phase for a single section. This procedure must then be repeated for all the sections. The advantage of holotomography with respect to tomography based exclusively on absorption is that 3-D structures of light materials can be reconstructed. Remarkable examples can be found in the literature. For example, 3-D reconstruction of a polystyrene foam fragment showing the internal structure of the cell can be found in [102].

4.2.7. X-Ray Photoelectron Microscopy

With an SXM, instead of measuring the transmitted intensity or the fluorescence, photoelectrons generated by the focused X-ray beam can be detected by suitable electron detectors, allowing accurate spectroscopic information related to composition and electronic state.

Alternatively, the sample can be illuminated uniformly by the X-ray beam without any X-ray optics, and the photoelectrons then are detected through a suitable electron optics, which raster the sample at high-spatial resolution. This last can reach even values as high as tens of nm. In both cases, a high vacuum environment is required, and only a thin surface layer is probed. Moreover, if artifacts are to be negligible, flat and slightly conductive samples must be used.

Very interesting applications recently have been implemented with this technique in the study of carbon nanotubes [104]. The electronic structure of multiwalled carbon nanotubes has been studied with a spatial resolution of the order of 90 nm with a scanning photoelectron microscope (SPEM) at the Elettra S.R. light source in Trieste (Italy). The microscope is equipped with FZPs and a hemispherical electron analyzer and can work both in spectroscopy mode and in imaging mode. The carbon nanotubes were aligned perpendicularly on a Si substrate. The SEM measurements and SPEM analysis were made on cross sections obtained by cleavage. Figure 25 shows a SEM micrograph. The valence band and the C1s spectra were measured with SPEM on spatially selected regions along the tube axes. The valence band spectra and the C1s photoelectron spectromicroscopy image are presented, respectively, in Figure 26a and b. The locations where the valence band spectra were measured are indicated in the spectromicroscopy image. It clearly appears that valence band spectra from the tips of the nanotubes have a substantially larger spectral intensity in the energy range about 1 eV below the Fermi edge with respect to spectra taken from the nanotube sidewalls. Taking into account a number of considerations not reported here, the authors interpret these results, assuming a higher density of dangling bonds at the spherically curved tips with respect to the defective density at the cylindrically curved sidewalls.

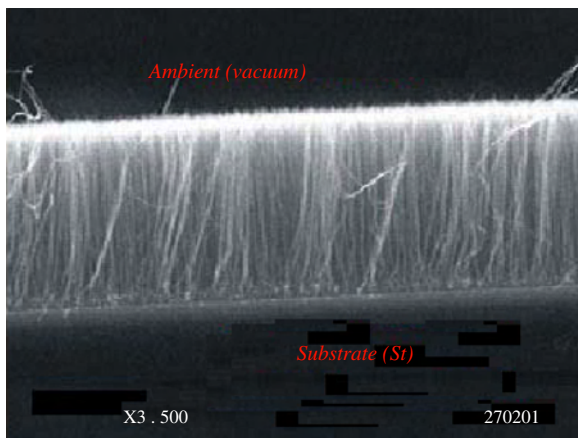


Figure 25. Scanning electron microscopy of a cross section of the aligned multiwall carbon nanotubes. (Courtesy of S. Suzuki).

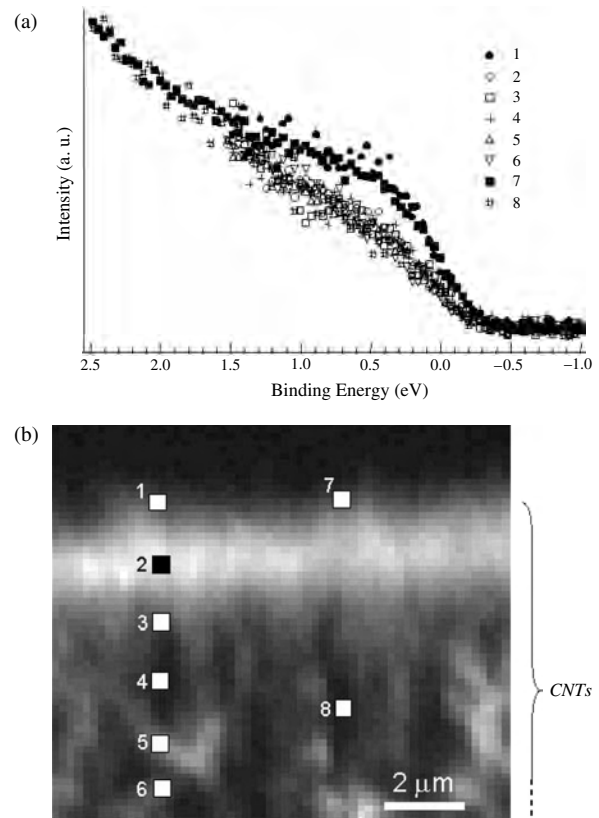


Figure 26. a) Valence band photoemission spectra in the vicinity of the Fermi level from spatially selected regions. b) C1s photoelectron spectromicroscopy image, where locations of the measurements are indicated by white spots. Note the difference of spectra taken in the 1 and 7 positions with respect to the other locations, indicating a larger spectral intensity about 1 eV below the Fermi edge. (Courtesy of S. Suzuki).

This example illustrates well the potentiality of a technique that combines high spatial resolution with spectroscopic capabilities.

5. X-RAY NANODIFFRACTION

The wavelength of hard X-rays ($\lambda \approx 0.1$ nm) is close to the interplanar spacings of crystalline materials. As already mentioned in Section 1, this allows the study of structural properties through Bragg diffraction. In nonhomogeneous samples, or in samples subjected to nonuniform stress, it can be of high interest to probe the local structural properties with high spatial resolution. This can be particularly important in interface problems or in ultra large scale integration (ULSI), where reduction of critical dimensions down to the order of 0.1μ and correlated technological steps can introduce unwanted strain field deleterious for device performance. Emerging nanotechnologies also requires development and improvement of structural microprobes. Since nanodiffraction requires hard X-rays, optics such as Kirkpatrick and Baez mirrors [17], waveguides [18], refractive lenses [16], and FZP are used. Tapered capillaries also are used, but for resolutions not better than 1μ , and we will not treat them here.

5.1. Monochromatic Beam

We first discuss Bragg nanodiffraction applications, which use a monochromatic beam. Examples with waveguides, FZP and mirrors will be reported.

5.1.1. Waveguides

As already mentioned, planar waveguides compress an incident X-ray beam of several tens of microns, reducing one of its dimensions of three orders of magnitude. A narrow line beam of a few tens of nanometers is thus produced. The beam is highly coherent and has a divergence of about 1 mrad. In the phase-contrast paragraph, we presented examples of high-resolution phase-contrast images obtained with this optics. We will discuss its application in nanodiffraction and, in particular, in studies of local strain measurements. To have high strain sensitivity, a high angular resolution is needed, which is incompatible with high angular divergence. However, significant angular divergence is only in the plane of compression (i.e., the vertical one) and the horizontal high collimation of the S.R. source is left unmodified by the waveguide. We now describe in some detail, a nanodiffraction experiment aimed at measuring local strain in Si substrate due to SiO₂ isolation micropatterning. Let the sample coordinates be x , y , and z , with the xy plane coinciding with sample surface, x in the vertical direction, y in the horizontal one, and z perpendicular to the surface (Fig. 27). The diffracting plane is yz , and the high spatial resolution of the Waveguide is along x . The projected beam size on the sample surface along y depend on the horizontal slit aperture and the Bragg angle. For typical incident beam size of $50 \times 50 \mu^2$ and Bragg angle of 20° [Si(400) reflection at 13 keV photon energy], the projected beam size along y is of the order of 150μ . Along x , the beam size depends strongly on the distance D_1 between the waveguide exit and the sample. Due to divergence, the

beam size increases about 0.1μ every 100μ of increasing distance. With such conditions, two modes of operation are possible: the projected mode and the scanning mode. The projected mode is very similar in concept to the projection microscopy as illustrated, with the only difference being that the two-dimensional detector will record the image of the diffracted beam instead of the image of the transmitted one. As in microscopy the magnification M is given by the ratio $M = (D_1 + D_2)/D_1$, where D_1 and D_2 are, respectively, the waveguide sample and the sample–detector distances. The projection mode relies on the coherence properties of the beam and requires a two-dimensional detector whose pixel size P is correlated to the spatial resolution r through the simple relation: $r = P/M$.

In the scanning mode, instead, the sample is simply scanned in front of the waveguide exit and diffracted intensities are recorded for each sample position by a standard detector (e.g., scintillator). In this case, the spatial resolution is given by the vertical beam size on the sample, which critically depends on distance D_1 due to the beam divergence. Both operation modes have been implemented. The samples consisted of narrow stripes aligned along y . In the first studies, LOCOS (local oxidation of silicon) SiO₂ stripes were analyzed, successively shallow trench isolation (STI) structures, more convenient for high-density packaging, were studied. Strain was measured by recording the diffracted intensity as a function of deviation from the Bragg angle [known as a rocking curve (R.C.) or diffraction profile]. The R.C. of a perfect crystal is the convolution of the theoretical Darwin reflectivity, with the instrumental function, which takes into account energy spread, incident beam divergence, reflectivity of a monochromator if any, etc. [70]. A strained lattice will give a R.C. with enhanced intensity or even additional peaks on the low-angle side of the Bragg peak if the strain is tensile (higher lattice parameter) or in the high-angle side in the case of a compressive strain. With our geometry (symmetric reflection), the ε_{zz} component of the matrix strain along the surface perpendicular has been probed. The spatial localization of strain is straightforward in the case of the scanning mode: a R.C. is recorded for each spatial position of the sample in a vertical scan, and strain information are extracted, analyzing the individual R.C. In the case of projection geometry, the diffracted intensity is recorded on a two-dimensional detector for each angular position of the sample during a R.C., then the images are analyzed to extract a diffraction profile for each vertical small portion of the sample within the allowable spatial resolution. In both cases, a number of diffraction profiles must be analyzed. In the analysis, the penetration of X-rays into the crystal must be taken into account. The diffraction profiles, therefore, reflect a strain information integrated in depth, and a strain depth profile should be obtained eventually. To do this, an analysis based on dynamical diffraction theory for deformed crystals [105, 106] has been carried out, which ideally divides the crystal into thin layers, each with its own strain value. The integrated strain in a LOCOS structure about 5μ wide and another about 1μ wide are presented in Figure 28, while Figure 29 reports the strain depth profile distribution for three locations a distance 100 nm from each other in the narrow structure [107]. These measurements were carried

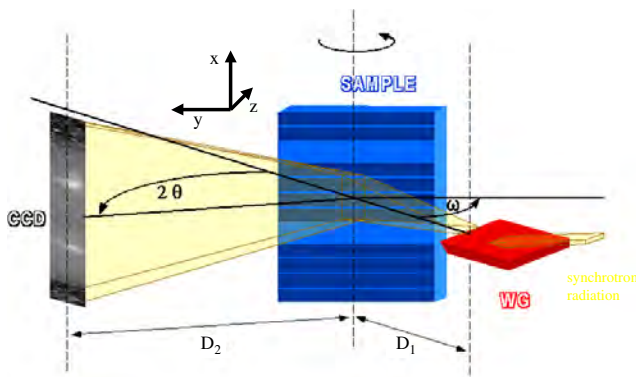


Figure 27. Schematic arrangement of X-ray microdiffraction with the waveguide in the projection geometry. The coherent beam from the waveguide impinges on the sample surface at an incident angle ω and is diffracted at an angle 2θ . The divergence in the vertical plane allows a magnification M given by $(D_2 + D_1)/D_1 \approx D_2/D_1$. The oxide stripes lying in the plane xy can be analyzed with high spatial resolution along x . Diffraction takes place in the horizontal plane where collimation of S.R. beam allows high angular resolution. The diffracted beam is imaged on the CCD detector for each angular position of the rocking curve (see text). (Reprinted with permission from [106], S. Di Fonzo et al., *Nature* 403, 638 (2000). © 2000, Macmillan Magazines Ltd.

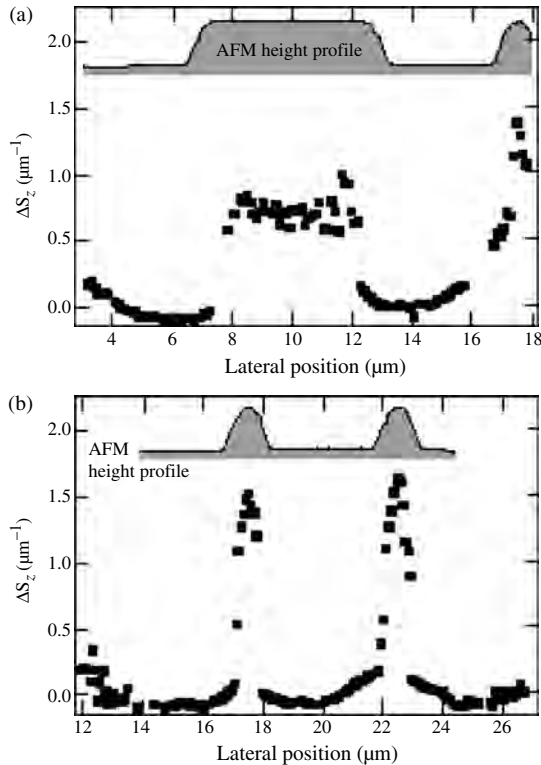


Figure 28. Spatial variation of depth-integrated strain under SiO_2 stripes of different widths w : a) $w \approx 5 \mu\text{m}$, b) $w \approx 1 \mu\text{m}$. Strain is indicated by the length of the variation of reciprocal space vector with respect to the undeformed substrate. Both in a) and b), an inset shows an atomic force microscopy height profile of the Si-oxide structures. Reprinted with permission from [106], S. Di Fonzo et al., *Nature* 403, 638 (2000). © 2000, Macmillan Magazines Ltd.

out in the projection mode. A narrow ($0.2 \mu\text{m}$) STI structure also was measured in the scanning mode. In this case, the spatial resolution was of the same order of magnitude of the structure, therefore, a single R.C. centered on the structure described its strain. A few words about the complexity of measurements and the comparison between projected and scanning modes: a key point to preserve spatial resolution is the proper alignment between a waveguide beam and

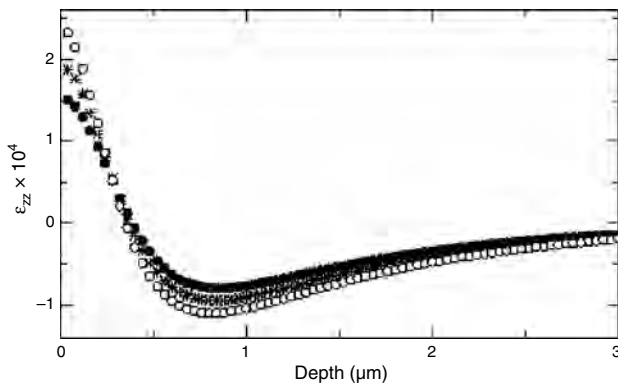


Figure 29. Strain depth profile for three adjacent lateral positions along x (see Fig. 29), distant 100 nm from each other in the $1 \mu\text{m}$ wide SiO_2 stripe of Figure 34. (Reprinted with permission from [106], S. Di Fonzo et al., *Nature* 403, 638 (2000). © 2000, Macmillan Magazines Ltd.

stripes along the y direction. A slight misalignment (typically larger than 1 mrad) could seriously deteriorate spatial resolution. The projected mode deserves, in principle (and also in practice), better spatial resolution. Distance D_1 is not so critical for resolution and values around few mm are acceptable. However, it requires higher brilliant sources and sensitive two-dimensional detectors. Scanning mode is less demanding on this point of view, but, on the counterside, the distance D_1 is much more critical and cannot be larger than a few tens of microns if high spatial resolution is desired. Anyway, in case of polycrystalline materials, the projection mode cannot be applied. We, therefore, used the scanning mode in studies of biomaterials where the aim was to study bone reconstruction at the interface with a Zr orthopedic prosthesis covered with bioglass. Interesting results about structural differences between native bone and bone reconstructed at the interface were found [108].

The method applied in biomaterials can also be applied to study single fibers. In particular, local studies on single cellulose fibers have shown the additional information that can be extracted by using micro- and nanodiffraction, with respect to other conventional techniques like electron microscopy.

Cellulose molecules aggregate, forming small crystals called microfibrils (a few nm in diameter). The arrangement of the microfibrils in single fibers (average diameter $20 \mu\text{m}$) is of great variability, and the main interest concerns the disorder, both inside the microfibrils and in their arrangement in the fiber. In each fibrils of a Kevlar fiber, the polymer chains form hydrogen-bonded sheets. A nanodiffraction experiment [109] on a single Kevlar fiber showed that the sheets present a radial organization around the fiber axis and form pleats along the fiber axis, with a periodicity of $0.5 \mu\text{m}$ and an angle of 170° between neighboring pleats.

The method described can be applied virtually to any monocrystalline or polycrystalline material, including hard and soft condensed matter. In particular, microdiffraction with waveguides is of particular interest where interface problems are of relevance, such as coatings, damaged surface layers, etc.

5.1.2. Zone Plates

An interesting experiment that studied local strain at grain boundaries in colossal magnetoresistive films by using a microbeam generated by a phase zone plate can be found in [110]. The measurements, taken at a spatial resolution of about $0.35 \mu\text{m}$, show that strain relaxation takes place at the grain boundaries, yielding a lattice constant different from that at the interior of the grain, thus supporting magnetic measurement results. Other microdiffraction experiment using zone plates were carried out on Cu interconnects where EM can have deleterious effects on device performance. The measurements, carried out with $0.2 \mu\text{m}$ spatial resolution, aimed at study strain close to the voids and hillocks created by EM. A strong influence of Ti adhesion layer on the Cu microstructure has been put in evidence [111].

5.2. White Beam

A completely different approach has been followed by Larson and coworkers [112]. They used a submicrometer white beam produced by Kirkpatrick and Baez mirrors

to generate a Laue (i.e., transmitted) diffraction pattern from the sample (either a polycrystalline or a monocrystalline one) recorded by a two-dimensional detector. With a white beam, many reflections are excited simultaneously, and the complex pattern is computer analyzed to determine Miller indices of reflections, crystallographic orientation, and stress/strain tensor [113]. To obtain high spatial resolution, a Pt wire $50\ \mu$ thick is scanned in front of the sample at a distance $D_{Pt} \ll D_D$, where D_D is the wire-detector distance. The wire is stepped in submicrometer steps, and at each step the pattern is recorded. The difference between two successive steps allows correlation of the individual CCD pixel to the element volume that contributed to this pixel differential intensity. The entire ensemble of the differential intensities allows reconstruction of the map of the individual volumes, which, along the path of the beam, gives rise to the Laue diffraction pattern. The method has been applied to analysis of hot-rolled Al alloy, giving quantitative information about grain sizes and inter and intragranular rotations. In the case of a cylindrically bent Si crystal, it provides depth-resolved measurement of elastic strain tensor.

White beam also is used in another recently developed technique, which allows tracking of individual nanocrystals by using diffracted X-rays (diffracted X-ray tracking [DXT] [114]. With this method, it has been possible to follow the dynamics of single DNA molecules [115]. The principle is the following: artificial nanoparticles, consisting of a Si-Mo multilayer were fabricated by using deposition techniques and reactive ion etching to reduce the lateral dimensions of the nanocrystals to about 30 nm [114]. The nanoparticles, dispersed in a gel, were illuminated with collimated white X-rays and diffracted spots from individual nanocrystals were imaged with a CCD camera. The rotational movements of the nanoparticles were then monitored following the displacement of the diffracted spots. In this way, the viscosity of supercooled liquid water at atmospheric pressure could be determined [114]. Even more interesting, single DNA molecules were attached to the nanocrystals, as depicted in Figure 30. In this way, the rotational motion (α and β degrees of freedom, see Fig. 30) of the DNA molecule could be monitored [115]; α corresponds to angular displacement ϑ , and β to angular displacement ω of the diffracted spots. By following the displacement of several diffracted spots, the investigators were able to conclude that the main motion was the α rotation, while the β movement was not detected and determined both the diffusion coefficient and the drift velocity of the nanoparticles. These two parameters essentially characterize the nature of the Brownian motion. It is expected that this technique can, in the future, give important information about biological processes in living cells.

5.3. Diffraction Microscopy

A new field “diffraction microscopy” is now emerging where far-field diffraction of nonperiodic objects are analyzed to reach the ultimate resolution limit in X-ray imaging. The starting point is the oversampling concept [116]. In Bragg diffraction from a periodic array, strong Bragg peaks are generated where constructive interference takes place, while destructive interference keeps intensity at very low levels in

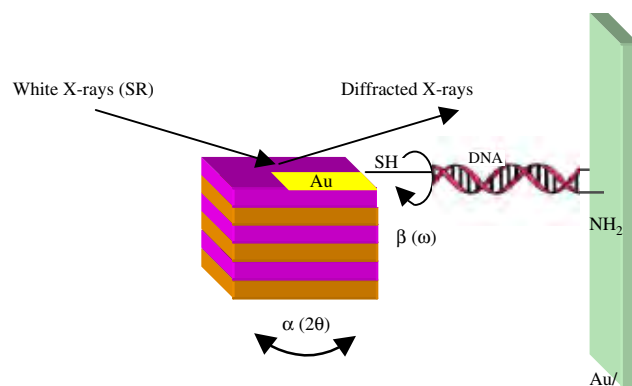


Figure 30. i) Schematic drawing of the diffracted X-ray tracking (DXT) method to detect motion of single DNA molecule in aqueous solution. The DXT traces the displacement of the single diffracted X-ray spot from the one-dimensional artificial Si-Mo nanocrystal, which is linked to the single DNA molecule. The diameters of the nanocrystal is about 30 nm and that of the DNA molecule, 2.5–3 nm. In the figure, the two rotational degrees of freedom α and β of the DNA molecule are indicated, corresponding, respectively, to angular displacements ϑ and ω of the diffracted spots. ii) The nanocrystals physically adsorbed on the Au-quartz substrate are used as a calibration of the system stability. iii) When the direction of the stacking period of the Si-Mo nanocrystals is parallel to the substrate, the diffraction spots cannot be monitored.

between the peaks. When crystal dimensions become smaller and smaller, the Bragg peaks become broader and broader and increasing intensity is found on Bragg peak tails. At the limit of nonperiodic objects, a continuous diffraction pattern is generated if the specimen is illuminated with coherent light. This continuous pattern can be sampled at frequencies finer than the Nyquist frequency, which corresponds to the inverse of the specimen size. At sufficiently small frequency, the phase can be retrieved by using an iterative algorithm [117, 118]. Experiments were carried out both in the soft [119] and in the hard X-ray region spectra [117, 120]. In [117], the experiment, which reached the record spatial resolution of 8 nm, was carried out at a wavelength of 0.2 nm (corresponding to an energy of about 6 keV) at the Spring-8 synchrotron light source in Japan. The sample, fabricated by electron beam lithography, consisted of two identical single-layered Ni nanostructure patterns separated by $1\ \mu$ in depth and rotated each other by 65° in plane. While in the SEM micrograph, only the upper pattern is visible, due to the small depth of focus of electron microscopy, the X-rays are capable of providing both the top and the bottom patterns, after reconstruction from the diffraction pattern. The microradiograph has a spatial resolution of 8 nm, but the two patterns are overlapped. Three-dimensional reconstruction also was carried out from a limited number (31) of two-dimensional diffraction patterns recorded at different angular setting of the sample from -75° to 75° in 5° steps. However, the spatial resolution of the 3-D reconstruction was of the order of 50 nm. The example reported here shows clearly the potentiality of the method that has, with respect to other forms of microscopy, the advantage of a higher penetration depth, which allows the nondestructive 3-D reconstruction. It is self-evident that this technique can give important contributions to biological

science where whole cells could be imaged at high resolution and in the nanoscience field, where, in principle, nano-dimensional structures could be imaged nondestructively in three dimensions at atomic resolution.

6. CONCLUSIONS

In this discussions, we have tried to give an idea about the state of the art of a research field that, though it has its origins at the beginning of last century, only in these last years started to show all its potentialities. In this respect, a virtuous circle has been set up: the big progress in S.R. pushed for the development in X-ray optics, which now leads to routine experiments in the nanometer range. On the other hand, the achievements reached in this field also pushed researchers to develop powerful and more brilliant laboratory sources that now can profit from the new X-ray optics available to reach deep submicrometer spatial resolution. We, therefore, look forward to more and more achievements and expansion of this field. In particular, X-ray microscopy and nanodiffraction will certainly be able to give significant contributions to nanoscience and nanotechnology. A new frontier is at the horizon: 4th generation S.R. sources such as the free electron lasers with pulses as short as a few tens of femtoseconds and peak brilliances 10 orders of magnitude higher than the present most powerful sources, are now under construction or are planned. The astonishing properties of these new radiation sources will literally open a new world (that of extremely short probes with extremely high brilliance), where experiments that are now impossible will become feasible. Fantasy at work.

GLOSSARY

Absorption contrast The contrast in X-ray radiography and microscopy due to spatial variations in the sample of the *imaginary* part of the refractive index, which causes *intensity* modifications of the transmitted wavefield.

Coherence Property of an electromagnetic field to maintain a specific relation of phase into a given spatial and temporal interval.

Coherence length The extension of the spatial region where the X-ray beam can be considered as coherent.

Coherent diffraction Diffraction from sampled regions smaller than the coherence length of the incoming X-ray beam.

Phase contrast The contrast in X-ray radiography and microscopy due to spatial variations in the sample of the *real* part of the refractive index, which causes *phase* modifications of the transmitted wavefield.

X-ray fluorescence microscopy X-ray microscopy technique based on the excitation of fluorescence radiation. Each element has characteristic fluorescence lines differing by their energies.

X-ray photoelectron microscopy X-ray microscopy technique based on the analysis of photoelectrons generated by the incoming X-ray beam.

X-ray spectromicroscopy X-ray microscopy technique based on the large variations of absorption coefficients at

absorption edges of the constituent elements. Requires image acquisition at different energies of the incoming X-ray beam.

X-ray tomography Three-dimensional reconstruction of the sampled volume obtained with a large number of radiographies, both in absorption or in phase contrast mode, taken at different orientation of the sample with respect to the incoming X-ray beam.

REFERENCES

1. G. Schmahl and P. Cheng, in "Handbook on Synchrotron Radiation" (S. Ebashi, M. Koch, and E. Rubenstein, Eds.), Vol 4. Elsevier Science, North-Holland, 1991.
2. D. Sayre and H. N. Chapman, *Acta Crystallogr. A* 51, 237 (1995).
3. R. Fitzgerald, *Phys. Today* 23 (2000).
4. (A. Meyer-Ilse, T. Warwick, and D. Attwood, Eds.). Proceedings of the Sixth International Conference on X-ray Microscopy, Vol. 507. 2000.
5. "Neutron and synchrotron radiation for condensed matter studies" (Hercules) (J. Baruchel, J. I. Hodeau, M. S. Lehmann, J. R. Regnard, and C. Schlenker, Eds.), Vol. 1. Les editions de Physique, Les Ulis Cedex A, France and Springer Verlag, Berlin-Heidelberg, 1993.
6. International tables for X-ray crystallography, eds. Intern. Union of Cryst. Kynoch Press, Birmingham, 1968.
7. L. G. Parrat, *Phys. Rev.* 95, 359 (1954).
8. M. Born and E. Wolf, "Principles of Optics." 6th ed. Pergamon, Oxford, 1980.
9. J. M. Cowley, "Diffraction Physics." North Holland, Amsterdam, 1975.
10. W. L. Bragg, *Proc. Cambridge Philos. Soc.* 17, 43 (1913).
11. S. C. Mayo, P. R. Miller, S. W. Wilkins, T. J. Davis, D. Gao, T. E. Guneyev, D. Paganin, J. Parry, A. Pogany, and A. W. Stevenson, *J. Microscopy* 207, 79 (2002).
12. L. Rymell and H. M. Hertz, *Opt. Commun.* 103, 105 (1993).
13. L. Malmqvist, L. Rymell, M. Berglund, and H. M. Hertz, *Rev. Sci. Instrum.* 67, 4150 (1996).
14. E. Anderson and D. Kern, in "X-Ray Microscopy" (A. G. Michette, G. R. Morrison, and C. J. Buckley Eds.), p. 75. Spring, Berlin, 1990.
15. V. Aristov, A. Snigirev, Y. A. Basov, and A. Y. Nikulin, *AIP Conf. Proc.* 147, 253 (1986).
16. A. Snigirev, V. Kohn, I. Snigireva, and B. Lengeler, *Nature (London)* 384, 49 (1996).
17. P. Kirkpatrick and A. V. Baez, *J. Opt. Soc. Am.* 38, 766 (1948).
18. S. Lagomarsino, W. Jark, S. Di Fonzo, A. Cedola, B. Muller, P. Engstrom, and C. Riekkel, *J. Appl. Phys.* 79, 4471 (1996).
19. R. W. Wood, "Physical Optics," edited by Macmillan, New York, 1914.
20. A. V. Baez, *J. Opt. Soc. Am.* 51, 405 (1961).
21. J. Thieme, in "X-ray Microscopy II" (D. Sayre, M. Howells, J. Kirz, and H. Rarback, Eds.), p. 70. Springer Verlag, Berlin, 1988.
22. O. E. Meyers, *Am. J. Phys* 19, 359 (1951).
23. E. Di Fabrizio, M. Gentili, L. Grella, M. Baciocchi, A. Krasnoperova, F. Cerrina, W. Yun, B. Lai, and E. Gluskin, *J. Vac. Sci. Technol., B* 12, 3979 (1994).
24. B. Lai, W. B. Yun, D. Legnini, Y. Xiao, J. Chrzas, P. J. Viccaro, V. White, S. Bajikar, D. Denton, F. Cerrina, E. Di Fabrizio, M. Gentili, L. Grella, and M. Baciocchi, *Appl. Phys. Lett.* 6116, 1877 (1992).
25. R. O. Tatchyn, "Springer Series in Optical Sciences," Vol. 43, pp. 40–50, Springer, Berlin, 1990.
26. J. Kirz, *J. Opt. Soc. Am.* 64, 301 (1974).
27. W. B. Yun and M. R. Howells, *J. Opt. Soc. Am. A* 4, 34 (1987).

28. D. Rudolph and G. Schmahl, *Ann. N. Y. Acad. Sci.* 342, 94 (1980).
29. Y. Vladimirovsky, E. Kallne, and E. Spiller, *SPIE Proc.* 448, 25 (1984).
30. D. Weiss, M. Peuker, and G. Schneider, *Appl. Phys. Lett.* 72, 1805 (1998).
31. E. Di Fabrizio, F. Romanato, M. Gentili, S. Cabrini, B. Kaulich, J. Susini, and R. Barret, *Nature (London)* 401, 895 (1999).
32. M. Peuker, *Appl. Phys. Lett.* 78, 2208 (2001).
33. C. David, B. Kaulich, R. Barret, M. Salomè, and J. Susini, *Appl. Phys. Lett.* 77, 3851 (2000).
34. S. J. Spector, C. J. Jacobsen, and D. M. Tenant, *J. Vac. Sci. Technol., B* 15, 2872 (1997).
35. C. David, B. Kaulich, R. Medenwaldt, M. Hettwer, N. Fay, M. Diehl, J. Thieme, and G. Schmahl, *J. Vac. Sci. Technol., B* 13, 2762 (1995).
36. E. H. Anderson, V. Boegli, and L. P. Muray, *J. Vac. Sci. Technol., B* 13, 2525 (1995).
37. P. Charalambous, P. Anastasi, R. E. Burge, and K. Popova, in "X-ray Microbeam Technology and Applications" (W. Yun, Ed.). Bellingham, Washington, 1995.
38. Z. G. Cheng, Ph. D. Thesis, University of Wisconsin-Madison, 1998.
39. A. Duvel, D. Rudolph, and G. Schmahl, *AIP Conf. Proc.* 507, 607 (2000).
40. C. David, B. Nohammer, and E. Ziegler, *Appl. Phys. Lett.* 79, 1088 (2001).
41. V. Aristov, Y. A. Basov, S. V. Redkin, A. Snigirev, and V. A. Yunkin, *Nucl. Instrum. Methods Sect. A* 261, 72 (1987).
42. V. Aristov, Y. A. Basov, G. N. Kulipanov, V. F. Pindyurin, A. Snigirev, and A. S. Socolov, *Opt. Commun.* 66, 183 (1988).
43. U. Bonse, C. Riekel, and A. Snigirev, *Rev. Sci. Instrum.* 63, 622 (1992).
44. A. Snigirev, *Rev. Sci. Instrum.* 66, 2053 (1995).
45. Y. Hartman, A. K. Freund, I. Snigireva, A. Souvorov, and A. Snigirev, *Nucl. Instrum. Methods Phys. Res., Sect. A* 385, 371 (1997).
46. S. Suehiro, H. Miyaji, and H. Hayashi *Nature (London)* 352, 385 (1991).
47. A. G. Michette, *Nature (London)* 353, 510 (1991).
48. B. X. Yang, *Nucl. Instrum. Methods Sect. A* 328, 578 (1993).
49. B. Lengeler, C. G. Schroer, B. Benner, A. Gerhardus, T. F. Gunzler, M. Kuhlmann, J. Meyer, and C. Zimprich, *J. Synchrotron Radiat.* 9, 119 (2002).
50. V. Aristov, M. Grigoriev, S. Kuznetsov, L. Shabelnikov, V. Yunkin, T. Weitkamp, C. Rau, I. Snigireva, A. Snigirev, M. Hoffmann, and E. Voges, *Appl. Phys. Lett.* 77, 4058 (2000).
51. I. Snigireva, A. Snigirev, C. Rau, T. Weitkamp, V. Aristov, M. Grigoriev, S. Kuznetsov, L. Shabelnikov, V. Yunkin, M. Hoffmann, and E. Voges, *Nucl. Instrum. Methods Phys. Res., Sect. A* 467, 982 (2001).
52. A. Iida and K. Hirano, *Nucl. Instr. and Meth. in Phys. Res. B* 114, 149 (1996).
53. O. Hignette, G. Rostaing, P. Cloetens, A. Rommeveaux, W. Ludwig, and A. Freund, *Proc. SPIE* 4499, (2002).
54. E. Spiller and A. Segmuller, *Appl. Phys. Lett.* 24, 60 (1974).
55. M. J. Bedzyk, G. M. Bommarito, and J. S. Schildkraut, *Phys. Rev. Lett.* 62, 1376 (1989).
56. J. Wang, M. J. Bedzyk, and M. Caffrey, *Science (Washington, D.C.)* 258, 775 (1992).
57. Y. P. Feng, S. K. Sinha, H. W. Deckman, J. B. Hastings, and D. P. Siddons, *Phys. Rev. Lett.* 71, 537 (1993).
58. Y. P. Feng, S. K. Sinha, E. E. Fullerton, G. Grubel, D. Abemathy, D. P. Siddons, and J. B. Hastings, *Appl. Phys. Lett.* 67, 24 (1995).
59. W. Jark, A. Cedola, S. Di Fonzo, M. Fiordelisi, S. Lagomarsino, N. V. Kovalenko, and V. A. Chernov, *Appl. Phys. Lett.* 78, 1192 (2001).
60. E. Pfeiffer, C. David, M. Burghammer, C. Riekel, and T. Salditt, *Science (Washington, D.C.)* 12, 230 (2002).
61. W. Jark, S. Di Fonzo, S. Lagomarsino, A. Cedola, E. Di Fabrizio, A. Brahm, and C. Riekel, *J. Appl. Phys.* 80, 4831 (1996).
62. A. Souvorov, I. Snigireva, and A. Snigirev, *Proc. SPIE* 3113, 476 (1997).
63. D. K. G. de Boer, *Phys. Rev. B* 44, 498 (1991).
64. P. Goby, *Cr. Acad. Sci. Paris* 156, 686 (1913).
65. P. Goby, *J. Roy. Mic. Soc.* August 373 (1913).
66. D. L. Spears and H. I. Smith, *Electron. Letters* 8, 102 (1972).
67. D. Rudolph, B. Niemann, G. Schmahl, and O. Christ, in "X-ray microscopy" (G. Schmahl and D. Rudolph, Eds.), p. 192. Springer Verlag, Berlin, 1984.
68. K. Kobayashi, K. Izumi, H. Kimura, S. Kimura, T. Ibuki, Y. Yokoyama, Y. Tsusaka, Y. Kagoshima, and J. Matsui, *Appl. Phys. Lett.* 78, 132 (2001).
69. M. Stampanoni, G. Borchert, R. Abela, and P. Ruegsegger, *J. Appl. Phys.* 92, 7630 (2002).
70. A. Authier, "Dynamical Theory of X-ray Diffraction," Oxford University Press, New York, 2001.
71. W. Meyer-Ilse, D. Hamamoto, A. Nair, S. A. Lelievre, G. Denbeaux, L. Johnson, A. L. Pearson, D. Yager, M. A. Legros, and C. A. Larabell, *J. Microscopy* 201, 395 (2000).
72. C. A. Larabell, D. Yager, and W. Meyer-Ilse, *AIP Conf. Proc.* 507, 107 (2000).
73. W. T. Lynch and L. A. Arledge, *Mater. Res. Soc. Symp. Proc.* 514, 11 (1998).
74. G. Schneider, D. Hambach, B. Niemann, B. Kaulich, J. Susini, N. Hoffmann, and W. Hasse, *Appl. Phys. Lett.* 78, 1936 (2001).
75. J. Thieme, C. Schmidt, and J. Niemeyer, *AIP Conf. Proc.* 507, 301 (2000).
76. P. Fischer, T. Eimuller, G. Schutz, P. Guttmann, G. Schmahl, and G. Bayreuther, *AIP Conf. Proc.* 507, 205 (2000).
77. P. Fischer, G. Denbeaux, H. Stoll, A. Puzic, J. Raabe, F. Nolting, T. Eimuller, and G. Schutz, *J. Phys. IV, France* 104, 471 (2003).
78. F. Zernike, *Z. technische Physik* 11, 454 (1935).
79. D. Gabor, *Nature (London)* 161, 777 (1948).
80. T. Wilhein, B. Kaulich, E. Di Fabrizio, F. Romanato, S. Cabrini, and J. Susini, *Appl. Phys. Lett.* 78, 2082 (2001).
81. G. Schmahl and D. Rudolph, in "X-ray Microscopy: Instrumentation and Biological Applications" (P. C. Cheng and G. J. Jan, Eds.). Springer, Berlin, 1987.
82. G. Schmahl, D. Rudolph, and P. Guttmann, in "X-Ray Microscopy II" (D. Sayre, M. Howells, J. Kirz, and H. Rarback, Eds.). Springer Verlag, Berlin, 1988.
83. D. Rudolph, G. Schmahl, and B. Niemann, in "Modern Microscopies" (P. J. Duke and A. G. Michette, Eds.). Plenum Press, London, 1990.
84. M. R. Howells, C. Jacobsen, J. Kirk, R. Feder, K. McQuaid, and S. Rothman, *Science (Washington, D.C.)* 238, 514 (1987).
85. A. Snigirev, I. Snigireva, V. Kohn, S. Kuznetsov, and I. Schelokov, *Rev. Sci. Instrum.* 66, 5486 (1995).
86. P. Cloetens, R. Barret, J. Baruchel, J. P. Guigay, and M. Schlenker, *J. Phys. D: Appl. Phys.* 29, 133 (1996).
87. S. Lagomarsino, A. Cedola, P. Cloetens, S. Di Fonzo, W. Jark, G. Soullie, and C. Riekel, *Appl. Phys. Lett.* 71, 2557 (1997).
88. S. W. Wilkins, T. E. Gureyev, D. Gao, A. Pogany, and A. W. Stevenson, *Nature (London)* 384, 335 (1996).
89. A. Cedola, Ph.D. Thesis, Universite Joseph Fourier, Grenoble I, 1999.
90. D. Paganin, S. C. Mayo, T. E. Gureyev, P. R. Miller, and S. W. Wilkins, *J. Microscopy*, 206, 33 (2002).
91. W. Coene, A. J. E. M. Janssen, T. J. J. Denteneer, M. Op de Beeck, and D. Van Dyck, *Microscopy Society of America Bulletin* 24, 472 (1994).

92. R. Spal, *Phys. Rev. Lett.* 86, 3044 (2002).
93. V. N. Ingal and E. A. Beliaevskaya, *J. Phys. D: Appl. Phys.* 28, 2314 (1995).
94. T. J. Davis, D. Gao, T. E. Gureyev, A. W. Stevenson, and S. W. Wilkins, *Nature (London)* 373, 595 (1995).
95. S. Bohic, A. Simionovici, R. Ortega, D. Heymann, C. G. Schroer, and A. Snigirev, ESRF Highlights 2000.
96. A. Hitchcock, *Am. Lab.* 33, 30 (2001).
97. G. E. Mitchell, L. R. Wilson, M. T. Dineen, S. G. Urquhart, F. Hayes, E. G. Rightor, A. P. Hitchcock, and H. Ade, *Macromolecules* 35, 1336 (2002).
98. H. Ade, X. Zhang, S. Cameron, C. Castello, J. Kina, and S. Williams, *Science (Washington, D.C.)* 258, 972 (1992).
99. C. G. Schroer, *Appl. Phys. Lett.* 79, 1912 (2001).
100. A. Simionovici, M. Chukalina, F. Gunzler, C. Schroer, A. Snigirev, I. Snirigeva, J. Tummler, and T. Weitkamp, *Nucl. Instrum. Methods Phys. Res., Sect. A* 467, 889 (2001).
101. C. Raven, A. Snigirev, I. Snigireva, P. Spanne, A. Souvorov, and V. Kohn, *Appl. Phys. Lett.* 69, 1826 (1996).
102. P. Cloetens, M. Pateyron-Salomé, J. Y. Buffière, G. Peix, J. Baruchel, F. Peyrin, and M. Schlenker, *J. Appl. Phys.* 81, 5878 (1997).
103. P. Cloetens, W. Ludwig, J. Baruchel, D. Van Dyck, J. Van Landuyt, J. P. Guigay, and M. Schlenker, *Appl. Phys. Lett.* 75, 2912 (1999).
104. S. Suzuki, Y. Watanabe, T. Ogino, S. Heun, L. Gregoratti, A. Barinov, B. Kaulich, M. Kiskinova, W. Zhu, C. Bower, and O. Zhou, *Phys. Rev. B* 66, 035414 (2002).
105. D. Taupin, *Bull. Soc. Fr. Miner. Cristallogr.* 87, 469 (1964).
106. S. Takagi, *Acta Crystallogr.* 15, 1311 (1962).
107. S. Di Fonzo, W. Jark, S. Lagomarsino, C. Giannini, L. De Caro, A. Cedola, and M. Muller, *Nature (London)* 403, 638 (2000).
108. A. Cedola, V. Stanic, M. Burghammer, S. Lagomarsino, F. Rustichelli, R. Giardino, N. Nicoli Aldini, and S. Di Fonzo, *Phys. Med. Biol.* 48, N37 (2003).
109. M. Muller, M. Burghammer, D. Flot, C. Riekel, C. Morawe, B. Murphy, and A. Cedola, *J. Appl. Crystallogr.* 33, 1231 (2000).
110. Y. A. Soh, P. G. Evans, Z. Gal, B. Lai, C. Y. Kim, G. Aeppli, N. D. Mathur, M. G. Blamire, and E. D. Isaacs, *J. Appl. Phys.* 91, 7742 (2002).
111. X. Zhang, H. Solak, F. Cerrina, B. Lai, Z. Cai, P. Ilinski, D. Legnini, and W. Rodrigues, *Appl. Phys. Lett.* 76, 315 (2000).
112. B. C. Larson, W. Yang, G. E. Ice, J. D. Budai, and J. Z. Tischler, *Nature (London)*, 415, 687 (2002).
113. N. Tamura, A. A. Mac Dowell, R. S. Celestre, H. A. Padmore, B. Valek, J. C. Bravman, R. Spolenak, W. L. Brown, T. Marieb, H. Fujimoto, B. W. Battermann, and J. R. Patel, *Appl. Phys. Lett.* 80, 3724 (2002).
114. Y. C. Sasaki, Y. Suzuki, N. Yagi, S. Adachi, M. Ishibashi, H. Suda, K. Toyota, and M. Yanagihara, *Phys. Rev. E: Stat. Phys., Plasmas, Fluids, Relat. Interdiscip. Top.* 62, 3843 (2000).
115. Y. C. Sasaki, Y. Okumara, S. Adachi, H. Suda, Y. Taniguchi, and N. Yagi, *Phys. Rev. Lett.* 87, 248102 (2001).
116. D. Sayre, in "Imaging Processes and Coherence in Physics, Springer Lecture Notes in Physics" (M. Schlenker et al. Eds.), Vol. 112, p. 229. Springer Verlag, Berlin, 1980.
117. J. Miao, T. Ishikawa, B. Johnson, E. H. Anderson, B. Lai, and K. O. Hodgson, *Phys. Rev. Lett.* 89, 88303 (2002).
118. J. Miao, D. Sayre, and H. N. Chapman, *J. Opt. Soc. Am. A* 15, 1662 (1998).
119. J. Miao, P. Charalambous, J. Kirz, and D. Sayre, *Nature (London)* 400, 342 (1999).
120. I. K. Robinson, I. A. Vartanyants, G. J. Williams, M. A. Pfeifer, and J. A. Pitney, *Phys. Rev. Lett.* 87, 195505 (2001).

X-Ray Photoelectron Spectroscopy of Nanostructured Materials

J. Nanda

Stanford University, Stanford, California, USA

Sameer Sapra, D. D. Sarma

Indian Institute of Science, Bangalore, India

CONTENTS

1. Introduction
2. X-Ray Photoelectron Spectroscopy
3. X-Ray Photoemission Spectroscopy
Applications to Nanostructured Materials
4. Conclusion
Glossary
References

1. INTRODUCTION

Photoemission spectroscopy has traditionally been a powerful technique for probing the electronic structure in both condensed and gas phase systems [1–4]. Apart from this, it can also provide useful information like elemental composition, chemistry, and oxidation states of surfaces, etc. [3]. This form of spectroscopy assumes an even greater significance in the case of nanomaterials, where the surface plays a dominant role in determining the material properties [5–7]. Despite the inherent limitations in applying this technique, especially for wide bandgap materials, there have been quite a number of studies in literature pertaining to X-ray photoemission spectroscopy (XPS) in nanomaterials [8–12]. Such studies can be broadly classified into two areas: 1) determining the detailed composition, nature of surfaces, and bonding of the nanostructured materials from both qualitative and quantitative analysis of the photoemission core levels; and 2) evolution of electronic structure as a function of size by studying the valence band/levels using both X-ray and ultraviolet photon energies. This article focuses primarily on the X-ray photoemission core level studies of various kinds of nanostructured materials like nanocrystallites (NC), nanotubes, and nanofilms. The organization of this article is as follows: Section 2 gives a brief outline of the various sample preparation techniques for XPS followed by Section 3, which has several subsections listing the XPS studies in a

wide variety of nanosystems, mainly semiconducting nanoparticle chalcogenides, oxides, metallic nanoparticles, nanotubes, and nanowires. Section 4 is the conclusion. However, we would like to point out that this chapter only discusses those systems where XPS has been used as an important tool for obtaining both qualitative and quantitative information, about the surface and bulk chemical nature and not merely as a characterizing tool used for chemical analysis.

2. X-RAY PHOTOELECTRON SPECTROSCOPY

2.1. Sample Preparation Techniques for XPS

Most of the semiconducting NCs, with the exception of those belonging to IV–VI groups, show strong quantum size effect within a size regime of 1–10 nm [5, 6]; in the case of IV–VI NC, such size effects can be observed for sizes that are even larger by a factor of 4 to 8 [13]. Growing these crystallites, using methods of colloid chemistry, has been the most widely used approach. Normally, this is achieved by arresting the growth of the NCs in solution either by capping the surface atoms by organic moieties, which directly bond to the surfaces of the crystallites, or using stabilizers to control their growth [14–16]. There are also reports of growing nanocrystallites within the cavity of micelles or vesicles [17, 18]. Such chemical synthetic procedures often lead to the production of free-standing powder of NCs that are stable for a considerable period of time. The NCs then consist of a semiconducting core, surrounded by an organic shell. Typically, performing photoemission experiments on such materials, which have a wide bandgap material in the core surrounded by an insulating organic layer, leads to the charging up of the sample. This is because, in the case of wide bandgap materials and insulators during the photoemission, photoelectrons are continuously ejected from the sample. However, the charge neutralization does not occur within the

time-scale of the experiment leading to the accumulation of positive charges on the sample. When this process continues over a period of time and sufficient charge accumulates on the surface, a dynamical equilibrium is reached at a certain potential difference between the sample and the ground, due to the electric field-induced charge compensation. However, the potential difference between the sample and the ground depends on the transport property of the sample and the photon intensity. Subsequent photoelectrons emitted from the sample experience the positive potential on the sample surface resulting in a shift of the kinetic energy of the emitting photoelectron to a lower value and thereby, resulting in an apparent increase in the observed binding energy of the photoelectron signals. In the case of highly insulating samples, the whole surface does not necessarily attain the same steady-state potential giving rise to an inhomogeneous charging. An inhomogeneously charged sample leads to a different extent of binding energy shifts for different parts of the sample, resulting in a broadening of the photoemission signal. Such binding energy shifts, and broadening of the signals make it difficult for any quantitative measurement of the absolute energy positions of the various levels and its comparison between different samples. In view of such problems, there have been a number of techniques reported in the literature for minimizing the effect of sample charging [19, 20]. One such method is to attach the individual nanocrystallites to a conducting surface like gold or aluminum using organic linker molecules like dithiols. The binding molecules place the nanocrystallites at approximately 10 Å from the conducting surface. Such distances supposedly allow the charge to tunnel between the nanocrystal and surface and thus compensate for the charging of the sample. Bowen Katari et al. [8] used this procedure for XPS study of CdSe NCs. The sample for photoemission was prepared by allowing the hexanedithiol to self assemble on the ion-etched gold evaporated on glass slides. These slides were then dipped into a solution of nanocrystals. The surfaces of the NC covalently bonds to the sulfur of the hexanedithiol.

Another method for charge compensation in the case of wide bandgap NCs like CdS and ZnS has been reported by Nanda and Sarma [9, 21]. This method consists of dispersing the NC powders uniformly in a graphitic matrix. The graphitic powders form a conducting network on the top of the crystallites and thus, dissipate the charges accumulated on the surface of the NC. In some cases, it was found that the presence of graphite alone was not enough for the removal of the charging. In those cases, a low-energy electron flood gun was used in addition to the graphitic coating to further minimize the charging. The efficacy of this method is demonstrated in Figure 1(a) and 1(b) for the case of bulk ZnS sample. The Zn $2p_{3/2}$ core level spectrum of bulk ZnS powder and graphite is shown in the spectrum labeled (1). This spectrum clearly exhibits multiple features spread over a wide energy range. The spectral shape clearly shows the presence of inhomogeneous charging. For example, the most intense peak appears at 1025.7 eV, while there is a broad shoulder near 1022.5 eV binding energy. This is in sharp contrast to the fact that the Zn $2p_{3/2}$ signal from pure bulk ZnS is expected to have a single feature. While mixing the sample with graphite does help in reducing the extent of

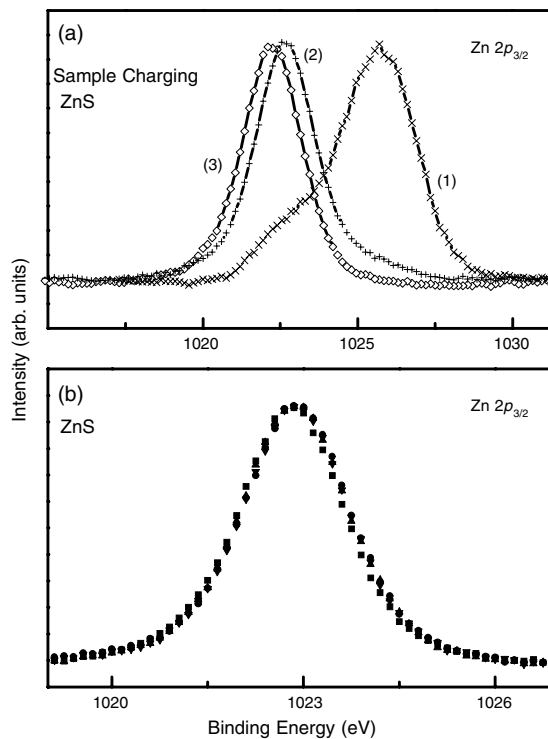


Figure 1. (a) Zn $2p_{3/2}$ core level spectra of bulk ZnS showing various stages of charging leading to minimal charging position. (b) Similar spectra collected at various time intervals at minimal condition showing the consistency of the method.

charging, this procedure alone was not sufficient in eliminating the charging. A low-energy electron flood gun was therefore used to eliminate the remnant charging of the sample. The presence of the sample charging was monitored by the shift in the peak position as well as by the full width at half maximum (FWHM) of the Zn $2p_{3/2}$ spectrum for different conditions of the flood gun as shown in the spectra labeled 2 and 3 in Figure 1a; the narrowest energy width was found to be the no-charging condition. Figure 1(b) shows the charge-compensated Zn $2p_{3/2}$ spectra collected at different time intervals during which the experiment was performed. This overlapping Zn $2p_{3/2}$ spectra shows the reproducibility of minimal charging states for such wide bandgap samples. Consequently, all the core level and valence band spectra were collected while maintaining such consistent position of the core level.

3. X-RAY PHOTOEMISSION SPECTROSCOPY APPLICATIONS TO NANOSTRUCTURED MATERIALS

3.1. Semiconductor Nanoparticles: Group II–VI

3.1.1. Chemical Composition and Core-Level Chemical Shifts

As discussed in the earlier part of the text, significant information about the chemical nature of the surfaces and composition of nanocrystallites can be obtained from the core

level analysis. X-ray photoemission spectroscopy is commonly used to study compositional analysis of materials. The XPS peak intensity from a single element for a homogenous sample is given by the expression [4]

$$I = nF\sigma\theta\lambda A\Phi T \quad (1)$$

where n is the number of atoms per cm^3 , F is the photon flux, σ is the photoelectric cross-section, θ is the detection angle, λ is the mean escape depth, which is a function of the electron kinetic energy, A is the area of the sample probed, Φ is the efficiency of photoelectrons with full kinetic energy, and T is the transmission factor. Equation (1) can be written as

$$n = I/S$$

where

$$S = \frac{1}{nF\theta\sigma\lambda\Phi T} \quad (2)$$

S is called the atomic sensitivity factor. Some of these factors, like the photoelectric cross-section, can be calculated theoretically and others depend on the experimental conditions, the design of the spectrometer, and its electronic detection system. The relative atomic composition is then determined by simply dividing each atomic core level peak intensity by the sensitivity factor. However, in the case of nanocrystallites, since the mean escape depths are comparable to the size, the intensities were calculated by multiplying the intensities at each point by an exponential factor, which decreases with depth from the sample surface. Bowen Katari et al. have reported a detailed composition analysis of various sizes of CdSe NC [8]. In their study, the calculated ratio of Cd: Se was 1.02 ± 0.14 and it did not vary systematically with size. The surface of the CdSe NCs of various sizes was chemically passivated by tri-*n*-octylphosphine oxide (TOPO). The surface coverage of the ligands on the surface of the nanocrystals was determined by comparing the Cd and P peaks. The ratio of Cd/P for various NC sizes fits best to a $1/r$ curve, implying that the ligands are on the surface. Furthermore, the ratio of P/Cd showed a systematic decrease with an increasing crystallite size showing the correct trend. The percent coverage of ligands on the nanocrystals decreases as the nanocrystal radius increases, reaching saturation coverage of around 20%. Characterization of the surface coverage by alternative techniques like NMR on CdSe NC surfaces also confirms such a trend [22].

These workers also studied the surface of CdSe NC as well as surface modifications upon exposure to the atmospheric conditions. This was performed by carefully studying the Cd and Se core levels of the NC over a period of time. These samples showed an oxidized Se peak after a typical exposure time of around one day. The binding energy of the oxide peak appears at the same position as seen for Se oxide on bulk CdSe. Figure 2 shows the Se $3d$ core level of different sizes of CdSe NCs. One of the interesting findings of their study was the gradual appearance and disappearance of the oxide peaks as a function of time. The surface properties of the CdSe NC changes drastically by extracting the TOPO-capped crystallites in Pyridine. In this case, Pyridine replaces the ligand in the solution. The XPS survey scans

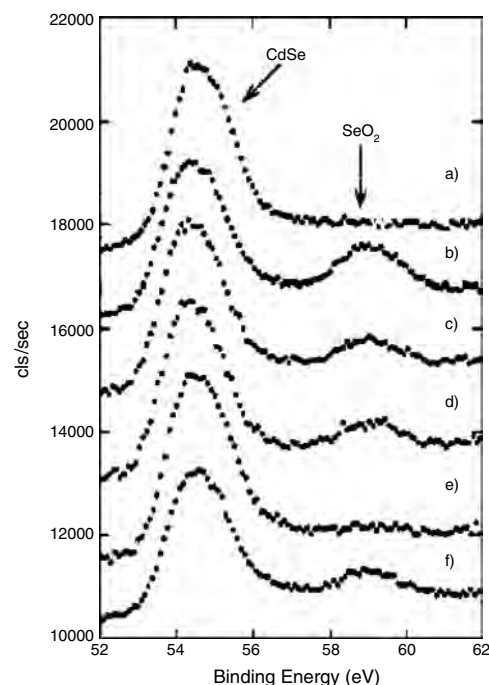


Figure 2. Oxidation of the CdSe nanocrystallite surface as evident from the Se $3d$ cores: (a) 13.1 NC as prepared; (b–f) after 24, 48, 72, 96, and 120 h in air. The oxide peak re-emerges after a finite time interval. Reprinted with permission from [8], J. E. Bowen Katari et al., *J. Phys. Chem.* 98, 4109 (1994). © 1994, American Chemical Society.

then show the absence of P. However, the close-up scan of the P region shows a small peak indicating a small amount of P on the nanocrystal surface. The absence of N $1s$ signal even in the narrow energy window suggested that when the sample was kept under vacuum, pyridine desorbs leaving behind a clean nanocrystal surface. When such samples were exposed under atmosphere, the surface Cd atoms also get oxidized as shown by the Cd $3d$ core level in Figure 3.

Nanda et al. [23] also carried out similar studies on CdSe NC thin films prepared by chemical and electro-chemical

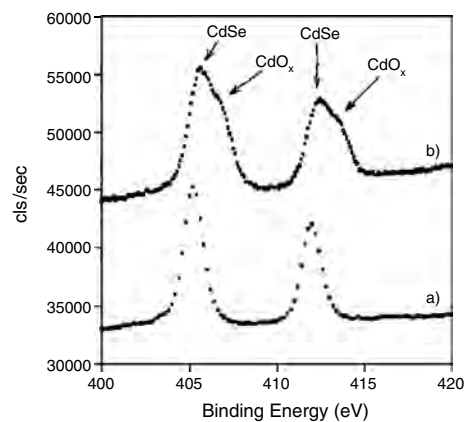


Figure 3. Oxidation of the CdSe surface: Cd $3d$ cores (a) 15.9 NC as prepared showing no oxide Cd component. (b) Same size NC after a few weeks under atmospheric condition. Reprinted with permission from [8], J. E. Bowen Katari et al., *J. Phys. Chem.* 98, 4109 (1994). © 1994, American Chemical Society.

depositions [24, 25]. X-ray photoelectron spectroscopy measurements were carried out on these films using a monochromatic Al K_{α} radiation at a photon energy of 1486.6 eV. The Cd $3d$ core level spectrum of CdSe NC films with an average particle size of about 5 and 15 nm exhibited single features as shown in Figure 4a, suggesting only one type of Cd species present in the sample. The $3d$ level signal has a doublet structure due to the spin-orbit interaction resulting in Cd $3d_{3/2}$ and $3d_{5/2}$ levels at binding energies of 405.6 and 412.35 eV, respectively. The Se $3d$ spectra of the corresponding sample are shown in Figure 4b. The experimental Se $3d$ spectrum could be fitted with three Gaussian doublets with each individual doublet signifying different types of Se species. The three selenium species, in order of increasing binding energies of 53.5, 54.6 and 59 eV, correspond to the bulk, surface, and oxide of Se, respectively [23]. A detailed discussion on these different species will be presented later in the text.

Detailed XPS core level studies of metal sulfide, semi-conducting NC like CdS and ZnS have been carried out by various groups [9–11]. Nanda et al. have studied extensively the surface structure and bonding of various sizes of CdS and ZnS NC [9, 10]. Nanocrystallites of different sizes were synthesized using the same capping agent, 1-thioglycerol, for both CdS and ZnS. By changing the ratio of sulfide to thiol, the NC sizes could be varied. The details of the sample preparation and characterization have been reported elsewhere [26]. The Zn and Cd core level spectra of different sizes of NC and bulk are shown in Figure 5a and b, respectively. When these levels are probed by relatively bulk-sensitive Al K_{α} radiation ($h\nu = 1486.6$ eV, as in this case), one sees only a single peak feature in each of the spin-orbit components without any second Zn or Cd species, similar to the spectrum of bulk. In the case of NC, the Zn $2p$ and Cd $3d$ levels are slightly broadened and also shifted towards lower binding energy. These broadening in NC can arise due to a combination of factors ranging from the intrinsic size distribution of the synthesized NC

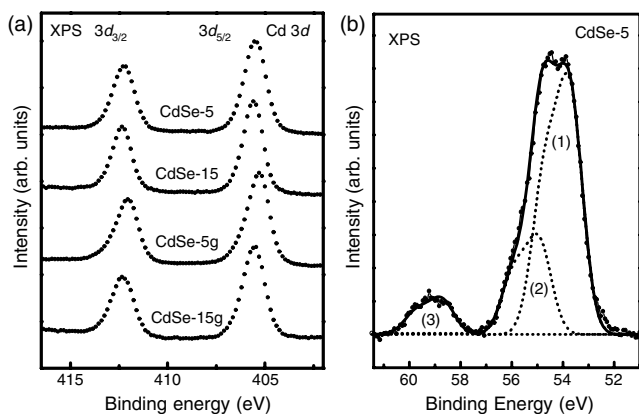


Figure 4. (a) Cd $3d$ core level spectra of 5- and 15-nm CdSe NC thin films. The spectrum labeled as CdSe-5 and 18 nm were chemically grown whereas CdSe-5g and 18g are electrodeposited on gold. (b) Se $3d$ core level spectrum of 5nm CdSe NC film. The circles are the experimental curve and the solid line is the overall fit. Dotted lines are the individual Se Components obtained from spectral decomposition as discussed in the text.

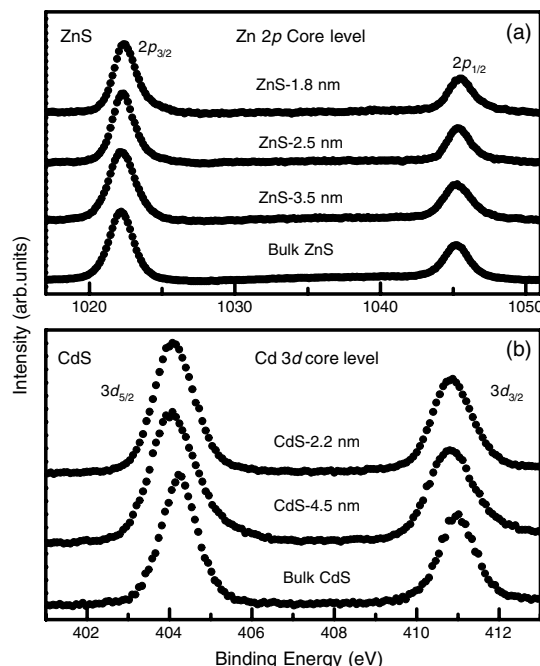


Figure 5. (a) XPS spectra of Zn $2p$ core level of bulk ZnS and three NC sizes of 3.5, 2.5, and 1.8 nm, respectively. (b) Cd $3d$ core level spectra of bulk CdS and two NC sizes of 4.5 and 2.2 nm, respectively.

(about 8–10% in this case) to some degree of uncompensated charging as discussed earlier in the text. The S $2p$ and S $2s$ of the NC provide valuable information about the surfaces. The inset in Figure 6a shows the S $2p$ spectrum of bulk CdS, which can be described by two Gaussians having the same FWHM of 0.44 eV separated by a spin-orbit splitting of 1.2 eV, as shown by the solid line. On the contrary, the S $2p$ spectra of the NC are broad and appear to have multiple features as illustrated in Figure 6a for 2.2 nm CdS NC. A single Gaussian doublet in this case cannot describe the S $2p$ spectrum as shown in the figure for 2.2 nm CdS NC. A good fit to the experimental spectrum was obtained with three sets of Gaussian doublets with the $2p_{3/2}$ signal centered at 161.8, 162.9, and 163.9 eV, respectively. In each case, the spin-orbit splitting turns out to be 1.2 eV, the same as in bulk CdS. The spectral decomposition procedure as discussed above is further justified by the fact that the experimental S $2s$ spectrum of the same sample could be fitted well with three single Gaussians with their energy separations and intensity ratios being fixed to those between the three components observed in the case of S $2p$, as shown in Figure 6b. The dotted lines in fitting are the spectra from individual sulfur species whose relative abundances are given by the areas under each of these curves labeled as (1), (2), and (3). The inset in this figure shows the S $2s$ spectrum of bulk CdS showing a single peak feature as expected. Based on the binding energy values of the various sulfur species, one can assign (1), (2), and (3) to the sulfur atoms belonging to the core, surface, and the thiols that cap the surface of the NC. This was further ascertained by recording the core levels using Mg K_{α} monochromatic radiation, which has a relatively high surface sensitivity. There was a marginal increase in the surface components compared to the aluminum X-ray source. Similar results were also obtained from XPS core

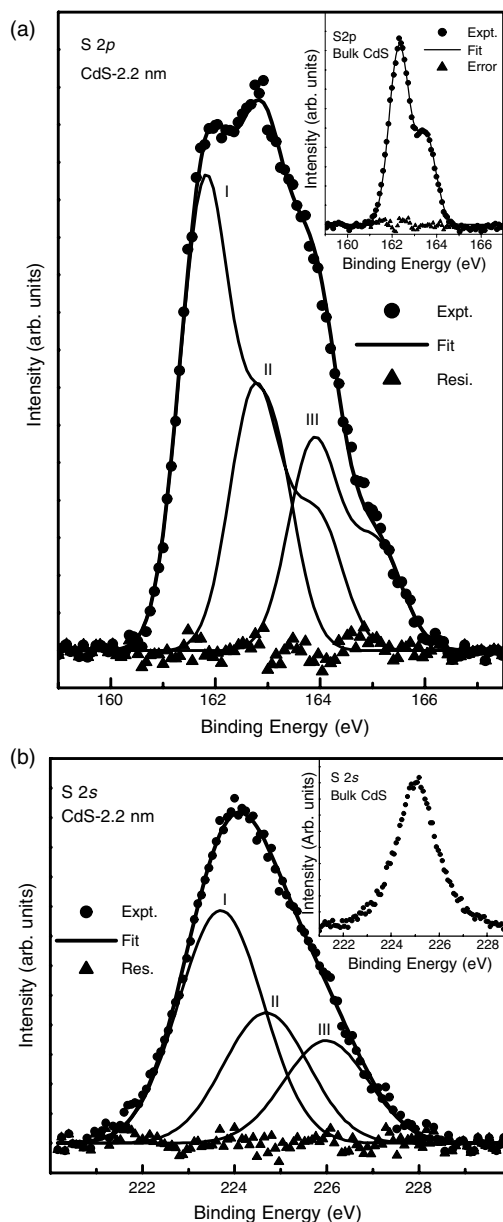


Figure 6. (a) S 2p core level spectrum of CdS-2.2-nm NC showing different sulfur species marked as I, II, III, respectively. Inset shows the S 2p core level of bulk CdS showing only a single sulfur species. The solid circles are the experimental points and the solid lines are the calculated fit. The triangles are the residuals at each point. (b) S 2s core level spectrum of 2.2 CdS NC showing different species of sulfur species labeled as I, II, and III, respectively. Inset shows the corresponding spectrum of bulk CdS showing only a single feature. The solid circles are the experimental points while solid lines are the calculated fit and the triangles show the residual of the fit at each point.

level studies on ZnS NC of various sizes synthesized by a similar procedure [9]. Sulfur species were also noticed in the case of 1.8 nm ZnS NC as illustrated in Figure 7. The inset shows the corresponding S 2s spectrum fitted using a consistent set of parameters as was discussed in the context of CdS NC.

In another study, similar to those of [9] and [10], Winkler et al. investigated NC surfaces by recording the core

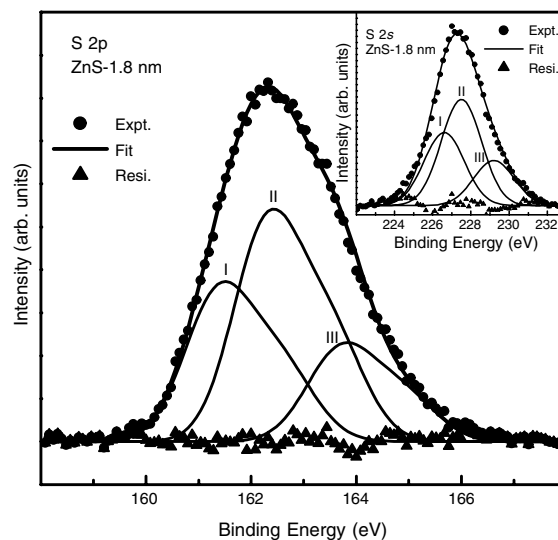


Figure 7. S 2p core level spectrum of 1.8 nm ZnS NC showing different sulfur species labeled as I, II, and III, respectively. The experimental spectra are shown by solid circles, the solid lines are the calculated fits. The triangles show the residual of the fit at each point.

levels spectra employing high-resolution X-ray photoelectron using a synchrotron source [11]. They also reported various sulfur species in CdS NC of various sizes similar to those reported by Nanda et al. [10, 21]. However, they could vary the surface sensitivity by tuning the incident photon energy and thereby being able to vary the degree of bulk and surface contributions in the core level spectrum. The different NC samples studied were approximately 7, 4, and 2.7 nm in diameter and were capped by mercaptopropionic acid. Interestingly, the Cd $3d_{5/2}$ core level spectra recorded with the maximum surface sensitivity ($h\nu = 445$ eV) revealed the existence of two components at 406.1 (A) and 406.6 (B) eV, as shown in the inset of Figure 8. These two Cd groups are assigned to the Cd in the bulk (A) and Cd atom bonding to the sulfur atoms capping agent (B). The S 2p spectra of 7 and 4 nm particle sizes showed three features corresponding to the sulfur atoms belonging to the bulk, surface, and capping of the NC, shown in Figure 8(a) and 8(b). However, the S 2p-core level in the case of the 2.7-nm diameter sample could be fitted to only four spin-orbit doublets (labeled I–IV) as shown in Figure 7c. While the origin of the first three components are the same as the corresponding numbered spectral components for 7- and 4-nm sized particles, the component IV is tentatively assigned to S–S bonds of the capping thiol group, which is abundant in the case of smaller sized particles due to an increased surface-to-volume ratio. Furthermore, the surface-sensitive S 2p spectra (recorded at $h\nu = 203$ eV) showed an oxidized peak at a binding energy of 168.8 eV in case of the larger 7- and 4-nm sized particles, whereas this feature was almost negligible in the case of 2.7 nm NC. This is most probably due to the less number of unsaturated S atoms in the case of the smaller NC. It is often required to anneal the chemically prepared NC for minimizing the defects in their surfaces leading to better emission efficiency. However, annealing methods can lead to a considerable change in the surface composition and structure; hence, there is a need to understand in detail

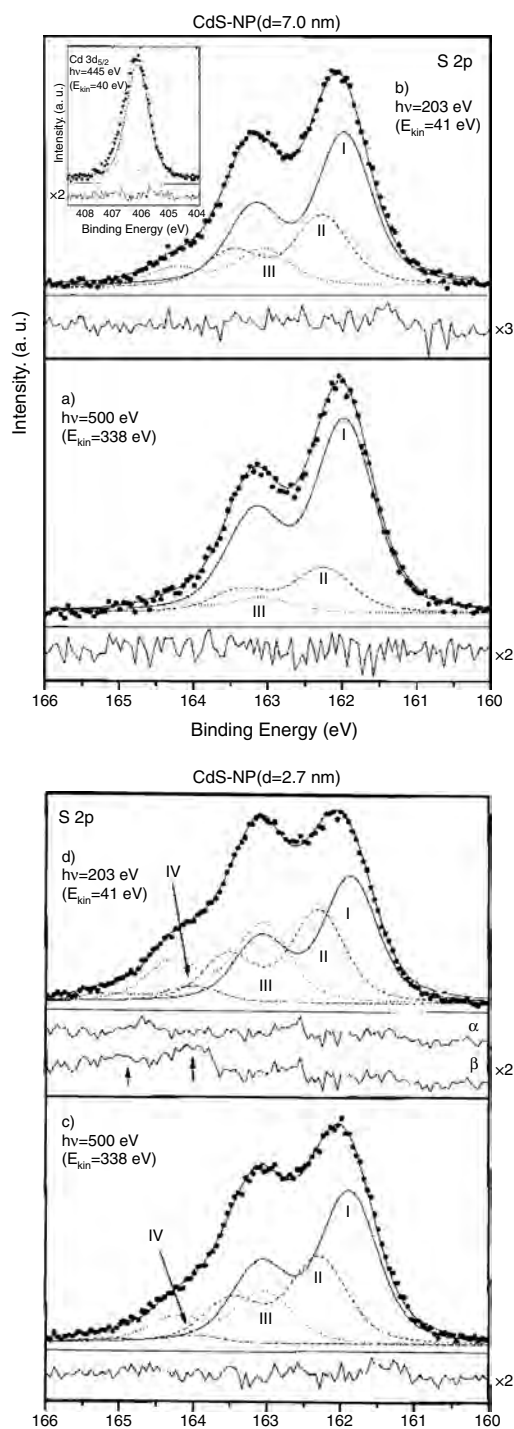


Figure 8. a–b S 2*p* XPS of CdS 7.0-nm particle. The photon energy was set (a) to $h\nu=500$ eV for the bulk sensitive measurements. The three different S 2*p* doublets labeled I–III are obtained from fitting as described in the text. The inset shows the Cd 3*d*_{5/2} spectrum displaying two different species of Cd. The residuals of the fitting results are shown below the corresponding spectral. Reprinted with permission from [11], U. Winkler et al., *Chem. Phys. Lett.* 306, 95 (1999). © 1999, Elsevier-Science. c–d S 2*p* core level spectra of 2.7-nm sized CdS nanoparticles showing four different S species. The residuals of the fitting are shown below each corresponding spectral. Reprinted with permission from [11], U. Winkler et al., *Chem. Phys. Lett.* 306, 95 (1999). © 1999, Elsevier-Science.

the surface of such systems. The above authors have also reported the thermal behavior and stability of CdS NC on similar sized CdS NC by closely monitoring the core level features of the NC [27]. Their results indicate that thermal annealing of CdS NC samples at 240 °C in ultra-high vacuum conditions modifies the surface from being sulfur-terminated at normal room temperature to that of Cd. This is possibly due to the desorption of the capping material at these temperatures or/and the segregation of Cd atoms from the interior of the particle to the surface.

The characterization and mechanism of nanoscale self-assembly is an important area of current research. X-ray photoemission spectroscopy studies have been performed to characterize the layer-by-layer self-assembly of composite thin films of CdS nanoparticles and alkanedithiol on gold substrate [28]. The layer-by-layer structure was confirmed by an angle-resolved photoemission technique at each composite film preparation step.

3.1.2. Particle Size and Structure Analysis from XPS

As discussed in the previous section, photoemission spectroscopy can provide important information on the surface composition and structure of NC. The mean escape depth of the photoelectrons from a sample depends on its kinetic energy and is approximately given by $d = 0.5(K.E)^{1/2}$ Å [1]. For example, the mean escape depth of an S 2*p* electron for AlK_α monochromatic radiation is about 18 Å. Since such length scales are comparable to the NC sizes, the core level spectrum contains signal from both the interior and surface of the NC. A quantitative analysis of such a core level spectrum will provide an estimate of the mean NC size. This was first realized by Nanda et al. [10] and they provided such an analysis in cases of CdS and ZnS NC [9, 10]. Here, we briefly summarize the method. As discussed in detail in section 1.2, the S 2*p*-core level of the NC shows three distinct species (Fig. 5b). The intensity of each component obtained from least-squared fitting of the S 2*p* spectrum is proportional to the relative number of atoms in each of the corresponding layers. The positions and normalized intensities of the three sulfur species, namely, the core, surface, and capping are listed in Table 1 for CdS and ZnS NC, respectively. Given these experimental intensities, one can also calculate the photoemission core level intensities corresponding to different regions of the NC. Assuming the NC to be spherical, one can model a typical nanocrystallite into a three-layer core-shell structure as shown in Figure 9 consistent with the three-sulfur region as evidenced from the sulfur core level.

Table 1. Experimentally obtained intensities of the three sulfur species, namely, the core (1), surface (2), and capping (3), in percentage of the total intensity as obtained from the S 2*p* core level fitting for CdS and ZnS nanoparticles.

Sample	I_{core}	I_{sur}	I_{cap}
CdS-I (4.5 nm)	63.3	21.0	15.7
CdS-II (2.2 nm)	49.8	28.0	22.2
ZnS-3.5	51.6	30.5	17.9
ZnS-2.5	46.7	36.9	16.3
ZnS-1.8	32.5	47.3	20.2

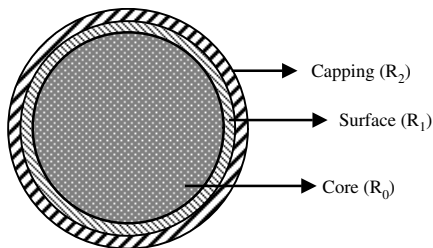


Figure 9. Schematic model of a nanocrystallite showing various regions, namely, the core a radius of R_0 , a shell of radius R_1 , and capping layers of radius R_2 .

The photoelectron intensity from a particular level of an atom is given by

$$dI = I_0 \exp\left(-\frac{z}{\lambda}\right) dv \tag{3}$$

where dI is the infinitesimal intensity contribution from a volume dv situated at a distance z from the surface. The prefactor I_0 depends on the type of atomic level, nature of the sample, and the details of the spectrometer such as the detection efficiency corresponding to a photoelectron of a particular kinetic energy, angle of acceptance, photon flux, etc. λ is the mean-free path of the photoionized electron. Integrating the above expression for the infinitesimal intensity contribution over suitable limits, one can obtain the total intensity corresponding to each of the three regions. Although the instrumental details, like the analyzer characteristics, etc., are the same for different regions of the crystallites, the number densities of the sulfur atoms are not the same in the bulk and the capping materials. This could easily be evaluated from the physical parameters of CdS or ZnS bulk and the capping material thioglycerol, as shown below:

$$\frac{I_o^{\text{Thio}}}{I_{\text{CdS}}^{\text{Cds}}} = \frac{\rho^{\text{Thio}}}{M^{\text{Thio}}} X \frac{M^{\text{CdS}}}{\rho^{\text{CdS}}} = 0.35 \tag{4}$$

In case of a spherical nanocrystallite, eq. (3), after integration, can be conveniently expressed in terms of spherical polar coordinates as

$$I = I_o \int_{R_1}^{R_2} \int_0^\pi \int_0^{2\pi} \exp\left(-\frac{f(r)}{\lambda}\right) r^2 dr \sin \theta d\theta d\phi \tag{5}$$

where, $f(r) = (R^2 - r^2 \sin^2 \theta)^2 - r \cos \theta$; on account of spherical symmetry, integration over ϕ gives only a factor of 2π and the integration over variables r and θ are over the suitable limits discussed below. The intensity ratios for the surface to the core and the capping to the core are given, respectively, by:

$$\frac{I_{\text{sur}}}{I_{\text{core}}} = \frac{I_0^{\text{CdS}} \int_{R_0}^{R_1} \int_0^\pi \exp\left[-\frac{f(r,\theta)}{\lambda}\right] r^2 dr \sin \theta d\theta}{I_0^{\text{CdS}} \int_0^{R_0} \int_0^\pi \exp\left[-\frac{f(r,\theta)}{\lambda}\right] r^2 dr \sin \theta d\theta} \tag{6}$$

$$\frac{I_{\text{cap}}}{I_{\text{core}}} = \frac{I_0^{\text{Thio}} \int_{R_1}^{R_2} \int_0^\pi \exp\left[-\frac{f(r,\theta)}{\lambda}\right] r^2 dr \sin \theta d\theta}{I_0^{\text{CdS}} \int_0^{R_0} \int_0^\pi \exp\left[-\frac{f(r,\theta)}{\lambda}\right] r^2 dr \sin \theta d\theta} \tag{7}$$

These integrals were evaluated numerically for different choices of R_0 , R_1 , and R_2 . The values of R_0 , R_1 , and R_2 were used as adjustable parameters for calculating the intensity ratios given in the above equations, and the set of values that match the experimental intensity ratios best provides one with the size of the core, surface, and the capping layers of the NC. A comparative tabulation of the sizes obtained from this method and the sizes obtained using independent techniques such as X-ray diffraction and transmission electron microscopy (TEM) is given in Table 2 for CdS and ZnS NC, respectively. The sizes of the nanocrystallites estimated from the analysis of the photoemission core level agree reasonably well with those from other methods.

3.2. Semiconductor Nanoparticles: III–V and Other Groups

Following the early approaches of [10] and [11], McGinley et al. have most recently studied the surface of colloiddally prepared InAs NC using photoelectron spectroscopy with synchrotron radiation [12]. These NC were in the size range of 30–60 Å passivated with trioctylphosphine (TOP). The phosphorous atom of TOP bonds with the surface atoms of the NC. Spectral decompositions of the As $3d$ and In $4d$ core levels at different photon energies provide qualitative information about the surface bonding and reconstruction. The core level spectra of In and As were fitted to a minimum number of Voigt functions, using a simplex optimization routine after a proper background subtraction (using a polynomial function in this case, shown in Figs. 2 and 3 of [12]). As illustrated in the figure, each of these spectra can be fitted with three Voigt components indicated by V, S_1 , and S_2 respectively. The higher kinetic energy component V is a well-resolved, spin-orbit doublet, with a spin-orbit splitting value of 0.69 eV in this case, while the lower kinetic energy components, S_1 and S_2 , are much broader to show the spin-orbit separation. The typical Gaussian widths of the Voigt function for these two components were 1.20 ± 0.05 and 1.20 ± 0.02 eV, respectively. The contributions of S_1 and S_2 to the total core-level signal decrease in the spectra with $h\nu = 483.3$ eV as compared to those with $h\nu = 118.3$ eV, as shown in the figure. With increasing nanocrystal size, the intensities of the surface components (S_1 and S_2) decrease in comparison to the volume component V, consistent with

Table 2. Sizes of the various regions in the nanocrystals, CdS-I, CdS-II, and ZnS obtained from the analysis of the photoelectron intensities of various sulfur components and their comparison with other experimental techniques. R_0 , R_1 , and R_2 are the radii of the various regions in the nanocrystals, R_0 , R_1 , and R_2 , as illustrated in Figure 9.

Sample	Core diameter $2R_0$ (nm)	Surface layer diameter $2R_1$ (nm)	Capping layer diameter	Diameter from other experiment (nm)
CdS-I (4.5 nm)	4.1	4.4	4.9	4.4
CdS-II (2.2 nm)	2.0	2.3	2.7	2.2
ZnS-3.5	3.5	4.0	4.6	3.5
ZnS-2.5	1.9	2.3	2.7	2.5
ZnS-1.8	1.5	2.0	2.4	1.8

the decrease in the surface-to-volume ratio. The component S_1 , which is shifted by 0.22 eV from the volume component V , is ascribed to the formation of As—As bonds on the surface, similar to the formation of As trimers in the case of clean bulk InAs surfaces [29]. Component S_2 is associated with the surface As atoms bonded to the passivating organic TOP. The magnitude of this core-level shift from the volume component V is about 1.4 eV, indicating a significant amount of charge transfer from As to P atoms. The In 4*d* core level spectra of the NC could also be described with three Voigt components, similar to the As 3*d* (Fig. 3, [12]). However, in this case, the surface components S_1 and S_2 are shifted by 0.44 and 2.4 eV with respect to V and the corresponding Gaussian widths were found to be 0.65, 1.90 ± 0.10 , and 1.60 ± 0.10 eV, respectively, for the V , S_1 , and S_2 . These authors have ascribed the S_1 components to a sp^2 bonding geometry of the surface In atoms, whereas S_2 is identified with In—P bonds at the nanocrystal/TOP interface.

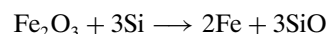
The origin of the extreme broadening of the surface core level spectra has been ascribed to the possibility of a number of different bonding geometries available for the surface atoms of a multi-faceted NC surface resulting in a distribution of bond lengths, distortions, and strain, which is collectively defined as the surface roughness by the above authors. Such inhomogeneity invariably gives rise to the broadening of the core level. However, such broadening is in addition to the broadening arising due to the distribution of pinning of the Fermi level by defect sites, which would broaden all the core levels to the same degree including the volume component.

Recently, Borchet et al. [30] have characterized the core shell nature of ZnS passivated InP NC by taking advantage of the variation of the escape depth on the energy of the photon. The detailed synthetic procedure is described elsewhere [31]. Their results demonstrate that the In atoms are in the core, while Zn is located in the surrounding shell. Using a similar analysis as reported by Nanda et al. [10], they have determined the average thickness of the core, shell, and capping layer. Furthermore, the ratio of the normalized intensities of In to Zn core levels showed an increase with increasing kinetic energy, demonstrating that at lower kinetic energy, the In intensity is screened by the surrounding Zn atoms. If the In and Zn atoms were randomly distributed in the NC as in the case of an alloy, the ratio of the normalized intensities should stay at a constant value determined by their atomic concentrations. Earlier, Hoener et al. had demonstrated a similar shell-core structure in the case of CdSe-ZnSe NC using X-ray and Auger spectroscopies [32]. The normalized XPS and Auger intensity ratios of Cd and Zn cations showed a marked difference in the case of core-shell NC than that of a random mixture of CdSe and ZnSe particles.

3.3. Nanoparticle Oxides

Oxides of semiconductors form an important category of materials that have important optoelectronic properties [33]. Nanoparticles of oxides are currently an important area of study as these materials might have tremendous impact in the area of magnetic semiconductors or spintronics, and memory devices [34]. One of the interesting areas in which

XPS has been used in these materials is to study their size, spatial distribution, as well as their functionality. This is often manifested as a change in the nature of the surface species of the nanoparticle assemblies, which can then be monitored and characterized by XPS. An example of such is reported by Prabhakaran et al. in the case of Fe_2O_3 nanoparticles on the surface of Si [35]. Fe_2O_3 nanoparticles were synthesized sonochemically and incorporated into Si wafers, leading to multiple light emissions and multiple functionality all at the same time. At an annealing temperature of 850 °C in UHV chamber and the Si wafer treated with Fe_2O_3 nanoparticles, the Fe^{3+} is reduced by the silicon, and desorbs as SiO, resulting in the formation of magnetic nanoparticles consisting predominantly of Fe^0 . The reduction of Fe_2O_3 to elemental Fe takes place by the following reaction:



During the reaction, an XPS core level of Si 2*p* and Fe 2*p* were monitored at several temperatures to study the reaction. The Si 2*p* core level is shown as an inset in Figure 10 showing the disappearance of the oxide contribution at an elevated temperature. The main figure shows the gradual reduction of the Fe_2O_3 peak (Fe^{3+}) with the temperature showing predominantly Fe^0 , which is chemically shifted by

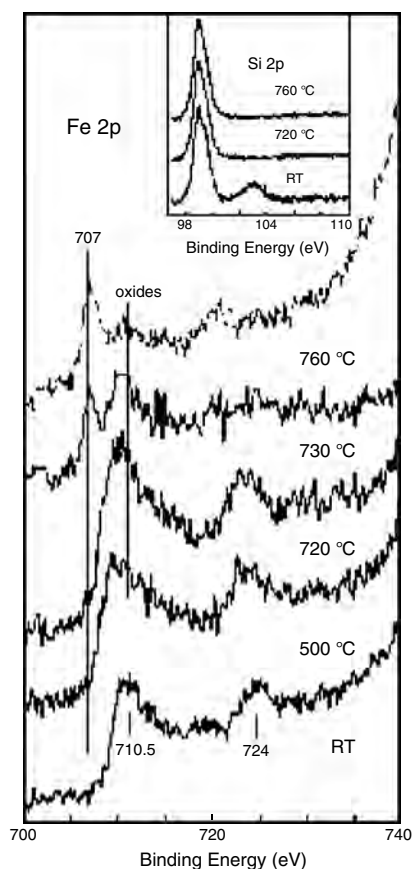


Figure 10. XPS measurement of Fe 2*p* core level as a function of temperature showing the reduction of Fe_2O_3 to Fe on Si (III) surface. The corresponding Si 2*p* spectra are shown in the inset. Reprinted with permission from [35], Prabhakaran et al., *Adv. Mater.* 13, 1859 (2001). © 2001, Wiley-VCH.

3.5 eV towards higher binding energy. The Si wafer with the as-incorporated amorphous Fe_2O_3 particles exhibits superparamagnetic behavior, which is characteristic of amorphous nanoparticles [36]. Upon annealing, the samples show soft ferromagnetic behavior.

Another interesting XPS study on oxide nanoparticle has been reported by Schmeisser et al., in which they have observed a large dipole moment at the interface of metal semiconductor core, which is manifested in the form of a core level shift [37]. This has been observed in the case of Sn/SnO_2 and $\text{Ta}/\text{Ta}_2\text{O}_5$ nanoparticles. The oxidic shell covering the metal cluster produces a high interface dipole moment whose origin is probably due to the charge difference between the metallic core and the substrate. The corresponding shift in the XPS core level is proportional to the strength of the dipole moment, which can vary depending on the size of the core and the oxide layer thickness. The smaller nanoclusters do not show a dipole shift and the Sn 3d core level spectra only shows the metallic (at 484.4 eV) and oxidic (486.7 eV) contribution (Fig. 2 of [37]). However, the larger clusters exhibit new peaks. The oxidic part is shifted to 488.8 eV from its usual position. Thus, the net shift induced by the interface dipole moment amounts to 2.1 eV when compared to the oxidic peak. The Sn 4d of the clusters shows a dipole-induced shift of about 5 eV compared to bare SnO_2 (100) single crystals and the valence band of the nanoparticle is shifted by 2.8 eV.

McGinley et al. have studied pure and Sb-doped SnO_2 nanoparticles using photoemission spectroscopy [38]. Photoelectron spectra with synchrotron radiation were recorded for Sn 3d, Sb 3d, and O 1s core levels. The O 1s core level spectrum of pure SnO_2 nanoparticles is shown in Figure 11a. The spectrum could be fitted with two Voigt components. With increasing photon energy, the relative contribution of the surface and bulk components changes as shown in Figure 11b. The lower kinetic energy component of the spectrum is due to O atoms in a surface environment and the bulk component, which shifted by $+1.30 \pm 0.05$ eV, has the same shift found for surface hydroxyl groups (OH^-) in a study of thin film SnO_2 [39]. Hence, it was suggested that the surface hydroxyl groups bond to the surface in a manner similar to that found for the O bridging atoms (O^{2-}) of the SnO_2 (110) surface [40]. It appears that there is no clear surface environment for Sn as the Sn 3d core level spectrum is fitted with only one Voigt function. This primarily suggests that Sn atoms are largely confined to the bulk of the nanoparticle with oxygen atoms remaining largely on the surface and participating in the surface bonding. Furthermore, these workers have addressed the important question of the dopant distribution in the nanoparticle and whether the oxidation state is similar throughout the structure. Figure 12 shows the Sb: Sn $3d_{3/2}$ core level intensity ratio as a function of photon energy for samples with two different Sb concentrations, namely, 9.1 and 16.7%. This shows an enrichment of Sb at the surface in SnO_2 nanoparticles for both concentrations. A quantitative analysis of Sb 3d core level done for nanoparticles synthesized from precursors containing Sb^{III} and Sb^{V} shows that Sb atoms located in the surface have a oxidation state of Sb^{V} . The photoemission features are, however, very broad with a Gaussian FWHM of 1 eV when the total experimental

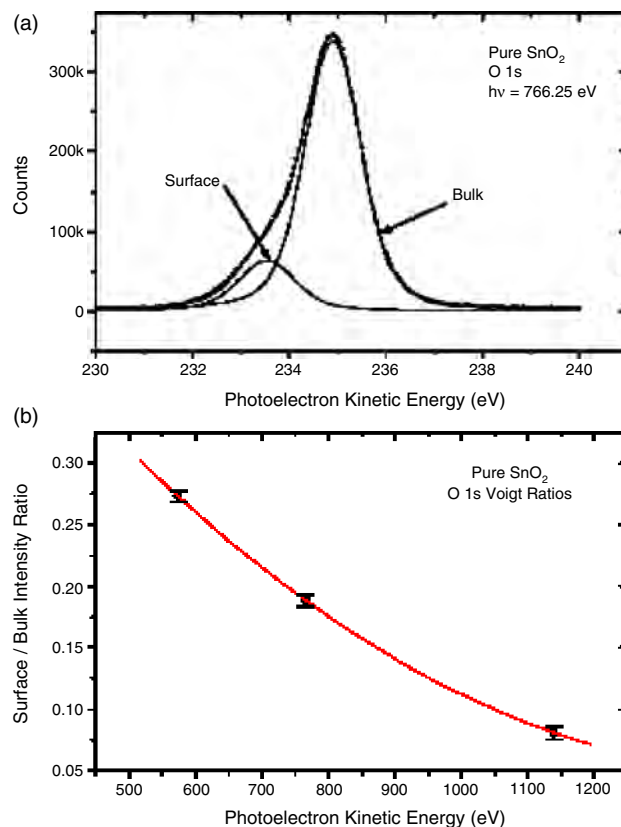


Figure 11. (a) O 1s core level spectrum of pure SnO_2 nanoparticles fitted with two Voigt functions. (b) Intensity ratio of the components in (a) as function of photon energy. Reprinted with permission from [38], McGinley et al., *Eur. Phys. J. D16*, 225 (2001). © 2001, Springer-Verlag.

resolution was set to 240 meV. This highlights the effect of the expected internal faceting on the photoemission core levels.

Bullen and Garrett have recently studied surface nature and composition of TiO_2 nanoparticle arrays using XPS [41]. Using close-packed polystyrene nanosphere masks, TiO_2 arrays were fabricated using a chemical route. The average composition of the particles was confirmed using XPS. Figure 13 shows the Ti 2p spectrum of a nanoparticle array grown on glass after removal of the polystyrene mask. The shape, binding energy, and the spin-orbit splitting of the Ti 2p photoemission spectrum are characteristic of the TiO_2 . Comparison with the spectrum of a TiO_2 (110) single crystal shown in (a) with that of the nanoparticle array reveals some evidence of Ti^{3+} species as indicated by a slight low BE shoulder on the Ti $2p_{3/2}$ peak. However, it was difficult to determine the percentage of Ti^{3+} on the surface because of the close proximity of Ti^{4+} (TiO_2) and Ti^{3+} binding energies. The large surface-to-volume ratio and high curvature of these particles suggests that the Ti^{3+} species may be associated with corner, edge, or terrace defect sites. There have also been a few reports on XPS study on other oxide nanoparticles, for example, ZnO, where it has been mainly used as a characterizing tool [42].

X-ray photoelectron spectroscopy study of nanostructured CeO_2 films was reported by Wang et al. [43]. Cerium oxide serves as an important catalyst in many chemical reactions

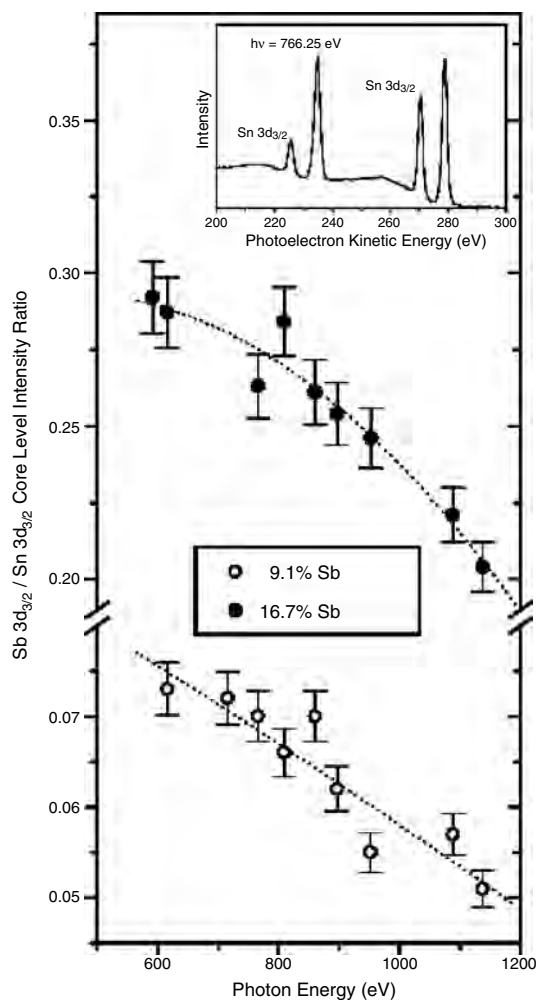


Figure 12. Sb: Sn 3d_{3/2} core level intensity ratio as a function of photon energy for samples with two different Sb concentrations. Lines are drawn as a guard to the eye. The inset shows a typical wide-range spectrum from which the core level intensities were calculated. Reprinted with permission from [38], McGinley et al., *Eur. Phys. J. D16*, 225 (2001). © 2001, Springer-Verlag.

and the chemical state of ceria is an important factor that controls the catalytic activity. The films were grown by the electrodeposition method and the average crystallite sizes were in the range of 6–8 nm. These authors have studied the Ce 3d, 4d, O 1s, and valence band XPS of these films at different sintering conditions. Their results indicate that the produced films were nonstoichiometric, with a typical value in the range of 1.90–1.98 for x in CeO_x. The photoelectron spectra also showed an increase of Ce⁴⁺ concentration at the surface with increasing sintering temperature.

3.4. Metallic Nanoparticles

Many interesting optical and electronic properties are observed in the case of nanometer-sized metal particles due to confinement of the free-charge carriers [44]. A particular example is the presence of a strong band in the visible region of the absorbance spectrum of noble metallic particles. This strong band is attributed to the surface plasmon

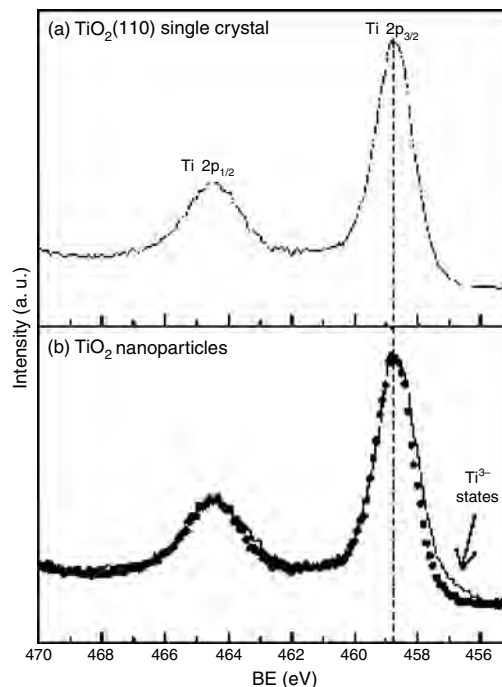


Figure 13. XPS comparison of Ti 2p region for a rutile TiO₂(110) single crystal and TiO₂ nanoparticle arrays on a glass substrate. The solid circles are the spectrum shown in (a) overlapped to highlight the presence of Ti³⁺ surface species on the nanoparticle. Reprinted with permission from [41], H. A. Bullen and S. J. Garret, *Nano Lett.* 2 (2002). © 2002, American Chemical Society.

oscillation modes of the conduction electrons in the particle, which are coupled through the surface to the external applied electromagnetic field. Because of this reason, the optical properties of the nanometer-sized gold, copper, and silver particles have been extensively studied in the recent past [45]. Ultra-fast dynamics of these metal colloids have also been studied in the recent past to understand the basic electron-phonon and electron-electron interactions and their relaxation mechanisms [46].

X-ray photoelectron studies have been performed recently on some of these metallic nanoparticles to study their reactivity and surface properties. Boyen et al. recently reported the unique, oxidation-resistant 55-atom gold cluster [47]. These authors have studied the size dependence of the oxidation behavior of gold nanoparticles using XPS. Generally, bulk gold is highly oxidation-resistant; however, it can form Au₂O₃ by electrochemical methods, by exposure to atomic oxygen delivered by molecular dissociation at a hot filament, or radicals provided by oxygen plasma [48, 49]. For this experiment, the Au nanoparticles were synthesized by a micellar technique giving a narrow size dispersion [50]. The samples were then exposed to oxygen plasma in order to remove the ligand shell thus allowing the study of the naked Au cluster of different sizes. Since we are interested in the response of such pure Au nanoparticles to highly reactive oxygen species, a flat Au (111) surface was first treated under identical condition for comparison. The XPS core-level spectra of bulk Au-4f region is shown in Figure 14A for two different take-off angles (having different surface sensitivities). Both spectra reveal

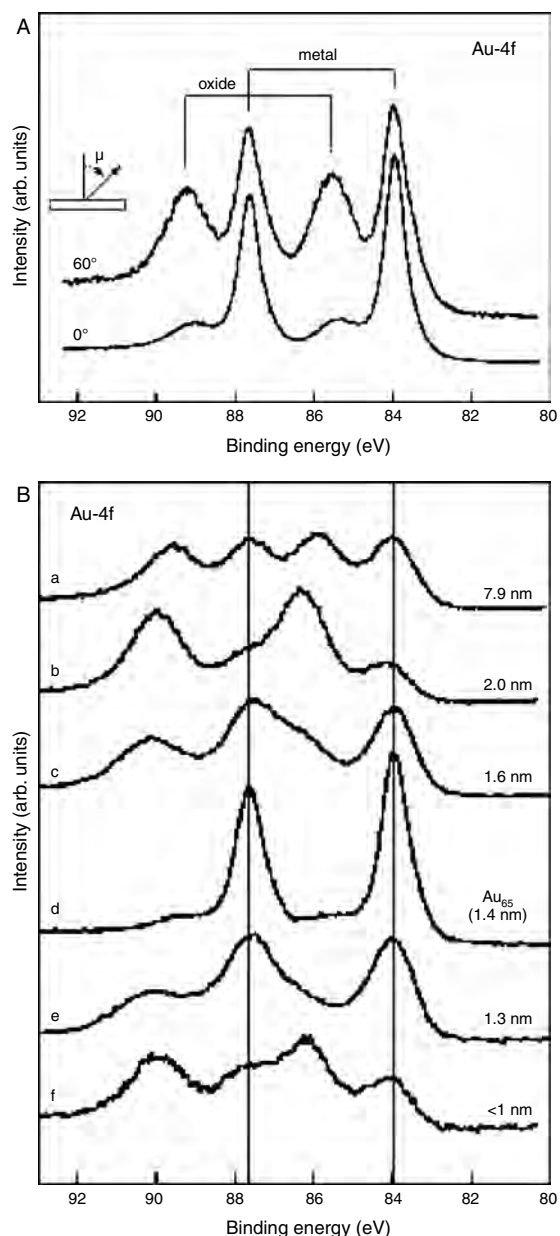


Figure 14. (A) Au 4f photoelectron spectra obtained from an Au (111) surface after treatment in an *in-situ* radiofrequency oxygen plasma. The different detection angles result in different surface sensitivities of the photoemission experiment. (B) After exposure of pure Au particles (size 1–8 nm) to reactive oxygen species provided by an *in-situ* rf plasma (exposure for 10 min at 50 W and 0.005 mbar). The vertical lines indicate the energy positions corresponding to elemental Au. Reprinted with permission from [47], Boyen et al., *Science* 297, 1533 (2002). © 2002, American Association for Advancement of Science.

four peaks originating from metallic Au (binding energy 84.0 and 87.7 eV) and the corresponding oxide (binding energies 85.8 and 89.5 eV) [51]. When the Au nanoparticles are exposed to such plasma, one expects spectroscopic signatures of both pure gold and the corresponding oxide with a concurrent increase of the oxide layer with a decrease in the size of the nanoparticles. The XPS core level spectra of different sized Au nanoparticles are illustrated in Figure 14B.

Upon exposure, the 7.9-nm sample (curve a) shows a pair of doublets originating from both elemental Au and the corresponding oxide. A quantitative analysis of the spectrum reveals an inner metal core of 6.5 nm with a 0.7-nm oxide formation on the surface due to the plasma treatment. With a reduction in the size of the cluster to 2.9 nm, the corresponding thicknesses are 1.6 nm and 0.65 nm oxide layer. Surprisingly, reduction in the particle size to 1.6 nm (curve c) shows a dramatic increase in the metallic contribution, pointing to an increased resistance to oxidation. This feature is even more spectacular in the case of Au₅₅ atom cluster (1.4 nm), which shows almost no oxide peak in the spectrum (curve d). With a further decrease in the particle size to 1.3 and <1 nm, again the dominant contribution is from the oxide behavior as in the case of bulk (curve e and f). In order to investigate whether electronic properties like the opening of the energy gap or structural properties like atomic closed structure are responsible for the stability of Au₅₅ clusters, valence band studies were carried out by these authors. The valence band of clean Au films, Au₂O₃ and Au₅₅ clusters, were compared taking the Au-5d feature as the common energy reference. The valence band of the cluster shows a step intensity at the Fermi level (E_F) indicating that the bare clusters have already formed a metallic system. Au₂O₃, on the other hand, shows a semiconducting behavior due to the opening of the gap at the Fermi energy position. These studies indicate that the extraordinary chemical stability of gold clusters is not caused by the size-induced modification in the electronic structure but rather due to the closing of the second atomic shell at this particular size. The other reason, according to these authors, could also be due to defect formations on the supporting matrix which are known to induce the reactivity of the clusters [52].

There are several reports in literature relating to the characterization of metallic and bimetallic nanoparticles using XPS technique. Kataby et al. have studied the catalytic properties of bare amorphous iron particles versus tridecanol-coated iron nanoparticles [53]. Figure 15 shows the XPS spectra of uncoated and alcohol-coated iron nanoparticles. An Fe 2p core level spectrum of bare iron particles is much broader than the case of coated nanoparticles due to the partial oxidation of uncoated iron. The binding energy position of zerovalent Fe is around 707 eV, and Fe₂O₃ peak has been reported at 710.9 eV. The coated nanoparticle spectrum shows a marked absence of the pure Fe peak and only

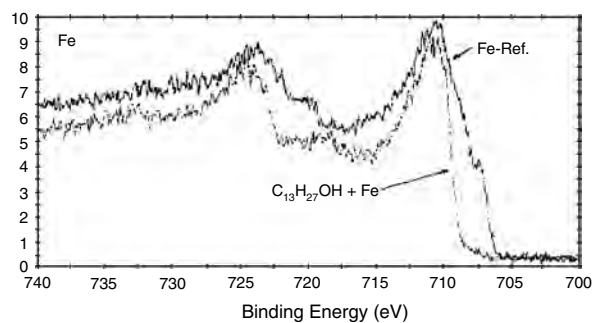


Figure 15. Fe (2p) XPS spectrum of amorphous iron and 1-tridecanol coated amorphous iron. Reprinted with permission from [53], Kataby et al., *Langmuir* 14, 1512 (1998). © 1998, American Chemical Society.

shows the oxide peak indicating the formation of Fe—O bonding on the surface. These authors have also examined the O 1s core level of coated and uncoated samples to further elucidate the surface bonding. Hemakanthi et al. [54] have studied the formation of Cu(0) nanoparticle using Langmuir–Blodgett films of octadecylsuccinic acid as the template. They have studied the composition and oxidation states of the Cu nanoparticles using XPS.

Several investigators have recently studied the properties of bimetallic and trimetallic nanoparticles [55–57]. Depending on the synthetic approach and the growth conditions, they can either have a core shell structure or form an alloy of two phases. The X-ray photoemission spectroscopy method has been used extensively to extract such information. In the case of alkanethiol-derivatized, Au-Ag bimetallic nanoparticles as synthesized by Han et al. [58]. The XPS core level study of the composite clusters showed a Ag-rich surface. Herein, the surface enrichment of a particular type of atom means that the surface composition of the bimetallic system is somewhat different from the inner part. Their studies were further confirmed by FTIR.

3.5. Nanotubes and Nanowires

X-ray photoelectron spectroscopy has been used in conjunction with other techniques in determining chemical state, surface bonding, and reactivity of nanotubes and wires. This section discusses some of the XPS work reported in literature pertaining to carbon nanotubes and semiconducting nanowires. Chen et al. have investigated the detailed electronic structure of carbon nanotubes using UPS and XPS [59]. The results were compared with graphite. The C 1s signal from graphite was detected at a BE of 284.6 eV, while in the case of nanotubes it shifts by 0.3 eV towards the lower binding energy. However, the FWHM of the 1s peak for nanotubes was 1.1 as 1.0 eV for graphite (Fig. 3 of [59]). The negative shift of the core level in the nanotubes was ascribed to weaker C—C binding caused by the curvature of graphene sheets, as well as the larger interlayer distance of the carbon nanotubes. The larger FWHM observed in the case of nanotubes indicates a shorter lifetime of the holes of C 1s photoemission in nanotubes in comparison to that of graphite. The energy loss spectra (not shown here), demonstrate a sharp peak at ~ 6.6 eV loss energy and a very broad loss feature around 27 eV, corresponding to the collective π and $\sigma + \pi$ plasma excitation, respectively [60, 61]. In comparison with those of graphite, both the loss features are stronger in the case of nanotubes as per earlier findings [62]. This appears to be related to the curved nature of the graphene sheets in carbon nanotubes.

Chemical functionalization of single-wall carbon nanotube (SWCNT) can change the electronic properties of the nanotubes significantly resulting in an enhanced performance in hydrogen storage, secondary battery, and super capacitor. The XPS study of fluorinated SWCNT has been reported recently by An [63]. The XPS data show a clear binding-energy shift towards the higher energy with increasing fluorination temperature. At low temperatures, up to 200 °C, they show an ionic bonding character and at higher temperatures, the bonding is covalent. C 1s spectra of fluorinated SWCNTs at different reaction temperatures are shown in Figure 16a.

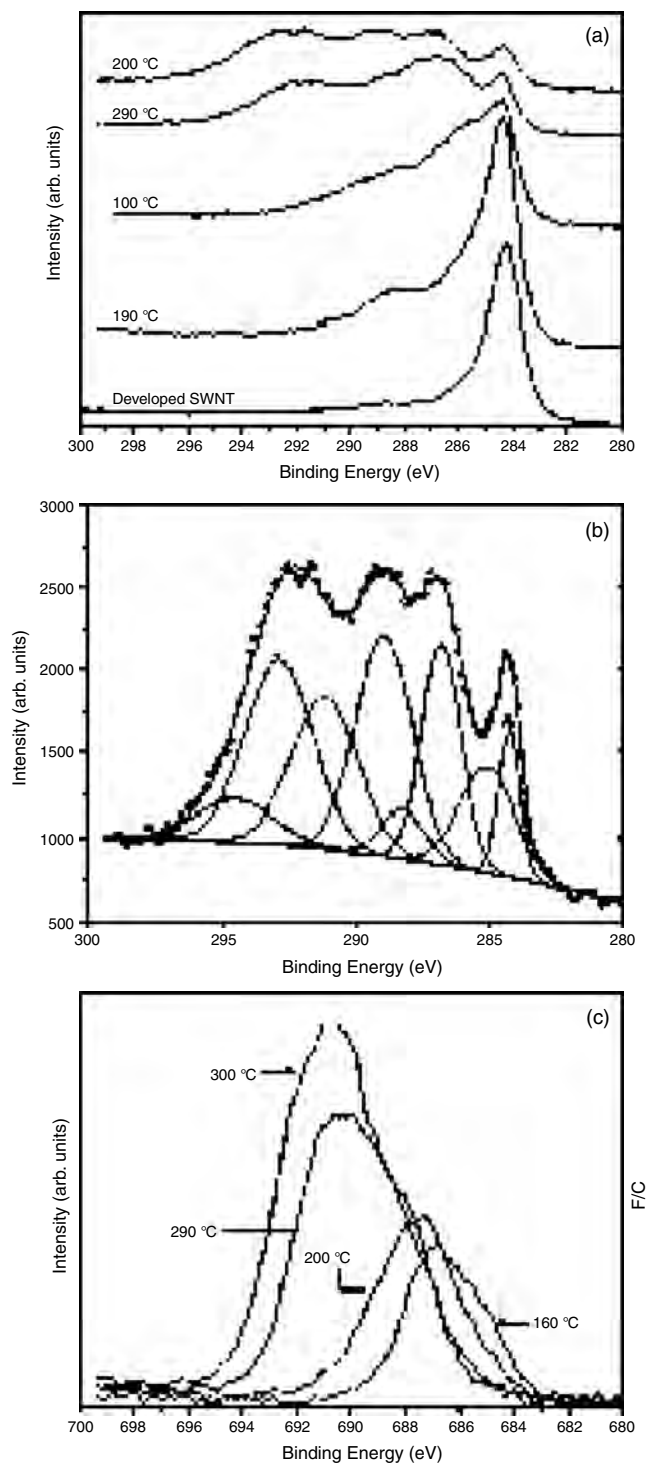


Figure 16. (a) C 1s XPS spectra of the undoped and fluorinated SWCNTs at various reaction temperatures. (b) XPS C 1s curve for the fluorinated SWCNTs at 300 °C. (c) F 1s XPS spectra of the undoped and fluorinated SWCNTs at various reaction temperatures. Reprinted with permission from [63], K. H. An et al., *Appl. Phys. Lett.* 80, 4235 (2002). © 2002, American Institute of Physics.

The spectrum of an undoped nanotube shows a sharp peak at 284.3 eV assigned to sp^2 carbon. The tail around 285 eV corresponds to the sp^3 carbon. With an increasing reaction temperature, the sp^2 peak significantly decreases and also

becomes broad. The subsequent appearance of the peaks at a higher binding energy with increasing temperature indicates the existence of several carbon species bonded to fluorine. Figure 16b shows the spectral decomposition of the various carbon species fluorinated at 300 °C. The peaks were fitted with several Gaussian curves, each Gaussian representing a distinct carbon component. Curve A is the sp^2 carbon, B relates to sp^3 peak, C-E are the oxygen-related peaks, and F-H relates to the formation of other types of CF_x bonds. The F 1s core level spectra of the samples are shown in Figure 16c. As is shown, the intensity of the F 1s peak increases and the binding energy shifts towards higher values with reaction temperatures. The binding energy shifts from 687 to 691 eV at temperatures above 200 °C. The peak at 687 eV is assigned to semi-ionic fluorine and 691 eV to covalent fluorine.

The growth and oxidation properties of Ge nanowires were studied by Hanrath and Korgel using XPS [64]. These workers have used alkanethiol-protected gold nanocrystal as the seed materials for the wire formation. Their studies indicate that prior to the atmospheric exposure, the Ge nanowires are not oxidized; however, after 24 h of atmospheric exposure, the wires oxidize to a significant degree, with 3 mole % O relative to Ge this value went up to 7 mole % upon 168 h of exposure. Zheng et al. have recently reported a new synthetic procedure for silicon-oxide nanowires where they have used XPS to characterize the SiO_x nanowires [65].

4. CONCLUSION

As previously discussed, it is quite evident that XPS serves a rather important tool for studying a wide range of nanostructured materials. With the advent of high intensity synchrotron sources, this technique has become even more powerful yielding valuable information about both surface and bulk properties of such samples. The specific examples of XPS application of nanomaterials as discussed in this text was just a brief overview of the work done in this area by a cross-section of researchers all over the world. There have been numerous reports in literature where XPS has been applied routinely to determine the composition and chemical state in a host of nanomaterials.

GLOSSARY

Al K_{α} Characteristic X-ray radiation emitting from aluminum. The typical energy of this radiation is 1486.6 eV.

Binding Energy Refers to the energy of an electron level in an atom in the ground state.

Capping material Organic moieties used to passivate the surface of the nanocrystallites to prevent aggregation.

Colloid chemistry A method generally used for making nanocrystallites of various sizes by growing them in an aqueous or nonaqueous medium.

Core level Electronic energy levels that are tightly bound to the core (or nucleus).

Mean escape depth Refers to the mean-free path traveled by the photoelectrons before they emit from the surface.

The escape depth mainly depends on the kinetic energy of the photoelectron and the properties of material.

Nanomaterial Materials whose typical sizes range from one nanometer to a few hundred nanometers.

Photoelectric cross-section Probability of the emission of an electron (corresponding to a particular energy level) from an atom due to incident photon. This strongly depends on the incident photon energy.

Sample charging Building up of excess charge on the surface of insulating samples upon exposure to X-ray radiation.

Semiconducting nanocrystallites Tiny fraction of a semiconductor having size ranging from 1–100 nm with a crystalline core.

Surface plasmon Oscillation due to the free electron clouds on the surface of small metal particles. The frequencies of this oscillation are different from that of bulk-free electron in the metal.

REFERENCES

1. S. Hüfner, "Photoelectron Spectroscopy: Principles and Application." Springer-Verlag, Berlin-New York, 1995.
2. M. Cardona and Ley, Eds., "Photoemission in Solids – I and II." Springer-Verlag, Berlin, 1978.
3. D. Briggs and M. P. Seah, "Practical Surface Analysis," 2nd ed., Vol. 1. John Wiley & Sons Ltd., New York, 1990.
4. C. D. Wagner, W. M. Riggs, L. E. Davis, J. F. Moulder, and G. E. Muilenberg, "Handbook of X-Ray Photoelectron Spectroscopy." Perkin-Elmer, Eden Prairie, MN, 1978.
5. H. Weller, *Angew. Chem. Int. Ed. Engl.* 32, 41 (1993).
6. A. P. Alivisatos, *J. Phys. Chem.* 100, 13 (1996).
7. S. A. Majetich and A. C. Carter, *J. Phys. Chem.* 97, 8727 (1993).
8. J. E. Bowen Katari, V. L. Colvin, and A. P. Alivisatos, *J. Phys. Chem.* 98, 4109 (1994).
9. J. Nanda and D. D. Sarma, *J. Appl. Phys.* 90 2504 (2001).
10. J. Nanda, B. A. Kuruvilla, and D. D. Sarma, *Phys. Rev. B* 59 7473 (1999).
11. U. Winkler, D. Eich, Z. H. Chen, R. Fink, S. K. Kulkarni, and E. Umbach, *Chem. Phys. Lett.* 306, 95 (1999).
12. C. McGinley, M. Riedler, T. Möller, H. Borchet, S. Haubold, M. Hasse, and H. Weller, *Phys. Rev. B* 65, 245308 (2002).
13. F. W. Wise, *Acc. Chem. Res.* 33, 773 (2000).
14. T. Vossmeier, L. Katsikas, M. Giersig, I. G. Popovic, K. Diesner, A. Chemseddine, A. Eychmuller, and H. Weller, *J. Phys. Chem.* 98, 7665 (1994).
15. C. B. Murray, D. J. Norris, and M. G. Bawendi, *J. Am. Chem. Soc.* 115, 8707 (1993).
16. M. T. Nenadovic, M. I. Comor, V. Vasic, and O. I. Micic, *J. Phys. Chem.* 94, 6390 (1990).
17. C. Petit, P. Lixon, and M. P. Pileni, *J. Phys. Chem.* 91, 257 (1987).
18. H. C. Fendler and F. C. Meldrum, *Adv. Mater* 7, 604 (1995).
19. A. Cros, *J. Electron Spectrosc. Relat. Phenom.* 59, 1 (1992).
20. M. N. Obrovac, Y. Gao, M. N. Richard, and J. R. Dahn, *Appl. Phys. Lett.* 71, 2262 (1997).
21. J. Nanda, Ph.D. thesis, India Institute of Science, Bangalore (2000).
22. L. R. Becerra, C. B. Murray, R. G. Griffin, and M. G. Bawendi, *J. Chem. Phys.* 100, 3297 (1994).
23. J. Nanda, S. Sapra, and D. D. Sarma. Unpublished results.
24. S. Gorer and G. Hodes, *J. Phys. Chem.* 98, 5338 (1994).
25. Y. Golan, G. Hodes, and I. Rubinstein, *J. Phys. Chem.* 100, 2220 (1996).
26. J. Nanda, S. Sapra, N. Chandrasekharan, and G. Hodes, *Chem. Mater.* 12, 1018 (2000).

27. U. Winkler, D. Eich, Z. H. Chen, R. Fink, S. K. Kulkarni, and E. Umbach, *Phys. Stat. Sol. A* 173, 253 (1999).
28. T. Nakanishi, B. Ohtani, K. Shimazu, and K. Uosaki, *Chem. Phys. Lett.* 278, 233 (1997).
29. C. B. M. Andersson, U. O. Karlsson, M. C. Hankansson, L. O. Olsson, L. Ilver, J. Kanski, and P. O. Nilsson, *Surf. Sci.* 347, 199 (1996).
30. H. Borchert, S. Haubold, M. Haase, H. Weller, C. McGinley, M. Riedler, and T. Moller, *Nano Lett.* 2, 151 (2002).
31. A. A. Guzelian, J. E. B. Katari, A. V. Kadavanich, U. Banin, K. Hamad, E. Juban, A. P. Alivisatos, R. H. Wolters, C. C. Arnold, and J. R. Heath, *J. Phys. Chem.* 100, 7212 (1996).
32. C. F. Hoener, K. A. Allan, A. J. Bard, A. Campion, M. A. Fox, T. E. Mallouk, S. E. Webber, and J. M. White, *J. Phys. Chem.* 96, 3812 (1992).
33. D. S. Ginley and C. Bright, *Mater. Res. Soc. Bull.* 25, 15 (2000).
34. P. D. Szurumi, *Science* 294, 2251 (2001) and related refs. therein.
35. K. Prabhakaran, K. V. P. M. Shafi, A. Ulman, and T. Ogino, *Adv. Mater.* 13, 1859 (2001).
36. S. Morup, *Europhys. Lett.* 28, 671 (1994).
37. D. Schmeisser, O. Bohme, A. Yfantis, T. Heller, D. R. Batchelor, I. Lundstorm, and A. L. Spetz, *Phys. Rev. Lett.* 83, 380 (1999).
38. C. McGinley, S. Al Moussalami, M. Riedler, M. Pflughoefft, H. Borchert, M. Hasse, A. R. B. de Castro, H. Weller, and T. Moller, *Eur. Phys. J. D* 16, 225 (2001).
39. G. Gaggiotti, A. Galdikas, S. Kaciulis, G. Mattogno, and A. Setkus, *J. Appl. Phys.* 76, 4467 (1994).
40. T. J. Goldin and J. P. LaFemina, *Phys. Rev. B* 47, 6518 (1993).
41. H. A. Bullen and S. J. Garrett, *Nano Lett.* 7 (2002).
42. R. F. Mulligan, A. A. Iliadis, and P. Kofinas, *POLY97* preprint (1997).
43. A. Q. Wang, W. Punchaipetch, R. M. Wallace, and T. D. Golden, *J. Vac. Sci. Tech.* (2002), submitted.
44. A. Henglein and P. Mulvaney, *Ber. Bunsen-Ges. Phys. Chem.* 98, 180 (1998).
45. Y. Sun and Y. Xia, *Science* 298, 2176 (2002) and refs. therein.
46. S. L. Logunov, T. S. Ahmadi, M. A. El-Sayed, J. T. Khoury, and R. L. Whetten, *J. Phys. Chem. B* 101, 3713 (1997).
47. H.-G. Boyen, G. Kastle, F. Weigl, B. Koslowski, C. Dietrich, P. Ziemann, J. P. Spatz, S. Riethmuller, C. Hartmann, M. Moller, G. Schmid, M. G. Garnier, and P. Oelhafen, *Science* 297, 1533 (2002).
48. D. D. Eley and P. B. Moore, *Surf. Sci.* 76, L599 (1978).
49. H. Ron and I. Rubinstein, *Langmuir* 10, 4566 (1994).
50. G. Schmid, *Inorg. Synth.* 7, 214 (1990).
51. J. J. Pireau, M. Liehr, P. A. Thiry, J. P. Delrue, and R. Caudano, *Surf. Sci.* 475, 1 (2001).
52. U. Heiz and W.-D. Schneider, *J. Phys. D Appl. Phys.* 33, R85 (2000).
53. G. Kataby, A. Ulman, R. Prozorov, and A. Gedanken, *Langmuir* 14, 1512 (1998).
54. G. Hemakanthi, A. Dhathathreyan, and T. Ramasami, *Bull. Mater. Sci.* 25, 1 (2002).
55. J. Matignier, J. Belloni, M. Delcourt, and J. Chevalier, *Nature* 317, 344 (1985).
56. D. De Caro and J. S. Bradley, *Langmuir* 14, 245 (1998).
57. P. Mulvaney, M. Giersig, and A. Henglein, *J. Phys. Chem.* 97, 7061 (1993).
58. S. W. Han, Y. Kim, and K. Kim, *J. Coll. Inter. Sci.* 208, 272, (1998).
59. P. Chen, X. Wu, X. Sun, J. Lin, W. Ji, and K. L. Tan, *Phys. Rev. Lett.* 82, 2548 (1999).
60. V. P. Dravid, X. Lin, Y. Wang, X. K. Wang, A. Lee, J. B. Ketterson, and R. P. H. Chang, *Science* 259, 1601 (1993).
61. J. Fink, Th. Muller-Heinzerling, J. Pfluger, and B. Scheerer, *Phys. Rev. B* 30, 4713 (1984).
62. P. M. Ajayan, S. Ijima, and T. Ichihashi, *Phys. Rev. B* 47, 6859 (1993).
63. K. H. An, J. G. Heo, K. G. Jeon, D. J. Bae, C. Jo, C. W. Yang, C. Y. Park, Y. H. Lee, Y. S. Lee, and Y. S. Chung, *Appl. Phys. Lett.* 80, 4235 (2002).
64. T. Hanrath and B. A. Korgel, *J. Am. Chem. Soc.* 124, 1424 (2002).
65. B. Zheng, Y. Wu, P. Yang, and J. Liu, *Adv. Mater.* 14, 122 (2002).

Yttrium Oxide Nanocrystals: Luminescent Properties and Applications

Fiorenzo Vetrone, John-Christopher Boyer, John A. Capobianco

Concordia University, Montreal, Canada

CONTENTS

1. Introduction
 2. Synthesis of Yttrium Oxide Nanocrystals
 3. Characterization of Yttrium Oxide Nanocrystals
 4. Luminescence and Optical Spectroscopy of Rare Earth Doped Yttrium Oxide Nanocrystals
 5. Applications
 6. Summary and Conclusions
- Glossary
References

1. INTRODUCTION

The scientific community will remember the 20th century for the advancement of nanoscience, science at the nanometer level, which has led to unprecedented understanding and control over the fundamental building blocks of nature. Recent progress in nanoscience has yielded the ability to not only study but manipulate these building blocks, atoms, and molecules, from which all things are made. This knowledge will no doubt one day change the way most things known to man are created thus allowing limitless possibilities of new discoveries. In the realm of materials science, the natural progression toward the nanoscale has opened up new and exciting possibilities. Many things that were once believed unattainable are now easily within our grasp and the field is quickly burgeoning and adapting. Nanocrystals are of interest both from a fundamental as well as applied point of view as the properties of the materials are drastically altered when the crystallite size reaches the nanometer regime. These particular systems represent a new class

of advanced materials showing particle size dependent phenomena that exhibit unique chemical and physical properties compared to the bulk material.

Over the past two decades, using size control to tailor the characteristics of semiconductor materials has been widely demonstrated [1]. It was shown that the optical properties of these materials could be changed by varying the particle size, thus stimulating a great deal of interest in both basic [2] and applied research [3]. In the early 1990s, Bhargava reported [4–6] that nanocrystalline ZnS:Mn²⁺ can yield high luminescence efficiencies and a spectacular lifetime shortening, which suggested that doped semiconductor nanoparticles formed a new class of luminescent materials for various applications. This effect was in part due to a change in the band structure of the semiconductor as the particle size is decreased. This quantum confinement effect [7], as it became known, led to an increase in the bandgap causing the edges of the bands to split into discrete energy levels [8]. Those findings were recently critically reviewed by Bol and Meijerink [9, 10] who showed substantial misinterpretation of the experimental results; however, this did not stem the tide and numerous papers on the quantum size effects in nanocrystalline semiconductors have since appeared.

The interest in nanoparticles was not only limited to semiconductor materials. Shortly thereafter, many papers appeared on nanocrystalline insulating materials doped with rare earth ions [11–20]. Rare earth doped inorganic materials are particularly suitable for any application which involves the generation of artificial light. The emission of light from the rare earth ions is due mainly to electric and magnetic dipole optical transitions within the $4f^n$ manifold or may also be of interconfigurational nature, involving configurations such as $4f^{n-1}5d$ [21]. The outer, less energetic $5s$ and $5p$ shells shield the f -electrons from the influence of external forces and as a result, the emission spectra consist of relatively sharp lines [22]. Although these $f-f$ transitions are by nature electric dipole forbidden, the crystal

field surrounding the dopant ion relaxes the selection rules so that luminescence is observed [23].

The search for novel light emitting materials, phosphors, has been the subject of continuous study since the early part of the previous century. Light amplification by single crystals doped with rare earth ions is well known. While these single crystals are one of the most common ways to amplify light, several limitations exist. The formation of large defect-free crystals can be time-consuming and the specialized equipment required to produce the crystals is quite costly. A simpler and more cost effective method to obtain phosphors is to use a solid state reaction or precipitation method to produce powders with crystal sizes in the micrometer (4–10 μm) range. Powder phosphors find uses in numerous lighting and display applications, particularly the cathode ray tube (CRT) used in conventional television sets. The resolution of images on a CRT display is related closely to the particle size of the phosphors and thus smaller particles are favorable for higher resolution [24]. However, in a conventional phosphor, a reduction in the particle size was achieved by mechanically grinding techniques, which had little or no control over the particle morphology and ultimately resulted in a decrease of the luminescence efficiency [25]. The grinding methods used for particle size reduction resulted in the formation of a surface dead layer, which provides nonradiative recombination routes thereby lowering the luminescence efficiency [26]. However, the development of techniques to synthesize the crystals directly in the nanometer regime has eliminated the need for such practices and as many electronic display devices are being reduced in size, the development of phosphors with nanometric particle sizes has become vital. Recently, the advent of new techniques allowing for the facile synthesis of nanosized phosphors has made it possible to control both the size and shape of many of the most commonly used luminescent materials. These phosphors with particle dimensions in the nanometer regime have of late become the focus of intense study since it was shown that the luminescence efficiency has been reported to be dependent on the size of the crystallite. Furthermore, the associated size restrictions and extraordinarily large surface areas incur changes in the spectroscopic properties of these materials.

There are two principal reasons for the change in the electronic properties of very small particles. One reason is the quantum size effect, which is a consequence of the strong reduction of quantum mechanical allowed states in a small particle, seen in an increased bandgap. The second reason is a much larger surface/volume ratio, which makes surface and interface effects dominant over volume effects [27]. Such interface effects can completely cover the expected quantum size effect. The large surface-to-volume ratio of nanometer-size particles determines the structure and chemistry of the particles, which in turn controls the structural, electronic, and optical properties of the materials. Studying these surface effects in microcrystalline phosphors would be quite difficult. However, it would be possible in nanocrystalline materials. Therefore, understanding the surface chemistry of nanocrystalline materials could lead to methods of controlling the defect chemistry at the surface [28]. Thus, besides their intrinsic interest, nanocrystalline materials also provide model systems for studying the effects of surfaces on bulk properties.

For many of these studies, nanocrystalline $\text{Y}_2\text{O}_3:\text{RE}^{3+}$ has been the material of choice owing to its favorable physical properties and ease of synthesis in the nanometer regime. The optical properties of yttrium oxide (single crystal and microcrystalline) doped with rare earth ions are very well known. Yttria is a favorable host for rare earth ion substitution for several reasons. It is a refractory oxide having a high melting point ($\sim 2400^\circ\text{C}$) [29] and very high thermal conductivity ($\kappa_{\text{Y}_2\text{O}_3} = 27 \text{ W/mK}$) [30, 31]. Due to its chemical stability and refractoriness, yttria has been considered for many applications, such as high temperature chemical resistant substrates, crucibles for melting reactive materials, and also nozzles for jet-casting molten rare earth–iron magnetic alloys [32]. Yttrium oxide is also optically isotropic, with a refractive index of 1.91 [33]. But perhaps the most important property of all is that yttrium oxide contains low phonon energies. In fact, the dominant phonon energy is 380 cm^{-1} , which is one of the smallest phonon energies among the oxides [34]. This relatively small vibrational energy allows for efficient radiative transitions between electronic energy levels of the rare earth ions.

In nanocrystalline form, the intensity of the rare earth luminescence [35] and lifetime of the excited states [36] have been shown to be inversely proportional to the size of the particles in this host. The luminescence efficiency of these materials is often limited by the dynamics of the rare earth ion, which depends on the interactions with the insulating host and therefore the rare earth dopant can be used as a sensitive probe of the chemistry and structure of its host. A detailed understanding of the structural properties of these materials is an important prerequisite for the elucidation of their optical spectroscopy, as an explanation for this behavior could lie in structural differences between the nanosized and bulk samples.

This chapter is divided into four main sections. The first section discusses the numerous preparation techniques used to synthesize yttrium oxide nanocrystals followed by a section on the methods used in characterizing the material. The third section deals with yttrium oxide nanocrystals doped with tripositive rare earth ions, specifically on the spectroscopy and optical properties of the material. The final section is devoted to some applications of nanocrystalline Y_2O_3 .

2. SYNTHESIS OF YTTRIUM OXIDE NANOCRYSTALS

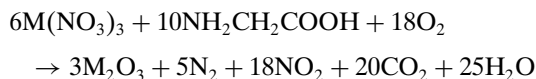
Yttrium oxide, both doped and undoped, can be synthesized by a variety of techniques. In this section we discuss the four major synthesis routes used to obtain yttrium oxide nanocrystals: the combustion method, a variety of wet chemical syntheses, chemical vapor synthesis techniques, and the use of sol–gels.

2.1. Combustion

The combustion synthesis technique used to prepare nanocrystalline yttrium oxide involves the exothermic reaction of an oxidizer and an organic fuel. Typical oxidizers include metal nitrates, ammonium nitrate, or ammonium perchlorate, while typical fuels may include urea ($\text{CH}_4\text{N}_2\text{O}$),

carbohydrazide ($\text{CH}_6\text{N}_4\text{O}$), or glycine ($\text{C}_2\text{H}_5\text{NO}_2$) [37]. One of the most attractive features of combustion synthesis is that nanocrystals are produced at relatively low temperatures with reduced processing time. Thus, a high temperature furnace is not required as the reaction is initiated at temperatures of 500 °C or less. In a typical reaction the precursor mixture of distilled water, oxidizer, and fuel decomposes, dehydrates, and ruptures into a flame after approximately 5 minutes creating a voluminous foamy powder. The combustion reaction is influenced by a number of parameters such as type of fuel, fuel-to-oxidizer ratio, use of excess oxidizer, ignition temperature, and water content of the precursor mixture [11, 38].

In the synthesis technique of rare earth doped yttrium oxide nanocrystals first used by Tao [39] and later adapted by Bettinelli [40–42], glycine served as the fuel for the combustion reaction, being oxidized by nitrate ions. The stoichiometric synthesis reaction is expressed as follows:



where M is Y and/or RE. In the combustion procedure, the reaction temperature has a great influence on the particle size of the material and by adjusting the glycine-to-metal nitrate molar ratio, the combustion flame temperature can be controlled. The stoichiometric molar ratio of glycine-to-metal nitrate can be calculated using the method of Jain et al. [43] where the ratio is expressed in terms of the elemental stoichiometric coefficient, Φ_e , defined as

$$\Phi_e = \left(\sum (\text{coefficient of oxidizing elements in specific formula}) \times (\text{valency}) \right) \\ / \left((-1) \sum (\text{coefficient of reducing elements in specific formula}) \times (\text{valency}) \right) \quad (1)$$

The mixture is stoichiometric when $\Phi_e = 1$, fuel-lean when $\Phi_e > 1$, and fuel-rich when $\Phi_e < 1$. Stoichiometric glycine-to-metal nitrate molar ratios produce the maximum temperature in the combustion process. The following equation can be used to approximate the adiabatic flame temperature, T_f , for a combustion reaction:

$$T_f = T_o + \frac{\Delta H_r - \Delta H_p}{c_p} \quad (2)$$

ΔH_r and ΔH_p are the enthalpies of formation of the reactants and products, respectively, and c_p is the heat capacity of the products at constant pressure. The reaction is initiated after the water in the precursor solution boils; thus, T_o is 373 K, the boiling point of water [44].

For rare earth oxides, it was shown that lower temperatures lead to smaller particle sizes. In the case of $\text{Y}_{1.80}\text{Eu}_{0.20}\text{O}_3$ produced by this method, average particle sizes of 8 and 40 nm were obtained for oxidant-rich glycine-to-metal nitrate molar ratios of 1.0:1 (reaction temperature of 1000 °C) and 1.3:1 (reaction temperature of 1320 °C),

respectively [39]. For a stoichiometric ($\Phi_e = 1$) glycine-to-metal nitrate molar ratio of 1.7:1 (reaction temperature of 1420 °C) $\text{Y}_2\text{O}_3:\text{Eu}^{3+}$ nanocrystals with an average particle size of 70 nm were produced. In the synthesis of nanocrystalline Y_2O_3 powders doped with RE_2O_3 (RE = Ce, Pr, Nd, Eu, Gd, Ho, and Er) prepared using the same procedure, a ratio of 1.2:1 was employed yielding nanocrystals with an average particle size of 20 nm with a yield of approximately 80% [40, 42]. The infrared (IR) spectra of the resultant powders indicated the presence of residual NO_3^- from the combustion reaction. The powders were subsequently treated at 500 °C for 1 hour to decompose the nitrate ions. Laser-excited Raman and Fourier transform IR (FTIR) spectroscopy showed that the treatment was sufficient to remove the residual nitrate ions [41].

The combustion process has been used by many to synthesize nanocrystalline yttrium oxide or its derivatives [32, 45–47]. The appearance of product was shown by Sun et al. [46] to be dependent on the molar ratio of glycine and rare earth in the precursor solution. When the ratio was less than 1, a light gray product was formed because the nitroxide was formed instead of the oxide due to the incomplete decomposition of the nitrate. A white, crisp foamy product was obtained when the glycine-to-rare earth ratio was between 1 and 2.5; however, when this ratio was larger than 3, much more glycine in the product made the product yellowish and hygroscopic because of the residual glycine. A study of the combustion synthesis of nanocrystalline yttrium oxide was carried out with yttrium nitrate as the oxidizer but using different fuels [48] (Table 1). A difference in particle size with the use of different fuels was observed and was shown to depend on the number of moles of gaseous products released during combustion. As more gas is freed, the agglomerates are disintegrated and more heat is carried from the system thus hindering particle growth [49]. A novel approach has been reported which does away with the furnace and makes use of microwaves to initiate a self-propagating combustion reaction [50]. The microwave irradiation couples with polar wet chemical precursors that have a high dielectric constant and produces the final product in a very short time.

A gel combustion process was employed by Roy and co-workers [51] to produce yttrium oxide nanocrystals with a mean particle size of 25 nm. They demonstrated that a combination of citrate and nitrate anions in the precursor of a gel combustion process led to a low temperature combustion reaction with low reaction enthalpies. The conventional

Table 1. Different fuels used with stoichiometric amounts of $\text{Y}(\text{NO}_3)_3$ in the combustion reaction.

Fuel	Chemical formula
Oxalodihydrazide (ODH)	$\text{C}_2\text{H}_6\text{N}_4\text{O}_2$
Malonodihydrazide (MDH)	$\text{C}_3\text{H}_8\text{N}_4\text{O}_2$
Glycine	$\text{C}_2\text{H}_5\text{NO}_2$
Diformylhydrazide (DFH)	$\text{C}_2\text{H}_4\text{N}_2\text{O}_2$
Tetraformal trisazine (TFTA)	$\text{C}_4\text{H}_{16}\text{N}_6\text{O}_2$
3-Methylpyrazol-5-one (3MP5O)	$\text{C}_4\text{H}_6\text{N}_2\text{O}$

chemical gelation route for synthesizing ceramic powders experiences problems like:

- (i) drying due to hygroscopy of the gels,
- (ii) adherence of the gels to glass surfaces,
- (iii) repeated calcination due to swelling.

However, the gel combustion process directly yielded decomposed-intermediate powders and therefore overcame the above difficulties. The gel was prepared by gelling an aqueous solution of solid yttrium nitrate [$Y(NO_3)_3 \cdot 6H_2O$] and anhydrous citric acid by evaporation of water at 80 ± 5 °C. A white precipitate was formed upon further heating under the same conditions. As soon as the precipitate was formed, the temperature of the hot plate was increased to 200 °C. The precipitates underwent a combustion process and yielded solid products along with the evolution of gases. The combusted products were calcinated at 750 °C in air for 2 hours at a heating rate of 350 °C per hour.

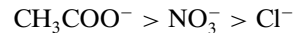
2.2. Wet Chemical Synthesis

Wet chemical processes are an attractive means of synthesizing yttrium oxide nanocrystals since they offer a new level of control over the particle size, crystallinity, and microstructure. A popular technique for the synthesis of yttrium oxide nanocrystals involves a combined method of coprecipitation and hydrothermal processes in the presence of a seed [52]. The coprecipitation method was employed to produce a gel in the presence of a surface modifier followed by the addition of Y_2O_3 seeds to the coprecipitated gel, which was then subjected to a hydrothermal treatment. Synthesis of nanocrystals via wet chemical methods requires control over the thermodynamics of the interfaces due to their tendency to minimize their surface energy by agglomerating or growing large particles. Using a surface modifier in highly alkaline media ($pH > 10$) is one of the approaches used to modify the surface of growing particles. Thus to control the particle size, addition of a surface modifier is necessary as it coats the surface of the particles and provides a barrierlike protection against agglomeration [53].

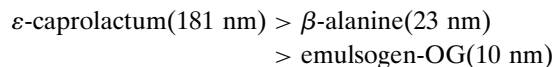
Europium doped yttrium oxide was synthesized via preparation of a precursor solution by dissolving a known amount of yttria salt and $Eu(NO_3)_3 \cdot 5H_2O$ in a solvent and was stirred for 2 hours. The modifier solution was prepared by dissolving 10 wt% of surface modifier (1:1 mixture of tween-80 and β -alanine, ϵ -caprolactum, or emulsogen-OG) with respect to Eu_2O_3/Y_2O_3 in 50 ml of aqueous ammonium hydroxide solution ($pH > 10$) and was stirred for 1 hour at room temperature. The precursor solution was then added to the modifier solution at a controlled rate with vigorous stirring, which converted into gel. The gel was then centrifuged (6000 rpm for 30 minutes) and the aqueous solution was removed by refluxing in toluene. The toluene was removed by evaporation and the resulting white powder was dried in an oven at 60 °C for 24 hours.

In this study [54] different solvents were used (ethanol and water) in the precursor solution, and it was found that the Eu^{3+} emission was higher when ethanol was used. Similarly, different precursor salts were studied—yttrium nitrate [$Y(NO_3)_3 \cdot 5H_2O$], yttrium acetate [$Y(CH_3COO)_3 \cdot 4H_2O$], and yttrium chloride ($YCl_3 \cdot 6H_2O$)—and it was determined

that the Eu^{3+} emission intensity decreased with the type of precursors used in the following order:



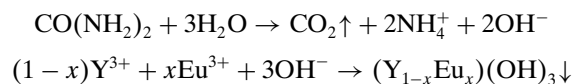
These effects on the luminescence and spectroscopy of the Eu^{3+} ion will be discussed in detail in Section 4. The modifier was shown to play an important role on the crystallite as the particle size decreased in the following order of modifiers used:



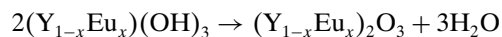
The concentration of the modifier was increased from 0 to 10 wt% with respect to Eu_2O_3/Y_2O_3 and the particle size was reduced from 6 μm to 10 nm [53]. The modifier protects the generated particles by forming a layer and significantly reduces the surface free energy of the particulate matter thus preventing interaction with neighboring particles. The size of yttrium doped nanocrystals can be successfully tailored using chemical wet synthesis in the presence of a modifier in different pH conditions [55]. The size and morphology of the particle are greatly influenced by the pH conditions, where low pH conditions were found to be favorable for obtaining nanocrystals with uniform morphology. Low pH (< 7) is suitable for obtaining the particles with large surface area and low pore size and volume.

This synthesis method was also employed by other groups to produce yttrium oxide nanocrystals doped with 10 mol% Nd, Gd, Tb, Ho, and Er [56, 57] and having an average particle size of about 10 nm.

A forced hydrolysis technique can be used to prepare $Y_2O_3:Eu^{3+}$ nanocrystals [58]. This synthesis method produces spherical particles and can effectively control the particle size. In this study, given concentrations of $Y(NO_3)_3$ and $Eu(NO_3)_3$ solutions were prepared by dissolving Y_2O_3 and Eu_2O_3 in nitric acid and diluting with deionized water to 0.05 mol/L. The resulting nitrate solution was mixed with 0.5 M urea solution, filtered, and heated for 3 hours in an isothermal oven. During the heating, the urea reacts with water to release OH^- thus allowing the Y^{3+} and Eu^{3+} cations to combine with the OH^- to form $(Y_{1-x}Eu_x)(OH)_3$ precipitates, which were amorphous particles at the processing temperature. The following reactions were involved in the processing of the particles:



The precipitates were separated by high speed centrifuging and were then washed with deionized water to remove residual urea and nitric ions. The resulting powder was washed with ethanol to remove water and fired at different temperatures to form $Y_2O_3:Eu^{3+}$:



The size of the nanocrystals increased as the firing temperature increased, and at 1400 °C each particle was in a single crystalline phase.

The urea homogenous precipitation method was also employed to prepare nanocrystals of Y_2O_3 doped with Er^{3+} , Er^{3+} co-doped with Yb^{3+} , and Eu^{3+} [59–62]. This method involves the addition of urea to an aqueous solution of $Y(NO_3)_3$ and $RE(NO_3)_3$ followed by heating at 80 °C for different amounts of time. The solution was separated by centrifugation and repeatedly washed. The obtained precipitate was dehydrated by freeze drying and calcined at 980 °C for 3 hours to obtain the nanocrystals. By controlling the reaction time of the homogeneous precipitation, different particle sizes could be obtained with longer reaction times yielding larger particles. Reaction times of 1, 1.5, 2, and 2.5 hours were employed and yielded nanocrystals with particles sizes of 43, 55, 68, and 71 nm, respectively.

A novel synthesis technique was reported by Silver et al. [63, 64] in which colloidal copolymers were used to produce $Y_2O_3:Eu$ nanocrystals. Copolymers of NIPAM (*N*-isopropylacrylamide) and AAc (acrylic acid) as well as NIPAM (*N*-isopropylacrylamide) and 2-acrylamido-2-methylpropane sulfonic acid were added to the aqueous solution of urea (10 wt%) when the temperature of decomposition of urea was reached (>80 °C). Under these conditions, the microgel was in its collapsed form having a relatively small hydrodynamic diameter and an increased charge density. The solution was kept boiling for 1 hour and then filtered. The precipitates were washed with deionized water and dried at 110 °C in an oven. To convert the powder from the hydroxycarbonate precursor to the oxide the product was fired at 980 °C for 6 hours.

Nanometer $Y_2O_3:Eu$ particles were also synthesized by firing a hydroxy carbonate precursor, which was prepared from two aqueous solutions [24]. One solution was composed of the metal nitrates $Y(NO_3)_3$ and $Eu(NO_3)_3$ while the other was an aqueous Na_2CO_3 solution. The two solutions were mixed and stirred for 10 minutes. The precipitate was separated by centrifugation at 3000 rpm for 15 minutes and was dried at 80 °C for 24 hours. The precursors were fired at 900 °C for 30 minutes in air and cooled rapidly to room temperature yielding particles with diameters of approximately 60 nm.

It was also possible to produce nanocrystals of $Y_2O_3:Eu^{3+}$ by colloidal chemical methods [65] involving precipitation of amorphous spherical precursor material, which was then fired to form the nanocrystalline material. Yttrium and europium chloride salts in water were adjusted to a pH of ~1 using HCl. An excess of urea, typically 15×, was dissolved in the solution and then heated to >80 °C for 2 hours. The urea was slowly decomposed and a burst of particle nucleation was achieved when a certain pH was reached (pH 4–5). The particles continued to grow uniformly until the cation supply was exhausted. The obtained precipitate was washed, flocculated, dried, and fired in air for 3 hours at temperatures greater than 1000 °C. The material consisted of agglomerations of nanocrystals with the size of the agglomerates being defined by the drying stage. It was also possible to produce nanocrystals in the 2–10 nm range by colloidal methods which were defect-free. The surface of the nanocrystals can provide nonradiative recombination routes. However, by using a surface-capping agent, these effects can effectively be minimized. To a solution of $EuCl_3 \cdot 6H_2O$ in methanol, an equal amount of triocetyl phosphine oxide

(TOPO) solution was added. The TOPO binds to the surface and has three functions:

- (i) It prevents particle agglomeration (steric passivation).
- (ii) It achieves electrical passivation.
- (iii) The ratio of TOPO to Eu^{3+} ions may be used to control the particle size.

Excitons migrating to the surface can deexcite, both radiatively and nonradiatively via surface dangling bonds, which may act as trap states. TOPO bound to the surface passivates these states and allows only recombination with the Eu^{3+} 4*f* shell. The solution was stirred for 10 minutes and the nanocrystals were precipitated by the addition of a controlled amount of methanolic NaOH solution (pH 5.5–6). The precipitation was carried out in a nonaqueous environment in order to reduce the possibility of hydroxide formation. When the colloidal precipitation reaction occurs in an alcoholic solution, the dehydrating properties of the alcohols result in formation of the oxide [66]. A TOPO:Eu³⁺ ratio of 1:1 resulted in particles in the 4 nm range.

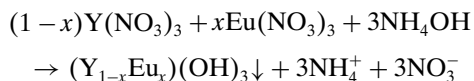
Eu-doped yttrium oxide nanocrystals were synthesized using the reverse microemulsion technique, which is a particularly attractive reaction medium in terms of being able to obtain monodispersed nanoparticles with controlled morphology [67]. Reverse microemulsion consists of an aqueous phase dispersed as microdroplets (<0.1 μm) surrounded by a monolayer of surfactant molecules in a continuous oil phase. The dispersed water droplets behave as nanoreactors for the synthesis and the surfactant monolayer restricts the growth of the particles [68]. In this study, the nanocrystals were prepared by mixing two nonionic reverse microemulsions consisting of:

- (i) poly(oxyethylene)₅ nonylphenyl ether (NP5)
- (ii) poly(oxyethylene)₉ nonylphenyl ether (NP9)

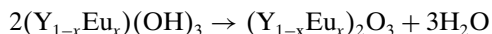
and $Y(NO_3)_3/Eu(NO_3)_3$ or ammonium hydroxide solutions and cyclohexane. Microemulsion I was prepared by mixing NP5/NP9 in a 2:1 weight ratio as the surfactant (20 wt%), cyclohexane as the continuous oil phase (62 wt%), and aqueous yttrium nitrate/europium nitrate salt solution as the dispersed aqueous phase (18 wt%). In microemulsion II, aqueous ammonium hydroxide solution (0.5 M) was used as the water phase with all other components identical to those in microemulsion I. Equal amounts of microemulsion I and II were mixed with continuous stirring at 30 °C for 2 hours followed by the addition of acetone to break the microemulsion and allow the yttrium–europium hydroxides to be sedimented. The sedimented particles were repeatedly washed with acetone and water to remove any oil and surfactant adsorbed on the surface of the particle. The particles were collected, dried at 90 °C for 3 hours, and crushed by a marble mortar. The yttrium–europium hydroxide particles were calcined at 900 °C for 2 hours for conversion to the oxide.

For reactions in reverse microemulsions, reactants are confined inside the dispersed water droplets and exchanges of those by collision and coalescence between droplets are needed. Chemical reaction inside the water droplets occurred by the following mechanism where $Y(NO_3)_3$ and

$\text{Eu}(\text{NO}_3)_3$ in the water droplet reacted with ammonium hydroxide to produce the precipitates:

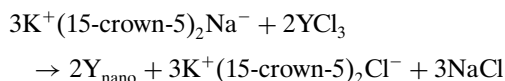


The Eu-doped yttrium hydroxide particles were converted into Eu-doped yttrium oxide nanocrystals (diameter of 20–30 nm) by calcination at 900 °C for 2 hours:



The microemulsion route has a remarkable advantage in comparison with other methods. All starting materials are mixed at the molecular level in a solution; therefore, nanocrystals with high chemical purity and a high degree of homogeneity are achievable. The microemulsions are greatly influenced by temperature [69]. As such, they were kept around 30 °C. Otherwise, phase separation or phase conversion can occur.

Nelson and co-workers [70] prepared nanocrystalline yttrium oxide by homogeneous alkalide reduction according to the following scheme:



The by-products (crown ether–15-crown-5) were removed by washing with aerated H_2O at ambient temperature. This process oxidized the metal to Y_2O_3 without any apparent evolution of gas. The resultant nanocrystals (11.8–20.1 nm) were separated from the wash via centrifuge.

Yttrium oxide nanocrystals co-doped with Er^{3+} and Yb^{3+} as well as nanocrystals of $\text{Y}_2\text{O}_3:\text{Eu}^{3+}$ were prepared using an emulsion liquid membrane system [71, 72]. The initial solution was made by mixing in a volume ratio of 1:2 the internal water phase (W1) for the emulsion (0.1 mol/L oxalic acid) and the organic membrane phase (O), which was composed of kerosene containing 5 wt% Span 83 (sorbitan sesquioleate) and 0.5 mol/L of DTMBPA [bis(1,1,3,3-tetramethylbutyl)phosphinic acid] or VA-10 (2-methyl-2-ethylheptanoic acid). Following this mixture, emulsification was achieved by means of a mechanical homogenizer (12,000 rpm) and the mean diameter of the internal water droplets produced was circa. 3 μm . The resulting W1/O emulsion (10 ml) was then poured into an external water phase, W2 [an aqueous solution containing 50 ml of $\text{RE}(\text{NO}_3)_3$ or RECl_3], and stirred vigorously, with a magnetic stirrer, to form the W1/O/W2 emulsion. The total metal concentration of the external solution was kept fixed at 4 mmol/L, but the feed molar ratio was varied. When VA-10 was used, CH_3COONa (0.02 mol/L) was added to the external phase for those cases to maintain the external water phase pH above 4. The size of the emulsion drops, dispersed in the external water phase, was less than 2 mm. After stirring for the required time, the W1/O emulsion was separated from the external aqueous solution and demulsified by adding approximately 50 ml of ethylene glycol or acetone. The particles, formed in the internal water droplets, were then separated by centrifuge, washed with acetone, and dried in a vacuum. The oxalate particles were finally calcined

in air, at 1073 K for 2 hours, to obtain the desired oxide particles, $\text{Y}_2\text{O}_3:\text{Yb}$, Er or $\text{Y}_2\text{O}_3:\text{Eu}$ with particle diameters in the 20–30 nm range.

2.3. Chemical Vapor Synthesis

Tissue's group [73] showed that nanocrystals of ZnO , Eu_2O_3 , and $\text{Y}_2\text{O}_3:\text{Eu}^{3+}$ could be synthesized by gas-phase condensation after directly vaporizing metal-oxide starting materials with a CO_2 laser yielding crystals with particle sizes between 3 and 30 nm depending on such preparation conditions as cold-finger temperature, distance between heated target and cold finger, and the atmosphere pressure [28]. The atoms or molecules, which are vaporized by the laser, are cooled due to collisions with inert-gas molecules (Ar, for example) and form clusters that are collected on a cold finger. This preparation process has the distinct advantage of avoiding reaction and contamination problems encountered when trying to heat high melting point oxides in crucibles [74]. Nanocrystalline monoclinic $\text{Y}_2\text{O}_3:\text{Eu}^{3+}$ was prepared by using a continuous wave CO_2 laser (22–50 W) focused with a ZnSe lens to a 2 mm diameter to vaporize pressed and sintered ceramic pellets of $\text{Y}_2\text{O}_3:\text{Eu}^{3+}$ under an N_2 atmosphere at 400 Torr. The starting materials were prepared by cold pressing mixtures of predried Eu_2O_3 and Y_2O_3 and sintering overnight in platinum crucibles at 1000 °C. The $\text{Y}_2\text{O}_3:\text{Eu}^{3+}$ pellets were ground in an agate mortar and pestle and resintered to improve homogeneity and were then placed on a slow rotating platform in a vacuum chamber and irradiated with the laser [75]. The nanocrystalline particles were produced at a rate of approximately 0.5 g/kW-hr and collected on a cold finger filled with water at a temperature of 50–60 °C, which kept the quenching temperature fairly constant [76].

A chemical vapor technique was developed by Konrad and co-workers [77] to produce yttrium oxide nanocrystals (10 nm diameter) with the cubic structure in a single processing step. Europium doped nanoparticles were synthesized in a tubular flow reactor by chemical vapor reaction using tetramethylheptanedionato yttrium, $\text{Y}(\text{C}_{11}\text{H}_{19}\text{O}_2)_3$, and tetramethylheptanedionato europium, $\text{Eu}(\text{C}_{11}\text{H}_{19}\text{O}_2)_3$, as starting materials [78]. The powder precursors at room temperature were stored in two separate vaporizers and submerged in separate oil baths, which were kept at a constant 438 and 428 K for Y and Eu, respectively. Argon was used as a carrier gas (200 ml/min) for the $\text{Y}(\text{C}_{11}\text{H}_{19}\text{O}_2)_3$ and $\text{Eu}(\text{C}_{11}\text{H}_{19}\text{O}_2)_3$ vapors. To prevent early condensation of the vaporized precursor, a ribbon heater was used to heat the tubes between the vaporizer and furnace. Pure O_2 was introduced into the furnace via a separate line. The reaction chamber, which consisted of an alumina tube with a cylindrical heating zone, was kept at a constant temperature of 1273 K. A water-cooled cylinder was installed at the end of the reaction chamber for collecting the synthesized powder (90% yield). The samples were annealed in air for 5 hours at 900 and 1100 °C resulting in grain growth to 20 and 50 nm, respectively [79]. Schmechel's group [27] used the same starting materials but synthesized nanocrystals of $\text{Y}_2\text{O}_3:\text{Eu}^{3+}$ in MCM-41 (pore size 2.7 nm). The precursors were dissolved in ethanol and the empty molecular sieve was dipped into the solution for 30 minutes. The sample was

dried and heat treated for 5 hours at 600 °C and nanocrystals with a mean particle diameter of 7 nm were obtained.

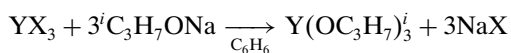
Yttrium oxide phosphor powders doped with Eu^{3+} and Tb^{3+} ions were prepared by supercritical CO_2 -assisted aerolization and pyrolysis [25] from aqueous solutions of $\text{Y}(\text{NO}_3)_3$, $\text{Eu}(\text{NO}_3)_3$, and $\text{Tb}(\text{NO}_3)_3$. The precursor nitrates were dissolved in water, forming a solution and the solution along with supercritical CO_2 were pumped into, and mixed, in a low-dead-volume tee at 1500 psi by an HPLC pump, forming a microemulsion of the aqueous solution with CO_2 . During decompression, the CO_2 expanded rapidly from the emulsion, forming a gas with a significant expansion in volume, which produced highly dense and fine aerosols. The aqueous metal nitrate aerosols were converted into spherical oxide particles by introducing them into a quartz tube furnace at high temperature (at 1010 °C) where they were desolvated; then, thermally induced reactions took place and resulted in the desired fine powder materials. Since the particles were prepared from each individually suspended aerosol droplet, agglomeration could be effectively minimized.

2.4. Sol-Gel Synthesis

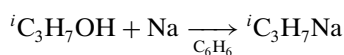
Rare earth doped yttrium oxide nanocrystals can also be synthesized using sol-gel methods. Bhargava et al. first showed that yttrium oxide nanocrystals doped with tripositive terbium could be synthesized using sol-gel processing techniques [35, 80]. Metallic sodium was reacted with isopropanol resulting in sodium isopropoxide, which was reacted with yttrium and terbium chlorides to obtain yttrium and terbium isopropoxides. The metal isopropoxides were combined in azeotropic distillation of butanol to exchange the isopropoxide to butoxide groups. A fivefold excess of *n*-butanol was used. The resulting yttrium *n*-butoxide was used as a stock solution and was combined with yttrium butoxide, which was prepared separately to vary the terbium concentration in the nanocrystals. This method produced nanocrystals of $\text{Y}_2\text{O}_3:\text{Tb}$ with particle sizes between 2.5 and 5.5 nm [81]. In order to study particle size effects, the nanocrystals were heated between 300 and 500 °C to induce agglomeration [82].

Nanocrystalline $\text{Y}_2\text{O}_3:\text{Er}^{3+}$ could be prepared by using commercial Y_2O_3 sol, which was composed of 14% colloidal Y_2O_3 dispersed in acetate solution at pH 7 with a nominal particle size of 10 nm [83]. The preformed Y_2O_3 sol colloidal dispersion was mixed with an appropriate amount of $\text{Er}(\text{NO}_3)_3$ and approximately 1% by mass of gelation catalyst (HNO_3) forming an opaque gel after 1 hour. The resulting white powders were obtained following a vacuum oven treatment and a series of higher temperature heat treatments.

Nanocrystalline $\text{Y}_2\text{O}_3:\text{RE}^{3+}$ could also be produced by a sol-gel process using yttrium isopropilate [$\text{Y}(\text{OC}_3\text{H}_7)_3$] [84]. The synthesis of $\text{Y}(\text{OC}_3\text{H}_7)_3$ may be represented as

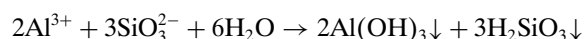


Sodium metal and benzene were added to the newly formed yttrium isopropilate at low temperature (0 °C) initiating the following reaction:



After the reaction was complete, YCl_3 was added to the mixture followed by a mixing period of 2 hours at the boiling point of benzene (80 °C) and the pH of the solution (pH < 7) was measured to ensure the reaction had gone to completion. The solution was left to stand for a few days while the precipitate separated from solution. Once again benzene was added to the precipitate, mixed, and centrifuged. The solutions were combined and the alcohol and benzene were evaporated followed by centrifugation. The dry $^i\text{C}_3\text{H}_7\text{OH}$ and acetylacetone were added to the obtained product in a 2:1 ratio. The hydrolysis of $\text{Y}(\text{OC}_3\text{H}_7)_3$ was performed at room temperature and the dilute solutions of RE salts were added under ultrasonic mixing. The obtained gels were dried at 90 °C resulting in powders whose crystallite size was in the range of 10–15 nm.

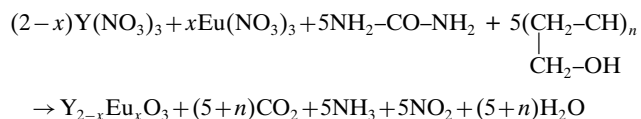
Nanocrystalline $\text{Y}_2\text{O}_3:\text{Eu}$ powders with 20 nm diameters were prepared by the polyacrylamide gel method. It is known that defects on the particle surface could reduce the luminescence efficiency of the material. Thus, to improve the luminescent efficiency, the powders were coated by dipping them in a solution of $\text{KAl}(\text{SO}_4)_2$ for 15 minutes so that Al^{3+} was absorbed on the surface of the nanocrystals [85]. Following centrifugation, the powders were dipped in a solution of Na_2SiO_3 for 15 minutes and initiated the following reaction on the surface:



After washing and separation, via centrifugation, the powders were calcined at 400 °C for 3 hours thereby improving the dispersity of the nanocrystals.

Nanometer $\text{Y}_2\text{O}_3:\text{Eu}^{3+}$ was synthesized by a simple sol-gel process involving the reaction of Y_2O_3 and Eu_2O_3 with diluted HNO_3 [86]. The amount of HNO_3 added was just enough to dissolve the oxides. Citric acid was then added to this solution with a 2:1 molar ratio of metal ions to citric acid. The concentration of metal ions in the obtained solution was 1 mol/L, and the pH was about 0.5. The solution was then heated at 95 °C for approximately 2 hours while stirring and a transparent gel was obtained, which was then dried at 95 °C for about 1 hour to obtain a gray fluffy powder. The dry gel was then calcined at a temperature of 600 °C for 3 hours and the nanocrystalline material with a mean crystallite size of 14 nm was obtained.

Another group utilized a sol-gel thermolysis method to similarly produce $\text{Y}_2\text{O}_3:\text{Eu}^{3+}$ nanocrystals with particle diameters in the 10–20 nm range [87]. The authors used urea as the fuel to produce high temperature PAM (polyacrylamide) and/or PVA (polyvinyl alcohol). The organic polymers not only served as the dispersing media but also functioned as a secondary fuel due to the presence of the alcohol or amide groups, which produced a strong exothermic reaction. The formation of Y_2O_3 nanocrystallites from the starting materials, for the PVA system as an example, occurred via the following reaction:



The mixed (Y/Eu)(NO_3)₃ stock solution was prepared using 0.13 M YNO_3 and 0.005 M EuNO_3 solutions obtained from

the corresponding oxides by dissolving dilute nitric acid. To this solution, 0.3375 M urea and 0.3375 M PAM (or 0.3375 M PVA) solutions were added and stirred thoroughly. This mixture was polymerized by adding 10 ml of 30% H_2O_2 initiator and heated to 60 °C in order to accelerate the polymerization process. The total reaction volume was 50 ml and the concentration of Eu^{3+} was fixed at an optimum value of 4%, with respect to Y^{3+} in all cases. For the sol-gel preparation, 1% ammonia solution was added to 10 ml of the stock solution in a beaker at a rate of 10 drops per minute to precipitate $\text{Y/Eu(OH)(CO}_3\text{)}$ gel and the excess water was evaporated at 100 °C. The prepared precursor was pyrolyzed at 400 °C for approximately 30 minutes. The product obtained upon combustion of this mixture produced a highly fluffy, voluminous carbonaceous mass. This carbonaceous mass was heated around 600 °C for approximately 2 hours so that the carbon was completely removed and produced fine grains of nanocrystalline $\text{Y}_2\text{O}_3\text{:Eu}^{3+}$. It should be noted that the nanocrystals were not further heat treated once synthesized.

3. CHARACTERIZATION OF YTTRIUM OXIDE NANOCRYSTALS

The material scientists of today have a large number of tools and techniques at their disposal to probe the physical properties of nanocrystalline materials such as yttrium oxide. X-ray diffraction (XRD) is a powerful tool for determining crystallite phase of the synthesized powders along with the degree of crystallinity and particle size. Transmission electron microscopy (TEM) and scanning electron microscopy (SEM) allow for visual probing of the nanocrystal morphology on the nanometer and micrometer scale, respectively. Because of its high resolution, TEM also allows for particle size determination to compliment that obtained from XRD techniques. Through Brunauer, Emmett, Teller (BET) analysis the surface area of the synthesized crystals may be determined which can also provide insight into their morphology. IR spectroscopy, thermogravimetric analysis (TGA), and differential thermal analysis (DTA) allow for the detection of adsorbed species on the nanocrystalline Y_2O_3 that may be detrimental to their performance as phosphors and catalysts. Through the use of these characterization methods, a detailed picture can be painted of the physical properties of Y_2O_3 nanocrystals.

3.1. X-Ray Diffraction

For the most part, powder XRD was utilized to determine the phase and degree of crystallinity of the yttria powders obtained from the various synthesis techniques. The majority of synthesis methods resulted in the formation of cubic yttria [39, 40, 54, 79], with the exception being the gas phase condensation method employed by Tissue et al. that resulted in monoclinic Y_2O_3 [28, 74]. The monoclinic Y_2O_3 lattice has a space group $C2/m$ and possesses three crystallographically distinct cation sites (A, B, and C) with sevenfold coordination, each having point group symmetry C_s (Fig. 1). The coordination of two cation sites (A and B) can be described

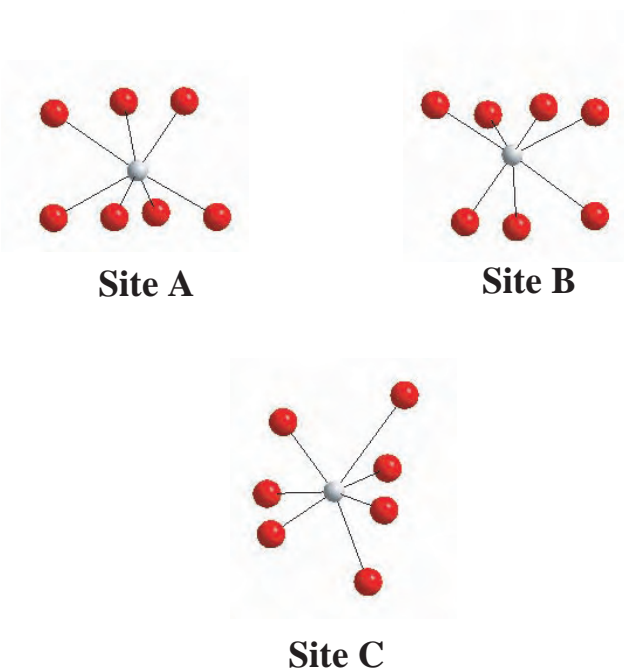


Figure 1. Pictorial representation of the three crystallographically distinct C_s cation sites (A, B, and C) with sevenfold coordination of the monoclinic Y_2O_3 lattice.

by six oxygens at the apices of a trigonal prism with a seventh oxygen lying along the normal to a face. The coordination of the third site (C) is described as a distorted octahedron with a seventh oxygen at a long distance [88]. Cubic Y_2O_3 crystallizes in the C bixbyite structure, with space group $Ia\bar{3}$. Y^{3+} ions occupy in the unit cell 24 sites with point symmetry C_2 and 8 sites with point symmetry C_{3i} [89, 90]. It should be noted that in ^{151}Eu Mössbauer studies on nanocrystalline $\text{Y}_2\text{O}_3\text{:Eu}^{3+}$, prepared by combustion synthesis, one group observed a preferential occupation of the dopant ions in the C_{3i} site [91]. A schematic representation of the two sites is shown in Figure 2. The XRD pattern of the as-synthesized powders from combustion reactions indicated that crystalline yttria was achieved without any calcinations step [32]. Further calcinations of the powders yielded an increase in crystallinity, which was

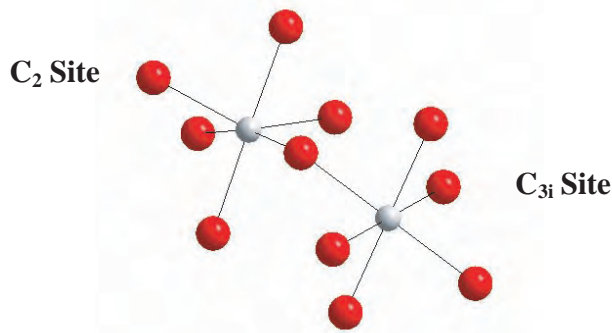


Figure 2. Pictorial representation of the C_2 and C_{3i} cation sites of the cubic Y_2O_3 lattice.

reflected in the diffraction pattern. Single cubic crystalline phase of space group $Ia\bar{3}$ was the result with no amorphous materials present.

Chemical methods also resulted in highly crystalline products with the absence of impurity phases [92] with diffractograms, which were almost identical to combustion samples [56]. In both cases an absence of preferential orientation was observed [57]. XRD results also revealed that the cell parameters of the cubic Y_2O_3 lattice increased with the ionic radius of the rare earth dopant ion independent of the synthesis route [56]. XRD of $Y_2O_3:Eu^{3+}$ particles synthesized using a copolymer of NIPAM and AAc also showed cubic Y_2O_3 [64]. As per results obtained with combustion samples, particles synthesized via a forced hydrolysis technique that were annealed at high temperatures exhibited higher crystallinity. The XRD peaks of these powders were smaller [full width at half maximum (FWHM)] than those of the particles fired at low temperatures [58].

XRD data from two $Y_2O_3:Eu^{3+}$ samples synthesized utilizing microemulsion techniques resulted in particles that were initially amorphous [67, 69]. Calcination of the powders in both cases led to a strong cubic crystalline nature. Huang et al. showed that powders calcinated at 600 °C or above demonstrated good crystallinity with little difference observed between 600, 800, and 1000 °C powders [69].

XRD of Eu(III) and Tb(III) doped yttrium oxide phosphor powders synthesized by supercritical CO_2 -assisted aerosolization and pyrolysis (at 1010 °C) showed that the as-prepared powders were crystalline with peaks corresponding to cubic Y_2O_3 [25]. Large width of peaks obtained indicated either small grain size or poor crystallinity. Annealing of powders at 1200 °C for 1 hour produced sharp diffraction peaks, which indicated growth in grain size and improved crystallinity.

A secondary use of X-ray diffraction is the measurement of line broadening to determine crystallite size. It is possible using Scherrer's equation,

$$B(2\theta) = \frac{0.94\lambda}{L \cos(\theta)} \quad (3)$$

where $B(2\theta)$ is the full width in radians subtended by the most intense peak in the X-ray diffraction pattern, λ is the X-ray wavelength, and L is the particle size broadening used to determine the crystallite size of the synthesized powders from their powder diffraction patterns. The technique is quite accurate in determining crystallite size with other techniques giving similar results thus confirming the validity of this method of particle size determination. Both combustion and chemical synthesis methods yield fine particle size powders less than 100 nm in diameter as indicated by the broad lines (Fig. 3) of the XRD patterns observed in several studies [48, 56, 57, 92].

3.2. Transmission Electron Microscopy and Scanning Electron Microscopy

TEM and SEM are quite useful in determining particle morphology and also particle size. SEM is capable of examining the morphology of the microstructure of nanoscale powders while TEM allows for the probing of materials

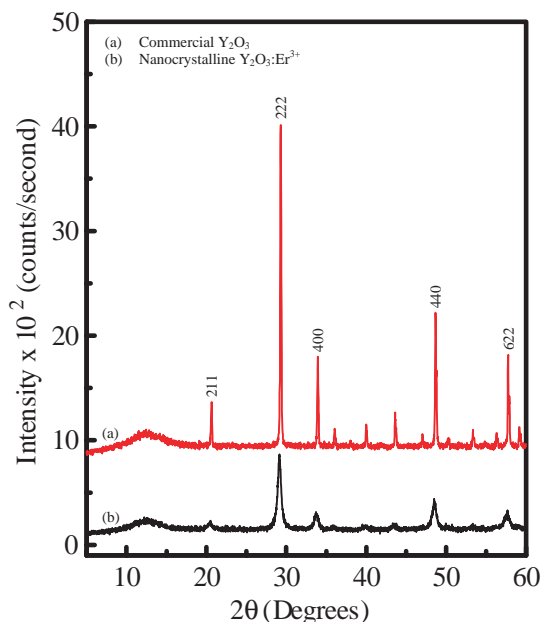


Figure 3. Powder X-ray diffraction pattern for (a) commercial Y_2O_3 and (b) nanocrystalline $Y_2O_3:Er^{3+}$ prepared via a wet chemical synthesis involving a combined method of coprecipitation and hydrothermal processes in the presence of a seed.

on the nanometer scale and confirmation of particle size determination.

SEM of the microstructure of combustion powders showed a foamy and porous structure typical of combustion derived powders [32]. Combustion yields very open, sponge-like structure with similar morphology over large range of magnifications [42]. The formation of the pores and voids that are observed in the spongelike structure were attributed to the escaping gas of the combustion reaction [44]. TEM of combustion samples revealed the fluffy and agglomerate nature of combustion powders on the nanometer scale. TEM analysis of combustion nanopowders revealed that crystallites had a spherical morphology and were randomly oriented in the lattice [51].

Several studies have also observed differences in the microstructures and particle sizes of combustion synthesized powders depending on the reaction conditions utilized. Differences in particle size and morphology have been attributed to the choice of fuel which alters the energetics/exothermicity of the combustion reaction and thus the properties of the combustion product [48]. The difference in particle size with the use of different fuels may also depend upon the number of moles of gaseous products released during combustion [44]. As more gases are liberated, the agglomerates are disintegrated and more heat is carried from the system, thereby hindering particle growth. The degree of agglomeration and porosity was also shown to be related to the fuel to metal nitrate ratio used in the combustion reactions [39, 51]. Larger ratios resulted in large particle sizes due to poor heat dissipation and an increase in agglomeration.

Calcination (annealing) of the as-synthesized powders resulted in an increase of particle size as observed by SEM.

Micrographs of heat treated powders made with carbonylhydrazide and urea fuel showed highly agglomerated, nonuniform particles with rough surfaces, as well as pores and cracks [44]. Annealing of particles made using glycine as the fuel at 1600 °C resulted in uniform particles that were interconnected by several small necks due to sintering [44]. In concurrence with BET analysis results, annealing of the powders at high temperatures resulted in particle agglomeration and an overall decrease in porosity of the materials, with the degree of agglomeration increasing directly with increasing annealing temperature.

It was also determined by SEM that the wet chemical method and combustion syntheses give powders with radically different morphologies. Unlike the voluminous, spongelike structure obtained by the combustion method, wet chemical samples resemble powdery, plateletlike material with a compact surface [57]. In the submicrometer scale the compact structure was revealed to be an aggregate of platelets about 200 nm large and 10 nm thick, arranged with some degree of orientation [57]. The platelets had an irregular shape and were made up of roughly rounded basic units that could merge together to give rise to larger particles. Sharma et al. also observed oval particle morphologies in the TEM micrograph of Eu^{3+} doped yttria powders obtained by a similar method. TEM of the individual platelets shows that they had a nonuniform density with an inner structure comprised of small agglomerates. In the nanometer scale they demonstrated a porous structure with pores that were about 2–4 nm in size randomly distributed inside the platelets [57]. It was also revealed that yttria samples show similar micro- and nanostructures regardless of the presence of rare earth dopants [57].

Similar results have been observed in the TEM of $\text{Y}_2\text{O}_3:\text{Eu}^{3+}$ powders obtained via a different wet chemical method by Wakefield et al. [65] where the nanoparticles tended to form agglomerates in the 70–100 nm size range, with the individual particles being free of defects with no detectable surface dead layer [65]. Particles synthesized by a precipitation method in the presence of EDTA were shown to have sizes between 50 and 160 nm and were shown to aggregate but not to sinter [60]. In the absence of EDTA particles had sizes of 600–800 nm. Crystallite size determined by TEM ranged from 46 to 58 nm dependent on the quantity of EDTA utilized in the synthesis.

SEM and TEM data on $\text{Y}_2\text{O}_3:\text{Eu}^{3+}$ particles synthesized using a forced hydrolysis technique also demonstrated the effect of annealing temperature on particle size and morphology [58]. Particle sizes of the samples exhibited a sharp increase with increasing firing temperature along with improved crystallinity and quality of the particles. Each individual particle in the specimen fired at 900 °C was found to consist of many nanocrystals. This behavior was attributed to a process of structural evolution from an amorphous solid to an ordered crystalline state [58]. As the firing temperature increased the size of the nanoparticles also increased until at 1400 °C each particle was composed of a single crystalline phase.

SEM of a microemulsion synthesized $\text{Y}_2\text{O}_3:\text{Eu}^{3+}$ powder revealed that after calcination, particles demonstrated a tendency to agglomerate forming a continuous network in which pores and voids can be seen [69]. The observed

morphology may be the result of outgas procession during calcination. TEM revealed that the individual particles were spherical and ranged in size from several to 50 nm. Particles calcinated at 800 or 1000 °C had a narrower particle size range compared to particles calcinated at 600 °C. Another microemulsion technique employed by Lee et al. to synthesize $\text{Y}_2\text{O}_3:\text{Eu}^{3+}$ nanocrystals resulted in particle morphology and size that were different than that encountered by Huang et al. SEM micrographs of the nanoparticles showed a narrow size distribution and spherical shape that formed densely packed agglomerates of 20–30 nm with few voids.

SEM on a laser-heated vaporization/condensation synthesis technique revealed the formation of small particles that had a tendency to agglomerate [28]. Small voids between the agglomerates were observed. Europium(III) and terbium(III) doped yttrium oxide phosphor powders synthesized by supercritical CO_2 -assisted aerosolization and pyrolysis (at 1010 °C) were shown to be composed of spherical particles with particle size ranging from ~ 0.1 to 1 μm in diameter by SEM [25].

3.3. Brunauer, Emmett, Teller Analysis

BET analysis is an experimental technique that allows for the measurement of particle surface area. Several studies have utilized BET to determine the surface area of Y_2O_3 nanopowders prepared through the various synthesis techniques as the increased surface area is one of the desired properties of nanoparticles. This technique is also interesting as it illustrates the difference in morphology of the nanocrystals obtained from the different synthesis methods. For instance, nanocrystalline Y_2O_3 obtained using a combustion synthesis normally has a large surface area due to its voluminous morphology. A decrease in the surface area was observed upon annealing (calcination) of these powders which was attributed to the reduction of the bulk porosity of the compound [51]. It was also determined that the reduction in surface area was directly related to the annealing temperature. However, the decrease in surface area was not necessarily due to crystallite growth as only a 3% change in crystallite size was observed while a 25% change in surface area was noticed upon annealing at 500–600 °C. This behavior was indicative of sintering of the nanocrystals [51].

Surface areas of combustion derived powders obtained by the BET analysis method ranging from 1 to 40 $\text{m}^2 \text{g}^{-1}$ have been reported in the literature depending on the reaction conditions [32, 44]. The type of fuel selected, along with the fuel-to-metal oxide ratio, had a profound effect on the microstructure, and hence the surface area, of the material obtained. Wet chemical methods were also excellent at producing powders with high surface areas. Results published range from 19 $\text{m}^2 \text{g}^{-1}$ by Polizzi et al. [57] to an astonishing 229 $\text{m}^2 \text{g}^{-1}$ by Sharma et al. [55]. The BET analysis of a reverse microemulsion synthesized powder also demonstrated that as calcination temperature was increased, particles grew and agglomerated leading to a decrease in surface area [67]. Although growth of the particles occurred during calcination, no change in their shape was observed.

3.4. Infrared Spectroscopy

The uncalcined powders obtained by combustion synthesis usually exhibit bands in the IR spectrum that may be attributed to residual nitrate ($-\text{NO}_3$) groups remaining from the reactants. Hydroxyl ($-\text{OH}$) and carbonate ($-\text{CO}_3$) groups were also detected in the corresponding IR spectrum of the uncalcined combustion synthesized powders [51]. As will be discussed later, these adsorbed species are detrimental to the optical properties of rare earth ions doped into the Y_2O_3 lattice as they lead to nonradiative (nonemissive) depopulation of the excited states thus reducing the overall efficiency of the materials. The adsorbed species may also hinder the catalytic properties of nanoscale Y_2O_3 as they may occupy possible binding sites for reactants. Though annealing of the powders removed the residual nitrates and the majority of the adsorbed water, the removal of the adsorbed carbon dioxide tends to be more difficult requiring higher annealing temperatures and longer annealing times that may lead to particle aggregation [93].

FTIR of chemically synthesized powders revealed M–OH stretching vibrations at 3300–3400 and 1640 cm^{-1} indicating adsorbed water on the surface of the powders [53, 54]. IR spectra showed peaks between 1250 and 1800 cm^{-1} which were attributed to C–H, C–O, and C–C bonding due to residual organic matter [53]. Annealing of the powders removed the residual organic matter but adsorbed CO_2 from the atmosphere was still detected [55].

3.5. Thermogravimetric Analysis and Differential Thermal Analysis

TGA measures weight changes in a material as a function of temperature (or time) under a controlled atmosphere. Its principal uses include measurement of a material's thermal stability and composition. Precise measurement of the weight change of Y_2O_3 nanocrystals as they are heated at a controlled rate can be used to determine the amount of adsorbed species or the remaining organic content after a wet chemical synthesis. Changes in mass are clear indications that H_2O , CO_2 , CO , and O_2 gases were being evolved either from adsorbed gas or from hydroxyl or carbonate groups [51].

DTA determines the precise temperature at which a reaction takes place or identifies a phase change. DTA involves heating a material at a controlled rate to a predetermined temperature and comparing any chemical emissions of heat (exothermic) or absorptions of heat (endothermic) from the material in comparison with a passive material such as alumina.

Several weight losses were also noticed upon heating of the as-synthesized wet chemical powders. A TG weight loss was observed to occur in three steps, 110–180 (removal of adsorbed water), 190–210 (loss of chemisorbed water), and 300–390 $^\circ\text{C}$ (removal of solvents and organic matter). The corresponding DTA revealed the presence of two endothermic peaks at 135 and 200 $^\circ\text{C}$, along with an exothermic peak at 380 $^\circ\text{C}$ [53, 55]. Huang et al. demonstrated similar results on nanocrystalline $\text{Y}_2\text{O}_3:\text{Eu}^{3+}$ synthesized using a microemulsion synthesis technique finding weight losses to occur at 230 (loss of water molecules), 230–350 (removal of

organic materials), and 500–620 $^\circ\text{C}$ (conversion of hydroxide to oxide) [69]. Little change in the mass of the powders was observed from 620 to 1000 $^\circ\text{C}$.

4. LUMINESCENCE AND OPTICAL SPECTROSCOPY OF RARE EARTH DOPED YTTRIUM OXIDE NANOCRYSTALS

Microcrystals of yttrium oxide doped with the tripositive europium ion are one of the most commonly used phosphor materials on the market in CRTs and fluorescent lighting. It follows therefore that many of the papers on nanocrystalline $\text{Y}_2\text{O}_3:\text{Eu}^{3+}$ in the literature deal with the characterization of the luminescent properties, one of the most important properties being catholuminescence efficiency, as they compare to the standard commercial phosphors or to a bulk material.

4.1. Catholuminescence

The catholuminescence efficiency of $\text{Y}_2\text{O}_3:\text{Eu}^{3+}$ nanocrystals was measured by Jiang et al. [58] as a function of firing time and temperature, Eu_2O_3 doping concentration, and electron voltage. Brightness data were obtained by bombarding the nanoparticles with a continuous electron beam and were converted into intrinsic efficiency according to

$$\text{efficiency}(\text{lm/W}) = \frac{100\pi L_0}{jV} \quad (4)$$

where L_0 is the brightness in Cd/m^2 , j is electron beam current density in ($\mu\text{A/cm}^2$), and V is the accelerating voltage in volts. In this study, the luminescent efficiency of the as-synthesized powder was highest when an accelerating voltage of 4 kV was used to bombard a $\text{Y}_2\text{O}_3:\text{Eu}$ sample with 2 mol% Eu_2O_3 doping that was fired for 2 hours at 1400 $^\circ\text{C}$. For comparison, the luminescence efficiency of a commercial phosphor ($\text{Y}_2\text{O}_2\text{S}:\text{Eu}$) was studied and it was shown that the $\text{Y}_2\text{O}_3:\text{Eu}^{3+}$ nanocrystals synthesized by the authors had higher efficiency. At 4 kV accelerating voltage, the efficiency of the $\text{Y}_2\text{O}_3:\text{Eu}^{3+}$ powder (11.6 lm/W) was determined to be approximately 50% higher than the commercial $\text{Y}_2\text{O}_2\text{S}:\text{Eu}$ standard (7.9 lm/W).

From catholuminescence (CL) measurements under electron beam excitation, $\text{Y}_2\text{O}_3:\text{Eu}$ nanocrystals displayed the characteristic red color of the phosphor [64]. The luminance (Cd/m) of the nanocrystals was measured as a function of the accelerating voltage from a pulsed electron beam (400–1500 V) for a commercial $\text{Y}_2\text{O}_3:\text{Eu}$ standard (3–5 μm), spherical $\text{Y}_2\text{O}_3:\text{Eu}$ (300 nm), and the nanocrystal samples synthesized by the authors with an average particle diameters of 50 nm. It was demonstrated that the method the authors employed to synthesize the nanocrystals yielded particles with very good luminance comparable with the commercial standard phosphors.

Xu and co-workers [25] studied the catholuminescence of $\text{Y}_2\text{O}_3:\text{Eu}$ phosphors by electrophoretically coating a thin layer of phosphor particles on an aluminium stub holder, exciting the sample with an electron gun, and measuring the light emitted as a function of increasing accelerating

voltage, and it was noted that the intensity of the as-synthesized nanocrystal $\text{Y}_2\text{O}_3:\text{Eu}^{3+}$ sample was more than twice as bright as that of the commercial $\text{Y}_2\text{O}_3:\text{Eu}$ phosphor. This large improvement in the brightness was attributed to an increase in the specific surface area of the nanocrystals compared to the standard phosphor. The increase in brightness as a function of increasing surface area is believed to be the result of surface-generated photons not undergoing reabsorption losses in the bulk material. Similarly, the catholuminescence of two different $\text{Y}_2\text{O}_3:\text{Eu}^{3+}$ samples in a vacuum ($<10^{-6}$ Torr) were studied [67]: a nanocrystalline sample prepared by reverse microemulsion (25 nm average particle diameter) and a bulk sample prepared using the precipitation method [68]. The electron voltage was varied from 200 to 700 V at a fixed current density of $50 \mu\text{A}/\text{cm}^2$ and it was observed that catholuminescence intensity of both phosphors increased with increasing accelerating voltages. However, the nanocrystalline sample prepared by reverse microemulsion showed a relatively higher improvement as the CL increased from 0.286 to 1.543 lm/W, whereas the bulk sample increased from 0.157 to 0.897 lm/W. The higher overall CL of the sample prepared by reverse microemulsion was ascribed to its smaller particle size, thus resulting in larger surface area in a given screen area and to a better crystalline structure of the sample compared to the bulk. The CL efficiencies as a function of current density at a fixed voltage of 400 V were measured and it was observed that both samples exhibit poor efficiencies at low current densities, which may have been attributed to the nonluminescent dead layer on the surface of the particles. With increasing electron-beam current, the efficiencies were gradually increased up to a maximum and then decreased which was due to the luminescent centers tending to saturate at high current densities. However, the nanocrystalline sample synthesized by reverse microemulsion decreased approximately 23% from the maximum efficiency whereas the bulk decreased by about 29%.

Under excitation of an electron beam, $\text{Y}_2\text{O}_3:\text{Eu}^{3+}$ displayed the characteristic red emission and the CL spectrum of the nanocrystalline material, collected in the voltage range from 400 to 15,000 V, was identical to that of a commercial $\text{Y}_2\text{O}_3:\text{Eu}$ phosphor [94]. The authors studied the effect of firing temperature on the luminance of their powders and they observed that it increased dramatically when the samples were fired between 800 and 1050 °C due to the better crystallinity obtained after firing. However, the luminance dropped dramatically after firing temperatures surpassed 1050 °C since the crystal grains grew larger and at the same time lost their spherical shape and began to sinter together.

A simple calculation of electron penetration depth at an accelerated voltage of 5 kV was used to determine the minimum crystallite size required for efficient luminescent properties in $\text{Y}_2\text{O}_3:\text{Eu}^{3+}$ nanocrystals synthesized by a wet chemical method [65]. The electron range in a solid, for electron acceleration voltages of 1–10 kV, is given by the empirical formula [95]

$$\text{Range}[\text{\AA}] = 250(A/\rho)(E/Z^{1/2})^n \quad (5)$$

where $n = 1.2/(1 - 0.29 \log_{10} Z)$, A is the atomic weight, ρ is the density of the material, Z is the atomic number, and E is

the accelerating voltage. According to Eq. (5), for $\text{Y}_2\text{O}_3:\text{Eu}$ at an accelerating voltage of 5 kV, the electron penetration depth is 56 nm. The CL data compared the nanocrystalline material to the bulk and it was observed that as the accelerating voltage was lowered, the $\text{Y}_2\text{O}_3:\text{Eu}^{3+}$ nanocrystals had improved efficiency over the bulk. At 1 kV, the efficiency of the nanocrystals (6.5 lm/W) was approximately 50% greater than that of the bulk material (4.5 lm/W). At voltages above 4 kV, both bulk and nanocrystalline materials had approximately equal efficiencies (10.5 lm/W). The authors expected that the nanocrystals would have had an even greater performance advantage upon lowering the accelerating voltage below 1 kV.

4.2. Charge Transfer Excitation of $\text{Y}_2\text{O}_3:\text{Eu}^{3+}$ Nanocrystals

The irradiation with ultraviolet (UV) light of nanocrystalline yttrium oxide doped with the Eu^{3+} ion into the charge transfer (CT), which yields intense red emission dominated by the $^5D_0 \rightarrow ^7F_6$ transition (Fig. 4), is a common theme in many research papers. In $\text{Y}_2\text{O}_3:\text{Eu}^{3+}$, the excited CT band is due to a local excitation where an electron from the $2p$ orbital of O^{2-} becomes excited to the $4f$ orbital of Eu^{3+} [96]. This Eu^{3+} -ligand electronic transition produces the CT band in the region between 220 and 280 nm.

Wakefield's group [65] compared the photoluminescence efficiency of $\text{Y}_2\text{O}_3:\text{Eu}^{3+}$ nanocrystals and a commercial

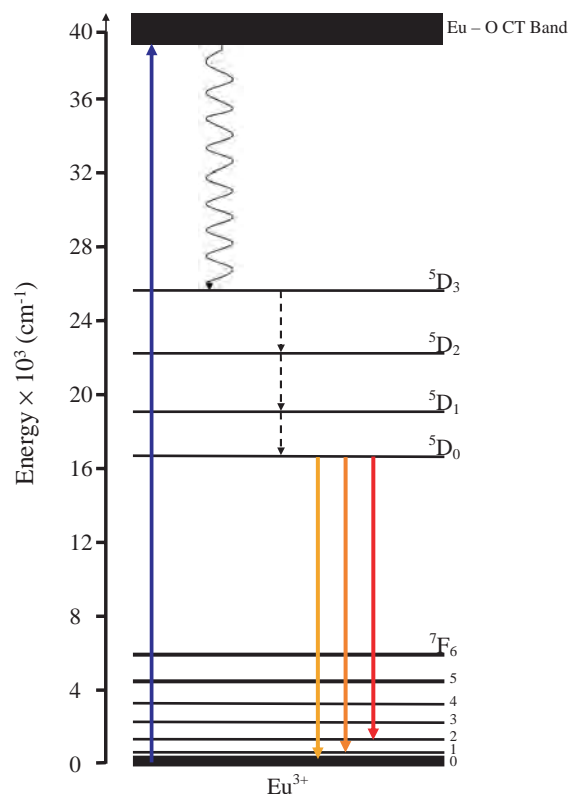


Figure 4. Energy level diagram of the Eu^{3+} ion in the cubic Y_2O_3 lattice showing excitation into the charge transfer band resulting in emission from the 5D_0 energy level.

phosphor with a particle diameter of 3.5 μm . In order to obtain comparative phosphor performance data, the samples were identically prepared by loading 0.1 g/cm^3 of phosphor in a silicone binder so that the amount of phosphor material in each case was identical. The authors observed that the nanocrystalline $\text{Y}_2\text{O}_3:\text{Eu}^{3+}$ sample showed a photoluminescence efficiency 10–20% higher than the commercial microcrystalline sample following excitation with 254 nm into the CT band.

Zhang et al. [86] measured the excitation spectrum of the red $^5D_0 \rightarrow ^7F_2$ transition ($\lambda_{\text{emission}} = 612 \text{ nm}$) in nanocrystalline $\text{Y}_2\text{O}_3:\text{Eu}^{3+}$ prepared via a simple sol–gel route. The excitation spectrum showed a wide band with a peak centered at approximately 233.5 nm, which was attributed to the charge transfer state transition due to Eu–O interaction. The authors investigated the emission spectrum following excitation with 233.5 nm and observed transitions from the 5D_0 level to the 7F_J ($J = 0, 1, 2, 3, 4$) level of the $4f^6$ configuration of the Eu^{3+} ion. The authors also studied the emission spectrum of a $\text{Y}_2\text{O}_3:\text{Eu}^{3+}$ phosphor, with identical concentration, prepared via traditional solid-state reaction and observed that the spectrum was similar to the nanocrystalline material. However, they noticed that the luminescence intensity in the emission spectrum of the nanocrystalline material was higher. The authors believed that the regular shape of the sol–gel-derived nanomaterial was one of the reasons for the increased luminescence as the scattering of light evolved from this material decreased and thus the luminescence was increased. Similarly, the luminescence intensity of Eu^{3+} doped yttrium oxide nanocrystals prepared via a standard gel coprecipitation method and having a crystallite size of approximately 54 nm was compared to a Sylvania $\text{Y}_2\text{O}_3:\text{Eu}^{3+}$ industrial standard phosphor [97]. The authors showed that a 50% luminescent peak intensity was achieved for the nanocrystals compared to the standard phosphor, which had an average particle size between 5 and 10 μm .

Lee et al. [68] showed the effects of crystallinity on the photoluminescence (PL) of $\text{Y}_2\text{O}_3:\text{Eu}^{3+}$ following excitation into the charge transfer band ($\lambda_{\text{exc}} = 255 \text{ nm}$). Samples prepared by reverse microemulsion and bulk precipitation, each calcined at 700 and 900 $^\circ\text{C}$, were compared and it was determined that the PL intensity was highest for the samples prepared by microemulsion which had the better crystallinity at relatively low temperature. The samples prepared by microemulsion consisted of more densely packed particles with very few voids.

Huang et al. [69] showed that the emission intensity of nanocrystalline $\text{Y}_2\text{O}_3:\text{Eu}^{3+}$ was directly related to the concentration of the Eu^{3+} activator. When the activator (Eu^{3+}) concentration was increased to a certain level, the luminescence began to quench. At elevated concentrations, the pairing or aggregation of activator atoms may change a fraction of the activators into quenchers thus inducing the quenching effects. The energy migration between the Eu^{3+} activators may sometimes be very efficient so as to carry the energy to a distant killer or to a quenching center, which exists at the surface of the crystal. For yttrium oxide nanocrystals doped with Eu^{3+} prepared via the microemulsion method, the authors observed that quenching started at an Eu^{3+} concentration of 10 mol%. On the other hand, in a conventional

$\text{Y}_2\text{O}_3:\text{Eu}^{3+}$ phosphor, quenching was observed beginning at 6–8 mol% while in a nanocrystalline $\text{Y}_2\text{O}_3:\text{Eu}^{3+}$ sample prepared via combustion synthesis, the onset of quenching began at 12 mol% [98]. The authors attributed this observation to a reduced energy transfer rate due to the interface effect of the nanoscale material, so that less energy could migrate to the quenching sites. This change in quenching concentrations also suggested that the close proximity of the surface did not introduce a large number of surface quenching defects.

The authors observed that all nanocrystalline samples showed the same relationship between emission intensity and calcination temperatures. For an 8 mol% Eu^{3+} sample without calcination, the main emission from the $^5D_0 \rightarrow ^7F_2$ transition was observed at 613 nm with very low intensity. Furthermore, the $^5D_0 \rightarrow ^7F_1$ (589, 594 nm) and $^5D_0 \rightarrow ^7F_4$ (700 nm) transitions were clearly visible. However, following calcination at 1000 $^\circ\text{C}$ for 2 hours, the main emission intensity was 16 times greater and the peak shifted from 613 to 610 nm. The $^5D_0 \rightarrow ^7F_1$ and $^5D_0 \rightarrow ^7F_4$ transitions were dramatically suppressed. Huang and co-workers attributed this drastic difference to the formation of the cubic form of yttria following the calcination and the 3 nm peak position shift was attributed to a change in the crystal field thus supporting their hypothesis. Huang's group also studied the effects of increasing the calcination temperature on the lifetimes of $\text{Y}_2\text{O}_3:\text{Eu}^{3+}$ nanocrystals. The authors stated that the lifetime is sensitive to local variations in electron density throughout a material and thus can be correlated to the defect density. For all samples under investigation, the same relationship between calcination temperature was observed. The lifetime of the emission corresponding to the $^5D_0 \rightarrow ^7F_2$ transition became longer with increasing calcination temperatures. This lengthening of the decay time was attributed to the improvement in the crystallinity and lower density of defects as the nanoparticles were calcined.

Li's group [59] observed a blueshift of the $^5D_0 \rightarrow ^7F_2$ emission peak position with decreasing size in nanocrystalline $\text{Y}_2\text{O}_3:\text{Eu}^{3+}$. The peak position was shifted from 610 to 614 nm as the size of the nanocrystals was increased from 43 to 71 nm. From the XRD measurements, the authors showed that the unit cell of nanocrystalline $\text{Y}_2\text{O}_3:\text{Eu}^{3+}$ became smaller as the size of the particle was decreased. With the decrease in the grain size, the surface area of the particle increased significantly, which resulted in increased surface tension and in turn led to a decrease in the lattice parameter. They stated that the changes in the unit cell affected the crystal field surrounding the Eu^{3+} ions and in turn caused the blueshift phenomena. Nanocrystalline $\text{Y}_2\text{O}_3:\text{Eu}^{3+}$ ($\sim 20 \text{ nm}$) was coated with a 2–3 nm layer of aluminum oxide [85] in an attempt to improve the luminescence. The FTIR spectrum of the noncoated nanocrystals showed a band at 558 cm^{-1} ascribed to the stretching vibration of Y(Eu)–O and a shoulder near 558 cm^{-1} , which the authors believed to be due to defects connected with Y(Eu)–O on the nanocrystalline surface. The defects in the nanocrystalline lattice are one of the main factors responsible for the decrease in the luminescence intensity. The shoulder at 558 cm^{-1} in the FTIR spectrum of the coated samples disappeared, indicating that the defects were largely

eliminated. The authors showed an increase in the luminescence intensity after the nanocrystals were coated. A broadening of the Y–O absorption bands was observed as the particle size was decreased [39]. The authors stated that the cause of the broadening in the FTIR spectra was due to the polarization charge induced at the particle surface by the external electromagnetic field. Therefore, as the size of the particle was decreased, the surface effects were enhanced so that the damping of the surface absorption mode increases causing the Y–O bands to broaden.

Konrad et al. [78] excited into the CT band and used the energy transfer process from the two crystallographically different C_2 and C_{3i} sites to check the europium content in nanocrystalline $Y_2O_3:Eu^{3+}$. The transfer of energy from the C_{3i} site to the C_2 gets stronger with increasing Eu^{3+} concentration; therefore the ratio of the emission intensity of the C_{3i} site to the emission intensity of the C_2 site decreases upon the addition of Eu^{3+} . The authors compared the ratio of ${}^5D_0 \rightarrow {}^7F_1$ emission of the C_{3i} site to the ${}^5D_0 \rightarrow {}^7F_0$ emission of the C_2 site for a coarse grained (reference, 5 μm) sample with a known concentration (4 wt%) to the nanocrystalline $Y_2O_3:Eu^{3+}$ sample. They showed that the ratio was much lower for the nanocrystalline sample, which indicated that the nanocrystals had a concentration of approximately 7 wt%. The excitation spectra for the ${}^5D_0 \rightarrow {}^7F_2$ emission of both the reference and nanocrystalline samples were presented. For the reference sample, they observed the direct excitation of the 5D levels of europium between 320 and 285 nm. However, in the range of 285–220 nm, the excitation via the charge transfer state of the Eu^{3+} ion and the oxygen ions in close proximity was dominant and was shown to be concentration dependent, with a maximum of 227 nm. The observed excitation band was a superposition of two excitation bands, the exciton absorption band and the charge transfer band. Below 220 nm, the exciton and the host lattice absorption were determined to be the reason for the excitation with a maximum of 213 nm, which is independent of the concentration. Similar to the reference, the excitation of the 5D levels of the europium ion was observed in the nanocrystalline sample. However, the charge transfer state and the host lattice had different features; specifically, in the charge transfer range, the maximum was determined to be 238 nm and in the host lattice absorption range, the excitation band showed a narrower structure with a maximum of 208 nm. Thus, they observed a redshift in the CT band and a blueshift, of 5 nm, in the host absorption. The diffuse reflection spectrum of the reference (2 and 4 wt%) confirmed that the charge transfer absorption occurred between 220 and 285 nm and that the absorption coefficient depended upon the europium content as the reflection increased with less Eu^{3+} content in the sample. The reflectance spectrum also showed that the europium content had no effect on the host lattice absorption, as the absorption of the doped and undoped samples was identical. Each sample showed two minima at 214 and 201 nm corresponding to exciton and interband assisted absorption, respectively. The reflection spectrum of the nanocrystalline sample also showed the charge transfer state; however, in this region the nanocrystalline sample with a concentration of 7 wt% had a higher reflection than the references with lower europium content. A lower reflection should have

been observed due to the higher Eu^{3+} concentration, the absence of which was described as being due to the small particle size of the nanocrystals. The scattering of the incident light is dependent on the size of the particle; thus decreasing the particle size would cause an increase in the scattering and reflection. In the region of the host lattice absorption, two minima were observed at 204 and 190 nm and were blueshifted relative to the reference sample. Furthermore, the authors observed a significant increase in the luminescence intensity with increasing grain size for both the excitation via the charge transfer state and for excitation via the host lattice [99]. The authors cited a reduction of surface fraction and crystal defects as possible reasons for the increased luminescence.

The quantum efficiency (QE) of the $Y_2O_3:Eu^{3+}$ nanocrystals was investigated [27] and for an excitation at 253 nm; a QE of 3–5% was obtained. The low QE was presumed to be due to an increase in the nonradiative transition rate ($k_{nonradiative}$), which was caused by structural imperfections. However, according to the lifetime data, the decay time of the 5D_0 was shown to increase as the particle size was decreased from bulk (1.1 ms) to nanocrystal (3.6 ms) but still remained single exponential. The lifetime, τ , of an excited state is related to the radiative and nonradiative transitions rates (k) by

$$\tau = \frac{1}{k_{nonradiative} + k_{radiative}} \quad (6)$$

and the quantum efficiency is given by

$$QE \propto \frac{k_{radiative}}{k_{nonradiative} + k_{radiative}} \quad (7)$$

Therefore, an increase in the lifetime with a decrease in the QE was believed to be caused by a decrease in the radiative transition rate. The ${}^5D_0 \rightarrow {}^7F_2$ transition is a hypersensitive forced electric dipole transition which according to the Judd–Ofelt framework [100, 101] means that this transition is very sensitive to changes in the crystal field. The authors concluded that changes in the crystal field drastically reduced the radiative transition rate thus causing a low QE. The authors also studied the luminescence properties of $Y_2O_3:Eu^{3+}$ nanocrystals in different inert host materials following excitation into the CT band ($\lambda_{exc} = 253$ nm) [102]. The emission spectra of 5 and 7.8 nm $Y_2O_3:Eu^{3+}$ nanocrystals as well as nanocrystalline $Y_2O_3:Eu^{3+}$ in porous silica, porous alumina, and MCM-41 (grain size ≥ 8 nm) were obtained and compared with a commercial bulk sample (5 μm). It was observed that the width of the ${}^5D_0 \rightarrow {}^7F_2$ emission band changed slightly with particle size and suggested that a distortion of the crystalline environment was present in comparison to the bulk. Also, the authors observed a slight shift in the emission line for the smallest grain size, which they believed was caused by the superposition of two neighboring emission lines. Two main structures were observed in the photoluminescence spectra, the Eu–O charge transfer band at approximately 240 nm and an exciton absorption in the Y_2O_3 host located around 210 nm. The results indicated a strong change in the relative amplitude of the charge transfer process compared to the excitonic process with the surrounding. The

bulk material showed a dominant CT process, whereas the spectra of the $\text{Y}_2\text{O}_3:\text{Eu}^{3+}$ nanocrystals were correlated with particle size and a decrease of the relative amplitude with decreasing particle size was observed. It should also be noted that a pronounced dominance of the excitonic transition in comparison to the charge transfer process for the caged materials was observed. Furthermore, the photoluminescence excitation spectra related to the excitonic process were extracted by elimination of the charge transfer band and a shift was observed ranging from 211 nm for the bulk material to 208 nm for the 8 nm sample to 205 nm for the 5 nm $\text{Y}_2\text{O}_3:\text{Eu}^{3+}$ sample.

Following UV excitation ($\lambda_{\text{exc}} = 250\text{--}260$ nm), Dhanaraj's group [87] observed that the $\text{Y}_2\text{O}_3:\text{Eu}$ nanocrystals and the bulk sample used for comparison yielded intense red emission dominated by the ${}^5D_0 \rightarrow {}^7F_2$ transition. Furthermore, the excitation spectrum monitoring the red emission (~ 610 nm) showed an asymmetric band, shifted to higher energy in the nanocrystalline material, with the maximum at 250 nm, corresponding to the charge transfer band lying in the bandgap region of the Y_2O_3 matrix. This asymmetric excitation band was reported to be due to the superposition of an additional excitation component, notably the fundamental absorption edge of the yttrium oxide host matrix, which sets in around 200 nm and has a tail, the Urbach tail. The Urbach tail in Y_2O_3 is due to the O^{2-} (valence band) to the Y^{3+} (conduction band) excitonic transition and sets in around 238 nm ($41\text{--}941$ cm^{-1}) at room temperature. Under UV excitation, these two processes compete against one another. Although the absorption coefficient of the excitonic process is much stronger than the charge transfer process, the excitonic process is strongly quenched at the many recombination sites at the particle surface, as the excitonic process is a surface process. Therefore, the CT band will dominate and feeds energy to the various localized $f\text{--}f$ levels of europium. The authors observed a shift in the excitonic band of 600 cm^{-1} to higher energy as the crystallite size is reduced as can be explained by the Urbach relation. Their findings were in excellent agreement with those of Konrad [78, 99] and Schmechel [27, 102].

Igarashi et al. [24] also showed the photoluminescence excitation spectra for the 611 nm emission (${}^5D_0 \rightarrow {}^7F_2$) of nanocrystalline and microcrystalline $\text{Y}_2\text{O}_3:\text{Eu}^{3+}$ but they observed a blueshift of 5 nm in the charge transfer state. This blueshift of the CT excitation band was reported to occur due to an increase in the ionicity in the nanocrystalline material. The CT band is closely related to the covalency between the O^{2-} and the Eu^{3+} ions and so a decrease in energy for electron transfer from O^{2-} to Eu^{3+} represents an increase in the covalency or the decrease in the ionicity between oxygen and Eu^{3+} . The lattice constant of both micro- and nanocrystalline $\text{Y}_2\text{O}_3:\text{Eu}^{3+}$ samples was determined to be 10.654 and 10.695 Å, respectively. Since the crystal structure of the samples under investigation was cubic, the lattice constant could be regarded as the average bond length, and therefore the increase in the lattice constant for the nanocrystalline samples indicated the increase in the ionicity. Interestingly, Beck et al. showed that the Raman line shifted to lower frequencies with decreasing crystallite sizes in yttrium oxide nanocrystals [103]. The Raman line shifted by approximately 5 cm^{-1} from 373.2 to

378.6 cm^{-1} as the size of the nanocrystals was increased from 4.9 to 100 nm. The shift in the Raman line was related to the lattice constant (a), which decreased from 10.654 Å in the 4.9 nm nanocrystals to 10.602 Å in the 100 nm nanocrystals.

On the other hand, the excitation spectra of nanocrystalline $\text{Y}_2\text{O}_3:\text{Eu}^{3+}$ prepared by combustion synthesis showed that the excitation peak position of ${}^5D_0 \rightarrow {}^7F_2$ shifted toward the red, from 239 to 250 nm, with decreasing particle size while the FWHM of the peaks became narrower [39]. In the sample with the smallest particle size (8 nm), a new peak was observed in the excitation spectrum. The authors described the redshift phenomenon as being due to the stability of the O^{2-} surrounding electrons. The position of the excitation peak is dependent on the nature of the surrounding O^{2-} ions, which in a crystal lattice is stabilized by the surrounding positive ions. As the size of the particle was decreased, the surface-to-volume ratio of atoms was also increased resulting in an increase of the degree of disorder of the nanocrystalline system. As a consequence, the O^{2-} was less stable and required less energy to remove an electron from an O^{2-} ion. Therefore, the authors claimed that the CT band is shifted to lower energy and is a manifestation of surface effects.

Qi and co-workers [45] also observed a size effect in nanocrystalline $\text{Y}_2\text{O}_3:\text{Eu}^{3+}$. The peak position of the ${}^5D_0 \rightarrow {}^7F_2$ transition was observed to be at 612 nm in a sample with a particle size of 40 nm. However, when the particle size was reduced to less than 10 nm, the emission spectrum had drastic changes. The emission consisted mainly of two broad bands in the region of 600–640 nm. One of the bands was located at 615 nm, which was the shoulder in the emission spectrum of the 40 nm sample, and the other band was located at 622 nm, which was a new emission band previously not observed. Similarly, the excitation spectrum showed obvious differences between the two samples. The maximum of the excitation band of the 10 nm sample was determined to be 277 nm while the maximum for the 40 nm sample was 262 nm. Therefore, the samples exhibited a redshift with decreasing particle size, which the authors stated was different from the normal case where the CT band has a blueshift upon decreasing particle size. The EXAFS results were used to explain their findings. The authors stated that the position of the charge transfer band in europium doped oxides is dependent on the Eu–O bond length and coordination environment around the Eu^{3+} ion. The coordination is more or less fixed in a 6 coordinate octahedral. In 8 coordination, it varies as a function of the host lattice, which is proportional to the Eu–O bond distance, and with increasing bond length the band shifts to lower energies. According to their EXAFS results, the Eu–O bond length became larger and Eu^{3+} had eightfold coordination as the size of the particle decreased. This changed the crystal field surrounding the Eu^{3+} ions and caused the observed redshift. Similarly, EXAFS studies on nanocrystalline Y_2O_3 (10 nm) [104] revealed that the oxygen coordination number was 5.3, almost 6 within error of the data analysis. The Y–O distances at approximately 2.45 Å were identified as Y–OH groups most likely located at the surface of the particles as similar Y–O distances were found in $\text{Y}(\text{OH})_3$.

Kang et al. presented the excitation spectra of nanocrystalline $\text{Y}_2\text{O}_3:\text{Eu}^{3+}$ prepared by spray pyrolysis [105]. The

nanocrystals absorbed excitation energy in the range from 220 to 280 nm, with a maximum excitation wavelength of 243 nm. The authors also presented the photoluminescence emission spectra of varying concentrations of $\text{Y}_2\text{O}_3:\text{Eu}^{3+}$ nanocrystals and it was determined that 6 at% was the optimum doping concentration. The effect on the luminescence intensity of annealing the nanocrystals (at 1000 °C for 3 hours) was investigated. The results indicated that while both heat treated and non-heat-treated samples had similar emission patterns, the annealed nanocrystals, at the optimum 6 at% Eu doping concentration, had approximately 30% higher emission intensity. The authors stated that the emission characteristics of the rare earth doped nanocrystals were strongly affected by the crystallinity of the particles and the doping efficiency of the activator. The effect of the preparation temperature on the luminescence efficiency of $\text{Y}_2\text{O}_3:\text{Eu}^{3+}$ (6 at%) nanocrystals was also investigated. They determined that the brightness of the nanocrystals increased with increasing temperatures (700–1400 °C) because the crystallinity of the samples improved at the higher temperatures. Kang's group also studied the PL efficiency of $\text{Y}_2\text{O}_3:\text{Eu}^{3+}$ nanocrystals synthesized by spray pyrolysis where the starting materials were prepared either via colloidal solution or conventional aqueous solution [106]. The nanocrystalline samples prepared from the colloidal solution were shown to have higher photoluminescence efficiencies in all cases.

In the spray pyrolysis synthesis outlined by Kang and co-workers, the flux materials used in the preparation affected the morphology and crystallinity and thus the brightness of the europium doped nanocrystals. However, the flux material had no influence on the crystallite size of the nanoparticles. The authors studied the effect of LiCl flux on the PL intensity and showed that the $\text{Y}_2\text{O}_3:\text{Eu}^{3+}$ nanocrystals made from solutions containing LiCl flux had higher luminescence than those prepared without flux [107]. However, they also showed that the PL intensity is strongly affected by the amount of flux used and had a maximum value of 20 wt%. They also investigated the effect of utilizing a mixture of LiCl/KCl flux on the PL efficiency of nanocrystalline $\text{Y}_2\text{O}_3:\text{Eu}^{3+}$ [108] prepared from colloidal and conventional aqueous solutions. The nanocrystals in decreasing order of their photoluminescence intensities were LiCl/KCl flux-added colloidal solution, then flux-added aqueous solution, followed by no LiCl/KCl flux-added colloidal solutions, and finally no-flux added aqueous solution. In another study, the PL spectra of Eu^{3+} nanocrystals prepared from solutions with and without different metal chloride (LiCl, KCl, and NaCl) fluxes, following excitation with 254 nm, showed that the flux clearly influenced the spectrum [109]. The maximum PL intensity was obtained from the nanocrystals prepared from the solution with a mixture of LiCl and KCl, which was 142% of that of the nanocrystals prepared from the solution without flux. Similarly, the authors studied the photoluminescence intensities of $\text{Y}_2\text{O}_3:\text{Eu}^{3+}$ nanocrystals prepared from solutions with metal carbonate (Li_2CO_3 , K_2CO_3 , and Na_2CO_3) fluxes [110]. Again, the photoluminescence intensities of the nanocrystals prepared from solutions with metal carbonate fluxes increased by approximately 25% in comparison to those prepared from solutions without flux. Finally, the photoluminescence excitation spectra of

$\text{Y}_2\text{O}_3:\text{Eu}^{3+}$ nanocrystals prepared from solutions with different amounts and ratios of polymeric solutions were presented [111]. The PL spectra were identical irrespective of the addition of polymeric precursors. The nanoparticles absorbed the excitation energy in the 200–280 nm range, with the maximum excitation wavelength at about 230 nm. Following excitation with 254 nm, the samples showed the typical red emission of Eu^{3+} and the samples with the better morphology had higher PL intensity. The samples prepared from the nitrate solution (with no polymeric precursor) had inferior morphological characteristics and showed PL intensity up to 56% lower than the samples prepared using the polymeric precursors. Including the precursors in the synthesis enhanced the morphology by decreasing the surface defects and induced crystallite growth.

Sun et al. co-doped $\text{Y}_2\text{O}_3:\text{Eu}^{3+}$ nanocrystals with Li^+ ions and observed a significant increase in the luminescence intensity compared to the nanocrystals without Li^+ [47]. The emission intensity of the $^5D_0 \rightarrow ^7F_2$ transition was greatly enhanced and a 40% increase was observed for $\text{Y}_{1.70}\text{Eu}_{0.20}\text{Li}_{0.10}\text{O}_3$ in comparison to a $\text{Y}_{1.80}\text{Eu}_{0.20}\text{O}_3$ sample. However, high concentrations of Li^+ also quenched the luminescence in much the same fashion as a high concentration of Eu^{3+} ions would. The effective ionic radii of Li^+ ions (76 pm) is smaller than that of Y^{3+} ions (89 pm). Therefore, it was assumed that the smaller Li^+ ions were introduced into the C_2 sites with higher population in the cubic Y_2O_3 lattice. Therefore, the sites available to the Eu^{3+} ions had a more reduced symmetry, which was able to lift the parity selection rule and resulted in enhanced luminescence. Furthermore, when lithium ions were doped into $\text{Y}_2\text{O}_3:\text{Eu}^{3+}$ nanocrystals, the replacement of Y^{3+} by Li^+ gave rise to the formation of a defective structure. The authors stated that the accompanied increase in the emission intensity might have been attributed to the increase in Li^+ deficiency and therefore the oxygen vacancies. The oxygen vacancies on the surface of the nanocrystals would decrease at first when Li^+ was added in minute amounts, which in turn decreased the quenching centers and increased the crystallinity, thereby increasing the emission intensity. Of course, as more Li^+ is added to the matrix, the oxygen vacancies of the host lattice greatly increased thus destroying the crystallinity, which led to lower luminescence.

4.3. Laser Spectroscopy of $\text{Y}_2\text{O}_3:\text{Eu}^{3+}$ Nanocrystals and Size Dependent Optical Properties

In $\text{Y}_2\text{O}_3:\text{Eu}^{3+}$ nanocrystals prepared via the combustion method, Shea's group studied the effects of the fuel/oxidizer ratio and flame temperature on the photoluminescence spectrum following excitation with 365 nm [44]. The PL emission spectra of nanocrystals produced from yttrium nitrate-carbohydrazide fuel-lean precursors with fuel/oxidizer ratios of 0.9, 1.0, 1.25, and 1.5 all showed the characteristic red emission from the Eu^{3+} ions. As the amount of fuel in the precursor mixture was increased, the light output of the resultant nanocrystals similarly increased. The authors stated that this was most likely due to the increase in flame temperature associated with the higher fuel/oxidizer ratios and with more complete combustion,

the development of $\text{Y}_2\text{O}_3:\text{Eu}^{3+}$ nanocrystals was of course facilitated.

Silver [62] used luminescence spectroscopy to investigate the anti-Stokes and the Stokes emissions of $\text{Y}_2\text{O}_3:\text{Eu}^{3+}$ nanocrystals following 632.8 nm excitation. The Eu^{3+} ion has no transitions originating from the 7F_0 ground state with energy corresponding to 632.8 nm. However, Stokes and anti-Stokes emissions were observed because the 7F_0 ground state of Eu^{3+} lies close to the 7F_1 , 7F_2 , and 7F_3 states and at room temperature these low-lying states may be thermally populated resulting in the population of the 5D_0 level. The temperature dependence of the spectra was studied and the authors observed that the intensities of all of the anti-Stokes and Stokes luminescence lines manifested temperature-dependent behavior. The authors showed that the relative populations of the ground and thermally excited states obey a Boltzmann distribution as given by

$$I = A \exp\left(-\frac{\Delta E}{kT}\right) \quad (8)$$

where I is the integrated intensity of any emission band due to a transition down from the 5D_0 level which is populated following optical excitation of thermally excited Eu^{3+} ions, E is the thermal energy, and k is Boltzmann's constant. A is the preexponential factor, which comprises a number of parameters including the radiative transition probabilities, the degeneracies of the levels involved in the absorption and emission steps, and the photon energies of the ${}^5D_0 \rightarrow {}^7F_J$ transitions. They determined that the thermally excited 7F_2 state had a population of only 0.2% of that of the ground state at room temperature, based on a value of 1300 cm^{-1} above the ground state. Thus, only approximately 1 in 500 of the doping Eu^{3+} ions present was thermally activated at room temperature. Furthermore, the authors observed identical temperature dependencies of the luminescence of the Eu^{3+} ions in both C_2 and C_{3i} sites.

Sharma et al. used a wavelength of 394 nm to excite the Eu^{3+} ions of nanocrystalline $\text{Y}_2\text{O}_3:\text{Eu}^{3+}$ into the 5D_0 energy level manifold [92]. The authors showed the pre- and post-calcination emission spectra of the nanocrystals prepared via wet chemical synthesis. The relative intensity of the 594 nm emission band (${}^5D_0 \rightarrow {}^7F_1$) compared to the 614 nm emission band (${}^5D_0 \rightarrow {}^7F_2$) in the precalcined samples was very different compared to the postcalcined nanocrystals. The authors observed a limited shift of wavelength in the calcined samples indicating that the energy levels of the inner $4f$ electrons, which are shielded by the outer $5s$, $5d$, and $5p$ electrons, were not strongly influenced by the nature of the host lattice into which the Eu^{3+} ions were placed. The emission intensity was also studied as a function of the calcination temperature and they observed that the intensity of the ${}^5D_0 \rightarrow {}^7F_2$ transition in the nanocrystals heated at 350 and 450 °C was stronger than that of the ${}^5D_0 \rightarrow {}^7F_1$ transition. In the uncalcined powders, the relative intensity was almost 1:1.

Sharma's group studied the effects of the solvent, precursor salt, concentration dopant, and modifier on the luminescence properties of $\text{Y}_2\text{O}_3:\text{Eu}^{3+}$ nanocrystals synthesized by a combined method of coprecipitation and hydrothermal processes [54]. Europium doped yttria was synthesized

using two different solvents, ethanol and water. Excitation of the ${}^5D_3 \leftarrow {}^7F_0$ absorption band using 394 nm radiation revealed that the emission intensity of the ${}^5D_0 \rightarrow {}^7F_2$ transition was greater in the nanocrystals produced by ethanol than in those prepared in water. The difference in emission was assumed to be due to signal quenching of the 5D_0 state by OH groups, which were shown to be present via FTIR spectra. The intensity of the bands due to metal-OH stretching vibrations ($3300\text{--}3400$ and 1640 cm^{-1}), which is a measure of the presence of adsorbed water, decreased with the change from water to ethanol. This was explained by the fact that the precursors, yttrium acetate and yttrium chloride, had little or no solubility in ethanol. Similarly, the luminescence intensity of the ${}^5D_0 \rightarrow {}^7F_2$ transition was observed to be at least two and five times more intense in the case of the nanocrystal material obtained using yttrium acetate as the precursor in the synthesis compared to yttrium nitrate and yttrium chloride, respectively. It was reported that these effects arose from an increased shielding of the Eu^{3+} ion from quenching collisions in yttrium acetate and the increase in asymmetry in the Eu^{3+} site. The emission was also determined to be directly proportional to the concentration of the acetate ion. While increasing the concentration of yttrium acetate in the synthesis had no effect on the particle size, the emission intensity was significantly affected. This was explained in terms of the relative affinity of the counterion for the inner coordination of the Eu^{3+} ion. It was shown that acetate ions are more effective at entering the inner coordination sphere, resulting in a lower rate of multiphonon relaxation, thus increasing the radiative emission intensity.

A dependence on the Eu^{3+} dopant concentration was observed in nanocrystalline $\text{Y}_2\text{O}_3:\text{Eu}^{3+}$. When the samples were produced using yttrium acetate as the precursor, the emission intensity of the ${}^5D_0 \rightarrow {}^7F_2$ transition increased as the europium concentration increased (1–5 mol%). However, in the particles produced using the chloride salt, the emission of the ${}^5D_0 \rightarrow {}^7F_2$ transition increased up to 3 mol% then decreased for higher concentrations. This effect occurs since cross-relaxation processes between Eu^{3+} ions quench the luminescence. This effect was somewhat minimized in certain complexes such as yttrium acetate due to an increase in the interionic separations relative to the uncomplexed ions.

The effect of different surface modifiers (tween-80 with β -alanine or ϵ -caprolactum or emulsogen-OG) on the emission intensity of the ${}^5D_0 \rightarrow {}^7F_2$ transition was studied. The modifier protects the generated particles by forming a layer and significantly reduces the surface free energy, which prevents interaction with neighboring particles. This plays an important role on the emission intensity, as the use of different modifiers will yield nanocrystals with different particle sizes and the nanocrystals with smaller particle sizes have higher luminescence than those with the larger particle size. The concentration of modifier (tween-80 with emulsogen-OG) was varied from 0 to 10 wt% with respect to $\text{Eu}_2\text{O}_3/\text{Y}_2\text{O}_3$, resulting in a reduction of particle size from 6 μm to 10 nm [53]. Furthermore, it was found that the luminescence intensity of the ${}^5D_0 \rightarrow {}^7F_2$ transition increased approximately fivefold as the particle size decreased from 6 μm to 10 nm. The fact that nanocrystals with smaller particle sizes had higher luminescence was explained in terms of

the amount of unit area being irradiated by the incident light as smaller particles have higher surface area than larger particles. The study showed that the particle size had no effect on the energy of the ${}^5D_0 \rightarrow {}^7F_1$ and 7F_2 transitions. However, the excitation spectra of the ${}^7F_2 \rightarrow {}^5D_0$ transition of the Eu^{3+} emission (~ 612 nm) showed that the position of the peak was blueshifted from 396 to 382 nm as the particle size decreased from 6 μm to 10 nm. This particle size dependent shift in the excitation spectra was determined to be due to quantum confinement. The ${}^5D_0 \rightarrow {}^7F_2$ transition was also found to be dependent on the pH of the modifier (tween-80 with ϵ -caprolactum), which was varied from 4 to 10. The luminescence intensity decreased with increasing pH revealing the sensitivity of the Eu^{3+} emission to the environment [55]. The change in intensity occurred for two reasons. First, with increased pH came a corresponding increase in the hydroxyl groups in the immediate vicinity of the Eu^{3+} ion as shown by FTIR spectroscopy. The resulting increase in nonradiative decay due to an increase in the OH stretching at 3300 cm^{-1} led to lower luminescence. Second, the pH affected the particle size of the $\text{Y}_2\text{O}_3:\text{Eu}^{3+}$ nanocrystals, which in turn affected the luminescence as described. Decreasing the pH of the modifier from 10 to 4 correspondingly decreased the particle size from 198 to 35 nm.

Hirai's group studied the photoluminescence of $\text{Y}_2\text{O}_3:\text{Eu}^{3+}$ nanocrystals prepared via an emulsion liquid membrane procedure [71] with a particle diameter between 20 and 30 nm. Following excitation with 254 nm, the authors observed the characteristic red emission of europium with the main emission peak at 614 nm. However, contrary to Sharma's findings where they observed an increase in the PL intensity with decreasing particle size, Hirai observed lower luminescence intensities for the smaller nanocrystals.

The emission of nanocrystalline $\text{Y}_2\text{O}_3:\text{Eu}^{3+}$ synthesized by a novel microwave combustion route following 457.9 nm excitation was studied as a function of Eu^{3+} concentration [50]. The authors observed that the luminescence intensity of the ${}^5D_0 \rightarrow {}^7F_2$ (611 nm) transition increased as the concentration of Eu^{3+} ions increased. For an Eu^{3+} concentration of up to 5 mol%, the intensity was quite low; however, it increased sharply between 5 and 10 mol% and was nearly saturated at 20 mol%.

Polizzi et al. [57] studied the luminescence properties of $\text{Y}_2\text{O}_3:\text{Eu}^{3+}$ nanocrystals prepared by the same synthesis technique following 488 nm laser excitation. The emission spectra obtained were similar to those obtained by Sharma using a conventional spectrofluorimeter, although the limited resolution of the latter prevented any comparisons from being made. It was reported that all emission bands of the samples prepared by wet chemical means were broader in comparison to the bulk sample. This phenomenon denoted a higher disorder in the crystalline environment of the Eu^{3+} ions in the nanocrystals. The ratio of the integrated intensities, R , of the ${}^5D_0 \rightarrow {}^7F_2$ and ${}^5D_0 \rightarrow {}^7F_1$ transitions was considered to be indicative of the asymmetry of the average coordination polyhedron of the Eu^{3+} ion and was denoted by

$$R = \frac{I({}^5D_0 \rightarrow {}^7F_2)}{I({}^5D_0 \rightarrow {}^7F_1)} \quad (9)$$

The R -value for the nanocrystalline $\text{Y}_2\text{O}_3:\text{Eu}^{3+}$ sample was determined to be 6.5 ± 0.1 compared to 5.3 ± 0.1 for the

bulk suggesting that, on average, the local environments of the Eu^{3+} ions were more distorted. This was attributed to the higher number of europium ions at or near the surface as a result of the higher surface-to-volume ratio in the nanocrystalline material.

The sesquioxide Y_2O_3 lattice has two distinct sites available for europium ion substitution, one with point-group symmetry C_2 and the other with point-group symmetry C_{3i} . The observed optical transitions within the $4f^n$ configuration are mainly attributed to electric dipole transitions, which are forced by the odd parity components of the crystalline electric field. For C_{3i} symmetry the parity of the electron wavefunction is an exact quantum number ($4f^6$ is even) and as such only magnetic dipole transitions should be observed. For these transitions, the selection rule $J = 0, 1 (J = 0 \rightarrow J = 0 \text{ forbidden})$ holds true. For the ${}^5D_0 \rightarrow {}^7F_1$ transition of the Eu^{3+} ion in the cubic bixbyite structure, five emission peaks should be present: two peaks that are attributed to Eu^{3+} ions residing in C_{3i} sites and three peaks for Eu^{3+} in C_2 sites. Due to the higher resolution spectra obtained, the presence of Eu^{3+} ions in both sites was observed in the luminescence spectra of the material.

Dilute aqueous suspensions of $\text{Y}_2\text{O}_3:\text{Eu}^{3+}$ nanoparticles [112] (mixed with SDS surfactant to minimize clustering) were filtered with a 200 nm syringe filter and a small volume ($\approx 200\ \mu\text{L}$) was spotted out on a clean fused quartz microscope slide. From the preparation stoichiometry (10:1 $\text{Y}_2\text{O}_3:\text{Eu}^{3+}$) and nominal particle size (2–15 nm), a significant fraction ($\geq 10\%$) of the yttrium oxide nanocrystals contained only a single Eu^{3+} ion. Dry $\text{Y}_2\text{O}_3:\text{Eu}^{3+}$ nanocrystals were continuously illuminated with the 514.5 nm line from an Ar^+ laser and probed by time-resolved fluorescence imaging techniques. The authors observed striking on-off blinking and multiple bright state luminescence that appeared to be related to thermal activation of the particle by the pump laser. They proposed that the discrete multilevel luminescence and oscillatory switching between levels from these crystals was derived from local symmetry fluctuations that modulated the electric dipole transition moment. Similar imaging experiments with different pump sources (488 and 454 nm) showed qualitatively different dynamics [113]. At the bluest pump wavelength, the luminescence appeared exclusively as very brief flashes and the authors speculated that the novel luminescence dynamics were associated with phonon interactions, which enhanced both the absorption and emission rates.

Tissue et al. have thoroughly investigated the spectroscopy of monoclinic Eu_2O_3 and $\text{Y}_2\text{O}_3:\text{Eu}^{3+}$ nanoparticles synthesized via a laser-heated vaporization/condensation technique. In several studies they noted that nanocrystal samples demonstrated vastly different spectroscopic properties compared to bulk (micrometer) crystalline samples.

In examining the laser spectroscopy of monoclinic nanocrystalline Eu_2O_3 and $\text{Y}_2\text{O}_3:\text{Eu}^{3+}$ Tissue et al. observed particle size dependent changes in the excitation and emission spectra [28, 74]. To aid in the comparison with $\text{Y}_2\text{O}_3:\text{Eu}^{3+}$ nanoparticles the spectroscopic properties of 5 and 14 nm Eu_2O_3 nanoparticles were first examined. The ${}^7F_0 \rightarrow {}^5D_0$ excitation spectra of 14 nm Eu_2O_3 particles exhibited no size effects when compared to a micrometer sized Eu_2O_3 sample, which consisted of only three sharp lines

corresponding to each of the three crystallographic cation sites in the monoclinic structure. However, the excitation spectra for 5 nm Eu_2O_3 particles showed broad and shifted bands that resembled the spectrum of a disordered material with the three sharp lines of the ${}^7F_0 \rightarrow {}^5D_0$ transition superimposed on them. It was found that excitation into any of the bands produced the same ${}^5D_0 \rightarrow {}^7F_2$ emission spectra while exciting into the broad luminescence produced a similar spectrum but with differing relative intensities of the peaks.

Low-temperature fluorescence excitation spectrum of 12 nm $\text{Eu}_{0.20}\text{Y}_{1.80}\text{O}_3$ particles showed two sets of lines: slightly broadened lines of Eu_2O_3 and an additional set of shifted sharp lines attributed to Eu^{3+} in monoclinic Y_2O_3 . In contrast, the excitation spectra of 5 nm $\text{Eu}_{0.20}\text{Y}_{1.80}\text{O}_3$ particles showed only a broad featureless band at 579.4 nm similar to the spectrum of 5 nm Eu_2O_3 . This broad spectrum was attributed to the small particle size in analogy to the Eu_2O_3 spectra [28, 74].

The ${}^5D_0 \rightarrow {}^7F_2$ fluorescence spectrum of the 12 nm $\text{Eu}_{0.20}\text{Y}_{1.80}\text{O}_3$ sample differed significantly from that obtained from the 14 nm Eu_2O_3 samples and was attributed to monoclinic $\text{Y}_2\text{O}_3:\text{Eu}^{3+}$. The ${}^5D_0 \rightarrow {}^7F_2$ fluorescence spectrum of the 5 nm sample was different from Eu^{3+} in the monoclinic phase with broadened and shift bands being observed. These observations were consistent with the same observations for the excitation spectrum, which indicated a disordered phase that was different from the crystalline monoclinic phase.

Differences in the spectra as a function of particle size, and thus preparation conditions, were attributed to different “phases” [28, 74]. Broadened lines observed in several of the smaller nanocrystalline samples (5 and 7 nm) indicated a large degree of disorder in the local environment of the Eu^{3+} probe ion, which could be due to structural disorder throughout the particles, disorder due to oxygen vacancies, or surface disorder. The authors eventually attributed line broadening in the case of the 5 nm samples to a range of particle sizes, with the narrow lines arising from larger crystalline particles and the broad features arising from smaller disordered particles. The fluorescence spectrum of the 5 nm species resulted from a summation of the contributions from all particles while for the 12 nm particles, the observations pointed toward a model of segregated surface atoms slightly displaced from their usual lattice positions.

To further explore the effects of the nanometer dimensions on the spectroscopy of rare earth doped Y_2O_3 , Tissue et al. initiated a concentration dependent study on monoclinic $\text{Y}_2\text{O}_3:\text{Eu}^{3+}$ [75]. Samples were prepared from 0.1%, 0.7%, 2%, and 5% Eu^{3+} doped Y_2O_3 starting material. The ${}^5F_0 \rightarrow {}^5D_0$ excitation spectra were recorded by monitoring the ${}^5D_0 \rightarrow {}^7F_2$ fluorescence of these materials at 624 nm using different boxcar delays to differentiate the contributions from the various sites and phases in the nanocrystals. At short delay times the peaks of the 5% sample were broadened and asymmetric, while at longer delays the spectral lines appeared symmetric and were shifted to longer wavelengths. This type of behavior was negligible in the 0.1% sample as the excitation lines were noted to remain sharp and symmetric. The results were assigned to contributions

to the three distinct cation sites for the monoclinic structure labeled as sites A, B, and C [75]. The excitation peaks attributed to sites B and C were also resolved in the spectrum of the 0.1% sample. The spectra of the 0.7%, 2%, and 5% samples showed a gradual increase in asymmetry and width of line profiles, along with a decrease in decay times. The authors concluded from these observations that nanocrystalline materials prepared by gas-phase condensation from starting materials containing 0.7% Eu^{3+} or higher had mixed phases [75].

A detailed site-selective spectroscopy study of the 0.1% Eu^{3+} doped Y_2O_3 nanocrystals was also carried out [75]. The particle size of the sample utilized in the study ranged in size from 7 to 30 nm, determined by TEM, and had an average particle size of 23 nm, determined by XRD. The results of the ${}^7F_0 \rightarrow {}^5D_0$ and ${}^7F_0 \rightarrow {}^5D_1$ excitation spectra are given in Table 2 along with the assignments to the A, B, and C sites. The ${}^5D_0 \rightarrow {}^7F_2$ fluorescence spectra when exciting the individual A, B, and C sites was also presented, the results of which are presented in Table 2. Exciting site A at 579.4 nm resulted in a rather complex spectrum consisting of more than 10 weak lines originating from all of the three sites indicating the presence of an energy transfer process occurring from site A to sites B and C. A broad line at 624.0 nm was also observed that overlapped with the strongest ${}^5D_0 \rightarrow {}^7F_2$ transitions of sites B (623.7 nm) and C (624.4 nm). Given the observed energy transfer from site A to sites B and C, the 624.0 nm line could not be assigned to site A with any degree of certainty.

The fluorescence decay times of the 5D_0 and 5D_1 transitions for the 0.1% Eu^{3+} doped Y_2O_3 nanocrystal sample are given in Table 3. The 5D_0 decay curves for each of the A, B, and C sites exhibited single exponential behavior. However, a short initial decay was observed in the case of site A, which was attributed to some portion of site A ions undergoing a very rapid nonradiative decay. The 5D_0 decay curves for the 0.7%, 2%, and 5% samples are given in Table 3. The 5D_0 decay times were shown to decrease as the concentration of Eu^{3+} increased in the nanocrystals due to an increase

Table 2. Energy levels of monoclinic $\text{Y}_2\text{O}_3:0.1\% \text{Eu}^{3+}$ at 10 K [75].

Energy level	Site A	Site B	Site C
5D_1	19,004	18,932	18,914
	18,960	18,918	18,911
		18,893	18,907
5D_0	17,259	17,161	17,158
7F_3	2171	1944	1921
	2123	1869	1868
	1983	1845	1828
	1937		
7F_2	1404	—	—
	1346	1324	1185
	1328	1128	1143
	1070	933	993
	860	915	890
7F_1	645	431	369
	350	383	346
	171	264	—
7F_0	0	0	0

Table 3. Fluorescence decay times of 5D_1 and 5D_0 levels in nanocrystalline monoclinic 0.1, 0.7, 2, and 5% $\text{Eu}^{3+}:\text{Y}_2\text{O}_3$ at 10 K [75].

Sample	Energy level	Site A	Site B	Site C
$\text{Y}_2\text{O}_3:0.1\% \text{Eu}^{3+}$	5D_1	$45 \pm 7 \mu\text{s}$	$117 \pm 9 \mu\text{s}$	$156 \pm 2 \mu\text{s}$
	5D_0	$1.75 \pm 0.12 \text{ ms}$	$1.23 \pm 0.09 \text{ ms}$	$1.32 \pm 0.06 \text{ ms}$
$\text{Y}_2\text{O}_3:0.7\% \text{Eu}^{3+}$	5D_0	—	$1.05 \pm 0.10 \text{ ms}$	$1.24 \pm 0.12 \text{ ms}$
$\text{Y}_2\text{O}_3:2\% \text{Eu}^{3+}$	5D_0	—	$0.82 \pm 0.08 \text{ ms}$	$1.13 \pm 0.11 \text{ ms}$
$\text{Y}_2\text{O}_3:5\% \text{Eu}^{3+}$	5D_0	—	$0.82 \pm 0.12 \text{ ms}$	—

in depopulation of excited states from ion–ion interactions. At low europium concentrations the decay mechanism was mainly radiative resulting in longer and single exponential decay curves. No interaction between sites B and C was observed at 10 K in 0.1% Eu^{3+} doped Y_2O_3 nanocrystals. However, significant energy transfer from site A to sites B and C was noted in the same sample which was attributed to phonon-assisted energy transfer.

The results of this study give insight to the difference in solubility of the Eu^{3+} ion in bulk and nanocrystal Y_2O_3 [75]. In the 0.1% Eu^{3+} nanocrystal sample there appeared to be a single phase, while doping with 0.7% Eu^{3+} formed a secondary Eu_2O_3 phase. The secondary phase was attributed to a kinetic effect of the gas-phase condensation method. The 10–30 nm $\text{Y}_2\text{O}_3:\text{Eu}^{3+}$ nanocrystals were found to fluoresce and were determined to be crystalline. There was no observed decrease of the 5D_0 lifetime in the nanocrystal samples due to quenching by surface defects although the luminescence from the nanocrystal $\text{Y}_2\text{O}_3:\text{Eu}^{3+}$ was visually weaker than that of the starting material (cubic $\text{Y}_2\text{O}_3:\text{Eu}^{3+}$).

The spectroscopy of a bulk monoclinic 0.1% Eu^{3+} doped Y_2O_3 sample was also examined in detail in order to provide reference spectra and excited-state lifetimes for the evaluation of the optical properties of Eu^{3+} doped Y_2O_3 nanocrystals of similar concentration [76]. The line positions for both the $^7F_0 \rightarrow ^5D_0$ and $^7F_0 \rightarrow ^5D_1$ excitation spectra of the 23 nm nanocrystalline material revealed a small shift toward shorter wavelengths (<1 nm) compared to those of the bulk material. The other significant difference was that the spectral lines of the nanocrystals were observed to be significantly broader than those of the bulk material due to inhomogeneous broadening caused by disorder. Increasing the sensitivity of the spectra led to the discovery of weak broad lines at approximately 580 nm ($^7F_0 \rightarrow ^5D_0$ and 526.5 nm ($^7F_0 \rightarrow ^5D_1$) in the nanocrystal sample. The intensity of these broad lines was shown to increase as the particle size decreased, eventually becoming dominant in the case of the ~5 nm diameter particles [28, 74], and were attributed to a different “phase” in the nanocrystalline samples.

The anomalies of site A noted in a previous study [75], such as the additional lines in the fluorescence spectra, were also observed in the case of the bulk sample and were attributed to the intrinsic features of the monoclinic phase of Y_2O_3 [76]. Energy transfer was observed from site A to sites B and C in the 0.1% Eu^{3+} doped Y_2O_3 nanocrystals but not in the bulk monoclinic material. This indicated that either the overall or local concentration of the europium ions was higher than 0.1% in the nanocrystal sample.

Excitation directly into the 5D_0 level of the bulk material resulted in single exponential lifetimes of 1.57, 0.78, and

0.82 ms for sites A, B, and C respectively. The 5D_1 fluorescence decay times for sites B and C were 112 and 138 μs respectively. The 5D_1 fluorescence decay of site A was determined from the rise of the 5D_0 decay after excitation into site A of the 5D_1 level and was found to be 71 μs . With the exception of the 5D_1 lifetime of site A, the lifetimes of both the 5D_0 and 5D_1 levels were noted to be the same or longer in the case of the nanocrystals compared to those of the bulk sample [76].

A detailed particle size study was also performed on monoclinic Eu^{3+} doped nanocrystals to determine the effects of the nanocrystal particle size on their spectroscopic properties [36]. Two significant changes in the spectra were observed as the particle size decreased. The widths of the three sharp monoclinic lines became broader as the particle size was decreased due to inhomogeneous broadening which was attributed to disorder induced by the increase in the surface area. The second was the appearance of secondary phases or sites. A line at 580.6 nm was also observed by the authors that was assigned to Eu^{3+} residing in the C_2 site of cubic Y_2O_3 . The presence of the cubic phase was explained on the basis of its more open nature, which accommodates the inherent disorder of the surface better than the monoclinic phase and provides a lower surface area. There was also a broad band that overlaps with the site A excitation line, which was most evident in the 7 and 10 nm particles but was also present in the 13 and 15 nm samples but at much weaker intensity.

The authors noted that excitation into site A in the 7 nm nanocrystal sample resulted in fluorescence from this site similar to the bulk sample, but also in broad features and emission lines originating from sites B and C. Emission from sites B and C was observed from all nanocrystal samples for site A excitation. The low concentration in the nanocrystals utilized in this study would normally not allow for energy transfer to occur. This indicated that the true concentration of the nanocrystals might have been higher than in the starting material or that the dopant ions were segregated in the nanocrystals leading to a higher local concentration that allows energy transfer [36].

In the case of the site B emission spectra of the 7 nm sample, site B emissions were observed at the same wavelengths as the bulk material along with additional weaker lines belonging to site C emissions. Similar behavior was observed upon site C excitation, where site C emissions dominated the spectrum while site B lines appeared as shoulders on the site C lines. The broad band that was observed in the site A spectrum also appeared in the sites B and C spectra but with decreased intensity. The behavior was attributed to the broadening of the sites B and C excitation lines in the

nanocrystals as the particle size was decreased. The overlap of the two excitation lines explained why emission from both sites B and C was observed in the emission spectra under selective excitation. It was found though that some selectivity was still possible by exciting into the sides of the broadened line which resulted in changes in the relative intensities of site B and C emission lines.

A broad emission was also noticed in all the fluorescence spectra of the nanocrystal samples that spanned from 605 to 635 nm that was not attributable to either the monoclinic or cubic phases. This band was strongest under site A excitation but was also noticeable under site B and C excitation. With the decrease in particle size, the intensity of this band increased similarly to what was observed in the excitation spectra. The origin of this broad feature was tentatively assigned by the authors to either a separate “phase,” a new “site” in the nanocrystal samples, or from Eu^{3+} ions at the surface of the particles [36].

The excitation and luminescence spectra of nanocrystal Y_2O_3 in this study showed three distinct phases:

- (i) sharp lines of the three sites of monoclinic Y_2O_3 , which dominated in the larger particles,
- (ii) the C_2 site of the cubic phase, which appeared in the small particles,
- (iii) broad bands due to an unidentified phase that increased in intensity as the particle size decreased.

The observation by the authors of distinct spectral lines from the monoclinic phase confirmed the presence of some crystalline phase for the entire range of particle sizes [36].

All decay transients obtained for the bulk, 23 nm, and 15 nm samples were single exponential and the reported decay times were obtained from single exponential fits. The decay curves for the 7 and 13 nm samples were not single exponential and the lifetimes were obtained from fits to the linear portion of the log plots of the transients. This nonexponential behavior indicated that the proximity of the surface may have quenched some fraction of the Eu^{3+} ions due to surface defects or Eu^{3+} segregation. However, there was no drastic lifetime shortening due to the increase in surface-to-volume ratio. The 5D_0 decay time was found to increase for all sites as the nanocrystal particle size decreased.

In the previous studies it was noted that the 5D_0 lifetimes in the monoclinic Y_2O_3 nanocrystal samples were significantly longer than in the bulk (micrometer) sample [36]. The significant difference observed in the lifetimes was explained by the change induced in the nanocrystals' refractive index by the medium surrounding the nanocrystals [114]. Since the particles were much smaller than the light wavelength, the local electric field acting on the Eu^{3+} was determined by the combined effects of the Y_2O_3 medium contained within the nanoparticles and that of the medium filling the voids. To determine the role of the external medium, Meltzer et al. compared the lifetime of the 5D_0 level of Eu^{3+} in monoclinic Y_2O_3 nanoparticles surrounded by air ($n = 1$) and when they were immersed in liquids with different refractive indices [114]. Methanol, CH_3OH ($n = 1.326$), and carbon disulfide, CS_2 ($n = 1.628$), were chosen as the other media. It was observed that changing the medium had a profound effect on the observed lifetime; the lifetime decreased as the index of the immersion medium was increased [114].

The radiative lifetime of electric dipole transitions of an ion embedded in a medium may be expressed by the formula

$$\tau_R \sim \frac{1}{f(\text{ED})} \frac{\lambda_0^2}{\left[\frac{1}{3}(n^2 + 2)\right]^2 n} \quad (10)$$

where $f(\text{ED})$ is the oscillator strength for the electric dipole transition, λ_0 is the wavelength in vacuum, and n is the refractive index of the medium. The dependence of τ_R on the refractive index, n , is caused by (i) the change in the density of states for the photons in the medium of reduced light velocity and (ii) the modification of the polarizability of the surrounding medium. To correlate the experimental results with Eq. (10), it was necessary for the authors to introduce an effective index of refraction for the medium, n_{eff} , which consisted of the index of Y_2O_3 and of the surrounding media n_{med} . The effective refractive index is given by $n_{\text{eff}}(x) = x \cdot n_{\text{Y}_2\text{O}_3} + (1 - x) \cdot n_{\text{med}}$, where x is the “filling factor” showing what fraction of space is occupied by the nanoparticles. One may replace n by n_{eff} when the average size of the particles in question is much smaller than the wavelength of light. The best fit to the experimental data corresponded to $x = 0.23$ indicating that the Y_2O_3 nanocrystals occupied only 23% of the sample space [114].

The authors found that the results in the case of the nanoparticles showed that the radiative lifetimes of the excited states of impurity ion strongly depended on the effective index of refraction of the media consisting of nanoparticles and the substance filling the space between them [114]. It is therefore possible according to Eq. (10) that the lifetime of any nanoparticle material could be increased from its bulk factor by a factor of $n(n^2 + 2)^2/9$ when the material is totally dispersed as individual particles in air (vacuum). For Y_2O_3 with $n = 1.91$, the maximum lifetime enhancement is a factor of 6.77. It may be possible to reduce the lifetime even more by placing the nanoparticles in a media with a greater index of refraction, as might be the case for nanoparticles embedded in glass or polymer matrices. This effect is usually hard to directly observe since changing the host matrix results in a change of the local structure of the impurity ion along with its oscillator strength. Nanocrystalline materials allow for a change in the refractive index of the medium without altering the impurities local structure. The effect may also be utilized in determining the fraction of the sample volume occupied by the nanocrystals.

In a continuation of this study Meltzer et al. examined the radiative lifetimes of monoclinic $\text{Y}_2\text{O}_3:\text{Eu}^{3+}$ nanocrystals dispersed in a siloxane polymer [115]. The sample utilized in the study was monoclinic 23 nm $\text{Y}_2\text{O}_3:0.1\% \text{Eu}^{3+}$ nanocrystals produced by condensation after laser evaporation, which were dispersed in a siloxane polymer. Similar to isolated $\text{Y}_2\text{O}_3:\text{Eu}^{3+}$ nanoparticles, the nanoparticles embedded in siloxane polymer form in loosely packed aggregates. No changes in the sharp line optical spectra of the $\text{Y}_2\text{O}_3:\text{Eu}^{3+}$ nanocrystals were observed upon embedding them in the siloxane polymer. The measured lifetime in the C sites of the 5D_0 state of Eu^{3+} in 23 nm monoclinic Y_2O_3 nanoparticles ($n = 1.91$) embedded in siloxane polymer ($n = 1.40$) was $\tau_R = 1.05$ ms compared to $\tau_R = 0.73$ ms in the bulk materials ($T = 300$ K) [115]. According to Eq. (10), this lifetime corresponds to an effective index of refraction of the media,

consisting of Y_2O_3 nanocrystals and polymer filling the space between them of $n_{\text{eff}} = 1.7$. The data obtained for the radiative lifetime of the 5D_0 state of Eu^{3+} in Y_2O_3 nanocrystals embedded in polymer were compared to the previous results in liquids. Assuming the 23% filling factor found in the first study [114], the observed radiative lifetime is smaller than that predicted for $n_{\text{med}} = 1.4$. However, the value is consistent with the assumption of a larger “filling factor” of 63%, which was attributed to compaction of the Y_2O_3 aggregates that occurred in the course of dispersal and polymerization [115].

The investigation of the spectroscopic properties of nanocrystal $\text{Y}_2\text{O}_3:\text{Eu}^{3+}$ was further advanced by Yang et al. who examined the effect of the nanocrystals' modified phonon spectrum on the relaxation rate of closely spaced electronic levels. This was performed by analyzing the decay rate due to one-phonon emission (the direct process) for electronic states with energy separations of 3 to 7 cm^{-1} by observing the time-resolved emission from 5D_1 to 7F_3 states for the C site in monoclinic $\text{Y}_2\text{O}_3:\text{Eu}^{3+}$ nanocrystals [116, 117]. The energy separation between the second and third levels and the lowest level of the 5D_1 manifold for Eu^{3+} ions located in C sites was 3 and 7 cm^{-1} , respectively. The authors utilized nanocrystals with an average size of 23 nm in the study since they were unable to support phonons with energies of 3 and 7 cm^{-1} due to their small size. Hence they anticipated that one-phonon emission would not be observed in these materials. For comparative purposes, the fluorescence transients for Eu^{3+} ions situated at the C site for micrometer scale $\text{Y}_2\text{O}_3:\text{Eu}^{3+}$ were also obtained. The lowest level $^5D_1(\text{I})$ possessed a single exponential decay with a lifetime of 137 μs which corresponded to previous work [76]. The transients for the second $^5D_1(\text{II})$ and third $^5D_1(\text{III})$ levels exhibited a rapid initial decay on a 100 ns time scale followed by a long tail of 134 and 132 μs , respectively. This type of behavior was attributed to a rapid direct relaxation process followed by thermalization [116, 117].

When examining the same decays in the nanocrystalline material it was found that the transient of the $^5D_1(\text{I})$ level was single exponential with a lifetime of 131 μs [116, 117]. The transient of the $^5D_1(\text{II})$, which was 3 cm^{-1} above the $^5D_1(\text{I})$, was fitted to a double exponential that had decay times of 27 and 113 μs , while the emission from the third level $^5D_1(\text{III})$ yielded decay times of 7 and 101 μs . These lifetimes were temperature independent in the range of 1.5 and 10 K, indicating that relaxation was due to neither an Orbach nor a Raman relaxation process. Possible mechanisms that were proposed for the residual relaxation included resonant coupling to modes of the nanoparticles cluster and nonresonant coupling to modes of the nanoparticles, which have been broadened due to interactions with cluster modes or other excitations [116]. The emission from the corresponding levels of the 5D_1 manifold for Eu^{3+} ions at the B site was noted to be extremely weak indicating a considerably fast relaxation rate compared to Eu^{3+} ions at the C site. It was thought that the 25 and 29 cm^{-1} energy gaps between these levels and the $^5D_1(\text{I})$ were sufficiently high to allow for electronic relaxation by one-phonon emission.

Hong et al. have examined the optical dephasing of monoclinic $\text{Y}_2\text{O}_3:\text{Eu}^{3+}$ nanocrystals synthesized via a laser vaporization/condensation method using transient spectral hole

burning, as a function of temperature and particle size (d) [118]. They observed a strongly enhanced optical dephasing rate that was dependent on $1/d^2$. This observation was indicative of an enhanced electron-phonon (e-p) interaction as particle size was decreased. The virtually exponential temperature dependence of the hole linewidth was described using a calculation for the two-phonon Raman scattering rate. Yet this same calculation was found insufficient to describe the particle size dependence observed by the authors. They observed that for a micrometer sized monoclinic $\text{Y}_2\text{O}_3:\text{Eu}^{3+}$ (0.1%) powder, the B/C sites had an instrument-limited linewidth of 5 MHz below 10 K. Above 15 K, the linewidth of these sites increased consistent with a T^7 Raman process. The linewidth of site A was observed to increase rapidly above 5 K also following a T^7 behavior, possibly indicating a stronger e-p interaction. A 20 nm nanocrystal sample was observed to have similar linewidth dependence as the micrometer sample except for a strong linear temperature dependence in the case of the A site. In the case of the 12 nm nanocrystals, the B/C sites showed a measurable low temperature linewidth of about 10 MHz that rapidly increased above 5 K while site A exhibited a large linear temperature dependence up to 5 K, which increased significantly above 5 K. These results demonstrated that as the particle size was decreased below 20 nm, a significant enhancement in the optical dephasing rate occurred [118]. The same behavior was noted in a 12 nm Eu_2O_3 sample suggesting that concentration did not have a profound effect on the optical linewidth. The authors observed that as the particle size was reduced, the Eu^{3+} probe ions in the main body of the particle experienced enhanced dephasing effects [118]. Alternatively, other localized resonant nodes at the surface may have a greater effect in the smaller particles. The observed temperature dependence along with the increase in the e-p interactions with reduced particle size could have been due to a local mode attributed to defects or with structure on the surface.

Another paper focused on how the size, preparation technique, and local structure of the monoclinic $\text{Y}_2\text{O}_3:\text{Eu}^{3+}$ nanocrystals affected their dynamical properties [119]. Spectral hole burning (HB) within inhomogeneously broadened optical transitions and fluorescence line narrowing (FLN) were utilized as these techniques allowed one to obtain homogeneous linewidths of optical transitions. These measurements provided direct information on the e-p interactions, which in turn greatly influenced the dynamics of the dopant ions. The authors carried out experiments on three different types of samples: (1) Y_2O_3 : 0.1% Eu^{3+} nanocrystals produced by gas-phase condensation following laser evaporation, (2) Y_2O_3 :0.5% Eu^{3+} nanocrystals produced by sol-gel techniques, and (3) sol-gel produced SiO_2 glass containing Y^{3+} and Eu^{3+} . All three materials displayed unique dynamical properties when examined through HB and FLN techniques. The particle size distributions of the monoclinic $\text{Y}_2\text{O}_3:\text{Eu}^{3+}$ nanocrystals obtained by condensation were 4, 7, and 12 nm. The 4 nm nanocrystal sample showed the presence of some cubic phase. The sol-gel produced cubic $\text{Y}_2\text{O}_3:\text{Eu}^{3+}$ nanocrystals varied in size between 5 and 10 nm (TEM and XRD results). Samples were also prepared using a sol-gel technique that produced SiO_2 glasses with the following compositions: SiO_2 :1% Eu;

SiO₂:1% Eu, 2.5% Y; SiO₂:1% Eu, 10% Y. It was anticipated that (Y, Eu)₂O₃ clusters may have formed making these materials analogous to the nanocrystalline samples. These samples were annealed at different temperatures, $T_{\text{ann}} = 200, 400, 600, 800, \text{ and } 900 \text{ }^\circ\text{C}$.

The hole widths for the ${}^7F_0 \rightarrow {}^5D_0$ transition of all three crystallographic inequivalent A, B, and C sites of the monoclinic nanocrystalline Y₂O₃:Eu³⁺ materials and a monoclinic micrometer powder were obtained at 1.5 and 6.5 K [119]. The authors found that the micrometer sized powder displayed minimal spectral dependence of the hole width while the monoclinic nanocrystals exhibited considerable spectral hole width variations, especially at $T = 6.5 \text{ K}$. Little spectral dependence was noted for site A except for $T = 5 \text{ K}$. From the observed larger spectral dependence at 6.5 K than at 1.5 K, they concluded that the hole width was highly wavelength dependent with the hole width being more pronounced far from the unperturbed B/C site resonances. The temperature dependencies of the hole widths for the ${}^7F_0 \rightarrow {}^5D_0$ transition of Eu³⁺ (C sites) in different nanocrystalline Y₂O₃ samples were also examined [119]. The hole width in the laser evaporation nanocrystal samples varied slightly below 5 K but was observed to become much faster ($\sim T^3$ dependence) at higher temperatures. When the laser frequency was tuned 0.04 nm to the long wavelength side of the C site's ${}^7F_0 \rightarrow {}^5D_0$ transition, the temperature dependence of the hole width was found to be much steeper. In the case of the sol-gel produced cubic nanocrystalline (5–10 nm) Y₂O₃ (C₂ site) the temperature dependence of the hole width was notably different, being described by a $\sim T^{0.6}$ dependence. It was also observed that the homogeneous linewidths did increase with a decrease of the particle size for any given temperature. The observations were explained tentatively by a two-phonon Raman scattering of phonons, involving size quantized vibrational excitations of the nanoparticles [119]. The observed temperature dependence of the hole width in the sol-gel produced cubic nanocrystals indicated the presence of significant disorder possibly associated with the surface of the nanocrystals [119]. The surface disorder resulted in the presence of a two-level system (TLS), similar to what is observed in the low temperature behavior of homogeneous linewidths in glasses and disordered crystals. In these systems the linewidth exhibits a power-law temperature dependence $\gamma_h \sim T^\alpha$ ($1 < \alpha < 2$). A power-law temperature behavior was observed in the sol-gel nanocrystals, but with $\alpha = 0.6$. The authors attributed this behavior to the interaction with the TLS but only toward the surface of the nanocrystals. This was due to the fact that the TLS might be at the surface and is spatially separated from the activator ions inside the crystalline particles.

The large differences observed in the spectral dependencies of the homogeneous linewidths between the micrometer size and nanocrystalline samples suggested a correlation between the location of the impurity ion in the nanoparticles and its spectral line position inside the inhomogeneously broadened line contour [119]. The authors explained the observed differences in the dynamical properties of different Eu³⁺ ions in nanoparticles by taking into account the fact that a significant fraction of Eu³⁺ ions in nanoparticles lie close to the surface and this fraction increased as the particle

size was reduced. The lowest frequency size resonant vibrational modes had large displacements near the surface and resulted in these ions experiencing larger electron-phonon interactions and a stronger temperature dependence in their hole widths. Thus, it was the presence of the size-quantized vibrational excitations near the surface of the nanocrystals that controlled their dynamics.

Although the authors anticipated that nanostructured behavior would also be observed in sol-gel produced Eu³⁺, Y³⁺ doped SiO₂ glass due to clusters of (Y, Eu)₂O₃, no indication of cluster formation was observed [119]. Of note was that persistent hole burning was observed in this material, which is unusual in Eu³⁺ doped glasses. The presence of the holes was attributed to a photophysical rearrangement of the Eu³⁺ local environment. The difference in the hole-burning results compared to regular glasses, besides its persistence, was the magnitude of the hole width which was more than 30 times broader in the sol-gel glass at 1.5 K. However, they did exhibit similar spectral and temperature dependences of the homogeneous width compared to regular glasses indicating a similar mechanism of broadening (interaction with TLS). The authors attributed the larger hole width in the sol-gel glasses to a higher TLS concentration and/or stronger coupling to the Eu³⁺ ions [119]. When comparing HB and FLN results, the authors observed much larger linewidths in the case of the HB technique. This difference in linewidths was attributed to a spectral diffusion process. The characteristic time scale of an FLN experiment is the fluorescence lifetime ($\sim 1 \text{ ms}$) while the HB experiment required a time scale of $\sim 100 \text{ s}$. They attributed the observed factor of three larger linewidth in the HB experiments to this difference in time scale [119].

Monoclinic 0.1% Y₂O₃:Eu³⁺ nanocrystals synthesized by condensation after laser evaporation dispersed in siloxane polymer were examined by Meltzer et al. to determine the difference in the homogeneous broadening of nanoparticles embedded in a matrix with that of free nanoparticles [120, 121]. To accomplish this, the width of spectral holes, γ_{HB} , burned in the ${}^7F_0 \rightarrow {}^5D_0$ transition of Eu³⁺ ions located on the C site ($\lambda = 582.8 \text{ nm}$) in 23 nm Y₂O₃ monoclinic crystallites dispersed in siloxane polymer and in free, as-prepared, nanocrystals of the same size were examined. The hole burning occurred due to redistribution of the population of the ground-state hyperfine levels of those ions whose hyperfine transitions were resonant with the laser.

Embedding the nanoparticles in the polymer resulted in an observed large increase in hole width and the $\sim T^3$ temperature dependence observed for isolated nanoparticles became $\sim T$ for the embedded nanoparticles. This nearly linear temperature behavior of γ_{HB} in nanoparticles surrounded by the polymer matrix was similar to what was observed for Eu³⁺ doped glasses, indicating that the dominant mechanism for the homogeneous broadening of the ${}^7F_0 \rightarrow {}^5D_0$ transition of Eu³⁺ in Y₂O₃ nanocrystals embedded in the polymer was the interaction with the TLS of the surrounding glass [120, 121]. The long-range elastic dipole-dipole TLS-RE ion interaction may be effective over the whole nanoparticle leading to the possibility that it may be responsible for the homogeneous broadening of the optical transitions of RE ions contained inside the nanocrystals.

The large changes observed to the magnitude and temperature dependence of the hole linewidth upon embedding the nanocrystals into a polymer ($\text{Y}_2\text{O}_3:\text{Eu}^{3+}$) supported this suggestion and provided direct evidence for the long-range character of the TLS-RE interaction [120].

4.4. Quantum Confinement in Y_2O_3 Nanocrystals

Bhargava and co-workers studied the optical properties of Tb^{3+} doped Y_2O_3 nanocrystals and showed that excitation of the $4f^7-5d$ absorption band was followed by multiphonon relaxation to the 5D_3 or 5D_4 states resulting in blue emission from the $^5D_4 \rightarrow ^7F_6$ transition and the characteristic green Tb^{3+} emission from the $^5D_4 \rightarrow ^7F_5$ transition [122]. The intraconfigurational $4f^8$ transition is parity and spin forbidden but due to the effects of the crystal field, a slight admixing of the 5D and 7F states leads to a partially allowed transition resulting in a transition lifetime on the order of a few milliseconds making Tb^{3+} an ideal candidate for various light emitting applications.

Bhargava et al. compared the PL spectra of terbium doped nanocrystalline Y_2O_3 to that of a standard phosphor, LaOBr:Tb , and showed that the light output of the nanocrystals was lower by a factor of two than that of the standard phosphor [123]. However, the photoluminescence excitation (PLE) data indicated that the concentration of the Tb doped nanocrystals was lower than the standard phosphor and it was anticipated that with an increase in Tb^{3+} concentration and better control of the nanocrystalline particle size and size distribution, the efficiency of nanocrystalline $\text{Y}_2\text{O}_3:\text{Tb}$ would exceed that of the standard Tb phosphor. The authors showed that the green PL peak of the nanocrystalline phosphor was shifted by 2 nm compared to the standard phosphor and attributed it to the quantum confinement of the dopant ion. However, the authors do not report that the shift of 2 nm may occur because the Tb^{3+} ions experience different crystal field effects from the two different hosts.

Later, Bhargava showed that a decrease in the particle size, from 10 to 4 nm, of nanocrystalline $\text{Y}_2\text{O}_3:\text{Tb}$ phosphor resulted in the corresponding increase of the photoluminescent efficiency and it was shown that the light output per Tb^{3+} ion in the doped nanocrystalline Y_2O_3 phosphor was higher than in the standard LaOBr:Tb^{3+} phosphor [35]. The increase in the efficiency varied as the square of the particle size (D) [8] as was expected from the quantum confinement model ($1/D^2$). The excited states of the localized terbium atoms in yttria could be strongly modulated as a result of quantum confinement in the nanocrystals, which can lead to changes in the overlap of wave functions with other atoms in the particle. Due to this modulation effect, the dopant terbium ions could interact more readily with the host lattice than in a bulk sample, which led to changes in both the electronic structure and transition probabilities. Furthermore, the authors observed differences in the absorption edge, a redshift, as the size of the $\text{Y}_2\text{O}_3:\text{Tb}^{3+}$ nanocrystals was reduced.

Terbium doped nanocrystals were reported to be able to downconvert X-ray photons to green luminescence when excited by incident X-rays with energies at the absorption edges of Tb (L edge) and Y (K edge) [81]. X-ray excited

luminescence (XEL) data showed pronounced changes and a significant difference between bulk and nanocrystalline $\text{Y}_2\text{O}_3:\text{Tb}^{3+}$ at the L edge but only a moderate difference at the K edge with lower XEL observed for the bulk material compared to the nanocrystals. The green Tb^{3+} emission showed sharp XEL edge jumps and the conversion of X-ray excitation to luminescence could have involved two distinct paths. One possible path may have involved the direct absorption of the incident photons by the Tb^{3+} ion, which gave rise directly to the Tb-activator edge jump. Conversely, the Y atom of the host material could have absorbed the incident photons followed by subsequent energy transfer to the Tb^{3+} ion, which caused the host edge jump. From the EXAFS results, it was possible that a large fraction of Tb ions occupied the sites near the surface of the nanocrystal and thus the energy transfer from the Y_2O_3 host to the surface Tb ions may have been hindered due to nonradiative energy losses.

Bhargava's group [122] reported that the effect of the quantum confinement on impurity ions depended critically on the size of the host crystal and as the size of the host decreased, the degree of confinement and its effect increased. In the chosen system $\text{Y}_2\text{O}_3:\text{Tb}^{3+}$, the electrons and holes of the host would not be considered either weakly or strongly confined since the Bohr diameter of electrons in Y_2O_3 is about 1 nm while the particle sizes were in the range of 5 nm. In the nanocrystalline material with particle sizes in the 2 to 5 nm range, a significant increase in the luminescence efficiency was observed. To explain these results, a new model of doped nanocrystals was proposed where the change in the oscillator strength was a result of the quantum confinement of a localized atom by the boundary of the host. The quantum confined atom was said to characterize a new class of materials where the properties of the localized impurity were modulated. This was attributed to the interaction between the excited states of the localized impurity and the induced carrier in the nanocrystal (quantum dot). The Tb^{3+} ion contains eight electrons (represented as $4f^8$), and as such the $4f$ shell readily releases an electron resulting in an intraionic $4f^8-4f^75d$ transition, which takes place at relatively low energy. The $5d$ orbit lies at the surface of the ion, and therefore it can be strongly influenced by the lattice. In the case of the excitation spectra associated with the green $^5D_4 \rightarrow ^7F_5$ emission, a transfer mechanism of the excited carriers from the $4f^7-5d$ bands to the $4f^8$ manifold of the Tb^{3+} ion was observed and occurred at 246 nm, which was quite different from bulk $\text{Y}_2\text{O}_3:\text{Tb}^{3+}$. The authors showed that following 254 nm excitation, the PL efficiency of bulk $\text{Y}_2\text{O}_3:\text{Tb}^{3+}$ was significantly lower than that of nanocrystalline $\text{Y}_2\text{O}_3:\text{Tb}^{3+}$, which was comparable to two well known green phosphors; $\text{Gd}_2\text{O}_3:\text{Tb}^{3+}$ and $\text{Y}_2\text{SiO}_5:\text{Tb}^{3+}$. The authors measured the photoluminescence excitation spectra of the blue $^5D_3 \rightarrow ^7F_5$ emission (417 nm) and of the green $^5D_4 \rightarrow ^7F_5$ (543 nm) emission and showed that the 417 nm emission had an excitation peak at 251 nm, while the 543 nm emission had a PLE peak at 246 nm. The 5 nm shift was believed to occur because a size distribution of particles was present.

To explain the results of the size dependent variation in the quantum efficiency, the authors used a standard configuration coordinate diagram for Tb^{3+} in Y_2O_3 . They included

the effect of the distortion imposed by quantum confinement on the $4f^7-5d$ bands represented by bulk, medium-sized nanocrystals (>5 nm) and small-size nanocrystals (<5 nm). A few key observations were made:

- (i) The PLE peaks shifted to lower energy as the particle size of $Y_2O_3:Tb^{3+}$ increased.
- (ii) The intensity of the PLE peak decreased as the peak position shifted to lower energy suggesting that the product of the absorption and emission intensity was largest for the smallest particles.
- (iii) As the particle size decreased, the transfer mechanism of the excited carriers shifted. For the bulk material, the carriers were directly relaxed in a Tb-ion energy manifold, which resulted in a slow process and since the $^5D_3 \rightarrow ^7F_5$ transition is forbidden, a weak 417 nm emission line was observed. However, as the particle size changed from bulk to medium-sized nanocrystals, the intensity of the 417 nm emission improved since the transfer to the 5D_3 level occurred directly without going through intermediate levels and was due to confinement of the Tb^{3+} ions imposed by the host boundary. When the size of the particle was reduced further, the transfer occurred directly toward the 5D_4 level and quenched the $^5D_3 \rightarrow ^7F_5$ transition thus improving the efficiency of the green emission.
- (iv) The changes were consistent with the fact that when the nanocrystals were heated, the resultant particle growth generated a decrease in efficiency.
- (v) The changes in the absorption in the UV region (oscillator strength) brought about by quantum confinement were only observed when the carriers were present in the host. The charge-transfer modulated the intraionic states such as $4f^7-5d$, and as a result there were no changes in the core $4f^8$ states.

In the model proposed by the authors, the excited states of the atom (dopant) provided a significant overlap with the host boundary. The overlap of the host wavefunctions and the extended excited states led to strong modulation of the excited states of the atom. Subsequently, this led to efficient and fast transfer of carriers from the host to the dopant. Furthermore, not only the $5d$ states of the Tb ion but also other higher excited states such as $6s$, $6p$, etc. begin to play a role in the transfer mechanism.

Bhargava's group reported that the surface-to-volume ratio of nanocrystal $Y_2O_3:Tb^{3+}$ could be controlled by varying the state of agglomeration through heat treatments [82]. To induce aggregation, the nanocrystals were heated between 300 and 500 °C. The photoluminescence efficiency of the $Y_2O_3:Tb^{3+}$ nanocrystals was at least five times higher than that of bulk $Y_2O_3:Tb^{3+}$ and when the nanocrystals were heated to temperatures over 550 °C their spectral features reverted back to bulk and the photoluminescence efficiency decreased significantly [124]. The following key differences between the bulk and nanocrystal samples were observed:

- (i) The PLE peak shifted from 250 to 310 nm in the bulk and from 220 to 250 nm in the nanocrystals.
- (ii) The intensity of the PLE peak was at least five times more intense than in the bulk material.
- (iii) The PL efficiency was at least five times more than in the bulk material.

These changes were explained by invoking that the excited states of the Tb^{3+} ion behaved like excitons in a semiconductor. In the case of Tb^{3+} ion, the $4f^7-5d$ absorption was involved in the intraionic transitions. These absorption bands were blueshifted by approximately 1 eV and this shift was assigned from $4f^7-5d$ to $4f^7-6s$. This excited intraionic absorption ($4f^7-6s$ and possibly $4f^7$ -higher excited states) could only have occurred when the electron occupancy of these excited states was modulated by the size reduction in nanocrystals to about 2–3 nm. The diameter of the $6s$ states in Tb^{3+} is about 0.5 nm while that of the $5d$ states is only about 0.15 nm. Thus the quantum mechanical overlap of the nanocrystals and excited states of the impurity enhanced the absorption (oscillator strength) beyond the bulk value of the $4f^7-5d$ states.

Konrad et al. [79] studied the luminescence of undoped bulk and nanocrystalline Y_2O_3 at room (300 K) and liquid nitrogen temperatures (80 K). The room temperature reflectance spectra in the range from 200–250 nm of 10, 20, 50 nm and 10 μm Y_2O_3 samples showed that the excitation maximum increased in energy as the size of the nanocrystal decreased. In fact, there was a 0.2 eV shift to higher energy as the size of the particle was decreased from 10 μm (5.85 eV) to 10 nm (6.05 eV). Since the absorption edge of nanocrystalline yttrium oxide was caused by exciton absorption, it was fitted with the classical Frank-Condon approximation by a Gaussian function in order to determine the exciton excitation energy and the width of the exciton absorption band. Similarly, the width of the absorption band was shown to decrease with increasing particle size. At 80 K, the same trends were observed in that for increasing particle size, the exciton excitation energy and the bandwidth decreased. However, the energy shifts of the exciton energy at room temperature were systematically larger than at 80 K. The room temperature emission spectra of the undoped nanocrystalline and bulk yttria samples following 207 nm excitation were obtained and no luminescence was observed for the 10 nm sample. The emission spectra of the remaining samples showed one broad Gaussian emission band whose intensity increased with increasing particle size. This peak was fitted with a single Gaussian function with a center corresponding to the emission energy (λ_{max}) and a width representing the emission width. The 20 nm sample showed an emission peak at approximately 3.66 eV with an emission width of 0.35 eV while the 50 nm sample showed an emission peak at approximately 3.70 eV with an emission width of 0.38 eV. The emission energy of the coarse grained bulk sample was 3.68 eV with an emission width of 0.39 eV. At 80 K, luminescence was observed for all samples and the same general trend was obtained. The highest luminescence intensity was observed for the coarse grained sample; however, the sample with the smallest grain size had the broadest emission band.

The absorption and emission mechanisms caused by a localized exciton or luminescence center were described by a quantum mechanical configurational coordinate diagram. As a consequence of the barrier-free self-trapping exciton in Y_2O_3 , the measured emission spectrum was significantly Stokes shifted relative to the absorption spectrum. Thus, the absorption and emission properties within the configurational coordinate diagram were explained by the ground

state and a single excited state parabola. The results were in agreement Blasse's results who found similarity between the optical transition behavior of Y_2O_3 and the charge transfer transition between oxygen $2p$ and the empty d orbitals of metal ions in oxo complexes [125].

In the range of weak quantum confinement, where the particle radius $R \geq 4a_B$ (a_B = excitonic Bohr radius), the energy upshift ΔE is given by

$$\Delta E = \frac{\eta^2 \pi^2}{2\mu} \frac{1}{R^2} \quad (11)$$

where ΔE is the particle size dependent energy shift of the exciton excitation energy due to quantum confinement and μ is the reduced mass of the exciton, which is equal to $0.634m_e$ (m_e is the mass of the electron). The authors showed that neither of the experimental results at 80 K, for which the exciton-phonon coupling had a much lower influence than at 300 K, are in the possible range of the quantum confinement effect. They therefore concluded that quantum confinement was not the main reason for the observed particle size dependence of the exciton excitation energies in nanocrystalline yttria. The increase of the bandwidth within the configurational coordinate diagram could be caused by a change in the lattice relaxation energy $S_v \hbar \omega_v$ of the excited state or the $S_u \hbar \omega_u$ of the ground state. However, the authors observed that the emission had neither a particle size dependence of the emission maximum nor a dependence of the bandwidth. The lattice relaxation energy of the ground state had no particle size dependence and remained unchanged. Thus, they concluded that the shift of the excitation energy and the increasing bandwidth resulted from an increase of the lattice relaxation energy $S_v \hbar \omega_v$ of the excited state with decreasing particle size. There were two key reasons, which the authors expected could lead to an increase in the lattice relaxation energy, $S_v \hbar \omega_v$. First, due to the surface of the nanocrystals, a hydrostatic pressure caused by the Gibbs-Thomson effect may lead to an increase in the phonon energy $\hbar \omega_v$ or the coupling constant S_v due to the presence of strain. Second, the exciton-phonon coupling constant may have a particle size dependence, increasing with decreasing particle size as observed in semiconductor nanocrystals.

4.5. Upconversion in Rare Earth Doped Yttrium Oxide Nanocrystals

The phenomenon of upconversion has been studied extensively over the past few years and it is an important process for the generation of visible light from near infrared radiation. Upconversion is defined as the optical illumination of an ion-doped material, which produces a population in an excited state, whose energy exceeds that of the pump photon [126]. The conversion of infrared radiation to visible has generated much of the current interest in upconversion as advances in both solid state lasers and semiconductor laser diodes have resulted in highly efficient sources of IR radiation [127]. Rare earth ions such as Pr^{3+} , Nd^{3+} , Sm^{3+} , Dy^{3+} , Ho^{3+} , Er^{3+} , and Tm^{3+} are particularly suited for upconversion as they possess several excited states with long lifetimes that are well matched to the emission wavelengths of several efficient pump laser sources. Co-doping with the

Yb^{3+} ion has been shown to improve the upconversion efficiency in singly doped systems, due to its high absorption cross-section in the near infrared (NIR) (circa. 980 nm) and efficient energy transfer rates [128]. Thus, trivalent rare earth ions doped in glasses and crystals are excellent candidates for upconversion. Upconversion can occur via three different mechanisms [129–131]:

- (i) excited state absorption (ESA)
- (ii) energy transfer upconversion (ETU)
- (iii) photon avalanche (PA)

The ESA model involves only a single ion and thus it is usually the only upconversion process which occurs in materials at low dopant concentrations. In this process, an incoming photon from the pump beam will bring the ion to an intermediate excited level ($|1\rangle$) and a second photon from the pump beam will bring it to an upper level ($|2\rangle$). In the framework of the proposed model, the population N_2 of level $|2\rangle$ is given by

$$N_2(t) = \frac{N_0 A_{01} A_{12} I_0^2}{\tau_2^{-1} (\tau_1^{-1} + A_{12} I_0)} \quad (12)$$

where N_0 is the initial population of the ion in the ground state ($|0\rangle$), and A_{ij} is a characteristic constant involving the oscillator strengths for the transitions from the initial state $|i\rangle$ to the final state $|j\rangle$. I_0 describes the density of photons in the pump beam while τ_1^{-1} and τ_2^{-1} are the intrinsic relaxation rates of levels $|1\rangle$ and $|2\rangle$, respectively. According to Eq. (12), we note that the upconverted luminescence varies quadratically with the pump beam (I_0) but varies linearly with the concentration of the emitting particle.

ETU proceeds according to a scheme in which two ions in close proximity are excited in an intermediate level $|1\rangle$ and are coupled by a nonradiative process in which one ion returns to the ground state $|0\rangle$ while the other is promoted to the upper level $|2\rangle$. Using the same symbols as in Eq. (12), the population of level $|2\rangle$ can be written as

$$N_2(t) = \frac{(N_0 A_{01} I_0)^2 \sigma_u}{\tau_2^{-1} (\tau_1^{-1})^2} \quad (13)$$

where σ_u is the rate constant for the ETU process. Similar to ESA, in the ETU process the population of level $|2\rangle$ varies quadratically with the density of photons in the pump beam (I_0) but, at variance with ESA, also varies quadratically with the dopant concentration N_0 .

PA is produced by absorption from an excited state of the rare earth ion. Thus the pump laser wavelength is resonant with a transition from the intermediate metastable level to a higher excited state. The absorption of the pump photons directly populates the higher excited state; therefore an energy transfer process is responsible for producing the population in the intermediate excited state [126]. In PA, one ion initially in the metastable state produces two ions in this state as a result of photon absorption and subsequent energy transfer. Under the right pumping conditions 2 ions can produce 4 in the metastable state, 4 can produce 8, the 8 can produce 16, etc. The avalanche process requires a minimum pump intensity and is characterized by a pump threshold. If this threshold is not achieved, the upconversion will be inefficient [132].

The efficiency of the upconversion is a function of the rate of multiphonon relaxation, which is dependent upon the energy gap separating the upper level and the next lower level and the highest phonon energy in the material. The rate of the multiphonon relaxation can be expressed as [133]

$$W_{\text{MPR}} = C \exp^{-\alpha \Delta E} \quad (14)$$

and

$$\alpha = -\frac{\ln(\varepsilon)}{h\nu} \quad (15)$$

where ΔE is the energy gap to the next lower level, $h\nu$ is the highest phonon energy of the material, and the parameters C and α are constants and can be derived from the measurements of the fluorescence lifetimes and the calculation of the W_{EDT} , the electric dipole transition rates. To obtain efficient upconversion, selecting a lattice with low phonon energies is essential. In a lattice with high phonon energies, the rare earth ion will predominantly decay from its excited level nonradiatively to the next lower lying level via the emission of phonons. On the other hand, in materials that possess low phonon energies, the probability of multiphonon relaxation is low and thus the ion will mainly decay radiatively via the emission of photons. The efficiency of the upconversion depends also on the spatial distribution of the dopant ions. Increasing the dopant concentration will result in an increased upconversion efficiency. However, this is successful only to a certain extent and cannot be considered as a viable solution to increasing the upconversion luminescence since at higher dopant concentrations, cross-relaxation between rare earth ions quenches the luminescence, thereby decreasing the effect of the increased concentration.

4.5.1. Optical Properties and Upconversion of $\text{Y}_2\text{O}_3:\text{Ho}^{3+}$ Nanocrystals

The optical spectroscopy and upconversion properties of Ho^{3+} doped nanocrystalline and bulk Y_2O_3 , as a function of holmium concentration (0.1, 0.5, 1, 2, 5, and 10 mol%) have also been investigated [134]. Nanosized Y_2O_3 crystals doped with 0.1, 0.5, 1, 2, 5, and 10 mol% Ho_2O_3 ($\text{Y}_{1.98}\text{Ho}_{0.002}\text{O}_3$, $\text{Y}_{1.99}\text{Ho}_{0.01}\text{O}_3$, $\text{Y}_{1.98}\text{Ho}_{0.02}\text{O}_3$, $\text{Y}_{1.96}\text{Ho}_{0.04}\text{O}_3$, $\text{Y}_{1.90}\text{Ho}_{0.10}\text{O}_3$, and $\text{Y}_{1.80}\text{Ho}_{0.20}\text{O}_3$, respectively) were prepared using a solution combustion synthesis procedure. The average crystallite size of the samples was in the range of 10 to 15 nm determined from line broadening of X-ray reflections. For comparison purposes, micrometer sized bulk $\text{Y}_{1.98}\text{Ho}_{0.02}\text{O}_3$ and $\text{Y}_{1.80}\text{Ho}_{0.20}\text{O}_3$ samples were prepared by conventional solid state reaction.

In the case of all samples under investigation, the authors observed that the room temperature visible luminescence spectra excited at 457.9 nm exhibited four distinct emission bands (Fig. 5): blue emission between 480 and 500 nm corresponding to the $^5F_3 \rightarrow ^5I_8$ transition; green emission in the region of 530–580 nm attributed to the $(^5F_4, ^5S_2) \rightarrow ^5I_8$ transition; red emission between 630 and 680 nm corresponding to the $^5F_5 \rightarrow ^5I_8$ transition; and NIR emission between 735 and 775 nm attributed to the $(^5F_4, ^5S_2) \rightarrow ^5I_7$ transition. The transition energies were observed to be similar for both the nanocrystalline and bulk samples; hence the crystal field

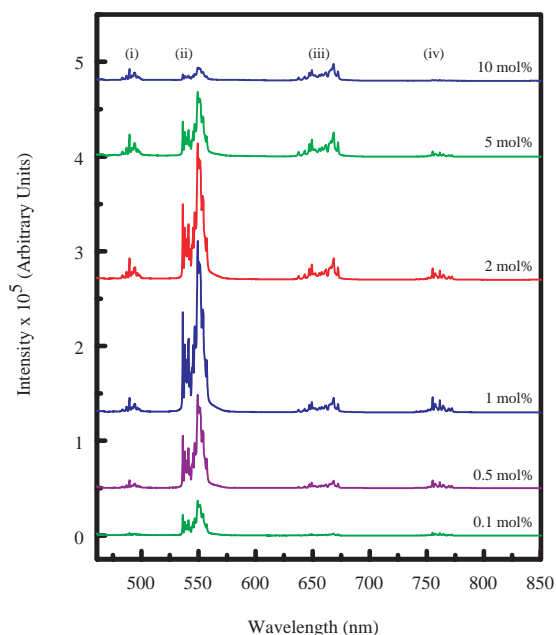


Figure 5. Room temperature luminescence of nanocrystalline $\text{Y}_2\text{O}_3:\text{Ho}^{3+}$ upon excitation at 457.9 nm. (i) $^5F_3 \rightarrow ^5I_8$, (ii) $(^5F_4, ^5S_2) \rightarrow ^5I_8$, (iii) $^5F_5 \rightarrow ^5I_8$, (iv) $(^5F_4, ^5S_2) \rightarrow ^5I_7$. Reprinted with permission [134], J. A. Capobianco et al., from *Chem. Mater.* 14, 2915 (2002). © 2002, American Chemical Society.

energy was reasonably similar for the nanocrystalline and bulk samples [134].

A change in the relative intensities of the green and red emission bands was observed between the bulk and nanocrystalline samples. The overall luminescence was also severely reduced by about one order of magnitude in the nanocrystal samples compared to the bulk samples. The authors attributed this type of behavior to an increase in multiphonon relaxation due to adsorbed atmospheric carbon dioxide and/or water [134].

The medium IR spectra of the nanocrystalline $\text{Y}_2\text{O}_3:\text{Ho}^{3+}$ samples investigated revealed bands around 1500 and 3350 cm^{-1} , which were attributed to stretching modes of carbonate and hydroxide ions, indicating that the materials have adsorbed atmospheric CO_2 and H_2O . These adsorbed ions on the surface of the nanocrystalline materials provide vibrational quanta of higher wavenumbers compared to the intrinsic phonons of yttria ($\approx 600 \text{ cm}^{-1}$) resulting in an increase of multiphonon relaxations from all excited levels. This larger nonradiative decay probability is thus responsible for the lower emission efficiencies observed in the nanocrystals.

Furthermore, the rapid quenching of the $(^5F_4, ^5S_2) \rightarrow ^5I_8$ transition relative to the $^5F_5 \rightarrow ^5I_8$ transition in the nanocrystalline samples was also attributed to the presence of these adsorbed atmospheric molecules. The energy gap between the 5S_2 and 5F_5 levels for the Ho^{3+} ion in Y_2O_3 single crystals [135] has been reported to be 2666 cm^{-1} . As five intrinsic phonons (about 600 cm^{-1}) were required in the bulk material to bridge this gap, the 5S_2 level was only slightly affected by multiphonon decay, while in the nanocrystals only two of the high energy carbonate ion

phonons available or just one hydroxide high energy phonon were required to span this gap making multiphonon relaxation of ($^5F_4, ^5S_2$) levels much more probable.

A rapid quenching of the ($^5F_4, ^5S_2$) \rightarrow 5I_8 transition was also observed relative to the $^5F_3 \rightarrow ^5I_8$ and $^5F_5 \rightarrow ^5I_8$ transitions in the bulk and nanocrystalline samples as the Ho^{3+} dopant concentration increased from 1 to 10 mol%. The authors stated that this type of behavior was related to an ion-pair cross-relaxation (energy transfer) process represented by the $^5S_2 \rightarrow ^5I_4$ and $^5I_7 \leftarrow ^5I_8$ transitions. In this energy transfer process a donor Ho^{3+} ion in the 5S_2 excited state relaxed nonradiatively to the 5I_4 state, while in another simultaneous nonradiative process an acceptor Ho^{3+} ion in the ground 5I_8 state was excited to the 5I_7 state, thereby quenching the luminescence of the ($^5F_4, ^5S_2$) level.

Room temperature emission decay curves of the ($^5F_4, ^5S_2$) \rightarrow 5I_8 transition upon 457.9 nm excitation were also reported for both the bulk and nanocrystalline samples [134]. The lifetimes are reported in Table 4. Decay curves for the bulk samples were fitted with a single exponential model. However, a deviation from first exponential behavior was observed by the authors in all decay curves obtained for the nanocrystalline samples. The difficulty in fitting with a single exponential model in the nanocrystalline samples was attributed to a distribution of dopant ions within the individual nanocrystals that are coupled in various degrees to the adsorbed surface molecules. This resulted in the dopant ions located close to the surface having faster decay times than those ions located inside the nanocrystals. Hence, a nonexponential decay was observed as a significant portion of the dopant atoms reside near the surface due to the particles' small size (about 10 nm). Furthermore, the lifetimes of the excited states were found to be significantly faster in the nanocrystal samples than in the bulk samples [134]. For example, the ($^5F_4, ^5S_2$) \rightarrow 5I_8 lifetime in the 1 mol% bulk sample was found to be 135 μs as opposed to 14 μs (first time constant) or 57 μs (second time constant) in the similarly doped nanocrystalline sample. This type of behavior was again attributed to the presence of adsorbed species on the surface of the nanocrystals that led to nonradiative relaxation of the excited states. The higher energy phonons that were present in the nanocrystals as opposed to the bulk samples resulted in a lower-order multiphonon process from the ($^5F_4, ^5S_2$) level to the 5F_5 level. The larger rate of

nonradiative processes in the nanocrystalline samples resulted in a shorter lifetime for the ($^5F_4, ^5S_2$) level.

Upon excitation with 646 nm radiation from a dye laser that populated the 5F_5 level, anti-Stokes emissions corresponding to the $^5F_3 \rightarrow ^5I_8$ and ($^5F_4, ^5S_2$) \rightarrow 5I_8 transitions were observed in both the bulk and nanocrystalline samples (Fig. 6). A power study of the upconverted blue and green emission indicated a two-photon upconversion process. The upconversion luminescence was thought to result from an ESA process involving the 5I_7 energy state as the intermediate level (Fig. 7). In the assigned mechanism the laser light brought the Ho^{3+} ion into the 5F_5 level, which then nonradiatively decayed to the 5I_7 level. An excited state absorption process brought the ion to the 5F_3 level. The ion then emitted through the $^5F_3 \rightarrow ^5I_8$ transition or nonradiatively decayed to the lower lying levels and the ($^5F_4, ^5S_2$) \rightarrow 5I_8 transition occurred [134].

The upconversion process was noted to be far less efficient in the nanocrystal samples which was attributed to an increase of multiphonon relaxations of excited levels due to the presence of the aforementioned adsorbed species on the surface of the nanocrystals. The populations of the intermediate levels from which a part of the excited ions can be re-excited to the upper emitting levels by ESA are substantially impacted by the nonradiative decay rate that increases as the lattice phonon energy becomes higher [136]. The highest available phonon energy not only affects quantum efficiencies of the emitting levels such as 5F_3 and 5S_2 levels but also impacts the upconversion efficiencies, which are primarily determined by populations of intermediate levels such as the 5I_6 and 5I_7 . The excitation populations of intermediate levels

Table 4. Decay times obtained from an exponential fit of the room temperature decay curves for the ($^5F_4, ^5S_2$) \rightarrow 5I_8 transition upon 457.9 nm excitation.

Bulk	Decay time (μs)	
$\text{Y}_{1.98}\text{Ho}_{0.02}\text{O}_3$	135	
$\text{Y}_{1.80}\text{Ho}_{0.20}\text{O}_3$	60	
Nanocrystalline	First decay time (μs)	Second decay time (μs)
$\text{Y}_{1.998}\text{Ho}_{0.002}\text{O}_3$	17	77
$\text{Y}_{1.99}\text{Ho}_{0.01}\text{O}_3$	20	73
$\text{Y}_{1.98}\text{Ho}_{0.02}\text{O}_3$	14	57
$\text{Y}_{1.96}\text{Ho}_{0.04}\text{O}_3$	9	40
$\text{Y}_{1.90}\text{Ho}_{0.10}\text{O}_3$	3	14
$\text{Y}_{1.80}\text{Ho}_{0.20}\text{O}_3$	2	4

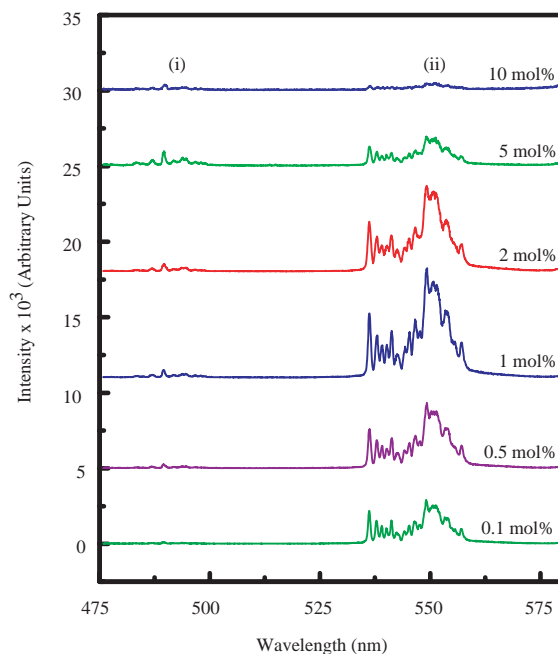


Figure 6. Upconverted emission of Ho^{3+} -doped Y_2O_3 nanocrystals at room temperature upon 646 nm excitation, showing (i) $^5F_3 \rightarrow ^5I_8$, (ii) ($^5F_4, ^5S_2$) \rightarrow 5I_8 . Reprinted with permission from [134], J. A. Capobianco et al., *Chem. Mater.* 14, 2915 (2002). © 2002, American Chemical Society.

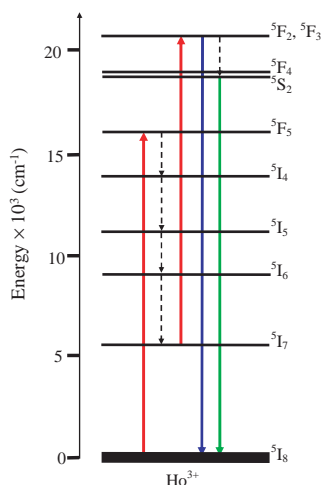


Figure 7. Mechanism for Ho^{3+} upconversion in Y_2O_3 for 646 nm excitation resulting in excited state absorption via the 5I_7 level.

and the quantum efficiencies of emitting levels of Ho^{3+} in a host crystal with a higher phonon energy are undoubtedly lower than those in a crystal with a lower phonon energy.

Capobianco's group also observed anti-Stokes emission corresponding to the $^5F_3 \rightarrow ^5I_8$, $(^5F_4, ^5S_2) \rightarrow ^5I_8$, and $^5F_5 \rightarrow ^5I_8$ transitions in the bulk samples upon excitation with 754 nm radiation from a titanium sapphire laser that excites the 5I_4 level (Fig. 8). Though strong luminescence was observed from the bulk samples no upconversion was noted in the nanocrystal samples. As mentioned previously, behavior of this type was attributed to an increase of multiphonon relaxations of excited levels due to the presence of carbonate and hydroxide ions on the surface of the nanoparticles.

The $(^5F_4, ^5S_2) \rightarrow ^5I_8$ transition demonstrated a quadratic dependence on the power of the pump beam indicating that two photons were involved in the excitation process. Again, an ESA process was thought to be the dominant mechanism. In this case there were two distinct ESA processes

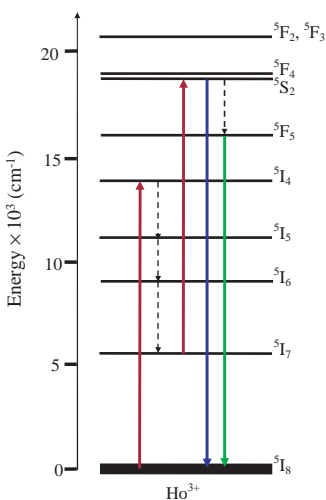


Figure 8. Mechanism for Ho^{3+} upconversion in Y_2O_3 for 754 nm excitation resulting in excited state absorption via the 5I_7 level.

occurring concurrently that originated from the 5I_6 and 5I_7 levels and could populate the 5G_6 , 3K_8 , and $(^5F_4, ^5S_2)$ levels, respectively. Therefore, the authors proposed the following mechanism. The laser light brought the Ho^{3+} ion into the 5I_4 level, which then nonradiatively decayed to the 5I_7 level. An excited state absorption process brought the ion to the $(^5F_4, ^5S_2)$ levels. The ion then emitted through the $(^5F_4, ^5S_2) \rightarrow ^5I_8$ transition or could have nonradiatively decayed to the lower lying levels and the $^5F_5 \rightarrow ^5I_8$ transition occurred. A second ESA process originating from the 5I_6 level was also possible. For the 754 nm excitation wavelength used in this study there was another possible resonant excited state absorption: $^5I_6 \rightarrow ^3K_8, ^5G_6$. It was most likely this ESA process, along with nonradiative relaxation, which was responsible for the weak blue emission from the 5F_3 level.

4.5.2. Optical Spectroscopy and Upconversion of Nanocrystalline $\text{Y}_2\text{O}_3:\text{Er}^{3+}$ and $\text{Y}_2\text{O}_3:\text{Er}^{3+}, \text{Yb}^{3+}$

The optical properties of cubic nanocrystalline Y_2O_3 doped with 10 mol% Er^{3+} prepared by combustion synthesis were studied and compared with a microcrystalline $\text{Y}_2\text{O}_3:\text{Er}^{3+}$ (bulk) of equal concentration synthesized by conventional solid state techniques [137]. The authors measured the diffuse reflectance spectra in the UV and visible regions for both the nanocrystalline and bulk samples. The reflectance spectrum of the nanocrystalline material was composed of a series of relatively sharp features in the visible region, accompanied by an absorption edge at approximately 350 nm (Fig. 9). The sharp bands were assigned to the intra-configurational $f-f$ transitions from the $^4I_{15/2}$ ground state to the excited states of the Er^{3+} ion, while the edge was assigned to the intrinsic absorption of the yttria host. The reflectance spectrum of the bulk sample was composed of the same $f-f$ transitions. However, it was more resolved and had an absorption edge extending from at least 400 nm. The onset of the intrinsic absorption of the Y_2O_3 host, assigned to band-to-band transitions, was shifted toward the blue for the nanocrystals, compared to the bulk sample. The authors believed that the reduced resolution of the spectral features in the reflectance spectrum of the $\text{Y}_2\text{O}_3:\text{Er}^{3+}$ nanocrystals samples could have been partly due to inhomogeneous broadening induced by the presence of disorder in the material.

The visible luminescence spectra of nanocrystalline and bulk $\text{Y}_2\text{O}_3:\text{Er}^{3+}$ excited at 488 nm, were presented and the features in the 520–570 nm region were assigned to the transition from the thermalized ($^2H_{11/2}, ^4S_{3/2}$) excited states to the $^4I_{15/2}$ ground state of Er^{3+} ions in the C_2 sites since the $f-f$ electric dipole transitions are forbidden in the C_{3i} sites due to its center of inversion. The overall shape of the emission bands for the two samples were similar except for a slight difference in the relative intensity of the peaks at 520–530 nm (assigned to emission from $^2H_{11/2}$), which were more intense for the nanocrystals. The authors believed this was caused by the hypersensitivity of the $^2H_{11/2} \rightarrow ^4I_{15/2}$ transition, whose intensity is strongly influenced by small distortions of the sites accommodating the Er^{3+} ions. Thus, they suggested that in the nanocrystalline sample, the degree

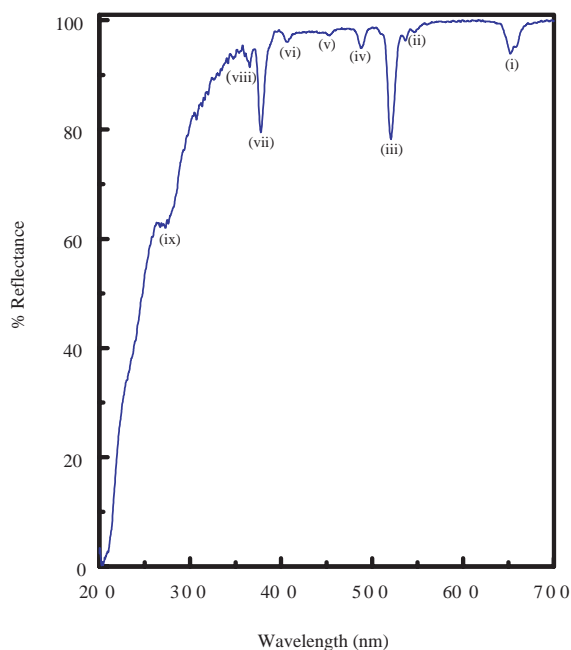


Figure 9. Diffuse reflectance spectrum of $\text{Y}_{1.80}\text{Er}_{0.20}\text{O}_3$ nanocrystalline sample. (i) ${}^4I_{15/2} \rightarrow {}^4F_{9/2}$, (ii) ${}^4I_{15/2} \rightarrow {}^4S_{3/2}$, (iii) ${}^4I_{15/2} \rightarrow {}^2H_{11/2}$, (iv) ${}^4I_{15/2} \rightarrow {}^4F_{7/2}$, (v) ${}^4I_{15/2} \rightarrow {}^4F_{5/2}$, (vi) ${}^4I_{15/2} \rightarrow {}^2H_{9/2}$, (vii) ${}^4I_{15/2} \rightarrow {}^4G_{11/2}$, (viii) ${}^4I_{15/2} \rightarrow {}^2K_{15/2}$, (ix) ${}^4I_{15/2} \rightarrow {}^4G_{9/2}$. Reprinted with permission from [137], J. A. Capobianco et al., *Phys. Chem. Chem. Phys.* 2, 3203 (2000). © 2000, The Royal Society of Chemistry on behalf of the PCCP Owner Societies.

of distortion of the C_2 sites, in which the dopant ions were found, was greater than in the bulk sample. Furthermore, sharp peaks in the red region (640–700 nm) of the spectra of the nanocrystalline and bulk materials were observed and assigned to the C_2 allowed ${}^4F_{9/2} \rightarrow {}^4I_{15/2}$ transition.

Bettinelli's group [40] studied the near infrared (NIR) emission of $\text{Y}_2\text{O}_3:\text{Er}^{3+}$ (10 mol%) nanocrystals prepared via the combustion synthesis. The authors observed strong features at 990 nm and 1570 nm assigned to transitions from the ${}^4I_{11/2}$ (A) and ${}^4I_{13/2}$ (B) excited states to the ${}^4I_{15/2}$ ground state, respectively. Comparison of the NIR emission spectrum of the nanocrystalline material to the bulk showed that the Stark structure of the observed transitions was identical. However, they observed remarkable differences in the relative intensities of the bands originating from the various excited states. The integrated intensity ratio [$R = I(\text{A})/I(\text{B})$] was distinctly lower for the nanocrystalline material ($R = 0.242$) than for the bulk ($R = 0.668$) and was attributed to different cross-relaxation properties in the nanocrystalline and bulk materials. A similar behavior was also observed between bulk and nanocrystalline $\text{Y}_2\text{O}_3:\text{Nd}^{3+}$.

The decay times of the thermalized (${}^2H_{11/2}$, ${}^4S_{3/2}$) \rightarrow ${}^4I_{15/2}$ transition were reported for the 10 mol% $\text{Y}_2\text{O}_3:\text{Er}^{3+}$ bulk and nanocrystalline samples as well as for 1, 2, and 5 mol% nanocrystalline samples (Table 5). The decay times of the nanocrystalline material were shown to be concentration dependent and the variation of the decay times with concentration was believed to be due to the ${}^2H_{11/2} + {}^4I_{15/2} \rightarrow {}^4I_{9/2} + {}^4I_{13/2}$ cross-relaxation mechanism, which caused significant depopulation of the excited state [137]. Furthermore, the

Table 5. Decay times of bulk and nanocrystalline $\text{Y}_2\text{O}_3:\text{Er}^{3+}$ obtained from an exponential fit of the room temperature decay curves for the (${}^2H_{11/2}$, ${}^4S_{3/2}$) \rightarrow ${}^4I_{15/2}$ transition upon 488 nm excitation.

Decay time (μs)	
Bulk	
$\text{Y}_{1.80}\text{Er}_{0.20}\text{O}_3$	56
Nanocrystal	
$\text{Y}_{1.98}\text{Er}_{0.02}\text{O}_3$	3.8
$\text{Y}_{1.96}\text{Er}_{0.04}\text{O}_3$	12
$\text{Y}_{1.90}\text{Er}_{0.10}\text{O}_3$	31
$\text{Y}_{1.80}\text{Er}_{0.20}\text{O}_3$	34

decay time of the 10 mol% $\text{Y}_2\text{O}_3:\text{Er}^{3+}$ bulk sample was more than one order of magnitude longer than the nanocrystal sample with an identical dopant concentration. The authors attributed this behavior to the fact that yttria powders could adsorb carbon dioxide and water from the atmosphere. The authors presented the FTIR spectrum of the $\text{Y}_2\text{O}_3:\text{Er}^{3+}$ nanocrystalline material (1 mol%), which showed the presence of a band at approximately 1500 cm^{-1} attributed to the presence of carbonate ions. The adsorption of CO_2 is efficient due to the large surface area ($64\text{ m}^2\text{ g}^{-1}$) of the nanocrystalline material prepared by the combustion synthesis technique. The presence of these CO_3^{2-} ions on the surface yields vibrational quanta of relatively high wavenumbers (1500 cm^{-1}) compared to the intrinsic phonons of yttria (having a cutoff wavenumber of 597 cm^{-1}), which are the only ones available in the bulk material. The authors state that the energy gap separating the ${}^4S_{3/2}$ state from the lower lying ${}^4F_{9/2}$ state was approximately 2795 cm^{-1} . Therefore, in the nanocrystalline material, the presence of the vibrational quanta of 1500 cm^{-1} made multiphonon relaxation of (${}^2H_{11/2}$, ${}^4S_{3/2}$) much more probable than for the bulk sample, where at least five phonons are required to bridge the gap.

The authors also briefly studied the upconverted luminescence following continuous wave excitation ($\lambda_{\text{exc}} = 815\text{ nm}$) into the ${}^4I_{9/2} \leftarrow {}^4I_{15/2}$ transition and observed anti-Stokes emission bands assigned to the ${}^2H_{11/2} \rightarrow {}^4I_{15/2}$, ${}^4S_{3/2} \rightarrow {}^4I_{15/2}$, and ${}^4F_{9/2} \rightarrow {}^4I_{15/2}$ transitions centered at 525, 550, and 660 nm, respectively. The spectral band shapes and position were identical to those obtained upon 488 nm excitation and the authors stated that sequential absorption of photons or energy transfer upconversion were the two mechanisms which may have been responsible for the upconversion.

The authors extended the spectroscopic investigation [93] by studying the effects of the Er^{3+} concentration (1, 2, 5, and 10 mol%) on the upconversion emission properties of nanocrystalline and bulk $\text{Y}_2\text{O}_3:\text{Er}^{3+}$. Continuous wave excitation with visible ($\lambda_{\text{exc}} = 488\text{ nm}$) or NIR radiation ($\lambda_{\text{exc}} = 815\text{ nm}$) produced green emission between 520 and 570 nm ascribed to ${}^2H_{11/2}$, ${}^4S_{3/2} \rightarrow {}^4I_{15/2}$ transition and red emission between 640 and 700 nm from the ${}^4F_{9/2} \rightarrow {}^4I_{15/2}$ transition (Figs. 10 and 11). The authors compared the spectra of all the samples under investigation and showed that although they were identical and unaffected by the pump wavelength, 488 or 815 nm, there was a notable reduction in the

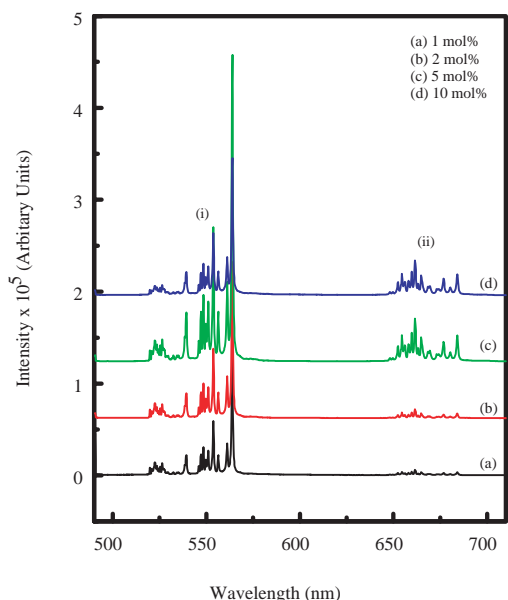


Figure 10. Room temperature luminescence of nanocrystalline $\text{Y}_2\text{O}_3:\text{Er}^{3+}$ upon excitation at 488 nm. (i) $(^2H_{11/2}, ^4S_{3/2}) \rightarrow ^4I_{15/2}$, (ii) $^4F_{9/2} \rightarrow ^4I_{15/2}$. Reprinted with permission from [93], J. A. Capobianco et al., *J. Phys. Chem. B* 106, 1181 (2002). © 2002, American Chemical Society.

overall luminescence when pumping with 815 nm. The authors presented the MIR spectrum of the yttria nanoparticles, which showed bands at approximately 1500 and 3350 cm^{-1} due to vibrational modes typical of carbonates and hydroxyl ions, respectively. The presence of these

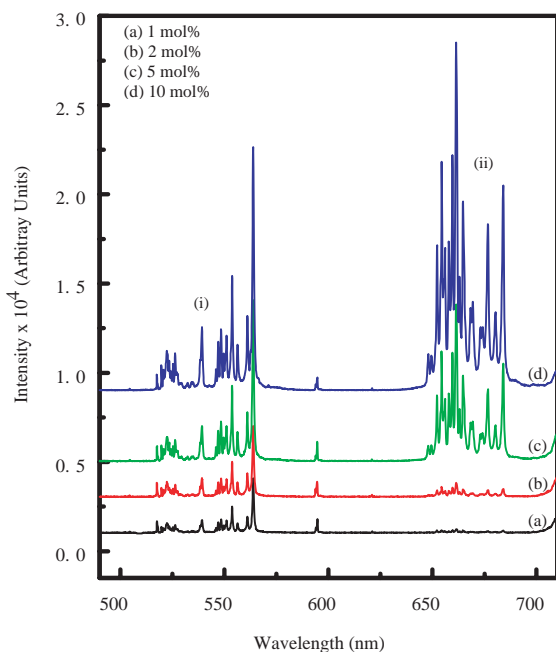


Figure 11. Upconverted emission of Er^{3+} -doped Y_2O_3 nanocrystals at room temperature, showing (i) $(^2H_{11/2}, ^4S_{3/2}) \rightarrow ^4I_{15/2}$ and (ii) $^4F_{9/2} \rightarrow ^4I_{15/2}$, $\lambda_{\text{exc}} = 815$ nm. Reprinted with permission from [93], J. A. Capobianco et al., *J. Phys. Chem. B* 106, 1181 (2002). © 2002, American Chemical Society.

groups on the surface yields vibrational quanta of relatively high wavenumbers compared to the phonons of pure yttria and increased the efficiency of multiphonon relaxation.

In order to reduce the amount of CO_3^{2-} and OH^- ions on the surface of the nanoparticles, the authors attempted different heat treatments on a nanocrystalline $\text{Y}_2\text{O}_3:\text{Er}^{3+}$ (10 mol%) sample. The nanosample was treated at 800 °C for 17 hours and then cooled to room temperature followed by a treatment at 1000 °C for 65 hours and then subsequently cooled to room temperature. The MIR spectra of the doped nanoparticles obtained after the heat treatments indicated that the surface contamination was reduced from the overall intensities of the bands at 1500 and 3350 cm^{-1} . However, the conditions used for the experiments were not sufficient to completely remove the contaminants (Fig. 12). The authors stated that longer heat treatment at higher temperatures was not possible as an aggregation of the nanoparticles could occur, a process in which they combine to form larger particles. In this case, as the spectroscopy of the nanocrystalline material is particle size dependent, a comparison between the luminescence of the heat-treated and non-heat-treated nanocrystalline materials would not be possible. It was noted that in the bulk sample no bands at 1500 and 3300 cm^{-1} were present.

The authors observed a concentration dependent enhancement of the red ($^4F_{9/2} \rightarrow ^4I_{15/2}$) upconverted emission following irradiation with 815 nm. In order to get a better idea of the mechanism(s) involved in the upconversion, the authors performed a power dependence study. It was shown that the intensity of the upconverted luminescence, I_o , is proportional to some power n of the excitation

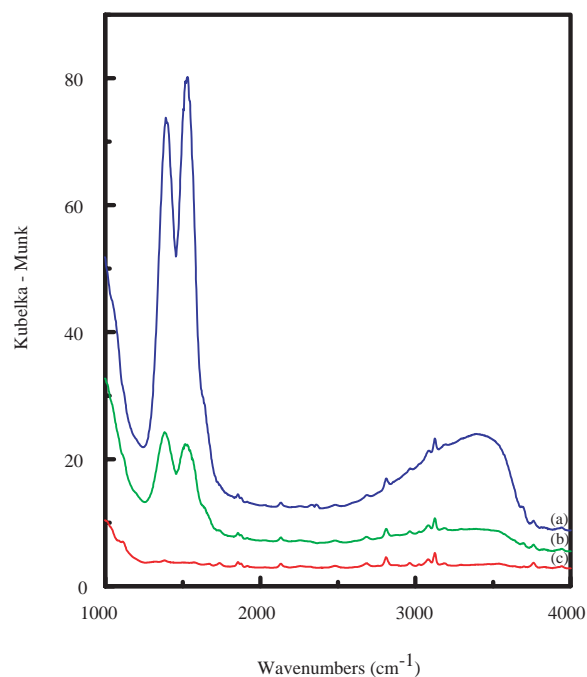


Figure 12. Diffuse reflectance spectra of nanocrystalline $\text{Y}_{1.80}\text{Er}_{0.20}\text{O}_3$ following sequential heat treatment: (a) 800 °C for 17 h, (b) 1000 °C for 65 h, (c) bulk $\text{Y}_{1.80}\text{Er}_{0.20}\text{O}_3$ sample shown for comparison. Reprinted with permission from [93], J. A. Capobianco et al., *J. Phys. Chem. B* 106, 1181 (2002). © 2002, American Chemical Society.

intensity, I_i , and can be written as

$$I_o \propto I_i^n \quad (16)$$

where $n = 1, 2, 3, \dots$. The superscript n is the number of photons required to populate the emitting state and was determined from the slope of the graph $\ln(\text{intensity})$ versus $\ln(\text{power})$. The fitting of the data yielded a straight line with a slope of approximately 2 for the $(^2H_{11/2}, ^4S_{3/2}) \rightarrow ^4I_{15/2}$ and the $^4F_{9/2} \rightarrow ^4I_{15/2}$ transitions in all samples under investigation. PA was immediately ruled out as a mechanism of upconversion as no power threshold was observed in the power study. Thus, the authors determined that the upconversion occurred via a two-photon ESA or ETU process. In the ESA and ETU mechanisms (Fig. 13), the laser light brought the Er^{3+} ion to the $^4I_{9/2}$ level, which then nonradiatively decayed to the $^4I_{11/2}$ level. After this nonradiative relaxation, either an energy transfer from a neighboring Er^{3+} ion in the $^4I_{9/2}$ state (ETU) or a second photon from the incident laser beam (ESA) brought the ion to the $^4F_{3/2}$ level. Alternatively, after the initial excitation, the Er^{3+} ion could nonradiatively decay down to the $^4I_{13/2}$ level. Again, either an energy transfer process from another Er^{3+} ion in the $^4I_{9/2}$ state or a second photon populated the $^2H_{11/2}$ level. Emission from the lower lying states can then be observed.

The authors noted that if the upconversion occurred only via the above mechanisms, upconversion spectra with identical relative intensities as in the direct emission ($\lambda_{\text{exc}} = 488 \text{ nm}$) would have been expected. This was clearly not the case as an enhancement of the red emission for the $^4F_{9/2}$ state with increasing Er^{3+} concentration was observed. This effect was demonstrated using a graph of the ratio of the integrated intensity of the green emission [$(^2H_{11/2}, ^4S_{3/2}) \rightarrow ^4I_{15/2}$] over that of the red emission [$^4F_{9/2} \rightarrow ^4I_{15/2}$], versus

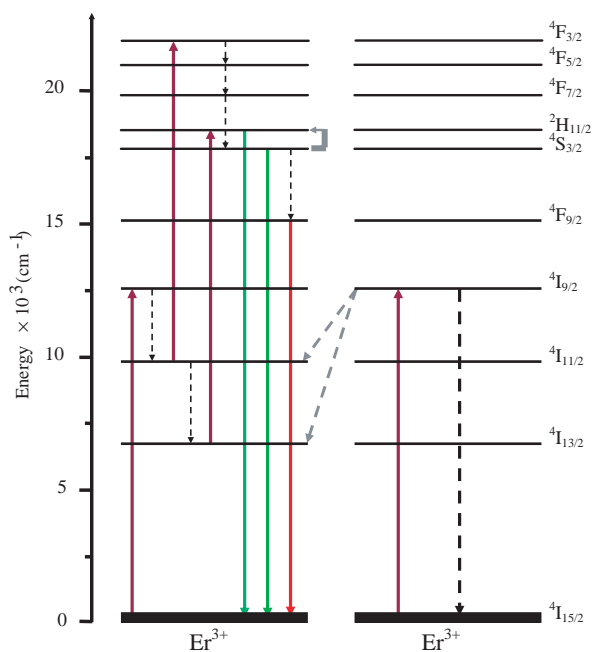


Figure 13. Mechanisms for Er^{3+} upconversion in Y_2O_3 for 800 nm excitation showing both excited state absorption via the $^4I_{11/2}$ or $^4I_{13/2}$ levels (left) or energy transfer upconversion from a second Er^{3+} ion (right).

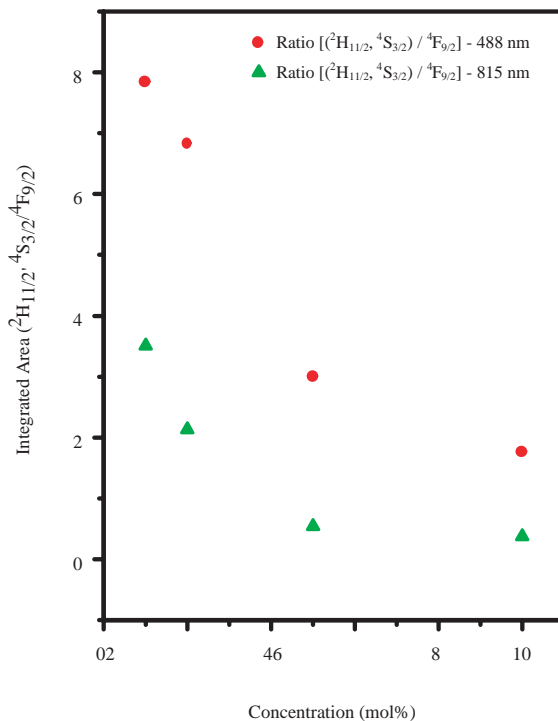


Figure 14. Graph of the ratio of the integrated areas of the $(^2H_{11/2}, ^4S_{3/2}) \rightarrow ^4I_{15/2}$ and $^4F_{9/2} \rightarrow ^4I_{15/2}$ bands [$(^2H_{11/2}, ^4S_{3/2}) / ^4F_{9/2}$] versus Er^{3+} concentration for the nanocrystalline material. Reprinted with permission from [93], J. A. Capobianco et al., *J. Phys. Chem. B* 106, 1181 (2002). © 2002, American Chemical Society.

Er^{3+} concentration at both (488 and 815 nm) wavelengths (Fig. 14). The authors observed that as the dopant concentration was increased in the nanocrystalline material, the difference in ratios became less significant and was indicative of presence of an emission enhancement. They postulated that a second mechanism was responsible for populating the $^4F_{9/2}$ level only. The laser light (815 nm) excited two neighboring ions to the $^4I_{9/2}$ state. One ion nonradiatively decayed to the $^4I_{11/2}$ state, while the other decayed to the $^4I_{13/2}$ state. A phonon-assisted energy transfer process occurred via two transitions, $^4I_{9/2} \rightarrow ^4I_{13/2}$ and $^4I_{11/2} \rightarrow ^4F_{9/2}$, and resulted in the population of the $^4F_{9/2}$ state (Fig. 15).

Silver's group studied the upconverting properties of nanocrystalline $\text{Y}_2\text{O}_3:\text{Er}^{3+}, \text{Yb}^{3+}$ following HeNe laser excitation at 632.8 nm into the $^4F_{9/2}$ state of the Er^{3+} ion [60] and observed that the intensity of the anti-Stokes luminescence was 1/15 that of the Stokes luminescence. The power dependence study showed that the upconversion occurred via a two-photon process thus populating the emitting level via ETU. The authors also observed that the Stokes and anti-Stokes luminescence lost intensity when Yb^{3+} was added to the $\text{Y}_2\text{O}_3:\text{Er}^{3+}$ matrix indicating the presence of a back transfer mechanism from Er^{3+} to Yb^{3+} . The authors [61] studied the dependence of the upconversion on the temperature in $\text{Y}_2\text{O}_3:\text{Er}^{3+}$ nanocrystals and predicted the relative populations of the $^4S_{3/2}$ and $^2H_{11/2}$ states using a three-level model. The model, comprised of the $^4S_{3/2}$ (Level 2) and $^2H_{11/2}$ (Level 3) states as well as the ground

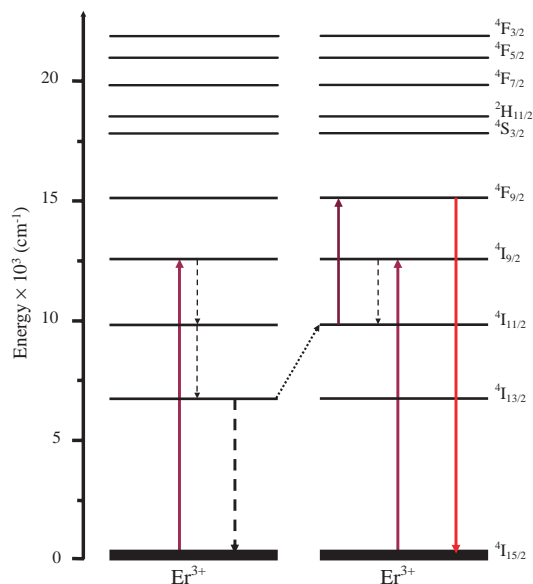


Figure 15. Energy level diagram of Er^{3+} ions in Y_2O_3 showing the two-photon energy transfer upconversion process responsible for populating the ${}^4F_{9/2}$ level ($\lambda_{\text{exc}} = 815 \text{ nm}$).

${}^4I_{15/2}$ state, can be written as

$$\frac{I_3}{I_2} = A \exp\left(-\frac{E_{32}}{kT}\right) \quad (17)$$

where I_2 and I_3 are the integrated emission intensities of the ${}^4S_{3/2} \rightarrow {}^4I_{15/2}$ and ${}^2H_{11/2} \rightarrow {}^4I_{15/2}$ transitions, respectively, E_{32} is the energy gap between the two states, T is the temperature, and k is Boltzmann's constant. The pre-exponential factor A is given as:

$$A = \frac{W_{R3}g_3h\nu_3}{W_{R2}g_2h\nu_2} \quad (18)$$

where W_{R2} and W_{R3} are the radiative transition probabilities of the two transitions, g_2 and g_3 are the $(2J + 1)$ degeneracies of the two levels, and $h\nu_2$ and $h\nu_3$ are the photon energies of the respective transitions from levels 2 and 3 to level 1. They showed that such an analysis for the C_2 and C_{3i} sites yielded straight lines and analysis of the C_2 site yielded an energy gap (E_{32}) of 628 cm^{-1} with a pre-exponential factor (A) of 7.6 while the C_{3i} site showed E_{32} equal to 244 cm^{-1} with a A equal to 0.5.

The upconversion properties of cubic nanocrystalline $\text{Y}_2\text{O}_3:\text{Er}^{3+}$ and $\text{Y}_2\text{O}_3:\text{Er}^{3+}, \text{Yb}^{3+}$ prepared by both the combustion and hydrolysis techniques were studied following excitation with 980 nm into the ${}^4I_{11/2} \leftarrow {}^4I_{15/2}$ transition of Er^{3+} and the ${}^2F_{5/2} \leftarrow {}^2F_{7/2}$ of Yb^{3+} [138]. The authors showed that the Stokes emission spectra of the co-doped bulk sample as well as the nanocrystalline samples prepared by the two different techniques following excitation with 488 nm were similar in both intensity and peak shape to their respective singly doped erbium Y_2O_3 spectra (Fig. 16). However, the NIR emission spectrum of the bulk $\text{Y}_2\text{O}_3:\text{Er}^{3+}, \text{Yb}^{3+}$ sample showed emission from the ${}^4I_{11/2} \rightarrow {}^4I_{15/2}$ transition centered at approximately 1000 nm but also provided evidence that an energy transfer process from the

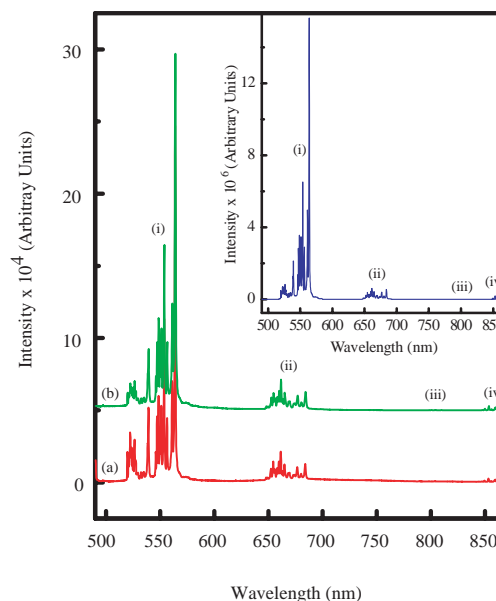


Figure 16. Room temperature Stokes luminescence of nanocrystalline $\text{Y}_2\text{O}_3:\text{Er}^{3+}, \text{Yb}^{3+}$ prepared via (a) propellant and (b) wet synthetic routes following excitation with 488 nm. (i) ${}^2H_{11/2}, {}^4S_{3/2} \rightarrow {}^4I_{15/2}$, (ii) ${}^4F_{9/2} \rightarrow {}^4I_{15/2}$, (iii) ${}^4I_{9/2} \rightarrow {}^4I_{15/2}$, (iv) ${}^4S_{3/2} \rightarrow {}^4I_{13/2}$. Inset: Room temperature Stokes luminescence of bulk $\text{Y}_2\text{O}_3:\text{Er}^{3+}, \text{Yb}^{3+}$. Reprinted with permission from [138], F. Vetrone et al., *J. Phys. Chem. B* in press.

excited Er^{3+} ions to the Yb^{3+} ions in the ground state was present. Following irradiation of the co-doped bulk sample with 488 nm, only the Er^{3+} ions should have been excited as Yb^{3+} has only one excited state in the NIR ($\sim 10,600 \text{ cm}^{-1}$) and therefore no emission from the Yb^{3+} ions should have been observed. However, peaks were observed in the NIR emission spectra and attributed to Yb^{3+} emission and thus the authors assumed that an energy transfer between the Er^{3+} and Yb^{3+} ions was operative. The Er^{3+} ion was initially excited to its ${}^4F_{7/2}$ state with the 488 nm pump photons. A cross-relaxation process of the form $({}^4F_{7/2}, {}^2F_{7/2}) \rightarrow ({}^4I_{11/2}, {}^2F_{5/2})$ occurred following the initial excitation. After the Yb^{3+} ion was excited to its ${}^2F_{5/2}$ state, it could emit radiatively, as evidenced by the NIR emission spectrum, or it could transfer its energy back to the Er^{3+} ion exciting it to the ${}^4F_{7/2}$ state once again. It was apparent from the intensity of the ${}^4S_{3/2} \rightarrow {}^4I_{15/2}$ transition compared to that of the ${}^4I_{11/2} \rightarrow {}^4I_{15/2}$ and ${}^2F_{5/2} \rightarrow {}^2F_{7/2}$ transitions that the back transfer from Yb^{3+} to Er^{3+} is favored over the radiative ${}^2F_{5/2} \rightarrow {}^2F_{7/2}$ emission from the Yb^{3+} ion. The authors noted that the peaks attributed to Yb^{3+} emission were very weak and barely detected in the nanocrystalline co-doped samples and were attributed to the high phonon energies from adsorbed H_2O and CO_2 inherent in this type of material. In the nanocrystalline material, the energy transfer from Er^{3+} to Yb^{3+} was severely limited due to the very efficient multi-phonon relaxation from the ${}^4I_{11/2}$ to the ${}^4I_{13/2}$ excited states. The high phonon energies significantly reduced the population reservoir in the ${}^4I_{11/2}$ state and since this mechanism involved this state, the process became highly inefficient.

The upconversion spectra of nanocrystalline and bulk $\text{Y}_2\text{O}_3:\text{Er}^{3+}, \text{Yb}^{3+}$ following excitation with 980 nm radiation

were presented, and the spectra exhibited three distinct emission bands centered at approximately 530, 560, and 670 nm and correspond to green emission from the ${}^2H_{11/2}$, ${}^4S_{3/2}$ and red emission from the ${}^4F_{9/2}$ excited states to the ${}^4I_{15/2}$ ground state of the Er^{3+} ions, respectively (Fig. 17). In the power study of the upconverted luminescence, the graph of $\ln(\text{intensity})$ versus $\ln(\text{power})$ showed no inflection point and yielded a slope of n equal to approximately 2 for all samples under investigation. Thus, the authors proposed that two photons were involved in the upconversion mechanism responsible for populating the green and red levels. Following 980 nm irradiation of Y_2O_3 , the Er^{3+} ion was excited to the ${}^4F_{7/2}$ state via two successive energy transfers from the Yb^{3+} ions in the ${}^2F_{5/2}$ state (Fig. 18). Thus, one Yb^{3+} ion transferred its energy to an Er^{3+} ion in the ground state, thereby exciting it to the ${}^4I_{11/2}$ state. This process was followed by a transfer of energy from another Yb^{3+} ion also in its excited state and resulted in the population of the ${}^4F_{7/2}$ state of the Er^{3+} ion. Of course, interactions between two Er^{3+} ions could not be ignored and the authors state that an NIR photon from the pump beam will also excite an Er^{3+} ion to its ${}^4I_{11/2}$ state. Another Er^{3+} ion also in the ${}^4I_{11/2}$ state and in close proximity would transfer its energy to the initial ion thereby exciting it to the ${}^4F_{7/2}$ state (Fig. 18). However, following the addition of Yb^{3+} ions to nanocrystalline $Y_2O_3:Er^{3+}$, this process was greatly diminished due to the large absorption cross-section of the ytterbium ions.

In the aforementioned mechanism, the authors expected the green emission to dominate the spectrum, as was the case when directly exciting the ${}^4F_{7/2}$ state with 488 nm radiation

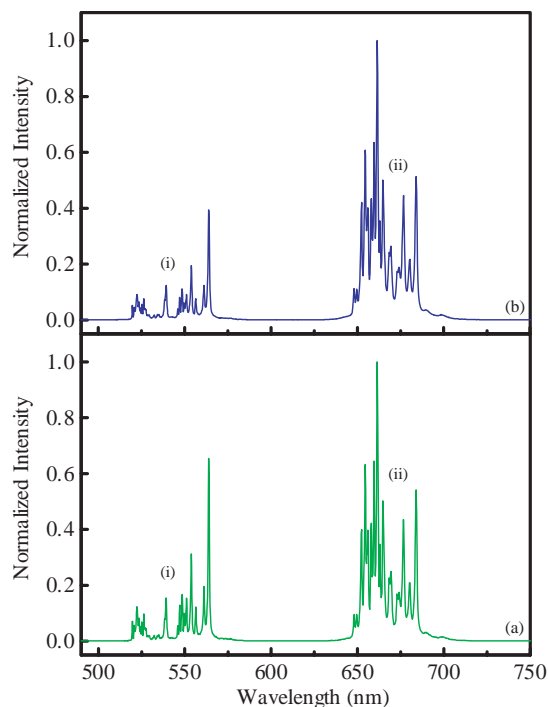


Figure 17. Room temperature anti-Stokes luminescence of nanocrystalline $Y_2O_3:Er^{3+}, Yb^{3+}$ prepared via (a) propellant and (b) wet synthetic routes following excitation with 978 nm. (i) ${}^2H_{11/2}, {}^4S_{3/2} \rightarrow {}^4I_{15/2}$, (ii) ${}^4F_{9/2} \rightarrow {}^4I_{15/2}$. Reprinted with permission from [138], F. Vetrone et al., *J. Phys. Chem. B* in press.

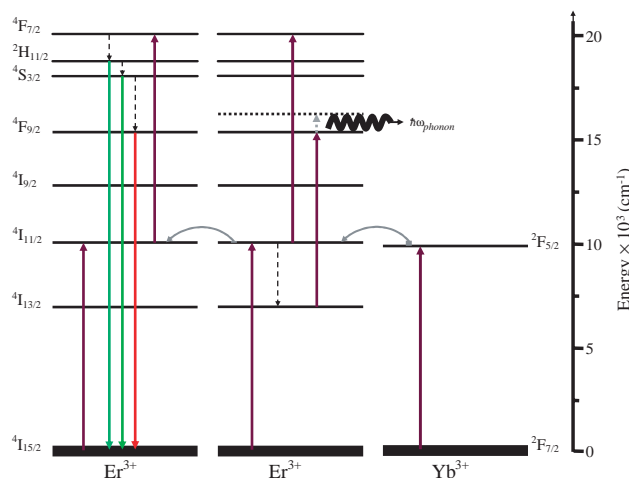


Figure 18. Mechanism for Er^{3+} upconversion in Y_2O_3 for 980 nm excitation showing the energy transfer upconversion between two Er^{3+} ions and the energy transfer from the Yb^{3+} to Er^{3+} ions responsible for populating both the ${}^4F_{7/2}$ and ${}^4F_{9/2}$ states.

since the ${}^4F_{9/2}$ state was populated via multiphonon relaxation from the ${}^4S_{3/2}$ state. The authors observed a change in the relative intensities between the green and red upconverted emissions in the nanocrystalline material in that the red emissions dominated the spectrum unlike the bulk sample where the green emission dominated. The authors proposed that an ion-pair process of the type $({}^4F_{7/2}, {}^4I_{11/2}) \rightarrow ({}^4F_{9/2}, {}^4F_{9/2})$ was responsible for directly populating the ${}^4F_{9/2}$ state and bypassing the green ${}^2H_{11/2}$ and ${}^4S_{3/2}$ states. A slight enhancement of the population in the ${}^4F_{9/2}$ state was also observed in the bulk sample albeit to a lesser extent than in the nanocrystalline material. The ion-pair process occurred via two energy transfer processes and thus should have occurred with equal probability in both the bulk and the nanocrystalline samples having the same dopant concentration. The authors state that this process did not account for the drastic differences in the magnitude of the red enhancement between the bulk and nanocrystalline samples.

The magnitude of the red enhancement was slightly different in the two nanocrystal samples prepared by different techniques and so the authors studied the microstructure of each sample determining that the microstructure played only a minor role in the upconversion. The distinguishing factor between the bulk and nanocrystal materials was the presence of the CO_3^{2-} and OH^- impurities on the surface of the nanocrystals. They proposed a mechanism which utilized these high-energy phonons. Following the initial energy transfer from the Yb^{3+} ion, the large vibrational quanta associated with these impurities allowed for an efficient depopulation of the ${}^4I_{11/2}$ state, which resulted in the subsequent population of the ${}^4I_{13/2}$ state. Since the gap between the ${}^4I_{11/2}$ and ${}^4I_{13/2}$ states is approximately 3600 cm^{-1} a few high-energy phonons in the nanocrystalline material could easily bridge the gap. In contrast, the bulk material required many more phonons to bridge the same gap as it utilized only the intrinsic phonons of yttria. Following the multiphonon relaxation to the ${}^4I_{13/2}$ state, another energy transfer from the Yb^{3+} ion in the ${}^2F_{5/2}$ state excited the Er^{3+} ion directly to the ${}^4F_{9/2}$ state. An excess energy of approximately 1600 cm^{-1}

was present, which was dissipated by the nanocrystal lattice to conserve energy (Fig. 18). In order to show that this mechanism was operative, the authors presented the upconversion spectrum of bulk $\text{Y}_2\text{O}_3:\text{Er}^{3+}, \text{Yb}^{3+}$ following excitation with 1064 nm and observed that ${}^4F_{9/2} \rightarrow {}^4I_{15/2}$ emission was more intense relative to the $({}^2H_{11/2}, {}^4S_{3/2}) \rightarrow {}^4I_{15/2}$ emission when compared to the spectrum obtained following excitation with 980 nm. The enhancement in the bulk material occurred because the ${}^4F_{9/2} \leftarrow {}^4I_{13/2}$ transition is nearly resonant with the 1064 nm line of the Nd:YAG laser. Since the excess energy in this transition was on the order of about 800 cm^{-1} , the probability of the process occurring in the bulk material was much greater thereby resulting in an enhancement of the ${}^4F_{9/2}$ population.

The infrared-to-visible upconversion of nanocrystalline $\text{Y}_2\text{O}_3:\text{Er}^{3+}, \text{Yb}^{3+}$ prepared using an emulsion liquid membrane was also studied by Hirai et al. [72] following excitation with 960 nm. The authors observed a predominantly red emission and attributed it to the $({}^4F_{7/2}, {}^4I_{11/2}) \rightarrow ({}^4F_{9/2}, {}^4F_{9/2})$ ion-pair energy transfer process, which bypassed the green $({}^2H_{11/2}$ and ${}^4S_{3/2})$ emitting levels. The authors showed the variation of the ${}^4F_{9/2} \rightarrow {}^4I_{15/2}$ transition intensity as a feed function of the Yb^{3+} ion by measuring the ratios of Yb concentration to the overall M^{3+} concentration, $\{\text{Yb}/(\text{Y} + \text{Yb} + \text{Er})\}_f$. The red emission was seen to increase slowly from a value of $\{\text{Yb}/(\text{Y} + \text{Yb} + \text{Er})\}_f = 0$ to a maximum of $\{\text{Yb}/(\text{Y} + \text{Yb} + \text{Er})\}_f = 0.08$, after which it decreased slowly. Thus, the authors state that the sensitization effect of the Yb ion on the activator Er ion varied with Yb ion concentration. At higher Yb concentrations, the Yb ions may act as trapping centers and dissipate the energy nonradiatively, instead of transferring it to the Er ion. Similarly, the authors studied the variation of the ${}^4F_{9/2} \rightarrow {}^4I_{15/2}$ transition intensity as a function of the Er^{3+} ion concentration. They showed that intensity increased rapidly from a starting value of $\{\text{Er}/(\text{Y} + \text{Yb} + \text{Er})\}_f = 0$ to a maximum at $\{\text{Er}/(\text{Y} + \text{Yb} + \text{Er})\}_f = 0.1$ and then decreased with further increase of Er^{3+} ions. This behavior may have been due to cross-relaxation or energy migration between activator ions or to quenching sites where the excitation energy was lost nonradiatively. These quenching sites could be impurities or defects within the lattice, which were invariably present.

5. APPLICATIONS

Yttrium oxide is a material with a wide range of applications. We have chosen to concentrate on the three main applications of nanocrystalline Y_2O_3 : optical and electrical, mechanical (refractories and ceramics), and catalytic. In each case the application will be briefly discussed along with the possible advantages of utilizing the nanosized version of the oxide. In the majority of cases, the nanosized particles exhibit significantly different properties from those of bulk materials.

5.1. Optical and Electrical

5.1.1. Display Devices

The visible-light-generating components of emissive, full color displays are called phosphors. Phosphors are composed of an inert host lattice and an optically excited activator, typically a $3d$ or $4f$ electron metal. The development

of new types of high resolution and high efficiency conventional and planar displays has created a need for optical phosphors with new or enhanced properties. For application in the emerging full color, flat panel display industry, thermally stable, high luminous efficiency, radiation resistant, fine particle size powders are required. The demands of these newer technologies have produced a search for new materials and synthesis techniques to improve the performance of phosphors. High efficiency phosphor materials are the key for development of these new devices [56].

Rare earth containing compounds have long found uses as phosphors in lamps and display devices due to sharp, intensely luminescent $f-f$ electronic transitions. Micrometer sized $\text{Y}_2\text{O}_3:\text{Eu}^{3+}$ phosphors have been used since the 1970s as the red component in television projection tubes and fluorescent lighting devices [139]. This material has been utilized for some time due to its efficient luminescence under UV and electron beam excitation [65]. The red emission is due to a ${}^5D_0 \rightarrow {}^7F_2$ transition within the europium impurity. Though Eu^{3+} is the most common utilized of the rare earth ions in oxide phosphors, it is possible to dope various other rare earth ions such as Er^{3+} , Tb^{3+} , Tm^{3+} , Dy^{3+} , Ho^{3+} , Pr^{3+} , and Sm^{3+} , either singularly or in combinations, to achieve visible luminescence. Thus, these materials are also possible candidates for use as phosphors in numerous lighting and display devices.

The CRT is still the most commonly used display device in the world today. A basic CRT utilizes a heated cathode, two sets of anodes (focusing and accelerating), and steering coils to produce and direct electrons at phosphors coated onto a screen to generate light and thus a picture. The commercial phosphors utilized in the majority of current CRTs are micrometer in size due to problems encountered such as decreased luminescence as one goes to smaller particle sizes. If it were possible to produce smaller spherical particles in the nanometer range with luminescent properties similar or improved over their current micrometer counterparts, then these particles could be easily processed into smaller pixels than those currently used in conventional CRT screens. This opens up the possibility of higher resolution which is desirable for the future of high definition television (HDTV) [94]. The potential for forming a densely packed layer (because of the size and shape of the particles and their self-assembly abilities) should also improve any aging problems encountered with traditional phosphors [94].

Plasma display panels (PDP) are a new generation of large flat panel displays. PDPs are based on multiple microdischarges working on the same basic principles as the aforementioned fluorescent tubes. These PDP modules consist of a cell structure where a combination of gases is confined. Each cell has electrodes that enable gas ionization under an electric field. The UV rays that are created from this plasma gas excite a phosphor layer that converts them into red, green, or blue color. The PDP is the only technology able to provide direct view displays with diagonals in the range 30 to 65 inches, which can be viewed under room-light or sunlight conditions. The high energy UV photons (147 nm, 8.5 eV) that impinge on the phosphor powders cause reduction in luminous efficiency of the display over time because of radiation damage induced in the material [44]. Thus, oxide phosphors were found to be optimal for

PDP devices compared to other conventional sulfide based phosphors which suffer from this type of degradation. It is also hoped that the proposed increase in luminescence in the nanocrystalline oxide phosphors will result in brighter and more energy efficient PDP displays.

The field emission display (FED) has been recognized as one of the most promising technologies for flat panel display. The FED functions on principles similar to the CRT as a beam of electrons are utilized to excite the phosphors, which then emit light. However, they differ in that the FED uses multiple electron emitters for each pixel arranged in a grid. This technology eliminates the beam steering system of the CRT and allows screens to be manufactured as thin as 10 mm. Another benefit over CRTs is that the electrons are not created by heat and thus the display does not need to warm up and produces much less unwanted heat. FEDs also have several advantages over the current choice for flat panel displays, liquid crystal devices: they require no back light, are very light, and have a wide viewing angle, a short response time, a very high contrast ratio, and excellent color properties.

Recent advances in FED technology have placed a requirement on the development of a corresponding screen technology. An important field of practical application of the FED is the development of phosphors, which show high efficiency and good stability at low-voltage electron excitation and high current density. However, phosphors synthesized through conventional methods are inappropriate for the FED due to reduced cathodoluminescent efficiency, large particle size, and lack of morphological control. Therefore, in recent years luminescent nanostructured materials have become attractive for FED applications.

Compared with a conventional CRT screen, an FED operates with lower energy (3–10 keV) but higher current density (1 mA/cm²) beams impinging on the phosphors. This requires more luminously efficient and thermally stable materials [44]. Luminous efficiency is defined as the ratio of the energy out (lumens) to the input energy. Due to the low excitation voltage, electron penetration into the luminescent particles is very shallow. This means that the effective luminescent region may be confined near the surface of particles and that the low voltage excitation favors small particles or large specific surface area. As a result, the small size of nanoparticles allows complete penetration by low-voltage electrons for efficient material utilization [67].

In addition, sulfide-based phosphors used in the traditional CRT are known to be rapidly degraded at high current density needed on FED. This outgassing from the highly efficient sulfide-based phosphors has been shown to degrade the cathode tip of the field emitter array and cause irreversible damage [44]. Thus, the study of oxide-based phosphors which are stable at the high current density has progressed in many fields [68]. There is, therefore, a need to develop oxide-based phosphors that display a higher efficiency than the materials conventionally used in CRT screens under low to medium electron accelerating voltages [65]. In the case of oxide-based red phosphors for FED application the most promising material to date is Y₂O₃:Eu³⁺ particles.

Another requirement is on the particle size distribution: there is a maximum and minimum particle size limitation to the powders. For FED applications about five particle layers

are required to achieve optimal light output. Large particles (>8 μm) require thicker layers, increasing the phosphor cost and also producing more light scattering. Additionally, the pixel pitch (~250 μm) places a maximum on particle size. It is therefore advantageous that the phosphor particle size be as small as possible as this potentially leads to higher screen resolution, lower screen loading, and a higher screen density [65]. Unfortunately, it is usually found that smaller particles (<0.2 μm) do not have a high luminous efficiency arising from grain boundary effects. The activator ion in the crystal is most efficient when located in the bulk material in a regular crystal field. Activators located on the surface or on the grain boundaries are thought to be nonluminescent or even luminescence quenching regions [44]. Thus claims of increased luminescence in rare earth doped nanocrystalline Y₂O₃ [124] have sparked interest in these materials throughout the scientific community.

5.1.2. Fluorescent Lamps

The use of rare earth doped Y₂O₃ as a phosphor in mercury-discharge lamps dates back almost 50 years. The commercial red-emitting phosphor for these fluorescent lamps is typically Y₂O₃ activated with Eu³⁺. The increase in the luminescence efficiency observed in nanocrystalline phosphor materials would make these devices more energy efficient, thus reducing energy consumption while at the same time improving overall brightness.

5.1.3. Thin Films

It should also be mentioned that Y₂O₃ has also been extensively studied as thin films deposited on various types of substrates. Due to its high dielectric constant (strength), Y₂O₃ oxide films have been evaluated for possible applications as high dielectric constant electric insulators in electronic devices. Though this subject is outside the scope of this chapter due to the wealth of information published on it alone, it at least deserves mention due to the fact that the deposited layer in many cases is <100 Å. Besides the possible use as an electronic insulator, Y₂O₃ thin films doped with Eu³⁺ have also been widely studied for use in the aforementioned FEDs. The idea here is that instead of laying out thin layers of Y₂O₃:Eu³⁺ particles the actual phosphor could be deposited as a thin film on the anode itself thereby simplifying the process. Though the process is feasible, it leads to lower efficiencies than depositing the phosphors themselves onto the screens.

5.2. Mechanical

In recent years, there has been an upsurge of interest in yttria as a refractory material because of its high melting point (2410 °C), which is higher than that of alumina, its high temperature stability (even in an oxidizing environment), and its low thermal expansion ($4 \times 10^{-7} \text{ K}^{-1}$), which is lower than that of alumina, magnesia, and zirconia [48]. An additional benefit is that it does not undergo any phase transformation. Yttrium oxide, because of its chemical stability and refractory nature, has a wide range of applications (e.g., high temperature chemical-resistant substrates, crucibles for melting reactive metals, and nozzles for

jet-casting molten, rare earth–iron magnetic alloys). Non-sinterable yttria is usually obtained through decomposition of yttrium compounds (yttrium carbonate, oxalate, nitrate, and hydroxide) at high temperatures. The chemical methods mentioned previously also yield fine sinter-active materials. The drawbacks of these hydrolysis techniques are that they are usually quite involved and require long processing times, expensive chemicals, and special equipment. It is also possible to produce nanoscale yttria by the low temperature initiated self-propagating, gas-producing exothermic reactions.

Improved sintering processes, especially for ceramics, have allowed for a better understanding of the relationship between various mechanical properties and the nanostructure of dense materials. The majority of research in this field has revolved around the study of mechanical and magnetic properties. For magnetic applications, the new properties found in some nanostructured materials have been easily developed for technological uses. However, since most processing methods result in the production of loose powders, major challenges still exist in the application of these solids as structural materials. For example, there are still difficulties in controlling the grain growth during densification or the amount of gaseous impurities that are adsorbed during the fabrication process [140].

It has been found though that nanocrystalline Y_2O_3 synthesized via a combustion reaction undergoes densification at lower temperatures than its micrometer commercial counterpart [32]. Normally, this procedure requires temperatures in excess of 1800 °C with the sought after fully dense, uniform microstructures not necessarily being attained. It was determined that by using nanocrystalline Y_2O_3 as the starting material this temperature could be lowered to 1600 °C producing results within 98% of the theoretical density as opposed to 80% for a commercial Y_2O_3 powder processed under the same conditions.

For the most part, yttria oxide's application in ceramic materials has been as an additive to other compounds to help stabilize or modify their mechanical and structural properties. A good example of this technique is yttrium stabilized zirconium. Zirconia as the binary oxide (ZrO_2) has little value as a ceramic due to the fact that it undergoes two phase transitions upon heating. At room temperature the undoped oxide is monoclinic but transforms to a tetragonal phase at 1170 °C and then to the cubic form at 2370 °C with both phase transformations accompanied by large volumetric changes. Zirconia is stabilized by the addition of Y_2O_3 resulting in a material with high strength and toughness that remains in one phase up until melting. As a result, Y_2O_3 stabilized zirconia finds uses in high temperature applications such as thermal barrier coatings for gas turbine parts [70]. Again, the volume of papers published on this subject alone is staggering and beyond the scope of this chapter.

5.3. Catalytic Activity

Along with its traditional uses as a phosphor and refractory material, the scientific community has also placed a growing significance on the study of nanoscale materials for use as potential catalysts for numerous chemical reactions. In many aspects nanoscale materials (and their understanding) could be the basis of revolutionary development in the field of

catalysis and electrocatalysis [140]. Many researchers have related improved or new properties observed in nanoscale materials to an increased number of atoms at the surface of the crystals relative to bulk samples, which imply an increased number of active sites. These nanostructured materials allow the possibility to design crystalline surfaces virtually on an atomic scale [140]. This allows for the construction of specific microstructures in order to achieve improvements on a given catalytic process.

As mentioned previously, there are numerous synthesis routes available to the materials scientist of today which produce large quantities of nanoscale materials. The choice of synthesis method and the following processing techniques employed allow for the precise control of the microstructure obtained. Unlike refractories, the application of nanoparticles as catalysts depends neither on the use of agglomerate-free powders nor upon the use of a fully dense solid. Rather, a carefully tailored nanostructured material is preferred while dealing with industrial processes concerning chemical production, energy conversion systems, and separation or purification processes [51]. The fabrication of a fully dense solid is not necessarily essential for application in the area of catalysis. The use of nanometer materials for catalysis is not necessarily a new field. In the time span of 10 to 50 years ago, catalysts based on fine microstructures with an average grain size from 1 to 20 nm were developed, an example being metallic nanoparticles dispersed on inert materials, such as Rh/Al_2O_3 or Pt/C [140]. These materials found uses in many industries such as for petrochemical production, automobile emission control, and fine chemical synthesis.

The process of catalysis involves a cyclic process whereby reactants enter a site on the catalyst. After their formation, the products are then desorbed thus returning the active site to its original configuration and continuing the cycle. In traditional catalytic materials, the active site may be composed of a group of adjacent surface atoms or an adsorbed species. These sites are associated with the surface structure, the lattice defects, and the edges or corners of crystallites [140]. As a result of their increased surface area, nanoscale materials seem to be ideal for this application due to the ability to synthesize them with a specific crystallite size. Furthermore, one has control over lattice parameters and the amount or type of internal defects. It is possible to obtain crystals with a large amount of atoms at the surface or at grain boundaries, for instance, crystallites with an average size of ~5 nm will have close to 50% of their atoms at the surface. Designing or modifying only the surface structure could, for some applications, be more desirable or, even in some cases, more feasible [140].

Though nanoscale materials seem to be viable catalysts, very little investigation has been performed into the use of nanoscale Y_2O_3 as a catalytic material. Roy et al. describe a gel combustion technique for synthesizing nanostructured yttria powders with structures suitable for catalytic applications [51]. They note that it possible to tailor the powders for different purposes depending on the observed level of porosity in the powders. The obtained powders could then be processed by the addition of dispersants for deagglomeration to achieve a fine dispersed powder [51].

Hussein et al. have investigated the acid-base and catalytic properties of porous Y_2O_3 samples formed from the

acetate, nitrate, and oxalate of yttrium utilizing infrared spectroscopy [141]. In their study the decomposition of 2-propanol was used as a catalytic test reaction because the selectivity for dehydration versus dehydrogenation provided a measure of the surface acid-base properties. They found that porous Y_2O_3 is basic and possesses catalytic properties that are dependent on the specific precursor utilized to synthesize the yttria with some preparations give selective 2-propanol dehydrogenation and others giving selective 2-propanol dehydration. This is a clear illustration on how it may be possible to tailor the nanocrystals using synthesis techniques to catalyze a specific chemical process.

The possible use of nanoscale Y_2O_3 as a catalyst reducing NO, CH_4 , and CO emissions from natural gas engine exhaust streams has also been investigated by Fokema et al. [142]. In this study high-surface-area Y_2O_3 powders were synthesized using a controlled chemical precipitation technique. The Y_2O_3 catalyst produced greater than 50% conversion of NO to N_2 in excess oxygen. The Y_2O_3 system was found to have superior hydrothermal stability compared to traditional noble metal and zeolitic catalysts.

6. SUMMARY AND CONCLUSIONS

In this chapter, we have reviewed many novel preparatory techniques for the synthesis of yttrium oxide nanocrystals ranging from the quite simple utilization of a muffle furnace and a combustion reaction to produce nanopowders in relatively short periods of time to very elaborate procedures. An ideal synthesis should be relatively simple and should produce defect-free crystals in large quantities in very little time. If it is to be adopted for industrial use, it should be as inexpensive as possible also. In the reviewed synthesis procedures, a few issues need to be addressed before the techniques become commercially viable. For example, although the combustion synthesis yields small particle size nanocrystals in gram quantities with relative ease, the contaminants on the surface have been shown to be detrimental to the luminescence efficiency. Eliminating the dangling bonds with some sort of coating has shown to increase the luminescence efficiency. If a relatively simple coating process could be combined with the simplicity and ease of the combustion synthesis to produce nanocrystals with higher luminescence efficiency than the current crop of commercial phosphors, Y_2O_3 nanocrystals would no doubt find many commercial applications.

Rare earth doped nanocrystals, in particular Y_2O_3 , continue to garner interest from both academic and industrial scientists. Yttrium oxide doped with Eu^{3+} is immensely popular with materials researchers as evidenced by the sheer volume of literature on the topic. Its popularity, of course, stems from its primary use as a red phosphor in various display devices. In fact, the synthesis and characterization of the nanocrystalline $Y_2O_3:Eu^{3+}$ phosphor are being made accessible to undergraduate students in inorganic synthesis courses [143]. However, many of the other rare earth ions have been largely overlooked for such applications. For example, the principle emission of $Y_2O_3:Pr^{3+}$ nanocrystals is also red and is due to the $^1D_2 \rightarrow ^3H_4$ transition between 600 and 700 nm. Similarly, the majority of the visible emissions of $Y_2O_3:Sm^{3+}$ are in the red region of the spectrum

from 550 to 700 nm and are attributed to the emission from the $^4G_{5/2}$ excited state to the $^6H_{9/2}$, $^6H_{7/2}$, and $^6H_{5/2}$ states. Nanocrystalline yttrium oxide doped with both these ions has not been explored for use as a red phosphor.

Nanocrystalline Y_2O_3 doped with other visible emitting rare earth ions has not been studied in any great detail either and such investigations would make an interesting addition to the scientific literature as well as add to our understanding of the behavior of rare earth ions in Y_2O_3 . Two ions of particular interest for certain imaging devices are Dy^{3+} and Tm^{3+} . Nanocrystalline $Y_2O_3:Dy^{3+}$ emits yellow radiation with a sharp peak at 573 nm from the $^4F_{9/2} \rightarrow ^6H_{15/2}$ transition. Similarly, $Y_2O_3:Tm^{3+}$ emits blue light at 488 nm from the $^1G_4 \rightarrow ^3H_6$ transition. Furthermore, Tm^{3+} -doped Y_2O_3 is especially interesting as it can undergo photon avalanche upconversion when irradiated with red light [144].

At the other end of the spectrum, luminescent materials that emit short wavelength visible or ultraviolet radiation are desired for many applications in imaging, lithography, optical data recording, scintillation, and displays [145]. The $5d \rightarrow 4f$ emission of Ce^{3+} is desirable as it combines the broad absorption and emission profiles of the transition metals with the high-energy emission properties of the rare earths. Nanocrystalline materials doped with Ce^{3+} would be attractive for such applications and, as mentioned previously, their small size would have positive effects on the resolution of the devices. Infrared emitting materials are also of technological importance. The neodymium ion is attractive as it emits at various IR wavelengths from the $^4F_{3/2}$ state when doped into Y_2O_3 nanocrystals. The long lifetimes of some of the excited states make this material useful for such applications as optical data storage.

While the scientific community as a whole has unearthed a great deal of information in rare earth doped Y_2O_3 nanocrystals, there is still much we need to learn. There is no doubt that such studies would add to the basic understanding of the physics and chemistry of these novel luminescent materials.

GLOSSARY

Catholuminescence Light generated following bombardment of electrons in a high vacuum environment.

Luminescence Light generated following irradiation with electromagnetic radiation.

Nano (nanometer) One billionth of a meter (10^{-9} meters).

Nanocrystals Polycrystalline materials with particle diameters or grain sizes of 100 nm or less.

Nanoscience Study of nanometer sized objects.

Phonon A quantum of acoustic (vibrational) energy.

Phosphor High-purity inorganic materials that emit light when exposed to various excitation sources such as photons, electrons, or an electric field.

Photoluminescence Light generated following irradiation with photons.

Rare earth elements Series of chemical elements of the periodic table with atomic numbers 57 through 71, and, named in order, are lanthanum (La), cerium (Ce), praseodymium (Pr), neodymium (Nd), promethium (Pm), samarium (Sm), europium (Eu), gadolinium (Gd),

terbium (Tb), dysprosium (Dy), holmium (Ho), erbium (Er), thulium (Tm), ytterbium (Yb), and lutetium (Lu). Yttrium (Y, atomic no. 39) and scandium (Sc, atomic no. 21) are sometimes included in the group of rare earth elements.

Spectroscopy Study of the interaction of matter with (electromagnetic) radiation of specific frequency and wavelength by making use of the emission, absorption, or scattering of the radiation.

Upconversion Emission of light with higher energy than the excitation pump wavelength.

ACKNOWLEDGMENTS

The authors gratefully and wholeheartedly acknowledge Dr. Adolfo Speghini and Professor Marco Bettinelli from the Università di Verona whose unprecedented mastery of the synthesis of inorganic nanocrystals and whose helpful scientific discussions have greatly increased our understanding of nanocrystalline $Y_2O_3:RE^{3+}$. The authors acknowledge the National Science and Engineering Research Council of Canada for the support of our research.

REFERENCES

1. A. P. Alivisatos, *J. Phys. Chem.* 100, 13226 (1996).
2. L. Brus, *J. Phys. Chem.* 90, 2555 (1986).
3. Y. Shen, C. S. Friend, Y. Jiang, D. Jakubczyk, J. Swiatkiewicz, and P. N. Prasad, *J. Phys. Chem. B* 104, 7577 (2000).
4. R. N. Bhargava, D. Gallagher, and T. Welker, *J. Lumin.* 60–61, 275 (1994).
5. R. N. Bhargava, D. Gallagher, X. Hong, and A. Nurmikko, *Phys. Rev. Lett.* 72, 416 (1994).
6. Y. L. Soo, Z. H. Ming, S. W. Hunag, Y. H. Kao, R. N. Bhargava, and D. Gallagher, *Phys. Rev. B* 50, 7602 (1994).
7. A. P. Alivisatos, *Endeavour* 21, 56 (1996).
8. R. N. Bhargava, *J. Lumin.* 72–74, 46 (1997).
9. A. A. Bol and A. Meijerink, *Phys. Rev. B* 58, R15997 (1998).
10. A. A. Bol and A. Meijerink, *J. Lumin.* 87–89, 315 (2000).
11. X. Yu, P. Xie, and Q. Su, *Phys. Chem. Chem. Phys.* 3, 5266 (2001).
12. W. Zhang, P. Xie, C. Duan, K. Yan, M. Yin, L. Lou, S. Xia, and J.-C. Krupa, *Chem. Phys. Lett.* 292, 133 (1998).
13. K. Riwotzki and M. Hasse, *J. Phys. Chem. B* 102, 10129 (1998).
14. G. K. Liu, H. Z. Zhuang, and X. Y. Chen, *Nano Lett.* 2, 535 (2002).
15. J. W. Stouwdam and F. C. J. M. van Veggel, *Nano Lett.* 2, 733 (2002).
16. H. X. Zhang, C. H. Kam, Y. Zhou, H. Q. Han, S. Buddhudu, and Y. L. Lam, *Opt. Mater.* 15, 47 (2000).
17. G. Yi, B. Sun, F. Yang, D. Chen, Y. Zhou, and J. Cheng, *Chem. Mater.* 14, 2910 (2002).
18. F. Vetrone, J. C. Boyer, J. A. Capobianco, A. Speghini, and M. Bettinelli, *J. Phys. Chem. B* 106, 5622 (2002).
19. C. M. Bender, J. M. Burlitch, D. Barber, and C. Pollock, *Chem. Mater.* 12, 1969 (2000).
20. J. A. Capobianco, F. Vetrone, J. C. Boyer, A. Speghini, and M. Bettinelli, *Opt. Mater.* 19, 259 (2002).
21. J. H. van Vleck, *J. Phys. Chem.* 41, 67 (1937).
22. S. Hüfner, "Optical Spectra of Transparent Rare Earth Compounds." Academic Press, New York, 1978.
23. G. Wakefield, H. A. Keron, P. J. Dobson, and J. L. Hutchison, *J. Colloid Interface Sci.* 215, 179 (1999).
24. T. Igarashi, M. Ihara, T. Kusunoki, and K. Ohno, *Appl. Phys. Lett.* 76, 1549 (2000).
25. C. Xu, B. A. Watkins, R. E. Sievers, X. Jing, P. Trowga, C. S. Gibbons, and A. Vecht, *Appl. Phys. Lett.* 71, 1643 (1997).
26. T. Hase, T. Kano, E. Nakazawa, and H. Yamamoto, *Adv. Electron. Electron Phys.* 79, 271 (1990).
27. R. Schmechel, H. Winkler, L. Xiaomao, M. Kennedy, M. Kolbe, A. Benker, M. Winterer, R. A. Fischer, H. Hahn, and H. von Seggern, *Scripta Mater.* 44, 1213 (2001).
28. B. M. Tissue and H. Eilers, *J. Soc. Inform. Displ.* 4, 213 (1996).
29. K. Petermann, G. Huber, L. Fornasiero, S. Kuch, E. Mix, V. Peters, and S. A. Basun, *J. Lumin.* 87–89, 973 (2000).
30. L. Laversenne, Y. Guyot, C. Goutaudier, M. T. Cohen-Adad, and G. Boulon, *Opt. Mater.* 16, 475 (2001).
31. L. Laversenne, S. Kairouani, Y. Guyot, C. Goutaudier, G. Boulon, and M. T. Cohen-Adad, *Opt. Mater.* 19, 59 (2002).
32. W.-J. Kim, J. Y. Park, S. J. Oh, Y. S. Kim, G.-W. Hong, and I.-H. Kuk, *J. Mater. Sci. Lett.* 18, 411 (1999).
33. Y.-N. Xu, Z.-Q. Gu, and W. Y. Ching, *Phys. Rev. B* 56, 14993 (1997).
34. N. Yamada, S. Shionoya, and T. Kushida, *J. Phys. Soc. Japan* 32, 1577 (1972).
35. E. T. Goldburt, B. Kulkarni, R. N. Bhargava, J. Taylor, and M. Libera, *J. Lumin.* 72–74, 190 (1997).
36. D. K. Williams, H. Yuan, and B. M. Tissue, *J. Lumin.* 83–84, 297 (1999).
37. E. Zych, *Opt. Mater.* 16, 445 (2001).
38. G. A. Hirata, F. Ramos, R. Garcia, E. J. Bosze, J. McKittrick, O. Contreras, and F. A. Ponce, *Phys. Status Solidi A* 188, 179 (2001).
39. Y. Tao, G. Zhao, W. Zhang, and S. Xia, *Mater. Res. Bull.* 32, 501 (1997).
40. G. Tessari, M. Bettinelli, A. Speghini, D. Ajò, G. Pozza, L. E. Depero, B. Allieri, and L. Sangaletti, *Appl. Surf. Sci.* 144–145, 686 (1999).
41. G. Fagherazzi, S. Polizzi, M. Bettinelli, and A. Speghini, *J. Mater. Res.* 15, 586 (2000).
42. S. Polizzi, G. Fagherazzi, M. Battagliarin, M. Bettinelli, and A. Speghini, *J. Mater. Res.* 16, 146 (2001).
43. S. R. Jain, K. C. Adiga, and V. R. Pai Verneker, *Combust. Flame* 40, 71 (1981).
44. L. E. Shea, J. McKittrick, and O. A. Lopez, *J. Am. Ceram. Soc.* 79, 3257 (1996).
45. Z. Qi, C. Shi, W. Zhang, W. Zhang, and T. Hu, *Appl. Phys. Lett.* 81, 2857 (2002).
46. L. Sun, J. Yao, C. Liu, C. Liao, and C. Yan, *J. Lumin.* 87–89, 447 (2000).
47. L. Sun, C. Qian, C. Liao, X. Wang, and C. Yan, *Solid State Commun.* 119, 393 (2001).
48. S. Ekambaran and K. C. Patil, *J. Mater. Chem.* 5, 905 (1995).
49. J. McKittrick, L. E. Shea, C. F. Bacalski, and E. J. Bosze, *Displays* 19, 169 (1999).
50. S. Dutta, Q. Mohammad, and S. S. Manoharan, *J. Mater. Sci. Lett.* 21, 1077 (2002).
51. S. Roy, W. Sigmund, and F. Aldinger, *J. Mater. Res.* 14, 1524 (1999).
52. P. K. Sharma, M. H. Jilavi, R. Nab, and H. Schmidt, *J. Mater. Sci. Lett.* 17, 823 (1998).
53. P. K. Sharma, M. H. Jilavi, R. Nass, and H. Schmidt, *J. Lumin.* 82, 187 (1999).
54. P. K. Sharma, R. Nass, and H. Schmidt, *Opt. Mater.* 10, 161 (1998).
55. P. K. Sharma, M. H. Jilavi, V. K. Varadan, and H. Schmidt, *J. Phys. Chem. Solids* 63, 171 (2002).
56. B. Allieri, L. E. Depero, A. Marino, L. Sangaletti, L. Caporaso, A. Speghini, and M. Bettinelli, *Mater. Chem. Phys.* 66, 164 (2000).
57. S. Polizzi, M. Battagliarin, M. Bettinelli, A. Speghini, and G. Fagherazzi, *J. Mater. Chem.* 12, 742 (2002).
58. Y. D. Jiang, Z. L. Wang, F. Zhang, H. G. Paris, and C. J. Summers, *J. Mater. Res.* 13, 2950 (1998).
59. Q. Li, L. Gao, and D. Yan, *Nanostruct. Mater.* 8, 825 (1997).

60. J. Silver, M. I. Martinez-Rubio, T. G. Ireland, G. R. Fern, and R. Withnall, *J. Phys. Chem. B* 105, 948 (2001).
61. J. Silver, M. I. Martinez-Rubio, T. G. Ireland, and R. Withnall, *J. Phys. Chem. B* 105, 7200 (2001).
62. J. Silver, M. I. Martinez-Rubio, T. G. Ireland, G. R. Fern, and R. Withnall, *J. Phys. Chem. B* 105, 9107 (2001).
63. M. I. Martinez-Rubio, T. G. Ireland, G. R. Fern, J. Silver, and M. J. Snowden, *J. Electrochem. Soc.* 149, H53 (2002).
64. M. I. Martinez-Rubio, T. G. Ireland, G. R. Fern, J. Silver, and M. J. Snowden, *Langmuir* 17, 7145 (2001).
65. G. Wakefield, E. Holland, P. J. Dobson, and J. L. Hutchison, *Adv. Mater.* 13, 1557 (2001).
66. G. Wakefield, H. A. Keron, P. J. Dobson, and J. L. Hutchison, *J. Phys. Chem. Solids* 60, 503 (1999).
67. M. H. Lee, S. G. Oh, S. C. Yi, D. S. Seo, J. P. Hong, C. O. Kim, Y. K. Yoo, and J. S. Yoo, *J. Electrochem. Soc.* 147, 3139 (2000).
68. M. H. Lee, S. G. Oh, and S. C. Yi, *J. Colloid Interface Sci.* 226, 65 (2000).
69. H. Huang, G. Q. Xu, W. S. Chin, L. M. Gan, and C. H. Chew, *Nanotechnology* 13, 318 (2002).
70. J. A. Nelson and M. J. Wagner, *Chem. Mater.* 14, 915 (2002).
71. T. Hirai, T. Hirano, and I. Komasa, *J. Mater. Chem.* 10, 2306 (2000).
72. T. Hirai, T. Orikoshi, and I. Komasa, *Chem. Mater.* 14, 3576 (2002).
73. H. Eilers and B. M. Tissue, *Mater. Lett.* 24, 261 (1995).
74. H. Eilers and B. M. Tissue, *Chem. Phys. Lett.* 251, 74 (1996).
75. B. Bihari, H. Eilers, and B. M. Tissue, *J. Lumin.* 75, 1 (1997).
76. D. K. Williams, B. Bihari, B. M. Tissue, and J. M. McHale, *J. Phys. Chem. B* 102, 916 (1998).
77. A. Konrad, T. Fries, A. Gahn, F. Kummer, U. Herr, R. Tidecks, and K. Samwer, *Chem. Vap. Deposition* 5, 207 (1999).
78. A. Konrad, T. Fries, A. Gahn, F. Kummer, U. Herr, R. Tidecks, and K. Samwer, *J. Appl. Phys.* 86, 3129 (1999).
79. A. Konrad, U. Herr, R. Tidecks, F. Kummer, and K. Samwer, *J. Appl. Phys.* 90, 3516 (2001).
80. E. T. Goldburt and R. N. Bhargava, in "Proceedings of the International Symposium on Advanced Luminescent Materials" (D. J. Lockwood, P. M. Fauchet, N. Koshida, and S. R. J. Brueck, Eds.), Vol. PV 95-25. Electrochemical Society, Chicago, 1995.
81. Y. L. Soo, S. W. Huang, Z. H. Ming, Y. H. Kao, G. C. Smith, E. Goldburt, R. Hodel, B. Kulkarni, J. V. D. Veliadis, and R. N. Bhargava, *J. Appl. Phys.* 83, 5404 (1998).
82. Y. L. Soo, S. W. Huang, Y. H. Kao, V. Chhabra, B. Kulkarni, J. V. D. Veliadis, and R. N. Bhargava, *Appl. Phys. Lett.* 75, 2464 (1999).
83. P. A. Tanner and R. W. Y. Sun, *J. Mater. Sci.* 36, 2253 (2001).
84. S. P. Feofilov, A. A. Kaplyanski, A. B. Kulinkin, A. B. Kutsenko, T. N. Vasilevskaya, and R. I. Zakharchenya, *J. Sol-Gel Sci. Technol.* 21, 135 (2001).
85. Q. Li, L. Gao, and D. Yan, *Chem. Mater.* 11, 533 (1999).
86. J. Zhang, Z. Tang, Z. Zhang, W. Fu, J. Wang, and Y. Lin, *Mater. Sci. Eng. A* 334, 246 (2002).
87. J. Dhanaraj, R. Jagannathan, T. R. N. Kutty, and C.-H. Lu, *J. Phys. Chem. B* 105, 11098 (2001).
88. H. L. Yakel, *Acta. Crystall. B* 35, 564 (1979).
89. R. W. G. Wyckoff, "Crystal Structures," 2nd ed., Vol. 2. Interscience, New York, 1964.
90. A. Saiki, N. Ishizawa, N. Mizutani, and M. Kato, *J. Ceram. Soc. Japan* 93, 649 (1985).
91. G. Concas, C. Muntoni, G. Spano, M. Bettinelli, and A. Speghini, *Z. Naturforsch.* 56, 267 (2001).
92. P. K. Sharma, M. H. Jilavi, H. Schmidt, and V. K. Varadan, *Int. J. Inorg. Mater.* 2, 407 (2000).
93. J. A. Capobianco, F. Vetrone, J. C. Boyer, A. Speghini, and M. Bettinelli, *J. Phys. Chem. B* 106, 1181 (2002).
94. X. Jing, T. Ireland, C. Gibbons, D. J. Barber, J. Siver, A. Vecht, G. Fern, P. Trowga, and D. C. Morton, *J. Electrochem. Soc.* 146, 4654 (1999).
95. C. Feldman, *Phys. Rev.* 117, 455 (1960).
96. G. Blasse and B. C. Grabmaier, "Luminescent Materials." Springer-Verlag, Berlin, 1994.
97. S. Erdei, R. Roy, G. Harshe, H. Juwhari, D. Agrawal, F. W. Ainger, and W. B. White, *Mater. Res. Bull.* 30, 745 (1995).
98. Y. Tao, G. Zhao, X. Ju, X. Shao, W. Zhang, and S. Xia, *Mater. Lett.* 28, 137 (1996).
99. A. Konrad, T. Fries, A. Gahn, F. Kummer, U. Herr, R. Tidecks, and K. Samwer, *Mater. Sci. Forum* 343-346, 494 (2000).
100. G. S. Ofelt, *J. Chem. Phys.* 37, 511 (1962).
101. B. R. Judd, *Phys. Rev.* 127, 750 (1962).
102. R. Schmechel, M. Kennedy, H. von Seggern, H. Winkler, M. Kolbe, R. A. Fischer, L. Xiaomao, A. Benker, M. Winterer, and H. Hahn, *J. Appl. Phys.* 89, 1679 (2001).
103. C. Beck, K. H. Ehses, R. Hempelmann, and C. Bruch, *Scripta Mater.* 44, 2127 (2001).
104. M. Winterer, R. Nitsche, and H. Hahn, *J. Phys. IV* 7, 1211 (1997).
105. Y. C. Kang, S. B. Park, I. W. Lenggoro, and K. Okuyama, *J. Mater. Res.* 14, 2611 (1999).
106. Y. C. Kang, H. S. Roh, and S. B. Park, *Adv. Mater.* 12, 451 (2000).
107. Y. C. Kang, H. S. Roh, S. B. Park, and H. D. Park, *J. Eur. Ceram. Soc.* 22, 1661 (2002).
108. Y. C. Kang, H. S. Roh, S. B. Park, and H. D. Park, *J. Mater. Sci. Lett.* 21, 1027 (2002).
109. Y. C. Kang, H. D. Park, and S. B. Park, *Jpn. J. Appl. Phys.* 39, L1305 (2000).
110. Y. C. Kang, H. S. Roh, D. J. Seo, and S. B. Park, *J. Mater. Sci. Lett.* 19, 1225 (2000).
111. H. S. Roh, Y. C. Kang, H. D. Park, and S. B. Park, *Appl. Phys. A* 76, 241 (2003).
112. M. D. Barnes, A. Mehta, T. Thundat, R. N. Bhargava, V. Chhabra, and B. Kulkarni, *J. Phys. Chem. B* 104, 6099 (2000).
113. A. P. Bartko, L. A. Peyser, R. M. Dickson, A. Mehta, T. Thundat, R. Bhargava, and M. D. Barnes, *Chem. Phys. Lett.* 358, 459 (2002).
114. R. S. Meltzer, S. P. Feofilov, B. M. Tissue, and H. B. Yuan, *Phys. Rev. B* 60, R14012 (1999).
115. R. S. Meltzer, W. M. Yen, H. Zheng, S. P. Feofilov, M. J. Dejneka, B. M. Tissue, and H. B. Yuan, *J. Lumin.* 94&95, 217 (2001).
116. H.-S. Yang, K. S. Hong, S. P. Feofilov, B. M. Tissue, R. S. Meltzer, and W. M. Dennis, *J. Lumin.* 83&84, 139 (1999).
117. H.-S. Yang, S. P. Feofilov, D. K. Williams, J. C. Milora, B. M. Tissue, R. S. Meltzer, and W. M. Dennis, *Physica B* 263-264, 476 (1999).
118. K. S. Hong, R. S. Meltzer, B. Bihari, D. K. Williams, and B. M. Tissue, *J. Lumin.* 76&77, 234 (1998).
119. K. S. Hong, R. S. Meltzer, S. P. Feofilov, R. I. Zakharchenya, W. Jia, H. Liu, B. Tissue, and H. B. Yuan, *J. Lumin.* 83&84, 393 (1999).
120. R. S. Meltzer, W. M. Yen, H. Zheng, S. P. Feofilov, M. J. Dejneka, B. M. Tissue, and H. B. Yuan, *Phys. Rev. B* 64, 100201/1 (2001).
121. R. S. Meltzer, W. M. Yen, H. Zheng, S. P. Feofilov, M. J. Dejneka, B. M. Tissue, and H. B. Yuan, *J. Lumin.* 94&95, 221 (2001).
122. R. N. Bhargava, V. Chhabra, B. Kulkarni, and J. V. D. Veliadis, *Phys. Status Solidi B* 210, 621 (1998).
123. E. T. Goldburt and R. N. Bhargava, *J. Soc. Inform. Displ.* 4, 365 (1996).
124. R. N. Bhargava, *J. Cryst. Growth* 214/215, 926 (2000).
125. G. Blasse and L. H. Brixner, *Eur. Solid State Inorg. Chem.* 28, 767 (1991).
126. R. Scheeps, *Progr. Quant. Electron.* 20, 271 (1996).
127. J. A. Capobianco, G. Prevost, P. P. Proulx, P. Kabro, and M. Bettinelli, *Opt. Mater.* 6, 175 (1996).

128. S. Taccheo, P. Laporta, S. Longhi, O. Svelto, and C. Svelto, *Appl. Phys. B* 63, 425 (1996).
129. J. S. Chivian, W. E. Case, and D. D. Eden, *Appl. Phys. Lett.* 35, 124 (1979).
130. F. Auzel, *C. R. Acad. Sci. Paris* 262, 1016 (1966).
131. N. Bloembergen, *Phys. Rev. Lett.* 2, 84 (1959).
132. M. F. Joubert, *Opt. Mater.* 11, 181 (1999).
133. L. A. Riseberg and H. W. Moos, *Phys. Rev.* 174, 429 (1968).
134. J. A. Capobianco, J. C. Boyer, F. Vetrone, A. Speghini, and M. Bettinelli, *Chem. Mater.* 14, 2915 (2002).
135. R. P. Leavitt, J. B. Gruber, N. C. Chang, and C. A. Morrison, *J. Chem. Phys.* 76, 4775 (1982).
136. K. Hirao, S. Kishimoto, K. Tanaka, S. Tanabe, and N. Soga, *J. Non-Cryst. Solids* 139, 151 (1992).
137. J. A. Capobianco, F. Vetrone, T. D'Alesio, G. Tessari, A. Speghini, and M. Bettinelli, *Phys. Chem. Chem. Phys.* 2, 3203 (2000).
138. F. Vetrone, J. C. Boyer, J. A. Capobianco, A. Speghini, and M. Bettinelli, *J. Phys. Chem. B* 107, 1107 (2003).
139. K. A. Franz, W. G. Kehr, A. Siggel, and J. Wiczoreck, in "Ullman's Encyclopedia of Industrial Chemistry" (B. Elvers, S. Hawkins, and G. Schulz, Eds.), Vol. A15. VCH, Weinheim, 1985.
140. M. L. Trudeau and J. Y. Ying, *Nanostruct. Mater.* 7, 245 (1996).
141. G. A. M. Hussein and B. C. Gates, *J. Catal.* 176, 395 (1998).
142. M. D. Fokema, J. Audrey, and J. Y. Ying, *NATO Science Ser.* 78 355 (2000).
143. D. B. Bolstad and A. L. Diaz, *J. Chem. Educ.* 79, 1101 (2002).
144. I. R. Martín, C. Goutaudier, S. Guy, Y. Guyot, G. Boulon, M.-T. Cohen-Adad, and M. F. Joubert, *Phys. Rev. B* 60, 7252 (1999).
145. Y. Shen, D. B. Gatch, U. R. Rodríguez Mendoza, G. Cunningham, R. S. Meltzer, W. M. Yen, and K. L. Bray, *Phys. Rev. B* 65, 212103/1 (2002).

Zinc Oxide Nanostructures

Chun-Hua Yan, Jun Zhang, Ling-Dong Sun

Peking University, Beijing, People's Republic of China

CONTENTS

1. Introduction
 2. Fabrication and Morphology of ZnO Nanostructures
 3. Optical Properties of ZnO Nanostructures
 4. Conclusion
- Glossary
References

1. INTRODUCTION

Nanostructured semiconductors, in particular their versatile fabrications and unique chemical or physical properties for potentially technological applications, have been stimulating considerable research interests in the past decade [1]. Tremendous progress has been made to understand the quantum-size behaviors and to investigate the size- and morphology-dependent properties. With this respect, great efforts and contributions from the fruitful groups, such as Yang's [2] and Wang's groups [3] for ZnO nanostructures, have been made persistently to enrich the diversiform morphological world of nanostructures and show their possibilities for versatile utilizations in room temperature laser and other highly technological fields. It is demonstrated so much that the properties of materials on nanoscale, especially those with one dimension less than 10 nm, are virtually dependent on their sizes and morphologies [4]. We therefore reasonably need to summarize the achievements obtained so far in the field of fabrication and morphology control of the most focused nanostructures of ZnO.

ZnO, known as a very important semiconductor with wide bandgap (3.37 eV) and large exciton binding energy of 60 meV [5] at room temperature, has been investigated extensively due to its wide technological applications from catalytic, electrical, optoelectronic, and photochemistry fields [6] to the room temperature blue-ultraviolet (UV) laser region [7]. For instance, ZnO as a gas sensing materials is sensitive to many sorts of gases with satisfactory stability [8], while as a promising material for dye-sensitized solar cells, ZnO demonstrates improved performance [9]. In the form of thin film, ZnO is a potential candidate for flat

display screen usage [10], and a recent report reveals that ZnO would be an alternative to the TiO₂ nanostructured electrode in Grätzel-type photocells [11]. Moreover, ZnO is also regarded as a hopeful material for realizing efficient light-emitting diodes, UV light-emitting diodes [12], and room temperature lasers, which has been demonstrated by several groups [2g, 2h, 13]. In addition, ZnO can be made as transparent and highly conductive, or piezoelectric components as well [14]. Therefore, studies with respect to synthesis and properties of ZnO nanostructures have been presented to meet the demands of potential applications on morphology of materials. So far, synthetic strategies including physical process-related methods such as chemical vapor deposition [15], thermal evaporation [16], vapor deposition [17], thermal decomposition [18], arc plasma [19], sputtering and laser ablation [13a, 20], molecular-beam epitaxy [21], hydrolysis [22], electrochemical deposition [23], and chemical route such as hydrothermal and solvothermal [24], solid state reaction [25], sol-gel [26], precipitation [27], templated-based and solution-based processes (discussed in detail later) have been employed to manufacture ZnO nanostructures. Well-defined nanostructures of ZnO with abundant morphological forms such as nanorods [28], nanobridges and nanonails [29], nanobelts [3b, 3h], hierarchical nanostructures [30], nanocables and nanotubes [3e], nanoneedle [31], and dendritic nanowires [32] have been achieved and other unusual morphological forms controlled as flower-, snowflake-, prism-, and prickly sphere-like shape have been presented as well [33]. The morphogenesis shows the possibility of controlling the morphology of ZnO nanostructures by employing suitable synthetic process.

To give an insight into the capability of controlling the size and morphology of ZnO nanostructures, it is desirable to integrate the knowledge of all aspects of the morphology controlling preparation. We hereby present this chapter and try to highlight fabrication and control strategies of ZnO nanostructures based on our efforts on morphologically controllable synthesis by solution-based routes [33a, 34].

For the purposes of this chapter, the synthetic methods can be tentatively classified into several categories according to a previous publication [3b]: vapor-phase growth including thermal evaporation, chemical vapor-phase deposition, metal-organic chemical vapor-phase deposition, arc-discharge, laser ablation, templated-based, sol-gel, and solution-based growth methods, etc. Among these synthetic

processes, the solution-based approach may be the simplest, without involving high temperature and expensive equipment, but powerful enough to lead to morphology control by adjusting the reaction conditions. This chapter will mainly review recent progress on synthesis and morphology control of ZnO by the solution-based route.

2. FABRICATION AND MORPHOLOGY OF ZnO NANOSTRUCTURES

2.1. Early Synthetic Route

ZnO being a useful semiconductor has been studied for a long time. Long before, attention was mostly paid to the synthesis of ZnO nanocrystallites and nanocrystalline epitaxial films, in which ultraviolet emission at room temperature was observed [2h, 13d, 13g, 13i]. Physical methods such as thermal decomposition, vapor evaporation, pyrolysis, laser ablation, arc plasma, etc. and chemical techniques such as hydro- or solvothermal, microemulsion, precipitation, sol-gel, etc. are popular ways used to achieve high quality ZnO crystals. For example, Meulenkamp et al. [35a] employed sol-gel method via the addition of LiOH into ethanolic solution of zinc acetate to prepare morphological well-defined ZnO nanoparticles. By finely controlling the water content and acetate anions, the nanoparticles size can be well controlled. Later, more combined methods, for instance a hydrothermal coupled with microemulsion method, were developed to prepare nanocrystallites with controllable morphology, which show novel optical and electrical properties attributed to the size reduction and the accordant quantum confinement effects. By high temperature physical methods, nano- or microwiskers are easy to obtain but mainly on the micrometer scale and with a wide size distribution [36]. In contrast, by wet chemical routes, more morphological forms rather than nanoparticles were achieved. However, less effort has been made on morphology controllable synthesis purposefully. Chittofrati et al. [33b] has achieved ZnO whiskers and intertwined morphologies by hydrothermally treating zinc nitrate solution in presence of alkali such as NaOH, KOH, NH_4OH , triethanolamine and ethylenediamine at elevated temperature. Wang et al. [37] fully investigated the growth mechanism of bipyramidal dumbbell-like twinning morphology of ZnO generated by the hydrothermal method, indicating that growth conditions may have crucial effects on final morphologies of ZnO, which preliminarily provides a possibility for morphology control of ZnO. A chemical precipitation method [38] was adopted to produce rodlike and other unusual morphologies of ZnO. Summarily, it is noticeable that early synthetic methods may focus on the preparation of spherical and rodlike related morphology of ZnO, which might be attributed to the inadequate understanding of the diversity of materials morphology and of its importance for finely tuning properties.

2.2. Vapor-Phase Growth

Vapor-phase growth is one kind of approach involving a high temperature process for synthesizing nanomaterials. Several methods can be assigned to this category, such as thermal evaporation [16], chemical vapor deposition [15],

and metal organic chemical vapor deposition [17i]. However, in consideration of morphology control, the innovative vapor deposition process and thermal evaporation method recently developed by Yang et al. and Wang et al. have been proved to be the two most effective approaches so far to obtain uniform ZnO nanostructures. Generally, vapor deposition is carried out by heating the mixture of ZnO and graphite powder to high temperature, normally around 1000 °C under a constant flow of argon, to make ZnO nanowires grow on a Au-coated silicon substrates. This method is employed by Yang et al. to prepare uniform ZnO nanowire arrays via a vapor-liquid-solid growth mechanism, in which the natural laser cavities are formed to give room temperature lasing action. With the catalyst of Au film on substrate, the diameter of ZnO nanowires with growing orientation along the *c*-axis can be controlled as 20–150 nm and length up to 40 μm . This process provides the possibilities to get short-wavelength nanolasers for potential applications in optical computing, information storage, and nanoanalysis [2]. The thermal evaporation process is in principle one technique to make source materials evaporate and then condense to finally obtain the materials on nanoscale. The experiments are conducted with rigid reaction parameters of temperature, pressure, carrier gas, substrate, and evaporation time, etc., whose settings will be ultimately crucial to the morphology and phase structure of as-prepared nanostructures. The process is employed successfully by Wang et al. to manufacture novel one-dimensional nanostructures called nanobelts. The unique geometrical configuration of nanobelts with a rectangle-like cross-section of 30 to 300 nanometers width and 5 to 10 width-to-thickness ratios, and lengths up to several millimeters, may potentially open up new application fields of nanostructures. The achievement of ZnO nanobelts thus further pushes the research developments forward in the synthesis of novel one-dimensional (1D) nanostructured candidates for fully understanding dimensional confinement effects and constructing nanodevices. Up to now, ZnO nanobelts tentatively used as nanocantilever, field-effect transistors have been demonstrated [3].

2.3. Template-Based Methods

Roughly the templates used for synthesis of nanostructures of ZnO can be divided into hard and soft features. Most common hard templates are based on anodic alumina membranes (AAM), which have hexagonally ordered porous structure (channel diameter below 10 to 200 nm, lengths from 1 to over 100 μm , and channel density in the range of 1010–1012 cm^{-2}) [39]. Since the nanochannel of AAM can be adjusted by finely varying preparation parameters and AAM itself possesses good chemical and thermal stabilities, it can be used as an ideal template to deposit desired materials on nanoscale based on the porous shape of AAM. Coupled with other techniques such as electrophoretic deposition [40] and electrochemical deposition [41], this method has been employed widely to build nanowires or nanoarrays. For this approach, the method of source material injection and porous structure of AAM are of vital importance for material size and morphology modulation. Li et al. [41c] reported the successful preparation of ZnO nanowire arrays

embedded in AAM by oxidizing Zn nanowire arrays electrodeposited in an AAM nanochannel. The nanowire arrays possessing polycrystalline feature with diameters from 15 to 90 nm exhibit blue emission. By using an anodic aluminum oxide (AAO) templated method coupled with the sol-gel process, uniform polycrystalline ZnO nanotubules were assembled in the membrane pores of AAO. Soft templates generally refer to those chemically formed structures without rigidity such as mesoporous silica [42], polymeric filter membranes [43], poly(styrene) beads [44], and copolymer [45]. These structures are normally on nanoscale with well-controlled shapes, which can be used as templates to do morphologically controllable synthesis. Zhang et al. have made the attempt to prepare ZnO nanoclusters in the channels of MCM-41 by high temperature calcinations of MCM-41 with zinc cations attachment. Zheng et al. employed an AAO membrane as the template for preparation of an array of zinc oxide (ZnO) and polyaniline coaxial nanowires, which shows enhanced photoluminescence. Neves and co-workers obtained the hollow structure of ZnO by the calcination of hydrozincite coated poly(styrene) beads. All soft templates afford versatile ways for achieving nanostructures with diverse morphologies.

2.4. Solution-Based Approaches

2.4.1. Overview

A solution-based approach has been attractive for many years for the achievement of ZnO nanostructures. In comparison with other methods, this approach possesses the advantages of relatively low cost, mild reaction conditions, inexpensive equipment, and easy control by simply adjusting the chemical process of reactions. Up to now, a solution-based approach might be one of the lowest cost ways but popular and powerful in the synthesis field of nanostructures. Recently much research on the synthesis of ZnO with novel and unusual morphologies via this synthetic method has been demonstrated. Boyle et al. [46] have grown perpendicularly oriented ZnO rods along the *c*-axis on thin ZnO template from aqueous solution of zinc acetate and hexamethylenetetraamine. The ZnO nanorods deposited on substrate exhibit more homogenous and ordered features than the previous reports in which ZnO was obtained by aqueous thermal decomposition of Zn²⁺ amino complex [47]. Vayssieres et al. showed a successful preparation of three-dimensional arrays of highly oriented crystalline ZnO microtubes by employing aqueous solution of Zn²⁺ ions and methenamine as starting materials [48]. Recently, there have been several continual reports [28] on the preparation of nanodots, regular nanorods, and columns of ZnO by solution-based methods with assistance of additives or microemulsions, indicating the versatile utilizations of the solution-based approach for morphology control.

Our preparation is based on the facts that previous reports on preparation of ZnO by a wet chemical route such as hydrothermal, sol-gel, and precipitation processes are mainly dependent on the decomposition of hydroxide or products of hydrolyzed zinc salt in pure water or a simple solvent system, which cannot lead to diversiform morphologies with uniform size distribution. Therefore, we like the

ideas of using a single precursor solution, a one-step process, and a low temperature condition with microemulsion modulation to realize morphology control of nanostructured ZnO. We employ simple Zn²⁺ complexes, Zn(OH)₄²⁻ and Zn(NH₃)₄²⁺, obtained at different pH values of Zn²⁺ in base solution dependent on the fact that Zn²⁺ is liable to form a soluble complex when the base is excessive, as precursors, since previous investigations on nanostructured ZnO formation suggest that Zn(OH)₄²⁻ is proposed to be the growth unit and can be directly incorporated into ZnO crystallites under given conditions [49]. The processes for precursor decomposition into ZnO nanostructures are simple in terms of chemical reaction. However, the advantages of this approach may be seen in several aspects: microemulsions and solvents as a driving force to modulate crystal nucleation and growth process, lower hydrothermal temperature to ensure sufficient crystallinity, and single source precursors to integrate into nanostructures with the desired building method. By adjusting parameters of solvent, precursor, solution basicity, reaction temperature, as well as time, the preparative process becomes controllable to get desired high quality ZnO with controllable morphologies.

In our preparation, Zn(OH)₄²⁻ precursor solution is prepared by mixing 0.5 mol/L ZnAc₂ and 5 mol/L NaOH solutions (volume ratio, v/v = 1:1, pH ≈ 14), while Zn(NH₃)₄²⁺ precursor is achieved by mixing 0.5 mol/L ZnAc₂ and fresh ammonia (pH ≈ 10 or 12). Typically, Zn(OH)₄²⁻ or Zn(NH₃)₄²⁺ precursor solution, surfactant cetyltrimethylammonium bromide (CTAB) (absence in some cases), cosurfactant *n*-hexanol (absence in some cases), and solvent were mixed with various ratio (see Table 1) to form a solution or microemulsion in a vessel under constant stirring. The mixture is then transferred into a 25 mL Teflon-lined autoclave for hydrothermal treatment to a given temperature for a certain time (see Table 1). After the reaction finished, the autoclave containing the samples is cooled to room temperature naturally. The white precipitate deposited on the bottom of the autoclave is collected and washed with absolute ethanol and distilled water several times. Finally, ZnO samples are obtained by centrifugation and dehydration of the precipitate in vacuum at 60–70 °C. All reaction parameters and morphologies are summarized in Table 1.

2.4.2. One-Dimensional Nanostructures

Nanorods By thermally treating Zn(OH)₄²⁻ precursor solution in a CTAB quaternary microemulsion-based system at various reaction conditions, ZnO nanorods with variable diameter and length can be produced [50]. Figure 1 shows a typical transmission electron microscopy (TEM) image of ZnO nanorods obtained by hydrothermally treating a microemulsion system consisting of 1 g CTAB, 1.2 mL Zn(OH)₄²⁻ solution, 5.0 mL *n*-hexanol, and 8.2 mL *n*-heptane at 180 °C for 13 h. From the low magnification TEM image shown in Figure 1a, it can be seen clearly that ZnO nanorods possessing a good crystallinity are formed and most of them are relatively uniform, with an average diameter less than 100 nm and length up to tens of micrometers. The high resolution TEM (HRTEM) shown in Figure 1b proves the wurtzite phased structure of ZnO with a deduced lattice spacing of 2.59 Å corresponding

Table 1. Summarized morphologies and reaction conditions.

Morphology	Reaction media	pH ^a	Temperature (°C)	Time (h)
Rodlike (Fig. 1)	1 g CTAB/1.2 mL Zn(OH) ₄ ²⁻ solution/ 5.0 mL <i>n</i> -hexanol/8.2 mL <i>n</i> -heptane	14	180	13
Rodlike (Fig. 3a)	1 g CTAB/1.2 mL Zn(OH) ₄ ²⁻ solution/ 2.0 mL <i>n</i> -hexanol/11.2 mL <i>n</i> -heptane	14	180	13
Rodlike (Fig. 3b)	1 g CTAB/1.2 mL Zn(OH) ₄ ²⁻ solution/ 2.0 mL <i>n</i> -butanol/11.2 mL <i>n</i> -heptane	14	180	13
Wireslike	1 g CTAB/1.2 mL Zn(OH) ₄ ²⁻ solution/ 3.0 mL <i>n</i> -hexanol/10.2 mL <i>n</i> -heptane	14	140	13
Tubelike	1.2 mL Zn(NH ₃) ₄ ²⁺ solution/ 13.2 mL ethanol	12	180	13
Tubelike	1 g CTAB/1.2 mL Zn(NH ₃) ₄ ²⁺ solution/ 3.0 mL <i>n</i> -hexanol/10.2 mL <i>n</i> -heptane	10	100	13
Flowerlike	1.2 mL Zn(OH) ₄ ²⁻ solution/ 13.2 mL H ₂ O	14	180	13
Snowflakelike	1.2 mL Zn(OH) ₄ ²⁻ solution/ 13.2 mL <i>n</i> -heptane	14	180	13
Prismlike	1.2 mL Zn(NH ₃) ₄ ²⁺ solution/ 13.2 mL ethanol	10	100	13
Prickly sphere-like	1.2 mL Zn(OH) ₄ ²⁻ solution/ 13.2 mL ethanol	14	100	13
Regular rodlike	1.2 mL Zn(OH) ₄ ²⁻ solution/ 13.2 mL ethanol	14	180	13
Columnlike	1.2 mL Zn(OH) ₄ ²⁻ solution/ 13.2 mL H ₂ O	14	180	10 min
Multiarm architecture	1.2 mL Zn(OH) ₄ ²⁻ solution/ 13.2 mL H ₂ O	14	180	2

^a The pH of Zn(OH)₄²⁻ or Zn(NH₃)₄²⁺ precursor solutions.

to the (002) plane, implying the preferred growth orientation of ZnO nanorods along the (002) plane. The electron diffraction (ED) pattern in the inset of Figure 1b indicates the single crystalline nature of ZnO nanorods. The X-ray diffraction (XRD) pattern in Figure 2a also reveals the wurtzite structure of ZnO (hexagonal phase, space group *P63mc*), which is consistent with the ED characterization shown in the inset of Figure 1b. All diffraction peaks can be well assigned to hexagonal-phase ZnO (JCPDS card, No. 36-1451). Compared with the standard diffraction pattern, as shown in Figure 2 (the bottom), the diffraction intensity differences along [101] and [002] directions may imply the preferred growth orientation of ZnO. By increasing the

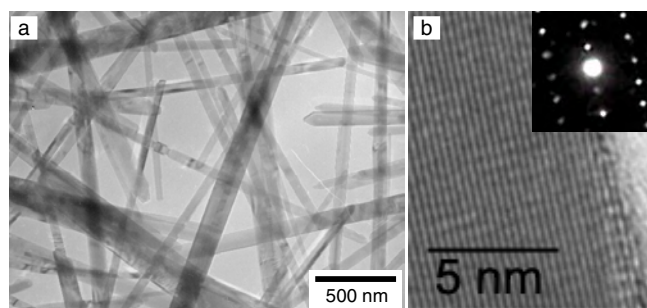


Figure 1. TEM (a) and HRTEM (b) images (the inset is ED pattern) of ZnO nanorods fabricated via a solution-based route (for detailed preparative information, see Table 1). The lattice spacing of 2.59 Å corresponds to (002) plane, implying the preferred growth orientation of ZnO nanorods along (002) plane.

ratio of *n*-heptane and hexanol from 8.2/5.0 to 11.2/2.0, but maintaining other compositions of microemulsion and reaction conditions, the diameters of ZnO nanorods achieved are gradually increased. Figure 3a shows the ZnO structures obtained at the ratio of 11.2/2.0, which exhibits rodlike morphology as well, but more uniform and with an average diameter (around 350 nm) larger than that of the

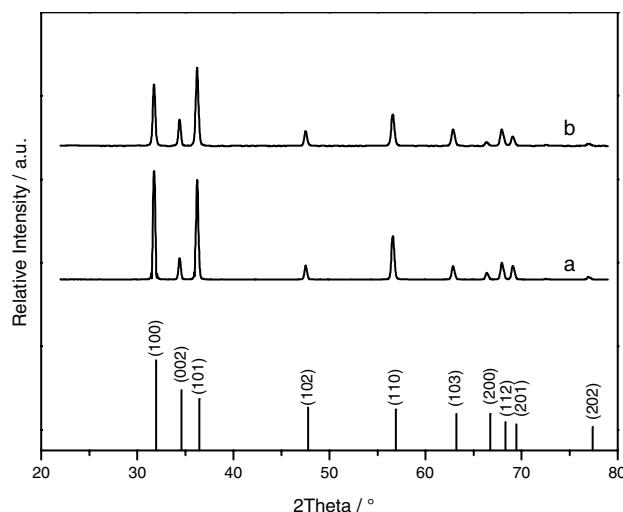


Figure 2. XRD patterns of ZnO nanorods fabricated via a solution-based route. (a) Sample shown in Figure 1 and (b) sample shown in Figure 3. The bottom is a standard XRD pattern of ZnO (JCPDS No.36-1451).

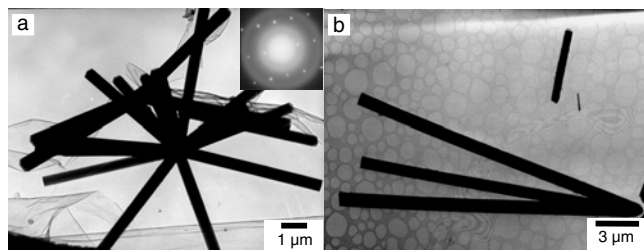


Figure 3. TEM images of ZnO nanorods fabricated via a solution-based route in different microemulsion systems of (a) 1 g CTAB, 1.2 mL $\text{Zn}(\text{OH})_4^{2-}$ solution, 2.0 mL *n*-hexanol, and 11.2 mL *n*-heptane, and (b) the same microemulsion compositions as (a) except replacing *n*-hexanol by *n*-butanol.

previous sample shown in Figure 1, indicating microemulsion compositions are of significant importance in modulating the morphology during the formation process of ZnO nanostructures. The ED pattern in the inset of Figure 3a displays the single crystalline nature of ZnO with the wurtzite phased structure consistent with the XRD result shown in Figure 2b. When replacing *n*-hexanol by butanol and maintaining other reaction conditions, the diameters of obtained ZnO nanorods (1 μm) become much larger than that of comparative samples, as shown in Figure 3b, confirming the modulation function of microemulsion compositions on ZnO morphology formation.

To fully understand the formation process of ZnO nanorods, the time-dependent experiments are carried out to monitor the evolving process by recording the shapes of the sample achieved at stepwise increased heating time from 10 min to 8 h. The series scanning electron microscopy (SEM) images in Figure 4 show the morphology evolution with prolonged reaction time. Figure 4a shows that when operating the reaction for 10 min, the aggregates of spherical morphology ZnO with an average diameter as smaller as 30 nm, other than nanorods, are observed. This implies that at this stage nanostructured ZnO forms in a fashion of spherical shape in microemulsion droplets and the interactions such as collision, conglutination, and amalgamation among the microemulsion droplets would lead to the aggregates of nanoparticles. Figure 4b indicates the morphology exhibition of ZnO obtained after 30 min heating treatment. At this stage, besides the aggregated nanoparticles, ZnO nanorods are observed, which indicates that parts of nanoparticles observed in Figure 4a have evolved into nanorods. Although the length and diameter of the nanorods are not uniform, it can be deduced from the image that the diameters of most nanorods do not exceed 100 nm. The reason for this observation is that with the extension of heating time, the nucleation of ZnO may gradually be completed and the directed aggregation growth mediated by microemulsion droplets might occur. By aggregation, the microemulsion droplets might connect into a linearlike shape, and then by experiencing an Ostwald ripen process, the linearlike aggregates recrystallize into perfect single-crystalline 1D structure along the preferred orientation.

For a synthetic strategy by employing microemulsion as reaction media, it is proved that the shape of a microemulsion droplet has important effects on morphology formation of nanostructures [51]. With the microemulsion composition

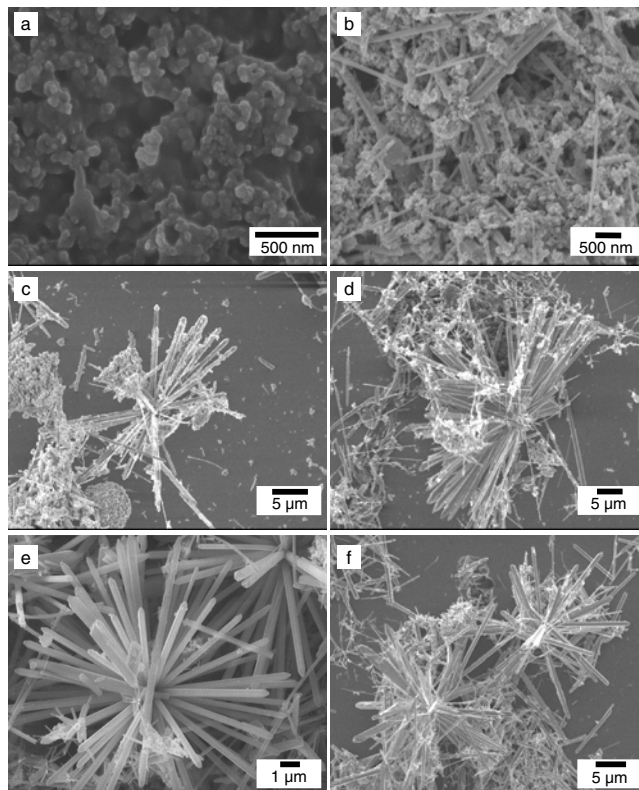


Figure 4. Series of SEM images of shape evolution of ZnO nanorods shown in Figure 3a with stepwise prolonged reaction time (a) 10 min, (b) 30 min, (c) 1 h, (d) 2 h, (e) 4 h, and (f) 8 h, exhibiting the evolution of ZnO nanoparticles to nanorods.

used in our preparation, the microemulsion droplets are liable to form spherical shape at room temperature and their sizes can be adjusted by changing the ratio of solvent to cosurfactant (*n*-hexanol to *n*-heptane in present case) or altering cosurfactant species [51]. With this regard, the diameter of ZnO nanorods can be adjusted by changing the size of microemulsion droplet. The proposed formation process is further proved by the morphological changes during continually extending reaction time to 1, 2, 4, and 8 h. The representative SEM images corresponding to each stage are shown in Figure 4c–f. Figure 4c shows uniform rod shape with an average diameter of about 200 nm after driving the reaction for 1 h. Figure 4d–f displays the Ostwald ripen processes of rodlike ZnO, which gradually makes the crystallinity improved and the diameter grow. With the Ostwald ripening, the ends of nanorods show the evolved tendency from pyramid- to prismlike shapes, which can be seen clearly from the comparison of images shown in Figures 4e and 3a. This accords with the crystal growth habit of ZnO with different growth velocities along different crystal planes [49, 52]. In addition, from images shown in Figure 4b–f, it can be seen that some nanorods are liable to form a homocentric bundle, which is more evident in Figure 4e. This phenomenon has also been observed in other shapes of ZnO, implying the detailed growth fashion [33a].

Nanowires In consideration of the strategies we used to adjust the diameters of nanorods, it is reasonably believed that by varying the reaction conditions, the nanowires can

be achieved. Based on the nanorod morphology, to get the nanowires, the Ostwald ripening process should be slowed down by decreasing the reaction temperature and the nuclei should be smaller as well. Then by aggregating smaller nanoparticles into 1D nanostructures, the nanowires would possibly be achieved. The nanowire preparation is carried out by thermally treating a microemulsion consisting of 1 g CTAB, 1.2 mL $\text{Zn}(\text{OH})_4^{2-}$ solution, 3 mL *n*-hexanol, and 10.2 mL *n*-heptane at 180 °C for 13 h [34b]. The representative image shown in Figure 5a reveals that the obtained sample exhibits nanowire structure with a diameter ranging from 30 to 150 nm. The aspect ratio of nanowires is estimated to be larger than 50, as a typical image in Figure 5c shows a single nanowire with aspect ratio more than 200 (diameter of 50 and length up to approximately 14 μm). The TEM image (Fig. 5b) shows another shorter single ZnO nanowire with a diameter of ~ 30 nm and a length up to 3 μm . The ED pattern (inset of Fig. 5b) indicates that the ZnO nanowires have a single crystal nature with preferred growth orientation along the (110) crystal plane based on the calculation of the diffraction dots. The blurry diffraction dots in the inset image might hint at the existence of branch crystallites around the nanowires. The XRD pattern of ZnO nanowires (Fig. 6) shows the same fashion as that of ZnO nanorods (Fig. 2). However, the obtained result of ZnO nanowire growth along (110) crystal plane deduced from the diffraction calculation is different from that of nanorods achieved from HRTEM before, which adopts oriented growth along (002) crystal plane, indicating the possibility to obtain 1D ZnO nanostructures with different orientated growth direction by the same approach. The same results of SnO_2 nanorods achieved via a solution-based route may be another good example to prove this [53]. It is believed that the nanowire formation mechanism is analogous to that of ZnO nanorods.

Nanotubes Apart from our works [34a], recently there have been several other reports concerning tubular ZnO nanostructures [16f, 22d, 39d, 43, 54]. The methods for preparing tubular ZnO are mostly based on the processes of pyrolysis, thermal reduction routes, or AAO based template methods. A low cost, solution-based approach for growing tubular ZnO still remains a big challenge. Our preparation is conducted with the mixture of $\text{Zn}(\text{NH}_3)_4^{2+}$ aqueous solution

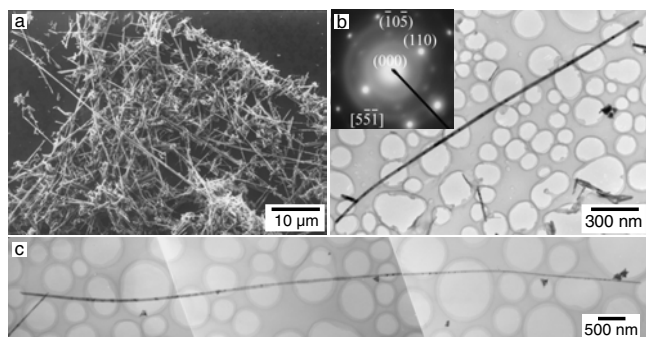


Figure 5. SEM (a) and TEM (b and c) images of ZnO nanowires synthesized via a solution-based route. The inset in (b) is an ED pattern of a single nanowire.

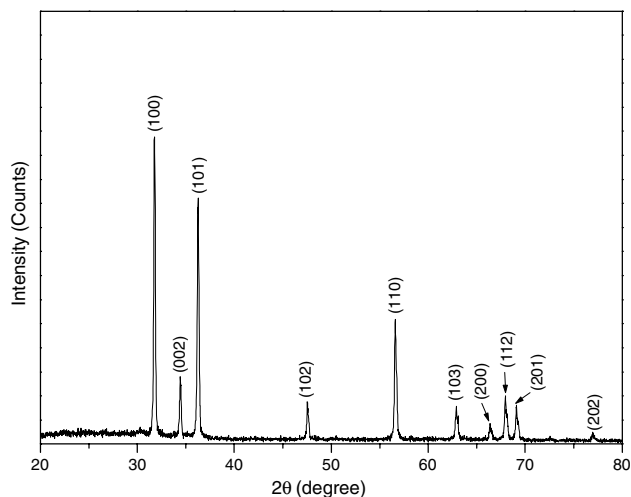


Figure 6. X-ray diffraction pattern of ZnO nanowires shown in Figure 5.

(pH ~ 12) and ethanol (v/v = 1/11) at 180 °C for 13 h. Following the typical preparation procedures, the tubular ZnO is obtained.

XRD structural characterization (Fig. 7) indicates the wurtzite phase (hexagonal, space group $P63mc$) with good crystallinity. Figure 8 displays the SEM and TEM images showing different aspects of the tubular structure of ZnO. The image in Figure 8a shows a few tubular ZnO coexisted with some small nanoparticles, while Figure 8b shows the magnified hollow structure of the individual tube marked by the arrow. From these two images it can be deduced that the outer and inner diameters of the hollow tube are about ~ 450 and ~ 250 nm, respectively. The average length of the tube is about ~ 4 μm . And the tube wall with thickness of ~ 100 nm is not smooth as it is built up by small polycrystalline nanoparticles. Figure 8c gives the TEM image of an individual tube with the destroyed ends, showing clearly the

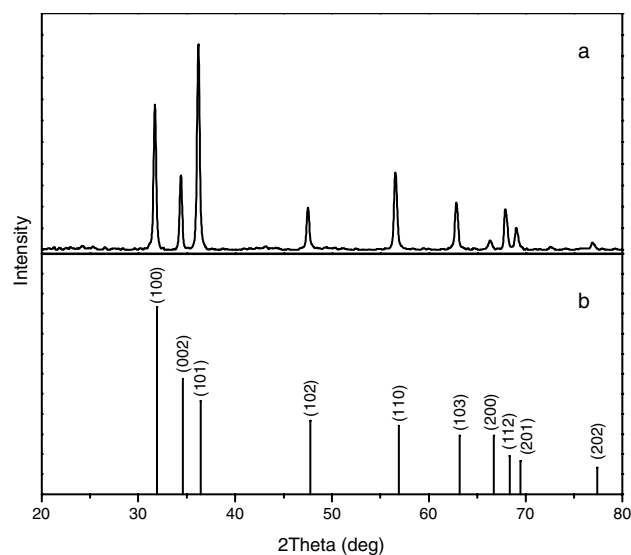


Figure 7. X-ray diffraction pattern of polycrystalline tubular ZnO fabricated via a solution-based route.

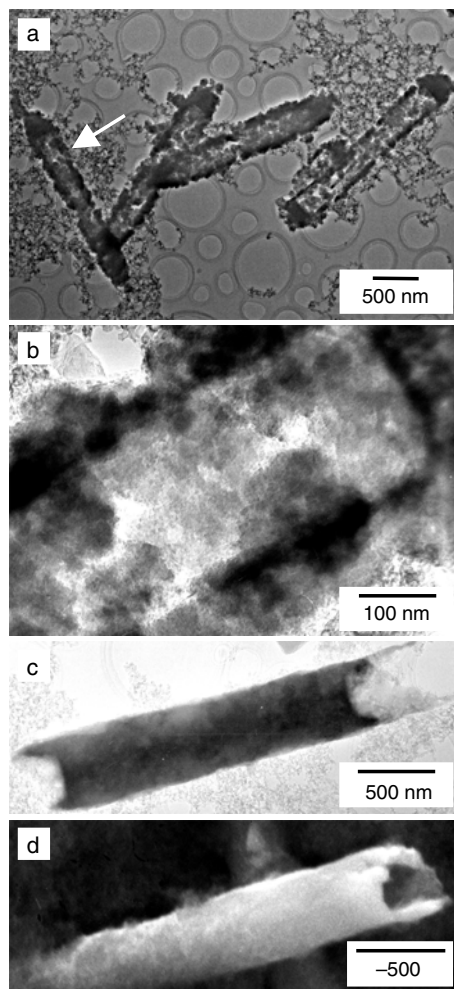


Figure 8. TEM (a, b and c) and SEM (d) images of polycrystalline tubular ZnO fabricated via a solution-based route.

hollow structure, and the SEM image in Figure 8d further affords a spatial view of the destroyed end of the tube.

The tubular sample is obtained by hydrothermal treatment of $\text{Zn}(\text{NH}_3)_4^{2+}$ precursor solution in ethanol to lead to the polycrystalline tubular ZnO. Interestingly, when changing the reaction media into microemulsion with compositions of 1 g CTAB, 1.2 mL $\text{Zn}(\text{NH}_3)_4^{2+}$ solution, 3.0 mL *n*-hexanol, and 10.2 mL *n*-heptane, and lowering the pH value of the precursor solution to around 10 and temperature to 100 °C, hexagonal structure ZnO microtubes with single crystalline nature are obtained. The SEM image in Figure 9a shows finely crystallized hexagonal structures, and some of them grow separately and others have the growing feature of embedded into each other. From the destroyed parts of the hexagonal structures, the hollow structure can be seen clearly. The embedded feature of hollow structures may be attributed to the homocentrically growing tendency of ZnO crystals under our reaction conditions, which is observed for the homocentrically growing branch of nanorods. Figure 9b shows the magnified image of hollow structures of one destroyed end of a ZnO microtube marked by a white pane in Figure 9a, displaying the evident hollow structure of ZnO single crystal microtubes. From

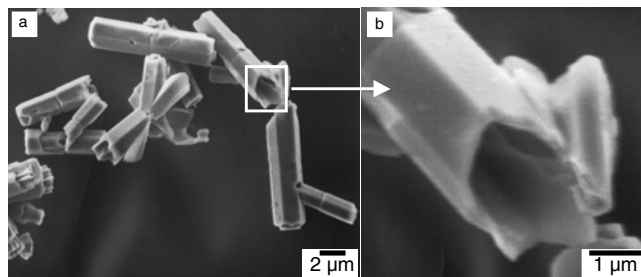


Figure 9. SEM images (a and b) of monocrystalline tubular ZnO fabricated via a solution-based route (for detailed preparative information, see Table 1). (b) The magnified image of the white pane part in (a), showing the hollow structure.

Figure 9, it can be deduced that the individual microtube of ZnO with a wall thickness of ~ 200 nm may be approximately 1–2 μm wide and 8–10 μm long. It is proposed that during the formation process, the decomposition of $\text{Zn}(\text{NH}_3)_4^{2+}$ precursor may result in the generation of NH_3 which may be responsible for the formation of hollow structures.

2.4.3. Other Unusual Morphologies

Flower- and Snowflake-Like Nanostructures Based on the successful preparation of 1D ZnO nanostructures via a solution-based route with the assistance of microemulsion modulation, it is reasonably believed that reaction media play an important role in modulating the morphology during the reaction process. Therefore, some pure solvents other than microemulsion were also employed to comparatively investigate the possibilities of morphologically controllable synthesis by varying reaction media. By employing the mixture of $\text{Zn}(\text{OH})_4^{2-}$ or $\text{Zn}(\text{NH}_3)_4^{2+}$ precursor solution and solvent according to the volume ratio of 1:11, some unusual nano- or microstructures are achieved by following the same reaction procedures. The summarized morphologies and reaction conditions are listed in Table 1.

By decomposing $\text{Zn}(\text{OH})_4^{2-}$ precursor in H_2O solvent at 180 °C for 13 h, flowerlike morphology of ZnO is achieved, as the representative SEM image shows in Figure 10a. The flowerlike ZnO with average size about ~ 1.5 μm displays a feature of homocentric growth due to multiple nuclei twinning at the onset of growth, which finally becomes an individual crystalline nucleus to make all branch growth at different directions. The flowerlike structure of ZnO is further confirmed by the TEM image shown in Figure 10b. The ED pattern inset in Figure 10b indicates the single crystalline nature and wurtzite structure of ZnO, which is consistent with the results of XRD characterization shown in Figure 11b. From the ED pattern, it is also deduced that the flowerlike shape of ZnO is not the simple aggregation of small crystallites but is formed by monocrystallines of nanorods growing homocentrically. The similar morphology of ZnO has been previously observed by Chittofrati et al. [33b] and appeared in a very recent publication [55]. Figure 10c and d gives the magnified SEM images of two individual flowerlike ones marked by a white pane in Figure 10a, showing the detailed features of two different growing patterns of ZnO flowers. When changing the polar solvent of H_2O by nonpolar solvent of *n*-heptane, snowflake-like structures of ZnO are observed, as

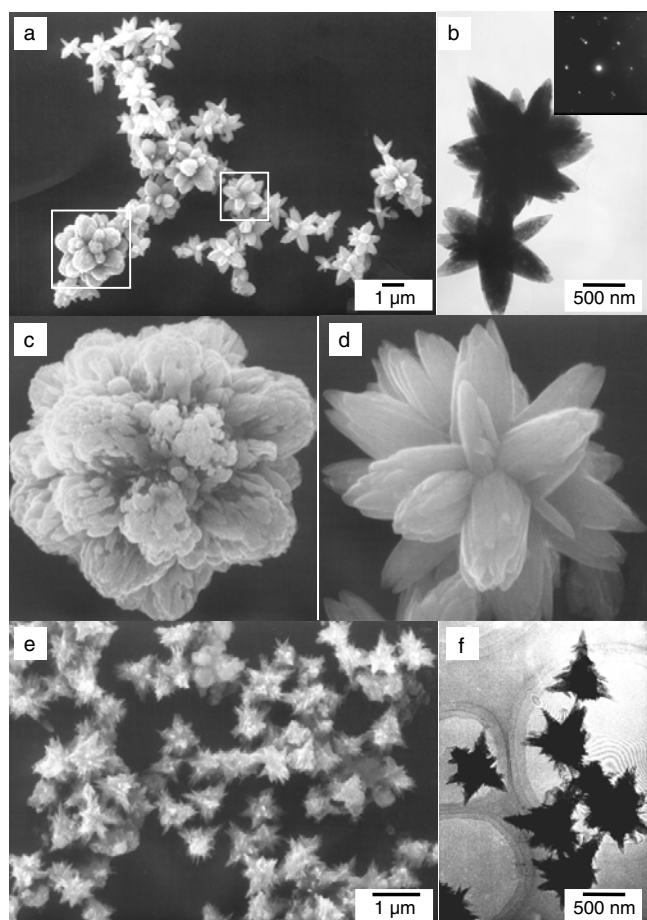


Figure 10. SEM (a, c, d, and e) and TEM (b and f) images of ZnO fabricated via a solution-based route. (a) and (b) General morphology of flowerlike ZnO. The inset of (b) is the ED pattern. (c) and (d) Magnified images of two individual ZnO flowers marked with the white pane in (a). (e) and (f) Snowflakelike ZnO (for detailed preparative information, see Table 1).

shown in Figure 10e and f. The size of snowflakelike morphology is in the range of 0.5–1.0 mm, having the same growth fashion but composed of needle ZnO nanocrystals. XRD in Figure 11c shows the wurtzite phase structure of ZnO.

Prism-, Prickly Sphere-, and Regular Rodlike Nanostructures When thermally treating the reaction media containing $\text{Zn}(\text{NH}_3)_4^{2+}$ precursor at 100 °C for 13 h, prismlike morphology of ZnO is obtained, with average diameter ~ 500 nm and length ~ 1 μm , as can be seen clearly from the SEM image in Figure 12a for the aspect ratio, and the TEM image in Figure 12b for the top view of the regular hexagonal shape of the prism. When operating the reaction at 100 °C for 13 h by decomposing $\text{Zn}(\text{OH})_4^{2-}$ in ethanol, prickly sphere-like instead of prismlike structures of ZnO are achieved. From the SEM image of Figure 12c, it can be deduced that the average diameter of prickly sphere-like ZnO is approximately 1.5 μm , while from the TEM image in Figure 12d, it is concluded that the surface of the prickly sphere-like ZnO is built up by needlelike rods several tens of nanometers in width. With identical reaction conditions

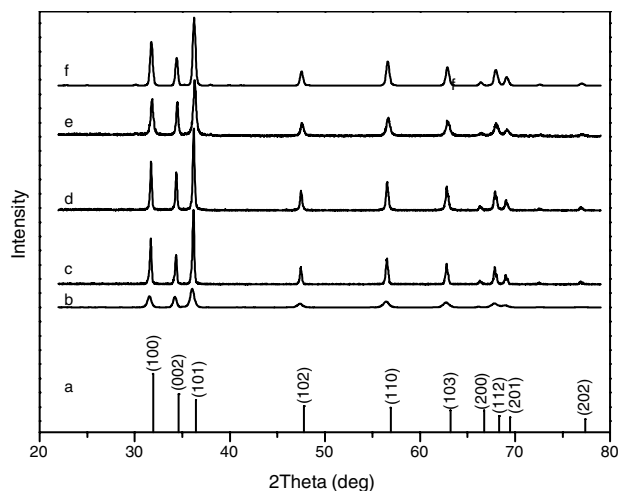


Figure 11. X-ray diffraction pattern of ZnO nanostructures with various morphologies. (a) Standard ZnO (JCPDS #36-1451), (b) flower-, (c) snowflake-, (d) prism-, (e) prickly sphere-, and (f) regular rodlike ZnO.

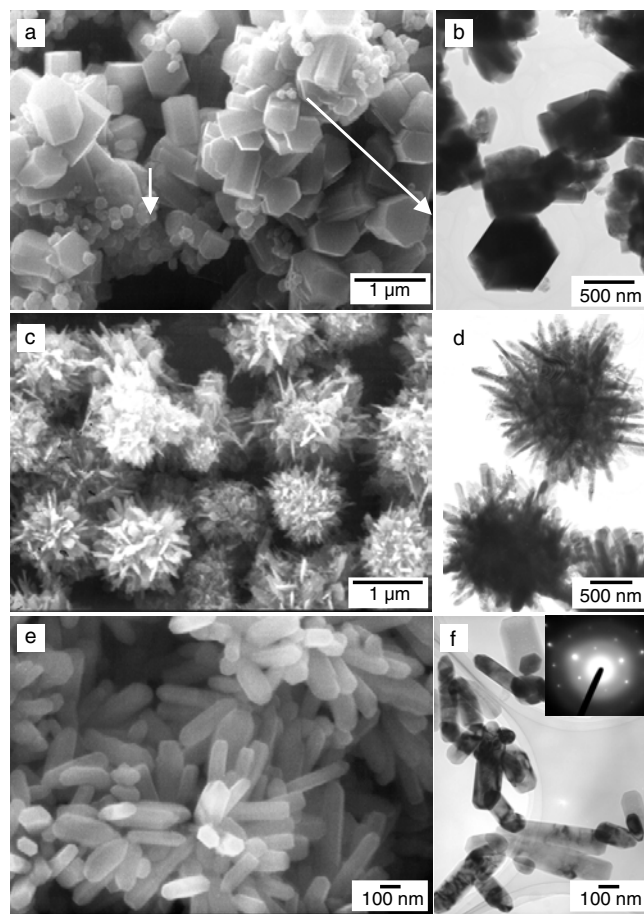


Figure 12. SEM (a, c and e) and TEM (b, d and f) images of ZnO fabricated via a solution-based route. (a) and (b) Prismlike morphology. (c) and (d) Prickly sphere-like morphology. (e) and (f) Regular rodlike morphology of ZnO (for detailed preparative information, see Table 1). The inset in (f) is an ED image.

for preparing a prickly sphere-like ZnO sample but increasing temperature to 180 °C, regular rodlike nanostructures of ZnO are formed, as SEM and TEM images show in Figure 12e and f. The regular nanorods of ZnO have unique aspect ratio near 5, with an average diameter of 100 nm and length of 500 nm. The ED pattern (the inset of Fig. 11f) shows the orientated growth of ZnO nanorods along the *c*-axis of hexagonal phase structured ZnO. XRD patterns in Figure 11d, e, and f show the wurtzite phase structures of prism-, prickly sphere-, and regular rodlike ZnO.

Columnlike Morphology and Multiarmed Architectures

While keeping all the preparative conditions for synthesizing flowerlike structures of ZnO, we conduct the experiments for 10 min at a higher basicity by adding one time more volume of NaOH solutions (5 M) to ZnAc₂ solution when preparing Zn(OH)₄²⁻ precursor solution. ZnO obtained at this condition exhibits the aggregated column feature composed of flakelike branches. The size of the column is up to several micrometers, as the SEM image shows in Figure 13a. When prolonging the reaction to 2 h at the same conditions, the columnlike ZnO totally evolves into uniform multiarmed architectures formed by branch rods sharing one growth center. The uniform ZnO multiarmed architecture seems to be formed by nanorods growing homocentrically, which is similar to the formation of flowerlike structure of ZnO (Fig. 10a), but the diameter of the rod (~300 nm) deduced from the SEM image in Figure 13b is smaller and

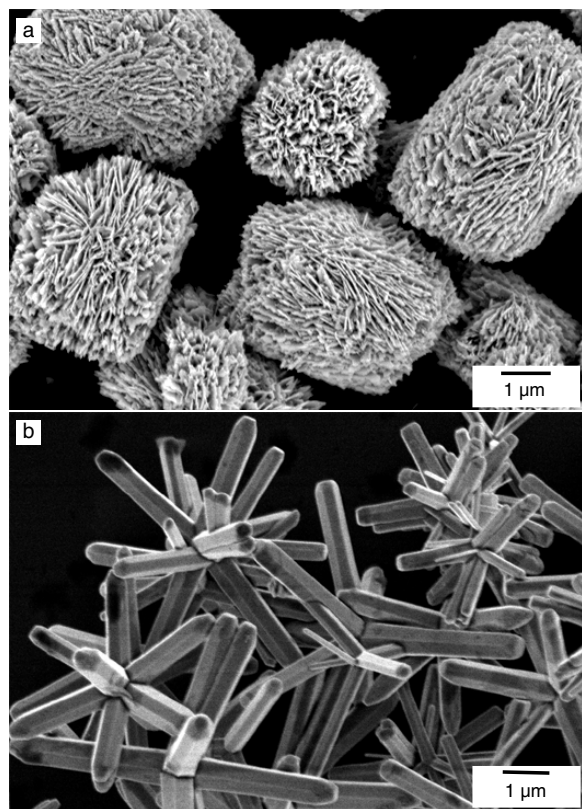


Figure 13. SEM images of (a) columnlike morphology and (b) multiarmed architecture of ZnO.

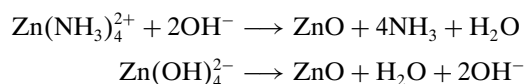
the aspect ratio is bigger. It is believed that the growth process of the multiarmed architecture is analogous to that of flowerlike shape but having a different crystal growth rate along a certain crystal face due to the effects of various solution basicities on crystal growth habit.

2.4.4. Formation Mechanism

In fact, for the solution-based route employed in our preparations, it can be expediently classified into two types of microemulsion- and solvent-based ways in terms of the reaction media in order to present the formation mechanism. To understand the formation mechanism of 1D nanostructures of ZnO achieved in microemulsion systems, the roles of microemulsion should be taken into consideration. In principle, the crystallization of ZnO shows a tendency toward 1D nanostructures under hydrothermal conditions [56], but without the assistance of additives. Most times irregular ellipsoidal shapes resulted and no regular nanorods can be obtained. To avoid these disadvantages, we employ the reaction media of microemulsions in consideration of modulating crystal formation. It is proposed that the formation of homogeneous ZnO nanorods and nanowires might be induced and achieved via a directed aggregation growth process mediated by the microemulsion droplets, as suggested in previous works [57]. Following this mechanism, the microemulsion may function both on the nucleation and growth stages of the formation of 1D ZnO nanostructures. On the nucleation stage, on the one hand, microemulsion droplets can act as microreactors and play a role in controlling nucleation rate and nuclei size, which would eventually affect the final morphologies of the samples. On the other hand, the characteristic kinetics processes of collision, conglutination, and amalgamation among microemulsion droplets may, as a result, result in the linear aggregations of ZnO nanoparticles. While in the growth stage, the linear aggregations will grow into the well-crystallized 1D nanostructures by experiencing a recrystallization of the Oswald ripen process confined by microemulsion droplets. Therefore, changing the microemulsion compositions to make droplet smaller, which means the nuclei would be smaller as well, may induce nanowires rather than nanorods. The formation mechanism for 1D nanostructures along the preferred growth orientation is analogous to another investigation [58] on the transformation process of nanodots to nanorods by experiencing an “oriented attachment” mechanism, but with a confinement of microemulsion droplets. Besides, it is also suggested that surfactant CTAB is beneficial to the transport and orderly stacking of the crystal growth units [16k].

The growth processes of ZnO samples under solvothermal reaction conditions are described as follows. At the initial heating stage, the temperature is comparatively low, and many individual nuclei are formed in the reaction media. During this stage, the formed nuclei are individually dispersed in the reaction media. Within the ramping range of the temperature until the solvent is boiling, the individual nuclei gradually grow and begin to amalgamate in an airtight autoclave. Since the boiled solvent exhibits the droplet-like dispersion in the autoclave under gas–liquid equilibrium, there are many nuclei in one droplet. Thus, all nuclei in one droplet have the tendency to amalgamate into a big

one. As the amalgamation of the nuclei occurred, the crystal growth also took place on various crystal faces with different growth rates. As a result, the dendrite of ZnO grew into rod-like form from one big center nucleus by the amalgamation of a large amount of nuclei in one droplet. Therefore, the morphological features of ZnO samples are liable to be dendriticlike, such as flowers, snow flakes, and prickly spheres. Of course, due to influences of variation of the precursors, solvents, and reaction condition, the growth habit of ZnO changes accordingly, which causes the variation of final morphologies of ZnO. The influences of solvents, precursors, reaction time, and temperature as well as basicity may have influence on the ZnO morphologies as discussed in detail in our previous publication [33a]. For the solvent, it is found that the polarity and saturated vapor pressure of solvents may affect the resulting morphology by adjusting the homogenization of the reactants in reaction medium, the amount of individual nucleus formation, the amalgamation, and the direction preference of growing nucleus. For the precursors, we employ two kinds of single source precursor of $\text{Zn}(\text{OH})_4^{2-}$ and $\text{Zn}(\text{NH}_3)_4^{2+}$ solutions. The precursors may follow different reaction equations to form ZnO nanostructures shown as follows:



The first reaction may produce a by-product of NH_3 , which may play a role in preventing the amalgamation of nucleus in the supersaturated solvents during reaction process. Therefore, it is easy to lead to dispersed morphology of prismatic or hollow tubular structures by using $\text{Zn}(\text{NH}_3)_4^{2+}$ as precursors. Time and temperature are the key factors responsible for morphology evolutions. Series images in Figure 14 record the process of morphology evolution of flowerlike ZnO from the morphology of sheetlike branch aggregates at 10 min (Fig. 14a), to rodlike branch aggregates at 2 and 4 h (Fig. 14b, c), and finally to a well-developed flowerlike shape (Fig. 14d) [33a]. For other morphologies of ZnO, it has the same evolution feature under solvothermal conditions. Figure 15a–d shows the initial shape of snowflake-, prickly sphere-, rod-, and prismatic ZnO, respectively, indicating the discrepancies of initial and final morphologies due to the crystal growth habits under different reaction conditions.

3. OPTICAL PROPERTIES OF ZnO NANOSTRUCTURES

As it is mentioned that ZnO is a wide bandgap semiconductor with a large exciton binding energy at room temperature, so it is a suitable candidate in forms of disordered particle, thin film, and nanowire arrays for the realization of ultraviolet lasing action. However, the photoluminescence of ZnO in the visible region of green instead of desired emission at UV range is often observed due to the high density of crystal defects, which may quench effective exciton emission by irradiative transition and cause a deep-level or trap-state emission [13i]. This deficiency hinders the progress of the applications of ZnO in optoelectronic and lasing devices. In this regard, the development of suitable

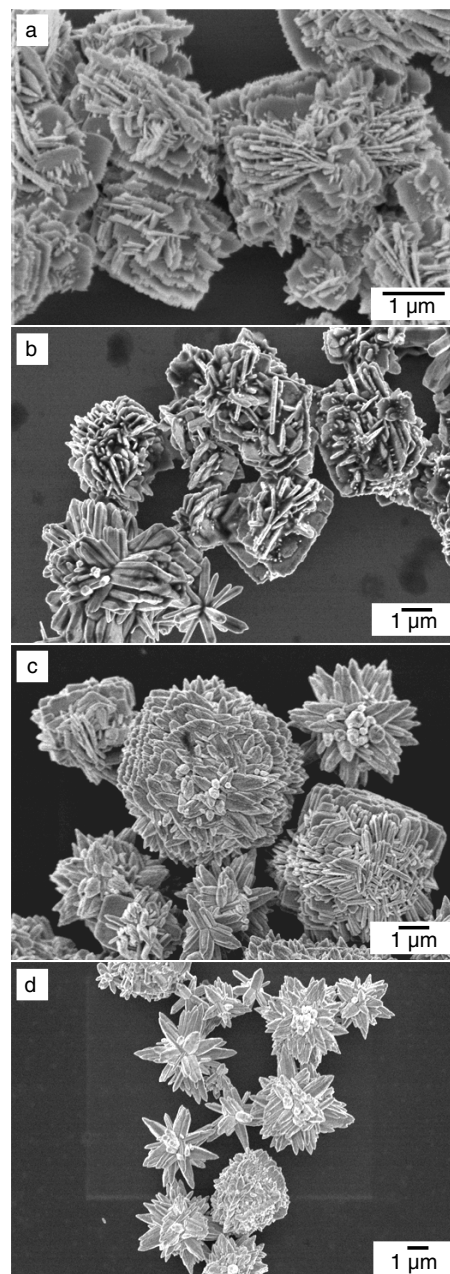


Figure 14. Series SEM images of morphology evolution of flowerlike ZnO with the stepwise prolonged reaction time (a) 10 min, (b) 2 h, (c) 4 h, and (d) 8 h.

synthetic approaches toward high quality ZnO is the basis of realizing UV emission and lasing. Our morphologically controllable synthesis may afford a possible way to solve this problem. The room temperature photoluminescence spectra of nanostructured ZnO with various morphologies are measured by using a Jobin Yvon–Labram spectrometer with a He–Cd laser focused to ca. 1 μm as the excitation source ($\lambda_{\text{ex}} = 325 \text{ nm}$).

The photoluminescence of ZnO nanowires shown in Figure 16 exhibits a strong UV emission at 385 nm arising from the recombination of excitonic center of the nanowires [2i], and a green emission at 485 nm attributed to

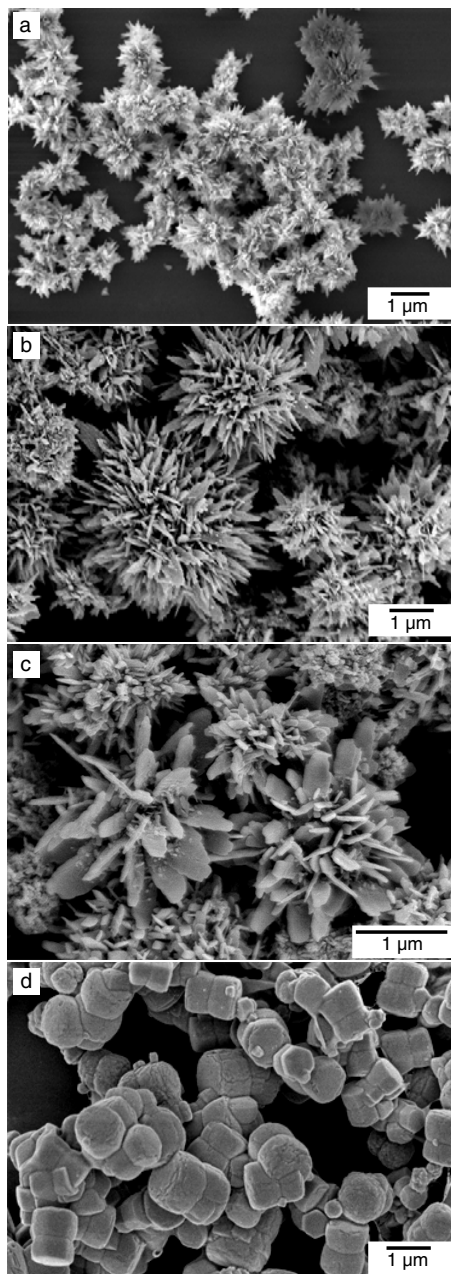


Figure 15. SEM images of morphology exhibitions of (a) snowflake-, (b) prickly sphere-, (c) regular rod-, and (d) prismatic ZnO when driving reaction for 10 min.

the radiative recombination of a photogenerated hole with an electron occupying the oxygen vacancy [59]. While the photoluminescence of polycrystalline tubular ZnO shown in Figure 17 displays a strong UV emission at 385 nm and no defect emission at the visible region is observed. The discrepancies of photoluminescence between 1D structure of ZnO nanowires and tubes may be ascribed to the crystal quality in association with size and morphology, since the tubular ZnO is built up by sufficiently crystallized nanoparticles, which may have less possibility to generate singly ionized oxygen vacancy to lead to green emission [2d]. The photoluminescence of other unusual morphologies is comparatively given in Figure 18. The photoluminescence has

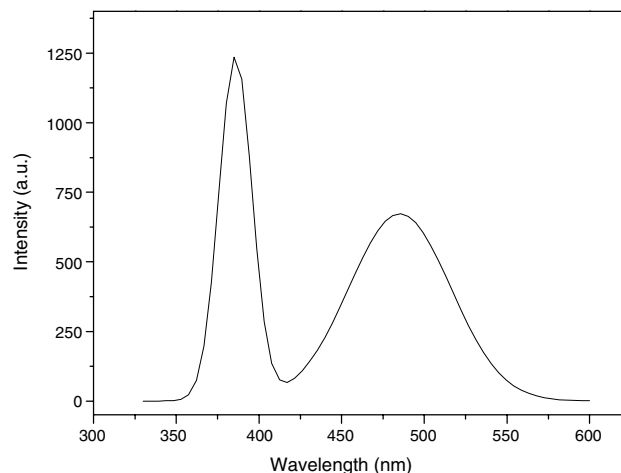


Figure 16. Room temperature photoluminescence of ZnO nanowires.

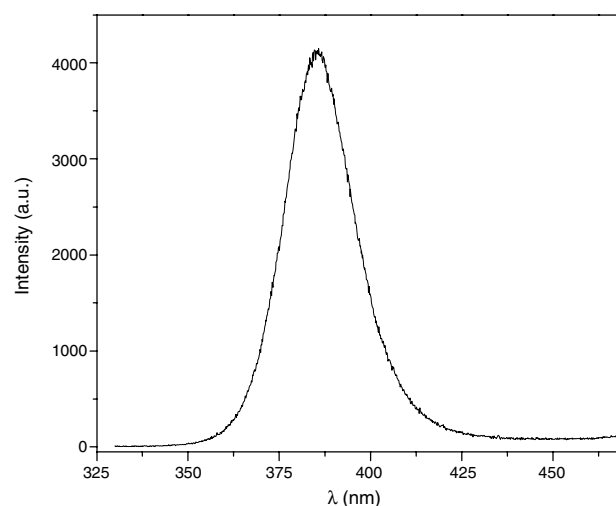


Figure 17. Room temperature photoluminescence of polycrystalline tubular ZnO.

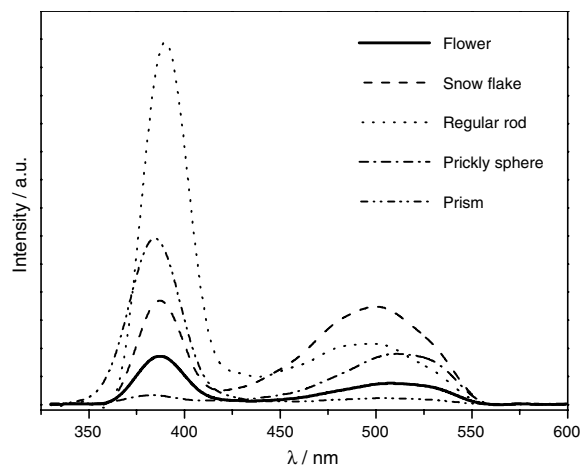


Figure 18. Room temperature photoluminescence of ZnO with unusual morphologies.

different features in UV and green emissions. The prism-like ZnO shows a strong UV emission at ca. 385 nm, due to its prismatic morphology with sufficient crystallization, which only results in the recombination of exciton. The regular rodlike ZnO exhibits a strong UV emission with a very weak green emission (ca. 510 nm) due to the recombination of electrons in singly occupied oxygen vacancies with photoexcited holes, as observed in ZnO nanowires. The relative density of oxygen vacancies can be estimated by comparing the green emission intensity. ZnO samples with three other kinds of morphologies (i.e., flower-, snowflake-, and prickly sphere-like) show both the UV and green emissions, but the relative intensity of UV emission gradually decreased with the morphology changing from flower-, snowflake-, to prickly sphere-like, which is a strong evidence indicating the increase of oxygen vacancies.

4. CONCLUSION

This chapter reviews the solution-based route by making use of the advantages of microemulsion and hydrothermal preparative techniques to reach the morphology control aim of ZnO micro- and nanostructures in our laboratory. The novel structures of ZnO including nanorods, nanowires, microtubes, and other unusual morphologies such as dendritic flower- and snowflake-, prickly sphere-, prism-, columnlike shape and multiarm architecture are successfully realized by adjusting the parameters of microemulsion compositions, solvent species, precursors, and other conditions such as time and temperature of solution synthesis. The growth mechanism for each kind of morphology formation under microemulsion-based conditions is basically understood by a microemulsion droplet mediated aggregation process and other morphology achieved in pure solvent can be considered as results in terms of competition of nuclei diffusion and aggregation process. The optical properties of various typical morphologies show a morphology-dependent features induced by the crystal quality due to morphology variations. Such an abundant morphology world of micro- and nanostructured ZnO obtained via the current approach may afford, in consideration of fundamental research, better understanding of crystal nucleation and growth mechanism from various aspects and would provide, in consideration of technological applications, possible candidates for nanodevice constructions for various utilizations. We believe this contribution would give some hints for fabrication and morphology control of other kinds of semiconductors.

GLOSSARY

Hydrothermal and solvothermal The term hydrothermal usually refers to any heterogeneous reaction in the presence of aqueous solvents of mineralizers under high pressure and temperature conditions to dissolve and recrystallize (recover) materials that are relatively insoluble under ordinary conditions. When the solvent is replaced by other matter, it is known as “solvothermal.”

Microemulsion A microemulsion is a thermodynamically stable dispersion of one liquid phase into another, stabilized by an interfacial film of surfactant. This dispersion may

be either oil-in-water or water-in-oil. Microemulsions are typically clear solutions, as the droplet diameter is approximately 100 nm or less. The interfacial tension between the two phases is extremely low.

Ostwald ripening processes Ostwald ripening is the process by which larger particles (or, for emulsions, droplets) grow at the expense of smaller ones because of the higher solubility of the smaller particles (Gibbs–Thomson or Kelvin effect) and molecular diffusion through the continuous phase.

Template-based synthesis In this approach, the matter functions as the template simply serves as a scaffold within (or around) which a different material is generated *in-situ* and shaped into a nanostructure with its morphology complementary to that of the template.

Vapor-phase growth Vapor-phase growth is one kind of approach toward crystal growth in which the crystal is grown by depositing material directly from the vapor or gaseous state (i.e., the immediate precursor is in a vapor or gaseous state). Several methods can be assigned to this category, such as thermal evaporation, chemical vapor deposition, and metal organic chemical vapor deposition.

ACKNOWLEDGMENTS

This work was supported by NSFC (20001002, 20023005, and 20221101), MOST (G19980613), MOE (the Foundation for University Key Teacher), and the Founder Foundation of PKU.

REFERENCES

1. C. M. Lieber, *Solid State Commun.* 107, 607 (1998); (b) J. Hu, T. W. Odom, and C. M. Liber, *Acc. Chem. Res.* 32, 435 (1999).
2. (a) J. Goldberger, R. R. He, Y. F. Zhang, S. W. Lee, H. Q. Yan, H. J. Choi, and P. D. Yang, *Nature* 422, 599 (2003). (b) H. Q. Yan, R. R. He, J. Pham, and P. D. Yang, *Adv. Mater.* 15, 402 (2003). (c) Y. Y. Wu, H. Q. Yan, and P. D. Yang, *Top. Catal.* 19, 197 (2002). (d) P. D. Yang, H. Q. Yan, S. Mao, R. Russo, J. Johnson, R. Saykally, N. Morris, J. Pham, R. R. He, and H. J. Choi, *Adv. Funct. Mater.* 12, 323 (2002). (e) J. C. Johnson, H. Q. Yan, R. D. Schaller, P. B. Petersen, P. D. Yang, and R. J. Saykally, *Nano Lett.* 2, 279 (2002). (f) Y. Y. Wu, H. Q. Yan, M. Huang, B. Messer, J. H. Song, and P. D. Yang, *Chem. Eur. J.* 8, 1261 (2002). (g) H. Kind, H. Q. Yan, B. Messer, M. Law, and P. D. Yang, *Adv. Mater.* 14, 158 (2002). (h) M. H. Huang, S. Mao, H. Feick, H. Q. Yan, Y. Y. Wu, H. Kind, E. Weber, R. Russo, and P. D. Yang, *Science* 292, 5523 (2001). (i) M. H. Huang, Y. Y. Wu, H. Feick, N. Tran, E. Weber, and P. D. Yang, *Adv. Mater.* 13, 113 (2001).
3. (a) W. L. Hughes and Z. L. Wang, *Appl. Phys. Lett.* 82, 2886 (2003). (b) Z. R. Dai, Z. W. Pan, and Z. L. Wang, *Adv. Funct. Mater.* 13, 9 (2003). (c) M. S. Arnold, P. Avouris, Z. W. Pan, and Z. L. Wang, *J. Phys. Chem. B* 107, 659 (2003). (d) Y. Berta, C. Ma, and Z. L. Wang, *Micron* 33, 687 (2002). (e) X. D. Wang, P. X. Gao, J. Li, C. J. Summers, and Z. L. Wang, *Adv. Mater.* 14, 1732 (2002). (f) P. X. Gao and Z. L. Wang, *J. Phys. Chem. B* 106, 12653 (2002). (g) K. Mcguire, Z. W. Pan, Z. L. Wang, D. Milkie, J. Menendez, and A. M. Rao, *J. Nanosci. Nanotech.* 2, 499 (2002). (h) Z. W. Pan, Z. R. Dai, and Z. L. Wang, *Science* 291, 1947 (2001).
4. H. Gleiter, *Acta Mater.* 48, 1 (2000).
5. D. C. Reynolds, D. C. Look, B. Jogai, J. E. Hoelscher, R. E. Sherriff, M. T. Harris, and M. J. Callahan, *J. Appl. Phys.* 88, 2152 (2000).

6. C. R. Lee, H. W. Lee, J. S. Song, W. W. Kim, and S. Park, *J. Mater. Synth. Process.* 9, 281 (2001); L. Vayssieres, k. Keis, A. Hagfeldt, and S. E. Lindquist, *Chem. Mater.* 13, 4386 (2001); D. S. King and R. M. Nix, *J. Catal.* 160, 76 (1996); T. Minami, *Mater. Res. Soc. Bull.* 25, 38 (2000); D. M. Bagnall, Y. F. Chen, Z. Zhu, T. Yao, S. Koyama, M. Y. Shen, and T. Goto, *Appl. Phys. Lett.* 70, 2230 (1997); J. Zhong, A. H. Kitai, P. Mascher, and W. Puff, *J. Electrochem. Soc.* 140, 3644 (1993).
7. Y. F. Chen, D. M. Bagnall, H. Koh, K. Park, K. Hiraga, Z. Zhu, and T. Yao, *J. Appl. Phys.* 84, 3912 (1998).
8. T. Seiyama and A. Kato, *Anal. Chem.* 34, 1502 (1962); L. F. Dong, Z. L. Cui, and Z. K. Zhang, *Nanostruct. Mater.* 8, 815 (1997); R. J. Shen, D. Z. Jia, K. Liang, X. Q. Xin, and J. Y. Wang, *Chin. J. Inorg. Chem.* 16, 906 (2000).
9. K. Hara, T. Horiguchi, T. Kinoshita, K. Sayama, H. Sugihara, and H. Arakawa, *Sol. Energy Mater. Sol. Cells* 64, 115 (2000).
10. D. S. Ginley and C. Bright, *Mater. Res. Bull.* 25, 15 (2000); B. G. Lewis and D. C. Paine, *Mater. Res. Bull.* 25, 22 (2000); A. J. Freeman, K. R. Poeppelmeier, T. O. Mason, R. P. H. Chang, and T. J. Marks, *Mater. Res. Bull.* 25, 45 (2000).
11. K. Keis, L. Vayssieres, S. E. Lindquist, and A. Hagfeldt, *Nanostruct. Mater.* 12, 487 (1999).
12. R. F. Service, *Science* 276, 895 (1997).
13. (a) P. Zu, Z. K. Tang, G. K. L. Wong, M. Kawasaki, A. Ohtomo, H. Koinuma, and Y. Segawa, *Solid State Commun.* 103, 459 (1997). (b) M. Kawasaki, A. Ohtomo, H. Koinuma, Y. Sakurai, Y. Yoshida, Z. K. Tang, P. Yu, G. K. L. Wang, and Y. Segawa, "Silicon Carbide III—Nitrides and Related Materials," Pts 1 and 2, Vol. 264-2, p. 1459 (1998). (c) A. Ohtomo, M. Kawasaki, Y. Sakurai, Y. Yoshida, H. Koinuma, P. Yu, Z. K. Tang, G. K. L. Wong, and Y. Segawa, *Mater. Sci. Eng. B* 54, 24 (1998). (d) Z. K. Tang, G. K. L. Wong, P. Yu, M. Kawasaki, A. Ohtomo, H. Koinuma, and Y. Segawa, *Appl. Phys. Lett.* 72, 3270 (1998). (e) M. Kawasaki, A. Ohtomo, I. Ohkubo, H. Koinuma, Z. K. Tang, P. Yu, G. K. L. Wong, B. P. Zhang, and Y. Segawa, *Mater. Sci. Eng. B* 56, 239 (1998). (f) V. A. Dijken, E. A. Meulenkaamp, D. Vanmaekelbergh, and A. Meijerink, *J. Lumin.* 87, 454 (2000). (g) Y. Sun, J. B. Ketterson, and G. K. L. Wong, *Appl. Phys. Lett.* 77, 2322 (2000). (h) A. Ohtomo and M. Kawasaki, *IEICE Trans. Electron.* E83C, 1614 (2000). (i) Y. C. Kong, D. P. Yu, B. Zhang, W. Fang, and S. Q. Feng, *Appl. Phys. Lett.* 78, 407 (2001). (j) A. Mitra and R. K. Thareja, *J. Appl. Phys.* 89, 2025 (2001). (k) A. Mitra, R. K. Thareja, V. Ganesan, A. Gupta, P. K. Sahoo, and V. N. Kulkarni, *Appl. Surf. Sci.* 174, 232 (2001).
14. M. Hiramatsu, K. Imaeda, N. Horio, and M. Nawata, *J. Vac. Sci. Technol. A* 16, 669 (1998).
15. S. C. Liu and J. J. Wu, *J. Mater. Chem.* 12, 3125 (2002); J. J. Wu, and S. C. Liu, *J. Phys. Chem. B* 106, 9546 (2002); J. Zhang, W. Y. Yu, and L. D. Zhang, *Phys. Lett.* 299, 276 (2002); J. J. Wu and S. C. Liu, *Adv. Mater.* 14, 215 (2002).
16. (a) H. T. Ng, B. Chen, J. Li, J. E. Han, M. Meyyappan, J. Wu, S. X. Li, and E. E. Haller, *Appl. Phys. Lett.* 82, 2023 (2003). (b) H. Kim and W. Sigmund, *Appl. Phys. Lett.* 81, 2085 (2002). (c) C. K. Xu, G. D. Xu, Y. K. Liu, and G. H. Wang, *Solid State Commun.* 122, 175 (2002). (d) Y. Dai, Y. Zhang, Q. K. Li, and C. W. Nan, *Chem. Phys. Lett.* 358, 83 (2002). (e) R. Wu, C. S. Xie, H. Xia, J. H. Hu, and A. H. Wang, *J. Cryst. Growth* 217, 274 (2000). (f) J. Q. Hu, Q. Li, X. M. Meng, C. S. Lee, and S. T. Lee, *Chem. Mater.* 15, 305 (2003). (g) J. S. Lee, M. I. Kang, S. Kim, M. S. Lee, and Y. K. Lee, *J. Cryst. Growth* 249, 201 (2003). (h) R. Wu, J. Wu, C. S. Xie, J. Zhang, and A. H. Wang, *Mater. Sci. Eng. A* 328, 196 (2002). (i) B. D. Yao, Y. F. Chan, and N. Wang, *Appl. Phys. Lett.* 81, 757 (2002). (j) H. J. Yuan, S. S. Xie, D. F. Liu, X. Q. Yan, Z. P. Zhou, L. J. Ci, J. X. Wang, Y. Gao, L. Song, L. F. Liu, W. Y. Zhou, and G. Wang, *Chem. Phys. Lett.* 371, 337 (2003). (k) X. M. Sun, Z. X. Deng, and Y. D. Li, *Mater. Chem. Phys.* 80, 366 (2003). (l) Y. K. Tseng, I. N. Lin, K. S. Liu, T. S. Lin, and I. C. Chen, *J. Mater. Res.* 18, 714 (2003).
17. (a) W. I. Park, D. H. Kim, S. W. Jung, and G. C. Yi, *Appl. Phys. Lett.* 80, 4232 (2002). (b) Y. J. Zhang, N. L. Wang, S. P. Gao, R. R. He, S. Miao, J. Liu, J. Zhu, and X. Zhang, *Chem. Mater.* 14, 3564 (2002). (c) S. C. Lyu, Y. Zhang, H. Ruh, H. J. Lee, H. W. Shim, E. K. Suh, and C. J. Lee, *Chem. Phys. Lett.* 363, 134 (2002). (d) W. I. Park, Y. H. Jun, S. W. Jung, and G. C. Yi, *Appl. Phys. Lett.* 82, 964 (2003). (e) K. Ogata, K. Maejima, S. Fujita, and S. Fujita, *J. Cryst. Growth* 248, 25 (2003). (f) S. Y. Li, C. Y. Lee, and T. Y. Tseng, *J. Cryst. Growth* 247, 357 (2003). (g) C. J. Lee, T. J. Lee, S. C. Lyu, Y. Zhang, H. Ruh, and H. J. Lee, *Appl. Phys. Lett.* 81, 3648 (2002). (h) W. Il Park, G. C. Yi, M. Y. Kim, and S. J. Pennycook, *Adv. Mater.* 14, 1841 (2002). (i) K. S. Kim and H. W. Kim, *Physica B* 328, 368 (2003).
18. N. Audebrand, J. P. Auffredic, and D. Louer, *Chem. Mater.* 10, 2450 (1998); P. D. Cozzoli, M. L. Curri, A. Agostiano, G. Leo, and M. Lomascolo, *J. Phys. Chem. B* 107, 4756 (2003).
19. L. F. Dong, Z. L. Cui, and Z. K. Zhang, *Nanostruct. Mater.* 8, 815 (1997).
20. P. Ayyub, R. Chandra, P. Taneja, A. K. Sharma, and R. Pinto, *Appl. Phys. A* 73, 67 (2001).
21. Y. W. Heo, V. Varadarajan, M. Kaufman, K. Kim, D. P. Norton, F. Ren, and P. H. Fleming, *Appl. Phys. Lett.* 81, 3046 (2002).
22. (a) O. Milosevic, V. Gagic, J. Vodnik, A. Mitrovic, L. Karanovic, B. Stojanovic, and L. Zivkovic, *Thin Solid Films* 296, 44 (1997). (b) X. Y. Zhao, S. C. Zhang, C. Z. Li, B. C. Zheng, and H. C. Gu, *J. Mater. Sci. Procs.* 5, 227 (1997). (c) S. Sakohara, M. Ishida, and M. A. Anderson, *J. Phys. Chem. B* 102, 10169 (1998). (d) J. J. Wu, S. C. Liu, C. T. Wu, K. H. Chen, and L. C. Chen, *Appl. Phys. Lett.* 81, 1312 (2002). (e) T. Tani, L. Madler, and S. E. Pratsinis, *J. Nanopart. Res.* 4, 337 (2002). (f) Y. H. Lin, Z. L. Tang, Z. T. Zhang, F. L. Yuan, Y. B. Ling, J. L. Lee, and S. L. Huang, *J. Am. Ceram. Soc.* 83, 2869 (2000).
23. R. Liu, A. A. Vertegel, E. W. Bohannon, T. A. Sorenson, and J. A. Switzer, *Chem. Mater.* 13, 508 (2001); L. Dloczik, R. Engelhardt, K. Ernst, S. Fiechter, I. Sieber, and R. Konenkamp, *Appl. Phys. Lett.* 78, 3687 (2001).
24. S. H. Yu, J. Yang, Y. T. Qian, and M. Yoshimura, *Chem. Phys. Lett.* 361, 362 (2002); W. J. Li, E. W. Shi, Y. Q. Zheng, and Z. W. Yin, *J. Mater. Sci. Lett.* 20, 1381 (2001); W. J. Li, E. W. Shi, M. Y. Tian, and W. Z. Zhong, *Sci. Chin. Ser. E* 41, 449 (1998); W. J. Li, E. W. Shi, M. Y. Tian, W. Z. Zhong, and Z. W. Yin, *J. Mater. Res.* 14, 1532 (1999); X. M. Sun, X. Chen, Z. X. Deng, and Y. D. Li, *Mater. Chem. Phys.* 78, 99 (2003).
25. R. J. Shen, D. Z. Jia, Y. M. Qiao, and J. Y. Wang, *J. Inorg. Mater.* 16, 625 (2001); Y. L. Du, M. S. Zhang, Y. Deng, Q. Chen, Z. Yin, and W. C. Chen, *Chin. Phys. Lett.* 19, 372 (2002); R. J. Shen, D. Z. Jia, K. Liang, X. Q. Xin, and J. Y. Wang, *Chin. J. Inorg. Chem.* 16, 906 (2000).
26. D. Mondelaers, G. Vanhoyland, H. V. Rul, J. D'Haen, M. K. Van Bael, J. Mullens, and L. C. V. Poucke, *Mater. Res. Bull.* 37, 901 (2002).
27. L. N. Wang and M. Muhammed, *J. Mater. Chem.* 9, 2871 (1999); Q. S. Yi, X. M. Wu, and Z. C. Tan, *J. Inorg. Mater.* 16, 620 (2001); J. E. Rodriguez-Paez, A. C. Caballero, M. Villegas, C. Moure, P. Duran, and J. F. Fernandez, *J. Eur. Ceram. Soc.* 21, 925 (2001).
28. L. Guo, Y. L. Ji, H. B. Xu, P. Simon, and Z. Y. Wu, *J. Am. Chem. Soc.* 124, 14864 (2002); B. Liu and H. C. Zeng, *J. Am. Chem. Soc.* 125, 4430 (2003); P. V. Radovanovic, N. S. Norberg, K. E. McNally, and D. R. Gamelin, *J. Am. Chem. Soc.* 124, 15192 (2002); Z. R. R. Tian, J. A. Voigt, J. Liu, B. Mckenzie, and M. J. Mcdermott, *J. Am. Chem. Soc.* 124, 12954 (2002).
29. J. Y. Lao, J. Y. Huang, D. Z. Wang, and Z. F. Ren, *Nano Lett.* 3, 235 (2003).

30. J. Y. Lao, J. G. Wen, and Z. F. Ren, *Nano Lett.* 2, 1287 (2002).
31. W. I. Park, G.-C. Yi, M. Y. Kim, and S. J. Pennycook, *Adv. Mater.* 14, 1841 (2002).
32. H. Q. Yan, R. R. He, J. Johnson, M. Law, R. J. Saykally, and P. D. Yang, *J. Am. Chem. Soc.* 125, 4728 (2003).
33. (a) J. Zhang, L. D. Sun, J. L. Yin, H. L. Su, C. S. Liao, and C. H. Yan, *Chem. Mater.* 14, 4172 (2002). (b) A. Chittofrati and E. Matijevic, *Colloid. Surf.* 48, 65 (1990).
34. (a) J. Zhang, L. D. Sun, C. S. Liao, and C. H. Yan, *Chem. Commun.* 3, 262 (2002). (b) J. Zhang, L. D. Sun, H. Y. Pan, C. S. Liao, and C. H. Yan, *New J. Chem.* 26, 33 (2002).
35. (a) E. A. Meulenkamp, *J. Phys. Chem. B* 102, 5566 (1998). (b) M. Hilgendorff, L. Spanhel, C. Rothenhäusler, and G. Müller, *J. Electrochem. Soc.* 145, 3632 (1998).
36. T. Matsushita, K. Kodaira, and J. Satio, *J. Cryst. Growth* 26, 147 (1974); S. D. Sharma and S. C. Kashyap, *J. Appl. Phys.* 42, 5302 (1971); N. Sakagami, *J. Cryst. Growth* 99, 905 (1990); H. Nishizawa, T. Tani, and K. Matsuka, in "Committee of the American Ceramic Society," 1984, p. C-99.
37. B. G. Wang, E. W. Shi, and W. Z. Zhong, *Cryst. Res. Tech.* 33, 937 (1998).
38. L. N. Wang and M. Muhammed, *J. Mater. Chem.* 9, 2871 (1999).
39. (a) Y. Li, G. S. Cheng, and L. D. Zhang, *J. Mater. Res.* 15, 2305 (2000). (b) G. Shi, C. M. Mo, W. L. Cai, and L. D. Zhang, *Solid State Commun.* 115, 253 (2000). (c) S. H. Yu and M. Yoshimura, *Adv. Mater.* 14, 296 (2002). (d) Z. Wang and H. L. Li, *Appl. Phys. A* 74, 201 (2002).
40. Y. C. Wang, I. C. Leu, and M. H. Hon, *J. Mater. Chem.* 12, 2439 (2002); Y. C. Wang, I. C. Leu, and M. H. Hon, *Electrochem. Solid St. S.* 5, C53 (2002); Y. C. Wang, I. C. Leu, and M. H. Hon, *J. Cryst. Growth* 237, 564 (2002).
41. (a) M. J. Zheng, L. D. Zhang, G. H. Li, and W. Z. Shen, *Chem. Phys. Lett.* 363, 123 (2002). (b) Z. X. Zheng, Y. Y. Xi, P. Dong, H. G. Huang, J. Z. Zhou, L. L. Wu, and Z. H. Lin, *Phys. Chem. Comm.* 9, 63 (2002). (c) Y. Li, G. W. Meng, L. D. Zhang, and F. Phillipp, *Appl. Phys. Lett.* 76, 2011 (2000). (d) W. Choi, T. W. Kang, and L. A. Nosova, *J. Korean Phys. Soc.* 42, S216 (2003).
42. W. H. Zhang, J. L. Shi, L. Z. Wang, and D. S. Yan, *Chem. Mater.* 12, 1408 (2000).
43. B. B. Lakshmi, P. K. Dorhout, and C. R. Martin, *Chem. Mater.* 9, 857 (1997); B. B. Lakshmi, C. J. Patrissi, and C. R. Martin, *Chem. Mater.* 9, 2544 (1997).
44. M. C. Neves, T. Trindade, A. M. B. Timmons, and J. D. P. de Jesus, *Mater. Res. Bull.* 36, 1099 (2001).
45. R. F. Mulligan, A. A. Iliadis, and P. Kofinas, *Abstr. Pap. Am. Chem. S.* 220, 278-PMSE (2000).
46. D. S. Boyle, K. Govender, and P. O'Brien, *Chem. Commun.* 80 (2002).
47. K. Keis, S. E. Lindquist, and A. Hagfeldt, *J. Phys. Chem. B* 105, 3350 (2001).
48. L. Vayssieres, K. Keis, A. Hagfeldt, and S. E. Lindquist, *Chem. Mater.* 12, 73 (2001).
49. W. J. Li, E. W. Shi, W. Z. Zhong, and Z. W. Yin, *J. Cryst. Growth* 203, 186 (1999).
50. J. Zhang, L. D. Sun, X. C. Jiang, C. S. Liao, and C. H. Yan, submitted for publication.
51. J. Zhang, L. D. Sun, C. S. Liao, and C. H. Yan, *Solid State Commun.* 124, 45 (2002).
52. W. Z. Zhong and J. Tang, *J. Cryst. Growth* 166, 91 (1996).
53. D. F. Zhang, L. D. Sun, J. L. Yin, and C. H. Yan, *Adv. Mater.*, in press.
54. J. Q. Hu and Y. Bando, *Appl. Phys. Lett.* 82, 1401 (2003); L. Vayssieres, K. Keis, A. Hagfeldt, and S. E. Lindquist, *Chem. Mater.* 13, 4395 (2001).
55. R. A. Bride, J. Melley, and D. E. Cormack, *J. Mater. Chem.* 13, 1196 (2003).
56. C. H. Lu and C. H. Yeh, *Ceram. Int.* 26, 351 (2000).
57. D. B. Zhang, L. M. Qi, J. M. Ma, and H. M. Cheng, *Chem. Mater.* 13, 2753 (2001); L. M. Qi, J. Li, and J. M. Ma, *Adv. Mater.* 14, 300 (2002).
58. C. Pacholski, A. Kornouski, and H. Weller, *Angew. Chem. Int. Ed.* 41, 1188 (2002).
59. K. Vanheusden, W. L. Warren, C. H. Seager, D. R. Tallant, J. A. Voigt, and B. E. Gnade, *J. Appl. Phys.* 79, 7983 (1996).